

Batteries

2018 Annual Progress Report

Vehicle Technologies Office

(This Page Intentionally left blank)

Disclaimer

This report was prepared as an account of work sponsored by an agency of the United States government. Neither the United States government nor any agency thereof, nor any of their employees, makes any warranty, express or implied, or assumes any legal liability or responsibility for the accuracy, completeness, or usefulness of any information, apparatus, product, or process disclosed or represents that its use would not infringe privately owned rights. Reference herein to any specific commercial product, process, or service by trade name, trademark, manufacturer, or otherwise does not necessarily constitute or imply its endorsement, recommendation, or favoring by the United States government or any agency thereof. The views and opinions of authors expressed herein do not necessarily state or reflect those of the United States government or any agency thereof.

Acknowledgements

The projects reported in this report were supported through various contracts funded by the U.S. Department of Energy, Vehicle Technologies Office. A list of contributing authors appears in the sections for specific projects in this report.

Acronyms

AABC	Advanced Automotive Batteries Conference
ABF	Annular bright-field (STEM)
ABMR	Advanced Battery Materials Research
ABR	Applied Battery research
AC	Alternating current
ACS	American Chemical Society
ADF-STEM	Annular dark-field – scanning transmission electron microscope
AEGIS	Analysis of Electrochemical Gassing by Infrared Spectroscopy
AES	Atomic emission spectroscopy
AFM	Atomic force microscopy
AH	Ampere hour
AIMD	Ab initio molecular dynamics
ALD	Atomic layer deposition
AMPED	Advanced Management and Protection of Energy Storage Devices
AMR	Annual Merit Review
ANL	Argonne National Laboratory
AOI	Area of Interest
APP	Ammonium polyphosphate
APS	Advanced Photon Source (laboratory)
ARC	Accelerated rate calorimetry
ARPA-E	Advanced Research Projects Agency - Energy
ARXPS	Angle-resolved XPS
ASI	Area-specific impedance
ASME	American Society of Mechanical Engineers
ASR	Area-specific resistance
ATR	Attenuated total reflection
BCDI	Bragg Coherent Diffraction Imaging
BET	Brunauer, Emmett, and Teller (surface area analysis)
BEV	Battery electric vehicle
BIT	Beijing Institute of Technology
BLI	Beyond Lithium-ion
BMF	Battery manufacturing facility
BMR	(Advanced) Battery Materials Research (program)
BN	Boron nitride
BNL	Brookhaven National Laboratory
BO	Bridging oxygen
BOL	Beginning of life
BP	Budget period
BTC	Battery Technology Center
BTFE	Bis(2,2,2-trifluoroethyl) ether
BTMS	Behind-the-Meter-Storage

BYU	Brigham Young University
CABS	Consortium for Advanced Battery Simulation
CAD	Computer-aided Design
CAEBAT	Computer-aided engineering of batteries
CAFE	Corporate Average Fuel Economy
CAMP	Cell analysis, modeling, and prototyping (facility)
CAN	Controller Area Network
CB	Carbon black
CBA	Carbon/binder additive (geometry)
CBD	Conductive binder domain
CC	Constant current
CCCV	Constant current, constant voltage
CCD	Charge-coupled device
CDFEM	Conformal decomposition finite element method
CE	Coulombic efficiency
CEI	Cathode electrolyte interfaces
CIP	Contact ion pair
CMC	Carboxymethyl cellulose
CMOS	Complementary metal oxide semiconductor
CN	Coordination number
CNC	Computer numeric control (machine)
CNF	Carbon nanofibers
CNT	Carbon nano-tubes
COTS	Commercial-off-the-shelf
C-PAN	Carbon poly(acrylic acid)
CPE	Constant phase element
C-PVDF	Carbon Polyvinylidene fluoride
CV	Cyclic voltammetry
CVD	Chemical vapor deposition
DCR	Direct current resistance
DD	Deep-dive
DEC	Diethyl carbonate
DEM	Discrete element method
DEMS	Differential electrochemical mass spectrometry
DES	Deep eutectic solvent
DFLM	Dark field light microscopy
DFT	Density function theory
DI	De-ionized (water)
DMA	Dopamine methacrylamide
DMC	Dimethyl carbonate
DME	Dimethyl ether
DMF	Dimethylformamide
DOD	Depth-of-discharge
DOE	Department of Energy
DOL	Dioxolane

DOS	Density of state
DP	Dry process
DPDMS	Diphenyldimethoxysilane
DRC	Democratic Republic of Congo
DRX	Disordered (rocksalt) transition metal oxides
DSC	Differential scanning calorimetry
DST	Dynamic stress test
EADL	Electrochemical Analysis and Diagnostic Laboratory (at ANL)
EB	Electron beam
EC	Ethylene carbonate
ECM	Equivalent circuit model
ECS	Electrochemical Society
ECT	Eelectrochemical-thermal
ED	Electrode domain
EDAX	Energy dispersive x-ray spectroscopy mapping
EDS	Energy dispersive spectroscopy
EDV	Electric Drive Vehicle
EDX	Energy-dispersive x-ray (spectroscopy)
EDXRD	Energy Dispersive X-ray Diffraction
EEI	Electrode/electrolyte interface
EELS	Electron energy loss spectroscopy
EERE	Energy Efficiency and Renewable Energy (DOE Office)
EIC	Energy Innovation Center
EIS	Electrochemical impedance spectroscopy
EM	Electro-mechanical
EMC	Ethylmethyl carbonate
EMSL	Environmental Molecular Sciences Laboratory
EOL	End of life
EPA	Environmental Protection agency
EQCM	Electrochemical quartz crystal microbalance
EV	Electric vehicle
EXAFS	Extended X-ray absorption fine structure
FCE	First cycle efficiency
FDES	Fluorinated Deep Eutectic Solvent
FEA	Finite element analysis
FEC	Fluoro ethylene carbonate
FEM	Finite element method
FFT	Fast Fourier-transform
FIB	Focused ion beam
FIB-SEM	Focused Ion Beam Scanning Electron Microscopy
FOA	Federal opportunity announcement
FSI	(Lithium) bis(trifluoromethanesulfonyl)imide
FSP	Flame spray pyrolysis
FTIR	Fourier transform infrared spectroscopy
FY	Fiscal year

GB	Grain boundary
GC-MS	Gas chromatography - molecular spectroscopy
GF	Glass fiber
GHG	Green-house gases
GITT	Galvanostatic intermittent titration
GO	Graphene oxide
GPC	Gel permeation chromatography
GREET	Greenhouse gas regulated energy and emissions and transpiration
HAADF	High-angle annular dark-field
HAXPES	Hard X-ray Photoelectron Spectroscopy
HCE	High concentration electrolyte
HCS	Hollow carbon spheres
HEV	Hybrid electric vehicle
HF	Hydrofluoric acid
HFDEC	Bis (2,2,2 trifluoroethyl) carbonate
HOPG	Highly oriented pyrolytic graphite
HPISE	Hybrid polymer-in-salt electrolyte
HPLC	High-performance liquid chromatography
HPNO	2-(2-hydroxyphenyl)-naphthoxazole
HPPC	Hybrid pulse power characterization
HRTEM	High-resolution transmission electron microscopy
HR-TEM	High resolution transmission electron microscopy
HT	High temperature
HVIST	High-voltage interface stabilizing testing
ICE	Internal combustion engine
ICL	Initial capacity loss
ICP	Inductively coupled plasma
IEEE	Institute of Electrical and Electronics Engineers
IFM	Inorganic filler molecules
INL	Idaho National Laboratory
IPA	Isopropyl alcohol
IR	Infra-red
JACS	Journal of the American Chemical Society
KF	Karl Fischer (titration)
KMC	Kinetic Monte Carlo (simulations)
LAMMPS	Large-scale atomic/molecular massively parallel simulator
LBNL	Lawrence Berkeley National Laboratory
LCA	Life cycle analysis
LCI	Life cycle inventory
LCO	Lithium cobalt oxide
LEDC	Lithium ethylene dicarbonate
LFO	Li ₅ FeO ₄
LFP	Li-iron phosphate
LHCE	Localized high concentration electrolyte
LIB	Lithium-ion battery

LIC	Lithium-ion conducting
LIO	Li_2IrO_3
LIPON	Lithium phosphorous oxy-nitride
LISO	$\text{Li}_2\text{Ir}_{1-y}\text{Sn}_y\text{O}_3$
LL	Layered-layered
LLATO	$\text{Li}_{0.33}\text{La}_{0.56}\text{Al}_{0.005}\text{Ti}_{0.995}\text{O}_3$
LLP	LiTFSI-LLZTO-PVDF
LLS	Layered-layered spinel
LLTO	$(\text{Li},\text{La})\text{TiO}_3$
LLZ	$\text{Li}_7\text{La}_3\text{Zr}_2\text{O}_{12}$
LLZMO	$\text{Li}_{6.5}\text{La}_3\text{Zr}_{1.75}\text{Mo}_{0.25}\text{O}_{12}$
LLZO	Lithium lanthanum zirconate
LLZTO	$\text{Li}_{6.75}\text{La}_3\text{Zr}_{1.75}\text{Ta}_{0.25}\text{O}_{12}$
LMA	Lithium metal anode
LMNO	Lithium manganese nickel oxide
LMNOF	Li-Mn-Nb-O-F
LMO	Lithium manganese oxide
LMR	Lithium manganese-rich (layered cathode material)
LMRPMC	Lithium- and manganese-rich nickel manganese cobalt oxide
LMTOF	Li-Mn-Ti-O-F
LNMO	$\text{LiNi}_{0.5}\text{Mn}_{0.5}\text{O}_2$
LNRO	$\text{Li}_{1.2}\text{Ni}_{0.2}\text{Mn}_{0.6}\text{O}_2$
LPS	B-Li ₃ PS ₄
LRLO	Lithium-rich layered oxide
LS	Low spin
LSB	Lithium sulfur batteries
LSV	Linear scanning voltammetry
LTO	Lithium titanate, $\text{Li}_4\text{Ti}_5\text{O}_{12}$
LUMO	Lowest unoccupied molecular orbital
MAS	Magic angle spinning
MCMB	Mesocarbon micro beads
MD	Molecular dynamics
MERF	Materials Engineering Research Facility
MOSS	Multibeam optical stress sensor
MPF	Metal porous foam
MRS	Materials Research Society
MSD	Mean square displacements
MSMD	Multi-scale, multi-domain
MT	Metric tons
NBO	Non-bridging oxygens
NCA	$\text{LiNi}_{0.8}\text{Co}_{0.15}\text{Al}_{0.05}\text{O}_2$
NCM	$\text{Li}_{1+w}[\text{Ni}_x\text{Co}_y\text{Mn}_z]_{1-w}\text{O}_2$
NDI	Naphthalene diimide
NEB	Nudged elastic band (method)
NETL	National Energy Technology Laboratory

NEV	New electric vehicle
NHTSA	National Highway Transportation Safety Administration
NMC	Nickel manganese cobalt (oxide)
NMC	$\text{LiNi}_{1/3}\text{Co}_{1/3}\text{Mn}_{1/3}\text{O}_2$
NMP	N-methylpyrrolidone
NMR	Nuclear magnetic resonance
NPD	Neutron power diffraction
NR	Neutron reflectometry
NREL	National Renewable Energy Laboratory
NREL	National Renewable Energy Laboratory
NSLS	National Synchrotron Light Source
OBD	On-board diagnostics
OCP	Open-circuit potential
OCV	Open circuit voltage
OEM	Original equipment manufacturer
OPLS	Optimized Potential for Liquid Simulation
ORNL	Oak Ridge National Laboratory
OWRK	Owens-Wendt-Rabel-Kaelble (method)
PAA	Polyacrylic acid
PAN	Polyacrylonitrile
PARC	Palo Alto Research Center
PDF	Pair density function
PDI	Polydispersity index
PDMS	Polydimethylsiloxane
PE	Polyethylene
PECVD	Plasma-enhanced chemical vapor deposition
PEG	Polyethylene glycol
PEO	Polyethyleneoxide
PES	Prop-1-ene-1,3-sultone
PET	Polyethylene terephthalate
PEV	Plug-in electric vehicle
PHEV	Plug-in hybrid electric vehicle
PI	Principal investigator
PLD	Pulsed laser deposition
PMA	Polyacrylamide (gel)
PMP	Polymethylpentene (coating)
PNNL	Pacific Northwest National Laboratory
POSS	Poly(acryloisobutyl polyhedral oligomeric silsesquioxane)
PS	Polystyrene
PSD	Pore size distribution
PTA-DDSA	Polysulfide trapping agent - directly derived sulfur assembled
PTFE	Poly(tetrafluoroethylene) (cathode)
PU	Polyurethane
PV	Photovoltaic
PVD	Physical vapor deposition

PVDF	Poly(vinylidene fluoride)
R&D	Research and Development
RDE	Rotating disk electrode
RF	Radiofrequency
RGB	Red, green, blue
RH	Relative humidity
RIXS	Resonant inelastic x-ray scattering
RMS	Root mean square
RPT	Reference performance test
RS	Rocksalt
RVE	Representative volume element
SAE	Society of Automotive Engineers
SAED	Selected area electrode diffraction
SAM	Self-assembled molecular (film)
SBIR	Small Business Innovation Research
SDS	Safety data sheet
SE	Solid electrolyte
SEI	Solid electrolyte interphase
SEM	Scanning electron microscopy
SEM-AFM	Scanning electron microscopy - atomic force microscopy
SERS	Surface-enhanced Raman spectroscopy
SHE	Self-healing elastomer
SHP	Self-healing polymer
SIG	Solvate ionogel
SIMS	Secondary ion mass spectrometry
SLAC	Stanford acceleration laboratory
SLMP	Stabilized lithium metal powder
SLSM	Sacrificial Li source material
SMPS	Scanning mobility particle sizing
SN	Succinonitrile
SNL	Sandia National Laboratories
SNS	Spallation Neutron Source
SOA	State of the art
SOC	State of charge
SOH	State of health (for battery)
SP	Silly Putty
S-PAN	Sulfurized poly-acrylonitrile
SPM	Scanning probe microscopy
SPRDE	Stationary probe rotating disk electrode
SRL	Surface reconstruction layer
SS	Solid-state
SSE	Solid-state electrolyte
SSIP	Solvent-separated ion pair
SSRL	Stanford Synchrotron Radiation Lightsource
SSRM	Solvent-separated ion pair

STEM	Scanning transmission electron microscopy
STL	StereoLithography
STTR	Small Business Technology Transfer Program
STXM	Scanning transmission X-ray microscopy
SUNY	State University of New York
TAC	Technical Advisory Committee
TAMU	Texas A&M University
TARDEC	(U.S. Army) Tank Automotive Research, Development and Engineering Center
TD	Transverse direction
TEGDME	Tetraethyleneglycoldimethyl
TEGMVC	Tetraethylene glycol methacrylate vinlyenecarbonate
TEM	Transmission electron microscopy
TERS	Tip-enhanced Raman spectroscopy
TES	Tender-energy x-ray absorption spectroscopy
TEY	Total electron yield
TFSI	Bistriflimide (anion)
TFY	Total fluorescence yield
TGA	Thermal gravimetric analysis
THF	Tetrahydrofuran
TIC	Total (negative) ion count
TM	Transition metal
TMC	Transition-metal cation
TMO	Transition metal oxide
TMS	Trimethylsilyl
TMSB	Tris(trimethylsilyl) borate
TMSMEC	Tris(trimethylsilyl) disilyl (ethyl) carbonate
TMSMMC	Tris(trimethylsilyl) disilyl (methyl) carbonate
TMSP	Tris(trimethylsilyl) phosphite
TNO	Titanium niobium oxide
TOF	Time-of-flight
TOF-SIMS	Time-of-flight SIMS
TR-XAS	TR-XRD and absorption
TR-XRD	Time-resolved X-ray diffraction
TTF	Tris(2,2,2,-trifluoroethyl)
TTFP	Tris(2,2,2,-trifluoroethyl)phosphite
TXM	Transmission X-ray microscopy
UCL	University College, London
UCSD	University of California, San Diego
UCV	Upper cutoff voltage
UHV	Ultra-high vacuum
UM	University of Michigan
UMD	University of Maryland
UMERC	University of Maryland, Energy Research Center
USABC	United States Advanced Battery Consortium
USCAR	United States Council for Automotive Research

USDRIVE	Driving Research and Innovation for Vehicle efficiency and Energy sustainability
USEPA	United States Environmental Protection Agency
UV	Ultraviolet
VC	Vinylene carbonate
VOC	Volatile organic compounds
VTO	Vehicle Technologies Office
WL	White line (energy)
WP	Wet polishing
WPI	Worcester Polytechnic Institute
XANES	X-ray absorption near edge structure
XAS	X-ray absorption spectroscopy
XCT	X-ray computed tomography
XFC	Extreme fast charging
XPS	X-ray photoelectron spectroscopy
XRD	X-ray diffraction
XRF	X-ray fluorescence (microscopy)
XTS	X-ray total scattering

Executive Summary

Introduction

The Vehicle Technologies Office (VTO) of the Department of Energy (DOE) conducts research and development (R&D) on advanced transportation technologies that would reduce the nation's use of imported oil and would also lead to reduced harmful emissions. Technologies supported by VTO include electric drive components such as advanced energy storage devices (batteries and ultracapacitors), power electronics and electric drive motors, advanced structural materials, energy efficient mobility systems, advanced combustion engines, and fuels. VTO is focused on funding early stage, high-reward/high-risk research to improve critical components needed for more fuel efficient (and consequently, also cleaner-operating) vehicles.

One of the major VTO objectives is to enable U.S. innovators to rapidly develop the next generation of technologies that achieve the cost, range, and charging infrastructure necessary for the widespread adoption of plug-in electric vehicles (PEVs). An important prerequisite for the electrification of the nation's light duty transportation sector is development of more cost-effective, longer lasting, and more abuse-tolerant PEV batteries. One of the ultimate goals of this research, and currently a strong trend in vehicle electrification, is an EV which can provide the full driving performance, convenience, and price of an internal combustion engine (ICE) vehicle. To achieve this, VTO has established the following overarching goal:

VTO supports early-stage R&D to identify new battery chemistries or a new cell technology with the potential to reduce the cost of electric vehicle batteries by more than half to less than \$100/kWh and increase the range to 300 miles while decreasing the charge time to less than 15 minutes by 2028.

The cost target supports a levelized cost of driving of a 300-mile BEV at \$0.28/mile, which is comparable to that for future ICEs at \$0.27/mile. The ultimate cost goal for a 300-mile BEV battery is \$80/kWh, which achieves \$0.26/mile.

VTO competitively awards funding through funding opportunity announcement (FOA) selections, and projects are fully funded through the duration of the project in the year that the funding is awarded. Directly-funded work at the national laboratories (also awarded competitively through a lab-call process) is subject to change based on annual appropriations. During the past year, VTO continued R&D in support of PEVs such as plug-in hybrid vehicles (PEHV), extended range electric vehicles (EREV), and all-electric vehicles (EVs), as well as some conventional hybrid electric vehicle (HEV) technologies, particularly the 12 volt start/stop hybrid.

Stakeholders for the VTO R&D activities include universities, national laboratories, other government agencies and members of industry including automakers, battery manufacturers, material suppliers, component developers, private research firms, and small businesses. VTO works with key U.S. automakers through the United States Council for Automotive Research (USCAR) – an umbrella organization for collaborative research consisting of Fiat Chrysler LLC, the Ford Motor Company, and the General Motors Company. Collaboration with automakers through the partnership known as U.S. Driving Research and Innovation for Vehicle Efficiency and Energy Sustainability (US DRIVE) attempts to enhance the relevance and the potential for success of the research portfolio.

This document summarizes the progress of VTO battery R&D projects supported during the fiscal year 2018 (FY 2018). In FY 2018, the DOE VTO battery R&D funding was approximately \$101 million. Its R&D focus was on the development of high-energy batteries for PEVs and very high-power devices for hybrid vehicles. The electrochemical energy storage roadmap (which is found at the EERE Roadmap web page <http://energy.gov/eere/vehicles/downloads/us-drive-electrochemical-energy-storage-technical-team-roadmap>) describes ongoing and planned efforts to develop electrochemical storage technologies for PEVs. To advance battery technology to improve the market penetration of PEVs and hybrid vehicles, the program focuses on overcoming specific technical barriers typically related to the battery's cost, performance, life (both calendar

life and cycle life), its tolerance to abusive conditions, and its recyclability/sustainability. Various battery chemistries are being investigated with that aim.

VTO R&D has lowered the cost of EV battery packs to \$197/kWh in 2018, representing more than 80% reduction since 2008, yet even further cost reduction in high-energy batteries is necessary for EVs to achieve head-to-head cost competitiveness with internal combustion engines (without Federal subsidies). In addition, today’s batteries also need improvements in such areas as their ability to accept charging at a high rate – or extreme fast charging (XFC) where this rate can approach a value of 400 kW; and a better ability to operate at low temperatures – so as to enable EVs an all-weather performance and “refueling” convenience similar to ICE vehicles. Research into “enhanced Li-ion” batteries which would provide such functionalities is one of the R&D focus areas. For even further gains in energy density and reduction in cost, VTO is funding research on both “next gen” chemistries (which employ an alloy anode and/or a high voltage cathode) and beyond lithium-ion (BLI) chemistries (which can employ a lithium metal anode). Current cycle and calendar lives of next gen and BLI chemistries are well short of the goals set for EVs – most cells employing a significant amount of silicon provide only 500 deep discharge cycles and less than two years of calendar life.

To quantify the improvements needed to accelerate large-scale adoption of PEVs and HEVs, certain performance and cost targets have been established. Some sample performance and cost targets for EV batteries, both at cell level and at system (pack) level, are shown in Table ES- 1.

Table ES- 1: Subset of EV requirements for batteries and cells.

Energy Storage Goals (by characteristic)	Pack Level	Cell Level
Cost @ 100k units/year (kWh = useable energy)	\$100/kWh*	\$75/kWh*
Peak specific discharge power (30s)	470 W/kg	700 W/kg
Peak specific regen power (10s)	200 W/kg	300 W/kg
Useable specific energy (C/3)	235 Wh/kg*	350 Wh/kg*
Calendar life	15 years	15 years
Deep discharge cycle life	1000 cycles	1000 cycles
Low temperature performance	>70% useable energy @C/3 discharge at -20°C	>70% useable energy @C/3 discharge at -20°C
	*Current commercial cells and packs not meeting the goal	

The batteries R&D effort includes multiple activities, ranging from focused fundamental materials research to prototype battery cell development and testing. It includes, as mentioned above, R&D on BLI and next-gen materials and cell components, as well as that on synthesis and design, recycling, and ways to address the high cost. Those activities are organized into mainly two inter-related (and complementary) program elements:

- Advanced Cell and Battery R&D
- Advanced Materials R&D

A short overview of work under each of those program elements is given below.

Advanced Cell and Battery Research and Development

The *Advanced Cell and Battery Research and Development* activity focuses on the development of robust battery cells and modules to significantly reduce battery cost, increase life, and improve performance. This work mainly spans the following general areas:

- United States Advanced Battery Consortium (USABC)-supported battery development & materials R&D (11 projects)
- Advanced processing (12 projects)
- Computer-aided engineering for batteries (CAEBAT) (seven projects)
- Recycling and sustainability (5 projects)
- Extreme fast-charging and behind the meter storage (7 projects)
- Testing and Analysis (8 projects)
- Small business innovative research (SBIR) (multiple Phase I and Phase II projects)

Chapter I of this report describes projects under the *Advanced Cell and Battery Research and Development* activity. Part of this effort occurs in close partnership with the automotive industry, through a cooperative agreement with the USABC. In FY 2018, via the USABC, VTO supported 11 cost-shared contracts with developers to further the development of PEV and HEV batteries and battery components. The estimated DOE share of those USABC contracts (over the life of the contracts) is approximately \$39M. These include lower cost, high energy lithium battery technology being developed by Zen Labs (previously called Envia Systems), high performance battery cells by 24M and Amprius, and cells incorporating recycling processes by Farasis Energy and Worcester Polytechnic Institute. The development of lithium-ion battery technology for 12V Start-stop system is being supported through R&D efforts with XALT Energy. Thicker cathode coatings are being developed by PPG and certain high capacity anode materials by Sinode Systems. Additional battery technologies are also supported, including two separator technologies being developed by Celgard, and benchmarking activities by Southwest Research Institute.

In addition to the USABC projects listed above, VTO also supports multiple *advanced processing* projects: including four battery and material supplier R&D projects which are funded/administered by the National Energy Technology Laboratory (NETL) and eight projects at the national labs and universities. Most strategies for increasing the performance and reducing the cost of lithium-ion batteries have focused on novel battery chemistries, material loading modifications, and increasing electrode thickness. Increasing electrode thickness is a known approach for increasing energy density (and in turn, the overall cell capacity). However, practical thicknesses are constrained by ionic transport limitations that occur with the increased thickness, limiting the cell power – as well as encountering processing issues. The project participants include the Palo Alto Research Center's (PARC), Group14, Miltec, PPG, University of Missouri, Vanderbilt University and several national labs (ANL, NREL, ORNL). The estimated value of those advanced processing projects (over project lifetime) is approximately \$35M.

The advanced cell and battery research activity also includes several projects categorized under the *Computer Aided Engineering for (Electric-Drive Vehicle) Batteries* (CAEBAT) Program – which recently evolved into the Advanced Computer Aided Battery Engineering Consortium. The Consortium seeks to enable safer design of batteries by enhancing the predictive capability of computationally efficient electrochemical models for mechanical/electrochemical/thermal simulation models of battery physiochemical processes (in the event of a vehicle crash or internal short/thermal runaway). The participants include the National Renewable Energy Laboratory (NREL), Argonne National Laboratory (ANL) and Sandia National Laboratories (SNL). The consortium for advanced battery simulation (CABS) is an integrated partnership between Oak Ridge National Laboratory (ORNL), Lawrence Berkeley National Laboratory (LBNL), and SNL. Its projects highlight new experiments to develop constitutive relations for mechanical response of constituent materials, effective transport properties for electrochemical behavior of electrodes under deformation, and coupled simulations at layer-resolved scale to predict the behavior of the damaged batteries. The approximate value of the CAEBAT and associated programs is \$14M.

The *Recycling and Sustainability* activity involves studies of the full life-cycle impacts and costs of Li-ion battery production/use; cost assessments and impacts of various recycling technologies; and the available material and cost impacts of recycling and secondary use. The participants include ANL and NREL and the associated value is approximately \$10M.

To become truly competitive with the internal combustion engine vehicle (ICEV) refueling experience, EV charging times must also be significantly shorter. A research project to understand/enable extreme fast charging (XFC) in enhanced Li-ion systems began in FY 2017 and it increased in scope during FY 2018. XFC, charging an EV at power rates of up to 400 kW, would decrease vehicle charging times and increase EV utility. Projects on numerous XFC topics are taking place at ANL, INL, NREL, ORNL, SNL and a “behind the meter” storage project is taking place by a team including NREL, INL, ORNL and SNL.

The *Battery Testing and Analysis* activity develops requirements and test procedures for batteries (to evaluate battery performance, battery life and abuse tolerance). Battery technologies are evaluated according to USABC-stipulated battery test procedures. Benchmark testing of an emerging technology is performed to remain abreast of the latest industry developments. The *battery testing* activity includes performance, life and safety testing, and thermal analysis and characterization. It currently includes the following 4 projects, based at ANL, INL, SNL, and NREL. The testing activity also supports the cell analysis, modeling, and prototyping (CAMP) projects at ANL, as well as benchmarking for CAMP and post-test analysis of lithium-ion battery materials which includes three labs (ANL, ORNL, and SNL). Other projects in this area include conducting testing (for performance, life and abuse) for contract deliverables, laboratory- and university-developed cells, and benchmark systems from industry; thermal analysis, thermal testing and modeling; cost modeling; other battery use and life studies; and the recycling of core materials. *Cost assessments and requirements analysis* includes an ANL project on developing the performance and cost model BatPaC. This ANL model, developed over time and rigorously peer-reviewed, is used to design automotive Li-ion batteries to meet the specifications for a given vehicle, and estimate the cost of manufacturing it. An analysis using BatPaC compared the estimated costs of cells and packs for different electrode chemistries (Figure ES- 1 shows the pack costs).

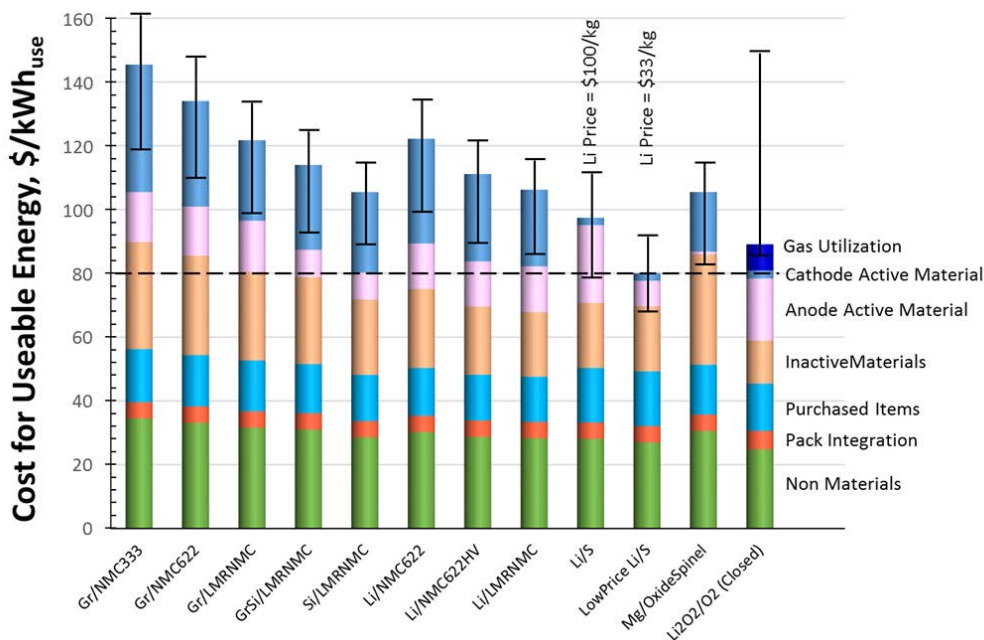


Figure ES- 1. Estimated costs of cells in automotive battery packs with different combination of electrodes. The packs are rated for 100 kWh_{Total} (85 kWh_{Useable}), 300 kW, 315 V, 168 cells, and produced at a plant volume of 100K packs/year.

VTO also supports several *Small Business Innovation Research* (SBIR) contracts in addition to the R&D described above. These SBIR projects focus on development of new battery materials/components and serve as

the source of new ideas and concepts. The section on SBIR projects includes a short list of recent Phase I and Phase II projects that were active during FY 2018.

Advanced Materials R&D

The *Advanced Materials Research & Development* activity addresses fundamental issues of materials and electrochemical interactions associated with rechargeable automotive batteries. It develops new/promising materials and it makes use of advanced material models to discover such materials (and their failure modes), utilizing scientific diagnostic tools and techniques to gain insight into the failure process. The researchers belong to various national labs, universities, and industry partners. The work spans mainly two general areas – “next gen” chemistries (which employ an alloy anode and/or a high voltage cathode) and beyond lithium-ion (BLI) chemistries (which employ a lithium metal anode). The projects are distributed as follows:

- Next generation (Next-gen) lithium-ion battery technologies (34 projects)
 - Advanced Electrodes (two projects)
 - Advanced Anodes (four projects)
 - Advanced Cathodes (12 projects)
 - Advanced electrolytes (three projects)
 - Diagnostics (seven projects)
 - Modeling (six projects)
- Beyond lithium-ion battery technologies (24 projects)
 - Metallic Lithium and Solid Electrolytes (10 projects)
 - Lithium sulfur (11 projects)
 - Lithium-Air Batteries (two projects)
 - Sodium-ion batteries (one projects)
 - Battery500 Consortium (five keystone projects and 16 seedling projects)

The *next generation lithium-ion battery* R&D area’s goal is to advance material performances, designs, and processes to significantly improve performance and reduce the cost of Li-ion batteries using an alloy or intermetallic anode and/or high voltage cathode. Specific areas of investigation include high-energy anodes (e.g., those containing silicon or tin), high voltage cathodes, high voltage and non-flammable electrolytes, novel processing technologies, high-energy and low-cost electrode designs, and certain other areas. This work spans a range of US DRIVE activities.

- *Advanced electrode R&D* research includes two projects. One of them is studying inactive components and processing conditions and looking at different binder sources, slurry viscosities, and other parameters to identify physics for a smooth laminate to meet specific performance requirements. The other project focuses on advanced polymer materials for Li-ion and correlative microscopy characterization of electrochemical hotspots in oxide electrodes.
- *Advanced anodes* R&D includes four multi-lab collaborative projects. In the first project, a team consisting of ANL, LBNL, ORNL, SNL, and NREL provides research facility support for the next-generation lithium-ion anodes. A second project, conducted by the five-member National Laboratory Consortium, includes the **silicon deep-dive** project. Silicon is a viable alternative to graphitic carbon as an electrode in lithium-ion cells and can theoretically store >3,500 mAh/g (i.e., about ten times more than graphite). However, lifetime problems severely limit its use in practical systems – this project is focused on those problems. A third project conducted by PNNL in collaboration with the University of Pittsburgh is focused at developing high capacity silicon-based anodes. The fourth collaborative project (NREL, ANL, ORNL, PNNL, LBNL Stanford University, and GM) is the **silicon electrolyte interface stabilization (SEISta)** project which develops a foundational understanding of the formation/evolution of the solid electrolyte interphase on silicon.
- *Advanced cathodes* R&D includes 12 projects. Three of those projects are geared to **enable high-energy/high-voltage cells** via new insights and/or understanding into the failure of present materials/systems. A fourth project on novel cathode materials and processing methods focuses on lithium- and manganese-rich, **‘layered-layered’ composite materials**. Of the remaining eight advanced

cathode projects, three are being conducted at LBNL, one each at PNNL, ORNL and BNL, one at Binghamton University, and another at the University of Texas at Austin.

- *Advanced Electrolyte R&D* includes three projects. Two of them are taking place at ANL to study NG-LiB cathode-liquid electrolyte interfaces, and fluorinated deep eutectic solvent (FDES)-based electrolytes. The third project at Daikin America researches high voltage electrolytes.
- *Diagnostics R&D* includes eight projects, including two which study interfacial processes and *in operando* thermal diagnostics of cells. Other projects study *in situ* diagnostic techniques for battery materials, correlative microscopy characterization of oxide electrodes, and microscopy investigation on the fading mechanism of electrode materials. There are two additional diagnostics projects: an advanced microscopy and spectroscopy project and another on the properties of solid electrolyte interphases for lithium metal systems.
- Of the six *modeling of electrode materials* projects, one is on novel electrode materials from first principles and another on large-scale *ab initio* molecular dynamics simulation of liquid and solid electrolytes. Yet another modeling project focuses on electrode materials design and failure prediction. There are also three more modeling projects based at various universities (including the University of California at Berkeley, Texas A&M University, and the Brigham Young University).

R&D on *beyond Li-ion battery technologies* includes solid-state technology, lithium metal systems, lithium sulfur, lithium air, and sodium-ion. The main areas of focus include new methods to understand/stabilize lithium metal anodes; lithium polysulfides to enable the use of sulfur cathodes; and developing electrolytes for lithium air and lithium sulfur cells. These systems offer further increases in energy and potentially reduced cost compared to the next-gen lithium-ion batteries. However, they also require additional breakthroughs in materials (often at a fundamental level) before commercial use. VTO is investigating the issues and potential solutions associated with cycling metal anodes. The main research topics include: coatings, novel oxide and sulfide-based glassy electrolytes, and *in situ* diagnostics approaches to characterize and understand Li metal behavior during electrochemical cycling.

- *Metallic lithium and solid electrolytes* R&D includes ten projects, one on mechanical properties at the protected lithium interface and another on composite electrolytes to stabilize metallic lithium anodes. Of the remaining, one focuses on dendrite suppression and another on improving the stability of lithium-metal anodes and inorganic-organic solid electrolytes. The remaining six projects are based at various universities including Texas A&M University (TAMU), University of Pittsburgh, West Virginia University, Pennsylvania State University, University of Michigan, and the University of Maryland.
- *Lithium Sulfur R&D* includes 11 projects – three of them at national laboratories and the remaining eight at various universities. The lab-based projects include one on lithium-selenium and selenium-sulfur couple (at ANL), advancing solid-solid interfaces (also at ANL), and the development of high energy lithium sulfur batteries (at PNNL). The eight universities with lithium sulfur projects include TAMU, the Stanford University, University of Wisconsin at Madison, the University of Texas at Austin, Stony Brook University, University of Washington, Rutgers University, and the University of Pittsburgh.
- Additional beyond Li-ion projects include two on *Lithium-Air batteries* and one on *Sodium-ion batteries*.

The *Battery500 Innovation Center* is a combined effort by a team of four National Labs (PNNL, INL, BNL and SLAC) and five universities (University of Texas-Austin, Stanford University, Binghamton University, University of Washington, and University of California, San Diego) with the goal to develop commercially viable Li battery technologies with a cell level specific energy of 500 Wh/kg while simultaneously achieving 1,000 deep-discharge cycles. The consortium keystone projects focus on innovative electrode and cell designs that enable maximizing the capacity from advanced electrode materials. The consortium works closely with the R&D community, battery/materials manufacturers and end-users/OEMs to ensure that these technologies align well with industry needs and can be transitioned to production.

Recent Highlights

Battery cost reduction. The 2018 DOE PEV battery cost reduction milestone of \$200/kWh was accomplished. DOE-funded research has helped reduce the current cost projection for an EV battery (for three DOE-funded battery developers) to an average of \$197/kWh of useable energy. This cost projection is calculated using ANL's public domain Battery Production and Cost model (BatPaC). It assumes a production volume of at least 100,000 batteries per year, the batteries meeting DOE/USABC system performance targets. DOE's goal is to continue to drive down battery cost to \$100/kWh by 2028.

Extreme Fast Charging in enhanced Li-ion systems. Extreme fast charging of EV batteries would provide a refueling experience similar to conventional gasoline powered vehicles. Research in this area started with a 2017 research project to understand XFC. More recently, DOE awarded nine projects to develop cells with EV energy densities but that are also capable of being fast charged. Table ES- 2 lists the projects awarded.

Table ES- 2: Extreme Fast Charging Project Awards

Awardee	Description	Funding
The Regents of the University of California, University of California San Diego	Research surface-acoustic wave turbulent electrolyte mixing during charging to enable rapid charging.	\$653,641
Pennsylvania State University	Research advanced battery cell designs and strategies to operate and improve life and fast charging at higher temperatures.	\$1,000,000
Regents of the University of Michigan	Research three-dimensional hierarchical graphite architectures for anodes for fast charging.	\$1,500,000
SLAC National Accelerator Laboratory	Research on an advanced electrolyte and optimized cell design to enable extreme fast charging.	\$1,500,000
Oak Ridge National Laboratory	Novel electrolyte research that increases the transport rate of lithium-ion from cathode to anode.	\$900,000
Microvast, Inc.	Develop new electrolyte additives, optimized active materials, and electrode formulations.	\$1,500,000
The Research Foundation for the SUNY Stony Brook University	Research to control lithium deposition over-potential on metal-coated graphite electrodes.	\$800,000
University of Tennessee	Research on high power, doped titanium-niobium oxide anodes.	\$720,000
Coulometrics, LLC	Research advanced battery cell designs with lower resistance to enable extreme fast charging.	\$1,000,000

Low Cobalt/No Cobalt cathode projects. Recognizing the issues of price volatility and supply reliability with cobalt, in 2018, DOE awarded six new projects to develop and optimize low cobalt cathode materials. The projects awarded are listed in Table ES- 3.

Table ES- 3: Low Cobalt/No Cobalt Project Awards

Awardee	Description	Funding
Cabot Corporation	Aerosol manufacturing technology for production of low-cobalt lithium-ion battery cathodes	\$2,989,057
NexTech Materials, Ltd. dba Nexceris, LLC	Cobalt-free lithium manganese nickel titanium oxygenate spinel cathodes for next generation lithium-ion batteries	\$2,466,547
Oak Ridge National Laboratory	Cobalt-free aluminum iron nickelate cathode materials for next generation lithium-ion batteries.	\$2,100,000
Penn State University Park	High-performance coated low-cobalt cathode materials for lithium-ion batteries	\$1,952,017
University of California: San Diego	Cobalt free cathode materials and novel architectures	\$2,500,000
University of California: Irvine	Enhancing oxygen stability in low-cobalt cathode materials	\$2,500,000
University of Texas at Austin	High-nickel cathode materials for high-energy, long-life, low-cost lithium-ion batteries	\$2,400,000

Recycling R&D Center. DOE launched the ReCell Battery Recycling R&D Center, a \$4M/year effort by a multiple lab consortium with ANL, NREL, and ORNL which will focus on novel approaches to recycling to maximize economic yield of batteries at their end of life. This is expected to increase the rate of recycling for lithium-ion batteries and decrease dependence on foreign sources for critical materials. The focus areas of the ReCell Center include direct recovery of cathode material, separation methods, battery design for recycling, recovery of other materials, and advanced characterization of recycled material.

Battery500 Cell Achieves 310Wh/kg and 275 cycles, 350Wh/kg and 150 cycles. The Battery500 team succeeded in preparing rechargeable Li metal batteries that achieved 275 cycles with an initial specific energy of 310 Wh/kg. A second generation Li metal/NMC811 cell that is currently cycling shows a beginning of life (BOL) specific energy of 350Wh/kg and has reached 150 cycles of operation with less than 10% capacity fade, see Figure ES- 2. PNNL prepared the cells and INL performed validation and electrochemical analysis.

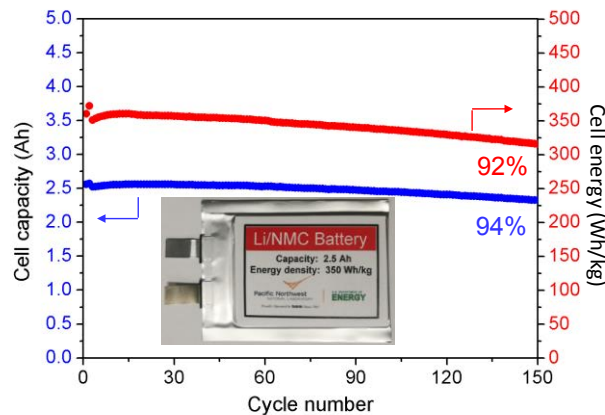


Figure ES- 2. Cell capacity (blue) and the energy (red) of a 2.5 Ah pouch cell as a function of cycling. The cell energy was measured based on the weight of the whole pouch cell including all cell components. The cell was charged within 10 hours (C/10) and discharged within 3 hours (C/3).

Collaborative Activities

In addition to the above, VTO has established extensive and comprehensive ongoing coordination efforts in energy storage R&D across all of the DOE complex and with other government agencies. It coordinates efforts on energy storage R&D with both the Office of Science and the Office of Electricity. Coordination and collaboration efforts also include membership and participation in the Chemical Working Group of the Interagency Advanced Power Group (IAPG), in program reviews and technical meetings sponsored by other government agencies, and inviting participation of representatives from other government agencies in the contract and program reviews of DOE-sponsored efforts. DOE coordinates such activities with the Army's Advanced Vehicle Power Technology Alliance, the Department of Transportation/National Highway Traffic Safety Administration (DOT/NHTSA), the Environmental Protection Agency (EPA), and the United Nations Working Group on Battery Shipment Requirements. Additional international collaboration occurs through the International Energy Agency's (IEA's) Hybrid Electric Vehicles Technology Collaboration Program (HEV TCP); the G8 Energy Ministerial's Electric Vehicle Initiative (EVI); and bilateral agreements between the U.S. and China. The *U.S. China Clean Energy Research Center* conducts collaborative research both on rechargeable lithium-ion and beyond lithium-ion battery technologies to help develop the next generation of advanced batteries to help expand electrification of vehicles and enable smart grids internationally and its main objective is to understand and develop advanced battery chemistries based on lithium-ion and beyond lithium ion that meet 300Wh/kg energy density.

Organization of this Report

This report covers all the FY 2018 projects as part of the advanced battery R&D (i.e., energy storage R&D) effort in VTO. We are pleased with the progress made during the year and look forward to continued cooperation with our industrial, government, and scientific partners to overcome the remaining challenges to delivering advanced energy storage systems for vehicle applications.



David Howell
VTO Director (Acting)
Vehicle Technologies
Office



Steven Boyd
Program Manager,
Batteries and
Electrification Program
Vehicle Technologies
Office



Tien Q. Duong
Manager, Advanced
Battery Materials
Research and VTO
Battery500 Consortium
Vehicle Technologies
Office



Peter W. Faguy
Manager, Applied Battery
Research and Advanced
Processing R&D
Vehicle Technologies
Office



Brian Cunningham
Manager, Battery Development; and Battery Testing, and Analysis and Design
Vehicle Technologies Office



Samuel Gillard
Manager, Battery Testing, Analysis and Design; and Small Business Innovation Research for Batteries
Vehicle Technologies Office

Table of Contents

Disclaimer	iii
Acknowledgements	iv
Acronyms	v
Executive Summary	xiv
Table of Contents	xxiv
List of Figures	xxix
List of Tables	xc
Vehicle Technologies Office Overview	xciii
Batteries Program Overview	xcv
I. Advanced Battery and Cell Research and Development	1
I.1 USABC Battery Development & Materials R&D	1
I.1.A High Energy Lithium Batteries for Electric Vehicles (Zenlabs Energy).....	1
I.1.B High-Performance Semi-Solid Cell for EV Applications (24M Technologies, Inc.).....	7
I.1.C Development of High Performance Li-ion Cell Technology for EV Applications (Farasis Energy).....	12
I.1.D Enabling Thicker Cathode Coatings for Lithium Ion EV Batteries (PPG)	17
I.1.E Advanced High-Performance Batteries for Electric Vehicle Applications (Amprius)	21
I.1.F Rapid Commercialization of High Energy Anode Materials (SiNode Systems)	26
I.1.G Advanced Separators for Vehicle Lithium Battery Applications (Celgard, LLC)	31
I.1.H Li-Ion Cell Manufacturing Using Directly Recycled Active Materials (Farasis Energy)..	37
I.1.I A Closed Loop Recycling Process for End-of-Life Electric Vehicle Li-ion Batteries (Worcester Polytechnic Institute).....	43
I.1.J Perform USABC/USCAR Benchmarking Activities (Southwest Research Institute)	49
I.1.K 12V Start-Stop Development Program (XALT Energy).....	52
I.2 Advanced Processing	58
I.2.A Low Cost Manufacturing of Advanced Silicon-Based Anode Materials (Group14 Technologies, Inc.).....	58
I.2.B Co-Extrusion (CoEx) for Cost Reduction of Advanced High-Energy-and-Power Battery Electrode Manufacturing (PARC).....	65
I.2.C Electrodeposition for Low-Cost, water-Based Electrode Manufacturing (PPG Industries, ANL, Navitas, ORNL).....	72
I.2.D Development of UV Curable Binder Technology to Reduce Manufacturing Cost and Improve Performance of Lithium Ion Battery Electrodes (Miltec UV International).....	78
I.2.E Towards Solventless Processing of Thick Electron-Beam (EB) Cured LIB Cathodes (ORNL)	84
I.2.F Performance Effects of Electrode Processing for High-Energy Lithium-Ion Batteries (ORNL)	90
I.2.G Advanced Active Battery Materials: Active Cathode Materials with Component Concentration Gradient Structures (ANL)	99

I.2.H	Process R&D for Droplet-Produced Powdered Materials (ANL).....	105
I.2.I	Integrated Flame Spray Process for Low Cost Production of Battery Materials for Lithium Ion Batteries and Beyond (University of Missouri).....	109
I.2.J	High Performance Li-Ion Battery Anodes from Electrospun Nanoparticle/Conducting Polymer Nanofibers (Vanderbilt University).....	114
I.2.K	Process R&D and Scale up of Critical Battery Materials (ANL).....	120
I.2.L	High Energy, Long Life Lithium-Ion Battery (NREL).....	128
I.3	Computer-Aided Engineering for Batteries (CAEBAT).....	135
I.3.A	Advanced Computer Aided Battery Engineering Consortium (NREL/ANL/SNL/Purdue Univ).....	135
I.3.B	Consortium for Advanced Battery Simulation (ORNL).....	146
I.3.C	Consortium for Advanced Battery Simulation (SNL).....	155
I.3.D	Consortium for Advanced Battery Simulation (ANL, LBNL).....	161
I.3.E	Advanced Tool for Computer Aided Battery Engineering (ANL).....	167
I.3.F	Advanced Tool for Computer Aided Battery Engineering (SNL).....	173
I.3.G	Development and Validation of a Simulation Tool to Predict the Combined Structural, Electrical, Electrochemical and Thermal Responses of Automotive Batteries (Ford Motor Company).....	177
I.4	Recycling and Sustainability.....	189
I.4.A	Life Cycle Assessment of Li-ion Batteries (ANL).....	189
I.4.B	Battery Production and Recycling Materials Issues (ANL).....	194
I.4.C	Closed-loop Battery Recycling Model (ANL).....	200
I.4.D	Li-ion Battery Recycling R&D Center (ANL).....	206
I.4.E	Lithium-ion Battery Recycling Prize Support (NREL).....	210
I.5	Extreme Fast Charge (XFC).....	214
I.5.A	XFC R&D: CAMP, Testing & Post-Test Characterization and Modeling (ANL).....	214
I.5.B	XFC R&D: Battery Testing Activities (INL).....	233
I.5.C	XFC R&D: MSMD Modeling & Thermal Testing (NREL).....	239
I.5.D	Novel Liquid/Oligomer Hybrid Electrolyte with High Li Ion Transference Number (Hi-LiT) for Extreme Fast Charging (ORNL).....	250
I.5.E	Research on high power, doped titanium-niobium oxide anodes (ORNL).....	257
I.5.F	Research three-dimensional hierarchical graphite architectures for anodes for fast charging (SNL).....	260
I.5.G	Beyond Batteries: Behind the Meter Storage (NREL, INL, ORNL, SNL).....	264
I.6	Small Business Innovation Research (SBIR).....	267
I.7	Testing and Analysis.....	273
I.7.A	BatPaC Model Development (ANL).....	273
I.7.B	Battery Performance and Life Testing (ANL).....	281
I.7.C	Electrochemical Performance Testing (INL).....	285
I.7.D	Battery Safety Testing (SNL).....	290
I.7.E	Battery Thermal Analysis and Characterization Activities (NREL).....	296
I.7.F	Cell Analysis, Modeling, and Prototyping (CAMP) Facility Research Activities (Argonne National Laboratory).....	303
I.7.G	Materials Benchmarking Activities for CAMP Facility (Argonne National Laboratory).....	316
I.7.H	Post-test Analysis of Lithium-Ion Battery Materials (ANL, ORNL, SNL).....	325

II. Advanced Materials R&D	330
II.1 Next-gen Lithium-ion: Advanced Electrodes R&D	330
II.1.A Higher Energy Density via Inactive Components and Processing Conditions (LBNL) ..	330
II.1.B Advanced Polymer Materials for Li-ion and Correlative Microscopy Characterization of Electrochemical Hotspots in Oxide Electrodes (SLAC)	335
II.2 Next Generation Lithium-Ion Batteries: Advanced Anodes R&D	341
II.2.A Next Generation Anodes for Lithium-Ion Batteries: Silicon (ANL, LBNL, ORNL, SNL, NREL).....	341
II.2.B Silicon Electrolyte Interface Stabilization (SEISta) (NREL, ANL, ORNL, LBNL, SNL).....	407
II.2.C Development of Si-based High-Capacity Anodes (Pacific Northwest National Laboratory).....	516
II.2.D Pre-Lithiation of Silicon Anode for High Energy Li Ion Batteries (Stanford University)	522
II.3 Next-Gen Lithium-Ion: Advanced Cathodes R&D	528
II.3.A Electrochemical Analysis and Evaluation (ANL, LBNL, ORNL).....	528
II.3.B Materials and Characterization (ANL, LBNL, ORNL)	537
II.3.C Theory and Modeling (ANL, LBNL, ORNL).....	544
II.3.D Studies on High Capacity Cathodes for Advanced Lithium-Ion (ORNL)	554
II.3.E High Energy Density Lithium Battery (Binghamton University)	564
II.3.F Development of High-Energy Cathode Materials (PNNL).....	571
II.3.G <i>In situ</i> Solvothermal Synthesis of Novel High-Capacity Cathodes (BNL).....	578
II.3.H Novel Cathode Materials and Processing Methods (ANL).....	586
II.3.I Advanced Cathode Materials for High Energy Lithium Ion Batteries (LBNL).....	593
II.3.J Lithium Batteries with Higher Capacity and Voltage (UTA)	599
II.3.K Discovery of High-Energy Li-Ion Battery Materials (LBNL)	604
II.3.L Model-System Diagnostics for High-Energy Cathode Development (LBNL)	612
II.4 Next-Gen Lithium-Ion: Advanced Electrolytes.....	621
II.4.A Stability of cathode/electrolyte interfaces in high voltage Li-ion batteries (ANL).....	621
II.4.B Fluorinated Deep Eutectic Solvent (FDES)-Based Electrolytes (ANL)	627
II.4.C Advanced Lithium Ion Battery Technology – High Voltage Electrolyte (Daikin America, Inc.).....	633
II.5 Next-Gen Lithium-Ion: Diagnostics	643
II.5.A Interfacial Processes (LBNL).....	643
II.5.B Advanced in situ Diagnostic Techniques for Battery Materials (BNL).....	651
II.5.C Advanced Microscopy and Spectroscopy for Probing and Optimizing Electrode- Electrolyte Interphases in High Energy Lithium Batteries (UCSD)	659
II.5.D Microscopy Investigation on the Fading Mechanism of Electrode Materials (PNNL)....	666
II.5.E In-Operando Thermal Diagnostics of Electrochemical Cells (LBNL).....	673
II.5.F Correlative Microscopy Characterization of Oxide Electrodes (SLAC National Accelerator Laboratory)	677
II.5.G <i>In situ</i> Diagnostics of Coupled Electrochemical-Mechanical Properties of Solid Electrolyte Interphases on Lithium Metal for Rechargeable Batteries (General Motors) 683	
II.5.H Development of high energy battery system with 300wh/kg (ANL)	694
II.6 Next-Gen Lithium-Ion: Modeling Advanced Electrode Materials.....	703

II.6.A	Electrode Materials Design and Failure Prediction (ANL).....	703
II.6.B	Predicting and Understanding Novel Electrode Materials from First Principles	710
II.6.C	First Principles Calculations of Existing and Novel Electrode Materials	715
II.6.D	Addressing Heterogeneity in Electrode Fabrication Processes (Brigham Young University)	722
II.6.E	Large scale ab initio molecular dynamics simulation of liquid and solid electrolytes (Lawrence Berkeley National Laboratory)	729
II.6.F	Dendrite Growth Morphology Modeling in Liquid and Solid Electrolytes (MSU).....	734
II.7	Beyond Li-ion R&D: Metallic Lithium and Solid Electrolytes.....	740
II.7.A	Mechanical Properties at the Protected Lithium Interface (ORNL).....	740
II.7.B	Solid electrolytes for solid-state and lithium-sulfur batteries (Univ. of Michigan, ORNL, ARL, Oxford U.).....	746
II.7.C	Composite Electrolytes to Stabilize Metallic Lithium Anodes (ORNL).....	753
II.7.D	High Conductivity and Flexible Hybrid Solid State Electrolyte (University of Maryland).....	758
II.7.E	Lithium Dendrite Prevention for Lithium Batteries (Pacific Northwest National Laboratory).....	765
II.7.F	Understanding and Strategies for Controlled Interfacial Phenomena in Li-Ion Batteries and Beyond (TAMU, Purdue).....	772
II.7.G	Engineering Approaches to Dendrite Free Lithium Anodes (University of Pittsburgh)..	778
II.7.H	Solid-State Inorganic Nanofiber Network-Polymer Composite Electrolytes for Lithium Batteries (WVU)	786
II.7.I	Electrochemically Responsive Self-Formed Li-ion Conductors for High Performance Li Metal Anodes (Penn State Univ).....	792
II.7.J	Improving the Stability of Lithium-Metal Anodes and Inorganic-Organic Solid Electrolytes (LBNL)	800
II.8	Beyond Li-ion R&D: Lithium Sulfur Batteries	810
II.8.A	Novel Chemistry: Lithium-Selenium and Selenium-Sulfur Couple (ANL).....	810
II.8.B	Development of High Energy Lithium-Sulfur Batteries (PNNL)	817
II.8.C	Nanostructured Design of Sulfur Cathodes for High Energy Lithium-Sulfur Batteries (Stanford University)	824
II.8.D	Addressing Internal “Shuttle” Effect: Electrolyte Design and Cathode Morphology Evolution in Li-S Batteries (TAMU, Purdue Univ).....	831
II.8.E	Mechanistic Investigation for the Rechargeable Li-Sulfur Batteries (U of Wisconsin)...	837
II.8.F	Statically and Dynamically Stable Lithium-sulfur Batteries (UTA).....	843
II.8.G	Dual Function Solid State Battery with Self-forming Self-healing Electrolyte and Separator (Stony Brook University).....	850
II.8.H	Advancing Solid-Solid Interfaces in Li-ion Batteries (Argonne National Laboratory) ...	857
II.8.I	Multifunctional, Self-Healing Polyelectrolyte Gels for Long-Cycle-Life, High-Capacity Sulfur Cathodes in Li-S Batteries (University of Washington).....	864
II.8.J	Self-Forming Thin Interphases and Electrodes Enabling 3-D Structures High Energy Density Batteries (Rutgers, the State University of New Jersey).....	873
II.8.K	Electrochemically Stable High Energy Density Lithium Sulfur Batteries (University of Pittsburgh).....	877
II.9	Beyond Li-ion R&D: Lithium-Air Batteries	888
II.9.A	Rechargeable Lithium-Air Batteries (Pacific Northwest National Laboratory).....	888

II.9.B	Lithium-Air Batteries (Argonne National Laboratory).....	895
II.10	Beyond Li-ion R&D: Sodium-Ion Batteries.....	900
II.10.A	Exploratory Studies of Novel Sodium-Ion Battery Systems (BNL).....	900
II.11	Beyond Li-ion R&D: Battery500.....	906
II.11.A	Battery500 Innovation Center (PNNL).....	906
II.11.B	Battery500 Seedling Projects (NAVSEA).....	920
List of Principal Investigators.....		934

List of Figures

Figure I.1.A.1 Current and projected cell development progression throughout the USABC program	3
Figure I.1.A.2 Cycle life performance for various high-energy build #3 cell designs.....	4
Figure I.1.A.3 Schematic of cell foot prints used in final cell build #4	5
Figure I.1.A.4 Normalized capacity versus cycles for large 50Ah and standard 11 Ah capacity footprint cells	6
Figure I.1.B.1 Full cell voltage drop and anode potential drop during discharge at different rates.....	9
Figure I.1.B.2 Discharge rate capability of R&D full cell using cathode with modified slurry composition	10
Figure I.1.C.1 DST Cycle life for nickle rich NCM with Si/C composite.....	14
Figure I.1.C.2 DCR for the Gen 1 deliverable chemistry & 2b) Rate capability	14
Figure I.1.C.3 Cycle life for Gen 1 deliverable chemistry	14
Figure I.1.C.4 Cycle life for the different electrolyte formulations	15
Figure I.1.C.5 Calendar life DCR for the Gen 1 deliverable chemistry & 4b) Capacity retention at 100%SOC @ 30° and 45°C	15
Figure I.1.C.6 a) Capacity of C1.1 with different amount of sacrificial Li source b) Cycle life of Ni rich NCM(C1.1) with 5% SLSM for Si (500mAh/g) and c) Si composite with capacity of 1000mAh/g.	16
Figure I.1.D.1 90°peel test result of PPG coating with different binder and mixing procedure	18
Figure I.1.D.2 Long term cycling of pouch cells with baseline thickness, 93/3/4 and with NMC622 cycled under C/3.....	19
Figure I.1.D.3 Nyquist Plot of EIS measurement on pouch cells fabricated at PSU	19
Figure I.1.D.4 Peel strength of the thick cathode coatings	20
Figure I.1.E.1 Electrolyte formulation was optimized for better Calendar and Cycle Life in Si/NCM (70% Ni) cells.....	23
Figure I.1.E.2 CAD drawing and prototype 40Ah cell with silicon nanowire anode	24
Figure I.1.E.3 Silicon nanowire cells with NCM811 and in large form factor achieve 375 Wh/kg.....	25
Figure I.1.F.1 Si anode failure mechanisms (left), SiNode graphene-wrapped advanced silicon anode architecture (right).	27
Figure I.1.F.2 1st cycle efficiency (FCE) and capacity (mAh/g) for a series of surface-treated SiOx materials.....	28
Figure I.1.F.3 Normalized full cell capacity versus cycles for SiNode-graphite blended anodes (1000 mAh/g) with NCA.....	28
Figure I.1.F.4 SiNode production and production capacity (left) and particle size distribution (PSD) measurements demonstrating consistent material production quality (right).	29

Figure I.1.F.5 10 Ah prototype cell with SiNode anode and NCA cathode. Commercial 18650 cell for comparison.....	29
Figure I.1.G.1 Cycling performance comparison between cells stored for 25 days at 4.6 V and a cell tested without storage.....	33
Figure I.1.G.2 SEM Images of PMP-coated separator produced under various trial conditions.....	34
Figure I.1.G.3 Residual capacity during OCV stand at 100% SOC vs. total thickness of AlO_x deposited on the experimental separators.....	35
Figure I.1.G.4 Discharging capacity of experimental and control separators in NCM523/Graphite 1.35 Ah pouch cells cycled at 45°C, between 3.5 and 4.4 V.....	35
Figure I.1.H.1 Pictorial representation of the direct recycling process which largely relies on physical separation processes; compared to other recycling technologies, the positive electrode active material is recovered intact, preserving some of the value added during its synthesis.....	38
Figure I.1.H.2 (a) Material recovery from positive electrode scrap, and (b) reversible electrochemical capacity of recycled NMC111, recovered using different process parameters (First discharge capacity, C/20, 4.2 - 3.0 V vs. Li metal counterelectrode). (c) Thermal tr.....	40
Figure I.1.H.3 Raman spectra and SEM images of NMC111 recovered from electrode scrap using a range of thermal treatment conditions.....	41
Figure I.1.I.1 Hardware Strategy of the Program.....	44
Figure I.1.I.2 Cycling of 1Ah cells with WPI cathode and control between 4.15V and 2.7V, 100% DOD, 45°C, +1C/-2C.....	45
Figure I.1.I.3 1-second DCR, 5C discharge, 45°C, 70%, 50%, and 20% SOC after 1 month of cycling ...	45
Figure I.1.I.4 Cycling of 10Ah cells with WPI cathode and control cathode between 4.15V and 2.7V, 100% DOD, 45°C, +1C/-2C.....	46
Figure I.1.I.5 HPPC of 10Ah cells with WPI cathode at 25°C and 0°C at 10s (a) and 1s (b).....	47
Figure I.1.I.6 Rate performance of 10Ah cells with WPI cathode powder and a reference cell at 25°C....	47
Figure I.1.J.1 High-voltage measurement schematic (left). Power electronics breakout for voltage and current measurement (right).....	50
Figure I.1.J.2 OBD e-PID messages have been deciphered.....	50
Figure I.1.K.1 2C/-2C, 100%DOD cycle life tests on D0.1 (1 Ah LMO-LTO cells) at 30°C, 45°C, and 55°C. Capacity Retention (left), impedance retention (right).....	53
Figure I.1.K.2 5C/-5C, 100%DOD cycle life tests on 1 Ah LMO-LTO cells at 30°C. Capacity Retention (left), impedance retention (right).....	54
Figure I.1.K.3 Charge and discharge power calculated from HPPC test at 30°C on 1Ah LMO-LTO cells and scaled to the 12V module using the appropriate BSF.....	54

Figure I.1.K.4 (Left): (a) -30°C impedance growth rate during the pulse cycle life test. (●-) denote values from 0.5s, 6KW pulse test, (-○-) denote values from 4s 4KW pulse test, (b) 30°C impedance growth from HPPC tests, (●-) denote values at 50%SOC and (-○-)	55
Figure I.1.K.5 Capacity fade of D0.1 (1Ah LMO-LTO cells) during calendar life testing at 100% SOC and 70% SOC, at both 30°C and 45°C .	55
Figure I.1.K.6 Impedance growth on D0.1 (1Ah LMO-LTO cells) during calendar life testing at 100% SOC and 70% SOC. (a) Impedance growth measured at 30°C from HPPC test for cells stored at 100%SOC, (b) Impedance growth measured at -30°C from cold crank test for cells stored at 100%SOC, (c) Impedance growth measured at 30°C from HPPC test for cells stored at 70%SOC, (d) Impedance growth measured at -30°C from cold crank test for cells stored at 70%SOC.	56
Figure I.1.K.7 Voltage profile during cold crank test at 50% SOC on 1 Ah LMO-LTO cell	57
Figure I.2.A.1 Volumetric energy density (Wh/L) in full cell coin cells for Si-C produced at lab-pilot scale.	60
Figure I.2.A.2 Gravimetric energy density (Wh/kg) in full cell coin cells for Si-C produced at lab-pilot scale.	60
Figure I.2.A.3 Example of device-level enhancement: cycle stability of pre-lithiated Si-C.	61
Figure I.2.A.4 Homogeneity within the Si-C composite as determined by SEM in combination with EDS.	61
Figure I.2.A.5 Raman (left) and XRD spectra (right) consistent with amorphous silicon and carbon within Si-C.	62
Figure I.2.B.1 3-D Microscope images of as-printed and dried (a) and post-calendered (b) cathode electrodes produced via CoEx. Images illustrate the corrugated topography that persists after the calendaring process.	66
Figure I.2.B.2 Comparison of the electrochemical rate performance of one-layer and two-layer thick graphite anodes ($\sim 6 \text{ mAh/cm}^2$) in half coin cells. Three cycles were run at each C rate. Each plotted data point represents the median of the 2nd cycle capacities for each cell group (3 cells for the baseline coating and 4 cells for the 30% Bottom/70% Top coating), while the error bars represent the group minimum and maximum. All cells were made with 1.2 M LiPF ₆ in 3:7 wt% EC/EMC electrolyte.	68
Figure I.2.B.3 Representative surface profile of CoEx cathode both before (blue) and after (red) calendaring.	69
Figure I.2.B.4 Electrochemical Performance of 1 Ah pouch cells, comparing thin and thick baselines vs. CoEx cathodes. Error bars represent +/- 1 standard deviation. Quadratic curve fits are intended to guide the eye. All cells were made with 1.2 M LiPF ₆ in 3:7 wt% E	70
Figure I.2.C.1 (a) Optical photograph of a 20 foot roll coated continuously on the mini-coater system at a line speed of 0.5 m/min. (b) A comparison of half-cell coin-cell performance of LFP electrodes fabricated using bench-scale equipment and the mini-coater system	74
Figure I.2.C.2 Film deposition rate increases proportionally to the increase in electric field strength demonstrated by (a) increasing voltage and (b) decreasing separation between electrodes.	74

Figure I.2.C.3 Aerial capacity measurements of electrode coatings fabricated by simultaneously coating both sides of the current collector foil on the mini-coater system and highlighting the top-to-bottom (i.e. side to side) and front-to-back uniformity for both (a) LFP and (b) NCM 622 formulations. Coin-cell performance of electrodes fabricated on the mini-coater using (c) LFP and (d) NCM 622 formulations. . 75

Figure I.2.C.4 (a) Residual water content of PPG electrocoated cathodes and ORNL NMP-processed NCM 333 cathodes subjected to different secondary drying conditions. Each data point is an average of two titrations, and the error bars represent the standard deviation. (b) Discharge rate performance results for single-layer pouch cells made with PPG electrocoated cathodes dried at 3 different conditions (100°C for 4h, 140°C for 4h, and 160°C for 16h) 76

Figure I.2.C.5 Cycling performance of electrocoated cathodes fabricated using bench-scale equipment compared to baseline cells assembled using conventional binders and drawdown method. An improvement to cycle life is observed for both (a) LFP formulations and (b) NCM 111 formulations by using electrocoat fabrication. 77

Figure I.2.D.1 Developed UV Web and Slot Die Process. 79

Figure I.2.D.2 Layer on Layer Cathode Coatings are not a problem, but the solution. Double layer coatings always retain capacity as well or better than single layer coatings..... 80

Figure I.2.D.3 Layer on layer UV Slot-Die Processing works with no loss in capacity. 94-4-3-NMC532-C-UV 7, 14, and 21 mg/cm²..... 80

Figure I.2.D.4 Power cathode (82-12-6:NMC(532)-C-UV, 4 mg/cm²) shows 75% capacity retention at 10C rate. UV cathode withstands high temperature (120°C), where a PVDF electrode would melt and flow. Three curves show tight consistency between cells..... 81

Figure I.2.D.5 UV LTO Anode (93-4-3:LTO-C-UV) with 3 mg/cm² loading. Three curves show tight consistency between cells. 81

Figure I.2.E.1 Voltage curves of the 1.5 Ah cells prepared from baseline sample (PVDF/NMP processing), sample B (acrylate polyurethane resin binder and EB cured at 500 fpm) and sample C (acrylate polyurethane resin, not cured)..... 86

Figure I.2.E.2 Cycling performance of 1.5 Ah cells prepared from baseline sample (PVDF/NMP processing), sample B (acrylate polyurethane resin binder and EB cured at 500 fpm) and sample C (acrylate polyurethane resin, not cured)..... 86

Figure I.2.E.3 Representative photos of the electrostatic sprayed samples after receiving from Keyland polymer. 88

Figure I.2.E.4 Areal loading of the electrode prepared by electrostatic spraying method versus the spraying time..... 88

Figure I.2.F.1 Capacity retention of five different cosolvent systems cycled in full pouch cells at 0.33C/-0.33C..... 92

Figure I.2.F.2 Comparison of crack formation for three different solvent systems showing a crack-free coating for the 90/10 wt% water/methyl acetate cosolvent dispersion. 92

Figure I.2.F.3 SEM micrographs of laser-structured NMC 532 cathodes with different pitches (left and center) and schematic of a bilayer NMC 532 cathode with a porosity gradient (right).	93
Figure I.2.F.4 Rate performance from 0.05C to 10C discharge rates of full graphite/NMC 532 pouch cells comparing laser structured cathodes and a structured bilayer cathode to an unstructured baseline.	93
Figure I.2.F.5 NMC 811 rate performance comparison between aqueous processed cathodes, NMP processing with water exposed cathodes, and NMP processed baseline charged to 4.2 V (left) and 4.4 V (right).	94
Figure I.2.F.6 XRD (left) and Raman spectroscopy (right) data of NMC 333 and NMC 811 pristine active material and after one week of water exposure showing no difference in bulk structure for either compound.....	94
Figure I.2.F.7 TEM images of pristine NMC 811 (top) and NMC 811 exposed to water for one week (bottom).	95
Figure I.2.F.8 Comparison of 0.33C/-0.33C cycle life between aqueous processed NMC 811, NMC 811 exposed to water for one week, and the NMP processed baseline showing that water exposure for a long period of time has a deleterious effect on capacity retention.	95
Figure I.2.F.9 Surface energy of various NMC 532 cathodes with different porosities compared to Conoco Phillips A12 graphite surface energy; surface energies not including the effect of electrode roughness (left) and apparent surface energies including surface porosit.....	96
Figure I.2.G.1 Thermal stability comparison between commercial NMC811 and 811 core-gradient using time resolved XRD	100
Figure I.2.G.2 Oxygen release comparison of normal NMC and core-gradient materials	100
Figure I.2.G.3 New synthesis approach toward Core-Multi Shell particle structure	101
Figure I.2.G.4 Electrochemical performance of synthesized core-multi shell materials	101
Figure I.2.G.5 Cycling comparison between commercial NMC and core-multi shell materials	102
Figure I.2.G.6 DSC comparison at 5 C/min rate.....	102
Figure I.2.G.7 Impedance analysis of core-multi shell materials	103
Figure I.2.G.8 Normalized average discharge capacities of commercial NMC811 and core-multi shell materials.....	103
Figure I.2.G.9 Average discharge capacity retention of commercial NMC811 and core-multi shell materials.....	104
Figure I.2.H.1 Mean particle diameter versus solids production rate for FSP synthesis of LLZO. All points except Sol40 are based on the LLZO-UM recipe. Sol40 is based on the LLZO-ANL recipe. The inset shows predicted particle size for SMPS versus BET-SA data.	107
Figure I.2.H.2 (SEM digital image of LLZO-ANL before and after annealing for 12 hours at 800°C) ...	107
Figure I.2.H.3 XRD patterns for LLZO-ANL green and annealed powder. The material was annealed in oxygen for 12 hours at the temperatures noted.	108

Figure I.2.H.4 XRD patterns for LNMO following annealing in Ar for 12 hours at 1000°C.....	108
Figure I.2.I.1 SEM images of NMC (111) powders made at different temperatures: Left –a wrinkled morphology at low temperature (500°C), and Right –a spherical morphology at high temperature (800°C).	110
Figure I.2.I.2 SEM images of NMC (111) powders made with two different precursors: Left – powders showing better spherical morphologies; Right – powders show “perfect” spheres, despite some wrinkled particles.	110
Figure I.2.I.3 Cycling tests (a) rate capability at various C rates, and (b) cycling performance at 1C.	111
Figure I.2.I.4 XRD patterns of the as-prepared LR1 and LR2 showing typical diffraction peaks of Li-rich materials.	111
Figure I.2.I.5 SEM image of a Ni-rich NMC powders and a mapping of the Al element on a particle surface, showing Al was uniform on the surface of the particle.	112
Figure I.2.I.6 Charge-discharge profiles on bare (previously presented) and Al ₂ O ₃ coated NMC powders (new results). The coated NMC shows improved stability.	112
Figure I.2.J.1 (a) Cycling results (discharge curve) for a Li-ion half-cell with anode prepared from a dual fiber Si-PAA/C-PAN mat. The first 5 cycles were carried out at 0.1C and the remaining 50 cycles at 1C; terminal discharge capacity at 1C was 604 mAh/g (gravimetric) and 1.58 mAh/cm ² (areal), (b) Photograph of the anode extracted from the cell after cycling at 1C, demonstrating excellent integrity of the fibrous structure, (c) Surface SEM image of the raw mat (51 wt.% Si, 9 wt.% C and 40 wt.% PAA+PAN in the fibers), and (d) Surface SEM of the compacted mat from Figure 1c.	116
Figure I.2.J.2 Cycling results for Li-ion half-cells with anodes prepared from the same C-PAN/Si-PAA dual fiber mat. Both cells were subjected to one charge/discharge cycle at 0.1C followed by 50 cycles at either 0.1C or 1C. The charge/discharge capacity after 50 cycles is above the project’s Go/No-Go target. The terminal discharge capacity for the anode cycled at 0.1C is 1000 mAh/g (gravimetric) and 2.4 mAh/cm ² (areal). The terminal discharge capacity at 1C is 611 mAh/g (gravimetric) and 1.5 mAh/cm ² (areal). The coulombic efficiency is in the range of 98-99% for the both anodes.	117
Figure I.2.J.3 (a) Surface SEM image of the raw mat obtained by concurrent electrospinning of Si-PAA and electrospaying of C-PVDF, (b) Surface SEM of the compacted/welded mat from Figure 3a, and (c) Cycling results (discharge curves) for two Li-ion half-cells with anodes (A200 and A201) prepared from the compacted/welded mat. The first 5 cycles were at 0.1C and the remaining 50 cycles at 1C; terminal discharge capacity at 1C was 600 mAh/g (gravimetric) and 1 mAh/cm ² (areal).	118
Figure I.2.J.4 (a) Surface SEM image of an as-spun mat of Si/PAA nanofibers (40 wt.% PAA in Si-PAA fibers), (b) Surface SEM of the welded/compacted mat from Figure 4a, and (c) (a) Cycling results (discharge curves) for Li-ion half-cells with anodes prepared from a thinner (5 μm and 0.46 mg/cm ²) and thicker (25 μm and 1.71 mg/cm ²) electrospun and compacted/welded Si-PAA fiber mats. The first 5 cycles were at 0.1C and the remaining 50 cycles at 1C; terminal discharge capacity at 1C was 1400 mAh/g (gravimetric) and 0.7 mAh/cm ² (areal), for the thinner anode and 600 mAh/g and 1.1 mAh/cm ² for the thicker anode,	119
Figure I.2.K.1 Batch synthesis of ethyl and propyl trifluoroethyl sulfones.	121

Figure I.2.K.2 Screening of flow synthesis conditions for propyl trifluoromethyl sulfone	122
Figure I.2.K.3 Batch Conditions for the Synthesis of H-TDI	122
Figure I.2.K.4 Conversion data for H-TDI as a function of time and temperature	122
Figure I.2.K.5 Reaction calorimetry data	123
Figure I.2.K.6 Structure of literature FSP precursors synthesized at MERF	123
Figure I.2.K.7 Route for novel disilylcarbonate electrolyte solvents invented and developed at MERF .	124
Figure I.2.K.8 Conversion dependence on reaction conditions for Me ₃ SiCH ₂ SiMe ₂ CH ₂ OC(O)OMe	124
Figure I.2.K.9 10% w/w TMSMSMMC and TMSMSMEC in Gen2, graphite//NCM523, 3.0 - 4.4 V cycling (Ch/DCh at C/3), 30°C.	125
Figure I.2.K.10 Synthesis of Si-containing carbonate solvents	125
Figure I.2.K.11 Cell performance of BTMSMC and DEGBTMSMC additives to Gen2 electrolyte.....	126
Figure I.2.L.1 Cycling of 400 mAh Si pouch cells at C/3 and room temperature with and without relithiation. The blue circles represent cycling with no relithiation. The green and red points represent cycling where triggered relithiation is performed during rest at 100 μ A when 75% capacity is reached.	131
Figure I.2.L.2 Cycling of 400 mAh Si pouch cells at C/3 and room temperature with and without continuous relithiation using passive control.....	131
Figure I.2.L.3 Comparison of cell resistance during cycling of 400 mAh Si pouch cells at C/3 and room temperature with and without continuous relithiation using passive control.....	132
Figure I.2.L.4 Measured lithium concentration within LFP/graphite 18650 cells after high-rate relithiation. Three coin cells were extracted from each of location of the cells' jellyrolls. A 2D Li-transport model prediction shown as blue dots/line. LFP/graphite chemistry is worst case scenario due to OCP plateaus of both the graphite and LFP electrodes.....	133
Figure I.2.L.5 Simulated lithium concentration within NMC/graphite 18650 cell relithiated at different rates. 20% of capacity can be recovered over 6 months or slower without concern for Li plating.	133
Figure I.2.L.6 Loss mechanisms for SOA high energy (5% Si - 85%Gr/NMC811) LG MJ1 cell	134
Figure I.3.A.1 Approach for microstructure characterization and modeling	137
Figure I.3.A.2 (a) Five layers of 114 μ m thick graphite electrode individually resolved in beamline XRD study. (b) Li concentration layer-by-layer during 1C charge and discharge, data (symbols) vs. model (lines).	138
Figure I.3.A.3 Comparison of experimentally measured stress-strain response of a 3 Ah pouch format cell against model predictions at various strain rates	139
Figure I.3.A.4 Comparison of the experimentally observed rise in temperature within a 5S1P module comprised of 3 Ah pouch format cells charged to 100% SOC.	139
Figure I.3.A.5 Force vs displacement of fully charged 5-Ah pouch cells. Little changed is observed up to 60°C, however a dramatic softening of the cell is observed at 120°C	140

Figure I.3.A.6 Electrode microstructural variations concurrently affect (a) electrochemical, (b) thermal and (c) chemical interactions. The electrode capacities are kept unchanged to identify the microstructural effects [11].	141
Figure I.3.A.7 Through-plane tortuosity factors of 7 positive NMC532 and 7 negative A12 graphite ANL CAMP electrodes, obtained with microstructure numerical homogenization (blue), macro-homogenous model fitting (orange), and direct measurement (red). Region of confidence	142
Figure I.3.A.8 Lithiation of anode with Superior graphite SLC1506T at 5C rate with snapshot taken at approximately 60% SOC. The 3D direct numerical electrochemical model solves for approximately 500,000 degrees of freedom.	143
Figure I.3.B.1 (a) Load vs. Displacement plots of 3-point bend tests of 4 cells (b) XCT results of Li-ion cells after 3-point bending	147
Figure I.3.B.2 Cross-sectional SEM images of an anode from a used cell after indentation (a) Low magnification image showing the Cu and fragmentation, (b) higher magnification of fracture point and rough surface, (c) rough surfaces of an unstressed area, (d) Low magnification image of a pristine anode, (e) Higher magnification to show smooth surfaces	148
Figure I.3.B.3 (a) XPS depth profiles of elements in a pristine collect collector, (b) XPS depth profiles of elements in a stressed current collector	148
Figure I.3.B.4 Drucker-Prager criterion in deviatoric stress-pressure coordinates.	149
Figure I.3.B.5 Unconstrained compression of battery electrode material. (a) experimental setup with die-set; and sample (b) axial compression; (c) lateral compression (Brazilian test).	149
Figure I.3.B.6 FIB-SEM cross-sectioning of positive electrodes. (a) SEM image of the cross-section; (b) EDS map showing carbon as signature for binder location	150
Figure I.3.B.7 (a) 1C charge and discharge capacity curves, 1C dQ/dV curves. (b) concentration profiles at the end of CC and CV charging conditions (c) CC charging for various C rates and the subsequent CV charging.	151
Figure I.3.B.8 Equivalent circuit model for lithium ion battery.	152
Figure I.3.B.9 Battery cell HPPC voltage data compared to ECM at ambient temperature of 25°C. Data from HPPC test shown as solid red line, ECM as dashed black line. Right plot is enlarged from 60% SOC region.	152
Figure I.3.B.10 Comparison of the module ECM (purple line) to the module US06 drive cycle data (red line). The voltage profile represents three modules connected in series.	153
Figure I.3.C.1 Enhanced workflow for converting 3D tomography to mesh including the CBD phase.	156
Figure I.3.C.2 Convergence and mesh refinement study for image-based mesoscale simulations for various effective properties. Reprinted from figure 13 of [2].	157
Figure I.3.C.3 Pore space tortuosity calculated for dense and nanoporous CBD phases using the binder morphologies from the next figure. Reprinted from figure 8 of [5].	158
Figure I.3.C.4 Binder morphologies generated from multiple approaches. Reprinted from figure 6 of [5].	158

Figure I.3.C.5 Snapshot of a coupled electrochemical-mechanical discharge simulation of an NMC cathode.	159
Figure I.3.C.6 (left) A CDFEM mesostructure including active material particles and CBD created from DEM simulations of electrode drying and compression. (right) Tortuosity versus porosity calculated from the image-based simulations compared to the initial DEM simulations, showing reasonable agreement.	159
Figure I.3.D.1 Tomography scan times overlaid on potential-time curve. (LBNL, ANL)	162
Figure I.3.D.2 Image postprocessing pipeline. Left to right: reconstruction, slice after edge detection, detection of central plane, detection of bounding planes, rotated and cropped electrode region. First four images show a region 320 microns across, last image shows a region 320 microns tall. (LBNL, ANL). 163	
Figure I.3.D.3 Upper left: Raw slice averages as a function of slice position. Upper right: Slice average curves aligned on current collector edge. Lower left: Slice average curves translated into relative linear absorption coefficient curves. Lower right: Local electrode expansion during initial charge. (LBNL, ANL)	164
Figure I.3.E.1 X-ray radiograph of the cell (a transverse cross section), showing the various components. The X-ray beams penetrate the cell from the left. Gaussian-shaped colored lines represent the actual profiles of the X-ray beam as determined from a radiograph intensity map and by the depth calibration. Layers L_n ($n = 0-4$ with n increasing in the direction of the electrode depth z away from the separator) are overlapping sections of the cell that are probed by the X-ray beams. During charge, a Li^+ ion current flows from the NCM523 cathode to the Gr anode (graphite lithiation); the reverse happens during discharge (graphite delithiation).	169
Figure I.3.E.2 Voltage-capacity plots for cycling of Gr/NCM523 cell at C/20 and 1C rates (cycles 2 and 5, respectively). Specific capacities of the graphite electrode are shown at the bottom, and the estimated cell average lithium content of this electrode is shown at the top. The arrows indicate the direction of the Li^+ ion current. For cycle 5, the red color corresponds to charge and the blue color corresponds to discharge of the cell.	169
Figure I.3.E.3 Experimental d-spacing (filled circles, axis to the left) for Li_xC_6 phases present in layer L0, observed during cycling at 1C rate and plotted as a function of the cell average lithium content \bar{x} in the matrix. The lithiation stages are color-coded as shown in the inset. The vertical dashed lines indicate the potentiostatic hold. Shown to the right in grey is the layer average lithium content x	170
Figure I.3.E.4 Layer average lithium content x in the ordered Li_xC_6 phases estimated using eq. 1 plotted as a function of the cell average lithium content x of the graphite matrix determined electrochemically. The layers are color coded as shown in the inset. The vertical dashed lines correspond to the potentiostatic hold periods (see voltage plot at the top). The arrow shows the direction of increasing depth. The open circles indicate the five-layer average, and the straight line is x	171
Figure I.3.E.5 Layer average Li content x in the ordered phases (filled circles, to the bottom) plotted vs. the median depth of these layers (to the left). Panel a is for charge and panel b is for discharge of the cell at 1C rate vs. the graphite electrode capacity. The numbers in the plot give the overall cell average lithium content x of the graphite matrix calculated based on the electrochemically measured cell capacity.	171

Figure I.3.F.1 Force vs displacement of fully charged 5 AH pouch cells. Little changed is observed up to 60°C, however a dramatic softening of the cell is observed at 120°C	174
Figure I.3.F.2 Drop tower commissioning	175
Figure I.3.F.3 Example propagation data provided to NREL for multi-cell modeling activities.	175
Figure I.3.G.1 Project schematic showing major constituents and progression of Alpha and Beta versions.	177
Figure I.3.G.2 Two models for the battery impact simulation. These models have the same settings except that different elements, (a) solid elements and (b) composite t-shell elements, are used in the cell bulk.	179
Figure I.3.G.3 Comparison of (a) voltage and (b) state of charge evolution in two types of models.	179
Figure I.3.G.4 Comparison of temperature distribution at 41 seconds in (a) the composite t-shell element model and (b) macro model.	179
Figure I.3.G.5 Both (a) composite tshell models and (b) macro models can use a small number of elements in the cell thickness direction. The difference is that in the former, the EM and thermal solvers rebuild a mesh internally to resolve each individual layers. In the latter, no internal mesh is needed, and each node contains two potential fields connected by either Randles circuit or short-circuit resistance depending on local parameters such as stress, strain or temperature.	180
Figure I.3.G.6 Comparison of the cell stresses in the (a) layered solid and (b, d) solid element assembly. In (b), the four top unit cells are resolved, and in (d) all unit cells are resolved. The layers in one unit cell is shown in (c).....	181
Figure I.3.G.7 X-ray tomography of deformed cells (a) cell sectioning, and (b) scanning.	182
Figure I.3.G.8 X-ray tomography of the internal damage in a sheared cell.....	182
Figure I.3.G.9 Experimental test for lateral compression of active material specimen.	183
Figure I.3.G.10 Experimental results for uniaxial and lateral compression test of active material specimens.....	184
Figure I.3.G.11 The uniaxial compression test response for LS-DYNA materials 145 and 193.....	184
Figure I.3.G.12 Characterization of microstructure characteristics based on image analysis.....	185
Figure I.3.G.13 Stochastic reconstruction of 3D microstructures. The reconstructed “porous phase” is shown in green pixel. The lamellae phase is not shown.	186
Figure I.3.G.14 Solid-beam hybrid model. Tension along the machine direction.	186
Figure I.3.G.15 Solid-beam hybrid model. Tension along the transverse direction.	187
Figure I.3.G.16 Simulation results: stress-strain curves on machine direction (MD) and transverse direction (TD).	187
Figure I.4.A.1 Process for NMC precursor production via co-precipitation.....	190
Figure I.4.A.2 Process for production of NMC cathode powder via calcination.....	191
Figure I.4.A.3 Share of total energy of Li-S cell production (excluding energy use for cell assembly) ..	192

Figure I.4.A.4 Cradle-to-gate LCA comparison of Li-S battery and conventional LIB on a per kWh basis	192
Figure I.4.B.1 Reduction in virgin material demand due to recycling.....	195
Figure I.4.B.2 Inter-relationship of recycling processes	198
Figure I.4.C.1 Schematic of ReCell model	201
Figure I.4.C.2 Potential cost savings of per kg cell production via battery recycling for different chemistries	202
Figure I.4.C.3 Potential SO _x emission savings from recycling NMC111 batteries	203
Figure I.4.C.4 Total energy reductions from recycling of Li-S batteries.....	204
Figure I.4.E.1 Process and Timeline for the Battery Recycling Prize	212
Figure I.5.A.1 Discharge capacity as a function of electrode loading (mAh/cm ²) and charge rate (left) and photos of lithium deposits on representative graphite electrodes (right). These results were obtained with capacity-matched cells using graphite negative electrodes and LiNi _{0.6} Mn _{0.2} Co _{0.2} O ₂ (NMC622) positive electrodes.	215
Figure I.5.A.2 Discharge capacity retention for the graphite materials selected in the coin-cell prescreening study under 6C charge and C/2 discharge between 3 – 4.1 V at 30°C (anode capacity of 2 mAh/cm ²). +cyclor issue	218
Figure I.5.A.3 Discharge capacity for the MAG-E3 graphite using CMC-SBR binder versus NMP-based PVDF binder in the coin-cell prescreening study under 6C charge and C/2 discharge between 3 and 4.1 V at 30°C (2 mAh/cm ²).....	220
Figure I.5.A.4 Discharge capacities for the 2nd Round coin cells (purple and blue) compared to the 1st Round coin cells (green) cycled under 6C (and 4C) charge rates (Superior Graphite SLC1506T vs. NMC532).	222
Figure I.5.A.5 Averaged and normalized capacities (based on NMC532) for the 2nd Round coin cells (purple and blue) compared to the 1st Round coin cells (green) cycled under 6C (and 4C) charge rates (Superior Graphite SLC1506T vs. NMC532).....	222
Figure I.5.A.6 Normalized capacities (based on NMC532) for the 2nd Round coin cells at increasing charge rates (Superior Graphite SLC1506T vs. NMC532).....	223
Figure I.5.A.7 Discharge capacities from formation cycles for 24 single-sided single-layer 2nd Round pouch cells (Superior Graphite SLC1506T vs. NMC532) delivered to INL.	223
Figure I.5.A.8 Raman spectrum of MAG E3. All spectrum displayed the same bands with different intensity ratios, including the band at ~2700 cm ⁻¹ (overtone/harmonic of D band at ~1350 cm ⁻¹).	224
Figure I.5.A.9 XRD patterns of the selected graphites in the 2θ range of 40 to 60°	225
Figure I.5.A.10 Relaxation time (τ^{δ}) vs. state of charge (SOC) for the discharge subcycle for MCMB graphite. The discharge voltage limits were 1.5 V to 5 mV and represented the lithiation process. Each dot represents the average of three cells.	226

Figure I.5.A.11 Relaxation time (τ^{δ}) vs. state of charge (SOC) for the charge subcycle for MCMB graphite. The discharge voltage limits were 5 mV to 1.5 V and represented the delithiation process. Each dot represents the average of three cells.	227
Figure I.5.A.12 Discharge A12 graphite half-cell GITT data and simulation in the LiC ₃₂ single-phase region (left) and the LiC ₆ -LiC ₁₂ two-phase region (right).	227
Figure I.5.A.13 Left: graphite electrode voltage compared to model simulation using indicated parameters for 10s 3C discharge and charge pulses on reference electrode cell. Right: NMC electrode voltage compared to model simulation.	228
Figure I.5.A.14 Left: graphite electrode voltage compared to model simulation from reference electrode cell for 1C discharge. Right: NMC electrode voltage compared to model simulation for 1C discharge.	229
Figure I.5.A.15 Comparison of cell cost estimates with material prices in 2017 and 2018.	230
Figure I.5.B.1 The respective C/1 and C/20 capacity fade results from the aging experiment (right) using the different charge protocols defined in Table I.5.B.1.	235
Figure I.5.B.2 Increased graphite capacity in stage 1 following over lithiation in a half-cell (left) and compared coulombic efficiency and Li stripping efficiency (right).	236
Figure I.5.B.3 Preliminary data showing acoustic signal for Li plating for cells cycled at 0.2C. LCO pouch cell at 8°C (a, with Li plating) and 21°C (b, no plating). Circles on the left show nucleation of Li metal, discharge of Li metal and Li ion de-intercalation	237
Figure I.5.B.4 Capacity over cycles, Right: Visual Lithium Confirmation	237
Figure I.5.C.1 Schematic of the various transport limitations during XFC that can result in poor charge acceptance, heat generation, lithium plating and capacity loss. Caption Credits/Source: NREL- Kandler Smith.	241
Figure I.5.C.2 Comparison of high rate charging performance of graphite/NMC 532 cells having a low loading of 1.5 mAh/cm ² -NMC. Model results are shown as solid lines and experimental results are dots. The graph on the left is for A12 graphite anode at 3,5, and 7C and the right is for Superior 1506T graphite anode that varies from 1 to 9C. Caption Credits/Source: NREL- Andrew Colclasure.	241
Figure I.5.C.3 Comparison of high rate charging performance of graphite/NMC 532 cells having a low loading of 1.5 mAh/cm ² -NMC. Model results are shown as solid lines and experimental results are dots. The graph on the left is for A12 graphite anode at 3,5, and 7C and Comparison of high rate charging performance of graphite/NMC 532 cells with higher loadings. Model results are shown as solid lines and experimental results are dots. The graph on the left is for A12 graphite anode at 4 different loadings all charging at 6C (two cells per condition). The right figure is for Superior 1506T graphite anode with a loading of 2.5 mAh/cm ² -NMC and charge rate varying from 1C up to 9C. Caption Credits/Source: NREL- Andrew Colclasure.	242
Figure I.5.C.4 Comparison of high rate charging performance of graphite/NMC 532 cells having a low loading of 1.5 mAh/cm ² -NMC. Model results are shown as solid lines and experimental results are dots. The graph on the left is for A12 graphite anode at 3,5, and 7C and	243
Figure I.5.C.5 Cell potential and intercalation fraction within A12 graphite anode during 1C in-situ XRD experiments performed by ANL. Experimental results are squares and model predictions are lines. Layer	

L0 refers to layer closest to separator and L4 is layer next to current collector. Each layer is approximately 20 microns. Caption Credits/Source: NREL- Andrew Colclasure..... 243

Figure I.5.C.6 Macro-homogeneous model predictions for useable SOC (left) and driving potential for lithium plating (right) as function of cell/cathode level loading at 4 and 6C. For the capacity plot, the line turns dashed when there is a driving potential for lithium plating. Caption Credits/Source: NREL- Andrew Colclasure..... 244

Figure I.5.C.7 Macro-homogeneous model predictions for useable SOC (left) and driving potential for lithium plating (right) as function of cell/cathode level loading at 4 and 6C. For the capacity plot, the line turns dashed when there is a driving potential for Model predictions for how normalized capacity (left) and energy density (right) achieved during XFC vary with electrode thickness/loading for current electrodes and electrolyte (dot-dash lines) and next generation (NG) electrodes and electrolyte (solid lines). Caption Credits/Source: NREL- Andrew Colclasure..... 245

Figure I.5.C.8 Model predictions for lithium plating during XFC as function of electrode thickness/loading for current electrodes & electrolyte (dot-dash lines) and next generation (NG) electrodes & electrolyte (solid lines). Caption Credits/Source: NREL- Andrew Colclasure 245

Figure I.5.C.9 (a) Microstructure-predicted tortuosity for several different electrodes. (b) Correlation of tortuosity with capacity at cycle number 500 for 6C charge, C/2 discharge of Round 1, 1.5mAh/cm² cells. Caption Credits/Source: NREL- Francois Usseglio-Viretta 246

Figure I.5.C.10 Model predictions for lithium plating during XFC as function of electrode thickness/loading for current electrodes & electrolyte (dot-dash lines) and next generation (NG) electrodes & electrolyte (solid lines). Correlation of tortuosity with the particle elongation, i.e. particle axis in the electrode through-plane direction divided by particle axis in the in-plane direction. Elongation of 1 indicates spherical particles; Less than 1 indicates ellipsoid or platelet particles misaligned with the through-plane direction leading to high tortuosity. Caption Credits/Source: NREL- Francois Usseglio-Viretta 246

Figure I.5.C.11 Model predictions for lithium plating during XFC as function of electrode thickness/loading for current electrodes & electrolyte (dot-dash lines) and next generation (NG) electrodes & electrolyte (solid lines). Correlation of tortuosity with the Left – Estimates for heat generation from I-V profiles. Right – Mathematical model was built to calculate heat generation rates. Captions Credits/Source: NREL - Shriram Santhanagopalan..... 247

Figure I.5.C.12 Model predictions for lithium plating during XFC as function of electrode thickness/loading for current electrodes & electrolyte (dot-dash lines) and next generation (NG) electrodes & electrolyte (solid lines). Correlation of tortuosity with the Left – Pouch cell microcalorimeter (left) and with an ANL CAMP cell (right) prepped for testing. Caption Credits/Source: NREL- Shriram Santhanagopalan 248

Figure I.5.D.1 (a) slurry mixture in a planetary mixer; (b) wet anode slurry coated onto Cu foil; (c) wet cathode slurry coated onto Al foil; (d) electrode coating densified through calendering machine..... 251

Figure I.5.D.2 left, the first three cycles of superior graphite 1520T electrodes; right, the first three cycles of NMC622 electrodes. 251

Figure I.5.D.3 Normalized cell voltage vs. capacity curves with different loadings charging at different C rates and discharging at 1C.	252
Figure I.5.D.4 left, capacity & voltage versus cycling number when the cells are cycled at +1C/-1C and +6C/-1C, respectively. Right, voltage versus capacity curves during cycling.	252
Figure I.5.D.5 Temperature rises inside a 600 mAh pouch cells during a 5A charge (through collaboration with Prof Guangsheng Zhang at University of Alabama in Huntsville).	253
Figure I.5.D.6 ^1H NMR spectra of Sty-TFSI- K^+	253
Figure I.5.D.7 Synthesis of single Li-ion conducting oligomer (compound 5).	254
Figure I.5.D.8 ^1H NMR spectrum of single Li-ion monomer (compound 4).	254
Figure I.5.E.1 Charge/discharge capacities and coulombic efficiencies of TNO at different current rates.	258
Figure I.5.E.2 Normalized capacity of NMC622 half coin cells at various charge protocols and areal loadings.	259
Figure I.5.F.1 Cooling plate fixture.	261
Figure I.5.F.2 Cell temperature (Kokam 5Ah pouch) during 6C charge, 2C discharge cycling, inside the cooling fixture.	262
Figure I.5.F.3 Baseline cell rate capability performance.	262
Figure I.5.F.4 Figure 4: $dQdV$ vs V for various cycles in baseline rate capability.	263
Figure I.5.F.5 Figure 5: $dQdV$ vs V for 1C discharge steps after each charge rate increase.	263
Figure I.5.G.1 Conceptual graphic describing the connections between fast charging and the related energy systems that can be bridged by behind the meter storage.	266
Figure I.7.A.1 Cost of cells and packs as a function of the production volume. See Table 1 for specifications.	275
Figure I.7.A.2 Cost of cells and packs as a function of the maximum allowable current density to avoid lithium deposition during charging. Production volume = 100,000 packs/year. See Table 1 for specifications.	276
Figure I.7.A.3 Cost of cells and packs as a function of the production volume, showing the effects of cathode price and pack size. See Table 1 for specifications.	276
Figure I.7.A.4 Specific energy density as a function of the upper cutoff voltage (UCV) [4].	277
Figure I.7.A.5 Pack costs vs. upper cutoff voltages (UCV vs Li/Li^+) for BEV and PHEV batteries. The ASI of all the cathode materials is held constant $12 \Omega\text{-cm}^2$ (at 20% SOC). Production Volume: 100,000 packs per year [4].	277
Figure I.7.A.6 Schematic of a process for the production of LiPF_6	278
Figure I.7.A.7 Impact of the cost of LiPF_6 on the cost of a 60 kWh lithium ion battery pack. (NMC622-Graphite electrodes, plant capacity of 100,000 packs per year).	279
Figure I.7.B.1 Schematic representations of the HPPC and Peak Power test profiles.	282

Figure I.7.B.2 (a) Relative resistance at 80% DOD from the peak power test from the calendar life test. The numbers in the legend represent the test temperature in °C. The best-fit line was forced to have a y-intercept of 1. (b) Arrhenius plot of the slopes from Figure I.7.B.2a 283

Figure I.7.B.3 (a) Relative resistance at 80% DOD vs. time. The numbers in the legend are the test temperatures. The best-fit line was forced to have a y-intercept of 1. The least-squares equations and values of r^2 are given on the plot. (b) Arrhenius plot of the slopes shown in Figure I.7.B.3a vs. $1/T$ 283

Figure I.7.D.1 Results of increasing SOC within 18650 cells 292

Figure I.7.D.2 Comparison for two cell sizes 293

Figure I.7.D.3 Failure SOC during overcharge testing. 293

Figure I.7.D.4 Failure temperature during overcharge. 293

Figure I.7.D.5 Failure temperature during thermal ramp 294

Figure I.7.D.6 dQ/dV vs SOC for cells charged at 1C and 1.5C. 294

Figure I.7.E.1 Efficiency summary of cells tested at 30°C in NREL’s calorimeters. Caption Credits/Source: NREL- Aron Saxon..... 298

Figure I.7.E.2 Efficiency of silicon blended cells tested at 30°C in NREL’s calorimeters under various charge/discharge currents. Caption Credits/Source: NREL- Aron Saxon 299

Figure I.7.E.3 Entropic response to NCM – 1:1:1 and high nickel content NCM cathodes paired with a graphite anode. Caption Credits/Source: NREL- Aron Saxon..... 300

Figure I.7.E.4 Efficiency comparison of a single cell compared to a 10-cell module at 30°C. Caption Credits/Source: NREL- Aron Saxon..... 300

Figure I.7.E.5 Infrared image of lithium battery cell at the end of a 2C discharge. Caption Credits/Source: NREL- Aron Saxon..... 301

Figure I.7.F.1 a) Voltage profile comparison and b) cycle performance comparison of NCM523/SiO and NCM523-LFO/SiO. The capacity of SiO/NCM523-LFO full cells are calculated based on the total weight of NCM523-LFO blend. 305

Figure I.7.F.2 Punched electrodes of ceramic-coated graphite anode. 307

Figure I.7.F.3 Cycle Life (left) and HPPC ASI at 50% SOC (right) for the ceramic-coated graphite electrodes evaluated in xx3450 single-layer pouch cells. 307

Figure I.7.F.4 Cycle Life (left) and HPPC ASI at 50% SOC (right) for the ceramic-coated graphite electrodes evaluated in coin cells in separator-free study for 3-4.1 V window. 308

Figure I.7.F.5 Cycle Life (left) and HPPC ASI at 50% SOC (right) for the ceramic-coated graphite electrodes evaluated in coin cells in separator-free study for 3-4.4 V window. 309

Figure I.7.F.6 White light images of the (a) pristine and (b) aged (400 cycles) electrode cross-sections; Raman maps were obtained in the portions indicated by the dashed red boxes. The Spot 02, Spot 15, and Spot 60 spectra in (c) were recorded at the locations shown in the color map to the right of (a). The red

and green spectra in (e) were representative of data recorded at the red and green areas, respectively, shown in the color map of (d).	310
Figure I.7.F.7 Sequence of steps for the quantitation of gas evolution by the Archimedes method.....	311
Figure I.7.F.8 Volume change of pouch bags containing (a) deionized water and NMP slurries, with and without 2.5 wt% PAA and (b) aqueous slurries with PAA and LiPAA (the extent of lithiation is indicated in the plot). (c) Example of data from the gas analysis experiments showing H ₂ as a dominant component. (d) Pouch containing the LiPAA80% slurry (shown in c) after 120 h. The NanoAmor silicon particles (30-50 nm) was used for all these experiments.	312
Figure I.7.F.9 Gas evolution from aqueous slurries containing LiPAA80% and silicon particles from Paraclete Energy with different surface coatings: graphene for nSi/Cg, silicon oxide for nSiO, and carbon for nSi/C. The gas evolution for the NanoAmor silicon (the same slurry constitution) is shown for comparison.....	313
Figure I.7.F.10 (Left) Cathode dimensions, interfaces, area, and perimeter information of the xx3450 and xx6395 pouch cells fabricated at the CAMP Facility. (Right) Image of the partially assembled xx3450 and xx6395 pouch cells side by side.....	313
Figure I.7.F.11 Cycle life performance (Left) and area specific impedance performance at 50% depth of discharge (DOD) which were acquired every 50 cycles (Right) for both the xx3450 and xx6395 pouch cells. Areal capacity of 3.5 mAh/cm ² for the anode and 3.1 mAh/cm ² for the cathode was used.	314
Figure I.7.G.1 Schematic diagram of (left) core-gradient nickel rich cathode material, and (right) charge and discharge voltage profiles of NMC811 and NMC811-CG.	318
Figure I.7.G.2 Cycling performance of conventional NMC811 and NMC-CG full cell	318
Figure I.7.G.3 ASI results of full cells containing (left) NMC811 and (right) NMC811-CG cathode during cycling test	319
Figure I.7.G.4 FSEM images from graphite raw materials: a) CPreme A12; b) XL40; c) XL20. Note the slightly different scale bars.	320
Figure I.7.G.5 Gr/NMC532 full-cell electrochemical cycling data following standard cycling protocols; filled points indicate discharge capacity while open points indicate Coulombic Efficiency. (a) Formation (C/10) and Rate studies. Rate studies used C/5 charging while discharge rate was varied as indicated. (b) C/3 cycling with C/10 then HPPC every 10 th cycle. Error bars represent n=3, ± 1σ.....	321
Figure I.7.G.6 Gr/NMC532 full-cell electrochemical cycling data following Fast-Charge protocols. (left) Charge capacity during Formation (C/10) and Fast-Charge studies (discharge rate was a constant C/5, while charge rate was varied as indicated, with a current cutoff of I ≤ 0.05C). Filled points indicate total charge capacity while open points indicate galvanostatic capacity. (right) Normalized galvanostatic vs total charge capacity fraction, Q _{gal} /Q _{tot} , as a function of cycle number and charge rate.....	322
Figure I.7.G.7 SEM images of graphite electrode containing (a) XL40 and (b) A12 graphite recovered after 100 cycles with 6C charge, C/3 discharge. The insets include photographs of the rinsed, recovered electrodes.	323
Figure I.7.H.1 SEM images of the anode surfaces from cells charged to 140% SOC. Figure (a) is from a cell containing a NMC532 cathode, and (b), from a cell containing an LFP cathode.	326

Figure II.1.A.1 Temperature versus time for laminates dried at different oven temperatures.....	331
Figure II.1.A.2 Drying time versus oven temperature.	331
Figure II.1.A.3 Photos of laminates dried at different temperatures.....	332
Figure II.1.A.4 Adhesion (green) and cohesion (orange) of the laminates dried at different temperatures as measured on a peel tester in N/m and N/m ² , respectively.....	332
Figure II.1.A.5 Area specific resistance as a function discharge % for laminates dried at different temperatures.....	332
Figure II.1.A.6 Nyquist plot of EIS data of electrodes dried at various temperatures.	333
Figure II.1.A.7 The atomic percentage of C and F measured on the surface of electrodes dried at different temperatures as measured by EELS.....	333
Figure II.1.A.8 X-ray data of PVDF films formed by drying from solutions at different drying temperatures.....	333
Figure II.1.A.9 Ionic conductivity of electrolyte in PVDF films prepared by drying from solutions at different temperatures.	334
Figure II.1.B.1 (a) Chemical structures of the polymer coatings used in this study. Coloring of the label corresponds to the chemical functionality of the polymer. (b) Diagram of the conditions used to study the initial stages of Li metal growth under polymer coatings.....	336
Figure II.1.B.2 (a) Chemical structures of the dynamic crosslinking of the dynamic crosslinking of the SHP and covalent crosslinking of the SHE. SEM images of 0.1 mAh/cm ² of lithium electrodeposited on polymer coated copper. The electrodes are coated with (b-c) a supramolecular adaptive coating and (d-e) a covalently crosslinked self-healing elastomer with similar chemistry to the supramolecular coating. Scale bars are 50 um for b and d, and 1 um for c and e.	337
Figure II.1.B.3 SEM images of 0.1 mAh/cm ² of lithium electrodeposited on copper with (a) no polymer coating, (b) PEO coating, (c) PVDF coating, (d) SHP coating, (e) PU coating, and (f) PVDF-HFP coating. Scale bars for all images are 5 um.	337
Figure II.1.B.4 (a) Exchange current density plotted against dielectric constant for various polymer coatings measured via microelectrode. (b) The average diameter of the Li deposited under various polymer coatings plotted against the surface energy of those coatings.	339
Figure II.1.B.5 Schematic of the factors influencing Li metal deposition through a polymer coating. Low surface energy coatings give rise to higher interfacial energies and encourage the growth of large surface area particles. Additionally, high dielectric constant polymers have higher exchange currents and promote larger Li metal deposits.....	340
Figure II.2.A.1 Battery Performance and Cost (BatPaC) model utilized to establish relevance by connecting pack to anode targets.	341
Figure II.2.A.2 Program participants including Laboratories, research facilities, and individual contributors.	342

Figure II.2.A.3 Electrochemical results of an experimental silicon electrodes fabricated by the CAMP Facility. These cells were cycled between 0.05 to 1.5 V vs. Li^+/Li . Graphite was not used in this electrode.	344
Figure II.2.A.4 Full cell results using the silicon deep dive protocol of the high-silicon graphite-free anode and 15 wt.% Si in graphite composite. Both cells were tested against a common capacity-matched NMC532 cathode. The anode to cathode capacity pairing for the electrode couples was based on the anode capacities achieved upon a 50-mV lithiation cutoff.	345
Figure II.2.A.5 Electrochemical results of the A-A017 high-silicon graphite-free electrode fabricated by the CAMP Facility. These cells were cycled between various lower cutoff voltages (LCV) to 1.5 V vs. Li^+/Li . Graphite was not used in this electrode.	346
Figure II.2.A.6 Installed 4 L hydro/solvothermal reaction system (a) and FT-IR result comparison of pristine NanoAmor Si particles and their hydrothermally treated product	347
Figure II.2.A.7 a) cycling performance of NMC532 Si/Gr cells with a) modified silicon anode with and without carbon coating in baseline electrolyte. b) modified silicon anode with carbon coating and PI binder in TEPA-based LHCE.	348
Figure II.2.A.8 (a) XRD patterns of Si films along with Cu foil reference, and (b) content of Si and O detected by EDS for Si films.	349
Figure II.2.A.9 CV curves of (a) Si-5, (b) Si-10, (c) Si-20, and (d) Si-30 films during the first two cycles. Insets are enlarged CV curves between 0.45 and 1.5 V	349
Figure II.2.A.10 (a) Voltage profiles, (b) CV curves of Si-Sn film,, (c) enlarged CV curves at 0.14 -1.5 V, (d) capacity, (e) capacity retention, and (f) CE of Si-Sn and Si films of similar thickness.	350
Figure II.2.A.11 1 L of 15% Si-graphite aqueous based slurry after 1-week storage. Gassing from the slurry caused foaming and subsequent drying as the slurry “snaked” out of the open container.	351
Figure II.2.A.12 a) The change in pressure vs time of W2 – water based nano Si/CB slurry (blue trace, circles), W5 – water based 325 mesh Si slurry (black trace, diamonds), W4 – water based Nano Si/CB/LiPAA slurry (green trace, triangles), W3 – water based nano Si/LiPAA slurry (green trace, triangles), W3 – water based nano Si/LiPAA slurry (fuchsia trace, hour glasses), W1 – water based Nano Si slurry (purple trace, upside-down triangles), and N1 – NMP based Nano Si/CB slurry (red trace, squares). B) plot of the first 30 hours (enlarged).	352
Figure II.2.A.13 a) Mass spectrum of gas collected from head space of mixing vessel for W2 (blue trace), W4 (green trace), and N1 (red trace), normalized to the N_2 signal of ambient air (black trace). B) plot of H_2 signal in mass spectrum from (a) C) plot of O_2 signal in mass spectrum from (a). C) plot of CO_2 signal in mass spectrum from (a).....	353
Figure II.2.A.14 XPS of Si 2p orbitals, Normalized to Si^{4+} at 103.6 eV, of various dried Si samples (untreated nano Si – brown trace, N1 – red trace, W1 – purple trace (overlapping with N1), W4 – green trace, W2 – blue trace)	354

Figure II.2.A.15 Voltage profile of Si-Li metal half cells comparing short-processed NA 70 – 130 Si (brown trace) and W2 (blue trace). Cycled at C/10 (0.25 A g ⁻¹) from 1.5 to 0.05 V vs Li metal.	355
Figure II.2.A.16 A representative schematic of several reactions that occur during processing of water based Si/CB slurry.	356
Figure II.2.A.17 Raman maps of the distribution of carbon black, c-Si, graphite, and a-Si in Si-Gr composite anodes after 1 full cycle (lithiation and delithiation). The top row maps an anode made with PAA binder and the bottom row maps an anode made with LiPAA binder. Each map is 50 μm x 50 μm and comprises 2500 spectra. The color scale indicates the relative fraction of each component at each location across the map.	357
Figure II.2.A.18 (a) Raman map of the intensity of the main band from crystalline silicon at 520 cm ⁻¹ in a silicon-graphite composite electrode after 1 charge-discharge cycle. The fraction of crystalline silicon increases from blue to red. (b) Two level map of the same data presented in (a). The red pixels are from the electrode areas with the highest concentration of crystalline silicon. (c) The average Raman spectra from regions with high and low concentrations of crystalline silicon is mapped in (b).	357
Figure II.2.A.19 SEM images of the different Cu-coated silicon electrodes obtained by applying the 6 different electrodeposition protocols collected in Table 2.	358
Figure II.2.A.20 Raman spectra of the different Cu-coated silicon electrodes obtained by applying the 6 different electrodeposition protocols collected in Table 2.	359
Figure II.2.A.21 XRD of as-synthesized Li ₇ Si ₃ , with a small amount of the slightly oxidized phase Li ₁₂ Si ₇	359
Figure II.2.A.22 (a) ⁷ Li NMR, (b) ²⁹ Si NMR, and (c) XRD results of pristine LS samples and their mixture with 10 wt% PVDF or LiPAA.	360
Figure II.2.A.23 (a) ¹ H, (b) ¹³ C, and (c) ¹⁹ F MAS NMR spectra of pristine LS samples and their mixture with 10 wt% PVDF.	360
Figure II.2.A.24 Images of gas-cathcing setup before, immediately after, and 1 day after the mixing of PVDF and Li ₇ Si ₃	361
Figure II.2.A.25 (a) ⁷ Li and (b) ²⁹ Si solid state MAS NMR for Li ₇ Si ₃ and its mixture with different electrolyte solvents.	362
Figure II.2.A.26 (a) ⁷ Li and (b) ²⁹ Si in-situ solid state MAS NMR for Li ₂₁ Si ₅ and different electrolyte solvents. ANL, unpublished results.	363
Figure II.2.A.27 Electrochemical profiles of Paraclete baseline silicon powder and carbon SP electrodes vs. Li metal half cells comparing Gen2 + 10% FEC and 1M LiTFSI in Triglylme electrolytes.	364
Figure II.2.A.28 (a) ⁷ Li and (b) ¹³ C solid state MAS NMR for post-electrochemistry Si loose-powder anodes after cycling between 0.01-1.5 and 0.05-1.5 V vs. Li respectively for 15 cycles, using 1 M LiTFSI in triglylme as the electrolyte. ANL, unpublished results.	365
Figure II.2.A.29 Electrode potential vs. capacity during lithiation (a) and delithiation (b) of a Gr-only electrode (grey line) and of a Si/Gr (15/73 w/w, red line) blended electrode cycled vs. Li metal. Operando XRD spectra (shown in the 3.2 to 3.8 Å d-spacing range) collected during the electrochemical cycling in	

(a) and (b) for the Gr-only (c) and Si-Gr (d) electrodes. Spectra collected on lithiation and delithiation are shown in black and blue coloring, respectively.	366
Figure II.2.A.30 Capacity (a) and specific capacity (b) of the Gr and Si components in a Si-Gr electrode during lithiation and delithiation. Note that the capacity increases during lithiation and decreases during delithiation. Regions 1 to 4 are indicated with the circled numerals in panel a. The percentages shown in panel (a) are the estimated expansions of Si particles.....	367
Figure II.2.A.31 Changes in the positive electrode potential during (a) cycle-life aging and (b) calendar-life aging of a NCM523/Si-Gr (10 wt% FEC) cell. The inset in (b) shows the top 50 mV of the plot. In both plots, the first 3 (formation) cycles are at a $\sim C/20$ rate. In (a), cycles 4-97 (aging) are at a $\sim C/3$ rate and cycles 98-100 are at a $C/20$ rate. In (b), cycle 4 includes a 600 h hold after charging to 4.1 V; the cycle 4 discharge and the final diagnostic cycles 5 and 6, are at a $C/20$ rate.....	368
Figure II.2.A.32 Synthesis of surface-functionalized SiNPs with methyl and epoxy terminal groups.....	370
Figure II.2.A.33 (a) FT-IR spectra and (b) TGA thermograms of pristine SiNPs, silanol-enriched SiNPs, and epoxy-SiNPs.....	371
Figure II.2.A.34 Initial capacity and Coulombic efficiency of Si/Li cells: (a) three $C/20$ formation cycles and (b) one-hundred $C/3$ cycles.	372
Figure II.2.A.35 EDX elemental mapping (Si, C, O, F, P) for Si/PAA electrodes with (a) pristine SiNPs, (b) Si-OH SiNPs and (c) epoxy-SiNPs after 100 cycles.	372
Figure II.2.A.36 Si _{2p} XPS spectra of the Si electrodes based on pristine SiNPs and epoxy-SiNPs before and after one formation cycle: (a) fresh Si electrode before cycling and (b) Si electrode after one formation cycle at delithiated state.	373
Figure II.2.A.37 (a) Adhesion strength of the Si anodes with pristine SiNPs, Si-OH SiNPs, epoxy-SiNPs, and CH ₃ -SiNPs as active materials, and (b) summarized data of average load per unit width (N/cm)....	374
Figure II.2.A.38 The voltage profiles of the functionalized electrodes. Cut-off: 2 hours lithiation, 1.5 V delithiation. Current density: 27.3 $\mu\text{A}/\text{cm}^2$	375
Figure II.2.A.39 Impedances of the surface treated electrodes, measured at the end of lithiation. The same electrolyte, Gen2 with 10% FEC, was used for all of electrochemical testing.	376
Figure II.2.A.40 (a) A representative voltage profile of Si wafer electrode. (b) (c) Nyquist plots of SEI-CH ₃ and SEI-COOH. EIS measurements were conducted at specific state of lithiation and delithiation marked by the red circles in (a).....	377
Figure II.2.A.41 Bode plots of silicon electrodes fictionalized by (a) -COOH and (b) -CH ₃	378
Figure II.2.A.42 Surface coating effects on the electronic conductivity. Resistivity depth profile in (a) was plotted as a function of depth. All of the measurements end at the point where the resistivity reaches $\sim 10^{-1} \Omega\text{cm}$, indicating that the AFM probe has touched the bulk Si electrode. The resistance profile in (b) was calculated and plotted as a function of the distance from the bulk Si electrode.	379
Figure II.2.A.43 Diagram for the synthesis of Li ₂ SiO ₃ -coated silicon nanoparticles.	380
Figure II.2.A.44 XRD patterns of silicate-coated Si with starting Si nanoparticles of different oxide layer thicknesses.	380

Figure II.2.A.45 Electrochemical performance of formation cycles for silicate-coated Si with different silicate layer thicknesses.	381
Figure II.2.A.46 SEM of silicate-coated Si with starting Si nanoparticles of different oxide layer thicknesses	382
Figure II.2.A.47 Electrochemical performance of formation cycles for high-energy-ball-milled silicate-coated Si with a) a thinner silicate layer and b) a thicker silicate layer.	382
Figure II.2.A.48 (a) Generic synthesis of poly(1-pyrenemethyl methacrylate-co-dopamine methacrylamide) (PPyMADMA). (b) Wide angle X-ray scattering (WAXS) of PPyMA and PPyMADMA polymers. (c) Carbon K-edge sXAS of PPyMA and PPyMADMA shows that the LUMO energy is intact in PPyMADMA, although non-conductive DMA groups are introduced.	384
Figure II.2.A.49 (a) Synthetic scheme, (b, c) physical appearance of PBzM, PNaM and P(AnM _x -co-BuM _y) polymer emulsions.	385
Figure II.2.A.50 a. A schematic of bi-functional additives. b. Formation of surface layer on the Si surface. c. Formation of bulk polymer. d. An example of vinylencarbonate polymerization to form polyvinylencarbonate bulk polymer.	386
Figure II.2.A.51 The bi-functional additives and their performance as an additive in a graphite or Si electrode with EC/DMC LiPF ₆ electrolyte and lithium metal counter electrode. There is no FEC additive in the electrolyte. a. VC reactive functional group class of bi-functional binder. c. Graphite electrode performance with different methacrylate series of additives. d. Si electrode performance with different methacrylate series of additives.	387
Figure II.2.A.52 A plot of pH vs. LiOH/COOH molar ratio (a) and the apparent viscosity vs. the shear rate (b) for 10 wt% aqueous solutions of PAA. The pH of the aqueous solutions is color coded in panel b. Mind the logarithmic scales in panel b. Mind the logarithmic scales in panel b.	389
Figure II.2.A.53 A viscosity plot for the PAA polymers at two different pHs.	390
Figure II.2.A.54 Specific delithiation capacity (a and c) and Coulombic efficiency profiles (b and d) of half cells assembled using lithiated PAA during formation cycles at a C/3 rate (a,b) and after 100 cycles at a C/3 rate (c,d). The pH of the PAA solutions (Figure II.2.A.53) is color coded in panel d.	390
Figure II.2.A.55 Specific discharge capacity (left) and Coulombic efficiency (right) for full cells. The pH of PAA solutions in Figure II.2.A.52 is indicated in the plot.	391
Figure II.2.A.56 The 180° peeling test for the Si-Gr electrode composed using different PAA binders (left). The load/width ratios averaged over a range of 50 mm for different electrodes (right). The pH of PAA solutions in Figure II.2.A.52 is indicated in the plots.	391
Figure II.2.A.57 Synthesis of P4VBA and Methylation for GPC Analysis.	392
Figure II.2.A.58 MOPAC Computed Conformations of PAA and P4VBA Dimers	392
Figure II.2.A.59 (a) Size exclusion chromatograms for synthesized P4VBA polymers; (b) The apparent viscosity vs. shear rate for 30 wt% P4VBA solutions in NMP. See the color coding in the plot.	393
Figure II.2.A.60 Specific discharge capacity (left) and Coulomb efficiency (right) for different half-cells (100 cycles at a constant C/3 rate).	393

Figure II.2.A.61 (a) The load/width ratio plotted vs. the extension and (b) the average ratio over the extension range for different S-Gr electrodes.	394
Figure II.2.A.62 Specific discharge capacity (to the left) and Coulombic efficiency (to the right) for different full-cells.....	394
Figure II.2.A.63 Specific discharge capacity (to the left) and Coulombic efficiency (to the right) for half cells using non-lithiated PAA binders during formation (a) and normal cycling (b).....	395
Figure II.2.A.64 Cathode capacity versus cycle number plot of two LFO weight percent blended NMC532 electrodes (as labeled) together with the non LFO-containing Si-graphite full cells. In each case the Si-graphite electrode is from CAMP (A-A013). Black markers show the baseline performance, where the NMC cathode is from CAMP (A-C013B). The colored markers use a glove-box cast electrode, with the magenta markers serving as a 0 % LFO proxy (baseline) for the LFO-containing cells. Note the glove-box cast electrodes (magenta (WD label)) match the performance of the CAMP full cells.....	396
Figure II.2.A.65 Cathode capacity versus cycle number plot (Si DD protocol) of three over-lithiated $\text{Li}_{1+x}\text{NMC532O}_2/\text{Si-graphite}$ full cells, and one black baseline cell. The x value represents the extra Li introduced into the cell (Li inventory) from prior electrochemical lithiation in a Li half cell. The labels are red markers (23 mAhg^{-1} ; $x = 0.09$, blue markers (46 mAhg^{-1} ; $x = 0.17$), and green markers (70 mAhg^{-1} ; $x = 0.26$). Note the black markers (baseline) is the matched NMC532/Si-graphite CAMP electrodes in a full cell.....	397
Figure II.2.A.66 Full cell potential profiles for the (a) first and (b) second charge and discharge of $\text{LiNi}_{0.5}\text{Mn}_{1.5}\text{O}_4$ and chemically lithiated $\text{Li}_{1.62}\text{Ni}_{0.5}\text{Mn}_{1.5}\text{O}_4$ versus a Si-graphite composite anode at a rate of C/10. Full cell (c) discharge capacity and (d) cycle efficiency over 100 cycles for $\text{LiNi}_{0.5}\text{Mn}_{1.5}\text{O}_4$ and chemically lithiated $\text{Li}_{1.62}\text{Ni}_{0.5}\text{Mn}_{1.5}\text{O}_4$ versus Si-graphite at a rate of C/10. Filled data symbols represent the average of two duplicate cells, with error bars showing the deviation between them. The open data symbols in (b) represent the region where a scheduled ~20 h power shutdown interrupted cycling of $\text{LiNi}_{0.5}\text{Mn}_{1.5}\text{O}_4$ and the subsequent cell recovery/break-in time (cycles 95-100). In this region, data is shown from the two cells separately since they were interrupted on different cycle numbers. Cycling conditions: 4.8 to 3.5 V, C/10, 30°C, and GEN2 electrolyte containing 10% FEC.....	398
Figure II.2.B.1 Pouch cells designed for gassing studies. The pouch has two wells—one for electrolyte and the other for material—to control initial mixing.....	411
Figure II.2.B.2 Buoyancy apparatus with a water bucket, indium wire to hang the pouch from the balance, and a bob (20 g dry).....	411
Figure II.2.B.3 IR gas cell used for kinetic measurements from two different angles. The path length through the cell is 11 cm, and the KBr windows are 25 mm in diameter by 2 mm thick from Sigma Aldrich. The injection port (circled in red) is sealed with a septum, and the outgas port (yellow) can be opened for purging, if necessary.....	412
Figure II.2.B.4 Plot of change in volume (calculated through buoyancy) of the nanostructured silicon compounds reacting with various electrolytes in pouches. The left plot is of the PECVD Si and the right is nanoamor silicon.....	413
Figure II.2.B.5 Characterization data for the gases produced in the reaction between the PECVD silicon LiPF_6 electrolyte. A. Kinetic IR (black = 14 min, red = 752 min, blue = 1,278 min), insets CO_2 and CO ,	

and SiF₄ and PF₃. B. Peak area vs time plot to illustrate any correlation between the evolution of the different gases. Inset is derivative of plot with respect to time. (In both, black = CO₂, purple = CO, red = SiF₄, and blue = PF₃). C. Mass spectrum was taken after 480 minutes (sample is red, helium is blue). Boxes around peaks correspond to various compounds (blue = CO, purple = O₂), SiF₄ (104 amu, 85 amu, 86 amu, 87 amu), PF₃ (69 amu), CO₂ (44 amu), F (19 amu), and H₂ (2 amu). 414

Figure II.2.B.6 Characterization data for the gases produced in the reaction between the nanoamor silicon and the electrolyte. A. Kinetic IR (black = 0.936 min, red = 126 min, blue = 559 min, purple = 818 min), insets CO₂, and SiF₄ and PF₃. B. Mass spectrum was taken after 14 days (sample is red, helium is blue). Boxes around peaks correspond to various compounds (yellow = H₂, black = F, blue = CO, purple = O₂, orange = CO₂, red = PF₃, green = SiF₄). SiF₄ (104 amu, 85 amu, 86 amu, 87 amu), PF₃ (69 amu), CO₂ (44 amu), F (19 amu), and H₂ (2 amu). C. Peak area vs time plot to illustrate any correlation between the evolution of the different gases. Inset is derivative of plot with respect to time. (In both, black = CO₂, red = SiF₄, and blue = PF₃)..... 415

Figure II.2.B.7 Characterization data for the gases produced in the reaction between the fumed silica and the electrolyte. A. Kinetic IR (black = 0.3 min, red = 184 min, blue = 1,019 min, purple = 1,147 min), insets CO₂, and SiF₄ and PF₃. B. Peak area vs time plot to illustrate correlation between the evolution of the different gases and trends. Inset: Derivative of plot with respect to time of peak area vs time plot. (In both, black = CO₂, red = SiF₄, and blue = PF₃). C. Mass spectrum was taken after 40 days (sample is red, helium is blue). Boxes around peaks correspond to various compounds (yellow = H₂, black = F, blue = CO, purple = O₂, orange = CO₂, red = PF₃, green = SiF₄). SiF₄ (104 amu, 85 amu, 86 amu, 87 amu), PF₃ (69 amu), CO₂ (44 amu), F (19 amu), and H₂ (2 amu). 416

Figure II.2.B.8 Characterization data for the gases produced in the reaction between the Stöber silica and the electrolyte. A. IR data as a function of time (black = 0.936 min, red = 126 min, blue = 559 min, purple = 818 min), the CO₂, SiF₄, and PF₃ peaks were nonexistent, as identified in the insets. B. Peak area vs time plot, the three gases produced (black = CO₂, red = SiF₄, and blue = PF₃). C. The mass spectrum was taken after 48 days, and the reaction gases were present in this spectrum, indicating that the reaction took longer than the run time of the IR experiment (sample is red and black, helium is blue). SiF₄ (104 amu, 85 amu, 86 amu, 87 amu), PF₃ (69 amu), CO₂ (44 amu), F (19 amu), and H₂ (2 amu). Boxes around peaks correspond to various compounds (yellow = H₂, black = F, blue = CO, purple = O₂, orange = CO₂, red = PF₃, green = SiF₄)..... 417

Figure II.2.B.9 Characterization data for the gases produced in the reaction between the Li₂SiO₃ and the electrolyte. A. IR data as a function of time (black = 0.936 min, red = 126 min, blue = 559 min, purple = 818 min), insets CO₂, and SiF₄ and PF₃. B. Peak area vs time plot. C. Derivative of plot with respect to time of peak area vs time plot. (In both, black = CO₂, red = SiF₄, and blue = PF₃). b) Mass spectrum was taken after 27 days (sample is red, helium is blue). Boxes around peaks correspond to various compounds (yellow = H₂, black = F, blue = CO, purple = O₂, orange = CO₂, red = PF₃, green = SiF₄). SiF₄ (104 amu, 85 amu, 86 amu, 87 amu), PF₃ (69 amu), CO₂ (44 amu), F (19 amu), and H₂ (2 amu). 418

Figure II.2.B.10 Characterization data for the gases produced in the reaction between the Li₄-SiO₄ and the electrolyte. A. Kinetic IR data as a function of time (black = 0.936 min, red = 126 min, blue = 559 min, purple = 818 min), insets CO₂, and SiF₄ and PF₃. B. Peak area vs time plot. Inset is derivative of plot with respect to time. (In both, black = CO₂, red = SiF₄, and blue = PF₃). C. Mass spectrum was taken after 19 days (sample is red, helium is blue). Boxes around peaks correspond to various compounds

(yellow = H ₂ , black = F, blue = CO, purple = O ₂ , orange = CO ₂ , red = PF ₃ , green = SiF ₄). SiF ₄ (104 amu, 85 amu, 86 amu, 87 amu), PF ₃ (69 amu), CO ₂ (44 amu), F (19 amu), and H ₂ (2 amu).	419
Figure II.2.B.11 FTIR data showing the proton-termination region of several representative materials.	420
Figure II.2.B.12 Left: Example FTIR data on chemical reactivity of plasma-grown Si nanoparticles (black) with 1.2 M LiPF ₆ in EC (blue) or (red) electrolyte. Right: Cartoons showing various functional groups identified in the solid state.	421
Figure II.2.B.13 DRIFTS spectra showing fumed SiO ₂ (top), nanoamor 30–50 nm particles (middle), and Stöber SiO ₂ (bottom) before (black) and after (red) exposure to electrolyte.	422
Figure II.2.B.14 DRIFTS spectra showing Li ₂ SiO ₃ and Li ₄ SiO ₄ before (black) and after (red) exposure to electrolyte.	422
Figure II.2.B.15 ATR IR spectra over exposure time for a) SiO ₂ , b) Li ₂ Si ₂ O ₅ , c) Li ₂ SiO ₃ , and d) Li ₃ SiO _x .	423
Figure II.2.B.16 FIB cross sections of Li ₃ SiO _x samples soaked for (a) 0 hour, (b) 3 hours, (c) 24 hours, and (d) 72 hours.	424
Figure II.2.B.17 Illustration of thickness and compositional changes of (a) SiO ₂ , (b) Li ₂ Si ₂ O ₅ , (c) Li ₂ SiO ₃ , and (d) Li ₃ SiO _x films soaked in electrolyte over time.	425
Figure II.2.B.18 XPS depth profile of Li ₃ SiO _x thin film.	425
Figure II.2.B.19 XPS sputter depth profiles for SiO ₂ (a) F 1s and (b) Li 1s; Li ₂ Si ₂ O ₅ (c) F 1s and (d) Li 1s; Li ₂ SiO ₃ (e) F 1s and (f) Li 1s; and Li ₃ SiO _x (g) F 1s and (h) Li 1s.	426
Figure II.2.B.20 XPS Si 2p, O 1s, F 1s, and C 1s binding energies with depth for SiO ₂ soaked for 0 hours (a–d), 30 minutes (e–h), 24 hours (i–l), and 72 hours (m–p).	427
Figure II.2.B.21 XPS Si 2p, O 1s, F 1s, and C 1s binding energies with depth for Li ₃ SiO _x soaked for 0 hours (a–d), 30 minutes (e–h), 24 hours (i–l), and 72 hours (m–p).	428
Figure II.2.B.22 1×1 μm AFM images from left to right: Native oxide pristine surface, after soaking in electrolyte, thermally grown 50-nm SiO _x wafer pristine surface, after soaking in electrolyte. A plot is shown displaying comparisons between linescans over surface islands on each sample.	432
Figure II.2.B.23 SSRM depth profiling on 15-nm SiO ₂ on c-Si sample after soaking in electrolyte for 7 days. Height image is shown at left, and resistivity image is shown at right. Electronic contrast between SiO ₂ and c-Si is manifest at a depth of 15 nm, showing that the integrity of the SiO ₂ film is retained after soaking in electrolyte.	432
Figure II.2.B.24 Calculated radial distribution functions g(r) and the corresponding integrals N(r) of Li-O(EC), Li-F(PF ₆ ⁻), Li-Li, Li-P(PF ₆ ⁻) pairs of (a) (b) 1.0 M LiPF ₆ in EC, and Li-O(EC), Li-F(PF ₆ ⁻), Li-P(PF ₆ ⁻), Li-O(FEC), Li-F(FEC) pairs of (c) (d) 1.0 M LiPF ₆ in EC with 10%mol FEC additive.	433
Figure II.2.B.25 (a) The calculated total coordination number for Li ⁺ in 1.0 M LiPF ₆ in EC with 0/5/10% FEC and 1.2 M LiPF ₆ in EC with 0/5/10% FEC with specifications of the contributions from EC, FEC and PF ₆ ⁻ . The representative solvation structures taken from MD simulation snapshots of (b) 1.0 M LiPF ₆ in EC and (c) 1.0 M LiPF ₆ in EC with 10% FEC.	433

Figure II.2.B.26 (a) Self-diffusion coefficients computed from MD simulations as compared with NMR experiments (1.0 M LiPF ₆ in EC) (b) Transference numbers for Li ⁺ and PF ₆ ⁻ from MD simulations and NMR experiments. The error bars represent the standard deviation of the data collected every 1 ns during the 5-ns production runs.....	434
Figure II.2.B.27 Measured FTIR spectra of the C=O breathing band of (a) pure EC and 1.0 M LiPF ₆ in EC, and (b) EC with 10% FEC and 1.0 M LiPF ₆ in EC with 10% FEC. (c–d) The corresponding calculated IR spectra as a comparison of the experimental results. Red, cyan, purple, green, grey, and dark grey lines correspond to uncoordinated EC, EC coordinated with Li ⁺ , uncoordinated FEC, FEC coordinated with Li ⁺ , C-H deformation, and total spectrum, respectively. Scatter points denote the original FTIR data points.	435
Figure II.2.B.28 Measured FTIR spectra of the P–F bond stretching band of (a) 1.0 M LiPF ₆ in EC, and (b) 1.0 M LiPF ₆ in EC with 10% FEC. (c) The corresponding calculated IR spectra for 1.0 M LiPF ₆ in EC as a comparison of the experimental results. Yellow, green, blue, and dark grey lines correspond to uncoordinated PF ₆ ⁻ , coordinated PF ₆ ⁻ , FEC ring deformation, and total spectrum, respectively. Scatter points denote the original FTIR data points.....	436
Figure II.2.B.29 Structures of EC molecules around a Li ion (a) in bulk and (b) at interface.....	437
Figure II.2.B.30 (a) The model Si anode interface, and (b) the voltage profile in the electrolyte region between the electrodes. The electric potentials are -0.47 V and +0.7 V at the negative and the positive electrodes, respectively. (c) Radial distribution functions and the coordination numbers (CN) of PF ₆ ions around a Li ion in bulk and at the neutral, negative and positive electrodes, from top to bottom, and the CN values are 0.3, 0.65, 0.4, and 0.45, respectively.....	438
Figure II.2.B.31 Contact ion pair (CIP) ratio in the bulk electrolyte and at SiO ₂ interface at temperatures of 400 K, 350 K, and 313 K. The CIP ratio increases from the bulk to interface. The neutral silicon interface shows the largest CIP ratio, and it becomes smaller at the charged interface.....	438
Figure II.2.B.32 Li-Si phase diagram.	439
Figure II.2.B.33 (a) ⁷ Li and (b) ²⁹ Si solid-state in-situ MAS NMR for Li ₇ Si ₃ and its physical with different electrolyte solvents.....	440
Figure II.2.B.34 (a) ⁷ Li and (b) ²⁹ Si in-situ solid-state MAS NMR for Li ₂₂ Si ₅ and different electrolyte solvents. ANL, unpublished results.	441
Figure II.2.B.35 Inset photo: Electrolyte drop on lithium silicide thin film on silicon wafer. Main plot: ATR-FTIR spectra of the FEC and Gen2-treated lithium silicide surface.....	441
Figure II.2.B.36 Bulk modulus of lithium silicates and lithium silicides.	442
Figure II.2.B.37 a) Photo of sputter targets, and b) diagram of sputter conditions in the process chamber of Lesker PVD75 system.	443
Figure II.2.B.38 Substrate holders used for sputter deposition. Left: Holder for Si chips, Right: Holder for KCl chemical test samples.	444
Figure II.2.B.39 Sputter system and sample transfer process.	444
Figure II.2.B.40 ICP-OES results for Li/Si ratio in each thin film at each power setting.	445

Figure II.2.B.41 FTIR spectra of all five sputtered lithium silicate compositions.....	446
Figure II.2.B.42 Gaussian-peak deconvolution of Li/Si =7.7 film.	447
Figure II.2.B.43 Gaussian-peak deconvolution of a) Li/Si = 4.8 film, b) Li/Si = 2.9 film, c) Li/Si = 1.9 film, and d) Li/Si = 1.4 film.....	448
Figure II.2.B.44 Percent of vibration modes relevant to lithium silicate film with for each composition.	449
Figure II.2.B.45 XPS a) O1s, b) Si 2p, and c) C 1s binding energy regions with depth profiling of Li/Si = 1.4 sample.	450
Figure II.2.B.46 XPS a) O1s, b) Si 2p, and c) C 1s binding-energy regions with depth profiling of Li/Si = 2.9 sample.	451
Figure II.2.B.47 XPS a) O1s, b) Si 2p and c) C 1s binding-energy regions with depth profiling of Li/Si = 4.8 sample.	452
Figure II.2.B.48 XPS a) O1s, b) Si 2p, and c) C 1s binding-energy regions with depth profiling of Li/Si = 7.7 sample.	453
Figure II.2.B.49 TOF-SIMS analysis of Li/Si = 1.4 thin film.	455
Figure II.2.B.50 TOF-SIMS analysis of a) Li/Si = 1.9 thin film, b) Li/Si = 2.9 thin film, c) Li/Si = 4.8 thin film, and d) Li/Si = 7.7 thin film.....	456
Figure II.2.B.51 TOF-SIMS depth profiling of Li ₂ O (left), Li ₃ SiO _x (middle), and Li ₂ SiO ₃ (right).....	457
Figure II.2.B.52 XPS depth profile analysis of LiF thin films on a Li foil (left) and a Pt-coated Si wafer (right).	457
Figure II.2.B.53 Morphologies and RMS roughness of individual SiEI components deposited on Pt-coated Si wafers.	458
Figure II.2.B.54 Ionic conductivity of individual SiEI components with varying temperature (left) and binding energy variation of a LiF thin film on a Li foil obtained from operando XPS (right).	459
Figure II.2.B.55 Average surface electronic resistivity (left) and nanoindentation depth (right) of individual SiE.....	460
Figure II.2.B.56 500×500-nm AFM images of the LiF surfaces before and after nanoindentation was performed, illustrating the AFM-based nanoindentation technique. Hardness results for each deposited film are plotted at right.	460
Figure II.2.B.57 1×1-μm SSRM images of the LiF surface showing resistance and height channels after SSRM resistivity vs. depth profiling was performed. Resistivity vs. depth profiles for LiF and Li ₂ O are plotted.	461
Figure II.2.B.58 EELS spectrum images of Li ₂ O film deposited on Pt on c-Si showing the Li K edge and O K edge maps.....	461
Figure II.2.B.59 EELS spectrum images of Li ₂ SiO ₃ film deposited on Pt on crystalline Si showing O K edge, Si L edge, and C K edge maps.	462

Figure II.2.B.60 XPS data showing little to no variation in chemical states present on the surface of the Si thin-film samples.	463
Figure II.2.B.61 TOF-SIMS profile data showing the apparent change in sputter rate of Si thin-film samples that have been aged in different gloveboxes across the five national laboratories; b) XPS profile data showing the difference between glovebox, control, and air exposed.	464
Figure II.2.B.62 (left) Photo of the silicon-supported electrodes; (right) Schematic of the electrode cross section.	465
Figure II.2.B.63 TOF-SIMS data collected on the as-prepared electrode.	466
Figure II.2.B.64 TOF-SIMS data collected for ^{18}O labeled electrodes aged for three hours in wet and dry electrolyte.	466
Figure II.2.B.65 NR data collected for $\text{Li}_2\text{Si}_2\text{O}_5/\text{Si}$ films as a function of time aging in electrolyte.	467
Figure II.2.B.66 Cyclic voltammetric response of 70-nm-thick amorphous $\text{Li}_2\text{Si}_2\text{O}_5$ films on a Si wafer in 1 M LiPF_6 1:1 EC:DMC at scan rate of 0.1 mV/s. Markers indicate the potential-dependent elastic modulus measured with an electrochemical AFM. The inset shows the change in optical properties with Li-Si substrate alloying.	468
Figure II.2.B.67 Operando AFM images on 70-nm-thick $\text{Li}_2\text{Si}_2\text{O}_5:\text{Si}$ electrodes undergoing lithiation and substrate alloying. Topography and effective elastic modulus a,b) prior to the Li-Si alloy threshold and c,d) after alloying at 50 mC/cm^2 , 90 mV (vs. $\text{Li}^{0/+}$).	469
Figure II.2.B.68 Scanning electron micrographs of a $\text{Li}_2\text{Si}_2\text{O}_5:\text{Si}$ electrode alloyed to 50 mC/cm^2 at 90 mV (vs. $\text{Li}^{0/+}$). a) Silicate film disruption (localized cracking and delamination) is induced by low-force AFM scanning but at a considerable distance from the imaging area. b–d) The morphology of the silicate is unchanged with electrochemical lithiation, early-stage alloying of the underlying Si, and low-force (nN) imaging.	470
Figure II.2.B.69 TOF-SIMS depth profiles (25-keV Bi^+ for analysis, 1-keV Xe^+ for milling) of $\text{Li}_2\text{Si}_2\text{O}_5:\text{Si}$ electrodes at various stages of LiSi alloying. a) 72-nm-thick silicate alloyed to 50 mC/cm^2 at 90 mV (vs. $\text{Li}^{0/+}$) left in the alloyed state. b) 72-nm-thick silicate alloyed to 8 mC/cm^2 , de-alloyed, repeatedly potentiodynamically cycled to 7 mC/cm^2 at 0.1 mV/s, and left in the de-alloyed state. c) 72-nm-thick silicate alloyed to 8 mC/cm^2 , de-alloyed, repeatedly potentiodynamically cycled to 12 mC/cm^2 at 0.1 mV/s, and left in the de-alloyed state. d) Comparison of F- ion yield for each of the electrodes. Dashed traces correspond to as-deposited silicate controls.	471
Figure II.2.B.70 Uncoated amorphous silicon galvanostatically cycled with 0.05 V cutoff voltage at C/100 rate.	472
Figure II.2.B.71 a) First-cycle CV for silicon anodes with silicate coatings and b) discharge profiles.	473
Figure II.2.B.72 First lithiation of silicate-coated silicon anodes at C/100 with replicates for each coating composition.	474
Figure II.2.B.73 CV plots for the a) second, b) seventh, and c) fourteenth cycle for each silicate coating cycling at a C/50 cycle rate.	475

Figure II.2.B.74 Discharge capacity per cycle calculated using area under CV curve with 0.08 V cutoff voltage.....	476
Figure II.2.B.75 Discharge capacity per cycle calculated using area under CV curve with 0.26 V cutoff voltage.....	477
Figure II.2.B.76 Discharge capacity per cycle for cycling data with a 0.26V cutoff voltage.....	477
Figure II.2.B.77 Discharge capacity change from the first to second and second to fourteenth cycle for cyclic voltammetry and constant current samples.	478
Figure II.2.B.78 XPS depth profile analysis of Li_xSiO_y composite thin film on copper foil for a) Si-rich region and b) Li-rich region. The top panels show binding-energy depth profile of O 1s (green), Si 2p (red), and Li 1s (blue). The bottom panel shows atomic percentage as a function of sputter depth.....	479
Figure II.2.B.79 a) Voltage profile of lithium-rich Li_xSiO_y composite film and silicon-rich Li_xSiO_y composite film; b) Impedance evolution of lithium-rich Li_xSiO_y composite and silicon-rich Li_xSiO_y composite as well as Si film.....	480
Figure II.2.B.80 a) Charge and discharge profile of Si and $\text{Li}_x\text{SiO}_y/\text{Si}$, with inset showing the schematic of double-layer thin film; b) Cycle performance and coulombic efficiency of double-layer thin film and pure silicon.....	481
Figure II.2.B.81 a) Evolution of XPS core-level spectra during in-situ lithiation of 50-nm $\text{SiO}_2/\text{Si}(001)$ wafer. b) AES depth profile of the lithiated sample reveals that the entire SiO_2 layer has been converted to a $\text{Li}_x\text{Si}_y\text{O}$ phase and that an underlying Li_xSi phase has also formed.	482
Figure II.2.B.82 Evolution of XPS core-level spectra during in-situ lithiation of an: a) sputter-cleaned Si(001) wafer, b) wafer with a native oxide, and c) Si (001) wafer with a 50-nm-thick thermally grown SiO_2 layer.	482
Figure II.2.B.83 Overpotential variations for the three different Si wafers tested: a) 50-nm SiO_2/Si (001) b) native oxide on Si (001) and c) sputter-cleaned Si (001). The black curve was acquired with the Li^+ ion gun current bias on and the red curve without. Binding-energy shifts can be used to estimate overpotentials of lithiation, and ultimately, Li diffusivity as a function of Li-Si-O phase.	483
Figure II.2.B.84 XPS core-level spectral evolution monitored as a function of lithiation time for three samples: bare Si(001), native oxide $\text{SiO}_x/\text{Si}(001)$, and 5-nm thermal-oxide $\text{SiO}_2/\text{Si}(001)$. The evolution of the core levels in the first two cases—and, in particular, the evidence for uptake of residual gas species by the exposed surfaces—shows that these surfaces are more reactive in comparison to the 5-nm $\text{SiO}_2/\text{Si}(001)$ sample.....	484
Figure II.2.B.85 XPS O 1s (upper left) and Si 2p (upper right) core levels recorded on the 5-nm $\text{SiO}_2/\text{Si}(001)$ sample before the Li ion gun was turned on and immediately after. The shifts in SiO_2 core levels reveal the overpotential associated with the 5-nm-thick SiO_2 layer. Changes in the Si^0 peak likely result from downward band bending in the p-type Si(001) wafer substrate, as illustrated in the schematic energy-band diagrams in the lower panel.	485
Figure II.2.B.86 Measured (symbols) and calculated (solid lines) ARXPS angular profiles of detected chemical states highlighting near-surface, intermediate, and buried phases (upper panels). The preliminary model structure shown in the lower left panel agrees well with the measured data and indicates that very	

little Li is incorporated into the SiO _x layer at early stages of lithiation. The colored circles in the ternary phase diagram (lower right) represent approximate compositions of detected phases based on XPS intensities.	485
Figure II.2.B.87 Structures of EC molecules around a Li ion (a) in the bulk and (b) at the interface.	487
Figure II.2.B.88 (a) The model Si anode interface, and (b) the voltage profile in the electrolyte region between the electrodes. The electric potentials are -0.47 V and +0.7 V at the negative and the positive electrodes, respectively. (c) Radial distribution functions and the coordination numbers (CN) of PF ₆ ions around a Li ion in bulk and at the neutral, negative, and positive electrodes, from top to bottom; the CN values are 0.3, 0.65, 0.4, and 0.45, respectively.....	488
Figure II.2.B.89 Contact ion-pair (CIP) ratio in the bulk electrolyte and at SiO ₂ interface at temperatures of 400, 350, and 313 K. The CIP ratio increases from the bulk to interface. The neutral silicon interface shows the largest CIP ratio, and it becomes smaller at the charged interface.....	488
Figure II.2.B.90 (a) The voltage profile and (b) differential capacity profile when lithiation to 60 mV. (c) The voltage profile and (d) differential capacity profile when using a cut-off voltage of 115 mV including both Regime 1 and Regime 2. (e) The voltage profile and (f) differential capacity profile when using a cut-off voltage of 400 mV including only Regime 1.	489
Figure II.2.B.91 The SEM morphology of es-SEI on the Si surface after cathodic cycling with the cut-off potential of (a) 400 mV and no rest, (b) 115 mV and no rest, as well as (c) 115 mV and long rest.	490
Figure II.2.B.92 The XPS spectra obtained from the es-SEI with the cut-off potential of 400 mV. The spectra show that the LiEDC starts to form at the potential higher than 400 mV.	491
Figure II.2.B.93 The XPS spectra obtained from the es-SEI after HVIST cycling with the cut-off potential of 115 mV and no rest. The spectra show that the SiO _x was reduced to Li _x SiO _y during the potential between 115 mV and 400 mV.....	492
Figure II.2.B.94 The XPS spectra obtained from es-SEI after HVIST cycling with the cut-off potential of 115 mV and long rest. During the long rest, the spectra show that the LiEDC was decomposed because the LiEDC reduced. It also shows that there is no lithiation on the Si wafer because the lithium silicide was not found in Si.	493
Figure II.2.B.95 (a) Cyclic voltammetry of 50-nm Si thin film in Gen 2 electrolyte (1.2M LiPF ₆ in EC:EMC 3:7 wt.%). Inset represents the comparison of the first-cycle voltage profile of the Si thin-film electrode and the bare-copper current collector. (b) First and second galvanostatic cycle of a 50-nm Si thin-film electrode cycled in 1.2M LiPF ₆ in EC:EMC 3:7 wt.% electrolyte at 5 μA cm ⁻² within the 0.05 V–1.5 V vs Li ⁺ /Li potential range.....	494
Figure II.2.B.96 Schematic representation of the electrode recovery and ATR-FTIR testing of unwashed (a) and washed (c) Si thin-film model electrodes. Cells have been cycled at 5 μA cm ⁻² employing 1.2 M LiPF ₆ in EC:EMC (3:7 wt.%) as electrolyte. Ex-situ ATR-FTIR analysis of cycled Si thin films at different states of charge during the first (de)lithiation process in the 1,900–1,000 cm ⁻¹ spectral region of unwashed (b) and washed (d) electrodes. (e) Schematic representation of LiEDC formation as a decomposition product of EC.[8].....	495
Figure II.2.B.97 (a) 3-D schematic of aNSOM experimental setup and operational principle. aNSOM 1-μm × 1-μm image of 50-nm silicon thin-film electrode cycled up to 0.05 V after the first lithiation	

- process. (b) Topography of a region of the surface film formed on the fully lithiated silicon thin-film electrode obtained by AFM. Near-field IR absorption maps over the same region at (c) $1,330\text{ cm}^{-1}$ and (d) $1,360\text{ cm}^{-1}$ wavenumbers. 497
- Figure II.2.B.98 Ex-situ ATR-FTIR analysis of cycled Si thin films at different states of charge during the first (de)lithiation process in the $1,000\text{--}700\text{ cm}^{-1}$ spectral region of unwashed (a) and washed (b) electrodes. (c) Ex-situ XAS analysis at the F K--edge collected in TEY mode. 498
- Figure II.2.B.99 Ex-situ ATR-FTIR analysis of cycled Si thin films in the fully lithiated and delithiated state upon the 1st and 2nd cycle in the $1,900\text{--}1,000\text{ cm}^{-1}$ (a) and $1,000\text{--}700\text{ cm}^{-1}$ (b) spectral regions. Cells have been cycled at $5\text{ }\mu\text{A cm}^{-2}$ employing 1.2M LiPF_6 in EC:EMC (3:7 wt.%) as electrolyte. 499
- Figure II.2.B.100 Ex-situ XAS analysis at the Si L-edge collected in TEY (a) and TFY (b) mode for the 50-nm Si thin film with native oxide. 499
- Figure II.2.B.101 Ex-situ ATR-FTIR analysis of unwashed cycled 50-nm Si thin films with 10-nm SiO_2 at different states of charge during the first (de)lithiation process (a) and following 2nd cycle (b). 500
- Figure II.2.B.102 A comparison of the EQCM-D data for a silicon film cycled in (a) Gen2, and (b) Gen2 +10 wt.% FEC. 501
- Figure II.2.B.103 AFM topography (blue box), TERS mapping of an individual band (orange box) and composite TERS map (grey box) of 1X, 5X, and 20X cycled a-Si samples. The topography and chemical imaging are on the same sample area. The intensity roughly indicates the concentration of each chemical moiety. The individual band TERS mapping quantifies the intensity of a band, after spectral background correction, of each vibrational signal scaled by the false color bar. From left to right (orange box), TERS mapping indicates the overlap of $-\text{CH}_2$ rocking, $-\text{OCO}$ and $-\text{COC}$ deformation bands ($\sim 740\text{ cm}^{-1}$), $-\text{CH}_2$ twisting, asymmetric CCO stretching bands ($1,281\text{ cm}^{-1}$) and $-\text{CH}_2$ twisting, asymmetric OCOO stretching bands ($\sim 1,407\text{ cm}^{-1}$) collected from 1X a-Si, respectively. For 5X a-Si, TERS mapping respectively shows the combination of $-\text{CH}_2$ bending band ($1,348\text{ cm}^{-1}$), $-\text{CH}_2$ twisting, asymmetric OCOO stretching bands ($\sim 1,429\text{ cm}^{-1}$) and $-\text{CH}_2$ twisting, asymmetric COO stretching, and C=O stretching bands ($1,566\text{ cm}^{-1}$). For 20X a-Si, TERS mapping exhibits the asymmetric $-\text{OCO}$ stretching band ($1,169\text{ cm}^{-1}$), bidentate asymmetric $-\text{COO}$ stretching band ($1,510\text{ cm}^{-1}$), and the monodentate asymmetric $-\text{COO}$ stretching bands ($1,583\text{ cm}^{-1}$). The right grey box shows the composite TERS maps for all samples. The number index of the composite map marks where the sample TERS spectrum was taken. 502
- Figure II.2.B.104 TERS spectra collected from various locations of (a) 1X sample, (b) 5X sample, and (c) 20X sample. The assignment for bands of interest are at the top of each plot. The Greek symbols denote corresponding vibrational modes: ν (stretching), δ (bending), χ (scissoring), τ (twisting), ρ (rocking), β (deformation), and ω (wagging). 504
- Figure II.2.B.105 SSRM resistivity vs. depth profiles of SEI formed on 15-nm SiO_2 and native oxide on Si wafers after one cycle. 505
- Figure II.2.B.106 STEM EELS areal density maps on SEI formed on two model Si systems. SEI formed on native oxide is comparably thicker and less laterally homogenous when compared to that formed on SiO_2 505

Figure II.2.B.107 An example of 3-D resistance mapping of SEI. (a) SSRM schematic, where spreading resistance (R_{sp}) \gg sample and back-contact resistance (R_{sb}). By using appropriately large probe forces, the contribution of the contact resistance (R_{ct}) is reduced to a stable level. Curved arcs around the probe represent potential contour arcs, indicating the sampling volume, in a semi-infinite uniform material. (b) Conceptual diagram depicting measurement technique. A resistance map is captured at intermediate probe forces, resulting in uniform milling of the surface material to a defined depth. A larger scan is then taken over the measurement area to determine the depth of the resistance map. (c) $0.5 \times 0.5 \mu\text{m}$ resistance map captured with a probe forces of $15 \mu\text{N}$ on SEI on Si with SSRM, measuring resistance of SEI at a depth of 9 nm. (d) $1.0 \times 1.0 \mu\text{m}$ height channel image (left) captured at a low contact force ($<1 \mu\text{N}$) over the location of the previously described resistance mapping raster scan, indicating the depth of the resistance map shown in (c). Resistance channel image (right) captured in the same scan shows relative contrast in the electronic properties between the superficial and deeper structures of SEI. Slightly higher resistivities are measured at the milled area when compared to (c) due to the contribution of contact resistance when scanning with low contact forces. (e) Example resistivity vs. depth profile obtained from resistance and depth measurements shown in (c) and (d), respectively. The datapoint obtained from resistivity and height data presented in (c) and (d) is indicated on the profile with an arrow. 506

Figure II.2.B.108 SIMS and SSRM data for doped α -Si:H on c-Si reference sample. (a) Dynamic SIMS P-concentrations measured with cesium and oxygen sputtering at 15 keV and 2 keV, respectively. (b) Inverse P-concentration, normalized to highest bulk resistivity, measured on “sister” co-deposition on glass. Sample schematic with thicknesses and bulk resistivities is shown in inset. (c) Line scans across overview height images captured during various stages of incremental SSRM profiling, showing three distinct depths within the structure. (d) $2 \times 2 \mu\text{m}$ height (left) and resistivity (right) overview images at three stages of incremental SSRM profiling, demonstrating contrast in electronic resistivities at different depths within the structure. (e) SSRM resistivity vs. depth profile for the sample. Box-smoothing of normalized inverse P-concentration data shows close agreement with SSRM data after smoothing to include 10 nm of previous points (to account for probe tip penetration and debris accumulation at the probe) and 40 nm of subsequent points (to account for the sampling volume of the spreading resistance). 507

Figure II.2.B.109 (Left) Scheme for lithium binding by HPNO fluorophore. (b) UV-vis spectra of 0.05 mM HPNO in propylene carbonate without lithium (purple) and increasing amounts of LiBr until the solution is saturated with LiBr (red). 508

Figure II.2.B.110 Synthesis of Li ion fluorescent sensors with tunable absorbance spectra. R groups represent strong electron withdrawing groups. n 508

Figure II.2.B.111 (top) Three new monomeric Li-ion fluorescent sensors developed in this program with “tunable” absorbance spectra over a range of ~ 100 nm. (Bottom) Sensitivity of the sensors to various LiBr concentrations. 509

Figure II.2.C.1 Voltage profile (a) and cycling performance (b) of the NMC532|| Si/Gr (CAMP electrodes) in TEPA-based LHCE. 517

Figure II.2.C.2 a) Cycling performance of NMC532|| Si/Gr cells with a) modified silicon anode with and without carbon coating in baseline electrolyte. b) Modified silicon anode with carbon coating and PI binder in TEPA-based LHCE. 518

Figure II.2.C.3 Cycling performance of NMC532 Si/Gr full cell with different additives.....	519
Figure II.2.C.4 In situ TEM characterization of the lithiation process of a typical CNT@Si microsphere. a) Si/MWNT composite particle before lithiation; b) partially lithiated particle; c, fully lithiated particle.	519
Figure II.2.C.5 In-situ SEM-AFM indentation of a CNT@Si@C particle. a) SEM image of the AFM Tip; b) high resolution of the CNT@Si@C particle; c) SEM image of the contact between AFM tip and the particle before the introduction of the force; d) SEM image of the particle after the introduction of the force.	520
Figure II.2.C.6 (a) Long-term cycling performance of the CNT@Si @C and Comm-Si electrodes. (b) Cycling performance of CNT@Si @C-Graphite electrodes with 30wt% CNT@Si @C in the composite.	520
Figure II.2.D.1 Stability of the Li_xSi /graphene foil. (a) Photographs of the Li metal and Li_xSi /graphene foil exposed to ambient air for different durations. (b) The areal capacity retention of a Li_xSi /graphene foil in the dry room for two weeks. The inset shows the trend of capacity decay of the Li_xSi /graphene foil (red) and $\text{Li}_x\text{Si}/\text{Li}_2\text{O}$ nanoparticles (black) with varying durations. (c) The areal capacity retention of the Li_xSi /graphene foil exposed to ambient air for three days. The inset shows the trend of capacity decay of Li_xSi /graphene foil (red) and $\text{Li}_x\text{Si}/\text{Li}_2\text{O}$ nanoparticles (black) with varying durations.	523
Figure II.2.D.2 Electrochemical performance of the Li_xSi /graphene foil. Half-cell cycling performance of Li_xSi /graphene foils with thicknesses of 12 and 19 μm at 0.1mAcm^{-2} . The Coulombic efficiency is plotted for the foil with the thickness of 19 μm only (purple).	524
Figure II.2.D.3 Electrochemical performance of the Li_xSi /graphene foil. a, The voltage profiles of Li_xSi /graphene foil- LiFePO_4 full cell and Li- LiFePO_4 half cell (LiFePO_4 : Super P: PVDF = 70:20:10 by weight) within a potential window of 2.5-3.8 V. The capacity and rate are both based on the mass of LiFePO_4 in the cathode. b, Rate capability of Li_xSi /graphene foil- LiFePO_4 and Li- LiFePO_4 cells at various rates from 0.2 to 20 C (1 C = 170 mA g^{-1} of LiFePO_4). c, Schematics and the corresponding cross-sectional view SEM images of the Li_xSi /graphene foil before and after being cycled and stopped at the delithiated and lithiated states.	525
Figure II.2.D.4 Characterization of the sulfur electrode and the sulfur batteries. a, SEM image of the graphitic carbon-encapsulated sulfur composites. b, TEM image of the graphitic carbon-encapsulated sulfur composite. Inset shows the magnified graphitic carbon lattice fringes. c, The voltage profiles of Li_xSi /graphene foil-S and Li-S cells at a rate of 0.5 C (1 C = 1.67 A g^{-1} of S; the capacity is based on the mass of graphitic carbon-encapsulated S in the cathode; the mass ratio of anode to cathode is 1.8:1). d, Cycling performance of Li_xSi /graphene foil-S and Li-S cells at a rate of 0.5 C. The Coulombic efficiency is plotted on the right y axis. e, XPS spectra of C 1s (left) and S 2p (right) performed on Li metal (top) and the Li_xSi /graphene foil (bottom) cycled in the sulfur batteries for 50 times.	526
Figure II.2.D.5 Photographs of the (a) Li_xSn /graphene foil and (b) Li_xAl /graphene foil. XRD patterns of the (c) Li_xSn /graphene foil and (d) Li_xAl /graphene foil.	527
Figure II.3.A.1 (Left Panel) Change in volume of NMC-811//Gr pouch cells due to gas evolution measured using Archimedes method. Gassing is significant in cells charged to 4.4 V with baseline Gen2	

electrolyte but less severe with electrolyte additives. (Right Panel) Capacity retention of NMC-811//Gr pouch cells charged to 4.4 V with baseline Gen2 electrolyte and electrolyte with additives.	530
Figure II.3.A.2 (Left Panel) Gases sampled from symmetric pouch cells (anode//anode and cathode//cathode) and full pouch cells after cycling. The gases were measured ex situ with GC-MS. Differences in gas composition between symmetric cells and full cells provide evidence for gas “cross-talk” in HE/HV cells. (Right Panel) Expanded view of the left panel.	530
Figure II.3.A.3 (Left) AEGIS reactor capable of continuously probing gas phase species without loss of solvent. (Right) Change in concentration of CO and CO ₂ with state of charge measured for a 0.2 Ah NMC-811//Gr cell.	531
Figure II.3.A.4 (Left Panel) - Voltage and electrode potential data from cells containing the (a) NMC811/LTO and (b) NMC811/Gr couples. For both couples, the profiles to the left show the formation (two C/10 and one C/25) cycles; the profiles to the right show the cycle with the first 100 h potentiostatic hold. (Right Panel) - Cell and electrode ASI change (from HPPC measurements) resulting from calendar-aging of (a-c) NMC811/LTO cells and (d-f) NMC811/Gr cells. The aging times are indicated in (c): after formation cycles (black), 100 h (red), 200 h (blue), and 400 h (green).	532
Figure II.3.A.5 (Left Panel) HAADF-STEM micrograph (5 nm scale bar) from a NMC-532 particles cycled in FE-3 electrolyte. (Right Panel) EELS analysis results from the oxides cycled with various electrolytes. Energy difference between the O-K edge and its pre-peak is plotted as a function of distance from the surface.	533
Figure II.3.A.6 (a) Capacity vs. cycle number for cells containing pristine graphite/F-Gr/G-Gr anodes, pristine cathodes, and Gen2 electrolyte. (b) Average CE for the final 5 C/3 cycles of each “aging set”, directly before the C/10 cycles. Each data point is the average of 3 cells with the standard deviation indicated by the error bars.	534
Figure II.3.B.1 SEM images of a) platelet-shaped and b) truncated-octahedron-shaped NMC crystals. .	538
Figure II.3.B.2 (a, b) Hard XAS spectra of pristine, delithiated, and aged NMC-333 particles, and (c) The relationship between Ni-K edge energy and aging time.	539
Figure II.3.B.3 K-edge energy shift of a) Ni, b) Mn and c) Co as a function of aging time in chemically-delithiated NMCs.	539
Figure II.3.B.4 (Right) ²⁷ Al NMR spectra of 5 wt.% Al ₂ O ₃ -coated NMC-622 and 811 annealed at 800°C for 8h, compared to Co-rich NCA, Ni-rich NCA and NCMA, and Co-rich NCMA. (Left) scheme of the evolution of surface coating.	540
Figure II.3.B.5 Summary of effects of different surface treatment conditions on electrochemical performance.	540
Figure II.3.B.6 Electrochemical performance of baseline NMC-532 with optimized coatings as per Figure II.3.B.5	541
Figure II.3.B.7 Electrochemical performance comparison of baseline with optimized cathodes.	542
Figure II.3.C.1 (a) Segregation trend for dopants in NMC-111. (b) Reactivity trend for dopants in NMC-111.	545

Figure II.3.C.2 (a) Dissolution concentrations in the electrolyte for different additives, electrolytes, and states of charge.....	546
Figure II.3.C.3 Formation energy as a function of c-direction expansion for pinned (a) $\text{Li}_2\text{Ni}_2\text{O}_4$ and (b) $\text{Li}_2\text{Co}_2\text{O}_4$ spinels on a NMC-111 (012) facet.....	546
Figure II.3.C.4 Adsorption configuration on partially delithiated NMC-111 of (a) TMSPi and (b) TMSPi decomposed by Si-O bond breaking pathway. Silver, blue, purple, green, light blue, gray, brown, white and small red spheres represent Ni, Co, Mn, Li, Si, P, C, H and O, respectively.....	547
Figure II.3.C.5 Change of NMC/ LiAlO_2 interface formation energy with the thickness of α - LiAlO_2 layer sandwiched between NMC and a disordered LiAlO_2 phase.....	550
Figure II.3.C.6 (a) Model slab for the (012) NMC-111 surface coated with 2 layers of α - LiAlO_2 . Light blue spheres represent Al, green-Li, purple-Mn, blue-Co, silver-Ni, and red-O. (b) TM layer configuration for NMC-111, (c) Al swapped with Mn, (d) Al swapped with Ni, (e) Al swapped with Co. The dashed circles represent the first and second nearest neighbors to Al atoms. The values of energy at the bottom of panels (c) to (e) represent the thermodynamic energy change after swapping Al from the surface layer with different TM centers in the bulk of NMC-111.....	550
Figure II.3.C.7 Positive SEI growth model compared to a 4.6 V hold on NMC//Gr coin cell at room temperature.....	551
Figure II.3.C.8 Left: Proposed side reaction mechanism from reference 1. Right: Full electrochemical model compared to 4.6 V hold on NMC//Gr coin cell at room temperature.....	551
Figure II.3.D.1 (a) Neutron diffraction and Rietveld refinement of a Mo-NMC composite cathode with $x = 0.15$. (b) Charge/discharge curves and (c) cycling stability of NMC compared with a Mo-NMC composite ($x = 0.10$) prepared either with or without an 850°C heat treatment as indicated. ¹	556
Figure II.3.D.2 Half-cell electrochemical characterization of Li_2MoO_3 thin film cathodes cycled in a liquid carbonate electrolyte. (a) Galvanostatic charge/discharge profiles and (b) differential capacity plots collected between 2.0 – 4.8 V vs. Li/Li^+ at a current density of $9.46 \mu\text{A}/\text{cm}^2$	557
Figure II.3.D.3 Ex-situ XPS spectra of pristine (i.e., uncycled) and cycled thin film Li_2MoO_3 thin film cathodes collected after 1 and 20 charge/discharge cycles showing core-level scans for (a) Mo 3d, (b) C 1s, and (c) F 1s. Note that F 1s core level scans were not collected for the pristine samples.....	558
Figure II.3.D.4 Electrochemical characterization at room temperature for an all-solid-state $\text{Li}_2\text{MoO}_3/\text{Lipon}/\text{Li}$ thin film battery showing (a) galvanostatic charge/discharge curves, (b) dQ/dV plots, and (c) cycling stability collected over 2.0 – 4.8 V at $10 \mu\text{A}/\text{cm}^2$	559
Figure II.3.D.5 Li^+ diffusion coefficient in Li_2MoO_3 at 80°C at various states of charge for a $\text{Li}_2\text{MoO}_3/\text{Lipon}/\text{Li}$ thin film battery as determined from EIS using the method reported by Ho et al. ³ Error bars represent the range of values determined from plots of either the reactance vs. $\omega^{-1/2}$ or resistance vs. $\omega^{-1/2}$	559
Figure II.3.D.6 Characterization of $\text{LiNi}_{0.5}\text{Mn}_{0.5}\text{O}_2$ (LNMO)-based cathodes with and without 1 at % Mo ($\text{LiNi}_{0.495}\text{Mn}_{0.495}\text{Mo}_{0.01}\text{O}_2$). (a) X-ray diffraction (XRD) patterns and galvanostatic charge/discharge curves over 50 cycles for (b) unmodified LNMO and (c) 1 at% Mo-doped LNMO. For the	

electrochemical characterization, the cathodes were galvanostatically cycled in half cells between 2.0 – 4.5 V vs. Li/Li^+ at 20 mA/g in an electrolyte containing 1.2 M LiPF_6 in EC/EMC (3/7).....	560
Figure II.3.D.7 (a) Cycling stability at 20 mA/g and (b) rate capabilities at 10 – 200 mA/g for LNMO cathodes which were modified by doping with 1 at% Mo and/or coating with 2 wt% MnPO_4 . Electrochemical characterization was performed by cycling the cathodes between 2.0 – 4.5 V vs. Li/Li^+ in half cells.	561
Figure II.3.E.1 The cycling behaviors of Sn-Fe-C anode composite synthesized with mechano-chemical synthesis.	565
Figure II.3.E.2 The cycling and rate performance of modified polyol approach synthesized Sn_yFe anode material.	565
Figure II.3.E.3 (left) The first cycle, (middle) the 1 st three cycles showing the rapid decay and (right) the ex-situ XAS showing the oxidation and reduction of Cu during the conversion and reconversion reactions. The decay of the Cu^{2+} peak at just under 9000 eV, shows the incomplete formation of CuF_2 on recharge.	566
Figure II.3.E.4 The rate capability on 1 st discharge of (left) a Li//CuF_2 cell and (right) a $\text{Li//CuF}_2\text{-VOPO}_4$ cell.	566
Figure II.3.E.5 The behavior of a $\text{Cu}_{0.5}\text{Fe}_{0.5}\text{F}_2$ electrode. From left to right: the first two cycles (and also indicating where the XAS measurements were made; the fade of the Cu^{2+} peak; the recovery of the Fe^{2+} peak on charging; and the cycling performance of the $\text{Cu}_{0.5}\text{Fe}_{0.5}\text{F}_2$ anode.	566
Figure II.3.E.6 The cycling and rate performance of solid-state synthesized Li_xVOPO_4 cathode with high energy ball milling with carbon and then annealed with different hours.	567
Figure II.3.E.7 Comparison of (a) the capacity and (b) the energy density of the $\text{Sn}_y\text{Fe//Li}_x\text{VOPO}_4$ cell vs. the baseline $\text{Sn}_y\text{Fe//LiFePO}_4$ cell.	568
Figure II.3.E.8 (a) Comparison of the cycling performance of a $\text{Sn}_y\text{Fe//Li}_x\text{VOPO}_4$ cell with different capacity ratios of cathode to anode; (b) comparison of the performance of $\text{Sn}_y\text{Fe//Li}_x\text{VOPO}_4$ vs. a graphite/ Li_xVOPO_4 Cell; (c) the voltage profile of $\text{Sn}_y\text{Fe//Li}_x\text{VOPO}_4$ cell with lithium metal prelithiation; (d) compare of the performance of $\text{Sn}_y\text{Fe//Li}_x\text{VOPO}_4$ cell with different amounts of lithium metal prelithiation indicating the quantity control is critical: a small excess is needed; (e) $\text{Sn}_y\text{Fe//Li}_x\text{VOPO}_4$ cells meet the 4 mAh capacity at both 0.1C and 0.3C; (f) the volumetric capacity and energy density of those two $\text{Sn}_y\text{Fe//Li}_x\text{VOPO}_4$ cells in (e).	569
Figure II.3.F.1 Electrochemical behavior of Li NMC76 cells using two different carbonate-based electrolytes at 0.33C current rate after three formation cycles at 0.1C rate. Comparison of cycling performance (A) and capacity retention (B) in the two electrolytes; voltage profiles of LMBs using (C) E-baseline and (D) E-optimized; comparison of midpoint voltage evolution (E) and energy density (F) between E-baseline and E-optimized based LMBs.	573
Figure II.3.F.2 Comparison of the cycling performance of Li NMC76 cells using two electrolytes under high charging/discharging current rates (A) 1C/1C, (B) 2C/2C, and (C) 5C/5C. (D) Rate performance at the same charge rate of 0.2C and gradually increased discharge rate from 0.1C to 10C, and then switched back to 0.1C. (E) Long-term cycling performance and CE of Li NMC76 cell using E-optimized over 1000 cycles at 2C charging rate.	574

Figure II.3.F.3 (a, d) Cycling performance of Ni-rich $\text{LiNi}_{0.76}\text{Mn}_{0.14}\text{Co}_{0.10}\text{O}_2$ cathode in (a) E-baseline (1 M $\text{LiPF}_6/\text{EC-EMC}$) and (d) E-optimized (0.6 M LiTFSI , 0.4 M LiBOB , and 0.05 M LiPF_6 in EC-EMC) electrolytes during cycling at C/3, 1C, 2C, 5C rates (after 3 formation cycles at C/10) between ~ 2.7 and ~ 4.5 V. (b, c; e, f) HAADF-STEM images of Ni-rich $\text{LiNi}_{0.76}\text{Mn}_{0.14}\text{Co}_{0.10}\text{O}_2$ after 100 cycles at C/3 between ~ 2.7 and ~ 4.5 V in (b, c) E-baseline electrolyte and (e, f) E-optimized electrolyte. 575

Figure II.3.F.4 (a) First cycle charge-discharge voltage profiles and (b) cycling performance of $\text{Li}||\text{NMC76}$ cells using E-baseline and four LiBOB -added electrolytes (E-n% LiBOB). (c) Comparison of long-term cycling performance of $\text{Li}||\text{NMC76}$ using E-baseline and E-2% LiBOB for 500 cycles under 0.2C charging and 5C discharging. (d-i) STEM-HAADF images of the surface layers of the NMC76 cathodes. (d) Pristine sample without cycling and (g) enlarged area from the region marked with red rectangle in (d). (e) After 200 cycles in E-baseline and (h) enlarged area from the region marked with red rectangle in (e). (f) After 200 cycles in E-2% LiBOB and (i) enlarged area from the region marked with red box in (f). The insets in panels (g), (h) and (i) are the structural models illustrating lattice transformation from surface into bulk. 576

Figure II.3.G.1 Schematic illustration of the experimental setup for in situ probing of local elemental diffusion, oxidation and ordering of cations during synthesis of Ni-Mn-Co (NMC) layered oxides. A new design of sample loading configuration and environment in in situ reactors was developed, allowing multimodal characterization of elemental diffusion, oxidation, structural ordering within individual particles, via a combination of synchrotron XRF imaging, XANES spectroscopy, XRD and XTS (coupled with pair distribution function (PDF) analysis). 579

Figure II.3.G.2 **Structural transformation during synthesis of the layered $\text{LiNi}_{0.73}\text{Mn}_{0.13}\text{Co}_{0.10}\text{O}_2$ (NMC771310) from the hydroxide precursor.** (a) Schematic of the transformation from layered hydroxide precursors (P-3m1) to layered oxides (R-3m), and the corresponding change in the basic building units (BBUs), from initial $\text{TM}(\text{OH})_6$ to the TMO_6 octahedra. (b) Temperature-resolved in situ synchrotron XRD patterns, showing three sequential stages during the entire synthesis process: I (below 250 °C), II (250–500 °C) and III (above 500 °C). (c) Contour plot of selected regions in XRD patterns (marked with red dashed rectangles). (d) Evolution of integrated intensities of (003) and (104) peaks (denoted as $I_{(003)}$ and $I_{(104)}$), being normalized to their corresponding values at 850 °C, which reflect the behaviors of cationic disordering/ordering (by $I_{(003)}$) and Li insertion (by $I_{(104)}$) as the temperature increases. (e) Schematic of atomic re-arrangement, inter-layer gliding, and Li/Ni mixing (illustrated by arrows) in the intermediate $(\text{Ni}_{0.77}\text{Mn}_{0.13}\text{Co}_{0.10}(\text{OH}_{1-x}\text{Li}_y)_2)$ during Stage II. 580

Figure II.3.G.3 **Dynamic process of local structural ordering within TMO_6 octahedra during synthesis of NMC771310.** (a) Temperature-resolved in situ PDF patterns in a wide r range, showing changes in long- and short-range ordering. (b) Enlarged low r range ($r = 1.5\text{--}3.5$ Å, marked by the dashed square in (a)), wherein the two peaks at 1.6–2.4 Å, and 2.5–3.5 Å correspond to the scattering signals of TM-O and TM-TM atomic pairs, respectively. (c) Positions of TM-O and TM-TM peaks as a function of temperature (curves with squares and circles, respectively), showing the evolution of the interatomic distances. (d) Integrated intensity of TM-O and TM-TM peaks (curves with squares and circles, respectively; denoted $I_{\text{TM-O}}$ and $I_{\text{TM-TM}}$) as a function of temperature. 581

Figure II.3.G.4 **Oxidation dynamics of the constituent cations during synthesis of NMC771310.** (a) Schematics of the transformation of the octahedra associated with the hydroxides, namely, $(\text{Ni}^{2+})(\text{OH})_6$, $(\text{Co}^{2+})(\text{OH})_6$, and $(\text{Mn}^{2+})(\text{OH})_6$ into octahedra associated with the layered oxides, $(\text{Ni}^{3+})\text{O}_6$, $(\text{Co}^{3+})\text{O}_6$, and

(Mn⁴⁺)O₆, which involves oxidation of the three constituent cations (Ni, Co, Mn). (b-c) Representative XANES spectra for Ni, Co, Mn K-edges from in situ measurements. (d) Normalized Ni²⁺, Co²⁺, and Mn²⁺ contents as a function of temperature. 582

Figure II.3.G.5 Reaction pathway, with cationic ordering coupled with reconstruction of NiO₆ octahedra, during synthesis of NMC771310, at the three sequential stages: I (below 250 °C); II (250 °C–500 °C); III (above 500 °C). The protons (H⁺), Li⁺ ions, and vacancies (V_O), are represented by magenta, green spheres and purple ellipses, respectively. 583

Figure II.3.G.6 In situ tracking of local cationic oxidation/ordering during synthesis of Ni-rich NMC with compositional heterogeneity. (a) RGB images reproduced from XRF maps of multiple particles and one selected particle (as marked by the yellow square). (b) Temperature-resolved K-edge XANES spectra for all the constituent elements (Ni, Co, Mn), recorded from the Ni-rich (core) and Mn-rich (surface) regions of a single particle (as shown in (a)). (c) Elemental re-distribution as temperature increases, demonstrated by the contour plots of the distribution of Ni, Co and Mn at representative temperatures (room temperature (RT), 500 °C and 850 °C). The X and Y axis were used to indicate the position of the single particle. Each of the sum of Ni, Co, and Mn XRF intensity was normalized to 1 for the convenience of comparison. 584

Figure II.3.H.1 (Left) Estimated cathode-oxide specific capacity and voltage requirements for next-gen EV targets (K. Gallagher). **(Right)** Pack-level cost for useable energy (\$/kWh) as a function of cell couple (S. Ahmed). Calculations performed using BatPaC (<http://www.cse.anl.gov/batpac/about.html>). 586

Figure II.3.H.2 (a) Cycle-life of NMC-532//Li and LLS//Li cells cycled between 4.45 – 2.5 V; the LLS//Li cells included a first-cycle activation between 4.6 – 2.0 V. All cycling was carried out at 15 mA/g. **(b)** LLS//LTO cycle-life between 2.9 – 1.0 V at C/10 **(c)**. LLS//Gr cell data between 4.4 – 2.5 V at C/2. All data was collected at 30°C. 587

Figure II.3.H.3 LLS//Li cell cycling data for baseline and surface-treated LLS samples under various cycling conditions (a) 1st cycle: 4.6 – 2.0 V ; All others: 4.45 – 2.5 V at 15 mA/g. **(b)** Capacity retention (%) after voltage opening test: 1st cycle 4.3 – 2.5 V; 2nd cycle 4.3 – 2.5 V; 3rd cycle cutoff 250 mAh/g; All others cycles 4.3 – 2.5 V at 15 mA/g. **(c)** Rate performance between 4.45 – 2.5 V; charge current was constant at 15 mA/g; discharge currents in mA/g are shown along the top of the figure. All data was collected at 30°C. 589

Figure II.3.H.4 (a) Cycle-life performance of an untreated LLS//Li baseline cell in traditional EC:EMC electrolyte (Gen2, red) and a high-voltage, fluorinated electrolyte (DFEC:FEMC, blue). All cycles were between 4.6 – 2.5 V at ~C/15 and 30°C. **(b-e)** SEM and EDX analysis of the cathodes cycled in Gen2 electrolyte (b, d) or fluorinated electrolyte (c, e). 590

Figure II.3.H.5 (a) LLS//Gr cell data for various treated and untreated samples collected using the HE/HV protocol. Each of the cells underwent an activation cycle between 4.5 – 2.0 V followed by continuous cycling between 4.4 – 2.5 V. **(b)** Comparison of the first-cycle dQ/dV of four cells containing untreated LLS (black), Al_100°C LLS (blue), 0.5% LiDFOB in Gen2 (red), and Al_100°C + 0.5% LiDFOB in Gen2 (green). **(c)** ASI as a function of voltage (SOC) on discharge, derived from the data in (a), for Al_100°C LLS cells using 0.5% LiDFOB in Gen2. 591

Figure II.3.I.1 In-situ heating XRD patterns of (a) 75% chemically delithiated NMC-622, **(b)** zoomed in sections of (a), and **(c)** 75% chemically delithiated NMC-811. 595

Figure II.3.I.2 Transition metal L-edge of thermal exposed to various temperatures of 75% chemically delithiated NMC 622 (a: Ni, b: Co, c: Mn) and NMC-811 (d: Ni, e: Co, f: Mn).....	596
Figure II.3.I.3 (a) soft XAS O K-edge in TEY mode which probes 5 nm of the surface and (b) X-ray Raman spectroscopy which probes the bulk of the NMC-811. Both analysis were done at 75% chemical delithiation.	597
Figure II.3.I.4 (a) In-situ heating experiments on 75% chemically delithiated NMC-811, probing the Ni oxidation changes using TXM. (b) Post heating TXM analysis on small 75% chemically delithiated NMC-811 particles, heated to 300°C.....	597
Figure II.3.J.1 Charge/discharge voltage curves of the bare and graphene-coated Cu current collectors at 0.5 mA cm ⁻² (discharge for 2 h, charge up to 2 V; 5th cycle).....	600
Figure II.3.J.2 SEM images of Li deposit on the bare and graphene-coated Cu current collectors. Li deposition was performed at 1 mA cm ⁻² for 6h at room temperature.	600
Figure II.3.J.3 Charge/discharge voltage curves of the Li//Li symmetric cells with the Al ₂ O ₃ - and LiZr ₂ (PO ₄) ₃ -filled LiTFSI:PEO membranes at the 10th cycle and 60°C.....	601
Figure II.3.J.4 Charge/discharge cycle performance of the Li//Li symmetric cells with the (a) Al ₂ O ₃ - and (b) LiZr ₂ (PO ₄) ₃ -filled LiTFSI:PEO membranes at 60 °C.	601
Figure II.3.J.5 Charge/discharge voltage curves of the Cu/Al ₂ O ₃ -filled LiTFSI:PEO membrane/Li cell at the 5 (blue), 50 (green), and 100th (red) cycles and 60 °C.....	602
Figure II.3.J.6 (a) Charge/discharge voltage curves of the LiTFSI/Cu(ClO ₄) ₂ -dissolved in PEG inside PVDF-HFP in contact with Cu foil. (Current: 20 μA). (b) Charge/discharge voltage curves of the LiTFSI/Cu(ClO ₄) ₂ -dissolved in PEG inside PVDF-HFP that is impregnated in the Cu foam. Carbon was added to the polymer membrane (red curves) to characterize its effect on the polarization. (Current: 40 μA).....	602
Figure II.3.K.1 CV plot of (a) LNMO, (b) LNRO, (c) LNRO-C, and (d) LNRO-BM. Cells were cycled between 4.8 and 2.0 V at 0.5 mV/s.	605
Figure II.3.K.2 In situ XRD patterns of LNRO during the 1 st cycle and 2 nd charge. Black curve on the bottom indicates the background from in situ pouch cell. In situ cell was cycled between 4.8 and 2.0 V at C/20 during the 1 st and 2 nd charge and C/10 during the 1 st discharge. Vertical solid and dash lines mark the pristine and new monoclinic C2/c phase, respectively.	606
Figure II.3.K.3 Structural characterization upon chemical delithiation and electrochemical cycling. (a) XRD patterns, Rietveld refinement of (b) x = 1.2, and (c) x = 0, (d, e) lattice parameters of chemically delithiated samples, and (f) XRD patterns of electrochemically cycled LNRO between 4.8 and 2.0 V, where the black and red lines in (f) mark the most representative peaks of pristine and new monoclinic C2/c phase, respectively.....	607
Figure II.3.K.4 Structural evolution during the first cycle. HAADF-STEM images of LNRO (a) at pristine state, (b) after 4.8 V charge, and (c) after 2.0 V discharge, scale bar in (a-c) is 1 nm; (d) line profiles of the regions highlighted by red dash lines in (a-c); (e) atomic models along [100], [110], and [110] zone axes of monoclinic C2/c structure; SAED patterns of LNRO (f) at pristine state, (g) after 4.8 V charge, (h) after 2.0 V discharge along [010] zone axis, insets are LNRO particles at corresponding states with a	

scale bar of 200 nm; and (i) corresponding line profiles of SAED patterns, demonstrating the reciprocal of the d spacing for (002) plane of LNRO at different states of charge.	608
Figure II.3.K.5 Microstructural evolution upon cycling. HAADF-STEM images of LNRO (a) at pristine state, (b) after 4.8 V charge, (c) after 2.0 V discharge, (d) after 10 cycles, (e, f) after 20 cycles; (g) and (h) line profiles of the regions highlighted by blue boxes in (e) and (f), respectively, where yellow arrows indicate the directions that line profiles are generated and red arrows indicate TM migration; (002) spacing in (h) region 3 is calculated between the maximum of two adjacent peaks; (i) atomic model along [100] zone axis of monoclinic C2/c structure, showing a distance of 0.43 nm between two adjacent pairs of TM in the TM layer and distance of 0.48 nm between two adjacent TM layers.	609
Figure II.3.K.6 (a) sXRD patterns, (b) voltage profiles, and (c) dQ/dV plots of $\text{Li}_{1.2}\text{Ni}_{0.8-x}\text{Ru}_x\text{O}_2$ ($x = 0.2, 0.4, 0.6$). Cells were cycled between 4.8 and 2.5 V at 5 mA/g.	610
Figure II.3.K.7 (a) In situ sXRD patterns of $\text{Li}_{1.2}\text{Ni}_{0.4}\text{Ru}_{0.4}\text{O}_2$ during the first cycle between 4.8 and 2.5 V at C/10, and (a) ex situ sXRD patterns of $\text{Li}_x\text{Ni}_{0.4}\text{Ru}_{0.4}\text{O}_2$ ($x = 1.2, 0.5, 0.2, \text{ and } 0$) prepared via chemical delithiation method.	611
Figure II.3.L.1 Cyclic voltammograms of $\text{Li}_{1.3}\text{Nb}_{0.3}\text{Mn}_{0.4}\text{O}_2$ half-cells cycled between 1.5 V and various upper cut off voltages of: a) 4.2 V, b) 4.4 V, c) 4.6 V and d) 4.8 V. The scan rate was 5 mV/min.	613
Figure II.3.L.2 Voltage profiles of $\text{Li}_{1.3}\text{Nb}_{0.3}\text{Mn}_{0.4}\text{O}_2$ half-cells cycled at 10 mA/g between the voltage window of: a) 1.5-4.2 V and b) 1.5-4.8 V, and c) Specific discharge capacity and average voltage as a function of cycle number.	614
Figure II.3.L.3 Diffusion coefficient and dQ/dV profile during: a) first charge and b) first discharge. Relationship between diffusion coefficient and cell voltage during the first 4 cycles of $\text{Li}_{1.3}\text{Nb}_{0.3}\text{Mn}_{0.4}\text{O}_2$ half cells: c) charge and d) discharge.	615
Figure II.3.L.4 O K-edge (a-f) and Mn L-edge (g-l) XAS profiles of chemically delithiated $\text{Li}_0\text{Nb}_{0.3}\text{Mn}_{0.4}\text{O}_2$ a), b), g), h) and $\text{Li}_{1.3}\text{Nb}_{0.3}\text{Mn}_{0.4}\text{O}_2$ cathodes charged to 4.8 V after various cycle numbers c), d), i), j). e) and f): Intensity of the $\text{TM}_{3d}\text{-O}_{2p}$ absorption band as a function of the cycle number. K) and l): Mn oxidation state determined from average L_3 and L_2 band.	616
Figure II.3.L.5 SEM images a) and d) and Rietveld refinement of b) and e) synchrotron XRD patterns, c) and f) neutron diffraction patterns of as-synthesized $\text{Li}_{1.2}\text{Nb}_{0.2}\text{Mn}_{0.6}\text{O}_2$ and $\text{Li}_{1.4}\text{Nb}_{0.4}\text{Mn}_{0.2}\text{O}_2$ samples. The X-ray wavelength is 0.414 Å.	617
Figure II.3.L.6 Voltage profiles a), c), e) and f) and incremental capacity (dQ/dV) profiles b), d), f) and h) of the half-cells cycled at 10 mA/g. a) and b) were collected during the first cycle, c) and d), e) and f), g) and h) were from $\text{Li}_{1.2}\text{Nb}_{0.2}\text{Mn}_{0.6}\text{O}_2$, $\text{Li}_{1.3}\text{Nb}_{0.3}\text{Mn}_{0.4}\text{O}_2$ and $\text{Li}_{1.4}\text{Nb}_{0.4}\text{Mn}_{0.2}\text{O}_2$ cells, respectively.	619
Figure II.4.A.1 (Stationary Probe Rotating Disk Electrode (SPRDE) System Coupled to Inductively Coupled Plasma Mass Spectrometry (ICP-MS).....	623
Figure II.4.A.2 (a) In situ dissolution currents for Co ion dissolution (magenta) from LiCoO_2 in 1.2 M LiPF_6 in 3:7 EC/EMC at increasing upper potential values during electrochemical polarization. Corresponding electrochemical current is shown in blue during the same polarization experiment. (b) Total mass of Co dissolved in each potential step window (left axis) and the corresponding excess positive charge measured on the disk attributed to electrolyte decomposition (right axis).	624

Figure II.4.B.1 Representative synthesis route for the proposed solvent and electrolyte based on fluorinated pyrrolidinium bis(fluorosulfonyl)imide (FDEFSI). (The proposed new synthesis is based on Lewis acid/base one-step reaction yielding highly pure FDEFSs.).....	628
Figure II.4.B.2 Capacity and capacity retention of 1 M LiFSI PMpipFSI for LiFP/Li cells (left) and charge/discharge voltage profiles (Cutoff voltage: 3.0-3.8 V; C/20 for 3 formation cycles and C/10 for 100 cycles).	629
Figure II.4.B.3 Capacity and capacity retention of 1 M LiFSI PMpipFSI for NMC532/Li cells (left) and Coulombic efficiency profiles (Cutoff voltage: 3.0-4.3 V; C/20 for 3 formation cycle and C/10 for 100 cycles).	629
Figure II.4.B.4 Capacity and capacity retention of 5 M LiFSI PMpipFSI for NMC532/Li cells (left) and Coulombic efficiency profiles (Cutoff voltage: 3.0-4.3 V; C/20 for 3 formation cycle and C/10 for 100 cycles).	630
Figure II.4.B.5 Cyclic voltammograms of the FDES/LiFSI electrolytes with 1 M, 2 M, 3 M, 4 M and 5 M LiFSI concentration. (Al electrode as working electrode and lithium as both counter and reference electrode; and glass fiber as the separator; the scan rate was 10 mV/s).....	630
Figure II.4.B.6 Cyclic voltammograms of the FDES/LiFSI electrolytes with 1 M, 2 M, 3 M, 4 M and 5 M LiFSI concentration. (SS electrode as working electrode and lithium as both counter and reference electrode; and glass fiber as the separator; the scan rate was 10 mV/s).....	631
Figure II.4.C.1 AES survey scan of an uncycled (left) and cycled (right) NMC622 cathode before (black) and after (red) a depth profile experiment.	635
Figure II.4.C.2 TOF-SIMS maps of positive ions in a cycled NMC622 cathode at 4.6 V with the hydrocarbon electrolyte. A) TIC B) Ni ⁺ C) Mn ⁺ D) Co ⁺ E) Al ⁺	636
Figure II.4.C.3 TOF-SIMS maps of negative ions in a cycled NMC622 cathode with the hydrocarbon electrolyte. A) TIC B) LiF ⁻ and LiF ₂ ⁻ C) O ⁻ D) PF ₆ ⁻ E) F ⁻	636
Figure II.4.C.4 TOF-SIMS maps of positive ions in a cycled NMC622 cathode at 4.6 V with a highly fluorinated electrolyte (1.2M LiPF ₆ , 60% EMC, 20% HFE, 20% FEC, 1% w/w PS). A) TIC B) Combined Li ⁺ C) C _x H _y O _z -Li ⁺ D) LiOH ₂ /LiOH ₃ ⁺	636
Figure II.4.C.5 TOF-SIMS maps of negative ions in a cycled NMC622 cathode with the fluorinated electrolyte. A) TIC B) C _x H _y O _z F _w C) C _x H _y O _z D) C _x H _y F _z P _w E) F ⁻	637
Figure II.4.C.6 SEM images of amorphous carbon films A) 1000 Å B) 5000 Å	638
Figure II.4.C.7 Elemental profiles of different spots on an NMC622 cathode (left). Solid lines represent that from a cycled cathode (4.6 V, fluorinated electrolyte), dashed lines from an uncycled cathode. Average AES signal of cycled NMC622 cathode (top right). Raw carbon AES signal from each depth profile (bottom right).	638
Figure II.4.C.8 Keyence thickness gauges have a linear voltage response to thickness changes in devices, up to 5 mm. These have a sub-millimeter resolution, and are capable of operating at elevated temperatures.	639

Figure II.4.C.9 200 mAh NCA cells cycled at .7C at r.t. as a function of FEC concentration (0-20% v/v) and voltage (4.2, 4.5, and 4.6).....	640
Figure II.4.C.10 Calendar life test (Δ OCV and Δ gas volume) at 55°C with 20% FEC at an OCV of 4.2 (left) and 4.6 V (right).....	641
Figure II.5.A.1 (a) AFM image, (b) XRD and (c) Raman spectrum of the NMC thin film electrode made by PLD.....	645
Figure II.5.A.2 (a) Voltammogram trace of the NMC thin film electrode and (b) FTIR-ATR spectrum of the pristine and 3 cycled NMC thin film electrode, tetraethylene glycol and polyethylene glycol standard, 1M LiPF ₆ EC/DEC=1/2 (v/v) electrolyte and EC/DEC=1/2.39 (v/v) solvent.....	645
Figure II.5.A.3 (a) CV profile of NMC thin film electrode. Scan rate: 0.2 mV s ⁻¹ Inserted plot presents a typical CV of NMC composite electrodes reported in [1], (b) <i>ex situ</i> Raman of NMC thin film electrodes at different state of charge: pristine, 1 st de-lithiation and 3 rd lithiation.....	646
Figure II.5.A.4 FTIR spectrum of cycled thin film electrode with different washing time. (a) after 3 cycles (discharge end), (b) after 1, 2 and 3 cycles, and (c) after 3 cycles vs. Li or MCMB anode.....	646
Figure II.5.A.5 (a,d) AFM morphology image of the pristine NMC thin film electrode, (b) AFM morphology image and (c) near-field IR absorbance image of cycled NMC thin film after 5s washing in DEC, (e) AFM morphology image and (c) near-field IR absorbance image of cycled NMC thin film with 5 min washing in DEC.....	647
Figure II.5.A.6 Experimental setup for impedance measurements of the NMC electrode under Ar atmosphere.....	648
Figure II.5.A.7 (a) Real-part AC impedance at 0.1Hz (b) ATR-FTIR spectra of thin-film NMC532 electrodes: pristine and after 3 and 10 cycles.....	648
Figure II.5.B.1 The minority phases identified by our data-mining approach. Panels (a) and (c) show the transmission images of the field-of-views covering particles (P37 and P46), which are identified by our method as minority phases. Panel (e) is the transmission image of another typical field-of-view that contains several normal LiCoO ₂ particles. Panels (b), (d), and (f) show the clustering results, with the four different clusters color coded to the corresponding inset. We compare the spectroscopic fingerprints of all the four clusters in panels (g) and (h). It is interesting to note that clusters 1# and 2# are both similar to LiCoO ₂ . The radar chart in panel (i) shows the differences in the spectroscopic fingerprints of all the 4 clusters are systematically captured by the data attributes extracted in our approach. The scale bar in panel (a) is 10 microns.....	653
Figure II.5.B.2 (a) Electrochemical profile of LiCoO ₂ charged to 4.6 V followed by a discharge to 3 V. The lower-left and the right insert show the structures of the pristine sample and the charged sample respectively. (b) Rietveld refinement of the NPD pattern of pristine sample and (c) Rietveld refinement of the NPD pattern of charged sample.....	654
Figure II.5.B.3 (a) xPDF data of pristine sample (symbol) and the O-O pair contribution (solid line) (b) nPDF data of both pristine and charged sample (symbol) and the O-O pair contribution (solid line). (c) The relative scattering power/length of Li, Co and O for X-ray and for neutron scattering. (d) The change of the shortest O-O pair distance from pristine sample to charged sample.....	655

Figure II.5.B.4 (a) Figure 1. Spatially resolved EELS mapping of concealed pore and exposed pore. (a) STEM-EELS mapping of a concealed pore. (i) ADF-STEM image of a concealed pore. (ii) The reference spectra used for linear composition of the Mn L _{2,3} spectra in (iv). (iii) The linear decomposition coefficient as a function of the vertical spatial location. (iv) The EELS spectra of Mn L _{2,3} edges across the surface and the concealed pore. (b) STEM-EELS mapping and atomic-resolution imaging of an exposed pore. (i) ADF-STEM image of an opened pore. (ii and iii) The Mn (ii) and oxygen (iii) composition extracted from the quantification of the EELS map. (iv) Atomic resolution image of the open pore	656
Figure II.5.C.1 STEM/ABF images of (a) uncoated LRLO and (b) LRLO material coated with 1wt% LLTO. (c) EELS Ti-L edge spectra at surface regions of LRLO sample coated with LLTO before and after cycling. (d, e) ABF and HAADF images of LRLO material coated with LLTO after cycling. (f) EELS O-K edge spectra of LRLO sample coated with LLTO after cycling collected at bulk and surface region, respectively	660
Figure II.5.C.2 First charging comparison of (a) electrochemical performance and (b) strain generation for LRLO electrode under different rate. (c, d) The strain distribution along the [003] direction inside of the nanoparticle charged at 50 mA/g for two representative states of charge. The scale bar is 100 nm.	661
Figure II.5.C.3 Operando evolution of a LRLO nanoparticle during electrochemical charge at different rates including the changes in the displacement field along q_{003} and the strain along the [001] direction (perpendicular to the layers) inside of the nanoparticle calculated from the 3D displacement fields.	661
Figure II.5.C.4 HRTEM image, ED, and intensity of reciprocal lattice from line-scanning on single particle for the LRLO sample after 50 cycles (a) and after heat treatment at 300°C (b). Models of cycled and heat treated LRLO for ED simulation (c). Simulated ED patterns for LRLO with different degree of stacking faults (d).....	662
Figure II.5.C.5 Correlation between voltage decay and defects generation. a. Schematic illustration of free energy differences due to different oxygen stacking sequences (green, Li; red, O; purple, Mn; blue, Ni). b. The Gibbs free energy for each delithiation composition of the supercell with O ₃ and O ₁ stacking. c. Calculated voltage of supercell $\text{Li}_{1-x}\text{Ni}_2\text{Mn}_5\text{O}_{18}$ ($0 \leq x \leq 4$) for stacking sequence O ₃ and O ₁ . d. Schematic illustration of the Gibbs free energy profiles for the conversion between pristine and cycled LRLO.	663
Figure II.5.C.6 Cryo-TEM images (a, b, d, e) with their corresponding area FFT analysis (c, f) of the deposited Li metal using electrolytes containing Cs ⁺ (a-c) and Zn ²⁺ (d-f) additives at 400 kx magnification.	663
Figure II.5.C.7 Compared XPS spectra of the survey (a), C 1s (b), F 1s (c), Li 1s (d), Cs 3d (e) and Zn 2p (f) with the deposited Li metal from the pristine, Cs ⁺ and Zn ²⁺ containing electrolytes.	664
Figure II.5.D.1 HAADF-STEM images of layered-to-disordered rock salt phase transition at the low cycling rate. (a) HAADF-STEM image of the pristine sample showing the majority of the bulk maintains $R\bar{3}m$ structure. The white and green arrows point to the TM layer and Li layer, respectively. (b and c) HAADF-STEM image of the 200-cycle sample at 0.33C and 1C, respectively. The blue dashed lines outline the boundary of the converted phase, below and above which are the disordered rock salt and layered structure, respectively. (d–g) The enlarged view of the pristine bulk, pristine surface, 0.33C 200-	

cycle surface, and 1C 200-cycle surface from area 1, 2, 3, and 4 in panels a–c, respectively. (h–j) Atomic structure corresponding to the panels d, e, and f, respectively 668

Figure II.5.D.2 Infusion of Li_3PO_4 into secondary particles eliminates structural degradation. The structural degradations are evaluated by a combination of SAED a-c, bright-field TEM imaging d-f, STEM-HAADF imaging g-i, and atomic-level STEM-HAADF imaging j-l (corresponding to the high magnification image of the redline marked regions). The left column corresponds to the pristine electrode without cycling, the middle column is the pristine electrode after 200 cycles, and the right column shows the Li_3PO_4 -infused electrode after 200 cycles. These observations demonstrate that after 200 cycles, the pristine electrode shows significant structural degradation, featuring intergranular cracking and formation of amorphous phase within the grain boundaries (e), formation of surface reaction layer on each grain surface (indicated in h by the yellow arrows), and layered-to-spinel transformation (k), while these degradation features do not occur in the Li_3PO_4 -infused electrode. The scale bars are 5 nm^{-1} in a-c, 500 nm in d-f, 100 nm in g-i, and 2 nm in j-l..... 669

Figure II.5.D.3 In situ heating-induced crack nucleation and propagation. The $\text{LiNi}_0.6\text{Mn}_0.2\text{Co}_0.2\text{O}_2$ (NMC622) was delithiated by charging to 4.7 V vs. Li metal. a and b High angle annular dark field (HAADF) images from delithiated NMC622 before heating (room temperature). c-f HAADF images after heating to 275 °C. Selected area electron diffraction (SAED) patterns and fast Fourier transformation images in (a), (c), and (e) show the overall lattice change during heating. d, e, and f show local lattice structure change at crack regions and crack-free regions. The scale bars are 200 nm in (a) and (c); 10 nm in (b) and (d); and 4 nm in (e) and (f). 670

Figure II.5.E.1 Design of 3-omega thermal sensors and how they are incorporated into an electrochemical battery pouch cell for in-operando measurements. 674

Figure II.5.E.2 Raw 3-omega data for an in-operando measurement of a full Li-ion battery showing the extended frequency range of our upgraded system..... 674

Figure II.5.E.3 Newly built Cut Bar system that uses linear heat flow to accurately measure the thermal conductivity of isolated battery components ex-situ. Bottom-right: data from Cut Bar measurements on dry cathode samples. By measuring samples of varying thickness, we can separate out the effects of thermal contact resistance and intrinsic thermal conductivity. 675

Figure II.5.F.1 **Reversible redox and phase behavior of $\text{Li}_{2-x}\text{IrO}_3$.** (a) Capacity-voltage curves of $\text{Li}_{2-x}\text{IrO}_3$ galvanostatically measured at a C/12 rate (17.58 mA g^{-1}) in 4.50-2.50 V for the initial three cycles and the stable phases during the two consecutive two-phase reactions of $\text{Li}_{2-x}\text{IrO}_3$ occurring at each voltage plateau obtained by combined XRD Rietveld refinements and DFT calculations. (b) *Operando* transmission XANES spectra of Ir L_3 edge for charging (left) and discharging (right) with two isosbestic points (arrows in insets). (c) Shift of the white line energy showing the continuous oxidation/reduction of iridium throughout the whole charge/discharge processes. Error (see methods) was determined to be reasonably small. (d) Linear combination analysis of the three end-members obtained through NMF, consistent with the phase behavior..... 679

Figure II.5.F.2 **Hybridized Ir-O redox in $\text{Li}_{2-x}\text{IrO}_3$.** (a) sXAS fluorescence yield spectra (solid lines) and STXM (scanning transmission X-ray microscopy)-XAS spectra (dashed lines) of O K edge of $\text{Li}_{2-x}\text{IrO}_3$ at various states of charge in the first cycle. From bottom to top, pristine (red, A), charged to 3.9 V (yellow, B), charged to 4.6 V (green, C), discharged to 3.7 V after being charged to 4.6 V (olive, D), discharged to

2.5 V after being charged to 4.6 V (blue, E). (b) Difference plot of sXAS obtained from A showing the hole population evolution of Ir $5d-O 2p t_{2g}$ and e_g^* hybridized state. (c) Ratio of the area of Ir $5d-O 2p t_{2g}$ peak and Ir $5d-O 2p e_g^*$ peak measured by RIXS, STXM and sXAS. (d) O K edge RIXS maps of Li_2IrO_3 , $LiIrO_3$ and $Li_{0.5}IrO_3$ showing conventional Ir-O cationic redox. The right bottom panel shows the RIXS spectra of each composition at 530.7 eV excitation energy where the anion redox feature is expected to appear.....	680
Figure II.5.F.3 (a) Charge/discharge profiles of $Li_{2-x}Ir_{1-y}Sn_yO_3$ ($y=0, 0.25, 0.5$) under a constant current density (C/10 rate) for a full cycle (black) and for an approximately 1.5 electron per Ir per f.u. cycle (pink). (b) In-plane and out-of-plane disorders quantified by iterative XRD Rietveld refinement for the LISO25 cycled in 4.60-2.50 V and 4.25-2.50 V and LIO cycled in 4.60-2.50 V, quantified by the total VM concentration. The scheme illustrates the in-plane (top) and out-of-plane (bottom) structural disordering mechanisms resulting in VM, with the migrated cation octahedron shaded yellow and the Wyckoff positions indicated in parentheses. (c) Operando transmission XANES spectra of Ir L3 edge for the first cycle showing the continuous Ir oxidation up to 4.25 V, no shift beyond 4.25 V, and the continuous Ir reduction during discharge.....	681
Figure II.5.G.1 Stress-thickness response during plating sequence and OCV hold of 5 consecutive symmetric cycles. a: -265uA/cm ² for 5hrs; b: -265uA/cm ² for 10hrs.	684
Figure II.5.G.2 Schematic of Li flow between the conductive paths and Li metal surface during plating/stripping cycles.	685
Figure II.5.G.3 Stress-thickness evolution predicted from the kinetic model.....	685
Figure II.5.G.4 (a-c) Finite element modeling of morphological evolution of SEI on Li metal anode (a) before 1st Li plating half-cycle; (b) after the 1st Li plating half-cycle; (c) after the 1st Li stripping half-cycle. (d) Stress×thickness response of the SEI.....	686
Figure II.5.G.5 A phase diagram of wrinkling and delamination of a thin film protective coating on a Li metal electrode.	687
Figure II.5.G.6 (a) The distribution of von Mises stress in bulk Li after nanoindentation. (b) Microstructure of an indent in a Li foil after it is stored inside an Ar-filled glovebox for 30 days at room temperature. The insert shows the stress distribution on Li surface along the red line direction.	687
Figure II.5.G.7 (a) The schematic diagram of a Swagelok cell. Microstructure of mossy Li plated under (b) 4.85 MPa and (c) 19.39 MPa.....	688
Figure II.5.G.8 XPS depth profiling spectra of plated Li surfaces after a half cycle (0.5 mA cm ⁻² , 4 mAh cm ⁻²) in 4 different electrolytes (4 M LiFSI DME, 0.4 LiTFSI + 0.6 M LiNO DOL-DME, 1 M LiTFSI DOL-DME, and 1 M LiPF ₆ EC-DEC)	689
Figure II.5.G.9 Self-forming nanocomposite has a unique nanostructure where LiF nanocrystals embedded in polymeric matrix (a); The cross-section image showing the coating is dense and has good adhesion to Li metal (b).	691
Figure II.5.G.10 The combination of the protective coating with high concentration LiFSi in DME enables the long cycle stability.	691

Figure II.5.H.1 XAS results of various elements in $\text{Li}_{1.2}\text{Ni}_{0.15}\text{Co}_{0.1}\text{Mn}_{0.55}\text{O}_2$ at different cycles. Transmission mode transition metal K-edge XAS spectra for Mn, Co and Ni, and fluorescence mode O K-edge XAS of samples at the 1st, 2nd, 25th, 46th, and 83th cycle. For each element, charged and discharged graphs are plotted using the same scale.	697
Figure II.5.H.2 Three-dimensional electron tomography reconstruction of $\text{Li}_{1.2}\text{Ni}_{0.15}\text{Co}_{0.1}\text{Mn}_{0.55}\text{O}_2$ materials. (a and b) volume rendition and progressive cross-sectional view of cathode particles at the (a) pristine state, and (b) after 15 cycles. (c and d) Internal pore size distribution of the pristine sample weighted by occurrence (c) and by volume (d). (e and f) Internal pore size distribution of the cycled sample (15 cycles) weighted by occurrence (e) and by volume (f). The green and orange lines in (c) and (e) are single-Gaussian and bi-Gaussian fitting of the pore size histogram. The reweighting by volume in (d and f) are applied to the fitted curves.	697
Figure II.5.H.3 (a) CV scan (black) of the fresh graphite electrode in 1 mol/L LiPF_6 EC/DMC at 1 mV/s from OCP (3.0 V) to 0.0 V, and the simultaneous EQCM responses (blue) recorded; (b) AFM topological imaging of HOPG during the CV scan, where the long white arrows indicate the scan directions, and the length of scale bar is 1.0 μm ; (c) Further analysis of first SEI formation scanning from 0.90 V to 0.36 V, and the length of scale bar is 1.0 μm ; (d) The height distribution (the black curve) of SEI on the stage labeled by a blue line, and the datum line of height (the red curve) is extracted from the first image of Figure 1b.	699
Figure II.5.H.4 the thermal stability of the PET-based separator	700
Figure II.5.H.5 Thermal runaway characterization of 25-Ah SC-NMC532/graphite cell	700
Figure II.6.A.1 (a) One dimensional model geometry for the electrode-electrolyte interfacial region; (b) phase field model converts the sharp interface into a continuous interfacial region by a phase parameter; (c) electrochemical reactions assumed for the Li_2S precipitation process in the battery discharge process; (d) electrochemical/ chemical reactions assumed for Li_2S removal during battery charge process.	705
Figure II.6.A.2 (a) Demonstration of inhomogeneous SEI resistance, which may have a sharp variation (black line) or a wide drop (red line). (b) Initial lithium-electrolyte interface, which is flat. (c) Sharp drop in SEI resistance leads to growth of a thin dendritic protrusion. (d) Wider variation in SEI resistance forms a thick dendritic protrusion.	706
Figure II.6.A.3 (a) Increase in height of dendritic protrusions with time for sharp and wide drop in SEI resistance. Growth of dendrites decrease with time because of increase in surface area and surface curvature induced suppression mechanisms. (b) As the surface energy between lithium and electrolyte increases, the width of the dendritic protrusion increase (red circles), and the aspect ratio of the protrusions drop (black squares).	706
Figure II.6.A.4 (a) Computational mesh used to understand the growth of dendritic protrusions under the presence of SEI layer. Internal heterogeneity of the SEI at the left boundary leads to faster transport of reacting species, which eventually leads to the growth of dendritic protrusions. (b) Potential distribution within the electrolyte during operation under specified conditions. (c) Concentration distribution within electrolyte under the same operating condition specified above the figures. Larger gradients of both potential and concentration are observed within the SEI.	707

Figure II.6.A.5 (a) Growth of dendritic protrusions with time under applied current density of $100\text{A}/\text{m}^2$. Increasing thickness of a stiff SEI layer helps to prevent dendrite growth. (b) Height of the dendritic protrusion with increasing SEI stiffness. Increase in applied current density helps to grow the dendritic protrusion. (c) Increasing surface energy density between lithium and electrolyte helps to suppress the dendritic protrusion. However, the impact of surface energy density minimizes at extremely high currents of operation ($\sim 100\text{A}/\text{m}^2$).	707
Figure II.6.A.6 (a) Modeled Li_2S film growth on the active carbon surface in the discharge, and Li_2S film removal in the charge; (b) Li_2S film thickness growth under different discharge current conditions: $100\text{mA}/\text{cm}^2$, $200\text{mA}/\text{cm}^2$ and $480\text{mA}/\text{cm}^2$; (c) Simulated Li_2S film thickness variation under different charge current conditions.	708
Figure II.6.A.7 Effect of the S_4^{2-} solubility on the evolution of Li_2S film thickness on top of carbon substrate. (a) During discharge, decreasing the solubility of S_4^{2-} helps to delay the surface passivation. (b) Similarly, at the time of charge, decreasing S_4^{2-} solubility slows down the dissolution of Li_2S film.	708
Figure II.6.B.1 Experimentally measured conductivity as a function of salt concentration for LiAsF_6 and LiPF_6 in dimethyl carbonate (DMC). The bottom rectangles (left to right) illustrate the neat solvent, an electrolyte with only associated salt (with dipole moments drawn as directed arrows), and finally an electrolyte with both associated (arrows) and dissociated salt (no arrows). [1]	711
Figure II.6.B.2 Free energy of dissociation for LiAsF_6 (black) and LiPF_6 (blue) into their respective free ions as computed from first principles using the polarizable continuum model (PCM). [1]	711
Figure II.6.B.3 Formation energy of crystalline and amorphous a) lithium silicides and b) lithium silicates, following lithiation path from Si and SiO_2 , respectively, as seen on the c) phase diagram.	712
Figure II.6.B.4 Predicted potential profiles for a) Si and b) SiO_2 as referenced to the phase diagram in Figure II.6.B.3.	713
Figure II.6.B.5 Li self-diffusivity diffusion coefficients in lithium silicides and lithium silicates as a function of voltage vs Li/Li^+ .	713
Figure II.6.C.1 LiCoO_2 - LiF phase diagram [6].	716
Figure II.6.C.2 (a) Local fluorine environments present in $\text{Li}_{1.125}\text{M}_{0.875}\text{O}_{1.75}\text{F}_{0.25}$ disordered rocksalt phases. (b) Superposition of the low fluorine region of the phase diagrams obtained for the Ti, V, Cr, Mn, Fe, Co, and Ni LMO systems [6].	717
Figure II.6.C.3 (a) XRD, (b) STEM-EDS mapping from $\text{Li}_2\text{Mn}_{2/3}\text{Nb}_{1/3}\text{O}_2\text{F}$, (c) SEM [1].	717
Figure II.6.C.4 (a) Electrochemical performance of LMNOF. (b) A schematic band structure of $\text{Li}_2\text{Mn}_{2/3}\text{Nb}_{1/3}\text{O}_2\text{F}$ [1].	718
Figure II.6.C.5 Computed phase diagram of MnO - Li_2VO_3 - LiF . [4].	718
Figure II.6.C.6 Computed voltage profile and evolution of Mn and V oxidation states (from DFT) [4].	719
Figure II.6.C.7 Comparison between observed and theoretical capacities for ST-LMVF20, ST-LMVO, MR-LMVF20, and LR-LMVF20 compounds [4].	720

Figure II.6.C.8 Distribution of (a) F-cation and (b) Li-anion environments by coordination number, among simulated partially charged structures derived from ST-LMVF20, according to the voltage at which they appear [4].....	720
Figure II.6.D.1 Large-format Shapeoko CNC stage produced by Carbide 3D, with a custom made N-line probe attachment.....	723
Figure II.6.D.2 Measured bulk conductivity and contact resistance values (with 95% confidence intervals) on ANL AC006 cathode film using both large-format (“Big Red”) and high-resolution stages, compared to results from the (old) rigid 4-line probe.....	724
Figure II.6.D.3 Converted Carbide 3D CNC stage with custom rolling N-line probe attachment.	724
Figure II.6.D.4 Conductance measurements over a 40-mm segment of battery electrode film, showing areas of no, minimal, and good contact. The measurement is repeated eight times with the probe rolled back forth over the same segment.....	725
Figure II.6.D.5 The experimental setup of a microprobe in contact with a sample of delaminated cathode.	726
Figure II.6.D.6 Nyquist spectra of different electrolyte samples with conductivities varying from 82 to 443 $\mu\text{S}/\text{cm}$	726
Figure II.6.D.7 Average MacMullin number versus localized ionic resistance for 7 different electrode films.	726
Figure II.6.D.8 Optical microscope images of probe surface (a) before durability tests, (b) after a total of 3,000 sampling points, (c) after a total of 7,000 points, and (d) after a total of 10,000 points.	727
Figure II.6.E.1 A sandwich system with Li-S and Mn hexaaminobenzene system with the maximum lithiation of 20 Li per 8 S atoms. The top view and side view. The green ball is Li and yellow ball is S.	730
Figure II.6.E.2 The energy landscape by pulling one Li through the system. One can use such landscape to estimate the barrier height.....	730
Figure II.6.E.3 The Li polysulphides free energies calculated with solvent model (Sol), compared with the results in vacuum (Vac), and the reference curve derived from experiment (Ref).	730
Figure II.6.E.4 A sandwich system with Li-S and Mn hexaaminobenzene system with the maximum lithiation of 20 Li per 8 S atoms. The top view and side view. The green ball is Li and yellow ball is S.	731
Figure II.6.E.5 The energy landscape by pulling one Li through the system. One can use such landscape to estimate the barrier height.....	731
Figure II.6.E.6 The mixing of the $\text{Li}_{10}(\text{GeS}_4)(\text{PS}_4)_2$ structure and the $\text{Li}_{10}(\text{GeO}_4)(\text{PO}_4)_2$ structure to form the $\text{Li}_{10}(\text{GeS}_4)(\text{PO}_4)_2$ structure.	731
Figure II.6.E.7 The chemical decomposition energy of $\text{Li}_{10}\text{GeP}_2\text{S}_{12-x}\text{O}_x$ system (green), and the moisture caused reaction energy (purple). Negative energy indicates the instability, while positive energy indicates the stability against the reaction.....	732

Figure II.6.E.8 Mean square displacements (MSD) of Li-ions along three different crystallographic directions as well as the overall value, obtained from the ab initio molecular dynamics trajectory at 800 K; within LGPSO: $\text{Li}_{10}(\text{GeS}_4)(\text{PO}_4)_2$ (a) and LGPS: $\text{Li}_{10}(\text{GeS}_4)(\text{PS}_4)_2$ (b). The a, b, c in (a) and (b) denotes for diffusion in the a, b, c directions. Inset shows the same for LSnPSO: $\text{Li}_{10}(\text{SnS}_4)(\text{PO}_4)_2$. (c) Li-diffusivity (D) at various temperature (T) are fitted linearly for: LGPS, LGPSO, LSnPSO and corresponding Li-migration barriers (in eV) are given.	733
Figure II.6.F.1 upper panel, the observed Li (left) and Mg (right) plating morphology from Yoo et al.[1]. Lower panel, the simulated morphology difference of Li and Mg plating.	735
Figure II.6.F.2 Improved cycle life with carbon coated Li-electrode.	736
Figure II.6.F.3 Compare the total density of states between bulk and slabs of (a) c-LLZO and (b) LIPON and (c) the solid electrolyte properties that relate to Li-dendrite resistance.	737
Figure II.6.F.4 Phase-field simulation results of Li dendrite growth and nucleation at straight grain boundaries with different widths under constant voltage condition at 100s: (a) Li dendrite morphology, (b) overpotential distribution, (c) Li-ion concentration distribution and (d-f) stress distribution.....	737
Figure II.6.F.5 (a) Voltage profiles of Li-Li symmetrical cells cycled in baseline electrolyte (1 M LiPF_6 in a mixture of ethylene carbonate and diethyl carbonate with a mass ratio of 1:2) with 5wt% additives. The current density is 1 mA cm^{-2} and the capacity density is 4 mAh cm^{-2} . (b) C 1s, F 1s, and S 2p XPS spectra and (c) schematic of SEI compositions associated with Li metal electrode after one charge in baseline electrolyte with 5wt% 1,2-propyleneglycol sulfite.	738
Figure II.7.A.1 Indentation of Li thin films. Plots at left are typical the load displacement curves to a maximum of $250 \mu\text{N}$, followed by 60 sec hold and unload. At right are average values for the hardness collected for many indents and different samples. The indentations were conducted at different strain rates and different thicknesses of Li films.	742
Figure II.7.A.2 Instron and sample setup for Li adhesion test (left). The area specific resistance of the Li/LLZO/Li determined by electrical impedance correlates with the Li-LLZO adhesion (right).	743
Figure II.7.A.3 Average CCD for our recent studies compared to earlier published results. Most of the studies showed little change with increasing temperatures (left). The Arrhenius plot (right) determines an activation energy.	743
Figure II.7.A.4 Indentation of Lipon thin films showing creep behavior for constant load at different displacements from the surface (left). The stress exponent (right) was determined for the power law dependence strain rate dependence.	744
Figure II.7.B.1 XPS analysis of LLZO before and after heat treatment at 400 and 500°C. a) C:(La+Zr) atomic ratio as a function of heat treatment temperature, b) O 1s and c) C 1s core levels, d) percentage of total composition of different oxygen species on the LLZO surface as a function of heat treatment temperature after wet polishing (WP).	747
Figure II.7.B.2 Contact angle measurements of molten metallic Li on a) Li_2CO_3 , b) DP-LLZO, c) WP-LLZO, d) WP-LLZO after heat treatment at 500°C.	748
Figure II.7.B.3 Calculated work of adhesion (W_{ad}), contact angle (θ), and atomic structure for the a) Li- Li_2CO_3 and b) Li-LLZO interfaces.	749

Figure II.7.B.4 a) Schematic of the all solid-state Li-LLZO-Li cell, b) the equivalent circuit used for modeling the EIS data c) representative Nyquist plot of the Li-LLZO-Li cell (for LLZO heat-treated at 500°C), as-assembled (○) and after preconditioning at 175°C (●). Markers indicate experimental data and dotted lines are simulated lines extrapolated from the equivalent circuit modeling using the circuit shown in b, d) the Li-LLZO interfacial resistance after preconditioning at 175°C versus the heat-treatment temperature. N=3 for each HT condition. Error bars represent standard deviations.	749
Figure II.7.B.5 a) DC cycling of Li-LLZO-Li cells (LLZO HT to 500°C after WP) at room temperature, stepping the current density from 0.01 to 1 mA.cm ⁻² , b) the critical current density versus Li-LLZO interfacial resistance comparing the result of this study with other studies available in the literature, c) Nyquist plots of Li-LLZO-Li cell after each 20 cycles for cell cycled 100 time, d) Galvanostatic cycling of Li-LLZO-Li at 0.2 mA.cm ⁻² for 100 cycles at 0.4 mAh.cm ⁻² . The blue dotted line shows the times at which EIS was collected and is shown in c.	750
Figure II.7.C.1 Tri-layer sample configuration (left). Comparison of area specific resistance dry and with DMC additive (center). Extracted resistance attributed to polymer-ceramic interface (right).	754
Figure II.7.C.2 Cycling of batteries comparing performance with PE-only with a bilayer electrolyte of PE coated CPE. Cycling capacities at 75°C (left). Voltage profiles for cycle 15 (right). Capacity is normalized to mass of the composite cathode.	755
Figure II.7.C.3 Ionic conductivity comparing dry and plasticized electrolytes of different compositions (left). DC symmetric cycling at +/- 50μA/cm ² for plasticized ceramic-free polymer gel versus composite gel (right).	756
Figure II.7.D.1 Characterization of garnet fibrous membrane: left, Reconstructed model of garnet membrane flatness generated by 3D laser scanning; right, Focus ion beam analysis of the typical fiber bundle structure.....	759
Figure II.7.D.2 Characterization of hybrid electrolyte membrane: left, AFM scanning of the hybrid electrolyte membrane; right, Thermal properties of the hybrid electrolyte membrane	760
Figure II.7.D.3 Sintered garnet nanofiber membrane from PAN fiber template. Sample was impregnated with epoxy.....	760
Figure II.7.D.4 Hybrid electrolyte membrane with ~11 μm thickness	760
Figure II.7.D.5 Electrochemical impedance of the Li/electrolyte/Li symmetrical cell at room temperature (left); Cycling of the cell at different current densities of 0.1 mA/cm ² , 0.5 mA/cm ² and 3 mA/cm ²	761
Figure II.7.D.6 Formation energy of point defects in LLZO (left) and Li ion diffusion in LLZO grain boundary (right) from atomistic modeling	762
Figure II.7.D.7 Hot map of Li dendrite formation in SSE with various microstructure features	762
Figure II.7.D.8 Electrochemical cycling of the Li/electrolyte/Li symmetrical cell, including low current density stabilization at 0.1 mA/cm ² and high current density cycling at 3 mA/cm ² (top); enlarged plot at 3 mA.cm ² for 500 cycles without lithium dendrite penetration (bottom)	763
Figure II.7.E.1 (a) Cross-sectional views of Li metal anodes retrieved from Li NMC cells after 100 cycles at 1.75 mA cm ⁻² using different dual-salt electrolytes. (b) cycling performances of the baseline LiPF ₆	

electrolyte and the four different dual-salt electrolytes at a current density of 1.75 mA cm^{-2} after three formation cycles at 0.175 mA cm^{-2} .	766
Figure II.7.E.2 (a) The average Li CE values of the LiTFSI-LiBOB/EC-EMC (7:3 by wt) electrolytes with single additive of LiPF_6 , VC, and FEC, and the combinational additives of $\text{LiPF}_6 + \text{VC}$, $\text{LiPF}_6 + \text{FEC}$, and $\text{LiPF}_6 + \text{VC} + \text{FEC}$. The weight percentages of LiPF_6 , VC, and FEC are 0.6, 2.0, and 2.0%, respectively. (b) Cycling performances of Li NMC cells using the three electrolytes of ELY-14, ELY-19, and ELY-13 at the same charge and discharge current density of 2.0 mA cm^{-2} after 3 formation cycles at 0.2 mA cm^{-2} at 60°C .	767
Figure II.7.E.3 (a) Average CE values of Li metal in electrolytes with LiDFP additive from 0 to 0.15 M. (b) Cycling stability of Li Li symmetric cells in the electrolytes without and with various contents of LiDFP additive at the current density of 1.0 mA cm^{-2} with 1 h plating/stripping time at 25°C . Inserted are SEM images of Li anodes in Li Li cells at 1.0 mA cm^{-2} with 1 h plating/stripping time for 100 cycles without and with LiDFP.	768
Figure II.7.E.4 (a) Cyclic voltammogram curves of Li Li Pt three-electrode cell containing HPISE at a scan rate of 0.5 mV s^{-1} in the voltage window of -0.2 V to 5.0 V at room temperature. (b) Temperature dependence of ionic conductivity of HPISE without and with GF separator. (c) Voltage profiles of a coin cell of Li NMC333 (2 mAh cm^{-2}) with GF separator soaked with HPISE cycled using a charge rate of C/5 and a discharge rate of C/3 between 3.0 V and 4.2 V at 60°C , where $1\text{C} = 2.0 \text{ mA cm}^{-2}$. (d) The corresponding cycling performance of the cell.	769
Figure II.7.F.1 Charge density difference profile when a Li ion is deposited on top of a defective Li surface. Yellow: charge density accumulation. Light blue: Charge density depletion.	773
Figure II.7.F.2 Atomic configuration and energy profile of a knocked-off Li atom entering the gap site. Panels (A) through (E) show atomic configurations of the diffusion pathway of the Li atom knocked-off by a Li entering the gap site. Orange, grey and red spheres represent Cu, C and O atoms, respectively. Li atoms adsorbed at the GO layer are shown in a line display style for clarity. The green and blue spheres represent the Li atoms entering the gap site and the displaced Li atoms, respectively. (F) Energy profile for the Li transport through gap site.	774
Figure II.7.F.3 (a) MD simulation setting (side views): anode surface (blue) covered by SEI (LiF , yellow). The SEI has a crack (shown as a blue spot in (a)). In green the electrolyte phase and Li ions are small purple spheres. Electrolyte (green) access the SEI crack in direct contact with the anode surface leading to Li^+ deposition and dendrite formation. (b), (c) and (d) show time evolution of the dendrite growth as the Li ions are deposited and plated in the crack region.	775
Figure II.7.F.4 (a) Electrodeposition morphology phase map for Li deposition as a function of Damkohler number. Yellow zone corresponds to $\text{Da} \gg 1$ (dendrite morphology), green zone corresponds to $\text{Da} \sim 1$ (island type deposits) and blue zone corresponds to $\text{Da} \ll 1$ (uniform film type deposits). Electrode operating regime for Li deposition on Li/Cu falls inside the white box. (b) KMC derived morphology map for Li deposition on the copper current collector in terms of local overpotential and surface self-diffusion, and four regions are presented: deposited Li can form metal film, needle-like Li, porous metal film, and dendrite. Purple is deposited Li, and red dots are Li-ions.	776

Figure II.7.F.5 Effect of the Li surface diffusion rate k_f on the electrodeposition rate and morphology of the deposited film; k_{f0} is the rate of diffusion calculated using activation energy of Li diffusion on the (100) plane.	776
Figure II.7.G.1 a) Coulombic Efficiency of Li plating on MPF with organic coating, without coating, and on an unmodified copper foil. b) Nucleation overpotential for Cu foil, Cu foam, and organic layer-Cu foam during the first 50 cycle.	779
Figure II.7.G.2 SEM images of (a) pristine lithium foil, (b) lithium foil imprinted with 300 grit sandpaper, and (c) 2500 grit.	780
Figure II.7.G.3 a) Nucleation potential for various surface modified lithium-metal foils at different current densities. Sand's time experiment showing potential vs time for symmetric Li/Li cells for a) P-Li and b) SE-Li.	780
Figure II.7.G.4 SEM images of a) surface engineered Lithium, b) Li plating on SE-Li and c) cycled SE-Li. d) Cycling behavior of LiMn_2O_4 cathode tested against P-Li and SE-Li.	781
Figure II.7.G.5 Voltage-time curve for symmetric Li/Li cells using composite polymer electrolytes a) CPE-III and b) CPE-VI (~200 cycles). SEM images of lithium-metal after cycling in symmetric Li/Li cells with c) CPE-III and d) CPE-VI after ~200 cycles).	782
Figure II.7.G.6 a) Variation of heterogeneous nucleation barrier with contact angle, b) Plating/ stripping behavior of an efficient electrode showing zero nucleation underpotential and invariant growth potential with time and cycle numbers, c) the charge/discharge capacity along with coulombic efficiency of an efficient electrode, d) Plating/stripping behavior of multicomponent alloy showing high coulombic efficiency.	784
Figure II.7.H.1 (a) Linear sweep voltammetry curve of the PEO/LiTFSI and PEO/LiTFSI/LLTO 15 wt% solid composite electrolytes. (b) Voltage profile of the continued lithium plating/stripping cycling of PEO/LiTFSI/LLTO 15% electrolyte tested at a current density of 0.5 mA cm^{-2} at 25°C (inset: voltage profiles of the PEO/LiTFSI/LLTO 15% electrolyte tested at 710–720 h).	787
Figure II.7.H.2 (a) Schematic illustration showing the structure with and without Li_3PO_4 coating on the LLTO nanofibers. (b) Voltage profile of $\text{Li} \text{PVDF-HFP} \text{LiTFSI}/\text{LLATO}/\text{Li}_3\text{PO}_4 \text{Li}$ at a current density of $0.5 \text{ mA}/\text{cm}^2$. (c) LSV curve of the FRPC electrolyte membrane to show the electrochemical stability window in the range of 0–6 V. (d) Voltage profile of $\text{Li} \text{PVDF-HFP} \text{LiTFSI}/\text{LLATO} \text{Li}$ at a current density of $0.5 \text{ mA}/\text{cm}^2$	788
Figure II.7.H.3 The procedure for synthesis of cross-linked poly(ethylene oxide) solid-state electrolyte (CLPSE).	789
Figure II.7.H.4 Schematic illustration of the CNF/S-PEO/LLTO bilayer structure: the top thin PEO/LLTO solid composite electrolyte layer acts as the Li-ion conductor, enabling fast ion transport between cathode and anode; and the bottom PEO filled CNF/S nanofiber layer with intimate triple-phase contact of electrical conductive current collector (CNF), active material (S) and solid polymer electrolyte (PEO), providing a balanced dual-conductive architecture for continuous electron/ion transfer. The entire bilayer structure can be placed on the top of the anode surface to form a Li-S full cell without the use of an additional electrolyte or a separator.	790

Figure II.7.I.1 Possible molecular conformation of aromatic-based Li organosulfide (a) and Li organopolysulfide (b) originating from PSD polymer; alkyl amine-based Li organosulfide (c) and Li organopolysulfide (d) originating from PST polymer.	793
Figure II.7.I.2 The photos of PSD-90-Ely before cycling (a) and after 1st cycle of Li plating/stripping: (b) with separator covering on stainless steel, (c) separator was peeled off.....	793
Figure II.7.I.3 Cycling performance of 2 wt% PSDs containing different sulfur contents as additives. ...	793
Figure II.7.I.4 Cycling performance of cells using electrolytes containing different contents of SCPs. ...	794
Figure II.7.I.5 Morphologies of Li metal deposited onto stainless steel substrates. SEM images of Li metal deposited onto bare stainless steel substrates in the control electrolyte (a-c), and the electrolyte containing 8 wt% PSD-90 (d-f) at a current density of 2 mA cm ⁻² and a deposition capacity of 2 mA h cm ⁻² after 10 cycles of Li plating/stripping.	794
Figure II.7.I.6 SEM images of the deposited Li after 100 cycles at a current density of 2 mA cm ⁻² and a deposition capacity of 2 mA h cm ⁻² . (a, b) Top view and cross-section view of deposited Li using the electrolyte containing 8wt% PSD-90. (c, d) Top view and cross-section view of deposited Li using the control electrolyte.	795
Figure II.7.I.7 The XPS spectra of SEI layers formed from the electrolytes containing different additives. S 2p XPS spectra (a), C 1s XPS spectra (b), and F 1s XPS spectra (c) of the SEI layers formed from different electrolytes.	795
Figure II.7.I.8 FT-IR of SEI layers obtained from the C-Ely (C-SEI) and the PSD-90-Ely (PSD-90-SEI).	796
Figure II.7.I.9 AFM images and indentation study of SEI layers obtained from C-Ely (a, c) and PSD-90-Ely (b, d). SEM images of SEI layers obtained from C-Ely (e) and PSD-90-Ely (f). The scan size for AFM images is 10 × 10 μm ²	796
Figure II.7.I.10 Cycling performances of Li deposition/dissolution using the PSD-90-Ely and C-Ely at a current density of 2 mA cm ⁻² and a deposition capacity of 2 (a) and 3 mA h cm ⁻² (b). (c) Voltage profiles (the first cycle) and (d) average voltage hysteresis of (b).	797
Figure II.7.I.11 Li deposition/dissolution cycling performances of the cells using PSD-90-Ely at a current density of 4 mA cm ⁻² with a deposition capacity of 4 mA h cm ⁻²	798
Figure II.7.I.12 Cycling performance of cells using PSD-90-Ely electrolyte.....	798
Figure II.7.I.13 Schematic illustration for the fabrication of polymer-PxSy protective layer on substrates.	798
Figure II.7.I.14 SEM images of the as prepared polymer-PxSy film on SS foil.....	798
Figure II.7.J.1 Synthesis scheme for PEO-POSS block copolymers.	801
Figure II.7.J.2 Chemical structure of the POSS-PEO-POSS triblock copolymer. The triblock synthesized during this study has a molecular weight of 5-35-5 [kg/mol].	802
Figure II.7.J.3 Ionic conductivity of PEO-POSS. Conductivity is plotted for organic-inorganic diblock copolymer electrolytes with PEO molecular weight 5 kg mol ⁻¹ and POSS 1, 1.9, 2.7, and 18 kg mol ⁻¹ (a) between 30°C and 130°C with [Li]/[EO] = 0.10 and (b) at 90°C with salt concentration ranging between	

[Li]/[EO] = 0.02 to 0.30. Conductivity decreases with POSS molecular weight and increases with temperature.	802
Figure II.7.J.4 Ionic conductivity of a POSS-PEO-POSS (5-35-5) electrolyte with LiTFSI salt concentration $r = [\text{Li}]/[\text{EO}] = 0.04$. The ionic conductivity is similar to previously studied polystyrene- <i>b</i> -poly(ethylene oxide) (PS-PEO) diblock copolymer electrolytes.	802
Figure II.7.J.5 Diffusion coefficient and transference number of the POSS-PEO-POSS (5-35-5) electrolyte. The values, marked by a star, are superimposed for comparison on a plot of previously reported values [1] for PEO homopolymer and PS-PEO diblock copolymer electrolytes.	803
Figure II.7.J.6 Transference number measurements of PEO-POSS(5-6) as a function of salt concentration.	803
Figure II.7.J.7 Comparison of charge passed before failure, C_d , between Li symmetric cells fabricated from a POSS-PEO-POSS (5-35-5 [kg/mol]) electrolyte and a polystyrene- <i>b</i> -poly(ethylene oxide) (PS-PEO) (115-172 [kg/mol]) electrolyte. Each cycle consisted of a 4 hour discharge at 0.175 mA cm^{-2} , 1 hour rest, 4 hour charge at 0.175 mA cm^{-2} , and 1 hour rest at 90°C	804
Figure II.7.J.8 Slice through a reconstructed volume imaged using X-ray tomography. This Li/POSS-PEO-POSS/Li cell was cycled at 0.175 mA cm^{-2} and failed after 17 cycles.	804
Figure II.7.J.9 Example of a routine used to test the limiting current of POSS-PEO-POSS (5-35-5). This 30 micron thick solid organic-inorganic polymer electrolyte was sandwiched between two lithium electrodes and polarized to electrodeposit Li from one electrode to the other. The current density was increased systematically until the potential diverged or the cell short-circuited.	805
Figure II.7.J.10 A schematic showing the three types of defects observed in this study: (a) a void defect, (b) a protruding lithium globule, and (c) a protruding non-globular dendrite. In each case, the triangle signifies a crystalline impurity particle, which is observed to be the nucleating site for defective deposition.	806
Figure II.7.J.11 Examples of defective lithium deposition observed by X-ray tomography. The top row shows an orthogonal cross-section through the defect. The bottom row shows a 3D rendered volume that includes the defect. In the 3D rendering, the lower interface between electrolyte and lithium is highlighted. The impurity particle, present in each tomogram, is colored green. Lithium is deposited from top to bottom. The current densities used to polarize the cells are indicated, along with the calculated average thickness of lithium, $h_{\text{Li,calc}}$, deposited on the bottom electrode. The yellow arrows are used to estimate the actual thickness of lithium deposited, using the impurity particle as a reference point. In the third cell, not enough lithium was deposited to label the figure. (a) a void defect, (b) a protruding lithium globule, and (c) a protruding non-globular dendrite.	806
Figure II.7.J.12 Representative cross section of cell polarized at $i = 0.04 \text{ mA cm}^{-2}$ for $t = 900 \text{ h}$ acquired using X-ray tomography. Lithium was deposited downward through the polymer electrolyte, which appears as a light band extending across the cell near the top of the cross-section. No lithium protrusions were observed. This cell did not short circuit. The yellow arrow shows the thickness of the electrochemically deposited lithium, $190 \mu\text{m}$, at a representative location based on the analysis of the tomograms, using the electrolyte's original position at the edge of the cell as a reference point. The light	

blue arrow shows, for comparison, the estimated thickness of electrochemically deposited lithium, 175 μm , based on the current passed through the cell.	807
Figure II.7.J.13 Correlation between current density and defect density in failed cells. The areal density of protruding defects, P , increases with current density.....	807
Figure II.7.J.14 Nature of observed lithium protrusions as a function of current density, i , and charge passed before failure, C_d . Observation of no protrusion nucleation at low current densities (yellow area), globules at medium current densities (green area) and non-globular dendrites at high current densities (blue area). The asterisk at $i = 0.04 \text{ mA cm}^{-2}$ indicates these cells had not failed at the time point used to calculate C_d , ($t = 900 \text{ h}$). Normalized current density, i/i_L , as a function of C_d , where i_L is theoretical limiting current (Eq. 1). [1].....	808
Figure II.8.A.1 Cycle performance of a Li/S cell in two different electrolytes at C/10 within 1.0-3.0 V voltage window at room temperature: (a) novel concentrated siloxane-based electrolyte and (b) 1M LiTFSI/DOL+DME+0.2M LiNO ₃ . Insets in (a) and (b) show results from polysulfide solubility test in the two electrolytes.	811
Figure II.8.A.2 SEM images of Li metal before (a) and after 20 cycles in (b) common ether-based electrolyte and (c) concentrated siloxane-based electrolyte. SEM images of S cathode before (d) and after 20 cycles in (e) common ether-based electrolyte and (f) concentrated siloxane-based electrolyte.	812
Figure II.8.A.3 SEM elemental mapping of Li metal after 20 cycles in (a) common ether-based electrolyte and (b) concentrated siloxane-based electrolyte. SEM elemental mapping of separator after 20 cycles in (c) common ether-based electrolyte and (d) concentrated siloxane-based electrolyte.....	813
Figure II.8.A.4 (a) 2D contour plot of in-operando Se K-edge XANES of Li/Se cell in concentrated siloxane-based electrolyte at C/10 within 1.0-3.0 V voltage window at room temperature and (b) corresponding phase composition analysis using linear combination fitting at different charge/discharge states.....	813
Figure II.8.A.5 In-operando Se K-edge EXAFS measurement of Li/Se cell in concentrated siloxane-based electrolyte at C/10 within 1.0-3.0 V voltage window at room temperature.....	814
Figure II.8.A.6 Snapshot of simulated structure of Li ₂ S ₆ in the concentrated siloxane-based electrolyte determined by ab initio molecular dynamics simulation.	814
Figure II.8.B.1 (a) Comparison of BET surface areas of pristine IKB/CNF carbon materials and those mixed with 10 wt% of different types of binders and (b) corresponding pore volume. (c) Cyclic voltammetry (CV) of IKB/CNF electrodes with PAA and PTFE binders (1.5-3.0 V, 0.05 mV/s), and (d) first discharge curves of sulfur electrodes with PAA and PTFE binders (sulfur loading >6.3 mg/cm ² , E/S=4 μL /mg, 0.05C).....	819
Figure II.8.B.2 (a) Cross-section view of the hybrid cell design, (b) electrochemical impedance of In-SE-In and In-SE-LE-Li (5 mv, 10 ⁵ -10 ⁻¹ Hz). (c) charge/discharge curves of LiIn-SE-LE-S. (0.1C, V _{InLi} vs. V _{Li} = 0.6V).	820
Figure II.8.B.3 Electrochemical impedance spectra (EIS) evolution in the first 20 hrs of In-SE-LE-SS cell with electrolytes (a) 1M LiTFSI/DME and (b) 1 M LiTFSI/DOL. (c) EIS evolution of InLi/SE/LE/SS and (d) InLi/SE/LE/S with 1 M LiTFSI/DOL. EIS test (5 mv, 10 ⁵ -10 ⁻¹ Hz).....	821

Figure II.8.B.4 (a) Cross-sectional SEM image of double-side coated Celgard 2500, (b) digital photographs of the static contact angles of the coated separators with electrolyte 1M LiTFSI/DOL/DME+0.3M LiNO ₃ , (c) effects of separator coating on sulfur utilization rate, and (d) cycling stability of cells at lean electrolyte conditions (E/S= 4 μl/mg) (S: 4 mg/cm ²).....	822
Figure II.8.C.1 ICP-AES data of S to Li atoms concentration ratio (a) remaining in supernatant solutions and (b) adsorbed onto candidate materials, after 3mM Li ₂ S ₆ adsorption test.	825
Figure II.8.C.2 (a) Commercially available APP used as fertilizer. (b) Digital image of the Li ₂ S ₆ (0.005 M) captured by PVDF and APP in DOL/DME solution. (c) UV/Vis absorption spectra of Li ₂ S ₆ solution before and after the addition of PVDF and APP. Chemical structures of (d) APP and (e) PVDF binders. Adsorption conformations and binding strengths for Li ₂ S ₆ on (f) APP and (g) PVDF polymers. (h) Binding strengths for APP and PVDF with various Li-S species. (i) Swelling ratios of the APP and PVDF binders.....	827
Figure II.8.C.3 The specific burning time test of sulfur electrodes with (a) S-PVDF electrode and (b) S-APP electrode. The time indicated in the pictures are counted as soon as the electrodes are exposed to the direct flame from a lighter (indicated by the white arrow in (a)). (c) The specific burning time of the sulfur cathodes with APP and PVDF binders. (d) Schematic showing the flame-retardant mechanism of the APP binder based sulfur electrode.	828
Figure II.8.C.4 (a) Chemical reaction for flame-retardant mechanism. (b) XPS spectra of the surface chemical composition of the S-APP electrode before and after burning. (c) S 2p XPS spectra of the S-PVDF electrode before and after burning. (d) SEM image and the corresponding (e) sulfur and (f) phosphorus elemental maps of the S-APP electrode after burning. (g) EDS of the S-APP electrode after burning. (h) SEM image and the corresponding (i) sulfur and (j) fluorine elemental maps of the S-PVDF electrode after burning. (k) EDS of the S-PVDF electrode after burning.....	829
Figure II.8.C.5 (a) Schematic of the electrochemical cell design that allows in-operando dark field light microscopy (DFLM) observation. (b and c) DFLM images of the metal grid (50 nm thick, 1 μm wide) fabricated on glass slide as a substrate for the electrochemical cell. (d) Voltage profile of the cell.....	830
Figure II.8.D.1 (a) Effects of porosity, sulfur loading, and morphology on cell performance. (b) Evolution of resistance modes during discharge: Surface passivation resistance (red), pore block resistance (green), concentration resistance (blue) and transport resistance (black). As any N resistance value goes to 1, the mode becomes dominant.....	832
Figure II.8.D.2 Anode chemical reactions and electrochemical interactions at 1C. (a) With chemical redox reactions at Li anode, capacity decreases as well as qualitative nature of the potential profile changes with changes in speciation. (b) The dominant mode of chemical reduction at Li metal anode correlates the form of sulfur present at that instance. (c) This effect has both reversible and irreversible components.....	833
Figure II.8.D.3 (a) Charge-discharge hysteresis is composed of dissimilar potential profiles and unequal capacities (b) Dissolution of Li ₂ S does not often proceed to completion as freshly precipitated S covers Li ₂ S surface (c) Both Li ₂ S isolation and shuttle effect fundamentally lead to such hysteresis.....	833
Figure II.8.D.4 (a) Lithium-sulfur bonding and lithium-carbon interaction at low lithium contents, (b) electronic charge distribution at low lithium contents. Color code: C grey, S yellow, Li purple. In (b) atoms are colored according to their electrostatic charge shown in the color bar.	834

Figure II.8.D.5 Multilayer graphene structure showing the incorporation of N into the C rings in pyridinic (not shown), graphitic (blue circle), and pyrrolic (green circle) positions and their interactions with Li. Note that: a) Graphitic N does not interact with Li. b) Pyrrolic N bonds to Li. c) C backbone also participates in the electrochemical reduction of S.	834
Figure II.8.E.1 The relative ratios of (RS5R+RS6R+RS7R+RS8R+S8)/(RS3R+RS4R) for electrolytes (containing 16 mM Li ₂ S ₆) without and with additives before and after contacted with Li metal for different period of time.	839
Figure II.8.E.2 Comparison of the reaction between dissolved polysulfide ions with metallic Li, Li-phosphorus and a proprietary Li containing anode (Li-XX). The HPLC peak on the far right (in the dash-line box) is elemental sulfur peak.	840
Figure II.8.E.3 The photograph of the synthesized S/Xant co-polymer with different sulfur contents (top); the cycle and rate performance of the co-polymer with 70% sulfur. The tests were done in a coin cell. .	841
Figure II.8.F.1 Scanning electron microscope (SEM) images of Li deposits using Li-Cu cells (a) with and (b) without the KW-stabilization layer at 3 mA cm ⁻² for 3 hours. Overpotential of Li-Li symmetric cells (c) with and (d) without the KW-stabilization layer at 2 mA cm ⁻² for 400 hours.	844
Figure II.8.F.2 Cyclability (a) with various E/L ratios from 45 to 9 μL mg ⁻¹ at a fixed Li ₂ S loading of 8 mg cm ⁻² and (b) with various Li ₂ S loadings from 2 to 8 mg cm ⁻² at a fixed E/L ratio of 9 μL mg ⁻¹ . E/L ratio and Li ₂ S loading of, respectively, 45 μL mg ⁻¹ and 2 mg cm ⁻² are the average values reported in published Li ₂ S papers. (c) Performances of the cells with a Li ₂ S loading of 8 mg cm ⁻² and an E/L ratio of 9 μL mg ⁻¹ at various cycling rates.	845
Figure II.8.F.3 (a) Cyclability of the cells fabricated with the carbon-paper cathodes with a sulfur loading, sulfur content, and E/S ratio of, respectively, (a) 13 mg cm ⁻² , 75 wt.%, and 4.0 μL mg ⁻¹ and (b) 17 mg cm ⁻² , 80 wt.%, and 3.9 μL mg ⁻¹	846
Figure II.8.F.4 (a) Sulfur cathodes fabricated for pouch-type Li-S cells. Electrochemical performance of the pouch-type Li-S cells: (b) voltage profiles and (c) cycling performance.	846
Figure II.8.G.1 Silver-lithium/iodine solid state dual function battery.	851
Figure II.8.G.2 Conductivity effects of additive.	852
Figure II.8.G.3 (a) Cycling of cells containing additive with and without Li metal added, b) Coulombic efficiency.	852
Figure II.8.G.4 (a) Intermittent charging and (b) AC impedance results for LiI electrolyte based cell.	853
Figure II.8.G.5 AC impedance of LiI cells with and without polymer.	853
Figure II.8.G.6 (a) Discharge curves, (b) AC impedance, and (c) impedance results for LiI composite containing cell.	854
Figure II.8.G.7 Schematic of cell as assembled and after charge.	854
Figure II.8.G.8 X-ray diffraction of negative and positive electrodes after charge of AgI cell.	855
Figure II.8.G.9 X-ray diffraction of negative and positive electrodes after charge of LiI cell.	855
Figure II.8.G.10 X-ray diffraction of positive electrode after charge of LiI cell.	855

Figure II.8.H.1 Ti 2p core level HAXPES spectra after Li deposition demonstrating orientation-dependent reactivity of epitaxial LLTO thin films.	858
Figure II.8.H.2 (a) C1s and (b) O 1s XPS core level before (labeled RT) and after heating to 500°C to remove surface contamination species. (c) XRD patterns of LLZO heated to 200°C (green) and 800°C (black).	859
Figure II.8.H.3 XPS core level spectra after Li deposition on clean LLZO surface. Reduction of (a) Nb and Zr in Nb:LLZO; (b) Zr in Al:LLZO; and (c) Zr in Ta:LLZO.	859
Figure II.8.H.4 EIS spectra of Li-Li symmetric cells with (a) Nb- and (b) Ta-doped LLZO at room temperature demonstrating the change in impedance over 72 hours due to reaction with Li metal.	860
Figure II.8.H.5 Examples of DFT optimized structures with Nb dopants (a) distributed in the bulk and (b) segregated towards the surface for Nb-doped LLZO in contact with Li. (c) Bar chart showing differences in dopant energy near the surface and in the bulk for Nb- and Ta-doped LLZO without and with Li present.	861
Figure II.8.H.6 Survey (left), S 2p (middle) and P 2p (right) core level XPS spectra before (red) and after (black) Li sputtering show clear reaction of LPS with Li metal	861
Figure II.8.H.7 The impedance spectrum of unpolished (left) and polished (right) Li-LPS-Li symmetric cells at room temperature.	862
Figure II.8.I.1 a) Molecular structure of SIG components with their abbreviated names. b) Cycling data (0.1 mA/cm ²) for Li Li symmetric cells with SIG separators, along with Li(G4)TFSI/glass fiber for comparison. All cells completed 100 cycles (600 hrs) without developing short circuits. SIG separators required less overpotential (normalized to separator thickness) for Li stripping/plating than the solvate ionic liquid alone. c) Photograph of a SIG/S/C cathode, where SIG is cured in-situ within the pores of the electrode. d) Galvanostatic cycling data (theoretical C/10 rate) for an all-solid-state Li-S cell containing SIG in both the cathode and separator. Capacity retention (81%, 2nd → 75th cycle) and coulombic efficiency (~97%) are encouragingly high even without anode passivating additives (i.e. LiNO ₃).	867
Figure II.8.I.2 a) Self-healing efficiency based on maximum tensile strength and, b) recovery of Young's modulus upon self-healing of composite films after heat treatment at different temperatures, c) Nyquist plots and curve fit of PP-1/Li(G4)TFSI at room temperature and recovery of PP-1/Li(G4)TFSI under 40°C for 12 h.	868
Figure II.8.I.3 a) Self-healing efficiency based on maximum tensile strength and, b) recovery of Young's modulus upon self-healing of composite films after heat treatment at different temperatures, c) Nyquist plots and curve fit of PP-1/Li(G4)TFSI at room temperature and recovery of PP-1/Li(G4)TFSI under 40°C for 12 h.	868
Figure II.8.I.4 (a) The discharge/charge voltage profiles of the MJ430-S and the 20% SH-MJ430-S electrodes based on S loading of 1 mg cm ⁻² at initial activation cycle (0.05 C) and 10th cycle (0.25C) and (b) the corresponding cycling performance within the first 300 cycles. (c) The discharge/charge voltage profiles and (d) the corresponding cycling performance of the MJ430-S and the 20% SH-MJ430-S electrodes based on S loading of 4 mg cm ⁻² . (e) The discharge/charge voltage profiles of the 20% SH-MJ430-S electrodes at various rates. (f) The discharge/charge voltage profiles of a series [SH]-MJ430	

with increasing weight percentage of thiol modifier, from 5% to 20%, controlled via reaction conditions. Thiol modification largely increases capacity retention.	870
Figure II.8.I.5 (a) ^7Li MAS NMR spectra of the Li_2S_8 solution interacting with MJ430 and the 20% SH-MJ430. (b) ^7Li MAS NMR spectra of the cathode materials with MJ430-S and 20% SH-MJ430-S from Li-S cells that are discharged to different voltages, with experimental data in solid lines, deconvolution peaks in dot lines, and the sum of deconvolution peaks in dash lines. High resolution S2p XPS spectra of (c) the MJ430-S and (d) the 20% SH-MJ430-S cathodes, obtained from Li-S cells discharged to 1.9 V after 100 cycles. EIS analysis of (e-f) the MJ430-S and (g-h) the 20% SH-MJ430-S cells at different stages of discharge within 40 cycles.	871
Figure II.8.J.1 Constant voltage charge (red) /constant current discharge (blue) profile representative of multicomponent structured architecture cells cycled between 1.75 and 3.5 V.	874
Figure II.8.J.2 Impact of transport additive composition on discharge capacities of solid state multicomponent nanolayered structured architecture cells in the 1 st , 2 nd and 5 th cycles. Additives A, B and C enhance ionic, electronic and mixed conductivity, respectfully. Cells cycled between 1.75 and 3.5V.	874
Figure II.8.J.3 Impact of electrode design, including electrode thickness and width, on the positive electrode utilization of 12 V <i>in-situ</i> cells. Cells were cycled between 7.5 and 13.5 V. By decreasing the aspect ratio of the electrodes and thereby increasing surface area, enhanced diffusion properties enabled access to previously electrochemically inactive areas leading to higher utilization.	875
Figure II.8.J.4 First cycle voltage profile for self-formed 12 V cell with improved transport pathways due to cell design modifications and increased reactive electrolyte thickness. The cell was charged up to 14 V before undergoing a stepped discharge protocol down to 7.5 V.	876
Figure II.8.K.1 a) Crystal structure of Li_3PO_4 and Li_3PS_4 with hopping pathways of Li-ions; 1b) potential energy for migration paths of Li-ions along c-axis interstitial channels in pure and doped Li_3PS_4 and Li_3PO_4 with Dop1; 1c) the same for vacancy hopping mechanism along a- and c-axis in pure Li_3PO_4 and doped Li_3PO_4 with Dop2 and Dop3.	880
Figure II.8.K.2 a) Nyquist plot from lithium ion conductivity measurements performed on the LIC membranes. b) Mechanical property analysis of the LIC membranes c) Electrochemical cycling performance of the LIC membranes.	881
Figure II.8.K.3 a) Crystal structure of the cubic garnet-type $\text{Li}_7\text{La}_3\text{Zr}_2\text{O}_{12}$ with partially occupied Li-ion sites denoted by arrows, 3b) potential energy for the migration paths of Li-ions in pure garnet and the oxide doped with dopants 1-4, 3c) Nyquist plot of the undoped and D ₁ -doped LLZO-LIC.	882
Figure II.8.K.4 a&b) TEM images of S-C4FM-1 at two different magnifications along with the corresponding SAED pattern (inset) and c&d) TEM images of S-C4FM-1 at two different magnifications along with the corresponding SAED pattern (inset).	883
Figure II.8.K.5. a) Cycling performance of S-C4FM-1 and S-C4FM-2 cycled at 0.2C rate, b) rate capability plot of S-C4FM-1 and S-C4FM, c) charge-discharge plot of S-C4FM-1 and d) charge-discharge plot of S-C4FM-2.	884
Figure II.8.K.6. a&b) TEM images of C4FM-3 at two different magnifications and c&d) TEM images of S-C4FM-3 at two different magnifications along with the corresponding SAED pattern (Figure II.M.8.6d inset).	885

Figure II.8.K.7.a) Cycling and rate capability plot of the S-C4FM-3 and b) Specific capacity plot of the S-C4FM-3.....	886
Figure II.9.A.1 (a) Schematic of the operation principle of the simple one-step electrochemical pre-charging treatment process for CNTs air electrode and Li metal anode. (b) TEM image of protective thin film produced on CNTs air-electrode after pre-treatment (4.3 V/10 min). (c) Atomic force microscopy (AFM) image of protective thin film produced on Li metal anode after pre-treatment (4.3 V/10 min). (d) Stable cycling life of Li-O ₂ cells without and with pretreatment cycled at 0.1 mA cm ⁻² in common 1 M lithium trifluoromethanesulfonate (LiTf) in tetraethylene glycol dimethyl ether (Tetra glyme) electrolyte at room temperature. Scanning electron microscopy (SEM) top-view images of Li metal anode with pre-treatment (4.3 V/10 min) after 110 cycles (e), and Li metal anode without pre-treatment after 70 cycles (f).	890
Figure II.9.A.2 (a) Cycling performance of Li-O ₂ cells with optimized RuO ₂ /CNT air electrode and LiFePO ₄ (LFP) counter electrode cycled at 0.1 mA cm ⁻² in 1 M LiTf-Tetra glyme electrolyte under capacity-fixed protocols of 1,000 mAh g ⁻¹ and 800 mAh g ⁻¹ , respectively. (b) SEM images of cycled air-electrode after 430th discharge (b) and 430th charge (c). XPS spectra of O 1s (d) and Ru 3p (e) of cycled air-electrodes.....	891
Figure II.9.A.3 (a, b) Optical images of as-prepared free-standing thin composite LiTFSI-LLZTO-PVDF (LLP) membrane with good flexibility. Cycling performance of Li-O ₂ cells composed of CNTs air-electrode and Li anode without LLP membrane (c, d), and with LLP membrane (e, f) cycled at 0.1 mA cm ⁻² under a limited capacity of 1,000 mAh g ⁻¹	892
Figure II.9.A.4 (a) Schematic of high energy-density Li-O ₂ cell design. (b) Cycling performance of Li-O ₂ cells containing optimal RuO ₂ /CNTs air electrodes (high loading: 4 mg cm ⁻²) and Li metal anodes with and without composite protective membrane (LiTFSI/LLZTO/PVDF) cycled in voltage window between 2.2 V and 4.2 V at a current density of 0.1 mA cm ⁻² in 1 M LiTf-Tetra glyme electrolyte at room temperature.	893
Figure II.9.B.1 Schematic of Pt modified MOF-derived catalysts. BND-Co@G = biphasic N-doped cobalt@graphene, Pt-SC-BND-Co@G = Pt surface-coating BND-Co@G, and Pt-BD-BND-Co@G = Pt bulk-doping BND-Co@G.)	897
Figure II.9.B.2 HRTEM image of annealed Ir ₈ clusters on an rGO cathode showing crystalline facets of the Ir nanoparticles.....	897
Figure II.9.B.3 Density functional calculation of the barrier for dissolution of O ₂ into the TEGDME....	898
Figure II.10.A.1 Na-driven structural behavior on cycling. (a) In situ XRD patterns collected during the first charge-discharge cycle for NaCrS ₂ , corresponding time vs. voltage profile is shown on the right. (The 2θ is converted to the corresponding angle for λ=1.54 Å (Cu-Kα) from the real wavelength λ=0.7747 Å used for synchrotron XRD experiments). (b) Evolution of lattice parameters calculated from the in situ X-ray diffraction during the first charge/discharge process.....	901
Figure II.10.A.2 Ex situ XAS Studies of Cr (b) and S (g) valance state during various charge-discharge stages.....	902

Figure II.10.A.3 X-ray diffraction patterns of $\text{Li}_x\text{Na}_{3-x}\text{VP}_3\text{O}_9\text{N}$ collected before starting and after each ion exchange (IE) process. The zooming (111) reflections are shown on the right side, the initial phase, second phase and third phase are labeled as A, B and C separately.	902
Figure II.10.A.4 In-situ X-ray diffraction patterns collected during the first charge/discharge and the second charge of $\text{Na}/\text{Na}_{0.66}\text{Mn}_{0.6}\text{Ni}_{0.2}\text{Mg}_{0.2}\text{O}_2$ cells at a current rate of 0.2 C in the potential range between 1.5 and 4.3 V.	903
Figure II.10.A.5 Charge compensation mechanism of MNM-2 during charge and discharge processes. a), b) and c) Mn and d), e) and f) Ni K-edge XANES of MNM-2 at various stages during the first charge/discharge and the second charge process, respectively. g) The half edge energy ($E_{0.5}$) at different content of Na in $\text{Na}_x\text{Mg}_{0.05}[\text{Mn}_{0.6}\text{Ni}_{0.2}\text{Mg}_{0.15}]\text{O}_2$. h) The charge compensation of different elements contribution during the charge and discharge process.	904
Figure II.11.A.1 (a) 1 st cycle charge/discharge voltage profiles of $\text{LiNi}_{0.94}\text{M}_{0.06}\text{O}_2$ at fresh and after exposure to a moist atmosphere for 14 and 30 days. (b) Cycling performance of Maxwell24 and Maxwell30, 2 cycles at C/10, then 3 rd - 50 th cycle at C/3, 2.8-4.4 V. (c) Comparison of rate capability and capacity of NMC811, NMC622 and NCA, 12 mg/cm ²	908
Figure II.11.A.2 DSC profiles of (a) NMC 811 and (b) NCA charged to different cut-off voltages. (c) Capacity retention of a graphite/NMC 811 cell, compared with a Li NMC 811 cell.	909
Figure II.11.A.3 Electrochemical performance of Li NMC811 with investigated electrolytes (a) cycling performance at C/3 charge/discharge processes (b) Different charge rate performance in ED1123 electrolyte with constant charge rate of C/3. (c) Different discharge rate performance in ED1123 electrolyte with constant charge rate of C/3, all Li NMC cells are cycled between 2.8 and 4.4 V vs. Li/Li^+	910
Figure II.11.A.4 Cross-section of cycled Li (100 cycles) collected from Li NMC811 cells with (a) baseline and (b) ED1123 electrolytes.	910
Figure II.11.A.5 SEM images of NMC811 electrodes fabricated with two different binders, PVDF-HFP copolymer and PVDF-HSV 900 homopolymer.	911
Figure II.11.A.6 Schematics (top) of LiF deposition on h-BN to heal the defects. This approach enables dense, void-free Li metal cycling (bottom, A). In contrast, Li deposits on bare Cu surface in a carbonate based electrolyte is dendritic and porous (bottom, B).	912
Figure II.11.A.7 Cycle life of cells (as specified by the cycle number at completely no capacity) as a function of electrolyte content (in g Ah ⁻¹) to illustrate the impact of electrolyte quantity on cycle aging.	912
Figure II.11.A.8 Cryo FIB-SEM images of the plated lithium at the first cycle and the corresponding cross-section images when the cells are cycled in (a, c) 1M LiPF_6 EC: DMC, and (b, d) 0.1M LiTFSI in fluoromethane: CO_2 19:1 with 0.1M Additive01	914
Figure II.11.A.9 Discharge curves at ~6 mA/cm ² to understand cathode utilization (right). Current density variation computations (left) cathode chemistries.	914
Figure II.11.A.10 Final deliverable cell for FY2018. The Li NMC pouch cell was still cycling at the end of FY2018	915

Figure II.11.B.1 Potential vs. time (bottom right), capacity vs. cycle number (bottom left), and columbic efficiency (top) plots of SPAN/LATSP+LiPON/Li half cells at 0.25 C rate.	925
Figure II.11.B.2 (a,d) Computer generated schematics, (b,e) stereomicroscope images of as-printed structures, and (c,f) SEM images of sintered structures for the (a-c) columns and (d-f) multilayer grid designs. (g-h) Modeling results predicting the electrode utilization during discharge as a function of time and feature diameter, from 6.25 to 150 μm . (i) Model results showing the enhancement of relative C-rate with smaller feature size at constant cathode layer porosity (85 v%) and loading. (j) Cycling at C/20 (10 mA/g) and C/7 (30 mA/g) rates with 3D printed garnet grid structure filled with 811 NMC on the cathode side with Li metal filling random pores on anode side	926
Figure II.11.B.3 (Top) - High performance of Directly Derived Doped Sulfur Architectures (DDSA) with polysulfide trapping agents (PTA); (Bottom) – weight analysis and cost analysis for large scale manufacturing and laboratory scale battery testing of the DDSA-PTA system at the Nanomaterials for Energy Conversion and Storage Technology (NECST) laboratories at the Energy Innovation Center (EIC), University of Pittsburgh.	928
Figure II.11.B.4 Schematic of direct alternating deposition of S/carbon and graphene by layer-on-layer via air-controlled electro spray (ACES) and enhanced cell performance (rate capability and capacity retention) of layered cathodes.	929
Figure II.11.B.5 Schematic of direct coating of PEDOT:PSS-rGO coating on a separator and enhanced cell performance due to the separator coating.....	929
Figure II.11.B.6 Electrodeposition of solvated Li (green) at constant potential. Top left: High density DME solvent (low LiTFSI salt concentration). Top right: Low density DME solvent (high LiTFSI salt concentration). Bottom left: LiTFSI in DOL solvent. Bottom right: LiNO ₃ in DME solvent. Color code: O: red, C: brown, F: light blue, H: white, Li: green, N: grey.....	930
Figure II.11.B.7 Preliminarily electrochemical results of the as-prepared 3-D MnO ₂ based cathode materials: (a) First three cycle charge-discharge profiles; (b) Capacity vs. cycle number plots. The cycling performance of monolayer MnO ₂ nanosheets without 3-D structure tested under the same conditions was plotted in (b) for comparison.	931
Figure II.11.B.8 First three cycles of galvanostatic charge and discharge (GCD) profiles of surface tuned Li ₂ S@graphene at A . E/S ratio of 2 with mass loading of 6.8 mg/cm ² B . A TEM image of Li ₂ S@Graphene.	931
Figure II.11.B.9 MoS ₂ nanosheet-carbon nanotube-sulfur composites. Left: conceptual figure, Right: scanning electron micrograph.	932
Figure II.11.B.10 Synchrotron tomographic images of aqueous freeze-cast LLZO scaffolds (subvolume view 1046x1403x128 μm). Left to right: 7.5% LLZO, 12.5% LLZO, and 17.5% LLZO loading in the aqueous slurries.....	933

List of Tables

Table I.1.B.1 Characteristics of the annual cell deliverables in the program	8
Table I.1.B.2 Phase 2 Deliverable Cell Initial Performance	11
Table I.1.D.1 Coating parameters	18
Table I.1.D.2 Coating parameters for thick cathodes.....	19
Table I.1.G.1 Properties of PMP-Coated Experimental Separator Conditions	33
Table I.1.G.2 Test Plan for Down Selection of Experimental Separators	34
Table I.1.H.1 Overview of Program Hardware Deliverables and Build Strategy.....	39
Table I.1.H.2 Properties of Recycled Positive Electrode Active Material.....	41
Table I.1.H.3 Properties of Recycled Negative Electrode Active Material	42
Table I.2.A.1 Summary of 1Q2018 Key Activities Related to Pilot-Scale Manufacturing of Si-C.	59
Table I.2.A.2 Improvements in Process and Product Parameters after Pilot-Scale Modifications.....	62
Table I.2.B.1 Predicted Improvement in 1 Ah Pouch Cells Based On Coin Cell Electrochemical Performance	67
Table I.2.B.2. Anode Slurry Formulations for Dual Layer Slot Die.....	68
Table I.2.B.3. Electrode Dimensions and Loadings for 1 Ah Pouch Cells	69
Table I.2.B.4. Energy Density of 1 Ah Pouch Cells, Comparing CoEx Cathodes to Conventionally Manufactured Thin and Thick Baseline Cathodes	70
Table I.2.E.1 Compositions of trial electrostatic spray coatings blended at ORNL and coated at Keyland Polymer.....	87
Table I.2.I.1 Structure parameters of the prepared Li-rich cathode materials	111
Table I.2.L.1 Summary of capacity recovery/efficiency for triggered relithiation of 400 mAh Si Pouch Cells with 20-60% capacity fade at a relithiation rate of 100 μ A.	130
Table I.4.A.1 Cradle-to-gate environmental impacts of 1kg NMC111 cathode powder	191
Table I.4.B.1 Projected material demand, compared to reserves	195
Table I.4.B.2 Challenges for Li-Ion Battery Recycling.....	196
Table I.4.D.1 Team Members and Responsibilities.....	207
Table I.4.D.2 List of Additional Facilities	208
Table I.4.D.3 Cross-cutting Capabilities.....	208
Table I.5.A.1 Graphite powders selected to elucidate causes of lithium plating during fast charges.....	217
Table I.5.A.2 Summary of capacity retention for selected graphites and binders in prescreening task. (Discharge capacity retention is based on the 10th cycle (6C Chg, C/2 Dchg).).....	219

Table I.5.A.3 Ratio of D:G bands of the selected graphite materials.	224
Table I.5.B.1 Fast Charge Protocols	235
Table I.5.E.1 NMC622 cathodes.....	258
Table I.5.F.1 Baseline cell cycling profile	261
Table I.7.A.1 Pack specifications used in BatPaC calculations	274
Table I.7.A.2 Electrode material costs to estimate the cost of battery packs.....	275
Table I.7.B.1 Status of Deliverables for Testing.....	282
Table I.7.C.1 Articles Tested for USABC	287
Table I.7.C.2 Articles Tested for Benchmark	287
Table I.7.C.3 Articles Tested for Applied Battery Research (ABR).....	287
Table I.7.F.1 Ceramic Materials Coated on Graphite Anode	306
Table I.7.F.2 Al ₂ O ₃ and MgO Coated on Graphite Anode for Separator-free Cell Study	308
Table I.7.G.1 Formation data for graphite half-cells cycled at C/10, 1.5–0.01 V vs Li ⁺⁰	320
Table I.7.H.1 Relative elemental compositions of anodes in LFP cells.....	326
Table I.7.H.2 Relative elemental compositions of anodes in NMC532 cells from Reference 10.	327
Table I.7.H.3 Proposed structural formulae.	327
Table I.7.H.4 Proposed structures from Reference 10.	327
Table II.1.B.1 Properties of the polymer coatings in the battery environment.	338
Table II.2.A.1 Summary of Slurry Samples and Selected Results.....	351
Table II.2.A.2 Electrodeposition protocols applied to prepare the Cu-coated silicon electrodes.	358
Table II.2.A.3 Chemical composition of SEI calculated using XPS spectra.	375
Table II.2.A.4 Loading density, initial specific capacity, initial Coulomb efficiency, capacity retention, and average capacity for half-cells.....	393
Table II.2.B.1 Summary of silicon-based materials used in this work	410
Table II.2.B.2 Peak assignments for XPS analysis on soaked SiO ₂ and Li ₃ SiO _x thin films	428
Table II.2.B.3 Vibration-Mode Assignments for FTIR Peaks	447
Table II.2.B.4 Peak Assignments for O 1s, C 1s, and Si 2p Binding-Energy Regions.....	454
Table II.2.B.5 Ionic Conductivities and Activation Energies of Individual SiEI Components.	459
Table II.2.B.6 Elemental Surface Analysis after Aging Si Thin Films for Five Days in Different Gloveboxes across Different National Laboratories. Controlled Unaged and Air-Exposed Samples are Shown for Comparison.	464
Table II.2.B.7 Fitting Results Show the Components in the Film	479

Table II.2.B.8 TERS spectral band assignment for cycled a-Si.....	503
Table II.2.C.1 Representative results of the key performance parameters of NMC532 Si/C/Gr full cells with LiFSi-TEPa based LHCE.....	518
Table II.2.C.2 Representative results of the key performance parameters of NMC532 Si/Gr full cells with different additives	519
Table II.3.C.1 Adsorption/reaction energies of select phosphorous-containing additives and decomposition products on the partially (25% Li content) delithiated (012) NMC surface.....	548
Table II.3.C.2 Adsorption energies (eV) of fluorinated and non-fluorinated electrolyte molecules on the (012) surface of NMC materials	549
Table II.3.I.1 Summary of structure changes in chemical delithiated NMCs using in-situ XRD heating experiments.....	595
Table II.4.B.1 Summary of Conductivity, Viscosity and Li ⁺ Transference Number.....	628
Table II.4.C.1 Summary of Conductivity, Viscosity and Li ⁺ Transference Number.....	634
Table II.5.G.1 DFT calculated energetics for different fully-relaxed interfacial supercells in comparison with the fracture energy of the bulk materials.....	689
Table II.7.I.1 Prepared SCPs with different contents of sulfur.....	793
Table II.7.I.2 The reduced modulus of SEI layers formed from the C-Ely and PSD-90-Ely.....	797
Table II.7.J.1 POSS-PEO diblock copolymers currently available with isobutyl-functionalized-POSS. The volume fraction of PEO is given and chain length <i>N</i> based on a reference volume of 0.1 nm ³	801
Table II.8.E.1 Summary of the recovery rate of elemental sulfur and the coulombic efficiency for several Li-S cells with and without different catholyte additives	840
Table II.8.E.2 Test results of ten synthesized co-polymers.....	842
Table II.8.G.1 Quarterly Milestones and Verification for Year 2.....	852
Table II.8.I.1 Composition/Properties of Five Novel SIGs in Comparison to Li(G4)TFSI.....	867
Table II.8.K.1 Battery Specifications for the Battery 500 Program.....	878
Table II.8.K.2 Ionic conductivity of different LIC membranes.....	881

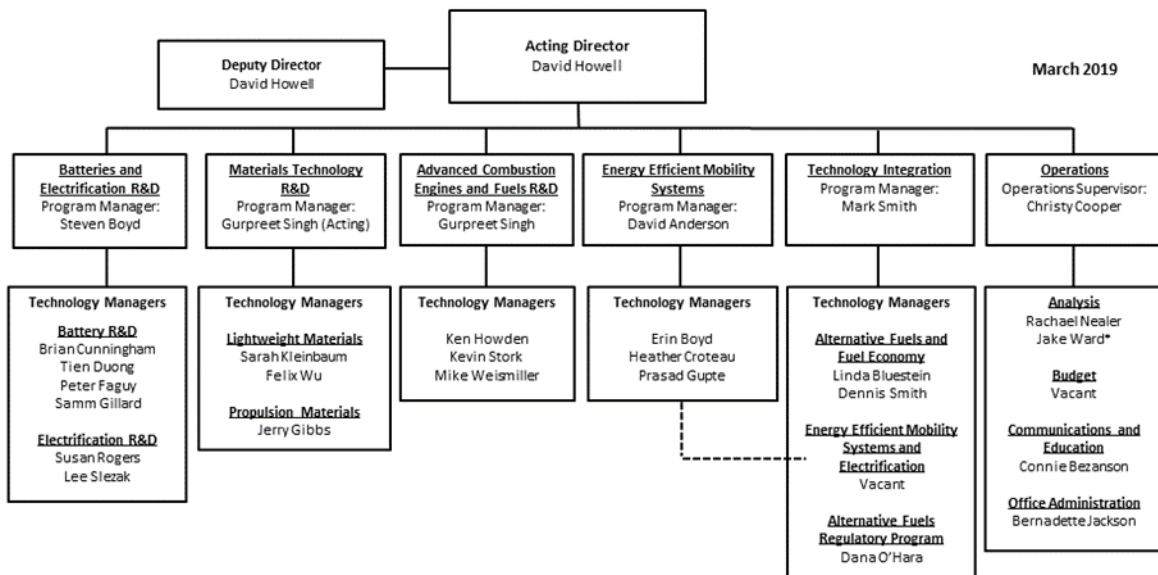
Vehicle Technologies Office Overview

Vehicles move our national economy. Annually, vehicles transport 11 billion tons of freight – more than \$32 billion worth of goods each day – and move people more than 3 trillion vehicle-miles. Growing our national economy requires transportation and transportation requires energy. The transportation sector accounts for 70% of U.S. petroleum use. The United States imports 20% of the petroleum consumed – sending more than \$15 billion per month overseas for crude oil. The average U.S. household spends nearly one-sixth of its total family expenditures on transportation, making transportation the most expensive spending category after housing.

To strengthen national security, enable future economic growth, improve energy efficiency, and increase transportation energy affordability for Americans, the Vehicle Technologies Office (VTO) funds early-stage, high-risk research on innovative vehicle and transportation technologies. VTO leverages the unique capabilities of the national laboratory system and engages private sector partners to develop innovations in electrification, including advanced battery technologies; advanced combustion engines and fuels, including co-optimized systems; advanced materials for lighter-weight vehicle structures; more efficient powertrains; and energy efficient mobility systems.

VTO is uniquely positioned to address early-stage challenges due to strategic public-private research partnerships with industry (e.g. U.S. DRIVE, 21st Century Truck Partnership) that leverage relevant expertise. These partnerships prevent duplication of effort, focus DOE research on critical R&D barriers, and accelerate progress. VTO focuses on research that industry does not have the technical capability to undertake on its own, usually due to a high degree of scientific or technical uncertainty or is too far from market realization to merit industry resources.

Organization Chart



(This page intentionally left blank)

Batteries Program Overview

Introduction

During the fiscal year 2018 (FY 2018), the Vehicle Technologies Office (VTO) battery program continued research and development (R&D) support of technologies for plug-in electric vehicles (PEVs), e.g., plug-in hybrids, extended range electric vehicles, all-electric vehicles, and some hybrid electric vehicles (including those with 12 volt start/stop hybrid). One of the objectives of this support is to enable U.S. innovators to rapidly develop the next generation of technologies that achieve the cost, range, and charging infrastructure necessary for the widespread adoption of PEVs. Stakeholders involved in VTO R&D activities include universities, national laboratories, other government agencies and industry partners – including automakers, battery manufacturers, material suppliers, component developers, private research firms, and small businesses. VTO works with key U.S. automakers through the United States Council for Automotive Research (USCAR) – an umbrella organization for collaborative research consisting of Fiat Chrysler LLC, the Ford Motor Company, and the General Motors Company. Collaboration with automakers through the US DRIVE (Driving Research and Innovation for Vehicle Efficiency and Energy Sustainability) partnership enhances the relevance and the success potential of the research platform. An important prerequisite for the electrification of the nation’s light duty transportation sector is the development of more cost-effective, longer lasting, and more abuse-tolerant PEV batteries and accordingly, VTO battery R&D is focused on the development of high-energy batteries for PEVs and very high-power devices for hybrid vehicles.

Goals

The goals of this research are to address barriers which hold back EVs from matching the full driving performance, convenience, and price of an internal combustion engine (ICE) vehicle. EVs have the advantage of a very high efficiency compared to other vehicle types, a simplified drive train, and a flexible primary energy source (i.e., the electricity needed to charge an EV can come from coal, natural gas, wind turbines, hydroelectric, solar energy, nuclear, or any other resource). Another current focus is the 12V start/stop (S/S) micro-hybrid architecture, in which the engine is shut down whenever a vehicle stops. Vehicles with the S/S functionality are being deployed worldwide. The 12V battery provides power for auxiliary equipment (e.g., the radio and air conditioning) and then restarts the engine when the vehicle moves. Current 12V S/S batteries, typically lead-acid batteries, have a poor life. Table 1 and Table 2 show a subset of the targets for EV and 12V start/stop micro hybrid batteries that have been set by U.S. DRIVE.

Table 1: Subset of EV requirements for batteries and cells.
(Cost and low temperature performance are critical requirements).

Energy Storage Goals (by characteristic)	System Level	Cell Level
Cost @ 100k units/year (kWh = useable energy)	\$100/kWh*	\$75/kWh*
Peak specific discharge power (30s)	470 W/kg	700 W/kg
Peak specific regen power (10s)	200 W/kg	300 W/kg
Useable specific energy (C/3)	235 Wh/kg*	350 Wh/kg*
Calendar life	15 years	15 years
Deep discharge cycle life	1000 cycles	1000 cycles
Low temperature performance	>70% useable energy @C/3 discharge at -20 °C	>70% useable energy @C/3 discharge at -20 °C
	*Current commercial cells do not meet this goal	

**Table 2: Subset of targets for 12V start/stop micro-hybrid batteries
(cost and cold cranking are critical requirements)**

Energy Storage Goals (by characteristic)	Under the hood	Not under the hood
Maximum selling price	\$220*	\$180*
Discharge pulse (1s)	6 kW	
Cold cranking power, (-30 °C)	6 kW for 0.5s followed by three 4 kW/4s pulses*	
Available energy	360 Wh	
Peak recharge rate (10s)	2.2 kW	
Sustained recharge rate	750 W	
Cycle life	450 k	
Calendar life	15 years at 45 °C*	15 years at 30 °C**
Maximum weight	10 kg	
Maximum volume	7 liters	
	*Current commercial cells do not meet this goal **Current cells almost meet this goal	

State of the Art

Battery R&D attempts to advance battery technology to help improve the market penetration of PEVs and hybrid vehicles by overcoming the current barriers. To accomplish this, it focuses on: (1) a significantly reduced battery cost, (2) increased battery performance, e.g., extreme fast charge (XFC) and low temperature performance for enhanced Li-ion, (3) improved life advanced chemistry cells, (4) increased tolerance to abusive conditions; and (5) more cost-effective recycling and sustainability.

The current status of the broad battery chemistry types (current Li-ion, next gen, and BLI) is summarized in Figure 1. Battery R&D spans mainly three areas:

- **Current Technology (enhanced) Li-ion:** Cells with today's materials (i.e., graphite anode/transition metal oxide cathode), but with features like XFC compatibility, low temperature performance and improved abuse tolerance.
- **Next-gen Li-ion:** Cells containing an alloy anode, usually Silicon-based, and/or a high voltage (>4.5 V) cathode.
- **Beyond Li-ion (BLI):** Cells containing Li metal anodes.

Over the past seven years, PEVs have become more commercially viable, with battery costs dropping almost 80% since 2010. Further cost reductions in high-energy batteries for PEVs are always desirable. In addition, although today's batteries approach very attractive cost numbers, they still need the ability to accept extreme fast charging (XFC) and to perform better in low-temperature operations, to favorably match ICEs in all-weather performance and "refueling" convenience. Research into "enhanced Li-ion" batteries (which would providing these functionalities) is one of the R&D focus areas. For further gains in energy density and cost reduction, research is needed in both "next gen" chemistries (which employ an alloy anode and/or a high voltage cathode) and BLI chemistries (see Figure 1). Cycle and calendar lives of next-gen and BLI chemistries are well short of EV goals. Most cells employing a significant amount of silicon provide (at most) 500 deep discharge cycles and less than two years of calendar life; BLI cells typically provide much less (a cycle life of 100 cycles or less). In addition, the requisite low temperature performance and extreme fast charge capability are lacking in all chemistries.

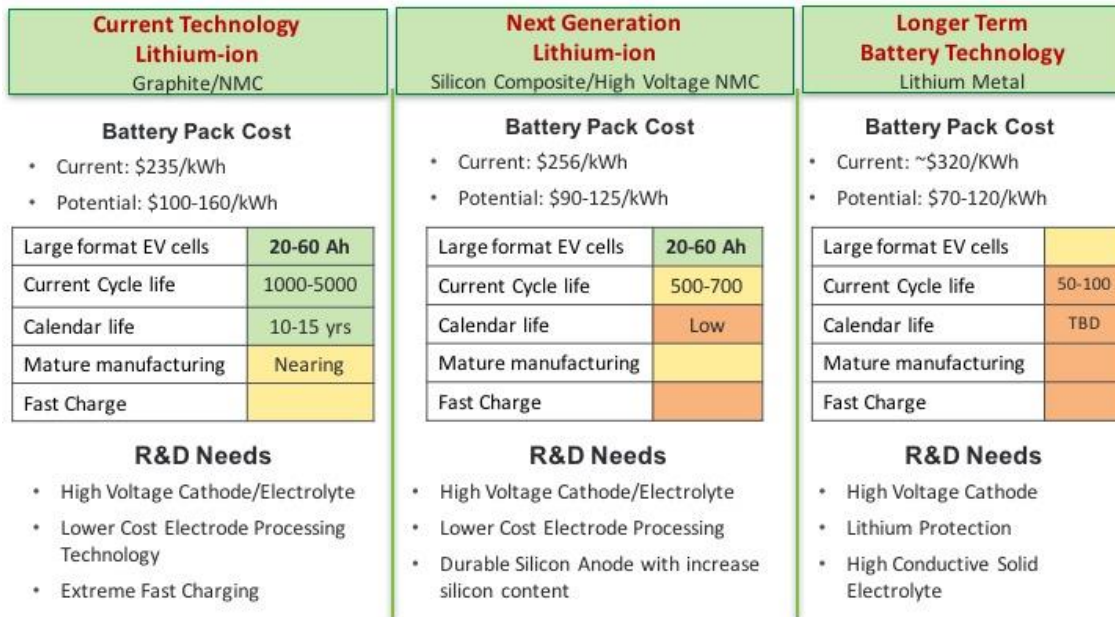


Figure 1. Chemistry classes, status, and R&D needs

An overview of the candidate battery technologies and their likely ability to meet the DOE cost goals are shown in Figure 2. Because of the large variation in different battery technologies, battery research also includes multiple activities focused to address remaining high cost areas within the entire battery supply chain.

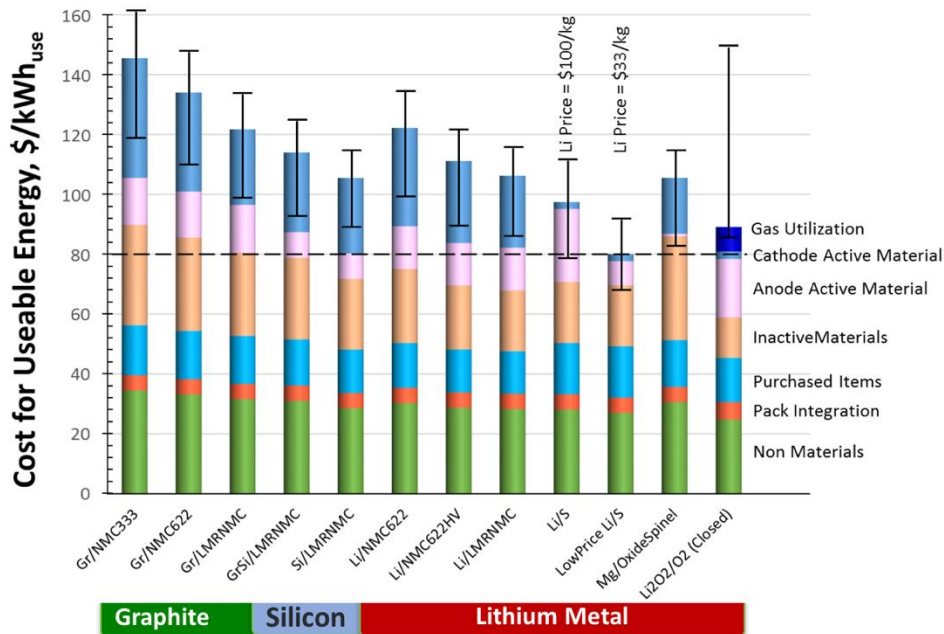


Figure 2. Potential for Future Battery Technology Cost Reductions

Battery Technology Barriers

The major remaining challenges to commercializing batteries for EVs and 12V SS micro-hybrid batteries are as follows:

A. Cost. The current cost of high-energy Li-ion batteries is approximately \$200 - \$300/kWh (on usable energy basis), a factor of two-three times too high from where it needs to be. The cost of Li-ion-based 12V micro-hybrid batteries (which offer significantly better life than conventional lead acid batteries) is approximately 50% too high compared to lead acid. The main cost drivers are the high cost of raw materials, costs associated with materials processing, the cell and module packaging, and manufacturing.

B. Performance. Historically, a higher energy density was needed to reduce the weight and volume of PEV batteries, but those weight and volume issues have been to a large degree been addressed. The use of higher energy materials is still an effective way to reduce costs further, but cell chemistries that provide higher energy have life and performance issues. Also, existing chemistries (e.g., graphite anodes paired with transition metal oxide cathodes) need improvement in XFC and low temperature performance to compete favorably with gas-powered vehicles in the areas of performance and customer convenience. The main performance issue with Li-ion 12V start/stop batteries is a challenging “cold start” requirement at -30°C coupled with high or room temperature life.

C. Life. The life issue for mature Li-ion technologies has mainly been mostly addressed. However, both next-gen and BLI cell technologies still suffer major cycle and calendar life issues. The life of Li-ion-based 12V start/stop micro-hybrid batteries is relatively good, however enhancing cold crank performance often shortens high temperature life.

D. Abuse Tolerance. Current Li-ion automotive batteries are generally used consistent with safe practices. Thus, although Li-ion is not intrinsically tolerant to abusive conditions (as is the case for gasoline as well), it can be engineered in a commercially acceptable product. The characteristics of next-gen and BLI chemistries to abusive conditions are not well understood. However, Li-metal-based batteries have a long history of problematic dendrite growth which can lead to internal shorts and thermal runaway.

E. Recycling and Sustainability. Currently, automotive OEMs pay a relatively large cost (5-15% of the battery cost) to recycle end of life PEV batteries. The various chemistries used in Li-ion cells results in variable backend value. Alternatively, unless they get recycled, Li-ion batteries could lead to a shortage of key materials (lithium, cobalt, and nickel) vital to the technology. Finding ways to decrease the cost of recycling could thus significantly reduce the life cycle cost of PEV batteries, avoid material shortages, lessen the environmental impact of new material production, and potentially provide low-cost active materials for new PEV battery manufacturing.

Program Organization Matrix

VTO's energy storage effort includes multiple activities, ranging from focused fundamental materials research to prototype battery cell development and testing. The R&D activities can involve either shorter-term pre-competitive research by commercial developers or exploratory materials research generally spearheaded by national laboratories and universities. The program elements are organized as shown in Figure 3. Battery R&D activities are organized into the following program elements: Advanced Batteries and Cells R&D, Battery Materials R&D, and new focus.

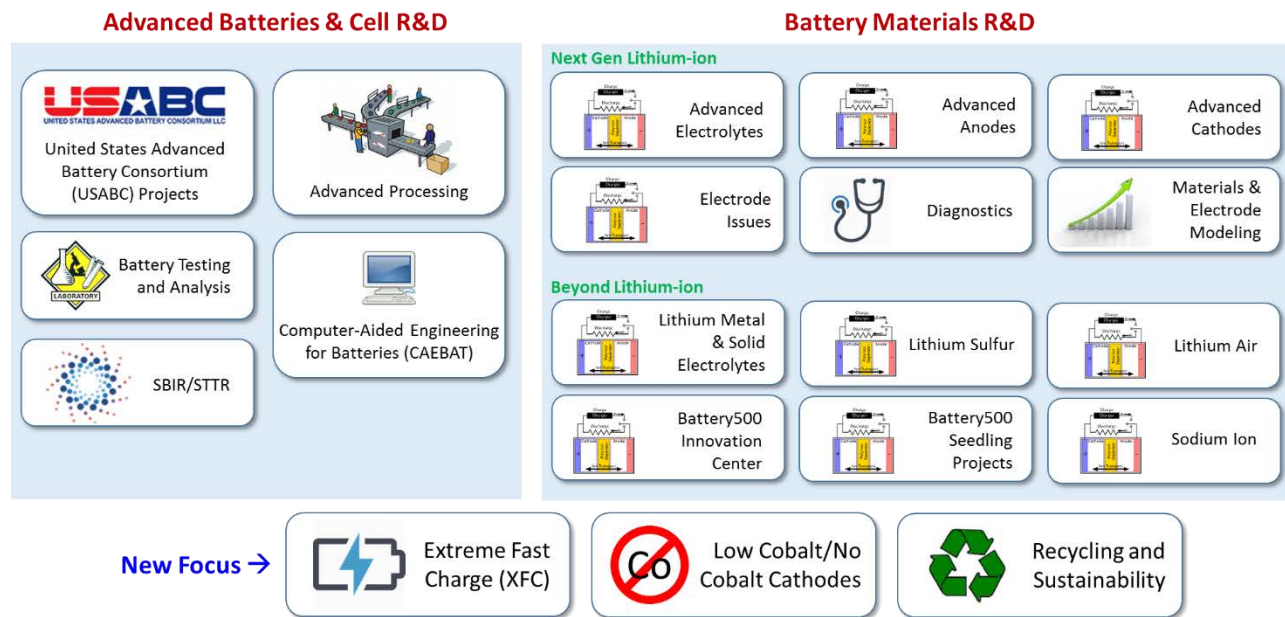


Figure 3. Battery R&D Program Structure

Advanced Cell and Battery Research and Development activity. This activity focuses on the development of robust battery cells and modules to significantly reduce battery cost, increase life, and improve performance. In this report, Part of this effort takes place in close partnership with the automotive industry, through a cooperative agreement with the *United States Advanced Battery Consortium* (USABC). In FY 2018, the USABC supported thirteen cost-shared contracts with developers to further the development of batteries and battery components for PEVs and HEVs. In addition to the USABC projects, DOE supports battery and material suppliers via contracts administered by the National Energy Technology Laboratory (NETL) and development of tools for the *computer aided engineering of batteries* (CAEBAT). The *Battery Testing and Analysis activity* has a supporting role toward the other battery programs. It works in close collaboration with USABC to develop requirements and test procedures. Other projects in this area include performance, life and abuse testing of contract deliverables, laboratory- and university-developed cells, and benchmark systems from industry; thermal analysis, thermal testing and modeling; cost modeling; secondary usage and life studies; and recycling studies for core materials. It evaluates battery technologies according to USABC-stipulated battery test procedures and performs benchmark testing of emerging technologies to remain abreast of the latest industry developments. The *Advanced Processing Science and Engineering* activity involves R&D on systematic material engineering and customized scaled processes to produce high quality material at kilogram-levels. Several *Small Business Innovation Research* (SBIR) projects, also supported by VTO, are focused on the development of new battery materials/components and are the source of new ideas and concepts and are covered in that chapter.

Advanced Materials Research activity. This activity addresses fundamental issues of materials and electrochemical interactions associated with rechargeable automotive batteries. It develops new/promising materials and uses advanced material models to discover them and their failure modes, as well as scientific diagnostic tools and techniques to gain insight into why they fail. This work is carried out by researchers at several national labs, universities, and by commercial entities. It includes the *Next Generation Lithium Ion* research activity focused on the optimization of next generation, high-energy lithium-ion electro-chemistries that incorporate new battery materials. It emphasizes identifying, diagnosing, and mitigating issues that impact the performance and lifetime of cells constituted of advanced materials. Research continues in six areas advanced anodes, advanced cathodes, advanced electrolytes, electrode issues, diagnostics, and modeling. The *Beyond Lithium Ion* (BLI) Technology activity addresses fundamental issues associated with lithium batteries, develops new/promising materials and uses advanced material models to discover such materials using

scientific diagnostic tools/techniques. It includes solid-state battery technologies, lithium metal, lithium sulfur, and lithium air systems. The newly-started VTO *Battery500* projects are also managed in conjunction with this program element.

New Focus. Currently there is new focus on three areas of battery research. The first area is concerned with enabling *extreme fast charging* (XFC) in enhanced Li-ion systems. It started with a 2017 research project to understand XFC and has been followed by a set of XFC awards (listed later in this section). In the second area, recognizing the issues of price volatility and supply reliability with cobalt DOE recently started new projects to develop and optimize low cobalt cathode materials. The third area consists of a set of recently-awarded *recycling and sustainability* projects, which involve studies of full life-cycle impacts and costs of battery production and use; cost assessments and impacts of various battery recycling technologies; and the material availability for recycling and secondary usage and their cost impacts.

As a further resource, the Electrochemical Energy Storage Roadmap describes ongoing and planned efforts to develop electrochemical storage technologies for PEVs and can be found at the EERE Roadmap page <http://energy.gov/eere/vehicles/downloads/us-drive-electrochemical-energy-storage-technical-team-roadmap>. VTO also has extensive ongoing *collaboration* efforts in energy storage R&D across the DOE and with other government agencies. It coordinates efforts on energy storage with the Office of Science, and the Office of Electricity. Coordination and collaboration efforts include membership and participation in the Chemical Working Group of the Interagency Advanced Power Group (IAPG), in program reviews and technical meetings by other government agencies, and the participation of representatives from other government agencies in the contract and program reviews of DOE-sponsored efforts. DOE also coordinates with the Department of Army's Advanced Vehicle Power Technology Alliance, the Department of Transportation/National Highway Traffic Safety Administration (DOT/NHTSA), the Environmental Protection Agency (EPA), and the United Nations Working Group on Battery Shipment Requirements. Additional international collaboration occurs through a variety of programs and initiatives. These include: the International Energy Agency's (IEA's) Hybrid Electric Vehicles Technology Collaboration Program (HEV TCP); the G8 Energy Ministerial's Electric Vehicle Initiative (EVI); and bilateral agreements between the U.S. and China. The collaborative activities with China under U.S. China CERC.

Battery Highlights from FY 2018

The following are some highlights associated with battery R&D funded by VTO (including highlights related to market developments, R&D breakthroughs, and commercial applications).

Battery cost reduction. The 2018 DOE PEV battery cost reduction milestone of \$200/kWh was accomplished. DOE-funded research has helped reduce the current cost projection for an EV battery (for three DOE-funded battery developers) to an average of \$197/kWh of useable energy. This cost projection is calculated using ANL's public domain Battery Production and Cost model (BatPaC). It assumes a production volume of at least 100,000 batteries per year, the batteries meeting DOE/USABC system performance targets. DOE's goal is to continue to drive down battery cost to \$100/kWh by 2028.

DOE awards to develop cells enabling extreme fast charge. Extreme fast charging of EV batteries would provide a refueling experience similar to conventional gasoline powered vehicles. To help achieve this capability, DOE awarded nine projects to develop cells with EV energy densities but that are also capable of being fast charged. The projects awarded are shown in Table 3.

Table 3: Extreme Fast Charging Project Awards

Awardee	Description	Funding
The Regents of the University of California, University of California San Diego	Research surface-acoustic wave turbulent electrolyte mixing during charging to enable rapid charging.	\$653,641
Pennsylvania State University	Research advanced battery cell designs and strategies to operate and improve life and fast charging at higher temperatures.	\$1,000,000
Regents of the University of Michigan	Research three-dimensional hierarchical graphite architectures for anodes for fast charging.	\$1,500,000
SLAC National Accelerator Laboratory	Research on an advanced electrolyte and optimized cell design to enable extreme fast charging.	\$1,500,000
Oak Ridge National Laboratory	Novel electrolyte research that increases the transport rate of lithium-ion from cathode to anode.	\$900,000
Microvast, Inc.	Develop new electrolyte additives, optimized active materials, and electrode formulations.	\$1,500,000
The Research Foundation for the SUNY Stony Brook University	Research to control lithium deposition over-potential on metal-coated graphite electrodes.	\$800,000
University of Tennessee	Research on high power, doped titanium-niobium oxide anodes.	\$720,000
Coulometrics, LLC	Research advanced battery cell designs with lower resistance to enable extreme fast charging.	\$1,000,000

DOE awards low Cobalt cathode projects. Recognizing the issues of price volatility and supply reliability with cobalt, in 2018, DOE awarded six new projects to develop and optimize low cobalt cathode materials. The projects awarded are listed in Table 4.

Table 4: Low Cobalt/No Cobalt Project Awards

Awardee	Description	Funding
Cabot Corporation	Aerosol manufacturing technology for production of low-cobalt lithium-ion battery cathodes	\$2,989,057
NexTech Materials, Ltd. dba Nexceris, LLC	Cobalt-free lithium manganese nickel titanium oxygenate spinel cathodes for next generation lithium-ion batteries	\$2,466,547
Oak Ridge National Laboratory	Cobalt-free aluminum iron nickelate cathode materials for next generation lithium-ion batteries.	\$2,100,000
Penn State University Park	High-performance coated low-cobalt cathode materials for lithium-ion batteries	\$1,952,017
University of California: San Diego	Cobalt free cathode materials and novel architectures	\$2,500,000
University of California: Irvine	Enhancing oxygen stability in low-cobalt cathode materials	\$2,500,000
University of Texas at Austin	High-nickel cathode materials for high-energy, long-life, low-cost lithium-ion batteries	\$2,400,000

DOE Establishes Recycling R&D Center. In 2019, VTO launched the ReCell Battery Recycling R&D Center, a \$4M/year effort by a multiple lab consortium with ANL, NREL, and ORNL which will focus on novel approaches to recycling to maximize economic yield of batteries at their end of life. This is expected to increase the rate of recycling for lithium-ion batteries and decrease dependence on foreign sources for critical materials. The focus areas of the ReCell Center include direct recovery of cathode material, separation methods, battery design for recycling, recovery of other materials, and advanced characterization of recycled material.

Battery500 Cell Achieves 310Wh/kg and 275 cycles, 350Wh/kg and 150 cycles. The Battery500 team succeeded in preparing rechargeable Li metal batteries that achieved 275 cycles with an initial specific energy of 310 Wh/kg. A second generation Li metal/NMC811 cell that is currently cycling shows a beginning of life (BOL) specific energy of 350Wh/kg and has reached 150 cycles of operation with less than 10% capacity fade, see Figure 4. PNNL prepared the cells and INL performed validation and electrochemical analysis.

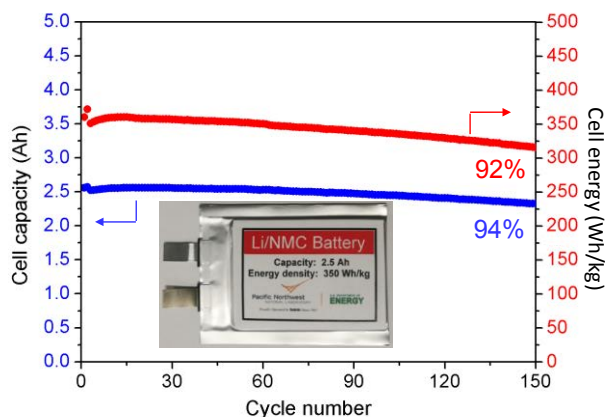


Figure 4. Cell capacity (blue) and the energy (red) of a 2.5 Ah pouch cell as a function of cycling. The cell energy was measured based on the weight of the whole pouch cell including all cell components. The cell was charged within 10 hours (C/10) and discharged within 3 hours (C/3).

Insights on the Stabilization of Nickel-rich NMCs. Researchers at ANL have developed a model system to monitor the stability of nickel at the surfaces of high Ni NMC-type cathodes in a working cell. Early results show that the prototypical ALD surface coating, Al_2O_3 , does not stabilize surface nickel which may help to explain why this strategy has not enabled long-term, high-voltage stability.

Stabilized Anode Interface Enables Improved High-Voltage Stability of NMCs: Researchers have shown that extremely robust anode SEI can be formed electrochemically using advanced, high-voltage, fluorinated electrolytes. The newly discovered interphases were found to reduce the effects of electrode crosstalk and improve cycle-life at high voltages, Figure 5.

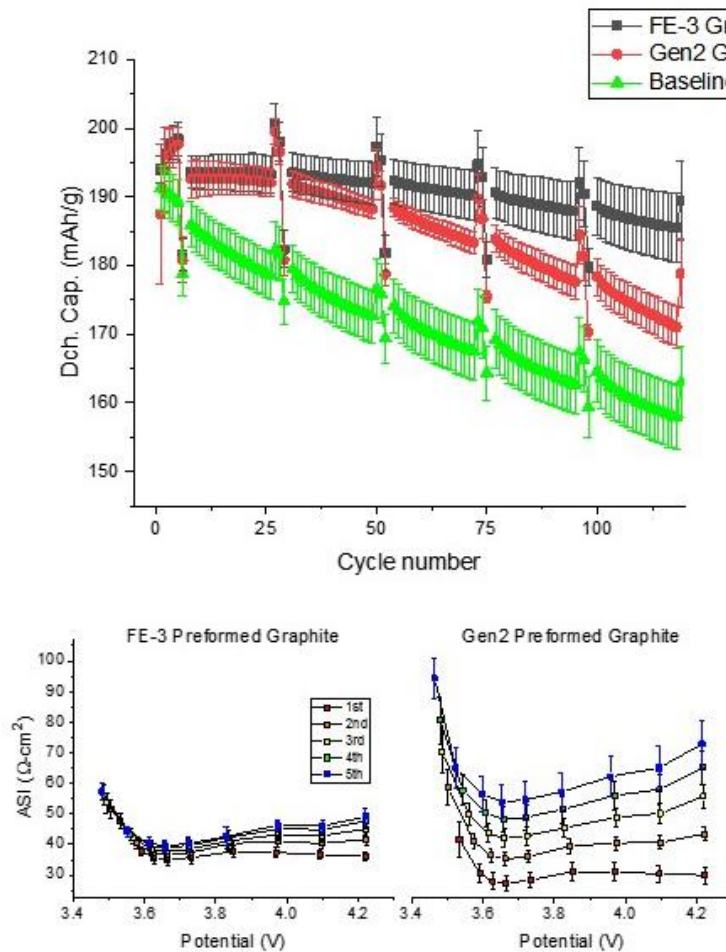


Figure 5. (Top) Battery cycle life for cells formed using a fluorinated electrolyte (FE-3), Gen2 electrolyte, or pristine graphite (baseline) showing better retention for FE-3 preformed graphite (FE-3 Gr). (Bottom) Impedance growth (power loss) over the course of the cycling shown in the top for cells containing FE-3 (left) and Gen2 (right) preformed graphite showing improved power retention on left.

Time-dependent Effects of Electrolyte Additives Reveal Improved Performance in High-Voltage NMC Cells. Researchers at ANL have discovered that certain additives, if allowed to properly “age” in common electrolyte formulations, undergo chemical transformations that result in the stabilization of NMC cathodes under high-voltage operation. These insights, supported by calculation, may lead to improved designs for high-voltage additives.

DFEC-Based Polyfluorinated Electrolyte for High Voltage Li-ion Cells. The oxidation stability of the new electrolyte suppresses transition metal dissolution and the deposition on the graphite anode affording a high voltage NMC/graphite cell with exceptional cycling stability, Figure 6.

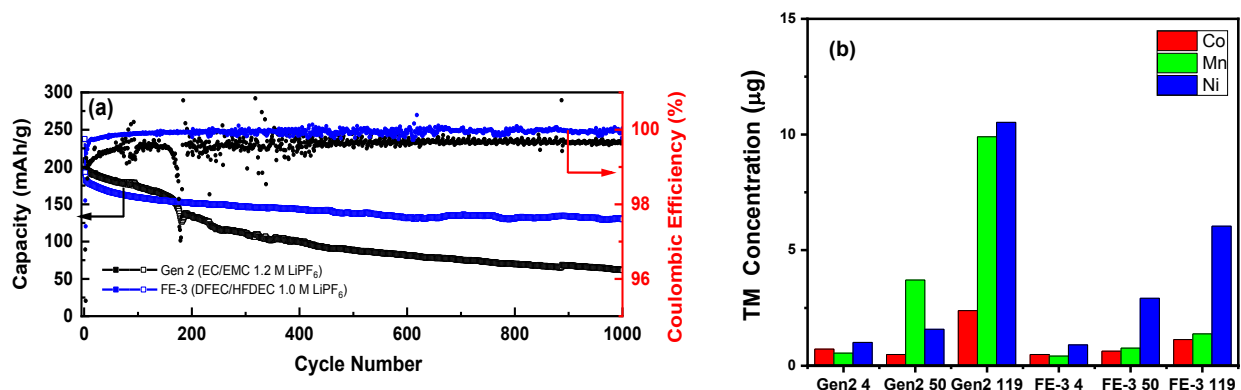


Figure 6. (a) Capacity retention and Coulombic efficiency of NMC532/graphite cells with Gen 2 and FE-3 electrolyte, and (b) TM (Ni, Co, Mn) dissolution at various testing conditions.

Production of low cost graphite: Coulometrics has developed a new technology to produce graphite that is safe for the environment and at a significantly lower cost. Coulometrics recently leveraged its SBIR work to establish an exclusive joint venture with Novonix, called PUREgraphite, to develop, manufacture and sell these high-performance anode materials into the global Li ion battery market. Coulometrics is projecting that their graphite should cost 50% as much as conventionally produced graphite. LIB cycling data at 40°C to 100% depth of discharge is shown in the Figure below and exhibits excellent stability to over 2,000 cycles, Figure 7.

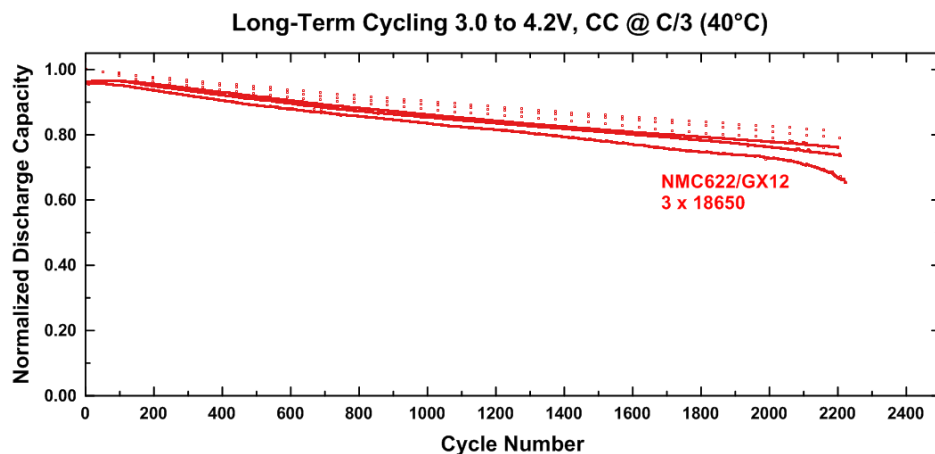


Figure 7. GX12 exhibiting excellent cycle stability with over 2,000 cycles at 40 °C.

40°C Extreme Fast Charge Cell. A team at Penn State University has devised an approach that enables 15-min fast-charging of Li-ion batteries at any temperatures (even at -50 °C) while still preserving cycle life (4,500 cycles, equivalent to >12 years of operation) thus making EVs truly weather-independent. The team uses a rapid internal fast-heating step prior to charging. The self-heating LiB structure has thin Ni foils embedded inside a cell that can create rapid and uniform heating. The Ni foil becomes an inherent component of a single cell along with the electrodes and electrolyte. It serves as an internal heating element, as well as an internal temperature sensor. The Ni foils only add 0.5% weight and 0.04% cost to a conventional LiB single cell. Figure 8 shows the total charge time to reach 80% SOC and the 1C specific energy in the subsequent discharge of each cycle. It can be seen that the Gen-1 cells sustained 700 XFC cycles before reaching 20%

energy loss. Earlier testing showed that higher power cells subjected to similar cycling reached end of life after 100 cycles without the internal heater vs. >800 cycles with it (data not shown).

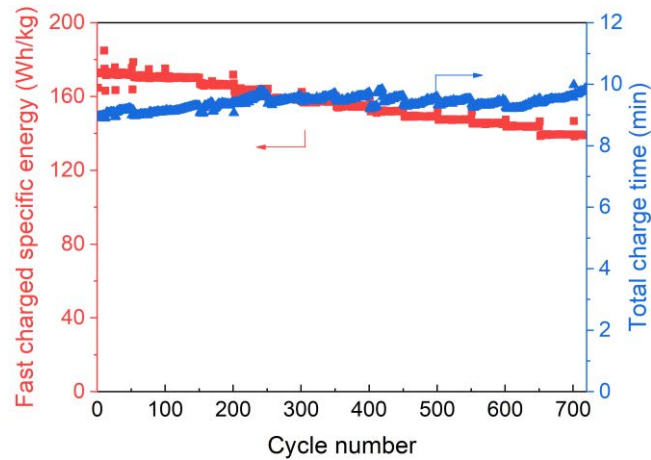


Figure 8. Dischargeable specific energy at 33Ah size and total charge time of each extreme fast charging cycle. The cell is charged at 6C to 80% state of charge in each cycle.

3D electrodes as Li metal hosts. 3D electrodes were prepared using ALD-coated hollow carbon spheres (HCS). The thin ALD coating seals the micropores of HCS to keep the electrolyte from contacting Li occupying the center; the liquid electrolyte only contacts the outer surface of ALD $\text{Al}_2\text{O}_3/\text{HCS}$. 500 cycles, over 3 months, was achieved without fluctuations in the Coulombic efficiency, see Figure 9.

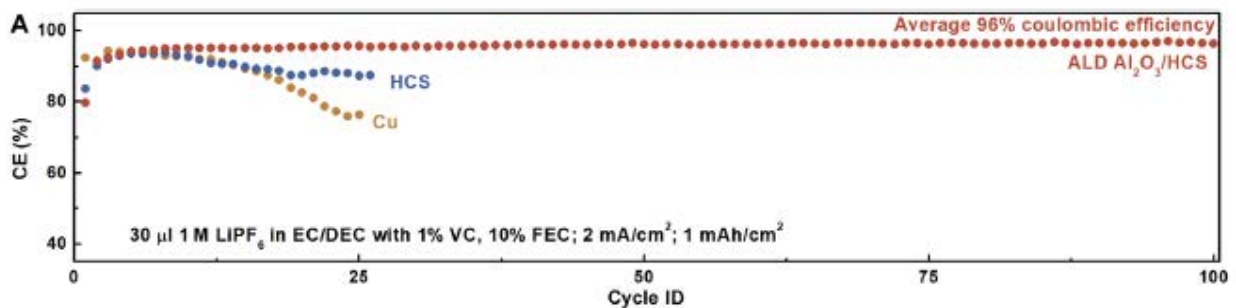


Figure 9. Cycling performance in carbonate electrolyte and study of failure mechanisms. (A) Coulombic efficiency versus cycle number plots of Cu, HCS, and ALD $\text{Al}_2\text{O}_3/\text{HCS}$ in 30 μl of EC/DEC electrolyte with 1 M LiPF_6 , 1% VC, and 10% FEC.

Predictive Modeling of Electrode Tortuosity (NREL). Under the XCEL fast-charge program, ANL observed differences in 6C charge performance from their library of graphite electrodes. To quantify the role of the graphite's microstructures, NREL used 3D geometries reconstructed from tomographic images to calculate multiple metrics of electrochemical performance. Differences in ionic tortuosity calculated by the microstructure model quantitatively explain differences in 6C charge capacity measured by ANL across the graphitic electrodes. Particle sphericity and the orientation of the particle long-axis with the electrode plane are key predictors of electrode tortuosity and thus fast-charge performance. The microstructure method, including a numerically generated carbon-binder inert phase developed under CAEBAT, was published in October in the *J. E. chem. Society* and validated versus several experimental measurements of tortuosity.

Passive Relithiation Doubles Lifetime of ANL's Si/Graphite-Blended Cell. High-energy Si electrode cells experience a loss of Li with cycling, therefore limiting their storage capacity as they age. Prelithiation strategies require costly and time-consuming manufacturing steps and can only be done once. In contrast, NREL's patent-pending Li-reservoir device is easily added during cell production and can relithiate the cell

multiple times or continuously throughout its lifetime. When the device was incorporated into a 400-mAh Si-Gr/NMC532 pouch cell produced by ANL's Cell Analysis, Modeling and Prototyping (CAMP) facility, the lifetime of two treatment cells undergoing passive relithiation experienced a 145% life extension compared to the baseline cell, see Figure 10. The passive relithiation was accomplished with no external controller or power source. Relithiation showed no effect on the cells' power fade. The technique shows promise to make high energy density Si-based cells market-ready for EVs.

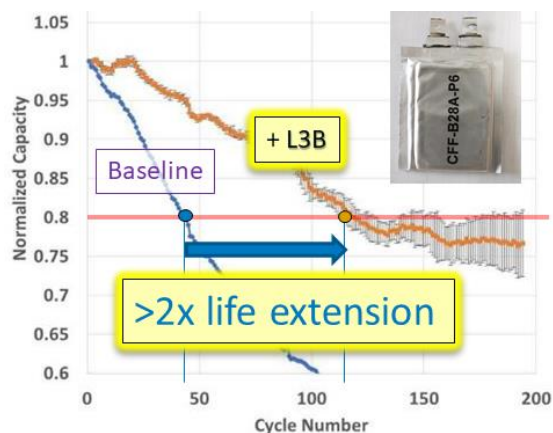


Figure 10. Demonstration of life extension for Si/graphite pouch cell using passive/internal release from Li reservoir.

Fast Charging Solid-State Lithium-Metal Batteries. Solid-state batteries are considered the future of energy storage because they enable the use of high capacity lithium-metal anodes and provide improved safety due to the nonflammable solid-state electrolytes. The limiting issue has been the high lithium-electrolyte interfacial resistance and the formation of lithium dendrite shorts at high current density. Researchers at the University of Maryland have addressed these issues by modifying the lithium-electrolyte interface and developing a unique 3D extended electrode-electrolyte structure achieving DOE's Fast Charge goal of 10 mA/cm² for lithium metal cycling across a nonflammable solid-ceramic electrolyte with low resistance and no degradation/shorting at room temperature.

Development of Low-cobalt Cathodes for High-energy-density Lithium-ion Batteries. The limited availability and the high cost of cobalt can become an impediment to the electrification of the transportation sector. A team at the University of Texas at Austin has developed oxide cathodes with an ultra-low cobalt content of less than 6 wt.% while increasing the energy density beyond the current lithium-ion technology with long cycle life in pouch cells paired with graphite anode, see Figure 11.

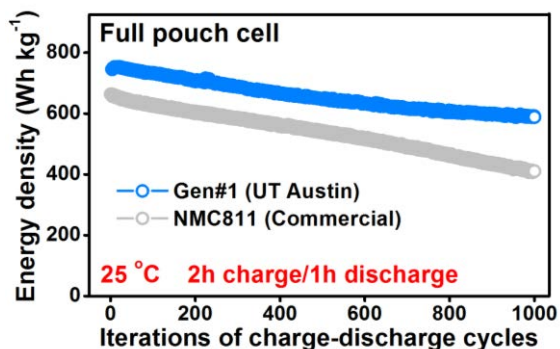


Figure 11. Energy density of generation 1 (Gen #1) proprietary, LiNi_{1-x}M_xO₂ ultralow-cobalt material compared with state-of-the-art commercial LiNi_{0.8}Co_{0.1}Mn_{0.1}O₂ (NCM811) cathode cycled in full pouch cells paired with graphite anodes.

Development of Lithium-sulfur Batteries with Practical Parameters. Sulfur is abundant and inexpensive, but the commercialization of lithium-sulfur batteries is hampered by poor cycle life. The high performances of lithium-sulfur cells reported in the literature are often obtained by using an insufficient sulfur loading of $< 4 \text{ mg/cm}^2$ and sulfur content of $< 60 \text{ wt.}\%$ and an excess electrolyte/sulfur (E/S) ratio of $> 11 \text{ }\mu\text{L/mg}$ along with the extra mass from the aluminum current collector ($\sim 5 \text{ mg cm}^{-2}$). All of these factors severely reduce the final cell energy density. A team at the University of Texas at Austin has developed lithium-sulfur batteries with high sulfur loading and content and lean electrolyte with competitive energy density. This work demonstrates a new concept by designing a three-dimensional, conductive cathode substrate with low surface area and nanoporosity that enables high sulfur loadings (13 and 17 mg/cm^2) and sulfur contents (75 and $80 \text{ wt.}\%$) with an extremely low electrolyte/sulfur ratio of $4.0 \mu\text{L/mg}$ (Figure 12).

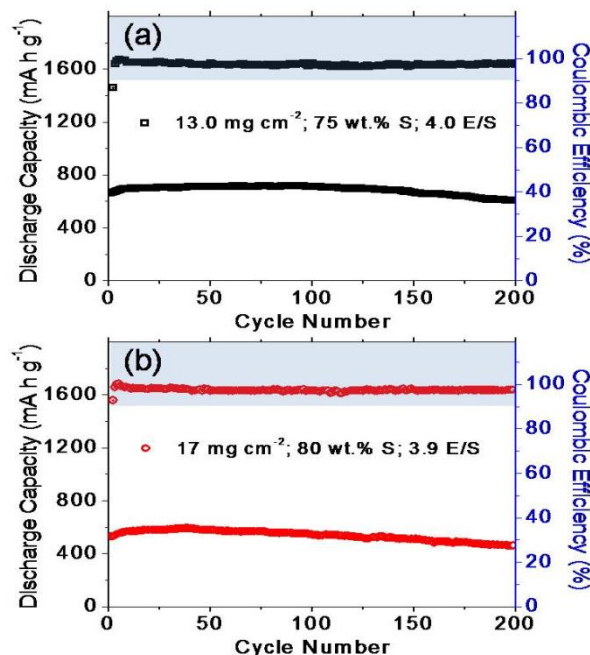


Figure 12. (a) Cyclability of the cells fabricated with the carbon-paper cathodes with a sulfur loading, sulfur content, and E/S ratio of, respectively, (a) 13 mg/cm^2 , $75 \text{ wt.}\%$, and $4.0 \mu\text{L/mg}$ and (b) 17 mg/cm^2 , $80 \text{ wt.}\%$, and $3.9 \mu\text{L/mg}$.

Water Processing of Low-Co NMC 811 Cathodes. A team at ORNL has investigated water processed low-Co-containing and high-energy NMC 811. XRD, Raman spectroscopy, XPS, and TEM studies verified that there was no change in the bulk structure of the 811 with long-term water exposure, and only small changes in the surface chemistry. Figure 13 shows the capacity retention (0.33C/-0.33C cycling) for single-layer pouch cells for NMC 811 aqueous processing compared to: 1) the NMP/PVDF processed baseline; and 2) NMC 811 exposed to water for 4 hours before processing with the standard NMP/PVDF formulation. The water exposed NMC 811 processed in NMP shows a similar capacity fade to the aqueous processed case. However, all three cases show excellent capacity retention. The aqueous processed cells and NMP processed cells exhibited $\sim 75\%$ and $\sim 80\%$ capacity retention through 1000 cycles, respectively. It was also observed that the differences in capacity fade for all three cases occur within the first ~ 100 cycles, and the capacity fade slopes were similar from that point on. It is thought that this slight difference in early capacity retention is due to surface chemistry changes of the NMC 811 during aqueous processing and could be remedied with shorter mixing times or a surface protective coating.

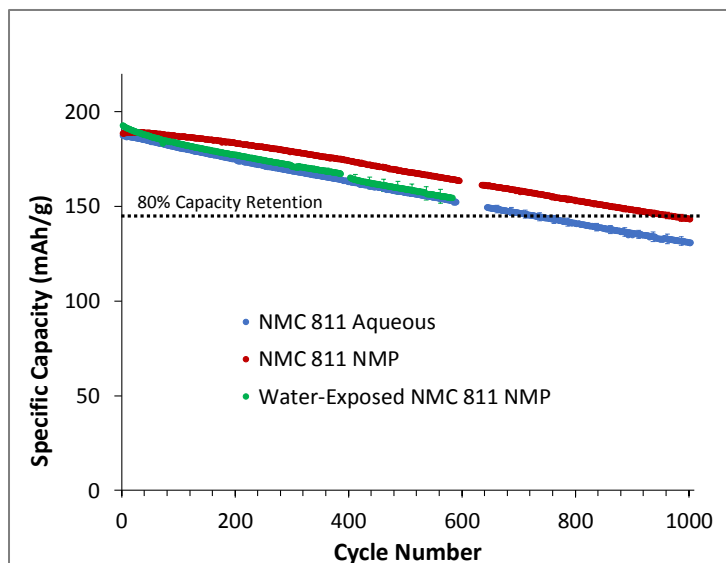


Figure 13. Capacity retention of NMC 811 / graphite pouch cells (11.3-11.6 mg-NMC/cm²) cycled at 0.33C/-0.33C up to 4.2 V. Comparison between standard processing (dark red line), water-exposed NMC 811 prior to NMP/PVDF processing (green line), and aqueous processing (blue line).

Cell using recycled NMC achieves >3000 cycles. A team consisting of Worcester Polytechnic Institute (WPI), Battery Resources and A123 Systems recycled more than 1 full pack each of spent GM Volt cells, Focus EV cells and FCA 500-e cells, generating several hundred kilograms of cathode powder. The powder was used to make multiple lots of 1Ah and 11Ah cells, each from a different combination of incoming cell chemistries, and to demonstrate the process' ability to make consistent NMC from a variable feedstock. Each build was accompanied by a control lot of equivalent cells made using commercial cathode powder for side-by-side evaluation. The data below, Figure 14, shows 3 lots of 1Ah cells using recycled NMC111 made from *different* input feeds, as well as the control group (purple) made from commercial NMC111. The recycled lots have achieved 3,800 cycles to date under an aggressive cycling regime, and all 3 exhibit less capacity fade than that of the control group.

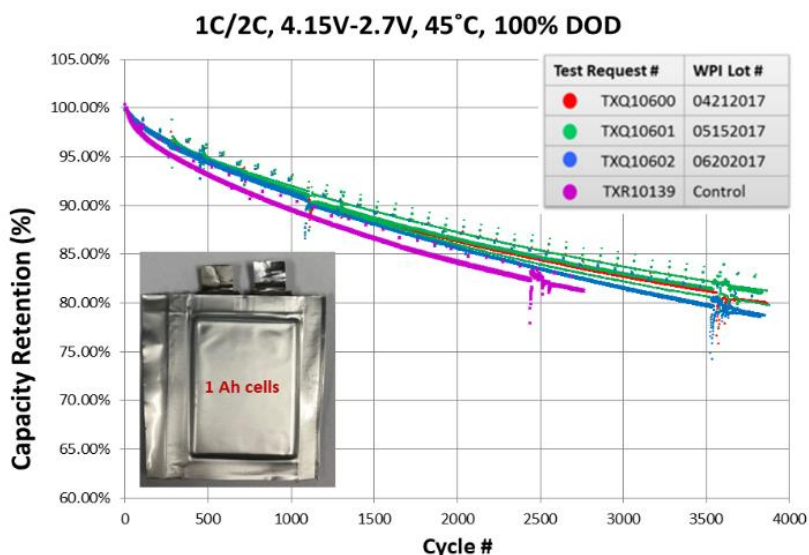


Figure 14. Results from 1Ah cells made with recycled cathode NMC111 shown in red, green and blue. Results from control cells made with commercial NMC111 shown in purple.

(This page left intentionally blank)

I. Advanced Battery and Cell Research and Development

I.1 USABC Battery Development & Materials R&D

I.1.A High Energy Lithium Batteries for Electric Vehicles (Zenlabs Energy)

Herman Lopez, Principal Investigator

Zenlabs Energy Inc.
3390 Gateway Blvd.
Fremont, CA 94538
E-mail: mherman@zenlabsinc.com

Brian Cunningham, DOE Technology Development Manager

U.S. Department of Energy
E-mail: Brian.Cunningham@ee.doe.gov

Start Date: June 1, 2014

End Date: December 31, 2018

Project Funding: \$7,700,000

DOE share: \$3,850,000

Non-DOE share: \$3,850,000

Project Introduction

In order to reduce our dependence on fossil fuels and decrease greenhouse gas emissions, electric vehicles (EVs) have received intense attention as a possible solution. One of the main barriers preventing widespread adoption of EVs relates to the lack of available high energy, low cost and safe energy storage. Lithium ion batteries (LIBs) are presently the best energy storage solution used in current EVs sold. Further improving the performance of LIBs by integrating high capacity active materials, novel passive components and unique cell designs will be critical for the success and mass adoption of EVs.

This project is developing a new battery system based on novel high capacity Ni-Co-Mn (NCM) cathodes and high capacity silicon-based anode composites that could meet the USABC EV cell performance targets for 2020. In order to enable high Si-content anodes, a manufacturable and cost effective pre-lithiation process will need to be developed to compensate for the high irreversible capacity loss (IRCL) of the anode. At the conclusion of the program, Zenlabs aims to demonstrate LIBs with usable specific energy greater than 300 Wh/kg while maintaining other performance requirements of EV cells, including power, calendar life, cycle life, safety and cost. This will be achieved through a collaborative effort across several organizations, where each organization provides expertise on specific components of the material, processing and cell. Ultimately, large format cells meeting the USABC goals will be built and delivered to the National Laboratories for testing.

Objectives

- Develop high capacity silicon-based anode composite electrodes capable of supporting long cycle life by controlling electrode pulverization, lithium consumption and conductivity loss.
- Develop high capacity NCM cathodes capable of supporting the energy, cycle life, calendar life, power, safety and low/high temperature cell requirements.
- Develop a manufacturable and cost effective pre-lithiation process that enables the fabrication of large-format high-capacity pouch cells.
- Screen and down-select best electrolyte and separator to support meeting the USABC performance, cost and safety cell targets.
- Design and optimize the active and passive cell materials along with the cell design to meet the USABC EV cell goals.

- Design and develop large format 50 Ah capacity pouch cells to meet the USABC EV cell goals.
- Build, deliver and test large format (11 Ah and 50 Ah capacity) pouch cells integrating high capacity Si-based anode and cathode composites along with optimized electrolyte, separator and pre-lithiation process that meet the USABC EV cell goals.

Approach

Zenlabs is utilizing a system-level approach to screen, develop and optimize the critical cell components (cathode, anode, electrolyte, separator), pre-lithiation process (process, dose), cell design (N/P ratio, electrode design) and cell formation and testing protocols that will enable meeting the USABC EV cell level goals for the year 2020. The development consists in integrating high capacity Ni-rich Ni-Co-Mn cathodes, pre-lithiated silicon-based high capacity anodes, high voltage electrolytes and separator into large capacity (10-60 Ah) pouch cells. The developed cells will exhibit high energy density and power, good cycle life and calendar life and acceptable low temperature performance while meeting the cell level cost and safety targets. Cells will be delivered and tested by three National Laboratories: Idaho National Laboratory (INL), Sandia National Laboratory (SNL) and National Renewable Energy Laboratory (NREL).

Zenlabs is leveraging its material, process and cell development expertise to develop, modify and engineer material and cell-level solutions to meet the cell specifications. During this project, Zenlabs partnered with leading companies like Daikin America (electrolyte), Asahi Kasei (separator), Nanoscale Components (pre-lithiation processing), A123 (cell manufacturing), 3M (Si alloys), and DuPont (n-Si composites), to screen and develop the best materials, processes and cells. Having the proper partnerships will increase the probability of meeting the USABC project goals by leveraging the strength of each of the partner, with Zenlabs mainly focusing on its core strengths of anode and cathode development, and cell design. Partnering with large OEMs also ensures that any developed technology will have a clear path to high volume production and commercialization.

The program has been structured in a way that as it progresses, the cell targets increase with respect to specific energy, energy density, cycle life and lower cell cost. The program consists of 5 cell builds that include 2 internal builds (#1 and #3) and 3 builds (baseline, #2 and #4) intended to deliver cells to the National Laboratories. The program has completed internal cell build #3, which is an internal cell build developing ~11 Ah capacity cells with specific energy >300 Wh/kg and a cycle life targeting 1000 cycles. The cell development of cell build #3 served to freeze the final cell design of the program (build #4).

Figure I.1.A.1 shows the measured and projected usable BOL (beginning of life) and EOL (end of life) specific energy, energy density, cycle life and cell cost for the various program cell builds. Different cell builds focused on different format and capacity cells. The baseline cell build consisted of 21Ah capacity cells, cell build #1 consisted of smaller 1.2 Ah capacity cells, cell build #2 and #3 consisted of 11 Ah capacity cells, while the remaining cell build #4 will focus on both 11 Ah and 50 Ah capacity cells. The equivalent 50 Ah capacity cell data is also shown in the figure for the different builds by the dotted boxes.

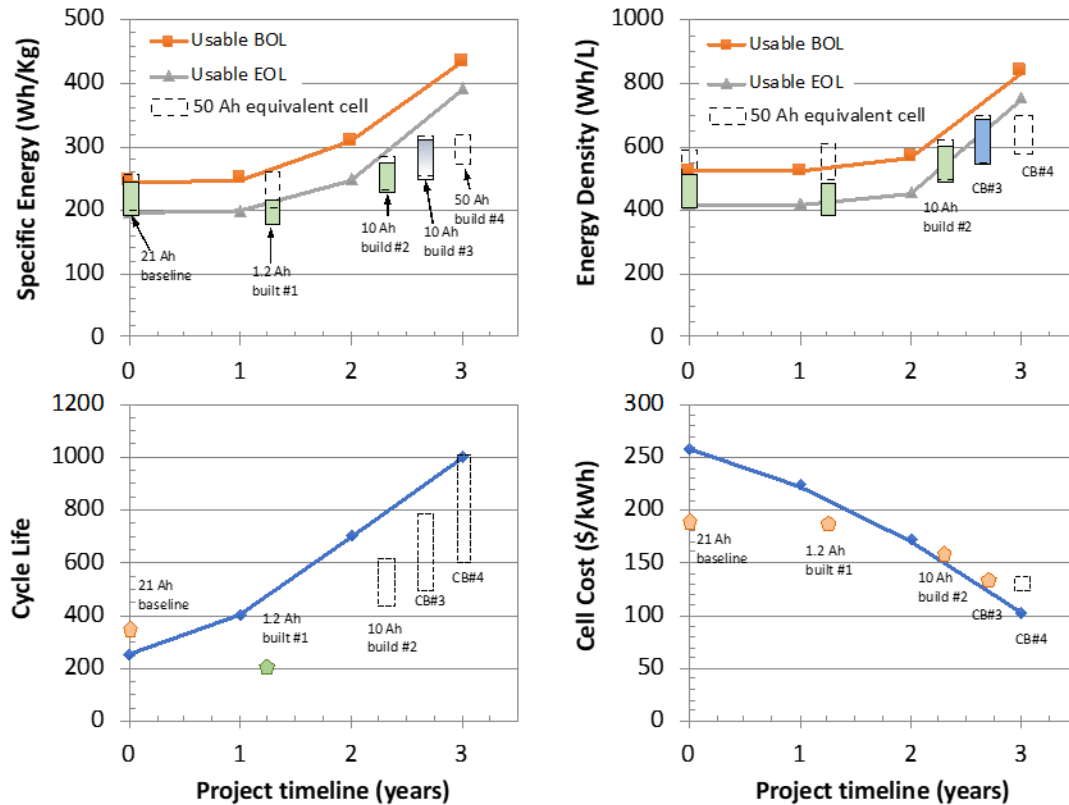


Figure I.1.A.1 Current and projected cell development progression throughout the USABC program

Results

Pre-lithiation Development: A consequence of working with high capacity silicon-based anodes, and especially with SiO_x -based materials, is an inherent high irreversible capacity loss (IRCL). In order to compensate for this loss, pre-lithiation of the anode is required specially when working with high percent containing SiO -based anode formulations. Zenlabs partnered with Nanoscale Components, which pre-lithiates anodes via a scalable, manufacturable and cost-effective roll-to-roll electrochemical process. Nanoscale has completed its larger pilot scale pre-lithiation line and has shown promising pre-lithiation results, but there have been challenges pre-lithiating the Zenlabs SiO_x -based anodes to the full required dose. The challenges are related to stress created on the electrode during the pre-lithiation process and pending concerns with aging and storage of the pre-lithiated electrodes prior to cell assembly. Even though the electrochemical pre-lithiation process is promising, it is currently not ready for implementation in the final cell deliverable of the program scheduled for delivery in December 2018. The final cell deliverable of the program (CB#4) will continue using lithium metal powder as the source for pre-lithiation. Zenlabs has extensive experience working with lithium metal powder as the pre-lithiation source. Unfortunately, there were some problems with the incoming material. The lithium powder was observed to have a different color, agglomerated particles and it was sticking during processing. These changes created problems in the pre-lithiation process, cell assembly and cell performance resulting in delays in the program. After a few iterations working with the vendor, the material properties were improved and the processing and cell performance was re-qualified. Using lithium metal powder continues to be the process that will be used for the final cell deliverable of the program.

Cell Development: Various 11 Ah capacity cell designs incorporating different NCM cathodes, SiO_x -C anode formulations and electrode and cell specifications have been evaluated as part of the internal cell build #3 (CB#3) development. Figure I.1.A.2 compares the normalized capacity versus cycles at a 1C rate for the different designs. C/3 rate is the standard rate for the USABC program, but it was agreed to use a faster 1C rate to expedite the cycle life feedback. All designs shown in Figure I.1.A.2 show a specific energy >300 Wh/kg

when tested at a $C/3$ rate and understandably lower < 300 Wh/kg at the higher 1C rate. Evaluating the cycling performance of the cells at a 1C rate produces cycling data two times faster than cycling at the slower $C/3$ rate. The final cells of the program will be tested according to USABC specification of $C/3$ rate both at Zenlabs and at the National Laboratories. The cycling data for Design F which is the highest energy cell design (320 Wh/kg at 1C rate) shows some of the worst cycling performance reaching 80% capacity retention in ~ 350 cycles. Design H which shows an energy of 290 Wh/kg at a 1C rate also shows similar poor cycling performance comparable to Design F. Both design G and E show improved cycling performance with Design E showing a higher energy of 295 Wh/kg at a 1C rate and approaching 600 cycles with a capacity retention above 80%. For these reasons Design E has been down selected as the final design of the program showing a specific energy > 300 Wh/kg at a $C/3$ rate and a cycle life approaching the target of 1000 cycles before reaching 80% capacity retention. The cycle life is expected to meet the 1000 cycle target, because cells are expected to show improved cycling when cycled at the lower $C/3$ rate compared to the 1C rate shown in Figure I.1.A.2. The down-selected Design E integrates a high active percentage SiO_x -based anode ($> 50\%$ SiO_x) and a Ni-rich NCM cathode.

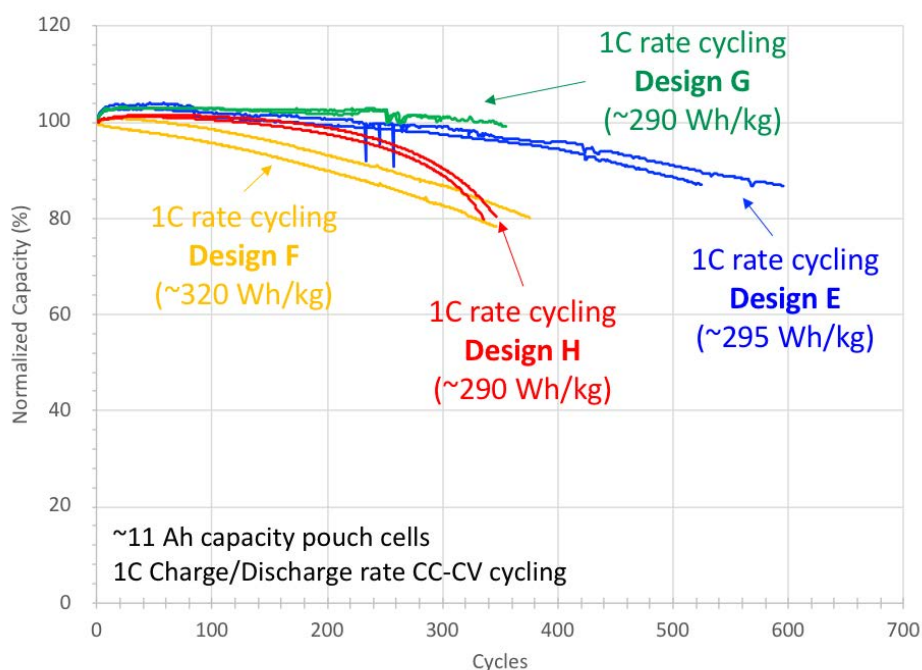


Figure I.1.A.2 Cycle life performance for various high-energy build #3 cell designs

The down-selected cell Design E will be built in the standard ~ 11 Ah capacity (64 mm width x 145 mm length) and larger ~ 50 Ah capacity (102 mm width x 320 mm length) cell footprints. Figure 3 shows a schematic of both cell footprints that are being built as the final cell deliverable (CB#4) of the program. The final cell deliverable of the program consists of delivering 28 (twenty-eight) ~ 11 Ah capacity cells and 5 (five) ~ 50 Ah capacity cells to the National Laboratories in December 2018 for independent testing.

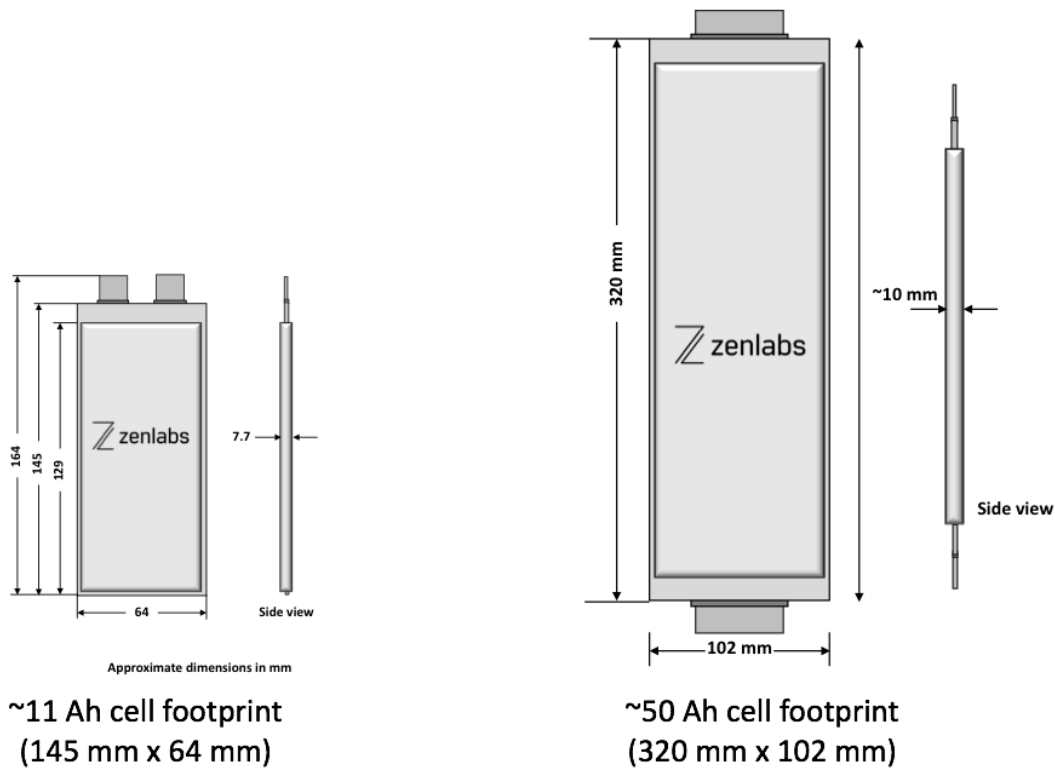


Figure I.1.A.3 Schematic of cell foot prints used in final cell build #4

Zenlabs has developed a larger footprint (102 mm width x 320 mm length) ~50 Ah capacity cell to be used in the final USABC program cell deliverable (Cell Build #4 - CB#4). The larger footprint cell will: a) enable a fair cell comparison to other USABC programs; b) deliver a production representative cell; c) deliver cells which are closer to customer needs; and d) enable gaining experience in building and testing large capacity cells. The exact dimensions for the large foot print cell were decided based on input from the USABC team.

Zenlabs built multiple iterations of the large capacity ~50Ah cells with the cells showing consistent electrochemical performance and physical characteristics meeting the design targets. The cycling performance of the 50 Ah capacity cells are closely matching the performance of the standard size ~11 Ah capacity cells. Figure I.1.A.4 shows the normalized 1C rate capacity versus cycles for two identical cell designs that incorporate the previous baseline NCM cathode blend and SiO_x anode composite in the standard ~11 Ah and larger 50 Ah capacity cell formats. The cycling data for both cell formats are identical nearing 600 cycles and still retaining >90% capacity retention. Cell development on the large 50 Ah capacity cells continues to optimize the reproducibility of the cells as Zenlabs prepares to build and deliver the final cells of the program.

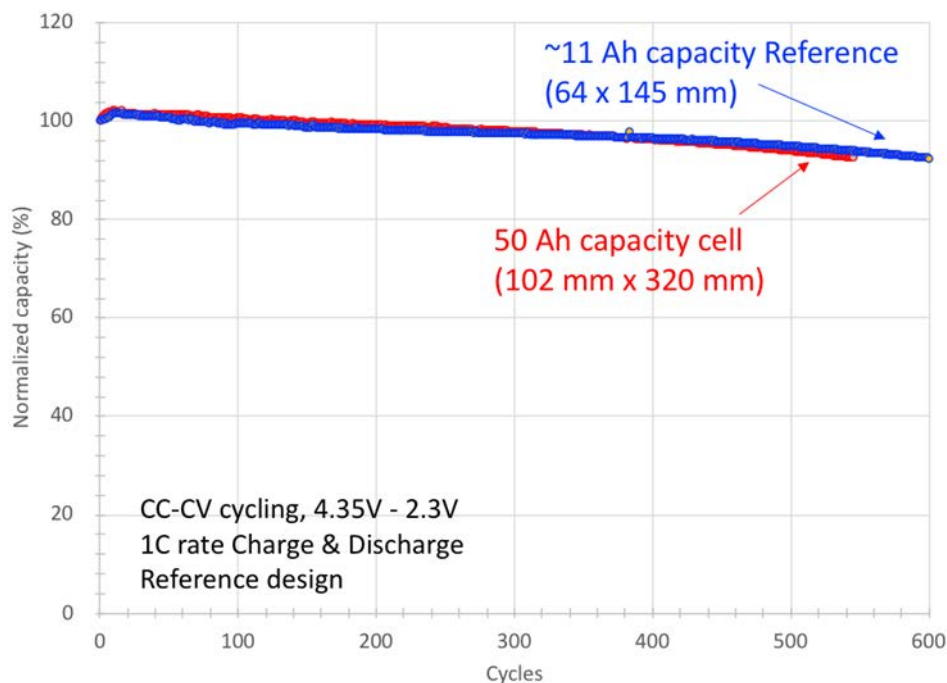


Figure I.1.A.4 Normalized capacity versus cycles for large 50Ah and standard 11 Ah capacity footprint cells

Conclusions

Zenlabs has completed cell build #3 development and has frozen the final cell design for the program. The final cell design will incorporate high capacity Ni-rich Ni-Co-Mn cathode and SiO_x -based anode. The anode will be pre-lithiated using the lithium metal powder process and the cells will be built at Zenlabs cell prototyping facility in Jiaxing, China. Zenlabs has developed and built large foot-print (102 mm x 320 mm) ~50Ah capacity cells that are showing consistency, meet the design targets with cycle life matching the smaller (64 mm x 145 mm) 11 Ah cells. The 50 Ah capacity cells cycling at a 1C rate are nearing 600 cycles and still showing ~90% capacity retention. As part of the final program cell deliverable, two different cell foot-prints (64 mm x 145 mm & 102 x 320 mm) are being built and both are expected to be delivered to the National Laboratories for independent testing in December 2018.

Key Publications

1. "High Energy Lithium Batteries for Electric Vehicles", ES247_Lopez_2018_p, US DOE Vehicle Technologies Program Annual Merit Review, AMR, 2018.
2. "High Energy Lithium Batteries for Electric Vehicles", ES247_Lopez_2017_p, US DOE Vehicle Technologies Program Annual Merit Review, AMR, 2017.
3. "High Energy Lithium Batteries for Electric Vehicles", ES247_Lopez_2016_p, US DOE Vehicle Technologies Program Annual Merit Review, AMR, 2016.
4. "High Energy Lithium Batteries for Electric Vehicles", ES247_Lopez_2015_p, US DOE Vehicle Technologies Program Annual Merit Review, AMR, 2015.

I.1.B High-Performance Semi-Solid Cell for EV Applications (24M Technologies, Inc.)

Mohamed Taggougui, Principal Investigator

24M Technologies, Inc.
130 Brookline Street
Cambridge, MA 02139
E-mail: Mtaggougui@24-m.com

Brian Cunningham, DOE Technology Development Manager

U.S. Department of Energy
E-mail: Brian.Cunningham@ee.doe.gov

Start Date: June 15, 2016
Project Funding: \$6,998,594

End Date: June 14, 2019
DOE share: \$3,499,297

Non-DOE share: \$3,499,297

Project Introduction

24M Technologies has developed a breakthrough manufacturing process that leverages proven and emerging chemistries to deliver lithium-ion batteries with lower cost and less inactive materials content than any existing lithium-ion cell. In this program, 24M will develop large-format, automotive-capable cells leveraging high-energy advanced lithium-ion chemistries. 24M's unique electrode and cell architectures are inherently capable of accommodating large volume-change active materials, and 24M's cells exhibit unprecedented levels of abuse tolerance. The manufacturing process requires less than one half the number of unit operations of conventional lithium-ion technology, and has been demonstrated in automated pilot production.

24M's proprietary flowable (semi-solid) electrode technology enables unique cell architectures with several advantages compared to conventional Li-ion batteries. For automotive applications, a key advantage is the novel manufacturing method, which dramatically reduces manufacturing complexity and cost. Additionally, it is readily scalable according to market demand. The small footprint for equipment and comparatively low capital equipment investment needed further reduce the manufacturing risk.

24M's unique electrode and cell architectures significantly lower the materials cost in each cell. 24M believes that its cell design has lower materials cost per energy (\$/kWh) than any Li-ion cell of comparable energy and power in the market or under development. Cells based on semi-solid electrodes have a higher ratio of active materials to inactive materials than conventional Li-ion cells, providing an inherent, sustainable advantage in the cell bill of materials.

Finally, unlike most development approaches in advanced batteries, 24M's core technologies are platforms for electrode and cell design and manufacturing that are not limited to any particular set of active materials. Therefore, 24M's cells can leverage all of the active materials available today and those developed in the future. As a platform player, 24M maintains the flexibility to drop-in next generation active material as lithium-ion chemistries evolve and as alternative chemistries (such as Na-ion or Mg-ion) emerge.

Objectives

24M will demonstrate that its novel electrode, cell and manufacturing approach can be applied to high-energy density lithium-ion chemistries to enable mass production of automotive-capable prismatic Li-ion cells with dramatically lower cost. The approach outlined below has been planned to develop high energy density semi-solid electrode formulations, and to demonstrate the manufacturing of prototype cells based on those formulations that meet or exceed the USABC targets outlined in Table I.1.B.1 Characteristics of the annual cell deliverables in the program for each phase of the program.

Table I.1.B.1 Characteristics of the annual cell deliverables in the program

	Phase 1	Phase 2	Phase 3
Cell Footprint (cm ²)	80	250	250
Capacity (Ah)	6	11	11
Energy Density* (Wh/L)	400	640	800
Specific Energy** (Wh/kg)	200	290	350
Number of Cells	30	18	18

*Assuming 87% volumetric packing efficiency

**Assuming 95% gravimetric packing efficiency

Approach

24M has planned activities designed to achieve the objectives identified in the preceding section. For each activity, the task-specific objectives and approaches are described.

1. High Energy Materials Evaluation and Selection

Developing new semi-solid electrode formulations utilizing high energy active materials requires evaluation and selection of materials comprising a semi-solid suspension – active materials, additives, and electrolyte – as well as developing an appropriate mixing procedure that yields a semi-solid suspension with excellent electrochemical performance. Different combinations of active materials and additives will be formulated into semi-solid suspensions where the physical properties will be evaluated and ranked. The rheology of the material suspension will also be tested in order to determine the consistency and repeatability of the electrode forming process. Candidate electrode formulations will then be used in cell fabrication to evaluate the electrochemical performance of the electrode. Ultimately, active materials and electrode formulations will be selected that optimally balance the tradeoffs of power performance, safety, processibility, and life (cycle and calendar) in a 24M automotive cell.

2. Processing Methods for Increased Active Solids Loading

Although increases in active solids loading may seem incremental, each time solids loading is increased, an entirely new formulation must be developed, and processing method evaluated to ensure that ion and electron transport and rheological properties are optimized for manufacturing and cell performance. In this activity, 24M's current and alternative mixing methods will be evaluated and developed to obtain semi-solid electrodes with active materials loadings necessary for target high energy densities while achieving cycle life and safety performance target. This activity is complementary to, but distinct from, the active material evaluation and selection activity outlined above. New mixing methods and equipment are continually developed at 24M and these will be evaluated, and as necessary, developed to achieve the active materials loading levels required for a cell meeting the USABC targets. 24M will create quality control metrics and measure electrochemical performance to evaluate the performance of the semi-solid suspensions from the various processing methods.

3. Electrode Architecture Development

24M's current electrode forming process is based on automated dispensing and coating of both anode and cathode semi-solid slurries, using conventional foil current collectors. This activity will evaluate alternative electrode forming methods and cell architectures, including current collectors and investigations into cell formats with increased volumetric efficiency. As 24M continues to transition from pilot manufacturing to high volume manufacturing methods, we anticipate continual improvements in the electrode and cell making operations. Additionally, the ideal processing methods for highly-loaded semi-solid slurries based on high-energy active materials may differ from those developed for earlier electrode formations. Initially, this activity will evaluate current electrode structure and forming methods for compatibility with high energy active materials. Throughout the program, there will be continual evaluations to ensure that the developed cells are capable of meeting or exceeding the automotive power performance requirements. Finally, this area of activity will include a specific focus on safety and abuse testing of the developed 24M automotive cell.

Results

We have achieved notable progress along numerous development pathways, some of the most notable being in the following categories:

Completed installation and commissioning of a new automated pilot manufacturing line: 24M USABC team in collaboration with 24M advanced manufacturing team designed, installed and commissioned a new automated pilot manufacturing line in 24M Cambridge, Boston location. The pilot line enabled 24M USABC team to cast high loading slurries. More than 2000 cathode and anode electrodes, 250cm² size, with area capacity up to 15mAh/cm² have been produced using this new capability. Both cathode and anode slurries are made with 24M proprietary and scalable mixing method and conditions. Slurries are coated using a continuous method.

Successfully identified High loading electrodes power limitation and implemented corrective actions:

The 24M USABC team identified that power limitations are dominated by the cathode, not the anode by using a reference electrode to analyze the voltage drop during high rate discharge. Figure I.1.B.1 shows the full cell voltage and anode potential drop during discharge at different rates. The voltage cutoff in discharge at high rates is dominated by the cathode, not the anode.

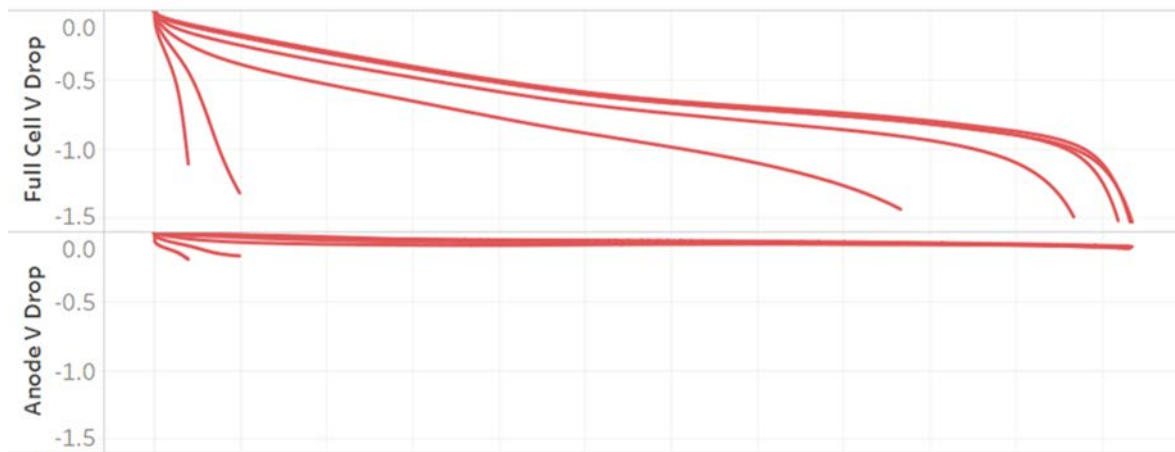


Figure I.1.B.1 Full cell voltage drop and anode potential drop during discharge at different rates

After exploring different semi-solid cathodes slurry compositions and mixing conditions, 24M USABC team successfully developed a cell design, with cathode area capacity of 8.5 mAh/cm², capable of achieving 80% capacity retention at 1C discharge rate (see Figure I.1.B.2).

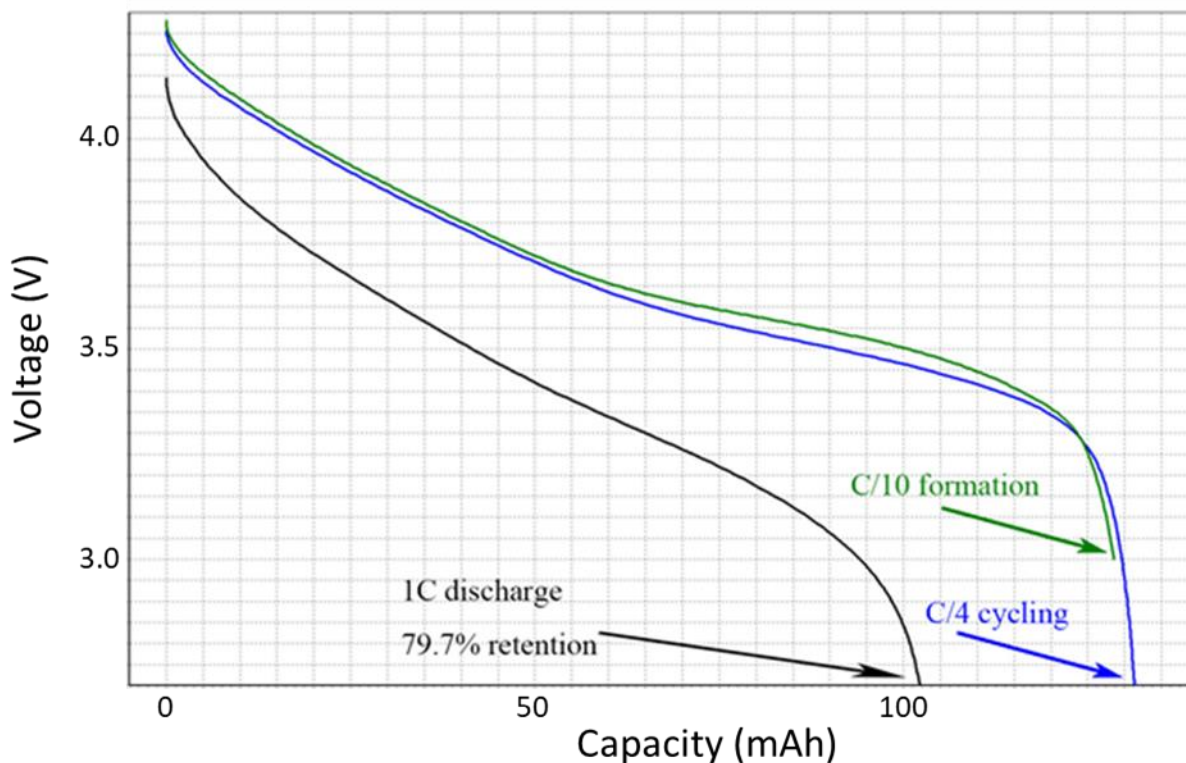


Figure I.1.B.2 Discharge rate capability of R&D full cell using cathode with modified slurry composition

Transitioned pilot manufacturing and processing procedures to NMC811 cathode active material:

The 24M USABC team began the process of transitioning the active material used in its semi-solid cathodes from NMC622 to NMC811 to further improve cell energy density. The difference in physical properties for the NMC811 chosen for development during active material screening compared to the NMC622 that was previously employed necessitated process optimization in order to mix and form semi-solid electrodes of the desired quality and quantity for project Phase 2 development. At the end of this optimization, the 24M build capability for NMC811 matched that achieved with NMC622 materials. Further, the relative ease of transition between NMC622 and NMC811 provides additional evidence that 24M's electrode and cell production method is chemistry agnostic and may be applied to a wide variety of cell chemistries.

Delivered Phase 2 deliverable cells of planned quantity and increased size on schedule:

Stacked cells with 24M's Phase 2 deliverable formulation were built using 24m's new automated pilot manufacturing line and delivered on schedule. The new automated pilot manufacturing capable of building large size electrode allowed 24M to increase phase 2 deliverable cell footprint from 80cm² to 250cm².

18 test units with a nominal reversible discharge capacity of 11.48Ah and a nominal total specific energy density of 257Wh/kg were shipped to designated USABC testing partners. To satisfy internal development needs and the external deliverables, 63 total stacked cells were built towards this milestone. The initial cells were used to validate the process scale-up and the remainder were used for internal testing and/or were yielded out. Table I.1.B.2 below summarize the initial performance of phase 2 deliverable cell.

Table I.1.B.2 Phase 2 Deliverable Cell Initial Performance

	Phase 2 Deliverable
Nominal Capacity, C/3, 25°C	11.48 Ah
Discharge Power Density, 30 s Pulse, 20%SOC	2152 W/L
Specific Discharge Power , 30 s Pulse, 20%SOC	1025 W/kg
Specific Regen Power , 10 s Pulse, 10%SOC	561 W/kg
Total Specific Energy @ C/3 Discharge Rate	257 Wh/kg
Areal Capacity	9.3 mA/cm ²
Nominal Roundtrip Energy Efficiency, C/3 rate	92%
Maximum Operating Voltage, Continuous/Pulse (V)	4.2/4.3
Minimum Operating Voltage, Continuous/Pulse (V)	2.7/2.5
Maximum Self-discharge	<1.5%/month

Confirmed Semi-solid technology creates sustainable cost advantage:

24M USABC team used the USABC cost model and confirmed phase 2 deliverable cells meet the phase target price. 24M semi-solid electrodes enable 25% lower cost (compared to the same design using traditional Li-ion technology) via reduced bill of materials and simplified manufacturing process.

Conclusions

In this program to date, 24M has successfully demonstrated that its unique manufacturing method and electrode format for lithium-ion battery is scalable and agnostic to cathode active material chemistry. Project Phase 2 deliverable cells were produced and delivered to USABC. In addition, the 24M team has made significant progress in improving the semi-solid electrode slurry active loading and cell discharge rate capability.

Key Publications

1. "Semi-solid Lithium-ion: A Breakthrough Battery and Manufacturing Platform," Naoki Ota (invited speaker), International Conference on Advanced Lithium Batteries for Automotive Applications, 2017.

I.1.C Development of High Performance Li-ion Cell Technology for EV Applications (Farasis Energy)

Madhuri Thakur, Principal Investigator

Farasis Energy
21363 Cabot Blvd, Hayward, CA 94545
Hayward, CA 94545
E-mail: kkepler@farasis.com

Brian Cunningham, DOE Technology Development Manager

U.S. Department of Energy
E-mail: Brian.Cunningham@ee.doe.gov

Start Date: February 1, 2017	End Date: September 30, 2019	
Project Funding: \$5,900,000	DOE share: \$2,950,000	Non-DOE share: \$2,950,000

Project Introduction

The goal of this project is to develop a high energy density, low cost Li-ion cell technology that meets the USABC goals for Advanced Batteries for EV's for 2020 commercialization. The major objective of this project, will develop a cell technology capable of providing 350 Wh/kg after 1000 cycles for End of Life (EOL) at a cost target of \$100/kWh. We are targeting a Beginning of Life (BOL) cell level energy density of ~400 Wh/kg in the final cells, giving us an approximately 12% available energy margin to meet the USABC EOL cell level targets. Farasis will head the development effort which will bring together technical contributions from many leaders in the Li-ion technology industry.

Objectives

- Develop a EV cell technology capable of providing 350 Wh/kg after 1000 cycles at a cost target of \$0.10/Wh.
- Develop high capacity cathode materials to meet USABC EV goals through collaborative development efforts with partner organizations.
- Optimization of electrode formulation and fabrication processes to incorporate high-capacity sacrificial Li-source.
- Comparative evaluation of positive and negative electrode active material blends.
- Optimization of negative electrode formulation for maximum energy density and cycle life.
- Investigate effect of Si incorporation on negative electrode conductivity and mechanical stability relative to graphite-only active material electrodes.
- Evaluation of new solvent and salt components for high voltage stability.
- Additive package development to optimize SEI formation on Si anodes.

Approach

- The key barriers of this project are achieving high energy density with stable chemistry to meet cycle life and calendar life goals as well as the manufacturing processes compatible of the new materials. To meet the USABC target of 400Wh/Kg, we need to use high capacity anode (Silicon) and cathode material. To achieve the desire energy density and cycle life, Farasis is doing the screening of critical cells components such as (cathode, anode, electrolyte and separators), Li source development for pre-

lithiation, optimization of Li source, electrode design, cell design as well as the optimization of formation and test protocols. During the first phase, the project focused on screening of the anode and cathode materials in coin cells. The capacity of the cathode should be higher than 200mAh/g and the anode in between 500-1800mAh/g. The materials will further go on screening in single layer pouch cells for its impedance, rate and cycle life. 18650 cells were built using baseline anode and cathode electrodes based on the capacity of the cathode and anode materials to be used for electrolyte optimization as well as for the relative safety of the materials. The results from this initial screening were used to narrow the electrolyte compositions best suited for this chemistry and to be used for further optimization in the second round of small cell builds for the down selected chemistry. Throughout the program Farasis is working on the synthesis of lithium source materials and incorporating them as a pre-lithiation source. A combination of device level testing and fundamental electrochemical measurements are used to guide the development of large form factor cells for Phase II of the project.

- Phase II of the project is scheduled for approximately 17 months and shifts to manufacturing and testing of larger format pouch cells using a refined subset of cell chemistries. Some ongoing chemistry development continued at this stage to address specific issues identified in Phase I builds and to pursue further optimization of cell level performance. This will occur in two iterations starting with capacity of 40 Ah Gen 1 cells and progressing to the final deliverable cells based on a larger pouch cell form factor, which will be capacity of 75Ah using the optimized high-energy cell chemistry. The program has finished the first two cell-builds (baseline and Gen1) and is currently working on final deliverable cell chemistry with pre-lithiation. Phase II will also include testing to guide system development in future applications; these tests will characterize cells in small groups to efficiently evaluate their behavior on a large scale where thermal management, cycling-induced gradients, and failure isolation become important.

Results

Gen 1 Cell Development: Farasis delivered baseline cells for testing during the first six months of the project. To meet the USABC target for Gen 1 (270-300Wh/Kg) deliverable goal, Farasis completed the assembly of 35Ah cells (270Wh/Kg specific energy). The cells are going through internal testing for cycle life, impedance, rate and calendar life. Farasis will deliver 40 Ah capacity pouch cells (17 cells to INL, 10 cells to SNL and 3 cells NREL) by November 2018. In order, to meet the USABC target we will continue to build multiple high capacity cells by implementing the improved chemistry from small pouch cell results (cycle life, impedance, rate and safety) and by optimizing other cells components.

Gen1 Positive and Negative Electrode Technology Development: Farasis has evaluated 12 cathode materials (High voltage NCM, LMR with NCM and Ni rich NCM) in a single layer pouch cell at a fixed capacity of Si anode with a target energy density of 270-300Wh/Kg in 40/75Ah form factor. Based on the results for cycle life, DCR and rate capability Farasis down-selected the cathode materials with a target energy density of 270 /300Wh/Kg in 40 /75Ah form factor. Farasis completed the assembly of the 35Ah pouch cell from the down-select chemistry. Before locking the Gen1 deliverable chemistry we have done a pre-build for the Gen1 with the downselected chemistry. At Farasis we are testing the cells for DST cycle life, impedance and the calendar life. The cell getting delivered to National Labs are 40Ah with energy density of 270Wh/Kg. Figure I.1.C.1 shows the DST cycling data for the Gen1 cells with Ni rich NCM and Si/C composite. In parallel, Farasis is using the down selected cathode material for further optimization of the lithium source in single layer pouch cells to improve cycle life and impedance of cells.

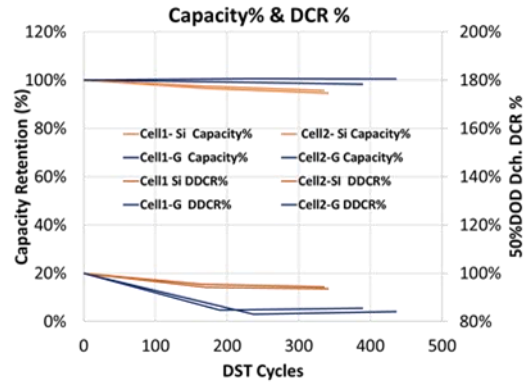


Figure I.1.C.1 DST Cycle life for nickle rich NCM with Si/C composite

The Gen1 cells with the Ni rich cathode and Silicon/Carbon composite anode cell are also tested for the DCR and rate capability. Figure I.1.C.2 shows the DCR and rate capability for the Ni rich cathode and Si/C composite cathode in 35Ah cells.

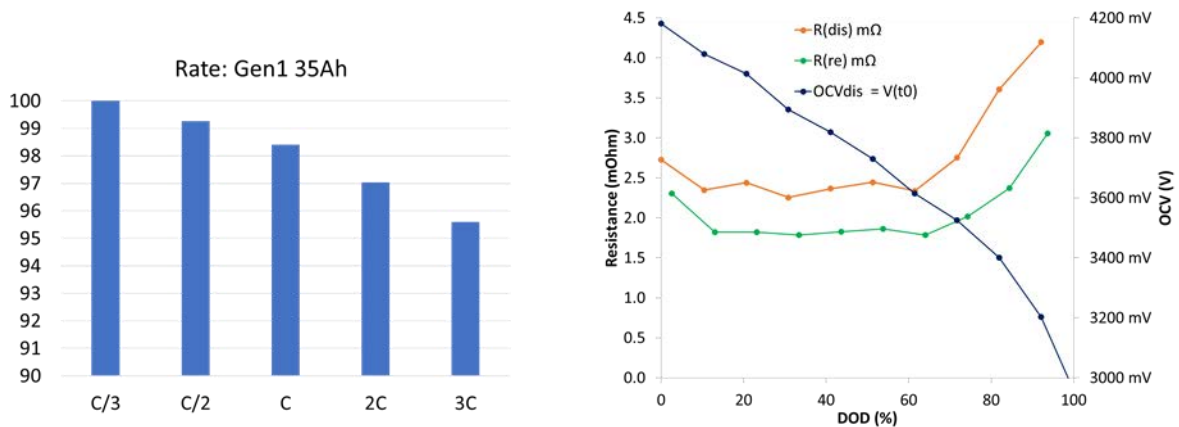


Figure I.1.C.2 DCR for the Gen 1 deliverable chemistry & 2b) Rate capability

The cells are charge/discharge for 1C. Figure I.1.C.3 shows the cycle life for the Ni rich cathode and Si/C anode in Gen1 deliverable cell.

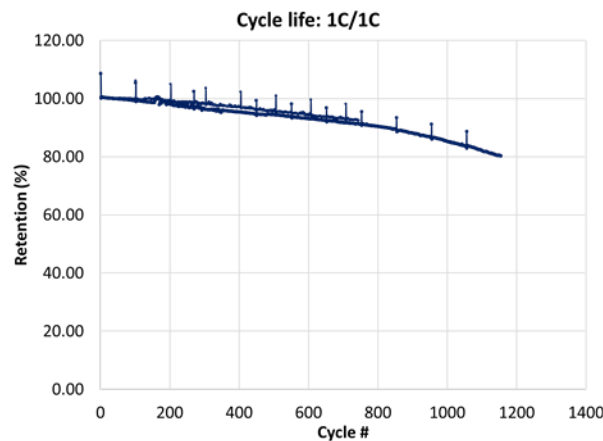


Figure I.1.C.3 Cycle life for Gen 1 deliverable chemistry

Electrolyte Technology Development

Farasis is performing electrolyte exploration, evaluation and optimization in 1Ah pouch cells. Figure I.1.C.4 shows selected results for 270Wh/Kg chemistry with Ni rich cathode and Si/C anode without pre-lithiation. Figure I.1.C.4 shows the cycle life for different electrolyte formulations with the down selected electrode chemistry.

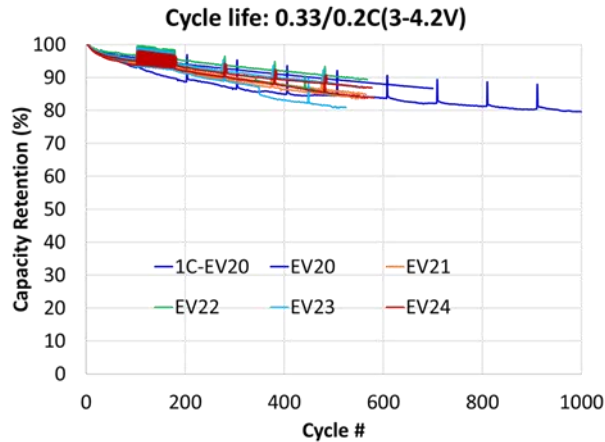


Figure I.1.C.4 Cycle life for the different electrolyte formulations

Farasis continues the optimization of the cell design and material selections to achieve high specific energy density > 300Wh/Kg and targeted USABC goals. Figure I.1.C.3–Figure I.1.C.4 shows the cycle life for (35Ah and 1Ah pouch cell targeting energy density of 270Wh/kg). The cycle life achieved at a 1C rate is higher than 1000 cycle before reaching 80% retention.

The calendar life for the cells are shown in Figure I.1.C.5 during the storage at 100% SOC at two temperature 30°C and 45°C. As the data indicate that the high temperature have considerable decrease in the capacity and the impedance of the cell increase.

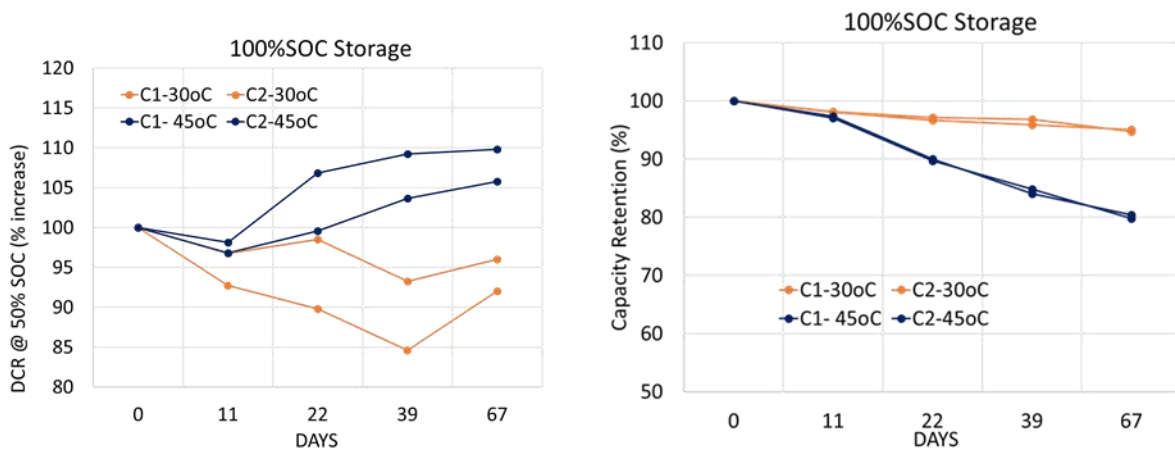


Figure I.1.C.5 Calendar life DCR for the Gen 1 deliverable chemistry & 4b) Capacity retention at 100%SOC @ 30° and 45 °C

Gen2 Cell Development

Electrode Development with Sacrificial Li Source: To achieve the specific energy of 400Wh/Kg we need the cathode with a capacity of $\geq 200\text{mAh/g}$ and anode capacity of $\geq 150\text{mAh/g}$. A consequence of working with high capacity silicon-based anodes, is an inherent high irreversible capacity loss. To compensate for this loss, pre-lithiation is a requirement. Farasis using the sacrificial Li source material (SLSM) as cathode additive to compensate the 1st cycle loss of Si anode. The addition of the Li source reduce the capacity of the cathode material and which leads to use the Si composite with the higher capacity and improving the cycle life of the cells. To understand the pre-lithiation we started with Gen1 down selected cathode (C1.1) $\sim 195\text{mAh/g}$. The mixing of the C1.1 with 5% of Li source bring down the capacity of cathode to 181mAh/g as shown in Figure I.1.C.6. Figure I.1.C.6 shows the cycle life of C1.1 with Li source vs Si alloy at a capacity of 500mAh/g. The results show that the pre-lithiation help to improve the cycle life whereas there is an increase in the impedance of the cells. The Gen2 cells need the Si composite with capacity of $\sim 1500\text{mAh/g}$. To make the progress towards the high capacity Si composite we tested C1.1 with anode (Si composite) of 1000mAh/g and shows the addition of the Li source improve the life by 100 cycles as compared to the controlled cells as shown in Figure I.1.C.6.

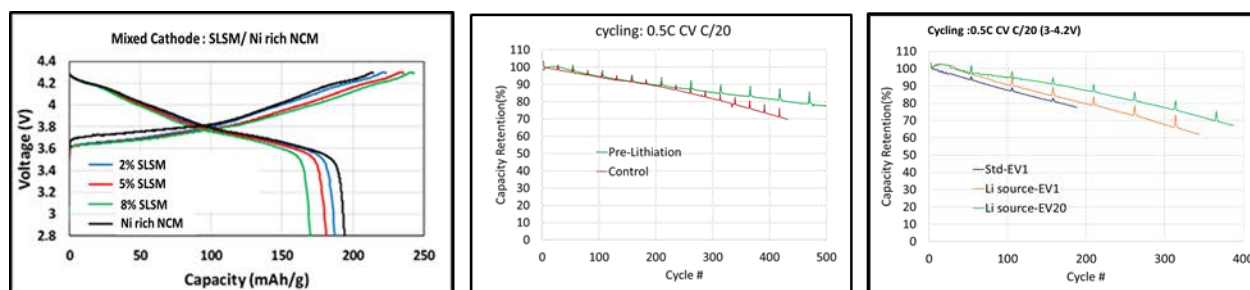


Figure I.1.C.6 a) Capacity of C1.1 with different amount of sacrificial Li source b) Cycle life of Ni rich NCM(C1.1) with 5% SLSM for Si (500mAh/g) and c) Si composite with capacity of 1000mAh/g.

Major challenge about the sacrificial Li source is its stability and compatibility to the existing manufacturing process. It has been seen that the reproducibility of the cells built with Li source is very poor. Farasis is working with Argon National Lab to stabilize the material and make it compatible with the manufacturing process. It is also seen that as we increase the amount of Si the cycle decreases and other cell components need to change to accommodate the swelling of the Silicon.

Conclusions

Farasis has delivered the baseline cells to the National Labs. Farasis has shown more than 1000 cycles before reaching 80% capacity retention of the Gen1 cell of capacity 40 Ah and specific energy of 270Wh/Kg. Farasis will deliver Gen1 40 Ah capacity pouch cells (INL, SNL and NREL) by November 2018. Further optimization in Gen1 chemistry is continuing for the different conductive additives and electrolyte additives. Farasis continues to use a system level approach to meet the USABC goals by optimization of material, cell components, pre-lithiation and cell design.

Key Publication

1. "Development of High-Performance Lithium-Ion Cell Technology for Electric Vehicle Applications", bat355_thakur_2018_p, US DOE Vehicle Technologies Program Annual Merit Review, AMR, 2018.

I.1.D Enabling Thicker Cathode Coatings for Lithium Ion EV Batteries (PPG)

Stuart Hellring, Principal Investigator

PPG Industries Inc
4325 Rosanna Drive
Allison Park, PA 15101
E-mail: hellring@ppg.com

Brian Cunningham, DOE Technology Development Manager

U.S. Department of Energy
E-mail: Brian.Cunningham@ee.doe.gov

Start Date: February 1, 2017	End Date: February 28, 2019	
Project Funding: \$1,200,000	DOE share: \$600,000	Non-DOE share: \$600,000

Project Introduction

To lower the overall cost of the electric vehicle (EV) lithium ion battery, PPG Industries, Inc. and partner LG Chem Power, Inc. will develop and demonstrate NMP-free cathode coatings with higher achievable thickness compared to conventional state of the art coatings. These thicker coatings will permit fabrication of higher energy density batteries without decreasing electrochemical performance. Additional cost savings and reduced environmental impact will be realized through the elimination of NMP-based manufacturing.

Objectives

The objective of this program is to develop solvent based binder systems for lithium ion cathode coatings that do not require the use of NMP and can be coated at a thickness of 150 μ . This cathode coating will demonstrate high flexibility and passed 1'' Mandrel bend test. The 90° peel strength of pressed coating is higher than 66N/m. Coatings and subsequent lithium ion cells will be manufacturable using existing standard industry equipment and demonstrate cell performance capability equivalent to current state of the art.

Approach

Reconfigure the electrode binder system into a novel NMP-free formulated product. This cathode formulation is stable chemically and possesses excellent shelf life. The unique design of PPG's NMP-free binders along with optimized processing parameters will mitigate film stress and enable the assembly of thicker, more flexible, homogeneous cathode coatings with higher active material loading per unit area.

PPG's binders are a combination with customized resins. The binder resins together form a composite that is designed to enhance dispersion stability and rheology to aid application, as well as final coating properties such as flexibility, cohesion, adhesion, etc., and electrochemical properties such as low resistance, and cycle and calendar life stability. Cell performance will be demonstrated in 1Ah pouch cells built in partnership with LG, and tested in accordance with the USABC EV test manual.

Results

PPG has successfully done several slurry scale-ups and enabled application line trials to prepare double-sided cathode coatings. PPG baseline coatings has shown good adhesion, flexibility and great capacity retention over cycling which meets the project baseline goal. Deliverable cells are being fabricated.

PPG developed and scaled-up several coatings with NMC 622 using PPG's NMP-free binder system at University of Michigan Energy Institute (UMEI). These coatings are with active/carbon/binder ratio of 93/3/4. The coatings parameters are listed in Table I.1.D.1 and their 90° peel strength are shown in Figure I.1.D.1.

We compared coatings with two different binders and two different mixing procedures. The "wet mix" procedure starts with a carbon dispersion in binder and active materials are added in the next step.

Alternatively, a “dry mix” starts with mixing of dry ingredients first and binder plus solvent are added in the next steps. All of the PPG coatings showed superior peel strength, as high as 550 N/m, which far exceeds the project goal of 66N/m. PPG also fabricated a graphite CMC/SBR anode with 97% graphite and CMC/SBR ratio of 1/1.

Among all the cathodes, we used NMC 622 dry A and NMC 622 dry B matched with this CMC/anode to fabricate 2.1 Ah capacity pouch cells. These cells were tested at Battery Innovation Center (BIC). Cell testing result suggest that cells with PPG binders have very good capacity retention when paired with waterborne CMC anodes. Figure I.1.D.2 shows the capacity retention vs. cycles for the cells cycled under C/3 at 30°C. All cells are between 97.5% and 98.1% capacity retention after about 330 cycles when cycled under C/3. The capacity retention results also suggest that PPG coatings with binder B start to deviate from PPG coatings with binder A. Binder B formulation was developed to improve PPG battery cycle performance by incorporating newly developed PPG additives, especially after extended cycles counts. From the capacity retention, the difference of binder A and B was not obvious until after 150 cycles However, the advantage of binder B became apparent as cell cycling continued.

EIS and DCR measurements were performed by Penn State University (PSU), who joined this project in August as our anode collaborator. PSU fabricated cells using another CMC/SBR anode. This anode has 96.5% graphite, 0.5% carbon, 2% CMC and 1% SBR. The EIS measurements were performed on these cells at 90% of SOC while DCR were measured at 50% SOC, with 5C charge and 3.75C discharge. Figure I.1.D.3 shows the Nyquist plot from the EIS measurement. Both cells showed two depressed semicircles and a straight sloping line at higher frequency on the Nyquist plot. While the difference between surface resistance, which is represented by the semicircle at higher frequency are relatively small between PPG dry A and PPG dry B, PPG dry B showed a slightly lower bulk resistance and lower charge transfer resistance. DCR results showed PPG dry A cells have 0.4% higher charge resistance and 0.3% higher discharge resistance compared to PPG dry B cells. These cell testing results demonstrate that PPG binder B successfully improved both the battery cycle performance and rate capability.

Table I.1.D.1 Coating parameters

Cathode	Coating Facility	Active/Carbon/Binder	PPG Binder	Carbon	Mass Loading (mg/cm ²)
NMC 622 wet A	UMEI	93/3/4	A	Litx 200	22.2
NMC 622 dry A	UMEI	93/3/4	A	Lixt 200	22.2
NMC 622 dry B	UMEI	93/3/4	B	Litx 200	22.2

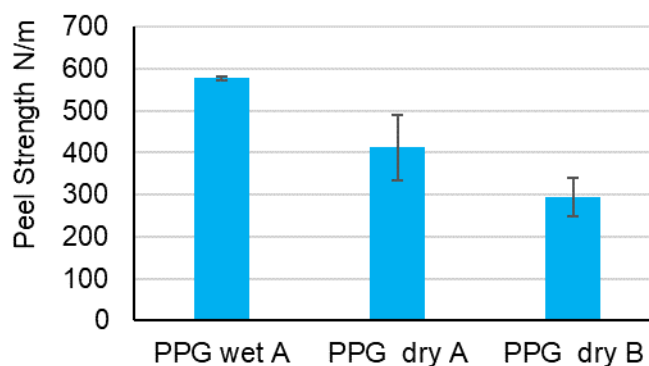


Figure I.1.D.1 90° peel test result of PPG coating with different binder and mixing procedure

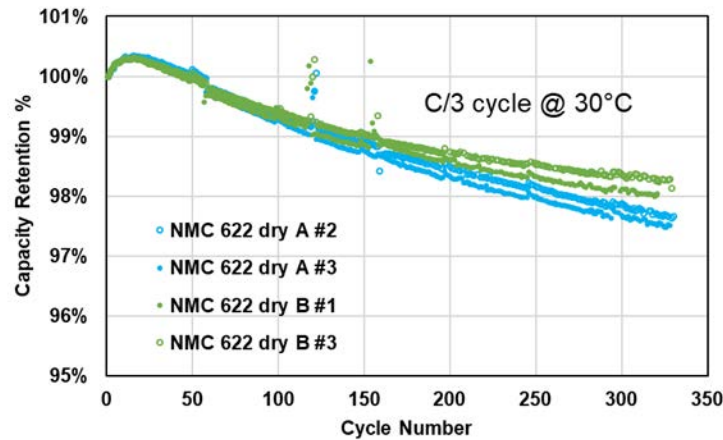


Figure I.1.D.2 Long term cycling of pouch cells with baseline thickness, 93/3/4 and with NMC622 cycled under C/3

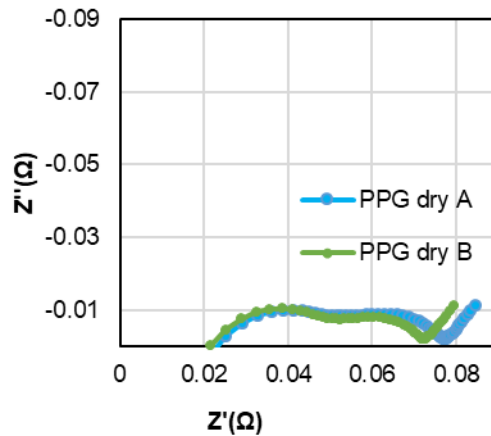


Figure I.1.D.3 Nyquist Plot of EIS measurement on pouch cells fabricated at PSU

With the good results from binder A and B, PPG started to look into coating thicker cathodes with these two binders. PPG prepared final target coatings with binder A and B at UMEI, both of which were mixed with a carbon dispersion method. The coating information of which is shown in Table I.1.D.2. Both coatings were successfully fabricated on pilot scale roll-to-roll coaters. The peel strength of the coatings are plotted in figure I.1.4. Both coatings have very good adhesion compared to the results of earlier versions of PPG binder. Binder B outperformed binder A in peel test and gave a peel strength as high as 98N/m. This trend is different from the peel strength results in baseline coatings, which were mixed with a dry mix procedure. Our observation suggest both the mixing procedures and the binder formulation have big impact on coating properties. Both coatings pass a 1/2 inch mandrel bend test. To this end, PPG has successfully met all out-of-cell coating targets for this project.

Table I.1.D.2 Coating parameters for thick cathodes

Cathode	Coating Facility	Active/Carbon/Binder	Binder	Carbon	Mass Loading
NMC 622 thick A	UMEI	93/3/4	PPG Binder A	Litx 200	40 mg/cm ²
NMC 622 thick B	UMEI	93/3/4	PPG Binder B	Litx 200	40 mg/cm ²

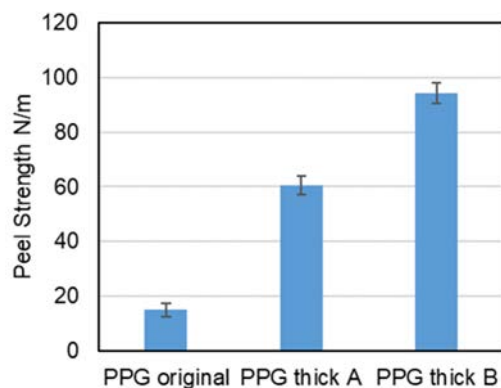


Figure I.1.D.4 Peel strength of the thick cathode coatings

The remaining challenge, however, is to fabricate cells that will meet the project cell-performance targets. In order to make cells using PPG thick cathode, a matching anode is required. PPG attempted to use a modified graphite-PVDF anode with 93/7 active/binder ratio to match these thick cathode coatings and fabricated some pouch cells. This modified anode has 2wt% more binder than a standard 95/5 graphite-PVDF binder to avoid the delamination of this thicker anode coating. 5Ah cells were fabricated with the aforementioned thick cathode and thick anode. We compared the rate capability result of these cells with a baseline cell. The baseline cell uses a PPG cathode at about 22mg/cm² and a 95/5 PVDF-graphite anode with matching capacity. The results show that cells with PPG thicker cathodes have worse performance at C-rates higher than C/3, which indicates PPG cells have larger resistance, especially with larger thicknesses. It is often observed that increasing the electrode loading results in reduced capacity at higher C-rates. The anode used to match the thicker cathode is with 7% binder while the anode to match thinner cathode is with 5% binder. This 40% increase in binder content likely contributes to this increase in resistivity. However, a more thorough understanding of the cause of high resistivity will require using the same anode formulation for both thick and thin coatings. Due to the high cell resistance, the cells are not expected to perform well enough to meet the project goal. In order to fabricate cells that meet the project goal, an anode will need to be developed to have a matching capacity without introducing a high electrical resistance. PPG will start to develop a thick anode by optimizing the CMC/SBR anode currently. Anode development will be our next step to move this project forward.

Conclusions

PPG demonstrated great cycle performance with PPG baseline coatings with NMC 622. Cells with 93/3/4 and binder A and B are at 97-98% with about 330 cycles when cycled under C/3. PPG developed Binder B which shows better battery cycle life and lower resistance than PPG binder A. The deliverable cells are being made and will be fabricated and ship to INL. PPG also successfully fabricated coatings with final target mass loading. These coatings meet the out-of-cell goal of the project. Currently, PPG is developing the matching anode to work with these thick cathodes. This anode will need not only to have a sufficiently large capacity, but also sufficiently small resistance in order to have good cell performance under higher power conditions.

I.1.E Advanced High-Performance Batteries for Electric Vehicle Applications (Amprius)

Ionel Stefan, Principal Investigator

Amprius, Inc.
225 Humboldt Court
Sunnyvale, CA 94089
E-mail: ionel@amprius.com

Brian Cunningham, DOE Technology Development Manager

U.S. Department of Energy
E-mail: Brian.Cunningham@ee.doe.gov

Start Date: January 1, 2015
Project Funding: \$5,500,000

End Date: September 30, 2018
DOE share: \$2,750,000

Non-DOE share: \$2,750,000

Project Introduction

Silicon has significant potential as a new anode material; silicon offers nearly 10 times the theoretical energy capacity of graphite. However, when charged with lithium ions, silicon swells up to four times its volume, causing capacity fade and mechanical failure. Because of swelling, conventional approaches to silicon anodes have not produced cells with the long cycle life required for electric vehicle applications. Amprius' rooted silicon nanowire structure mitigates material and mechanical issues, and enables high energy density products with reasonable cycle life. Amprius proposed to match its silicon nanowire anode with a high capacity NMC cathode, to achieve 2020 USABC goals for EV performance at the cell level.

Objectives

- Amprius engaged in a 45 month, USABC project to develop and deliver vehicle-size cells that meet USABC's technical requirements goals for year 2020. Throughout the project, Amprius targeted improvements of its silicon nanowire anode material and cell performance in a baseline cell, and then transfer learnings to larger cells. At project's end, Amprius planned to deliver ~40 Ah cells with end of life specific energies of 350 Wh/kg and energy densities of 750 Wh/L.
 - The project addresses the key performance and production challenges to the commercialization of high-capacity cells and batteries with silicon nanowire anodes. Barriers addressed:
 - Energy: Low Wh/kg & Wh/L
 - Cycle Life: <1,000 Cycles
 - Size: Small Anodes and Cells
 - Cost: High \$/kWh
- Amprius' goal is to deliver cells that meet USABC's EV battery goals. Amprius' will deliver high-capacity pouch cells at the conclusion of the project's first, second and third years. Idaho National Laboratory will independently test the performance and safety of Amprius' cells according to USABC's test protocols.
 - Specific technical targets:
 - Available Energy Density @ C/3 Discharge Rate: 750 Wh/L
 - Available Specific Energy @ C/3 Discharge Rate: 350 Wh/kg
 - DST Cycle Life: 1,000 Cycles
 - Peak Discharge Power Density, 30 s Pulse: 1500 W/L
 - Peak Specific Discharge Power, 30 s Pulse: 700 W/kg
 - Peak Specific Regen Power, 10 s Pulse: 300 W/kg

- Calendar Life: 15 Years
- Selling Price @ 100K units: \$100
- Operating Environment: -30°C to +52°C
- Normal Recharge Time: < 7 Hours
- High Rate Charge: 80% ΔSOC in 15 min
- Peak Current, 30 s: 400 A
- Unassisted Operating at Low Temperature: > 70% Useable Energy @ C/3 Discharge Rate at -20°C
- Survival Temperature Range, 24 Hr: -40°C to+ 66°C
- Maximum Self-discharge: < 1%/month

Approach

Amprius has innovative silicon technology – an anode made of silicon nanowires attached to the current collector – that mitigates silicon swelling, unlocking silicon’s potential, and meeting USABC’s commercialization criteria.

Amprius’ technology is unique in three respects: material, structure, and results. First, Amprius’ anode material is made of silicon rather than graphite or a graphite-silicon composite. Second, Amprius’ anode structure is composed of nanowires physically attached to the current collector, rather than particles. Third, Amprius has demonstrated both high energy and long cycle life in full cells with silicon nanowire anodes.

Amprius’ unique, patent-protected material and structure – nanowires that are “growth-rooted” (i.e. grown directly on the current collector, without binders) – addresses swelling by enabling silicon to successfully expand and contract internally. Because the nanowires are attached to the current collector, Amprius does not rely on particle-to-particle contact and is able to achieve not only long cycle life, but also high electrical conductivity and power.

Before the USABC project, Amprius achieved >700 Wh/L at start of life and >400 cycles at C/2 rate and 100% depth of discharge (DOD). To meet USABC goals, during the project Amprius will:

- Increase specific energy and energy density by tuning anode structure and using advanced components (e.g. thinner substrates and separators). Amprius will also transition from LCO to NCM.
- Extend cycle life by optimizing anode structure and identifying and/or developing electrolyte formulations that improve Solid Electrolyte Interphase (SEI) stability and cell performance.
- Increase anode and cell size by developing methods for handling larger anodes; improving the uniformity of silicon growth and deposition technologies; reducing defect density; and utilizing manufacturing methods that inherently scale to larger dimensions.

Results

Amprius reduced the main gaps in performance, cycle life and calendar life, by identifying electrolyte additives that improve solid electrolyte interphase (SEI) stability and reduced gassing.

In FY2018, Amprius screened over 100 electrolyte formulations that included a variety of additives, solvents and salts. The main focus was on reducing reactions that produce gases at the cathode, especially at high state of charge and high temperature. These reactions are particularly accelerated at high capacity NMC cathodes that are rich in nickel. The task is complicated by the fact that the electrolyte composition has to include additives that are beneficial to the cycle life of silicon anodes, additives which are not necessarily stable at high voltage, high temperature or on catalytically active cathodes. Thus, cathode additives were explored, as well as coatings on the cathode materials.

For screening, Amprius measured the relative capacity retention after either storing the cells at full charge at 50°C or after cycling the cells at 50°C for a number of cycles. In parallel, cell volume increase was measured by an immersion method, to evaluate the volume of gasses evolved at high temperature. For concentration

optimization, Amprius used a design of experiment methodology to reduce the number of combinations. In cycling, Amprius uses a typical test method: CC-CV at C/2 rate with 10% current taper and C/2 discharge rate, over the full voltage range (2.85-4.25V).

A sample set of results are shown in Figure I.1.E.1. Formulation ELY280 was developed in Year 2 for 10Ah cells because it had very good room temperature and low temperature (not shown here) performance. However, a new formulation had to be developed in FY2017 and FY2018 (Year 2 and 3) to improve performance at high temperature (both Calendar and Cycle Life). Formulation ELY572 was selected for Year 2 deliverable cells. Electrolyte formulation development was done in Si/NCM cells with a 70% Ni-content cathode.

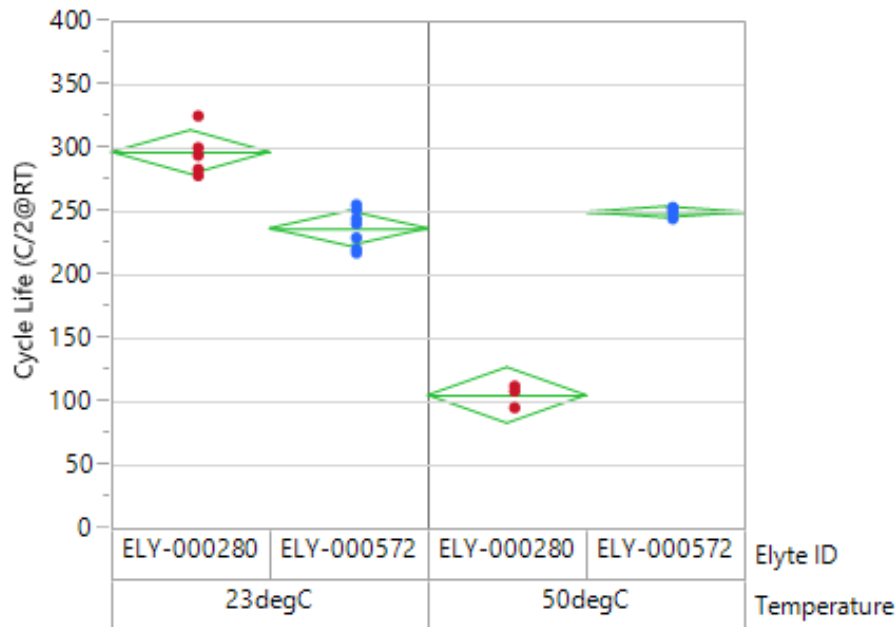


Figure I.1.E.1 Electrolyte formulation was optimized for better Calendar and Cycle Life in Si/NCM (70% Ni) cells

Amprius built and delivered to DOE for testing Silicon-NCM cells with average capacities of 10.6 Ah, specific energies of 345 Wh/kg, and energy densities of 860 Wh/L, and increase of 12% compared to previous year.

Amprius continued the cell design and development work started in Year 2 of the project by iterative design optimization of larger form factor. The Year 2 form factor, a 10Ah cell, required a doubling in length and thickness of the cell tested in Year 1.

In parallel, more energy dense cathode materials were evaluated, including materials with high content of Ni (60 to 80% content). Amprius delivered a larger number of cells compared to that scheduled, to allow a comparison of the effects of Ni-content on cell performance and safety, and tests at Idaho National Laboratory (INL) confirmed a significant increase in Calendar Life (7 months at 50°C and ongoing) compared to the previous round of testing. Amprius also achieved an increase of about 10% in specific energy and energy density in Year 3 cells compared to Year 2 cells.

Amprius started the development the project's final, Year 3 cells, to achieve a target capacity of ≥ 40 Ah. Amprius selected the VIFB—/99/300 form factor for ≥ 40 Ah cells. This cell is a pouch cell with tabs on opposite sides (see Figure I.1.E.2). Amprius will use cell components (e.g. separator, pouch material and electrolyte) selected and/or optimized in smaller Year 1 and Year 2 form factors. The main effort of the task in FY2017 and FY2018 was to scale up the equipment and tooling for the 40Ah form factor. In particular, Amprius started producing anode foils of larger size both in its batch, laboratory process, as well as in the newly developed roll-to-roll anode pilot line.

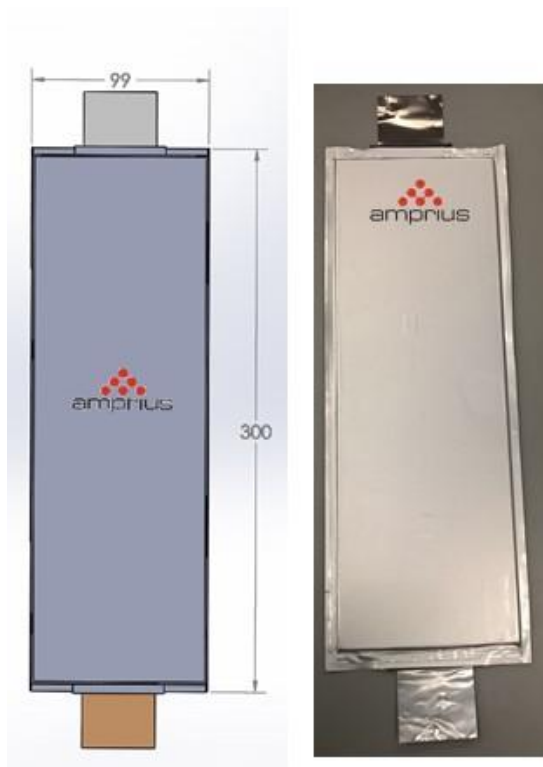


Figure I.1.E.2 CAD drawing and prototype 40Ah cell with silicon nanowire anode

In parallel with the form factor efforts, Amprius continued evaluation of new cathode powders. Among the more successful types was an NMC811 cathode coated with aluminum oxide by Forge Nano. The result was a similar cycle life with the previous 70%-Ni NMC and an increase in specific energy. This cathode combined with the larger form factor significantly exceeds the 2020 USABC targets at the beginning of life. Figure I.1.E.3 illustrates a comparison of cell form factors and cathode types evaluated.

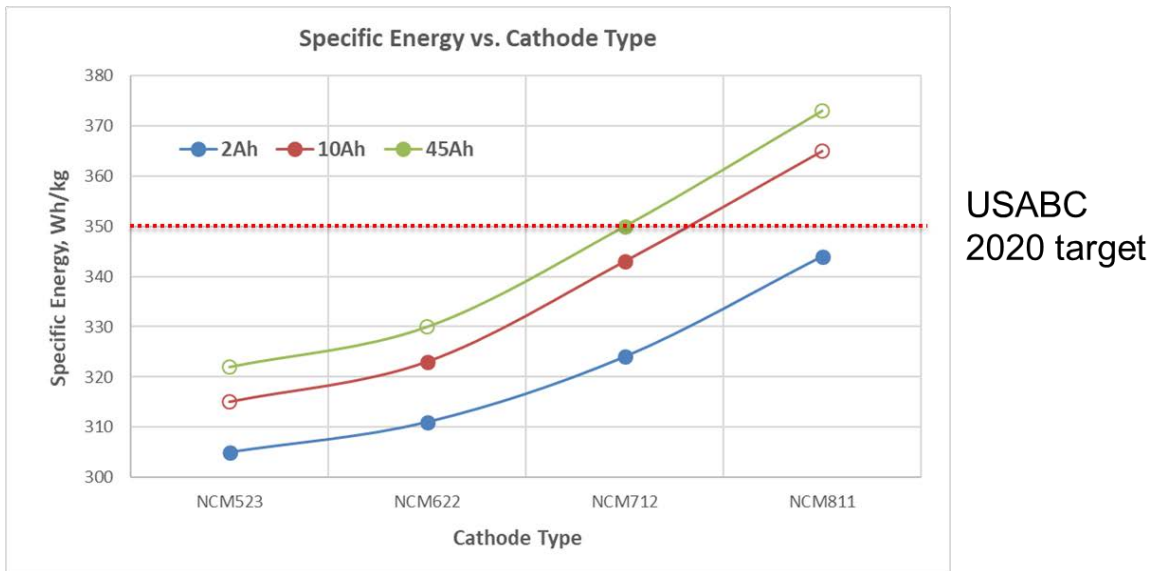


Figure I.1.E.3 Silicon nanowire cells with NCM811 and in large form factor achieve 375 Wh/kg

At the end of the project (September 2018), cycle life was increased to about 500 cycles (to be verified by INL on Year 3 cells) and calendar life was increased to over 7 months at 50°C (test ongoing). The silicon nanowire cells also meet the High-Rate Charge test requirements (>80% charge in 15 minutes), Storage, Low and High temperature exposure and Low Temperature requirements.

Conclusions

During the project's last year, Amprius continued to make significant progress increasing cell energy, extending cell cycle life, and demonstrating that its silicon nanowire anode-based cells exceed USABC's goals. Amprius built and delivered 18 cells for testing by Idaho National Laboratory. The evaluation at Idaho National Laboratory of Year 2's cells confirmed Amprius' results, including achievement of the initial power and energy targets.

Although silicon nanowire cells meet most of the USABC 2020 technical goals, cycle life and calendar life fall short. Amprius made significant improvements over the last two years and there are good reasons to believe that Calendar Life targets can be achieved with improved electrolyte formulations. Cycle life, however, will need more development at the material/silicon structure level, to mitigate the effects of surface morphology changes and associated reactions. Amprius has already started work along these directions.

Key Publications

1. "Advanced High-Performance Batteries for Electric Vehicle (EV) Applications", ES41_Stefan_2018_p, US DOE Vehicle Technologies AMR, 2018.

Acknowledgements

Amprius wishes to acknowledge the support provided by Matthew Denlinger, USABC Program Manager, and Brian Cunningham, DOE Technology Manager, as well as by Harshad Tataria (General Motors), Carrie Okma (FCA), Matt Shirk (INL) and Leigh Anna Steele (SNL) for helpful direction and collaboration in the development and testing of Amprius cells.

I.1.F Rapid Commercialization of High Energy Anode Materials (SiNode Systems)

Cary Hayner, Principal Investigator

SiNode Systems
3440 S. Dearborn Street, #113N
Chicago, IL 60616
E-mail: caryhayner@sinode-systems.com

Brian Cunningham, DOE Technology Development Manager

U.S. Department of Energy
E-mail: Brian.Cunningham@ee.doe.gov

Start Date: May 1, 2016	End Date: October 31, 2018	
Project Funding: \$1,707,310	DOE share: \$853,655	Non-DOE share: \$853,655

Project Introduction

As global usage of electric vehicles steadily increases, so does the power/energy requirement to meet mainstream needs. Performance trajectories of traditional lithium-ion technology, despite an annual 3-5% improvement in energy density since inception, suggest that long-term electric vehicle needs will not be met without an evolution beyond traditional energy storage materials (i.e. graphitic anodes). SiNode Systems has developed a novel Si-based, negative-electrode material which can enable a quantum leap in battery energy and power density, and significantly impact battery weight and run-times that burden today's electric vehicles.

Objectives

The project entitled "Rapid Commercialization of High Energy Anode Materials" has been established with the aim of extending, benchmarking, and demonstrating the performance of SiNode System's advanced silicon-based anode materials in battery form factors and designs relevant for electric vehicle applications.

Approach

SiNode Systems has demonstrated a novel high energy density (>1,000 mAh/g) Si-based negative-electrode materials technology with a long-term potential to replace graphitic-based anodes in lithium-ion batteries. SiNode's technology uses a proprietary silicon alloy-graphene material architecture to achieve: i) category-leading performance and ii) solutions to long-standing Si anode technical hurdles. The proprietary combination of silicon-based alloys and a flexible 3D graphene network helps to stabilize the active material during charge and discharge (see Figure I.1.F.1) by providing an interfacial barrier between the active material and the electrolyte which can accommodate large volumetric changes through a laminar graphene sliding mechanism. The 3D graphene-silicon architecture results in a minimization of capacity losses due to electrical disconnection, significantly improved active utilization (mAh/g), and partial stabilization of the SEI interface with a flexible physical barrier between electrolyte and active material.



Figure I.1.F.1 Si anode failure mechanisms (left), SiNode graphene-wrapped advanced silicon anode architecture (right).

SiNode has made continuous improvements against key USABC advanced electrode metrics over time, and has demonstrated an attractive trajectory towards USABC advanced electrode goals. The goal of the program is the advancement and commercialization of advanced silicon-based active materials for high energy / high power EV batteries. Specifically, the program aims to demonstrate that SiNode technologies can exceed USABC electric vehicle performance targets in USABC-recognized form factors, be produced at-scale by commercially viable methods and reach USABC cost targets at scale. To this end, a series of tasks have been developed to address the core technology gaps and their associated barriers: Task 1: Materials Stabilization and Analysis, 2. Manufacturing Scale-Up, 3. System Cost Reduction, 4. Cell Prototype Evaluation, 5. Downstream Cell Process Optimization and 6. Cell Characterization and Performance Evaluation.

SiNode has two strategic partners for this program. A123 Systems works with SiNode on Tasks 4 and 6, the pouch cell deliverables and PPG works with SiNode on Tasks 2 and 3 to scale up the anode material.

Results

During FY18, SiNode further developed and improved their novel SiO_x precursor material with high stability that was integrated into SiNode's 3D graphene architecture. Additionally, SiNode developed a surface treatment for stabilizing the SEI and improving the energy density of the active particles, prior to graphene addition (Figure I.1.F.2). Recently, this process was further refined and improved to increase anode capacity and better understand the impact of the treatment on the electrochemical cycling performance of the final composite. As shown in Figure I.1.F.3, SiNode has been able to achieve more than 350 cycles to 80% capacity retention and has confirmed this result in 1 Ah pouch cell prototypes. Additionally, SiNode has scaled up production of this material and integrated the technology into a 10 Ah prototype cell deliverable.

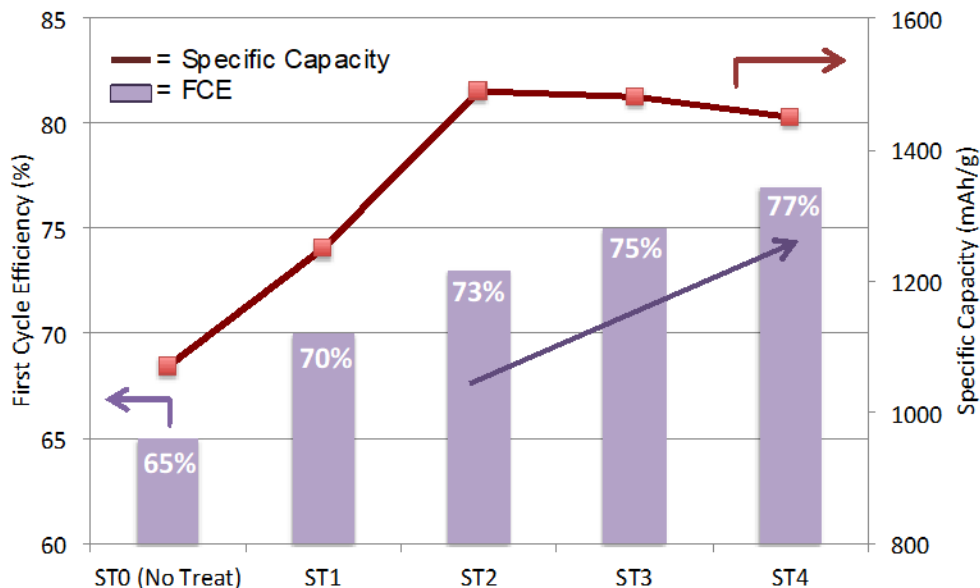


Figure I.1.F.2 1st cycle efficiency (FCE) and capacity (mAh/g) for a series of surface-treated SiOx materials.

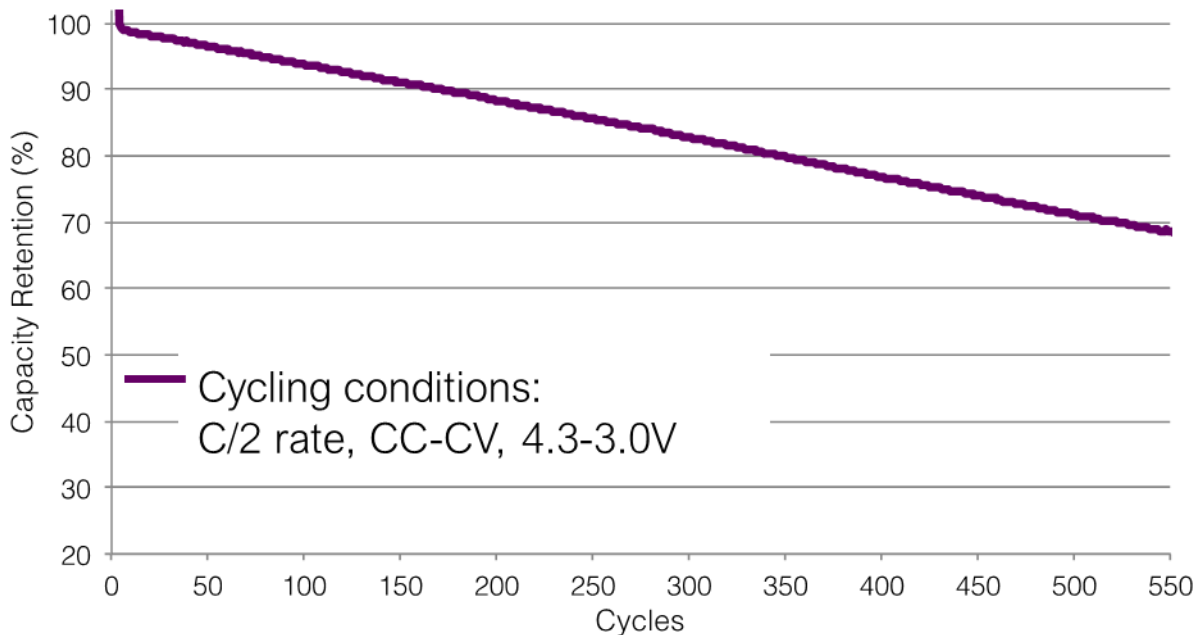


Figure I.1.F.3 Normalized full cell capacity versus cycles for SiNode-graphite blended anodes (1000 mAh/g) with NCA.

SiNode also focused on production scale-up and cost reductions. During FY 2018, SiNode successfully completed installation and validation of pilot-scale equipment capable of producing >25 kg/month to enable production of large format cells (Figure I.1.F.4). Additionally, SiNode focused on developing quality control processes to monitor product quality and ensure consistent material production and reproducibility.

Finally, the project team has developed a cost model that indicates cell level costs of \$100/kWh can be achieved by 2025. Material component costs are forecasted to decrease through increasing market penetration

from 2019-2025, coupled with improvements in key cost drivers. The model assumes a gradual market penetration, plus process, quality, and supply chain improvements over time.

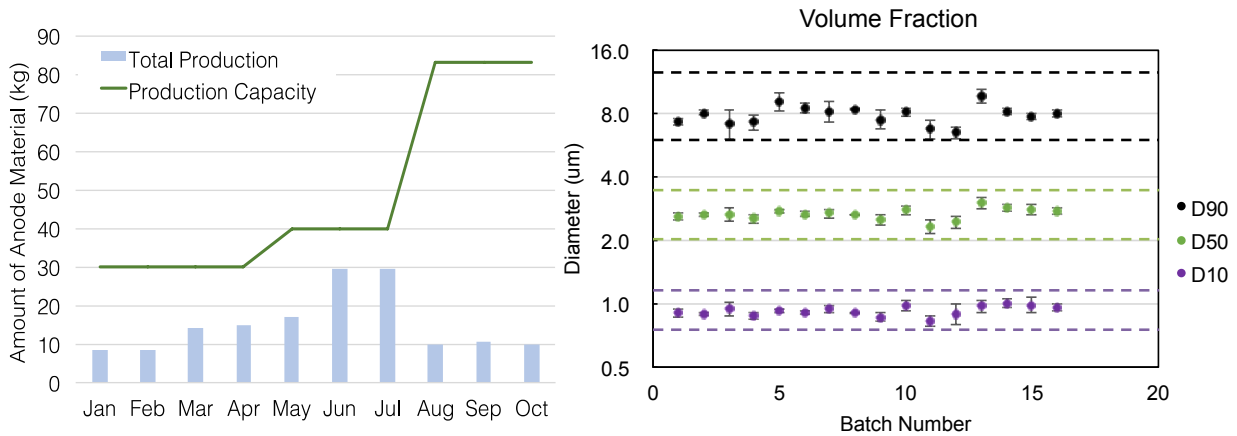


Figure I.1.F.4 SiNode production and production capacity (left) and particle size distribution (PSD) measurements demonstrating consistent material production quality (right).

As a deliverable, SiNode has produced a set of 10 Ah cells in partnership with A123 (Figure I.1.F.5). The 10 Ah cell design contains SiNode’s scaled-up surface-treated SiOx material paired with an NCA cathode. SiNode delivered 18 10 Ah cells to Argonne National Laboratory in November 2018 for analysis. The 10 Ah cells are expected to achieve performance that is in-line with the results shown in Figure I.1.F.3. SiNode continues to optimize materials selection (anode, cathode, binder, electrolyte, etc.) as well as cell design (electrode formulation, loading, porosity, balance, etc.) to improve cycle life and energy density for automotive applications.



Figure I.1.F.5 10 Ah prototype cell with SiNode anode and NCA cathode. Commercial 18650 cell for comparison.

Conclusions

SiNode has concluded the 30th month of the 30-month-long project. The 10 Ah cell deliverables will be delivered this quarter. In FY18, major milestones were achieved in improving cycle life and energy density, materials scale-up, and 10 Ah cell production.

Several challenges remain to be overcome, including consistent improvements to achieve DOE/USABC targets of 1000 DST cycles with high energy (750 Wh/L and 350 Wh/kg). Additionally, successful battery electrode design, electrode expansion, safety testing, and ton-scale production with line-of-sight on materials cost reductions (i.e., graphene and silicon) is required.

SiNode has demonstrated a cadence of innovation and product development of the past year, and looks optimistically towards demonstration of viable performance in commercially-relevant EV cells.

Key Publications

1. “High Energy Anode Material Development for Li-ion Batteries”, BAT240_Hayner_2018, US DOE Vehicle Technologies AMR, 2018.
2. “High Energy Anode Material Development for Li-ion Batteries”, ES240_Hayner_2017, US DOE Vehicle Technologies AMR, 2017.

I.1.G Advanced Separators for Vehicle Lithium Battery Applications (Celgard, LLC)

Eric White, Principal Investigator

Celgard, LLC.
13800 South Lakes Dr.
Charlotte, NC 28273
E-mail: eric.white@celgard.com

Brian Cunningham, DOE Technology Development Manager

U.S. Department of Energy
E-mail: Brian.Cunningham@ee.doe.gov

Start Date: March 3, 2017

End Date: March 20, 2020

Project Funding: \$2,500,000

DOE share: \$1,130,000

Non-DOE share: \$1,370,000

Project Introduction

Increasing cell voltage and electrode capacity may be the most effective approaches to increasing the energy density of lithium ion batteries. Increasing cell voltage, however, would accelerate degradation of cell components including electrolyte, separator, electrode binder, conductive carbon, etc. With recent advancements in electrolytes, the separator becomes a new limiting factor in advancing toward a high voltage (5 V class) battery system. When operated at high voltages, particularly at elevated temperatures, lithium ion cells may demonstrate degradation that is partially attributed to the oxidation of the separator or to the deterioration in separator performance. During extended cycling at high voltages, especially at elevated temperatures, separators can suffer from intensified electrochemical oxidation on the surface facing the positive electrode, as well as degradation due to the strongly reducing environment on the surface facing the negative electrode.

Objectives

To enable the technical evolution towards 5.0 V lithium batteries, Celgard proposed to develop advanced separators that are cost-effective and durable at high voltages, in collaboration with battery manufacturers. Two integrated approaches to the project are proposed, to maximize chances for success. The first is a unique coating technology capable of creating continuous, nanometer coatings on a base separator. The second approach is a novel separator comprised of polymers that are stable in a 5.0 V Li-ion battery. Present separator/coating technologies will be used as comparison baseline for these advanced development concepts. Celgard will then select the most suitable material. Evaluation of the material will be conducted in conjunction with USABC and Farasis Energy, Inc. of Hayward, CA, USA. The battery maker subcontractor (Farasis) will provide a reproducible 5.0 V battery system to be used for testing during the program.

Approach

This body of work will address the development of a product specifically designed to accommodate 5.0 V lithium batteries. The work focuses on moving the current state of the art separator products from PE and PP, with binder and solvent based ceramic coatings to an Advanced Product and Process. Two basic approaches will be taken. The first approach includes a new type of coatings, made through a new advanced method for continuous deposition of nanometer size coatings, which will be used to protect the PP and/or PE from high voltage attack. The second approach includes the evaluation of novel polymers capable of withstanding a voltage of 5.0 V in a lithium battery environment.

Rationale Novel Coatings - In this proposed research, Celgard will address such issues by developing several strategies to mitigate chemical and electrochemical attacks on separators: 1). High efficiency blocking mechanism. Celgard will develop a nanometer-scale, ultra-dense coating on current polyolefin separators that will be highly efficient in protecting the polyolefin materials (such as PE and/or PP) from chemical attacks without sacrificing porosity/ionic conductivity of the separators. 2). Chemical/free radical scavenging

mechanism. The nanometer-scale coating will serve as a chemical/free radical scavenger that will quickly decrease the local concentration of free radicals before the oxidizing Mn^{+} and/or free radicals attack the separator material. The migration of side-reaction products from the high voltage spinel cathode to the graphite anode is responsible for much of the parasitic reaction damage at the graphite SEI and the consumption of active Li^{+} in the cells. The proposed method for delivering the coating or layer is physical vapor deposition. This method is commonly accepted to produce very thin layers on plastic film materials and is proposed to be similarly deployed for the case of Celgard's battery separator films. The resulting coatings are extremely thin (nanometer-scale vs. micron-scale as may be used with current slurry based technologies), binder-free and homogeneous.

Rationale Novel Polymers - Besides polyolefin microporous membranes, a variety of new polymers have been used for preparing microporous membranes for lithium ion batteries in the past decade. The three most reported ones are polyvinylidene fluoride (PVDF), polyacrylonitrile (PAN), and poly(methyl methacrylate) (PMMA). Many of them, such as microporous PVDF membranes, are proven to be chemically and electrochemically stable in lithium ion batteries using today's conventional technologies. In this proposed research, Celgard will investigate the application of separators with the two new materials (PMP and PVDF) in high voltage lithium ion batteries. Celgard will develop the two new separator materials and evaluate their stability in high voltage lithium ion batteries.

For these candidate new separator materials, their fabrication and performance in 5.0 V batteries will be demonstrated and evaluated in this project. It is challenging for any new polymers to be fabricated into battery separators, since the resulting membranes must possess appropriate porosity and mechanical strength. While Celgard has demonstrated that both PVDF and PMP can be processed through Celgard's technology, the membrane properties need further improvement. A similar internal R&D effort is ongoing at Celgard, to demonstrate PVDF-based separators. Despite the potential challenges, these new polymer separators have advantages when compared to PP and PE separators. For example, PVDF membranes are mechanically strong and have great wettability due to good affinity of PVDF to liquid electrolyte solutions.

Results

Separators harvested from 5 V LMNO cells cycled by Farasis during FY2017 and their accompanying deposits were analyzed at the beginning of FY2018. Mn and Ni deposits were found on both the cathode and anode sides, which is evidence that the transition metal (TM) ions dissolved from the LNMO electrode have migrated through the separator to the anode. The TM dissolution was greater in cells stored at full state of charge prior to cycling, as shown in Figure I.1.G.1. In order to minimize the deposition of transition metal ions from the cathode, Celgard has begun working with ANL on the development of an ALD coating of the LNMO particles with AlF_3 . This coating may provide a stable electrode-electrolyte interface, thus enabling LNMO//graphite cells to be used in the evaluation of the down-selected experimental separators.

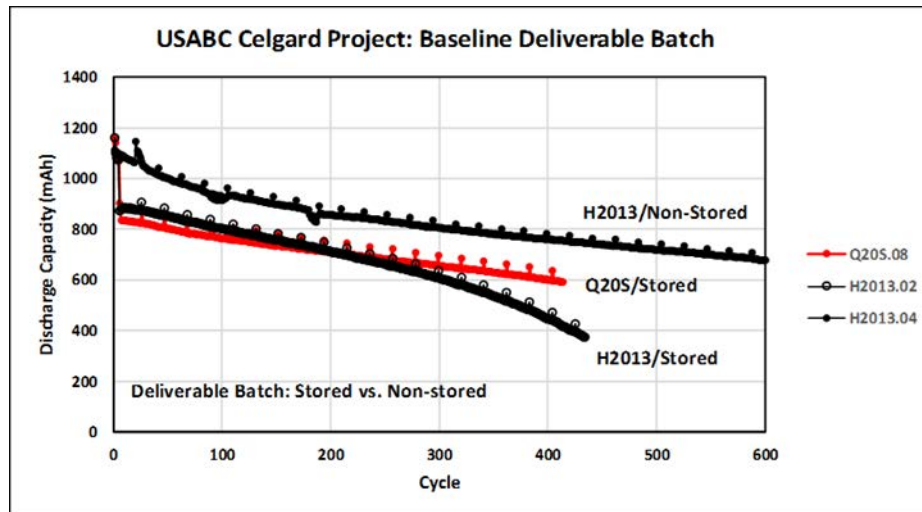


Figure I.1.G.1 Cycling performance comparison between cells stored for 25 days at 4.6 V and a cell tested without storage.

Celgard completed a PMP-PP composite test trial at a local toll coating facility in February 2018, which produced 4 rolls of samples with different loadings with PMP. Full characterization of the PMP-PP composite films was also completed by the Celgard QC lab and is displayed in Table I.1.G.1. Thermal shrinkage of the films at high temperatures appears to be improved, as is the stiffness of the films, which is indicated in the table by the increase in modulus. Figure I.1.G.2 shows the SEM images of the coated separators and indicates little or no pore clogging. These films were evaluated in cells operating to 4.4 V, as part of the separator down-selection detailed below.

Table I.1.G.1 Properties of PMP-Coated Experimental Separator Conditions

Sample		Control	1	2	3	4
Thickness	µm	11.6	10.4	11.5	11.6	11.9
Electrical Resistance	Ωcm ²	0.4	0.6	0.5	0.5	0.7
MD Modulus	kg/cm ²	5,042	5,409	5,214	3,521	5,235
TD Modulus	kg/cm ²	3,098	3,772	3,660	2,563	3,708
Puncture Strength	g	205	210	216	194	225
MD Shrinkage	% @ 90 °C	5.8	6.4	5.8	6.4	5.5
	% @ 120 °C	15.3	14.1	11.8	15.7	11.8
	% @ 150 °C	50.9	36.0	35.9	47.8	32.1

Celgard’s candidate separators were evaluated in an attempt to down-select the designs for further testing in a 5.0 V cell, by using NCM523/Graphite 1.35Ah pouch cells tested with an upper voltage limit of 4.4 V. A total of 6 experimental separators using physical vapor deposition and PMP coating were evaluated along with 2 reference separators. Table I.1.G.2 lists the separators evaluated. Characterization of the PMP coated separators tested is detailed above while characterization of PVD coated separators tests was detailed in the 2017 DOE report for the program.

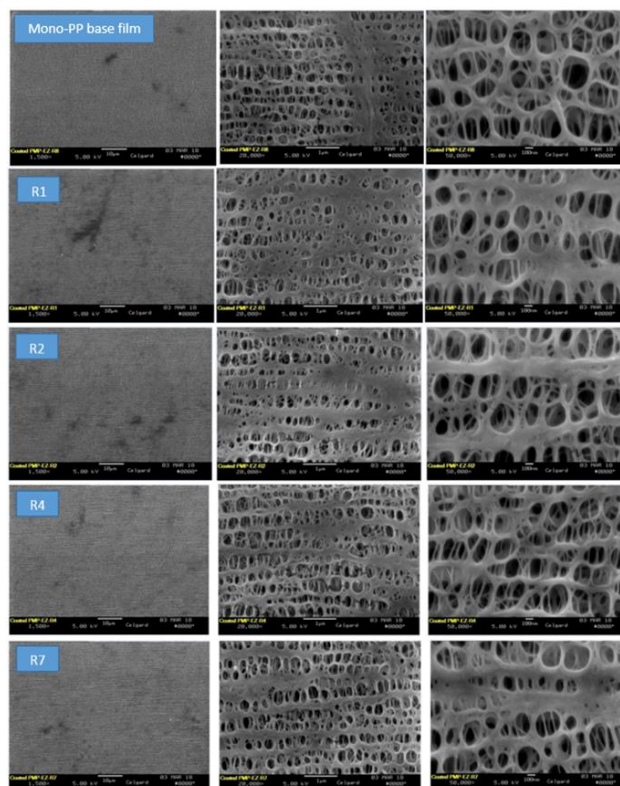


Figure I.1.G.2 SEM Images of PMP-coated separator produced under various trial conditions.

Table I.1.G.2 Test Plan for Down Selection of Experimental Separators

Sample	Cells Tested, 45 °C Cycling	Cells Tested, 45 °C OCV Stand at 100% SOC	Separator Description
26-R2	3	3	H2013 + 15nm AlO _x
27-R2	3	3	H2013 + 30nm AlO _x
27-R4	3	3	H2013 + 15nm AlO _x + 15nm AlO _x
28-R4	3	3	H2013 + 30nm Al + 15nm AlO _x
28-R1	3	3	H2013 + 30nm Al
PP-PMP	1	1	Monolayer PP with 2-sided PMP coating
H2013	3	3	Control #1, Commercial Tri-Layer Separator
Q20S1	3	3	Control #2, Commercial Ceramic Coated Separator

PVD coated separators lead to worse performance relative to the reference separators, when evaluated in a stable 4.4 V cell chemistry. As seen in Figure I.1.G.3, the residual capacity of cells with the PVD coated separators during OCV stand testing decreased as the amount of deposited AlO_x increased. A similar degradation pattern can be seen in discharge capacity of cells in Figure I.1.G.4.

Formation issues with the PMP coated separators reviewed above resulted in only 2 of 10 cells being suitable for testing. The two cells were split between the cycling and OCV testing. A combination of hard and soft shorts caused the issue with cell formation. We believe this is related to the low insulation strength of the

separator due to a high porosity open pore structure used to promote a more uniform coating performance. Results from the cycling and OCV stand testing showed performance with no statistical difference relative to the control samples.

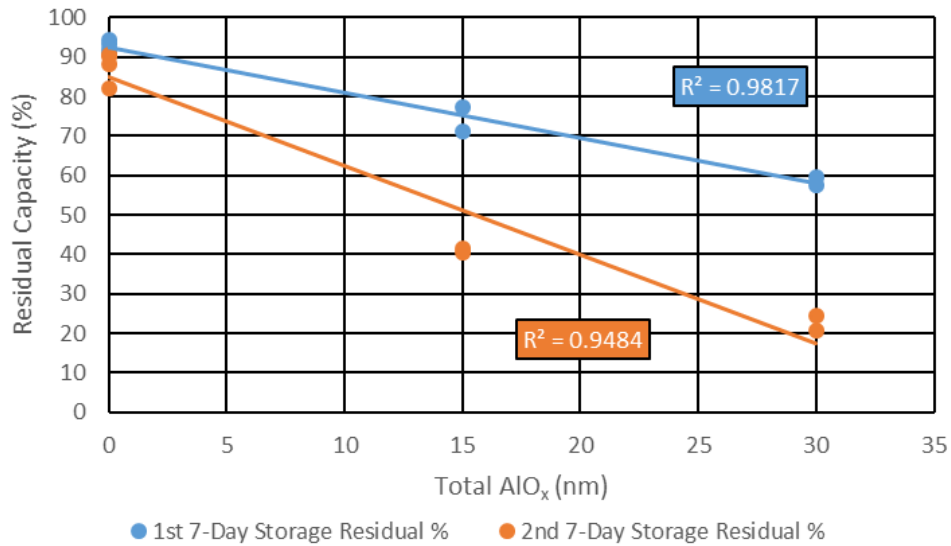


Figure I.1.G.3 Residual capacity during OCV stand at 100% SOC vs. total thickness of AlO_x deposited on the experimental separators.

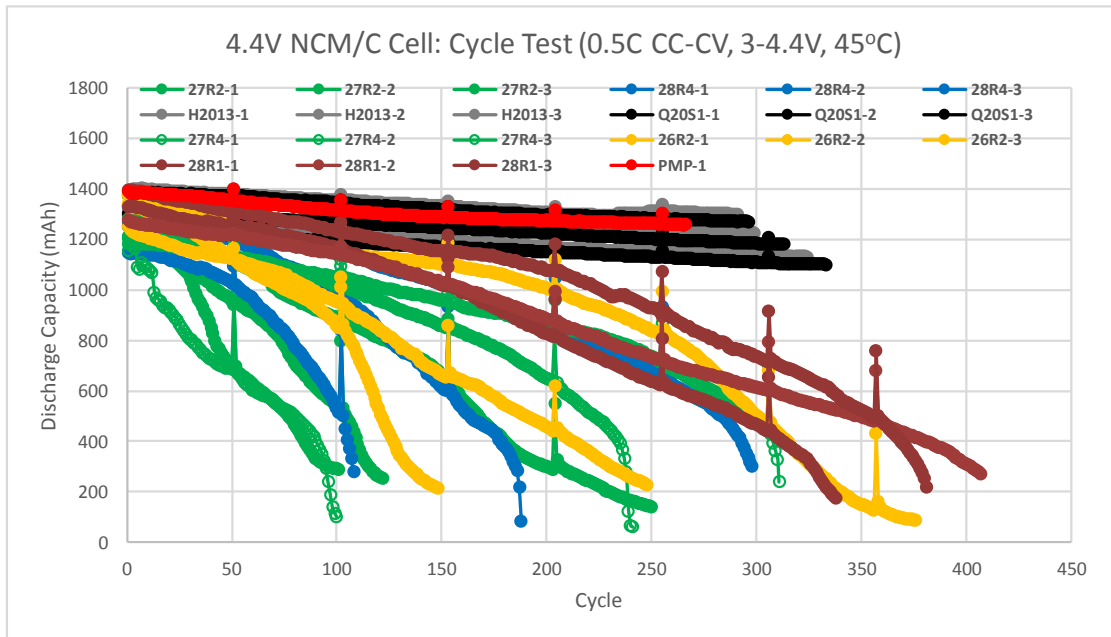


Figure I.1.G.4 Discharging capacity of experimental and control separators in NCM523/Graphite 1.35 Ah pouch cells cycled at 45 °C, between 3.5 and 4.4 V.

Conclusions

Conclusions so far:

- Polyolefin separators coated with a PVD nano-size AlO_x layer showed a decrease in performance during cycling and OCV-stand in batteries with commercial electrodes, when tested to 4.4 V, which is related to the amount of PVD deposited material. Aluminum coated separators showed a similar, but somewhat lesser reduction in capacity retention during cycling in the same cell type. Due to the relative performance to the control separators these are not believed to be a viable candidate for a 5V system.
- Separators coated with PMP are not viable due to manufacturing difficulties during the cell assembly process. These issues are likely not correctable, given the high porosity required during separator manufacturing which can be directly related to the high rate of hard and soft shorts seen during cell assembly.
- Current the LMNO//graphite cell chemistry is unable to provide a stable test platform for the evaluating separators at 5 V. Stabilization of the cathode-electrolyte interface is necessary to provide a stable cell chemistry, for evaluation of separators at 5 V.

I.1.H Li-Ion Cell Manufacturing Using Directly Recycled Active Materials (Farasis Energy)

Michael Slater, PhD, Principal Investigator

Farasis Energy, Inc.
21363 Cabot Blvd
Hayward, CA 94545
E-mail: m Slater@farasis.com

Brian Cunningham, DOE Technology Development Manager

U.S. Department of Energy
E-mail: Brian.Cunningham@ee.doe.gov

Start Date: February 1, 2017
Project Funding: \$1,639,044

End Date: February 1, 2019
DOE share: \$819,522

Non-DOE share: \$819,522

Project Introduction

The rapid performance gains of Li-ion batteries in the past few decades has led to accelerating implementation of this electrochemical energy storage technology on an unprecedented scale. For this growth to be sustainable, the entire life cycle of the batteries must be accounted for, from raw material sourcing to end-of-life disposal and reuse. So far, the cost associated with end-of-life disposition of these batteries has not been included in the product price; coupled with a drive to use less costly materials in the batteries themselves we are arriving at a situation in which there is less intrinsic value in the elemental composition of the battery than it costs to recycle/dispose of them in a responsible manner. Thus there is a need for a recycling method that goes beyond treating the battery as an ore and can harvest some of the additional value that is invested in the product during complex raw material and cell manufacturing processes.

Objectives

There are four main objectives for this project:

1. Optimize direct recovery processes at larger scale (>8 kg cell/module input)
2. Optimize electrode formulations to make best use of refurbished active materials
3. Manufacture full-size LiBs on commercial production line using direct-recycled active materials
4. Quantify impacts of using recycling active materials on technology cost

Approach

Farasis Energy has been working on recycling technology for Li-ion batteries for a number of years. We have addressed the challenges of closing the loop of the Li-ion product life cycle by developing methods for recovery and reuse of valuable components in the batteries largely based on the direct recycling approach. "Direct Recycling" refers to battery recycling technology in which material recovery is performed using physical separation processes and active materials are reused with minimal processing, ideally without the need for extensive chemical transformation. In this way, some of the value invested in the materials (*e.g.*, synthesis process energy, particle size distribution and shape) can be recovered without the need to resynthesize these materials from their lowest value elemental form. Figure I.1.H.1 shows a flow chart for a straightforward direct recycling process used to recover the high value components of the Li-ion battery. In this approach the entire cell or module is shredded after being fully discharged and deactivated. Safety is a key requirement for this step, and therefore measures to prevent release of hazardous materials and fires are a primary consideration. The shredded material is subjected to a solvent extraction step, which removes the electrolyte while also stabilizing the cell chemistry by removing a source of hydrofluoric acid, which can

damage the valuable active materials upon exposure to air and water during subsequent processing. The shredded mass is then screened/sieved to remove other battery components from the micron-sized active materials. This leaves the “Black Mass,” a mixture of active anode and cathode powders with some binder, carbon, and small amounts of other components as contaminants. In this state, the recovered active materials are not immediately ready for use in new lithium ion cells; the recovered cathode material is missing some lithium due to the inherent losses during the formation process and extended cycling while the graphite active material contains some lithium and surface species generated during the formation and cycling processes. Separation of the cathode and anode active materials from each other is achieved using a liquid with density between that of graphite and the metal oxide. This is followed by purification of the active materials by removing contaminants, restoring the lithium inventory, and final annealing in which the structural integrity of the materials is returned to its pristine state. Farasis has developed proprietary approaches to achieve these final steps that are chemistry independent and have demonstrated the capability to achieve good separation yields, high purity and high performance materials.

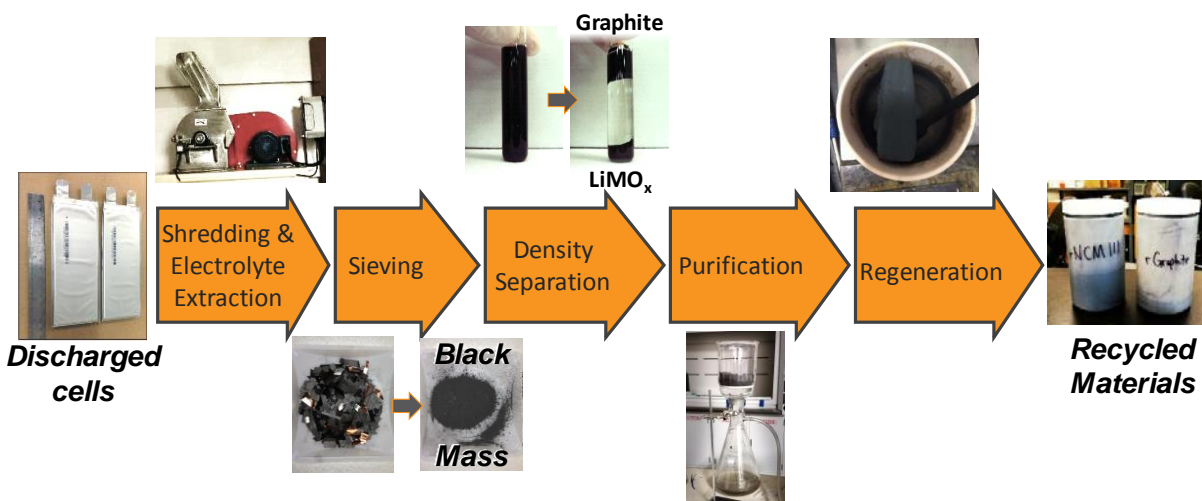


Figure I.1.H.1 Pictorial representation of the direct recycling process which largely relies on physical separation processes; compared to other recycling technologies, the positive electrode active material is recovered intact, preserving some of the value added during its synthesis.

Available evidence to-date suggests that modified surface chemistry of the isolated active materials is the primary technological challenge to address from a process perspective, while any intervention in this domain also provides an opportunity for improvements over the properties of the pristine materials. Detailed structural investigations as to the nature of material changes during recycling processes are being explored in collaboration with Robert Kostecki at Lawrence Berkeley National Laboratory. The suite of analytical tools that will be used to inform the optimization of the recycling steps include:

- High resolution X-ray instrumentation at DOE’s Synchrotron User Facilities, enabling detailed investigation of structural parameters such as microstrain and lattice defects
- SEM will be used for imaging particle morphology and surface chemical analysis by EDAX
- Electrochemical Impedance Spectroscopy will be used to determine intrinsic conductivity of materials and for electrode-level characterization during formulation research with recycled materials
- Particle size distribution measurements and gas adsorption analysis will be used to determine material physical characteristics such as particle size, surface area, and internal microporosity

- Raman spectroscopy will be used to study surface and near surface changes in material structure and chemistry which are difficult to characterize by other methods
- Neutron diffraction will be employed in conjunction with XRD to more accurately characterize the structure of Li-containing materials. Due to the extremely weak scattering cross section of Li for X-rays, neutron diffraction is required to positively locate Li in the crystal structures

The direct recycled active materials will be used in iterative cell builds through which insight will be gained on how to best incorporate recycling technologies in battery manufacturing, resulting in more environmentally friendly, lower cost production of Li-ion batteries. A high-level summary of project deliverables (internal and external) may be found in Table I.1.H.1.

Table I.1.H.1 Overview of Program Hardware Deliverables and Build Strategy

Hardware Deliverable	Description	Source Material	Quantity ANL/FEI*	Delivery Date
Cell Build 1 (66 x ~ 2 Ah cells)	Control: pristine NMC/pristine Gr	commercial powders	9/12	Month 21
	recycled NMC/recycled Gr	manufacturing scraps	9/12	Month 21
	recycled NMC/pristine Gr	manufacturing scraps	0/12	Month 21
	pristine NMC/recycled Gr	manufacturing scraps	0/12	Month 21
Cell Build 2 (54 x ~2 Ah cells)	Control : pristine NMC/pristine Gr	commercial powders	9/12	Month 23
	100 % recycled NMC/100% recycled Gr	BOL cells/QC rejects	9/12	Month 23
	blended: TBD % of recycled/TBD % new	BOL cells/QC rejects	0/12	Month 23
Final Build (54 x 25 Ah cells)	Control: 25 Ah FEI production cells	commercial powders	15/12	Month 25
	25 Ah cells with optimized (maximum) recycled content in each electrode	EOL cells and module parts	15/12	Month 25

* Each build will include cells for external (USABC/ANL) and internal (Farasis Energy) testing and evaluation

The measure of success of the program is being quantified by measuring the gap between recovered material and equivalent control test articles made using commercial grade active materials, which will be included with each build to allow comparative evaluation. While not included in the final deliverables, there will be development work addressing how best to handle mixed chemistry feed streams, which is an inherent challenge for direct recycling processes. Specifically, recovery of feed streams with NMC532 and mixed NMC/spinel compositions will be studied. Another important outcome of the program will be to refine current assumptions of a scaled production process (including milling, separation, purification and regeneration operations) and evaluate revenue potential against capital and energy requirements and operating costs, thus ensuring that the technology is economically relevant.

Results

Direct recycling process optimization for recovery of active materials from scrap electrode feedstocks is complete. Critical process parameters were identified in the course of scaling the process to handle kg of materials and some additional optimization was performed to refine material characteristics. In the first phase of this project, we optimized processes around a feedstock of scrap electrodes (manufacturing waste), which reduces the complexity of the process considerably. Process parameter variations affect both the yield and material properties of recovered materials. Figure I.1.H.2 illustrates these effects for both positive and negative electrode scrap feedstocks. Part (a) shows that thermal processing parameters have a small impact on yield from positive electrode scrap, while part (b) details the electrochemical characteristics which are strongly dependent on processing conditions. Similar data for negative electrode scrap is presented in parts (c) and (d); processing the negative electrode scrap in air can lead to oxidation of the copper substrate, concomitant with combustion of the graphite, leading to copper oxide fines in the graphite product. The electrochemical signature of these oxides is evident as irreversible capacity at *ca.* 1.2 V (vs. Li/Li⁺) in the first reduction of the material. While this contamination can be largely eliminated with optimized thermal processing conditions,

some amount of Cu in the graphite product is difficult to eliminate. Farasis has also developed chemical processing technology that can be used to further reduce the Cu contamination, if required.

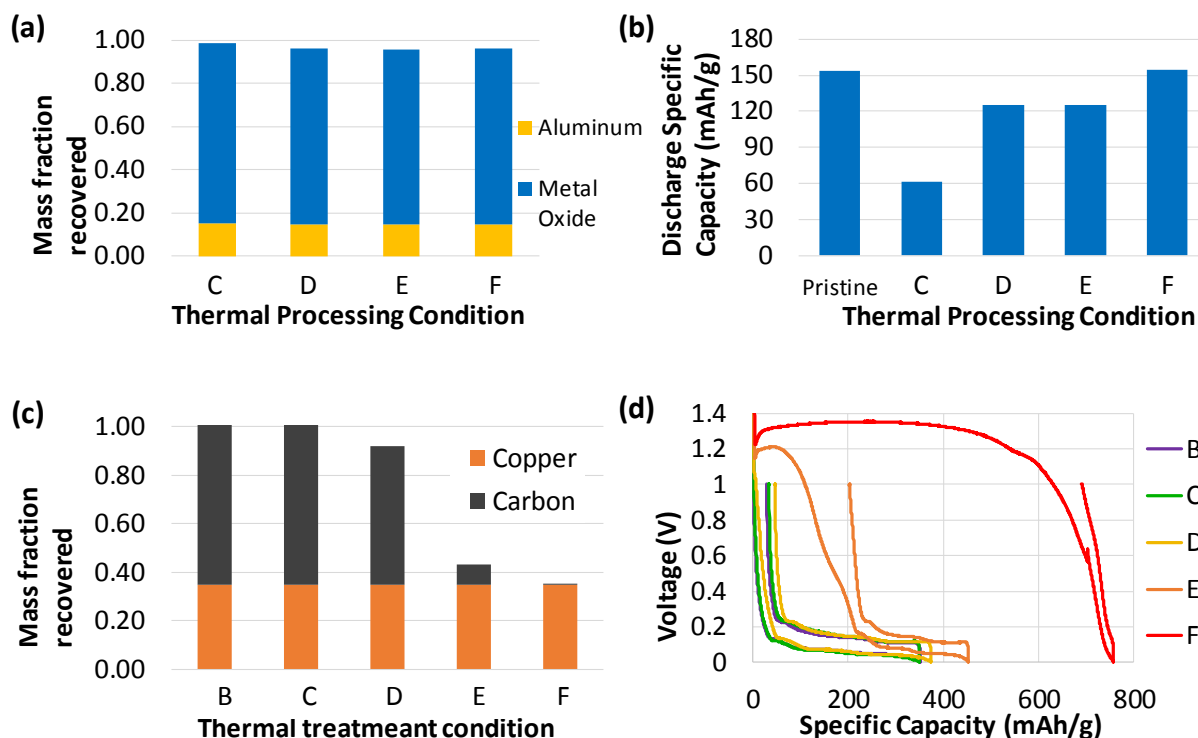


Figure I.1.H.2 (a) Material recovery from positive electrode scrap, and (b) reversible electrochemical capacity of recycled NMC111, recovered using different process parameters (First discharge capacity, C/20, 4.2 - 3.0 V vs. Li metal counter-electrode). (c) Thermal treatment conditions effect on material recovery from scrap negative electrodes; (d) First cycle of recovered anode materials vs. Li metal counter-electrode (C/20, 0.05 - 1.0 V vs. Li/Li+).

Further analysis of recycled NMC111 by researchers at Lawrence Berkeley National Laboratory aids in understanding the underlying physical phenomena responsible for observed differences in electrochemical performance. Figure I.1.H.3 displays SEM images and Raman spectroscopy studies of a series of recycled NMC111 samples recovered using different process conditions. With increasing thermal treatment temperature, the surfaces of the materials become progressively cleaner, with less soft material apparent in the crevices between crystallites. This soft material is a mixture of carbonaceous compounds that burns off with greater thermal exposure. Vibrational Raman spectroscopy analyzes the particle surfaces and can clearly detect the presence of carbon compounds there. This clearly shows that the carbons are completely removed with sufficiently high processing temperature.

A summary of the material properties for active materials recovered from positive and negative electrode scrap is presented in Table I.1.H.2 and Table I.1.H.3, respectively. For the recycled NMC111, the properties of the recycled material are nearly identical to the pristine version of the material. The process of converting NMC into electrodes and eventually batteries does leave its mark on the material however, evident as a slight decrease in tap density and an increase in specific surface area in the recycled material; both of these changes are thought to be due to crushing during the calendaring process which alters the particle size distribution of the active material (although this can be reversed to some extent during the recycling process). There is also a slight decrease in specific capacity and first cycle efficiency which are due to surface chemical changes during the recycling process. Despite these differences, the recycled material is within the acceptable range for manufacturing new Li-ion cells. Similarly, the recycled graphite has parameters very close to the pristine version. The main differences are decreased tap density and increased specific surface area, which are thought

to be due to residual nanocarbons. Unlike with the metal oxide cathode material, the graphite active material can not be arbitrarily heated to force combustion of carbon contaminants. These can be accounted for, however, when formulating electrodes using the recycled graphite.

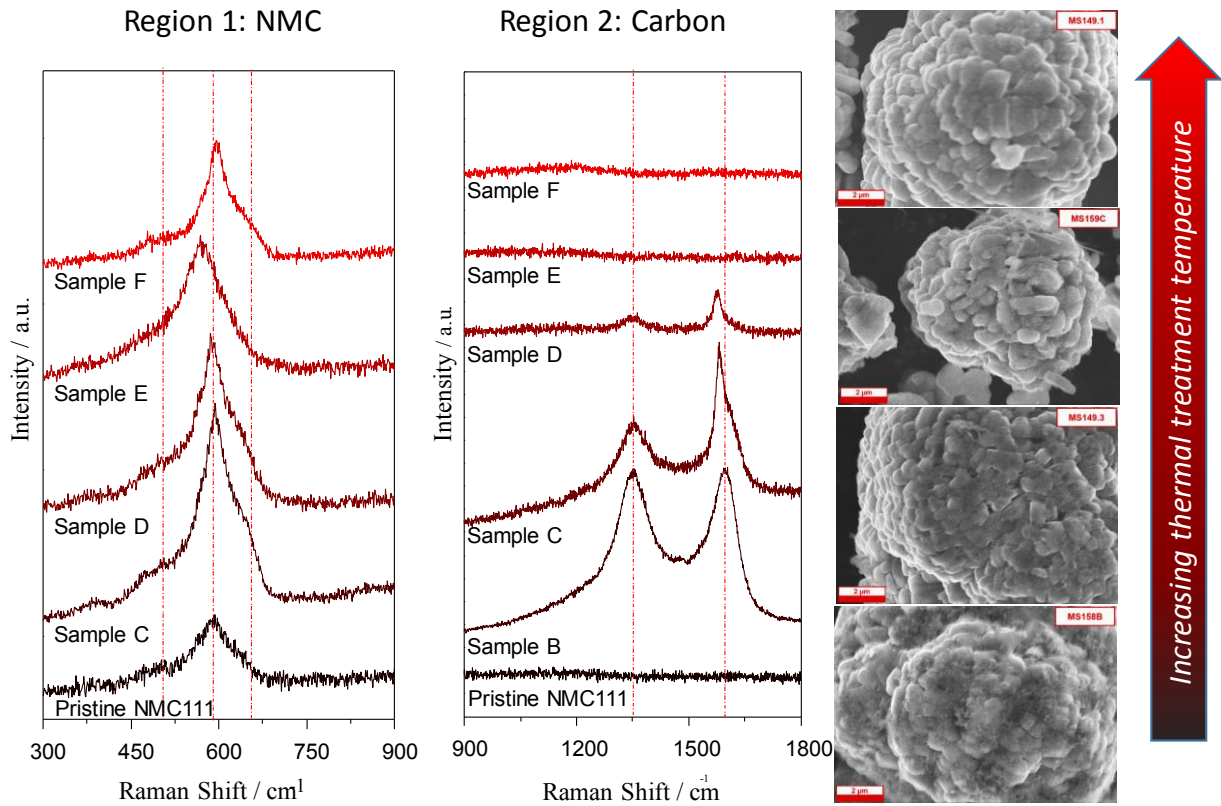


Figure I.1.H.3 Raman spectra and SEM images of NMC111 recovered from electrode scrap using a range of thermal treatment conditions.

Table I.1.H.2 Properties of Recycled Positive Electrode Active Material

Characteristic	Units	Pristine	Recycled NMC
Particle size (D_{50})	μm	9.4	10.4
Tap Density	(g/cm^3)	2.5	2.3
Reversible capacity (4.2 - 3.0 V vs. Li/Li ⁺ , 0.1 C)	(mAh/g)	150	145
Specific Surface Area (BET method)	(m^2/g)	0.23	0.26
First cycle efficiency	%	91	88
Impurities	%w/w	Na < 1 Mg < 0.4 Ca < 0.5 Fe < 0.2 Cu < 0.01	Na < 1 Mg < 0.4 Ca < 0.5 Fe < 0.2 Cu < 0.01
pH assay	$-\log [\text{H}^+]$	11.2	11.3

Table I.1.H.3 Properties of Recycled Negative Electrode Active Material

Characteristic	Units	Pristine	Recycled Graphite
Particle size (D ₅₀)	μm	15	14
Tap Density	(g/cm ³)	1.2	0.94
Reversible capacity	(mAh/g)	322	315
First Cycle Efficiency	%	89	88
Specific Surface Area	(m ² /g)	1.13	2.56
Ash content	%w/w	0.09	0.4

The next phase of the project will incorporate these recovered materials in deliverable test articles. Process optimizations on the more complex feedstocks comprised by aged cells and complete battery systems have begun and will lead to additional builds of cells to further refine direct recycling approaches for Li-ion batteries.

Conclusions

A recycling process for direct recovery and reuse of Li-ion battery active materials has been scaled up and is being applied to multiple commercially-relevant feedstocks. Initial processing of manufacturing residues has demonstrated that recovery of active materials with properties nearly identical to pristine materials is practical using commercially relevant Graphite//NMC cell chemistries. Cell builds with recycled active materials will provide data for quantitative technology valuation.

Key Publications

1. “Li-Ion Cell Manufacturing Using Directly Recycled Active Materials,” bat356_Slater_2018_p, US DOE Vehicle Technologies Program Annual Merit Review, 2018.

Acknowledgements

Farasis Energy would like to extend special thanks to Renata Arsenault, who manages this project for USABC, for her collaboration and dedicated effort to advance Li-ion battery recycling technology. The PI would also like to extend special recognition to Benjamin Little and Martin Grodzicki, both researchers at Farasis, who contribute to the progress of this project on a daily basis.

I.1.1 A Closed Loop Recycling Process for End-of-Life Electric Vehicle Li-ion Batteries (Worcester Polytechnic Institute)

Yan Wang, Principal Investigator

Worcester Polytechnic Institute
100 Institute Road
Worcester, MA 01609
E-mail: yanwang@wpi.edu

Brian Cunningham, DOE Technology Development Manager

U.S. Department of Energy
E-mail : Brian.Cunningham@ee.goe.gov

Start Date: February 2, 2016	End Date: September 15, 2018	
Project Funding: \$1,024,740	DOE share: \$512,370	Non-DOE share: \$512,370

Project Introduction

The purpose of this USABC project was to successfully recycle multiple 30 kg size batches of end of life EV batteries consisting of different incoming cathode chemistries via the recycling process developed at WPI, and produce PHEV format cells of a single chemistry using the recovered NMC111 cathode. Over the course of the two year development program, WPI/A123 systems/Battery Resourcers would improve the performance of the recovered cathode materials so that they achieve performance equivalent to current commercial materials, as confirmed by A123 and National lab testing using USABC PHEV test procedures. Other materials including lithium, steel, copper, aluminum, etc. would also be recycled where possible.

Objectives

The objective of this program was to scale up and demonstrate WPI's novel and efficient Li-ion battery recycling process, verify its claim of no or minimal sorting, and develop PHEV cell designs with a lower cost structure for improved industry sustainability. The USABC development program was structured to advance the WPI technology through the completion of three major tasks: 1) optimize the synthesis parameters of the recovered $\text{LiNi}_{0.33}\text{Mn}_{0.33}\text{Co}_{0.33}\text{O}_2$ (NMC111) cathode materials for improved particle density and electrochemical performance; 2) improve the recycling efficiency of cathode materials and lithium and 3) scale the process from the initial (pre-program) 1 kg scale to a 30 kg scale or greater, as required.

Approach

WPI collaborated with A123 Systems and Battery Resourcers. To execute the project. WPI's primary focus was developing the recycling process and recovering NMC111 powder, A123's focus was on powder characterization and cell fabrication, and Battery Resourcers' focus was on scale up and cost analysis. The recycling process and recovery of cathode materials followed a patented process developed at WPI. The development strategy of the program is shown in Figure I.1.1.1. The project included 3 phases: initial scale-up, optimization and final deliverables. During the initial scale-up, the synthesis parameters of NMC111 precursor and cathode materials were determined and electrochemical testing were conducted with coin cells. During the optimization phase, 4 different spent battery streams (30kg each) were utilized for recycling experiments to generate NMC111 for 1Ah cells. At the same time, virgin NMC111 was used to fabricate 1Ah control cells for side by side evaluation. For final deliverables phase, two spent battery streams, with intentionally different input chemistry combinations, were utilized for recycling experiments to generate NMC111 for 10Ah cells. At the same time, virgin NMC111 was again used to fabricate 10Ah control cells.

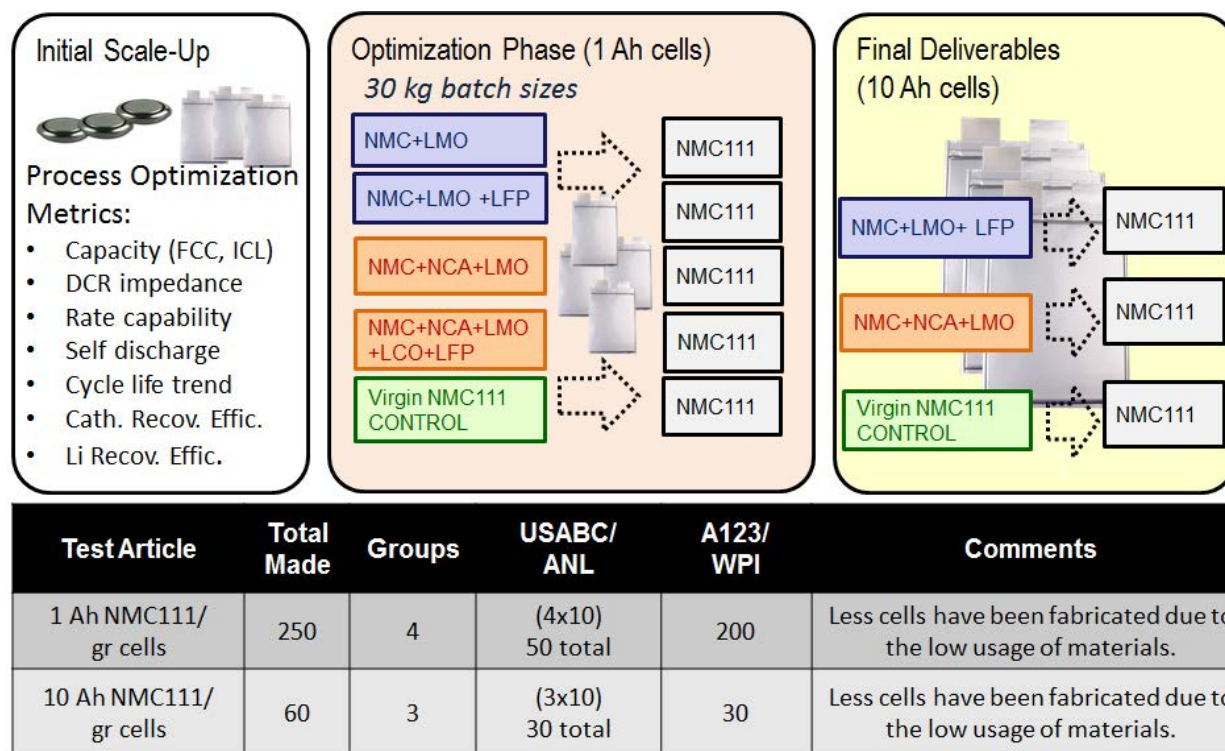


Figure I.1.1.1 Hardware Strategy of the Program

Results

All required powder was recycled from spent batteries and delivered to A123 for 1Ah and 10Ah cell fabrication. Below are detailed cell performance results from cells made with WPI recovered NMC111 and control NMC111.

1Ah - A123 Internal Testing Results (cycle life): The cycle life of the 1Ah cells can be seen in Figure I.1.1.2. All three builds with WPI powder show above 80% capacity retention to 2200 cycles of +1C/-2C cycling between 4.15V-2.7V at 45°C. It is expected that these cells will reach ~3200 cycles before hitting 80% retained capacity if current cycling trends continue. All three lots of WPI NCM111 also show consistent cycling behavior between and within groups. The control group has cycled just over 2000 cycles but is exhibiting poorer capacity retention than any and all of the WPI lots, as shown below.

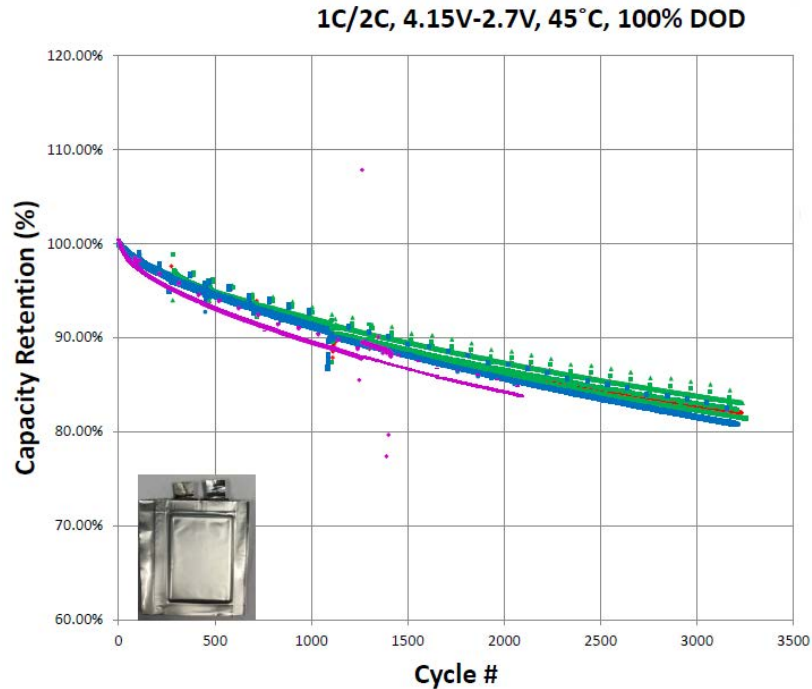


Figure I.1.1.2 Cycling of 1Ah cells with WPI cathode and control between 4.15V and 2.7V, 100% DOD, 45 °C, +1C/-2C

During cycle life testing, a SOH check is performed every month which involves a 5C discharge pulse for 20 seconds at 70%, 50%, and 20% SOC. Figure I.1.1.3 shows the DCR measurements during the first SOH check for the cells in Figure I.1.1.2. The 1s DCR resistance is lowest in WPI lot 04212017 and highest in lot 06202017. This difference in resistance does not seem to have any impact on the cycling performance of the cells.

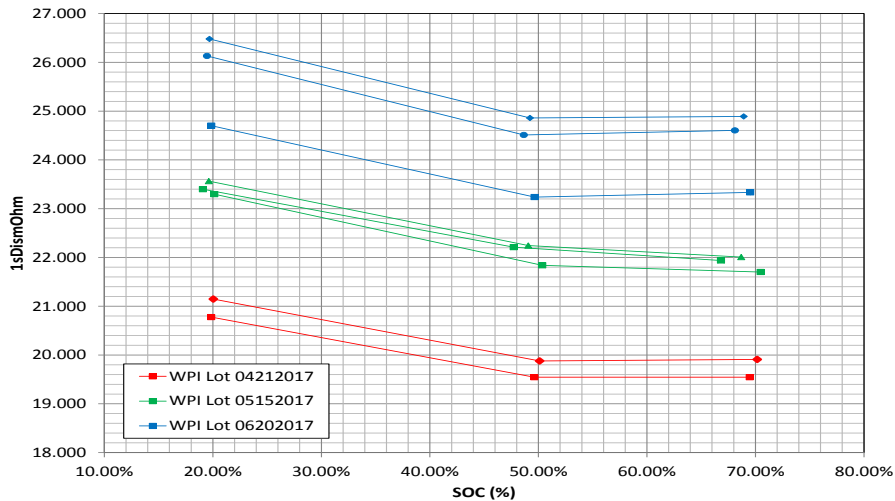


Figure I.1.1.3 1-second DCR, 5C discharge, 45 °C, 70%, 50%, and 20% SOC after 1 month of cycling

10Ah - A123 Internal Testing Results: The cycle life performance of the 10Ah builds can be seen in Figure I.1.1.4. For the 10Ah cycling, two of the data sets correspond to builds with WPI recycled powder and one data set reflects the A123 selected commercial control powder. The same cycling parameters were used as with the 1Ah cells (4.15V-2.7V, 45°C, +1C/-2C, 100%DOD). Each group has two cells cycling and, with the exception of one control cell, all cells remain above 80% capacity retention at 1100

cycles. One control cell experienced a sudden drop in capacity retention around 800 cycles and was removed from testing. It was assumed that the cell failure was due to a cell assembly error and not a material issue. However, with only two cells in each group, it was not possible to make any meaningful conclusions. At the very least, it does seem that the builds with the WPI powder perform similar to the cells with control powder, consistent with trends seen in all smaller format results. It was also observed that 10Ah cells were exhibiting worse cycle retention than the 1Ah cells, contrary to typical behavior whereby larger format cells would yield better results. A123 have surmised that the most likely cause of the poor 10Ah cell performance is related to the anode coating used for these cells. The anodes used for the 10Ah cells were coated using A123's 'large scale' (pilot) coater which has fewer drying zones than the smaller R&D coater used for the 1 Ah cell anodes. The pilot coater drying capacity, while adequate for the solvent based coatings used for the cathode, has proven inadequate for the water based anode systems. It is assumed that the superior drying parameters available on the R&D coater resulted in a better quality (1Ah) anode, improving qualities such as adhesion, which in turn resulted in better cycle life of the smaller cells. A123 plans on increasing the number of drying zones on the large scale coater prior to the Phase 2 cell builds in order to enable more conventional cycling trends for the follow-on program's large format cells.

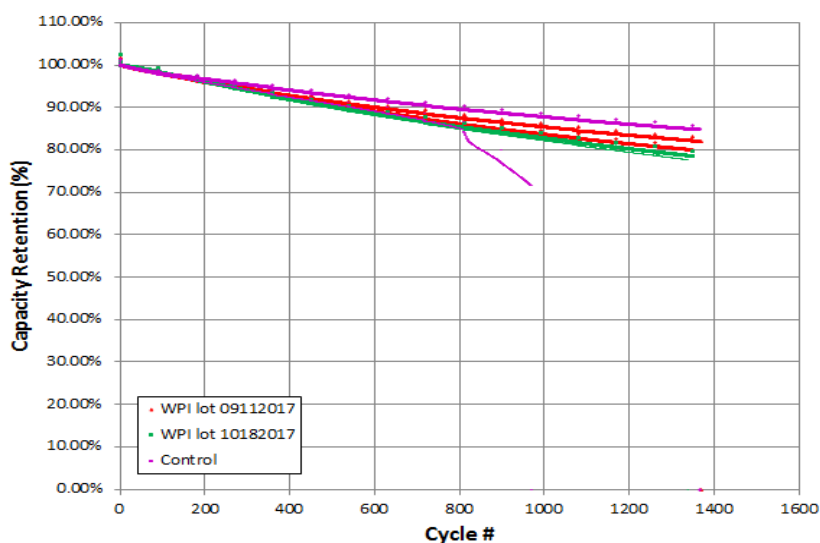


Figure I.1.1.4 Cycling of 10Ah cells with WPI cathode and control cathode between 4.15V and 2.7V, 100% DOD, 45 °C, +1C/-2C

HPPC: Two different HPPC protocols were used on the 10Ah cells with WPI powder. The first was HPPC at 25°C from 100%SOC to 0%SOC with -5C discharge pulses for 30 seconds with +3.75C 30 second charge regen. The second was HPPC at 0°C 100%SOC to 0%SOC with -5C discharge pulses for 30 seconds with +1.5C 30 second charge regen. The DCR at both 1s and 10s can be seen in Figure I.1.1.5. Both builds with WPI cathode show 50%SOC DCR to be about 3 mOhm at 1 second and 3.9 mOhm at 10 seconds. When conducted at 0°C, the build from lot 09112017 has slightly lower DCR at both 1 second and 10 second discharge (~8.5mOhm vs 9.3mOhm at 1 second and 9.6mOhm vs 10.4mOhm at 10 seconds). Both groups show expected DCR trends, with higher DCR at lower SOC and at lower temperatures.

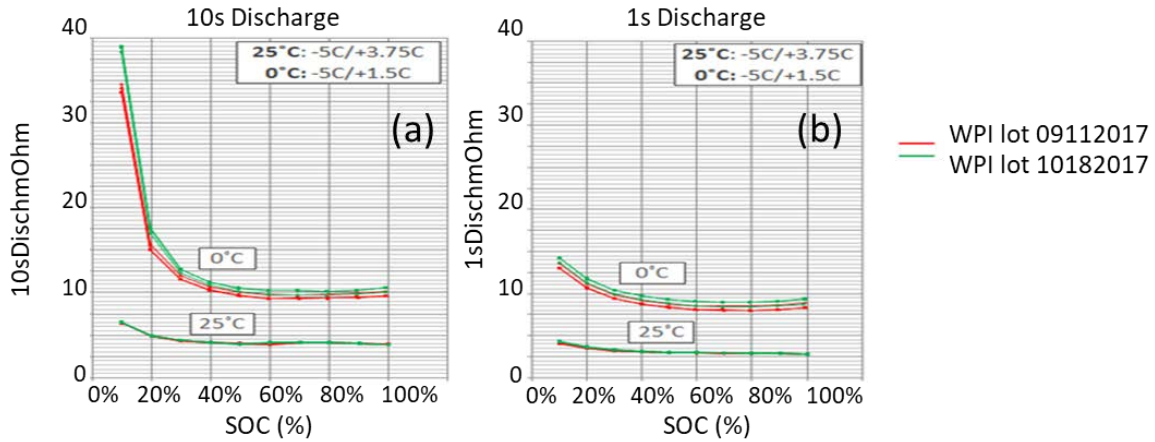


Figure I.1.1.5 HPPC of 10Ah cells with WPI cathode at 25 °C and 0 °C at 10s (a) and 1s (b)

Rate Performance: Both lots 09112017 and 10182017 showed excellent rate performance, consistent with results observed in coin cell-level powder evaluations throughout the program. Cells were subjected to currents between 1C and 9C and the resulting discharge curves can be seen in Figure I.1.1.6. The cells were then compared to a reference cell since there were not enough control cells beyond the USABC deliverables for internal A123 testing. The reference cell used was a 26Ah commercially available product with a similar chemistry. The results were plotted as DOD% relative to the capacity at the 1C discharge, to compensate for the different capacities of the program cells and commercial reference. Both cells from WPI recycled powder show very similar performance, with lot 10182017 showing slightly better rate performance between 5C and 9C. Both groups discharge above 60% of the 1C capacity at 5C and almost 30% of the 1C capacity at 9C. The cells with WPI cathodes have better rate retention than the 26Ah commercial cells. The cells with WPI powder actually show slightly better capacity retention at 9C than the reference cell shows at 7C. As noted, this trend has been observed throughout the program and is believed to be attributed to the internal void space within the WPI powder particles.

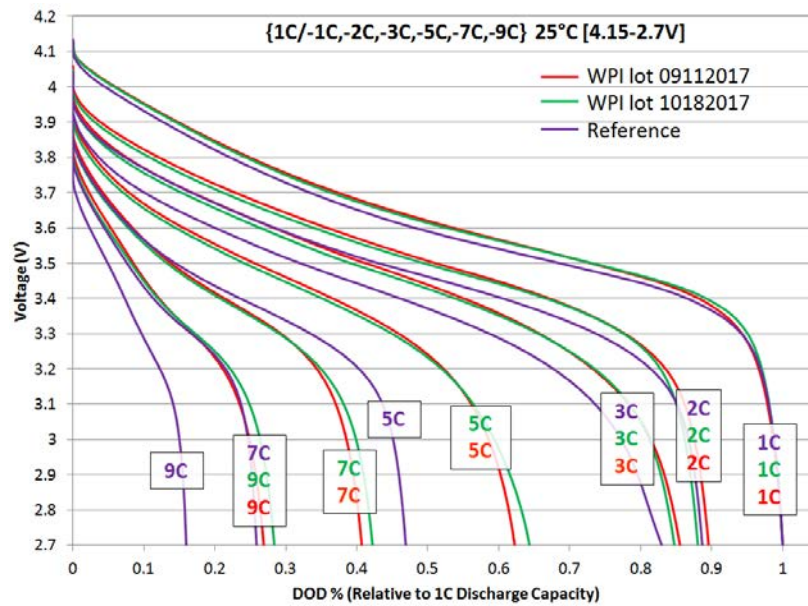


Figure I.1.1.6 Rate performance of 10Ah cells with WPI cathode powder and a reference cell at 25 °C

Conclusions

In this USABC project, the team successfully recycled multiple 30 kg size batches of end of life EV batteries consisting of different incoming cathode chemistries via the recycling process developed at WPI, producing NMC111 powder that was used by A123 to fabricate 1 Ah and 10Ah cell deliverables. Over the course of the two-year development program, WPI/A123 systems/BRs continually improved the performance of the recovered cathode materials so that they now exhibit comparable performance to current commercial materials, according to extensive powder and cell level characterizations conducted by A123. The deliverables (1 Ah and 10 Ah) will allow confirmation of the A123 test results via independent national lab testing using USABC xEV test procedures. Other materials including lithium, steel, copper, aluminum, etc. can also be recycled with the WPI process. To date, this process has been scaled to a 30 kg scale (30 kg shredded battery feed per lot) at WPI, and has generated recovered cathode materials with low impurity concentrations, dense particles, and electrochemical properties closely approaching those of new commercial materials.

Key Publications

1. Zhangfeng Zheng, Mengyuan Chen, Qiang Wang, Yubin Zhang, Xiaotu Ma, Chao Shen, Dapeng Xu, Jin Liu, Yangtao Liu, Paul Gionet, Ian O'Connor, Leslie Pinnell, Jun Wang, Eric Gratz, Renata Arsenault, Yan Wang, High Performance Cathode Recovery from Different Electric Vehicle Recycling Streams, ACS Sustainable Chemistry & Engineering, DOI: 10.1021/acssuschemeng.8b02405

Acknowledgements

The development team (WPI/A123/BRs) would like to thank the following for all of the help, advice, support and suggestions: USABC program manager Renata Arsenault (Ford) and USABC work group members Ron Elder (FCA), Jake Porter (FCA), Nakia Simon (FCA), Peter Karlson (GM), David Maxwell (GM), Brian Cunningham (DOE), Samuel Gillard (DOE) and David Robertson (ANL).

I.1.J Perform USABC/USCAR Benchmarking Activities (Southwest Research Institute)

Bapiraju Surampudi, Principal Investigator

Southwest Research Institute
6220 Culebra Rd.
San Antonio, TX 78258
E-mail: bapiraju.surampudi@swri.org

Ian Smith, Principal Investigator

Southwest Research Institute
6220 Culebra Rd.
San Antonio, TX 78258
E-mail: ian.smith@swri.org

Brian Cunningham, DOE Technology Development Manager

U.S. Department of Energy
E-mail: Brian.Cunningham@ee.doe.gov

Start Date: May 4, 2018
Project Funding: \$529,253

End Date: March 8, 2019
DOE share: \$150,000

Non-DOE share: \$379,253

Project Introduction

Development of new powertrains for hybrid electric vehicles requires knowledge of similar and past powertrains' proficiencies and shortcomings. This knowledge is gained through benchmarking and additional data analysis can help drive the direction of product development and influence goals and targets such as range and production price for the U.S. Department of Energy Vehicle Technologies Program. A vehicle- and component-level powertrain benchmark study and detailed cost analysis of the battery is performed on the 2018 Audi A3 eTron plug-in hybrid electric vehicle (PHEV).

Objectives

Vehicle-level benchmarking includes on-road testing at various battery pack state of charge (SOC) to examine vehicle performance (acceleration and regenerative braking) along with chassis dynamometer testing to determine vehicle fuel economy over various emissions certification drive cycles.

Component-level benchmarking includes battery pack performance testing (static capacity and HPPC), pack teardown and cost analysis and motor performance testing.

Approach

For vehicle-level benchmarking the PHEV is instrumented to acquire voltage and current at various locations in the high-voltage system (battery pack, electric motor, inverter, etc.) and 12 V system. CAN data on the engine, transmission, electric motor, inverter and power electronics is also recorded. The vehicle will be tested at Southwest Research Institute's (SwRI) test track and chassis dyno facility in addition to a third-party test track in Texas.

For component-level testing the motor and battery subsystems of the vehicle will be removed and installed in test cells for evaluation. The electric motor and inverter will be sent CAN data such that it believes it is installed in-vehicle for accurate performance results. The battery pack will be tested in accordance with the voltage and current limitations gleaned from vehicle test data.

Component cost analysis will be conducted at a third-party vendor.

Results

In 2018 the vehicle was acquired and instrumented for vehicle/on-track testing. Instrumentation included current sensors and voltage taps on each phase of the electric motor, high voltage battery pack, high-voltage accessories (air conditioning compressor & PTC heater), on-board charger and DC/DC converter. The electric motor and high-voltage battery pack were connected to a power analyzer in order to determine the power factor and efficiency of the electric motor. Thermocouples were placed in various locations along the cooling circuit for the high-voltage system along with flow meters to accurately account for the cooling requirements for this powertrain.

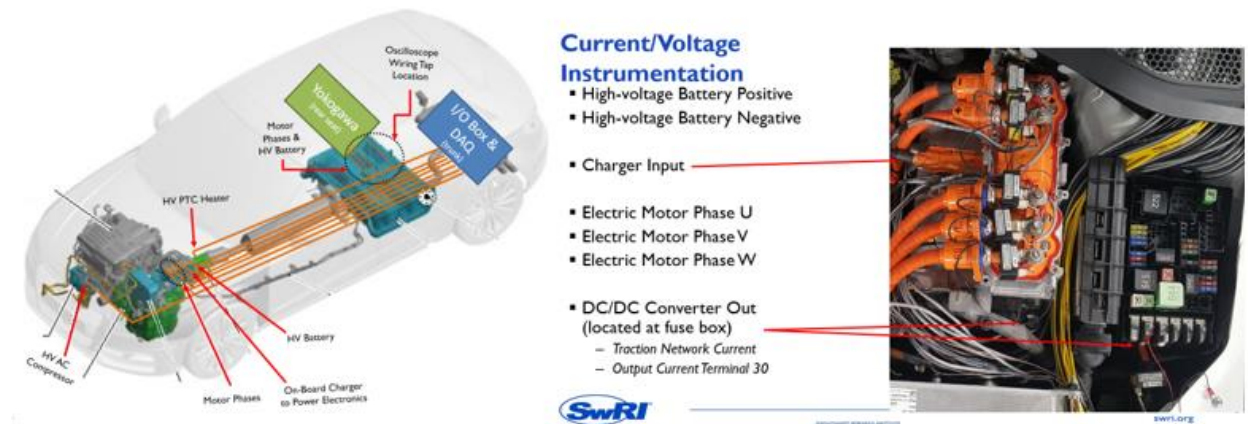


Figure I.1.J.1 High-voltage measurement schematic (left). Power electronics breakout for voltage and current measurement (right).

Over 55 OBD-II extended PID messages have been deciphered on the engine, transmission, electric drive, battery and steering assist modules. A sample of these messages is shown in the figure below. These messages include electric motor commanded torque and speed, driver requested torque, transmission input/output speeds, battery temperatures and various currents and voltages.

Battery	Engine	Electric Drive	Auto Trans
Current of H-V/hybrid battery*	Throttle Valve Position	Phase current U*	Engine Speed*
Battery Temperature	Absolute load value	Phase current V*	Transmission Output Speed*
Battery Charge Condition	Normed load value	Phase current W*	Accelerator position*
H-V battery voltage	Selected Gear-Bits 0-7	RPM of electric machine*	Brake pressure*
Temperature Sensors 1	Coolant Temperature at Radiator	E-machine speed: actual value*	Transmission fluid temperature
Temperature Sensors 2	Engine oil temperature	Temperature of electric machine*	Driver Request Torque*
Temperature Sensors 3	High fuel pressure	Torque: current value*	Transmission Input Speed*
Temperature Sensors 4	Low fuel pressure	Specified torque*	Vehicle Speed Sensor
Temperature Sensors 5	Throttle valve position: normed	Calculated actual torque of electric machine*	Trans Input Speed Shaft 1*
Temperature Sensors 6	Shift lever position	Output current of DCDC converter*	Trans Input Speed Shaft 2*
Temperature Sensors 7	Vehicle Speed	Electric Motor; electric power*	Trans Output Speed Shaft 1*
Temperature Sensors 8	Engine Torque*	Electric motor: RMS current*	Trans Output Speed Shaft 2*
Cell 1 SOC	Pedal Travel	DC/DC Converter circuit voltage	Current of Gear Solenoid A*
...	Brake Pressure		Current of Gear Solenoid B*
Cell 96 SOC			Current of Gear Solenoid C*
Min Cell SOC			Current of Gear Solenoid D*
Max Cell SOC			
Cell 1 Voltage			
...			
Cell 96 V			
Min Cell V			
Max Cell V			

ABS

CAN Input Signal Brake

Vehicle Speed*

Steering Assist

Steering Wheel Steering Angle

*Indicates investigating HS CAN buses for this signal.

The more messages you request the more traffic on the OBD CAN bus and the slower the response.

Some messages found on multiple modules.

POWERTRAIN ENGINEERING

swri.org

Figure I.1.J.2 OBD e-PID messages have been deciphered.

In addition to the OBD-II CAN traffic that is being requested, SwRI has tapped into two high-speed CAN bus lines (the Powertrain CAN bus and Hybrid CAN bus) located under the hood. Unlike OBD, these two buses

openly broadcast hundreds of frames of messages with update rates ranging from 2 milliseconds to 0.5 seconds. SwRI is in the process of relating these high-speed CAN messages to messages requested over OBD-II using proprietary algorithms.

Conclusions

The fully instrumented vehicle is currently undergoing mileage accumulation for vehicle break-in and on-road testing.

I.1.K 12V Start-Stop Development Program (XALT Energy)

Dr. Veselin Manev, Principal Investigator

XALT Energy
750 South Blvd E
Pontiac, MI 48341
E-mail: vmanev@xaltenergy.com

Dr. Kevin Dahlberg, Principal Investigator

XALT Energy
750 South Blvd E
Pontiac, MI 48341
E-mail: kdahlberg@xaltenergy.com

Brian Cunningham, DOE Technology Development Manager

U.S. Department of Energy
E-mail: Brian.Cunningham@ee.doe.gov

Start Date : April 13, 2018	End Date : April 30, 2021	
Project Funding: \$4,611,158	DOE share: \$2,305,579	Non-DOE share: \$2,305,579

Project Introduction

The fundamental challenge that is currently preventing widespread market penetration of lithium-ion based Start/Stop (S/S) batteries, is meeting the cold-crank power density at an adoptable sales price. The solution to a cost-effective S/S battery requires the ability to optimize the active materials as well as the cell design. LMO-LTO chemistry is the most suitable choice of active materials for the S/S application, if the challenges related to LMO degradation and LTO gassing are addressed, specifically at high temperatures. Cold crank power can be achieved by employing high surface area LMO and LTO materials, but will challenge high temperature durability.

Today, XALT delivers an outstanding cell based on NMC-LTO chemistry with no gassing problem and this knowledge will be leveraged to design the LMO-LTO cell system that addresses LTO-based gassing. To optimize the high surface area active materials for durability, XALT is partnering with Forge Nano (FN), a global leader in low-cost interfacial material design that will employ the Atomic Layer Deposition (ALD) process for stabilizing LMO. XALT will also pursue advanced active material synthesis methods by collaborating with Amastan Technologies to synthesize high quality LTO using Plasma Spray Pyrolysis (PSP) to produce powders with precisely tunable particle size, crystallite size, and surface area, at a low cost.

Objectives

The overall objective of this project is to develop an LMO-LTO Start/Stop battery that will meet all the requirements for 'Not Under Hood' applications [1] in a duration of 3 years. The project will be conducted in two phases. The goal for Phase 1 (ending in September 2019) is to deliver 1 Ah cells that meet all the 12V S/S goals for 'Not Under Hood'. In addition, these cells will demonstrate desired cold crank power at 50% state of charge (SOC) at the end of 2000, 100% DOD cycles with lower than 20% capacity fade, conducted at 55°C.

The goals for phase 2 are: (a) to deliver 45Ah cells that meet all the 12V S/S goals for 'Not Under Hood' in Oct 2020. In addition these cells will demonstrate desired cold crank power at 50% SOC at the end of 4000, 100% DOD cycles with lower than 20% capacity fade, conducted at 55°C, and (b) to deliver 3 prototype packs in April 2021.

Approach

To deliver the high power requirements for S/S applications and to meet the phase 1 and 2 goals, XALT are employing LMO and LTO active materials with high surface area. These high surface area active materials will be optimized for durability at high temperatures by using Atomic Layer Deposition (ALD) process to stabilize LMO, by partnering with Forge Nano. XALT will also capitalize on the proprietary processes used in the current state of the art NMC-LTO technology to mitigate gassing, thus ensuring cycle life and calendar life stability in the LMO-LTO cells.

Results

The first generation of 1Ah cells (denoted as D0.1) built with high surface area LMO and LTO materials were tested for cycle life and calendar life and as well for cold crank performance at beginning of life (BOL).

Accelerated Cycle Life Performance

Cells were tested for 100% DOD cycle life at 2C/2C charge/discharge rates at 30°C, 45°C and 55°C (Figure I.1.K.1). The cells show a capacity retention of ~99% at 30°C at 4500 cycles, greater than 95% at 45°C at 4500 cycles and, about 88% at 55°C at 4900 cycles (Figure I.1.K.1, left). The corresponding impedance retention shows about 21% impedance rise at 30°C, 38% increase at 45°C and about 63% rise at 55°C (Figure I.1.K.1, right). 4500 cycles at this test condition equals 40 weeks of cycling.

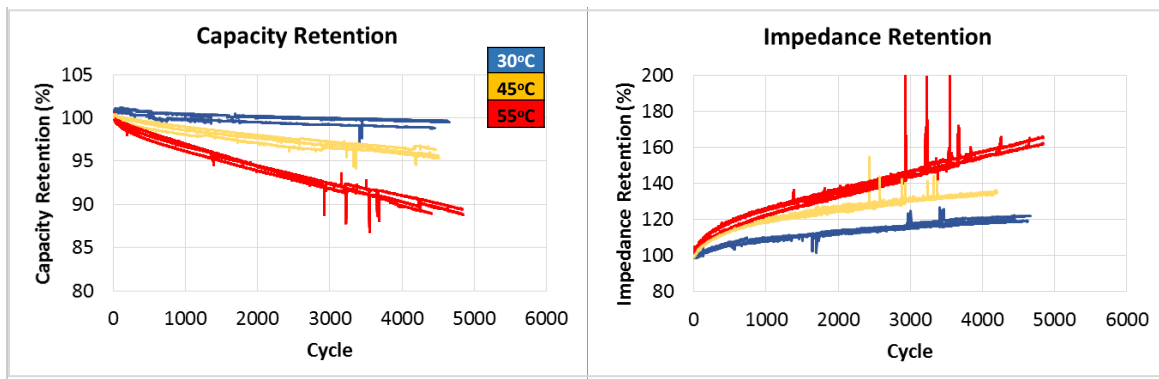


Figure I.1.K.1 2C/-2C, 100%DOD cycle life tests on D0.1 (1 Ah LMO-LTO cells) at 30°C, 45°C, and 55°C. Capacity Retention (left), impedance retention (right)

Cells were also tested at 5C/-5C charge/discharge rates to 100% DOD and have completed 4500 cycles at 30°C (Figure I.1.K.2). The results from this test show that the cells are capable of sustaining these high rates with stable capacity retention (Figure I.1.K.2, left) for 4500 cycles, which equals 13 weeks of cycling. At 13 weeks of cycling, the impedance growth at 5C/-5C rates similar to the impedance growth at 2C/-2C rate cycling at 30°C (~1500 cycles).

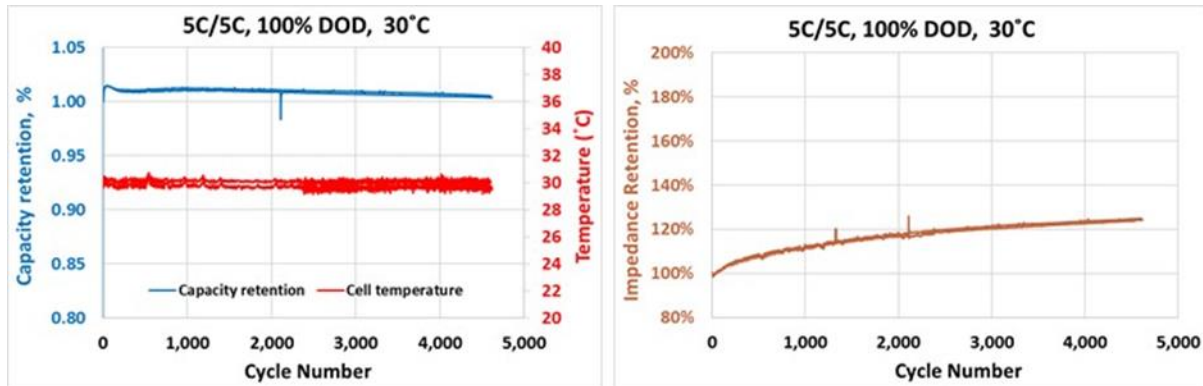


Figure I.1.K.2 5C/-5C, 100%DOD cycle life tests on 1 Ah LMO-LTO cells at 30°C. Capacity Retention (left), impedance retention (right)

Cycle Life Test on D0.1 cells

The D0.1 1 Ah cells have also been subjected to cycle life testing as per the USABC S/S cycle life test profile (Section 3.10), at an SOC of 95%. This SOC was selected based on the results from the HPPC test (Section 3.4) as shown in Figure I.1.K.3. At 5% DOD or 95% SOC, the cells are capable of delivering the required discharge power of 6KW and charge power of 2KW.

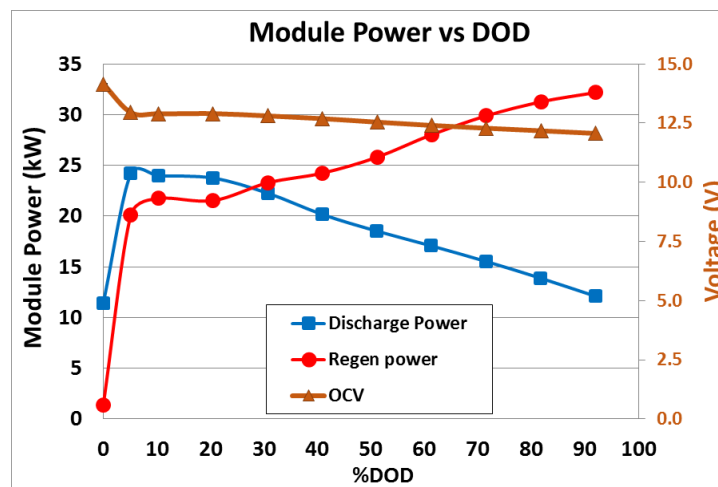


Figure I.1.K.3 Charge and discharge power calculated from HPPC test at 30°C on 1Ah LMO-LTO cells and scaled to the 12V module using the appropriate BSF.

These cells have completed 100,000 S/S cycles. The results from the RPTs are shown in Figure I.1.K.4 and indicate that impedance growth (Figure I.1.K.4 left (b)) and capacity fade ((Figure I.1.K.4, right) measured at 30°C during the RPTs are minimal. At 70,000 cycles, which is an equivalent of ~13 weeks, the impedance grew by 5% at most, and the capacity fade was at 1%. The impedance at -30°C (Figure I.1.K.4 left (a)) increased at a higher rate compared to 30°C, by 30% for the 4KW pulse and by 40% for the 6KW pulse. However, after reaching peak values at around 70,000 cycles the low temperature impedance growth stabilizes.

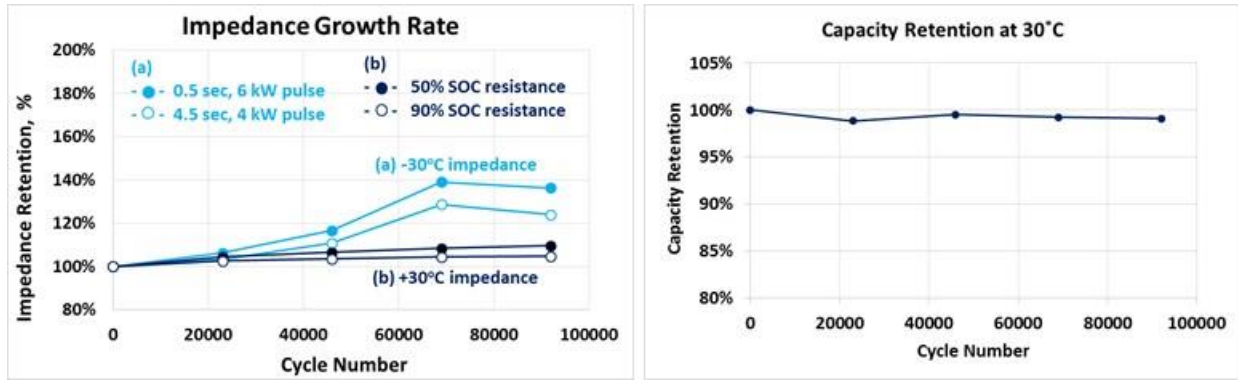


Figure I.1.K.4 (Left): (a) -30°C impedance growth rate during the pulse cycle life test. (-●-) denote values from 0.5s, 6KW pulse test, (-○-) denote values from 4s 4KW pulse test, (b) 30°C impedance growth from HPPC tests, (-●-) denote values at 50%SOC and (-○-) at 90%SOC.

Calendar Life Test performance of D0.1 cells

Calendar life test was conducted on D0.1 cells. The test included initial capacity, impedance and power measurements at 30°C, and cold crank at -30°C, followed by rest at OCV at 100% SOC at 30°C and 45°C, as well as at 70% SOC, also at 30°C and 45°C. After 35 weeks of calendar life, the capacity fade in the cells was observed to be minimal as shown in Figure I.1.K.5.

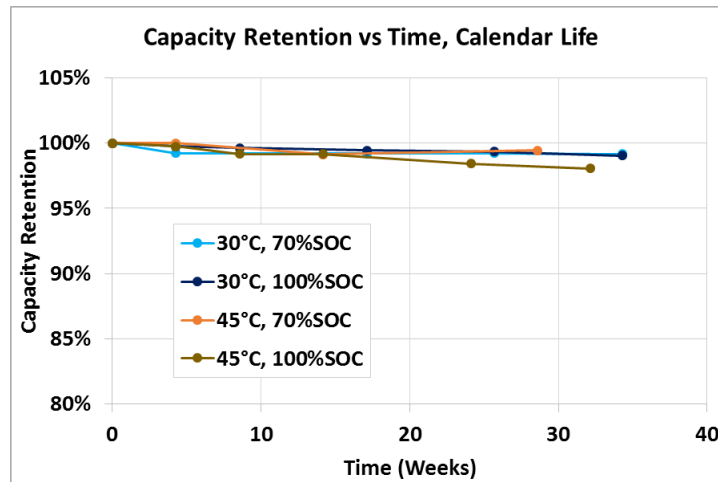


Figure I.1.K.5 Capacity fade of D0.1 (1Ah LMO-LTO cells) during calendar life testing at 100% SOC and 70% SOC, at both 30°C and 45°C.

The impedance growth for the same cells at 30°C as calculated from HPPC tests and, at -30°C as calculated from cold crank tests for all four conditions is shown in Figure I.1.K.6. Figure I.1.K.6 (a) and (c), at 100% SOC and 70% SOC storage, show that after about 35 weeks of calendar life test, the 30°C impedance growth is about 15% for 30°C storage and less than 20% for 45°C storage. Figure I.1.K.6(b) shows that at 100% SOC storage, the -30°C impedance growth is 40% for both 30°C storage and for 45°C storage. However, at 70% SOC storage, as seen Figure I.1.K.6 (d), the -30°C impedance growth is about 40% for 30°C storage and almost 200% for 45°C storage.

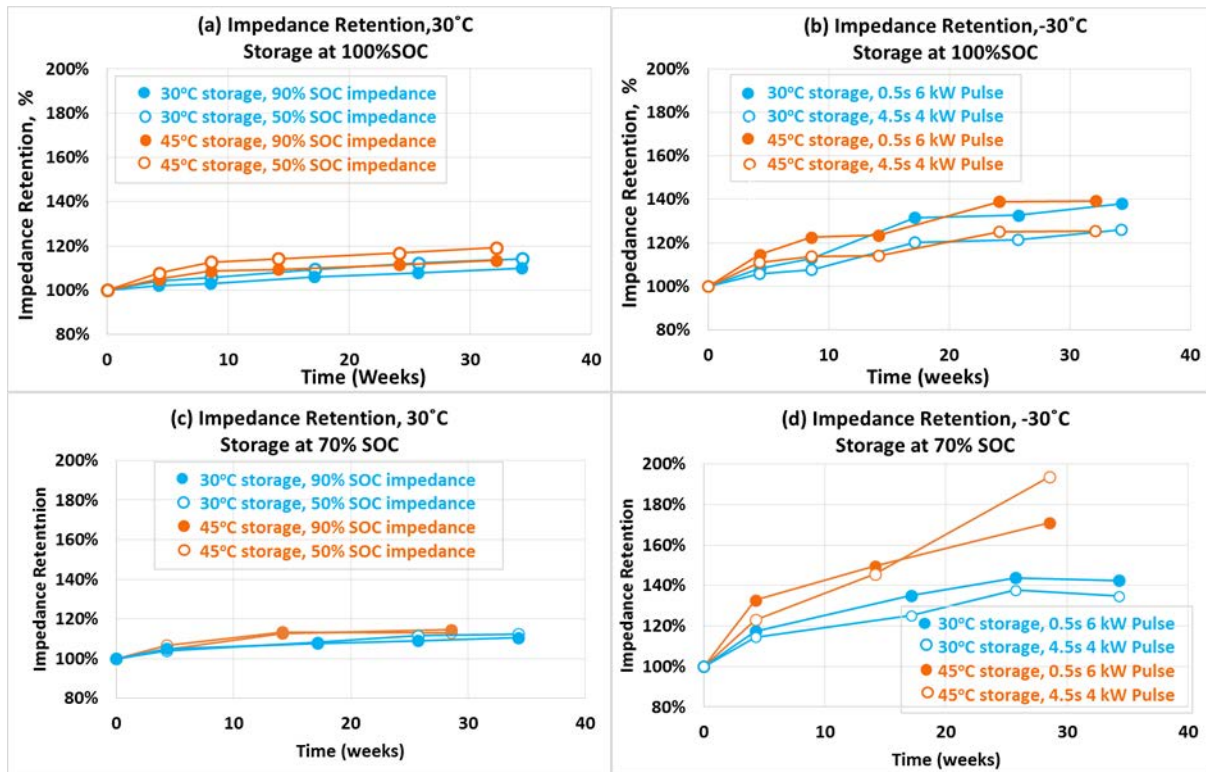


Figure I.1.K.6 Impedance growth on DO.1 (1Ah LMO-LTO cells) during calendar life testing at 100% SOC and 70% SOC. (a) Impedance growth measured at 30 °C from HPPC test for cells stored at 100%SOC, (b) Impedance growth measured at -30 °C from cold crank test for cells stored at 100%SOC, (c) Impedance growth measured at 30 °C from HPPC test for cells stored at 70%SOC, (d) Impedance growth measured at -30 °C from cold crank test for cells stored at 70%SOC.

Cold crank performance on DO.1

Cold crank test was performed on the 1Ah cells by scaling the power requirements using a Battery Scale Factor (BSF) as per the instructions in the S/S manual ([1], Section 3.10), at 50% SOC. As shown in Figure I.1.K.7, at BOL and at 50% SOC, the DO.1 cells are capable of delivering the scaled 4kW pulse power for 4s and 6kW pulse power for 0.5s.

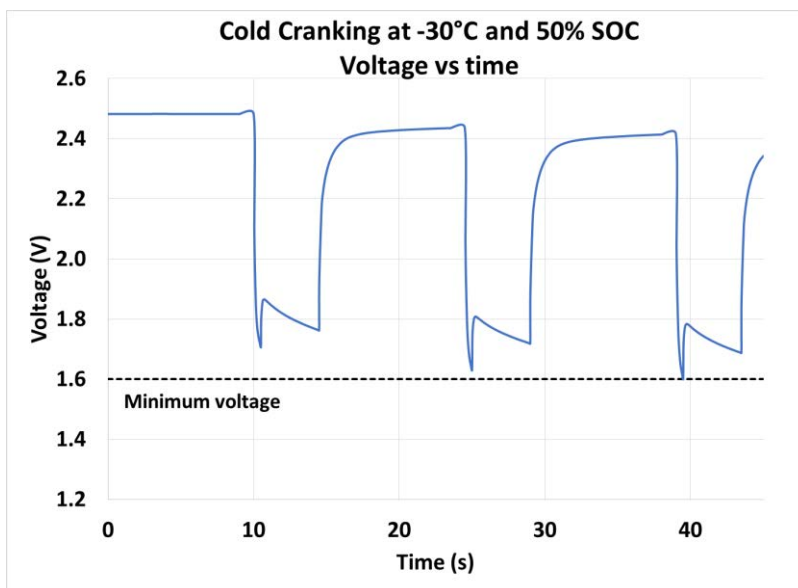


Figure I.1.K.7 Voltage profile during cold crank test at 50% SOC on 1 Ah LMO-LTO cell.

Conclusions

The first generation of 1 Ah LMO-LTO cells built with high surface area active materials demonstrate stable cycle life performance at 30°C, 45°C, and 55°C. High temperature durability was enhanced by employing XALT's proprietary electrochemical interface stabilization methods used in the NMC-LTO product. These cells will be able to complete cycle life and calendar life per the S/S profile as given in the manual [1] with less than 10% capacity fade. At BOL, these cells are capable of delivering cold crank power at 50% SOC.

To achieve the cold crank power at lower than 50% SOC, XALT will employ active materials with higher surface area than those used in D0.1 cells. This increase in surface area of the active materials may affect durability at high temperature. To address this issue, XALT will employ ALD coatings and in the next 6 months demonstrate good cold cranking capability combined with improved high temperature cycle life and calendar life performance.

References

1. Idaho National Lab, U.S Department of Energy, Vehicle Technologies Program. 2015. Battery Test Manual for 12V Start/Stop Vehicles. U.S. Department of Energy, Assistant Secretary for Energy Efficiency and Renewable Energy (EERE), Idaho Operations Office. n.d. "Battery Test Manual for 12V Start/Stop Vehicles."

Acknowledgements

Individuals who are contributing to this project in addition to the PIs include, Susmitha Gopu, Maithri Venkat, Nishanth Bharadwaj and John Camardese from XALT Energy; Arrelaine Dameron from Forge Nano; and Gregory Wrobel from Amastan Technologies. This program is also supported by the USABC work group that include, Jack Deppe (Department of Energy), Josh Lamb (Sandia National Lab), Lee Walker (Idaho National Lab), Matt Denlinger (Ford) and Carrie Okma (FCA).

I.2 Advanced Processing

I.2.A Low Cost Manufacturing of Advanced Silicon-Based Anode Materials (Group14 Technologies, Inc.)

Henry R. Costantino, Ph.D., Principal Investigator

Group14 Technologies, Inc.
100 NE Northlake Way, Suite 300
Seattle, WA 98105
E-mail: rcostantino@group14technologies.com

Peter Faguy, DOE Technology Development Manager

U.S. Department of Energy
E-mail: Peter.Faguy@ee.doe.gov

Start Date: January 1, 2016	End Date: June 30, 2019	
Project Funding: \$4,040,000	DOE share: \$2,810,000	Non-DOE share: \$1,230,000

Project Introduction

Despite substantial investment in Lithium-Ion Battery (LIB) technology, most commercial cells still rely on graphite anodes – originally deployed in the ‘90’s, because of their low cost and acceptable lithium capacity. A shift is underway to replace the graphite anode with a silicon containing material, but due to elaborate manufacturing techniques current costs exceed \$100/kg. It is our vision to develop new anode materials that are high performance, and also easily scalable, employing low-cost materials and manufacturing processes. To this end, we have launched Group14 Technologies, spun out of EnerG2 Inc., a leader in carbon materials development, manufacturing, and commercialization. Group14’s strategy is to develop low cost processes for manufacturing silicon-carbon (Si-C) composite materials that will enable a dramatic reduction in the cost structure of silicon-carbon anodes, i.e., by an order of magnitude, while maintaining the high performance that the LIB industry demands of these advanced anodes.

Objectives

The objective of this project is to develop a new low cost production process that is capable of mass-producing silicon-based lithium ion battery (LIB) anode material that can reach 1000 mAh/g after 1000 cycles and with a cell level cost target of < \$125/kWh, validate performance in LIB full cells, and prove the cost basis at pilot scale.

Approach

At Group14, we are leveraging EnerG2’s carbon technology as our foundation to develop new approaches for low-cost manufacturing of high-performing Si-C composites. These Si-C composites comprise nano-sized and/or nano-featured silicon. Our approach focuses on raw materials that are low cost and readily sourced. Likewise, our approach focuses on manufacturing processes that are low-cost and readily scalable. Specifically, both carbon and silicon components within the Si-C composite are based on low-cost precursors.

Our approach is to down-select Si-C composite materials and manufacturing processes at lab-scale, supported by robust characterization, including electrochemical characterization with a focus on electrochemical testing of the Si-C composite anode materials in full cell Li-ion batteries such as coin cells or pouch cells. Our philosophy for the electrochemical characterization is to employ relatively standard procedures and materials, i.e., industry-standard electrolyte, cathode, and battery cycling conditions. While we are interested in potential synergies with our Si-C composite materials and the next generation of other battery materials (cathodes, electrolyte, etc.) our current intent is that our Si-C composite materials are a “drop-in” replacement for graphite powder as an anode materials, compatible with current commercial anode and Li-ion battery manufacturing lines.

Consistent with our project plan, we have down-selected materials and processes, and have established a facility for manufacturing Si-C at pilot scale (~kg). We are currently producing materials for external and internal performance evaluations. The latter includes electrode and device development towards achieving our final DOE project goal.

Results

The focus during the first quarter of 2018 (Jan-Mar 2018) was completing installation and commissioning of equipment at pilot scale (~kg). Regarding the progress towards scale-up, a summary of the key activities is provided in Table I.2.A.1. As described in previous reports and discussions with the DOE, we previously completed a successful factory acceptance test for the compounding reactor, and the equipment was subsequently shipped and received at our Woodinville, WA pilot production facility. During the first quarter of 2018, we completed all required facility upgrades, equipment installation, and equipment operational commissioning as detailed in Table I.2.A.1.

Table I.2.A.1 Summary of 1Q2018 Key Activities Related to Pilot-Scale Manufacturing of Si-C.

Item/Activity	Status	Next Steps/Deliverable
Equipment Specification	Complete	Reactor and critical auxiliary equipment ordered.
Equipment Procurement	Complete	Equipment successfully completed factory acceptance test and was shipped to Woodinville site.
Site Selection	Complete	Identified and procured ~4,000sf MFG site in Woodinville, WA.
Site Readiness	Complete	Facility upgrades completed to facilitate pilot plant commissioning.
Raw Materials Procurement	Complete	Ongoing procurement, as necessary, to support future reporting periods.
Permitting	Complete	N/A
Process Safety Management	Complete	N/A
Installation and Commissioning	Complete	Identify and stabilize pilot production at optimal processing conditions.

Another important aspect of pilot manufacturing addressed in the first quarter of 2018 was sourcing of raw materials. In the case of the current Si-C composite material, Group14 produces both the carbon and silicon comprising the composite. To that end, Group14 has procured access to precursor materials in quantities sufficient to support pilot process development and projected pilot scale manufacturing to complete DOE project goals. As described in prior progress reports, we made the decision regarding our silicon precursor to procure the raw material as a pre-blended material, based on the anticipated substantially reduced facility costs and permitting requirements. Consequently, within the first quarter of 2018 we completed all requirements and obtained permitting to allow for pilot manufacturing operations.

Also within the first quarter of 2018, we completed all critical aspects of our process safety management plan. These aspects included site-specific items such as our chemical hygiene plan, our emergency plan, procurement and training on all specified safety equipment, and so on. All installation, commissioning, and ongoing pilot manufacturing operations are subject to prior, pro-active review in the form of a failure mode effects analysis (FMEA).

The primary focus during the second quarter of 2018 (Apr - Jun 2018) was ongoing process optimization of Si-C composite production at pilot scale. This topic was discussed at a meeting held at the Woodinville, WA process manufacturing facility on May 9th, 2018. At that meeting, we discussed our progress on identifying critical process variables, and optimizing those parameters. The next steps discussed included combing our

cumulative process learning towards production of ~kg Si-C material, confirmation of reproducibility of optimized processing, implementation of pilot bath operations per DOE project requirements, and ongoing process improvements.

Also at the May 9th meeting (in addition to our poster at the AMR meeting June 18-21), we presented an update on ongoing monitoring of the performance of our Si-C composite materials produced at lab-pilot scale (~10 g scale). These results are presented in Figure I.2.A.1 (Wh/L vs. cycle) and Figure I.2.A.2 (Wh/kg vs. cycle) for three representative samples (denoted A, B, and C). These data are for full cell coin cells cycled at C/2 rate over a voltage window of 2.5–4.2 V, with I/2 hold, with a C/10 cycle conducted every 20 cycles, employing an electrolyte comprising 1M LiPF₆ in EC:DEC w/10% FEC, LiNiCoAlO cathode (provided by ANL), and a 5-15% anode excess (anode=5% CMC-SBR, 5% Super-C45, with the remainder of mass comprising ~16-19% Si-C, ~71-74% graphite). As can be seen, consistent with previous demonstrations, the G14 Si-C composite is capable of at least 500 cycle stability. For comparison, a representative graphite sample is also presented. It can be seen that the samples comprising a blend of the Si-C in graphite are capable of at least 20-30% improvement in energy density compared to graphite alone.

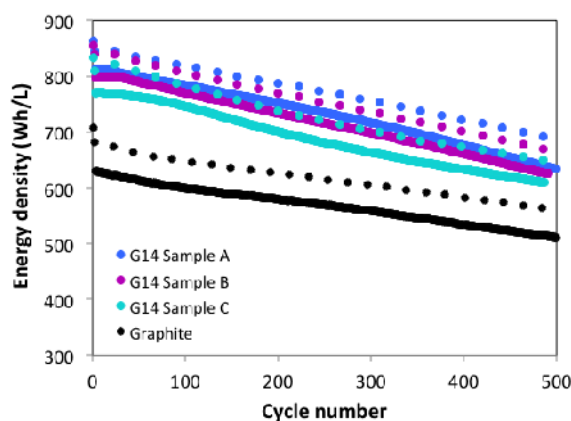


Figure I.2.A.1 Volumetric energy density (Wh/L) in full cell coin cells for Si-C produced at lab-pilot scale.

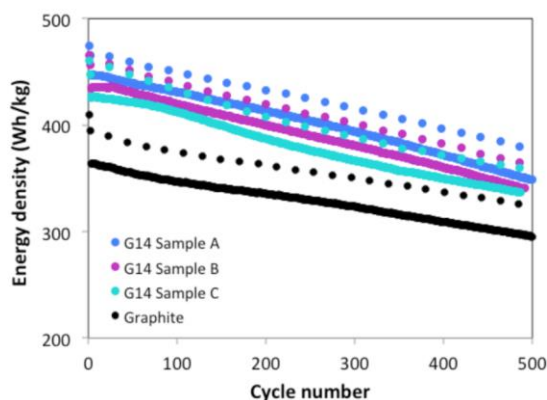


Figure I.2.A.2 Gravimetric energy density (Wh/kg) in full cell coin cells for Si-C produced at lab-pilot scale.

Further data presented at the May 9th meeting (in addition to our poster at the AMR meeting June 18-21) demonstrated an example of device-level enhancement in combination with the Si-C composite. Specifically, we explored the effect of prelithiation of an anode comprising a blend of Si-C and graphite. In this instance, the pre-lithiation was accomplished by an electrochemical contacting method prior to cell assembly. The data are presented in Figure I.2.A.3 as retention for full cell coin cycling employing similar methods as described

above. For comparison, a representative graphite sample is also presented. As can be seen, the G14 Si-C composite when blended with graphite in an anode is capable of at least 1000 cycle stability when employing pre-lithiation as an example of a device-level enhancement.

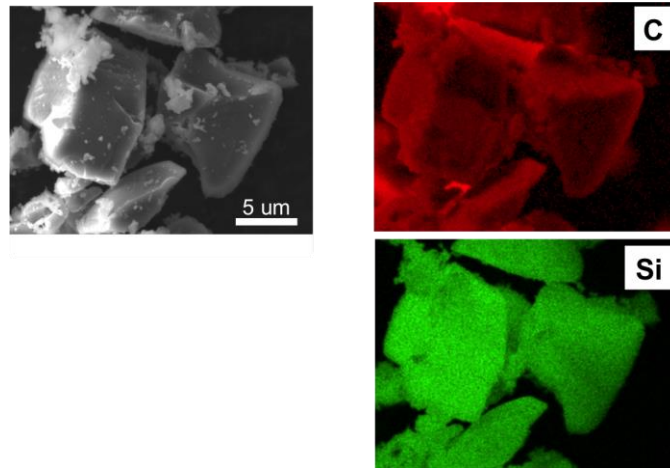


Figure I.2.A.3 Example of device-level enhancement: cycle stability of pre-lithiated Si-C.

Even further data presented at the May 9th meeting (in addition to our poster at the AMR meeting June 18-21) were regarding our collaboration with University of Washington (graduate student Matt Lim and Professor Peter Pauzauskis). First, we presented data demonstrating the homogeneity of Si-C material (Figure I.2.A.4).

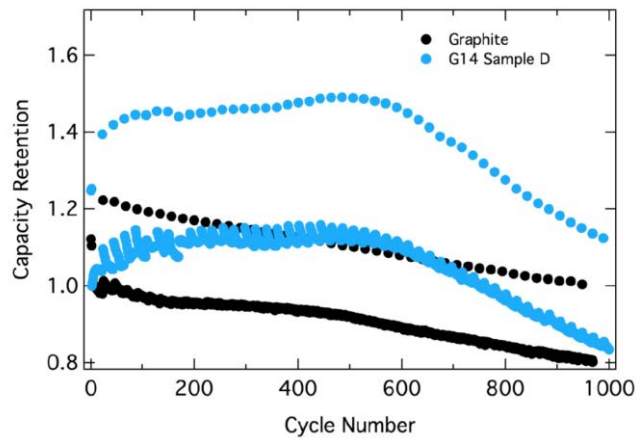


Figure I.2.A.4 Homogeneity within the Si-C composite as determined by SEM in combination with EDS.

Homogeneity of silicon within the Si-C composite was examined by SEM in combination with energy-dispersive X-ray spectroscopy (EDS) to allow for elemental analysis and mapping. The data suggest uniform distribution of carbon (C) and silicon (Si) throughout each particle. Also presented were data regarding the ability to achieve amorphous composite. To this end, Raman and X-ray diffraction spectra (Figure I.2.A.5) were presented that were consistent with amorphous silicon and carbon throughout the Si-C composite.

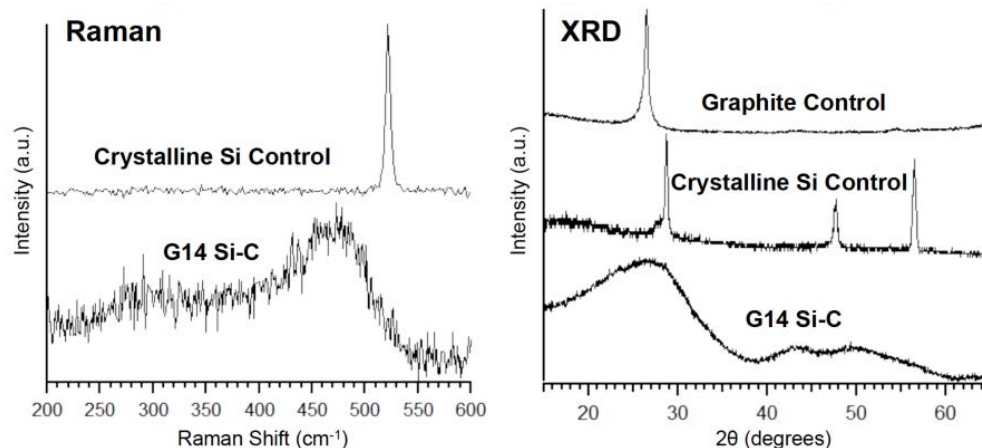


Figure I.2.A.5 Raman (left) and XRD spectra (right) consistent with amorphous silicon and carbon within Si-C.

Over the third quarter of 2018 (Jul – Sep 2018) we confirmed a new approach to dramatically improve the performance of our pilot scale reactor. This new approach has led to the development of various modifications to the pilot scale equipment as well as the pilot scale manufacturing process. Furthermore, the pilot scale equipment and process modifications will allow for facilitating further scale up, i.e., to commercial scale. The dramatic improvements achieved are further described in Table I.2.A.2, wherein data for various process and product parameters are summarized for both before and after developing the pilot-scale modifications.

Table I.2.A.2 Improvements in Process and Product Parameters after Pilot-Scale Modifications.

Process/Product Parameter	Prior to Modifications	After Modifications
Particle Elutriation	Up to 8 to 106 g/h	Negligible
Temperature Uniformity for Product During Reaction	> +/- 50 C	As low as < +/- 5 C
Large Si particles	Average = 28%	Negligible
% Silicon loading by TGA	20% +/- 12%	44+/-4%
% Nano silicon by TGA	67% +/- 28%	85% +/- 17% (94% +/- 5% for consecutive n=12)
Coulombic Efficiency (Cycle 7-25, 60:20:20 formula)	Up to 0.9951	Up to 0.9984 (Many data pending)

As can be seen, there were dramatic improvements observed as a result of the modifications. For instance, prior to the modifications, there was substantial elutriation, i.e., loss of product from the pilot reactor; obviously, such losses are not acceptable. Following implementation of the pilot scale equipment and process improvements, the resulting elutriation is now negligible. As another example, prior to the pilot scale modifications, the temperature uniformity for the material in the reactor varied widely, in excess of +/- 50 C. After implementation of modifications to the pilot scale equipment and processes, there was a dramatic improvement, i.e., reduction, in the temperature uniformity for the material in the reactor, up to as low as +/- 5 C. Another important parameter that was improved was the extent of large particles within the final product. For instance, prior to the pilot scale modifications, there was an average of about 30% of the final product that was retained above a 355 um sieve, i.e., could not be passed through this size sieve even with application of force on the material. In contrast, with the pilot scale equipment and process modifications in place, the vast majority of product could be easily passed through a 355 sieve; the large Si particle content is now negligible.

We also observed dramatic improvements in Si-C physicochemical and electrochemical properties as a result of the pilot scale equipment and process modifications. From thermogravimetric analysis (TGA), it can be seen that the Si loading was much more consistent in the desired range after (44% +/-4%) vs. before (20% +/- 12%)

implementing the modifications. Furthermore by TGA, it can be seen that the % nano silicon was consistently in the desired, higher range after (85% +/-17%) vs. before (67% +/- 28%) implementing the modifications. Importantly, for a series of a dozen runs towards the end of the reporting period, the achieved % nano silicon was 94% +/- 5%. Overall, the loading and quality (i.e., % nano sized) silicon achieved after implementing the pilot scale equipment and process modifications matches or exceeds our experience at smaller scale (1-10 g scale, comprising lab and lab-pilot scale). Importantly, these same pilot scale equipment and process modifications facilitate further scale-up, i.e., to commercial scale manufacturing, in the future.

Electrochemical characterization of G14 Si-C produced after implementation of the pilot scale equipment and process modifications is underway. To this end, data is currently available in half-cell coin cell format, and full cell performance evaluation is underway. For comparison, consider Figure I.2.A.1 which depicts half-cell data for three Si-C batches produced at 1-10 g scale (these particular batches were chosen since they have been previously presented to DOE). For this analysis, anode electrodes were produced employing our previously described 60:20:20 system (anode comprising 60% Si-C, 20% CMC-SBR as binder and 20% Super-C45 as conductivity enhancer). These three batches, denoted as G14 sample A, G14 sample B, and G14 sample C exhibited max capacity of 1492, 1340, and 1450 mAh/g, respectively. These materials exhibited relatively high average Coulombic efficiency over cycles 7-20 (0.9985, 0.9983, 0.9914, respectively) as well as relatively high capacity retention at cycle 20 (97, 97, and 83%, respectively).

The half-cell performance achieved for recent pilot scale Si-C matches or exceeds the performance at lab / lab-pilot scale. This can be seen in Figure I.2.A.2, which depicts half-cell data for three pilot-scale Si-C batches. Identical to the methodology above, anode electrodes were produced employing our previously described 60:20:20 system (anode comprising 60% Si-C, 20% CMC-SBR as binder and 20% Super-C45 as conductivity enhancer). These three batches, denoted as Pilot scale sample A, Pilot scale sample B, and Pilot scale sample C exhibited max capacity of 1336, 1558, and 1665 mAh/g, respectively. These materials also exhibited relatively high average Coulombic efficiency over cycles 7-20 (0.9984, 0.9983, 0.9982, respectively) as well as relatively high capacity retention at cycle 20 (99%, 98%, and 98%, respectively).

Conclusions

Group14 Technologies is developing low-cost, high-performing Si-C composite materials suitable as a drop-in for Li-ion battery anodes. We have successfully down-selected samples for scale up, and we have advanced to pilot scale manufacturing. Over the course of pilot scale process development, substantial modifications were made to equipment and processes that resulted in dramatic improvements in key process and product parameters. As a result, we have established the ability to manufacture in the pilot-scale equipment Si-C that matches or exceed key product attributes. Electrochemical characterization of Si-C produced in the pilot-scale equipment is ongoing, including investigation of device-level improvements. The latter have been shown capable of achieving Si-C cycle stability of 1000 cycles for material produced at lab scale. Our current focus is on production of Si-C in the pilot-scale equipment and as-necessary material, electrode and device development to achieve final project milestones.

Key Publications

1. Poster entitled “Low Cost Manufacturing of Advanced Silicon-Based Anode Materials,” presented on June 19, 2018 at the Annual Merit Review (AMR) meeting in Washington, DC.
2. US provisional patent application 62/641871, filed 12-Mar-2018.

References

DOE Site Visit for Project ES268, “Low Cost Manufacturing of Advanced Silicon-Based Anode Materials,” presented on April 9, 2018 at Woodinville, WA.

Acknowledgements

The PI thanks Avery Sakshaug, Chris Timmons, and Dr. Abirami Dhanabalan (Group14 Technologies, Inc) for critical contributions to the project. The PI also thanks Dr. Matt Lim and Professor Peter Pauzauskie (University of Washington) for investigations on material properties as described herein.

I.2.B Co-Extrusion (CoEx) for Cost Reduction of Advanced High-Energy-and-Power Battery Electrode Manufacturing (PARC)

Ranjeet Rao, Principal Investigator

Palo Alto Research Center (PARC)
3333 Coyote Hill Road
Palo Alto, CA 94304
E-mail: ranjeet.rao@parc.com

Peter Faguy, DOE Technology Development Manager

U.S. Department of Energy
E-mail: Peter.Faguy@ee.doe.gov

Start Date: December 1, 2015

End Date: August 31, 2019

Project Funding: \$3,790,000

DOE share: \$3,000,000

Non-DOE share: \$790,000

Project Introduction

Most strategies for increasing the performance and reducing the cost of lithium-ion batteries have focused on novel battery chemistries, material loading modifications, and increasing electrode thickness. Increasing electrode thickness is a known approach to increase energy density and in turn overall cell capacity. However, practical thicknesses are constrained by ionic transport limitations that occur with increasing thickness, limiting cell power. We believe PARC's Co-Extrusion (CoEx) technology can overcome this limitation, enabling a substantial improvement in the performance of thick electrodes for most lithium-ion chemistries. CoEx has the potential to disrupt current manufacturing processes and enable the DOE 2022 goal of \$125/kWh by enabling the simultaneous deposition of alternating regions of high ionic transport and high lithium density.

Objectives

Our overall project objectives are to demonstrate Co-Extrusion (CoEx) printing technology at electric vehicle (EV) relevant scales by assembling large, 14 Ah pouch cells. These pouch cells will demonstrate an estimated $\geq 30\%$ reduction in \$/kWh costs through thick, structured high energy and high power electrodes, and a gravimetric energy density improvement of $\geq 20\%$ relative to conventional electrodes of the same chemistry.

Approach

Co-Extrusion (CoEx) Cathode

Co-Extrusion (CoEx) is a deposition technology developed at PARC that uses engineered fluidic channels to cause multiple streams of dissimilar fluids to impart shape to one another [1]. The result is a high-speed, continuous deposition process that can create fine structures much smaller than the smallest physical feature within the printhead. By eliminating the small channels necessary for conventional extrusion and injection processes, CoEx is able to deposit highly loaded and viscous pastes at high process speeds under reasonable operating pressures. Depending on particle size, the CoEx process is capable of direct deposition of features as small as 25 μm with aspect ratios of 5 or greater, and print speeds > 400 mm/s (~ 80 ft./min). A CoEx printhead can serve the same function as the slot die printhead in modern battery manufacturing lines, depositing the electrode slurry onto the current collector web in a continuous roll-to-roll process. The thicknesses, widths, and lengths of the deposited CoEx features are dependent on the internal printhead geometry, slurry rheology, and process conditions. The precise flow paths are constructed out of a stack of replaceable printhead layers that can be easily exchanged, allowing for precise tailoring of the final deposited features within a single printhead design. PARC's scale-up of CoEx batteries for EVs builds on a solid base of experience in applying CoEx to solar cell manufacturing [2]. We have chosen a commercially relevant chemistry, $\text{LiNi}_{0.5}\text{Mn}_{0.3}\text{Co}_{0.2}\text{O}_2$ (NMC 532) and our strategy will be to scale the technology from coin cells (BP1) to 14Ah pouch cells (BP3) by project completion. Our partner, Ford Motor Company, will provide PARC with baseline cell specifications in addition to EV-relevant cell characterization on the pouch cells developed during the course of the project.

High Capacity Graphite Anode

While PARC will use CoEx to develop thick, high performance cathode electrodes, ORNL will develop the thick, high capacity anode that will match the CoEx cathode. In addition, they will utilize ORNL's Battery Manufacturing Facility (BMF) to fabricate small scale pouch cells in BP2 and assist PARC with technology scale-up on ORNL's roll coater, in addition to running electrochemical rate and cycling tests. As part of the anode development, ORNL will refine graphite-based anode slurries for improved coating adhesion, agglomerate cohesion, and high ionic and electronic conductivity by modifying binder and conductive additive. Anodes will be prepared with an NMP/PVDF solvent/binder system and slot-die coated to a sufficient thickness to balance the CoEx cathodes. Beginning with baseline anode coatings with targets of 50-80 μm in thickness after calendaring, 2.5-3.0 mAh/cm² in loading, and capacity > 350 mAh/g, ORNL will then work to demonstrate anodes that are thick (125 – 200 μm) to match the high capacity CoEx cathodes. These anodes will be shown to maintain their integrity after drying and calendaring to 30-40% porosity

Results

CoEx Cathode Printing for Half-Cells

As was described in the FY2017 annual report, work in BP1 focused on developing the CoEx cathodes and thick conventional anodes separately at PARC and ORNL, respectively. In this way, CoEx cathodes were tested in half-cell configuration and structure-performance relationships were tested without concern that anode limitations would obscure results. The CoEx printhead takes two inks or slurries as inputs, and interdigitates the fluid streams to create a patterned thick film on a substrate. By depositing inks with different solvent loadings, we are able to create films that, after drying, result in a cathode electrode with periodic grooves. These grooves get filled with electrolyte during battery assembly, and these periodic regions of reduced tortuosity result in overall improved utilization of a highly loaded electrode.

Figure I.2.B.1 is a 3-D microscope (Keyence VHX-500) image of a representative CoEx electrode region both before (a) and after (b) calendaring. In these images, one can see the general topology of the CoEx electrode, with a narrow groove or "valley" and a wider, thicker "ridge" region. This image also illustrates that CoEx features survive the calendaring process. Modeling work done in the first budget period [3] provided guidance on the types of CoEx structures to make, indicating that the best performance, in terms of gravimetric and volumetric energy density, would be achieved by having a ridge:valley width ratio ≥ 4 and with an electrode thickness $\sim 120 \mu\text{m}$. We control the relative width ratio of these ridge and valley regions by controlling the relative input pressures and thus volumetric flow rates of the two inks.

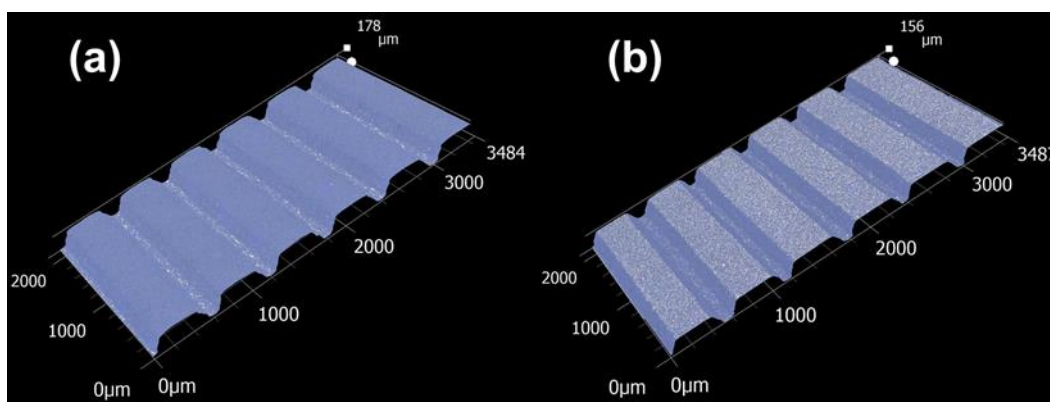


Figure I.2.B.1 3-D Microscope images of as-printed and dried (a) and post-calendared (b) cathode electrodes produced via CoEx. Images illustrate the corrugated topography that persists after the calendaring process.

With this in mind, coin cells were prepared with a variety of CoEx cathode geometries and tested electrochemically. For these tests, CoEx cathodes (active material loading 22-25 mg/cm² NMC) were compared to thinner baseline electrodes ($\sim 16 \text{ mg/cm}^2$ loading) as well as thicker baseline electrodes (~ 22

mg/cm² loading). A summary of these previously reported findings is shown in Table I.2.B.1, which tabulates the predicted improvement of 1 Ah pouch cells based on the coin cell electrochemical results. These improvements in gravimetric and volumetric energy density are due to the reduced number of current collector and separator layers needed to attain 1 Ah capacity with thicker electrodes. When compared to the thin baseline, CoEx cathodes are predicted to provide up to 10% improvement in capacity at low discharge rates, with slightly negative performance at 1D discharge rates. This is due to the reduced performance of the thicker CoEx cathodes relative to the thin baseline at higher discharge rates. The specific benefits of CoEx structuring are seen when compared to the thicker baseline electrode, which is of similar loading to the CoEx electrode but is homogeneous. In this case, the performance is similar at discharge rates $\leq D/2$, but CoEx electrodes are dramatically better at 1D and 2D discharge rates. This result shows how CoEx addresses the traditional tradeoff between power and energy density with conventional battery electrode manufacturing. Increasing the thickness of the battery electrode improves performance at low (D/10) discharge rates with a tradeoff of significantly reduced capacity at $> D/2$ discharge rates. CoEx, on the other hand, achieves similar improvements at low discharge rates with minimal dropoff at 1D discharge rate. The next step (achieved in FY2018) is to validate these coin cell results for full cell pouch cells.

Table I.2.B.1 Predicted Improvement in 1 Ah Pouch Cells Based On Coin Cell Electrochemical Performance

Discharge Rate	CoEx Vs. Thin Baseline			CoEx Vs. Thick Baseline		
	mAh/g	Wh/kg	Wh/L	mAh/g	Wh/kg	Wh/L
D/10	9%	10%	9%	2%	1%	-1%
D/5	8%	9%	8%	1%	2%	-1%
D/3	9%	9%	8%	3%	3%	0%
D/2	8%	6%	5%	3%	4%	1%
1D	2%	-3%	-4%	35%	36%	33%
2D	-46%	-44%	-44%	119%	136%	130%

Thick Anode Development

Earlier work on anode development focused on selecting an appropriate graphite active material, based on both electrochemical performance as well as adhesion in thick films. After testing over 10 different candidate materials, Superior SLC 1520T graphite was chosen as the best anode material. While this graphite material resulted in graphite electrodes with the best combination of performance and adhesion compared to the other graphite materials tested, adhesion issues did limit performance of thicker coatings. For this reason, a double-layer coating method was used to try and optimize the performance of the thick anode electrode. Two different slurry formulations (Figure I.2.B.2) were sequentially deposited using the dual-layer slot die setup. The bottom slurry formulation included a slightly higher PVDF content as well as a small amount of oxalic acid, both of which serve to promote adhesion of the graphite electrode to the copper foil. If the two slurry formulations are deposited at the same rate (50% bottom / 50% top), the overall dried anode formulation will be the same as our original baseline, 92/6/2 graphite/PVDF/carbon black by weight. Figure I.2.B.2 shows electrochemical performance of this two layer structure (in this case, 30% bottom / 70% top) compared to a single layer coating. The results show improved performance of the double-layer anode, which may be due to improved adhesion and reduced contact resistance. (See Table I.2.B.2.)

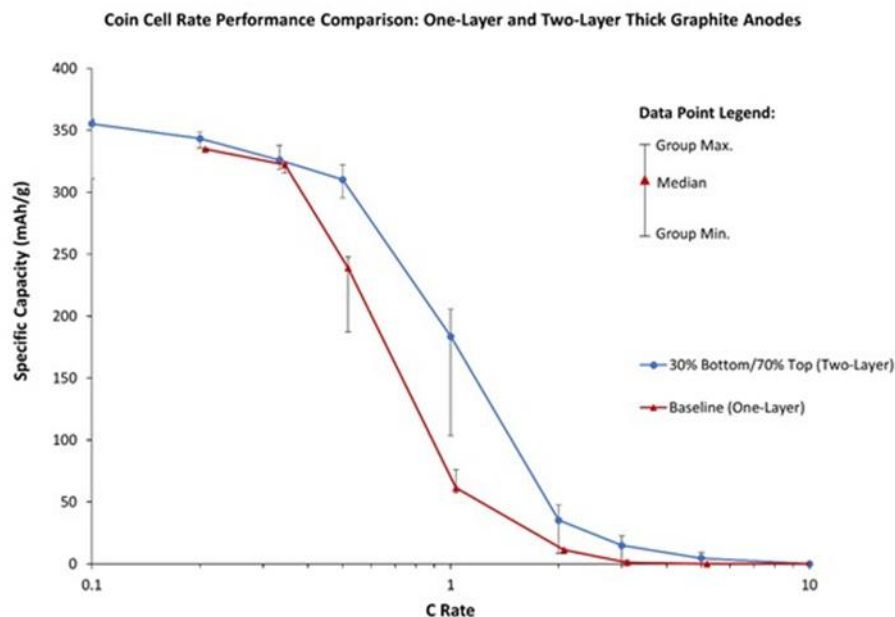


Figure I.2.B.2 Comparison of the electrochemical rate performance of one-layer and two-layer thick graphite anodes (~ 6 mAh/cm²) in half coin cells. Three cycles were run at each C rate. Each plotted data point represents the median of the 2nd cycle capacities for each cell group (3 cells for the baseline coating and 4 cells for the 30% Bottom/70% Top coating), while the error bars represent the group minimum and maximum. All cells were made with 1.2 M LiPF₆ in 3:7 wt% EC/EMC electrolyte.

Table I.2.B.2. Anode Slurry Formulations for Dual Layer Slot Die

	Superior SLC1520T Graphite (wt%)	Imerys C-Nergy Super C65 Carbon Back (wt%)	Kureha 9300 PVDF (wt%)	Oxalic Acid (wt%)
Bottom Layer (Current Collector Side)	89.93	2	8	0.17
Top Layer (Separator Side)	94	2	4	0

CoEx Printhead Scale-Up and Pouch Cell Development

The CoEx coin-sized half cells described above were assembled from electrodes produced with PARC's prototype CoEx printhead, with a nominal print width of 20 mm. As part of achieving the overall goals of creating high capacity pouch cells, major project tasks include scaling up the printhead hardware to enable larger format battery cells. This year we have designed, fabricated, and tested a CoEx printhead with a 90 mm print width (CoEx90), sufficient to make 1 Ah pouch cells (nominal cathode dimensions of 56.0 x 84.4 mm), and have designed a larger, 180 mm wide printhead (CoEx180) that will be used to manufacture electrodes for 10+ Ah pouch cells (nominal cathode dimensions of 110 x 175 mm). As part of this process development, we have demonstrated print speeds as high as 400 mm/s (24 m/min) as well as the capability for double-sided printing in batch mode at PARC. Figure I.2.B.3 shows a representative surface profile of a print made with the CoEx90 printhead, measured with a STIL confocal profilometer. In this profile we focus on a 5 mm wide region of the print, and we superimpose the profile of the as-dried and the calendered electrode. After calendaring, the topography of the electrode is still maintained, with less thickness variation in the thickest region of the print.

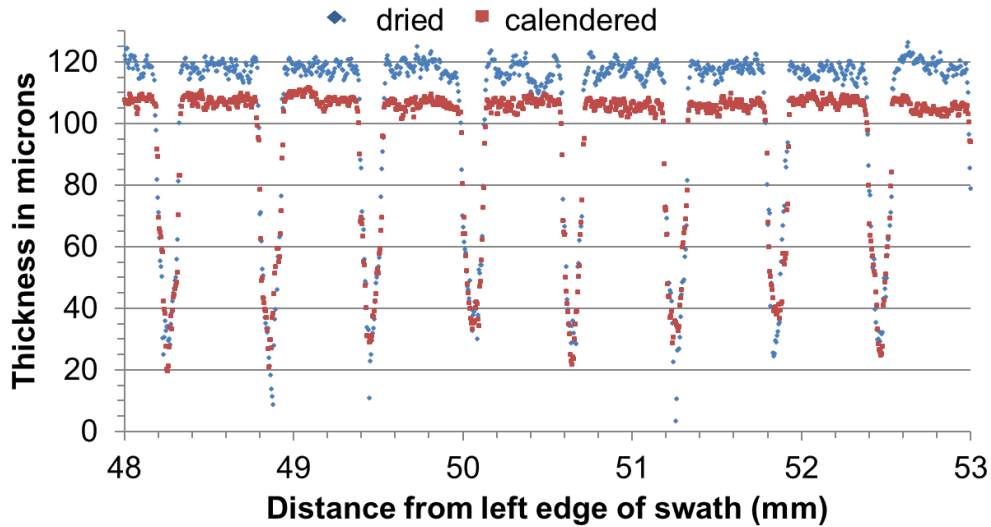


Figure I.2.B.3 Representative surface profile of CoEx cathode both before (blue) and after (red) calendaring.

Table I.2.B.3. Electrode Dimensions and Loadings for 1 Ah Pouch Cells

	CoEx		Baseline		Thick Baseline	
	NMC532	Graphite	NMC532	Graphite	NMC532	Graphite
Active Material Loading (mg/cm ²)	24.2	12.3	13.2	6.9	24.8	12.3
Electrode Thickness (µm)	111	109	55	63	106	109
# of Cathode Layers	6		10		6	

Using the CoEx90 printhead, double-sided CoEx cathodes were printed, calendered, and sent to ORNL for assembly into 1 Ah pouch cells. Cathodes were paired with thick matching anodes (N:P of 1:1.1) produced with a dual layer slot die as described above. Table I.2.B.3 lists relevant loading, porosity, and physical electrode information for the three types of pouch cells, while Figure I.2.B.4 shows the rate performance of the CoEx pouch cells along with baseline and thick homogeneous cathodes for comparison. Referring to Figure I.2.B.3, both the CoEx and thick baseline cells have similar thicknesses and electrode loadings, approximately twice that of the thinner baseline. As a result, 40% fewer electrode layers are required to reach 1 Ah capacity, with a concurrent decrease in the number of current collector and separator layers. With regards to electrochemical performance, all pouch cells show high utilization at low discharge rates, with similar performance out to approximately D/2 discharge rate. At higher discharge rates, the thick baseline shows much reduced capacity compared to both the CoEx (which contains cathodes of the same thickness and loading) and the baseline pouch cells, again showing that structuring the cathode electrode results in improved utilization of the active material. These electrochemical results, combined with the physical parameters of the pouch cells (mass, thickness) can be used to calculate the performance in terms of gravimetric and volumetric energy density. Table I.2.B.4 summarizes this data, showing how the CoEx pouch cells compares to the thin and thick baseline cells. Since the CoEx pouch cell needs fewer electrode layers in order to achieve a 1 Ah capacity, it contains fewer current collector and separator layers, resulting in improved energy density at discharge rates $\leq 1D$. The improved ionic transport within the CoEx cathodes improves performance relative to the thick baseline pouch cells, with gains of 15% and 17% at 1D discharge in gravimetric and volumetric energy density, respectively. At higher discharge rates (2D), the energy density of CoEx pouch cells is even greater, 2.5x that of the thick baseline cells. To summarize, we have tested the effect of doubling cathode layer thickness and loading via two different cathode manufacturing methods. For a conventional cathode produced

via slot die coating, doubling the cathode thickness resulted in improvements of 13% to 17% (gravimetric and volumetric, respectively) in energy density at low (D/10) discharge rates, with a tradeoff of 14% & 10% *reduced* capacity at 1D discharge rate. The CoEx cathode performs similarly at low discharge rates with *no* tradeoff at 1D discharge rates.

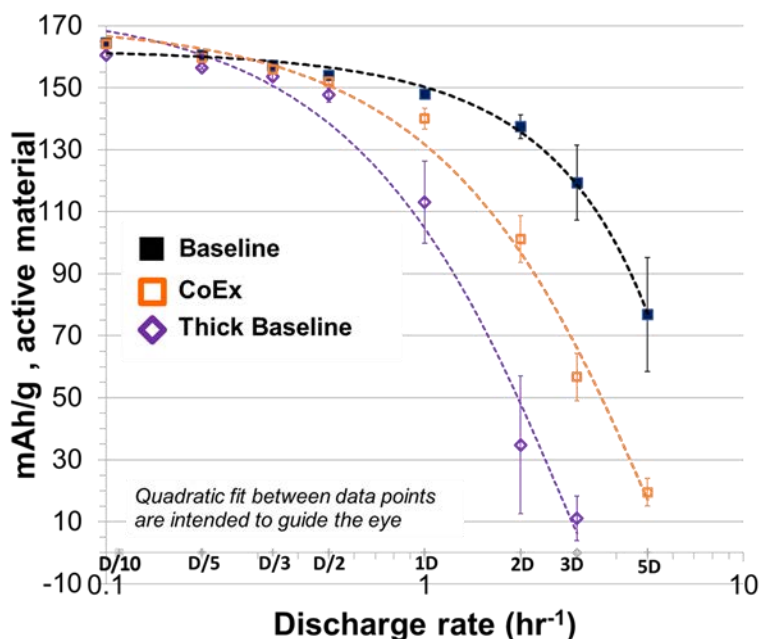


Figure I.2.B.4 Electrochemical Performance of 1 Ah pouch cells, comparing thin and thick baselines vs. CoEx cathodes. Error bars represent +/- 1 standard deviation. Quadratic curve fits are intended to guide the eye. All cells were made with 1.2 M LiPF₆ in 3:7 wt% E

Table I.2.B.4. Energy Density of 1 Ah Pouch Cells, Comparing CoEx Cathodes to Conventionally Manufactured Thin and Thick Baseline Cathodes

Discharge Rate	CoEx Vs. Thin Baseline			CoEx Vs. Thick Baseline		
	mAh/g	Wh/kg	Wh/L	mAh/g	Wh/kg	Wh/L
D/10	11%	12%	15%	0%	-1%	-2%
D/5	10%	11%	14%	0%	-1%	-3%
D/3	10%	10%	13%	-1%	-2%	-4%
D/2	10%	8%	11%	0%	-1%	-3%
1D	5%	1%	3%	21%	17%	15%
2D	-18%	-26%	-24%	184%	163%	159%

Conclusions

PARC, ORNL, and Ford are collaborating to create a pilot scale demonstration of PARC's CoEx battery manufacturing technology for structured high energy and high power cathodes for cost-effective EVs. This year, we have successfully scaled up our electrode printing process to the 1 Ah pouch cell level, and demonstrated that CoEx structuring leads to improved utilization over homogeneous (*i.e.* non-structured) electrodes of similar loading. Our earlier results based on half-cell measurements have been validated at the full cell level, and indicate an improvement in energy density of 10-15% over a baseline pouch cell for discharge rates $\leq 1D$. We are continuing to scale-up our deposition processes, and are working towards EV-relevant, 10+ Ah pouch cells for further testing.

Key Publications

1. Cobb, C.L. and Scott E. Solberg, "Analysis of Thick Co-Extruded Cathodes for Higher-Energy-and-Power Lithium-Ion Batteries," *J. Electrochem. Soc.*, **164** (7), A1339-A1341, 2017
2. Rao, R.B., "Co-Extrusion of Electrodes for Both Energy and Power." Presentation, *U.S. Drive Electrochemical Energy Storage Technology Discussion*, Southfield, MI, May 16, 2017
3. Cobb, C.L., "Co-Extrusion: Advanced Manufacturing for Energy Devices." Presentation, *2016 AIChE Annual Meeting, Battery and Energy Storage Technologies*, San Francisco, CA, November 14, 2016. (Session Keynote)
4. Cobb, C.L., "Modeling Co-extruded Cathodes for High Energy Lithium-ion Batteries." Presentation, *229th ECS Meeting*, San Diego, CA, June 1, 2016.
5. Rao, R.B. *et al.*, "Thick Co-Extruded Cathode Electrodes for High Energy Lithium-Ion Batteries." Presentation, *2018 Fall MRS Meeting and Exhibition*, Boston, MA, November 27, 2018

References

1. Fork, David, and Thomas Hantschel. Extrusion/dispensing Systems and Methods. US Patent US7765949B2, filed May 17, 2007, and issued September 21, 2010.
2. L.P. Richter *et al.*, "Progress in Fine Line Metallization by Co-extrusion Printing on Cast Mono Silicon PERC Solar Cells," *Solar Energy Materials and Solar Cells*, 142 (2015): 18-23.
3. Cobb, C.L., and Scott E. Solberg, "Analysis of Thick Co-Extruded Cathodes for Higher-Energy-and-Power Lithium-Ion Batteries." *Journal of The Electrochemical Society* 164, no. 7 (2017): A1339-A1341

I.2.C Electrodeposition for Low-Cost, Water-Based Electrode Manufacturing (PPG Industries, ANL, Navitas, ORNL)

Stuart Hellring, Principal Investigator

PPG Industries
4325 Rosanna Drive
Allison Park, PA 15101
E-mail: hellring@ppg.com

Peter Faguy, DOE Technology Development Manager

U.S. Department of Energy
E-mail: Peter.Faguy@ee.doe.gov

Start Date: January 1, 2016
Project Funding: \$2,399,034

End Date: June 30, 2019
DOE share: \$1,399,275

Non-DOE share: \$999,759

Project Introduction

The state of the art for the manufacture of lithium ion battery (LIB) cathodes is slot-die coating of a high-viscosity slurry of active battery materials, conductive additives, and a polymeric binder that is dissolved in N-methyl-2-pyrrolidone (NMP). NMP is an expensive consumable in electrode manufacturing with serious health concerns. Together with the high cost of raw materials, this approach results in LIB costs that exceed the DOE target. In order to realize cost-effective, environmentally friendly processes for battery electrode manufacture, binder systems must be developed that enable compatibility of lithium-ion active materials with water and are amenable to coating processes that reduce the cost of electrode manufacturing compared to the current state of the art. One promising approach to achieve this is the use of waterborne binder systems applied to metal foils using electrocoat. Electrocoat is a process widely recognized to be a high-throughput, low cost coating application method. This project addresses materials processing and manufacturing costs.

Solvent-based electrodeposition of pre-formed cathode active powders for producing electrodes for secondary lithium ion batteries has been evaluated by several groups. Cathodes produced by solvent-based electrodeposition showed promising battery performance for metrics which include discharge capacity/rate capability, coulombic efficiency and cycle life retention. However, the use of volatile organic solvents for manufacturing electrode coatings by electrodeposition has a number of serious drawbacks including volatile organic compound (VOC) emissions, explosion risk, health risks from worker exposure, and cost. Using waterborne coatings significantly mitigates most of the concerns associated with organic solvent-based coating formulations. Benefits include lower voltage/current, better process temperature control and faster deposition rates due to a higher dielectric constant. Binder design, proprietary additives, and electrochemical processing methods are used to ensure quality during manufacturing, to disperse pigment particles and stabilize the aqueous formulation bath against agglomeration and settling.

Objectives

The objective of the project is to develop and demonstrate novel binders to enable a low-cost, water-based, electrodeposited lithium ion battery electrode coating system and manufacturing process capable of reducing cell costs by at least 3% while improving battery performance. This project will demonstrate these improvements by designing and constructing a pilot-scale roll-to-roll system based on this process. In addition, the project will demonstrate a battery supply chain model that mirrors traditional automotive OEM supply chain models to reduce the risk of electric vehicles (EVs) and increase adoption. During this year, specific objectives for this project are as follows:

- Construct a pilot-scale electrocoat roll-to-roll coater (i.e. 'mini-coater').
- Operate the mini-coater to produce electrodes for pouch cell evaluation.

- Complete evaluation of the long-term cycling behavior of LFP and NCM electrodes fabricated using bench-scale electrocoat.
- Evaluate high-nickel NCM active materials in the electrocoat system.
- Optimize the drying conditions of electrocoated electrodes.

Approach

Electrocoat offers several manufacturing advantages over conventional slot-die or roll-coater application processes. Electrocoat processes can coat both sides of a foil simultaneously as electric fields are the driving force for particle assembly. Another advantage is a greater coating density. Because electrophoretic deposition moves solid components to the substrate and dewateres a coating as it deposits, high density coatings with 90% by weight solids content are produced routinely from dilute formulation baths that have low viscosity. Finally, electrocoat affords simple slurry and bath management. The low viscosity of the electrocoat bath enables simple mixing and the dilute nature of the bath ensures no particle or binder agglomeration. Unlike electroplating, electrocoat formulations are comprised of preformed and prequalified materials such as cathode-active powders, conductive carbon additives and binders that are deposited together to form the cathode coating.

A viable electrodeposition process has been developed and electrodepositable binders with sufficient flexibility and ionic mobility have been designed and synthesized. The remainder of this project will establish electrodeposition process parameters and validate the performance and economics of the technology at a 1Ah scale to ensure a path to commercialization. Argonne National Laboratory provides guidance and assistance developing and selecting active materials that are compatible with the waterborne electrocoat process. Oak Ridge National Laboratory develops optimized drying conditions for electrocoat films through residual water analysis and pouch cell testing. Navitas Systems provides the fabrication and testing of larger format cells and establishes baseline cell level performance with commercial binder systems.

Budget Period (BP) 1 included bench-scale development of the materials necessary for a successful electrocoated electrode. Work was split between concurrent active material selection and electrocoat system development. At the end of BP 1, commercially available active materials were identified along with compatible electrocoat formulations. Budget Period 2 continued bench-scale activity to refine the electrocoat system to improve baseline performance. A pilot roll-to-roll electrocoat system was designed and constructed to enable high throughput production of electrocoated cathode coatings with a comparable line speed to pilot-scale slot-die coating systems. The remainder of Budget Period 3 will optimize the coating system components to the point that large format cells will be built and evaluated using electrodes from the pilot roll-to-roll system. This budget period includes obtaining optimized, representative electrodes that will be tested for performance properties both independently and within cells.

Results

Installation and operation of the mini-coater system

The construction of the mini-coater system was completed and the system was installed at the PPG research facility. The mini-coater was successfully operated to continuously coat over 20 feet of double-sided cathode electrode coating with in-line baking at a speed of 0.5 m/min (Figure I.2.C.1). The electrocoat system consisted of two 12 in. x 18 in. aluminum counter electrodes situated on either side of a 4" wide, 20 μm thick aluminum foil placed in tension across an electrocoat deposition chamber, a rinse chamber, and an infrared oven. Anodic electrocoating of the cathode film was performed using an application of 100 volts and a 10% solids solution comprised of 92% LFP or NCM active material and 8% carbon/binder. The film build rate was adjustable using operational parameters such as the line speed and electrocoat conditions. LFP electrodes electrocoated on the mini-coater were assembled into coin-cell half-cells and the performance was compared to coatings fabricated using bench-scale equipment with identical deposition parameters. Comparable capacity, rate

performance, and cycle life was observed between both electrodes indicating no loss of performance in the mini-coater system (Figure I.2.C.1).

a. 20 feet of electrocoat cathode



b.

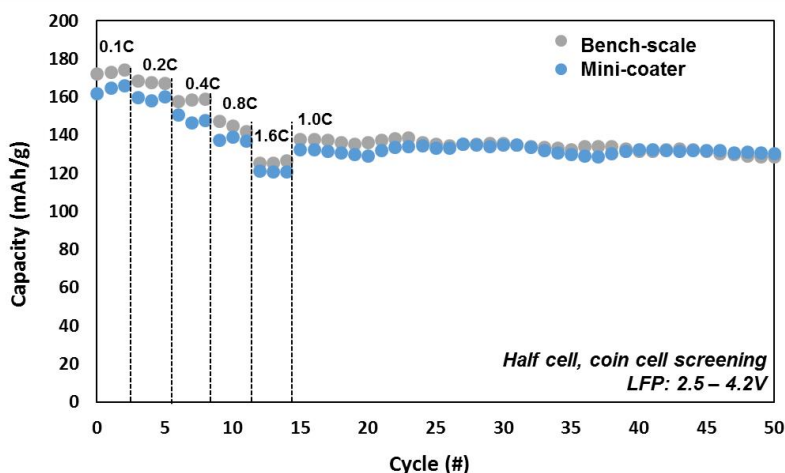


Figure I.2.C.1 (a) Optical photograph of a 20 foot roll coated continuously on the mini-coater system at a line speed of 0.5 m/min. (b) A comparison of half-cell coin-cell performance of LFP electrodes fabricated using bench-scale equipment and the mini-coater system

In comparison to traditional slot-die coating, film formation in electrocoat is driven by electric field mediated processes which are easily adjustable. This formation mechanism enables unique deposition parameters to be used to adjust coating thickness and density. The film build rate in an electrocoat system is directly related to the rate of water electrolysis which can be tuned during operation without making changes to the line operation. The deposition rate can be increased by lowering the resistance between electrodes or by increasing the applied voltage. The relationship between applied voltage and the film-build rate was quantified on the mini-coater system using a voltage range of 30 – 100V and a fixed line speed of 0.5 m/min. An increase in the applied voltage by 1 volt increased the film build rate by approximately 0.1 mg/cm²/s per side (Figure I.2.C.2). Similarly, counter-electrode separation can impact the deposition rate by lowering the resistance between electrodes. A reduced counter electrode separation also resulted in a thicker film build for a fixed voltage and deposition time (Figure I.2.C.2).

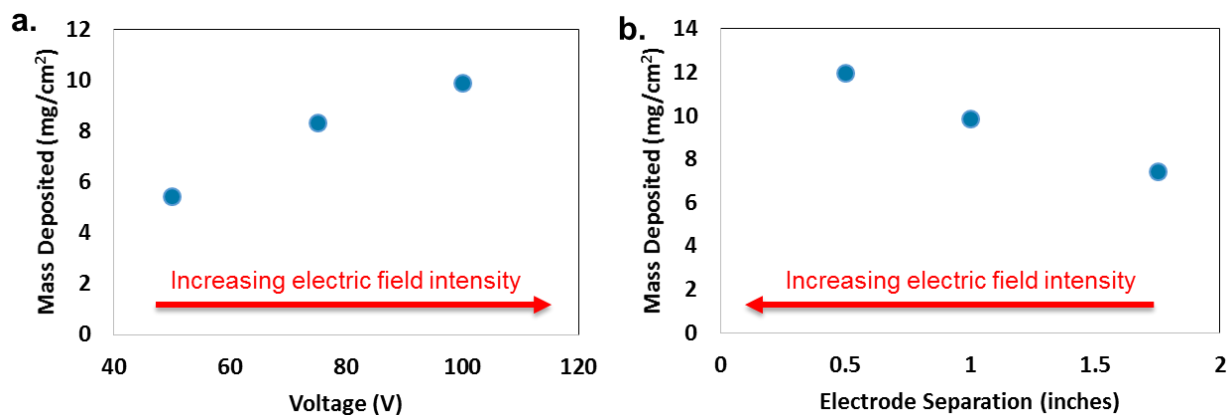


Figure I.2.C.2 Film deposition rate increases proportionally to the increase in electric field strength demonstrated by (a) increasing voltage and (b) decreasing separation between electrodes.

The uniformity of electrode components is a critical factor to ensure long cycle life and good performance of battery coatings. A number of electrocoat parameters must be controlled to ensure a uniform film build rate across the entire electrode surface. Both the electrocoat bath agitation conditions and the electrocoat deposition parameters were optimized for both LFP and NCM 622 active material formulations. The mini-coater system achieved a top-to-bottom uniformity of $\pm 3.0\%$ using NCM 622 formulations and $\pm 3.7\%$ using LFP formulations. Similarly, a front-to-back uniformity of $\pm 2.6\%$ was obtained using NCM 622 formulations and $\pm 3.8\%$ using LFP formulations (Figure I.2.C.3). The battery performance of both LFP and NCM 622 electrodes was evaluated in coin-cell half-cells. LFP electrodes fabricated on the mini-coater delivered comparable capacity and rate performance to electrodes fabricated on the bench-scale (Figure I.2.C.3). NCM 622 electrodes delivered comparable rate performance and cycling retention, however, the gravimetric capacity of the coating is low compared to electrodes fabricated on the bench-scale (Figure I.2.C.3). The diminished gravimetric capacity is attributed to higher levels of binder and carbon in the electrocoated film compared to the electrocoat bath.

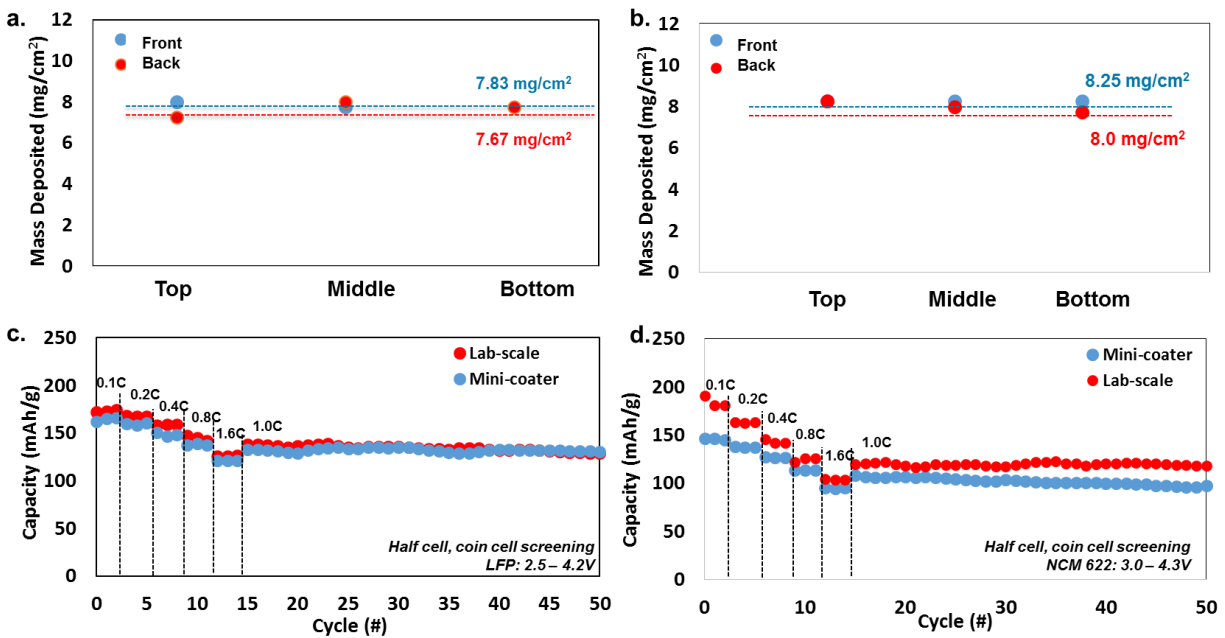


Figure I.2.C.3 Aerial capacity measurements of electrode coatings fabricated by simultaneously coating both sides of the current collector foil on the mini-coater system and highlighting the top-to-bottom (i.e. side to side) and front-to-back uniformity for both (a) LFP and (b) NCM 622 formulations. Coin-cell performance of electrodes fabricated on the mini-coater using (c) LFP and (d) NCM 622 formulations.

Drying conditions for electrocoat electrodes

ORNL performed a comprehensive secondary drying study on electrocoated cathodes received from PPG. The residual water in the samples was measured by Karl Fischer (KF) titration after drying at four different temperatures (100°C, 120°C, 140°C, 160°C) for two different time periods (4h and 16h). The KF titration results for the PPG electrocoated cathodes are plotted in Figure I.2.C.4, along with results from ORNL NCM 333 cathodes made with N-methylpyrrolidone (NMP) for comparison. As expected, drying the PPG cathodes at the lowest temperature for the shortest amount of time (100°C for 4h) resulted in the highest residual water content. However, this water content is still relatively low (132 ppm) and represents a 63% reduction compared to the control. The 4h and 16h time series show slightly different trends with increasing temperature. For the 4h series, the residual water content decreases with increasing temperature, and drying at 160°C results in only 63 ppm of water—an 82% reduction compared to the control. However, for the 16h series, drying at 120°C, 140°C, and 160°C all result in very similar residual water content (57, 50, and 55 ppm, respectively). These values correspond to an 84-86% reduction compared to the control and represent the lowest overall

residual water content achieved at any of the drying conditions. The PPG cathodes compare favorably with the standard ORNL NMP-processed NCM 333 electrodes, showing slightly less residual water than the ORNL cathodes when dried at the lowest temperature (120°C) and slightly more when dried at the highest temperature (160°C). These results indicate that the PPG cathodes can be easily dried to the same degree as standard NMP-processed cathodes. Pouch cells were fabricated from electrodes dried at each temperature. All of the pouch cells demonstrated similar rate performance at lower C rates (< 1C), but cells made with cathodes dried at 140°C for 4h perform best at C rates > 1C, reaching 77% of their original capacity at 5C (compared to 69% for cells made with cathodes dried at 100°C for 4h and 64% for cells made with cathodes dried at 160°C for 16h). (See Figure I.2.C.4.)

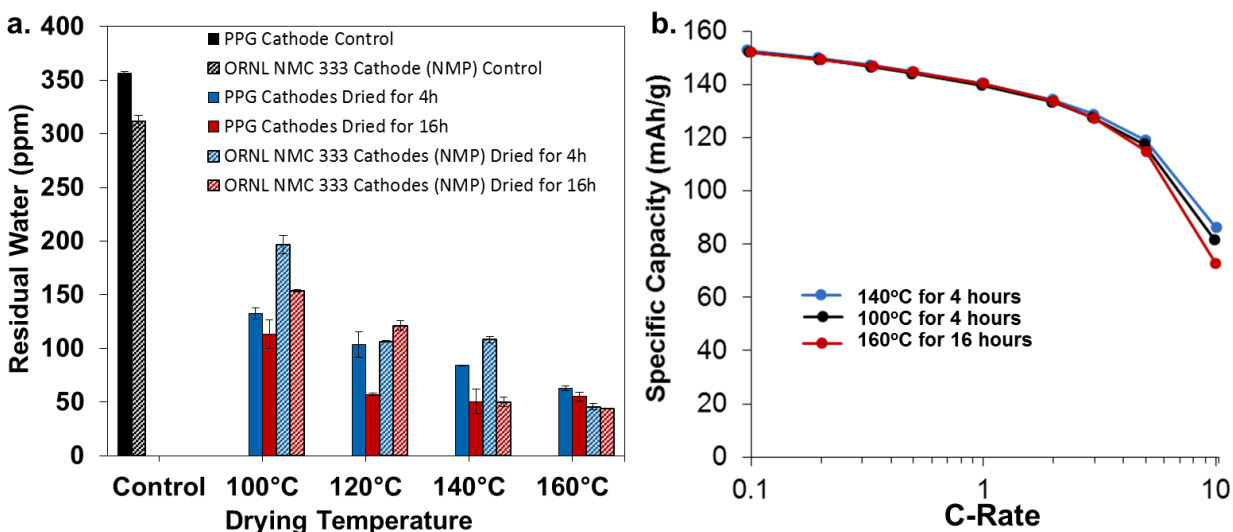


Figure I.2.C.4 (a) Residual water content of PPG electrocoated cathodes and ORNL NMP-processed NCM 333 cathodes subjected to different secondary drying conditions. Each data point is an average of two titrations, and the error bars represent the standard deviation. (b) Discharge rate performance results for single-layer pouch cells made with PPG electrocoated cathodes dried at 3 different conditions (100°C for 4h, 140°C for 4h, and 160°C for 16h)

Pouch cell testing of NCM and LFP

Navitas Systems evaluated PPG electrocoated NCM 111 and LFP cathodes in full cell pouch cells. Electrocoated NCM111 electrodes were assembled using a graphite anode and the performance was compared to baseline cells assembled using identical active materials and formulations with an aqueous PVDF latex binder. After extended cycling, the electrocoated NCM cells demonstrated improved cycle ability compared to cells fabricated with the PVDF latex. Electrocoated cells retained 65% of the original capacity after 1200 cycles compared to control samples which retained only 60%. Electrocoated LFP cells were also evaluated by Navitas Systems. Electrocoated LFP electrodes were assembled with a graphite anode and the performance was compared to baseline cells assembled using identical active material and formulation with a NMP-PVDF binder. Electrocoated LFP cells retained 92% of the original capacity after 1200 cycles compared to the control which retained only 60%. (See Figure I.2.C.5.)

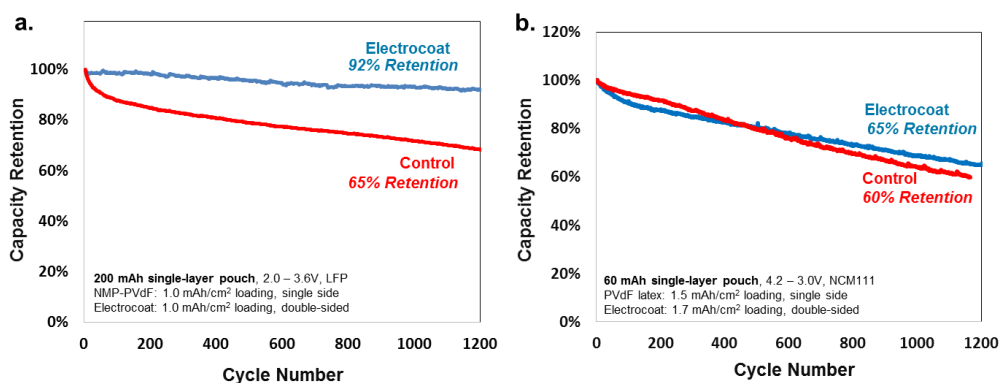


Figure I.2.C.5 Cycling performance of electrocoated cathodes fabricated using bench-scale equipment compared to baseline cells assembled using conventional binders and drawdown method. An improvement to cycle life is observed for both (a) LFP formulations and (b) NCM 111 formulations by using electrocoat fabrication.

Conclusions

The viability of electrocoat to fabricate battery electrodes at commercially relevant formulations has been demonstrated using both bench-scale equipment and a pilot-scale roll-to-roll system. Electrocoated LFP and NCM 111 materials were evaluated for over 1000 cycles in full cell pouch cells using electrodes fabricated on bench-scale equipment. These results demonstrate that the electrocoat binder has improved cycling performance compared to NMP-PVDF for LFP cathodes. Similarly, the electrocoat binder has improved cycling performance compared to a commercial waterborne PVDF latex for NCM 111 cathodes. A drying study completed by ORNL demonstrated that waterborne electrocoat binders do not retain more moisture than NMP-PVDF binders.

A pilot-scale roll-to-roll electrocoat system was constructed and evaluated to demonstrate the commercial feasibility of this assembly process. Coin-cell evaluation of electrodes fabricated using the mini-coater system demonstrated comparable rate and cycling performance compared to electrodes fabricated using bench-scale equipment. Continuous roll-to-roll electrocoat of both LFP and NCM 622 produced over 20 feet of electrode material with the desired areal capacity and uniformity for pouch cell evaluation. Next steps include a full evaluation of electrodes fabricated on the mini-coater system will be completed by Navitas Systems, and the electrocoat conditions will be optimized to produce 47 prismatic pouch cells > 1 Ah.

Key Publications

1. Poster presentation at the 2018 Annual Merit Review

Acknowledgements

Landon Oakes, Haley Orlor and Peter Votruba-Drzal at PPG. Mike Wixom, Pu Zhang, and Robert Sosik at Navitas Systems. Ozge Kahvecioglu and Andy Jansen at ANL. David Wood III, Marissa Wood, Jianlin Li at ORNL.

I.2.D Development of UV Curable Binder Technology to Reduce Manufacturing Cost and Improve Performance of Lithium Ion Battery Electrodes (Miltec UV International)

Dr. John Arnold, Principal Investigator

Miltec UV International
146 Log Canoe Circle
Stevensville, MD 21666
E-mail : jarnold@miltec.com

Peter Faguy, DOE Technology Development Manager

U.S. Department of Energy
E-mail: Peter.Faguy@ee.doe.gov

Start Date: December 1, 2015
Project Funding: \$2,568,200

End Date: January 31, 2019
DOE share: \$1,742,560

Non-DOE share: \$513,640

Project Introduction

Previously identified UV curable binders and associated curing technology have been shown to reduce the time required to cure electrode coatings from tens of minutes to less than one second. This revolutionary approach can result in dramatic increases in process speeds and significantly reduced capital costs (a factor of 10 to 20) and operating costs, reduced energy requirements and reduced environmental concerns and costs due to the virtual elimination of volatile organic solvents and associated solvent dryers and recovery systems.

The accumulated advantages of higher speed, lower capital cost, lower operating cost, reduced footprint, lack of VOC recovery, and reduced energy cost is a reduction of 50-85% in the manufacturing cost of electrodes. When commercialized, the resulting cost reduction in Lithium ion batteries will allow storage device manufacturers to expand their sales in the market and thereby accrue the energy savings of broader utilization of HEVs, PHEVs and EVs in the U.S., and a broad export market is also envisioned. In addition to equipment required to make and UV cure hand drawn cathode samples on high speed web conveyors with UV lamps; Miltec UV has a continuous coating and UV curing system (three very high intensity UV lamps) to demonstrate the primary objectives of the project.

Objectives

The primary objective of this project is to provide performance data sufficient for Lithium ion battery manufacturers to commit to the first steps of making their own HEV, PHEV and/or EV Lithium ion batteries with a UV process. This project involves an iterative R&D effort: making coin cells and pouch cells, followed by testing and analyses, then by adjustments in chemistry, mixing, coating, and UV curing to produce layered pouch cells at high processing speeds (200-300 fpm) with performance equal or greater than that of a conventional PVDF cell. This effort focuses on cathodes made with UV curable binders and is also investigating UV curable binders in the manufacturing of LTO based anodes.

As a supplemental effort, Miltec and its team will investigate high speed coating techniques to demonstrate consistent thickness and edge control and will also conduct supplemental research on applying a UV cathode layer on top of an existing UV cathode layer to produce a thicker high energy cathode.

Approach

A major innovation of the use of UV curable binders in LIB electrode manufacturing is the potential for much higher processing speeds. Miltec UV and its partners have shown that once a condition for complete UV curing is determined (speed, thickness, number of lamps, etc.) then there is a linear correlation between process speed and number of UV lamps. For example, it has been shown that if UV curable coating completely

cures at a cathode coating thickness of 20 μm with 1 lamp (600 W/in lamp) at a speed of 100 fpm, then that same 20 μm coating will completely cure at a speed of 300 fpm with 3 lamps.

Based on the difficulty of coating UV curable binder with slot die at higher speeds (>150 fpm), it is believed that coating technology other than slot die will most likely be required to achieve the very high process speeds made possible by UV curable binders (100 meters/minute). Miltec will evaluate and adapt the best from two coating processes from the printing industry, flexography and letterpress printing.

Another potentially important innovation made possible with UV curable binders is the ability to make cathodes with multiple layers of coating. This is made possible by the fact that, unlike a solvent based system, the second or subsequent layers can be applied without the solvent in the second layer dissolving material in the layer below and the time between application and cure is so short that the second layer of liquid coating does not have time to flow into the pores of the first layer. Multilayered coating introduces the ability to make thicker, higher active material loading cathodes for EV applications. It also introduces the ability to change porosities and other characteristics such as material composition (active material and carbon) between layers. Miltec and ORNL will investigate and evaluate multilayered coatings and the potential advantages in this project.

The expected outcome of the project is to generate performance data from multilayer pouch cells (0.5–1.0 Ahr) fabricated using UV curable binder to demonstrate capacity, long term cycling, rate capacity, impedance, and repeatability equal to or better than a pouch cell with cathodes made using PVDF as a binder. Miltec is in contact with battery manufacturers and it is our belief that they will take the next steps once we demonstrate equivalent pouch cell performance. The most likely next step after the completion of this project would be the addition of a UV curing system to an existing cathode manufacturing line as a demonstration project; or possibly a stand-alone demonstration unit because of the relatively low capital and operating cost of a UV curing system.

Results

Miltec UV international developed a web-based slot die UV process to coat not only single layers but layers on layers (Figure I.2.D.1).



Figure I.2.D.1 Developed UV Web and Slot Die Process.

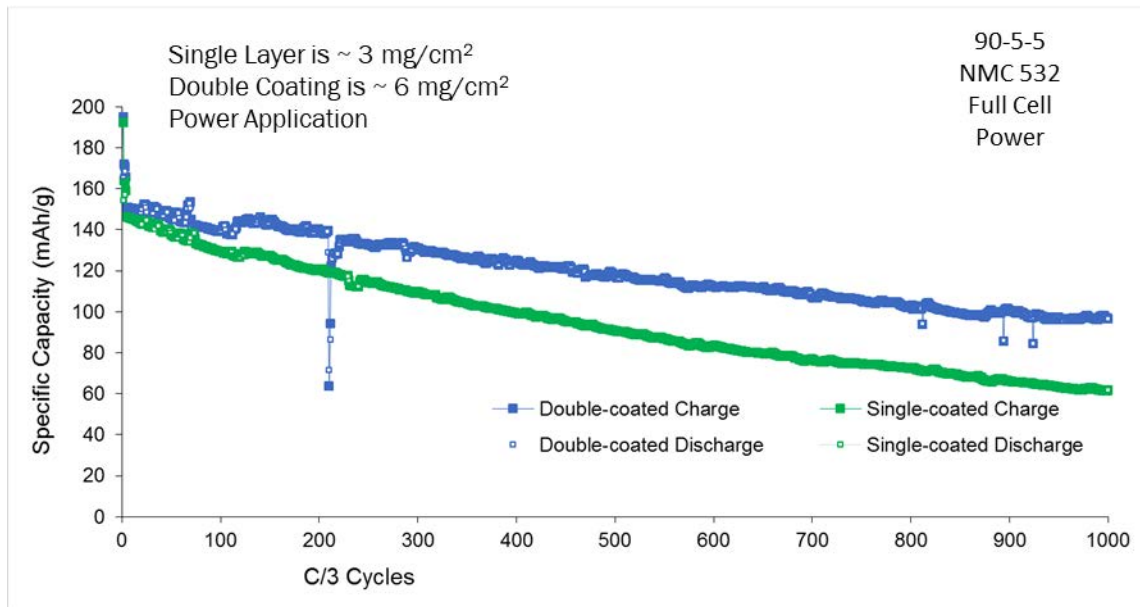


Figure I.2.D.2 Layer on Layer Cathode Coatings are not a problem, but the solution. Double layer coatings always retain capacity as well or better than single layer coatings.

Our research has proven that Layer on Layer coating improves capacity cycling (as shown in Figure I.2.D.2 for 1000 cycles).

Our layer on layer technology allows us to exceed the limits of UV curing in single layers and allows to make quality 94-3-3 NMC-C-UV electrodes of 7, 14, and 21 mg/cm^2 (Figure I.2.D.3). And our final report will include data with 10, 20, and even 30 mg/cm^2 94-3-3 NMC, in 1, 2, and 3 layers respectively.

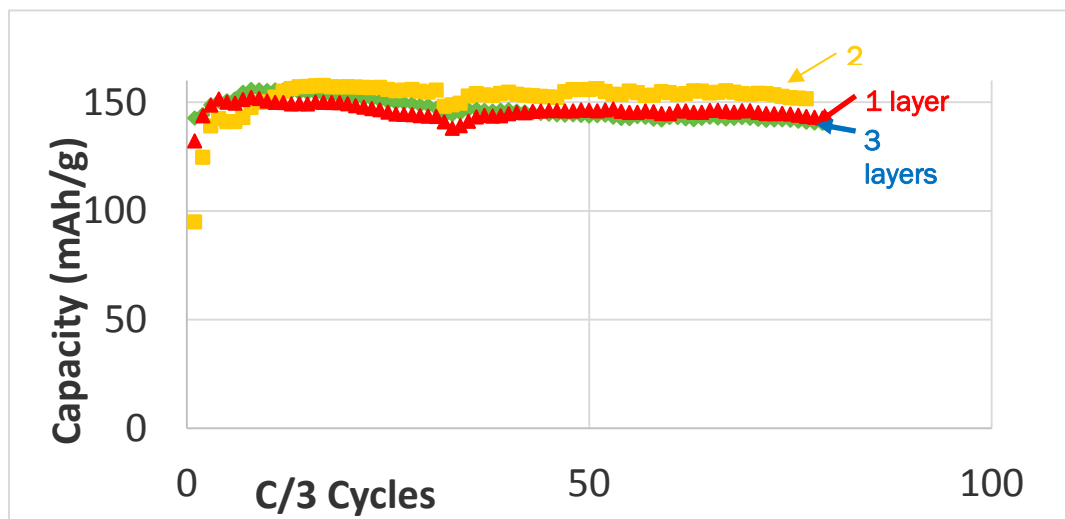


Figure I.2.D.3 Layer on layer UV Slot-Die Processing works with no loss in capacity. 94-4-3-NMC532-C-UV 7, 14, and 21 mg/cm^2 .

We made great strides in power electrodes, which are more problematic due to the greater carbon content. We finished our power work with 82-12-6 NMC-C-UV power cells that had a 75% capacity retention with a 10C rate (Figure I.2.D.4).

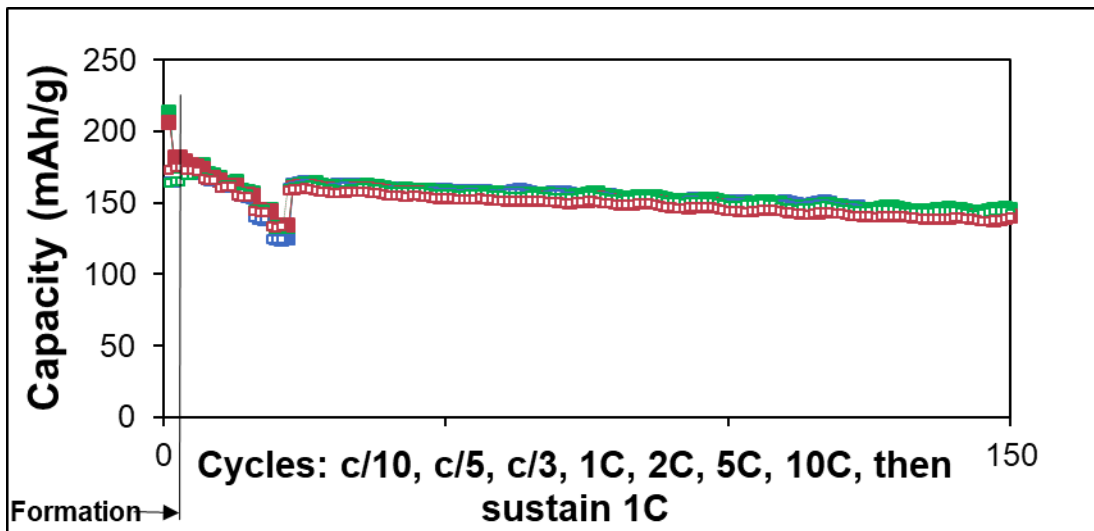


Figure I.2.D.4 Power cathode (82-12-6:NMC(532)-C-UV, 4 mg/cm²) shows 75% capacity retention at 10C rate. UV cathode withstands high temperature (120 °C), where a PVDF electrode would melt and flow. Three curves show tight consistency between cells.

Earlier results showed that graphite electrodes were problematic due to the absorption of UV and small UV curing molecules by the graphite. We have been able to demonstrate that LTO anodes are very compatible with UV curing (Figure I.2.D.5)

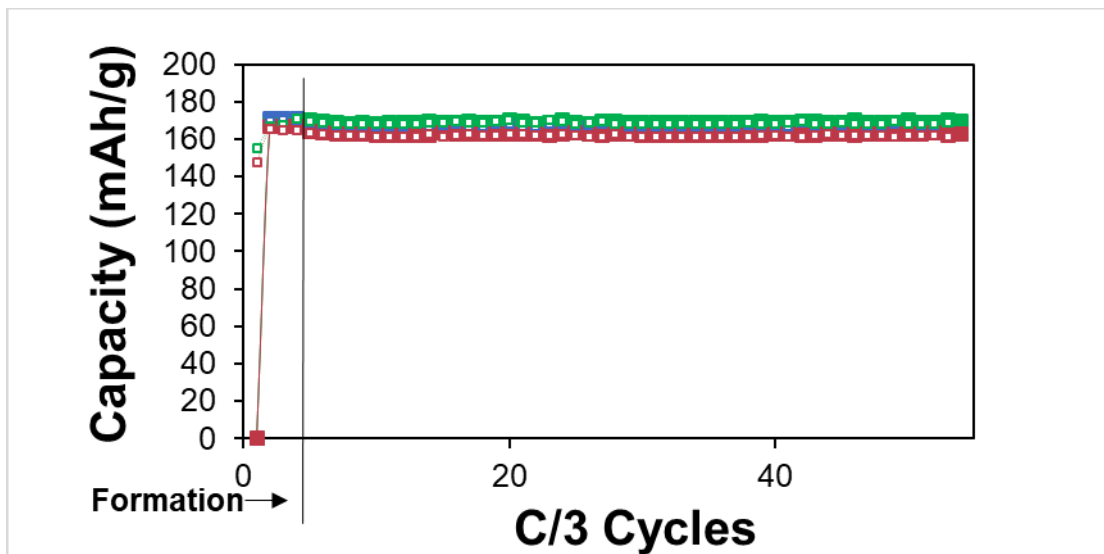


Figure I.2.D.5 UV LTO Anode (93-4-3:LTO-C-UV) with 3 mg/cm² loading. Three curves show tight consistency between cells.

Conclusions

During this approximate three-year project, the substantial benefits of using UV curable binders to replace conventional binders like PVDF and the associated NMP solvent in Lithium ion battery electrodes has been demonstrated and the next step is full commercialization. The goals of the project have been met. The iterative research and development effort led by Miltec UV with support from ANL and ORNL has established several noteworthy conclusions:

- The electrode manufacturing cost savings due to the reduced capital and operating costs (elimination of huge drying ovens and NMP recovery); reduced energy consumption; increased operating speeds and dramatically smaller footprints are 65-85% not including raw materials and 20-25% when including raw materials in the total electrode cost.
- The UV binders have been found compatible with a wide array of active cathode materials; including NMC, LMO, LCO, and LFP. The resultant UV cathodes exhibit electrochemical performance equal to conventional PVDF cathodes.
- Cathode coatings using UV curable binders can be made with 6, 5, 3, 2, and even 1% binder by weight. The higher binder concentrations are used for high carbon power electrodes, which is true with conventional PVDF batteries as well. The cathodes of <2% binder exhibit reasonable adhesion, resistance and other characteristics but the best consistent performance is in the 3-2% range. Very high power and very high energy cells have been demonstrated ranging from energy cells of 94/3/3 (active cathode material/carbon/UV binder) loading to 83/12/5 75% capacity retention at a 10C rate power cells.
- With every electrode composition there is a practical limit to achieving full curing of the UV binder. This limit is a result of limitations on even the very high intensity UV light to effectively penetrate beyond this depth in a very opaque high solids content coating. For NMC energy cathodes this equates to a material loading of approximately 10 mg/cm² per layer. This is not an absolute limit, it is the limit that we expect reliable electrode production. So, 20 mg/cm² requires 2 UV layers and 30 mg/cm² requires 3 UV layers with NMC.
- The 2-3% UV binder levels achievable with a cathode are not achievable with a graphite or carbon anode. At the present state of development UV curable binder for graphite anodes is not practical.
- LTO anodes made with UV curable binder exhibit the same electrochemical performance as LTO anodes made with conventional binders.
- Miltec UV International and Argonne National Laboratory and Oak Ridge National Laboratory have made significant progress toward meeting the goals of this project. A three lamp UV curing system with slot die coater and an interchangeable letterpress coater with a reel to reel control system is operational. Cathode coatings of 3%, 2 and 1% UV binder have been prepared; made into pouch cells and cycled with performance equal to PVDF reference cells. Double layered cathode coatings have been made with performance equal or greater than equivalent single-layer electrodes. This shows there is no hypothetical barrier between the first and second layer. In addition, Miltec has demonstrated the ability to make LTO anodes using UV binder with performance equal to conventional LTO anodes. The coating and UV curing system in place will allow Miltec UV to complete the optimization and demonstrate the full potential of this technology. Miltec UV intends to vigorously pursue full development and commercialization of UV systems as applied to Lithium ion battery electrodes.

In addition, Miltec UV has identified additional areas where UV Processing and Chemistry can help the current technology move to Battery 500 goals

- The UV curable materials formulated by Miltec UV can be used as Solid and Gel Polymer Electrolyte (SPE/GPE) binder combinations

- UV curing of SPEs and GPEs were demonstrated directly on the lithium metal surface in an argon-inerted environment
- Sulfur cathodes, 90 μm thick, were made with our UV chemistry and process and are in test.

Publications

Miltec UV made various public releases of project results during the last year. These include:

- Presentation at the DOE Annual Merit Review sponsored by the Vehicle Technology Office in June of 2017.
- Miltec UV had an exhibit with visuals and a video presenting the progress on UV binder for LIB electrodes at the International Battery Conference, Fort Lauderdale, FL March 2018 and the Battery Show, Novi, MI September 2018.
- Miltec UV has a fully operating website presenting details on the performance and potential for LIB electrodes made with UV curable binder. <http://www.miltec.com/technology/battery/cathode-binders/>

Acknowledgements

The author would like to recognize the contributions of Miltec UV investigators Allen Shariaty, Taylor Xu and Kelly Hillen.

I.2.E Towards Solventless Processing of Thick Electron-Beam (EB) Cured LIB Cathodes (ORNL)

David L. Wood, III, Principal Investigator

Oak Ridge National Laboratory
 Energy & Transportation Science Division
 2370 Cherahala Blvd., NTRC-2, MS-6479
 Knoxville, TN 37932
wooddl@ornl.gov

Zhijia Du, Principal Investigator

Oak Ridge National Laboratory
 Energy & Transportation Science Division
 2370 Cherahala Blvd., NTRC-2, MS-6479
 Knoxville, TN 37932
duz1@ornl.gov

Peter Faguy, DOE Technology Development Manager

U.S. Department of Energy
 E-mail: Peter.Faguy@ee.doe.gov

Start Date: October 1, 2014	End Date: September 30, 2019	
Project Funding (FY18): \$350,000	DOE share: \$350,000	Non-DOE share: \$0

Project Introduction

There are a variety of technical attributes to electron beam (EB) curing of LIB binders. EB curing uses solvent-free compositions that have low emissions (VOCs, etc.) and are recognized by federal, state and local governments as being a more desirable technology. Solvent or water-based processing requires high drying energy and results in significant CO₂ emissions. EB curing offers significant process energy savings, is ultra-high speed, and utilizes much more compact equipment than conventional drying ovens (much less plant floor space required). Furthermore, it is a relatively cool process and is compatible with heat-sensitive substrates. Conventional thermal drying of LIB electrodes is typically conducted using multiple temperature stages; however, EB can be conducted in a single step. Solvent-free electrode compositions are rated as non-flammable, which translates into lower insurance costs, less stringent storage requirements and, a reduction in handling hazards.

EB treatment is a fast, robust materials processing technology that commonly delivers low cost and excellent performance for high-volume materials production. Based on decades of development and commercial deployment, self-shielded machines routinely operate with high reliability and low maintenance in industrial roll-to-roll production environments. ORNL is developing, demonstrating, and transitioning technology for high-speed roll-to-roll EB processing of LIB electrodes (i.e. coating formation and binder curing). Further specific advantages of this processing route for LIBs are:

- Unmatched throughput – We estimate ≥ 600 m²/min throughput can be achieved based on ≥ 300 m/min line speed for roll widths up to 2 m (\$1.5-2.0M installed with machine footprint ~ 10 m²).
- Thicker electrodes (synergy with Task 1) – Up to 150 microns can be achieved at the throughput rate mentioned above. Coatings of several hundred microns could be processed at higher capital cost per unit throughput, modest reduction in energy efficiency, and larger equipment footprint.
- Excellent energy efficiency – Electrical efficiencies $\geq 60\%$ are possible, including voltage transformer losses (i.e., $\geq 60\%$ of electrical line energy is converted to productive EB energy).

- Environmentally friendly – EB processing requires no solvent and no initiator and has low emissions.

Objectives

- Significant LIB electrode processing energy savings.
- Ultra-high electrode processing speed (~5-10× conventional coating speeds).
- Utilize much more compact equipment than conventional drying ovens (considerable capital equipment savings and battery plant space reduction).

Approach

ORNL is working on a multiphase approach to develop, demonstrate, and transition EB processing of roll-to-roll battery materials.

- Phase 1 – Demonstrate the technology’s key differentiating attributes of high throughput and thick layer processing (FY15-16).
- Phase 2 – Address the key challenges of EB curing parameters and resulting material performance; develop coating methods requiring little or no solvent. (FY17-18).
- Phase 3 – Demonstrate an optimized curing system in conjunction with a high-speed coating line together with a key equipment partner and battery manufacturer (FY19).

Results

NMC 532 slurries were prepared in a planetary mixer (Ross, PDM ½) with solid components of NMC 532/carbon black/radiation curable binder = 90/5/5 wt%. A small amount of CMC (0.5 wt% of the solid content) was used as a thickening agent. Adequate amounts of deionized water and isopropyl alcohol were added to adjust the rheological properties and surface tension of the slurries. The electrode was prepared by spreading the slurry onto a 15 µm thick Al foil using the ORNL pilot slot-die coater (Frontier Industrial Technology, Inc.) with an a real loading of 25 mg/cm² after drying.

High-speed EB curing was conducted to avoid the effect of excess oxygen inhibition on the curing process by placing a 15 µm thick clear film (Stretch-Tite) on top of the entire electrode. (Excess oxygen is detrimental to the EB curing process by forming oxygen containing radicals in the presence of the high energy electrons.) The film was then taped around the periphery of the samples using clear packaging tape. Prior to taping down the last side of the clear films, the sample was purged several times with nitrogen. Then the film was pressed down along the length of the sample to remove most of the nitrogen and quickly taped closed to minimize any air intrusion. The EB curing conditions were 60 kGy dosing at 275 keV energy at a line speed of 500 ft/min.

Electrochemical performance of 1.5 Ah cells prepared from three different electrodes is shown in Figure I.2.E.1. The high-speed EB cured sample showed similar charging/discharging behavior compared to the baseline PVDF/NMP processed electrode. However, the uncured sample exhibited more than 20% capacity loss during the first cycle, which was due to the poor binding integrity of the uncured resin. During the first 100 cycles, the NMP/PVDF processed electrode had about 3% capacity fade and the cured one had about 15%. Although most of the resin was cured during the high-speed EB curing trial, a small portion of uncured acrylate group remained in the resin, which may be the reason for the greater capacity fade of the EB cured sample compared to the baseline. The small portion of uncured resin results in poor cohesion of electrode constituents (i.e. conductive carbon black and active material), which could lead to electrical isolation of these particles during initial cycling. Hence, greater capacity fade was observed during this period compared to the PVDF/NMP baseline electrode. Once the uncured portion of the electrode is completely electrically isolated, the remaining cured resin functions like the baseline PVDF binder, which explains the identical capacity fade rate after 100 cycles for both electrode types. This finding suggests that equally good cycling performance can be achieved from high-speed EB cured electrode when all the resin is cured.

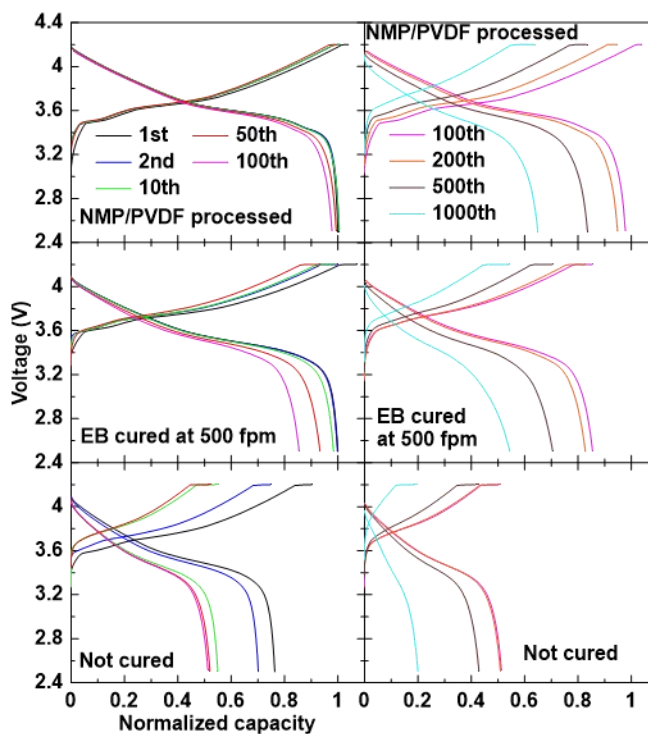


Figure I.2.E.1 Voltage curves of the 1.5 Ah cells prepared from baseline sample (PVDF/NMP processing), sample B (acrylate polyurethane resin binder and EB cured at 500 fpm) and sample C (acrylate polyurethane resin, not cured).

Figure I.2.E.2 shows the long-term cycling results at 0.33C/-0.33C vs. cycle number for the same 1.5 Ah cells. The uncured sample showed poor performance with only 50% capacity retained after 10 cycles. For the high-speed EB cured sample, higher capacity fade was observed up to 100 cycles as compared to the NMP/PVDF baseline. However, the capacity fade rate of the former cathode from 100-1000 cycles was identical to the latter, with the former achieving 80% capacity retention after 300 cycles (FY18 stretch milestone). It is hypothesized that the effect from the small portion of uncured resin diminished after the first 100 cycles, and the short-term capacity retention of EB-cured thick cathodes can be improved to the baseline level if complete EB curing (cross-linking) is achieved.

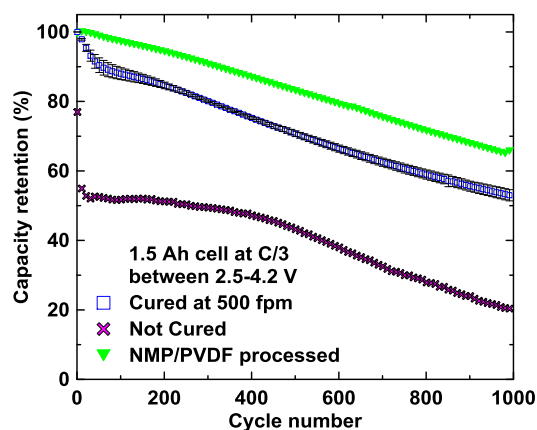


Figure I.2.E.2 Cycling performance of 1.5 Ah cells prepared from baseline sample (PVDF/NMP processing), sample B (acrylate polyurethane resin binder and EB cured at 500 fpm) and sample C (acrylate polyurethane resin, not cured).

The importance of achieving complete cross-linking of the radiation curable resin during EB exposure has been determined. Solutions for further performance improvement will be implemented to overcome oxygen radical inhibition, which include:

- Increasing EB dose. [1],[2] Oxygen inhibition can be reduced by using a high EB dose, which can produce a high concentrations of free radicals that react with oxygen. Increasing the EB dose also results in higher degree of crosslinking of the binder resin.
- Inerting environment. [3] This is the most efficient method to overcome oxygen inhibition. Nitrogen is commonly used to flush the EB curing chamber continuously. However, one disadvantage is the increased cost due to the large volume of nitrogen required.
- Addition of thiols and amines. [2],[4] The lack of oxygen inhibition in thiol-ene and amine polymerizations has been well studied. The peroxy radicals, which are not reactive towards addition reactions, are reactive towards hydrogen abstraction. The chemicals with thiol and amine groups contain easily abstractable hydrogen atoms.
- EB curable cationic resins. [5],[6] EB curable cationic resin systems react via a cationic mechanism which is different from the free-radical polymerization of acrylate resin systems. Photoinitiators, which are photo-acid generators, are required for this system. Upon radiation exposure, the photoinitiator is converted into a strong acid species which initiates polymerization. Therefore, the curing of these resin systems is not inhibited by oxygen.

Another difficult problem with applying EB curing to LIB electrode coatings is finding a coating method that is compatible with the high line speed (≥ 500 ft/min or 5-10 \times faster than conventional slot-die coating with baseline PVDF/NMP). ORNL has chosen electrostatic spraying with industrial partner Keyland Polymer as a potential method for replacing slot-die coating, which is suitable for high line speeds. In order to increase the areal loading of the electrostatically sprayed electrodes, three additional cathode powders were prepared and sent to Keyland for electrostatic spraying trials, and their compositions are shown in Table I.2.E.1 below.

Table I.2.E.1 Compositions of trial electrostatic spray coatings blended at ORNL and coated at Keyland Polymer.

Sample	NMC	Carbon black	resin	Resin type
A	217.5 g	12.5 g	20 g	Keyland Polyester
B	220 g	12.5 g	17.5 g	Keyland polyester*
C	261 g	20	28.6 g	Ucecoat 7689

These powders were sprayed using an electrostatic powder coating gun followed by melting. Powder A was difficult to spray and did not adhere well to the substrate (it required significantly more passes of the gun to get any powder to stick to the Al foil substrate). Because of the difficulty associated with processing this powder, it was not subjected to further testing. Powder B had the best adhesion to the substrate, and four samples of it were prepared with increasing spraying time for film building. For Powder C, it was also somewhat difficult to obtain good adhesion to the substrate. Due to unoptimized fluidity of the three powder types, the gun needed to be gently shaken during the spraying process to keep the powder flowing through the nozzle.



Figure I.2.E.3 Representative photos of the electrostatic sprayed samples after receiving from Keyland polymer.

As the loading of sprayed electrode is increased, the challenge with electrostatic application of small particle size is the carrying capacity of the charge is directly proportional to the size of the particle. Figure I.2.E.4 shows that areal loading increases with the spraying time for short to moderate spray durations, but it decreases afterwards, which is possibly due to limited charge attraction as the coating thickness builds up.

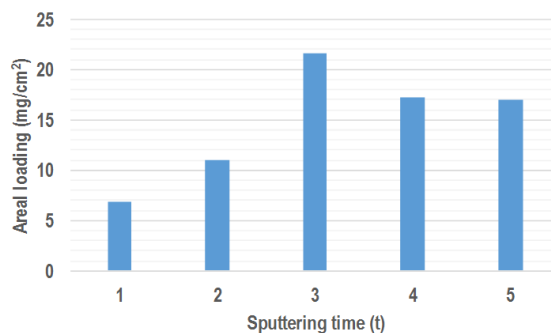


Figure I.2.E.4 Areal loading of the electrode prepared by electrostatic spraying method versus the spraying time.

Conclusions

This research demonstrated the feasibility of using high speed electron beam (EB) curing to manufacture thick LIB cathodes, which can significantly reduce the manufacturing cost compared to conventional fabrication processes. Pilot-scale manufacturing equipment was used to validate the suitability of the EB scaling process. Oxygen radical inhibition of the cross-linking reaction led to the poor adhesion in the cathode coating. With improvement in nitrogen protection, a high speed EB curing at 500 ft/min with 60 kGy dose under 275 kV was successfully implemented. The electrochemical performance was tested in NMC 532/graphite 1.5-Ah pouch cells produced at the DOE Battery Manufacturing R&D Facility at ORNL (BMF). High speed EB cured electrodes showed similar cycling performance after 100 cycles compared to PVDF/NMP baseline processing. The capacity fade during the first 100 cycles for the EB cured electrode likely resulted from a small portion of uncured resin. Further improvement strategies were discussed, such as high-speed-compatible electrostatic spray coating, so EB curing technology can be fully utilized for manufacturing low-cost and high energy density LIB electrodes.

Key Publications

1. Z. Du, C.J. Janke, J. Li, C. Daniel, and D. L. Wood III, "High speed EB curing of thick electrode for high energy density Li-ion batteries" *Advanced Engineering Materials*, submitted.

2. Zhijia Du, Christopher J. Janke, Jianlin Li, Claus Daniel, and David L. Wood. "Towards Solventless Processing of Thick Electron-Beam (EB) Cured Lithium-Ion Battery Electrodes." In Meeting Abstracts, no. 6, pp. 578-578. The Electrochemical Society, 2017.
3. Zhijia Du, Marissa Wood, Yangping Sheng, Seong Jin An, Jianlin Li, Claus Daniel, and David L. Wood. "The Importance of Surface Tension Control in Slurry Preparation for Thick Electrode Manufacturing." In Meeting Abstracts, no. 6, pp. 570-570. The Electrochemical Society, 2017.
4. Zhijia Du, Jianlin Li, Marissa Wood, Chengyu Mao, Claus Daniel, and D. L. Wood III. "Three-dimensional conductive network formed by carbon nanotubes in aqueous processed NMC electrode." *Electrochimica Acta* 270 (2018): 54-61.

References

1. Awokola, M.; Lenhard, W.; Löffler, H.; Flosbach, C.; Frese, P. UV Crosslinking of Acryloyl Functional Polymers in the Presence of Oxygen. *Prog. Org. Coatings* **2002**, *44* (3), 211–216.
2. O'Brien, A. K.; Cramer, N. B.; Bowman, C. N. Oxygen Inhibition in Thiol-Acrylate Photopolymerizations. *J. Polym. Sci. Part A Polym. Chem.* **2006**, *44* (6), 2007–2014.
3. Wight, F. R. OXYGEN INHIBITION OF ACRYLIC PHOTOPOLYMERIZATION. *J Polym Sci Polym Lett Ed* **1978**, *16* (3), 121–127.
4. Cramer, N. B.; Bowman, C. N. Kinetics of Thiol-Ene and Thiol-Acrylate Photopolymerizations with Real-Time Fourier Transform Infrared. *J. Polym. Sci. Part A Polym. Chem.* **2001**, *39* (19), 3311–3319.
5. Lopata, V. J.; Saunders, C. B.; Singh, A.; Janke, C. J.; Wrenn, G. E.; Havens, S. J. Electron-Beam-Curable Epoxy Resins for the Manufacture of High-Performance Composites. *Radiation Physics and Chemistry*. 1999, pp 405–415.
6. Saunders, C.; Lopata, V.; Barnard, J.; Stepanik, T. Electron Beam Curing - Taking Good Ideas to the Manufacturing Floor. *Radiat. Phys. Chem.* **2000**, *57* (3–6), 441–445.

Acknowledgements

The co-PIs are grateful to Mike Knoblauch, President of Keyland Polymer Material Sciences, LLC and Christopher Janke of ORNL for valuable data collection and analysis.

I.2.F Performance Effects of Electrode Processing for High-Energy Lithium-Ion Batteries (ORNL)

David L. Wood, III, Principal Investigator

Oak Ridge National Laboratory
Energy & Transportation Science Division
2370 Cherahala Blvd., NTRC-2, MS-6479
Knoxville, TN 37932
E-mail: wooddl@ornl.gov

Jianlin Li, Principal Investigator

Oak Ridge National Laboratory
Energy & Transportation Science Division
2370 Cherahala Blvd., NTRC-2, MS-6479
Knoxville, TN 37932
E-mail: lij4@ornl.gov

Peter Faguy, DOE Technology Development Manager

U.S. Department of Energy
E-mail: Peter.Faguy@ee.doe.gov

Start Date: October 1, 2014

End Date: September 30, 2019

Project Funding (FY18): \$700,000

DOE share: \$700,000

Non-DOE share: \$0

Project Introduction

This project at the DOE Battery Manufacturing R&D Facility (BMF) at ORNL builds on past research successes on battery electrode process development and optimization, cost reduction, and cell energy density and manufacturability improvements, which support the Vehicle Technologies Office (VTO) and Electrochemical Energy Storage Tech Team ultimate targets of \$80/kWh-usable system cost, 500 Wh/kg cell energy density, 800 W/kg cell power density, and 10-15 min extreme fast charging times. Our goal is to perform the science needed to reduce high-risk, high-payoff technologies to lower risk levels, such that U.S. industry will consider their integration in future products. Once a new material, process, or concept has demonstrated feasibility for integration and scaling, the BMF will work to make it a viable processing methodology (preferably with an industry partner) with validated performance in a full pouch cell design. While doing so, the BMF will leverage a large array of complimentary projects and sponsors that will provide additional experience and a fast, efficient methodology for solving problems faced by the domestic lithium-ion battery (LIB) industry.

Objectives

To generate a deep understanding of process-property-performance relationships that lead to lower cost and higher performing lithium-ion cells:

- To improve cell energy and power density and reduce battery pack cost by implementing tailored electrode architectures via aqueous processing while simultaneously utilizing high-energy, high-voltage cathode materials.
- Fabricate thick and crack-free 4-8 mAh² composite cathodes via aqueous processing.
- Create laser structured electrodes.
- Evaluate compatibility and broad application of low-Co NMC active materials with aqueous processing.

- Characterize surface energy of electrodes and electrolyte uptake properties.
- Demonstrate energy density ≥ 225 Wh/kg (cell level).

Approach

- Fabricate crack-free electrodes with high areal loading (4-8 mAh/cm²) via aqueous processing.
- Create laser structured electrodes to overcome liquid-phase lithium-ion mass-transport limitations.
- Correlate measured energy and power density of laser structured electrodes with mathematical modeling.
- Evaluate stability of high-energy, high-voltage cathodes (NMC 622 and NMC 811) during aqueous processing.
- Incorporate aqueous processing to fabricate NMC 811 cathodes.
- Characterize surface energy of composite electrodes and dependence on calendaring parameters to provide insights into electrolyte wetting.
- Characterize electrode microstructure.

Evaluate rate performance and long term cyclability in pouch cells Results

Aqueous processing of thick electrodes

Crack-free thick NMC 532 cathodes were successfully demonstrated via a co-solvent approach where 90% water was mixed with 10% isopropyl alcohol (IPA) or methyl acetate (MA). This methodology lowers the surface tension of the solvent system and reduces the tendency of residual-stress related cracks to form in the cathode coating. Figure I.2.F.2 shows coatings from a pure water dispersion, a 90/10 wt% water/methyl acetate dispersion, and the baseline pure NMP dispersion, and it is seen that the cosolvent approach yields a crack-free coating at 4 mAh/cm². In Figure I.2.F.1, corresponding cycle life testing is shown for five of the cathode solvent systems evaluated in graphite/NMC 532 pouch cells. The two co-solvent systems with IPA were found to perform identically to the NMP baseline formulation through ~700 0.33C/-0.33C USABC cycles with excellent capacity retention of about 80%, while the MA cosolvent system degraded at a much faster rate. It is seen that the water/MA cosolvent system degrades at an even faster rate than the pure water system containing a high degree of cracking (see Figure I.2.F.2). The reason for this degradation was found to be a substantial increase in proton concentration and associated pH decrease from 12.4 to 9.0 after 4 h of mixing. Further investigation with NMR revealed that the methyl acetate was undergoing hydrolysis into acetic acid and methanol to an extent of about 8%. It was determined that this may be a fundamental limitation of using MA in cathode aqueous processing. However, it was predicted that crack-free 5 mAh/cm² (32 mg/cm²) NMC coatings can be made with the 80/20 H₂O/IPA system via surface tension measurements of the co-solvent systems. It is the intent to explore this approach for reaching the ultimate goal of 6-8 mAh/cm² for NMC 811 cathode coatings.

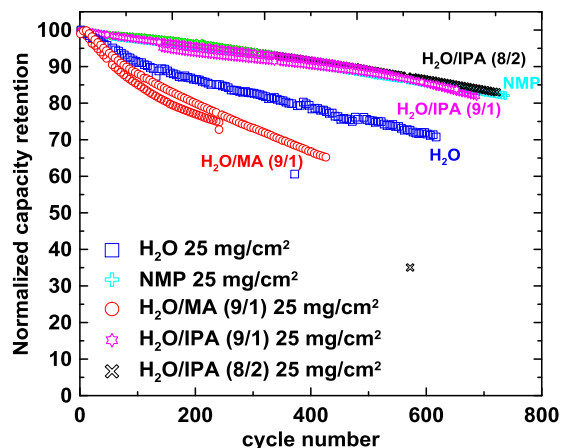


Figure I.2.F.1 Capacity retention of five different cosolvent systems cycled in full pouch cells at 0.33C/-0.33C.

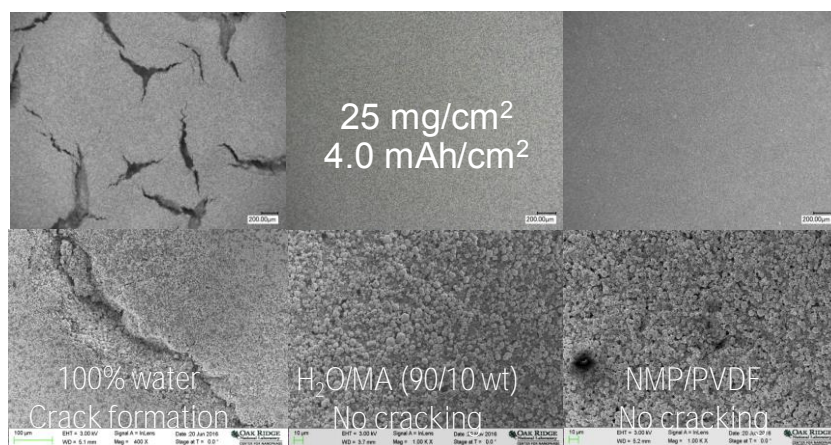


Figure I.2.F.2 Comparison of crack formation for three different solvent systems showing a crack-free coating for the 90/10 wt% water/methyl acetate cosolvent dispersion.

Laser-structured cathodes

In collaboration with Karlsruhe Institute of Technology (KIT), laser patterned NMC 532 cathodes were produced and evaluated in full pouch cells. Cathodes with a 250-micron pitch (width of electrode between laser etched regions) and 500-micron pitch were compared to an unstructured baseline and a structured bilayer with porosity gradient. Figure I.2.F.3 shows SEM micrographs of the laser patterned cathodes and a schematic of the structured bilayer cathode. The structured bilayer had an active material loading of 25 mg/cm² and the other three electrodes had a loading of 29.7 mg/cm² and thickness of 126 microns. Figure I.2.F.4 shows the rate performance results of these four cathodes, and it is seen that there was a slight improvement (>70% rated capacity vs. 55-60% rated capacity at a 2C discharge rate) for the 250-micron-pitch case over the other two cases with 29.7 mg/cm² loading. It is also seen that the structured bilayer cathode performs much worse despite having a lower cathode active material loading, and it is thought to be due to high contact resistance between the two layers. In addition, it is expected that more improvement with laser patterning will be seen with the thicker 6-8 mAh/cm² areal cathode loadings and with even narrower pitches, although an optimum pitch width is expected to preserve volumetric energy density. With these cells, ORNL achieved a key FY18 milestone of ≥ 225 Wh/kg gravimetric energy density based on a scaling factor up to 14 Ah and dimensions of 110 mm \times 148 mm.

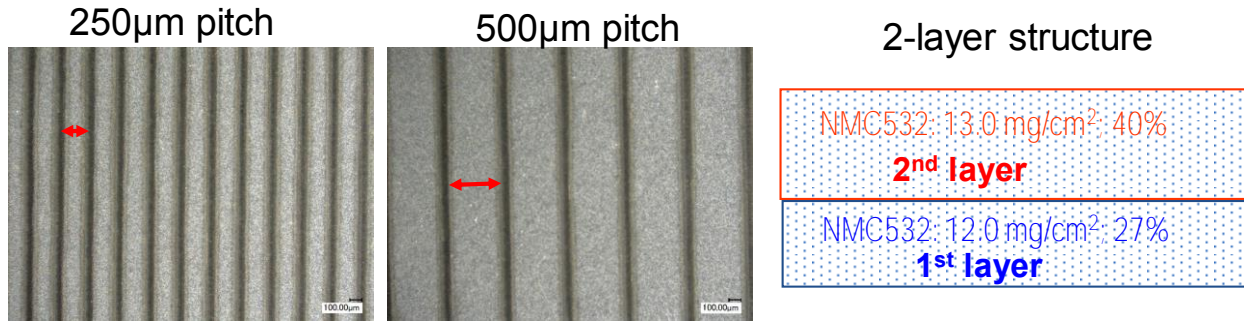


Figure I.2.F.3 SEM micrographs of laser-structured NMC 532 cathodes with different pitches (left and center) and schematic of a bilayer NMC 532 cathode with a porosity gradient (right).

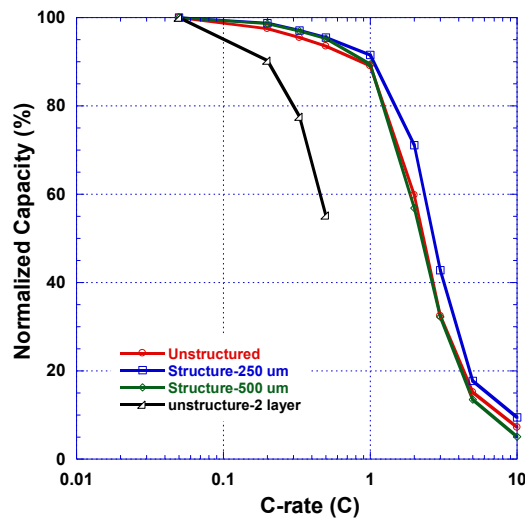


Figure I.2.F.4 Rate performance from 0.05C to 10C discharge rates of full graphite/NMC 532 pouch cells comparing laser structured cathodes and a structured bilayer cathode to an unstructured baseline.

NMC 811 water stability studies and long-term cycling

During FY18, ORNL moved towards low-Co-containing and high-energy NMC 811 and away from NMC 532 for conducting water stability studies. Figure I.2.F.5 shows rate performance data for three different cases of NMC 811 cathodes paired with graphite in single-layer pouch cells charged to an upper cutoff voltage of either 4.2 V or 4.4 V. The difference between the cell groups were that one was made based on ORNL’s standard aqueous processing methodology and compared to both an NMP processing baseline and a case where the NMC 811 had been exposed to water for the same amount of time as the aqueous processing case but processed in NMP. This latter case was conducted to determine if the primary differences in rate performance that had been observed in the past were due to further optimizations needed in formulation chemistry or surface/structural changes in the NMC 811 itself. All cathode active material loadings were between 11.3-11.6 mg/cm². It is seen in Figure I.2.F.5

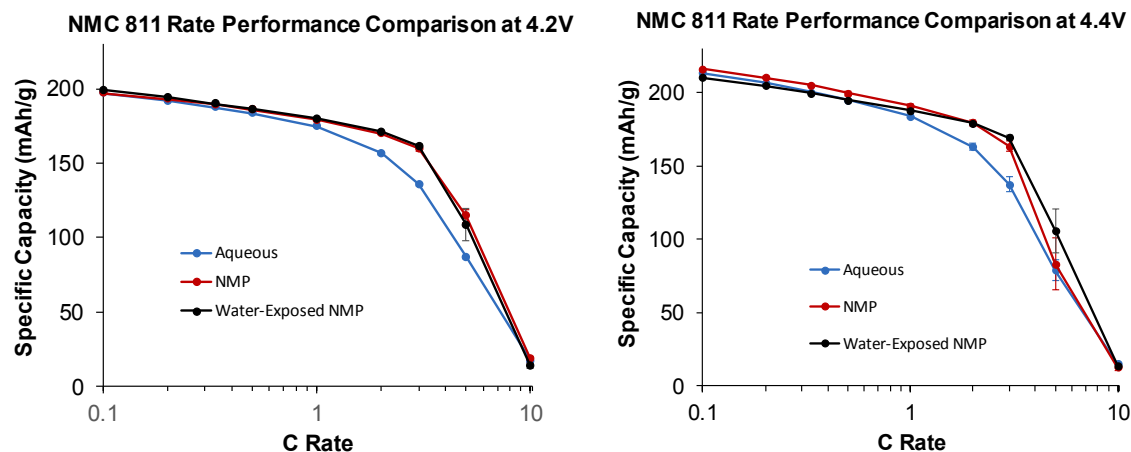


Figure I.2.F.5 NMC 811 rate performance comparison between aqueous processed cathodes, NMP processing with water exposed cathodes, and NMP processed baseline charged to 4.2 V (left) and 4.4 V (right).

that the rate performance of the aqueous processed case, although quite good through 2C discharge rates, is slightly lower than the two NMP processed cases. However, the case where the NMC 811 was exposed to water prior to NMP processing was identical to the NMP baseline for both upper cutoff voltages, which suggests that it is formulation optimization that is needed rather than a fundamental surface chemistry or bulk structural change preventing the processing of Ni-rich NMCs in water. Supporting this hypothesis is the XRD and Raman spectroscopy data in Figure I.2.F.6, which show no changes in bulk structure for NMC 333 or NMC 811 after one week of exposure in DI water when compared to the pristine active materials. However, it was observed that there were changes in the surface features of NMC 811 after one week of water exposure when compared to the pristine active material as shown in the Figure I.2.F.7 TEM images. It is seen that the thickness of an amorphous layer (likely Li_2CO_3 , LiOH , or a combination of the two due to Li leaching from the NMC 811) increases by about $3\times$ after the water exposure. These findings strongly suggest that the length of time that the NMC 811 is exposed to water could be playing a role in rate capability results shown in Figure I.2.F.5. It is further thought that with shorter mixing times and high solids loadings that NMC 811 will be compatible with aqueous processing, and only the formulation needs to be optimized to obtain similar rate capability to the NMP baseline.

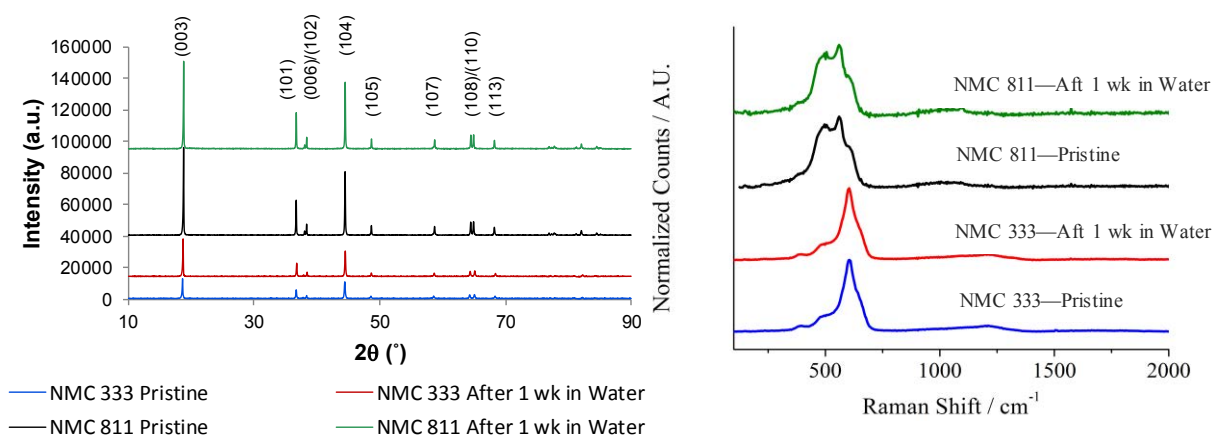


Figure I.2.F.6 XRD (left) and Raman spectroscopy (right) data of NMC 333 and NMC 811 pristine active material and after one week of water exposure showing no difference in bulk structure for either compound.

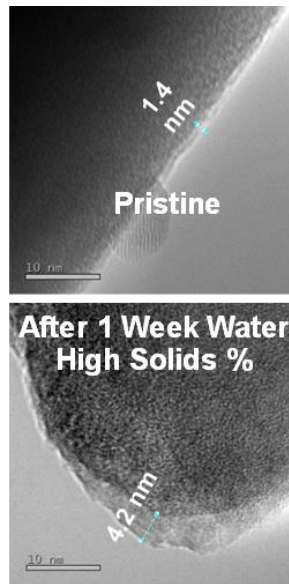


Figure I.2.F.7 TEM images of pristine NMC 811 (top) and NMC 811 exposed to water for one week (bottom).

Figure I.2.F.8 shows the capacity retention (0.33C/-0.33C USABC long-term cycling) for single-layer pouch cells for NMC 811 aqueous processing compared to the NMP processed baseline. Contrary to the rate capability data in Figure I.2.F.5, the water exposed NMC 811 processed in NMP shows a similar capacity fade to the aqueous processed case. However, all three cases show excellent capacity retention through 600 cycles and the aqueous processed cells and NMP processed cells exhibited ~75% and ~80% capacity retention through 1000 cycles, respectively. It was also observed that the differences in capacity fade for all three cases occur within the first ~100 cycles, and the capacity fade slopes were similar from that point on.

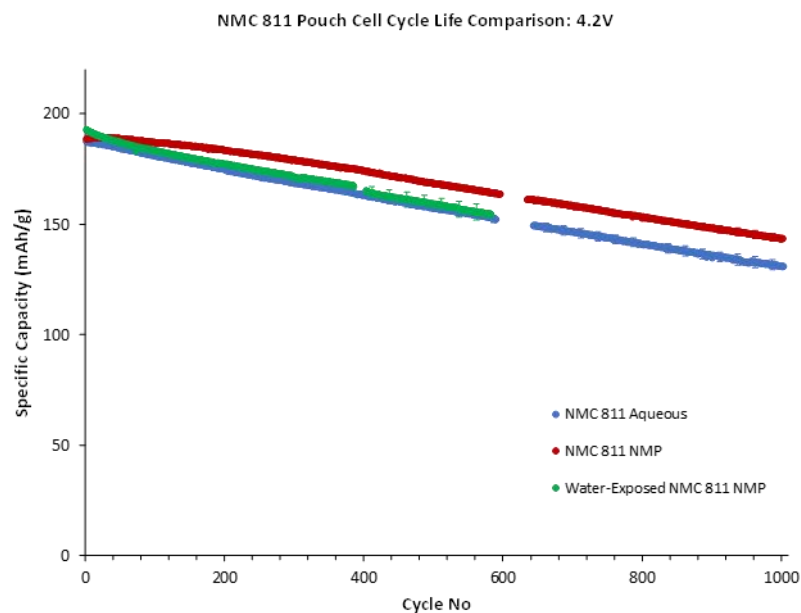


Figure I.2.F.8 Comparison of 0.33C/-0.33C cycle life between aqueous processed NMC 811, NMC 811 exposed to water for one week, and the NMP processed baseline showing that water exposure for a long period of time has a deleterious effect on capacity retention.

Cathode and anode surface chemistry and electrolyte wettability

Advanced surface energy measurements were carried out in collaboration with Binghamton University on NMC 532 cathodes and Conoco Phillips A12 anodes using the Owens-Wendt-Rabel-Kaelble (OWRK) method for both aqueous processing and baseline NMP processing at different extents of calendaring. The OWRK approach allows for calculating the apparent (or true) solid surface energy of a porous electrode when accounting for the interaction of a liquid with the surface pore volume *and* the surface roughness. Surface roughness and porosity were calculated using optical profilometry, which was selected over AFM due superior measurement consistency. It was also found that the surface porosity was dramatically lower than the interior bulk density of the electrodes. Figure I.2.F.9 (left) shows a comparison of the polar and dispersive surface energy components of the aqueous and NMP processed cathodes and anodes in an uncalendered state (55-56% porosity), without accounting for surface roughness and porosity. It is seen that the cathode has a substantially higher total surface energy and polar component (related to hydrophilicity and electrolyte uptake) than the anode. In addition, it was found that the aqueous processed electrodes were more hydrophilic (greater polar surface energy component) than their NMP processed counterparts (74.1% surface energy increase for the NMC 532 cathode and 48.2% increase for the A12 anode). Figure I.2.F.9 (right) shows the surface energies of the same electrodes when surface roughness and porosity is accounted for using the OWRK method. The surface energies increased substantially by ~6-8 mN/m for the cathodes and 12-15 mN/m for the anodes, and the hydrophilicity of the cathodes decreased with increased extent of calendaring (decreasing porosity for the NMP processed cathodes and increased slightly for the aqueous processed cathodes). These findings suggest that aqueous processing is beneficial for the rate of electrolyte wetting and the extent of wetting into the mesopores of the electrodes during the electrolyte filling and wetting steps.

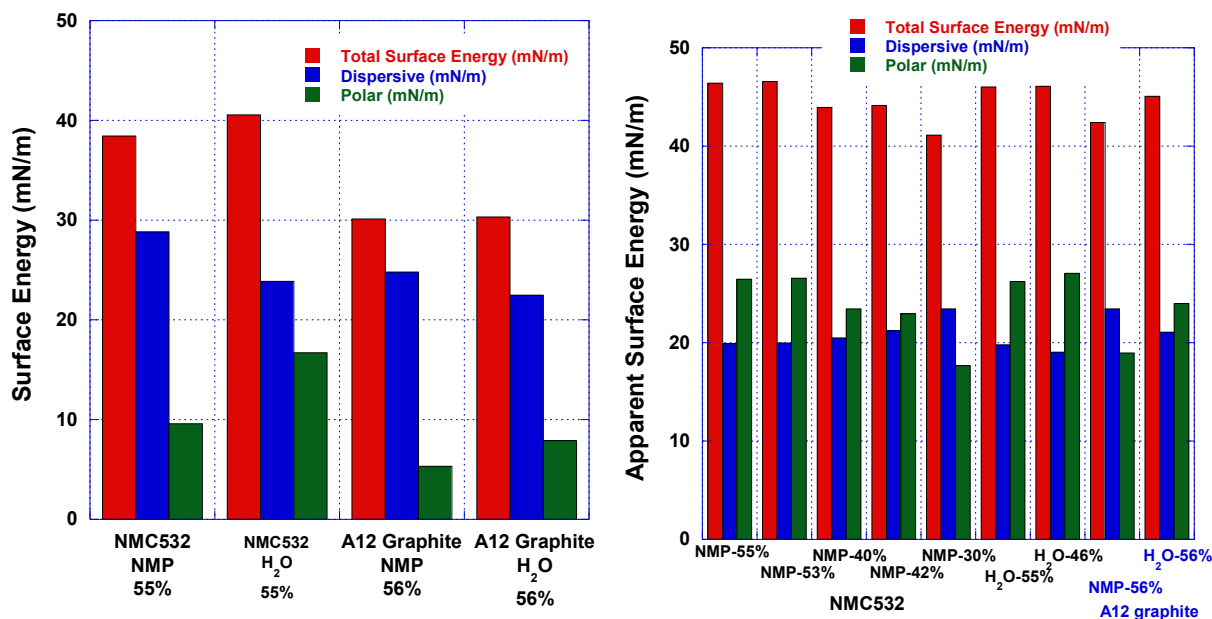


Figure I.2.F.9 Surface energy of various NMC 532 cathodes with different porosities compared to Conoco Phillips A12 graphite surface energy; surface energies not including the effect of electrode roughness (left) and apparent surface energies including surface porosity

Conclusions

The cosolvent approach to aqueous processing was implemented to reach the 4-5 mAh/cm² FY18 goal for cathode areal loading. It was found that a solution of 90/10 wt% isopropyl alcohol (IPA) performed equal to the NMP baseline under long-term pouch cell cycling at 0.33C/-0.33C, and a solution of 90/10 wt% methyl acetate (MA) exhibited the best rate performance. However, the MA suffered from hydrolysis when mixed with water, which negatively affected the long-term capacity retention. Laser structured cathodes were

produced in collaboration with KIT, and it was found that optimization of the pitch width was a key parameter to achieving high-rate performance improvement. In addition, it was concluded that the cathodes must have electrode loadings much greater than $\sim 30 \text{ mg/cm}^2$ for the full effectiveness of the laser patterns to be realized. Extensive NMC 811 water stability studies were concluded (pH change vs. exposure time, lithium leaching vs. exposure time, transition metal leaching vs. exposure time, active material structural characterization with XRD and Raman spectroscopy, and surface characterization with XPS and TEM), which culminated with testing single-layer graphite/NMC 811 pouch cells through 1000 cycles. The durability of the aqueous processed cathodes was found to be excellent with a capacity retention of $\sim 75\%$ obtained through 1000 0.33C/-0.33C USABC cycles with an upper cutoff voltage of 4.2 V. The NMP baseline cells also showed excellent cycling behavior and had about 80% capacity retention. Finally, extensive surface energy characterization of cathodes and anodes was conducted in collaboration with Binghamton University, where the OWRK method was used to account for the effect of surface roughness and porosity on total solid surface energy and the polar component. The polar component accounts for hydrophilicity and electrolyte uptake rate, and it was concluded that aqueous processing increases the electrode surface energy and increased extent of calendaring of NMP processed electrodes decreases surface energy.

Key Publications, Patents, and Invited Presentations

1. C. Mao, S.J. An, H.M. Meyer, III, J. Li, M. Wood, R.E. Ruther, and D.L. Wood, III, "Balancing Formation Time and Electrochemical Performance of High Energy Lithium-Ion Batteries," *Journal of Power Sources*, **402**, 107–115 (2018).
2. A. Davoodabadi, J. Li, Y. Liang, R. Wang, H. Zhou, D.L. Wood, III, T.J. Singler, and C. Jin, "Characterization of Surface Free Energy of Composite Electrodes for Lithium-Ion Batteries," *Journal of The Electrochemical Society*, **165**, A2493–A2501 (2018).
3. L. David, R.E. Ruther, D. Mohanty, H.M. Meyer, III, Y. Sheng, C. Daniel, and D.L. Wood, III, "Identifying Failure Mechanisms in Lithium-Ion Batteries with Coating Defects at the Cathode," *Applied Energy*, **231**, 446–455 (2018).
4. C. Mao, M. Wood, L. David, Y. Sheng, Z. Du, H.M. Meyer, III, R.E. Ruther, and D.L. Wood, III, "Selecting the Best Graphite for Long-Life, High-Energy Li-Ion Batteries," *Journal of The Electrochemical Society*, **165**, A1837–A1845, 2018.
5. Z. Du, A.J. Kukay, M. Wood, J. Li, C. Daniel, and D.L. Wood, III, "Three-Dimensional Conductive Network Formed by Carbon Nanotubes in Aqueous Processed NMC Electrode," *Electrochimica Acta*, **270**, 54–61, 2018.
6. P. Rupnowski, M. Ulsh, B. Sopori, B. Green, D.L. Wood III, J. Li, and Y. Sheng, "In-Line Monitoring of Li-Ion Battery Electrode Porosity and Areal Loading Using Active Thermal Scanning – Modeling and Initial Experiment," *Journal of Power Sources*, **375**, 138–148 (2018).
7. Jianlin Li, "Advanced materials processing and manufacturing for lithium-ion batteries", Department of Chemical and Materials Engineering, University of Kentucky, Lexington, KY, August 29, 2018. (Invited)
8. Jianlin Li, "Toward low-cost and high energy density batteries", Department of Mechanical Engineering, University of Arkansas, Fayetteville, AR, August 10, 2018. (Invited)
9. David Wood, Marissa Wood, Zhijia Du, and Jianlin Li, "Electrode structuring and processing challenges of advanced lithium secondary batteries with ultra-high energy densities," Beyond Lithium-Ion XI, Cleveland, OH, July 26, 2018. (Invited)

10. David Wood, Marissa Wood, Jianlin Li, Zhijia Du, Peter Smyrek, Yijing Zheng, Jan-Hendric Rakebrandt, Wilhelm Pfleging, Ranjeet Rao, and Scott Solberg, “Novel R2R Manufacturing Approaches for Lithium Ion Battery Electrodes,” 2018 ASME Power & Energy Conference & Exhibition, Orlando, FL, June 28, 2018. (Invited)
11. Z. Du, C. Daniel, J. Li, and D.L. Wood, III, “Manufacturing of Thick Composite Electrode using Solvent Mixtures,” Filed April 27th, 2018, U.S. Patent Application No. 15/965,242 (UT-Battelle, LLC).
12. Jianlin Li, “Technical and economic analysis of solvent-based lithium-ion electrode drying with water and NMP”, 2018 International Battery Seminar, Fort Lauderdale, FL, March 26-29, 2018. (Invited) Jianlin Li, “Electrode processing and engineering for low cost and high energy density lithium-ion batteries”, Biological and Chemical Processing Group, Idaho National Laboratory, Idaho Falls, ID, October 9, 2017. (Invited)

Acknowledgements

The co-PIs are grateful to ORNL team members Marissa Wood, Zhijia Du, and T.J. Christensen for valuable data collection and analysis, KIT for providing laser patterned cathodes, and Binghamton University for completing the OWRK surface energy measurements.

I.2.G Advanced Active Battery Materials: Active Cathode Materials with Component Concentration Gradient Structures (ANL)

Gregory K Krumdick, Principal Investigator

Argonne National Laboratory
9700 South Cass Avenue
Argonne, IL, 60439-4837
E-mail: gkrumdick@anl.gov

Peter Faguy, DOE Technology Development Manager

U.S. Department of Energy
E-mail: Peter.Faguy@ee.doe.gov

Start Date: October 1, 2017	End Date: September 30, 2018	
Project Funding (FY18): \$1,200,000	DOE share: \$1,200,000	Non-DOE share: \$0

Project Introduction

Newly-invented active battery materials that are not yet commercially available are being synthesized in gram quantity at bench-scale without quality control and reproducibility. These chemistries need to be tested and validated in large format prototype cells before going to high-volume manufacturing which needs a fair amount of material. Moreover, for in-depth material characterizations and further material modification such as surface coating, kilogram scale stocks of these materials are necessary as baseline materials. Therefore, the supplement of newly-invented materials with high quality and large quantity is critical for both fundamental research and industrial validation for commercialization.

From material engineering perspective, the development of a tailored synthesis process and composition optimization are the key issues to produce sufficient quantities of these newly-invented materials with high quality and reproducibility. Challenges and barriers addressed in this project are synthesis route selection, process and composition optimization, quality control with reproducibility and manufacturing cost reduction. The systematic material engineering and customized scaled process that we develop, will resolve the scale-up constraints of these materials and bridge the gap between basic material research and commercialization.

Objectives

The program is a key missing link between discovery of advanced active battery materials, market evaluation of these materials and high-volume manufacturing to reduce the risk associated with their commercialization. We provide systematic process and material engineering researches to develop cost-effective customized processes and to produce sufficient quantities of target materials with high quality by optimizing synthesis process and material composition, evaluating material purity profile and applying emerging manufacturing technologies. The technical targets of this program are developing customized synthesis processes for each material selected, scaling up multi-kilogram material with reproducibility under rigorous quality control and evaluating emerging manufacturing technologies to assist the fundamental research of R&D groups and reduce the commercialization risk of newly-invented active battery materials.

Approach

Advanced active battery materials with component concentration gradient structures were selected as target materials which are composed of Ni-rich core and Mn-rich outer layer. This type of materials have been reported to have the potential of a high capacity with more than 200 mAh/g whereas exhibit improved thermal stability. We synthesized these materials in a variety of particle structures and performed advanced material characterization as particle cross-sectional mapping as well as electrochemical performance evaluation such as discharge capacity, capacity retention, thermal stability, impedance rise, oxygen release. At the same time, a tailored synthesis process is being developed to enable industrial scale production of selected material using various synthesis process equipment installed in Material Engineering Research Facility (MERF) at ANL.

Results

To stabilize this high-capacity Ni-rich cathode material, as an approach, particle shape with component concentration gradient structures has been implemented. This approach can improve capacity retention during cycling and thermal-abuse tolerance of Ni-rich cathode materials. To determine the possibility, we first compared the thermal stability of the synthesized 811 core-gradient material with the commercial NMC811 using time-stable XRD through collaborative research with Dr. Seongmin Bak at BNL. Figure I.2.G.1 shows that the (003) peak shift during heating shows typical phase transition from layered to spinel structure. Both commercial 811 and 811 core-gradient show the phase transition at around 200 °C. However, we can see the peak broadening of 811 core-gradient which indicates more structural inhomogeneity. As another analytical approach to determining the stability of gradient materials, temperature dependent oxygen release was measured as shown in Figure I.2.G.2. 622 core-gradient and 811 core-gradient materials represent a more broaden form of oxygen release at temperatures higher than commercial 622 and 811. Thus, core-gradient materials show improved thermal stability. So, we saw the potential for gradient materials and began to synthesize more advanced types of gradient materials.

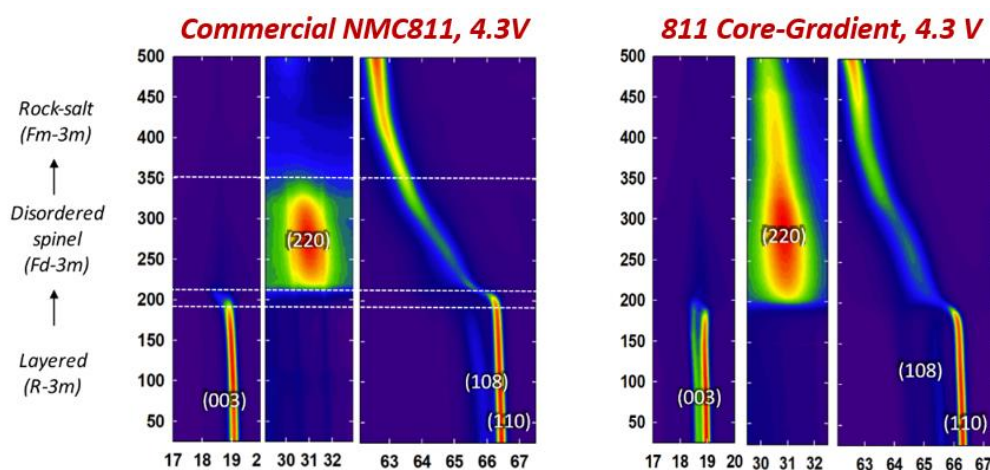


Figure I.2.G.1 Thermal stability comparison between commercial NMC811 and 811 core-gradient using time resolved XRD

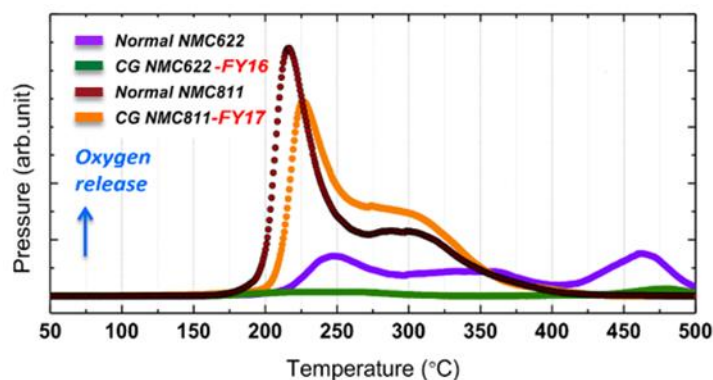


Figure I.2.G.2 Oxygen release comparison of normal NMC and core-gradient materials

Figure I.2.G.3 shows a new synthesis approach toward core-multi shell particle structure. First, we synthesized NMC90/5/5 as a core material to enable high capacity. Then, core-multi shell particles were made on the NMC90/5/5 core, with one shell of 811, with two shells of 811 and 622, and with three shells of 811, 622, and 333. Thus, the overall Ni concentration of synthesized materials are gradually lowered from 90% to 86%, 80% and 63%. Cross-sectional line scan and mapping for Ni reveals that as the number of shells increases, the Ni concentration on the surface decreases. On the other hand, Co and Mn concentrations increase on the surface

as the shell count increases. We analyzed and compared the electrochemical performance of these four materials.

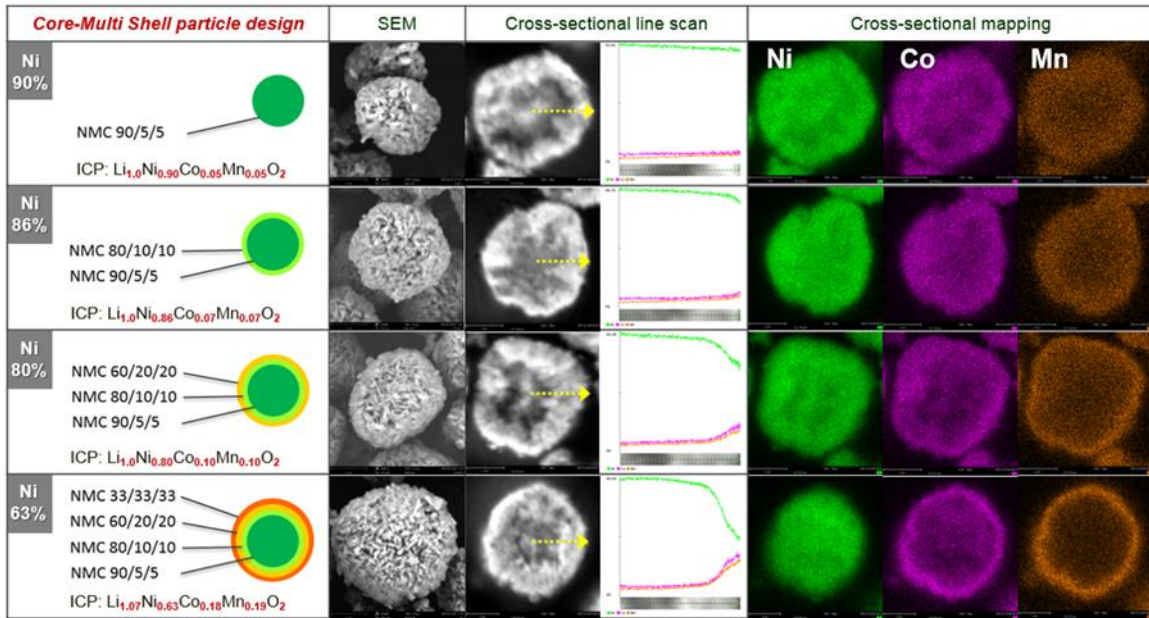


Figure I.2.G.3 New synthesis approach toward Core-Multi Shell particle structure

All cathode laminates prepared for coin half cell are composed of 90% active material and have a thickness of 34µm and a porosity of 43%. The cut-off voltage window between 2.7 and 4.4 was used to clearly show the performance difference of each material. As shown in Figure I.2.G.4, the voltage profile indicates that as the Ni content decreases, the discharge capacity decreases as expected. The C/2 cycling results show the highest normal discharge capacity of 90/5/5, but the fastest capacity fade. However, as the content of manganese and cobalt increases near the surface of the particles, the capacity retention is better due to more stable shell composition.

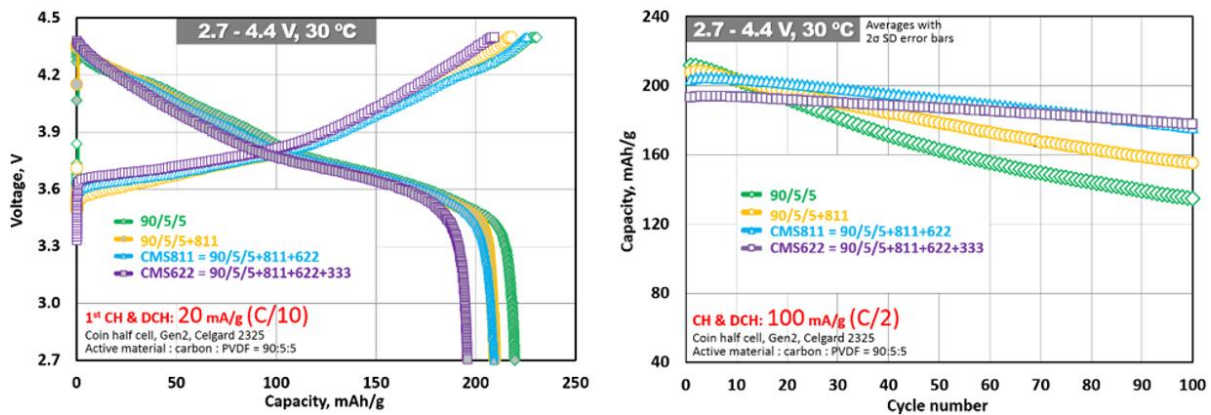


Figure I.2.G.4 Electrochemical performance of synthesized core-multi shell materials

Figure I.2.G.5 compares the cycling performance of the synthesized core-multi shell 811 and core-multi shell 622 with commercial 811 and 333. In the C/2 cycling graph, the commercial 811 and 333 are black and red. Core-multi shell 811 and 622 are blue and purple. Commercial 811 and core-multi shell 811 have the same overall composition, but there is a big difference in capacity retention. It is also noteworthy that the core-multi shell 622 and commercial 333, which have the same surface composition, have similar capacity retention

trend. This shows that the surface composition of core-multi shell particle structure significantly affects the cycle performance.

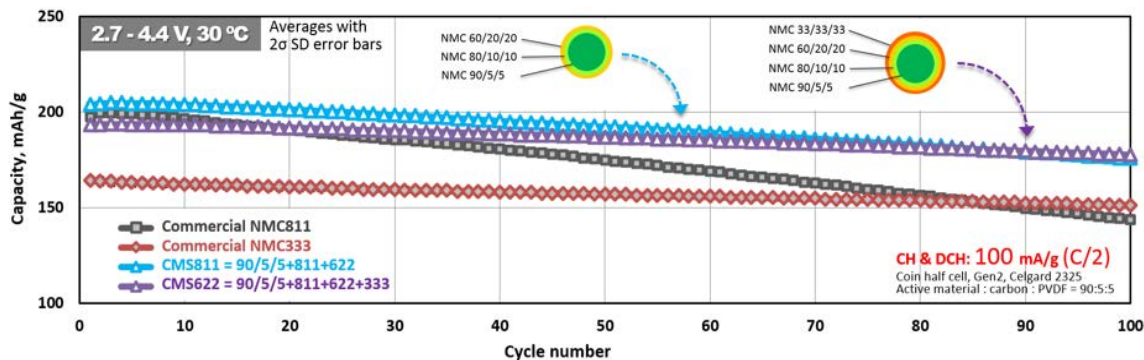


Figure I.2.G.5 Cycling comparison between commercial NMC and core-multi shell materials

We performed thermal stability test using DSC for the core-multi shell materials. As shown in Figure I.2.G.6, the lower the Ni content, the less the amount of heat release and the higher the peak temperature. The thermal stability improvement of the core-multi-shell 811 is impressive. It reduces energy release by 50% than the commercial 811.

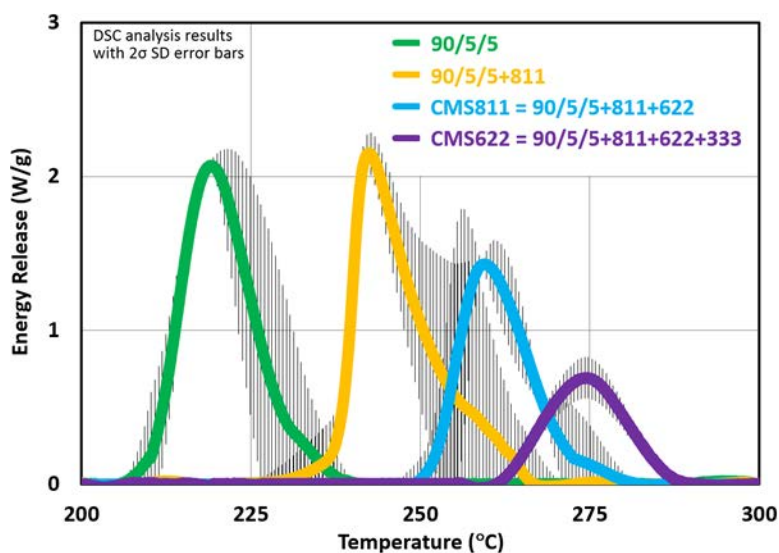


Figure I.2.G.6 DSC comparison at 5 C/min rate

Figure I.2.G.7 shows an impedance analysis of the core-multi shell materials. Comparing the results of the first charged to that of the 60th cycled measurement, we identified that the lower the Ni content on the particle surface, the more the impedance rise is suppressed as the cycle progresses. This low impedance growth of the core-multi shell materials means longer cycle life and lowers the cooling requirements of the battery pack. Through this impedance analysis, once again, we can see that there is a shell layer made up of different composition. In other words, as the cycle progresses, a resistive shell layer appears.

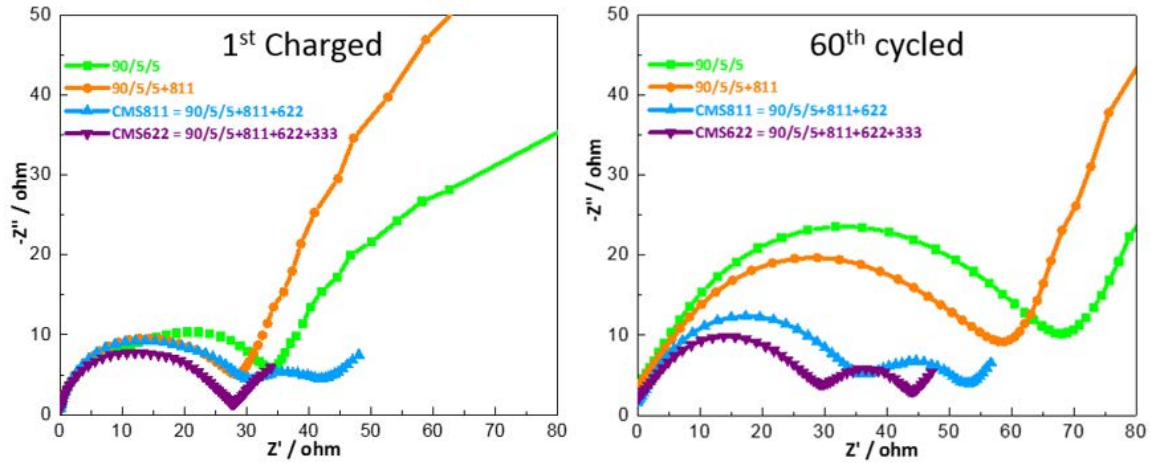


Figure I.2.G.7 Impedance analysis of core-multi shell materials

We selected 811 core-shell, 811 core-gradient, core-multi shell 811 and core-multi shell 622 materials for electrochemical evaluation in pouch cell format. Each of these four materials were scaled up to 100 g level, and the pouch cell test is now under way at Argonne CAMP. Figure I.2.G.8 and Figure I.2.G.9 show the partial results for the scaled up materials. The initial capacity of gradient materials is lower, compared to the commercial 811, but their capacity retentions are significantly better as shown in Figure I.2.G.9.

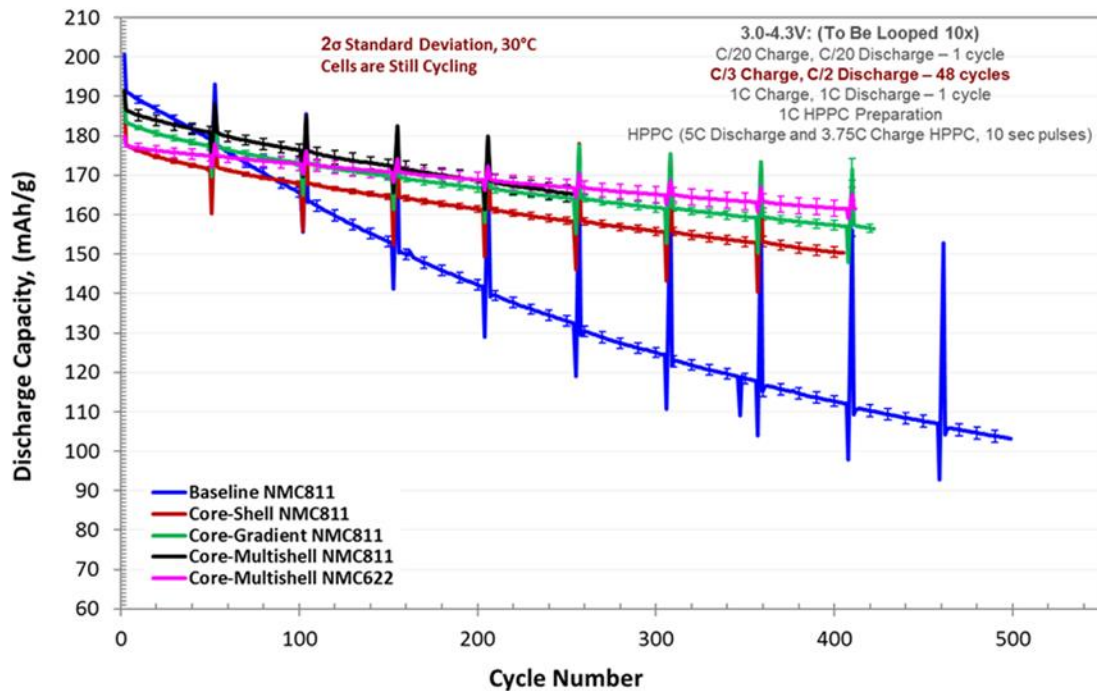


Figure I.2.G.8 Normalized average discharge capacities of commercial NMC811 and core-multi shell materials

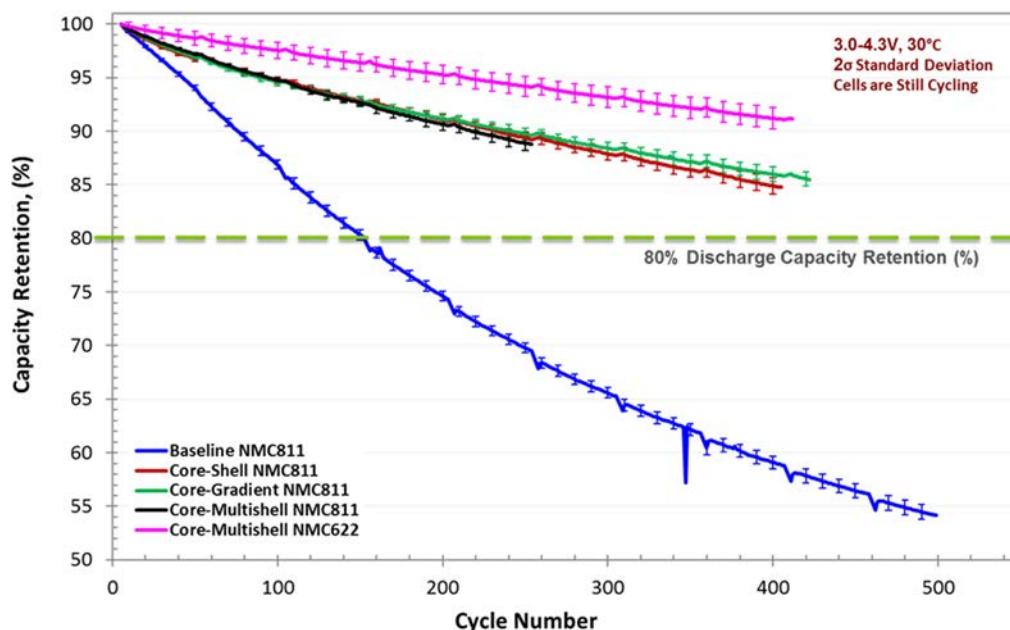


Figure I.2.G.9 Average discharge capacity retention of commercial NMC811 and core-multi shell materials

Conclusions

As a new synthetic approach to component concentration gradient material, we developed and synthesized core-multi shell particle structured material using NMC90/5/5 as a core composition to enable high capacity. The synthesized core-multi shell materials have superior capacity retention and thermal stability and show lower impedance rise compared to materials with the same overall elemental composition and uniform constitution across the particle. The selected four gradient materials were scaled up to 100 g each at ANL MERF and pouch full cell evaluation was performed at ANL CAMP. Based on 400 cycles, scale-up gradient materials show significantly improved capacity retention than commercial NMC811. In the future, depending on the needs of the battery community, we will select the core-multi-shell material with the most desirable particle structure and proceed with kilogram production.

Key Publications

1. Youngho Shin and Gregory K. Krumdick, “Tangent gradient concentration material for battery, digital gradient concentration material for battery”, US Patent filed (2018)
2. Youngho Shin, Youngmin Chung, “Active battery material with banded particle structure, method for producing the same, and lithium secondary battery comprising the same”, Invention disclosure IN-18-067
3. Youngho Shin, Ozgenur K. Feridun and Gregory K. Krumdick, “Pressurized Taylor vortex reactor”, US Patent filed (2018)
4. M. M. Thackeray, J. R. Croy, E. Lee, A. Gutierrez, Meinan He, J. S. Park, B. T. Yonemoto, B. R. Long, J. D. Blauwkamp, C. S. Johnson, Youngho Shin and W. I. F. David “The quest for manganese-rich electrodes for lithium batteries: strategic design and electrochemical behavior, Sustainable Energy Fuels”, 2, 1375–1397 (2018)

Acknowledgements

Dr. Youngho Shin was the lead researchers in this project responsible for synthesis process development and material production. Youngmin Chung, a postdoctoral appointee has been instrumental to characterization and evaluation of the prepared composition gradient materials. CAMP team prepared electrodes, assembled and evaluated pouch cells.

I.2.H Process R&D for Droplet-Produced Powdered Materials (ANL)

Joseph Libera, Principal Investigator

Argonne National Laboratory
9700 S. Cass Avenue
Lemont, IL 60439
E-mail: jlibera@anl.gov

Peter Faguy, DOE Technology Development Manager

U.S. Department of Energy
E-mail: Peter.Faguy@ee.doe.gov

Start Date: October 1, 2017

End Date: September 30, 2019

Project Funding (FY18): \$500,000

DOE share: \$500,000

Non-DOE share: \$0

Project Introduction

Combustion synthesis by flame spray pyrolysis is a materials synthesis process that uses solution of organic and/or inorganic metal salts. The liquid solution is atomized using oxygen and combusted to atomic species from which particles condense and are collected in exhaust filters. The composition of the particles is precisely determined by the solution composition. Any ceramic oxide can be produced by this method as well as reduced phases. This technique is amenable to continuous powder manufacture and is used to industrial scale production of carbon black, silica and titania, for example. LLZO, LMO, and LNMO have been successfully manufactured in the ANL FSP facility. The particle size range is in 30-140 nm for these materials. The particle size increase with solution concentration up to the limit of solubility of the precursor chemicals. Modifications to existing burner including increasing temperature of the flame zone in a controlled manner and utilizing pressurized combustion will be explored to increase the particle size range to 500 nm. Both of these enhancements will also permit the use of lower enthalpy combustion solutions that will facilitate the use of low-cost raw chemicals.

Objectives

To develop processes and produce customized and optimized LLZO and low cobalt large crystal-domain cathode powders for the advanced battery research community.

Approach

Flame Spray Pyrolysis is a commodity scale powder production method and is successfully deployed for simple materials. Adoption of this technology for complex materials such as multi-element battery electrolyte or cathode active materials is challenging due to the greater number of possible materials phases. However, there are two viable strategies both of which can produce a useful product that can be used in the production of energy storage devices. Ideally, the target phase with optimized crystal structure and particle size is obtained and used directly in applications. However, even when the desired final phase is not produced, the resulting powder which may consist of several phases, will be a nano-mixed material that is amenable to sintering to the final desired product. FSP can take advantage of rapid quenching inherent in the flame synthesis process which allows in some cases metastable phases to be synthesized.

The ANL FSP facility has features that allow for convenient and high throughput sample production. A glovebox design filter box allows for collection of nanomaterials and restoration of the filter media within 15 minutes of a run completion allowing for up to 6 generated and collected samples per workday. Material that deposits on the walls of the reactor does not significantly cross-contaminate from sample to sample. On a day to day basis, a clean-in-place brushing fixture allows for the combustion tube to be cleaned of wall deposits for changeover to new material systems further assuring no cross contamination between runs.

The ANL FSP facility has been designed to produce powder materials in an industrially relevant way using liquid spray (droplet) combustion which can produce materials at the highest possible rate compared to ultrasonic atomization or gas-fed precursor introduction. In order to best navigate the complexities of spray combustion, the ANL FSP facility has been provided with a suite of in-situ advanced diagnostics: (a) laser diagnostic system for Filtered Rayleigh Scattering (FRS) and Planar Laser Induced Fluorescence (PLIF) imaging of temperature and species distribution respectively, (b) Optical Emission Spectroscopy (OES) of the flame zone, (c) particle size analysis using Scanning Mobility Particle Sizing (SMPS). Ex-situ diagnostics are also applied including (a) XRD and temperature programmed XRD, (b) BET-SA, (c) DSC-IR/MS, (d) electrochemical testing and electron microscopy (SEM and TEM).

Several FSP process modifications are being deployed to decouple the flame zone engineering from the solution enthalpy: (a) radiation shielding and (b) pressurized combustion. The use of radiation shielding to prevent rapid cooling of the flame and thus sustain higher flame zone temperatures is a means to (a) improve spray combustion properties, (b) engineer the high-temperature traverse through the complex phase space of multi-element condensation and (c) enable the tolerance of low-enthalpy solutions that will facilitate the use of aqueous/organic mixtures using low cost metal precursors. Pressurized combustion is being utilized to (a) provide flame zone temperature control similar to radiation shielding and (b) achieve larger produced particle size targeting FSP particles sizes up to 500 nm.

Results

The ANL FSP facility was first used to develop Al-doped LLZO powder. State of the art synthesis based on University of Michigan (UM) reports (Yi et al.) was reproduced at their reported 3% ceramic yield solutions and then extended to 6% and 9% ceramic yield solutions (recipe LLZO-UM). A maximum LLZO production yield of 89 grams per hours was achieved using the 9% solution. All samples were annealed for 12 hours at 700, 800 and 1050°C. Tetragonal LLZO was observed at 700 and 800°C and cubic was obtained at 1050°C consistent with the UM results.

Variations in the LLZO-UM recipe as well as a new solution chemistry (recipe LLZO-ANL) were discovered that give the cubic phase LLZO at temperatures as low as 670°C (48 hours). In all the samples discussed above, 50% excess lithium and aluminum dopant was used and the annealing was performed in magnesia crucibles. For select recipes that provide the cubic phase at 800°C or lower, the recipes were adjusted to 5% excess lithium with no change in the annealing result to the cubic phase. The ability to process LLZO green powders into the cubic phase at lower temperatures avoids loss of Lithium by evaporation during higher temperature annealing. Efforts to sinter the LLZO into full density pellets for electrochemical evaluations are ongoing. Efforts to optimize LLZO for slurry processing by various means into porous structures suitable for solid state battery application are ongoing.

The particle size obtained by the FSP process was mapped over a wide range of concentrations using the LLZO-UM recipe and is shown in Figure I.2.H.1. The data were obtained using in-situ sampling and analysis with a TSI scanning mobility particle sizer (SMPS). The highest concentration for the LLZO-UM recipe was 9% and could not be further increased due to solubility limits. For comparison, a data point for LLZO-ANL is included in the figure.

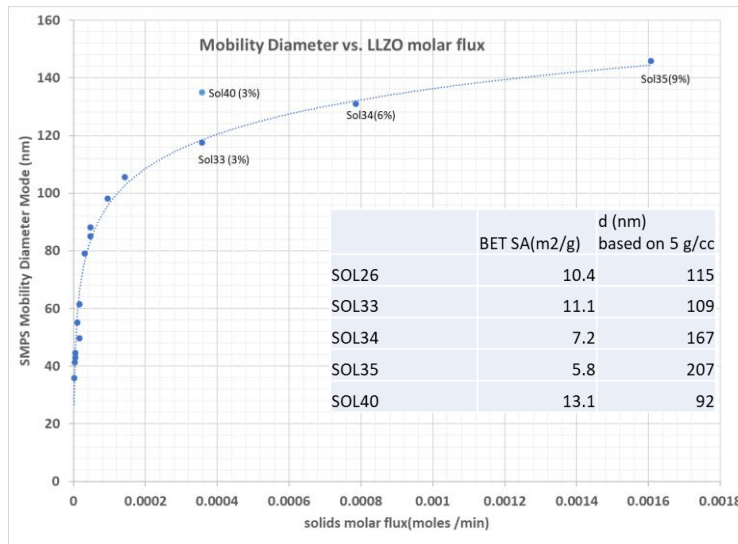


Figure I.2.H.1 Mean particle diameter versus solids production rate for FSP synthesis of LLZO. All points except Sol40 are based on the LLZO-UM recipe. Sol40 is based on the LLZO-ANL recipe. The inset shows predicted particle size for SMPS versus BET-SA data.

The morphology of LLZO-ANL green powder before and after annealing is shown in Figure I.2.H.2 where each image is taken at the same magnification. The as-synthesized material is a fine nanopowder whereas the annealed material shows the strong tendency for sintering as continuous domains at the micron scale are evident. The challenge to obtain a full density solid is complicated by the need for excess lithium which has to be exactly evaporated during annealing at high temperatures such as 1050°C in order to avoid a second phase in the solid LLZO.

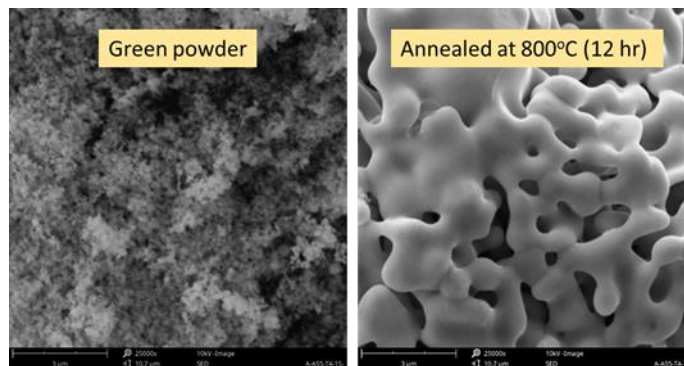


Figure I.2.H.2 (SEM digital image of LLZO-ANL before and after annealing for 12 hours at 800°C)

The annealing behavior of LLZO-ANL was characterized by XRD as shown in Figure I.2.H.3. In this figure the XRD patterns for the as-synthesized green powder and subsequent annealing for 12 hours at 700 and 800°C are shown. For both the LLZO-UM and LLZO-ANL recipes, the as-synthesized material is composed of a distorted lanthanum zirconium oxide (LZO) and lithium carbonate. The aluminum dopant is not identified in the XRD. The XRD pattern for the 700°C anneal shows a mixture of the green powder and cubic-LLZO phases indicating more time is needed at 700°C for complete conversion to cubic-LLZO. At 800°C the green powder is fully converted to cubic-LLZO.

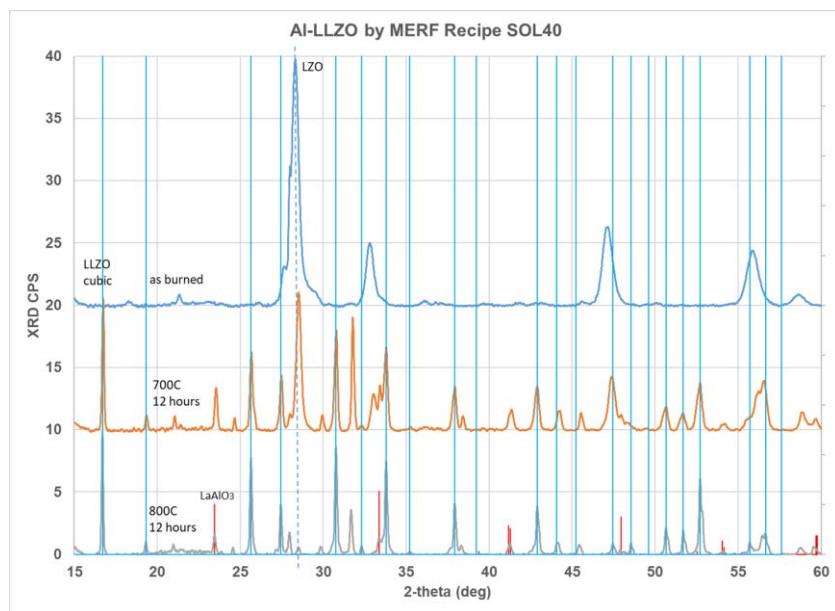


Figure I.2.H.3 XRD patterns for LLZO-ANL green and annealed powder. The material was annealed in oxygen for 12 hours at the temperatures noted.

Preliminary material synthesis efforts for cathode powders was also started in the first year of this project. Lithium manganese oxide was produced using a solutes of manganese acetylacetonate and lithium propionate with the solvents acetonitrile and 2-ethylhexanoic acid. In this synthesis the as-synthesized material was cubic LiMn_2O_4 . Niobium ethoxide was added to this recipe targeting the disordered rock salt lithium manganese niobium oxide cathode material. The as-synthesized material did not yield the target rock salt phase but annealing in Ar at 1000°C did produce the target phase as shown in Figure I.2.H.4.

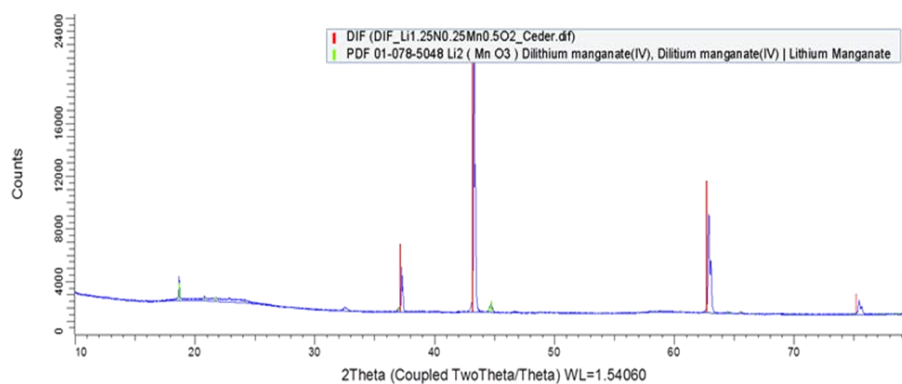


Figure I.2.H.4 XRD patterns for LNMO following annealing in Ar for 12 hours at 1000°C .

Conclusions

A capability for energy storage material synthesis using flame spray pyrolysis has been established at the MERF facility. The facility uses industrially relevant processing and is configured with a suite of advanced diagnostics to gain a deeper understanding of the synthesis mechanisms and help guide material optimization. The facility provides convenient and efficient production of samples for distribution to collaborators for application development. Single samples of 10-20 grams can be produced up to six times per day or up to 500 gram samples of a single chemistry per day can be made in one day. The system has been used to synthesize LLZO over a wide range of concentrations and a new recipe was discovered with promising properties for application to solid state batteries. Preliminary work into cathode powder synthesis was started.

I.2.I Integrated Flame Spray Process for Low Cost Production of Battery Materials for Lithium Ion Batteries and Beyond (University of Missouri)

Yangchuan Xing, Principal Investigator

University of Missouri
416 S. 6th Street
W2028 Lafferre Hall
Columbia, MO 65211
E-mail: xingy@missouri.edu

Peter Faguy, DOE Technology Development Manager

U.S. Department of Energy
E-mail: Peter.Faguy@ee.goe.gov

Start Date: January 1, 2016	End Date: December 31, 2019	
Project Funding: \$2,526,250	DOE share: \$2,215,556	Non-DOE share: \$310,694

Project Introduction

Flame (combustion) processes have been demonstrated to be the most economic way to produce fine powders. Pigment titanium oxide and fused silica are produced in millions of tons per year worldwide using flame processes. One of the challenges in these flame processes is that multiple metal oxides, like those used in lithium ion batteries, are difficult to produce due to the lack of appropriate gasified chemical precursors. As a result, oxides of multiple metals are often produced in flame spray pyrolysis processes in which liquid precursors of metal salts dissolved in water are used. The precursor salt solutions are then atomized and sprayed into a flame and are burned to make metal oxide powders. These processes consume a large amount of water and are prone to producing pollutants. They also do not show advantages in cost reduction.

This project is aimed at developing an integrated flame spray process (iFSP) to produce battery materials. The technology is based on our innovations in spray processes, chemical precursors, and process integrations. The process is a green chemical process and does not use water. It has the potential to reduce the cost of battery materials significantly. A full-scale production process beyond the performance period is expected to reduce cathode powder cost by 50%.

Objectives

The overall objective of this project is to develop an advanced process technology for battery materials production at low cost and in a green chemical process using glycerol as solvent to replace water. The specific objective in 2018 was to understand the process science in powder synthesis from the deep eutectic solvent (DES) chemical precursors and powder materials performance.

Approach

Our approach is to develop the iFSP process into a cost effective process to produce battery materials. The innovations of the proposed technology can be summarized in the following three technical aspects:

1. DES as novel chemical precursors.
2. Innovative spray process.
3. Integrated downstream processing.

Results

Powders from iFSP Processes

The powders of NMC111 have been synthesized in our iFSP process. The flame reactor was designed to spray glycerol-based DES precursors. The chemical precursors were prepared from metal acetates dissolved in glycerol that is a byproduct in biodiesel production. Process conditions were studied to control powder morphology. It was observed that temperatures have a significant effect on powder morphologies. Powders made at a low temperature (e.g., 500°C) show a wrinkled morphology, but powders made at a high temperature (800°C) mainly have a spherical morphology. Figure I.2.1.1 shows typical morphologies of the produced powders. It was assumed that the wrinkles were formed due to a slow drying process where surface tension can create non-uniform surface structures as a result of high viscosity of the glycerol-based DES precursors. At high temperatures, the wrinkles were smoothed out leading to spherical particles. Depending on needs, the powder morphologies can be controlled to certain degree through temperature control in the flame reactor.

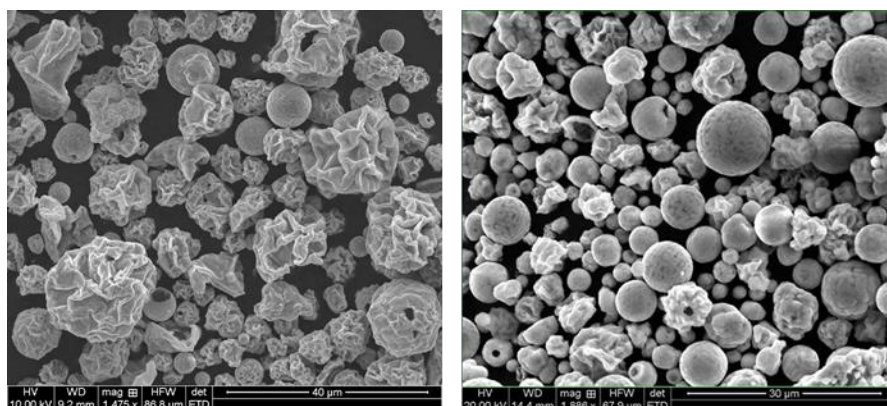


Figure I.2.1.1 SEM images of NMC (111) powders made at different temperatures: Left – a wrinkled morphology at low temperature (500 °C), and Right – a spherical morphology at high temperature (800 °C).

In addition to the temperature control, efforts have also been made to understand the precursor effects during the powder synthesis processes. Modification of the DES precursors yielded other morphologies as shown in Figure I.2.1.2. Powder can be produced with few wrinkles at a lower temperature (700°C). On the other hand, another precursor produced some “perfect” spheres, despite the lower temperature. A higher temperature should be able to produce more spherical morphology.

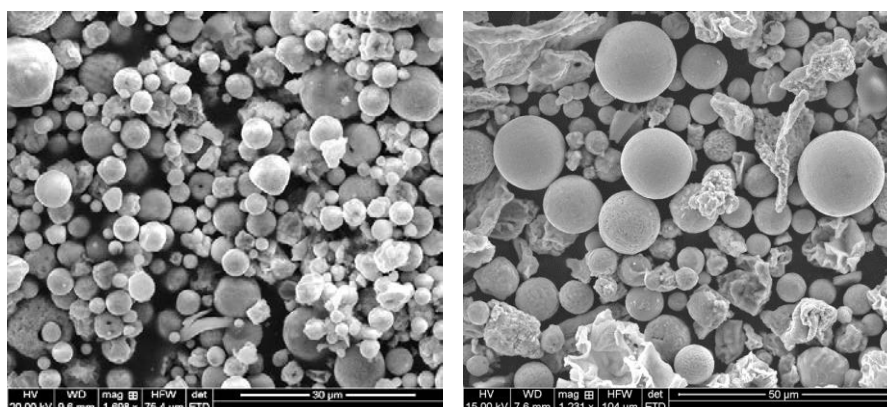


Figure I.2.1.2 SEM images of NMC (111) powders made with two different precursors: Left – powders showing better spherical morphologies; Right – powders show “perfect” spheres, despite some wrinkled particles.

Powders from DES Precursor Thermal Pyrolysis

The glycerol-based DES precursors were pyrolyzed in a thermal process to produce Li-rich materials. Two lithium-rich cathode materials $\text{Li}_{1.2}\text{Mn}_{0.51}\text{Ni}_{0.145+x}\text{Co}_{0.145-x}\text{O}_2$, with $x=0.0725$ (sample LR1) or 0 (sample LR2), were prepared with gelling reagent. Both materials have typical Li-rich material phases with good crystallinity, but the particle size and morphology are different. The LR1 sample has less Co but showed (Figure I.2.I.3) an increasingly improved discharge capacity at 0.1C up to 15th cycle, followed by 93.5% capacity retention up to 48th cycle. At 1C discharge rate its capacity increased steadily from 127 mAh/g (1st discharge cycle) to 152 mAh/g (80th discharge cycle) and ended at 149 mAh/g (98% capacity retention) in the 100th cycle. The superior performance of LR1 was attributed to the continuous activation of the Li_2MnO_3 . Overall, the Li-rich battery materials from our process showed much less cationic mixing, evidenced in XRD results in Table I.2.I.1 and Figure I.2.I.4. This was attributed to the formation of crystalline structures at much lower temperatures, which leads to metal ions immobilization in the structures.

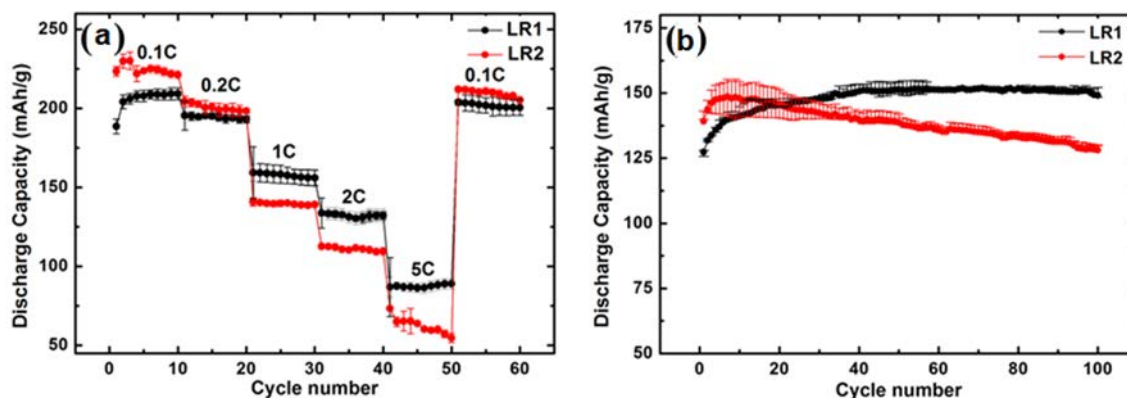


Figure I.2.I.3 Cycling tests (a) rate capability at various C rates, and (b) cycling performance at 1C.

Table I.2.I.1 Structure parameters of the prepared Li-rich cathode materials

Samples	<i>a</i> (Å)	<i>c</i> (Å)	<i>c/a</i>	<i>I</i> ₍₀₀₃₎ / <i>I</i> ₍₀₀₄₎
LR1	2.8552	14.2299	4.984	1.7736
LR2	2.8525	14.2193	4.985	1.6406

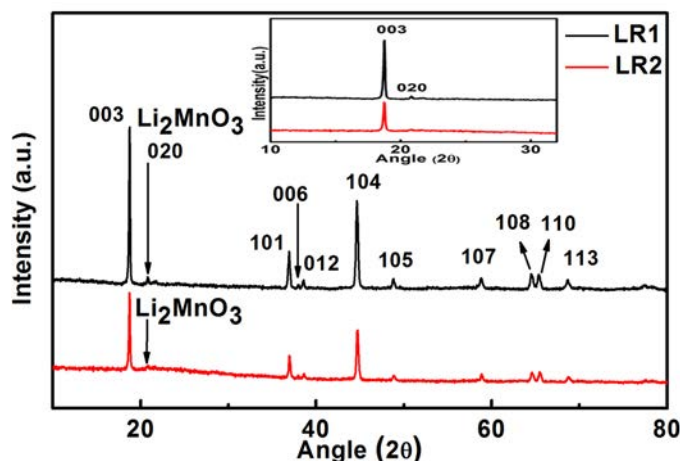


Figure I.2.I.4 XRD patterns of the as-prepared LR1 and LR2 showing typical diffraction peaks of Li-rich materials.

Solution-based Coating Process to Stabilize Battery Powders

Effort has been made to study a solution-based coating process for stabilizing active powders. This effort makes it convenient to design coating conditions with a chosen coating material. Figure I.2.I.5 shows a result on Al_2O_3 nanocoating on a nickel-rich NMC material that was prepared in a co-precipitation process. Elemental mapping shows that alumina (0.8wt.%) was uniformly coated on the surface of the powders.

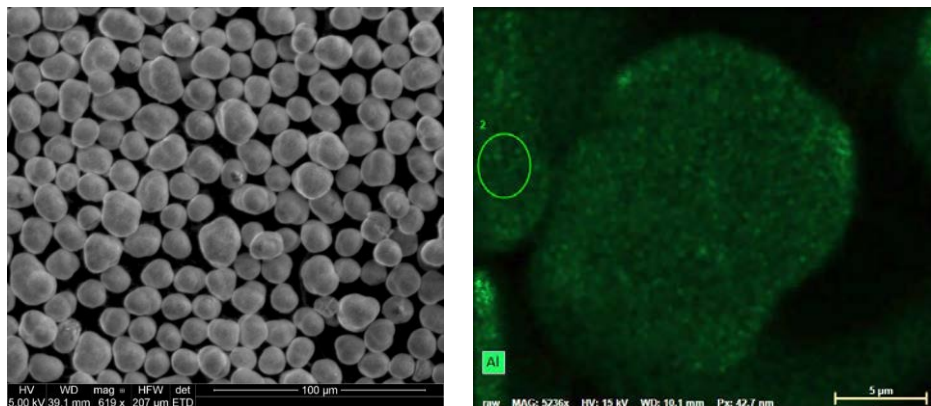


Figure I.2.I.5 SEM image of a Ni-rich NMC powders and a mapping of the Al element on a particle surface, showing Al was uniform on the surface of the particle.

Coin cell tests showed improved material performance in term of stability, as shown in Figure I.2.I.6. The charge-discharge curves are from the 1st cycle to 100th cycle. The powder as prepared showed a large capacity loss during cycling, but the Al_2O_3 coated powders showed much less percentage loss. The stability of the Al_2O_3 coated NMC powders is obviously improved. There is a decrease in overall capacity of the powders after Al_2O_3 coating, which was attributed to that Al_2O_3 is not an active material and therefore it would somewhat compromise the specific capacity.

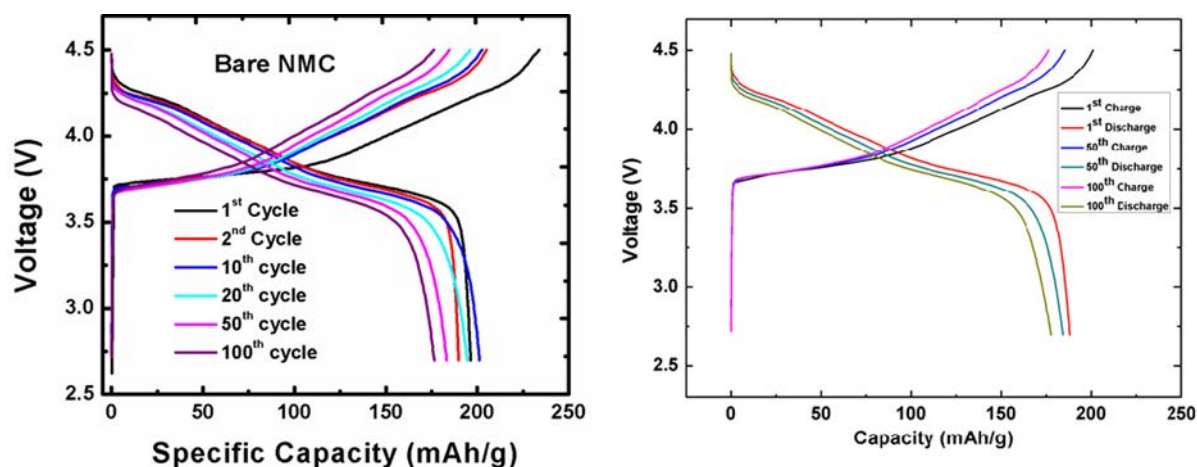


Figure I.2.I.6 Charge-discharge profiles on bare (previously presented) and Al_2O_3 coated NMC powders (new results). The coated NMC shows improved stability.

The coating process is a solution-based process and can coat various materials on powders. It does not involve expensive equipment and can be adapted to different chemical precursors, including metal alkyls and metal alkoxides. The coating thickness can be controlled from a few nanometers to a few tens of nanometers.

Conclusions

1. Study on the flame spray process showed that the NMC111 powder morphology can be controlled by controlling the flame reactor temperatures. In particular, low temperatures tend to produce wrinkled particles with a high surface area, but high temperatures tend to generate smooth spherical particles.
2. Study also showed that the DES precursors can have a large effect on powder morphology. In particular, the particles can be made into spheres with a change in the DES precursors.
3. The DES chemical precursors were also studied in thermal pyrolysis to make Li-rich powders. It was shown that the powders have good electrochemical performances with a continuous activation process. Furthermore, the produced powders showed low cationic mixing, demonstrating that the DES chemical precursors have their uniqueness in the synthesis of battery powders.
4. It was demonstrated that our coating process can coat battery powders with different materials. The Al₂O₃ nanocoatings showed they can stabilize Ni-rich materials.

Key Publications

1. Hamad, K.I. and Xing, Y., “Effect of Cobalt and Nickel Contents on the Performance of Lithium Rich Materials Synthesized in Glycerol Solvent”, *Journal of The Electrochemical Society*, 165, A2470-A2475, 2018.
2. Xing, Y. (invited), “Renewable Solvents to Replace Water in the Synthesis of Battery Materials”, presented at the 8th World Congress on Particle Technology, Orlando, FL, April 22-26, 2018.
3. Hamad, K.I. and Xing, Y. “Lithium Ion Cathode Materials Prepared Using Glycerol as Solvent and Reactant”, presented at the 2018 AIChE Annual Meeting, Pittsburg, PA, October 28 - November 2, 2018.

Acknowledgements

EaglePicher Technologies is a partner in this project with Dr. Hyun Joo Bang as project lead. We thank program manager Walter G. Parker at NETL and technology managers Dr. Ahmad Pesaran and Dr. Jack B. Deppe for their project management and support in this work.

I.2.J High Performance Li-Ion Battery Anodes from Electrospun Nanoparticle/Conducting Polymer Nanofibers (Vanderbilt University)

Peter N. Pintauro, Principal Investigator

Vanderbilt University
 Department of Chemical and Biomolecular Engineering
 Nashville, TN 37235
 E-mail: pn.pintauro@vanderbilt.edu

Peter Faguy, DOE Technology Development Manager

U.S. Department of Energy
 E-mail: Peter.Faguy@ee.doe.gov

Start Date: October 1, 2015

End Date: September 20, 2019

Project Funding: \$706,062

DOE share: \$590,000

Non-DOE share: \$116,062

Project Introduction

Si is an attractive replacement for graphite in Li-ion battery anodes due to its high theoretical capacity (3,600 mAh/g for $\text{Li}_{15}\text{Si}_4$ vs. 372 mAh/g for LiC_6) and low operating potential (< 0.5 V vs. Li/Li+). However, Si-based anodes often exhibit poor stability during charging and discharging due to large volume changes and particle pulverization during cycling as well as instabilities associated with the solid electrolyte interphase (SEI) layer. The use of Si nanoparticles and nanowires has shown promise, but the active material loading in such nano-Si anodes is low, resulting in low areal and volumetric capacities. Thus, there is a need for new anode designs which can tolerate Si volumetric changes while maintaining high gravimetric, areal, and volumetric capacities over many charge/discharge cycles at low and high C-rates.

Objectives

The objectives of this project are to fabricate an electrospun Li-ion battery nanofiber anode and demonstrate its superior performance in half-cell and full-cells. The fiber mat anode is expected to outperform current state-of-the-art thin film slurry anodes, in terms of volumetric capacity and rate capability, and could enable a substantial reduction in the weight and size of an electric vehicle battery. The project will also demonstrate that the fiber mat anode can be manufactured in large scale at a commercial electrospinning facility. Experiments will focus on optimizing the composition and morphology of Si-based nanofiber anodes with a non-conducting polymer binder for lithium ion batteries. Such anodes will be designed for high gravimetric and volumetric energy densities, e.g., an initial capacity of 1,200 mAh/g and 1-2 mAh/cm² with 90% capacity retention after 200 cycles at 0.1C and a capacity of 500 mAh/g after 200 cycles at 2C which is recoverable to at least 1,000 mAh/g at the lower charge rate of 0.1C. The project will also generate useful correlations and insightful understandings regarding the composition, structure, and performance of electrospun Si anodes.

Approach

This project is an extension of the PI's prior successes in using neat polymer and particle/polymer nanofiber electrospinning for membranes and electrodes in electrochemical devices. In prior published studies, fiber-based Li-ion battery electrodes were prepared by carbonizing polymeric electrospun fiber precursors at high temperature. In particle/polymer electrospinning, there is no fiber pyrolysis; the electrospinning and post-processing are performed at room temperature to preserve the beneficial properties of the polymer binder and to insure an electrode with a high fiber volume fraction. High gravimetric, areal, and volumetric capacities are achieved at fast charge/discharge rates through the use of thick, densely packed particle/polymer nanofiber mats. Four key tasks will be performed in the project: (1) Synthesis, optimization and testing of conducting polymer binders; (2) Electrospinning and post-processing of composite nanofiber mat anodes of Si nanoparticles with a conducting binder or with electrically conducting carbon powder and a non-conducting binder; (3) Evaluation of short-term and long-term performance of electrospun anodes in half-cells and full-cells (with a NMC cathode) followed by post-mortem characterization; and (4) Preliminary scale-up of anode

fiber mat manufacturing at a commercial electrospinning facility, where the resultant materials meet the project performance targets. Experiments during this reporting period focused on: (a) single fiber mats composed of Si and carbon particles in a suitable polymer binder; (b) dual fiber mat anodes, where one fiber type contains Si nanoparticles and binder and the second fiber is composed of carbon powder and binder; and (c) an electrospayed anode composed of Si nanoparticles and carbon powder with a new thermally crosslinked polymer binder. The national laboratory partner on this project is Dr. Jagjit Nanda at Oak Ridge National Laboratory (ORNL) who is overseeing electrode characterization experiments. eSpin Technologies, Inc. is a subcontractor on the project and will be prepare fiber mat anodes on their commercial electrospinning equipment.

Results

Electrospinning and Testing of Dual Fiber Anodes

Dual fiber anodes were the major subject of the reported year's (2018) work. Experiments were carried out to increase both the quality and the performance of Si-poly(acrylic acid) (abbreviated as PAA) and C-PAN fibers. Specifically, an increase in areal capacity from 0.7 mAh/cm² achieved in 2017 with dual fiber anodes to >1 mAh/cm², was a major undertaking in 2018. Improvements in C-PAN and Si-PAA fiber quality was accomplished through ink composition and electrospinning conditions optimization. This led to improvement in the uniformity of fibers in an electrospun dual fiber mat. Experiments also dealt with the optimization of mat compaction pressure and organic DMF vapor exposure time. At the present time, the best post-electrospinning steps for a dual fiber mat are 1 hr DMF vapor exposure at room temperature, followed by 1 min. 28 MPa pressure.

A representative example of a well-performing dual fiber anode is shown in Figure I.2.J.1. The anode was fabricated concurrent electrospinning suspensions containing Si-PAA in n-propanol/methanol and Vulcan XC72R-PAN in DMF/DMSO. The flowrates of the two spinning suspensions (1.2 ml/h for Si-PAA and 0.2 ml/g for C-PAN) were fixed to obtain a mat containing 51 wt.% Si, 9 wt.% C and 40 wt.% PAA+PAN binders. After DMF vapor exposure and hydraulic press densification, 10 mm discs were cut, annealed for 2h at 120°C, and then transferred to a glovebox for half-cells assembly. Generation 2 electrolyte was employed (1.2 M LiPF₆ in 3/7 EC/EMC with 10 wt.% FEC additive) along with Celgard separators and Li metal disks that served as counter/reference electrodes. The half cells were galvanostatically charged/discharged between 0.015 V and 1.5 V, typically for 5 cycles at a rate of 0.1C and then for 50 cycles at a rate of 1C. An example cycling performance of one of the best dual fiber anodes is shown in Figure I.2.J.2a. The terminal discharge capacity after 50 cycles at 1C is 604 mAh/g (gravimetric) and 1.58 mAh/cm² (areal). The anode showed no visible damages after the cycling and extraction from the cell (Figure 2b). The surface of the raw dual fiber Si-PAA/C-PAN mat is shown in Figure I.2.J.2c; fibers of uniform diameter are evident. In Figure I.2.J.2d, a SEM image of the surface of the compacted anode is shown. A significant level of densification, as compared to that of the raw mat can be seen, however, the exact porosity is unknown.

Due to a relatively narrow range of compositions for well-formed Si-PAA and C-PAN fibers, most of the dual fiber mats that exhibited good cycling stability had a terminal gravimetric capacity of 500-700 mAh/g and an areal capacity of 0.8-1.5 mAh/cm² after 50 cycles at 1C. In the final year of this project, capacities will be increased to at least 1000 mAh/g and 2.0 mAh/cm² by: (1) decreasing the content of the PAA and PAN binders in the mat, (2) decreasing the amount of carbon powder (decreasing the number of carbon fibers) in a dual fiber mat, and (3) increasing the mat compaction level (decreasing the residual mat porosity).

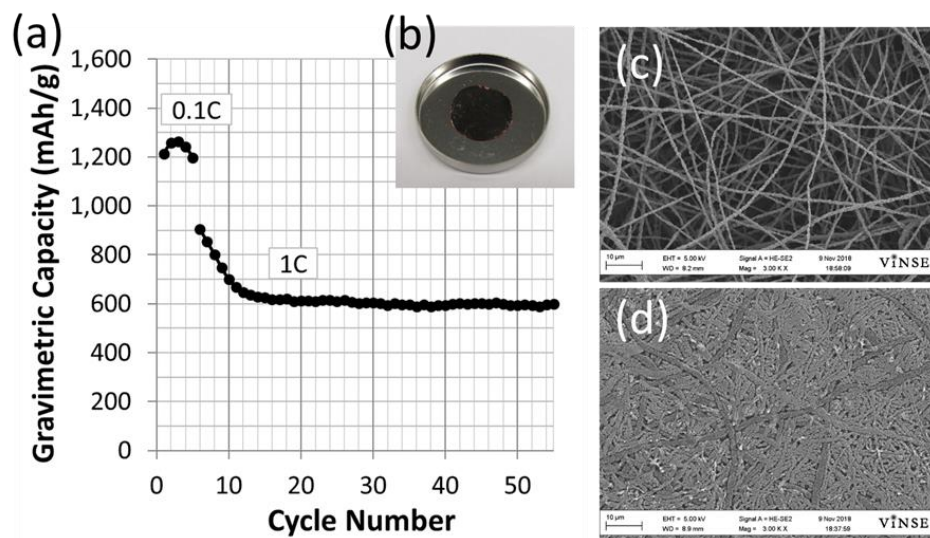


Figure I.2.J.1 (a) Cycling results (discharge curve) for a Li-ion half-cell with anode prepared from a dual fiber Si-PAA/C-PAN mat. The first 5 cycles were carried out at 0.1C and the remaining 50 cycles at 1C; terminal discharge capacity at 1C was 604 mAh/g (gravimetric) and 1.58 mAh/cm² (areal), (b) Photograph of the anode extracted from the cell after cycling at 1C, demonstrating excellent integrity of the fibrous structure, (c) Surface SEM image of the raw mat (51 wt.% Si, 9 wt.% C and 40 wt.% PAA+PAN in the fibers), and (d) Surface SEM of the compacted mat from Figure 1c.

Demonstrating an Electrospun Anode that Meets the Go/No-Go 2018 Milestone

The September 2018 Go/No-Go milestone for this project is: “Demonstrate a discharge capacity above 750 mAh/g after 50 cycles at 0.1C charge/discharge rate, and a capacity above 500 mAh/g after 50 cycles at 1C with an areal capacity of 1-2 mAh/cm².” This Go/No-Go milestone was successfully met with a dual-fiber Si-PAA/C-PAN electrospun fiber mat anode. The mat was electrospun from separate suspensions of carbon black and Si nanopowder. The carbon suspension was composed of 7.4 wt.% Vulcan XC-72R, 1 wt.% conductive carbon from US Research Nanomaterials, 5.4 wt.% polyacrylonitrile (PAN) binder, 61.6 wt.% of DMF and 24.6 wt.% DMSO. The Si suspension was composed of 8.8 wt.% Si nanoparticles (50 nm diameter), 6.1 wt.% poly(acrylic acid) (PAA), 48.6 wt.% n-propanol and 36.5 wt.% methanol. The flowrates were 0.6 ml/h and 0.9 ml/h, for the carbon and Si suspensions, respectively. The resultant mat had the following (calculated) composition: 26 wt.% C, 34 wt.% Si and 40 wt.% binders (a combination of PAN and PAA). The mat was cut into rectangles 3.5 cm x 4.5 cm and each rectangular piece was compressed at 24,000 lb. for 1 min. The densified anodes were exposed to methanol vapor and then to DMF vapor for 20 min each (to weld intersecting fibers), then dried under vacuum at 70°C for 15 min (the solvent vapor step was used to weld fibers). The welded samples were heated at 120°C under vacuum for 1 hour and 1 cm diameter discs were cut, weighed and reheated at 120°C under vacuum for an additional 1 hour before transferring to a glovebox for half-cell assembly. As can be seen in Figure I.2.J.2, this anode performed well with a terminal gravimetric capacity of 1000 mAh/g after 50 cycles at 0.1C and a capacity of 611 mAh/g after 50 cycles at 1C. The terminal areal capacity was 2.4 mAh/cm² at 0.1C and 1.5 mAh/cm² at 1C, better than the Go/No-Go target of 1 mAh/cm².

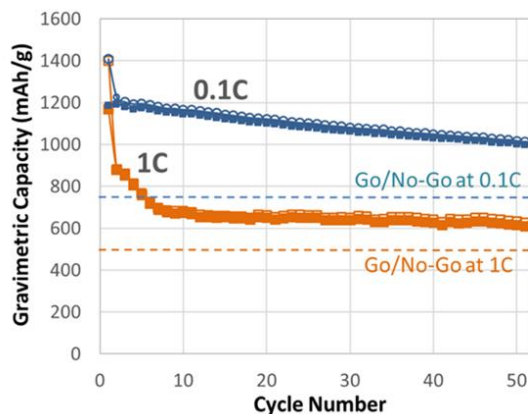


Figure I.2.J.2 Cycling results for Li-ion half-cells with anodes prepared from the same C-PAN/Si-PAA dual fiber mat. Both cells were subjected to one charge/discharge cycle at 0.1C followed by 50 cycles at either 0.1C or 1C. The charge/discharge capacity after 50 cycles is above the project's Go/No-Go target. The terminal discharge capacity for the anode cycled at 0.1C is 1000 mAh/g (gravimetric) and 2.4 mAh/cm² (areal). The terminal discharge capacity at 1C is 611 mAh/g (gravimetric) and 1.5 mAh/cm² (areal). The coulombic efficiency is in the range of 98-99% for the both anodes.

Anodes Fabricated by Concurrent Electrospinning of Si-PAA and Electrospaying of C-PVDF

The creation of well-formed electrospun particle/polymer fiber systems is more demanding than electrospinning of polymers, in that it operates within a narrow range of operational parameters (humidity, temperature, flowrate, and spinneret-collector distance) and it typically requires a significant fraction of a polymeric binder in the electrospinning solution. High polymer loading improves anode robustness but at the same time imposes a limit on its charge storage capacity. As part of the Y2018 effort, an experiment was performed to explore combined electrospaying and electrospinning for the fabrication of a Si/C anode. A mat was fabricated from electrospun Si-PAA fiber (40 wt.% PAA) and electrospayed C-PVDF droplets (37 wt.% PVDF). The SEM images of an as-spun mat and compacted/welded anode mat are shown in Figure I.2.J.3a and Figure I.2.J.3b, respectively. Well-developed Si-PAA fibers can be seen, whereas C-PVDF was distributed through the mat as either sub-micron clusters or very fine beads that deposited onto the Si-PAA fibers. Fiber mat samples were exposed to DMF vapor for 1 h (to weld intersecting fibers), compressed for 1 min to increase the fiber volume fraction, and then heated at 120°C under vacuum for 2 hours to remove residual solvent. Raw mat densification was moderate (Figure I.2.J.3b) and thus the anode porosity was relatively high compared to that of a typical dual fiber anode (cf. Figure I.2.J.1d). The resultant anode had the following (calculated) composition: 36 wt.% Si, 26 wt.% C, and 38 wt.% binders (a combination of PVDF and PAA). As can be seen in Figure I.2.J.3c, duplicate half-cells with this anode performed well; during the initial formation at 0.1C the gravimetric capacity increased to slightly above 1000 mAh/g and after switching to 1C rate, the capacity decreased to 600 mAh/g within seven cycles and stabilized at this level throughout the cycling. The terminal areal capacity was 1.0 mAh/cm² after 50 cycles at 1C.

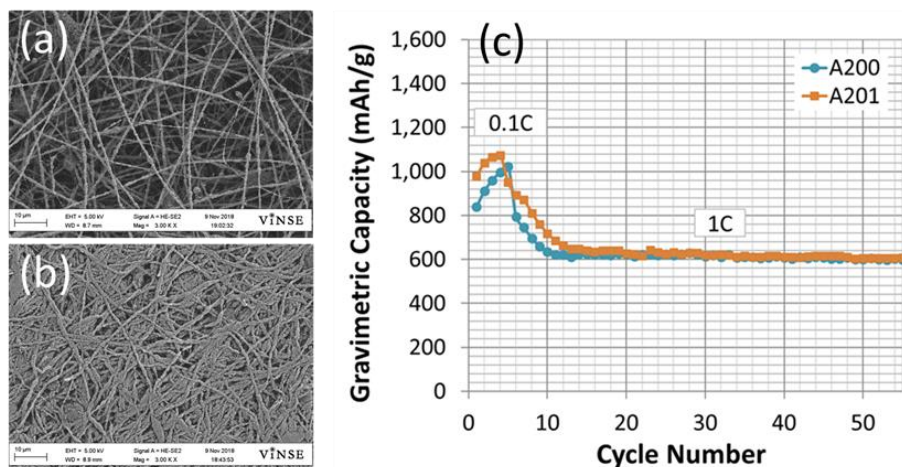


Figure I.2.J.3 (a) Surface SEM image of the raw mat obtained by concurrent electrospinning of Si-PAA and electrospinning of C-PVDF, (b) Surface SEM of the compacted/welded mat from Figure 3a, and (c) Cycling results (discharge curves) for two Li-ion half-cells with anodes (A200 and A201) prepared from the compacted/welded mat. The first 5 cycles were at 0.1C and the remaining 50 cycles at 1C; terminal discharge capacity at 1C was 600 mAh/g (gravimetric) and 1 mAh/cm² (areal).

Fabricating and Testing Si-PAA Fiber Anodes with No Carbon

In order to analyze the separate contributions of Si-PAA and C-PAN fibers to the overall Li storage capacity of electrospun dual fiber anodes, Si-PAA single fiber anodes of different Si loading were electrospun, compacted, welded and tested in half-cells. The raw mats Figure I.2.J.4a were exposed to DMF vapor for 1 h at room temperature (to weld intersecting fibers) followed by compaction at 28 MPa for 1 minutes and annealing for 2 h at 120°C. The resulting compacted welded mat is shown in Figure I.2.J.4b. Anodes were kept overnight at 70°C under vacuum before coin cell assembly in a glove box. Surprisingly, the carbon-less anodes performed well in these coin cell experiments, with a stable charge-discharge capacity at 1C for at least 50 cycles. Representative examples of two Si/PAA fiber anodes with a Si content of 64% (an areal loading of 0.46 mg/cm²) or 60 wt.% (a thicker anode with an areal loading of 1.71 mg/cm²) are shown in Figure I.2.J.4c. As can be seen, the thinner anode showed a very high and stable gravimetric capacity of 1,400 mAh/g over 55 cycles at 1C, (with a terminal areal capacity of 0.66 mAh/cm²). The thicker anode also exhibited very good performance, with a gravimetric capacity of 600 mAh/g after 55 cycles at 1C, with a terminal areal capacity of 1.06 mAh/cm². These results are better than those reported in the literature for binderless Si nanofiber-based papers with/without carbon coating [1].

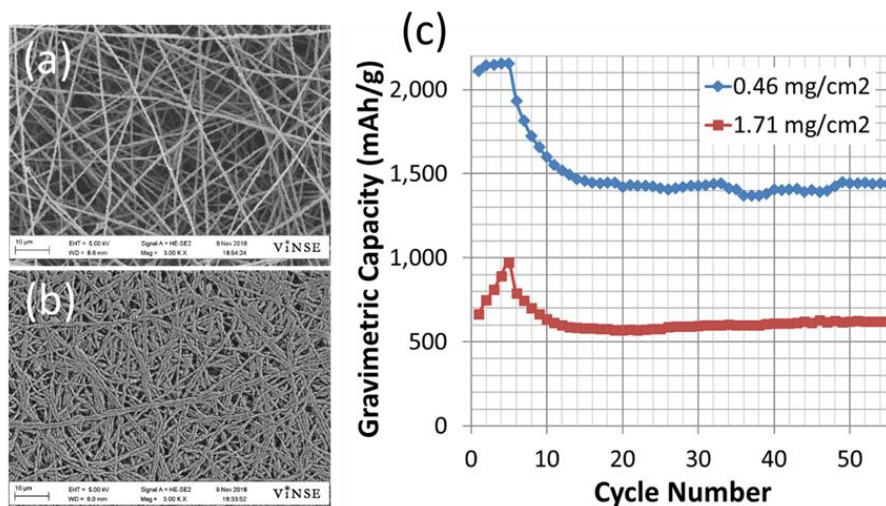


Figure 1.2.J.4 (a) Surface SEM image of an as-spun mat of Si/PAA nanofibers (40 wt.% PAA in Si-PAA fibers), (b) Surface SEM of the welded/compacted mat from Figure 4a, and (c) (a) Cycling results (discharge curves) for Li-ion half-cells with anodes prepared from a thinner ($5\ \mu\text{m}$ and $0.46\ \text{mg}/\text{cm}^2$) and thicker ($25\ \mu\text{m}$ and $1.71\ \text{mg}/\text{cm}^2$) electrospun and compacted/welded Si-PAA fiber mats. The first 5 cycles were at 0.1C and the remaining 50 cycles at 1C ; terminal discharge capacity at 1C was $1400\ \text{mAh}/\text{g}$ (gravimetric) and $0.7\ \text{mAh}/\text{cm}^2$ (areal), for the thinner anode and $600\ \text{mAh}/\text{g}$ and $1.1\ \text{mAh}/\text{cm}^2$ for the thicker anode

Conclusions

(1) The areal capacity of a dual fiber electrospun Si-based anode (with Si-PAA and C-PAN fibers) has been double this year, from 0.7 to $1.6\ \text{mAh}/\text{cm}^2$, (2) single fiber Si-PAA anodes with no electrically conductive carbon powder performed surprisingly well in half-cell tests, with a gravimetric capacity of $660\ \text{mAh}/\text{g}$ and an areal capacity of $1.06\ \text{mAh}/\text{cm}^2$ after 50 cycles at 1C , and (3) The 2018 Go/No-Go gravimetric capacity milestone has been met/exceeded with a dual fiber electrospun mat. For next year, experiments will focus on: (1) Selecting the best electrospun Si-fiber anode system (single fiber or dual fiber), with an increase in gravimetric capacity (to $1,000\ \text{mAh}/\text{g}$) and areal capacity (to $2.0\ \text{mAh}/\text{cm}^2$) after 100 cycles at 1C . Full cell tests will be performed with lithiated PAA and a NMC cathode from Argonne National Laboratory.

Key Publications

1. Pintauro et al., Dual Fiber Electrospun Anodes for Li-Ion Batteries (2018) – in preparation
2. Pintauro et al., Electrospun Si-PAA Fiber Anodes for Li-Ion Batteries (2018) – in preparation

References

1. Z. Favors et al., “Towards Scalable Binderless Electrodes: Carbon Coated Silicon Nanofiber Paper via Mg Reduction of Electrospun SiO_2 Nanofibers,” Scientific Reports, 5:8246 (2014). <https://www.nature.com/articles/srep08246.pdf>

Acknowledgements

The PI would like to acknowledge Dr. Abhishek Mondal and Dr. Ryszard Wycisk from Vanderbilt University and Dr. Ethan Self and Dr. Jagjit Nanda from ORNL for their contributions to the project.

I.2.K Process R&D and Scale up of Critical Battery Materials (ANL)

Gregory Krumdick, Principal Investigator

Argonne National Laboratory
9700 S Cass Avenue
Lemont, IL 60439
E-Mail: gkrumdick@anl.gov

Peter Faguy, DOE Technology Development Manager

U.S. Department of Energy
E-mail: Peter.Faguy@ee.doe.gov

Start Date: October 1, 2017

End Date: September 30, 2018

Project Funding (FY18): \$950,000

DOE share: \$950,000

Non-DOE share: \$0

Project Introduction

New, experimental materials are being constantly invented to improve the safety, energy density, cycle, and calendar life of lithium ion batteries for HEV and PHEV applications. These materials are typically synthesized in discovery laboratories in small batches providing amounts sufficient only for limited basic evaluation but not in quantities required for full scale validation and prototyping. In addition, bench-scale processes are often un-optimized, not validated, and generate materials with inconsistent purity and yield. The project is aim to assist advanced battery research community by enabling access to larger quantities of high quality innovative materials.

Objectives

The objective of this project is to conduct research toward scaling up production of advanced materials for Li-ion batteries originally created in small quantities by discovery scientist. Scaling up the original route used by discovery scientists requires often an extensive modification of the bench-scale chemistry and systematic, scientific-based process R&D to allow for safe and cost effective production, development of an engineering flow diagram, design of a mini-scale system layout, construction of the experimental system, and validation of the optimized process. The experimental system will be assembled and the materials will be manufactured in quantities sufficient for full scale industrial evaluation. The materials produced by the program will be fully characterized to confirm chemical identity and purity. Analytical methods will be developed for quality control. The electrochemical performance of the materials will be validated to confirm that the properties match the original sample generated by the discovery scientist. Sample of the materials produced by the project will be available to advanced LIBs research community to support basic development and large scale performance validation.

Approach

New materials for experimental electrolyte formulations often have complex molecular structure that translates frequently into increased synthesis difficulties and cost. Materials Engineering Research Facility (MERF) at Argonne is evaluating emerging production technologies to address the challenges. A comprehensive, systematic approach to scale-up of advanced battery materials has been defined. This approach starts with the original route the new material was first made in the discovery lab and initial electrochemical evaluation. This determines if the material is to be added to the inventory database, ranked, prioritized and selected for scale up. MERF prioritizes new materials based on level of interest, validated performance and scale up feasibility. The new candidate materials for scale up are discuss with DOE for final approval. MERF evaluates several approaches, including non-standard manufacturing technologies, to determine the best approach to scale up each particular material. One of such technology is Continuous Flow Chemical Reactor that enables the continuous synthesis of materials from discovery through process development and production scale. Continuous flow reactor can be used for rapid screening of reaction condition to better understand fundamentals of process kinetic and thermodynamic. The technology offers cost-effective and safer alternative

to traditional batch processes by improving material and energy usage and minimize environmental impact of the manufacturing operation. At this point, the scale-up process begins with a feasibility study, followed by proof of concept testing, 1st stage scale-up and final 2nd scale scale-up. Several Go/No Go decisions are located after feasibility determination and electrochemical validation testing. For each material, we will develop a scalable manufacturing process, analytical methods and quality control procedures. We will also prepare a “technology transfer package” which includes detailed procedure of the revised process for material synthesis, materials balance, analytical methods and results (Specification Sheet) and SDS for the material. The detailed process description allows for preliminary estimates of production cost, an important factor for decision making in industry. We apply the newly developed process to make kilogram quantities of the material. We will fully characterize chemically each material and make samples available for industrial evaluation and to the research community. We will also provide feedback to discovery chemist helping guide future research.

Results

1. Flow Chemistry Synthesis of Sulfone Electrolyte Solvents Ethyl and Propyl Trifluoromethyl Sulfone.

As reported last year, these solvents are promising solvents for high voltage LIBs electrolyte formulations, however, there are only a very few references to these compounds [1], [2], [3], [4]. MERF had successfully scaled-up these materials in batch processes, but concluded that the current process is extremely exothermic and is not suitable for larger scale production.

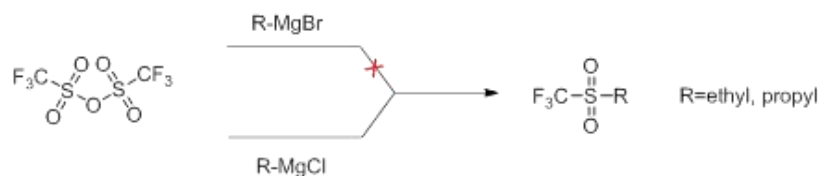


Figure I.2.K.1 Batch synthesis of ethyl and propyl trifluoroethyl sulfones.

We have now investigated continuous flow reactor processes as a technology platform to manufacture ethyl and propyl trifluoromethyl sulfones. Several challenges were encountered. Unlike batch processes, flow chemistry is extremely sensitive to the presence of solid particles, which readily clog the narrow diameter channels and thereby shut down the process. This precluded the use of microchannel flow reactors, but allowed the use of standard tube flow reactor equipment. Acceptable conversions to propyl trifluoroethyl sulfone are obtained in these tubular flow synthesis reactors under non-cryogenic conditions.

We found a preferred temperature regime at 0-5°C where the product is generated in the highest yields (Figure I.2.K.2). Higher temperatures result in greater side products, while lower temperatures appear to inhibit the reaction. Even with these short reaction times, there is substantial byproduct accumulation which complicated the purification.

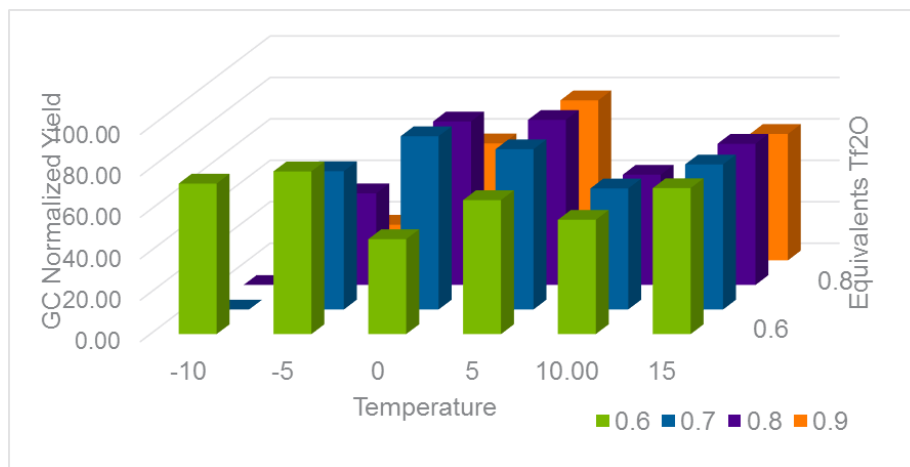


Figure I.2.K.2 Screening of flow synthesis conditions for propyl trifluoromethyl sulfone

2. Flow Chemistry Synthesis of Lithium TDI.

Recently, Li-TDI (Lithium 4,5-dicyano-2-(trifluoromethyl)imidazole) has been reported as an electrolyte stabilizing additive [5]. The batch process (Figure I.2.K.3) involved an initial cold step, followed by heating the intermediate to form the cyclized form. We re-investigated the synthesis of the parent acid (H-TDI) using a flow chemistry platform, with the premise that a dual flow ship system could reproduce the dual temperature profile of the batch synthesis.

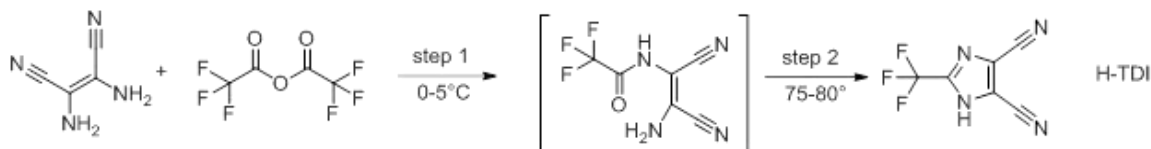


Figure I.2.K.3 Batch Conditions for the Synthesis of H-TDI

Initial results indicated that the temperature of the first microreactor chip was not a critical factor- unlike the batch process which depended on a low temperature (0=5°C) profile to ensure a clean acylation, but also that the first chip temperature could be run as high a 60°C with good results. This is likely a function of the better mixing profile of flow reactors relative to batch processes. The overall process was performed in good conversion using high (160-170°C) temperature in THF (tetrahydrofuran) at a relatively high pressure of 12-15 bar.

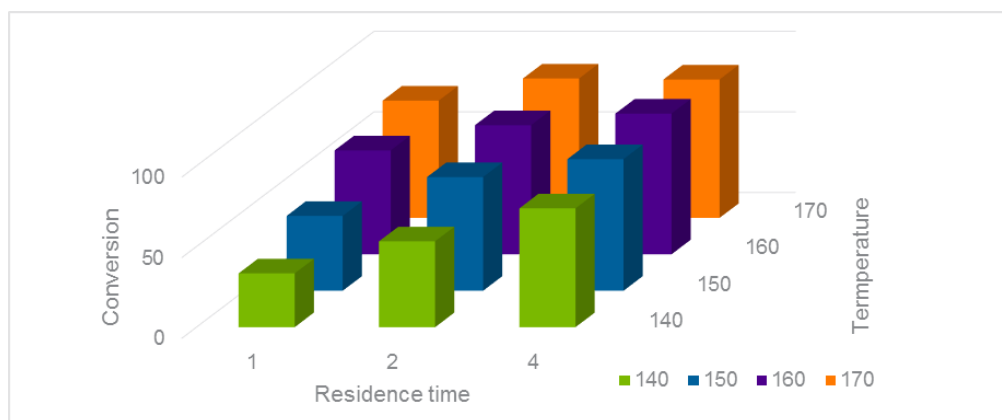


Figure I.2.K.4 Conversion data for H-TDI as a function of time and temperature

3. Large Scale Synthesis of Al-LLZO Precursors

Al-doped LLZO (lithium lanthanum zirconium oxide, $\text{Li}_7\text{La}_3\text{Zr}_2\text{O}_{12}$) remains a much sought-after material for use in solid state lithium ion batteries [6], [7]. One synthesis methodology for this compound is flame spray pyrolysis (FSP), which requires specialized metal precursors. MERF has successfully scaled up multiple materials for this as well as developing new precursor solutions for use. It was found that not only are there solubility and solution stability drawbacks in using lanthanum and zirconium isobutyrate in the FSP process, there are unreported reaction hazards as well. Lanthanum oxide was measured by reaction calorimetry to react with isobutyric acid with an average heat of reaction of 370 kJ/mol; as the average energy release over 5 separate but non-equal charges of La_2O_3 .

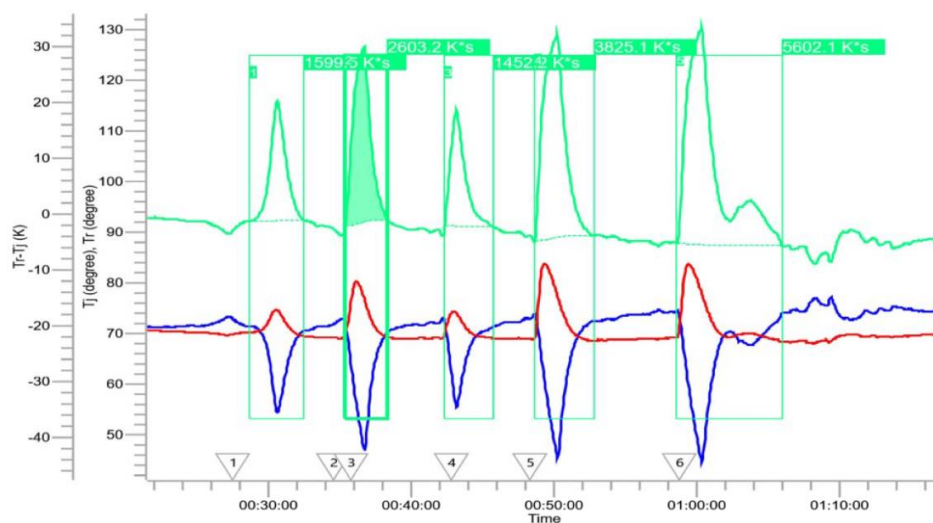


Figure I.2.K.5 Reaction calorimetry data

MERF successfully developed a newer safe procedure and supplied several batches of material ranging from 50-400g for all the requested propionate and isobutyrate metal precursors (Figure I.2.K.6).

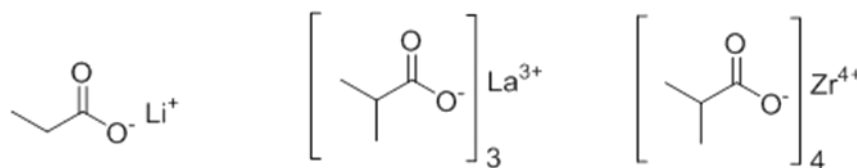


Figure I.2.K.6 Structure of literature FSP precursors synthesized at MERF

Early analysis of the MERF-developed metal-containing FSP precursors showed higher solubility, better stability, and equivalent performance in the liquid-feed FSP experiments. Importantly, the synthetic processes developed for these materials did not exhibit any large exothermic events, and were operationally less complex than the literature propionate and isobutyrate processes. These materials were provided in multi-kilo amounts to the FSP facility.

4. Novel silicon-containing carbonate solvents in continuous flow and batch

In the quest for materials that offer improved safety without sacrificing performance we are continuing to synthesize and investigate a series of electrolyte carbonate solvents containing silicon atoms. Earlier work focused on the transesterification of dimethyl carbonate with (trimethylsilyl)methanol [8], which was evaluated as candidate for a continuous flow manufacturing process. Screening of several catalysts and various reaction conditions in batch and continuous flow mode revealed that the material can be made in continuous flow reactor in more feasible manner than in batch and was successfully scaled up in continuous mode using a solid

catalyst reactor. In a similar vein, similar materials with two silicon atoms was developed (Figure I.2.K.7). We assume that increasing number of Si atoms in the molecule should enhance the desired property of the material (flame retarding/propagation).

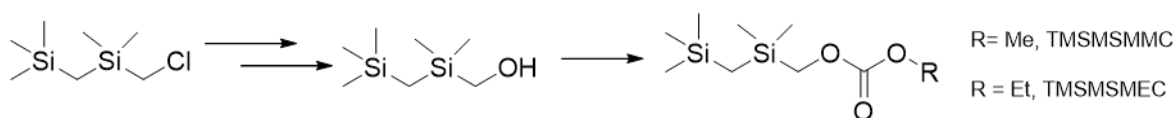


Figure I.2.K.7 Route for novel disilylcarbonate electrolyte solvents invented and developed at MERF

The new disilyl-substituted alcohol was screened in our flow system, using dimethyl carbonate as a reactant and solvent, evaluating the effect of reaction time, temperature and concentration on the reaction conversion (Figure I.2.K.8). As expected, higher temperatures, longer reaction times, and greater ratios of dimethylcarbonate to substrate all contribute positively to higher conversion to the desired silicon-containing carbonate.

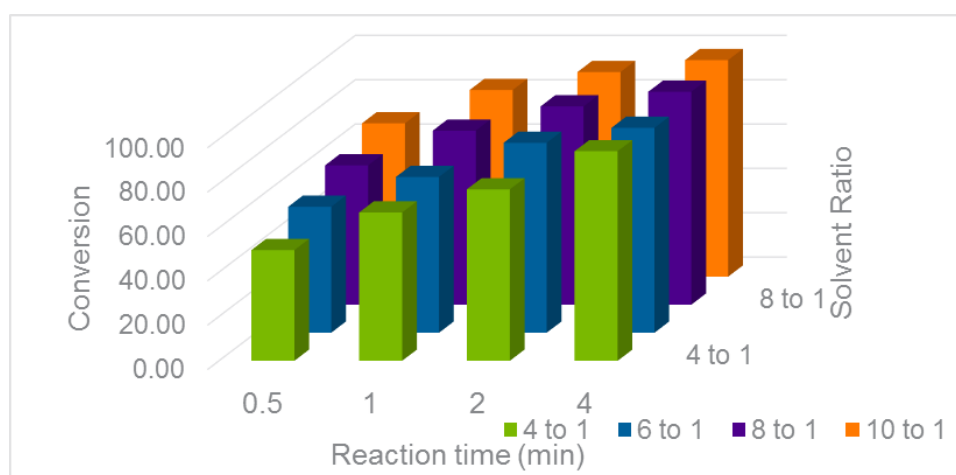


Figure I.2.K.8 Conversion dependence on reaction conditions for $\text{Me}_3\text{SiCH}_2\text{SiMe}_2\text{CH}_2\text{OC(O)OMe}$

These materials were then evaluated in coin cells for basic electrochemical performance relative to the standard Generation 2 (Gen 2) electrolyte. These molecules with two silicon atoms showed increased safety properties such as higher flash point and boiling points, but also showed slightly lower electrochemical performance evidenced in a slightly lower capacity. In contrast with the monosilylated compounds, the disilyl (ethyl) carbonate (TMSMSMEC) showed slightly better performance than the methyl carbonate (TMSMSMMC). Up to 10 wt % replacement of TMSMSMMC in Gen 2 electrolyte formulation did not show an appreciable loss of performance of the cell (Figure I.2.K.9).

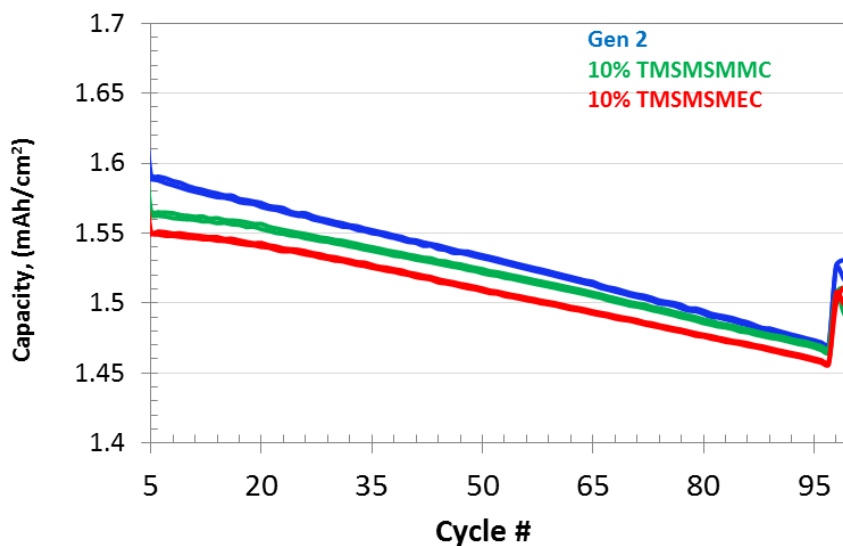


Figure I.2.K.9 10% w/w TMSMSMMC and TMSMSMEC in Gen2, graphite//NCM523, 3.0 - 4.4 V cycling (Ch/DCh at C/3), 30°C.

We plan for extensive safety evaluation of the new electrolyte formulation in various cell chemistries.

Several other silicon-containing carbonate solvents have been invented, synthesized and tested at MERF using a different synthetic processes (Figure I.2.K.10). This process, based on the sequential reaction of two alcohol substrate with 1,1'-carbonyldiimidazole (CDI), is useful for producing a wide range of symmetric and non-symmetric carbonates.

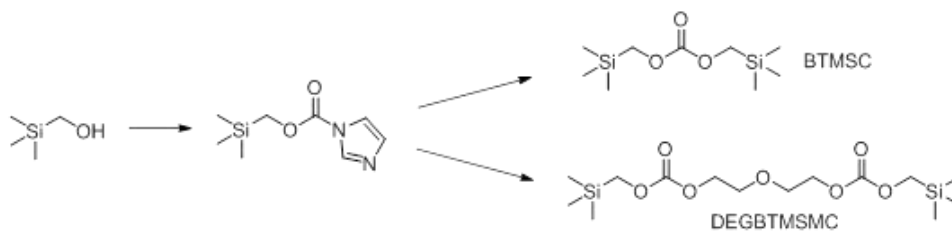


Figure I.2.K.10 Synthesis of Si-containing carbonate solvents

These materials were evaluated for electrochemical performance as well, and revealed that up to 10% EMC with DEGBTMSC in the Gen2 electrolyte formulation did not show a dramatic decrease in the cell performance (Figure I.2.K.11). Replacement of 5% EMC with BTMSC, however, actually evidenced an increased performance of the cell (CR2032, gr/NCM523, 3.0 - 4.4 V, C/3, 30°C) over the plain Gen2 electrolyte.

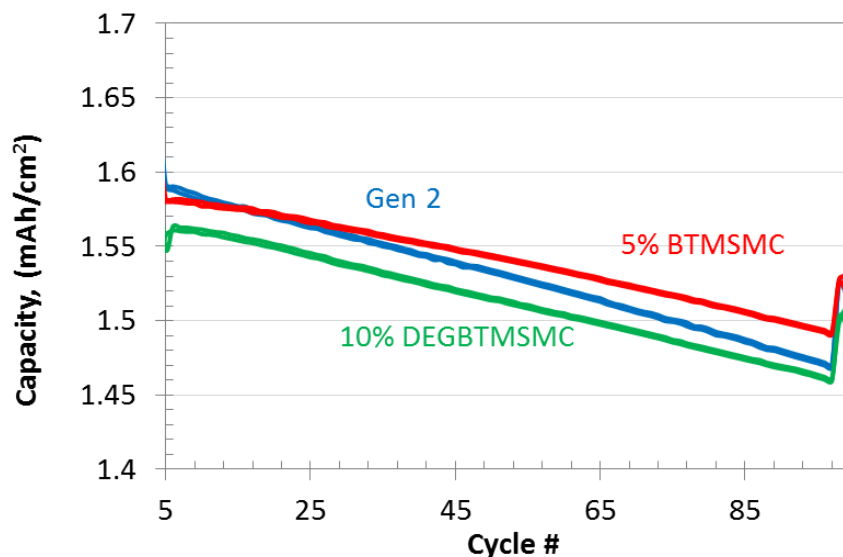


Figure I.2.K.11 Cell performance of BTMSMC and DEGBTMSMC additives to Gen2 electrolyte.

Samples of selected electrolyte formulations containing the new materials will be provided to Argonne's CAMP facility for thorough evaluation. Materials (electrolyte formulations) with acceptable electrochemical performance will be used to manufacture larger cell formats for safety and abuse tolerance tests.

Conclusions

MERF's experimental materials scale-up program assists the battery research community and allows for a comprehensive evaluation of new materials by industrial laboratories as well as supports basic research. In FY18 the program provided several new, not commercially available materials. Samples of high, uniform quality materials were distributed for further evaluation and research. Over 130 samples, ranging from grams to hundreds of grams of experimental battery materials have been provided to researchers since the program inception.

MERF continues to design and synthesize new compounds in a series of silicon-containing carbonate solvents. The materials have significantly higher flash point than solvents commonly used to formulate LIBs electrolytes. Preliminary electrochemical evaluation revealed that the materials can improve safety of LIBs without performance degradation.

Evaluate emerging manufacturing technologies such as continuous flow reactors, microwave assisted reactions, acoustic mixing or reactive distillations to improve product quality while lowering manufacturing costs are all under consideration. MERF utilized recently acquired a customized Syrris ASIA320 and Corning Advanced-Flow™ continuous flow chemical reactors to develop expedient manufacturing processes for new electrolyte solvents, salts and additives by improving safety, minimize waste stream and lower material and energy cost.

Key Publications

Issued Patents

1. Dzwiniel, Trevor; Pupek, Krzysztof; Krumdick, Gregory "Process For The Production Of High Voltage Electrolyte Solvents For Li-Ion Batteries" US Patent 10,099,994 October 16, 2018.
2. Krumdick; Gregory K., Dzwiniel; Trevor L., Pupek; Krzysztof "High Voltage Redox Shuttles, Method For Making High Voltage Redox Shuttles" US 10,008,743 June 26, 2018.

Patent Applications

1. Dzwiniel, Trevor L.; Pupek, Krzysztof; Krumdick, Gregory K. "Process For Producing Fluorinated Electrolyte Solvent" U.S. Pat. Appl. Publ. (2018), US 20180079708 A1 20180322

Invention Disclosures

1. Joseph A. Libera, Trevor L. Dzwiniel, Krzysztof Pupek, Gregory K. Krumdick, and Stephen Cotty "Combustion Synthesis Of Aluminum Doped Lithium Lanthanum Zirconium Oxide With Annealing Properties For Cubic LLZO Formation At 700°C" ANL Case #: IN-18-046.

Presentations

1. Dzwiniel, Trevor; Pupek, Krzysztof; Krumdick, Gregory "Continuous Flow Processes: An Advanced Manufacturing Platform for Electrolyte Materials" 232nd ECS Meeting, National Harbor, MD, Oct 2-5, 2017.

References

1. Xu, Wu, et.al. "Non-Aqueous Electrolytic Solutions And Electrochemical Cells Comprising The Same" U.S. Pat. Appl. Publ. (2009), US 2009001738 (Ferro).
2. Li, Wentao "Use Of Lithium Bis(Fluorosulfonyl) Imide (LiFSI) In Non-Aqueous Electrolyte Solutions For Use With 4.2V And Higher Cathode Materials For Lithium Ion Batteries" U.S. Pat. Appl. Publ. (2015), US Li (BASF).
3. Xu, Kang and Angell, C. Austen "Sulfone-Based Electrolytes for Lithium-Ion Batteries" J. Electrochem. Soc. (2002), 149 (7) A920-A926.
4. Chi-Cheung Su, Meinan He, Paul C. Redfern, Larry A. Curtiss, Ilya A. Shkroba and Zhengcheng Zhang "Oxidatively Stable Fluorinated Sulfone Electrolytes For High Voltage High Energy Lithium-Ion Batteries" Energy and Environ. Sci. 2017, 10, 900.
5. Xu, Chao, et.al. "The Role of LiTDI Additive In $\text{LiNi}_{1/3}\text{Mn}_{1/3}\text{Co}_{1/3}\text{O}_2$ /Graphite Lithium-Ion Batteries At Elevated Temperatures" J. Electrochem. Soc (2018), 165 (2) A40-A46.
6. Liu, Q. et.al "Challenges And Perspectives Of Garnet Solid Electrolytes For All Solid-State Lithium Batteries" J. Power Sources 389 (2018) 120-134.
7. Eongyu Yi, Weimin Wang, John Kieffer and Richard M. Laine "Flame made nanoparticles permit processing of dense, flexible, Li^+ conducting ceramic electrolyte thin films of cubic- $\text{Li}_7\text{La}_3\text{Zr}_2\text{O}_{12}$ (c-LLZO)" J. Mater. Chem. A, 2016 (4) 12947.
8. Miura, Hitoshi; Sakano, Fumihiro; Yahagi, Akira; Yamamoto, Taketsugu; Jpn. Kokai Tokkyo Koho (1998), JP 10172610 A 19980626.

I.2.L High Energy, Long Life Lithium-Ion Battery (NREL)

Kandler Smith, Principal Investigator

National Renewable Energy Lab
15013 Denver West Parkway
Golden, Co 80401
E-mail: Kandler.Smith@nrel.gov

Brian Cunningham, DOE Technology Development Manager

U.S. Department of Energy
E-mail: Brian.Cunningham@ee.doe.gov

Start Date: October 1, 2016

End Date: September 30, 2019

Project Funding (FY18): \$506,791

DOE share: \$506,791

Non-DOE share: \$0

Project Introduction

Energy-dense, long-life energy storage is needed to improve market readiness and enable higher penetration of electric vehicles. Today's state-of-the-art lithium-ion EV battery lasts around 10 years and provides just 100-250 miles range, both inferior to conventional vehicles. Across virtually all of today's Li-ion chemistries, Li loss capacity fade is the dominant mechanism that limits lifespan. High-energy Li-ion electrode materials presently under research and development (e.g., silicon) suffer even shorter life than today's materials because of large volume change during cycling that fractures electrode surface films and accelerates Li loss. In addition to lifetime challenges, large irreversible Li loss on the first cycle limits the beginning-of-life performance of these high-energy electrodes. To boost initial capacity, these materials presently require prelithiation as an extra manufacturing step, adding unwanted cost to the cell. This project seeks to overcome the barrier presented by limited useable Li inventory in order to enable higher energy, longer life batteries.

Objectives

The objective of the High-Energy, Long-Life Li-ion Battery (L3B) Project is to increase cycle and calendar lifetime of both graphite and silicon (Si) based Li-ion cells. For cells employing Si, the proposed technology will also increase initial capacity. The L3B device will be low cost, passively controlled, and occupy minimal weight and volume. Specific objectives include:

- Extend calendar and cycle life by 50% for Li-ion graphite/NMC (nickel-manganese-cobalt) and Si-X/NMC systems
- Re-lithiate the Si anode following formation cycle to increase Si-anode Li-ion cell energy density by 20%
- Design the system such that it adds less than 5% to the cost, weight, and volume of Li-ion cells, and is compatible with cell manufacturing and safety
- Use modeling and experiments to quantify the uniformity of lithium distribution throughout the cell at multiple rates of relithiation
- Pending resources, work with commercialization partner in year 3 to transition the technology to the marketplace.

Approach

The proposed objectives will be met by introducing an excess Li reservoir into Li-ion cells that can be released to boost capacity upon demand, increasing initial performance and extending lifetime. Different from previous concepts, the proposed technology is controlled by a passive internal circuit and can deliver a slow, continuous release of Li ions throughout the cell lifetime and/or a faster, triggered release of Li ions on demand. The

device is projected to add less than 1% to the cost, weight, and volume of today's cells. In addition to extending lifetime, the device is a practical way to prelithiate Li-starved systems to boost their initial capacity, addressing a present roadblock hindering commercialization of high-energy anode materials such as silicon. The project is demonstrating the proposed device on cells using both today's graphite-based and tomorrow's high-energy Si-based negative electrode material presently under investigation by the DOE Applied Battery Research for Transportation (ABRT) program.

The team leverages unique expertise at NREL and ANL. NREL is a recognized expert in the electrochemical characterization and model-based design of electrochemical couples and large-format cells under DOE's CAEBAT program, including diagnosis and modeling of degradation mechanisms in automotive systems and environments. ANL's Cell Analysis, Modeling, and Prototyping (CAMP) laboratory is the leading DOE facility for producing high-quality electrochemical couples in partnership with DOE's Si Deep-Dive project. (See Section II.H.1 of this report for additional description of the CAMP facility.) ANL's high energy density Si anodes when demonstrated together with NREL's supplemental Li technology may represent the best progress to date amongst labs, universities, and industry to reach DOE's VTO Battery500 Strategic Goal for EV batteries of 500Wh/kg and 1000 cycles.

Results

The L3B device is a combination of excess lithium reservoir and passive control. Experiments have been conducted with and without the passive control. During FY 2018, NREL demonstrated significant life extension for Si/graphite-NMC based cells using L3B. Capacity recovery was initially performed in a triggered fashion using a second cyler channel with the cell resting in a deep discharged state. As the year progressed, NREL starting using the passive control to continuously release lithium during cycling. Major accomplishments for the year include:

- >2X life extension for 400 mAh Si-based pouch cells with passive control. The cells were fabricated by ANL-CAMP and, with 73% graphite and 15% Si, have an anode specific capacity of 600 mAh/g
- 50% capacity recovery demonstrated for Si-based pouch cells using multiple triggered relithiations
- Prototype cells built with Li reservoir and passive control inserted inside of cell packaging
- Measurement of lithium distribution via extensive coin cell harvesting after relithiation within 18650 commercial graphite cells and Si pouch cells after high rate relithiation.
- Continued development of 2D transport model through comparison with experimentally measured results. Used model to predict distributions at lower rates that have not been measured within the program due to time constraints (experiments would take several years)
- Submitted technical manuscript to *Electrochimica Acta* that has been accepted with minor revisions. Article investigates fade mechanism for state-of-the-art (SOA) high energy density 18650 cell.

To prove the capability of the proposed Li reservoir/passive control, NREL started inserting metallic lithium electrodes into ANL-CAMP fabricated Si/graphite-NMC pouch cells. NREL received an initial batch of 33 cells. The anodes consisted of 15 wt% Si, 73 wt% graphite, 2 wt% carbon black and 10% binder with a specific capacity of ~600 mAh/g-electrode. The anode had a high porosity of 44% to allow for expansion of Silicon during lithiation. The high porosity is also beneficial for enabling uniform relithiation. Baseline data was collected for the cells without the device inserted and with the device inserted but idle. In either case, the cell capacity rapidly faded to 80% of the initial value in only 40-50 cycles.

The capacity of Si cells was initially recovered by pausing cycling at various levels of capacity fade and using a second cyler channel to control relithiation from the Li reservoir. During relithiation, the cell was resting in a deeply discharged state. Initial recovery was done at a relatively high rate of 100 μ A discharge for Li. For

these cells, this would represent 20% lithium capacity inserted in one month. The results of these initial triggered, externally controlled relithiations are summarized in Table I.2.L.1. Capacity recovery of 7-10% was demonstrated for these 6 cells. The relithiation efficiency metric in Table I.2.L.1 quantifies the discharge capacity gained divided by the lithium capacity removed from reservoir. Ideally, this efficiency would be >90% indicating lithium is uniformly inserted throughout the entire cell and is also not consumed by any side reactions. The relithiation efficiency tends to increase as the applied Li current is reduced. For instance, at 100 μA the average efficiency was 72% and at 200 μA was 65%.

Cells were then relithiated multiple times using triggered, externally controlled release. A possible concern for cells with Si-based anodes is that other physical phenomena besides loss of lithium could result in significant capacity loss, such as loss of active material or electrolyte dry out. The large volume expansion of Si can result in tremendous stress and cracking of SEI layers. This process results in continuous SEI growth and loss of lithium, for which the reservoir can be used to recover capacity. The large stresses can also crack particles and isolate them from electronic percolation paths leading to a loss of active material. Further, SEI growth may result in too much electrolyte consumption and lead to dry out. To investigate, two cells that had faded to around 150 mAh capacity from 350 mAh were relithiated at 100 μA multiple times. The capacity of

Table I.2.L.1 Summary of capacity recovery/efficiency for triggered relithiation of 400 mAh Si Pouch Cells with 20-60% capacity fade at a relithiation rate of 100 μA .

Cell #	Relative Capacity after Cycle Aging under Various Conditions	Capacity Gained with 1 Month Relithiation at 100 μA	Relithiation Efficiency
1	43%	8.8%	69%
2	83%	6.5%	67%
3	81%	7.7%	73%
4	42%	9.5%	72%
7	52%	9.1%	71%
9	80%	8.8%	76%

both cells was restored to 300+mAh. These tests showed a very large amount of capacity can be restored with relithiation and that at least 75% of the capacity fade for these Si cells was due to loss of available lithium. Other degradation mechanisms play a minor role compared to Li inventory loss.

Figure I.2.L.1 shows cycling experiments where cells were relithiated once an end of life capacity of 75% was reached. The multiple relithiations extended the end of life capacity from 60 cycles to 180+ cycles – a 3x improvement. The ability to replenish lithium throughout cell lifetime is one of the major benefits of the proposed technology compared to prelithiation.

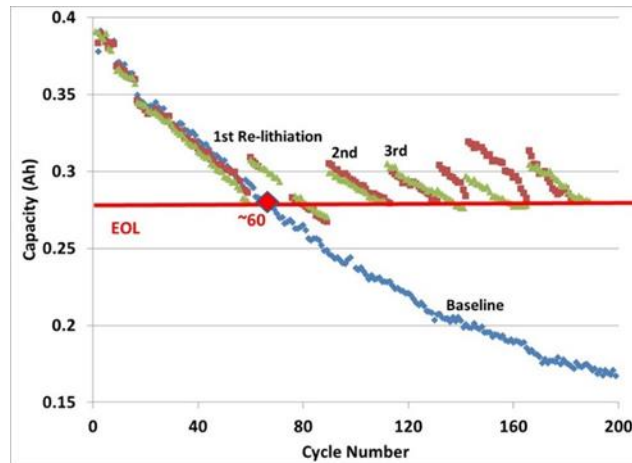


Figure I.2.L.1 Cycling of 400 mAh Si pouch cells at C/3 and room temperature with and without relithiation. The blue circles represent cycling with no relithiation. The green and red points represent cycling where triggered relithiation is performed during rest at 100 μ A when 75% capacity is reached.

In a separate experiment demonstrating passive control, the Li reservoir was used to extend life during continuous cycling within 400 mAh Si cells. In Figure I.2.L.2 the blue dots/line represent cycling for the baseline cell which rapidly falls to 80% capacity in \sim 40 cycles. The orange circles/line represent the average of two cells cycling with continuous relithiation using passive control. The bars on individual circles represents the standard deviation for replicate cells. The end of life capacity of 80% is reached after 110+ cycles.

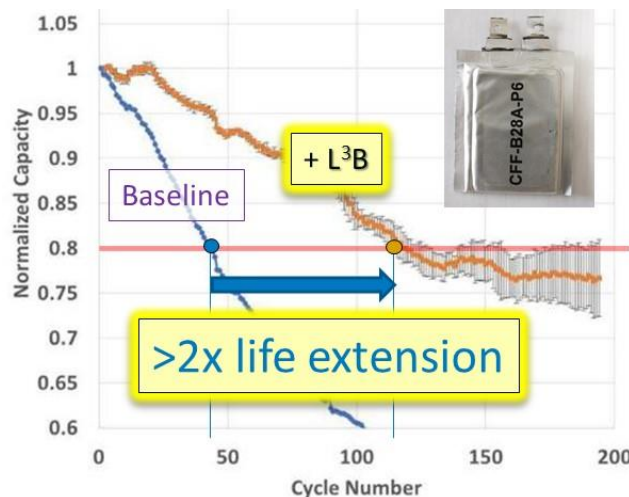


Figure I.2.L.2 Cycling of 400 mAh Si pouch cells at C/3 and room temperature with and without continuous relithiation using passive control

Resistance growth was also tracked during these experiments to test the baseline cell's resistance growth and monitor whether relithiation affected the cell's power fade characteristics. Figure I.2.L.3 shows that relithiation causes no discernable change to the cell's resistance growth. Total cell resistance plotted in Figure I.2.L.3 is calculated from the voltage difference between the charge and discharge directions and is a metric of energy efficiency. A separately measured 10-second pulse resistance showed similar trends, with no discernable difference between the baseline and relithiated cells. So while the L3B technology is not helping reduce power fade, it is not exacerbating the problem either.

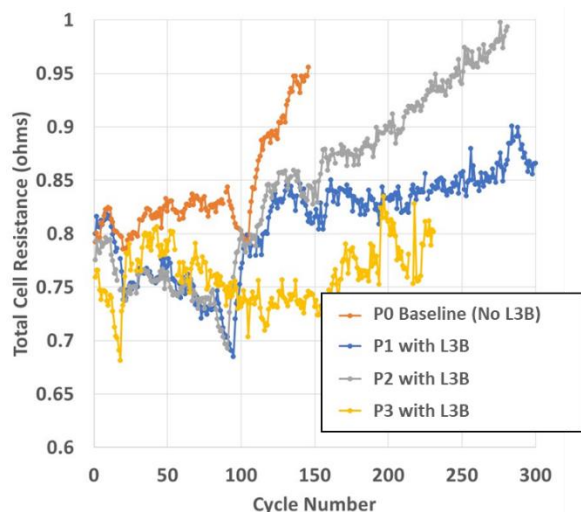


Figure I.2.L.3 Comparison of cell resistance during cycling of 400 mAh Si pouch cells at C/3 and room temperature with and without continuous relithiation using passive control

With the lithium reservoir placed on the edge of the jellyroll, a concern of the proposed technology is the ability to uniformly insert lithium throughout the entire cell. Due to relatively slow in-plane electrolyte transport properties, lithium will preferentially insert near the lithium reservoir when the recovery/lithium discharge rate is too high. The discharge/charge capacity of harvested coin cells was used to measure lithium concentration as a function of distance from the reservoir. For the ANL pouch cells, the lithium must only move across a total distance of 3.2 cm for the 3450 cell. Further, the porosity of the cells is relatively high and there is a large variation in anode and cathode OCP with intercalation fraction that promotes uniformity. These 3 factors resulted in a very uniform lithium distribution even at a high recovery rate of 100 μA .

In contrast, systems such as graphite and lithium iron phosphate (LFP) have quite flat potentials and will thus be the most challenging to relithiate uniformly. The lithium concentration for two graphite/LFP 18650 jelly rolls was measured after relithiation at a fast rate of 200 μA and is shown in Figure I.2.L.4. The relative moles of lithium are the moles of lithium divided by the number of moles present in the cell initially within the fully discharged cathode. The measured concentration at each distance is the average of 3 coin cells per jellyroll. The lithium concentration variation is considerably higher for these 18650 cells due to longer transport distance of 6+ cm and the OCP plateaus of both the LFP and graphite chemistries promoting non-uniformity. Also shown in Figure I.2.L.4 is a 2D transport model prediction for lithium concentration. The 2D model overpredicts the nonuniformity and the model also predicts a sudden jump in concentration. The model assumes uniform cell properties (SOC, temperature, electrode properties, etc.) at the beginning of relithiation – a possible reason for discrepancy. Nonetheless, the model captures the trend and magnitude of Li nonuniformity.

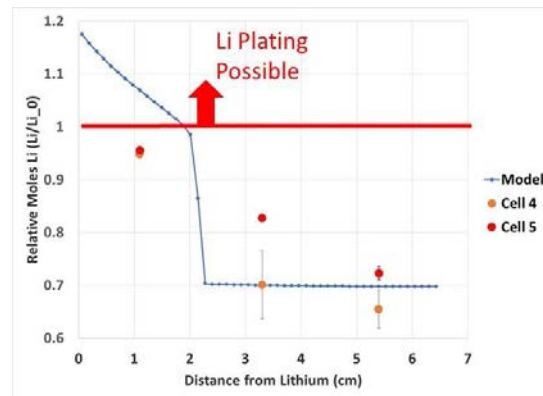


Figure I.2.L.4 Measured lithium concentration within LFP/graphite 18650 cells after high-rate relithiation. Three coin cells were extracted from each of location of the cells' jellyrolls. A 2D Li-transport model prediction shown as blue dots/line.

LFP/graphite chemistry is worst case scenario due to OCP plateaus of both the graphite and LFP electrodes.

Shown in Figure I.2.L.5, the 2D transport model was used to estimate lithium concentration distribution for high density NMC/graphite cells as a function of recovery rate. If the lithium reservoir is discharged at 500 μA or a rate to recover 20% capacity in 1 month, then lithium distribution is predicted to be non-uniform with relative lithium content varying from 1.3 to 0.8 across the cell. Conversely, when the recovery is done over the course of 1 year, then the variation is only predicted to be from 0.85 to 0.97 and lithium plating is not expected.

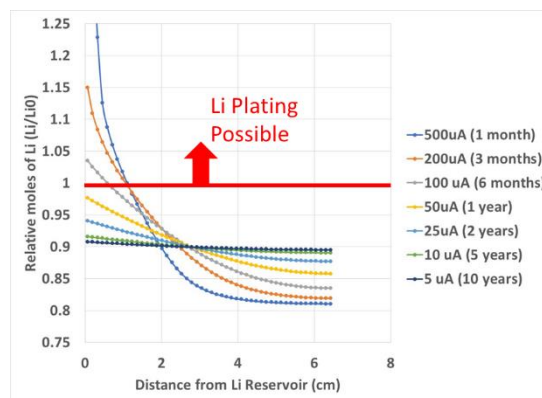


Figure I.2.L.5 Simulated lithium concentration within NMC/graphite 18650 cell relithiated at different rates. 20% of capacity can be recovered over 6 months or slower without concern for Li plating.

NREL is also investigating commercial high-energy cells. The SOA LG MJ1 18650 cell under investigation has a high capacity of 3.4 Ah and energy density of 270 Wh/kg. To support incorporating this device into these cells, NREL performed a detailed analysis to estimate the amount of capacity fade from various loss mechanisms and to understand electrode chemistry. These results have been written into a manuscript entitled: "Degradation Mechanisms of High Capacity 18650 Cells Containing Si-Graphite Anode and Nickel-Rich NMC Cathode." Chemical analysis shows the anode is composed of graphite and 5 wt% Si and the cathode is NMC 811. Fade estimates from various physical phenomena were estimated from dV/dQ incremental capacity analysis and coin cell harvesting.

Figure I.2.L.6 is taken from the manuscript and illustrates the amount of capacity loss from active material loss, loss of lithium, and impedance rise. The relative amount of capacity fade from active cathode material loss, anode material loss, and loss of lithium were roughly equivalent. The article has been accepted with minor revision to the technical journal *Electrochimica Acta*.

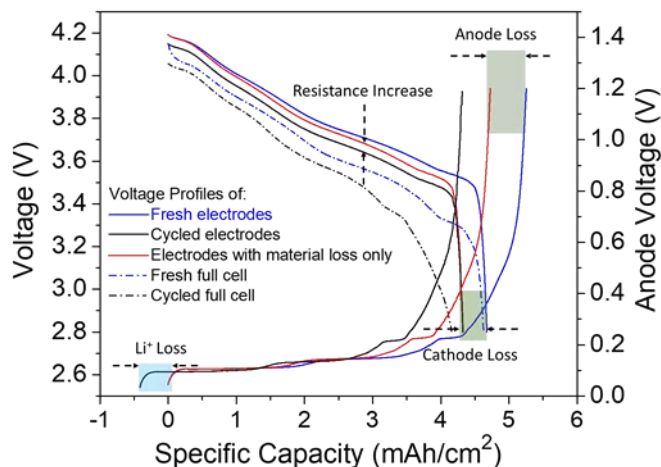


Figure 1.2.L.6 Loss mechanisms for SOA high energy (5% Si - 85%Gr/NMC811) LG MJ1 cell

Conclusions

NREL has demonstrated significant life extension and capacity recovery for Si based cells using the proposed L3B Li reservoir and passive control. More specifically, a life extension of >2X and capacity recovery of 50% have been demonstrated for 400 mAh pouch cells with anodes containing 15 wt% Si. The technology has also been demonstrated with more conventional graphite type cells. The variation of lithium concentration from relithiation has been measured for a worst-case scenario at high rate and with electrodes having flat OCP. A 2D lithium-transport model compared well with the result for the tested graphite/LFP cells. For high energy density graphite/NMC cells, the 2D model prediction shows relithiation over the course of 1 year or more should result in relatively uniform lithium distribution and avoid concerns of lithium plating. The team investigated chemistry and loss mechanisms for SOA commercial Si-Gr/NMC LG MJ1 18650 cells and a journal article has been accepted. In FY19, the team will work with commercial material and cell vendors to demonstrate L3B life extension benefits on SOA commercial cells and materials.

Key Publications

1. X. Li, A. Colclasure, D. Finnegan, D. Ren, Y. Shi, X. Feng, L. Cao, Y. Yang, and K. Smith. "Degradation Mechanisms of High Capacity 18650 Cells Containing Si-Graphite Anode and Nickel-Rich NMC Cathode." Accepted in *Electrochimica Acta*.
2. M. Keyser, A. Colclasure, X. Li, D. Finegan, K. Smith, "High-Energy Long-Life Li-ion Battery: L3B," DOE Innovation XLab Energy Storage Summit, SLAC National Accelerator Laboratory, Sept. 18-19, 2018.

Acknowledgements

Co-authors: Andrew Colclasure, Xuemin Li, Donal Finegan. Thanks to Drs. Andy Jansen, Bryant Polzin and Steven Trask of the ANL-CAMP facility for supplying high-quality Si cells and for helpful discussions regarding Si chemistry.

I.3 Computer-Aided Engineering for Batteries (CAEBAT)

I.3.A Advanced Computer Aided Battery Engineering Consortium (NREL/ANL/SNL/Purdue Univ)

Dr. Kandler Smith, Principal Investigator

National Renewable Energy Laboratory
15013 Denver West Pkwy
Golden, Colorado 80401
E-mail: kandler.smith@nrel.gov

Dr. Shriram Santhanagopalan, Principal Investigator

National Renewable Energy Laboratory
15013 Denver West Pkwy
Golden, Colorado 80401
E-mail: shriram.santhanagopalan@nrel.gov

Dr. Daniel Abraham, Principal Investigator

Argonne National Laboratory
9700 Cass Ave,
Lemont, IL 60439
E-mail: abraham@anl.gov

Dr. Joshua Lamb, Principal Investigator

Sandia National Laboratory
1611 Innovation Pkwy SE
Albuquerque, NM 87185
E-mail: jlamb@sandia.gov

Dr. Partha P. Mukherjee, Principal Investigator

Purdue University
585 Purdue Mall
West Lafayette, IN 47907
E-mail: pmukherjee@purdue.edu

Brian Cunningham, DOE Technology Development Manager

U.S. Department of Energy
E-mail: Brian.Cunningham@ee.doe.gov

Start Date: October 1, 2016

End Date: September 30, 2019

Project Funding: \$5,150,000

DOE share: \$5,150,000

Non-DOE share: \$0

Project Introduction

Building upon previous work under DOE's Computer Aided Engineering for Electric-Drive Vehicle Batteries (CAEBAT) Program, the current project seeks to (1) enhance and validate the predictive capability of computationally efficient electrochemical models for thick electrode designs as a path to lower battery cost and increase energy density; (2) develop and validate mechanical/electrochemical/thermal simulation models that describe the physiochemical processes encountered by batteries in the event of vehicle crash, possible internal short and thermal runaway, providing better understanding and enabling safer designs; (3) develop 3D models of electrochemical processes on the electrode microstructure length scale, providing better understanding of electrode morphology and inhomogeneous electrode utilization that leads to performance limitations and premature degradation. With NREL as lead, the Advanced Computer Aided Battery Engineering Consortium includes partner laboratories Argonne National Laboratory (ANL) and Sandia National Laboratories (SNL)

conducting complementary experimental studies and Purdue University conducting complementary mesoscale modeling studies. ANL and SNL experimental studies are described in further detail in separate sections of this report, respectively I.C.5 and I.C.6. The project has resulted in 16 archival publications, an open-source electrode microstructure library and an open-source plug-in for the FEniCS finite-element software used for 3D microstructure simulation.

Objectives

The Advanced Computer Aided Battery Engineering Consortium is working to develop modeling capabilities that help industry accelerate development of electric-drive vehicle (EDV) batteries, promote deeper and quantitative physical understanding and thereby improve battery performance, energy density, cost, safety and life. The project is divided into three tasks with the following objectives:

1. **Computationally Efficient Electrochemical Modeling** – Build upon recently published multiscale multidomain (MSMD) 3-D battery electrochemical-thermal simulation models with 100 to 1000-fold speedup and develop electrochemical parameter libraries for NMC523 and graphite electrodes from ANL Cell Analysis, Modeling and Prototyping (CAMP) facility. Demonstrate the accuracy of those models to capture the electrochemical performance of the CAMP electrode library with electrode loadings ranging from 1.6 to 7.5 mAh/cm². Identify tortuosity and other rate limitations inherent to these thick electrode designs to promote future lower cost, higher energy density batteries. Develop new *in operando* diagnostics to resolve heterogeneity of electrode utilization and validate models.
2. **Mechanical/Electrochemical/Thermal Abuse** – With SNL, build and experimentally validate simulation tools to predict the thermal-runaway behavior of lithium ion cells after a crash-induced crush. Include rate-dependent mechanical failure of individual cell components coupled with electrical, thermal and electrochemical reactions. Capture changes in cell behavior with aging. Implement battery crash abuse models in LS-DYNA coupling solid mechanics response with electrochemical/ thermal abuse user-defined functions. Partner with the USCAR Crash Safety Work Group (CSWG) to evaluate models, obtain feedback, and ensure they meet the needs of crash safety engineers.
3. **Microstructure Modeling** – Use microscopy and tomography to characterize the microstructure of Ni_{0.5}Co_{0.3}Mn_{0.2} (NMC523) and graphite porous electrodes with varying thickness, recipe and calendaring from the ANL CAMP library. With Purdue and ANL, identify and elucidate critical factors of electrode microstructure influencing rate limitations and inhomogeneous utilization using microstructural analysis, stochastic reconstruction, homogenization and direct numerical simulation of electrochemical physics on the complex 3-D geometry.

Approach

1. **Computationally Efficient Electrochemical Modeling** – Leveraging commercial materials and electrode designs from other DOE programs, the ANL CAMP facility produced high-quality electrodes of varying thickness and porosity. Negative electrodes with ConocoPhillips CGP-A12 graphite loadings ranged from 2.0 to 7.5mAh/cm² and in uncalendered and calendered variants with porosities of 51% and 37%, respectively. Positive electrodes utilized Toda Li_{1.03}(Ni_{0.5}Co_{0.3}Mn_{0.2})_{0.97}O₂ active material, loadings ranged from 1.6 to 5.8 mAh/cm² and uncalendered/calendered variants of similar porosity. All cells used Gen II electrolyte, 1.2M LiPF₆ in EC:EMC (3:7,w/w). All electrodes underwent electrochemical testing that consisted of galvanostatic intermittent titration (GITT) and constant current discharge rate tests. For modeling, the baseline thin electrode GITT and C/100 data were used to extract solid state thermodynamic, transport and reaction kinetic properties. Thick electrode data were used to validate macro-homogeneous electrochemical models and provide an estimate of tortuosity, a difficult to quantify parameter controlling effective electrolyte transport rate capability in the porous electrode. X-ray diffraction

experiments were carried out at the Advanced Photon Source (APS) facility to measure heterogeneity of Li concentrations across thick A12 graphite electrodes while charging and discharging.

2. **Mechanical/Electrochemical/Thermal Abuse** – Previous efforts to simulate the coupled mechanical-electrochemical-thermal response of batteries relied upon solving the mechanical model equations separate from the electrochemical-thermal (ECT) equations and implementing the results from the latter as user-defined material models in LS-DYNA to incorporate the effects of ECT response on the mechanical behavior of the cell components. This year, a more direct approach that involved introducing potential and heat generation rate as additional degrees of freedom in user-defined elements within LS-DYNA enabled simulation of a complete discharge at the cell level on a 3D CAD geometry of a 6 Ah prismatic cell in under 20 minutes.
3. In FY18, this part of the project focused on i) measuring mechanical response of cell components under complex loading conditions (e.g., strain rates greater than 100/s) ii) effect of long term (5 years) aging on component properties, and iii) validation of single-cell and multi-cell failure-propagation simulations.
4. **Microstructure Modeling** – Figure I.3.A.1 shows the overall approach for microstructure characterization and modeling. Microstructure geometries are either experimentally or numerically generated. ANL and University College of London (Prof. Paul Shearing) generated FIB-SEM and X-ray computed tomography (CT) images of the ANL CAMP electrodes, resolving different length scales. CT imaging reasonably captures active material geometry (~0.5 to 100 μ m) however is not capable of resolving carbon/binder additive (CBA) geometry due to inadequate resolution and phase contrast. To overcome this limitation, Purdue University (Prof. Partha P. Mukherjee) has developed a set of algorithms to numerically generate the CBA and match its properties to FIB-SEM and electrochemical data. The microstructure geometry is used for several purposes: (1) for 3D electrochemical simulation on NREL's high performance computer (HPC), Peregrine, and (2) for calculation of effective properties that are applied in macro-homogeneous electrochemical models. Macro models are well suited to wide design space searches. The micro models inform the macro models and provide deeper physical understanding how electrode morphology influences performance and degradation. In FY18 the team completed a study of tortuosity of the ANL CAMP electrodes that also included experimental measurements performed by Brigham Young University (Prof. Dean Wheeler).

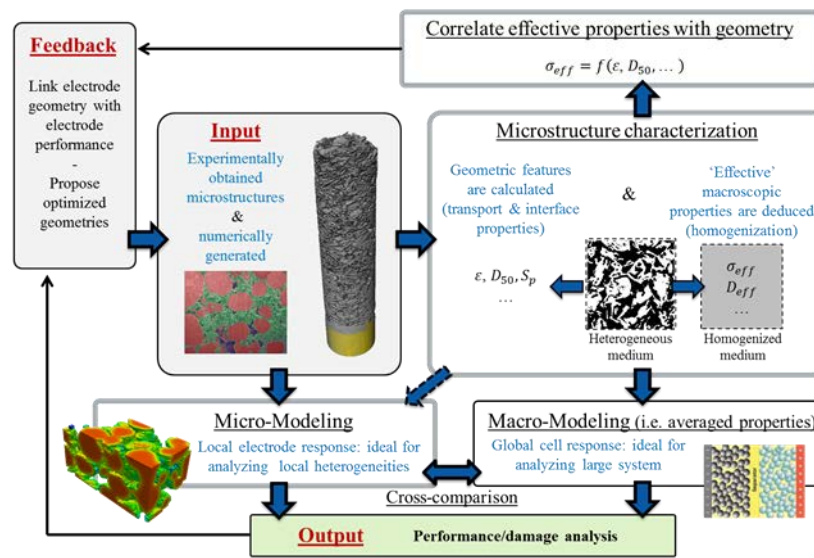


Figure I.3.A.1 Approach for microstructure characterization and modeling

Results

1) Computationally Efficient Electrochemical Modeling

In FY16-17, electrodes and experimental data provided by ANL-CAMP were used to (1) develop parameter sets for the electrochemical models and validate the computationally efficient models [11] for electrodes of varying thickness and (2) conduct a tortuosity study validating microstructure model-based tortuosity prediction methods. In FY18, (3) the tortuosity study was completed and published [13], (4) a microstructure library was published on NREL's website [15], and (5) a beamline XRD study was conducted and manuscript accepted [16] measuring sub-electrode-level heterogeneity and provide model validation data.

The beamline XRD study, funded by this CAEBAT project, is fully described in section I.C.5 of this report. In brief, the X-ray at Argonne's APS user facility provided in operando Li concentration and phase information for five $\sim 20\mu\text{m}$ slices of a $114\mu\text{m}$ thick graphite electrode during 1C charge and discharge (Figure I.3.A.2). The X-ray "slicing" revealed steep gradients in the net and phase specific lithium content for five separate layers of the electrode (Figure I.3.A.2). This thick graphite electrode was one of interest for the extreme fast charge (XFC) project and a simulation study was carried out under the XFC project and is described in detail in section I.E.3. Figure I.3.A.2 shows reasonable agreement between model and data, with the model slightly over-predicting heterogeneity across the electrode during intercalation.

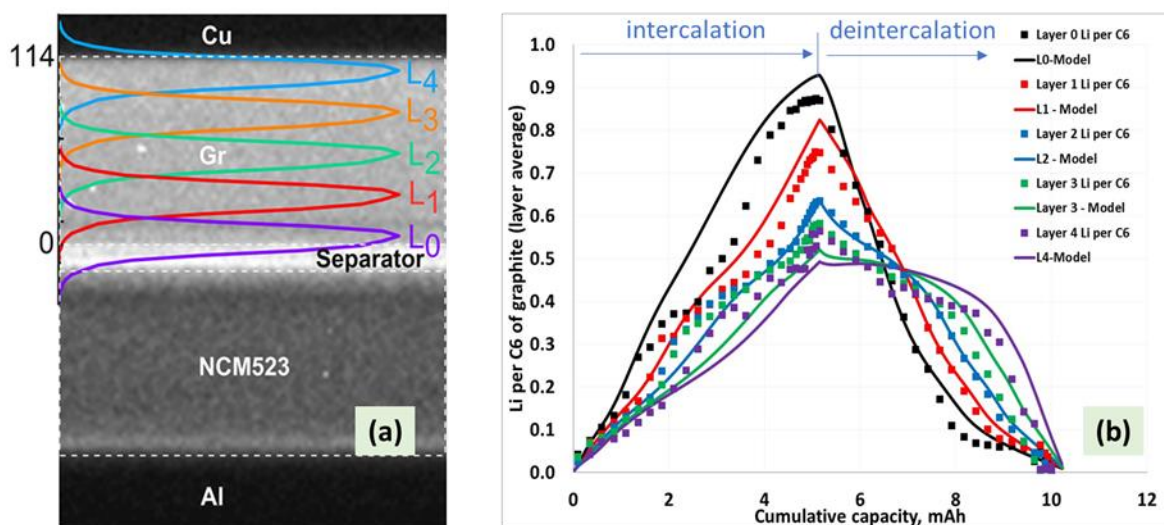


Figure I.3.A.2 (a) Five layers of $114\mu\text{m}$ thick graphite electrode individually resolved in beamline XRD study. (b) Li concentration layer-by-layer during 1C charge and discharge, data (symbols) vs. model (lines).

2) Mechanical/Electrochemical/Thermal Abuse

For low strain-rates tested in previous years, there was no significant strain-rate dependence detected at the electrode level. The original set of model equations proposed in 2016 were able to capture the cell-level response within 10% differences on the stress-strain curves (Figure I.3.A.3). However, the response at strain rates higher than $100/\text{s}$ was considerably different, indicative of a different failure mode of the electrodes (e.g., debonding of the coating from the electrode surface due to sudden infusion of energy) at these extreme strain rates. This data is included directly as a set of calibration curves on the LS-DYNA data card.

Validation of model predictions at the single-cell and multi-cell levels was initiated this year as well. The experimental data set for all cell-level and multi-cell modules were provided by Sandia National Laboratory (SNL). One example of comparison of temperature rise within a module is shown in Figure I.3.A.4. The figure in the inset shows the location of the thermocouples. The heat transfer coefficients between the cooling plates and the cells are difficult to measure and contribute to the differences between the maximum temperatures predicted by the models, and experimental measurements.

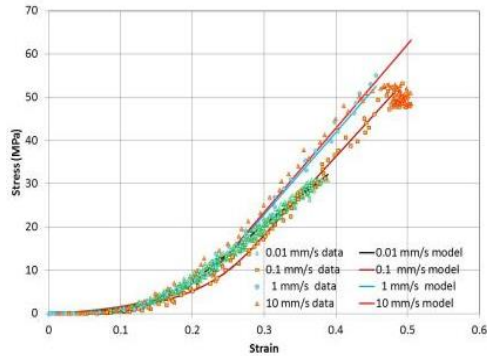


Figure I.3.A.3 Comparison of experimentally measured stress-strain response of a 3 Ah pouch format cell against model predictions at various strain rates

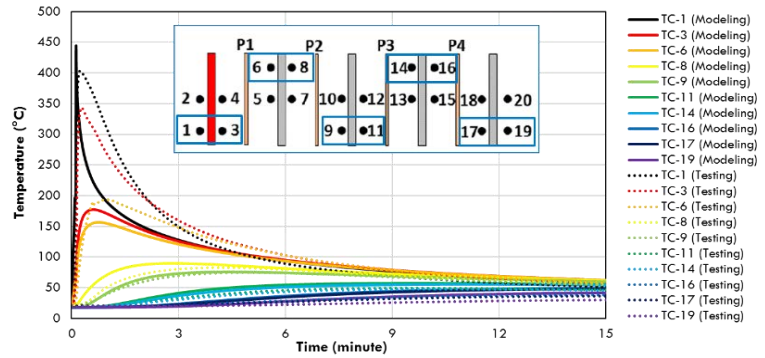


Figure I.3.A.4 Comparison of the experimentally observed rise in temperature within a 5S1P module comprised of 3 Ah pouch format cells charged to 100% SOC.

Further described in section I.C.6, Sandia National Laboratories developed and performed mechanical abuse testing to support CAEBAT modeling efforts to provide both parameterization and validation of mechanical abuse models. Current work focuses on understanding of the mechanical response of cells at elevated temperatures and the development of dynamic impact testing.

Figure I.3.A.5 shows the impact of temperature on fully charged 5-Ah pouch cells. Previous work has shown little change in the mechanical behavior of these cells when evaluated at temperatures within typical operating ranges of lithium ion batteries. This new work evaluated cells above normal operating temperatures. The cells were compressed at a rate of 0.1 mm/sec with a 24.4 mm radius cylindrical impactor. Cells were tested at both 100% SOC and 0% SOC. 100% SOC cells were compressed until thermal runaway was observed, while cells at 0% SOC were compressed to the average deformation required to create thermal runaway. The current results show little change in the overall mechanical behavior of the cells up to 100 °C, however at 120 °C we observed a significant reduction in the force required to deform the battery. We also observed that a slightly higher displacement before thermal runaway occurred at elevated temperatures.

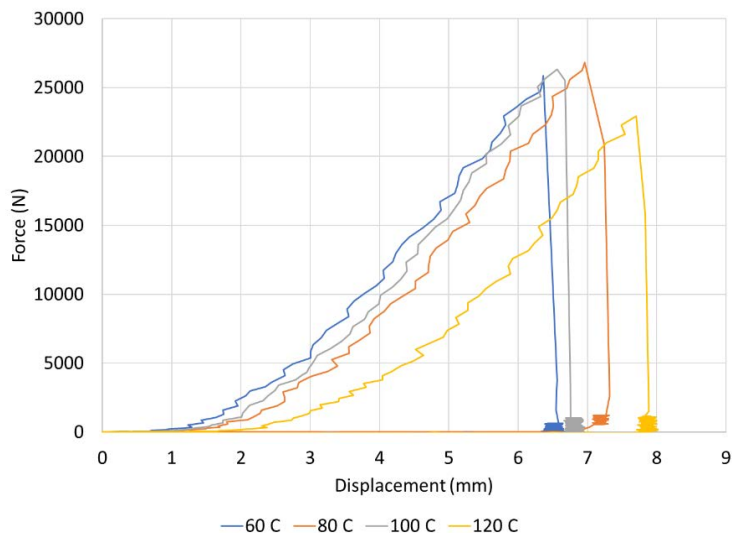


Figure I.3.A.5 Force vs displacement of fully charged 5-Ah pouch cells. Little change is observed up to 60°C, however a dramatic softening of the cell is observed at 120°C

The observations here suggest that temperature would have minimal impact on the resilience of cells to mechanical deformation at more moderate temperatures. This and previous data show little apparent change in the behaviors at lower temperatures suggesting that, until 120°C we wouldn't expect the susceptibility to mechanical crush to change significantly. On-going testing is looking at this elevated temperature testing at different rates and orientations to provide a complete picture on this susceptibility.

3) Microstructure modeling

Mesoscale modeling – In lithium-ion battery composite electrodes, relevant species/charge transport as well as reaction kinetic interactions take place at the pore-scale. Hence, variation in the pore-scale geometry, i.e., microstructure, alters such interactions and in turn, leads to observable differences at electrode and cell levels. Cell level observables represent capacity, temperature rise and irreversible capacity loss due to lithium plating at the anode. Multi-modal microstructural effects [10],[11] are studied for composite porous electrodes as well as the coupled response of the two electrodes in a full cell setting. It is found that the anode is ionically transport limited given the distorted pore-network formed due to platelet graphite particles, while the NMC cathode is both kinetically and ionically transport limited. The secondary solids, i.e., conductive binder domains (CBD), are present in many different interfacial arrangements and accordingly they alter reaction and speciation signatures during operation. Purdue University explored these interactions using meso-scale models.

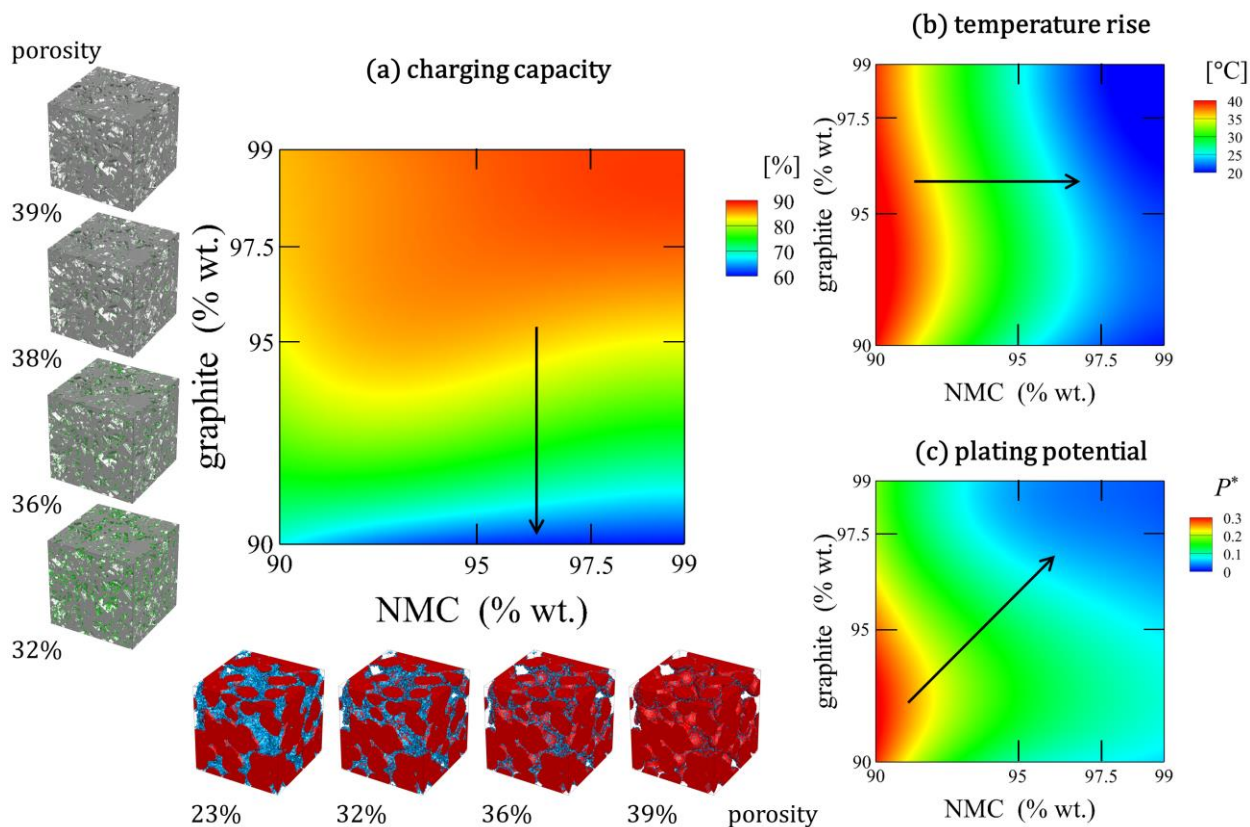


Figure I.3.A.6 Electrode microstructural variations concurrently affect (a) electrochemical, (b) thermal and (c) chemical interactions. The electrode capacities are kept unchanged to identify the microstructural effects [11].

Electrode recipes implicitly change the microstructural arrangement. To explicitly examine these microstructural effects, identical capacity electrodes are considered in Figure I.3.A.6 [11]. Active material weights and respective porosities are highlighted along with representative microstructures. Figure I.3.A.6a outlines the microstructural effect on finite rate capacity, which appears to be strongly dependent on anode microstructure. As porosity decreases for the anode, transport becomes severe, leading to a higher resistance to intercalation (i.e., for charging) and, equivalently, a smaller achievable capacity. The corresponding thermal response is shown in Figure I.3.A.6 b where cathode microstructure appears to be the dominant contributor. As NMC weight percent decreases, CBD amount increases and in turn available active area decreases due to surface area coverage with CBD. Decreased active area increases kinetic heating, which leads to a higher temperature rise. Plating, which is believed to be an anode-centric phenomenon, is in fact affected by both anode and cathode microstructures as both contribute barriers to ionic transport. Lower porosity cathodes have a higher electrolyte phase potential drop which in turn lowers the anode potential and increases the plating propensity. These meso-scale modeling results show microstructural effects are important to consider when designing for cell-level performance targets.

Tortuosity Prediction from Microstructure – Ionic transport limitations due to microstructure tortuosity reduces accessible capacity for energy-dense thick electrodes, especially during fast charging. In macroscopic models, tortuosity is treated as an effective parameter that must be tuned to test data. The tortuosity literature is scattered depending on the modeling or experimental method chosen. To gain predictive insight into how microstructure effects tortuosity, we published a study comparing multiple tortuosity measurements compared to our predictive method based on 3D microstructure geometry including the effect of the inert CBD phase [13].

Figure I.3.A.7 shows tortuosity factors for the ANL CAMP electrodes, obtained from three different methods: (1) numerical homogenization from 3D-tomography-based microstructures enhanced with numerically generated CBD (NREL & Purdue University), (2) tortuosity parameter fitting to rate data with a 1D-macro-homogenous electrochemical model (NREL), and (3) direct measurement with electrochemical impedance spectroscopy of symmetric cell infiltrated with a non-intercalating electrolyte (Brigham Young University). CBD impact on tortuosity factor has been quantified through a morphology and porosity-dependent corrective parameter determined for a wide range of microstructures and enables a better agreement with the two other methods thanks to a comprehensive error analysis. Within the range of possible CBD morphologies, we find CBD morphology for these ANL-CAMP electrodes tends towards a web-like, rather than film-like structure.

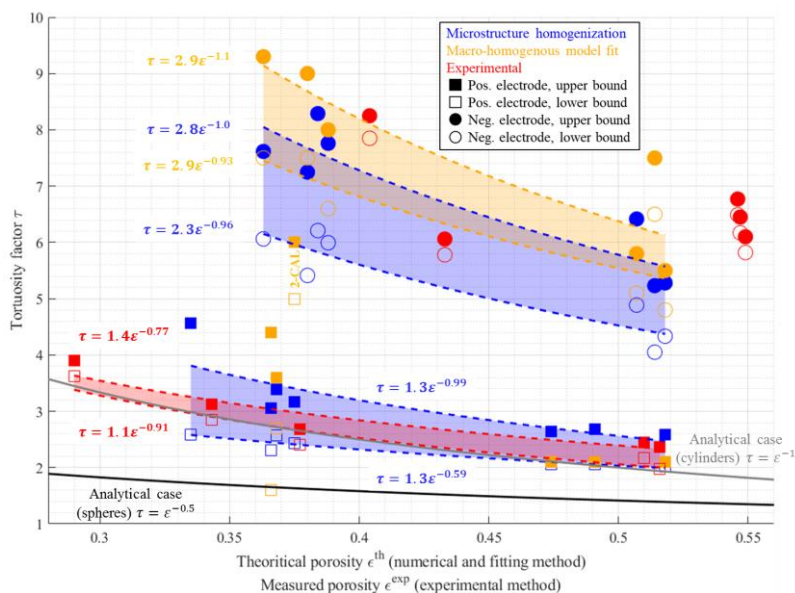


Figure I.3.A.7 Through-plane tortuosity factors of 7 positive NMC532 and 7 negative A12 graphite ANL CAMP electrodes, obtained with microstructure numerical homogenization (blue), macro-homogenous model fitting (orange), and direct measurement (red). Region of confide

The microstructure predictive method has been further applied and validated under the Extreme Fast Charge Program (section I.E.3), where 5 additional graphites were analyzed and differences in predicted ionic tortuosity quantitatively explained differences in 6C charge capacity measured by ANL across the different graphites. In addition, this work led to publication of an open-source electrode microstructure library [17]. A separate microstructure characterization Matlab toolbox (with a user-friendly graphic user-interface) is under development and will be made available online in FY19.

3D Electrochemical Modeling – While many microstructural influences can be captured through homogenization and upscaling, 3D direct numerical simulation is still necessary to fully capture coupled concentration/reaction heterogeneity and its influence on degradation processes such as mechanical fracture and Li plating. NREL previously described a 3D electrochemical direct numerical simulation model created in the FEniCS finite-element open-source environment implemented on NREL’s high performance computer, Peregrine. The model is being used to probe how different microstructures contribute to concentration and reaction heterogeneities and how microstructures can be tuned to reduce the onset of mechanical fracture and Li plating. Similar to other works in the literature, scaling the 3D model to a representative volume size with millions of degrees of freedom and obtaining results within days (rather than weeks) remains a challenge.

In FY18, numerical stability and speed of the 3D electrochemical direct numerical simulation model created in the FEniCS finite-element open-source environment have been significantly improved. Collaborators from NREL’s Computational Sciences Center developed an open-source block preconditioner plug-in for FEniCS,

available on GitHub [18]. When solving simultaneously for multiple governing equations, the software applies separate preconditioners to separate parts of the matrix. The method recently enabled 50X speedup for the 3D model on a limited number of processors. We are evaluating scalability. Figure I.3.A.8 shows an example result from the 3D electrochemical direct numerical simulation model. The model reveals significant in-plane heterogeneity (not visible with 1D macro-homogeneous models) during fast charging and discharging, as well as correlations between electrochemical local response and local morphology (e.g.: local drop of potential difference due to a local tortuosity increase, which thus increases the lithium-plating likelihood). Representative Volume Element (RVE) analysis performed on superior graphite SLC1506T indicates the RVE size for electrochemical simulation is rate-dependent, which is particularly important to assess the model results level of confidence. Current work is focused on achieving RVE-size simulations and evaluating impact of various electrode morphology (e.g. secondary pore network and particle size distributions) on electrochemical performances and effective parameters.

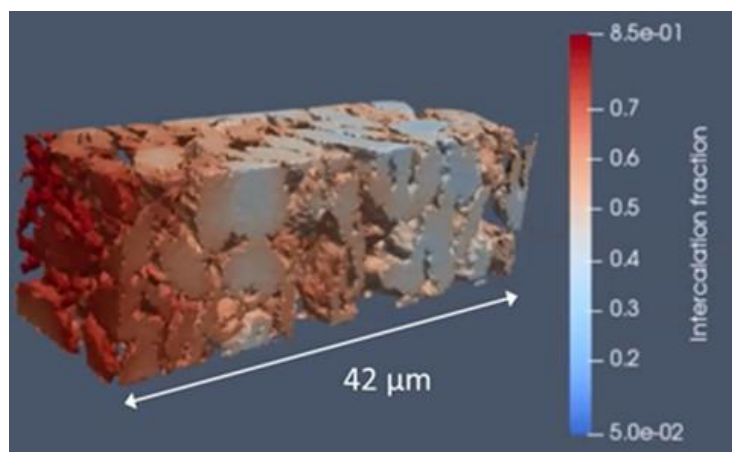


Figure I.3.A.8 Lithiation of anode with Superior graphite SLC1506T at 5C rate with snapshot taken at approximately 60% SOC. The 3D direct numerical electrochemical model solves for approximately 500,000 degrees of freedom.

Conclusions

The Advanced Computer Aided Battery Engineering Consortium – a partnership between NREL, ANL, SNL and Purdue University, with additional collaborators at UCL and BYU – continues to develop and validate simulation models that promote deeper understanding of battery physics and enable acceleration of next generation designs. In this third year of the four-year project, beamline XRD provided new sub-electrode validation data for model predictions of heterogeneity across thick electrodes, and mechanical abuse models were enhanced to capture high-strain rate abuse response of aged cells. In the final year, those models will be validated versus off-axis and high-speed crush tests at SNL. This year, the team further published a comparative study quantifying electrode tortuosity using different modeling and experimental methods. In the final project year, the 3D electrochemical microstructure model will be compared to additional beamline validation datasets and the combined model toolset will be applied in studies to promote deeper physical understanding of electrode inhomogeneity and enable higher energy density and higher rate designs.

Key Publications

1. G-H. Kim, K. Smith, J. Lawrence-Simon, and C. Yang, “Efficient and Extensible Quasi-Explicit Modular Nonlinear Multiscale Battery Model: GH-MSMD,” *J. Electrochem. Soc.*, A1076-1088, 2017.
2. A. Verma, K. Smith, S. Santhanagopalan, D. Abraham, K.P. Yao, P.P. Mukherjee, “Galvanostatic Intermittent Titration and Performance Based Analysis of LiNi_{0.5}Co_{0.2}Mn_{0.3}O₂ Cathode,” *J. Echem. Soc.*, 164 (13), A3380 – A3392, 2017.

3. Z. Wu, L. Cao, J. Hartig, S. Santhanagopalan, "Effect of Aging on Mechanical Properties of Lithium-Ion Battery Components," *ECS Trans.*, 77 (11) 199-208 (2017).
4. C. Zhang, J. Xu, L. Cao, Z. Wu and S. Santhanagopalan, "Constitutive Behavior and Progressive Mechanical Failure of Electrodes in Lithium-ion Batteries," *J. Power Sources*, 2017.
5. C. Zhang, S. Santhanagopalan, and A. Pesaran, "Simultaneously Coupled Mechanical-Electrochemical-Thermal Simulation of Lithium-Ion Cells," *ECS Trans.*, 72 (24) 9-19 (2016).
6. S. Santhanagopalan, C. Zhang, M.A. Sprague, and A. Pesaran, "A Representative-Sandwich Model for Simultaneously Coupled Mechanical-Electrical-Thermal Simulation of Lithium-ion Battery Cell under Quasi-Static Indentation Tests." *J. Power Sources*, 298, p. 102-113 (2016).
7. F. Usseglio-Viretta, K. Smith, "Quantitative Microstructure Characterization of a NMC Electrode," *ECS Transactions*, 77 (11) 1095-1118 (2017).
8. A. Mistry, D. Juarez-Robles, M. Stein IV, K. Smith, and P.P. Mukherjee, "Analysis of Long-Range Interaction in Lithium-Ion Battery Electrodes," *J. Echem. Energy Conversion & Storage*, 13 (3) 031006, 2016.
9. C.-F. Chen, A. Verma and P. P. Mukherjee, "Probing the Role of Electrode Microstructure in the Lithium-ion Battery Thermal Behavior", *J. Electrochem. Soc.*, 164 (11), E3146 – E3158 2017.
10. A. Mistry, K. Smith and P. P. Mukherjee, "Secondary-Phase Stochastics in Lithium-ion Battery Electrodes", *ACS Appl. Mater. Interfaces*, 10 (7), 6317 – 6326, 2018.
11. A. Mistry, K. Smith and P. P. Mukherjee, "Electrochemistry Coupled Mesoscale Complexations in Electrodes Lead to Thermo-Electrochemical Extremes", *ACS Appl. Mater. Interfaces*, 10 (34), 28644 – 28655, 2018.
12. A. Mistry and P. P. Mukherjee, "Probing Spatial Coupling of Resistive Modes in Porous Intercalation Electrodes through Impedance Spectroscopy", *Phys. Chem. Chem. Phys.* In press (doi: 10.1039/C8CP05109G), 2018.
13. F. L. E. Usseglio-Viretta, A. Colclasure, A. N. Mistry, K. P. Y. Claver, F. Pouraghajan, D. P. Finegan, T. M. M. Heenan, D. Abraham, P. P. Mukherjee, D. Wheeler, P. Shearing, S. J. Cooper, and K. Smith, "Resolving the Discrepancy in Tortuosity Factor Estimation for Li-Ion Battery Electrodes through Micro-Macro Modeling and Experiment", *J. Electrochem. Soc.*, 165 (14) A3404 – A3426, 2018.
14. B. L. Trembacki, A. N. Mistry, D. R. Noble, M. E. Ferraro, P. P. Mukherjee, and S. A. Roberts, "Mesoscale Analysis of Conductive Binder Domain Morphology in Lithium-ion Battery Electrodes", *J. Electrochem. Soc.*, 165 (13), E725 – E736, 2018.
15. Qibo Li, Chuanbo Yang, Shriram Santhanagopalan, Kandler Smith, Joshua Lamb, Leigh Anna Steele, and Loraine Torres-Castro, "Numerical Investigation of Thermal Runaway Mitigation through a Passive Thermal Management System" (submitted)
16. Koffi P.C. Yao, John S. Okasinski, Kaushik Kalaga, Ilya A. Shkrob, and Daniel P. Abraham, "Quantifying lithium concentration gradients in the graphite electrode of Li-ion cells using operando energy dispersive X-ray diffraction", *Energy and Environmental Science*, accepted for publication (2018).

17. “Battery Microstructures Library,” <https://www.nrel.gov/transportation/microstructure.html>

18. “pFIBS: A Parallel FEniCS implementation of Block Solvers,” <https://github.nrel.gov/jallen/pfibs>

Acknowledgements

We wish to thank collaborators from Univ. College of London (Paul Shearing group) for microstructure imaging and Brigham Young University (Dean Wheeler group) for tortuosity measurement. We also wish to thank Drs. Andrew Jansen, Bryant Polzin, Steven Trask and Alison Dunlop from the ANL-CAMP facility for providing electrodes and cells for this effort. The co-authors of this report include Andrew Colclasure, Francois Usseglio-Viretta, Chuanbo Yang, Jeff Allen, Justin Chang, Peter Graf, Aashutosh Mistry, Koffi Pierre Yao Claver, and Leigh Anna Steele.

I.3.B Consortium for Advanced Battery Simulation (ORNL)

John A. Turner, Principal Investigator

Oak Ridge National Laboratory
1 Bethel Valley Rd.
Oak Ridge, TN, 37831-6164
E-mail: turnerja@ornl.gov

Brian Cunningham, DOE Technology Development Manager

U.S. Department of Energy
E-mail: Brian.Cunningham@ee.doe.gov

Start Date: October 1, 2015

End Date: September 30, 2018

Project Funding (FY18): \$800,000

DOE share: \$800,000

Non-DOE share: \$0

Project Introduction

CABS is an integrated partnership between Oak Ridge National Laboratory (ORNL), Lawrence Berkeley National Laboratory (LBNL), and Sandia National Laboratories (SNL). The project report is divided into three sections (I.C.2, I.C.3, I.C.4) that includes contributions from individual Laboratories. Sections I.C.3 and

I.C.4 also report updates from industry-led projects. Mechanically induced internal short-circuit is believed to be the main cause of battery failure and thermal runaway in crashes involving electric vehicles. To accurately predict the internal-short we need to capture the deformed material variations and its influence on the transport properties. In this report, we highlight new experiments conducted to develop constitutive relations for mechanical response of constituent materials, effective transport properties for electrochemical behavior of electrodes under deformation, coupled simulations at layer resolved scale to predict the behavior of the damaged batteries.

Objectives

The objective of this project is to characterize the failure of the cells under various mechanical loading, develop upscaled coupled simulation tools to predict electrochemical behavior, and develop constitutive relations and failure criterion for mechanical response. The progress towards these objectives is achieved by delivering the following milestones for FY18:

1. Experimental data and diagnosis on deformation leading to mud-cracks.
2. Evaluation of electrode material properties for construction mechanical constitutive relations.
3. Development of framework to model primary effects under fast charge condition.

Approach

To address some of the critical impediments in understanding the battery failure, we first developed new experimental protocols to measure mechanical properties of electrode materials and cell components. This ensures that we have gathered all the necessary material parameters for the constitutive relations used in the models. During the previous year, we reported progress on development of new experimental protocols to study failure leading to internal short circuit. In the current year, we conducted indentation tests till failure and followed with microscopy experiments for diagnostic analysis. The diagnosis from this experimental evidence is used to develop formulation of new models for mechanical behavior of battery components. These various efforts allowed us to investigate some of the challenging internal short simulations under extreme mechanical deformations and predict the behavior of the batteries. Also, as part of improving the capability of models deployed through VIBE, we have demonstrated the coupling of lower order models with physics-based models in simulating the dynamic discharge of the battery modules.

Results

We conducted 3-point bending tests with an incremental approach to the final failure. The cells were examined using non-destructive x-ray tomography scans. These experimental methods allowed us to pin-point the failure point and associated materials behaviors. The refined simulation includes the bulk constitutive model leading to the failure and a detailed chain reaction of different layers during the final failure.

Li-ion cells in aluminum cans for small electronic appliances were used in the single-side indentation tests with 650-670 mAh in capacity. The mechanical load frame with an actuator driven by a servomotor and a 5000 lb load cell that measures the indentation force is employed. The load vs. Time plots of four cells with incremental displacements from 1.91 mm to 3.81 mm are shown in Figure I.3.B.1(a). They all followed the same loading curves and showed very repeatable mechanical responses.

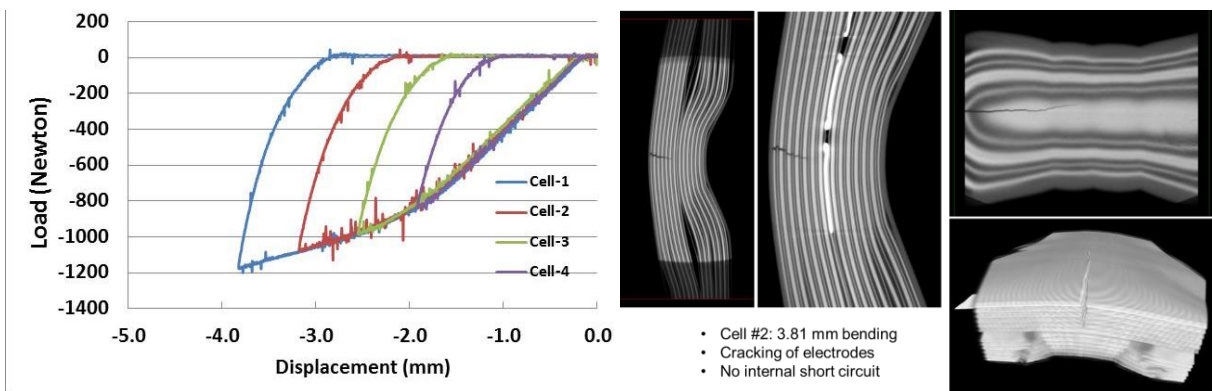


Figure I.3.B.1 (a) Load vs. Displacement plots of 3-point bend tests of 4 cells (b) XCT results of Li-ion cells after 3-point bending

We also carried out preliminary XCT scans of the cells after 3-point bending. In Figure I.3.B.1(b) shows images of a cell with 3.81 mm displacement. Although the cell was not shorted, through-thickness cracks were observed. In the XCT images of the cells with incremental deformation, cracks were observed in 3 out of the four cells.

In summary, indentation tests were carried out to incrementally study the deformation of the Li-ion cells. The first 60-70% deformation can be simulated using a constituent model. The follow-on x-ray tomography revealed details of the internal layer deformation under indentation. The hidden fragmentations of the copper layers were observed by XCT. It helped to pin-point the origin of failure at the cathodes and to refine the failure criteria in our simulation. Preliminary XCT results of cells subjected to 3-point bending test indicated through layer cracking.

Microscopic Analysis of Cu Current Collectors

Large, areal, brittle fracture of copper current collector foils has been observed by 3D x-ray computed tomography (XCT) of a spherically indented Li-ion cell. The cracking of copper foils could not be immediately confirmed when the cell is opened for post-mortem examination. However, 3D XCT on the indented cell reveals “mud cracks” within the copper layer and an X-ray radiograph on a single foil of the Cu anode shows clearly that the copper foil has broken into multiple pieces [1]. This failure mode of anodes in Li-ion cell has very important implications on the behavior of Li-ion cells under mechanical abuse conditions. In addition to 3D X-ray tomography, scanning electron microscopy (SEM), transmission electron microscopy (TEM) and X-ray photoelectron spectroscopy (XPS) were carried out to confirm this observation. In Figure I.3.B.2, we show SEM images of the fragmented copper foils and a pristine copper foil. A clear interface area after chemical reaction/corrosion was observed in the stressed (/cycled) material. In comparison, the pristine material is smooth with no signs of chemical reaction. The graphite/copper interface area of the anode was studied by SEM and TEM. In the element mapping of interface area, we observe the transition area between carbon and

copper, oxygen and phosphorus. There is also presence of phosphorus in the bulk region of the copper indicating it is also an alloying element. The O and P detected at the interface areas are likely residuals and diffusion species from the electrolyte.

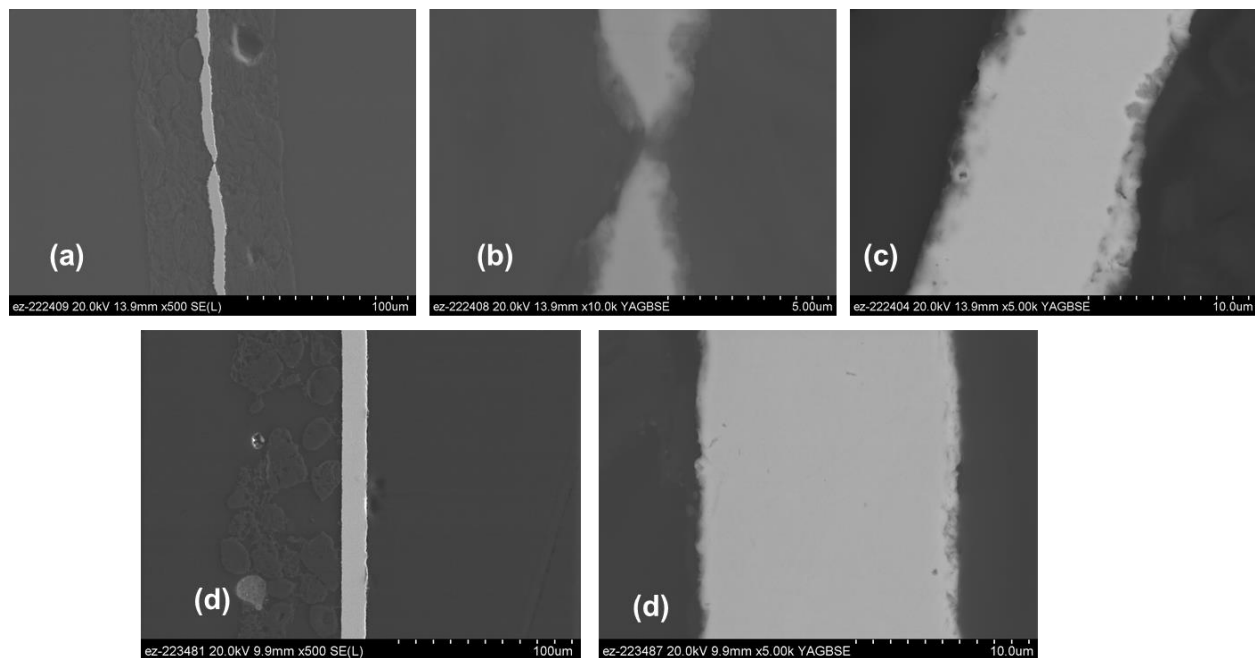


Figure I.3.B.2 Cross-sectional SEM images of an anode from a used cell after indentation (a) Low magnification image showing the Cu and fragmentation, (b) higher magnification of fracture point and rough surface, (c) rough surfaces of an unstressed area, (d) Low magnification image of a pristine anode, (e) Higher magnification to show smooth surfaces

We also analyzed two XPS depth profiles of a pristine collect collector and a stressed electrode. The XPS has the capability to pick up lighter elements such as Li and F. The profile of the pristine sample showed copper is the main element and other elements are un-detectable except for carbon in the first few nanometers. On the other hand, the stressed electrode showed the presence of Li, F, O, P and Na in the first 50 nm and some element were still present at 100 nm. The extra carbon was due to residual deposits on the surface that was not sputtered away by the ion beam. The carbon started to decrease after 500 nm.

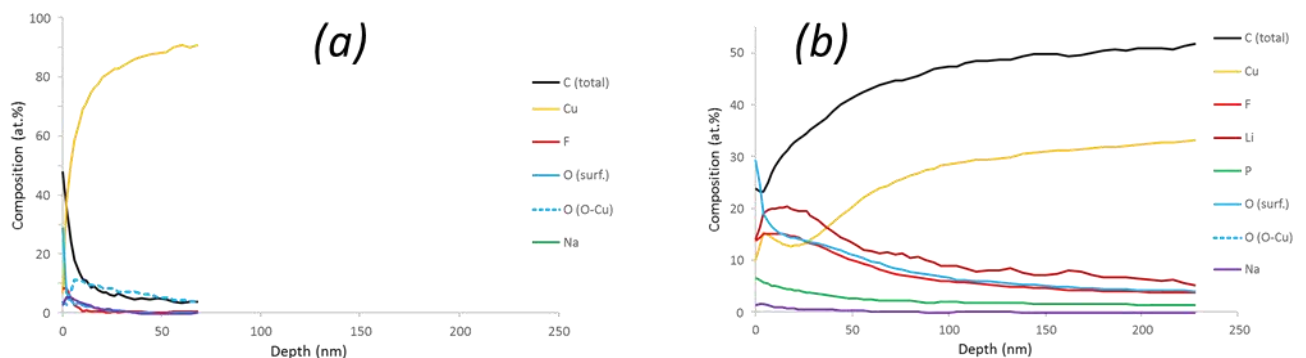


Figure I.3.B.3 (a) XPS depth profiles of elements in a pristine collect collector, (b) XPS depth profiles of elements in a stressed current collector

In summary, the microscopy studies showed an interface area between the graphite and copper in the used/cycled cells with microstructure characteristic of corrosion and chemical reactions. Elements such as O, P were detected by SEM and TEM, XPS analysis also showed the presence of Li, F and Na. Some of these

elements diffused into the copper foil. The diffusion of the elements caused embrittlement of the copper foil. Cracking under compressive force led to the observed mud cracks by X-ray tomography. This observation is helpful to the understanding of failure mechanisms of the Li-ion batteries under mechanical deformation.

Constitutive mechanics models for battery materials

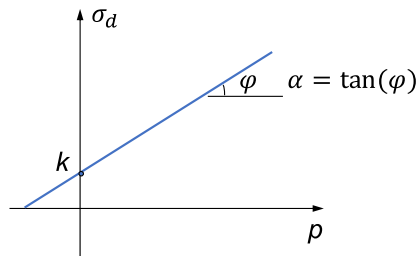


Figure I.3.B.4 Drucker-Prager criterion in deviatoric stress-pressure coordinates.

Mechanical behavior of a battery cell and response to the external mechanical loading is in large part dictated by mechanics of electrode coating materials, which constitute up to 80% of the jelly-roll by volume. The electrode coatings are porous particulate composite materials consisting of a hard phase (active electrode material) and visco-elastic binder with conductive additive (carbon black) to enhance electronic conductivity of the system. Considering that the active materials are layered metal oxides and have high hardness and elastic modulus, the electrode coating represents a mix of materials with very different mechanical properties. In this regard, the mechanical behavior of such material is best described by the models of cohesive-friction granular materials, i.e. similar to asphalt or concrete. In such materials

the strength and shear behavior are pressure-sensitive, which results in higher strength in compression (increase in cohesion) compared to tension. In this case the models that do not consider confinement pressure (i.e. Tresca and Von-Mises) are not applicable. Models based on generalized Mohr-Coulomb criterion are used instead with Drucker-Prager model being commonly utilized to describe behavior of such materials.

$$f(\sigma) = \sigma_d + \alpha p - k \leq 0 \quad (1)$$

where σ_d and p are the deviatoric stress and hydrostatic pressure correspondingly. The schematic of the Drucker-Prager criterion is shown in Figure I.3.B.4 with α representing the friction coefficient and k being cohesion. Determination of these parameters can be done by performing unconstrained compression tests. For that purpose, we fabricated cylindrical samples of electrode composite material consisting of NMC 532/PVDF binder/carbon black in 90/5/5 wt% ratio. The slurry was dispensed into the plastic cylindrical molds, pre-treated with the Buehler release agent. The resulting samples were 25 mm in diameter and 15 mm height. Two tests were performed on these samples: axial compression and lateral compression (Brazilian test) commonly used in mechanics of granular materials. A small die-set with guiding linear bearings was built to ensure orthogonal application of the load to the sample as shown in Figure I.3.B.5 together with the results of the tests. The friction angle (φ) and Drucker-Prager cohesion (k) were determined from the above experiments as 1.29rad and 1.77 MPa respectively.

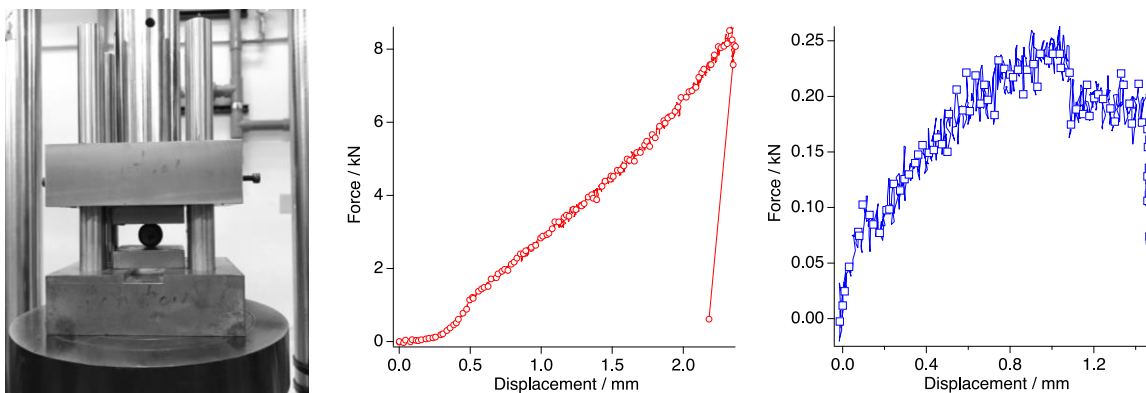


Figure I.3.B.5 Unconstrained compression of battery electrode material. (a) experimental setup with die-set; and sample (b) axial compression; (c) lateral compression (Brazilian test).

Resolving microstructure of electrodes

Microstructure of composite electrode coatings dictates the effective properties such as electronic and ionic conductivity and thus the performance of the electrochemical cell. It is expected that the significant role is played by the fraction and more importantly distribution of binder with conductive additive for electron transport. Methods of non-destructive reconstruction of microstructure such as X-Ray Computed Tomography (XCT) do not provide information on binder distribution as it is “transparent” for the X-Ray radiation and thus becomes indistinguishable from the pores in the electrodes. In our previous work we attempted to map the binder by using nano-indentation on a large grid by utilizing the orders of magnitude difference in modulus of layered metal oxide particles and binder. While providing good estimate for the modulus of NMC, the method did not result in sufficient resolution. In addition, in order to perform such modulus mapping the electrode needs to be filled with metallographic epoxy and polished, a process which could change the interparticle distance and thus result in erroneous information on microstructure. As an alternative, we utilized cross-sectioning with Focused-Ion beam (FIB) and subsequent elemental mapping. The method does not require filling the electrode; in addition, the decision was made to perform ion milling from the current collector side of the electrode which provided smooth surface and eliminated need for tungsten or carbon deposition on the surface. Based on the composition of Polyvinylidene fluoride (PVDF) binder we initially expected fluorine as a good “marker” in Energy Dispersive X-Ray Spectroscopy (EDS) mapping of electrode cross-sections. It was however determined later that carbon provided much better signature for detection of binder within the microstructure. A representative cross-section is shown in Figure I.3.B.6 demonstrating correlation between FIB-SEM and EDS mapping. The slicing was performed using Hitachi NB500 dual-beam FIB/SEM. Cross-sections were taken every 200 nm resulting in total depth of 26 μm . The electrode in Figure I.3.B.6 has been calendered to final porosity of 30%. The team is working on processing the images to create 3D maps and ultimately meshes from FIB cross-sections and we plan to analyze microstructure of as-cast as well as calendered to other porosities cathodes of the same composition.

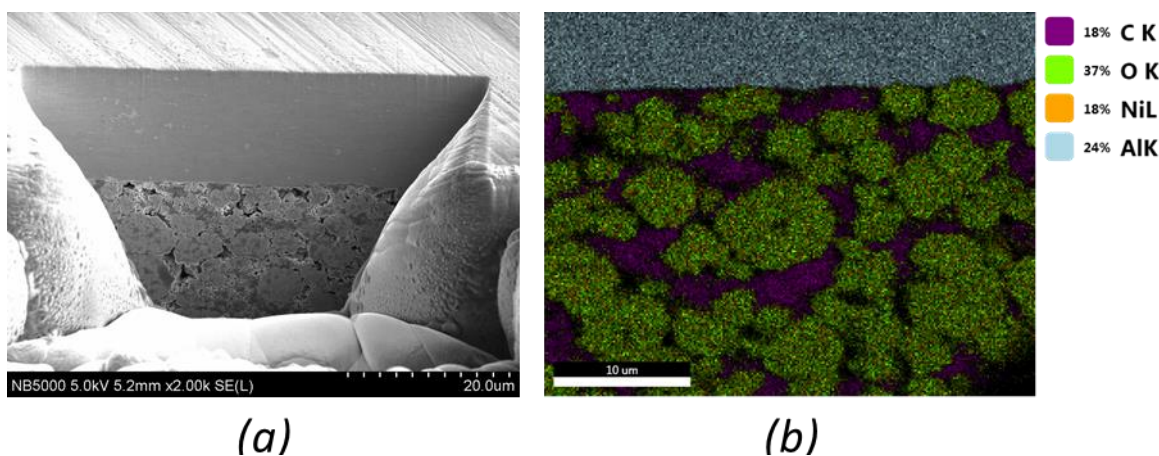


Figure I.3.B.6 FIB-SEM cross-sectioning of positive electrodes. (a) SEM image of the cross-section; (b) EDS map showing carbon as signature for binder location

Modeling the inhomogeneity and degradation in batteries

Inhomogeneity and degradation play an important role in battery lifetime, performance, and reliability of the lithium-ion batteries. There are various factors that will have impact on the lithium intercalation process which plays the critical role in the battery charge cycle. Therefore, quantitatively analyzing the lithium distributions under various stages in battery charge cycle, and how charge or discharge rates impact the lithium distributions, is an important step toward understanding the cause of lithium plating and other degradation mechanism. The previously developed electrochemical model based on volume averaging of Newman’s model [2] has been used for comparison of calculated lithium concentration profiles as a function of graphite electrode thickness to the experimental line profiles of the neutron attenuation [3]. We initiated development of model for plating and degradation based on the initial experimental studies performed at Battery

Manufacturing facility at ORNL using a large-format 0.5Ah NMC532/graphite pouch cell [4]. The cell has thickness values of 60 μm for anode, 25 μm for separator, and 60 μm for cathode. In Figure I.3.B.7 we show the charge/discharge profiles and associated dQdV plots from these studies that will serve the validation purpose for the simulations.

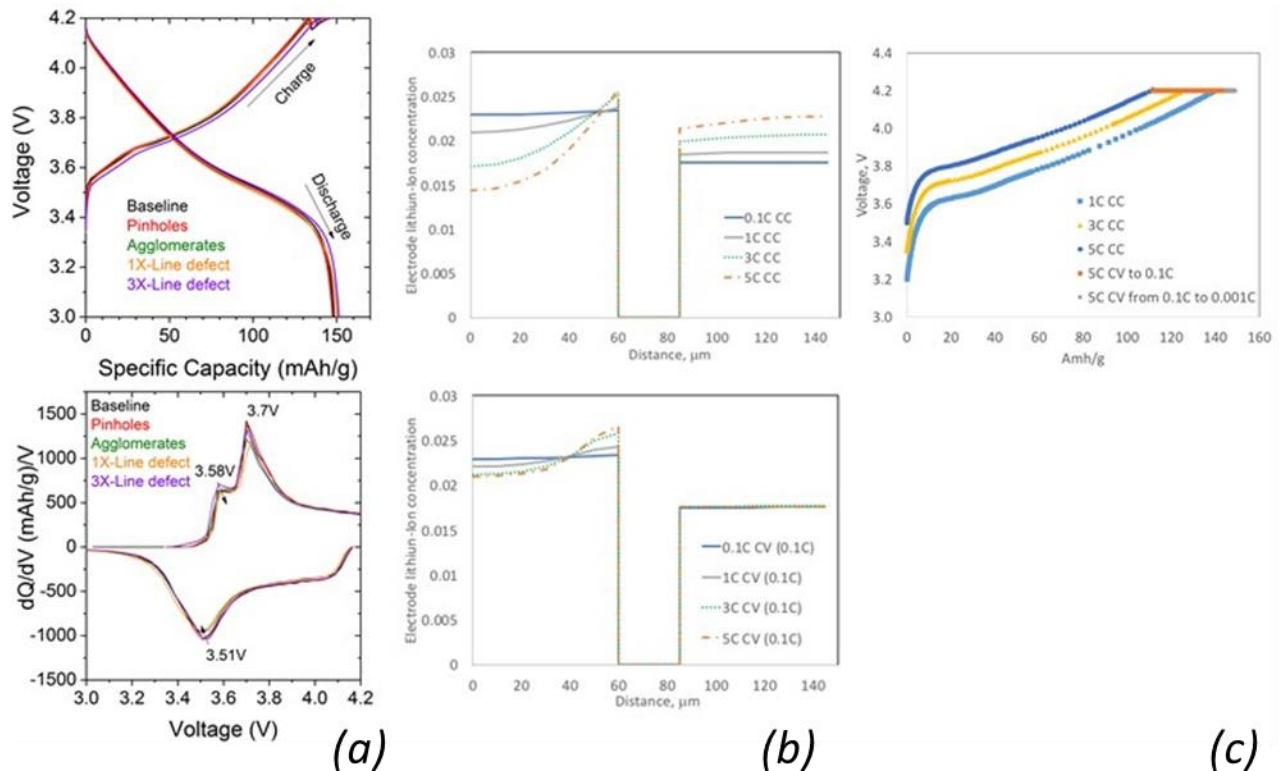


Figure I.3.B.7 (a) 1C charge and discharge capacity curves, 1C dQ/dV curves. (b) concentration profiles at the end of CC and CV charging conditions (c) CC charging for various C rates and the subsequent CV charging.

The initial focus has been on the detailed lithium-ion concentration distributions in both electrode and electrolyte at different phases of the battery charge cycle: discharge, constant current charge, and constant voltage charge, rest period, etc., under various discharging and charging C rates, and with or without defects. As the discharge progresses, lithium ions reduce in anode and increase in cathode. In the charging process, the reverse occurs as the lithium moves back from cathode to anode through the separator. As shown in Figure I.3.B.7, for charging, either constant current (CC) or constant voltage (CV), lithium ions intercalate back to anode from cathode. A CC charging with a lower C rate, makes the intercalation and de-intercalation more complete and cause less gradients on both anode and cathode sides. The subsequent CV charging, if necessary, continues the intercalation and de-intercalation and at the meantime lowers the gradients. For any given charging rate, the lithium concentration gradient in anode is larger than that in the cathode. The gradient introduced after CC is larger than that after discharge with the same C rate, this means that the charging insufficiency after a fast charging is more significant than the capacity loss in discharge with a high C rate. In Figure I.3.B.7 shows the CC and the subsequent CV for a few different C rates. In theory, time requirement for CC charge is approximately the same as time for discharge for the same C rate. This is generally true for a low C rate, such as 0.1C. As C rate increases, charging takes less time for CC charging than in discharge, leaving higher gradients in the lithium distribution, and consequently restoring less capacity back to the battery cell, i.e., 75% capacity for 5C CC alone. CV (e.g., with 0.1C termination current) charging which makes up the most lost capacity requires a longer time if it follows a high C rate CC charging. Various reaction mechanism for degradation must be added to the model to predict the capacity fade at higher current charge rates.

Development of composite models for dynamic discharge of battery modules

An equivalent circuit model (ECM) was developed from Hybrid Performance Pulse Characterization (HPPC) test data for a battery cell. The HPPC test exercises the dynamic behavior of the battery cell during discharge and regen pulses. The pulse tests for this work were conducted at various temperatures to understand the battery behavior under "real-world" conditions. A diagram of the equivalent circuit is shown below in Figure I.3.B.8 where the cell's voltage drop under load is accounted for by the series resistance R_0 while diffusion voltages are represented by the R_1C_1 and R_2C_2 sub-circuits.

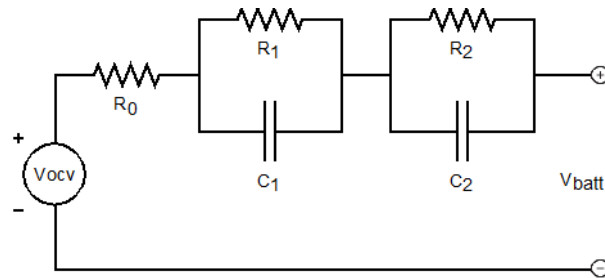


Figure I.3.B.8 Equivalent circuit model for lithium ion battery.

Based on the above circuit, the ECM for the cell and module is represented by the equations shown below where parameters v_1 , R_1 , C_1 are associated with the first sub-circuit and v_2 , R_2 , C_2 represent the second sub-circuit. Model parameters at each 10% SOC are determined by a non-linear least squares curve fit of the HPPC voltage profile. A comparison of the ECM results to experimental data is provided in Figure I.3.B.9.

$$\frac{dz}{dt} = \frac{-i(t)\eta(t)}{Q} \quad (2)$$

$$\frac{dv_1}{dt} = -\frac{1}{R_1C_1}v_1 + \frac{1}{C_1}i \quad (3)$$

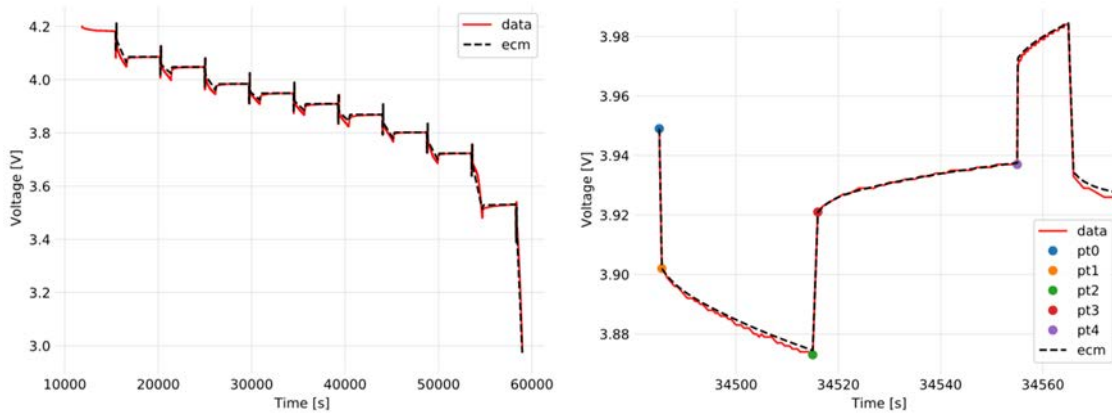


Figure I.3.B.9 Battery cell HPPC voltage data compared to ECM at ambient temperature of 25°C. Data from HPPC test shown as solid red line, ECM as dashed black line. Right plot is enlarged from 60% SOC region.

$$\frac{dv_2}{dt} = -\frac{1}{R_2C_2}v_2 + \frac{1}{C_2}i \quad (4)$$

$$v_{ecm}(t) = v_{ocv}(z(t)) - v_1(t) - v_2(t) - i(t)R_0 \quad (5)$$

The module ECM was evaluated at US06 drive cycle conditions as shown in Figure I.3.B.10. The experimental data represents three modules connected in series; therefore, the module ECM was adapted to account for the voltage increase of the system. We will finally couple this ECM model with thermal transport to predict the temperature distribution of the battery packs during US06 discharge cycle.

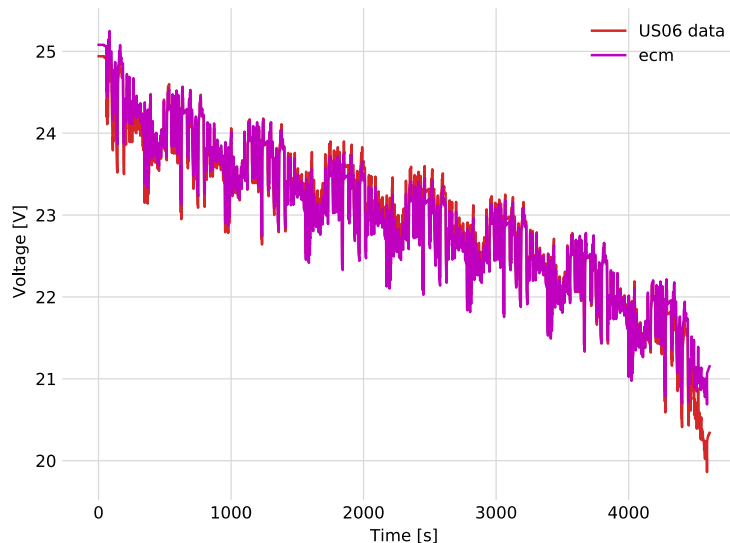


Figure I.3.B.10 Comparison of the module ECM (purple line) to the module US06 drive cycle data (red line). The voltage profile represents three modules connected in series

Conclusions

During this year, we have conducted the diagnostic studies on the origin of failure of battery components and evaluated properties which were used in the constitutive relations of the mechanical simulations. We have also started developing physics-based models for understand the fast charge behavior and associated plating mechanisms. Also, composite models for simulations of battery module and packs under realistic driving conditions are introduced into the software release.

Key Publications

1. Wang, Hsin, Thomas R. Watkins, Srdjan Simunovic, Philip R. Bingham, Srikanth Allu, and John A. Turner. "Fragmentation of copper current collectors in Li-ion batteries during spherical indentation." *Journal of Power Sources*, 364 (2017): 432-436

References

1. Wang, Hsin, Thomas R. Watkins, Srdjan Simunovic, Philip R. Bingham, Srikanth Allu, and John A. Turner. "Fragmentation of copper current collectors in Li-ion batteries during spherical indentation." *Journal of Power Sources*, 364 (2017): 432-436
2. Allu, S., S. Kalnaus, S. Simunovic, J. Nanda, J. A. Turner, and S. Pannala. "A three-dimensional meso-macroscopic model for Li-Ion intercalation batteries." *Journal of Power Sources* 325 (2016): 42-50.
3. Zhou, Hui, Ke An, Srikanth Allu, Sreekanth Pannala, Jianlin Li, Hassina Z. Bilheux, Surendra K. Martha, and Jagjit Nanda. "Probing multiscale transport and inhomogeneity in a lithium-ion pouch cell using in situ neutron methods." *ACS Energy Letters* 1, no. 5 (2016): 981-986.

4. David, Lamuel, Rose E. Ruther, Debasish Mohanty, Harry M. Meyer III, Yangping Sheng, Sergiy Kalnaus, Claus Daniel, and David L. Wood III. "Identifying degradation mechanisms in lithium-ion batteries with coating defects at the cathode." *Applied Energy* 231 (2018): 446-455.

Acknowledgements

Srikanth Allu (ORNL), Hsin Wang (ORNL), Sergiy Kalnaus (ORNL), Srdjan Simunovic(ORNL), Kevin Lai (ORNL) and Gavin Wiggins (ORNL) contributed to this project.

We would like to acknowledge CABS team members from Sandia National Laboratory and Lawrence Berkeley Laboratory for their contributions towards the milestones and supporting the efforts as part of the consortium. We also like to thank NREL CAEBAT team members for sharing experimental data and technical discussions.

I.3.C Consortium for Advanced Battery Simulation (SNL)

Scott A. Roberts, Principal Investigator

Sandia National Laboratories
1515 Eubank SE
Albuquerque, NM 87123-0836
Email: sarober@sandia.gov

Brian Cunningham, DOE Technology Development Manager

U.S. Department of Energy
E-mail: Brian.Cunningham@ee.doe.gov

Start Date: October 1, 2015	End Date: September 30, 2019	
Project Funding (FY18): \$1,500,000	DOE share: \$1,500,000	Non-DOE share: \$0

Project Introduction

Multi-physics simulations of battery performance are typically performed at the macroscale, including entire cells, cells stacks, batteries, packs, and modules. Classically, these types of simulations model the electrodes using homogenized equations and properties, often utilizing porous electrode theory. These electrodes, however, are comprised of packs of active material particles, polymeric binders, and conductive additives. These materials are combined to form a complex mesostructure that is influenced by material choices and processing conditions. This mesostructure strongly influences the macroscopic performance of the electrode and is of particular importance in abuse scenarios, where it is difficult to experimentally determine mesostructure evolution and properties and during extreme fast charge, where transport through this complex mesostructure and be rate limiting.

Study of the influence of these mesoscale effects on the macroscale behavior of electrodes is the focus of this project. We are utilizing microtomography of NMC cathodes to create detailed simulation domains within Sandia's Sierra/Aria code suite using the Conformal Decomposition Finite Element Method (CDFEM). These imaging-derived particle networks are augmented with a conductive binder morphology that we designed. We are also creating discrete element method (DEM) capabilities informed by image data to computationally predict electrode mesostructures. Physics simulations are then performed on these mesostructures, including the calculation of effective properties (e.g. electrical conductivity, ionic tortuosity, Young's modulus) and fully coupled electrochemical-mechanical (dis)charge simulations. The results of these simulations are upscaled to feed into macroscale models developed by our ORNL teammates.

Objectives

The objective of this project is to improve the fidelity of battery-scale simulations of abuse scenarios through the creation and application of microscale (particle-scale) electrode simulations. Our specific FY2018 objectives are twofold:

1. Progress towards an accurate, robust coupled electrochemical-mechanical simulation of NMC discharge at the mesoscale, including the active binder phase.
2. Investigate mesoscale mechanics impact on electrode-scale mechanical behavior.

Successfully accomplishing these objectives will impact the VTO by improving the ability to assess battery response to abuse scenarios (e.g. crush) computationally, enabling many parametric computer tests rather than expensive and dangerous experiments.

Approach

Our approach centers around simulations performed using Sandia's Sierra Mechanics suite of codes. In particular, physics simulations are performed using the Sierra/Aria multi-physics code and the mesoscale

geometric representation is performed using CDFEM implemented within Sierra/Krino. Additionally, we have begun the use of the LAMMPS code for DEM-based predictions of electrode mesostructures.

Experimentally gathered electrode tomography data forms the foundation of our mesostructure representation. We are in the process of utilizing data gathered within the scope of this project by our CABS teammates and collaborators at Lawrence Berkeley National Laboratory (LBNL) and Argonne National Laboratory (ANL) [6]. For the work shown here, however, we have utilized microtomography from Vanessa Wood's group from ETH-Zurich. Specifically, Ebner *et al.* [7], published and made publicly available a high-quality data set of NMC electrodes. Material properties were gathered from a variety of sources detailed in our FY2016 report.

Computational representations of the NMC particle mesostructures are created using the CDFEM algorithm. This workflow has been discussed in detail in two journal publications [1],[2], but will be summarized here for completeness. The commercial software Avizo (Thermo Fisher Scientific) is used to binarize images, label individual particles, and create a smooth surface mesh for each particle which can then be exported as a faceted STL file. The faceted STL representation of each particle is then superimposed on top of a regular tetrahedral background mesh. CDFEM is used to decompose the background mesh to be conformal to the particles. This approach has been thoroughly verified, the mesh resolution requirements quantified, and the representative volume element size determined in a recent publication [3].

Conductive binder domain (CBD) phases are added to the mesostructure mesh using the “binder bridge” morphology approach [4]. This algorithm involves manipulating the level-set field representation of each particle to create a pendular ring or bridge of CBD that connects each particle, again conformally meshed using CDFEM. A new addition to the CBD approach this year is to appropriately include the effects of nanoporosity and compare this morphology approach to other stochastic methods [5], a comparison that will be discussed in more detail in the results section. A visualization of the workflow and a resulting mesh is shown in Figure I.3.C.1.

We have additionally this year begun generating mesostructures using particle-based DEM simulations, with a goal of generating cathode mesostructures including the CBD phase from physics-based colloidal and granular dynamics, rather than the geometry manipulation used in the binder bridge approach. The LAMMPS simulation code is used to uniaxially compress a collection of NMC particles (modeled using 10-micron

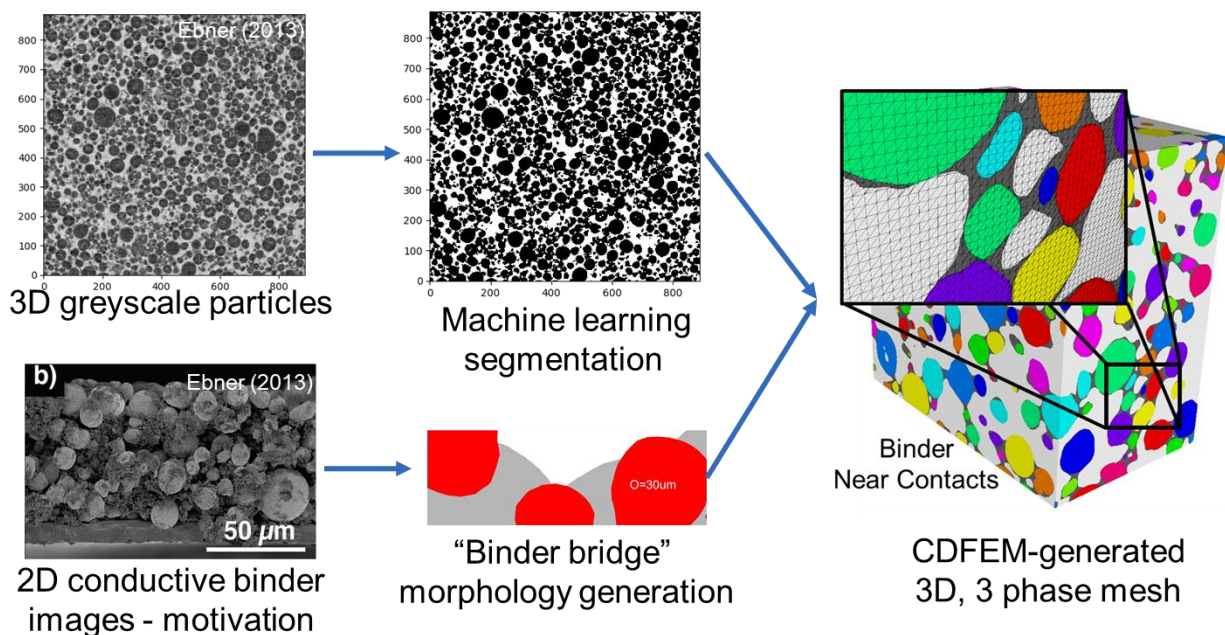


Figure I.3.C.1 Enhanced workflow for converting 3D tomography to mesh including the CBD phase.

diameter spheres) and coarse-grained CBD particles (modeled as 500 nm cohesive colloidal particles) from the as-coated condition (roughly 90% porous) all of the way through calendaring (as low as 20% porosity). Results of these simulations will be discussed in the following sections.

Results

The key technical results arising from our FY2018 research is presented in the following subsections.

Mesostructure simulation mesh resolution and representative volume element analysis

In a paper recently published in the Journal of Computational Physics [3], we verified the multi-material CDFEM approach to mesoscale simulations. One key aspect of performing credible mesoscale simulations is understanding what mesh resolution is required for a required degree of accuracy. The results of this study for an image-based mesostructure is shown in Figure I.3.C.2. Near-optimal convergence is achieved for all quantities of interest. While it is relatively easy (in terms of mesh resolution) to calculate geometric quantities with low error (subfigures a-c), much higher mesh resolutions are required for the effective property calculations (subfigures d-f). The recommended mesh resolution is that of the original image resolution, approximately 1/3 micron edge length. We also showed in [3] that relatively large domains are required to get low variability and a statistically representative volume element (RVE), and recommend simulations of at least 100 microns cubed.

Effect of CBD morphology and nanoporosity on electrode effective properties

In a paper published in the Journal of The Electrochemical Society and jointly produced with our collaborators at Purdue University as part of section I.C.1 of this report, we studied the effect of binder morphology on effective transport properties. We combined a uniform coating approach (which is commonly found in the literature), Sandia's binder bridge approach, and the stochastic representation of Purdue university to create a continuum of binder morphologies, highlighted in Figure I.3.C.4.

Using the representations shown in Figure I.3.C.4, we calculated many effective transport properties for both

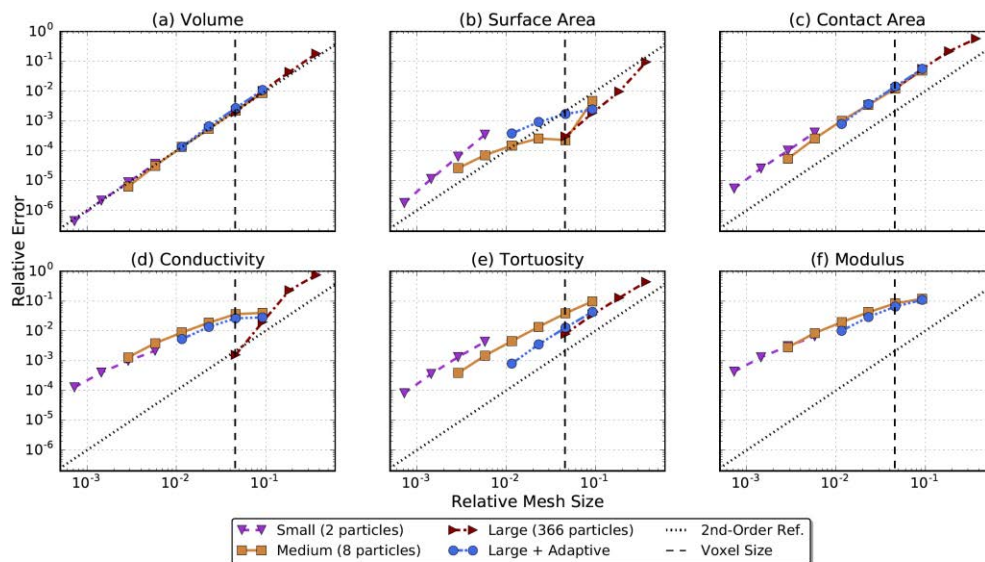


Figure I.3.C.2 Convergence and mesh refinement study for image-based mesoscale simulations for various effective properties. Reprinted from figure 13 of [2].

dense binders and ones containing nanoporosity [8],[9]. A key parameter extracted from these studies is the tortuosity, with its value as a function of binder morphology shown in Figure I.3.C.3. A few general observations can be made. First, the dense CBD morphology is always less tortuous than the nanoporous

morphology. This is due to the fact that the nanoporous morphology has 2x the volume of CBD, and even though it is now porous, its ionic diffusivity is only 5% that of pure electrolyte. The doubling of volume more than makes up for the small diffusivity through it. Second is that the CBD morphologies where the CBD is more closely adhered to the particles leads to a lower tortuosity. When the CBD preferentially adheres to itself rather than the particles, it tends to agglomerate in the pore throats, blocking them to transport and causing the ions to take a much longer pathway through the mesostructure.

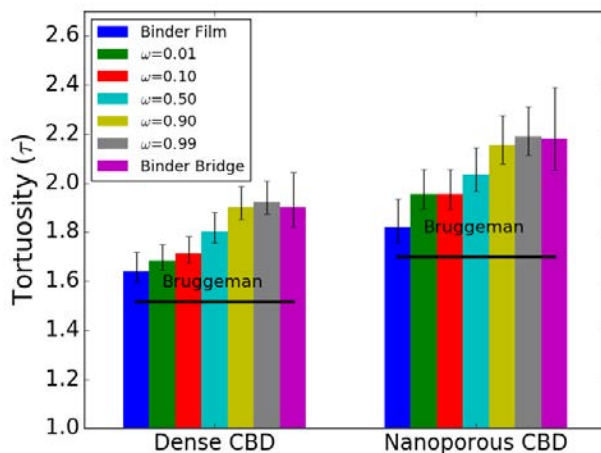


Figure I.3.C.3 Pore space tortuosity calculated for dense and nanoporous CBD phases using the binder morphologies from the next figure. Reprinted from figure 8 of [5].

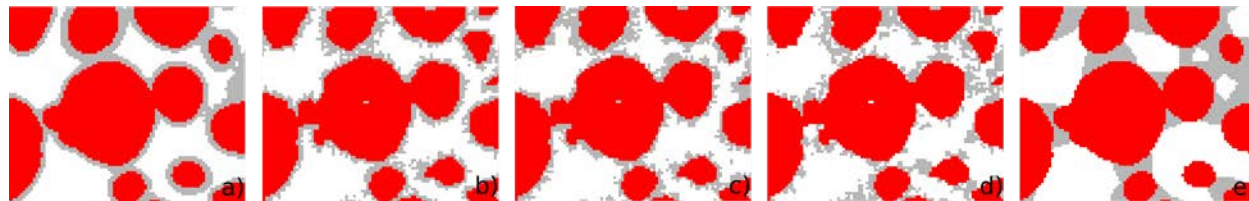


Figure I.3.C.4 Binder morphologies generated from multiple approaches. Reprinted from figure 6 of [5].

Mesostructure creation using DEM simulations

Our previous approach to generating mesostructures involves using 3D image data (expensive to gather), image processing and meshing (time intensive), and an ad-hoc CBD placement algorithm (which brings with it significant uncertainty). To alleviate some of these concerns, we have begun the development of DEM-based techniques of generating the entire mesostructure computationally in a physics-based approach. The simulation technique and setup were previously described in the approach section.

A snapshot of the resulting CDFEM mesh and simulation comparisons between the image-based approach and the DEM-based approach are shown in Figure I.3.C.6. Qualitatively, the mesostructure resulting from the DEM simulations look consistent with the image-based mesostructures. The resulting CBD morphology depends strongly on cohesion between CBD particles and adhesion between CBD and NMC particles, and can result in mesostructures that span the range of uniform coatings to binder bridges. Fortunately, the effective properties predicted from these DEM simulations (Figure I.3.C.6, right image) are consistent with those from the image-based simulations. These DEM simulations were a preliminary, proof-of-concept set of simulations. More representative and detailed simulations are an area for future work.

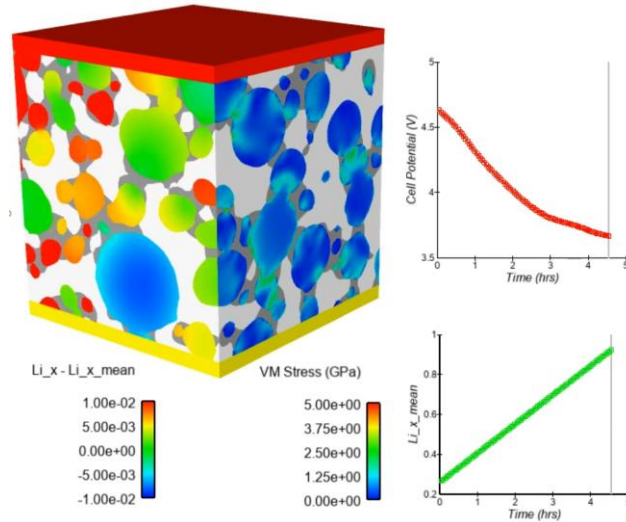


Figure I.3.C.5 Snapshot of a coupled electrochemical-mechanical discharge simulation of an NMC cathode.

Electrochemical-mechanical simulations to study mechanics impact

A primary objective of this project is to develop coupled electrochemical-mechanical simulations of electrode (dis)charge to study the impact of the mesostructure on macroscale properties. We have now developed the framework to perform coupled electrochemical-mechanical simulations of a statistically significant RVE using the image-based plus binder bridge mesostructure approach. A snapshot of an example simulation is shown in Figure I.3.C.5. The left slice of the image highlights the variability in lithium concentration on a per-particle basis, while the right slice shows concentrations of stress at particle-particle contacts. Full-scale simulations varying calendaring pressure and binder loading are ongoing, as is statistical analysis of the results on a per-particle basis to extract key insights and generating upscaling behavior.

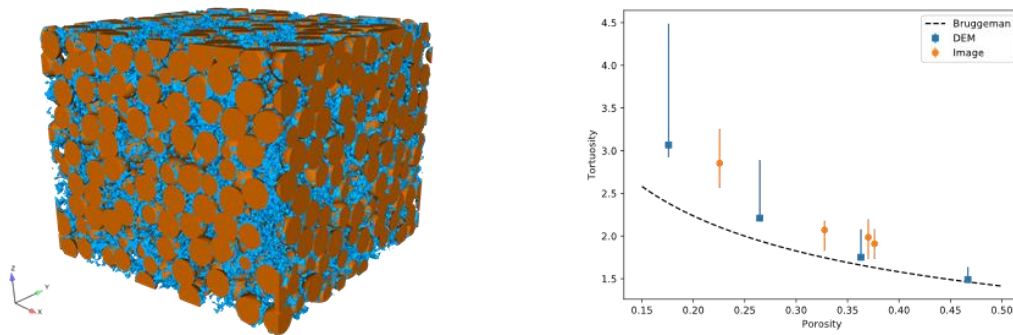


Figure I.3.C.6 (left) A CDFEM mesostructure including active material particles and CBD created from DEM simulations of electrode drying and compression. (right) Tortuosity versus porosity calculated from the image-based simulations compared to the initial DEM simulations, showing reasonable agreement.

Conclusions

We have significantly extended our approach for representing both experimentally derived and DEM simulated battery electrode mesostructures in a computational framework suitable for performing coupled multi-physics battery performance simulations. We have built up the confidence in this approach through careful solution verification and model comparisons.

Key Publications

1. S. Roberts, V. Brunini, K. Long and A. Grillet, "A Framework for Three-Dimensional Mesoscale Modeling of Anisotropic Swelling and Mechanical Deformation in Lithium-Ion Electrodes," *Journal of The Electrochemical Society*, vol. 161, pp. F3052-F3059, 2014.
2. S. Roberts, H. Mendoza, V. Brunini, B. Trembacki, D. Noble and A. Grillet, "Insights Into Lithium-Ion Battery Degradation and Safety Mechanisms From Mesoscale Simulations Using Experimentally Reconstructed Mesostructures," *Journal of Electrochemical Energy Conversion and Storage*, vol. 13, pp. 031005--031005, 2016.
3. S. A. Roberts, H. Mendoza, V. E. Brunini and D. R. Noble, "A verified conformal decomposition finite element method for implicit, many-material geometries," *Journal of Computational Physics*, pp. 352 - 367, 2018.
4. B. Trembacki, D. Noble, V. Brunini, M. Ferraro and S. Roberts, "Mesoscale Effective Property Simulations Incorporating Conductive Binder," *Journal of The Electrochemical Society*, vol. 164, pp. E3613-E3626, 2017.
5. B. L. Trembacki, A. N. Mistry, D. R. Noble, M. E. Ferraro, P. P. Mukherjee and S. A. Roberts, "Editors' Choice—Mesoscale Analysis of Conductive Binder Domain Morphology in Lithium-Ion Battery Electrodes," *Journal of The Electrochemistry Society*, pp. E725-E736, 2018.

References

1. K. Higa, S.-L. Wu, D. Parkinson, Y. Fu, S. Ferreira, V. Battaglia and V. Srinivasan, "Comparing Macroscale and Microscale Simulations of Porous Battery Electrodes," *Journal of The Electrochemical Society*, vol. 164, pp. E3473-E3488, 2017.
2. M. Ebner, F. Geldmacher, F. Marone, M. Stampanoni and V. Wood, "X-Ray Tomography of Porous, Transition Metal Oxide Based Lithium Ion Battery Electrodes," *Advanced Energy Materials*, vol. 3, pp. 845--850, 2013.
3. L. Zielke, T. Hutzenlaub, D. Wheeler, C.-W. Chao, I. Manke, A. Hilger, N. Paust, R. Zengerle and S. Thiele, "Three-Phase Multiscale Modeling of a LiCoO₂ Cathode: Combining the Advantages of FIB-SEM Imaging and X-Ray Tomography," *Advanced Energy Materials*, vol. 5, p. 1401612, 2015.
4. A. M. Grillet, T. Humplik, E. K. Stirrup, S. A. Roberts, D. A. Barringer, C. M. Snyder, M. R. Janvrin and C. A. Apblett, "Conductivity Degradation of Polyvinylidene Fluoride Composite Binder during Cycling: Measurements and Simulations for Lithium-Ion Batteries," *Journal of The Electrochemical Society*, vol. 163, no. 9, pp. A1859-A1871, 2016.

Acknowledgements

We would like to acknowledge members of the Sandia CAEBAT team, namely Bradley Trembacki, Mark Ferraro, Ishan Srivastava, and David Noble. We also appreciate our collaboration through the CAEBAT project, including ORNL partners John Turner and Srikanth Allu and our co-authors at Purdue Partha Mukherjee and Aashutosh Mistry. Sandia National Laboratories is a multi-mission laboratory managed and operated by National Technology and Engineering Solutions of Sandia, LLC., a wholly owned subsidiary of Honeywell International, Inc., for the U.S. Department of Energy's National Nuclear Security Administration under contract DE-NA0003525.

I.3.D Consortium for Advanced Battery Simulation (ANL, LBNL)

Venkat Srinivasan, Principal Investigator

Argonne National Laboratory
9700 S. Cass Ave.
Lemont, IL 60439
E-mail: vsrinivasan@anl.gov

Brian Cunningham, DOE Technology Development Manager

U.S. Department of Energy
E-mail: Brian.Cunningham@ee.doe.gov

Start Date: October 1, 2015	End Date: September 30, 2018	
Project Funding (FY18): \$170,000	DOE share: \$170,000	Non-DOE share: \$0

Project Introduction

Porous battery electrode thickness affects ion transport and therefore battery performance. Some recent battery models (see, for example, [1]) have incorporated electrode volume changes using submodels based on limited experimental data, such as active material volume change as a function of state-of-charge (SOC). However, recognizing that volume changes at the electrode level may be influenced by multiple interacting factors, we have undertaken an effort to use X-ray microtomography, simultaneous electrochemical cycling, and a novel analytical approach in order to obtain a quantitative understanding of electrode volume changes--not just of overall electrode thickness, but of local changes throughout the electrode. Our findings should lead to more realistic treatment of electrode volume change in battery models.

Objectives

Our FY18 objective for the Consortium for Advanced Battery Simulation (CABS) program was to obtain electrode image data from cycled electrode material. The objective for our “CD-adapco” subproject was to develop a postprocessing pipeline for tomographic reconstructions of cycled electrodes.

Approach

An electrode fabricated in FY16 by CABS teammate Sergiy Kalnaus (ORNL), using NMC532 active material and calendered to approximately 40% porosity, was cut to a 1 cm² square. Andrew Jansen at the Cell Analysis, Modeling, and Prototyping (CAMP) facility at ANL incorporated this electrode into a pouch cell suitable for imaging by hard X-ray microtomography, containing a lithium metal anode and a 1M solution of LiPF₆ in a mixture (1:1 by mass) of ethylene carbonate and diethyl carbonate.

With the guidance of beamline scientist Xianghui Xiao (formerly at ANL/APS 2-BM, now at BNL), the pouch cell was sandwiched between rigid acrylic plates and mounted approximately vertically on a rotating sample platform. This approach prevented the NMC electrode from being partially obscured by the adjacent material for the entire rotation, which would otherwise require that the electrode be oriented perfectly horizontally with respect to the camera. However, this change in sample orientation required changes to the postprocessing strategies developed for this project FY16 and FY17. In addition, the pouch cell was also connected to a galvanostat in a way that prevented the leads from obscuring the cell during rotation.

The region of interest was restricted to the NMC electrode, and over 66 hours of cycling (at rates ranging from 0.1C to 5C), 152 tomography data sets were obtained (blue dots overlaid on potential-time curve in Figure I.3.D.1). Image acquisition was started before cycling, instrument clocks were synchronized. This in situ experiment exceeded our FY18 CABS milestone of obtaining electrode image data from cycled electrode material. The TomoPy package (supplied by APS) was used in filtering and reconstruction.

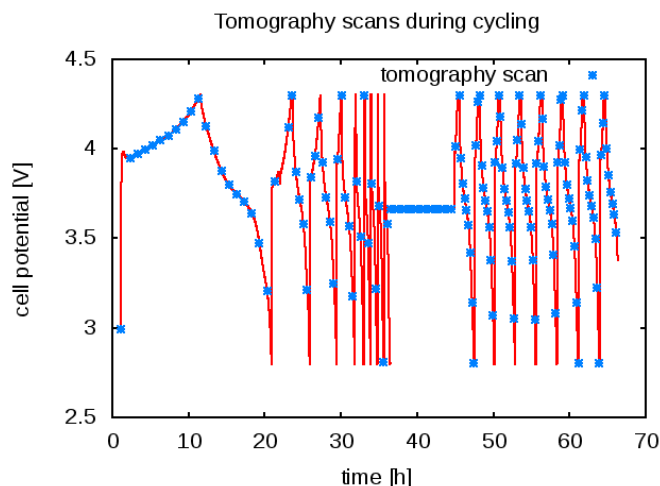


Figure I.3.D.1 Tomography scan times overlaid on potential-time curve. (LBNL, ANL)

It was found that the pouch cell was slightly angled with respect to the vertical plane, and that the sample moved slightly over the course of the 66-hour experiment. This was the first challenge to be addressed through postprocessing, as image alignment facilitates quantitative comparison of image results.

Automation of the postprocessing pipeline, as also performed under the “CD-adapco” subproject in previous years, provides several benefits. It precisely documents the postprocessing activity, improves consistency by reducing the influence of researcher subjectivity, and saves time in analyzing large amounts of data requiring similar treatment. The automated postprocessing was implemented in Python 2, and made use of the NumPy and SciPy packages.

Unlike in tomography images obtained in our FY16 and FY17 experiments, average voxel values in the electrode region and in surrounding regions were very similar, and therefore not useful as a means of detecting the electrode location within the image data. However, the electrode region clearly showed less spatial uniformity. Canny edge detection (as implemented in SciPy) was therefore used to roughly highlight the electrode regions. Effective detection parameters were found by trial-and-error, but consistent parameter values could be used for all data sets because all images were similar. This procedure was performed only for the bounding slices of each image data set, as it was observed that the electrode was nearly planar and therefore its location could be well-described by its corners.

Although the previous procedure was sufficient to highlight voxels within the electrode region, further processing was needed to get the computer to recognize these voxels not as a collection of edges internal to the electrode region, but as part of a larger planar region. After filtering the images to remove noise, the pixels in the monochrome edge images were reinterpreted as data points in Cartesian space. A linear least-squares fit with a linear function was then sufficient to approximately identify the central plane through the electrode.

As the electrode was observed to have nearly uniform thickness, the central plane was recognized as being well-aligned with the edges of the electrode region. By “walking” across the images and summing pixel values along lines parallel to the central plane, we obtained an indicator of electrode edge location: rapid changes in sums. These sums were then subjected to k-means clustering (kmeans2 as implemented in SciPy) in order to automatically detect edge locations.

Having identified the electrode boundary edges, one can readily calculate the rotation angles needed to align the electrode edge planes with voxel block axes. An ImageJ/Fiji [\[2\]\[3\]](#) script was used to perform these rotations and crop the resulting voxel blocks to the electrode regions. This fulfilled the “CD-adapco” milestone of developing an automated image processing pipeline for processing of images of cycled electrodes, enabling

quantitative comparisons of corresponding imaging and electrochemical data, as described in the following section.

The pipeline described above is illustrated in Figure I.3.D.2.

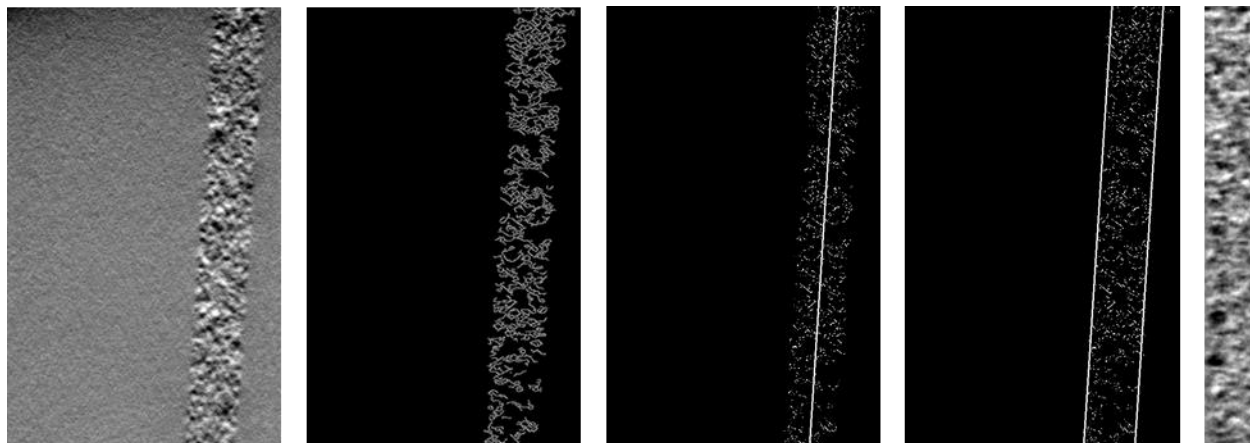


Figure I.3.D.2 Image postprocessing pipeline. Left to right: reconstruction, slice after edge detection, detection of central plane, detection of bounding planes, rotated and cropped electrode region. First four images show a region 320 microns across, last image shows a region 320 microns tall. (LBNL, ANL)

Results

The cropped, rotated electrode images showed thickness changes during the experiment, and suggested a complicated relationship between SOC and thickness. Understanding these results will provide unique information to modelers who are working to incorporate realistic strain into battery simulations.

Ideally, the voxel value information in our tomography data would be linear absorption coefficients that can be related to material identity in a straightforward way. Unfortunately, due to the filtering and reconstruction built into TomoPy to provide useful contrast, the relationship between voxel values and X-ray transmission is very complicated and effectively unknown, so individual voxel values cannot be interpreted quantitatively.

However, we believe that quantitative analysis of this data is still possible. We begin with a very mild assumption: that despite the uncertainty in interpreting the value of any single voxel, that over large numbers of voxels, a higher average value indicates a volume of less transmission than does a lower average value. In this particular case, we take averages over 1-voxel-thick “slices” that are parallel to the electrode plane, since we expect conditions to be fairly uniform within each slice.

To reduce complexity, we restrict our attention to only the first 12 image sets, corresponding to the initial charging process. Computing slice averages as a function of slice position in the image data, we obtain continuous curves and approximately monotonic changes from one side of the electrode to the other, but no clear correlation with SOC, along with negative average values that therefore cannot be linear absorption coefficients (Figure I.3.D.3, upper left).

We make a further assumption: that electrode changes will be most limited near the current collector due to transport limitations during operation, although we note that the location of the current collector during the experiment was not recorded. This suggests that the electrode will see most expansion on the separator side, and since lower slice average values correspond to greater transmission (corresponding to lower material density), we should see a decrease in slice average values close to the separator. As a first approximation, all curves of slice averages as a function of slice position were shifted to an arbitrary common value at one electrode edge. It turns out that alignment on only one of the edges is associated with the expected increasing

transmission along the other edge, providing identification for the current collector and separator sides of the electrode (Figure I.3.D.3, upper right).

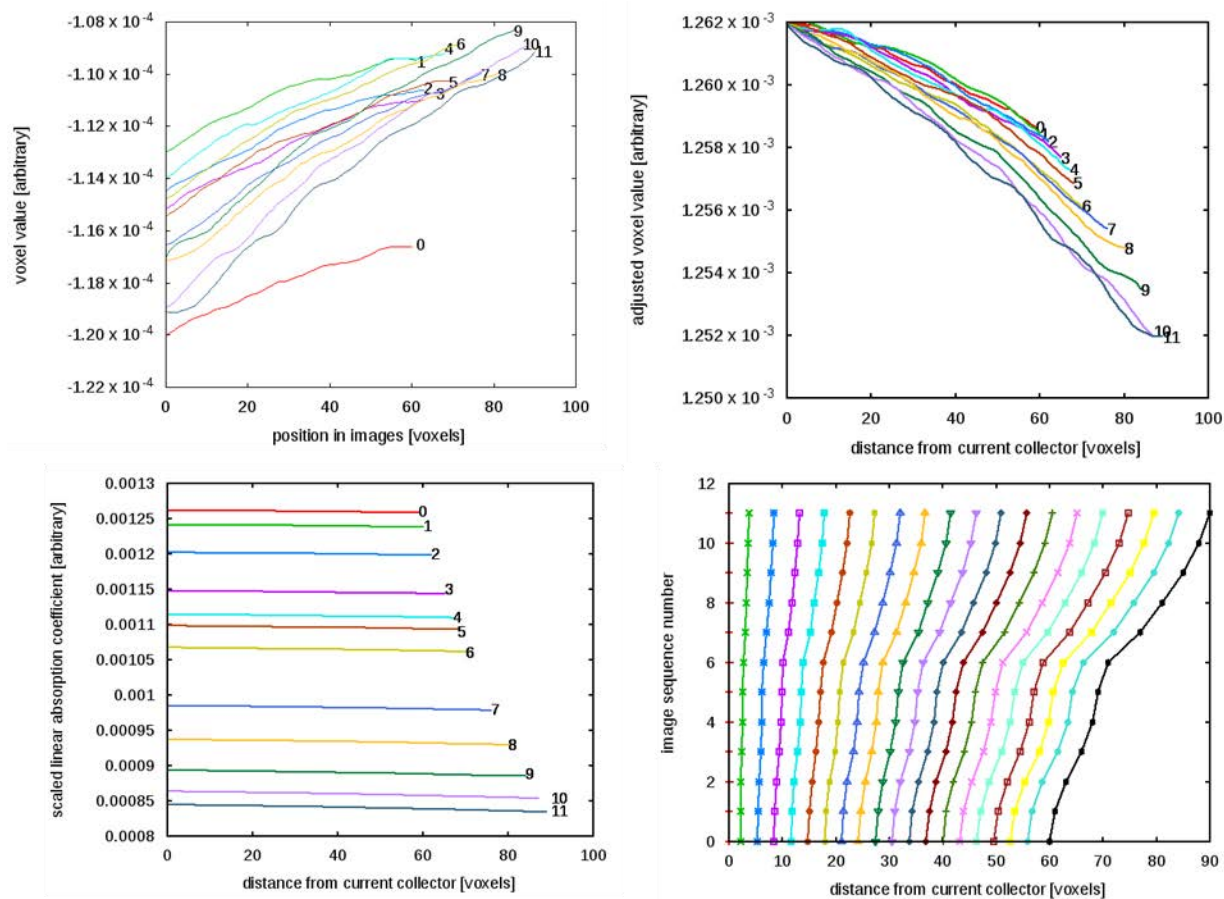


Figure I.3.D.3 Upper left: Raw slice averages as a function of slice position. Upper right: Slice average curves aligned on current collector edge. Lower left: Slice average curves translated into relative linear absorption coefficient curves. Lower right: Local electrode expansion during initial charge. (LBNL, ANL)

Observing that differences in voxel values within a single curve appear to be reproducible among different curves and are therefore probably physically meaningful, even if the slice-averaged values lack absolute meaning, we adopted the strategy of using differences in average voxel values within each curve to quantify spatial variation in transmission.

By examining published NMC532 data showing volume and density changes as a function of lithium content [4], and by combining this data with X-ray transmission calculator results [5][6], we first determined that the change in transmission due to chemical changes was negligible relative to the effect of electrode expansion on transmission.

Recognizing that total transmission through the electrode should be unaffected by physical expansion alone, relaxing the assumption of negligible expansion near the current collector, representing the linear absorption coefficient as an expansion of an unknown function of voxel value differences, and then performing fits using a minimal number of parameters, we then developed a quantitative relationship between voxel value and linear absorption coefficient (to within an arbitrary scaling).

Replotting the slice average value data in light of this relationship shows that expansion is fairly uniform throughout the electrode, and significant even near the current collector (Figure I.3.D.3, lower left). By

tracking points of fixed cumulative absorption, we could further distinguish material regions to quantify local expansion (Figure I.3.D.3, lower right). This has demonstrated that electrode expansion is not very smooth on the initial charge, which suggests that creating accurate models will be challenging.

Conclusions

Our in situ tomography imaging of a pouch cell exceeded our CAEBAT milestone of obtaining image data of cycled electrodes, and we met the “CD-adapco” subproject milestone through the development of a new automated pipeline for processing the resulting images.

Despite known limitations on quantitative interpretation of individual voxel values in the tomography images, we developed a method, based on clear and reasonable assumptions, that permitted quantitative comparison of different images, providing an unprecedented examination of local electrode volume change during the in situ experiment. We have also demonstrated that, counterintuitively, electrode volume changes during initial charge are in the opposite direction of changes in active material volume.

Key Publications

1. M. Chintapalli, K. Higa, X. C. Chen, V. Srinivasan, and N. P. Balsara. 2017. "Simulation of local ion transport in lamellar block copolymer electrolytes based on electron micrographs." *J. Polym. Sci. Part B: Polym. Phys.*, 55, 3, 1099
2. Sung Un Kim and Venkat Srinivasan. 2016. "A Method for Estimating Transport Properties of Concentrated Electrolytes from Self-Diffusion Data." *J. Electrochem. Soc.*, volume 163, issue 14, A2977-A2980
3. K. Higa, S.-L. Wu, D. Y. Parkinson, Y. Fu, S. Ferreira, V. Battaglia, and V. Srinivasan. 2017. "Comparing Macroscale and Microscale Simulations of Porous Battery Electrodes." *J. Electrochem. Soc.*, volume 164, issue 11, E3473-E3488; doi: 10.1149/2.0501711jes; <http://jes.ecsdl.org/content/164/11/E3473.short>
4. Z. Feng, K. Higa, K. S. Han, and V. Srinivasan. 2017. "Evaluating Transport Properties and Ionic Dissociation of LiPF₆ in Concentrated Electrolyte." *J. Electrochem. Soc.*, volume 164, issue 12, A2434-A2440; doi: 10.1149/2.0941712jes; <http://jes.ecsdl.org/content/164/12/A2434.short>

References

1. T. R. Garrick, K. Higa, S.-L. Wu, Y. Dai, X. Huang, V. Srinivasan, and J. W. Weidner. 2017. *J. Electrochem. Soc.* 164, 11, E3592-E3597
2. J. Schindelin, I. Arganda-Carreras, E. Frise, V. Kaynig, M. Longair, T. Pietzsuch, S. Preibisch, C. Rueden, S. Saalfeld, B. Schmid, J. Y. Tinevez, D. J. White, V. Hartenstein, K. Eliceiri, P. Tomancak, and A. Cardona. 2012. *Nat. Methods.*, 9(7), 676
3. C. A. Schneider, W. S. Rasband, and K. W. Eliceiri. *Nat. Methods*, 9(7), 671
4. O. Dolotko, A. Senyshyn, M. J. Mühlbauer, K. Nikolowski, H. Ehrenberg. 2014. "Understanding structural changes in NMC Li-ion cells by in situ neutron diffraction." *Journal of Power Sources*, 255, 197-203
5. E. Gullikson. 1995-2010. "X-Ray Interactions with Matter." http://henke.lbl.gov/optical_constants/.
6. B.L. Henke, E.M. Gullikson, and J.C. Davis. 1993. "X-ray interactions: photoabsorption, scattering, transmission, and reflection at E=50-30000 eV, Z=1-92." *Atomic Data and Nuclear Data Tables*, Vol. 54 (no.2), 181-342

Acknowledgements

Kenneth Higa (LBNL), Zhange Feng (formerly at ANL), and Pallab Barai (ANL) contributed to this project.

We gratefully acknowledge:

- Kee Sung Han (PNNL/EMSL) for past and ongoing pulsed field gradient NMR electrolyte solution transport property measurements. A portion of the research was performed using EMSL (Ringgold ID 130367), a DOE Office of Science User Facility sponsored by the Office of Biological and Environmental Research.
- Sergiy Kalnaus (ORNL), our CABS teammate for fabricating the electrodes use in imaging experiments.
- Andrew Jansen (ANL/CAMP) for constructing the pouch cell used in the *in situ* imaging experiment.
- Xianghui Xiao (previously at ANL/APS 2-BM, now at BNL) for his guidance in performing the *in situ* X-ray microtomography experiment. This research used resources of the Advanced Photon Source, a U.S. Department of Energy (DOE) Office of Science User Facility operated for the DOE Office of Science by Argonne National Laboratory under Contract No. DE-AC02-06CH11357.
- Dula Parkinson and Harold Barnard (LBNL/ALS beamline 8.3.2) for their assistance with earlier X-ray microtomography experiments. This research used resources of the Advanced Light Source, which is a DOE Office of Science User Facility under contract no. DE-AC02-05CH11231.
- This work was supported by the Assistant Secretary for Energy Efficiency and Renewable Energy, Vehicle Technologies Office, of the U.S. Department of Energy under Contract Nos. DE-AC02-05CH11231 and DE-AC02-06CH11357, under the CAEBAT3 Program.

I.3.E Advanced Tool for Computer Aided Battery Engineering (ANL)

Dr. Daniel Abraham, Principal Investigator

Argonne National Laboratory
9700 Cass Ave
Argonne, IL 60439
E-mail: abraham@anl.gov

Brian Cunningham, DOE Technology Development Manager

U.S. Department of Energy
E-mail: Brian.Cunningham@ee.doe.gov

Start Date: October 1, 2016	End Date: September 30, 2018	
Project Funding (FY18): \$300,000	DOE share: \$300,000	Non-DOE share: \$0

Project Introduction

The main goals of DOE's Computer Aided Engineering for Electric-Drive Vehicle Batteries (CAEBAT) Program were introduced in section I.C.1. In this section we describe the experimental studies conducted at Argonne National Laboratory (ANL) to support the development of 3D models of electrochemical processes on the electrode microstructure length scale and to provide an understanding of factors that limit electrode performance and cause premature degradation. These studies are intended to complement and enhance the experimental and computational work being conducted at the partner national laboratories and universities.

Objectives

The key objectives of our work can be summarized as follows:

1. To provide the positive and negative electrodes needed to accomplish the various tasks listed in section I.C.1.
2. To characterize the electrodes using conventional electrochemical techniques, both in half-cell and full-cell configurations, and to provide the data for the development of 3D electrochemistry models.
3. To develop advanced tools, including spectroscopy and diffraction, to obtain deeper insights on the correlations between electrode microstructure and electrochemical performance.

Approach

Commercial lithium-ion batteries (LIBs) predominantly use porous graphite (Gr) anodes (negative electrodes) and layered metal oxide cathodes (positive electrodes). At cycling rates below 1C (full discharge in 1 hour), these LIBs can go through hundreds of cycles of operation with minimal performance degradation. However, at higher cycling rates, the capacity, cycle life, and thermal stability of these LIBs is known to degrade. Theoretical studies of lithium intercalation using Newman-type models attribute these effects to lithium plating, kinetic losses, and Li^+ concentration gradients (causing polarization of the cell) occurring both in the electrolyte filling the matrix pores and in the graphite electrode itself. Our focus was the latter gradients that are a complex function of Li^+ diffusion coefficients, intercalation rates, ion transference numbers, and the electrode thickness (t), porosity (ϵ), and tortuosity (τ). For example, low porosity and high tortuosity in the electrode decrease the effective diffusion coefficient $D_{eff} = (\epsilon/\tau)D_{bulk}$ of the Li^+ ions in the matrix relative to the solvent bulk. At high charge rates, this lower mobility leads to greater differentials in lithium concentration in the direction of the flowing Li^+ ion current (that we take as the z -direction of the laboratory frame with $z = 0$ corresponding to the electrode surface near the separator between the electrodes).

While there have been many modeling studies of concentration gradients developing in LIBs during high-current cycling, the experiments directly observing and quantifying these gradients are still lacking. With this

study, we seek to close this gap in knowledge. To this end, we used energy dispersive X-ray diffraction (EDXRD) to spatially-resolve Li concentration profiles in an *operando* fashion during cycling of a Li-ion cell at 1C rate. With this technique, narrowly focused polychromatic (“white light”) beams of synchrotron photons are used to obtain diffraction patterns at a fixed angle θ , so the Bragg condition, $2d \sin\theta = n\lambda$, is satisfied for some wavelengths λ in the light continuum. This method is complementary to the commonly used angle-dispersive XRD method, which uses monochromatic X-ray beams and scans the angle θ to satisfy the Bragg condition. As lithium intercalates into the graphite crystal, it fills layers between the graphene sheets (“staging of the graphite”) yielding distinctive, ordered Li_xC_6 phases ($0 \leq x \leq 1$) that can be easily recognized even from a single Bragg peak. The intensities of these peaks can be used to quantify the concentration of each Li_xC_6 phase, and through such quantification we determine the exact phase composition of each probed layer in the solid matrix. As only ordered Li_xC_6 phases contribute to the diffraction signal, this method is blind to Li^+ ions in the electrolyte and/or potential disordered solid compounds in the matrix. Using the EDXRD technique, the succession of Li_xC_6 phases formed during the electrochemical lithiation and delithiation of graphite has been studied with a spatial resolution of 20 μm and a time resolution of one minute.

A standard 2032-type coin cell, containing a Gr based anode and a $\text{Li}_{1.03}(\text{Ni}_{0.5}\text{Co}_{0.2}\text{Mn}_{0.3})\text{O}_2$ (NCM523) based cathode, was used in our experiments. Briefly, the anode contained 92 wt% graphite, 2 wt% conductive carbon particles, and 6 wt% polymer binder, while the NCM523 cathode contained 90 wt% oxide, 5 wt% conductive carbon particles, and 5 wt% polymer binder. The slurries were prepared by mixing the particles in a planetary centrifugal mixer using *N*-methyl-2-pyrrolidone as a solvent. Electrode laminates were fabricated by casting these slurries onto a 10 μm battery grade copper foil for the Gr electrode and 20 μm battery grade aluminum foil for the NCM523 counter electrode, using a battery coater at the Cell Analysis, Modeling and Prototyping (CAMP) facility at Argonne National Laboratory. After drying of the solvent, the Gr electrode was calendered to obtain uniform thickness. The NCM523 cathode was not calendered, in order to retain maximum porosity in the matrix and ensure minimal interference during the high rate cycling. Before cell assembly, the electrodes were dried at 120 °C for 12 h, and the separator was dried at 70 °C for 24 h, both in a vacuum oven. The assembled cell contained 40 μL of 1.2 M LiPF_6 in ethyl carbonate/ethyl methyl carbonate mixture (3:7 w/w). This electrolyte filled a microporous Celgard 2325 separator sandwiched between the two electrodes (1.58 cm^2 areas). A positive-to-negative electrode capacity ratio of 1.13 was chosen to enable deep lithiation and delithiation of the graphite electrode.

The cycling tests were conducted at 30 °C. The C-rates, state-of-lithiation, and cell capacities were calculated with respect to the theoretical capacity of the Gr, which is 372 mAh/g. The applied current of 5.6 mA corresponded to a ~1C rate for the full cell. Prior to the *operando* XRD experiment, the cell was cycled twice at a C/20 rate in the 3–4.1 V range, in order to stabilize the solid electrolyte interphase (SEI) on the graphite electrode. Three additional cycles were conducted during the XRD experiment: the cycling was performed in a galvanostatic regime until an upper cut voltage of 4.4 V or a lower cut voltage of 3.0 V were attained on charge (Gr lithiation) and discharge (Gr delithiation), respectively. Upon attainment of the set voltages, the cell operated in a potentiostatic regime for 30 min (referred to as “potentiostatic hold”).

Results

The EDXRD setup at beamline 6BM-A of the Argonne’s Advanced Photon Source was used to observe the diffraction patterns of the pristine graphite and ordered Li_xC_6 phases in an operating Gr/NCM523 cell described above. The X-ray photons with energies between 5 and 250 keV (that corresponds to 47 to 1 Å in d-spacing) readily transmit through the stainless steel casing of the coin cell. A Ge detector placed at a fixed angle $\theta \approx 3^\circ$ in the vertical plane with respect to the incident X-ray beam collected and averaged the diffraction patterns at a rate of 1 min per acquisition for a total period of 3 h per charge/discharge cycle. The probe X-ray beam was 20 μm x 1045 μm ; this beam propagated along the plane of the Gr electrode “slicing” it in steps of 25 μm , to give a total of five minimally-overlapping layers numbered from L_0 to L_4 in Figure I.3.E.1 As shown in the figure, layer L_0 was adjacent to the separator and layer L_4 was adjacent to the Cu current collector. To position the X-ray beams in the transverse direction with respect to the Cu current collector, the latter was scanned in small steps, and the maximum intensity of the scattered (002) peak from Cu

was taken as the midsection of the foil. To obtain the profile of the beam as it crosses the Gr matrix, a radiograph through the cell was collected (Figure I.3.E.1). The pixel intensity map represents the beam intensity distribution, which is overlaid onto the radiograph. The five layers were sampled in a round-robin fashion.

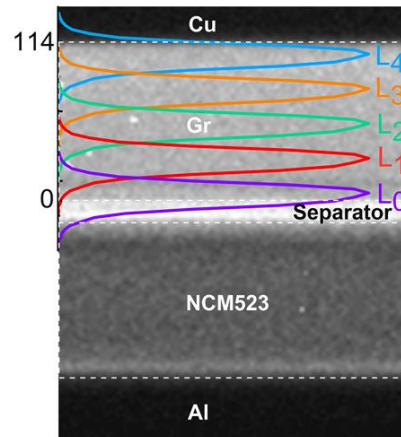


Figure I.3.E.1 X-ray radiograph of the cell (a transverse cross section), showing the various components. The X-ray beams penetrate the cell from the left. Gaussian-shaped colored lines represent the actual profiles of the X-ray beam as determined from a radiograph intensity map and by the depth calibration. Layers L_n ($n = 0-4$ with n increasing in the direction of the electrode depth z away from the separator) are overlapping sections of the cell that are probed by the X-ray beams. During charge, a Li^+ ion current flows from the NCM523 cathode to the Gr anode (graphite lithiation); the reverse happens during discharge (graphite delithiation).

The voltage-capacity curves from the Gr/NCM523 cell during cycling at a C/20 rate (cycle 2, 3-4.1 V) and a 1C rate (cycle 5, 3-4.4 V) are shown in Figure I.3.E.2. From the measured specific capacity, one can calculate the cell average lithium content \bar{x} that we express in Li atoms per C_6 unit of the graphite present in the electrode; the \bar{x} value is given at the top of Figure I.3.E.2. During 1C galvanostatic charging, the upper cut-off voltage of 4.4 V was attained at $\bar{x} = 0.58$, which increased to $\bar{x} = 0.68$ at the end of the 30 min potentiostatic hold. During the 1C discharge, the lower cut voltage of 3.0 V was attained at $\bar{x} = 0.1$, which decreased to $\bar{x} = 0.02$ at the end of the 30 min hold.

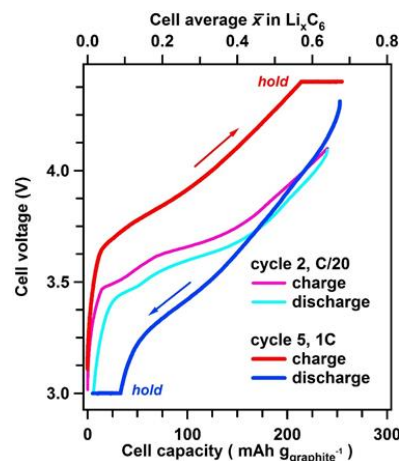


Figure I.3.E.2 Voltage-capacity plots for cycling of Gr/NCM523 cell at C/20 and 1C rates (cycles 2 and 5, respectively). Specific capacities of the graphite electrode are shown at the bottom, and the estimated cell average lithium content of this electrode is shown at the top. The arrows indicate the direction of the Li^+ ion current. For cycle 5, the red color corresponds to charge and the blue color corresponds to discharge of the cell.

The voltage-capacity curves shown in Figure I.3.E.2 reveal characteristic steps attributable to the graphite electrode (known as "stages"); the stages of graphite correspond to progressive filling of spaces between the adjacent graphene sheets. The d -spacings obtained from the XRD patterns collected during the operando experiments are shown in Figure I.3.E.3. The various stages/phases formed by Li intercalation into graphite are stage I', stage IV/III, stage III (LiC₁₈), stage II (LiC₁₂), and stage I (LiC₆); the peaks of the dilute Li stages I', IV/III, and III overlap in d -spacing and cannot be easily resolved. For convenience, the concentrations of the Li_{*x*}C₆ phases reported below have been adjusted by the fractional Li content f_j of the phases; therefore these concentrations reflect the availability of Li in each phase averaged in a given layer.

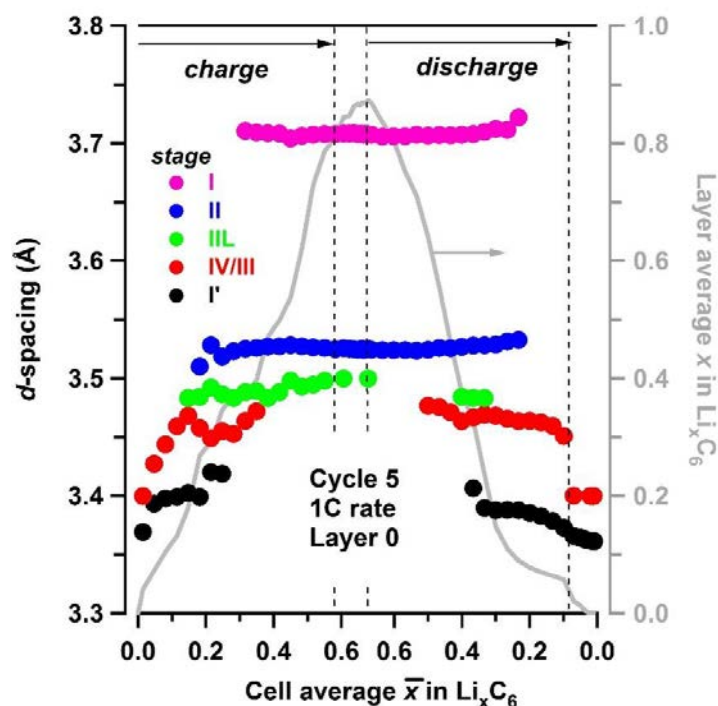


Figure I.3.E.3 Experimental d -spacing (filled circles, axis to the left) for Li_{*x*}C₆ phases present in layer L₀, observed during cycling at 1C rate and plotted as a function of the cell average lithium content \bar{x} in the matrix. The lithiation stages are color-coded as shown in the inset. The vertical dashed lines indicate the potentiostatic hold. Shown to the right in grey is the layer average lithium content x .

Using the concentration of each phase, the *layer* average Li content of layers L₀ through L₄ can be determined and compared with the *cell* average Li content \bar{x} determined electrochemically (see Figure I.3.E.4). We reason that for sufficiently smooth concentration profiles the arithmetic average of these layers would be sufficiently close to the cell average (open circles in Figure I.3.E.4), i.e. the two metrics are expected to be close to each other (straight black lines in Figure I.3.E.4). This is indeed the case during charge. It is also seen from these plots that at the peak of charge, x for L₀ is considerably above the cell average \bar{x} , whereas x for L₄ is significantly below \bar{x} . The inhomogeneity in the quantity of individual phases in each layer across the graphite electrode (greater amount of LiC₆ at the electrode surface compared to deeper layers for example) is reflected in the calculated Li content of the layers, with significant difference observed only when $\bar{x} > 0.2$. A surprising feature of Figure I.3.E.4 is the asymmetry of the traces: the delithiation of the electrode does not mirror the lithiation run "in reverse"; this asymmetry becomes even more noticeable for the deepest layers. Most strikingly, during the rapid discharge (in contrast to charge) the arithmetic mean of layer averages (open symbols in Figure I.3.E.4) strongly deviates from \bar{x} for $\bar{x} > 0.3$.

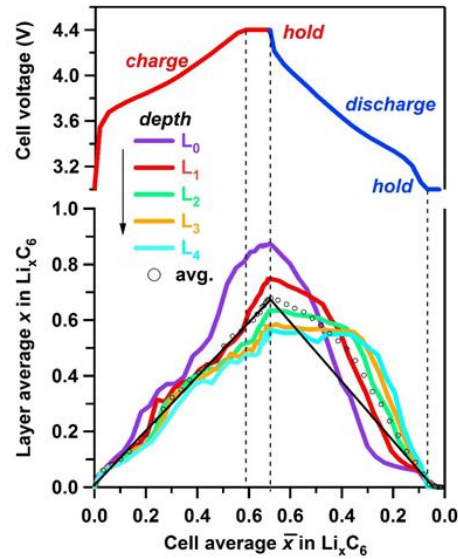


Figure I.3.E.4 Layer average lithium content x in the ordered Li_xC_6 phases estimated using eq. 1 plotted as a function of the cell average lithium content \bar{x} of the graphite matrix determined electrochemically. The layers are color coded as shown in the inset. The vertical dashed lines correspond to the potentiostatic hold periods (see voltage plot at the top). The arrow shows the direction of increasing depth. The open circles indicate the five-layer average, and the straight line is \bar{x} .

To better visualize the inhomogeneities across the electrode, in Figure I.3.E.5. we plot Li content in each layer at different states of charge as a function of the median depth z of the five layers (L_0 to L_4 , filled color symbols).

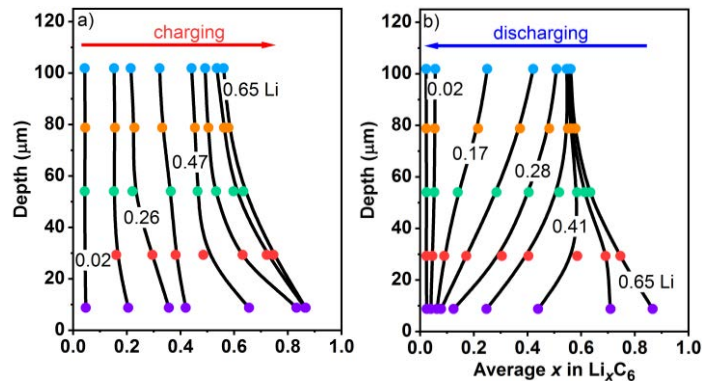


Figure I.3.E.5 Layer average Li content x in the ordered phases (filled circles, to the bottom) plotted vs. the median depth of these layers (to the left). Panel a is for charge and panel b is for discharge of the cell at 1C rate vs. the graphite electrode capacity. The numbers in the plot give the overall cell average lithium content \bar{x} of the graphite matrix calculated based on the electrochemically measured cell capacity.

In the initial stages of charging (Figure I.3.E.5 a), the Li content is nearly uniform across the electrode. As the cell is charged further, a concentration gradient develops, with more lithium present near the surface (L_0) than at the back (L_4). This transformation nearly coincides with the moment when LiC_6 becomes the prevalent phase near the surface in this particular graphite electrode. During cell charge, the gradient $d[\text{Li}]/dz$ remains negative across the electrode depth. During cell discharge, there is Li depletion near the surface that gradually spreads deeper into the matrix until it reaches the back of the cell. After that, the Li gradients once again become lower, and in the advanced stages of delithiation they become too small to observe. The complex shape of Li profiles during the cell discharge compared to the profiles during the cell charge is the primary

reason for the asymmetries seen in Figure I.3.E.4, including the behavior of the arithmetic average of layer averages. Put together, our data indicate strong inhomogeneity of Li insertion and de-insertion, both in the net Li content and in the individual Li_xC_6 phases.

Conclusions

We present an experimental methodology for quantifying spatial and phase heterogeneity of lithium intercalation into graphite during rapid cycling. The X-ray “slicing” of a 114 μm thick graphite electrode reveals steep gradients in the net and phase specific lithium content. The greatest inhomogeneity is observed for the LiC_6 phase. Under certain charging conditions, this phase accounts for all Li present at the surface; deeper in the electrode, the concentration exponentially falls towards the current collector. This Li inhomogeneity can have detrimental effects on cell performance, including low utilization of the active material and Li plating in the regions that are close to the electrode surface. Our data on concentration profiles in the individual phases Li_xC_6 as a function of lithiation can serve as a benchmark for modeling of electrochemical processes in LIBs. While some of the features observed have been anticipated by modelers, other features are less expected, such as the surprising persistence of Li_xC_6 phases during the potentiostatic hold at the end of discharge. Another peculiarity that awaits full explanation is the striking asymmetry between the charge and discharge, which suggests that the complex character of phase transitions during the high-rate delithiation may involve less ordered phases. While our method is eminently suitable to characterize phase dynamics on the scale of tens of microns, it does not provide sufficient insight into the processes occurring in the individual graphite particles, where different phase domains can coexist and affect each other. In fact, it is somewhat surprising that our analysis (neglecting such complexities) appears to adequately capture the phase dynamics under strongly non-equilibrium conditions. We hope that the insight this approach provides into electrochemical processes in practical lithium-ion cells, will spark renewed interest in validation and improvement of the cell models. Although only planar cells with single-sided electrodes were studied, our methodology can be extended to characterize heterogeneity of Li transport in more complex, multi-layer, prismatic and cylindrical battery cells.

Key Publications

1. Koffi P.C. Yao, John S. Okasinski, Kaushik Kalaga, Ilya A. Shkrob, and Daniel P. Abraham, “Quantifying lithium concentration gradients in the graphite electrode of Li-ion cells using *operando* energy dispersive X-ray diffraction”, *Energy and Environmental Science*, *accepted for publication* (2018).

Acknowledgements

Use of the Advanced Photon Source (APS) at Argonne is supported by the U. S. Department of Energy, Office of Science, Office of Basic Energy Sciences, under Contract No. DE-AC02-06CH11357. The electrodes used in this article are from Argonne’s Cell Analysis, Modeling and Prototyping (CAMP) Facility, which is supported within the core funding of the Applied Battery Research (ABR) for Transportation Program. We are grateful to our colleagues (Stephen Trask, Bryant Polzin, Andrew Jansen, Dennis Dees, Jonathan Almer, Andrew Chuang, Kandler Smith, Francois Usseglio-Viretta, Andrew Colclasure) for their support and guidance during this effort.

I.3.F Advanced Tool for Computer Aided Battery Engineering (SNL)

Joshua Lamb, Principal Investigator

Sandia National Laboratories
1515 Eubank SE
Albuquerque, NM 87185
E-mail: jlamb@sandia.gov

Brian Cunningham, DOE Technology Development Manager

U.S. Department of Energy
E-mail: Brian.Cunningham@ee.doe.gov

Start Date: October 1, 2017	End Date: September 30, 2018	
Project Funding (FY18): \$200,000	DOE share: \$200,000	Non-DOE share: \$0

Project Introduction

This project aims to provide experimental support, including support for validation and parameterization, for mechanical failure modeling work as part of DOE's Computer Aided Engineering for Electric-Drive Vehicle Batteries (CAEBAT) program. This work involves mechanical deformation testing on both charged and discharged cells, including abusive mechanical testing leading to battery failure. The mechanical data generated is provided to the modeling teams to provide empirical parameterization as well as validation for newly developed models. Testing fully charged cells and packs (abusive battery testing) also allows for a better understanding of what conditions are most likely to lead to a potentially hazardous thermal runaway event.

Objectives

Experimental determination of mechanical properties of lithium ion batteries and materials

Experimentally validate simulation tools used to predict thermal runaway events caused by crash induced crush. This includes rate-dependent mechanical failure and properties of individual cells as well battery packs. Provide collected data to the consortium to aid in model development. Partner with the USCAR Crash Safety Work Group to obtain feedback on experimental methods as well as develop new tests that may be of relevance to crash safety engineers.

Approach

Sandia's Battery Abuse Test Laboratory was used to perform mechanical testing on full cells and packs for this project. This facility can contain and withstand thermal runaway of lithium ion cells and packs of up to 1 kWh of total energy. Mechanical test capabilities include a 100 klbf large crush fixture and a 10 klbf nail penetration and small-scale crush fixture. Recording capabilities include force, displacement, temperature and voltage measurements at rates of up to 1 kHz. Data recording rates varied depending on duration of testing.

Mechanical deformation results collected at Sandia have been provided to NREL and the technical working groups. This has also included collaboration and information sharing with the USCAR Crash Safety Working Group, with the ultimate goal of understanding what hazards lithium ion batteries may pose during extreme mechanical deformation events, such as an auto collision. Quarterly meetings also provide information sharing and collaboration with the broader consortium, including NREL, ANL, SNL and Purdue University, as well as members of the ORNL consortium.

Results

Mechanical/electrochemical/thermal abuse

Sandia National Laboratories developed and performed mechanical abuse testing to support CAEBAT modeling efforts to provide both parameterization and validation of mechanical abuse models. Current work focuses on understanding of the mechanical response of cells at elevated temperatures and the development of dynamic impact testing.

Figure I.3.F.1 below shows the impact of temperature on fully charged 5 AH pouch cells. Previous work has shown little change in the mechanical behavior of these cells when evaluated at temperatures within typical operating ranges of lithium ion batteries. This new work evaluated cells above normal operating temperatures. The cells were compressed at a rate of 0.1 mm/sec with a 24.4 mm radius cylindrical impactor. Cells were tested at both 100% SOC and 0% SOC. 100% SOC cells were compressed until thermal runaway was observed, while cells at 0% SOC were compressed to the average deformation required to create thermal runaway. The current results show little change in the overall mechanical behavior of the cells up to 100°C, however at 120°C we observed a significant reduction in the force required to deform the battery. We also observed a slightly higher displacement before thermal runaway occurred at elevated temperatures.

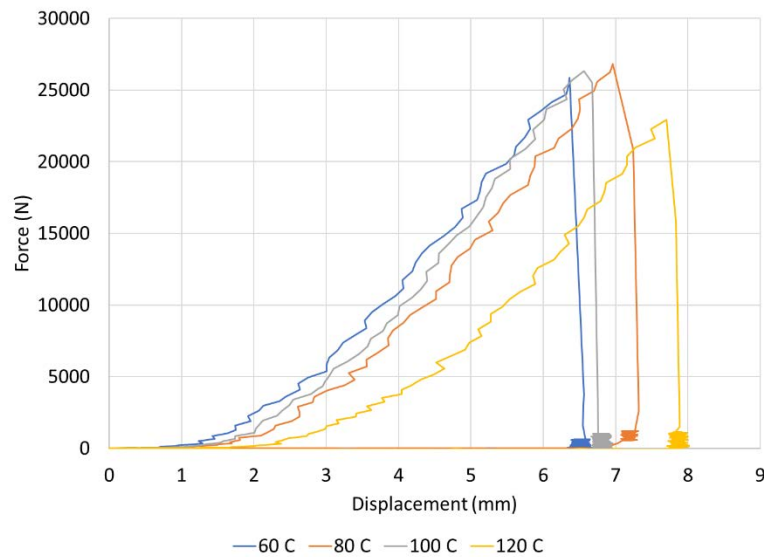


Figure I.3.F.1 Force vs displacement of fully charged 5 AH pouch cells. Little change is observed up to 60°C, however a dramatic softening of the cell is observed at 120°C

The observations here suggest that temperature would have minimal impact on the resilience of cells to mechanical deformation at more moderate temperatures. This and previously collected data show little apparent change in the behaviors at lower temperatures suggesting that until 120°C we wouldn't expect the susceptibility to mechanical crush to change significantly. On-going testing is looking at this elevated temperature testing at different rates and orientations to provide a complete picture on this susceptibility.



Figure I.3.F.2 Drop tower commissioning

Figure I.3.F.2 shows the commissioning progress on the drop tower to perform dynamic impact testing on cells and packs. The final deliverables pursued for this project in FY19 will be to perform drop tower testing on relevant cells and packs to provide parameterization and validation of behaviors under dynamic conditions.

Information sharing with NREL continues as well. Propagation testing data collected as part of this and other projects have been shared and developed into a publication detailing the behavior of cell to cell thermal runaway. Figure I.3.F.3 shows a sample of the data that has been provided. The intent is to provide sufficient data to further the analysis and understanding of multi-cell thermal runaway, particularly that introduced through mechanical failure.

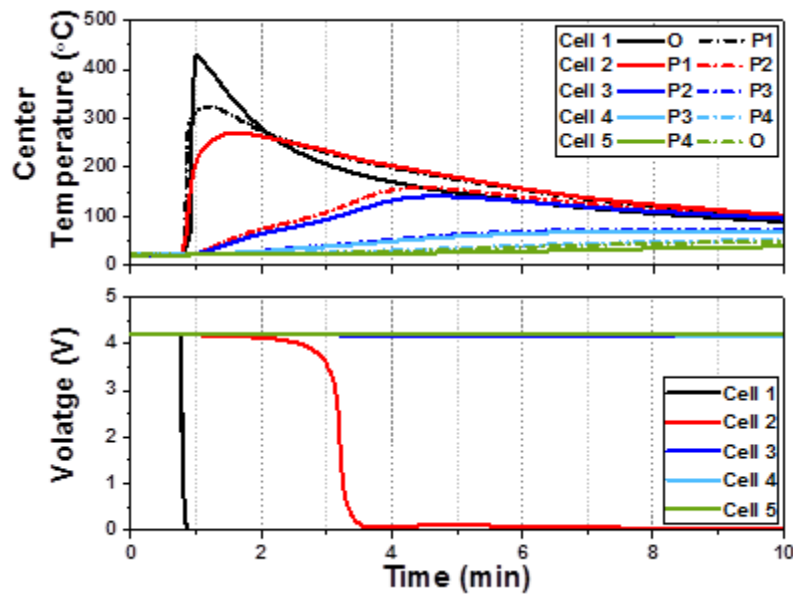


Figure I.3.F.3 Example propagation data provided to NREL for multi-cell modeling activities.

Conclusions

Sandia continues to provide experimental validation results to the NREL consortium as well as providing a broader understanding of the conditions likely to cause a potentially dangerous thermal runaway event in lithium ion batteries. The current work shows that mechanical compression events continue to be the most likely to cause a thermal runaway event. There was little observed dependence on temperature with cell mechanical behavior up to 100°C. However, at elevated temperatures a the cell was observed to require less force to drive the cell into thermal runaway suggesting softening of the constituent materials at that temperature. Sandia also continues to participate in information sharing with NREL partners as well as the USCAR Crash Safety Work Group.

Acknowledgements

Sandia Co-authors

Mohan Karulkar
Lorraine Torres-Castro
June Stanley
Chris Grosso
Lucas Gray

National Lab collaborators

Shriram Santhanagopalan
Chuanbo Yang
Kandler Smith
Matt Keyser
Daniel Abraham

I.3.G Development and Validation of a Simulation Tool to Predict the Combined Structural, Electrical, Electrochemical and Thermal Responses of Automotive Batteries (Ford Motor Company)

Dr. Chulheung Bae, Principal Investigator

Ford Motor Company
 Energy Storage Research
 2101 Village Road
 Dearborn, MI 48121
 E-mail: cbae@ford.com

Brian Cunningham, DOE Technology Development Manager

U.S. Department of Energy
 E-mail: Brian.Cunningham@ee.doe.gov

Start Date: January 1, 2016	End Date: December 31, 2019	
Project Funding: \$4,375,000	DOE share: \$3,500,000	Non-DOE share: \$875,000

Project Introduction

This is the third year of a three-year project to develop a practical simulation tool for predicting battery abuse response. However, due to unexpected problems in cell testing, model validation fell behind schedule, and a one-year no-cost extension was approved. The project will now conclude by the end of 2019.

The project plan including major constituents and progression based on case studies is shown in Figure I.3.G.1. The first half of the project was focused on developing an Alpha version of the model. This included developing new, battery-specific keywords within LS-DYNA, identifying electrical, thermal, and mechanical input parameters, validating the model for performance situations where the cells are cycling in their intended operating mode, demonstrating preliminary abuse simulations for external short and crush, and enhancing the composite element formulations within LS-DYNA to provide accurate representations of battery material mechanics. Importantly, one-way coupling mechanisms linking the structural response to the electrical and thermal response were implemented and initial simulation predictions compared to test results from previous studies to confirm that the solvers are directionally accurate. Physical testing of full cells, begun for model validation in the second year, was insufficient and will be completed early in the next year.

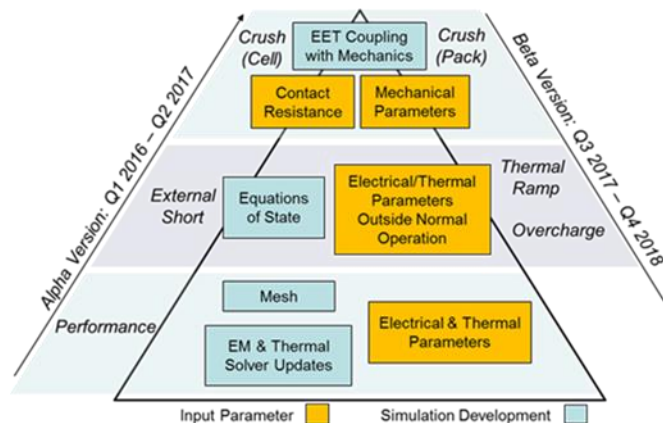


Figure I.3.G.1 Project schematic showing major constituents and progression of Alpha and Beta versions.

Objectives

Develop and validate a simulation tool to predict the combined structural, electrical, electrochemical and thermal (SEET) response of automotive batteries to crash-induced crush and short circuit, overcharge, and thermal ramp, and validate it for conditions relevant to automotive crash.

Approach

Develop material constitutive models and finite element method (FEM) element formulations that capture the mechanical response of cell components, including the case material, electrodes, separator, and their interactions with electrolyte.

Clearly identify the required input parameters for the constitutive models, FEM element formulations, and exothermic, electrochemical reaction state equations governing multi-physics phenomena during crush-induced electrical short, thermal ramp, and overcharge conditions.

Design and execute a test matrix encompassing automotive crash strain rates, at a number of kinetic energy levels and physical orientations likely to occur in vehicle impacts.

Develop integrated modeling tools that demonstrate high-fidelity predictions of the onset of thermal runaway from the experimental test matrix using commercially available cells, modules, and packs, spanning multiple chemistries relevant to automotive applications.

Maintain high-fidelity predictions while exploring methods to reduce the computational complexity of the model, and deliver a practical tool that is integrated with the laboratory's Open Architecture Software (OAS), for a broad customer base within automotive product development.

Results

Development of LS-DYNA Solvers

Work continued in refining the mechanical, EM and thermal solvers with composite t-shell elements. Models with composite t-shell elements under different abuse scenarios were developed to demonstrate the performance of composite t-shell elements and their advantages compared with solid elements in battery safety simulations. One example of an abuse event is that of a pouch cell impacted by a semi-sphere indenter, see Figure I.3.G.2. Models with either solid elements or composite t-shell elements are built with the same in-plane mesh size and boundary conditions. Results show that using composite t-shell elements can achieve comparable results in all three solvers (see Figure I.3.G.3 and Figure I.3.G.4) and reduce computational time by orders of magnitude in the mechanical solver. Since the mechanical solver takes the majority of time in impact simulations, improving efficiency in the mechanical solver significantly reduces the computational time for the entire simulation that involves three solvers. Moreover, it is found that using composite t-shell elements is more numerically stable at large deformation than solid elements due to their better aspect ratio. Numerical stability is critical to battery safety simulations that involve large deformation such as impact simulations. Similar features are also found in other scenarios where a cell is impacted by a semi-cylinder indenter. These advantages of the composite t-shell element allow us to build reliable and efficient models for battery safety.

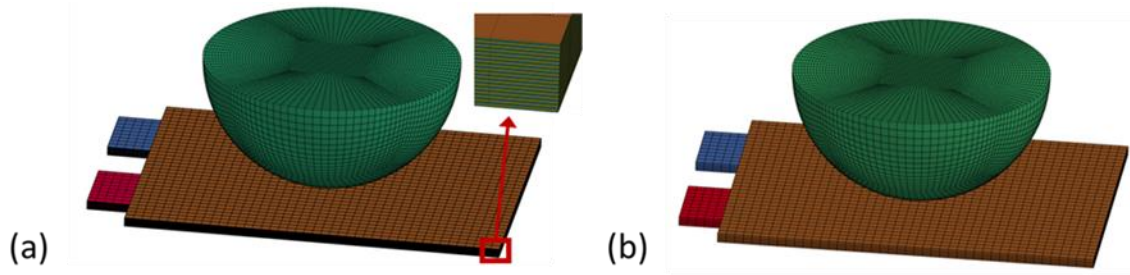


Figure I.3.G.2 Two models for the battery impact simulation. These models have the same settings except that different elements, (a) solid elements and (b) composite t-shell elements, are used in the cell bulk.

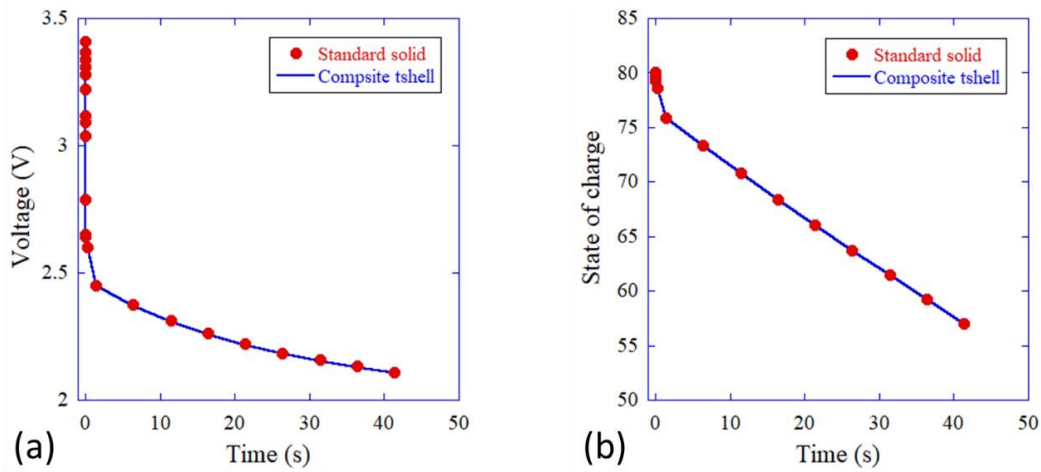


Figure I.3.G.3 Comparison of (a) voltage and (b) state of charge evolution in two types of models.

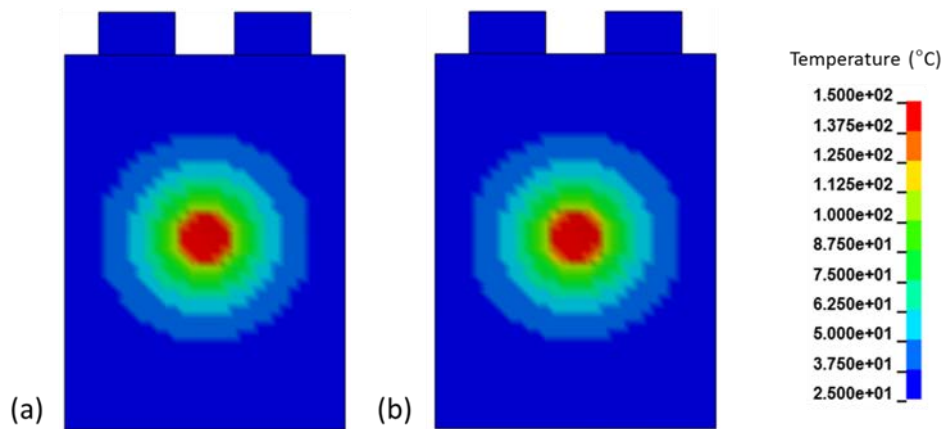


Figure I.3.G.4 Comparison of temperature distribution at 41 seconds in (a) the composite t-shell element model and (b) macro model.

The development of the macro model was initiated. The aim of the macro model is to improve the computational efficiency of EM and thermal solvers, and its difference from the composite t-shell element model is illustrated in Figure I.3.G.5. Early benchmark simulations show that the macro model can capture essential features of battery behaviors and save computational time by more than one order of magnitude compared with composite t-shell element model in an impact simulation that involves three solvers. Currently, the development of the macro model is still in its early stage. For instance, it only works for solid elements and

has limited short-circuit conditions. It is expected that after improving the capabilities of the macro model, it will be very attractive to large-scale simulations such as module and pack level simulations.

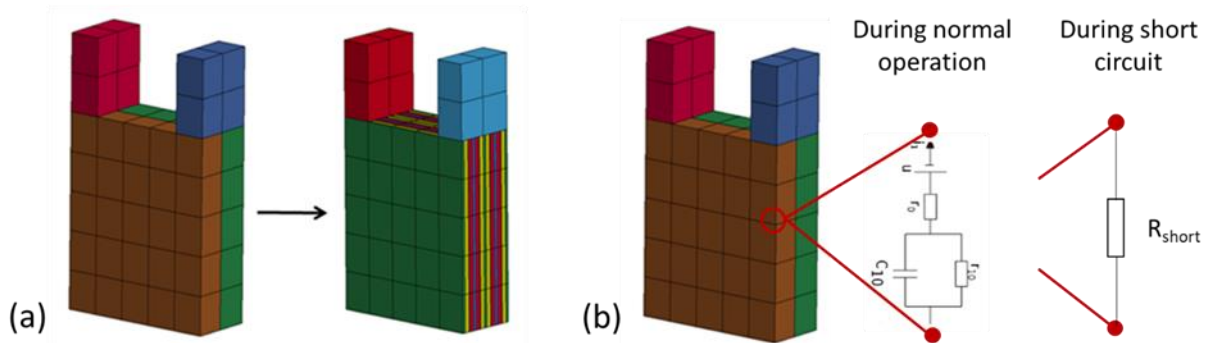


Figure I.3.G.5 Both (a) composite tshell models and (b) macro models can use a small number of elements in the cell thickness direction. The difference is that in the former, the EM and thermal solvers rebuild a mesh internally to resolve each individual layers. In the latter, no internal mesh is needed, and each node contains two potential fields connected by either Randles circuit or short-circuit resistance depending on local parameters such as stress, strain or temperature.

Development of Layered Solid Elements for Battery Cells

Layered solid finite element formulation has been under development for battery cells. (Note that ORNL uses the term layered solid element while Ford uses composite t-shell element. They are the same and can be used interchangeably). The element accounts for cell component layers within its integration points and integrate their response into the finite element. An accurate model of the cell assembly would be to use separate solid finite elements for each component layer of the cell, although such models are computationally extremely expensive. In fact, multiple elements may be needed across each layer but such models are even more impractical. We use these solid element assemblies as benchmarks against the layered solid element formulation. In Figure I.3.G.6, we show an example stress distribution under a rigid sphere that is indenting a battery cell. The repeated unit is shown in Figure I.3.G.6c. In the layered solid element formulation, each integration point through the thickness of the element contains different material model. However, the element only has eight nodes and 24 degrees of freedom. In the solid element model, two discretization schemes were used. In one, only four top cell repeated units (Figure I.3.G.6c) were resolved with solid elements, and the remaining layers were modeled with a homogenized material model. In the other solid element model, all 17 repeated cell units through cell thickness were discretized by solid elements.

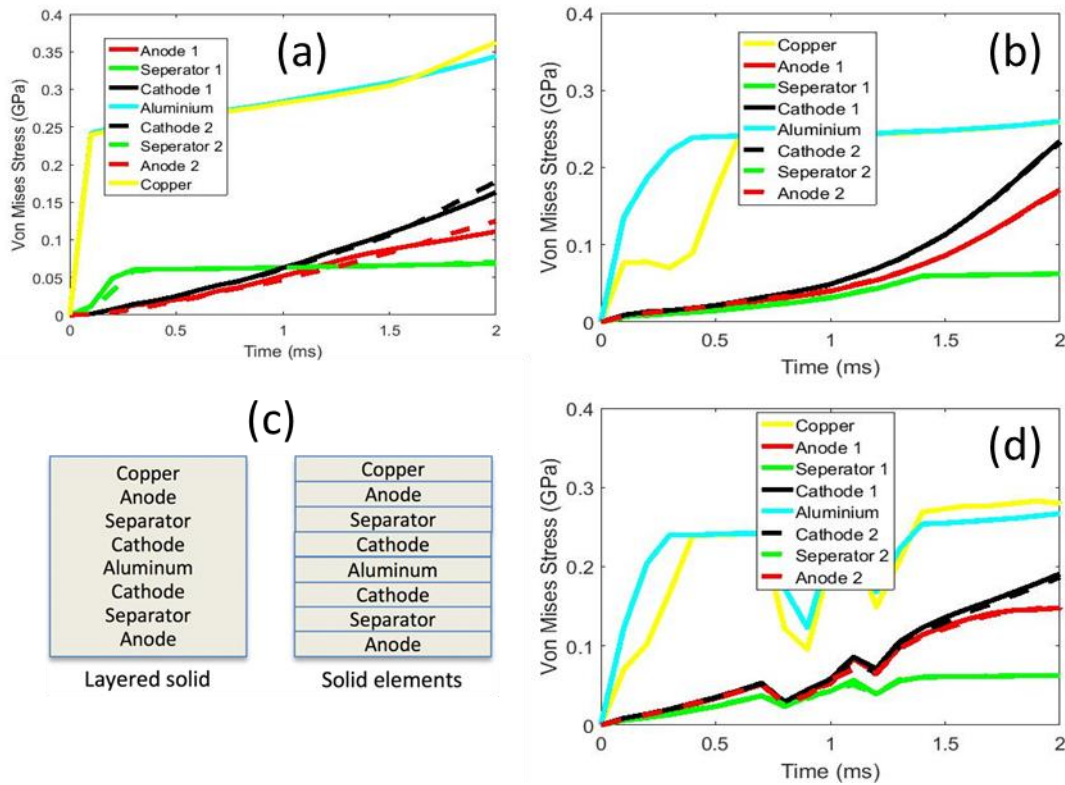


Figure I.3.G.6 Comparison of the cell stresses in the (a) layered solid and (b, d) solid element assembly. In (b), the four top unit cells are resolved, and in (d) all unit cells are resolved. The layers in one unit cell is shown in (c).

The layered solid model shows good correlation with the solid assembly counterparts but it requires orders of magnitude less computational time. It can also be seen that the model with solid element discretization of all layers has strong oscillations that are not expected in the actual mechanical response and lead to computational instabilities with increased indentation.

X-Ray Tomography of Deformed Battery Cells

X-Ray tomography was used to investigate characteristics of internal deformation and failure in battery cells. The pouch cells were tested in shear up to different depths and the X-ray tomography was conducted in the regions where the shear deformation was concentrated. The cells' regions of interest were cut (Figure 7a) and placed in the X-ray tomography instrument (Figure I.3.G.7b).

Figure I.3.G.8 shows characteristic views in the region of cell tearing. The mode and extent of the breaks as a function of deformation type and extent are used to determine constitutive model types and failure models.

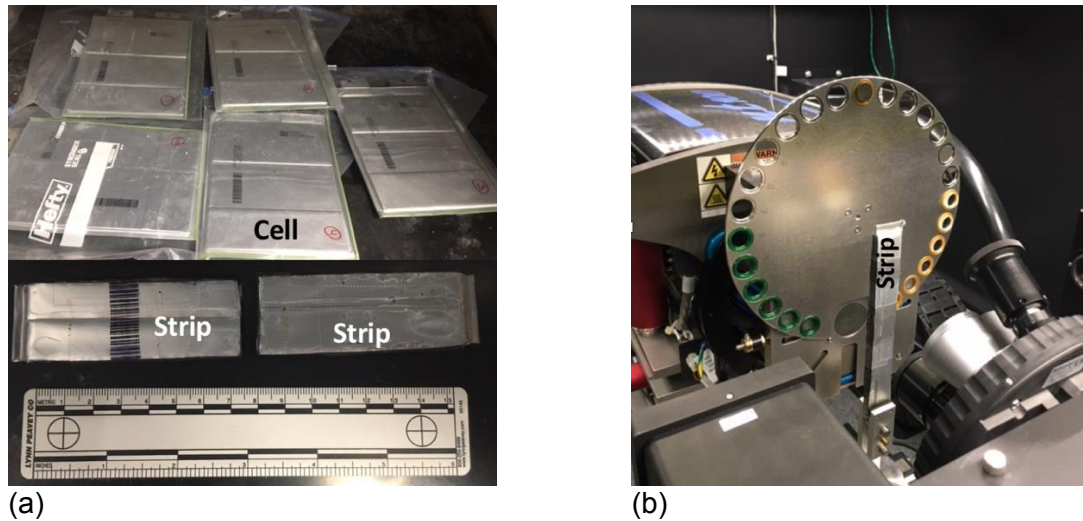


Figure I.3.G.7 X-ray tomography of deformed cells (a) cell sectioning, and (b) scanning.

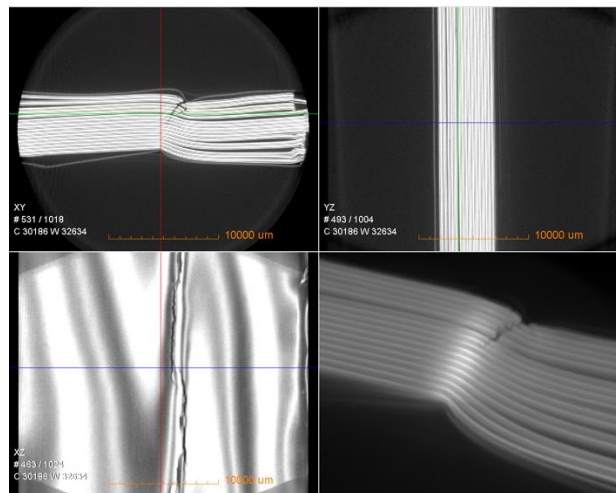


Figure I.3.G.8 X-ray tomography of the internal damage in a sheared cell.

Analysis of the three-dimensional tomography scans indicates significant compression in the active materials and the formation of slanted failures that are similar to the soil or concrete-type materials. The active materials are usually particulate aggregates of active substance with bonding additives, so that it is reasonable that they exhibit large compressibility and sensitivity to shear. Based on the observations from the X-ray scans, we are investigating constitutive models in LS-DYNA that are used for modeling of soils and concrete and using them in the cell deformation and crush models. The limit surfaces in these models are being investigated for modeling the onset of failure in cells.

Constitutive Material Model Development for Active Materials

Material properties and models of the other cell components (foils, separators) are relatively well established. Isotropic and anisotropic elastoplastic material models for these cell components have shown good agreement with the experimental data. The properties and models for current collectors (metal foils) are well established in the literature [1]. The models for tearing and failure of thin metal foils also exist [2], and they are implemented in commercial codes through various failure criteria. Anisotropic elasto-plastic material models for separators have developed [4] in related battery safety projects and applied in the analysis of cell deformation. However, the material models for active materials have not yet been established. The experiments on battery cells have shown that active materials have mechanical response similar to cohesive granular

materials [7], such as soil, rocks and concrete. The experience with such material models is not prevalent in automotive engineering. LS-DYNA has several constitutive models that are used for soils and concrete, and we are analyzing the feasibility of that class of material models for modeling active materials in battery cells. Because the material parameters for granular material models are measured on length scales orders of magnitude larger than the scale of active materials in the battery cells, new tests need to be developed for characterizing active materials, as well.

Material models MAT 25, 145, 173 and 193 in LS-DYNA are relevant to modeling cohesive granular materials. Out of the group, MAT 145, *MAT_SCHWER_MURRAY_CAP_MODEL, has ability to model material after onset of failure. However, the material has a large number of parameters that have to be determined and require extensive experimental program and numerical calibration. On the other hand, MAT 193, *MAT_DRUCKER_PRAGER, has limited number of parameters and requires much simpler experiments. A recent paper [8] has reported material parameters measurements for MAT 193, and our experiments shown in Figure I.3.G.9, have also been used to derive properties of anode active materials.

Given that the MAT 145 provides the most flexibility for modeling active material deformation, onset of failure, and post failure behavior, we have used MAT 193 model and measured properties to calibrate corresponding parameters for MAT 145. The two materials use similar formulations, however, the yield functions and material parameters had to be mapped from MAT 193 to MAT 145 to produce similar response.

The result of this formulation and parameter mapping for the two material is shown in Figure I.3.G.11. The graph shows the effective uniaxial stress versus time for uniaxial compression for the two materials. The response of the two material is essentially the same.

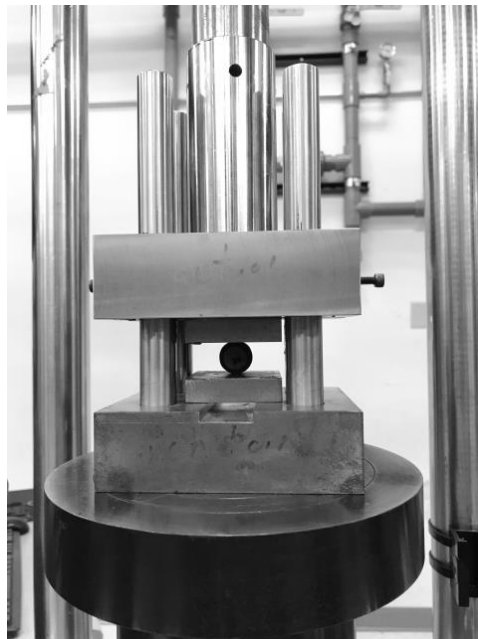


Figure I.3.G.9 Experimental test for lateral compression of active material specimen.

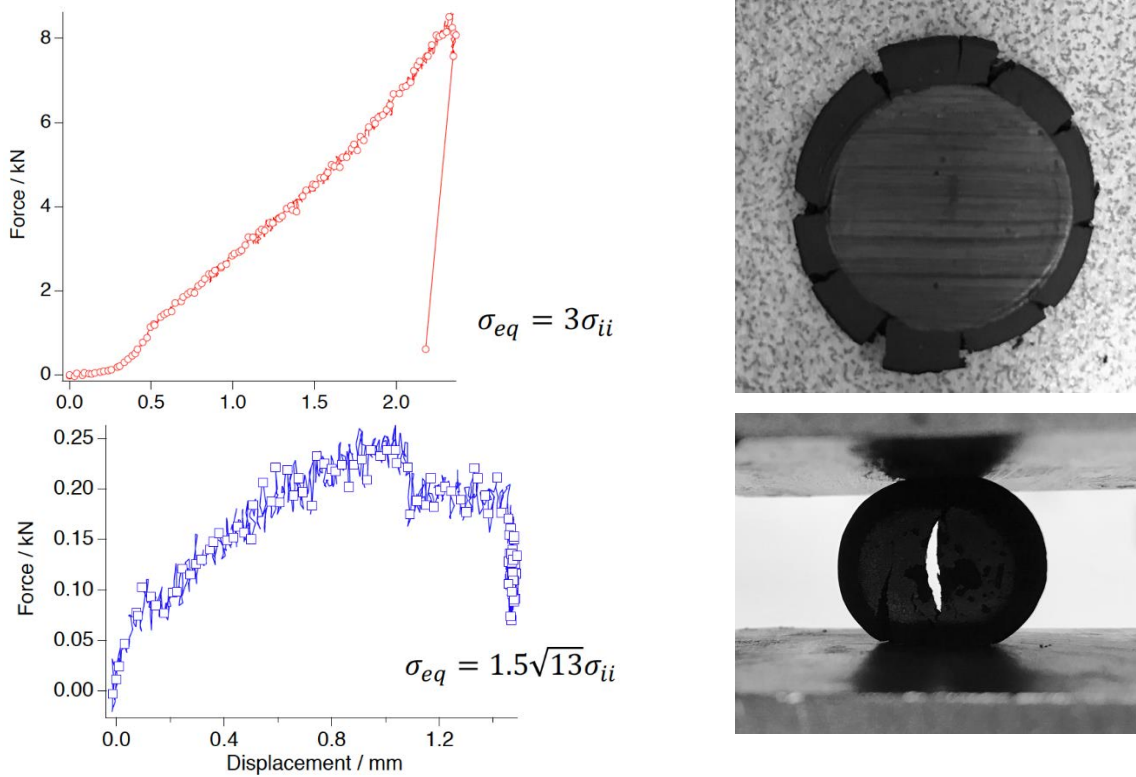


Figure I.3.G.10 Experimental results for uniaxial and lateral compression test of active material specimens.

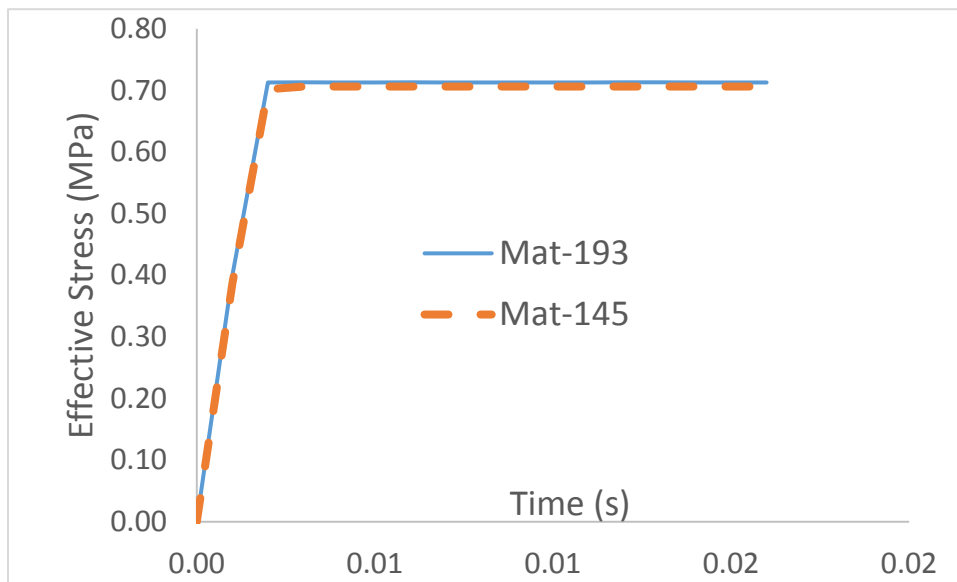


Figure I.3.G.11 The uniaxial compression test response for LS-DYNA materials 145 and 193.

Development of a 3D Microstructure Model for Battery Separators

The 3D microstructure modeling approach consists of three major steps: (1) image-based statistical characterization, (2) stochastic reconstruction, and (3) FEA with a solid-beam hybrid model. In the first step, microstructure characteristics are characterized from the processed microscopic images (Figure I.3.G.12). In the processed image, the lamellae phase is represented by black pixels and the “porous phase” (thin fibrils and voids) are represented by white pixel clusters. The size of the “porous phase” is characterized using t-copula model, as the height and width of the white clusters are correlated random quantities. The profile of the “porous phase” boundaries, which can be considered of a curve with randomness, is characterized using Gaussian copula random process model.

In the second step, 3D microstructure reconstructions are generated based on the statistical models of microstructure characteristics. The size and geometry of each “porous phase” cluster is determined by sampling the statistical models obtained in the previous step. The “porous phase” and the lamellae phase are modelled by voxels of different values.

In the third step, the reconstructed 3D microstructure is converted into a Finite Element mesh in LS-DYNA and a solid-beam hybrid model is developed. The voxels representing the lamellae phase are converted into solid elements, and the thin fibrils are modeled by beam elements. Orthotropic elastic-plastic material model is used for the solid elements, and elastic model is used for the beam elements. Compared to the pure solid element models, the solid-beam hybrid model has significantly less number of elements, so it enables the modeling of a larger physical domain ($1.043 \mu\text{m}^3$). We have tested the model in two simulations: uniaxial tension along the machine direction (Figure I.3.G.14), and uniaxial tension along the transverse direction (Figure I.3.G.15).

The simulated material properties are compared to the experimental testing data reported in literature (Figure I.3.G.16). It is demonstrated that the 3D microstructure model can successfully capture the anisotropic behavior of the microstructure model. However, the prediction accuracy needs to be improved by calibrating the constitutive models.

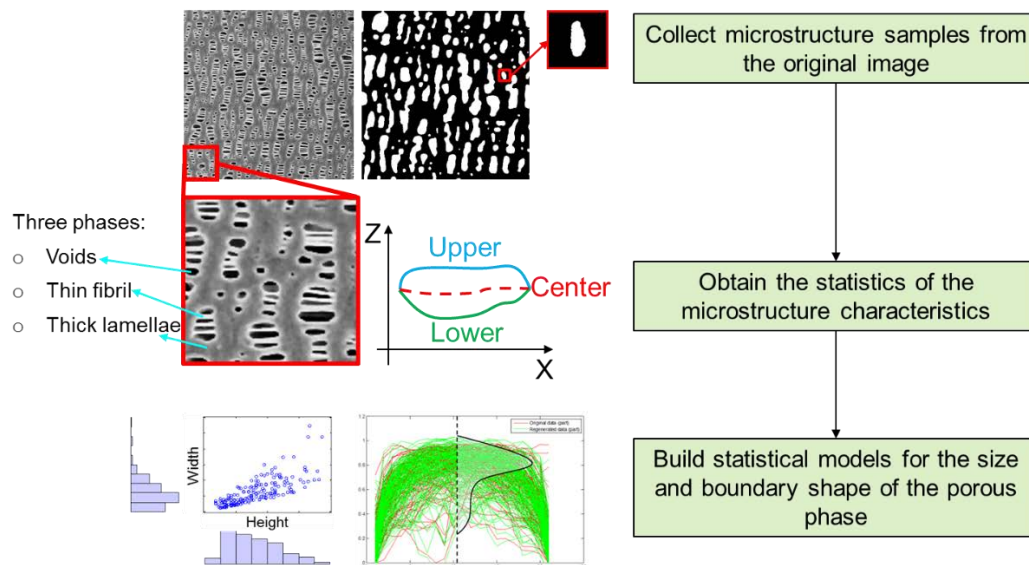


Figure I.3.G.12 Characterization of microstructure characteristics based on image analysis.

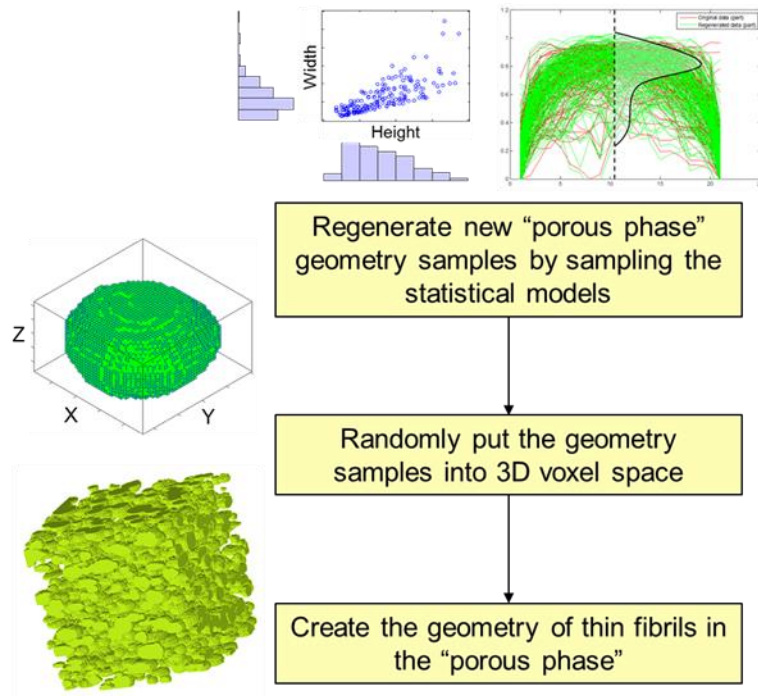


Figure I.3.G.13 Stochastic reconstruction of 3D microstructures. The reconstructed “porous phase” is shown in green pixel. The lamellae phase is not shown.

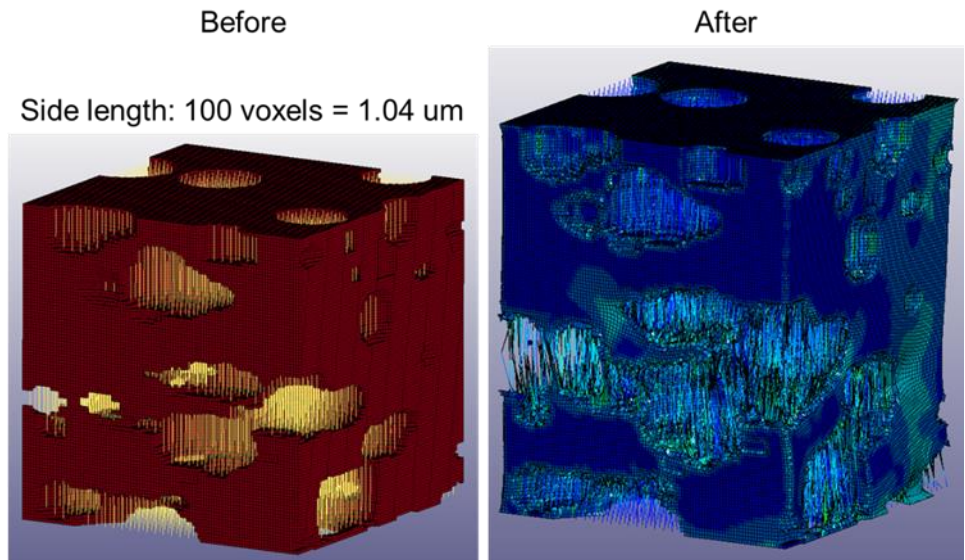


Figure I.3.G.14 Solid-beam hybrid model. Tension along the machine direction.

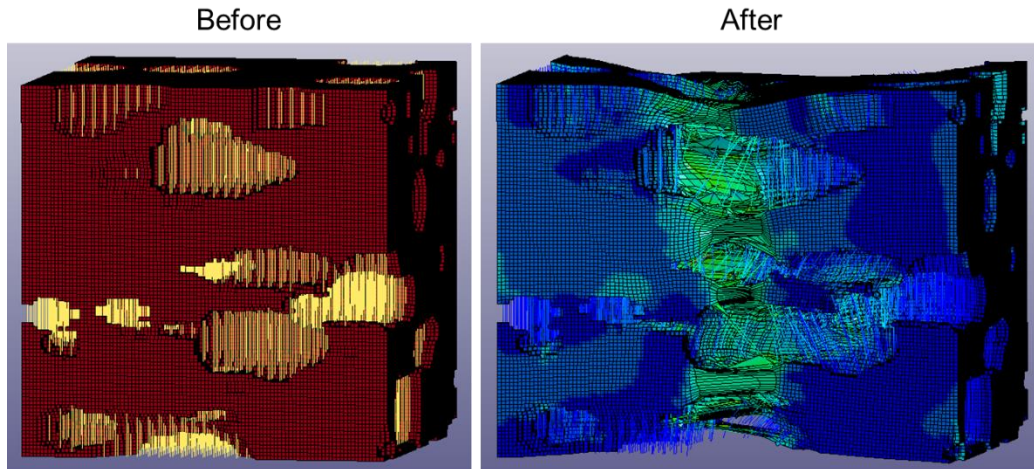


Figure I.3.G.15 Solid-beam hybrid model. Tension along the transverse direction.

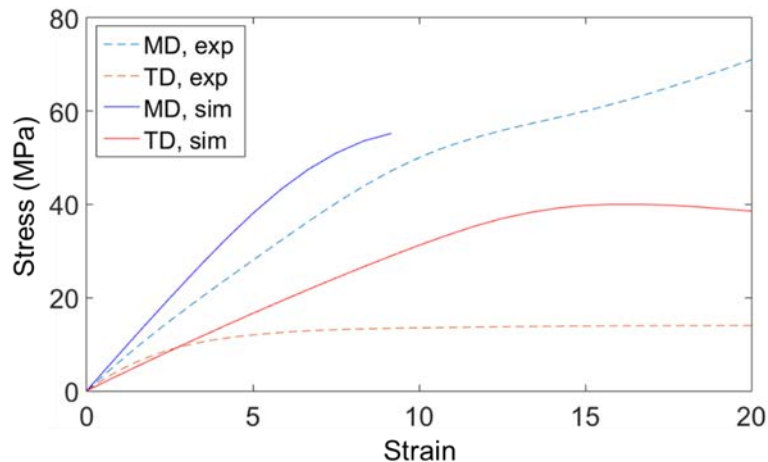


Figure I.3.G.16 Simulation results: stress-strain curves on machine direction (MD) and transverse direction (TD).

Conclusions

The third year has been successful, with the project essentially on track and nearly all milestones accomplished. Validation testing was conducted at Intertek, but was not sufficiently rigorous; testing was switched to Southwest Research Institute and should be complete in the next few months. Spending continues to be below estimated (but will increase with testing). It is expected that the final year will result in a validated, practical simulation tool that can be used to predict battery response to abuse.

The use of composite t-shell elements in mechanical, electromagnetic and thermal solvers has been demonstrated to greatly reduce computation while maintaining accuracy. Material input parameters for the new models and solvers have been obtained through experimental tests and modeling, including the newly developed modelling of the 3D microstructure of commercial separators. Additionally we initiated the development of the macro model that aims to improve computational efficiency of the EM and thermal solvers, used X-ray tomography to investigate damage in individual cell layers under shear and compression, and developed new material models that treat active materials as granular materials with parameters chosen to yield good results compared to experiments.

Key Publications

1. Jie Deng, Chulheung Bae, James Marcicki, Alvaro Masias, Theodore Miller, “Safety modelling and testing of lithium-ion batteries in electrified vehicles”, *Nature Energy*, 3, 261-266, 2018.
2. Jie Deng, Chulheung Bae, Theodore Miller, Pierre L’Eplattenier, Sarah Bateau-Meyer, “Accelerate battery safety simulations using composite tshell elements”, *Journal of The Electrochemical Society*, 165, A3067-A3076, 2018.
3. Jie Deng, Min Zhu, Chulheung Bae, Theodore Miller, Pierre L’Eplattenier, Sarah Bateau-Meyer, “Safety modeling of lithium-ion batteries under mechanical abuse”, *Proceedings of 15th International LS-DYNA Users Conference*, 2018.
4. Sarah Bateau-Meyer, Pierre L’Eplattenier, Jie Deng, Min Zhu, Chulheung Bae, Theodore Miller, “Randles circuit parameters set up for battery simulations in LS-DYNA”, *Proceedings of 15th International LS-DYNA Users Conference*, 2018.
5. Chulheung Bae made a presentation on this project at the Department of Energy Annual Merit Review on June 4, 2018.
6. Jie Deng gave a presentation at the 15th International LS-DYNA Users Conference in Dearborn, MI on June 12, 2018.

References

1. Merchant HD, Khatibi G, Weiss B. Elastic and elastoplastic response of thin copper foil. *Journal of Materials Science*. 2004;39:4157-70.
2. Atkins AG. Thin Sheet Fracture. In: Milne I, Ritchie R, Karihaloo B, editors. *Comprehensive Structural Integrity*: Elsevier; 2003.
3. Andreasson E, Kao-Walter S, Stahle P. Micro-mechanisms of a laminated packaging material during fracture. *Engineering Fracture Mechanics*. 2014;127:313-26.
4. Kalnaus S, Wang YL, Turner JA. Mechanical behavior and failure mechanisms of Li-ion battery separators. *Journal of Power Sources*. 2017;348:255-63.
5. Kalnaus S, Kumar A, Wang YL, Li JL, Simunovic S, Turner JA, et al. Strain distribution and failure mode of polymer separators for Li-ion batteries under biaxial loading. *Journal of Power Sources*. 2018;378:139-45.
6. Kalnaus S, Wang YL, Li JL, Kumar A, Turner JA. Temperature and strain rate dependent behavior of polymer separator for Li-ion batteries. *Extreme Mechanics Letters*. 2018;20:73-80.
7. Wang H, Simunovic S, Maleki H, Howard JN, Hallmark JA. Internal configuration of prismatic lithium-ion cells at the onset of mechanically induced short circuit. *Journal of Power Sources*. 2016;306:424-30.
8. Zhu JE, Li W, Xia Y, Sahraei E. Testing and Modeling the Mechanical Properties of the Granular Materials of Graphite Anode. *Journal of the Electrochemical Society*. 2018;165:A1160-A8.

I.4 Recycling and Sustainability

I.4.A Life Cycle Assessment of Li-ion Batteries (ANL)

Jarod C. Kelly, Principal Investigator

Argonne National Laboratory
9700 S. Cass Avenue
Lemont, IL 60439
E-mail: jkelly@anl.gov

Samuel Gillard, DOE Technology Development Manager

U.S. Department of Energy
E-mail: Samuel.Gillard@ee.doe.gov

Start Date: October 1, 2017 End Date: December 31, 2020
Project Funding (FY18): \$125,000 DOE share: \$125,000 Non-DOE share: \$0

Project Introduction

The U.S. electric light duty vehicle fleet, which includes battery electric vehicles (BEV) and plug-in hybrid electric vehicle (PHEV), is expected to grow from 0.66 million vehicles in 2017, to 9 million vehicles by 2030 [1]. Although vehicle electrification is touted as a promising strategy to reduce petroleum consumption and emissions from the transportation sector, the environmental impacts of lithium-ion batteries (LIB) remains an unresolved research area. The findings from existing life cycle analyses (LCA) of LIBs exhibit large uncertainties, which call for continued efforts to improve the transparency and robustness of life cycle inventory (LCI) data for LIBs, especially battery materials [2]. Evaluations of emerging LIB technologies are also necessary to inform stakeholders as the battery industry progresses towards higher specific energy and lower production cost. This project continues Argonne's efforts to quantify and understand the life-cycle energy consumption and pollutant emissions from electric vehicles, by integrating more industry LCI data representative of current LIB production and conducting preliminary analyses of next-generation LIBs.

Objectives

The objectives of this project are to 1) quantify the energy use and emissions associated with LIB production, accounting for scale of production and technological progression, and 2) identify major environmental burden contributors and bottlenecks for battery production, thereby helping the Vehicle Technologies Office and other stakeholders guide future battery research and development (R&D) efforts, with Argonne's Greenhouse gases, Regulated Emissions, and Energy use in Transportation (GREET[®]) model.

Approach

To improve the understanding of the energy use and emissions pertaining to LIB production, we continue to update battery LCI data, through communications with the battery industry and our Chinese collaborators. Since battery material LCI data that is representative of large-scale industrial production is particularly lacking in existing battery LCA studies, and active cathode materials can account for over 80% of the cradle-to-gate environmental impacts of LIBs [2], in FY 2018, we updated LCI data for cathode materials, which include the production of cobalt precursors for cathode materials, and the production of cathode powders.

The cobalt precursor production update was based on recent literature, industry statistics, and company reports, and covers material and energy flows associated with cobalt ore mining, cobalt ore processing, cobalt chemicals production, cobalt metal production, and pertinent transportation activities. The cathode powder production update was based on our site visit to one leading cathode material producer, literature, and industry reports, and covers the production of lithium cobalt oxide (LCO), lithium nickel cobalt manganese oxide (NMC), and lithium nickel cobalt aluminum oxide (NCA). Both of the updates represent the current status of industrial production of LIB cathode materials, and were incorporated into GREET 2018.

To guide battery R&D efforts towards a more sustainable future, in FY 2018, we also conducted a preliminary LCA study on lithium sulfur (Li-S) batteries, one of the most promising next-generation energy storage technologies beyond conventional LIBs. The bill-of-material for the Li-S was compiled based on design parameters reported in literature, and the environmental impacts for Li-S production were evaluated with the GREET model.

Results

The LCI of cobalt precursor production was compiled based on the materials and energy flows associated with 1) cobalt ore mining and refining in three major copper-cobalt mines in the Democratic Republic of Congo (DRC), and 2) refined cobalt chemicals production by the top producer in China. The compiled LCI shows that the production of 1 kg CoSO_4 , the precursor for NMC and NCA materials, consumes 28.9 MJ of purchased energy, while the production of 1 kg Co_3O_4 , the precursor for LCO material, consumes 71.8 MJ of purchased energy.

The LCI of cathode powder production was based on data collected from our site visit to a leading LIB cathode materials producer in China, and their environmental impacts assessment report. The collected data show that the production of 1 kg of LCO material from Co_3O_4 and Li_2CO_3 by calcination consumes 6 kWh of electricity. For NMC and NCA materials, the production processes consist of two stages. The first stage, producing $\text{NMC}(\text{OH})_2/\text{NCA}(\text{OH})_2$ from Ni/Mn/Co salts via co-precipitation, consumes 44.9 MJ of heat, while the second stage, producing NMC and NCA materials from their hydroxide precursors and lithium salts via calcination, consumes 7-8 kWh of electricity.

The industrial production of cathode materials is more energy-intensive than previously estimated. The NMC/NCA hydroxide precursor production processes deployed by the industry, depicted in Figure I.4.A.1, are more complex than what had been reported in literature, and thus consume more energy, mostly because the lab/bench-scale production processes reported in literature do not consider wastewater treatment, which is, in fact, a major concern of the battery materials producers, and can account for 45% of the plant's energy demand. In contrast, the battery powder production processes used by the industry, depicted in Figure I.4.A.2, align well with those reported in literature. The higher process energy requirement arises from challenges for large-scale industrial production, including, among others, limited equipment choices, and more difficult process control than lab/bench-scale production, which results in multiple calcination stages to ensure product quality.

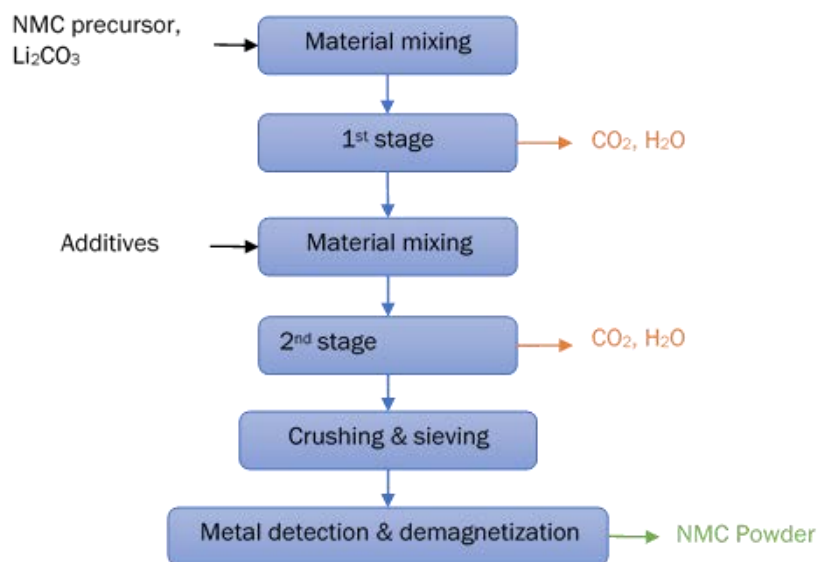


Figure I.4.A.1 Process for NMC precursor production via co-precipitation

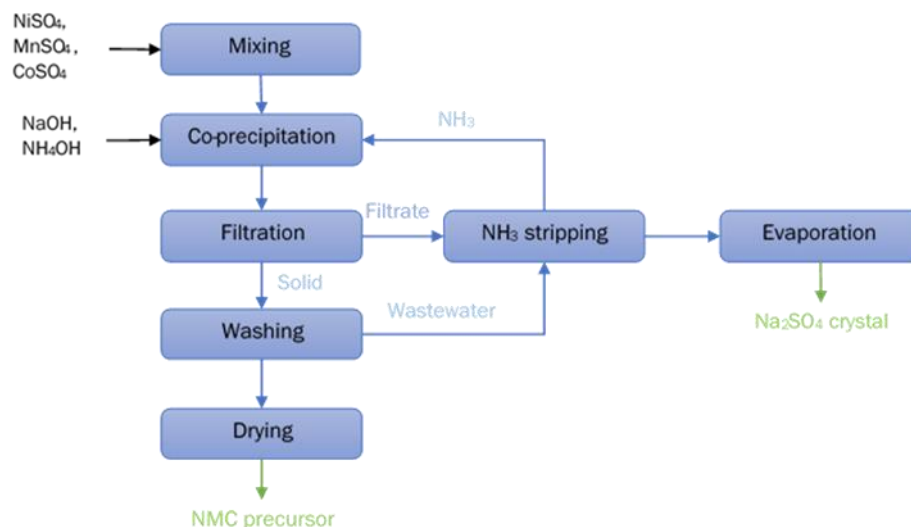


Figure I.4.A.2 Process for production of NMC cathode powder via calcination

The environmental impacts of the production of 1kg $\text{LiNi}_{1/3}\text{Mn}_{1/3}\text{Co}_{1/3}\text{O}_2$ (NMC111) powder evaluated using GREET before and after the cathode materials updates are summarized in Table I.4.A.1. The results show that the increased process energy demand leads to increased total energy consumption, and GHG emissions. The industrial production process for cathode materials also consumes more water than previously estimated, because the updates account for processes that were missing in GREET 2017. However, the industrial process of cathode materials production gives less SO_x emissions than originally thought, because as of 2017, cobalt ore processing in the DRC involves capturing SO_2 emissions from ore roasting for sulfuric acid production, instead of emitting them to the atmosphere, which was assumed in GREET 2017.

Table I.4.A.1 Cradle-to-gate environmental impacts of 1kg NMC111 cathode powder

	Total energy (MJ)	Water Consumption (L)	GHG emissions (kg CO ₂ e)	SO _x emissions (kg SO ₂)
GREET 2017	179	85.2	13.3	0.610
GREET 2018	231	132	16.1	0.288

Preliminary results for the LCA of Li-S batteries are shown in Figure I.4.A.3 and Figure I.4.A.4. The assumed Li-S cell consists of 28% sulfur, 15% copper, 11% dimethyl ether, 11% aluminum, 10% metallic lithium, and 8% graphene by weight. Since metallic lithium, aluminum, and graphene are all energy-intensive to produce, they represent the major contributors to the total energy for cell production, as can be observed in Figure I.4.A.3. Nevertheless, although the use of graphene and metallic lithium in a Li-S battery incurs substantial environmental burdens, since Li-S batteries can deliver five times the energy density of conventional LIBs. When compared to their conventional LIB counterpart on a per kWh basis, Li-S batteries offer considerable reductions in total energy consumption, and significant reductions in air pollutant emissions, as shown in Figure I.4.A.4.

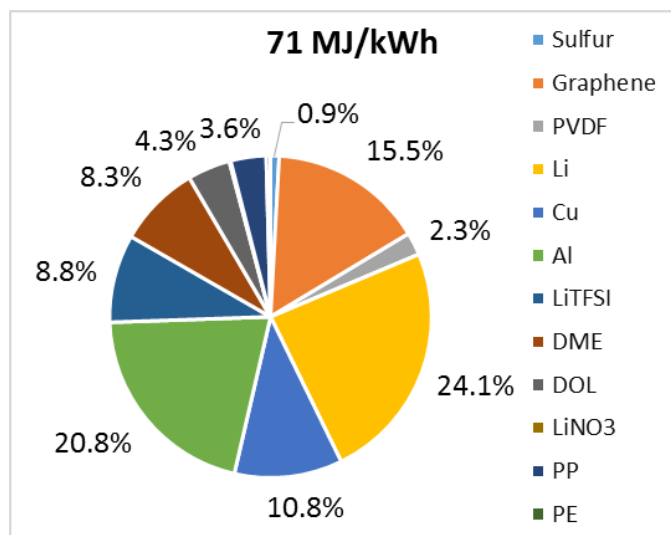


Figure I.4.A.3 Share of total energy of Li-S cell production (excluding energy use for cell assembly)

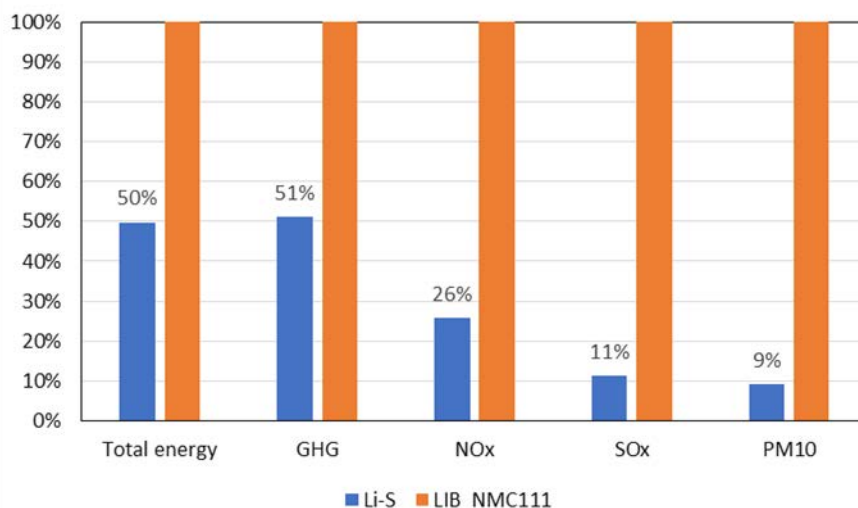


Figure I.4.A.4 Cradle-to-gate LCA comparison of Li-S battery and conventional LIB on a per kWh basis

Conclusions

The results of our FY 2018 efforts reinforce the importance of using LCI data representative of current and large-scale industrial practice in the LCA studies of LIBs and electric vehicles. Such data can help bridge the knowledge gaps and capture technological progression trends of the industry, thereby enhancing the completeness and robustness of the LCA study. Interactions with stakeholders are key to understanding and acquiring such data and should remain a focus of our future LIB LCA research. LCA studies of next-generation energy storage technologies can help identify major contributors to environmental impacts and illuminate improvement opportunities, thereby facilitating improved battery design and informing future battery R&D activities.

Key Publications

1. Dai, Qiang, Jarod C. Kelly, and Amgad Elgowainy. “Cobalt Life Cycle Analysis Update for the GREET® Model”. 2018. Argonne White Paper. https://greet.es.anl.gov/publication-update_cobalt

2. Dai, Qiang, Jarod C. Kelly, Jennifer Dunn, and Pahola Benavides. “Update of Bill-of-materials and Cathode Materials Production for Lithium-ion Batteries in the GREET® Model”. 2018. Argonne White Paper. https://greet.es.anl.gov/publication-update_bom_cm
3. Kelly, Jarod C. “Argonne National Lab: Battery Advancements, Costs and Recycling”. North Central Clean Cities Meeting, Chicago, IL Oct 17, 2018.
4. Dai, Qiang, Jennifer Dunn, Linda Gaines, Jarod C. Kelly, Amgad Elgowainy, and Michael Wang. “Life Cycle Analysis of Automotive Lithium-ion Batteries: the Real Story”. LCA XVIII Conference, Fort Collins, CO, Sep 26, 2018.

References

1. Energy Information Administration. “Annual Energy Outlook 2018”. Accessed Nov 12, 2018. <https://www.eia.gov/outlooks/aeo/index.php>
2. Peters, Jens F., and Marcel Weil. “Providing a Common Base for Life Cycle Assessments of Li-Ion Batteries.” *Journal of Cleaner Production* 171 (January 10, 2018): 704–13. <https://doi.org/10.1016/j.jclepro.2017.10.016>.

Acknowledgements

Dr. Qiang Dai from Argonne National Laboratory was instrumental to the execution of this project.

I.4.B Battery Production and Recycling Materials Issues (ANL)

Linda Gaines, Principal Investigator

Argonne National Laboratory
9700 S. Cass Avenue
Argonne, IL 60439
E-mail: lgaines@anl.gov

Samuel Gillard, DOE Technology Development Manager

U.S. Department of Energy
E-mail: Samuel.Gillard@ee.doe.gov

Start Date: April 1, 2008

End Date: December 31, 2019

Project Funding (FY18): \$125,000

DOE share: \$125,000

Non-DOE share: \$0

Project Introduction

Examination of the production of batteries from raw material acquisition to assembly illuminates the stages of this supply chain that incur the greatest energy and environmental burdens. Recycling of material from spent batteries will be a key factor in alleviating potential environmental and material supply problems. We examine battery material production, battery assembly, and battery recycling processes that are available commercially now or have been proposed. Battery materials, assembly, and recycling processes are compared on the basis of energy consumed and emissions, suitability for different types of feedstock, and potential advantages relating to economics and scale. We compare the potential of recycling processes to displace virgin materials at different process stages, thereby reducing energy and scarce resource use, as well as potentially harmful emissions from battery production. Although relatively few automotive batteries have been produced to date, viable processes will be required to recycle them when they are no longer usable. Secondary use of the batteries could delay return of material for recycling. Economic and institutional factors impact recycling as well.

Objectives

- Follow developing and potential material scarcity issues that may influence viability of automotive lithium-ion batteries
- Characterize lithium-ion battery recycling in the United States and abroad to identify the most promising recycling technologies as they evolve, barriers to recycling, and influence of recycling on material scarcity
- Engage with the international battery recycling community to exchange information and identify paths to advancing battery recycling technology and enabling adoption
- Postulate improved recycling processes to maximize material recovery
- Determine impact of battery reuse on recycling processes and economics
- Formulate actions to address developing technical and institutional issues concerning used batteries

Approach

We estimated the maximum reasonable demand for battery materials, based on extremely aggressive scenarios for penetration of electric-drive vehicles. We combined vehicle demand growth with detailed battery designs and looked at how lithium demand might grow world-wide. We also estimated how much material could be recovered by recycling, thus reducing demand for virgin materials. We determined that cumulative world demand for lithium to 2050 would not strain known reserves. More recent estimates of material demand for all uses also identifies cobalt as a key material. Cobalt supplies could be a significant constraint; the envisioned

move away from chemistries containing large quantities of cobalt reduces but does not alleviate potential problems. Table I.4.B.1 shows that cobalt demand is slowed by a shift to NMC111, but electronics demand for LCO keeps the total high. Recycling can reduce demand for virgin material, but only in the long term (see Figure I.4.B.1).

Table I.4.B.1 Projected material demand, compared to reserves

Element	Projected Demand to 2025 (1000 tons)		Reserves (1000 tons)	% of Reserves
	If all NMC is 811	If all NMC is 111		
Lithium	230	230	14,000	1.6
Cobalt	790	910	7,000	14 (111)
Nickel	580	340	78,000	0.7 (811)

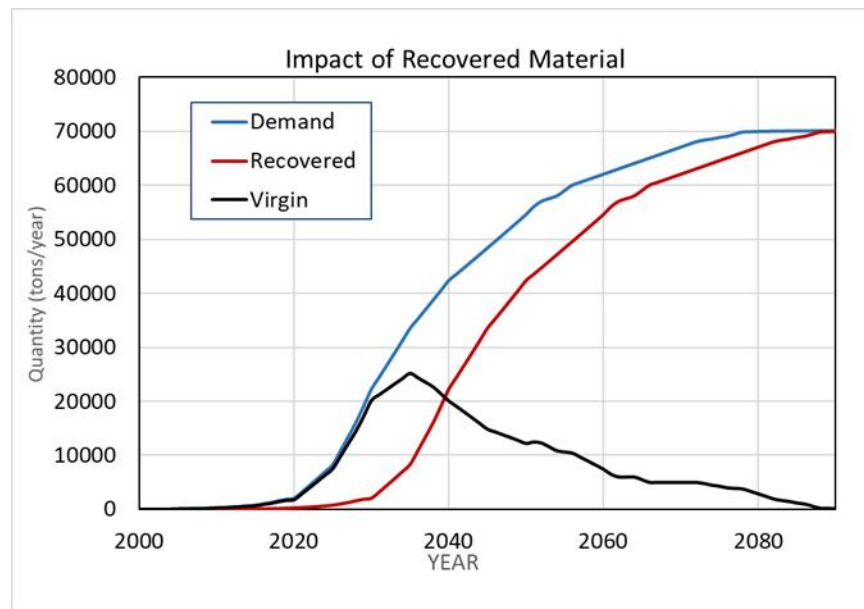


Figure I.4.B.1 Reduction in virgin material demand due to recycling

Life cycle analysis (LCA) was used to further identify potential environmental and economic roadblocks to battery production, and to compare energy savings and emissions reductions enabled by different types of recycling processes. Economic analysis of recycling processes revealed cathode recovery as a way to achieve economic viability for recycling of low-Co cathodes. This research forms the basis for the work of the planned battery recycling research center. Examination of environmental impacts determined that emissions of sulfur oxides could be minimized by recycling any of the transition metals generally smelted from sulfide ores.

Close interactions with stakeholders are sustained to remain on top of technological and legislative developments associated with LIB production and recycling, and to maintain Argonne’s position as the world’s leader in battery recycling research and analysis. During FY18, Argonne staff 1) gave invited talks and presentations to government, industry, and academia, and to numerous visitors; 2) organized a session at Electrochemical Society meeting; 3) planned an international battery recycling discussion; 4) contributed to a DOE report on recycling technology gaps; 5) served on SAE and NAATBATT recycling committees and the

Science Advisory Board of the Responsible Battery Coalition; 6) negotiated potential battery recycling and modeling work with several organizations; and 7) responded to countless requests for information. Argonne has also examined recycling processes and businesses for other battery types to determine what lessons can be learned from successfully established systems.

Results

Based on our analysis, recycling provides energy conservation benefits and reduces the local impacts of metal recovery and purification. Benefits differ by recycling process and increase as more materials are recovered. Recycling is especially beneficial when cathode materials contain nickel or cobalt. In the case of LiCoO_2 , the recovery and purification of the metal dominates the overall energy consumption of producing this cathode material, so recycling results in significant energy savings (and sulfur emission reductions).

Stakeholders at the 2016 Argonne battery recycling workshop agreed on several points that require additional work. Although recycling technologies have been demonstrated, basic process R&D is needed to determine the optimal recycling method for each Li-ion chemistry, especially lower cobalt cathode materials. For such materials, it appears that direct recycling, still only demonstrated at bench scale, offers the only real prospect of being economically feasible, but a segregated feed stream would be required. For any process, the goal is to maximize the yield of valuable materials at lower recycling cost. Optimized processes would then require demonstration on a larger scale, but this might not be sufficient because manufacturers are skeptical about putting recycled material back into batteries. Therefore, we need to develop product specifications that recycled materials must meet. Furthermore, there is not yet enough material available to support full-scale infrastructure for collection and processing. There should be enough material from consumer electronics, but those batteries are generally not getting collected, let alone recycled. The potential for restrictive government regulations also hinders recycling business development, so the industry could consider pre-emptive self-regulation. Some of the challenges to Li-ion battery recycling are shown in Table I.4.B.2, with proposed R&D to address them.

Table I.4.B.2 Challenges for Li-Ion Battery Recycling

Challenge	Proposed R&D
Many of the constituents have low market value	Process development to recover multiple high-value materials
Low value of mixed streams	Separation of mixed cathode material
Obsolete cathode recovered	Convert to new configuration

Detailed understanding of recycling processes will be necessary to maximize material recovery. A simple experiment was conducted to demonstrate how pH and temperature affect the loss of Li in cathode material. High pH has no impact, but low pH (acid conditions) remove much of the lithium; this information will help enable efficient recycling process design. Additional experiments are proposed to fully characterize properties of potentially recoverable materials. Low-temperature processes that can recover usable cathode material are of particular interest.

In FY 2018, we maintained interactions with Chinese stakeholders to stay informed of the legislative and technological developments for battery production and recycling in China, as China emerges as the world's top battery producer, and the largest market for electric vehicles (EV). In January 2018, China issued the *Provisional Regulation on the Recycling and Reuse of Traction Batteries for New Energy Vehicles (NEVs)*, which became effective on August 1 2018. The regulation 1) demands that NEV manufacturers will be responsible for the collection, sorting, storage, and transportation of spent traction batteries; 2) determines who is responsible for what along the supply chain of traction batteries; 3) establishes a traction battery tracking system, for which each traction battery will be assigned an identification number, which battery manufacturers, NEV manufacturers, and battery repurposers are to maintain and update in the tracking system; 4) and encourages “reuse then recycle”, for maximum economic benefit.

To better understand the implications of the regulation for the Chinese battery industry, we visited two battery materials producers and four battery manufacturers. We learned that hydrometallurgical recycling continued to be the only commercialized recycling technology in China. The companies commented that recovered Ni and Co materials via the hydrometallurgical route can be cheaper than virgin materials, and can be used for new battery production without compromising the battery electrochemical properties. Therefore, all of the companies have been actively pursuing recycling, either alone or in partnership with other stakeholders. In terms of technological development, in addition to Co, Ni, and Mn, some recyclers started recovering Li, due to recent surges of lithium compounds prices.

The regulation encourages “reuse then recycle”, but some companies believe that for $\text{LiNi}_{1-x-y}\text{Mn}_x\text{Co}_y\text{O}_2$ (NMC) and $\text{LiNi}_{0.8}\text{Co}_{0.15}\text{Al}_{0.05}\text{O}_2$ (NCA) batteries, it is best to recycle them directly after they reach their end-of-service on EVs, while 2nd life applications are more preferable for spent EV LiFePO_4 (LFP) batteries. It is because with hydrometallurgical recycling, the cost of LFP battery recycling outweighs the revenue obtainable from recycled materials. Reuse/repurpose spent LFP batteries before recycling can help offset some of the recycling cost. In addition, LFP batteries have longer cycle life, which makes 2nd life applications more viable. Possible 2nd life applications include low-speed vehicles and energy storage. Spent automotive batteries, which typically have 80% of the original capacity left, can be used for these 2nd life applications until their capacity drop to 20-30% of the original, before they finally get recycled, most likely via physical separation focusing on Al and Cu recovery only.

The Chinese battery industry has been moving towards Ni-rich cathode chemistries. The battery materials producers already started mass-producing $\text{LiNi}_{0.8}\text{Mn}_{0.1}\text{Co}_{0.1}\text{O}_2$ (NMC811) cathode powder. The battery manufacturers planned to use NMC811 on consumer electronics, in addition to cars, and have been working diligently to develop NMC811 cells that can be produced at industrial scale, and can pass required safety tests.

Most of the Li and Ni demands from the Chinese battery industry in the next decade will have to come from virgin materials, since before 2017, the dominant chemistry for traction batteries in China was LFP, which does not contain Ni, and is not an economical source of Li with current recycling technology. As for the Co demand, if batteries based on Ni-rich chemistries can gain a fast and deep penetration in the consumer electronics market, Co recycled from spent consumer electronics batteries, which has been predominantly based on LiCoO_2 , can be a substantial source of Co to sustain future battery production in China.

In contrast, LIB recycling has yet to be fully commercialized in the U.S. Retrieval operates a plant that recovers black mass (see Figure I.4.B.2), but it is not running at capacity. Europe relies primarily on pyrometallurgy. Great Britain and Australia are exploring their options. In the US, direct recycling technology is under development at laboratory-scale because it has the biggest potential to be economic and to reduce energy use and environmental impacts of LIB. Barriers to growth of LIB recycling in the U.S. include low collection rate of spent LIB, unstandardized LIB designs, confusion over liability for LIB recycling, and uncertainty in the market for recovered materials. Several companies are moving forward with plans for hydrometallurgical recycling in the US, and each employs a different set of process steps. We continue to gather detailed recycling process information to include in our ReCell closed-loop lifecycle, which will serve as a useful tool in comparing process costs and environmental impacts. Transportation cost is another issue, which leads to our new interest in pretreatment to enable cheaper transport.

6. Symposium Organizer and Chair: Materials Recycling for Energy Conversion and Storage, Electrochemical Society, Seattle, WA, (May 14, 2018)
7. Presentation: Key technical issues for lithium-ion battery recycling, Electrochemical Society, Seattle, WA, (May 14, 2018)
8. Workshop keynote: A Tour Around the Li-Ion Battery Life Cycle, Battery Recycling Discussion, NREL (May 30, 2018)
9. Presentation: Recycling of Li+ Batteries – State of the Science, RBC new member orientation, Milwaukee, WI (August 14, 2018)
10. Paper: Lithium-Ion Battery Recycling Processes: Research towards a Sustainable Course <https://www.sciencedirect.com/science/article/pii/S2214993718300629?via%3Dihub> , Sustainable Materials and Technologies, (September 2018)
11. Presentation by J. Dunn: Emerging Issues in Automotive Lithium-Ion Battery Life Cycle Analysis, Conference on Circular Economy of Battery: Production and Recycling, Gothenburg, SE (September 24-26, 2018)
12. Paper: Key issues for lithium-ion battery recycling MRS Energy and Sustainability (Fall 2018)
13. Panel: Storage and the Grid- Current Options, Applications, and Possible Futures, Energy Security Meeting, NREL (October 2, 2018)

I.4.C Closed-loop Battery Recycling Model (ANL)

Jeffrey Spangenberg, Principal Investigator

Argonne National Laboratory

9700 S. Cass Avenue

Lemont, IL 60439

E-mail: jspangenberg@anl.gov

Samuel Gillard, DOE Technology Development Manager

U.S. Department of Energy

E-mail: Samuel.Gillard@ee.doe.gov

Start Date: July 1, 2017

End Date: December 31, 2019

Project Funding (FY18): \$250,000

DOE share: \$250,000

Non-DOE share: \$0

Project Introduction

The cumulative U.S. electric vehicle (EV) sales surpassed 0.4 million units in 2015, with 0.2 million battery electric vehicle (BEV) sales, and 0.2 million plug-in hybrid electric vehicle (PHEVs) sales [1]. Assuming a lifespan of just over a decade for EVs, an average battery pack weight of 300 kg for BEVs, and an average battery pack weight of 200 kg for PHEVs, by 2025, 0.1 million metric tons of EV batteries would reach their end-of-life (EOL) in the U.S. Beyond 2025, the volume of spent EV batteries is expected to increase markedly, as future EV sales in the U.S. continue to grow explosively through 2050 [2]. Although battery recycling has the potential to significantly mitigate the environmental impacts of battery production, via recovery of materials such as cobalt, nickel, and lithium, no industrial-scale EV battery recycling processes currently exist in the U.S., as battery collection, transportation, and recycling pose substantial challenges to the automotive battery and EV manufacturers. Since cost and eco-friendliness are two major performance metrics for battery recycling technologies, Argonne has developed the ReCell model to evaluate the economic and environmental impacts of battery recycling, aiming to help expedite the development of a sustainable and revenue-positive battery recycling infrastructure.

Objectives

The objectives of the project are to 1) provide insight into the economic and environmental impacts of battery recycling from a life-cycle perspective, 2) help stakeholders make more informed battery recycling decisions, and 3) help accelerate the development of a more sustainable supply chain for automotive batteries.

Approach

To better inform the stakeholders of the performances of battery recycling technologies, we continue to advance and expand the capabilities of the ReCell model. In Q4 2017, we added to the ReCell model two new battery chemistries, $\text{LiNi}_{0.8}\text{Co}_{0.15}\text{Al}_{0.05}\text{O}_2$ (NCA) and $\text{LiNi}_{0.8}\text{Mn}_{0.1}\text{Co}_{0.1}\text{O}_2$ (NMC811), as Ni-rich materials are touted to be one of the next-generation cathode materials for EV batteries [3]. In FY 2018, we 1) added to ReCell a module to evaluate the cost and environmental footprints for the production of cathode powders, including NCA, NMC811, $\text{LiNi}_{0.6}\text{Mn}_{0.2}\text{Co}_{0.2}\text{O}_2$ (NMC622), and $\text{LiNi}_{1/3}\text{Mn}_{1/3}\text{Co}_{1/3}\text{O}_2$ (NMC111); 2) expanded ReCell to enable evaluations of all battery life-cycle stages in different geographical regions, accounting for differences in building, labor, equipment, capital, transportation, and utilities costs; and 3) expanded the recycling module and cathode production module in ReCell to allow for processes scaling up/down.

To better engage the stakeholders, we also continue to improve the usability and user-friendliness of the model. Throughout Q4 FY 2017 and FY 2018, we have been actively seeking inputs from the stakeholders, to ensure that 1) the assumptions made and data used in the model are reasonable, and 2) the model is easy to use.

In an effort to direct battery research and development towards a more sustainable future, in FY 2018, we also conducted a preliminary study on recycling of lithium sulfur (Li-S) batteries, one of the most promising next-generation energy storage technologies beyond conventional lithium-ion batteries (LIBs).

Results

An updated ReCell model, along with the user's manual, was completed in June 2018, and was made available to selected stakeholders to solicit feedback and suggestions on areas for improvement. The schematic of the updated ReCell model is depicted in Figure I.4.C.1. The ReCell model currently covers 1) seven battery chemistries including LiCoO₂ (LCO), LiMn₂O₄ (LMO), LiFePO₄ (LFP), NCA, NMC111, NMC622, and NMC 811, and 2) three recycling technologies including pyrometallurgical (pyro), hydrometallurgical (hydro), and direct recycling.

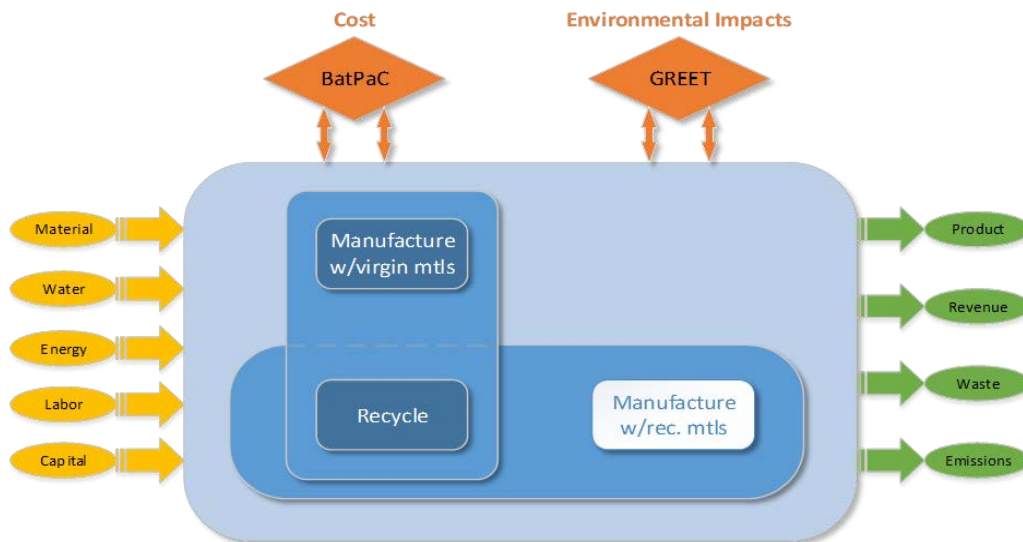


Figure I.4.C.1 Schematic of ReCell model

ReCell cost evaluation for the production of 7,000 metric tons of NMC111 cells per year in the U.S. shows that materials cost accounts for ~70% of the total cell production cost, followed by building and equipment depreciation, the second largest cost contributor. Of the materials cost for cell production, active cathode material accounts for 48%, followed by separator, active anode material, copper foil, and electrolyte, accounting for 14%, 13%, 10%, and 9%, respectively. For NMC111 cathode powder production, materials cost also represents the single largest contributor, accounting for 65% of the total NMC111 cathode powder production cost. It is therefore confirmed that recycling technologies that are able to recover materials from spent batteries, especially cathode materials containing cobalt and nickel, can be economically viable, if the recovered materials can be reused for the production of new batteries without extensive and expensive processing.

ReCell cost evaluation for the recycling of 7,000 metric tons of NMC111 cells per year in the U.S. indicates that spent battery collection and transportation may be a barrier to the development of large-scale EV battery recycling. Currently, LIBs are characterized as class 9 hazardous material [4]. The transportation of spent EV batteries therefore can incur significantly higher cost, compared with the transportation of non-hazardous materials, and can account for up to 50% of the total recycling cost, if the battery transportation distance surpasses 500 miles. Making the battery exempt from the class 9 materials transportation requirements, and/or shortening the transportation distance, therefore represent the best opportunity to reduce battery recycling cost. At the recycling plant level, increasing the recycling throughput is an effective strategy to reduce recycling cost, before the plant capacity reaches around 10,000 metric tons per year, where the per kg battery recycling

cost starts to level off. Building the recycling plant in a place where building and equipment costs are relative cheap also helps, as capital cost dominates the total cost at the recycling plant.

From a life-cycle perspective, assuming all spent batteries are collected and recycled, and all of the recovered materials are re-incorporated into the battery supply chain, substantial cost savings and significant environmental benefits can be achieved, as shown in Figure I.4.C.2. and Figure I.4.C.3.

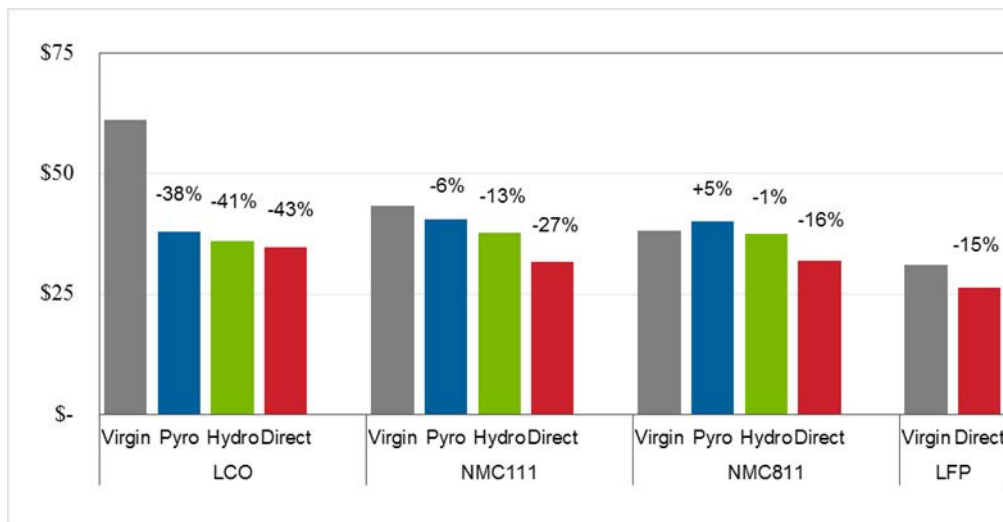


Figure I.4.C.2 Potential cost savings of per kg cell production via battery recycling for different chemistries

It can be observed from Figure I.4.C.2. that as we move towards less cobalt content in the cathode chemistry, the cost reduction achievable through recycling decreases. Due to the high price of cobalt materials, current battery recycling technologies focus on cobalt materials recovery. As we move towards Ni-rich cathode chemistries in the future, additional incentives may be needed to encourage recyclers to take batteries that are low in cobalt content and develop recycling processes that can recover a wider variety of battery materials. It can be also observed from Figure I.4.C.2. that direct recycling, which recovers cathode material as is, becomes increasingly promising as the battery cobalt content decreases. In fact, for cathode materials that do not contain cobalt, direct recycling appears to be the only economically feasible option among known recycling technologies. Focused and sustained efforts in the R&D of direct recycling processes, could therefore be critical to a sustainable and revenue-positive battery recycling infrastructure.

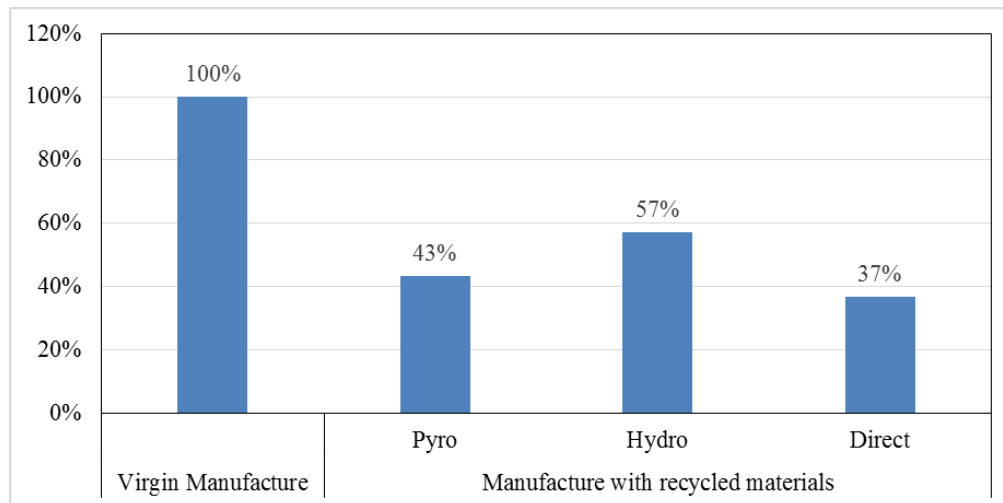


Figure I.4.C.3 Potential SO_x emission savings from recycling NMC111 batteries

Compared with cost savings, battery recycling may offer higher reductions in some of the environmental impacts categories. Since mining and refining of nickel and cobalt materials are quite energy-intensive and associated with large amounts of SO₂ emissions, recovered nickel and cobalt materials from spent batteries can displace primary materials production, which can result in over 60% reduction in SO_x emissions, as shown in Figure I.4.C.3.

Potential energy benefits of recycling major components of Li-S batteries are shown in Figure I.4.C.4. Li-S batteries use the same materials for current collectors, separator, and cell casing as conventional LIBs. Therefore, with currently available recycling technologies, aluminum and copper can be recovered and reused for new battery production, and plastics and binder materials can be recovered and used for energy or other low-value applications. In contrast, sulfur, the predominant cathode material for Li-S batteries, is abundant and inexpensive, so it may not make economic sense to recover sulfur from spent Li-S batteries. Graphene, a commonly used carbonaceous material in the cathode for Li-S batteries, is expensive and extremely energy-intensive to produce, which provides incentives to recycle. In fact, graphene has been reportedly recycled from cycled Li-S batteries, by removing elemental sulfur, polysulfides, and binder from the cathode material [5]. For the anode material, metallic lithium could be recycled with currently available recycling technologies. However, due to the presence of a surface coating, and possible deposition of polysulfides on the surface, the recovered lithium anode may need to undergo vacuum distillation to improve the purity to battery grade.

Figure I.4.C.4 shows that if graphene, aluminum, and copper are recycled and reused as is in new batteries, lithium is recycled as metal, goes through vacuum distillation, and reused in new batteries, recycling can reduce total energy consumption by up to 60%, compared with batteries produced with 100% virgin materials. This would help further reduce the environmental impacts of the transportation sector and shape a more sustainable future.

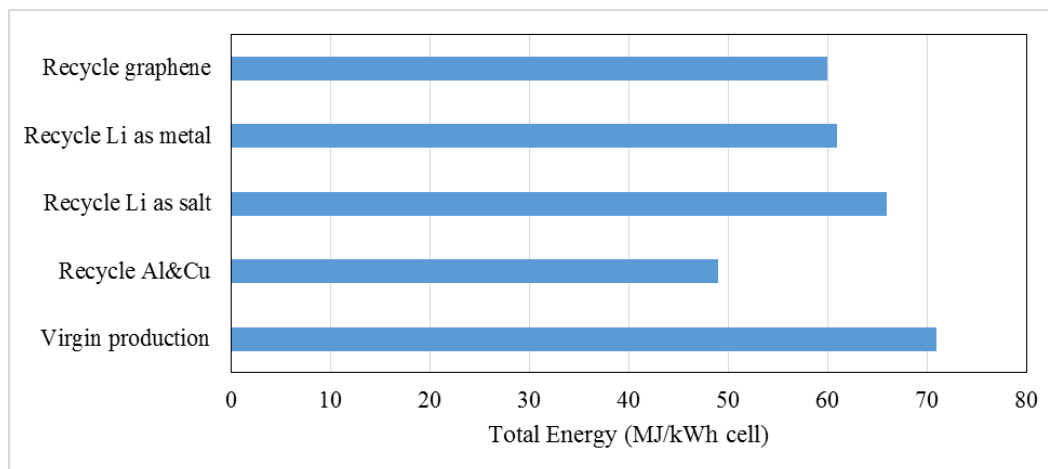


Figure I.4.C.4 Total energy reductions from recycling of Li-S batteries

Conclusions

By identifying key contributors to the cost and environmental burdens of battery recycling processes, and recognizing potential areas of improvements, ReCell can help the stakeholders make more informed recycling decisions. By providing a holistic picture of the sustainability of batteries over their entire life-cycle, ReCell can also facilitate design-for-recycling activities and encourage the development of a more sustainable battery supply chain. Interactions with the stakeholders are key to continuing improvement of the ReCell model, and will remain a focus of our future ReCell development activities. We will also continue to enhance and expand the capabilities of the ReCell model, to help accelerate the development of a sustainable and economically feasible battery recycling infrastructure.

Key Publications

1. Spangenberg, Jeffrey, Linda Gaines. "Comparison of Lithium-ion Battery Recycling Processes Using the ReCell Model". 35th International Battery Seminar and Exhibit. Ft. Lauderdale, FL. March 27, 2018
2. Dai, Qiang, Jeffrey Spangenberg, and Linda Gaines. "ReCell: a Closed-loop Battery Recycling Economics and Environmental Impacts Model". The 233rd ECS Meeting, Seattle, WA, May 14, 2018.
3. Spangenberg, Jeffrey, Qiang Dai, and Linda Gaines. "Closed-loop Battery Recycling Model". International Recycling Workshop, Golden CO. May 30, 2018
4. Spangenberg, Jeffrey. "Comparison of Lithium-ion Battery Recycling Processes Using the ReCell Model". Battery Show North America 2018. Novi, MI. September 13, 2018

References

1. International Energy Agency. "Global EV Outlook 2017". Accessed Nov 12, 2018. <https://www.iea.org/publications/freepublications/publication/GlobalEVOutlook2017.pdf>
2. Energy Information Administration. "Annual Energy Outlook 2018". Accessed Nov 12, 2018. <https://www.eia.gov/outlooks/aeo/index.php>
3. Andre, Dave, Sung-Jin Kim, Peter Lamp, Simon Franz Lux, Filippo Maglia, Odysseas Paschos, and Barbara Stiaszny. "Future Generations of Cathode Materials: An Automotive Industry Perspective." *Journal of Materials Chemistry A* 3, no. 13 (March 17, 2015): 6709–32. <https://doi.org/10.1039/C5TA00361J>.

4. Huo, Haibo, Yinjiao Xing, Michael Pecht, Benno J. Züger, Neeta Khare, and Andrea Vezzini. "Safety Requirements for Transportation of Lithium Batteries." *Energies* 10, no. 6 (June 9, 2017): 793. <https://doi.org/10.3390/en10060793>.
5. Ma, Zhaoling, Shuo Dou, Anli Shen, Li Tao, Liming Dai, and Shuangyin Wang. "Sulfur-Doped Graphene Derived from Cycled Lithium–Sulfur Batteries as a Metal-Free Electrocatalyst for the Oxygen Reduction Reaction." *Angewandte Chemie International Edition* 54, no. 6 (February 2, 2015): 1888–92. <https://doi.org/10.1002/anie.201410258>.

I.4.D Li-ion Battery Recycling R&D Center (ANL)

Jeffrey Spangenberg, Principal Investigator

Argonne National Laboratory

9700 S. Cass Avenue

Argonne, IL 60439

E-mail: jspangenberg@anl.gov

Samuel Gillard, DOE Technology Development Manager

U.S. Department of Energy

E-mail: Samuel.Gillard@ee.doe.gov

Start Date: September 30, 2018

End Date: December 31, 2021

Project Funding (FY18): \$1,225,000

DOE share: \$1,225,000

Non-DOE share: \$0

Project Introduction

Plug-in vehicles have great potential to increase the United States' energy security, economic vitality, and quality of life. Recycling of the vehicles' lithium-ion batteries will remove a barrier to widespread deployment. This project will help to reduce the cost of electric vehicle batteries towards DOE's target of \$80/kWh.

By 2020, more than 575,000 electric drive vehicles are estimated to be sold annually in the United States. This number is expected to climb to more than 1,375,000 by 2025. As recycling of lithium-ion vehicle batteries is not currently a revenue positive business and relies on fees for profitability, the economic, environmental, and safety issues with this wave of batteries for recycling will only escalate. Industry has not yet invested heavily in developing advanced recycling processes because the risk-to-reward ratio is too high. A coherent R&D effort is needed so that an economic and environmentally sound recycling process will be available to industry and consumers. A U.S. Department of Energy (DOE)-led lithium-ion battery recycling effort would connect academic research, industry knowledge, and national laboratory effort and facilities to demonstrate a scalable and profitable recycling process. The result of this program will reduce the risk industry faces, and encourage state-of-the-art technologies to transition to commercialization. The Center will effectively start operations at the beginning of FY19.

Objectives

The objective of this project is to establish the DOE Closed-loop Battery Recycling R&D (CBRRD) Center, headquartered at Argonne National Laboratory (Argonne), to focus on developing cost-effective recycling technologies for current and future batteries.

Argonne, NREL, ORNL, and university partners (Michigan Technological University, University of California at San Diego, and Worcester Polytechnic Institute) will work together to raise the value that xEV batteries have at end-of-life, without compromising safety or the environment. Together the team will:

- Establish dedicated battery recycling laboratories and personnel for bench-scale and pilot-scale research, development, and demonstration of battery recycling techniques and processes.
- Develop new processes to enable cathode-to-cathode recycling of cathode powders using temperatures below 900°C;
- Develop new processes to recover currently discarded battery materials;
- Create new electrode and cell designs, enabling cell rejuvenation and more effective material recovery at end of life; and
- Establish and use advanced characterization techniques to improve and accelerate battery recycling technologies

This work will result in new technologies, incorporated into a Scale-up Facility at the Center, and demonstrate a complete, integrated process for lithium-ion battery recycling, ready for assessment by industry.

Approach

There are currently two methods of recycling lithium-ion batteries: pyrometallurgical and hydrometallurgical. Pyrometallurgical recycling (smelting) uses high-temperature furnaces to create an alloy of valuable metals and can handle mixed battery chemistries. Cobalt and nickel are the most valuable elements, but these must be leached and separated from the alloy prior to reuse. Other elements, such as lithium and aluminum, are lost to the slag. To operate this process at an industrial-scale a large investment is required.

Hydrometallurgical recycling involves dissolving the active materials into solution and then separating them into transition metal compounds and lithium salts. It is potentially economical at smaller scale due to lower operating temperatures, lower capital investment, and recovery of more products than smelting. However, the recovered compounds require significant further processing to produce usable battery materials and the majority of revenue is also from cobalt and nickel.

The existing recycling solutions cannot cost-effectively process lithium ion xEV batteries, and require the battery owner to pay about \$1 per pound at end-of-life for disposal. As battery chemistries move away from cobalt-rich systems, the impetus for recycling using current methods will decline. This center will work to reduce recycling costs while increasing product revenues. The center will work in all areas that show potential to increase the cost-effectiveness. However there are four key focus areas the Center will address: Direct cathode recycling, recovery of additional materials, design for recycle and advanced characterization.

This program will establish a Center to develop and scale-up new processes to enable direct recycling of multiple battery materials (cathode, anode, salts) for current and future batteries. We will also investigate new electrode and cell designs, enabling cell rejuvenation and more effective material recovery at end-of-life. Because the work we are proposing is very challenging, multiple solutions are being explored.

Results

We have assembled an unprecedented team of national laboratories and universities that will allow us to achieve the program objectives in the 3-year performance period. Roles and responsibilities of the team members, which leverage their core capabilities, are shown below in Table I.4.D.1.

Table I.4.D.1 Team Members and Responsibilities

Team Member	Responsibility
Argonne	Cathode-to-cathode processes, cell design, recycle process modeling, and housing the Closed-loop Battery Recycling R&D (CBRRD) Center.
NREL	Thermal analysis, End-of-life materials analysis, and supply chain modeling
ORNL	Design of cells and electrodes for recyclability, and materials recovery
WPI	Cathode recovery and compositional adjustment through solution chemistry
MTU	Physical methods for cathode-cathode separations
UCSD	Regeneration process for cathode powders

The team will utilize its labs' unique world-class facilities to maximize research potential. Experience, capabilities, and knowledge at Argonne's MERF in materials processing, characterization, and scale-up R&D

for advanced battery materials will be applied directly to this program. A dedicated Battery Recycling R&D Lab and Scale-up Facility will be established within the MERF, providing a focal point for the materials and process research at multiple levels. The Table I.4.D.2 below shows additional state-of-the-art facilities the team will leverage to advance the Center's research.

Table I.4.D.2 List of Additional Facilities

Facility	Lab	Description
CAMP	Argonne	DOE VTO-funded cell fabrication facility focused on materials evaluation in a variety of cell formats
BMF	ORNL	DOE VTO-funded battery manufacturing facility with an emphasis on electrode formulations, coating technology, and electrode architectures in high-capacity cells
EADL	Argonne	Computerized facility designed to test cells from 2 mAh to 80 kWh
Post Test	Argonne	Combines microscopy, spectroscopy and chromatography in a controlled-atmosphere glove box to preserve sample integrity for analysis
TTF	NREL	World's most accurate battery calorimeters, thermal imaging, and cell testing
APS	Argonne	Third generation synchrotron that enables unparalleled descriptions of material
SNS	ORNL	Two of the world's most powerful neutron powder diffractometers

Crosscutting research takes advantage of established facilities and capabilities of individuals and combines them together to accelerate R&D for deployment into industry. This project uses crosscutting capabilities to address specific tasks in the projects, to enable a successful outcome in the allotted timeframe. This program will leverage prior efforts at the labs, funded by lab LDRD's, CEMAC, AMO, and VTO programs. (See Table I.4.D.3.)

Table I.4.D.3 Cross-cutting Capabilities

Capabilities	Funding	Work Description
Modeling	\$500,000	Intergrate and use BatPaC, BLAST, B2U, MSMD, ReCell, and NREL's Supply Chain Model for guidance in project decisions. In return, models will be refined as project data are generated for industry benefit.
CAMP Facility	\$100,000	Provide material, electrodes, and cells based upon the needs of the project. This covers baseline and experiment materials.
Argonne Advanced Characterization	\$100,000	Utilize Argonne's NMR Center and Analytical Chemistry Laboratory to characterize materials to determine damage/repair from processing.
Post Test Facility	\$175,000	Analyze materials from spent and recycled cells to understand the process effects on them by using microscopy, spectroscopy and chromatography techniques.
TTF	\$150,000	Evaluate processed materials looking for thermal signatures of impurities and support the modeling effort.

Additional facilities that the team will leverage at no cost to this project are the EADL, APS, and SNS. The team will utilize its internal access to these facilities to address the needs of the project, such as cell testing and analysis of the cathode structure.

Conclusions

The Closed-loop Battery Recycling Research and Development Center, consisting of a team from Argonne, NREL, ORNL, and three university collaborators has been selected by DOE-VTO to work together, and with industry, to increase the cost-effectiveness of lithium-ion battery recycling. This will be done by focusing on four key areas: direct cathode recycling, recovery of other materials within the battery, design for recycle, and

advanced characterization. Dedicated battery recycling laboratories will be made available for collaborative recycling work from bench-scale through pilot-scale R&D and demonstration. This center and its facilities is to be considered a user facility to enable fast and efficient development of battery recycling technologies. The success of the Center will be visible through an increase in recycling facilities in the United States, reduces recycling costs and increased product revenues. These successes will translate to a reduction in energy consumption, reduction in emissions, and lower overall battery cost to DOE's goal of \$80/kWh.

A kick-off meeting for the Center was scheduled for Nov. 1-2, 2018.

Key Publications

No publications on the Battery Recycling Center have been made available at the time of writing.

I.4.E Lithium-ion Battery Recycling Prize Support (NREL)

Ahmad Pesaran, Principal Investigator

National Renewable Energy Laboratory
15013 Denver West Parkway
Golden, Colorado 80401
E-mail: ahmad.pesaran@nrel.gov

Samuel Gillard, DOE Technology Development Manager

U.S. Department of Energy
E-mail: Samuel.Gillard@ee.doe.gov

Start Date: September 1, 2018 End Date: June 30, 2022
Project Funding (FY18): \$2,500,000 DOE share: \$2,500,000 Non-DOE share: \$0

Project Introduction

There is a growing demand for lithium ion batteries for use in a variety of applications including electric vehicles, consumer electronics and grid storage. Lithium ion batteries contain a substantial amount of cobalt, a critical material that is both expensive and dependent on foreign sources for production. In 2017, average annual cobalt prices more than doubled; The Democratic Republic of Congo supplies 59% of the world's cobalt; and China is the world's leading producer of refined cobalt and a leading supplier of battery imports to the United States. Unlike lead-acid batteries, which are collected and recycled at a rate of 99%, lithium ion batteries are only collected and recycled at a rate of less than 5%. Recycled material could potentially provide one third of our cathode material needs for lithium ion batteries by 2023. In order to address today's very limited infrastructure for collection, storing, and transporting discarded lithium ion batteries for eventual recycling, a Battery Recycling Prize was established by the Vehicle Technologies Office (VTO) to be directed and administered by the National Renewable Energy Laboratory (NREL). This effort is complementary to the early-stage laboratory, university, and industry research to develop low-cobalt (or no cobalt) active cathode materials for next-generation li-ion batteries (see the associated sections) and the Lithium Battery R&D Recycling Center (see the associated sections) with the aim of developing closed-loop cost-effective recycling processes to recover critical lithium battery materials.

Objectives

The proposed Battery Recycling Prize is designed to incentivize American entrepreneurs to find innovative solutions to solve current challenges associated with collecting, storing, and transporting discarded lithium ion batteries for eventual recycling. The objective of the Prize is to develop and demonstrate processes that, when scaled, have the potential to profitably capture 90% of all lithium-based battery technologies in the U.S., covering consumer electronics, stationary, and transportation applications.

Approach

The Battery Recycling Prize has a rapid iteration prize structure that makes it easier for our nation's entrepreneurs to transform innovative research from early-stage concepts to mature technology primed for industry adoption through a series of down-selecting phases. In collaboration with VTO, EERE's Advanced Manufacturing Office will also support this Prize to address the issue of critical materials for affordable and reliable American energy. The program offers a cash prizes to contestants, in three phases for approximately three years. The three consecutive innovation phases will accelerate entrepreneurs' efforts to develop, explore, and evaluate disruptive solutions to collect, store, and transport 90% of discarded lithium ion batteries. In each phase, the winners are determined by a panel of experts evaluating results based pre-determined criteria on the feasibility of collection, storage and transporting processes, cost to implement, and potential impact.

Phase I: Incubation (6 months):

The first stage prize winners will be promising startups or entrepreneurs that have identified potential high impact solutions. The purpose of the first stage of the prize is for participating contestants to identify a clear business model and technology plan toward profitable collection, storing, and transporting of discarded lithium ion batteries. The outcome of this first phase is further refinement and improvement of the 20 concepts so contestants can pitch their enhanced solutions to a panel of experts for evaluation and entry to the next phase.

Phase II: Prototyping and Partnering (1 year):

Up to 10 contestants from Phase I will receive cash prizes to further develop, improve, and prove their prototypes. The prototyping and partnering period is 1 year. The proof of concept system can include modeling, simulation, and analysis in addition to hardware prototyping. The outcome for each contestant is to substantially advance their solutions to a functional level and develop relationships with potential pilot partners. The outcome of this phase is the selection of the best concepts to proceed to the “Pilot Validation” phase.

Phase III: Pilot Validation (1 year):

The final prize supports two contestants to demonstrate a pilot test of their technology within 1 year. This could include building, demonstration, and analysis to validate a small-scale pilot prototype with focus on solutions under real-world applications and scenarios. The outcome of this final phase is for the two contestants and their partners to exhibit that their validated small-scale pilot prototype has pathways to recovering, storing, and transporting 90% of discarded lithium ion batteries.

Since NREL has already been approved to administer prizes and has established a framework for Solar Prize funded by EERE’s Solar Energy Technologies Office, NREL will also administer the Battery Recycling Prize for VTO.

Results

This project was funded in September 2018. We have initiated utilizing the framework of the Solar Prize (<https://americanmadechallenges.org/solarprize.html>) that NREL has developed in partnership with the DOE’s Solar Energy Technology Office. As part of this effort we have initiated the following approaches:

- Develop innovative business and technology strategies that make collecting, sorting, safely storing and affordably transporting lithium-based batteries profitable;
 - Develop business models to incentivize the collection of 90% of lithium-based batteries in the U.S. at their end of use,
 - Implementation of cost-effective, automated methods or technologies for separation and sorting of various collected battery types and sizes,
 - Developing cost-effective methods or technologies that will render lithium-based batteries safe or inert during storage,
 - Investigate technologies that reduces the hazardous classification of lithium-based batteries in order to reduce shipping cost,
- Enable U.S.-based recyclers to reach economies of scale in their processes by providing higher volume feedstocks;
- Attract private, public, state, and local dollar investments to scale collection, storage, and transportation of discarded lithium ion batteries;

- Incentivize networks across municipalities, states, and the country to support recovering critical materials for lithium ion battery technology for transportation applications.

While the prize purpose is to test disruptive solutions to collect, store, and transport 90% of discarded lithium ion batteries, it is not to develop the science and technology for recycling processes. Concurrent with this prize competition, DOE is sponsoring early-stage research with National Laboratories, universities and industry to develop the recycling processes.

Based on the prize structure, we have established the following process and timeline for execution of the prize's objectives, subject to modification and adjustments. (See Figure I.4.E.1.)



Figure I.4.E.1 Process and Timeline for the Battery Recycling Prize

Conclusions

The Battery Recycling Prize is established to enable collection, storing, and transporting of discarded lithium ion batteries from electric vehicles, consumer electronics, and grid storage applications for eventual recycling. The proposed contest will award cash prizes to contestants in three phases over approximately three years. NREL will administer the prize process using the established framework for the Solar Prize. In FY19, we will establish the rules and guidelines for each phase of the program, announce the Prize, launch the Battery Recycling Prize website, received applications for the first phase of the contest of incubation, select judges, and select 20 contestants to complete the incubation during a 6-month period. The eventual goal of the Prize is Incentivize American entrepreneurs to develop and demonstrate a process that, when scaled, has the potential to profitably capture 90% of all lithium-based battery technologies in the U.S., covering consumer electronics, stationary, and transportation applications.

Key Publications

Presentation on Battery R&D and Recycling Prize to Chief of Staff, EERE Assistance Secretary, September 2018.

References

1. <https://minerals.usgs.gov/minerals/pubs/commodity/cobalt/mcs-2018-cobal.pdf>
2. https://www.epa.gov/sites/production/files/2016-11/documents/2014_smmfactsheet_508.pdf
3. <https://www.call2recycle.org/>

4. EIA Annual Energy Outlook 2018, Light-Duty Vehicle Sales by Technology Type
5. <https://about.bnef.com/electric-vehicle-outlook/>
6. http://cii-resource.com/cet/AABE-03-17/Presentations/BRMT/Pilot_Christophe.pdf
7. <https://www.bloomberg.com/graphics/2018-cobalt-batteries/?cmpId=flipboard>
8. M. Mann, A. Mayyas, D. Steward, “Impact of Li-Ion Recycling on the Supply Chain, NREL, presented at the International Li-Ion Battery Recycling Workshop,” Golden, CO, May 30-31, 2018
9. L. Gaines and P. Nelson, “Lithium-Ion Batteries: Examining Material Demand and Recycling Issues,” TMS 2010 Annual Meeting and Exhibition, Seattle, WA (February 2010)

I.5 Extreme Fast Charge (XFC)

I.5.A XFC R&D: CAMP, Testing & Post-Test Characterization and Modeling (ANL)

Venkat Srinivasan

Argonne National Laboratory
9700 S. Cass Ave.
Lemont, IL 60439
E-mail: vsrinivasan@anl.gov

Samuel Gillard, DOE Technology Development Manager

U.S. Department of Energy
E-mail: Samuel.Gillard@ee.doe.gov

Start Date: October 1, 2018	End Date: September 30, 2021	
Project Funding (FY18): \$800,000	DOE share: \$800,000	Non-DOE share: \$0

Project Overview

DOE-EERE has identified fast charge as a critical challenge in ensuring mass adoption of electric vehicles with a goal of 15-min recharge time. Present day high energy cells with graphite anodes and transition metal cathodes in a liquid electrolyte are unable to achieve this without negatively effecting battery performance. There are numerous challenges that limit such extreme fast charging at the cell level, including Li plating, rapid temperature rise, and possible particle cracking. Of these, Li plating is thought to be the primary culprit. This project aims to gain an understanding of the main limitations during fast charge using a combined approach involving cell builds, testing under various conditions, characterization, and continuum scale mathematical modeling. Expertise from three National Labs are utilized to make progress in the project.

Cells are built at the Cell Analysis, Modeling, and Prototyping (CAMP) facility at Argonne National Lab (ANL) using various carbons, different cell designs, in both half-cell and full cell configuration and with reference electrodes. Cells are tested at both Idaho National Lab (INL) and ANL under various operating conditions (c-rate, temperature) and under different charging protocols with the aim of identifying the onset of plating, to quantify the extent of the problem, and to determine parameters and test data for mathematical models. Tested cells are opened and various advanced characterizing performed at ANL to determine the extent of plating and to determine if other failure models, such as particle cracking, also play a role.

A critical part of the project is the use of continuum scale mathematical models to understand the limitations at high charge rates and therefore suggest possible solutions that can be pursued. Both macro-scale approaches and microstructure-based simulations are pursued and serve to complement each other. Macromodeling at National Renewable Energy Lab (NREL) is used to test cell designs, accompanied by microstructure models to provide deeper insights into the phenomenon in the battery. This is complemented with development of models incorporating of new physics, such as phase change and SEI growth, at ANL.

Finally, two exploratory projects aim to study ways to detect Li *in situ* during operation. NREL will pursue the use of microcalorimetry to detect heat signatures during plating. INL will work with Princeton University to examine the use of acoustic methods to determine if plating leads to a signature in the acoustic signal.

Here we describe the projects at ANL related to the fast charge program, specifically related to the CAMP facility, cell testing, post-test characterization, and continuum modeling. This composite effort is further divided into three distinct projects as follows:

- Project 1: CAMP Facility Electrode and Cell Development for Fast Charge – contributors: Alison Dunlop, Andrew Jansen, Dave Kim, Bryant Polzin, and Steve Trask (Argonne)

- Project 2: Testing and Post-Test Analysis – contributors: Alison Dunlop, Andrew Jansen, Dave Kim, Bryant Polzin, and Steve Trask (Argonne)
- Project 3: Mathematical Modeling – contributor: Venkat Srinivasan (Argonne)

Accordingly, each section of this write-up is divided according to one of those three projects.

Introduction

Project 1: CAMP Facility Electrode and Cell Development for Fast Charge

In this first year's effort, the Cell Analysis, Modeling, and Prototyping (CAMP) Facility's objective was to develop experimental electrodes that will be used to identify causes of lithium plating at fast charges in single-layer pouch cells. Earlier work at Argonne by Gallagher et al. [1] had studied the influence of capacity loading on material utilization at various discharge rates. This work also touched on the effect of charge rate on capacity retention and lithium plating, which is summarized in Figure I.5.A.1. These single-layer pouch cells were originally charged for 285 cycles at a C/3 rate, after which the charge rate was increased to C/1 (followed by trickle charging to 4.2 V) up to 549 cycles, and for the surviving cells, the charge rate was further increased to 1.5C. The discharge rate was held at C/3 rate in all cases to remove that rate as a variable. As can be seen in Figure I.5.A.1, it is clear that the electrodes with loadings higher than ~ 3 mAh/cm² could not sustain a charge rate higher than C/1.

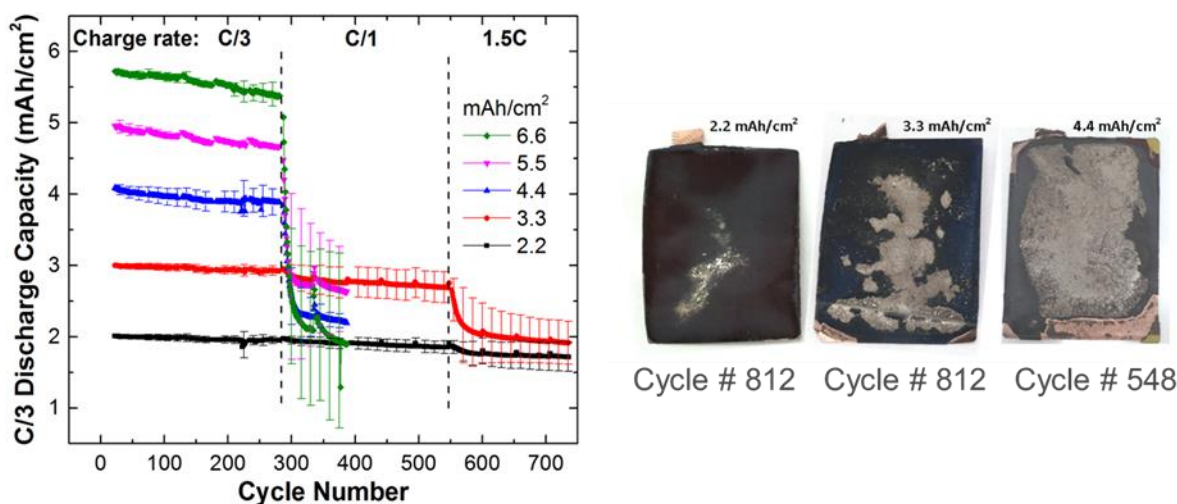


Figure I.5.A.1 Discharge capacity as a function of electrode loading (mAh/cm²) and charge rate (left) and photos of lithium deposits on representative graphite electrodes (right). These results were obtained with capacity-matched cells using graphite negative electrodes and LiNi_{0.6}Mn_{0.2}Co_{0.2}O₂ (NMC622) positive electrodes.

Evidence of lithium plating was sought for these cells by disassembling representative cells in a dry room after a 24-h voltage hold at 3.75 V and then washing with dimethyl carbonate. As expected, cells with the largest capacity fade exhibited the most lithium deposits as can be seen in Figure I.5.A.1. Surprisingly, fully discharging one of the 4.4 mAh/cm² cells at a low rate before disassembly did not remove the lithium deposits from the negative electrode surface, which suggests that the lithium deposits become electrically isolated from the graphite electrode.

Project 2: Testing and Post-Test Analysis

As consumer acceptance of electric vehicles (EVs) increases, EVs will have to provide an experience that consumers have grown used to in internal-combustion-engine-powered (ICE) vehicles. These include availability and driving experience. Of key note is the refueling experience. Here, people will expect to "refuel," that is, recharge, the EV in about the same amount of time that it typically takes to refuel an ICE-powered vehicle, about 6-10 minutes.

Project 3: Mathematical Modeling

Electrochemical modeling uses continuum based transport equations combined with kinetic and thermodynamic expressions to allow the potential, concentration, and current distributions to be determined throughout a cell. The recent focus of the electrochemical modeling effort is to improve an existing phase change model developed for graphite active materials [2]. The previous model treats graphite active materials as multiple phases, also referred to as stages for graphite, where the well-known Avrami equation was introduced to describe the phase changes as a function of lithium concentration. Further, the model effectively correlated lithium diffusion and phase change during galvanostatic intermittent titration technique (GITT) studies. However, based on limited half-cell (i.e., graphite//lithium metal cell) data with an MCMB graphite electrode, the model tended to underestimate the performance of the graphite at high current rates.

Objectives

Project 1: CAMP Facility Electrode and Cell Development for Fast Charge

The goal of the FY18 work was to determine the influence of graphite selection on fast charge capability, at an even faster rate of 6C. Initial expectations are that the physical properties of the graphite particles in the negative electrode will affect the onset of lithium dendrites. These properties include the surface area, particle size, size distribution, surface coatings/modifications, and source of graphite, i.e., natural graphite versus artificial graphite.

Project 2: Testing and Post-Test Analysis

One of the objectives of these projects is to determine how small pouch cells, which contain selected graphite anodes and oxide cathodes, respond to extreme fast charging. One of the key points here is to detect lithium plating as soon as it occurs using electrochemical methods. Another aspect is to provide materials characterization data, such as X-ray diffraction, Raman spectra, and diffusion coefficient measurements, which can be used for better understanding the observed performance response and for modeling. Another objective is to determine the physical and chemical changes that extreme fast charging causes. These changes will be characterized by post-test analysis of the fast-charged cells. A suite of materials and surface characterization techniques will be used.

Project 3: Mathematical Modeling

To use continuum-based transport equations combined with kinetic and thermodynamic expressions to allow the potential, concentration, and current distributions to be determined throughout the cell.

Approach

Project 1: CAMP Facility Electrode and Cell Development for Fast Charge

The CAMP Facility has a range of graphite powders suitable for this study that can provide a basis of comparison for these properties. At least four different graphite powders will be made into negative electrodes and evaluated for fast charge performance against a standard NMC532 positive electrode. This screening test will be performed in coin cells. The best performing graphite material will then be used in single-sided single-layer pouch cell builds and delivered to battery testing labs in this program for complete electrochemical characterization under fast charge conditions.

A second single-sided single-layer pouch cell build will be performed based on the preliminary results of the coin-cell graphite screening results and the first pouch cell build. This second cell build will either use a different graphite or a higher electrode mass loading (thicker). These pouch cells will also be delivered to the battery test labs for evaluation and analysis.

Project 2: Testing and Post-Test Analysis

The approach to this work will consist of materials science techniques, such as Raman and X-ray diffraction, to characterize selected graphites. To understand the electrochemical limitations of the graphite, the galvanostatic

intermittent titration technique (GITT) will be performed to estimate the diffusion coefficients for lithium intercalation and de-intercalation. These data will also be used in the modeling sections of the project.

Project 3: Mathematical Modeling

The initial efforts on electrochemical modeling focused on improving the graphite phase change model. Two improvements on the model were identified. However, they did not significantly improve the model's performance at high current rates. Paralleling the phase change model modifications, an existing improved data set was utilized to develop a new parameter set for a ConocoPhillips CGP-A12 graphite. The graphite electrode, fabricated at the CAMP Facility, has exhibited reasonably good fast charge characteristics. Further, it is thin enough that electrochemical model simulations indicate that the electrode is not limited by lithium ion transport through the electrolyte at a 6C rate.

Results

Project 1: CAMP Facility Electrode and Cell Development for Fast Charge

Prescreening of Available Graphite Powders

Table I.5.A.1 lists the available properties for the graphite powders selected in the prescreening tests initiated at the start of this fiscal year. Since several of these powders were already incorporated into the CAMP Facility's Electrode Library, it was decided to evaluate these materials using the Library's anode capacity loading of 2 mAh/cm² against capacity-matched NMC532 positive electrodes also in the Library. The negative-to-positive electrode capacity (n:p) ratios were ~1.1 to 1.2. Graphite materials not in the Electrode Library were designed and developed at the same capacity loading (and added to the Library).

Table I.5.A.1 Graphite powders selected to elucidate causes of lithium plating during fast charges.

Trade Name	Co.	Type	Particle shape or morphology	Tap Density, [g/mL]	Surface Area, [m ² /g]	Particle Size D10, [μm]	Particle Size D50, [μm]	Particle Size D90, [μm]
SLC1506T*	Superior Graphite	coated, natural graphite	spherical graphite powder	1.03	1.936	5.37	8.06	13.15
SLC1520P	Superior Graphite	coated, natural graphite	spherical graphite powder	1.19	0.89	11.03	16.94	26.76
MagE3	Hitachi	artificial graphite, combines hard graphite additive		0.90	3.9	-	22.4	-
MCMB	Gelon	Artificial, Mesocarbon Microbeads standard type-G15	MesoCarbon MicroBeads	1.324	2.022		17.649	
CPG-A12	Phillips 66	natural graphite core coated with surface treatment	potato	-	2 to 4	-	9 to 12	-
BTR-BFC-10	BTR	Artificial Graphite High Energy Fast Charge [Targray-SPGPT805]	TBD	0.770	2.487	6.539	11.196	18.891

Coin cells were assembled with 14 mm diameter cathodes and 15 mm diameter anodes using Celgard 2320 separator (20 μm , PP/PE/PP) and Tomiyama 1.2 M LiPF_6 in EC:EMC (3:7 wt%) “Gen2” electrolyte. Four duplicate coin-cells were made for each graphite. The coin cells were then cycled in the 3.0 to 4.1 V window with 3 formation cycles at C/10 (w/ C/20 trickle charge), followed by 250 cycles of fast charging at 6C with trickle charge down to C/5 until a maximum charge time of 10 minutes was reached, with C/2 discharges. 2 minute open circuit rests were used between charge and discharge steps. This profile was repeated until <80% of the capacity measured at the 10th cycle remained.

At this relatively low loading, all of the graphite materials in Table I.5.A.1 were able to cycle under a 6C charge rate for 750 cycles, at which point they were removed from testing and given to the Post-Test Facility for tear down and inspection. A comparative summary of their capacity over cycling is best illustrated in Figure I.5.A.2, which is the average of the cells (with standard deviations) for each graphite. This data was also analyzed in terms of capacity retention, and is summarized in Table I.5.A.2. Cycle 10 was used as the common cycle in normalizing this data, which is a point where the majority of cells were considered to be stabilized. Surprisingly, nearly all cells have reached 750 cycles with 80% capacity retention. A few conclusions can be postulated here based on this data, namely: 1) these selected graphites are statistically similar at this relatively low capacity loading (2 mAh/cm²); 2) the difference between natural graphite and synthetic graphite is not significant; and 3) SLC1506T graphite and MCMB graphite appear to have higher capacity utilization compared to the other graphite materials. It should be pointed out that none of these electrodes were designed for fast charging. It remains to be seen if these observations hold true at higher capacity loadings. A decision was made in January 2018 to use the SLC1506T graphite from Superior Graphite for the first pouch cell build deliverable in order to meet the deadline for delivery of these pouch cells to the battery testing labs.

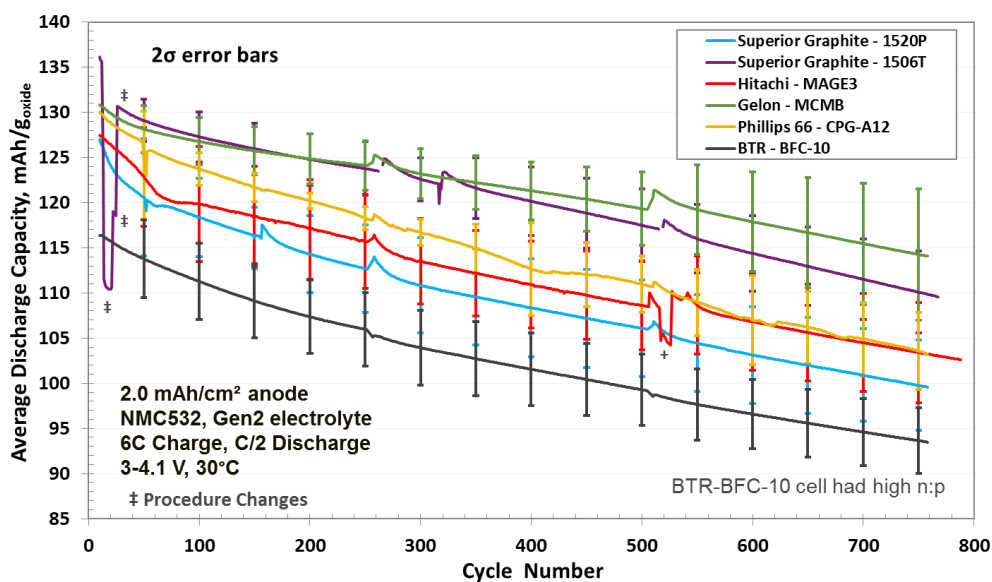


Figure I.5.A.2 Discharge capacity retention for the graphite materials selected in the coin-cell prescreening study under 6C charge and C/2 discharge between 3 – 4.1 V at 30 °C (anode capacity of 2 mAh/cm²). †cyclers issue

Table I.5.A.2 Summary of capacity retention for selected graphites and binders in prescreening task. (Discharge capacity retention is based on the 10th cycle (6C Chg, C/2 Dchg).)

		Average Discharge Capacity Retention (%)		
Graphite Type	Coating Loading (mg/cm ²)	At Cycle 750 (%)	# of Cells in Average	2 σ [+/-] Standard Deviation at Cycle 750 (%)
Superior Graphite 1520P	6.3	78.5 %	4	3.22
Superior Graphite 1506T	6.4	80.9 %	3	2.12
Hitachi MAGE3 with PVDF	6.4	81.1 %	4	4.34
Hitachi MAGE3 with CMC-SBR	6.3	84.9 %	3	3.06
Gelon MCMB	6.4	87.3 %	5	5.61
CPG A12	6.1	79.7 %	3	4.77
BTR BFC-10	7.2	80.5 %	4	0.22

Earlier work [1] that addressed the effects of capacity loading on rate performance had indicated that cathode capacity loadings above 2 mAh/cm² experienced lithium plating at charge rates as low as 1.5C. This appeared to be in conflict with the observations from the early prescreening results obtained at the beginning of this fiscal year. One difference noted was that the electrodes in reference [1] were made by an outside vendor using an aqueous CMC-SBR binder, while the CAMP Facility electrodes use an NMP-based PVDF binder. To test the binder effect, the CAMP Facility remade the MAG-E3 graphite electrode using a CMC-SBR binder. This electrode was then tested at the 6C charge rate in the same manner as the prescreening graphite materials presented in Figure I.5.A.2. The results of this binder comparison are presented in Figure I.5.A.3, where one can conclude that there is no significant difference in the capacity fade rate for either binder system. Although the CMC-SBR cells seem to behave in a predictable manner, representative cells from each of these cell sets were opened in a glove box and inspected for signs of plating. The result is shown in the insets of Figure I.5.A.3. There were clear signs of lithium plating near the perimeter of the graphite electrode in the cell with PVDF binder, but only a light “halo” near the perimeter for the CMC-SBR cell. The influence of binder type should be explored later in cells with higher capacity loadings.

Coin-cell GITT Study

Lithium-ion diffusion coefficients through these different graphite materials are needed to accurately model the electrochemical processes taking place during fast charges. One of the best methods to obtain these coefficients is via the Galvanic Interruption Titration Technique (GITT). The CAMP Facility is providing 15 duplicate coin-cells for each of the graphite materials listed in Table I.5.A.1 to Argonne’s Electrochemical Analysis and Diagnostics Laboratory (EADL) (Ira Bloom). The results of this on-going study are presented in the EADL report. The coin cells were assembled with 15 mm diameter graphite electrodes and 15.6 mm diameter lithium metal counter electrodes using Celgard 2325 separator (25 μ m, PP/PE/PP) and Tomiyama 1.2 M LiPF₆ in EC:EMC (3:7 wt%) “Gen2” electrolyte. No formation cycles or other cycles were applied to these coin cells so that the EADL could capture the first lithiation electrochemical response. The cells were delivered to EADL and put on test within a few hours of assembly to minimize corrosion of the copper current collector. The list of graphite coin cells produced for this GITT study so far are: MCMB (A-A010), delivered 10/25/17; SLC1506T (A-A015), delivered 12/18/17; SLC1520P (A-A005A), delivered 12/19/17; and MAG-E3 (A-A016), delivered 2/22/18. The BTR-BFC-10 and A12 graphite cells will be produced later if needed.

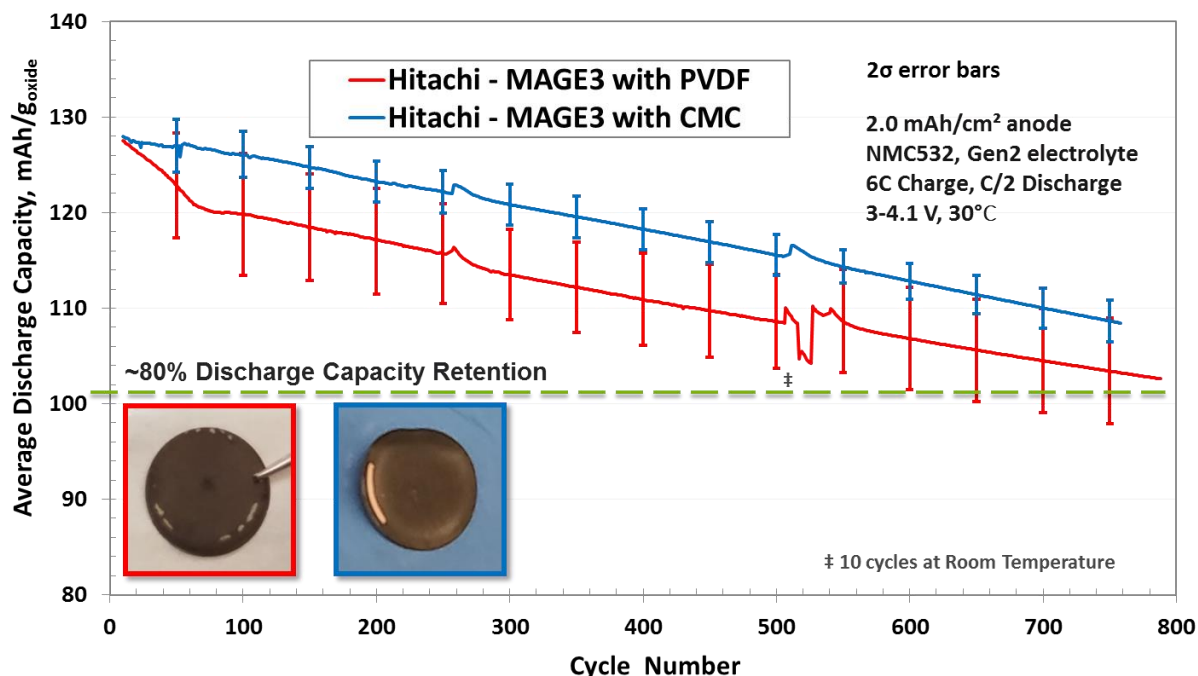


Figure I.5.A.3 Discharge capacity for the MAG-E3 graphite using CMC-SBR binder versus NMP-based PVDF binder in the coin-cell prescreening study under 6C charge and C/2 discharge between 3 and 4.1 V at 30 °C (2 mAh/cm²).

Round 1 Pouch Cell Deliverables (Single-sided Single-layer)

Pouch cells were assembled with 14.1 cm² single-sided cathodes (0.145 grams of NMC532 per pouch cell) and 14.9 cm² single-sided graphite anodes (SLC1506T from Superior Graphite) using Celgard 2320 separator (20 μm, PP/PE/PP) and 0.5 mL of Tomiyama 1.2 M LiPF₆ in EC:EMC (3:7 wt%) “Gen2” electrolyte. The n:p ratio is between 1.12 and 1.22 for this voltage window (3.0 to 4.1 V). After assembly, the pouch cells underwent formation cycles at ~4 psi in the 3.0 to 4.1 V window as follows: 1.5 V tap charge and hold for 15 minutes, followed by a 12 hour rest, and then 3 cycles at C/10, followed by 3 cycles at C/2. The cells were then brought to a safe state of charge by constant voltage charging to 3.5 V for 6 hours, and then degassed, and prepared for shipping/delivery to the battery test labs. A nominal C/3 capacity of 19 mAh was recommend for future tests.

Idaho National Laboratory (INL) requested 30 of these pouch cells for testing. These 30 cells were received at INL the week of 2/13/18. Argonne’s EADL requested 16 of these pouch cells for testing in February. These 16 cells were delivered to Argonne on 2/15/18 in 4 test fixtures at ~4 psi. An additional 16 pouch cells were assembled and kept dry (no electrolyte) for Argonne’s EADL for future rounds of testing. These additional cells were later filled with electrolyte and electrochemically formed by the CAMP Facility and delivered to EADL on 5/17/18.

In addition, the National Renewable Energy Laboratory (NREL) requested 4 of these pouch cells fully formed similar to INL and Argonne’s EADL pouch cells for micro-calorimetry studies. They also requested 2 dry pouch cells and several punched pristine anodes and cathodes that are used in the pouch cells. All of these cells and electrodes were shipped to NREL at the end of February. NREL also requested 4 graphite (SLC1506T) half-cell pouch-cells and 4 NMC532 half-cell pouch-cells, which were assembled with no electrolyte (dry) and shipped to NREL the week of 5/28/18.

Round 2 Pouch Cell Deliverables (Single-sided Single-layer)

Several options were available in designing the second pouch cell build. These options included changing the graphite, binder, and electrode capacity loading. Since the results from designing the first cell build indicated that the choice of graphite and binder was not the dominant driving factor in the fast charge performance, it was decided to focus on increasing the electrode capacity loading. As in the 1st pouch cell build, a quick screening was performed to determine an electrode loading that would yield at least a few hundred fast charge cycles. The CAMP Facility searched through their available electrodes with varying electrode loadings to find suitable capacity-matched anode-cathode pairs. Four sets of matched A12 Graphite versus NMC532 were found with nominal loadings of 1.5, 3.0, 4.5, and 5.5 mAh/cm². Coin cells were made with these electrodes and formed at C/10 rate, after which they were subjected to several 6C charges. It was quite clear from the resulting capacity utilizations that cathode electrode loadings above ~2.5 mAh/cm² were not able to charge at a true 6C rate. (This data was presented at the recent DOE-EERE-VTO Annual Merit Review in June.) Thus, it was decided that the 2nd pouch cell build would use a graphite electrode loading of 3.0 mAh/cm² with the same graphite (SLC1506T from Superior Graphite) and PVDF binder.

Single-sided anode and cathode electrodes were then made with capacity loading of 3.0 and 2.7 mAh/cm², respectively; the n:p ratios were 1.07 to 1.16. Coin cells were assembled with 14 mm diameter cathodes and 15 mm diameter anodes using Celgard 2320 separator (20 μm, PP/PE/PP) and Tomiyama 1.2 M LiPF₆ in EC:EMC (3:7 wt%) “Gen2” electrolyte. Eight replicate coin-cells were made and then cycled in the 3.0 to 4.1 V window with 3 formation cycles at C/10 (w/ C/20 trickle charge) followed by 3 cycles at C/2 (w/ C/10 trickle charge). Four of these cells were cycled at a 4C rate, and the remaining four were cycled at a 6C rate with trickle charge down to C/5 until a maximum charge time of 15 or 10 minutes, respectively, was reached, and with C/2 discharges and 2 minute open circuit rests between charge and discharge steps, for 250 cycles (with 3 cycles at C/2 in between). This profile was repeated until <80% of the capacity measured at the 10th cycle remained.

Figure I.5.A.4 is a summary of the 2nd Round coin cells compared to the 1st Round coin cells. While the higher capacity loading coin cells (2nd Round) are able to achieve over 700 cycles at a 6C rate, these cells did not perform equally, unlike the 1st Round coin cells, which show little cell-to-cell variance in capacity over cycles. Several of the 2nd Round coin cells failed early on and were removed from the figure. In addition, note the large loss of capacity utilization between the cells charged at the 6C rate versus the 4C rate. It will be interesting to see if the 2nd Round pouch cells exhibit similar behavior. The data in Figure I.5.A.4 was averaged and normalized to the cathode capacity and is shown in Figure I.5.A.5.

Additional coin cells were built to test the rate capability of the 2nd Round electrodes in full cells. A protocol was written to cycle these cells for 10 cycles at a 1C charge (60 minutes total), then 10 cycles at a 2C charge (30 minutes total), then likewise for 3C, 4C, 5C, and 6C. A C/2 discharge rate was used for each charge cycle. These results are shown in Figure I.5.A.6 normalized against the weight of NMC532. Data files from this study were provided to NREL for their modeling development.

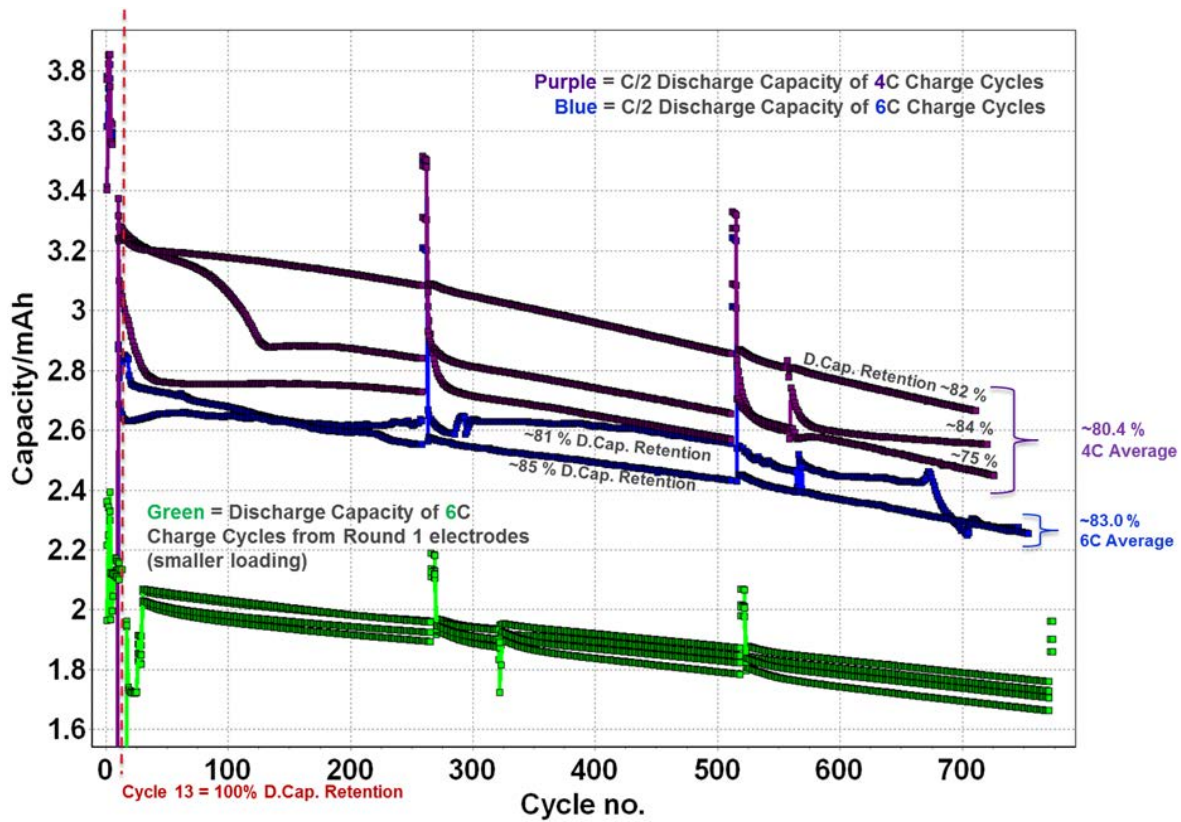


Figure I.5.A.4 Discharge capacities for the 2nd Round coin cells (purple and blue) compared to the 1st Round coin cells (green) cycled under 6C (and 4C) charge rates (Superior Graphite SLC1506T vs. NMC532).

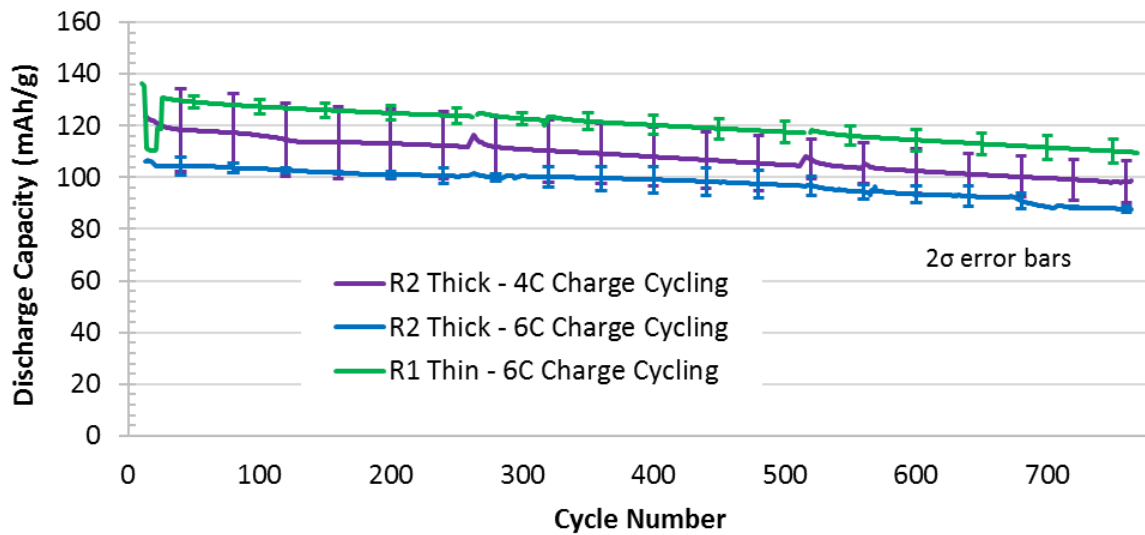


Figure I.5.A.5 Averaged and normalized capacities (based on NMC532) for the 2nd Round coin cells (purple and blue) compared to the 1st Round coin cells (green) cycled under 6C (and 4C) charge rates (Superior Graphite SLC1506T vs. NMC532).

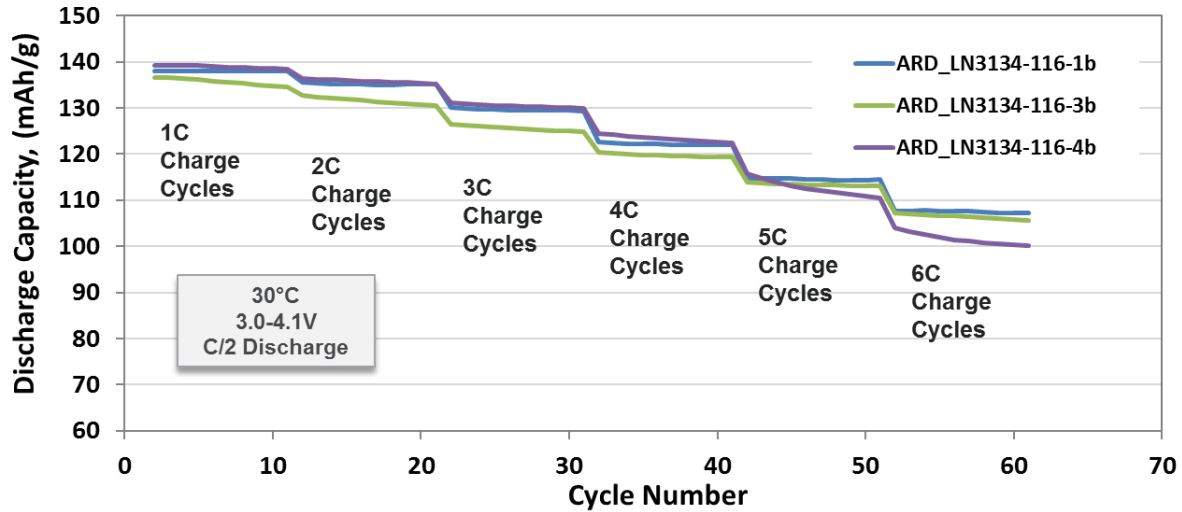


Figure I.5.A.6 Normalized capacities (based on NMC532) for the 2nd Round coin cells at increasing charge rates (Superior Graphite SLC1506T vs. NMC532).

Pouch cells were assembled with 14.1 cm² single-sided cathodes (0.236 grams of NMC532 per pouch cell) and 14.9 cm² single-sided graphite anodes (SLC1506T from Superior Graphite) using a Celgard 2320 separator (20 μm, PP/PE/PP) and 0.615 mL of Tomiyama 1.2 M LiPF₆ in EC:EMC (3:7 wt%) “Gen2” electrolyte for an electrolyte-to-pore volume factor of 4.20. The n:p ratio is between 1.07 and 1.16 for this voltage window (3.0 to 4.1 V). After assembly, the pouch cells underwent formation cycles at ~4 psi in the 3.0 to 4.1 V window as follows: 1.5 V tap charge and hold for 15 minutes, followed by a 12 hour rest, and then 3 cycles at C/10, followed by 3 cycles at C/2. The cells were then brought to a safe state of charge by constant voltage charging to 3.5 V for 6 hours, and then degassed, and prepared for shipping/delivery to the battery test labs. A nominal C/2 capacity of 32 mAh was recommended for future tests. A plot of the discharge capacities during the formation cycles applied to the 24 pouch cells delivered to INL is shown in Figure I.5.A.7.

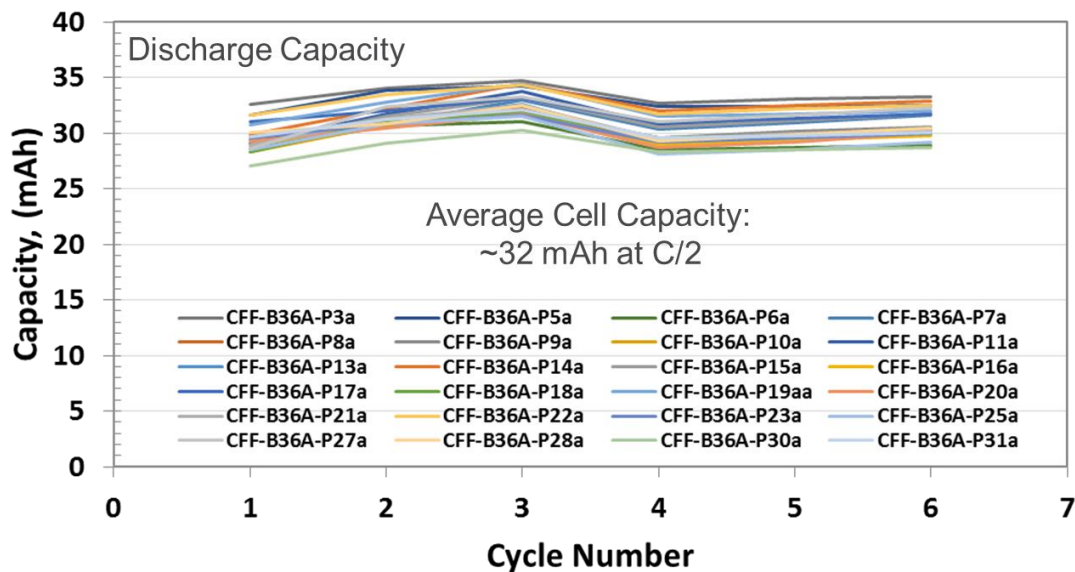


Figure I.5.A.7 Discharge capacities from formation cycles for 24 single-sided single-layer 2nd Round pouch cells (Superior Graphite SLC1506T vs. NMC532) delivered to INL.

INL requested 24 of the 2nd Round pouch cells for testing. These 24 cells were received at INL the week of 6/18/18. Argonne's EADL requested 16 of the 2nd Round pouch cells, which were assembled, formed, and delivered to EADL on 9/10/18. In addition, NREL requested 4 of the 2nd Round pouch cells fully formed similar to INL's pouch cells for micro-calorimetry studies, which were received at NREL the week of 6/18/18. They also requested 4 dry pouch cells and several punched pristine anodes and cathodes that are used in the pouch cells, as well as 4 graphite (SLC1506T) half-cell pouch cells and 4 NMC532 half-cell pouch cells. These 2nd Round specialty pouch cells were assembled and shipped to NREL on 9/21/18.

Project 2: Testing and Post-Test Analysis

Materials Characterization. Four graphite materials were selected as part of the modeling effort of the cell performance under extreme fast charging conditions. They were MAG E and E3 (Hitachi), MCMB (Gelion G15), Superior Graphite SLA1506 (coated, natural, and spherical graphite), and Superior Graphite SLC1506T. These materials were characterized by using Raman spectroscopy and X-ray diffraction (XRD) to determine if there were any physical characteristics that could be related to differences in performance.

Since all are graphitic materials, the Raman spectra were very similar. A typical spectrum is shown in Figure I.5.A.8. The ratio of the area of the D and G bands varied from sample to sample. These ratios are given in Table I.5.A.3.

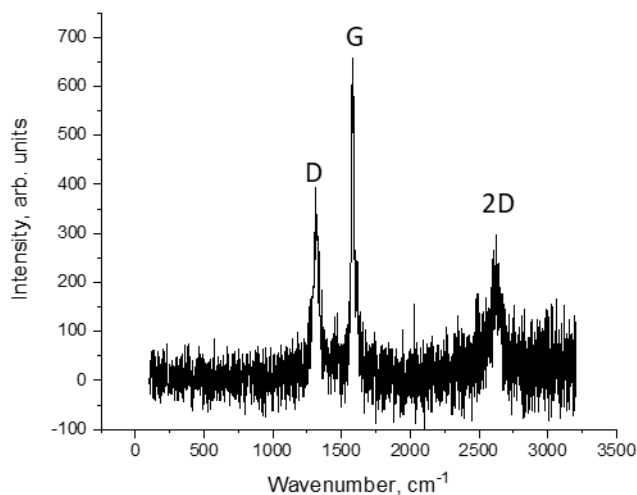


Figure I.5.A.8 Raman spectrum of MAG E3. All spectrum displayed the same bands with different intensity ratios, including the band at $\sim 2700\text{ cm}^{-1}$ (overtone/harmonic of D band at $\sim 1350\text{ cm}^{-1}$).

Table I.5.A.3 Ratio of D:G bands of the selected graphite materials.

Graphite	Ratio of D:G bands
MAG E	1.00
MAG E3	1.08
MCMB	1.35
SLC1506T	1.89
SLA1506	2.01

The graphites were also characterized using XRD. In general, the patterns were similar. Most of the lines in the patterns could be indexed in space group $P6/mmc$. There were additional reflections in the 2θ range of 40° to 60° (see Figure I.5.A.9) that could not be indexed in that space group. All but MCMB contained extra reflections. The crystallographic parameters and interslab distances were calculated from the XRD data. There

was not sufficient variation in these parameters among the graphites to make this technique useful for the correlation of electrochemical properties.

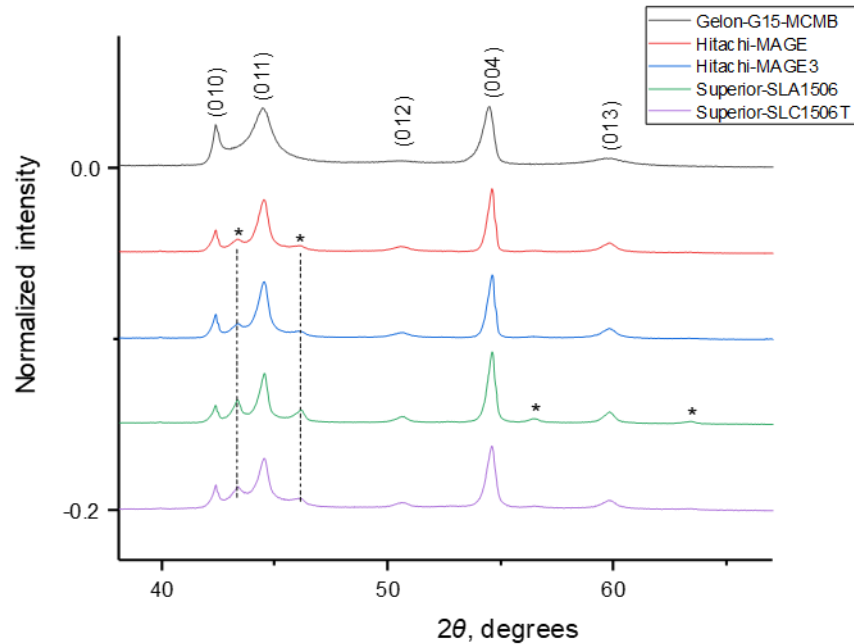


Figure I.5.A.9 XRD patterns of the selected graphites in the 2θ range of 40 to 60°.

At face value, the numbers shown in Table I.5.A.3 indicate that there may be a way to simply distinguish between graphites by Raman spectroscopy. However, based on the physics behind Raman spectroscopy, the intensity of the D band is inversely proportional to particle size. At small particle sizes, the selection rules that govern which vibrational modes are active in the Raman break down (k-selection rule) [3]. Thus, the D:G ratio is indicative of particle size and is not necessarily unique to a given graphite.

Diffusion coefficient measurements. Coin half-cells were constructed from CAMP laminates of the selected anode materials. After two formation cycles at the C/20 rate, a GITT experiment was performed at 25, 35, 45, and 55°C. Here, cells were charged and discharged using C/20 currents. The current was on for 15 min and off for 90 min.

Because the graphites were not a single phase in most of the compositional range, the usual GITT equation, shown below, could not be used to estimate the diffusion coefficient.

$$D = \frac{4}{\pi} \left(\frac{I V_M}{n F S} \right)^2 \left[\frac{\frac{dE_{OCV}}{d\delta}}{\frac{dE_{POL}}{d\sqrt{t}}} \right]^2$$

Instead, a depolarization analysis [4][5][6] was performed. The model used is shown below.

$$\ln(|E(t) - E(t = \infty)|) = \text{constant} - \frac{t}{\tau\delta}$$

$$\tau\delta = \frac{L^2}{\pi^2 D_{Li^+}}$$

This model is based on the relaxation of concentration gradients and should be less susceptible to interference from phase response. Here, $E(t)$ and $E(t=\infty)$ are the electrode potentials at time t and at infinite time, respectively, τ^δ is the relaxation time constant for the process, L is the characteristic length, and D_{Li^+} is the diffusion coefficient for Li^+ (in cm^2/s). L was calculated from the BET surface area (A_{BET}) and the density of carbon, as shown below.

$$\frac{1}{L} = 10000 \times A_{\text{BET}} \times \text{density}$$

The density of carbon was 2.267 g/cm^3 and the BET surface area of MCMB was $2.022 \text{ m}^2/\text{g}$. This calculation method does not assume a fixed particle geometry. With all the pores in graphite, one cannot assume that each particle is spherical.

Figure I.5.A.10 and Figure I.5.A.11 show the relaxation time constant, τ^δ , as a function of state of charge and temperature for both the charge and discharge subcycles. From the plots, there appears to be changes in the τ^δ vs. state of charge (SOC) curve at approximately the states of charge where phase changes would be expected. Additionally, τ^δ during lithiation (discharge) appeared sensitive to temperature at the extrema more so than at intermediate states of charge. There was almost no sensitivity to temperature during delithiation.

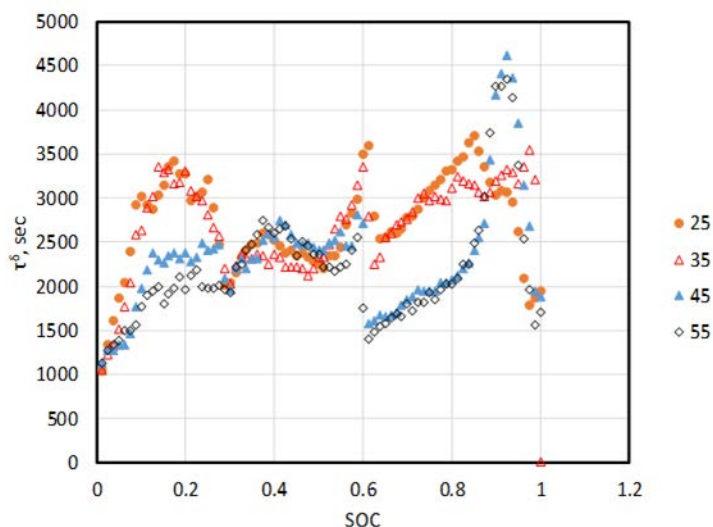


Figure I.5.A.10 Relaxation time (τ^δ) vs. state of charge (SOC) for the discharge subcycle for MCMB graphite. The discharge voltage limits were 1.5 V to 5 mV and represented the lithiation process. Each dot represents the average of three cells.

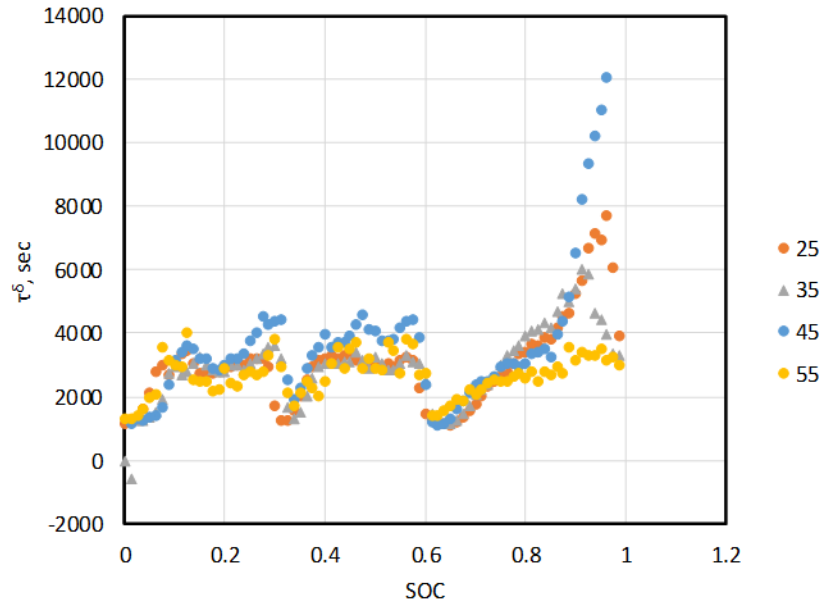


Figure I.5.A.11 Relaxation time (τ^δ) vs. state of charge (SOC) for the charge subcycle for MCMB graphite. The discharge voltage limits were 5 mV to 1.5 V and represented the delithiation process. Each dot represents the average of three cells.

Calculating the diffusion coefficients, D , from the above data leads to values in the range of 10^{-14} cm^2/s , which may be too slow for use in a fast-charge application. Only 1520P showed values of D that are significantly higher, in the range of 10^{-10} to 10^{-9} cm^2/s .

Project 3: Mathematical Modeling

The half-cell GITT study (i.e., repeated C/18 current for 16 minutes followed by 45 minute rest) was modeled with the phase change electrochemical model. In general, half-cell data can be problematic because the lithium electrode is generally unstable during cycling. Comparison of charge and discharge GITT data strongly indicated that lithium electrode instability effects were small. A typical fit of discharge data in the LiC_{32} single-phase region and the LiC_6 - LiC_{12} two-phase regions using the phase change half-cell model is shown in Figure I.5.A.12. Observations of note include the diffusion coefficient for the single phases varied from 1.2 to 2.0×10^{-13} cm^2/s , based a graphite active surface area equal to the BET surface area. In addition, the rate of phase change on charge was much faster than discharge. Previous work assumed equal rates for charge and discharge.

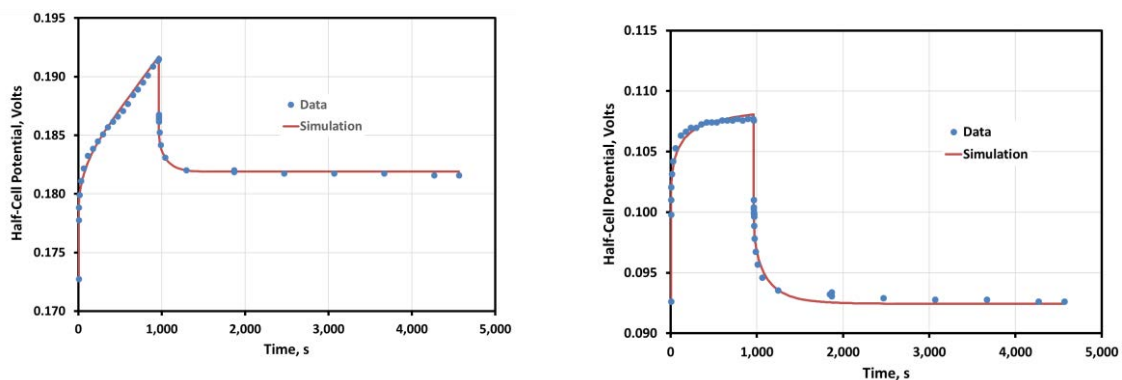


Figure I.5.A.12 Discharge A12 graphite half-cell GITT data and simulation in the LiC_{32} single-phase region (left) and the LiC_6 - LiC_{12} two-phase region (right).

Data from a full reference electrode (i.e., lithiated 25 micron copper wire between two separator layers) cell (NMC532 cathode//A12 graphite anode) with the above-described GITT study graphite electrode indicates that the cell can be easily charged at 1C without lithium deposition. Exercising the full cell electrochemical model with the GITT-derived graphite electrode parameters indicated that the full reference electrode cell cannot be charged at 1C without the graphite electrode dropping below lithium potential. Comparing the hybrid pulse power characterization (HPPC)-like studies performed with reference electrode cells having graphite electrodes to simulations with the full cell model using the GITT-derived graphite active material parameter set was problematic, as shown in Figure I.5.A.13. The lithium diffusion coefficients for each phase needed to be increased by more than an order of magnitude to fit the HPPC data. Instead of using the GITT-derived diffusion coefficients, the HPPC data was examined to establish the lithium diffusion coefficient and also the kinetic exchange current density for each of the graphite phases. Also shown in Figure I.5.A.13 is the fit for the intercalation positive electrode that was used to develop the NMC532 lithium diffusion and kinetic parameters.

The C/1 charge and discharge data for the graphite in the reference electrode cell was used to examine the GITT-derived phase change parameters, which only needed minor adjustments to improve the fit, as shown in Figure I.5.A.13 for the discharge data. Also shown in Figure I.5.A.13 is the error in the simulation at low SOC's caused by assuming only three phases in the model (LiC_{32} , LiC_{12} , and LiC_6). The GITT-derived thermodynamic parameters were not adjusted. The electrochemical model fit for the positive NMC532 electrode at C/1 discharge is also shown in Figure I.5.A.14. Using the HPPC-developed parameter set, the model agreement at the C/5 rate is excellent. However, graphite diffusional effects are relatively small in this case. The model varies from 4C to 6C rate data at higher SOC's. To obtain good agreement at the 4C rate, the diffusion coefficients for the LiC_{12} and LiC_6 phases would have to be increased another order of magnitude. Another possibility for some of the variance can also be attributed to lithium plating in part of the cell.

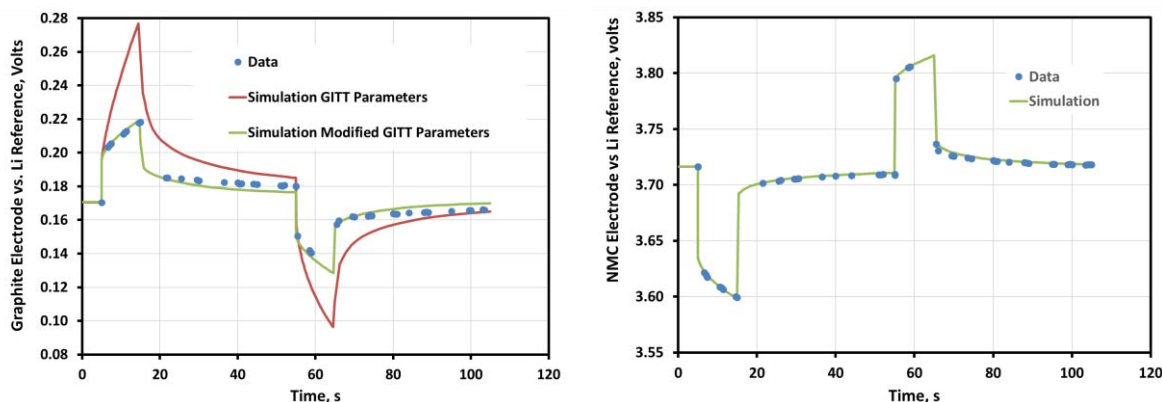


Figure I.5.A.13 Left: graphite electrode voltage compared to model simulation using indicated parameters for 10s 3C discharge and charge pulses on reference electrode cell. Right: NMC electrode voltage compared to model simulation.

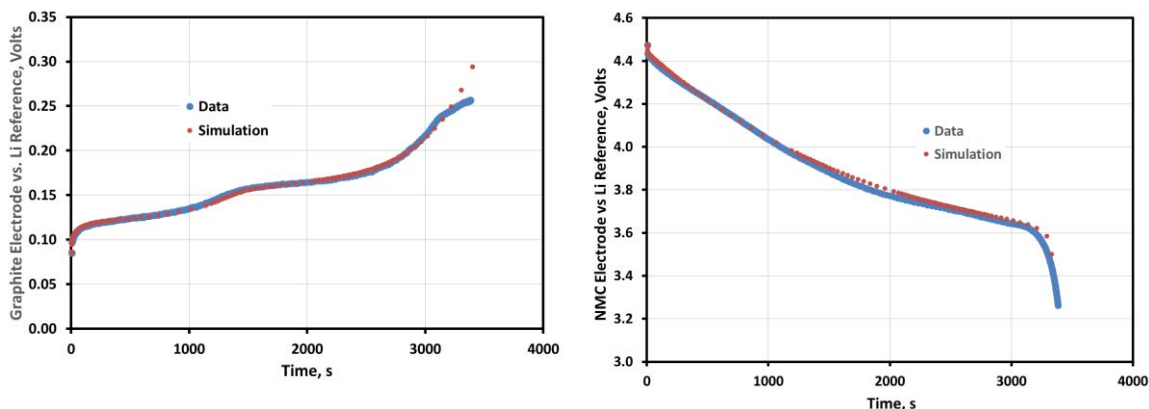


Figure I.5.A.14 Left: graphite electrode voltage compared to model simulation from reference electrode cell for 1C discharge. Right: NMC electrode voltage compared to model simulation for 1C discharge.

Having established a complete parameter set for the NMC532//A12 graphite cell, the electrochemical model was used to examine low porosity (i.e., more dense) and gradient porosity electrodes. For a fixed loading, lowering the electrode porosity reduces electrode thickness and the lithium transport length through the electrolyte, but increases tortuosity. The Bruggeman equation ($\tau = \epsilon^{-0.5}$) was used to account for electrode tortuosities. Since the electrolyte current is highest at the separator interface and goes to zero at the current collector, having an electrode with varying porosity could allow for higher currents. While the linear gradient used in this study is definitely not optimum, it does represent a significant challenge to manufacture. In general, based on capacity, the higher porosity electrodes outperformed the lower porosity electrodes for the same loading. In addition, changing the positive porosity had very little impact. Further, the gradient porosity electrode improved performance and decreasing the separator thickness (i.e., 25 to 10 micron) increased capacity. While this is certainly not an exhaustive study, it does indicate that gains in electrolyte transport would most likely need to come from reduced tortuosity electrodes or by improved electrolytes.

Performance and Cost Modeling

The Battery Performance and Cost model (BatPaC) was developed for lithium ion battery packs used in automotive transportation [7]. The model designs the battery for a specified power, energy, and type of vehicle. The cost of the designed battery is then calculated by accounting for every step in the lithium ion battery manufacturing process. It was used in 2017 to estimate the cost of batteries capable of fast charging, defined as being able to recharge 80% of the battery's capacity (from 15% to 95% SOC) in a given time [8].

The issue of lithium plating usually generates the question of whether lithium titanate (LTO) anodes (instead of graphite) can offer the solution for fast charging. Analysis has shown that the lower specific capacity of the LTO combined with the lower cell voltage of the NMCxxx-LTO chemistry leads to higher costs at the cell level. A simple example of this is demonstrated by examining the cell level costs of a 100 kWh, 300 kW pack, 900 V (240 cells in series). The graphite anode cells cost \$107/kWh as compared to 175 for the LTO technology. The packs were designed to be capable of raising the SOC by 80% in ~15 minutes. Use of the LTO allows the use of thicker electrodes.

Based on available data, it was estimated that the BatPaC battery design was constrained by a maximum allowable current density of 4 mA/cm² to prevent lithium deposition in the graphite anode [9]. These calculations were revisited recently to reflect the changes incorporated in the latest version of BatPaC Version 3.1 (released June, 2018). The changes include the prices of the materials used in the cells. Figure I.5.A.14 compares the cost estimates for the years 2017 and 2018. The 2018 estimate suggests a non-fast-charging battery cost of \$100/kWh_{Use} based on the following input specifications: [100 kWh_{Total}, 85 kWh_{Use}, 300 kW, Graphite-NMC622, 168 cells, 315V, production volume of 100K packs per year]. This is \$10/kWh cheaper than the baseline estimate from 2017.

Tests conducted on the cells from a Ford C-MAX battery [10] pack have shown charging up to 80% of the capacity at 5C rate (12 mA/cm²). However, the data does not include the sustainability of repeated charges at this rate. If we assume that a state-of-the-art anode material in 2018 is capable of sustainably charging at 9 mA/cm², then the cost of the cells is estimated at ~\$115/kWh_{Use}. The curves also indicate a sharp rise in cell costs at the lower allowable current densities.

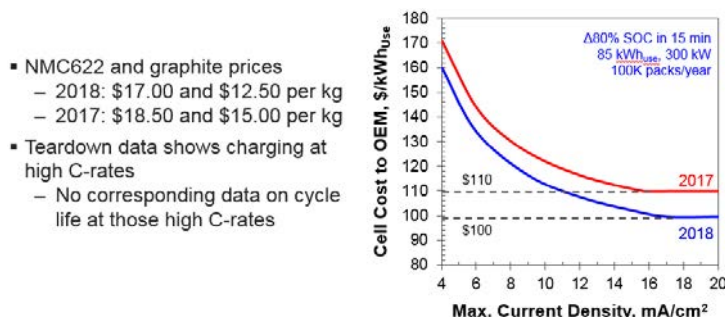


Figure I.5.A.15 Comparison of cell cost estimates with material prices in 2017 and 2018.

Conclusions

Project 1: CAMP Facility Electrode and Cell Development for Fast Charge

Six different graphite negatives were chosen from the CAMP Facility's Electrode Library for fast-charge prescreening and GITT study in coin-cells. Surprisingly similar fade rates were observed at the 6C charge for many of these graphite materials. All of the selected graphites were able to achieve 750 cycles with 80% capacity retention. A decision was made early in the prescreening study to use SLC1506T graphite from Superior Graphite for the first single-sided single-layer pouch cell build using a 2 mAh/cm² graphite loading.

The discharge capacity of the CMC-SBR vs. PVDF binder showed little difference at the 2 mAh/cm² graphite loading.

Over 70 single-sided single-layer pouch cells were fabricated and delivered to lab partners (INL, ANL, and NREL) for fast charge testing with a recommended 19 mAh capacity at the C/3 rate. Half-cell pouch cells were also designed, fabricated, and delivered to NREL.

Prescreening of anode-cathode pairs with varying electrode capacity loading indicated that loadings over ~2.5 mAh/cm² were not able to charge at a true 6C rate. Thus, the 2nd Round pouch cell build was designed with a graphite loading of 3.0 mAh/cm². Twenty-four of these 2nd Round pouch cells were delivered to INL and 4 were delivered to NREL. Sixteen of the 2nd Round pouch cells were formed and delivered to Argonne's EADL.

In August of FY18, the XCEL team met with the Awardees from the DOE-EERE-VTO FOA and Lab Call projects related to fast charge. The CAMP Facility has begun supplying these teams with electrodes and pouch cells from the 1st and 2nd Round builds.

Project 2: Testing and Post-Test Analysis

Selected graphites were characterized by Raman spectroscopy and X-ray diffraction in an attempt to find a simple method to distinguish one graphite from another. Neither was found to serve the intended purpose.

Diffusion coefficients were estimated with data from a GITT experiment using coin, half cells, and depolarization analysis. Most graphites displayed values of D in the range of 10^{-14} cm²/s, which may be too slow for use in a fast-charge application. Only 1520P showed values of D that are significantly higher, in the range of 10^{-10} to 10^{-9} cm²/s. This experiment should be repeated using a lithium reference electrode cell.

Project 3: Mathematical Modeling

The initial phase change electrochemical model modifications did not yield the needed improved rate capability. While the phase change model was successfully applied to GITT studies on an A12 graphite half-cell, model simulations with the new parameters still indicated it was underperforming at high rates. Electrochemical modeling of full reference electrode cell studies indicated that the lithium diffusion coefficient through graphite increases with applied current rate. A phase change model parameter set for A12 graphite was developed for high rate charging studies that is useable over a wide range of currents. Further, an intercalation model parameter set for NMC532 positive was developed. Modeling studies indicate the need for a fundamental understanding of increasing diffusion coefficient of lithium through graphite with applied current rate. An atomistic level study has been initiated to address this phenomenon.

The BatPaC model has demonstrated its utility in the design of battery packs for fast charge. Further, it can be used to establish the impact of possible technology and design changes on overall battery pack cost. Updates of BatPaC calculations again emphasize the importance of charge current limitations on pack costs.

Key Publications

1. "Enabling Fast Charging – A Battery Technology Gap Assessment", Shabbir Ahmed, Ira Bloom, Andrew N. Jansen, Tanvir Tanim, Eric J. Dufek, Ahmad Pesaran, Andrew Burnham, Richard B. Carlson, Fernando Dias, Keith Hardy, Matthew Keyser, Cory Kreuzer, Anthony Markel, Andrew Meintz, Christopher Michelbacher, Manish Mohanpurkar, Paul A. Nelson, David C. Robertson, Don Scoffield, Matthew Shirk, Thomas Stephens, Ram Vijayagopal, Jiucui Zhang, *J. Power Sources* **367**, 250-262 (2017).

References

1. "Optimizing Areal Capacities through Understanding the Limitations of Lithium-ion Electrodes", Kevin G. Gallagher, Stephen E. Trask, Christoph Bauer, Thomas Woehrle, Simon F. Lux, Matthias Tschech, Bryant J. Polzin, Seungbum Ha, Brandon Long, Qingliu Wu, Wenquan Lu, Dennis W. Dees, and Andrew N. Jansen, *Journal of The Electrochemical Society* **163**(2), A138-A149 (2016).
2. K.G. Gallagher, D.W. Dees, A.N. Jansen, D.P. Abraham, and S.-H. Kang, *Journal of The Electrochemical Society*, **159** (12) A2029-A2037 (2012)
3. F. Tuinstra and J. L. Koenig, *J. Chem. Phys.*, 53 (1970) 1126-1130.
4. C. Wagner, Proc. 7th Meeting Int. Comm. on Electrochem. Thermodynamics and Kinetics, Lindau 1955, Butterworth, London, 1957.
5. I. Yokota, *J. Phys. Soc. Japan*, 16 (1961) 2213.
6. J. Maier, *Physical Chemistry of Ionic Materials: Ions and Electrons in Solids*, Wiley, Chicester, England (2004).
7. P. Nelson, K. Gallagher, I. Bloom, D. Dees and S. Ahmed, "BatPaC: A Lithium-Ion Battery Performance and Cost Model for Electric-Drive Vehicles," 2018. [Online]. Available: <http://www.cse.anl.gov/batpac/>.
8. S. Ahmed, I. Bloom, A. Jansen, T. Tanim, E. Dufek, A. Pesaran, A. Burnham, R. Carlson, F. Dias, K. Hardy, M. Keyser, C. Kreuzer, A. Markel, A. Meintz, C. Michelbacher, M. Mohanpurkar, P. Nelson, D. Robertson, D. Scoffield, M. Shirk, T. Stephens, R. Vijaygopal and J. Zhang, "Enabling fast charging e A battery technology gap assessment," *Journal of Power Sources*, vol. 367, pp. 250-262, 2017.
9. K. Gallagher, S. Trask, C. Bauer, T. Woehrle, S. Lux, M. Tschech, P. Lamp, B. Polzin, S. Ha, B. Long, Q. Wu, W. Lu, D. Dees and A. Jansen, "Optimizing Areal Capacities through Understanding

the Limitations of Lithium-Ion Electrodes," *Journal of The Electrochemical Society*, vol. 163(2), pp. A138-A149, 2016.

10. Ricardo, "2013 MY Ford C-MAX Energi Battery Cell Teardown Analysis," 2016.

Acknowledgements

Key contributors to this work include: Alison Dunlop, Andrew Jansen, Bryant Polzin, and Steve Trask (all from Argonne National Laboratory). We thank K. Pierre Yao and Alison Dunlop for suggesting the depolarization method to calculate the diffusion coefficients (KPY) and for help making coin cells for the GITT experiment (ARD).

I.5.B XFC R&D: Battery Testing Activities (INL)

Eric Dufek, Principal Investigator

Idaho National Laboratory
2525 Fremont Ave
Idaho Falls, 83415
E-mail: eric.dufek@inl.gov

Samuel Gillard, DOE Technology Development Manager

U.S. Department of Energy
E-mail: Samuel.Gillard@ee.doe.gov

Start Date: October 1, 2017	End Date: September 30, 2019	
Project Funding (FY18): \$250,000	DOE share: \$250,000	Non-DOE share: \$0

Project Introduction

Extreme fast charging (XFC) of Li-ion batteries can create life and safety issues (Ahmed et al. 2017). With respect to performance loss one of the key complications is plating of Li metal on the negative electrode during fast charging. When this occurs there is a pronounced loss of Li inventory and subsequent enhanced electrolyte degradation due to the reaction of electrolyte molecules with Li metal. The detection and monitoring of Li plating onset and evolution over aging is a significant challenge. In operando detection schemes to understand the dynamics of Li plating and the role that aging has on Li plating are vital to enable fast charging of high specific energy cells.

Discreetly identifying Li plating is difficult without performing a destructive post-test analysis. The objective of the Battery Testing Activity at Idaho National Laboratory (INL) and Princeton is to overcome these limitations using electrochemical analysis and non-destructive ultrasonic acoustic methods that can be directly applied *in operando* to understand onset and growth of Li plating during XFC. The team is closely coordinating with other efforts at the National Renewable Energy Lab (NREL) and Argonne National Lab (ANL) to understand the key limitations that enhance the probability of Li plating. The effort is directed at understanding the interplay between materials, electrode structure and use conditions. The ability to understand the complex interactions will be distinctly aided in this project using the joint electrochemical and ultrasonic tools which ultimately advance the scientific understanding required to facilitate the XFC of batteries for electric vehicles.

Electrochemical methods which can be used to identify Li plating include the use of differential capacity (dQ/dV), both direct (DC) and alternating current (AC) impedance measurement, and quantitative analysis of the cells charge and discharge profiles. These tools give pertinent information associated with both kinetic and thermodynamic processes which occur in batteries, and as such provide direct ability to better understand how variation in materials and electrodes have an impact across the life of a battery. There are limitations on the type of techniques which can be used to compliment electrochemistry *in operando* using standard cell formats. One method which is showing promise is the use of ultrasonic measurements. Ultrasonic measurements rely on acoustic waves propagating through a structure, such as an electrode, which are modulated by its properties and encode structure/property relationship data. These relationships are directly tied to the material and mechanical changes which occur in a cell during cycling and can be used to characterize change in a non-destructive, real time manner. Coupling ultrasonic and electrochemical measurements will enable a more complete evaluation of the impacts of XFC to be understood. In particular both electrochemical and acoustic methods are expected to produce distinct and complimentary signals which signal the deposition of Li on the negative electrode of a battery during aggressive charging conditions. Tracking changes with the coupled ultrasonic and electrochemical methods over life and as batteries age will provide information related to the distinct conditions which drive Li plating during XFC.

Objectives

This work is focused on non-destructive, principle-based evaluation methods that can be used to better identify, quantify and advance understanding of performance fade for cells which undergo XFC. Key objectives are detection of the early stages of Li metal plating on graphite negative electrodes, quantifying the cycle-to-cycle evolution of plating and understanding reproducibility of plating. With respect to detection, both electrochemical and acoustic techniques are being evaluated to provide complimentary information on cycling performance and mechanical changes within the cell. Secondary objectives lie in advancing the understanding of how to minimize ion transport limitations in cells using different charging protocols and temperature regimes. At the end of the project a combined set of quantitative, non-destructive methods will be advanced to understand fade from extreme fast charging.

Approach

This effort is a joint collaboration that includes researchers from INL, ANL, NREL and Princeton. For analysis at INL, cells and electrode laminate prepared at ANL were used for all studies with a base chemistry of graphite/NMC 532. The first round of cells received from ANL had negative electrode loading of 2 mAh/cm². The second round of cells had higher loading which exceeded 3 mAh/cm². Both rounds of cells had a negative-to-positive electrode ratio greater than 1. After receipt from ANL cells were cycled using commercial battery cyclers or coin cells were prepared with laminate. Cycling focused on fast charging scenarios and different means to modify the transport of ions in the cell in a systematic manner. Different charging regimes which either used variable rates or distinct relaxation periods were used. All cycling at INL was performed at a constant temperature (25°C). During cycling, periodic reference performance tests (RPTs) were used to gauge the combined thermodynamic and kinetic degradation of the cell performance. The RPTs included slow cycling steps for both charge and discharge to look for distinctive losses from Li plating and to better quantify the full set of losses in the cell over cycling.

Activities at Princeton focused on obtaining acoustic signals using commercial ultrasound transducers during cycling of commercial and ANL prepared cells. Cells were cycled at different temperatures and rates to better understand the acoustic time-of-flight (TOF) response from different conditions and the plating of Li metal. For both the INL and Princeton work, targeted post-test characterization of electrodes using cell disassembly was performed to identify regions of Li plating and to analyze for other degradation modes present due to fast charge.

Results

The ability to understand the role of charging protocol and ultimately ionic transport within cells during fast charging is crucial to probe the key scientific limitations of XFC. To advance understanding on the hypothesis that fast charge capability can be influenced by transport, multiple charge profiles were developed to specifically probe different mechanisms by which ion distribution near the negative electrode could be altered. Prior to performing analysis of the procedures it was necessary to uniformly evaluate the cells to ensure that there was not introduced bias to the evaluation due to variable cell performance. When evaluating round 1 cells at the beginning of life it was found that the cells had less than 3% variability at both a C/1 and C/20 rate. The rate capability of the cells was also evaluated and from this analysis the components of the overvoltage were characterized as being due to cell impedance or due to transport. For transport two different regimes (data not shown) were identified where above 7C a sharp increase in transport related overvoltage occurred. This information was used to construct 7 different charge protocols (Table I.5.B.1). The different protocols were designed to enhance overall transport by relaxing gradients within the cell using either decreasing rates as the cell state-of-charge (SOC) increased or using distinct pauses in the charge.

The seven procedures were then used to cycle cells. During non-RPT portions of the cycling the total charge time was maintained at 10 minutes or less with RPTs repeated every 25 cycles near the beginning of life and every 50 cycles after RPT3. The data for the capacity fade at C/1 and C/20 are shown in Figure I.5.B.1.

Supporting the transport hypothesis there are distinct differences across the protocols. Better performance was seen using the protocols (6.8C MS1, 9C MS1 and 9C MS5) which had a decreasing currents as the SOC of the cell increased. Differential capacity (dQ/dV) analysis of the RPT data found that the cells with the lowest fade displayed primarily loss of lithium inventory (LLI) the higher fade cells also displayed loss of active material (LAM) primarily from the positive electrode side of the cell. This loss of utilization from the positive electrode is most likely attributed by the inability to fully lithiate the NMC during the discharge of the cell due to enhanced LLI. Further analysis (data not shown) highlights that simply looking at capacity and charge-discharge data is insufficient to fully characterize fade. As an example overvoltage data and impedance spectroscopy were jointly used to identify changes which occurred. The overvoltage analysis showed only slight shift in the transport within the cell linked with liquid and solid state diffusion. Likewise, the ohmic impedance had only slight shifts while there was a distinct increase in the charge transfer impedance.

Table I.5.B.1 Fast Charge Protocols

Cell	Label	Current Profile
4, 5, 6	6.8C CCCV	CCCV
8, 9, 10	6.8C MS1	2 step current
11, 12, 13	6.8C MS2	Pulsed current
14, 161, 17	9C CCCV	CCCV
18, 20, 21	9C MS1	2 step current
22, 23, 24	9C MS2	Pulsed Current
15, 19	9C MS5	5 step current

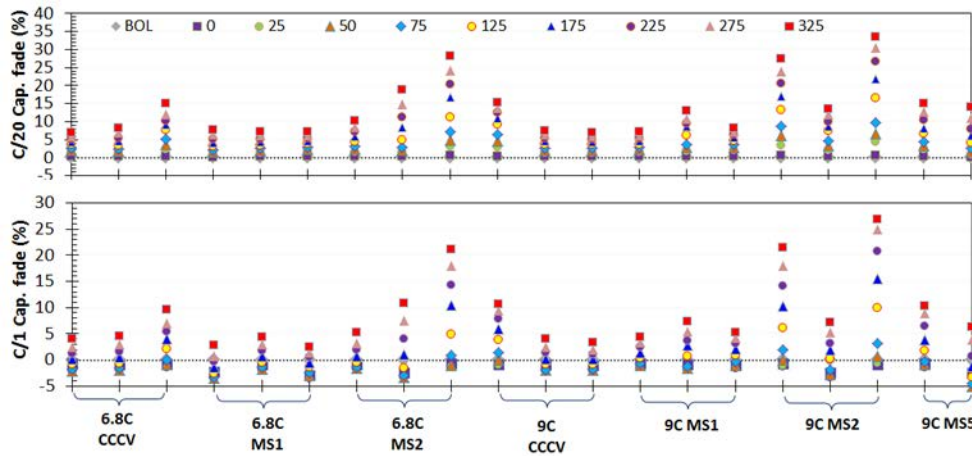


Figure I.5.B.1 The respective C/1 and C/20 capacity fade results from the aging experiment (right) using the different charge protocols defined in Table I.5.B.1.

Following cycling during post-test analysis at both INL and ANL it was found that the majority of the round 1 cells did not show distinct, visual evidence of Li metal plating when using the protocols seen in Table I.5.B.1. Only for the cells which experienced roughly 20% capacity fade was Li observed and in those cases it was non-uniformly distributed across the negative electrode. Samples and data from the round 1 cycling were shared with multiple researchers at ANL, NREL and other institutions to aid in identification of Li plating and to help validate electrochemical and multi-physics models.

As part of the RPTs for the aging study, dQ/dV analysis was performed to identify the presence of reversibly plated Li metal. Over the duration of cycling (400 fast charge cycles) there was no direct indication of reversible Li plating. To better understand the distinct limits for detecting reversible Li metal plating during fast charging a set of coin cell studies was performed. In the coin cell experiments the graphite anodes were purposefully overlithiated and the subsequent Li stripping efficiency (electrochemical reversibility) was evaluated. Two distinct outcomes from the work are noted. First, during the first few lithiation cycles the overall delithiation capacity of the graphite increased and readily approached the theoretical limit of graphite (372 mAh/g) and exceed the beginning of life lithiation capacity (for just the graphite, Figure I.5.B.2). This result suggests that for these cells and electrode configurations that full lithiation of the graphite is only achieved at potentials at which some level of Li metal plating occurs. For low levels of Li plating a distinct signature from the electrochemical stripping of metallic Li is not observed. In the analogous fast charge experiment it is likely that observing Li stripping would also be problematic using dQ/dV for low levels of Li plating. Currently work is on-going to further refine this analysis.

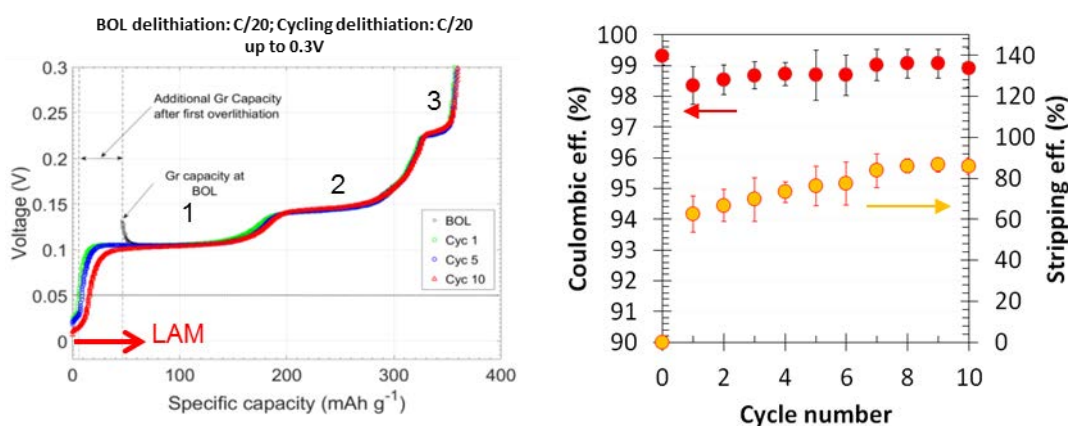


Figure I.5.B.2 Increased graphite capacity in stage 1 following over lithiation in a half-cell (left) and compared coulombic efficiency and Li stripping efficiency (right).

The second notable occurrence in the half-cell experiments was that evidence of Li metal stripping was not evident on the dQ/dV curve until the extent of overlithiation approached 5%. From this signature and the overall charge passed it is possible to characterize both the coulombic efficiency and the Li stripping efficiency (Figure I.5.B.2, right). When Li plating occurs a distinct, slight decrease in the coulombic efficiency is observed for the first few cycles, but the coulombic efficiency increases with further cycling. A similar trend is seen for the Li stripping efficiency though the overall efficiency falls well below the overall coulombic efficiency of the cell. Both the stripping efficiency and coulombic efficiency increase as multiple overlithiation cycles occur. Efforts are underway to understand the complex dynamics of the graphite lithiation and the reversibility of Li metal plating with respect to the efficiency of Li stripping.

Near the end of the fiscal year, a second round of cells was received from ANL. These cells underwent similar characterization at the beginning-of-life and were found to have less than 1% variability at different rates. During the rate performance evaluation it was found that the cells, which had higher negative electrode loading, performed worse at higher rates. This expected result, was used to modify the protocols in Table I.5.B.1. Currently the cycling performance of these cells is still underway.

The FY18 Princeton component of the work focused on the detection of Li metal plating using acoustic methods. As a first characterization the team used small multilayer pouch cells (16 layers and 210 mAh) which were cycled at a C/2.5 rate at 8°C to reduce the diffusion coefficient of Li and intentionally plate Li on the graphite negative electrode (Figure I.5.B.3). Using these conditions two distinct shifts in the transmitted wave were observed with the standard operating frequency of 2.25 MHz. A 1µs TOF shift over a period of 10 minutes was observed in the ultrasonic signal in the cells cycled at 8°C with no signal observed when the same charging protocol was used at 21°C. This data suggests Li plating and was used to design additional experiments to more clearly probe Li plating.

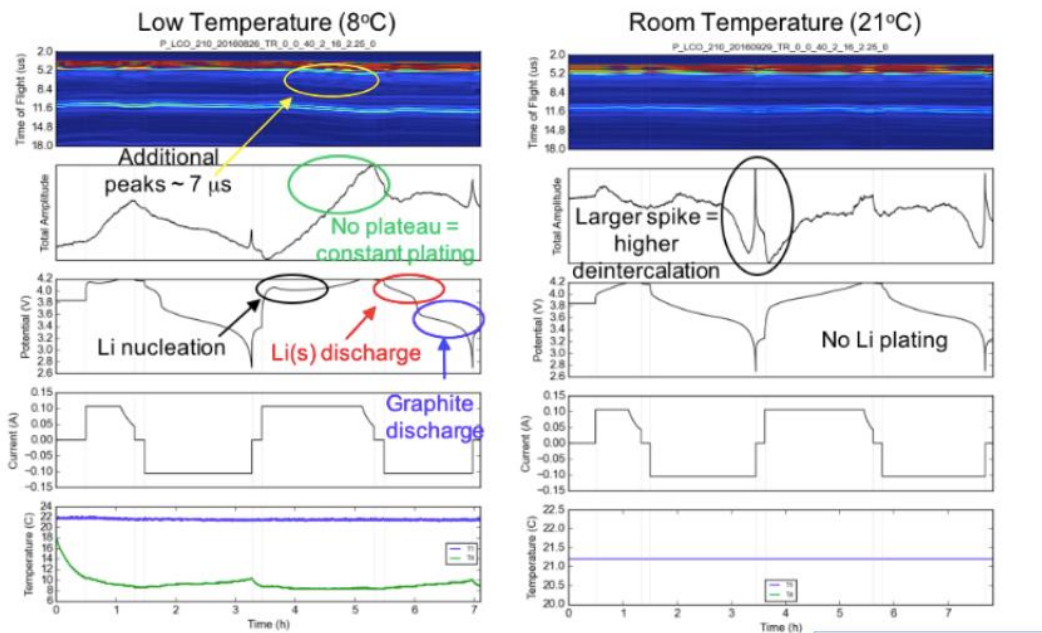


Figure I.5.B.3 Preliminary data showing acoustic signal for Li plating for cells cycled at 0.2C. LCO pouch cell at 8°C (a, with Li plating) and 21°C (b, no plating). Circles on the left show nucleation of Li metal, discharge of Li metal and Li ion deintercalation

During experiments with multiple cycles (Figure I.5.B.4) using similar 210 mAh cells at 5°C (2C CCCV charge protocol) a gradual decline in capacity is observed. During the charge the acoustic signal is distinctly mutated and altered greatly during the initial cycle (data not shown). At the completion of 10 cycles at 2C the presence of plated Li was optically verified on the surface of the negative electrode (Figure I.5.B.4, right). For cells cycled at 1 C CCCV there is no lithium optically detected and the TOF shift is not observed.

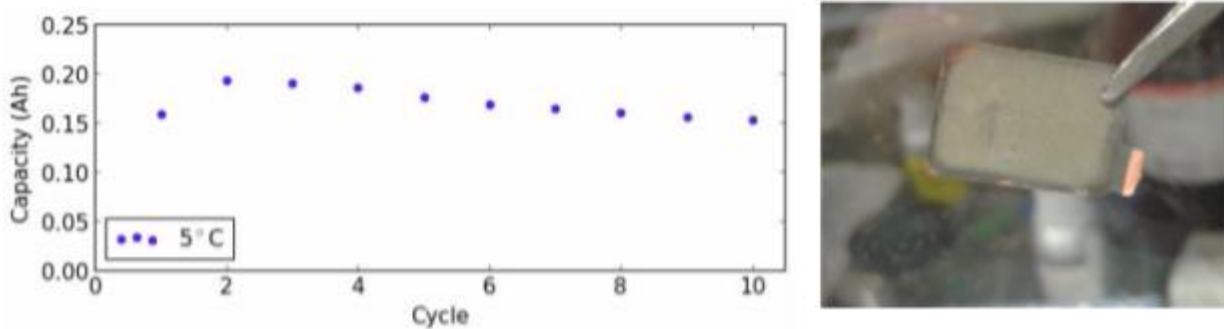


Figure I.5.B.4 Capacity over cycles, Right: Visual Lithium Confirmation

Following confirmation using thicker, commercial cells the Princeton team focused on the evaluation of the single layer pouch cells from ANL. The dimensionality of these cells paired with the existing transducers at

Princeton produced little TOF shift as well as no electrochemical or optical evidence of lithium plating and deposition. There was no visible change in the cycle profile of these cells after 50 cycles at 10C. This aligns with the INL data suggesting that it is likely that little to no Li was being plated for this cell design. To increase sensitivity Princeton is in the process of refining the experimental apparatus for single layer pouch cell investigations.

Conclusions

Research activities have identified distinct differences in fast charging performance as different charging protocols are used. It was found that for the cells with more accelerated aging that the primary modes of failure were loss of lithium inventory with some impact due to loss of positive electrode active material. For low loading negative electrodes there is little evidence of Li metal plating during most charging profiles though the extent of capacity fade varies considerably as extensive cycling occurs. Analysis of the overlithiation of graphite suggests that full, theoretical lithiation of graphite only occurs in the potential range where Li metal deposition occurs. For low levels of Li plating there is no distinct dQ/dV signature of plating which may lead to difficulty in detection during fast charging experiments unless significant quantities of Li are reversibly plated on the negative electrode. Acoustic analysis has shown that it is possible to detect Li metal plating in thicker commercial cells at low temperatures. Currently efforts are underway to further improve resolution to enable detection in single layer pouch cells from ANL.

References

1. Ahmed, Shabbir, Ira Bloom, Andrew N. Jansen, Tanvir Tanim, Eric J. Dufek, Ahmad Pesaran, Andrew Burnham, et al. 2017. "Enabling Fast Charging – A Battery Technology Gap Assessment." *Journal of Power Sources* 367 (Supplement C): 250–62. <https://doi.org/10.1016/j.jpowsour.2017.06.055>.

Acknowledgements

The work has been supported by Tanvir Tanim, Charles Dickerson, Michael Evans, Ryan Jackman and Sean Wood at INL. At Princeton efforts were led by Daniel Steingart and Clement Bommier. The INL team would also like to thank ANL for pouch cells and electrode material and the other team members from ANL and NREL for discussions.

I.5.C XFC R&D: MSMD Modeling & Thermal Testing (NREL)

Matthew Keyser, Principal Investigator

National Renewable Energy Laboratory
15013 Denver West Pkwy
Golden, CO 80401
E-mail: matthew.keyser@nrel.gov

Samuel Gillard, DOE Technology Development Manager

U.S. Department of Energy
E-mail: Samuel.Gillard@ee.doe.gov

Start Date: October 1, 2017

End Date: September 30, 2018

Project Funding (FY18): \$800,000

DOE share: \$800,000

Non-DOE share: \$0

Project Introduction

A 2017 DOE technology gap assessment report [1] established goals for next-generation electric vehicle (EV) batteries, namely battery cost of \$80/kWh, energy density of 275 Wh/kg and 550 Wh/L, vehicle range of 300 miles, and charge time of 80% ΔSOC in 15 minutes. Compared to thin electrodes, thick electrodes are preferred due to less inert material, higher energy density and lower cost. Unfortunately today's thick electrodes cannot tolerate fast charge rates. The thick electrodes have increased distance for ionic transport through the liquid electrolyte. Thin electrode batteries are capable of fast charge, however they come at a almost 2x increase in cell cost (from \$103/kWh to \$196/kWh) and have around 20% less energy density (180Wh/kg vs. 220 Wh/kg) [1]. In addition to polarization and low capacity, electrolyte transport limitations can lead to lithium plating, a side reaction with degradation and safety consequences. It is uncertain what graphite materials can best tolerate fast charge and why. At the system level, fast charging presents thermal management challenges to remove the heat generated during charging.

Objectives

- Achieve 6C (10 minute) charging of low cost, thick electrodes with loadings approaching 4 mAh/cm²
- Identify material-, electrolyte- and electrode-level barriers to reach these goals
- Validate NREL's multi-scale multi-dimensional microstructure and macro-homogeneous electrochemical models versus data from Argonne National Laboratory (ANL) and Idaho National Laboratory (INL) for cells with various materials, loadings and charged under different rates
- Use modeling tools to identify what changes are needed to material, electrode architecture and electrolytes to enable 6C fast charging
- Use isothermal calorimetry to measure heat generated at various charge rates
- Combine microcalorimetry with EIS to detect the onset of lithium plating.
- Provide design feedback to experimentalists

Approach

MSMD Modeling

NREL is leveraging multi-scale multi-dimensional (MSMD) modeling tools developed under DOE's Computer-Aided Engineering of Batteries (CAEBAT) project. (See section I.C.1 of this document.) For the material and electrode length-scales questions presently under XFC investigation, NREL mainly applied

1. Macro-homogeneous models, describing electrochemical/thermal transport/reaction physics
2. Microstructure characterization models, calculating effective properties such as tortuosity and material morphology statistics based on 3D computed-tomography imaging of electrodes.

To gain a realistic understanding of the design space and physical constraints on electrode XFC performance, the NREL team compared macro-homogeneous model predictions with experimental test data from ANL and INL for cells with the following properties and charging conditions:

- Cell/cathode NMC532 loadings of 1.5 to 5 mAh/cm²-NMC
- Charge rates from C/5 up to 9C
- Anodes composed of Superior 1506T and A12 graphite

For a loading of 1.5 mAh/cm² and 1506T graphite at 30°C, cells are capable of withstanding 6C constant current (CC) charging with relatively high capacity of 103 mAh/g and are free from lithium plating. (Electrode loadings are reported herein on a cathode basis. The anode is oversized by a factor of 1.25.) When the loading is increased to 2.5 mAh/cm², the achieved capacity at 6C falls to 51 mAh/g. Also, ANL and INL data show these cells plate lithium after only 5-10 cycles. The model accurately predicts the falloff in capacity with loading under XFC and shows this falloff is due to electrolyte transport limitations. Requirements for electrolyte transport properties needed to enable XFC of high energy density cells are reported based on model outputs. The report also compares macro-homogenous model predictions with novel in-situ XRD measurements from ANL resolving localized SOC variations across a thick anode.

NREL's microstructure characterization models – based on 3D microstructure geometry – were used to calculate tortuosity for a variety of graphite anodes produced by ANL's Cell Analysis, Modeling and Prototyping (CAMP) facility. Tortuosity almost directly correlates with initial capacity observed by ANL-CAMP across the graphite material library. In order to provide design feedback, tortuosity is further correlated to graphite particle morphology and alignment within the electrode. In FY19, the validated models will be applied to span the design space and assess best approaches to achieve 6C charging of energy-dense 3-4 mAh/cm² electrodes. These include requirements for next generation electrolytes and electrode architectures. Finally, multi-layer pouch cells received in Q4FY18 will be tested in FY19 using isothermal calorimetry under various extreme fast charging protocols.

Results

Figure I.5.C.1 illustrates 3 main transport limitations that can occur during XFC and their consequences. During charging lithium ions de-intercalate from the NMC positive electrode active particles and transfer into the electrolyte phase. These lithium ions migrate and diffuse from the positive through the separator and into the negative electrode where they intercalate into the active graphite particles. At the high current densities required to support XFC of $>10\text{mA}/\text{cm}^2$, large concentration and electrolyte potential gradients develop to drive the necessary flux of lithium ions within the electrolyte. Sustained fast charge can result in electrolyte Li-ion depletion within the negative and/or saturation within the positive electrode. These electrolyte transport limits can also occur at lower charge rates at low temperature and/or for cell designs when electrolyte conductivity is low, electrolyte diffusivity is low, electrode tortuosity is high, porosity is low, and/or electrode thickness is high. Due to limited solid-state diffusivity for graphite and NMC, lithium ions can become saturated at the graphite surfaces and depleted at the NMC surfaces. Saturation of Li ions at the graphite particle surface along with sluggish kinetics can result in lithium plating, causing cell degradation and safety concerns.

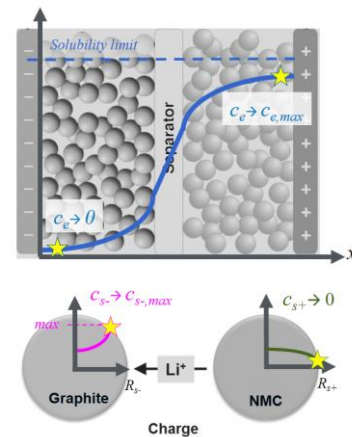


Figure I.5.C.1 Schematic of the various transport limitations during XFC that can result in poor charge acceptance, heat generation, lithium plating and capacity loss. Caption Credits/Source: NREL-Kandler Smith

The macro-homogeneous model was first compared to high rate charging data for single layer pouch cells with a low loading of $1.5\text{mAh}/\text{cm}^2$ and results are illustrated in Figure I.5.C.2. Results are shown for cells with both A12 and Superior 1506T graphite. The anode and cathodes for these two cells are between 40-45 microns with porosities between 33-37%. Both cells have an active area of 14.1cm^2 . The cell with an A12 based anode capacity falls off more when increasing charge rate from 3C to 7C (70% retention) compared to 1506T graphite (80% retention). This is due to the lower tortuosity of the 1506T superior graphite anode that is comprised of more spherical particles. The specific cathode capacity achieved for the 1506T cell at 1,3,5,7, and 9C was 128, 118, 108, 97, and 82 mAh/g-NMC. The model predicts these cells do not suffer from electrolyte depletion.

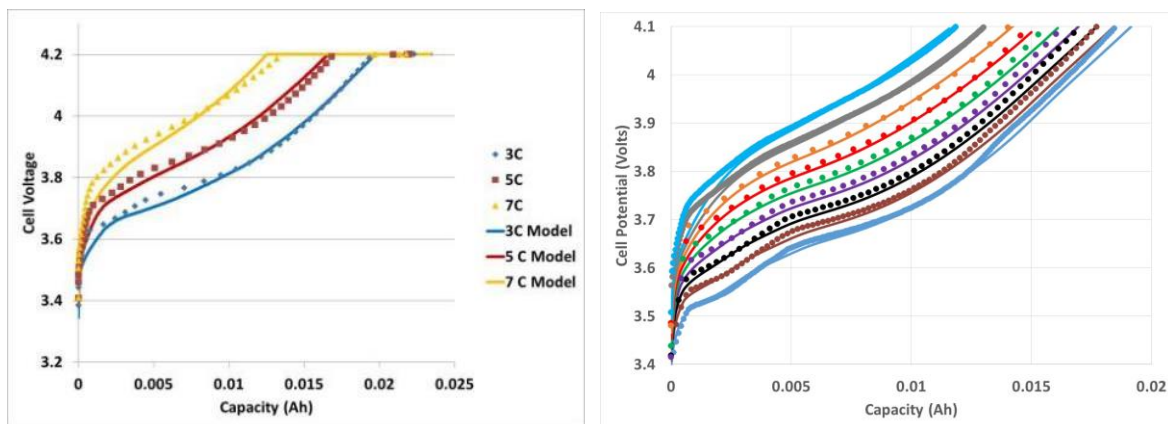


Figure I.5.C.2 Comparison of high rate charging performance of graphite/NMC 532 cells having a low loading of $1.5\text{mAh}/\text{cm}^2$ -NMC. Model results are shown as solid lines and experimental results are dots. The graph on the left is for A12 graphite anode at 3,5, and 7C and the right is for Superior 1506T graphite anode that varies from 1 to 9C. Caption Credits/Source: NREL- Andrew Colclasure

Next, the model was compared with experimental data for cells with higher loadings and these results are summarized in Figure I.5.C.3. All cells had an N/P ratio of ~ 1.1 - 1.2 and similar porosities of 30-35%. The falloff in capacity with high rate charging for the higher loading cell is well captured by the model. At 6C CC, the specific capacity for A12 cells with a loading of 1.5, 2.8, 4.3, and 5 mAh/cm² are 117, 30, 12, and 6 mAh/g-NMC. For the 1506T cell with 2.5 mAh/cm² loading, the specific capacity at 1, 3, 5, 7, and 9C was 134, 112, 73, 35, and 17. Thus, the achievable capacity for XFC dramatically reduces with electrode loading. The model predicts this falloff is from electrolyte transport limitations resulting in electrolyte depletion/saturation. This depletion/saturation results in electrodes being preferentially used near the separator interfaces. Electrode material near the current collectors is essentially un-used. While capable of capturing capacity changes, the model significantly under predicts the charge voltage for cells where electrolyte transport is limiting. This could be due to factors such as: uncertainties in electrolyte properties at high concentrations, rate dependent solid diffusivity from cracking/thermal effects, neglecting lithium-graphite phase transitions, and the model using lower tortuosity than predicted by microstructure calculations.

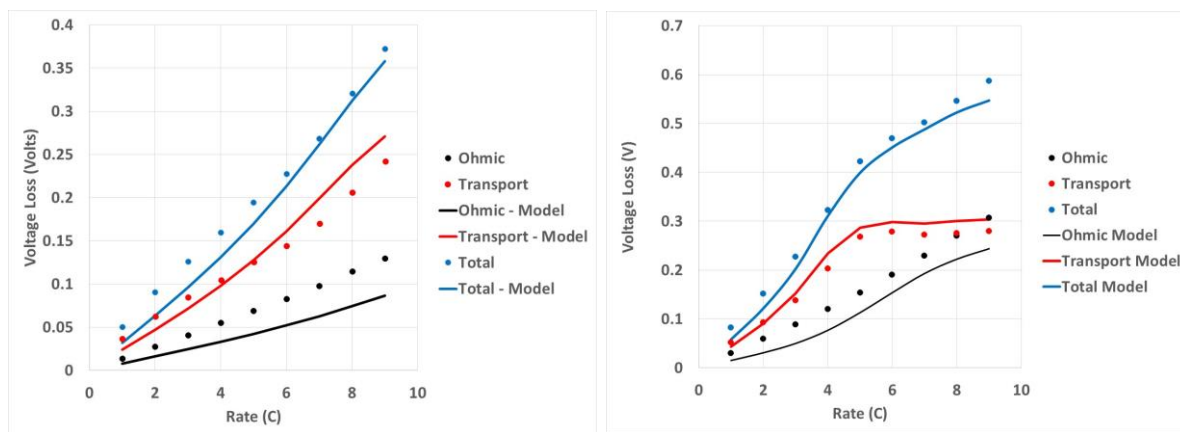


Figure I.5.C.3 Comparison of high rate charging performance of graphite/NMC 532 cells having a low loading of 1.5 mAh/cm²-NMC. Model results are shown as solid lines and experimental results are dots. The graph on the left is for A12 graphite anode at 3, 5, and 7C and Comparison of high rate charging performance of graphite/NMC 532 cells with higher loadings. Model results are shown as solid lines and experimental results are dots. The graph on the left is for A12 graphite anode at 4 different loadings all charging at 6C (two cells per condition). The right figure is for Superior 1506T graphite anode with a loading of 2.5 mAh/cm²-NMC and charge rate varying from 1C up to 9C. Caption Credits/Source: NREL-Andrew Colclasure

NREL's macro-homogeneous model was compared with INL measurements for voltage losses/overpotentials for 1506T cells with 1.5 mAh/cm² and 2.5 mAh/cm² loading and Figure I.5.C.4 illustrates the results. INL used rest data after 4.1V cutoff was reached to separate out the voltage losses. The immediate voltage change once current is stopped is an ohmic voltage loss. While the transport loss is measured based on the voltage change after 15 minutes of the cell resting. For the 1.5 mAh/cm², the ohmic and transport losses increase with charge rate. However, for the 2.5 mAh/cm² loading, the transport losses plateau above 4C indicating major transport limitations.

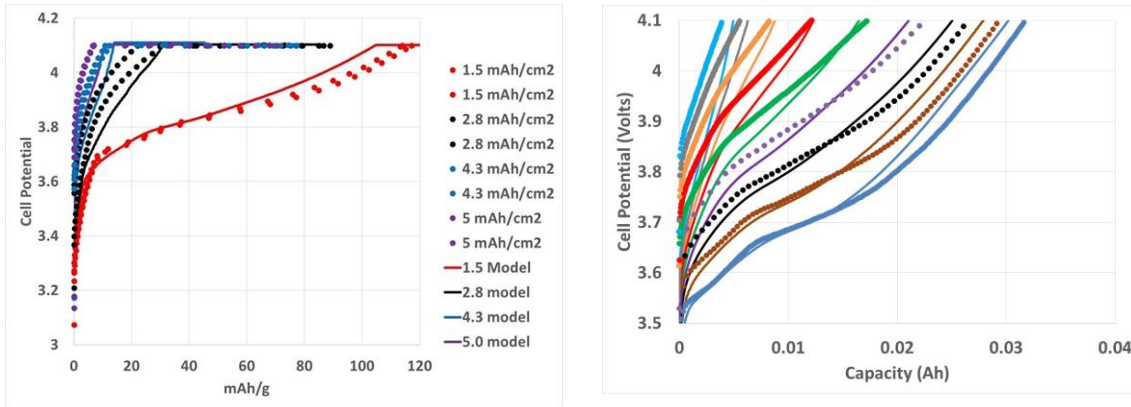


Figure I.5.C.4 Comparison of high rate charging performance of graphite/NMC 532 cells having a low loading of 1.5 mAh/cm²-NMC. Model results are shown as solid lines and experimental results are dots. The graph on the left is for A12 graphite anode at 3,5, and 7C

ANL performed in-situ XRD experiments on the Advanced Photon Source (APS) beamline to measure intercalation fraction/SOC within a thick graphite anode during electrochemical cycling. The cell consisted of a 114-micron graphite anode, 25-micron separator, and 111-micron cathode. The cell stage was tilted at different angles to measure the intercalation fraction average within 5 distinct layers during 1C cycling at 30°C. There was a discrepancy encountered during the discharge portion of the experiment. The intercalation fraction from the 5-layer average did vary linearly with discharge and was higher than expected based on capacity. NREL has had discussions with ANL to try and better understand this discrepancy but the exact cause is unknown. Thus, to compare with the model, the raw values were divided by a corrective factor such that the measured average matched the expected value. Layer 0 represents the layer next to the separator and Layer 4 is next to the copper current collector. During charge, lithium is preferentially inserted into the layers closer to the separator. At the end of 1C charging, the intercalation fraction near the separator is 0.9 and only 0.5 at the current collector side due to electrolyte transport limitations. During discharge, lithium is first mainly extracted from the graphite anode near the separator and then eventually lithium is extracted from near the current collector, but only after a significant delay. A 3.0V hold at the end of discharge is needed to remove all the lithium from near the current collector. There is a reasonably good fit between the model predicted intercalation fraction and that measured with in-situ XRD. The model predicts slightly more heterogeneity than measured experimentally. Future experiments are planned to measure the intercalation fraction heterogeneity during higher rate charging, which will require more frequent sampling with better spatial resolution.

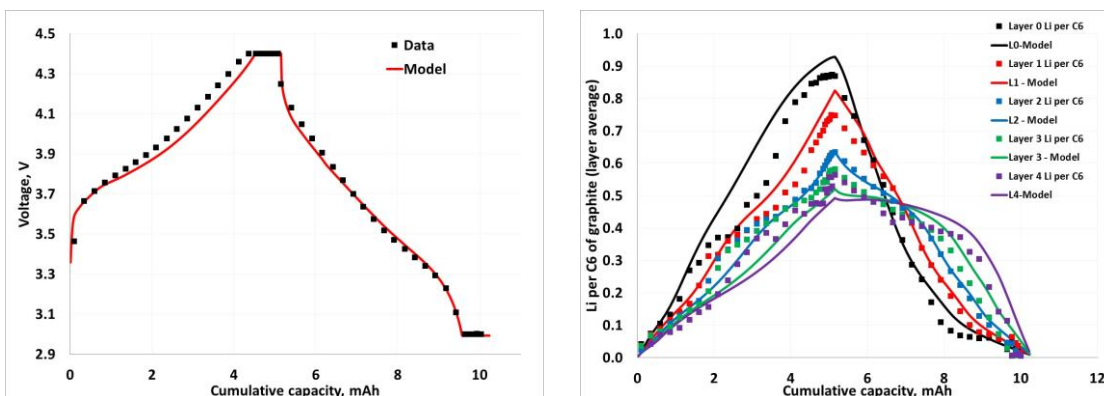


Figure I.5.C.5 Cell potential and intercalation fraction within A12 graphite anode during 1C in-situ XRD experiments performed by ANL. Experimental results are squares and model predictions are lines. Layer L0 refers to layer closest to separator and L4 is layer next to current collector. Each layer is approximately 20 microns. Caption Credits/Source: NREL- Andrew Colclasure

After fitting the model to all available data, the macro-homogeneous model is used to predict achieved capacity/SOC and driving potential for lithium plating as a function of loading for 4 and 6C charging (Figure I.5.C.6). The simulations were run up to a charge cutoff of 4.1 V. The cathode and anode porosities were set to 33% and 38%, respectively. Using the Superior graphite 1506T results in slightly better rate capability at moderate loadings of up to 10% SOC. The model predicts the round 2 (2.5 mAh/cm²-NMC) cells at 30°C are right on the verge of having lithium plating. For electric vehicle (EV) applications, a loading of 3.5 mAh/cm² or higher is desired. This corresponds to electrodes that are approximately 100 microns thick. The model predicts with the standard Gen2 electrolyte operating at 30°C cells with this loading cannot be effectively charged at 6C.

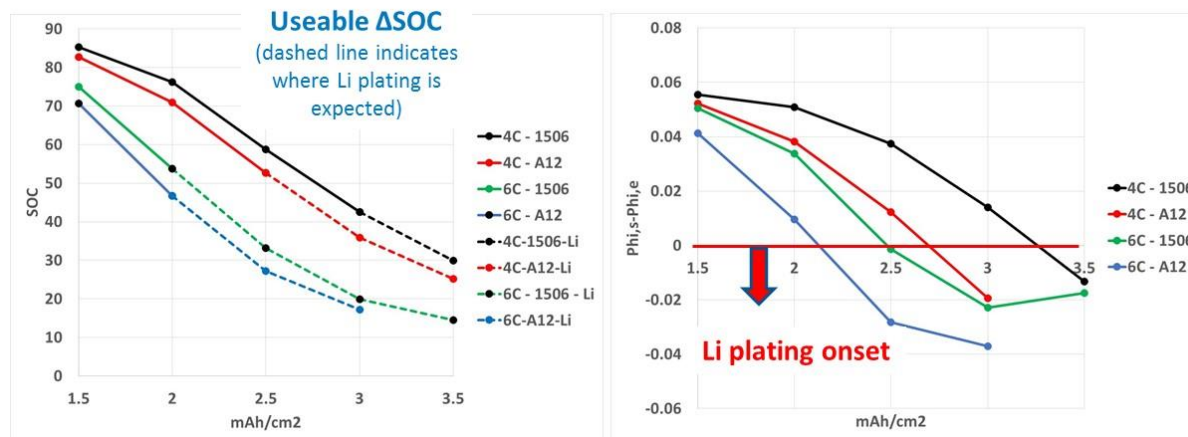


Figure I.5.C.6 Macro-homogeneous model predictions for useable SOC (left) and driving potential for lithium plating (right) as function of cell/cathode level loading at 4 and 6C. For the capacity plot, the line turns dashed when there is a driving potential for lithium plating. Caption Credits/Source: NREL- Andrew Colclasure

To enable XFC of energy dense cells with high loadings, it is important to improve electrolyte properties and reduce negative electrode tortuosity. Figure I.5.C.7 and Figure I.5.C.8 illustrate how a next generation electrolyte and negative electrode could improve the charge rate capability of thick electrodes. At 30°C and ~1M, the present Generation 2 electrolyte (LiPF₆ in 30% wt EC/70 wt% EMC) achieves an electrical conductivity of 10 mS/cm and diffusivity of 1.5e-10 m²/s. The hypothetical next generation electrolyte has a conductivity of 15 mS/cm and diffusivity of 4.5e-10 m²/s at 30°C at ~1M and negative electrode has a Bruggeman exponent of 2 (compared to the present negative electrode whose Bruggeman exponent is ~2.5). The model predicts these improvements help prevent lithium plating and electrolyte saturation/depletion for electrodes as thick as 100 μm and at charge rates up to 7C. Other researchers have noted the importance of enhancing electrolyte properties to enable XFC within high energy density cells. Recently, Jeff Dahn and coworkers have published results indicating incorporating ethers as a co-solvent improves electrolyte conductivity with values reported up to 13 mS/cm at 30°C enabling slightly higher rate charging without plating [2],[3]. The addition of ethers is also shown to reduce viscosity and thus likely improve diffusivity since the two are inversely related. It should be noted, the present estimate for lithium plating considers very fast lithium intercalation kinetics (as_{io} = 6 A/cm³ at 50% intercalation fraction). Further, the model only considers the potential of the electrode phase relative to the electrolyte phase and simple chemistry. More detailed models incorporating SEI chemistry, SEI potential drop, and multiple lithium-graphite phases will be adopted as needed during the XFC project to more accurately predict the onset of lithium plating.

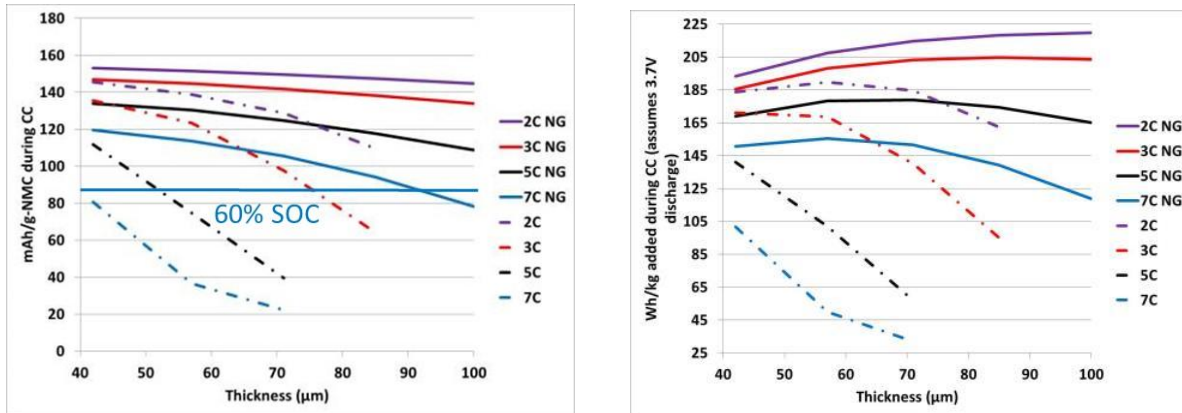


Figure I.5.C.7 Macro-homogeneous model predictions for useable SOC (left) and driving potential for lithium plating (right) as function of cell/cathode level loading at 4 and 6C. For the capacity plot, the line turns dashed when there is a driving potential for Model predictions for how normalized capacity (left) and energy density (right) achieved during XFC vary with electrode thickness/loading for current electrodes and electrolyte (dot-dash lines) and next generation (NG) electrodes and electrolyte (solid lines). Caption Credits/Source: NREL- Andrew Colclasure

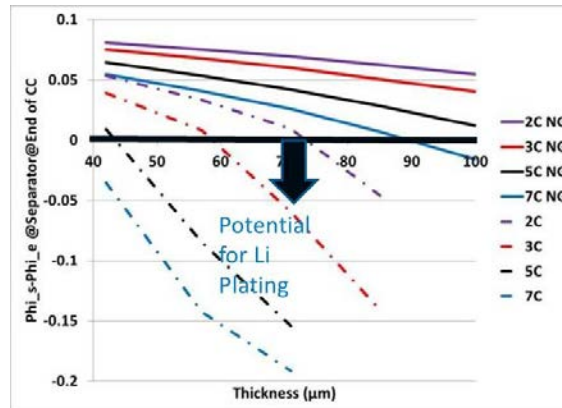


Figure I.5.C.8 Model predictions for lithium plating during XFC as function of electrode thickness/loading for current electrodes & electrolyte (dot-dash lines) and next generation (NG) electrodes & electrolyte (solid lines). Caption Credits/Source: NREL- Andrew Colclasure

To quantitatively understand tortuosity of various graphites, NREL also performed detailed microstructure reconstruction/simulations of 6 anode samples from ANL. By combining with electrochemical experimental data, this analysis provides insight into the effect of microstructure properties on the ability of electrodes to handle XFC. First, computed tomography imaging was performed by the University College of London on the anode samples. Then NREL performed segmentation of the images to construct a 3D volume representation. A drawback of the imaging is that it does not distinguish between pores and the carbon binder domain. This phase can have a significant impact on electrode tortuosity. In separate work under the CAEBAT program [4], NREL worked with Purdue University to numerically generate an appropriate carbon/binder phase. Homogenization calculations were performed to determine the effective diffusivity through the 3D microstructure and thus calculate the electrodes' tortuosity. Figure I.5.C.9a summarized the calculated tortuosity values. Figure I.5.C.9b shows that the tortuosity for the five different graphites strongly correlate with capacity of the Round 1 cells built and tested by ANL-CAMP (see Section I.E.1 of this document). A similar analysis was carried out for other graphite screening metrics (e.g. particle size, surface area, surface coating). None of the other metrics correlated with 6C capacity. Predicting tortuosity is the key factor for predicting fast charge performance.

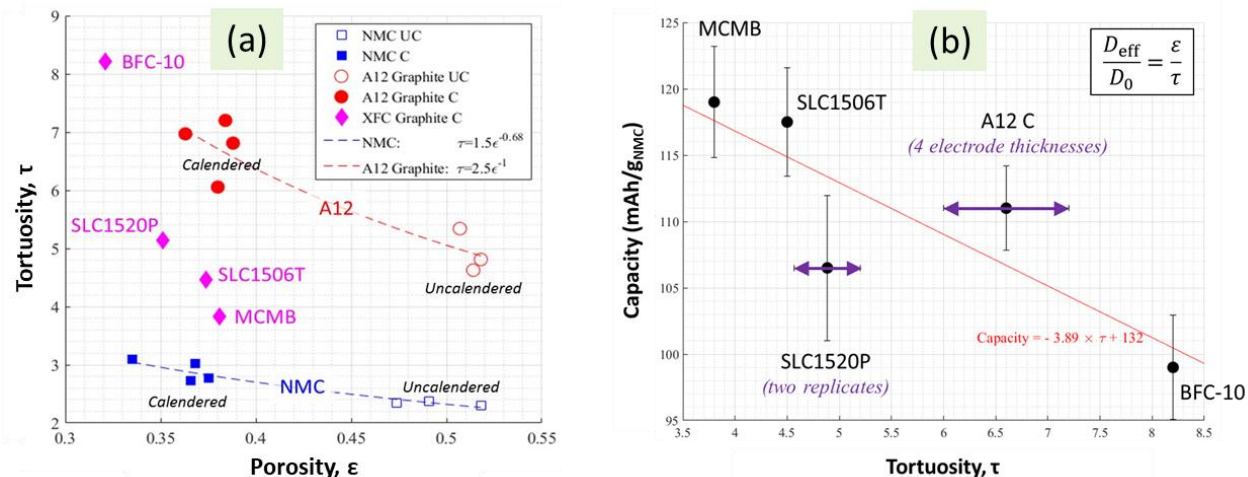


Figure I.5.C.9 (a) Microstructure-predicted tortuosity for several different electrodes. (b) Correlation of tortuosity with capacity at cycle number 500 for 6C charge, C/2 discharge of Round 1, 1.5mAh/cm² cells. Caption Credits/Source: NREL- Francois Usseglio-Viretta

Figure I.5.C.10 explains why different graphite materials have such different tortuosity factors. A discrete particle algorithm was used to identify each individual particle within the CT-imaged 3D geometry. Next, the axis of each particle in the through-plane direction was compared to the axis in the in-plane direction. A “particle elongation” metric – dividing the average through-plane axis by the average in-plane axis – shows strong correlation with tortuosity. Particle elongation of 1 indicates spherical particles; Less than 1 indicates ellipsoid or platelet particles aligned with the in-plane direction leading to high tortuosity. The BFC-10 and A12 graphite electrodes in Figure I.5.C.10 consist of platelet-like particles that lay flat with the electrode current collector, hindering ionic transport in the electrode through-plane direction. The SLC1506T and MCMB graphite materials are more spherical, yielding lower tortuosity. Even lower tortuosity is possible with perfectly spherical particles, or with secondary pore channels, an advanced electrode architecture to be analyzed by the team in FY19.

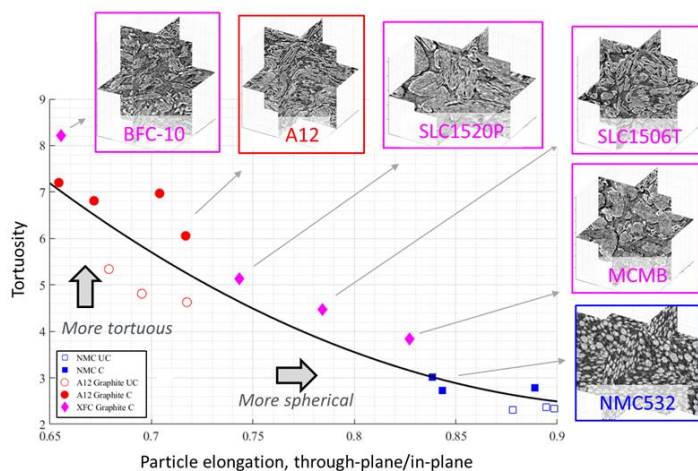


Figure I.5.C.10 Model predictions for lithium plating during XFC as function of electrode thickness/loading for current electrodes & electrolyte (dot-dash lines) and next generation (NG) electrodes & electrolyte (solid lines). Correlation of tortuosity with the particle elongation, i.e. particle axis in the electrode through-plane direction divided by particle axis in the in-plane direction. Elongation of 1 indicates spherical particles; Less than 1 indicates ellipsoid or platelet particles misaligned with the through-plane direction leading to high tortuosity. Caption Credits/Source: NREL- Francois Usseglio-Viretta

Thermal Testing

NREL is exploring utilizing heat signatures from different cell components (e.g., thermal losses due to transport limitations in the electrolyte Vs, increase in thermal impedance across the interface) to study the onset of lithium plating under different operating conditions. We are attempting to use a micro-calorimetry setup in combination with an electrochemical impedance spectroscopy (EIS) unit to detect/calibrate plating parameters for different mechanisms under different temperatures and C-rates.

During FY18, we identified sensitivity targets for heat measurements with the calorimeter to distinguish different sources of heat within the cell, as well as to detect the onset of lithium plating. Heat generated during the onset of plating was estimated at $\sim 10 \mu\text{W}$ over a 1 in^2 electrode area (geometric). Under normal operating conditions (e.g., constant current charge at 6C) these heats are very small, making in operando measurements difficult. However, developing a test-protocol, that serves as a non-intrusive off-line diagnostic technique to distinguish between electrodes with and without plating is possible. This protocol tracks heat generation across different frequencies over a set period of time, to identify different sources of heat within the cell.

Our initial modeling efforts allowed us to obtain estimates for heat generation by comparing differences in I-V profiles for cells with and without plating – shown in Figure I.5.C.11. The difference in area between the two cases was integrated to obtain the wattage associated with plating of lithium on the anode, and associated changes in the interface. These heat generation values were of the order of $10\text{-}15 \mu\text{W}$ and were too small to be measured using existing calorimetric experimental setups. Basically, calorimetric measurement techniques that track cumulative heats over an extended period of time only yield average heat generation rates. Thus, calibrating out the ohmic contributions required us to impose frequency dependent input signals to electrically excite the cell, EIS. We developed a protocol to impose these voltage signals over periods of seconds (at MHz range frequencies) to a few hours (at the mHz range frequencies). The frequencies were chosen based on the Nyquist response of the cell to correlate with the time-constants for the reaction heats of interest. For this to be successful, we needed to design a calorimeter for small pouch cells provided by ANL.

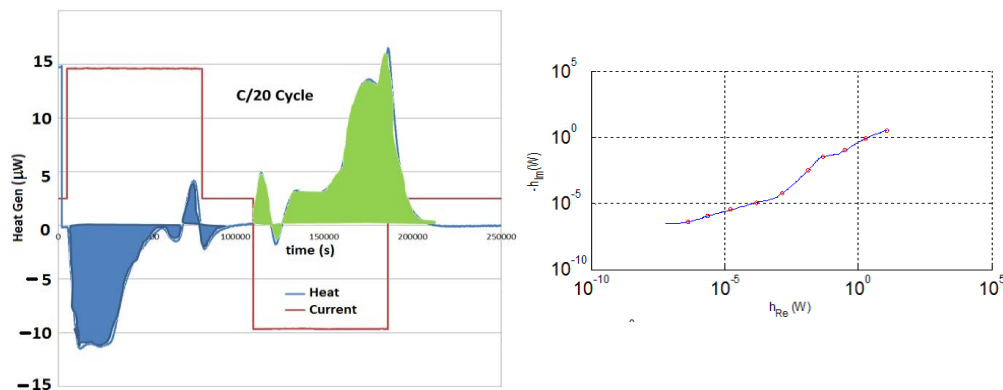


Figure I.5.C.11 Model predictions for lithium plating during XFC as function of electrode thickness/loading for current electrodes & electrolyte (dot-dash lines) and next generation (NG) electrodes & electrolyte (solid lines). Correlation of tortuosity with the Left – Estimates for heat generation from I-V profiles. Right – Mathematical model was built to calculate heat generation rates. Captions Credits/Source: NREL - Shriram Santhanagopalan

A NREL prototype microcalorimeter geared towards pouch-cells has been designed and the unit is under calibration. Off-the-shelf units NREL identified were either not able to detect small quantities of heat and/or had very high signal-to-noise ratios for us to study calorimetric signatures from gradual changes in the electrolyte that precede onset of lithium plating. The work with the calorimeter, shown in Figure I.5.C.12, is on-going and we are working to overcome a few challenges: 1) controlling the signal-to-noise ratios on a large surface area with intermittent contact between the pouch and the TEG plates is difficult compared to a small aluminum case we have previously used with the coin-cells, 2) making the chamber design flexible in order to accommodate pouch cells of various dimensions resulted in additional handling issues that are being resolved, and 3) the large area for heat dissipation also means that the diagnostic protocols must be revised according to the re-design specs.



Figure I.5.C.12 Model predictions for lithium plating during XFC as function of electrode thickness/loading for current electrodes & electrolyte (dot-dash lines) and next generation (NG) electrodes & electrolyte (solid lines). Correlation of tortuosity with the Left – Pouch cell microcalorimeter (left) and with an ANL CAMP cell (right) prepped for testing. Caption Credits/Source: NREL- Shriram Santhanagopalan

In summary, we performed a scoping study to understand the calorimetry tools required to detect lithium plating in pouch format cells produced by ANL. In concert, we re-designed our coin cell calorimeter to be able to test pouch cells and the unit is currently being calibrated – results from the re-designed unit will be summarized in the March 2019 milestone.

Conclusions

NREL's macro-homogeneous electrochemical model was compared to extensive experimental data collected by ANL and INL. Across multiple graphite materials and electrode loadings, the model is found to fit data relatively well including cell capacity, measured voltage losses, and intercalation fraction. The model tends to underpredict cell potential during initial charging for thick electrodes and/or high rates with electrolyte transport limitations. Uncertainties that could be responsible include: unknowns in electrolyte properties at high concentrations, thermal/mechanical effects, model using lower anode tortuosity than predicted from microstructure analysis, particle cracking, and simplified electrochemistry. Nonetheless, discrepancy is small. The model further agrees with qualitative observations of lithium plating seen from cell tear downs, though further quantitative testing and modeling analysis of lithium plating onset and plating rate are warranted.

The model predicts that, with standard Gen2 electrolyte and 6C charging, electrode loading must be limited to ≤ 2.5 mAh/cm²-NMC. Higher loadings are predicted to have very poor charge capacity acceptance and to plate lithium. Requirements for a hypothetical next generation electrolyte are discussed to enable 6C charging of 100-micron electrodes. Lastly, microstructure analysis/calculations are shown to estimate tortuosity for numerous electrodes. Key to enabling XFC is using electrodes with low tortuosity. For traditional porous electrode architectures, spherical shaped graphite particles provide the lowest tortuosity. Preliminary studies indicate that 6C charge is possible thick 3-4 MAh/cm² cells only by combining both improved electrolyte transport properties and lower tortuosity for anode and cathode. Charging at 45°C also partially alleviates

transport limitations. Microstructure studies/analysis in FY19 will help to determine possible electrode architectures that have required tortuosity needed for XFC.

References

1. “Enabling Fast Charging: A Technology Gap Assessment” U.S. DOE, October 2017.
2. ER Logan, EM Tonita, KL Gering, J. Li, X. Ma, LY Beaulieu, and JR Dahn. “A study of the Physical Properties of Li-Ion Battery Electrolytes Containing Esters.” *J. Electrochem. Soc.* **165**, A21-A30 (2018).
3. X Ma, RS Arumugam, L Ma, E Logan, E Tonita, J Xia, R Petibon, S Kohn, and JR Dahn. “A study of Three Ester Co-Solvents in Lithium-Ion Cells.” *J. Electrochem. Soc.* **164**, A3556-A3562 (2017).
4. F.L.E. Usseglio-Viretta, A. Colclasure, A.N. Mistry, K.P. Yao Claver, F. Pouraghajan, D.P. Finegan, T.M.M. Heenan, D. Abraham, P.P. Mukherjee, D. Wheeler, P. Shearing, S.J. Cooper, K. Smith, “Resolving the Discrepancy in Tortuosity Factor Estimation for Li-Ion Battery Electrodes through Micro-Macro Modeling and Experiment,” *J. Electrochem. Soc.* **165**, A3403-A3426 (2018)

Acknowledgements

Co-authors: Andrew Colclasure, Kandler Smith, Francois Usseglio-Viretta. We wish to acknowledge Samm Gillard and DOE for sponsoring these efforts. We would also like to acknowledge the co-authors of this report – Andrew Colclasure, Kandler Smith, Francois Usseglio-Viretta, and Shriram Santhanagopalan. We wish to acknowledge the XFC team from ANL and INL who contributed substantial test prototypes and data to this project. (See sections I.E.1 and I.E.2.) For tortuosity studies, we further wish to acknowledge CAEBAT collaborators (section I.C.1 and co-authors of [\[4\]](#)) from Purdue University (Mukherjee group), ANL (Abraham group), Univ. College of London (Shearing group), Brigham Young University (Wheeler group) and Imperial College of London (Cooper).

I.5.D Novel Liquid/Oligomer Hybrid Electrolyte with High Li Ion Transference Number (Hi-LiT) for Extreme Fast Charging (ORNL)

Zhijia Du, Principal Investigator

Oak Ridge National Laboratory
One Bethel Valley Road
Oak Ridge, TN 37830
E-mail: duz1@ornl.gov

Brian Cunningham, DOE Technology Development Manager

U.S. Department of Energy
E-mail: Brian.Cunningham@ee.doe.gov

Start Date: August 15, 2018	End Date: August 14, 2020	
Project Funding (FY18): \$1,000,000	DOE share: \$900,000	Non-DOE share: \$100,000

Project Introduction

This project focuses on development of novel electrolyte to address AOI 2 (Batteries for Extreme Fast Charging (XFC)) in DE-FOA-0001808. The DOE has ultimate goals for EV batteries, which include reducing the production cost of a BEV cell to \$80/kWh, increasing the range of BEVs to 300 miles, and decreasing the charging time to 15 minutes or less. Increasing electrode thickness is an effective way to achieve these goals; however, thicker electrodes present several barriers to fast charging. This project is to implement a novel high-Li-ion-transport (Hi-LiT) electrolyte and enable a 10-minute charge of 180 Wh/kg energy density with less than 20% fade after 500 cycles (144 Wh/kg). The targeted improvements in the Hi-LiT electrolyte will be increasing Li ion transference number from 0.363 to 0.7-0.75 while maintaining a relatively high conductivity of 4-10 mS/cm. The improvement in electrolyte formulation will suppress the Li plating issue during cycling. This electrolyte will be implemented into high energy density Li-ion cells.

Objectives

The objective of this project is the increase of Li ion transference number from 0.3-0.4 to 0.7-0.75 while maintaining high conductivity of non-aqueous electrolyte at 4-10 mS/cm through novel Li salt synthesis, anion receptors additives screening and solvent systems optimization, which will significantly increase the Li ion mass transport from cathode to anode during XFC to avoid abrupt end of charging and Li plating/dendrite growth. The implementation of this novel non-aqueous electrolyte system in high energy density Li-ion cells meet the battery performance goal of delivering 180 Wh/kg of stored energy to the cell in 10-minute charging at the beginning of life and achieving less than 20% fade in specific energy after 500 cycles (144 Wh/kg).

Approach

1. Innovative Li salts to suppress anion mobility and increase Li ion transference number.
2. Formulations with multiple solvent systems to provide better Li ion mobility and suppress Li plating.
3. Anion receptor additives to further immobilize anions and dissociate cations in electrolyte.

Results

Electrode preparation

NMC622 electrodes were coated at the Battery Manufacturing R&D Facility with formulation of NMC622/carbon black/PVDF in 94/3/3 wt%. Graphite electrodes were coated with formulation of Superior graphite (1520T)/carbon black/PVDF in 94/1/5 wt%. PVDF was dissolved in NMP prior to the slurry mixing to formed binder solution. The slurries were coated on 15 μm thick aluminum foil (for NMC622) or 10 μm thick copper foil (for graphite) with 8" width. Three different cathode loadings were made, and the anode loadings were adjusted based on N/P ratio at 1.15. Both coating processes went smoothly, and the electrodes

were calendared to about 30% porosity. Figure I.5.D.1 shows (a) the slurry mixing, (b) wet anode slurry spreading on Cu foils, (c) wet cathode slurry spreading on Al foils, and (d) calendaring process to densify the electrodes.

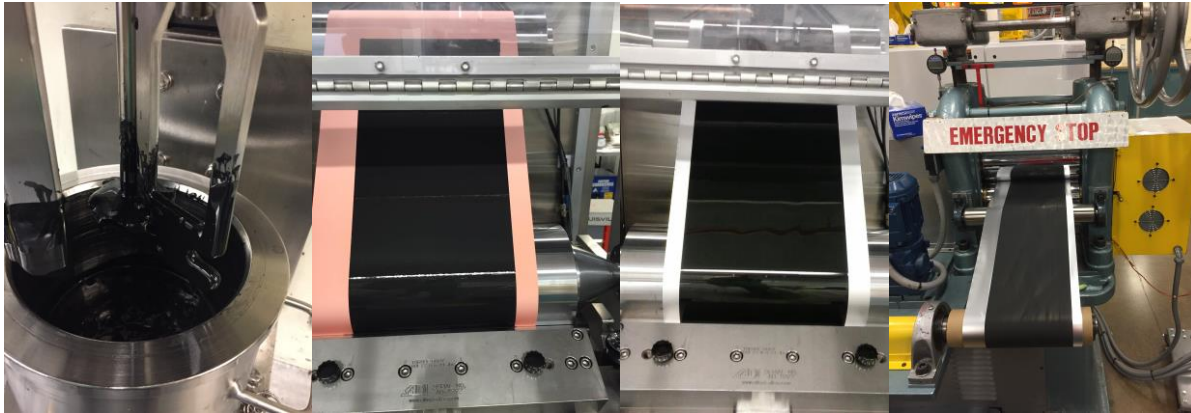


Figure I.5.D.1 (a) slurry mixture in a planetary mixer; (b) wet anode slurry coated onto Cu foil; (c) wet cathode slurry coated onto Al foil; (d) electrode coating densified through calendaring machine.

Baseline cell performance testing

The electrochemical behavior of the NMC622 and graphite electrode were studied by assembling half coin cells and the voltage curves are shown in Figure I.5.D.2. The graphite electrode shows typical three plateaus from intercalation reaction with LiC_{18} , LiC_{12} and LiC_6 formed at the end of each plateau. The first cycle intercalation/de-intercalation capacity is 325/302 mAh/g with a Coulombic efficiency of 92.7%. The capacity is increased gradually to 343 mAh/g. The NMC622 electrode shows typical sloping voltage curves which is due to the oxidation of Ni^{2+} to Ni^{3+} and Ni^{4+} , and Co^{3+} to Co^{4+} . The first deintercalation/intercalation capacity is 198/175 mAh/g with a Coulombic efficiency of 88%. The capacity is stable at 175 mAh/g.

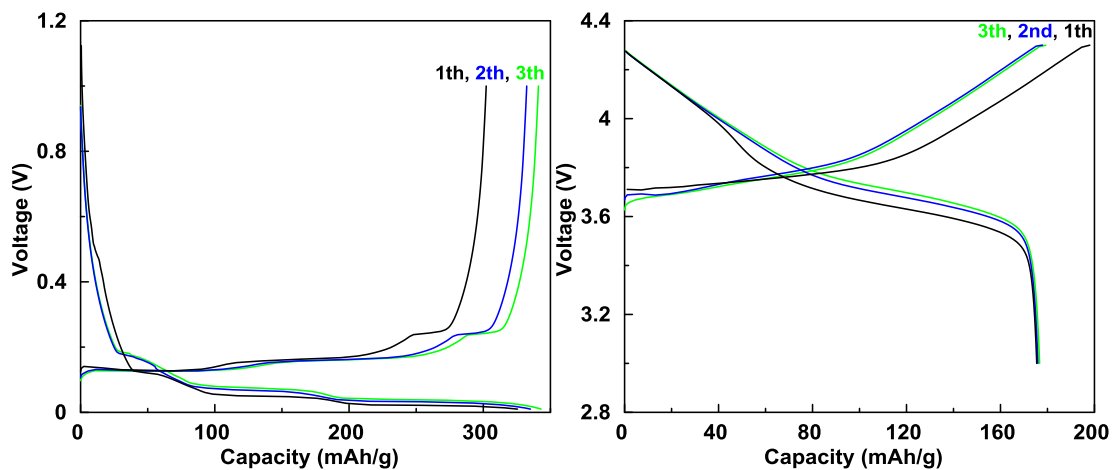


Figure I.5.D.2 left, the first three cycles of superior graphite 1520T electrodes; right, the first three cycles of NMC622 electrodes.

NMC622 cathodes with three different loadings were prepared and denoted as Loading L (2.0 mAh/cm^2), M (2.2 mAh/cm^2) and H (2.5 mAh/cm^2). Pouch cells were assembled using one layer of anode, one layer of cathode and one layer of separator (Celgard 2325). The cells were vacuum filled with the electrolytes. Cell assembly was carried out inside a dry room with a dew point of less than -50°C and relative humidity (RH) of 0.1 % at BMF. The cells were cycled between 2.5 and 4.2 V using the battery cycler, Maccor Series 4000, coupled with an environmental chamber set at 30°C . Figure I.5.D.3 shows the fast charging capability of the

cells with three different loadings. The cell capacity is normalized to its capacity under 1C charge for clear comparison. Under 1C and 2C charge, the three cells show similar behavior and the cell voltage gradually increased during the constant current (CC) charge and reached the cut-off voltage for trickle charge (constant voltage, CC). However, they started to differentiate from each other under 3C (20 minutes) charge and the difference became greater with higher charging rate (less charging time). Under 10 minute charge, the loading L has the most CC charge section which translates to a higher discharge capacity. With increasing electrode loading, the CC section becomes shorter and thus less capacity is obtained for cell discharge. However, thinner electrode (low loading) electrode may increase cell cost and lower energy density. Trade-off is yet to be made.

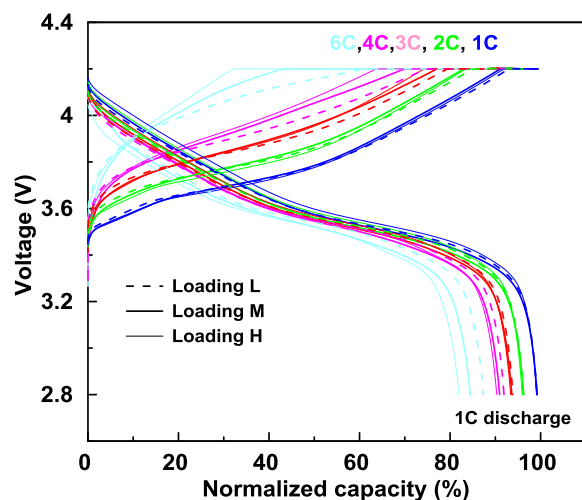


Figure I.5.D.3 Normalized cell voltage vs. capacity curves with different loadings charging at different C rates and discharging at 1C.

Cycling performance comparison was shown in Figure I.5.D.4 with two identical cells cycling under +1C/-1C and +6C/-1C, respectively. The cells have the NMC622 electrode loading of 2.2 mAh/cm^2 . The cell cycling performance is very good under +1C/-1C with no capacity fading. However, the cell under +6C/-1C cycling is not good with capacity dropping constantly from around 75 mAh at cycle No. 5 to 55 mAh at cycle No. 90. The cell voltage profiles are shown in the right figure. The voltage profile is unchanged for the cell running at +1C/-1C while the capacity/voltage fading can be clearly seen when the cell is running at +6C/-1C.

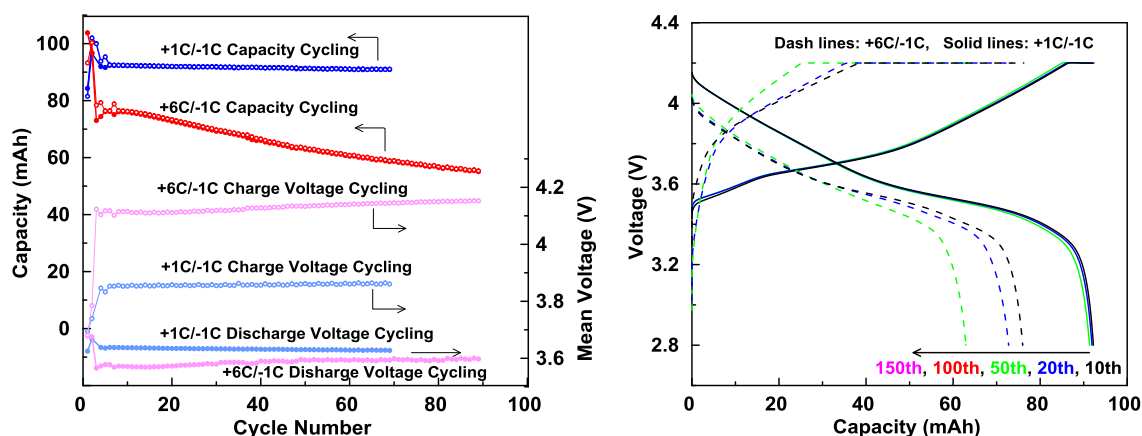


Figure I.5.D.4 left, capacity & voltage versus cycling number when the cells are cycled at +1C/-1C and +6C/-1C, respectively. Right, voltage versus capacity curves during cycling.

Temperature measurement

Fast charging also has effect on cell temperature increasing. A 600 mAh pouch cell was assembled with two thermal couple sensors embedded into the cells: one is at the very center of the jelly roll, one is at the surface of the jelly roll but inside the pouch. A third sensor was used outside the pouch cell. Since the cell is relatively thin and small, a current of 5A was applied to the cell to magnify the internal temperature rise during fast charging. The temperature rises significantly when the 5A current is applied. The temperature rise inside the cell is also greater than the surface of the cell. This heat generation during fast charging will causes electrolyte degradation and need to be closely studied.

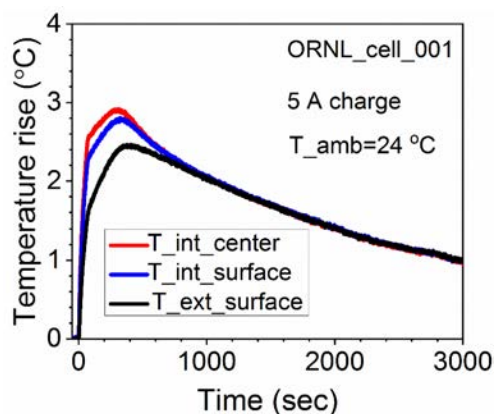


Figure I.5.D.5 Temperature rises inside a 600 mAh pouch cells during a 5A charge (through collaboration with Prof Guangsheng Zhang at University of Alabama in Huntsville).

Li salt synthesis

A monomer with delocalized negatively charge can be synthesized, where cations are the mobile ions. The special care needs to be taken for the monomer of Li-ion as the cation (Sty-TFSI-Li⁺) due to chemical instability when exposing to moisture. Therefore, we synthesized the monomer with potassium ion as the counter ions (Sty-TFSI-K⁺) as shown. The 1H NMR spectrum of Sty-TFSI-K⁺ was shown in Figure I.5.D.6, and integration of each peak is consistent with the proton ratio in the monomer, which confirms the successful synthesis of pure Sty-TFSI-K⁺

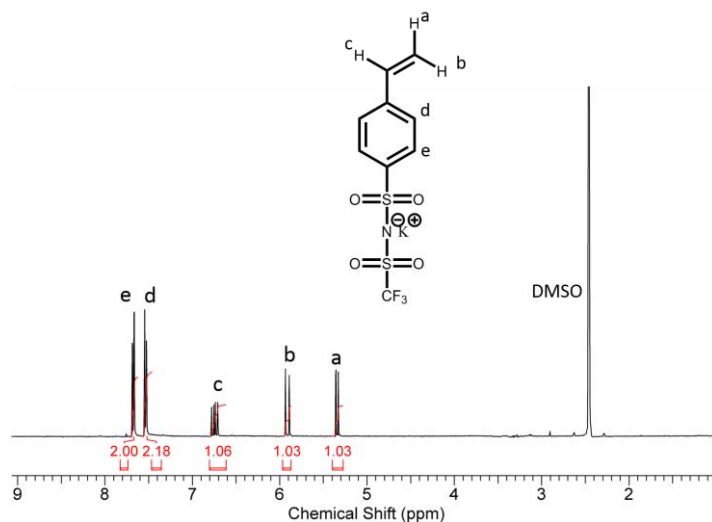


Figure I.5.D.6 ¹H NMR spectra of Sty-TFSI-K⁺

Oligomer was synthesized from radical polymerization of the Sty-TFSI-K⁺ using a thermal initiator in DMF, and the unreacted initiator and monomers were removed several times' washing by the mixing solvent of toluene and THF. Subsequently, the counter ion exchange was performed using LiClO₄, in THF, which transfer the oligo-Sty-TFSI-K⁺ to oligo-Sty-TFSI-Li⁺. Disappearance of the proton signals of double bond (5.0 ppm to 6.0 ppm) from the ¹H NMR spectrum suggested the formation of the oligomers and no residual monomers. The DP_n of the resulting oligomers is calculated to be 3, 4, and 5.

The oligomer was dissolved in the mixed solvent of EC/EMC (3:7) with concentration of 1 mol/L, and the conductivity of the electrolytes are currently investigated.

The detailed synthesis of single Li-ion conducting methacrylate oligomer (oligo-MA-TFSI-Li⁺) is shown as follows. It should be noted that various small details described here are crucial to synthesize this compound.

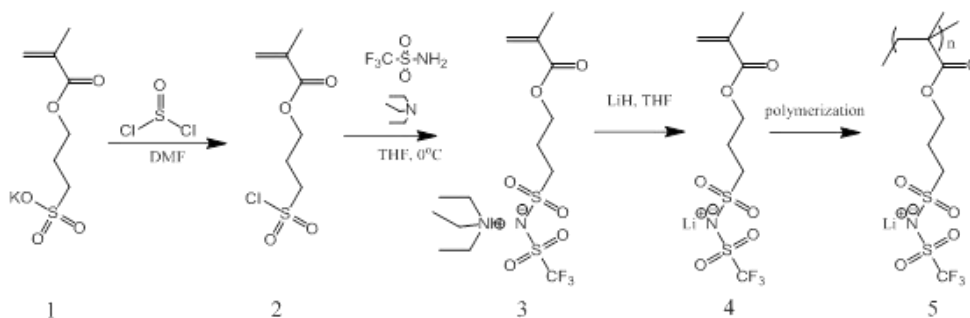


Figure I.5.D.7 Synthesis of single Li-ion conducting oligomer (compound 5).

The first step involves the synthesis of 3-(chlorosulfonyl)propyl methacrylate (2), using the previous reference with minor modification. [1] Potassium 3-(methacryloyloxy)propane-1-sulfonate (1) is reacted with thionyl chloride with the presence of 4-tertbutylcatechol as an inhibitor. After rigorous purification, the compound 2 is obtained. The purified compound 2 is further reacted with trifluoromethanesulfonamide with the presence of triethylamine as an acid scavenger, which results in triethyl ammonium 1-[3-(methacryloyloxy)propylsulfonul]-1-(trifluoromethane-sulfonyl)imide (3). [2] After a few purification steps and dried over anhydrous sodium sulfate, the compound 3 is exchanged with a suspension of lithium hydride to produce lithium 1-[3-(methacryloyloxy)propylsulfonul]-1-(trifluoromethane-sulfonyl)imide (4) by following a modified procedure. [3] The obtained viscous oil is thoroughly dried to obtain the desired monomer in a powder form. ¹H NMR confirmed the structure and purity of the monomer (Figure I.5.D.7). Our team has synthesized this monomer in a good quantity with high yield.

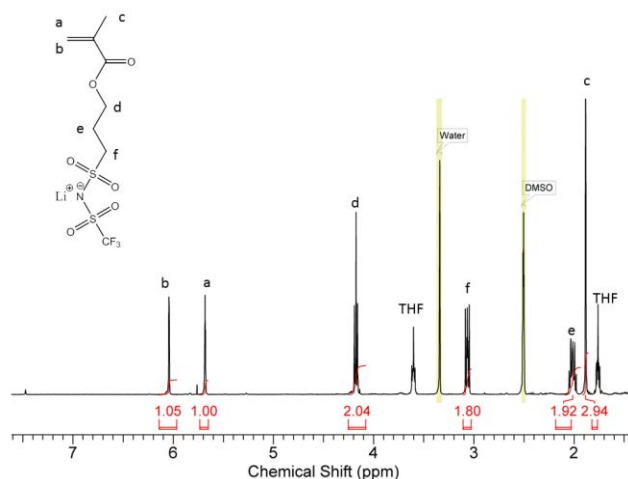


Figure I.5.D.8 ¹H NMR spectrum of single Li-ion monomer (compound 4).

The final step of synthesis involves a free radical polymerization of compound 4 with a thermal initiator, to produce single Li-ion conducting oligomer (compound 5). After rigorous purification, our first attempt resulted in ~ 1800 g/mol of compound 5 (based on ¹H NMR), which is still larger than our final target. By tailoring the reaction condition and employing a controlled polymerization, [4] we will be able to prepare precisely tailored single lithium-ion conducting oligomer with high Li-ion conductivity.

Our team also has been studying single-ion conducting cationic electrolytes including imidazolium and quaternary ammonium polymerized ionic liquids (PILs) with various counter anion. [5] Our preliminary data shows half an order of magnitude higher diffusion of the counter ion (in this case, anion), even with the trimer form. Thus, t_{Li^+} can be increased to 0.75 by making oligomeric anions. By tailoring the degree of polymerization in the oligomer form and other modified imide anions, these oligomer anions can be readily dissolved into non-aqueous solvents and significantly increase t_{Li^+} .

Conclusions

- Established baseline electrodes and cell testing.
- Studied the effect of charging time and electrode loading on cell performance.
- Studied the temperature rise during fast charging.
- Synthesis of styrene(Sty)-typed monomer and methacrylate(MA)-typed monomer
- Polymerization of Sty-typed monomer to form oligomers with different DP_n

Key Publications

1. Mao, C., Ruther, R. E., Li, J., Du, Z., & Belharouak, I. (2018). Identifying the limiting electrode in lithium ion batteries for extreme fast charging. *Electrochem. Comm.*, 97, 37-41.

References

1. K. Arimitsu, M. Yonekura, M. Furutani, Acid-amplifying polymers: synthesis, characterization, and application to environmentally stable chemical amplification positive (ESCAP) resists, *RSC Adv.* 5 (2015) 80311
2. A.S. Shaplov, P.S. Vlasov, M. Armand, E.I. Lozinskaya, D.O. Ponkratov, I.A. Malysheva, F. Vidal, O. V. Okatova, G.M. Pavlov, C. Wandrey, I.A. Godovikov, Y.S. Vygodskii, Design and synthesis of new anionic “polymeric ionic liquids” with high charge delocalization, *Polym. Chem.* 2 (2011) 2609. doi:10.1039/c1py00282a
3. L. Porcarelli, A.S. Shaplov, M. Salsamendi, J.R. Nair, Y.S. Vygodskii, D. Mecerreyes, C. Gerbaldi, Single-Ion Block Copoly(ionic liquid)s as Electrolytes for All-Solid State Lithium Batteries, *ACS Appl. Mater. Interfaces.* 8 (2016) 10350–10359. doi:10.1021/acsami.6b01973.
4. P.F. Cao, Z. Wojnarowska, T. Hong, B. Carroll, B. Li, H. Feng, L. Parsons, W. Wang, B.S. Lokitz, S. Cheng, V. Bocharova, A.P. Sokolov, T. Saito, A star-shaped single lithium-ion conducting copolymer by grafting a POSS nanoparticle, *Polym. (United Kingdom)*. 124 (2017) 117–127. doi:10.1016/j.polymer.2017.07.052.
5. F. Fan, W. Wang, A.P. Holt, H. Feng, D. Uhrig, X. Lu, T. Hong, Y. Wang, N.G. Kang, J. Mays, A.P. Sokolov, Effect of molecular weight on the ion transport mechanism in polymerized ionic liquids, *Macromolecules.* 49 (2016) 4557–4570. doi:10.1021/acs.macromol.6b00714.
6. F. Fan, Y. Wang, T. Hong, M.F. Heres, T. Saito, A.P. Sokolov, Ion Conduction in Polymerized Ionic Liquids with Different Pendant Groups, *Macromolecules.* 48 (2015) 4461–4470. doi:10.1021/acs.macromol.5b00257.

7. C. Gainaru, E.W. Stacy, V. Bocharova, M. Gobet, A.P. Holt, T. Saito, S. Greenbaum, A.P. Sokolov, Mechanism of Conductivity Relaxation in Liquid and Polymeric Electrolytes: Direct Link between Conductivity and Diffusivity, *J. Phys. Chem. B.* 120 (2016) 11074–11083. doi:10.1021/acs.jpcc.6b08567.
8. Z. Wojnarowska, H. Feng, M. Diaz, A. Ortiz, I. Ortiz, J. Knapik-Kowalczyk, M. Vilas, P. Verdía, E. Tojo, T. Saito, E.W. Stacy, N.G. Kang, J.W. Mays, D. Kruk, P. Włodarczyk, A.P. Sokolov, V. Bocharova, M. Paluch, Revealing the Charge Transport Mechanism in Polymerized Ionic Liquids: Insight from High Pressure Conductivity Studies, *Chem. Mater.* 29 (2017) 8082–8092. doi:10.1021/acs.chemmater.7b01658.

I.5.E Research on High Power, Doped Titanium-niobium Oxide Anodes (ORNL)

Sheng Dai, Principal Investigator

University of Tennessee
354 Buehler Hall
Knoxville, TN 37996
Email: sdai@utk.edu

Xiao-Guang Sun, Principal Investigator

Oak Ridge National Laboratory
One Bethel Valley Road
Oak Ridge, TN 37831
E-mail: sunx@ornl.gov

Jianlin Li, Principal Investigator

Oak Ridge National Laboratory
One Bethel Valley Road
Oak Ridge, TN 37831
E-mail: lij4@ornl.gov

Brian Cunningham, DOE Technology Development Manager

U.S. Department of Energy
E-mail: Brian.Cunningham@ee.doe.gov

Start Date: July 1, 2018	End Date: June 30, 2020	
Project Funding (FY18): \$800,000	DOE share: \$720,000	Non-DOE share: \$80,000

Introduction

Commercial lithium ion batteries (LIBs) using graphite as an anode can easily result in lithium plating during extreme fast charging or abuse conditions, leading to fast battery fading and safety issues. To eliminate lithium plating issue in LIBs, we proposed to use doped titanium niobium oxide (TNO) as anode, which has not only an operation voltage of 1.66 V vs. Li/Li⁺ that is far from the lithium plating but also a high theoretical capacity of 387 mAh g⁻¹.

Objectives

The main objective of this project is to synthesize TNO that has a nanoporous structure with porous channels for rapid lithium diffusion, enabling extreme fast charging. The focus of this project is to improve the electronic conductivity and ion diffusion coefficient in TNO to achieve high capacities under extreme fast charge conditions. In addition, electrolytes with additives will be formulated to promote stable interphase formation on NMC cathode surface to improve long cycling stability. Overall, the optimized TNO and NMC based lithium ion batteries will have high capacity and long cycling stability under extreme fast charging conditions, achieving less than 20% energy fade after 500 6C charge/1C discharge cycles.

Approach

The objectives outlined above will be accomplished by the following approaches:

- Enhance the electronic conductivity and lithium diffusion coefficient of TNO by doping.
- Enhance the electronic conductivity of doped TNO by surface carbon coating.
- Improve the long cycling stability of TNO and NMC based lithium ion batteries by formulating electrolytes with commercially available additives and new lithium malonateborate salts additive.

Results

This is a new start project from July 1 in FY 18. In the past three months, we have performed initial work on synthesis of TNO using alternative low-cost precursor and evaluation of NMC cathode.

Synthesis of TNO with low-cost precursor

Previously, niobium ethoxide ($\text{Nb}(\text{OCH}_2\text{CH}_3)_5$), a very expensive precursor (\$517/50g from Aldrich), was used for small scale synthesis of TNO. [1] It would be too expensive to be used in large scale synthesis for practical applications. Therefore, our first task is to find alternative niobium precursors to synthesize TNO with the same battery performance as that synthesized using niobium ethoxide. Here we used niobium chloride (\$494/500g), which is ten times cheaper than that of niobium ethoxide, to synthesize TNO. Ethanol was used as both solvent and reactant, which not only in-situ generate niobium ethoxide but also generate HCl catalyst that would be added for TNO synthesis with the niobium ethoxide. [1] The synthesized TNO has a surface area of $48 \text{ m}^2/\text{g}$, a pore size of 27 nm, and a pore volume of $0.17 \text{ cm}^3 \text{ g}^{-1}$, which are similar to that synthesized with niobium ethoxide. [1] Figure I.5.E.1 shows the rate capability of the newly synthesized TNO, delivering reversible capacities of 273, 262, 253, 213, 182 mAh g^{-1} at 0.1C, 1C, 2C, 5C and 10C, respectively. These values are lower than earlier report. [1] On the one hand, this may be due to its double loading of active materials as compared to previous report; on the other hand, it underlines the importance of improving the electronic conductivity of TNO for high rate performance, which is one of the main focuses of this project.

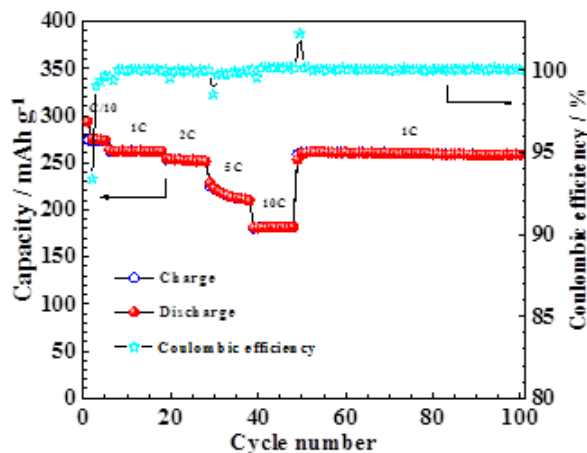


Figure I.5.E.1 Charge/discharge capacities and coulombic efficiencies of TNO at different current rates.

Cathode fabrication and evaluation

In this project, we use NMC as cathode and TNO as anode to assemble pouch cells. First, we investigate $\text{LiNi}_{0.6}\text{Mn}_{0.2}\text{Co}_{0.2}\text{O}_2$ (NMC622, D50=10 μm , Targray), which was mixed and coated via a slot die coater with various loadings following our published procedure. [2] Table I.5.E.1 details the electrode information.

Table I.5.E.1 NMC622 cathodes.

Electrode	Solvent	Electrode Composition	Loading
NMC622-11.5	NMP	NMC622/Denka Carbon Black/5130 PVDF in 90/5/5 wt%	11.5 mg/cm^2
NMC622-15.0	NMP	NMC622/Denka Carbon Black/5130 PVDF in 90/5/5 wt%	15.0 mg/cm^2
NMC622-20.0	NMP	NMC622/Denka Carbon Black/5130 PVDF in 90/5/5 wt%	20.1 mg/cm^2
NMC622-25.0	NMP	NMC622/Denka Carbon Black/5130 PVDF in 90/5/5 wt%	24.6 mg/cm^2

NMC622 half coin cells was assembled with 1.2 M LiPF_6 in (EC/EMC 3/7 wt) as the electrolyte. The cells were cycled at 30°C between 3.0 and 4.3V. Various test protocols were investigated on charge capability of the electrodes. The cells went through 5 cycles charge and discharge at C/5 (1C=175 mA/g) to verify cell capacity. Then, various charge protocols at different constant currents and constant voltage charge (CCCV) were performed while maintaining total charge time at 10 min. The discharge rate was kept at C/3. Triple kites were assembled for each areal loading and each protocol has 5 cycles. All cells with various areal loadings showed great reproducibility. For the cells with areal loading of 11.5 and 15.0 mg/cm^2 , the charge and discharge capacity were identical at C/5, demonstrating >180 mAh/g. They started decreasing to 175 and 146 mAh/g when further increasing the areal loading to 20.0 and 25.0 mg/cm^2 , respectively. For the 10 min charge, it generally follows a trend where lower capacity was observed at higher constant current rate, which indicate the contribution of constant current charge is more significant than the constant voltage charge to the overall charge capacity. Figure I.5.E.2 shows the normalized capacity to that at C/5 at various charge protocols. 72% capacity can be retained when charged at CCCV with 5C current for the areal loading of 11.5 mg/cm^2 . The capacity retention dropped to 50% at 20C. The fast charge capacity decreased dramatically with increasing areal loading. The ones with 25 mg/cm^2 only have < 55% capacity retention at 10 min charge.

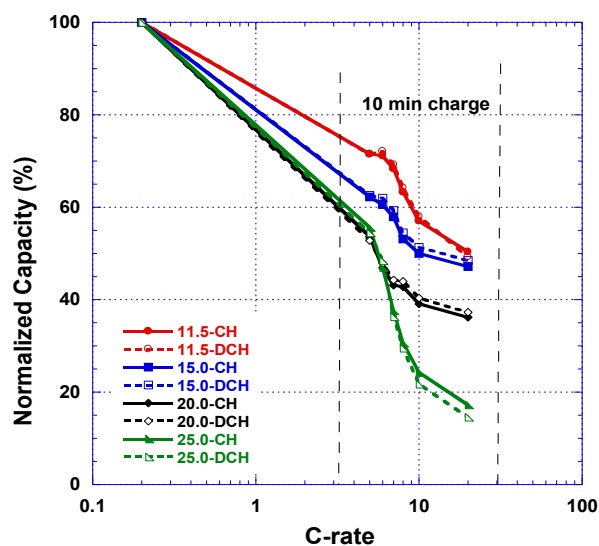


Figure I.5.E.2 Normalized capacity of NMC622 half coin cells at various charge protocols and areal loadings.

References

1. Guo, B. K.; Yu, X. Q.; Sun, X. G.; Chi, M. F.; Qiao, Z. A.; Liu, J.; Hu, Y. S.; Yang, X. Q.; Goodenough, J. B.; Dai, S., A long-life lithium-ion battery with a highly porous TiNb_2O_7 anode for large-scale electrical energy storage. *Energy Environ. Sci.* **2014**, 7 (7), 2220-2226.
2. Li, J. L.; Daniel, C.; An, S. J.; Wood, D., Evaluation Residual Moisture in Lithium-Ion Battery Electrodes and Its Effect on Electrode Performance. *Mrs Advances* **2016**, 1 (15), 1029-1035.

I.5.F Research three-dimensional hierarchical graphite architectures for anodes for fast charging (SNL)

Mohan Karulkar, Principal Investigator

Sandia National Laboratories
1515 Eubank Dr. SE, M/S 0613
Albuquerque, NM, 87185
E-mail: mpkarul@sandia.gov

Brian Cunningham, DOE Technology Development Manager

U.S. Department of Energy
E-mail: Brian.Cunningham@ee.doe.gov

Start Date: May 1, 2018

End Date: September 30, 2018

Project Funding (FY18): \$40,000

DOE share: \$40,000

Non-DOE share: \$0

Project Introduction

With current lithium ion batteries optimized for performance under relatively low charge rate conditions, implementation of XFC has been hindered by drawbacks including Li plating, kinetic polarization, and heat dissipation. This project will utilize model-informed design of 3-D hierarchical electrodes to tune key XFC-related variables like 1) bulk porosity/tortuosity 2) vertical pore diameter, spacing, and lattice 3) crystallographic orientation of graphite particles relative to exposed surfaces 4) interfacial chemistry of the graphite surfaces through “artificial SEI” formation using ALD 5) current collector surface roughness (aspect ratio, roughness factor, etc.).

A key aspect of implementing novel electrodes is characterizing them in relevant settings. For this project, ultimately led out of University of Michigan by Neil Dasgupta, that includes both coin cell and 2+ Ah pouch cell testing, as well as comparison testing against baselines. Sandia National Labs will be conducting detailed cell characterization on iterative versions/improvements of the model-based hierarchical electrodes, as well as COTS cells for baseline comparisons. Key metrics include performance under fast charge conditions, as well as the absence or degree of lithium plating. Sandia will use their unique high precision cycling and rapid EIS capabilities to accurately characterize performance and any lithium plating during 6C charging and beyond, coupling electrochemical observations with cell teardown. Sandia will also design custom fixturing to cool cells during rapid charge, to decouple any kinetic effects brought about by cell heating and allow comparisons between different cells and charge rates. Using these techniques, Sandia will assess HOH electrodes from the University of Michigan, as well as aiding in iterative model and electrode design.

Objectives

- Work with University of Michigan to establish cadence for receiving improved-electrode cells for characterization via in-person kickoff and weekly update meetings.
- Develop and validate a custom rapid cooling plate fixture to allow the best possible temperature control of cells during fast charging, regardless of cell design, charge current, and environmental conditions.
- Begin baseline COTS cell fast charge characterization.
- Demonstrate high fidelity dQdV measurements during 6C charging using high precision coulometry.

Accomplishments

- Attended project kick-off in Ann Arbor, MI where SNL PI Mohan Karulkar presented initial data on SNL’s cooling fixture design.

- Attended weekly teleconferences with the University of MI team to discuss progress and propose next steps.
- Demonstrated effective temperature control of cell using custom cooling plate hardware.
- Performed baseline rate capability and capacity retention cycling on 5Ah COTS cells, combining high precision coulometry with the rapid cooling fixture, calculating high fidelity dQdV data

Approach

To perform baseline cell testing and establish testing protocols for the study moving forward, a combined rate capability and cycle life approach was used. Cells were cycled with increasing charge rates, followed by a charge taper to C/20, followed by a 1C discharge. After the rate capability portion, the cell was cycled at 1C charge / 1C discharge to a total of 100 cycles to monitor capacity retention after the high rate charge cycles (See Table I.5.F.1). The first baseline cell chosen was a commercial Kokam 5Ah NMC/Graphite cell, with measured energy density values of 112 Wh/kg and 211 Wh/L. Cycling was performed with the Arbin high precision cyler developed through an ARPA-E AMPED program with SNL, Ford, Arbin, and Montana Tech.

Table I.5.F.1 Baseline cell cycling profile

Cycle	CC Charge Rate	CV Charge Taper	CC Discharge
1-3	0.5 C	C/20	1 C
4-6	1 C	C/20	1 C
7-9	1.5 C	C/20	1 C
10-12	2 C	C/20	1 C
13-16	3 C	C/20	1 C
16-18	4 C	C/20	1 C
19-21	5 C	C/20	1 C
22-24	6 C	C/20	1 C
25-100	1 C	C/20	1 C

To minimize effects of cell heating, a rapid-response cooling plate fixture was designed specifically with University of Michigan prototype cells in mind, but flexible to accommodate the baseline cells as well. A 50/50 WEG solution was used with a chiller and circulated through channeled brass blocks, with temperature monitoring on the cell surface, sides, and tabs. (Figure I.5.F.1)

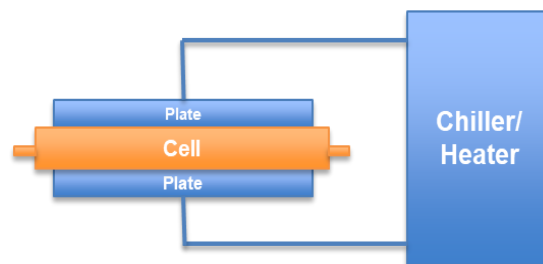


Figure I.5.F.1 Cooling plate fixture.

Results

Figure I.5.F.2 shows temperatures during 6C/2C (charge/discharge) cycling of a Kokam baseline cell in the cooling fixture, for purposes of fixture validation. The cell edge showed the largest temperature swing of about 3°C during the 6C charge, compared to 7-8°C swings with environmental chamber alone. Then negative tab showed about 1.5°C temperature swing and the cell-plate interfaced showed almost no swing at all. The stable

cooling bath temperature and intimate cell contact allow for much more precise control / steadying of cell temperature than is possible in an environmental chamber. The cooling fixture is a key part of continuing cell assessment, since cell heating can otherwise affect kinetics during charging and complicate the effort of comparing cell performance between different charge rates, as well as cell performance between improvement iterations.

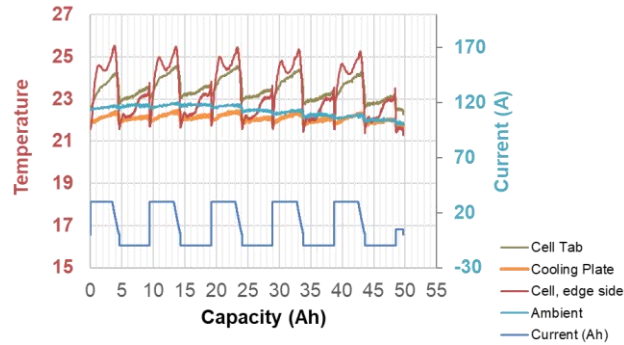


Figure I.5.F.2 Cell temperature (Kokam 5Ah pouch) during 6C charge, 2C discharge cycling, inside the cooling fixture.

Figure I.5.F.3 shows the result of cycling a Kokam 5Ah baseline cell according to the cycling profile in Table I.5.F.1. The orange line shows the capacity from just the high rate portion of the charge, while the blue line shows the charge capacity with the high rate and taper step together. The gray line (overlapped with blue) shows the 1C discharge capacity. The data shows that the baseline cell was able to accommodate charge rates up to 6 C, though polarization lowered the charge passed during that step. The overall cell capacity and efficiency remained mostly unchanged, with an efficiency of > 99.9%.

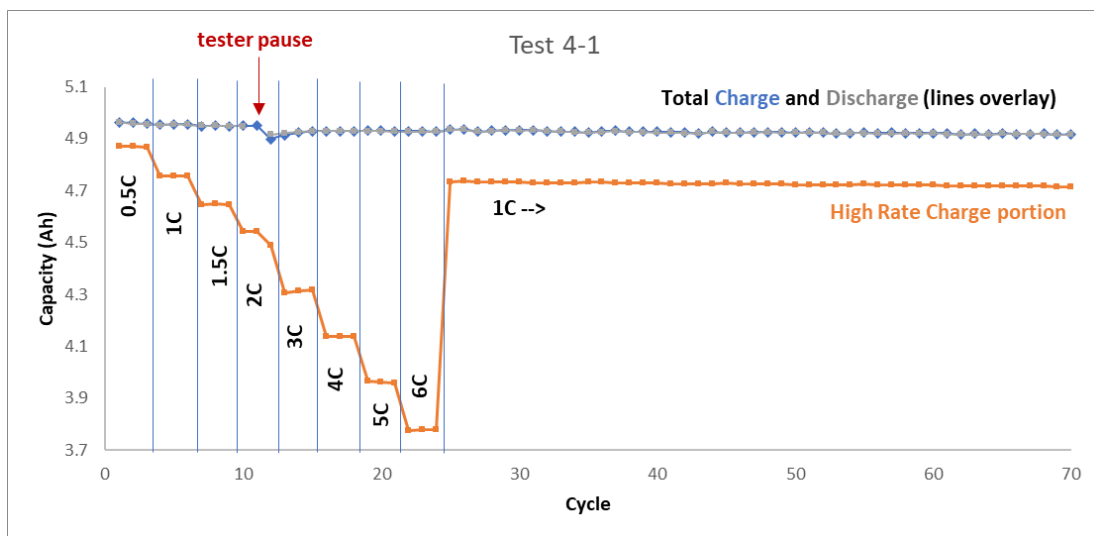


Figure I.5.F.3 Baseline cell rate capability performance.

Figure I.5.F.4 shows dQ/dV vs V for charge rates of 0.5C, 1C, and 6C during the rate capability, as well as the subsequent 1C discharge cycles, and the first 1C/1C cycle *after* the rate capability (cycle 25). Of note is the general line smoothness and clear representation of peaks, a benefit of Sandia's high precision cycling capability. Peaks are seen to shift right with increasing charge rate, a reflection of cell polarization. 1C discharge steps are identical, showing a lack of fundamental electrode changes that would alter discharge steps throughout the cycling profile. Likewise, the 1C charges at cycle 3 and 25 are identical, showing no changes due to the subsequent charge steps. Figure I.5.F.5 shows the 1C discharge step after every step change in charge rate (line reflected to positive axis for ease of viewing). In every case, the discharge dQ/dV pattern is identical, suggesting a lack of lithium plating that would otherwise cause distinct lithium stripping peaks.

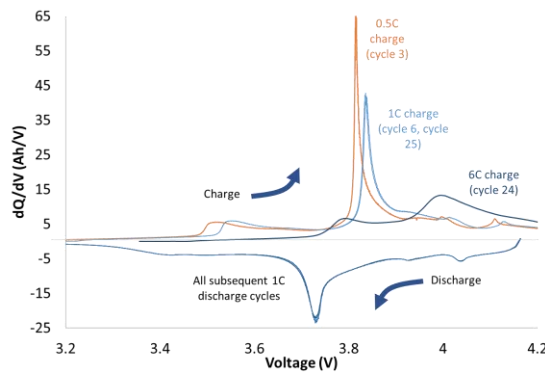


Figure I.5.F.4 Figure 4: dQ/dV vs V for various cycles in baseline rate capability.

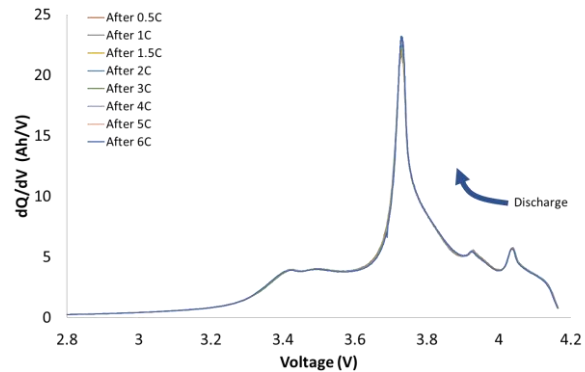


Figure I.5.F.5 Figure 5: dQ/dV vs V for 1C discharge steps after each charge rate increase.

Conclusions

The baseline COTS cell was able to accommodate 6C charge with no issue other than expected cell polarization, but it is important to note that the cell sports 112 Wh/kg, well below DOE targets. Experience has shown that cells with more aggressive design perform much worse at high charge rates, often polarizing to an extreme where almost no charge is passed, or degrading rapidly via heating and lithium plating. Our baseline cells also showed no evidence of cell damage or lithium plating in dQ/dV analysis, however we should note that the taper step during charge may have allowed time for plated lithium to diffuse into the graphite, making it invisible to subsequent charge steps. Further testing is underway without the taper or any rest steps to try and capture lithium plating that could have been missed.

Importantly, the dQ/dV techniques developed during this short first FY will be used to assess optimized project cells for such negative effects, and quantify the improvements seen through HOH applications. Additionally, the rapid cooling plate fixture showed excellent temperature control, with only 3°C temperature increase during the highest charge rates. This ensures that, moving forward, cells made in different iterations and cycled at different charge rates will be absent of temperature-driven inconsistencies.

Acknowledgements

Sandia co-authors: Josh Lamb, Loraine Torres-Castro, June Stanley, Chris Grosso, Lucas Gray, and Christopher Orendorff

Sandia National Laboratories is a multi-mission laboratory managed and operated by National Technology and Engineering Solutions of Sandia, LLC., a wholly owned subsidiary of Honeywell International, Inc., for the U.S. Department of Energy's National Nuclear Security Administration under contract DE-NA0003525.

I.5.G Beyond Batteries: Behind the Meter Storage (NREL, INL, ORNL, SNL)

Anthony Burrell

National Renewable Energy Laboratory
15013 Denver West Parkway
Golden, CO 80401
E-mail: anthony.burrell@nrel.gov

Samuel Gillard , DOE Technology Development Manager

U.S. Department of Energy
E-mail: Samuel.Gillard@ee.doe.gov

Start Date: October 1, 2018	End Date: September 30, 2022	
Project Funding (FY18): \$2,190,000	DOE share: \$2,190,000	Non-DOE share: \$0

Project Introduction

This initiative, referred to as Behind-the-Meter-Storage (BTMS), will focus on novel critical-material-free battery technologies to facilitate the integration of EV charging, and energy-efficient buildings while minimizing both costs and grid impacts. For extreme fast charging at levels of 350kW or higher, novel approaches are required to avoid significant negative cost and resiliency impacts. However, it is reasonable to assume BTMS solutions would be applicable to other intermittent renewable energy generation sources or short duration high power demand electric loads.

BTMS research is targeted at developing innovative energy storage technology specifically optimized for stationary applications below 10MWh that will minimize the need for significant grid upgrades. Additionally, avoiding excessive high-power draws will eliminate excess demand charges that would be incurred during 350kW fast charging using current technologies. The key to achieving this is to leverage battery storage solutions that can discharge at high power but be recharged at standard lower power rates, acting as a power reservoir to bridge to the grid and other on-site energy generation technologies such as solar photovoltaic (PV), thereby minimizing costs and grid impacts. To be successful, new and innovative integration treatments must be developed for seamless interaction between stationary storage, PV generation, building systems, and the electric grid.

Key components of BTMS will address early-stage research into new energy generation and building integration concepts, critical materials free battery energy storage chemistries, and energy storage designs with a focus on new stationary energy storage strategies that will balance performance and costs for expanded fast charging networks while minimizing the need for grid improvements.

Objectives

A cohesive multidisciplinary research effort to create a cost effective, critical materials free, solution to BTMS by employing a whole systems approach will be taken. The focus of this initiative is to develop innovative battery energy storage technologies with abundant materials applicable EVs, and high-power charging systems. Solutions in the 1-10 MWh range will eliminate potential grid impacts of high power EV charging systems, and lower installation costs and costs to the consumer.

Although many lessons learned from EV battery development may be applied to the BTMS program, the requirements for BTMS systems are unique, carrying their own calendar-life, cycle-life, and cost challenges. For example, EV energy storage systems need to meet very rigorous energy density and volume requirements in order to meet consumer transportation needs. Despite that, current stationary storage systems use batteries designed for electric vehicles due to high volumes driving the costs down. This creates another market demand for EV batteries, further straining the EV battery supply chain and critical material demand.

Considering BTMS electrochemical solutions could be optimized for these applications with less focus on energy density in mass and volume, the potential for novel battery solutions is very appealing. Furthermore, the balance-of-plant for a BTMS battery system, or the cost of everything minus the battery cells, is thought to be upwards of 60% of the total energy storage system cost. Whereas the EV's balance-of-plant costs makeup roughly 30% of the total battery cost. Therefore, BTMS will also need to focus on reduction of balance-of-plant cost through system optimization in order to realize desired cost targets.

The design parameters are needed to optimize the BTMS system for performance, reliability, resilience, safety, and cost.

The objectives for the project are:

- Produce behind the meter battery solutions that can be deployed at scale and meet the functional requirement of high power EV charging.
- Battery Storage: Utilize a total systems approach to develop and identify the draft functional requirements for BTMS battery solutions that will provide novel battery systems in the 1-10 MWh range at \$100/kWh installed cost and able to cycle twice per day, discharging for at least 4 hours, with a lifetime of roughly 20 years or at least 8,000 cycles.

Approach

A cohesive multidisciplinary research effort, involving NREL, INL, SNL and ORNL, will create a cost effective, critical materials free, solution to BTMS by employing a whole systems approach will be taken. The focus of this initiative is to develop innovative battery energy storage technologies with abundant materials applicable to PV energy generation, building energy storage systems, EVs, and high-power charging systems. Solutions in the 1-10 MWh range will enable optimal integration of PV generation from a DC-DC connection, increase building energy-efficiency, eliminate potential grid impacts of high power EV charging systems, and lower installation costs and costs to the consumer.

Although many lessons learned from EV battery development may be applied to the BTMS program, the requirements for BTMS systems are unique, carrying their own calendar-life, cycle-life, and cost challenges. For example, EV energy storage systems need to meet very rigorous energy density and volume requirements in order to meet consumer transportation needs. Despite that, current stationary storage systems use batteries designed for electric vehicles due to high volumes driving the costs down. This creates another market demand for EV batteries, further straining the EV battery supply chain and critical material demand.

Considering BTMS electrochemical solutions could be optimized for these applications with less focus on energy density in mass and volume, the potential for novel battery solutions is very appealing. Furthermore, the balance-of-plant for a BTMS battery system, or the cost of everything minus the battery cells, is thought to be upwards of 60% of the total energy storage system cost. Whereas the EV's balance-of-plant costs makeup roughly 30% of the total battery cost. Therefore, BTMS will also need to focus on reduction of balance-of-plant cost through system optimization in order to realize desired cost targets.

Integration of battery storage with PV generation, energy-efficient buildings, charging stations, and the electric grid will enable new and innovative control strategies. The design parameters are needed to optimize the BTMS system for performance, reliability, resilience, safety, and cost.

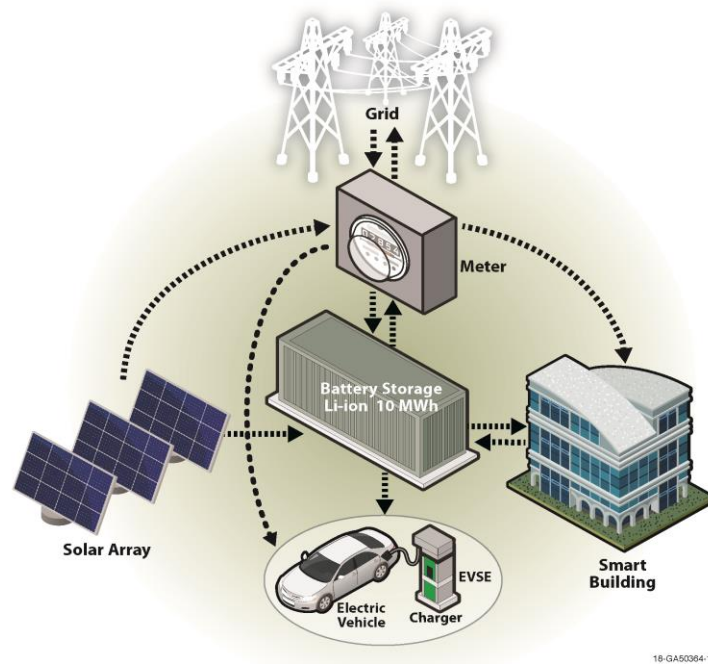


Figure I.5.G.1 Conceptual graphic describing the connections between fast charging and the related energy systems that can be bridged by behind the meter storage.

Results

This project began in the last month of FY18 and as such much of the work consisted of establishing the work plans within the team and a kick-off meeting in late September.

I.6 Small Business Innovation Research (SBIR)

Samuel Gillard, DOE Technology Development Manager

U.S. Department of Energy

E-mail: Samuel.Gillard@ee.doe.gov

Objectives

Use the resources available through the Small Business Innovation Research (SBIR) and Small Business Technology Transfer (STTR) programs to conduct research and development of benefit to the advanced batteries effort within the Vehicle Technologies Office.

Project Introduction

The advanced batteries effort of the Vehicle Technologies Office supports small businesses through two focused programs: Small Business Innovation Research (SBIR) and Small Business Technology Transfer (STTR). Both programs are established by law and administered by the Small Business Administration. Grants under these programs are funded by set aside resources from all Extramural R&D budgets; 3.0% of these budgets are allocated for SBIR programs while 0.45% for STTR grants. These programs are administered for all of DOE by the SBIR Office within the Office of Science. Grants under these programs are awarded in two phases: a 6-9 month Phase I with a maximum award of \$150K and a 2 year Phase II with a maximum award of \$1M. Both Phase I and Phase II awards are made through a competitive solicitation and review process.

The advanced batteries team participates in this process by writing a topic which is released as part of the general DOE solicitation. Starting in FY12, the advanced batteries team decided to broaden its applicant pool by removing specific subtopics and allowing businesses to apply if their technology could help advance the state of the art by improving specific electric drive vehicle platform goals developed by the DOE with close collaboration with the United States Advanced Battery Consortium.

Results

Phase II Awards Made in FY 2018

Under the SBIR/STTR process, companies with Phase I awards made in FY 2017 are eligible to apply for a Phase II award in FY 2018. The following two Phase II grants were awarded in FY 2018 (from among the four Phase I grants that were conducted in FY 2017):

Amastan Technologies (North Andover, MA). For electric vehicles to be widely adopted as a common mode of transportation, the price of the battery packs must be reduced to \$125 per kilowatt hour. Prices are currently around \$200 per kilowatt hour. One path to reduced cost per kilowatt hour is by reducing cathode cost and improving their energy density. Cathode materials account for up to 25% of the battery pack cost. Cost reductions can be achieved by reducing raw material costs, reducing production costs, and increasing specific capacity of cathode materials with nickel rich materials. Cathode materials will be manufactured with a single-step continuous microwave-generated plasma materials processing technology (UniMelt™). The processing technique processes each precursor droplet within the same thermal path and thermal history, leading to tight control of phase purity, size and size distribution, and performance of the product for cost effective manufacture of commercially relevant quantities of cathodes for electric vehicle batteries. Phase I work successfully met the defined objectives to validate the feasibility and versatility of UniMelt as a low-cost high-performance production method capable of producing commercially viable materials for lithium ion batteries in electric vehicles. Traditional and high energy Ni-rich cathode materials were produced using the UniMelt process, and their electrochemical performance was verified. The proposed Phase II work is aimed to reduce battery cost per kilowatt hour by: (i) demonstrating process scale-up, (ii) validating the proposed cost-models, (iii) strengthening US-based cathode end-user relationships/collaborations aimed at continuing this work beyond the Phase II timeline and into commercial production. For this Phase II project, the cathode materials of focus are high nickel content materials which are the current and upcoming industry standard rechargeable lithium batteries. Lower cost batteries help enable further adoption of sustainable technologies such as electric

vehicles and grid energy storage where the purchase price per item is strongly related to the battery prices. Success of the proposed work will help reduce the overall usage of fossil fuels throughout the US and world.

Giner, Inc (Newton, MA). Conventional lithium-ion batteries demonstrate great potential for applications in electrical vehicles, but they face some major challenges such as low energy density and high cost. It is worthwhile to pursue alternative strategies to address the barriers of cost and energy density. We propose to develop advanced rechargeable lithium-sulfur (Li-S) batteries that have much higher theoretical energy density and lower cost. We will improve the practicality and cycle life of Li-S batteries to make them more commercially viable. In the Phase I project, we have improved the energy density and cycle life of Li-S batteries using button cells. First, highly conductive lithium-ion exchange (LIE) films have been used as battery separators. Second, concentrated Li electrolytes has been applied to the sulfur electrodes. These efforts have prevented cathode sulfur loss due to the polysulfide diffusion, thus significantly enhancing the cycle life of Li-S batteries. In the Phase II project, we will further develop this technology using more advanced and low-cost lithium-ion exchange (LIE) separators and ionomers to further reduce polysulfide diffusion. We will then increase the S loading, fabricate pouch cells and evaluate their energy density and cycle life under more realistic EV conditions. **Commercial Applications and Other Benefits.** The proposed lithium-sulfur technology will address two major barriers of electrical vehicles, cost and energy density; therefore it may directly facilitate the deployment and commercialization of electrical vehicles. They may also be applicable in the consumer market to portable electronics and communication devices.

pH Matter (Columbus, OH). Wider adoption of electric vehicles can be achieved with lower cost batteries that have higher specific energy and better durability. In the proposed project, pH Matter, LLC and the University of Akron will partner to develop lithium ion batteries that will increase their specific energy and capacity by greater than 50%. The anode components will be based on a combination of nanostructured materials developed at pH Matter, and polymers developed by the University of Akron. The new components will be consistent with existing manufacturing approaches for lithium ion batteries. **Commercial Applications and Other Benefits:** The technologies being developed on this project will be used in electric vehicles, military / aerospace applications, and portable electronics. Wider adoption of electric vehicles, enabled by better performing batteries, will reduce our nation's dependence on fossil fuels, and reduce air pollution associated with combustion engines. Better batteries for military / aerospace energy storage will enable advanced features and capabilities for end users.

CAMX Power (Lexington, MA). "Successful commercialization and market adoption of electric drive vehicles (EVs) requires development of fast-charge capable Li-ion storage technologies that can deliver >350Wh/kg, well above what can be achieved with current battery materials. Implementation of next generation cathode and anode materials is needed to further increase specific energy of Li-ion cells. However, without pre-lithiation, some of the most promising anode materials that have high capacity but low efficiency cannot be used. CAMX Power proposes to develop a safe and scalable pre-lithiation technology that will enable the use of very high capacity, long life, but low first cycle efficiency Si-based anodes to demonstrate lithium-ion cells capable of meeting specific energy, power, and life targets for EV batteries. Moreover, this prelithiation technology will enable the use of fast-charge capable but low first cycle efficiency carbon anodes that have a potential to achieve extreme fast charge EV batteries. We will leverage our CAM-7[®] cathode material and our work on Si-based and carbon anodes to demonstrate lithium-ion cells that utilize pre-lithiation and are able to meet the 350Wh/kg target while providing fast charge capability. The Phase I program demonstrated the feasibility of the pre-lithiation technology for substantially improving cell specific energy for the EV applications and potential improvement in achieving long life during fast charge operation. Specifically, during the Phase I effort, we assessed the impact of active materials on the extent of pre-lithiation achieved and tested different pre-lithiation process parameters and environmental stability of pre-lithiated electrodes. Pre-lithiation was then demonstrated with a Si containing anode, first in coin cells and then in 200mAh pouch cells, to show how this technology can be scaled. **Commercial Applications and Other Benefits**

Proposed technology will enable production of fast-charge capable batteries with >350Wh/kg specific energy making it extremely attractive for implementation in both portable power and EV batteries. By increasing the energy density of EV batteries, and thus increasing the driving range of vehicles between recharges, while bringing EV charge rates closer to refueling times for ICE vehicles we anticipate this technology will further lead to increased market adoption of electric vehicles.

Hazen Research (Golden, CO). "To increase the utilization of electric vehicles, the US Department of Energy is seeking to reduce the cost of electric vehicle batteries to less than \$125/kWh by 2022. To achieve this goal, the costs of cathode materials, which account for approximately 30% of the cost of vehicle batteries, must be reduced significantly. To address the challenge of lowering the costs of advanced lithium battery cathode materials, we will demonstrate an improved, scalable, and continuous method to develop nickel-rich cathodes with superior performance. This method will use a single source solution precursor, which will be modified to achieve ideal nickel, manganese, and cobalt ratios and compositional gradient to affect the cathode performance and cost. In Phase I, new single source metal inorganic organic composite precursors were developed and a semi-continuous process was demonstrated using a vertical spray pyrolysis and a fluidized-bed reactor that formed well-crystallized cathode particles smaller than 5 μm . These cathodes showed initial capacity greater than 200 mAh/g, voltage stability in the range 3.0–4.5 V, energy density greater than 800 Wh/kg, columbic efficiency over 90%, and 70% capacity retention after 25 cycles. In Phase II, the equipment will be modified and the method will be scaled up to produce at least 250 g cathode powders as a continuous process. Higher precursor concentrations and different spray pyrolysis and fluidized-bed reactor conditions will be evaluated to produce approximately 15 μm particles to increase the capacity retention to more than 90% over 250 cycles in greater than 1 Ah capacity pouch cells. A capital and operating cost analysis estimate will be performed and energy and resource inputs will be quantified to compare the cost benefits of the developed process with state-of-art manufacturing methods. Commercial Applications and Other Benefits The low-cost production of high performance cathodes will enable its widespread adoption in electric vehicle batteries. It will improve the US competitiveness in the fields of advanced materials and manufacturing and energy storage technologies, as well as create jobs, reduce dependence on fossil fuels, and enhance energy security and environmental sustainability. The process is adaptable and will improve manufacturing processes for other advanced functional materials used in diverse technologies.

Phase I Awards Made in FY 2017

Nine Phase I grants were awarded in the Summer of FY 2018.

TDA Technologies (Wheat Ridge, CO). Electric drive vehicles can drastically improve fuel efficiency compared to internal combustion engines, but their performance and safety is limited by available battery technology. Rechargeable lithium and lithium-ion batteries can fail violently when they are overheated, crushed, overcharged / over discharged or they are subjected to an internal electrical short. The violent nature of these failures is exacerbated by their highly flammable conventional liquid electrolyte solvents. The goal of this project is to develop a high-performance non-flammable lithium electrolyte based on the combination of a non-flammable ionic liquid solvent and a novel nanoporous solid polymer material. This project will develop an ionic liquid – nanoporous polymer hybrid electrolyte that will be far safer than conventional electrolytes, have a high conductivity, the ability to safely operate at extreme temperatures and that can be used with a lithium metal anode in a rechargeable battery for electric vehicles. In Phase I we will develop and test polyelectrolyte membrane separators containing non-flammable ionic liquids, in full lithium metal batteries greater than 200 mAhr in size.

Cuberg, Inc (Mountain View, CO). Widespread adoption of electric vehicles is hindered by the weight, size, and cost of battery technology. Lithium-ion battery technology is plateauing in performance, and next-generation solutions are required to deliver step change improvements. Lithium metal batteries promise greatly reduced weight compared to lithium-ion, but they suffer from serious performance, cycle stability, and safety issues because of incompatibility with conventional organic electrolytes. This project proposes a lithium metal rechargeable battery based on a non-flammable and chemically stable electrolyte that has demonstrated

enhanced compatibility with lithium metal anodes and high-voltage cathodes. The objective of the project is to improve the rate capability of the electrolyte with the use of different co-solvents that improve physical properties while maintaining oxidative stability at high voltage and cycling stability with lithium metal. This work will bring the cycling performance and rate capability of the lithium metal battery chemistry much closer to commercial viability for electric vehicle applications. The proposed project will identify and screen the most promising and commercially viable co-solvents for use in a high-voltage lithium metal chemistry. Based on the electrochemical data collected in the screening process, the most promising candidates will be down-selected for an expanded experimental study. That work will focus on further optimization of the co-solvent content as well as assessing the benefits of combining multiple co-solvents. The most promising electrolyte compositions will be assessed in rate and cycle life tests in commercially representative coin cells, and the best-performing electrolytes will finally be cycled and studied in single-layer pouch cells.

Navitas Systems (Ann Arbor, MI). Higher performance batteries are needed to support commercialization of electric vehicles. Battery performance can be improved through cell chemistry innovations that raise the discharge voltage without sacrificing cost or safety. This DOE SBIR will demonstrate innovative high voltage and high temperature non-carbonate electrolytes. Combined with stabilized high voltage cathode materials, this will enable higher energy density cell designs able to meet USABC goals for electric vehicle batteries. Non-carbonate electrolytes will be synthesized. Protective coatings will be applied to high nickel content cathode materials. These components will be incorporated into prototype pouch cells of >200 mAh which will be fabricated, filled and formed using materials and methods compatible with high volume automated cell production. Cell performance and abuse tolerance will be evaluated.

CAMX Power (Lexington, MA). Broad commercialization and adoption of electric drive vehicles (EVs) that meet the market requirements for driving range requires development of electrochemical storage technologies that can deliver high energy density while providing requisite power, cycle life and calendar life at a low cost. Lithium-ion (Li-ion) batteries are the current technology of choice for both consumer electronics and emerging EVs. However, the highest energy density Li-ion cells currently used for commercial portable power applications are still well over 100 \$/kWh in cost. On a \$/kWh basis, Li-ion costs are more greatly driven by cathode materials than by any other component, and therefore lower cost, high-performance next generation cathode materials are needed to provide higher energy density, lower cost Li-ion cells. CAMX Power is developing a novel low-cost, high voltage Li-ion cathode chemistry with long cycle life. This novel chemistry produced via a low-cost manufacturing process, enables Li-ion electric drive vehicle batteries that are lower cost and higher energy density. CAMX Power will resolve historical challenges of high voltage cathodes by developing an inexpensive manufacturing process, developing protective coatings based on ionically and electronically conducting materials to boost high temperature cycle life, and by developing electrolyte formulations that are stable for high voltage operation. In Phase I, we will optimize the process for synthesis of the high voltage spinel cathode and explore different techniques for coating the material with the protective layer. Best-performing materials will be evaluated with high voltage-stable electrolytes and implemented in 200mAh pouch cells for program demonstration.

Beltech (Chicago, IL). Rechargeable lithium-ion batteries with low cost (\$100/kWh) and high energy density (500 Wh/kg) are critically desired to meet the ever-increasing needs for energy. One way to achieve the goals is to enable lithium metal as the anode for lithium-ion batteries owing to its ultrahigh theoretical capacity (3,860 mAh/g) and the high negative potential (-3.04 V vs. standard hydrogen electrode). However, the problems of lithium dendrite formation and low Coulombic efficiency (CE) during electrochemical cycling prevent the wide deployment of lithium anodes. In order to tackle the two problems of lithium anodes, researchers have pursued a number of strategies including electrolyte additives, solid polymer electrolyte and different coatings acted as artificial solid electrolyte interphase (SEI) layers. Making artificial SEI layers is a most promising and effective strategy to enable the use of lithium anodes. In the proposal, ultrathin lithium will be used and advanced coatings will be prepared with excellent properties, including great mechanical strength, high dielectric constant and high lithium-ion conductivity, to greatly suppress lithium dendrites and stabilize the interface of the lithium/electrolyte for ultrahigh CE. In Phase I, different advanced coatings will

be directly prepared onto the ultrathin lithium metal. Such protected Li will be assessed in lithium-ion batteries and lithium-sulfur batteries (coin cells and pouch cells) at practical current rates for 300-400 cycles. Scanning electron microscope (SEM) images for the cycled anodes will be taken to check if there is any dendrite formation.

Glacigen (Bozeman, MO). Despite all of the advantages that electric vehicles bring, better battery performance remains a requirement of widespread commercial adoption. Areas of specific interest include improved specific energy and energy density coupled with improved manufacturing processes which reduce costs and increase throughputs. This project aims to demonstrate a unique processing method, freeze tape casting, which is applicable an array of anode and cathode materials. The process is derived from traditional tape casting which speaks to commercial viability but produces entirely unique microstructures which impart important functional advantages to the battery. These advantages ultimately manifest as improvements in specific energy and energy density. In this project, the freeze tape casting technique will be applied to relevant materials for the production of a solid-state lithium ion demonstration cell. This project will provide proof of concept for this specialized processing approach as well as preliminary performance characterization from the subject cell. These results will further provide the basis for Phase II collaboration with established battery developers with whom active discussion is already occurring. Within Phase I formulations for freeze tape casting of the anode and cathode materials will be developed, prototype electrodes will be produced, complete cells assembled, and electrochemical characterization performed. The outcome of the proposed work is two-fold. First, the project will have demonstrated a novel, high-performance solid state, battery architecture. Second, the project will have provided an important basis in the freeze tape casting battery electrodes which will enable the company to provide technical services and freeze tape casting equipment to battery developers with an enhanced technical knowledge base. This commercial application will be of interest to developers of electric vehicle drive batteries and beyond.

Triton Systems(Berkeley, CA). The integration of silicon anodes, with their high theoretical specific capacity (4200 mAh/g vs. 372 mAh/g for the conventional graphite anode), into Li-ion cells and subsequent battery packs can significantly increase their energy density, which will assist in extending the range of electric vehicles. However, they suffer from low rapid capacity fade (low cycle-life) due to physical (mechanical fracturing) and chemical (Solid Electrolyte Interface [SEI] layer overgrowth) degradation during repeated cycling. To increase the cycle-life of Si as an anode in Li-ion batteries, we propose to develop a novel Si anode with an advanced artificial SEI layer to prevent the physical and chemical degradation experienced during battery charge and discharge cycles. In Phase I, Triton Systems Inc. will explore a family of Si anode materials with electron and Li- ion conducting properties. Once characterized, the advanced Si material will be deposited on a Cu current collector to be used as an anode material in full-cell battery coin-cell prototypes that are greater than 200mAh in size. Battery prototypes will be tested in accordance with applicable test procedures as published by the Department of Energy (DOE) and the U.S Advanced Battery Consortium (USABC) found at www.uscar.org/guest/article_view.php?articles_id=86.

Xilectric (Fall River, MA). Large Li-ion factories are being built around the world in an attempt to dramatically lower cost through economies of scale. At the same time, new market opportunities are becoming accessible to Li-ion as the technology improves. For many of these technologies, the levelized cost of energy storage is the primary metric, not \$/kWh. Cycle life varies tremendously depending on cycling conditions, chemistry, cell design, and manufacturing quality. Cell manufacturers and storage integrators are very interested in new technologies that can improve the abuse tolerance of Li-ion batteries resulting in improved cycle life. But proving new technologies or even iterating on existing formulations is challenging given that under some load profiles Li-ion chemistries can cycle for many years. Such long evaluation timeframes are not conducive to technical advancement. New characterization techniques are required that provide rapid insight on capacity loss and degradation mechanisms with sufficient clarity to make informed design decisions. This project will develop a new battery characterization tool that allows the measuring of capacity loss rates of Li-ion batteries under a variety of specific use scenarios. Xilectric's proposed characterization technique provides insights not available from existing techniques providing a more complete picture of the capabilities of the

variant of Li-ion chemistry under test. In particular, our technique is able to provide several measures of fidelity under realistic cycling conditions while avoiding artificial accelerated aging conditions such as extreme temperatures and potentials as well as full depth of discharge cycling. The information provided by the new test can be used to develop better battery management algorithms, to improve on cell design, and to select Li-ion formulations best suited to the end-user application. Once validated, Xilectric would expect strong commercial interest in the new device from various Li-ion cell manufacturers, end-users, researchers, and academic institutions.

SafeLi (Shorewood, WI). Electric vehicle manufacturers and the Department of Energy want safer, longer-lasting batteries that utilize new, low-cost materials that are compatible with current battery manufacturing infrastructure and industry standardization. Lithium-ion batteries dominate the current electric vehicle market. The applicant, LLC holds an exclusive license to patented materials that have favorable properties for use in these batteries. In addition, these materials can also improve batteries for portable tools and electronics, medical implants, military and aerospace applications. The applicant's founders are developing recently patented multiphase composite materials—composed of graphene monoxide, graphene, and transition metal oxides—into marketable products for novel lithium-ion anodes. With these anodes, battery performance will surpass current lithium-ion batteries because the composite materials facilitate both lithium⁺ and electron transfer and actively store and release lithium⁺ during charge/discharge cycles. The new materials are compatible with graphite and silicon-graphite, enabling development of novel, lighter, and safer anode materials that will charge faster and increase battery energy and power densities. We will use 2 approaches to constrain costs: (1) maintain compatibility with existing anode manufacturing infrastructure and (2) initially enter the market as an additive to improve silicon-graphite anode performance. As economies of scale reduce the cost, the applicant's materials will become a larger-volume fraction of active anode materials. The applicant envisions itself as a materials company that operates in the Chemical and Materials market of lithium-ion batteries. The specific market is advanced Anode Materials with application in electric, plug-in, and hybrid vehicles. Market research projects that the lithium-ion battery market will reach ~\$46 B worldwide by 2022, and that its anode segment will reach \$1.2 B by 2020 and then will outpace the cathode segment. The applicant's primary customers are companies that assemble active materials into battery cells and design high-voltage battery packs for automotive applications. Additives can be an entry point into the market while material production scales up and costs decrease. Similarly, establishing with a regional strategic partner that the anodes work well in power tools will enable the applicant to approach enterprise-scale companies that manufacture materials in-house to build on national relationships and explore licensing options. Improved anode materials will result in better batteries, which in turn will make electric vehicles more affordable and convenient to drive. In addition to the economic benefits (such as job creation) from the innovative electric vehicle industry, political and environmental benefits include decreased dependence on foreign oil and reduced air pollution.

I.7 Testing and Analysis

I.7.A BatPaC Model Development (ANL)

Shabbir Ahmed, Principal Investigator

Argonne National Laboratory
9700 S. Cass Avenue,
Argonne IL 60439
E-mail: ahmeds@anl.gov

Samuel Gillard, DOE Technology Development Manager

U.S. Department of Energy
E-mail: Samuel.Gillard@ee.doe.gov

Start Date: October 1, 2015

End Date: October 31, 2020

Project Funding (FY18) : \$900,000

DOE share: \$900,000

Non-DOE share: \$0

Project Introduction

A performance and cost model (BatPaC [\[1\]](#)) was developed at Argonne to design automotive Li-ion batteries that can meet the specification of a given vehicle, and then to estimate the cost of manufacturing such batteries. It is the product of long-term research and development at Argonne through sponsorship by the U.S. Department of Energy.

Over a decade, Argonne has developed methods to design Li-ion batteries for electric-drive vehicles based on modeling with Microsoft® Office Excel spreadsheets. These design models provided all the data needed to estimate the annual materials requirements for manufacturing the batteries being designed. This facilitated the next step, which was to extend the effort to include modeling of the manufacturing costs of the batteries.

The BatPaC model has been peer reviewed and is available on the web. It captures the interplay between design and cost of Li-ion batteries for transportation applications. It is used to estimate the impact of R&D advances on the mass, volume, and cost of lithium ion batteries. Moreover, BatPaC is the basis for the quantification of battery costs in U.S. EPA and NHTSA 2017-2025 Light-Duty Vehicle Technical Assessment. This assessment is then used to determine what mileage (i.e. CAFE) and CO₂ emission standards are optimal from a cost-benefit analysis.

Objectives

To develop and utilize efficient simulation and design tools for lithium ion batteries to predict

- Overall and component mass and dimensions
- Cost and performance characteristics when manufactured in large volume

Approach

The battery pack design and cost calculated in BatPaC represent projections for a specified level of annual battery production (10,000-500,000). As the goal is to predict the future (~5 years) cost of manufacturing batteries, a mature manufacturing process is assumed. The model designs a manufacturing plant with the sole purpose of producing the battery being modeled. The assumed battery design and manufacturing facility are based on common practice today but also assume some problems have been solved to result in a more efficient production process and a more energy dense battery. Our proposed solutions do not have to be the same methods used in the future by industry. We assume the leading battery manufacturers, those having successful operations in the near future, will reach these ends by some means.

For a selected battery chemistry, BatPaC solves the governing equations to determine the size of each layer, cell, and modules that make up the battery pack that can meet the desired requirements for power and energy.

This allows the calculation of the mass of each material, the volume of the components, and the heat removal needed during discharge. The cost of the pack is then estimated based on a predefined manufacturing process.

Current effort is directed at

- Improving the design capability by including correlations derived from continuum modeling and updating the default material properties to reflect recent experimental and industrial performance data
- Reducing the uncertainty of model predictions by setting up independent models of the manufacturing processes
- Validating the results through discussions with manufacturers and component developers.
- Updating the cost of materials used in BatPaC calculations.

Collaborations are taking place with:

- Pacific Northwest National Laboratory, Idaho National Laboratory, National Renewable Energy Laboratory, USEPA, DOT/NHTSA, International Energy Agency, B&W-MEGTEC

Results

Key Accomplishments

- The cost of BEV batteries and its sensitivity to key variables was studied.
- The potential of high voltage cathode materials was studied to estimate the mass and cost savings of PHEV and BEV batteries.
- A process model for the production of lithium hexafluorophosphate (LiPF_6) has been developed.

Cost of Cells and Packs from BatPaC Simulations

The BatPaC model was used to estimate the future cost of cells for automotive battery packs. The effects of electrode thickness, the maximum allowable current density (to avoid lithium deposition on the graphite electrode during charging), and the production volume were studied. The specifications for the battery pack and the prices of materials used in calculations are shown in Table I.7.A.1 and Table I.7.A.2.

Table I.7.A.1 Pack specifications used in BatPaC calculations

Specifications	Item	Unit
Electrodes	NMC622-Graphite	-
Energy Storage Capacity	100 (85)	kWh _{Total} (kWh _{Useable})
Power	300	kW
No. of Cells (120S-2P)	240	
Pack Voltage	450	Volts
Fast Charge ($\Delta\text{SOC} = 80\%$)	30	minutes
Max. Allowable Current Density	4	mA/cm ²

Table I.7.A.2 Electrode material costs to estimate the cost of battery packs.

Materials	Price	Unit
NMC622	17.00	\$/kg
Carbon	6.60	\$/kg
Binder PVDF	9.50	\$/kg
Binder Solvent (NMP)	3.10	\$/kg
Graphite	12.50	\$/kg
Carbon Black	6.60	\$/kg
Binder	10.00	\$/kg
Positive Current Collector	0.30	\$/m ²
Negative Current Collector	1.20	\$/m ²
Separator	1.10	\$/m ²
Electrolyte	15.00	\$/L

Figure I.7.A.1 shows the cost of the cells and packs as a function of the production volume between 10,000 to 150,000 packs per year. For 30,000 packs per year, the cell level cost is seen to be ~\$140 per kWh_{Useable} while the pack level cost is ~\$172 per kWh_{Useable}. The costs are sharply higher at lower production volumes. The error bars on the curve for the pack costs represent a 15% variability. Figure I.7.A.1 shows the effect of the price of the cathode active material, NMC622, and the effect of the pack size. The blue curve represents the base case conditions of Table I.7.A.1. If the price of NMC622 increases to \$20/kg, the cell cost will increase to \$146 per kWh_{Useable}, at a production volume of 30K packs/year. If the plant produced 30K packs/year of 51 kWh_{Useable} (60 kWh_{Total}) capacities, the cost will be \$156 per kWh_{Useable}.

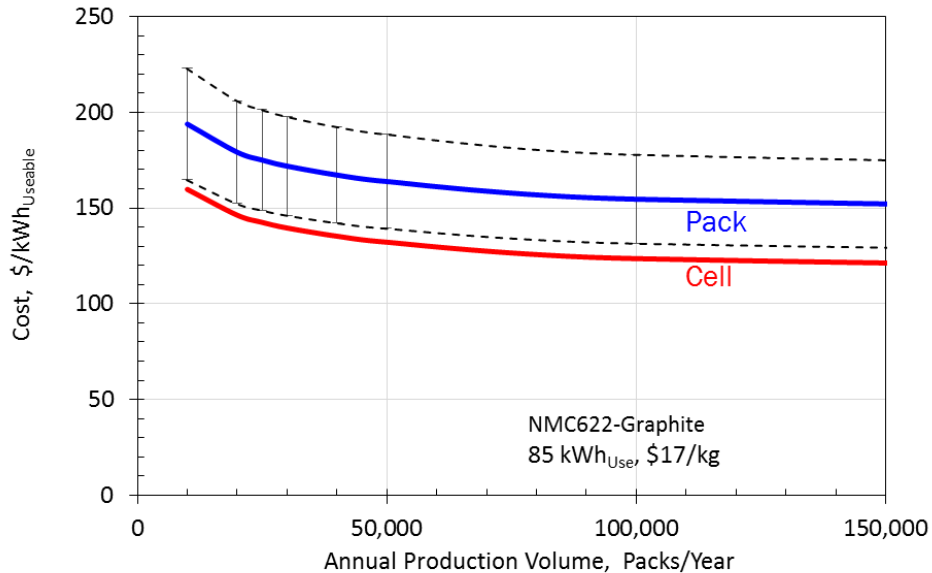


Figure I.7.A.1 Cost of cells and packs as a function of the production volume. See Table 1 for specifications.

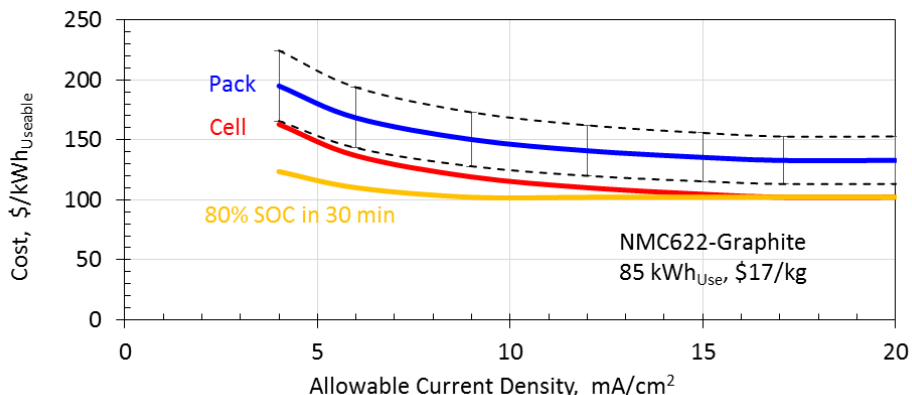


Figure I.7.A.2 Cost of cells and packs as a function of the maximum allowable current density to avoid lithium deposition during charging. Production volume = 100,000 packs/year. See Table 1 for specifications.

Fast charging capability using graphite anodes is challenged by the hazard / problem of lithium deposition. This problem can be avoided by limiting the current density during charging. The results presented above assumed a charging time of 30 minutes and an allowable current density of 4 mA/cm². The USABC target for recharging BEVs in the year 2020 is 80% ΔSOC in 15 minutes [2]. This requirement together with the constraint on the allowable current density increases the electrode area and reduces the thickness of the electrodes, which results in increased processing costs and the need for more inactive materials. Figure I.7.A.3 shows the cost of the cells and packs as a function of the allowable current density. The red and blue curves represent the costs for a 15-minute charge capability. If the electrode can tolerate allowable current densities (≥ 17.1 mA/cm²) without lithium deposition, the electrode thickness would not be limited by current density and the design would then be constrained by the sustained power specification. In such cases, the electrodes can be much thicker and the cost would be low (\sim \$100/kWh_{Useable}). For comparison, the orange curve represents the cell level costs when the charge requirement is relaxed to 30 minutes, and indicates that these cells cost considerably less, especially if the allowable current density is small. Teardown data suggests that commercial automotive LIBs may be capable of charging at >10 mA/cm² without lithium plating [3].

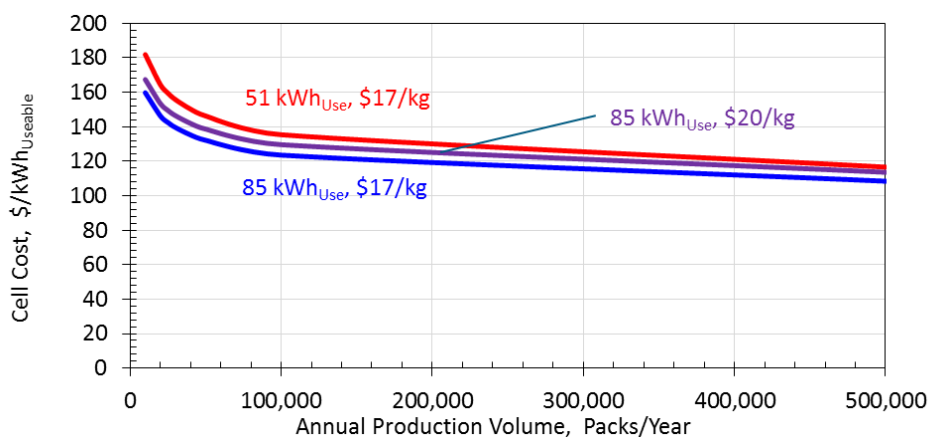


Figure I.7.A.3 Cost of cells and packs as a function of the production volume, showing the effects of cathode price and pack size. See Table 1 for specifications.

Impact of Cathode Materials at Higher Upper Cutoff Voltage (UCV)

Extending the upper cutoff voltage of lithium ion cells is a strategy that can yield a significant improvement in the specific energy while reducing the cost. A number of material related challenges are being addressed by developers, which include finding a combination of electrolyte and cathode materials that can operate reliably

and repeatedly at the higher voltage. An experimental study was conducted by Argonne researchers at the Cell Analysis, Modeling, and Prototyping (CAMP) facility to evaluate the performance of several cathode materials [4]. These materials were tested at UCVs between 4.2 and 4.7 V vs. Li/Li⁺. Figure I.7.A.4 shows the specific energy density during discharge for eight cathode materials tested in half cells. At UCV = 4.7 V vs. Li/Li⁺, the LMRNMC showed the highest specific energy density of ~900 mWh/g, followed by the NMC622 and NMC811 at ~840 mWh/g. The performance data (specific capacity, voltage) from CAMP experiments were used in BatPaC to project the mass, volume and cost of automotive batteries (BEV and PHEV). The area specific impedance (ASI) for the automotive cells were assumed to be 12 Ω·cm² [4]. The projected cost of these packs are shown in Figure I.7.A.6. The cost estimates indicate that if/when the challenges of high voltage operation can be resolved, the order of preference for the tested cathode materials at UCV > 4.5 V vs. Li/Li⁺ is LMRNMC > NMC811 > NMC622 > NCA, NMC111.

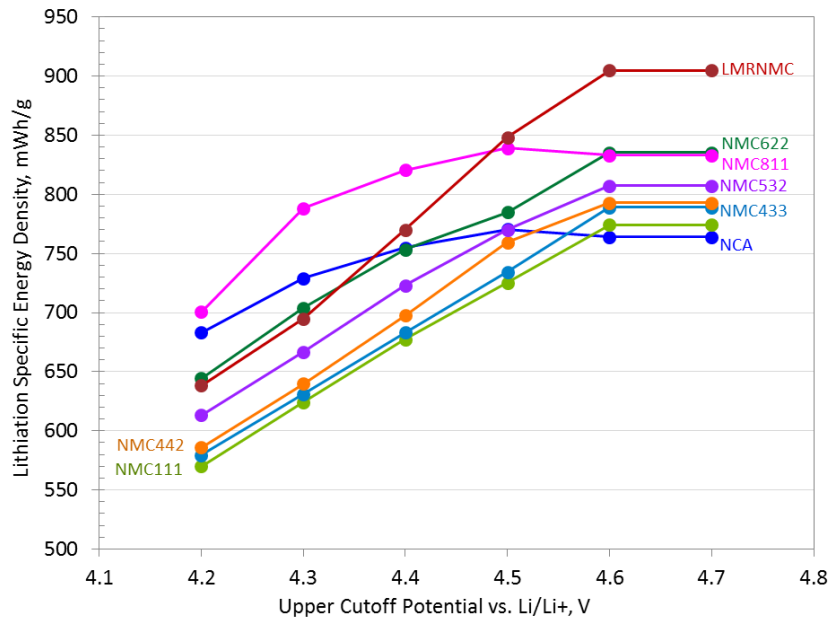


Figure I.7.A.4 Specific energy density as a function of the upper cutoff voltage (UCV) [4].

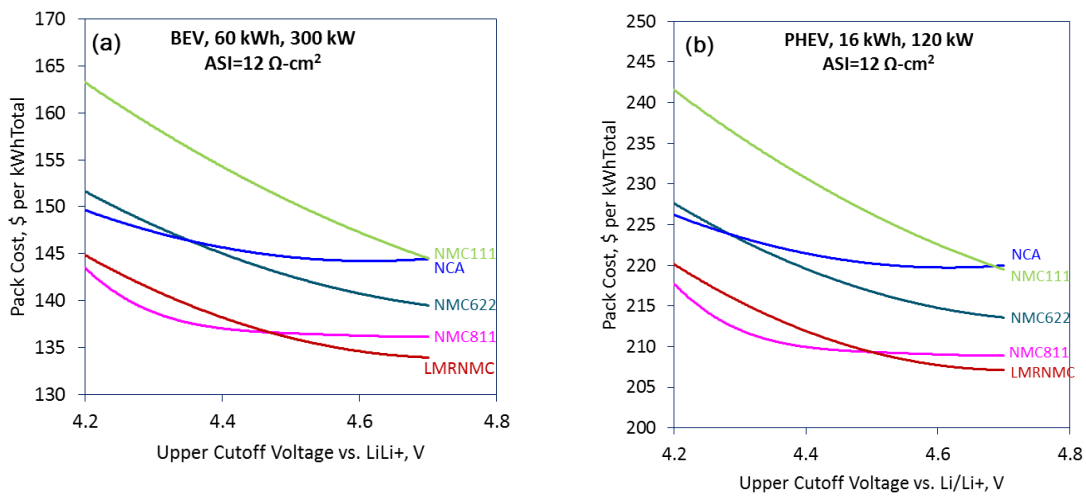


Figure I.7.A.5 Pack costs vs. upper cutoff voltages (UCV vs Li/Li⁺) for BEV and PHEV batteries. The ASI of all the cathode materials is held constant 12 Ω·cm² (at 20% SOC). Production Volume: 100,000 packs per year [4].

BatPaC 3.1 Release

A new version of BatPaC (3.1) was released in June 2018. It includes improvements in calculations for fast-charging cells, the inventory of recyclable materials, and updates on the price of materials.

Production of LiPF₆

The production of LiPF₆ was studied to estimate the manufacturing cost, energy demand, and environmental impact. For this, detailed process models and flowsheets were developed for three different processes and techno-economic analysis was performed to strategize the reduction of manufacturing cost. The minimum manufacturing cost of LiPF₆ with a baseline plant capacity of 10,000 MT per day was estimated to be \$20 per kg of LiPF₆ using the process as shown in Figure I.7.A.6. The cost of equipment contributes less than 4% but procuring raw materials and the cost for solvent recycling contributes ~65% of the overall manufacturing cost. Also, the cost of manufacturing LiPF₆ changes by \$1.75/kg for every \$1/kg change in the price of PCl₅, which is one of the key raw materials. It was observed that solvent recycling has a significant impact on the cost of manufacturing, e.g. for every \$1/kg change in the price of solvent recycling, the cost of LiPF₆ manufacturing changes by \$4/kg. Of the three processes studied, the process shown in Figure I.7.A.6 was found to be the cheapest (\$20 vs. \$26 & \$29 /kg LiPF₆) but has relatively higher greenhouse gas emissions computed in terms of equivalent CO₂ (80 MT/day vs. 50 & 70 MT/day). However, the process shown in Figure 6 was identified as the safest process as it uses the minimum amount of hazardous chemical, HF, and uses the least hazardous solvent (acetonitrile vs. liquid SO₂ & anhydrous HF).

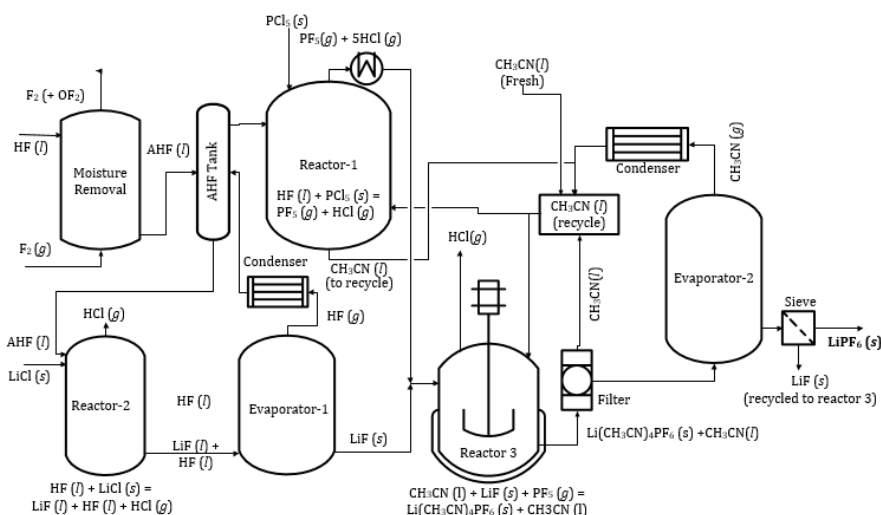


Figure I.7.A.6 Schematic of a process for the production of LiPF₆.

Figure I.7.A.7 shows the sensitivity of the cost of LiPF₆ on the cost of a 60 kWh battery pack (with NMC622-Graphite, produced at a scale of 100K packs per year). It shows that the cost (\$/kWh) of the battery pack would change by ~10 cents/kWh for every dollar change in the cost of the LiPF₆.

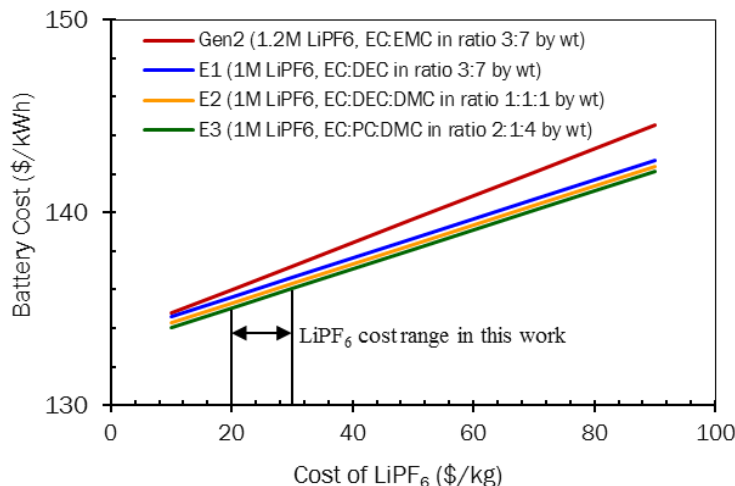


Figure I.7.A.7 Impact of the cost of LiPF₆ on the cost of a 60 kWh lithium ion battery pack. (NMC622-Graphite electrodes, plant capacity of 100,000 packs per year)

Conclusions

Increasing deployment of electric vehicles will increase the demand for lithium ion batteries and its constituent materials leading to lower costs. BatPaC studies on the effect of the production volume, fast charge requirements, and cathode price indicate that these are important parameters that affect the battery costs. Higher volume production will enable economies of scale. The development of anode materials that can tolerate higher current densities will enable thicker electrodes thereby lowering the cost of inactive materials and the electrode processing cost.

An experimental and BatPaC-simulation study shows that the LMRNMC and NMC811 are attractive cathode materials that can lead to lower cost cells if /when the suitable electrolytes and other cycle-life-limiting issues of high voltage cells are resolved.

Modeling a process for the production of the electrolyte salt LiPF₆ suggests the cost would range around \$30 per kg. For every dollar change in the cost of LiPF₆, the cost of a 60 kWh battery would change by ~10 cents per kWh.

Key Publications

1. Ahmed, Shabbir, Stephen Trask, Dennis Dees, Paul Nelson, Wenquan Lu, Alison Dunlop, Bryant Polzin and Andy Jansen, "Cost of automotive lithium-ion batteries operating at high upper cutoff voltages," *Journal of Power Sources*, 403 (2018) 56–65.
2. Wood III, David L., Quass Jeffrey, Li Jianlin, Shabbir Ahmed, David Ventola and C. Daniel. "Technical and Economic Analysis of Solvent-based Lithium-ion Electrode Drying with Water and NMP," *Drying Technology* 36 2018: 234-244.
3. Susarla, N., Ahmed, S., Dees, D. W. "Modeling and analysis of solvent removal during Li-ion battery electrode drying," *Journal of Power Sources*, 378 (2018), 660-670.
4. D. Santini, A. Burnham, P. Nelson, Y. Zhou, S. Ahmed, J. Miller, M. Rood, "Evolving Estimates of Emerging Eminence of Electrified Vehicles," *Proceedings of The 31st International Electrical Vehicles Symposium and Exhibition (EVS31)*, 2018, Kobe, Japan.

References

1. P. Nelson, K. Gallagher, I. Bloom, D. Dees and S. Ahmed, "BatPaC: A Lithium-Ion Battery Performance and Cost Model for Electric-Drive Vehicles," 2018. [Online]. Available: <http://www.cse.anl.gov/batpac/>.
2. USCAR, "Energy Storage System Goals," 2017. [Online]. Available: http://uscar.org/guest/article_view.php?articles_id=85. [Accessed July 2017].
3. Ricardo, "2013 MY Ford C-MAX Energi Battery Cell Teardown Analysis," 2016.
4. S. Ahmed, S. Trask, D. Dees, P. Nelson, W. Lu, A. Dunlop, B. Polzin and A. Jansen, "Cost of automotive lithium-ion batteries operating at high upper cutoff voltages," *Journal of Power Sources*, vol. 403, pp. 56-65, 2018.
5. W.-J. Zhang, "A review of the electrochemical performance of alloy anodes for lithium-ion batteries," *Journal of Power Sources*, vol. 196, pp. 13-24, 2011.
6. A. Casimir, H. Zhang, O. Ogoki, J. Amine, J. Lu and G. Wu, "Silicon-based anodes for lithium-ion batteries: Effectiveness of materials synthesis and electrode preparation," *Nano Energy*, vol. 27, pp. 359-376, 2016.
7. A. Gonzalez, N.-H. Yang and R.-S. Liu, "Silicon Anode Design for Lithium-Ion Batteries: Progress and Perspectives," *The Journal of Physical Chemistry C*, vol. 121, pp. 27775-27787, 2017.

Acknowledgements

P. Nelson, N. Susarla, D. Dees, S. Trask, W. Lu, A. Dunlop, B. Polzin, A. Jansen, G. Henriksen

I.7.B Battery Performance and Life Testing (ANL)

Ira Bloom, Principal Investigator

Argonne National Laboratory
9700 South Cass Avenue
Argonne, IL 60439
E-mail: ira.bloom@anl.gov

Samuel Gillard, DOE Technology Development Manager

U.S. Department of Energy
E-mail: Samuel.Gillard@ee.doe.gov

Start Date: October 1, 2017	End Date: December 31, 2020	
Project Funding (FY18): \$1,500,000	DOE share: \$1,500,000	Non-DOE share: \$0

Project Introduction

Batteries are evaluated using standard tests and protocols that are transparent to technology. These protocols are based on those developed by the USABC [1], [2], [3], [4].

Objectives

- Provide DOE, USABC, and battery developers with reliable, independent and unbiased performance and life evaluations of cells, modules and battery packs.
- Benchmark battery technologies that were not developed with DOE/USABC funding to ascertain their level of maturity.

Approach

The batteries are evaluated using standardized and unbiased protocols, allowing a direct comparison of performance within a technology and across technologies. For those tested using the USABC methods, the performance of small cells can be compared to that of larger cells and full-sized pack by means of a battery scaling factor [1], [2].

Results

Batteries, which were fabricated during programs with developers, are sent to Argonne for evaluation. Here, the purpose of evaluation is two-fold: to provide confirmation of other test information and to provide an independent assessment of the state of the given battery technology, that is, how does it compare to the USABC [1], [2], [3], [4] and/or project goals? A list of program deliverables associated with Argonne is given in Table-1, along with their status.

Table I.7.B.1 Status of Deliverables for Testing

Developer	Sponsor	Quantity x System Level	Application	Status
Maxwell	USABC	15 x Cell	12-V S/S	on-going
Maxwell	USABC	15 x Module	12-V S/S	complete
24-M	USABC		EV	expected
Navitas	DOE FOA	24 x Cell	EV	complete
XALT	DOE FOA	24 x Cell	EV	complete
WPI	USABC	40 x Cell	Recycling/PHEV-20	on-going
WPI	USABC	30 x cell	Recycling/PHV-20	On-going
SiNode	USABC	9 x Half cell	EV	on-going
SiNode	USABC	8 x Cell	EV	on-going
SiNode	USABC	20 x Cell	EV	expected
Farasis	USABC	68 x Cell	Recycling/PHEV-20	expected
Daikin	DOE	9 x Cell	EV/PHEV	on-going
ANL-CAMP	DOE	48 x half cell	XCEL - GITT	complete
ANL-CAMP	DOE	30 x Cell	XCEL - 6C fast charge	complete
ANL-CAMP	DOE	15 x cell	XCEL - 6-C fast charge	complete

The USABC is always improving its test methods, keeping up with changing applications. Recently, the USABC added a modified HPPC test to those used to characterize the performance of EV batteries [5] in addition to the Peak Power test [3], [4], [5]. The test profiles used in these tests are shown in Figure I.7.B.1. A full description of these tests is given in Ref. 5 and will not be repeated here. The HPPC test was added as a means of characterizing the regenerative braking power capability of a battery under test; the Peak Power test did not have that ability. Another difference between the two tests, as shown in Figure I.7.B.1, the HPPC profile starts at the zero current level after a long rest period (~1 h) and the Peak Power test always has a small current (labeled base current in the Figure) flowing through the battery.

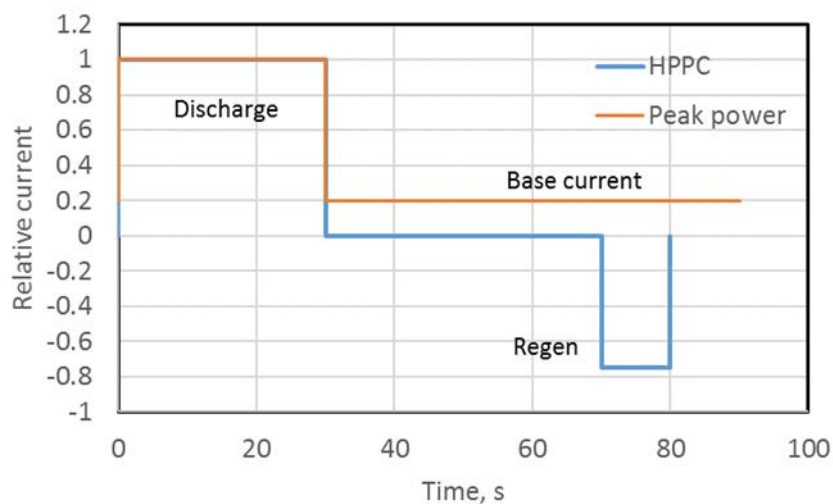


Figure I.7.B.1 Schematic representations of the HPPC and Peak Power test profiles.

Since both tests are meant to characterize the performance of a battery under test, a question remains, how do their results compare? To answer this, we conducted an EV test that incorporated both. For the sake of

simplicity, the discussion will be limited to a calendar life test only. The calendar life test used three temperatures, 30, 40, and 50°C. The principles are also applicable to cycle life testing.

The power capability of a given cell at 80% DOD is usually the prime metric for USABC testing. However, the two test protocols employ different methods to calculate this value. Changes in relative resistance, the basic performance parameter obtained in both tests and from which power is calculated, are discussed below.

Peak Power Resistance at 80% DOD. A plot of relative resistance at 80% DOD vs. time for the calendar life test is given in Figure I.7.B.2a. Least-squares regression using these values show that cell resistance increases linearly with time. Indeed, plotting the slopes of the lines from Figure I.7.B.2a on an Arrhenius plot produced Figure 2b. From the best-fit line in Figure I.7.B.2b, the value of r^2 is 0.97; from the slope of the line, the energy of activation is 49.4 kJ/mol. This appears to a thermally-activated process.

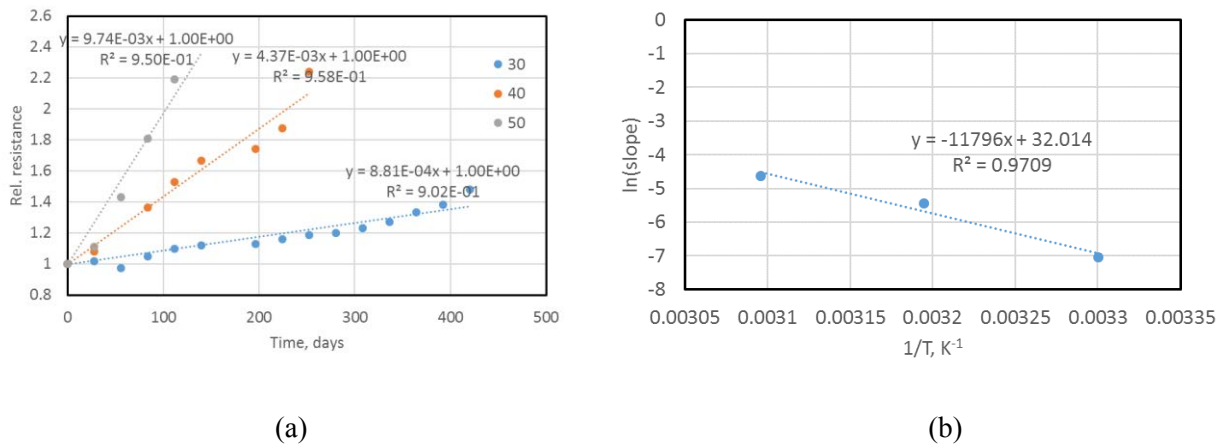


Figure I.7.B.2 (a) Relative resistance at 80% DOD from the peak power test from the calendar life test. The numbers in the legend represent the test temperature in °C. The best-fit line was forced to have a y-intercept of 1. (b) Arrhenius plot of the slopes from Figure I.7.B.2a.

HPPC Resistance at 80% DOD. The relative resistance at 80% DOD was calculated from the HPPC tests for a direct comparison to the standard USABC metric. A plot of these values as they change with time is given in Figure I.7.B.3a.

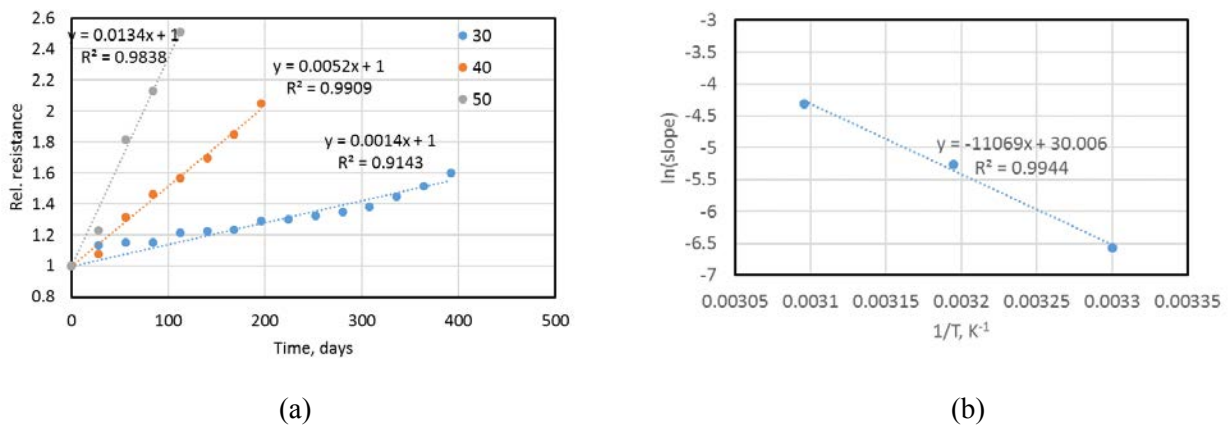


Figure I.7.B.3 (a) Relative resistance at 80% DOD vs. time. The numbers in the legend are the test temperatures. The best-fit line was forced to have a y-intercept of 1. The least-squares equations and values of r^2 are given on the plot. (b) Arrhenius plot of the slopes shown in Figure I.7.B.3a vs. 1/T.

Plotting the $\ln(\text{slope})$ vs. $1/T$ and performing least-squares fitting (Figure I.7.B.3b) show that Arrhenius-like kinetics are present, implying that resistance increase process is a thermally-activated, diffusion-controlled process. From the slope of the line shown in Figure I.7.B.3b, the energy of activation is 46.3 kJ/mol.

Comparing Figure I.7.B.2a and Figure I.7.B.3a shows similarities and differences. Both sets of data yield good linear fits with time, indicating linear-with-time kinetics. However, they differ in the magnitude of the resistance increase. Taking the 30°C data as an example, Figure I.7.B.2a (peak power) shows a total relative increase of about 0.4. On the other hand, Figure I.7.B.3a (HPPC) shows a total relative increase of about 0.6. Incorporating these results into life estimation models will produce different results.

Cell resistance (impedance) can be divided into a number of components, such as those given in Eq. 1.

$$R_{\text{cell}} = R_{\text{ohmic}} + R_{\text{charge transfer}} + R_{\text{mass transfer}} + R_{\text{reaction}} \quad \text{Eq. 1}$$

Here, R_{ohmic} is the resistance from just the electrode materials; $R_{\text{charge transfer}}$ is the resistance to charge movement across the electrolyte/electrode interface; $R_{\text{mass transfer}}$ is the resistance to material diffusion in to and out of the electrochemically active site; and R_{reaction} is the resistance due to the chemical kinetics of the reaction. It should be noted that, for the purposes of this discussion, the terms in Eq. 1 contain contributions from both electrodes, and, where possible, from the electrolyte. The only term in Eq. 1 that is not sensitive to current is R_{ohmic} . The other terms are. The resistance of the cell will be governed by the slowest step [6]. If current exceeds the rate of the process, such as mass transfer, there will be an increase in resistance due to that process.

The HPPC test used a discharge pulse current of 95 A and that of the Peak Power test, 285 A. Based on the simple argument shown above, one would expect the calculated resistance from the latter test to be higher. The power capability calculated from these tests would follow suit: higher resistances lead to lower power.

Conclusions

The current USABC EV test manual contains both the peak power and HPPC tests. Comparing them shows similarities and difference. At 80% DOD, both seem to produce data that would lead to linear-with-time kinetic laws. However, the magnitude of resistance increase would differ in the same amount of time, leading to different life estimates.

References

1. FreedomCAR Battery Test Manual for Power-Assist Hybrid Electric Vehicles, DOE/ID-11069, October 2003.
2. FreedomCAR Battery Test Manual for Plug-In Hybrid Electric Vehicles, June 2010.
3. Electric Vehicle Battery Test Procedures Manual, Revision 2, January 1996.
4. Battery Test Manual for 12 Volt Start/Stop Vehicles, Rev. 1, May 2015, INL/EXT-12026503.
5. Battery Test Manual for Electric Vehicles, Rev. 3, June 2015, INL/EXT-15-34184.
6. A. J. Bard and L. R. Faulkner, *Electrochemical Methods*, John Wiley and Sons, 1980, NY, p. 16ff.

Acknowledgements

Co-Investigators: John Basco, Panos Prezas, LeRoy Flores and David Robertson (Argonne National Laboratory)

I.7.C Electrochemical Performance Testing (INL)

Lee Walker, Principal Investigator

Idaho National Laboratory
2525 Fremont Ave
Idaho Falls, ID 83402
E-mail: lee.walker@inl.gov

Samuel Gillard, DOE Technology Development Manager

U.S. Department of Energy
E-mail: Samuel.Gillard@ee.doe.gov

Start Date: October 1, 2017

End Date: September 30, 2018

Project Funding (FY18): \$4,000,000

DOE share: \$4,000,000

Non-DOE share: \$0

Project Introduction

The advancement of battery technologies which can meet the emerging demands for vehicle electrification requires in-depth understanding of the performance of early stage pre-commercial batteries, state-of-the-art commercial cells and the ability to adapt evaluation methods as mobility needs change. The Battery Test Center (BTC) at Idaho National Laboratory (INL) has been supporting the evolution of electrified transportation through high-quality, independent testing of electrical energy storage systems for more than 30 years. Independent testing provides data for quantitative assessment of the fundamental technology gaps which exist in early stage battery development. Test methods and techniques are continuously improved to offer data on relevant metrics as vehicle applications evolve and as new core gaps are identified. Advancing electrified powertrain transportation including understanding both high energy battery chemistries and high power, extreme fast charging needs, is a top priority in advancing how people and goods are transported in the United States. As a designated core capability and lead test facility for the Vehicle Technologies Office (VTO), the BTC at INL directly supports the US Advanced Battery Consortium (USABC) and other VTO programs by providing discrete information on failure modes, mechanisms and shortfalls in emerging technologies. Gaps in performance relative to targets are used as a metric to guide future R&D priorities.

Objectives

The activities at the INL BTC are focused on providing high fidelity, science-based performance and life testing, analysis, modeling, and reporting. To ensure the alignment with future industry and government needs, it is a key objective to update test and analysis procedures as new concepts and design space become achievable. Refined procedures help identify promising future research paths and identify key fundamental gaps which need to be addressed.

Approach

With 20,000 square feet of laboratory space, the INL BTC is equipped with over 800 test channels for advanced energy storage testing at the cell-level (e.g., up to 7V, 300A), module-level (e.g., up to 65V, 250A), and pack-level (e.g., 500-1000V, 500A). Test equipment is programmed to perform distinct test profiles while simultaneously monitoring for compliance with operating limits such as voltage, current and temperature. The output from such tests enables principles-based analysis to be performed that can aid in identification of key technology gaps.

To ensure high quality, repeatable and dependable data is used for analysis, batteries and other energy storage devices are typically subjected to specific test sequences while housed inside precision thermal chambers. To enhance performance testing across a wide range of thermal conditions, driven by automotive usage scenarios, the thermal chambers can be operated across a broad temperature range (e.g., -70 to 200°C). This temperature range enables key information to be extracted by modifying the chemical kinetic degradation rates within the evaluated items and enables accelerated aging analysis.

Successful performance testing and accurate life modeling are highly dependent on the fidelity of the acquired test data. The INL BTC has developed advanced calibration verification and uncertainty analysis methodologies to ensure that voltage, current, and temperature measurements are within the tolerance specified by the test equipment manufacturer (e.g., 0.02% of the full scale). These measured test parameters are subsequently used in various mathematical combinations to determine performance capability (e.g., resistance, energy, power, etc.). INL has also quantified the error associated with these derived parameters using the accuracy and precision of the relevant measured parameter (e.g., voltage) to ensure high-quality and repeatable results and meaningful presentation.

The INL BTC is also equipped with facilities that enable the characterization of batteries in aggressive use cases. One such use case is vibration which mimics what would be seen over the life of a battery in a typical automotive setting. Analysis of vibration on batteries at INL utilizes a high capacity vibration table to perform non-destructive tests to understand reliability and safety of new cell topologies to mechanical vibration and shock. Emerging cell designs which vary from current state of the art cell designs are the main focus of mechanical vibration and shock testing at INL.

Adjacent to the vibration table are two fire-rated isolation rooms that can be used for tests that push the known limits of battery operation. These aggressive use cases include extreme fast charging, subtle over- or under-charging, high-temperature thermal characterization for under-hood systems, among many others. The isolation rooms allow for safe testing of emerging cell technologies at or near the design limits and help characterize future use cases. The rooms also enable identification of key changes in performance fade which may emerge in aggressive use cases that can directly inform future rounds of early stage material and cell development activities. These complimentary non-destructive evaluation capabilities comprise INL's Non-Destructive Battery Evaluation Laboratory.

Results

The INL BTC continues to test articles of various sizes and configurations using standardized test protocols developed by INL with industry partnerships for different electric drive vehicle application. Tables 1 and 2 summarize the testing activities under the USABC and Benchmarking programs, respectively, for FY-18. Technologies developed through USABC contracts are aged and tested against the appropriate application target (EV, HEV, PHEV, 12V S/S, 48V HEV) and, where applicable, they are compared to previous generations of test articles from the same developer. 192 articles were tested for USABC in FY-18, including 3 modules and 189 cells. The vibration table in the Non-Destructive Battery Evaluation Laboratory was used to evaluate 2 sets of USABC deliverables and demonstrated the level of resilience of these emerging technologies to mechanical vibration. The purpose of the Benchmark program is to evaluate device technologies that are of interest to VTO within DOE, but are not deliverables developed under a contract. In some cases, Benchmark devices are used to validate newly developed test procedures and analysis methodologies. Benchmark activities also are used to understand which gaps need to be fundamentally addressed to improve cell performance. 90 cells were tested for the Benchmark program in FY-18. Cells from the Applied Battery Research (ABR) program were life and performance tested at INL, using modified testing procedures based on ABR program goals. These early stage development cells were designed to improve performance of batteries to meet goals for high energy design. Within the framework of ABR testing, the INL BTC tested and reported on 63 cells.

Analysis was performed for all articles tested, and results were presented regularly at quarterly review meetings and USABC Technical Advisory Committee (TAC) meetings to USABC representatives from different automotive manufacturers, DOE VTO representatives, developers, and national laboratory staff. INL worked with the USABC test methods committee to develop the methodology and update the manual for testing 12V Start/Stop batteries and to start modifications on other manuals including in the area of fast charging.

Table I.7.C.1 Articles Tested for USABC

Developer	Application	System	Number of Articles Tested	Status at Year End
NOHMS	PHEV	Cell	18	Complete
24M	EV	Cell	3	Complete
Envia	EV	Cell	17	Complete
NOHMS	PHEV	Cell	4	Complete
SAFT	HEV	Cell	13	Ongoing
SAFT	12V Stop/Start	Cell	15	Ongoing
LG/CPI	12V Stop/Start	Cell	15	Ongoing
SAFT	12V Stop/Start	Cell	15	Ongoing
SAFT	12V Stop/Start	Cell	4	Ongoing
Amprius	EV	Cell	24	Ongoing
Amprius	EV	Cell	13	Ongoing
LG/CPI	12V Stop/Start	Cell	15	Ongoing
LG/CPI	12V Stop/Start	Module	3	Ongoing
SAFT	12V Stop/Start	Module	3	Ongoing
FARASIS	EV	Cell	8	Ongoing
Xalt	12V Stop/Start	Cell	18	Ongoing
Amprius	EV	Cell	4	Ongoing

Table I.7.C.2 Articles Tested for Benchmark

Developer	Application	System	Number of Articles Tested	Status at Year End
LG/CPI	PHEV	Cell	13	Complete
EIG LTD	12V Stop/Start	Cell	20	Complete
Fisker	EV	Cell	9	Complete
Toshiba	EV	Cell	3	Ongoing
Toshiba	EV	Cell	18	Ongoing
Toshiba	12V Stop/Start	Cell	12	Ongoing
LG/CPI	EV	Cell	15	Ongoing

Table I.7.C.3 Articles Tested for Applied Battery Research (ABR)

Developer	Application	System	Number of Articles Tested	Status at Year End
Penn State	PHEV	Cell	15	Complete
Farasis	EV	Cell	12	Complete
Farasis	PHEV	Cell	12	Complete
ANL	PHEV	Cell	12	Complete
Envia	EV	Cell	12	Complete

A key focal area for FY-18 at INL was expanded fade analysis as part of the Benchmark and USABC activities. The analysis was focused on more directly quantifying different levels of performance fade

associated with more aggressive use cases. In both instances the work directly capitalized on the isolation chambers in the Non-Destructive Battery Evaluation Laboratory. Two programs were jointly identified through discussion of INL and VTO to undergo more extensive analysis on modes of performance fade. The two programs were chosen due to initial, high performance in fast charge and high energy. In both programs analysis expanded on traditional reference performance tests to include differential capacity analysis, expanded analysis of cell impedance, and close monitoring of thermal changes during key portions of the use profile. The analysis of these different data streams enabled the identification of enhanced loss of lithium inventory and loss of active materials as key emergent fade mechanisms which were accelerated as the rate of charging increased beyond normal operating conditions. Currently additional programs are undergoing this evolution in analysis to continually provide additional information as part of evaluation.

In addition to the activities looking at performance analysis, INL worked with the National Renewable Energy Lab and Argonne National Laboratory to finalize and publish a set of manuscripts defining the key technology gaps which exist and which need to be addressed by early stage R&D to enable extreme fast charging. The analysis resulted in five peer review manuscripts which were published to Journal of Power Sources.

Conclusions

The ability to perform discrete performance and life evaluation of emerging technologies in an independent, reliable manner is a direct aid to the identification of key technology gaps. Over the course of FY-18 the INL BTC was able to directly support many different endeavors within VTO with a keen focus on advancing battery technologies for emerging trends in electrified transportation. As a core capability in performance and life analysis for VTO, INL has identified key performance fade modes which exist in cells used for fast charging and has advanced the understanding of performance and evaluation protocols for multiple programs funded by VTO and USABC. A total of 345 devices were tested in FY-18. The work also resulted in the update of the USABC 12V Start/Stop test manual and the submission/acceptance of 7 peer reviewed manuscripts. In FY-19, INL plans to continue this level of support for multiple programs with broad support for the USABC and Benchmark programs in particular, having completed support of ABR testing. FY-19 activities will also look to more discretely probe key failure modes and how they relate to cell design and evaluation. Additional testing activities will be started to support XCEL and BTMS activities. INL will also continue developing and refining standard test protocols and analysis procedures in collaboration with USABC and on providing information on core fundamental performance gaps which need to be addressed across VTO programs.

Key Publications

1. "Fast Charge Implications: Pack and Cell Comparison and Analysis" Tanvir R. Tanim, Matthew Shirk, Randy L. Bewley, Eric J. Dufek and Boryann Liaw, *J. Power Sources*, 381 (2018), 56-65
2. Battery Test Manual for 12 Volt Start/Stop Vehicles, Idaho National Laboratory, February 2018, INL/EXT-12-26503
3. "Enabling fast charging – Introduction and Overview" Christopher Michelbacher et. al. *J. Power Sources*, 367 (2017), 214-215
4. "Enabling fast charging – A battery technology gap assessment" Shabbir Ahmed et. al. *J. Power Sources*, 367 (2017), 250-262
5. "Enabling fast charging – Vehicle Considerations" Andrew Meintz et. al. *J. Power Sources*, 367 (2017), 216-227.
6. "Enabling fast charging – Battery Thermal Considerations" Matthew Keyser et.al. *J. Power Sources*, 367 (2017), 228-236.

7. “Enabling fast charging – Infrastructure and Economic Considerations” Andrew Burnham et. al. J. Power Sources, 367 (2017) 237-249
8. Ed Thomas et. al. Predicting Memoryless Degradation Under Variable Stress, accepted to Journal of Quality Technology.

Acknowledgements

The following staff at INL supported this work: Matthew Shirk, Tanvir Tanim, Shrikant Nagpure, Sergiy Sazhin, Eric Dufek, Boryann Liaw, Randy Bewley, Charles Dickerson, Chinh Ho, Ryan Jackman, Michael Evans, Clair Ashton, and David Jamison.

I.7.D Battery Safety Testing (SNL)

Joshua Lamb, Principal Investigator

Sandia National Laboratories
1515 Eubank Dr. SE, M/S 0613
Albuquerque, NM, 87185
E-mail: jlamb@sandia.gov

Samuel Gillard, DOE Technology Development Manager

U.S. Department of Energy
E-mail: Samuel.Gillard@ee.doe.gov

Start Date: October 1, 2017

End Date: September 30, 2018

Project Funding (FY18): \$800,000

DOE share: \$800,000

Non-DOE share: \$0

Project Introduction

Abuse tests are designed to determine the safe operating limits of HEV/PHEV energy storage devices. Testing is intended to achieve certain worst-case scenarios to yield quantitative data on cell/module/pack response, allowing for failure mode determination and guiding developers toward improved materials and designs. Standard abuse tests with defined start and end conditions are performed on all devices to provide comparison between technologies. New tests and protocols are developed and evaluated to more closely simulate real-world failure conditions.

While robust mechanical models for vehicles and vehicle components exist, there is a gap for mechanical modeling of EV batteries. The challenge with developing a mechanical model for a battery is the heterogeneous nature of the materials and components (polymers, metals, metal oxides, liquids). Our work will provide empirical data on the mechanical behavior of batteries under compressive load to understand how a battery may behave in a vehicle crash scenario. This work is performed in collaboration with the U.S. Council for Automotive Research (USCAR) and Computer Aided Engineering of Batteries (CAEBAT). These programs have supported the design and development of a drop tower testing apparatus to close the gap between cell/string level testing and full scale crash testing with true dynamic rate effects.

This work is discussed in further detail in the CAEBAT annual report section. Additional modeling efforts lie in being able to better predict failure propagation within larger battery systems. Sandia's battery safety testing provides testing support to better aid in thermoelectrical model development at NREL and SNL.

Materials characterization to better understand batteries that have undergone abusive conditions is of interest. Our partnerships with Argonne National Lab (ANL) and Oakridge National Lab (ORNL) through the Post Test Analysis Program for ABR, spans the building of cells with known materials (ORNL), overcharge testing to various states (SNL), and the posttest analysis of the cells (ANL). In addition, testing to support the Si-Deep Dive Program has been leveraged to gain a better understanding of the safety implications for these materials.

Calorimetry testing has historically been performed on 18650 cells of ~1.5 AH or lower. Testing has been performed to understand how best to apply data from this testing to larger scale formats and cells of increasing energy density. This will inform future work performing ARC testing of new high energy chemistries and how those results might apply to larger format cells.

The ability to fast charge electric vehicles addresses two major points of consumer EV adoption: range anxiety and convenience. However, fast charging also introduces new degradation mechanisms in the battery, and may contribute to new failure mechanisms. In fact, adverse effects seen during fast charge resemble battery abuse in several ways. In the cathode, fast charging is known to cause localized heating, which can lead to breakdown of active materials, electrolyte, and binder. It can also cause localized over-delithiation, damaging the cathode structure. In the anode, the primary danger is lithium plating, which occurs if lithium diffusion into the cathode

can't keep pace with high rate Li⁺ delivery to the anode. The anode can also be host to Li⁺ depletion in the adjacent electrolyte, causing unexpected electrolyte changes and double layer effects. Two common abuse scenarios, overcharge and thermal ramp, result in similar effects. Overcharge is known to cause high voltage breakdown of separator, binder, electrolyte, and cathode material. It also causes over-delithiation in the cathode, as well as lithium plating on the anode. Thermal ramp causes cathode and separator breakdown, SEI layer breakdown, and other electrolyte effects. Because of the shared effects between fast charging and abuse, a project was undertaken to quantify the effects of fast charging on abuse response.

Objectives

- Provide independent abuse testing support for DOE and USABC
- Abuse testing of all deliverables in accordance with the USABC testing procedures
- Evaluate the impact of scale of stored energy on the thermal runaway characteristics of lithium ion batteries, with an eye to informing how to interpret accelerating rate calorimetry data of developmental cells.
- Develop initial test methods for evaluating the impact of high rate charging on battery safety performance.
- Provide testing data to support failure propagation model (NREL)
- Provide testing support for ABR Post Test program (INL/ANL)

Accomplishments

- Completed testing of all USABC deliverables to date and reported results to the USABC TAC
- Current abuse testing procedures published as a Sandia report SAND
- Developed method to use a laser to induce a short within cells
- Testing support for CAEBAT activities
- Extended failure propagation modeling efforts with NREL using testing data
- Provided testing support for several cell chemistry types (NMC, LFP, and Si) to varied levels of overcharge in support of the ABR post test program (ORNL, SNL, and ANL)
- Evaluated impact of extended high rate charging on abuse response of pouch format cells
- Impact of cell scale and state of charge on Accelerating Rate Calorimetry results examined

Approach

Abuse tolerance tests evaluate the response to expected abuse conditions. The goals of abuse and safety testing include a) testing to failure of energy storage devices and documentation of conditions that caused failure, b) systematic evaluation of failure modes and abuse conditions using destructive physical analysis (DPA), c) provide quantitative measurements of cell/module response, d) document improvements in abuse response, and e) develop new abuse test procedures that more accurately determine cell performance under most probable abuse conditions. Electrical (overcharge/overvoltage, short circuit, over discharge/voltage reversal, and partial short circuit), mechanical (controlled crush, penetration, blunt rod, drop, water immersion, laser induced short circuit, mechanical shock and vibration) and thermal abuse (thermal stability, simulated fuel fire, elevated temperature storage, rapid charge/discharge, and thermal shock cycling) cover the main categories of possible conditions evaluated. These techniques are applied to USABC deliverables and the results reported to DOE and USABC.

Research and development batteries used for simulating internal short circuits, propagation testing (alternative initiators and passive thermal management), impact of cell scale evaluation, and safety impacts of elevated charging rates are based on commercial-off-the-shelf (COTS) LiCoO₂ 18650 and pouch cells, NMC and NCA 18650 and pouch cells, and LFP 18650 (designed for energy) and 26650 (designed for power) cells. Cell failure and thermal runaway initiated by various methods were investigated this FY, including overcharge, laser initiation, and mechanical nail penetration into a single cell within a pack.

Results

The impact of total energy within cells on thermal runaway as well as the scalability of Accelerating Rate Calorimetry (ARC) testing was examined by testing cells of various capacities as well as cells at various states of charge. ARC has been used by Sandia to evaluate the total energy as well as the onset and kinetics of thermal runaway processes, however the bulk of this testing has been done largely on 18650 format cells with less than 1.5 AH of capacity. This work is to better understand how testing of cylindrical format cells can be applied to large format pouch cells, and how the thermal runaway scales as the energy density of a cell increases. This testing was performed on commercial off the shelf (COTS) NMC cells. Summary of these results are shown in Figure I.7.D.1-Figure I.7.D.2.

Figure I.7.D.1 shows the results of increasing state of charge within 18650 cells, and in particular shows how lower states of charge impacts thermal runaway. The behavior at 40% SOC shows behavior similar to that seen for higher states of charge, albeit at lower total heating rates. At 20% SOC, an onset similar to that observed for higher states of charge was observed, however the overall kinetics and total energy was significantly reduced, with a relatively low peak heating rates observed. At 0% SOC the exothermic reactions are limited primarily to the effects of electrolyte decomposition as seen in Figure I.7.D.1 (right). This shows a fairly high onset of any exothermic reactions, as well as relatively limited peak heating rates. Some effects are still observed, however, showing that some exothermic behaviors are still possible even in absence of stored energy.

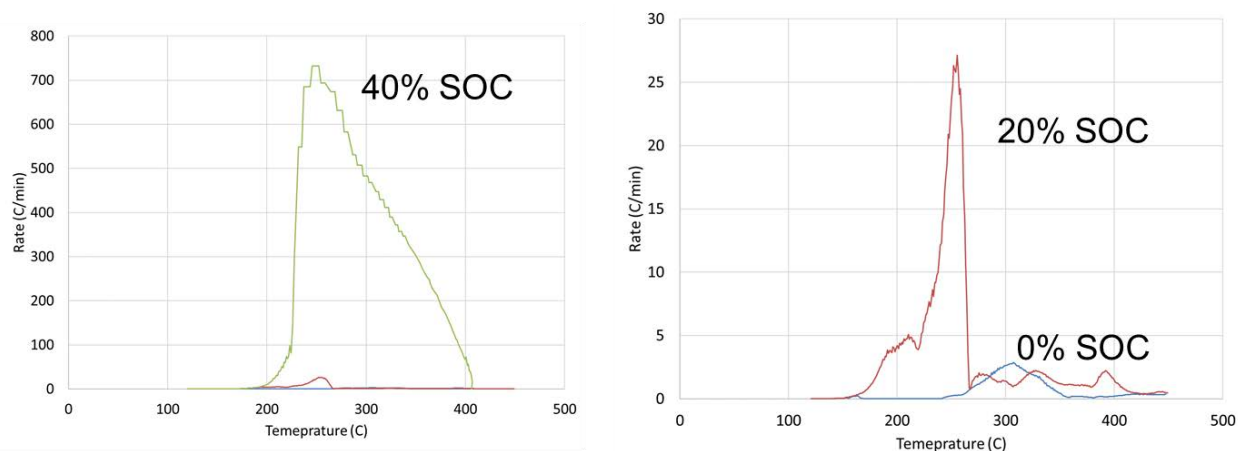


Figure I.7.D.1 Results of increasing SOC within 18650 cells

Comparison of cells of varying size is ongoing, with 15 AH and 10 Ah cells shown in Figure I.7.D.2 below. The kinetics in this case do not show expected patterns with regards to size, with fairly high heating rates observed in both cases. The higher heating rate however was observed in the lower capacity cell, which also had a lower onset of thermal runaway than the larger format cell. This is an early indication that there may be a limit on at least how rapid thermal runaway can occur in large format cells. An evaluation of the total energy of these cells shows a more linear relationship, with the 10 AH cell having a total enthalpy of runaway of ~142 kJ and the 15 AH cell having a total enthalpy of ~189 kJ. While the runaway of the larger cell was at a lower rate, it drove the cell to a significantly higher temperature with the increased energy content.

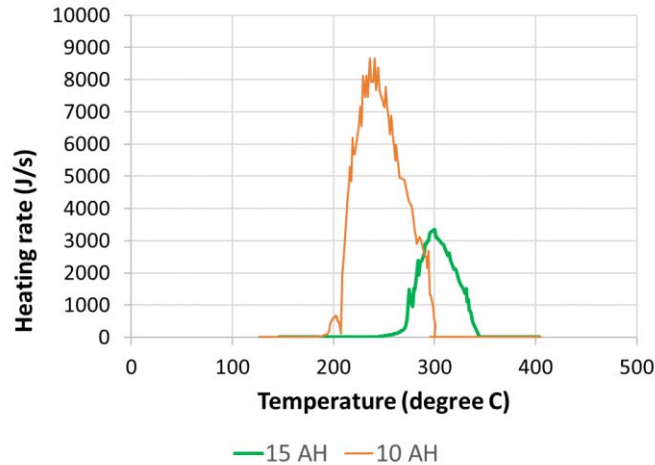


Figure I.7.D.2 Comparison for two cell sizes

To establish the relationship between fast charge and abuse response, we cycled 10Ah commercial off-the-shelf (COTS) cells up to 300 cycles with charge rates of both maximum specification (1C) and 1.5x maximum specification (1.5C). COTS cells were chosen for ease of procurement and cost constraints. Relevancy to automotive cells was established by observing that COTS cells are typically over-designed, thus adverse effects in COTS cells would only be amplified in automotive cells. 1.5C was chosen as the high charge current due to limitations in cell rate capability. Abuse response, voltage profile, and dQ/dV were analyzed to look for effects on abuse response and markers of cell damage.

Figure I.7.D.3 highlights the relationship seen between charge current, cycle number, and overcharge failure SOC. During overcharge tests, it was observed that with increased cycling, cells failed at lower SOC. Some data suggested earlier failure (thermal runaway) with higher charge rate, but the data was not consistent. It should be noted that even after 300 cycles, runaway SOC was still 175%, well beyond the normal stopping point for cell charging. Runaway temperature during overcharge also decreased as cycles increased.

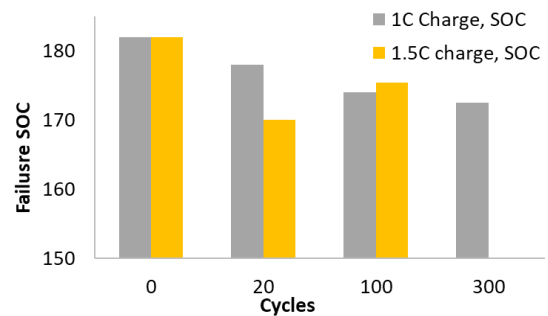


Figure I.7.D.3 Failure SOC during overcharge testing.

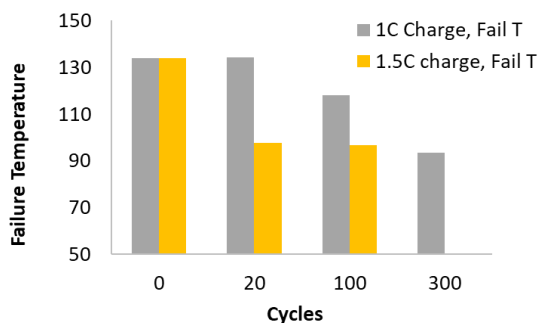


Figure I.7.D.4 Failure temperature during overcharge.

Figure I.7.D.4 shows the effect of cycles and cycling current on failure temperature during overcharge. Like SOC, failure temperature also decreased with higher cycles. There was also a clearer decrease in failure temperature with higher charge rate. The worst case showed runaway at about 90°C, which was a 30% drop in runaway temperature. This suggests that processes within the cell during fast charge are lowering the resistance of the cell, causing less heat to be generated during otherwise comparable degrees of overcharge.

Figure I.7.D.5 shows the effect of fast charge cycles on thermal ramp failure temperature. One outlier was observed but otherwise the failure temperature was unchanged. This further confirms that changes in the cell affected cell resistance, but did not introduce chemical changes such that failure occurred at lower temperature during the ramp.

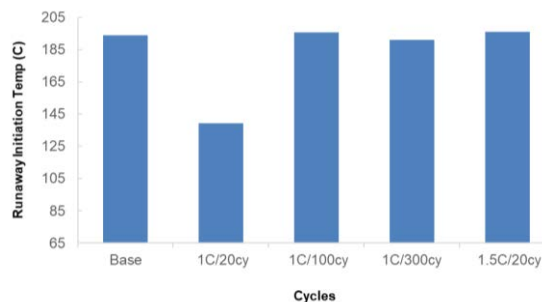


Figure I.7.D.5 Failure temperature during thermal ramp.

dQ/dV analysis (Figure I.7.D.6) reveals a signature process at about 8% SOC; that peak shows a lower dQ/dV energy flux at later cycles for the fast charged cell compared to the base cell, further indicating a general lowering of resistance in the fast charged cell. Also, the fast charged cell shows a second dQ/dV hump about 15-20% SOC not seen at all in the standard-charged cell. This could be sign of a key process that changes the fast charged cell's resistance, and consequently its failure behavior.

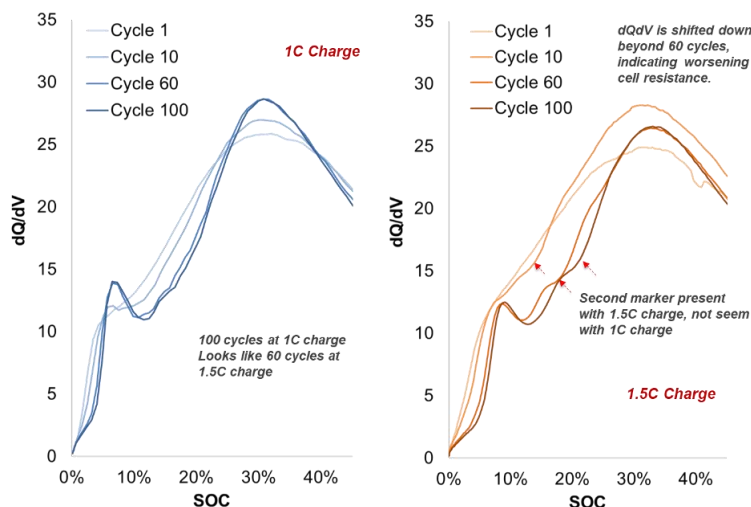


Figure I.7.D.6 dQ/dV vs SOC for cells charged at 1C and 1.5C.

Conclusions

Development and testing of higher energy, larger format cells and modules continues for USABC developers in hopes to meet the EV Everywhere 2022 goals. We provide a means to field the most inherently safe chemistries and designs to help address the challenges in scaling up lithium-ion technologies of interest. This has required careful control and monitoring of tests with the potential of high energy release as well as standing up a larger facility at SNL to support module level testing this FY. This has provided critical information to cell developers to aid in the development of increasingly abuse tolerant cell chemistries and module designs. This independent testing is also necessary to perform objective evaluations of these various designs and chemistries by the DOE and US automobile manufacturers. SNL has completed abuse testing support for all USABC deliverables to date.

The impact of varying energy contents on ARC results was explored to get a better understanding of how to consider the scaling issues around testing of smaller developmental cells. This work explored both varying states of charge as well as cells of various size. Initial work indicates there may be some limitations to the kinetics, that while the increased energy content of large cells provides more energy to thermal runaway, the heating rate will not necessarily increase as a function of cell size. The heating rate however is highly dependent upon state of charge, with elevated states of charge dramatically increasing the likelihood of high rate thermal runaway.

A study of the impact of elevated charge rate cycling was performed as a feasibility study to identify changes to abuse behavior with different charge rates and numbers of cycles. We identified a small lowering of failure SOC and a 30% drop in failure temperature during overcharge., but no effect on failure temperature during thermal ramp. We theorize that this indicates a changing cell resistance during faster charging. This thought is further supported by dQ/dv vs SOC data showing lowered energy of a 10% SOC process and an entirely new process at 15-20% SOC in the faster charged cell. For future work, more robust cells will be used, with a goal of achieving 6C charge rates. dQ/dV will be used to identify markers of lithium plating, and possibly explain the abuse response changes seen in this work.

SNL continues to provide testing support and data to help build and validate models with other national lab partners through the CAEBAT VTO program. Additional abuse testing support for the VTO post mortem program and Si-Deep Dive expanded this year, which included overcharging cells of various chemistries manufactured by ORNL to different states followed by posttest analysis done by ANL. Also, initial abuse testing of Si based cells has been achieved to better understand the safety impacts of this emerging chemistry.

Key Publications

1. Lamb, J. et. Al. “Consequences mitigation and detection of propagating battery failure” MRS Fall Meeting, November 2017
2. Lamb, J. et. Al. “Understanding battery safety through abusive battery testing” Energy Storage Systems Safety and Reliability Forum, March 2018
3. Lamb, J. et. Al. “Battery Safety and Abuse Testing” DOE Vehicle Technologies Annual Merit Review, June 2018
4. Lamb, J. et. Al. “Examining and Controlling the Behavior of Thermal Runaway in Multi Cell Systems” ECS Spring Meeting, May 2018
5. Karulkar, M. et. Al. “Characterization of Abuse Response during Fast Charge of Lithium Ion Batteries” ECS Spring Meeting, May 2018
6. Torres-Castro, L. “Investigations of the structural and electrochemical properties of overcharged Li-ion batteries” ECS Spring Meeting, May 2018
7. Lamb, J. et. Al. “Abuse Testing to Understand High Energy Battery Failure” AABC 2018, June 2018
8. Karulkar, M. et. Al. “Multiscale Battery Diagnostics for Improved Safety and Performance” AABC 2018, June 2018
9. Lamb, J. et. Al. “Evaluating the Impact of Initiation Methods on Propagating Thermal Runaway in Lithium-Ion Batteries” Battery Safety 2018, October 2018

Acknowledgements

Sandia co-authors: Mohan Karulkar, Loraine Torres-Castro, June Stanley, Chris Grosso, Lucas Gray, Christopher Orendorff

National Lab Collaborators: Ira Bloom (ANL), Matt Keyser (NREL), Shriram Santhanagopalan (NREL), Eric Dufek (INL), Lee Walker (INL)

Sandia National Laboratories is a multi-mission laboratory managed and operated by National Technology and Engineering Solutions of Sandia, LLC., a wholly owned subsidiary of Honeywell International, Inc., for the U.S. Department of Energy’s National Nuclear Security Administration under contract DE-NA0003525.

I.7.E Battery Thermal Analysis and Characterization Activities (NREL)

Matthew Keyser, Principal Investigator

National Renewable Energy Laboratory
15013 Denver West Parkway
Golden, CO 80401
E-mail: Matthew.Keyser@nrel.gov

Samuel Gillard, DOE Technology Development Manager

U.S. Department of Energy
E-mail: Samuel.Gillard@ee.doe.gov

Start Date: October 1, 2017

End Date: September 30, 2018

Project Funding (FY18): \$500,000

DOE share: \$500,000

Non-DOE share: \$0

Project Introduction

While EDVs promise to curb America’s need for imported oil, designing high-performance, cost-effective, safe, and affordable energy-storage systems for these cars can present challenges, especially in the critical area of battery thermal control. As manufacturers strive to make batteries more compact and powerful, knowing how and where heat is generated becomes even more essential to the design of effective thermal-management systems. NREL’s thermal characterization activities provide developers, manufacturers and OEMs with the knowledge necessary to assure that batteries are designed to perform strongly, last a long time, and operate at maximum efficiency.

The Vehicle Technologies Office has a goal to reduce the cost of electric vehicle battery packs by 2022 to less than \$150/kWh with technologies that significantly reduce or eliminate the dependency on critical materials (such as cobalt) and utilize recycled material feedstocks [1]. In order to meet these metrics, the battery packs will need to have higher energy densities resulting in a very compact system. Even if the energy efficiency of the next generation of batteries increases, because of the compactness of these batteries more heat is being generated per unit volume with less heat transfer area. Thus, more advanced heat rejection systems are needed to keep the battery temperatures in the “goldilocks” zone that prevents acceleration of the aging mechanisms within the battery.

The chemistries of advanced energy-storage devices—such as lithium-based batteries—are very sensitive to operating temperature. High temperatures degrade batteries faster while low temperatures decrease their power and capacity, affecting vehicle range, performance, and cost. Understanding heat generation in battery systems—from the individual cells within a module, to the inter-connects between the cells, and across the entire battery system—is imperative for designing effective thermal-management systems and battery packs.

Inadequate or inaccurate knowledge of the thermal characteristics of batteries makes it difficult to design effective thermal-control systems. This can negatively affect lifespan, safety, and cost, ultimately resulting in negative consumer perception and reduced marketability. In 2012, Nissan had to address problems with the battery for its Leaf fully-electric vehicle (EV) losing capacity in the hot Arizona climate. Many attributed this issue to inadequate battery-thermal management.

Accurately measuring battery thermal performance under various electrical loads and boundary conditions makes it possible for battery-system engineers to design effective thermal-management systems. NREL, with the funding from DOE VTO, has developed unique capabilities to measure the thermal properties of cells and evaluate thermal performance of active, air, and liquid cooled battery packs. Researchers also use electro-thermal finite element models to analyze the thermal performance of battery systems in order to aid battery developers with improved thermal designs. In addition, our lumped capacitance multi-node battery-vehicle-ambient model can predict the temporal temperature of batteries as a function drive cycle, ambient

temperature, and solar radiation. These one-of-a-kind tools allow NREL to work with the battery manufacturers and OEMs to meet stringent EDV life, performance, cost, and safety goals

Objectives

- Thermally characterize battery cells and evaluate thermal performance of battery packs provided by USABC developers.
- Provide technical assistance and modeling support to USDRIVE/USABC and developers to improve thermal design and performance of energy storage systems.
- Evaluate extreme fast charging effects on battery thermal performance.
- Quantify the impact of temperature and duty-cycle on energy storage system life and cost.
- Address high energy storage cost due to battery packaging and integration costs
- Reduce the cost, size, complexity, and energy consumption of thermal management systems
- Optimize the design of passive/active thermal management systems—explore new cooling strategies to extend the life of the battery pack.

Approach

NREL has measured the thermal properties of the cells and batteries with many different chemistries (lead acid, NiMH, and many versions of lithium cells) through heat generation, heat capacity, and infrared thermal imaging; conducted performance thermal testing of battery and ultracapacitor modules and packs; analyzed the thermal performance of cells and modules; and developed thermal models. Researchers perform thermal testing, analysis, and modeling (1) to assist DOE/USABC battery developers in designing cells/modules/packs for improved thermal performance, and (2) to evaluate and validate the thermal performance of cell/module/pack deliverables from DOE/USABC battery developers and suppliers.

NREL's equipment can benchmark how changing the design of the cell using a different cathode, anode, current collector, electrolyte, additive, or separator affects the overall performance of the cell. The information garnered from these tests helps battery and advanced vehicle manufacturers improve their designs, while providing critical data for the development of thermal management systems that will reduce the life-cycle cost of battery systems. Using NREL's unique R&D 100 Award-winning calorimeters and infrared thermal imaging equipment, we obtain thermal characteristics of batteries and ultracapacitors developed by USABC battery developers and other industry partners. NREL supports the Energy Storage Technical Team by participating in various work groups such as the Amprius, Zenlabs, Saft, Farasis, 24M and USABC Working Groups.

Results

The following narrative outlines some of the more interesting insights garnered from NREL's testing over the past year. The outline below is not meant to be an exhaustive study of NREL's work but rather to help the reader understand how NREL's unique thermal characterization technologies are used to improve the energy storage technologies in conjunction with industry and USABC.

Calorimeter Testing

Figure I.7.E.1 shows an efficiency summary of cells tested at NREL at a calorimeter temperature of 30°C. The lithium ion cells were fully discharged from 100% SOC to 0% SOC under a C/2, C/1, and 2C currents. It should be noted that the cells in the figure are for both power and energy cells and have been developed for HEV, PHEV, EDV, and/or the 12 Volt Start/Stop programs within USABC. The graph indicates that the HEV power cells are the most efficient due to the use of thinner electrodes and that lithium titanate oxide (LTO) anodes are among the most efficient anodes on the market today. The next efficiency grouping of cells

involves the state-of-the-art PHEV and EV NMC/Graphite cells. Over the discharge c-rates tested, the efficiency of these cells is between 97% and 93%. Finally, the least efficient cells are those that combine higher energy NMC/MCN materials with a silicon anode. The high silicon content cells approach discharge efficiencies of 78% at a 2C discharge rate – much below industry state-of-the-art cells. The silicon and silicon blended cells were designed with energy density as a primary consideration contributing to these systems having slightly lower efficiencies. Even after adjusting for the electrode thickness, the general trend still shows that the stable structure of LTO systems allows for higher energy efficiencies and confirms that the silicon systems may require improvements with regards to their electrical conductivity when used under conditions such as fast charge. DOE and USABC are investigating each of these chemistries to improve energy density, power density, cycle life and/or cost benefits. NREL's calorimeters provide the fundamental understanding of whether the inefficiencies shown below are due to chemistry or cell design.

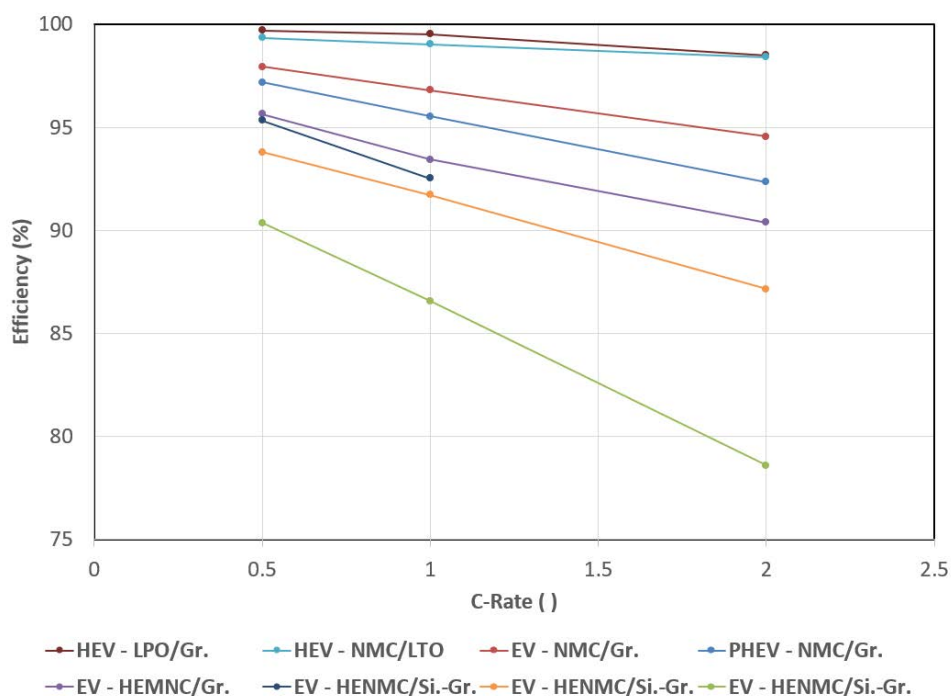


Figure I.7.E.1 Efficiency summary of cells tested at 30 °C in NREL's calorimeters. Caption Credits/Source: NREL- Aron Saxon

Figure I.7.E.2 shows the full charge and discharge efficiencies of a blended silicon cell tested at NREL – the anode silicon percentage for this cell is greater than 50%. The data trends indicate that the discharge and charge efficiencies are approximately equivalent when the cell is new. For a C/1 charge and discharge current, the efficiency is approximately 93% for the fresh cell. For comparison, state-of-the-art commercially available cells typically have C/1 charge and discharge efficiencies greater than 98%. After the cells are aged with approximately fifty C/3 charge/discharge cycles, the charge and discharge efficiencies drop to below 87% - on par with NiMH technologies. It should be noted that the aged cell under charge has slightly higher efficiencies as compared to discharge. Under a CC/CV charge, the charge current tapers at the end of charge decreasing the RMS current for the cycle. Nonetheless, the expansion and contraction of the silicon anode affects not only the life but the electrical and ionic diffusion pathways within the cell.

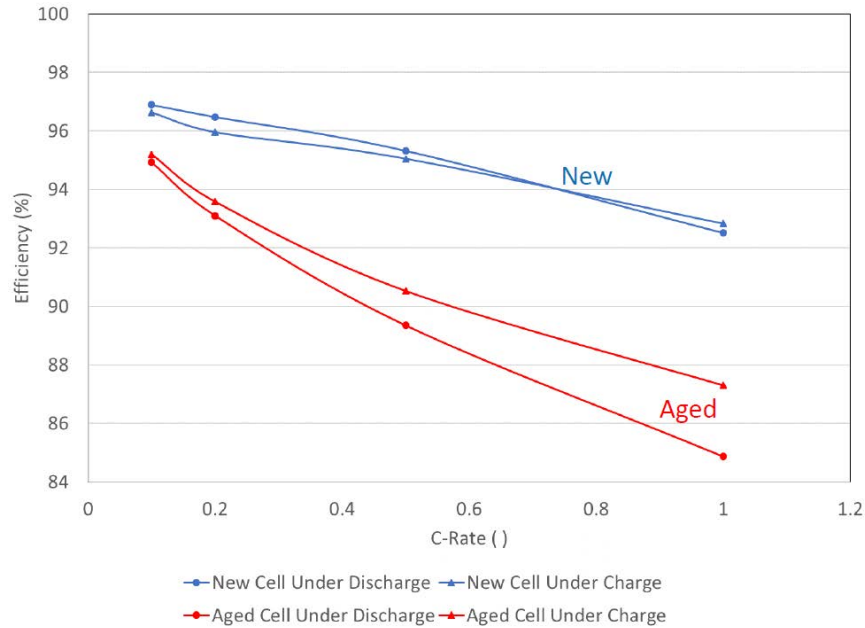


Figure I.7.E.2 Efficiency of silicon blended cells tested at 30 °C in NREL's calorimeters under various charge/discharge currents.

Caption Credits/Source: NREL- Aron Saxon

NREL's calorimeters were designed to be accurate enough to measure the electrochemical response from batteries under test – this capability allows NREL to understand benefits associated with design and chemistry changes to the cell. Figure I.7.E.3 shows the entropic heat generation rates normalized to the Ah capacity of the cell for two different cathodes – NCM – 1:1:1 and high nickel content NCM - at 30°C and under a constant current charge. The cells in this figure were cycled over their entire state-of-charge range at a very low current – minimizing the current decreases the joule heating of the cell and allows for the entropic heat signature to be assessed. As shown in the figure, the cells can undergo endothermic and exothermic heat generation over the cycling range. The endothermic/exothermic heat signatures from the two versions of the cell are primarily due to the electrochemical (phase) changes in the anode. However, the cathode material also has effects on the entropic signature of the cell. In particular, the endothermic response at the beginning of charge for the high nickel content NCM is reduced and even minimized when compared to the NCM – 1:1:1 cathode material. Furthermore, the heat generation of the cells decrease after about 60% SOC for both NCM versions even though the charge current remains constant. When the current is minimal, the entropic response dominates despite the impedance increase at higher states-of-charge. The entropic testing can provide insights into the chemical processes occurring within the cell for different materials and additives.

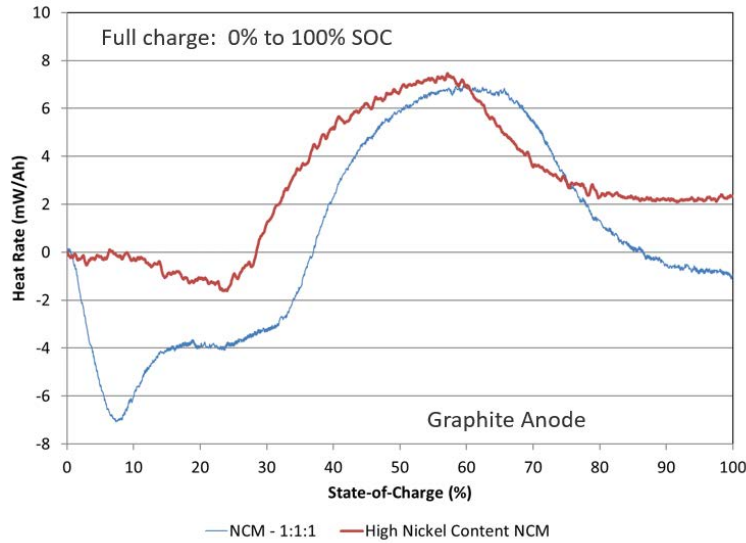


Figure I.7.E.3 Entropic response to NCM – 1:1:1 and high nickel content NCM cathodes paired with a graphite anode.
Caption Credits/Source: NREL- Aron Saxon

Module efficiencies can be heavily influenced by the interconnect design. To understand the heat generation in a module due to the battery interconnects, the heat generation of a single cell was measured and compared the heat generation of a 10-cell module when using the same cell. The module was designed for high power applications and the cells are power cells with a power-to-energy ratio of greater than 10 – the power-to-energy ratio is defined as the maximum battery power for a known period divided by the overall energy stored in the battery. Figure I.7.E.4 shows an efficiency comparison between a single cell and the efficiency for the module at various charge currents – the difference in the efficiency is due to the interconnects between the cells in the module. In this module, the interconnects are well designed – the efficiency varies by less than 1% at the 4C charge rate. An interconnect design optimized for high power/current can minimize the heat from ancillary sources and limits safety concerns for future extreme fast charging applications.

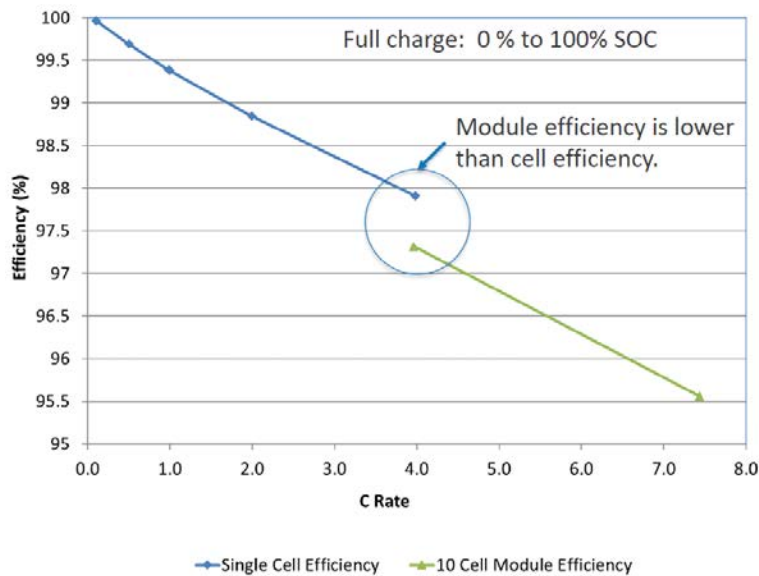


Figure I.7.E.4 Efficiency comparison of a single cell compared to a 10-cell module at 30°C.
Caption Credits/Source: NREL- Aron Saxon

Infrared Imaging of Cells

NREL performs infrared (IR) thermal imaging of battery manufacturer’s cells to determine areas of thermal concern. We conduct IR thermal imaging under a set of prescribed procedures and environments to minimize the error from different sources such as reflective cell surfaces, radiation from surrounding surfaces, and cooling from the power cables attached to the cell. NREL combines the IR imaging equipment with a battery cycler to place the cells under various drive cycles, such as a US06 charge depleting cycle for a PHEV, to understand the temperature differences within the cell. We then make recommendations to the battery manufacturers and USABC on how to improve the thermal design of the cell to increase its cycle life and safety.

Figure I.7.E.5 shows a lithium battery at the end of a 2C discharge. Each IR image has a temperature spread associated with it – by decreasing the temperature spread a visual reference can be used to determine where the heat is preferentially being generated within the cell. For this cell, the heat generation is biased towards the top between the two terminals. The point of thermal concern on this cell is due to a unique tab welding technique that was being used to reduce cost. During the IR imaging, we also assess the temperature uniformity across the cell surface. When the cell temperature is not uniform and consistent, individual cells within modules and packs age differently affecting the cycle life of the module. NREL is working with battery developers to understand how temperature non-uniformities affect the efficiency and cost of the cell over its life.

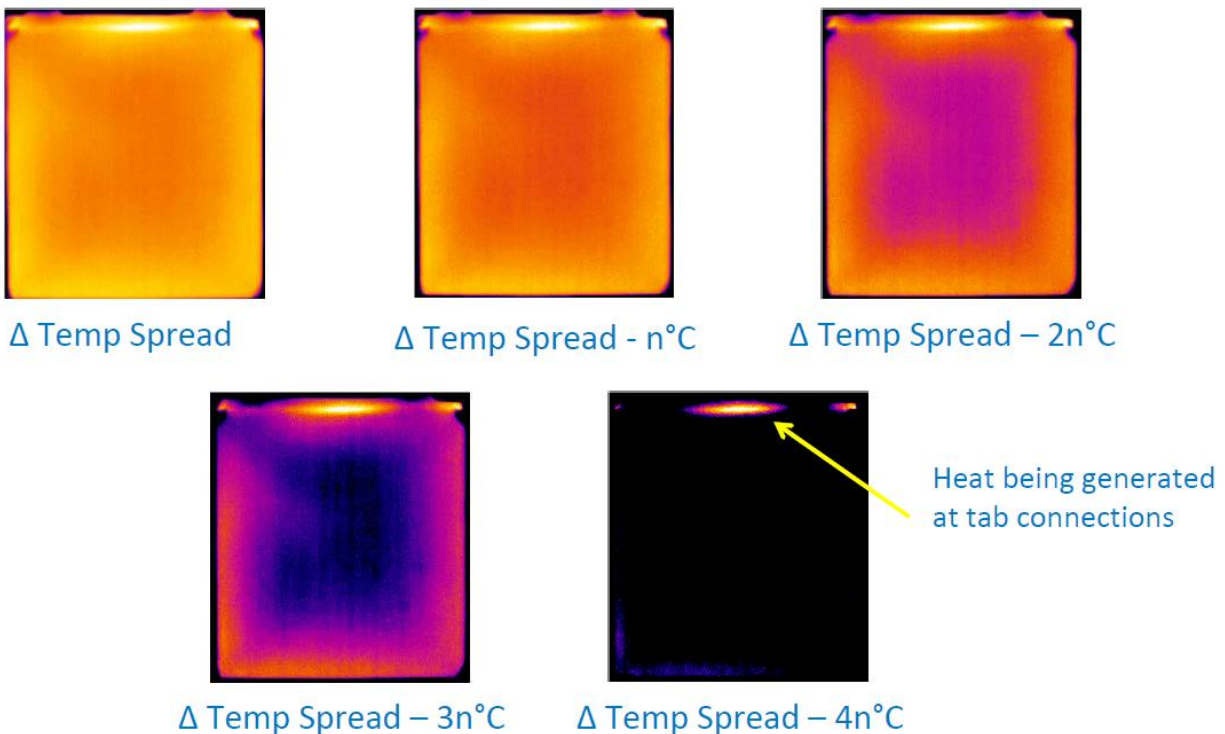


Figure I.7.E.5 Infrared image of lithium battery cell at the end of a 2C discharge.
Caption Credits/Source: NREL- Aron Saxon

Conclusions

NREL has thermally tested cells and modules from Amprius, Zenlabs, Saft, Farasis, and 24M during FY18. We’ve provided critical data to the battery manufacturers and OEMs that can be used to improve the thermal design of the cell, module, pack and their respective thermal management systems. The data included heat generation of cells under typical profiles for HEV, PHEV, EV, and 12 Volt Start/Stop applications, which is essential for designing the appropriately sized battery thermal management system. In FY19, NREL will

continue to thermally characterize cells and modules for USABC, DOE, and USDRIVE but the focus will shift to fast charging applications and the heat generation differences between chemistries.

Key Publications

1. 2018 DOE Annual Peer Review Meeting Poster on Battery Thermal Analysis and Characterization Activities
2. Quarterly meeting presentations to the battery working group and manufacturers.

References

1. David Howell, Electrochemical Energy Storage R&D Overview, Annual Merit Review, Washington DC, 2018

Acknowledgements

We wish to acknowledge Samm Gillard and DOE for sponsoring these efforts. We would also like to acknowledge the co-authors of this report – Aron Saxon, Ying Shi, and Thomas Bethel.

I.7.F Cell Analysis, Modeling, and Prototyping (CAMP) Facility Research Activities (Argonne National Laboratory)

Andrew N. Jansen, Principal Investigator

Argonne National Laboratory
9700 S. Cass Ave
Lemont, IL 60439
E-mail: Jansen@anl.gov

Peter Faguy, DOE Technology Development Manager

U.S. Department of Energy
E-mail: Peter.Faguy@ee.doe.gov

Start Date: October 1, 2014	End Date: September 30, 2019	
Project Funding (FY18): \$1,400,000	DOE share: \$1,400,000	Non-DOE share: \$0

Project Introduction

The “valley of death” is a phrase often used to describe the path a new discovery must traverse to become a commercial product. This is especially true for novel battery materials invented in research laboratories around the world. Often researchers are resource limited and are only able to make gram quantities of their new material. The CAMP Facility is appropriately sized to enable the design, fabrication, and characterization of high-quality prototype cells using just a few hundred grams of the latest discoveries involving high energy battery materials. Prototype cells made in the CAMP Facility generally have 400-mAh capacity, which straddles the gap between coin cells and industrially-sized cells nicely – two orders of magnitude from each end point. Thus, a realistic and consistent evaluation of candidate chemistries is enabled in a time-effective manner with practical quantities of novel materials in cell formats commonly used in industry.

The CAMP Facility is an integrated team effort designed to support the production of prototype electrodes and cells, and includes activities in materials validation (benchmarking), modeling, and diagnostics. It is not the aim of this facility to become a small battery manufacturer, but instead to be a laboratory research facility with cell production capabilities that adequately evaluate the merits and limitations of new lithium-ion chemistries in a close-to-realistic industrial format. The source of these materials (anodes, cathodes, electrolytes, additives, separators, and binders) may originate from the ABR and BMR Programs, as well as from other domestic and foreign organizations such as universities, national labs, and industrial vendors. Electrochemical couples with high power and energy density are given extra priority. Lately efforts have focused on silicon-based anodes, and nickel-manganese-cobalt (NMC) cathodes that are high in nickel and operating at higher potentials.

The CAMP Facility has the capability to make three prototype cell formats in their 45 m² dry room: pouch cells (xx3450 format, with capacity around 0.5 Ah; and xx6395, with capacity around 2 Ah) and 18650 cells (with capacity around 2 Ah). Pouch cells are generally easier to assemble, and are a great indicator of gassing problems in a cell during cell aging and cycling. Central to this effort is a pilot-scale coating machine that operates with slurry sizes that range from 20 grams to a couple kilograms. This is a key feature of the CAMP Facility that enables a professional evaluation of small quantities of novel materials. If needed, the Materials Engineering Research Facility (MERF) is available for scaling up materials for these prototype cell builds.

Objectives

The objective of this core-funded effort is to design, fabricate, and characterize high-quality prototype electrodes and cells that are based on the latest discoveries involving high energy anode and cathode battery materials. Using this multi-disciplined facility, analytical diagnostic results can be correlated with the electrochemical performance of advanced lithium-ion battery technologies for electric vehicle (EV) applications.

- Link experimental efforts through electrochemical modeling studies.
- Identify performance limitations and aging mechanisms.
- Support lithium-ion battery projects within the DOE-EERE-VTO

Approach

The general approach used in this effort is to start small and grow large in terms of cell size and amount of resources devoted to each novel battery material. At various points in the development process, decisions are made to either advance, modify, or terminate studies to maximize utilization of available resources.

Coin cells (2032 size) are used for materials validation purposes with initial studies performed at 30°C. After formation cycles, the coin cells go through rate capability testing, HPPC testing, and limited cycle life testing. Additional temperatures and test conditions are employed if warranted.

Using the results obtained by the materials validation of promising materials, single-sided electrodes are fabricated on the larger dry-room coater for diagnostic study. The new cell chemistries are studied in detail using advanced electrochemical and analytical techniques, including the employment of micro-reference electrode cells. Factors are identified that determine cell performance and performance degradation (capacity fade, impedance rise) on storage and on extensive deep-discharge cycling. The results of these tests are used to formulate data-driven recommendations to improve the electrochemical performance/life of materials and electrodes that will be incorporated in the prototype cells that are later fabricated in the dry room. This information also lays the foundation for electrochemical modeling focused on correlating the electrochemical and analytical studies, in order to identify performance limitations and aging mechanisms.

If the results from diagnostics and modeling still look promising, full cell builds are conducted using double-sided electrodes. The electrodes are then either punched in the case of pouch cells, or slit in the case of 18650 cells and assembled into full cells in the dry room using semi-automated cell assembly equipment. Formation procedures are conducted on the cells to encourage electrolyte wetting and uniform solid-electrolyte-interface (SEI) formation. These cells undergo rigorous electrochemical evaluation and aging studies under the combined effort of the CAMP Facility team, and Argonne's Electrochemical Analysis and Diagnostic Laboratory (EADL) and Post-Test Facility. After testing, select cells are destructively examined by the Post-Test Facility to elucidate failure mechanisms. This information is then used to further improve the new chemistry, as well as future electrode and cell builds.

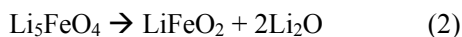
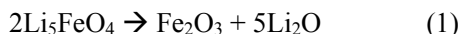
Results

The CAMP Facility is designed to work closely with materials researchers across the many electrochemical energy storage programs throughout the DOE-EERE-VTO. In addition to its own yearly R&D tasks, it actively coordinates its efforts to provide support to other national lab teams such as: the High-Energy High-Voltage, the Next Generation Anodes, Fast Charge (XFC/XCEL), and the CAEBAT programs. The Materials Benchmarking Activities (Section II.H.2) is a segment of the CAMP Facility. The CAMP Facility also complements the capabilities of other DOE support facilities such as: the Materials Engineering Research Facility (MERF - ANL), the Post-Test Facility (PTF - ANL), the Battery Abuse Testing Lab (BATLab - SNL), and the Battery Manufacturing Facility (BMF - ORNL). More information about these projects can be found in the relevant chapters and sections of this annual report. The remainder of this CAMP Facility section will discuss the results of the CAMP Facility deliverables for FY18, and include results of related topics.

Develop Methods to Fabricate Pre-lithiated High-Energy Electrode Couples

Li_5FeO_4 has been synthesized in our lab and investigated as a cathode prelithiation reagent. Li_5FeO_4 possesses a theoretical capacity of 867 mAh/g and potentially can release up to 5 lithium ions per mole to the cell upon the first charge via reaction (1), but it was found that the practical limit is 4 lithium ions via reaction (2) (see ref [1]). An advantage of LFO is that unlike some prelithiation reagents which may only work with certain

cathode active materials (such as Li_2O_2 , which requires the catalytic surface of NCM to obtain lithiation at a reasonable voltage), LFO appear to work well with different cathode active materials.



In this work, we demonstrate the use of Li_5FeO_4 in addressing the irreversible capacity loss of silicon monoxide (SiO). Li_5FeO_4 was mixed with $\text{LiNi}_{0.5}\text{Co}_{0.2}\text{Mn}_{0.3}\text{O}_2$ (NCM523) cathode materials. The resulting cathode was then paired with a SiO anode. The impact of Li_5FeO_4 addition on the electrochemical performance of the cell was then carefully analyzed.

Figure I.7.F.1 compares the first cycle voltage profiles and cycle performance of SiO/NCM523 and SiO/NCM523-LFO full cells. The specific capacity of SiO/NCM523-LFO full cells shown in Figure I.7.F.1 is based on the weight of NCM523-LFO blend. As shown in Figure I.7.F.1a, comparative to SiO/NCM523, SiO/NCM523-LFO shows an increased first cycle charge and discharge capacity. Figure I.7.F.1b compares the complete electrochemical performance for SiO/NCM523 and SiO/NCM523-LFO full cells. Fast capacity fade in the initial three formation cycles was observed for both SiO/NCM523 and SiO/NCM523-LFO. The fast capacity fade of SiO electrodes in the initial cycles can be attributed to the capacity loss from incomplete delithiation of SiO due to large volume change during cycling. As the SiO anode stabilizes, the capacity retention of the cells improve. During the cycle test, SiO/NCM523 showed a capacity retention of 90.94% for 50 cycles, while the addition of LFO improved the capacity retention to 98.93% for 50 cycles.

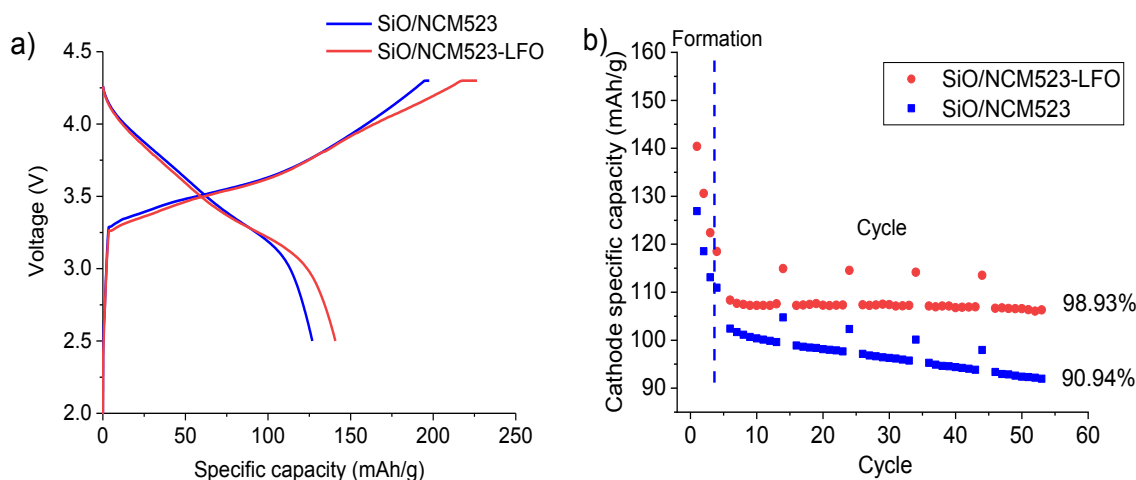


Figure I.7.F.1 a) Voltage profile comparison and b) cycle performance comparison of NCM523/SiO and NCM523-LFO/SiO. The capacity of SiO/NCM523-LFO full cells are calculated based on the total weight of NCM523-LFO blend.

Develop Methods to Direct Coat Ceramics onto Lithium-Ion Electrodes

Lithium-ion batteries have steadily advanced over the last three decades with great advancements in energy density and cycle life, while still maintaining acceptable safety tolerances. Further advances will continue to rely on creative uses of materials' properties such as developing multi-layer electrode-separator systems. These systems could: potentially replace the polymer separator, improve the safety of the cell, reduce or minimize the effects of electrolyte decomposition products, suppress lithium dendrite formation and eventually lead to a fully solid state battery. In FY18, one of the CAMP Facility's tasks was to start to explore the processing of ceramic coatings on electrodes and to determine their electrochemical stability under various cycling conditions. A variety of ceramic materials were selected as possible candidates due to their refractory and insulating properties. These materials (see Table I.7.F.1) were mainly oxides, silicates and nitrides.

The anode used in this work was from CAMP Facility's Electrode Library, S-A001, which has a formulation of 89.8 wt% Phillips66 A12 graphite, 4 wt% Timcal Super P Li carbon black, 6 wt% Kureha 9300 PVDF, and 0.17 wt% oxalic acid, with a coating loading of 6.06 mg/cm². This electrode was calendered to a thickness of 42 microns (26 % porosity). Small batches of slurries were made with a composition of 95 wt% ceramic particles and 5 wt% Solvay 5130 PVDF binder for each ceramic and then hand coated onto the graphite anode sheet. The wet gap of the hand coater was set at 50 microns. The electrodes were then lightly calendered to ensure that the ceramic coating was bonded to the graphite and to reduce the porosity of ceramic layer.

Table I.7.F.1 Ceramic Materials Coated on Graphite Anode

Electrode	Foil Thickness (microns)	Graphite Thickness (microns)	Ceramic Coating Thickness (microns)	Total Thickness (microns)	Graphite Loading (mg/cm ²)	Ceramic Coating Loading (mg/cm ²)
Baseline Graphite	10	42	0	52	6.06	0
Zirconium (IV) Oxide			35	87		9.27
Aluminum Silicate (Mullite)			40	92		5.55
Zirconium(IV) Silicate			33	85		5.67
Boron Nitride			36	88		3.64
Aluminum Oxide (10um)			36	88		7.06
Aluminum Nitride			33	85		5.60
Ohara Glass LICGC			27	79		4.89
Aluminum Oxide (Comma Coated)			25	77		4.29
Magnesium Oxide (Comma Coated)			24	76		2.51

Two materials (aluminum oxide and magnesium oxide) were selected to do further process development work using our pilot-scale reverse-comma coater to see if we could better control the ceramic coating loading. While a better coating was achieved, the resulting process abraded the steel coating roll during the transfer of the ceramic slurry onto the electrode. Even though this method did produce a thin and consistent coating on the graphite electrode, it was decided that the damage to the coater was not acceptable. New coating methods such as gravure, knife-over-roll, spray, and slot die are now being considered.

After the electrodes were coated, SEM images of the electrode surface and the cross section were taken of each ceramic-coated electrode. The surface SEM images indicated that the surface was completely covered and that there was no exposed graphite particles. Electrodes were then punched for an xx3450-sized pouch cell for each ceramic-coated electrode (see Figure I.7.F.2). These electrodes were assembled into single layer pouch cells with a capacity-matched NMC532 cathode and cycled between 3 to 4.1 V. In all of these pouch cells a single layer of Celgard 2325 separator was used between the ceramic-coated graphite and the NCM523 cathode electrode as a precaution against possible shorting. The pouch cells went through Formation, Rate, HPPC, and then Cycle Life Testing. All of the ceramic-coated cells made it through the Formation, Rate, and HPPC test, with the only exception being the Ohara LICGC material. These cells started to fade during the formation process for reasons that are not fully understood at this time - further analysis is needed.



Figure I.7.F.2 Punched electrodes of ceramic-coated graphite anode.

These single-layer pouch cells were cycled between 3 and 4.1 V using a protocol that consisted of one cycle at C/20 followed by 47 cycles at C/2 charge & discharge, and then one HPPC test. This series is repeated until the cells reach 80% capacity fade. The HPPC test was performed approximately every 50 cycles to track the impedance of the cells as they age. The results of these tests are shown in Figure I.7.F.3. The baseline cell (plain graphite) had an initial (cycle 50) impedance of ~20 ohm-cm² and all of the ceramic-coated electrodes had an impedance slightly higher. We observed that the Ohara LICGC coated electrode had high initial impedance and low capacity. The zirconium (IV) oxide sample had a higher impedance but this is most likely due to the higher ceramic loading on the graphite electrode (see Table I.7.F.1). Additionally, because the capacity fade rate and impedance response is similar to the baseline cell, we do not believe that the majority of these ceramic materials are reacting or decomposing at this stage of exploration.

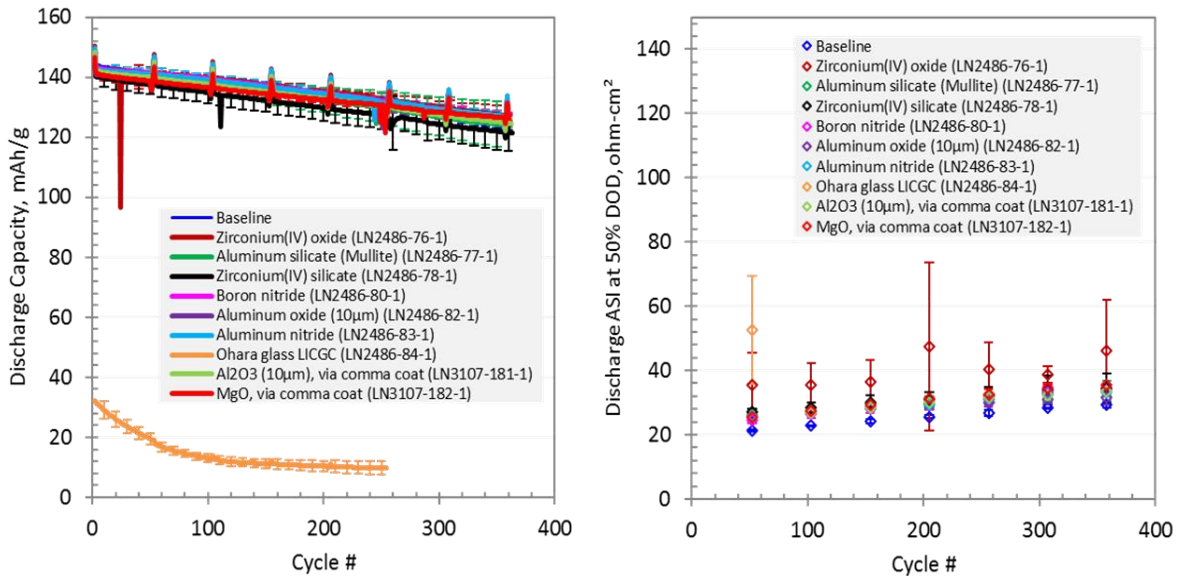


Figure I.7.F.3 Cycle Life (left) and HPPC ASI at 50% SOC (right) for the ceramic-coated graphite electrodes evaluated in xx3450 single-layer pouch cells.

Aluminum oxide (10 micron) and magnesium oxide were selected for further study in a cell system with no polymer separator. In this study the anode used was from CAMP Facility's Electrode Library, A-A002B. This has a formulation of 91.8 wt% Phillips66 A12 Graphite, 2 wt% Timcal C45 carbon black, 6 wt% Kureha 9300 PVDF, and 0.17 wt% Oxalic Acid with a coating loading of 6.07 mg/cm². This electrode was calendered to a coating thickness of 43 microns (34.5 % porosity). These two ceramic materials were coated on this graphite electrode and lightly calendered as before. Table I.7.F.2 summarizes these three electrodes.

Table I.7.F.2 Al₂O₃ and MgO Coated on Graphite Anode for Separator-free Cell Study

Electrode	Foil Thickness (microns)	Graphite Thickness (microns)	Ceramic Coating Thickness (microns)	Total Thickness (microns)	Graphite Loading (mg/cm ²)	Ceramic Coating Loading (mg/cm ²)
Baseline Graphite	10	43	0	53	6.07	0
Aluminum Oxide (10um)			40	93		5.82
Magnesium Oxide			25	78		2.12

CR2032 coin cells were made with the baseline graphite and these two ceramic-coated anodes to test the feasibility of using ceramic coatings in-place of the traditional polyolefin/polymer separator. The baseline graphite cell used a Celgard 2325 separator, while the two ceramic-coated graphite cells did not have a separator. These cells were then tested as above, but under two voltage conditions, 3-4.1 V and 3-4.4V, to examine the stability of the ceramic coating. Figure I.7.F.4 shows the performance of the three cell sets at 3-4.1V, and Figure I.7.F.5 shows the performance for the cell set cycled between 3 to 4.4 V. Note that in the higher voltage cell sets, a lower mass-loading NMC532 cathode was used to maintain a consistent n:p ratio.

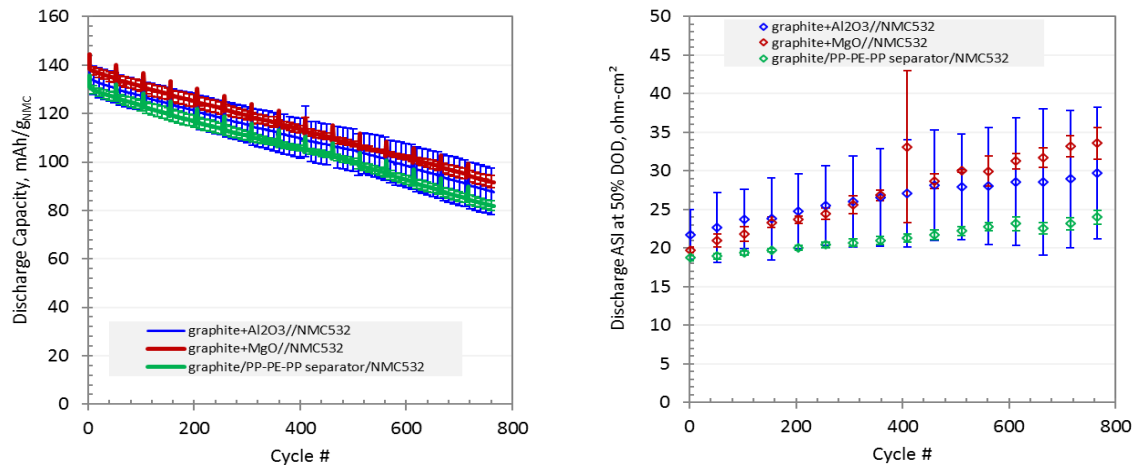


Figure I.7.F.4 Cycle Life (left) and HPPC ASI at 50% SOC (right) for the ceramic-coated graphite electrodes evaluated in coin cells in separator-free study for 3-4.1 V window.

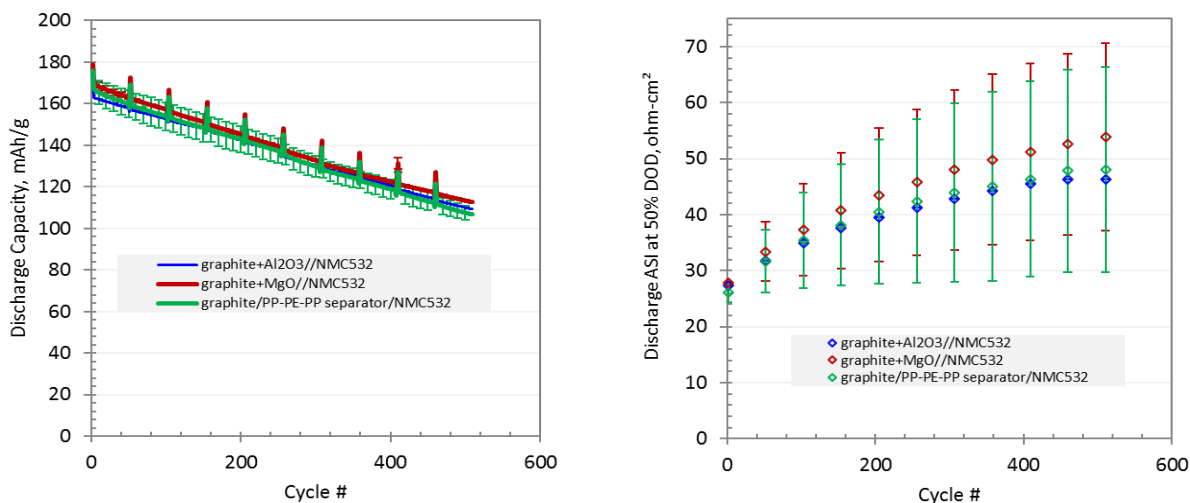


Figure I.7.F.5 Cycle Life (left) and HPPC ASI at 50% SOC (right) for the ceramic-coated graphite electrodes evaluated in coin cells in separator-free study for 3-4.4 V window.

From these studies, it can be concluded that the ceramics coated directly onto a graphite electrode can provide electrical insulation for necessary separation from the positive electrode, while still achieving similar performance of a typical polymer separator-containing cell. In fact, in this case the ceramic-coated anodes with no separator had slightly better capacity retention than the baseline graphite/separator/NMC523 cells. Looking further at the HPPC data, one might speculate that the aluminum oxide and magnesium oxide coatings increase the impedance of the cells slightly. Nevertheless, it is worth expanding this effort but with better roll-to-roll coating systems.

Use Raman Spectroscopy to Examine (In)Homogeneity in Pristine and Cycled Oxide Electrodes

Typically, Raman spectroscopy of lithium-ion cell electrodes are conducted in the top-down mode. In this approach, one obtains information mainly from the electrode surface because of the limited penetration depth of the excitation wavelength (in the range of a few microns). In contrast, micro-Raman measurements conducted on ion-milled electrode cross-sections provide information from regions that span the full thickness of the electrode. Here, we present data from two $\text{LiNi}_{0.5}\text{Co}_{0.2}\text{Mn}_{0.3}\text{O}_2$ (NMC523) samples: (a) a pristine electrode, which was never exposed to an electrolyte, and (b) an aged electrode, from a NMC523/graphite full cell that underwent 400, 3.0-4.4 V cycles at 30°C.

Whole-area Raman maps of the pristine laminate and the aged electrode are presented in Figures H.1.6a and 6b, respectively. The color image to the right of the white light image shows where the “Spot 2”, “Spot 15”, and “Spot 60” spectra in Figure I.7.F.6c were obtained. Spectra throughout the green colored areas are like that of Spot 15, which are at the centers of NMC523 agglomerates. Spectra in the magenta areas are like that of Spot 60, which is characteristic for the C45 carbon. Spectra in the dark areas (e.g. Spot 2) are mainly a mix of the Spot 15 and Spot 60 spectra, indicating an overlap of the NMC523 particles and the carbon-containing matrix.

In Figure I.7.F.6b the boxed rectangle reveals the location of a whole-area map of the aged electrode. The red areas and green areas in the color image (Figure I.7.F.6d) are characterized, respectively, by spectra (1) and (2) in Figure I.7.F.6e. It is noteworthy that the red and green areas in Figure I.7.F.6d comprise mostly a single large NMC523 aggregate. The spectral differences between the part of this aggregate closest to the electrode surface and the part closest to the interior of the cross-section indicate that even within a single secondary particle aggregate there can be composition differences for the aged electrodes. Clearly, the NMC523 oxide in the aged/discharged electrode has not been restored to the same chemical state present in the pristine laminate and there is localized compositional variability even across a single large secondary particle aggregate. The data from the highly aged electrodes indicate that the oxide particles near the electrode surface (closest to the

separator) have relatively low Li^+ contents compared to those deeper into the electrode. We propose that the highly-delithiated particles, which are near the electrode surface, have very high impedance and respond very slowly during cell cycling, i.e., they are effectively “dead” except at very slow cycling rates. In contrast, the oxide particles, deeper in the electrode, have lower impedance and still accept Li^+ .

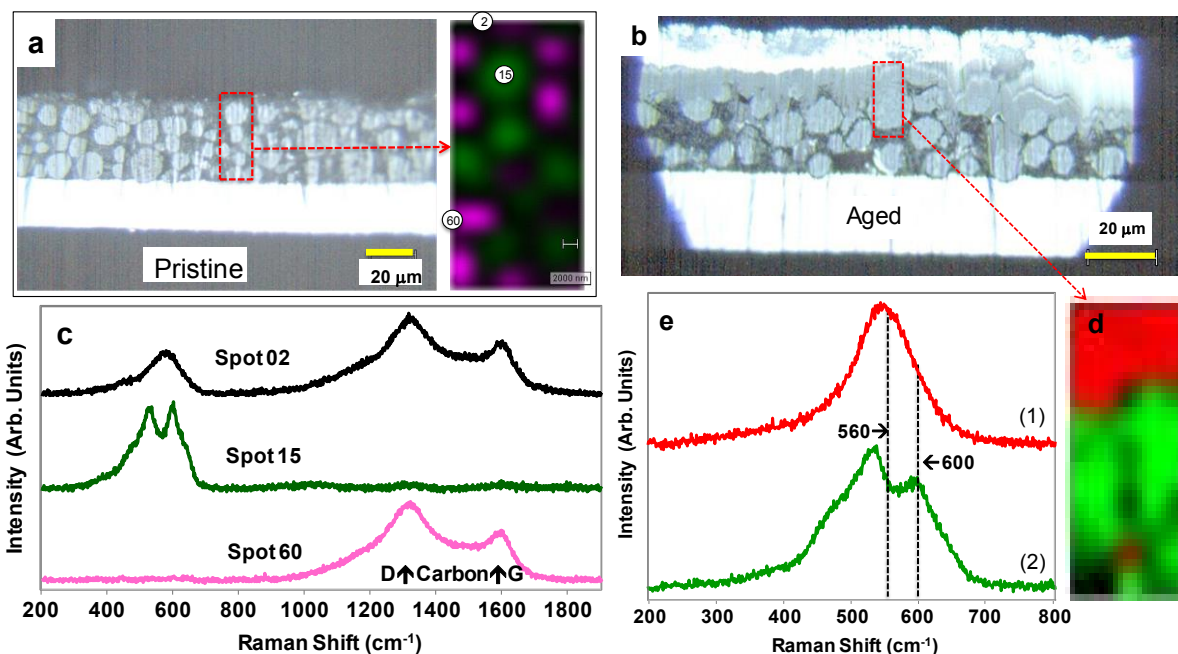


Figure I.7.F.6 White light images of the (a) pristine and (b) aged (400 cycles) electrode cross-sections; Raman maps were obtained in the portions indicated by the dashed red boxes. The Spot 02, Spot 15, and Spot 60 spectra in (c) were recorded at the locations shown in the color map to the right of (a). The red and green spectra in (e) were representative of data recorded at the red and green areas, respectively, shown in the color map of (d).

The key finding of this work is the difference observed between the Raman spectra of oxide particles from aged electrodes measured in the top-down mode and the spectra measured on ion-milled cross sections. The top-down spectra are often obscured by electrode surface films containing organic and inorganic electrolyte/separator decomposition products. The cross section spectra, on the other hand, provide more comprehensive information on the electrodes through-thickness. An important conclusion from our data is the composition/SOC variation across the electrode is observed in cross section. The composition heterogeneity revealed by the Raman data is a manifestation of impedance heterogeneity that develops in the electrode during electrochemical cycling.

Quantifying Gas Generation from Slurries used in Fabrication of Advanced Electrodes

As the CAMP Facility continues to explore advanced battery materials, several processing concerns occasionally occur that need to be addressed. One key concern is the generation of gases during the slurry mixing process. In this fiscal year, we devoted a portion of our effort to developing a method to quantify gas generation that could occur during the typical time of mixing in the CAMP Facility (minutes to ~4 hours). Silicon powders are a good choice for this study since some samples have been observed to generate gas in certain mixing processes. Four silicon powders in total were obtained from Nanostructured & Amorphous Materials, Inc. (NanoAmor) and Paraclete Energy Inc. The three Paraclete samples presented different surface structures: carbon coated (nSi/C), graphene coated (nSi/Cg) and silicon dioxide coated (nSiO). Poly(acrylic acid) and lithiated PAA with different extents of proton exchange (LiPAA20% and LiPAA80%, according to the mole fraction of H^+/Li^+ substitution) were selected, which are macromolecular binders commonly used in Si-containing electrodes. PAA was obtained from Sigma-Aldrich ($M_v \sim 450,000$). LiPAA was prepared by

titration of PAA with 1 M LiOH in an aqueous solution. Deionized (DI) water for aqueous slurries and dry *N*-methyl-2-pyrrolidone (NMP) for nonaqueous slurries were used as solvents.

The sequence of steps involved in the gas quantitation experiments is depicted in Figure I.7.F.7. The slurries were first thoroughly homogenized using a planetary mixer, then transferred into a pre-weighed pouch bag (xx3450 format, 3.5 mm thickness), which was partially evacuated and sealed. The porosity of the slurries was determined using a portable meter kit from Oakton Instruments. Volume changes of the pouch bag were monitored using a Sartorius YDK03 Density Determination Kit coupled to a Practum analytical balance, with deionized water serving as the immersion medium. The chemical composition of gases generated in the pouch was determined using a Pfeiffer OMNI Star GSD230 Residual Gas Analyzer with a QMG220 Quadrupole Mass Spectrometer (MS) and Secondary Electron Multiplier.

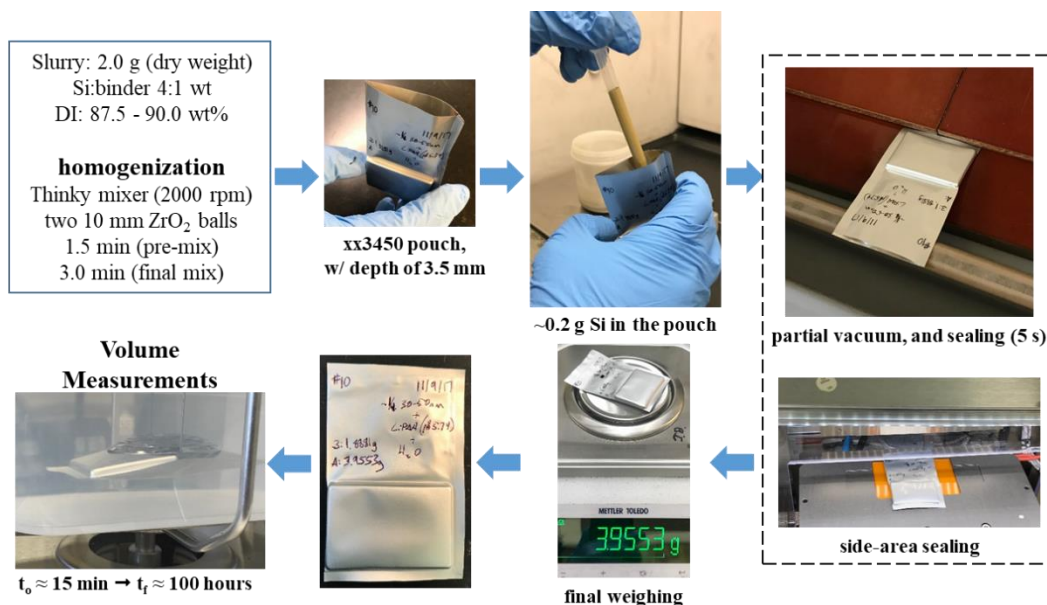


Figure I.7.F.7 Sequence of steps for the quantitation of gas evolution by the Archimedes method.

The volume evolution of pouch bags containing the NanoAmor silicon (30-50 nm) exposed to either water or NMP solutions is shown in Figure I.7.F.8a. For the deionized water, there was a continuous ballooning of the pouch bag, amounting to ~12 mL/g_{Si} after 102 h, while the NMP sample exhibited a slight deflation. The divergent behavior indicates the importance of water for the gas generation reactions. Residual gas analysis (for example, Figure H.1.8c) confirmed the presence of gaseous hydrogen in the pouch bag. For NMP, the deflation can be attributed to the consumption of residual oxygen by silicon. Figure I.7.F.8a also shows gas evolution with 2.5 wt% PAA present in the solvent. The same trends are observed in these PAA solutions as in the neat solvents, although the volume change is somewhat smaller. In the aqueous slurries, the gas evolution is more rapid at the beginning of the reaction. During the first hour, the pouch bags expanded linearly in time, at rates of 0.79 mL/g_{Si}h (DI water) and 0.45 mL/g_{Si}h (PAA solution). At longer measurement times, the gas evolution gradually becomes slower without quite reaching the zero.

Prelithiation of polycarboxylate binders is known to improve electrochemical performance of Si and Si-graphite electrodes. The proton exchange by Li⁺ ions minimizes the extent of electrochemical reduction of the residual -CO₂H groups during the first lithiation, improving coulombic efficiency and reducing H₂ release in the formation cycles. Additionally, this lithiation disrupts the H bond network in the PAA, reducing coiling of the polymer chains and improving their adhesion to the particles. However, Figure I.7.F.8b indicates that this lithiation also markedly increases the rate of gassing from the Si slurries, and this effect is proportional to the extent of PAA lithiation. Our data show that the net volume expansion after 5 h is maximum for LiPAA80%,

with the release of over 27 mL/g_{Si}. To put these estimates in perspective, at our fabrication facility, slurries for Si-graphite composite anodes can be prepared in batches as large as ~40 g of silicon, which would generate 1 L of gas during the electrode fabrication. This estimate exemplifies the scale of the problem that gas evolution can present to the production. The gas evolution is amplified by time as seen from Figure I.7.F.8d, which shows the image of a ballooned pouch containing the LiPAA80% slurry (with the NanoAmor 30-50 nm Si particles) after 120 h.

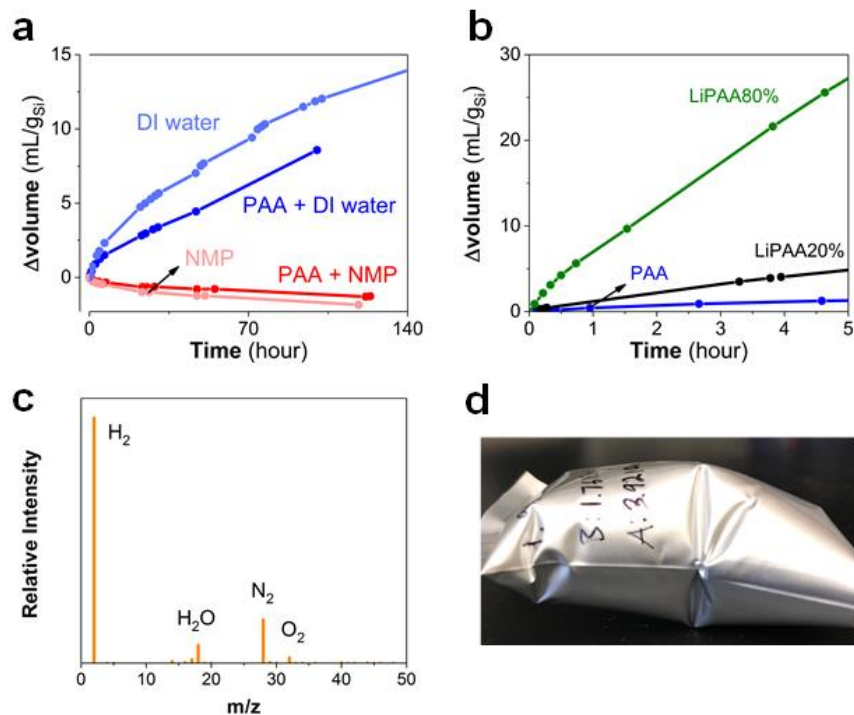


Figure I.7.F.8 Volume change of pouch bags containing (a) deionized water and NMP slurries, with and without 2.5 wt% PAA and (b) aqueous slurries with PAA and LiPAA (the extent of lithiation is indicated in the plot). (c) Example of data from the gas analysis experiments showing H₂ as a dominant component. (d) Pouch containing the LiPAA80% slurry (shown in c) after 120 h. The NanoAmor silicon particles (30-50 nm) was used for all these experiments.

Silicon from Paraclete Energy consists of primary particles (150 nm) that are more than three times larger than the material obtained from NanoAmor, and have carbon (nSi/C), graphene (nSi/Cg) or SiO₂ (nSiO) coatings. The volume changes for these silicon materials in the aqueous LiPAA80% slurries are shown graphically in Figure I.7.F.9. Among these three types of silicon particles, nSi/Cg shows the fastest change in volume. Even for this material, however, the volume change after 5 h was ~1/10 of the one observed for the NanoAmor silicon (Figure I.7.F.9, dashed line). Thus, larger Si particles (with their lower specific surface) appear to generate hydrogen at a lower rate. Furthermore, nSi/Cg-coated particles yielded much more H₂ than the oxide-protected material (nSiO), while carbon-covered particles yielded negligible amounts of gas.

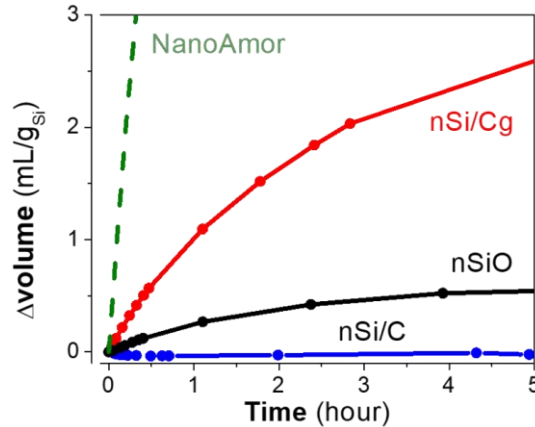


Figure I.7.F.9 Gas evolution from aqueous slurries containing LiPAA80% and silicon particles from Paraclete Energy with different surface coatings: graphene for nSi/Cg, silicon oxide for nSiO, and carbon for nSi/C. The gas evolution for the NanoAmor silicon (the same slurry constitution) is shown for comparison.

Compare Performance of xx3450 (~0.5 Ah) and xx6395 (~1.5 Ah) -Sized Pouch Cells

The CAMP Facility recognized and responded to the need for making >0.5 Ah pouch cells for DOE and USABC programmatic calls to the battery community. In FY18, the CAMP Facility demonstrated equipment acquired in FY17 to wind multilayer pouch cells larger than xx3450. The equipment has the capability to wind “small” xx3450 (~0.5 Ah) cells, but also has the ability to wind “big” xx6395 (~2 Ah) cells, all while utilizing the industrially proven winding method of the zig-zag (or z-fold) technique.

To demonstrate the initial xx6395 pouch cell build at the CAMP Facility, identical electrodes, composition, chemistry, electrolyte, etc., were used. Pouch cells with the xx3450 format were fabricated as the baseline to compare against (Figure I.7.F.10) since the majority of pouch cells assembled at the CAMP Facility before the new winder were of the xx3450 format. The only design difference between the two cell builds were the stamp dimensions. The study was designed to solely focus on the impact of cell size on performance.

	xx3450	xx6395
cathode height, cm	4.5	8.35
cathode length, cm	3.13	5.55
cathode area, cm ²	14.1	46.3
cathode perimeter length, cm	15.26	27.79
# of interfaces in cell	12	12
Total Cell Cathode Area, cm ²	169	556
Total Cathode Perimeter Length, cm	183	334
Area : Perimeter	0.92	1.7

Figure I.7.F.10 (Left) Cathode dimensions, interfaces, area, and perimeter information of the xx3450 and xx6395 pouch cells fabricated at the CAMP Facility. (Right) Image of the partially assembled xx3450 and xx6395 pouch cells side by side.

Several cells of each configuration were then filled with electrolyte (1.2 M LiPF₆ in EC:EMC, 3:7 by wt.; “Gen2”) and put through identical testing, including formation, de-gassing post formation, rate study, HPPC, and then cycle life testing with RPT at intervals of every 50 cycles. The cells were cycled between 3.0 and 4.1 V.

The cell performance between the xx6395 and xx3450 pouch cells were remarkably similar (Figure I.7.F.11). The cells had nearly identical capacity fade rates and initial cell impedances. Our study showed a slightly higher impedance rise for the xx6395 cells during the cycle life. The average voltages and energy densities were also similar between the two builds (not shown here). The results demonstrated that the electrochemical performance of small (xx3450) and big (xx6395) pouch cells are very similar and implies that when materials are limited and only xx3450 cells are possible to be made, the results are both relevant and valid.

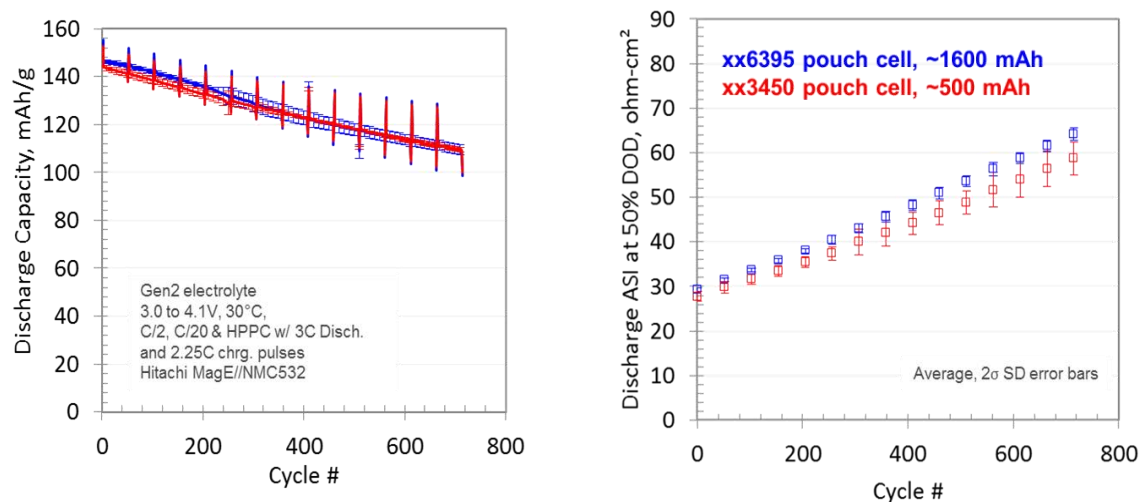


Figure I.7.F.11 Cycle life performance (Left) and area specific impedance performance at 50% depth of discharge (DOD) which were acquired every 50 cycles (Right) for both the xx3450 and xx6395 pouch cells. Areal capacity of 3.5 mAh/cm² for the anode and 3.1 mAh/cm² for the cathode was used.

Conclusions

The CAMP Facility has had another very productive year in the R&D of advanced lithium-ion electrochemical energy storage systems. We were also critical to the support of other numerous DOE-EERE programs, much of which was performed through the CAMP Facility's Electrode Library. A summary of some of the key successes in FY18 are as follows:

- Demonstrated that prelithiating an NMC cathode with Li₅FeO₄ (LFO) can improve the capacity retention of a cell with a SiO_x-based anode. LFO remains a viable method of prelithiating cell systems.
- Proved ceramic-coated anodes worked well under variety of testing conditions. All but one of the ceramics selected held up under the 3-4.1V full cell cycling conditions. Post-test analysis is needed to search for indications of ceramic corrosion.
- Demonstrated that full cells can operate without polymer-based separators.
- Identified problems using reverse-comma coater for coating ceramics due to hardness of ceramic powders and wetting of the porous graphite electrode.
- Showed that Raman spectroscopy combined with ion-milling is a method capable of detecting composition changes across the cathode electrode.
- Developed an Archimedes-based method to quantify the gas generated during slurry mixing of reactive materials.

- Demonstrated that electrochemical performance of small (xx3450) and big (xx6395) pouch cells are very similar, which means results from smaller pouch cells made with limited material quantities are still valid.
- Provided numerous experimental electrodes and cells to DOE programs.

Key Publications

1. Ahmed, Shabbir, Stephen Trask, Dennis Dees, Paul Nelson, Wenquan Lu, Alison Dunlop, Bryant Polzin and Andy Jansen. "Cost of automotive lithium-ion batteries operating at high upper cutoff voltages," *Journal of Power Sources*, **403** (2018): 56–65.
2. L. Zhang, W. Dose, A. Vu, C. Johnson, and W. Lu. "Mitigating the Initial Capacity Loss and Improving the Cycling Stability of Silicon Monoxide Using Li_5FeO_4 ," *J. Power Sources* **400** (2018): 549-555.
3. M.-T.F. Rodrigues, S.E. Trask, I.A. Shkrob, D.P. Abraham, "Quantifying gas generation from slurries used in fabrication of Si-containing electrodes for lithium-ion cells", *J. Power Sources* **2018**, *395*, 289–294.
4. J.A. Gilbert, V.A. Maroni, Y. Cui, D.J. Gosztola, D.J. Miller, D.P. Abraham, "Composition and Impedance Heterogeneity in Oxide Electrode Cross-sections detected by Raman Spectroscopy", *Adv. Mater. Interfaces* **2018**, p. 1701447.
5. K. Kalaga, I.A. Shkrob, R.T. Haasch, C. Peebles, J. Baro, D.P. Abraham, "Auger Electrons as Probes for Composite Micro and Nanostructured Materials: Application to Solid Electrolyte Interphases in Graphite and Silicon-Graphite Electrodes", *J. Phys. Chem. C* **2017**, *121*, 23333–23346.
6. J. Bare, I.A. Shkrob, J.A. Gilbert, M. Klett, D.P. Abraham, "Capacity Fade and Its Mitigation in Li-ion Cells with Silicon-Graphite Electrodes", *J. Phys. Chem. C* **121** (2017), pp 20640-20649.
7. M. Klett, J.A. Gilbert, K.Z. Pupek, S.E. Trask, D.P. Abraham, "Layered Oxide, Graphite and Silicon-Graphite Electrodes for Lithium-ion Cells: Effect of Electrolyte Composition and Cycling Windows", *J. Electrochem. Soc.* **164** (2017) A6095-6102.
8. S. Ahmed, I. Bloom, A.N. Jansen, T. Tanim, E.J. Dufek, A. Pesaran, A. Burnham, R.B. Carlson, F. Dias, K. Hardy, M. Keyser, C. Kreuzer, A. Markel, A. Meintz, C. Michelbacher, M. Mohanpurkar, P.A. Nelson, D.C. Robertson, D. Scofield, M. Shirk, T. Stephens, R. Vijayagopal, and J. Zhang, "Enabling fast charging—A battery technology gap assessment", *J. Power Sources* **367** (2017) 250-262.

References

1. C.S. Johnson, S.-H. Kang, J.T. Vaughey, S.V. Pol, M. Balasubramanian, and M.M. Thackeray. "Li₂O Removal from Li_5FeO_4 : A Cathode Precursor for Lithium-Ion Batteries," *Chemistry of Materials* **22**, no. 3 (2010): 1263-70.

Acknowledgements

Key contributors to this work include: Daniel Abraham, Shabbir Ahmed, Javier Bareno, Ira Bloom, Dennis Dees, Nancy Dietz-Rago, Fulya Dogan, Wesley Dose, Alison Dunlop, Arthur Dysart, Trevor Dzwiniel, Andrew Jansen, Gerald Jeka, Chris Johnson, Ozge Kahvecioglu Feridun, Kaushik Kalaga, Joel Kirner, Gregory Krumdick, Wenquan Lu, Paul Nelson, Bryant Polzin, Kris Pupek, Yan Qin, YoungHo Shin, Ilya Shkrob, Steve Trask, Pierre Yao, John Zhang, and Linghong Zhang

I.7.G Materials Benchmarking Activities for CAMP Facility (Argonne National Laboratory)

Wenquan Lu, Principal Investigator

Argonne National Laboratory
9700 S. Cass Ave.
Lemont, IL 60439
E-mail: luw@anl.gov

Peter Faguy, DOE Technology Development Manager

U.S. Department of Energy
E-mail: Peter.Faguy@ee.doe.gov

Start Date: October 1, 2014	End Date: September 30, 2019	
Project Funding (FY18): \$400,000	DOE share: \$400,000	Non-DOE share: \$0

Project Introduction

High energy density electrode materials are required in order to achieve the 40-mile all electric range for electric vehicle (EV) within the weight and volume constraints established by DOE and the USABC. One would need a combination of anode and cathode materials that provide 420mAh/g and 220mAh/g, respectively, as predicted by Argonne's battery design model (BatPac), if one uses a 20% margin for energy fade over the life of the battery assuming an average cell voltage of 3.6 volts. Therefore, the search for new high energy density materials for lithium ion batteries (LIB) is the focus of this material benchmarking project. In addition to electrode materials, other cell components, such as separators, binders, current collectors, etc., are evaluated to establish their impact on electrochemical performance, thermal abuse, and cost.

This benchmarking effort is conducted as part of the Cell Analysis, Modeling, and Prototyping (CAMP) Facility (Refer to the relevant Chapter) to identify and support promising new materials and components across the "valley of death", which happens when pushing a new discovery towards a commercial product. The CAMP Facility is appropriately sized to enable the design, fabrication, and characterization of high-quality prototype cells, which can enable a realistic and consistent evaluation of candidate chemistries in a time-effective manner. However, the CAMP Facility is more than an arrangement of equipment, it is an integrated team effort designed to support the production of prototypes electrodes and cells. In order to utilize the facility more efficiently and economically, cell chemistries are validated internally using coin type cells to determine if they warrant further consideration.

Objectives

- The primary objective is to identify and evaluate low-cost materials and cell chemistries that can simultaneously meet the life, performance, and abuse tolerance goals for batteries used in EV applications.
- The secondary objective is to enhance the understanding of the impact of advanced cell components and their processing on the electrochemical performance and safety of lithium-ion batteries.
- This project also provides the support for CAMP Facility for prototyping cell and electrode library development, and the MERF facility for material scale up.

Approach

Under materials benchmarking activities, we constantly reach out to or approached by material developers to seek opportunities to test their advanced or newly released products. By leveraging ANL's expertise in electrode design and cell testing, we can provide not only a subjective third opinion to material suppliers, but also deeper understanding on their materials, which can aid their material development. This deep

understanding becomes even more important when the material developers are small companies or new players, who often overlook overall requirements of battery materials.

In addition to industrial partners, we also work closely with scientists from various research institutes, such as universities and research laboratories. They often come up with novel materials with advanced electrochemical performance, but small quantities, which is only enough for validation purpose. These test results help us to determine how much effort should be expanded to explore the material potential.

In general, we will validate any potential cell material, which has impact on the cell performance, mainly in terms of electrochemical performance, electrode optimization, and thermal stability. The electrochemical performance is the centerpiece of the materials benchmarking activities, which will be tested using 2032 coin type cells under test protocol derived from USABC PHEV 40 requirements [Battery Test Manual For Plug-In Hybrid Electric Vehicles, Idaho National Laboratory]. The freshly made coin cells will undergo three formation cycles at a C/10 rate. The cells are then tested for the rate performance. For the rate test, the charging rate is set at C/5, while the discharge rate varies from C/5, C/3, C/2, 1C to 2C. Three cycles are performed for each discharge rate. After the rate test, the cells then undergo cycling test at C/3 rate. During the cycling test, we change the current rate to C/10 every 10th cycle to check the rate effect. Also, Hybrid Pulse Power Characterization (HPPC) is conducted every 10th cycle, which will be used to calculate the Area Specific Impedance (ASI).

This fiscal year, we have investigated various battery materials, such as cathode, anode, and conductive additives. In this report, selective work, including nickel rich cathode material and synthetic graphite, will be presented.

Results

Nickel-Rich High Energy Cathode Materials (NMC)

Nickel-rich $\text{LiNi}_x\text{Mn}_y\text{Co}_z\text{O}_2$ (NMC) is gaining momentum as high energy cathode materials for electric vehicle applications. Following NMC532, NMC622 is penetrating the market, and NMC811 is expected to be the next generation high energy cathode material. However, the higher energy density of nickel rich NMC comes at the expense of lower surface activity and thermal stability. The MERF at ANL is working on core-gradient concepts to coat the nickel-rich core with low nickel NMC to mitigate these issues (refer to chapter [II.G.2](#) for details). The concept of core-gradient nickel rich cathode material is illustrated in Figure I.7.G.1. The core-gradient NMC811 (NMC811-CG) has fixed nickel rich composition (90%) for the core, but concentration gradient for its shell ending with 33% Ni. The average nickel/manganese/cobalt ratio of the whole particle is equivalent to 80%/10%/10%.

The electrochemical performance of the NMC811-CG was tested and compared with regular NMC811 materials (Targay, Canada). These two cathode materials were made into laminates with 90 wt.% active material, 5 wt.% PVDF binder, and 5 wt.% carbon black. The 2032 coin type cells were fabricated and electrochemically tested between 3.0 V and 4.3 V. The specific capacity for these two materials are around 200 mAh/g. The voltage profiles of half cells (vs. lithium metal) of these two samples during the third formation cycle are shown in Figure I.7.G.1. The similar voltage profiles of these two NMC materials suggest that they have almost the same chemistry, which confirmed that the core-gradient NMC does have designed composition. The slight difference in voltage profiles between two materials could be attributed to the local chemistry effect.

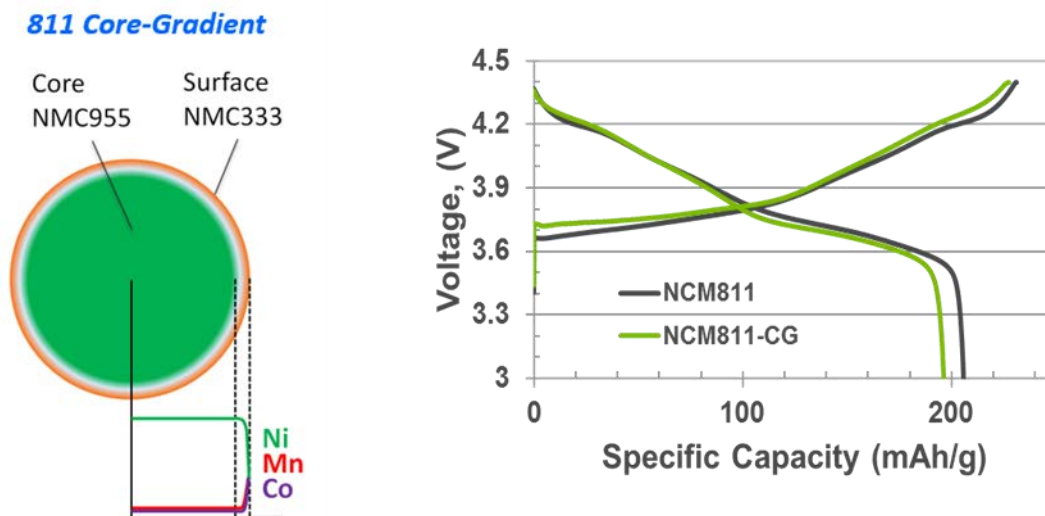


Figure I.7.G.1 Schematic diagram of (left) core-gradient nickel rich cathode material, and (right) charge and discharge voltage profiles of NMC811 and NMC811-CG.

In order to obtain the true electrochemical performance, two sets of full cells using NMC811 cathode and NMC811-CG, coupled with graphite electrode, were fabricated and tested in 2032 coin type cells. These two sets of cells underwent 3 formation cycles, 15 rate cycle, and 50 cycling test as described in approach section. The discharge capacity as a function of cycle number is shown in Figure I.7.G.2. Some capacity variation can be seen during 3 formation cycles, which can be attributed to the wetting process. During the rate, the better rate performance was observed for regular NMC811. Except for rate, similar cycling performance was observed for both NMC811 and NMC811-CG cells.

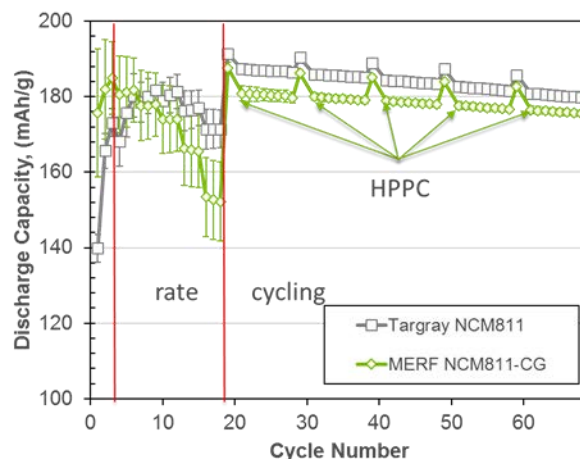


Figure I.7.G.2 Cycling performance of conventional NMC811 and NMC-CG full cell

We further calculated area specific impedance (ASI) from Hybrid Pulse Power Characterization (HPPC) test, which was conducted every 10th cycle during the cycling test. The ASI values as a function of cell voltage, equivalent to state of charge (SOC), were plotted in Figure I.7.G.3 for both NMC811 and NMC811-CG. It can be seen that the ASI values of NMC811 cells are lower than that of NMC811-CG at the beginning of the cycling test, which is consistent with its better rate performance. However, the ASI value of NMC811 cells increases much faster during cycling test, which suggests the vulnerable surface property of nickel rich NMC cathode material. The slower ASI rise rate of NMC811-CG cells could be attributed to the core-gradient structure. The low nickel content at the shell of the NMC811-CG particle will mitigate the surface/structure

degradation of cathode material, which will have positive effect on the cycle life. This material is being studied at the CAMP Facility.

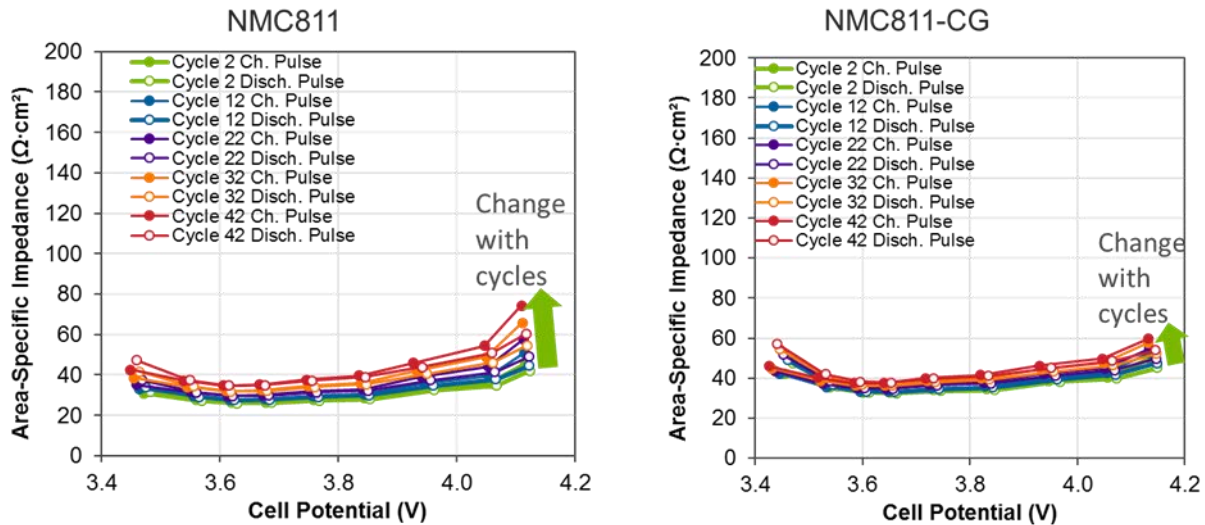


Figure I.7.G.3 ASI results of full cells containing (left) NMC811 and (right) NMC811-CG cathode during cycling test

Synthetic graphite Anode

In state-of-the-art EV LIBs, the negative electrode active material tends to be graphite, and the positive electrode tends to be lithium metal oxides, LiMO_2 (M: Ni, Co, Mn). The solid-state Li^+ diffusion coefficients in, for example, $\text{LiNi}_{0.5}\text{Mn}_{0.3}\text{Co}_{0.2}\text{O}_2$ (NMC532) and graphite have been estimated to be on the order to 10^{-10} and 10^{-13} cm^2/s , respectively. As such, graphite is generally considered to be the kinetic-limiting component of lithium-ion batteries. What's more, the low electrochemical potential for the lithiation of graphite relative to $\text{Li}^{+}/0$ means that polarization at high charge rate carries the risk of lithium plating, which accelerates capacity fade and reduces safety.

Natural graphite is the current dominant anode material due to its high energy density and low cost. Though expensive compared to natural graphite, synthetic graphite is worthy of investigation for LIBs due to its higher purity and different properties. Two synthetic graphite materials were obtained and tested in coin type full cell using natural graphite A12 as a control. Electrochemical characterization of 3 different commercial graphite samples in full-cell batteries with a focus on fast-charging capability were thoroughly investigated.

All three raw graphite (Gr) materials were characterized by SEM, with results shown in Figure I.7.F.4. The A12 material exhibits potato-shaped particles with diameters roughly 10 μm . The XL40 material exhibits globular, irregular particle morphology, with slightly lower average particle size than A12, and the XL20 material exhibits larger, stacked flake-like morphology.

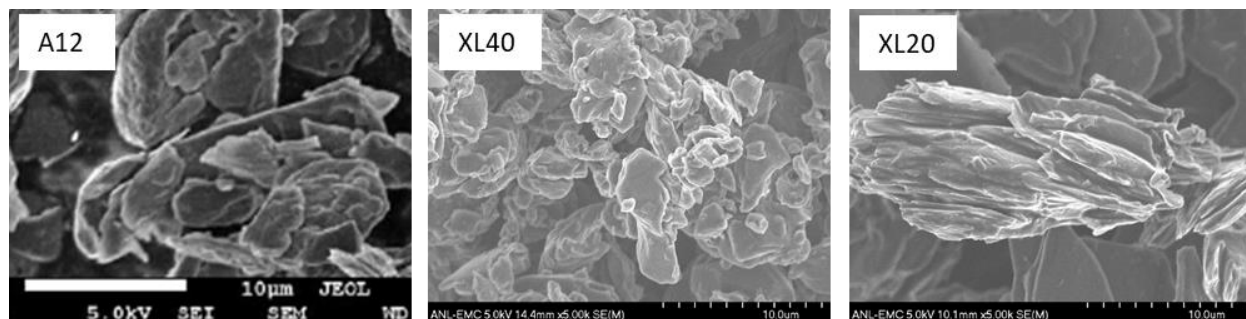


Figure I.7.G.4 FSEM images from graphite raw materials: a) CPreme A12; b) XL40; c) XL20. Note the slightly different scale bars.

To begin, all three graphite materials were tested in half cells to record their voltage profiles and reversible capacities (from their 3rd, C/10 formation cycle) with voltage window between 1.50 and 0.01 V vs Li^{+/0}. Negative electrodes each consisted of 96 wt% graphite, 2 wt% carbon black (C45, Timcal), and 6 wt% PVDF (KF-9300, Kureha) on copper foil. Half-cell formation data for the 3 different graphite materials (averaged from 3 cells for each material) are provided in Table I.7.G.1. Note that A12 shows the highest reversible capacity, and all are below the theoretical specific capacity of pure LiC₆, 372 mAh/g. XL20 shows the highest 1st cycle Coulombic Efficiency (CE), which is not surprising given that XL20 has the lowest surface area (Table I.7.G.1), and therefore may be expected to have the least irreversible capacity loss caused by reduction reactions at the solid–electrolyte interface.

Table I.7.G.1 Formation data for graphite half-cells cycled at C/10, 1.5–0.01 V vs Li^{+/0}.

Material	1 st Cycle Delithiation Capacity* (CE)	3 rd Cycle Delithiation Capacity* (CE)
A12 Gr	348 ± 10 mAh/g (91.1%)	364 ± 1 mAh/g (99.2%)
XL40 Gr	319 ± 4 mAh/g (91.0%)	327 ± 1 mAh/g (99.3%)
XL20 Gr	345 ± 3 mAh/g (93.3%)	351 ± 1 mAh/g (99.5%)

*specific capacity calculated per mass of graphite, $n=3 \pm 1\sigma$.

Gr/NMC532 full cells were studied according to our standardized testing protocols as outlined in approach section above. NMC532 cathodes were prepared by the CAMP Facility at Argonne, using semi-automated pilot scale battery production equipment in a moisture-controlled dry room. The NMC532 cathodes consisted of 90 wt% LiNi_{0.5}Mn_{0.3}Co_{0.2}O₂ (“NMC532”, TODA), 5 wt% C45, and 5 wt% PVDF on aluminum foil. Electrochemical results are provided in Figures below. Figure I.7.G.5a plots the discharge capacity (filled data points) and Coulombic Efficiency (open points) as a function of cycle number and varied discharge rate (including C/10 formation cycles) obtained from full cells containing the 3 different graphite materials.

Because these full-cells all use the same positive electrode laminate which limits capacity, we expect all full-cells to have the same initial capacity. However, 2 of the 3 cells containing the A12 graphite negative electrodes exhibited a capacity “break-in” period (capacity increases with formation cycles), which may be associated with electrode misalignment (13), wettability, or some unknown factor. This “break-in” skews the A12 data in early cycles towards lower capacity. Cells lose capacity at higher rates because polarization causes the cells to reach the lower cut-off (LCV) before the full capacity is extracted. Accounting for the “break-in” mentioned above, all three graphite materials in Figure I.7.G.5a exhibit qualitatively comparable percent capacity loss at higher discharge rates.

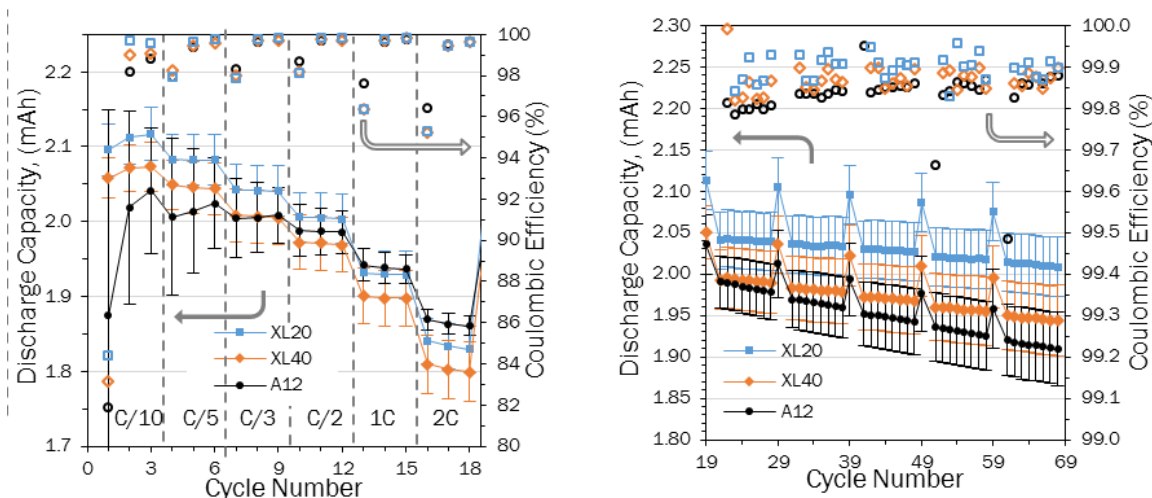


Figure I.7.G.5 Gr/NMC532 full-cell electrochemical cycling data following standard cycling protocols; filled points indicate discharge capacity while open points indicate Coulombic Efficiency. (a) Formation (C/10) and Rate studies. Rate studies used C/5 charging while discharge rate was varied as indicated. (b) C/3 cycling with C/10 then HPPC every 10th cycle. Error bars represent $n=3, \pm 1\sigma$.

Figure I.7.G.5b shows subsequent cycling data with HPPC testing. Spikes in capacity every 10th cycle correspond to a C/10 cycle prior to HPPC testing. There is a clear, gradual capacity loss with continued cycling. While 1σ error bars overlap, it is clear that the average irreversible capacity loss is greatest for A12 graphite and least for XL0.

A second batch of Gr/NMC532 full cells was prepared and studied by fast-charge cycling protocols. Note that in all protocols, constant current and constant voltage (CCCV) charging was used (i.e., charging was galvanostatic until the upper cut-off (UCV) was reached, then potentiostatic at the UCV until current decayed to $I \leq 0.02C$). We note that, due to the CV charge portion, total charge times were slightly longer than that predicted by the C-rate. For example, at the highest charge rate of 10C, the UCV was reached in ≤ 6 min, but the total charge times with CV charging were ~ 20 min.

Figure I.7.G.6a plots both the cells' total charge capacity (filled points), as well as the galvanostatic charge capacity (open points). We note that, if no CV charge portion were used, the cells' capacities would essentially be the galvanostatic value. Due to the slightly different total capacities, the values are normalized in Figure H.2.6b by plotting the galvanostatic vs total charge capacity fraction, Q_{gal}/Q_{tot} . This is essentially an indirect measure of the graphite electrodes' polarization. A larger polarization will cause the cell to reach its UCV at a lower SOC, and therefore result in a lower Q_{gal}/Q_{tot} value. Figure I.7.G.6b indicates that all 3 sets of cells are capable of charging to $\sim 80\%$ of their total capacity within 10 min (6C rate). This is an encouraging result, in light of the Vehicle Technology Office's goal for EV charging times of 15 min or less (2). However, we note that commercial electrode loadings (and therefore current densities at a given C-rate) are likely higher than those used here, which will lead to higher polarization at a given C-rate.

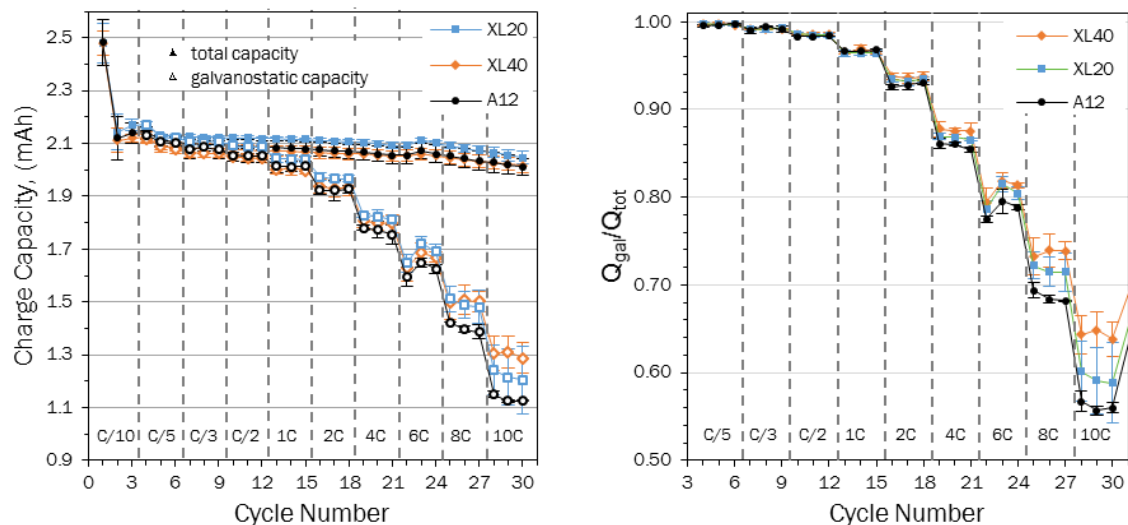


Figure I.7.G.6 Gr/NMC532 full-cell electrochemical cycling data following Fast-Charge protocols. (left) Charge capacity during Formation (C/10) and Fast-Charge studies (discharge rate was a constant C/5, while charge rate was varied as indicated, with a current cutoff of $I \leq 0.05C$). Filled points indicate total charge capacity while open points indicate galvanostatic capacity. (right) Normalized galvanostatic vs total charge capacity fraction, Q_{gal}/Q_{tot} , as a function of cycle number and charge rate.

The differences in fast-charge performance between different graphite materials indicated in Figure I.7.G.6b are small relative to the error bars. This is somewhat surprising, given the large particle size differences between XL20 and XL40, for example. If we hypothesize that solid-state Li^+ diffusion in graphite is the rate-limiting step to fast-charging, then we would expect more polarization for the larger particle size (longer distance for Li^+ to travel) of XL20 relative to XL40 and A12. However, this is not observed. Instead the synthetic graphite materials, XL20 and XL40, both show lower polarization than the nature graphite, A12. One remaining hypothesis is that the proprietary surface treatment of A12, claimed to maximize capacity retention, may somehow enhance polarization at high current. What's more, one recent modeling study suggests that polarization attributed to Li^+ transport in the electrolyte and across the solid–electrolyte interface, rather than solid-state diffusion, may dominate under fast-charging conditions. If true, one might expect tortuosity or active material surface area, respectively, to play a larger role in fast-charging performance than particle size.

In order to test the possibility of Li^0 plating, graphite electrodes were harvested, rinsed, and analyzed by SEM after 100 fast-charge cycles. Visual inspection of the electrodes (Figure I.7.G.7 insets) revealed surprising differences, given the relatively similar cycling performance and only a small difference in full-cell ASI. An A12 graphite electrode (Figure I.7.G.7b) showed a white ring, whereas XL40 (Figure I.7.G.7a) showed no evidence of such a ring. Inspection of the white ring on A12 by SEM revealed a high prevalence of Li dendrites in this region. Dendrites were also present throughout the middle of the electrode, though less prevalent. By contrast, very few dendrites were observed on the XL40 electrode. The appearance of a Li^0 dendrite ring is consistent with previously calculated inhomogeneity of current and concentration distribution, expected as a result of the oversized, 15 mm anode relative to the 14 mm cathode.

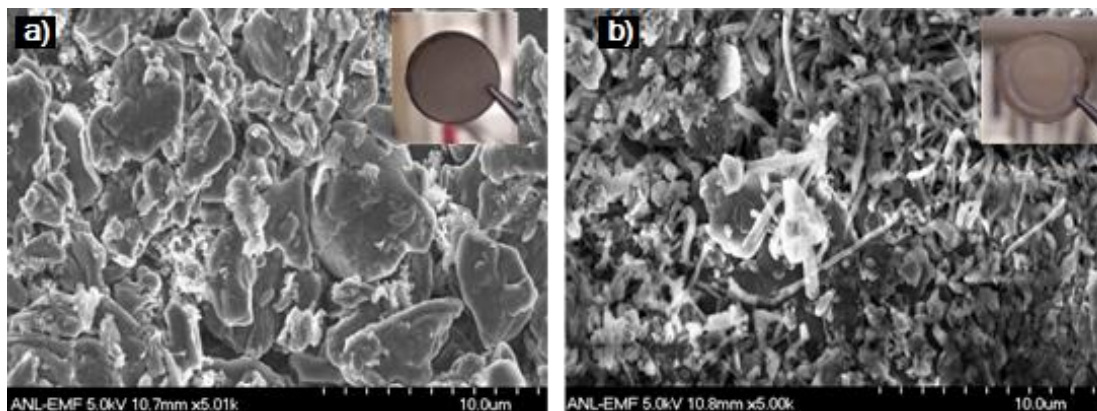


Figure I.7.G.7 SEM images of graphite electrode containing (a) XL40 and (b) A12 graphite recovered after 100 cycles with 6C charge, C/3 discharge. The insets include photographs of the rinsed, recovered electrodes.

Conclusions

Concentration gradient NMC811 from MERF was tested using graphite/NMC811-CG coin type full cells. Compared to conventional NMC811 cells, NMC811-CG full cells demonstrated similar electrode chemical performance, including specific capacity and capacity retention. Furthermore, much less impedance rise during cycling test was obtained, which suggests that the core-gradient structure can stabilize the nickel rich NMC material.

Two synthetic graphite were tested as anode materials. Compared to natural graphite (A12), detectable differences in fast-charging performance when testing in Gr/NMC532 full-cells. In general, two synthetic graphite samples (XL40, XL20) exhibited slightly superior fast-charge performance (e.g., slightly higher galvanostatic capacity at a given C-rate, slightly lower ASI) than a sample of natural graphite (A12). A surprising result was the observation of significantly more Li^0 on A12 graphite electrodes after fast-charge cycling compared to XL40, despite relatively small differences in ASI.

Key Publications

1. Joel Kirner, Yan Qin, Xin Su, Linghong Zhang, Yangxing Li, and Wenquan Lu, Analysis of graphite materials for fast-charging capabilities in lithium ion batteries, ECS Trans., 2018 85(13): 33-44; doi:10.1149/08513.0033ecst.
2. Linghong Zhang, Yan Qin, Yuzi Liu, Qi Liu, Yang Ren, Wenquan Lu, Capacity fading mechanism of silicon monoxide as the anode for lithium ion batteries, 233rd ECS Meeting, Seattle, May 13 -17, 2018
3. Joel Kirner, Yan Qin, Xin Su, Linghong Zhang, Yangxing Li, and Wenquan Lu, Analysis of graphite materials for fast-charging capabilities in lithium ion batteries, 233rd ECS Meeting, Seattle, May 13 - 17, 2018
4. Wenquan Lu, Linghong Zhang, Yan Qin, and Andrew Jansen, Calendar and Cycle Life of Lithium Ion Batteries Containing Silicon Monoxide Anode, J. Electrochem. Soc., 2018, 165 (10) A2179-A2183
5. Linghong Zhang, Yan Qin, Yuzi Liu, Qi Liu, Yang Ren, Andrew N. Jansen, and Wenquan Lu, Capacity Fading Mechanism and Improvement of Cycling Stability of the SiO anode for Lithium-ion Batteries, J. Electrochem. Soc., 2018, 165 (10), A2102-A2107
6. Wenquan Lu, Joel Kirner, Linghong Zhang, Yan Qin, Steve Trask, Alison Dunlop, Bryant Polzin, and Andrew Jansen, Materials benchmarking activities for CAMP facility, 2018 U.S. Department of

Energy Vehicle Technologies Office Annual Merit Review and Peer Evaluation Meeting Washington D.C., Jun 18th – 21st, 2018.

7. Xin Su, Fulya Dogan, Jan Ilavsky, Victor A. Maroni, Yan Qin, David J. Gosztola, Wenquan Lu, Lithium Dendrite Growth Mechanisms on Carbon Anode for Lithium Ion Batteries, ABAA10, Chicago 2017.

Acknowledgements

Key contributors to this work include: Daniel Abraham, Shabbir Ahmed, Javier Bareno, Ira Bloom, Dennis Dees, Nancy Dietz-Rago, Fulya Dogan, Wesley Dose, Alison Dunlop, Arthur Dysart, Trevor Dzwiniel, Andrew Jansen, Gerald Jeka, Chris Johnson, Ozge Kahvecioglu Feridun, Kaushik Kalaga, Joel Kirner, Gregory Krumdick, Wenquan Lu, Paul Nelson, Bryant Polzin, Kris Pupek, Yan Qin, YoungHo Shin, Ilya Shkrob, Steve Trask, Pierre Yao, John Zhang, and Linghong Zhang

I.7.H Post-test Analysis of Lithium-Ion Battery Materials (ANL, ORNL, SNL)

Ira Bloom, Principal Investigator

Argonne National Laboratory
9700 South Cass Avenue
Argonne, IL 60439
E-mail: ira.bloom@anl.gov

David L. Wood, Principal Investigator

Oak Ridge National Laboratory
P.O. Box 2008
Oak Ridge, TN 37831
E-mail: wooddl@ornl.gov

Kyle R. Fenton, Principal Investigator

Sandia National Laboratories
P.O. Box 5800
Albuquerque, NM 87185
E-mail: krfento@sandia.gov

Peter Faguy, DOE Technology Development Manager

U.S. Department of Energy
E-mail: Peter.Faguy@ee.doe.gov

Start Date: October 1, 2015

End Date: September 30, 2018

Project Funding (FY18): \$3,375,000

DOE share: \$3,375,000

Non-DOE share: \$0

Project Introduction

The surface of the electrodes in a lithium-ion cell affects performance [1], and, most likely, the abuse response of the cell. Usually, the surface of the electrode is covered with a passivating or solid electrolyte interphase (SEI) layer. The SEI layer consists of electrolyte reaction products: at the positive, those formed by oxidation and, at the negative, by reduction [2], [3], [4]. The SEI is a complex, structurally and chemically, under normal operating conditions [5], [6], [7], [8]. However, there is very little information about the changes that occur in the SEI during overcharge. One would expect that these changes would depend on cell chemistry, including the binder in the electrode. Understanding these changes would very useful from the view point of safety. The information gained by studying these changes may help us design more robust SEI layers, possibly mitigating the consequences of overcharge.

Objectives

The overall objective of the project is to understand the physical and chemical changes that occur during overcharging and how changes in the cell chemistry, such as binder and cathode, alter the response. As part of our systematic study of overcharging lithium-ion cells, we reported the changes that occur as Li(Ni_{0.5}Mn_{0.3}Co_{0.2})O₂ (NMC532) /graphite cells were charged to 100, 120, 140, 160, 180, and 250% SOC. We showed that the nature of the binder has a pronounced effect on the overcharge response. This year, we investigated how electrode cross-talk impacts the nature of the surface layer on the anode during overcharging.

Approach

1.2-Ah lithium-ion cells containing LiFePO₄ (LFP)/graphite chemistry were fabricated and formed at Oak Ridge National Laboratory. The 1.2-Ah capacity rating represented 95+% of the theoretical amount of lithium in the cathode material. They were charged to 100, 120, 140, 160, 180 and 250% SOC at Sandia National Laboratories. After discharging to 3.0V, the cells were dismantled in an inert-atmosphere glove box at

Argonne National Laboratory. The changes to the graphite anode were characterized using scanning-electron microscopy (SEM), X-ray photoelectron spectroscopy (XPS) and liquid chromatography.

Results

Under the SEM, the surface of overcharged anodes appears very different. For example, Figure I.7.H.1 shows images of the anode surfaces from (a) a cell containing an NMC532 cathode [9] and (b) a cell containing an LFP cathode. Both contained polyvinylidene difluoride binders.

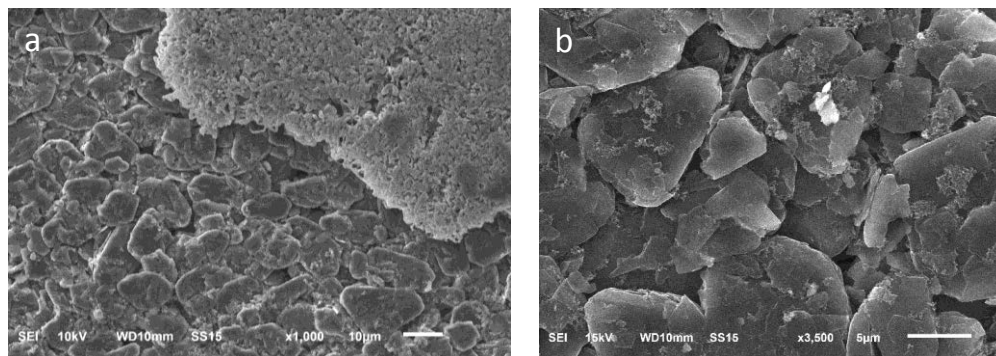


Figure I.7.H.1 SEM images of the anode surfaces from cells charged to 140% SOC. Figure (a) is from a cell containing a NMC532 cathode, and (b), from a cell containing an LFP cathode.

In the NCM532 case, dendrites, which incorporated transition metals, were clearly seen on the anode surface as islands. We assume that the islands were produced when the separator was pulled away from the anode during disassembly. Examination of the separator from this cell also showed islands of dendrites, which made our initial assumption seem reasonable. On the other hand, the surface of the anode from the LFP-containing cell was much cleaner, showing only small particles.

The dependence of relative elemental concentrations with %SOC are presented in Table I.7.H.1. From these data, the concentrations of fluorine and lithium tend to increase with extent of overcharge, while the concentration of carbon tends to decrease. These values were calculated from a multiple-gaussian fit of reach region.

The XPS results from the companion work using NMC532 cathodes [10] are shown below in Table I.7.H.2 to aid comparisons. Comparing the data in Table I.7.H.1 and Table I.7.H.2 shows that there is, at SOC's less than 180%, more phosphorus on the anode in the LFP versus those from the NMC532 cells.

Table I.7.H.1 Relative elemental compositions of anodes in LFP cells.

%SOC	C, at%	F, at%	O, at%	P, at%	Li, at%	Fe, at%
100	47.35	21.66	7.35	1.87	19.96	1.82
120	29.17	17.15	19.69	3.9	28.86	1.43
140	42.90	16.48	17.41	2.13	19.53	1.54
160	33.11	15.68	19.49	3.14	27.39	1.19
180	12.82	27.98	8.26	2.13	46.38	2.49
250	8.34	32.01	6.91	1.66	48.30	2.78

Table I.7.H.2 Relative elemental compositions of anodes in NMC532 cells from Reference 10.

%SOC	C, at%	F, at%	O, at%	P, at%	Li, at%
100	68.09	14.51	7.4	1.55	8.46
120	45.96	14.77	19.13	1.69	18.44
140	35.37	22.57	17.32	1.43	23.31
160	28.41	27.44	13.67	2.12	28.36
180	39.4	16.97	20.95	3.87	18.81
250	9.64	44.13	8.8	2.2	35.23

The organic part of the solid electrolyte interphase (SEI) layer was extracted from the anodes and characterized using liquid chromatography coupled to a mass spectrometer detector. Many species were observed; however, only four were organic and displayed a dependence on SOC. Table I.7.H.3 shows the proposed structural formulae for these organics as H⁺ or Na⁺ adducts. [11] For the reader's convenience, the proposed structural formulae from Reference 10 are shown in Table I.7.H.4.

Comparing Table I.7.H.3 and Table I.7.H.4 shows that more compounds were formed in the cell containing the LFP cathode than in the NMC532 case. Organophosphites/ates [12] were formed in both cases. Additionally, the -P(=O)F₂ bonding motif is clearly apparent in the LFP case. The larger number of phosphorus atoms in compounds A, B, C, in general, is consistent with the XPS results, showing a greater concentration of phosphorus on the anode surface in the LFP cells.

More telling of the change in the cathode is the extent of polymerization shown in compounds A, B, and C as compared to E and F. During charging, Ni⁴⁺ is formed in the NMC532 cathode and Fe³⁺ in the LFP cathode. The difference in extent of polymerization may indicate that Ni⁴⁺ was more effective than Fe³⁺ in oxidizing a common intermediate before it could polymerize.

Table I.7.H.3 Proposed structural formulae.

Label	Proposed structural formula
A	[F ₂ P(=O)OCH ₂ CH ₂ OP(=O)(OCH ₂ CH ₂ OH)OCH ₂ CH ₂ OP(=O)(OCH ₂ CH ₂ OH)OCH ₃]H ⁺
B	[F ₂ P(=O)OCH ₂ CH ₂ OP(=O)(OCH ₂ CH ₂ OCH ₃)OCH ₂ CH ₂ OP(=O)(OCH ₂ CH ₂ OH)(OCH ₂ CH ₂) ₃ OH]Na ⁺
C	[F ₂ P(=O)OCH ₂ CH ₂ OP(=O)(OCH ₂ CH ₂ OH)(OCH ₂ CH ₂) ₆ OH]H ⁺
D	[F ₂ P(=O)O(CH ₂ CH ₂ O) ₄ CH ₃]H ⁺

Table I.7.H.4 Proposed structures from Reference 10.

Label	Proposed structures
E	[HOCH ₂ CH ₂ OCH ₂ CH ₂ OP(=O)(OCH ₂ CH ₂ OCH ₂ CH ₂ OCH ₂ CH ₃) ₂]H ⁺
F	[HOCH ₂ CH ₂ OP(=O)(OCH ₂ CH ₂ OH)OCH ₂ CH ₂ OCH ₂ CH ₂ OP(=O)CH ₂ CH ₂ CH ₃)OC ₂ H ₅]Na ⁺

Conclusions

Small, pouch cells containing LFP cathodes were systematically charged to 100, 120, 140, 160, 180 and 250% SOC. After charging, the graphite anode surface was characterized, looking for changes in surface microstructure and composition. These were compared to similarly charged cells containing NMC532 cathodes. In general, the surface of the anodes from the LFP cells were much simpler and did not contain dendritic formations. The SEI layer on these anodes apparently consisted of more compounds which were more highly polymerized organophosphates than found in the NMC532 cells.

Key Publications

1. Effect of overcharge on lithium-ion cells containing Li(Ni_{0.5}Mn_{0.3}Co_{0.2})O₂ cathodes: NMP-soluble binder. I. Microstructural Changes in the Anode, Nancy Dietz Rago, Javier Bareno, Ira Bloom, Jianlin Li, David L. Wood, III, Leigh Anna Steele, Joshua Lamb, Scott Spangler, Christopher Grosso, Kyle Fenton, J. Power Sources, 385 (2018) 145-155. DOI: 10.1016/j.jpowsour.2018.01.009

2. Effect of overcharge on lithium-ion cells containing $\text{Li}(\text{Ni}_{0.5}\text{Mn}_{0.3}\text{Co}_{0.2})\text{O}_2$ cathodes: NMP-soluble binder. II — Chemical changes in the anode, Ira Bloom, Javier Bareno, Nancy Dietz Rago, Fulya Dogan, Donald G Graczyk, Yifen Tsai, Seema R Naik, Sang-Don Han, Eungje Lee, Zhijia Du, Yangping Sheng, Jianlin Li, David L Wood III, Leigh Anna Steele, Joshua Lamb, Scott Spangler, Christopher Grosso, Kyle R Fenton, J. Power Sources, 385 (2018) 156-164. DOI: 10.1016/j.jpowsour.2017.12.015
3. Effect of overcharge on NMP-processed $\text{Li}(\text{Ni}_{0.5}\text{Mn}_{0.3}\text{Co}_{0.2})\text{O}_2$ / Graphite lithium ion cells with PVDF binder. III — Chemical changes in the cathode, Javier Bareño, Nancy Dietz Rago, Fulya Dogan Key, Donald Graczyk, Yifen Tsai, Seema Naik, Sang Don Han, Eungje Lee, Zhijia Du, Yangping Sheng, Jianlin Li, David Wood , Leigh Anna Steele, Joshua Lamb, Scott Spangler, Christopher Grosso, Kyle Fenton, Ira Bloom, J. Power Sources, 385 (2018) 165-171, DOI information: 10.1016/j.jpowsour.2017.12.061

References

1. L. Gireaud, S. Grugeon, S. Pilard, P. Guenot, J.-M. Tarascon, and S. Lareulle, *Anal. Chem.*, 78 (2006) 3688–3698.
2. M. Morita, O. Yamada, and M. Ishikawa, *J. Appl. Electrochem.*, 28 (1998) 209–213.
3. S.W. Song, G.V. Zhuang, and P.N. Ross, Jr., *J. Electrochem. Soc.*, 151 (2004) A1162–A1167.
4. D. Aurbach, *J. Power Sources*, 89 (2000) 206–218.
5. E. Peled, *J. Electrochem. Soc.*, 126 (1979) 2047.
6. J.G. Thevenin and R.H. Muller, *J. Electrochem. Soc.*, 134 (1987) 273.
7. S.J. An, J. Li, C. Daniel, D. Mohanty, S. Nagpure, and D.L. Wood, *Carbon*, 105 (2016) 52–76.
8. D. Aurbach, I. Weissman, A. Zaban, and O. Chuzid (Youngman), *Electrochim Acta*, 39 (1994) 51.
9. N. Dietz Rago, J. Bareno, I. Bloom, J. Li, D. L. Wood, III, L. A. Steele, J. Lamb, S. Spangler, C. Grosso, K. Fenton, *J. Power Sources*, 385 (2018) 145-155.
10. I. Bloom, J. Bareno, N. Dietz Rago, F. Dogan, D. G. Graczyk, Y. Tsai, S. R. Naik, S.-D. Han, E. Lee, Z. Du, Y. Sheng, J. Li, D. L. Wood III, L. A. Steele, J. Lamb, S. Spangler, C. Grosso, K. R. Fenton, *J. Power Sources*, 385 (2018) 156-164.
11. The H^+ and Na^+ came from the acidic mobile phase used in the chromatography experiment or from Na_2CO_3 used as part of sample preparation.
12. During sample preparation, the aqueous extract from the anode is exposed to air. Any organophosphites present would be quickly converted to phosphates.

Acknowledgements

Co-investigators: Nancy Dietz Rago (Argonne), Jianlin Li (Oak Ridge) and Joshua Lamb (Sandia)

We gratefully acknowledge support from the U. S. Department of Energy (DOE), Office of Energy Efficiency and Renewable Energy, Vehicle Technologies Office. Argonne National Laboratory is operated for DOE Office of Science by UChicago Argonne, LLC, under contract number DE-AC02-06CH11357.

The work at Oak Ridge National Laboratory was sponsored by U. S. Department of Energy (DOE), Office of Energy Efficiency and Renewable Energy, Vehicle Technologies Office, Applied Battery Research. Oak

Ridge National Laboratory is managed by UT Battelle, LLC, for the U.S. Department of Energy under contract DE-AC05-00OR22725.

Sandia National Laboratories is a multi-mission laboratory managed and operated by National Technology and Engineering Solutions of Sandia, LLC., a wholly owned subsidiary of Honeywell International, Inc., for the U.S. Department of Energy's National Nuclear Security Administration (NNSA) under contract DE-NA0003525.

II. Advanced Materials R&D

II.1 Next-gen Lithium-ion: Advanced Electrodes R&D

II.1.A Higher Energy Density via Inactive Components and Processing Conditions (LBNL)

Vincent Battaglia, Principal Investigator

Lawrence Berkeley National Laboratory

1 Cyclotron Road

Berkeley, CA 94720

E-mail: vsbattaglia@lbl.gov

Peter Faguy, DOE Technology Development Manager

U.S. Department of Energy

E-mail: Peter.Faguy@ee.doe.gov

Start Date: October 1, 2016

End Date: September 30, 2019

Project Funding (FY18): \$1,250,000

DOE share: \$1,250,000

Non-DOE share: \$0

Project Introduction

Improved energy density is considered a critical metric to increasing the demand for electric vehicles. One way to increase the energy density is to fabricate cells with thicker, higher-loading electrodes. Higher loading electrodes reduce the fraction of inactive components in a cell of a given size thereby increasing the energy density. The problem with this, which is what we seek to address, is that thicker electrodes cannot be produced using the same binder and solvent content used in traditional Li-ion cell fabrication. More specifically, the present conditions are not viscous enough to allow for thick, free standing films and prevent material sedimentation during drying.

Objectives

This research will identify processing steps that impact electrode quality in terms of mechanical and electrochemical performance. It will point to the underlying physics that is responsible for changes in performance as a function of changes in electrode thickness. Ultimately, the research will establish processing conditions that lead to the best compromise between electrode quality and speed of fabrication.

Approach

The approach to conducting this research was to methodically go through every step of the electrode fabrication process and identify those processes with the greatest impact on the ability to produce a quality thick electrode based on its mechanical and electrochemical performance using tools available at a national lab. Upon identifying the processes with the greatest impact, we performed the research necessary to establish the root cause of limited ability to fabricating thick electrodes. For the first two years, we investigated the impact of binder supplier on binder solubility, the effect of binder molecular weight, the effect of slurry viscosity, the effect of slurry casting speed, the use of carbon fiber, the effects of calendaring at different temperatures, the effect of doctor blade height on final electrode thickness, and the impact of the presence of electrolyte on electrode swelling in a coin cell. During the past year we studied the effect of drying temperature with all other conditions held constant on electrode quality. The tools utilized to date include standard electrode fabrication techniques, UV-VIS, rheology, electrode cross sectioning, EELS, synchrotron x-rays, peel tests, bend tests, and electrochemical testing. Through this combination of testing protocols and analysis we were able to identify several sources that limit production and performance of thick electrodes.

Results

The focus of this third year of the project was drying rate on electrode quality and performance. To start, a methodology was needed for drying lab-scale laminates in a way similar to that found in an industrial setting. Up until now, all drying was performed on the draw down coater under ambient glove-box conditions over night. According to our industrial contacts, laminates are presently dried at approximately 30 meters per minutes using staged, dry-air, convective heating that sweeps up the volatile NMP. For a 100 m oven, it takes about 3 minutes to dry. To simulate this condition, our group still prepares laminates on a draw-down coater located in a glove box, but in order to dry at industry speeds, it was important to transfer freshly cast laminates into a convection oven. This is performed by casting the slurry on a current collector that is resting on a thin plate of aluminum (*ca.* 3/16 in. thick). Once cast, the entirety is moved to a rack in a convection oven operating at a set temperature. A thermocouple is placed between the rack and the aluminum plate and the temperature recorded. We have found that the best way to dry the plate without disturbing the slurry that rests on top is by having the air in the oven impinge on the aluminum plate from below. The laminates are dried in the oven at different temperature set points and the time at which the laminate appears completely dry is recorded. Several drying temperatures were established between 80°C to 180°C. The morphology of the dried laminates was characterized by optical microscopy and scanning electron microscopy. The mechanical performance of each laminate was studied through use of a bend test. The electrochemical performance of the final electrode was tested for rate capability, ASR as a function of DOD, and cycling capability. The temperature of the laminate as a function of time for a number of oven set-point temperatures is provided in Figure II.1.A.1.

One sees in the figure that the temperature reaches the set-point temperature in about 2 minutes. This does not mean that the laminate is dry, just up to the set point temperature. A bar graph of the time to dry for each oven set-point temperature is provided in Figure II.1.A.2. A fit to the data suggests a drying time that drops exponentially with temperature.

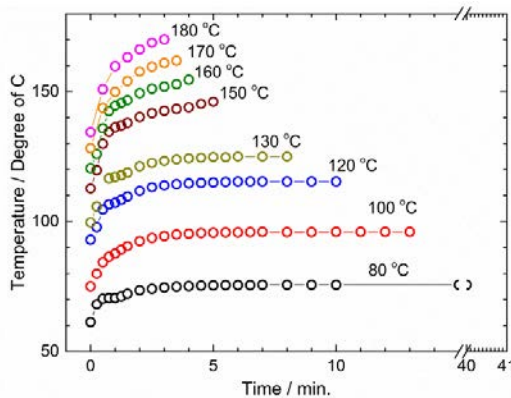


Figure II.1.A.1 Temperature versus time for laminates dried at different oven temperatures.

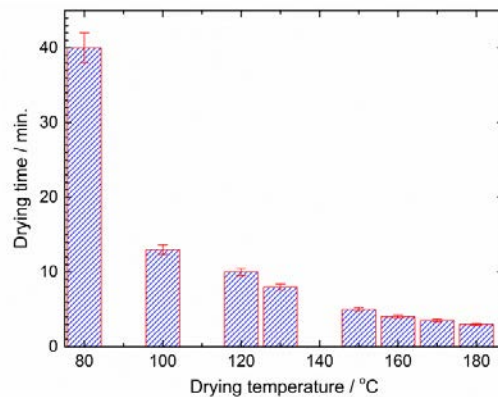


Figure II.1.A.2 Drying time versus oven temperature.

Figure II.1.A.3 shows the quality of the laminates. One can see that for laminates dried at a temperature greater than 150°C, major cracking occurs. The root cause of this cracking is thought to be the result of competing surface tension and viscous forces and will be further investigated in the next year.

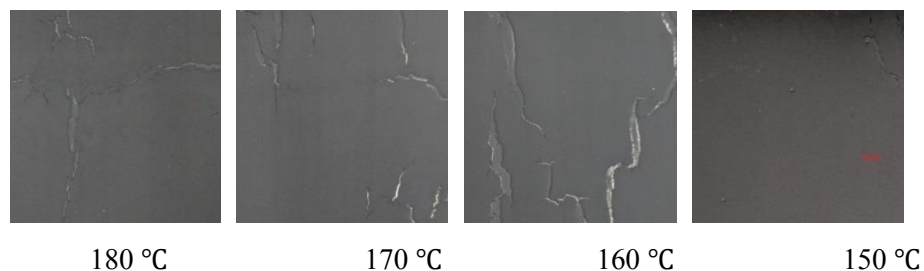


Figure II.1.A.3 Photos of laminates dried at different temperatures.

Thus our drying technique allows for the laminates to reach oven temperature within the first two minutes of being introduced; the laminates were dried within 40 and 3 minutes at oven temperatures between 80 and 180°C, respectively. Briefly, what we discovered is that thick electrodes (of 5 mAh/cm² loadings) displayed “mud cracking” when dried at a temperature greater than 130°C. Next, we measured the mechanical properties and electrochemical performance (30-sec pulse-power resistance as a function of DOD) of the laminates.

The adhesion is measured on a peel tester where the face of the laminate sample is attached to a vertical substrate, tape is attached to back of the current collector, and the tape is pulled vertically straight up with an arm that can measure force. Figure II.1.A.4 shows the adhesion of the laminate to the current collector in N/m and the cohesion of the laminate after the current collector is removed in N/m² for electrodes dried at different temperatures. One immediately sees that the adhesion and cohesion forces mimic each other and that there is a peak in the data at 130°C. This corresponds to the maximum temperature that the electrodes can be dried without displaying mud cracking. Thus, as the drying temperature is increased, the mechanical properties improve up until 130°C, at which point the mechanical properties deteriorate.

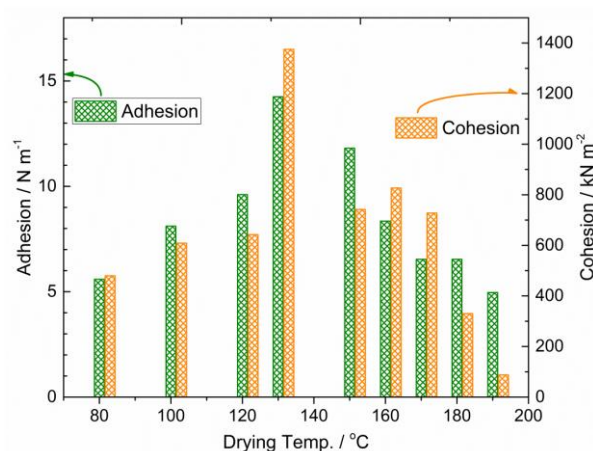


Figure II.1.A.4 Adhesion (green) and cohesion (orange) of the laminates dried at different temperatures as measured on a peel tester in N/m and N/m², respectively.

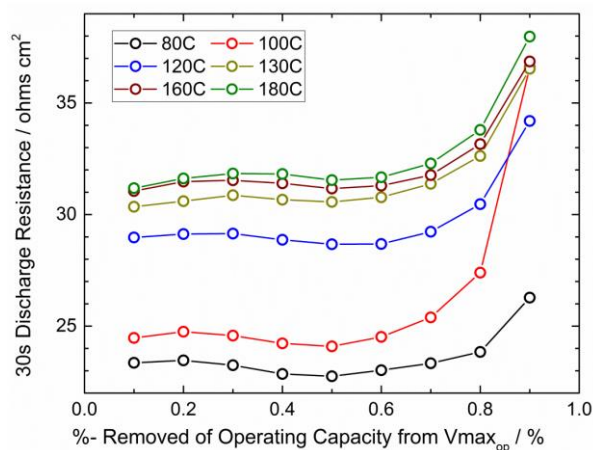


Figure II.1.A.5 Area specific resistance as a function discharge % for laminates dried at different temperatures.

Figure II.1.A.5 shows the 30-second pulse-power resistance data as a function of depth-of-discharge for laminates dried at different temperatures. The resistance is measured by applying a current pulse for 30 seconds and dividing the voltage difference of the cell at the beginning and end of the current pulse. Contrary to the mechanical properties, the resistance of the electrodes increases with laminate drying temperature starting at 80°C but levels out at 130°C. Going forward, we hope to shed light on the differences in trends between the mechanical and electrochemical properties.

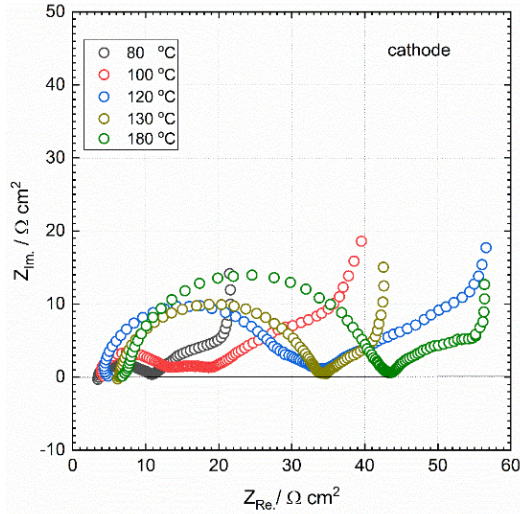


Figure II.1.A.6 Nyquist plot of EIS data of electrodes dried at various temperatures.

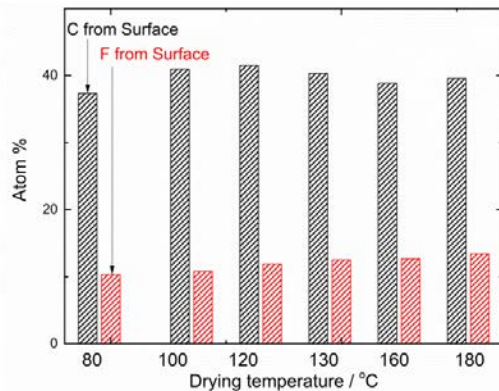


Figure II.1.A.7 The atomic percentage of C and F measured on the surface of electrodes dried at different temperatures as measured by EELS.

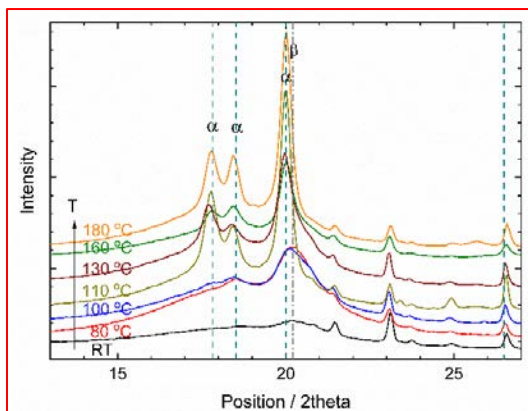


Figure II.1.A.8 X-ray data of PVDF films formed by drying from solutions at different drying temperatures.

To better understand the rise in resistance with drying temperature, we built cells with reference electrodes and utilized EIS. The results of the EIS for the cathode *versus* the reference electrode are provided in Figure II.1.A.6. One sees in this figure that the impedance follows roughly the same trend of increasing with temperature as the pulse power data from the HPPC tests. However, this set of data is quite confusing as it does not systematically show an increase in any one particular frequency space. Further work is needed to help comprehend the variations of different contributions.

We also conducted electron energy loss spectroscopy (EELS) on the surface of the laminates to help understand changes with drying temperature; the results of this analysis are provided in Figure II.1.A.7. Here, one sees a slight but continuous increase in F found at the surface of the electrode with drying temperature. Since these electrodes have never been placed in a cell, the only source of F is from the binder. This suggests that the binder is migrating to the surface faster with increase in drying temperature.

As noted, the electrochemical performance of a thick cathode laminate indicates less pulse power capability for electrodes dried at higher temperatures, although better mechanical properties. We also reported slightly higher fluorine concentrations at the surface of electrodes dried at higher temperatures and higher impedance based on ac-impedance data. It is possible that the better mechanical properties as indicated by peel tests are a result of more binder at the surface. This could also explain the poorer rate performance if the binder is prohibiting the transport of electrolyte through the surface of the electrode.

It is well known that PVDF is crystalline at room temperature and solubilizes in NMP. What we recently learned is that if PVDF is precipitated out of a solvent, the temperature at which the solvent is removed, impacts its crystalline structure (1). These structures are referred to as α , β , γ and δ . What is reported is if the polymer slurry dried below 70°C, β -phase is formed; if dried between 70 and 110°C, α - and β -phases are present; and if dried above 110°C, α phase is predominant. Our electrodes in the previous reported work were dried in an oven set at temperatures between 80 and 150°C.

To understand the impact of drying temperature on the polymer crystallinity and the ionic conductivity through the polymer when swollen with electrolyte, thin films of polymer were produced from slurries dried between 80 and 180°C. After drying, the films were subjected to x-ray

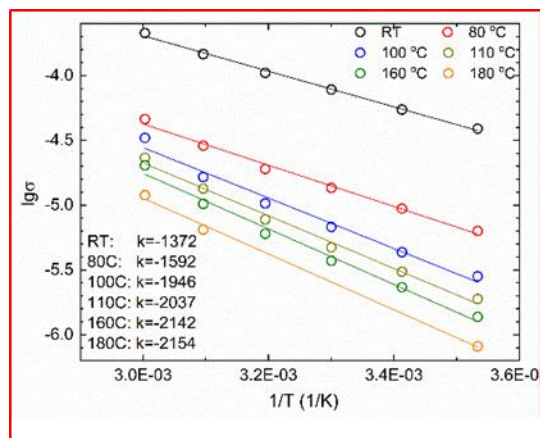


Figure II.1.A.9 Ionic conductivity of electrolyte in PVDF films prepared by drying from solutions at different temperatures.

from solutions at high temperatures.

diffraction; the results are provided in Figure II.1.A.8. Here we see confirmation of the formation of α and β phases dependent on drying temperature.

Once dried, electrolyte was added to the laminates and the conductivity measured in a cell with two blocking electrodes. The temperature of the electrochemical cell was varied from 10 to 110°C in acquiring the high frequency intercept and using that data in an Arrhenius plot to extract the activation energy of the conductivity. The results of this effort are provided in

. Here, one clearly sees that the conductivity of the polymer films decrease with drying temperature and that the slope of the data on the Arrhenius plot increases with drying temperature up until 100°C, indicating the activation energy for ionic conductivity increases with drying temperature, and hence that ionic motion is inhibited when the binder is dried

Conclusions

The conditions of battery electrode fabrication, which are strongly temperature and solvent fraction dependent, can lead to slightly differing electrode morphologies that in turn lead to significantly different electrode performance. To produce high-performing thick electrodes at today's speeds or faster will require a complete understanding of this relationship. We believe that viscosity, buoyancy, surface tension, and polymer crystallinity, which are all impacted by temperature, play critical roles.

Key Publications

1. "Effect of excess lithium in LiMn₂O₄ and Li_{1.15}Mn_{1.85}O₄ electrodes revealed by quantitative analysis of soft X-ray absorption spectroscopy," Zengqing Zhuo, Paul. Olalde-Velasco, Timothy Chin, Vincent Battaglia, Stephen J. Harris, Feng Pan, and Wanli Yang, *Appl. Phys. Lett.* **110**, 093902 2017, doi.org/10.1063/1.4977502
2. "Multi-hierarchical nanosheet-assembled chrysanthemum-structured Na₃V₂(PO₄)₃/C as electrode materials for high-performance sodium-ion batteries," Y Ruan, J Liu, S Song, N Jiang, V Battaglia, *Ionics*, Volume **24**, Issue 6, pp 1663–1673, 2018, doi.org/10.1007/s11581-017-2342-0
3. "Understanding the crack formation of graphite particles in cycled commercial lithium-ion batteries by focused ion beam - scanning electron microscopy," Na Lin, Zhe Jia, Zhihui Wang, Hui Zhao, GuoAi, Xiangyun Song, Ying Bai, Vincent Battaglia, Chengdong Sun, Juan Qiao, Kai Wu, Gao Liu, *Journal of Power Sources* **365**, Pages 235-239, 2017, doi.org/10.1016/j.jpowsour.2017.08.045
4. "Ultrahigh-Capacity Organic Anode with High-Rate Capability and Long Cycle Life for Lithium-Ion Batteries," Yan Wang, Yonghong Deng, Qunting Qu, Xueying Zheng, Jingyu Zhang, Gao Liu, Vincent S. Battaglia, and Honghe Zheng, *ACS Energy Lett.* **2**, pages 2140-2148, 2017, DOI: 10.1021/acsenderglett.7b00622

References

1. Rinaldo Gregorio, Jr. , *Journal of Applied Polymer Science*, Vol. **100**, 3272–3279 (2006).

II.1.B Advanced Polymer Materials for Li-ion and Correlative Microscopy Characterization of Electrochemical Hotspots in Oxide Electrodes (SLAC)

Zhenan Bao, Principal Investigator

Stanford University
443 Via Ortega, Shriram Center
Stanford, CA 94305
E-mail: zbao@stanford.edu

Yi Cui, Principal Investigator

Stanford University
476 Lomita Mall, McCullough Building
Stanford, CA 94305
E-mail: yicui@stanford.edu

Tien Duong, DOE Technology Development Manager

U.S. Department of Energy
E-mail: Tien.Duong@ee.doe.gov

Start Date: October 1, 2017	End Date: September 30, 2018	
Project Funding (FY18): \$300,000	DOE share: \$300,000	Non-DOE share: \$0

Project Introduction

Li easily reacts with electrolyte components to form a natural SEI, which is full of defects and ‘hot spots’ with higher current density. This leads to faster Li deposition and formation of dendrites. Additionally, large volume change of Li metal anodes during stripping/plating will expose fresh Li surface to electrolyte. The irreversible and uncontrollable parasitic reactions between Li metal and electrolyte components aggravate Li consumption, further forming dead Li, lowering the CE, and devastating the cycle life of Li metal anodes. [1], [2], [3] These problems are major obstacles against their practical application. With the implementation of a polymer-based protective layer which functions as an artificial SEI with desired properties, we were able to enhance the performance of Li metal electrodes.

Objectives

This project will develop new polymer materials for batteries. The team will develop polymer coatings with specific mechanical properties that can accommodate the volume expansion and contraction of the Li-metal anode associated with deposition and stripping (charging and discharging).

Approach

The project uses soft polymer coatings with dynamic crosslinking to give the resulting polymers liquid-like rheological properties and stretchable and self-healing properties. In previous work, the project has shown that such coatings resulted in uniform deposition/stripping of lithium metal and improved cycling stability of Li-metal electrodes. To understand the design rules for effective polymer coatings, we chose a few representative polymers to systematically understand structure property relationships. Here, we investigate the correction between surface energy of the polymer and exchange current for lithium deposition.

Results

Selection of polymers for systematic understanding. In order to develop a clear fundamental picture of the processes affecting Li metal deposition, we prepared a number of polymer coatings with various chemical and mechanical properties to investigate the importance of these parameters to the quality of the electrodeposited Li metal. For this study, we systematically chose several different polymers that have been previously used in battery applications. Poly (ethylene oxide) (PEO) is a common solid polymer electrolyte, and polyurethane (PU) and poly (vinylidene fluoride) (PVDF) are common gel electrolytes. Additionally, PVDF and poly

(vinylidene fluoride-co-hexafluoropropylene) (PVDF-HFP) are also common binder materials for composite electrodes. Poly (dimethylsiloxane) (PDMS) was tested because it has been used previously as a coating to stabilize Li metal. We also modified the mechanical properties of our previously reported adaptive (self-healing) polymer (SHP) coating with chemical crosslinking to obtain a self-healing elastomer (SHE) with different mechanical properties but almost identical chemistry. The thermal and mechanical properties of the polymers were characterized in detail, and the following distinct groupings can be observed (Figure II.1.B.1). PEO, PVDF, and PVDF-HFP are rigid, semi-crystalline solids exhibiting high initial modulus and plastic deformation after strain is applied. They are characterized by frequency-independent storage modulus and clear first order phase transitions corresponding to the melting of the crystalline domains. The stress-strain curves show that these properties will give rise to tough, but deformable polymer coatings at room temperature. The SHP and PDMS coatings are highly adaptable to mechanical strain due to the viscoelastic nature of these two polymers. Both polymers have liquid-like mechanical properties at low frequencies with the loss modulus dominating over the storage modulus. While the SHP is a flowable viscoelastic material, the SHE is a covalently crosslinked elastic solid. Similarly, the PU used here is a soft elastomer with high stretchability and low glass transition temperature (T_g). These elastic coatings should be able to deform and potentially recover from applied strain, but these films will not have the adaptive qualities of the SHP and PDMS due to solid-like properties of both elastomers. Even at long time scales, the SHE and PU both behave as solids and will not significantly flow or adapt without external stimuli. Overall, PEO, PVDF, and PVDF-HFP have the mechanical properties of traditional thermoplastics, PU and SHE are soft elastomers, and PDMS and SHP are viscoelastic materials.

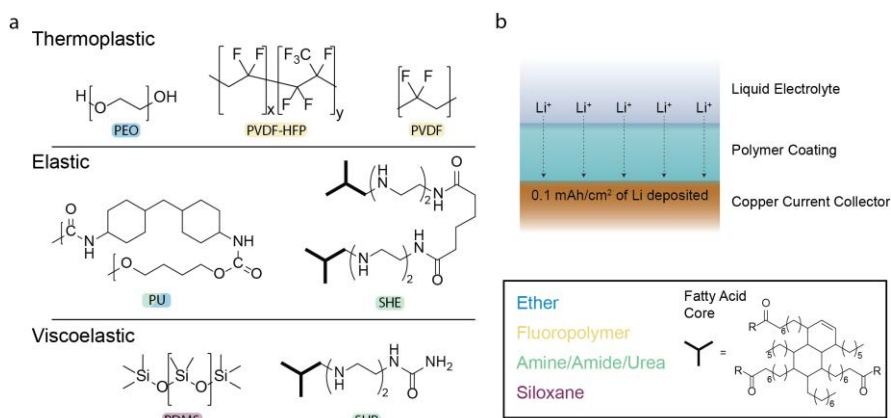


Figure II.1.B.1 (a) Chemical structures of the polymer coatings used in this study. Coloring of the label corresponds to the chemical functionality of the polymer. (b) Diagram of the conditions used to study the initial stages of Li metal growth under polymer coatings

Coating Chemistry and Li Morphology. We compared the SHP and SHE coatings to understand the effects of polymer coating mechanics on Li deposition. Both polymers have similar chemistry, but the SHP is a flowable viscoelastic material while the SHE is a covalently crosslinked elastic solid. The high density of hydrogen bonding groups in the SHE still allows for self-healing to occur. We observed that the overall uniformity of the Li deposition was very poor for the SHE compared to the flowable SHP (Figure II.1.B.2b,d), indicating that the mechanical properties and coating quality of a polymer film are important for uniform deposition. However, when closely examining the individual Li deposits we noticed that both the SHP and SHE coatings grew Li with nearly identical shapes (Figure II.1.B.2c,e). This suggests that the chemical functionality of the polymer is a main factor dictating the local Li morphology.

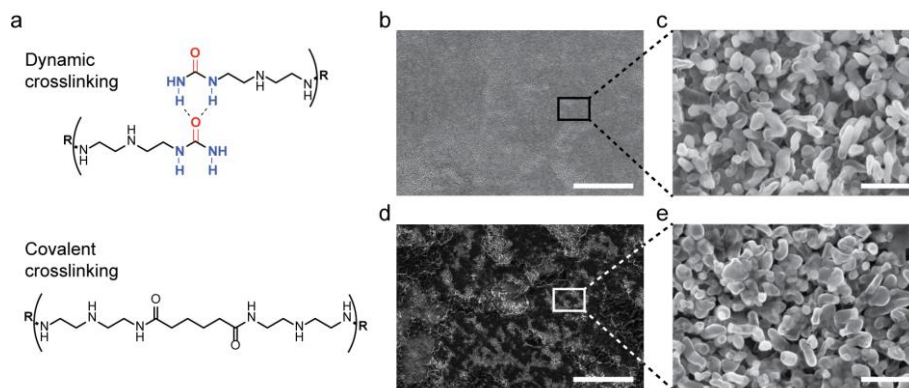


Figure II.1.B.2 (a) Chemical structures of the dynamic crosslinking of the SHP and covalent crosslinking of the SHE. SEM images of 0.1 mAh/cm² of lithium electrodeposited on polymer coated copper. The electrodes are coated with (b-c) a supramolecular adaptive coating and (d-e) a covalently crosslinked self-healing elastomer with similar chemistry to the supramolecular coating. Scale bars are 50 μm for b and d, and 1 μm for c and e.

To further investigate the effects of the chemistry of the polymer coating we tested the other polymers described above. Every polymer coating tested was found to improve the coverage of initial Li deposits on the electrode over that of uncoated Cu, which showed many exposed regions of bare surface (Figure II.1.B.3a). This suggests that the polymer coatings increased the density of lithium nucleation, leading to more uniform electrode coverage. However, this increased density of Li particles is not correlated to increases in the overpotential measured for the deposition as one would expect from classical nucleation theory.

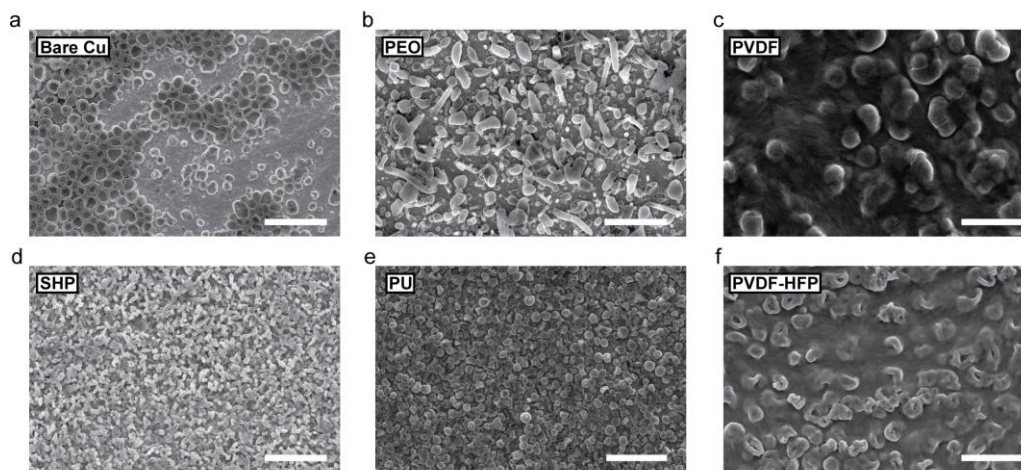


Figure II.1.B.3 SEM images of 0.1 mAh/cm² of lithium electrodeposited on copper with (a) no polymer coating, (b) PEO coating, (c) PVDF coating, (d) SHP coating, (e) PU coating, and (f) PVDF-HFP coating. Scale bars for all images are 5 μm.

Interestingly, we also noticed that the shape or size of the Li particles changed depending on the polymer coating. For example, SHP and PEO altered the Li deposits to be very small in diameter (10² nm) and nearly filamentary or rod-like in shape (Figure II.1.B.3b,d), while PVDF and PVDF-HFP changed the Li particles to be much larger (10³ nm) and globular (Figure II.1.B.3c,f). Since there is no clear correlation of the Li deposit behavior with the modulus or viscoelasticity, it suggests that the polymer mechanical properties do not solely dictate Li morphology and cannot fully predict the intricate chemistry of lithium growth dynamics. This is especially clear when comparing the PEO and PVDF polymer coatings. Even though these materials have similar modulus and stress-strain behavior, the size and shape of the Li deposits differed drastically. These differences in particle size depend on both the nucleation and growth processes of the Li metal, which are influenced by the specific coating chemistry and will be discussed in later sections. Ideally, lithium metal

would be deposited as a dense, uniform film on the electrode to minimize the contact area with the electrolyte and the potential for forming dead lithium particles electronically separated from the electrode. Coatings that promote this type of growth and are electrochemically stable over long-term battery cycling should provide the best performance.

Exchange Current Density. Initially, we presumed that the difference in nuclei size was a result of changes in the nucleation overpotential, as per classical nucleation theory. However, we found that the differences in the overpotential for the Li nucleation event measured from the galvanostatic charging were not enough to explain the variation in nuclei size, let alone their shape or morphology. This galvanostatic nucleation overpotential is a combination of all of the different overpotential components present in the coin cell including competition between the double layer capacitance and the nuclei growth. In order to more accurately characterize the electrochemical processes occurring in the system, we turned to measuring the Li exchange current density which reflects the direct interaction of the polymer coating with the Li metal surface and can provide more precise information about the overpotential in the system. (See Table II.1.B.1.) Generally, lower values of the exchange current density mean that the surface of the Li metal is inhibited or passivated, and in the field of electrodeposition inhibition represents the degree to which additive molecules absorb to the active metal surface and suppress the reduction reaction. In the case of our control system (ether electrolyte with 1 wt.% LiNO₃), the LiNO₃ acts as an inhibitor, which promotes the growth of rounded Li particles and improves the coulombic efficiency. For Li deposition on polymer-coated electrodes, the specific polymer coatings take on the role of inhibitors because they are directly in contact with the Li surface at the onset of and throughout deposition. Thus, the exchange current densities measured would ideally represent the level of inhibition or the strength of absorption and interaction of the polymers with the as-deposited Li metal and provide some relation to the Li morphology observed.

Table II.1.B.1 Properties of the polymer coatings in the battery environment.

Polymer	Overpotential ^a [mV]	j_0 ^b [mA/cm ²]	Swelling [%]	σ ^c [mS/cm]	Size [um]
PU	76.8	20	595.0	0.10	0.54
PVDF-HFP	80.2	39	27.2	0.07	2.85
PEO	87.8	22	Soluble	0.27	0.41
PDMS	121.3	5	28.0	0.10	1.26
SHP	129.9	27	Soluble	0.15	0.26
PVDF	151.0	27	27.5	0.06	3.32

^a Nucleation overpotential determined from galvanostatic cycling. ^b Exchange current density. ^c

It is challenging to accurately measure the exchange current density in traditional coin cell geometries because of SEI forming reactions that occur on the surface of the Li metal. Fast sweep rates would allow this limitation to be overcome, but are generally not possible due to mass transport limitations. Here we utilized a homebuilt microelectrode, a technique known to overcome the mass transport limitations, to perform cyclic voltammetry sweeps at high rates of 200 mV/s. At these high sweep rates the freshly deposited Li is in direct contact with the polymer coating because the short timescale (~2 s) of the scan minimizes any reactions of the Li metal and electrolyte that may occur. These quick scan rates prevent resistive SEI formation from influencing the experiment and provide accurate measurement of the exchange current density, which reflects how the polymer coating interacts with the Li metal surface.

Exchange current, Surface energy, and Li particle size As mentioned above, the mechanical properties of the polymer coating and the overpotential measured from galvanostatic deposition could not accurately predict the size of the Li particles that were deposited. We also found that the swelling, ionic conductivity, or resistance of the film did not follow any discernable trend (Figure II.1.B.4b). However, we observed that the

exchange current increased with dielectric constant of the polymer coating (Figure II.1.B.4b and Figure II.1.B.4a). PVDF-HFP contains a high density of polarizable fluorinated groups and has a higher dielectric constant of 15. PVDF-HFP also exhibited the highest measured exchange current. PDMS has a much lower

dielectric constant of 2.7 because of the nonpolar nature of the siloxane chemistry and exhibited the lowest exchange current measured. The other polymers tested have intermediate dielectric constants and their exchange current densities fell in between that of PVDF-HFP and PDMS. We hypothesize that the relationship between dielectric constant and exchange current is due to the better solvation of Li^+ ions at the lithium-polymer interface from improved charge screening by the high dielectric constant coatings. This allows for easier dissolution and solvation of the Li from the metal electrode surface and could also increase the concentration of Li^+ ions available for deposition locally. These phenomena would cause an increase in exchange current between the Li metal surface and the electrolyte and are different effects from the adsorption-based inhibition that happens in the case of low concentration additives added to electrolyte solutions.

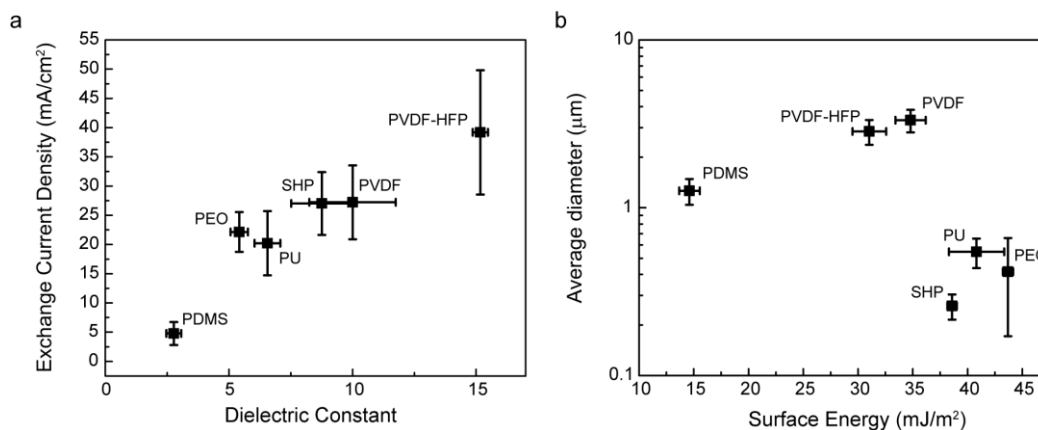


Figure II.1.B.4 (a) Exchange current density plotted against dielectric constant for various polymer coatings measured via microelectrode. (b) The average diameter of the Li deposited under various polymer coatings plotted against the surface energy of those coatings.

We also noticed that in general, the size of Li deposits increased for the polymer coatings with higher exchange current. However, PDMS presents a notable exception. Even though it has a very low exchange current due to a low dielectric constant, the Li deposited under the PDMS coating grows into large particles around 1.26 μm in size. When we reexamined the relationship between deposit size and other polymer properties, we found that PU, PEO, and SHP coatings all had high surface energy and promoted the growth of small Li particles around 100-400 nm in size (Figure II.1.B.4b). The higher surface energy coatings should have enhanced adhesion to the Li metal surface compared to the lower surface energy polymers, and this stronger polymer-Li interaction serves to stabilize the Li-polymer interface. When both surface energy and exchange current are considered as relevant parameters, the anomalous size of the Li in the presence of the PDMS coating can be understood. The low surface energy of PDMS (14.6 mJ m⁻²) resulted in a larger average particle size than the other polymers with low dielectric constants, but smaller than the ~3 μm particles from intermediate surface energy, high dielectric constant PVDF and PVDF-HFP.

Simultaneously, polymers with low surface energies have a weaker interaction with the Li metal, and therefore do not reduce the polymer-Li interfacial energy as much as high surface energy polymers. With increased interfacial energy, the Li will deposit as larger particles to minimize surface area and reduce the total energy of the Li-polymer interface. Figure II.1.B.5 schematically illustrates the effects of the exchange current and interfacial energy on the Li particle size as described through the polymer dielectric constant and surface energy. In general, larger Li particles deposited under polymer coatings correspond to polymers with high dielectric constant and low surface energy.

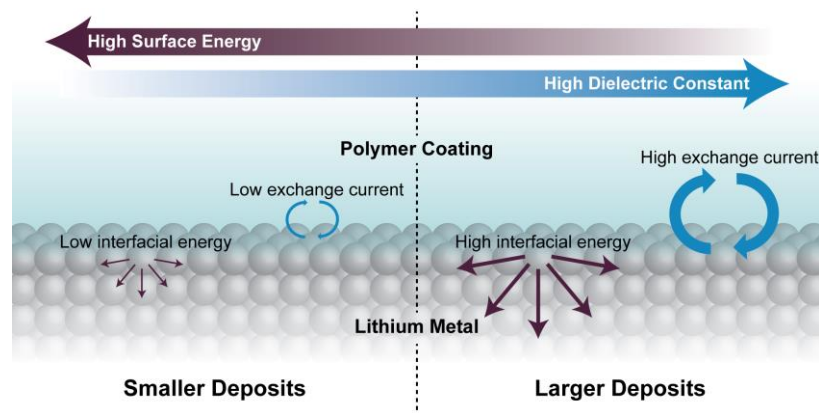


Figure II.1.B.5 Schematic of the factors influencing Li metal deposition through a polymer coating. Low surface energy coatings give rise to higher interfacial energies and encourage the growth of large surface area particles. Additionally, high dielectric constant polymers have higher exchange currents and promote larger Li metal deposits.

Conclusions

By examining the initial stages of Li deposition and growth in the presence of polymer coatings we have found that the chemistry of a polymer coating has significant impact on Li electrodeposition. The chemical functionality of a polymer coating resulted in different local Li deposit morphology, but coating mechanical properties, including modulus and flowability, and uniformity are still very important for the global deposition quality. We additionally found that the dielectric constant, and thus the solvation environment of the Li^+ ions, of the respective coatings determine the exchange current in the presence of polymer coatings. Furthermore, the size of the Li particles is dependent on both the dielectric constant, due to effects of the exchange current on nucleation, and surface energy, due to energetics of the Li-polymer interface, of the polymer coatings. Finally, both coating thickness and reactivity should additionally be considered as they both have large effects on coating performance. Moving forward, new coatings should be designed with high dielectric constant, low surface energy, and low reactivity. Ideally, a coating would also be soluble in nonpolar solvent or amenable to melt processing below lithium's T_m at 180°C . This would allow for direct coating on the Li metal surface, which is important for the fabrication of practical lithium metal batteries that are unlikely to be anodeless. The insight provided here should serve as a starting point for further systematic investigation into soft organic coatings that can potentially help to enable the uniform and reversible deposition of lithium metal at high rates and over long times.

Key Publications

1. J. Lopez, A. Pei, J. Y. Oh, G.-J. N. Wang, Y. Cui, Z. Bao "Effects of Polymer Coatings on Electrodeposited Lithium Metal", *J. Am. Chem. Soc.*, 140, 11735-11744, (2018)
2. D. G. Mackanic, W. Michaels, M. A. Lee, D. Feng, J. Lopez, J. Qin, Y. Cui, Z. Bao, "Crosslinked Poly(tetrahydrofuran) as a Loosely-Coordinating Polymer Electrolyte", *Adv. Energy Mater.*, 8, 1800703 (2018)

References

1. Xu, W. et al. Lithium metal anodes for rechargeable batteries. *Energy Environ. Sci.* 7, 513–537 (2014).
2. Lin, D., Liu, Y. & Cui, Y. Reviving the lithium metal anode for high-energy batteries. *Nat. Nanotechnol.* 12, 194–206 (2017).
3. Xu, K. Electrolytes and Interphases in Li-Ion Batteries and Beyond. *Chem. Rev.* 114, 11503–11618 (2014).

II.2 Next Generation Lithium-Ion Batteries: Advanced Anodes R&D

II.2.A Next Generation Anodes for Lithium-Ion Batteries: Silicon (ANL, LBNL, ORNL, SNL, NREL)

Jack Vaughey, Principal Investigator

Argonne National Laboratory
 9700 South Cass Avenue
 Argonne, IL 60439
 E-mail: vaughey@anl.gov

Brian Cunningham, DOE Technology Development Manager

U.S. Department of Energy
 E-mail: Brian.Cunningham@ee.doe.gov

Start Date: October 1, 2017 End Date: September 30, 2018
 Project Funding (FY18): \$300,000 DOE share: \$300,000 Non-DOE share: \$0

Project Introduction

Silicon has received significant attention as an alternative to graphitic carbon negative electrode in a lithium-ion battery due to its high capacity and availability.[1] Compared to graphitic carbons, elemental silicon has nearly an order of magnitude higher capacity (~3600 mAh/g Silicon vs 372 mAh/g Graphite), however, several problems have been identified that limit its utility including a large crystallographic expansion (~320%) upon lithiation, slow lithium diffusion, and high reactivity at high states of charge. Together these physical properties can result in particle cracking, particle isolation, electrolyte reactivity, and electrode delamination issues. These chemical reactivity and volume changes are manifested in SEI stability and cycling efficiency issues for the cell. Keeping this in mind, the large number of studies focused on silicon based electrodes is a testament to the opportunity it presents but also the size of the challenge and innovation it inspires on multiple fronts.

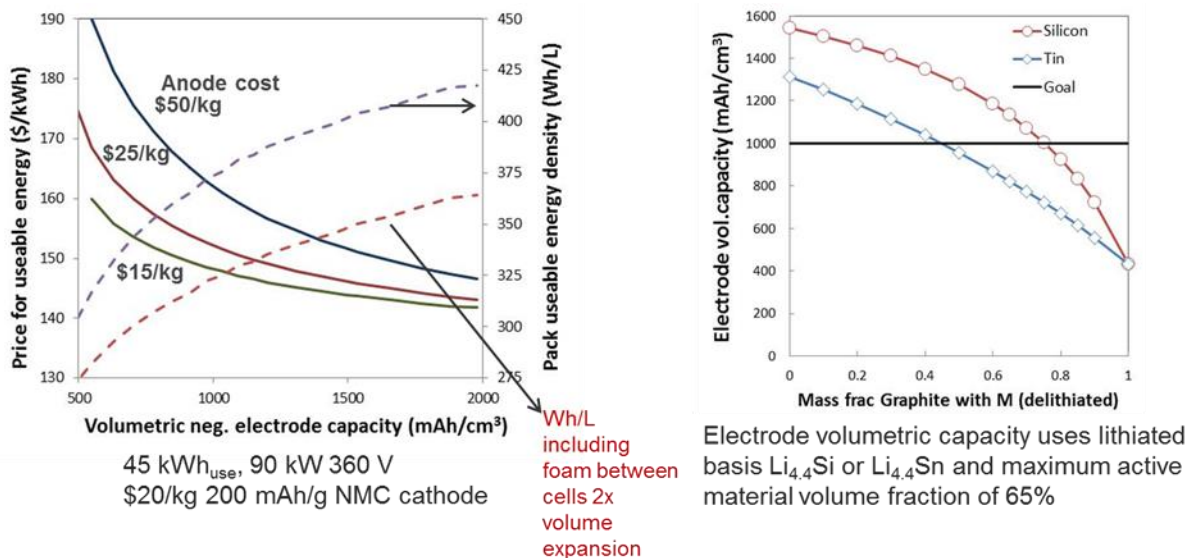


Figure II.2.A.1 Battery Performance and Cost (BatPaC) model utilized to establish relevance by connecting pack to anode targets.

BatPaC [2], a techno-economic program designed to model lithium-ion battery performance and cost, was utilized to establish program relevance by connecting DOE/USABC pack performance targets to anode targets. To set goals for the program, BatPac was used to (see Figure II.2.A.1, left frame), show that anode volumetric

capacities greater than 1000 mAh/cm³ generally minimizes battery cost when coupled to an advanced NMC cathode. Note that higher capacities result in diminishing savings in cost. The analysis (right frame) also predicts that silicon-graphite electrodes with less than 75 wt% graphite can achieve the 1000 mAh/cm³ target.

Next Generation Anodes for Lithium-Ion Batteries, also referred to as the Silicon Deep Dive Program, is a consortium of five National Laboratories assembled to tackle the barriers associated with development of an advanced lithium-ion negative electrode based upon silicon as the active material. This research program has several goals including baselining promising silicon materials that can be either developed by a team member or obtained in quantities sufficient for electrode preparation by the consortiums facilities, developing a composite Si-Gr electrode that meets BatPac specifications, and executing full cell development strategies that leverage DOE-EERE-VTO investments in electrode materials and characterization. The primary objective of this program is to understand and eliminate the barriers to implementation of a silicon based anode in a lithium-ion cell. The five National Laboratories involved are focused on a single program with continuous interaction, clear protocols for analysis, and targets for developing both an understanding and a cell chemistry associated with advanced negative electrodes for lithium-ion cells. This undertaking is a full electrode/full cell chemistry project leveraging baseline electrodes prepared at the consortium facilities. All efforts are directed to understanding and developing the chemistry needed for advancing silicon-based anodes operating in full cells. Materials development efforts include active material development, binder synthesis, coatings, safety, and electrolyte additives. Efforts include diagnostic research from all partners, which span a wide range of electrochemical, chemical and structural characterization of the system across length- and time-scales. Specialized characterization techniques developed with DOE-EERE-VTO funding, include neutrons, MAS-NMR, optical, and X-ray techniques being employed to understand operation and failure mechanisms in silicon-based anodes. In addition, several strategies to mitigate lithium loss are being assessed. The project is managed as a single team effort spanning the Labs, with consensus decisions driving research directions and toward development of high-energy density lithium-ion batteries. A detailed list of participants is given in Figure II.2.A.2.

Research Facilities			
▪ Post-Test Facility (PTF)	▪ Materials Engineering Research Facility (MERF)	▪ Cell Analysis, Modeling, and Prototyping (CAMP)	▪ Battery Manufacturing Facility (BMF)
		▪ Battery Abuse Testing Laboratory (BATLab)	

Contributors			
▪ Daniel Abraham	▪ Steve George	▪ Min Ling	▪ Ilya A. Shkrob
▪ Eric Allcom	▪ Jinghua Guo	▪ Gao Liu	▪ Caleb Stetson
▪ Seong Jin An	▪ Binghong Han	▪ Wenquan Lu	▪ Wei Tong
▪ Chunmei Ban	▪ Atetegeb Meazah	▪ Maria Jose Piernas Muñoz	▪ Stephen Trask
▪ Ira Bloom	▪ Haregewoin	▪ Jagjit Nanda	▪ Jack Vaughey
▪ Anthony Burrell	▪ Andrew Jansen	▪ Kaigi Nie	▪ Gabriel Veith
▪ Peng-Fei Cao	▪ Haiping Jia	▪ Ganesan Nagasubramanian	▪ Yimin Wu
▪ Yang-Tse Cheng	▪ Sisi Jiang	▪ Bryant Polzin	▪ Taeho Yoon
▪ Dennis Dees	▪ Christopher Johnson	▪ Krzysztof Puppek	▪ Ji-Guang Zhang
▪ Fulya Dogan Key	▪ Kaushik Kalaga	▪ Marco-Tulio F. Rodrigues	▪ Liang Zhang
▪ Wesley Dose	▪ Baris Key	▪ Philip Ross	▪ Lu Zhang
▪ Zhijia Du	▪ Joel Kirner	▪ Rose Ruther	▪ Zhengcheng Zhang
▪ Alison Dunlop	▪ Robert Kostecki	▪ Niya Sa	▪ Tianyue Zheng
▪ Kyle Fenton	▪ Jianlin Li	▪ Yangping Sheng	
	▪ Xiaolin Li	▪ Youngho Shin	

Support for this work from Battery R&D, Office of Vehicle Technologies, DOE-EERE, is gratefully acknowledged – Brian Cunningham, Steven Boyd, and David Howell



Figure II.2.A.2 Program participants including Laboratories, research facilities, and individual contributors.

Objectives

- Understand and overcome the science and technology barriers to the use of silicon-based anodes in high-energy density lithium-ion batteries for transportation applications.
 - Stabilize the SEI
 - Stabilize the electrode
- Demonstrate functional prototype lithium-ion cell chemistries that include a silicon-containing anode which meet the DOE/USABC performance targets.

Approach

Sandia National Laboratories (SNL), Oak Ridge National Laboratory (ORNL), National Renewable Energy Laboratory (NREL), Lawrence Berkeley National Laboratory (LBNL), and Argonne National Laboratory (ANL) have teamed together to form an integrated program dedicated to identifying, developing an understanding, and proposing solutions to the problems associated with the commercialization of silicon as an active component of a lithium-ion electrochemical cell. Technical targets have been developed and regular communications have been established across the team. Throughout the program, there is a planned focus on understanding, insights into, and advancement of silicon-based materials, electrodes, and cells. All anode advancements will be verified based on life and performance of full cells. Toward that end, baseline silicon-based materials, electrodes, and cells have been adopted, along with uniform full cell testing protocols.

In examining improvements, changes to the baseline cell technology will be minimal but will be updated to reflect advances, new suppliers, and treatments. Studies of the present baseline systems have adopted a testing protocol from the literature [3] that has worked well for lithium-ion cells with silicon containing anodes. The test starts with three slow (C/20) formation cycles, an HPPC cycle, and then the C/3 aging cycles. The test ends with another HPPC cycle and three more slow (C/20) cycles. All constant current cycling is symmetric between charge and discharge rates. The tests are run at 30°C. If there is little or no aging in the first 100 cycles, the protocol can be repeated. This protocol effectively examines capacity, impedance, and aging effects in about a month's worth of testing. The present baseline silicon was developed and produced by Paraclete Energy (Chelsea, MI) and has been made available to all participants. The cathode is a commercial 532 NMC Cathode available from CAMP, and the electrolyte is 1.2M LiPF₆ in a 3:7 ratio of EC/EMC by weight (Gen2) plus 10 wt% FEC. Scale-up of materials, incorporation of materials advancements into electrodes, prototype cells, characterization, safety evaluation, abuse tolerance and testing of cells, are part of a wide range of integrated studies supported by battery research facilities at the National Labs working closely with the program. These research facilities include the Battery Abuse Testing Laboratory (BATLab), the Battery Manufacturing Facility (BMF), the Cell Analysis, Modeling, and Prototyping (CAMP), the Materials Engineering Research Facility (MERF), and the Post-Test Facility (PTF).

The fundamental understanding of silicon-based electrode active materials is based on extensive electrochemical and analytical diagnostic studies on components, electrodes, and cells conducted within the program. This effort contains in-situ and ex-situ studies on full and specialty cells, including reference electrode cells. Overall, the diagnostic studies are intended to help establish structure-composition-property relationships, including lithium-rich surface compounds, bulk transport, and kinetic phenomena. Together they form the basis for accurately assessing component and electrode failure modes and sets a path for advancements. Supported by the diagnostic studies, materials development on silicon-based materials, electrodes, and cells has been focused on enhancement of interfacial stability, accommodation of volume changes on lithiation, improvements in overall performance and life. A key avenue of research for this goal is the development and testing of surface coatings and electrolyte additives designed to modify and stabilize the dynamic silicon-electrolyte interface. In addition, functional polymer binders designed to accommodate volume changes, increase conductivity, and improve adherence are being developed and analyzed. Finally, the

program is exploring active material development including silicon composites, compounds, and the advantages of adding additional lithium inventory into the cell are being developed.

Communication of programmatic progress to battery community is critical. This will generally be accomplished through publications, presentations, reports, and reviews. Further, the program is open to industrial participation and/or collaboration that does not limit program innovation or the free flow of information. Finally, this program is highly integrated with the SEISta program, a sister program focused on stabilization of the silicon SEI layer. Generally, SEISta is focused on the development and characterization of model systems, surface analysis, well-defined active area thin film electrodes, lithium transport, and interfacial silicate phases and phenomena.

Results

1. Active Silicon-based Materials

Baseline Silicon Studies

Efforts in developing silicon-graphite composite electrodes consistently yielded significant capacity fade when utilizing the majority of silicon capacity contributions down to ~ 50 mV vs. Li^+/Li . Initial thoughts were that lower amounts of silicon (i.e. 15 wt.%) in a majority graphite-based electrode could result in reasonable cycle life while still maintaining an increase in capacity. The CAMP Facility first started evaluating high silicon content electrodes (~ 70 wt.%) in 2012 to the level of nearly full lithiation (~ 5 mV vs. Li^+/Li). These early cells provided impressive capacities, but would have significant capacity fade within 30 cycles. Capacity limitations to 1,000 mAh/g provided longer cycle life, but still only to around 100 cycles. Due to the poor performance observed with these high silicon-content electrodes, the majority of the CAMP Facility's efforts focused on developing silicon-graphite composite electrodes with the intention to prolong cycle life. While many variables including various silicon powders, binders, graphites, etc. have been investigated, the consistently poor cycle life performance suggested that the path forward to a better understanding of the silicon-based electrode lies with graphite-free silicon electrodes.

The CAMP Facility's revisiting of the high-silicon (graphite-free) electrode concept started with experimental coatings using Paraclete Energy's silicon powder with a composition of $\sim 71:10:19$ wt.% (silicon : conductive additive : LiPAA binder). The cells were cycled between 0.05 and 1.5 V to be able to directly compare against the performance of the 15 wt.% silicon-graphite electrode fabricated earlier in the project. The half-cell performance is shown in Figure II.2.A.3.

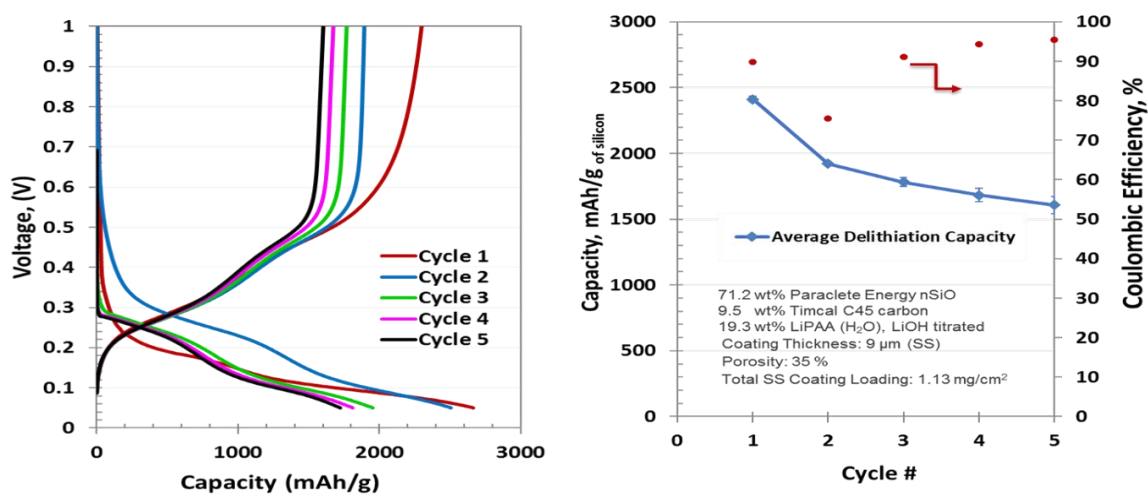


Figure II.2.A.3 Electrochemical results of an experimental silicon electrodes fabricated by the CAMP Facility. These cells were cycled between 0.05 to 1.5 V vs. Li^+/Li . Graphite was not used in this electrode.

After observing the electrode's capacity on a mAh/g and mAh/cm² basis, it was determined that the capacity match was close enough to the Silicon Deep Dive's NMC532 cathode baseline for full cell testing. Figure II.2.A.4 shows the resulting full cell performance of both the 15 wt.% silicon-graphite and high-silicon graphite-free anodes. The initial capacities of the high-silicon graphite-free cells are lower, however, the capacity fade rate is less such that the high-silicon graphite-free cells have higher capacity retention beyond the 70th cycle.

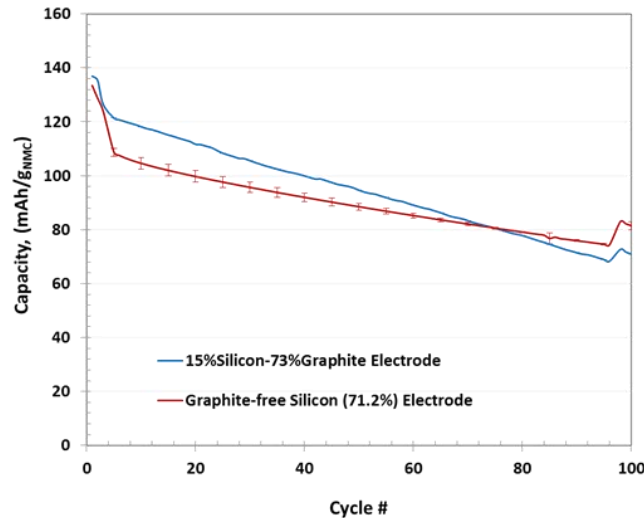


Figure II.2.A.4 Full cell results using the silicon deep dive protocol of the high-silicon graphite-free anode and 15 wt.% Si in graphite composite. Both cells were tested against a common capacity-matched NMC532 cathode. The anode to cathode capacity pairing for the electrode couples was based on the anode capacities achieved upon a 50-mV lithiation cutoff.

This promising result led the CAMP Facility to fabricate high-silicon (80 wt%) graphite-free electrode (A-A017) using the large batch (4 kg) of silicon powder acquired in FY18 from Paraclete Energy. Further studies of the A-A017 electrode included an evaluation of the degree of lithiation via half-cell voltage cutoffs and the resulting impact on capacity retention. Lower cutoff voltages of 0 mV, 50 mV, 100 mV, and a capacity limitation of 1,000 mAh/g were used to study this concept. The performance, shown in Figure II.2.A.5, suggests that indeed, limiting the utilization of a high-silicon graphite-free electrode improved cycling performance. The 100 mV lower cutoff limit provides reasonably high capacities in the initial cycles (higher than the 1000 mAh/g limit), while also showing more cycling stability compared to the 0 and 50 mV cutoff voltages. This result provides important information for the design targets for future high-silicon graphite-free electrode development.

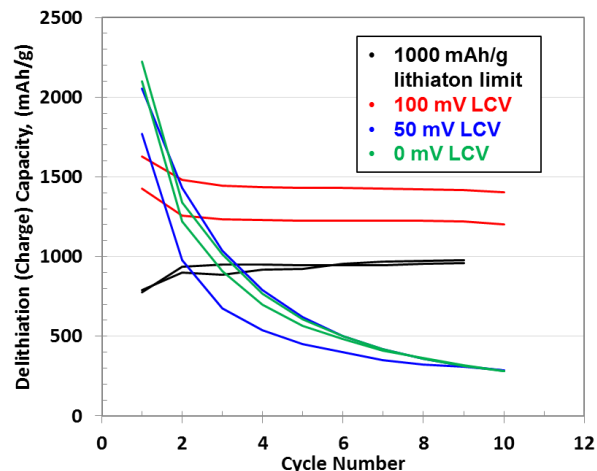


Figure II.2.A.5 Electrochemical results of the A-A017 high-silicon graphite-free electrode fabricated by the CAMP Facility.

These cells were cycled between various lower cutoff voltages (LCV) to 1.5 V vs. Li⁺/Li. Graphite was not used in this electrode.

These cells were cycled between various lower cutoff voltages (LCV) to 1.5 V vs. Li⁺/Li. Graphite was not used in this electrode.

Silicon Scale-up

In addition to the commercial Paraclete silicon samples we obtained, there is programmatic interest in securing an internal supplier for evaluation, testing, and modification that is controlled by the Laboratories. One alternative is development of an advanced bench-scale hydrothermal or solvothermal-based synthesis system to produce engineered silicon nanoparticles and composites. This method needs to be validated and materials characterized for surface passivation, purity, and scalability. The synthetic capability to be developed would be based on the design and construction of a turnkey hydrothermal or solvothermal-based synthesis reactor system capable of batch production of 10 to 50 g of nanoparticles per run.

Initial development centered on design and installation of a four liter hydrothermal or solvothermal-based system. Seen in Figure II.2.A.6(a), the high-temperature, high-pressure system was installed with significant safety devices in a walk-in hood. System stability and performance of the installed equipment were confirmed by adding 15 grams of NanoAmor Si particles (CAMP - Lot # 0142-071510, 130 nm) were injected into the reactor using water as a solvent, and heating to anticipated temperatures and pressures. The reaction mixture was allowed to stand for 1 hour at a reaction temperature of 392°C, a reaction pressure of 3500 psi and a stirring speed of 500 rpm. After cooling, the water and hydrothermally treated 15 grams of NanoAmor Si particles were evaluated and characterized.

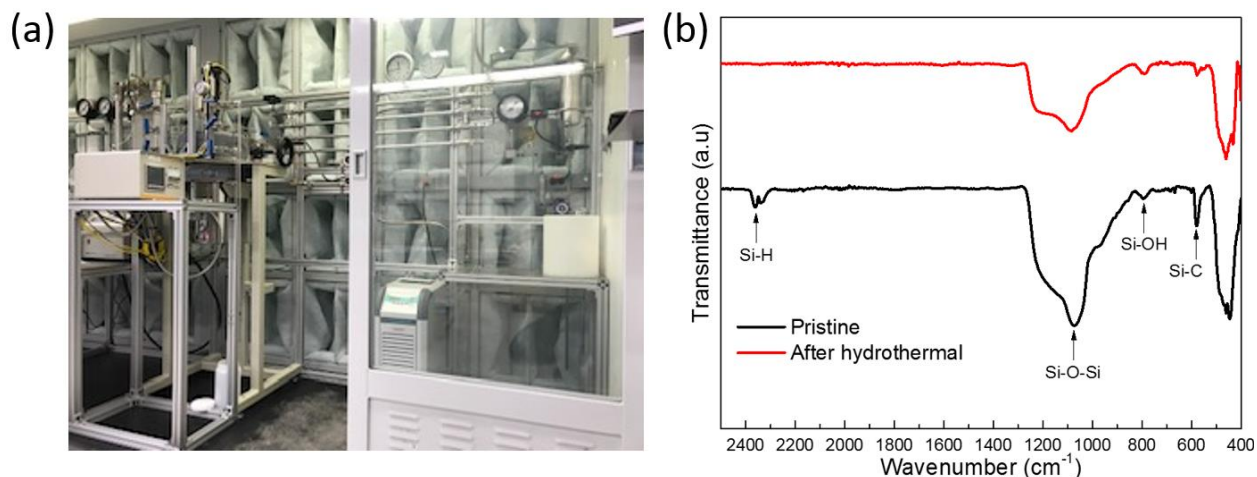


Figure II.2.A.6 Installed 4 L hydro/solvothermal reaction system (a) and FT-IR result comparison of pristine NanoAmor Si particles and their hydrothermally treated product

FTIR analysis of the Si particles before and after exposure to the high temperature high pressure water process showed little change in the Si-C (600 cm^{-1}) and Si-H (2350 cm^{-1}) peaks. Previous MAS-NMR studies had shown that while these NanoAmor samples are approximately 50% SiO_2 by weight, due to their small size and high surface area, the silica surface appears stable to the treatment.

Additional reaction studies, new solvents, alternative precursors, and detailed analysis of product stream are underway. This test has confirmed stable operation of the installed four liter hydrothermal or solvothermal-based synthesis system, stability of a passivated version of our desired product.

Porous Silicon

The cycle life and calendar life of Silicon-based anodes for Li-ion batteries are related to the surface area and passivation layer of the silicon used. By designing a stable porous Si structure in conjunction with an artificial SEI layer coated onto the surface of porous Si particles a more effective anode can be achieved. The degradation mechanism of Si anodes during shelf storage was systematically investigated using a highly porous structured Si that avoid pulverization during cycling process. However, the large surface area of micron sized porous Si particles may lead to continuous reactions between lithiated silicon and electrolyte, leading to continuous growth of SEI layer and an increase in cell impedance. We sought to minimize the surface area of Si while identifying additives necessary for long term stability of Si based Li-ion batteries. These materials, created by the high temperature reaction of magnesium with silica, have shown good performance compared to other silicon materials built with a combination of nanoscale porosity and a stable passivation coating.

In a full cell, additional information on the surface binder binding and the reactivity of the lithiated species is tied to the electrolyte used. Inspired by the similarity of the low potential and large volume change between Si and lithium metal, the localized high concentration electrolyte (LHCE) concept was used to try to enhance the stability of the baseline silicon. The LHCE chosen, an electrolyte composed of a mixture of triethyl phosphate (TEPa) and a miscible non-coordinating fluoroether (1.2M LiFSi/TEPa-3BTFE (E-313)), was used to test Si based anodes obtained from the CAMP facility. Initial results indicated that the TEPa-based localized high concentration electrolytes were not stable with the electrodes prepared using a LiPAA binder due to a reaction between the polymer binder and the TEPa

Replacing the LiPAA binder with a polyimide binder (PI) system, and carbon-coating the Paraclete silicon (with 10 wt% CVD carbon) to enhance surface binding on Si active was identified as a more stable model system to evaluate the LHCE electrolyte with silicon concept. The PI-based electrode was made to have a similar composition as those provided by ANL-CAMP facility. Using full cells based on NMC532 – Si(15)/Gr in baseline Gen2 + 10% FEC electrolyte showed that the PI binder in addition to the carbon coating was

needed to achieve a high first cycle efficiency and improved the cycling stability (Figure II.2.A.7a). On the other hand, the LHCE electrolyte demonstrated high stability with PI binder alone, and even better performance with the carbon coating on the silicon (Figure II.2.A.7b), indicating the importance of a full system optimization.

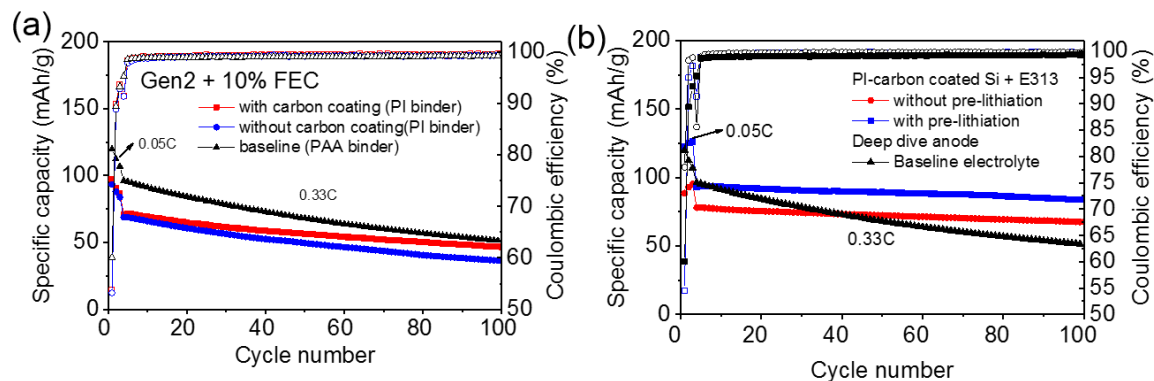


Figure II.2.A.7 a) cycling performance of NMC532 | Si/Gr cells with a) modified silicon anode with and without carbon coating in baseline electrolyte. b) modified silicon anode with carbon coating and PI binder in TEPA-based LHCE.

Silicon-Tin Composites

The Dahn group (Dalhousie University, Halifax, NS) has identified amorphous Si-Sn films with Sn content lower than 40 mol% as a series of compositions that show acceptable reversible capacities while demonstrating low irreversible capacity. For example the composition $\text{Si}_{0.64}\text{Sn}_{0.36}$ was shown to demonstrate a capacity of ~ 1900 mAh/g with a low irreversible capacity of ~ 100 mAh/g during the 1st cycle. [3] Ahn *et al.* later confirmed amorphous Si-Sn nanocomposite electrodes produced by magnetron co-sputtering method also demonstrated improved cycling when compared to an amorphous Si film at a similar thickness. [4] In general the advantage of the Si-Sn composite anode system arise from combining the large gravimetric capacity of Si with the excellent electrical conductivity and good ductility of Sn. [5], [6] Experiments to understand the lithiation / delithiation process and interplay between the two lithiated species in more detail have been initiated driven by the nanoscale interactions between the immiscible crystalline Si and Sn metals. Initial efforts have focused on thin film studies to assess non-homogeneous phases, stability, and electrochemical performance before developing a splat quenching method to produce bulk phases.

Before the synthesis of Si-Sn thin films, we first optimized Si thin film deposition by a DC magnetron sputtering method. Physical and electrochemical properties of the as-produced Si films were investigated using X-ray diffraction (XRD), scanning electron microscopy (SEM), energy-dispersive X-ray spectroscopy (EDS), and electrochemical methods to identify the optimal synthesis condition. Coin cells were assembled directly using the as-produced Si films deposited on Cu foils (1.6 cm^2) as the working electrodes, Li metal foil as the counter electrode, and 1 M LiPF_6 in ethylene carbonate (EC)-diethyl carbonate (DEC) (50: 50 wt%) as the electrolyte without the use of fluoroethylene carbonate (FEC) additive. The cells were cycled between 1.5 and 0.01 V at $C/20$ based on the experimental capacity. Cyclic voltammetry (CV) was carried out between 2 and 0.01 V at a scan rate of 0.1 mV/s.

A layer of 100 nm oxide is present on the Si wafer before deposition meanwhile, a layer of Si appears on the top of the oxide layer after the deposition. The thickness of the deposited Si is ~ 160 nm. Varied deposition times yielded controllable sample thicknesses in the range 40 - 240 nm, respectively. SEM images of the Si thin films display similar morphological features. It is believed that the surface roughness originates from the underlying Cu foil. As shown in Figure II.2.A.8, all the Si films appear amorphous to powder X-ray diffraction and have approximately the same O content. Investigations on the source of oxygen are inconclusive but probably include surface silica or copper oxide on the copper foil.

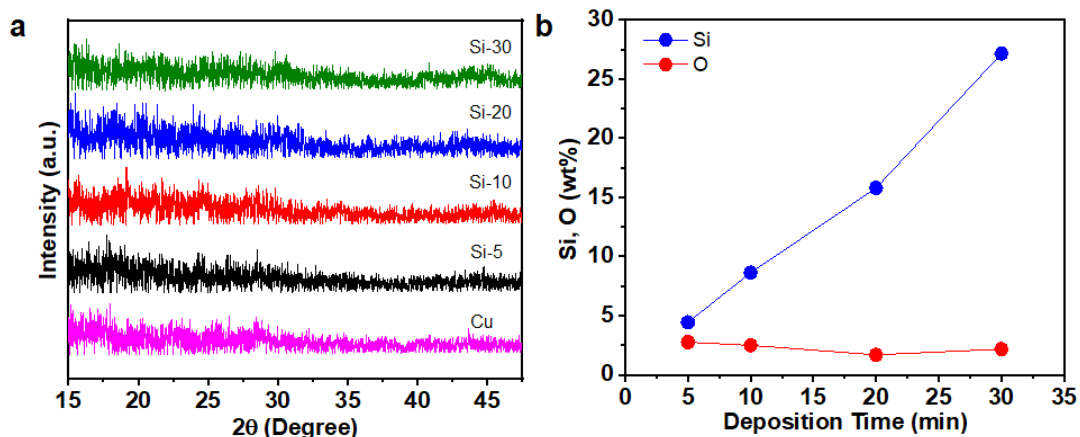


Figure II.2.A.8 (a) XRD patterns of Si films along with Cu foil reference, and (b) content of Si and O detected by EDS for Si films.

Figure II.2.A.9 presents the CV curves of the as-produced Si films during the first two cycles. The small cathodic peaks at $\sim 0.7 - 0.8$ V are attributed to electrolyte decomposition and/or SEI formation during the 1st cycle (insets in Figure II.2.A.9a-d). All the films demonstrate typical lithiation of amorphous Si (a-Si), leading to the formation of amorphous Li_xSi (a- Li_xSi) at $\sim 0.2 - 0.3$ V, whereas all anodic curves show two broad peaks at ~ 0.3 and 0.5 V, corresponding to the extraction of Li from a- Li_xSi .

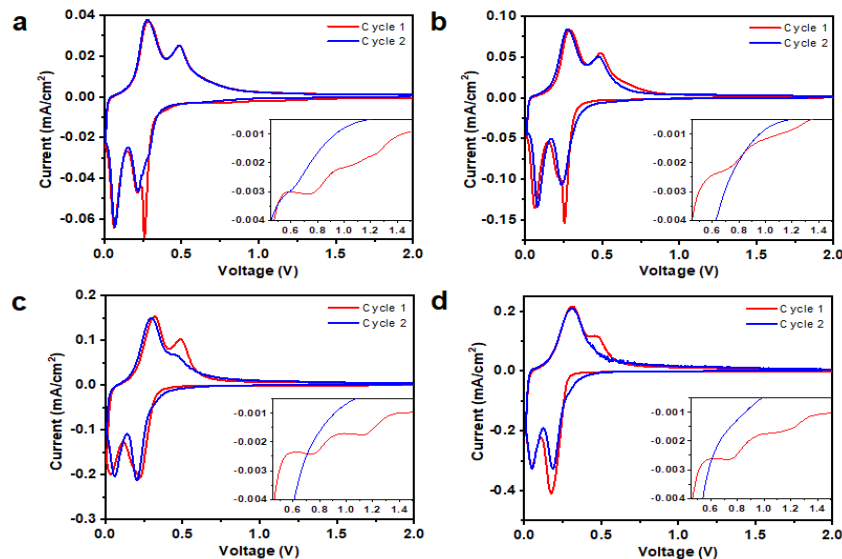


Figure II.2.A.9 CV curves of (a) Si-5, (b) Si-10, (c) Si-20, and (d) Si-30 films during the first two cycles. Insets are enlarged CV curves between 0.45 and 1.5 V

Based on the deposition method used to produce Si thin films, Si-Sn thin films were deposited on Cu foil. Figure II.2.A.10 shows the electrochemical performance of the as-produced Si-Sn film. From the cross-sectional SEM image, the thickness of Si-Sn film is ~ 140 nm. The voltage profiles and CV curves (Figure II.2.A.10a,b) exhibit similar amorphous features to Si films, with an improved initial CE of $\sim 87\%$, compared to 82% for the earlier Si films. A close comparison of the CV curves for the 140 nm Si-Sn vs. 160 nm Si film reveals small differences near the SEI formation region around 0.75 V, perhaps implying the possible difference in the passivating behavior between Si and Sn. Overall the Si-Sn film exhibits much better cycling stability than the Si films of similar thickness with no obvious difference in CE, consistent with the earlier reports of Ahn, et al. These results highlight that the incorporation of tin (and lithiated tin) into the matrix

improves the electrochemical performance of the active Si species. Further scale-up studies and studies to discern the role the interactions between the lithiated phases has on the increased stability are underway.

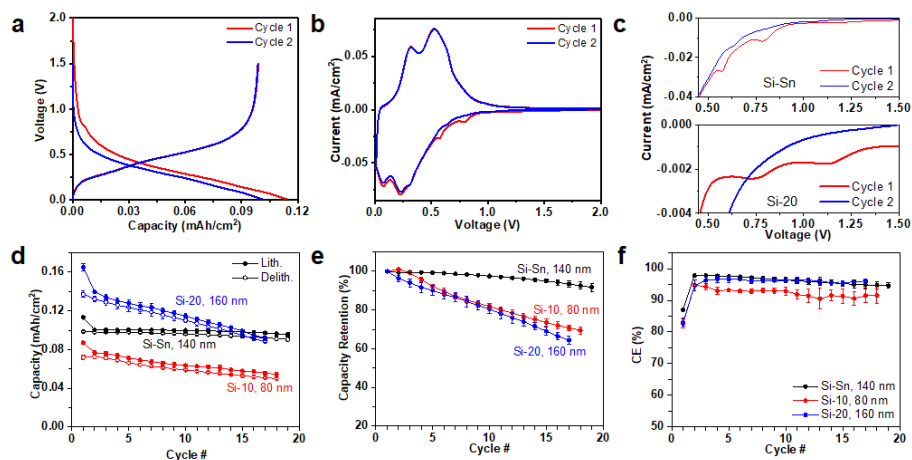


Figure II.2.A.10 (a) Voltage profiles, (b) CV curves of Si-Sn film,, (c) enlarged CV curves at 0.14 -1.5 V, (d) capacity, (e) capacity retention, and (f) CE of Si-Sn and Si films of similar thickness.

2. Silicon-based Electrodes

Electrode Processing of Silicon Containing Anodes

Whereas as traditional graphite anodes are formulated in an *N*-methyl-2-pyrrolidone (NMP) based slurry with carbon black and polyvinylidene fluoride binder on Cu foil [7], industry has been moving towards using water based slurries to lower costs [8], [9]. The dispersion of Si in water based graphite slurries has been assumed to fall directly from the graphitic carbon system, however most of the work in the literature was focused on small batches of materials whereas working at larger scale often introduces new challenges. Indeed, recent studies have observed H₂ gas formation during larger scale preparation (> 1 L) in water based Si slurries [10], [11] with proposed deeper oxidation of the Si particles being the source of the gas [10], [11], producing a thick oxide layer that can decrease the materials theoretical capacity and cause additional first Coulombic losses.

This gassing during electrode processing likely goes unnoticed when working at laboratory scale but becomes problematic in a manufacturing setting. The occurrence of H₂ poses safety concerns, as current production methods involve mixing slurries in large sealed planetary mixers, allowing for pressurization of this flammable gas. Furthermore, slurries are not necessarily coated immediately after they are mixed. This allows for continued oxidation of the Si during slurry storage, which will lead to loss of material capacity as well as changes in weight loadings. The conversion of a 5 nm thick shell of Si to SiO₂, on a 110 nm Si particle, lends to a ~25% capacity decrease. Understanding these reactions and their impact on the properties of the silicon electrodes will lead to better and more consistent electrodes if water –based processing is to become the standard for silicon electrodes.



Figure II.2.A.11 1 L of 15% Si-graphite aqueous based slurry after 1-week storage. Gassing from the slurry caused foaming and subsequent drying as the slurry “snaked” out of the open container.

Figure II.2.A.11 demonstrates the negative impact of gassing on the storage of Si/graphite aqueous based slurry. Open storage, to prevent pressurization of the gassing slurry, resulted in ejection of the slurry over a 1-week period. These observations motivated this research to understand specifically what components of the slurry manufacturing lead to gassing and how it could be minimized. To emulate high energy mixing needed for dispersing Si, the slurries were mixed on a roller mill with the zirconia media, in a custom pressure vessel, allowing in-situ pressure monitoring and post-processing gas analysis by mass spectroscopy. Because Si tends to easily agglomerate, high energy mixing methods, such as planetary ball milling, are often used to better disperse the Si amongst carbon additives and binder. This technique does not match the energy of planetary ball milling, likely leading to lower overall gassing reactions. A summary of the prepared slurries and selected results can be found in Table II.2.A.1. Samples are identified utilizing designations given in this table. Conditions were selected to represent various mixing conditions and solvents.

Table II.2.A.1 Summary of Slurry Samples and Selected Results

sample id	Si particle	CB	binder	solvent	ΔP 100 h (atm)	ΔP 20 h (atm)
N1	NA 70-130 ^b	Yes	No	NMP	-0.03	-0.01
W1	NA 70-130	No	No	water	-0.01	0
W2	NA 70-130	Yes	No	water	0.22	0.04
W3	NA 70-130	No	Yes	water	-0.01	-0.01
W4	NA 70-130	Yes	Yes	water	0.47	0
W5	AA 325 ^c	No	No	water	1.27	0.16

a) Based Scherrer analysis of Si (111) reflection; b)NA 70-130 = NanoAmor 70 – 130 nm; c)AA 325 = Alfa Aesar 325 mesh.

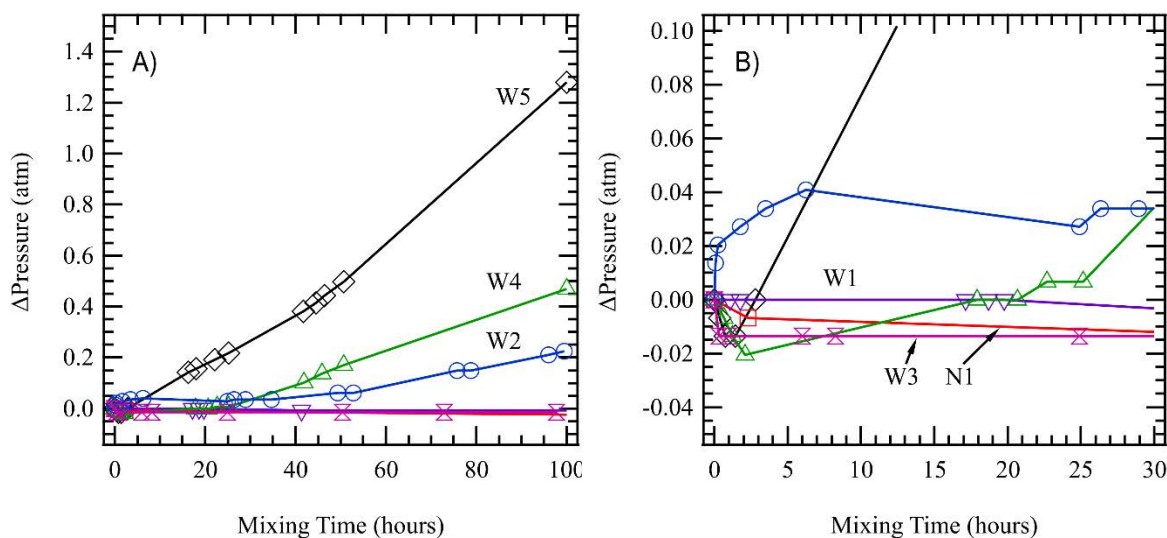


Figure II.2.A.12 a) The change in pressure vs time of W2 – water based nano Si/CB slurry (blue trace, circles), W5 – water based 325 mesh Si slurry (black trace, diamonds), W4 – water based Nano Si/CB/LiPAA slurry (green trace, triangles), W3 – water based nano Si/LiPAA slurry (green trace, triangles), W3 – water based nano Si/LiPAA slurry (fuchsia trace, hour glasses), W1 – water based Nano Si slurry (purple trace, upside-down triangles), and N1 – NMP based Nano Si/CB slurry (red trace, squares). B) plot of the first 30 hours (enlarged).

Figure II.2.A.12a shows the change in pressure in the mixing vessel of various Si slurries (100 hours mixing time). This data shows the change in cell pressure with time as the reaction occurs. W5 caused the greatest pressure increase of ~ 1.27 atm, followed by the W4 and W2 at ~ 0.47 atm and ~ 0.22 atm, respectively. W1, W3, and N1 caused the pressure to decrease by 0.01, 0.01, and 0.03 atm, respectively. A closer examination of the first 30 hours of mixing, (Figure II.2.A.1b), shows that the W4 and W5 also caused a pressure decrease in the vessel before increasing to the above-mentioned pressures, indicating a competing reaction that absorbs gas(es). Unlike the other mixtures, W2 caused a pressure increase in the initial mixing time, with a slight pressure decrease of 0.01 atm after 20 hours. In a separate experiment, even after the mixing was halted on a nano Si/CB water based slurry, pressure continued rising at a rate of $0.012 \text{ atm day}^{-1}$. This observation is important, as this reveals that the reaction does not stop when mixing is ceased.

The gases from the vessels were analyzed by mass spectroscopy to determine the cause of the pressure changes. Figure II.2.A.13 shows the mass spectra collected from W2, W4, and N1. These were all normalized to the N_2 peak intensity of ambient air inside the vessel (the N_2 peak exceeds the y axis of Figure II.2.A.13a). The gas collected from W2 and W4 show large spikes at 2 AMU, due to H_2 production (Figure II.2.A.13b). No additional H_2 was present in the vessel of NMP based slurry, indicating the H_2 must come from H_2O , according to eq. 1:

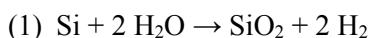
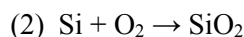


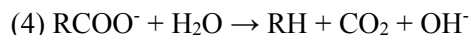
Figure II.2.A.13c focuses on the O_2 signal at 32 AMU. Both the water based and NMP bases slurries resulted in a decrease in the O_2 concentration by 2% and 7%, respectively, relative to ambient air. Since this O_2 consumption occurs independent of solvent choice, it is must come from residual air inside vessel, according to eq. 2:



This finding is emphasized by the fact that the O₂ consumption aligns with the pressure decrease of the N1 and W4 (Figure II.2.A.13b). The same immediate pressure drop was not observed for sample W2, but the rapid H₂ production may have outweighed the O₂ consumption, resulting in an overall positive pressure trend, following eq. 3:



In addition to the generation of H₂ by W4, Figure II.2.A.13d also indicates an increase of CO₂ not present in W2. The addition of LiPAA binder in W4 is likely the source of the CO₂, as this is not included in the gas composition of W2. Decarboxylation of polyacrylic acid has been demonstrated in aqueous solutions, according to eq 4: [\[13\]](#)



This reaction may not only lead to the decomposition of the binder, but also drives the pH of the slurry towards more basic conditions.

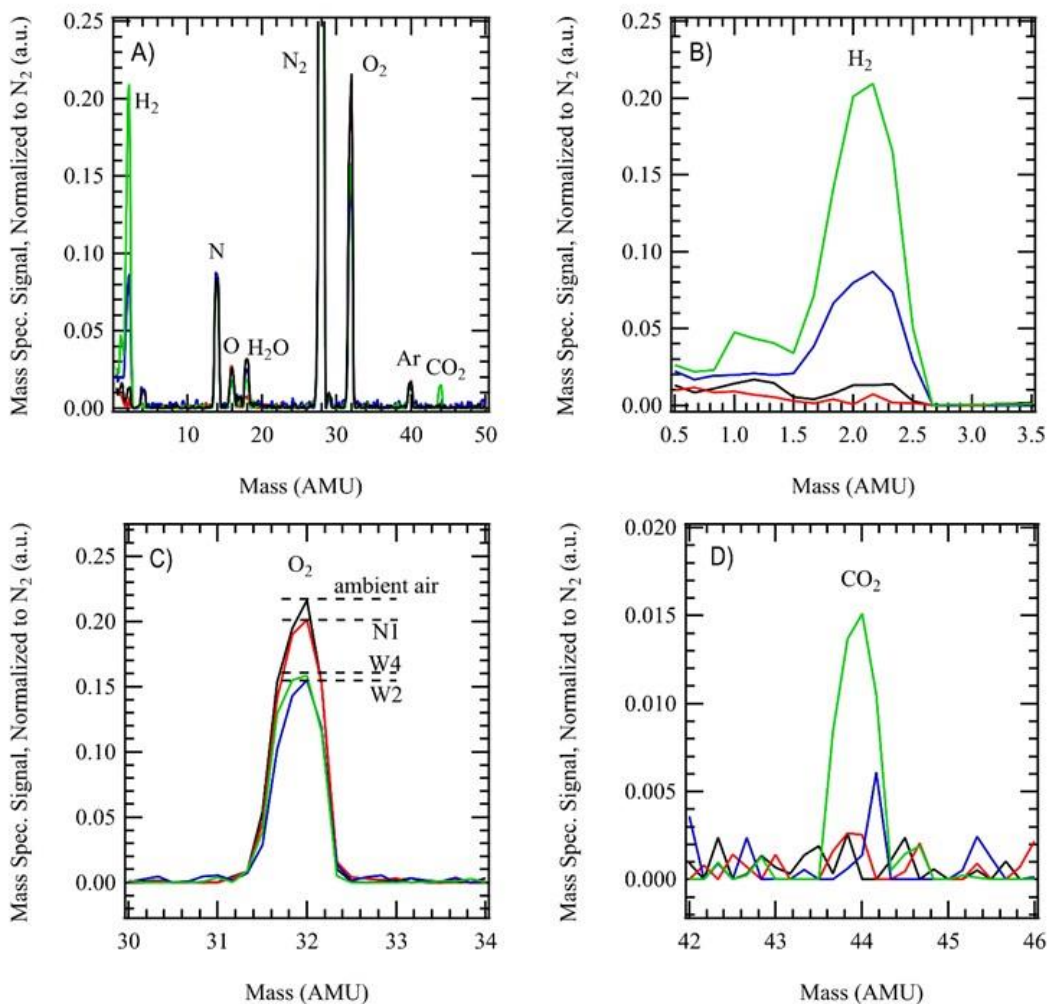


Figure II.2.A.13 a) Mass spectrum of gas collected from head space of mixing vessel for W2 (blue trace), W4 (green trace), and N1 (red trace), normalized to the N₂ signal of ambient air (black trace). B) plot of H₂ signal in mass spectrum from (a) C) plot of O₂ signal in mass spectrum from (a). D) plot of CO₂ signal in mass spectrum from (a).

XPS data (Figure II.2.A.14) were collected on dried powders to determine the change in oxidation of the NA 70-130 Si after mixing. All plots were normalized to SiO₂ 2p peak at 103.6 eV. The variations in the intensities of peaks at 99.3 eV were caused by changes in the Si⁰. The spectra can be fitted to a 3 peak model coordinating with Si, SiO₂, and an oxygen deficient form of silica deemed SiO_x (~102 eV). The untreated Si comprised of Si, SiO₂, and SiO_x. After treatment in water, the Si⁰ signal decreased, signifying either the oxidation of Si or a buildup of products at the surface attenuating the Si⁰ signal. The untreated Si shows the greatest Si⁰ signal, followed by a decrease in W1 and N1 (which are largely overlapped in Figure II.2.A.14). The fact that these spectra are so well overlapped lends towards the first scenario (Si oxidation), since N1 contains CB and there is no visible change in profile compared to W1, which contains only Si. If the CB was uniformly coating Si, it would be expected that the Si⁰ peak of N1 would be smaller. In addition, the XRD and NMR also support a thicker oxide (see below). The XPS data from W1 and N1 also show an increase in the shoulder at 102 eV when compared to other samples, which implies that a greater extent of the oxide shell is converted to the less oxidized SiO_x phase. This means that the reaction leads to a different oxide composition depending on whether the oxidation occurs by O₂ consumption (eq. 1) or H₂O (eq. 2). W2 and W4 display even greater loss in the Si⁰ signal, meaning the oxidation by water results in an oxide shell that penetrates even further into the Si particle. It is also interesting to note that the addition of LiPAA in W4 has little effect on the Si⁰ signal. Like the CB, this implies that the binder is not uniformly coating the Si particles, which may have implications towards the cycle-ability of Si based anodes.[\[14\]](#)

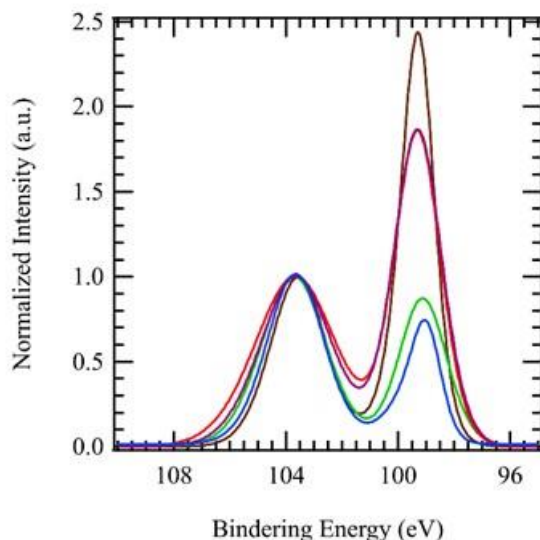


Figure II.2.A.14 XPS of Si 2p orbitals, Normalized to Si⁴⁺ at 103.6 eV, of various dried Si samples (untreated nano Si – brown trace, N1 – red trace, W1 – purple trace (overlapping with N1), W4 – green trace, W2 – blue trace)

Knowing that processing Si in water, under certain conditions, causes a change in the oxide content and surface chemistry, we cycled Si based half cells with and without the 100 hours of mixing. NA 70 – 130 Si, with a much shorter processing time, was compared to W2 to identify differences in electrochemical performance. In the voltage profile, shown in Figure 5, the half-cell containing the unprocessed Si has a 1st cycle delithiation capacity of 1392 mAh g⁻¹. The 2nd cycle delithiation capacity decreases to 1128 mAh g⁻¹. The half-cell containing W2 has 1st and 2nd delithiation capacities of 566.9 and 417.4 mAh g⁻¹, respectively. While this slurry formulation was not optimized, accounting for the lower than theoretical capacity, it is immediately noticeable that the 1st cycle delithiation capacity of the short-processed Si is more than twice the capacity of W2. This could arise due to some portion of the Si particles becoming electrochemically inactive, due to a thick oxide shell, or because whole particles are electronically isolated because of poor mixing. The first circumstance seems more likely, because W2 was mixed for 100 h, compared to the short-processed sample which was only mixed for a few minutes. Moreover, there is a larger hysteresis between the lithiation

and delithiation curves of the half-cell containing W2. This also supports a thicker oxide shell on the Si particles that would decrease its electronic conductivity, leading to a larger IR drop. In addition to capacity, the 1st cycle coulombic efficiency of the half-cell using the unprocessed Si is 64%, whereas W2 is 40%. This difference may result from the additional SiO_x in W2, which undergoes an electrochemical conversion to Li₂O, Li₂SiO₃, and Li₄SiO₄, or by the decomposition of more organic electrolyte.^[9] Overall the half-cell containing W2 only lost 149.5 mAh g⁻¹ between the 1st and 2nd delithiation compared to 264.1 mAh g⁻¹ for the short-processed Si. This improved capacity retention between the 1st and 2nd cycle could result from better dispersion of W2, less electrochemically active Si overall in this electrode, elimination of reactive sites, or less SEI.

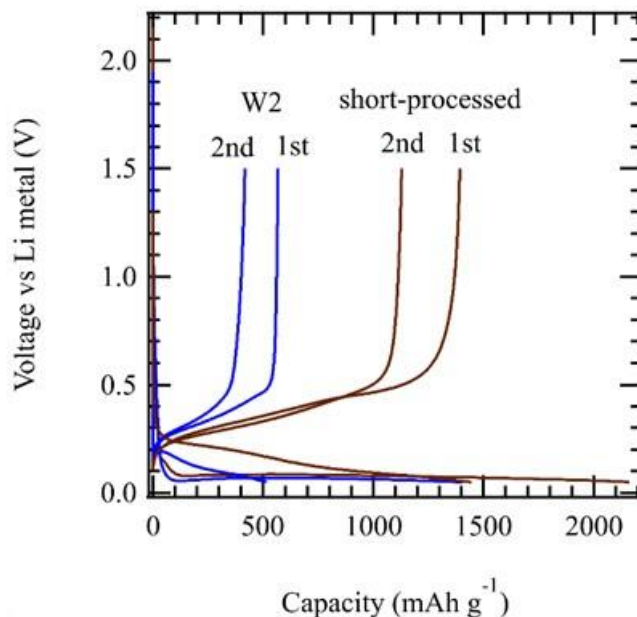
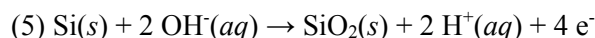
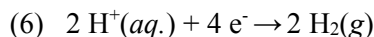


Figure II.2.A.15 Voltage profile of Si-Li metal half cells comparing short-processed NA 70 - 130 Si (brown trace) and W2 (blue trace). Cycled at C/10 (0.25 A g⁻¹) from 1.5 to 0.05 V vs Li metal.

The generation and consumption of gas in these slurries is, for the most part, a direct result of Si oxidation during slurry preparation. Furthermore, solvent contribution alone is not the limiting factor (Table II.2.A.1), rather the addition of CB played a role in promoting the oxidation of the Si particles. Based off gassing results of the NA 70 - 130 Si particles from the water slurries, the W2 and W4 (contained CB) suffered the greatest amount of oxidation while W1 and W3 (no CB) showed the least, confirming CB is a key reagent. Though W4 produced more gas than W2, W4 also produced CO₂, which cannot be decoupled from the pressure of H₂ in Figure II.2.A.15. In fact, both W2 and W4 displayed similar oxidation based off XRD and XPS, meaning this difference gas production of 0.25 atm, after 100 h, could, in part, be caused by CO₂. We believe the CB acts as a high surface area catalytic site in which a proton coupled, charge transfer could take place,^[16] following the scheme found in Figure II.2.A.16. Both OH⁻ and H⁺ readily diffuse through amorphous SiO_x.^{[17], [18]} Despite the acidic environment, the natural dissociation of water provides sufficient OH⁻ ions, which could diffuse through the amorphous SiO_x and oxidize the Si⁰ core according to eq. 5:



This reaction is followed by the reverse diffusion of H⁺ opposed to molecular H₂, which alleviates the need for additional porosity to allow the escape of gas. The diffusion of 2 H⁺ out of the SiO_x occurs in tandem with a 4 e⁻ transfer to the local CB, providing a site for aqueous H⁺ reduction, eq. 6:



In this proposed scenario the CB lowers the activation energy needed to reduce the protons, which may not take place on the SiO_x surface alone.

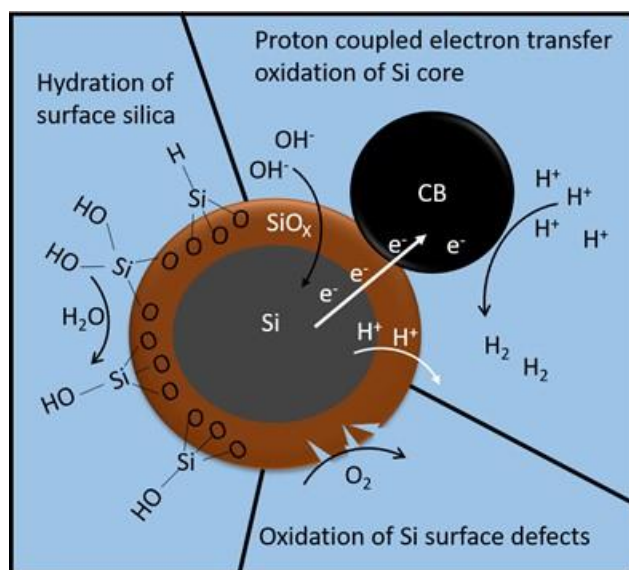


Figure II.2.A.16 A representative schematic of several reactions that occur during processing of water based Si/CB slurry.

Electrode Characterization: Raman Spectroscopy

Raman spectroscopy has been used as a tool to characterize heterogeneity in silicon-graphite composite electrodes. Our Raman results clearly show evidence for phase segregation and non-uniform electrochemical cycling of the active silicon component, indicative of a greater need to understand how the slurry properties effect the formation of the final composite electrodes when materials with such different surface chemistries are used. Electrode heterogeneity and non-uniform lithiation is a primary driver of battery failure.

Binder: Processing the electrodes with PAA binder in NMP yielded a more uniform composite than water-based processing with LiPAA binder. The anodes processed from water showed higher levels of segregation for the silicon and graphite phases. In general, NMP-based processing resulted in better wetting and dispersion of silicon nanoparticles and carbon black in the slurry, which was reflected in the dried electrode. Despite differences in the quality of the pristine coatings, the first-cycle lithiation proceeded identically independent of the electrode binder (Figure II.2.A.17). Both electrodes contained c-Si after one cycle, which indicates that some Si did not participate in the electrochemical reaction and convert to amorphous phases. Regions of electrochemically inactive Si were similar in size and extent in electrodes with PAA and LiPAA binder. Based on these data, the electrode uniformity and reactivity during the first cycle cannot explain the improvements in long-term performance of the LiPAA-based anodes compared to the PAA-based anodes and we believe factors such as residual moisture in the electrode appear to dominate.

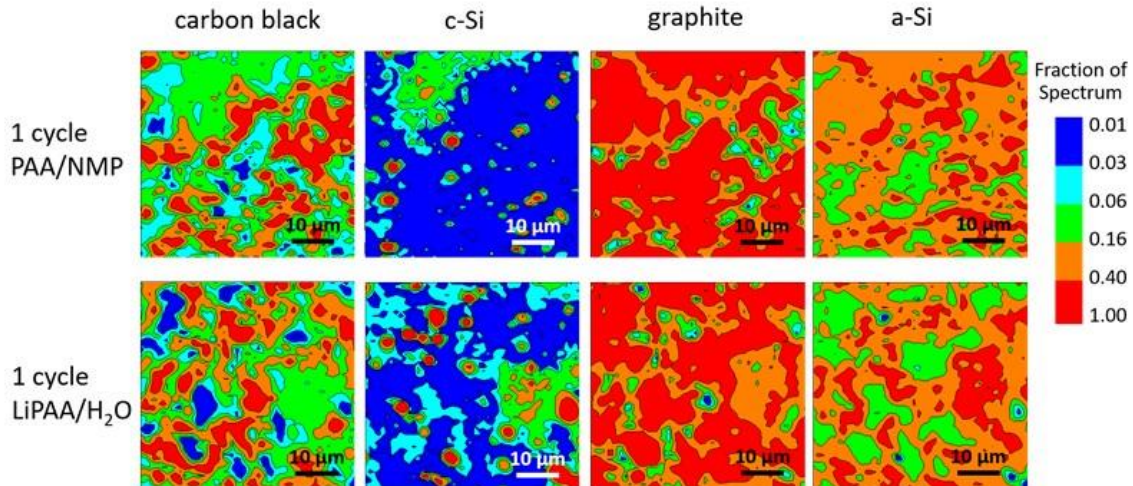


Figure II.2.A.17 Raman maps of the distribution of carbon black, c-Si, graphite, and a-Si in Si-Gr composite anodes after 1 full cycle (lithiation and delithiation). The top row maps an anode made with PAA binder and the bottom row maps an anode made with LiPAA binder. Each map is $50\ \mu\text{m} \times 50\ \mu\text{m}$ and comprises 2500 spectra. The color scale indicates the relative fraction of each component at each location across the map.

On cycling, we observed domains of crystalline Si in the cycled composite anodes (Figure II.2.A.18), indicative that some fraction of the Si is electrochemically inactive (does not lithiate) and thus does not undergo a crystalline to amorphous transition. Inactive Si was observed even after 100 cycles in full cells and in half cells with a virtually infinite supply of active lithium. To understand if the inactive regions of the electrode could be electronically isolated, we collected Raman spectra from a large area ($50 \times 50\ \mu\text{m}$, 2500 pixels) and broke it into two groups to separate out the spectra with the largest fraction of crystalline silicon (Figure II.2.A.17b). No difference in the intensity of the bands from carbon and graphite were observed in the spectra with the most crystalline silicon compared to all other regions of the electrode (Figure II.2.A.17c). Differences in carbon content do not explain why some Si is electrochemically inactive and suggest that electronic conductivity is not the limiting factor. This points to a need to further improve electrode processing.

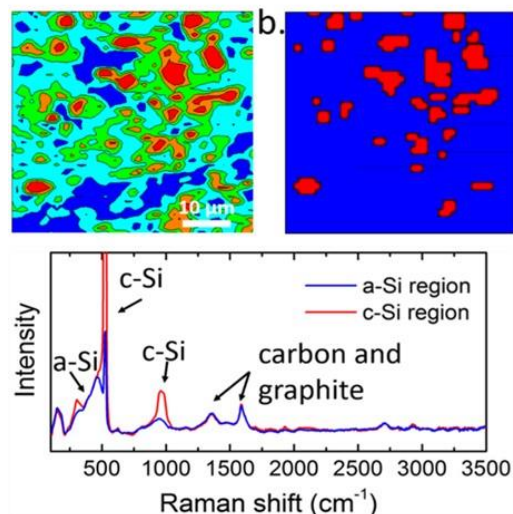


Figure II.2.A.18 (a) Raman map of the intensity of the main band from crystalline silicon at $520\ \text{cm}^{-1}$ in a silicon-graphite composite electrode after 1 charge-discharge cycle. The fraction of crystalline silicon increases from blue to red. (b) Two level map of the same data presented in (a). The red pixels are from the electrode areas with the highest concentration of crystalline silicon. (c) The average Raman spectra from regions with high and low concentrations of crystalline silicon is mapped in (b).

In addition to using Raman spectroscopy to elucidate the uniformity of the electrode and level of particle isolation, it also can be used to study the solid electrolyte interphase (SEI) layer. In this context, we characterized the SEI layer on silicon by using surface-enhanced Raman spectroscopy (SERS). Although SERS normally introduces metallic islands in the SEI layer that may lead to non-representative results, it is a powerful tool that may under certain conditions yield insights into the SEI layers structure and composition. In this study, we utilized Cu nanoparticles on the surface to increase the Raman signal. Copper was chosen as the metal nanoparticle surface because it does not react with lithium and is already a constituent in the cell.

The silicon laminate electrode was provided by the CAMP Facility at Argonne. It consisted of 70.7 wt% NanoAmor Si particles (70 nm to 130 nm), 9.4 wt% Timcal C-45 conductive additive and 19.9 wt% polyacrylic acid-lithium salt (LiPAA). The methodology followed to prepare the Cu-coated electrodes utilized a solution-based reduction in an aqueous solution of $\text{Cu}(\text{SO}_4)_2$ with application of the appropriate voltage and current. With the purpose of finding the optimum Cu electrodeposition, six different protocols were examined, as shown in Table II.2.A.2.

Table II.2.A.2 Electrodeposition protocols applied to prepare the Cu-coated silicon electrodes.

Sample	Voltage (mV) vs. Ag^+/Ag	Charge (C/in^2)
1	-461	0.2
2	-711	0.2
3	-961	0.2
4	-711	0.6
5	-711	1.8
6	-961	0.6

The copper distribution and size varied from sample to sample, as a function of the protocol employed (see Figure II.2.A.19). Samples 1, 3 and 4 exhibited a more evenly dispersed copper than samples 2, 5 and 6, in which the copper particles were randomly distributed. At higher magnifications (bottom images of Figure II.2.A.19), the size of copper particles varied from tens (sample 4) or hundreds of nanometers (sample 3) to micron size (sample 2), for instance.

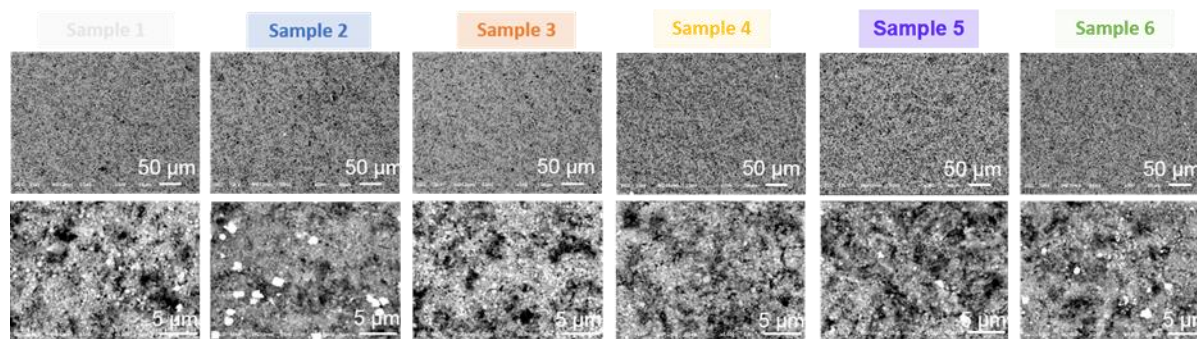


Figure II.2.A.19 SEM images of the different Cu-coated silicon electrodes obtained by applying the 6 different electrodeposition protocols collected in Table 2.

For these samples, only sample 1 showed a signal enhancement. As copper is only weakly active for the purpose of SERS-based signal enhancement when compared to the more commonly used silver or gold nanoparticles (Figure II.2.A.20). For the sample that showed the most enhancement, the signal strength (related to the amount of copper deposited) was insufficient to significantly enhance any additional peaks compared to the baseline samples.

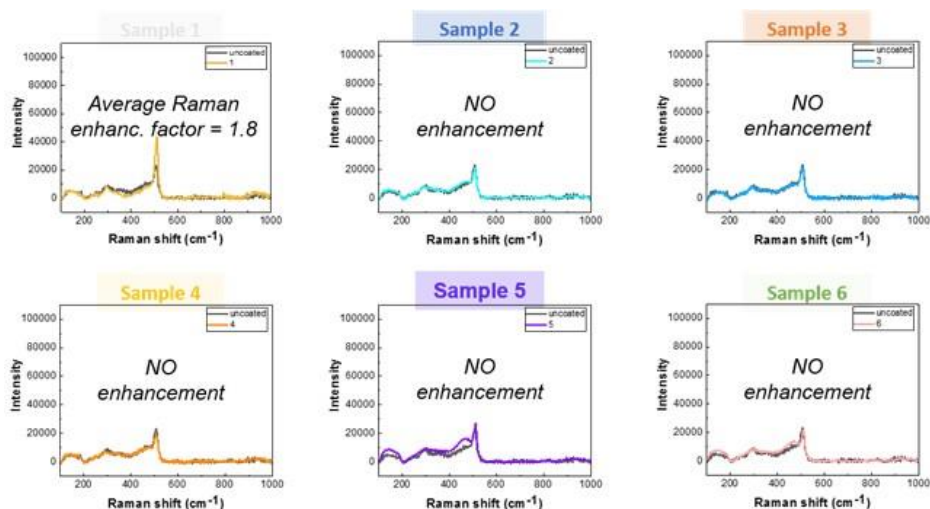


Figure II.2.A.20 Raman spectra of the different Cu-coated silicon electrodes obtained by applying the 6 different electrodeposition protocols collected in Table 2.

Charged Silicon Electrode Reactivity

One of the core problems associated with Li-Si chemistry in Li-ion batteries is the inherent reactivity of the lithium silicides, the active material that forms upon the lithiation. These phases can react with almost all battery components such as binders, electrolytes, additives and impurities such as moisture and air, which cause Li loss and irreversible capacity, as well as continuously low Coulombic efficiencies during cycling, leading to electrode death.

To systematically study the reactivity of different battery components (including binders and electrolyte solvents) in direct contact with lithiated Si electrodes, crystalline lithium silicide (LS) with the Li_7Si_3 composition is synthesized as the model compound, which is associated with voltage of approximately 350 mV (vs Li). [19] Li-Si phase diagram and crucible studies were used to optimize the material synthesis conditions and procedures. The chosen process was found to be a stoichiometric mixture of Si and Li, Ta crucibles, with a heating ramp to 750 °C, followed by a one-hour hold, all under an argon atmosphere. Initial samples were near single phase Li_7Si_3 by powder X-ray diffraction (XRD) and ^{29}Si NMR. After this method was identified, we started to re-focused on a scale-up synthesis of crystalline LS compounds for team members to use these in the continued stability studies. The XRD of the as-synthesized scale-up LS sample is shown in Figure II.2.A.21, which are mainly Li_7Si_3 phase with a little less-lithiated $\text{Li}_{12}\text{Si}_7$ phase.

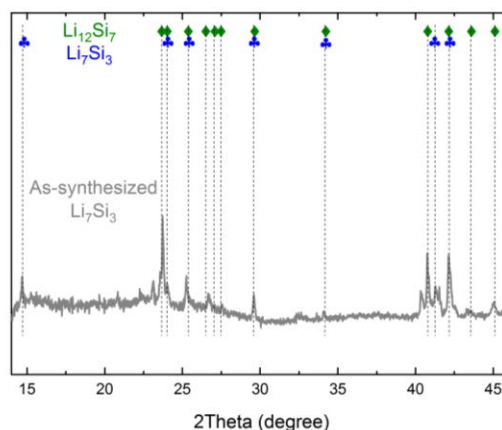


Figure II.2.A.21 XRD of as-synthesized Li_7Si_3 , with a small amount of the slightly oxidized phase $\text{Li}_{12}\text{Si}_7$.

To study the reactivity of different binder materials in contact with lithiated Si electrodes, X-ray diffraction and Solid State Magic Angle Spinning (MAS) NMR spectroscopy have been used to qualitatively and quantitatively study the evolution after grinding the lithium silicides model compounds with different binder materials, such as LiPAA and PVDF, under the Ar environment. It is found that compared with PVDF, LiPAA lead to less chemical shifts in ^7Li and ^{29}Si MAS NMR and less structural evolution in XRD results after mixed and ground with Li_7Si_3 model compounds (see Figure II.2.A.22). Particularly, compared with the $\text{Li}_7\text{Si}_3 + \text{LiPAA}$ mixture, the main ^7Li peak at ~ 16 ppm moved to much higher ppm after mixing Li_7Si_3 with PVDF, which according to the previous NMR study [20], [21] representing more delithiation of lithium silicides and worse chemical stability in contact with the charged Si species. Meanwhile, the new ^7Li peak appeared at ~ 0 ppm in the $\text{Li}_7\text{Si}_3 + \text{PVDF}$ mixture indicating the formation of new diamagnetic Li species coming from the degradation of PVDF. In general, PVDF showed less chemical stability when in contact with lithiated Si species compared with LiPAA, indicating PVDF is a less preferable binder material used for Si anode.

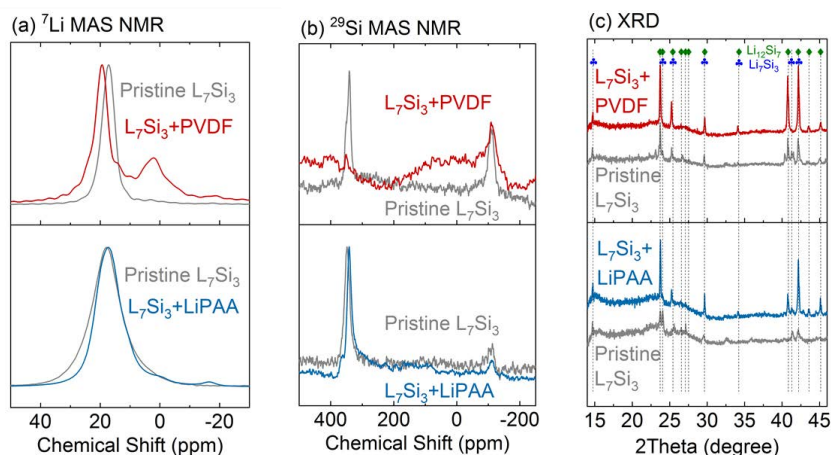


Figure II.2.A.22 (a) ^7Li NMR, (b) ^{29}Si NMR, and (c) XRD results of pristine LS samples and their mixture with 10 wt% PVDF or LiPAA.

To explore the degradation mechanism of PVDF in contact with the lithiated Si electrodes, the ^1H , ^{13}C and ^{19}F MAS NMR spectra of the mixture of Li_7Si_3 and PVDF were measured, as shown in Figure II.2.A.23. Compared with the pristine PVDF, the mixture of Li_7Si_3 and PVDF showed a broadened ^1H peak and several new ^{13}C peaks, indicating the potential breaking of C-H and C-C bonds in the PVDF ($-\text{CH}_2-\text{CF}_2-$) $_n$ structure. In the case of ^{19}F NMR results, although the relative peak intensities changed after mixing PVDF with Li_7Si_3 , no obvious peak broadening or new chemical environment, including LiF, was observed, indicating that the C-F bonds are relatively stable during the degradation of PVDF in contact with Li_7Si_3 .

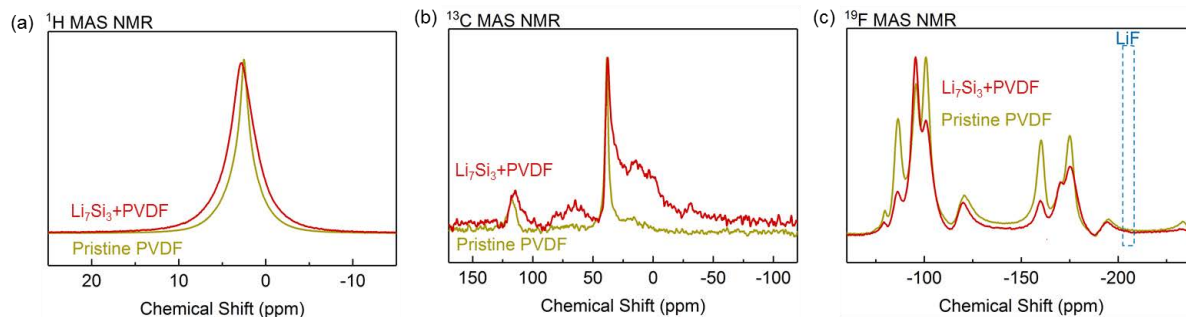


Figure II.2.A.23 (a) ^1H , (b) ^{13}C , and (c) ^{19}F MAS NMR spectra of pristine LS samples and their mixture with 10 wt% PVDF.

The potential breaking of C-H bonds by the extremely reducing Si anions in LS may lead to the formation of H₂. To confirm this hypothesis, we designed a special gas-trapping setup to catch the potential gas generation after mixing PVDF with Li₇Si₃. Initially, pristine PVDF powder and pristine ground LS powder were put at the two ends of a glass vial, as shown in the top left image in Figure II.2.A.24, to minimize their contact before mixing. A hole was drilled on the cap of the vial, and a totally-flat balloon was bonded to the cap to catch the generated gas. The cap was tightly screwed onto the glass vial, with additional parafilm sealing to prevent the gas leaking. Then the sealed system was hand-shaked for 10 min to physically mix the PVDF with LS. Due to the loose contact and limited mixing between LS and PVDF after the hand shaking, no clear gas generation was observed immediately after the mixing, as shown in the bottom left image in Figure II.2.A.24. After sitting in the glovebox for 1 day, notable gas formation was observed with the balloon being inflated, as shown in the right image in Figure II.2.A.24.

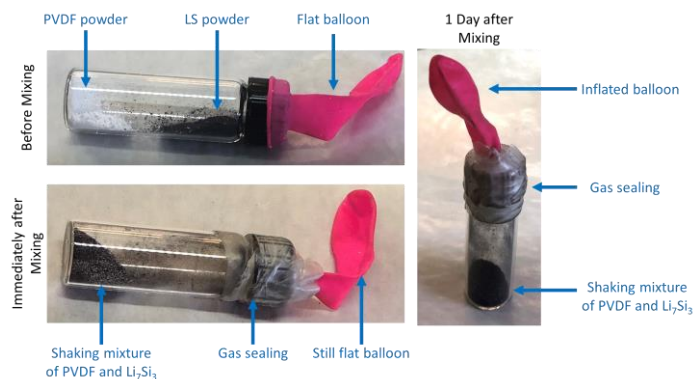
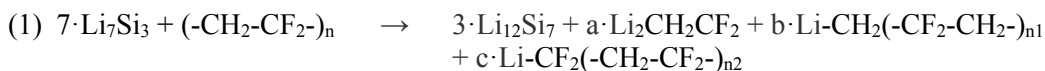
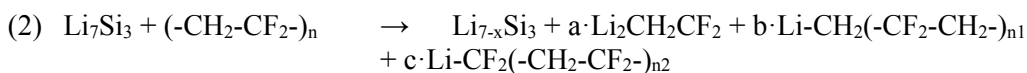


Figure II.2.A.24 Images of gas-catching setup before, immediately after, and 1 day after the mixing of PVDF and Li₇Si₃.

Based on the above characterization results, here we proposed several potential reaction mechanisms between Li₇Si₃ and PVDF after physical mixing. In one possibility, the severe delithiation of Li₇Si₃ in contact with PVDF may cause its transformation to a lower-Li-concentration phase such as Li₁₂Si₇. Meanwhile, the C-C bonds may be broken and lithiated to form organolithium complexes. The reaction could be written as below:

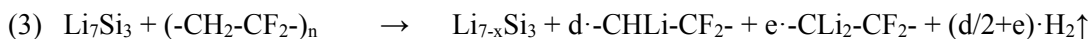


Here $a + b + c = 13$, representing different amounts of Li complexes formed. Since the phase transition from Li₇Si₃ to Li₁₂Si₇ requires a big change in the Si skeleton, such reaction maybe kinetically hindered. In another possibility, Li may leave the Li₇Si₃ structure without disturbing the Si skeleton too much, forming a less-lithiated silicide phase with crystal, semi-crystal, or even amorphous structures. This will give us:

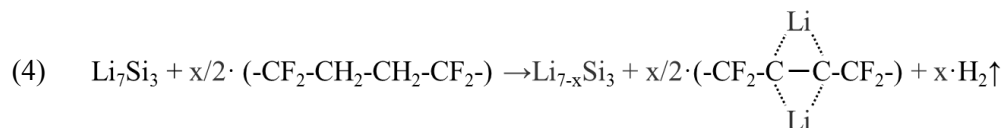


Here $a + b + c = x$.

In addition to the C-C bonds, the C-H bonds could also be broken and lithiated after mixing LS with PVDF, with protons being reduced to H₂, as shown in Figure 2. The potential reaction can be written as below:



Moreover, in PVDF there are usually some structural defects, such as the existence of $-\text{CF}_2-\text{CH}_2-\text{CH}_2-\text{CF}_2-$ sequence.^{35, 36} The replacement of two adjacent C-H bonds with C-Li bonds may overly reduce the C-C bond to a $\text{C}\equiv\text{C}$ triple bond, as is shown below:



In all reaction equations listed above, the C-F bonds were kept intact, because no sign of loss of fluoride from the PVDF or LiF formation was observed in ^{19}F NMR after the reaction between Li_7Si_3 and PVDF. To screen out the real PVDF degradation mechanism, further characterization supports from FTIR, Raman and XPS techniques will be applied in the future.

In addition to the binder materials, we also used LS model compounds to investigate the stability of electrode solvents in contact with lithiated Si electrodes. Figure II.2.A.25 shows the ^7Li and ^{29}Si MAS NMR results of the LS model compound and its mixture with different electrolyte solvents, including EC, EMC, FEC and triglyme. The results showed the highest Li loss and bulk reaction for EC and the lowest for FEC/triglyme after mixing with Li_7Si_3 . Furthermore, no LiF at ~ 0 ppm in ^7Li NMR was detected in the $\text{Li}_7\text{Si}_3 + \text{FEC}$ experiment, contrary to common belief that FEC de-fluorination reaction would be prevalent in the presence of lithiated Si species. The FEC results suggest either Li_7Si_3 of about 300-400mV potential vs. Li is not reducing enough and/or a flow of electrons is also required for FEC passivation reaction.

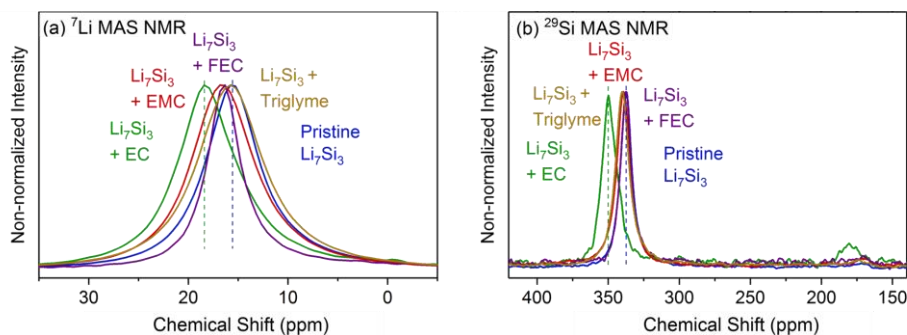


Figure II.2.A.25 (a) ^7Li and (b) ^{29}Si solid state MAS NMR for Li_7Si_3 and its mixture with different electrolyte solvents.

To test the hypothesis that the Li_7Si_3 -stable solvents such as FEC may react with more deeply lithiated Si species, new LS model compound with higher Li contents (i.e. representing lower charging potential) were synthesized. The newly synthesized lithium silicide was identified as $\text{Li}_{21}\text{Si}_5$ according to its ^7Li MAS NMR spectrum shown in Figure II.2.A.26a, which corresponds to about 0.05-0.1 V vs. Li during the lithiation of Si electrodes [22], [23]. The ^7Li and ^{29}Si MAS NMR results of the mixture of $\text{Li}_{21}\text{Si}_5$ and different electrolyte solvents, including EC, FEC and triglyme, are shown in Figure II.2.A.26. After mixing with EC, the main ^7Li peak of $\text{Li}_{21}\text{Si}_5$ at ~ 75 ppm shifted by ~ 4 ppm, indicating EC is still pretty reactive in contact with $\text{Li}_{21}\text{Si}_5$. Meanwhile, unlike the minor ^7Li and ^{29}Si NMR shifts previously observed after mixing Li_7Si_3 with FEC and triglyme (see Figure II.2.A.25), this time clear positive peak shifts and notable broadening were observed after mixing $\text{Li}_{21}\text{Si}_5$ with FEC and triglyme, indicating that although FEC and triglyme might be relative stable when in contact with the slightly-lithiated Si anode, it could react with the Si anode lithiated to lower voltages. In addition, in the ^7Li MAS NMR spectra shown in Figure II.2.A.25a, a clear diamagnetic ^7Li peak around 0 ppm (representing LiF) appeared after mixing $\text{Li}_{21}\text{Si}_5$ with FEC. This means our earlier observation that the mixing of FEC and Li_7Si_3 causes no LiF formation is because Li_7Si_3 is not reducing enough. When the Si anodes are further lithiated and more reducing LS such as $\text{Li}_{21}\text{Si}_5$ are formed, FEC will start to react with the charged anodes, forming LiF through the defluorination process, which is consistent with the common belief mentioned earlier.

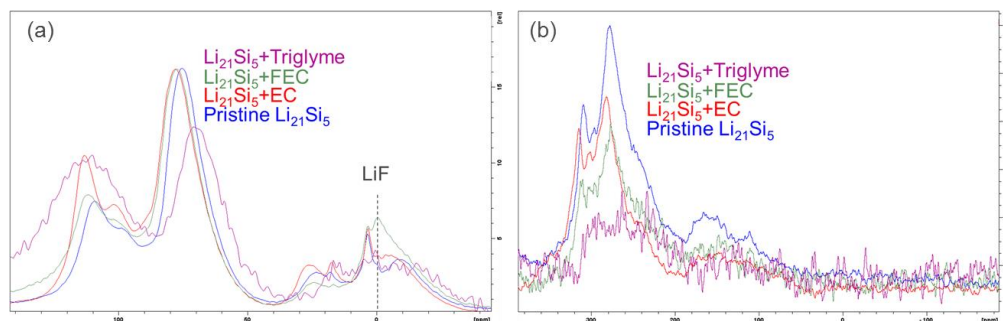


Figure II.2.A.26 (a) ^7Li and (b) ^{29}Si in-situ solid state MAS NMR for $\text{Li}_{21}\text{Si}_5$ and different electrolyte solvents. ANL, unpublished results.

Based on the reactivity study results and due to the lack of literature results on glymes and silicon electrodes, a preliminary test of the electrochemical performance of a triglyme-based electrolyte formulation (1M LiTFSI in triglyme) was studied via a simple baseline silicon powder and hard carbon mixture in half cells. Figure II.2.A.27a show the electrochemical profile comparison of the new triglyme-based electrolyte vs. the baseline Gen 2 + 10wt% FEC electrolyte, suggesting no major changes in the overall lithiation and delithiation electrochemistry. The 1st cycle electrochemical performance, shown in Figure II.2.A.27a, was about 75% higher in discharge capacities than the baseline electrolyte (Gen 2 + 10wt% FEC). This result alone is consistent with the hypothesis that the inertness of the electrolyte system could minimize side reactions and improve the overall capacity that can be obtained from silicon. While the baseline electrolyte capacities are lower in the first few cycles, they rapidly stabilize and are consistent for 10+ cycles, whereas the triglyme electrolyte performances are never found to stabilize and decay fast, with much lower coulombic efficiency (see Figure II.2.A.27b). This behavior could be explained by a lack of passivation on the electrode surface and/or Li-salt side reactions on the Li metal when using the new triglyme-based electrolyte. Figure II.2.A.27c illustrates an attempt to simply incorporate a passivation aid, FEC, to the system, which improved the initial coulombic efficiency (Figure II.2.A.27d) but did not improve the overall cyclability. The instability of triglyme-based electrolyte is consistent with the $\text{Li}_{21}\text{Si}_5$ highly-lithiated model compound test results shown in Figure II.2.A.27 that the Li_7Si_3 -stable solvents like FEC and triglyme can be reactive in contact with more deeply lithiated Si species. The above results suggest triglyme solvents are not stable enough as the electrolyte solvent for Si anodes. New carbonate electrolyte formulations are required to further improve the coulombic efficiency. Meanwhile, more basic characterization studies are required to study the degradation of triglyme-based electrolytes (e.g. full-cell electrochemistry, NMR, electron microscopy, FTIR and XPS) in order to optimize the triglyme-based electrolyte for Si electrode applications.

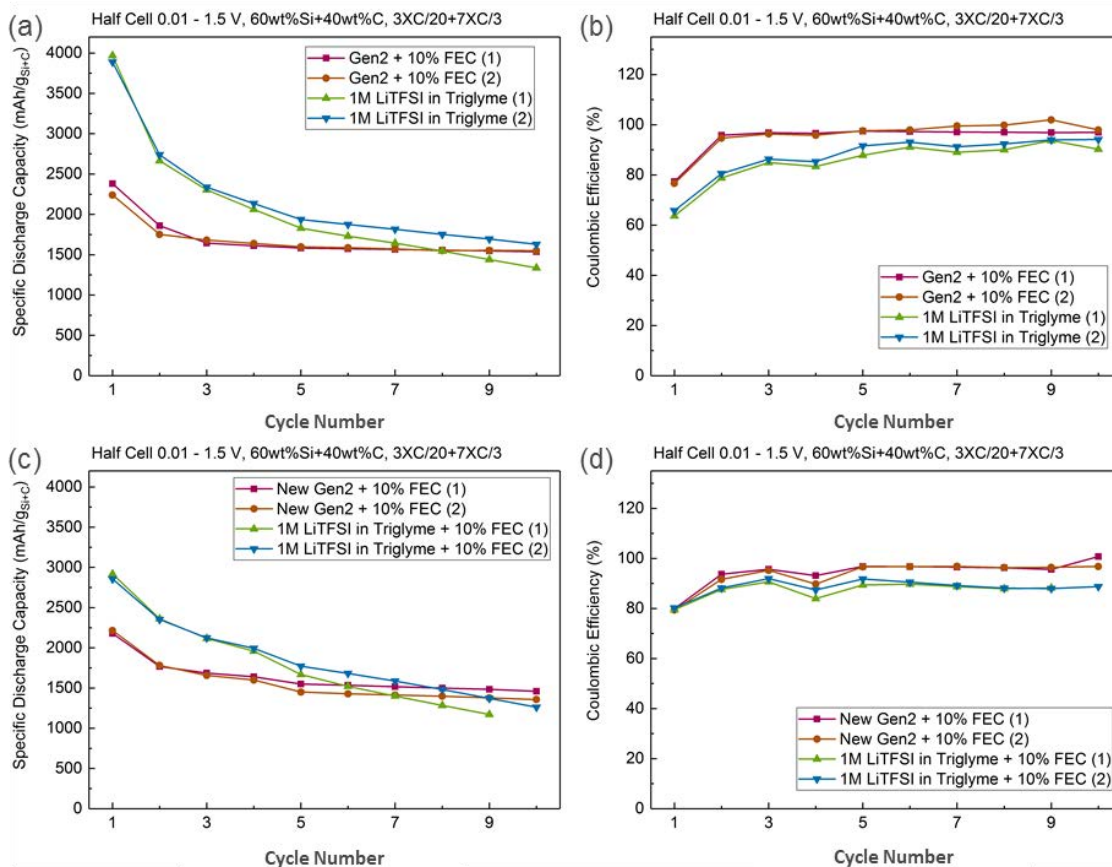


Figure II.2.A.27 Electrochemical profiles of Paraclete baseline silicon powder and carbon SP electrodes vs. Li metal half cells comparing Gen2 + 10% FEC and 1M LiTFSI in Triglyme electrolytes.

To understand the potential degradation mechanism of triglyme-based electrolytes used for Si electrodes, we measured the chemistry evolution of the Si anodes in half cells cycled between 0.01-1.5 and 0.05-1.5 V vs. Li respectively for 15 cycles using 1 M LiTFSI in triglyme as the electrolyte, as shown in Figure II.2.A.28. The ^{13}C NMR results indicated that the reaction between triglyme solvents and charged Si anodes could cause the degradation of triglyme into ethylene glycol and some other organic compounds. Additionally, lower cut-off voltage of 0.01 V for Si anode charging process led to the formation of a new ^7Li peak at ~ 10 ppm compared with that charged to 0.05 V vs. Li, implying that more reducing lithium silicides could trigger additional reactions with the electrolyte solvents. In the future, further NMR characterizations together with microscopy, FTIR and XPS techniques will be applied to understand the true degradation mechanism of triglyme system in contact with charged Si anodes in both half-cell and full-cell electrochemistry measurements.

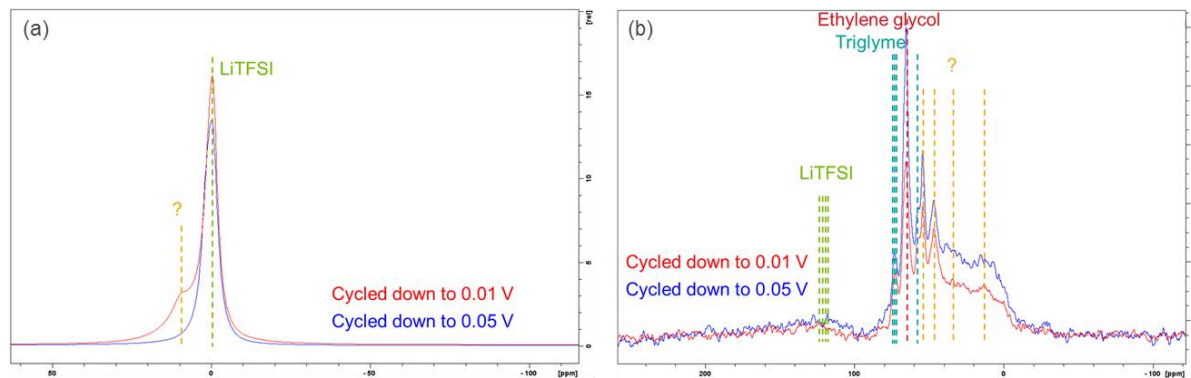


Figure II.2.A.28 (a) ${}^7\text{Li}$ and (b) ${}^{13}\text{C}$ solid state MAS NMR for post-electrochemistry Si loose-powder anodes after cycling between 0.01-1.5 and 0.05-1.5 V vs. Li respectively for 15 cycles, using 1 M LiTFSI in triglyme as the electrolyte. ANL, unpublished results.

Silicon Electrode Electrochemistry

The use of blended silicon-graphite (Si-Gr) negative electrodes increases the energy density of lithium-ion cells over those containing only graphite (Gr) electrodes. However, the potentials and kinetics of lithium insertion into (and extraction from) Si and Gr are known to be different. Silicon is active in the entire 1.0-0.0 V range, whereas Gr is active only at potentials < 0.25 V vs. Li/Li⁺ during electrochemical cycling in (half) cells containing a Li-metal counter electrode. However, the relative lithiation/delithiation behavior of the Si and Gr components in blended electrodes is not well understood. Knowledge of the distribution of Li⁺ ions in the Si and Gr components is important because (in addition to electrode porosity) it determines the volume expansion of the blended electrode during electrochemical cycling. One reason for the knowledge gap is the amorphization of crystalline Si that occurs during lithium insertion, which makes it difficult to track the evolution of the component by techniques such as X-ray diffraction. We conducted operando energy dispersive X-ray diffraction (EDXRD) to quantify lithiation/delithiation of Gr in a 15 wt% Si-Gr (Si-Gr) blended electrode; then, by taking into account the measured coulometric capacity of the cell we inferred the lithiation/delithiation behavior (and hence the volume changes) of the Si component. In parallel, we also conducted operando studies on a Gr electrode and used the data to calibrate behavior of the Gr component in the blended electrode. The EDXRD data were collected on cells containing a Li-metal counter electrode (*half* cells) at the 6BM-A beamline of Argonne's Advanced Photon Source (APS). The 2032-type coin cell was used without any modification as the white beam (5-250 keV) penetrates the stainless steel casing.

The volume changes in the Si particles that occur during cycling causes deterioration of the solid-electrolyte interphase (SEI) layer on the particles resulting in further electrolyte reduction that immobilizes Li⁺ ions and, therefore, capacity fade. A natural question to ask is whether the observed fast capacity fade in Si-Gr electrodes vs. Gr electrodes (for which the volume variation is $< 10\%$) is solely due to the volume changes, or if there are other compounding factors that are specific to Si particles alone? To answer this question we developed a calendar-aging test, which included a potentiostatic hold. Full cells with Si-Gr and Gr negative electrodes (and Li_{1.03}(Ni_{0.5}Co_{0.2}Mn_{0.3})_{0.97}O₂ containing positive electrodes) were assembled, tested, and compared using complementary cycle-life and calendar-life aging protocols. Because the Si particles volume changes are not expected to occur during a potentiostatic hold, by comparison of data from the cycle-life and calendar-life aging tests we were able to assess the role of volume changes in the deterioration of cell cycling performance. In order to gain insights into the capacity loss mechanisms we examined the cell electrolytes after completion of the electrochemical tests. The electrolyte samples were collected into polypropylene containers, diluted 1:10 v/v with CD₃CN, and analyzed by nuclear magnetic resonance (NMR) spectroscopy. ${}^{19}\text{F}$ and ${}^{31}\text{P}$ NMR spectroscopy data were obtained on the electrolyte samples to track PF₆⁻ hydrolysis, as the products have different chemical shifts from the parent compound. For accurate integration of the ${}^{19}\text{F}$ and ${}^{31}\text{P}$ NMR resonances, 10-15 s delays were introduced between the excitation radiofrequency pulses. For comparison purposes, we also conducted measurements on the fresh electrolytes, and on samples from as-

prepared full cells that were held at open circuit for ~ 130 h after assembly *but never cycled*. These latter samples provided information on changes in the electrolyte during electrode “soaking”, which was compared with changes to the electrolyte after formation cycling (~ 130 h is the time elapsed for three C/20 formation cycles).

The electrode potential vs. capacity profiles and the XRD data from the operando lithiation and delithiation cycles are displayed in Figure II.2.A.29. Prior to collecting these data, the 2032-type coin cells were cycled two times at a $\sim C/20$ rate in the 1.50-0.01 V vs. Li/Li^+ (abbreviated as V_{Li}) range to form the SEI on the Gr (or Si-Gr).

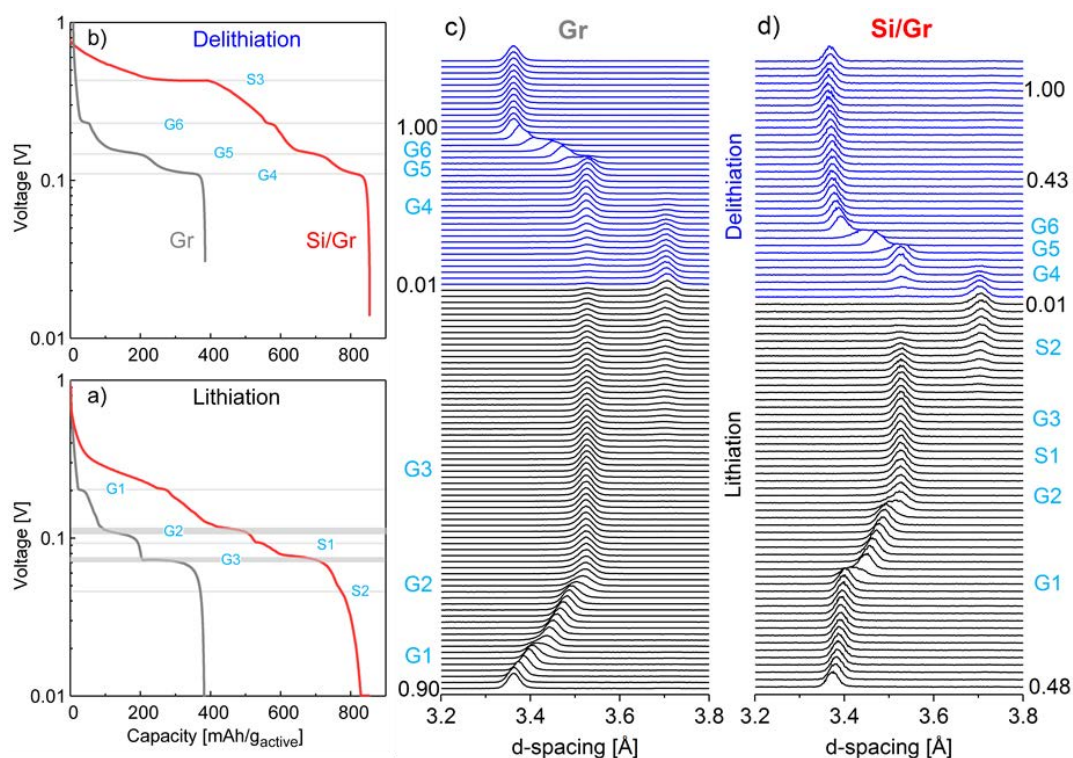


Figure II.2.A.29 Electrode potential vs. capacity during lithiation (a) and delithiation (b) of a Gr-only electrode (grey line) and of a Si/Gr (15/73 w/w, red line) blended electrode cycled vs. Li metal. Operando XRD spectra (shown in the 3.2 to 3.8 Å d-spacing range) collected during the electrochemical cycling in (a) and (b) for the Gr-only (c) and Si-Gr (d) electrodes. Spectra collected on lithiation and delithiation are shown in black and blue coloring, respectively.

The electrochemistry data in Figure II.2.A.28 shows several plateaus in the voltage profile. On lithiation at $\sim C/30$ rate (Figure II.2.A.29a), starting from ~ 1.5 V to a 10 mV cut-off, three major plateaus are seen for the Gr-only electrode, at 0.202 (G1), 0.106 (G2), 0.072 V_{Li} (G3). For the Si-Gr electrode, five plateaus are observable at voltages values of 0.206 (G1), 0.116 (G2), 0.094 (S1), 0.078 (G3), 0.047 V_{Li} (S2). The delithiation (Figure II.2.A.29b) profile shows three plateaus for the Gr-only electrode at 0.111 (G4), 0.150 (G5), and 0.232 (G6) V_{Li} . These same three plateaus are also seen in the Si/Gr electrode data. In addition, the plateau at 0.429 V_{Li} (S3) is seen only in the Si/Gr electrode data. Plateaus S2 and S3 have been attributed to the crystallization of amorphous Li_xSi_y to $\text{Li}_{15}\text{Si}_4$ below ~ 50 mV during lithiation and its subsequent delithiation above ~ 400 mV, respectively. The plateau S1 likely arises from structural changes in the (amorphous) Si component that continue during the change in graphite potential from the plateau G2 to G3.

XRD data collected during the electrochemical cycling are presented in Figure II.2.A.29c and Figure II.2.A.29d. Given that the strongest diffraction peaks belonging to the (00l) family of planes of the Li-Gr intercalation system occur within the range 3.2-3.8 Å, only this region is presented. It is worth noting that no

spectral peaks were observed that could be attributed to a crystalline phase of Si; this observation is in agreement with prior research, which indicates that the crystalline Si becomes X-ray amorphous after the initial lithiation. The Gr electrode data (Figure II.2.A.29c) shows the following: (i) the average d-spacing increases in the early stages of lithiation prior to the G2 point. (ii) At the onset of plateaus G1 and G2, the diffraction peak broadens indicating the appearance of additional phases with intermediate spectral features. (iii) Between the G2 and G3 points, a Bragg peak centered at 3.54 Å is observed; the position of this peak does not change between the plateaus. Past the G3 (iv) point, in addition to this 3.54 Å peak, a new peak at 3.70 Å emerges. From these observations, we conclude that at least five ordered phases (known as the lithiation stages) are formed during Li intercalation between the graphene layers in the graphite. These same phases are also observed during Gr delithiation (Figure II.2.A.29c). The similarity between the stages observed during Gr lithiation and delithiation is consistent with the well-known reversible nature of Li^+ ion intercalation into graphite. As lithiation progresses the sequential formation of dilute stage I (denoted I'), stage IV/III, stage III, stage II, and stage I has been reported. Of these stages, the stoichiometry of stages II and I has been determined as LiC_{12} , and LiC_6 ; ambiguity exists as to the exact stoichiometry of the other three stages. In our analysis below we assume the following stoichiometries: stage I' (Li_xC_6 , $0 < x < 0.1$), stage IV/III (Li_xC_6 , $0.1 < x < 0.22$, represented by LiC_{30} , and stage III (LiC_{18}).

A custom computer code was written to deconvolute the Li_xC_y phases observed in the XRD patterns. After this deconvolution, the average Li^+ content (i.e., capacity) of the Gr component was quantified from the XRD peak intensities. For the Si-Gr electrode, the lithium content of the Si-component was obtained by subtracting the Gr capacity from the total cell capacity: the results are as portrayed in Figure II.2.A.30. Figure II.2.A.30a shows that during the initial lithiation (region 1, 1.0 – 0.20 V_{Li}), Li mainly reacts with the Si; the lithiation ratio $\text{Li}_{\text{Si}}/\text{Li}_{\text{Gr}}$ of Si vs. Gr is 0.96/0.04 in this range. That is, when the electrode capacity during lithiation is 1.5 mAh, the capacity of the Si and Gr components are ~1.44 mAh and ~0.06 mAh, respectively. In region 2, the relative fraction of Gr lithiation increases as the electrode potential decreases to 0.20 V_{Li} , below which most of the Gr lithiation is expected. In this region (0.01 – 0.2 V_{Li}), the average $\text{Li}_{\text{Si}}/\text{Li}_{\text{Gr}}$ is ~0.58/0.42; i.e., the lithiation of Si occurs preferentially over Gr even in this region. During the initial delithiation (region 3, 0.01 – 0.22 V_{Li}), almost all Li^+ ions are extracted from Gr, and the $\text{Li}_{\text{Si}}/\text{Li}_{\text{Gr}}$ ratio is zero. In region 4, almost all Li^+ ions are extracted from Si, and in this region (0.22 – 1.0 V_{Li}) the $\text{Li}_{\text{Si}}/\text{Li}_{\text{Gr}}$ ratio is ~0.97/0.03.

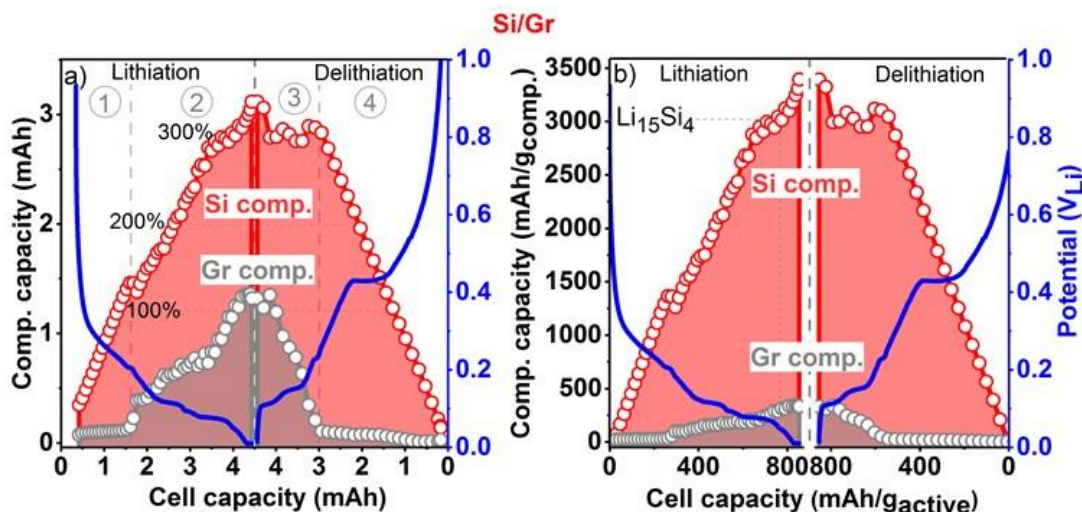


Figure II.2.A.30 Capacity (a) and specific capacity (b) of the Gr and Si components in a Si-Gr electrode during lithiation and delithiation. Note that the capacity increases during lithiation and decreases during delithiation. Regions 1 to 4 are indicated with the circled numerals in panel a. The percentages shown in panel (a) are the estimated expansions of Si particles.

These results indicate that delithiation of the Si-Gr electrode occurs sequentially, first from the Gr and then from the Si. This behavior has practical implications for electrode cycling. Figure II.2.A.30b shows the specific capacity in the individual components plotted as a function of the net specific capacity. When the potential reaches 0.2 V_{Li} during lithiation, the specific capacity in the Gr is negligible, whereas for the Si particles it is ~1350 mAh·g⁻¹Si, which corresponds to a volume expansion of 135 % (assuming a linear expansion rate of 100% per 1000 mAh·g⁻¹Si). When the potential is 0.01 V_{Li} during lithiation, the specific capacity of the Gr is ~340 mAh·g⁻¹Gr, whereas for the Si particles it is ~3400 mAh·g⁻¹Si, which corresponds to a volume expansion of 340 %. On delithiation, the Si particles remain at ~340 % expansion until the electrode potential reaches 0.20 V_{Li} since Li⁺ ions are extracted only from the Gr particles in the 0.01–0.2 V_{Li} range. The Si particles begin to contract only when the potential is in the 0.2–1.0 V_{Li} range. Previous research has shown that volumetric changes in the Si particles during electrochemical cycling greatly accelerate capacity fade. With that in mind, Figure II.2.A.30b can be used to design cycling regimes to minimize such changes by avoiding the formation of the expanded Li₁₅Si₄ phase, in this way extending the cycle life of the cell. Note, that the plots in Figure II.B.1.30b will be affected by the Si content, which will alter capacity contributions of the Gr and Si components.

Calendar-life versus Cycle-life aging of Lithium-ion Cells with Silicon-Graphite Composite Electrodes

Potential profiles for the positive electrode from a NCM523/Si-Gr (10 wt% FEC) cell that underwent cycle-life aging is shown in Figure II.2.A.31a and from a similar cell that underwent calendar-life aging is shown in Figure II.2.A.30b. The negative electrode potential is simply the difference between the cell voltage and positive potential at any given instant. For example, cycle 2 in Figure II.2.A.31a indicates that the positive potential changes from 3.68 V to 4.22 V (as a result of oxide delithiation), when the cell is charged from 3.0 to 4.1 V; the negative potential correspondingly changes from 0.68 V to 0.12 V (indicating lithiation of the Si-Gr electrode). The reverse process happens during cell discharge from 4.1 to 3.0 V; the positive potential changes from 4.22 V to 3.68 V (as a result of oxide lithiation), and the negative potential correspondingly changes from 0.12 V to 0.68 V (indicating delithiation of the Si-Gr electrode).

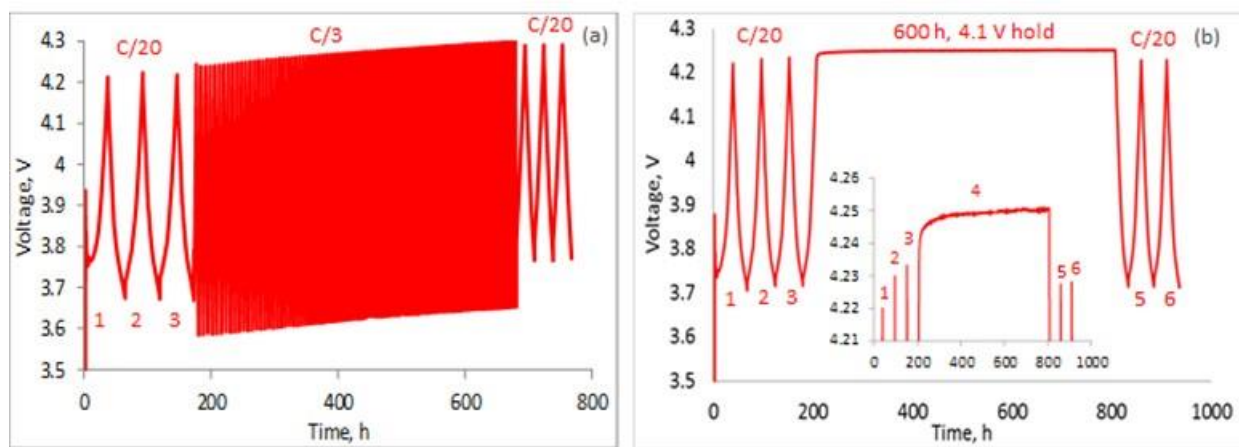


Figure II.2.A.31 Changes in the positive electrode potential during (a) cycle-life aging and (b) calendar-life aging of a NCM523/Si-Gr (10 wt% FEC) cell. The inset in (b) shows the top 50 mV of the plot. In both plots, the first 3 (formation) cycles are at a ~C/20 rate. In (a), cycles 4–97 (aging) are at a ~C/3 rate and cycles 98–100 are at a C/20 rate. In (b), cycle 4 includes a 600 h hold after charging to 4.1 V; the cycle 4 discharge and the final diagnostic cycles 5 and 6, are at a C/20 rate.

As the cell is cycled, the positive potentials at the end of charge and discharge gradually increase over the 100 cycles, and the cycling window narrows. For example, when the cell is charged from 3.0 to 4.1 V at cycle 99, the positive potential changes from 3.77 V to 4.29 V (Figure II.2.A.31a). The higher upper potential (4.29 V vs. 4.22 V at cycle 2) indicates increasing delithiation of the oxide during cycling and the narrower cycling window (0.52 V vs. 0.54 V at cycle 2) indicates ongoing capacity loss. The observed changes can be obtained by the electrode potential shifts (known as “voltage slippage”) that occur during cell cycling. This slippage,

results from a net loss of mobile Li^+ ions, as they become incorporated into the solid electrode phase (SEI) of the Si-Gr negative electrode. The capacity loss (cycle 99-cycle 2, C/20 rate) for the cell is ~44 %.

For the calendar-life test cell, electrode potential changes during the formation cycles are similar to that of the cycle-life cell, as expected. During the potentiostatic hold the positive electrode potential of this cell also increases, indicating increasing delithiation of the oxide (Figure II.2.A.31b). However, after the potentiostatic hold, the positive potentials at the end of charge and discharge are *slightly lower* than those before the hold. For example, the highest potential for cycle 5 is 4.227 V vs. 4.233 V for cycle 3; the lowest potential for cycle 5 is 3.714 V vs. 3.716 V for cycle 3. The capacity change during the 600 h potentiostatic hold was obtained through measurements of small parasitic currents, flowing through the cell: in Figure II.2.A.31b, 11.1 mAh/g_{oxide} charge was transferred between the electrodes during the 600 h potentiostatic hold.

A possible explanation for the observation in Figure II.2.A.31b is as follows: additional sites for Li^+ ion insertion in the negative electrode become available during the potentiostatic hold. These “higher impedance” sites, presumably in the silicon, are not accessible during typical charging, even at a C/20 rate. Lithiation of these “additional” sites lead to increased delithiation of the oxide resulting in a higher potential at the positive electrode. However, SEI formation would also be expected at these newer sites, leading to some irreversible loss of Li^+ ions. The measured capacity loss of cycle 4 (4.5 mAh/g) is the difference between the additional charge from accessing new sites and the charge consumed during SEI formation. The lower positive electrode potential during the fourth discharge results from the insertion of an additional charge into the oxide particles.

The mole fractions of the PO_2F_2^- anion were determined for various electrolyte samples. This anion forms because the electrolyte salt LiPF_6 is hydrolytically unstable and reacts with the water contained in the LiPAA binder. As expected, no detectable PO_2F_2^- was observed in the freshly prepared electrolytes. For the cell after three formation cycles, the mole fraction of PO_2F_2^- anions in solution was low, ca. 2%. After cycle-life aging, this fraction increased to 6%. For the calendar-life aged cell (which was held at 4.1 V for 600 h) this PO_2F_2^- fraction was considerably higher, ca. 25%. When the FEC electrolyte was simply put in contact with the electrode (no cycling) for 130 h (equivalent to time for formation cycles), the PO_2F_2^- mole fraction was 11%. This value is considerably *higher* than the fraction in the cycle-life aged cells but *lower* than in the calendar-life aged cells.

These data indicate that the extent of LiPF_6 hydrolysis in the electrolyte is ~ 4 times greater for calendar-life cells than for the cycle-life cells; that is, the chemical evolution of the electrolyte is different during calendar-life aging than during cycle-life aging. We propose the following explanation for the observations. When the Si-Gr cell is cycled and particle volumes change, the SEI becomes unstable, so HF can access and reacts with the surface. These reactions decrease the concentration of HF in the electrolyte. In contrast, during the potentiostatic hold, the SEI is not restructured so both water and HF can access the surface of the lithiated Si particles only slowly (by diffusion through the “static” SEI). Consequently, water has no reaction sink other than LiPF_6 hydrolysis; this is why the LiPF_6 hydrolysis becomes so efficient. However, even during the potential hold, some HF can reach the Li_xSi particle surface, where it corrodes the protective layer causing electrolyte reduction and the small (~3%) capacity fade mentioned above.

3. Silicon Surface Modifications

Silane-based Surface Modifications – Synthesis

The chemical and electrochemical reaction on the surface of the silicon (Si) and lithiated silicon (Li_xSi) with electrolyte solvent/additive plays a significant role in the battery performance of silicon anode. The non-volatile reaction products deposit on the particle and form the so-called solid-electrolyte-interface (SEI). For the traditional graphite-based anode, this exclusively Li^+ -conducting SEI layer passivates the surface of the lithiated graphite and prevents the further reactions with electrolyte thus enables the reversible lithiation / delithiation chemistry of lithium ion battery. However, due to the huge volume expansion/contraction of silicon-based anode, the surface passivation is not established since the SEI cracks and reforms with cycling

which consumes considerable amount of active lithium resource from the cathode leading to the rapid capacity decay.

The overall goal of this project is to develop sustainable high-energy density of Si-based nanocomposite electrodes for electric vehicle application. Specifically, in this work, we try to engineer the Si surface chemistry through different approaches with a target to stabilize the interface affording a Si anode with extended cycle life. The first approach is to develop new electrolyte/additive that could chemically / electrochemically decomposes and deposits on the lithiated Si surface forming a resilient SEI layer that stabilizes the interfacial reactivity of Li_xSi and electrolyte. Fundamental understanding of how the reactivity of electrolyte/additive with Si anode and how the chemical composition of SEI affects the cell performance will be systematically performed. The second approach is to functionalize the surface of Si particles through organic silane chemistry with a target to stabilize the interface affording a Si anode with extended cycle life.

A two-step approach was employed to introduce the epoxy group to the surface of commercial silicon nanoparticles. The SiNPs were first treated by hydrogen peroxide (H_2O_2) to enrich the surface silanol (Si-OH) group followed by a surface hydrolysis/condensation reaction with the epoxy-containing silane precursor. For comparison, methylsilane surface-modified SiNPs were also synthesized by the same procedure and the impact on the cycling performance was directly compared in coin cell tests. Post-test analysis included Fourier-transform infrared spectroscopy (FT-IR), X-ray photoelectron spectroscopy (XPS), thermogravimetric analysis (TGA), and scanning electron microscopy/energy-dispersion X-ray spectroscopy (SEM/EDX). The results shed light on the source of the improved electrochemical performance of the epoxy-functionalized SiNPs anode materials.

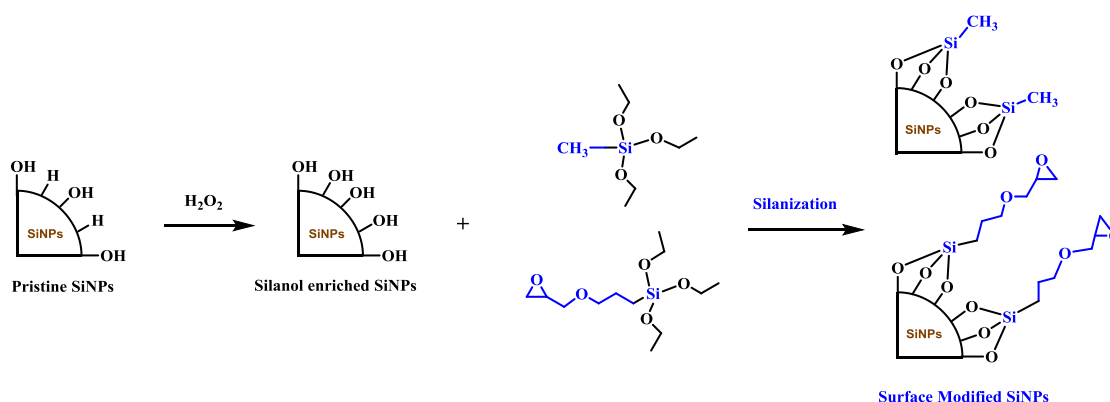


Figure II.2.A.32 Synthesis of surface-functionalized SiNPs with methyl and epoxy terminal groups.

Figure II.2.A.32 outlines the synthesis route for the surface-functionalized silicon nanoparticles. Commercial SiNPs were first treated by hydrogen peroxide solution to convert Si-H and Si-O-Si groups to silanol (-Si-OH) group following a literature procedure. The Si-OH SiNPs are subject to surface hydrolysis/condensation reaction with glycidylpropyltriethoxysilane. The pristine SiNPs showed a broad peak at 1100 cm^{-1} (expands from 1000 cm^{-1} to 1250 cm^{-1}) in the FT-IR spectrum (Figure II.2.A.29a), which is a typical stretching vibration peak for the Si-O-Si bond and indicates the existence of a native SiO_x layer on the pristine SiNPs. [24] After the hydrogen peroxide treatment, the increase in Si-OH peak intensity ($\sim 3300\text{ cm}^{-1}$) indicates that more silanol group was generated on the surface of the pristine SiNPs [25] and confirms the successful enrichment of surface silanol group. During the synthesis of epoxy-terminated SiNPs, a hydrolysis and condensation reaction formed a new Si-O-Si bond on the surface of the particle. The FT-IR spectrum of epoxy-SiNPs is also shown in Figure II.2.A.33a. The band at $1250\text{-}1500\text{ cm}^{-1}$ originated from the ring expansion or breathing of the epoxy ring [26], [27], [28] and typical C-H vibration bands of the alkyl group appear at 2923 cm^{-1} and 2880 cm^{-1} . The TGA data further confirmed the successful attachment of the epoxy group. As shown in Figure II.2.A.33b, negligible weight loss (0.3%) was observed for the pristine SiNPs. However, this value increased to 3.2% for the epoxy-SiNPs.

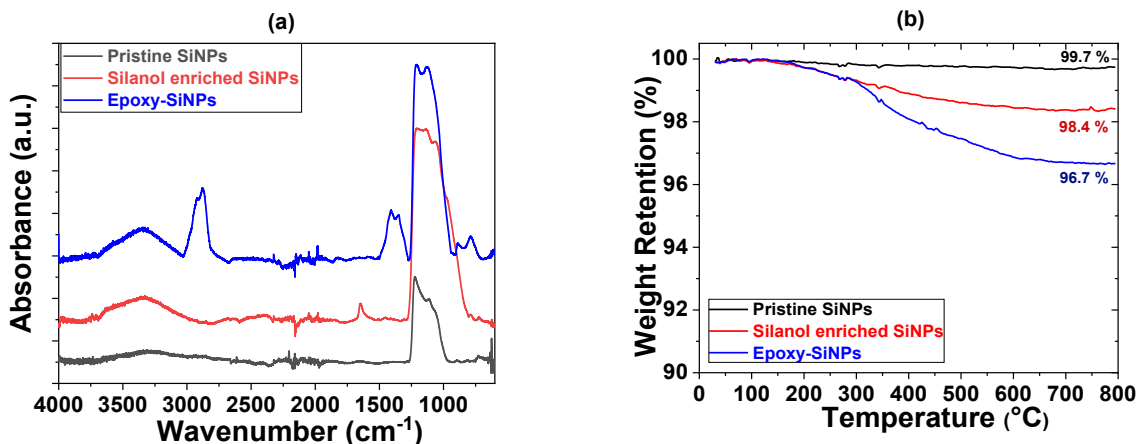


Figure II.2.A.33 (a) FT-IR spectra and (b) TGA thermograms of pristine SiNPs, silanol-enriched SiNPs, and epoxy-SiNPs.

To determine the electrochemical performance, Si electrodes were coated with pristine SiNPs, CH_3 -SiNPs, and epoxy-SiNPs as active anode materials. After three $C/20$ formation cycles, the Si/Li cells were operated for 100 cycles at a $C/3$ rate. Cell capacity and Coulombic efficiency for three formation cycles at $C/20$ rate are shown in Figure II.2.A.34a, and the cycling performance for one 100 cycles at the $C/3$ rate is shown in Figure 33b. The pristine SiNPs electrode shows an initial delithiation capacity of 1989 mAh/g and an average capacity

1890 mAh/g for 100 cycles. Both values for the epoxy-SiNPs electrode are much higher (initial capacity of 2294 mAh/g and average capacity of 2169 mAh/g) than those for the pristine anode. Surprisingly, the CH_3 -SiNPs electrode exhibited rapid fade in capacity with increasing cycle number (initial capacity of 1976 mAh/g and average capacity of 1212 mAh/g) (Figure II.2.A.34b). These data clearly indicate that the functional group on the surface of the SiNPs dictates the electrochemical performance of the Si electrode. The cell performance agrees well with our initial approach of introducing epoxy group on the surface of SiNPs to promote the integration of active particles with the binder, current collector, and other cell components. To further verify this positive impact, the chemical reaction between the epoxy-SiNPs and PAA binder was examined by mixing the SiNPs and PAA binder with the same composition used in the anode slurry and stirring at room temperature for overnight. The reacted SiNPs were isolated by high-speed centrifugation and subjected to TGA analysis. For the CH_3 -SiNP particles, the TGA profiles are almost identical before and after the reaction with PAA binder (data not shown); nevertheless, an additional weight loss was observed for the PAA treated epoxy-SiNPs. This indicates that PAA segments were attached to the surface of the epoxy-SiNPs particles via the ring-opening addition reaction of the epoxy group with the hydroxyl group from the PAA binder.

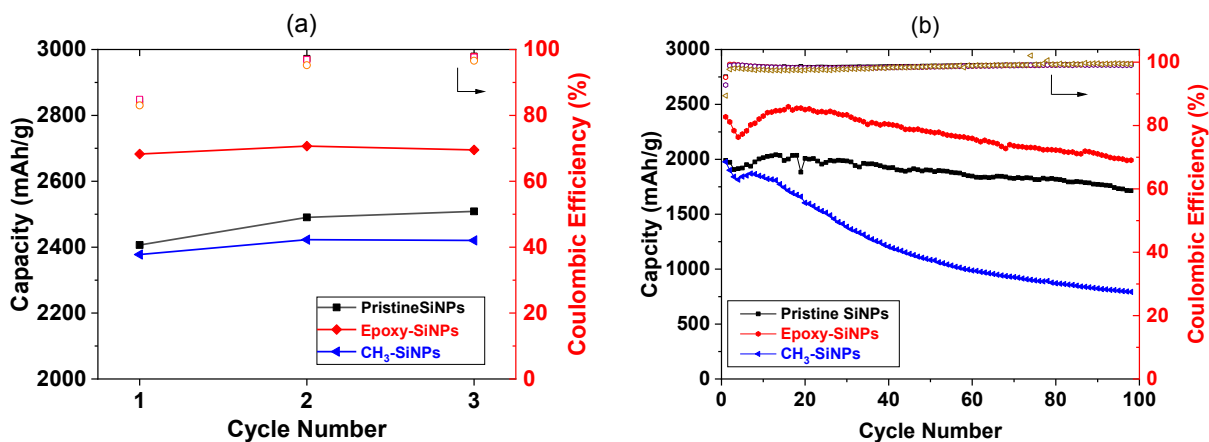


Figure II.2.A.34 Initial capacity and Coulombic efficiency of Si/Li cells: (a) three C/20 formation cycles and (b) one-hundred C/3 cycles.

Figure II.B.1.35 shows the surface chemical composition of the cycled electrodes: pristine SiNPs, Si-OH SiNPs, and epoxy-SiNPs. For all three electrodes, the detectable surface Si amount decreased, indicating the formation of a thick SEI layer. Fluorine and phosphate were detected from the surface of all three cycled electrodes due to the decomposition of the electrolyte. The surface of the electrode made from epoxy-SiNPs has much less fluorine and phosphate content than that of the other two electrodes, as shown in Figure II.2.A.35c. This finding suggests that the surface modification of SiNPs mitigated the continuous reduction/decomposition of the electrolyte. It is notable that the fluorine content on the surface of the electrode made from Si-OH SiNPs is much higher than that on the surfaces of the other two electrodes (Figure II.2.A.35b). We speculate that the surface silanol group tends to eliminate water via a condensation reaction during repeated cycling, leading to severe hydrolysis of the LiPF₆ electrolyte salt at the electrode surface.^[29]

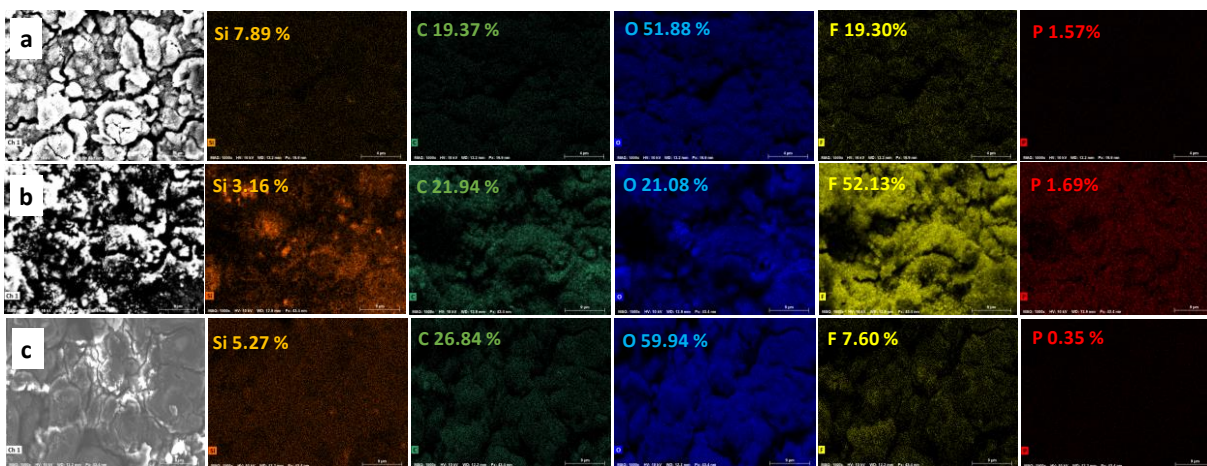


Figure II.2.A.35 EDX elemental mapping (Si, C, O, F, P) for Si/PAA electrodes with (a) pristine SiNPs, (b) Si-OH SiNPs and (c) epoxy-SiNPs after 100 cycles.

The surface of the cycled electrodes was examined by XPS. Figure II.2.A.36a show the Si_{2p} spectra of the pristine SiNPs and epoxy-SiNPs electrode before cycling. The peaks related to elemental silicon (99.4 eV) and oxidized silicon SiO_x (103.5 eV) resemble the spectra of their corresponding nanoparticles, indicating that the epoxy-SiNPs nanoparticles remain inert after exposure to the aqueous slurry. After one formation cycle, new peaks appeared in both spectra at 102 eV (Figure II.2.A.36b), a characteristic peak of Li_xSiO_y formed by irreversible reduction of SiO_x at the electrode surface.^{[30], [31]} However, a lower intensity Li_xSiO_y peak was

observed for the epoxy-SiNPs electrode. In addition, the presence of a new peak at a binding energy of 98 eV (Li_xSi) from the pristine SiNPs electrode implies that not all the lithium was extracted from the pristine SiNPs electrode. Without the surface group, the pristine SiNPs tends to react with the lithiated silicon causing impedance buildup and the polarization of the electrode. In contrast, the epoxy-functionalized SiNPs reduced the parasitic reactions with Li_xSi and enabled the reversible lithium insertion and extraction. Actually, the Li_xSi peak was not observed on the XPS spectrum of the epoxy-SiNPs electrode at the fully delithiation state. Surface modification of silicon nanoparticles could mitigate the irreversible reduction of SiO_x during lithiation and facilitate the extraction of lithium during delithiation. Since both Li_xSiO_y and Li_xSi species contribute to the irreversible capacity in the first lithiation/delithiation cycle, the XPS results are in good agreement with the higher initial capacity and Coulombic efficiency of the epoxy-SiNPs electrode.

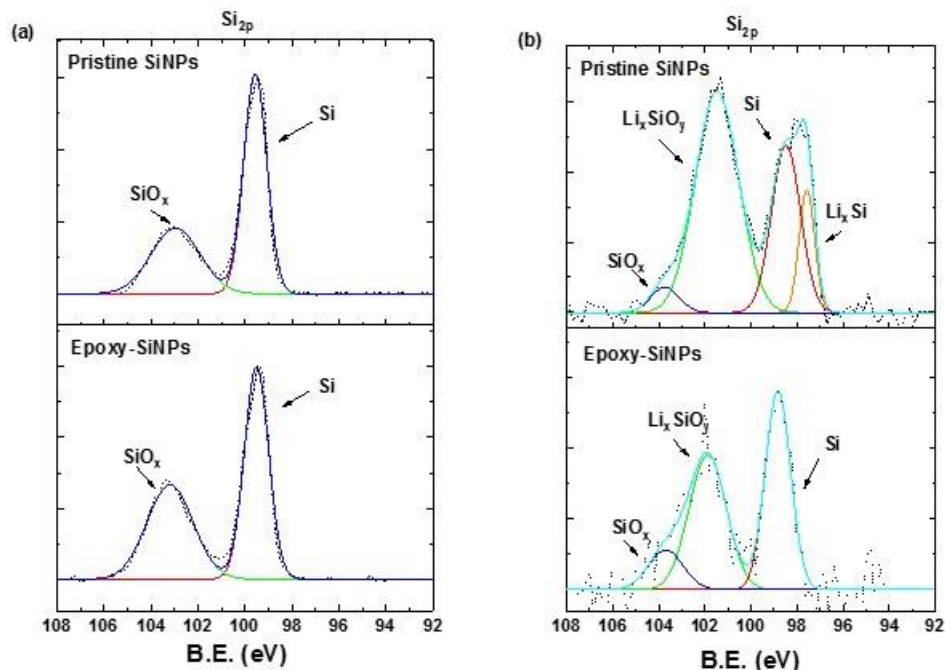


Figure II.2.A.36 Si_{2p} XPS spectra of the Si electrodes based on pristine SiNPs and epoxy-SiNPs before and after one formation cycle: (a) fresh Si electrode before cycling and (b) Si electrode after one formation cycle at delithiated state.

The binding strength is critical to the electrochemical performance of the Si-based electrode since strong bonding between the active particles and the particle/current collector help maintain the electrical contacts and the integrity of the Si anode.^[32] A peel test was employed to evaluate the adhesive strength of the Si/PAA anode. A continuous force was applied to the surface of the electrode and when the Si/PAA anode was peeled off of the current collector (copper foil in this case), the resulting load/width (N/cm) reflects the adhesive strength of the whole electrode. Figure II.2.A.37 summarizes the test results. The epoxy-SiNPs showed the strongest adhesion among the tested three electrodes, which is attributed to the high reactivity and strong interaction of the epoxy group with hydroxyl groups from the PAA binder and the Cu current collector. This result confirms one of our initial material design ideas, i.e., introducing an epoxy group onto the surface of nanosilicon particles will maintain the electrode integrity and thus exert a positive impact on the electrochemical performance.

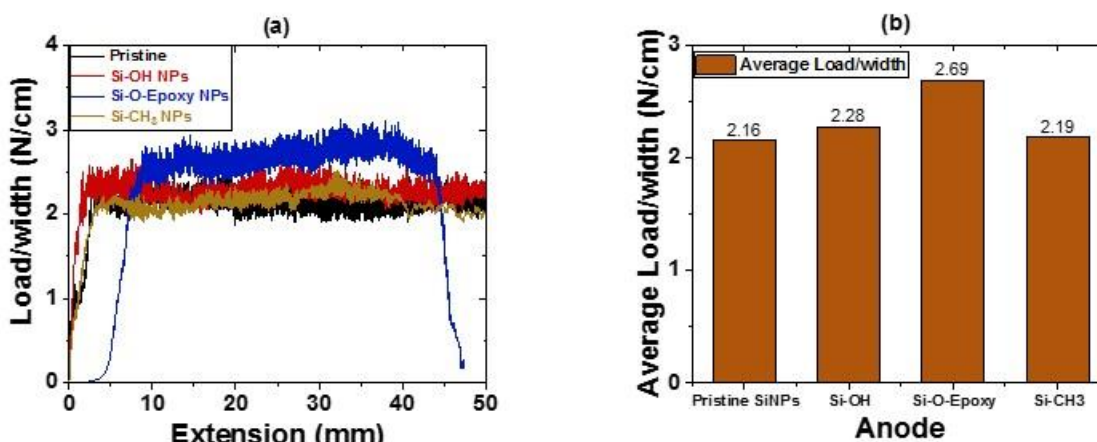


Figure II.2.A.37 (a) Adhesion strength of the Si anodes with pristine SiNPs, Si-OH SiNPs, epoxy-SiNPs, and CH₃-SiNPs as active materials, and (b) summarized data of average load per unit width (N/cm).

Silane-based Surface Modifications – Characterization

The project aims to develop a systematic understanding and synthesis of surface coating materials to chemically or physically change the surface of the silicon (Si) materials, in order to manipulate the interphase chemistry for enhanced electrochemical reversibility and mechanical integration in Si-based electrodes. Continuous decomposition of electrolyte on the silicon surface is one of the factors dictating the electrochemical performances of Si electrode. Tremendous efforts have been dedicated in our collaborative project to stabilizing the surface: (i) depositing an artificial protective layer by using atomic layer deposition (ALD) or molecular layer deposition (MLD), (ii) using a polymeric binder that mitigates electrolyte decomposition, and (iii) introducing electrolyte additives that sacrificially decompose to generate a protective film. To study the fundamental roles of the surface species on the electrochemical and physical properties of the electrodes, we devoted FY 18 research to develop the liquid-phase deposition process to functionalize the silicon surface. The liquid-phase deposition are capable to explore various functional groups and can be applied for both laminated electrodes and the nanoparticles. The in-depth understanding from these studies will help establish effective mitigation to address the key challenges in Si-based electrodes; and develop strategies to deploy high-energy silicon materials and composite electrode configurations in the full Li-ion cells.

Three functional groups (-CH₃, -CF₃, and -COOH), which are usually found in the functional polymer binding materials, have been selected and deposited on the surface of our Si (100) wafer electrodes by spinning coating or by directly immersing the samples into the liquid bath. The corresponding silane compounds with the selected functional groups were used as the precursors, including silanescarboxyethylsilanetriol, n-propyltriethoxysilane, and trimethoxy(3,3,3-trifluoropropyl)silane. A self-assembled molecular (SAM) film forms on the surface of the Si electrodes. The SAM film is assembled on the surface of Si wafer through the formation of the Si-O-Si bond between the silanol and the native silicon oxide on the surface of the Si wafer. The covalently attachment enhances the adhesion of the silane film on the surface of silicon, which ensures the coating effects during the electrochemical process. A variety of SAM films can be assembled by changing the functional groups in the corresponding silane compounds.

Electrochemical behavior of the surface-modified electrodes was characterized by using galvanostatic cycling tests. Figure II.2.A.38 displays the voltage profiles of the functionalized Si electrodes, cycled in the Gen2 (1.2 LiPF₆ in EC: DEC 3:7) electrolyte with 10 wt% FEC additive. Each electrode was lithiated for 2 hours and delithiated up to 1.5 V (vs. Li/Li⁺) with a current density of 27.3 μA/cm². The Coulombic efficiencies (CE) of the functionalized electrodes are slightly higher than CE in the pristine electrode, -CF₃ (92.9%) > CH₃ (92.2%) > COOH (91.8%) > Pristine (90.9%). The lithiation of the crystalline Si starts below 0.1 V (vs. Li/Li⁺), which

is much lower than the reduction potential of the carbonate electrolyte (>0.5 V) and the lithiation of native silicon oxide. Thus, the majority of capacity gained above 0.1 V can be attributed to the side reactions related to the interphase formation. Figure II.2.A.38b shows an enlarged plot of Figure II.2.A.38a. It is clearly seen that less activities were observed in the treated electrodes above 0.1 V, as compared to the pristine electrode. The behavior in the surface-treated Si electrodes is attributed to the insulating properties of the SAM layer at the top of Si electrodes; that is, the SAM layer hinders the electron transfer from the bulk to the surface of the Si electrode.

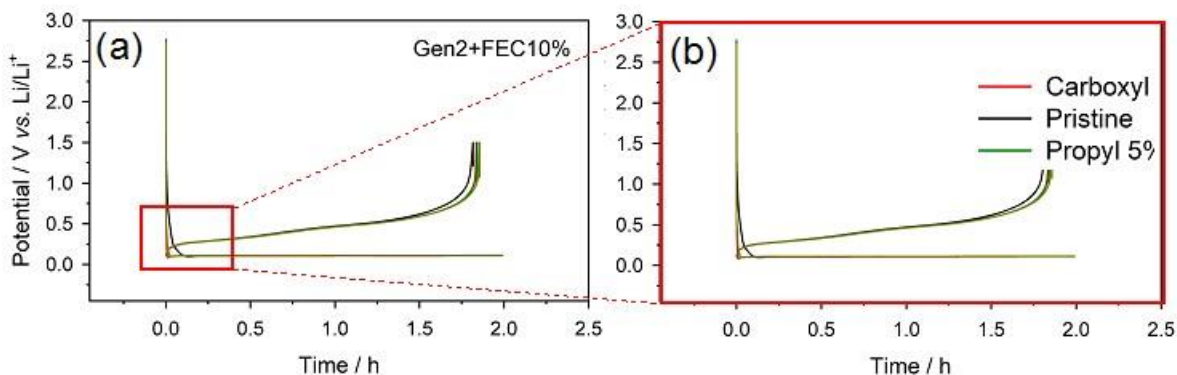


Figure II.2.A.38 The voltage profiles of the functionalized electrodes. Cut-off: 2 hours lithiation, 1.5 V delithiation. Current density: $27.3 \mu\text{A}/\text{cm}^2$.

Reduction of the carbonate electrolyte and its interaction with the surface species of the Si electrodes lead to the formation of solid electrolyte interphase (SEI). Due to the different functional groups used for surface modification, distinct SEI layers could be expected for each surface-modified Si electrode. X-ray photoelectron spectroscopy (XPS) with high sensitivity to the surface species has been performed to characterize the chemical structure of the SEI on the surface-modified Si electrodes. Table II.2.A.3 summarizes the composition of the surface layer, based on the XPS results. The SEI on the pristine electrode is enriched by Li and F, identified as LiF based on the binding energy of each element. As mentioned in previous sections, FEC was used in the galvanostatic testing. FEC has been known to be decomposed sacrificially prior to EC or DMC, generating LiF-rich SEI with minor ingredients of poly (VC), Li_2CO_3 and $\text{Li}_2\text{C}_2\text{O}_4$ on the surface. [33] As compared in Table II.2.A.3, XPS data show negligible impacts of the functional groups on the chemical composition of the interphase. It is interesting to note that the interphase formed on the treated Si electrodes are also dominated by LiF as the interphase of the pristine electrode does. Minor changes are observed in C, O, and Li spectra (not presented) especially on the surface of the CH_3 -treated electrode, implying the different concentration of Li_2CO_3 or $\text{Li}_2\text{C}_2\text{O}_4$ in the interphase.

Table II.2.A.3 Chemical composition of SEI calculated using XPS spectra.

Element	Pristine	-CH ₃	-COOH	-CF ₃
C 1s	8.8	13.9	10.5	11.2
Li 1s	35.8	34.1	35.6	35.3
F 1s	38.2	29.4	34.8	34.7
O 1s	9.6	15.7	12.9	12.3
P 2p	0.8	0.9	1.1	0.8
Si 2p	6.9	6.0	5.2	5.6

Electrochemical impedance spectroscopy (EIS) was used to evaluate the impact of the functional groups on the interfacial resistance of the Si electrodes. The Si electrodes surface-modified with different functional groups were cycled in a 3-electrode cell to measure impedance without the interference from a counter electrode reactions. The EIS data were collected at the end of lithiation using 3-electrode cells. In the Nyquist plot in Figure II.2.A.39, the semi-circle in the high frequency region reflects the interface resistance; SEI (R_{SEI}) and charge transfer resistance (R_{ct}). The spike in the low frequency region is Warburg impedance of Li^+ diffusion in the electrochemical active material—Si electrode. Although the chemical compositions of the SEIs are comparable and dominated by LiF, the interface resistances are significantly different. The interface resistance increases in the order of $-\text{CH}_3$ (420Ω) > Pristine (180Ω) > $-\text{CF}_3$ (140Ω) > $-\text{COOH}$ (100Ω).

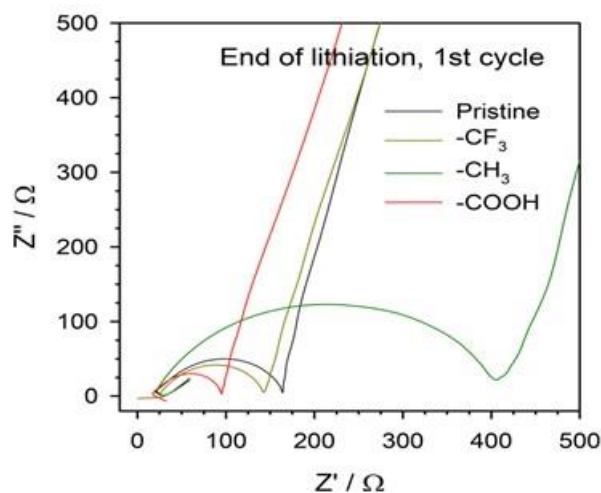


Figure II.2.A.39 Impedances of the surface treated electrodes, measured at the end of lithiation. The same electrolyte, Gen2 with 10% FEC, was used for all of electrochemical testing.

In Figure II.2.A.40, the ionic conductivity of the Si electrodes functionalized by $-\text{CH}_3$ and $-\text{COOH}$ shows the largest and smallest values, respectively. Then, these two electrodes were selected to run the quasi in-situ EIS for further understanding the impedance evolutions during lithiation/delithiation. A representative voltage profile of Si wafer is provided in Figure II.2.A.38a. EIS was conducted at the different potential, highlighted in red dots in Figure II.2.A.40a. The SEI layer formed on $-\text{CH}_3$ (or $-\text{COOH}$) modified surface is denoted as SEI- CH_3 (or SEI- COOH) hereafter. In Figure II.2.A.38a b and c, the Nyquist plots visualize the evolution of surface resistance during 1st lithiation and delithiation. As aforementioned, the first semi-circle in Nyquist plot reflects the SEI resistance. It shows that the SEI resistances for both SEI- CH_3 and SEI- COOH shows negligible changes during lithiation and delithiation. However, the resistance of the SEI- CH_3 is about 4 times larger than that of SEI- COOH , as indicated in Figure II.2.A.39, Figure II.2.A.40b and Figure II.2.A.40c. While the SEI resistance is distinctive in the Nyquist plots, the charge transfer resistance is hard to be distinguished. Charge transfer resistance is usually observed in the mid-frequency range. In our case, the charge transfer resistance is likely overlapping with either SEI resistance appeared in a higher frequency range or Warburg diffusion resistance shown in a lower frequency range.

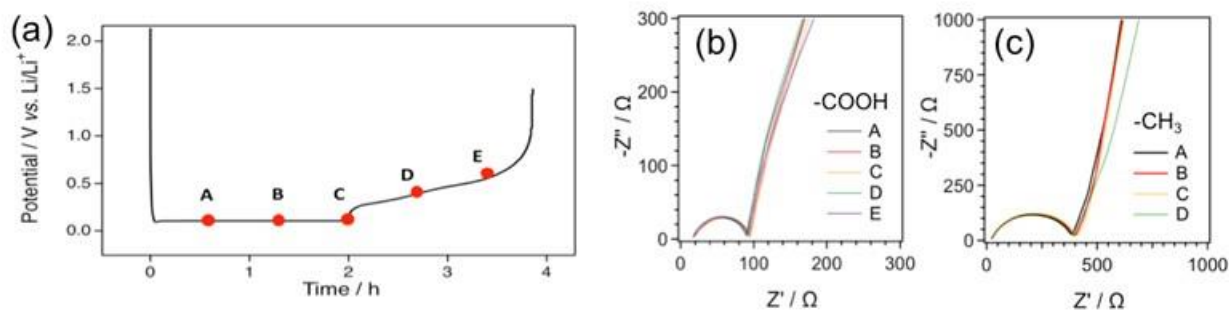


Figure II.2.A.40 (a) A representative voltage profile of Si wafer electrode. (b) (c) Nyquist plots of SEI-CH₃ and SEI-COOH. EIS measurements were conducted at specific state of lithiation and delithiation marked by the red circles in (a).

Nyquist plot has been widely used to evaluate the SEI and charge transfer resistance, without providing details about the formation process of SEI and the charge transfer reaction on electrodes' surfaces. In this study, we introduce Bode plots to compensate for the limitations inherent in Nyquist plot, provide the information about the interphase structure and formation process. Bode plots collected from both -CH₃ and -COOH treated Si electrodes are presented in Figure II.2.A.41, in which the phase angle is plotted versus frequency. Due to the frequency dependency, the Bode plots offer a better means to distinguish the individual electrochemical response that has a different time constant. The high-frequency region from $10^6 \sim 10^1$ Hz is attributed to the SEI layer. As indicated in Figure II.2.A.40a, the responses for the SEI-COOH are slightly different from those found in the SEI-CH₃. The peaks for both SEI-CH₃ and SEI-COOH locate about 10^4 Hz, which reflect the similar mobility of lithium ions in both SEI layers. As described in earlier section, LiF and Li₂CO₃ are the dominate species for both SEI-CH₃ and SEI-COOH layers, thus leading to the similar mobility for lithium ions. However, the SEI-COOH layer shows a shoulder in the higher frequency range in the Bode plot. The shoulder in the Bode plot of SEI-COOH is related to the ionic diffusion through the -COOLi layer between the top SEI layer and the Si surface. It is known that the -COOH SAM film can be lithiated ($-\text{COOH} + \text{Li}^+ + \text{e}^- \rightarrow \text{COOLi} + \text{H}_2$) [33], resulting in the formation of the interlayer of lithium carboxylate between the Si surface and FEC-driven SEI. Regarding the -CH₃ treated electrode, a longer tail is observed in the lower frequency range, indicating a layer forming between the top SEI and the Si surface. It is believed that the functional group -CH₃ involves in the formation of the layer. However, the frequency range where the shoulder appears is higher than that for the tail in the -CH₃ treated Si. We expect that the overall lithium ion mobility would be higher in the -COOLi layer than that in the -CH₃-incorporated layer.

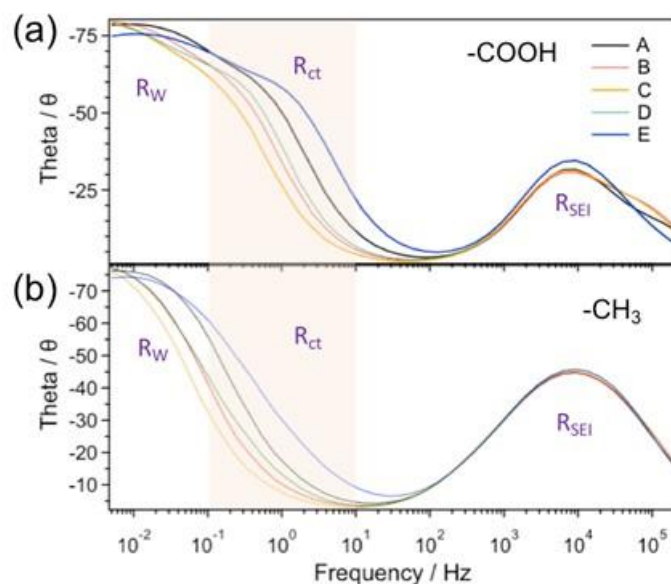


Figure II.2.A.41 Bode plots of silicon electrodes fictionalized by (a) -COOH and (b) -CH₃.

Charge transfer reaction on composite Si electrode is usually seen as a separated semi-circle in Nyquist plot. But the semi-circle is overlapped with Warburg resistance for these Si wafer electrodes (Figure II.2.A.40b). Here, we used Bode plot to identify the charge transfer process, considering the charge transfer process occurs in the mid-frequency range $10^1 \sim 10^{-1}$ Hz. In Figure II.2.A.41a, a shoulder-like peak in the range of $10^1 \sim 10^{-1}$ Hz is observed for the SEI-COOH, especially at the beginning of lithiation (labelled as A). As the reaction proceeds, the charge transfer resistance at the interphase becomes reduced (denoted C in Figure II.2.A.41a). But the plateau become more noticeable at the end of delithiation—denoted as E in Figure II.2.A.41a. In a strong contrast, the smooth linear Bode curve is observed for SEI-CH₃ at that frequency range, as shown in Figure II.2.A.41b. It indicates that the much smaller charge transfer resistance is observed for the SEI-CH₃ layer, as compared to that of the SEI-COOH layer.

Combining the data from Nyquist and Bode plots, we found that the SEI-COOH interphase has a smaller SEI resistance (higher lithium ion mobility across the layer), but a higher charge transfer resistance than that of SEI-CH₃. It is known that the charge transfer resistance includes the lithium ion transfer at the interface between the SEI layer and the bulk Si electrode, as well as the solvation/desolvation process at the interface between the electrolyte and the SEI layer. Due to the similar chemical composition on both SEI-CH₃ and SEI-COOH, we expect a similar solvation/desolvation process at the surface of both SEI layers. Therefore, the high charge transfer resistance, observed for the SEI-COOH, should be attributed to the lithium ion transfer at the interface between the SEI layer and the bulk Si electrode.

In addition to the lithium ion conductivity, the electronic resistivity of the interphase also plays an important role in governing electrochemical reversibility of Si electrode. The electron-insulating property of the SEI layer can block the electron transfer, then suppress parasitic reactions at the surface of the SEI layer. However, the direct measurement of the electronic resistivity is extremely challenging, majorly because of the absence of methodology for such measurements. Recently, NREL SEISTa team has developed a technique which scanning spreading resistance microscopy (SSRM) was customized to directly measure the SEI electronic resistivity. By applying a small voltage bias between the sample and a nanoscale AFM probe, the current response will be monitored and used to calculate the electronic resistivity based on the instrument parameters and sample dimensions. The most important feature of SSRM is to provide the electronic resistance of a nanometric scale of sampling volume. By moving the AFM probe, the technique can be applied for the

electronic conductivity mapping of SEI layers. Furthermore, the technique has been used to detect the evolution of the electronic resistance along the thickness of the sample, providing a depth profile of the electronic resistance. The details about the technique have been submitted.[\[34\]](#)

Here, SSRM was used to investigate the electronic conductivity of the SEI layers on the surface-treated Si electrodes. The resistivity/resistance from SEI-CH₃, SEI-COOH, and SEI-CF₃ (treated with trimethoxy(3,3,3-trifluoropropyl)silane) is plotted as a function of the depth—from the top of the SEI layer, and the distance from the bulk Si, as shown in Figure II.2.A.42. The resistivity continuously reduces, finally reaches $\sim 10^{-1}$ Ω cm—the resistivity of the bulk Si wafer. Therefore, the thickness of the interphase can be determined by the point at which the resistivity reaches to that of the bulk Si wafer. Resistivity, which shows the intrinsic property of the material, has also been calculated based on the formula, $R = \rho l/A$, in which R is the resistance, ρ is the resistivity, l is the length, and A is the area of the sample. The comparison of the resistance data in Figure II.2.A.41a reveals that the SEI-COOH has a higher resistivity than the other surface-treated electrodes. In addition, Figure II.2.A.41a indicates that the SEI-COOH layer is much thicker than those observed in the SEI-CH₃ and CH-CF₃. Furthermore, the resistance R per unit area was plotted as a function of distance from the bulk Si electrode. The interface between the bulk Si and the SEI layer was defined as '0' at the x-axis. The inner sections of the SEI-CH₃ and the SEI-CF₃ layers actually is more insulating than that of the SEI-COOH layer, while the outer section of the SEI-COOH shows the highest electronic resistance than the other two SEI layers. This peculiar growth at the latter stage of SEI formation is likely due to a chemical reaction in which electron transfer is not involved, considering the SEI resistance already reaches $\sim 10^5$ Ω before the sudden increase. The underlying mechanism is still not clear and require more investigation.

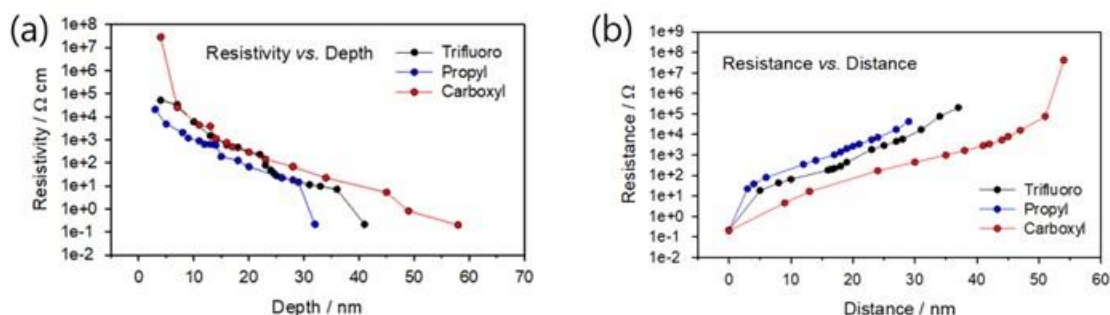


Figure II.2.A.42 Surface coating effects on the electronic conductivity. Resistivity depth profile in (a) was plotted as a function of depth. All of the measurements end at the point where the resistivity reaches $\sim 10^{-1}$ Ω cm, indicating that the AFM probe has touched the bulk Si electrode. The resistance profile in (b) was calculated and plotted as a function of the distance from the bulk Si electrode.

The results from both EIS and SSRM confirms that the SEI-COOH layer with a thickness about 60 nm has the highest ionic conductivity but the lowest electronic conductivity, as compared to the other surface-treated Si electrodes. Therefore, the -COOH terminated Si surface very likely facilitates forming a passivate SEI layer that can prevent electron transfer but allow fast ion transfer across the SEI layer. The results provide new insights on the working mechanism underlying the improved cycling performance found in the Si particle functionalized by -COOH groups and the Si electrode employing PAA or CMC binders.[\[35\]](#), [\[36\]](#)

Silicon Oxide and Lithium Silicate-based Surface Modifications

In our previous work, we investigated the stability of partially oxidized silicon nanoparticles in aqueous slurries and optimized the oxide layer thickness of silicon nanoparticles for optimal electrochemical performance. However, the silicon oxide layer is electronic and ionic insulating material, which will affect the rate performance. The silicon oxide layer could also potentially cause the side reaction, which will adversely affect the coulombic efficiency.

A Li₂SiO₃ coating has been reported to be beneficial for Li-ion batteries. When such a coating is present for a LiNi_{0.6}Co_{0.2}Mn_{0.2}O₂ cathode, improvement in both rate and cycle performance is observed owing to the

excellent ionic conductivity of Li_2SiO_3 as well as the enhanced structural stability it provides [37]. A coating containing Li_2SiO_3 has also been applied to the Si anode. The resulting material showed improved capacity retention, however, with a compromised specific capacity. [38] Nonetheless, the improved capacity retention suggests that the Li_2SiO_3 coating may improve the mechanical stability of the Si nanoparticles. In this work, we will convert the silicon oxide layer to lithium silicates and its impact on the electrochemical performance will be investigated.

Figure II.2.A.43 shows the diagram for the synthesis of silicate-coated silicon nanoparticles. To obtain silicate-coated silicon nanoparticles of different silicate layer thicknesses, the Si nanoparticles with an average diameter of 80 nm were first treated at 400, 500, and 600°C in the air for 15 hours to obtain a surface oxide layer with different thicknesses. The silicon oxide thicknesses of all three samples, plus pristine Si were estimated to be 2.2, 2.8, 3.7, and 5.8 nm from low to high temperature treatment. All four Si nanoparticles were then mixed with Li_2CO_3 with a molar ratio of $n(\text{Si in SiO}_2) : n(\text{Li in Li}_2\text{CO}_3) = 1:2$, and lithium silicate formation reaction was carried out at 800°C under Ar atmosphere for 6 hours before collection for characterization.



Figure II.2.A.43 Diagram for the synthesis of Li_2SiO_3 -coated silicon nanoparticles.

The silicate-coated Si nanoparticles were then characterized by x-ray diffraction performed at Advanced Photon Source at Argonne National Laboratory. The x-ray wavelength is 0.1173 Å. Figure II.2.A.44 shows the x-ray diffraction patterns of silicate-coated Si nanoparticles with different initial oxide layer thicknesses of 2.2 nm, 2.8 nm, 3.7 nm and 5.8 nm, corresponding to pristine, treated at 400°C, treated at 500°C, and treated at 600°C in air. The peaks corresponding to Si, Li_2SiO_3 and Li_4SiO_4 are labeled in the figure. A formation of Li_2SiO_3 (majority) and Li_4SiO_4 (minority) are observed in all samples, which are also confirmed by the FTIR results. As the thickness of the initial oxide layer increases, the peaks corresponding to silicates also increases in intensity, suggesting the formation of thicker silicate layers with thicker initial oxide layers.

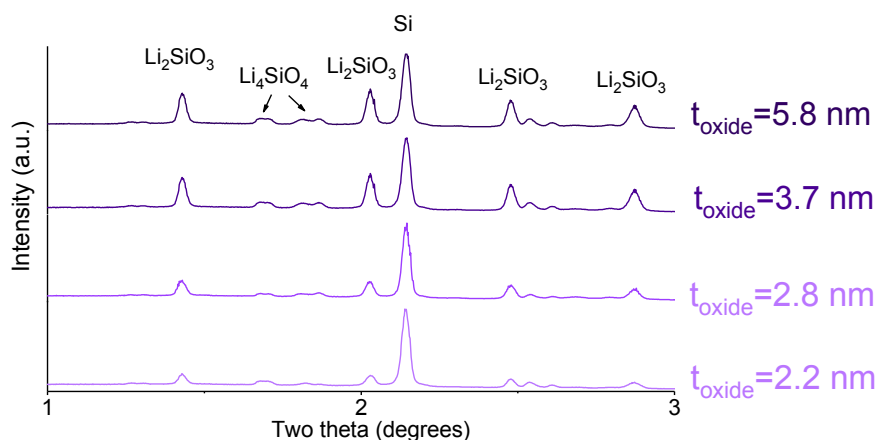


Figure II.2.A.44 XRD patterns of silicate-coated Si with starting Si nanoparticles of different oxide layer thicknesses.

The silicate-coated Si nanoparticles were then fabricated into laminates with 20 wt% LiPAA and 10 wt% C45. The electrodes were then tested in half-cell configuration with Gen II electrolyte (1.2 M LiFP₆ in EC:EMC=3:7) with 10 wt% FEC. The cells underwent three formation cycles at C/10 rate between 1.5 V and 0.01 V. Figure II.2.A.45 shows the electrochemical performance of formation cycles for silicate-coated Si nanoparticles with different silicate layer thicknesses. As the oxide layer increases, the capacity obtained from the electrode decreases. Although a lower capacity (but better cycling stability) is expected for silicon nanoparticles with a thicker oxide layer, the capacity observed for all samples were lower than expected values. A likely cause of the compromised capacity is the formation of large aggregates from the solid-state reaction between Si nanoparticles and Li₂CO₃.

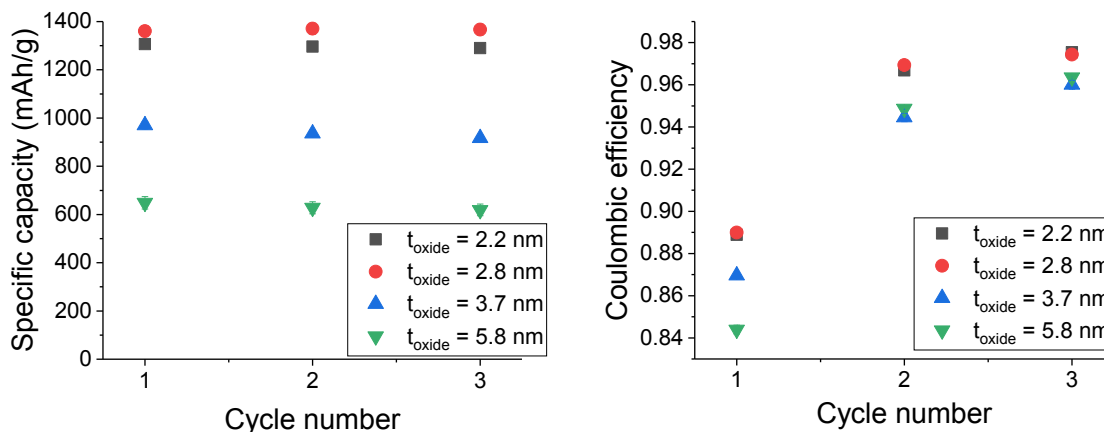


Figure II.2.A.45 Electrochemical performance of formation cycles for silicate-coated Si with different silicate layer thicknesses.

The silicate-coated silicon sample was then characterized by scanning electron microscopy (SEM). Figure II.2.A.46a shows that large agglomerates of 50-100 μm were present after the solid-state reaction between the silicon nanoparticles and the Li₂CO₃. The presence of such agglomerates in the electrodes may result in difficulty of accessing the active silicon material inside the agglomerates, leading to low capacity in the electrochemical testing. We then investigated the effect of high-energy ball milling at breaking up the aggregates with help from the CAMP Facility at ANL. The silicate-coated silicon sample was first milled in an air-filled zirconia container containing 20 zirconia balls (2mm in diameter) for 5 minutes at 500 rpm using a Retsch Mill, and then milled in water for another 20 minutes. The resulting milled silicate-coated silicon sample was then collected and characterized under SEM. Figure II.2.A.46b shows the SEM image of the ball milled silicate-coated silicon. Unlike the silicate-coated silicon after the solid-state reaction, the ball milled silicate-coated silicon showed no major agglomerates. The dynamic light scattering also confirmed the absence of larger agglomerates, further supporting the effectiveness of high-energy ball milling to break agglomerates.

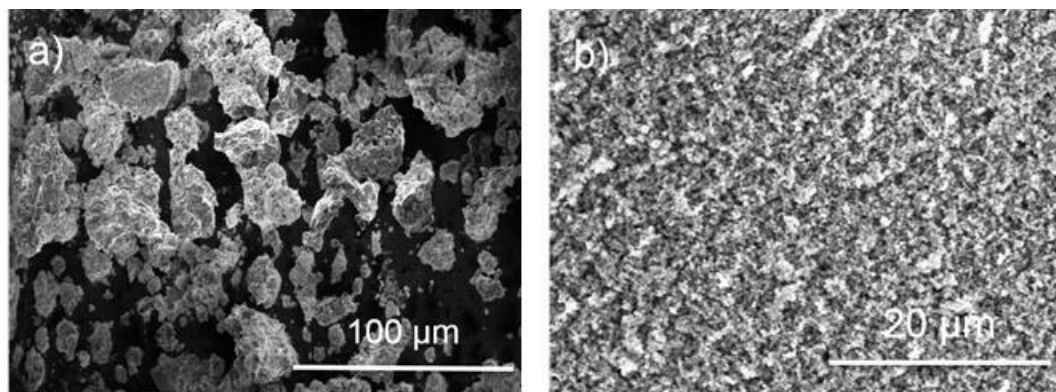


Figure II.2.A.46 SEM of silicate-coated Si with starting Si nanoparticles of different oxide layer thicknesses

To test the effect of high-energy ball milling on the electrochemical performance of silicate-coated silicon, silicate-coated silicon samples of two different silicate thicknesses were synthesized. The silicate-coated silicon with a thinner silicate layer was obtained from the reaction between Li_2CO_3 and Si nanoparticles with an oxide layer of 2.2 nm. The silicate-coated silicon with a thicker silicate layer was obtained from the reaction between Li_2CO_3 and Si nanoparticles with an oxide layer of 5.8 nm. To fabricate the laminates for electrochemical testing, the silicate-coated Si samples were ball-milled with 20 wt% LiPAA and 10 wt% C45 using the Retsch Mill. The laminates were coated after different milling times. The electrodes were then punched from the laminates and tested in the half-cell configuration with Gen II electrolyte (EC: EMC=3:7, 1.2 M LiPF₆) with 10 wt% FEC. For formation test, the cells underwent three cycles at C/10 rate between 1.5 V and 0.01 V. Figure II.2.A.47 compares the electrochemical performance of the electrodes made using the regular Thinky Mixer and the electrodes made using the Retsch Mill. Both silicate-coated silicon with a thinner silicate layer (shown in Figure II.2.A.47a) and the silicate-coated silicon with a thicker silicate layer (shown in Figure II.2.A.47b) showed worsened performance with high-energy ball milling process. The worsened performance suggest that the agglomeration may not be the key factor that leads to the poor electrochemical performance of the silicate-coated silicon.

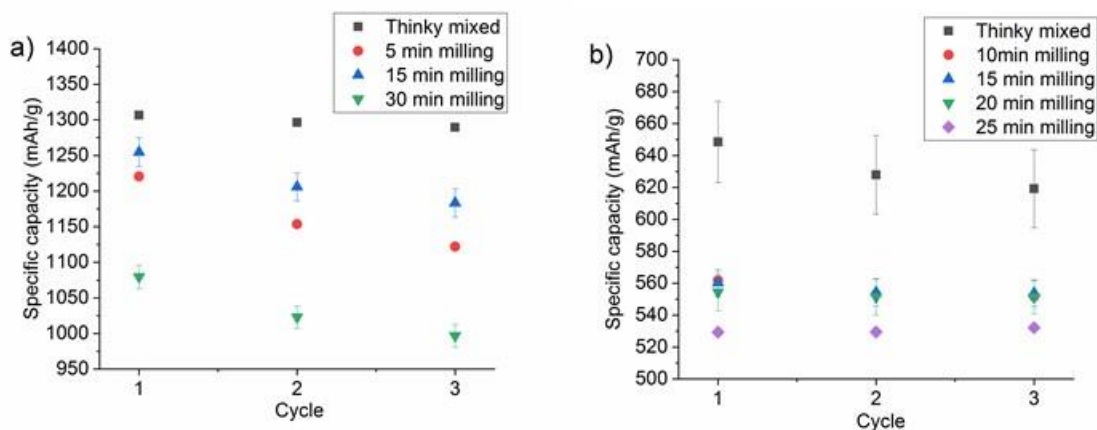


Figure II.2.A.47 Electrochemical performance of formation cycles for high-energy-ball-milled silicate-coated Si with a) a thinner silicate layer and b) a thicker silicate layer.

4. Electrode Construction

Binder Development

Electrolyte decomposition products play a critical role in the stabilization of the negative electrodes in lithium-ion batteries, as the negative electrode is operated outside the stability window of the electrolyte. The electrolyte decomposition products form insoluble SEI layer, which stabilizes the electrode and electrolyte interface. Silicon materials has large volume expansion and surface reactions with the electrolyte when it is electrochemically lithiated. When delithiated, the silicon volume shrinks and surface area also decreases. This dynamic surface change causes excessive side reactions with the electrolyte.^[39] Moreover, some of the key electrolyte decomposition products are soluble in the electrolyte rather than solid precipitates.^[40] Surface coatings on Si materials by organic and ceramic have demonstrated improved surface stability towards electrolytes. Nano-sizing the Si materials can successfully prevent cracking of Si material. The Si particles are assembled by a functional polymeric binder to further improve the electrode stability in a composite electrode.^[41]

This project is aimed to gain a comprehensive understanding of electrolyte decomposition products to SEI property relationship and understand the electrode binder's effect during electrochemical process, and to guide the design and synthesis of new electrolytes and additives and electrode binder for Si based materials. New electrolyte design with consideration of the SEI structure and functions on the Si materials can lead to enhanced Si performance over the traditional mixed carbonate based electrolyte. Both Si surface coating and functional electrode binders can enhance cyclability of the Si based composite electrode. Our recent development of an aqueous based dispersion binder can provide good point-to-point binding with the Si particle surface and allow the Si particles to expand and contract during cycling process. Surface coating on Si can prevent electrolyte interaction with the reactive surface and slow down the side reactions at the interface. Here, we propose to further reduce the Si surface reactivity by investigating electrolyte and additive functions to SEI formation and stabilization.

Designing organic molecules with preferred decomposition pathways during electrochemical process can lead to controlled SEI formation on Si surface.^[42] One consideration is to vary the composition of the decomposition products to produce SEI with different flexibility to understand if a flexible SEI can be a better choice to reduce Si surface reaction. The other consideration is to strengthen the adhesion force between the decomposition products and Si materials to prevent dissolution of the electrolyte decomposition products to achieve a robust SEI layer. The bonds between the SEI layer and the Si materials need to be both strong and flexible to accommodate large volume change. Emphasis will also be on understanding the adhesion force and nature of bond between Si and organic decomposition products. This information can also be used to further development of electrode binders.

Functional binders: Pyrene (Py)-based polymers derived from 1-pyrenemethyl methacrylate (PyMA) were established as candidate electrically-conducting polymers. The flexible chain backbone of these polymers allows self-assembly of the Py side chains into ordered structures, realizing electron conductivity via the side chain π - π stacking force of the aromatic Py moieties. A versatile radical-based polymerization was used to synthesize PPyMA and also facilitated the incorporation of additional functional groups. For adhesion, we used the building block of dopamine methacrylamide (DMA) synthesized based on a literature procedure. Poly(1-pyrenemethyl methacrylate-co-dopamine methacrylamide) (PPyMADMA) was synthesized through free-radical polymerization where the adhesive monomer, DMA, accounts for 36 mol% of this copolymer (1H-nuclear magnetic resonance spectroscopy) (Figure II.2.A.48a). PPyMADMA had a number-average molecular weight of 29,000 Dalton and a polydispersity index of 1.9, while being soluble in solvents such as tetrahydrofuran (THF) and N-methylpyrrolidone (NMP). The data for PPyMA in Figure II.2.A.48b and Figure II.2.A.48c were shown in our previous publication,⁴ and are incorporated here for comparison. Wide-angle X-ray scattering (WAXS) results show the ordered phase characteristic of the pyrene in both PPyMA and PPyMADMA (Figure II.2.A.48b). Diffraction peaks are located at $\sim 0.95 \text{ \AA}^{-1}$ and $\sim 1.02 \text{ \AA}^{-1}$, respectively. This corresponds to a lattice spacing of ~ 0.6 nanometers (nm). The broadening of the diffraction peak for the

PPyMADMA sample indicates that the crystal grain size is smaller when copolymerized with DMA (Figure II.2.A.48b).

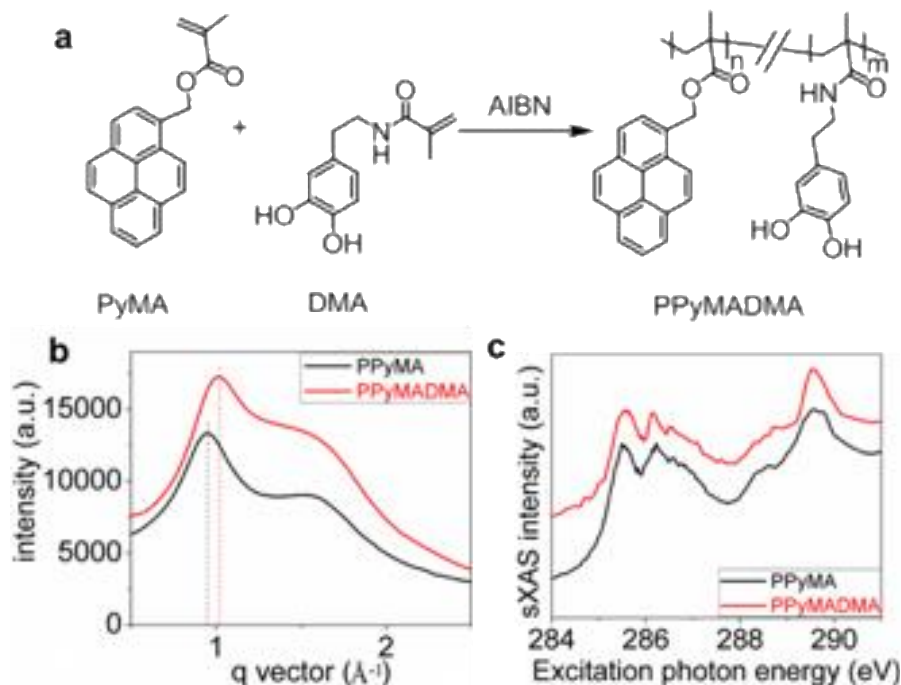


Figure II.2.A.48 (a) Generic synthesis of poly(1-pyrenemethyl methacrylate-co-dopamine methacrylamide) (PPyMADMA). (b) Wide angle X-ray scattering (WAXS) of PPyMA and PPyMADMA polymers. (c) Carbon K-edge sXAS of PPyMA and PPyMADMA shows that the LUMO energy is intact in PPyMADMA, although non-conductive DMA groups are introduced.

To ensure that the newly-designed PPyMADMA binder still maintains the electronic conductivity, we studied the electronic structure of both the PPyMA and PPyMADMA polymers using synchrotron-based x-ray absorption spectroscopy (sXAS). sXAS is a direct probe of the excitations of core level electrons to the unoccupied valence states. Previous results demonstrate that sXAS is the tool-of-choice to reveal the critical electron state associated with the electric properties of polymer binder materials in batteries. The methodology is based on the principle that the lowest-energy sXAS feature directly corresponds to the state of the lowest unoccupied molecular orbital (LUMO), which defines the electric properties of the polymers.⁷ We also note that a comparative sXAS measurement between polymers with different functional groups is reliable without the core-hole potential concerns. Figure II.2.A.48c shows such a comparison of the sXAS spectra of PPyMA and PPyMADMA. The splitting peaks around 285-286 eV correspond to the $\pi^*C=C$ bonds with conjugation, and the features around 288 eV are from $\pi^*C=O$.⁷ Focusing on the low-energy sXAS features corresponding to the LUMO states, it is obvious that incorporating the DMA group does not change the lowest-energy features in sXAS, indicating the LUMO of the PPyMA polymer is intact in PPyMADMA. Except for a finite change at high energies away from the LUMO states, the consistency of the overall line-shape implies that the electron states close to the Fermi level are dominated by the pyrene-based PPyMA states.

Latex Binders: To combine the advantages of conductive polymer binders and aqueous battery electrode coating processes, a versatile emulsion polymerization method is developed to prepare conductive polymer binder emulsions in water for lithium ion battery applications. These polymer emulsions are used as-is as the binder for silicon containing anode materials. Aqueous process of conductive polymer binders has been realized for silicon containing anode materials. Emulsion polymerization methods have been developed to prepare a series of conductive polymer emulsions in water. The final binder emulsions can be used as is for slurry mixing and electrode coating without further treatment. It combines the advantages of both conductive polymer binders and aqueous process, saving energy and time while making the electrode fabrication process

low-cost and environmentally friendly for silicon containing materials. Both homopolymer and copolymer emulsions in water have been synthesized and successfully been used as the binder for silicon containing anodes materials. These polymers bear different aromatic units in the polymer structure, which has shown to affect the resulting battery performance. The electrodes using these polymer emulsions as the binder show promising performance for both pure silicon and silicon/graphite composite materials. The resulting electrodes can achieve an initial capacity of about 880 mAh/g and 75% capacity retention after 200 cycles for the electrode containing 17% silicon and 83% graphite after optimization.

In order to perform the emulsion polymerization, the monomers are normally liquid or gas. However, while the benzyl methacrylate (BzM) is a fluid liquid, the 1-naphthalenemethyl methacrylate (NaM) is a viscous liquid and the 1-anthracenemethyl methacrylate (AnM) is a solid. Therefore, BzM and NaM were used directly to produce homo-polymer emulsions (Figure II.2.A.49a, P1 and P2) and AnM was dissolved in butyl methacrylate (BuM) before the reaction to finally produce co-polymer emulsions (Figure II.2.A.49a, P3 ~ P8). Besides the monomers and water, surfactants with high hydrophile-lipophile balance (HLB) values were used together with CMC as the stabilizer in the reaction mixture to form a stable colloidal system. And potassium persulfate (KPS) was used as the water-borne initiator. Finally, a series of polymer emulsions in water are obtained, as shown in Figure II.2.A.49b and Figure II.2.A.49c.

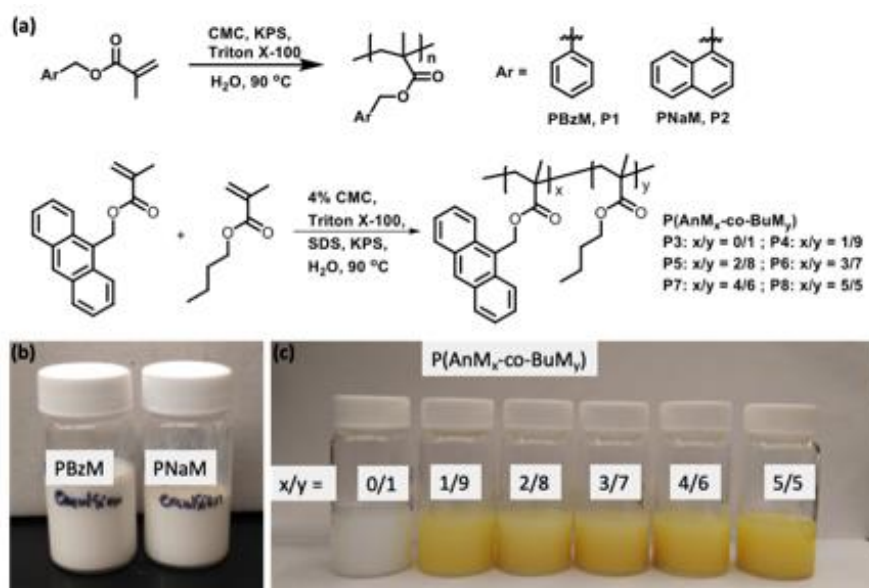


Figure II.2.A.49 (a) Synthetic scheme, (b, c) physical appearance of PBzM, PNaM and P(AnM_x-co-BuM_y) polymer emulsions.

New Bi-Functional Electrolyte Additives This research is aimed to gain a comprehensive understanding of electrolyte decomposition products to SEI property relationship, and to guide the design and synthesis of new electrolytes and additives for Si based materials. New electrolyte design with consideration of the SEI structure and functions on the Si materials can lead to enhanced Si performance over the traditional mixed carbonate based electrolyte. Designing organic molecules with preferred decomposition pathways during electrochemical process can lead to controlled SEI formation on Si surface. [4] An effort to construct a bi-functional additive toolbox is underway (Figure II.2.A.50).

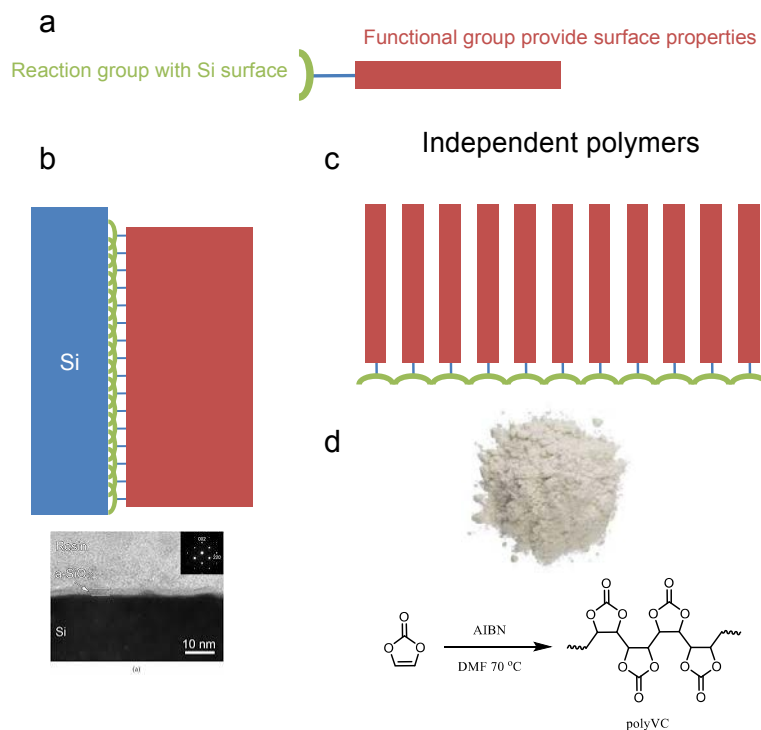


Figure II.2.A.50 a. A schematic of bi-functional additives. b. Formation of surface layer on the Si surface. c. Formation of bulk polymer. d. An example of vinylenecarbonate polymerization to form polyvinylenecarbonate bulk polymer.

The bi-functional additive molecules have one reaction functional group to form coating on the surface of Si particles at low potentials, and another functional group to provide desired surface properties for the SEI layers. The reaction functional groups can also react with each other to form bulk polymer in a controlled organic chemistry environment. Figure II.2.A.50d describes our previous work to synthesize bulk polyvinylenecarbonate (PolyVC) polymers. PolyVC can be used as binder and surface modifier for graphite based negative electrode to prevent propylene carbonate solvent molecules intercalation into the graphite layers.

Two groups of bi-functional additives have been investigated based on either a vinylenecarbonate or a methacrylate reactive groups and a hydrophilic or hydrophobic functional group (Figure II.2.A.51). Three new VC reactive functional additives are synthesized, and five new methacrylate reactive functional additives were identified. In the VC series (Figure II.2.A.51a), the first one is MVC with an additive methyl group at the 3 position. The C8MVC has an extended hydrophobic alkyl group at the 3 position, whereas the TEGMVC has an extended hydrophilic ethyleneoxide group at the 3 position. In the methacrylate series (Figure II.2.A.51b), dodecyl and butyl side chains give the additive coating a hydrophobic nature on the active materials surface, whereas, the ethyleneoxide segments side chains give the additive coating a hydrophilic nature. Both VC and methacrylate functional groups can react with the Si surface at low potential to form surface coating. The hydrophilic and hydrophobic chains can tune the properties of the either graphite or Si surface. The synthetic scheme is developed and the intermediate and final products are

qualified by the ^1H NMR spectroscopy. The methacrylate series of additives results are highlight in Figure II.2.A.51c,d. When the methacrylate based additives are used with graphite based electrode (Figure II.2.A.51), testing results show similar coulombic efficiencies (CE) but lower capacities due to the development of resistive film on the surface of the graphite material. The CE for the graphite electrode is very high ($\sim 99.7\%$), therefore, the CE difference between the additives cannot be detected for graphite electrode. However, when the methacrylate based additives are used with Si based electrode (Figure II.2.A.51d), testing results show higher CE of the ones with hydrophobic additives (DoMAA and BuMM). The higher efficiency is due to the hydrophobic effect of the coating, which tends to expel electrolyte from the active materials surface.

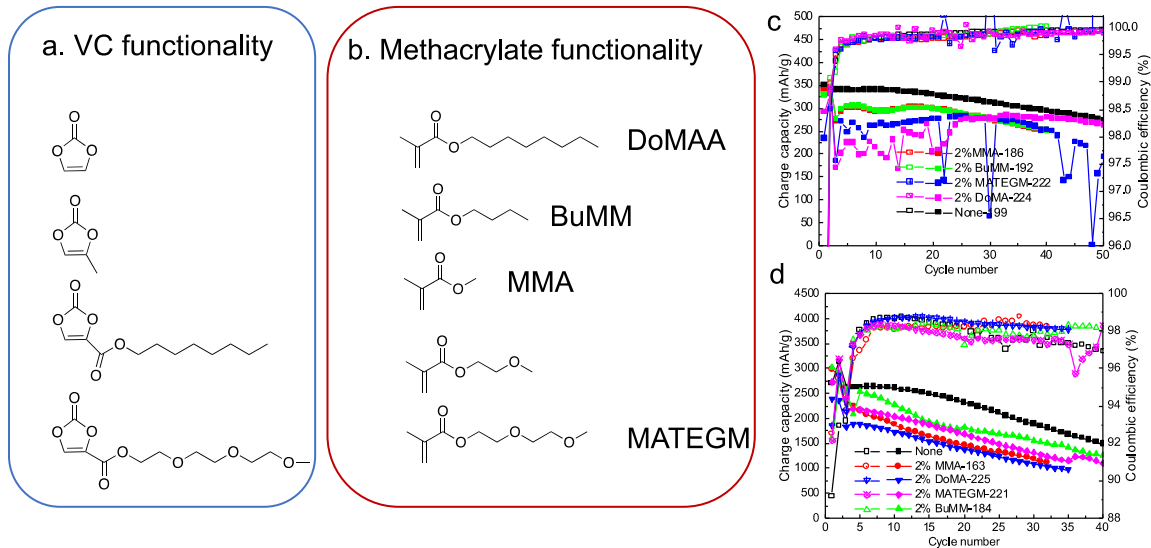


Figure II.2.A.51 The bi-functional additives and their performance as an additive in a graphite or Si electrode with EC/DMC LiPF₆ electrolyte and lithium metal counter electrode. There is no FEC additive in the electrolyte. a. VC reactive functional group class of bi-functional binder. c. Graphite electrode performance with different methacrylate series of additives. d. Si electrode performance with different methacrylate series of additives.

A novel designing practice of functional conductive binders and latex binders for lithium ion batteries has been conducted. A series of conductive polymer binder emulsions in water has been prepared using emulsion polymerization methods. These polymer emulsions have been further used for lithium ion battery applications. The electrode coating process is water-based without using any organic solvents, which is lower in cost and more environmentally friendly. Using these polymer emulsions as the binder, silicon materials, solely or together with graphite materials, have been fabricated into electrodes showing promising cycling performance.

A rational design, synthesis and testing of electrolyte additives have been conducted. Two classes of bi-functional electrolyte additives with surface reaction functional group and coating functional group on one molecule have been synthesized. A toolbox is under construction with different reactive groups and hydrophobic and hydrophilic surface coating groups. The preliminary results show the surface reactive groups are able to form surface coating on the active materials, whereas the film functional groups can provide designed interaction with the electrolyte. Advanced diagnostic and full cell testing will be applied to these bi-functional electrolyte additives to further elucidate the molecular level interactions and quantify their electrochemical performances.

Polycarboxylate polymers, such as alginate, carboxymethyl cellulose (CMC) and poly(acrylic acid) (PAA), show greater promise as their functional groups form strong covalent bonds with siloxyl (SiOH) groups on the Si surface maintaining cohesion during volumetric changes. Among these polymers, PAA is particularly attractive due to a combination of excellent performance as a binder and low cost. As a matter of fact, PAA has been selected as the standard binder materials for the Silicon Deep Dive program. While PAA is becoming increasingly used, the factors controlling its performance in the LIBs are not fully understood. Meanwhile, the performance of silicon lithium-ion batteries using PAA binders is still far from meeting the requirement of practical use. Therefore, it is of paramount importance to gain in-depth understanding of the factors controlling the performance of PAA binders and evolving those binders towards improved cell performance for silicon lithium-ion batteries. In this year, we have conducted extensive efforts under those directions. Firstly, followed the molecular weight study,^[43] another important factor, the pre-lithiation of PAA binder, has been carefully investigated and the property changes of the lithiated/non-lithiated polymer in solution, slurries, and the electrode matrix have been comprehensively characterized. Secondly, the re-engineered PAA binders, such as the cross-linked PAA, stiff poly(4-vinylbenzoic acid) (P4VBA), have been continuously pursued and evaluated in both half cells and full cells. Thirdly, initial efforts have been conducted to investigate the surface compatibility between the Si particles and binders.

Pre-lithiation of PAA binders is common practice for silicon lithium-ion batteries, which could benefit the large scale lamination process and enable the fabrication of mechanically robust electrodes. However, lithiation processes involves strong basic lithium hydroxide, LiOH, which dramatically impact the pH values of PAA polymers, consequently leading to the properties changes of the pH-responsive PAA binders and causing side reactions. For instance, the surface of the Si particles is more venerable against hydroxide under basic environment and can lead to formation of silicon oxide and generation of hydrogen. In addition, non-lithiated PAA films have been shown to have a higher tensile strength than the fully lithiated PAA films (the Young moduli were 1.4 vs. 1.0 GPa, respectively),^[44] suggesting that the former material has better mechanical resistance to volumetric changes in the Si particles. Therefore, we decided to quantify the effects of lithiation on the properties the PAA polymers and the performance of silicon-graphite (Si-Gr) composite electrodes containing such binders. A composite electrode was used in this study which contained ~15 wt% Si. For fair comparison, we have standardized the preparation of the polymer, the fabrication and coating of the slurries, the thermal treatment of the electrode matrices, and the testing protocols.

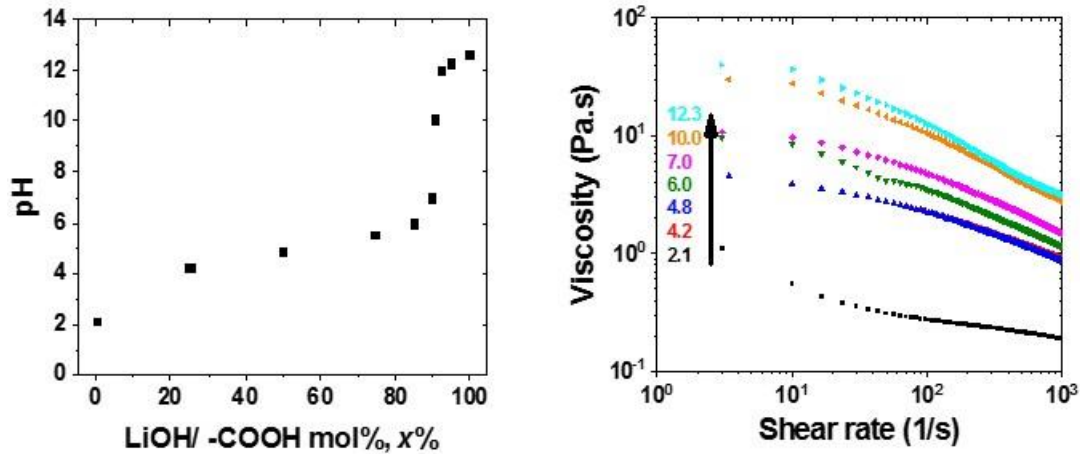


Figure II.2.A.52 A plot of pH vs. LiOH/COOH molar ratio (a) and the apparent viscosity vs. the shear rate (b) for 10 wt% aqueous solutions of PAA. The pH of the aqueous solutions is color coded in panel b. Mind the logarithmic scales in panel b. Mind the logarithmic scales in panel b.

Lithiated PAA samples ($M_n = 147$ kDa, PDI = 4.9) were prepared by mixing the aqueous PAA solutions with LiOH. Figure II.B.1.52a gives pH of these solutions as a function of the molar ratio $x\%$ of LiOH relative to the $-\text{CO}_2\text{H}$ groups. This pH dependence is reminiscent of a strong base - weak acid titration curve. Below $x = 90\%$, the pH slowly increases from 2 to 6, which is followed by an abrupt change from 6 to 12 when x increases from 90% to 92%. As the Li^+ substitution progresses further, the pH increases from 12.0 to 12.6. The observed equivalence point of 92% is lower than expected from the stoichiometry which we attribute to structural defects in the PAA polymer. Figure II.2.A.52b shows the apparent viscosity of these polymer solutions as a function of the shear rate. As seen from this plot, the viscosity of the solution systematically increases with the lithiation, the biggest increase seen between pH 2 and 4. This increase can be attributed to tighter packing of polymer chains in coils for neutral PAA compared to ionized one. In rheology, shear thinning refers to the non-Newtonian behavior of complex fluids whose viscosity decreases under shear strain. According to the power-law model,

$$\eta(\dot{\gamma}) = K(\dot{\gamma})^{n-1}, \quad (1)$$

where η is the apparent viscosity, $\dot{\gamma}$ is the shear rate, K is the consistency index, and n is the flow index. The fluid is pseudoplastic (shear thinning) when $n < 1$, and a smaller n indicates stronger shear thinning. The parameters in eq. 1 were determined by fitting the apparent viscosity in the shear rate range of $10^2 - 10^3 \text{ s}^{-1}$. It is seen that n decreases from ~ 0.83 at pH = 2.1 to ~ 0.40 for pH 12.3, indicating that the lithiation increases shear thinning effect. Rheology data in Figure II.2.A.53 indicate that aqueous Si-Gr slurries formulated using PAA polymers in Figure II.2.A.52b also exhibit shear thinning, and the viscosities of these slurries remain in the acceptable range for all practically significant shear rates. While higher viscosity and shear thinning are favorable physical properties for blending of Si nanoparticles in thick suspensions, slowing down their sedimentation, there seem to be no decisive advantages of lithiated vs. non-lithiated PAA from the processing standpoint.

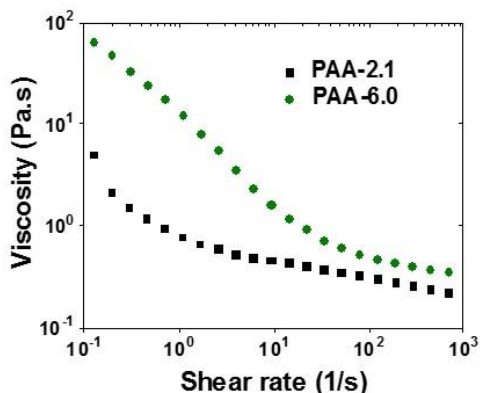


Figure II.2.A.53 A viscosity plot for the PAA polymers at two different pHs.

The lithiated PAA binders were then used to fabricate Si/graphite electrodes and later were assembled into half cells. The polymer solutions were then used to fabricate Si-Gr composite electrodes (15% Silicon), and the electrochemical performance was evaluated in half cells. The loading densities of these electrodes were similar around 2.7~3.0 mg/cm². As expected, their half cells performance was very different. The cells containing less lithiated PAA polymers demonstrated higher initial delithiation capacity, average capacity, and capacity retention. (Figure II.2.A.54). During the formation cycles (Figure II.2.A.54a), PAA-2.1 cell exhibited the highest initial specific capacity of 695 mAh/g. As pH increased to 7.0, the initial capacity decreased to 598 mAh/g. For pH >4, there was approximately linear decrease of the initial capacity with the increasing pH. For PAA-10.0 and PAA-12.3 cells the initial capacities were 353 mAh/g and 265 mAh/g, respectively. From the capacity profiles (Figure II.2.A.54c), it is obvious that the cells with less lithiated binders (lower pH value) generally afford better cycling performance. As shown in Figure II.2.A.54c and Figure II.2.A.54d, less lithiated PAA binders also demonstrate better capacity retention and coulombic efficiency. The capacity retention decreases from 60% to 40% as pH increases from 2 to 7.

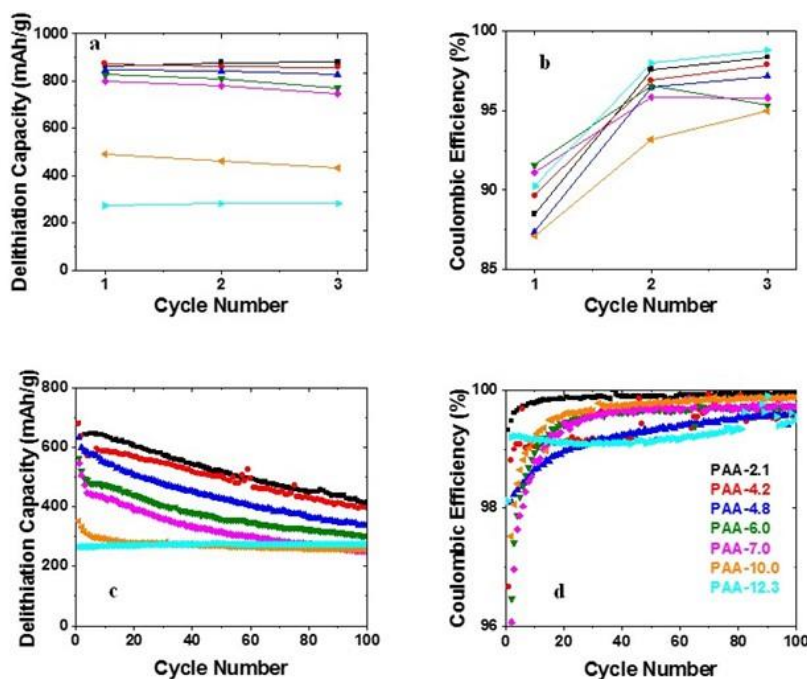


Figure II.2.A.54 Specific delithiation capacity (a and c) and Coulombic efficiency profiles (b and d) of half cells assembled using lithiated PAA during formation cycles at a C/3 rate (a,b) and after 100 cycles at a C/3 rate (c,d). The pH of the PAA solutions (Figure II.2.A.53) is color coded in panel d.

The cycling performance of the full cells, in which the Si-Gr electrode is paired with an NCM523 cathode, is shown in Figure II.2.A.55. Low pH cells still exhibited the superior performance and PAA-2.1 cell is the best among them. As pH increased, the cycling performance decreased except for PAA-6.0 cell, which demonstrated arguably the second best performance. Compared to the half-cell results, this relative unclear trend may partly due to the inconsistent cathode/anode matching issues.

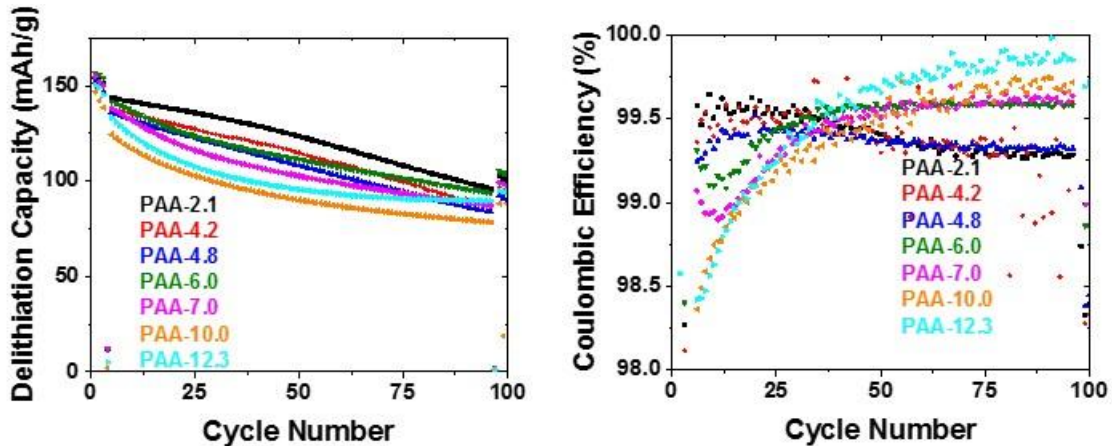


Figure II.2.A.55 Specific discharge capacity (left) and Coulombic efficiency (right) for full cells. The pH of PAA solutions in Figure II.2.A.52 is indicated in the plot.

It is reasonable to suggest that these trends could reflect the ability of the polymer binder to provide structural cohesion in the matrix. In Figure II.2.A.56, the peeling test was used to assess the adhesive/cohesive strength of the electrode. This test suggests that the increased lithiation of PAA decreases the cohesion in the matrix. This can be attributed to the reduced number of $-CO_2H$ groups that esterify siloxyl groups on the surface of Si particles, forming strong bonds between the polymer chains and the Si nanoparticles. Clearly, the reduced cohesion also makes the polymer binder less efficient in countering the effects of volumetric changes of Si particles in the electrode matrix. We remind that according to previous report lithiated PAA is 40% less stiff than non-lithiated PAA, so the two trends (the cohesion and tensile strength) act in the same direction.

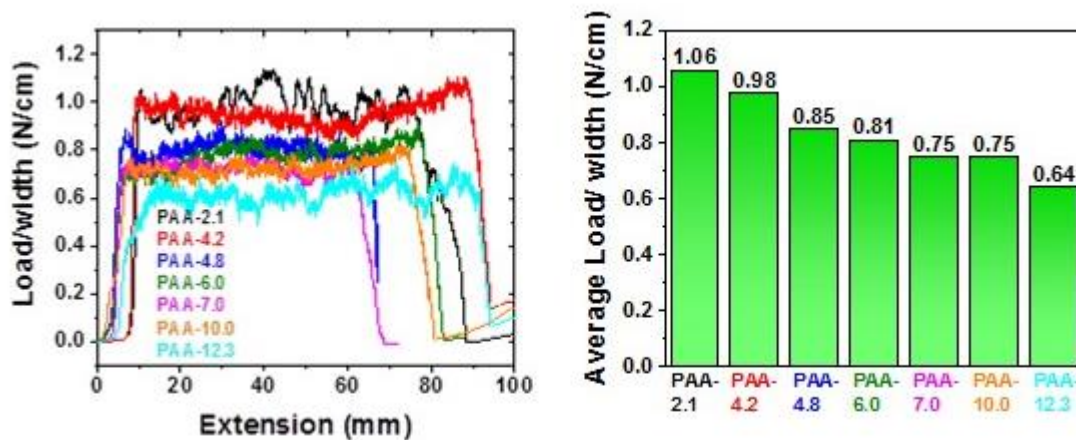


Figure II.2.A.56 The 180° peeling test for the Si-Gr electrode composed using different PAA binders (left). The load/width ratios averaged over a range of 50 mm for different electrodes (right). The pH of PAA solutions in Figure II.2.A.52 is indicated in the plots.

Polybenzoic Acids: While there has been rapid progress in developing water-soluble polymer binders for Si-based electrodes, developing polymer binders that allow water-free processing from organic solvents has

lagged behind. Such alternatives are desirable, as the wet processing introduces hard-to-remove moisture that leads to acid corrosion of Si during electrochemical cycling, resulting in rapid capacity fade. Here we demonstrate the use of poly(4-vinylbenzoic acid) (P4VBA) to fabricate high quality Si/graphite composite electrodes from 1-methyl-2-pyrrolidinone (NMP) slurries. Compared to PAA binders, P4VBA provides higher initial and average capacities and better capacity retention. We believe that P4VBA offers the urgently needed alternative to wet processing of the Si-based electrodes.

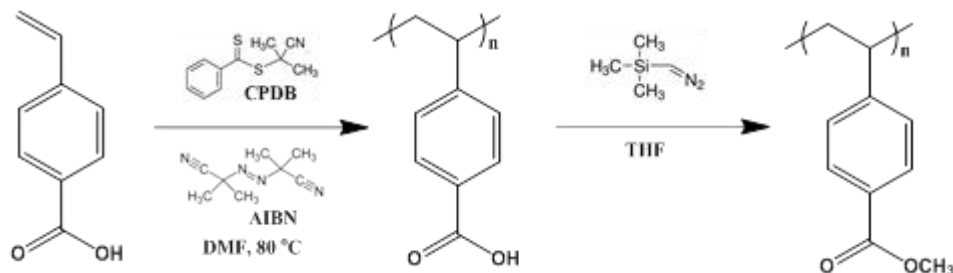


Figure II.2.A.57 Synthesis of P4VBA and Methylation for GPC Analysis

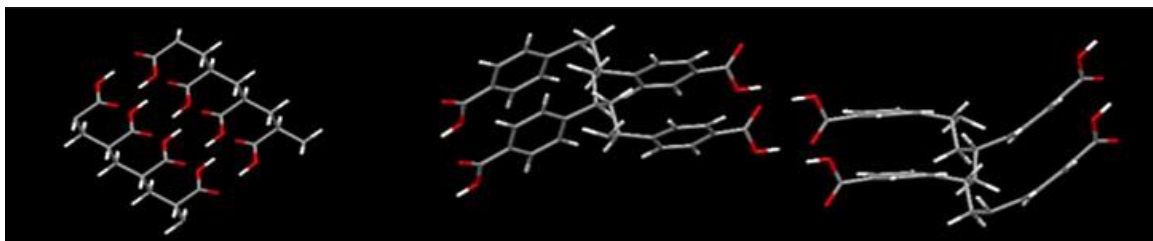


Figure II.2.A.58 MOPAC Computed Conformations of PAA and P4VBA Dimers

Polymer chains of varied length were synthesized in a manner analogous to the bifunctional additives (as shown in Figure II.2.A.57). The arene rings improve stiffness of these polymers (which is important for countering the effects of volume changes) and favor their syndiotacticity. As a result, neighboring P4VBA chains can interlock by H bonding more strongly compared to PAA chains as illustrated in Figure II.2.A.58, resulting in greater cohesion. Below we demonstrate that NMP-processed P4VBA-containing Si/graphite composite (Si-Gr) electrodes considerably outperform PAA-containing electrodes in our electrochemical tests. Three batches of P4VBA with different molecular weights were prepared and characterized as described in the preceding section. Size exclusion chromatograms for these polymers are shown in Figure II.2.A.59a, which also gives the estimates for Mn and PDI. We will refer to these samples as P4VBA-1 (63.5 kDa), P4VBA-2 (29.3 kDa) and P4VBA-3 (11.8 kDa). For comparison, we also used protiated PAA polymer (29.1 kDa) which had Mn close to P4VBA-2. Figure II.2.A.59b shows the apparent viscosity of 30 wt% P4VBA solutions in NMP plotted as a function of the shear rate. As expected, the viscosity rapidly increases with Mn. While P4VBA-2 and PAA have similar Mn, the viscosity was lower for the PAA solution, especially at high shear rates. The P4VBA solutions behave as Newtonian fluids at the shear rates $< 102 \text{ s}^{-1}$, and they show negligible shear thinning at higher rates (in contradistinction to the PAA solutions). As this shear thinning can cause uneven deposition of ink during coating of the laminates, in these NMP solutions the P4VBA binder shows better rheological properties than the PAA binder.

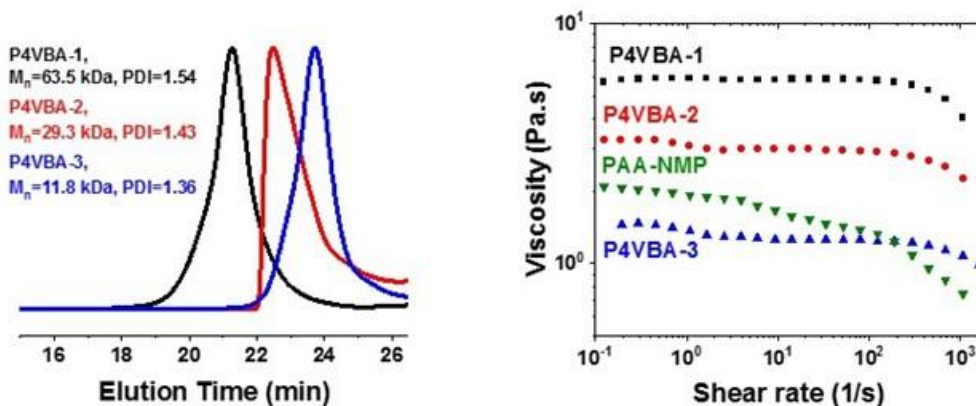


Figure II.2.A.59 (a) Size exclusion chromatograms for synthesized P4VBA polymers; (b) The apparent viscosity vs. shear rate for 30 wt% P4VBA solutions in NMP. See the color coding in the plot.

The performance of Si-Gr electrodes fabricated from NMP-polymer slurries was evaluated in half-cells over 100 charge/discharge cycles (Figure II.2.A.56). While the loading densities (Table II.2.A.4) were similar, the cycling behaviors were quite different. The P4VBA cells containing higher M_n polymers exhibited higher initial and average specific capacities and better capacity retention over 100 cycles (Table II.2.A.4). This trend is consistent with what we observed for water-based PAA polymers. In contrast to these P4VBA polymers, NMP-processed PAA electrodes performed very poorly, with ca. 70% loss of capacity after 25 cycles. The differential capacity (dQ/dV) plots for cycle 25 shown in indicate the complete loss of the 0.44 V feature from $Li_{15}Si_4$ phase in the latter case, whereas this feature is clearly seen in the P4VBA cells.

Table II.2.A.4 Loading density, initial specific capacity, initial Coulomb efficiency, capacity retention, and average capacity for half-cells.

Cell/binder	M_n kDa	Loading density, mg/cm ²	Initial specific capacity, ^a mAh/g	Average capacity, mAh/g ^b	Initial Coulombic efficiency, % ^c	Capacity retention, % ^d
P4VBA-1	63.5	2.5	818	527	97.8	49
P4VBA-2	29.3	2.4	787	452	95.8	46
P4VBA-3	11.8	2.6	650	343	95.8	46
PAA	29.1	2.6	611	230	90.9	33

a) for the third formation cycle at a C/20 rate; b) average capacity over 100 cycles at a C/3 rate; c) Coulomb efficiency immediately after the formation cycles; d) capacity retention after 100 cycles at a C/3 rate.

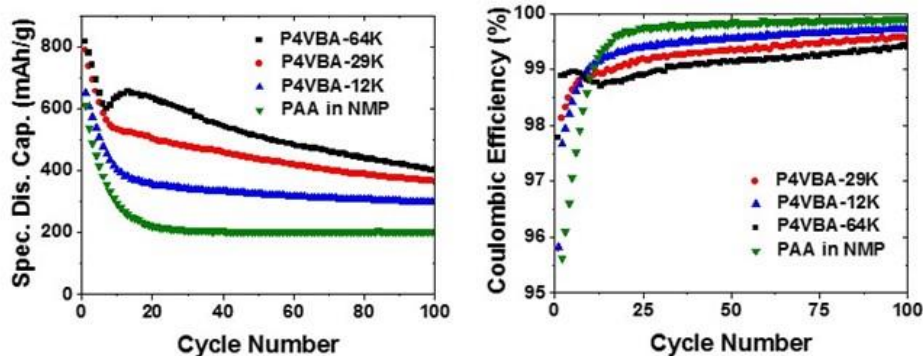


Figure II.2.A.60 Specific discharge capacity (left) and Coulomb efficiency (right) for different half-cells (100 cycles at a constant C/3 rate).

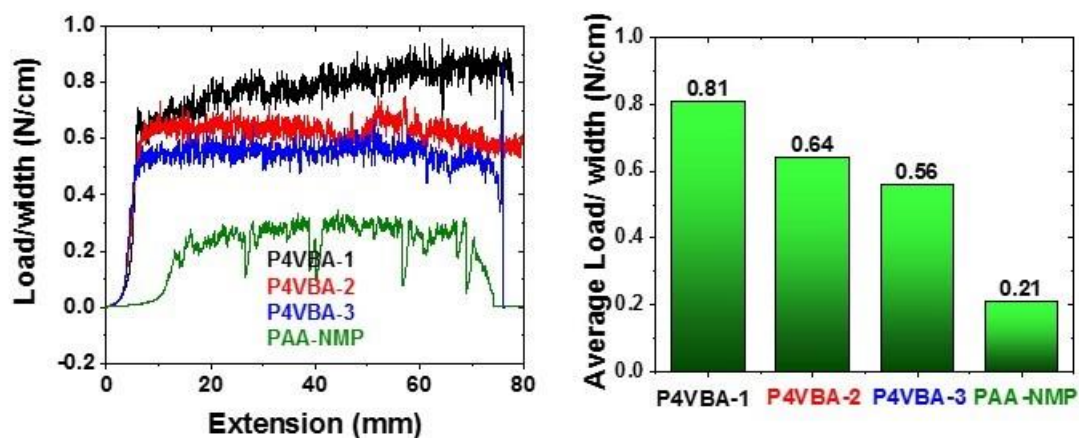


Figure II.2.A.61 (a) The load/width ratio plotted vs. the extension and (b) the average ratio over the extension range for different S-Gr electrodes.

To measure the adhesive/cohesive strength of the electrode a peel strength test was administered using a single column Instron 3343 universal testing system. As suggested by Figure II.2.A.61a and Figure II.2.A.61b, the cohesive strength of the P4VBA electrodes is much higher than the PAA electrode, and this strength increases by 45% from P4VBA-3 to P4VBA-1 in the order of the increasing Mn. The full-cell tests are briefly summarized in Figure II.2.A.62, which shows the same trends as our tests for half-cells. Once again, the P4VBA-1 cell showed the best cycling performance, whereas the PAA cell showed the worst cycling performance.

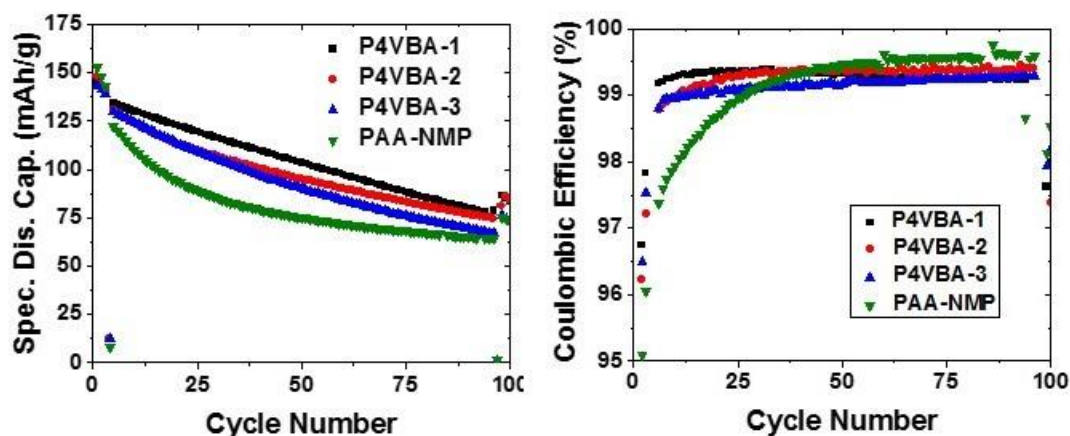


Figure II.2.A.62 Specific discharge capacity (to the left) and Coulombic efficiency (to the right) for different full-cells.

Initial investigation of the surface reaction between Si particle and binders: It has become more and more recognized that the Si particle's surface chemistry is very sensitive to conditions and often played important roles in influencing the electrode matrix. As a directly interacting component, binders are interacting or reacting to the surface of Si and the resulting binder-Si particle "bonding" often dictates the stability of electrode matrix and the final cycling performance. In some case, when Si particles change, the same binder could behave totally differently. For instance, the same PAA binders can lead to totally different or even reverse cycling performance on different Si particles. In a related study of PAA lithiation,^[45] the lithated PAA performed much better compared to the non-lithated PAA binders, which is contradicting to our own results in section 1. The major difference was the Si particle used in both studies. Our study used NanoAmor Si particle, which has high content of pure silicon and limited amount of SiO_x, while in the other study, the Si particle was purchased from Sigma-Aldrich, which has a thick layer of SiO_x based on the XPS results. It is obvious that different source of Si particles can afford different composition and more importantly different surface properties. Therefore, understanding the relationship of the Si particle surface and binders property becomes a

crucial challenge that can provide guidance for further optimization of the related materials. Here, we present some initial results toward this target.

Paraclete Si particles were used due to the availability of its large amount and better quality control. Those particles were heat-treated to form controlled SiO₂ layers. In this way, the silicon nanoparticles are oxidized in a controlled manner to obtain different thicknesses of SiO₂ layers.^[46] Three samples were studied including the pristine, 400°C, and 600°C treated samples. The growing SiO₂ layers can lead to better protection of the Silicon as well as changes of the surface of the particles, therefore are excellent platforms to study the surface chemistry. Those samples were then used to fabricate Silicon anodes (70% Silicon) with PAA binders. As shown in Figure II.2.A.63, half cells fabricated with non-lithiated PAA binders were firstly evaluated in half-cells. As expected, 400°C and 600°C cells delivered lower initial capacities, but higher Columbic efficiency and better capacity retention. More importantly, they all seem to work well with non-lithiated PAA binders. While these are preliminary results, we speculate that lithiated PAA may give much different cycling performance. More experiments are ongoing and more detailed analysis will be discussed shortly when results are available.

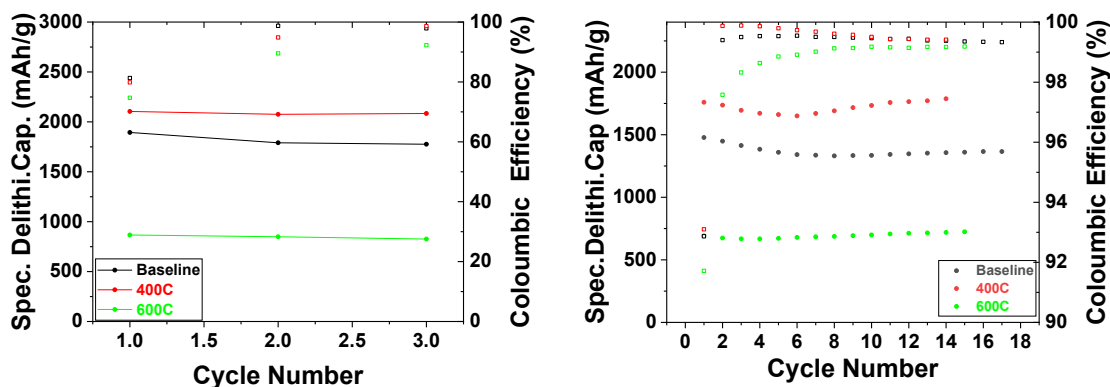


Figure II.2.A.63 Specific discharge capacity (to the left) and Coulombic efficiency (to the right) for half cells using non-lithiated PAA binders during formation (a) and normal cycling (b).

Lithium Inventory

Lithium inventory control is an issue that is part of the Si deep dive (DD) project. Si/graphite blended electrodes require careful cell-capacity balancing to begin to enable the technology. Typically this requires much thicker (and heavier) cathodes to account for first cycle irreversible capacity losses (ICL). One would like to use a pre-lithiation component either in the anode or the cathode to allow less weight (less heavy) cathodes by negotiating the first cycle irreversible capacity loss on the anode side. In addition, pre-lithiation has been observed to help the cycle life. Another problem to address using pre-lithiation, is electrode voltage slippage; the SOC is hard to control, and cell capacity can be compromised. The usable capacity begins to shrink in the cell, and eventually Li-trapping in the Si material wins out, and lifetime is exhausted. The behavior must be understood and then addressed by the lithium inventory team as part of the overall project. This past year we focused on (1) continued understanding lithium inventory through use of a LiFePO₄ quasi-CE/RE in Si-graphite composite full cells, and (2) alternative methods to Li₅FeO₄ for introducing extra lithium into the cell from the cathode side. Alternative methods include using (a) Li_{1+x}NMC532O₂ electrodes where x is added Li for the cell, and (b) Li_{1+y}Ni_{0.5}Mn_{1.5}O₄ (lithiated 5 V spinel) wherein y represents the additional Li introduced into the Si-graphite full cell.

Completing the LiFePO₄ (LFP) part of the project culminated in two articles published ^[47], ^[48]. These papers show the effectiveness of LiFePO₄ as a diagnostic tool in order to assay the quantity of Li consumption in a full cell as marked by the percent loss of lithium per cycle via SEI growth and/or SEI consumption and re-formation. The LFP work was presented in last year's annual report (FY17).

To wrap up the FY18 year we also accomplished three year-long objectives that were important to understand Li inventory and its effectiveness to help the Si-graphite anode-containing full cell demonstrate cycle improvement over the baseline.

LFO•NMC532/Si-graphite cell: Lithium iron oxide Li_5FeO_4 (LFO) was added to a NMC532 blended electrode laminate with two different examples of pre-lithiation amounts. The first was 3.3 wt.% LFO (86.7 wt.% 532) which is calculated to eliminate the first cycle ICL (irreversible capacity loss), and the second, 7.1 wt.% LFO (82.9 wt.% 532) which makes the n/p ratio 1.04, which is quite close to the goal of 1.1 ratio match, but will not be enough to detrimentally plate Li on the first charge. The results of Si protocol deep dive cycling (3.0 to 4.1 V) are shown in Figure II.2.A.64.

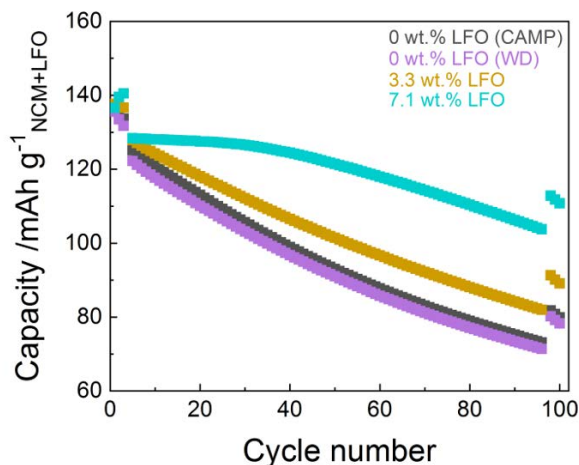


Figure II.2.A.64 Cathode capacity versus cycle number plot of two LFO weight percent blended NMC532 electrodes (as labeled) together with the non LFO-containing Si-graphite full cells. In each case the Si-graphite electrode is from CAMP (A-A013). Black markers show the baseline performance, where the NMC cathode is from CAMP (A-C013B). The colored markers use a glove-box cast electrode, with the magenta markers serving as a 0 % LFO proxy (baseline) for the LFO-containing cells. Note the glove-box cast electrodes (magenta (WD label)) match the performance of the CAMP full cells.

The findings indicate that the inclusion of LFO improves the utilization of NMC. Mitigating the ICL (3.3 wt.% LFO; gold markers) increases the capacity of the cell, but the capacity fades at the same rate as the baseline. Maximizing the Li inventory (7.1wt.% LFO; cyan markers) increases the capacity and delays the capacity fade. The capacity retention after 100 cycles for 7.7wt.% LFO full cell is 80%. LFO•NMC cathodes exhibit lower impedance rise across 100 cycles, as determined by HPPC, and show higher rate performance. Thus Li inventory into the Si-graphite cell using LFO can indeed improve the capacity within these parameters. Future investigations will, together with the CAMP facility, focus on scaling up the LFO•NCM laminate casting and seek to better understand the role of LFO in lowering the impedance.

$\text{Li}_{1+x}\text{NMC532O}_2$ /Si-graphite cell: As LFO located within the cathode compartment of the cell (after Li release on the first charge) adds dead inactive weight to the cell with cycling, we hypothesized that over-lithiated NMC532 may be a good way to introduce Li into the cell, but not add dead weight. Thus to do this experiment, we discharge the NMC532 electrode first in a Li half-cell, then extract the over-lithiated NMC (x is amount of Li added into the system) electrode, after which a full cell is then rebuilt with the Si-graphite anode. Note we can control the amount of x inserted into the NMC532 layer by limiting the first discharge of pristine NMC532. Figure II.B.1.65 shows the result on the cycling properties with the electrochemically produced over-lithiated NMC532 in a full cell at a few different x values (see caption Figure II.2.A.65).

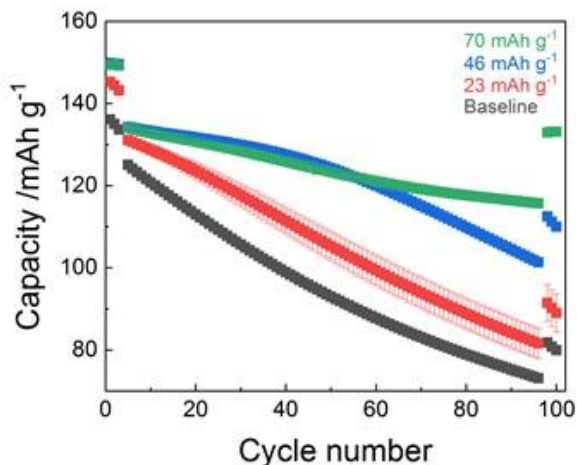


Figure II.2.A.65 Cathode capacity versus cycle number plot (Si DD protocol) of three over-lithiated $\text{Li}_{1+x}\text{NMC5320}_2/\text{Si}$ -graphite full cells, and one black baseline cell. The x value represents the extra Li introduced into the cell (Li inventory) from prior electrochemical lithiation in a Li half cell. The labels are red markers (23 mAh g^{-1} ; $x = 0.09$), blue markers (46 mAh g^{-1} ; $x = 0.17$), and green markers (70 mAh g^{-1} ; $x = 0.26$). Note the black markers (baseline) is the matched NMC532/Si-graphite CAMP electrodes in a full cell.

The experiments demonstrate the following observations. Increasing the Li inventory (either by 46 or 70 mAh g^{-1}) delays the capacity fade. A 70 mAh g^{-1} over-lithiation capacity yields 89% capacity retention over 100 cycles compared to 59% for baseline cell. The capacity retention in early cycles correlates well with high Coulombic efficiency, and is due to a Li reserve on the anodes compensating for capacity losses in early cycles. An independent measurement of impedance via HPPC cycle indicates that the over-lithiated NMC has a similar impedance rise over cycling from cycle 4 to cycle 97.

$\text{Li}_{1+y}\text{Ni}_{0.5}\text{Mn}_{1.5}\text{O}_4/\text{Si}$ -graphite cell: Chemical lithiation using lithium metal dissolved in liquid ammonia was introduced this past year as a viable, potentially scalable method to over-lithiate cathode materials, in this case, the 5V spinel $\text{Li}_{1+y}\text{Ni}_{0.5}\text{Mn}_{1.5}\text{O}_4$ (LNMO or LiNMO). [49] In this formula the value of y represents the amount of extra lithium inserted into the spinel. Such over-lithiated cathodes can subsequently be used to pre-lithiate high-energy anodes in a lithium-ion battery configuration during the first charge step. Lithiated 5V spinel $\text{Li}_{1+y}\text{Ni}_{0.5}\text{Mn}_{1.5}\text{O}_4$ cathode materials prepared by this technique show higher first delithiation capacities, confirming the chemically inserted lithium is electrochemically active. Full cells with a Si-graphite anode and the $\text{Li}_{1+y}\text{Ni}_{0.5}\text{Mn}_{1.5}\text{O}_4$ ($y=0.62$) cathode show a 23 % higher reversible capacity in the first cycle than $\text{LiNi}_{0.5}\text{Mn}_{1.5}\text{O}_4$ baseline cells, and improved capacity retention. The extra, chemically inserted lithium therefore sacrificially compensates for the loss of lithium at the anode allowing higher utilization of the cathode capacity in following cycles.

Pre-lithiation becomes more important when the ICL of the anode is large. To illustrate this, the first and second cycle potential profiles of Si-graphite/ $\text{Li}_{1.04}\text{NMO}$ and Si-graphite/ $\text{Li}_{1.62}\text{NMO}$ full cells are shown in Figure II.2.A.66a and Figure II.2.A.66b. Due to the larger ICL of the Si-graphite electrode, the Coulombic efficiency for $\text{Li}_{1.04}\text{NMO}$ is 57 % (charge and discharge capacity of 147 and 85 $\text{mAh g}^{-1}\text{LNMO}$, respectively). Conversely, with pre-lithiation the first charge capacity of $\text{Li}_{1.62}\text{NMO}$ is 201 $\text{mAh g}^{-1}\text{LNMO}$, with a reversible capacity of 104 $\text{mAh g}^{-1}\text{LNMO}$. The reversible capacity is therefore 19 $\text{mAh g}^{-1}\text{LNMO}$ higher for the cells where the ICL is compensated by the cathode pre-lithiation; a 23 % improvement. The increased first discharge capacity carries over into subsequent cycles (Figure II.2.A.65b), and after 100 cycles at C/10 the cells with $\text{Li}_{1.62}\text{NMO}$ deliver 44 $\text{mAh g}^{-1}\text{LNMO}$ of capacity (Figure II.2.A.65c and Figure II.2.A.65d). This is 18 $\text{mAh g}^{-1}\text{LNMO}$ higher than the baseline $\text{Li}_{1.04}\text{NMO}$ case. Additionally, the capacity retention over 100 cycles is higher for $\text{Li}_{1.62}\text{NMO}$ relative to $\text{Li}_{1.04}\text{NMO}$ (42 % and 30 %, respectively).

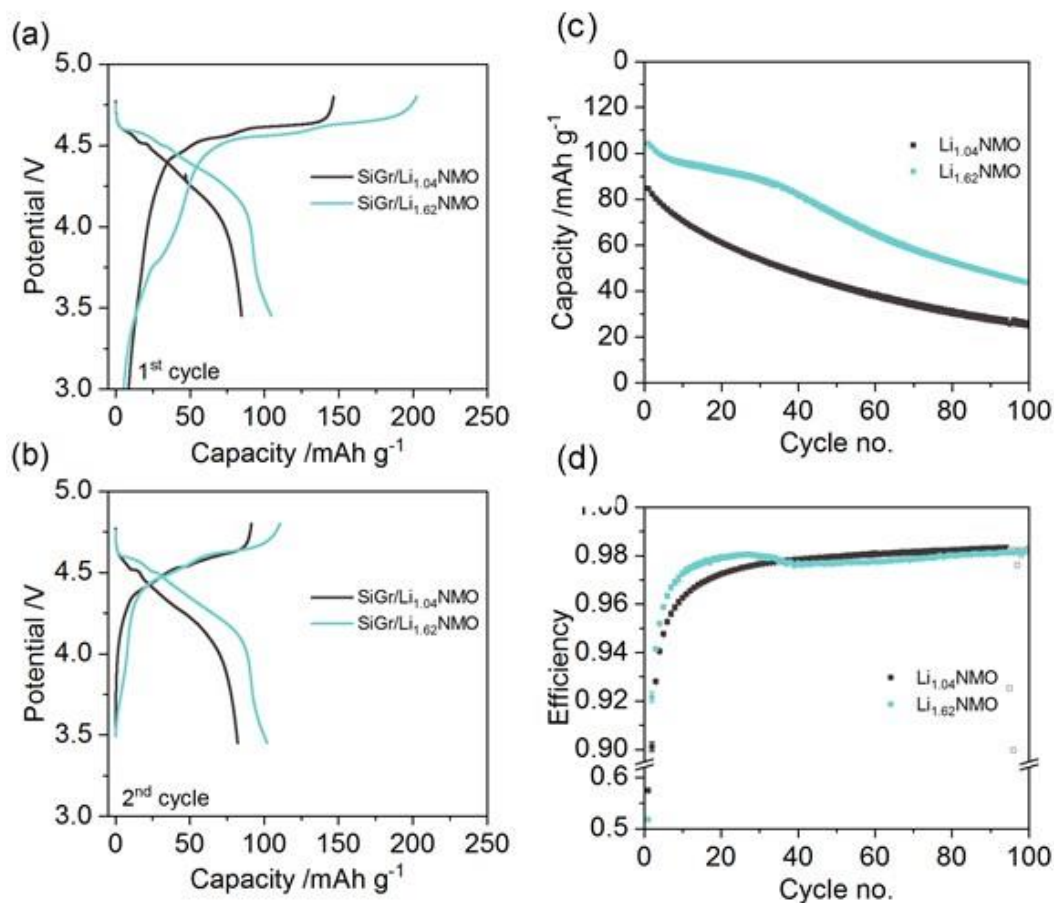


Figure II.2.A.66 Full cell potential profiles for the (a) first and (b) second charge and discharge of $\text{LiNi}_{0.5}\text{Mn}_{1.5}\text{O}_4$ and chemically lithiated $\text{Li}_{1.62}\text{Ni}_{0.5}\text{Mn}_{1.5}\text{O}_4$ versus a Si-graphite composite anode at a rate of C/10. Full cell (c) discharge capacity and (d) cycle efficiency over 100 cycles for $\text{LiNi}_{0.5}\text{Mn}_{1.5}\text{O}_4$ and chemically lithiated $\text{Li}_{1.62}\text{Ni}_{0.5}\text{Mn}_{1.5}\text{O}_4$ versus Si-graphite at a rate of C/10. Filled data symbols represent the average of two duplicate cells, with error bars showing the deviation between them. The open data symbols in (b) represent the region where a scheduled ~20 h power shutdown interrupted cycling of $\text{LiNi}_{0.5}\text{Mn}_{1.5}\text{O}_4$ and the subsequent cell recovery/break-in time (cycles 95-100). In this region, data is shown from the two cells separately since they were interrupted on different cycle numbers. Cycling conditions: 4.8 to 3.5 V, C/10, 30 °C, and GEN2 electrolyte containing 10% FEC.

Conclusions

Active Silicon-based Materials

We have evaluated and distributed a new baseline silicon electrode system using U.S. silicon supplier, Paraclete Energy, as a materials source. Paraclete provided multiple samples, including scale-up versions of the needed materials, for evaluation and screening. Paraclete Energy has demonstrated their ability to control particle size and customize processing steps to target surface chemistries. Electrochemical data is comparable to our earlier electrode performance. We have created high silicon content electrodes with the Paraclete scaled up silicon sample and have made them available to the DeepDive program.

A 4L hydrothermal/solvothermal-based synthesis system was installed and a preliminary performance evaluation of the reactor was successfully performed at 3500 psi, 392°C, and 500 rpm. During the testing process, pristine NanoAmor SiO_x particles were hydrothermally treated. The system was able to maintain specifications while no obvious decomposition or modification of the silicon / silica surface was noted.

Investigations using porous silicon electrodes indicated that the interactions of the active material and the electrolyte were critical to control to maximize performance. The study indicated that using a highly concentrated electrolyte system was not possible with a LiPAA-based binder but worked well with a polyimide based system, especially if the baseline silicon was modified to have a thin carbon-film based coating.

Silicon and silicon-tin composite films with the thickness ranging from a few tens to a few hundred nanometers were prepared by direct deposition on Cu foils. The DC sputtering method used generated films with low O content and stable cycling performance during early cycles. Silicon-tin composite films were prepared by extrapolation from Si film study. The as-produced Si-Sn exhibits improved 1st cycle CE and cycling stability, compared to similar silicon films. Future work will be focused on using splat cooling to scale up the materials.

Silicon-based Electrodes

Operando energy dispersive XRD was conducted on 2032-type coin cells to monitor the evolution of the Gr-component in a composite Si/Gr (15/73, w/w) electrode during lithiation/delithiation cycling. Deconvolution of the Gr peaks combined with quantitative XRD analysis allowed us to monitor of the (de)lithiation fraction in each active component. The lithiation begins with Li⁺ ion storage mainly in Si; the Gr intercalates Li⁺ ions only at potentials <0.20 V. In the 0.20–0.01 V range, the relative lithiation of Si and Gr are ~58% and 42%, respectively. On delithiation, Li⁺ extraction occurs mainly from Gr in the 0.01–0.23 V range (region 3) and from Si in the >0.23 – 1.50 V range; that is, the delithiation current is carried sequentially, first by graphite and then by silicon. This type of information can be used for the rational selection of electrochemical cycling windows that limits volumetric expansion in Si particles and thereby extending cell life.

The calendar-life and cycle aging behavior of several cells with a NCM523-based positive electrode and a Si-containing (or a Gr-based) negative electrode were compared. The cells contained the baseline Gen2 electrolyte (1.2 M LiPF₆ in EC:EMC 3:7 w/w) with or without 10 wt% FEC. Our data indicated that the capacity fade was greater for the cycle-life tests than for the calendar life tests. The fade mainly results from immobilization of Li⁺ ions in the negative electrode SEI. Furthermore, a small parasitic current flow was observed in the cell during the potentiostatic hold; after ~100 h, the current flow was infrequent, indicating an SEI that is passivating for most of the time. However, periods of cell activity seen as random bursts of current flow indicate some charge loss to the SEI. Electrolytes harvested from the cycle aged and calendar aged cells were examined. Our data showed that the concentration of LiPF₆ hydrolysis products (PO₂F₂⁻ anion, specifically) was significantly greater in the electrolyte from the calendar-life cells. Also, electrolytes that were simply in contact with the electrode (no cycling) showed significant amounts of the PO₂F₂⁻ anion, indicating that the Si-Gr electrodes are a source of water in the cell (even though they are dried at 150°C in a vacuum oven). The HF generated during LiPF₆ hydrolysis can diffuse through the SEI and react with the Si particle surfaces. Such corrosion is more likely during cycle-life aging (which causes continuous restructuring of the SEI) than during calendar-life aging (wherein the SEI slows down, but does not prevent, HF access to the particle surfaces).

Developing an understanding of how the lithiated Si species within the electrode interacts with their environment is critical to the SEI layer formation and the cyclability of the Si electrodes. We have synthesized and scaled up lithium silicides model compounds that represent the silicon electrode at various states of charge, and used MAS-NMR and X-ray diffraction to assess the stability of different battery components, including binders and electrolyte solvents, in contact with the highly-reactive lithiated Si electrodes. NMR results showed that the contacting between PVDF and LS would cause the breaking of C-C and C-H bonds in PVDF, formation H₂ gas and lithium complexes, leading to the degradation of PVDF and the final failure of Si anodes. Several potential reaction mechanisms between PVDF and Li₇Si₃ were proposed. In comparison, LiPAA showed good chemical stability in contact with the LS model compounds, implying it can be a better binder material for Si anode. In addition, the quantification study of the reactivity of Li₇Si₃ vs. carbonates (EC, EMC and FEC) and triglyme showed that exposure Li₇Si₃ to triglyme or FEC induced the least structural and chemical changes, whereas the reactions with EMC and EC are more pronounced. However, triglyme and FEC

become much more reactive after mixed with the more deeply lithiated model compound $\text{Li}_{121}\text{Si}_5$. Triglyme-based electrolytes were prepared and showed much higher initial capacity, outperformed the baseline by 75%. However, electrochemistry results suggest that interface passivation for the triglyme-based electrolytes is inadequate and cell performances decay rapidly.

Analysis of the electrodes via Raman Spectroscopy indicated that issues associated with homogeneity and electronic isolation exist as different parts of the electrode were found to have different levels of lithiation after cycling. Utilization of copper nanoparticles electrodeposited on the surface was identified as a method to increase the sensitivity of Raman Spectroscopy signal by the SERS effect with minimal chance of introducing new materials or altering the SEI deposition. Unfortunately, the enhancement associated with the Cu-coated electrodes was not significant enough to identify additional species.

The generation and consumption of gas in these slurries is, for the most part, a direct result of Si oxidation during slurry preparation. Furthermore, solvent contribution alone is not the limiting factor rather the addition of Carbon Black (CB) played a role in promoting the oxidation of the Si particles. Based on gassing results of the NanaAmor Si particles from the water slurries, the samples containing carbon black suffered the greatest amount of oxidation confirming CB is a key reagent. The CB-samples may be producing more gas as there was additional evidence that the CB containing samples had more CO_2 in the gas stream. We believe the CB acts as a high surface area catalytic site in which a proton coupled, charge transfer could take place. Both OH^- and H^+ readily diffuse through amorphous SiO_x . Despite the acidic environment, the natural dissociation of water provides sufficient OH^- ions, which could diffuse through the amorphous SiO_x and oxidize the Si core.

In this proposed scenario the CB lowers the activation energy needed to reduce the protons, which may not take place on the SiO_x surface alone.

Silicon Surface Modifications

Surface functionalized SiNPs were designed and synthesized via a silanization reaction between functional trialkoxysilane and Si-OH-enriched SiNPs. The epoxy-functionalized SiNPs showed much improved performance compared with the pristine and methyl-substituted Si particles due to the formation of covalent bonding between the epoxy group and the hydroxyl group from the polyacrylic acid binder. Furthermore, the surface functionalization protected the parasitic reactions of the Li_xSi with electrolyte and enabled the reversible insertion and extraction of lithium with much improved initial capacity and capacity retention compared with the anode prepared with pristine Si particles. Additionally, the enhanced chemical stability of the functionalized silicon particles enabled a successful aqueous slurry making/electrode coating process with no observed gassing or foaming issues. This research provided insight that the surface functionalization on the particle level of the silicon anode is a feasible approach to mitigate the parasitic reactions of the pristine Si powder and Li_xSi with the electrolyte, tailor the formation and chemical composition of SEI, and manipulate the interaction of active material with other electrode components to enable Si anode materials in next generation lithium-ion batteries with improved electrochemical performance.

Li_2SiO_3 -coated Si nanoparticles were successfully synthesized via solid-state reaction with Li_2CO_3 . The silicate-coated Si showed compromised capacity in the initial electrochemical tests, with decreased capacity obtained with increased silicate layer thickness. A likely cause of the low capacity is the presence of aggregates due to the solid-state reaction.

The Coulombic efficiencies of the surface-coated electrodes (termination groups— $-\text{CH}_3$, $-\text{COOH}$, or $-\text{CF}_3$) are similar to the pristine un-treated Si electrode for the 1st cycle; $-\text{CF}_3$ (92.9%), CH_3 (92.2%), COOH (91.8%), Pristine (90.9%). The chemical compositions of the SEI layers are comparable based on the XPS analysis. Surprisingly, the ionic conductivity from EIS measurement and electronic conductivity obtained by using SSRM show significant differences in these treated Si electrodes. The SEI-COOH layer has much higher ionic conductivity, but lower electronic conductivity, than the other two surface-treated electrodes. This integrated functionalization and characterization approach provides a systematic methodology to investigate the effect of

surface functional groups on the SEI formation, the electrochemical behavior, lithium ion conductivity, and the interfacial resistance of the Si electrode.

Electrode Construction

A novel designing practice of functional conductive binders and latex binders for lithium ion batteries has been conducted. A series of conductive polymer binder emulsions in water has been prepared using emulsion polymerization methods. These polymer emulsions have been further used for lithium ion battery applications. The electrode coating process is water-based without using any organic solvents, which is lower in cost and more environmentally friendly. Using these polymer emulsions as the binder, silicon materials, solely or together with graphite materials, have been fabricated into electrodes showing promising cycling performance.

A rational design, synthesis and testing of electrolyte additives have been conducted. Two classes of bi-functional electrolyte additives with surface reaction functional group and coating functional group on one molecule have been synthesized. A toolbox is under construction with different reactive groups and hydrophobic and hydrophilic surface coating groups. The preliminary results show the surface reactive groups are able to form surface coating on the active materials, whereas the film functional groups can provide designed interaction with the electrolyte. Advanced diagnostic and full cell testing will be applied to these bi-functional electrolyte additives to further elucidate the molecular level interactions and quantify their electrochemical performances.

Lithium inventory in Si-containing full cells has been evaluated from the standpoint of diagnostic tools with LiFePO_4 as a quasi-CE/RE in Si-graphite blended composite anode-containing cells, and from loading the cell with extra lithium sources introduced at the cathode side such as Li_5FeO_4 , $\text{Li}_{1+x}\text{NMC532O}_2$, and $\text{Li}_{1+y}\text{Ni}_{0.5}\text{Mn}_{1.5}\text{O}_4$ spinel. All three methods of lithium introduction works in the Si-graphite cell at some level. From our results we find that the more Li introduced into the cell will increase the lifetime of the Si-containing cell to the extent that the extra Li is exhausted from SEI reactions. We need significant improvement to the SEI stability to mitigate irreversible Li consuming processes occurring on each cycle. Reversible SEI stripping and reformation without Li loss on every cycle would be excellent. Finally, if one can leak Li into the cell over the lifetime of the battery, perhaps dosing every 100 cycles, then we surmise that a better performance will be achieved.

Extensive efforts have been conducted towards gain in-depth understanding of the factors controlling the performance of PAA binders and evolving those binders towards improved cell performance for silicon lithium-ion batteries. Firstly, PAA binders were used to study the effect of Li^+ exchange in the polymer binder (the pre-lithiation of PAA) on the properties and electrochemical cycling of cells containing Si-Gr composite electrodes. From the standpoint of material chemistry, the pre-lithiation of PAA does not confer significant benefits and can be detrimental. For instance, it increases the viscosity and shear thinning of aqueous solutions and slurries and reduced the cohesion between the particles in the electrode matrices. Furthermore, for both half cells and full cells, sparse lithiation of the binder notably improves the cycling performance. For half cells, there is severe depletion of Si nanoparticles for Li^+ substitution $> 95\%$ (pH 7) due to corrosion during fabrication of the electrode. The optimum pH range is between 2 and 4, and the best results are obtained without any pre-lithiation. The peeling test of the fabricated electrodes showed that the pre-lithiation can adversely affect the mechanical strength of the prepared binders. Thus, it appears that contrary to the current practice of pre-lithiation of PAA by titration of the solutions to pH 7 (lithiation ratio > 0.9), little to no pre-lithiation may be more favorable for improved performance for Si-Gr composite anode batteries. Secondly, NMP-soluble poly(4-vinylbenzoic acid) (P4VBA) polymers were synthesized and used as binders to fabricate high-quality Si/graphite composite electrodes from water-free slurries. Compared to PAA, these P4VBA polymers (of the equivalent or higher Mn) have higher viscosity and lower shear thinning in the NMP solutions, yielding good quality electrode coatings with superior adhesive strengths (4X over PAA). The initial and average capacity, Coulombic efficiencies, and capacity retention were also much better for these P4VBA polymer binders, and our post-mortem SEM examination suggests that the longer chain P4VBA polymers inhibit morphological deterioration of the electrode matrix during electrochemical cycling. Our results indicate

that long-chain (~64 kDa) P4VBA can serve as an excellent polymer binder for fabrication of Si-based electrodes from NMP, which makes this polymer an appealing alternative to water-soluble polycarboxylate binders that introduce moisture leading to faster degradation of Si particles through the formation of corrosive HF.

Key Publications

1. K. Kalaga, M.-T. Rodrigues, S.E. Trask, I.A. Shkrob, D.P. Abraham, "Calendar-life versus Cycle-life aging of Lithium-ion Cells with Silicon-Graphite Composite Electrodes", *Electrochimica Acta* **280** (2018) p. 221.
2. K. Kalaga, I.A. Shkrob, R.T. Haasch, C. Peebles, J. Baro, D.P. Abraham, "Auger Electrons as Probes for Composite Micro and Nanostructured Materials: Application to Solid Electrolyte Interphases in Graphite and Silicon-Graphite Electrodes", *J. Phys. Chem. C* **121** (2017), p. 23333.
3. J. Bare, I.A. Shkrob, J.A. Gilbert, M. Klett, D.P. Abraham, "Capacity Fade and Its Mitigation in Li-ion Cells with Silicon-Graphite Electrodes", *J. Phys. Chem. C* **121** (2017) p. 20640.
4. K.P.C. Yao, J.S. Okasinski, K. Kalaga, J.D. Almer, D.P. Abraham, "Operando Quantification of (De)Lithiation Behavior of Silicon-Graphite Blended Electrodes for Lithium-Ion Batteries", *Advanced Energy Materials* (2018), under review.
5. Caleb Stetson, Taeho Yoon, Jaclyn Coyle, William Nemeth, Matt Young, Andrew Norman, Svitlana Pylypenko, Chunmei Ban, Chun-Sheng Jiang, Mowafak Al-Jassim, Anthony Burrell, submitted
6. Zhao, H.; Wei, Y.; Wang, C.; Qiao, R. M.; Yang, W. L.; Messersmith, P. B.; Liu, G., Mussel-Inspired Conductive Polymer Binder for Si-Alloy Anode in Lithium-Ion Batteries. *Acs Applied Materials & Interfaces* **2018**, *10* (6), 5440-5446.
7. Zhang, G. Z.; Yang, Y.; Chen, Y. H.; Huang, J.; Zhang, T.; Zeng, H. B.; Wang, C. Y.; Liu, G.; Deng, Y. H., A Quadruple-Hydrogen-Bonded Supramolecular Binder for High-Performance Silicon Anodes in Lithium-Ion Batteries. *Small* **2018**, *14* (29).
8. Yao, K.; Ling, M.; Liu, G.; Tong, W., Chemical Reduction Synthesis and Electrochemistry of Si-Sn Nanocomposites as High-Capacity Anodes for Li-Ion Batteries. *J. Phys. Chem. Lett.* **2018**, *9* (17), 5130-5134.
9. Yang, S. M.; Gu, Y. Y.; Qu, Q. T.; Zhu, G. B.; Liu, G.; Battaglia, V. S.; Zheng, H. H., Engineered Si@alginate microcapsule-graphite composite electrode for next generation high-performance lithium-ion batteries. *Electrochim. Acta* **2018**, *270*, 480-489.
10. Wang, Y.; Zheng, X. Y.; Qu, Q. T.; Liu, G.; Battaglia, V. S.; Zheng, H. H., A novel maleic acid/graphite composite anode for lithium ion batteries with high energy and power density. *Carbon* **2018**, *132*, 420-429.
11. Sabisch, J. E. C.; Anapolsky, A.; Liu, G.; Minor, A. M., Evaluation of using pre-lithiated graphite from recycled Li-ion batteries for new LiB anodes. *Resour. Conserv. Recycl.* **2018**, *129*, 129-134.
12. Gao, X. M.; Ding, Y. L.; Qu, Q. T.; Liu, G.; Battaglia, V. S.; Zheng, H. H., Optimizing solid electrolyte interphase on graphite anode by adjusting the electrolyte solution structure with ionic liquid. *Electrochim. Acta* **2018**, *260*, 640-647.
13. Fang, S.; Li, N.; Zheng, T. Y.; Fu, Y. B.; Song, X. Y.; Zhang, T.; Li, S. P.; Wang, B.; Zhang, X. G.; Liu, G., Highly Graphitized Carbon Coating on SiO₂ with a π -Stacking Precursor Polymer for High Performance Lithium-Ion Batteries. *Polymers* **2018**, *10* (6).

14. Chen, H.; Ling, M.; Hencz, L.; Ling, H. Y.; Li, G. R.; Lin, Z.; Liu, G.; Zhang, S. Q., Exploring Chemical, Mechanical, and Electrical Functionalities of Binders for Advanced Energy-Storage Devices. *Chem. Rev.* **2018**, *118* (18), 8936-8982.
15. Liu, D.; Fina, M.; Guo, J. H.; Chen, X. B.; Liu, G.; Johnson, S. G.; Mao, S. S., Organic light-emitting diodes with carbon nanotube cathode-organic interface layer. *Applied Physics Letters* **2009**, *94* (1), 3.

References

1. *Alloy Negative Electrodes for Li-Ion Batteries*. M.N. Obrovac and V.L. Chevrier, *Chem, Rev.* 2014, *114*, 11444-11503.
2. *Modeling the Performance and Cost of Lithium-Ion Batteries for Electric-Drive Vehicles*. Second Edition, Argonne National Laboratory Report, ANL-12/55.
3. Hatchard, T. D.; Dahn, J. R., Study of the Electrochemical Performance of Sputtered Si_{1-x}Sn_x Films. *Journal of the Electrochemical Society* 2004, *151* (10), A1628-A1635.
4. Ahn, H.-J.; Kim, Y.-S.; Park, K.-W.; Seong, T.-Y., Use of Sn-Si nanocomposite electrodes for Li rechargeable batteries. *Chemical Communications* 2005, (1), 43-45.
5. Yao, K.; Ling, M.; Liu, G.; Tong, W., Chemical Reduction Synthesis and Electrochemistry of Si-Sn Nanocomposites as High-Capacity Anodes for Li-Ion Batteries. *The Journal of Physical Chemistry Letters* 2018, *9* (17), 5130-5134.
6. Xu, J.; Ling, M.; Terborg, L.; Zhao, H.; Qiu, F.; Urban, J. J.; Kostecki, R.; Liu, G.; Tong, W., Facile Synthesis and Electrochemistry of Si-Sn-C Nanocomposites for High-Energy Li-Ion Batteries. *Journal of The Electrochemical Society* 2017, *164* (7), A1378-A1383.
7. Li, J. L.; Daniel, C.; Wood, D., Materials processing for lithium-ion batteries. *Journal of Power Sources* 2011, *196*, 2452-2460.
8. Porcher, W., Lestriez, R., Jouanneau, S., Guyomard, D. *J. Power Sources* 2010, *195*, 2835-2843.
9. Wood, D. L.; Li, J.; Daniel, C. *Journal of Power Sources* 2015, *275*, 234-242.
10. Toudjine, A.; Morcrette, M.; Courty, M.; Davoisne, C.; Lejeune, M.; Mariage, N.; Porcher, W.; Larcher, D., Partially Oxidized Silicon Particles for Stable Aqueous Slurries and Practical Large-Scale Making of Si-Based Electrodes. *J. Electrochem. Soc.* 2015, *162*, A1466-A1475.
11. Zhang, L.; Liu, Y.; Key, B.; Trask, S. E.; Yang, Z.; Lu, W., Silicon Nanoparticles: Stability in Aqueous Slurries and the Optimization of the Oxide Layer Thickness for Optimal Electrochemical Performance. *ACS Appl. Mater. Interfaces* 2017, *9*, 32727-32736.
12. Xun, S.; Song, X.; Wang, L.; Grass, M. E.; Liu, Z.; Battaglia, V. S.; Liu, G., The Effects of Native Oxide Surface Layer on the Electrochemical Performance of Si Nanoparticle-Based Electrodes. *J. Electrochem. Soc.* 2017, *164*, A1733-A1742.
13. Gurkaynak, A.; Tubert, F.; Yang, J.; Matyas, J.; Spencer, J. L.; Gryte, C. C., High-temperature degradation of polyacrylic acid in aqueous solution. *Journal of Polymer Science Part A: Polymer Chemistry* 1996, *34*, 349-355.
14. Porcher, W.; Chazelle, S.; Boulineau, A.; Mariage, N.; Alper, J. P.; Van Rompaey, T.; Bridel, J.-S.; Haon, C., Understanding Polyacrylic Acid and Lithium Polyacrylate Binder Behavior in Silicon Based Electrodes for Li-Ion Batteries. *J. Electrochem. Soc.* 2017, *164*, A3633-A3640.

15. Philippe, B.; Dedryvere, R.; Allouche, J.; Lindgren, F.; Gorgoi, M.; Rensmo, H.; Gonbeau, D.; Edstrom, K., Nanosilicon Electrodes for Lithium-Ion Batteries: Interfacial Mechanisms Studied by Hard and Soft X-ray Photoelectron Spectroscopy. *Chem. Mat.* 2012, 24, 1107-1115.
16. Cabaniss, G. E.; Diamantis, A. A.; Murphy, W. R.; Linton, R. W.; Meyer, T. J., Electrocatalysis of Proton Coupled Electron Transfer Reactions at Glassy Carbon Electrodes. *J. Am. Chem. Soc.* 1985, 107, 1845-1853.
17. Hofstein, S. R., Proton and Sodium Transport in SiO₂ Films. *IEEE Trans. Electron Devices* 1967, ED14, 749+.
18. Seidel, H.; Csepregi, L.; Heuberger, A.; Baumgärtel, H., Anisotropic Etching of Crystalline Silicon in Alkaline Solutions: I. Orientation Dependence and Behavior of Passivation Layers. *J. Electrochem. Soc.* 1990, 137, 3612-3626.
19. C. J. Wen, R. Huggins, *J. Solid State Chemistry*, 1981, 37, pp 271-278.
20. B. Key, R. Bhattacharyya, M. Morcrette, V. Seznec, J-M. Tarascon, C. P. Grey, *J. Am. Chem. Soc.*, 2009, 131 (26), pp 9239-9249
21. B. Key, M. Morcrette, J-M. Tarascon, C. P. Grey, *J. Am. Chem. Soc.*, 2011, 133 (3), pp 503-512
22. Multinuclear Solid-State Nuclear Magnetic Resonance of Inorganic Materials, Volume 6, 1st Edition, Authors: Kenneth MacKenzie M.E. Smith
23. Q. Zhang, Y. Cui, E. Wang. Modelling Simul. Mater. Sci. Eng. 2013, 21, 074001S. Xun et al. "Improved Initial Performance of Si Nanoparticles by Surface Oxide Reduction for Lithium-Ion Battery Application", *Electrochemical and Solid-State Letters*, 2011, 14(5)
24. Zhang, L.; Liu, Y.; Key, B.; Trask, S. E.; Yang, Z.; Lu, W., Silicon Nanoparticles: Stability in Aqueous Slurries and the Optimization of the Oxide Layer Thickness for Optimal Electrochemical Performance. *ACS Appl. Mater. Interfaces* 2017, 9 (38), 32727-32736.
25. Aguiar, H.; Serra, J.; González, P.; León, B., Structural study of sol-gel silicate glasses by IR and Raman spectroscopies. *J. Non-Cryst. Solids* 2009, 355 (8), 475-480.
26. Vreugdenhil, A. J.; Balbyshev, V. N.; Donley, M. S., Nanostructured silicon sol-gel surface treatments for Al 2024-T3 protection. *Journal of Coatings Technology* 2001, 73 (915), 35-43.
27. Mu, J.; Liu, Y.; Zheng, S., Inorganic-organic interpenetrating polymer networks involving polyhedral oligomeric silsesquioxane and poly(ethylene oxide). *Polymer* 2007, 48 (5), 1176-1184.
28. Oliver, M. S.; Blohowiak, K. Y.; Dauskardt, R. H., Molecular structure and fracture properties of ZrO_x/Epoxy silane hybrid films. *J. Sol-Gel Sci. Technol.* 2010, 55 (3), 360-368.
29. Higgins, T. M.; Park, S. H.; King, P. J.; Zhang, C.; McEvoy, N.; Berner, N. C.; Daly, D.; Shmeliov, A.; Khan, U.; Duesberg, G.; Nicolosi, V.; Coleman, J. N., A Commercial Conducting Polymer as Both Binder and Conductive Additive for Silicon Nanoparticle-Based Lithium-Ion Battery Negative Electrodes. *ACS Nano* 2016, 10 (3), 3702-3713.
30. Philippe, B.; Dedryvère, R.; Allouche, J.; Lindgren, F.; Gorgoi, M.; Rensmo, H.; Gonbeau, D.; Edström, K., Nanosilicon Electrodes for Lithium-Ion Batteries: Interfacial Mechanisms Studied by Hard and Soft X-ray Photoelectron Spectroscopy. *Chem. Mater.* 2012, 24 (6), 1107-1115.

31. Philippe, B.; Dedryvère, R.; Gorgoi, M.; Rensmo, H.; Gonbeau, D.; Edström, K., Role of the LiPF₆ Salt for the Long-Term Stability of Silicon Electrodes in Li-Ion Batteries – A Photoelectron Spectroscopy Study. *Chem. Mater.* 2013, 25 (3), 394-404.
32. Wu, M.; Xiao, X.; Vukmirovic, N.; Xun, S.; Das, P. K.; Song, X.; Olalde-Velasco, P.; Wang, D.; Weber, A. Z.; Wang, L. W.; Battaglia, V. S.; Yang, W.; Liu, G., Toward an Ideal Polymer Binder Design for High-Capacity Battery Anodes. *J. Am. Chem. Soc.* 2013, 135 (32), 12048-12056.
33. L. Michan, B. S. Parimalam, M. Leskes, R. N. Kerber, T. Yoon, C. P. Grey, and B. L. Lucht, *Chemistry of Materials*, 28 (22), 8149-8159 (2016)
34. Caleb Stetson, Taeho Yoon, Jaclyn Coyle, William Nemeth, Matt Young, Andrew Norman, Svitlana Pylypenko, Chunmei Ban, Chun-Sheng Jiang, Mowafak Al-Jassim, Anthony Burrell, submitted
35. Cao Cuong Nguyen, Taeho Yoon, Daniel M Seo, Pradeep Guduru, Brett L Lucht, *ACS Applied Materials & Interfaces* 8 (19), 12211-12220
36. K. W. D. Kaveendi Chandrasiri, CC Nguyen, BS Parimalam, S Jurng, BL Lucht, Journal of The Electrochemical Society 165 (10), A1991-A1996 Aiken, C. P.; Xia, J.; Wang, D. Y. H.; Stevens, D. A.; Trussler, S.; Dahn, J. R., An Apparatus for the Study of In Situ Gas Evolution in Li-Ion Pouch Cells. *J. Electrochem. Soc.* **2014**, 161, A1548-A1554.
37. Wang et al. “Enhanced electrochemical performance of lithium metasilicate-coated Li(NiCoMn)O₂ Ni-rich cathode for Li-ion batteries at high cutoff voltage”, *Electrochimica Acta*, 2016, 222, 806-819
38. Lee. et al., “High-performance silicon-based multicomponent battery anodes produced via synergistic coupling of multifunctional coating layers”, *Energy Environ. Sci.*, 2015, 8, 2075-2084
39. Gu, M.; Xiao, X. C.; Liu, G.; Thevuthasan, S.; Baer, D. R.; Zhang, J. G.; Liu, J.; Browning, N. D.; Wang, C. M., Mesoscale Origin of the Enhanced Cycling-Stability of the Si-Conductive Polymer Anode for Li-ion Batteries. *Sci Rep* **2014**, 4, 7.
40. Shi, F. F.; Ross, P. N.; Zhao, H.; Liu, G.; Somorjai, G. A.; Komvopoulos, K., A Catalytic Path for Electrolyte Reduction in Lithium-Ion Cells Revealed by in Situ Attenuated Total Reflection-Fourier Transform Infrared Spectroscopy. *Journal of the American Chemical Society* **2015**, 137 (9), 3181-3184.
41. Park, S. J.; Zhao, H.; Ai, G.; Wang, C.; Song, X. Y.; Yuca, N.; Battaglia, V. S.; Yang, W. L.; Liu, G., Side-Chain Conducting and Phase-Separated Polymeric Binders for High-Performance Silicon Anodes in Lithium-Ion Batteries. *Journal of the American Chemical Society* **2015**, 137 (7), 2565-2571.
42. Zhao, H.; Park, S. J.; Shi, F. F.; Fu, Y. B.; Battaglia, V.; Ross, P. N.; Liu, G., Propylene Carbonate (PC)-Based Electrolytes with High Coulombic Efficiency for Lithium-Ion Batteries. *J. Electrochem. Soc.* **2014**, 161 (1), A194-A200.
43. B. Hu, I. A. Shkrob, S. Zhang, L. Zhang, J. Zhang, Y. Li, C. Liao, Z. Zhang, W. Lu and L. Zhang, *Journal of Power Sources*, 2018, 378, 671-676.
44. W. Porcher, S. Chazelle, A. Boulineau, N. Mariage, J. P. Alper, T. Van Rompaey, J.-S. Bridel and C. Haon, Journal of the Electrochemical Society, 2017, 164, A3633-A3640.
45. Z.-J. Han, K. Yamagiwa, N. Yabuuchi, J.-Y. Son, Y.-T. Cui, H. Oji, A. Kogure, T. Harada, S. Ishikawa, Y. Aoki and S. Komaba, *Physical Chemistry Chemical Physics*, 2015, 17, 3783-3795.

46. L. Zhang, Y. Liu, B. Key, S. E. Trask, Z. Yang and W. Lu, *ACS Applied Materials & Interfaces*, 2017, 9, 32727-32736.
47. W. M. Dose, V. A. Maroni, M. J. Piernas-Muñoz, S. E. Trask, I. Bloom, and C. S. Johnson “Assessment of Li-Inventory in cycled Si-Graphite anodes using LiFePO₄ as a diagnostic cathode”, , *J. Electrochem. Soc.*, (2018), **165**, A2389-A2396.
48. W. M. Dose, M. J. Piernas-Munoz, V. A. Maroni, S. E. Trask, I. Bloom and C. S. Johnson “Capacity fade in high energy silicon-graphite electrodes for lithium-ion batteries”, *Chemical Communications*, (2018), **54**, 3586-3589.
49. W. M. Dose, J. Blauwkamp, P. Senguttuvan, C. S. Johnson “Liquid ammonia chemical lithiation: an approach for high energy and high voltage Si-graphite | Li_{1+x}Ni_{0.5}Mn_{1.5}O₄ Li-ion batteries”, Submitted (2018).

II.2.B Silicon Electrolyte Interface Stabilization (SEISta) (NREL, ANL, ORNL, LBNL, SNL)

Anthony Burrell, Principal Investigator

National Renewable Energy Laboratory
15013 Denver West Parkway
Golden, CO 80401
E-mail: anthony.burrell@nrel.gov

Brian Cunningham, DOE Technology Development Manager

U.S. Department of Energy
E-mail: Brian.Cunningham@ee.doe.gov

Start Date: October 1, 2017 End Date: September 30, 2020
Project Funding (FY18): \$4,150,000 DOE share: \$4,150,000 Non-DOE share: \$0

Introduction

This report documents the Silicon Electrolyte Interface Stabilization team's approach in 1) characterizing the early-stage silicon-electrolyte interphase (SEI) including progress on identifying the specific reaction pathways present in the formation of the SEI layer, and 2) establishing a procedure for measuring SEI growth rate at fixed potentials and different cycling regimes.

Silicon is a viable alternative to graphitic carbon as an electrode in lithium-ion cells and can theoretically store >3,500 mAh/g. However, lifetime problems have been observed that severely limit its use in practical systems. The major issues appear to involve the stability of the electrolyte and the uncertainty associated with the formation of a stable SEI at the electrode. Recently, calendar-life studies have indicated that the SEI may not be stable even under conditions where the cell is supposedly static. Clearly, a more foundational understanding of the nature of the silicon/electrolyte interface is required if we are to solve these complex stability issues. A new multi-lab consortium has been formed to address a critical barrier in implementing a new class of materials used in lithium-ion batteries that will allow for smaller, cheaper, and better performing batteries for electric-drive vehicles. This consortium, named the Silicon Electrolyte Interface Stabilization (SEISta) project, was formed to focus on overcoming the barrier to using such anode materials. Five national laboratories are involved: the National Renewable Energy Laboratory (NREL), Argonne National Laboratory (ANL), Lawrence Berkeley National Laboratory (LBNL), Oak Ridge National Laboratory (ORNL), and Sandia National Laboratories (SNL).

The SEISta project was specifically developed to tackle the foundational understanding of the formation and evolution of the solid-electrolyte interphase on silicon. This project will have as its primary goal an understanding of the reactivity of the silicon and lithiated silicon interface with the electrolyte in lithium-ion systems. It consists of researchers from multiple national laboratories (NREL, ANL, LBNL, ORNL, and SNL) working toward clear unified goals. The Silicon Deep-Dive team, which focuses on the science and technology barriers in functional electrodes, is a critical partner in this work. Many of the researchers are shared between both teams, and we hold joint meetings to ensure effective communication between the teams.

The current goals of SEISta are:

- Quarter 1 Milestone:
 - Have completed selection and characterization (X-ray photoelectron spectroscopy [XPS], secondary-ion mass spectrometry [SIMS], infrared [IR] and Raman spectroscopy), including determination of the surface-termination chemistry and impurity levels of the SEISta model research samples to be used by all members of the team in FY18. (100% complete)
- Quarter 2 Milestone:

- Have characterized (XPS, SIMS, IR, and Raman) the surface chemistry and composition of the SEISta model research samples after contact with the electrolyte, before cycling, including the nature of the electrolyte decomposition products. (100% complete)
- Quarter 3 Milestone:
 - Completed characterization (electrochemistry, IR, and Raman) of the early-stage silicon-electrolyte interphase formation on the SEISta model research samples, specifically by establishing and demonstrating a procedure for quantitatively measuring the solubility of SEI on silicon surfaces. (100% complete)
- Quarter 4 Milestones:
 - Established and demonstrated a procedure for measuring the growth rate of silicon SEI components at fixed potentials and during cycling. (100% complete)
 - Determined how the physical properties of the silicon/electrolyte interface are influenced by the nature of the silicon surface on the SEISta model samples. (100% complete)

For FY18, all milestones are 100% complete.

Objectives

The critical issues that SEISta is attempting to determine are:

- What are the properties of the lithiated silicon/electrolyte interface?
- What is the silicon SEI actually made of and what reactions are contributing to it?
- How fast does the silicon SEI grow?
- Does it stop growing?
- Is it soluble?
- Can it be stabilized?

For FY18, the team focused on three broad tasks:

Materials Standardization – This task is critical to the development and deployment of standardized samples and experimental procedures across the team. We will continue to provide full characterization to any new sample that is to be used for SEI studies to ensure reproducibility and full understanding of the material. This quarter's work focused on developing new oxide coatings and methods to control the thickness and density of oxide samples. In addition, work on the silicon nanoparticles has made progress with the enhancement of the materials collection and handling system in the plasma reactor. *Although this work dominated the early part of the project and is still critical to its success, it is now only a minor part of the work and this is reflected in the relative balance of this quarterly report.*

Model Materials Development and Characterization – The nature of the electrode-electrolyte interaction in silicon electrodes is at the heart of the formation and stability of the SEI. The inherent chemical reactivity of silicon with common electrolytes has been a focus for this team and will be a primary focus moving to quarter 2. The synthesis of well-defined silicon nanoparticles and the different chemical markups of lithiated silicon surfaces is being probed by preparing model compounds and thin films that may/can exist in silicon anodes. Lithium silicides, silicates, and other inorganic material (LiF, Li₂O) are being prepared, and their reactivity

with electrolytes is being determined. These materials also act as standard spectroscopy samples for the researchers who are looking at the formation of the SEI on different silicon materials.

SEI Characterization – The overall objective for SEISta is to understand the nature and evolution of the SEI on silicon anodes. The materials standardization and model compounds will enable the researchers to systematically investigate the formation of the solid-electrode interphase using a wide variety of the spectroscopy techniques—from different optical, microscopy, and electrochemistry—to determine how the SEI forms based on the nature of the silicon surface, and how it evolves over time. This section of work will continue to grow in scope as we move beyond the sample-characterization phase of the project and toward understanding the nature and evolution of the SEI. *This part of the project now represents the bulk of the work and, as such, this quarterly report is largely reporting on work leading to this outcome.*

Approach

The SEISta team works to ensure that protocols for sample preparation, experimental design, and implementation as well as data reporting are consistent across the whole team. Each laboratory is working toward the same set of quarterly milestones using its own specific talents and capabilities in a concerted effort with the other team members. This joint focus results in multiple researchers interacting to produce and analyze data to ensure that individual experimental variations will not lead to erroneous results. Critical to the success of this effort is the use of standard samples that can be shared by all parties. In the first FY, a round-robin sample test was established to ensure that data could be duplicated at the different laboratories by different researchers. In addition to weekly whole-team video presentations, we have held on-site face-to-face meetings each quarter for all team members and other interested parties to brainstorm and sort out issues with existing experiments and jointly develop new experimental plans.

The outcomes from FY17 indicated that the nature of the silicon starting materials has major implications for the formation and evolution of the SEI. This is most clearly seen in the inherent chemical reactivity of the silicon materials with electrolytes before electrochemistry. Much of our focus for FY18 will be in looking at the initial chemistry of the silicon on contact with electrolytes. This will then lead to an understanding of how the electrode/electrolyte interface changes upon applied voltage and how the SEI forms and evolves.

The overall objective of the SEISta project is to better understand the formation and evolution of the solid-electrolyte interphase (SEI) on silicon anodes. Silicon is a viable alternative to graphitic carbon as an electrode in lithium-ion cells and can theoretically store >3,500 mAh/g. However, lifetime problems have been observed that severely limit its use in practical systems. The major issues appear to involve the stability of the electrolyte and the uncertainty associated with the formation of a stable SEI at the electrode. Recently, calendar-life studies have indicated that the SEI may not be stable even under conditions where the cell is supposedly static. Clearly, a more foundational understanding of the nature of the silicon/electrolyte interface is required if we are to solve these complex stability issues. A multi-lab consortium has been formed to address a critical barrier in implementing a new class of materials used in lithium-ion batteries that will allow for smaller, cheaper, and better performing batteries for electric-drive vehicles. This consortium—the Silicon Electrolyte Interface Stabilization (SEISta) project—was formed to focus on overcoming the barrier to using such anode materials. Five national laboratories, led by the National Renewable Energy Laboratory (NREL), are involved: NREL, as well as Argonne (ANL), Lawrence Berkeley (LBNL), Oak Ridge (ORNL), and Sandia National Laboratories (SNL).

Results

SEISta Section 1: Intrinsic Chemical Reactivity of Silicon Electrodes—Very Initial Stages of SEI Growth

Although the bottle may say silicon on the label, it is becoming increasingly clear that not all “silicon” materials are the same. The variation in silicon chemistry—influenced by manufacturing process, history, and processing—results in dramatic variations in performance, stability, and processability of silicon electrodes. In addition, we suspect that the surface chemistry of the silicon contributes to calendar life, binder interactions, and the general variability in the silicon literature.

Due to the increasingly apparent correlation of silicon source and performance, we have undertaken a series of studies to understand the intrinsic reactivity of various well-defined silicon-based materials. The goal is to answer the following questions:

- How does reactivity change depending on surface termination?
- How does the initial surface chemistry direct the SEI formation?
- What surface terminations are most stable?
- Can we develop approaches to stabilize the surface and direct SEI formation?

To address these questions, we are working with a series of silicon materials including: hydrogen- and hydrocarbon-terminated silicon, silicon dioxide made by flame pyrolysis and solution precipitation, stoichiometric lithium silicates, Li-Si line compounds, and thin-film and wafer silicon. We hypothesize that the surface chemistry helps to direct the very initial stages of SEI growth *and* stability of the cell during formation cycling. These studies will provide a foundation to predict and explore stable surface chemistries as well as establish a basis to begin to understand the variation of results reported in the literature and technical reports.

Well-defined or commercially available silicon-based materials in large quantities were used in this work. Table II.2.B.1 lists the representative silicon-containing materials used in these studies. Where possible, commercial materials were purchased. In other cases, they were manufactured using synthesis methods described below. For the aging studies, materials were exposed to standard SEISta electrolytes (1.2M LiPF₆ in 3:7 ethylene carbonate:ethyl methyl carbonate (EC/EMC), and 1.0M LiTFSI in 3:7 EC/EMC). For some experiments, LiClO₄ salt was added to a 3:7 EC/EMC solvent mixture to explore the role of fluorine in the observed chemical reactions.

Table II.2.B.1 Summary of silicon-based materials used in this work

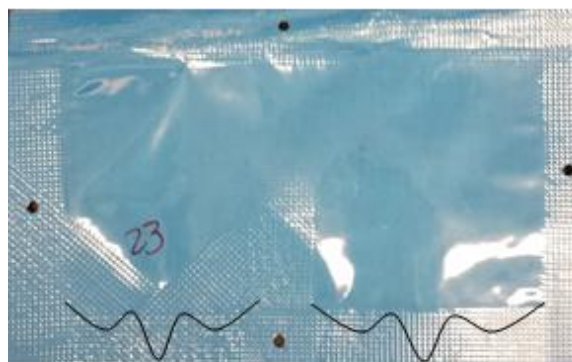
Material	Description/Synthesis	Ref
Si-H	Synthesized by plasma-enhanced chemical vapor deposition (PECVD). Particles 10 nm in diameter and materials mostly free of oxygen termination	1
Si powder	Milled silicon produced by nanoamor	
SiO ₂ – Stöbber	Synthesized through the controlled hydrolysis of tetraethyl orthosilicate (S5505 – Sigma Aldrich)	2
SiO ₂ – Fumed	Commercial SiO ₂ prepared by flame pyrolysis of SiCl ₄	
Li ₂ SiO ₃	Prepared by solid-state synthesis between SiO ₂ and Li ₂ CO ₃	
Li ₄ SiO ₄	Prepared by solid-state synthesis between SiO ₂ and Li ₂ CO ₃	
Li-Si alloy	Prepared by high-temperature reaction between Li metal and Si	
Si wafer	Commercial (100) wafer	
Li-Si-O films	Sputter-deposited lithium silicates	
Li-Si films	Evaporation of Li onto silicon film	

Chemical Reactions with Electrolyte

It has been observed in the past that extensive gassing occurs upon sealing of a pouch cell, presumably based on chemical reactions that occur before electrochemical cycling. We believe that this is the very initial stages of SEI growth and that by exploring these reactions, one can predict surfaces that would be stable and direct the formation of a suitable SEI layer.

To evaluate the extent of gassing, sealed Surlyn pouches (same material used for pouch cells) were assembled. The pouches consisted of two wells—one chevroned and holding the powdered sample, and the other holding

the liquid electrolyte—to be sealed with a pathway for the liquid to flow through as the pouch was turned on its side (Figure II.2.B.1). This was to keep the reactants separate because the reaction occurred immediately upon mixing. Samples were prepared in the glovebox by placing the silicon material (~0.2 g) in the pouch, followed by 400 μL of electrolyte. The pouches were sealed in the box and removed to atmosphere, where they were sealed again as a precaution. **(NOTE – hydrofluoric acid was measured in some cells, so suitable precautions should be taken when using these cells.)** The volume of gas produced was determined using the Archimedes buoyancy method. A photo of the experimental apparatus is shown in Figure II.2.B.2



Chevron side: powder

Figure II.2.B.1 Pouch cells designed for gassing studies. The pouch has two wells—one for electrolyte and the other for material—to control initial mixing.



Figure II.2.B.2 Buoyancy apparatus with a water bucket, indium wire to hang the pouch from the balance, and a bob (20 g dry).

To follow the gassing reaction rates and mechanisms, infrared (IR) experiments were run on an Agilent Technologies Cary 680 Fourier transform infrared (FTIR) spectroscope. These studies could track CO , CO_2 , SiF_4 , PF_3 , HF , and electrolyte, but not H_2 or O_2 gas. In a glovebox, a known amount of silicon-based material (~0.2 g) is weighed and transferred onto a boat (40 mm \times 13 mm \times 2 mm). The boat is inserted into the IR gas cell (Figure II.2.B.3). The cell had KBr windows as well as a septum (SupleCo GR-2 septum, 6 mm) for the injection port. A small syringe is filled with electrolyte (400 μL) and brought out of the glovebox along with the gas cell. The cell is placed on the holder in the IR spectrometer, and a background scan is taken. The electrolyte is injected through the injection port, first making sure that the boat is situated under the port inside the cell. Once the electrolyte is injected, the kinetic experiment is started. The data were taken as follows: a scan every 10 s for 30 min, then every 60 s for 60 min, then 120 s for 60 min, then 300 s for 600 min, and

finally, 600 s for 80 min. The range of scans was from 4,000 to 350 cm^{-1} , and the resolution was 4 cm^{-1} . After the scans were taken, the peaks of interest were integrated to track their intensity over time.

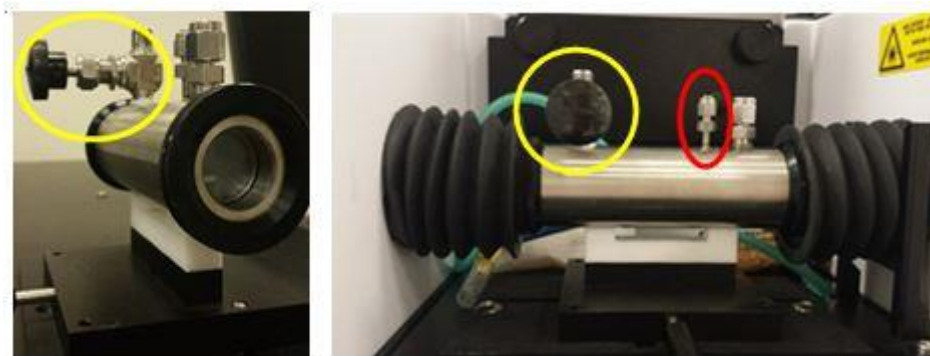


Figure II.2.B.3 IR gas cell used for kinetic measurements from two different angles. The path length through the cell is 11 cm, and the KBr windows are 25 mm in diameter by 2 mm thick from Sigma Aldrich. The injection port (circled in red) is sealed with a septum, and the outgas port (yellow) can be opened for purging, if necessary.

The CO_2 calibration curve was constructed by purging the gas cell with Ar gas, with a needle and hose leading through the injection port, and the outgas port open. The outgas port was closed, and the needle removed to take the background, and then a known concentration of CO_2 gas was flowed into the gas cell. Scans were taken with the outgas port closed and the injection needle removed so that there was no interference from the incoming gas or escaping gas in the resulting spectrum.

PECVD and Milled Silicon

The volume of gas produced between the plasma-enhanced chemical-vapor-deposited (PECVD) Si and the electrolyte, as measured from the buoyancy method, as a function of time is shown in Figure II.2.B.4. All reactions were duplicated to confirm reproducibility. The data show that PECVD Si produced gas immediately upon contact with the electrolyte, which indicates the extreme reactivity of the native silicon surface. The addition of 10% fluorinated ethylene carbonate (FEC), a known additive that leads to a more stable SEI, has no influence on the extent of gassing. However, removing the LiPF_6 salt from the electrolyte eliminates the gassing, thus indicating that the PF_6^- anion plays a major role in the observed gas formation. To confirm these results, LiTFSI-based electrolytes were explored. The TFSI electrolyte showed slight gassing with the rate being 115 times slower than LiPF_6 . The TFSI electrolyte evolved only 0.02 mL gas, so we conclude that the identity of the anion does matter in producing gas.

In comparison to the PECVD silicon, the oxide-terminated nanoamor took much longer (days to weeks) to begin gassing (see Figure II.2.B.4, right). However, once the reaction with milled silicon began, it produced a much larger volume of gas (4 mL vs 0.4 mL). This was an order-of-magnitude more gas produced than with PECVD, although it was much slower, suggesting that the oxide layer influences the kinetics and mechanism.

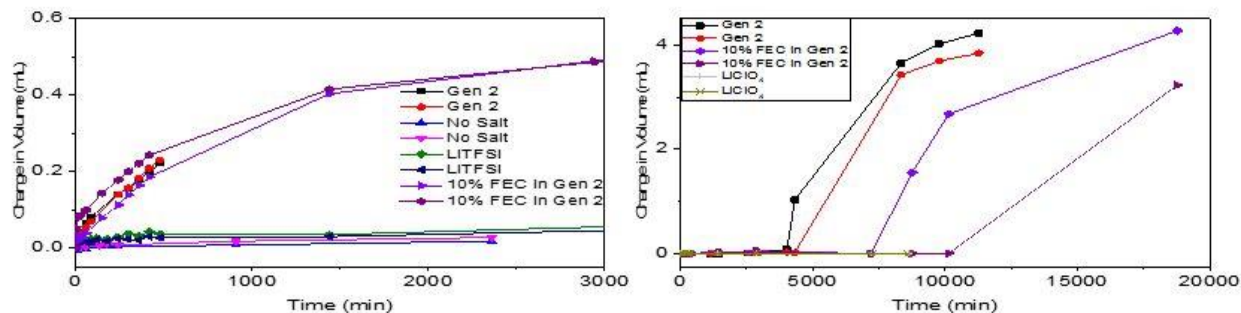


Figure II.2.B.4 Plot of change in volume (calculated through buoyancy) of the nanostructured silicon compounds reacting with various electrolytes in pouches. The left plot is of the PECVD Si and the right is nanoamor silicon.

Here, we saw that the FEC doubled the time delay for gas production, but the same amount of gas was produced. Replacing the PF_6^- anion with ClO_4^- prevented the reaction from occurring, again indicating that the LiPF_6 salt is an integral part of the reaction. Note that the analysis of reactions between TFSI salt with nanoamor revealed a large amount of HF gas formation.

To explore the reactions with silicon, further mass spectrometry and IR spectroscopy measurements were employed. *In-situ* IR spectra of the gas evolution was recorded in real time. Representative transient spectra are shown in Figure II.2.B.5A because many more spectra were taken to accurately follow the evolution over time. Within the data, most peaks are attributed to solvent vapor. Because the solvent is volatile, the referenced background was taken. Peaks that appeared at later times and grew throughout the reaction were attributed to products of the reaction, such as carbon dioxide ($2,350\text{ cm}^{-1}$), carbon monoxide ($2,200\text{ cm}^{-1}$), silicon tetrafluoride (725 cm^{-1}), and phosphorous trifluoride (475 cm^{-1}). The insets on the IR plot give a representative view of the products over time. Figure II.2.B.5B shows the integrated signal intensity as a function of time for CO, CO₂, SiF₄, and PF₃. For the first 500 minutes, the only product changing is carbon monoxide. Around 500 minutes, CO starts to increase, as CO₂ decreases. From 900 minutes, all curves begin to increase, with CO, SiF₄, and PF₃ peaks flattening slightly at 1,150 minutes. From this, it can be determined that the evolution of the gases is highly correlated. Further proof of their correlation can be found in the derivative plot, which is an inset of Figure II.2.B.5B. All four curves line up from 650 to 950 minutes, and then begin to rise at varying slopes from there. There is a spike in CO, SiF₄, and PF₃ at 1,190 minutes, corresponding to the bump in the integrated signal vs time plot. The CO₂ peak went negative before growing, indicating that initial concentrations of the gas were used in the reaction, or simply dissolved into the solution, because CO₂ is known to be highly soluble in carbonates. Mass spectroscopy was conducted on the gases in the pouch cells. Figure II.2.B.5C shows the mass spectrum of the PECVD Si pouch after 480 minutes. The gases evolved in the pouch were found to be O₂ (32 amu) and CO/ethylene (28 amu), known decomposition products of a similar electrolyte. The quick evolution of CO gas in the IR spectrum agrees with the rapid expansion of pouch cell and the high CO count in the MS.

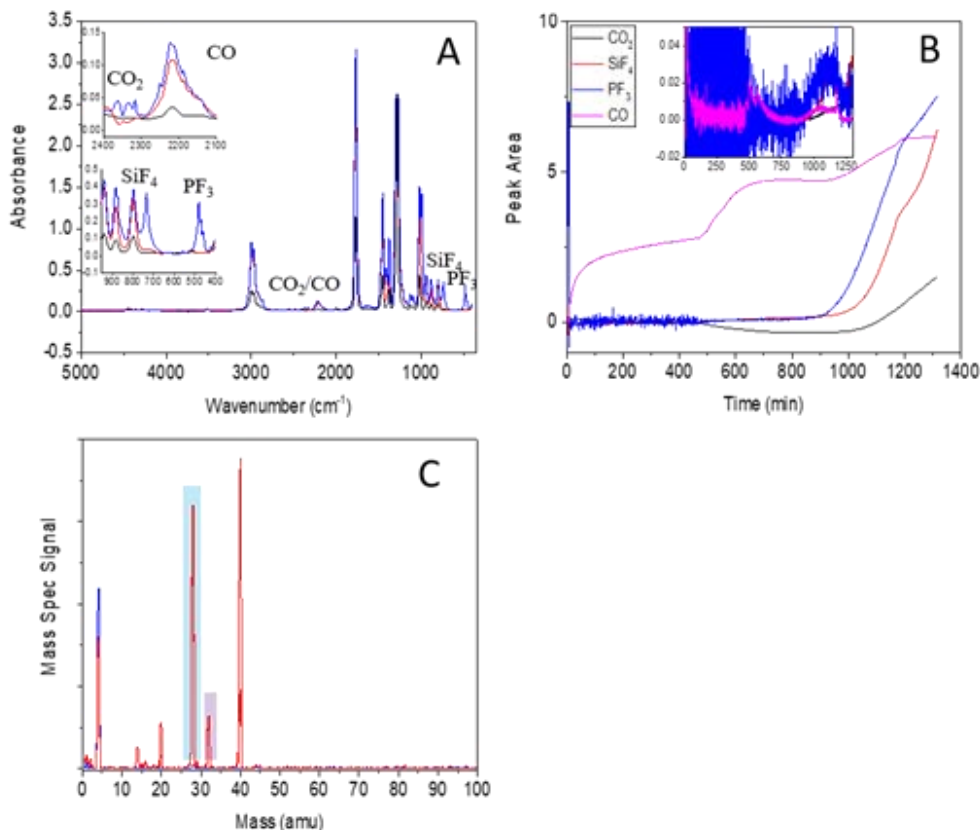


Figure II.2.B.5 Characterization data for the gases produced in the reaction between the PECVD silicon LiPF₆ electrolyte. A. Kinetic IR (black = 14 min, red = 752 min, blue = 1,278 min), insets CO₂ and CO, and SiF₄ and PF₃. B. Peak area vs time plot to illustrate any correlation between the evolution of the different gases. Inset is derivative of plot with respect to time. (In both, black = CO₂, purple = CO, red = SiF₄, and blue = PF₃). C. Mass spectrum was taken after 480 minutes (sample is red, helium is blue). Boxes around peaks correspond to various compounds (blue = CO, purple = O₂), SiF₄ (104 amu, 85 amu, 86 amu, 87 amu), PF₃ (69 amu), CO₂ (44 amu), F (19 amu), and H₂ (2 amu).

In contrast to the PECVD, the milled silicon showed dramatically different products. Figure II.2.B.6A shows representative FTIR spectra collected as a function of time. From these data, we did not observe the formation of CO, which directly contrasts with the PECVD data. Furthermore, the data show the immediate decomposition of salt to produce PF₃ and of silicon to produce SiF₄. The PF₃ evolves the fastest, but begins to slow down around 100 minutes when the CO₂ and SiF₄ rate increases. Just after 200 minutes, the CO₂ reaction increases in rate again, and the SiF₄ decreases until equilibrium is presumably reached. The PF₃ gas begins to disappear around 500 min, suggesting its consumption for another reaction. The small amount of PF₃ in the MS may be from the continued consumption of PF₃ gas for the next two weeks before reaching the point that the mass spectrum was taken. Clearly, the mechanism of electrolyte degradation is different between the two Si particles. The major difference between the particles is the surface state. For nanoamor, the surface is covered by a native oxide layer having -OH, -O termination, whereas that of the PECVD Si is terminated with surface -H. These results highlight opportunities to direct the surface reactivity.

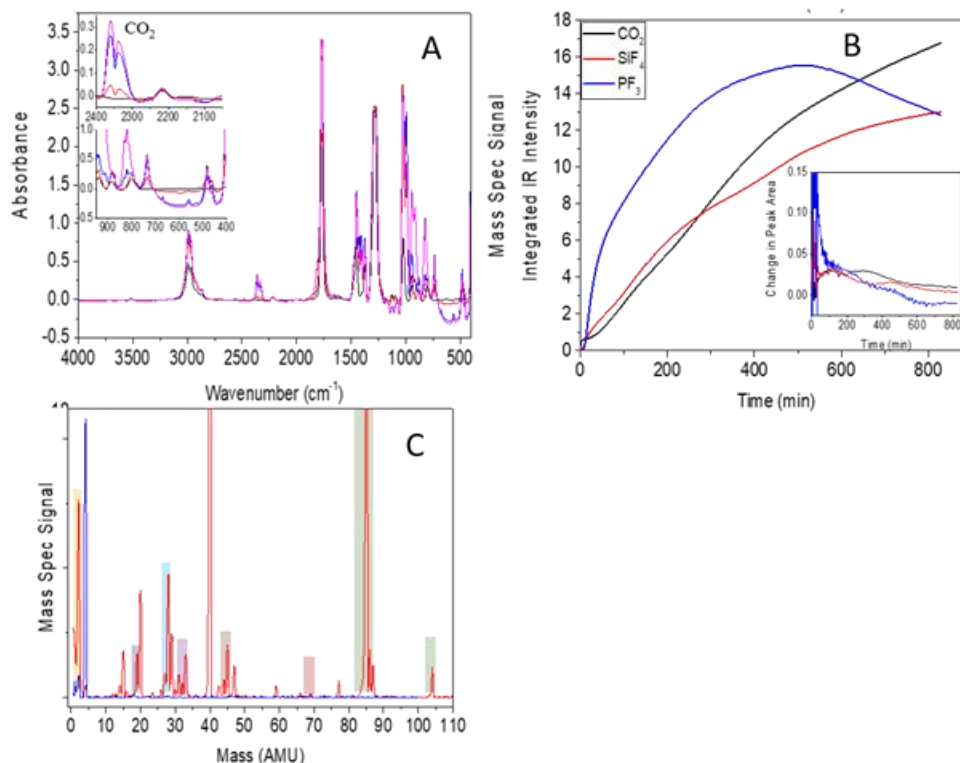


Figure II.2.B.6 Characterization data for the gases produced in the reaction between the nanoamorphous silicon and the electrolyte. A. Kinetic IR (black = 0.936 min, red = 126 min, blue = 559 min, purple = 818 min), insets CO₂, and SiF₄ and PF₃. B. Mass spectrum was taken after 14 days (sample is red, helium is blue). Boxes around peaks correspond to various compounds (yellow = H₂, black = F, blue = CO, purple = O₂, orange = CO₂, red = PF₃, green = SiF₄). SiF₄ (104 amu, 85 amu, 86 amu, 87 amu), PF₃ (69 amu), CO₂ (44 amu), F (19 amu), and H₂ (2 amu). C. Peak area vs time plot to illustrate any correlation between the evolution of the different gases. Inset is derivative of plot with respect to time. (In both, black = CO₂, red = SiF₄, and blue = PF₃).

Intrinsic Reactivity of SiO₂

To test the theory of the importance of the native oxide layer for producing CO₂, multiple silica compounds were tested in the same fashion. Fumed silica (S5505, Sigma Aldrich) was dried in a glovebox antechamber before use. From the selected plots from the kinetic IR Figure II.2.B.7A, the reaction clearly produces CO₂, SiF₄, PF₃, and CO, as seen in the previous reactions. Therefore, the solvent is still reacting to decompose, and the salt has access to the silicon to react with it, forming SiF₄. The plot of the integrated intensity vs time is shown in Figure II.2.B.7B. The CO₂ curve closely resembles that of the silane-sourced silicon. First, the curve is flat, indicating that any CO₂ produced is remaining in the solvent or in equilibrium with surrounding CO₂ gas dissolving in and out of the solvent. At 750 minutes, the CO₂ begins to disappear, again corresponding to the onset of SiF₄ production. As the CO₂ begins to increase again at 850 minutes, the SiF₄ peak has a plateau that jumps again as the CO₂ flattens off at 1,150 minutes. The PF₃ curve follows the same plateau and increase pattern as the SiF₄, indicating that the evolution of all three gases is connected. Figure II.2.B.7C shows the mass spectrum of the gas evolved in the pouch reaction between the S5505 and the Gen 2 electrolyte after 40 days. The products were found to be CO, CO₂, H₂, PF₃, and SiF₄: SiF₄ (104 amu, 85 amu, 86 amu, 87 amu), PF₃ (69 amu), CO₂ (44 amu), O₂ (32 amu), CO (28 amu), F (19 amu), and H₂ (2 amu). These results indicate that both the decomposition reaction of the solvent and the salt reaction with the silicon substrate are occurring.

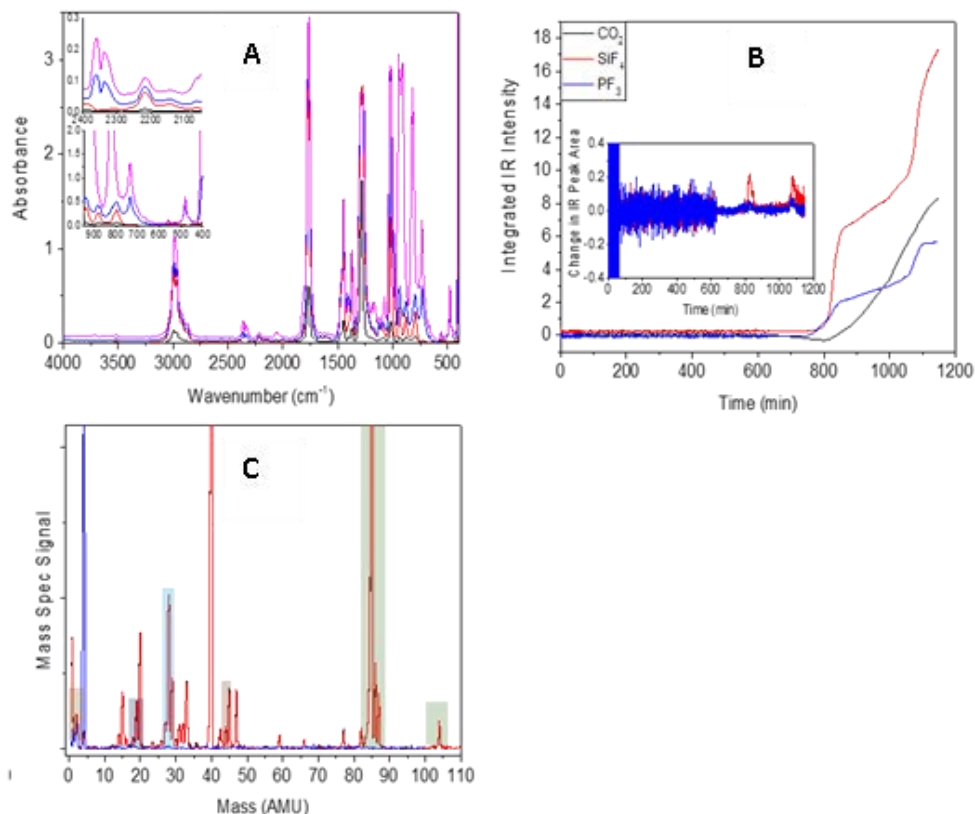


Figure II.2.B.7 Characterization data for the gases produced in the reaction between the fumed silica and the electrolyte. A. Kinetic IR (black = 0.3 min, red = 184 min, blue = 1,019 min, purple = 1,147 min), insets CO₂, and SiF₄ and PF₃. B. Peak area vs time plot to illustrate correlation between the evolution of the different gases and trends. Inset: Derivative of plot with respect to time of peak area vs time plot. (In both, black = CO₂, red = SiF₄, and blue = PF₃). C. Mass spectrum was taken after 40 days (sample is red, helium is blue). Boxes around peaks correspond to various compounds (yellow = H₂, black = F, blue = CO, purple = O₂, orange = CO₂, red = PF₃, green = SiF₄). SiF₄ (104 amu, 85 amu, 86 amu, 87 amu), PF₃ (69 amu), CO₂ (44 amu), F (19 amu), and H₂ (2 amu).

Silica prepared by the Stöber method was used as a comparison to determine if morphology influenced the gassing. Figure II.2.B.8A shows the IR spectra collected at several times. From the inset plots in Figure 8A, the CO₂ is decreasing in intensity, indicating that the initial amount present in the background spectrum is either dissolving into the solvent, or reacting to form another product. The CO peak is much stronger next to the decreasing CO₂, and the SiF₄ and PF₃ peaks do not appear to be changing. Figure II.2.B.8B, which is the IR integrated signal vs time plot, does not indicate any correlation between the gassing of each product relative to the others, which is supported by the derivative plot. After an extensive period of time, the mass spectrometry data (Figure II.2.B.8C) of gases evolved were determined to be CO, O₂, CO₂, SiF₄, F, and H₂. The CO, O₂, CO₂, and H₂ can all be attributed to solvent decomposition or the reaction of the termination layer on the silica. The excess of CO and O₂ compared to the CO₂ may indicate the decomposition of the CO₂, or simply that the solvent molecule decomposing, either the EC or the EMC, prefers to form CO than CO₂. Again, the SiF₄ results from the reaction between the LiPF₆ salt and the silicon in the electrode. Interestingly, there is no presence of PF₃, a natural product of the reaction generating the SiF₄. It is possible that the PF₃ formed is used in a further reaction related to passivation of the silica. Another interesting detail from this reaction was that an orange liquid formed in both the pouch and the IR cell. Although the exact identification of this liquid is unclear, some phosphorous compounds such as P₂H₄ are orange.^[15] In the pouches, an orange gas is also present, which is corrosive and has a negative effect on the mass spectrometer. This would indicate the

presence of a fluorinated compound, but it is unclear from the data gathered at this time what is the exact composition.

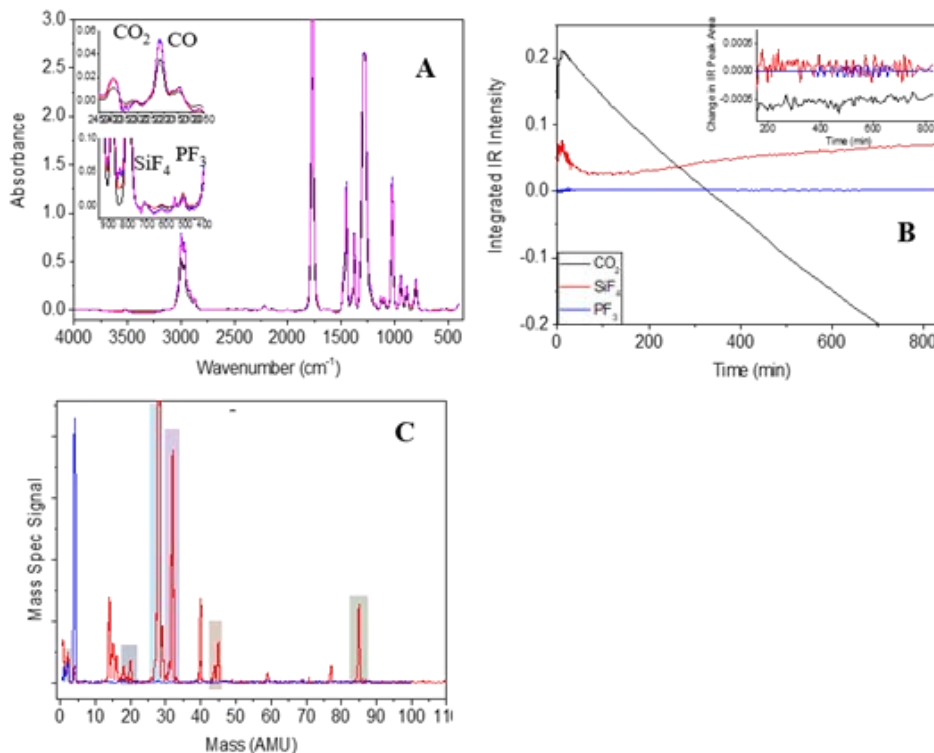


Figure II.2.B.8 Characterization data for the gases produced in the reaction between the Stöber silica and the electrolyte. A. IR data as a function of time (black = 0.936 min, red = 126 min, blue = 559 min, purple = 818 min), the CO₂, SiF₄, and PF₃ peaks were nonexistent, as identified in the insets. B. Peak area vs time plot, the three gases produced (black = CO₂, red = SiF₄, and blue = PF₃). C. The mass spectrum was taken after 48 days, and the reaction gases were present in this spectrum, indicating that the reaction took longer than the run time of the IR experiment (sample is red and black, helium is blue). SiF₄ (104 amu, 85 amu, 86 amu, 87 amu), PF₃ (69 amu), CO₂ (44 amu), F (19 amu), and H₂ (2 amu). Boxes around peaks correspond to various compounds (yellow = H₂, black = F, blue = CO, purple = O₂, orange = CO₂, red = PF₃, green = SiF₄).

Lithium Silicates

One potential silicon termination involves the formation of lithium silicates. Several known phases exist (Li₂SiO₃, Li₂Si₂O₅, Li₄SiO₄). Two end members of this series were investigated. Figure II.2.B.9A shows IR data collected at various times, along with the corresponding insets. The data indicate that the only gas produced was CO₂, with resonance peaks appearing beyond the normal peak at 2,350 cm⁻¹. The peak that appears around 650 cm⁻¹ in the inset plot, usually attributed to SiF₄ and PF₃ peaks, can be attributed to CO₂ harmonics. Very little SiF₄ and PF₃ evolved in the reaction, as indicated by the small IR signal, which could also be seen in the integrated IR signal vs time plot (Figure II.2.B.9C and D). The double-y axes allow for the trends between the materials to be compared, even as the change in the CO₂ is much greater than that of the other two. The carbon dioxide curve shows an increase in CO₂ over time, but the derivative plot shows the rate of evolution to be decreasing throughout the reaction. After 28 days, the mass spectroscopy data (Figure II.2.B.9 B) indicated the formation of CO, CO₂, H₂, and O₂ from solvent decomposition. However, the mass spectrum does not indicate the presence of SiF₄ or PF₃, even after the 28 days of reacting in the pouch. As with the Stöber silica, the CO evolution is rapid initially, but remains level at about 2.5 area units for the duration of the reaction.

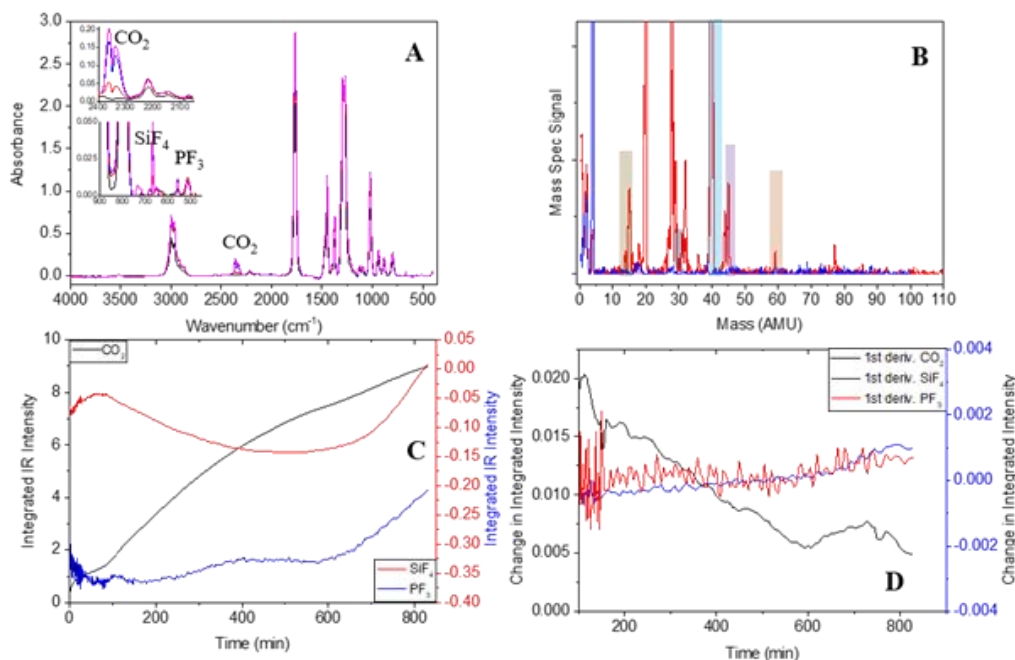


Figure II.2.B.9 Characterization data for the gases produced in the reaction between the Li_2SiO_3 and the electrolyte. A. IR data as a function of time (black = 0.936 min, red = 126 min, blue = 559 min, purple = 818 min), insets CO_2 , and SiF_4 and PF_3 . B. Peak area vs time plot. C. Derivative of plot with respect to time of peak area vs time plot. (In both, black = CO_2 , red = SiF_4 , and blue = PF_3). b) Mass spectrum was taken after 27 days (sample is red, helium is blue). Boxes around peaks correspond to various compounds (yellow = H_2 , black = F, blue = CO, purple = O_2 , orange = CO_2 , red = PF_3 , green = SiF_4). SiF_4 (104 amu, 85 amu, 86 amu, 87 amu), PF_3 (69 amu), CO_2 (44 amu), F (19 amu), and H_2 (2 amu).

Similar stability is observed for the lithium orthosilicate (Li_4SiO_4) as for the metasilicate. Figure II.2.B.10 A shows the spectra from the kinetic IR experiment, where once again the only gases evolving are CO and CO_2 , not SiF_4 or PF_3 . This trend is further visible in Figure II.2.B.10 B, the plot of integrated intensity vs time, where the SiF_4 and PF_3 curves are flat lines, and the CO_2 peak increases to 0.8 area units, and stays relatively constant for the remainder of the reaction. This is also the case with the CO curve. Figure II.2.B.10 C shows the mass spectrometry data, collected after 19 days. The evolution of CO , CO_2 , and O_2 from the reaction with the electrolyte in the pouch is confirmed. There is no evidence of SiF_4 or PF_3 in the mass spectrum, indicating again that only the electrolyte solvent is decomposing. The fluorine peak seen in the mass spectrum is an artifact from the column, as the HF from other pouches started appearing in all spectra. The pouch data shows almost no growth over time, and the IR plots show very consistent behavior for each product throughout the reaction time, indicating that there was almost no reaction.

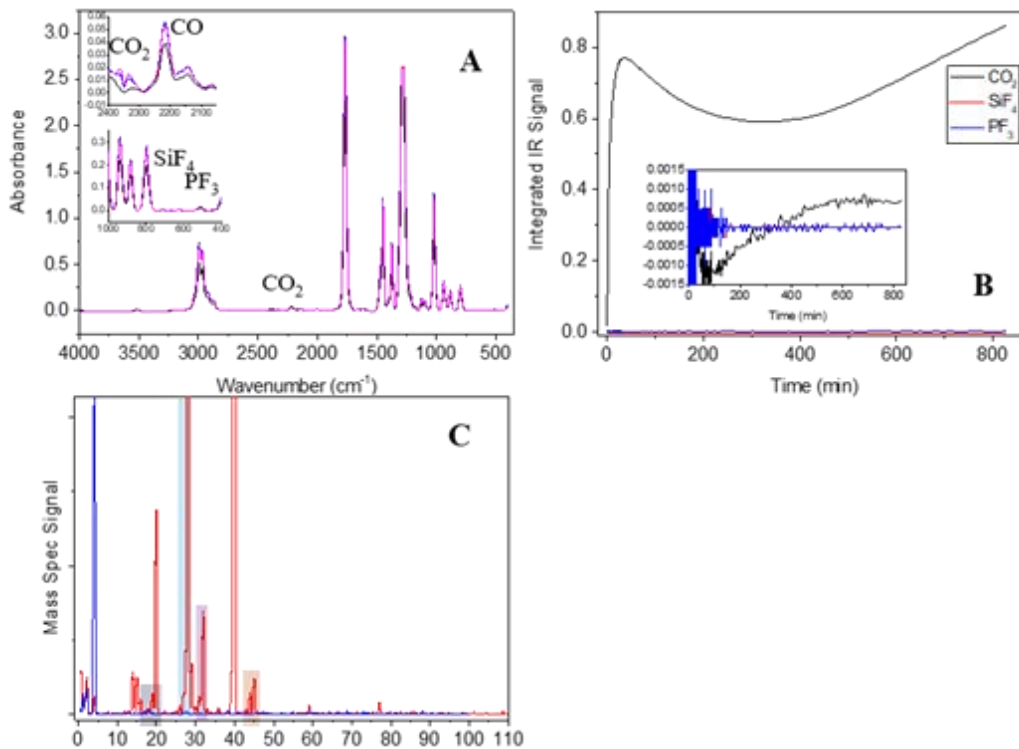


Figure II.2.B.10 Characterization data for the gases produced in the reaction between the $\text{Li}_4\text{-SiO}_4$ and the electrolyte. A. Kinetic IR data as a function of time (black = 0.936 min, red = 126 min, blue = 559 min, purple = 818 min), insets CO_2 , and SiF_4 and PF_3 . B. Peak area vs time plot. Inset is derivative of plot with respect to time. (In both, black = CO_2 , red = SiF_4 , and blue = PF_3). C. Mass spectrum was taken after 19 days (sample is red, helium is blue). Boxes around peaks correspond to various compounds (yellow = H_2 , black = F, blue = CO, purple = O_2 , orange = CO_2 , red = PF_3 , green = SiF_4 , SiF_4 (104 amu, 85 amu, 86 amu, 87 amu), PF_3 (69 amu), CO_2 (44 amu), F (19 amu), and H_2 (2 amu).

From the results described above, one can clearly see radical differences in reaction rates and reaction mechanisms. Furthermore, the reactions are strongly correlated in that the onset of a new gas evolution product corresponds with the loss of another product. The question is why and how we can use this to our advantage. From the low level of gas evolved in the pouch, and the lack of SiF_4 and PF_3 peaks in the mass and IR spectra, it can be determined that the addition of lithium to the silicate compound helps prevent the reaction of the silicon with the LiPF_6 salt. This provides a possible pathway to neutralize gas evolution. Furthermore, characterization of the starting materials indicates widely different proton terminations (see Figure II.2.B.11). Subsequent studies were performed to explore this issue.

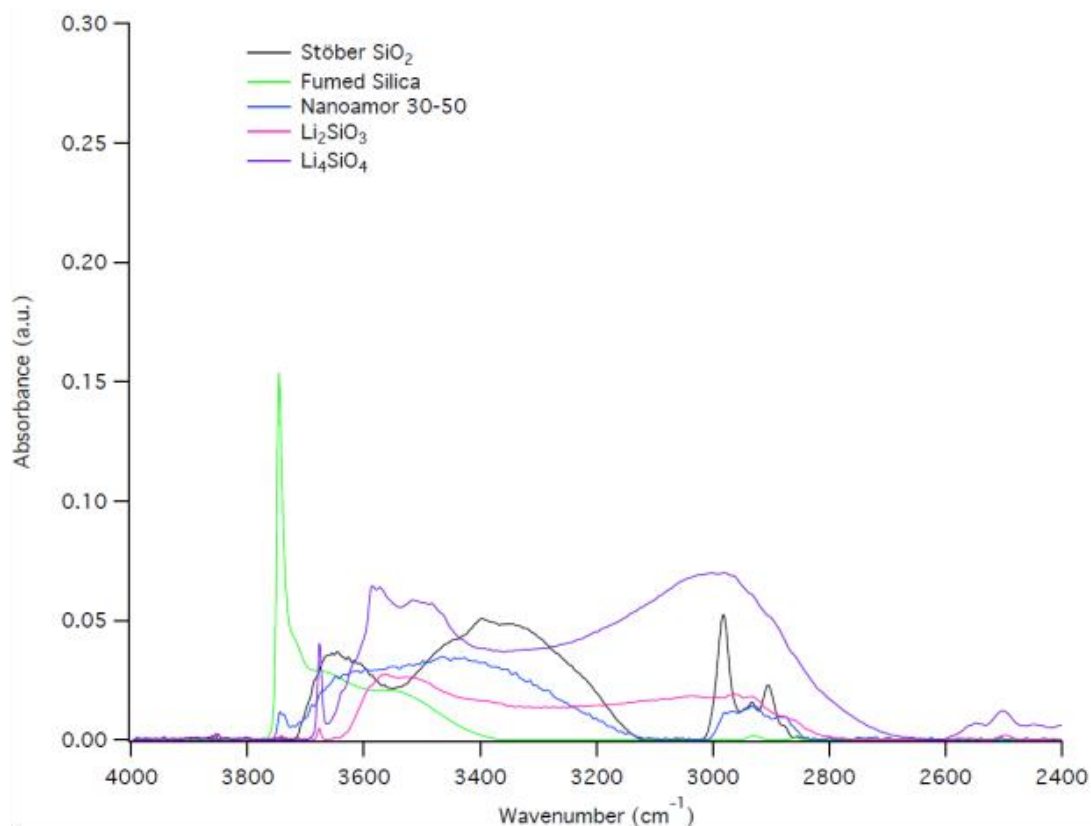


Figure II.2.B.11 FTIR data showing the proton-termination region of several representative materials.

Surface Species after Chemical Reactions

The evolution of gas is an inherently surface-derived process. After the reaction, residual species are likely to be formed or trapped on the electrode surface. We suspect that the remaining species will be stable with respect to future reactions and could lead to insights into stable silicon surfaces that would prevent oxidation or decomposition reactions and may provide guidance into the choice of surface terminations that might lead to directed SEI formation reactions. To probe this hypothesis, the same materials discussed previously (PECVD Si–H, nanoamor 30-50, fumed SiO₂, Stöber SiO₂, Li₂SiO₃, and Li₄SiO₄) were investigated using surface-sensitive IR spectroscopy after electrolyte exposure. All materials were exposed to either 1.2 M LiPF₆ in EC or standard electrolyte for 1–3 days to closely mimic that gas-evolution studies. Samples were well-washed with dimethyl carbonate, and subsequently subjected to surface characterization by diffuse reflectance Fourier transform infrared spectroscopy (DRIFTS) to evaluate the resulting surface chemistry.

Reactivity of Si Nanoparticles

DRIFTS spectra of as-prepared *SiH_x-Si nanocrystals (NCs) exhibit a broad peak corresponding to the Si–H stretching region (2,000–2,200 cm⁻¹), with peaks at 2,138 cm⁻¹ and 2,110 cm⁻¹ characteristic of the *SiH₃ and *SiH₂ surface terminations,^[3] as well as Si–H scissor (910, 863 cm⁻¹) and wag (669 cm⁻¹) modes (Figure II.2.B.12). As-prepared Si NCs are highly oxophilic, with a broad peak at 1,110 cm⁻¹ assignable to the Si–O–Si stretching vibration due to surface oxidation resulting from reaction with trace impurities in the glovebox atmosphere apparent after two weeks.

Exposing as-prepared Si NCs in electrolyte at room temperature for 1–3 days followed by washing (to remove excess LiPF₆ and carbonate) showed that the particles react significantly with the electrolyte, which is evident by the large differences (Figure II.2.B.12), consistent with the hypothesis of surface residue. Starting with the Si–H stretching region, the new shoulder at 2,244 cm⁻¹ is assigned to a *Si surface atom bound to oxygen, *Si(O)–H. The C=O stretching region shows low-energy peaks at 1,730 and 1,681 cm⁻¹ that do not correspond

to features in the electrolyte. We assign the feature at $1,730\text{ cm}^{-1}$ to a $^*\text{Si-OC(O)R}$ ester and that at $1,681\text{ cm}^{-1}$ —which is too low energy for an anhydride, ester, ketone, or aldehyde—to Li^+ or $^*\text{Si}$ coordination. For example, the C=O stretch in 2-butanone is known to shift from $1,712$ to $1,687\text{ cm}^{-1}$ as well as give rise to an even lower-energy carbonyl feature at $1,610\text{ cm}^{-1}$ upon coordination to a surface $^*\text{Si}$ atom via a hypervalent interaction (i.e., a 5-coordinate Si^*) in Si NCs. Similarly, the C-H bending region exhibits two new intense peaks at $1,457$ and $1,375\text{ cm}^{-1}$ likely resulting from ring-opening of EC^4 and/or reaction with EMC via radical-based processes to give either alkoxy- or carboxylate-functionalized Si NCs. Smaller but still evident C(O)-O resonances at $1,308$, $1,294$, $1,257$, $1,239$, and $1,147\text{ cm}^{-1}$ at the high-energy side of the very broad Si-O-Si stretch centered at $1,110\text{ cm}^{-1}$ speak to the complex nature of the reactivity of the electrolyte with $^*\text{SiH}_x\text{-Si}$ NCs. As-prepared $^*\text{SiH}_x\text{-Si}$ NCs were additionally soaked in 1.2 M LiPF_6 in EC, and new C=O modes ($1,749$ and $1,681\text{ cm}^{-1}$), C-H bends ($1,457$ and $1,375\text{ cm}^{-1}$), C(O)-O stretches ($1,294$, $1,263$, and $1,147\text{ cm}^{-1}$), and the Si-O-Si stretch ($1,092\text{ cm}^{-1}$) were observed (blue spectrum, Figure II.2.B.12).

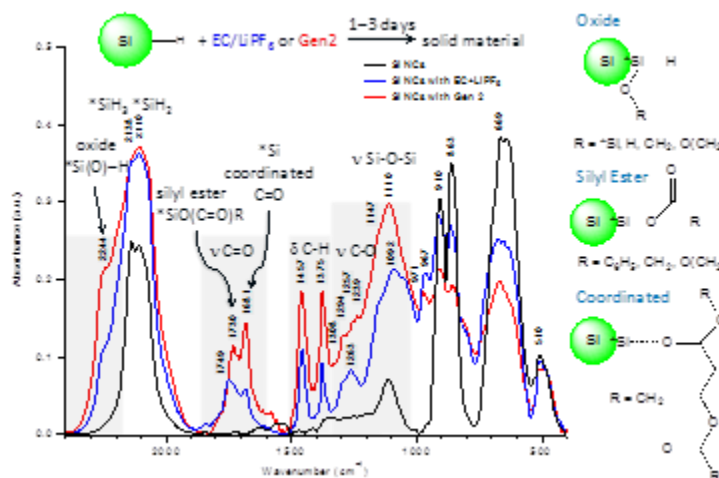


Figure II.2.B.12 Left: Example FTIR data on chemical reactivity of plasma-grown Si nanoparticles (black) with 1.2 M LiPF_6 in EC (blue) or (red) electrolyte. Right: Cartoons showing various functional groups identified in the solid state.

Next, we probed the reaction of electrolyte with three different silica samples (in which we include nanomorph because the surface largely comprises SiO_2 ; see Figure II.2.B.11). All samples exhibit a broad Si-O-Si stretch from $\sim 1060\text{--}1210\text{ cm}^{-1}$ prior to reaction with electrolyte. Surprisingly, fumed SiO_2 —prepared by dry O_2 flame pyrolysis of SiCl_4 —completely dissolved upon soaking in Gen 2 electrolyte. A colorless solid was precipitated and isolated using acetonitrile/toluene solvent/antisolvent and appears to be comprised largely of C-O stretches ($1,265$ and $1,167\text{ cm}^{-1}$) with no Si-O-Si stretching mode (blue-shaded regions, Figure II.2.B.13) and an intense, broad new feature at 724 cm^{-1} (yellow-shaded region, Figure II.2.B.13). However, the low-intensity peaks in the carbonyl ($1,816$, $1,788$, and $1,755\text{ cm}^{-1}$) and C-H bending ($1,481\text{--}1,377\text{ cm}^{-1}$) regions suggest that dissolution of fumed SiO_2 particles does not retain structural features from EC/EMC. The nanomorph particles exhibit a less intense Si-O-Si stretch relative to other peaks following electrolyte reaction as well as distinct C-O stretches ($1,206$ and $1,167\text{ cm}^{-1}$; blue-shaded region, Figure II.2.B.13) and a broad, intense peak at 739 cm^{-1} (yellow-shaded region, Figure II.2.B.13) that is similar in shape and intensity to that at 724 cm^{-1} in the reaction fumed SiO_2 with electrolyte. In addition, the nanomorph particles clearly contain $^*\text{SiH}_x$ and $^*\text{Si(O)-H}$ stretches both before and after electrolyte exposure (grey-shaded region, Figure II.2.B.13). The peak corresponding to unoxidized $^*\text{SiH}_x$ at $2,106\text{ cm}^{-1}$ is more intense than the oxidized $^*\text{Si(O)-H}$ stretch at $\sim 2,260\text{ cm}^{-1}$ following reaction, all of which demonstrate that SiO_2 at the surface of nanomorph particles dissolves in electrolyte. Additional work will be required to fully assess the molecular structure of this dissolved SiO_2 that is tentatively assigned to the C-H stretching modes from $2,855\text{--}2,957\text{ cm}^{-1}$ and broad intense feature at $\sim 730\text{ cm}^{-1}$ observed for fumed SiO_2 and nanomorph particles. In contrast, Figure II.2.B.13 show that Stöber SiO_2 particles display a low reactivity with carbonates (as evidenced by trace C=O and C-O stretching and hydrocarbon bending modes) and very similar Si-O-Si stretching region before and after electrolyte exposure.

The very weak C–H stretching region and absence of the feature at $\sim 730\text{ cm}^{-1}$ following exposure to electrolyte provide further evidence that this form of SiO_2 —prepared via a sol-gel process in which tetraethyl orthosilicate $\text{Si}(\text{OEt})_4$ is hydrolyzed in alcohol (typically methanol or ethanol) using ammonia as catalyst—is robust against dissolution.

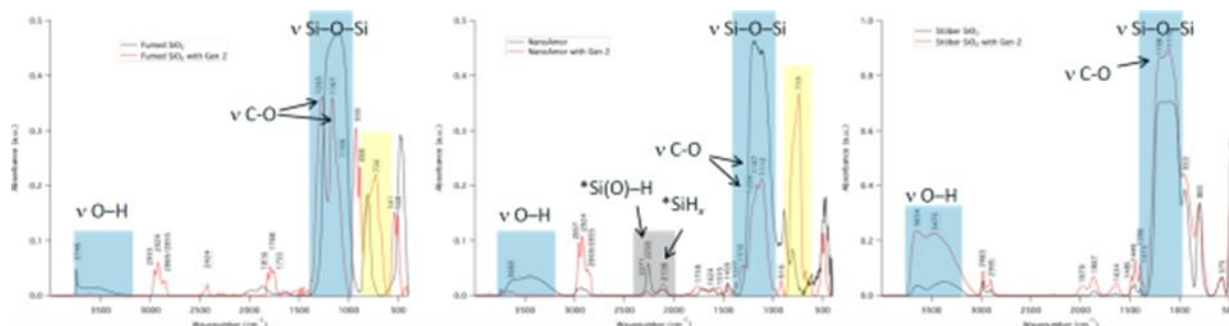


Figure II.2.B.13 DRIFTS spectra showing fumed SiO₂ (top), nanoamor 30–50 nm particles (middle), and Stöber SiO₂ (bottom) before (black) and after (red) exposure to electrolyte.

Reactivity of Lithium Silicates

Finally, we probed the reactivity of lithium silicate phases Li_2SiO_3 and Li_4SiO_4 with electrolyte. As can be seen in Figure II.2.B.14, lithium silicate FTIR spectra have many unique features distinct from SiO_2 . The Li_2SiO_3 sample appears to coordinate carbonates as evidenced by key new features at 1,814 and 1,781 cm^{-1} (comparable to the uncoordinated/coordinated C=O stretches at 1,807/1,773 cm^{-1} in electrolyte), C–H bending modes from 1,485–1,363 cm^{-1} (comparable to C–H bending modes in EC and EMC), and C(O)–O stretching modes at 1,300 and 1,210 cm^{-1} (comparable to EMC and ring EC coordination modes at 1,306 and 1,195 cm^{-1} , respectively). In contrast, very minimal differences between the Li_4SiO_4 samples before and after electrolyte exposure are observed. The results correlate very well with the gassing studies performed above and provide a general reactivity trend for the purported SEI components. More specifically, this work provides insight into the types of chemical species present in the SEI layer that either afford stability or lead to its dissolution. This work provides a foundation for FY19 planned work on tailoring the surface chemistry of Si nanoparticles and understanding electrochemical reactivity.

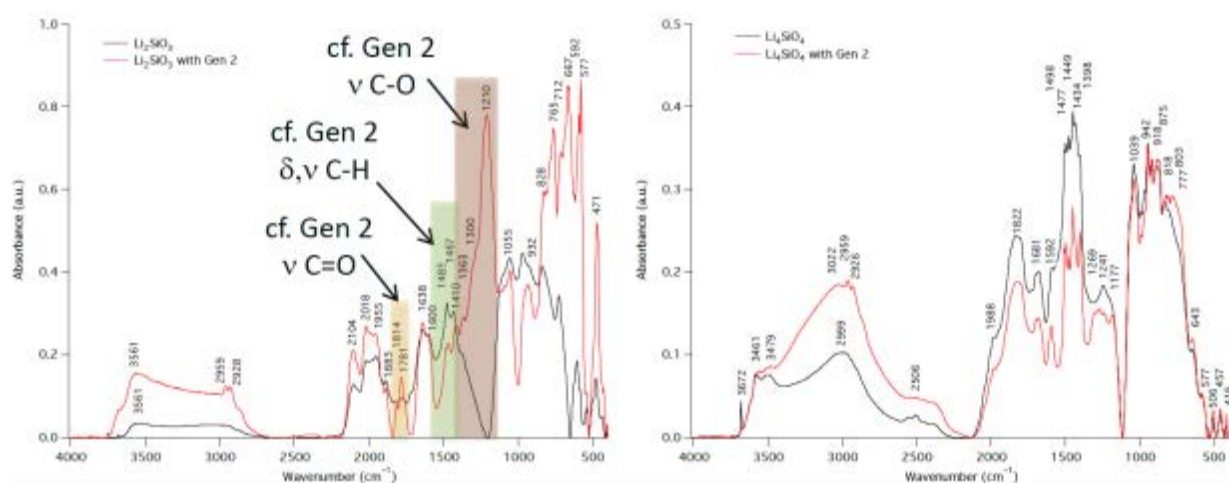


Figure II.2.B.14 DRIFTS spectra showing Li_2SiO_3 and Li_4SiO_4 before (black) and after (red) exposure to electrolyte.

Chemical Reactivity of Li-Si-O

Given the apparent stability of the lithium silicates, greater focus was placed on understanding the reactivity of various Li-Si-O and SiO_2 materials. These studies used thin films of Li-Si-O compounds to improve surface-

characterization studies and to facilitate modeling. Lithium silicate thin-film samples were deposited onto substrates by physical-vapor deposition using SiO_2 and Li_2O targets. Deposition times were controlled to achieve the desired thickness for each film. Inductively coupled plasma–mass spectroscopy (ICP-MS) was chosen to confirm composition. Samples were placed in 20-mL clear borosilicate glass bottles (VWR) and exposed to 3 mL of 1.2M LiPF_6 in 3:7wt% EC:EMC electrolyte for 0.5, 3, 24, 48, and 72 hours in an inert-atmosphere glovebox. The samples were removed with tweezers, rinsed with dimethyl carbonate (DMC) (Sigma Aldrich), and dried in the glovebox's insertion chamber for 10 minutes. The soak times were chosen because they indicate the amount of time a typical cell may rest in a research setting.

The thin films had linearly increasing lithium content corresponding to an increased Li_2O to SiO_2 target power ratio to produce films with the following compositions: $\text{Li/Si} = 1.3, 1.8, \text{ and } 2.8$. We refer to these films as $\text{Li}_2\text{Si}_2\text{O}_5$, Li_2SiO_3 and Li_3SiO_x , respectively. Deposition times were controlled to achieve a 40-nm thickness for each composition with deposition times ranging from 1.5 to 4 hours. Depositions with higher lithium-to-silicon ratio used lower target powers and thus required longer deposition times. Attenuated total reflectance (ATR) IR spectroscopy was used to observe changes in the bulk structure of the silicate films exposed to electrolyte over time. Figure II.2.B.15 shows the IR spectrum for each film composition at 0, 3, 24, 48, and 72 hours of exposure time.

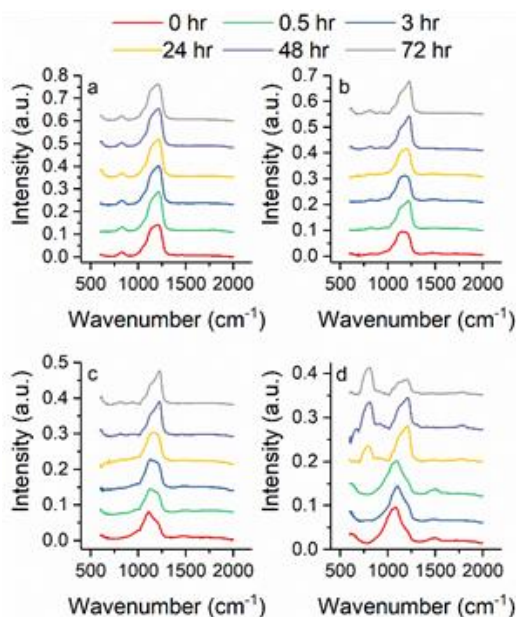


Figure II.2.B.15 ATR IR spectra over exposure time for a) SiO_2 , b) $\text{Li}_2\text{Si}_2\text{O}_5$, c) Li_2SiO_3 , and d) Li_3SiO_x .

The absorption peaks detected in the range of $900\text{--}1,200\text{ cm}^{-1}$ by IR spectroscopy are characteristic of silicate vibrational modes.^{[5], [6], [7]} As reported in our previous work, the vibrational modes that are the most illustrative of the effect of lithium modifying the silicate network in the lithium silicates are the vibrational modes of non-bridging oxygens (NBO) and bridging oxygens (BO), or $\nu(\text{Si-O}^-)$ and $\nu_{\text{as}}(\text{Si-O-Si})$, at $\sim 1,000\text{ cm}^{-1}$ and $1,200\text{ cm}^{-1}$, respectively.^[8] As more lithium is incorporated into the silicate network, the wide amorphous peak in the silicate region shifts toward $\sim 1,000\text{ cm}^{-1}$ because lithium breaks apart the Si-O-Si network, creating more NBO. This can be observed in the silicate samples with initial 0-h exposure time. Li_3SiO_x starts with a silicate peak centered more closely to the NBO-indicative region, whereas the SiO_2 film has a relatively sharp peak at $\sim 1,200\text{ cm}^{-1}$ because it has the most intact silicate network. The lithium silicate films also feature small peaks of $\sim 1,450\text{ cm}^{-1}$, which are characteristic of Li_2CO_3 species.^[9] In Figure II.2.B.15a, the silicate peaks for the SiO_2 thin film remain steady with increasing electrolyte exposure time all the way up to 72 hours. No peaks from typical SEI components, solvents, or salts appear, indicating that the bulk structure of the sputter-deposited SiO_2 film is relatively chemically stable against the electrolyte. The

same is not true for the two films with lower lithium content, $\text{Li}_2\text{Si}_2\text{O}_5$ in Figure II.2.B.15b and Li_2SiO_3 Figure II.2.B.15c. For both lithium silicate compositions, at about 24 hours of soaking time, the silicate vibrations that were initially shifted toward NBO begin to shift back toward BO, with both compositions having comparable silicate peaks after 72 hours. The shift of the silicate network peaks toward BO is even more evident for Li_3SiO_x in Figure II.2.B.12d. At 24 hours, there is an abrupt shift of the silicate peaks for Li_3SiO_x from being centered at $\sim 1,083\text{ cm}^{-1}$ to being centered at $\sim 1,200\text{ cm}^{-1}$. At 24 hours, this silicate peak shift is accompanied by the appearance of a significant peak at $\sim 800\text{ cm}^{-1}$, a small peak at $\sim 1,780\text{ cm}^{-1}$, and the disappearance of the Li_2CO_3 peak at $1,450\text{ cm}^{-1}$. The small peak at $\sim 1,780\text{ cm}^{-1}$ is characteristic of C=O bonds that have previously been shown to be dominant peaks for EC. [10] The large amorphous peak at $\sim 850\text{ cm}^{-1}$ is characteristic of several vibrations including alkyl phosphites, carbonate bending, Si-F bonds, or residual LiPF_6 . [11], [12], [13], [14], [15] This peak increases with continued exposure time, especially relative to the shifted silicate peak. The large amorphous silicate peak that initially shifts at 24 hours starts to degrade, or lose intensity, with continued exposure up to 72 hours. This degradation and shifting of the silicate network—combined with the appearance of peaks attributed to carbonates, phosphates, or fluorinated species and the disappearance of the Li_2CO_3 peak—indicates that after 24 hours, a significant breakdown occurs of the silicate network in the bulk of the Li_3SiO_x film. This breakdown is possibly due to the introduction of fluorinate, phosphate, or carbonate species. The disappearance of the Li_2CO_3 characteristic peaks also shows that this surface species may participate or be consumed by the reactions occurring at the surface of the thin film.

The nature of the composition of the reaction species observed by ATR IR, as well as their spacing with depth in the films, was confirmed by XPS depth profiling. Before this depth analysis could be completed accurately, focus ion beam (FIB) cross sections of SiO_2 , $\text{Li}_2\text{Si}_2\text{O}_5$, Li_2SiO_3 , and Li_3SiO_x films for all six soaking times were examined. Cross sections taken of the Li_3SiO_x films at 0, 3, 24, and 72 hours are shown in Figure II.2.B.16a–d. The initial thickness and the change in thickness over time were determined for each composition and visualized by the column heights in Figure II.2.B.17a–d. As opposed to the 36% loss of thickness that the Li_3SiO_x film underwent over 3 days, the SiO_2 thin film remained relatively close to its initial pre-soaking thickness measurements of around 45 nm. The overall change in thickness after 3 days of soaking increases from almost no change in SiO_2 to $\sim 25\%$ loss for $\text{Li}_2\text{Si}_2\text{O}_5$ and $\sim 33\%$ for Li_2SiO_3 . The change in thickness over soaking time trends increasingly with increased initial lithium content in the silicate films. This is evidence that the reaction dominating the degradation of the silicate thickness depends on the lithium content of the silicate.

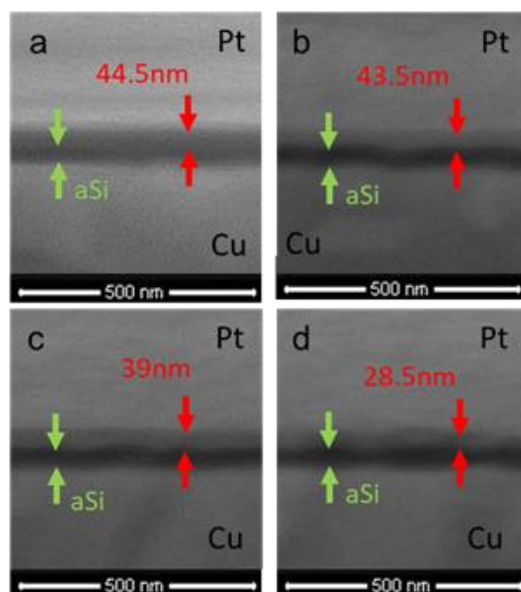


Figure II.2.B.16 FIB cross sections of Li_3SiO_x samples soaked for (a) 0 hour, (b) 3 hours, (c) 24 hours, and (d) 72 hours.

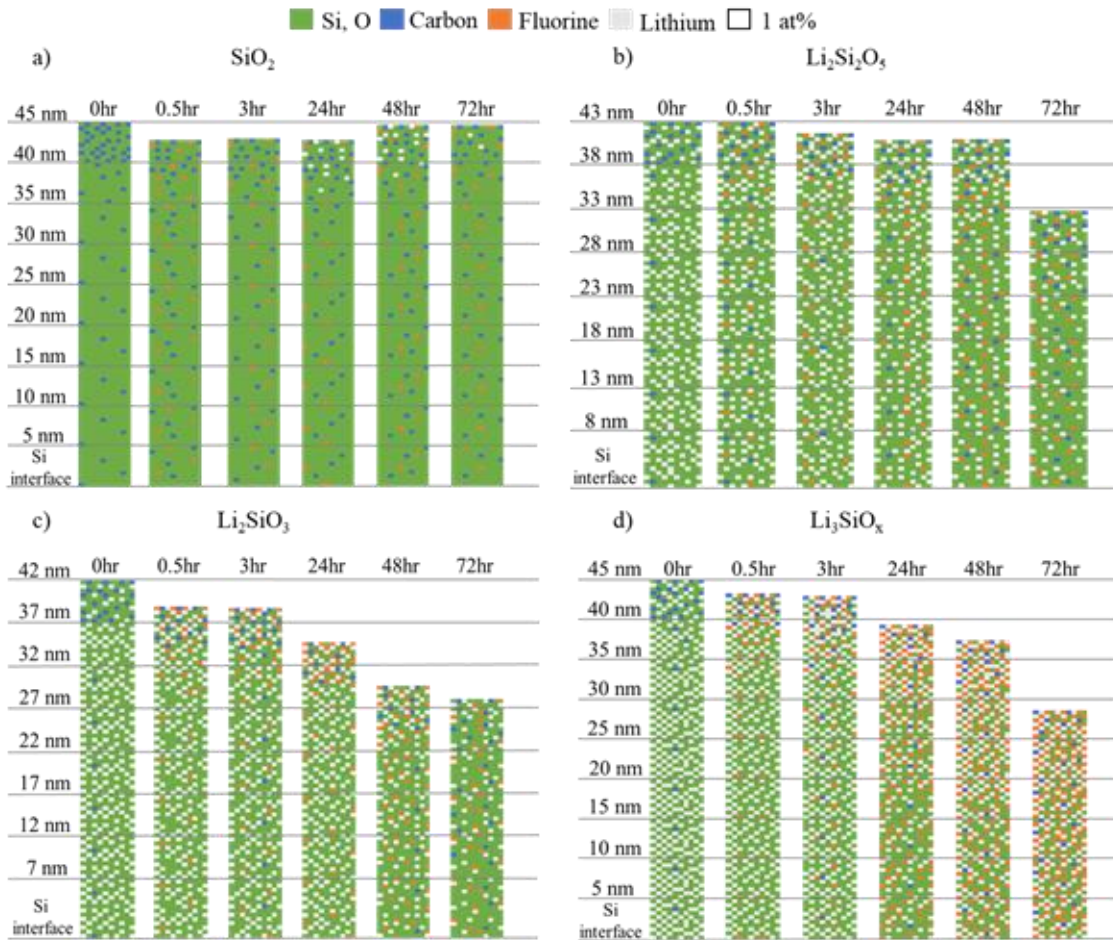


Figure II.2.B.17 Illustration of thickness and compositional changes of (a) SiO_2 , (b) $\text{Li}_2\text{Si}_2\text{O}_5$, (c) Li_2SiO_3 , and (d) Li_3SiO_x films soaked in electrolyte over time.

XPS depth profiling provides more specific surface characterization with depth to clarify the bulk structure changes observed with ATR IR. XPS with argon depth profiling was performed on samples soaked for 0, 0.5, 3, 24, 48, and 72 hours for each thin-film composition. Figure II.2.B.18 is the depth profile of the C 1s, F 1s, Li 1s, O 1s, and Si 2p binding regions with depth of the initial unsoaked Li_3SiO_x film.

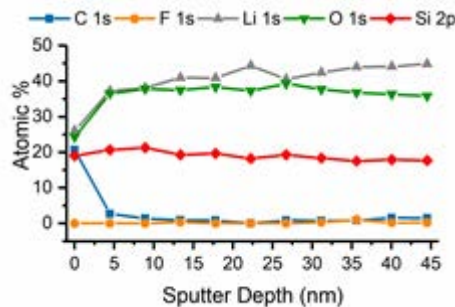


Figure II.2.B.18 XPS depth profile of Li_3SiO_x thin film.

All the silicate films started with a similar lack of fluorine in the bulk of the film. The atomic percent of Li, F, C, Si, and O was calculated for ~5-nm sections throughout the thickness of each composition at each soaking time and represented by separately colored squares that approximate ~1 atomic percent in each section in the

illustration in Figure II.2.B.14. From this representation of the combined FIB cross-section thickness measurements and XPS depth profile composition measurements, the overall reactivity response for each composition of silicate thin films with depth is more clearly represented. The silicate degradation and fluorination observed in ATR IR is shown in the figure to be a process that occurs throughout the depth of the films, not just at the surface. From Figure II.2.B.17, it appears that the lithium content in the bulk of the film decreases with soaking time whereas the fluorine content in the film increases.

To more closely examine this trend, the atomic percent of fluorine and lithium with depth for each soaking time for all four compositions is plotted in Figure II.2.B.19. As seen in Figure II.2.B.19, there is no fluorine present at the surface or in the bulk of any of the silicate thin films prior to exposure.

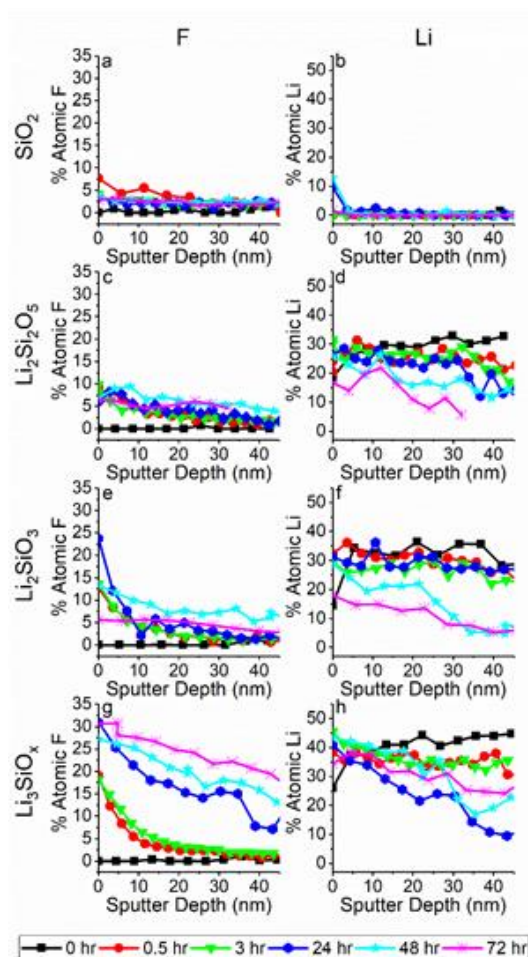


Figure II.2.B.19 XPS sputter depth profiles for SiO_2 (a) F 1s and (b) Li 1s; $\text{Li}_2\text{Si}_2\text{O}_5$ (c) F 1s and (d) Li 1s; Li_2SiO_3 (e) F 1s and (f) Li 1s; and Li_3SiO_x (g) F 1s and (h) Li 1s.

The lithium and fluorine content in the SiO_2 film remains relatively low compared to the other silicates. However, there is still about 8 atomic percent fluorine species in the SiO_2 starting at only 30 minutes of electrolyte exposure. Lithium insertion into SiO_2 happens at a similarly low atomic percent of about 10–12 atomic percent, but does not appear in XPS depth measurements until about 24 hours of exposure time. This lithium insertion into the SiO_2 film is concentrated at the surface and it drops down to less than 1 atomic percent deeper than 5 nm into the SiO_2 film. Conversely, the fluorine species are observed at about 3 atomic percent through the bulk of the film. As the initial lithiation of the silicates increases, the lithium content and fluorination of the thin films have more intense changes over soaking time. For each of the lithium silicates, just as for the SiO_2 , fluorine species are observed at 30 minutes of exposure to electrolyte. The amount of

fluorine present at the surface at 30 minutes increases from 9% on $\text{Li}_2\text{Si}_2\text{O}_5$ to 13% on Li_2SiO_3 to 19% on Li_3SiO_x then tapers off into the bulk of each film. This trend indicates that the more lithium that is initially incorporated in the film, the faster the rate of incorporation of fluorine species into the film. It also becomes more apparent with increasing lithium content that there is a large jump in the rate of fluorination over time from 3 hours to 24 hours. This jump in fluorine content is shown in the Li_3SiO_x film in Figure II.2.B.20g, when the atomic percent of fluorine at the surface jumps from 18 atomic percent at 3 hours to 30 atomic percent at 24 hours. This increase at the surface is matched by an increase from around 2–3 atomic percent in the bulk of the film at 3 hours to around 15 atomic percent in the bulk at 24 hours. As this fluorination occurs, there is a corresponding loss of lithium in the bulk of each silicate. In the initial lithium silicate films, there is a lower lithium atomic percent at the surface than in the bulk, likely due to adventitious surface carbonates. With continued exposure to electrolyte, this lower atomic percent of lithium at the surface transitions to excess lithium at the surface compared to the bulk of the film. It appears that the same mechanism that allows for fluorination of the silicates starting at the surface and extending into the bulk of the film also facilitates lithium leaving the bulk of the film, gathering at the surface, and possibly being leached into the electrolyte.

XPS binding energy spectra with depth for Si 2p, O 1s, F 1s, and C 1s for SiO_2 and Li_3SiO_x are plotted in Figure II.2.B.20 and Figure II.2.B.21 to investigate the molecular composition of the species observed during depth profiling. The peak assignments for XPS binding energies made in this work are summarized in Table II.2.B.2.

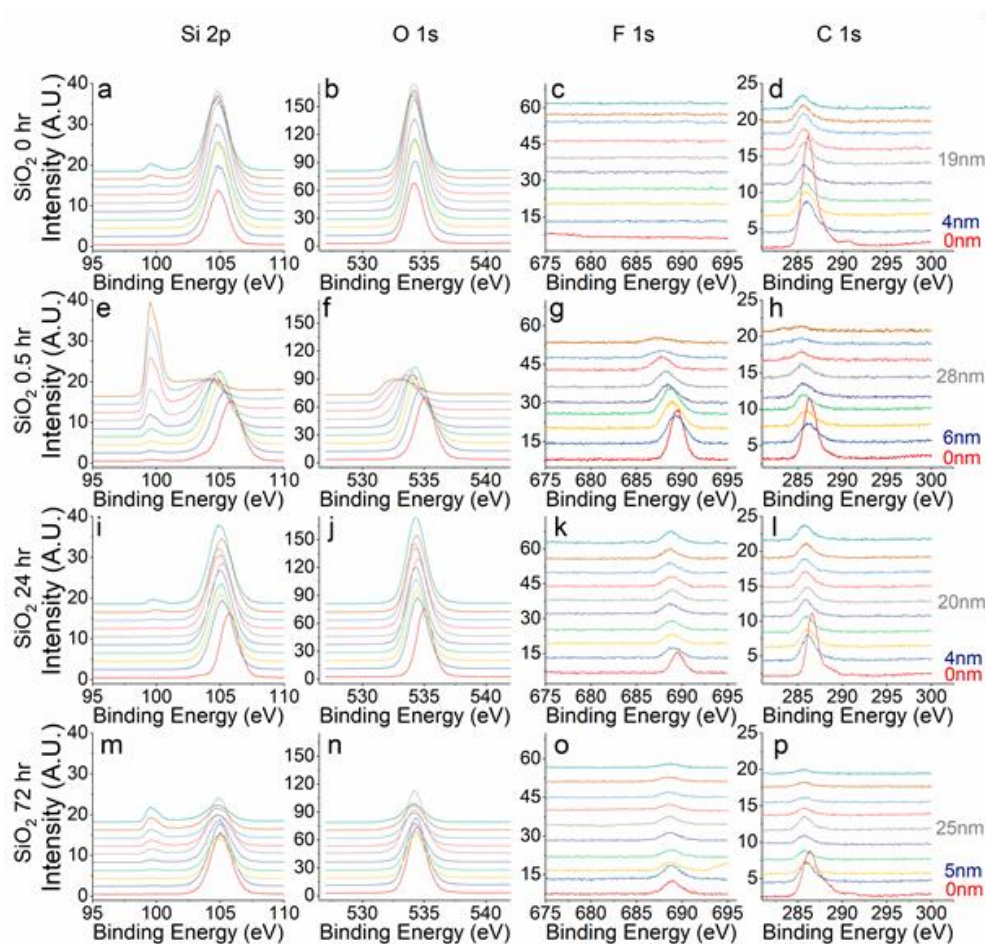


Figure II.2.B.20 XPS Si 2p, O 1s, F 1s, and C 1s binding energies with depth for SiO_2 soaked for 0 hours (a–d), 30 minutes (e–h), 24 hours (i–l), and 72 hours (m–p).

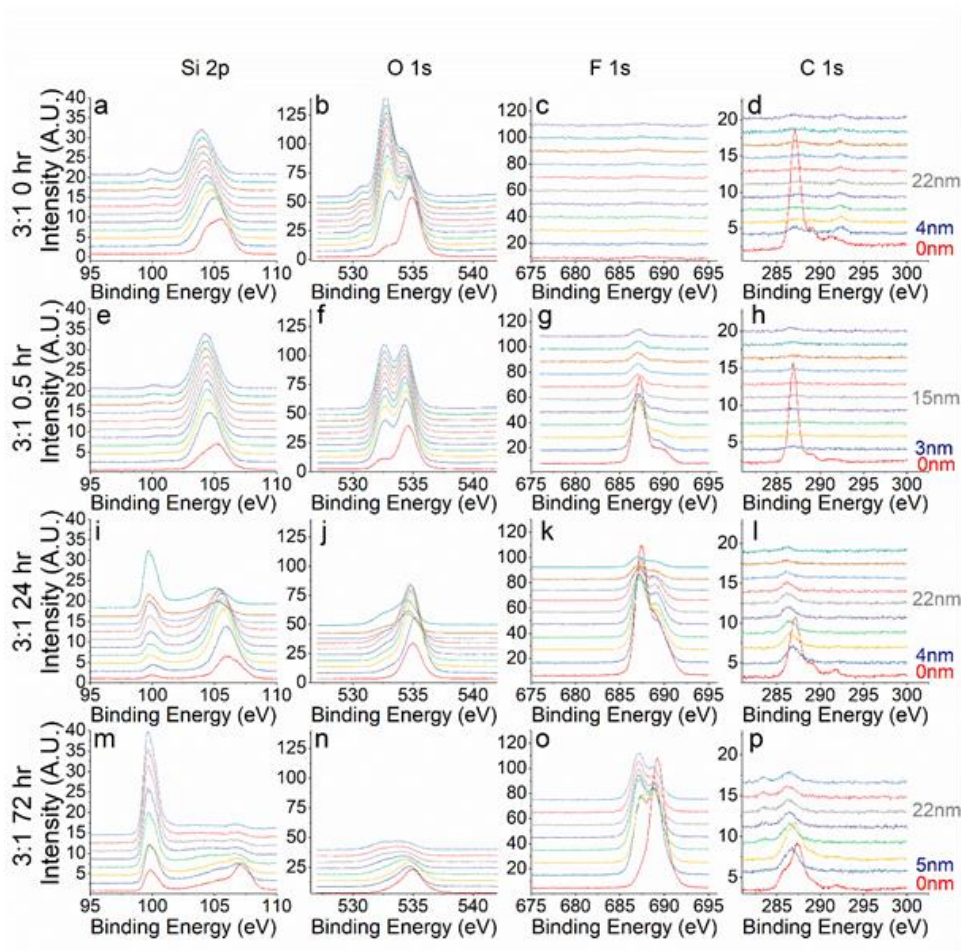


Figure II.2.B.21 XPS Si 2p, O 1s, F 1s, and C 1s binding energies with depth for Li_3SiO_x soaked for 0 hours (a–d), 30 minutes (e–h), 24 hours (i–l), and 72 hours (m–p).

Table II.2.B.2 Peak assignments for XPS analysis on soaked SiO_2 and Li_3SiO_x thin films

Assignments	Si 2p (eV)	O 1s (eV)	F 1s (eV)	C 1s (eV)	References
SiO_x	104	533–534			16–17
C–O		534–535		286	18–20
Li_2CO_3		532–534		290–291.5	21–22
Si–F	107		687		23
Si–Si	99				18, 23
Li–O		534–535			18
Li_xPF_y			688		21–22
$\text{Li}_x\text{PF}_y\text{O}_z$		535			24
Si–C	100			283	25
C=O		533		287	19–20

SiO_2 Binding Energy Analysis

Figure II.2.B.20 XPS Si 2p, O 1s, F 1s, and C 1s binding energies with depth for SiO_2 soaked for 0 hours (a–d), 30 minutes (e–h), 24 hours (i–l), and 72 hours (m–p). shows the binding energies for the SiO_2 thin films for samples soaked for 0, 0.5, 24, and 72 hours. For the initial SiO_2 samples before any electrolyte exposure, the Si 2p and O 1s binding-energy regions in Figure II.2.B.20a–b have peaks at 104.8 eV and 534 eV, which correspond to Si–O bonds in the well-connected silicate network expected in the SiO_2 film. The sample starts

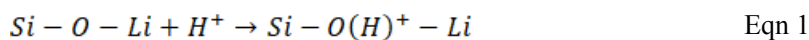
with no fluorine peaks, a small CO_3 peak and a large C-O bond at the surface. The carbonate peaks appear at 290 eV and 286.4 eV, respectively, and are expected to form from surface adsorption during storage and/or exposure to low pressures during sample transfer.^[8] The Si-O peaks remain steady in the bulk of the film (>5 nm from surface) with extended soaking time. At the surface of the SiO_2 film, which is marked 0 nm on the right side of Figure 20, there is a slight shift to higher binding energies starting at 30 minutes of soaking time. This is likely associated with the F 1s peaks at 688 eV that also appear on the SiO_2 surface at 30 minutes. This peak at 688 eV is assigned to LiPF_6 or Li_xPF_y species and it also continues with less intensity into the bulk of the film. This fluorinate peak remains about the same for the duration of the rest of the soaking time for the SiO_2 samples. The C 1s binding-energy region for the SiO_2 samples does not show any significant change from the initial surface adsorption peaks until about 72 hours of soaking. The peaks at the surface for the C 1s binding-energy region broaden and decrease in intensity, indicating that the carbonate surface species are being consumed or changed by surface reactions with the electrolyte. The C 1s peak at around 286 eV in the bulk of the SiO_2 thin film is likely from process-chamber contamination and does not change with exposure time. Carbonate species do not seem to penetrate past the surface area of the SiO_2 thin films, unlike the fluorinate species, which maintain a < 5 atomic percent presence throughout the bulk of the film starting at 30 minutes of soaking and continue through the rest of the 72 hours of soaking.

Li₃SiO_x Binding-Energy Analysis

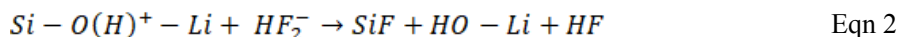
The addition of lithium as a silicate network modifier in the Li_3SiO_x significantly effects the stability of the silicate against electrolyte as demonstrated in Figure II.2.B.21. Figure II.2.B.21 XPS Si 2p, O 1s, F 1s, and C 1s binding energies with depth for Li_3SiO_x soaked for 0 hours (a–d), 30 minutes (e–h), 24 hours (i–l), and 72 hours (m–p). The Li_3SiO_x starts with a wide Si 2p peak in the Si-O binding-energy region as well as peaks at 535 eV and 533 eV in the O 1s binding-energy region that correlate to Si-O and Li-O bonds, respectively. This film also starts with no fluorine peak prior to being exposed to the electrolyte along with typical carbonate soaking peaks. There is a stronger signal around 290 eV in the C 1s binding-energy region for lithiated silicates because Li_2CO_3 forms more facily on lithium silicate surfaces due to their sensitivity to CO_2 ^{[26], [27], [28]} The surface of the pre-soaked Li_3SiO_x has a smaller Si-O peak in the O1s binding-energy region compared to the bulk of the film due to these surface carbonates. The Si-O peak also has a higher intensity than the Li-O peak for the unsoaked Li_3SiO_x through the bulk of the film. This ratio of Si-O to Li-O peaks is reversed starting at just 30 minutes of soaking time. The peaks in the O 1s binding-energy region all decrease over soaking time, but the Si-O peak decreases in intensity compared to the Li-O much more quickly. By 24 hours of soaking time, the Si-O peak is just a shoulder compared to the Li-O peak. For the 72-hour samples, there is only a single small wide peak centered around the Li-O binding-energy region. The decrease in oxygen bonding is accompanied by peak shifts in the Si 2p binding energy away from Si-O bonds and by an increase of fluorine species peaks. At 24 hours, the Si 2p binding peak shifts from ~105 eV toward 106 eV, and there is also a corresponding appearance of a small peak at ~100 eV, which is characteristic of Si-Si or Si-C bonds. By 72 hours, the Si-O peak has almost entirely shifted or been replaced by a peak at ~107 eV, which is characteristic of Si-F bonds and by Si-Si or Si-C bonds at 100 eV at the surface and throughout the bulk of the film. This degradation of the silicate bonds appears with the advent of significant peaks in the F 1s binding-energy region starting at 30 minutes of exposure time. At 30 minutes of exposure time, the fluorine species are concentrated at the surface as shown in Figure II.2.B.20g. These species appear as a sharp peak at 687 eV with a smaller shoulder peak at ~689 eV. These peaks are characteristic of F-Si and Li_xPF_y species, respectively. As the soaking time is increased to 24 hours and the silicate network appears to begin to break down, both F 1s binding-energy region peaks increase in intensity, particularly the shoulder at ~689 eV, and extend further into the bulk of the film. At 72 hours of soaking time, both peaks are about equal in intensity and are significantly present throughout the bulk of the Li_3SiO_x film. At the surface of the 72-hour sample, the Si-C or Li_xPF_y peak dominates the F 1s binding-energy region, with the F-Si peak only appearing as a shoulder. This is accompanied by a shift of the peaks in the C 1s binding-energy region that had been stable up to 72 hours. These C 1s peaks shift toward ~291 eV, or Li_2CO_3 species, as well as the appearance of a small peak at ~283 eV, which is assigned to Si-C peaks. Because C-O carbonate species at ~286 eV only appear as a small peak in the bulk of the Li_3SiO_x film at 24 hours and do not increase in intensity as rapidly as the fluorine species, it can be assumed that most of the peak at ~100 eV that is shared by Si-C and Si-Si species can be attributed to the

latter. There is a single peak at the surface of the Li_3SiO_x samples after 72 hours at 689 eV without a shoulder at 687 eV, which indicates a lack of silicon at the surface and of a higher concentration of Li_xPF_y at the surface than in the bulk. These trends observed in the binding-energy regions shown in Figure II.2.B.20 and Figure II.2.B.21 are clear evidence that, unlike the SiO_2 film, this lithiated silicate appears to undergo a process in which the Si-O bonds are etched away and replaced with Si-F, Li_xPF_y , and Si-C species.

A mechanism for etching vitreous SiO_2 in an aqueous HF solution, which is analogous to the type of etching observed in this study, was proposed by Knotter et al. [29] This mechanism is applicable to the experimental setup in this study because lithium-ion battery electrolytes such as the one used in this work are known to contain HF due to reaction of the LiPF_6 salt with water. Although efforts are made to make these electrolyte solvents non-aqueous, water can infiltrate the electrolyte over long-term storage even when it is stored in an inert-atmosphere glovebox. [30] The process for silicon dioxide etching proposed by the Knotter et al. study involved a nucleophilic substitution reaction, or a two-step reaction involving an elimination reaction followed by the addition of a nucleophile. This mechanism can be applied to the SiO_2 thin film and lithium silicate thin films because it assumed that the silicon dioxide surface includes some impurities leading to oxygens that are only linked to one silicon, or non-bridging oxygens. As discussed in our previous work, the structure of lithium silicates consists of a silicate network broken apart into non-bridging oxygens that are loosely bonded to lithium. [31] The etching reaction for these lithium silicates in an electrolyte that likely contains HF, based on the mechanism proposed by Knotter et al., begins with the protonation of a surface oxygen atom bound to one silicon atom and one lithium atom as seen in Equation 1:



The following reaction is possible under the assumption that there is enough H_2O contamination in the electrolyte to make it an aqueous solution that would allow HF to dissociate into H^+ , F^- , and HF_2^- species. [32] After the protonation of the surface oxygen, there is a nucleophilic attack by HF_2^- on the electrophilic silicon described in Equation 2:



This produces a stable leaving group of LiOH , which could be incorporated into the electrolyte solution and would account for the loss of lithium, with continued soaking/etching time for the lithium silicates shown in Figure II.2.B.14 and Figure II.2.B.16. The reaction rate for the first two steps of this proposed etching mechanism is a function of reactant concentration, or $[\text{SiO}(\text{H})^+\text{Li}]$ and $[\text{HF}_2^-]$, and of the concentration of active surface sites according to Knotter et al. Because the films for this study were all deposited by the same method, it is safe to assume that the reactant concentration, not the concentration of active surface sites, is the dominating factor for etching rates. For the unlithiated SiO_2 film, this etching mechanism would rely on surface impurities such as C or H instead of lithium in the previous equations. It follows that with increased network modifiers, or lithium, the etching rate increases. This is confirmed by the FIB cross-section thickness measurements that provide evidence that with increasing lithium content in these silicate films, more material is etched away from the film over the same amount of time. XPS analysis from Figure II.2.B.20 and Figure II.2.B.21 also confirms that Si-O bonds decrease in quantity whereas Si-F bonds increase in quantity over time just as this etching mechanism predicts.

The etching of the silicate network in these films occurs simultaneously with other side reactions with the electrolyte that account for the significant Li_xPF_y or relatively smaller C-Si peaks in the XPS spectrum. Because each sample is rinsed in DMC for an equal amount of time and LiPF_6 is soluble in DMC, it is most likely that these Li_xPF_y -type species are bound into the reaction layer, not just residual LiPF_6 salt from rinsing. These Li_xPF_y species have been observed in previous aging studies using LiPF_6 salt and can be attributed to hydrolysis products from salt decomposition or as products of the decomposition reaction of LiPF_6 with Li_2CO_3 . [22], [33] The genesis of the small C-Si peaks is less clear, but it could be from the exposure of dangling bonds in the etched silicate being exposed to the carbonate solvents, or from dissolved CO_2 in the

electrolyte, which provides an analogous pathway to attack of the NBO and subsequent substitution of the C into the Si network. More study to elucidate this is necessary.

In summary, in this study we synthesized four different thin-film silicates with increasing levels of lithium content from Li/Si = 0 to Li/Si = 3. These silicates were used to model the surface chemical reactivity of the potentially lithiated native oxide of a silicon anode against a typical carbonate electrolyte. The reaction products that occur from exposure to electrolyte for these silicate thin films are not isolated to just the surface of the film. XPS depth-profiling analysis confirms that reaction species penetrate the bulk of the films as early as at 30 minutes of exposure time. This indicates that the films are either quite porous or that there is a significant breakdown in the film integrity or density as soon as it is introduced to the electrolyte solution. The initial C-O or Li₂CO₃ contamination species at the surface of these silicate films are relatively stable against the electrolyte until about 72 hours of exposure, at which point they appear to be consumed by surface reactions to form more complex carbonates or Li_xPF_y species. The most significant effect on the model silicates came from HF etching of the Si-O bonds in the bulk and at the surface of the film that resulted in Si-O bonds being replaced by Si-F, loss of lithium potentially through the formation of LiOH that leaches into the electrolyte, and dramatic decreases in thickness of the films. A trend was observed that correlated increased reaction rate with lithium content in the film. It is theorized that this increased reaction rate is a function of the amount of non-bridging oxygens terminated by lithium metal ions in the silicate film. The reaction rate of the films also seems to undergo a waterfall effect that culminates in a considerable jump in content of reaction species in the films after 24 hours of electrolyte exposure time.

Together, these data show that Li-Si-O surfaces may react with the electrolyte, but trap the F species, thus preventing the loss/generation of SiF₄ and PF₃ gases.

Surface Species after Chemical Reactions

Continuing the investigation of oxide surface termination, the effect of oxide type on a silicon wafer was explored. In this study, we explored silicon wafers. The first wafer had a native (~2-nm) oxide. The second wafer had a thermally grown oxide (50-nm) Si wafer. Both materials were exposed to electrolyte (LiPF₆-based) and were analyzed with atomic force microscopy (AFM) to investigate electrolyte decomposition. After soaking in electrolyte, island-like accumulations of possible electrolyte decomposition products and residual salts were found on both surfaces as shown in Figure II.2.B.22. However, on the 50-nm SiO₂ surface, the particles showed greater density and more uniform size than on the native-oxide surface, which is likely a result of a rougher pristine surface with more initial adhesion and nucleation sites. Studies are being performed to analyze this surface chemistry. An experiment to investigate stability of the thermally grown oxide immersed in electrolyte for 2 days and 7 days showed that in the absence of electrochemical reactions, the oxide film is completely stable in electrolyte, and thus, the disappearance of the oxide film in the cycled samples results from the electrochemical reaction. A scanning spreading resistance microscopy (SSRM) depth profile of a 15-nm SiO₂ on crystalline-Si (c-Si) sample after soaking in electrolyte for 7 days can be seen in Figure II.2.B.23, demonstrating the electronic contrast visible between the intact SiO₂ layer and the underlying c-Si after mechanically milling down to the interface. The results illustrate that the mechanical and electronic properties were not significantly altered by immersion in electrolyte. Future studies are planned using vapor-grown films and contrasting the results with thermally grown oxides. We hypothesize that the differences in surface chemistry due to growth mechanisms may direct electrolyte decomposition.

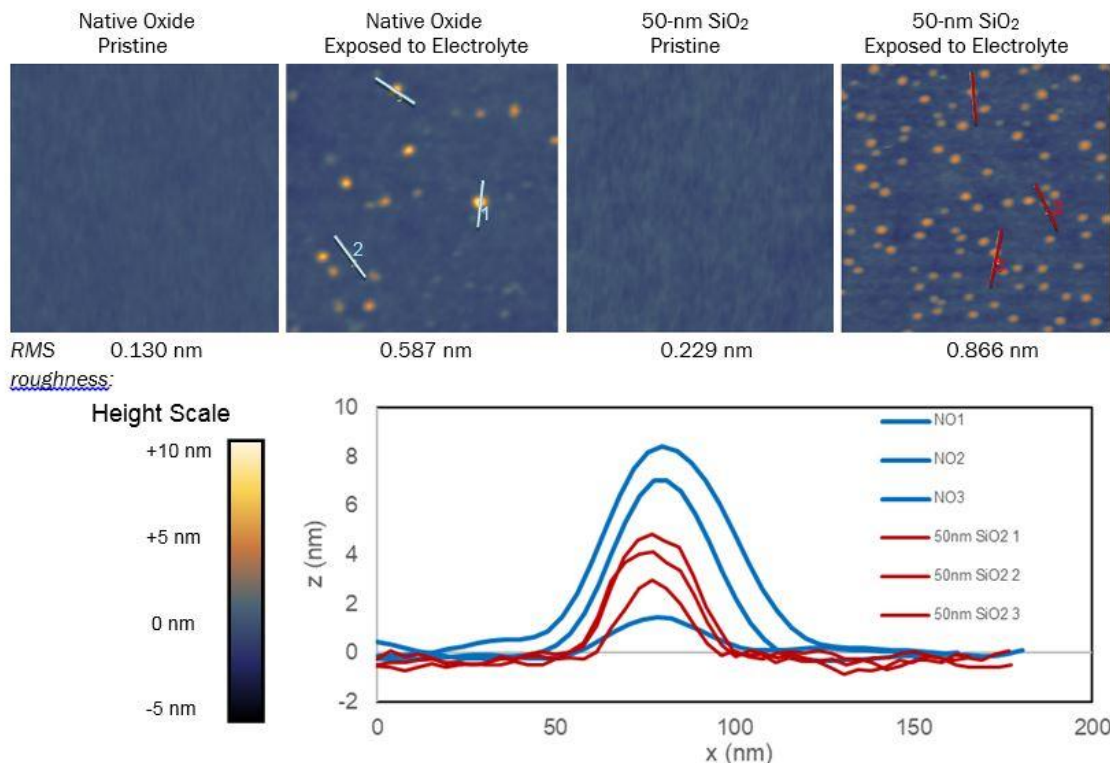


Figure II.2.B.22 $1 \times 1 \mu\text{m}$ AFM images from left to right: Native oxide pristine surface, after soaking in electrolyte, thermally grown 50-nm SiO_x wafer pristine surface, after soaking in electrolyte. A plot is shown displaying comparisons between linescans over surface islands on each sample.

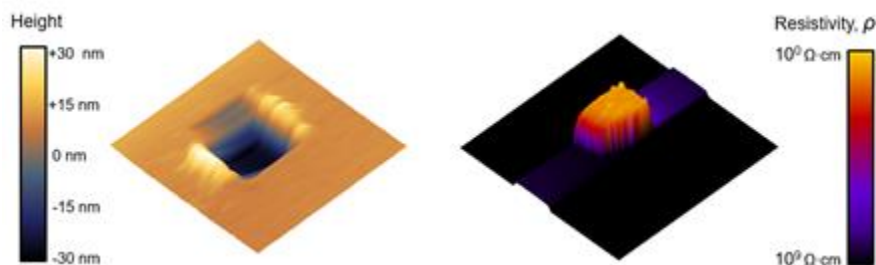


Figure II.2.B.23 SSRM depth profiling on 15-nm SiO_2 on c-Si sample after soaking in electrolyte for 7 days. Height image is shown at left, and resistivity image is shown at right. Electronic contrast between SiO_2 and c-Si is manifest at a depth of 15 nm, showing that the integrity of the SiO_2 film is retained after soaking in electrolyte.

Simulation of Surface Interactions

As part of this study, density functional theory (DFT) was applied to explore the possible mechanisms of reactivity over the pure silicon (PECVD Si). The modeling was designed to capture the electrolyte-electrode interactions whereas infrared spectroscopy was used to support the simulation/validate some of the results. Fluoroethylene carbonate (FEC) was recently proposed as an effective electrolyte additive that significantly enhances the stability and flexibility of the solid-electrolyte interphase layer for Si anodes. However, uncertainties remain on the exact mechanism through which FEC alters the electrolyte decomposition and SEI formation mechanism. Herein, the influence of FEC on LiPF_6/EC electrolytes for Si anodes is investigated through classical molecular dynamics (MD) simulations, FTIR measurements, and quantum chemical calculations.

A sequential simulation for 1.0/1.2 M LiPF_6 in EC with 0/5/10 % FEC was conducted to investigate the influence of FEC to the solvation structures of LiPF_6/EC electrolyte. The radial distribution function $g(r)$ and the corresponding integrals $N(r)$ of Li-X ($X = \text{O}(\text{EC}), \text{F}(\text{PF}_6^-), \text{Li}, \text{P}(\text{PF}_6^-)$ for EC and $X = \text{O}(\text{EC}), \text{F}(\text{PF}_6^-), \text{O}(\text{FEC}), \text{P}(\text{PF}_6^-), \text{F}(\text{FEC})$ for EC with FEC) pairs are summarized in Figure 24. The dominant peak of the Li-F pair at $\approx 2.11 \text{ \AA}$ shown in Figure II.2.B.24a suggests that for 1.0 M LiPF_6 in EC, most of the LiPF_6 salt forms solvent-separated ion pairs (SSIP), whereas the contact ion pairs (CIP) present as minority species (Figure 25b). In addition, a trace amount (less than 1%) of aggregate solvates (AGG) were also observed during the simulation. By integrating the $g(r)$ to 3.0 \AA , the total coordination number (CN) for Li ion is obtained as shown in Figure 25a. Interestingly, although most of the first solvation shell is occupied by EC solvent molecules (5.84 out of 5.90) with a most-probable distance of 2.08 \AA to Li^+ , the Li^+ solvation sheaths also present an average of 0.06 PF_6^- anions, most of which form monodentate structures coordinated through a fluorine. The simulation produced a longer distance of 2.11 \AA for the Li-F pair, illustrating that EC molecules take closer positions in solute complexes. The AGG species are rare, indicating an almost negligible number of Li ions that coordinate with more than one PF_6^- anion. Hence, the corresponding CIP ratio is estimated as 6%, with a SSIP ratio of 94%, in agreement with common assumptions that LiPF_6 is a weakly coordinating salt compared to LiBF_4 and well dissociated in EC solutions.

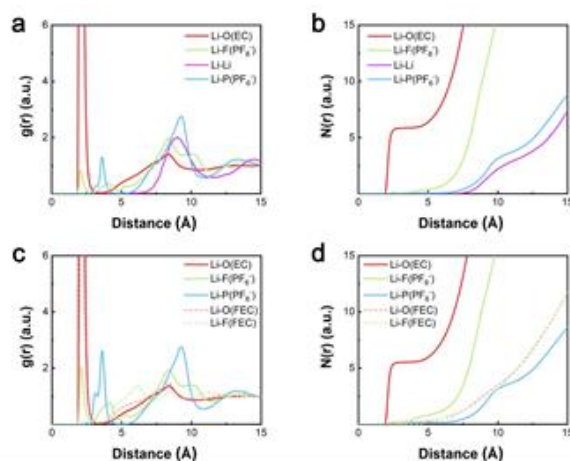


Figure II.2.B.24 Calculated radial distribution functions $g(r)$ and the corresponding integrals $N(r)$ of Li-O(EC), Li-F(PF_6^-), Li-Li, Li-P(PF_6^-) pairs of (a) (b) 1.0 M LiPF_6 in EC, and Li-O(EC), Li-F(PF_6^-), Li-P(PF_6^-), Li-O(FEC), Li-F(FEC) pairs of (c) (d) 1.0 M LiPF_6 in EC with 10%mol FEC additive.

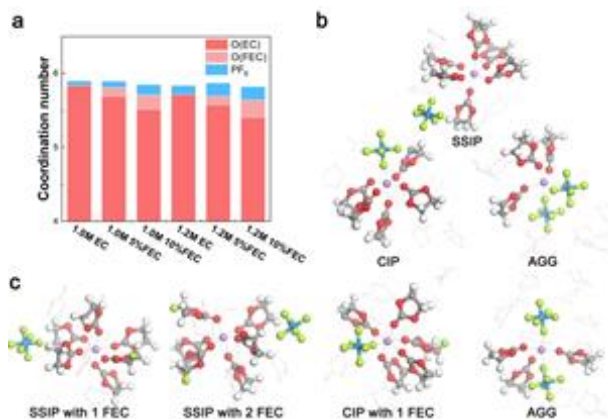


Figure II.2.B.25 (a) The calculated total coordination number for Li^+ in 1.0 M LiPF_6 in EC with 0/5/10% FEC and 1.2 M LiPF_6 in EC with 0/5/10% FEC with specifications of the contributions from EC, FEC and PF_6^- . The representative solvation structures taken from MD simulation snapshots of (b) 1.0 M LiPF_6 in EC and (c) 1.0 M LiPF_6 in EC with 10% FEC.

Upon addition of 10% FEC into the LiPF₆/EC electrolyte, the solvation structure is evidently altered in several ways, primarily due to the weakened donor ability of FEC. Besides the similar solvation structures as shown in Figure II.2.B.25b, other solute complex structures with FEC included were also observed in the snapshots of the MD simulation (Figure II.2.B.25c). Intriguingly, it is the carbonyl O in FEC that binds with the Li ion rather than F binding, which means that the composition difference of the solvent molecule does not radically alter the binding behavior as compared with the parent EC molecule. However, the average CN for Li-O(EC) pair decreases from 5.84 to 5.51, allowing for an average Li-O(FEC) pair contribution of 0.19 to the first solvation shell. A maximum in $g(r)$ of 2.0 is observed for the Li-O(FEC) pair, suggesting a weaker interaction between Li-FEC as compared to Li-EC. Notably, the CIP ratio doubles from 6% to 14%, which significantly changes the population statistics of the SEI formation reaction precursors, indicating a prominent role of FEC, even as a minority species. Similar to the EC electrolyte, the simulation with FEC additive results in a same Li-EC distance. Yet, the Li-FEC distance is slightly farther away (2.12 Å as compared to the Li-EC counterparts, which results in a “looser” structuring of the first solvation shell. EC electrolytes are known to promote salt dissociation due to its high dielectric constant ($\epsilon = 90$), as well as donor number. In contrast, FEC exhibits a lower dielectric constant ($\epsilon = 78.4$), which results in less dissociation of LiPF₆ and weakened donor ability (i.e., smaller CN of Li⁺-solvent). If we compare all six simulated compositions listed in Figure II.2.B.25a, it is obvious that a higher LiPF₆ concentration gives a higher CIP ratio. Somewhat less obviously, we surmise that when 5% of FEC is added to the system, the CIP ratio is elevated, and a non-negligible percentage of the solute complexes are modified with fluorine-containing FEC that occupy the first solvation shell.

The inclusion of 10% of FEC further reduces the solvating strength of the composite electrolyte and allows for more CIPs, i.e., for PF₆⁻ to directly contact/interact with Li⁺. The coordination number for the Li-FEC pair increases to ~0.2, which means that 20% of the solvate structures on average now contains at least one FEC. We argue that this content change of the solute complex significantly changes the reduction potentials of the electrolyte constituents.

Based on the mean square displacement (MSD) of each component during the simulation, the self-diffusion coefficients and transference numbers were calculated and plotted along with the reference experimental results by collaborator Nanda's group in Figure II.2.B.26. Both 1.0 M and 1.2 M simulation results indicate that the diffusion coefficients of all components within the EC electrolyte and EC/FEC mixture exhibit similar values (Figure II.2.B.26a). The trends for the three components EC, PF₆⁻, and Li⁺ are in good agreement with the simulation results obtained by the generalized AMBER force field (GAFF) as well as the trend from nuclear magnetic resonance (NMR) results in that solvent diffusivities are 2~5× larger than ion diffusivities. Although the simulations predict overall slower dynamics than the experimental results, the difference is within one order of magnitude (10^{-10} ~ 10^{-11} m² s⁻¹), illustrating that the classical MD simulation is adequately accurate to reproduce or predict the dynamical property trends of this system.

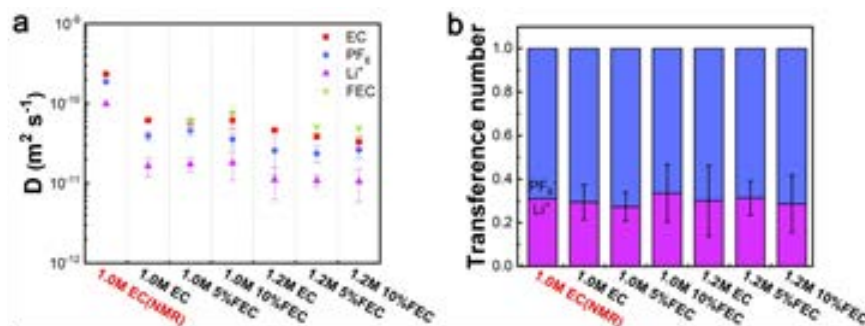


Figure II.2.B.26 (a) Self-diffusion coefficients computed from MD simulations as compared with NMR experiments (1.0 M LiPF₆ in EC) (b) Transference numbers for Li⁺ and PF₆⁻ from MD simulations and NMR experiments. The error bars represent the standard deviation of the data collected every 1 ns during the 5-ns production runs.

It is noteworthy that when FEC is added into the system, there is no significant variation of diffusion properties. EC and FEC exhibit almost the same diffusion coefficients within the calculation uncertainties, and we surmise that the intermolecular interaction behaviors of EC and FEC are similar due to the common cyclic carbonyl structures with only one different substituent. Hence, adding FEC does not directly affect the transport property of the electrolyte. On the other hand, FEC inclusion implicitly promotes the formation of CIPs; however, CIP species still remains a minority species in the electrolyte. According to the Nernst–Einstein relation, an 8% CIP ratio increase from EC electrolyte to EC with 10% FEC will lead to approximately the same percentage (8%) decrease in Li^+ ionic conductivity, and no conspicuous change in transference number was observed. In contrast, the salt concentration clearly affects the ionic diffusivity, decreasing by an average of 10% from 1.0 to 1.2 M. As for the transference number, all the six electrolyte systems give similar results and coincide well with the NMR experimental value of 0.31. Hence, both the self-diffusion coefficient and the transference number results demonstrate the weak dependence of transport properties on the FEC additive up to 10%, elucidating that FEC modifies the solvation structure without greatly affecting the ion transport ability.

To verify the theoretical simulation results, the Nanda group performed FTIR measurements for a range of EC and EC/FEC electrolytes. The peaks from the FTIR spectrum are deliberately deconvoluted to quantitatively estimate the population proportion of each electrolyte species. In parallel, we performed quantum chemical calculations to obtain the theoretical IR vibrational information for each solvation structure observed in the MD simulations. The calculated spectral profiles are further linearly combined using the population ratios obtained from MD simulation that result in predicted theoretical IR spectra. In general, there are two major characteristic peaks that are shifted after the inclusion of FEC: 1) the C=O breathing band at $710\text{--}730\text{ cm}^{-1}$, and 2) the P-F bond stretching band at $840\text{--}880\text{ cm}^{-1}$. The C=O breathing vibrational band at $710\text{--}730\text{ cm}^{-1}$ can be used to distinguish the responses from different C=O binding states. Peaks from experimental results (Figure II.2.B.27a and b) were designated as coordinated ones and uncoordinated ones based on our calculations and reference, which provide detailed information of the solvation structure.

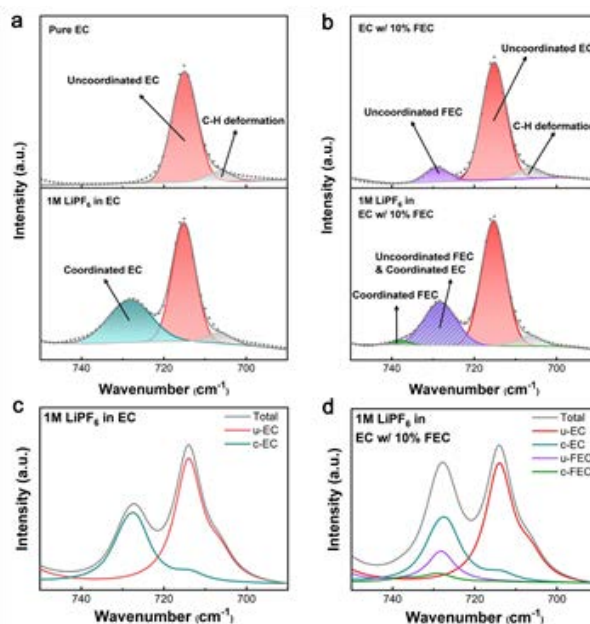


Figure II.2.B.27 Measured FTIR spectra of the C=O breathing band of (a) pure EC and 1.0 M LiPF_6 in EC, and (b) EC with 10% FEC and 1.0 M LiPF_6 in EC with 10% FEC. (c–d) The corresponding calculated IR spectra as a comparison of the experimental results. Red, cyan, purple, green, grey, and dark grey lines correspond to uncoordinated EC, EC coordinated with Li^+ , uncoordinated FEC, FEC coordinated with Li^+ , C-H deformation, and total spectrum, respectively. Scatter points denote the original FTIR data points.

First, we note that the experimental results are in good agreement with the calculated spectra (Figure II.2.B.27c, d), and identical peaks are found in the spectra from both methods, despite small deviations in the absolute frequency values. For the EC electrolyte (Figure II.2.B.27a), two peaks at 728 cm^{-1} and 715 cm^{-1} were identified as coordinated EC and uncoordinated EC, which were accompanied by a small C-H deformation peak at 706 cm^{-1} . By analyzing the measured peak area integrals, it was found that 38.1% of EC molecules are coordinated with Li^+ , which corresponds to a CN of 5.13 for Li-EC. Although the calculated CN (5.84) from MD simulations is slightly higher than the experimental result, it is notable that both approaches indicate a CN over 5 for the EC electrolyte system. When 10% of FEC is included, an additional peak arises at 738 cm^{-1} , corresponding to the coordinated FEC. Meanwhile, a free FEC breathing band at 729 cm^{-1} overlaps with the coordinated EC vibration band (Figure II.2.B.27b), which makes it difficult to deconvolute the peaks and obtain the exact percentage of the coordinated EC and uncoordinated FEC. Nonetheless, by comparing the peak of the uncoordinated EC, we estimate an increase in uncoordinated EC area by 6.6% as compared to the 1M LiPF_6 in EC system, which further supports the decrease in CN of Li^+ -EC with respect to the EC electrolyte. Additionally, the CN of FEC to Li^+ is directly calculated as 0.21 from the green area, which corresponds well with our previous calculation results (0.19) from the MD simulations.

In addition to the CN of solvents, contact ion pairing was probed by analyzing the P–F bond stretching band. As shown in Figure II.2.B.28, the peak at $838\text{--}840\text{ cm}^{-1}$ is identified as the response from uncoordinated PF_6^- , whereas two peaks at 878 cm^{-1} and 834 cm^{-1} arise through coordinated PF_6^- . For the EC electrolyte (Figure 28a), coordinated PF_6^- contributes 6.4%, showing an excellent agreement with our simulated 6% CIP ratio. With the inclusion of FEC in the EC electrolyte (Figure II.2.B.28b), an FEC ring-deformation vibration band appears at 862 cm^{-1} , which complicates the integral area calculation. By carefully deconvoluting the peaks, we estimate that 7.2% of the total PF_6^- ions are in the form of coordinated structure with Li^+ .

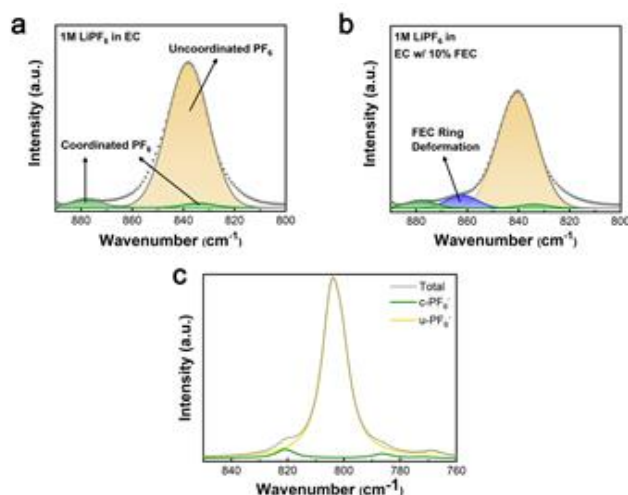


Figure II.2.B.28 Measured FTIR spectra of the P–F bond stretching band of (a) 1.0 M LiPF_6 in EC, and (b) 1.0 M LiPF_6 in EC with 10% FEC. (c) The corresponding calculated IR spectra for 1.0 M LiPF_6 in EC as a comparison of the experimental results. Yellow, green, blue, and dark grey lines correspond to uncoordinated PF_6^- , coordinated PF_6^- , FEC ring deformation, and total spectrum, respectively. Scatter points denote the original FTIR data points.

Interfacial properties of 1.0 M LiPF_6/EC at the Si anode at the initial charging step are studied with classical MD. We first investigated the solvation structure close to the neutral (uncharged) interface. An OPLS force field is employed for the electrolyte constituents, and the anode interface is represented by neat c-Si covered with a thin, native silicon oxide layer. We found that the solvation structure of Li^+ changes quite significantly from the bulk to the interface, such that the overall Li^+ coordination changes from about 6 to about 4 (Figure II.2.B.29a and b). This effect is due to two components: 1) a significant interaction between the SiO_2 oxygen and Li ion reduces the EC coordination number (CN) from 5.5 to 2.5, and 2) the Li-F CN increases from 0.4 in bulk to 1.2 at the interface. Because the PF_6^- anion can donate more than one F to each Li, the CIP ratio

increases from ~ 0.3 to ~ 0.65 from the bulk to the interface. We also find that the CIP ratio in bulk increases from 0.07 to 0.3 with temperature increasing from 300 K to 400 K, which we attribute to a decrease in the dielectric constant of the solvent.

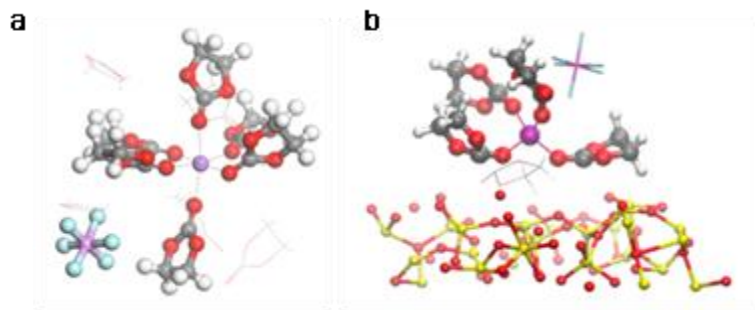


Figure II.2.B.29 Structures of EC molecules around a Li ion (a) in bulk and (b) at interface.

We then analyzed the solvation structure of electrolyte molecules for an interface with a constant charge. As previously, the chemical characteristics of the Si anode interface is modeled with an amorphous SiO₂ layer on top of the c-Si bulk electrode. The equilibrium MD simulation is performed for 1 M LiPF₆ in EC at 400 K (Figure II.2.B.30a). The applied voltage is modeled by assigning a uniform charge, $\pm 6.25 \times 10^{-4} e$, to each silicon atom at the negative/positive electrodes so that the voltage applied at the negative silicon electrode is ~ -0.47 V (Figure II.2.B.30b). Interestingly, the constant charged interface causes a reduction in the CIP ratio between the bulk and the interface as compared to the neutral case. Both a negatively as well as positively charged SiO₂ interface result in a CIP ratio of 0.4 and 0.45 at the negative- and the positive-charged electrode interface, respectively (Figure II.2.B.31), which should be compared to the neutral case of 1.2. Nevertheless, it should be stressed that the CIP ratio still is increased as compared to the bulk for both charged (marginally) and neutral (substantially) SiO₂ interfaces. Furthermore, similar to the neutral electrode, the CIP ratio increases from bulk to interface with increasing temperature, spanning 313, 350, and 400 K (see Figure II.2.B.30c). In summary, the neutral silicon SiO₂ interface exhibits the largest CIP ratio, and it becomes smaller at the charged interface. Specific interaction between ions and SiO₂ enhances the CIP forming at the interface, which provides a hint toward preferential reaction pathways of the early SEI formation.

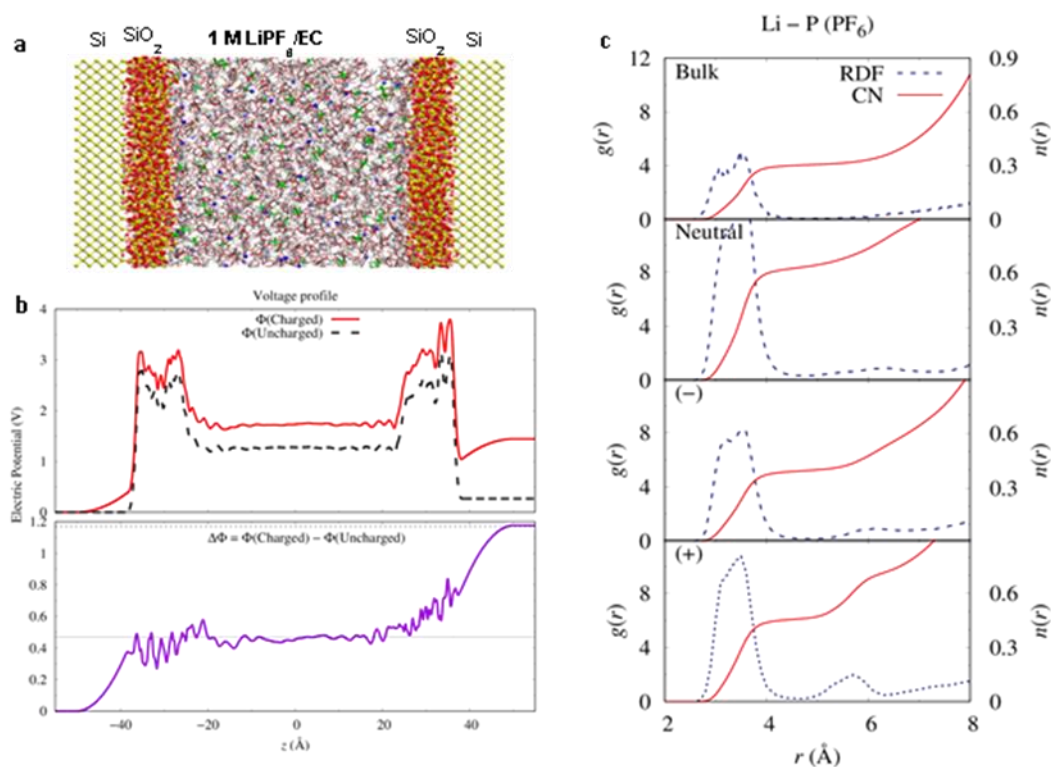


Figure II.2.B.30 (a) The model Si anode interface, and (b) the voltage profile in the electrolyte region between the electrodes. The electric potentials are -0.47 V and +0.7 V at the negative and the positive electrodes, respectively. (c) Radial distribution functions and the coordination numbers (CN) of PF₆ ions around a Li ion in bulk and at the neutral, negative and positive electrodes, from top to bottom, and the CN values are 0.3, 0.65, 0.4, and 0.45, respectively.

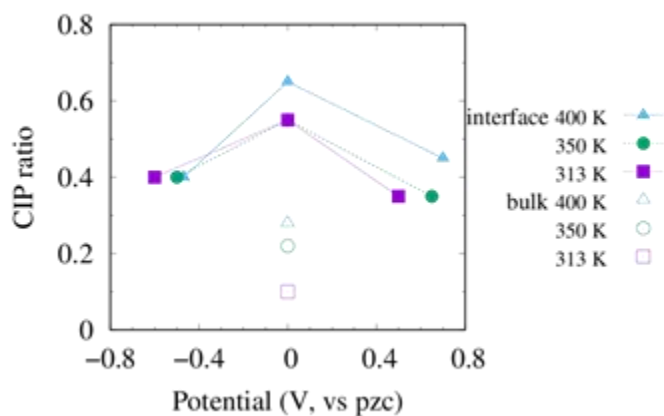


Figure II.2.B.31 Contact ion pair (CIP) ratio in the bulk electrolyte and at SiO₂ interface at temperatures of 400 K, 350 K, and 313 K. The CIP ratio increases from the bulk to interface. The neutral silicon interface shows the largest CIP ratio, and it becomes smaller at the charged interface.

We find the total solvation number of Li in EC to be close to 6 in the bulk electrolyte, and it reduces to 4 at the interface. Explicit interaction between the SiO₂ interface and electrolyte results in a higher CIP ratio at the interface. The CIP ratio increases from the bulk to the SiO₂ interface. The neutral silicon interface shows the

largest CIP ratio, which decreases for a charged interface; however, it is still larger than the bulk value. Enhanced CIP at the SiO₂ interface hints at reaction pathways of SEI formation.

In summary, collaborative FTIR experiments and the MD simulations provide consistent solvation structure information. Both approaches demonstrate that the LiPF₆/EC electrolyte with or without FEC results in a Li⁺ CN of 5–6. Furthermore, our results conclusively suggest that adding FEC increases the CIP ratio without significantly impacting the transport properties of either Li⁺ and PF₆⁻ ions. This minority FEC coordination with Li⁺ is important because the Li⁺ solvate complex serves as a key precursor for electrode-surface reduction reactions. The inclusion of FEC in the first solvation shell, even as a minority species, increases the reduction potential of FEC due to its close proximity of Li⁺, as compared to a freely solvated FEC.

Reactivity of Lithium Silicides

One possible approach to stabilizing silicon anodes against lithium losses is through prelithiation. However, this once again introduces new problems due to SEI formation and stability with electrolyte and electrode components. To explore this issue, we have focused on the synthesis of Li-Si materials and evaluated their reactivity with various solvents and binders. It is possible to form a range of lithium-silicon alloys as a series of Zintl phases as noted in the phase diagram, Figure II.2.B.32. Previous work by Key et al. has shown that although average lithium content reflects the state of charge, the underlying structure of the electrode is a mixture of various Zintl anions that reflect the components of the various anions in the salts from the phase diagram. To assess the reactivity of these charge electrode components, we synthesized several of the compounds as bulk phases. Li₇Si₃ is the highest-melting binary in the phase diagram and reflects the predominant species around 300 mV vs Li.

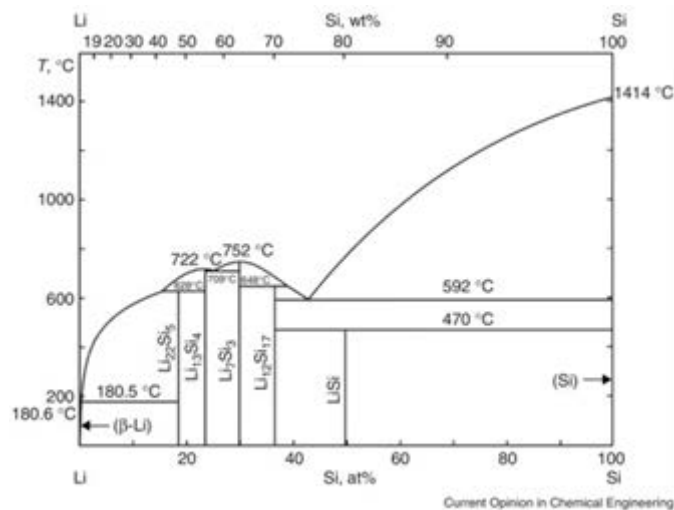


Figure II.2.B.32 Li-Si phase diagram.

Li₇Si₃ was synthesized by a direct stoichiometric reaction of lithium metal (FMC lithium) and micron-sized silicon powder (Sigma–Aldrich). Best synthetic conditions were identified as the following:

- Vertical Ta tubes with a BN cap
- Heating to 760°C, slow cooling to 700°C
- Radiative cool to room temperature.

For other compounds evaluated (Li₂₂Si₅, Li₁₃Si₄) were synthesized in a similar manner with temperatures determined by phase-diagram data. Purity was determined by powder X-ray diffraction and general stability was determined by storing the powder in a low-O₂ glovebox and examining the material on an irregular basis

by powder diffraction. To systematically study the reactivity of different battery components (including binders and electrolyte solvents) in direct contact with lithiated Si electrodes, Li_7Si_3 composition (voltage of about 350 mV vs. Li) was mixed with various solvents and polymers. ^7Li and ^{29}Si MAS NMR data were collected.

Figure II.2.B.33 shows the *in-situ* ^7Li and ^{29}Si MAS NMR results of the bulk LS model compound and its mixture with different electrolyte solvents, including EC, EMC, FEC, and triglyme. The bulk Li content of lithium silicides has previously been shown to be directly correlated with ^7Li NMR shifts, where a positive increase in shift indicates Li loss from the bulk. [34], [35] The results showed the highest Li loss and bulk reaction for EC and the lowest for FEC/triglyme after mixing with Li_7Si_3 . Furthermore, no LiF at ~ 0 ppm in ^7Li NMR (and ^{19}F NMR, data not shown) was detected in the Li_7Si_3 + FEC experiment, contrary to the common notion that a FEC defluorination reaction would be prevalent in the presence of lithiated Si species. The FEC results suggest that Li_7Si_3 of ~ 300 – 400 mV potential vs. Li is either not reducing enough and/or a flow of electrons is also required for FEC passivation reaction. The results confirm the hypothesis that EC may not be the best solvent choice for Li-Si chemistry in the absence of SEI passivation and leads to major coulombic inefficiencies and Li loss. The results suggest that more inert electrolytes could lead to better coulombic efficiencies and to improved electrolyte formulations specifically designed for silicon anodes.

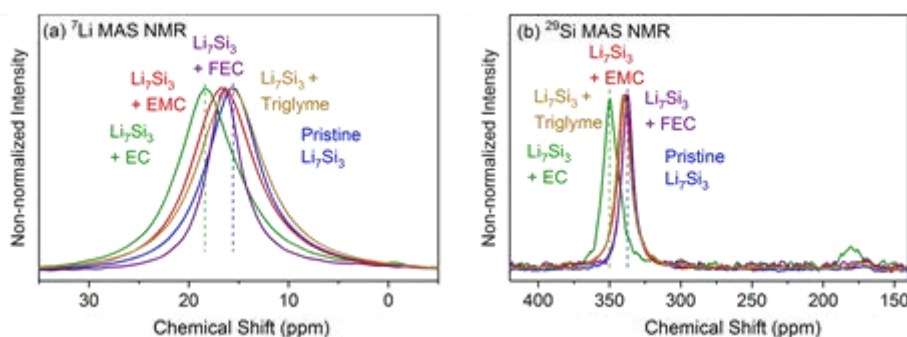


Figure II.2.B.33 (a) ^7Li and (b) ^{29}Si solid-state *in-situ* MAS NMR for Li_7Si_3 and its physical with different electrolyte solvents.

To test the above hypothesis, a new lithium silicide compound with higher Li contents (i.e., representing lower charging potential, $\text{Li}_{13}\text{Si}_4$) were synthesized, and then mixed with FEC and other solvents. Because of the excess Li in the reaction container to mitigate Li loss, the newly synthesized lithium silicide was instead identified as $\text{Li}_{22}\text{Si}_5$ according to its ^7Li MAS NMR spectrum shown in Figure II.2.B.34, which corresponds to about 0.05–0.1 V vs. Li. The ^7Li and ^{29}Si MAS NMR results of the mixture of $\text{Li}_{22}\text{Si}_5$ and different electrolyte solvents, including EC, FEC and triglyme, are shown in Figure II.2.B.34. After mixing with FEC or EC, the main ^7Li peak of $\text{Li}_{22}\text{Si}_5$ at ~ 75 ppm shifted by ~ 4 ppm, indicating the lithium loss caused by the reaction between $\text{Li}_{21}\text{Si}_5$ and FEC/EC. Meanwhile, unlike the minor ^7Li and ^{29}Si NMR shifts previously observed after mixing Li_7Si_3 with triglyme, this time we observed clear positive peak shifts and notable broadening after mixing $\text{Li}_{21}\text{Si}_5$ with triglyme. Such obvious peak evolution indicated that although triglyme might be relatively stable when in contact with the slightly charged Si anode, it could react with the Si anode charged to lower voltages. It must be noted that $\text{Li}_{22}\text{Si}_5$ NMR shifts are non-diamagnetic and the shift mechanism is due to conduction-band electrons at the Fermi level, i.e., a Knight shift; therefore, a simple interpretation of shift changes to higher or lower frequencies cannot be easily made as in the case of Li_7Si_3 . Still, the results indicate a bulk reaction and can partially explain our earlier observation that in half-cell tests using 1M LiTFSI in triglyme as the electrolyte, the capacity of Si anodes dropped faster over cycles compared with the LiPF_6 electrolyte + 10% FEC electrolyte. In addition, in the ^7Li MAS NMR spectra shown in Figure II.2.B.34, a clear diamagnetic ^7Li peak around 0 ppm (could be ascribed to LiF, ^{19}F NMR pending) appeared after mixing $\text{Li}_{21}\text{Si}_5$ with FEC. This means that our earlier observation that the mixing of FEC and Li_7Si_3 causes no LiF formation results from the Li_7Si_3 not being sufficiently reducing enough to break a C-F bond. The above results suggest that triglyme alone may not be stable/passivating enough for high-Li-content Li_xSi .

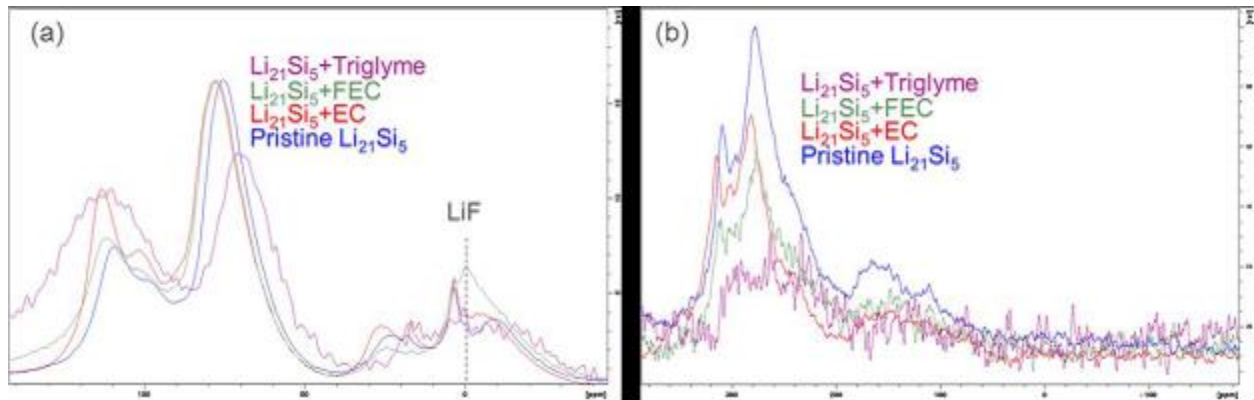


Figure II.2.B.34 (a) ^7Li and (b) ^{29}Si in-situ solid-state MAS NMR for $\text{Li}_{22}\text{Si}_5$ and different electrolyte solvents. ANL, unpublished results.

In parallel, thin films of Li-Si were prepared by evaporating lithium onto 50-nm Si films supported on a copper substrate. Specific capacity was calculated by the total mass of lithium and silicon. Electrolytes were dropped on the surface of the lithium silicide thin film, which was deposited on a Pt-coated silicon wafer. Attenuated total reflection-Fourier transform infrared spectroscopy (ATR-FTIR) was performed with a Bruker Alpha spectrometer under argon atmosphere in a glovebox. Figure II.2.B.35 shows the ATR-FTIR spectra of FEC and LiPF_6 EC/EMC electrolyte on lithium silicide. Peak assignment was referred to a previous ATR-FTIR study³ of lithium metal immersed in electrolytes. FEC helps form the uniform surface and suppresses the decomposition of PF_6^- . Similar findings are observed in this study. More organic phases formed with FEC and more inorganic phases formed in LiPF_6 electrolyte. In addition, LiPF_6 electrolyte generated more F⁻-containing phases than FEC. XPS also shows similar composition with ATR-FTIR. This study shows that FEC, EC, and DEC can be chemically reduced by lithium silicide. This result and the NMR studies indicate that the Li content in the silicide needs to be controlled to optimize the reduction potential.

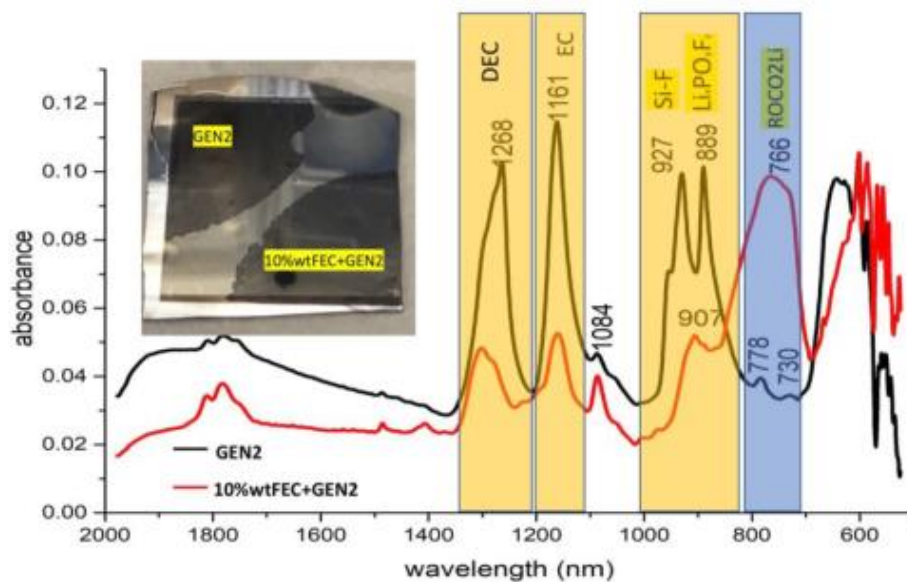


Figure II.2.B.35 Inset photo: Electrolyte drop on lithium silicide thin film on silicon wafer. Main plot: ATR-FTIR spectra of the FEC and Gen2-treated lithium silicide surface.

SEISta Section 2: The Influence of the Oxide Layer on the Formation and Stability of the SEI on Silicon

Theoretical Predictions for Li-Si-O

Understanding the underlying atomistic mechanisms for the Si anode performance is crucial for improving current materials and incorporating higher-capacity anodes into future, improved lithium-ion technology. Current research focuses on the formation of the silicon/electrolyte interface (SEI) and its constituents, but fewer publications exist on modifications to the bulk Si. Dopants and alloys can be an effective way of modifying electrochemical properties. For that, we utilize theoretical and computational approaches including the density functional theory (DFT) calculation and molecular dynamics simulation methods. Our efforts will focus on identifying systems with lower volumetric expansion.

Computation of the bulk moduli shows that lithium silicates are stiffer than the silicides (Figure II.2.B.36). The higher modulus of the silicates suggests that the native SiO₂ oxide is less accommodating to expansion. As Li penetrates into the Si and forms Li_xSi, the volumetric expansion will build internal pressure, ultimately resulting in the fracture of the silicate layer. This is consistent with two observations. First, that the particles that make up a Si electrode crack during the first few lithiation cycles and expose more surface area, which is observed especially in Si films. Second, the SiO₂ layer can be used to restrict expansion of the silicide phases, as demonstrated by Wu et al. when encasing a Si nanotube in SiO₂ to prevent outward expansion of the Si interior during lithiation.^[36]

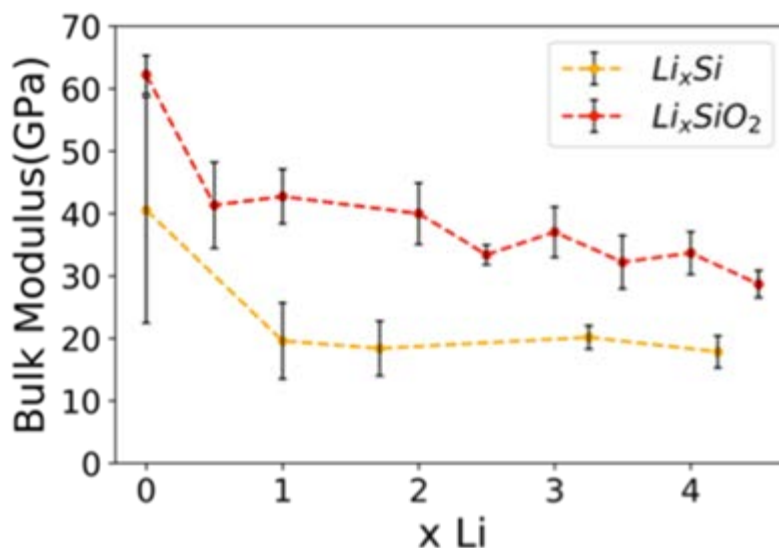


Figure II.2.B.36 Bulk modulus of lithium silicates and lithium silicides.

Synthetic Methods for Producing Li-Si-O (Coyle, Teeter)

The method used to synthesize the model lithium silicate thin films was chosen to control composition and thickness of the films. The deposition method also needed to provide uniform, defect-free thin films with minimal exposure to ambient atmosphere. Sputter deposition was identified as the optimal available method.

A radiofrequency (RF) magnetron co-sputtering technique was used to provide more freedom in the range of composition used and to prevent preferential sputtering seen in other studies attempting to sputter lithium silicates.^[38] Magnetron sputtering uses magnets installed behind the negatively charged electrode to trap more free electrons in a magnetic field above the target surface, which facilitates the ionization of neutral gas atoms and increases the rate at which material can be removed from the target and deposited onto a substrate. An RF power source was chosen due to the insulating nature of the target materials.

The deposition used for this thesis was a Kurt J. Lesker PVD 75 system with two RF sputter targets capable of sputtering at the same time. The sputter targets were oriented to sputter upward, as demonstrated in Figure II.2.B.37.

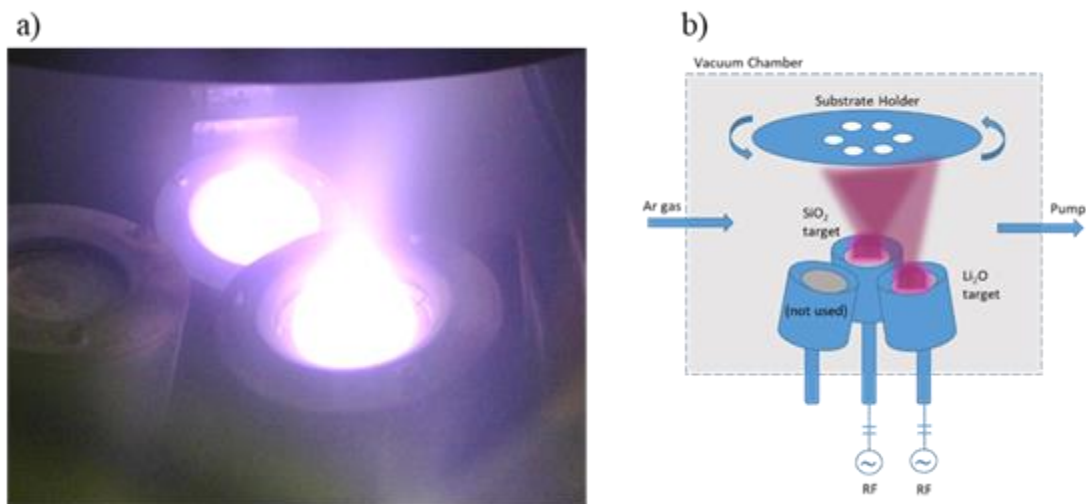


Figure II.2.B.37 a) Photo of sputter targets, and b) diagram of sputter conditions in the process chamber of Lesker PVD75 system.

Films were sputtered from a SiO₂ (99.995%, Kurt J. Lesker) target and a fabricated Li₂O target in a pure argon (99.999%, Airgas) atmosphere. The Li₂O target was made from pressed disks of lithium dioxide powder (97% 9060 mesh, Aldrich). These disks were calcined at 900°C for 10 hours separated by mica sheets to prevent disks from fusing together. The SiO₂ target was sputtered under a range of powers from 9–28 W whereas the Li₂O target was sputtered under a constant power of 20 W for all compositions to achieve different Li/Si ratios. Both targets were sputtered for at least 40 minutes with a shutter in place before actual deposition to avoid cross-contamination. During deposition, the substrate holder was rotated to achieve homogeneous films. Two substrate holders were designed to fit diverse deposition needs. These substrate holders are pictured in Figure II.2.B.38. Film deposition rates varied between 3 to 7.5 angstroms/minute. Deposition times were controlled to achieve the desired thickness for each film. Substrates were introduced to an inert atmosphere glovebox from atmosphere, loaded into the substrate holders, and placed in the secondary load-lock chamber that opens directly into the glovebox. The load-lock chamber was pumped down to suitably low vacuum ($\sim 10^{-6}$ torr) using a combination of roughing and turbo pumps. A gate valve was opened between the transitional load-lock chamber and the main process chamber, which was kept at a low vacuum ($\sim 10^{-8}$ torr), and the substrates were passed into the process chamber using an automated retractable arm. This process, along with the reverse process, allowed for thin-film samples to be removed from the deposition chamber directly into an inert atmosphere glovebox. Figure II.2.B.39 depicts the sputter system and the glovebox used for this study with the sample transfer process labelled.

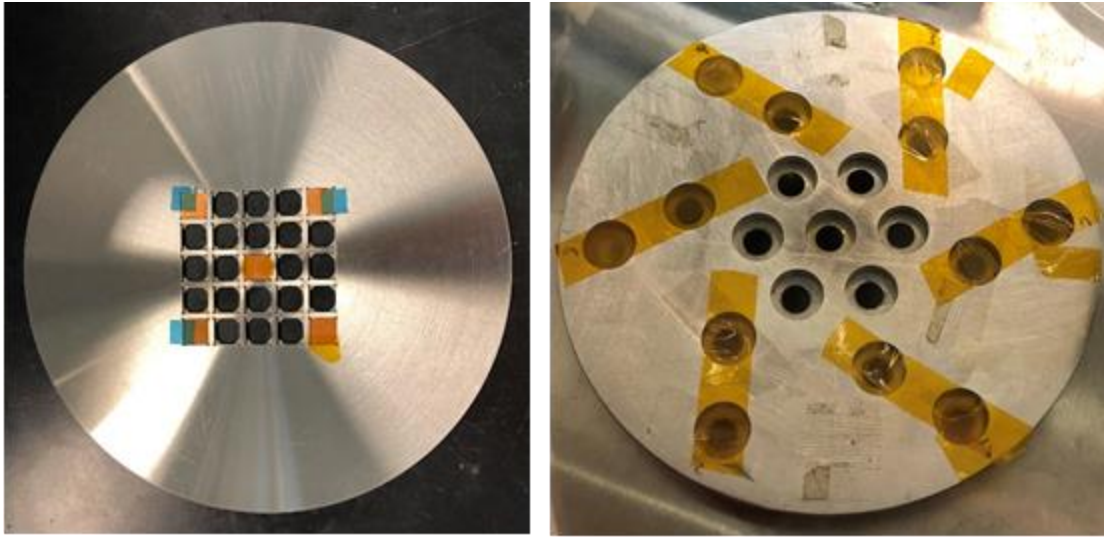


Figure II.2.B.38 Substrate holders used for sputter deposition. Left: Holder for Si chips, Right: Holder for KCl chemical test samples.

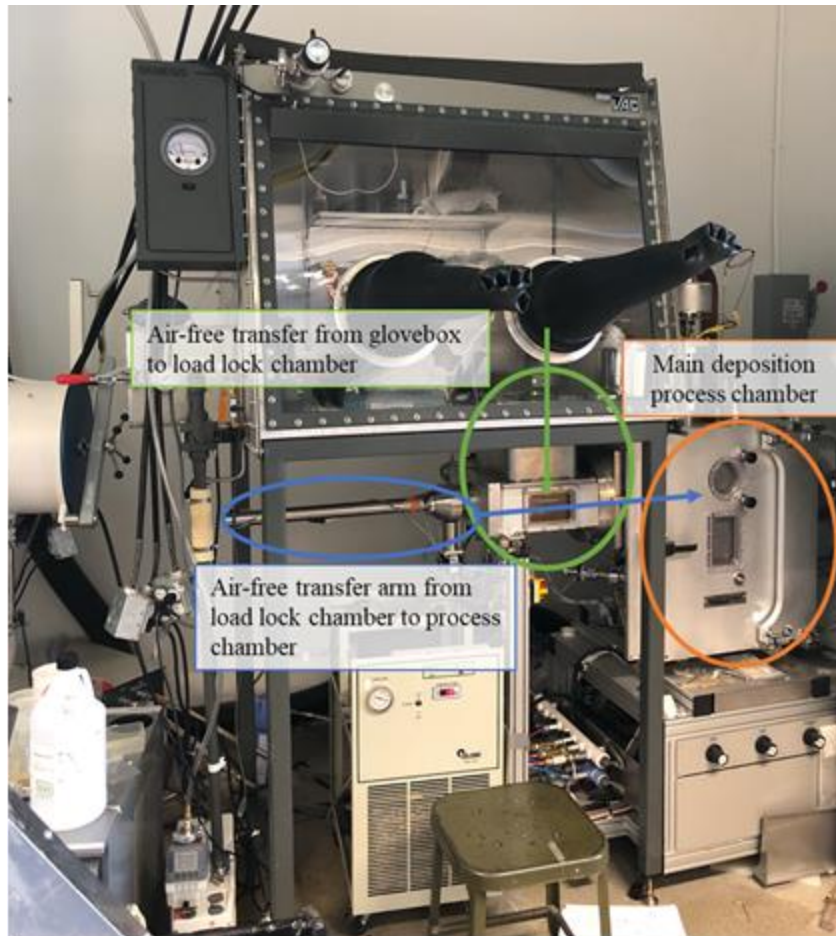


Figure II.2.B.39 Sputter system and sample transfer process.

RF magnetron sputter conditions were controlled to determine the effect of deposition time and power ratios on the structure and composition with depth of the thin films produced. The results of this study allowed for evaluation of whether this synthesis technique gave adequate control over the material synthesis (and thus, material performance) for a model SEI on a silicon anode. Five different compositions of lithium silicates with distinct structures were produced, and the deposition time was controlled to create films with a desired thickness. Results from this thesis indicate that the co-sputtering technique still results in surface contamination and that target synthesis has a direct effect on the purity of these films; but otherwise, this technique provides uniform reproducible amorphous films ideal for this study.

The first effort was to characterize the thin sputtered silicates for composition and quality. This was done in several ways by several different partner institutions in the program. Amorphous lithium silicate films about 550 nm thick were deposited for chemical analysis, and 50-nm-thick silicate films were deposited for all other analyses. Film thickness measurements were made with a Dektak 3030 profilometer. Each sample was replicated at least six times for reproducibility and error analysis. Inductively coupled plasma optical emission spectrometry (ICP-OES), Fourier transform infrared spectroscopy (FTIR), X-ray photoelectron spectroscopy (XPS) and time-of-flight secondary-ion mass spectrometry (TOF-SIMS) measurements were used to characterize the films.

The ICP-OES results for the thin films sputtered onto KCl substrates are shown in Figure II.2.B.40. From elemental analysis, there is a linear relationship between the ratio of powers on the Li_2O and SiO_2 target and the lithium-to-silicon ratio in the thin films. There is only a small error associated with each power setting intended for the following compositions: $\text{Li/Si} = 1.4, 1.9, 2.9, 4.8,$ and 7.7 . The error bars indicate compositional variation across multiple depositions. The data in Figure II.2.B.41 represent seven different deposition runs for each composition. Film deposition rates varied between 3 to 7.5 angstroms/minute based on the power ratio on the targets. Deposition times were controlled to achieve the desired thickness for each film (~550 nm). The time for each deposition ranged from 14 to 26 hours, with runs using higher $\text{Li}_2\text{O/SiO}_2$ target ratios requiring longer deposition times to achieve the desired thickness.

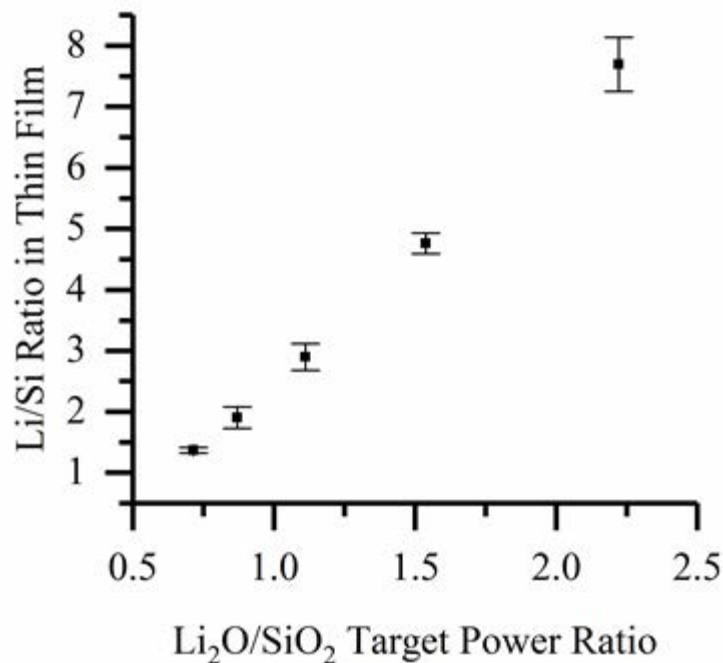


Figure II.2.B.40 ICP-OES results for Li/Si ratio in each thin film at each power setting.

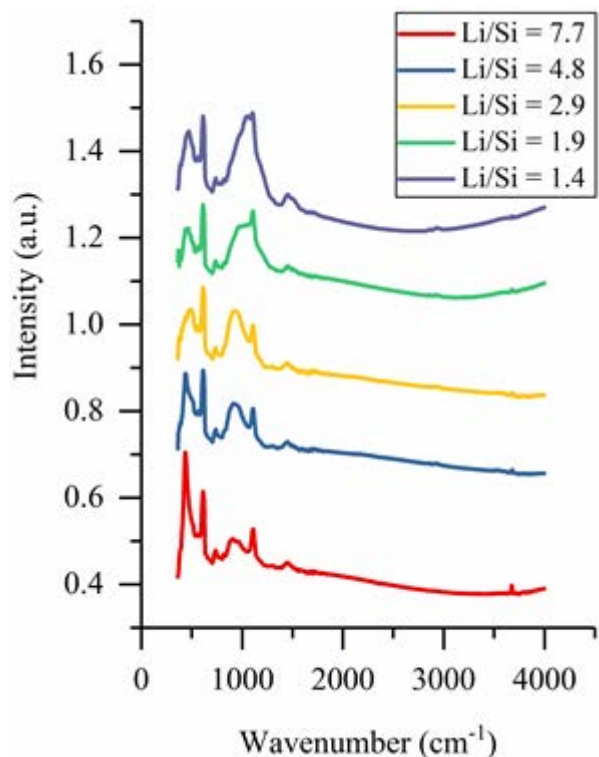


Figure II.2.B.41 FTIR spectra of all five sputtered lithium silicate compositions.

Structure/Composition in the Bulk and with Depth

FTIR in transmission mode was used to examine the bulk structure of the sputtered lithium silicate samples. Figure II.2.B.41 shows a representative FTIR spectrum for each of the five compositions of sputtered lithium silicates. The peaks at $\sim 1,450\text{ cm}^{-1}$ and $\sim 880\text{ cm}^{-1}$ are observed in all five film compositions and are characteristic of a Li_2CO_3 species.^[38] The small, but visible, peak at $\sim 3,700\text{ cm}^{-1}$ results from O-H stretching vibrations and is characteristic of LiOH species.^[39] Because these spectra are obtained using bulk transmission-mode infrared (IR) spectroscopy, there is no information on whether the Li_2CO_3 and LiOH species are found in the bulk of the film or result from surface contamination during transfer to the FTIR spectrometer. This issue will be further addressed in conjunction with the results of the surface analysis in this chapter.

The absorption peaks detected in the range of $400\text{--}1,200\text{ cm}^{-1}$ by FTIR are characteristic of silicate vibrational modes as well as Li-O type bonds, and their measured ratio is used to evaluate the structural changes to the silicate network as the Li content is increased. The vibrational modes associated with each absorption peak in this region are previously reported and summarized in Table II.2.B.3.^{[40], [41], [42], [43]}

The symmetric or asymmetric stretching modes (ν_s or ν_{as}) near 1160 , 1100 , 1000 , 900 , and 740 cm^{-1} are attributed to $\nu_{as}(\text{Si-O-Si})$, $\nu'_{as}(\text{Si-O-Si})$, $\nu_s(\text{O-Si-O})$, $\nu(\text{Si-O-})$, and $\nu_{as}(\text{Si-O-Si})$, respectively. The lower wavenumber band near 600 cm^{-1} corresponds to the $\nu_s(\text{Si-O-Si})$ mode, and the spectral features in the range of 500 to 560 cm^{-1} correspond to deformation vibrations associated with $\delta(\text{O-Si-O})$ or $\delta(\text{S-O-Si})$ modes. The vibrational bands centered around 440 cm^{-1} result from deformation of the non-bridging oxygen Si-O-(Li⁺) type bonds and the Li-O symmetric stretching mode. Due to the constraints of the FTIR instrument used, the asymmetric stretching modes of these Li-O bonds under 400 cm^{-1} that are observed in higher-order lithium silicates^{[44], [45]} could not be detected. The location of all vibrational modes shifts to slightly lower frequencies as the lithium content in each thin-film composition increases. Because lower frequencies correspond to lower bond strengths and the number of weak Li bonds are increased in the structure, the entire bulk network weakens, resulting in a uniform redshift of the vibrational spectrum.

Table II.2.B.3 Vibration-Mode Assignments for FTIR Peaks

Wavenumber (cm ⁻¹)	Vibration Mode Assignment
~440	$\delta(\text{Si-O}-(\text{Li}^+)) \nu(\text{Li-O})$
~500, ~560	$\delta(\text{O-Si-O}) \delta(\text{S-O-Si})$
~600	$\nu_s(\text{Si-O-Si})$
~740	$\nu_{as}(\text{Si-O-Si})$
~900	$\nu(\text{Si-O-})$
~1,000	$\nu_s(\text{O-Si-O})$
~1,100	$\nu'_{as}(\text{Si-O-Si})$
~1,160	$\nu_{as}(\text{Si-O-Si})$

To evaluate the ratio of each type of bond in these amorphous thin-film materials, Gaussian-peak deconvolution is necessary to decompose and identify overlapping peaks. Once the peaks for each vibration mode are assigned and integrated, structural analysis of the lithium silicates can be completed. The Gaussian-peak deconvolution of this lithium silicate characteristic region for the thin film with a Li/Si = 7.7 composition ratio is shown in Figure II.2.B.42 as an example for this method.

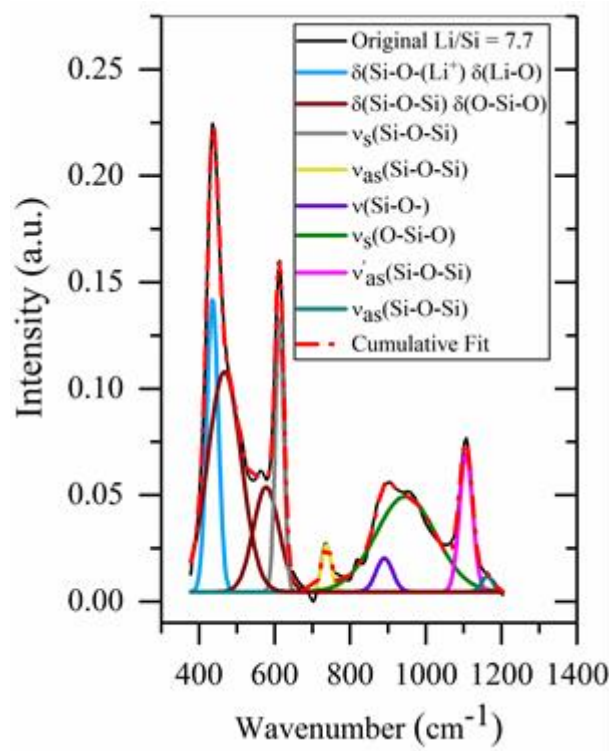


Figure II.2.B.42 Gaussian-peak deconvolution of Li/Si = 7.7 film.

The Gaussian peak fits were also completed for the other four compositions as well, with similar results. See Figure II.2.B.43 for the Gaussian-peak deconvolution of the other four film compositions.

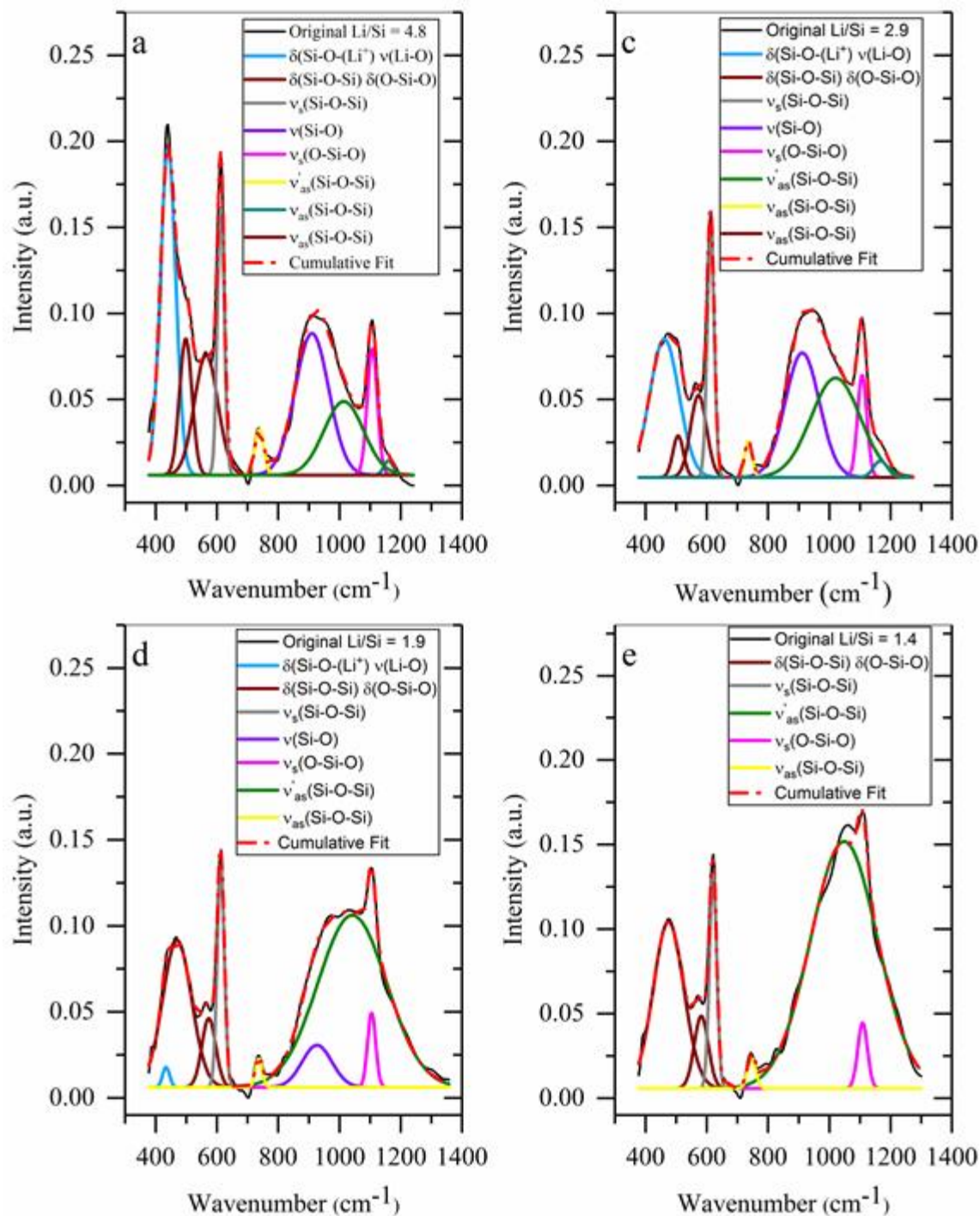


Figure II.2.B.43 Gaussian-peak deconvolution of a) Li/Si = 4.8 film, b) Li/Si = 2.9 film, c) Li/Si = 1.9 film, and d) Li/Si = 1.4 film.

The peak positions remained the same as those described in Table II.2.B.3 for all five compositions, but the intensity of the peaks shifted in a way that indicated increasing non-bridging oxygens (NBOs) as lithium content was increased in the thin films. A quantitative look at how these peaks shifted is shown in Figure II.2.B.44 by comparing the peak integration for the most-relevant vibration modes to the thin-film structure as the lithium content increases.

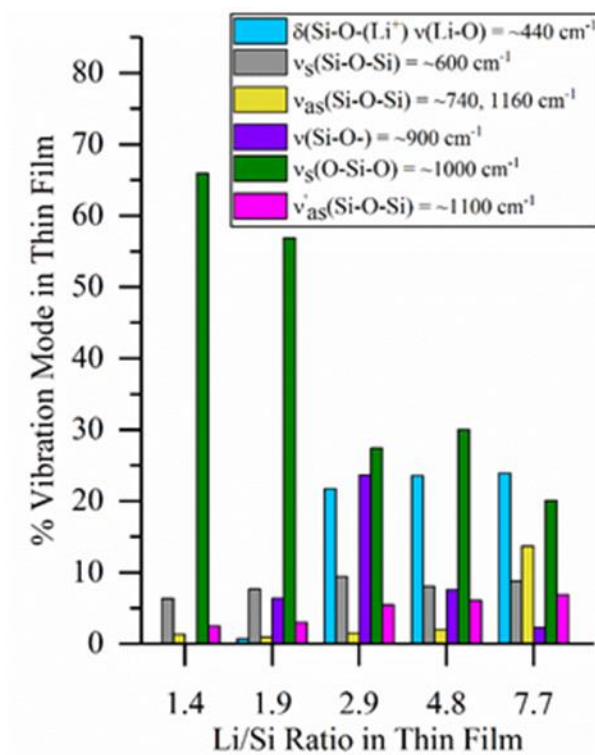


Figure II.2.B.44 Percent of vibration modes relevant to lithium silicate film with for each composition.

The peaks that show minimal variation across the film compositions (~ 600 , 740 , and 1100 cm^{-1}) are also too sharp to be associated with an amorphous material. Because sharp peaks in FTIR indicate a more-ordered structure, these bands are assigned to the crystalline-silicon substrate that is detected in transmission mode.

The vibrational modes that are most indicative of the structure of the lithium silicate films are $\nu(\text{Si-O-})$ at $\sim 900 \text{ cm}^{-1}$, and $\delta(\text{Si-O-(Li}^+))$ and $\nu(\text{Li-O})$ at $\sim 440 \text{ cm}^{-1}$ for the relative amount of NBOs in the material versus $\nu_s(\text{O-Si-O})$ at ~ 1000 for the relative amount of bridging oxygens (BOs) in the material. The fraction of $\nu_s(\text{O-Si-O})$ at $\sim 1000 \text{ cm}^{-1}$ in Figure II.2.B.44 (green) indicates that the number of BOs in the thin film decreases steadily as lithium is added, thus breaking up the silicate network. Up to $\text{Li/Si} = 3$, as lithium is added to the silicate network and the silicate chains break apart, more NBO bonds are observed; increased Li-O vibrations are observed, as well.

As more lithium is added past $\text{Li/Si} = 3$, sufficient lithium is now introduced such that it is possible for O^{2-} species to begin to form, which could create a decrease in NBOs as they dissociate from Si^{4+} altogether. This process can be observed by analyzing the variation in the $\nu(\text{Si-O-})$ mode at 900 cm^{-1} (shown in purple) as it increases in intensity up to $\text{Li/Si} = 3$ and then decreases for films with higher lithium content. In conjunction with this trend, the $\delta(\text{Si-O-(Li}^+))$ and $\nu(\text{Li-O})$ at $\sim 440 \text{ cm}^{-1}$ (shown in blue) increases as the lithium content is increased, suggesting that more lithium is bonding with the silicate network. The $\delta(\text{Si-O-(Li}^+))$ and $\nu(\text{Li-O})$ vibrational modes) at $\sim 440 \text{ cm}^{-1}$ are not observed to increase as much as might be expected for films with $\text{Li/Si} > 3$. The ratio of Li-O-type bonds in these higher-lithium-content films may not be fully represented in these spectra because there are Li-O bonds at frequencies $< 400 \text{ cm}^{-1}$ that are not observed due to limitation in the wavenumber range of the FTIR spectrometer used in this study. These results provide significant insight into how increasing lithium content acts to break apart the silica network, and they provide an important building block in understanding how lithium moves through the lithium silicate thin films.

XPS and TOF-SIMS was also used to further characterize the co-sputtered thin films and to assess the nature of the carbonate vibrational modes seen in FTIR, i.e., whether they are a surface or bulk impurity. XPS was

performed on Li/Si = 1.4, 2.9, 4.8, and 7.7 compositions with depth profiling using an argon ion beam. Lithium silicates are electronically insulating, so a low-energy electron flood source was used to compensate for the positive charge that accumulated during depth profiling. For each sample, the uppermost carbonate and oxide contamination layer was removed (~ 120 -second sputter time) to examine the chemistry of the underlying thin film. Figure II.2.B.45 shows the O 1s, Si 2p, and C 1s spectra of the Li/Si = 1.4 lithium silicate. See Figure II.2.B.46, and Figure II.2.B.48 for the XPS spectra of the other three film compositions. Table II.2.B.4 is a list of peak assignments for these spectra derived from literature. [46], [47], [48] Each set of spectra shows two relatively discrete layers within the films composed of the surface contamination layer on top of the film and the bulk film. Binding energy shifts show the transition zone at around 120 s of sputtering (green line).

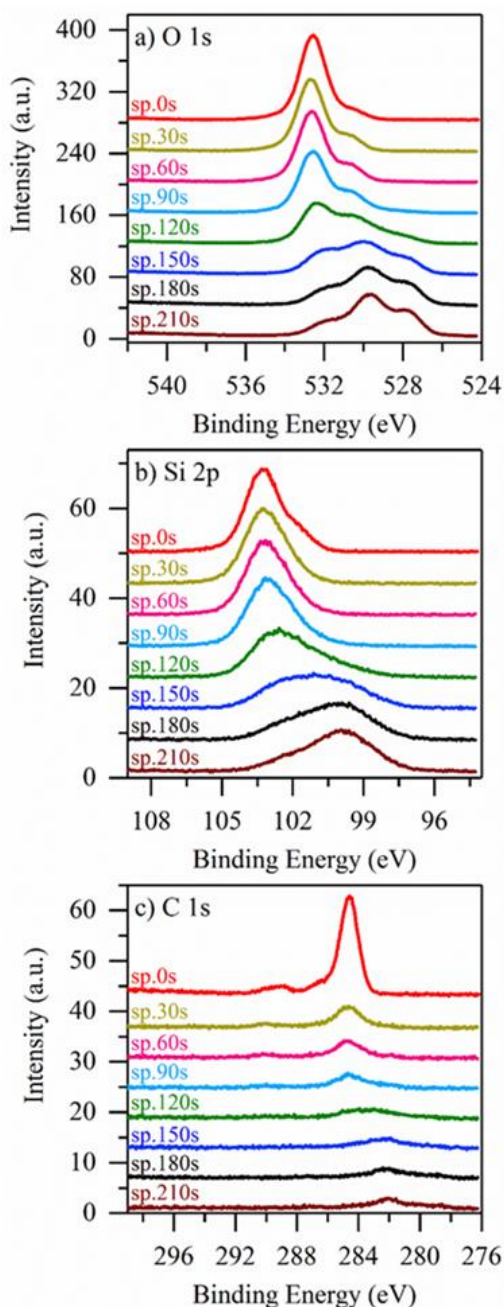


Figure II.2.B.45 XPS a) O1s, b) Si 2p, and c) C 1s binding energy regions with depth profiling of Li/Si = 1.4 sample.

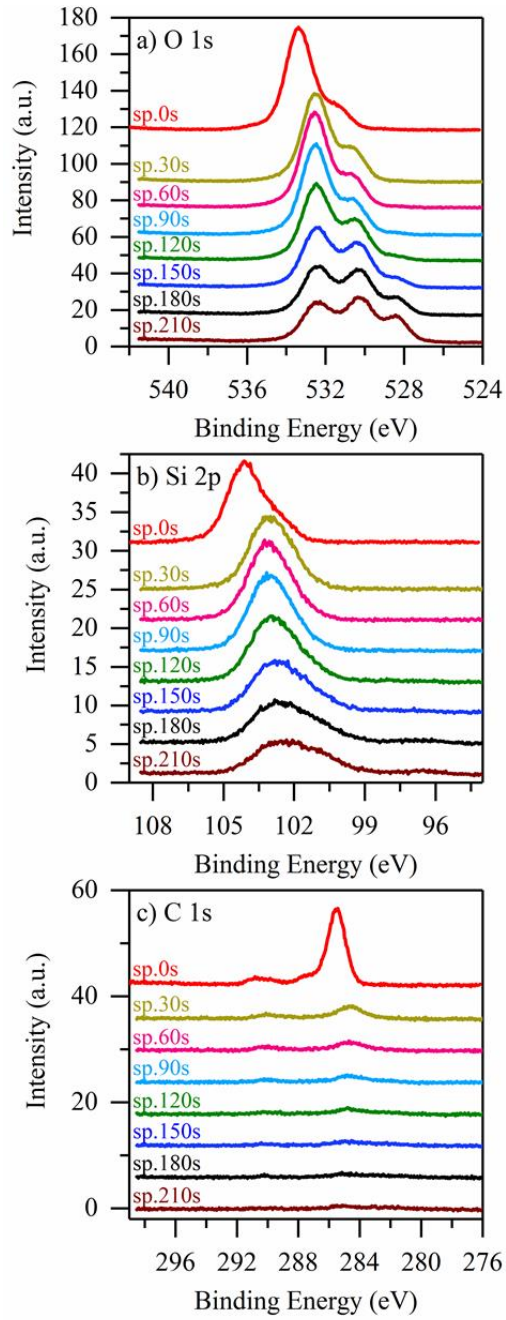


Figure II.2.B.46 XPS a) O 1s, b) Si 2p, and c) C 1s binding-energy regions with depth profiling of Li/Si = 2.9 sample.

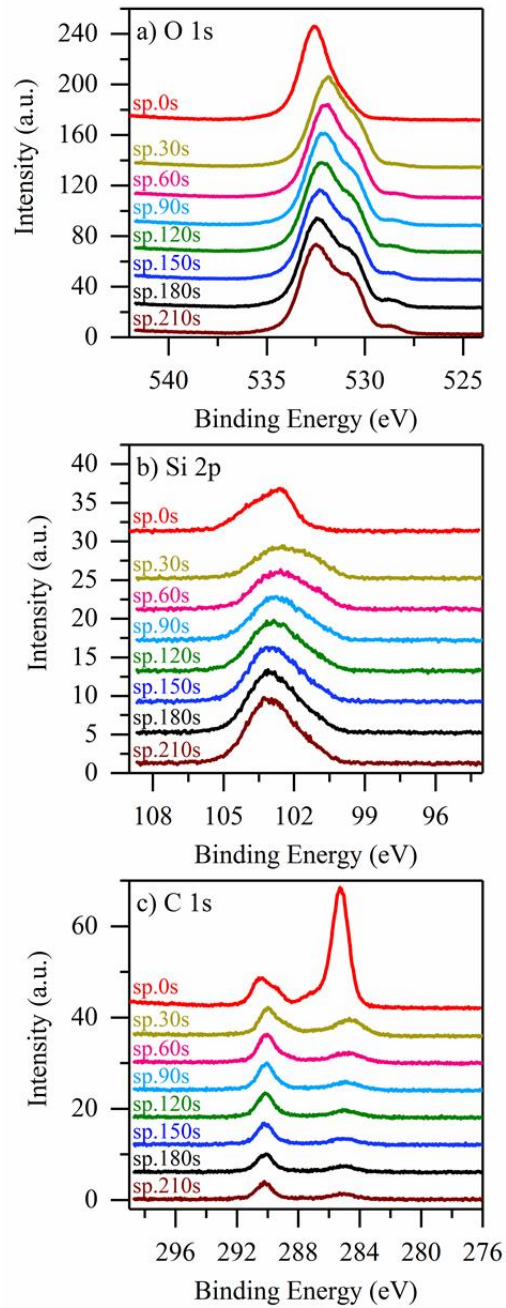


Figure II.2.B.47 XPS a) O1s, b) Si 2p and c) C 1s binding-energy regions with depth profiling of Li/Si = 4.8 sample.

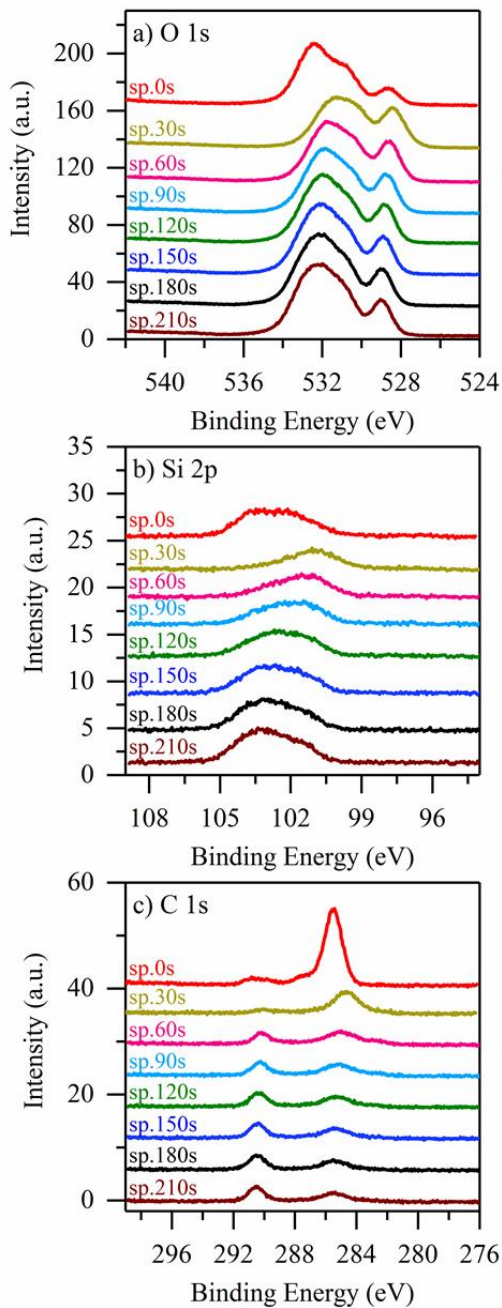


Figure II.2.B.48 XPS a) O1s, b) Si 2p, and c) C 1s binding-energy regions with depth profiling of Li/Si = 7.7 sample.

Table II.2.B.4 Peak Assignments for O 1s, C 1s, and Si 2p Binding-Energy Regions

Binding-Energy Region	Peak (eV)	Assignment
O 1s	532.7	SiO ₂
	531	LiOH
	531.5	Li ₂ CO ₃
	530–530.5	Li _x SiO _y
	528–528.5	Li ₂ O
C 1s	290	Li ₂ CO ₃
	288.5	CO ₂
	286.5	C-O
	284.6	C-C
Si 2p	103.2	SiO ₂
	100.5–101.3	Li _x SiO _y

The analysis for these XPS depth profiles begins with the spectra characteristic of the surface contamination layer (<120-s sputter). From the O 1s spectra shown in Figure II.2.B.45a, peaks are resolved at 532.7, 531.5, and 531 eV, indicating that the surface layer of the lithium silicate films consists of SiO₂, Li₂CO₃, and LiOH, respectively. The peak at around 103.2 eV observed in the Si 2p spectra in Figure II.2.B.45b and the peak at around 290 eV observed in the C 1s spectra in Figure II.2.B.45c also support the presence of Li₂CO₃ and SiO₂ at the surface of the thin film. The C 1s spectra in Figure II.2.B.45c (red line) shows some carbon surface contamination. Peaks are observed at 288.5, 286.5, and 284.6 eV assigned to CO₂, C-O-type bonds, and C-C bonds, respectively. The Li₂CO₃, CO₂, and C-O bonds are expected from surface adsorption during storage and/or exposure to low pressures during sample transfer. C-C bonds are observed into the bulk of the lithium silicate thin-film material, indicating a bulk contamination of higher-order carbon, such as graphite, in the thin film.

As the analysis transitioned into the bulk of the material (>120-s sputter time), some effect of charging became evident. This is most likely caused by differential charging that occurs in layered systems where the conductivity varies with each layer.^{[49], [50]} The charging results in the peaks in the bulk of the thin film appearing at lower binding energies due to the charge neutralizer, and they are broadened. This makes it challenging to assign these peaks to specific bonding structures. For this analysis, assigned peaks were chosen based on a uniform shift to lower binding energies that correlate to the shift in binding energies from known materials on the surface that are also present in the bulk of the film. Li 1s spectra were collected for these samples, but were confounded by the broadening and shifting of peaks due to charging—to the point that they could not be considered in this analysis. There are three main peaks that occur between 528 and 532 eV in the bulk of the thin film for the O 1s spectra. Taking into account a slight shift to lower eV as mentioned, the peaks were assigned to SiO₂ (532.7 eV), Li_xSiO_y (530–530.5 eV), and Li₂O (528–528.5 eV). The presence of SiO₂ as well as Li_xSiO_y can be explained by the fact that the Li/Si = 1.4 thin film has the lowest amount of lithium in the silicate network of the compositions studied in this work. This indicates that there may be some nanoscale phase separation in these films. The Li₂O is most likely also a reduced product from adventitious oxygen on the surface or weakly bound oxygen in the thin film, charge neutralization, X-ray exposure, or argon bombardment.

The thin film's bulk Si 2p spectra show a decrease in the SiO₂ binding energy at 103.2 eV and a shift toward Li_xSiO_y at 100.5–101.3 eV. The components found by XPS in the surface contamination layer and bulk of the

thin films agree with the silicate, Li_2CO_3 , and LiOH vibration-mode peaks observed in FTIR spectroscopy. The depth profiling provided by XPS confirms that the carbonate peaks observed in FTIR come from both surface and bulk carbon contaminations.

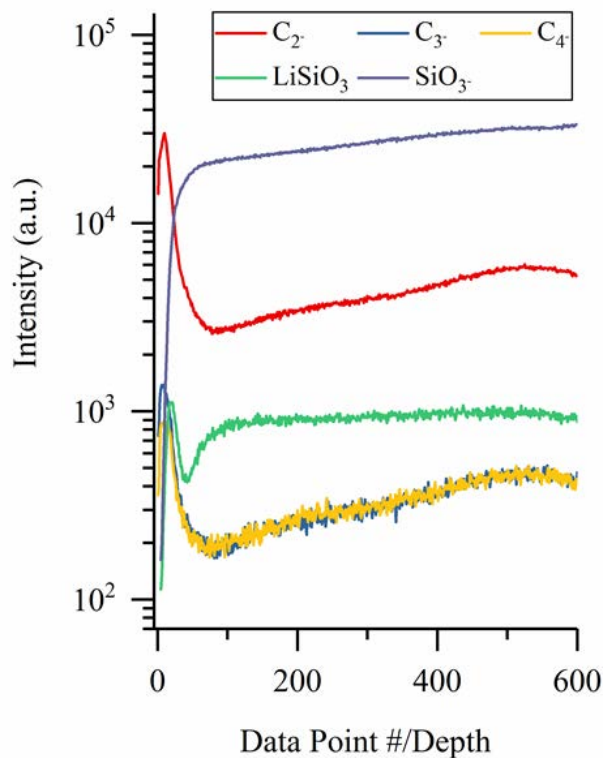


Figure II.2.B.49 TOF-SIMS analysis of Li/Si = 1.4 thin film.

The high-order carbon contamination observed in C 1s spectra in Figure II.2.B.45c was verified with TOF-SIMS. Figure II.2.B.49 shows that high-order carbon species even up to C_4 are present in the bulk of the lithium silicate film Li/Si = 1.4. These highly ordered carbon species were seen in all five compositions of the lithium silicates prepared in this work. See Figure II.2.B.50 for the TOF-SIMS analysis of the other four film compositions.

It is very unlikely that such highly ordered carbon would come from air contamination or handling of samples. Instead, this contamination is proposed to result from the sintering step during the synthesis process used to prepare the Li_2O target itself. The Li_2O target disks were separated by graphite sheets in the furnace to prevent incidental contact and unwanted reactivity such as melting. The graphite sheets visibly transferred some carbon onto the surface of the targets. The targets were mechanically abraded to remove any visible graphite and then sputtered for 24 hours prior to thin-film deposition; but evidence of graphite contamination is verified by our TOF-SIMS analysis. However, although this carbon exists within the films, there is no reason to expect it to adversely impact the structural analysis reported herein.

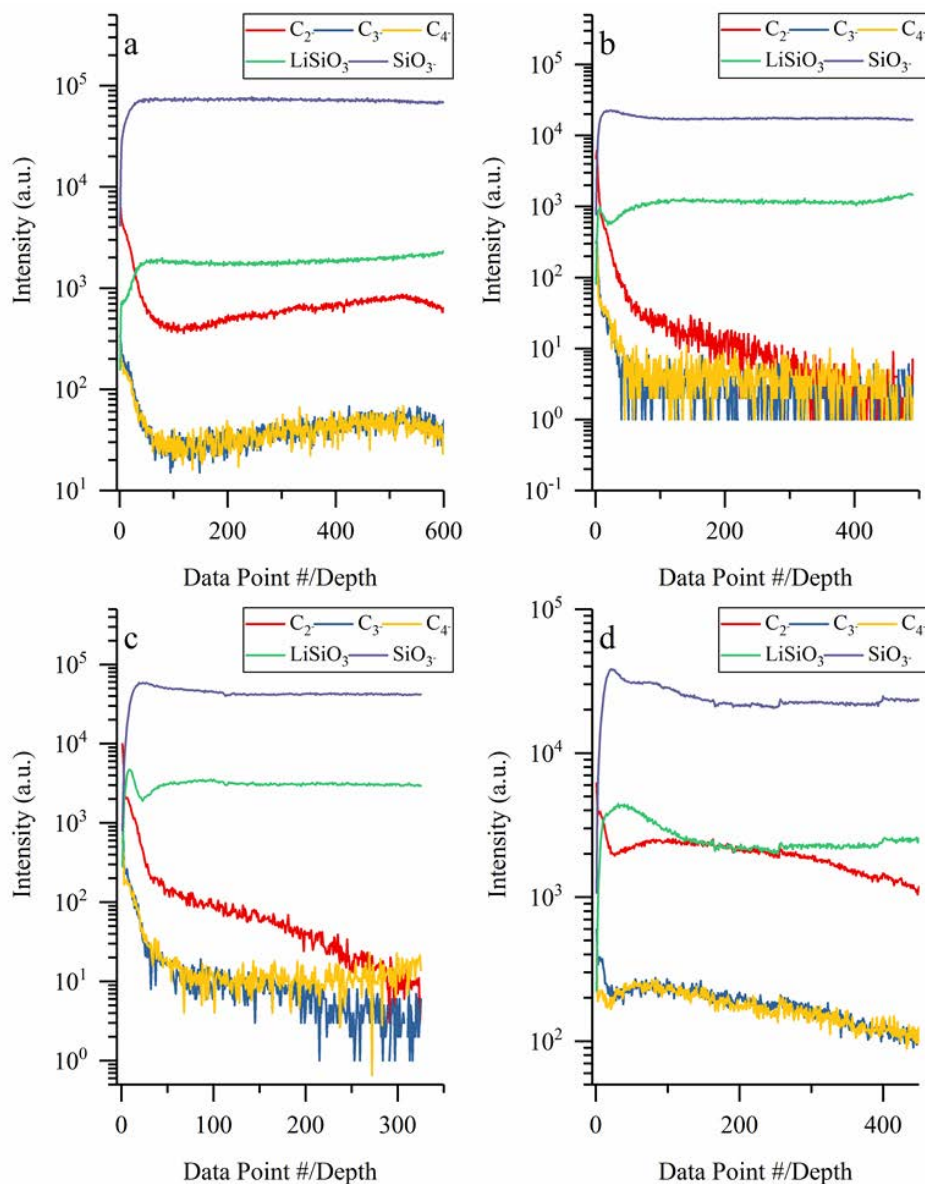


Figure II.2.B.50 TOF-SIMS analysis of a) Li/Si = 1.9 thin film, b) Li/Si = 2.9 thin film, c) Li/Si = 4.8 thin film, and d) Li/Si = 7.7 thin film.

Similar studies were carried out at NREL using TOF-SIMS and XPS and similar results were observed. They also used additional characterization techniques on the films to better understand ion mobility in the silicates, and they compared them to other stoichiometric compositions. The chemical composition and homogeneity of prepared individual SiEI component thin films were analyzed first, which can influence their intrinsic properties. Figure II.2.B.51 shows representative TOF-SIMS depth-profiling analysis of Li_2O , Li_3SiO_x , and Li_2SiO_3 thin films deposited on IPEs. In general, TOF-SIMS has ppm or better sensitivity, and negligible impurities were detected in the deposited films. In addition, similar chemical composition was confirmed for

the deposited thin film in between and on top of Pt digits. XPS depth profiling was used to analyze the chemical composition of deposited thin films of individual SiEI components.

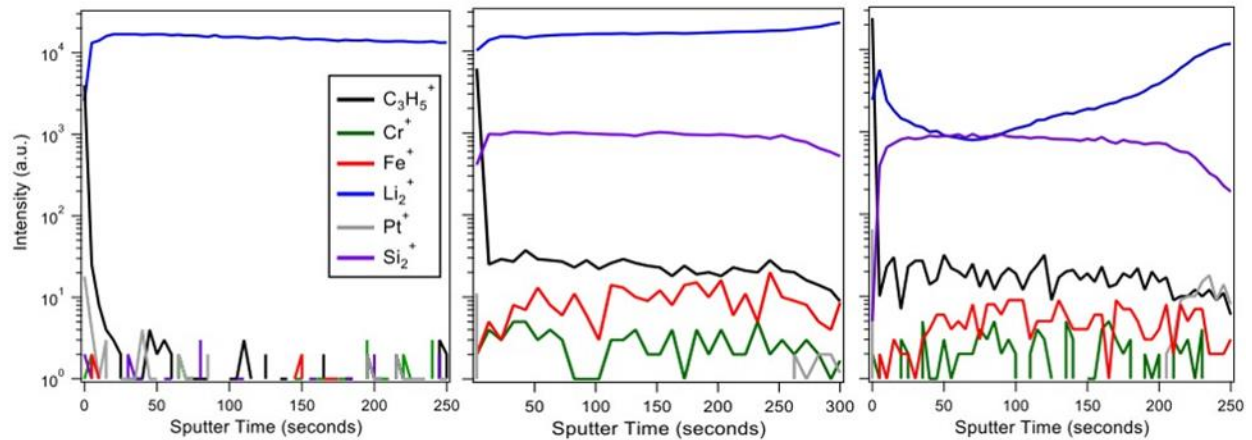


Figure II.2.B.51 TOF-SIMS depth profiling of Li_2O (left), Li_3SiO_x (middle), and Li_2SiO_3 (right).

Figure II.2.B.52 demonstrates that LiF was successfully grown on both a Li foil and Pt-coated Si wafer. Analysis of the change in binding energy (ΔBE) between the LiF peak in the F 1s and Li 1s was identical (629.41 eV) regardless of substrate, even though differences in surface charging occur because of the electrically insulating nature of LiF. Interesting, both of these films were deposited during the exact same run, but exhibited a difference in thickness of almost 6x. This is likely due to the reaction between the native Li surface and the evaporated LiF and/or the rough surface morphology of Li substrate.

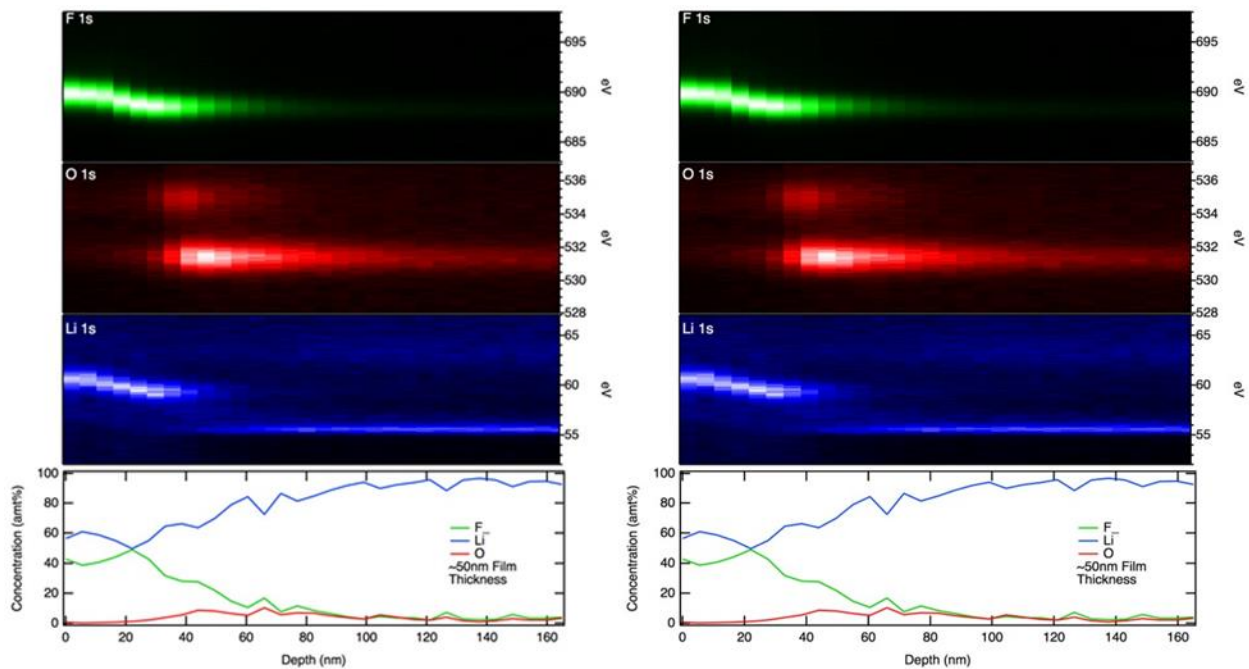


Figure II.2.B.52 XPS depth profile analysis of LiF thin films on a Li foil (left) and a Pt-coated Si wafer (right).

A similar set of experiments was outlined for other SiEI components (e.g., SiO_2 , $\text{Li}_2\text{Si}_2\text{O}_5$, Li_2SiO_3 , Li_3SiO_x , and Li_2O), and analysis of these sputter-deposited films demonstrated that the intended phase was present when deposited on a Pt-coated Si wafer.

The morphology and root-mean-square (RMS) roughness of the well-prepared thin-film samples were analyzed using atomic force microscopy (AFM), and the thickness of several samples was determined using scanning spreading resistance microscopy (SSRM) resistivity mapping and depth profiling. Unlike the surface morphologies of SiO_2 and LiF , those of lithium silicates and Li_2O display different nanoscale features (Figure II.2.B.53, $1 \times 1 \mu\text{m}$): $\text{Li}_2\text{Si}_2\text{O}_5$ shows small-scale features; Li_2SiO_3 shows large-scale features; Li_3SiO_x shows intermediate-scale features; and Li_2O shows the largest-scale features. The RMS roughness values of the Pt-coated Si wafer (as a blank sample for comparison), LiF , SiO_2 , $\text{Li}_2\text{Si}_2\text{O}_5$, Li_2SiO_3 , Li_3SiO_x , and Li_2O are 2.48, 2.77, 3.98, 13.4, 17.6, 26.6, and 69.1 nm, respectively. For lithium silicate surfaces, an increased Li:Si ratio has the trend of increased roughness, and Li_2O has the greatest roughness of all samples. One possible explanation for the largest-scale features and the greatest roughness of Li_2O thin film is that the sample was prepared with a relatively higher deposition rate, where the atoms do not have sufficient time to diffuse when they reach the substrate.

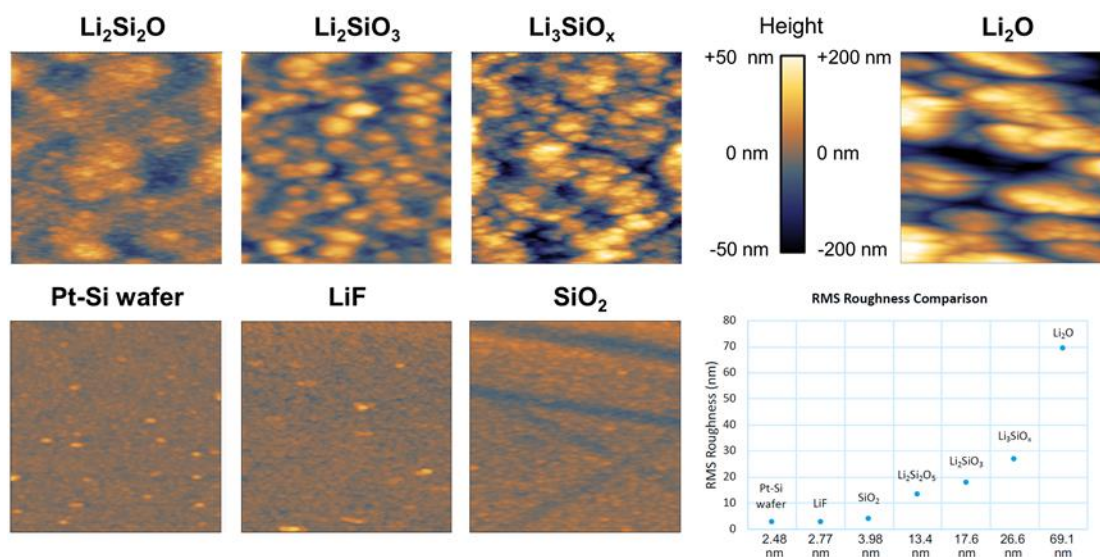


Figure II.2.B.53 Morphologies and RMS roughness of individual SiEI components deposited on Pt-coated Si wafers.

SSRM depth profiles were carried out to investigate deposition uniformity and thickness. Depositions showed uniformity of electronic properties throughout the deposited layers, and deposited layer thickness was measured at 100 and 200 nm for LiF and Li_2O , respectively, which shows good agreement with estimated deposition thickness.

The physical and electrochemical properties (e.g., ionic conductivity and activation energy) of individual SiEI component thin films (deposited on IPEs) were characterized using an EIS. The ionic conductivities with varying temperature and the activation energies (from Arrhenius relationship) of each thin film are shown in Figure II.2.B.54 and noted in Table II.2.B.5, respectively. In the case of a LiF thin film, increasing conductivity rates (in terms of slope) are different in two temperature regions (468–498 K vs. 528–588 K), possibly due to phase transition (e.g., growth of large grains, based on previous studies[37], [38]) at around 508 K. To verify this, XRD analysis was performed for as-prepared LiF and annealed LiF (at 523 K). Annealing of the LiF film with thermally induced reordering slightly shifts the (111) reflection peak toward a higher angle, which corresponds to a smaller lattice spacing. The shift very likely originates from residual stresses present in the film, as shown in previous research.[51]

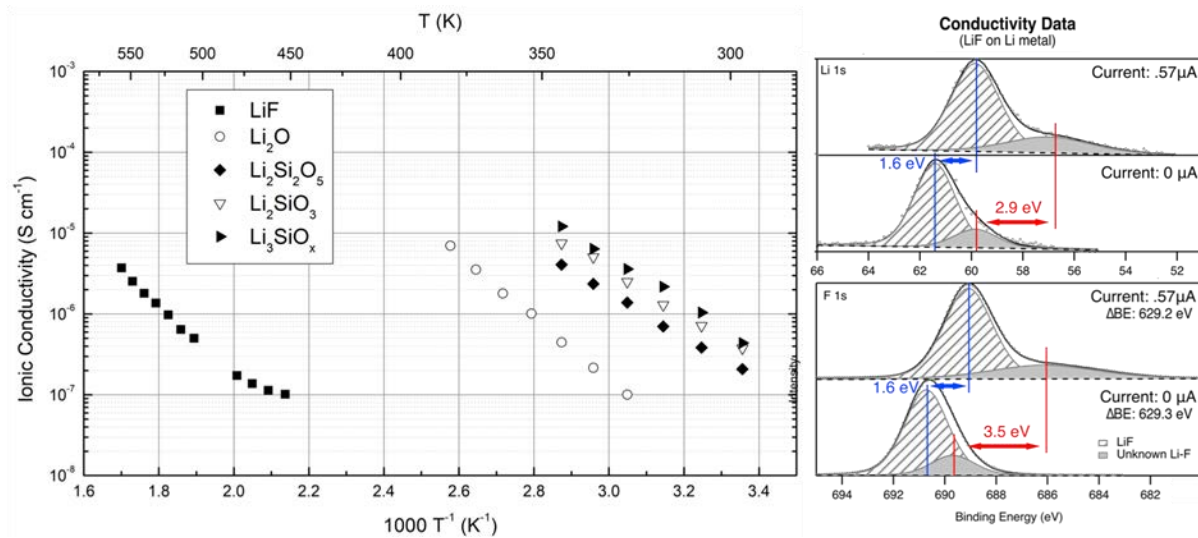


Figure II.2.B.54 Ionic conductivity of individual SiEI components with varying temperature (left) and binding energy variation of a LiF thin film on a Li foil obtained from operando XPS (right).

A complementary experiment using *operando* XPS has been designed to probe electronic/ionic conductivity. This novel technique uses sample biasing by creating a negative surface charge using an electron gun to measure shifts in binding energy, which can be related to either ionic or electronic conductivity (Figure II.2.B.54). [52]

Table II.2.B.5 Ionic Conductivities and Activation Energies of Individual SiEI Components.

Component	Conductivity (S cm ⁻¹)	Activation Energy (mV)
Li ₃ SiO _x	1.20×10 ⁻⁶ (at 298 K)	0.53 (298–348 K)
	2.20×10 ⁻⁵ (at 348 K)	
Li ₂ SiO ₃	9.49×10 ⁻⁷ (at 298 K)	0.56 (298–348 K)
	2.15×10 ⁻⁵ (at 348 K)	
Li ₂ Si ₂ O ₅	4.81×10 ⁻⁷ (at 298 K)	0.53 (298–368 K)
	9.52×10 ⁻⁶ (at 348 K)	
Li ₂ O	7.66×10 ⁻⁷ (at 348 K)	0.61 (348–408 K)
	1.42×10 ⁻⁵ (at 408 K)	
LiF	1.02×10 ⁻⁷ (at 468 K)	0.36 (468–498 K)
	~2.00×10 ⁻¹⁰ (at 298 K) ²	

¹at infinite temperature; ²obtained from *operando* XPS measurements

Overall, the following order is observed for increasing ionic conductivities of individual SiEI components with varying temperature:



It is noted that the ionic conductivities increased from low-lithium-content Li₂Si₂O₅ (1:1 Li/Si) to high-lithium-content Li₃SiO_x (3:1 Li/Si). Compared with surface electronic resistivity values in Figure II.2.B.55, the ionic conductivities of each sample (e.g., lithium silicates and LiF) are several orders of magnitude higher than the electronic conductivities of them, which is in accordance with our assumption for ionic conductivity measurements. Resistivity mapping at moderate forces at the surfaces of the deposited layers shows very low resistance for Pt-coated Si wafer, and very high resistivity (above the instrumental resolution limit, 10¹⁰ Ω·cm) for SiO₂ and LiF (Figure II.2.B.55).

AFM-scanning probe microscopy (SPM)-based nanoindentation was carried out at a determined force, 30 μN , exerted for 10 seconds (Figure II.2.B.55). At this force, no indentation was measured on a Pt-coated Si wafer, indicating a high measure of hardness. Relatively minor indentation was measured on lithium silicates and SiO_2 for this force (5–16 nm). LiF showed the least hardness among six samples, with the force resulting in an indentation of 36 nm. It is critical to note that all physical, electrochemical, and mechanical property values in this study are relative ones, for comparison only, among six inorganic amorphous thin-film samples. So, the relativity may be changed if we consider other known SiEI components (in particular, organic ones) or other types of samples (prepared with different methods).

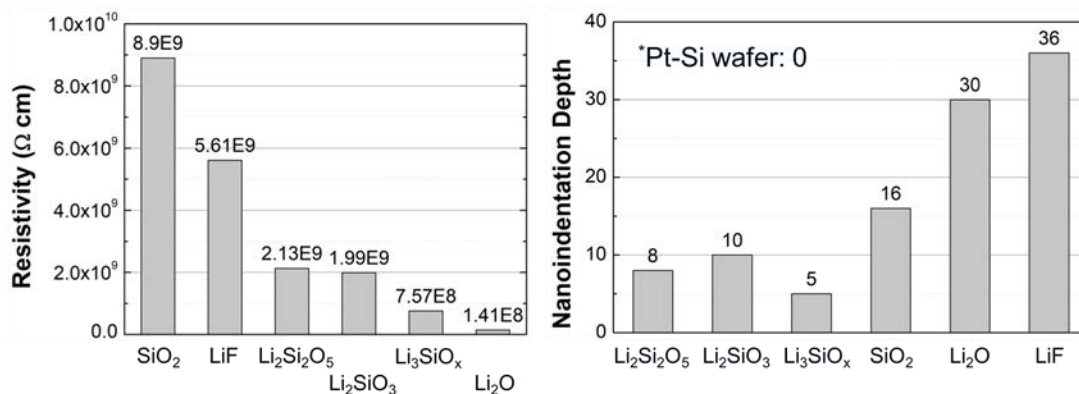


Figure II.2.B.55 Average surface electronic resistivity (left) and nanoindentation depth (right) of individual SiE

Nanoindentation was carried out on the as-deposited silicate films with a SPM nanoprobe by exerting a force of 30 μN for 10 seconds on the surface of the sample, then measuring the indentation depth of the probe. The results of these measurements are shown in Figure II.2.B.56.

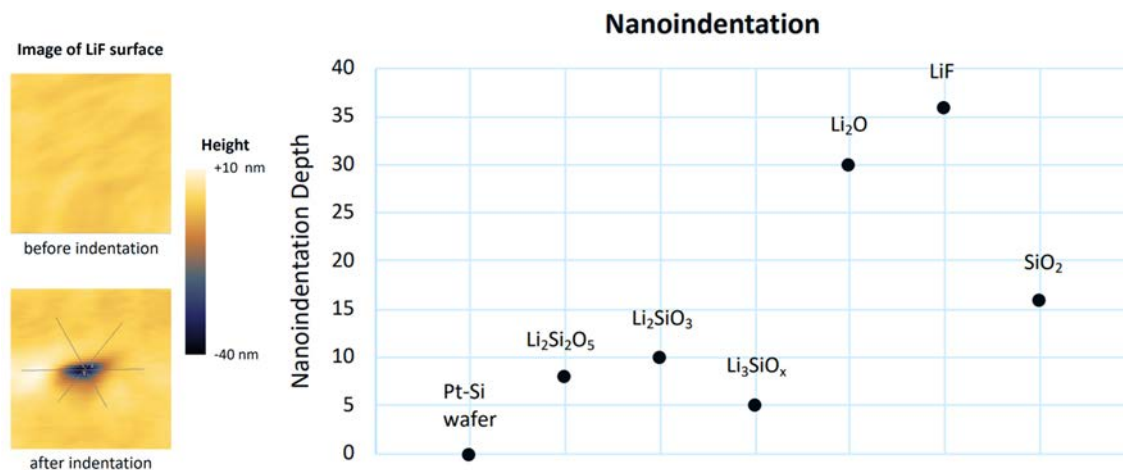
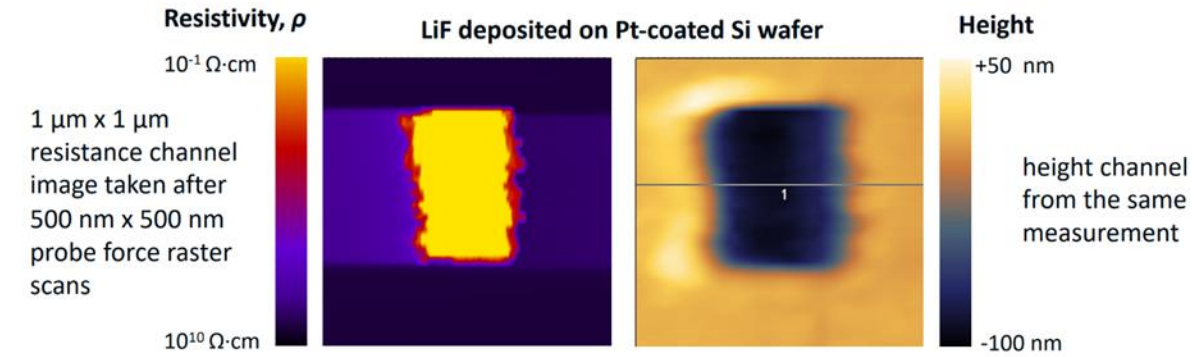


Figure II.2.B.56 500 \times 500-nm AFM images of the LiF surfaces before and after nanoindentation was performed, illustrating the AFM-based nanoindentation technique. Hardness results for each deposited film are plotted at right.

SSRM resistivity profiling on LiF and Li_2O deposited on Si wafers showed high resistivity ($10^9 \Omega \cdot \text{cm}$ and $10^8 \Omega \cdot \text{cm}$, respectively) with consistency throughout the film thickness, shown in Figure II.2.B.57.



SSRM profiles show good agreement with deposition estimate of thickness!

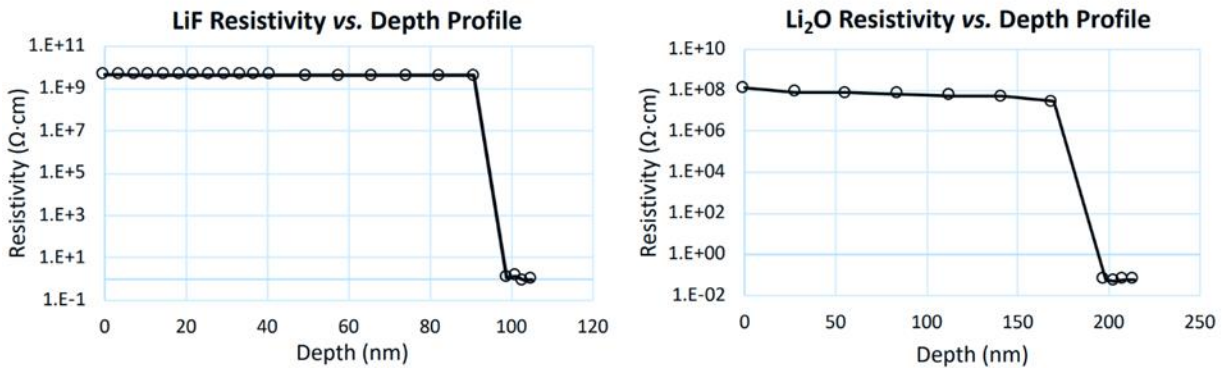


Figure II.2.B.57 $1 \times 1\text{-}\mu\text{m}$ SSRM images of the LiF surface showing resistance and height channels after SSRM resistivity vs. depth profiling was performed. Resistivity vs. depth profiles for LiF and Li₂O are plotted.

Several of the deposited films (Li₂O and Li₂SiO₃) were also examined in scanning transmission electron microscopy (STEM) electron energy loss spectroscopy (EELS). Results showed Li₂O to be nonuniformly deposited. EELS O K edge maps and Li K edge maps of the Li₂O sample showed oxygen to be located predominately in the Li₂O film, while significant amounts of Li had migrated into the e-beam Pt while exposed to the electron beam. See Figure II.2.B.58.

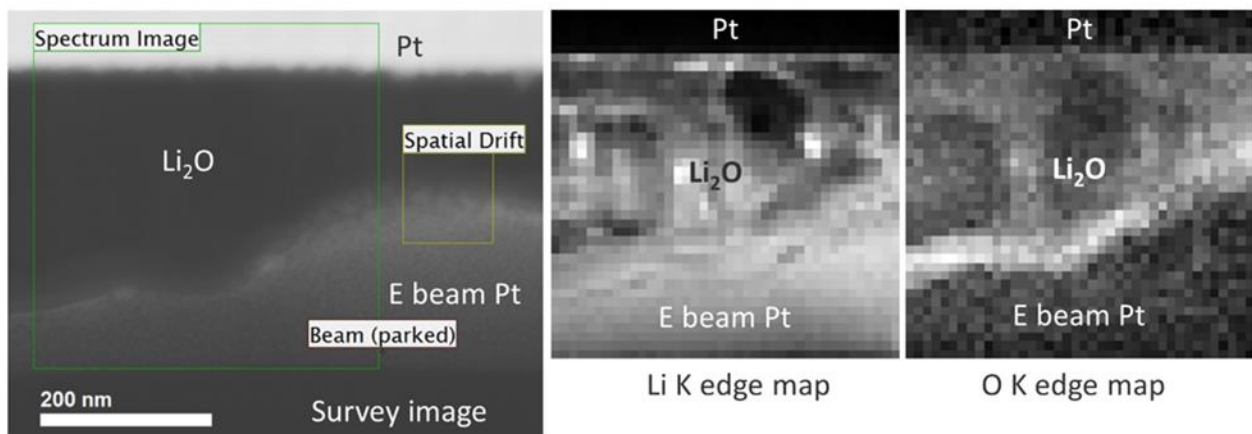


Figure II.2.B.58 EELS spectrum images of Li₂O film deposited on Pt on c-Si showing the Li K edge and O K edge maps.

EELS O K edge maps, Si L maps, and C K maps of the Li_2SiO_3 sample showed high O and Si content in the Li_2SiO_3 film. However, the Li K edge was unable to be mapped, likely because the Li migrated into nearby Pt layers due to electron-beam exposure. Atomic percent ratio calculations for this sample, obtained via Gatan Digital Micrograph EELS Analysis Software, showed Li to range from 58–63 at.%, whereas Si ranged from 37–42 at.%. The deposited film thickness showed greater continuity in this sample. See Figure II.2.B.59.

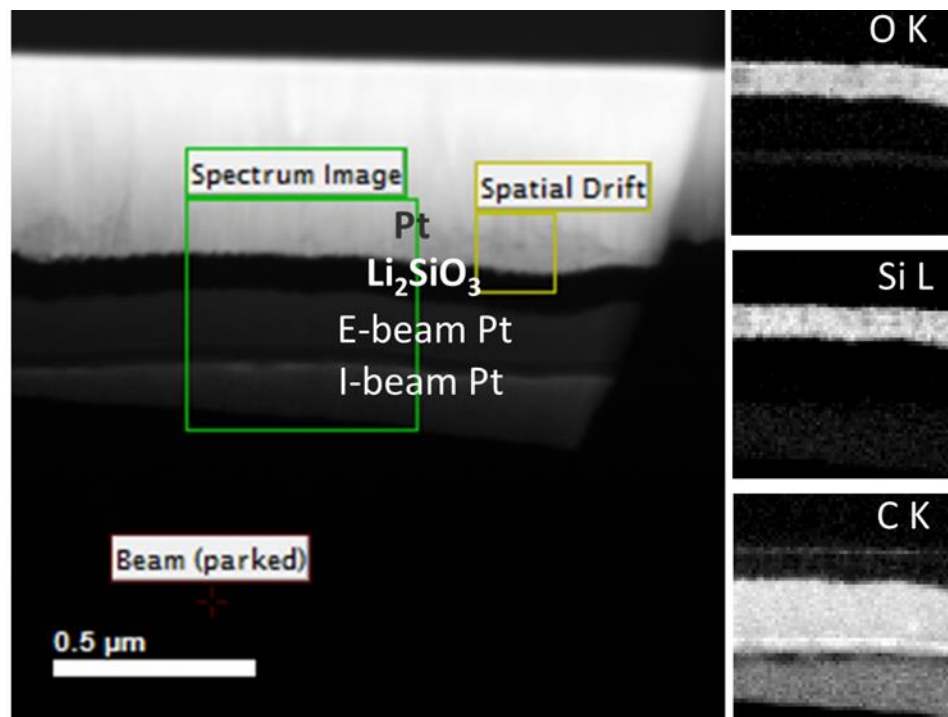


Figure II.2.B.59 EELS spectrum images of Li_2SiO_3 film deposited on Pt on crystalline Si showing O K edge, Si L edge, and C K edge maps.

To measure nanoscale electronic resistivity of SEI, an experimental approach was developed using SSRM to characterize SEI formed on Si. Reference samples were designed and measured to validate the technique and better understand instrumental resolution. The approach was implemented on SEI and results were compared to STEM results. Electronic resistivity of SEI is highly dependent on formation conditions (electrolyte mixture, cycling parameters, and original Si surface). But, in general, it shows a layered structure with high electronic resistivity at the surface, decreasing toward the SEI/Si interface.

Reactivity of Si surfaces exposed to electrolyte was investigated with AFM and SSRM. AFM measurements showed island-like accumulations of possible decomposition products and salts on the surfaces of both native oxide on crystalline Si (c-Si) and thermally grown SiO_2 on c-Si. However, immersion of a 15-nm-thick, thermally grown SiO_2 film on c-Si for 2 days and 7 days showed no decomposition of the film when investigated with SSRM resistivity vs. depth profiling.

Early-stage SEI characterized with SPM showed distinct trends with respect to alterations to resting protocol, cutoff voltage limit, and total number of cycles. These trends showed that resting the cell after cycling decreased roughness, increased thickness, and formed a less-resistive SEI. Using a higher cutoff-voltage limit led to the formation of SEI with decreased roughness and thickness, and less electronic resistivity. Continued cycling served to decrease surface roughness, increase thickness, and increase SEI resistivity.

SEI formed on a thin film of SiO_2 on c-Si showed interesting electronic, structural, and chemical properties when compared to that formed on native oxide on c-Si. Electronic resistivity measured via SSRM resistivity

vs. depth profiling showed that a thinner, more-resistive SEI formed on the SiO₂ model system. STEM characterization verified the thickness trend and also indicated a higher composition of C and O and lower levels of F in this SEI. High electronic resistivity may thus be a result of greater relative organic composition. Moreover, these results suggest that the initial SEI formation mechanism on SiO₂ depends on an intermediate Li_xSiO_y phase that forms during lithiation, because the SiO₂ film is no longer present after cycling. SEIs formed on these two model Si systems were also investigated with SSRM in their lithiated and delithiated states. Comparison showed lithiated SEI, after the first half cycle, is thinner and more resistive when compared to delithiated SEI after one full cycle.

Sputter-deposited films representative of proposed components of SEI on Si were characterized using AFM, SSRM, and STEM. Surface morphology, electronic resistivity, and mechanical hardness were measured for seven depositions using AFM and SSRM. Structure and chemical composition of several films were investigated with STEM to study the structure and elemental composition of the films.

STEM was used to characterize particulate materials for Si anodes. Elemental composition, particle size, and particle crystallinity were investigated. Additional samples were prepared to study the effects of exposure purely to glovebox environments, with no electrolyte or electrochemical cycling at all. In this case, the staff at Oak Ridge National Laboratory (ORNL) made thin-film Si (~200-nm) on Cu foil substrates and distributed samples from the same deposition run to each of the five partner national laboratories. Upon receipt by the different national laboratories, the thin-film samples were opened in gloveboxes and exposed for 5 days. After this 5-day period, the samples from each laboratory were sealed and shipped to NREL for surface analysis with XPS and TOF-SIMS. Each national laboratory partner also received the materials needed to make three Si-Li coin cell samples. These samples were electrochemically tested to establish correlations between the electrochemistry and surface chemistry.

After receiving samples from the various national laboratories, a control sample (sent directly to NREL from ORNL and not subjected to a 5-day glovebox exposure) was analyzed first, followed by each sample from the five partner laboratories. Normalized XPS surface spectra are shown in Figure II.2.B.60 (note that intensities are normalized for clarity). From this dataset, it is clear that the only new chemical states present on the surface are associated with F, whereas the Si, O, and C chemical states change very little. However, significant differences are observed in the relative atomic concentrations of these species on the surface.

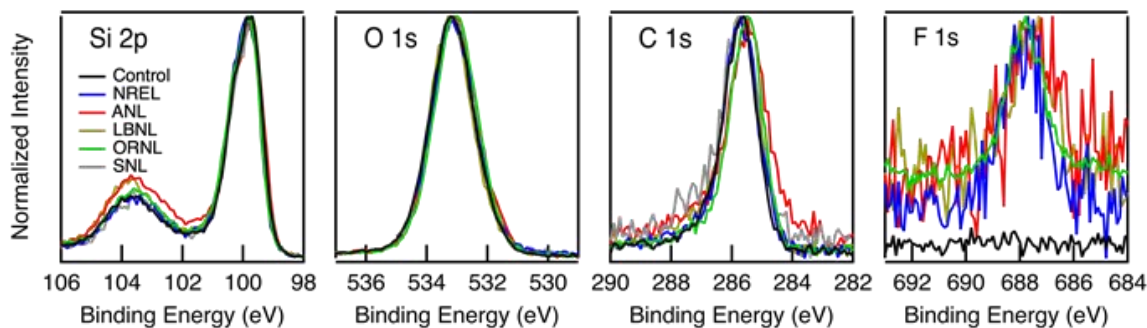


Figure II.2.B.60 XPS data showing little to no variation in chemical states present on the surface of the Si thin-film samples.

The atomic concentrations for each aged Si thin film are shown in Table II.2.B.6. These data show that storing a Si thin-film sample in any glovebox environment unsealed causes significant changes to the ratios of surface chemical states. Some boxes appear to introduce less surface contamination than others, whereas the relative amount of Si present at the surface always decreases with glovebox aging, while F, C, and O (O in every glovebox but one) increases. Consistent results were observed in the TOF-SIMS surface spectra. Perhaps even more interestingly, storing a Si thin-film sample in air caused the surface C and F content to decrease dramatically.

Table II.2.B.6 Elemental Surface Analysis after Aging Si Thin Films for Five Days in Different Gloveboxes across Different National Laboratories. Controlled Unaged and Air-Exposed Samples are Shown for Comparison.

	SNL	NREL	ORNL	ANL	LBNL	Control	Air Exposed
Si	54.0	53.4	51.3	50.9	45.2	56.5	51.7
C	19.2	20.9	20.5	13.5	22.6	17.2	12.6
O	26.5	24.6	26.1	34.9	31.4	25.9	35.7
F	0.1	1.2	2.2	0.7	0.8	0.0	0.0

TOF-SIMS and XPS analyses also reveal interesting changes in the aged materials' behavior with regard to apparent sputter rates. The sputter-depth scales for each technique were calibrated by correlating the sputter time to a sputter rate obtained from separate measurements on a smooth 100-nm-thick SiO₂ reference film on a Si wafer, because the films in this study were too rough for optical or stylus profilometry measurements. As seen in Figure II.2.B.61a, all of the glovebox-aged Si thin-film samples sputtered more quickly than the control, giving the appearance that the films thinned with aging. This effect might be due to 1) a relative increase in sputter rate that results from changes in film chemistry induced by the different ambient glovebox environments that altered aggregate bond strength in the films; or 2) the expulsion of water vapor, causing these films to densify. [53] By comparison, data in Figure II.2.B.61b show that it takes longer to sputter through the air-aged film than it does to sputter through the glovebox-aged samples or the unaged control. This interesting result might indicate that glovebox-aged films do in fact densify, because the partial pressure of water vapor will be much higher in air than in an Ar glovebox environment, thereby leading to a larger driving force for water expulsion during glovebox storage.

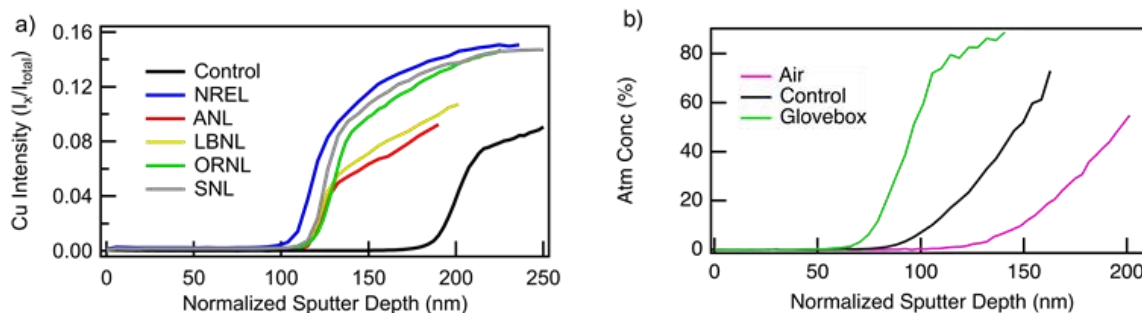


Figure II.2.B.61 TOF-SIMS profile data showing the apparent change in sputter rate of Si thin-film samples that have been aged in different gloveboxes across the five national laboratories; b) XPS profile data showing the difference between glovebox, control, and air exposed.

XPS and TOF-SIMS measurements demonstrated that exposure of Si thin films to ambient glovebox environments can lead to significant changes in the surface chemistry and film properties. Unsurprisingly, results showed that different gloveboxes produced varying degrees of surface contamination, whereas the chemical states associated with observed contamination were nearly identical for each glovebox in the study. When comparing glovebox storage to samples stored in air, air-stored films had more O present at the surface, but significantly less C and F. Further analysis of these materials revealed that glovebox storage might lead to film densification, while air storage might cause the reverse effect. Preliminary analysis of electrochemical data shows a trend suggesting that different surface chemistries indeed affect electrochemical performance.

There appears to be a link between the amount of C present on the surface of the sample and the amount of observed capacity obtained in the first half-cycle; higher C content tends to increase capacity.

Electrolyte Exposure Results (Harvey, Coyle, Han, Veith, Stetson, Zavadil)

Once the samples had been analyzed for composition and stability, the next step was exposure to electrolyte. Most of the laboratories involved in the study did some level of direct electrolyte exposure without electrochemical cycling, just to determine the chemical effects of exposure to unstable electrolyte on the silicates. The first set of these, a collaboration between ORNL and NREL, slightly modified the sample preparation from above to address where oxygen was coming from in the growth and modification of the SiEI. In this particular case, the oxide was grown with isotopically pure ^{18}O , rather than standard oxygen. The oxygen contained in the electrolyte was not isotopically enhanced, so differences in the positions of ^{18}O vs. ^{16}O could give some indication as to where oxygen was coming from during the growth and modification of the film. Virtually all silicon electrode materials are terminated with an oxide coating. The thickness and composition of the oxide ($x = ?$ in SiO_x) in most materials is not known. Furthermore, identifying the true oxide is difficult due to the challenges in elucidating the silicon oxidation state and proton termination of the oxides. One of the unanswered questions regarding the interfacial chemistry of silicon is what is the role of this SiO_x surface termination layer on the SEI formation reaction, lifetime, and cyclability on the starting film. Modeling data from Perrson (see above) indicates that with lithiation, one should proceed through the formation of Li-Si-O phases before lithiating the metallic silicon. Thus far, there have been multiple sets of conflicting information regarding the influence of the SiO_2 and whether this SiO_2 reacts to form a lithium silicate on the Si surface. There is IR and NMR spectroscopy data that show the growth of Li-Si-O species. In contrast, X-ray absorption data shows the absence of Li-Si-O with cycling.

The goal of this work is to identify the presence or absence of Li-Si-O as well as its location within the electrode and its role in SEI formation. The reactions are predicted to occur at open-circuit voltage from the chemical reaction with Li-salt or during lithiation. To answer these questions, we are performed experiments using ^{18}O -terminated silicon electrodes. The benefit of this isotope labeling is that it will enable us to identify where the potential Li-Si-O is forming, and also, where the oxygen used to form the Li-Si-O materials comes from—specifically, oxygen from the termination of the silicon electrode or oxygen from the carbonate solvent used in the electrolyte.

Samples were fabricated using physical vapor deposition. Pre-sectioned silicon wafers were fabricated at Sandia National Laboratories and battery-grade copper foil was used to grow the electrodes for this study. Figure II.2.B.62 shows a photo of the silicon-wafer-supported electrodes fabricated for this study and a cross-section schematic of the electrodes. The amorphous silicon was 50 nm thick whereas the oxide thickness varied depending on deposition time. These materials were distributed to Silicon Electrolyte Interface Stabilization (SEISta) team members for cycling and chemical characterization.

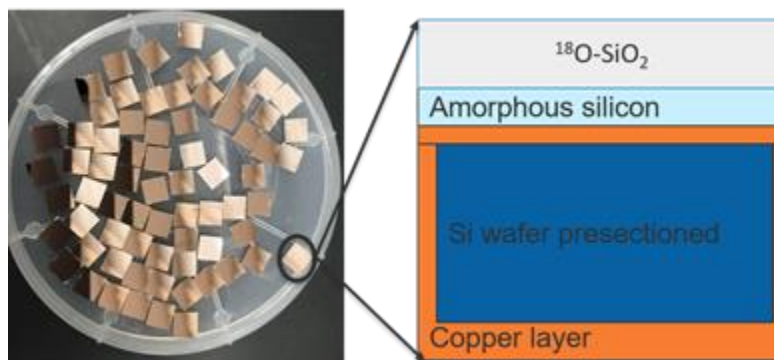


Figure II.2.B.62 (left) Photo of the silicon-supported electrodes; (right) Schematic of the electrode cross section.

Figure II.2.B.63 TOF-SIMS data collected for the as-prepared sample grown on a silicon wafer. The data show a 50-nm-thick silicon layer supported on a copper film. The surface oxide shows a large signal originating from the ^{18}O layer (black line). The apparent signal enhancement at the Cu/Si interface is likely due to matrix effects from the conductive copper underlayer.

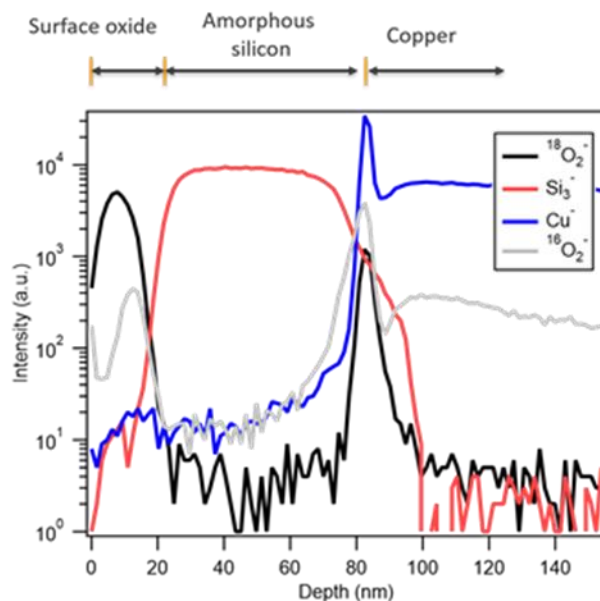


Figure II.2.B.63 TOF-SIMS data collected on the as-prepared electrode.

The samples were exposed to the GEN2 electrolyte used in the SEISta program (1.2M LiPF_6 3:7 wt% ethylene carbonate/ethylmethyl carbonate) for 1, 3, and 19 hours. To match electrode reaction conditions, we used a “dry” electrolyte (3 ppm H_2O) and a “wet” electrolyte (500 ppm H_2O). Figure II.2.B.64 shows TOF-SIMS data collected on samples aged for 3 hours in the wet and dry electrolytes. These data are shown in two plots for clarity. We observe several trends from these data. First, the electrode exposed to wet electrolyte slowly dissolves with time. This is observed by the smaller ^{18}O trace for the wet sample versus the dry sample, indicating the shrinking of the oxide coating.

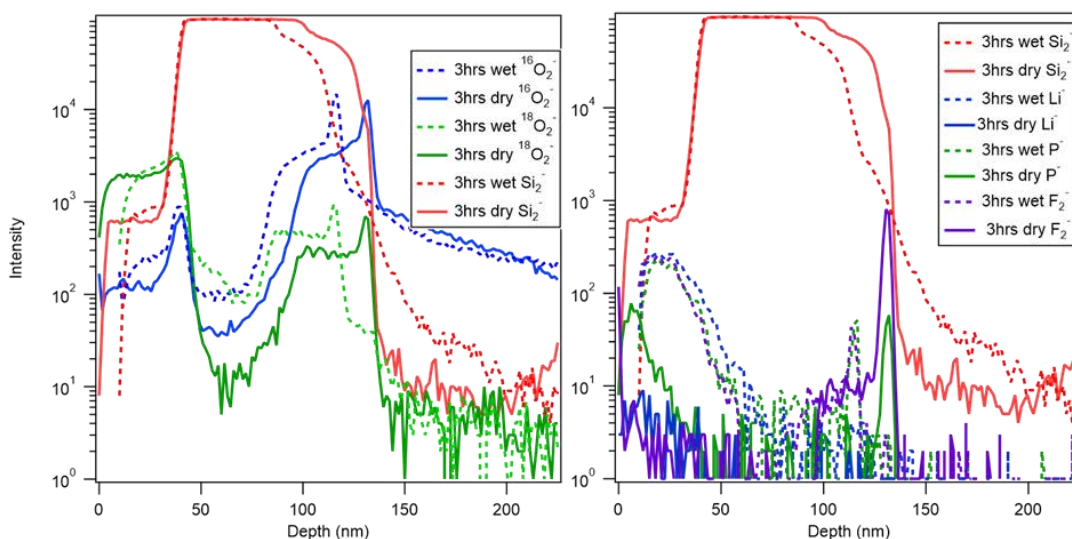


Figure II.2.B.64 TOF-SIMS data collected for ^{18}O labeled electrodes aged for three hours in wet and dry electrolyte.

The second trend we observe is the clear evidence for Li incorporation within the Si^{18}O_2 layer. This incorporation of lithium matches the same incorporation with P and F from the electrolyte and C and ^{16}O from the carbonate solvent. Interestingly, under the dry conditions, we do not see Li incorporation within the Si^{18}O_2 layer. Furthermore, we observe an apparent concentration of P and F for the dry samples at the silicon/copper interface. Together, these data indicate that the water is promoting the salt decomposition and reaction at the interface. This does not indicate the formation of Li-Si-O's at open-circuit voltage, so this is not a major component of the initial SEI formation reaction.

Stability of Lithium Silicate – $\text{Li}_2\text{Si}_2\text{O}_5$

Films of $\text{Li}_2\text{Si}_2\text{O}_5$ were specifically synthesized on amorphous silicon by sputtering. In this study, the samples were subjected to an aging study using dry electrolyte and investigated using neutron reflectometry (NR). In neutron reflectometry, the specular reflection of neutrons from an interface is measured as a function of the wave vector transfer, $Q = 4\pi\sin(\theta)/\lambda$, perpendicular to the sample surface. The angle of incidence θ is between the incoming neutron beam and the sample surface, and λ is the wavelength of the neutron. Analyzing the neutron reflectivity gives us information about the thickness and composition of the film layers.

Figure II.2.B.65 shows NR data collected for the as-prepared sample and sample soaked in electrolyte for 3 hours and 71 hours. The peaks in the NR data are called Kessing fringes and are due to constructive and destructive interference of the scattering pattern as a function of angle. The position is related to layer thickness whereas the amplitude is due to nuclear cross-section. In Figure A, the most-intense peak is highlighted. As one can see, the data are changing with time. Indeed, the position is shifting to lower Q values and the intensities are changing. This shift to lower Q values indicates a thickening of the oxide or a mixing of the surface and the underlying silicon layer. The structure is complex and difficult to fit due to the diffusion of Li within the structure or some other chemical changes to the layer chemistry.

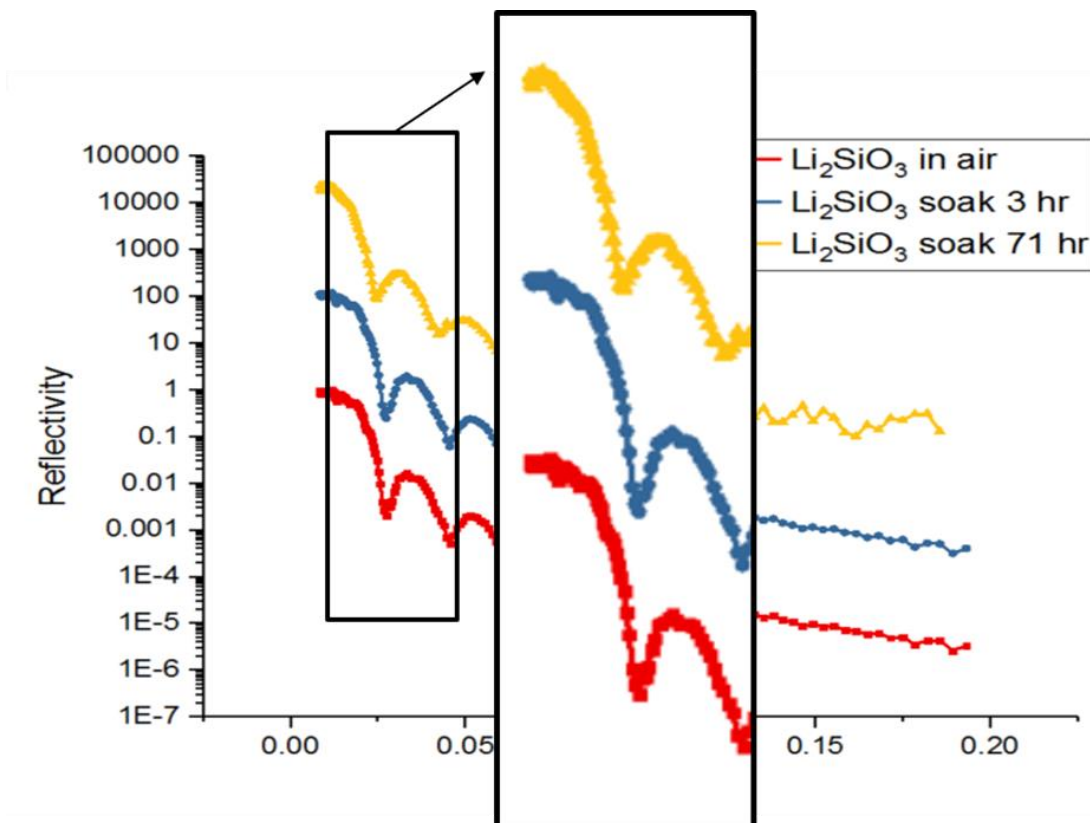


Figure II.2.B.65 NR data collected for $\text{Li}_2\text{Si}_2\text{O}_5/\text{Si}$ films as a function of time aging in electrolyte.

Amorphous silicate films ranging from 40 to 72 nm in thickness sputtered onto Si wafers were used as electrodes for this study. Imaging of the lithiation and alloying process was monitored using an electrochemical AFM (Bruker Dimension) to track morphology change. A cantilever sensitive to measuring surface deformation for materials with an elastic module of 1 to 100 MPa was used to both image and capture the mechanical response of the silicate film. A typical cyclic voltammogram (scan rate = 100 $\mu\text{V/s}$) generated for the first several cycles into the onset of Li-Si substrate alloy formation is shown in Figure II.2.B.66. Minimal reductive current is generated until the silicate film is polarized to ~ 100 mV, at which point the current increases in magnitude, which signals the onset of alloy formation. The return potential sweep exhibits anodic current due to de-alloying. Subsequent potential cycles demonstrate a lower potential onset for alloy formation, indicating that the initial barrier to Li^+ transport and alloy nucleation imposed by the silicate is significantly reduced. Details of the extent to which this process occurs can be learned by conducting *operando* imaging while conducting electrochemistry coupled with subsequent *ex-situ* analysis of the morphology, structure, and composition of the cycled silicate film.

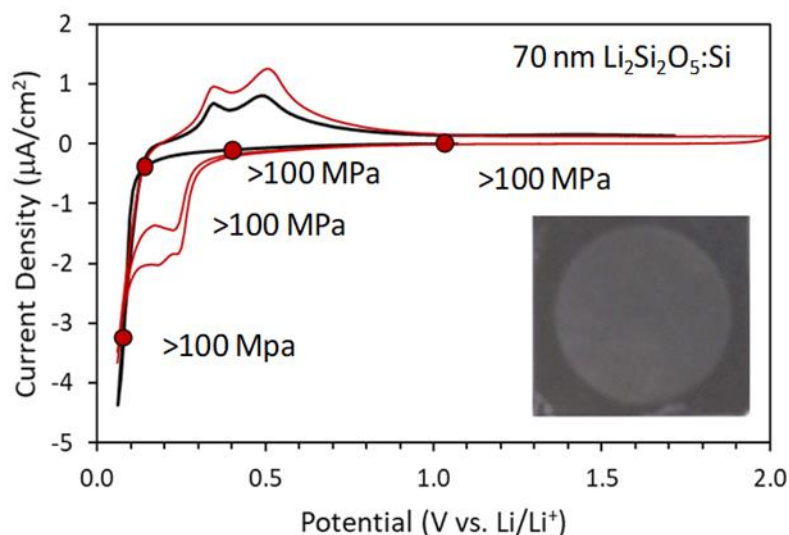


Figure II.2.B.66 Cyclic voltammetric response of 70-nm-thick amorphous $\text{Li}_2\text{Si}_2\text{O}_5$ films on a Si wafer in 1 M LiPF_6 1:1 EC:DMC at scan rate of 0.1 mV/s. Markers indicate the potential-dependent elastic modulus measured with an electrochemical AFM. The inset shows the change in optical properties with Li-Si substrate alloying.

Operando AFM imaging was used to track morphological and mechanical property changes with silicate lithiation and Si substrate alloying. AFM images were acquired for the $\text{Li}_2\text{Si}_2\text{O}_5$ film by sweeping to and holding the potential at select values based on the typical voltammetric response (labeled markers in Figure II.2.B.66). Minimal change in morphology is observed for this film up to the alloying threshold, and the elastic modulus of the silicate remains greater than 100 MPa, above the upper sensitivity limit of the AFM cantilever. With sufficient alloying at 90 mV (increased time of potential hold), the nodular morphology of the $\text{Li}_2\text{Si}_2\text{O}_5$ is preserved, but the elastic modulus of the silicate:LiSi bilayer decreases to 20 MPa, signaling “softening” or an increased mechanical compliance. Similar softening transitions are observed for the higher-Li-content amorphous silicates, including Li_2SiO_3 and Li_3SiO_x . AFM imaging shows that the basic morphology of the film is largely unchanged, shown in Figure II.2.B.67.

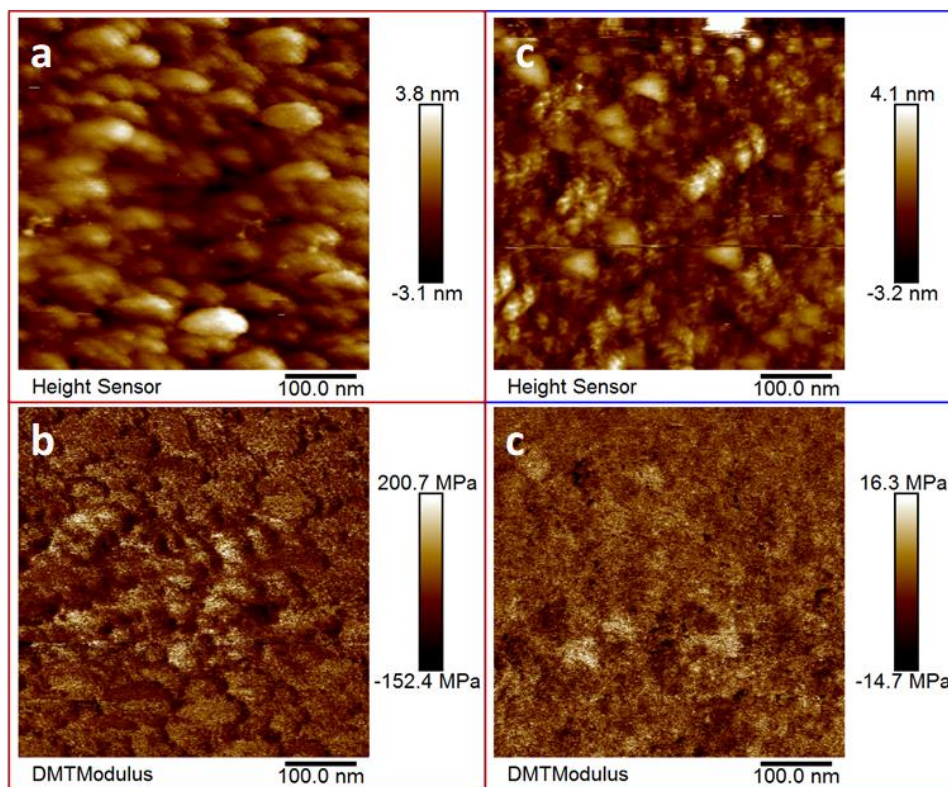


Figure II.2.B.67 Operando AFM images on 70-nm-thick $\text{Li}_2\text{Si}_2\text{O}_5\text{:Si}$ electrodes undergoing lithiation and substrate alloying. Topography and effective elastic modulus a,b) prior to the Li-Si alloy threshold and c,d) after alloying at 50 mC/cm², 90 mV (vs. Li^{0/+}).

The extracted, rinsed, and dried electrode was transferred under argon to a scanning electron microscope (SEM) to confirm that the silicate film remained intact on the wafer surface. Figure II.2.B.68 shows the original area imaged during the AFM experiment. This location was readily identified by a unique pattern of film disruption to either side of the AFM cantilever but projected outward at a distance of 15 μm . In the *operando* imaging, we demonstrated that displacement of the tip and scanning reproducibly recreated this pattern numerous times. SEM imaging showed that the silicate film morphology is unchanged with respect to the original (as-deposited) silicate, arguing that the silicate film does indeed remain intact during early-stage alloying of the underlying substrate. We interpret the decrease in modulus to detection of the more-compliant Li-Si alloy forming below the silicate. As depicted in Figure II.2.B.68, we hypothesize that the relatively rigid silicate film vibrates on top of the compliant alloy, yielding an effective decrease in elastic modulus of the silicate:LiSi bilayer. The observed mechanical disruption displaced from the tip likely corresponds to a node at which stress is concentrated, resulting in local fracture of the silicate. Such fracture could be correlated with the thickness of the silicate film because we have not observed this phenomenon on thinner 40-nm-thick films. We also argue that the flat nature of these films contributes to their stability. Silicate films on particles, a more representative geometry for a practical Si anode, will experience curvature and stress concentration, likely yielding film fracture.

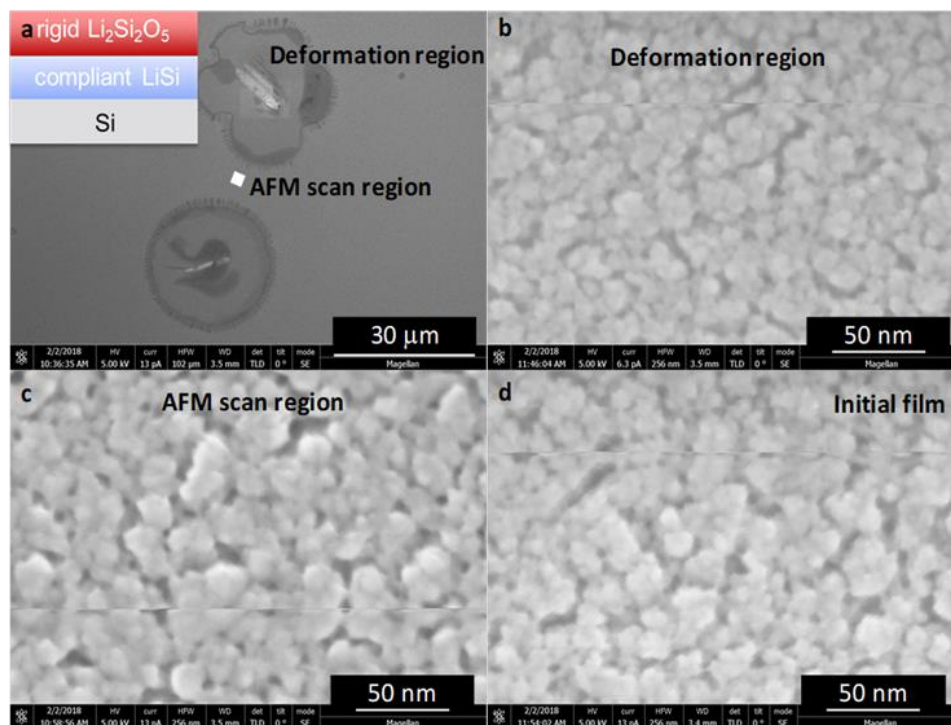


Figure II.2.B.68 Scanning electron micrographs of a $\text{Li}_2\text{Si}_2\text{O}_5:\text{Si}$ electrode alloyed to $50 \text{ mC}/\text{cm}^2$ at 90 mV (vs. $\text{Li}^{0/+}$). a) Silicate film disruption (localized cracking and delamination) is induced by low-force AFM scanning but at a considerable distance from the imaging area. b–d) The morphology of the silicate is unchanged with electrochemical lithiation, early-stage alloying of the underlying Si, and low-force (nN) imaging.

The fate of the silicate film under lithiation and substrate alloying conditions can also be tracked through compositional profiling of the electrode after removal from the electrochemical environment. TOF-SIMS depth profiles are shown in Figure II.2.B.69 that highlight the silicate film indicated by SiO^+ (shown) and $\text{LiSiO}^+/\text{LiO}^+$ (not shown for simplicity) ion yield, the silicate/Si interface where ion milling produces Li accumulation as indicated by LiSi^+ yield, and the bulk Si wafer with Si^+ yield apparent at the greatest depths. SIMS provides a clear signature for alloying of the substrate as the Si interface systematically shifts to greater relative depth with increased extent of alloying: from 5 nm at $6 \text{ mC}/\text{cm}^2$ (Figure II.2.B.69c) to 20 nm at $50 \text{ mC}/\text{cm}^2$ (Figure II.2.B.69a). Electrodes left in the alloyed state exhibit enhanced, depth-distributed LiSi^+ ion yield (Figure II.2.B.69a) as the direct measure of the alloy, whereas de-alloyed electrodes (Figure II.2.B.69c) yield a modest enhancement in LiSi^+ yield. We find minor variation in ion yield for the LiSiO^+ and LiO^+ families of ions with depth, arguing minimum modification of the basic composition and structure of the silicate film and emphasizing the stability of these films when used in this flat form factor. The silicate film appears resilient to repeated cycling (14 cycles) into the early stage of alloying over time (70 h), exhibiting minor compositional change (Figure II.2.B.69b,c).

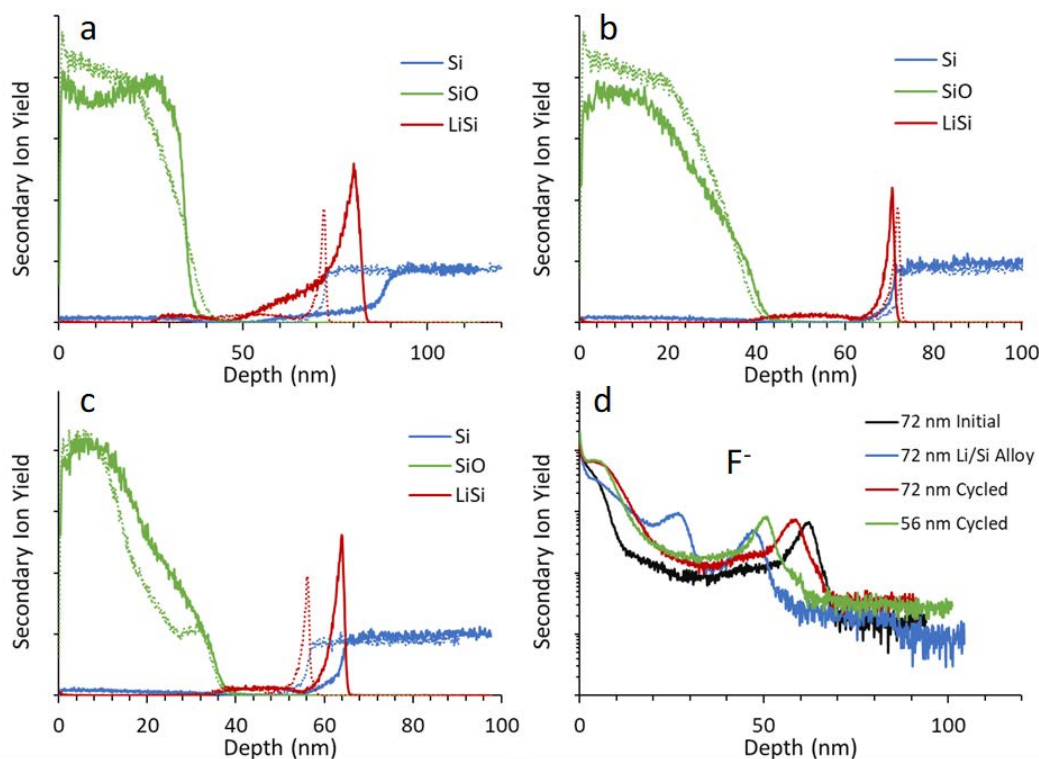


Figure II.2.B.69 TOF-SIMS depth profiles (25-keV Bi⁺ for analysis, 1-keV Xe⁺ for milling) of Li₂Si₂O₅:Si electrodes at various stages of Li/Si alloying. a) 72-nm-thick silicate alloyed to 50 mC/cm² at 90 mV (vs. Li^{0/+}) left in the alloyed state. b) 72-nm-thick silicate alloyed to 8 mC/cm², de-alloyed, repeatedly potentiodynamically cycled to 7 mC/cm² at 0.1 mV/s, and left in the de-alloyed state. c) 72-nm-thick silicate alloyed to 8 mC/cm², de-alloyed, repeatedly potentiodynamically cycled to 12 mC/cm² at 0.1 mV/s, and left in the de-alloyed state. d) Comparison of F⁻ ion yield for each of the electrodes. Dashed traces correspond to as-deposited silicate controls.

Measurable but small amounts of fluoride incorporation in the silicate are observed beyond the near surface and silicate/Si interface residual levels observed for the as-deposited silicate, signaling a degree of chemical reaction between silicate and electrolyte. The extent of interaction appears to increase with extent of alloying as opposed to contact time with electrolyte. Minimal compositional change is also observed for the higher-Li-content Li₂SiO₃ and Li₃SiO_x silicates with early-stage alloying, consistent with the observed short-term structural stability of these films.

Cycling Results (Coyle, Han, Stetson, Teeter, Veith, Zavadil, Xu)

No previous studies have conducted electrochemical analysis on the impact of lithium silicates at the surface of the silicon anode. To magnify the electrochemical effects of lithiated silicates at the silicon anode surface, this study uses model lithium silicate thin films deposited onto thin-film silicon anodes. Much of this analysis focuses on the discharge of the half cells, or lithiation of the silicon anode, particularly the first lithiation. This is because this work is an attempt to understand how the lithiation of the native oxide, which theoretically occurs during the first lithiation, affects the silicon anode performance. Analysis of more-extended cycling based on the native oxide lithiation is touched on here, but in-depth analysis of the stability of lithium silicates with cycling or their effect on the overall stability of the silicon anode was beyond the scope of this work.

The synthesis and composition verification of the 40-nm-thick SiO₂, Li₂Si₂O₅, Li₂SiO₃, and Li₃SiO_x thin films for this study will be published in the near future. As a reminder, these films were deposited on degenerately doped silicon (p⁺, boron, 0.004 to 0.04 Ωcm) substrates with 500-nm gold sputtered on their backside, as well as 20-nm Ti deposited on the front side as an adhesion layer for 500-nm copper coated with 40-nm evaporated

amorphous silicon. Silicate-coated silicon thin films were assembled in coin cells in half-cell configuration using a Celgard 2325 separator and 1.2M LiPF₆ EC:EMC 3:7 wt% electrolyte in an argon-filled glovebox. Galvanostatic cycling was completed with a constant current of 0.5 μA to provide a C/100 cycle rate. A voltage window of 0.26 V to 1.5 vs Li/Li⁺ was chosen to prevent additional reactions from volume expansion of silicon and to avoid undesirable side reactions with the c-Si substrate. Half cells with each composition of model thin film were in triplicate to provide assurance against any outliers in the results. For cyclic voltammetry, coin cells in half-cell configuration were swept from 1.5 V to 0.08 V vs Li⁺/Li at a 0.01 mV/s scan rate, or at an approximately C/50 cycle rate.

The high cut-off voltage of 0.26 V for the galvanostatically cycled cells was applied to ease the degradation from volume expansion and contraction, but it also served another purpose. Half cells that we attempted to lithiate below 0.26 V at a constant current at a C/100 rate experienced a voltage hold phenomenon, as seen in Figure II.2.B.70.

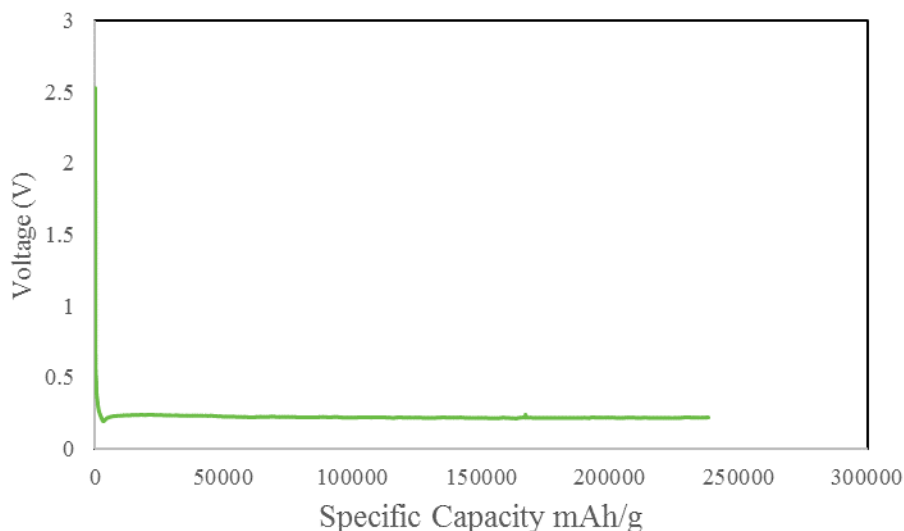


Figure II.2.B.70 Uncoated amorphous silicon galvanostatically cycled with 0.05 V cutoff voltage at C/100 rate.

Once the cells with or without any of the four silicate coatings reached ~0.21 V, a side reaction occurred resulting in the potential holding at ~0.21V for up to weeks at a time. This reaction could be due to unintentional lithiation of the underlying c-Si substrate, unintentional lithiation of the Au layer on the backside of the substrates, or an unknown SEI formation reaction. This reaction is not observed in CV, possibly due to the nature of the cycling (controlling current in cycling vs controlling voltage in CV) or due to the cycle rate. Given the observed behavior, the issue of continuous discharging was mitigated by limiting the voltage window before the voltage hold begins. Further study outside the scope of this work is necessary to verify the cause of this voltage hold for these substrates.

Cyclic voltammetry plots for the first cycle of thin-film silicon anodes with SiO₂, Li₂Si₂O₅, Li₂SiO₃, and Li₃SiO_x thin-film coatings are presented in Figure II.2.B.71.

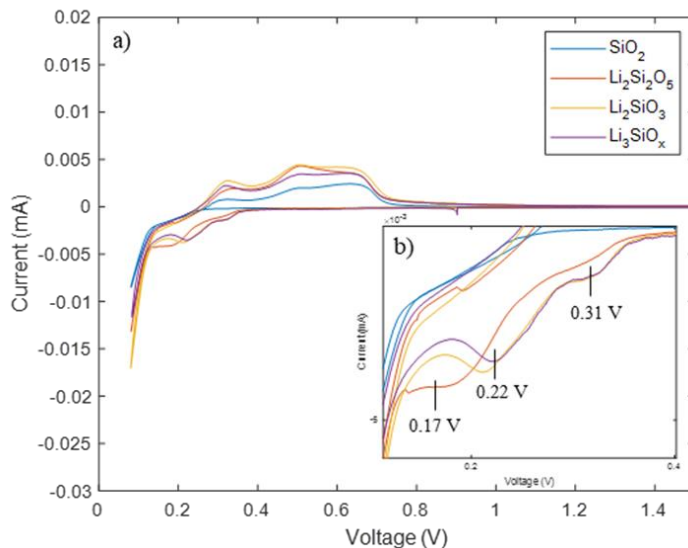


Figure II.2.B.71 a) First-cycle CV for silicon anodes with silicate coatings and b) discharge profiles.

Figure II.2.B.71b is a closer look at the discharge, or reduction, peaks for the first lithiation for each composition. The silicon anode with SiO₂ thin film does not show significant reduction current until about 0.23 V, whereas the lithiated silicate-coated silicon anodes show the onset of reduction current occurring around 0.4 V, with peaks associated with lithiation occurring at voltages as high as 0.31 V. This is evidence that the lithiated silicates provide a lower barrier to lithium-ion insertion than the unlithiated SiO₂, which makes sense considering their ionic conductivities. There is a sharp difference in the lithiation/delithiation mechanism of SiO₂ in comparison to the lithiated silicates. However, there is a less significant difference in the electrochemical performance as the lithium increases in the lithium silicate coatings. All anodes with the three different lithium silicate coatings exhibited step-wise lithium insertion into amorphous silicon, with reduction peaks or shoulders at around 0.31, 0.22, and 0.1 V, forming amorphous Li_xSi. [54] The silicon anode with an SiO₂ coating has only a small shoulder starting at ~0.23V with a sharp lithiation peak at ~0.1 V. This may be due to the higher impedance of the SiO₂ film at the surface compared to the Li_xSiO_y requiring lower potentials to overcome this transport barrier.

A closer look at the step-wise insertion peaks for lithium-silicate-coated anodes in Figure II.2.B.71b shows some subtle trends with increasing lithium content. The lowest-lithium-content film, Li₂Si₂O₅, has only a small shoulder at ~0.31V and a wave-type peak centered at ~0.17 V. Wave-like peaks show that a reaction that is causing the current to form a wave-like peak is not diffusion-controlled; additional overpotential does not increase the current because it is limited by the kinetics at the surface and current is not lost because there is no shortage of reactants. This shows that whereas Li₂Si₂O₅ provides a lower barrier to lithiation than SiO₂, it is not as low a barrier as the two higher-lithium-content silicates. These higher-lithium-content coatings, Li₂SiO₃ and Li₃SiO_x, show more complete lithiation reactions at 0.31 V and 0.22 V because they have a more-distinct shoulder and sharper peak at each respective potential. The difference between Li₂SiO₃ and Li₃SiO_x-coated silicon anodes is minimal. The silicon anode with a Li₂SiO₃ coating has a slightly larger peak at 0.22V than the Li₃SiO_x-coated silicon anode. This may indicate that the impedance presented by a Li₂SiO₃ coating is very similar to the impedance presented by a Li₃SiO_x coating. The delithiation, or oxidation, part of the first cycle from each silicate coating shows similar peaks for all compositions. Each silicate coating has broad delithiation peaks at 0.33 V, 0.5 V, and 0.68 V, which indicate lithium extraction from amorphous Li_xSi. [55] The differences in heights of these peaks correlate to the extent of lithiation of the silicon anodes during the discharge part of the cycle. That is why the SiO₂ coating has the lowest-intensity oxidation peaks. However, the delithiation peaks for the lithiated silicates increase in order from Li₃SiO_x to Li₂Si₂O₅ to Li₂SiO₃, which is not the same order as the depth of the lithiation peaks, as expected. This shows that the delithiation of the

silicon anode following the first round of SEI formation is less dependent on the initial lithium content of the film than the first lithiation.

CV samples are controlled to spend a specific amount of time scanning across voltages and are reported with respect to current generated at each voltage. Because of this, CV plots only observe electrochemical reactions that produce current through the silicon anode. Chemical or thermodynamic reactions, such as electrolyte degradation or SEI formation—which consume electrons or lithium ions but do not produce measurable current—are not documented by the CV technique. Constant-current (CC) samples have a controlled current applied to them and are free to hold at any voltage in the cut-off voltage window for the time that is required to complete the reactions that occur at said voltage. The raw data for CC samples is reported with regard to time (hours), then converted to capacity (mAh/g) using the mass of the anode and current applied. CC plots depend on the capacity, or time, consumed by any reaction (electrochemical, thermal or chemical) at a certain voltage instead of just the current produced by electrochemical reactions. So, they present a more comprehensive picture of what is occurring at the silicon anode during charge or discharge. When comparing CV and CC plots, it is important to remember that the CV curves represent only electrochemical reactions (typically just lithium-silicon alloying) whereas the CC curves describe both silicon-lithium alloying and chemical SEI formation reactions.

In Figure II.2.B.72, the first lithiation of a set of SiO_2 , $\text{Li}_2\text{Si}_2\text{O}_5$, Li_2SiO_3 , and Li_3SiO_x coatings on silicon cycled at a constant current at a C/100 cycle rate are plotted. This graph shows a similar pattern as Figure II.2.B.71 regarding the effect of the lithiation resistance of each silicate with a key additional piece of information.

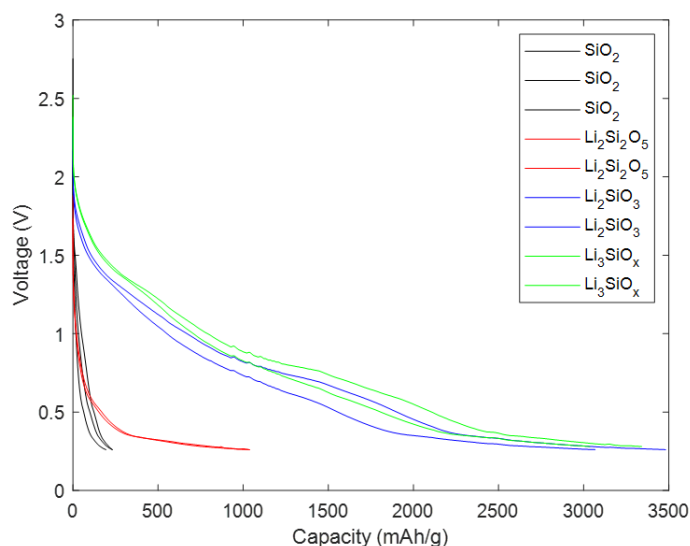


Figure II.2.B.72 First lithiation of silicate-coated silicon anodes at C/100 with replicates for each coating composition.

As in the CV lithiation reduction peaks, the plateaus that indicate lithiation in this graph occur at a lower potential for SiO_2 (in black) than for the lithiated silicates. Similarly, the $\text{Li}_2\text{Si}_2\text{O}_5$ curves (in red) have a slightly lower plateau than the higher-lithium silicates (high capacity blue and green curves). The three SiO_2 curves on the left side of Figure II.2.B.72 do not actually show a significant lithiation plateau because the voltage cutoff of 0.26 V is above 0.23 V, where silicon coated with SiO_2 starts to lithiate according to the CV plots in Figure II.2.B.71. The key additional piece of information gained from the cycling data even with the low cutoff voltage is the evidence of a large amount of capacity loss for the higher-lithium-content lithium silicates. According to the area under the CV curve in Figure II.2.B.71, which indicates the electrochemical capacity of the first discharge, the capacity from lithium-silicon alloying for a Li_3SiO_x -coated silicon anode during the first lithiation is only ~ 500 mAh/g. When examining the capacity from both current-producing

lithium-silicon alloying and SEI formation as in Figure II.2.B.72, the overall capacity for the first lithiation cycle for Li_3SiO_x -coated silicon anode is $\sim 3,000$ mAh/g. This shows that a great deal of the capacity shown for the Li_3SiO_x -coated silicon anodes in Figure II.2.B.72 comes from electrolyte degradation and formation of the SEI. This large capacity loss from SEI formation is evident for both Li_3SiO_x and Li_2SiO_3 -coated silicon anodes. The higher-order silicate coatings result in a more-reactive surface that consumes more electrolyte to create more SEI than the lower-order silicates.

Continued Cycling Analysis

Further cycling for CV samples is summarized in Figure II.2.B.73—with Figure II.2.B.73a showing the second cycle, Figure II.2.B.73b showing the seventh cycle, and Figure II.2.B.73c showing the fourteenth cycle for each composition of silicate coating.

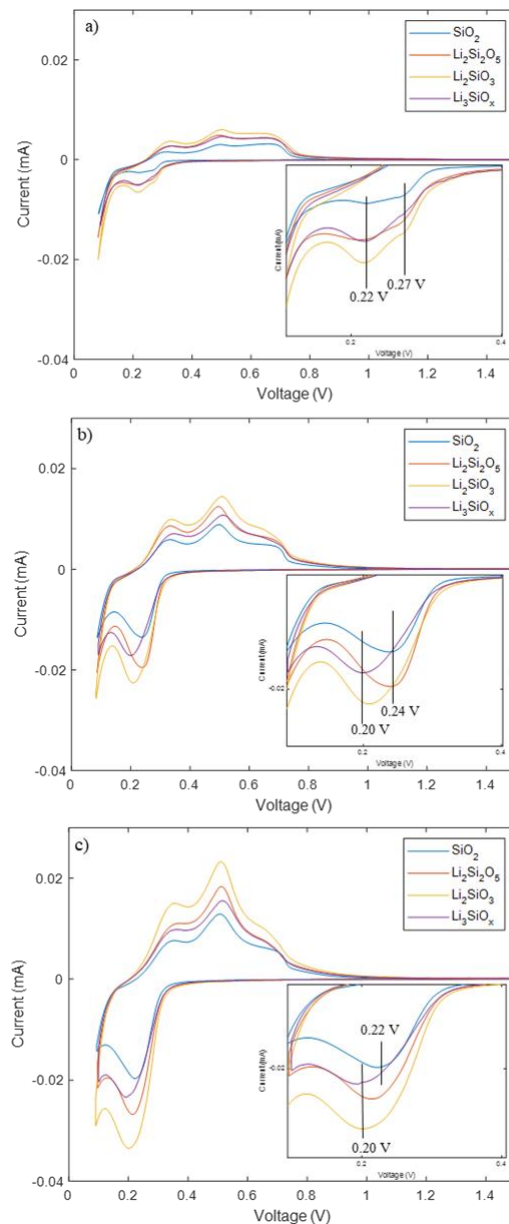


Figure II.2.B.73 CV plots for the a) second, b) seventh, and c) fourteenth cycle for each silicate coating cycling at a C/50 cycle rate.

The scale of the y-axis, or current, for each set of CVs is kept constant to illustrate that the area under the CV curve is increasing for each composition with continued cycling from Figure II.2.B.73a to Figure II.2.B.73c. This increase indicates increased silicon alloying with more cycling. From the insets of each graph in Figure II.2.B.73, it is also clear that the peaks for amorphous-silicon lithiation shift to lower potentials with continued cycling. The peaks shift from between 0.31 V and 0.22 V in the first cycle, to between 0.27 V and 0.22 V in the second cycle, to between 0.24 V and 0.20 V for the seventh cycle, and finally, between 0.22 V and 0.20 V for the fourteenth cycle. This shift to lower lithiation potentials is a sign of silicon anode and electrolyte degradation. Volume expansion from the silicon anode leads to electrical disconnection of sections of the silicon, and the SEI that forms may have a higher barrier to lithium-ion diffusion than the initial silicates, resulting in a higher overpotential upon subsequent cycling. Both of these processes lead to less active silicon material, which means that the remaining active silicon material must lithiate to higher lithium-to-silicon ratios to retain the same storage capacity. These lithium-rich alloys are formed at lower potentials, as seen in the potential shifts in Figure II.2.B.73. [56]

Figure II.2.B.74 is the capacity per cycle calculated from the area under the CV curves in Figure II.2.B.73c and Figure II.2.B.74 for a full CV scan, or with a 0.08 V cutoff voltage. Figure II.2.B.75 is the capacity per cycle calculated from the area under the CV curves with a 0.26 V cutoff voltage for comparison with cycled cells cut off at the same voltage.

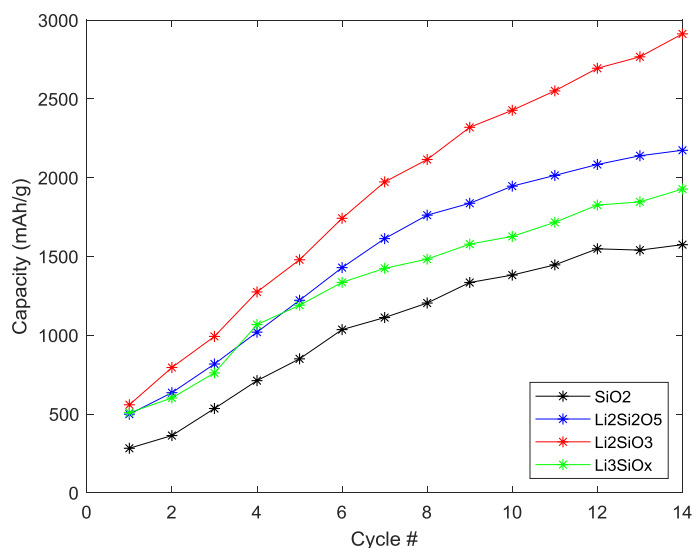


Figure II.2.B.74 Discharge capacity per cycle calculated using area under CV curve with 0.08 V cutoff voltage.

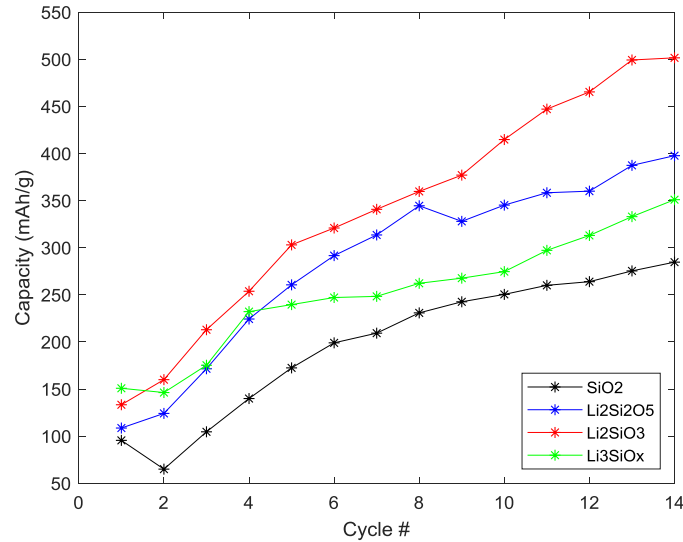


Figure II.2.B.75 Discharge capacity per cycle calculated using area under CV curve with 0.26 V cutoff voltage.

Figure II.2.B.74 and Figure II.2.B.75 both show an increase in capacity with cycling for all compositions of silicate coatings. Figure II.2.B.75 illustrates that capacities per cycle with the higher cutoff voltage of 0.26 V have lower values than the capacities with a full CV scan to 0.08 V. This is because the high cutoff voltage at 0.26 V cuts off some of the main lithiation peaks observed in CV scans for all four compositions of silicate coatings.

Figure II.2.B.76 is the discharge capacity per cycle for constant-current cycling data with a 0.26 V cutoff voltage. Figure II.2.B.75 and Figure II.2.B.76 can be used to examine the differences in capacity from lithium-silicon alloying to capacity loss from SEI formation.

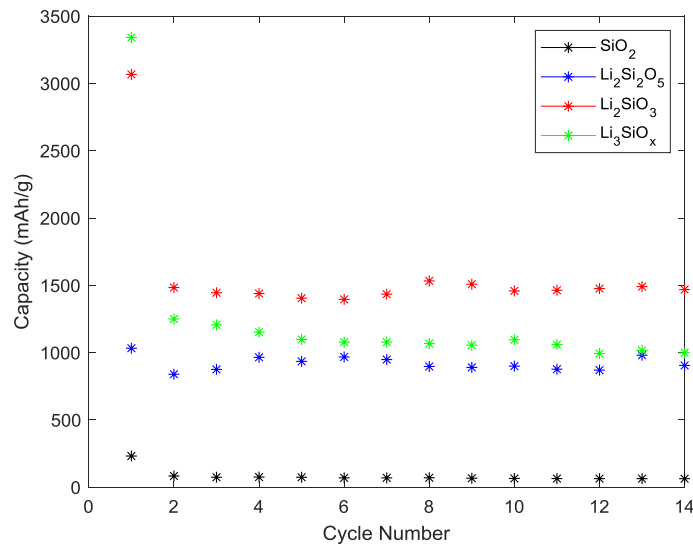


Figure II.2.B.76 Discharge capacity per cycle for cycling data with a 0.26V cutoff voltage

There is a very clear difference in the capacity trends for CC and CV cycling. The CV capacity for each silicate coating, representing current from lithium-silicon alloying, increases with cycling. The capacity from

CC cycling for each silicate coating, which includes SEI formation, is higher on the first cycle, drops 20%–60% from the first to second cycle (depending on the composition), and then remains relatively stable up to fourteen cycles compared to the initial capacity loss.

From Figure II.2.B.75, Figure II.2.B.76, and Figure II.2.B.77, it appears that although the capacity from lithium-silicon alloying increases with cycling, the overall capacity (including SEI formation) does not increase or decrease as dramatically. If the SEI continued to cause as great a capacity loss as in the first to second cycle, the capacities in Figure II.2.B.76 would trend upward, along with the increasing capacity in Figure II.2.B.75. This is evidence that with continued cycling, the SEI causes less capacity loss. There are also some trends for capacity loss per cycle that depend on the initial lithium content of the silicate coatings.

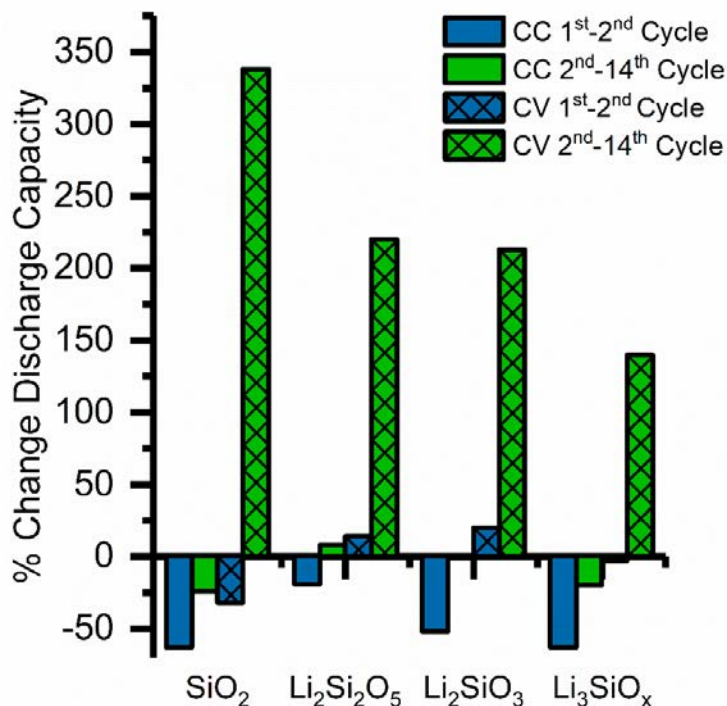


Figure II.2.B.77 Discharge capacity change from the first to second and second to fourteenth cycle for cyclic voltammetry and constant current samples.

As demonstrated by the solid blue columns in Figure II.2.B.77, the discharge capacity loss from the first to second cycle for cells with Li_xSiO_y coatings cycled at CC with a 0.26 V cutoff voltage increase with lithium content from 20% for an $\text{Li}_2\text{Si}_2\text{O}_5$ -coated silicon anode to 63% for an Li_3SiO_x -coated silicon anode. A SiO_2 -coated anode has a capacity loss of 63%, just like a Li_3SiO_x -coated silicon anode. These same trends are not observed in the capacity change from the first to second cycle for the CV cells, represented by the blue-hatched columns in Figure II.2.B.77. This suggests that the trend of increasing capacity loss with increasing lithium content in the silicate coatings and the high capacity loss of SiO_2 are mostly due to their SEI formation mechanism during the first lithiation process.

A more extensive study on identical samples was done by the NREL group, using both cycling and EIS. XPS was collected for two films with different Li/Si ratios. In Figure II.2.B.78, depth profiles are shown for Li 1s, Si 2p and O 1s core-level spectra, for both lithium-rich and silicon-rich regions of the thin film. From the XPS depth profile, significant oxidation was observed at the surface, even though the samples were protected from ambient atmosphere during the transfer from the deposition to the characterization instrument. Compositions obtained via peak fitting these spectra are listed in Table II.2.B.7. As can be seen from the XPS fitting results in Table II.2.B.7, for both lithium-rich and silicon-rich side of the film, lithium silicate and lithium silicide are

the main components in the film, with some contribution from SiO_2 . The average compositions for lithium-rich area and silicon-rich area are $\text{Li}_{4.88}\text{Si}_{2.85}\text{O}_{2.52}$ and $\text{Li}_{1.58}\text{Si}_{1.31}\text{O}_{1.95}$, respectively. Hence, the thin film is subsequently referred to as a Li_xSiO_y composite film. We note that the lithium-rich area has more lithium and more O compared to the silicon-rich area. Higher oxygen content in the lithium-rich area results from the higher affinity of lithium to oxygen.

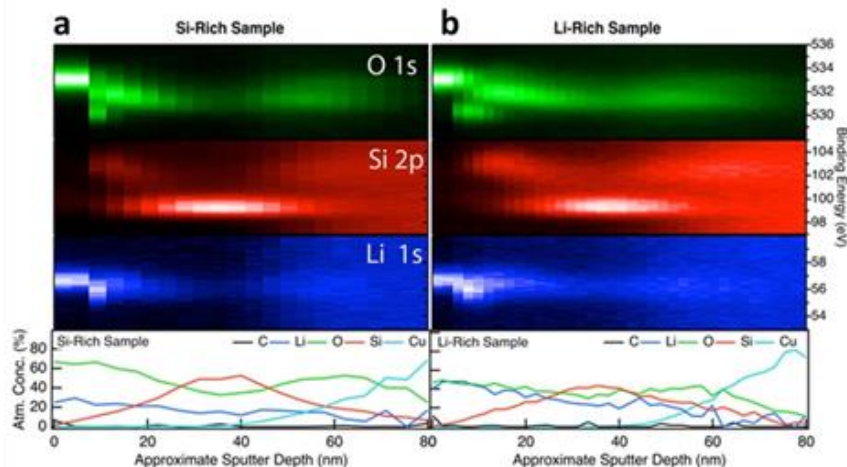


Figure II.2.B.78 XPS depth profile analysis of Li_xSiO_y composite thin film on copper foil for a) Si-rich region and b) Li-rich region. The top panels show binding-energy depth profile of O 1s (green), Si 2p (red), and Li 1s (blue). The bottom panel shows atomic percentage as a function of sputter depth.

Table II.2.B.7 Fitting Results Show the Components in the Film

Li-Rich		Si-Rich	
Li_2SiO_4	58.01%	Li_2SiO_3	63.68%
$\text{Li}_{12}\text{Si}_7$	31.56%	LiSi_2	32.72%
SiO_2	10.43%	SiO_2	3.6%
Film composition	$\text{Li}_{4.88}\text{Si}_{2.85}\text{O}_{2.52}$	Film composition	$\text{Li}_{1.58}\text{Si}_{1.31}\text{O}_{1.95}$

Electrochemical Impedance and Cycling

Chemical reactivity of Li_xSiO_y was studied indirectly by EIS. A 50-nm-thick sample was assembled into a coin cell and investigated by impedance spectroscopy and by galvanostatic charge and discharge measurements (Figure II.2.B.79). Capacity is not normalized in this work because all the films have the same thickness and area. As shown in Figure II.2.B.79a, a low amount of lithium could be extracted from the film even up to 1.5 V during the first charge cycle. This high open-circuit voltage is due to the lower electrochemical potential of lithium in Li_xSiO_y , which has part of the lithium bonded with oxygen. To investigate the reaction of the Li_xSiO_y composite film with electrolyte, it was measured by AC impedance at the open-circuit voltage, as shown in Figure II.2.B.79b. When the Li_xSiO_y composite film comes into contact with electrolyte, the charge transfer resistance increases with time. In contrast, for the silicon electrode, the impedance is not time dependent at open-circuit voltage.

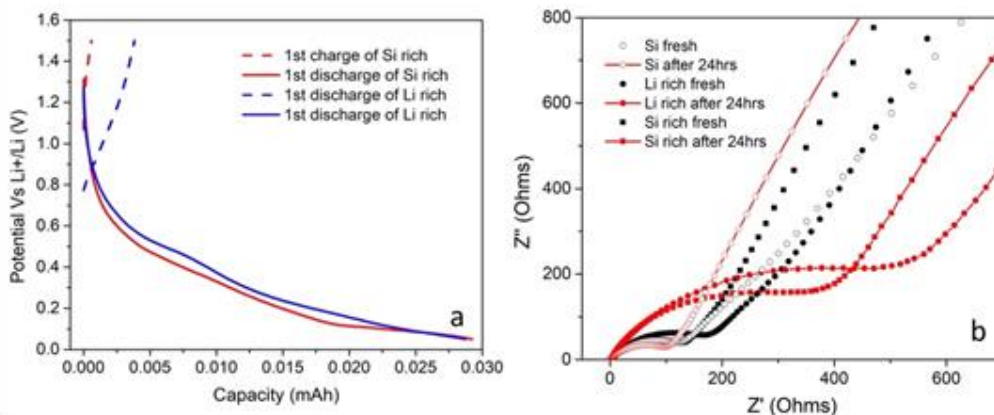


Figure II.2.B.79 a) Voltage profile of lithium-rich Li_xSiO_y composite film and silicon-rich Li_xSiO_y composite film; b) Impedance evolution of lithium-rich Li_xSiO_y composite and silicon-rich Li_xSiO_y composite as well as Si film.

To correlate the measured Li_xSiO_y properties with the electrochemical cycling performance of an electrode with Li_xSiO_y at the surface, a double-layer sample was deposited with Li_xSiO_y on top of a silicon thin film and then compared to a Si film. The thickness of Li_xSiO_y was set to 10 nm to emulate the native-oxide thickness, and the thickness of the silicon thin film was set to 50 nm, as shown in the inset in Figure II.2.B.80a. As shown in Figure II.2.B.80a, during the first-cycle discharge profile, $\text{Li}_x\text{SiO}_y/\text{Si}$ exhibited a lower open-circuit voltage of only 1.5 V (compared to 2.5 V for Si) due to the existing lithium on the silicon surface. The difference of the CV profiles above 0.25 V (before Si starts lithiating) results from the surface reaction between Li_xSiO_y and electrolyte. Both low potential of Li_xSiO_y and its reaction products make the electrochemical reduction different than that in the silicon case. The lower potential range profiles for both films are very similar because the same thickness of silicon film was deposited. The cycling of $\text{Li}_x\text{SiO}_y/\text{Si}$ showed a lower coulombic efficiency and less stable performance as compared to the bare silicon (Figure II.2.B.80b). We note that the coulombic efficiency of silicon is higher than that of the Li_xSiO_y -coated Si, indicating that the Li_xSiO_y film exhibits a greater reactivity with electrolyte Figure II.2.B.80. We hypothesize that the Li_xSiO_y composite film continuously reacts with the electrolyte, preventing the stabilization of the SEI on the silicon electrode. These results suggest that SiO_2 does not help stabilize the surface of the Si electrode, because the lithiation products are not stable upon cycling. Previously, there has been study² of the effect of SiO_2 with various thickness—from 2 nm, to 7 nm, to 10 nm. Only the 7-nm SiO_2 -coated Si showed improved performance compared to Si. This is a complementary result due to both mechanical property and reactivity. More studies of the reactant product between Li_xSiO_y and electrolyte are in progress to clarify the role of Li_xSiO_y in the functionality and SEI stabilization of the Si anode.

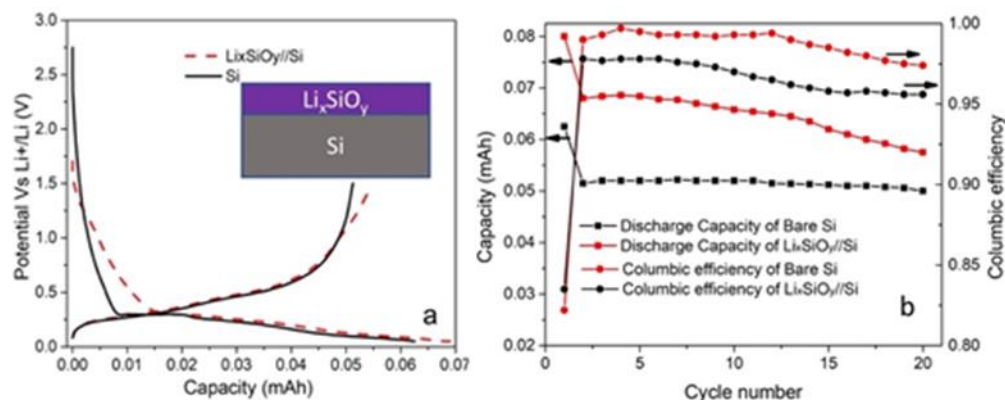


Figure II.2.B.80 a) Charge and discharge profile of Si and Li_xSiO_y/Si, with inset showing the schematic of double-layer thin film; b) Cycle performance and coulombic efficiency of double-layer thin film and pure silicon.

Finally, an interesting “cycling” of native oxides to produce silicates was performed by using a charged Li⁺ beam as the anode in a cycle and injecting ionized lithium into various surface layers with low (10-eV) incident energy—essentially performing an atomic beam lithiation of the film. To investigate the lithiation of SiO₂/Si(001), in a “SEISta round-robin,” a 50-nm SiO₂/Si(001) sample was subjected to a flux of 10-eV Li⁺ ions while performing XPS measurements. Current through the sample was ~20 nA, and the Li⁺ spot size was on the order of 2 mm in diameter. The XPS results during lithiation are shown in Figure II.2.B.81a. From these data, a clear charging effect can be observed during the initial lithiation: all peaks shift to higher binding energy by ~7.5 eV, corresponding to a positive increase in the surface electrochemical potential of 7.5 V. This overpotential drops to near zero after about 200 minutes of lithiation, which likely indicates that the SiO₂ layer has been fully converted to one or more Li_xSi_yO_z phases. In the O 1s spectral profile Figure II.2.B.81a; green), evolution in the chemical states can be observed between 300–500 min. In that region, the peak initially centered at ~533 eV splits into two peaks around 534.5 and 531.5 eV. This might be due to the formation of a more Li-rich Li_xSi_yO_z phase. On the other hand, the data also indicate that Li₂O may be forming during this time. After the XPS *in-situ* lithiation measurement, the sample was depth profiled using Auger electron spectroscopy (AES), as shown in Figure II.2.B.81b. These data clearly show three compositionally distinct regions within the sample, including a Li_xSi_yO_z phase at the surface, a buried Li_xSi layer, and the bulk Si wafer.

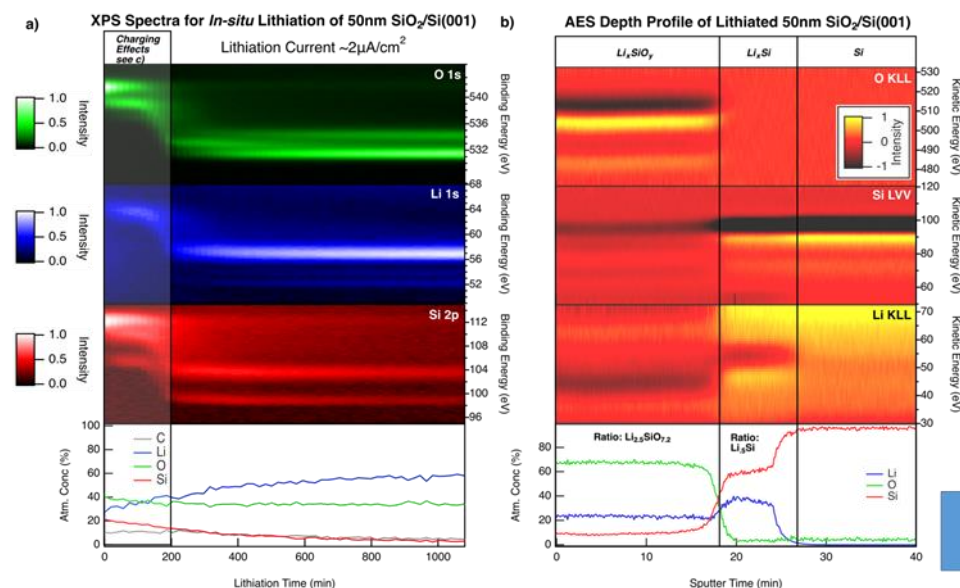


Figure II.2.B.81 a) Evolution of XPS core-level spectra during *in-situ* lithiation of 50-nm SiO₂/Si(001) wafer. b) AES depth profile of the lithiated sample reveals that the entire SiO₂ layer has been converted to a Li_xSi_yO phase and that an underlying Li_xSi phase has also formed.

In addition to the measurements summarized above for 50-nm SiO₂/Si(001), preliminary *in-situ* lithiation experiments have also been completed on native oxide/Si(001) and on sputter-cleaned Si(001). The XPS data sets comparing evolution of these different surfaces during *in-situ* lithiation are shown in Figure II.2.B.82. From these data, it is clear that differences in the XPS spectra—corresponding to differences in evolution of various Li-Si-O phases—can be observed that depend on the initial condition of the Si wafer. Perhaps the most striking difference is a low binding-energy peak in the Li 1s core level. This peak, possibly associated with Li-rich Li-Si phases, is significantly more intense when less surface oxide is present. To our knowledge, these Li 1s peaks have not yet been described in the literature; additional studies will be needed to conclusively assign them to particular phases.

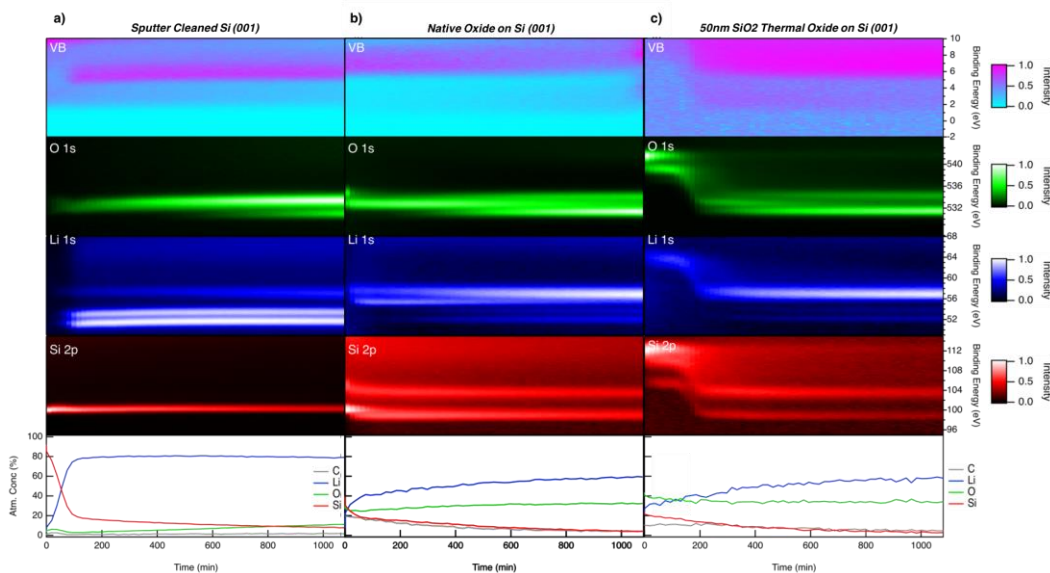


Figure II.2.B.82 Evolution of XPS core-level spectra during *in-situ* lithiation of an: a) sputter-cleaned Si(001) wafer, b) wafer with a native oxide, and c) Si (001) wafer with a 50-nm-thick thermally grown SiO₂ layer.

Comparing spectra acquired with and without Li^+ ion gun current bias enables determination of overpotentials associated with lithiation for the various Si wafer samples that were studied. As can be seen in Figure II.2.B.83, the overpotential associated with lithiation of the 50-nm SiO_2/Si (001) is ~ 7.5 V. Compared to the native oxide/Si(001) sample, this overpotential is over 100x larger in magnitude, even though the SiO_2 layer (estimated ~ 2 nm for native oxide) is only ~ 25 x thicker. This observation supports the conclusion that excessively thick SiO_2 layers will significantly increase cell overpotentials during the first cycle of a Si-based anode.

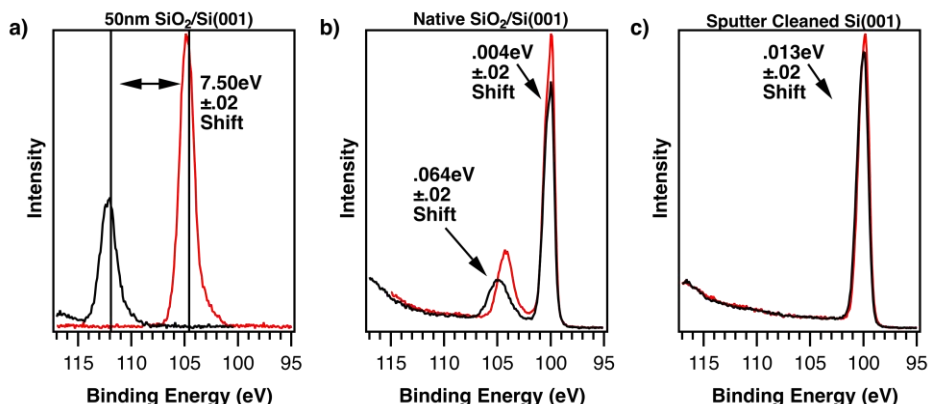


Figure II.2.B.83 Overpotential variations for the three different Si wafers tested: a) 50-nm SiO_2/Si (001) b) native oxide on Si (001) and c) sputter-cleaned Si (001). The black curve was acquired with the Li^+ ion gun current bias on and the red curve without. Binding-energy shifts can be used to estimate overpotentials of lithiation, and ultimately, Li diffusivity as a function of Li-Si-O phase.

In Q4, to further investigate the role of SiO_x in SEI formation during early-stage lithiation, three types of samples were studied: bare Si(001) substrates, native-oxide SiO_x/Si samples, and thermal-oxide (5–100-nm) SiO_2/Si (001) samples.

Evolution of the Si 2p, O 1s, Li 1s, and C 1s core levels as a function of lithiation time reveals that the three samples shown in Figure II.2.B.84 behave quite differently. All of the samples show evidence for the formation of Li_xSi phases, although it appears that different Li_xSi phases form depending on the initial oxide composition and thickness. Specifically, both the bare Si(001) and native-oxide SiO_x/Si (001) samples show evidence for a Li_xSi phase characterized by a peak doublet in the range of 50–55 eV. On the other hand, a higher-binding-energy Li 1s peak (~ 55 eV) is observed in both the native-oxide SiO_x/Si (001) and 5-nm SiO_2/Si (001) samples. The cause of this variability is not yet understood, but nevertheless, it reveals that the nature of the SEI can influence the formation and evolution of particular Li_xSi phases. The surface of the bare Si(001) wafer appears to be the most reactive, as evidenced by the appearance and growth of peaks in the O 1s and C 1s core-level spectra, due to reactions with trace residual gases (primarily H_2O , CO, and CO_2) in the XPS chamber. The native-oxide SiO_x/Si (001) sample appears to be less reactive. For example, the C peak associated with surface contamination that is initially present attenuates as lithiation progresses, indicating that the C contamination is being progressively covered by other phases, and that new C-containing phases are not forming due to reaction with residual gases. On the other hand, peaks in the Li 1s and O 1s core-level spectra are consistent with the growth of Li_2O , indicating that O-containing residual-gas species such as H_2O are likely reacting with the surface. The surface of the 5-nm SiO_2/Si (001) is the least reactive, and, in fact, there is no evidence for any uptake of residual gases by this surface. This seems to indicate that the surface remains chemically passivated indefinitely, although Li^+ migration through the lithiated SiO_2 is apparent.

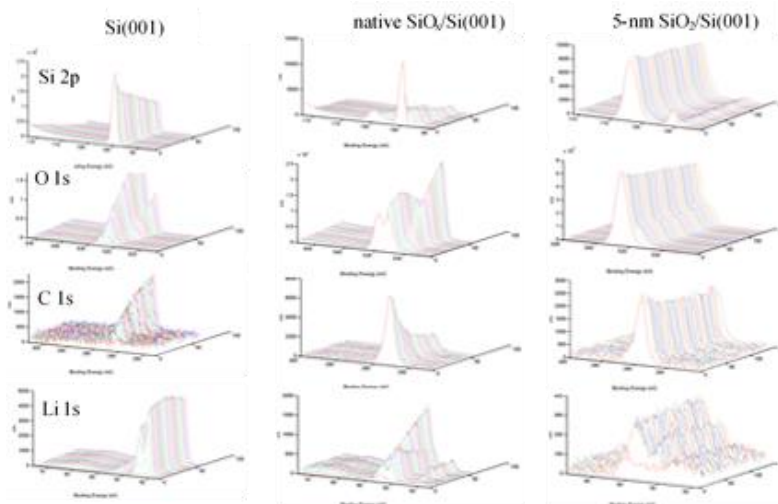


Figure II.2.B.84 XPS core-level spectral evolution monitored as a function of lithiation time for three samples: bare Si(001), native oxide $\text{SiO}_x/\text{Si}(001)$, and 5-nm thermal-oxide $\text{SiO}_2/\text{Si}(001)$. The evolution of the core levels in the first two cases—and, in particular, the evidence for uptake of residual gas species by the exposed surfaces—shows that these surfaces are more reactive in comparison to the 5-nm $\text{SiO}_2/\text{Si}(001)$ sample.

As illustrated in Figure II.2.B.85 shifts in O 1s and Si 2p core levels measured before and after the Li^+ ion gun is turned on reveal peak shifts associated with the overpotential required to drive Li^+ ion through the SiO_2 layer. In the case of 5-nm SiO_2 , with an estimated Li^+ -ion current density of 500 nA/cm^2 , the measured overpotential is $\sim 2.2 \text{ eV}$. Accounting for the SiO_2 thickness and dielectric properties, we estimate that the resulting electric field within the SiO_2 layer is $\sim 10^6 \text{ V/cm}$, which is approaching the dielectric breakdown threshold. Figure II.2.B.85 also reveals interesting changes in the Si^0 peak in the Si 2p core level that accompanies Li^+ ion gun current bias. The Si 2p peak broadens and shifts to higher binding energy, which likely results from downward band bending in the Si(001) substrate in response to the surface charge associated with Li^+ current bias. Following the *in-situ* lithiation measurements, samples were analyzed with angle-resolved XPS (ARXPS) measurements. This non-destructive technique leverages the surface sensitivity of XPS measurements to reveal the depth distribution of detected phases. Nine distinct chemical states were observed in the XPS spectra, and curve fitting enabled preliminary identification of specific phases (e.g., SiO_x , Li_ySiO_x , and Li_xSi), each with distinctive angular intensity profiles as shown in Figure II.2.B.86. For the lithiated 5-nm $\text{SiO}_2/\text{Si}(001)$ sample, preliminary results reveal a layered structure composed of a layer of surface C contamination, a Li_ySiO_x layer, a SiO_x layer (possibly Li-doped), and a Li_xSi layer.

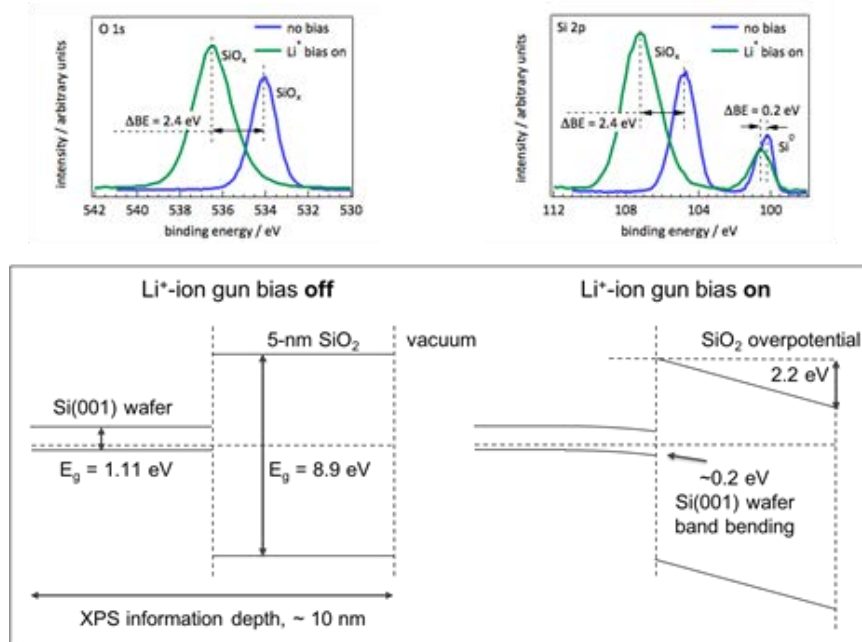


Figure II.2.B.85 XPS O 1s (upper left) and Si 2p (upper right) core levels recorded on the 5-nm SiO₂/Si(001) sample before the Li ion gun was turned on and immediately after. The shifts in SiO₂ core levels reveal the overpotential associated with the 5-nm-thick SiO₂ layer. Changes in the Si⁰ peak likely result from downward band bending in the p-type Si(001) wafer substrate, as illustrated in the schematic energy-band diagrams in the lower panel.

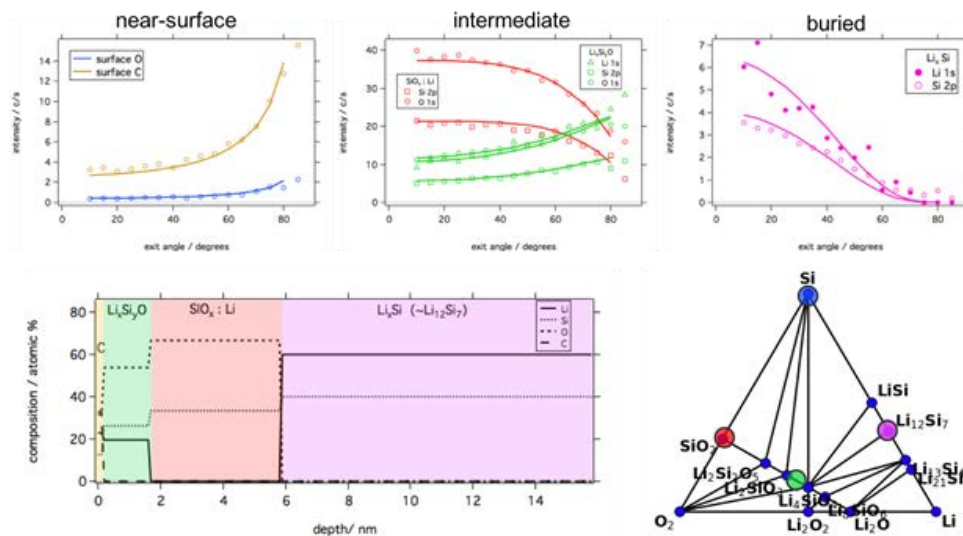


Figure II.2.B.86 Measured (symbols) and calculated (solid lines) ARXPS angular profiles of detected chemical states highlighting near-surface, intermediate, and buried phases (upper panels). The preliminary model structure shown in the lower left panel agrees well with the measured data and indicates that very little Li is incorporated into the SiO_x layer at early stages of lithiation. The colored circles in the ternary phase diagram (lower right) represent approximate compositions of detected phases based on XPS intensities.

The finding that the SiO_x layer remains largely intact during the initial phase of lithiation is somewhat surprising, but we emphasize that this is a preliminary result. To validate and refine the ARXPS modeling results, in FY19 we will apply a more rigorous data-analysis algorithm such as the Maximum-Entropy Method

or use suitable software such as Simulation of Electron Spectra for Surface Analysis (SESSA, developed by NIST).

We observed evidence that Li-containing Si-based electrodes drive electrolyte decomposition reactions at the electrode surface. By comparison, in some cases, SiO₂ layers on Li-free Si electrodes appear to be etched by the electrolyte solution, leaving behind Si and a surface layer consisting of adsorbed organics. Furthermore, this behavior in the Si-only electrodes is observed for both the GEN2 electrolyte and the electrolyte containing an FEC additive. Conversely, the FEC additive appears to make a difference in the decomposition product on the surface of Li-containing Si electrodes by reducing the amount of LiF and increasing the amount of organic functionalities.

A novel method for studying the fundamental lithiation processes of Si-based anode materials was demonstrated. Preliminary results show that *in-situ* lithiation via a Li⁺ ion gun combined with XPS measurements effectively probes the lithiation of Si-based electrode materials. These data will help with phase identification, validation of theoretical Li-Si-O ternary phase-diagram predictions, and the quantification of fundamental lithiation properties (e.g., chemically resolved overpotentials, impedances, and Li⁺ diffusivities).

The virtual-electrode approach has been further developed as a means for studying fundamental lithiation mechanisms in Si-based anode materials by monitoring the lithiation process *in-situ* with XPS, while delivering Li⁺ ion to the surface using a low-energy Li⁺ ion gun. With this method, it is possible to directly observe the formation of Li_xSi phases and to assess overpotentials necessary to drive lithiation. Initial results presented here show that SiO_x layer thickness influences surface reactivity: for the bare Si(001) and native-oxide SiO_x/Si(001) samples, all core levels evolve continuously throughout the course of the lithiation process due to reactions with trace residual gases present in the XPS chamber during the experiment. In contrast, the 5-nm-thick SiO₂ layer appears to chemically passivate the surface, at least with respect to residual gases. Preliminary analysis of ARXPS data from the lithiated 5-nm SiO₂/Si(001) sample suggests a layered structure comprising Li_ySiO_x, SiO_x (possibly Li-doped), and Li_xSi. Additional ARXPS data modeling to validate and refine these initial results is in progress.

Nature and Evolution of the Silicon SEI

The objective of this project is to develop a systematic understanding of solid-electrolyte interphases (SEIs) for silicon (Si) electrode materials and to provide practical strategies for stabilization of the SEI in Si-based electrodes. The SEI layer begins to form as soon as the Si electrode contacts the electrolyte. In fact, the reductive decomposition of the electrolyte in lithium-ion systems employing silicon anodes is inevitable, because the working potential of the electrode lies far below the electrochemical stability window of the electrolyte components. In principle, the insoluble decomposition products precipitate on the electrode surface, and if sufficiently insulating, result in the formation of a passivating surface film, which suppresses further electrolyte decomposition.^{[57], [58]} The SEI comprises the products from many reduction reactions of salts, solvents, and electrolyte additives. These reduction reactions compete with each other; and their kinetics depend heavily on current density, overpotential, and the catalytic properties of the electrode surface, which finally determine the composition and structure of a SEI layer. Moreover, the phase transformation and mechanical deformation caused by the Si lithiation/delithiation process present additional challenges in investigating the SEI layer. The continuous reduction of electrolyte observed in Si-based composite electrodes may be attributed to the never-ending appearance of fresh surfaces during the volume changes, which continuously consumes electrolyte and leads to cell failure by loss of cyclable lithium.^[59] These reactions create a mix of soluble and insoluble organic and inorganic decomposition products that produce the SEI layer.

This chapter aims to summarize the results and progress made in investigating the chemistry, physical properties, and formation mechanism of SEI for the Si anodes. The discussion explores three main themes including: 1) solvation structure of the carbonate electrolytes by using molecular dynamic computation, 2) SEI chemistry, which covers the formation of early-stage SEI, SEI chemistry evolution, and reduction of fluoroethylene carbonate additive, and 3) SEI inhomogeneity by using tip-enhanced Raman spectroscopy. In

addition, two new techniques—scanning spread-resistance microscopy (SSRM) and fluorescent probes for fluorescence microscopy—have been developed and are summarized in this report. In addition, a variety of characterization techniques have been employed and further developed to better understand the SEI, including X-ray photoelectron spectroscopy (XPS), X-ray absorption spectroscopy (XAS), Fourier-transform infrared spectroscopy (FTIR and ATR-FTIR), and apertureless IR near-field scanning optical microscopy (aNSOM), tip-enhanced Raman spectroscopy (TERS), scanning transmission electron microscopy (STEM), and electrochemical quartz-crystal microbalance (EQCM). All the techniques have been discussed and employed in our previous study; thus, they are not elaborated in this report. The Si samples used in this study are our SEISTa model samples: Si(100)-doped wafers with a native oxide, which have been studied and selected in FY2017. The cleaning protocol established in FY2017 has been used in this study.

SEISTa Section 3: Nature and Evolution of Silicon SEI

Solvation structure of the carbonate electrolytes

To elucidate the dominant early SEI formation reaction pathways, we examine the majority- as well as minority-specie solvation structures of the Li-ion electrolyte at the bulk electrolyte and at the interface. The solvation structure of the electrolyte (1.0 M LiPF₆/EC) has been studied with the classical molecular dynamic (MD) method. We first investigated the solvation structure close to the neutral (uncharged) interface at the Si anode, during the initial charging step. An OPLS force field is employed for the electrolyte constituents, and the anode interface is represented by neat crystalline-Si (c-Si) covered with a thin, native silicon oxide layer. We found that the solvation structure of Li⁺ changes quite significantly from the bulk to the interface, such that the overall Li⁺ coordination changes from about 6 to about 4 (Figure II.2.B.87a and 1b). This effect is due to two components: 1) a significant interaction between the SiO₂ oxygen and Li ion reduces the EC coordination number (CN) from 5.5 to 2.5, and 2) the Li-F CN increases from 0.4 in the bulk to 1.2 at the interface. Because the PF₆⁻ anion can donate more than one F to each Li, the contact ion-pair (CIP) ratio increases from ~0.3 to ~0.65 from the bulk to the interface. We also find that the CIP ratio in bulk increases from 0.07 to 0.3 with temperature increasing from 300 K to 400 K, which we attribute to a decrease in the dielectric constant of the solvent.

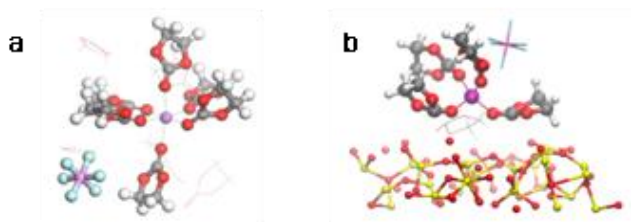


Figure II.2.B.87 Structures of EC molecules around a Li ion (a) in the bulk and (b) at the interface.

We then analyzed the solvation structure of electrolyte molecules for an interface with a constant charge. As previously, the chemical characteristics of the Si anode interface is modeled with an amorphous SiO₂ layer on top of the c-Si bulk electrode. The equilibrium MD simulation is performed for 1 M LiPF₆ in EC at 400 K (Figure II.2.B.88a). The applied voltage is modeled by assigning a uniform charge, $\pm 6.25e^{-4}$, to each silicon atom at the negative/positive electrodes so that the voltage applied at the negative silicon electrode is ~ -0.47 V (Figure II.2.B.88b). Interestingly, the constant charged interface causes a reduction in the CIP ratio between the bulk and the interface, as compared to the neutral case. Both a negative as well as positively charged SiO₂ interface result in a CIP ratio of 0.4 and 0.45 at the negative- and the positive-charged electrode interface, respectively (Figure II.2.B.89), which should be compared to the neutral case of 1.2. Nevertheless, it should be stressed that the CIP ratio still is increased as compared to the bulk for both charged (marginally) and neutral (substantially) SiO₂ interfaces. Furthermore, similar to the neutral electrode, the CIP ratio increases from bulk to interface with increasing temperature—spanning 313, 350, and 400 K (Figure II.2.B.88c). In summary, the neutral silicon SiO₂ interface exhibits the largest CIP ratio, and it becomes smaller at the charged interface.

Specific interaction between ions and SiO₂ enhances the CIP forming at the interface, which provides a hint toward preferential reaction pathways of the early SEI formation.

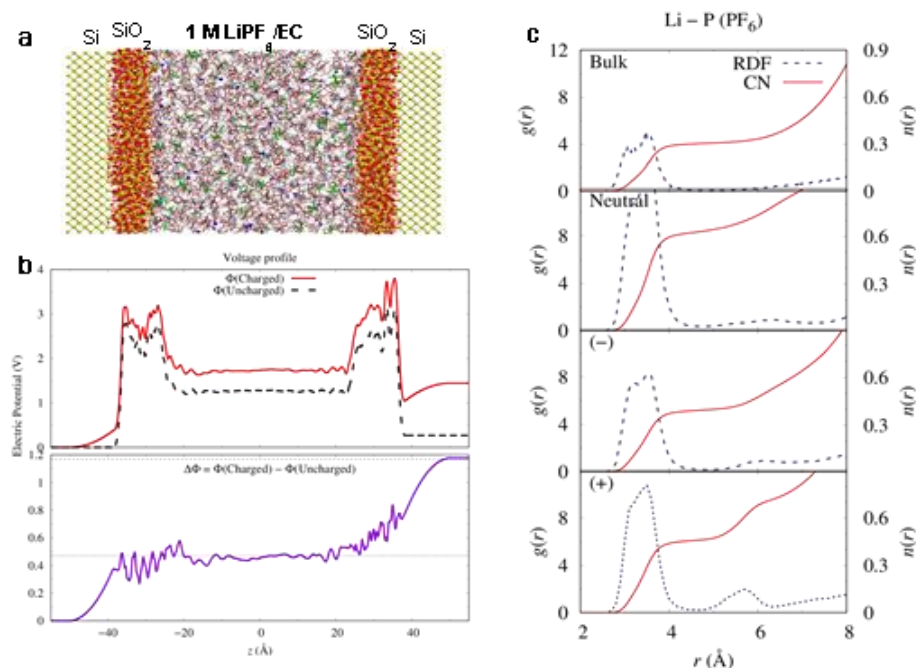


Figure II.2.B.88 (a) The model Si anode interface, and (b) the voltage profile in the electrolyte region between the electrodes. The electric potentials are -0.47 V and +0.7 V at the negative and the positive electrodes, respectively. (c) Radial distribution functions and the coordination numbers (CN) of PF₆ ions around a Li ion in bulk and at the neutral, negative, and positive electrodes, from top to bottom; the CN values are 0.3, 0.65, 0.4, and 0.45, respectively.

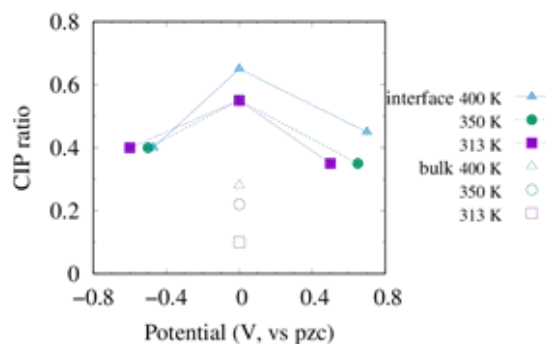


Figure II.2.B.89 Contact ion-pair (CIP) ratio in the bulk electrolyte and at SiO₂ interface at temperatures of 400, 350, and 313 K. The CIP ratio increases from the bulk to interface. The neutral silicon interface shows the largest CIP ratio, and it becomes smaller at the charged interface.

Chemistry in the SEI layer

Early-stage SEI formation

The electrolyte reduction and its interaction with electrode materials are involved in the early stage of SEI formation for Si anodes. To better understand the early-stage SEI chemistry, a new methodology has been developed here to decouple the lithiation-induced mechanical deformation from the SEI formation, to directly investigate the interphase formation and evolution. Galvanostatic reduction was performed on the Si anode

with a specific cut-off voltage before Si lithiation voltage, which allows the formation of an early-stage SEI (es-SEI) without the mechanical deformation.

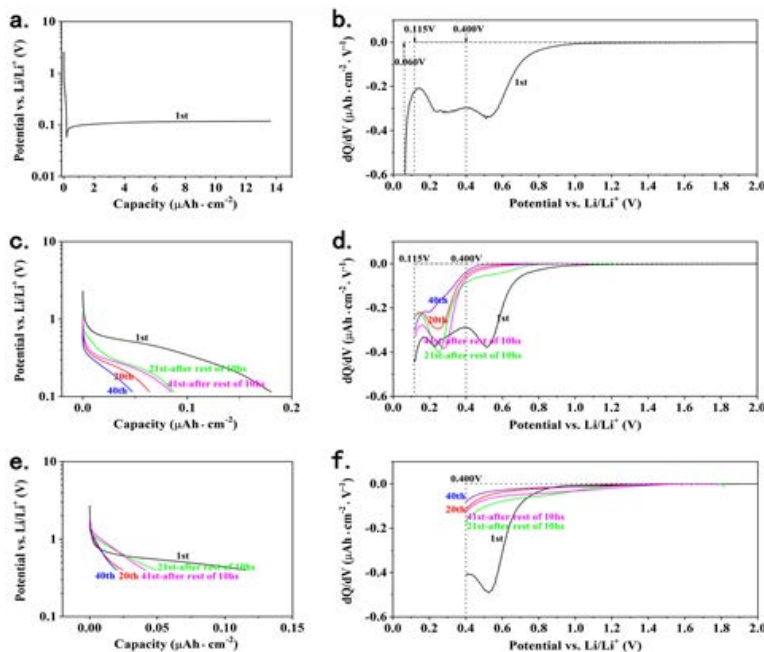


Figure II.2.B.90 (a) The voltage profile and (b) differential capacity profile when lithiation to 60 mV. (c) The voltage profile and (d) differential capacity profile when using a cut-off voltage of 115 mV including both Regime 1 and Regime 2. (e) The voltage profile and (f) differential capacity profile when using a cut-off voltage of 400 mV including only Regime 1.

A typical electrochemical procedure has been applied on the Si wafer anode: apply a galvanostatic reduction current of 6.82 mA cm^{-2} and keep it for the time up to 2 hours, then rest for 10 hours and repeat the above steps for 20 cycles. Figure II.2.B.90a shows the voltage profile as the function of capacity under this regular condition including both the electrolyte reduction and Si lithiation. The slope section of this voltage profile is ascribed to the reduction of electrolyte, and the low-voltage plateau section of this voltage profile corresponds to the two-phase region when the lithiated amorphous Si is formed. Figure II.2.B.87a well agrees with the initial lithiation behavior of c-Si reported in literature.^[68] Figure II.2.B.90b shows the differential capacity profile of this Si anode. There are two peaks at the potential of 250 mV and 550 mV shown in the profile, respectively. The deep dropping of this differential capacity profile at the potential of 60 mV is derived from the initiating Si lithiation.

To quantitatively study the reduction behavior of the electrolyte and Si anode, we divide this differential capacity profile into the following three regimes by the voltage range: 1) Regime 1 ranges from 400 mV to the open-circuit potential (OCP), which corresponds to the reduction behavior around the peak at 550 mV; 2) Regime 2 ranges from 115 mV to 400 mV, which corresponds to the reduction behavior around the peak at 250 mV; and 3) Regime 3 ranges from 60 V to 115 mV, which corresponds to the initiating Si lithiation. We focus on Regimes 1 and 2 in this work to understand the chemistry involved in the es-SEI formation. Therefore, we have designed a two-step electrochemical experiment: 1) Apply a galvanostatic reduction current of 6.82 mA cm^{-2} from OCP to the cut-off voltage of 115 mV (or 400 mV), then rest for 3 hours, and repeat the above steps for 20 cycles; and 2) Interval long rest for 10 hours. Figure II.2.B.90c and Figure II.2.B.90d show the voltage profile and the differential capacity profile when using a cut-off voltage of 115 mV, including Regime 1 and Regime 2. Figure II.2.B.90e and Figure II.2.B.90f show the voltage profile and the differential capacity profile when using a cut-off voltage of 400 mV, including only Regime 1. Both Figure II.2.B.90c and Figure II.2.B.90e show the slope curves because of involving Regime 1 and Regime 2. In these well-designed experiments, the Si wafer samples only experience the reduction of electrolyte and the

interaction with the electrolyte in an absence of the lithiation process—no plateau curve is observed in the voltage profile. The Si wafer samples were collected after the aforementioned electrochemical reduction process and were characterized using scanning electron microscopy (SEM). Figure II.2.B.91 exhibits the three SEM images from the samples at (a) 400 mV, (b) 115 mV, as well as (c) 115 mV and a 20-hour rest. The sample collected at 400 mV has a very smooth surface as compared to the samples collected at 115 mV. Surprisingly, the surface of the sample collected at 115 becomes much smoother after the 20-hour rest. The surface morphology evolves during the rest, indicating instability of some SEI components in the carbonate electrolyte.

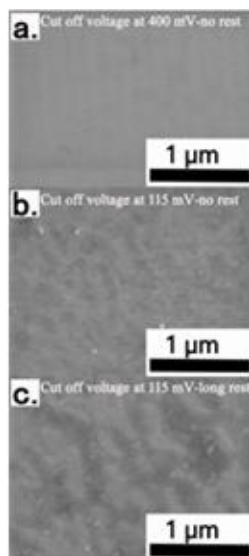


Figure II.2.B.91 The SEM morphology of es-SEI on the Si surface after cathodic cycling with the cut-off potential of (a) 400 mV and no rest, (b) 115 mV and no rest, as well as (c) 115 mV and long rest.

For the Si sample collected at 400 mV, the XPS spectra reveal the formation of both organic and inorganic components in the es-SEI, as shown in Figure II.2.B.92. Peak fitting has been carried out taking spin-orbit splitting into account for both the Si and P peaks and a constant binding-energy separation between elements belonging to the same chemical species. This allows corrections to eventual small charging effects or differential charging as described in Wood et al.[\[57\]](#)

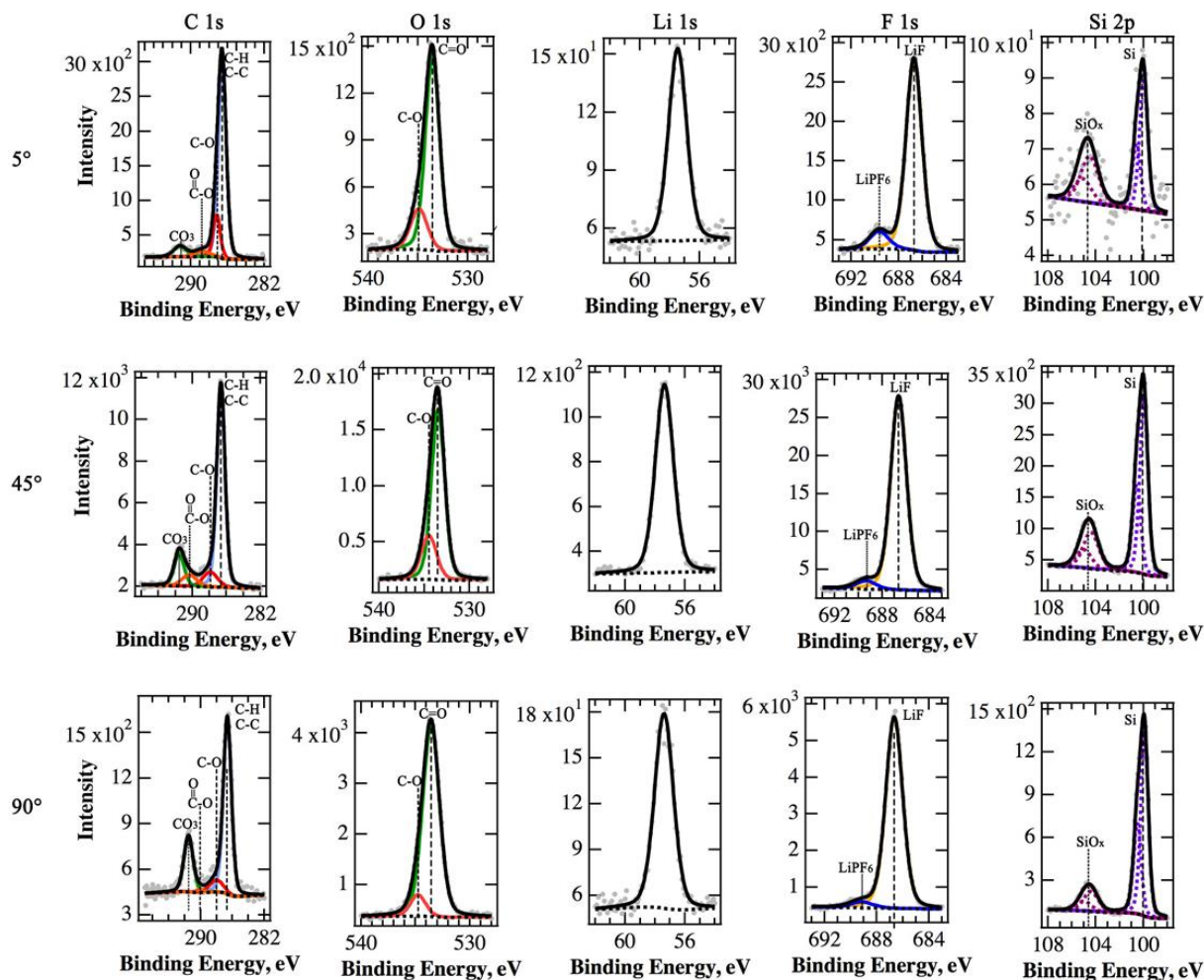


Figure II.2.B.92 The XPS spectra obtained from the es-SEI with the cut-off potential of 400 mV. The spectra show that the LIEDC starts to form at the potential higher than 400 mV.

The outcome of the analysis of the C 1s core levels shows that carbonate groups (CO_3) with the peak at 292 eV, ester groups ($\text{O}=\text{C}=\text{O}$) with the peak at 290–291 eV, ether ($\text{C}-\text{O}$) with the peak at 288–289 eV, and aliphatic ($\text{C}-\text{C}/\text{C}-\text{H}$) with the peak at 286–287 eV are present as organic components. The O 1s spectra include the peaks at 535 eV and 533 eV, showing the existence of $\text{C}=\text{O}$ and $\text{C}-\text{O}$, respectively, which is consistent with the carbonate/ester and ethers suggested by C 1s spectra. Regarding the carbonate groups, both organic carbonates such as LiEDC and inorganic carbonates such as Li_2CO_3 might be present. LiF is also the part of es-SEI, being accountable for the vast majority of the fluorine signal. LiPF_6 is present as well, but only in trace quantity. This might be due to residual salt that was not thoroughly washed out during the gentle rinsing procedure with DMC. The es-SEI appears to be a relative thin layer, as demonstrated by the fact that the signal of the underlayer SiO_x with the peak at 104–105 eV and the Si substrate with the peak at ~ 100 eV are still visible even on the most surface-sensitive measurements at 5° .

Figure II.2.B.93 summarizes the XPS results from the Si sample collected at 115 mV. It shows that the es-SEI appears to be thicker, with the underlying SiO_x/Si not visible in the most surface-sensitive measurements (5°) and its signal being much more attenuated in the more depth-probing measurements. Qualitatively, the es-SEI composition is different, as well: the organic components appear to be more pronounced and the amount of carbonates and ester species is much higher for this sample in comparison to the 400-mV/no-rest sample. LiF and a trace amount of LiPF_6 are also present in the es-SEI.

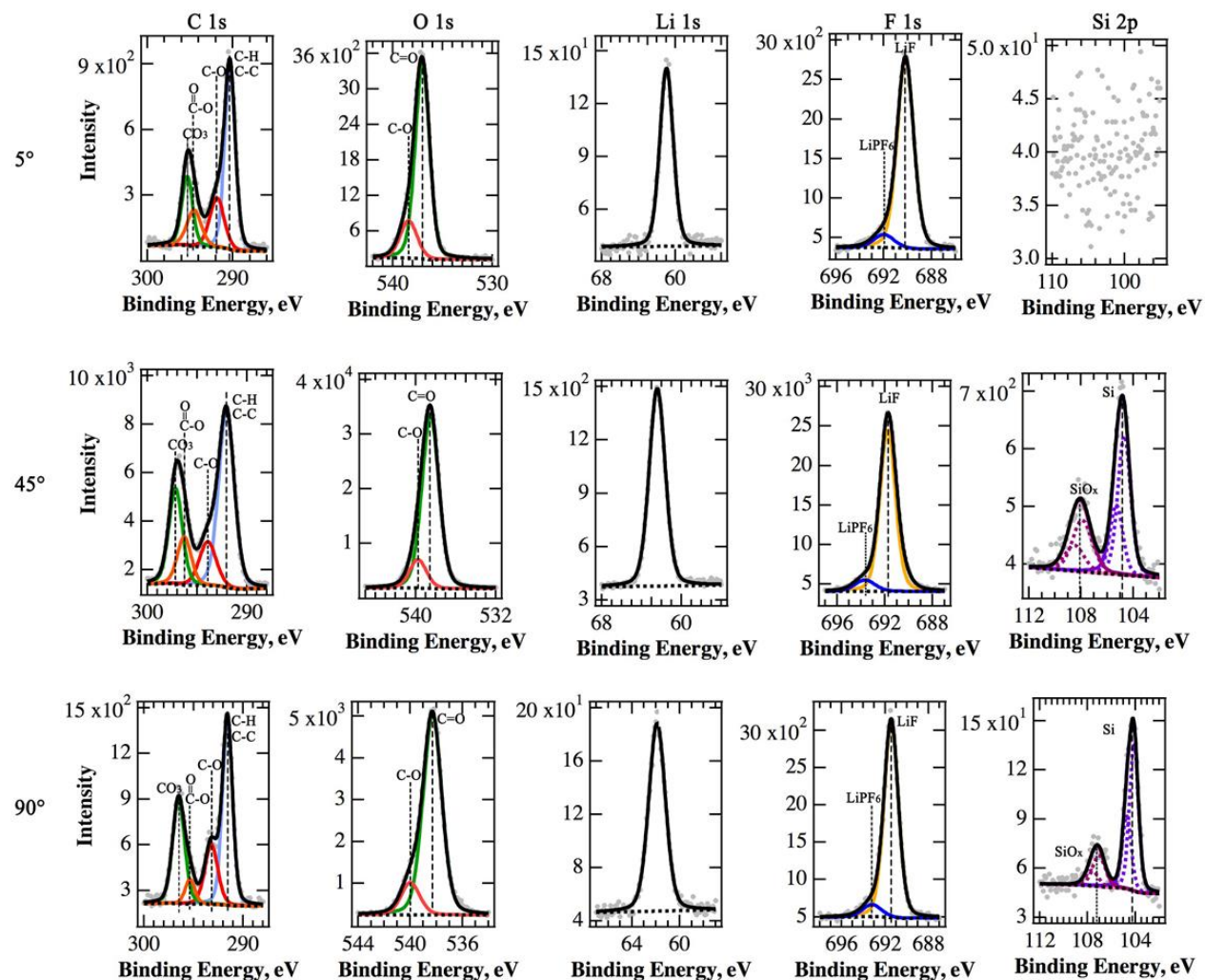


Figure II.2.B.93 The XPS spectra obtained from the es-SEI after HVIST cycling with the cut-off potential of 115 mV and no rest. The spectra show that the SiO_x was reduced to Li_xSiO_y during the potential between 115 mV and 400 mV.

Being similar to the 115-mV/no-rest sample, the 115-mV/long-rest sample also shows a thicker es-SEI in comparison to the es-SEI formed on the 400-mV/no-rest sample, as displayed in Figure II.2.B.94. It demonstrates that the signal of the underlying Si layer is not detectable for the samples measured at grazing exit and attenuated for the other take-off angles. Comparison between the 115-mV/no-rest sample and the 115-mV/long-rest sample shows that the composition of the es-SEI with long rest and no rest is different. The sample with no rest shows a much higher concentration of carbonate/ester group species compared to the sample after long rest. LiF is the other major component in the es-SEI. There are trace amounts of LiPF_6 and trace amounts of another F-containing species that could not be identified at present.

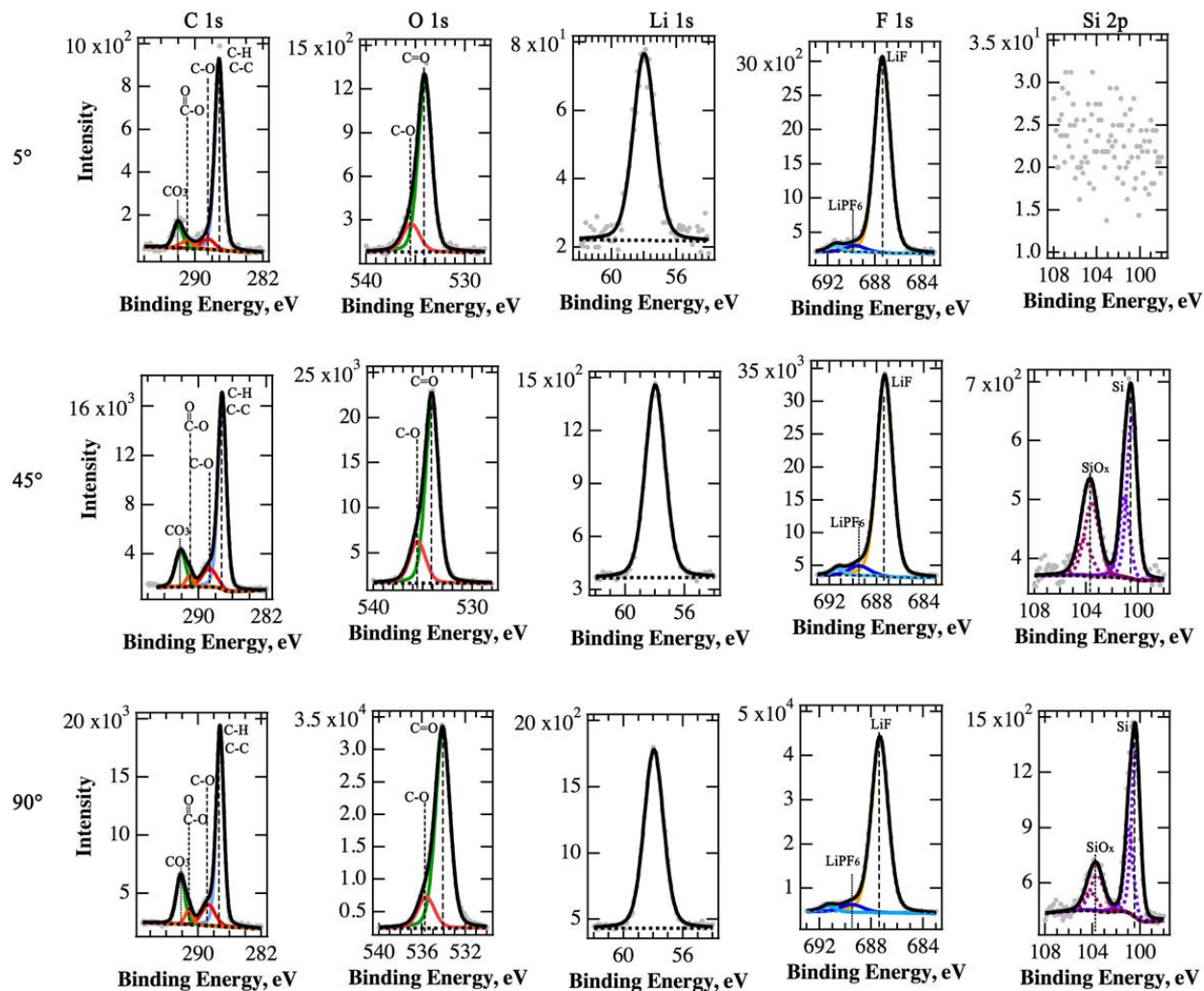


Figure II.2.B.94 The XPS spectra obtained from es-SEI after HVIST cycling with the cut-off potential of 115 mV and long rest. During the long rest, the spectra show that the LiEDC was decomposed because the LiEDC reduced. It also shows that there is no lithiation on the Si wafer because the lithium silicide was not found in Si.

Chemical evolution of the SEI layer

The electrochemical processes occurring upon (de-)lithiation and the SEI formation mechanism on the silicon electrodes have been investigated by cyclic voltammetry (CV) and galvanostatic cycling test.

Figure II.2.B.95a displays the CV profile obtained by cycling the 50-nm Si thin film for 10 cycles at a scan rate of 0.1 mV s^{-1} within the 0.05 V–1.5 V potential range using 1.2 M LiPF_6 in EC:EMC 3:7 wt.% as electrolyte solution. At 0.4 V, a small feature is observed and is most likely related to an early stage of lithiation of silicon.^[58] At low voltage values, i.e., 0.2 V and 0.08 V, the two main characteristic peaks of lithiation of amorphous silicon are observed. The two redox processes are also detected in the delithiation process at about 0.26 V and 0.48 V. The reductive decomposition of the electrolyte evolves through two main peaks at about 1.4 V and 0.8 V, attributable to the decomposition of EMC and EC, respectively. It is worth mentioning that for thin-film electrodes, a non-negligible contribution also arises from the interaction of the electrolyte with the copper current collector.^[59] Indeed, we also observe electrolyte reduction within the 2.0–0.5 V voltage range by cycling the bare-copper current collector in the same condition as the silicon thin-film electrode (see inset above Figure II.2.B.87a). The compared voltage signatures, reported in the inset of Figure

II.2.B.95a, show an overlapping behavior, with a small fraction of extra current attributable to the inherent reactivity of silicon toward carbonate-based electrolytes.

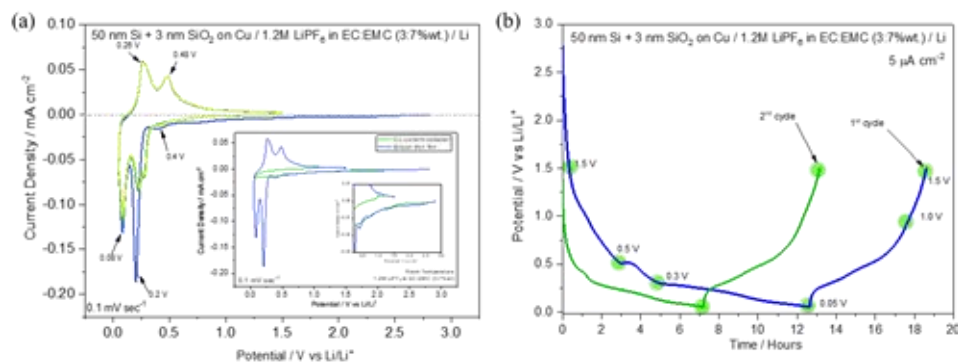


Figure II.2.B.95 (a) Cyclic voltammety of 50-nm Si thin film in Gen 2 electrolyte (1.2M LiPF₆ in EC:EMC 3:7 wt.%). Inset represents the comparison of the first-cycle voltage profile of the Si thin-film electrode and the bare-copper current collector. (b) First and second galvanostatic cycle of a 50-nm Si thin-film electrode cycled in 1.2M LiPF₆ in EC:EMC 3:7 wt.% electrolyte at 5 μA cm⁻² within the 0.05 V–1.5 V vs Li⁺/Li potential range.

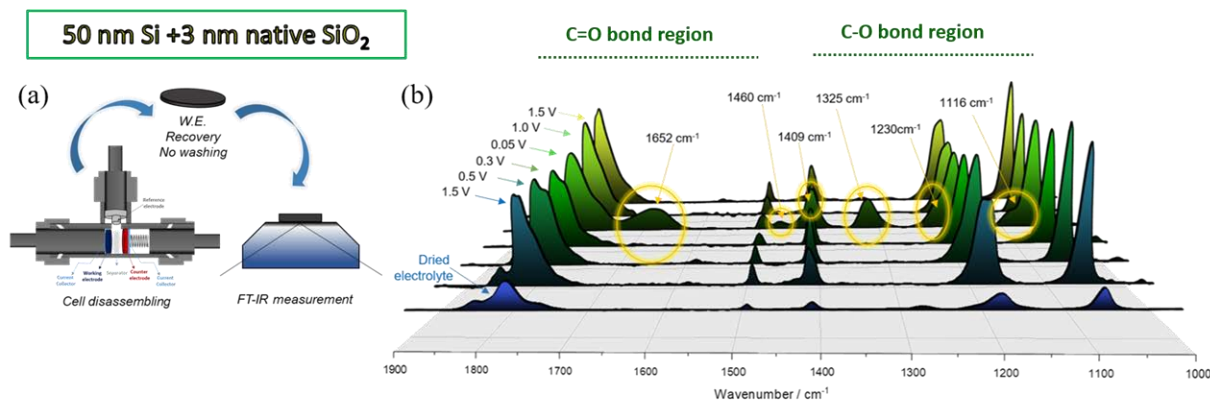
Upon further cycling, a stable electrochemical behavior is observed that is characterized by a decrease of the current involved in the electrolyte reduction region and a constant and reversible lithiation and delithiation process. The latter one is attributed to the properties of the thin-film electrode. Indeed, it is generally reported that the magnitude of the lithiation and delithiation peaks increase upon cycling due to the increased electrochemical reactivity of freshly exposed silicon generated by the cracking effect. However, in our study, this behavior is not observed due to the structural stability of the electrode conferred by the limited thickness of the thin films in which the cracking effect is well buffered. [58] This fundamental property of the 50-nm-thick thin film enables the study of the silicon reactivity toward the electrolyte, avoiding any possible effect related to the volume expansion experienced by the active material upon cycling.

Figure II.2.B.95b reports the voltage profile of the first and second (de)lithiation process obtained applying a constant current of 5 μA cm⁻² within the 0.05 V–1.5 V potential range. The cycling behavior is a good match with the CV analysis. Indeed, all the redox peaks observed during CV are also well defined in the constant-current-mode test. The green dots represent the different state of charge at which the electrode surface has been analyzed. The interfacial properties of the 50-nm Si thin-film model electrodes have been investigated by *ex-situ* ATR-FTIR analysis at different states of charge during the first (de)lithiation process.

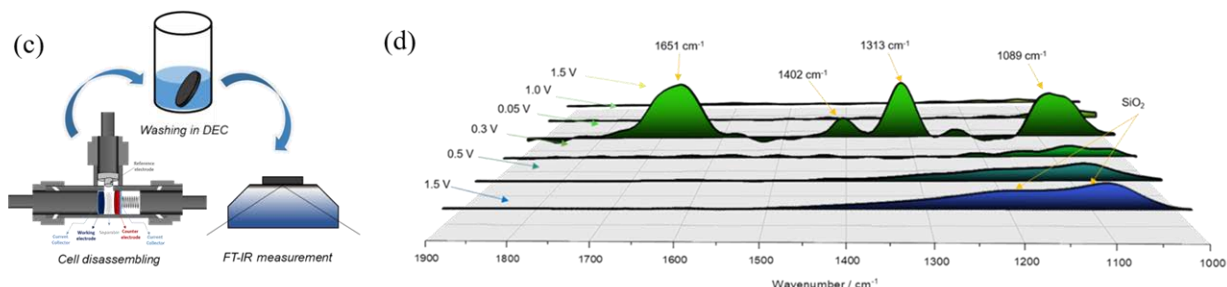
Figure II.2.B.96 reports the *ex-situ* ATR-FTIR spectra collected at 1.5, 0.5, 0.3, and 0.05 V during the reduction process and at 1.0 and 1.5 V in the following oxidation. The electrodes have been analyzed as recovered from the cell without any washing treatment to remove electrolyte residuals (see schematic in Figure II.2.B.96a). The spectra have been recorded after a drying step, enabling the evaporation of the most volatile solvent of the electrolyte, represented by EMC. For comparative purpose, the reference spectra of the so-called “dried” electrolyte is also reported; it is considered to be a more representative reference spectra for the *ex-situ* ATR-FTIR analysis performed on the recovered dried electrodes. The absorption peaks characterizing the spectra obtained at 1.5, 0.5, and 0.3 V mostly belong to electrolyte residuals as compared with the peaks of the dried electrolyte spectra. However, the analysis reported in Figure II.2.B.96b offers the ability to detect some major changes in the 1,000–1,900 cm⁻¹ spectral region in the fully lithiated state, i.e., 0.05 V. Three new main features appear at about 1,652 cm⁻¹ (ν C=O), 1,460 cm⁻¹ (δ C-H), and 1,325 cm⁻¹ (ν C=O), whereas broadening of the electrolyte peaks is observed at 1,409 cm⁻¹ (ν O-C-O and δ C-H), 1,230 cm⁻¹ (ν C-O or ν P=O, P-O-C), and 1,116 cm⁻¹ (ν C-O-C). The new contributions observed in the fully lithiated state are attributed to the presence of lithium ethylene dicarbonate ((CH₂OCO₂Li)₂-LiEDC) on the electrode’s surface. LiEDC was firstly proposed by Aurbach et al. [58], [59] as the primary decomposition product of EC-containing electrolytes. Indeed, it has been reported that LiEDC is the result of a single-electron reduction

process of EC (see schematic in Figure II.2.B.96e), which has been detected on noble metals and the surface of lithium electrodes.[62], [63] Later, the presence of LiEDC on lithium electrodes was further confirmed and implemented, with its detection also on nickel surfaces[64] and more recently on carbonaceous[63] and silicon-based electrodes,[64] suggesting LiEDC as a main component of the passivating film formed on the surface of working electrodes when using EC-containing electrolytes.

SEI on un-washed Silicon thin film electrodes: Visualization of the SEI evolution



SEI on washed Silicon thin film electrodes: Detection of the insoluble SEI components



Identifying LiEDC as main electrolyte decomposition product of 1.2 M LiPF₆ EC:EMC 3:7 wt. %

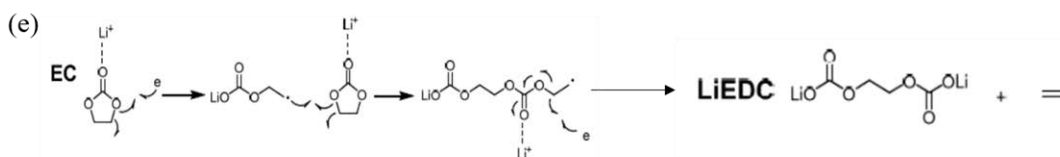


Figure II.2.B.96 Schematic representation of the electrode recovery and ATR-FTIR testing of unwashed (a) and washed (c) Si thin-film model electrodes. Cells have been cycled at $5 \mu\text{A cm}^{-2}$ employing 1.2 M LiPF₆ in EC:EMC (3:7 wt. %) as electrolyte. Ex-situ ATR-FTIR analysis of cycled Si thin films at different states of charge during the first (d)lithiation process in the 1,900–1,000 cm^{-1} spectral region of unwashed (b) and washed (d) electrodes. (e) Schematic representation of LiEDC formation as a decomposition product of EC.[8]

Although the detection of LiEDC does not itself represent a new finding, Figure II.2.B.96b offers a fundamental observation related to the instability of the passivating film formed on silicon electrodes. Indeed, the new features assigned to LiEDC in the spectra obtained at 0.05 V disappear upon delithiation both at 1.0 V and 1.5 V. This new fundamental observation leads to the correlation between the presence of LiEDC on the surface film and its passivating properties, making it one of the components most likely responsible for the poor passivating properties of silicon electrodes. Interestingly, in the 1,900–1,000 cm^{-1} spectral region, no other relevant features are observed in all the spectra collected at different states of charge. This can be explained considering the high solubility of the electrolyte decomposition products, which then diffuse into the

electrolyte. The latter ones may indeed either solubilize in the solvents or detach from the electrode's surface, thus inhibiting the formation of a stable passivating film.

In an effort to detect further hidden components of the surface layer and investigate the solubility of the formed products, two different approaches have been undertaken. The first one is a physical approach consisting in a rinsing step of 10 seconds in DEC followed by a drying process in a glovebox under inert atmosphere (see Figure II.2.B.96c). The FTIR analysis on the rinsed electrode is reported in Figure II.2.B.96d. The washing process adopted leads to the disappearance of all the electrolyte features on the silicon surface, disclosing the appearance of the native SiO₂ layer features at 1.5 V and 0.5 V and 0.3V. Indeed, it is believed that the surface-layer thickness at these states of charge is fairly limited and most likely constituted by soluble products, which totally disappear upon rinsing. Interestingly, it is seen that in the fully lithiated state, at 0.05 V, the features attributed to LiEDC are still present.

Indeed, as previously reported,^[64] the lithiated silicon represents a suitable surface for the deposition of LiEDC, which results in an insoluble product of the SEI because its main absorption features at about 1,651 cm⁻¹, 1,402 cm⁻¹, 1,313 cm⁻¹, and 1,089 cm⁻¹ can still be detected even after the washing process.

It is worth mentioning that generally, one of the main challenges while performing *ex-situ* analysis is represented by the rinsing step. The use of a carbonate-based solvent to eliminate electrolyte residuals is seen as a necessary step to avoid the massive contribution of electrolyte species, which may hinder the detection of hidden compounds associated with the film formation. On the other hand, the rinsing process may deeply affect and modify the film composition, especially at a high degree of lithiation of the electrodes, when the electrode is more likely to further react and may also further solubilize other film components. To enable the detection of hidden compounds, while avoiding the side effects possibly induced by the rinsing step, we adopted an additional approach, consisting in a mathematical subtraction of the electrolyte peaks from the spectra obtained at different states of charge, thus avoiding any possible side reaction with the solvent during the washing step. The subtraction analysis (data not reported here) shows that for all the spectra—except the one for the fully lithiated silicon electrode—there is no evidence of other components on the surface layer. The only detectable features appear for the fully lithiated sample at 0.05 V at about 1,654 cm⁻¹, 1,326 cm⁻¹, 1,110 cm⁻¹, and 1,062 cm⁻¹, which can still be attributed to LiEDC.

The surface of the fully lithiated silicon thin-film electrode has been investigated with an apertureless near-field scanning optical microscopy (aNSOM), employing a metallized AFM tip in contact with the sample surface as an optical probe for high-resolution spectroscopy and imaging measurements. The technique offers the extraordinary ability to combine the unique capability of infrared near-field microscopy with FTIR spectroscopy to map the chemical distributions on the electrode's surface, while guaranteeing the detection of single components at high spatial resolution (see Figure II.2.B.97a).^{[65], [66]}

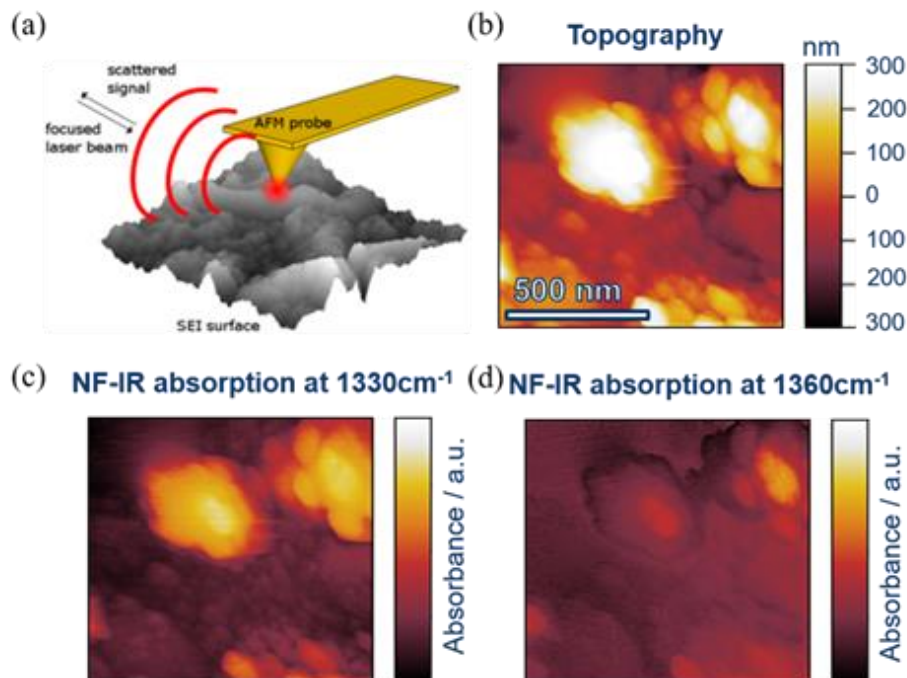


Figure II.2.B.97 (a) 3-D schematic of aNSOM experimental setup and operational principle. aNSOM $1\text{-}\mu\text{m} \times 1\text{-}\mu\text{m}$ image of 50-nm silicon thin-film electrode cycled up to 0.05 V after the first lithiation process. (b) Topography of a region of the surface film formed on the fully lithiated silicon thin-film electrode obtained by AFM. Near-field IR absorption maps over the same region at (c) $1,330\text{ cm}^{-1}$ and (d) $1,360\text{ cm}^{-1}$ wavenumbers.

Figure II.2.B.97b reports the obtained AFM topography image of the SEI layer on the lithiated silicon thin film. The morphology of the detected surface layer is characterized by a nonuniform distribution and roughness.

Figure II.2.B.97c and Figure II.2.B.97d report the variation in contrast as a function of IR wavelength, indicating changes in surface structure and composition. Indeed, by using a $1,330\text{ cm}^{-1}$ excitation wavelength, corresponding to an adsorption peak of LiEDC, i.e., $\nu\text{ C=O}$ (see Figure II.2.B.96), a strong absorbance is detected; however, changing the wavelength to $1,360\text{ cm}^{-1}$ revealed no significant absorbance, as indeed observed in the ATR-FTIR analysis reported in an earlier Figure, which does not present any IR feature at $1,360\text{ cm}^{-1}$. Indeed, it can be observed that the contrast in the corresponding IR images in Figure II.2.B.97c and Figure II.2.B.97d shows a direct correlation of specific features in the topography to chemical properties, which vary according to the IR absorption at different wavenumbers. The absorbing aggregates observed, which are most likely composed of round-shaped primary particles, are highlighted at $1,330\text{ cm}^{-1}$ in Figure II.2.B.97c, whereas they undergo a contrast inversion in Figure II.2.B.97d at $1,360\text{ cm}^{-1}$. This observation represents a direct observation of LiEDC aggregates on the electrode's surface, thus confirming our ATR-FTIR analysis and further implementing it with the gained spatial distribution on the electrode's surface.

In addition to the $1,900\text{--}1,000\text{ cm}^{-1}$ spectral region, the low-frequency region within the $1,000\text{--}700\text{ cm}^{-1}$ region has also been investigated by ATR-FTIR. This spectral region is generally characterized by P-F- and Si-O-bond-containing compounds. The analysis has been performed on both unwashed and washed electrodes and is reported in Figure II.2.B.98a and Figure II.2.B.98b, respectively.

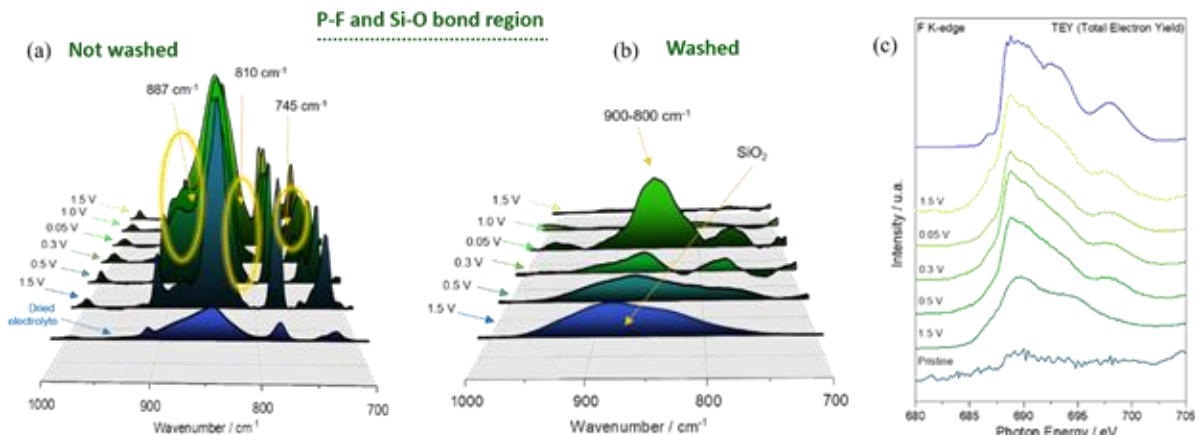


Figure II.2.B.98 Ex-situ ATR-FTIR analysis of cycled Si thin films at different states of charge during the first (de)lithiation process in the 1,000–700 cm^{-1} spectral region of unwashed (a) and washed (b) electrodes. (c) Ex-situ XAS analysis at the F K-edge collected in TEY mode.

The spectra recorded at different states of charge clearly indicate an accumulation of species that are IR active within the 800–900 cm^{-1} spectral region, most likely related to P-F- and P-O-F-containing compounds. It is generally accepted that LiPF_6 precipitates in the form of Li_xPF_6 and LiF after reduction. Moreover, the eventual presence of water traces generally catalyzes the formation of PF_5 and POF_3 species.^{[67], [68], [69]}

The detection of P-F- and P-O-F-containing compounds have been previously observed;^{[67], [68], [69]} however, our analysis offers more insights on a clear accumulation of P-F- and P-O-F-containing species upon cycling. Indeed, it is observed that upon lithiation, already starting at 1.5 V, the IR-band centered at about 850 cm^{-1} starts to broaden and becomes larger. The largest observed contribution is visible in the fully lithiated state (0.05 V). During the delithiation process, the band intensity decreases; however, the process is not totally reversible, leading to the deposition and accumulation of P-F- and P-O-F-containing species on the electrode's surface and suggesting a dynamic growth and disappearance of the surface layer. In addition, in the analysis performed on washed samples, it is clearly observed that primarily all the features disappear to be replaced by the Si-O contributions of the native SiO_2 layer, suggesting a solubility of the P-F and P-O-F species in the solvent used to wash the electrodes. The prominent feature observed at about 850 cm^{-1} in the fully lithiated state can be still attributed to the presence of LiEDC, as previously reported.^[62]

In relation to fluorine-containing compounds, X-ray absorption spectroscopy (XAS) at the fluorine K-edge has been performed. The analysis suggests the formation of LiF (see reference spectra in blue in Figure II.2.B.98c), starting at 1.5 V and accumulating upon cycling. XAS offers the ability to detect LiF as a stable SEI component, which is otherwise not detectable by FTIR because it is a non-active FTIR compound.

Our investigation leads to a fundamental observation related to the dynamic evolution of the SEI upon cycling, most likely related to the formation and disappearance of LiEDC and P-F- and P-O-F-containing compounds.

To corroborate our hypothesis linking the passivation properties of the surface layer formed on silicon electrodes with the presence of LiEDC and the P-F/P-O-F-containing species, we also further investigated the behavior of the silicon thin-film model electrodes during the second cycle.

In the 1,900–100 cm^{-1} spectral region, three main peaks and additional smaller features are observed to constantly appear and disappear upon (de)lithiation, during both the first and second cycle (see Figure II.2.B.99a). All the features are related to the formation and disappearance of LiEDC on the electrode's surface. In addition, the dynamic growth and dissolution of P-F/P-O-F-containing species is observed in the 1,000–700 cm^{-1} spectral region (see Figure II.2.B.99b).

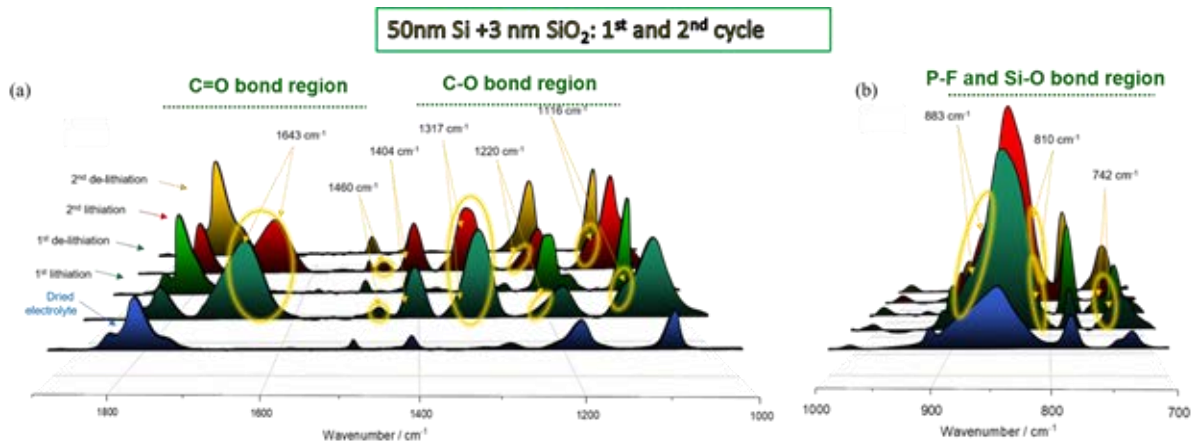


Figure II.2.B.99 Ex-situ ATR-FTIR analysis of cycled Si thin films in the fully lithiated and delithiated state upon the 1st and 2nd cycle in the 1,900–1,000 cm^{-1} (a) and 1,000–700 cm^{-1} (b) spectral regions. Cells have been cycled at $5 \mu\text{A cm}^{-2}$ employing 1.2M LiPF₆ in EC:EMC (3:7 wt.%) as electrolyte.

The results discussed here represents a step forward in understanding the stability of the SEI. The accumulation and following disappearance of different species on the electrode's surface clearly suggest a dynamic SEI formation and "dissolution." The "breathing" mode of the passivating layer on top of the silicon thin films has also been detected by XAS.

The analysis of the silicon L-edge employing a total electron yield (TEY) detector—which is surface-sensitive (with a detection depth on the order of a few nanometers)—clearly reveals the formation and thickening of a surface layer upon lithiation. Upon delithiation, it reduces considerably in thickness, further confirming the dynamic growth and disappearance of the surface layer (see Figure II.2.B.100a).

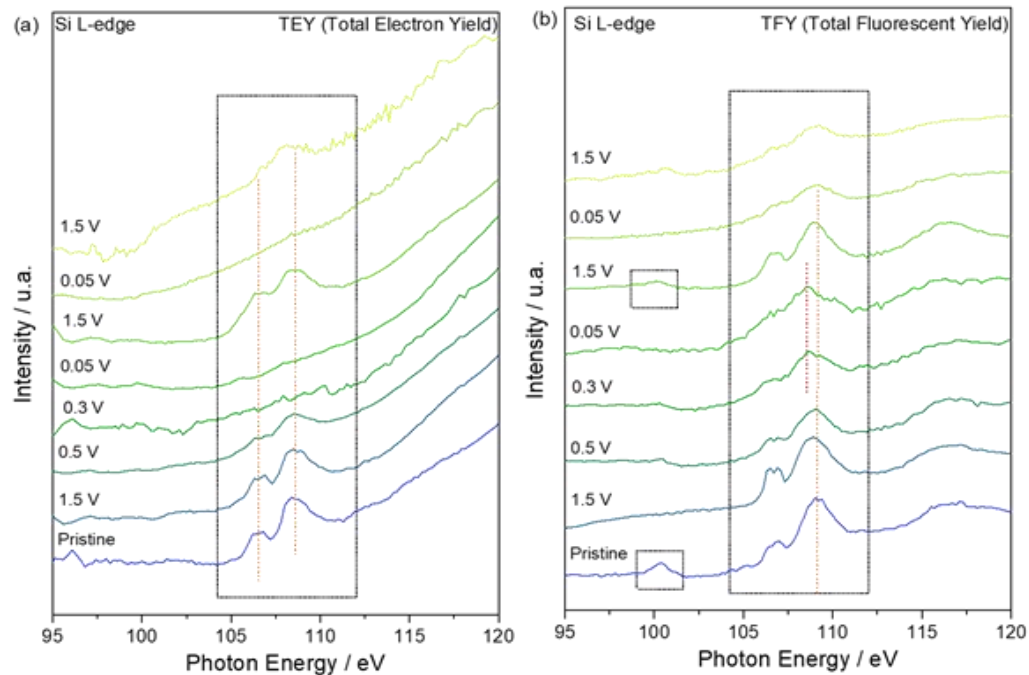


Figure II.2.B.100 Ex-situ XAS analysis at the Si L-edge collected in TEY (a) and TFY (b) mode for the 50-nm Si thin film with native oxide.

Indeed, the typical double feature of SiO₂ gradually disappears upon lithiation and further reappears upon delithiation. A total fluorescence yield (TFY) detector (see Figure II.2.B.100b) is more bulk-sensitive than the TEY, but still has a detection depth in the order of nanometers. Its use gives further insight on the behavior of both the SiO₂ (see peaks within 106–111 eV) and Si underneath the native oxide layer (see peak at about 100 eV). In Figure II.2.B.100b, the breathing effect is visualized following the peak related to the silicon, which disappears upon lithiation, to then reappear in the delithiated state. In addition, the typical double feature of SiO₂ undergoes some minor changes both in terms of shape and peak position. The changes are reversible, and in the delithiated state, the pristine features are recovered.

A change in the XAS spectra in the Si L-edge may indicate a change in the electronic state of the native SiO₂ surface layer on top of the silicon thin-film model electrodes.^[70] It has been proposed that the SiO₂ may undergo a conversion reaction upon lithiation, leading to the formation of Li₂O and metallic silicon by forming intermediate stoichiometric or non-stoichiometric silicate species.^{[71], [72], [73]}

To evaluate the hypothesis of the silicate formation, a new model electrode has been adopted. The electrode presents a thicker SiO₂ layer on top of the 50-nm Si thin film. ATR-FTIR analysis has been performed upon cycling and the related results are reported in Figure II.2.B.101.

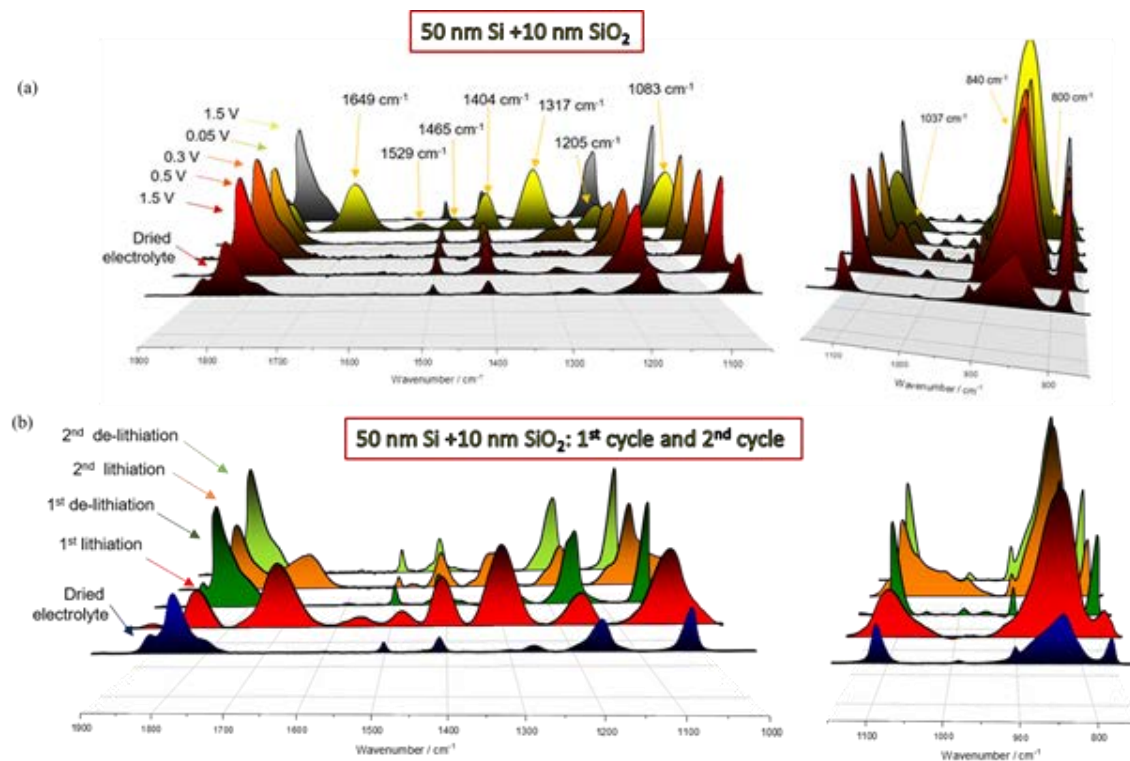


Figure II.2.B.101 Ex-situ ATR-FTIR analysis of unwashed cycled 50-nm Si thin films with 10-nm SiO₂ at different states of charge during the first (de)lithiation process (a) and following 2nd cycle (b).

The 50-nm Si thin films with a 10-nm SiO₂ layer have been investigated at different states of charge during the first lithiation and delithiation (see Figure II.2.B.101a) and also during the 2nd cycle (see Figure II.2.B.101b).

Interestingly, it is observed that the 1,900–1,000 cm⁻¹ spectral region is fairly comparable with the model electrode presenting only the native oxide layer (see Figure II.2.B.96), suggesting that the formation of LiEDC is not affected by the SiO₂ layer. In addition, a comparable presence of P-F/P-O-F-containing species is observed; however, new peaks at about 1,037 cm⁻¹ are also detected starting at 0.5 V until the fully lithiated state (see Figure II.2.B.101a), to then disappear again during the delithiation process. In addition to the P-F/P-

O-F-containing compounds, the new features may be related to the presence of other electrolyte decomposition products, such as DEDOHC,^[58] or the eventual presence of non-stoichiometric silicates. Interestingly, upon further cycling, the accumulation of these species in the fully lithiated state is enhanced, and a clear broad signal is detected that was not observed with the previous model electrodes (see Figure II.2.B.101b). It is worth mentioning that in this spectral region, features related to the presence of silicates have been proposed in the literature.^[74] However, work toward identifying and assigning these peaks is still in progress. In addition to the discussion related to the eventual formation of silicates, it is important to mention that our study is mainly focused on understanding the effect of the silicates on the silicon-passivating properties. The assignment of the observed features to silicates may lead to an important observation linked to the breathing behavior of silicon. Indeed, silicates, as well as LiEDC and P-F/P-O-F-containing compounds, may be linked to the breathing effect of the SEI and can be indicated as the SEI components responsible of the poor passivating properties of silicon electrodes and the poor stability of the SEI layer. Further studies in this regard are still in progress.

Reduction of fluoroethylene carbonate (FEC)

In this study, we are seeking to assess the role of adding FEC to the electrolyte and how it changes the physical properties of the SEI. Recent NMR and FTIR work on silicon cells cycled with FEC in the electrolyte have shown that whereas the initial reaction to activate the FEC is a defluorination reaction to create insoluble LiF and a vinoxyl radical, the majority of the FEC is then involved in a radical vinoxyl-driven polymerization of the FEC to form a cross-linked poly(fluoro-carbonate).^{[74], [75], [76]} In the absence of FEC, common carbonate battery solvents, such as ethylene carbonate (EC), appear to give co-polymers between a vinylene carbonate (VC)-derived species and PEO-like species.^[74] The latter reaction also resulted in a series of soluble PEO oligomers that dissolve into solution.^[76] In our EQCM study on similar materials and with similar FEC concentrations, we are able to note (see Figure II.2.B.102) that the silicon electrode responds, without FEC, as a stable mass increase on cycling (SEI formation) and an increase in dissipation that tracks the weight changes. The dissipation tracks film density. Consistent with previous observations, the Gen2 electrolyte forms a porous film on the silicon anode. In contrast, the addition of FEC has been noted to improve cycling whereas NMR data have noted that the film formed is more cross-linked (denser) and stable. The EQCM data are consistent with that interpretation because the initial gain of film weight stabilizes, whereas the dissipation data are consistent with the film formed being less porous and likely to have trapped solvent or electrolyte components. The percentage of FEC did not appear to have a significant impact on the data (up to 20% evaluated) although it should have an effect on electrolyte conductivity.

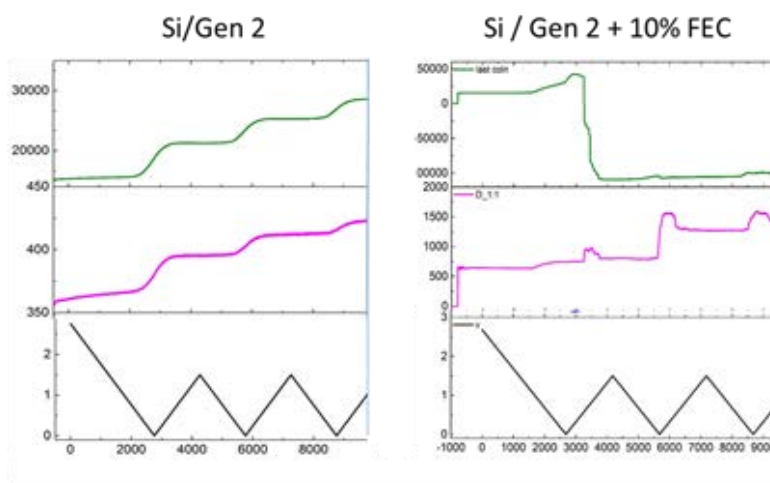


Figure II.2.B.102 A comparison of the EQCM-D data for a silicon film cycled in (a) Gen2, and (b) Gen2 +10 wt.% FEC.

Inhomogeneous chemistry of the SEI layer

Despite such progress, a unified picture encompassing the morphology, phase, and chemical composition of SEI is still lacking, and most studies still refer to the schematic cartoon proposed by Peled for SEI on graphite anodes in 1991. [77], [78] In Fiscal Year 2018, we implemented tip-enhanced Raman spectroscopy (TERS) experiments on pristine and cycled amorphous silicon (a-Si) samples. [79] And we successfully demonstrated that the SEI has structural and chemical heterogeneity in nanoscale on the a-Si surface.

Figure II.2.B.103 shows the topography (a, f, and k) and the intensity mapping of a few individual bands from the principal chemicals of SEI from each a-Si sample. The right-hand columns in Figure II.2.B.103 show the dominant vibrational species as observed for each cycled a-Si sample. The topography and chemical imaging are on the same sample area, with the spatial resolution given by the scale bar in each map. The intensity of each vibrational signal is given by the color bar, which indicates the concentration of each chemical moiety. Those bands and their associated principal chemical components are summarized in Table II.2.B.8.

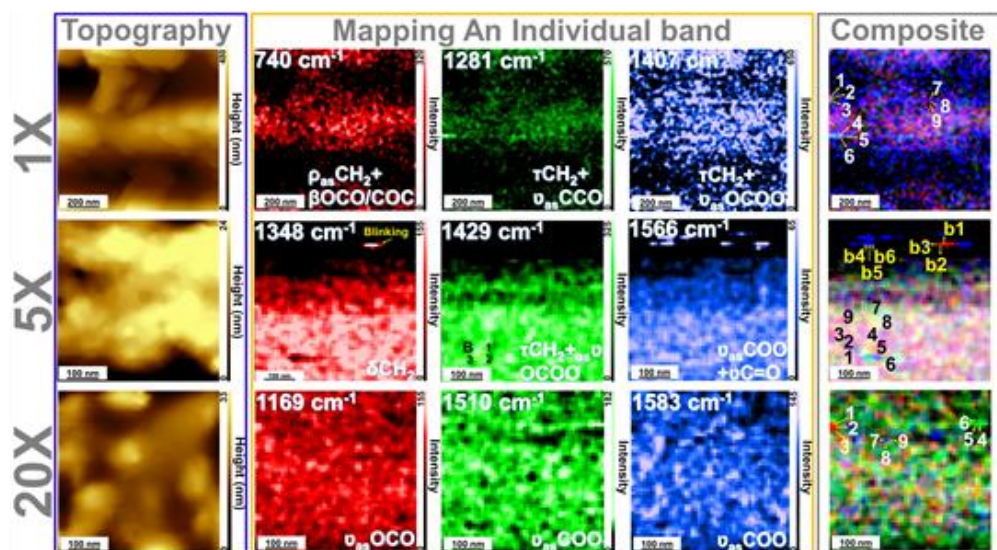


Figure II.2.B.103 AFM topography (blue box), TERS mapping of an individual band (orange box) and composite TERS map (grey box) of 1X, 5X, and 20X cycled a-Si samples. The topography and chemical imaging are on the same sample area. The intensity roughly indicates the concentration of each chemical moiety. The individual band TERS mapping quantifies the intensity of a band, after spectral background correction, of each vibrational signal scaled by the false color bar. From left to right (orange box), TERS mapping indicates the overlap of $-\text{CH}_2$ rocking, $-\text{OCO}$ and $-\text{COC}$ deformation bands ($\sim 740 \text{ cm}^{-1}$), $-\text{CH}_2$ twisting, asymmetric CCO stretching bands ($1,281 \text{ cm}^{-1}$) and $-\text{CH}_2$ twisting, asymmetric OCOO stretching bands ($\sim 1,407 \text{ cm}^{-1}$) collected from 1X a-Si, respectively. For 5X a-Si, TERS mapping respectively shows the combination of $-\text{CH}_2$ bending band ($1,348 \text{ cm}^{-1}$), $-\text{CH}_2$ twisting, asymmetric OCOO stretching bands ($\sim 1,429 \text{ cm}^{-1}$) and $-\text{CH}_2$ twisting, asymmetric COO stretching, and $\text{C}=\text{O}$ stretching bands ($1,566 \text{ cm}^{-1}$). For 20X a-Si, TERS mapping exhibits the asymmetric $-\text{OCO}$ stretching band ($1,169 \text{ cm}^{-1}$), bidentate asymmetric $-\text{COO}$ stretching band ($1,510 \text{ cm}^{-1}$), and the monodentate asymmetric $-\text{COO}$ stretching bands ($1,583 \text{ cm}^{-1}$). The right grey box shows the composite TERS maps for all samples. The number index of the composite map marks where the sample TERS spectrum was taken.

Table II.2.B.8 TERS spectral band assignment for cycled a-Si

Number of Cycles	Spectral Position (cm ⁻¹)	Principal Chemical/Vibrational Signature of SEI from TERS	Band Assignment
1X	740	LEDC	$\rho_{\text{as}}(\text{CH}_2) + \beta(\text{OCO/COC})$
	1,281	PEO	$\tau(\text{CH}_2) + \nu_{\text{as}}\text{CCO}$
	1,407	LEDC	$\tau(\text{CH}_2) + \nu_{\text{as}}\text{OCOO}$
	1,433	LEDC	$\tau(\text{CH}_2) + \nu_{\text{as}}\text{OCOO}$
5X	1,348	PEO/LEDC	$\delta(\text{CH}_2)$
	1,429	LEDC	$\tau(\text{CH}_2) + \nu\text{OCOO}$
	1,491	LEDC	$\chi(\text{CH}_2)$
	1,566	LEDC	$\nu_{\text{as}}(\text{COO}) + \nu(\text{C=O})$
	1,588	LEDC	$\nu_{\text{as}}(\text{OCO})$
	822	R ₂ POF	$\nu(\text{PF})$
	929	RPOF ₂	$\nu(\text{PF})$
20X	1,169	LEDC	$\nu_{\text{as}}(\text{OCO})$
	1,460	monodentate carboxylate	$\omega(\text{CH}_3)$
	1,510	bidentate carboxylate	$\nu_{\text{as}}(\text{COO})$
	1,565	Bridging + monodentate carboxylate	$\nu_{\text{as}}(\text{COO})$
	1,583	monodentate carboxylate	$\nu_{\text{as}}(\text{COO})$
	1,632	monodentate carboxylate	$\nu_{\text{as}}(\text{COO})$

To highlight the heterogeneous SEI chemical signatures at the nanoscale, we took nine spectra from nine spots (denoted by 1–9) for each a-Si sample, with each set of three spots 10 nm apart from each other. The spectra taken from those spots of each a-Si sample are shown in Figure II.2.B.88.

An immediate observation for 1X a-Si (cycled for once) TERS mapping (Figure II.2.B.103) is that the distribution of the selected chemical moieties in each TERS mapping follows the AFM topography, in which the band intensity tends to distribute on top of the ridge-like a-Si, whereas this trend is not observed for 5X and 20X samples. This might be due to a thicker SEI grown on the latter two a-Si samples. For 1X a-Si, the band at 740 cm⁻¹ is assigned to the –OCO/COC deformation mode of LEDC (Figure II.2.B.103a).^[80] The convolution of –CH₂ rocking mode with this band cannot be ruled out at this frequency range.^[80] The band centered at 1,281 cm⁻¹ is the combinational mode of CH₂ twisting and –CCO asymmetric vibration, ascribed to PEO-like oligomer species in the SEI. It is clear that the distribution of the 1,281 cm⁻¹ band on the 1X a-Si surface is different from that of the 740 cm⁻¹ band, indicating different local distributions of the LEDC and PEO components in SEI in nanoscale.

For 5X a-Si, we demonstrate that the more dominant species is LEDC in SEI, and the AFM topography does not correlate well to the TERS mapping like 1X a-Si. AFM topography and TERS mappings of three different vibrational modes of the 5X a-Si (Figure II.2.B.103), namely –CH₂ bending (1,348 cm⁻¹), the hybrid of –CH₂ twisting and –OCOO stretching (1,429 cm⁻¹), and the hybrid of asymmetric –COO stretching and C=O stretching (1,566 cm⁻¹), are shown in Figure II.2.B.103 middle row (also see Figure II.2.B.104b). The first

band stems from PEO oligomer or LEDC, and the latter two are from LEDC monomer or dimer.[81] More detailed inspection of the spectra taken from the line pattern (spot b1 to b6 in the combined TERS mapping) indicates that the corresponding bands are of much higher TERS intensity (up to 7-fold increase) than those taken from other places, attributed to the TERS “blinking” phenomenon in which extreme TERS intensity of probed species shows up intermittently.[81]

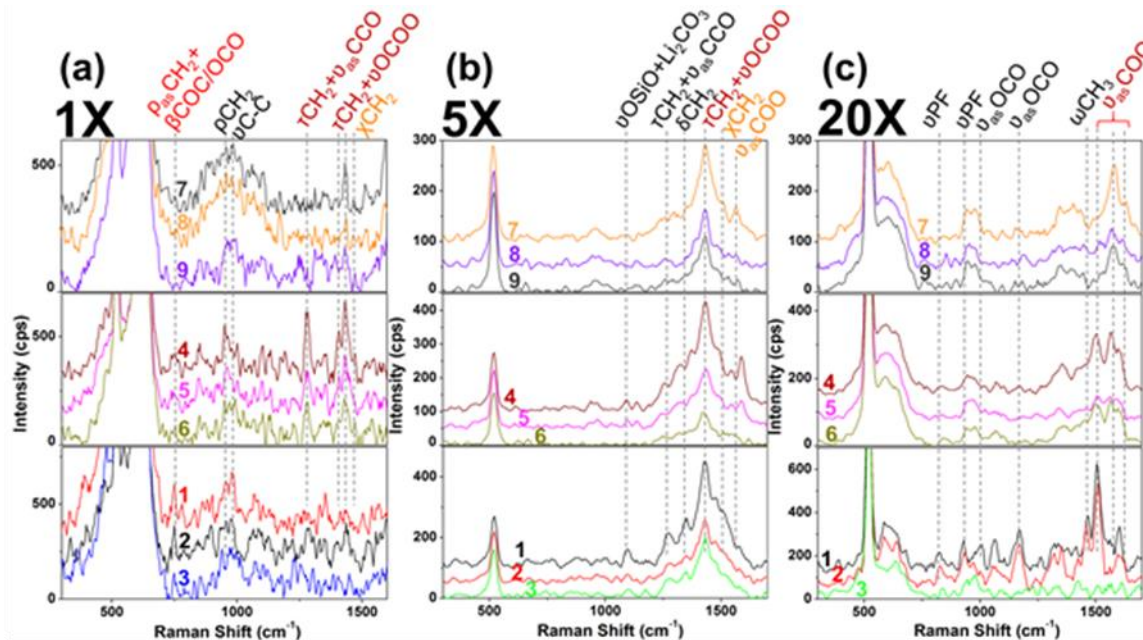


Figure II.2.B.104 TERS spectra collected from various locations of (a) 1X sample, (b) 5X sample, and (c) 20X sample. The assignment for bands of interest are at the top of each plot. The Greek symbols denote corresponding vibrational modes: ν (stretching), δ (bending), χ (scissoring), τ (twisting), ρ (rocking), β (deformation), and ω (wagging).

For 20X a-Si, the most exciting findings include that the local dominant species evolves into carboxylate (RCO_2Li) compounds and fluorinated species ($\text{Li}_x\text{PO}_y\text{F}_z$). The nanoscale carboxylate molecular conformational change can be depicted by TERS, as confirmed by density functional theory (DFT) simulation (data provided by Prof. Kristin Persson’s group and not shown here). Figure 17 bottom row shows the 20X a-Si AFM topography and TERS mapping of $-\text{OCO}$ asymmetric stretching ($1,169\text{ cm}^{-1}$), bidentate $-\text{COO}$ asymmetric stretching ($1,510\text{ cm}^{-1}$), and monodentate $-\text{COO}$ asymmetric stretching ($1,583\text{ cm}^{-1}$) (Figure 18c). Several vibrational modes between $1,450\text{ cm}^{-1}$ and $1,650\text{ cm}^{-1}$ gain in intensity, which cannot be assigned to either PEO or LEDC, as observed in the case of 1X and 5X samples. Those bands are most likely ascribed to various carboxylate compounds (RCO_2Li),[81] which are formed either by thermal decomposition of the LEDC per prolonged galvanostatic cycling[82] or by ester radicals coordinating to Li^+ . [84]

Morphology and physical properties of the SEI layer

Morphology of SEI layer formed on the two model Si wafer samples—including the Si wafer with a 15-nm SiO_2 thermally grown layer and Si wafer with a native oxide layer—have been obtained by using STEM, while the resistivity as a function of depth was monitored by using the SSRM technique. The Si wafer electrodes were lithiated at a constant current of $22\text{ }\mu\text{A cm}^{-2}$ for 5 hours. Figure II.2.B.105 compares the resistivity obtained from these two Si electrodes. When using the Si sample with a 15-nm SiO_2 layer, higher resistivity was detected in the SEI layer, as compared to the SEI later on the Si sample with a native oxide. STEM high-angle annular dark-field images and energy-dispersive X-ray spectroscopy (EDS) images were captured from these two samples and are shown in Figure II.2.B.106. EDS maps show a higher content of C and O and a lower content of F in the SEI layer formed on the Si electrode with a 15-nm SiO_2 layer, when compared to the SEI formed on a Si electrode with a native oxide layer. The high-content C and O in the Si electrode with a 15-

nm SiO₂ layer indicate the formation of organic components in the SEI layer, resulting in more insulating behavior.

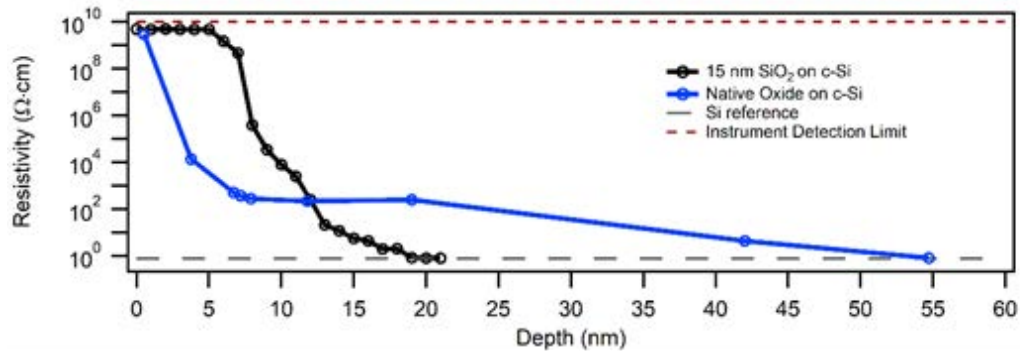


Figure II.2.B.105 SSRM resistivity vs. depth profiles of SEI formed on 15-nm SiO₂ and native oxide on Si wafers after one cycle.

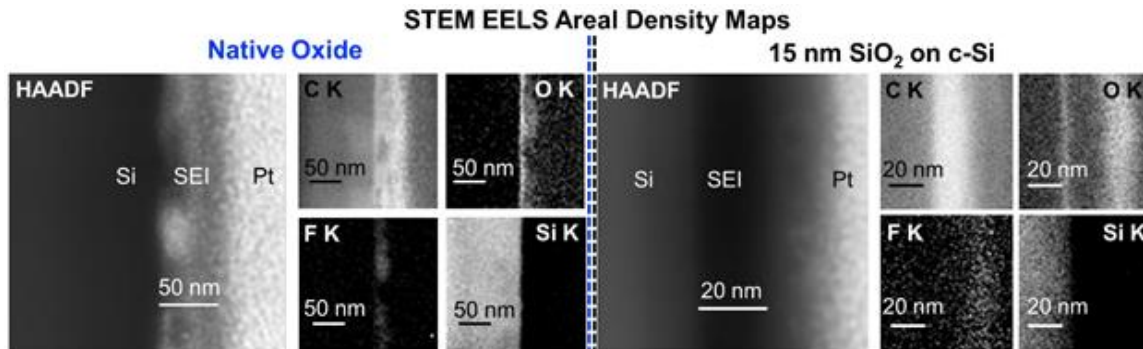


Figure II.2.B.106 STEM EELS areal density maps on SEI formed on two model Si systems. SEI formed on native oxide is comparably thicker and less laterally homogenous when compared to that formed on SiO₂.

Development of Characterization Techniques

Scanning Spreading Resistance Microscopy (SSRM) Technique Development: 3D Resistivity Mapping

To characterize the electronic resistivity of SEI, an experimental approach was developed using SSRM. The technique is described in Figure II.2.B.107. We found that the electronic resistance is uniform in the lateral direction (plane view) within an order of magnitude. However, the resistance decreases steeply (up to 10 orders of magnitude) with depth, from the top surface toward the Si electrode (Figure II.2.B.107e). The profile should qualitatively or semi-quantitatively reflect the resistivity change due to the different material compositions deposited by electrochemical reactions at different voltages in the lithiation/delithiation cycles. This resistivity profile also changes with SEI cycling conditions and electrolyte chemical composition, illustrating the material dependence of local 3-D resistivity.

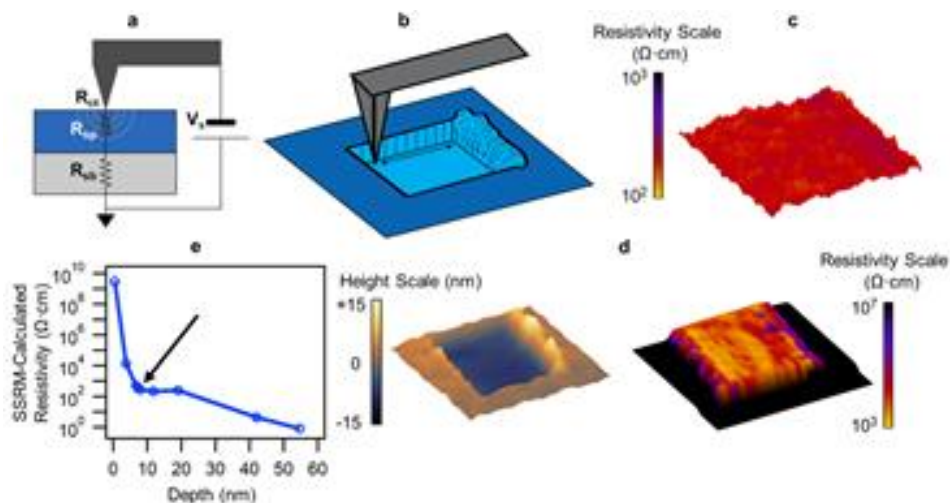


Figure II.2.B.107 An example of 3-D resistance mapping of SEI. (a) SSRM schematic, where spreading resistance (R_{sp}) \gg sample and back-contact resistance (R_{sb}). By using appropriately large probe forces, the contribution of the contact resistance (R_{ct}) is reduced to a stable level. Curved arcs around the probe represent potential contour arcs, indicating the sampling volume, in a semi-infinite uniform material. (b) Conceptual diagram depicting measurement technique. A resistance map is captured at intermediate probe forces, resulting in uniform milling of the surface material to a defined depth. A larger scan is then taken over the measurement area to determine the depth of the resistance map. (c) $0.5 \times 0.5 \mu\text{m}$ resistance map captured with a probe forces of $15 \mu\text{N}$ on SEI on Si with SSRM, measuring resistance of SEI at a depth of 9 nm. (d) $1.0 \times 1.0 \mu\text{m}$ height channel image (left) captured at a low contact force ($< 1 \mu\text{N}$) over the location of the previously described resistance mapping raster scan, indicating the depth of the resistance map shown in (c). Resistance channel image (right) captured in the same scan shows relative contrast in the electronic properties between the superficial and deeper structures of SEI. Slightly higher resistivities are measured at the milled area when compared to (c) due to the contribution of contact resistance when scanning with low contact forces. (e) Example resistivity vs. depth profile obtained from resistance and depth measurements shown in (c) and (d), respectively. The datapoint obtained from resistivity and height data presented in (c) and (d) is indicated on the profile with an arrow.

To validate the technique and determine its resolution, a reference sample was designed featuring an α -Si:H layer stack. Analysis of the sample with film resistivity measurement (to determine resistivities of individual layers), secondary-ion mass spectrometry (SIMS), and SSRM allowed validation of the SSRM 3-D resistivity mapping and determination of SSRM resolution with 10–50 nm in lateral and ~ 50 nm in vertical directions (Figure II.2.B.108).

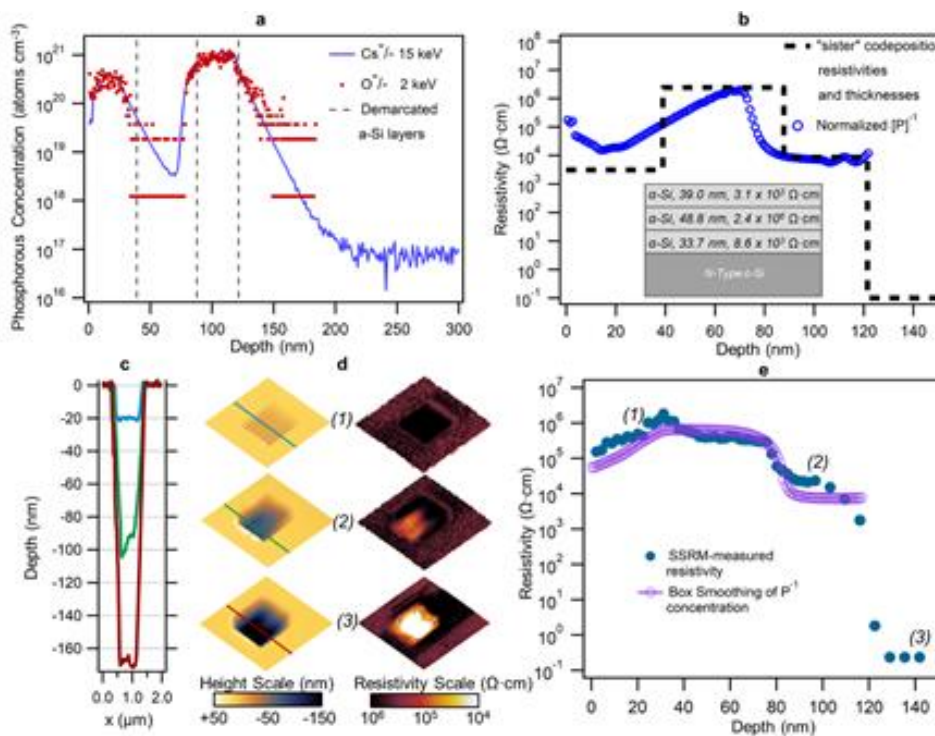


Figure II.2.B.108 SIMS and SSRM data for doped α -Si:H on c-Si reference sample. (a) Dynamic SIMS P-concentrations measured with cesium and oxygen sputtering at 15 keV and 2 keV, respectively. (b) Inverse P-concentration, normalized to highest bulk resistivity, measured on "sister" co-deposition on glass. Sample schematic with thicknesses and bulk resistivities is shown in inset. (c) Line scans across overview height images captured during various stages of incremental SSRM profiling, showing three distinct depths within the structure. (d) $2 \times 2 \mu\text{m}$ height (left) and resistivity (right) overview images at three stages of incremental SSRM profiling, demonstrating contrast in electronic resistivities at different depths within the structure. (e) SSRM resistivity vs. depth profile for the sample. Box-smoothing of normalized inverse P-concentration data shows close agreement with SSRM data after smoothing to include 10 nm of previous points (to account for probe tip penetration and debris accumulation at the probe) and 40 nm of subsequent points (to account for the sampling volume of the spreading resistance).

Development of fluorescence probes

A variety of methods have been employed to characterize the properties of lithium ions because they are relevant to battery technology. But these techniques often either require highly specialized equipment (neutron scattering, neutron tomography), do not have the spatial resolution to probe micro- and nanostructured ion transport pathways (NMR), or do not probe the lithium ions themselves, but rather, assumed ion-transport tunnels (scanning probe microscopy, X-ray tomography). Very recently, fluorescence microscopy was proposed as a tool that could potentially satisfy all of these technical obstacles by providing information on high spatial and time resolution about the distribution of lithium ions using relatively accessible equipment.^[85] However, many technical obstacles remain before such a technique could be employed *in operando* or even for *post-mortem* analysis to assess structural information in lithium-ion batteries.

In this work, we set out to develop fluorescent probes that would help determine how components of the silicon SEI layer evolve with cycling. The work specifically contributed to the SEISta project milestones by complimenting existing strategies to quantitatively measure soluble components of the SEI as well as measure the growth rate of the SEI components at fixed potentials and during cycling. In FT2018, work commenced with the synthesis of a model fluorescent probe recently described in the literature (Figure II.2.B.109) that is highly sensitive and specific to lithium ions.^[86] The organic molecule 2-(2-hydroxyphenyl)-naphthoxazole (HPNO) reportedly binds lithium in a 2:1 stoichiometry and maintains tetrahedral geometry, but the binding planarizes the organic molecule, which in turn red shifts its absorbance and fluorescence spectra. Following the

synthesis and characterization of HPNO this quarter, we verified the response of its optical properties to increasing lithium ion concentration with simple solution absorbance measurements. As can be seen in Figure II.2.B.109, absorbance red-shifts more than 40 nm in the presence of LiBr, and absorbance intensity scales with LiBr concentration.

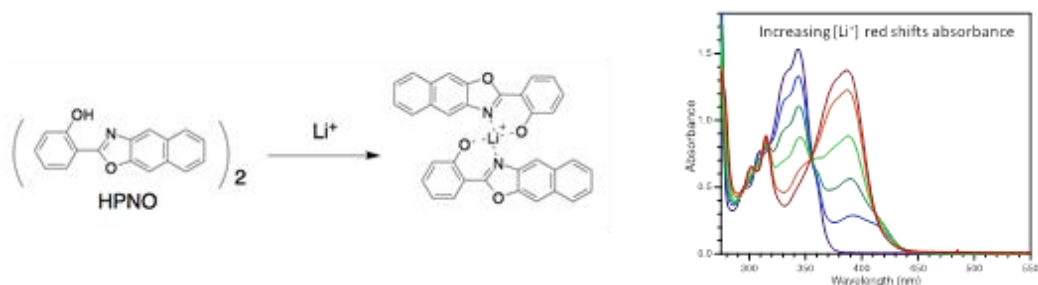


Figure II.2.B.109 (Left) Scheme for lithium binding by HPNO fluorophore. (b) UV-vis spectra of 0.05 mM HPNO in propylene carbonate without lithium (purple) and increasing amounts of LiBr until the solution is saturated with LiBr (red).

We then designed and implemented experimental routes for the synthesis of two new Li ion fluorescent sensors based on a modified literature design for tuning chromophore fluorescence.^[86] The strength of the different electron donating and withdrawing groups on these monomers (Figure II.2.B.110) would in principle allow the emission spectra of these compounds to be tuned so they do not significantly overlap with the background fluorescence of the SEI layer. As these compounds have not previously been reported in the literature, synthetic procedures were refined for each step.

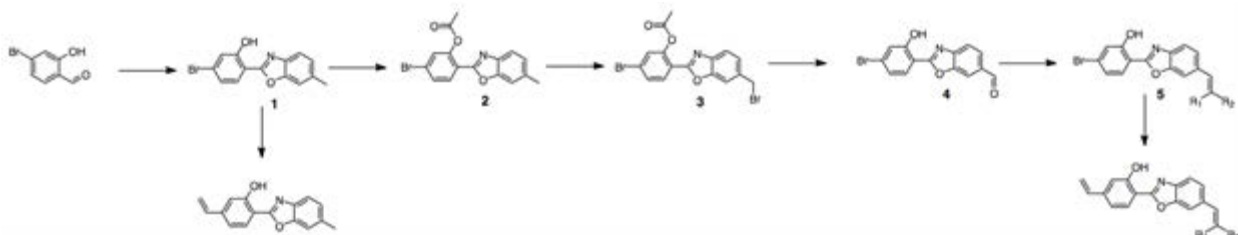


Figure II.2.B.110 Synthesis of Li ion fluorescent sensors with tunable absorbance spectra. R groups represent strong electron withdrawing groups. n

A series of three monomeric fluorophores (M1–M3) were completed with a range of electron donating/withdrawing substituents, whose strength allowed the absorbance and emission spectra of these compounds to be tuned so they would not significantly overlap with the background fluorescence of the SEI layer. As can be seen in Figure II.2.B.111 (top), where the absorbance spectra of each sensor was recorded in the presence of a large excess of Li salt, the “push-pull” effect of the strong electron-withdrawing cyano and ester group in the M3 sensor dramatically red-shifted the onset of absorbance by nearly 100 nm compared to the electron-donating effect of a methyl group (M1). The extended conjugation in M2 results in a very slight red-shift in absorbance relative to M1 by ~10–20 nm. The results indicate that excellent tunability of this sensor can be achieved over a range of 100 nm. The bottom half of Figure II.2.B.111 illustrates that the sensitivity of each fluorophore to increasing concentrations of LiBr are all similar, although the new sensor M3 actually has a slightly increased sensitivity to lower concentrations of LiBr. For example, 0.05 mM of sensors M1 and M2 do not detect the presence of 10 eq. of LiBr (compare blue and purple traces), whereas M3 does begin to respond to this low concentration of Li salt.

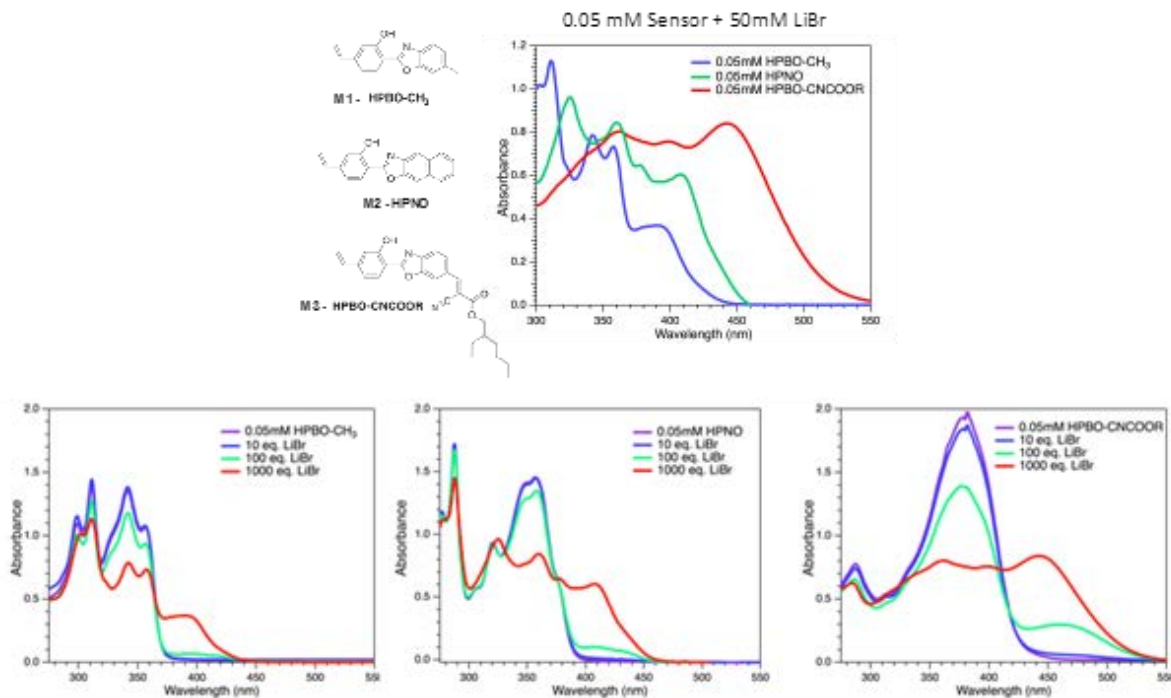


Figure II.2.B.111 (top) Three new monomeric Li-ion fluorescent sensors developed in this program with “tunable” absorbance spectra over a range of ~100 nm. (Bottom) Sensitivity of the sensors to various LiBr concentrations.

Recently, the fluorophores have been incorporated into poly(methyl acrylate) and poly(acrylic acid) gels. The preliminary data from the absorbance/fluorescence spectra in the solid state indicate that the absorbance spectra are more responsive to small Li concentrations in the solid state than in solution (because the Li fluorophore is not “competing” for coordination with solvent molecules). Preliminary qualitative fluorescence data also indicate that too much Li salt can actually have a quenching effect on fluorescence, but smaller concentrations turn fluorescence “on.” We are currently studying the effects of different counteranions (LiBr vs. LiPF₆ vs. LiTFSI), both in PMA gels and PAA gels where the fluorophore represents 2 mol% of the binder. We have also begun some spectroelectrochemistry experiments with Mike Carrol, although the data are quite preliminary.

Conclusions

The study of the solvation structure of the carbonate electrolyte has identified the total solvation number of Li in bulk EC to be close to 6, whereas it reduces to 4 at the interface. Explicit interaction between the SiO₂ interface and electrolyte results in higher CIP ratio at the interface. Enhanced CIP at the SiO₂ interface hints at reaction pathways of SEI formation. By decoupling the early-stage SEI formation from the lithiation process, we have investigated the chemistry and electrochemical reduction of the early-stage SEI. Both the LiEDC and Li₂CO₃ are verified as the main components of early-stage SEI formed by the EC reductive reaction occurring at around 550 mV. At lower voltage of about 250 mV, Li_xSiO_y is observed due to the interaction between the surface silicon oxide and the electrolyte. Surprisingly, the EC reduction repeatedly occurs at the Si surface, although the reactivity dramatically reduces after the first cathodic process. Meanwhile, Li_xSiO_y continuously forms even after many cycles of cathodic process. During a long rest after the cathodic process, the carbonaceous-based components found in the early-stage SEI layer leave the surface of the Si electrode, resulting in a clean, smooth surface. We expect that some components of the early-stage SEI may decompose or dissolve in the electrolyte. The chemical instability of the early-stage SEI would contribute to low coulombic efficiency.

The chemistry of SEI—formed during the Si lithiation process, at a voltage below 50 mVA—has also been studied. Among the components found in the SEI, lithium ethylene dicarbonate (LiEDC) has been identified as the only insoluble product of electrolyte reduction, observed only on the fully lithiated state (0.05 V), and it was concluded to be the primary component of the passive layer. In addition to LiEDC, P-F- and P-O-F-containing compounds were detected but were soluble and easily washed from the electrodes with EMC. LiF is not IR active and no conclusions related to it can be made here. We concluded that P-F and P-O-F compounds probably do not contribute to passivity, but reactions leading to these products would contribute to low coulombic efficiency. More importantly, the LiEDC features were lost upon delithiation to 1.5 V, and they reappeared upon subsequent lithiation back to 0.05 V. To date, the focus has been on correlating the properties of the silicon SEI film with the constituents of the electrolyte. We have noted that the interaction of the solvents (EC or FEC) are different with the charged silicon electrode surface. Correlating reported NMR data with the EQCM data indicates that the EC-derived film is much more porous and has steadier growth than the FEC-derived film, which appears denser.

The SEISta project has demonstrated the first TERS study of SEI, providing both topographical and chemical mapping of a-Si at nanoscale with extremely high sensitivity and surface selectivity, in contrast to ensemble-averaged information obtained from bulk spectroscopic techniques such as Raman and IR. TERS analysis of 1X, 5X, and 20X cycled a-Si shows that SEI composition gradually evolves with progressive cycling. The dominant SEI species at probed area are LEDC and PEO-like oligomer for 1X a-Si, LEDC for 5X a-Si, and carboxylate compounds for 20X a-Si. In addition to TERS, two characterization techniques—including SSRM and fluorescent probes—have been developed to help determine how components of the silicon SEI layer evolve with cycling. The work specifically contributed to the SEISta project milestones by complementing existing strategies to quantitatively measure soluble components of the SEI as well as measure the growth rate of the SEI components at fixed potentials and during cycling.

References

1. Wheeler, L.M., N.C. Anderson, P.K.B. Palomaki, J.L. Blackburn, J.C. Johnson, and N.R. Neale, Silyl Radical Abstraction in the Functionalization of Plasma-Synthesized Silicon Nanocrystals. *Chem. Mat.* 27 (2015): 6869–6878.
2. Veith, G.M., B.L. Armstrong, H. Wang, S. Kalnaus, W.E. Tenhaeff, and M.L. Patterson, Shear Thickening Electrolytes for High Impact Resistant Batteries. *ACS Energy Letters* (2017): 2084–2088.
3. Wheeler, L.M., N.C. Anderson, P.K.B. Palomaki, J.L. Blackburn, J.C. Johnson, and N.R. Neale, Silyl Radical Abstraction in the Functionalization of Plasma-Synthesized Silicon Nanocrystals. *Chem. Mater.* 27 (2015): 6869–6878.
4. Jarry, A., S. Gottis, Y.-S. Yu, J. Roque-Rosell, C. Kim, J. Cabana, J. Kerr, and R. Kostecki, The Formation Mechanism of Fluorescent Metal Complexes at the $\text{Li}_x\text{Ni}_{0.5}\text{Mn}_{1.5}\text{O}_{4-\delta}$ /Carbonate Ester Electrolyte Interface. *J. Am. Chem. Soc.* 137 (2015): 3533–3539.
5. Wang, S.N., D.K. Wang, S. Smart, and J.C.D. da Costa, Ternary Phase-Separation Investigation of Sol-Gel Derived Silica from Ethyl Silicate 40. *Sci Rep-Uk* 5 (2015).
6. Koroleva, O.N., M.V. Shtenberg, and P.V. Khvorov, Vibrational Spectroscopic and X-Ray Diffraction Study of Crystalline Phases in the $\text{Li}_2\text{O-SiO}_2$ System. *Russ J Inorg Chem* 59 (2014): 255–258.
7. Li, X.Y., H.M. Yang, Morphology-Controllable Li_2SiO_3 Nanostructures. *Crystengcomm* 16 (2014): 4501–4507.
8. Coyle, J., C. Apblett, M. Brumbach, J. Ohlhausen, and C. Stoldt, Structural and Compositional Characterization of RF Magnetron Cosputtered Lithium Silicate Films: From $\text{Li}_2\text{Si}_2\text{O}_5$ to Lithium-Rich Li_8SiO_6 . *Journal of Vacuum Science & Technology A* 35 (2017).

9. Brooker, M.H. and J.B. Bates, Raman and Infrared Spectral Studies of Anhydrous Li_2CO_3 and Na_2CO_3 . *J Chem Phys* 54 (1971): 4788–.
10. Shi, F.F., P.N. Ross, H. Zhao, G. Liu, G.A. Somorjai, and K. Komvopoulos, A Catalytic Path for Electrolyte Reduction in Lithium-Ion Cells Revealed by In Situ Attenuated Total Reflection-Fourier Transform Infrared Spectroscopy. *J Am Chem Soc* 137 (2015): 3181–3184.
11. Xiao, A., L. Yang, B.L. Lucht, S.H. Kang, and D.P. Abraham, Examining the Solid Electrolyte Interphase on Binder-Free Graphite Electrodes. *J Electrochem Soc* 156 (2009): A318–A327.
12. Nie, M.Y., D. Chalasani, D.P. Abraham, Y.J. Chen, A. Bose, and B.L. Lucht, Lithium Ion Battery Graphite Solid Electrolyte Interphase Revealed by Microscopy and Spectroscopy. *J Phys Chem C* 117 (2013): 1257–1267.
13. Yang, J.F., N. Solomatin, A. Kraytsberg, and Y. Ein-Eli, In-Situ Spectro-Electrochemical Insight Revealing Distinctive Silicon Anode Solid Electrolyte Interphase Formation in a Lithium-Ion Battery. *Chemistryselect* 1 (2016): 572–576.
14. Profatilova, I.A., C. Stock, A. Schmitz, S. Passerini, and M. Winter, Enhanced Thermal Stability of a Lithiated Nano-Silicon Electrode by Fluoroethylene Carbonate and Vinylene Carbonate. *J Power Sources* 222 (2013): 140–149.
15. Reiche, M., M. Wiegand, and U. Gosele, Infrared Spectroscopic Analysis of Plasma-Treated Si(100)-Surfaces. *Mikrochim Acta* 133 (2013): 35–43.
16. Radvanyi, E., E. De Vito, W. Porcher, and S.J.S. Larbi, An XPS/AES Comparative Study of the Surface Behaviour of Nano-Silicon Anodes for Li-Ion Batteries. *J Anal Atom Spectrom* 29 (2014): 1120–1131.
17. Park, J.K., E.T. Lee, B.K. Kim, S.W. Jeong, and Y. Roh, Characteristics of Hf-Silicate Interfacial Layers Formed by Wet Etching. *J Korean Phys Soc* 55 (2009): 1022–1025.
18. Pfeiffer, H., P. Bosch, J.A. Odriozola, A. Lopez, J.A. Ascencio, and S. Bulbulian, Sol-Gel Synthesis of Li-ZrSiO₄. *J Mater Res* 15 (2000): 1490–1495.
19. Nie, M.Y., J. Demeaux, B.T. Young, D.R. Heskett, Y.J. Chen, A. Bose, J.C. Woicik, and B.L. Lucht, Effect of Vinylene Carbonate and Fluoroethylene Carbonate on SEI Formation on Graphitic Anodes in Li-Ion Batteries. *J Electrochem Soc* 162 (2015): A7008–A7014.
20. Stankovich, S., D.A. Dikin, R.D. Piner, K.A. Kohlhaas, A. Kleinhammes, Y. Jia, Y. Wu, S.T. Nguyen, and R.S. Ruoff, Synthesis of Graphene-Based Nanosheets via Chemical Reduction of Exfoliated Graphite Oxide. *Carbon* 45 (2007): 1558–1565.
21. Bryngelsson, H., M. Stjerndahl, T. Gustafsson, and K. Edstrom, How Dynamic is the SEI? *J Power Sources* 174 (2007): 970–975.
22. Andersson, A.M. and K. Edstrom, Chemical Composition and Morphology of the Elevated Temperature SEI on Graphite. *J Electrochem Soc* 148 (2001): A1100–A1109.
23. Pereira, J., L.E. Pichon, R. Dussart, C. Cardinaud, C.Y. Duluard, E.H. Oubensaid, P. Lefaucheu, M. Boufnichel, and P. Ranson, In Situ X-Ray Photoelectron Spectroscopy Analysis of SiO_xF_y Passivation Layer Obtained in a SF₆/O₂ Cryoetching Process. *Appl Phys Lett* 94 (2009).

24. Andersson, A.M., M. Herstedt, A.G. Bishop, and K. Edstrom, The Influence of Lithium Salt on the Interfacial Reactions Controlling the Thermal Stability of Graphite Anodes. *Electrochim Acta* 47 (2002): 1885–1898.
25. Wang, Y.Y., K. Kusumoto, and C.J. Li, XPS Analysis of SiC Films Prepared by Radio Frequency Plasma Sputtering. *Physcs Proc* 32 (2012): 95–102.
26. Rodriguez-Mosqueda, R., and H. Pfeiffer, Thermokinetic Analysis of the CO₂ Chemisorption on Li₄SiO₄ by Using Different Gas Flow Rates and Particle Sizes. *J Phys Chem A* 114 (2010): 4535–4541.
27. Essaki, K., K. Nakagawa, M. Kato, and H. Uemoto, CO₂ absorption by Lithium Silicate at Room Temperature. *J Chem Eng Jpn* 37 (2004): 772–777.
28. Alcantar-Vazquez, B., P.R.D. Herrera, A.B. Gonzalez, Y.H. Duan, and H. Pfeiffer, Analysis of the CO₂-H₂O Chemisorption in Lithium Silicates at Low Temperatures (30-80 Degrees C). *Ind Eng Chem Res* 54 (2015): 6884–6892.
29. Knotter, D.M., Etching Mechanism of Vitreous Silicon Dioxide in HF-Based Solutions. *J Am Chem Soc* 122 (2000): 4345–4351.
30. Xu, K., Electrolytes and Interphases in Li-Ion Batteries and Beyond. *Chem Rev* 114 (2014): 11503–11618.
31. Coyle, J., C. Apblett, M. Brumbach, T. Ohlhausen, and C. Stoldt, Structural and Compositional Characterization of RF Magnetron Cosputtered Lithium Silicate Films: From Li₂Si₂O₅ to Lithium-Rich Li₈SiO₆. *JVST A* 35 (2017).
32. Warren, L.J., Measurement of Ph in Acid Fluoride Solutions and Evidence for Existence of (Hf)₂. *Anal Chim Acta* 53 (1971): 199–.
33. Duncan, H., D. Duguay, Y. Abu-Lebdeh, and I.J. Davidson, Study of the LiMn_{1.5}Ni_{0.5}O₄/Electrolyte Interface at Room Temperature and 60 Degrees C. *J Electrochem Soc* 158 (2011): A537–A545.
34. Key, B., R. Bhattacharyya, M. Morcrette, V. Seznéc, J.-M. Tarascon, and C.P. Grey, Real-Time NMR Investigations of Structural Changes in Silicon Electrodes for Lithium-Ion Batteries. *J. Am. Chem. Soc.* 131 (2009): 9239–9249.
35. Key, B., M. Morcrette, J.-M. Tarascon, and C.P. Grey, Pair Distribution Function Analysis and Solid State NMR Studies of Silicon Electrodes for Lithium Ion Batteries: Understanding the (De)lithiation Mechanisms. *J. Am. Chem. Soc.* 133 (2011): 503–512.
36. Wu, H., G. Chan, J.W. Choi, I. Ryu, Y. Yao, M.T. McDowell, S.W. Lee, A. Jackson, Y. Yang, L. Hu, and Y. Cui. Stable Cycling of Double-Walled Silicon Nanotube Battery Anodes through Solid–Electrolyte Interphase Control. *Nat. Nanotechnol.* 7 (5), (2012): 310–315.
37. Dudney, N.J., J.B. Bates, and J.D. Robertson. Radiofrequency Magnetron Sputtering of Pure and Mixed Targets of Li₄SiO₄, Li₃PO₄, and Li₂O. *Journal of Vacuum Science & Technology A-Vacuum Surfaces and Films* 11(2), (1993): 377–389.
38. Brooker, M.H. and J.B. Bates, Raman and Infrared Spectral Studies of Anhydrous Li₂CO₃ and Na₂CO₃. *Journal of Chemical Physics* 54(11), (1971): 4788.

39. Parker, S.F., et al. Assignment of the Vibrational Spectra of Lithium Hydroxide Monohydrate, LiOH Center Dot H₂O. *Journal of Chemical Physics* 134(8), (2011): 084503
40. Mahmoud, M.M., et al., Crystallization of Lithium Disilicate Glass Using Microwave Processing. *Journal of the American Ceramic Society* 95(2), (2012): 579–585.
41. Wang, S.N., et al., Ternary Phase-Separation Investigation of Sol-Gel Derived Silica from Ethyl Silicate 40. *Scientific Reports* 5 (2015): 14560.
42. Li, X.Y. and H.M. Yang, Morphology-Controllable Li₂SiO₃ Nanostructures. *Crystengcomm* 16(21), (2014): 4501–4507.
43. Koroleva, O.N., M.V. Shtenberg, and P.V. Khvorov, Vibrational Spectroscopic and X-Ray Diffraction Study of Crystalline Phases in the Li₂O-SiO₂ System. *Russian Journal of Inorganic Chemistry* 59(3), (2014): 255–258.
44. Carella, E. and M.T. Hernandez, High Lithium Content Silicates: A Comparative Study Between Four Routes of Synthesis. *Ceramics International* 40(7), (2014): 9499–9508.
45. Nocun, M. and M. Handke, Identification of Li-O Absorption Bands Based on Lithium Isotope Substitutions. *Journal of Molecular Structure* 596 (2001): 145–149.
46. Young, B.T., et al., Hard X-ray Photoelectron Spectroscopy (HAXPES) Investigation of the Silicon Solid Electrolyte Interphase (SEI) in Lithium-Ion Batteries. *ACS Applied Materials & Interfaces* 7(36), (2015): 20004–20011.
47. Philippe, B., et al., Role of the LiPF₆ Salt for the Long-Term Stability of Silicon Electrodes in Li-Ion Batteries – A Photoelectron Spectroscopy Study. *Chemistry of Materials* 25(3), (2013): 394–404.
48. Jaumann, T., et al., SEI-Component Formation on Sub 5 nm Sized Silicon Nanoparticles in Li-Ion Batteries: The Role of Electrode Preparation, FEC Addition and Binders. *Physical Chemistry Chemical Physics* 17(38), (2015): 24956–24967.
49. Kelly, M.A., Analyzing Insulators with XPS and AES, in *Surface Analysis by Auger and X-ray Photoelectron Spectroscopy*, J.T.G. D. Briggs, Editor. 2003, IM Publications: Chichester. p. 191–210.
50. Metson, J.B., et al., Suppression of Molecular-Ions in the Secondary Ion Mass-Spectra of Minerals. *Surface and Interface Analysis* 5(5), (1983): 181–185.
51. G. Baldacchini, M. Cremona, S. Martelli, R.M. Montereali, and L.C. Scavarda Do Carmo, *Phys. Stat. Sol.* 151 (1995): 319.
52. U. Kaiser, N. Kaiser, P. Weißbrodt, U. Mademann, E. Hacker, and H. Müller, *Thin Solid Films* 217 (1992): 7.
53. Wood, K.N., K.X. Steirer, S.E. Hafner, C. Ban, S. Santhanagopalan, S.-H. Lee, and G. Teeter, *Nat. Commun.* 9 (2018): 2490.
54. Nguyen, C.C. and B.L. Lucht, Comparative Study of Fluoroethylene Carbonate and Vinylene Carbonate for Silicon Anodes in Lithium Ion Batteries. *Journal of the Electrochemical Society* 161(12), (2014): A1933–A1938.
55. Obrovac, M.N. and L.J. Krause, Reversible Cycling of Crystalline Silicon Powder. *Journal of the Electrochemical Society* 154(2), (2007): A103–A108.

56. Delpuech, N., et al., Critical Role of Silicon Nanoparticles Surface on Lithium Cell Electrochemical Performance Analyzed by FTIR, Raman, EELS, XPS, NMR, and BDS Spectroscopies. *Journal of Physical Chemistry C* 118(31), (2014): 17318–17331.
57. Wood, K.N. and G. Teeter, *ACS Applied Energy Materials* 1(9), (2018): 4493–4504.
58. Schroder, K.W., H. Celio, L.J. Webb, and K.J. Stevenson, *J. Phys. Chem. C* 116 (2012): 19737–19747.
59. Ferraresi, G., L. Czornomaz, C. Villevieille, P. Novák, and M. El Kazzi, *ACS Appl. Mater. Interfaces* 8 (2016): 29791–29798.
60. Aurbach, D., Y. Gofer, M. Ben-Zion, and P. Aped, *J. Electroanal. Chem.* 339 (1992): 451–471.
61. Aurbach, D., *J. Electrochem. Soc.* 141, L1–L3 (1994).
62. Zhuang, G.V., K. Xu, H. Yang, T.R. Jow, and P.N. Ross, *J. Phys. Chem. B* 109 (2005): 17567–17573.
63. Zhuang, G.V., H. Yang, B. Blizanac, and P.N. Ross, *Electrochem. Solid-State Lett.* 8 (2005): A441–A445.
64. Shi, F. P.N. Ross, G.A. Somorjai, and K. Komvopoulos, *J. Phys. Chem. C* 121 (2017): 14476–14483.
65. Ayache, M. S.F. Lux, and R. Kostecki, *J. Phys. Chem. Lett.* 6 (2015): 1126–1129.
66. Ayache, M. D. Jang, J. Syzdek, and R. Kostecki, *J. Electrochem. Soc.* 162 (2015): A7078–A7082.
67. Yang, H., G.V. Zhuang, and P.N. Ross, *J. Power Sources* 161 (2006): 573–579.
68. Veith, G.M., M. Doucet, R.L. Sacci, B. Vacaliuc, J.K. Baldwin, and J.F. Browning, *Sci. Rep.* 7 (2017): 6326–6341.
69. Solchenbach, S., M. Metzger, M. Egawa, H. Beyer, and H.A. Gasteiger, *J. Electrochem. Soc.* 165 (2018): A3022–A3028.
70. Kasrai, M., W.N. Lennard, R.W. Brunner, G.M. Bancroft, J.A. Bardwell, and K.H. Tan, *Applied Surface Science* 99 (1996): 303–312.
71. Saint, B.J., M. Morcrette, D. Larcher, L. Laffont, S. Beattie, J.P. Pèrès, D. Talaga, M. Couzi, and J.M. Tarascon, *Adv. Funct. Mater.* 17 (2007): 1765–1774.
72. Schroder, K.W., A.G. Dylla, S.J. Harris, L.J. Webb, and K.J. Stevenson, *ACS Appl. Mater. Interfaces* 6 (2014): 21510–21524.
73. Philippe, B., R. Dedryèvre, J. Allouche, F. Lindgren, M. Gorgoi, H. Rensmo, D. Gonbeau, and K. Ed, *Chem. Mater.* 24 (2012): 1107–1115.
74. Jin, Y., N.-J.H. Kneusels, P.C.M.M. Magusin, G. Kim, E. Castillo-Martínez, L.E. Marbella, R.N. Kerber, D.J. Howe, S. Paul, T. Liu, and C.P. Grey, *J. Am. Chem. Soc.* 139 (2017): 14992–15004.
75. Yohannes, Y.B., S.D. Lin, and N.-L. Wu, *Journal of The Electrochemical Society* 164 (2017): A3641–A3648.
76. Michan, A.L., M. Leskes, and C.P. Grey, *Chemistry of Materials* 28 (2016): 385–398.

77. An, S.J., J. Li, C. Daniel, D. Mohanty, S. Nagpure, and D.L. Wood III, The State of Understanding of the Lithium-Ion-Battery Graphite Solid Electrolyte Interphase (SEI) and Its Relationship to Formation Cycling. *Carbon* 105 (2016): 52–76.
78. Peled, E. and S. Menkin, SEI: Past, Present and Future. *J. Electrochem. Soc.* 164 (7), (2017): A1703–A1719.
79. Jagjit Nanda, G.Y., D. Voylov, T. Hou, R.E. Ruther, M. Naguib, K. Persson, G.M. Veith, and A. Sokolov, Unraveling Nanoscale Chemical and Morphological Heterogeneity of Solid Electrolyte Interphase on Electrochemically Cycled Amorphous Silicon (*In preparation*) (2018).
80. Zhuang, G.V., K. Xu, H. Yang, T.R. Jow, and P.N. Ross, Lithium Ethylene Dicarboxylate Identified as the Primary Product of Chemical and Electrochemical Reduction of EC in 1.2 M LiPF₆/EC: EMC Electrolyte. *J. Phys. Chem. B* 109 (37), (2005): 17567–17573.
81. Socrates, G., *Infrared and Raman Characteristic Group Frequencies: Tables and Charts*. John Wiley & Sons: 2001.
82. Agapov, R.L., A.V. Malkovskiy, A.P. Sokolov, and M.D. Foster, Prolonged Blinking with TERS Probes. *J. Phys. Chem. C* 115 (18), (2011): 8900–8905.
83. Yoon, T., M.S. Milien, B.S. Parimalam, and B.L. Lucht, Thermal Decomposition of the Solid Electrolyte Interphase (SEI) on Silicon Electrodes for Lithium Ion Batteries. *Chem. Mater.* 29 (7), (2017): 3237–3245.
84. Schroder, K.W., H. Celio, L.J. Webb, and K.J. Stevenson, Examining Solid Electrolyte Interphase Formation on Crystalline Silicon Electrodes: Influence of Electrochemical Preparation and Ambient Exposure Conditions. *J. Phys. Chem. C* 116 (37), (2012): 19737v19747.
85. Padilla, N.A., M.T. Rea, M. Foy, S.P. Upadhyay, K.A. Desrochers, T. Derus, K.A. Knapper, N.H. Hunter, S. Wood, D.A. Hinton, A.C. Cavell, A.G. Masias, and R.H. Goldsmith, Tracking Lithium Ions via Widefield Fluorescence Microscopy for Battery Diagnostics. *ACS Sens.* 2 (2017): 903–908.
86. Seo, J., S. Kim, and S. Young Park, Strong Solvatochromic Fluorescence from the Intramolecular Charge-Transfer State Created by Excited-State Intramolecular Proton Transfer. *JACS*, 126 (2004): 11154.

II.2.C Development of Si-based High-Capacity Anodes (Pacific Northwest National Laboratory)

Ji-Guang Zhang, Principal Investigator

Pacific Northwest National Laboratory
902 Battelle Blvd, Mail Stop K2-44,
Richland, WA 99352
E-mail: Jiguang.Zhang@pnnl.gov

Xiaolin Li, Principal Investigator

Pacific Northwest National Laboratory
902 Battelle Blvd, Mail Stop K2-44
Richland, WA 99352
E-mail: Xiaolin.li@pnnl.gov

Brian Cunningham, DOE Technology Development Manager

U.S. Department of Energy
E-mail: Brian.Cunningham@ee.doe.gov

Start Date: October 1, 2017 End Date: September 30, 2020
Project Funding (FY18): \$300,000 DOE share: \$300,000 Non-DOE share: \$0

Project Introduction

Nano Si or highly porous structured Si has been widely used to avoid pulverization of Si particles during cycling process. However, large surface area of nano Si or micron sized porous Si may also lead to a continuous reaction between lithiated Si and electrolyte. As a result, this reaction may lead to continuous growth of SEI layer and increase of cell impedance. Another possible degradation mechanism is the cross talk between Si anode and cathode. The mitigation of dissolved Mn in cathode may poison Si anode; FEC additive which is highly effective in forming a stable SEI layer on Si may also form an unstable cathode electrolyte interface (CEI) on cathode surface and degassing during long term cycling. Therefore, minimize the surface area of Si and find a stable electrolyte additive are critical for long term stability of Si based Li-ion batteries.

Objectives

The objectives of this project are to enhance the cycle life and calendar life of Si based Li-ion batteries by designing a stable porous Si structure and develop an artificial SEI layer coated on the surface of porous Si particles. A more stable electrolyte additive or solvent mixture will be developed to minimize the detrimental effect of FEC currently used in Si based Li-ion batteries. The degradation mechanism of Si anodes during shelf storage will be systematically investigated. New insight on these mechanisms and the new approaches developed in this work will speed up the deployment of high energy Li-ion battery with Si-based anodes and increase market penetration of EVs and PHEVs as required by DOE/EERE.

Approach

- Investigate the effects of electrolyte additives on the cycle life of Si anode provided by ANL/CAMP facility. More than 20 functional additives that may form better SEI/CEI layer on anode/cathode and mitigate the HF generation or gas release have been investigated.
- Use localized high concentration electrolyte (LHCE), which has been known to be effective in Li metal protection, are used to enhance the stability of Si anodes obtained from CAMP facility prepared in PNNL with a modified electrode structure.
- Design Hierarchical structured CNT@Si microspheres with limited structure swelling and exceptional mechanical stress.

- Synthesize a hierarchically structured CNT@Si microsphere by using thermic reduction to accommodate the swelling of silicon particles and stabilize its structural and electrolyte integrity.
- Design CNT@Si@C-graphite composite to achieve excellent long-term cycling performance at high loading condition.

Results

1.1 Localized high concentration electrolytes (LHCEs) for Si anodes

Inspired by the similarity of the low potential and large volume change between Si and lithium metal, the LHCEs developed for Li metal anode have been investigated for their potential application for Si anodes. In one effort, LHCEs were used directly on as-received anodes provided by ANL/CAMP. In another effort, we have modified the anodes by applying new binder and carbon coating on Si active material (Paraclete Energy). The compatibility of LHCE with the modified Si anodes was also investigated.

The LHCE of 1.2M LiFSi/TEPa-3BTfE (E-313), which has been known to be effective in Li metal protection was used to test Si anodes received from ANL/CAMP. The result shows that the TEPa-based localized high concentration electrolytes is not stable with the electrodes prepared with water based binder (LiPAA) (Figure II.2.C.1). It is possible that TEPa reacts with the PAA binder which contributes to the failure of the cells. Fundamental understanding of the failure mechanism in this system will be investigated later.

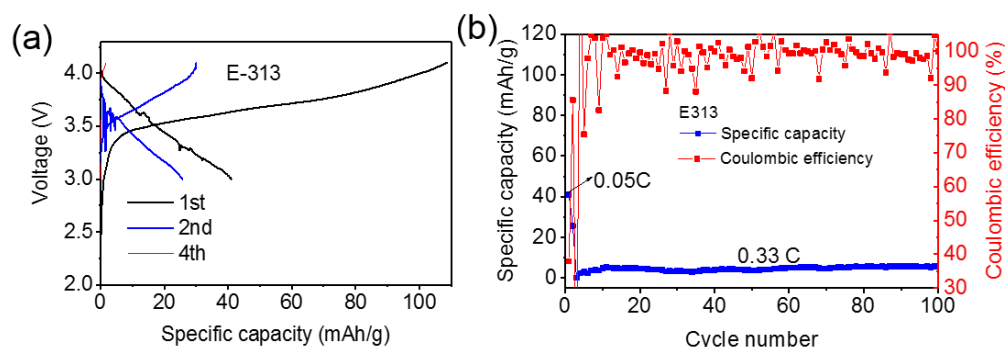


Figure II.2.C.1 Voltage profile (a) and cycling performance (b) of the NMC532 || Si/Gr (CAMP electrodes) in TEPa-based LHCE.

To overcome the incompatibility problem between LHCE and LiPAA based binder, polyimide (PI) binder were used to replace LiPAA binder to prepare Si based anode. The effect of CVD carbon coating (10 wt% carbon) on Si active material (Paraclete Energy Silicon) was also used to study the surface chemistry effect on battery performance. The modified anode has similar composition as those provided by ANL-CAMP facility except additional carbon coating on Si powder and the use of alternative binder (PI). The results of the NMC532 || Si/Gr cells tested in baseline electrolyte showed that anode prepared with pristine Si particle and PI binder exhibits a low FCE and low specific capacity, while anode prepared with CVD carbon coated Si particle and PI binder exhibits a higher FCE and improved the cycling stability (Figure II.2.C.2a). On the other hand, the E-313 electrolyte has demonstrated high stability with PI binder. The cells using an anode with carbon coated Si and PI binder showed significantly improved cycling stability when E-313 electrolyte is used as compared with the cells using the same anode and baseline electrolyte (Figure II.2.C.2b and Table II.2.C.1). The full cell (NMC532 || Si/Gr) with Si anodes pre-cycled against Li metal in half cells (3 formation cycles) showed specific capacity of ~92 mAh/g, similar to the baseline specific capacity. In future, we will continue optimize the new electrolyte and identify the working mechanism of the new electrolyte systems through in-depth collaboration with the teams in the Si consortium.

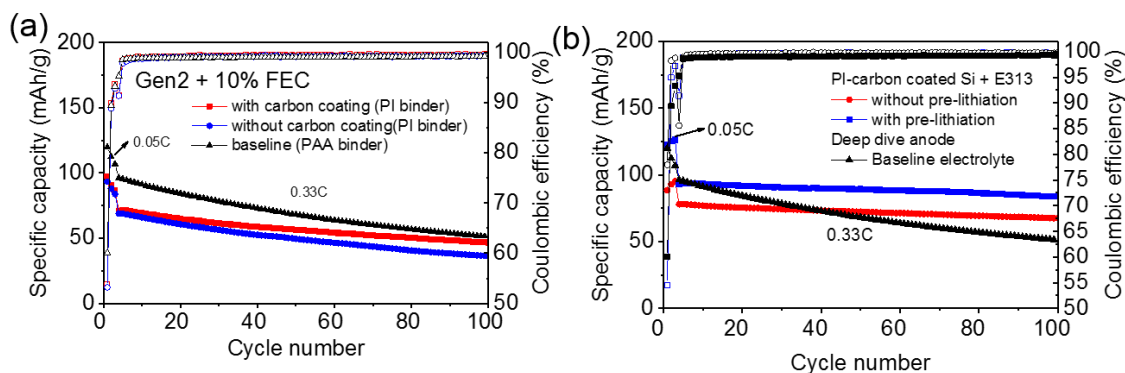


Figure II.2.C.2 a) Cycling performance of NMC532 || Si/Gr cells with a) modified silicon anode with and without carbon coating in baseline electrolyte. b) Modified silicon anode with carbon coating and PI binder in TEPA-based LHCE.

Table II.2.C.1 Representative results of the key performance parameters of NMC532 || Si/C/Gr full cells with LiFSi-TEPA based LHCE.

Design of experiments summary table						
Anodes	Prelithiation	Electrolyte		FCE	Specific capacity @ 4th cycle	Retention @ 100th cycle
Deep dive anode Si-PAALi	No	Baseline	1.2M LiPF ₆ in EC/EMC-10% FEC	60%	96.3	53.4%
PI-carbon coated Si	No	E-313	1.2M LiFSi/TEPA-3BTFE (molar ratio to TEPA)	55%	78	86.5%
	Yes	E-313		78%	92.8	90.3%

1.2 The effects of electrolyte additives on the cycle life of Si anode

Electrolyte additive is one of the critical factors that have significant impact on the composition and stability of SEI layer formed on Si anode surface as demonstrated by the success of the FEC additive. During the last year, we have investigated the effects of various electrolyte additives on the cycle life of Si anode using NMC532||Si/Gr full cells where both Si/Gr anode and NMC cathode were provided by ANL/CAMP facility. The cell tests were done following the same protocol suggested by ANL. The electrolyte amount was controlled at ~45 μ l. More than 20 functional additives including Tris(trimethylsilyl) borate (TMSB), Succinonitrile (SN), Fumaronitrile (FN), Tris(trimethylsilyl) phosphite (TMSP), Diphenyldimethoxysilane (DPDMS), Prop-1-ene-1,3-sultone (PES) have been investigated. Many of them are known to be effective in forming better SEI layer and/or mitigating the HF generation or gas release. The performance were compared to the baseline electrolyte of 1.2M LiPF₆ in EC: EMC (3:7, by weight) with 10% FEC (referred to E-control). Table II.2.C.2 and Figure II.2.C.3 compare the effects of the selected additives on the long term cycling stability of the additives on the performance of NMC532||Si/Gr full cells. TMSB and SN additives can effectively improve the first cycle Coulombic efficiency (FCE) of the cells, while the overall cycling performances of these cells are comparable to those of baseline electrolyte. TMSP and PES improve the cycling stability for the first 50 cycles. DPDMS stands out as the best additive with increased the cycling performance after 100 cycles.

Table II.2.C.2 Representative results of the key performance parameters of NMC532 || Si/Gr full cells with different additives

Experimental table-cycle test					
#	Electrolyte	Additive Concentration	FCE	Retention at 50 cycles (%)	Retention at 100 cycles (%)
Baseline	1.2M LiPF ₆ in EC/EMC-10% FEC		60-65	71.2	53.4
1	Plus, TMSB	1wt %	71-72	71.1	50
2	SN	1wt %	74-75	67.1	47.9
3	FN	1wt %	67	61.4	42.7
4	TMSP	1wt %	65	72.6	52.1
5	PES	1wt %	64	74.3	52.8
6	DPDMS	1wt %	64	74	54.5

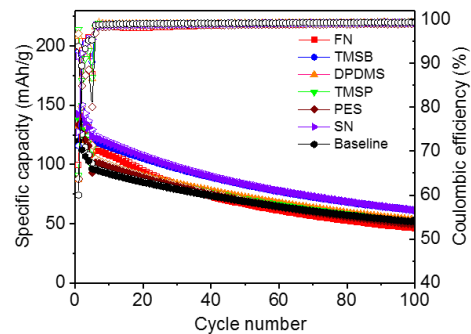


Figure II.2.C.3 Cycling performance of NMC532 || Si/Gr full cell with different additives.

1.3 Hierarchical structured CNT@Si microspheres

Hierarchical structured CNT@Si porous microspheres of extraordinary mechanical strength and excellent cycle life were prepared using micro-emulsion and controlled thermite reduction technologies (see our last year's report for the details of preparation procedures). The swelling and mechanical property of the CNT@Si anodes are studied to understand the correlation between the structure and electrochemical performance. In situ TEM characterization was carried out to observe the particle volume expansion during the lithiation process. Figure II.2.C.4a-c showed TEM images of the CNT@Si particles taken at different lithiation stages. The primary Si nanoparticles are fully lithiated after an extended period of lithiation, and the apparent volume expansion of the secondary spheres is only ~18.5% indicating the hierarchical structure developed in this work is effective in mitigating the swelling and pulverization of Si materials. The electrode is expected to have limited swelling and hence good mechanical and electrical integrity during cycling.

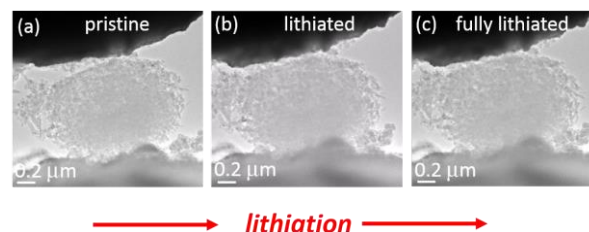


Figure II.2.C.4 In situ TEM characterization of the lithiation process of a typical CNT@Si microsphere. a) Si/MWNT composite particle before lithiation; b) partially lithiated particle; c, fully lithiated particle.

To avoid surface oxidation during further investigation, the CNT@Si was coated with carbon by CVD process. The CNT@Si@C demonstrated exceptional mechanical strength due to the introduction of carbon nanotubes and the fabrication of microsphere particles. Figure II.2.C.5 shows the in-situ SEM-AFM measurement of the compressing of a typical CNT@Si@C microsphere of ~ 8 micron. The stiffness of the particle can be calculated according to the displacement of AFM tip when the particle cracks. The particle did not show severe morphology deformation during the compressing and can withstand a pressure over 220 MPa. The excellent mechanical strength of the particles enables them to maintain their integrity during electrode calendaring process and can further boost the capacity density of anode for practical application.

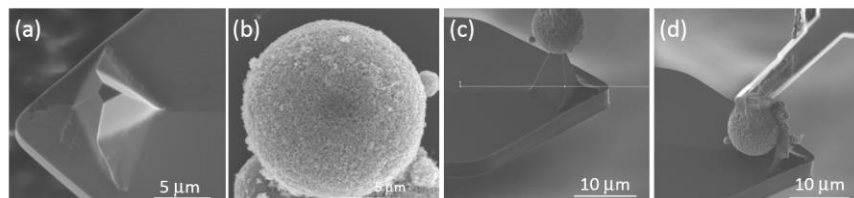


Figure II.2.C.5 In-situ SEM-AFM indentation of a CNT@Si@C particle. a) SEM image of the AFM Tip; b) high resolution of the CNT@Si@C particle; c) SEM image of the contact between AFM tip and the particle before the introduction of the force; d) SEM image of the particle after the introduction of the force.

The unique structure of the CNT@Si@C with limited swelling and excellent mechanical strength enables its remarkable electrochemical performance. The CNT@Si@C electrodes demonstrate excellent cycling stability over 750 cycles at a mass loading of 0.53 mg/cm^2 (Figure II.2.C.6a). After 750 cycles, the electrode delivers a reversible capacity of $> 1386 \text{ mAh/g}$, which is more than three times the theoretical capacity of graphite. The thick electrodes ($\sim 3 \text{ mAh/cm}^2$) of CNT@Si@C-Graphite also exhibit promising cycling stability. The electrode delivers a reversible capacity of $\sim 700 \text{ mAh/g}$ with 30 wt% Si@CNT@C in the composite electrode. The capacity retention is more than 98% from 4th to 200th cycle at a current density of 0.75 mA/cm^2 (Figure II.2.C.6b).

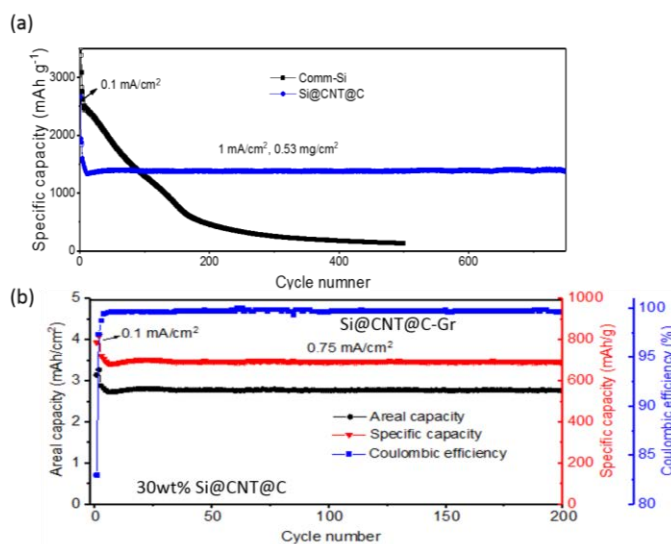


Figure II.2.C.6 (a) Long-term cycling performance of the CNT@Si@C and Comm-Si electrodes. (b) Cycling performance of CNT@Si@C-Graphite electrodes with 30wt% CNT@Si@C in the composite.

Conclusions

In summary, we have developed advanced electrolyte additive and electrolyte systems to improve the resistance of the SEI at the electrode-electrolyte interface. LHCEs based on TEPA can improve the cycling stability of the modified deep dive anodes (PI binder-carbon coated Si). In addition to the electrolyte work, hierarchical structured CNT@Si with limited structured swelling, exceptional mechanical strength as well as excellent cycling stability was developed.

Key Publications/patents

1. Haiping Jia, Jianming Zheng, Junhua Song, Langli Luo, Ran Yi, Luis Estevez, Wengao Zhao, Rajankumar Patel, Xiaolin Li, Ji-Guang Zhang, A novel approach to synthesize micrometer-sized porous silicon as a high performance anode for lithium-ion batteries, *Nano Energy*, 2018, 50, 589-597
2. Junhua Song, Xiaolin Li, Ji-Guang Zhang, Silicon-based anodes for advanced lithium-ion batteries, book chapter for *Inorganic Battery Materials*. Wiley. Accepted.

II.2.D Pre-Lithiation of Silicon Anode for High Energy Li Ion Batteries (Stanford University)

Yi Cui, Principal Investigator

Department of Materials Science and Engineering
McCullough 343, 476 Lomita Mall
Stanford University
Stanford, CA 94305
E-mail: yicui@stanford.edu

Tien Duong, DOE Technology Development Manager

U.S. Department of Energy
E-mail: Tien.Duong@ee.doe.gov

Start Date: October 1, 2017

End Date: September 30, 2018

Project Funding (FY18): \$300,000

DOE share: \$300,000

Non-DOE share: \$0

Project Introduction

Rechargeable lithium-ion batteries (LIBs) are widely used for consumer electronics and exhibit great potential for electrical vehicle and grid-scale energy storage. In existing lithium-ion technology, Li is provided by Li-intercalated cathode materials. Graphite is the most commonly used anode material. Various alternative high-capacity anode materials such as silicon, with a theoretical capacity more than ten times of graphite, have been well studied and have already shown promise in potential applications. The formation of a solid electrolyte interphase (SEI) layer on the anode surfaces is a critical process that occurs prior to regular battery operations and consumes a significant amount of Li. Graphite anodes exhibit an irreversible capacity loss of 5–10% from the initial battery charging process, while for high-capacity anode materials, the first-cycle Li loss is even higher (e.g., 15–35% for Si). Low first-cycle Coulombic efficiency leads to the consumption of an excess amount of cathode material solely for the first cycle and thereby, significantly reduces the energy density. It is also challenging to effectively compensate for the Li loss through loading excessive cathode materials as a result of kinetic limitations on the cathode thickness. Accordingly, there is a strong motivation to develop high-capacity materials to prestore a large amount of Li in either cathode or anode to compensate for the initial loss. Alloy anodes with much higher capacity have been recognized as promising alternatives to graphites. Without prestored Li in anodes, the energy density is limited by the low capacity of Li metal oxide cathodes. Recently, Li metal has been revived as a high-capacity anode, but faces many challenges resulting from its high reactivity and uncontrolled dendrite growth.

Objectives

Prelithiation of high capacity electrode materials such as Si is an important means to enable those materials in high-energy batteries. This study pursues two main directions: 1) developing facile and practical methods to increase first-cycle Coulombic efficiency of lithium-ion batteries, and 2) synthesizing fully lithiated Si and other lithium compounds for pre-storing lithium.

Approach

Usually, prelithiation of cathode materials was previously achieved by treating spinel cathode materials or metal oxides with chemical reagents, like n-butyllithium, LiI, or molten Li. However, the prestored capacity is still relatively low (100–800 mAh/g). Anode materials are more attractive Li reservoirs because of the high specific capacities. In previous studies, there have been three main approaches to realize anodes with prestored Li. One approach is electrochemical prelithiation by shorting electrolyte-wetted anodes with Li foil. Another approach is to incorporate microscale stabilized lithium metal powder (SLMP; FMC Lithium Corp.) into anodes. However, synthesis of SLMP in the research laboratory is difficult. In our previous report, we showed chemically synthesized $\text{Li}_x\text{Si}/\text{Li}_2\text{O}$ core shell nanoparticles (NPs) as an effective prelithiation reagent. The NPs maintained their capacities only in the dry air but that their capacities were reduced drastically after exposure

to ambient air. To further improve the environmental stability, we develop a high temperature and gas phase surface fluorination reaction to synthesize LiF-Li_xSi NPs. The dense and crystalline LiF coating improves the stability of Li_xSi NPs in both humid air and regular slurry solvent (NMP), indicating that LiF-Li_xSi NPs are compatible with industrial electrode fabrication processes.

In addition, alloy anodes with much higher capacity have been recognized as promising alternatives to graphites. Without prestored Li in anodes, the energy density is limited by the low capacity of Li metal oxide cathodes. Recently, Li metal has been revived as a high-capacity anode, but faces many challenges resulting from its high reactivity and uncontrolled dendrite growth. Therefore, we develop an air-stable and free-standing Li_xM (M = Si, Sn, or Al) /graphene foil as an alternative to Li metal, inheriting the desirable properties of alloy anodes and pure metal anodes.

Similar to our previous study, Li_xSi nanoparticles were synthesized on the gram-scale, by heating a stoichiometric mixture of Li metal and Si nanoparticles under mechanical stirring in an argon glovebox. Li_xSi nanoparticles were mixed with graphene sheets and poly(styrene-butadiene-styrene) (SBS) rubber (80:10:10 by weight) in toluene to form a slurry, which was then casted on a polyethylene terephthalate (PET) release film. After drying, the Li_xSi/graphene can be easily peeled off as a large free-standing foil. Thin layers of graphene sheets were coated on the double sides of the foil to ensure that even the Li_xSi nanoparticles on the surface were fully protected. This foil preparation process is also applicable to other Li alloy forming materials, such as Al and Sn.

Results

Free-standing Li_xSi/graphene foil shows excellent electrochemical and environmental stability

The Li_xSi/graphene foil is stable in air, owing to the unique structure as well as the hydrophobicity and gas impermeability of graphene sheets. The colour of Li_xSi/graphene foil remains the same even after 48 h, while the colour of Li metal turns black after exposure to ambient air for just 3 min (Figure II.2.D.1a). To investigate the dry-air stability, the foil was stored in the dry room for two weeks and its remaining capacity was examined over time. After two weeks, it still maintained 94.3% of its original capacity (Figure II.2.D.1b). Besides, with the protection of the graphene sheets, the Li_xSi/graphene foil exhibits excellent stability even in air with a high humidity level (20-60% relative humidity). After being exposed to ambient air for 3 days, the foil still exhibits a high areal capacity of 3.1 mAh cm⁻² (Figure II.2.D.1c).

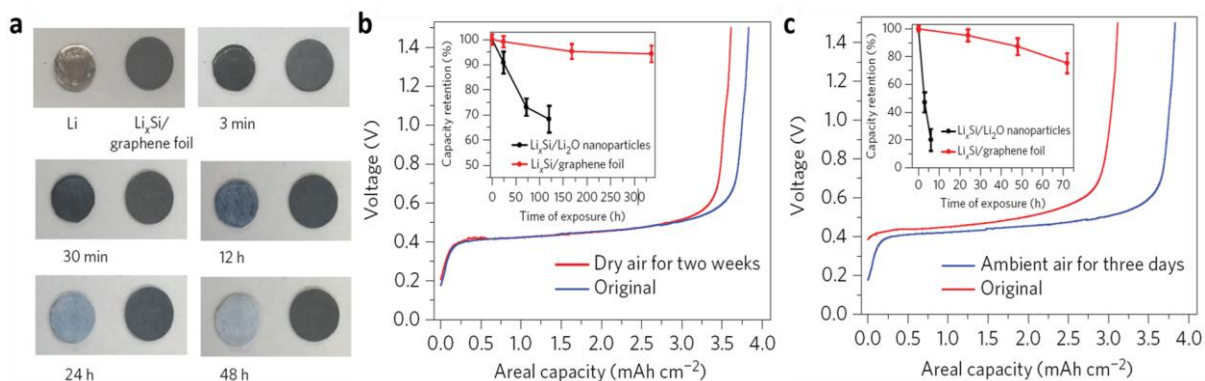


Figure II.2.D.1 Stability of the Li_xSi/graphene foil. (a) Photographs of the Li metal and Li_xSi/graphene foil exposed to ambient air for different durations. (b) The areal capacity retention of a Li_xSi/graphene foil in the dry room for two weeks. The inset shows the trend of capacity decay of the Li_xSi/graphene foil (red) and Li_xSi/Li₂O nanoparticles (black) with varying durations. (c) The areal capacity retention of the Li_xSi/graphene foil exposed to ambient air for three days. The inset shows the trend of capacity decay of Li_xSi/graphene foil (red) and Li_xSi/Li₂O nanoparticles (black) with varying durations.

The first-cycle delithiation capacities of Li_xSi/graphene foils with thicknesses of 19 and 42 μm were 3.8 and 8.3 mAh cm⁻² in half cells, respectively (Figure II.2.D.2a). From the 4th to the 400th cycle at a current density

of 1 mA cm^{-2} , the capacity retention of the $19\text{-}\mu\text{m}$ -thick foil is $\sim 98\%$, which is due to the high conductivity of graphene sheets and the already fully lithiated and expanded state of Si. Besides, the early and later cycle CE is (99.92% for later cycles) greatly improved, benefited from that Li_xSi nanoparticles are packed densely in a cluster form and encapsulated by graphene sheets to lower the surface accessible to the electrolyte and therefore reduces the side reactions.

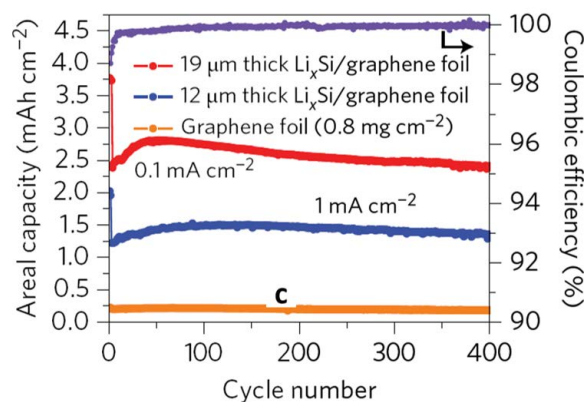


Figure II.2.D.2 Electrochemical performance of the Li_xSi /graphene foil. Half-cell cycling performance of Li_xSi /graphene foils with thicknesses of 12 and $19 \mu\text{m}$ at 0.1 mA cm^{-2} . The Coulombic efficiency is plotted for the foil with the thickness of $19 \mu\text{m}$ only (purple).

Free-standing Li_xSi /graphene foil shows excellent rate capability

The rate capability of the Li_xSi /graphene foil is also excellent and superior to bare lithium foil. We paired our Li_xSi /graphene foil with a traditional LiFePO_4 cathode (LiFePO_4 : conductive carbon (Super P): polyvinylidene fluoride (PVDF) = 70:20:10 by weight). Figure II.2.D.3a shows the voltage profiles of Li_xSi /graphene foil- LiFePO_4 and Li - LiFePO_4 cells between 2.5 and 3.8 V. The voltage drop of the full cell is due to the higher voltage plateau ($\sim 0.4 \text{ V}$) of Li_xSi . The full and half cells show similar capacities of 132.2 mAh g^{-1} and 130.6 mAh g^{-1} at 1 C (the capacity and rate are both based on the mass of LiFePO_4). The rate capability was tested at various rates from 0.2 to 20 C (Figure II.2.D.3b). At low rate, the capacities of LiFePO_4 in full and half cells are similar. Compared with half cells, LiFePO_4 in the full cell exhibits higher capacity especially at a high rate ($\sim 91.7 \text{ mAh g}^{-1}$ at 10 C and 84.0 mAh g^{-1} at 20 C), which can be attributed to the superior electrical conductivity of graphene. Besides, the morphology change of individual Li_xSi clusters during delithiation/lithiation process is indicated by the cross-sectional SEM images (Figure II.2.D.3c). A Li_xSi cluster ($\sim 5 \mu\text{m}$) is encapsulated by graphene sheets. Void space is created during the delithiation process, which accommodates further volume expansion of the subsequent lithiation process. Therefore, the foil voids the intrinsic problems of volume expansion that plague alternatives such as Li metal or unlithiated Si.

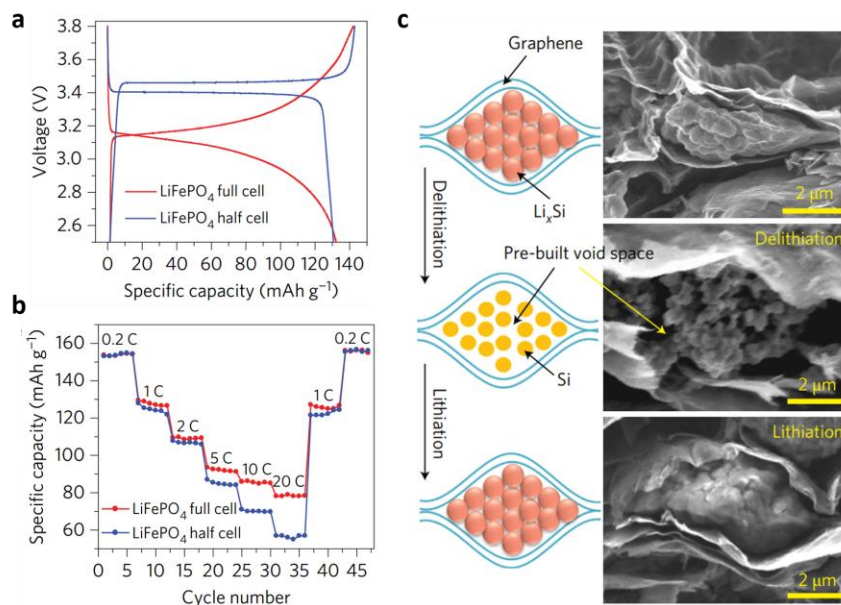


Figure II.2.D.3 Electrochemical performance of the Li_xSi /graphene foil. a, The voltage profiles of Li_xSi /graphene foil- LiFePO_4 full cell and Li - LiFePO_4 half cell (LiFePO_4 : Super P: PVDF = 70:20:10 by weight) within a potential window of 2.5–3.8 V. The capacity and rate are both based on the mass of LiFePO_4 in the cathode. b, Rate capability of Li_xSi /graphene foil- LiFePO_4 and Li - LiFePO_4 cells at various rates from 0.2 to 20 C (1 C = 170 mA g^{-1} of LiFePO_4). c, Schematics and the corresponding cross-sectional view SEM images of the Li_xSi /graphene foil before and after being cycled and stopped at the delithiated and lithiated states.

Free-standing Li_xSi /graphene foil shows excellent cycling stability for Li-S full cell

The excellent performance of the Li_xSi /graphene foil in half cells makes it possible to be used in full cells. The Li_xSi /graphene foil paired with sulfur can achieve stable full-cell cyclability. The graphitic carbon-encapsulated sulfur composite indicates sulfur can permeate into the graphitic carbon cage by capillary force and the composite maintains the original morphology of the cage (Figure II.2.D.4a). TEM confirms that the sulfur particles are well encapsulated by the graphitic carbon shell (>20 layers; Figure II.2.D.4b). Figure II.2.D.4c shows the voltage profile of the Li_xSi /graphene foil-S cell between 1.3 and 2.6 V, which shows a specific capacity of 1,086 mAh g^{-1} with an average voltage of ~ 1.8 V (the capacity is based on the mass of graphitic carbon-encapsulated S in the cathode). The mass ratio of anode to cathode is 1.8:1. Therefore, the estimated energy density is around 490 Wh kg^{-1} . There are two discharge voltage plateaus at 2.1 and 1.7 V, which agree with the Li-S discharge plateaus (2.4 and 2.1 V) and Li-Si (0.4 V) in half cells. The foil-S cell (Figure II.2.D.4d) demonstrates excellent cycling stability at 0.5 C and maintains a capacity of 858 mAh g^{-1} after 110 cycles with a CE of 99.5%, higher than that of the half cell (98.8%), indicating its great potential to replace Li metal in sulfur batteries (1 C = 1,672 mA g^{-1} of S). In the Li-S cell, the highly soluble polysulphides can easily diffuse from cathode to anode, and form a deposit of $\text{Li}_2\text{S}_2/\text{Li}_2\text{S}$ on the Li metal, which is confirmed by the XPS spectrum of S 2p (Figure II.2.D.4e). The counts of Li_2S_2 and Li_2S peaks are highly suppressed for the foil, which indicates that the protective action of the chemically stable graphene sheets minimizes the shuttle effect significantly. The relatively lower peaks of O-C=O and SO_3^{2-} confirm that the decomposition of Li salt is also suppressed in the foil-S cell.

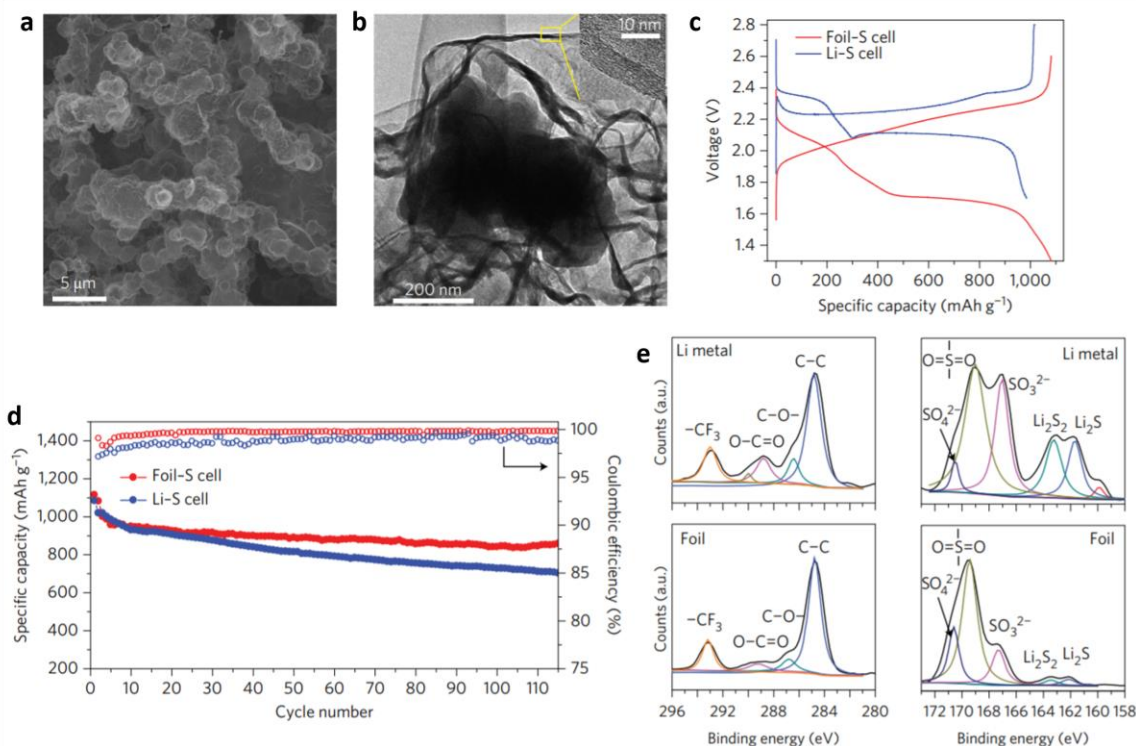


Figure II.2.D.4 Characterization of the sulfur electrode and the sulfur batteries. a, SEM image of the graphitic carbon-encapsulated sulfur composites. b, TEM image of the graphitic carbon-encapsulated sulfur composite. Inset shows the magnified graphitic carbon lattice fringes. c, The voltage profiles of $\text{Li}_x\text{Si}/\text{graphene}$ foil-S and Li-S cells at a rate of 0.5 C (1 C = 1.67 A g^{-1} of S; the capacity is based on the mass of graphitic carbon-encapsulated S in the cathode; the mass ratio of anode to cathode is 1.8:1). d, Cycling performance of $\text{Li}_x\text{Si}/\text{graphene}$ foil-S and Li-S cells at a rate of 0.5 C. The Coulombic efficiency is plotted on the right y axis. e, XPS spectra of C 1s (left) and S 2p (right) performed on Li metal (top) and the $\text{Li}_x\text{Si}/\text{graphene}$ foil (bottom) cycled in the sulfur batteries for 50 times.

Free-standing $\text{Li}_x\text{Sn}/\text{graphene}$ or $\text{Li}_x\text{Al}/\text{graphene}$ foil as an alternative to lithium metal anodes

We report a facile process to fabricate large-scale and freestanding $\text{Li}_x\text{Si}/\text{graphene}$ foil anode materials, which exhibit excellent environmental and electrochemical stability. Here, we show that the whole foil preparation process is applicable to other materials. Li_xM was synthesized by heating a stoichiometric mixture of M nanoparticles and Li metal under an inert atmosphere. Although M refers to Sn and Al (and Si in our previous example), other materials that form alloys with Li can be potentially used. The $\text{Li}_x\text{M}/\text{graphene}$ foil is prepared via vacuum filtration of a suspension of Li_xM and graphene sheets in toluene. (Figure II.2.D.5a, b) Thin layers of graphene sheets were coated on the double sides of the foil to ensure that even the Li_xSn or Li_xAl nanoparticles on the surface were fully protected. The previously adopted slurry coating and peeling-off approach is also suitable. The XRD pattern of the $\text{Li}_x\text{Sn}/\text{graphene}$ foil indicates that it is made of $\text{Li}_{22}\text{Sn}_5$ (PDF no. 01-081-6569) and graphitic carbon (Figure II.2.D.5c). The XRD pattern of the $\text{Li}_x\text{Al}/\text{graphene}$ foil confirms the existence of Li_3Al_2 (PDF no.04-007-1619) and graphitic carbon (Figure 1.5d).

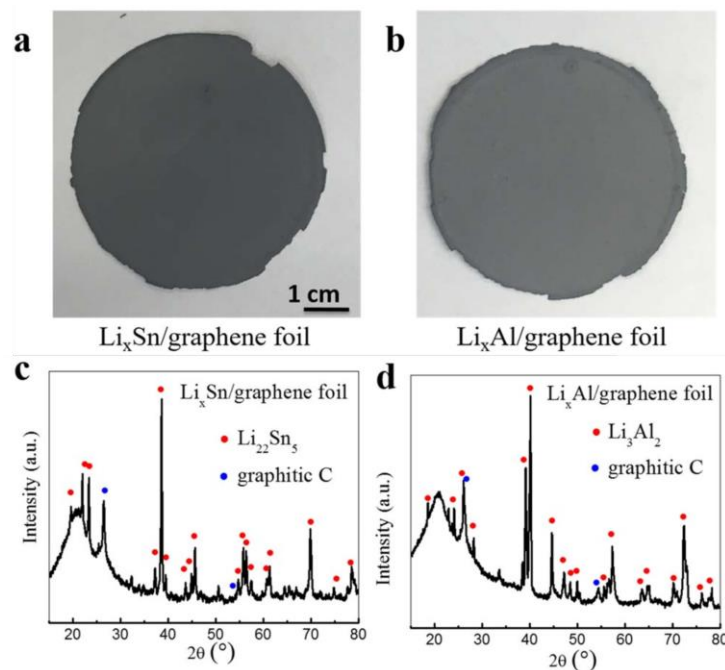


Figure II.2.D.5 Photographs of the (a) Li_xSn /graphene foil and (b) Li_xAl /graphene foil. XRD patterns of the (c) Li_xSn /graphene foil and (d) Li_xAl /graphene foil.

Conclusions

In the past year, we have developed a facile process to fabricate large-scale and free-standing Li_xM /graphene anodes with the unique foil structure comprising densely packed Li_xM nanoparticles encapsulated by large graphene sheets. M refers to Si, Sn, and Al, but other materials that can form alloys with Li can potentially be used. With its long-term cyclability and high CE in half cells, the Li_xSi /graphene foil has been successfully paired with high-capacity Li-free cathodes (sulfur) to achieve stable full-cell cyclability. The Li_xM /graphene foil is highly stable in different air conditions due to its unique structure in which each Li_xM cluster is surrounded and protected by the large graphene sheets. The air-stability could be further improved by atomic layer deposition of oxides or fluorides on the double sides of the foils. By addressing the electrochemical and environmental stability simultaneously, our Li-containing anodes should be attractive alternatives to Li metal anodes.

Key Publications

1. J. Zhao#, G. Zhou#, K. Yan, J. Xie, Y. Li, L. Liao, Y. Jin, K. Liu, P-C Hsu, J. Wang, H-M Cheng, and Yi Cui, "Air-stable and freestanding lithium alloy/graphene foil as an alternative to lithium metal anodes", *Nat. Nanotech.* 12, 993 (2017).
2. J. Zhao#, J. Sun#, A. Pei, G. Zhou, K. Yan, Y. Liu, D. Lin, and Y. Cui, "A general prelithiation approach for group IV elements and corresponding oxides", *Energy Storage Materials*, 10, 275, 2018.

II.3 Next-Gen Lithium-Ion: Advanced Cathodes R&D

II.3.A Electrochemical Analysis and Evaluation (ANL, LBNL, ORNL)

Daniel P. Abraham, Principal Investigator

Argonne National Laboratory
9700 S. Cass Avenue
Lemont, IL 46039
E-mail: abraham@anl.gov

Peter Faguy, DOE Technology Development Manager

U.S. Department of Energy
E-mail: Peter.Faguy@ee.doe.gov

Start Date: October 1, 2014

End Date: September 30, 2018

Project Funding (FY18): \$4,000,000

DOE share: \$4,000,000

Non-DOE share: \$0

Project Introduction

The inability to charge commercially available $\text{Li}_{1+x}\text{Ni}_a\text{Mn}_b\text{Co}_c\text{O}_2$ (NMC-abc, where x is typically <0.05), cathode materials beyond ~ 4.3 V (vs. graphite, Gr) without incurring excessive surface damage, electrolyte decomposition, structural instabilities, gassing, and loss of lithium inventory is a significant challenge in meeting next-generation energy storage targets. This multi-institutional effort aims to understand the underlying failure mechanisms associated with these issues that prevent state-of-the-art Li-ion battery systems from achieving higher practical energy densities than are currently obtainable. This work is intended to help "enable" high-energy/high-voltage (HE/HV) cells via new insights and/or understanding, not currently available, of why present materials/systems fail. This chapter deals with electrochemical investigations focused on gaining such insights and understanding; more specifically, studies relating to electrolyte and surface stability including solvents, additives, gassing, solid electrolyte interphases, and transition metal (TM) dissolution are presented.

Objectives

- Develop a fundamental understanding of gas generation and reactivity in HE/HV cells. These insights will allow better control over SEI/CEI chemistry, improve stability at electrode interfaces, and minimize impedance rise. Develop techniques to characterize gas composition *in situ* and *ex situ*.
- Formulate experiments to examine the various cross-talk processes during cycling. Identify effects of transition metals in the electrolyte on cell performance
- Advance understanding of mechanisms leading to cell impedance rise by answering questions such as the following: "is impedance rise affected by the type of anode in the cell?"
- Characterize the behavior of fluorinated solvents, which are stable at high potentials (oxidation resistant) but not stable at the graphite anode (easily reduced). Examine effect of highly fluorinated electrolyte on the impedance rise and capacity retention of NMC//Gr full cells using "preformed" graphite anodes.
- Identify additives, which when incorporated into our baseline electrolyte (Gen2), consisting of 1.2M LiPF_6 in EC:EMC (3:7 w/w), reduces cell degradation. Provide an understanding of electrolyte-additive mechanisms through closely-coupled experimental and computational techniques.

Approach

The objectives listed above were pursued through the following experimental thrusts:

- Systematic study and evaluation of various *additive systems* including:

- Previously identified and new additive combinations
- Electrochemical evaluation under standard project protocols
- Mechanistic determination of additive performance
- Investigation of *fluorinated electrolytes* and their electrochemical stability including:
 - Various electrolyte formulations
 - Measurements of oxidative stability
 - Characterization of cathode surface stability
- Examination role of *electrode cross-talk* on cell performance during aging including:
 - Transition metal dissolution from the oxides and deposition at the negative electrode
 - Origin and role of gasses generated in the cell
 - Symmetric cells to separately study the role of the positive and negative electrodes

Results

Fundamental understanding of gas generation and reactivity in HE/HV cells

A system to monitor gasses continuously over longer-term cycling was developed utilizing FTIR. The gas-forming reactions were monitored in 100 mAh and 500 mAh NMC-811//Gr pouch cells built at the ORNL BMF using electrodes coated in-house. The cells were cycled using the standard HE/HV protocol with voltage windows of 3.0-4.2 or 3.0-4.4 V. Cells with the baseline Gen2 electrolyte were compared to cells with common electrolyte additives (VC, TMSPi, and FEC). To isolate gas formation at the anode and cathode, symmetric cathode-cathode and anode-anode pouch cells were built. Symmetric cells were constructed by discharging NMC-811//Gr pouch cells to 50% SOC after formation. The partially charged electrodes were harvested inside an argon-filled glove box and built into symmetric cells.

The gas-forming reactions that occur in high-energy NMC-811//Gr cells depend on several factors including the cut-off voltage and electrolyte composition. Figure II.3.A.1 (Left Panel) shows the change in volume of NMC-811//Gr pouch cells due to gas evolution measured using the Archimedes method. No measurable volume change occurs in cells cycled with a 4.2 V cut-off, but significant gas evolution occurs in cells cycled to a higher cut-off voltage of 4.4 V. The change in volume peaks after 20 cycles and then slowly decreases due to consumption at the counter electrode. The maximum change in volume is $> 1\text{ mL/g}_{\text{NMC}}$ which is comparable to the volume of electrolyte. Interestingly, all the electrolyte additives tested significantly reduced the initial spike in gas generation for the same cut-off voltage of 4.4 V. Gas analysis of full cells and symmetric cells (cathode//cathode and anode//anode) provides clear evidence for cross-talk (Figure II.3.A.2). Most of the gas detected is generated at the cathode after the initial formation cycles. Symmetric cathode//cathode cells generated about twice as much gas per gram of NMC as full cells with graphite

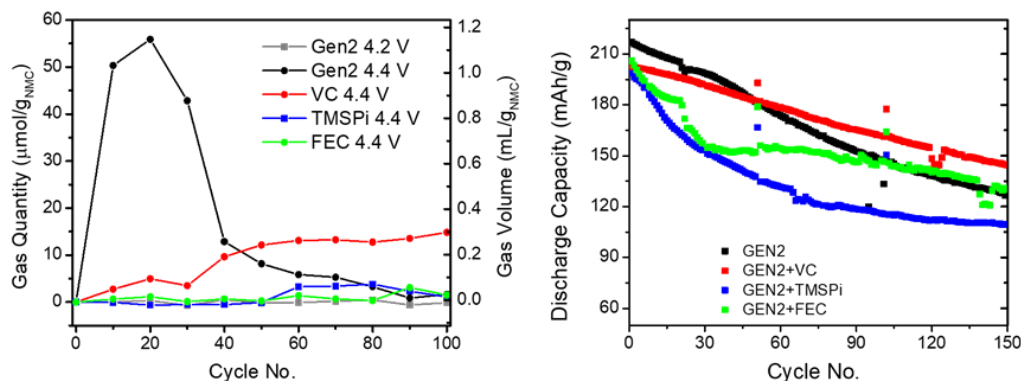


Figure II.3.A.1 (Left Panel) Change in volume of NMC-811//Gr pouch cells due to gas evolution measured using Archimedes method. Gassing is significant in cells charged to 4.4 V with baseline Gen2 electrolyte but less severe with electrolyte additives. (Right Panel) Capacity retention of NMC-811//Gr pouch cells charged to 4.4 V with baseline Gen2 electrolyte and electrolyte with additives.

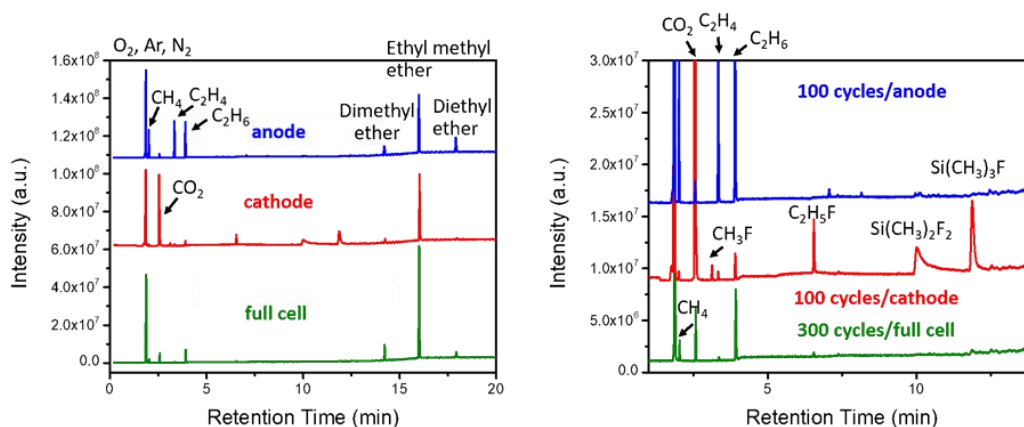


Figure II.3.A.2 (Left Panel) Gases sampled from symmetric pouch cells (anode//anode and cathode//cathode) and full pouch cells after cycling. The gases were measured ex situ with GC-MS. Differences in gas composition between symmetric cells and full cells provide evidence for gas “cross-talk” in HE/HV cells. (Right Panel) Expanded view of the left panel.

GC-MS analysis of full and symmetric cells illustrates how reactive gases generated at one electrode are consumed by the counter electrode (Figure II.3.A.2). The anode produces reduced gases including methane, ethane, and ethylene, while the cathode forms oxidized gases including CO_2 and fluorocarbons. Full cells have lesser amounts of both reduced and oxidized gases due to electrode cross-talk. No new gases are detected in the full cells. Because of electrode cross-talk, gas generation and impedance rise in symmetric cells do not correlate with cycling performance in full cells.

In situ measurements are needed to further understand gas generation and reactivity. In this work, a new AEGIS (Analysis of Electrochemical Gassing by Infrared Spectroscopy) reactor was built, capable of continuously probing the gas phase species without loss of solvent and drying out of the cell (Figure II.3.A.3, left panel). The pouch cell is sealed within a pressure vessel containing IR-transparent NaCl windows. *In situ* measurements of 0.5 Ah NMC-811//Gr pouch cells showed the change in the amount of CO and CO_2 with state of charge (Figure II.3.A.3, right panel). CO and CO_2 are typical products of electrolyte decomposition and Li_2CO_3 oxidation. Notably, the rate of CO production changes once the cell is charged above 3.8 V. The rate of CO_2 production changes once the cell is charged above 4.0 V. These changes point to a complex set of reactions that are beginning to be understood. Other cells have been studied over 1 week of continuous cycling.

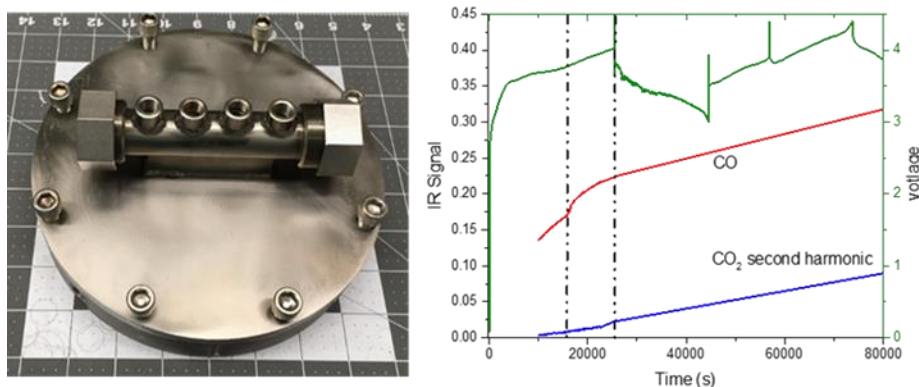


Figure II.3.A.3 (Left) AEGIS reactor capable of continuously probing gas phase species without loss of solvent. (Right) Change in concentration of CO and CO₂ with state of charge measured for a 0.2 Ah NMC-811//Gr cell.

Anode-Dependent Impedance Rise in Layered-Oxide Cathodes of Lithium-ion Cells

Electrodes used in this work are from Argonne's CAMP facility. The positive electrode active material was either LiNi_{0.8}Mn_{0.1}Co_{0.1}O₂ (NMC-811), LiNi_{0.5}Mn_{0.3}Co_{0.2}O₂ (NMC-532), or LiNi_{0.8}Co_{0.15}Al_{0.05}O₂ (NCA), and the negative electrode active material was either graphite or Li₄Ti₅O₁₂ (LTO). The separator used was Celgard 2325 separator and the electrolyte was the baseline Gen2. The electrochemical tests were conducted in cells containing a reference electrode, which provides electrode impedances, along with the *full* cell impedance. The aging procedure (Figure II.3.A.4, Left Panel) contains a series of potentiostatic holds and reference performance tests (RPTs), which include C/25 charge-discharge cycles to determine cell capacity, and hybrid pulse power characterization (HPPC) cycles to determine cell impedance. Area specific impedance (ASI) data from NMC-811//LTO and NMC-811//Gr cells, which were progressively exposed to potentiostatic holds for 100, 200 and 400 hours, are shown in (Figure II.3.A.4, Right Panel). Note that the upper cutoff voltage (UCV) for cycling was chosen such that the positive electrode potential during the potentiostatic hold was similar (~4.48 V vs. Li/Li⁺). The main conclusions from the data are as follows: (i) Cell impedance increases as the potentiostatic hold (calendar-aging) duration increases. The impedance rise comes almost entirely from the NCM-811 electrode (cathode); the anode (either Gr or LTO) shows negligible impedance increase even after 400 hours of calendar aging. (ii) The magnitude of the cathode impedance increase is higher for the cell containing the LTO anode as compared to the cell containing the graphite anode, i.e., the evolution of cathode impedance in a full-cell configuration is dependent on the identity of the anode. These data provide a striking example of the *cross-talk* between the two electrodes in a lithium-ion cell.

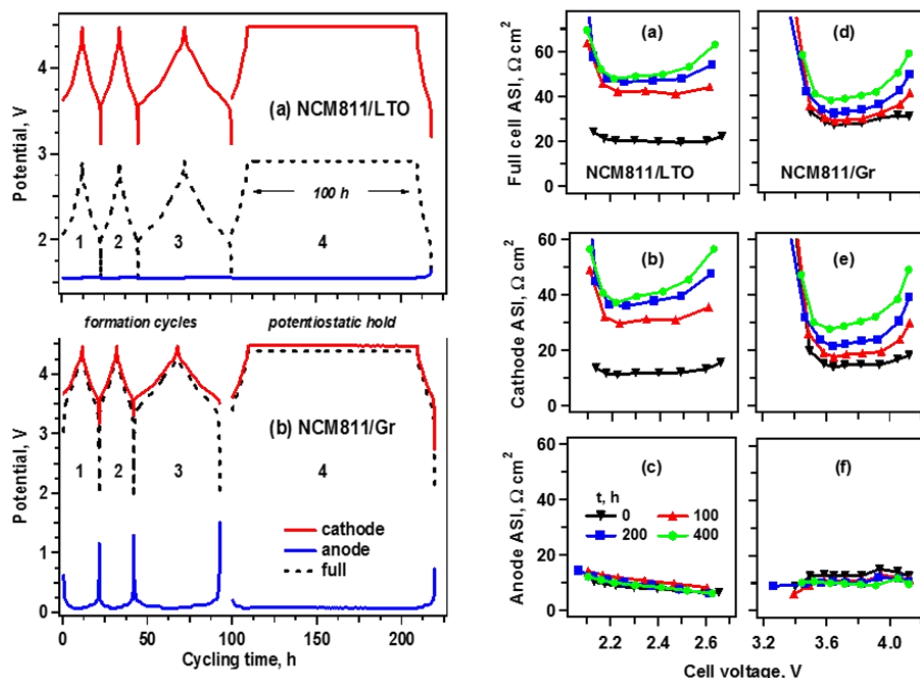


Figure II.3.A.4 (Left Panel) - Voltage and electrode potential data from cells containing the (a) NMC811/LTO and (b) NMC811/Gr couples. For both couples, the profiles to the left show the formation (two C/10 and one C/25) cycles; the profiles to the right show the cycle with the first 100 h potentiostatic hold. (Right Panel) - Cell and electrode ASI change (from HPPC measurements) resulting from calendar-aging of (a-c) NMC811/LTO cells and (d-f) NMC811/Gr cells. The aging times are indicated in (c): after formation cycles (black), 100 h (red), 200 h (blue), and 400 h (green).

During the potentiostatic hold tests all the LTO cells showed small *gains* in capacity after 400 h aging, while for the Gr cells the discharge capacity decreased steadily over time. The observed increase in capacity for the NMC//LTO cells is a consequence of electrolyte oxidation during the high-voltage potential hold. The electrons removed from the carbonate solvent by oxidation are compensated by the injection of Li^+ ions from the electrolyte into the electrodes, thereby increasing the inventory of cyclable lithium ions. The protons released during solvent oxidation compensate the PF_6^- anions in solution. Note that electrolyte oxidation during the high-voltage hold also occurs in the Gr cells. In these cells, the measured capacity loss is the difference between the lithium-inventory gain from electrolyte oxidation and lithium-inventory depletion from continual SEI formation. These oxidation and reduction processes in the Gr cells result in depletion of the electrolyte that could lead to premature cell failure. Cell failure from electrolyte depletion is well-known in Li-metal cells (colloquially known as “drying” of the cell), but is not commonly discussed for lithium-ion cells. This phenomenon is especially important for commercial cells, which typically are “electrolyte-starved” to increase energy density. The problem is aggravated by higher cell voltages, which increases the rate of electrolyte oxidation at the positive electrode.

Electrolyte composition effect on oxide surface reconstruction during high-voltage holds

Crystal structure degradation of layered oxides exposed to high voltage has been established in the literature. This process proceeds through oxygen loss from the surface, electrolyte oxidation by the released oxygen, and surface change of the cathode material. This work examines three electrolytes, which span the range of reactivity with oxygen, to evaluate the electrolyte role in oxygen loss at the cathode surface.

NMC-532// $\text{Li}_4\text{Ti}_5\text{O}_{12}$ cells were exposed to potentiostatic holds at 4.6 V vs. Li/Li^+ with the following electrolytes: a polyfluorinated electrolyte consisting of 1M LiPF_6 in a 3:7 w/w ratio of difluoroethylene carbonate and hexafluorodiethyl carbonate, collectively referred to as “FE-3”, the baseline Gen2 electrolyte, and the Gen2 electrolyte with an easily oxidizable additive, TTFP, that has been shown to incorporate oxygen

in its oxidized form. After the potentiostatic hold was completed, the cells were disassembled and the cathodes were evaluated in atomic resolution high-angular annular field imaging and electron energy loss spectroscopy to determine crystal structure degradation.

The current during the potentiostatic hold is representative of oxidation reactions at the cathode. In our data the FE-3 electrolyte showed the lowest current, the Gen2 + TTFP electrolyte showed the highest current, with the Gen2 current in the middle. A High-Angle Annular Dark Field (HAADF)-Scanning Transmission Electron Image (STEM) micrograph (Figure II.3.A.5, Left Panel) showed that the crystal structure at the oxide particle edges was different from that of the bulk. Electron energy loss spectra (EELS) shows how the cathode oxygen environment changed depending on both electrolyte identity and distance from the surface (Figure II.3.A.5, Right Panel). A smaller ΔE indicates lower average TM oxidation states consistent with rock-salt degradation, so the data indicates that the Gen2 + TTFP leads to significant oxygen loss and cathode degradation, while the FE-3 electrolyte leaves a mostly intact crystal structure. The Gen2 also shows oxygen loss at the top layer of the cathode, but this degradation does not extend as far into the bulk of the particle as was seen with cathodes exposed to the oxidizable additive, TTFP.

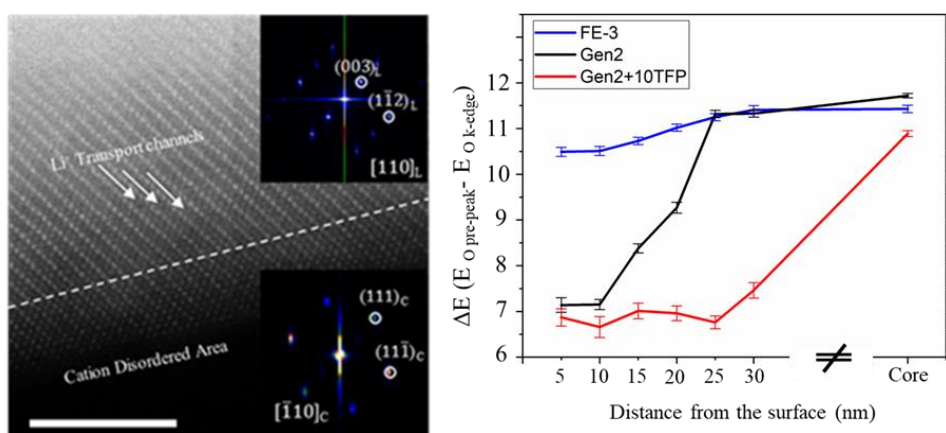


Figure II.3.A.5 (Left Panel) HAADF-STEM micrograph (5 nm scale bar) from a NMC-532 particles cycled in FE-3 electrolyte. (Right Panel) EELS analysis results from the oxides cycled with various electrolytes. Energy difference between the O-K edge and its pre-peak is plotted as a function of distance from the surface.

Preformed Anodes: Fluorinated Electrolytes, Cross-talk, and the Origins of Impedance Rise

Graphite electrodes were preformed by five cycles with NMC-532 cathodes in either a polyfluorinated electrolyte consisting of 1M LiPF₆ in a 3:7 w/w ratio of difluoroethylene carbonate and hexafluoroethyl carbonate, collectively referred to as “FE-3”, or the baseline Gen2 electrolyte. After the preforming protocol, the cells were deprimed, and the harvested graphite electrodes were combined with a pristine cathode, new separator, and fresh Gen2 electrolyte. These cells were then cycled according to the HE/HV protocol. After cycling, the cells were disassembled for analysis.

Figure II.3.A.6a shows the cycling protocol results with both preformed (both polyfluorinated and baseline electrolytes) and pristine graphite when combined with pristine cathodes and fresh Gen2 electrolyte. Graphite pretreated with the FE-3 electrolyte (FE-3 Gr) and graphite pretreated with the Gen2 electrolyte (Gen2 Gr) both show a high initial CE of 87.5% as well as discharge capacities of ~ 197 mAh/g. Both FE-3 Gr and Gen2 Gr containing cells maintain this high discharge capacity for a number of cycles before showing any capacity fade, in contrast to the baseline cells with pristine graphite electrodes, which show capacity fade immediately. The final capacities for the preformed graphite cells are 189 mAh/g and 179 mAh/g for the FE-3 Gr and Gen2 Gr containing cells, respectively. The CEs of both FE-3 Gr and Gen2 Gr containing cells start higher than the baseline, although Figure II.3.A.6b shows that FE-3 Gr cells approach a higher CE (99.88%) during the final aging cycles compared with the Gen2 Gr containing cells (99.71%), which is lower than that of the baseline (99.75%).

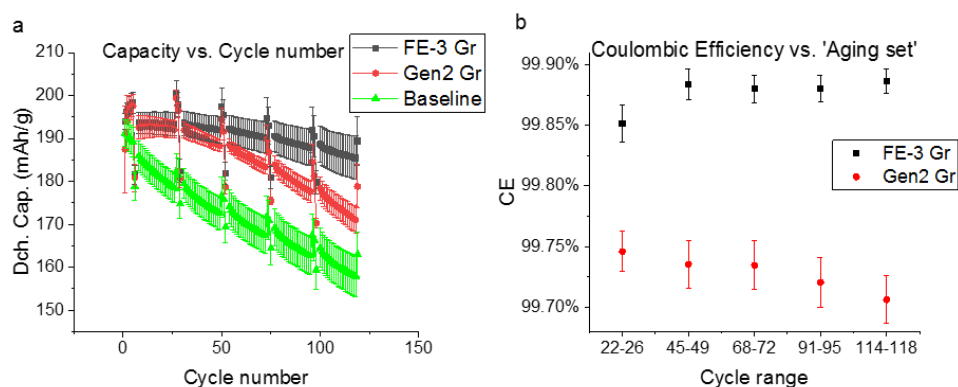


Figure II.3.A.6 (a) Capacity vs. cycle number for cells containing pristine graphite/F-Gr/G-Gr anodes, pristine cathodes, and Gen2 electrolyte. (b) Average CE for the final 5 C/3 cycles of each "aging set", directly before the C/10 cycles. Each data point is the average of 3 cells with the standard deviation indicated by the error bars.

Impedance data on the pretreated graphite cells were obtained from HPPC tests. Compared to the well-characterized baseline (Gen2) system (with pristine electrodes), the initial ASI for both the preformed graphite cells was higher, with FE-3 Gr leading to an ASI at ~ 3.7 V of $36 \Omega\text{-cm}^2$ compared to $29 \Omega\text{-cm}^2$ for Gen2 Gr. However, the impedance rise from the first HPPC (cycle 7) to the final HPPC (cycle 99) is dramatically lower for the FE-3 Gr compared to Gen2 Gr (13% vs. 92%). In addition, the impedance across all voltages for FE-3 Gr cells was lower than Gen2 Gr cells.

Conclusions

- Gases that are generated at the positive and negative electrode were isolated using symmetric cells and GC-MS. These studies demonstrated how electrode cross-talk changes the gas composition in full cells. Most gas evolution and impedance rise occurred at the cathode in NMC-811//Gr cells. Common electrolyte additives were found to significantly reduce gas evolution and impedance rise in these cells.
- The first in situ measurements of gas evolution using FTIR and a newly designed AEGIS reactor were demonstrated. FTIR enables monitoring of the rates of gas generation and consumption without electrolyte drying. This system will also enable deliberate introduction of reactive gases to further understand the complex chemical equilibria that occur in lithium-ion cells.
- Layered-oxide cathodes were paired with Gr and LTO anodes and it was observed that cells using LTO have higher impedance than cells using Gr during calendar-aging at sufficiently high (> 4.2 V vs. Li/Li⁺) oxide potentials. These results suggest that gases generated in the cell play an important role in this impedance rise. In Gr-containing cells, the gases are gradually depleted by reactions at the Gr electrode. In contrast, the build-up of gases in cells utilizing LTO degrades the electron conduction network and oxide-electrolyte interfaces within the cathode causing the observed impedance rise. The calendar-aging also alters cell capacity, with losses observed in the Gr cells and gains observed in the LTO cells.

- Three electrolytes, that span the range of reactivity with layered oxides, were tested using high-voltage potentiostatic-hold tests with NMC-532 cathodes. The most reactive electrolyte (Gen2 + TTFP) caused oxygen loss and surface degradation, while the fluorinated electrolyte preserved the oxide structure.
- Gr anodes preformed with a polyfluorinated electrolyte have better capacity retention than anodes preformed with the baseline Gen2 electrolyte. Additionally, cells with the fluorinated electrolyte displayed lower impedance rise, indicating that soluble reduction products from an unstable anode-electrolyte interface can influence impedance rise at the cathode-electrolyte interface (i.e., *cross-talk*).

Key Publications

1. A. Tornheim, C. Peebles, J.A. Gilbert, R. Sahore, J.C. Garcia, J. Bareño, H. Iddir, C. Liao, D.P. Abraham, "Evaluating electrolyte additives for lithium-ion cells: A new Figure of Merit approach", *J. Power Sources* 365C (2017) pp. 201-209.
2. Tornheim, R. Sahore, M. He, J.R. Croy, Z. Zhang, "Preformed Anodes for High-Voltage Lithium-Ion Battery Performance: Fluorinated Electrolytes, Cross-talk, and the Origins of Impedance Rise", *J. Electrochem. Soc.* 2018 165, A3360-A3368.
3. Tornheim, S. Sharifi-Asl, J.C. Garcia, J. Bareño, H. Iddir, R. Shahbazian-Yassar, Z. Zhang, "Effect of electrolyte composition on rock salt surface degradation in NMC cathodes during high-voltage potentiostatic holds", *Nano Energy*, in Press, (2018).
4. Tornheim, V. A. Maroni, M. He, D. J. Gosztola, and Z. Zhang, "Enhanced Raman Scattering from NCM523 Cathodes Coated with Electrochemically Deposited Gold", *J. Electrochem. Soc.*, 164, 13, A3000-A3005, 2017.
5. Mao, S.J. An, H.M. Meyer, J. Li, M. Wood, R.E. Ruther, D.L. Wood, "Balancing formation time and electrochemical performance of high energy lithium-ion batteries", *Journal of Power Sources* 2018, 402, 107-115.
6. Mao, M. Wood, L. David, S.J. An, Y. Sheng, Z. Du, H.M. Meyer, R.E. Ruther, D.L. Wood, "Selecting the Best Graphite for Long-Life, High-Energy Li-Ion Batteries", *J. Electrochem. Soc.* 2018, 165 (9), A1837-A1845.
7. Mao, R.E. Ruther, J. Li, Z. Du, I. Belharouak, "Identifying the limiting electrode in lithium ion batteries for extreme fast charging.", *Electrochemistry Communications* 2018, 97, 37-41.
8. Peebles, R. Sahore, J.A. Gilbert, J.C. Garcia, A. Tornheim, J. Bareño, H. Iddir, C. Liao, D.P. Abraham, "Tris(trimethylsilyl) Phosphite (TMSPi) and Triethyl Phosphite (TEPi) as Electrolyte Additives for Lithium Ion Batteries: Mechanistic Insights into Differences during LiNi_{0.5}Mn_{0.3}Co_{0.2}O₂-Graphite Full Cell Cycling", *J. Electrochem. Soc.* 164 (2017) A1579.
9. Peebles, J. Garcia, A.P. Tornheim, R. Sahore, J. Bareño, C. Liao, I. A. Shkrob, H.H. Iddir. D.P. Abraham, "Chemical Pickling of Phosphite Additives Mitigates Impedance Rise in Li Ion Batteries", *J. Phys. Chem. C*, 2018, 122, 9811–9824.
10. J.A. Gilbert, V.A. Maroni, Y. Cui, D.J. Gosztola, D.J. Miller, D.P. Abraham, "Composition and Impedance Heterogeneity in Oxide Electrode Cross-sections detected by Raman Spectroscopy", *Adv. Mater. Interfaces* 2018, 1701447.
11. J.A. Gilbert, I.A. Shkrob, D.P. Abraham, "Transition Metal Dissolution, Ion Migration, Electrocatalytic Reduction and Capacity Loss in Lithium-Ion Full Cells", *J. Electrochem. Soc.* 164 (2017) A389-399.

12. J.A. Gilbert, J. Bareño, T. Spila, S.E. Trask, D.J. Miller, B.J. Polzin, A.N. Jansen, D.P. Abraham, "Cycling behavior of NCM523//Graphite lithium-ion cells in the 3-4.4 V Range – Diagnostic studies of Full Cells and Harvested Electrodes", *J. Electrochem. Soc.* 164 (2017) A6054-A6065.
13. M.-T.F. Rodrigues, K. Kalaga, S.E. Trask, I.A. Shkrob, D.P. Abraham, "Anode-Dependent Impedance Rise in Layered-Oxide Cathodes of Lithium-Ion Cells", *J. Electrochem. Soc.* 2018, 165, A1697-A1705.
14. R. Sahore, C. Peebles, D.P. Abraham, J. Gilbert, I. Bloom, "Additive Effects in High-Voltage Layered-Oxide Cells: A Statistics of Mixtures Approach", *J. Power Sources* 362 (2017) pp. 342-348.
15. R. Sahore, A. Tornheim, J. Bareno, C. Peebles, J. Garcia, D. C. O'Hanlon, F. D. Key, C. Liao, H. Iddir, Z. Zhang, I. Bloom, "Methodology for understanding interactions between electrolyte additives and cathodes: a case of the tris(2,2,2-trifluoroethyl)phosphite additive", *Journal of Materials Chemistry A* 6 (2018) 198.

Acknowledgements

Chapter Acknowledgments D.P. Abraham, S.J. An, J. Bareño, I. Belharouak, I. Bloom, J.R. Croy, Y. Cui, L. David, Z. Du, J.C. Garcia, J.A. Gilbert, D.J. Gosztola, M. He, H. Iddir, A.N. Jansen, K. Kalaga, F. D. Key, J. Li, C. Liao, C. Mao, V. A. Maroni, H.M. Meyer, D.C. O'Hanlon, C. Peebles, B.J. Polzin, M.-T.F. Rodrigues, R.E. Ruther, R. Sahore, Y. Sheng, I. A. Shkrob, A. Tornheim, S.E. Trask, G. Veith, M. Wood, D.L. Wood, Z. Zhang.

II.3.B Materials and Characterization (ANL, LBNL, ORNL)

John Vaughey, Principal Investigator

Argonne National Laboratory
9700 S. Cass Avenue
Lemont, IL 46039
E-mail: vaughey@anl.gov

Guoying Chen, Principal Investigator

Lawrence Berkeley National Laboratory
1 Cyclotron Road
Berkeley, CA 94720
E-mail: GChen@lbl.gov

Peter Faguy, DOE Technology Development Manager

U.S. Department of Energy
E-mail: Peter.Faguy@ee.doe.gov

Start Date: October 1, 2014	End Date: September 30, 2018	
Project Funding (FY18): \$4,000,000	DOE share: \$4,000,000	Non-DOE share: \$0

Project Introduction

Charging $\text{Li}(\text{Ni}_a\text{Mn}_b\text{Co}_c)\text{O}_2$ (NMC) cathode materials beyond ~ 4.3 V (vs. graphite, Gr) is associated with excessive surface damage, electrolyte decomposition, structural instabilities, gassing, and loss of lithium inventory to side reactions and SEI formation at the anode. Overcoming these issues represent significant challenges to researchers in meeting next-generation energy storage targets. This project aims to understand the underlying failure mechanisms associated with these issues that prevent state-of-the-art Li-ion battery systems from achieving higher practical energy densities than currently obtainable. To this end, several research thrusts have been established to focus on areas of interest including cathodes, electrolytes and additives, surface modifications, interfacial characterization, testing and analysis, modeling, and cell fabrication. In addition, cross-cutting collaborations have been formed targeting information on the failure mechanisms of NMC//Gr cells that affect systems-level performance. This project is intended to enable high-energy/high-voltage (HE/HV) cells via new insights and an understanding of why present NMC systems fail above ~ 4.3 V. This chapter deals with the materials synthesis and characterization component of the project; more specifically, detailed studies of the structure and behavior of NMC surfaces, and their interactions with their environment, are presented.

Objectives

- Understand the effects on electrochemical performance of various cathode compositions where cathode interfaces are modified by (1) aqueous coating process or (2) a non-aqueous coating processes
- Understand the effects of cathode composition on surface segregation, coating efficiency, and electrochemical performance of Ni-rich cathodes
- Understand the complex relationships between NMC particle morphology and the associated, facet-dependent electrochemical properties
- Devise and create crystalline thin film model systems designed to test theoretical predictions by designing, synthesizing, and characterizing materials that allow for unique, atomic-scale insights into the reactivity of select NMC surfaces

Approach

The goals listed above will be pursued through the following experimental thrusts:

- Synthesis of *model systems* that allow for detailed experimental and theoretical characterization of NMC surfaces including:
 - Single-crystal, NMC particles with well-defined compositions, sizes, and morphologies
 - Surface-modified particles
 - Thin-film, NMC cathodes
- Systematic studies of *coated NMC particles* using Al_2O_3 as a baseline, to include:
 - NMC composition (442, 532, 622, 811, NCA, LCO)
 - Aqueous vs. non-aqueous solvents coupled with various Al precursors with oxidizing and non-oxidizing associated anions
 - Structure and morphology of coatings as a function of the above variables

Results

Reactivity of NMC Surfaces A variety of NMC single-crystal samples were synthesized using either a coprecipitation method or a molten-salt method (see FY17 HE/HV Annual Report for more detail) and made available to program participants. Here, facet-specific interactions between an NMC surface and a liquid electrolyte were probed through comparative studies performed on platelet-shaped crystals with dominant (001) termination surfaces and truncated-octahedron-shaped crystals with (012) dominated facets. Both samples had the same average particle size of 200–300 nm, as shown in the SEM images in Figure II.3.B.1.

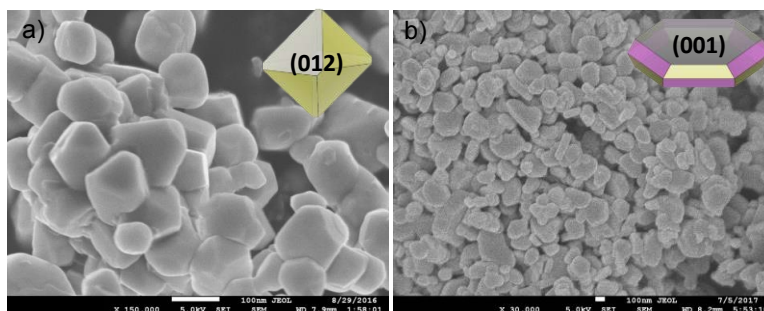


Figure II.3.B.1 SEM images of a) platelet-shaped and b) truncated-octahedron-shaped NMC crystals.

To avoid interference from binders or carbon additives in typical composite electrodes, chemical oxidation with NO_2BF_4 (~ 5.1 V vs. Li/Li^+) was used to extract Li from the NMC crystals. The fully-delithiated NMC crystals (20 mg) were then mixed with 1.5 ml of Gen2 electrolyte (1.2 M LiPF_6 in EC:EMC 3:7 w/w) and aged at room temperature in an Ar-filled glovebox, mimicking the aging process of a fully charged NMC cathode in a Li-ion cell. The particles were sampled at an interval of 2 weeks and analyzed by a range of analytical techniques. Figure II.3.B.2a shows Ni *K*-edge hard X-ray absorption spectroscopy (hXAS) profiles collected on the pristine, delithiated, and several aged NMC-333 particles having dominant (001) surfaces. The edge energy, determined relative to the intensity at 0.5 in the normalized spectra, shifted from 8342.0 to 8344.7 eV upon delithiation (Figure II.3.B.2a and b), consistent with an increase of Ni oxidation state. With aging, the Ni *K*-edge shifted towards lower energy by a total of 0.5 eV in 8 weeks, suggesting Ni reduction resulting from side reactions between the highly charged NMC particles and the electrolyte. A non-linear decay behavior was observed over time with a much faster decrease in oxidation state at the beginning of the aging process (Figure II.C.2.2c); likely reflecting a reduction in surface reactivity due to surface passivation.

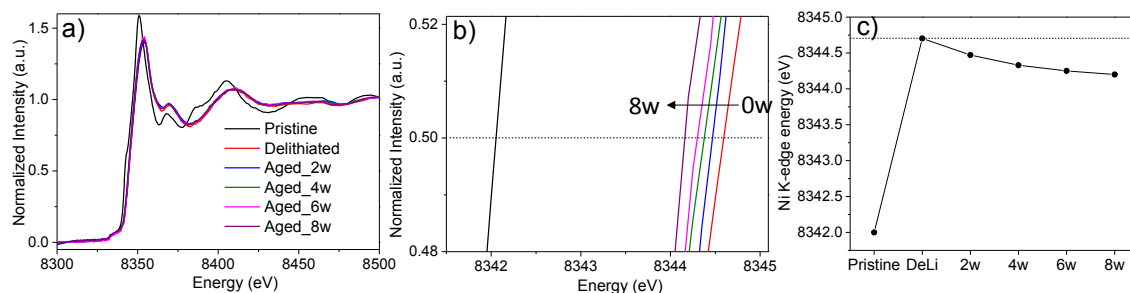


Figure II.3.B.2 (a, b) Hard XAS spectra of pristine, delithiated, and aged NMC-333 particles, and (c) The relationship between Ni-K edge energy and aging time.

The aging process was compared over a series of fully-delithiated NMC samples, including (001)-surface NMC-333, NMC-532, NMC-631, NMC-622, and NMC-613 as well as (012)-surface NMC-333 and NMC-532. Figure II.3.B.3 summarizes the *K*-edge energy shift as a function of aging time, where the shift was determined based on the energy difference relative to the corresponding chemically delithiated sample before aging. For all samples, no significant changes were observed for Mn or Co edges (Figure II.3.B.3 b and c), however, the Ni edge gradually shifted to lower energy with aging (Figure II.3.B.3a) for all samples, suggesting all compositions experience Ni reduction when charged and placed in contact with the electrolyte. The samples with the (012) dominant surface had notably more shift compared to those having (001) dominated surfaces, revealing higher surface reactivity in the former. These data clearly demonstrate the impact of chemical composition and morphology (facet-dependence) on the surface stability of NMCs.

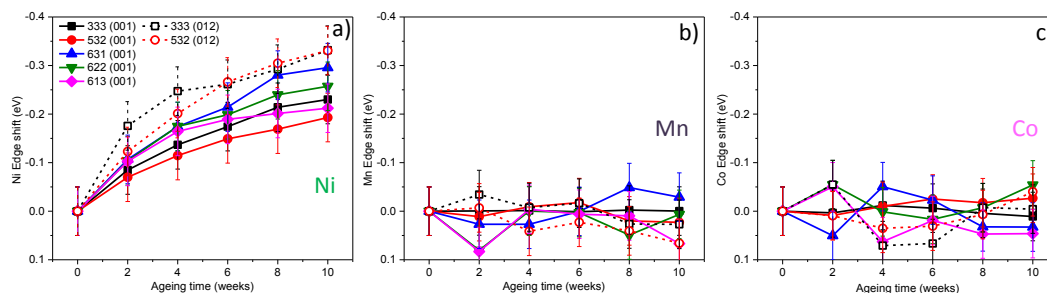


Figure II.3.B.3 K-edge energy shift of a) Ni, b) Mn and c) Co as a function of aging time in chemically-delithiated NMCs.

Using the *K*-edge reference spectra collected on $\text{Ni}^{+2/+3/+4}$ oxides, Ni oxidation state in each sample was estimated. Assuming no other processes contribute to transition metal (TM) reduction, the associated extent of particle re-lithiation can be estimated. The calculated amount of re-inserted Li, and the rate of re-lithiation as a function of aging time, shows that after 10 weeks the re-inserted Li content ranged from 0.03 to 0.09 per formula unit of NMC, depending on the type of surface and content of Ni in the sample. A similar trend was observed on the re-lithiation rate which decelerates with aging time.

Systematic Studies of NMC Coatings The effect of NMC metal ratios on surface and bulk composition, morphology, and electrochemical performance for aluminum coated and doped samples was studied with NMC-532, 622, and 811 with coatings prepared by different synthesis techniques, varying aluminum contents, and annealing temperatures. Surface elemental distributions, local chemical and atomic structures, surface species, and bulk changes were examined by SEM, TEM, XRD, and solid-state nuclear magnetic resonance spectroscopy (NMR). Results show that with compositional change from 532 to 811, the Al_2O_3 coatings begin to diffuse into the bulk on high-temperature annealing due to Al compatibility with Ni-rich materials (Figure II.3.B.4). ^{27}Al NMR data showed formation of a surface LiAlO_2 phase for all compositions when annealing temperatures increased to 800°C . The diffusion of Al into the lattice was found to negatively affect

electrochemical performance, indicating the importance of compatibility between surface coatings and bulk oxides.

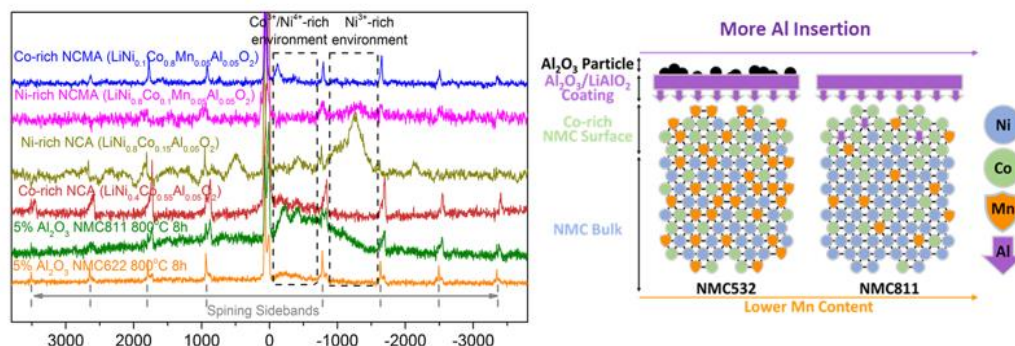


Figure II.3.B.4 (Right) ^{27}Al NMR spectra of 5 wt.% Al_2O_3 -coated NMC-622 and 811 annealed at 800°C for 8h, compared to Co-rich NCA, Ni-rich NCA and NCMA, and Co-rich NCMA. (Left) scheme of the evolution of surface coating.

The effect of the different surface treatment conditions on interphase chemistry, composition, local environment, and morphology was studied on NMC-532 with variable weight % of Al-nitrate and Al-isopropoxide as aluminum sources and ethanol, methanol, and xylene as solvents. Previous studies (see FY17 HE/HV Annual Report) showed that aqueous processing results in a measureable amount of ion exchange between surface-lithium cations and protons. Non-aqueously coated samples were annealed at 400°C and 800°C to study the temperature effect on coating composition and electrochemical performance. After visiting almost 40 different surface treatment routes, the combined structural electrochemical characterization results, performed on both half cells and full cells, showed that improvements in electrochemical performance could be obtained if the optimization of coating technique was undertaken separately for each cathode composition. Results show that surface-lithium content after annealing is indeed influenced by choice of solvent (Figure II.3.B.5) and that particle morphologies are altered when changing both solvent and aluminum precursor; ultimately affecting electrochemical performance.

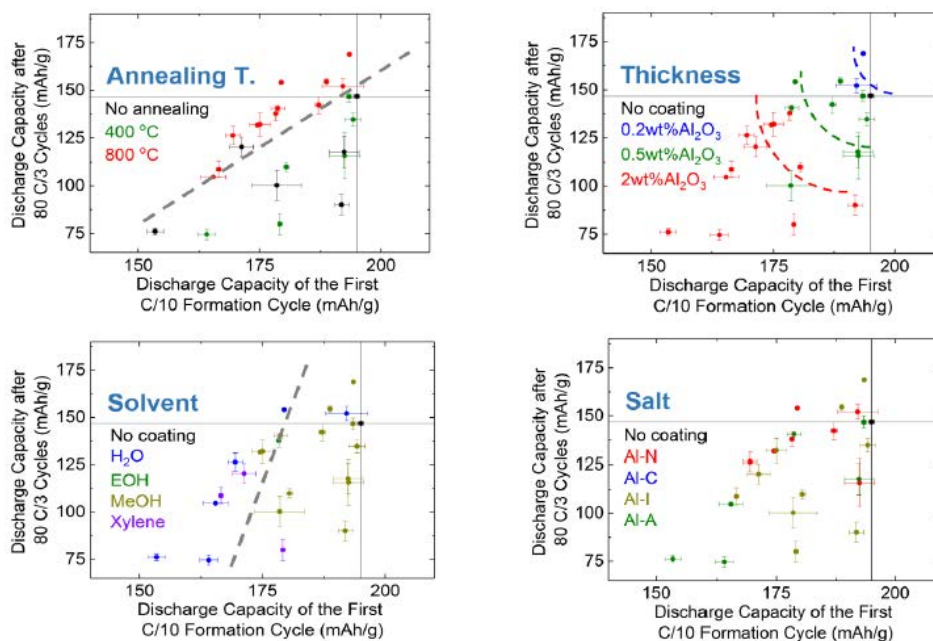


Figure II.3.B.5 Summary of effects of different surface treatment conditions on electrochemical performance.

The optimized Al-based coating strategy was applied to NMC-532 for both aqueous and non-aqueous samples, made into electrodes by CAMP researchers, and studied in full-cell electrochemical tests with capacity-matched graphite-based anodes, with and without the addition of the optimized electrolyte additive TMSPi studied by the electrolyte thrust. As shown in Figure II.3.B.6, these Al-based coatings show moderate improvements in fade rate and impedance over the untreated baseline. The data herein demonstrate the critical need for similar, systematic studies in the search for new coating materials. Such studies should be focused on a fundamental understanding of cathode-specific design criteria, as presented herein, with respect to protecting cathode interfaces at high operating voltages.

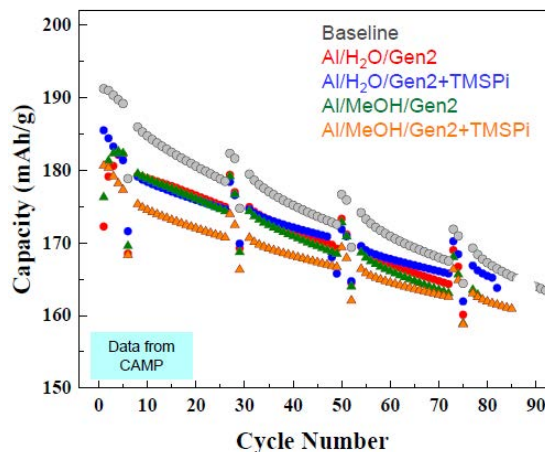


Figure II.3.B.6 Electrochemical performance of baseline NMC-532 with optimized coatings as per Figure II.3.B.5

Thin Film Cathodes: NMC thin films can be very useful in identifying the chemistry of the cathode-electrolyte interface (CEI) which is normally hidden in laminated composite electrodes by the spectroscopic signals arising from the components. For instance, carbon black, despite being less than a few percent of the electrode composition, makes up almost 90% of the surface area of the electrode. Due to this high fraction of the surface area it is difficult to separate reactions occurring on the cathode material from reactions on the carbon. This work was focused on developing thin film electrodes free from carbon. The advantage of this approach is that only study the CEI reaction on the electrode itself will be studied. Furthermore, in a planar configuration the cathode can be investigated and analytically evaluated using impedance spectroscopy because it is free of pores and capacitive effects which influence data analysis.

Heterostructure thin films were prepared by sequential DC magnetron sputtering of Co, Pt, Au, or Cr targets and RF magnetron sputtering of in-house made ceramic targets. The relative Li content of all the films decreased after annealing (700°C, 1hr) due to Li sublimation. This was mitigated by using a 60% Li excess target to make an NMC-622 film. The best performing electrodes were prepared by DC sputtering 20 nm of Co on both sides of the alumina wafer followed by 500 nm of Pt on top of the Co layer. This cobalt layer was critical to the formation of the electrodes.

Cycling data for the thin films and composite material are shown in Figure II.3.B.7 for a voltage window of 2.5 – 4.2 V vs. Li/Li⁺. A typical cycle at 10 mA/g (C/20) demonstrates poorly defined voltage plateaus for films on a thin (200 nm) layer of Pt (shown in blue in Figure II.3.B.7a, magnified by 10 for clarity). A somewhat improved specific discharge capacity of 78 mAh/g can be achieved with films on a thicker (1500 nm) layer of Pt, but the discharge plateau remains sloping and unresolved (Figure II.3.B.7a). The addition of a Co interlayer enables the NMC-622 films to match the voltage plateaus of the composite electrode material and greatly improves the specific discharge capacity to 118 mAh/g. Redox peaks are more apparent in the differential capacity plot, with both the composite cell and thin film on Pt:Co:Al₂O₃ having a primary peak at around 3.7 V (Ni^{2+/3+} oxidation) (Figure II.3.B.7b). A secondary peak around 3.75 V has been assigned to the Ni^{3+/4+} oxidation step.

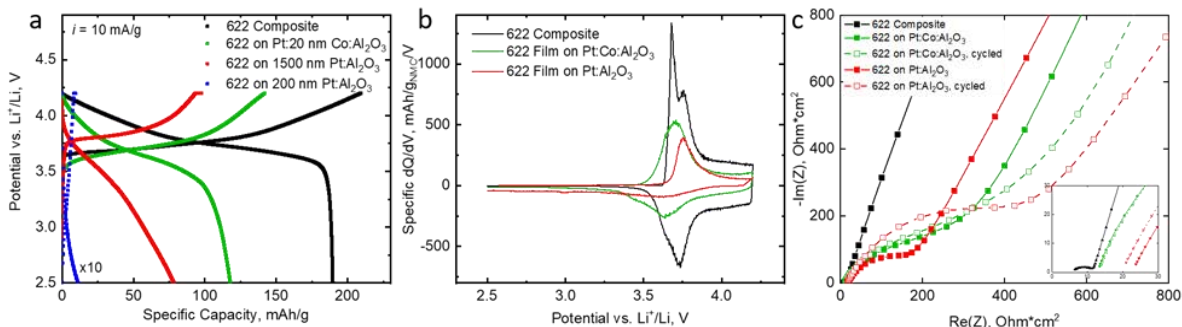


Figure II.3.B.7 Electrochemical performance comparison of baseline with optimized cathodes.

Conclusions

The effect of the NMC particle surface facet was demonstrated by its reactivity with the liquid electrolyte. On charged Ni-rich NMC cathodes, nickel cations were found to be the only constituent that was reduced on extended exposure to electrolyte, which was used to quantify the side reactions at high voltages. Kinetic data showed that the reduction was time dependent, an indication that diffusion and access to the organic electrolyte components were critical.

A better understanding of the effects of coating techniques, heat treatment conditions, and TM composition of cathodes on battery performance was developed. In addition, the TM (Ni, Mn, Co) composition of cathodes was shown to heavily influence coating-based, surface-dopant mobility based on cation ordering and local magnetic effects, which, in turn influenced cathode performance. A systematic study of the surface lithium content, interphase composition, and the electrochemical performance of coated NMC cathodes, with changing cathode composition and coating processes, was completed. The study demonstrated that the effectiveness of surface coating layers was highest for those created using non-aqueous methods.

Thin film NMC-622 electrodes were synthesized and contrasted against a standard composite electrode of the same active material. Crystalline orientation was influenced by the addition of a Co substrate under-layer, resulting in more facile Li^+ diffusion. Electrochemical performance of the thin film electrodes was comparable to that of the composite electrode and are suitable for surface studies of CEI layers.

Key Publications

1. Binghong Han, B. Key, S. Lapidus, J. Garcia, H. Iddir, J. Vaughey, F. Dogan. "From Coating to Dopant: How the Transition Metal Composition Affects Alumina Coatings on Ni-rich Cathodes." *ACS Applied Materials & Interfaces* 9, 2017: 41291-41302
2. B Han, AR Dunlop, SE Trask, B Key, JT Vaughey, F Dogan, Tailoring Alumina Based Interphases on Lithium Ion Cathodes, *Journal of The Electrochemical Society* 2018 165 (14), A3275-A3283
3. G. Chen, "Achieving Higher Energy in Lithium-Ion Battery Cathodes," 2018 International Battery Seminar & Exhibit, Fort Lauderdale, FL, March 2018 (invited).
4. J. Zhu and G. Chen, "Advanced High-energy Cathode Materials for Lithium-ion Batteries," 2017 Bay Area Battery Summit, Livermore, CA, November 2017.
5. B. Han, C. Peebles, T. Paulauskas, J.T.Vaughey, F. Dogan, Characterization of Al_2O_3 Coatings on Li-ion Cathodes: Effects of Annealing Temperature and Composition, 2017 MRS, Phoenix, April 17th (2017).
6. Han, Binghong, Baris Key, Saul Lapidus, Juan Garcia, Hakim Iddir, John Vaughey and Fulya Dogan. "Investigation of Al_2O_3 Wet-Chemical Coatings on Cathode Materials of Lithium-ion Batteries." 233rd Electrochemical Society Meeting, Seattle, WA US, May 13, 2018 - May 17, 2018.

7. Binghong Han, B. Key, S. Lapidus, J. Garcia, H. Iddir, J. Vaughey, F. Dogan. "From Coating to Dopant: How the Transition Metal Composition Affects Alumina Coatings on Ni-rich Cathodes" 256th American Chemical Society National Meeting and Exposition, Boston, MA US, August 19, 2018 - August 23, 2018.

Acknowledgements

Chapter Acknowledgments B. Han, A. Tornheim, J. Zhang, R. Sahore, I. Bloom, A. Dunlop, S. Trask, N., J.R. Croy, Phillip, G. Veith, J. Zhu, G. Chen, F. Dogan, J. Vaughey

II.3.C Theory and Modeling (ANL, LBNL, ORNL)

Hakim Iddir, Principal Investigator

Argonne National Laboratory
9700 S. Cass Avenue
Lemont, IL 46039
E-mail: iddir@anl.gov

Peter Faguy, DOE Technology Development Manager

U.S. Department of Energy
E-mail: Peter.Faguy@ee.doe.gov

Start Date: October 1, 2014 End Date: September 30, 2018
Project Funding (FY18): \$4,000,000 DOE share: \$4,000,000 Non-DOE share: \$0

Project Introduction

The inability to charge commercially available $\text{Li}_{1+x}\text{Ni}_a\text{Mn}_b\text{Co}_c\text{O}_2$ (NMC-abc, where x is typically <0.05), cathode materials beyond ~ 4.3 V (vs. graphite) without incurring excessive surface damage, electrolyte decomposition, structural instabilities, gassing, and loss of lithium inventory is a significant challenge in meeting next-generation energy storage targets. This project aims to understand the underlying failure mechanisms associated with these issues that prevent state-of-the-art Li-ion battery systems from achieving higher practical energy densities than are currently obtainable. To do so, a more complete description of the atomic-level structure and reactivity of NMC surfaces are needed. This report is divided into two major sections. The first section covers atomistic modeling focused on understanding material surfaces, particle shapes, material-coating interfaces, and material surface-electrolyte and additive interactions. The second section presents electrochemical modeling studies at the cell level.

Objectives

- Determination of surface structures and driving forces for surface elemental segregation
- Theoretical predictions of electrolyte- and additive-NMC surface interactions
- Effect of transition metal (TM) composition on the synthesis of Al_2O_3 -based NMC coatings
- Screen for potential dopants that can stabilize the surface at high delithiation levels
- Understand the effects of side reactions and electrode cross-talk through electrochemical modeling

Approach

The goals of this project will be accomplished through atomistic and electrochemical. All atomistic calculations were carried out by spin-polarized density functional theory (DFT) as implemented in the Vienna Ab Initio Simulation Package (VASP). The exchange-correlation potentials are treated by the generalized gradient approximation (GGA) parametrized by Perdew, Burke, and Ernzerhof (PBE). The interaction between valence electrons and ion cores is described by the projected augmented wave (PAW) method. Furthermore, the GGA+U scheme is used for applying the on-site correlation effects among 3d electrons of the TMs, where the parameter of (U-J) is set to 5.96 eV, 5.00 eV, and 4.84 eV for Ni, Co, and Mn, respectively. The wave functions were expanded in the plane wave basis up to a kinetic energy of 500 eV. All surface calculations were performed using a periodically repeating slab separated by vacuum layers along the surface normal. A vacuum thickness of 10 Å was adopted to remove interaction between the slab layers. The lattice parameter of the supercell was fixed at its bulk value. All ions were allowed to relax until the total energy differences were no more than 0.003 eV. After geometry optimization within the DFT+U framework,

electronic relaxation was performed using a single point calculation with the hybrid functional HSE06 to determine the surface energy at that level of theory.

NMC-111 is used as a model material because the TM-layer, ionic configuration is known. A k-point mesh of $3 \times 3 \times 3$ was found sufficient to get accurate electronic energies for bulk calculations on this unit cell. Each ion has six neighbors consisting of groups of the three other TMs arranged in a triangular shape. This ordering was found to be the most favorable using solid state NMR. This structure was also confirmed by DFT calculations of an initial set of 30 lowest energy configurations determined based on electrostatic interactions only.

Adsorption and reaction energies (ΔE) were calculated using the following expression:

$$\Delta E = E_{\text{surf+adsorbate}} - E_{\text{surf}} - E_{\text{adsorbate}} \quad (1)$$

Where $E_{\text{adsorbate}}$ is the energy of the isolated molecule in the vacuum, E_{surf} is the energy of the bare slab, and $E_{\text{surf+adsorbate}}$ is the total energy of the molecule adsorbed on the slab. Bulk solvent effects were accounted for by using an implicit solvation model as implemented in the DFT code VASP. Calculations of reactions in solution were performed with the Gaussian 09 implementation of DFT at the B3LYP/6-31+G(d,p) level of theory. Frequency calculations were performed for all structures in order to determine the nature of the stationary points. The ultrafine integration grid was employed in all calculations.

Results

Effect of dopants on NMC surface reactivity: This work focuses on the segregation of dopants in NMC and its effect on surface reactivity. A screening of several dopants substituting several TMs in a NMC-111 matrix was performed. For each substitution three different sites were tested: Bulk, surface, and subsurface layer. For each configuration the formation energy of an oxygen vacancy was computed as a proxy of surface reactivity. Figure II.3.C.1 summarizes the trend in segregation; more negative values indicate a larger thermodynamic driving force for surface segregation. Figure II.3.C.1b summarizes the trend in surface reactivity for several dopants, more negative values indicate a more reactive surface. The ideal dopant should hence preferentially segregate to the surface and reduce the oxygen vacancy formation energy, such as Fe and V. The screening of dopants is ongoing to aid the development of next-generation, high-energy cathode materials.

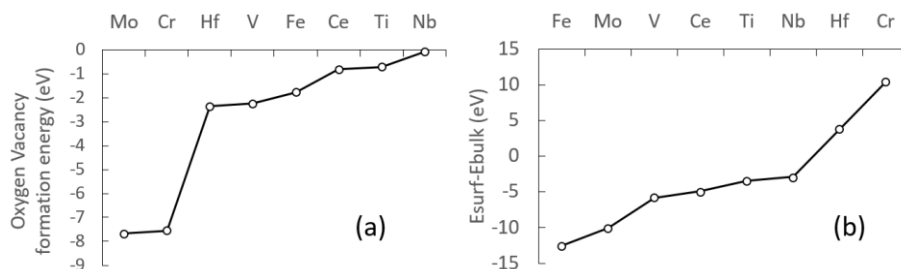


Figure II.3.C.1 (a) Segregation trend for dopants in NMC-111. (b) Reactivity trend for dopants in NMC-111.

Insights on TM dissolution: The presence of Lithium acetylacetonate (Liacac) in the electrolyte solvent was observed to dramatically change TM dissolution trends (Figure II.3.C.2). Liacac is able to form complexes with the three TMs of NMC. The strength and configuration of such complexes can explain the increased Mn dissolution compared to other additives such as TTFP or TMPSI. Stable $\text{TM}(\text{acac})_2$ complexes were found for Ni, Co and Mn. $\text{TM}(\text{acac})_3$ complexes are only stable for Ni and Co, with $\text{TM}(\text{acac})_3$ complexes being more stable than $\text{TM}(\text{acac})_2$. This could explain the increased Co dissolution with Liacac (Co^{3+}). The increased Mn dissolution with Liacac can be explained by the formation of not only Mn^{2+} complexes (conventional dissolution mechanisms), but also via Mn-oxo complexes (Mn^{4+}). TM-oxo complexes paths are hindered for Ni and Co due to the “oxo wall”. The $\text{MnO}(\text{acac})_2$ complex was found to be stable in an implicit solvent model. However, the Mn-oxo complex reacts in the presence of an explicit ethyl carbonate molecule, producing an oxidized electrolyte molecule and a $\text{Mn}(\text{acac})_2$ complex. TTFP can be oxidized to the phosphate TTFPa via the formation of a P-O bond, taking oxygen directly from the surface of the cathode and reducing

the TM at the surface. Hence, in the charged state TTFP oxidation would preferentially reduce Ni ions, which explains the increased Ni content in the solution.

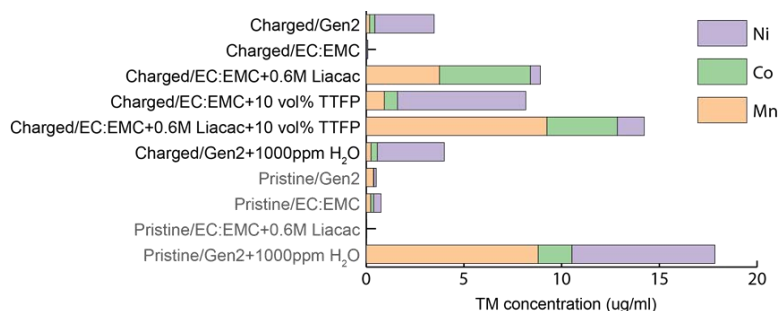


Figure II.3.C.2 (a) Dissolution concentrations in the electrolyte for different additives, electrolytes, and states of charge.

Facet-dependent elemental segregation: Experimental results based on high-resolution electron microscopy and electron energy loss spectroscopy have shown a preferential elemental segregation of Co to (104) facets in NMC-442, and Ni segregation to the (012) facets. DFT calculations from this project show that Co segregation to (104) is driven by the gain in surface energy resulting from intermediate Co spin states at the surface. The reduction of surface energy with increased Co concentration is due to a change in the occupation and energy levels of the t_{2g} and e_g orbitals of Co in the new pyramidal configuration, compared to the low spin octahedron configuration of Co in the bulk. Ni segregation to the (012) facet however, cannot be explained using the crystal field energy stabilization argument used for Co. It was found that Li-Ni exchange, energetically favored near the surface, is instead at the origin of such segregation. Higher Ni (Li-Ni anti-sites) concentrations near the surface would form a spinel-like reconstruction layer, such as over-lithiated $\text{Li}_2\text{M}_2\text{O}_4$ phases. This surface reconstruction layer (SRL) is further stabilized by the strain resulting from the NMC lattice.

Figure II.3.C.3a shows the total energy of the system as a function of the strain applied to the SRL. The unstrained phases lie at a c lattice fraction equal to 1. The SRL is considered a thin film that is allowed to relax in the direction perpendicular to the surface. This film shrinks in the direction perpendicular to the surface in response to the applied tensile strain, stabilizing the spinel phase with respect to the layered counterpart.

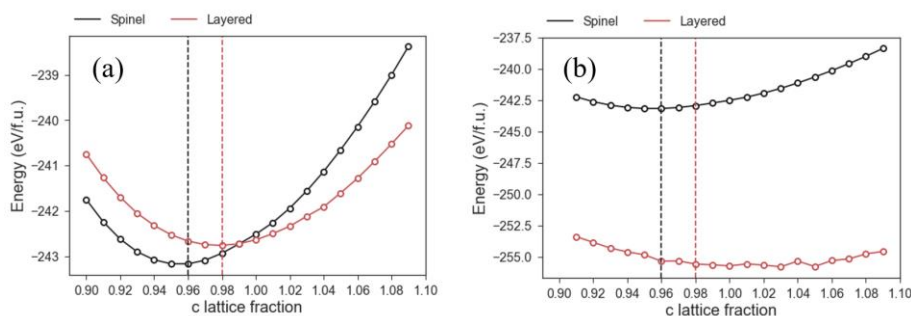


Figure II.3.C.3 Formation energy as a function of c -direction expansion for pinned (a) $\text{Li}_2\text{Ni}_2\text{O}_4$ and (b) $\text{Li}_2\text{Co}_2\text{O}_4$ spinels on a NMC-111 (012) facet.

Phosphorus-containing additives on NMC: DFT simulations were performed to investigate the interactions between electrolyte additive molecules and NMC cathode surfaces. A state of charge corresponding to 75% delithiation was used to model a high-voltage state. To build confidence in the molecule-surface model, an initial TMSPi molecule-surface configuration, followed by ab-initio molecular dynamic simulations at 700K for a few pico-seconds, was used to explore a wider set of configurations (local minima) and locate the most likely configuration with the lowest energy state. Further energy minimization was performed at the GGA+U level using the steepest descent to obtain the lowest energy for the molecule-surface configuration.

Figure II.3.C.4 shows the adsorption configurations and their corresponding energies for TMSPi and a representative TMSPi decomposition product. TMSPi presents a very low adsorption energy $E_{ads} = -0.08\text{eV}$ which is evidence of a weak interaction. The phosphorus atom in the phosphite is sterically hindered from reaching the oxygen atoms at the surface (Figure II.3.C.4a). The tris(methylsilyl) groups do not form any bonds with the surface. Hence, the formation of a stable film composed of TMSPi on the surface is unlikely. One of the TMSPi decomposition pathways requires the reaction with HF or PF₅. Such reactions can proceed with the O-Si bond breaking pathway or the O-P bond breaking pathway. Previous work showed that the preferred pathway is the O-Si bond breaking to produce (TMSO)₂POH, consistent with the calculations. Nevertheless, the products of the O-P bond breaking (TMSO)₂PF may also be in equilibrium in the complex mixture generated by the multiple reaction system. Hence, products such as (TMSO)₂PO⁻ species can also adsorb on the surface. The adsorption energy of this molecule on the (012) surface of NMC is -1.2eV (see Figure II.3.C.4b), indicating a thermodynamically favorable chemisorption process. In this case, the molecule forms a phosphate specie, with an oxygen atom from the surface. The single bond formed between the phosphorus atom from the phosphite group and the oxygen atom from the surface is strong enough to keep the molecule on the surface, providing the desired surface passivation.

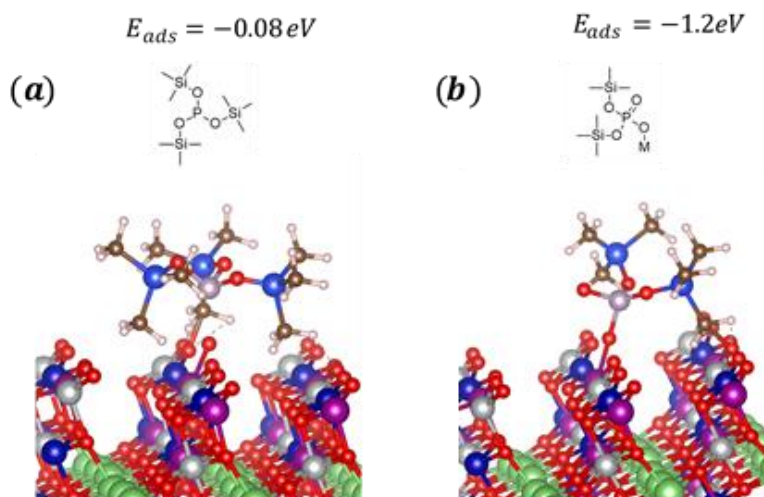


Figure II.3.C.4 Adsorption configuration on partially delithiated NMC-111 of (a) TMSPi and (b) TMSPi decomposed by Si-O bond breaking pathway. Silver, blue, purple, green, light blue, gray, brown, white and small red spheres represent Ni, Co, Mn, Li, Si, P, C, H and O, respectively.

Further aging of the TMSPi additive (beyond 3 weeks) allows for its reaction with HF or PF₅ to proceed all the way to forming PF₃ or P(OH)₃ compounds. Calculations show that there is a strong interaction of PF₃ and P(OH)₃ molecules with the surface of a charged cathode (75% delithiation level), to form stable, free phosphate or fluoride molecules by removing an oxygen atom from the NMC surface. An oxygen vacancy is hence produced during this process leaving two unpaired electrons in the lattice, and reducing the surface TMs. Table II.3.C.1 shows the computed adsorption energies for TMSPi and several of its decomposition products on NMC. Removal of oxygen atoms from the surface would be detrimental to the impedance rise and in general to the electrochemical performance of the cell, as it could increase metal dissolution and surface reconstruction. Thus, the passivation of the surface is possible only when specific TMSPi derivatives are present; derivatives that are produced during a specific aging timeframe.

Table II.3.C.1 Adsorption/reaction energies of select phosphorous-containing additives and decomposition products on the partially (25% Li content) delithiated (012) NMC surface.

Molecule	Adsorption/reaction Energy (eV)
TMSPi (adsorption)	-0.08
tris(trimethyl)phosphate TMSPa (adsorption)	0.15
(TMSO) ₂ PO ⁻ (adsorption)	-1.20
TMSOPF ₂ (adsorption)	-1.26
TMSOP(OH) ₂ (adsorption)	-1.28
TTFPi (adsorption)	-0.04
TTFPi (oxidation → TTFPa)	-3.1
TTFPi (H abstraction)	0.08
(OCH ₂ CF ₃) ₂ PO ⁻ (adsorption)	-1.28
TEPi (oxidation → TEPa)	-3.8
TEPi (H abstraction)	-0.02
TEPa (H abstraction)	-0.24

For an intermediate aging time, the TMSPi molecule would probably be completely consumed: One, two or three phosphite branch scission products would compose the solution mix. Note however, that the HF scavenging effect of the “fresh” TMSPi and its first derivatives (not PF₃ for instance) remains active as it has been documented previously, and hence fresh TMSPi would still be beneficial to the performance of the cell.

Contrary to TMSPi, similar calculations show that TEPi readily oxidizes to TEPa (Table II.3.C.1). However, it does not form a passivation film on the positive electrode, given the weak binding energy between TEPa and the surface. The steric effect may explain the differences between TMSPi and TEPi. For TMSPi, scission of the TMS groups leaves behind a smaller P-O structure that easily attaches to the oxide surface. For TEPi, the phosphorous center is able to reach an oxygen atom from the surface leading to the formation of the stable phosphate TEPa. Another possible reaction of TEPi is the abstraction of an oxygen atom from its alkyl group. However, the reaction energy of -0.02eV indicates this process, although possible, is thermodynamically less favorable than the reaction with the surface oxygen. Another additive considered in this study was TTFPi. H abstraction from TTFPi is not thermodynamically favorable (see Table II.3.C.1). On the pristine NMC surface, The CF₃ groups from TTFPi do not bind to any Li, TM or oxygen atom. However, a strong interaction is observed when 75% of the lithium is removed from the cathode. A stable free phosphate molecule is produced by the removal of an oxygen atom from the surface, reducing the surface TMs. Based on the TMSPi aging results, one would also consider investigating a derivative of TTFPi, such as ((OCH₂CF₃)₂PO⁻) that would be formed by cleaving one of the CH₂CF₃ groups from the TTFPi molecule. Indeed, subsequent calculations show that such a derivative would also produce a stable phosphate bound to the surface oxygen.

Fluorinated vs. non-fluorinated electrolytes: DFT calculations were used to estimate the interaction of the fluorinated and non-fluorinated solvent molecules with the NMC surfaces for several compositions, namely, NMC-532, NMC-622, and NMC-811. Table II.3.C.2 summarizes the adsorption energy of the fluorinated and non-fluorinated electrolyte molecules, for the lowest energy configurations of the potential energy surface. EC adsorbs strongly to the surface of the NMC-532. The negative adsorption energy denotes an exothermic process. The adsorption is even stronger on a delithiated surface and the molecule proceeds readily through a barrier-less H-abstraction process, producing an intermediate radical. This radical is highly reactive, for example in the presence of an alkene the intermediate polymerizes until a termination step is provided.

Table II.3.C.2 Adsorption energies (eV) of fluorinated and non-fluorinated electrolyte molecules on the (012) surface of NMC materials

Li content (%)	NMC-532				NMC-622		NMC-811	
	EC	FEC	DFEC	HFDC	EC	DFEC	EC	DFEC
100	-0.72	-0.11	0.02	-0.01	-0.71	0.06	-0.81	-0.02
75	-1.35	-0.16	-0.12	-0.05	-	-	-	-
50	-1.79	-0.19	-0.16	-0.08	-	-	-	-
25	-1.96	-0.33	-0.22	-0.12	-1.99	-0.19	-2.03	-0.27

The EC-surface interaction on NMC-622 has values of adsorption energies ranging from -0.71 to -1.99eV, which are similar to the energies on NMC-532. However, the interaction of EC with 811 produces a slightly more favorable oxidation process ranging from -0.81 to -2.03eV (see Table II.3.C.2). The differences in adsorption/reaction energies between the different NMC compositions are small but reveal a clear trend with Ni content.

Contrary to the non-fluorinated electrolytes, the fluorinated compositions FEC, DFEC, and HFDEC present weaker interactions with the NMC surfaces. FEC presents the strongest interaction among the fluorinated species with adsorption energies ranging from -0.11 for the lithiated material to -0.33eV for the 75% delithiated material. These values are much smaller than that for EC and no decomposition of the fluorinated compositions was observed. Therefore, the fluorinated molecules do not react with either the lithiated surface nor the partially delithiated surface. There is no charge transfer during this interaction and, hence, no TM metal reduction is expected. Less damage to the cathode surface is expected for the fluorinated electrolytes compared to the non-fluorinated counterpart.

Alumina-NMC interface: A slab model was used for the (012) surface (Figure II.C.3.6a) consisting of 5 layers of NMC-111 and two layers of α -LiAlO₂ on each side of the slab (symmetric). This configuration was chosen because α -LiAlO₂ is isomorphic with NMC. In order to model the system, a disordered α -LiAlO₂ phase was built as this can be considered as a precursor to a phase transformation to γ -LiAlO₂. The interface energy (E_i) between the LiAlO₂ layer and the NMC part of the material was computed as:

$$E_i = E_{LiAlO_2-surface} + E_{NMC-bulk} - E_{NMC-LiAlO_2}$$

Where $E_{LiAlO_2-surface}$ is the energy of a LiAlO₂ slab, $E_{NMC-bulk}$ is the energy of a bulk NMC-111 model with the same number of unit cells as the slab model, and $E_{NMC-LiAlO_2}$ is the energy of the NMC slab surface with a LiAlO₂ coating film. Figure II.3.C.5 shows the change in the interface energy with the thickness of the α -LiAlO₂ region layer. The energy decreases with the increase of the α -LiAlO₂ thickness. This result indicates that beyond a limited thickness (~4 atomic layers) of the α -LiAlO₂ phase, a different phase, such as the γ -LiAlO₂, could form on top of the α -LiAlO₂ phase. The modeling results, predict the formation of an interfacial α -LiAlO₂ buffer layer between NMC and a different phase, such as γ -LiAlO₂.

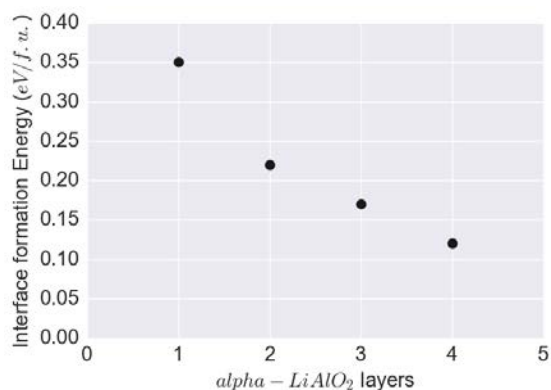


Figure II.3.C.5 Change of NMC/LiAlO₂ interface formation energy with the thickness of α -LiAlO₂ layer sandwiched between NMC and a disordered LiAlO₂ phase

The ion ordering within the TM layer of NMC-111 is shown in Figure II.3.C.6b. This configuration allows the simulation of different environments around Al. Different transition metal cations (from NMC) are swapped with Al from the surface LiAlO₂ layers. The only thermodynamically favorable configuration is the interchange of Al with Mn as shown in Figure II.3.C.6c. In this configuration: Ni and Co exclusively surrounds Al, while the second nearest neighbors within the TM layer maintain the NMC-111 configuration. All the configurations with Mn as a first neighbor (to Al) produce a positive change in energy with respect to the reference configuration (Figure II.3.C.6 d and e). This result shows that Al prefers to be surrounded by Co and Ni cations (not Mn) in the TM layers of NMC. The existence of Mn in the TM layer can therefore greatly block the diffusion of Al from the surface to the bulk of the NMC particles, as shown by NMR studies (see [II.C.2](#) report).

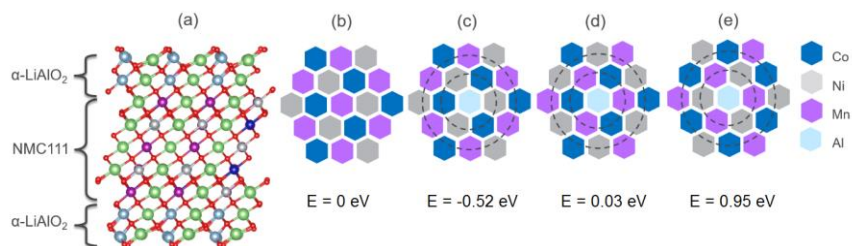


Figure II.3.C.6 (a) Model slab for the (012) NMC-111 surface coated with 2 layers of α -LiAlO₂. Light blue spheres represent Al, green-Li, purple-Mn, blue-Co, silver-Ni, and red-O. (b) TM layer configuration for NMC-111, (c) Al swapped with Mn, (d) Al swapped with Ni, (e) Al swapped with Co. The dashed circles represent the first and second nearest neighbors to Al atoms. The values of energy at the bottom of panels (c) to (e) represent the thermodynamic energy change after swapping Al from the surface layer with different TM centers in the bulk of NMC-111.

Electrochemical Modeling

Electrochemical modeling is aimed at associating electrochemical performance measurements with diagnostic studies conducted on lithium-ion cells. Essentially, continuum based transport equations are combined with kinetic and thermodynamic expressions to allow the potential, concentration, and current distributions to be determined throughout the cell. The focus this year is continuing on side reactions and cross-talk in lithium-ion cells. As described previously, a series of constant high-voltage hold current relaxation studies on NMC//Gr, Li, an LTO standard, reference electrode, special coin, and pouch cells were conducted over a wide range of voltages and conditions [7], [8], [9]. Most noteworthy from these studies, is the long relaxation time constant of 10s of hours and the final $\mu\text{A}/\text{cm}^2$ level currents. The reproducibility of long time current relaxation studies within this program, including a recent study involving successive voltage holds with limited cycling between holds [9], may lead one to expect the process to be governed by a single phenomenon. As described below, a

number of modeling studies this year indicate that the relaxation current levels result from a combination of multiple side reactions.

Several conclusions can be made from earlier modeling studies. Specifically, all time constants associated with the main cell reaction are on the order of hours or less. In addition, edge effects from using an oversized negative cannot account for the long time constant. Further, if lithium is consumed at a $\mu\text{A}/\text{cm}^2$ current in these NMC//Gr cells, then most the capacity would be gone in 1000 hours. Because the negative open circuit voltage is relatively flat, the hold current at long times is equal to the side reactions at the positive in NMC//Gr, Li, or LTO cells. Finally, a current on the order of $0.1 \mu\text{A}/\text{cm}^2$ for the solvent reduction side reaction on the negative can be estimated for NMC//Gr cells cycled between 4.25 and 3.0 V [10].

As shown in Figure II.3.C.7, applying a simple solvent (E) reaction film (F) or SEI growth model on the positive gives a surprisingly good fit of representative NMC//Gr current relaxation data, especially for times greater than 40 hours. However, the model results in final positive SEI thickness being greater 100 nm and, assuming complete reaction of the side reaction product (R^+) at the negative, will reduce lithium by 0.2 mAh/cm². Neither result is supported by experimental observations.

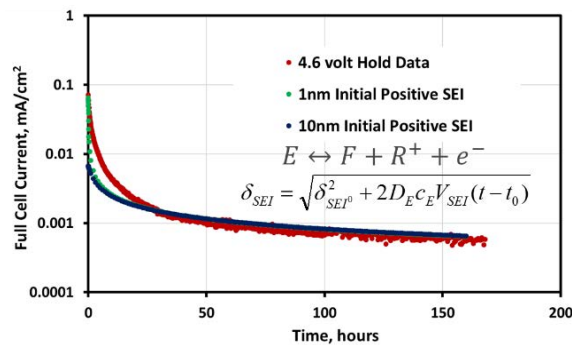


Figure II.3.C.7 Positive SEI growth model compared to a 4.6 V hold on NMC//Gr coin cell at room temperature.

The simple positive SEI growth model was expanded to include cross-talk of reaction products and negative electrode side reactions as shown in Figure II.3.C.8. In the model, the long time constant for the current relaxation is generally associated with a slow change in the concentration of the side reaction products (R and R^+) and most of the cell current goes into the cross-talk redox reactions of the side reaction products. The SEI generation reactions are at least an order of magnitude lower than the cross-talk reactions. Therefore, most of current goes into redox of side reactants (i.e., R cross-talk reactions) and not SEI growth that affects the cyclable lithium. Multiple side reactions are needed to improve the fit (i.e. R_1, R_2, R_3, \dots).

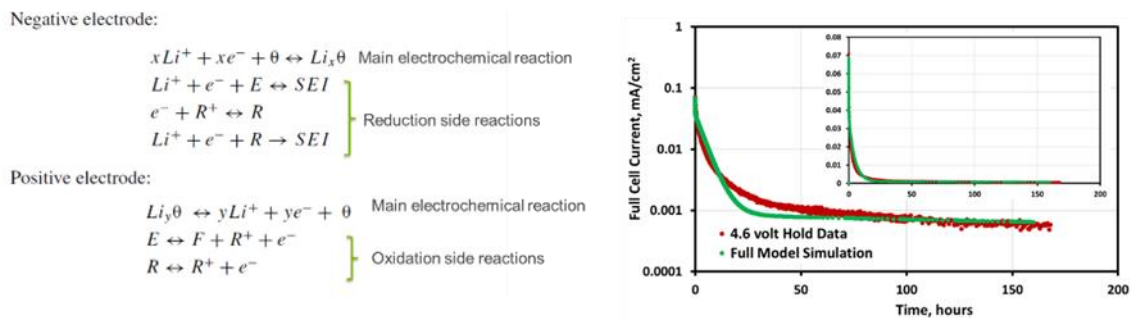


Figure II.3.C.8 Left: Proposed side reaction mechanism from reference 1. Right: Full electrochemical model compared to 4.6 V hold on NMC//Gr coin cell at room temperature.

The above model addresses much of the types of side reactions occurring in the cell, but does not address oxygen loss or TM dissolution that have been observed on the surface of the positive active material. As an initial step, an electrochemical model was developed with oxygen loss or TM dissolution side reactions on the

positive. The negative electrode side reactions included solvent reduction resulting in SEI growth and TM dissolution. It was further assumed that the TM dissolution was much slower than the oxygen loss. In order to support the relaxation cell current the oxygen depletion zone would need to be more than 10% of the bulk positive active material during the simulation, which is not supported by experimental observation.

This modeling effort suggests that the primary degradation reactions constitute only a fraction of the total observed relaxation current. Future efforts will continue to examine the impact of electrolyte stability and surface degradation reactions on electrode cross-talk and capacity retention. Existing models will be combined in a manner to retain salient features, have the ability to expand capabilities, and not add too much complexity. Further model calibration is needed, especially with new electrode materials as they become available.

Conclusions

DFT calculations have been used to provide a better understanding of the structure of NMC cathode surfaces. It was found that, in Gen2, EC preferentially oxidized relative to EMC via H abstraction and subsequent reduction of surface TMs. Conversely, select, fluorinated solvents (HFDEC, DFEC) were found to interact only weakly with the cathode surface. Oxidation of the phosphite additive molecule, TTFP, was found as a possible trigger to surface oxygen loss and phase transformation, whereas TMSPi, was found to decompose and create a passivating phosphate-based layer on the (012) surface. Interestingly, the use of a different phosphite molecule, TEPi, led to higher TM dissolution and impedance rise.

Studies on TM segregation have revealed a driving force for Co segregation to the (104) facet, while the observed tendency for Ni segregation to the (012) facet of some NMCs is found to be correlated to the increased tendency for Li/Ni ant-site defect formation near the surface. Surface reconstruction layers were found to be stabilized by the strain produced by pinning a spinel-like phase to an NMC (012) surface. However, the film must be thin enough with a capacity to release energy by changing the lattice spacing in the direction perpendicular to the surface.

Calculations of Al₂O₃-based coatings on NMCs suggest that an interfacial buffer, α -LiAlO₂ phase, between NMC surfaces and the bulk coating phase, could stabilize surface structures such as γ -LiAlO₂. In addition, substitution of Al into the surfaces of NMCs favors Al surrounded by Co and Ni (e.g., Mn/Al exchange).

Key Publications

1. Tornheim, A.; Sharifi-Asl, S.; Garcia, J. C.; Bareño, J.; Iddir, H.; Shahbazian-Yassar, R.; Zhang, Z. Effect of Electrolyte Composition on Rock Salt Surface Degradation in NMC Cathodes during High-Voltage Potentiostatic Holds. *Nano Energy* **2019**, *55*, 216–225.
2. Peebles, C.; Garcia, J.; Tornheim, A. P.; Sahore, R.; Bareño, J.; Liao, C.; Shkrob, I. A.; Iddir, H. H.; Abraham, D. P. Chemical “Pickling” of Phosphite Additives Mitigates Impedance Rise in Li Ion Batteries. *The Journal of Physical Chemistry C* **2018**.
3. Sahore, R.; Tornheim, A.; Peebles, C.; Garcia, J.; Dogan, F.; O’Hanlon, D. C.; Liao, C.; Iddir, H.; Zhang, Z.; Bareño, J.; et al. Methodology for Understanding Interactions between Electrolyte Additives and Cathodes: A Case of Tris(2,2,2-Trifluoroethyl) Phosphite Additive. *J. Mater. Chem. A* **2018**, *A6*, 198.
4. Han, B.; Key, B.; Lapidus, S. H.; Garcia, J. C.; Iddir, H.; Vaughey, J. T.; Dogan, F. From Coating to Dopant: How the T Composition Affects Alumina Coatings on Ni-Rich Cathodes. *ACS Appl. Mater. Interfaces* **2017**.
5. Tornheim, C. Peebles, J.A. Gilbert, R. Sahore, J.C. Garcia, J. Bareño, H. Iddir, C. Liao, D.P. Abraham, “Evaluating electrolyte additives for lithium-ion cells: A new Figure of Merit approach”, *J. Power Sources* **365C** (2017) pp. 201-209.

6. Peebles, R. Sahore, J.A. Gilbert, J.C. Garcia, A. Tornheim, J. Bareño, H. Iddir, C. Liao, D.P. Abraham, “Tris(trimethylsilyl) Phosphite (TMSPi) and Triethyl Phosphite (TEPi) as Additives for Lithium Ion Batteries: Mechanistic Insights into Differences during LiNi_{0.5}Mn_{0.3}Co_{0.2}O₂-Graphite Full Cell Cycling”, *J. Electrochem. Soc.* **164** (2017) A1579.
7. N. Vadivel, S. Ha, M. He, D. Dees, S. Trask, B. Polzin, and K. Gallagher, *J. Electrochem. Soc.*, **164** (2) (2017) 508.
8. A. Tornheim, S. Trask, and Z. Zhang, et al., *J. Electrochem. Soc.*, **163** (8) A1717-A1722 (2016)
9. M. Rodrigues, K. Kalaga, S. Trask, I. Shkrob, and D. Abraham, *J. Electrochem. Soc.*, **165** (9) A1697-A1705 (2018)
10. B. Long, S. Rinaldo, K. Gallagher, D. Dees, S. Trask, B. Polzin, A. Jansen, D. Abraham, I. Bloom, J. Bareño, and J. Croy, *J. Electrochem. Soc.*, **163** (14) (2016) A299.

Acknowledgements

Chapter Acknowledgments J. Garcia, H. Iddir, A. Tornheim, S. Sharifi-Al, J. Bareño, R. Shahbazian-Yassar, Z. Zhang, C. Peebles, R. Sahore, C. Liao, I.A. Shkrob, D.C. O’Hanlon, D.P. Abraham, J.A. Gilbert, F. Dogan, J.R. Croy, B. Han, B. Key, J.T. Vaughey, S.H. Lapidus, G. Chen, D. Dees.

II.3.D Studies on High Capacity Cathodes for Advanced Lithium-Ion (ORNL)

Jagjit Nanda, Principal Investigator

Oak Ridge National Laboratory
1 Bethel Valley Road
Oak Ridge, TN 37831-6124
E-mail: nandaj@ornl.gov

Peter Faguy, DOE Technology Development Manager

U.S. Department of Energy
E-mail: Peter.Faguy@ee.doe.gov

Start Date: October 1, 2017 End Date: September 30, 2018
Project Funding (FY18): \$400,000 DOE share: \$400,000 Non-DOE share: \$0

Project Introduction

The overall project goal is development of high energy density lithium-ion battery electrodes for EV and PHEV applications that meet and/or exceed the DOE energy density and life cycle targets based on the USDRIVE/USABC roadmap. Specifically, this project aims to mitigate the technical barriers associated with high voltage/high capacity cathodes, including lithium-rich transition metal (TM) based oxides and multi-lithium compositions such as $\text{Li}_2\text{M}_x^{\text{I}}\text{M}_{1-x}^{\text{II}}\text{O}_2$ and $\text{Li}_2\text{M}_x^{\text{I}}\text{M}_{1-x}^{\text{II}}\text{O}_3$ where M^{I} and M^{II} are TMs that may or may not include Ni, Mn, and/or Co. Major emphasis is placed on developing new materials modifications and synthetic approaches for stabilizing high voltage cathodes to enable reversible capacities in the range of 250 mAh/g at an average nominal voltage > 3.7 V vs. Li/Li^+ . Major technical barriers that will be addressed include (i) preventing the structural transitions during repeated electrochemical cycling, (ii) improving the oxidative stability at higher redox potential by addressing interfacial stability and (iii) reducing voltage hysteresis by improving kinetics and transport at the materials level. The cathode synthesis and optimization will utilize various advanced characterization and diagnostic methods at the electrode and/or cell level for studying cell and/or electrode degradation under abuse conditions. The techniques include electrochemical impedance spectroscopy, micro-Raman spectroscopy, aberration corrected electron microscopy combined with EELS, X-ray photoelectron spectroscopy, ICP-AES, X-ray absorption near edge spectroscopy (XANES), and X-ray and neutron diffraction (XRD and ND, respectively).

Objectives

1. Complete neutron powder diffraction, microstructural analysis and gas evolution studies of Li_2MoO_3 cathodes synthesized using solid state/sol-gel method as well as sputtered thin film electrodes with no binders and carbon. Evaluate and analyze oxygen stability between 4.3 – 4.8 V.
2. Synthesize and test the electrochemical performance of at least two composition of Mo-doped Ni-rich NMC composition. Initially Mo doping will be varied between 3 – 10 %.
3. Synthesize one particular class and composition of disorder composite cathodes with Li_2MoO_3 as a structural unit for stabilizing the NMC cathodes. Continue looking for stable phases with the compositional space $x\text{Li}_2\text{MoO}_3 \cdot (1-x)\text{LiMO}_2$; with $x = 0.2 - 0.4$ and $\text{M} = \text{Mn}, \text{Ni}, \text{Co}$.
4. Undertake structural and electrochemical performance analysis of disorder cathodes of few selected composition of $x\text{Li}_2\text{MoO}_3 \cdot (1-x)\text{LiMO}_2$ to gain a mechanistic understanding of the oxygen stability and the role of disorder.

Approach

We employ various synthesis routes including solid state, hydrothermal, solvothermal, and sol-gel reactions to produce cathode materials. The cathode compositions and phases are selected based on: (i) phase diagram

analysis and modeling from work by G. Ceder and others, (ii) thermal safety, and (iii) materials availability and cost. When appropriate, we utilize ORNL's expertise to produce thin film electrodes with these new chemistries. Thin film electrodes do not require polymer binders or conductive carbon additives and therefore facilitate our understanding of the intrinsic properties of the cathode material. We also have an active interest in developing coatings that can improve cathode properties such as conductivity or interfacial stability. For optimizing our cathode synthesis process and improving cell level performance, we correlate electrochemical properties with information obtained from advanced characterization methods including micro-Raman spectroscopy, mass spectrometry, microscopy, and X-ray and neutron diffraction.

Results

Synthesis and Structural Characterization of Composite $x\text{Li}_2\text{MoO}_3 \cdot (1-x)\text{LiNi}_{1/3}\text{Mn}_{1/3}\text{Co}_{1/3}\text{O}_2$ Cathodes

As we showed during FY17, the Li storage properties and excellent oxidative stability of Li_2MoO_3 make it a promising candidate as a structural stabilizer in composite $x\text{Li}_2\text{MoO}_3 \cdot (1-x)\text{LiMO}_2$ cathodes. As an initial investigation of these new materials, composite cathodes containing Li_2MoO_3 and $\text{LiNi}_{1/3}\text{Mn}_{1/3}\text{Co}_{1/3}\text{O}_2$ (NMC) subunits with $x = 0.10 - 0.15$ were prepared by ball-milling the two endmembers followed by heat treatment under Ar. The NMC powder used in the composites was synthesized via a sol-gel route and was phase-pure with R-3m symmetry (results not shown). The ball-milled composite consisted of separate Li_2MoO_3 and NMC phases with a cubic Li_3MoO_4 impurity phase (space group Fm-3m, present at ca. 5%) as determined from Rietveld refinement of neutron diffraction data (Figure II.3.D.1a). The presence of a multi-phase structure was confirmed by XRD data which showed splitting of the (0 0 3) reflection. A one-pot sol-gel synthesis route using metal acetate and ammonium molybdate precursors was also explored to prepare the Li_2MoO_3 -NMC composite. However, this approach resulted in over-oxidation of the Mo to the 6+ state (i.e., formation of Li_2MoO_4 , results not shown) and was thus not further explored. Figure II.3.D.1c compare the electrochemical properties of a baseline NMC cathode ($x = 0$) with that of composite cathodes ($x = 0.10$) prepared by ball-milling NMC and Li_2MoO_3 endmembers followed by either: (i) no heat treatment or (ii) heating at 850°C for 15 h under Ar. The NMC showed a high initial capacity of 177 mAh/g with an average operating potential of 3.9 V vs. Li/Li^+ when cycled between 2.0 – 4.5 V. The composite which was not heat treated exhibited a plateau ~ 3.9 V and a sloping profile in the range of 2.0 - 3.5 V. This profile is essentially a superposition of the charge/discharge behavior of the two endmembers, indicating the unheated composite consisted of sequestered Li_2MoO_3 and NMC domains. On the other hand, the composite which was heated at 850°C showed a single voltage plateau ~ 3.9 V with no appreciable capacity below 3.5 V. This result suggests Ni/Mn/Co were the main redox centers of the heated composite, and the Mo provided negligible charge compensation despite comprising 10% of the structure. Compared to NMC, the heated composite had a 24% lower reversible capacity during the first cycle (135 vs. 177 mAh/g for NMC) but showed improved cycling stability with 84% capacity retention over 20 cycles (compared to only 76% for NMC). These results demonstrate Li_2MoO_3 can effectively stabilize conventional LiMO_2 cathodes when incorporated into a composite structure. Ongoing work with these Mo-containing composites is focused on optimizing the cathode's performance by exploring various synthesis routes and degrees of Mo-substitution. From these experiments, a fundamental understanding of how Li_2MoO_3 affects the cathode's structural stability at high states of charge will be developed.

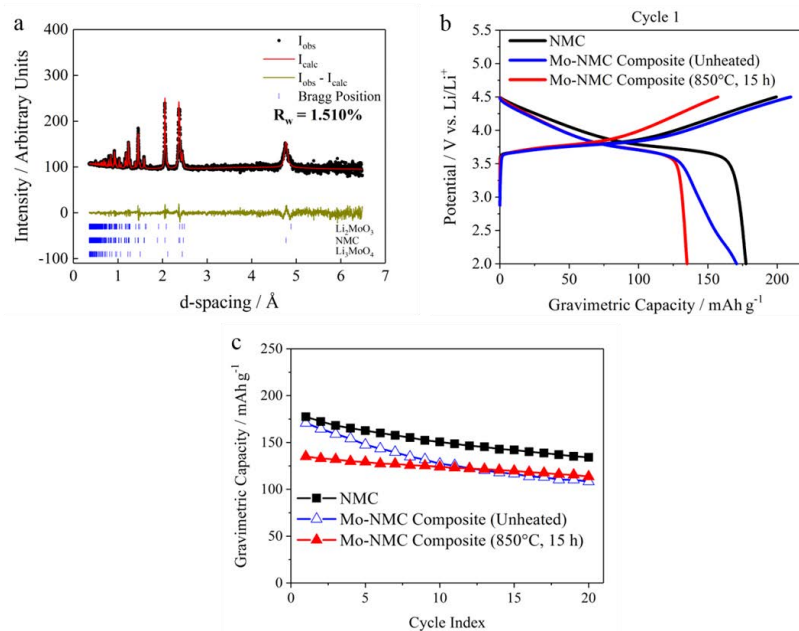


Figure II.3.D.1 (a) Neutron diffraction and Rietveld refinement of a Mo-NMC composite cathode with $x = 0.15$. (b) Charge/discharge curves and (c) cycling stability of NMC compared with a Mo-NMC composite ($x = 0.10$) prepared either with or without an 850°C heat treatment as indicated.¹

Investigation of Sputtered Thin Film Li_2MoO_3 Cathodes

Conventional Li-ion battery electrodes contain a blend of active material, carbon additives, and polymer binder which are cast onto a metal foil current collector. Evaluating the electrochemical properties (e.g., capacity, operating potential, etc.) of new active materials is straightforward using these slurry cast electrodes, but the presence of inactive electrode components often complicates studying fundamental changes in the electrode structure and electrode/electrolyte interface through methods such as Raman spectroscopy and X-ray photoelectron spectroscopy (XPS).

In the present study, Li_2MoO_3 thin film cathodes were fabricated and characterized to understand changes in the electrode structure and electrode/electrolyte interface which occur during charge/discharge cycling. The average film thickness was $1.23\ \mu\text{m}$, and the films were phase-pure with R-3m symmetry as indicated by XRD and Raman spectroscopy (results not shown). Furthermore, the Raman spectra of the thin films was extremely uniform with very little variation over a large electrode area ($50 \times 50\ \mu\text{m}^2$ with $1\ \mu\text{m}^2$ resolution), indicating the presence of a high-quality cathode layer suitable for electrochemical characterization.

The electrochemical properties of Li_2MoO_3 thin film cathodes were evaluated in CR2016 coin cells using a Li metal anode and liquid carbonate electrolyte (1.2 M LiPF_6 in 3/7 EC/EMC). To better understand how the Li_2MoO_3 structure and cathode/electrolyte interface evolve at conditions relevant for high voltage cathodes such as $x\text{Li}_2\text{MoO}_3 \cdot (1-x)\text{LiNi}_{1/3}\text{Mn}_{1/3}\text{Co}_{1/3}\text{O}_2$, the present study focuses on Li_2MoO_3 thin film cathodes charged to very positive electrochemical potentials (i.e., 4.8 V vs. Li/Li^+). During the first charge, the thin film cathodes exhibited two plateaus near 2.6 and 3.6 V with a total capacity of 196 mAh/g (see Figure I.1.2a). Upon discharge, the cathode showed a sloping profile with a reversible capacity of 166 mAh/g which faded to 98 mAh/g after 20 cycles. Most of the charge compensation during cycling occurred $\sim 2.0 - 3.5$ V due to the reversible Mo^{x+} redox center, but small irreversible oxidation plateaus were also observed near ~ 3.6 V throughout the first 20 cycles. These features (shown more clearly on the differential capacity plots in Figure II.3.D.2b) are likely due to the gradual amorphization of Li_2MoO_3 which was confirmed using *ex-situ* Raman spectroscopy (results not shown). Overall, the electrochemical properties of the thin film Li_2MoO_3 cathodes are consistent with our previous report on slurry cast Li_2MoO_3 cathodes.¹ [1]

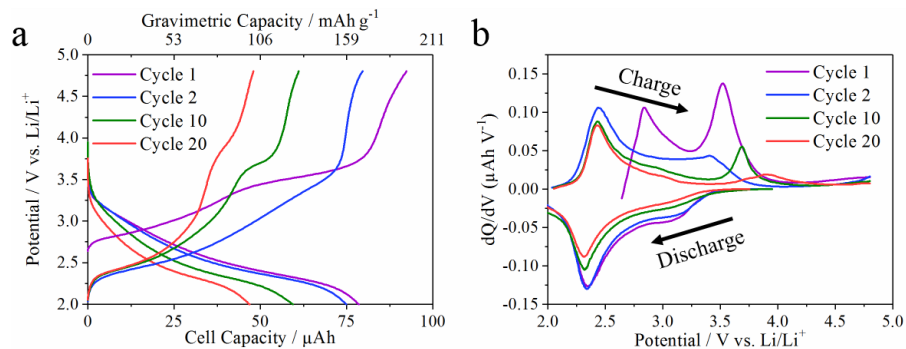


Figure II.3.D.2 Half-cell electrochemical characterization of Li_2MoO_3 thin film cathodes cycled in a liquid carbonate electrolyte. (a) Galvanostatic charge/discharge profiles and (b) differential capacity plots collected between 2.0 – 4.8 V vs. Li/Li^+ at a current density of $9.46 \mu\text{A}/\text{cm}^2$.

In addition to amorphization of Li_2MoO_3 , the irreversible oxidation processes also include decomposition of the electrolyte which is thermodynamically unstable beyond ~ 4.5 V vs. Li/Li^+ . While much research has investigated formation of the solid-electrolyte interphase (SEI) layer at the anode, comparatively little is known regarding the cathode/electrolyte interphase (CEI) layer and its evolution during electrochemical cycling. The properties of the CEI layer are influenced by the cathode and electrolyte chemistry, and a detailed study of the CEI layer on a Li_2MoO_3 surface has not yet been reported. In this regard, Li_2MoO_3 thin film cathodes represent a model system to study the electrode/electrolyte interface due to the absence of carbon and binder.

XPS was used to study the evolution of the CEI layer on the thin film cathodes cycled in a liquid electrolyte. Figure II.3.D.3a shows the Mo 3d core level spectra of pristine Li_2MoO_3 powder and Li_2MoO_3 thin film cathodes at the following conditions: (i) pristine (i.e., uncycled), (ii) after 1 cycle, and (iii) after 20 cycles. The spectra were fit with four peaks associated with the $3d_{5/2}$ and $3d_{3/2}$ orbitals associated with Mo^{6+} and Mo^{4+} . Li_2MoO_3 is expected to only contain Mo in the 4+ oxidation state, but the XPS measurements indicated substantial amounts of Mo^{6+} were present in the pristine Li_2MoO_3 powder and thin film. While the Li_2MoO_3 had the desired bulk R-3m structure, the XPS results suggest that partial oxidation of Li_2MoO_3 to Li_2MoO_4 occurred near the surface during sample preparation. Compared to the pristine material, the Mo 3d spectra for the cycled samples exhibited significant band broadening with convolution of the $3d_{5/2}$ and $3d_{3/2}$ peaks. This result is consistent with the formation of a cycling-induced amorphous structure containing a range of local bonding environments. Furthermore, the Mo 3d peaks were much weaker for the cycled cathodes. This observation suggests formation of electrolyte oxidation products on the cathode surface which attenuated the Mo 3d signal.

Analysis of the C 1s and F 1s core level scans provides some insight to the CEI layer's composition. The pristine samples contained Li_2CO_3 at the surface as indicated by the peak at a binding energy of 290 eV, but the cycled electrodes surprisingly showed no such peak. The lack of a peak at 293 eV in the C 1s scan (Figure II.3.D.3b) indicates the CEI layer did not contain a C-F bonding environment. Thus, the electrolyte oxidation products on the Li_2MoO_3 surface most likely consist of carbon with C-C and/or C-O-C functionalities. Analysis of the F 1s peak (Figure II.3.D.3c) for the cycled samples indicates the CEI also contains LiF (peak at 685 eV) and Li_xPF_y as evidenced by the feature at 688 eV which appeared after extended cycling.² [2] To the best of our knowledge, this is the first report of the chemical functionality of the CEI layer formed on Li_2MoO_3 cathodes cycled in a liquid electrolyte.

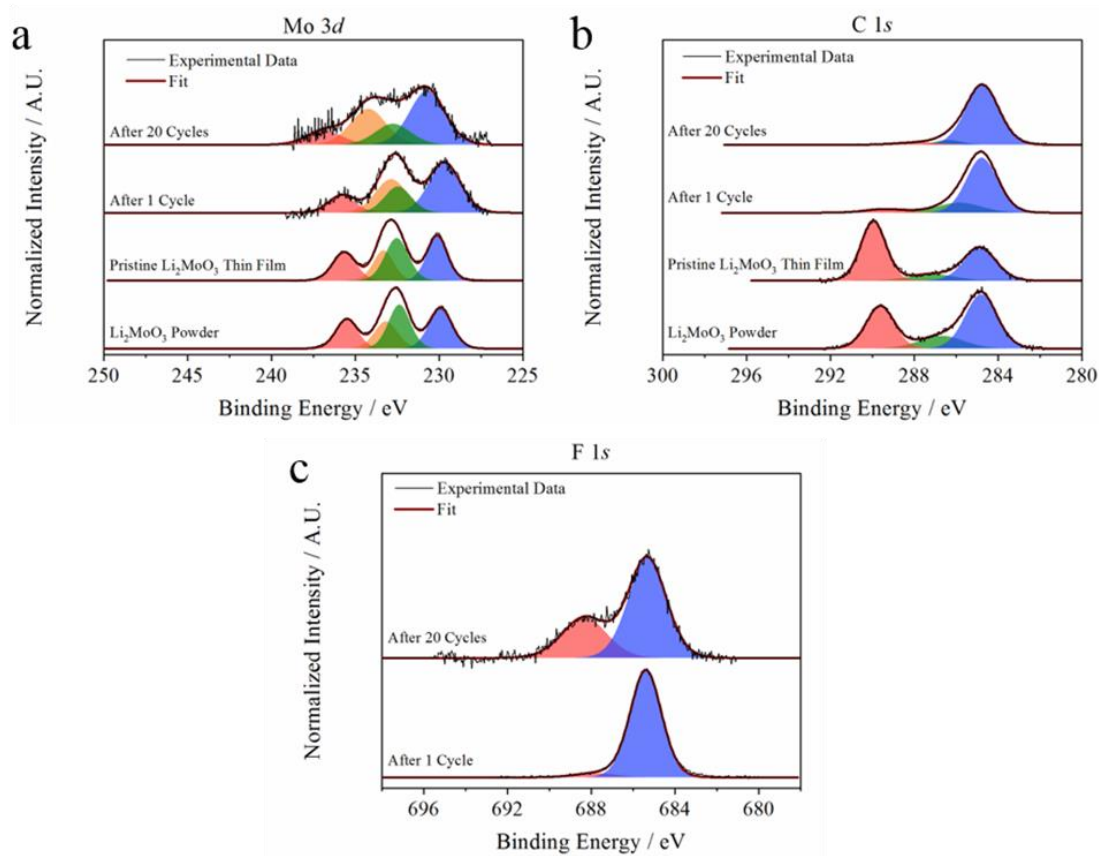


Figure II.3.D.3 Ex-situ XPS spectra of pristine (i.e., uncycled) and cycled thin film Li_2MoO_3 thin film cathodes collected after 1 and 20 charge/discharge cycles showing core-level scans for (a) Mo 3d, (b) C 1s, and (c) F 1s. Note that F 1s core level scans were not collected for the pristine samples.

To understand how different electrolytes influence the performance of Li_2MoO_3 thin film cathodes, all-solid-state devices containing a lithium phosphorus oxynitride (Lipon) solid electrolyte were also fabricated and tested. The cycling profiles of the $\text{Li}_2\text{MoO}_3/\text{Lipon}/\text{Li}$ thin film batteries (Figure II.3.D.4a) exhibit a sloping profile with most of the charge compensation occurring $\sim 2.5 - 3.5$ V vs. Li/Li^+ . However, analysis of the dQ/dV plots shows that the Li_2MoO_3 cycled in the all-solid-state device differs from that of the liquid electrolyte which showed a clear peak ~ 3.7 V. This discrepancy is not fully understood at this time but may be due to a liquid electrolyte-mediated reaction. When cycled using a solid electrolyte, the Li_2MoO_3 thin film showed excellent cycling stability with negligible fade over 45 cycles. In comparison, the cathode cycled in a liquid electrolyte showed 40% capacity loss after only 20 cycles (Figure II.3.D.2a). These results clearly demonstrate that the cathode's performance greatly depends on the nature of the cathode/electrolyte interface.

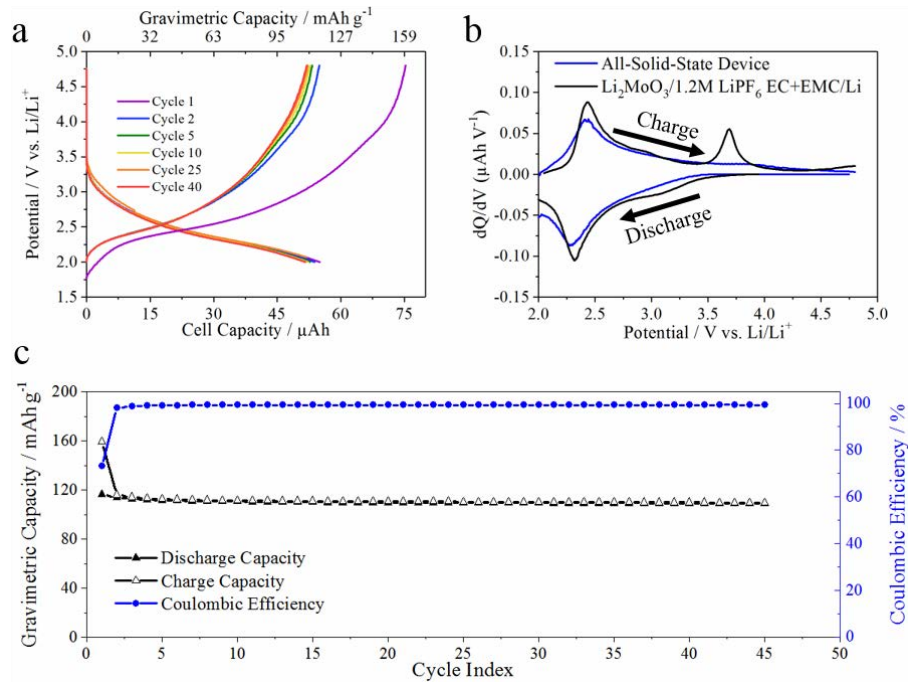


Figure II.3.D.4 Electrochemical characterization at room temperature for an all-solid-state $\text{Li}_2\text{MoO}_3/\text{Lipon}/\text{Li}$ thin film battery showing (a) galvanostatic charge/discharge curves, (b) dQ/dV plots, and (c) cycling stability collected over 2.0 – 4.8 V at $10 \mu\text{A}/\text{cm}^2$.

Compared to conventional porous electrode architectures, the planar geometry of thin film batteries greatly simplifies interpretation of electrochemical impedance spectroscopy (EIS) data. In particular, the Li^+ diffusion coefficient in the cathode structure can be determined from the slope of reactance (or resistance) plotted as a function of $\omega^{-1/2}$. A detailed mathematical derivation of this relationship is given by Ho et al.³ [3] By carefully analyzing the impedance response of $\text{Li}_2\text{MoO}_3/\text{Lipon}/\text{Li}$ thin film batteries, the Li^+ diffusion coefficient in the Li_2MoO_3 at various states of charge was reported for the first time with the summarized results provided in Figure II.3.D.5. Note that this dataset was collected at 80°C to expedite data acquisition by increasing the frequency at which the semi-infinite diffusion boundary conditions were satisfied. In the fully discharged state, the measured Li^+ diffusivity was $4.36 \times 10^{-11} \text{ cm}^2/\text{s}$ and decreased 2 orders of magnitude to $4.51 \times 10^{-13} \text{ cm}^2/\text{s}$ after charging to 3.6 V. Upon relithiation of the Li_2MoO_3 , the Li^+ diffusivity gradually increased, indicating that the Li^+ transport rates are greatly dependent on the cathode's state-of-charge.

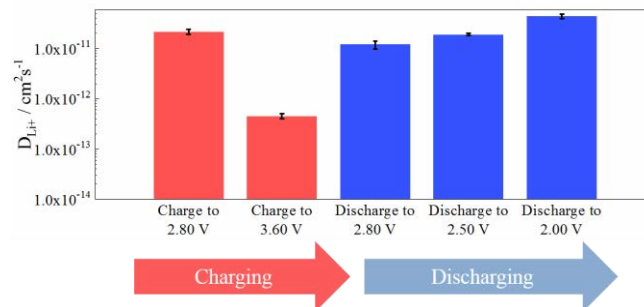


Figure II.3.D.5 Li^+ diffusion coefficient in Li_2MoO_3 at 80°C at various states of charge for a $\text{Li}_2\text{MoO}_3/\text{Lipon}/\text{Li}$ thin film battery as determined from EIS using the method reported by Ho et al.³ Error bars represent the range of values determined from plots of either the reactance vs. $\omega^{-1/2}$ or resistance vs. $\omega^{-1/2}$.

Synthesis and Characterization of Co-Free Cathode Chemistries

As the demand for LIBs in EV/PHEV applications continues to grow, the amount of Co, a toxic and limited resource, used in the cathode must be reduced. To address this need, a sol-gel synthesis procedure to produce a model Co-free cathode system ($\text{LiNi}_{0.5}\text{Mn}_{0.5}\text{O}_2$, abbreviated as LNMO) was developed. Motivated by our promising findings on the oxidative stability of Li_2MoO_3 , the LNMO structure was also doped with 1 – 5 at% Mo. The unmodified and 1 at% Mo doped LNMO were phase-pure with a layered R-3m structure as indicated by the X-ray diffraction (XRD) patterns shown in Figure II.3.D.6a. Cathodes with higher Mo doping levels (2 – 5 at%) contained Li_2MoO_4 phase impurities (results not shown here).

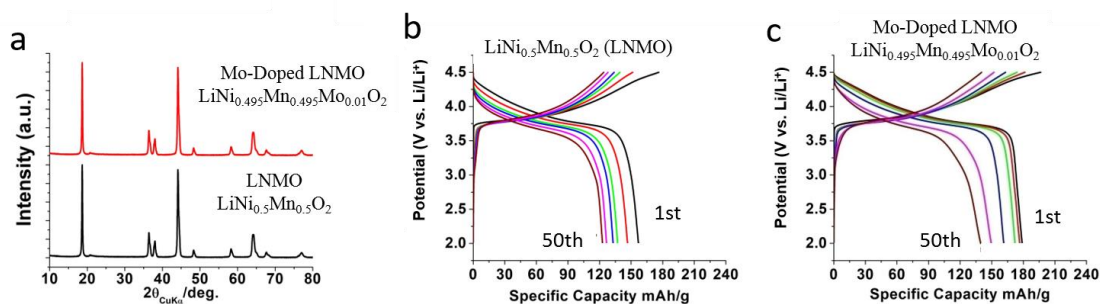


Figure II.3.D.6 Characterization of $\text{LiNi}_{0.5}\text{Mn}_{0.5}\text{O}_2$ (LNMO)-based cathodes with and without 1 at% Mo ($\text{LiNi}_{0.495}\text{Mn}_{0.495}\text{Mo}_{0.01}\text{O}_2$). (a) X-ray diffraction (XRD) patterns and galvanostatic charge/discharge curves over 50 cycles for (b) unmodified LNMO and (c) 1 at% Mo-doped LNMO. For the electrochemical characterization, the cathodes were galvanostatically cycled in half cells between 2.0 – 4.5 V vs. Li/Li^+ at 20 mA/g in an electrolyte containing 1.2 M LiPF_6 in EC/EMC (3/7).

The electrochemical properties of LNMO and 1 at% Mo-doped LNMO were evaluated in half cells containing a Li metal/counter reference and liquid carbonate electrolyte (1.2 M LiPF_6 in EC/EMC, 3/7). As shown in Figure II.3.D.6b, the unmodified LNMO exhibited a reversible capacity of 155 mAh/g with an average operating potential ~ 3.9 V vs. Li/Li^+ which is consistent with previous literature reports.^{4,5} [4], [5] Interestingly, the Mo-doped LNMO had a much higher specific capacity (180 mAh/g) when cycled over the same potential window (2.0 – 4.5 V vs. Li/Li^+ , see Figure II.3.D.6c). The Mo-doped sample also showed superior rate capabilities with a reversible capacity of 110 mAh/g at a specific current of 100 mA/g compared to 85 mAh/g for the unmodified LNMO. Both samples exhibited moderate voltage and capacity fade during extended cycling, likely due to irreversible structural transformations and/or formation of electrolyte oxidation products on the cathode surface. Decreasing the upper cutoff voltage to 4.2 V improved the cycling stability at the expense of a $\sim 25\%$ lower capacity (118 and 130 mAh/g for the unmodified and Mo-doped cathode, respectively, results not shown here). Overall, the performance of the LNMO and Mo-doped LNMO was extremely reproducible over multiple sample batches and electrochemical tests.

The fundamental mechanism by which Mo increases the LNMO capacity is not currently well-understood, but the electrochemical measurements in Figure II.3.D.6 suggest that the Mo dopant reduces the cathode's overpotential during battery operation. Two plausible explanations for this behavior include: (i) enhanced Li^+ and/or e^- conductivity of the active material and/or (ii) enhanced reaction kinetics for the Mo-doped system, although these hypotheses are largely speculative at this point. Ongoing experiments conducted through external collaborations with ANL, UC-Berkeley, and PNNL will provide additional characterization of these LNMO-based cathodes to better understand their fundamental structure/property relationship. More specifically, X-ray absorption spectroscopy (XAS), transmission electron microscopy (TEM), XPS, and differential electrochemical mass spectrometry (DEMS) will be used to study the cathodes' charge compensation mechanism, structural evolution, cathode/electrolyte interface, and gas evolution (e.g., O_2) during charge/discharge cycling. These findings will be detailed in an upcoming manuscript during FY19.

To improve the cycling stability of the Mo-doped LNMO cathode, a 2 wt% MnPO₄ coating was applied using a sol-gel synthesis route. Preliminary cycling performance of a LNMO cathode containing 1 at% Mo dopant and a 2 wt% MnPO₄ coating is shown in Figure II.3.D.7. The MnPO₄ coating did not substantially affect the cathode's capacity at a low rate of 10 mA/g, but at higher rates (20 – 200 mA/g), the MnPO₄ coated + Mo-doped material showed higher capacities than the uncoated system (e.g., 120 mAh/g at 200 mA/g). Furthermore, the MnPO₄ substantially improved the cycling stability as shown in Figure II.3.D.7a. Collectively, these results suggest the MnPO₄ coating improved the cathode's electrochemical performance by stabilizing the cathode/electrolyte interface. Ongoing experiments with these MnPO₄ coated cathodes will: (i) optimize the coating composition and loading and (ii) evaluate the coating thickness/uniformity using TEM.

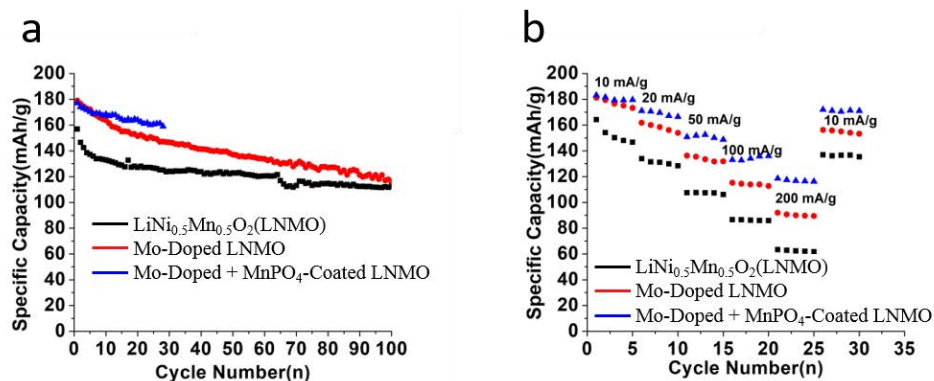


Figure II.3.D.7 (a) Cycling stability at 20 mA/g and (b) rate capabilities at 10 – 200 mA/g for LNMO cathodes which were modified by doping with 1 at% Mo and/or coating with 2 wt% MnPO₄. Electrochemical characterization was performed by cycling the cathodes between 2.0 – 4.5 V vs. Li/Li⁺ in half cells.

Conclusions

Experiments conducted during FY18 explored three different Mo-containing cathode systems including: (i) composite layered-layered structures (i.e., xLi₂MoO₃•(1-x)LiNi_{1/3}Mn_{1/3}Co_{1/3}O₂), (ii) Li₂MoO₃ thin films, and (iii) Mo-doped LiNi_{0.5}Mn_{0.5}O₂. For system (i), the effect of different synthesis conditions on the cathode structure was carefully studied using neutron diffraction. The electrochemical results from these studies demonstrate that Li₂MoO₃ improves the structural stability of layered cathodes (e.g., NMC111) at high states-of-charge.

To better understand the fundamental electrochemical properties and interface in Mo-containing cathodes, thin film Li₂MoO₃ cathodes were prepared using RF magnetron sputtering. The chemical nature of the cathode electrolyte interphase (CEI) layer formed on Li₂MoO₃ when cycling in a liquid electrolyte was probed using XPS. All-solid-state thin film Li₂MoO₃/Lipon/Li batteries were also fabricated. Interestingly, the cathodes cycled with the solid electrolyte exhibited superior cycling stability, demonstrating the critical role the cathode/electrolyte interface plays in governing device performance. Values for Li⁺ diffusivity in Li₂MoO₃ were reported for the first time through detailed EIS analysis of the thin film batteries.

LiNi_{0.5}Mn_{0.5}O₂ (LNMO) cathodes were also investigated as a model Co-free layered cathode system. The introduction of 1 at% Mo dopant into the LNMO structure resulted in a 16% increase in the cathode's reversible capacity. Furthermore, a synthesis route to coat the LNMO-based cathodes with MnPO₄ was developed to stabilize the cathode/electrolyte interface.

Overall, these studies broadly demonstrate the challenges associated with high energy density cathode systems, where there is close interplay between structure, transport, and oxygen loss that limits their use for advanced lithium-ion systems.

Key Publications

1. Probing Multiscale Transport and Inhomogeneity in a Lithium-ion Pouch Cell Using In-situ Neutron Methods, H. Zhou, K. Ann, S. Allu, S. Pannala, J. Li, H. Z. Bilheux, S. K. Martha, J. Nanda, *ACS Energy Letters* 1, 981 (2016)
2. High Capacity Cathodes for Advanced Lithium-ion: Challenges and Opportunities 11th Lithium Battery Power & Safety Conference, Nov 1- 4, 2016, Baltimore, MD [Invited]
3. Electrochemical Energy Storage Materials: From Transportation to Grid Storage, J. Nanda, *International Society on Advances in Electrochemical Science & Technology (ISAEST-11)*, December 7 - 9, 2016, Chennai, India [Invited]
4. High Capacity Multi-lithium Cathodes for Advance Lithium-ion, J. Nanda and R. E. Ruther, *US Drive Highlights (Energy Storage)*, DOE (2016)
5. High Capacity Multi-Lithium Oxide Cathodes and Oxygen Stability, R. E. Ruther, E. C. Self, and J. Nanda, *AMR Peer-Review Meeting*, June 5 - 9, 2017, Washington, DC
6. Structural Transformations in High-Capacity $\text{Li}_2\text{Cu}_{0.5}\text{Ni}_{0.5}\text{O}_2$ Cathodes, R. E. Ruther, A. S. Pandian, P. Yan, J. N. Weker, C. Wang, J. Nanda, *Chem. Mater.* 29, 2997 (2017)
7. Meso and micron scale chemical and morphological heterogeneities in high capacity battery materials, *MRS Spring Meeting*, April 17 - 21, 2017, Phoenix, AZ [Invited]
8. Structural Transformations in High Capacity $\text{Li}_2\text{Ni}_{0.5}\text{Cu}_{0.5}\text{O}_2$ Cathodes, R. Ruther, J. Nanda et al. *ECS Spring Meeting*, May 28 - June 1, 2017, New Orleans, LA
9. Oxygen Stability of Disordered, Multi-Lithium Oxide Cathodes for Li-ion Batteries, E. C. Self, R. E. Ruther, G. M. Veith, and J. Nanda, *ECS Fall Meeting*, Oct. 1 - 5, 2017, National Harbor, MD
10. Crystal Chemistry and Electrochemistry of $\text{Li}_x\text{Mn}_{1.5}\text{Ni}_{0.5}\text{O}_4$ Solid Solution Cathode Materials, W. H. Kan, S. Kuppam, C. Dhital, J. Nanda, A. Huq and G. Chen, *Chem. Mater.* 29, 6818 (2017)
11. Engineering Redox Potential of Lithium Clusters for Electrode Material in Lithium-Ion Batteries, A. K. Kushwaha, M. R. Samal, J. Nanda and S. K. Nayak, *J. Clust. Sci.* 28, 2779 (2017)
12. High Capacity Multi-Lithium Oxide Cathodes and Oxygen Stability, R. E. Ruther, E. C. Self, and J. Nanda, *AMR Peer-Review Meeting*, June 13 - 15, 2018, Washington, DC
13. Synthesis, Electrochemical, and Structural Investigations of Oxidatively Stable Li_2MoO_3 and $x\text{Li}_2\text{MoO}_3 \cdot (1-x)\text{LiMO}_2$ Composite Cathodes, E. C. Self, L. Zou, M. Zhang, R. Opfer, R. E. Ruther, G. M. Veith, B. Song, C. Wang, F. Wang, A. Huq, and J. Nanda, *Chem. Mater.* 30, 5061 (2018)
14. Synthesis and Characterization of Li Excess Mo-Based Cathodes for Li-ion Batteries, E. C. Self, L. Zou, M.-J. Zhang, R. Opfer, R. E. Ruther, G. M. Veith, B. Song, C. Wang, F. Wang, A. Huq, J. Nanda, *MRS Spring Meeting*, April 2 - 6, 2018, Phoenix, AZ
15. D. Darbar, E. C. Self, and J. Nanda. Unpublished Results (2018).

References

1. Self, E. C.; Zou, L.; Zhang, M.-J.; Opfer, R.; Ruther, R. E.; Veith, G. M.; Song, B.; Wang, C.; Wang, F.; Huq, A.; Nanda, J. *Chem. Mater.* **2018**, *30*, 5061.
2. Edström, K.; Gustafsson, T.; Thomas, J. O. *Electrochim. Acta* **2004**, *50*, 397

3. Ho, C.; Raistrick, I. D.; Huggins, R. A. *J. Electrochem. Soc.* **1980**, *127*, 343.
4. Shaju, K. M.; Subba Rao, G. V.; Chowdari, B. V. R. *Electrochim. Acta* **2003**, *48*, 1505.
5. Xiao, L.; Liu, X.; Zhao, X.; Liang, H.; Liu, H. *Solid State Ionics* **2011**, *192*, 335.

Acknowledgements

We would like to thank our collaborators including: Drs. Chongmin Wang and Pengfei Yan (electron microscopy, Pacific Northwest National Laboratory), Dr. Feng Wang (X-ray synchrotron and microscopy, Brookhaven National Laboratory), Dr. Johanna Nelson Weker (synchrotron X-ray microscopy and 3D microstructure, *Stanford Linear Accelerator Center*), Dr. Ashfia Huq (neutron scattering, Oak Ridge National Laboratory), and Drs. Gabriel Veith and Harry Meyer III (XPS, Oak Ridge National Laboratory).

II.3.E High Energy Density Lithium Battery (Binghamton University)

M. Stanley Whittingham, Principal Investigator

Binghamton University (SUNY)
85 Murray Hill Road
Vestal, NY, 13850
E-mail: stanwhit@binghamton.edu

Tien Duong, DOE Technology Development Manager

U.S. Department of Energy
E-mail: Tien.Duong@ee.doe.gov

Start Date: October 1, 2014

End Date: June 30, 2018

Project Funding: \$1,265,773

DOE share: \$1,265,773

Non-DOE share: \$0

Project Introduction

The project objectives are to develop the anode and cathode materials for high-energy density cells for use in plug-in hybrid electric vehicles (PHEVs) and in electric vehicles (EV) that offer substantially enhanced performance over current batteries used in PHEVs and with reduced cost. Specifically, the goal of this project is to enable cells with an energy density exceeding 1 kWh/liter. The carbon anode in today's Lithium-ion cells will be replaced with a tin-based anode with double the volumetric capacity of carbon. Similarly, the present intercalation cathodes will be replaced by materials, which are capable of reacting with up to two lithium ions per redox ion. Moreover, these cell reactions will occur within the stability limit of today's electrolytes, leading to longer-lived batteries.

Objectives

We propose to develop the anode and cathode materials for high-energy density cells for use in plug-in hybrid electric vehicles (PHEVs) and in electric vehicles (EV) that offer substantially enhanced performance over current batteries used in PHEVs and with reduced cost. Specifically the primary objectives are to:

- Increase the volumetric capacity of the anode by a factor of 1.5 over today's carbons by using a SnFeC composite conversion reaction anode
- Increase the capacity of the cathode by using a high capacity conversion reaction cathode, CuF_2 , and/or using a high capacity 2 Li intercalation cathodes, VOPO_4 .
- Enable cells with an energy density exceeding 1 kWh/liter.

Approach

The approach of this "beyond Li-ion" battery concept is (a) to remove the volume intensive intercalation-based carbon anode in today's Li-Ion batteries, and replace it with a conversion reaction based material, and (b) to replace the present cathodes that mostly react with less than one Li ion per transition metal ion with cathode materials that can react with more than one Li ion. This latter is similar to the concept of using the divalent magnesium with its two-electron transfer. However, we believe that moving two of the much more mobile singly charged lithium ions is more viable, and moreover today's electrolytes, SEI additives and cell technology can be used. Attainment of the goals proposed here will lead to a 50-100% increase in the volumetric and gravimetric energy storage capability of both the anode and the cathode, which will allow for the realistic attainment of the next generation batteries for PHEV vehicles. At the same time, the science generated will be applicable to other energy storage systems, such as anodes for Li/S. The anode and cathode components in this approach are:

1. A SnFeC composite for the anode which reacts by a conversion mechanism giving Li_xSn and Fe.

2. A CuF_2 containing material for the cathode which reacts with 2 Li ions by a conversion mechanism giving Cu and LiF.
3. A VOPO_4 containing cathode which reacts with up to 2 Li ions by an intercalation mechanism giving Li_2VOPO_4 .

The optimized anode and cathode from the above will then be combined in a full cell.

Results

The results are described on the following pages, first for the individual components, and then for the full cell.

The Sn_yFe Anode

We have demonstrated more than 500 cycles of the Sn_yFe anode at a volumetric capacity exceeding 1.5 times that of carbon. Two different approaches were used to synthesize the SnFe /carbon composite

- The results for the mechanochemical synthesis approach are shown in Figure II.3.E.1. This composite shows both higher volumetric and gravimetric capacities than standard graphite.
- The results for a modified polyol approach to form the Sn_yFe anode material are shown in Figure II.3.E.2. This material shows excellent cycling, capacity and capacity retention even at 1C rates
 - 414 mAh/g after 500 cycles, which is 1.2 Ah/cc, 1.5 times of 0.8 Ah/cc for graphite
 - About 400 mAh/g at 2C rate

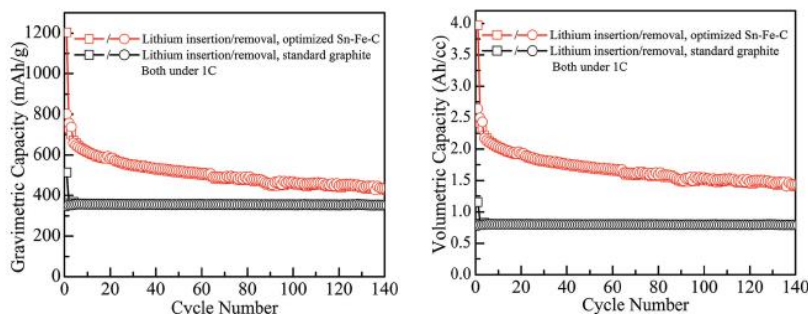


Figure II.3.E.1 The cycling behaviors of Sn-Fe-C anode composite synthesized with mechano-chemical synthesis.

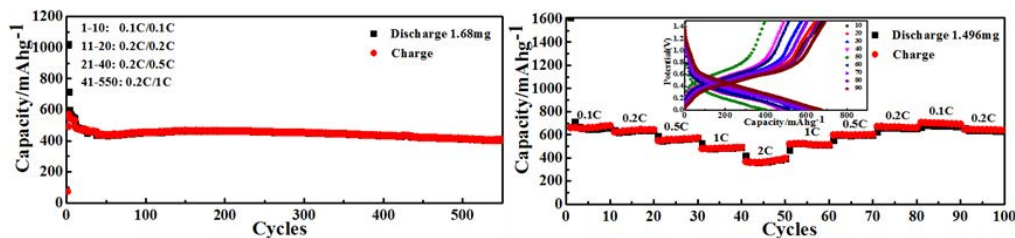


Figure II.3.E.2 The cycling and rate performance of modified polyol approach synthesized Sn_yFe anode material.

The CuF_2 Cathode

We have demonstrated that for CuF_2 , the full capacity of 500 mAh/g is achievable on the first discharge (Figure II.3.E.3), and at high rates (Figure II.3.E.4). XAS showed that the Cu was not fully recharged. In contrast when the Cu was partially replaced by Fe, the cell retained its capacity better. Further studies on CuF_2 were halted until a Cu^+ free electrolyte is found. Specifically, we determined that Cu^+ transport through the electrolyte is the failure mode for pure CuF_2 reversion and that Fe substitution can help the reversibility of the reaction:

- CuF_2 reacts to form Cu and LiF , but most does not revert back to form CuF_2 (Figure II.3.E.3)
 - The majority of the Cu transported as Cu^+ through the electrolyte (both liquids and solids) to the anode side
- The reversibility of $\text{Cu}_{1-y}\text{Fe}_y\text{F}_2$ mainly comes from the Fe redox potential (Figure II.3.E.5)
 - Fe oxidizes beyond Fe^{2+} to Fe^{3+}

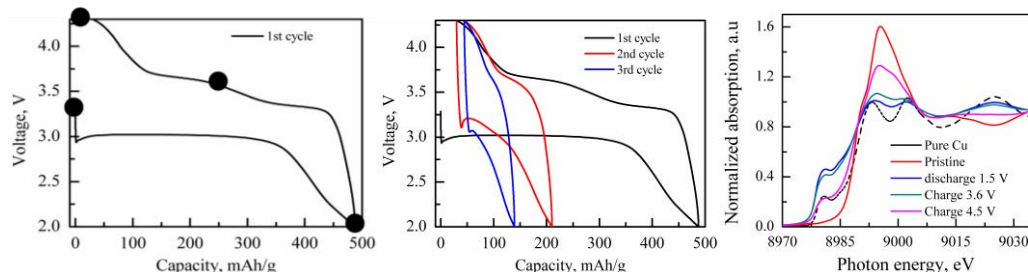


Figure II.3.E.3 (left) The first cycle, (middle) the 1st three cycles showing the rapid decay and (right) the ex-situ XAS showing the oxidation and reduction of Cu during the conversion and reconversion reactions. The decay of the Cu^{2+} peak at just under 9000 eV, shows the incomplete formation of CuF_2 on recharge.

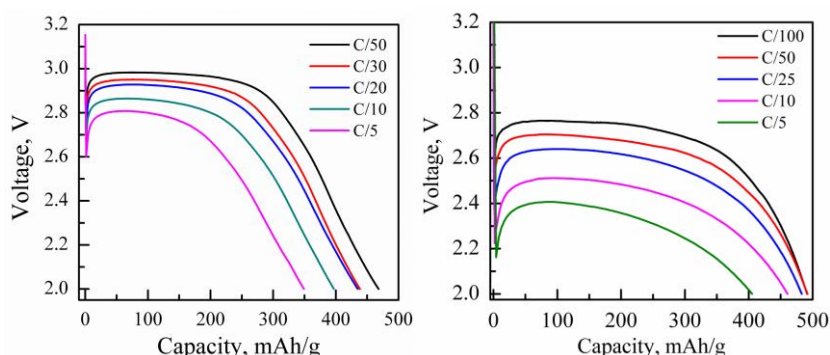


Figure II.3.E.4 The rate capability on 1st discharge of (left) a Li/CuF_2 cell and (right) a $\text{Li}/\text{CuF}_2\text{-VOPO}_4$ cell.

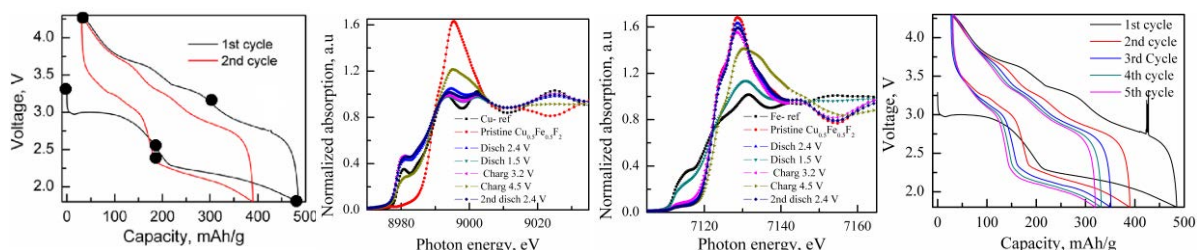


Figure II.3.E.5 The behavior of a $\text{Cu}_{0.5}\text{Fe}_{0.5}\text{F}_2$ electrode. From left to right: the first two cycles (and also indicating where the XAS measurements were made); the fade of the Cu^{2+} peak; the recovery of the Fe^{2+} peak on charging; and the cycling performance of the $\text{Cu}_{0.5}\text{Fe}_{0.5}\text{F}_2$ anode.

The VOPO_4 Cathode

Vanadium is the 4th most abundant transition metal in nature, so is a mineral-wise viable cathode for batteries. We have demonstrated that up to two Li can be reversibly reacted for the Li_xVOPO_4 cathode, contributing to a reversible capacity approaching 300 mAh/g ; good cycling and rate performance was obtained after optimization.

Ball milling and annealing improves electrochemical performance (Figure II.3.E.6)

- Ball milling reduces the particle sizes but introduces defects
 - A lot of defects hinders Li mobility
- Annealing at moderate temperatures decreased the defects and retains the small particle size

The theoretical capacity of 305 mAh/g was achieved by a synthesis modification discovered in our related fundamental understanding program funded by DOE-BES-EFRC-NECCES. This was accomplished using a solvothermal approach, where the ball milling and annealing steps were eliminated.

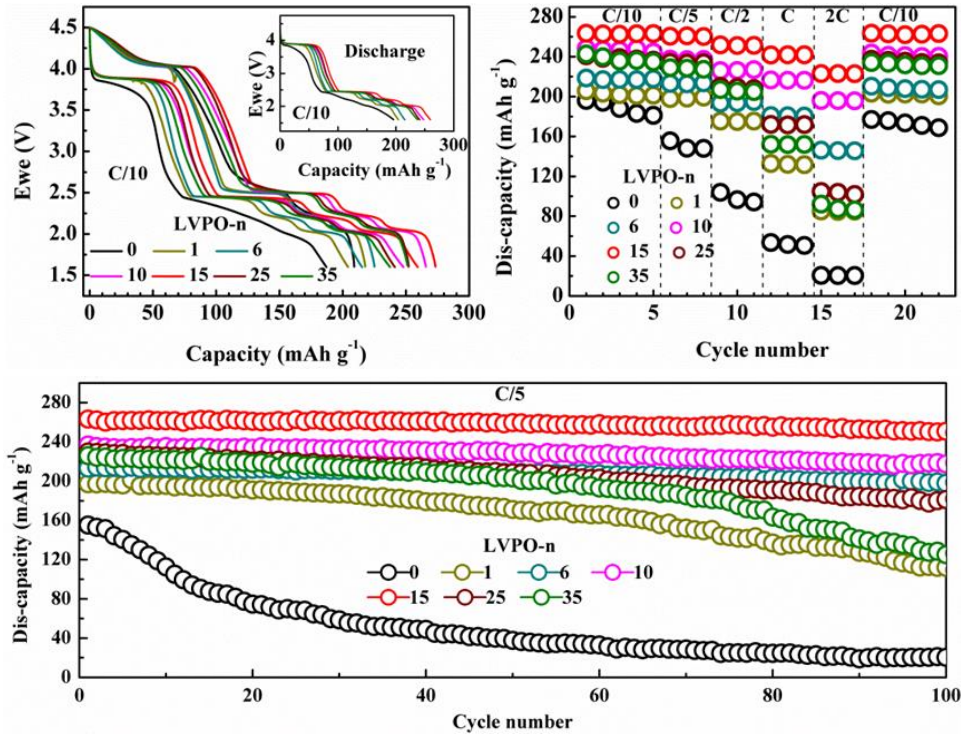


Figure II.3.E.6 The cycling and rate performance of solid-state synthesized Li_xVOPO_4 cathode with high energy ball milling with carbon and then annealed with different hours.

The $\text{Sn}_y\text{Fe}_z/\text{Li}_x\text{VOPO}_4$ Full Cell

We have demonstrated that the full $\text{Sn}_y\text{Fe}_z/\text{Li}_x\text{VOPO}_4$ cell has much higher energy density than the baseline LiFePO_4 cell (Figure II.3.E.7). The original target of 4 mAh can be achieved in a coin cell at either 0.1C or 0.3C and the calculated energy density of the cell approaches 600 Wh/kg.

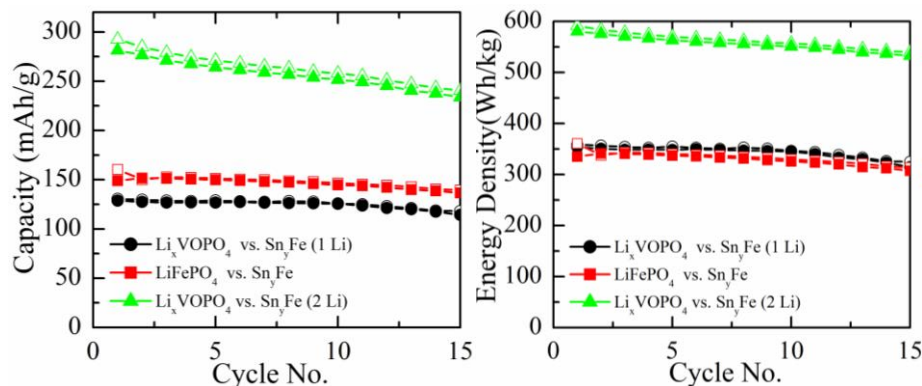


Figure II.3.E.7 Comparison of (a) the capacity and (b) the energy density of the $\text{Sn}_y\text{Fe}/\text{Li}_x\text{VOPO}_4$ cell vs. the baseline $\text{Sn}_y\text{Fe}/\text{LiFePO}_4$ cell.

Some key results are shown in Figure II.3.E.8.

- One of the electrodes had to be pre-lithiated
 - Adding a little excess Li metal to the SnFe anode was most effective
 - A small excess of Li was needed, but too much is detrimental (Figure II.3.E.8 (d))
 - The ratio of cathode and anode is important (Figure II.3.E.8 (a))
 - Anode capacity need to be slightly in excess
- Cell cyclability needs to be improved
 - Decay was determined to be coming from the Li_xVOPO_4 cathode. Figure II.3.E.8 (b) shows that the capacity fade is the same for both a graphite anode and the SnFe anode, indicating that the fade comes from the cathode. Figure II.3.E.8 (c) shows the discharge and charge curves for the $\text{SnFe}/\text{Li}_x\text{VOPO}_4$ cell over 20 cycles.
- The initial capacity and energy goals have been met.
 - Figure II.3.E.8.(e) shows that the goal of a 4 mAh cell has been achieved at rates of C/10 and C/3 in a full cell.
 - Figure Figure II.3.E.8.(f) shows the calculated volumetric energy densities of the two cells from the data in Figure II.3.E.8.(e). The volumes of both the anode and cathode were taken into account. This shows that our $\text{Sn}_y\text{Fe}/\text{Li}_x\text{VOPO}_4$ cell can attain an energy density of 1 kWh/L

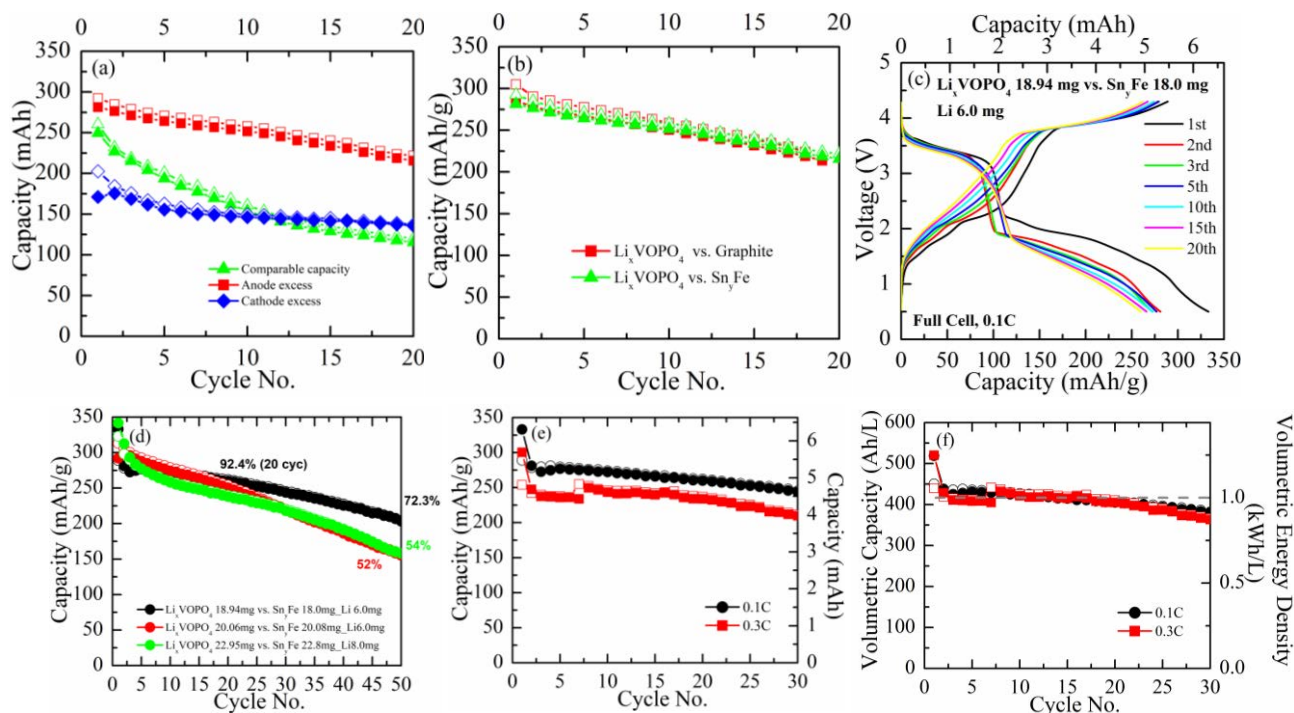


Figure II.3.E.8 (a) Comparison of the cycling performance of a $\text{Sn}_7\text{Fe}/\text{Li}_x\text{VOPO}_4$ cell with different capacity ratios of cathode to anode; (b) comparison of the performance of $\text{Sn}_7\text{Fe}/\text{Li}_x\text{VOPO}_4$ vs. a graphite// Li_xVOPO_4 Cell; (c) the voltage profile of $\text{Sn}_7\text{Fe}/\text{Li}_x\text{VOPO}_4$ cell with lithium metal prelithiation; (d) compare of the performance of $\text{Sn}_7\text{Fe}/\text{Li}_x\text{VOPO}_4$ cell with different amounts of lithium metal prelithiation indicating the quantity control is critical: a small excess is needed; (e) $\text{Sn}_7\text{Fe}/\text{Li}_x\text{VOPO}_4$ cells meet the 4 mAh capacity at both 0.1C and 0.3C; (f) the volumetric capacity and energy density of those two $\text{Sn}_7\text{Fe}/\text{Li}_x\text{VOPO}_4$ cells in (e).

Conclusions

This project has shown that a metal alloy composite anode can be cycled the desired 500 cycles for electric vehicle use, and at rates exceeding the required C/3 discharge rate. It also showed the feasibility of using 2 Li cathodes, but side reactions will need to be eliminated before commercial use is viable. Copper fluoride was shown not to be a viable cathode material, because of transport of cuprous ions through all electrolytes considered, both liquid and solid.

Key Publications

1. “Electrochemical Performance of Nanosized Disordered LiVOPO_4 ”, ACS Omega, 3(7), 7310–7323 (2018). Yong Shi, Hui Zhou, Ieuan D. Seymour, Sylvia Britto, Jatinkumar Rana, Linda W. Wangoh, Yiqing Huang, Qiyue Yin, Philip J. Reeves, Mateusz Zuba, Youngmin Chung, Fredrick Omenya, Natasha A. Chernova, Guangwen Zhou, Louis F. J. Piper, Clare P. Grey and M. Stanley Whittingham.
2. “ ϵ - and β - LiVOPO_4 : Phase Transformation and Electrochemistry”, ACS Appl. Mater. & Interfaces, 9, 28537–28541 (2017). Hui Zhou, Yong Shi, Fengxia Xin, Fredrick Omenya, and M. Stanley Whittingham. DOI: 10.1021/acsami.7b07895
3. Zhixin Dong, R. Zhang, D. Ji, N. A. Chernova, K. Karki, S. Sallis, L. Piper, M. S. Whittingham: The anode challenge for lithium-ion batteries: a mechanochemically synthesized Sn-Fe-C composite anode surpasses graphitic carbon. Advanced Science, 3, 1500229, 2016.

Acknowledgements

The key postdocs and students who performed this work are thanked: F. Omenya, H. Zhou, F. Xin, Z. Dong, Y. Shi, and N. Zagarella. The Advanced Photon Source (Argonne National Laboratory) and the National Synchrotron Light Source II (Brookhaven National Laboratory) were used to determine the phases formed in both ex-situ and operando electrochemical cells. The University of Colorado, Boulder (Se-Hee Lee) and the University of Michigan (Jeff Sakamoto) provided some of the electrolytes used.

II.3.F Development of High-Energy Cathode Materials (PNNL)

Ji-Guang Zhang, Principal Investigator

Pacific Northwest National Laboratory
902 Battelle Blvd., Richland, WA 99354
E-mail: jiguang.zhang@pnnl.gov

Jianming Zheng, Principal Investigator

Pacific Northwest National Laboratory
902 Battelle Blvd., Richland, WA 99354
E-mail: jianming.zheng@pnnl.gov

Peter Faguy, DOE Technology Development Manager

U.S. Department of Energy
E-mail: Peter.Faguy@ee.doe.gov

Start Date: October 1, 2017

End Date: September 30, 2018

Project Funding (FY18): \$150,000

DOE share: \$150,000

Non-DOE share: \$0

Project Introduction

Lithium (Li) ion batteries (LIBs) have been widely used in consumer electronics and electric vehicles due to their high energy density, high voltage, and environmentally friendly nature. Although significant progress has been made, the driving range of EVs using the state-of-the-art LIBs is still far below those of vehicles using internal combustion engines. Therefore, the energy density and power capability of LIBs must be improved to increase the driving range and decrease the recharging time. As one of the most promising cathode materials, the Ni-rich $\text{LiNi}_x\text{Mn}_y\text{Co}_{1-x-y}\text{O}_2$ (NMC, $x > 0.6$) has attracted much attention due to its high capacity and energy density. Ni-rich NMC offers a high discharge capacity of more than 200 mAh g^{-1} and the energy density of $\sim 800 \text{ Wh kg}^{-1}$ (calculated based on cathode only). However, several technical challenges, such as fast capacity fading and high voltage instability, hinder their large-scale application. This fade is directly related to the instability of cathode/electrolyte interface induced by the continuous oxidation of electrolyte as well as the structural degradation and the dissolution of transition metals. In FY18, we used several effective methods to address the above problems, including optimum synthesis condition of cathode material, use novel electrolytes, and choose appropriate electrolyte additives.

Objectives

- Develop high-energy cathode materials with improved safety for PHEV and EV applications
- Choose proper electrolytes to stabilize electrode/electrolyte interfaces for long cycle life of Lithium-ion batteries

Approach

- Identify an optimized electrolyte that could efficiently stabilize the electrode/electrolyte interface of Ni-rich NMC cathodes.
- Search for electrolyte additive to stable both Li-metal anode and Ni-rich NMC cathodes for high energy density LIBs.

Results

(1) Tailoring the electrode/electrolyte interface to improve the cycle life of Ni-rich NMC cathodes

The electrode/electrolyte interfacial stability of the Ni-rich NMC cathode, i.e., $\text{LiNi}_{0.76}\text{Mn}_{0.14}\text{Co}_{0.10}\text{O}_2$ was enhanced by using an optimized electrolyte (E-optimized) composed of 0.6 M lithium bis(trifluoromethanesulfonyl)imide (LiTFSI), 0.4 M lithium bis(oxalate)borate (LiBOB), and 0.05 M LiPF_6 in ethylene carbonate (EC)-ethyl methyl carbonate (EMC) (4:6 by wt.), leading to significantly enhanced electrochemical performance.

In order to investigate the effects of the electrolytes on the electrochemical performance of $\text{Li}||\text{NMC76}$ cells, the charge/discharge behavior of $\text{Li}||\text{NMC76}$ cells using E-optimized and E-baseline (1M $\text{LiPF}_6/\text{EC-EMC}$) were investigated in detail. The electrochemical performances of $\text{Li}||\text{NMC76}$ cells using the two different electrolytes are presented in Figure II.3.F.1. Three initial formation cycles at 0.1C ($1\text{C} = 200\text{ mA g}^{-1}$) were conducted on the cells prior to the subsequent cycling under higher charge/discharge current densities (0.33C). The cell based on E-optimized exhibits a higher capacity (Figure II.3.F.1A) and a higher CE than that using E-baseline during the formation (0.1C) and following cycles (0.33C), indicating the fast electrode redox reaction kinetics in E-optimized. The Ni-rich NMC76 is able to deliver a high discharge capacity of 220 mAh g^{-1} in E-optimized, corresponding to an energy density (integrating the area under the voltage-capacity profile shown in Fig. 1) of 846 Wh kg^{-1} , which is higher than the 213 mAh g^{-1} (corresponding to an energy density of 769 Wh kg^{-1}) that is obtained in E-baseline. Figure II.3.F.1B indicates that the cell using E-optimized exhibits a capacity retention of 90.12% at the 200th cycle, which is much higher than the 85.05% obtained for the E-baseline cell. Figure II.3.F.1C-D shows the charge/discharge profile evolutions for $\text{Li}||\text{NMC76}$ during long-term cycling. The cell using E-baseline shows obvious capacity fade and continuous increase of cell overpotential during cycling, suggesting the formation of more resistive SEI and cathode electrolyte interphase (CEI) layer on the LMA and the cathode, respectively. In comparison, the cell using E-optimized exhibits much less increase in cell overpotential (Figure II.3.F.1D), indicating that the electrode/electrolyte interphase layer formed in E-optimized is much more conductive for Li^+ ion transport than that formed in E-baseline. The evolution of midpoint voltages of $\text{Li}||\text{NMC76}$ cells using different electrolytes are compared in Figure II.3.F.1E. Apparently, the midpoint voltage in the LMB using E-optimized is very stable for 200 cycles. Due to the smaller voltage fade and the better protection for Li metal and/or the cathode, the $\text{Li}||\text{NMC76}$ cell using E-optimized exhibits a much better retention in energy density (752 Wh kg^{-1} at 200th cycle) than that using E-baseline (626 Wh kg^{-1} at 200th cycle) (Figure II.3.F.1F).

The cycling performance of the $\text{Li}||\text{NMC76}$ cells using these two electrolytes is also investigated at an elevated temperature of 60°C at 0.5C rate. The $\text{Li}||\text{NMC76}$ cell using E-baseline exhibits a drastic drop of discharge capacity after about 40 cycles, accompanied by a sudden drop in CE. In addition to the poor stability of E-baseline toward Li metal as reported previously, the aggressive side reactions between Ni-rich NMC76 material (especially the highly reactive Ni^{4+}) and E-baseline at the high temperature is another critical reason for the accelerated capacity decay. In contrast, the $\text{Li}||\text{NMC76}$ cell using E-optimized shows limited capacity degradation and very stable CE during cycling. Overall, the $\text{Li}||\text{NMC76}$ cells using E-optimized exhibit significantly superior electrochemical performance in terms of discharge capacity, capacity retention, voltage stability, and high-temperature performance in comparison with E-baseline cells at 0.33C rate.

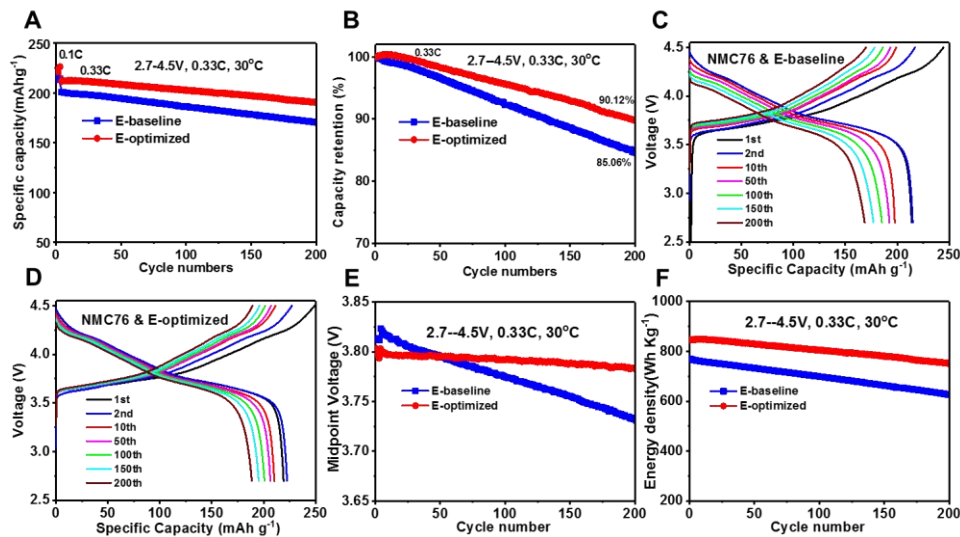


Figure II.3.F.1 Electrochemical behavior of Li||NMC76 cells using two different carbonate-based electrolytes at 0.33C current rate after three formation cycles at 0.1C rate. Comparison of cycling performance (A) and capacity retention (B) in the two electrolytes; voltage profiles of LMBs using (C) E-baseline and (D) E-optimized; comparison of midpoint voltage evolution (E) and energy density (F) between E-baseline and E-optimized based LMBs.

In order to further confirm the improved compatibility of the Ni-rich NMC76 cathode with the optimized dual-salt electrolyte, the long-term cycling stability of Li||NMC76 cells was also tested at high charge/discharge current rates of 1C/1C, 2C/2C, and 5C/5C as shown in Figure II.3.F.2A-C. It is clearly seen that LMBs using E-baseline undergo an abrupt capacity drop after 150 cycles, 80 cycles, and 15 cycles at 1C, 2C, and 5C, respectively. Although the degradation of Ni-rich NMC76 may also contribute to the capacity fade during cycling, the accelerated capacity fading at high charge current densities could be primarily ascribed to the quick corrosion of the LMA and the consequential increase in the overall cell resistance. In comparison, the Li||NMC76 cells using E-optimized show greatly enhanced cycling stability even at a high current rate of 5C (1000 mA g⁻¹) for both charge and discharge. These cells still deliver high reversible capacities of 180.4 mAh g⁻¹, 159.3 mAh g⁻¹, and 129.2 mAh g⁻¹ at 1C, 2C, and 5C after 300 cycles, corresponding to capacity retentions of 93.32%, 91.79%, and 91.37%, respectively, as shown in Figure II.3.F.2A-C. To further understand the rate capability of the LMBs using these two electrolytes, the charging/discharging performance at other C rates was also evaluated. The Li||NMC76 cell using E-optimized exhibits discharging capability superior to that using E-baseline even at 10C rate as shown in Figure II.3.F.2D. The reversible capacity remains stable after high current rate cycling and can recover to the original capacity when the current density returns to 0.1C, substantiating the excellent structural integrity of NMC76 in E-optimized for rapid Li⁺ ion extraction/insertion. The long-term stability of Li||NMC76 cells using E-optimized was further investigated at both high charge and discharge currents of 2C/2C within the voltage window of 2.7~4.5 V. Surprisingly, the Li||NMC76 cell using E-optimized can retain 80.61% capacity over 1000 cycles and exhibits a stable CE of more than 99.5% (Figure II.3.F.2E). To the best of our knowledge, this cycling performance is one of the best ever reported for LMBs based on a high-energy-density, Ni-rich NMC cathode at a high current rate and a high cutoff voltage. We also investigated the cycling performance of NMC622 and NMC811 using E-optimized and the results are pretty stable as well. The Li||NMC622 cell delivers the capacity retention of 86.9% after 500 cycles under 2C/2C charge/discharge rates, while the Li||NMC811 cell exhibits the capacity retention of 83.5% after 500 cycles at the same test condition. Therefore, the Li||NMC batteries combining the high-energy-density, Ni-rich NMC cathode and the highly stable electrolyte E-optimized will be a promising energy storage system.

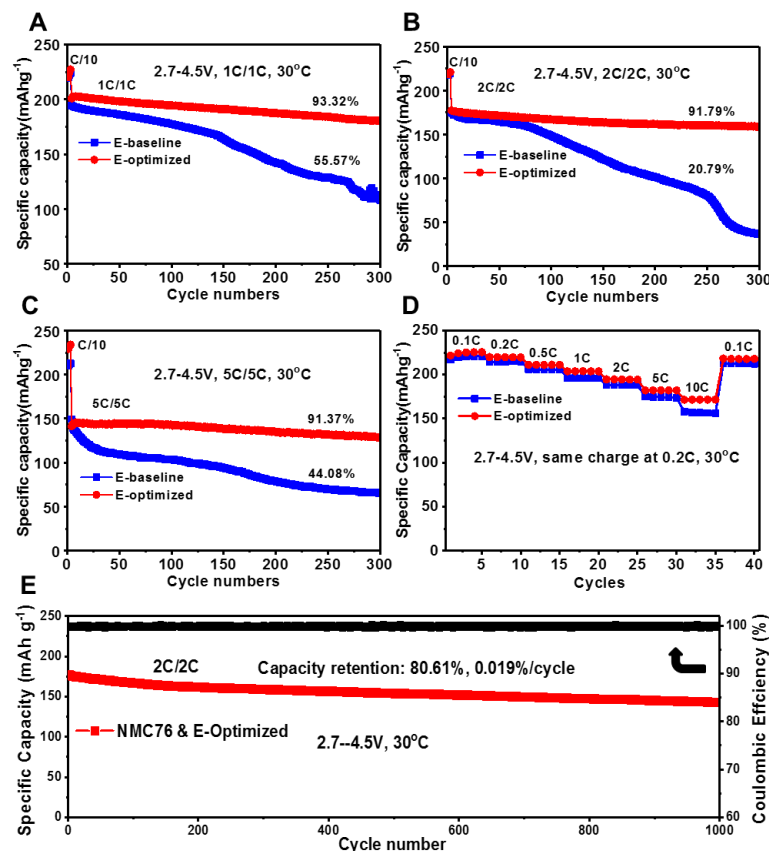


Figure II.3.F.2 Comparison of the cycling performance of Li | NMC76 cells using two electrolytes under high charging/discharging current rates (A) 1C/1C, (B) 2C/2C, and (C) 5C/5C. (D) Rate performance at the same charge rate of 0.2C and gradually increased discharge rate from 0.1C to 10C, and then switched back to 0.1C. (E) Long-term cycling performance and CE of Li | NMC76 cell using E-optimized over 1000 cycles at 2C charging rate.

The electrochemical performance data showed that, using optimized electrolyte, the Ni-rich $\text{LiNi}_{0.76}\text{Mn}_{0.14}\text{Co}_{0.10}\text{O}_2$ was able to deliver an initial discharge capacity of 220 mAh g^{-1} and achieve 86.9% capacity retention after 250 cycles, far superior to those (215 mAh g^{-1} , 75.2% retention after 250 cycles) obtained in baseline electrolyte (1 M $\text{LiPF}_6/\text{EC-EMC}$) (Figure II.3.F.3a,d). Meanwhile, the advantage of using E-optimized for Ni-rich NMC is further evidenced by the much improved stability in long-term cycling at higher charge/discharge C rates of 1C, 2C, and 5C, as compared to those using E-baseline (Figure II.3.F.3a, d). The mechanism of improved cyclability of the NMC cathode using E-optimized electrolyte was systematically investigated using SEM, TEM, x-ray photoelectron spectroscopy (XPS), and EIS. E-optimized has been previously proven to be much more stable with the Li metal anode, thereby suppressing the polarization increase occurring on the anode side. In addition, the E-optimized electrolyte greatly enhanced the surface structural stability of $\text{LiNi}_{0.76}\text{Mn}_{0.14}\text{Co}_{0.10}\text{O}_2$. Although similar particle cracking was observed in the two electrolytes, less corrosion and much less structural transformation (from R-3m layered to Fm-3m disordered rock salt) were detected at the particle surface of Ni-rich NMC cycled in E-optimized (Figure II.3.F.3e,f), as compared to those observed in E-baseline (Figure II.3.F.3b,c). This improvement can be ascribed to the absence of HF acidic species that could etch the cathode particle surface, resulting in the phase transformation from layered to disordered rock-salt phase. The enhanced surface structural/interfacial stability is regarded as the primary reason for the improved capacity retention and mitigated voltage decay of Ni-rich $\text{LiNi}_{0.76}\text{Mn}_{0.14}\text{Co}_{0.10}\text{O}_2$. The results highlight the importance of maintaining the particle surface structural/interfacial stability to enable the sustainable operation of Ni-rich cathode materials for high-energy-density Li-ion batteries.

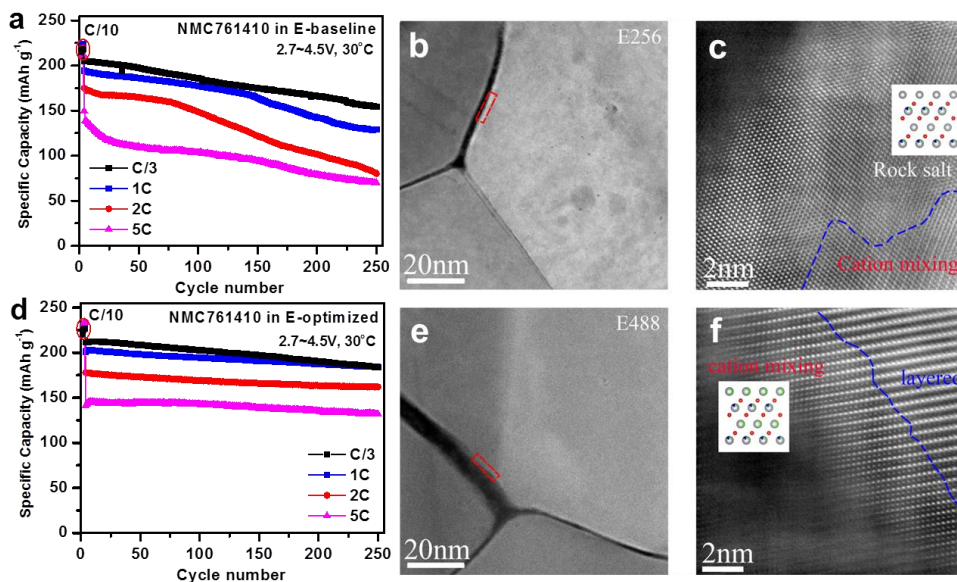


Figure II.3.F.3 (a, d) Cycling performance of Ni-rich $\text{LiNi}_{0.76}\text{Mn}_{0.14}\text{Co}_{0.10}\text{O}_2$ cathode in (a) E-baseline (1 M $\text{LiPF}_6/\text{EC-EMC}$) and (d) E-optimized (0.6 M LiTFSI , 0.4 M LiBOB , and 0.05 M LiPF_6 in EC-EMC) electrolytes during cycling at C/3, 1C, 2C, 5C rates (after 3 formation cycles at C/10) between ~ 2.7 and ~ 4.5 V. (b, c; e, f) HAADF-STEM images of Ni-rich $\text{LiNi}_{0.76}\text{Mn}_{0.14}\text{Co}_{0.10}\text{O}_2$ after 100 cycles at C/3 between ~ 2.7 and ~ 4.5 V in (b, c) E-baseline electrolyte and (e, f) E-optimized electrolyte.

(2) Stabilizing both Lithium anode and Ni-rich NMC cathode by LiBOB additive to enhance the cycle life of batteries

Lithium bis(oxalato)borate (LiBOB) has been confirmed as an effective additive to the LiPF_6 -based electrolyte for enhancing the long-term cycling performance, rate capability and voltage stability of the Ni-rich $\text{LiNi}_{0.76}\text{Mn}_{0.14}\text{Co}_{0.10}\text{O}_2$ (NMC76) based Li metal batteries. With 2% LiBOB in the electrolyte, the $\text{Li}||\text{NMC76}$ is able to achieve a high capacity retention of 96.8% after 200 cycles under C/3 rate ($1\text{C} = 200 \text{ mA g}^{-1}$), which is one of the best results reported for batteries based on Ni-rich NMC cathode and Li metal anode. The significantly improved electrochemical performances could be attributed to the stabilization of both NMC76 cathode/electrolyte and Li metal anode/electrolyte interfaces. On the one hand, LiBOB-containing electrolyte facilitates the formation of a more compact solid electrolyte interphase on the Li metal surface that largely alleviates the corrosion of Li metal anode. On the other hand, LiBOB additive enables formation of a thinner cathode electrolyte interface layer, which efficiently prevents the corrosion of cathode interface and mitigates the formation of disordered rock-salt phase after cycling. The fundamental findings of this work highlight the importance of identifying the dual effects of electrolyte additives on stabilizing the cathode and anode interfaces at the same time, so as to enhance the long-term cycle life of high energy density battery systems.

LiBOB additive facilitates the formation of a more compact solid electrolyte interphase on the Li metal surface that largely alleviates the corrosion of Li metal anode, moreover, LiBOB additive also favor the formation of a thinner cathode electrolyte interface layer, which efficiently prevents the corrosion of cathode interface and mitigates the formation of disordered rock-salt phase after cycling. The comparisons of the first cycle charge-discharge voltage profiles and the long-term cycling performances of $\text{Li}||\text{NMC76}$ cells using E-baseline and the electrolytes with various LiBOB contents in the voltage of 2.7-4.5 V are shown in Figure II.3.F.4a and b. The cells using electrolytes without and with 0.5%-2% LiBOB deliver similar initial discharge capacity. With the addition of LiBOB in the baseline electrolyte, the discharge capacity of the cell is much more stable with cycling than those using the baseline electrolyte. When LiBOB content is increased from 0.5% to 2% in the electrolyte, the stability of the $\text{Li}||\text{NMC76}$ cell improves. However, further increasing LiBOB content to 5% leads to faster capacity fading. The cell with 2% LiBOB exhibits the highest capacity and the most stable cycling performance among all these cells. In order to verify the enhanced cycling performance of $\text{Li}||\text{NMC76}$

cells with E-2%LiBOB, the long-term cycling and rate performance have been investigated under different current densities. All of the testing results show that the cells using E-2%LiBOB deliver more stable cycling performance and higher rate performance. When cycling the cells under C/5 charging and 5C discharging (Figure II.3.F.4c), the Li||NMC76 cell with E-2%LiBOB shows an excellent capacity retention reaching 86.1% along with stable CEs (99.6%) for 500 cycles, while the cell with E-baseline is completely dead after 300 cycles. To better understand the functionality of LiBOB toward the cathode and the anode, the following measurements have been carried out:

- The long-term cycle performance test under C/3 current rate has been interrupted every 50 cycles with 2 cycles under C/10 current rate to identify the polarization effect on the capacity retention of the cells using the electrolytes with and without LiBOB additive.
- Electrochemical impedance spectra (EIS) were also employed to further confirm the evolution of cell polarization during cycling process of Li||NMC76 cells using E-baseline and E-2%LiBOB.
- The surface morphologies and corrosion layers of Li metal anodes harvested from cells after 200 cycles using electrolytes with and without LiBOB additive were investigated by scanning electron microscopy (SEM).
- X-ray photoelectron spectroscopy (XPS) was employed to investigate the compositions of the CEI layer on the cycled electrodes.
- The structure stability of the NMC76 cathode were investigated through scanning transmission electron microscopy (STEM), and the comparison among the pristine electrode, the electrodes cycled in E-baseline and E-2%LiBOB after 200 cycles is shown in Figure II.3.F.4d-i. The pristine NMC76 particle (Figure II.3.F.2d, 2g) exhibits a slight $\text{Li}^+/\text{Ni}^{2+}$ cation mixing layer (< 2 nm) due to the similar radius of Li^+ (0.76 Å) and Ni^{2+} (0.69 Å) in Ni-rich NMC cathodes. After 200 cycles in E-baseline, an obvious cation mixing layer and large quantity of disordered rock-salt phase were discovered on the surface of NMC76 particles. The Ni-rich NMC cathode particles cycled in E-2%LiBOB demonstrate a very thin cation mixing layer without obvious rock salt phase being found. The reduced formation of disordered rock-salt phase could well explain the better stabilized voltage profiles of the NMC76 layered cathode in E-2%LiBOB.

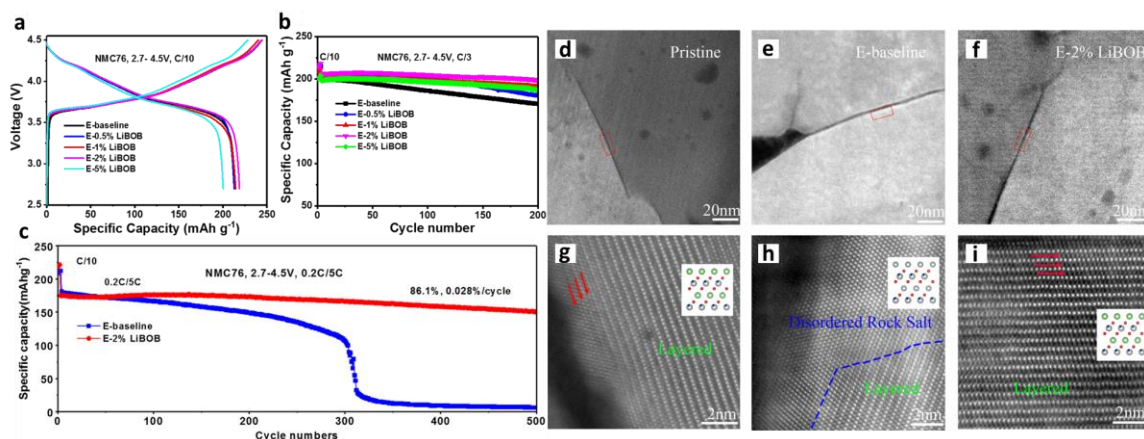


Figure II.3.F.4 (a) First cycle charge-discharge voltage profiles and (b) cycling performance of Li||NMC76 cells using E-baseline and four LiBOB-added electrolytes (E-n%LiBOB). (c) Comparison of long-term cycling performance of Li||NMC76 using E-baseline and E-2%LiBOB for 500 cycles under 0.2C charging and 5C discharging. (d-i) STEM-HAADF images of the surface layers of the NMC76 cathodes. (d) Pristine sample without cycling and (g) enlarged area from the region marked with red rectangle in (d). (e) After 200 cycles in E-baseline and (h) enlarged area from the region marked with red rectangle in (e). (f) After 200 cycles in E-2%LiBOB and (i) enlarged area from the region marked with red box in (f). The insets in panels (g), (h) and (i) are the structural models illustrating lattice transformation from surface into bulk.

Conclusions

Several approaches have been adopted to improve the structural and interfacial stability of high-energy-density Ni-rich NMC cathode materials for LIBs. In one approach, an optimized electrolyte (0.6 M LiTFSI, 0.4 M LiBOB, and 0.05 M LiPF₆ in EC-EMC) was used to improve the stability of electrolyte/electrode interface of Ni-rich LiNi_{0.76}Mn_{0.14}Co_{0.10}O₂. The optimized electrolyte significantly improved the long-term cycling stability of LiNi_{0.76}Mn_{0.14}Co_{0.10}O₂ at different C rates ranging from C/3 to 5C. Remarkably, these Li||NMC76 cells can deliver a high discharge capacity of >220 mAh g⁻¹ (846 Wh kg⁻¹) and retain more than 80% capacity after 1000 cycles at high charge/discharge current rates of 2C/2C (1C = 200 mA g⁻¹). This excellent electrochemical performance can be attributed to the greatly enhanced structural/interfacial stability of both the Ni-rich NMC76 cathode material and the Li metal anode using the optimized electrolyte. LiBOB additive has also been used to further improve the stability of Ni-rich based Li||NMC76 cells. The significantly improved electrochemical performances could be ascribed to the stabilization of both NMC76 cathode/electrolyte and Li metal anode/electrolyte interfaces. On the one hand, LiBOB-containing electrolyte facilitates the formation of a more compact solid electrolyte interphase on the Li metal surface that largely alleviates the corrosion of Li metal anode. On the other hand, LiBOB additive enables the formation of a thinner cathode electrolyte interface layer, which efficiently prevents the corrosion of cathode interface and mitigates both cathode and anode interfaces largely enhance the long-term cycle life of high energy density battery systems.

Based on the above fundamental understanding, future work will be focused on further improve the interfacial stability of electrode/electrolyte through surface coatings, novel electrolytes/additives. EIS and AFM will be used to perform in situ study on the interphase kinetics and stability of Ni-rich NMC cathode materials.

Key Publications

1. W. Zhao, J. Zheng, L. Zou, H. Jia, B. Liu, M.H. Engelhard, and C. Wang, Wu Xu, Y. Yang, J.-G. Zhang., "High Voltage Operation of Ni-Rich NMC Cathodes Enabled by Stable Electrode/Electrolyte Interphases." *Advanced Energy Materials* 8, no. 19:1800297, doi:10.1002/aenm.201800297,07/05/2018.
2. W. Zhao, L. Zou, J. Zheng, H. Jia, J. Song, M.H. Engelhard, and W. Xu, Yang Yong, Ji-Guang Zhang, "Simultaneous Stabilization of LiNi_{0.76} Mn_{0.14}Co_{0.10}O₂ Cathode and Lithium Metal Anode by Lithium Bis(oxalato)borate as Additive." *ChemSusChem* 11, no. 13:2211-2220, doi:10.1002/cssc.201800706,07/11/2018.
3. J. Zheng, P. Yan, L. Estevez, C. Wang, and J.-G. Zhang. "Effect of Calcination Temperature on the Electrochemical Properties of Nickel-rich Cathode LiNi_{0.76}Mn_{0.14}Co_{0.10}O₂ for Lithium-ion Batteries." *Nano Energy* 49, doi:10.1016/j.nanoen.2018.04.077,07/01/2018.
4. P. Yan, J. Zheng, T. Chen, L. Luo, Y. Jiang, K. Wang, and M. Sui, Ji-Guang Zhang, Sulin Zhang & Chongmin Wang, "Coupling of Electrochemically Triggered Thermal and Mechanical Effects to Aggravate Failure in a Layered Cathode." *Nature Communications* 9, no. 2437:Epup, doi:10.1038/s41467-018-04862-w, 06/22/2018.

II.3.G *In situ* Solvothermal Synthesis of Novel High-Capacity Cathodes (BNL)

Feng Wang, Principal Investigator

Brookhaven National Lab
Sustainable Energy Technologies Department
Upton, NY 11973
E-mail: fwang@bnl.gov

Jianming Bai, Principal Investigator

Brookhaven National Lab
National Synchrotron Light Source II
Upton, NY 11973
E-mail: jmbai@bnl.gov

Peter Faguy, DOE Technology Development Manager

U.S. Department of Energy
E-mail: Peter.Faguy@ee.doe.gov

Start Date: October 1, 2015

End Date: September 30, 2018

Project Funding (FY18): \$1,050,000

DOE share: \$1,050,000

Non-DOE share: \$0

Project Introduction

There has been considerable interest in developing new electrode materials for Li-ion batteries (LIBs), and many promising materials were predicted through *ab-initio* calculations with indicated high Li-storage capacity and/or reduction in cost, but very few of them have been brought into the real world through synthesis and indeed commercialized for use in LIBs. The challenge lies in the fact that synthesis is such a complex process being affected by a variety of parameters (precursor concentration, temperature, pressure, *pH* value, cation type and reaction time ...), and often undertaken under *non-equilibrium* conditions that has been found hard to predict by theoretical computations. So far, making new materials often relies on trial and error. *In situ*, real-time probing of the intermediate phases and their structural evolution as the materials are being synthesized can provide the details of the synthesis process, elucidating how temperature, pressure, time and the precursor concentrations affect the reaction pathways. Building on the established *in situ* capabilities/techniques for synthesizing and characterizing electrode materials, this project will undertake *in situ* studies of synthesis reactions under real conditions to identify the intermediates and to quantify the thermodynamic and kinetic parameters governing the reaction pathways. The results of such studies will enable strategies to ‘dial-in’ desired phases and properties, opening a new avenue for developing novel high-capacity cathodes through synthetic control of the phase, stoichiometry, and morphology.

Objectives

The goal is to develop novel high-capacity cathodes through synthetic control of the phase, stoichiometry and morphology.

Approach

One unique approach taken in this project is to develop new battery materials through *in situ* probing and kinetic control of synthesis reaction using the world-leading facilities at Brookhaven and other national laboratories. More specifically, synchrotron x-ray, neutron-based *in situ* techniques are developed and applied to studies of synthesis reaction and kinetic pathways during preparation of high-capacity cathode materials. Insights obtained from *in situ* studies will provide knowledge on how the synthesis conditions affect the kinetics and pathways of synthesis reaction. Such studies will be combined with detailed structural and electrochemical characterization of the synthesized materials, to gain understanding of how structure, composition, and synthesis affect their electrochemical properties, eventually enabling design and synthesis of phase-pure cathode materials of desired stoichiometry and morphology.

Results

Development of *in situ* multimodal techniques for probing synthesis reaction *In situ* cells for studying synthesis reaction are mostly designed for bulk synchrotron x-ray measurements, *i.e.* collecting x-ray diffraction (XRD) or other spectral data from a large amount of materials, and not suited for studying local structural/chemical evolution in heterogeneous materials. Starting with the cell design for *in situ* XRD measurements, a new design of the sample loading configuration and environment was developed, allowing for multimodal characterization of solid-state synthesis reaction under controlled atmosphere. Such type of cells have been tested in studying synthesis of Ni-rich Ni-Mn-Co (NMC) layered oxides with, using a combination of *in situ* x-ray fluorescence (XRF) imaging, x-ray absorption near-edge structure (XANES) spectroscopy, XRD, and x-ray total scattering (XTS) techniques (Figure II.3.G.1). Multimodal characterization of a same synthesis process allows obtaining important information about local cationic diffusion and ordering, by capturing elemental distribution, oxidation and ordering of the constituent transition metal cations within individual particles as they are being synthesized.

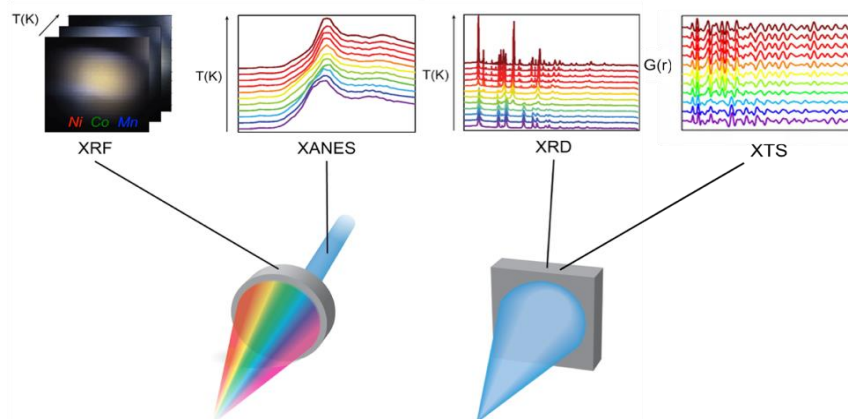


Figure II.3.G.1 Schematic illustration of the experimental setup for *in situ* probing of local elemental diffusion, oxidation and ordering of cations during synthesis of Ni-Mn-Co (NMC) layered oxides. A new design of sample loading configuration and environment in *in situ* reactors was developed, allowing multimodal characterization of elemental diffusion, oxidation, structural ordering within individual particles, via a combination of synchrotron XRF imaging, XANES spectroscopy, XRD and XTS (coupled with pair distribution function (PDF) analysis).

***In situ* XRD studies of synthesis of Ni-rich NMC: topotactic transformation.** A multimodal *in situ* x-ray characterization approach is employed to investigate the synthesis process in preparing $\text{LiNi}_{0.77}\text{Mn}_{0.13}\text{Co}_{0.10}\text{O}_2$ (NMC771310) from its hydroxide counterpart, at scales varying from the long range to local individual octahedral units. Temperature-resolved *in situ* synchrotron XRD was first applied to follow the structural evolution in hydroxide precursors and intermediates during the heating process; some of the results were presented in Figure II.3.G.2. Overall, the hydroxide precursors underwent 3 stages as temperature increased: at Stage I ($< 250\text{ }^\circ\text{C}$), there was no phase transformation but the lattice of the transition metal hydroxides continuously shrank in an anisotropic way; at Stage II ($250\text{--}500\text{ }^\circ\text{C}$), abrupt phase transformation occurred, from hydroxides to an intermediate $\text{Ni}_{0.77}\text{Mn}_{0.13}\text{Co}_{0.10}(\text{OH}_{1-x}\text{Li}_y)_2$ and then layered oxide, but with serious Li/Ni mixing at octahedral sites. At Stage III ($> 500\text{ }^\circ\text{C}$), the layered phase underwent a fast Li/TM ordering process, with TM ions in the Li layers migrating to TM layers.

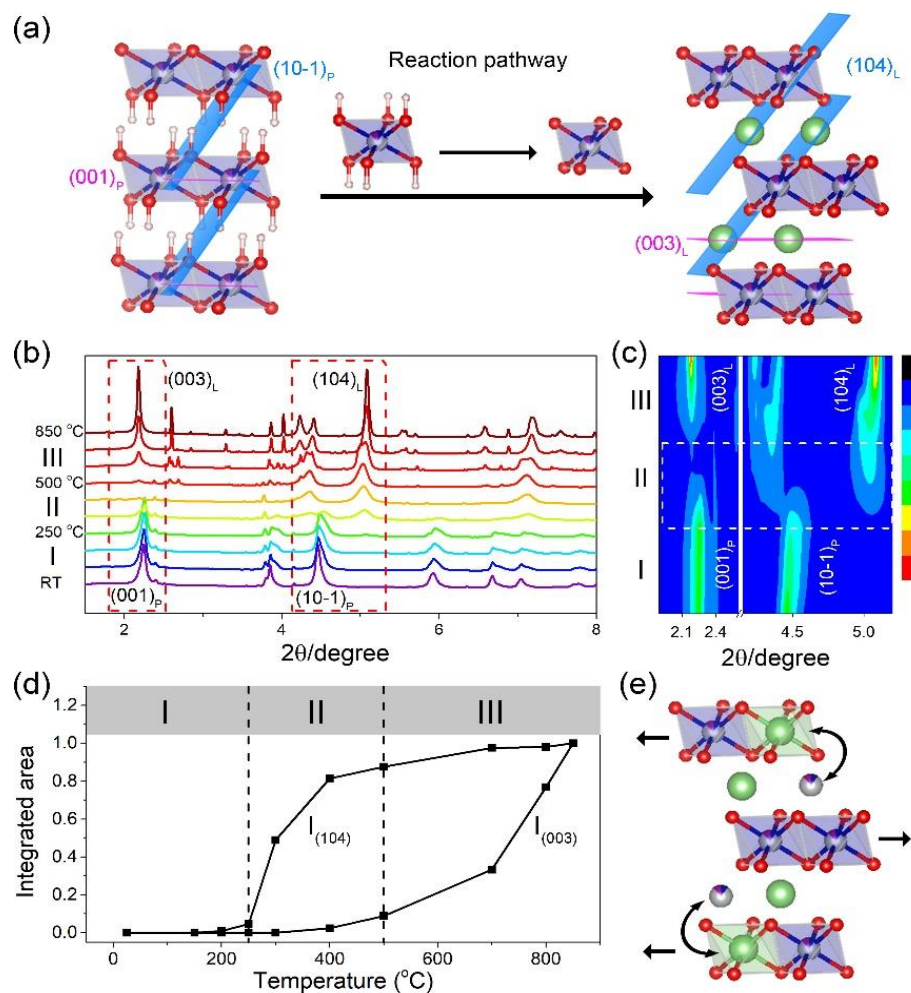


Figure II.3.G.2 **Structural transformation during synthesis of the layered $\text{LiNi}_{0.73}\text{Mn}_{0.13}\text{Co}_{0.10}\text{O}_2$ (NMC771310) from the hydroxide precursor.** (a) Schematic of the transformation from layered hydroxide precursors (P-3m1) to layered oxides (R-3m), and the corresponding change in the basic building units (BBUs), from initial $\text{TM}(\text{OH})_6$ to the TMO_6 octahedra. (b) Temperature-resolved in situ synchrotron XRD patterns, showing three sequential stages during the entire synthesis process: I (below 250 °C), II (250–500 °C) and III (above 500 °C). (c) Contour plot of selected regions in XRD patterns (marked with red dashed rectangles). (d) Evolution of integrated intensities of (003) and (104) peaks (denoted as $I_{(003)}$ and $I_{(104)}$), being normalized to their corresponding values at 850 °C, which reflect the behaviors of cationic disordering/ordering (by $I_{(003)}$) and Li insertion (by $I_{(104)}$) as the temperature increases. (e) Schematic of atomic rearrangement, inter-layer gliding, and Li/Ni mixing (illustrated by arrows) in the intermediate $(\text{Ni}_{0.77}\text{Mn}_{0.13}\text{Co}_{0.10}(\text{OH}_{1-x}\text{Li}_y)_2)$ during Stage II.

In the intermediate $\text{Ni}_{0.77}\text{Mn}_{0.13}\text{Co}_{0.10}(\text{OH}_{1-x}\text{Li}_y)_2$, a significant amount of Li has been inserted into the structure, but highly mixed with Ni at octahedral sites. Inter-layer gliding between neighboring TM layers occurred (driven by Li insertion); while the layered framework of the hydroxide precursor did not break down throughout the synthesis process, in contrast to the decomposition process reported in other types of precursors (such as acetate-based precursors; being reported previously in this project). Such a process resembles a topotactic transformation that have been commonly observed during electrochemical intercalation in NMC cathodes, or traditional epitaxial or topotactic growth at high temperatures. The observation of the topotactic transformation, with the retention of the layered framework, should be common during the solid-state synthesis of NMC layered oxides when the hydroxides are used as precursors (despite their different compositions). The retention of the layered framework through topotactic transformation may provide advantage for preparing NMC oxides.

***In situ* PDF studies of synthesis of Ni-rich NMC: cationic ordering within TMO_6 octahedra.** Results from *in situ* XRD analysis indicate that the overall framework (built on the edge-sharing octahedra) was preserved during the transformation from layered hydroxides to oxides. Nevertheless, the local structure/chemical evolution in the intermediates is complex, involving proton/ Li^+ exchange, and the related cationic disordering, and could not be resolved from XRD alone. Therefore, the local synchrotron x-ray probing technique, total scattering coupled with PDF analysis, was also applied to gain details about local structural evolution during synthesis (using the same heating procedure as for *in situ* XRD). Figure II.3.G.3 shows the temperature-resolved x-ray PDF patterns obtained from Fourier transform of the total scattering data, showing not only the overall evolution in the long range (as from the *in situ* XRD), but additional details about local structural ordering. Specifically, the shift of the TM-O and TM-TM peaks to small r direction indicates TM-O bond length and TM-TM interatomic distance are both shortening as the temperature increases (Figure II.3.G.3b). In contrast to the gradual decrease of the TM-O bond length due to the oxidation of TMs, the TM-TM interatomic distance decreases abruptly between 200-300 °C, by a factor of ~ 10 , cannot be solely explained by the oxidation but by the increase of O-TM-O bond angle in TMO_6 , arising from the phase transformation from the hydroxide to the layered phase. Consequently, the abrupt decrease of the TM-TM distance (and so the fast increase of the atomic density), leads to the quick increase of integrated intensity of TM-TM peak.

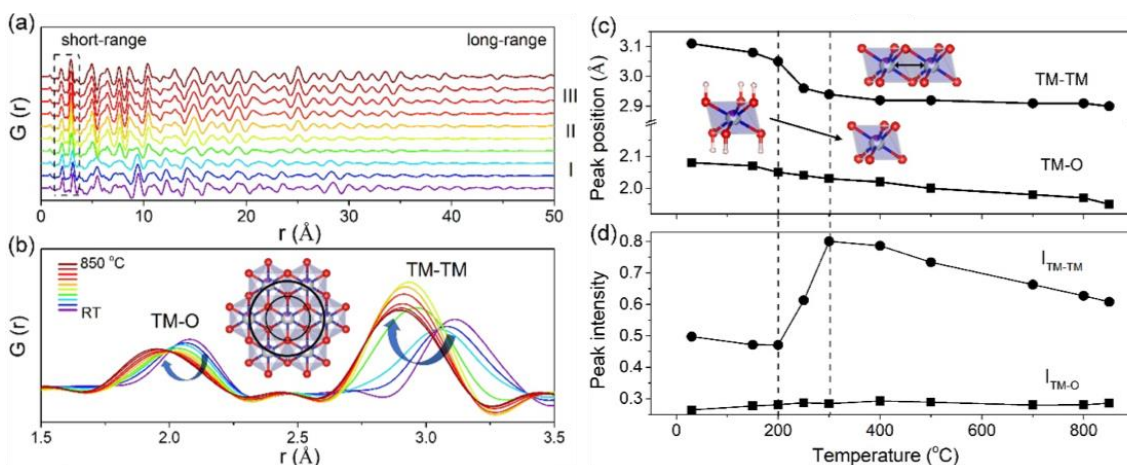


Figure II.3.G.3 **Dynamic process of local structural ordering within TMO_6 octahedra during synthesis of NMC771310.** (a) Temperature-resolved in situ PDF patterns in a wide r range, showing changes in long- and short-range ordering. (b) Enlarged low r range ($r = 1.5\text{--}3.5$ Å, marked by the dashed square in (a)), wherein the two peaks at 1.6–2.4 Å, and 2.5–3.5 Å correspond to the scattering signals of TM-O and TM-TM atomic pairs, respectively. (c) Positions of TM-O and TM-TM peaks as a function of temperature (curves with squares and circles, respectively), showing the evolution of the interatomic distances. (d) Integrated intensity of TM-O and TM-TM peaks (curves with squares and circles, respectively; denoted $I_{\text{TM-O}}$ and $I_{\text{TM-TM}}$) as a function of temperature.

***In situ* XANES studies of synthesis of Ni-rich NMC: preferential oxidation within TMO_6 octahedra.**

From *in situ* PDF, the local structural changes within TMO_6 octahedra, including the variations of bond lengths and angles, and the atomic density increase, should be closely related to the site-dependent oxidation of cations in the TMO_6 octahedra. Nevertheless, the scattering factors of the three types of TMs (Ni, Mn, Co) to x-ray are similar, so the oxidation of Ni, Mn, Co cannot be distinguished by PDF. To better understand of the local cationic oxidation and ordering in TMO_6 octahedra (involving Ni, Mn, Co), elemental-specific XANES analysis was carried out. The main results are presented in Figure II.3.G.4. The K-edges of the 3 elements (Ni, Co and Mn) all shift to high energies, indicating oxidation from the initial $2+$ in the hydroxides to their high oxidation states; however, their oxidation behaviors are different: the Ni^{2+} was not oxidized until the temperature increases to 250 °C (Stage I); it then slowly oxidizes in Stages II and III. In contrast, Co and Mn quickly oxidize almost fully to Co^{3+} and Mn^{4+} respectively (by Stage I). Such an observation of preferential

oxidation to Co and Mn over Ni may explain the cationic disordering and ordering during the topotactic transformation process (as to be discussed below).

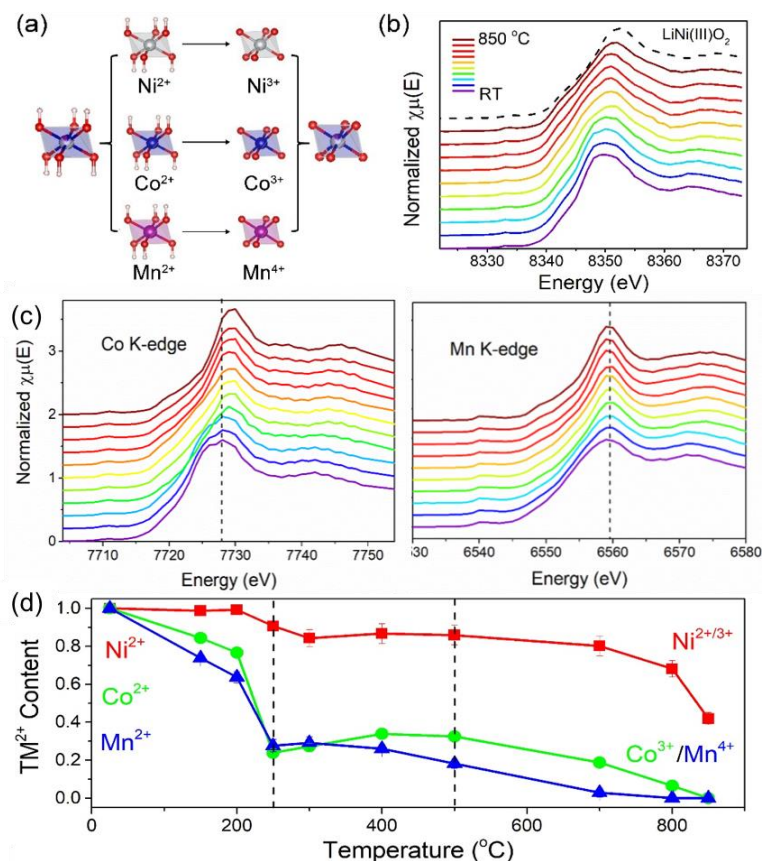


Figure II.3.G.4 **Oxidation dynamics of the constituent cations during synthesis of NMC771310.** (a) Schematics of the transformation of the octahedra associated with the hydroxides, namely, (Ni²⁺)(OH)₆, (Co²⁺)(OH)₆, and (Mn²⁺)(OH)₆ into octahedra associated with the layered oxides, (Ni³⁺)O₆, (Co³⁺)O₆, and (Mn⁴⁺)O₆, which involves oxidation of the three constituent cations (Ni, Co, Mn). (b-c) Representative XANES spectra for Ni, Co, Mn K-edges from in situ measurements. (d) Normalized Ni²⁺, Co²⁺, and Mn²⁺ contents as a function of temperature.

Cationic ordering coupled to reconstruction of basic building units during synthesis of Ni-rich NMC.

Results from combined XRD, PDF and XANES analysis provide details about the local change within octahedra, as schematically illustrated in Figure II.3.G.5. Simply put, the preferential oxidation of (Co²⁺)(OH)₆ and (Mn²⁺)(OH)₆ octahedra in Stage I (< 250 °C) induces partial Li insertion, which is essential to maintaining the layered framework in the intermediate phase. On the other hand, the slow oxidation of Ni triggers O loss and symmetry breaking of NiO₆ octahedra, which further leads to Li/Ni mixing. In Stage III (>500 °C), further oxidation of Ni induces cationic ordering and, concomitantly, the symmetry reconstruction of the octahedra from NiO_{6-x} to NiO₆. The two processes couple with each other, eventually leading to a highly ordered structure. The symmetry breaking due to the decomposition of Ni(OH)₆ into NiO_{6-x} and then reconstruction from NiO_{6-x} to NiO₆ octahedra determines the reaction pathway, featuring Li/Ni mixing/ordering from low to high temperatures. Through first-principles calculations (not shown here), very low activation energy for Ni²⁺ migration, with a value comparable to that of Li⁺ migration was predicted and attributed to the symmetry breaking of NiO₆ octahedra.

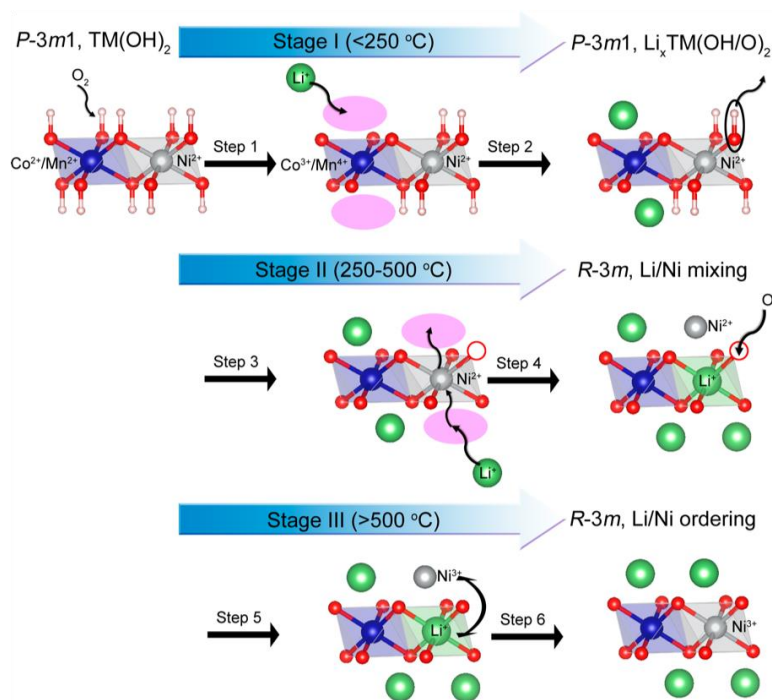


Figure II.3.G.5 **Reaction pathway, with cationic ordering coupled with reconstruction of NiO₆ octahedra, during synthesis of NMC771310**, at the three sequential stages: I (below 250 °C); II (250 °C–500 °C); III (above 500 °C). The protons (H⁺), Li⁺ ions, and vacancies (V_o), are represented by magenta, green spheres and purple ellipses, respectively.

Findings from this study highlight the vital importance of tuning the symmetry of NiO₆ octahedra during synthesis of high-Ni layered oxides of high structural ordering. For example, if one could avoid the symmetry breaking of NiO₆ octahedra by inhibiting the decomposition of Ni(OH)₆ octahedra, or making Ni(OH)₆ oxidize like Co(OH)₆ and Mn(OH)₆, Li/Ni mixing could be alleviated and even completely prevented in the initial phase transformation at low temperatures. The idea could potentially be implemented by providing a strong oxidizing environment or doping to lower the energy barrier for oxidation of Ni(OH)₆ octahedra. The findings from this study may help to pave the way for making high-Ni layered oxides without Li/Ni mixing.

Tracking cationic inter-diffusion during synthesis of Ni-rich NMC by *in situ* spectro-imaging. The new cell design (Figure II.3.G.1) not only enables tracking the structural evolution within multiple particles, but also spectro-imaging of both elemental distribution and valence evolution in a single particle using sub-micron x-ray absorption near edge spectroscopy (micro-XANES) and fluorescence (XRF) microscopy. By taking the advantage of high flux at NSLS-II, temperature-resolved spectro-images were successfully taken from individual particles during preparing Ni-rich layered oxides with compositional heterogeneity, as shown in Figure II.3.G.6. Local oxidation dynamics and re-distribution of the TMs were obtained from the spectro-images taken from the selected center and surface areas of a single particle (representing Ni-rich and Mn-rich areas, respectively). The local-position-dependent oxidation behavior of Ni²⁺ should be related with the elemental distribution, particularly the different Mn content in the core and at the surface. Since Mn²⁺ tends to be oxidized to Mn⁴⁺ at low temperatures (below 250 °C; as verified by *in situ* XANES experiments), Ni stayed as 2+ for the charge compensation at the near-surface region where Mn⁴⁺ is highly concentrated.

Re-distribution of Ni, Co and Mn also occurred as temperature increased. The Ni content at the center continuously decreased, indicated by the color change from dark red to red; correspondingly, the Mn content at the center continuously increased. The distribution of Co content also became more uniform with the increasing temperature. In short, the inter-diffusion of transition metals (Ni, Co and Mn) with the increase of temperature was clearly observed during the calcination. The diffusion of the three elements was all along the

directions from high concentration area to low concentration area, indicating that the driving force is the concentration gradient. Quantitative analysis is underway for understanding of the intrinsic role of interplay between cationic ordering and diffusion in governing compositional gradient, and findings from such studies may provide guidance to synthetic design of Ni-rich layered oxide cathodes of desired compositional and structural properties.

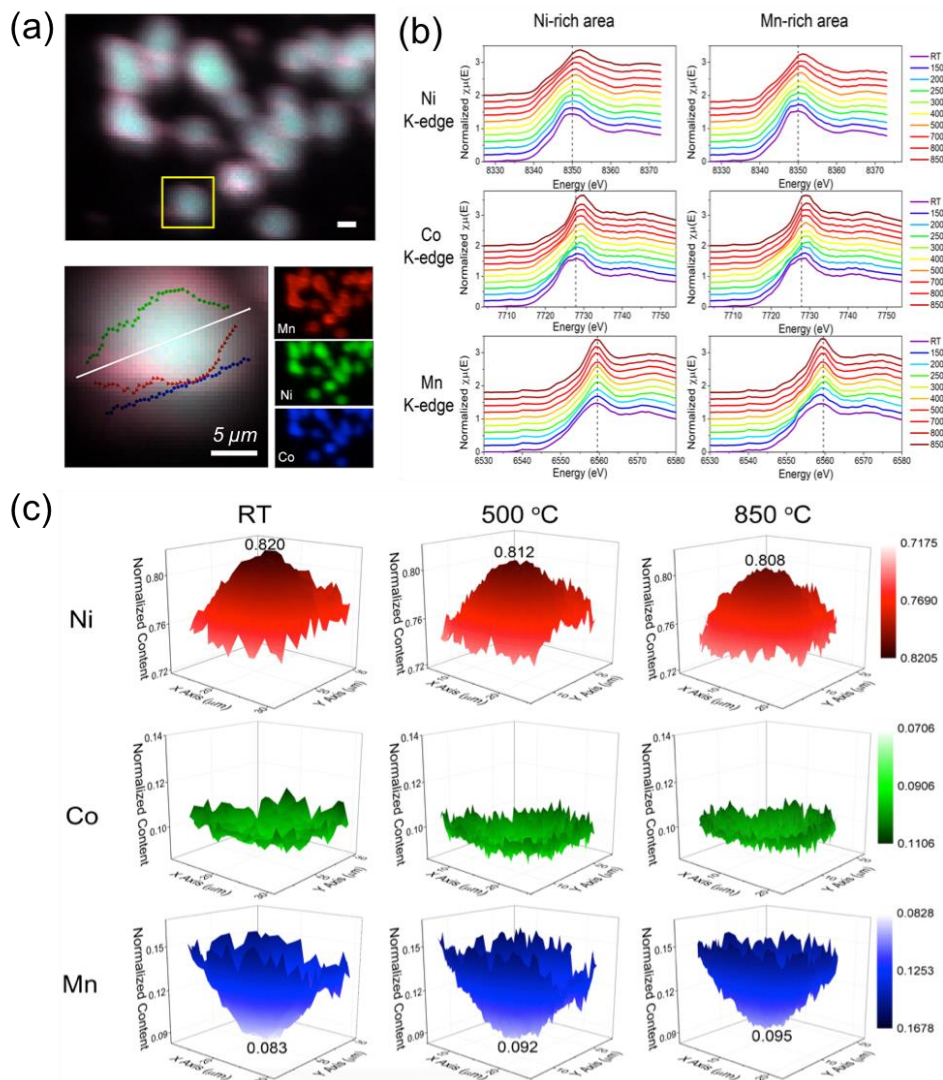


Figure II.3.G.6 **In situ tracking of local cationic oxidation/ordering during synthesis of Ni-rich NMC with compositional heterogeneity.** (a) RGB images reproduced from XRF maps of multiple particles and one selected particle (as marked by the yellow square). (b) Temperature-resolved K-edge XANES spectra for all the constituent elements (Ni, Co, Mn), recorded from the Ni-rich (core) and Mn-rich (surface) regions of a single particle (as shown in (a)). (c) Elemental re-distribution as temperature increases, demonstrated by the contour plots of the distribution of Ni, Co and Mn at representative temperatures (room temperature (RT), 500 °C and 850 °C). The X and Y axis were used to indicate the position of the single particle. Each of the sum of Ni, Co, and Mn XRF intensity was normalized to 1 for the convenience of comparison.

Conclusions

In FY18, *in situ* multimodal synchrotron x-ray techniques were developed and employed for studying the synthesis reaction and kinetic pathway in preparing Ni-rich NMC layered oxides. [ENREF 24](#) Significant efforts have been given to *in situ* studies synthesis of $\text{LiNi}_{0.77}\text{Mn}_{0.13}\text{Co}_{0.10}\text{O}_2$ from hydroxide precursors, using the developed multiple techniques, including x-ray diffraction, pair distribution function analysis, and

absorption near-edge spectroscopy. Through *in situ* studies, details about long- and short-range chemical and structural evolution, down to individual basic building units, were obtained, providing evidence showing a topotactic transformation from hydroxides to the layered oxides. Despite the retention of the layered framework, significant change occurred locally within TMO₆ octahedra. Especially, preferential oxidation of Co and Mn over Ni, led to symmetry breaking and reconstruction of NiO₆ octahedra, and, concomitantly, induced Li/Ni mixing/ordering throughout the synthesis process. Findings from this study highlight the fact that cationic disordering is intrinsic to high-Ni layered NMC, generated upon formation of the layered oxides as a result of symmetry breaking in NiO₆ octahedra, and so it is of vital importance to tune the symmetry of NiO₆ octahedra in order to achieve high cationic ordering.

In this fiscal year, another new development is the *in situ* spectro-imaging techniques, specialized for studying local cationic diffusion and ordering, by capturing elemental distribution, oxidation and ordering of the constituent transition metal cations within individual particles as they are being synthesized. The techniques have been applied to studying synthesis of NMC layered oxides with compositional heterogeneity, and quantitative data analysis is now under the way. The results will be reported in the future. Following the efforts in FY18 on *in situ* probing and kinetic control of cationic ordering in the bulk, this project will shift the focus onto synthetic control of local structural ordering and stoichiometry within individual particles, aiming at synthetic design of surface-stabilized high-Ni NMC layered oxides.

Key Publications

1. Y. Duan, L. Yang, M-J. Zhang, Z. Chen, J. Bai, K. Amine, F. Pan and F. Wang “Insights into Li/Ni Ordering and Surface Reconstruction during Synthesis of Ni-rich Layered Oxides” (*submitted*).
2. D. Wang, C. Xin, M-J. Zhang, J. Bai, J. Zheng, R. Kou, J.P. Ko, A. Huq, G. Zhong, C. Sun, Y. Yang, Z. Chen, Y. Xiao, K. Amine, F. Pan and F. Wang “Intrinsic Role of Cationic Substitution in Tuning Li/Ni Mixing in Ni-rich Layered Oxides” (*submitted*).
3. M.J. Zhang, G. Teng, Y.C.K. Chen-Wiegart, Y. Duan, J.Y.P. Ko, J. Zheng, J. Thieme, E. Dooryhee, Z. Chen, J. Bai, K. Amine, F. Pan, F. Wang, Cationic Ordering Coupled to Reconstruction of Basic Building Units during Synthesis of High-Ni Layered Oxides”, **J. Am. Chem. Soc.** 140 (2018) 12484.
4. E.C. Self, L. Zou, M.J. Zhang, R. Opfer, R.E. Ruther, G.M. Veith, B. Song, C. Wang, F. Wang, A. Huq and J. Nanda, 2018. Synthesis and Electrochemical and Structural Investigations of Oxidatively Stable Li₂MoO₃ and xLi₂MoO₃·(1-x)LiMO₂ Composite Cathodes. **Chem. Mater.** 30 (2018) 5061.
5. J. Zheng, W. Zhang, F. Wang, X-Y. Yu, "Enabling liquid solvent structure analysis using hard x-ray absorption spectroscopy with a transferrable microfluidic reactor" **J. Phys. Condens. Matter** 30 (2018), 18LT01.
6. M. Li, J. Liu, T. Liu, M. Zhang and F. Pan, “A versatile single molecular precursor for the synthesis of layered oxide cathode materials for Li-ion batteries” **Chem. Commun.** 54 (2018) 1331.
7. X. Fan, E. Hu, X. Ji, Y. Zhu, F. Han, S. Hwang, J. Liu, S. Bak, Z. Ma, T. Gao, S-C. Liou, J. Bai, X-Q. Yang, Y. Mo, K. Xu, D. Su and C. Wang, “High energy-density and reversibility of iron fluoride cathode enabled via an intercalation-extrusion reaction”, **Nat. Commun.**, 9 (2018) 2324 .

Acknowledgements

The work was supported by the Energy Efficiency and Renewable Energy, Office of Vehicle Technologies of the U.S. Department of Energy under contract DE-SC0012704. We thank the contribution by the team members, Mingjian Zhang, J. Patrick Looney, Yandong Duan, Chong Yin, Yusuf Celebi, and by collaborators, Yu-chen Karen Chen-Wiegart, Juergen Thieme, Eric Dooryhee, Lijun Wu, Yimei Zhu (Brookhaven Nat. Lab), Feng Pan (Peking U.), Khalil Amine, Zonghai Chen, Yang Ren, Chengjun Sun (Argonne National Lab), Jagjit Nanda, Ashfia Huq (Oak Ridge Nat. Lab), Peter Ko (Cornell High Energy Synchrotron Source).

II.3.H Novel Cathode Materials and Processing Methods (ANL)

Jason R. Croy & Arturo Gutierrez, Principal Investigators

Argonne National Laboratory
9700 South Cass Avenue
Lemont, IL 60439
E-mail: croy@anl.gov

Peter Faguy, DOE Technology Development Manager

U.S. Department of Energy
E-mail: Peter.Faguy@ee.doe.gov

Start Date: October 1, 2015
Project Funding (FY18): \$400,000

End Date: September 30, 2018
DOE share: \$400,000

Non-DOE share: \$0

Project Introduction

Current state-of-the-art (SOA), Li-ion cathodes typically deliver $<700 \text{ Wh/kg}_{\text{oxide}}$ (● in Figure II.3.H.1, left). However, in order to meet next-generation transportation targets, less expensive chemistries with energies $>800 \text{ Wh/kg}_{\text{oxide}}$ need to be realized. $\text{LiNi}_a\text{Mn}_b\text{Co}_c\text{O}_2$ (NMC-abc) materials, with $a > 0.6$, show promise in this respect and are currently in development. Nevertheless, it is still uncertain whether safety issues can be adequately addressed as nickel contents increase above $\sim 60\%$ (e.g., NMC-811). In addition, strong growth in the Li-ion market, coupled with increasing demand for Ni-rich cathodes, could lead to issues of supply/demand as well as cost related to Ni-rich NMCs. Figure II.3.H.1 (right) shows techno-economic modeling data performed using ANL's BatPaC platform. Calculations of pack-level energies reveal that layered-layered (LL), $x\text{Li}_2\text{MnO}_3 \cdot (1-x)\text{LiNMCO}_2$ materials represent viable options for Ni-rich chemistries. Previous work in this project has shown that integration of spinel components to form complex $y[x\text{Li}_2\text{MnO}_3 \cdot (1-x)\text{LiNMCO}_2] \cdot (1-y)\text{LiM}_2\text{O}_4$, LL-spinel (LLS) electrodes can further enhance the properties of LL cathodes towards future targets. Furthermore, these LLS compositions are composed of inexpensive, abundant, and safe Mn in concentrations of 50% or more. The work herein reports on continued progress at ANL to stabilize surfaces of LLS systems, further enabling them as alternative high-energy options to nickel-rich NMCs

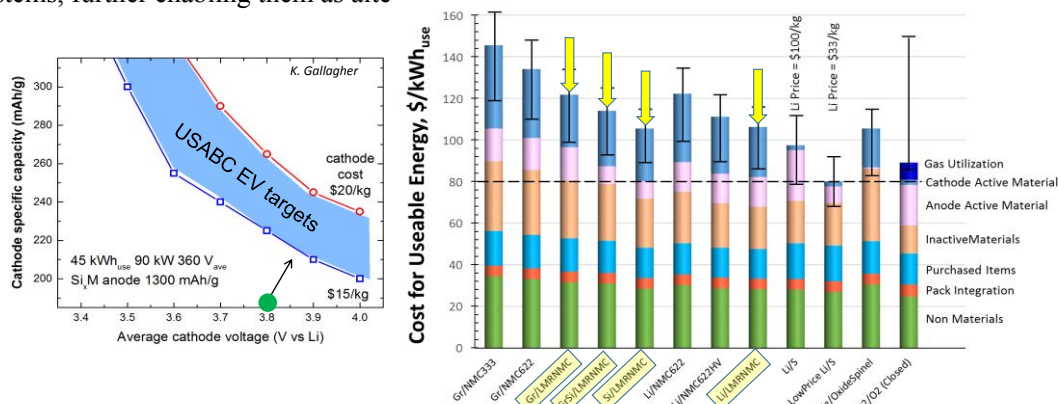


Figure II.3.H.1 (Left) Estimated cathode-oxide specific capacity and voltage requirements for next-gen EV targets (K. Gallagher). (Right) Pack-level cost for useable energy ($\$/\text{kWh}$) as a function of cell couple (S. Ahmed). Calculations performed using BatPaC (<http://www.cse.anl.gov/batpac/about.html>).

Objectives

- To develop low-cost, high-energy and high-power Mn-oxide-based cathodes for lithium-ion batteries that will meet the performance requirements of PHEV and EV vehicles

- Improve the design, composition and performance of advanced electrodes with stable architectures and surfaces, facilitated by an atomic-scale understanding of electrochemical degradation processes

Approach

Exploit the concept and optimize the performance of structurally-integrated “composite” electrode structures with a prime focus on LLS materials. Alternative processing routes will be investigated and Argonne National Laboratory’s comprehensive synthesis and characterization facilities will be used to explore novel surface and bulk structures in the pursuit of advancing the properties of SOA cathode materials.

Results

Electrochemical Validation of High-Energy LLS Electrodes: The baseline LLS used for this project has a nominal composition of $\sim\text{Li}_{1.18}\text{Mn}_{0.54}\text{Ni}_{0.28}\text{Co}_{0.18}\text{O}_y$ with an integrated $\sim 6\%$ spinel component. The sample was prepared via co-precipitation in a continuous stirred tank reactor (CSTR). CSTRs are commonly used in industry to optimize particle morphology and subsequently electrode density. Particle size analysis revealed a D_{50} (μm) = 20.7 and a reasonably high tap density of 2.0 g/cc.

Figure II.3.H.2 shows the cycle life of the baseline LLS in several types of cell configurations collected at 30°C. LLS//Li-metal cell data (Figure II.3.H.2a) was collected between 4.45 – 2.5 V at 15 mA/g, after an activation cycle between 4.6 – 2.0 V. For comparison, similar data was collected on an industrially-prepared, Ni-rich, NMC-532 as the cathode electrode with all cycles between 4.45 – 2.5 V, also at 15 mA/g. Both cells exhibited relatively stable capacity over the 50-cycle test with the LLS delivering a higher capacity (~ 205 mAh/g) compared to the NMC-532 (~ 185 mAh/g). dQ/dV plots of the 1st, 2nd, and 50th cycles for each of the materials are shown in the inset. The redox peaks for NMC-532 remained relatively stable throughout the test with some signs of impedance rise and capacity fade near the end of cycling. For the LLS, growth of low-voltage capacity (voltage fade) was apparent with cycling. However, all capacity was delivered above ~ 2.8 V for all cycles and the LLS achieved consistently higher energy than the NMC-532. At the completion of 50 cycles the LLS oxide-energy was 740 Wh/kg_{oxide} vs. 697 Wh/kg_{oxide} for the NMC-532.

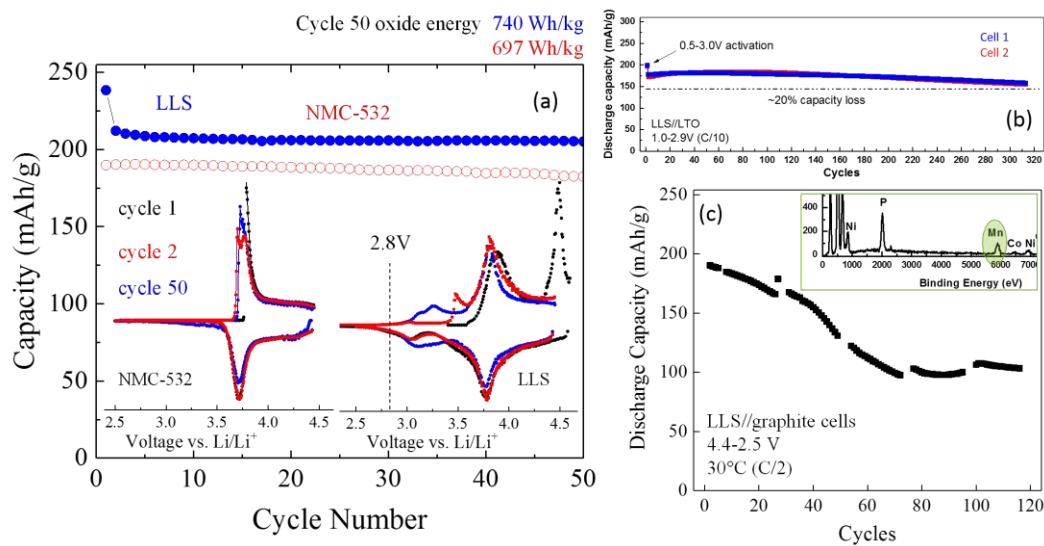


Figure II.3.H.2 (a) Cycle-life of NMC-532//Li and LLS//Li cells cycled between 4.45 – 2.5 V; the LLS//Li cells included a first-cycle activation between 4.6 – 2.0 V. All cycling was carried out at 15 mA/g. (b) LLS//LTO cycle-life between 2.9 – 1.0 V at C/10 (c). LLS//Gr cell data between 4.4 – 2.5 V at C/2. All data was collected at 30 °C.

The baseline LLS was also tested against $\text{Li}_4\text{Ti}_5\text{O}_{12}$ (LTO) anodes. Such cells allow more reliable, extended cycling by avoiding, to a large extent, harmful secondary reactions such as those that occur with the use of graphite (Gr) anodes; e.g., cross-talk, as will be demonstrated below. LLS//LTO cell results are shown in Figure II.3.H.2b. This cell configuration delivered ~ 200 mAh/g on the first-cycle (activation between 3.0 – 0.5

V) and ~180 mAh/g on subsequent cycling in a reduced window of 2.9 – 1.0 V. The LLS//LTO cells (2 cells shown) reveal promising, long-term stability of LLS cathodes, achieving 320 cycles with ~85% capacity retention.

The electrochemical results above demonstrate the viability of LLS electrodes as promising high-energy cathodes. However, as is now well-known, Mn-rich materials suffer from the effects of TM dissolution and loss of active lithium due to side reactions at the surfaces of Gr anodes. Figure II.C.9.2c shows electrochemical testing of LLS//Gr full-cells using a cycling protocol developed by DOE's deep dive program "*Enabling High-Energy/High-Voltage Li-ion Cells for Transportation Applications (HE/HV)*" (Chapters II.C.1-3 of this report). In brief, the protocol consists of five sequential blocks, each block containing three different types of tests with explicit purposes as follows: 1) hybrid pulse power characterization (HPPC) tests to measure the area specific impedance (ASI) of cells as a function of state of charge (SOC) and cycle number; 2) slow (C/10) cycles, performed before the HPPC cycling, to show the evolution of the voltage profiles and true capacity loss while minimizing impedance effects; and 3) C/3 ageing cycles, with a three-hour voltage hold at the top of each cycle to exacerbate the effects of high-voltage (SOC) and accelerate degradation. An initial activation cycle (not shown) was added for the LLS//Gr cells between 4.5 – 2.0 V. HPPC cycles are represented by the breaks in the data every 20 cycles and will be discussed below. The initial capacity of the C/3 ageing cycles was ~190 mAh/g and, unlike the LLS//LTO and LLS//Li cells, this capacity was rapidly lost, reaching ~20% loss within the first 45 cycles. After completion of the full cycling protocol (~120 cycles) the electrodes were harvested in an argon filled glovebox and washed with dimethyl carbonate, dried, and further characterized in two ways: 1) SEM/EDX analysis, and 2) rate testing after reassembling against a fresh Li-metal anode in LLS//Li cells. The EDX analysis of the Gr anode after cycling revealed high levels of Mn (Figure II.3.H.2c, inset). In addition, extremely poor rate performance (not shown), relative to fresh Gr//Li cells, confirmed that the anode was negatively impacted by Mn contamination. These results identify Mn dissolution as a major factor in the degradation of LLS//Gr cells and emphasize the need for stabilization against dissolution and cross-talk phenomena.

Surface Stabilization of Mn-Rich, LLS Electrodes: In order to address the issues related to surface instabilities, different surface-modification strategies were pursued. Presented herein are data sets from two of those strategies including a wet-chemical surface treatment and the use of fluorinated materials in the way of a high-voltage, fluorinated electrolyte and a fluorine containing additive. Both methods were initially investigated using LLS//Li cells.

Wet-chemical treatments included materials such as phosphates, oxides, fluorides, and metal-doped derivatives. Of the numerous tests undertaken several main conclusions could be drawn; 1) almost every material studied, when deposited as a relatively thin, uniform layer, showed some enhanced electrochemical performance with respect to untreated baseline cells – when tested against Li-metal anodes. This observation was particularly true of high-rate data, revealing that facile surface reactions can be easily altered and rate capability improved; 2) for each treatment, subsequent annealing resulted in improved performance for lower, rather than higher, annealing temperatures. This observation emphasizes the need to understand coating material interactions with particular cathode chemistries, where secondary phase formation and/or diffusion into the cathode bulk of coating materials could prove undesirable; and 3) relatively few surface treatments showed the same cycle-life benefits in LLS//Gr cells as compared to LLS//Li cells, revealing the complex, electrode-dependent role of cross-talk in these cells.

Figure II.3.H.3 shows the LLS baseline material after a wet-chemical surface treatment in DI water containing $\text{Al}(\text{NO}_3)_3$. The LLS powder was stirred in the solution for several hours and subsequently heated to various temperatures between 100 – 550°C. Cycle-life testing of each treatment, in LLS//Li cells, was conducted and the results are shown in Figure II.3.H.3a. The cells were first charged between 4.6 – 2.0 V followed by continuous cycling between 4.45 – 2.5 V at 15 mA/g and 30°C. The cycle-life of the material systematically improved as the post-treatment annealing temperature decreased. As observed in the figure, the lowest temperature treatment of 100°C resulted in the best overall performance. Figure II.3.H.3b shows additional

cycling data of the low-temperature (100°C) sample with a cycling protocol intended to expose the surface to harsher conditions (i.e. longer times at higher voltage). The upper cutoff voltage was incrementally increased for the first two cycles from 4.3 to 4.4 V while keeping the lower cutoff voltage constant. The 3rd cycle was then capacity-limited to 250 mAh/g. Subsequent ageing cycles were conducted between 4.5 – 2.5 V at 15 mA/g and 30°C. The low-temperature treatment on LLS enabled a capacity retention of ~99% while the untreated baseline cell lost 20% of its initial capacity in ~40 cycles.

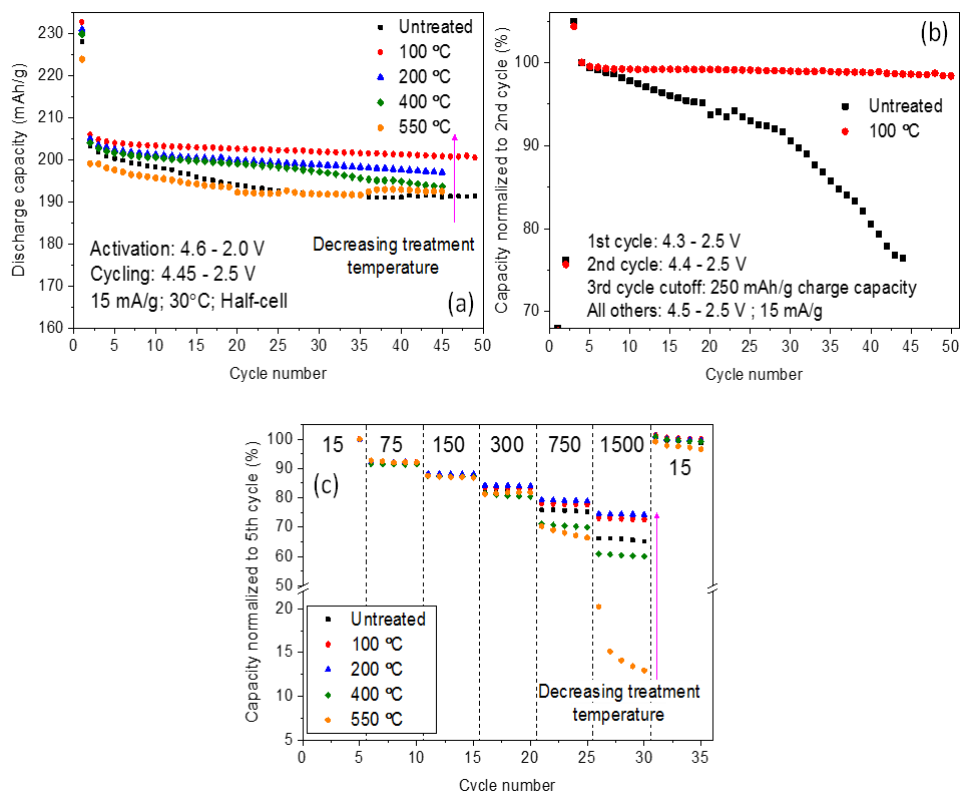


Figure II.3.H.3 LLS//Li cell cycling data for baseline and surface-treated LLS samples under various cycling conditions (a) 1st cycle: 4.6 – 2.0 V ; All others: 4.45 – 2.5 V at 15 mA/g. (b) Capacity retention (%) after voltage opening test: 1st cycle 4.3 – 2.5 V ; 2nd cycle 4.3 – 2.5 V ; 3rd cycle cutoff 250 mAh/g ; All others cycles 4.3 – 2.5 V at 15 mA/g. (c) Rate performance between 4.45 – 2.5 V ; charge current was constant at 15 mA/g ; discharge currents in mA/g are shown along the top of the figure. All data was collected at 30°C.

Figure II.3.H.3c shows the dependence of rate performance on the temperature of post-treatment annealing for the Al(NO₃)₃ treated cathodes. Each LLS//Li cell underwent an activation cycle between 4.6 – 2.0 V followed by rate testing between 4.45 – 2.5 V for all current rates tested (30°C). The charge current was constant at 15 mA/g while the discharge current was varied as indicated along the top of Figure II.3.H.3c. The rate performance was similar for each of the treatments until discharge currents of 300 mA/g were reached. In general, similar to the cycle-life data, cells delivered a greater percentage of the capacity (normalized to capacity delivered with 15 mA/g current) as the processing temperature of the surface treatment decreased. Some samples treated at higher temperatures (≥ 400 °C) were inferior in terms of rate capability to the baseline. The cycle-life and rate performance of the LLS cathode, surface-treated at 100°C, make it a viable candidate for testing in LLS//Gr configurations. This data will be presented below.

Fluorinated Materials for LLS Stabilization: A major factor in cell degradation related to capacity loss is TM dissolution and the associated cross-talk phenomena. Preventing reactions with cathode surfaces, via cathode surface modifications, is one strategy to mitigate dissolution. Another strategy is the development of high-voltage electrolytes that are far less reactive when in contact with delithiated cathode surfaces. Figure II.3.H.4a

compares the capacity retention of a baseline LLS//Li cell cycled continuously between 4.6 – 2.5 V (~C/15, 30°C) in two different electrolyte formulations. The LLS//Li system that used the traditional Gen2 (LiPF₆ in EC:EMC) electrolyte retained ~90% of its original capacity after 50 cycles, while a second LLS//Li cell utilizing a fluorinated (LiPF₆ in DFEC:FEMC) electrolyte formulation exhibited >95% capacity retention. The SEM of the cathode and EDX analysis of the anode reveal key differences between the Gen2 (Figure II.3.H.4b, d) and the fluorinated (Figure II.3.H.4c, e) electrolytes. After cycling at high voltage, the cathode particles tested in Gen2 underwent cracking (Figure II.3.H.4b) while the particles tested in the fluorinated electrolyte exhibited no such degradation (Figure II.3.H.4c). Additionally, the Gen2 cells showed particles having surface deposits after cycling, most likely from unwanted side reactions with the electrolyte, while the particles tested in the fluorine-containing electrolyte revealed much cleaner surfaces. Moreover, the anode tested in Gen2 contained high levels of Mn, evidence of excessive dissolution. The anode tested with the fluorinated electrolyte showed minor levels of Mn, attesting to the usefulness of protecting the cathode surface through the use of fluorine containing electrolytes. This data reveals that stabilization of LLS surfaces can be greatly enhanced through advanced electrolyte formulations and suggest that these materials may be good high-energy cathode options for Li-ion cells utilizing Li-metal anodes.

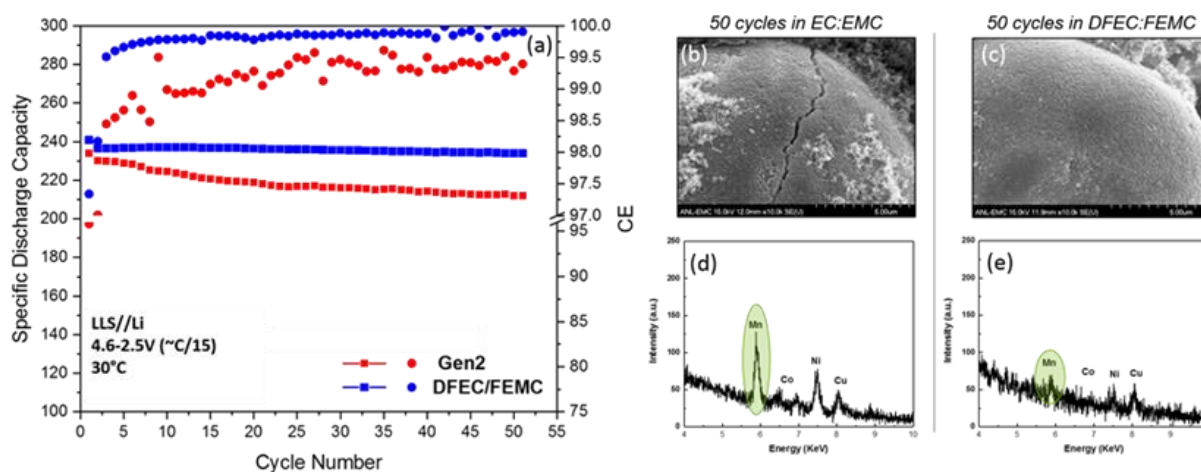


Figure II.3.H.4 (a) Cycle-life performance of an untreated LLS//Li baseline cell in traditional EC:EMC electrolyte (Gen2, red) and a high-voltage, fluorinated electrolyte (DFEC:FEMC, blue). All cycles were between 4.6 – 2.5 V at ~C/15 and 30 °C. (b-e) SEM and EDX analysis of the cathodes cycled in Gen2 electrolyte (b, d) or fluorinated electrolyte (c, e).

The wet-chemical treatment of LLS in Al(NO₃)₃, followed by annealing at just 100°C (hereafter, Al_100°C), performed well when coupled with Li-metal anodes. Figure II.3.H.5a shows the performance of these electrodes against Gr (blue symbols), cycled under the HE/HV protocol discussed above, and compared to a baseline LLS//Gr cell (black symbols). As shown in the figure, some level of improvement in cycle-life, as well as impedance (not shown), was obtained with the use of the coating. However, further enhancement is clearly required.

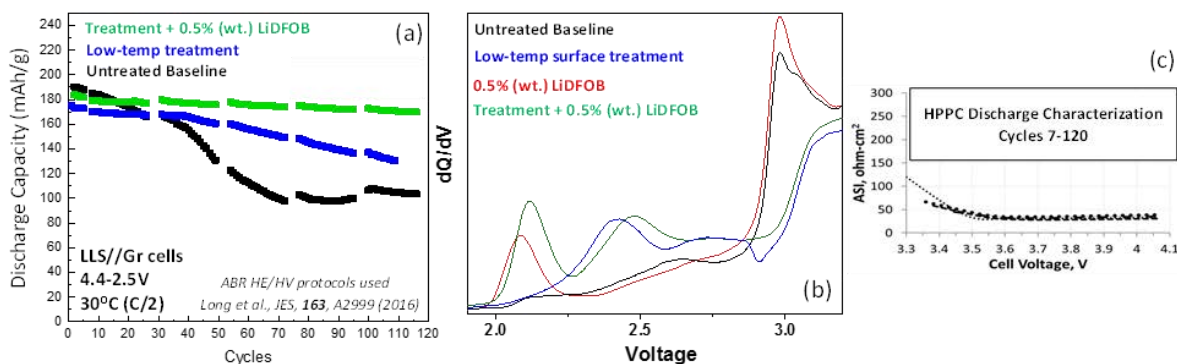


Figure II.3.H.5 (a) LLS//Gr cell data for various treated and untreated samples collected using the HE/HV protocol. Each of the cells underwent an activation cycle between 4.5 – 2.0 V followed by continuous cycling between 4.4 – 2.5 V. (b) Comparison of the first-cycle dQ/dV of four cells containing untreated LLS (black), Al₁₀₀°C LLS (blue), 0.5% LiDFOB in Gen2 (red), and Al₁₀₀°C + 0.5% LiDFOB in Gen2 (green). (c) ASI as a function of voltage (SOC) on discharge, derived from the data in (a), for Al₁₀₀°C LLS cells using 0.5% LiDFOB in Gen2.

A continuation of the study of fluorinated materials was carried out looking at the effects of the fluorinated electrolyte additive, lithium difluoro(oxalato)borate (LiDFOB), in LLS//Gr cells. The additive was dissolved in Gen2 electrolyte and cells were assembled using the untreated LLS baseline as the cathode. The effect of increasing amounts of additive (reported as a weight percent of the total electrolyte weight) were investigated. The overall results of the study (not shown) found that the capacity retention of the system increased and the ASI decreased as the amount of LiDFOB increased from 0.5% to 3%. However, increasing the concentration of LiDFOB also led to concomitant and significant decreases in coulombic efficiency, suggesting continuous decomposition of the additive with cycling. Despite the lower coulombic efficiency, the 3% LiDFOB cell exhibited improved capacity retention when compared to the untreated LLS and Al₁₀₀°C samples.

The effect of combining the wet-chemical treatments and fluorinated materials strategies was also tested using Al₁₀₀°C LLS electrodes with just 0.5% LiDFOB added to the Gen2 electrolyte. The capacity retention improved dramatically and >90% capacity retention was achieved over 120 cycles on test compared to only 54% retention achieved by the untreated baseline cell (Figure II.3.H.5a). As shown in Figure II.3.H.5b, the combination of the low temperature Al(NO₃)₃ treatment and just 0.5% LiDFOB results in unique processes early in cycling that act to synergistically improve the surfaces of the LLS cathodes. In addition, and perhaps most dramatic, the growth in ASI with cycling, as shown in Figure II.3.H.5c, was virtually eliminated over the 120 cycles on test. Though neither of the above treatments, Al(NO₃)₃ nor LiDFOB, alone could substantially improve cell performance, the combination of the two leads to dramatic improvements where just 0.5% of the fluorinated additive is needed when combined with the Al treatment.

Conclusions

The Mn-rich, layered-layered-spinel materials presented herein represent viable options for high-energy, low-cost cathode materials for lithium-ion applications. Techno-economic modeling as well as standardized electrochemical testing reveal that these compositions may already prove competitive with commercial materials such as NMC-532. Stabilization of Mn-rich, LLS surfaces has been demonstrated through several strategies including wet-chemical treatments and advanced electrolyte designs. Furthermore, combinations of surface treatments and electrolyte formulations enable long-term, high-voltage cycling of LLS//Gr cells; validated under established DOE protocols. Ongoing work in the development of LLS cathodes is focused on further stabilization of bulk and surface structures as well as advanced particle synthesis and characterization. The work herein shows significant progress has been made in stabilizing Mn-rich cathodes and continued advances towards next-generation cathode targets are expected.

Key Publications

1. M.M. Thackeray, J.R. Croy, Eungje Lee, A. Gutierrez, M. He, J.S. Park, B.T. Yonemoto, B.R. Long, J.D. Blauwkamp, C.S. Johnson, Y. Shin, and W.I.F. David, *The Quest for Manganese-Rich Electrodes for Lithium Batteries: Strategic Design and Electrochemical Behavior*, Sustainable Energy Fuels, **2**, 1375 (2018).
2. Gutierrez, B. Yonemoto, M. He, E. Lee, H. Iddir, R. Benedek, J.R. Croy, and M.M. Thackeray, *Li- and Mn-Rich Cathodes for Lithium-Ion Batteries: Approaches to Stabilization*, ABAA-10 Meeting (Oakbrook, IL), 22 – 25 October 2017.
3. R. Benedek, *First-Cycle Simulation for Li-Rich Layered Oxide Cathode Material $x\text{Li}_2\text{MnO}_3 \cdot (1-x)\text{LiMO}_2$ ($x=0.4$)*, J. Electrochem. Soc., **165**, A2667 (2018).
4. M.M. Thackeray and J.R. Croy, *Tailoring Integrated Layered and Spinel Electrode Structures for High Capacity Lithium-Ion Cells*, BAT049, DOE Vehicle Technologies Program Annual Merit Review (Arlington, VA), 18-21 June 2018.
5. Michael M. Thackeray and Jason R. Croy, *The Quest for Manganese-Rich Electrodes for Li Batteries: Strategic Design and Electrochemical Behavior – PART I*, DST Energy Storage Workshop, Greenway Woods Resort (White River, Mpumalanga, South Africa) Oct. 12-13th, 2017. **Invited**
6. Jason R. Croy and Michael M. Thackeray, *The Quest for Manganese-Rich Electrodes for Li Batteries: Strategic Design and Electrochemical Behavior – PART II*, DST Energy Storage Workshop, Greenway Woods Resort (White River, Mpumalanga, South Africa) Oct. 12-13th, 2017. **Invited**

Patents

1. A. Mane, J.R. Croy, J. Elam, and M. Balasubramanian, COMPOSITE BI-LAYER COATINGS FOR HIGH CAPACITY CATHODES AND ANODES, Pending 15/968,314.

Acknowledgements

Chapter Acknowledgments Arturo Gutierrez, Meinan He, Eungje Lee, Roy Benedek, John Zhang, Mike Thackeray, Jason R. Croy

II.3.I Advanced Cathode Materials for High Energy Lithium Ion Batteries (LBNL)

Marca M. Doeff, Principal Investigator

Lawrence Berkeley National Laboratory
1 Cyclotron Road, M/S 62R0100
Berkeley, CA 94720
E-mail: mmdoeff@lbl.gov

Peter Faguy, DOE Technology Development Manager

U.S. Department of Energy
E-mail: [E-mail: Peter.Faguy@ee.doe.gov](mailto:Peter.Faguy@ee.doe.gov)

Start Date: October 1, 2015

End Date: September 30, 2018

Project Funding (FY18): \$625,000

DOE share: \$625,000

Non-DOE share: \$0

Project Introduction

The recent development and adoption of large-scale energy storage applications including electric vehicles and smart electric grids have bolstered the need for higher energy dense lithium-ion battery systems. As a result, stringent requirements have been placed to develop next generation battery materials with high specific energy, high energy density, stable cycle life, and improved safety. Of the next generation battery cathode materials, Nickel (Ni)-rich NMC ($\text{LiNi}_x\text{Mn}_y\text{Co}_z\text{O}_2$; $x+y+z \approx 1$, $x \geq y+z$) layered oxide cathodes offer promising theoretical energy densities. Depending on their Ni content and the voltage limits used, the practical capacity can be higher than 200 mAh/g. However, as the Ni content increases, the cathode exhibits decreases in capacity retention upon cycling, poorer structural stability, and poorer thermal stability.^[1] The extraction of Li from the cathode causes the material to undergo significant phase transformations that hinders its performance as well as reducing its thermal stability. The aim of this project is to understand the surface, interfacial, and bulk properties of Ni-rich NMCs, in particular those of NMC-622 and NMC-811, as a function of lithium content, and how these affect thermal stability.

Operando synchrotron x-ray diffraction (sXRD) experiments using NMC-622 versus lithium coin cells demonstrate complex phase transformations similar to those seen in NMC-333, LiNiO_2 , and NCA counterparts.^[2] During electrochemical cycling the NMC-622 undergoes a volume expansion of 4%, redox of transition metals (particularly Ni and Co), and surface reconstruction. The surface reconstruction is a consequence of higher oxygen reactivity on the surface than in the bulk. The depth profiling experiments using soft x-ray absorption spectroscopy (XAS) clearly distinguish the transition metal and oxygen reactivity from the surface and bulk, which provide vital information about the transition metal reactivity in Ni-rich cathodes.

Our expertise in the chemical delithiation process of cathode materials for lithium ion batteries was leveraged to investigate various characteristics of cathode material in the absence of binder and conductive additive,^[3] which can complicate interpretation of the materials behavior. This is evident when comparing the surface chemistry of electrochemically delithiated NMC-622 to its chemically delithiated counterpart. Soft XAS showed that the Ni on particle surfaces was more reduced than that in the bulk for the pristine and electrochemically prepared samples. Conversely, there was significantly less discrepancy for the chemically delithiated NMC-622 compared to pristine powder. To further investigate changes that occur in the bulk, hard XAS was used on electrochemically delithiated electrodes and chemically delithiated powders, which further validated the need to utilize a model system when investigating surface and bulk characterization techniques. The knowledge gained from our work on NMC-622 (FY 2017) was applied to studying the thermal properties of Ni-rich NMCs. In FY 2018 we focused on investigating the thermal properties of chemically delithiated NMC-622 and NMC-811 as a function of lithium content. An array of synchrotron characterization techniques were used to understand the role of the transition metals on structure stability at elevated temperatures. The in-situ heating experiments capture both chemical and morphological changes within the material that yield key information on thermal stability as a function of Ni and Li content and particle size. The bulk and surface

sensitive techniques also give important information regarding changes in electronic structure in intermediate states, which occur at lower temperatures than the phase transitions that are observed, and serve as indicators that thermally induced changes are about to occur.

Objectives

Objectives are to understand what limits the cycling behavior of Ni-rich NMCs and to gain a deeper understanding of their thermal properties. Once this is done, methods to improve the robustness of the materials can be developed, ranging from partial substitution with Ti (for example), coatings, and synthetic strategies to reduce surface Ni content.

Approach

In order to fully investigate the thermal properties on Ni-rich NMCs, a highly collaborative approach was taken. The materials were synthesized at LBNL by classic co-precipitation methods or by spray pyrolysis. The materials were subject to rigorous structural characterization and electrochemical testing before any chemical delithiation process occurred. Lithium half-cell configurations were used to test electrochemical properties. An array of synchrotron radiation techniques (in collaboration with D. Nordlund, T. Kroll, D. Sokaras and Y. Liu at SSRL) was used to understand the surface and bulk characteristics of the NMCs. Several physical techniques (XRD, TGA, SEM, OES-ICP, etc.) were also used to characterize materials before and after electrochemical cycling under a variety of conditions. In house in-situ heating XRD experiments were used to investigate the structural changes that occur in the Ni-rich NMCs as a function of temperature. Using a single sample, one can see all the phase transformations that occur upon heating. In-situ heating experiments using Nanotomographic imaging (Transmission x-ray microscopy, TXM) at SSRL were used to determine oxidation state gradients in particles and correlate them with the materials structure changes as a function of thermal exposure. Depth profiling soft x-ray absorption spectroscopy (XAS) experiments carried out at SSRL were used to probe oxidation states of transition metals at or near particle surfaces as a function of lithium content and thermal exposure. In situ heating experiments using X-ray Raman spectroscopy were used to probe transition metal L-edges and oxygen K-edge deeper into particles. This technique combines the sensitivity of soft XAS with the ability to probe the bulk. For a full overview of the behavior of NMCs, the PI works closely with other PIs in the Advanced Battery Materials Research program, including W. Tong (novel materials), B. McCloskey (differential electrochemical mass spectroscopy to measure gas evolution), and C. Ban (NREL, atomic and molecular layer deposition for protective layers on cathode materials).

Results

A comprehensive study of the thermal properties of Ni-rich NMCs as a function of lithium content materials was carried out in FY2018. Our goal was to study the true thermal properties of the chemically delithiated NMCs to avoid contributions from the conductive carbon and binder. NMC-622 and -811 were chemically delithiated to various levels. Here we concentrate primarily on the samples delithiated to 75% removal of lithium. Figure II.3.I.1 and Figure II.3.I.2 show the results of the thermal studies conducted on 75% chemically delithiated NMC-622 and NMC-811 by in situ hot stage x-ray diffraction and XAS. The 50% and 75% chemically delithiated NMC-811 are two phase mixtures of H2 and H3. In contrast, delithiated samples of NMC-622 are single phase and appear to be more thermally stable when delithiated to the same level. In the case of 75% delithiated NMC-811, partial conversion to spinel at begins to occur at 120°C and is then followed by M_3O_4 formation, and rock salt formation at higher temperatures. These changes occur at higher temperatures for the 75% delithiated NMC-622. Table II.3.I.1 summarizes the phase transformations that occur in each material upon heating. Several of these phase transformations involve loss of oxygen, and thermogravimetric analysis shows that the NMC-811 75% chemically delithiated sample lost 14% percent of its mass after heating to 500°C, consistent with M_3O_4 and rock salt formation. These phase conversions also involve overall reduction of the average transition metal oxidation state, although XRD data gives little information about which metals are involved. In contrast, XAS is a sensitive monitoring tool to investigate changes in electronic states occurring during thermal exposure. Figure II.3.I.2 shows the Ni, Co, and Mn K-edge energies as a function of temperature for both NMC-622 and 811. In general, shifts to higher energies are correlated with higher average oxidation states and vice versa. As the temperature increased from 20°C to

120°C (where spinel formation begins) the Ni actually oxidized slightly in 75% delithiated NMC-811, then reduced at higher temperatures. A slight reduction in Ni oxidation state was observed in 75% delithiated NMC-622 heated to 170°C, near the temperature where spinel formation begins. The Ni then reduced more obviously as the temperature increased to 350°C. In both samples, the prepeak in the Co K-edge increased in intensity, at temperatures consistent with M_3O_4 formation. This suggests that Co migrates from the octahedral site to a tetrahedral site in the M_3O_4 spinel because of the association of increased intensity of this peak with non-centrosymmetric coordination of the probed element. There is also evidence of Co reduction at these temperatures. In contrast, relatively little change is seen for Mn for either sample upon heating.

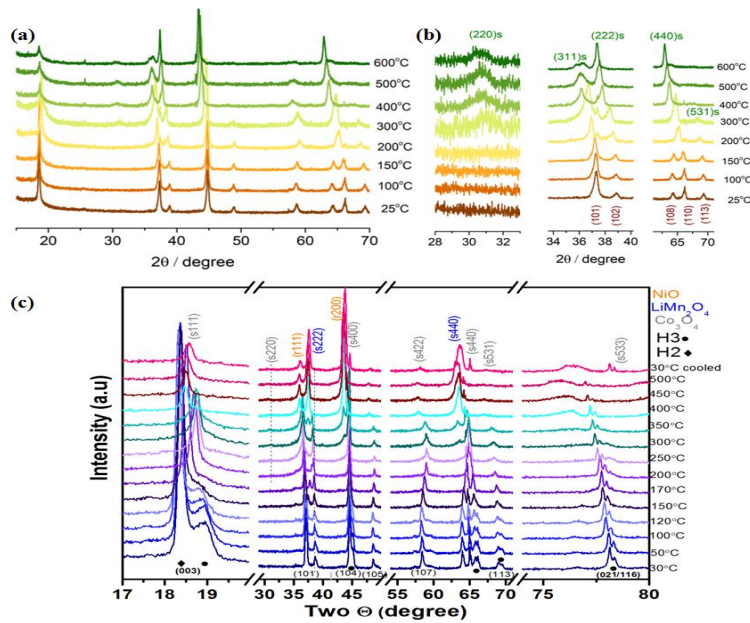


Figure II.3.I.1 In-situ heating XRD patterns of (a) 75% chemically delithiated NMC-622, (b) zoomed in sections of (a), and (c) 75% chemically delithiated NMC-811.

Table II.3.I.1 Summary of structure changes in chemical delithiated NMCs using in-situ XRD heating experiments.

Degree of Delithiation %	Onset temp of phase change NMC-811	Onset temp of phase change NMC-622
50	Room Temp (2 layered)	200°C (spinel)
	200°C (1 layered, spinel)	300°C ($M_2O_4^*$)
	400°C (spinel, MO*)	
75	Room Temp (2 layered)	150°C (spinel)
	120°C (1 layered, spinel)	300°C ($M_3O_4^*$, MO*)
	150°C, 200°C,	
	350°C (layered to spinel to MO*)	

*implies oxygen loss.

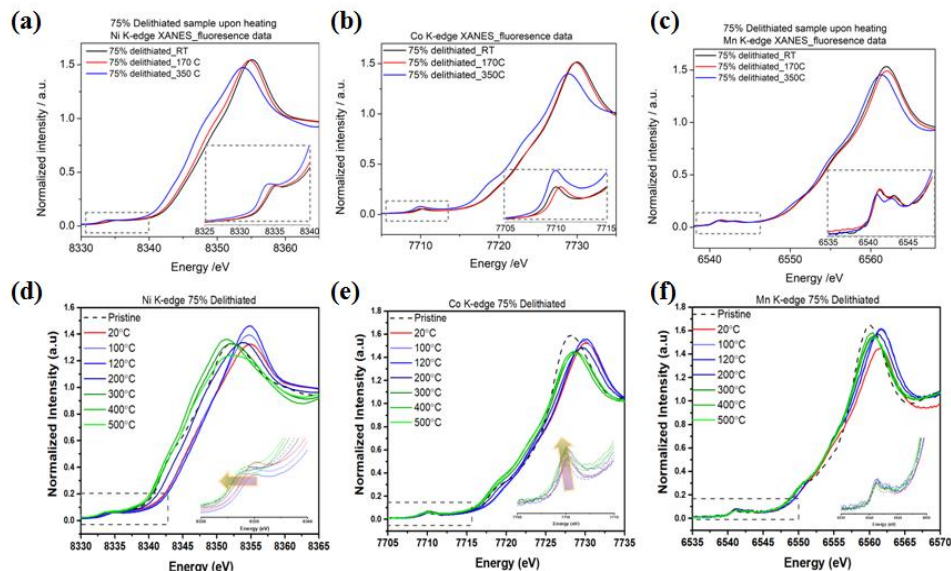


Figure II.3.I.2 Transition metal L-edge of thermal exposed to various temperatures of 75% chemically delithiated NMC 622 (a: Ni, b: Co, c: Mn) and NMC-811 (d: Ni, e: Co, f: Mn)

Soft XAS is a surface characterization and depth profiling technique (TEY mode ~ 5 nm, FY mode ~ 50 nm) that was used to further investigate these changes. Discrepancies between surface and bulk Ni oxidation states in the unheated delithiated samples imply surface reconstruction to a rock salt phase. For the 75% delithiated NMC-622 sample, heating to 170°C causes some reduction close to the surface (probably associated with loss of oxygen), but slight oxidation occurs deeper in the sample. Significant reduction in the Ni oxidation state was observed after heating to 350°C for the NMC-622 sample. On the other hand, the NMC-811 75% delithiated sample slightly oxidizes both at the surface and deeper into the bulk of the material upon heating to 100-120°C. Little change was observed for Co or Mn upon heating to the lower temperatures for either sample, but there was evidence of reduction of Co above 200°C. This suggests that Co is present in reduced phases on the particle surfaces. The O-K edge was further investigated for the 75% chemically delithiated NMC-811. The O-K-edge gives information on TM3d-O2p bond changes in the 525-536 eV range. By comparing to transition metal-containing standards, we were able to qualitatively analyze the thermal effects on this sample. The apparent oxidation of Ni at low temperatures (100-120°C) was also confirmed in both the FY and TEY modes for the O-K edge. This is interesting because this occurs somewhat before phase changes are observed in the bulk. When the temperature increased to 200°C, the intensity of the band associated with the Ni³⁺-O bond decreased while the Ni²⁺-O bond increased. This trend continued as the temperature was raised, consistent with the formation of reduced metal oxides. Co was also reduced as the temperature increased past 200°C, as evidenced by the rise in the Co²⁺-O peak at approximately 531 eV.

X-ray Raman spectroscopy was utilized to investigate the electronic structure in the bulk. The advantage of this technique is the improved sensitivity of soft X-ray experiments compared to hard XAS, combined with the ability to probe into the bulk. Similar to soft XAS, the peak at 530 eV is due to the TM3d-O2p bonds (Figure II.3.I.3b shows results for NMC-811, 75% chemically delithiated). The in-situ heating experiments show that as the temperature was increased to 120°C, the peak intensity decreased, owing to an increase in oxygen activity. There is a further decrease in intensity upon heating to 300°C associated with structural changes. These results, taken together with the soft and hard XAS results suggest that there is a covalency change in TM3d-O2p bonds that can serve as a sensitive indicator that a phase change is about to occur.

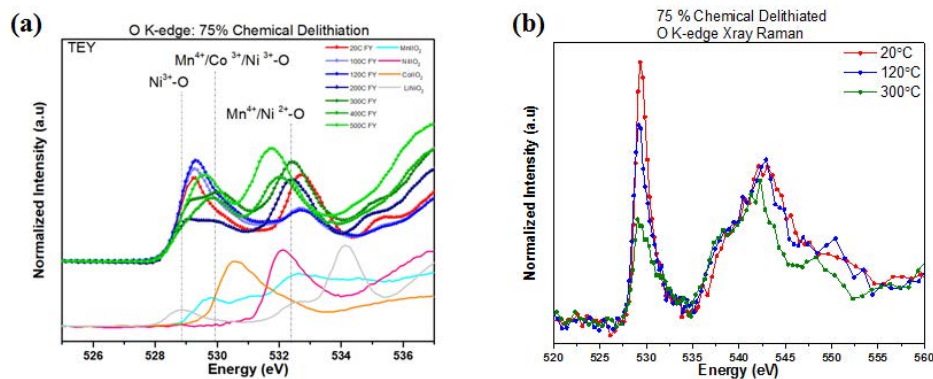


Figure II.3.1.3 (a) soft XAS O K-edge in TEY mode which probes 5 nm of the surface and (b) X-ray Raman spectroscopy which probes the bulk of the NMC-811. Both analysis were done at 75% chemical delithiation.

Synchrotron X-ray transmission x-ray microscopy (TXM) was used to further investigate oxidation state changes during heating. Figure II.3.1.4a shows Ni oxidation state mapping for particles as they underwent heating in the beamline. Again, higher energies are associated with higher oxidation states. A slight overall oxidation of Ni occurs upon heating to 120°C, but then reduction occurs at 300°C, consistent with the XAS and X-ray Raman results. It is also evident from these images that the smaller particles exhibited more drastic changes than the large main particle, indicating that they reacted more quickly. Some changes in morphology also occurred during heating. Another sample was examined after heating to 300°C, confirming the observation that smaller particles were more reactive than larger ones. TXM experiments carried out on 50% delithiated NMC-622 also show evidence of Ni migration near 350°C (not shown), as phase changes occur.

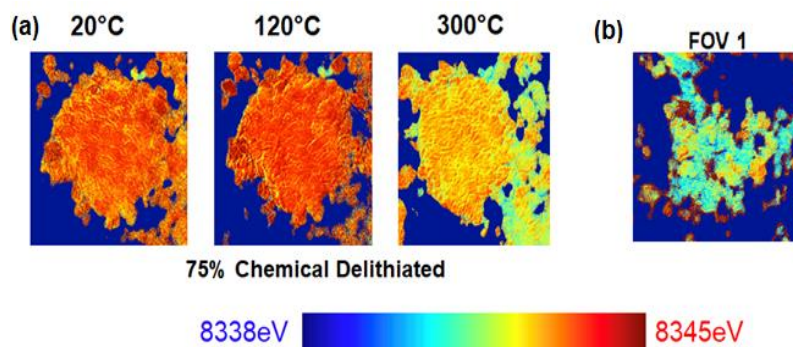


Figure II.3.1.4 (a) In-situ heating experiments on 75% chemically delithiated NMC-811, probing the Ni oxidation changes using TXM. (b) Post heating TXM analysis on small 75% chemically delithiated NMC-811 particles, heated to 300°C.

Conclusions

Upon heating, partially delithiated Ni-rich NMCs undergo a series of phase transformations to progressively reduced phases (layered to spinel to M_3O_4 -type spinel to rock salt). As Ni content is raised or Li content is lowered, the temperatures at which these transitions occur decrease, with changes observed as low as 120°C for some materials. Surprisingly, XAS and X-ray Raman experiments indicate that Ni first oxidizes at or below temperatures associated with phase transition to spinel, and then undergoes reduction. A comparison with O K-edge XAS and X-ray Raman data suggests that this apparent oxidation is associated with a change of covalency of the TM-O bond, which serves as a sensitive indicator that a phase change is about to occur. TXM confirms the apparent oxidation of Ni at lower temperatures and also indicates that small particles react more rapidly than larger particles and that migration of Ni occurs at below 350°C.

Key Publications

1. “Depth-Dependent Redox Behavior of $\text{LiNi}_{0.6}\text{Mn}_{0.2}\text{Co}_{0.2}\text{O}_2$ ” C. Tian, D. Nordlund, H. L. Xin, Y. Xu, Y. Liu, D. Sokaras, F. Lin and M. Doeff, **J. Electrochem. Soc.** 165 (3), A696-A704 (2018).
2. “Electrochemical Characteristics of Layered Transition Metal Oxide Cathode Materials for Lithium Ion Batteries: Surface, Bulk Behavior, and Thermal Properties” C. Tian, F. Lin, and M. M. Doeff, **Acc. Chem. Res.** 51, 89 (2018).
3. “Charge Heterogeneity and Surface Chemistry in Polycrystalline Cathode Materials” C. Tian, D. Nordlund, Y. Xu, F. Lin, Z. Dun, Y. Liu, and M. Doeff, **Joule** 2,464 (2018).
4. “Oxygen Release Induced Chemomechanical Breakdown of Layered Cathode Materials” L. Mu, R. Lin, R. Xu, L. Han, D. Sokaras, J. D. Steiner, T.-C Weng, D. Nordlund, M. M. Doeff, K. Zhao, H. L. Xin, and F. Lin, **Nano Letters**, 10.1021/acs.nanolett.8b01036 (2018).
5. “Propagation Topography of Redox Phase Transformations in Heterogeneous Layered Oxide Cathode Materials” L. Mu, Q. Yuan, C. Tian, P. Pianetta, M. M. Doeff, Y. Liu, and F. Lin **Nature Commun.**, 9, 2810 (2018).

References

1. F. Lin, I. Markus, D. Nordlund, T.-C. Weng, M. Asta, H. L. Xin, and M. M. Doeff, **Nature Commun.** 5:3529, DOI: 10.1038/ncomms4529 (2014).
2. C. Tian, D. Nordlund, H. Xin, Y. Xu, Y. Liu, D. Sokaras, F. Lin, and M. Doeff, **J. Electrochem. Soc.** 165, A696 (2018).
3. C. Tian, D. Nordlund, Y. Xu, F. Lin, Z. Dun, Y. Liu, and M. Doeff, **Joule** 2,464 (2018).

II.3.J Lithium Batteries with Higher Capacity and Voltage (UTA)

John B. Goodenough, Principal Investigator

The University of Texas at Austin
204 E. Dean Keeton St.
Austin, TX 78712
E-mail: jgoodenough@mail.utexas.edu

Peter, DOE Technology Development Manager

U.S. Department of Energy
E-mail: Peter.Faguy@ee.doe.gov

Start Date: Oct. 1, 2017

End Date: Sept. 30, 2018

Project Funding (FY18): \$120,000

DOE share: \$120,000

Non-DOE share: \$0

Project Introduction

An all-electric road vehicle that is powered by a rechargeable battery and is competitive in cost, safety, and convenience with today's road vehicles powered by a fossil fuel in an internal combustion engine would reduce the distributed air pollution generated on the highways of the world. The large-scale battery would also allow storage of electric power generated by sun-light and wind energy for backing up the grid. The Li-ion battery of the wireless revolution is used in hybrid road vehicles, but it has safety problems and is still too costly with too low a cycle life and too slow a charging time. Today's solid electrolytes, with the exception of a hydrophilic glass, require battery operation above 50°C, so there is need to continue to explore lithium batteries with a liquid electrolyte.

Objectives

The ability to plate/strip a dendrite-free lithium electrode from a liquid electrolyte would provide a safe battery cell with a fast charging time. Therefore, there is interest in the development of a low-cost, long-cycle-life lithium battery cell with a liquid electrolyte that has a sufficient volume density of stored energy to deliver a discharge power, $P=IV$ for a time Δt that can provide a driving range of 350 miles between 10-minute charges at driving speeds of at least 60 miles per hour. The ability to transfer reversibly lithium between two electrodes at a finite voltage for a sufficient Δt would provide the simplest low-cost cell. This concept should be possible in an all-solid-state cell operating at 60°C.

Approach

Investigate the problem associated with plating/stripping a lithium anode from a liquid and a solid electrolyte on a Cu current collector to investigate the feasibility of a Li/Cu cell with a liquid or with a solid electrolyte.

Results

The project has been conducted in collaboration with others in my group besides those supported by the BMR project. We have reported previously only results obtained with milestones specified by this project. Here, we report results placed in the broader context of our collaboration effort.

First, we have investigated the problem of plating/stripping of dendrite-free lithium on an electrode, with emphasis on a copper current collector. According to the literature, a common problem with plating from a liquid electrolyte is that the nucleation density of the lithium deposit is not high compared to the total available surface of the current collector. This is considered to be a condition for dendrite growth, which suggests the need to develop a uniform plating. In previous work, we show that a dendrite-free lithium anode can be plated from an organic-liquid electrolyte through a porous cellulose-based membrane that is wet by the lithium metal. [1] Wetting occurs where a bond between an alkali metal and a solid on contact is stronger than the bond of an alkali metal to itself. Li_3N is wet by lithium owing to the same reason and can eliminate lithium dendrites. [2]

To promote the wetting of lithium on the Cu current collector, we have coated a thin graphene film on a clean Cu current collector with CVD. We have tested half-cells with a liquid electrolyte, 1M LiPF₆ in EC/DEC (1/1) at room temperature. Galvanostatic lithium deposition showed notable contrasts between the bare and graphene-coated Cu current collectors. Figure II.3.J.1 shows charge/discharge voltage curves at 0.5 mA cm⁻² (discharge for 2 h, charge up to 2 V; 5th cycle). Coulombic efficiencies and average Li deposition voltage of the bare and graphene-coated Cu current collectors are 94.6 vs. 96.2% and -27.7 vs. -22.3 mV, respectively. It is apparent that the graphene film is effective to reduce electrochemical polarization and enhance charge/discharge reversibility.

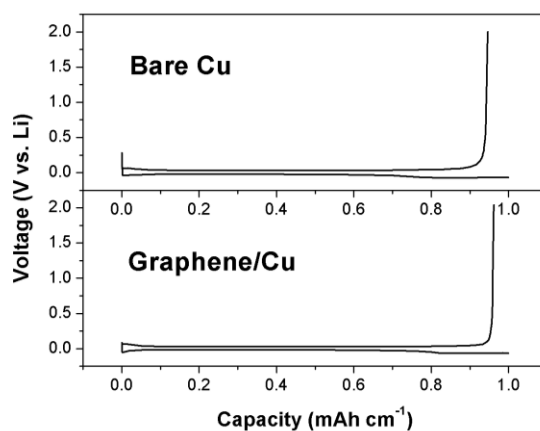


Figure II.3.J.1 Charge/discharge voltage curves of the bare and graphene-coated Cu current collectors at 0.5 mA cm⁻² (discharge for 2 h, charge up to 2 V; 5th cycle)

To explain the contrasts in the electrochemistry, we have observed surface morphologies of the lithium deposits on Cu current collectors with/without graphene. In this experiment, shown in Figure II.3.J.2, lithium metal was deposited at 1 mA cm⁻² for 6 h. The graphene layer was not effective to prohibit dendritic lithium growth, although utilization of the current collector was remarkably different with the presence of graphene. Scattered island-type lithium growth was observed on the bare Cu, but the lithium deposition on the graphene-coated Cu is much more uniform. Moreover, mechanical adhesion of lithium deposit on the graphene-coated Cu is far stronger. The morphological characterization suggests that the better lithium deposition kinetics and higher coulombic efficiencies on the graphene-coated Cu are mainly the result of better bonding of metallic lithium to the carbon than to copper.

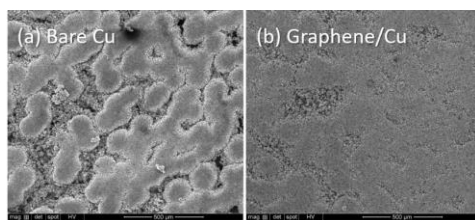


Figure II.3.J.2 SEM images of Li deposit on the bare and graphene-coated Cu current collectors. Li deposition was performed at 1 mA cm⁻² for 6 h at room temperature.

Second, besides the Li deposition on contact with a liquid electrolyte, we have also investigated ceramic/polymer composite membranes as a solid-state Li⁺ conductor to evaluate the effect of ceramic fillers on the ionic conductivity and the Li deposition on contact with a solid electrolyte. Al₂O₃ and LiZr₂(PO₄)₃ powder (15 wt.%) were added to LiTFSI:PEO (1:2 weight ratio) to contrast the ionic conductivity with the different fillers. However, both separator membranes had almost identical Li⁺ conductivities of ~0.3 mS cm⁻¹ at 60°C, which indicates that the Li⁺ conductivities of the ceramic fillers do not have an immediate impact on the total ionic conductivity.

Lithium plating/stripping cycle properties of the membranes were characterized with Li//Li symmetric cells. Figure II.3.J.3 shows the charge/discharge voltage curves of the cells at the 10th cycle at 60°C. Instead of the AC impedance technique, we have studied the voltage drop (iR drop) upon the current switch from charge to discharge to compare the charge-transfer resistances at the membrane/Li interfaces. Here, we have only focused on the iR drop during the initial 60 seconds. The calculated R_{ct} values are 335.6 Ω and 165.3 Ω for the Al_2O_3 - and $LiZr_2(PO_4)_3$ -filled LiTFSI:PEO membranes, respectively. Although the measured bulk Li^+ conductivity was almost the same, the interfacial charge transfer resistance was very different. The Li^+ -conducting ceramic particles help the interfacial Li^+ transfer not only by increasing the electrochemical surface area, but also by providing Li^+ ions directly to the interface; Li wets the ceramic.

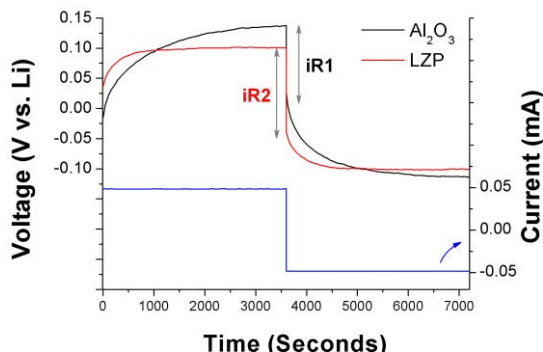


Figure II.3.J.3 Charge/discharge voltage curves of the Li//Li symmetric cells with the Al_2O_3 - and $LiZr_2(PO_4)_3$ -filled LiTFSI:PEO membranes at the 10th cycle and 60°C.

The cycle life in Figure II.3.J.4 also shows an interesting contrast. The Al_2O_3 -filled sample failed at 57th cycle, but the $LiZr_2(PO_4)_3$ -filled sample ran >440 cycles. Since surface-morphology changes of the Li metal electrode during cycling is a critical factor for long-term cycling, the enhanced charge transfer kinetics may have played a key role to stabilize the surface morphology and to increase the cycle life.

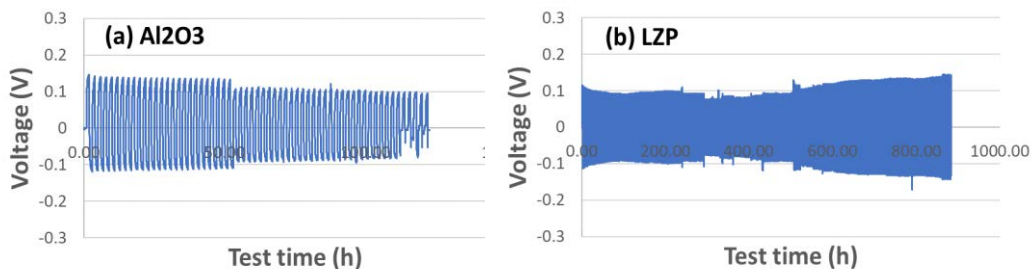


Figure II.3.J.4 Charge/discharge cycle performance of the Li//Li symmetric cells with the (a) Al_2O_3 - and (b) $LiZr_2(PO_4)_3$ -filled LiTFSI:PEO membranes at 60 °C.

Third, we switched our focus to the copper cathode that is in contact with a solid electrolyte. We tested the relative energies of the Cu^+/Cu^0 redox couple contacting the different solid electrolytes and their reversibility during an electrochemical reaction. Half-cells with Li as the anode and Cu as the cathode were assembled. We have tested several polymer electrolyte membranes including an Al_2O_3 -incorporated LiTFSI:PEO (1:2 weight ratio) membrane. All the cells were cycled galvanostatically at 60°C. The PEO-based solid electrolyte showed cycle-dependent changes in the coulombic efficiencies (Figure II.3.J.5): ~20% for the initial 30 cycles and later saturated to ~95% after cycling. It turned out that the electrochemically fed Cu^+ ions diffused out from the Cu cathode to the anode side due to the concentration gradient. With sufficient aging of the electrolyte by cycling, the redox reaction becomes more reversible.

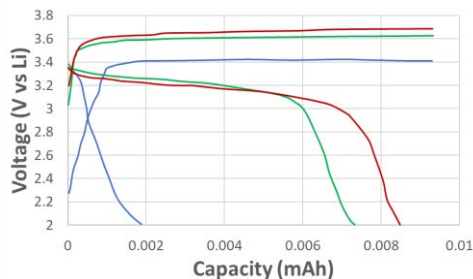


Figure II.3.J.5 Charge/discharge voltage curves of the Cu/Al₂O₃-filled LiTFSI:PEO membrane/Li cell at the 5 (blue), 50 (green), and 100th (red) cycles and 60 °C.

Lastly, we made a low-cost, 3V cell with a copper current collector as cathode and the Li⁺ gel polymer electrolyte membrane as the separator. Compared to the previous all-solid-state cell configuration, several modifications have been made. First, the electrochemical cell contains gel-polymer electrolyte membrane (Cu²⁺ salt dissolved in PEG inside PVDF-HFP polymer network). The gel polymer electrolyte membrane enables fast Li⁺/Cu²⁺ cation transports at room temperature. Second, as the PVDF-HFP gel polymer membrane cannot block the penetration of lithium dendrites, Li₃N particles were deposited on the anode lithium foil to remove the dendrites by wetting. All the cells were tested at room temperature.

The quasi-solid-state cathode electrolyte in contact with the Cu metal was LiTFSI/Cu(ClO₄)₂ dissolved in PEG inside PVDF-HFP. A separate layer of gel polymer membrane without the Cu salt was introduced on top of the Li anode to avoid a short-circuit. Although the thin Cu foil could be made very thin, (i) the electrochemical area was limited and (ii) a concentration polarization was observed during discharge as is shown in Figure II.3.J.6a. In contrast, the cathode gel-polymer-electrolyte-impregnating Cu foam exhibits stable voltage curves without a notable overpotential during discharge (the black voltage curve in Figure II.3.J.6b), which indicates that the increased surface area is beneficial to reduce effectively the Cu²⁺ diffusion length to and from the Cu surface during the redox reactions. Moreover, it was attempted to enhance the charge transfer kinetics of the Cu foam electrode by adding carbon black into the cathode polymer network. The voltage curve (red) in Figure II.3.J.6b shows the benefit of adding carbon in the cathode polymer: it shows less voltage polarization during charge and discharge. The carbon can facilitate electronic conduction in the cathode, so the Cu²⁺ ions can be deposited on carbon with the electrochemical potential in equilibrium with that of the Cu current collector.

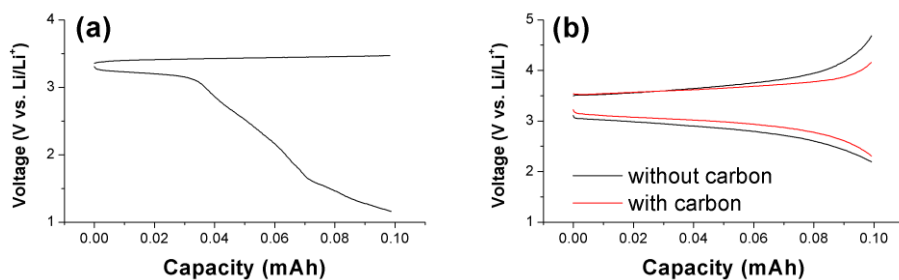


Figure II.3.J.6 (a) Charge/discharge voltage curves of the LiTFSI/Cu(ClO₄)₂-dissolved in PEG inside PVDF-HFP in contact with Cu foil. (Current: 20 μA). (b) Charge/discharge voltage curves of the LiTFSI/Cu(ClO₄)₂-dissolved in PEG inside PVDF-HFP that is impregnated in the Cu foam. Carbon was added to the polymer membrane (red curves) to characterize its effect on the polarization. (Current: 40 μA)

Conclusions

Investigation of a new cell concept has been performed: It consists of plating/stripping of metallic lithium on the anode and of metallic copper on a copper cathode with a quasi-solid-electrolyte system. The new cell chemistry delivers a low-cost and scalable 3V solid-state cell. It was identified that (i) the Cu/solid-electrolyte

interface is an important factor for the cell resistance, and (ii) the diffusion of Cu^{2+} in the polymer membrane determines the reversible capacity and charge-transfer kinetics. Moreover, regarding the lithium plating on the Cu current collector, the graphene coating can increase the nucleation density and wettability, and hence, make uniform Li deposits with a good mechanical adhesion.

Key Publications

1. K. Park, Y. Li, N. Wu, J. B. Goodenough, "A novel solid-state battery with Cu cathode", *under preparation*.

References

1. Yu, B. C., Park, K., Jang, J. H., Goodenough, J. B. "Cellulose-based porous membrane for suppressing Li dendrite formation in Li-sulfur battery." *ACS Energy Letters* 1, (2016) 633-637.
2. Park, K., Goodenough, J. B. "Dendrite-suppressed lithium plating from a liquid electrolyte via wetting of Li_3N ." *Adv. Energy Mater.* 7 (2017) 1700732.

II.3.K Discovery of High-Energy Li-Ion Battery Materials (LBNL)

Wei Tong, Principal Investigator

Lawrence Berkeley National Laboratory
1 Cyclotron Rd. MS62R0203
Berkeley, CA 94720
weitong@lbl.gov

Peter Faguy, DOE [Program/Technology Development] Manager

U.S. Department of Energy
E-mail: Peter.Faguy@ee.doe.gov

Start Date: October 1, 2015

End Date: September 30, 2018

Project Funding (FY18): \$1,500,000

DOE share: \$1,500,000

Non-DOE share: \$0

Project Introduction

Currently, the commercial Li-ion batteries adopt a wide use of intercalation cathodes such as layered lithium metal oxide, spinel-type lithium manganese oxide, and olivine-type lithium iron phosphate. However, these cathodes can only deliver a reversible capacity of 140 - 170 mAh/g based on the cationic redox. Attempt to charge layered oxides to higher potentials (> 4.7 V) results in a higher initial capacity (> 200 mAh/g), but leads to an irreversible phase transformation and ultimately a capacity decay. Recently, Li-, Mn-rich layered oxides have demonstrated a high reversible capacity of > 250 mAh/g, which outperforms most of the commercially available Li-ion cathodes. However, this family of compounds experience a series of structural rearrangement and gas evolution, demonstrating continuous voltage/energy decay over the extended cycles. In this project, we propose to develop new Li-rich metal oxides that utilize $\text{Ni}^{2+}/\text{Ni}^{4+}$ redox, meanwhile, incorporate a second transition metal (TM) that is located on the first and second row in the periodic table, which is designed to stabilize the crystal structure and/or contribute electrochemical redox. The presence of Li excess in the structure is expected to increase the number of Li diffusion paths, therefore, enable more accessible Li.

Objectives

- Develop a cathode that can cycle > 200 mAh/g while exhibiting minimal capacity and voltage fade
 - Target at Li-rich compositions in Li-Ni-O chemical space that utilizes $\text{Ni}^{2+}/\text{Ni}^{4+}$ redox to potentially overcome capacity limitation per TM
 - Integrate a second TM on the first and second row to improve structural stability and/or contribute electrochemical redox
- Gain in-depth understanding on the correlation between composition and electrochemistry in Li-rich metal oxides
 - Understand the participation/contribution of cationic and anionic redox in electrochemistry
 - Investigate the potential impact of TMs on oxygen reactivity

Approach

This project integrates material design, synthesis, physical and electrochemical evaluation to search for new high capacity cathodes within Li-Ni-O chemical space. We initiated our material synthesis efforts with Li, Mn-rich layered oxide to identify the optimal synthetic condition via a facile solid-state reaction that is ultimately employed for the synthesis of Li-rich Ni based metal oxides. Integration of a second TM is expected to stabilize structure and/or contribute electrochemical redox. The materials are subjected to a variety of synchrotron based radiation and spectroscopy techniques to characterize the crystal structure and electronic structure of both TMs and oxygen.

Results

Currently, the emerging oxygen redox has been considered as one of the prevailing theories along with structural rearrangement for voltage decay in Li-rich layered oxides. We have previously observed completely different anionic oxygen behavior in Li-rich layered oxides, $\text{Li}_{1.2}\text{Ni}_{0.2}\text{TM}_{0.6}\text{O}_2$ (TM = Mn, Ru), with active oxygen redox in Mn-based sample (LNMO), but not in Ru-based sample (LNRO). In FY18, we probed the origin of the voltage decay in $\text{Li}_{1.2}\text{Ni}_{0.2}\text{Ru}_{0.6}\text{O}_2$, a structurally and electrochemically relevant compound to Li, Mn-rich layered oxide, but exhibiting no oxygen activity. Such intriguing characteristic allowed us to explicitly decouple the contribution of anionic oxygen redox and structural evolution to voltage decay in Li-rich layered oxides. We first modified $\text{Li}_{1.2}\text{Ni}_{0.2}\text{Ru}_{0.6}\text{O}_2$ (LNRO) by reducing particle size via ball milling method (LNRO-BM) or use of conductive carbon matrix (LNRO-C). As shown in Figure II.3.K.1, voltage decay upon cycling was clearly visible in the cyclic voltammetry (CV) plots of all LNRO samples along with LNMO for comparison. Here, the CV curves during the first formation cycle were removed for figure clarity. However, the voltage decay phenomenon was much more severe in LNMO sample compared to LNRO samples. We clearly observed a continuous shift of the reduction peak centered around 3.6 to 2.9 V for LNMO from the 2nd to 90th cycle, while LNRO sample exhibited a much smaller voltage drop, with the reduction peak of ~ 3 V for the 90th cycle. Indeed, voltage decay is more noticeable in modified LNRO-BM sample with a much smaller primary particle size.

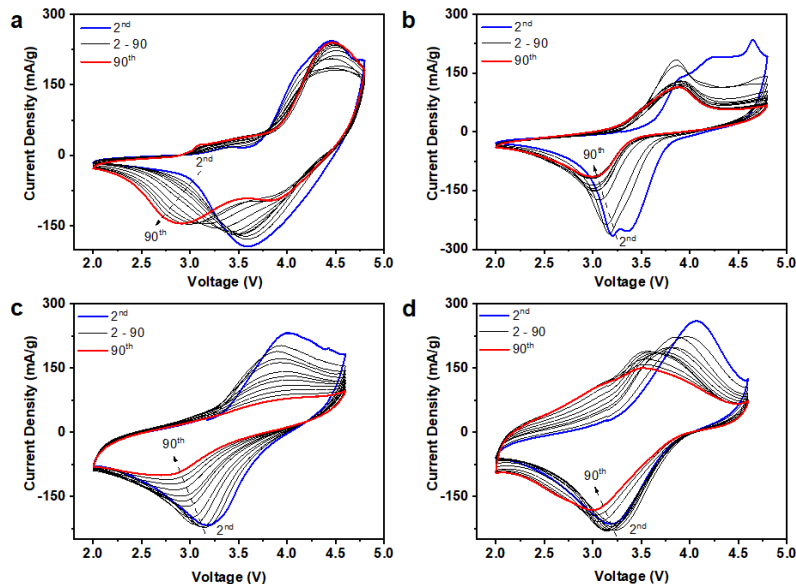


Figure II.3.K.1 CV plot of (a) LNMO, (b) LNRO, (c) LNRO-C, and (d) LNRO-BM. Cells were cycled between 4.8 and 2.0 V at 0.5 mV/s.

Once the voltage decay in LNRO was verified even with the absence of oxygen redox, the structural evolution of LNRO upon delithiation/lithiation was studied to gain more insights into the origin of voltage decay from the structural point of view. The structural evolution of the bulk LNRO during the 1st cycle and the 2nd charge was initially investigated by *in situ* XRD (Figure II.3.K.2). The *in situ* XRD results were analyzed along the electrochemical cycling, including the 1st charge (4.8 V), 1st discharge (2.0 V) and 2nd charge (4.8 V), guided by the horizontal red, blue, and green lines, respectively. First of all, all the XRD peaks of pristine LNRO (highlighted by vertical solid lines) could be indexed to monoclinic $C/2c$ space group, although the superlattice peaks around 13.5° ($\lambda =$) originating from Li/TM ordering in the TM layers partially overlapped with the background from *in situ* cell. Upon electrochemical cycling, the most pronounced feature related to structural evolution was the intense (002) Bragg peak, located at $\sim 11.5^\circ$. Upon the initial lithium extraction, (002) peak mostly remained, while a new peak developed at $\sim 12.1^\circ$ ($\lambda = 0.9762$) long with a set of relatively small diffraction peaks, indicating formation of a new phase (highlighted by vertical dash lines) upon further lithium extraction. Additionally, this second phase appeared to grow at the expense of pristine

$C/2c$ phase along with the broadening of XRD peaks upon further lithium extraction towards the end of the 1st charge (green *in situ* patterns). Upon subsequent discharge, the characteristic peaks of the second phase (highlighted by vertical dash lines) gradually disappeared, instead, Bragg peaks relating to pristine phase (highlighted by vertical solid lines) re-appeared at the end of the 1st discharge (guided by horizontal blue line), indicating a reversible structural change during the first charge-discharge process. During the 2nd charge, the sample underwent a similar structural change, a transition from pristine to the second phase at highly charged states, further suggesting such a biphasic process was reversible in the subsequent cycling process.

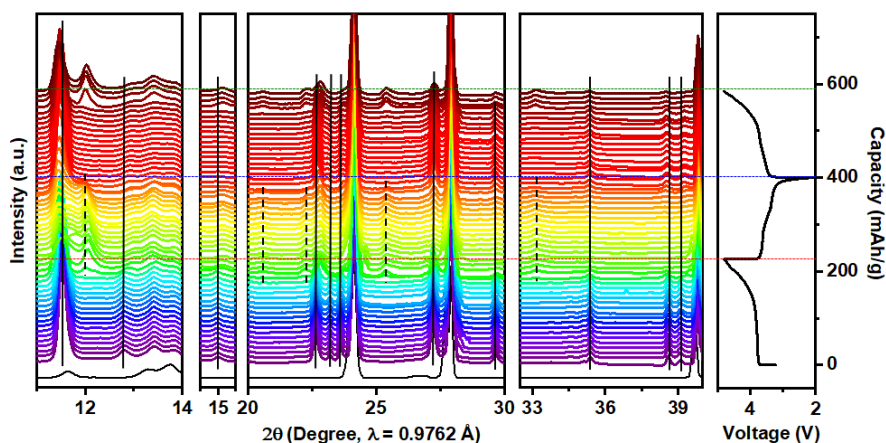


Figure II.3.K.2 In situ XRD patterns of LNRO during the 1st cycle and 2nd charge. Black curve on the bottom indicates the background from in situ pouch cell. In situ cell was cycled between 4.8 and 2.0 V at C/20 during the 1st and 2nd charge and C/10 during the 1st discharge. Vertical solid and dash lines mark the pristine and new monoclinic C2/c phase, respectively.

As noted above, some of the characteristic peaks of LNRO, particularly the super-lattice peaks around 13.5° ($\lambda = 0.9762 \text{ \AA}$), overlap with the *in situ* pouch cell background and disturbed through structural analysis. Therefore, a series of chemical delithiated $\text{Li}_x\text{Ni}_{0.2}\text{Ru}_{0.6}\text{O}_2$ ($x = 1.0, 0.8, 0.6, 0.4, 0.2$ and 0) samples were prepared by reacting LNRO with NO_2BF_4 oxidant. The chemically delithiated samples demonstrated a similar trend in the phase transformation to that upon electrochemical lithium extraction. The original C2/c phase was initially remained and gradually transformed to the second phase at highly delithiated states (Figure II.3.K.3a). Rietveld refinement analysis of the XRD pattern of the nominal $\text{Li}_0\text{Ni}_{0.2}\text{Ru}_{0.6}\text{O}_2$ suggested that the monoclinic C2/c structure was still preserved after near full delithiation (Figure II.3.K.3b, c). The significant shift of the XRD peaks was consistent with the brutal change in the lattice parameters of pristine ($a = 5.0418(5) \text{ \AA}$, $b = 8.7566(5) \text{ \AA}$, $c = 9.8624(6) \text{ \AA}$, $\beta = 99.830(6)^\circ$) and new phase ($a = 5.1153(5) \text{ \AA}$, $b = 8.5908(9) \text{ \AA}$, $c = 9.378(1) \text{ \AA}$, $\beta = 100.14(2)^\circ$), resulting in a total decrease of 5.43% in unit cell volume. The XRD patterns of $\text{Li}_x\text{Ni}_{0.2}\text{Ru}_{0.6}\text{O}_2$ samples of $0.6 \leq x \leq 0.2$ could be refined based on the model of mixed pristine and new C2/c phase. Overall, a subtle change in a and b axis, but a large decrease in c lattice parameter from pristine to new C2/c phase was revealed, accompanied by the oxidation of Ru⁴⁺ to Ru⁵⁺ and Ni²⁺ to Ni⁴⁺, in principle, towards full delithiation state (Figure II.3.K.3d, e). Furthermore, such phase transformation between pristine and new C2/c phase was further confirmed to be reversible, particularly the super-lattice peaks were still visible even after a few electrochemical cycles (Figure II.3.K.3f).

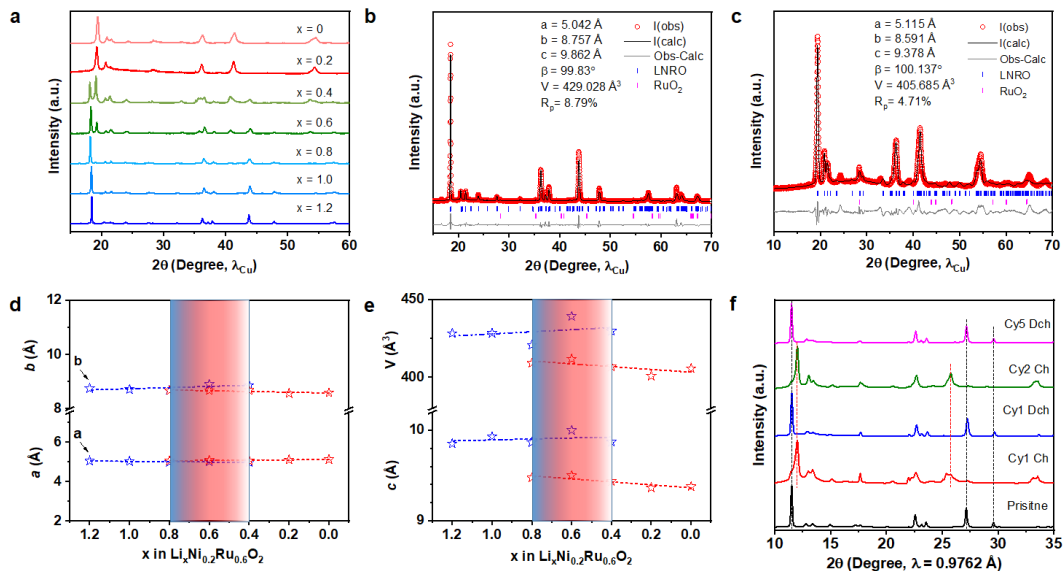


Figure II.3.K.3 Structural characterization upon chemical delithiation and electrochemical cycling. (a) XRD patterns, Rietveld refinement of (b) $x = 1.2$, and (c) $x = 0$, (d, e) lattice parameters of chemically delithiated samples, and (f) XRD patterns of electrochemically cycled LNRO between 4.8 and 2.0 V, where the black and red lines in (f) mark the most representative peaks of pristine and new monoclinic $C2/c$ phase, respectively.

Moreover, the microstructural change was studied at complementary length scale by high resolution transmission electron microscopy (HR-TEM) and high-angle annular dark field-scanning transmission electron microscopy (HAADF-STEM). Atomic structure of LNRO after 4.8 V charge and 2.0 V discharge were examined by HAADF-STEM (Figure II.3.K.4a-c). The line profile at pristine state (d) showed a spacing of 0.14 nm between the two adjacent TMs that form a TM-TM dumbbell and the light Li metals between the TM-TM dumbbells are invisible. Projections of $[110]$, $[100]$, and $[1\bar{1}0]$ zone axes co-existed in the bulk of pristine monoclinic LNRO. The atomic models along $[100]$, $[110]$, and $[1\bar{1}0]$ zone axes of monoclinic $C2/c$ are presented in Figure II.3.K.4e. The stacking faults along the c -axis $[002]$ of $C2/c$ structure can also be seen from pristine LNRO (Figure II.3.K.4a). After initial charge and discharge, such two-dimensional layered structure with stacking faults still remained (Figure II.3.K.4b, c). Meanwhile, the Li/TM ordering in the TM layer was also persevered even after the initial charge (Figure II.3.K.4d), consistent with the characteristic supper lattice reflections shown in the XRD pattern of charged LNRO. Selected area electron diffraction (SAED) patterns of LNRO samples at pristine, 4.8 V charge and 2.0 V discharge are shown in Figure II.3.K.4f-h, again, all LNRO samples remained a crystal structure of monoclinic $C2/c$. The distance between the two neighboring peaks in Figure II.3.K.4i, equivalent to the reciprocal of the d -spacing of (002) plane, increased from pristine to charged state (4.8 V), corresponding to a decrease in d -spacing. Clearly, (002) d -spacing was recovered when discharged to 2.0 V (Figure II.3.K.4i). SAED patterns attested the two-phase transformation, furthermore, c lattice parameter at pristine, 4.8 V charge and 2.0 V discharge was calculated to be 9.91, 9.34 and 9.81 Å, respectively, in close agreement with XRD refinement results.

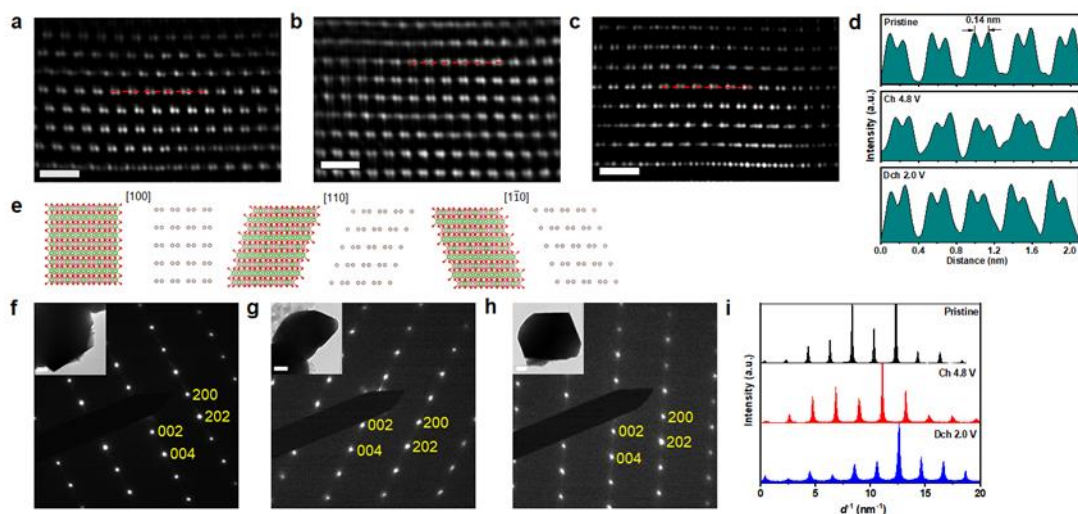


Figure II.3.K.4 Structural evolution during the first cycle. HAADF-STEM images of LNRO (a) at pristine state, (b) after 4.8 V charge, and (c) after 2.0 V discharge, scale bar in (a-c) is 1 nm; (d) line profiles of the regions highlighted by red dash lines in (a-c); (e) atomic models along [100], [110], and $[1\bar{1}0]$ zone axes of monoclinic C2/c structure; SAED patterns of LNRO (f) at pristine state, (g) after 4.8 V charge, (h) after 2.0 V discharge along $[0\bar{1}0]$ zone axis, insets are LNRO particles at corresponding states with a scale bar of 200 nm; and (i) corresponding line profiles of SAED patterns, demonstrating the reciprocal of the d spacing for (002) plane of LNRO at different states of charge.

The cycled LNRO electrodes were further examined to study the microstructural evolution from the surface towards the bulk. From the HAADF-STEM image, a thin layer (~ 1 nm) of spinel and/or rocksalt phase was found at the surface of pristine LNRO (Figure II.3.K.5a). Upon cycling, the layered structure in the bulk was well maintained, in contrast, the thickness of the surface layer gradually increased to ~ 1.5 and 4 nm after the 1st and 10th cycle, respectively (Figure II.3.K.5b-d). Such phase transformation continued to occur upon further cycling and the boundary between layered bulk and spinel/rocksalt surface was less pronounced after 20 cycles, indicating such phase transformation initiated at the particle surface then propagated into the inner bulk. Figure II.3.K.5e shows a HAADF-STEM image of LNRO electrode after 20 cycles at high magnification, exhibiting an overview of atomic arrangement from the surface to the depth of ~ 15 nm. The line profiles were collected along the [002] direction (orange arrows) in several areas from the very surface (area 1) toward the subsurface (area 2-4). For ideal C2/c with no Li/TM mixing, a spacing of 0.48 nm between the maxima of two adjacent peaks is anticipated (Figure II.3.K.5g and pink highlight in Figure II.3.K.5i). At the surface (area 1 in Figure II.3.K.5e), evidence of TM migration into the intermediate tetrahedral or Li sites between the neighboring TM layers was clearly revealed. At subsurface in Figure II.3.K.5g-2, 3, 4, the spacing between the maxima of two adjacent peaks is mostly ~ 0.48 nm in area 2 – 4, with evidence of TM migration into the intermediate tetrahedral or Li sites between TM layers (red arrows). HAADF-STEM images were also acquired at a lower magnification to examine wider area towards the bulk (Figure II.3.K.5f), and stacking faults were more visible. Line intensity profiles were collected along [010] and [002] direction, corresponding to area 1 and 2, respectively. Spacing between two adjacent dumbbells is 0.43 nm (orange highlight in Figure II.3.K.5i). The peaks in Figure II.3.K.5h-1 along [010] direction show a spacing of 0.43 nm started to be discernable at a distance of ~ 5.5 nm (estimated boundary marked by red dash line). However, Along [002] direction, the slab spacing obtained in both area 2 and 3 (Figure II.3.K.5h-2, 3) slightly deviated from 0.48 nm, a rough boundary of ~ 6.5 nm was marked as surface layer by red dash line in area 2 (Figure II.3.K.5h-2). Starting from this boundary, inner area had (002) d-spacing of 0.48 nm. Figure II.3.K.5f area 3 represented a region of more than 30 nm underneath from the surface. From the intensity profile of area 3 along [002] direction, we found some shoulders peaks as asymmetric peaks (marked by red arrows in Figure II.3.K.5h-3). We can also clearly see a spacing of < 0.48 nm in the domains composed of asymmetric peaks (marked by red arrows), corresponding to a slight contraction in spacing between the TM slabs due to subtle TM migration into the intermediate tetrahedral or Li sites between TM layers. Here, our STEM results clearly showed that

TM migration took place in LNRO upon electrochemical cycling, despite the absence of oxygen activity. Such migration seemed to start from the surface and propagate into the inner bulk particle. Therefore, the microstructural evolution, mostly relating to the TM migration, can indeed induce the undesirable voltage decay. Our results suggest that such decay originating from TM migration mechanism in LNRO is significantly less severe compared to that in Li, Mn-rich layered oxides, implying the coupling between TM migration and oxygen activity in oxygen-redox electrodes is highly possible.

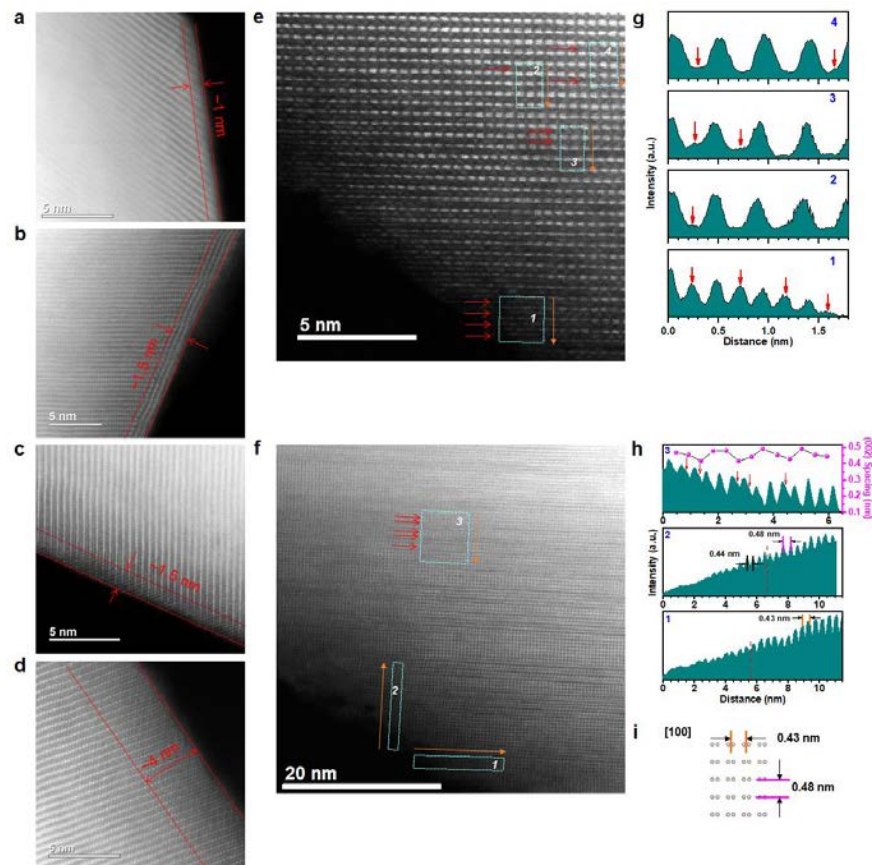


Figure II.3.K.5 Microstructural evolution upon cycling. HAADF-STEM images of LNRO (a) at pristine state, (b) after 4.8 V charge, (c) after 2.0 V discharge, (d) after 10 cycles, (e, f) after 20 cycles; (g) and (h) line profiles of the regions highlighted by blue boxes in (e) and (f), respectively, where yellow arrows indicate the directions that line profiles are generated and red arrows indicate TM migration; (002) spacing in (h) region 3 is calculated between the maximum of two adjacent peaks; (i) atomic model along [100] zone axis of monoclinic $C2/c$ structure, showing a distance of 0.43 nm between two adjacent pairs of TM in the TM layer and distance of 0.48 nm between two adjacent TM layers.

We also designed and synthesized alternative Li-rich Ni-based oxide cathodes of varied Ni/Ru ratios to understand the correlation between anionic oxygen and TM redox. $\text{Li}_{1.2}\text{Ni}_{0.8-x}\text{Ru}_x\text{O}_2$ ($x = 0.2, 0.4, 0.6$) samples were prepared *via* a solid state reaction. Here, different combination of Ni/Ru oxidation state was anticipated due to the necessity of charge balance, so do the TM and O redox contribution during the electrochemistry. All the reflections of $\text{Li}_{1.2}\text{Ni}_{0.2}\text{Ru}_{0.6}\text{O}_2$ sample could be well indexed based on monoclinic $C2/c$ space group. Decreasing Ru to $x = 0.4$ and 0.2 led to similar patterns to that of $\text{Li}_{1.2}\text{Ni}_{0.2}\text{Ru}_{0.6}\text{O}_2$ (Figure II.3.K.6a). However, the super-lattice peaks, characteristic of monoclinic $C2/c$ structure, in the region of $5 - 6.5^\circ$ ($\lambda = 0.4142 \text{ \AA}$) became completely invisible for $x = 0.4$ and 0.2 . Meanwhile, the relative intensity of the reflections around 5 and 11.5° varied with Ni/Ru ratio. Such difference could be due to either the complete disordering in TM layer or change of crystal structure of the final products. Rietveld refinement analysis on the XRD pattern of $\text{Li}_{1.2}\text{Ni}_{0.4}\text{Ru}_{0.4}\text{O}_2$ sample suggested it could be indexed to layered $R\bar{3}m$ space group with $\sim 7.4\%$ Li/Ni

intermixing. A better fitting was obtained based on mixed layered $R\bar{3}m$ (70 mol%) and rocksalt $Fm\bar{3}m$ (30 mol%). The first cycle voltage profiles and dQ/dV plots of $\text{Li}_{1.2}\text{Ni}_{0.8-x}\text{Ru}_x\text{O}_2$ samples are shown in Figure II.3.K.6a, b. Of all three samples, $\text{Li}_{1.2}\text{Ni}_{0.4}\text{Ru}_{0.4}\text{O}_2$ displayed the best initial performance, as evidenced by a capacity of 288 and 228 mAh/g during the charge and discharge, corresponding to 1.12 and 0.89 Li^+ , respectively. Moreover, a higher operating voltage with two pairs of oxidation/reduction peaks around 4.2/4.0 and 3.8/3.7 V during charge and discharge was observed. This seemed consistent with the Ni redox in conventional layered oxides, somehow showing agreement with the structural analysis. The possible TM combination in $\text{Li}_{1.2}\text{Ni}_{0.4}\text{Ru}_{0.4}\text{O}_2$ is $\text{Ni}^{2+}/\text{Ru}^{5+}$ or $\text{Ni}^{3+}/\text{Ru}^{4+}$ based on the charge balance, which in principle enables maximal 0.8 Li^+ , by assuming the full $\text{Ni}^{2+}/\text{Ni}^{4+}$ or combined $\text{Ni}^{3+}/\text{Ni}^{4+}$ and $\text{Ru}^{4+}/\text{Ru}^{5+}$ redox. Therefore, it is possible to facilitate the oxygen redox activity in $\text{Li}_{1.2}\text{Ni}_{0.4}\text{Ru}_{0.4}\text{O}_2$.

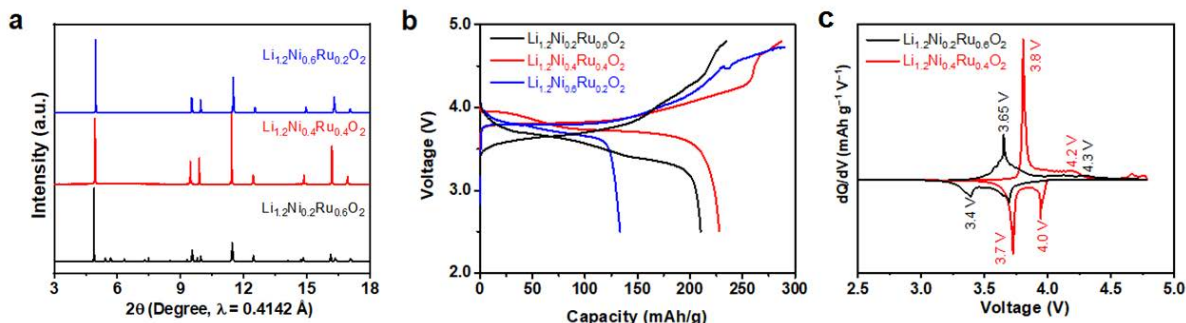


Figure II.3.K.6 (a) sXRD patterns, (b) voltage profiles, and (c) dQ/dV plots of $\text{Li}_{1.2}\text{Ni}_{0.8-x}\text{Ru}_x\text{O}_2$ ($x = 0.2, 0.4, 0.6$). Cells were cycled between 4.8 and 2.5 V at 5 mA/g.

Crystal structural evolution of $\text{Li}_{1.2}\text{Ni}_{0.4}\text{Ru}_{0.4}\text{O}_2$ sample upon electrochemical cycling was further explored by *in situ* and *ex situ* synchrotron X-ray diffraction (sXRD). Figure II.3.K.7a shows *in situ* sXRD patterns of $\text{Li}_{1.2}\text{Ni}_{0.4}\text{Ru}_{0.4}\text{O}_2$ during the first delithiation and lithiation along with that of the *in situ* cell background (black pattern on the bottom). First of all, the as-produced $\text{Li}_{1.2}\text{Ni}_{0.4}\text{Ru}_{0.4}\text{O}_2$ sample did not display the super-lattice reflections, characteristic of monoclinic $C2/c$ structure, instead, all sXRD reflections of $\text{Li}_{1.2}\text{Ni}_{0.4}\text{Ru}_{0.4}\text{O}_2$ at pristine state seemed consistent with those of conventional $R\bar{3}m$ layered structure. Interestingly, $\text{Li}_{1.2}\text{Ni}_{0.4}\text{Ru}_{0.4}\text{O}_2$ sample exhibited different structural evolution behavior compared to conventional layered oxides. As opposed to an increase in c lattice of conventional layered oxides upon delithiation, $\text{Li}_{1.2}\text{Ni}_{0.4}\text{Ru}_{0.4}\text{O}_2$ did not exhibit such a shift to a smaller 2θ angle upon nearly full delithiation. In contrast, there was a minimal shift in (003) reflection, implying a robust crystal structure of $\text{Li}_{1.2}\text{Ni}_{0.4}\text{Ru}_{0.4}\text{O}_2$ sample upon delithiation. *In situ* sXRD clearly demonstrated a unique isotropic change in crystal lattice for the as-produced $\text{Li}_{1.2}\text{Ni}_{0.4}\text{Ru}_{0.4}\text{O}_2$. In fact, a, c lattice of $\text{Li}_{1.2}\text{Ni}_{0.4}\text{Ru}_{0.4}\text{O}_2$ after delithiation exhibited a subtle change, only $\sim 1\%$, indicating a “low-strain” characteristic. As noted above, some of the characteristic peaks of $\text{Li}_{1.2}\text{Ni}_{0.4}\text{Ru}_{0.4}\text{O}_2$ partially overlapped with the *in situ* pouch cell background, therefore, chemically delithiated $\text{Li}_x\text{Ni}_{0.4}\text{Ru}_{0.4}\text{O}_2$ ($x = 1.2, 0.5, 0.2$, and 0) samples were prepared for a detailed study on the structural evolution (Figure II.3.K.7b). Clearly, chemical delithiation study showed consistent crystal structural evolution with that obtained from *in situ* electrochemical cell. All peaks displayed a minimal shift upon delithiation. Sample of $x = 0.2$ exhibited very similar crystal structure to pristine state, further confirming the robustness of $\text{Li}_{1.2}\text{Ni}_{0.4}\text{Ru}_{0.4}\text{O}_2$ upon electrochemical cycling. Detailed analysis of the crystal structure at pristine state needs to be conducted in the future.

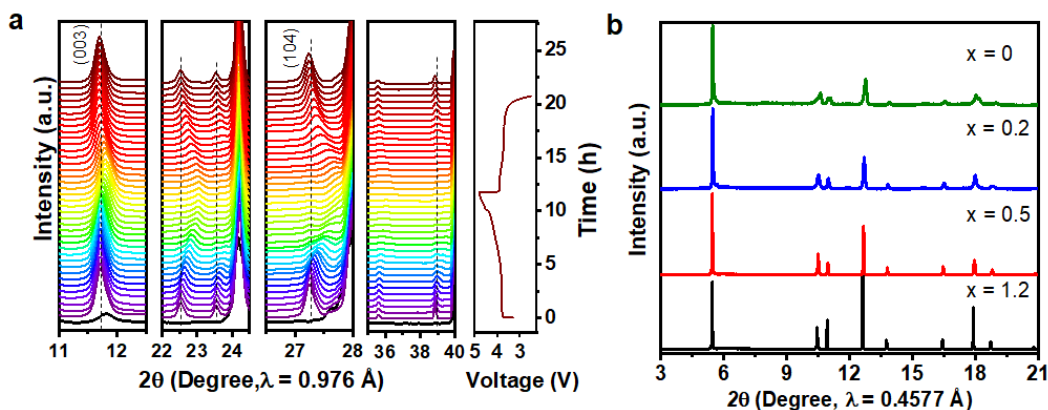


Figure II.3.K.7 (a) In situ sXRD patterns of $\text{Li}_{1.2}\text{Ni}_{0.4}\text{Ru}_{0.4}\text{O}_2$ during the first cycle between 4.8 and 2.5 V at C/10, and (a) ex situ sXRD patterns of $\text{Li}_x\text{Ni}_{0.4}\text{Ru}_{0.4}\text{O}_2$ ($x = 1.2, 0.5, 0.2, \text{ and } 0$) prepared via chemical delithiation method.

Conclusions

In summary, we have investigated the origin of the voltage decay in $\text{Li}_{1.2}\text{Ni}_{0.2}\text{R}_{0.6}\text{O}_2$, showing structural and electrochemical relevance to Li, Mn-rich layered oxide but no oxygen activity, by eliminating the effect of oxygen activity. We demonstrate the capacity and voltage decay in LNRO upon cycling, but to a much less extent than Li, Mn-rich layered oxide, implying the additional role of oxygen activity in voltage decay. Meanwhile, the absence of oxygen redox in LNRO allows us to explicitly decouple the contribution of anionic oxygen redox and structural evolution to voltage decay in Li-rich layered oxides. Our study highlights a role that microstructural evolution, specifically TM migration from the octahedral sites in the TM slabs to the interstitial tetrahedral or lithium octahedral sites between TM slabs, plays in the voltage decay during electrochemical cycling. We also studied alternative $\text{Li}_{1.2}\text{Ni}_{0.8-x}\text{Ru}_x\text{O}_2$ compounds of varied Ni/Ru ratio, and $\text{Li}_{1.2}\text{Ru}_{0.4}\text{Ni}_{0.4}\text{O}_2$ delivers the highest capacity as well as isotropic structural evolution upon electrochemical cycling, which largely differs from conventional and Li-rich layered oxide cathodes. Additional studies on its crystal structure and charge compensation mechanism need to be carried out to gain further understanding of the utilization of TM and O redox in such structurally favorable Li-rich layered oxides.

Key Publications

1. N. Li, S. Hwang, M. Sun, Y. Fu, V. S. Battaglia, D. Su, and W. Tong*, "Decoupling the Contribution of Oxygen Redox and Structural Evolution to Voltage Decay in Li-rich Layered Metal Oxide Cathodes," submitted to *Joule*.
2. C. Deng, P. Skinner, Y. Liu, R. Hunt, M. Lau, M. Sun, C. Ma, W. Tong, J. Xu, and H. Xiong, "Li-Substituted Layered-Spinel Cathode Material for Sodium-Ion Batteries," *Chemistry of Materials*, DOI: 10.1021/acs.chemmater.8b02614.
3. J. Xu, M. Sun, R. Qiao, S. E. Renfrew, L. Ma, T. Wu, S. Hwang, D. Nordlund, D. Su, K. Amine, J. Lu, B. D. McCloskey, W. Yang, W. Tong*, "Elucidating Anionic Oxygen Activity in Li-Rich Layered Oxides," *Nature Communications*, 9, 947 (2018).

Acknowledgements

Collaboration with Dr. Dong Su at Brookhaven National Laboratory on STEM work is greatly appreciated.

II.3.L Model-System Diagnostics for High-Energy Cathode Development (LBNL)

Guoying Chen, Principal Investigator

Lawrence Berkeley National Laboratory
1 Cyclotron Road
Berkeley, CA 94720
E-mail: GChen@lbl.gov

Peter Faguy, DOE Technology Development Manager

U.S. Department of Energy
E-mail: Peter.Faguy@ee.doe.gov

Start Date: October 1, 2016

End Date: September 30, 2019

Project Funding (FY18): \$500,000

DOE share: \$500,000

Non-DOE share: \$0

Project Introduction

To meet DOE targets for Li-ion batteries intended for vehicular applications, electrode materials with high-energy density and high stability are needed. Critical performance issues associated with electrode structural and morphological instabilities, side reactions with the electrolyte, and transport limitations are sensitive to material's properties such as chemical compositions, crystal structures, surface facets, and particle sizes. Advances in materials development, therefore, require a better understanding of these relationships between properties and functions, yet this has been difficult to achieve on conventional aggregated secondary particles. This project addresses these challenges in a systematic way, by synthesizing single-crystal version of the commercially promising yet complex electrode materials, obtaining new insights into the materials utilizing state-of-the-art analytical techniques that are mostly inapplicable or ineffective on conventional secondary particles, and subsequently establishing the relationships between structure and function. The goal is to use these findings to rationally design and synthesize advanced electrode materials with improved performance.

Objectives

This project will use a rational, non-empirical approach to design and synthesize next-generation high-energy, high-voltage cathode materials. Combining a suite of advanced diagnostic techniques with model cathode materials and model electrode/electrolyte interfaces, the project will perform systematic studies to achieve the following goals: 1) obtain new insights into solid-state chemistry, particularly cationic and/or anionic redox activities during charge and discharge of lithium transition-metal oxides, 2) gain fundamental understanding on cathode/electrolyte interfacial chemistry and charge transfer process as well as the impact of operating voltage window, 3) reveal performance- and stability-limiting properties and processes in high-energy, high-voltage cathodes, and 4) develop strategies to mitigate the structural and interfacial instabilities.

Approach

Prepare single crystals of Li-rich transition-metal oxides with well-defined physical attributes. Perform advanced diagnostic and mechanistic studies at both bulk and single-crystal levels. Global properties and performance of the samples will be established from the bulk analyses, while the single-crystal based studies will utilize time- and spatial-resolved analytical techniques to probe material's redox transformation and failure mechanisms.

Results

Layered Li- and Mn-rich (LMR) oxide cathodes have met significant challenges in commercialization due to performance deterioration associated with structural changes. Recent interest has turned to a class of alternative Li-excess oxides with a cation-disordered rock-salt crystal structure. Our previous investigation on a model rock-salt compound, $\text{Li}_{1.3}\text{Nb}_{0.3}\text{Mn}_{0.4}\text{O}_2$ ($\text{Li}_{1.3}\text{NMO}$), revealed that the high capacity was delivered through a two-step redox process: dominating $\text{Mn}^{3+}/\text{Mn}^{4+}$ redox activities at low state of charge (SOC) and oxygen redox at voltages above 4.3 V vs. Li^+/Li . To evaluate the performance and stability of these newer Li-

excess cathodes, various electrochemical analyses were performed. First, the extent of O redox participation in $\text{Li}_{1.3}\text{NMO}$ was systematically varied by performing cyclic voltammetry (CV) scans between 1.5 V and varying upper cut-off voltage (UCV) of 4.2, 4.4, 4.6 and 4.8 V. As shown in Figure II.3.L.1a, stable cycling with an anodic peak centered at ~ 3.2 V and a cathodic peak at ~ 3.0 V was observed when the voltage limit was set to 4.2 V, suggesting full reversibility of the cation redox. Increasing the limit to 4.4 V triggered a new anodic peak at the cut off voltage which signals the activation of O redox (Figure II.3.L.1b). Although stability mostly maintains, slight upper voltage shift of the anodic peak and current reduction of the cathodic peak was observed with cycling. Further increasing the voltage limit to 4.6 and 4.8 V largely increases the participation of O redox, as evidenced by the much larger anodic peak centered at ~ 4.5 V (Figure II.3.L.1c and Figure II.3.L.1d). With cycling, the intensity of this peak decreased quickly, suggesting that the O redox is largely irreversible. Furthermore, the anodic peak centered at ~ 3.2 V continued to shift towards high voltage while the cathodic peak at ~ 3.0 V was gradually replaced by a weak reduction peak at ~ 2.2 V. After 25 cycles, the CV profiles were dominated by a pair of redox peaks separated by more than 2 V. The results demonstrate a clear correlation between O anionic redox participation, voltage fade and hysteresis/path dependence. Voltage fade and hysteresis begin only after triggering anionic redox, which grows progressively with either deeper oxidation of oxygen at higher potential or extended cycling. This is remarkably similar to what was observed on the layered LMR materials, suggesting that the negative impact of O redox is not limited to the layered structure.

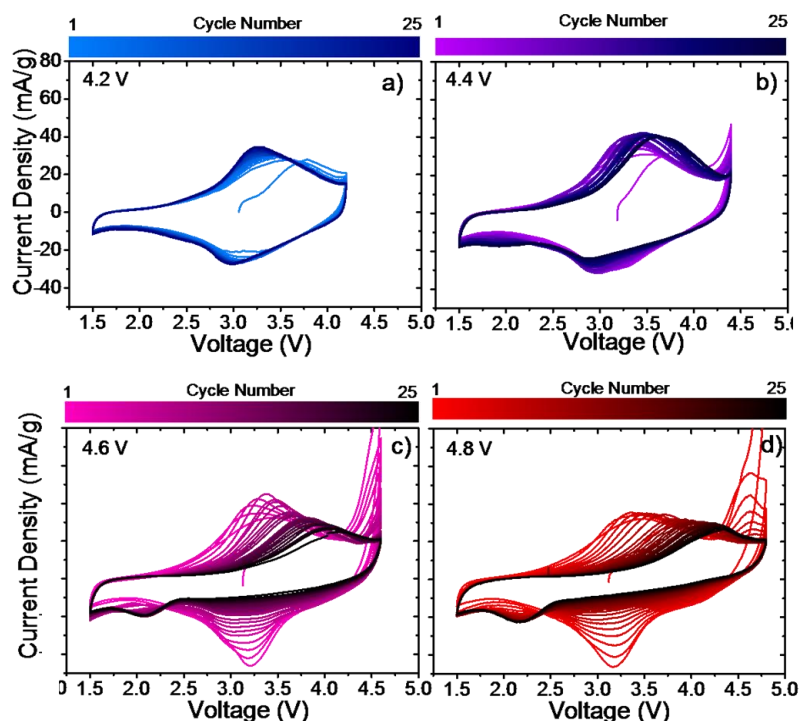


Figure II.3.L.1 Cyclic voltammograms of $\text{Li}_{1.3}\text{Nb}_{0.3}\text{Mn}_{0.4}\text{O}_2$ half-cells cycled between 1.5 V and various upper cut off voltages of: a) 4.2 V, b) 4.4 V, c) 4.6 V and d) 4.8 V. The scan rate was 5 mV/min.

The correlation between upper limit voltage and performance deterioration was further evidenced by charge/discharge cycling of $\text{Li}_{1.3}\text{Nb}_{0.3}\text{Mn}_{0.4}\text{O}_2$ half-cells. Figure II.3.L.2a and Figure II.3.L.2b show the voltage profiles of the cells cycled to 4.2 and 4.8 V, respectively. While stable cycling was achieved at the 4.2 V cutoff voltage, significant capacity fade and voltage decay were observed in the cell cycled to 4.8 V. The involvement of oxygen redox led to a high initial discharge capacity of ~ 275 mAh/g but only ~ 70 mAh/g remained after 50 cycles, as shown in Figure II.3.L.2c.

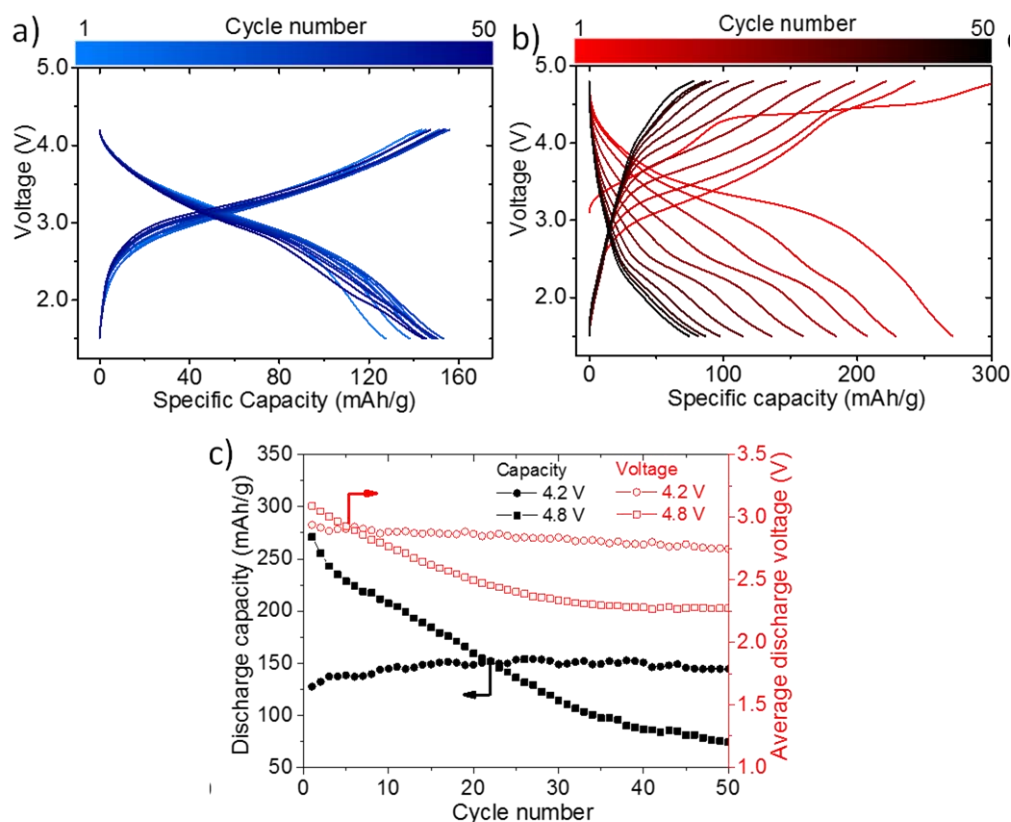


Figure II.3.L.2 Voltage profiles of $\text{Li}_{1.3}\text{Nb}_{0.3}\text{Mn}_{0.4}\text{O}_2$ half-cells cycled at 10 mA/g between the voltage window of: a) 1.5-4.2 V and b) 1.5-4.8 V, and c) Specific discharge capacity and average voltage as a function of cycle number.

Potentiostatic intermittent titration technique (PITT) measurements were then carried out to evaluate the kinetics of cationic and anionic redox reactions contributing to the charge storage capacity. For $\text{Li}_{1.3}\text{Nb}_{0.3}\text{Mn}_{0.4}\text{O}_2$ half-cells, a step size of 50 mV was used in both voltage windows of 1.5-4.2 V and 1.5-4.8 V. At each step, the potential was held until the current reached a corresponding rate of $C/150$. Figure II.3.L.3 shows the calculated chemical diffusion coefficients as well as the derived dQ/dV profiles from the measurements. In first charging to 4.2 V (Figure II.3.L.3a), a broad anodic peak centered at ~ 3.2 V was observed on the dQ/dV profile, corresponding to the oxidation of the transition metal (TM) cation (Mn^{3+} in this case). The diffusion coefficient during the oxidation process was approximately $1 \times 10^{-10} \text{ cm}^2/\text{s}$. When the charging voltage was extended to 4.8 V, a new strong peak centered at ~ 4.5 V along with a low voltage peak centered at ~ 3.6 V were observed on the dQ/dV profile, corresponding to the oxidation of oxygen and TM, respectively. While the diffusion coefficient for TM oxidation remains unchanged at $1 \times 10^{-10} \text{ cm}^2/\text{s}$, the oxygen oxidation process had a value of approximately $1 \times 10^{-12} \text{ cm}^2/\text{s}$, nearly two orders of magnitude lower. This suggests that Li diffusion is significantly slower during oxygen redox. For the subsequent discharging process (Figure II.3.L.3b), the dQ/dV profiles in both voltage windows show a single broad cathodic peak centered at ~ 3.0 - 3.2 V, consistent with the results previously obtained from CV studies. The primary difference lies in the current density, with significant current boost observed when oxygen oxidation was activated at the UCV of 4.8 V. For the diffusion coefficient in the voltage window of 1.5-4.2 V, it remained fairly stable at $\sim 1 \times 10^{-10} \text{ cm}^2/\text{s}$ during the reduction of TM. With the activation of oxygen, the value was significantly reduced to about $1 \times 10^{-12} \text{ cm}^2/\text{s}$. Furthermore, the diffusion coefficient in the entire voltage window decreased by nearly an order of magnitude. These results suggest that the reduction processes of TM and O are likely coupled rather than being separated. Involving oxygen redox leads to broad kinetic reduction in the entire voltage window.

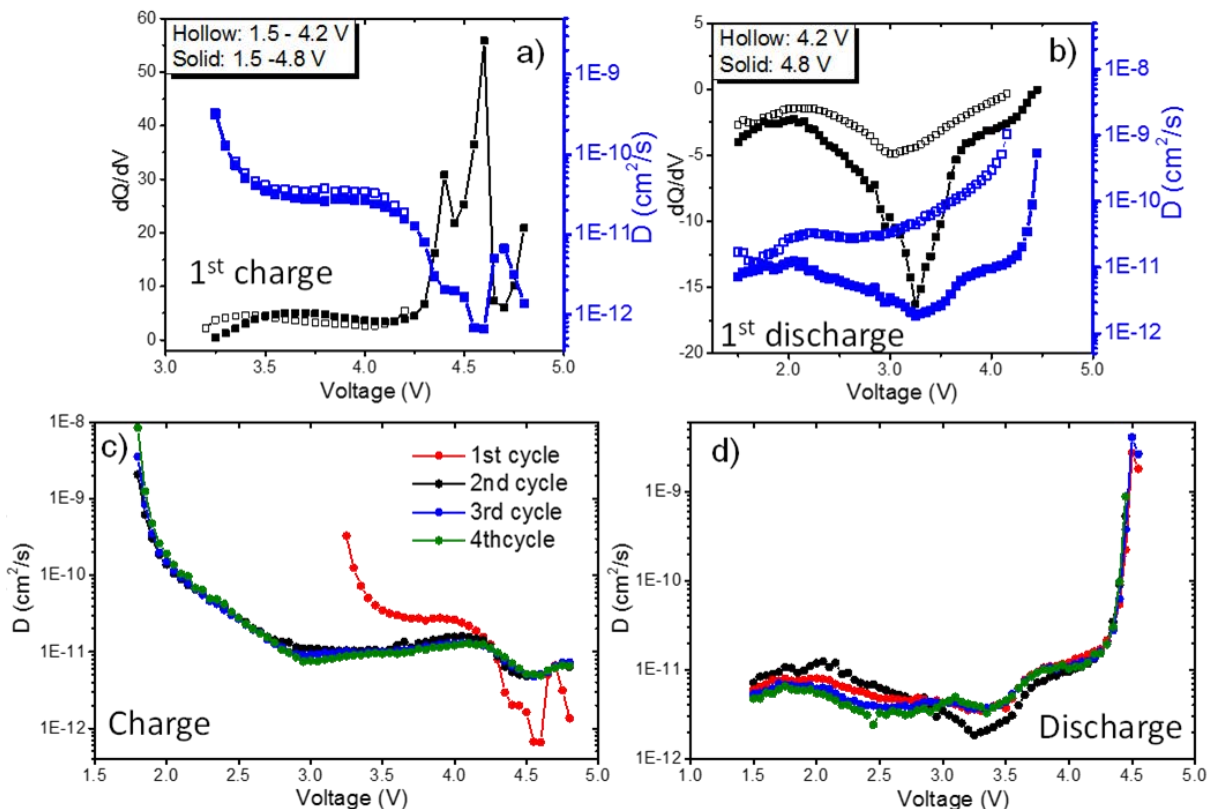


Figure II.3.L.3 Diffusion coefficient and dQ/dV profile during: a) first charge and b) first discharge. Relationship between diffusion coefficient and cell voltage during the first 4 cycles of $\text{Li}_{1.3}\text{Nb}_{0.3}\text{Mn}_{0.4}\text{O}_2$ half cells: c) charge and d) discharge.

Changes in Li diffusion kinetics as a function of cycle number between 1.5 and 4.8 V were also evaluated. Figure II.3.L.3c and Figure II.3.L.3d show the relationships during the first 4 cycles of charge and discharge, respectively. The profiles during the subsequent charging are considerably different from that during the first charge. Particularly, diffusion during oxygen oxidation appears to be much faster in the following cycles. This is likely due to the decreased contribution from the slow oxygen gas evolution occurring in the first charge. Li diffusion during TM oxidation, however, becomes slower with cycling. A gradual reduction in kinetics was also observed during discharge. These results suggest that repeated cycling involving oxygen redox leads to kinetic deterioration in the entire voltage window.

The chemical origin of the cycling instability was investigated by surface sensitive soft X-ray absorption spectroscopy (XAS) technique. Figure II.3.L.4a-Figure II.3.L.4d show the O K -edge spectra collected in both total electron yield (TEY) and fluorescent yield (FY) modes, which probe the electronic structures of the specified element with a depth of ~ 5 and 50 nm, respectively. The pre-edge feature centered at ~ 530 eV is attributed to the transitions between O_{1s} to $\text{TM}_{3d}\text{-O}_{2p}$ hybrid orbitals, which is strongly correlated to the changes in valence electrons of both oxygen and TM, or the covalency between them. Monitoring the intensity changes in the $\text{TM}_{3d}\text{-O}_{2p}$ peak, therefore, provides direct insights on oxygen redox activities. On both TEY and FY spectra, the chemically delithiated sample shows the highest $\text{TM}_{3d}\text{-O}_{2p}$ pre-edge intensity (Figure II.3.L.4a and Figure II.3.L.4b). The lower intensity observed on the cycled electrodes (Figure II.3.L.4c and Figure II.3.L.4d) suggests less electron extraction or charge compensation from these hybrid orbitals. While the TEY intensity of $\text{TM}_{3d}\text{-O}_{2p}$ pre-edge decrease drastically with cycling, with only $\sim 60\%$ and $\sim 30\%$ remaining after the 1st and 40th cycles, respectively, the reduction in FY intensity was much slower, with 90% remaining after the 1st cycle and 50% remaining after the 40th cycle (Figure II.3.L.4e and Figure II.3.L.4f). This clearly indicates that the irreversibility in oxygen related activities is more severe on the surface than that in the sub-surface region.

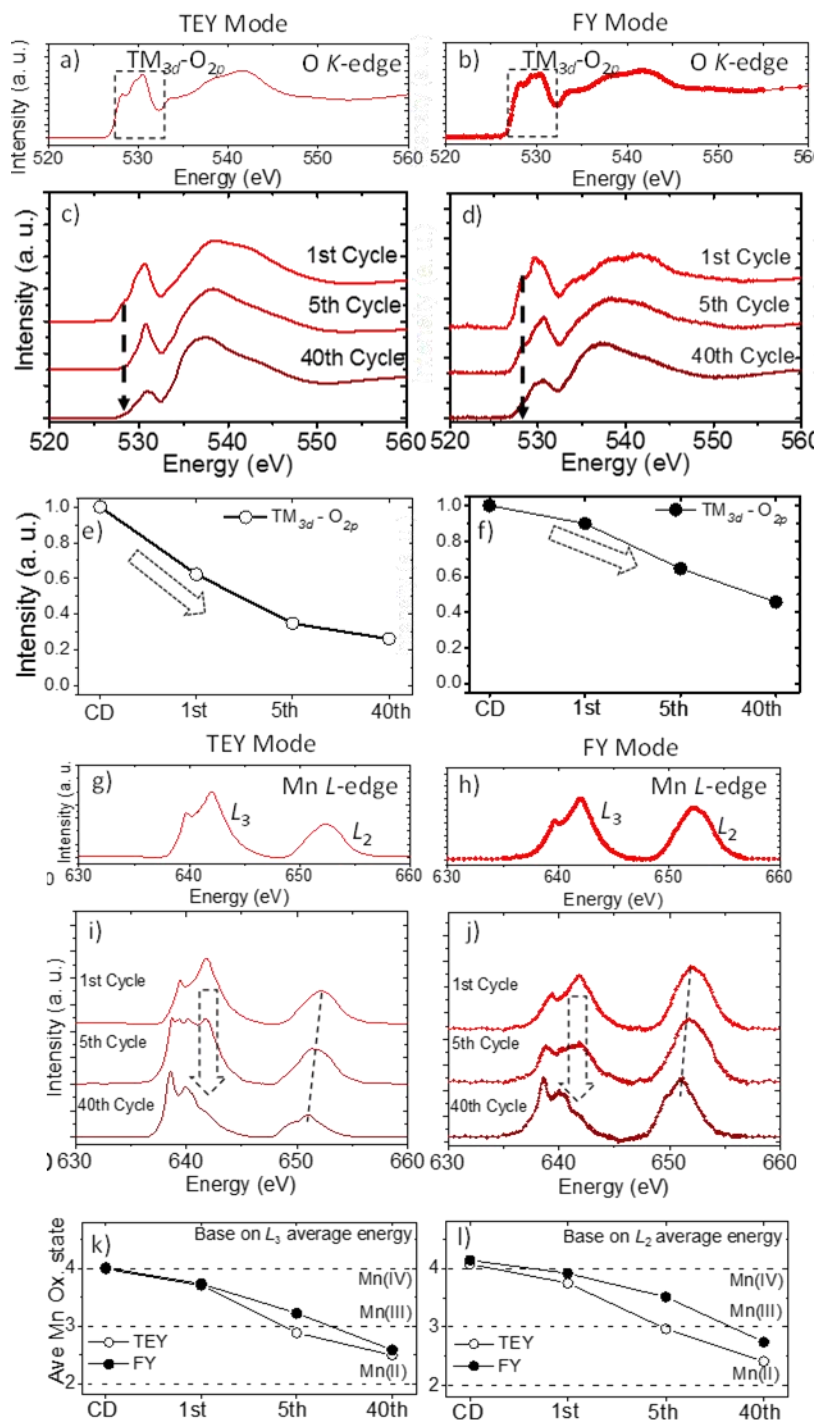


Figure II.3.L.4 O K-edge (a-f) and Mn L-edge (g-l) XAS profiles of chemically delithiated $Li_0.3Nb_0.3Mn_0.4O_2$ (a, b, g, h) and $Li_{1.3}Nb_{0.3}Mn_{0.4}O_2$ cathodes charged to 4.8 V after various cycle numbers (c, d, i, j). e) and f): Intensity of the $TM_{3d}-O_{2p}$ absorption band as a function of the cycle number. k) and l): Mn oxidation state determined from average L_3 and L_2 band.

Mn L-edge soft XAS measurements were also performed to further compare the chemical changes on surface and in the sub-surface region. Figure II.3.L.4g and Figure II.3.L.4h show the spectra collected on fully chemically delithiated oxide while Figure II.3.L.4i and Figure II.3.L.4j show electrochemically charged $Li_{1.3}Nb_{0.3}Mn_{0.4}O_2$ after 1, 5, and 40 cycles. Mn oxidation state, derived from average L_2 (transition from Mn

$2p_{1/2}$) and L_3 (transition from Mn $2p_{3/2}$) band energies, is plotted as a function of cycle number in Figure II.3.L.4k and Figure II.3.L.4l. While Mn is fully oxidized to 4+ in both chemically delithiated $\text{Li}_0\text{Nb}_{0.3}\text{Mn}_{0.4}\text{O}_2$ and $\text{Li}_{1.3}\text{Nb}_{0.3}\text{Mn}_{0.4}\text{O}_2$ electrode after the first charge to 4.8 V, the L_2 and L_3 band features on TEY and FY indicate gradual reduction with cycling. After 5 cycles, the presence of Mn(III) multiplets along with Mn(IV) doublet was clearly observed. Mn was further reduced to below 3+ after 40 cycles, as evidenced by the presence of a peak center at ~ 639 eV, signature of Mn(II) species. The broadly observed differences between the TEY and FY spectra suggest that Mn reduction is also more severe on the surface compared to that in the sub-surface region.

Unlike the layered LMR compounds where stoichiometry is largely fixed, in the rock-salt structure Li and TM cations share the same crystallographic sites which makes it feasible to adjust the TM/Li ratio and subsequently, the contribution of TM and O redox. To this end, two oxides with a composition of $\text{Li}_{1.2}\text{Nb}_{0.2}\text{Mn}_{0.6}\text{O}_2$ and $\text{Li}_{1.4}\text{Nb}_{0.4}\text{Mn}_{0.2}\text{O}_2$ were prepared to evaluate the effect of oxide chemistry on O redox activities in the cation-disordered $\text{Li}_{1.4-x}\text{Nb}_{0.4-x}\text{Mn}_{0.2+2x}\text{O}_2$ system. The samples were synthesized using the same molten-salt method which produced large uniform crystals with a similar particle size of ~ 5 μm (Figure II.3.L.5a and Figure II.3.L.5d). Rietveld refinement of the synchrotron XRD and neutron diffraction patterns (Figure II.3.L.5b-Figure II.3.L.5f) confirms the cation-disordered rock-salt crystal structure free of impurities.

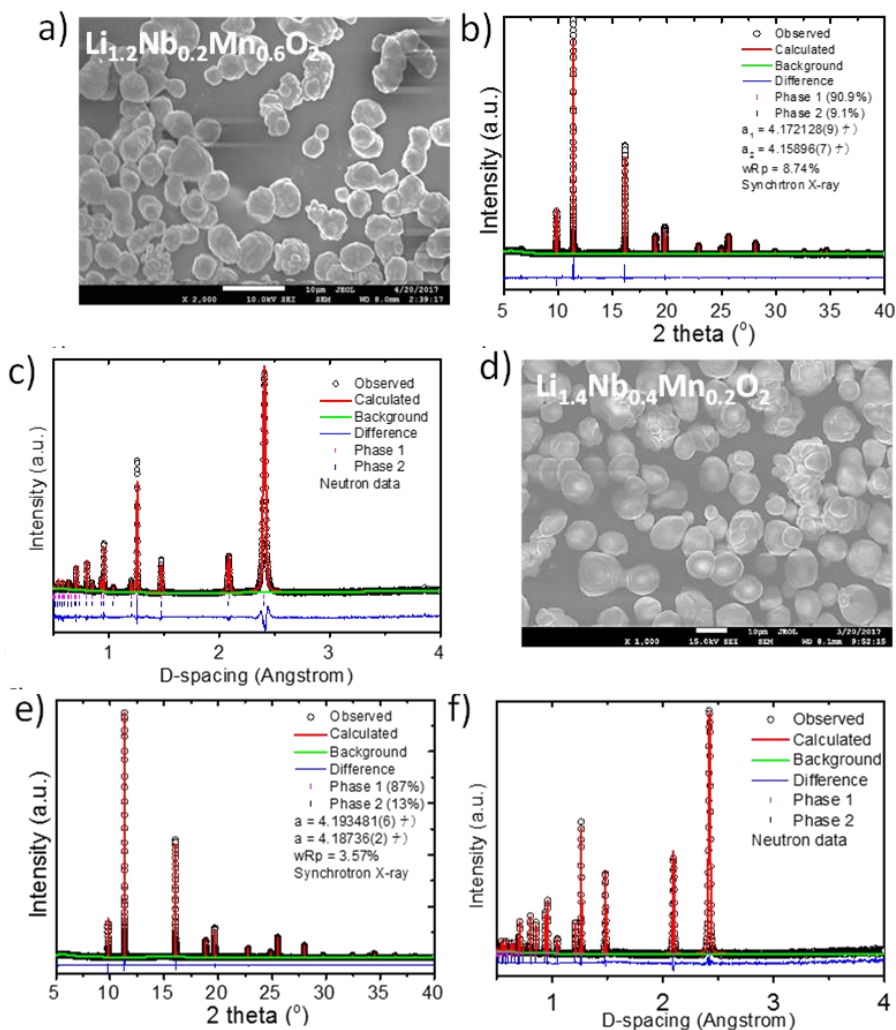


Figure II.3.L.5 SEM images a) and d) and Rietveld refinement of b) and e) synchrotron XRD patterns, c) and f) neutron diffraction patterns of as-synthesized $\text{Li}_{1.2}\text{Nb}_{0.2}\text{Mn}_{0.6}\text{O}_2$ and $\text{Li}_{1.4}\text{Nb}_{0.4}\text{Mn}_{0.2}\text{O}_2$ samples. The X-ray wavelength is 0.414 Å.

Figure II.3.L.6a compares the 1st cycle voltage profiles of the oxide half cells cycled at 10 mA/g between 1.5 and 4.8 V. As the Mn content (x) increases in $\text{Li}_{1.4-x}\text{Nb}_{0.4-x}\text{Mn}_{0.2+2x}\text{O}_2$, charge capacity obtained from the slopy region below 4.2 V also increases, with approximately 80, 120 and 180 mAh/g for $x=0$, 0.1 and 0.2 respectively. On the other hand, charge capacity obtained from O oxidation in the plateau region above 4.2 V increases with Li content and decreases with the Mn content, with approximately 300, 200 and 100 mAh/g for $x=0$, 0.1 and 0.2 respectively. Although the highest initial charge capacity was obtained on $x=0$, both discharge voltage and capacity were lower compared to that of $\text{Li}_{1.3}\text{Nb}_{0.3}\text{Mn}_{0.4}\text{O}_2$, suggesting higher hysteresis and lower columbic efficiency of O redox as compared to that of the Mn redox. For $x=0.2$, the lower initial charge capacity also led to a lower discharge capacity. The effectiveness of using Li/TM ratio to manipulate 1st cycle Mn and O redox is further shown in the dQ/dV profiles in Figure 6b. While the intensity of the Mn oxidation peak gradually increased along with the Mn content, that of the O oxidation peak decreases.

Figure II.3.L.6c-Figure II.3.L.6h compare the cycling stability of the $\text{Li}_{1.4-x}\text{Nb}_{0.4-x}\text{Mn}_{0.2+2x}\text{O}_2$ oxide cathodes. With the highest Mn redox contribution in $\text{Li}_{1.2}\text{Nb}_{0.2}\text{Mn}_{0.6}\text{O}_2$, the cathode maintained its initial discharge capacity of ~230 mAh/g during the first 20 cycles (Figure II.3.L.6c). On the dQ/dV profiles (Figure 6d), the anodic and cathodic peaks experienced little voltage shift and current decay after the 1st cycle, suggesting high redox reversibility and cycling stability. On the other hand, the charge and discharge profiles of $\text{Li}_{1.4}\text{Nb}_{0.4}\text{Mn}_{0.2}\text{O}_2$ cathode changed significantly with cycling (Figure II.3.L.6g) and the discharge capacity decreased from 270 to 140 mAh/g during the first 20 cycles, a near 50% reduction. On the dQ/dV profile (Figure II.3.L.6h), the anodic peak gradually shifted towards higher voltage at an approximate rate of 150 mV per cycle. The primary cathodic peak suffers from significant decay, and after mere 4 cycles, it was replaced by two lower-voltage cathodic peaks with much smaller current density. Comparing to the electrochemical performance of $\text{Li}_{1.3}\text{Nb}_{0.3}\text{Mn}_{0.4}\text{O}_2$ (Figure II.3.L.6e and Figure II.3.L.6f), performance degradation in $\text{Li}_{1.4}\text{Nb}_{0.4}\text{Mn}_{0.2}\text{O}_2$ was significantly worse. The observed differences suggest that in Li-rich rock-salt oxides, capacity contribution from TM and O redox can be readily tuned *via* cation stoichiometry, which subsequently impact the balance between capacity and stability. Such correlation offers a opportunity in designing electrode materials with minimized performance issues associated with utilizing the high capacity brought upon by oxygen redox.

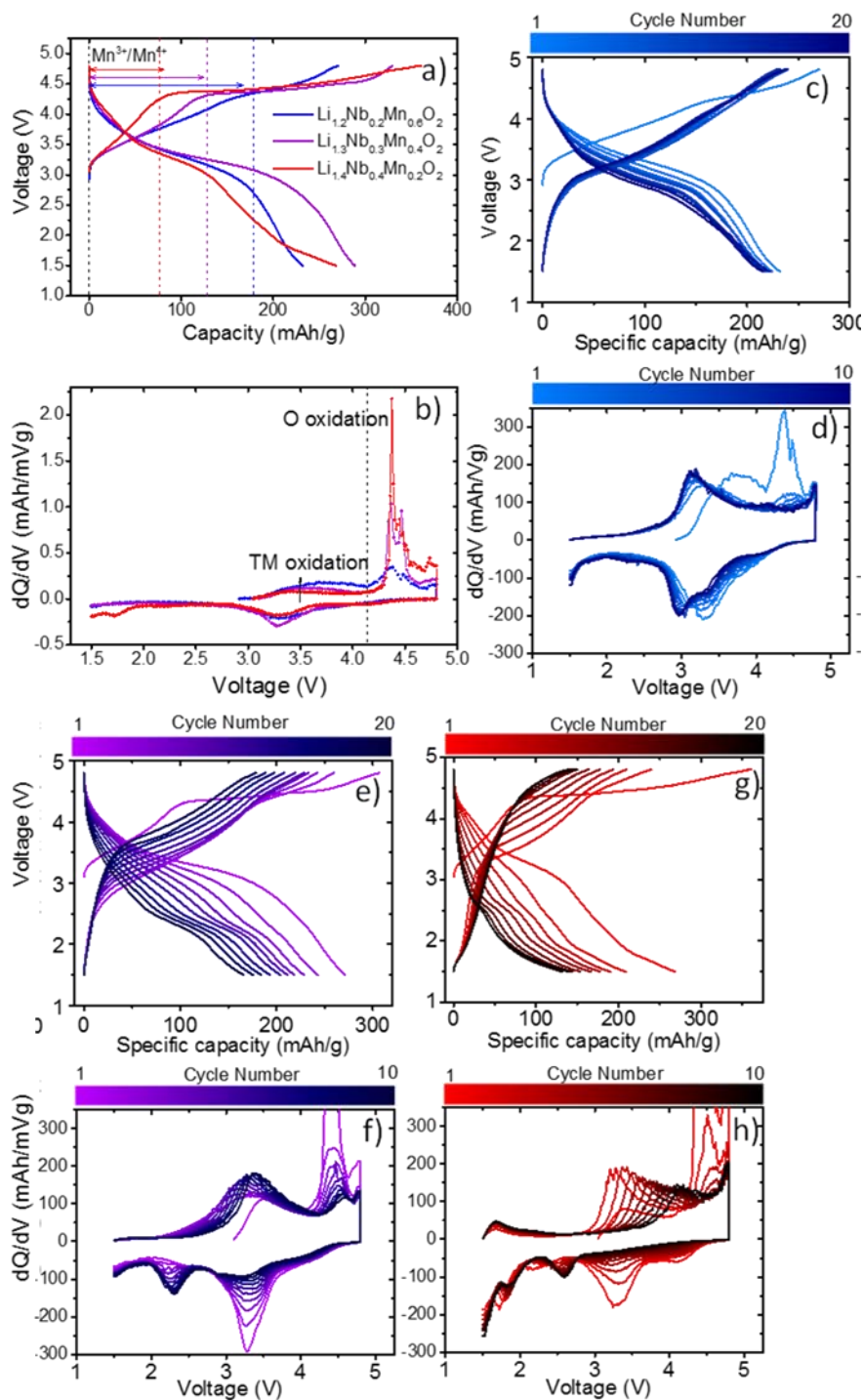


Figure II.3.L.6 Voltage profiles a), c), e) and f) and incremental capacity (dQ/dV) profiles b), d), f) and h) of the half-cells cycled at 10 mA/g. a) and b) were collected during the first cycle, c) and d), e) and f), g) and h) were from $\text{Li}_{1.2}\text{Nb}_{0.2}\text{Mn}_{0.6}\text{O}_2$, $\text{Li}_{1.3}\text{Nb}_{0.3}\text{Mn}_{0.4}\text{O}_2$ and $\text{Li}_{1.4}\text{Nb}_{0.4}\text{Mn}_{0.2}\text{O}_2$ cells, respectively.

Conclusions

In conclusion, the origin of performance and stability deterioration on a model Li-rich cation-disordered rock-salt oxide system, $\text{Li}_{1.3}\text{Nb}_{0.3}\text{Mn}_{0.4}\text{O}_2$, was evaluated. It was found that cathode capacity increases with the increase of O redox activities, but it comes at the expense of performance issues such as hysteresis, voltage and

capacity fade. While TM redox is intrinsically stable with cycling, involving oxygen redox causes irreversibility and kinetic hinderance of the redox processes. The results reveal incredible similarity between the well-studied layered LMR and the cation-disordered oxide cathodes. Soft XAS studies showed significant reduction of Mn oxidation state as a result of oxygen activities, especially on the surface. Net TM site migration, commonly reported in LMR cathodes, was not detected as new phases were not found in the cycled oxide. It was postulated that the unique combination of extensive chemical reduction of TM and reduced quality of the Li percolation network are the origins of cathode performance degradation in this rock-salt structured cathode functioning with a 3D Li diffusion network. These understandings on the relationships between oxygen redox, electrochemical behavior, Li diffusion mechanism, chemical and structural changes provide us with valuable insights on how to utilize the high capacity brought upon by oxygen redox without sacrificing stability. Two new oxides, $\text{Li}_{1.2}\text{Nb}_{0.2}\text{Mn}_{0.6}\text{O}_2$ and $\text{Li}_{1.4}\text{Nb}_{0.4}\text{Mn}_{0.2}\text{O}_2$, were synthesized. The comparative study of the $\text{Li}_{1.4-x}\text{Nb}_{0.4-x}\text{Mn}_{0.2+2x}\text{O}_2$ ($x=0, 0.1$ and 0.2) system showed that owing to the unique cation-disordered structure, fine tuning the cation-site chemistry may be used to balance capacity and stability in this new class of cathode materials.

Key Publications

1. W. H. Kan, D. Chen, J. K. Papp, A. K. Shukla, A. Huq, C. M. Brown, B. McCloskey and G. Chen, "Unravelling Solid-State Redox Chemistry in $\text{Li}_{1.3}\text{Nb}_{0.3}\text{Mn}_{0.4}\text{O}_2$ Single-Crystal Cathode Material," *Chemistry of Materials* **30**, 1655 (2018). DOI: 10.1021/acs.chemmater.7b05036.
2. W. H. Kan, B. Deng, Y. Xu, A. K. Shukla, T. Bo, S. Zhang, J. Liu, P. Pianetta, B.-T. Wang, Y. Liu and G. Chen, "Visualizing the Effect of Local Short-Range Ordering on Lithium-Ion Diffusion in $\text{Li}_{1.3}\text{Nb}_{0.3}\text{Mn}_{0.4}\text{O}_2$ Single-Crystal Cathode," *Chem* **4**, 2108 (2018). DOI:10.1016/j.chempr.2018.05.008
3. Y. Shin, W. H. Kan, M. Aykol, J. K. Papp, B. McCloskey, G. Chen and K. A. Persson, "Alleviating Oxygen Evolution from Li-excess Oxide Materials through Theory-guided Surface Protection," *Nature Communications* **9**, 4597 (2018). DOI: 10.1038/s41467-018-07080-6.
4. W. H. Kan, S. Kuppan, L. Cheng, M. Doeff, J. Nanda, A. Huq and G. Chen, "Crystal Chemistry and Electrochemistry of $\text{Li}_x\text{Mn}_{1.5}\text{Ni}_{0.5}\text{O}_4$ Solid Solution Cathode Materials," *Chemistry of Materials* **29** (16), 6818 (2017). DOI: 10.1021/acs.chemmater.7b01898.
5. D. Chen, W. H. Kan and G. Chen, "Understanding Performance Degradation in Li-Rich Rock-Salt Cathodes," under review (2018).
6. P. Yan, M. Su, J. Zheng, N. Song, A. Devaraj, B. Liu, Y. Wang, G. Chen, X. Li, Z. Xu, K. Amine, J.-G. Zhang, and C.-M. Wang, "Anionic Redox Enhanced Vacancy Injection and Condensation in Bulk Lattice of Layered Cathodes," under review (2018).
7. D. Chen, J. Zhu and G. Chen, "Strategies for Developing High-Energy Lithium-Ion Battery Cathodes," 232nd ECS Meeting, National Harbor, MD, October 2017.
8. J. Zhu and G. Chen, "Advanced High-energy Cathode Materials for Lithium-ion Batteries," 2017 Bay Area Battery Summit, Livermore, CA, November 2017.
9. G. Chen, "Achieving Higher Energy in Lithium-Ion Battery Cathodes," 2018 International Battery Seminar & Exhibit, Fort Lauderdale, FL, March 2018 (invited).
10. G. Chen, "Model System Diagnostics for High-Energy Cathode Development," 2018 Vehicle Technologies Office Annual Merit Review Meeting, Arlington, VA, June 2018.

II.4 Next-Gen Lithium-Ion: Advanced Electrolytes

II.4.A Stability of cathode/electrolyte interfaces in high voltage Li-ion batteries (ANL)

Dusan Strmcnik, Principal Investigator

Argonne National Laboratory
9700 S Cass Ave
Lemont, IL 60439
E-mail: strmcnik@anl.gov

Nenad Markovic, Principal Investigator

Argonne National Laboratory
9700 S Cass Ave
Lemont, IL 60439
E-mail: markovic@anl.gov

Vojislav Stamenkovic, Principal Investigator

Argonne National Laboratory
9700 S Cass Ave
Lemont, IL 60439
E-mail: vrstamenkovic@anl.gov

Peter Faguy, DOE Technology Development Manager

U.S. Department of Energy
E-mail: Peter.Faguy@ee.doe.gov

Start Date: October 1, 2016

End Date: September 30, 2019

Project Funding (FY18): \$600,000

DOE share: \$600,000

Non-DOE share: \$0

Project Introduction

Li-ion batteries have become very important in the last two decades and represent the power source of choice for most portable electronic devices. However, an improvement of this technology is still necessary to be durably introduced onto new markets such as electric vehicles (EVs) and hybrid electric vehicles (HEVs). One of the viable options to meet the high energy density demands of the new Li-ion technology are the high voltage Li-ion batteries, which utilize the cathode materials that can operate at voltages higher than 4.5 V vs. Li/Li⁺. A major problem with these high voltage cathode materials is the incompatibility with “conventional” Li-ion electrolytes, which commonly consist of a combination of lithium hexafluorophosphate (LiPF₆) salt with a binary solvent mixture of cyclic and linear alkyl carbonates such as ethylene carbonate (EC) and ethyl methyl carbonate (EMC). These electrolytes undergo severe degradation at high voltages which is often remedied by cathode passivation additives. Another approach, is to develop new solvents which are intrinsically stable at high voltages. Both approaches, however, demand a much better fundamental understanding of the underlying degradation mechanisms of the Li-ion cathode/electrolyte interfaces, which would be on par with understanding of aqueous electrochemical interfaces.

Objectives

The main goal of this project is to establish fundamental mechanistic understanding of the principles that govern the decomposition and properties of cathode/electrolyte interfaces and relate them to the performance of high voltage Li-ion cells.

In order to achieve this goal, we will divide our work into five objectives:

- Investigate the chemistries of individual electrolyte components of a Li-ion battery on a variety of materials, from well-defined metal single crystals to realistic TMO samples at high potentials, relevant for high voltage LiB. These individual components will range from different solvents, electrolyte salts to impurities that can either be present in the electrolyte from the beginning or contaminate the system during battery operation (e.g. metals from the cathode side).
- Investigate how the experimental conditions influence these individual chemistries or how they enhance or diminish individual processes in the case of overlapping chemistries.
- By utilizing both theoretical as well as experimental tools, establish thermodynamic and kinetic windows of stability of individual components. Furthermore, an attempt will be made to include mass transport effects into the understanding of the interface stability in various electrochemical environments.
- Combine the thermodynamic, kinetic and mass transport properties of a certain chemistry under specific experimental conditions to build an EEI with specific properties.
- Test the performance of the EEI in coin cells.

Approach

The number one priority of this proposal is to extend the state of the art of understanding how individual components of the cathode/electrolyte interface behave at potentials relevant for high-voltage Li-ion batteries and how these individual components interact with each other. A long-term goal, however, is to implement this knowledge into next generation high-voltage cathode materials and electrolytes. While there are many studies available in the literature exploring the electrolyte as well as cathode material decomposition, most of the attempts focused on real materials in real cells. Although such complex phenomena can be ‘tested’ in real systems, the only way to resolve, apply and connect the underlying fundamental processes with real cell performance would be possible with unique experimental-computational approach. To the best of our knowledge, a deeper fundamental understanding about the structure and properties of cathode side electrode-electrolyte-interphase at the atomic/molecular level is still lacking and would be of high importance for the development of next generation LiBs.

Our approach differs significantly from the well-established testing approach, incorporating three critical steps: (i) utilization of model well-defined systems to assess fundamental descriptors for the decomposition of the electrolyte as well as cathode components; (ii) probing more complex electrolytes and electrode materials with different morphologies; and (iii) exploring the properties of cathode materials that are currently, or are potential candidates, to be used in LIB.

Results

Dissolution of transition metal oxides in organic electrolytes

The elucidation of physicochemical parameters (descriptors) that control the functional links between the activity and stability of electrochemical interfaces in aqueous environments forms an increasingly active segment of contemporary surface electrochemistry. Among the various ex situ and in situ experimental techniques suited to establish activity–stability relationships at atomic and molecular levels, the stationary probe rotating disk electrode coupled to inductively coupled plasma mass spectrometry (SPRDE-ICP-MS) method, which has been developed in our laboratory, has provided the most detailed information to date. The power of this technique lies in the ability to simultaneously monitor the reaction kinetics on the rotating disk electrode (RDE) and the dissolution dynamics of the transition-metal cations (TMCs) from an oxide-based electrode material by means of ICP-MS. In doing so it is possible to obtain real-time information about relationships between the activity and stability of anode and cathode materials that are of vital importance to

the development of new renewable energy technologies. For this project, the SPRDE technique has been adapted for organic electrolytes (see Figure II.4.A.1).

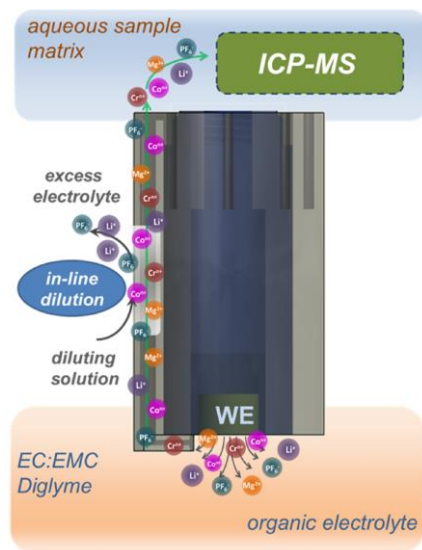


Figure II.4.A.1 (Stationary Probe Rotating Disk Electrode (SPRDE) System Coupled to Inductively Coupled Plasma Mass Spectrometry (ICP-MS)

The stationary probe (SP) consists of a PCTFE capillary tube (400 μm i.d.) positioned at the edge of the disk electrode, less than 1 mm distant from the disk surface, with electrolyte flow direction perpendicular to the electrode surface normal direction. To avoid any height adjustments between the probe and electrode surface, as it would change collection efficiency (N), the whole probe was precisely machined and easily inserted into the probe holder fixed in the rotator case (Pine Instruments MSR). This setup led to N values with no more than 5% variation between each experiment. To adapt the SPRDE-ICP-MS technique for use in organic electrolytes, the system was modified such that the electrolyte is pumped out of the electrochemical cell with a PTFE-lined peristaltic pump (Cole-Parmer) at $10 \mu\text{L s}^{-1}$ by the probe capillary connected to an ETFE tube (0.010 in. ID) directly to the inline dilution system. PCTFE mixing tees (VICI) are used as mixing and separation elements in the dilution system, while the flow of species into and out of the tees is controlled by an ESI MP2 microperistaltic pump to achieve the desired dilution ratio. Because of the addition of the sample dilution and flow conditions, the transport time between the electrode surface and the ICP-MS detections was fixed at 30s. To keep the total cell volume constant, fresh electrolyte is replenished by another peristaltic pump flowing at the same rate as it is pumped out through the SPRDE.

The current understanding of activity–stability relationships for transition-metal-based oxides that serve as host frameworks for intercalation/deintercalation of mobile (working) cations in organic environments remains inadequate, thus far relying solely on the separate evaluation of potential-dependent “charging currents” and post mortem determination of the concentration of TMCs (e.g., Mn, Ni, and Co) dissolved in the electrolyte or deposited at the anode.^{[1], [2], [3], [4], [5]} Although these ex situ studies provide some useful information about the potential-dependent stability of TMCs during multiple discharge–charge cycles in Li-ion batteries (LIBs), such measurements do not allow for reliable quantification of dissolved TMCs nor do they reveal the true dynamics of TMC dissolution. Such measurements of high-voltage oxide stability are further complicated by the common use of the two electrode “coin cell” geometry, which makes it impossible to identify electrochemical processes intrinsic to the oxide material due to crossover of decomposition products generated at both electrodes. As a result of this knowledge gap, there is currently no consensus on the mechanisms that may lead to TMC dissolution.^{[1], [4], [5], [6], [7]} Further complications arise from the ever-present possibility of electrolyte decomposition, whose individual contribution to the charge/discharge reactions is impossible to measure solely from galvanostatic cycling measurements. What is undisputable in the literature, however, is

that the dissolved cations can be deposited on the graphite anode, which, in turn, can lead to voltage fade and early cell failure. Here, by developing the SPRDE-ICP-MS method for use inorganic environments, we demonstrated that it is possible to easily follow the dynamics of cobalt dissolution from LiCoO_2 in 1.2 M LiPF_6 in 3:7 ethylene carbonate/ethyl methyl carbonate (EC/EMC) electrolyte. Representative current–time curves are summarized in Figure II.4.A.2 and correspond either to the Co^{nt} “ionic” dissolution current measured by the ICP-MS (in Figure 1a expressed in $\mu\text{A cm}^{-2}$) or to the total electrochemical current that is simultaneously recorded on the RDE (in Figure II.4.A.1b expressed in mA cm^{-2}). To the best of our knowledge, this is the first experiment of its kind that provides real-time, quantitative analysis of cation dissolution in organic environments. As we describe further later, it is also possible to determine the excess faradaic charge relative to Li intercalation/deintercalation and the simultaneous dissolution of Co^{nt} , which can provide important insights into the functional links between cathode stability and electrolyte decomposition.

We first explored the dynamics of Co dissolution during potential step transients from 3 V vs Li/Li^+ up to a maximum of 5 V (in 0.2 V increments) with 300 s per potential step. Note that the potential limits were purposely chosen to ensure that both Li deintercalation and intercalation take place to simultaneously evaluate the electrolyte decomposition currents. Figure II.4.A.2a reveals that the potential-dependent ionic current response for Co dissolution evolves from transient to steady-state behavior. The first three potential steps (4.0 to 4.4 V) exhibit a small, yet clearly discernible, amount of transient Co^{nt} dissolution (nanogram level) that quickly decays to the same level as the background. Beginning at 4.6 V, however, large, transient Co^{nt} dissolution rates are followed by rapid relaxation to a measurable, steady-state value, signaling that constant Co^{nt} dissolution takes place above 4.6 V. Note that the corresponding current–time profile recorded on the disk electrode shows that measurable disk currents are also only observed above 4.6 V, indicating that there is no measurable electrolyte decomposition below that potential limit. In addition, the results in Figure II.4.A.1a demonstrate that the Co dissolution current is almost three orders of magnitude smaller than the electrochemical current (only $\sim 0.15\%$ of the total current at 5 V), emphasizing the power of the SPRDE-ICPMS method to monitor, almost atom-by-atom, the dynamics of TMC dissolution that are otherwise inaccessible from typical charge/discharge measurements.

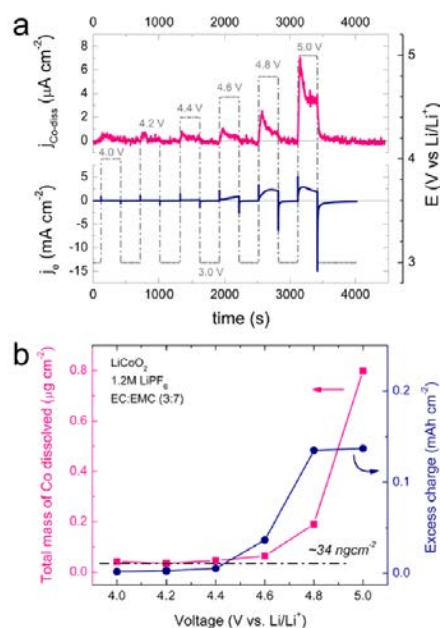


Figure II.4.A.2 (a) In situ dissolution currents for Co ion dissolution (magenta) from LiCoO_2 in 1.2 M LiPF_6 in 3:7 EC/EMC at increasing upper potential values during electrochemical polarization. Corresponding electrochemical current is shown in blue during the same polarization experiment. (b) Total mass of Co dissolved in each potential step window (left axis) and the corresponding excess positive charge measured on the disk attributed to electrolyte decomposition (right axis).

An important consequence of being able to measure Co dissolution rates independently from the electrode current is that it enables correlations between TMC oxide dissolution, the nature of the electrolyte, and its decomposition rate. The excess charge observed in Figure II.4.A.1b can be related to electrolyte decomposition by calculating the difference between the charge under the forward potential step (charging step) and the charge passed during the immediate step back to 3 V (discharge step), as expected. What has not been established before now is that electrolyte decomposition and $\text{Co}^{\text{n+}}$ corrosion take place simultaneously, and our independent measurements of electrolyte decomposition and electrode corrosion enable quantitative analysis of their individual contributions to parasitic losses during charge/discharge. On the basis of this evidence, two distinct corrosion pathways can be proposed. The first is that either electrolyte decomposition triggers Co dissolution or intrinsic LiCoO_2 surface instability initiates electrolyte decomposition. The second pathway requires a promoter of cobalt dissolution, for example, impurity HF or O_2 redox from within the oxide host, with HF-induced “attack” on cation surface centers (defects) or oxygen recombination and release of $\text{Co}^{\text{n+}}$ and O_2 leading to $\text{Co}^{\text{n+}}$ surface dissolution. In either case the remaining surface defects become the active centers for electrolyte decomposition and, in the case of O_2 redox, CO_2 release. Our results clearly demonstrate that Co dissolution is potential dependent, suggesting that a purely chemical corrosion process (e.g., HF attack) is unlikely, as it would take place regardless of electrode polarization. Regardless of the exact corrosion reaction mechanism, our unique capability for monitoring, in situ, Co dissolution and electrolyte decomposition from LiCoO_2 as well as the ability to correlate these phenomena in real time, will provide new avenues for exploring the stability of even more relevant high energy oxides, such as those containing Ni, Mn, and Co in varying stoichiometry.

Conclusions

In summary, we demonstrated the ability of in situ SPRDE-ICP-MS method as a unique means of extracting activity–stability relationships in organic systems that are on a par with those established in aqueous environments. In particular, we have shown that this technique can simultaneously and rapidly measure the onset and dynamic evolution of TMC host corrosion kinetics, deintercalation of the working cation, and electrolyte stability over a wide potential range under experimental conditions that are relevant for real applications. This capability will certainly open a new window of opportunities to rationalize, and ultimately understand, fundamental processes that control the stability and reversibility Li-ion battery systems.

Key Publications

Pietro P. Lopes, Milena Zorko, Krista L. Hawthorne, Justin G. Connell, Brian. J. Ingram, Dusan Strmcnik, Vojislav R. Stamenkovic, and Nenad M. Markovic, *Real-Time Monitoring of Cation Dissolution/Deintercalation Kinetics from Transition-Metal Oxides in Organic Environments*, *J. Phys. Chem. Lett.* 2018, 9, 4935–4940

References

1. Wandt, J.; Freiberg, A.; Thomas, R.; Gorlin, Y.; Siebel, A.; Jung, R.; Gasteiger, H. A.; Tromp, M. *Transition Metal Dissolution and Deposition in Li- Ion Batteries Investigated by Operando X-Ray Absorption Spectroscopy*. *J. Mater. Chem. A* 2016, 4, 18300–18305
2. Amatucci, G. G.; Tarascon, J. M.; Klein, L. C. *Cobalt Dissolution in LiCoO_2 -Based Non-Aqueous Rechargeable Batteries*. *Solid State Ionics* 1996, 83, 167–173
3. Evertz, M.; Horsthemke, F.; Kasnatscheew, J.; Winter, M.; Nowak, S. *Unravelling Transition Metal Dissolution of $\text{Li}_{0.4}\text{Ni}_{1/3}\text{Co}_{1/3}\text{Mn}_{1/3}\text{O}_2$ (NCM 111) in Lithium Ion Full Cells by Using the Total Reflection X-Ray Fluorescence Technique*. *J. Power Sources* 2016, 329, 364–371.
4. Kasnatscheew, J.; Evertz, M.; Streipert, B.; Wagner, R.; Nowak, S.; Cekic Laskovic, I.; Winter, M. *Changing Established Belief on Capacity Fade Mechanisms: Voltage Conditions*. *J. Phys. Chem. C* 2017, 121, 1521–1529.

5. Michalak, B.; Berkes, B.; Sommer, H.; Brezesinski, T.; Janek, J. *Electrochemical Cross-Talk Leading to Gas Evolution and Capacity Fade in $\text{LiNi}_{0.5}\text{Mn}_{1.5}\text{O}_4$ /Graphite Full-Cells*. *J. Phys. Chem. C* 2017, 121, 211–216.
6. Aurbach, D.; Markovsky, B.; Rodkin, A.; Levi, E.; Cohen, Y. S.; Kim, H.-J.; Schmidt, M. *On the Capacity Fading of LiCoO_2 Intercalation Electrodes: The Effect of Cycling, Storage, Temperature, and Surface Film Forming Additives*. *Electrochim. Acta* 2002, 47, 4291–4306.
7. Choi, S. S.; Lim, H. S. *Factors That Affect Cycle-Life and Possible Degradation Mechanisms of a Li-Ion Cell Based on LiCoO_2* . *J. Power Sources* 2002, 111, 130–136.

Acknowledgements

We would like to acknowledge Dr. Pietro P. Lopes for the development of the SPRDE-ICP-MS technique and its adaptation for organic battery electrolytes.

II.4.B Fluorinated Deep Eutectic Solvent (FDES)-Based Electrolytes (ANL)

Zhengcheng Zhang

Argonne National Laboratory
9700 S. Cass Ave.
Lemont, IL 60439
E-mail: zzhang@anl.gov

Peter Faguy, DOE Technology Development Manager

U.S. Department of Energy
E-mail: Peter.Faguy@ee.doe.gov

Start Date: October 1, 2018

End Date: September 30, 2021

Project Funding (FY18): \$350,000

DOE share: \$350,000

Non-DOE share: \$0

Project Introduction

The next generation lithium-ion battery for vehicle application requires high energy density with excellent cycling performance, low cost and significantly enhanced safety. For the PHEV application, lithium-ion chemistries with energy density around 175~250 Wh/kg are currently the most promising choice. The most efficient way to raise the energy density of a battery is to increase the voltage and/or capacity of the cathode. Several high-voltage cathode materials have been developed such as $\text{LiNi}_{0.5}\text{Mn}_{1.5}\text{O}_4$ (4.8 V) spinel and LiCoPO_4 (5.1 V) olivine. Other candidate cathodes that have potential of providing desired energy is the nickel (Ni)-based layered oxides with less or zero cobalt (Co) since these Ni-rich cathodes could deliver even higher capacity when the charging voltages are beyond >4.4 V vs Li^+/Li as well as their low cost due to the absence or low content of expensive cobalt. $\text{LiN}_{0.5}\text{Mn}_{0.3}\text{Co}_{0.2}$ (NMC532, theoretical capacity 287 mAhg⁻¹), a representative of this class of materials, could offer much higher energy had it been charged to higher potentials (4.4~4.8 V) instead of 4.2 or 4.3 V vs Li^+/Li , making it another promising candidate for next generation high energy Li-ion battery. Nevertheless, these high energy cells suffer from fast deterioration in capacity retention at such high potentials mainly due to the instability of the electrode/electrolyte interface. Designed for 4 V-class Li-ion chemistry, the conventional organic carbonate electrolyte is thermodynamically instable at the charged cathode surface higher than 4.3 V vs Li^+/Li . Oxidative decomposition of organic carbonates leads to the generation of gaseous products and water causing severe cell swelling and transition metal dissolution. TM dissolution was also observed in the 4 V-class Li-ion cells mainly due to the trace amount of the moisture existing in the initial electrolyte, but it gets significantly worse when the cycling voltage is elevated.

Objectives

The objective of this project is to develop fluorinated deep eutectic solvent (FDES)-based electrolytes (Figure II.4.B.1) as new high voltage electrolytes to address the high reactivity of conventional organic electrolyte at the surface of the charged cathode and the safety concern associated with the organic electrolyte. The design and synthesis of the new electrolytes are directed by the all-atom polarizable Drude model and molecular engineering, and the proposed FDES are designed to provide thermodynamic stability on the charged cathode surface affording a stabilized cathode/electrolyte interface. More importantly, the new electrolytes are highly compatible with the anode including graphite and Si. The proposed FDES is a new room-temperature molten salt comprising of new fluorinated organic cations and new fluorinated organic anions with a wide liquid window. FDES has superior thermal stability with no vapor pressure even heated to 300-400°C, and excellent fluidity at temperature lower than -20°C. Not only high performance, the proposed FDES are non-flammable with significantly enhanced safety characteristic.

Approach

To address the instability of cathode/electrolyte interface, we propose to develop a new electrolyte system based on the fluorinated deep eutectic solvents (FDES) (also called fluorinated ionic liquid-based aprotic

electrolytes) that have substantially high voltage tolerance. Aided by the quantum chemistry modeling and molecular engineering, the proposed FDES are designed to provide thermodynamic stability on the charged cathode surface affording a stabilized cathode/electrolyte interface. More importantly, the new electrolytes are highly compatible with the anode including graphite and silicon. The proposed FDES is a new room-temperature molten salt comprising of new fluorinated organic cations and new fluorinated organic anions with a wide electrochemical window and a wide liquid window. FDES has superior thermal stability with no vapor pressure even heated to 300-400°C, and excellent fluidity and conductivity at temperatures lower than -20°C. Not only high performance, the proposed FDES are non-flammable with significantly enhanced safety characteristic. This proposal is targeting to develop a high performance electrolyte material which could enable the next generation high energy high voltage lithium-ion battery for electric vehicle application.

Results

Figure II.4.B.1 showed the general synthetic route for the proposed FDES. The baseline FDES was first synthesized using this new, one-step reaction by mixing N-methylpyrrolidine (cation precursor) and methyl fluorosulfonylimide (MeFSI) in stoichiometric ratio without any further treatment. This process affords extremely high purity of the solvent since the individual reagent of this reaction could be made very pure by traditional methods. ^1H -, ^{13}C - and ^{19}F -NMR and Raman confirmed the identity and the purity of the synthesized solvents. The solvents were dried in lyophilizer for at least 2 days, then stored over 4 Å molecular sieves and filtered before use. The water content was less than 20 ppm measured by Karl-Fischer coulometric titrator.

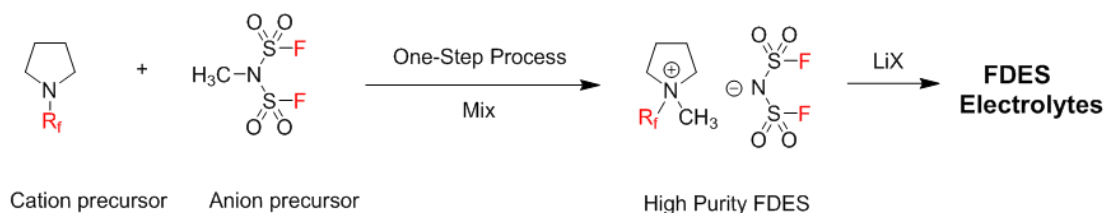


Figure II.4.B.1 Representative synthesis route for the proposed solvent and electrolyte based on fluorinated pyrrolidinium bis(fluorosulfonyl)imide (FDESFSI). (The proposed new synthesis is based on Lewis acid/base one-step reaction yielding highly pure FDESs.)

Table II.4.B.1 summarizes the physical properties of the synthesized FDES electrolytes with various LiFSI salt concentrations. It is evident that with increasing salt concentration, the viscosity and the conductivity of the electrolyte decrease monotonically. However, the Li^+ transference number showed the opposite trend, i.e., at higher salt concentration (5 M or 3.8 mol/kg), the t_{Li^+} jumped to 0.475 from 0.164 for 1 M or 0.76 mol/kg electrolyte. A high transference number benefits from the electrolyte concentration polarization and thus increases the cycling efficiency of the battery.

Table II.4.B.1 Summary of Conductivity, Viscosity and Li^+ Transference Number

Molality of LiFSI (mol/kg)	Li^+	PMpip ⁺	FSI ⁻	Viscosity (cP)	Conductivity (S/cm)	t_{Li^+}
0	0	0.50	0.50	87.25	3.50	-
0.76	0.10	0.40	0.50	133.5	2.24	0.164
1.5	0.16	0.34	0.50	249.0	1.25	0.185
2.3	0.21	0.29	0.50	396.0	0.819	0.340
3.0	0.25	0.25	0.50	601.3	0.555	0.344
3.8	0.28	0.22	0.50	936.6	0.353	0.475

1.0 M LiFSI PMpipFSI electrolyte showed high stability in the LiFePO₄/Li cells with high capacity retention of 99.1 % for 100 cycles (determined based on the 1st cycle at C/10 specific discharge capacity) as shown in Figure II.4.B.2. The scattered Coulombic efficiency with cycling number is due to the lithium dendrite formation caused by the use of thick glassfiber separator. However, when switched to a higher voltage cathode NMC532 with higher charging voltage, the same electrolyte showed low stability as indicated in Figure II.4.B.3.

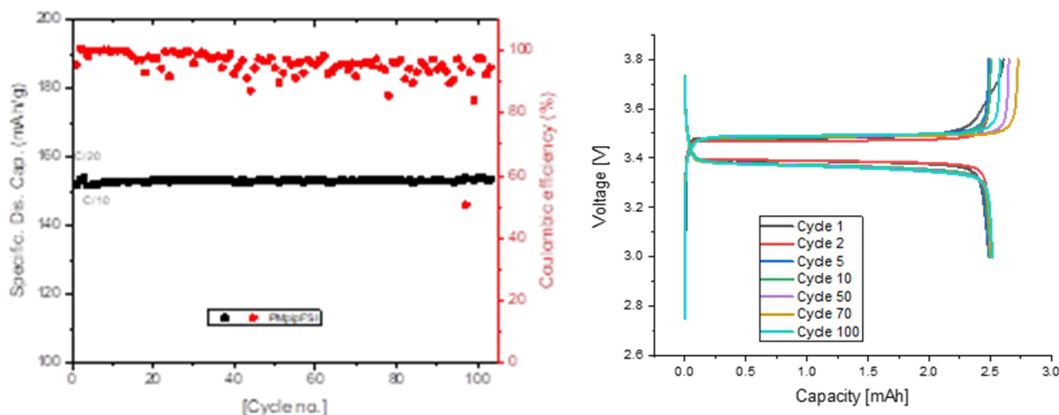


Figure II.4.B.2 Capacity and capacity retention of 1 M LiFSI PMpipFSI for LiFP/Li cells (left) and charge/discharge voltage profiles (Cutoff voltage: 3.0-3.8 V; C/20 for 3 formation cycles and C/10 for 100 cycles).

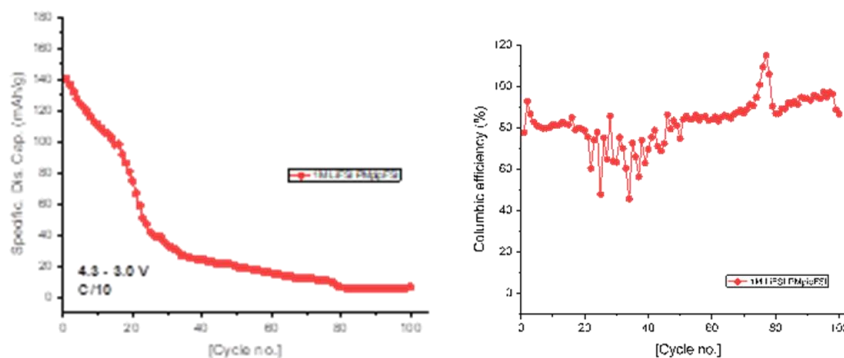


Figure II.4.B.3 Capacity and capacity retention of 1 M LiFSI PMpipFSI for NMC532/Li cells (left) and Coulombic efficiency profiles (Cutoff voltage: 3.0-4.3 V; C/20 for 3 formation cycle and C/10 for 100 cycles).

Surprisingly, the 5 M LiFSI PMpipFSI electrolyte showed much improved cell performance in NMC532/Li cell compared with 1 M electrolyte cell. As shown in Figure II.4.B.4, not only the capacity retention improves significantly, the Coulombic efficiency increases from about 80% for 1 M electrolyte cell to 92% for 5 M electrolyte cell. Based on the linear sweep voltammetry (LSV) experiment data (not shown), the oxidation stability of the new electrolyte could sufficiently support the NMC redox up to 4.3 V vs Li⁺/Li. The improved performance of NMC cell with 5 M electrolyte clearly indicates the passivation behavior for the metals existing in the cell system was altered. Figure II.4.B.5 is the summary of the corrosion experiment using Al as working electrode and Li as counter and reference electrode. It shows that 1 M, 2 M, 3 M, 4 M and 5 M electrolytes all could well passivate the Al electrode (used as current collector for cathode) as Gen 2 electrolyte (SOA electrolyte) does. We speculated at this stage that stainless steel (SS) (used as spacer in the 2320 coin cell format) corrosion issue might be responsible for the poor performance of 1 M electrolyte cell. The cyclic

voltammetry data using a SS working electrode unveiled the secret. As shown in Figure II.4.B.6, Gen 2 electrolyte could well passivate SS, whereas all the DES electrolytes showed corrosion phenomena. Nevertheless, the corrosion current was significantly suppressed for the 5 M electrolyte compared with that of 1 M electrolyte. The kinetic suppression of the SS corrosion leads to the good cycling performance as well as the Coulombic efficiency for the 5 M electrolyte cell (Figure II.4.B.4).

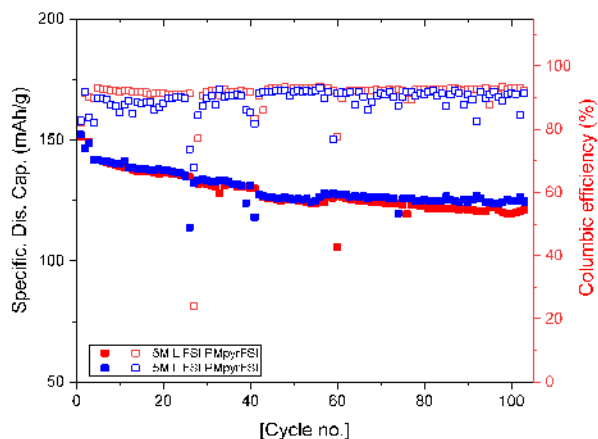


Figure II.4.B.4 Capacity and capacity retention of 5 M LiFSI PMpipFSI for NMC532/Li cells (left) and Coulombic efficiency profiles (Cutoff voltage: 3.0-4.3 V; C/20 for 3 formation cycle and C/10 for 100 cycles).

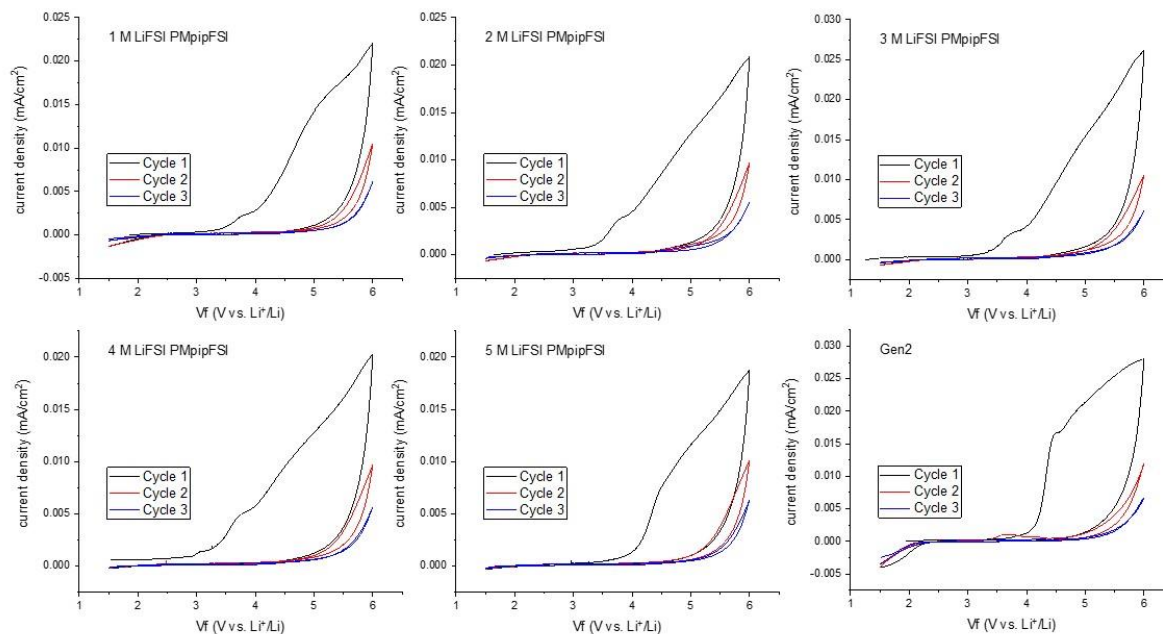


Figure II.4.B.5 Cyclic voltammograms of the FDES/LiFSI electrolytes with 1 M, 2 M, 3 M, 4 M and 5 M LiFSI concentration. (Al electrode as working electrode and lithium as both counter and reference electrode; and glass fiber as the separator; the scan rate was 10 mV/s).

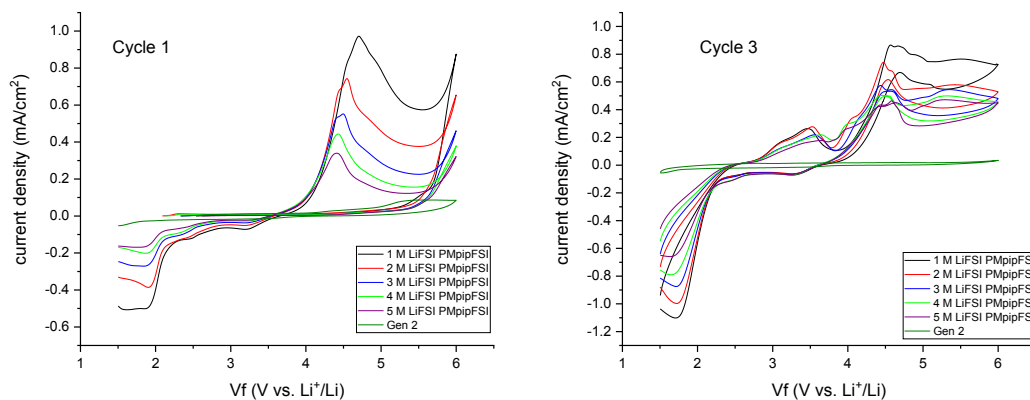


Figure II.4.B.6 Cyclic voltammograms of the FDES/LiFSI electrolytes with 1 M, 2 M, 3 M, 4 M and 5 M LiFSI concentration. (SS electrode as working electrode and lithium as both counter and reference electrode; and glass fiber as the separator; the scan rate was 10 mV/s).

We will continue to evaluate the high voltage performance of the high concentration FDES electrolytes in NMC532 cells with end of charging voltages of 4.5 V and 4.7 V, respectively. Also, we are planning to perform molecular dynamic (MD) simulation to understand the 3-D cation-anion-Li⁺ network for the high concentration FDES electrolyte as well as Raman, FT-IR and NMR analysis.

Conclusions

In summary, we have established a one-step synthesis of the FDES (or IL) solvent with extremely high purity. FDES/LiFSI electrolyte with various salt concentrations were formulated and their electrochemical performance was evaluated in LFP and NMC532 cells. It is evident that all the FDES/LiFSI electrolytes could passivate the Al current collector as the SOA electrolyte does; however, there is an issue for the stainless steel working electrode. The stainless steel corrosion study revealed the underlined reason for the improved cell performance for FDES/5.0 M LiFSI electrolyte due to its kinetic stability against stainless steel spacer in the coin cell.

Key Publications

1. Liu *et al.*, Ionic liquid-LiFSI based electrolyte for high voltage lithium ion battery, in preparation.

References

1. Michel Armand, Frank Endres, Douglas R. MacFarlane, Hiroyuki Ohno and Bruno Scrosati. Ionic-liquid materials for the electrochemical challenges of the future. *Nature Materials*, 2009, **8**, 621-629.
2. Daniela Molina Piper, Tyler Evans, Kevin Leung, Tylan Watkins, Jarred Olson, Seul Cham Kim, Sang Sub Han, Vinay Bhat, Kyu Hwan Oh, Daniel A. Buttry & Se-Hee Lee. Stable silicon-ionic liquid interface for next-generation lithium-ion batteries. *Nature Communications*, 2015, **6**, 6230.
3. Giuseppe Antonio Elia, Ulderico Ulissi, Sangsik Jeong, Stefano Passerini and Jusef Hassoun. Exceptional long-life performance of lithium-ion batteries using ionic liquid-based electrolytes. *Energy Environmental Science*, 2016, **9**, 3210-3220.

Acknowledgements

We gratefully acknowledge the support from Dr. Peter Faguy at Vehicle Technologies Office, Office of Energy Efficiency and Renewable Energy, the U. S. Department of Energy (DOE). Argonne National Laboratory is operated for DOE Office of Science by UChicago Argonne, LLC, under contract number DE-

AC02-06CH11357. We'd like to thank Dr. Wei Jiang and Dr. Ying Li at the Argonne Leadership Computing Facility (ALCF) for the molecular dynamic simulation work.

II.4.C Advanced Lithium Ion Battery Technology – High Voltage Electrolyte (Daikin America, Inc.)

Ron Hendershot, Principal Investigator

Daikin America, Inc.
2749 Highway 20 West
Decatur, Alabama 35601
E-mail: hendershot@daikin-america.com

Joseph Sunstrom, Principal Investigator

Daikin America, Inc.
2749 Highway 20 West
Decatur, Alabama 35601
E-mail: sunstrom@daikin-america.com

Alec Falzone, Principal Investigator

Daikin America, Inc.
2749 Highway 20 West
Decatur, Alabama 35601
E-mail: afalzone@daikin-america.com

Tien Duong, DOE Technology Development Manager

U.S. Department of Energy
E-mail: Tien.Duong@ee.doe.gov

Start Date: October 1, 2017	End Date: September 30, 2018	
Total Project Cost: \$1,826,895	DOE share: \$1,250,000	Non-DOE share: \$576,895

Project Introduction

The use of electrolytes containing small fluorinated molecules to enable stable high voltage (> 4.3 V) battery operation is the focus of this project. Previously, Daikin has shown that it is possible to operate lithium ion batteries utilizing several different cathode chemistries up to 4.5 V. This is accomplished by reducing the gas generation originating from electrolyte decomposition at high voltage. The primary mechanism for this is not completely understood, but the hypothesis is that the fluorinated molecules form a film on the highly oxidizing cathode. It is known that battery cycle performance above 4.5 V drops significantly, however the source of the observed performance loss is not yet understood. The target for this project is to achieve 300 cycles above 80% capacity retention at 4.6 V. A better understanding of gas evolution, which happens above 4.3 V and the failure mode above 4.5 V, is sought in order to propose mitigation strategies which will facilitate better high voltage performance in lithium ion batteries.

The battery industry trend for cathode materials is toward reducing the overall cobalt content (i.e. higher nickel) for a variety of reasons. Some of which include: increasing cost, loss of supply, and human rights issues. The experiments proposed for this project will encompass a range of cathode materials with successfully higher nickel content. This will be performed in order to comprehend how fluorinated electrolyte interacts with various cathode surfaces. This is with the anticipation that the lithium ion battery industry will move towards nickel-rich cathodes, which can operate at higher voltage in order to achieve more energy-dense batteries.

Objectives

The three-year project can be divided into three main milestone topics, each spanning one fiscal year: 1) understanding of gassing mechanisms and kinetics, 2) examining physical and chemical aspects of film formation, and 3) observation of chemical and structural evolution of electrode surfaces at various operating

conditions. The FY2018 focus is the characterization of the SEI layer formed on the cathode surface as a function of voltage, electrochemical performance, and electrolyte formulation. Cycling cells at high voltage results in a protective film forming on the surface of the highly oxidized cathode surface, which is derived from the highly fluorinated Daikin electrolyte. We aim to determine which electrolyte formulation produces an ideal SEI layer on the cathode, in addition to their characteristics. Efforts to develop methods to measure both film thicknesses and compositions (elemental and chemical) will help us understand the relationship between desired SEI layer characteristics and optimized electrochemical performance. Determination of the film thickness and elemental characterization will be carried out using Auger electron spectroscopy (AES), transmission electron microscopy (TEM) and scanning electron microscopy (SEM). Chemical analysis of cathode films will utilize both time-of-flight secondary ion mass spectrometry (TOF-SIMS) and X-ray photoelectron spectroscopy (XPS). Cell thickness changes related to non-gassing mechanisms throughout cycle life testing are measured using a voltage-based contact sensor. Properties of films derived from different electrolytes (i.e. hydrocarbon vs. fluorinated) will be compared which will assist in submitting interim cells with significant improvement in cycle performance at 4.6 V.

Table II.4.C.1 Summary of Conductivity, Viscosity and Li⁺ Transference Number

Milestone	Type	Description	Target Completion Date
Film composition (elemental) vs. time/voltage complete	Technical	Assemble four dimensional plots of film composition (element concentrations) as a function of performance parameters (voltage, initial capacity, cycle #) to understand effect of film composition on performance. Draw elemental maps of film surface as a function of voltage and cycle number.	07/30/2018 Complete
Film thickness vs. time/voltage complete	Technical	Assemble four dimensional plots of film thickness as a function of performance parameters (voltage, initial capacity, cycle #) to understand effect of film thickness on performance.	08/12/2018 Complete
Battery thickness (non- gas) vs. time/voltage complete	Technical	Assemble four dimensional plots of cell thickness as a function of performance parameters (voltage, initial capacity, cycle #) to understand effect of cell swelling on performance. Propose formulations based on learnings in Budget period 1 and 2.	10/01/2018 In Progress
Interim cells achieve a significant improvement in cycles at 4.6 V.	Go/No Go	Interim Cells achieve a significant improvement over initial cells submitted at the beginning of the project cycled at 4.6 V.	12/31/2018 To be Submitted

Approach

The baseline of current best-practice fluorinated electrolyte was determined by reviewing already obtained data from high-voltage lithium ion batteries from a previously funded project (DOE EE0006437). In parallel, an up-to date literature and patent review has also been performed to explore other cutting edge developments in 2017. Three electrolytes were selected as standards for this project: 1.2 M LiPF₆ ethylene carbonate (EC)/ethyl methyl carbonate (EMC) 80:20 (v/v %), 1.2 M LiPF₆ EC/EMC/fluoroether (FE) 20:60:20 (v/v %) and 1.2 M LiPF₆ FEC/EMC/FE 20:60:20 (v/v %). These represent electrolytes with zero, one and two fluorinated solvents added, respectively. All electrolytes also contain propane sultone (PS) (1% w/w) as an additional anti-gassing additive. 200 mAh dry wound cells have been purchased as test vehicles. The cathode chemistries studied (with increasing mole fractions of nickel are: LiCoO₂ (LCO), LiNi_xMn_yCo_zO₂ (NMC xyz = 111, 532, 622) and LiNi_{0.8}Co_{0.15}Al_{0.05}O₂ (NCA) all paired with artificial graphite anodes. Analysis of the

gases produced at high voltage (> 4.3 V) will be completed and compared to cells cycled at a baseline voltage of 4.2 V, which is the current battery industry standard. Post mortem analysis of the cathode materials will be carried out to determine the presence and characteristics of any protective film on the surface. Cycled cells will be compared to processed, uncycled cathodes to correlate surface properties to electrochemical testing and electrolyte formulation. A mass balance approach to the cells will be used in order to propose performance limiting factors and strategies to overcome them.

Results

Film Composition (Elemental) vs. Time/Voltage – Milestone 1

During FY2017, efforts were focused on investigating gassing mechanisms observed during high voltage operation of lithium ion batteries. Throughout these studies varying compositions of electrolyte were tested and compared to the baseline, hydrocarbon (HC) electrolyte (1.2M LiPF₆, 80% EMC, 20% EC, 1% w/w PS). Analysis of the electrochemical data supports the hypothesis that a more fluorinated electrolyte results in better performance above 4.5 V compared to the hydrocarbon electrolyte. One contributing factor in the high-voltage performance of lithium ion batteries utilizing a highly fluorinated electrolyte is the formation of a protective film, or SEI layer, on the cathode surface.

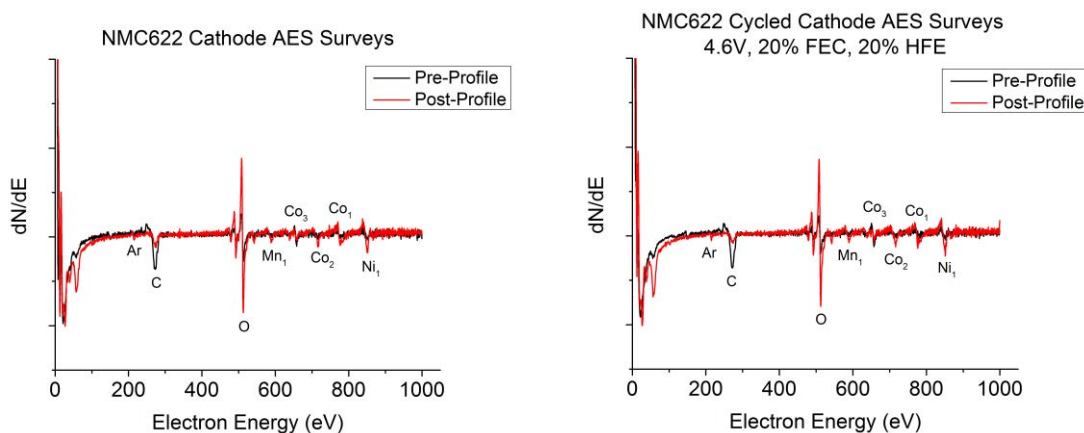


Figure II.4.C.1 AES survey scan of an uncycled (left) and cycled (right) NMC622 cathode before (black) and after (red) a depth profile experiment.

Determination of the SEI layer's elemental composition uses Auger Electron Spectroscopy (AES) as the first method of analysis. Figure II.4.C.1 depicts the elemental survey scans of a dried, uncycled NMC622 cathode (left) and a NMC622 cathode cycled at 4.6 V with a highly fluorinated electrolyte (right) both before and after a depth-profile experiment. In addition to AES identifying the elemental components of the SEI layer, it also serves as a technique to determine the film's thickness. AES depth profile experiments study changes in the surface composition as a function of depth of the material.

As seen in survey scans pre-depth profiling (Figure II.4.C.1), the surface elemental composition is almost identical, even after cycling at 4.6 V. The strongest signal comes from Carbon, and is present in many forms (adventitious, carbon black, PVDF binder, SEI layer, etc.). Oxygen also has a strong Auger signal, largely from the bulk NMC622 cathode material. Lithium (cathode, SEI layer, and electrolyte), fluorine (PVDF, SEI layer, and electrolyte), cobalt (cathode), and nickel (cathode) also contribute to the surface Auger signal.

Following the depth profile, the Auger signal from the transition metals (Mn, Co, and Ni) and oxygen are stronger as the SEI layer is sputtered away, exposing more of the bulk metal oxide material. Carbon's intensity is diminished, in both the cycled and uncycled cathode. Due to the presence of PVDF binder and conductive carbon black throughout the material, the carbon signal is measureable after sputtering. Although the elemental composition of the SEI layer is identical to that of an uncycled cathode, the differences lie in the chemical

composition and overall thickness of the amorphous film on the surface. Time-of-Flight Secondary Ion Mass Spectrometry (TOF-SIMS) imaging was performed in collaboration with Physical Electronics, USA (PHI). Investigating the surface composition of NMC622 cathodes through TOF-SIMS provides high-resolution mass spectra in all areas of interest.

Positive mode depth-profile data from an NMC622 cathode cycled at 4.6 V with the hydrocarbon electrolyte is depicted in Figure II.4.C.2. The metal oxide particles are represented by the transition metals (Ni, Mn, and Co) in addition to Al from the current collector. Aluminum was not detected in any of the cycled cathodes with fluorinated electrolyte, suggesting the protective SEI layer in these cells is thicker and more uniform, and prevents exposure of the current collector after electrochemical testing.

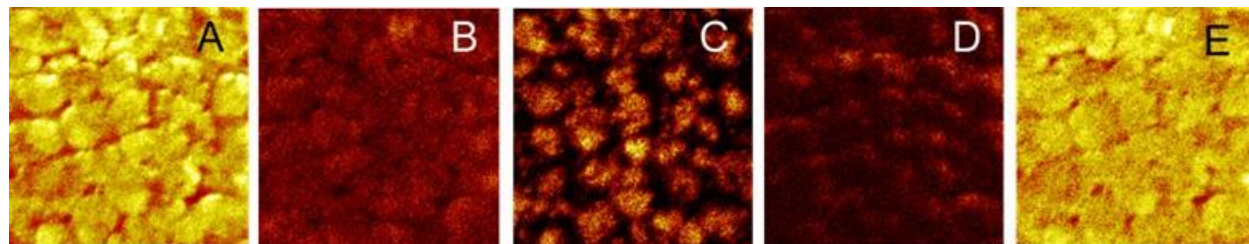


Figure II.4.C.2 TOF-SIMS maps of positive ions in a cycled NMC622 cathode at 4.6 V with the hydrocarbon electrolyte. A) TIC B) Ni⁺ C) Mn⁺ D) Co⁺ E) Al⁺

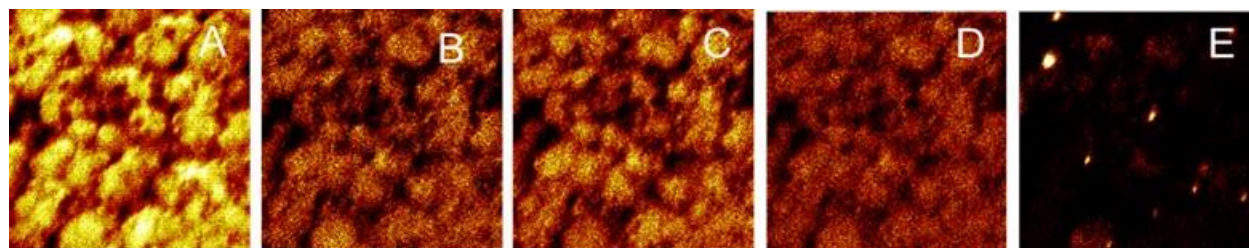


Figure II.4.C.3 TOF-SIMS maps of negative ions in a cycled NMC622 cathode with the hydrocarbon electrolyte. A) TIC B) LiF⁻ and LiF₂⁻ C) O⁻ D) PF₆⁻ E) F⁻

Figure II.4.C.3 displays the negative mode ions detected using TOF-SIMS in the identical spatial region depicted in Figure II.4.C.2. Various lithium salts (LiF and LiF₂ for example) are evident both on the surface of the particles, and also in the depressed areas between them. Like that of the transition metal signals, oxygen is largely present on the particles. Residual PF₆⁻ is the result of salt deposition following the evaporation of organic components in the electrolyte. F⁻ is heavily prevalent in e, originating from both the PF₆⁻ salt and PVDF binder. No organic fragments with measurable intensity were detected on the NMC622 cathode with the hydrocarbon electrolyte. This suggests that if there is an SEI layer on the surface, it is either disordered or too fragile to be analyzed under identical TOF-SIMS conditions.

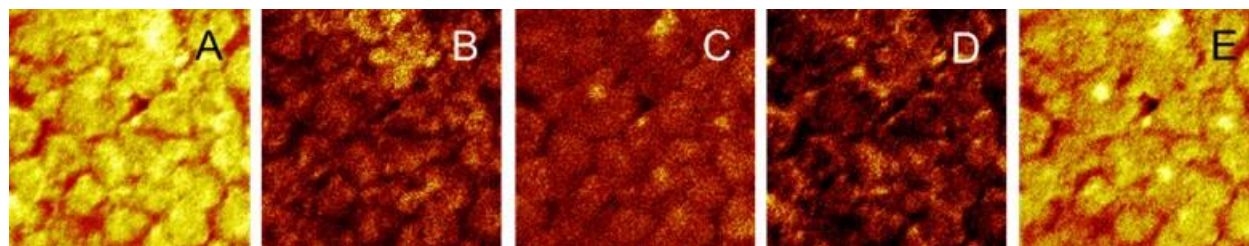


Figure II.4.C.4 TOF-SIMS maps of positive ions in a cycled NMC622 cathode at 4.6 V with a highly fluorinated electrolyte (1.2M LiPF₆, 60% EMC, 20% HFE, 20% FEC, 1% w/w PS). A) TIC B) Combined Li⁺ C) C_xH_yO_z-Li⁺ D) LiOH₂/LiOH₃⁺

In the depth-profile depicted in Figure II.4.C.4, organic fragments ionized with lithium were observed with significant intensity. These fragments are of similar composition $(C_xH_yO_z-Li)^+$, with a varying amount of carbon and hydrogen ($m/z = 78, 81, 83$). These fragments are located spatially on the surface of the cathode particles, which suggests they are a component of the SEI layer. Lithium ions complexed with water and hydronium are evident in the valleys between particles in Figure II.4.C.4D.

Figure II.4.C.5 represents the spatial distribution of negative ions on a cycled NMC622 cathode with a fluorinated electrolyte at 4.6 V. The total negative ion count (TIC) depicted in Figure II.4.C.5A is of similar intensity to that Figure II.4.C.3 A (hydrocarbon electrolyte), however the chemical composition of the SEI layer is dissimilar. Evident in Figure II.4.C.5B are organic fragments comprised of: carbon, hydrogen, oxygen, and fluorine ($m/z = 79, 80, 81$) whereas these are absent from the SEI layer on the cathode with a hydrocarbon electrolyte.

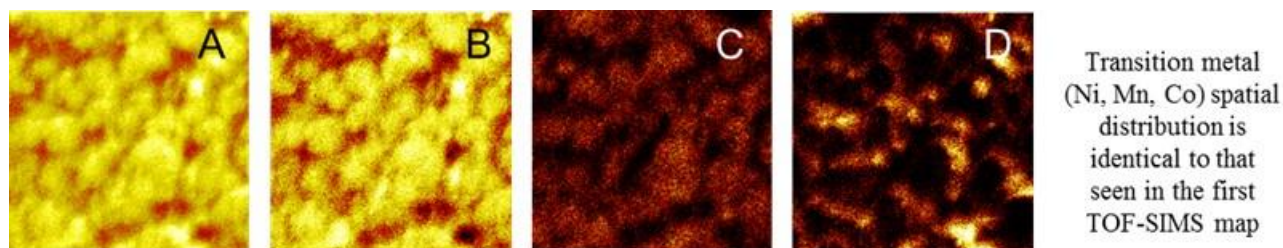


Figure II.4.C.5 TOF-SIMS maps of negative ions in a cycled NMC622 cathode with the fluorinated electrolyte. A) TIC B) $C_xH_yO_zF_w$ C) $C_xH_yO_z$ D) $C_xH_yF_zP_w$ E) F^-

Additional organic film fragments in Figure II.4.C.5C ($m/z = 26, 45, 82$) and D ($m/z = 103, 105, 108$) are only present in the cathode with fluorinated electrolyte, further suggesting the surface composition is electrolyte-dependent. Data analysis of NMC622 cathodes cycled at 4.2 V and with additional electrolyte formulations is ongoing and will provide additional insight into operating condition effects on cathode SEI layer formation.

Film Thickness vs. Time/Voltage – Milestone 2

Argon ion sputtering, traditionally calibrated to 1000 Å of O in SiO_2 , coupled with AES is a widely used method to determine material thicknesses. This method serves as the initial approach to measuring the SEI layer in cathode materials. AES survey scans coupled with TOF-SIMS profiling suggest the SEI layer more closely resembles that of a carbon-like material than an oxide layer. Amorphous carbon films of various thicknesses were grown on a silicon wafers (UHV Sputtering Inc.), and serve as the sputter rate determinant material. AES depth profiles of the carbonaceous films will then be compared to that of various cathode materials.

Three carbon film thicknesses were fabricated (500, 1000, and 5000 Å) in order to provide a comprehensive understanding of different conditions. Low resolution SEM images are depicted in Figure II.4.C.6 of the 1000 (A) and 5000 (B) Å films. The underlying silicon substrate is visible on the left, and the bright layer on the right is a sputtered gold layer which serves as an imaging contrast. The black area between the two bright layers is the carbon film. Current efforts are focused on confirming the thickness of these samples using FIB-SEM in collaboration with the Missouri University of Science and Technology.

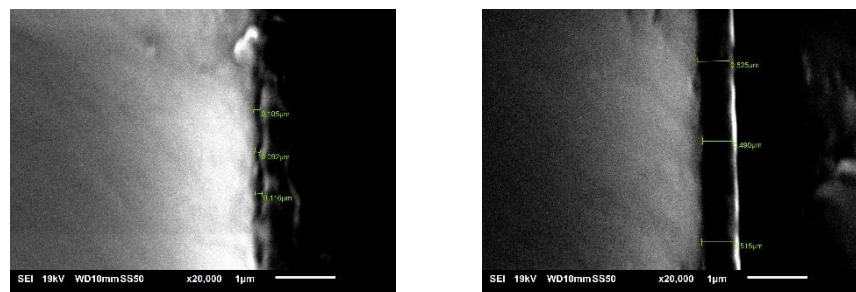


Figure II.4.C.6 SEM images of amorphous carbon films A) 1000 Å B) 5000 Å

The AES depth profile displays the elemental signal as a function of Argon ion sputtering through the material. Figure II.4.C.7 depicts the average signal from depth profile experiments of cycled (fluorinated electrolyte, 4.6 V) and uncycled NMC622 cathodes using AES. Carbon, oxygen, and nickel were the analytes of interest for Auger analysis. Initial AES survey scans suggest the surface composition of both cycled and uncycled cathode materials is carbonaceous, and the bulk cathode material a metal-oxide. Independent depth profile experiments were carried out on each cathode in order to develop a statistically meaningful understanding of the surface chemistry of each condition. The difference in the average argon ion current to reach the C-O intercept is proportional to the SEI layer thickness on the surface of a cycled cathode. This difference of 4.1×10^{14} argon ions will be compared to the depth profiles of the amorphous carbon film standards in order to calculate the thickness of the SEI layer.

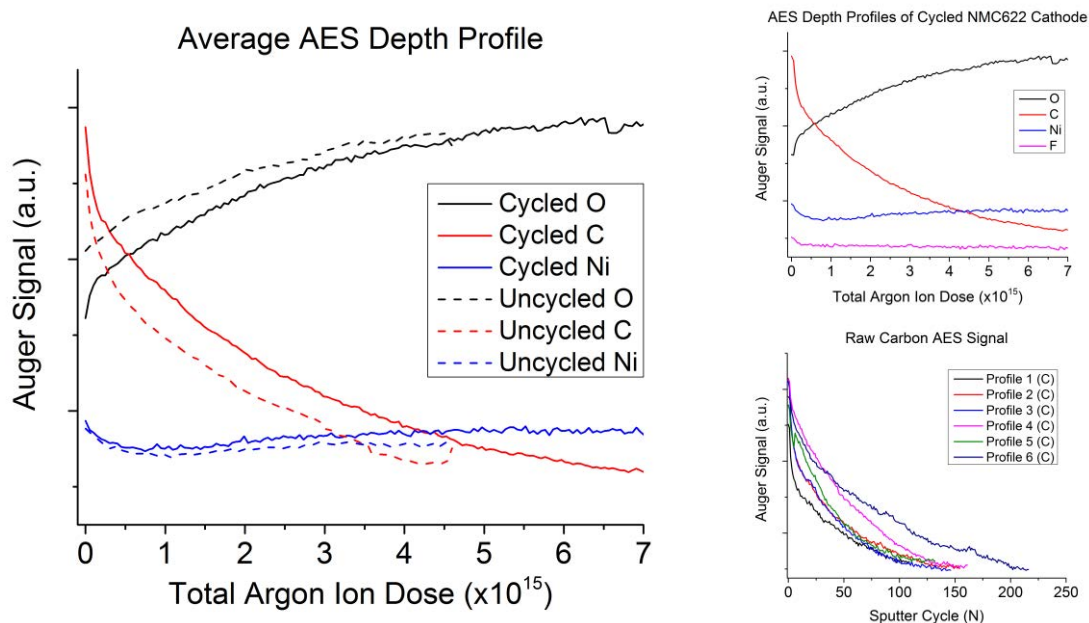


Figure II.4.C.7 Elemental profiles of different spots on an NMC622 cathode (left). Solid lines represent that from a cycled cathode (4.6 V, fluorinated electrolyte), dashed lines from an uncycled cathode. Average AES signal of cycled NMC622 cathode (top right). Raw carbon AES signal from each depth profile (bottom right).

In addition to internal experiments to determine film thicknesses, collaborative efforts with Dr. Yi Cui at Stanford University using other analytical techniques are ongoing.

Battery Thickness (Non-Gas) vs. Time/Voltage – Milestone 3

Current efforts to measure the dynamic thicknesses of cycling 200 mAh cells are ongoing. The approach utilizes a Keyence optical displacement gauge (one per cell) to record the swelling in the anode/cathode as a function of charging and discharge the cell. These thickness gauges are calibrated to materials of known

thicknesses in order to generate a calibration curve. The housing for these gauges have been custom fabricated to fit an Arbin battery tester, and utilizes two channels per cell/gauge combination.



Figure II.4.C.8 Keyence thickness gauges have a linear voltage response to thickness changes in devices, up to 5 mm. These have a sub-millimeter resolution, and are capable of operating at elevated temperatures.

Gassing Kinetics of FEC – NCA Cathode

In addition to investigating the LCO, NMC111, 532, and 622 cathode materials as reported in the FY2017 report, NCA is also a cathode of interest. NCA is a common cathode for electric vehicle applications, which to date is not capable of long-term operation at high voltage. Preliminary experiments on NCA batteries with a few different electrolytes show promising results optimized this throughout the project (Figure II.4.C.9).

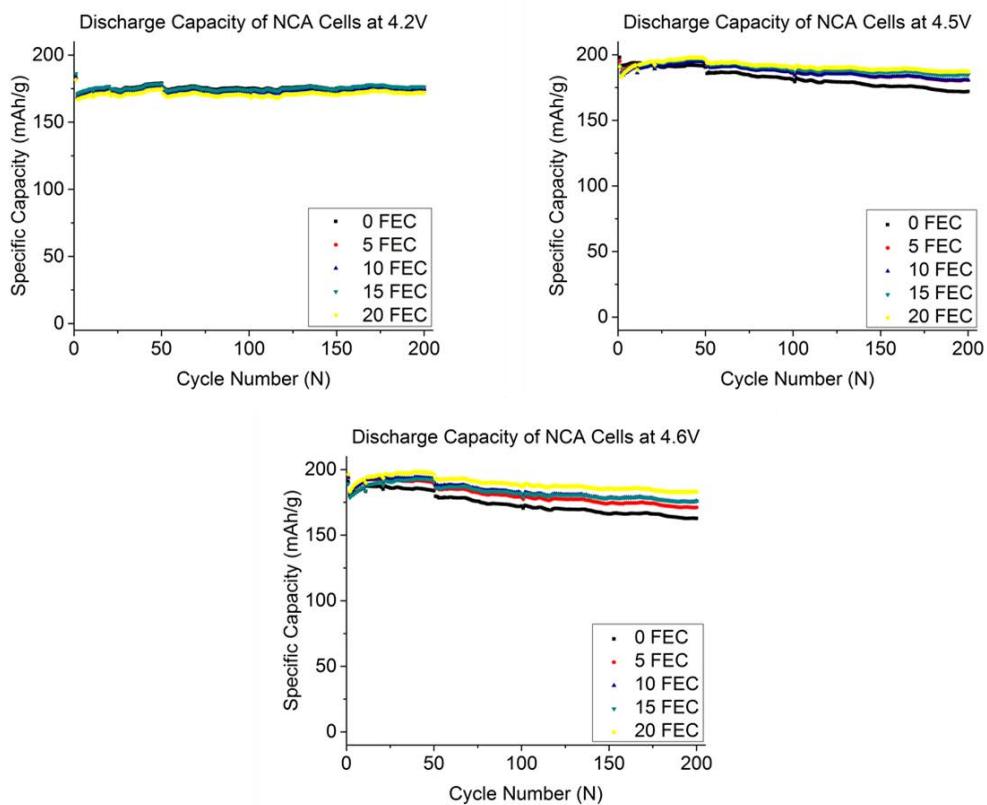


Figure II.4.C.9 200 mAh NCA cells cycled at .7C at r.t. as a function of FEC concentration (0-20% v/v) and voltage (4.2, 4.5, and 4.6)

As seen with our previously reported work (NMC111, 532, and 622 cells cathodes), cycling above 4.2V requires an electrolyte with a minimum of 10% FEC, with an optimal concentration between 10 and 15% (v/v). Cells are able to retain >85% capacity at high voltage (4.5 V and 4.6 V) after 200 cycles; however, they do exhibit significant gassing. Efforts to identify and quantify this gas are underway. Figure II.4.C.10 shows OCV drop and gas volume change results in a 55°C calendar life test at 4.2 and 4.6 V.

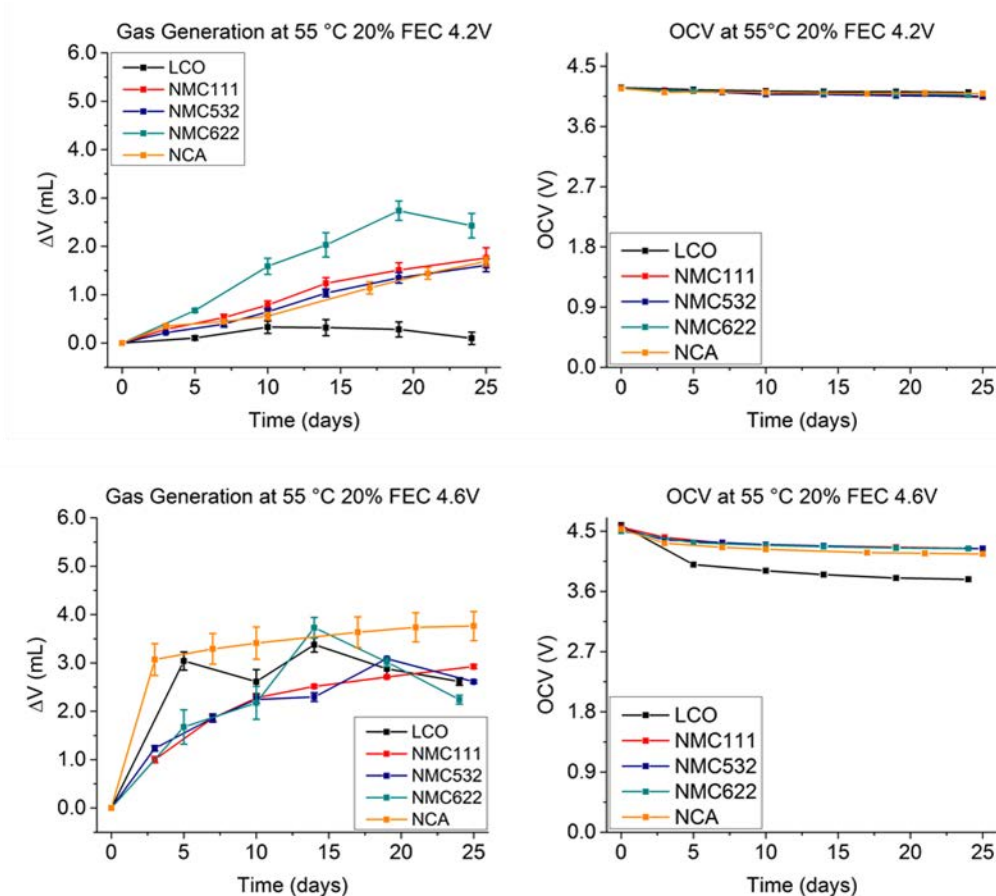


Figure II.4.C.10 Calendar life test (Δ OCV and Δ gas volume) at 55 °C with 20% FEC at an OCV of 4.2 (left) and 4.6 V (right)

Conclusions

Significant work at Daikin in the second year involved setup and validation and training for equipment needed to complete this project. This included the commissioning of several new pieces of equipment supporting analysis of the SEI layer, AES and XPS. In addition, several collaborations have been initiated to utilize their expertise and capabilities for film thickness and chemical analysis measurements. In FY2018 we also experienced significant personnel changes, which included the onboarding and continuous training of four team members. Gas composition and electrochemical testing have been completed for additional cathode materials (NMC111, 532, and NCA) initiated in FY2017. All contain significant amounts of CO, CO₂, CH₄ and O₂ along with select fluorinated hydrocarbons attributed to the decomposition of FEC in the electrolyte at high voltage. The analysis of this data has allowed us to choose chemistries/electrolyte formulations to fulfill the Go/No Go FY2018 milestone.

The surface elemental composition is identical in both a cycled and uncycled battery. The strongest signal comes from carbon, and is present in many forms (adventitious, carbon black, PVDF binder, SEI layer, etc.). Oxygen also has a strong Auger signal, largely from the bulk cathode material. Lithium (cathode, SEI layer, and electrolyte), fluorine (PVDF, SEI layer, and electrolyte), cobalt (cathode), and nickel (cathode) are also present. However, the chemical composition varies greatly, and is a function of the electrolyte formulation. There is a protective, fluorinated film that is present on the surface in cathodes when using the highly fluorinated (HFE and FEC) electrolyte. This film is not present when the baseline, hydrocarbon electrolyte is used.

Multiple methods for film thickness determination have been identified and implemented. The AES depth profile calibrations to known carbon thickness standards have been successful, and have aided in our deconvolution of the SEI layer's properties on the cathode. Preliminary analysis of the data set suggest the film's thickness in a fluorinated electrolyte after cycling at 4.6 V is < 100 nm, with additional quantification work ongoing.

Following our observation of electrochemical testing in NMC622 and LCO cells, the addition of FEC to electrolyte results in increased cycle life and capacity retention in NMC111, 532, and NCA cells. The full cycling performance benefit of FEC in the electrolyte is realized at a 10% (v/v %), and can be marginally increased with additional FEC. The data obtained thus far for NCA cells (OCV loss, gas evolution, etc.) suggests that the significant amount of gassing observed is an inherent property of the cathode material.

Key Publications

1. Sunstrom, J.; Falzone, A. J.; Hendershot, R., Daikin Advanced Lithium Ion Battery Technology – High Voltage Electrolyte. *2018 DOE- VTO AMR Meeting*, Arlington, VA, June 18-21, 2018
2. Falzone, A. J.; Sunstrom, J.; Hendershot, R.; Meserole, C.; Grumbles, E.; Haque, A.; Costa, M., Advancing Lithium Ion Battery Technologies: Development of a High-Voltage Electrolyte. *2018 Solid State Chemistry Gordon Research Conference*, New London, NH, July 22-27, 2018

References

1. Li, Y.; Li, Y.; Pei, A.; Yan, K.; Sun, Y.; Wu, C.; Joubert, L.; Chin, R.; Koh, A. L.; Yu, Y.; Perrino, J.; Butz, B.; Chu, S.; Cui, Y. *Science*, **2017**, *358*, 506-510
2. Xu, M.; Fujita, D.; Gao, J.; Hanagata, N. *ACS Nano*, **2010**, *4*, 2937-2945) Kalaga, K.; Shkrob, I. A.; Haasch, R. T.; Peebles, C.; Bareño, J.; Abraham, D. P., *J. Phys. Chem. C*, **2017**, *121*, 23333-23346
3. Tang, C.; Ma, Y.; Haasch, R. T.; Ouyang, J.; Dillon, S. J., *J. Phys. Chem. Lett.*, **2017**, *8*, 6226-6230
4. Philippe, B.; Hahlin, M.; Edström, K.; Gustafsson, T.; Siegbahn, H.; Rensmo, H., *J. Electrochem. Soc.*, **2016**, *163*, A178-A191
5. Andersson, A. M.; Abraham, D. P.; Haasch, R.; MacLaren, S.; Liu, J.; Amine, K., *J. Electrochem. Soc.*, **2002**, *149*, A1358-A1369

II.5 Next-Gen Lithium-Ion: Diagnostics

II.5.A Interfacial Processes (LBNL)

Robert Kostecki, Principal Investigator

Lawrence Berkeley National Laboratory
1 Cyclotron Rd.
Berkeley, CA 94720
E-mail: r_kostecki@lbl.gov

Tien Duong, DOE Technology Development Manager

U.S. Department of Energy
E-mail: Tien.Duong@ee.doe.gov

Start Date: October 1, 2015

End Date: September 30, 2018

Project Funding (FY18): \$440,000

DOE share: \$440,000

Non-DOE share: \$0

Project Introduction

Li-ion batteries are inherently complex and dynamic systems. Although often viewed as simple devices, their successful operation relies heavily on a series of complex mechanisms, involving thermodynamic instability in many parts of the charge/discharge cycle and the formation of metastable phases. This paradigm of Li-ion system operation usually drives the battery toward irreversible physical and chemical conditions that lead to battery degradation and failure.

The requirements for long-term stability of Li-ion batteries are extremely stringent and necessitate control of the chemistry at a wide variety of temporal and structural length scales. Progress towards identifying the most efficient mechanisms for electrical energy storage and the ideal material depends on a fundamental understanding of how battery materials function and what structural/electronic properties limit their performance. This in turn necessitates the development and use of new characterization tools to monitor these processes.

The design of the next generation of Li-ion batteries requires a fundamental understanding of the physical and chemical processes that govern these complex systems. Although some significant advances have been made to prepare and utilize new materials efforts towards the understanding of their operation mechanisms and degradation modes have been insufficient and/or unsuccessful.

This project provides better understanding of the underlying principles that govern the function and operation of battery materials, interfaces and interphases, which is inextricably linked with successful implementation of high energy density materials such as $\text{Li}[\text{Ni}_x\text{Mn}_y\text{Co}_z]\text{O}_2$ compounds (NMCs) in Li-ion cells for PHEVs and EVs. A systematic evaluation of the NMC material composition, and cell history on the surface reconstruction, transition metal dissolution, oxygen loss phenomenon is proposed for this work, using in situ surface-sensitive optical spectroscopy and microscopy. These results will supplement other characterization efforts within this Task and ultimately will be used to design and synthesize robust NMC materials that can cycle stably to high potentials and deliver >200 mAh/g at coulombic efficiency close to 100%.

Objectives

This collaborative project involves the development and application of advanced experimental methodologies to study and understand the mechanism of operation and degradation of high capacity NMC materials for Li-ion cells for PHEV and EV applications. The main objective of this task is to apply *in situ* and *ex situ* far- and near-field optical multifunctional probes to obtain detailed insight into the active material structure and the physico-chemical phenomena at electrode/electrolyte interfaces of stoichiometric NMCs with high Ni contents such as 622 and 523 compositions materials at a spatial resolution that corresponds to the size of basic chemical or structural building blocks. The primary goal of these studies is to unveil the structure and

reactivity at hidden or buried interfaces and interphases that determine material, composite electrode and full cell electrochemical performance and failure modes. A better understanding of the underlying principles that govern these phenomena is inextricably linked with successful implementation of high energy density materials such as Si and high voltage cathodes in Li-ion cells for PHEVs and EVs. The proposed work constitutes an integral part of the concerted effort within the BMR Program and it supports development of new cathode materials for high-energy Li-ion cells. Specific technical objectives include:

- Develop advanced experimental methodologies to study and understand the mechanism of operation and degradation of high capacity materials for rechargeable cells for PHEV and EV applications.
- Apply *in situ* and *ex situ* far- and near-field optical multifunctional probes to obtain detailed insight into the active material structure and the physio-chemical phenomena at electrode/electrolyte interfaces at a spatial resolution that corresponds to the size of basic chemical or structural building blocks.
- Design new diagnostic techniques and experimental methodologies that are capable to unveil the structure and reactivity at hidden or buried interfaces and interphases that determine material, composite electrode and full cell electrochemical performance and failure modes.

Approach

- Develop, apply and couple advanced characterization techniques, such as optical (Raman, ATR-FTIR) and scanning probe spectroscopy and microscopy (near-field IR) with standard electrochemical methods to determine function, operation and degradation of materials, electrodes and battery cells.
- Construct ultra-smooth, defined model cathodes by pulsed laser deposition (PLD) to permit the use of novel investigative techniques during operation.
 - Study interfacial reactions and organic film formation between organic electrolytes and Ni-rich NMC.
 - Obtain detailed insights into the organic film composition, distribution and contribution on impedance in Ni-rich NMC cathodes.

Results

We deposited NMC thin films on Al substrate by pulsed laser deposition (PLD) and demonstrated that it is a suitable approach for studying electrode/electrolyte interfaces in rechargeable batteries. The electrode's surface morphology was analyzed by AFM (Figure II.5.A.1a). The film consists of densely packed 100 nm grains with surface roughness ca. 10.9 nm (RMS). The XRD (Figure II.5.A.1b) and Raman (Figure II.5.A.1c) analysis both confirmed the NMC layered structure with a pronounced preferred crystal orientation along $\langle 003 \rangle$ direction. The chemical analysis of the thin film, performed by ICP resulted in Ni: Mn: Co ratio equal to 50.1: 29.2: 20.7 (%weight), which confirmed the same composition as the pristine NMC532 powder used for target in the PLD system.

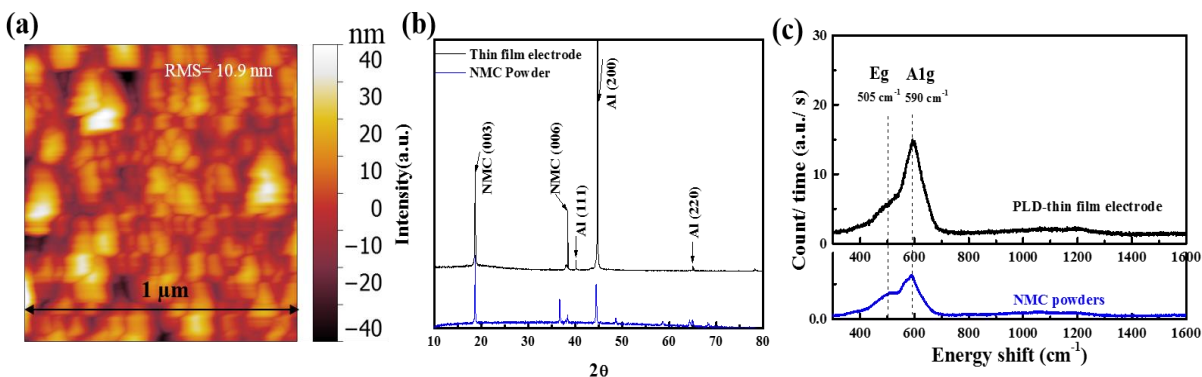


Figure II.5.A.1 (a) AFM image, (b) XRD and (c) Raman spectrum of the NMC thin film electrode made by PLD.

Electrochemical tests of the thin film electrodes were performed in a Swagelok cell. Lithium foil was used as counter electrode and 1M LiPF₆ in EC/DEC=1/1 (v/v) as electrolyte. The cyclic voltammogram (Figure II.5.A.2a) exhibits a main reduction and oxidation peak at 3.7 V and 4 V respectively, which are similar to those typically observed for NMC composite electrodes.

The binder and carbon additive free PLD thin film electrodes allow selective and specific chemical analysis of electrode/electrolyte interfaces without interference from other active and passive components. The FTIR-ATR spectrum of the pristine- and the cycled- electrode are shown in Figure II.5.A.2b. Each adsorption peak was indexed with certain vibration modes characteristic for specific functional groups. The pristine thin film electrode shows small amount of Li₂CO₃, which is a common impurity at NMC surface. After 3 cycles, many adsorption peaks emerged and most of them can match well with spectral features of glycols (blue band), ν(P-F) (purple band) and ν(C=O) (orange band). The formation of glycol species has also been previously reported for LiMn₂O₄ [11], however here, it is reported for the first time in NMC electrode by IR analysis. It is known that polyethylene glycol species exhibit Li⁺ conductivity. Indeed, they have also been employed as components for gel-based electrolytes in Li-ion batteries [2]. Thus, glycol species in the surface film may not be responsible for the observed impedance rise due to ion diffusion limitations. However, their poor electronic conductivity may contribute to the raise of the contact resistance between particles in the composite electrodes, resulting in the electrode and cell performance degradation.

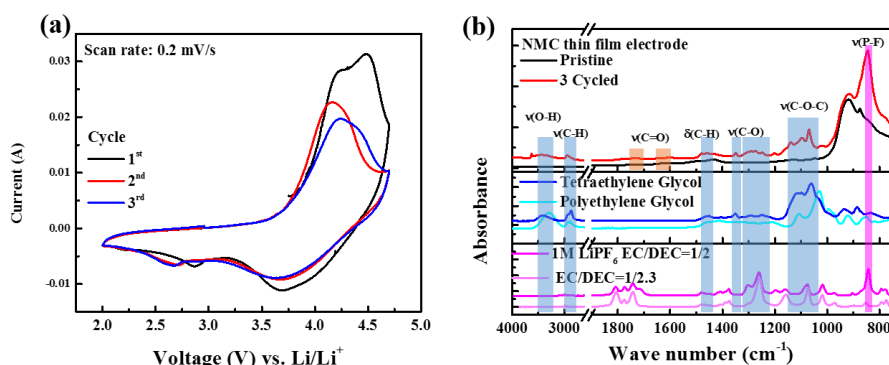


Figure II.5.A.2 (a) Voltammogram trace of the NMC thin film electrode and (b) FTIR-ATR spectrum of the pristine and 3 cycled NMC thin film electrode, tetraethylene glycol and polyethylene glycol standard, 1M LiPF₆ EC/DEC=1/2 (v/v) electrolyte and EC/DEC=1/2.39 (v/v) solvent.

We correlated the electrochemical behavior of the model NMC thin film electrodes obtained by PLD with their structural properties. The electrochemical response of NMC thin film electrodes was investigated in a Swagelok cell, employing Li-foil as counter and reference electrodes and 1M LiPF₆ in EC:DEC (1:2 wt)

electrolyte. The cyclic voltammetry profile (Figure II.5.A.1a) shows the main redox peaks, which are also observed for the NMC composite electrode (see inset Figure II.5.A.3a) [3]. *Ex situ* Raman analysis (Figure II.5.A.3b) shows a red shift of the E_g and A_{1g} peaks going from the pristine to charged state, and a blue shift back from charged to discharged state., which correspond to the lithiation-delithiation process of the $R\bar{3}m$ layer structure, in accordance with already reported *in situ* Raman study of NMC composite electrode [4].

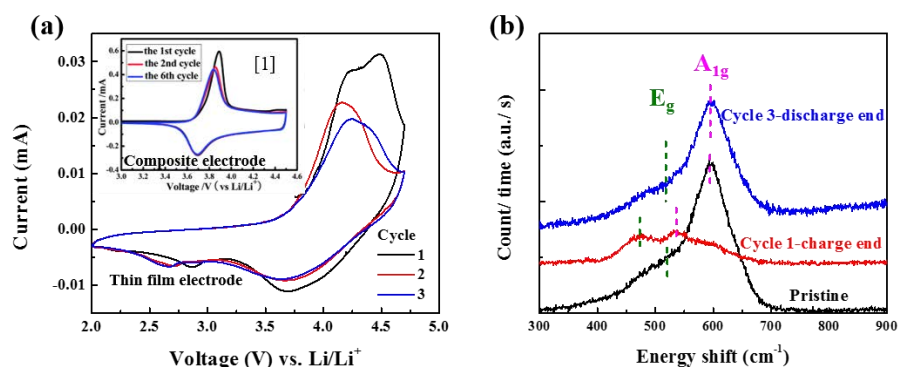


Figure II.5.A.3 (a) CV profile of NMC thin film electrode. Scan rate: 0.2 mV s^{-1} Inserted plot presents a typical CV of NMC composite electrodes reported in [1], (b) *ex situ* Raman of NMC thin film electrodes at different state of charge: pristine, 1st de-lithiation and 3rd lithiation.

The surface of the cycled NMC thin film electrodes were then studied by FTIR. Figure II.5.A.4a presents FTIR spectra of a thin film electrode cycled 3 obtained after 5 s and 5 min. washing in DEC. The FTIR spectrum of the sample washed for 5 s presents spectral characteristics of glycol species, while the spectra from the sample washed for 5 min show an additional set of adsorption C=O, C-O and C-O-C vibration modes. This simple washing procedure reveals a double layer film structure that forms on the NMC surface. The characterized peaks that can differentiate these two layers are associated to the vibrations of C-O-C bonds (1080 cm^{-1} for outer layer and 1150 cm^{-1} for inner layer). Besides, the double layers film was observed not only for the initial charge process but also during subsequent cycles (Figure II.5.A.4b). It has been previously reported that the organic film formed on the NMC surface might be associated with the electrolyte reactions at the Li anode side and “chemical shuttle” effect [5]. To investigate this possibility, the NMC thin film electrodes were cycled with a graphite anode instead of lithium. However, the FTIR surface analysis (Figure II.5.A.4c) does not reveal any obvious difference of the organic layer structure and composition when compared to the one obtained using Li anode. Thus, we conclude that the observed film formation is intrinsic to reactions between NMC and electrolyte during the de-lithiation process.

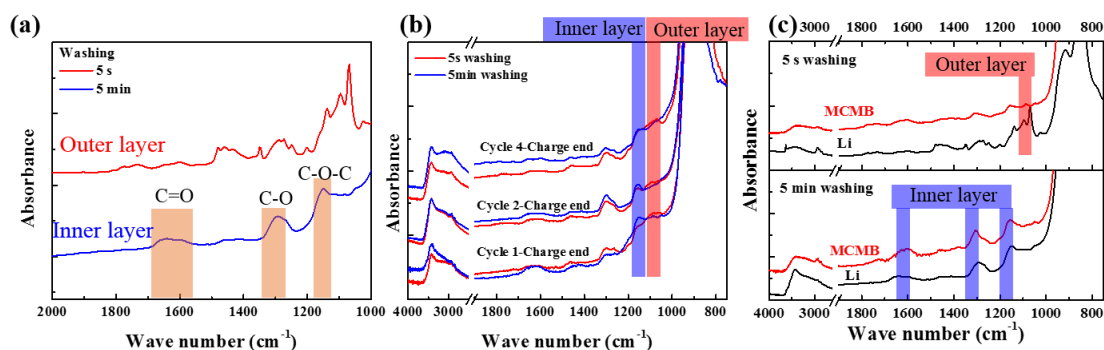


Figure II.5.A.4 FTIR spectrum of cycled thin film electrode with different washing time. (a) after 3 cycles (discharge end), (b) after 1, 2 and 3 cycles, and (c) after 3 cycles vs. Li or MCMB anode.

We characterized the morphology and chemical composition of the organic CEI layer on thin-film NMC532 electrode after 3rd cycle by Neaspec scattering-type scanning near-field optical microscopy (NeaSNOM). Electrode potential was scanned by cyclic voltammetry between 2 - 4.7 V with Li-foil as CE in 1M LiPF₆ in EC:DEC (1:2 wt.%) electrolyte in a Swagelok cell. After 3rd cycle (end at fully lithiated state), the electrode was washed in DEC for 5s or 5min to expose specifically the outer or inner organic CEI layer. The AFM images show the pristine thin-film NMC532 electrode (Figure II.5.A.5a, Figure II.5.A.5d) that consists of closely packed 50-100 nm nanoparticles with surface roughness <10 nm.

The cycled NMC532 electrode after soft (5s) DEC washing (Figure II.5.A.5b) shows clusters ca. 2~4 μm wide and 100 nm thick, unevenly distributed at the electrode surface. The corresponding IR absorbance image acquired by NeaSNOM of the same area is shown in Figure II.5.A.5c. The bright areas indicate higher IR adsorption whereas dark locations show no IR absorbance at the selected wavelength. Direct comparison of morphology (Figure II.5.A.5b) and IR images (Figure II.5.A.5c) reveals an overlap of the large clusters with the highly IR absorbing areas of the film at 1080 cm^{-1} , which corresponds to $\nu(\text{C-O-C})$ from polyethylene glycol-type compounds.

To study the inner organic CEI layer, the non-uniform outer CEI film was removed by washing in DEC for 5 min. The AFM image (Figure II.5.A.5e) gives no indication of thick deposits and displays similar surface morphology as the pristine electrode (Figure II.5.A.5d). To unveil the surface chemical composition, NeaSNOM imaging was used again at 1320 cm^{-1} , which corresponds to $\nu(\text{C-O})$ of the compounds observed in the inner organic layer. The IR absorbance image (Figure II.5.A.5f) displays a uniform distribution of IR adsorption at the surface, indicating the organic species in the inner CEI layer are evenly spread out over the NMC532 surface. In summary, the near-field IR analysis of the cycled thin-film NMC532 surface revealed stratified CEI film that consists of thick glycol-type outer layer and thin inner layer.

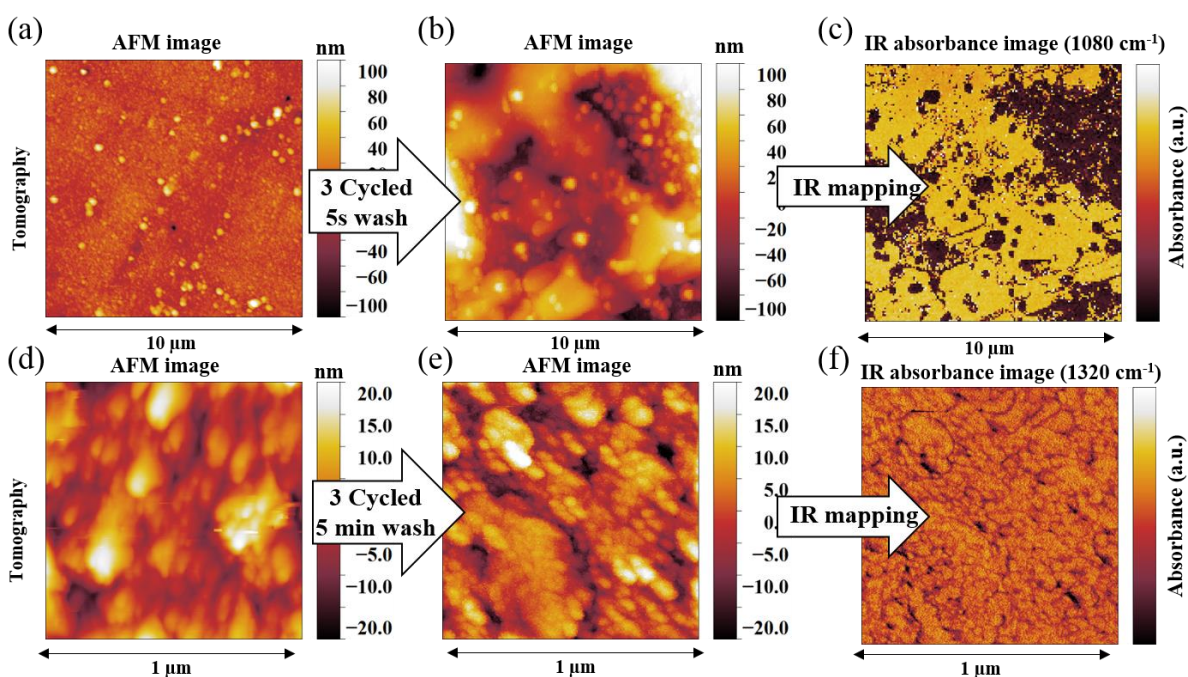


Figure II.5.A.5 (a,d) AFM morphology image of the pristine NMC thin film electrode, (b) AFM morphology image and (c) near-field IR absorbance image of cycled NMC thin film after 5s washing in DEC, (e) AFM morphology image and (c) near-field IR absorbance image of cycled NMC thin film with 5 min washing in DEC.

We analyzed impedance of the organic film formation on the thin-film NMC532 model electrode after electrochemical cycling and washing in DEC. Thin-film NMC532 electrode was cycled by in the cyclic voltammetry regime between 2-4.7 V in 1M LiPF₆ in EC:DEC (1:2 wt.%) electrolyte against Li-foil anode. Then, they were washed by DEC for 5 min to expose a homogeneous inner CEI layer (for details see our FY18 Q2 and Q3 reports). To evaluate CEI layer contribution to the electrode impedance, we've designed and built a new experimental setup (Figure II.5.A.6). The system was assembled by sandwiching the NMC electrode between two flat metal current collectors. The impedance measurements of dry NMC electrodes were carried out under Ar.

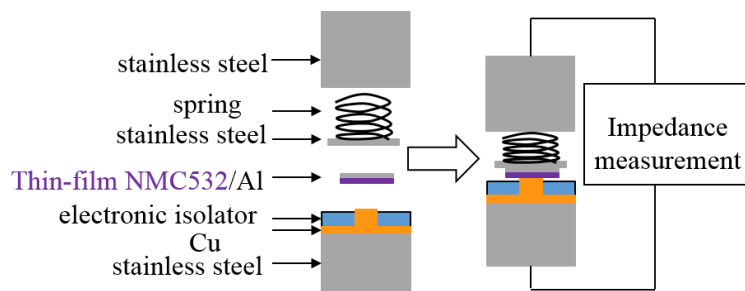


Figure II.5.A.6 Experimental setup for impedance measurements of the NMC electrode under Ar atmosphere.

The real part of AC impedance at 0.1 Hz of the pristine model thin-film NMC532 electrode and after 3 and 10 cycles in 1M LiPF₆ in EC:DEC is shown in Figure II.5.A.7a. The electrode impedance increases gradually from 0.5 Ω for the pristine electrode to 1 and 3 Ω after 3 and 10 cycles, respectively. To correlate these impedance results with the observed organic inner layer formation, corresponding ATR-FTIR spectra of the thin-film NMC532 electrode after 3 and 10 cycles were recorded and normalized vs. Al₂O₃ background peak at 900 cm⁻¹ (Figure II.5.A.7b). The increased intensity of -C-O vibration at ca. 1300 and 1150 cm⁻¹ indicates that the thickness of the inner layer that consists of β-diketone, LiEDC or ROCO₂Li increase with cycling. These semi quantitative electrode impedance/CEI film thickness correlation directly demonstrates the detrimental effect of the electrolyte oxidation and surface film formation on the NMC cathode long-term electrochemical performance.

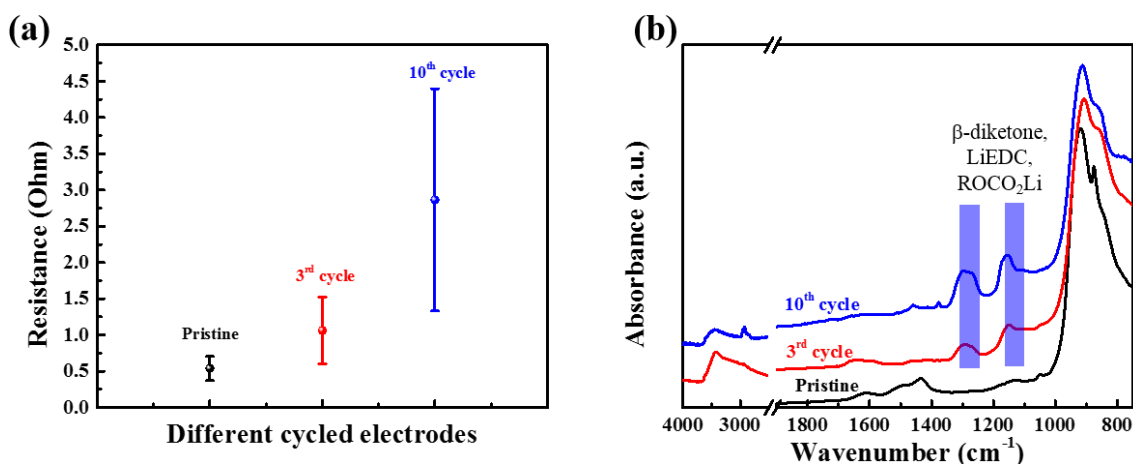


Figure II.5.A.7 (a) Real-part AC impedance at 0.1Hz (b) ATR-FTIR spectra of thin-film NMC532 electrodes: pristine and after 3 and 10 cycles.

Conclusions

- Thin-film NMC532 model electrodes were successfully produced by Pulsed Laser Deposition. The model NMC532 electrode exhibits a similar structure, chemical composition and electrochemical properties as commercial NMC532 powder.
- Cathode electrolyte interphase (CEI) on the NMC532 model electrode after cycling exhibits a stratified composition and structure.
 - Polyethylene glycol-based outer CEI layer, which is distributed non-uniformly on the electrode surface may affect adversely contact resistances in the composite cathode. On the other hand it may enhance local Li-ion conductivity.
 - A uniform and dense inner CEI layer consists mainly of ROCO_2Li , ROLi and β -diketone species. It can form an effective barrier for charge and mass transfer at the electrode/electrolyte interface.
 - The increasing thickness of the CEI inner layer correlates with the electrode impedance rise during cycling.

This study not only determines the mechanism of the CEI layer film formation but also offers unique insight into its direct and indirect impact on the electrochemical performance and interrelated mechanism of interfacial phenomena at high-voltage NMC cathodes.

Key Publications

1. T. N. Stanislavchuk, Derek S. Middlemiss, Jaroslaw Syzdek, Yuri Janssen, R. Basisty, A. A. Sirenko, Peter Khalifah, Clare P. Grey and Robert Kostecki, "Infrared-active optical phonons in LiFePO_4 single crystals", *Journal of Applied Physics*, **122**, 045107 (2017); <https://doi.org/10.1063/1.4995282>
2. Lei Cheng, Huaming Hou, Simon Lux, Robert Kostecki, Ryan Davis, Vassilia Zorba, Apurva Mehta, and Marca Doeff, "Enhanced Lithium Ion Transport in Garnet-type Solid State Electrolytes", *Journal of Electroceramics*, (2017) pp1-8. doi:10.1007/s10832-017-0080-3
3. Rung-Chuan Lee, Chixia Tian, Marca Doeff and Robert Kostecki, "The Mechanism of Impedance Increase in Nickel-rich NMC Cathodes", 232nd Electrochemical Society (ECS) Meeting, October 3, 2017, National Harbor, MD, USA
4. Jagjit Nanda and Robert Kostecki, "Multiscale Raman Imaging Applied to High Capacity Battery Materials and Electrodes", 232nd ECS Meeting, October 1-6, 2017, National Harbor, MD, USA
5. Robert Kostecki, "Probing Charge and Mass Transport Phenomena Across Interfaces and Interphases "International Workshop on Phase Interfaces for Highly Efficient Energy Utilization", Gaylord Resort & Convention Center, MD, USA, on October 6, 2017.
6. Robert Kostecki, Maurice Ayache, Hans A. Bechtel, , Michael C. Martin, Philip N. Ross, "Near- and Far-field IR Spectroscopy and Imaging of Interfaces and Interphases in Li-ion Electrodes", 649 WE-Heraeus-Seminar: In-operando characterization of energy materials, Physikzentrum Bad Honnef, Germany, August 23-27, 2017
7. Robert Kostecki, "Probing charge and mass transport phenomena across interfaces and interphases in Li-ion batteries", 5th International Conference on Nanomaterials and Advanced Energy Storage Systems, Astana, Kazakhstan, August 9-11, 2017,
8. Rung-Chuan Lee and Robert Kostecki, 2017 Bay Area Battery Summit (BABS), Livermore, CA (November 14, 2017): "Study the Degradation Mechanism of NMC Cathodes in Li-ion Batteries";

References

1. Y.M. Liu, B.G. Nicolau, J.L. Esbenschade, A.A. Gewirth, *Anal Chem*, 88 (2016) 7171-7177.
2. W.H. Meyer, *Adv. Mater.*, 10 (1998) 439.
3. X. F. Li, J. Liu, M. N. Banis, A. Lushington, R. Y. Li, M. Cai and X. L. Sun, *Energ. Environ. Sci.*, 7, 768 (2014).
4. M. Otoyama, Y. Ito, A. Hayashi and M. Tatsumisago, *Electrochemistry*, 84, 812 (2016).
5. E. Bjorklund, D. Brandell, M. Hahlin, K. Edstrom and R. Younesi, *J. Electrochem. Soc.*, **164**, A3054 (2017).

Acknowledgements

This work has been performed in close collaboration with:

- V. Battaglia: ABMR program leads
- ABMR Cathode and Anode Task Groups
 - ANL, LBNL, SUNY, UP, HQ, NREL and UU.
 - R-C. Lee, J. Franklin, G. Chen, V. Battaglia, M. Doeff, K. Persson, V. Zorba, W. Yang, C. Ban, N. Balsara, B. McCloskey)
- Advanced Light Source (H. Bechtel, E. Rotenberg, E. Crumlin)
- Nanyang Technological University (M. Srinivasan)
- University College London (P. Shearing, J. Franklin)
- University of California, Berkeley
 - Umicore, Farasis Energy, Inc.

II.5.B Advanced in situ Diagnostic Techniques for Battery Materials (BNL)

Xiao-Qing Yang, Principal Investigator

Chemistry division, Brookhaven National laboratory
 Bldg. 555, Brookhaven National Lab.
 Upton, NY 11973
 E-mail: xyang@bnl.gov

Seongmin Bak, Principal Investigator

Chemistry division, Brookhaven National laboratory
 Bldg. 555, Brookhaven National Lab.
 Upton, NY 11973
 E-mail: smbak@bnl.gov

Tien Duong, DOE Technology Development Manager

U.S. Department of Energy
 E-mail: Tien.Duong@ee.doe.gov

Start Date: October 1, 2017

End Date: September 30, 2018

Project Funding (FY18): \$500,000

DOE share: \$500,000

Non-DOE share: \$0

Project Introduction

This project has been focused on developing advanced diagnostic characterization techniques to investigate the issues, limiting the performance, life, and safety characteristics of lithium batteries by obtaining in-depth fundamental understanding of the mechanisms governing the relationship between the structure and the performance, and providing guidance and approaches to solve these problems. This project is uniquely oriented to the development and application of combined synchrotron based in situ X-ray techniques such as x-ray diffraction (SXR), pair distribution function (PDF), hard and soft x-ray absorption (XAS and SXAS), together with other imaging and spectroscopic tools such as high resolution transmission electron microscopy (HRTEM), scanning transmission electron microscopy (STEM), mass spectroscopy (MS), X-Ray fluorescence microscopy (XRF) and transmission x-ray microscopy (TXM). For advanced Li-ion battery technologies, the revolutionary approaches using new generation of materials for cathode, anode, electrolyte, and separator are in the horizon. The new generation of cathode materials such as high Ni content NMC high voltage spinels ($\text{LiMn}_{2-x}\text{Ni}_x\text{O}_4$) and/or Li-rich high energy density $\text{Li}_{1+x}(\text{NiMnCo})\text{O}_2$ (NMC) composite materials together with high energy density Si-based and Li metal anode materials will significantly increase the energy density of the lithium battery cells. However, many technical barriers must be overcome before the large-scale commercialization of these new materials can be realized. This project will use the time-resolved x-ray diffraction TR-XRD and absorption (TR-XAS) developed at BNL to study the kinetic properties of these materials with structural sensitivity (TR-XRD) and elemental selectivity (TR-XAS). This project will develop and apply the HRTEM, TXM and PDF techniques to study the mechanism of capacity and performance fading of cathode and anode materials. Another important issue is the thermal stability of new cathode materials which is closely related to the safety of the batteries. This problem will be studied using the combined TR-XRD, TR-XAS with mass spectroscopy (MS). This project has also been developing a novel in situ X-ray fluorescence (XRF) microscopy combined with X-ray absorption spectroscopy (XAS) technique, which can track the morphology and chemical state changes of the electrode materials during cycling. This project has also been further developing this novel technique utilizing the new unique capability of TES beamline at NSLS II, with better signal/noise ratio and spatial resolution to do diagnostic studies of the cathode and anode materials of advanced Li-ion batteries. In summary, this proposed project supports the goals of VTO, the Battery and Electric Drive Technologies, and Advanced Materials R&D program by developing new diagnostic technologies and applying them to the advanced Li-ion battery systems to provide guidance for new material development.

Objectives

The primary objective of this project is to develop new advanced in situ material characterization techniques and to apply these techniques to support the development of new cathode and anode materials with high energy and power density, low cost, good abuse tolerance, and long calendar and cycle life for the next generation of lithium-ion batteries (LIBs) to power plug-in hybrid electric vehicles (PHEV). The diagnostic studies will be focused on issues relating to capacity retention, thermal stability; cycle life and rate capability of advanced Li-ion batteries.

Approach

- Using nano-probe beamline at NSLSII to study the elemental distribution of new solid electrolyte materials for Li-ion and Na-ion batteries
- Using the pair distribution function (PDF) to study the high energy density LiCoO_2 with high charging voltage limit. Using both x-ray (x-PDF) and neutron (n-PDF) probes to study the mechanism of anionic redox reaction (ARR) in cathode materials for Li-ion batteries and explore the potential of using this material for high energy density cells.
- Using transmission x-ray microscopy (TXM) to do multi-dimensional mapping of cathode materials
- Using A combination of time resolved X-ray diffraction (TR-XRD) and mass spectroscopy (MS), together with *in situ* soft and hard X-ray absorption (XAS) during heating to study the thermal stability of the electrode materials
- Using *in situ* XRD and XAS, to study the new concentration gradient cathode materials to improve the cycle life of Li-ion batteries
- Design and carry out three dimensional (3D) STEM tomography experiments to study high energy density $\text{Li}_{1.2}\text{Ni}_{0.15}\text{Co}_{0.1}\text{Mn}_{0.55}\text{O}_2$ cathode materials at pristine state and after multiple cycling.

Results

1. TXM studies of LiCoO_2 cathode materials

In FY2018, BNL has been focused on the designing and developing of in-situ transmission X-ray Microscopy (TXM) imaging technique for battery material research. We designed and constructed a special pouch cell setup for TXM study and used this setup to study the inhomogeneity of the charged states of LiCoO_2 cathode material among large number of particles using data mining technique to detect the under (over) reacted minority regions. Among all the particles scanned in our experiment, the clustering algorithm identified four clusters of pixels (the cluster maps are shown in Figure II.5.B.1b, Figure II.5.B.1d and Figure II.5.B.1f; the corresponding spectra are shown in Figure II.5.B.1.g and Figure II.5.B.1h). The first two clusters are anticipated and cover over 98% of the data, but cluster analysis identified two spectrally distinct particles (clusters 3# and 4# in P37 and P46, respectively). We would emphasize here that it is not possible to identify P37 and P46 as distinct from the rest of the particles by just analysis of each of the data attributes individually, or by examination of the transmission images (see Figure II.5.B.1a, Figure II.5.B.1c and Figure II.5.B.1e for transmission images collected at 7850 eV). In Figure II.5.B.1a, Figure II.5.B.1c and Figure II.5.B.1e, we notice the highest contrast in P37, P46 and P14, which actually contain all the four different clusters. It again echoes our discussion regarding the importance of data attribute weighting for emphasizing the chemical heterogeneity rather than the density. As we show in the radar chart in Figure II.5.B.1i, the differences in the spectroscopic signatures of the unanticipated species are fully captured only by combining several of the extracted data attributes, which also highlights the effectiveness of our data mining analysis approach.

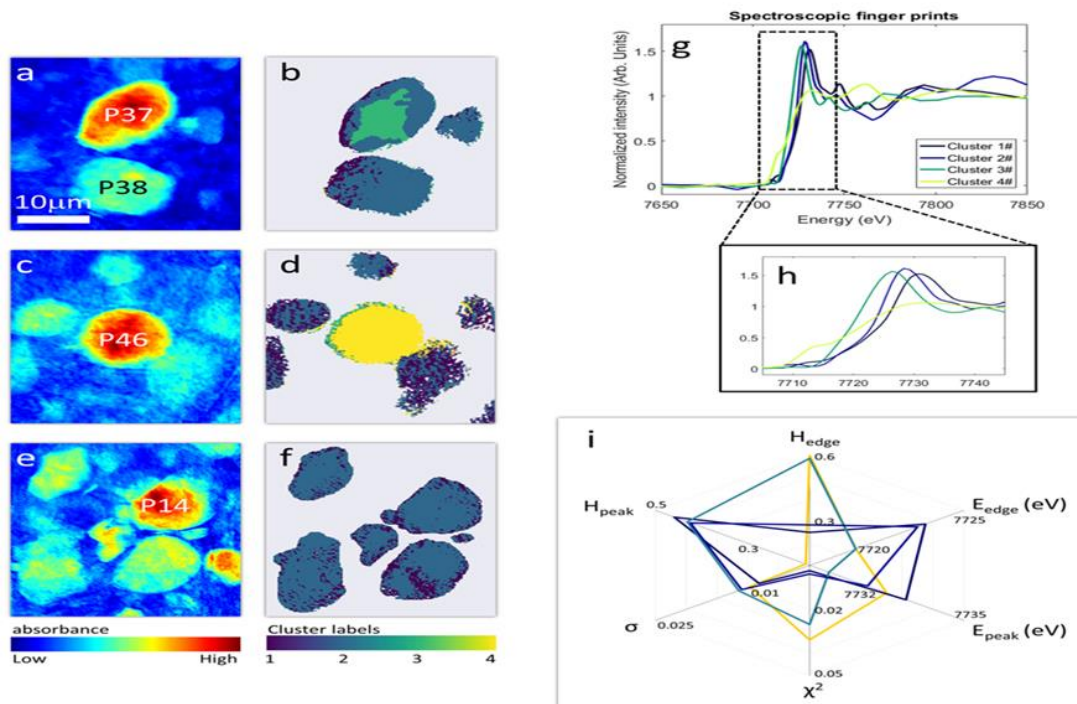


Figure II.5.B.1 The minority phases identified by our data-mining approach. Panels (a) and (c) show the transmission images of the field-of-views covering particles (P37 and P46), which are identified by our method as minority phases. Panel (e) is the transmission image of another typical field-of-view that contains several normal LiCoO_2 particles. Panels (b), (d), and (f) show the clustering results, with the four different clusters color coded to the corresponding inset. We compare the spectroscopic fingerprints of all the four clusters in panels (g) and (h). It is interesting to note that clusters 1# and 2# are both similar to LiCoO_2 . The radar chart in panel (i) shows the differences in the spectroscopic fingerprints of all the 4 clusters are systematically captured by the data attributes extracted in our approach. The scale bar in panel (a) is 10 microns

In FY2018, BNL also carried out the studies of structure change associated with the oxygen related redox reaction. The LiCoO_2 cathode was charged to 4.6V to reach a deeply delithiated state. As shown in Figure II.5.B.2(a), when LiCoO_2 is charged to 4.6 V, a capacity of 225 mAh/g was obtained, corresponding to 0.83 Li extraction. Upon discharge, a capacity of 205 mAh/g was reached, corresponding to 0.76 Li re-inserted. This indicates that the electrochemical reaction is mostly reversible. To understand the phase transition route during Li extraction, neutron power diffraction (NPD) was carried out on both the pristine sample and the *ex situ* sample charged to 4.6 V high voltage. The resultant diffraction patterns were fitted against model structures using Rietveld refinement as shown in Figure II.5.B.2(b). For the pristine sample, the structure has the space group of R-3m, with Li located at 3a site, Co at 3b site and O at 6c site. In terms of oxygen layer stacking sequence, it can be described as ABCABC... as illustrated in the lower-left corner of Figure II.5.B.2(a). Upon charging to 4.6 V, the oxygen layer stacking sequence changes into ABABCACABCBC as illustrated on the right panel of Figure II.5.B.2(a).

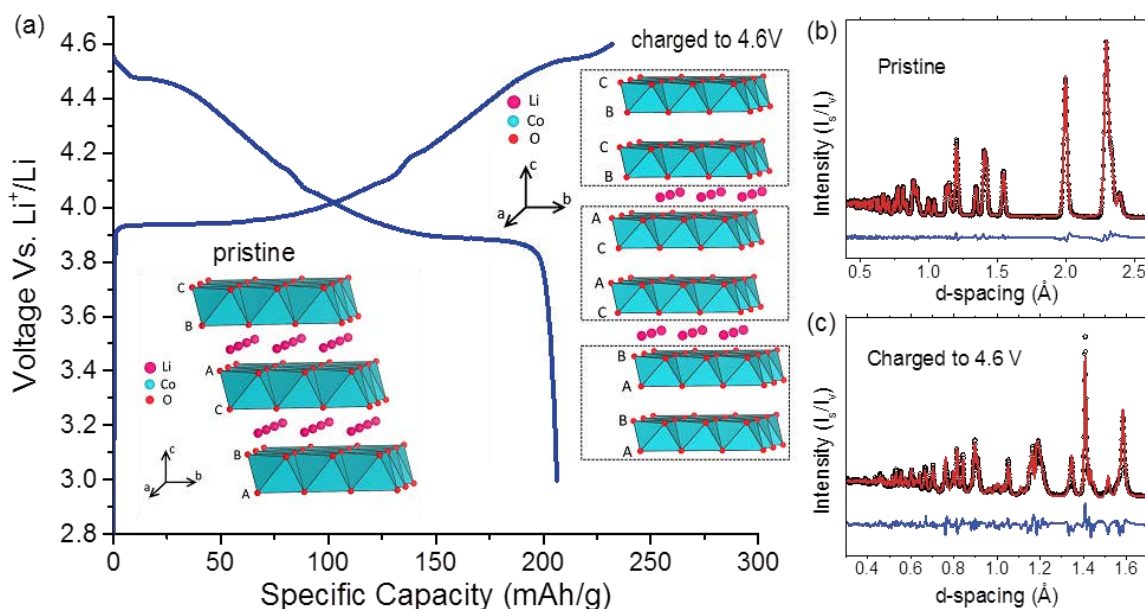


Figure II.5.B.2 (a) Electrochemical profile of LiCoO_2 charged to 4.6 V followed by a discharge to 3 V. The lower-left and the right insert show the structures of the pristine sample and the charged sample respectively. (b) Rietveld refinement of the NPD pattern of pristine sample and (c) Rietveld refinement of the NPD pattern of charged sample.

In FY2018, BNL has completed the studies of structure change associated with the oxygen related redox reaction. The LiCoO_2 cathode was charged to 4.6V to reach a deeply delithiated state. Understanding the role of oxygen anions during electrochemical reaction requires a local probe. Both X-ray and neutron pair distribution function analysis (xPDF and nPDF) were applied to the pristine sample and *ex situ* sample after charged to 4.6 V with the data shown in Figure II.5.B.3(a) and Figure II.5.B.3(b) respectively. In Figure II.5.B.3(a), xPDF data (upper panel) and nPDF data (lower panel) are plotted along with the contribution from O-O pairs. It can be clearly seen that in xPDF, O-O pairs make a minimum contribution to the whole pattern due to the small x-ray scattering cross section of oxygen. In contrast, the whole pattern of nPDF for the same sample is dominated by contribution from O-O pairs. Such difference can be understood by comparing the relative scattering power of Li, Co and O for X-ray with those for neutron as shown in Figure II.5.B.3(c). It can be seen from the lower panel of Figure II.5.B.3(b) that there is an obvious peak (peak A) at around 2.63 Å which is attributed to the shortest distanced O-O pairs. By checking with the structure determined from our NPD results, it is identified that the O-O pairs featuring such distance are those shared edges between neighboring CoO_6 octahedra as shown in Figure II.5.B.3(d). Upon charging, peak A shifts to the left, becoming peak A' located at around 2.47 Å. Interestingly, this value is very close to the O-O bond distance (2.45 Å) observed previously by McCalla in lithium-rich layered Li_2IrO_3 , suggesting the possibility of the formation of O-O dimers at the deeply delithiated state of conventional layered LiCoO_2 material.

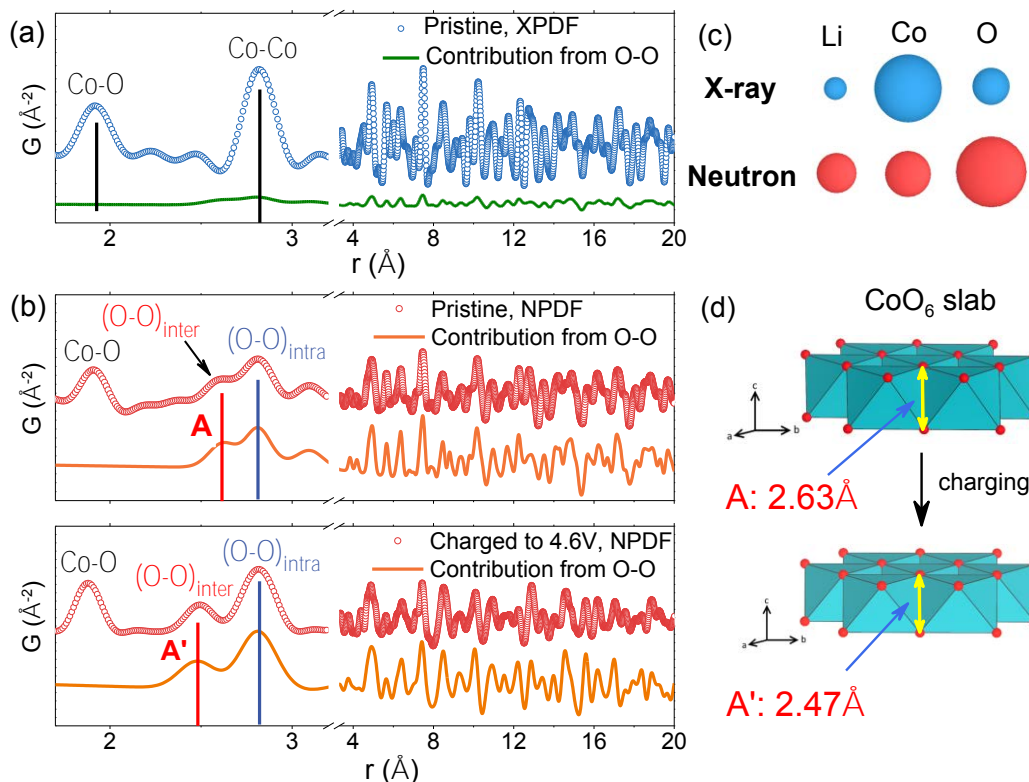


Figure II.5.B.3 (a) xPDF data of pristine sample (symbol) and the O-O pair contribution (solid line) (b) nPDF data of both pristine and charged sample (symbol) and the O-O pair contribution (solid line). (c) The relative scattering power/length of Li, Co and O for X-ray and for neutron scattering. (d) The change of the shortest O-O pair distance from pristine sample to charged sample.

In FY2018, BNL team completed the experimental design, data collection and analysis of three-dimensional (3D) STEM tomography studies of high energy density $\text{Li}_{1.2}\text{Ni}_{0.15}\text{Co}_{0.1}\text{Mn}_{0.55}\text{O}_2$ cathode materials at pristine state and after multiple cycling, especially on the studies of structure change associated with the oxygen loss during cycling. To clarify the origin of pores observed in STEM images, STEM-EELS mapping of a concealed pore and an exposed pore was performed as shown in Figure II.5.B.4. Figure II.5.B.4a shows the STEM-EELS mapping results over a concealed pore in bulk and the exposed pore at the surface of the particle. The EELS map of the concealed pore shows that there is only a very thin shell of Mn^{2+} build-up around the pore (Figure II.5.B.4a). Since a significant number of small pores were observed in the pristine sample before cycling, it is assumed these internal concealed pores are formed during synthesis and changed their sizes and shapes during cycling due to the oxygen release initiated near them. In contrast, for the opposite extreme situation in an exposed pore, the entire pore surface area is exposed to the electrolyte, as shown in Figure II.5.B.4b, a thick layer of spinel/rock-salt structure phase was formed through the interaction between the pore surface and the electrolyte. The EELS relative concentration mapping shows that there is a significant increase in Mn relative concentration close to the surface volume. Based on the observed increased number of pores with large volume size, we can speculate that large number of pores are not completely concealed or exposed, but partially exposed internal pores with oxygen pathways nearby in the form of microstructural defects such as dislocation, grain boundaries, and micro cracks. During cycling, these partially exposed internal pores will grow in size and number, together with those completely exposed pores at the surface, contributing to the propagation of the structural phase transitions, facilitating the further oxygen loss and self-feed the further microstructural defects formations, and accelerating the voltage fade

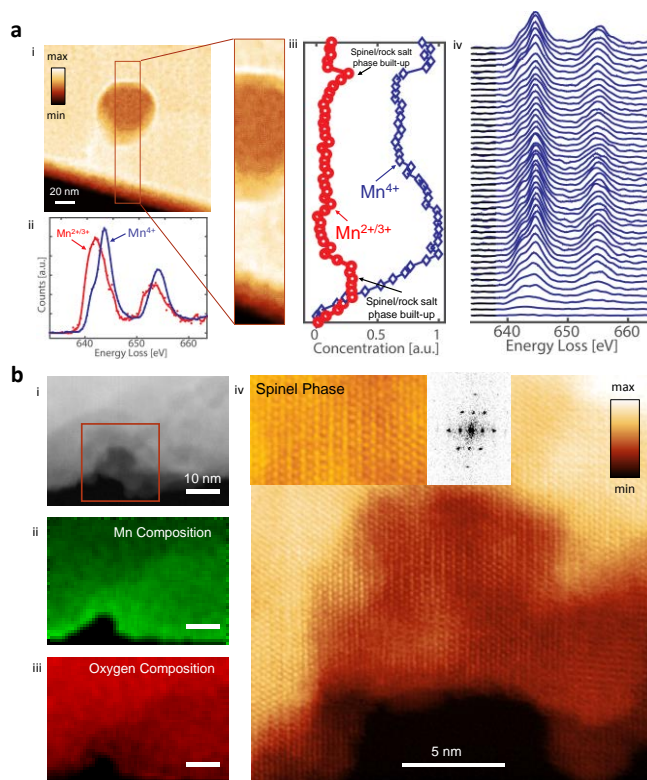


Figure II.5.B.4 (a) Figure 1. Spatially resolved EELS mapping of concealed pore and exposed pore. (a) STEM-EELS mapping of a concealed pore. (i) ADF-STEM image of a concealed pore. (ii) The reference spectra used for linear composition of the Mn L_{2,3} spectra in (iv). (iii) The linear decomposition coefficient as a function of the vertical spatial location. (iv) The EELS spectra of Mn L_{2,3} edges across the surface and the concealed pore. (b) STEM-EELS mapping and atomic-resolution imaging of an exposed pore. (i) ADF-STEM image of an opened pore. (ii and iii) The Mn (ii) and oxygen (iii) composition extracted from the quantification of the EELS map. (iv) Atomic resolution image of the open pore

Conclusions

1. Studies of LiCoO₂, a widely used cathode material have been carried out using TXM technique
2. Studies of ion exchange synthesis mechanism of Li₂Mg₂P₃O₉N have been carried out
3. The correlations between transition metal chemistry and structure in Li₂Ru_{0.5}Mn_{0.5}O₃ has been investigated in a wide voltage window.
4. The complexities of structural changes in layered oxide cathode materials for Li-ion batteries during fast charge–discharge cycling and heating were investigated using synchrotron based XRD and XAS, as well as TEM.

Key Publications

1. Yingchun Lyu, Enyuan Hu, Dongdong Xiao, Yi Wang, Xiqian Yu*, Guiliang Xu, Steven N. Ehrlich, Khalil Amine, Lin Gu*, Xiao-Qing Yang, and Hong Li* Correlations between Transition Metal Chemistry, Local Structure and Global Structure in Li₂Ru_{0.5}Mn_{0.5}O₃ Investigated in a Wide Voltage Window, *Chem. Mater.*, Publication Date (Web): October 20, 2017, DOI: 10.1021/acs.chemmater.7b02299,
2. Kai Zhang, Fang Ren, Xuelong Wang, Enyuan Hu, Yahong Xu, Xiao-Qing Yang, Hong Li, Liquan Chen, Piero Pianetta, Apurva Mehta, Xiqian Yu*, Yijin Liu*, “Finding a Needle in the Haystack:

- Identification of Functionally Important Minority Phases in an Operating Battery”, *Nano Lett.*, 2017, 17 (12), pp 7782–7788, Publication Date (Web): November 8, 2017. DOI: 10.1021/acs.nanolett.7b03985
3. Ji-Lei Shi, Dong-Dong Xiao, Mingyuan Ge, Xiqian Yu, Yong Chu, Xiaojing Huang, Xu-Dong Zhang, Ya-Xia Yin, Xiao-Qing Yang, Yu-Guo Guo, Lin Gu, and Li-Jun Wan, “High-Capacity Cathode Material with High Voltage for Li-Ion Batteries”, *Advanced Materials*, Publication Date: January 15, 2018. DOI: 10.1002/adma.201705575
 4. Enyuan Hu, Xuelong Wang, Xiqian Yu, and Xiao-Qing Yang, “Probing the Complexities of Structural Changes in Layered Oxide Cathode Materials for Li-Ion Batteries during Fast Charge–Discharge Cycling and Heating”, *Account of Chemical Research*, 2018, 51 (2), pp 290–298, DOI: 10.1021/acs.accounts.7b00506, Publication Date (Web): January 19, 2018.
 5. Shuai Liu, Xin Feng, Xuelong Wang, Xi Shen, Enyuan Hu, Ruijuan Xiao, Richeng Yu, Haitao Yang, Ningning Song, Zhaoxiang Wang, Xiao-Qing Yang, and Liquan Chen, Another Strategy, Detouring Potential Decay by Fast Completion of Cation Mixing, *Adv. Energy Mater.* Publication Date: February 12, 2018, DOI: 10.1002/aenm.201703092.
 6. Jue Liu*, Liang Yin, Xiao-Qing Yang*, and Peter G. Khalifah, “Li₃VP₃O₉N as a Multielectron Redox Cathode for Li-Ion Battery”, *Chemistry of Materials*, DOI: 10.1021/acs.chemmater.8b01114, Publication Date (Web): May 23, 2018
 7. Jue Liu*, Lei Yu, Enyuan Hu, Beth S. Guiton, Xiao-Qing Yang, and Katharine Page*, “Large-Scale Synthesis and Comprehensive Structure Study of δ -MnO₂”, *Inorg. Chem.*, 2018, 57 (12), pp 6873–6882, DOI: 10.1021/acs.inorgchem.8b00461, Publication Date (Web): May 30, 2018..
 8. Xiulin Fan, Enyuan Hu, Xiao Ji, Yizhou Zhu, Fudong Han, Sooyeon Hwang, Jue Liu, Seongmin Bak, Zhaohui Ma, Tao Gao, Sz-Chian Liou, Jianming Bai, Xiao-Qing Yang, Yifei Mo, Kang Xu, Dong Su & Chunsheng Wang, “High energy-density and reversibility of iron fluoride cathode enabled via an intercalation-extrusion reaction”, *Nature Communications*, DOI: 10.1038/s41467-018-04476-2, Publication Date (Web): June 13, 2018.
 9. Seong-Min Bak, Zulipiya Shadike, Ruoqian Lin, Xiqian Yu, Xiao-Qing Yang, In situ/operando synchrotron-based X-ray techniques for lithium-ion battery research, *NPG Asia Materials*, 2018, DOI 10.1038/s41427-018-0056-z, Publication Date (Web): July 03, 2018.
 10. Enyuan Hu, Xiqian Yu, Ruoqian Lin, Xuanxuan Bi, Jun Lu, Seongmin Bak, Kyung-Wan Nam, Huolin L. Xin, Cherno Jaye, Daniel A. Fischer, Kahlil Amine, and Xiao-Qing Yang, “Evolution of redox couples in Li- and Mn-rich cathode materials and mitigation of voltage fade by reducing oxygen release”, *Nature Energy*, volume 3, pages690–698 (2018), Doi: 10.1038/s41560-018-0207-z, Published date: July 30, 2018
 11. Fei Wang, Wei Sun, Zulipiya Shadike, Enyuan Hu, Xiao Ji, Tao Gao, Xiao-Qing Yang, Kang Xu, and Chunsheng Wang, “How Water Accelerates Bivalent Ion Diffusion”, *Angewandte Chemie*, DOI: 10.1002/anie.201806748, Publication Date (Web): July 31, 2018.
 12. Jun-Yu Piao, Yong-Gang Sun, Shu-Yi Duan, An-Min Cao, Xue-Long Wang, Rui-Juan Xiao, Xi-Qian Yu, Yue-Gong, Lin Gu, Yutao Li, Zhen-Jie Liu, Zhang-Quan Peng, Rui-Min Qiao, Wan-Li Yang, Xiao-Qing Yang, John B. Goodenough, Li-Jun Wan, “Stabilizing Cathode Materials of Lithium-Ion Batteries by Controlling Interstitial Sites on the Surface”, *Chem*, Volume 4, Issue 7, 12 July 2018, Pages 1685-1695, DOI: 10.1016/j.chempr.2018.04.020.

13. Xin-Yang Yue, Wei-Wen Wang, Qin-Chao Wang, Jing-Ke Meng, Zhao-Qiang Zhang, Xiao-Jing Wu, Xiao-Qing Yang, Yong-Ning Zhou, “CoO nanofiber decorated nickel foams as lithium dendrite suppressing host skeletons for high energy lithium metal batteries”, *Energy Storage Materials*, 14 (2018) 335–344, DOI: 10.1016/j.ensm.2018.05.017, publication date: September 2018.

II.5.C Advanced Microscopy and Spectroscopy for Probing and Optimizing Electrode-Electrolyte Interphases in High Energy Lithium Batteries (UCSD)

Ying Shirley Meng, Principal Investigator

University of California, San Diego
9500 Gilman Dr.
La Jolla, CA 92093
E-mail: shmeng@ucsd.edu

Tien Duong, DOE Technology Development Manager

U.S. Department of Energy
E-mail: Tien.Duong@ee.doe.gov

Start Date: April 1, 2017

End Date: March 31, 2021

Project Funding (FY18): \$360,000

DOE share: \$327,600

Non-DOE share: \$36,400

Project Introduction

The earliest developed LiCoO₂ layered oxide cathode material sparked the development of other layered cathode materials, dominating the positive electrode materials for lithium ion batteries. Within the practical operating conditions of today, the current generation layered oxide materials do not meet the future energy storage demands of 350 Wh kg⁻¹ at cell level. Li-rich layered oxide (LRLO) materials have the potential to meet the high energy demands. Unlike the classical layered oxides, LRLO materials exhibit capacities that go beyond conventional topotactic mechanistic theoretical values [1]. Despite its high capacities, this material has several challenges (voltage fading, structural instability, sluggish kinetics, cathode electrolyte interphase instability, etc.) that must be overcome in order to reach commercialization. In the past five years, our research group has made great progress on developing advanced characterization techniques coupled with atomic scale modeling to properly characterize the dynamic phenomena that govern the performance limitations of LRLO materials. Furthermore, our efforts have guided the material synthesis and surface modification to improve capacity retention. By carefully controlling the oxygen activities through the creation of uniform oxygen vacancies, we were able to avoid structural decomposition in LRLO. Our materials deliver a discharge capacity as high as 306 mAh g⁻¹ with an initial coulombic efficiency of 90.6% [2]. Furthermore, they do not exhibit obvious capacity decay with a reversible capacity over 300 mAh g⁻¹ after 100 cycles at 0.1 C-rate. Our approach demonstrates the critical needs for advanced diagnosis and characterization. It is through the in-depth understanding of these high voltage cathode materials at atomistic and molecular level and their dynamic changes during the operation of batteries; we can successfully formulate strategies to further optimize this class of cathode materials, especially for the voltage instabilities. The diagnostic tools developed here can also be leveraged to study anode materials such as Li metal anode. The challenge of probing Li metal is the low dose tolerance (high beam sensitivity) of Li metal. We will have to apply cryogenic method (low-temperature) and low-dose electron microscopy and specialized camera to enable the characterization of the lithium metal.

Objectives

The proposed research aims to develop advanced microscopy and spectroscopy tools to probe, understand, and optimize the anion activities that govern the performance limitations such as capacity and voltage stabilities in high energy Li-excess transition metal (Ni, Co, Mn, etc.) oxides cathode materials. Our approach uniquely combines atomic resolution scanning transmission electron microscopy (STEM), electron energy loss spectroscopy (EELS), operando Bragg Coherent Diffraction Imaging (BCDI), and first principles computation to probe anion redox and oxygen evolutions in Li-excess NMC materials. Furthermore, we will track the lithium and oxygen dynamics under electrochemical testing via operando neutron diffraction which will enhance the understanding of the overall structural changes due to anion activities. Ultimately, this will hone in on the synthesis efforts to produce the modified materials with the optimum bulk compositions and surface characteristics at large scale for consistently good performance. The above mentioned characterization tools will be extended to diagnose various anode types, such as Li metal anode.

Approach

This unique approach combines STEM/EELS, operando BCDI, and Ab initio computation as diagnostic tools for probing anion redox and oxygen evolutions in Li-excess NMC materials. This allows for pinning down the atomistic/molecular mechanism of anion oxidation and determining the speciation compositions and surface characteristics for enabling high rate and long life in the proposed materials. Neutron enables the characterization of bulk material properties to enhance and further optimize high energy electrode materials. This work funds collaborations on EELS (Miaofang Chi, Oakridge National Lab); neutron diffraction (Ke An, ORNL); soft XAS (Marca Doeff, Lawrence Berkeley National Laboratory). It supports collaborative work with Zhaoping Liu and Yonggao Xia at Ningbo Institute of Materials Technology and Engineering China. It also supports collaboration with Battery500 consortium.

Results

The following progress has been achieved:

Investigation of nanoscale LLTO surface coating effect on LRLO

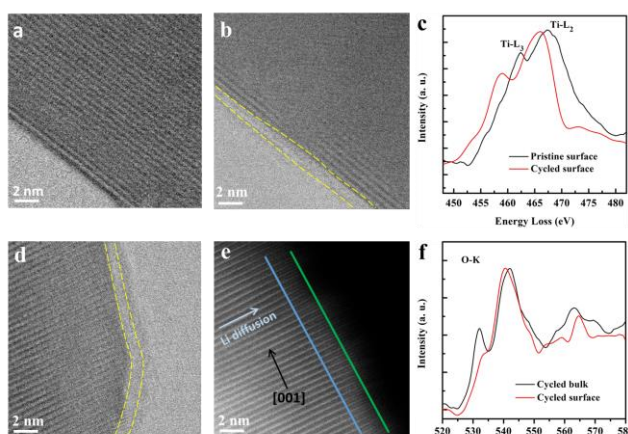


Figure II.5.C.1 STEM/ABF images of (a) uncoated LRLO and (b) LRLO material coated with 1wt% LLTO. (c) EELS Ti-L edge spectra at surface regions of LRLO sample coated with LLTO before and after cycling. (d, e) ABF and HAADF images of LRLO material coated with LLTO after cycling. (f) EELS O-K edge spectra of LRLO sample coated with LLTO after cycling collected at bulk and surface region, respectively

Experimentally, coating LRLO material ($\text{Li}_{1.13}\text{Ni}_{0.3}\text{Mn}_{0.567}\text{O}_2$) with LLTO could significantly improve cycling coulombic efficiency and capacity retention. As shown in our previous report, the uncoated LRLO shows only 74.2% capacity retention after 200 cycles, while the LLTO coating improves the capacity retention to 82.3%. Understanding the effect of LLTO coating is of extreme importance to eventually solve the cycling issues in this material. Annular bright-field STEM (ABF/STEM) images were applied to the uncoated and LRLO material coated with 1wt% LLTO to confirm the uniformity of the coating. As shown in Figure II.5.C.1a and b, the uncoated particles have a clean surface with Li and TM layers extending to the outermost surface. After LLTO coating, there is a uniform nanoscale layer (around 1 nm in thickness) found on the particle surface. There is a clear Ti-L edge peak in the spectra obtained on the surface region of the coated sample, where Ti-L_3 and Ti-L_2 were induced by the electron transitions from $2p^{3/2}$ and $2p^{1/2}$, respectively, to unoccupied 3d orbitals. Surprisingly,

the coating layer on LRLO particles is still conformal even after 200 cycles at a current density of 25 mA/g. After cycling, the positions of Ti-L edges shift to a lower energy region, indicating that the reduction of Ti ions. A thin amorphous cathode SEI layer was also observed for the cycled sample (to the right of the yellow dashed line in Figure II.5.C.1d), which mainly contains LiF as confirmed by F-K and Li-K EELS spectra (not shown here). More importantly, transition metal ions migration into the Li layer was only found within the 2 nm region from the surface (see Figure II.5.C.1e). There is a clear O-K edge pre-peak in the spectrum obtained in bulk of the particles after cycling. While the pre-peak decreases when it comes to the reconstruction region, which is due to oxygen vacancy formation. In other words, the coating layer effectively prevents oxygen vacancy generation as well as cation rearrangement during cycling, which ultimately improves the structure integrity and cycling stability.

BCDI characterization on single particle of LRLO during electrochemical cycling

In order to investigate strain network generation dynamics in LRLO material, operando BCDI was carried on single particle when the battery was charged at different rate. No obvious difference was found in the voltage curve until ~ 4.35 V (see Figure II.5.C.2a). While only 20% of total lithium is deintercalated from the structure after 4.4 V at higher rate, which is substantially smaller than that of material charged at lower rate. It well illustrates the sluggish charging process during the plateau region which is dominated by the oxygen activity. Figure II.5.C.2b shows that the average strain grows dramatically after 4.3 V for the sample under lower charging rate only. Note that the percentage strain for both charging rates is normalized to the pristine state. The strain field distribution further confirms that no obvious strain is built in the bulk of the particles during the higher rate charging process, which manifests the strain network formation is highly correlated to the oxygen activity. The more oxygen redox participates, the larger bulk strain grows.

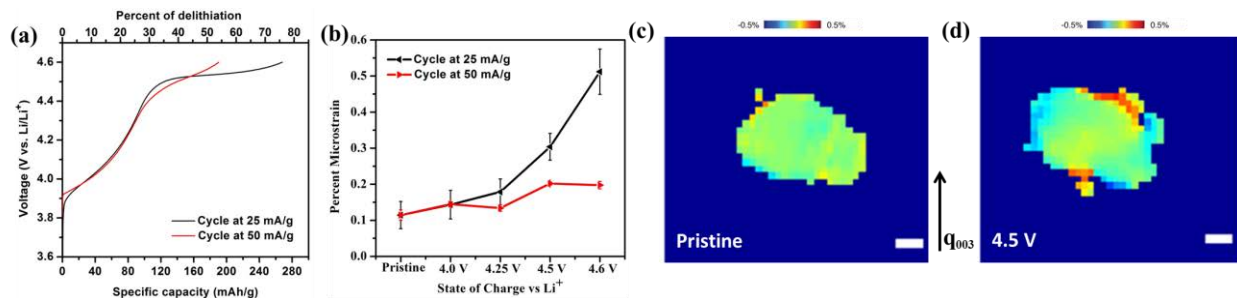


Figure II.5.C.2 First charging comparison of (a) electrochemical performance and (b) strain generation for LRLO electrode under different rate. (c, d) The strain distribution along the [003] direction inside of the nanoparticle charged at 50 mA/g for two representative states of charge. The scale bar is 100 nm.

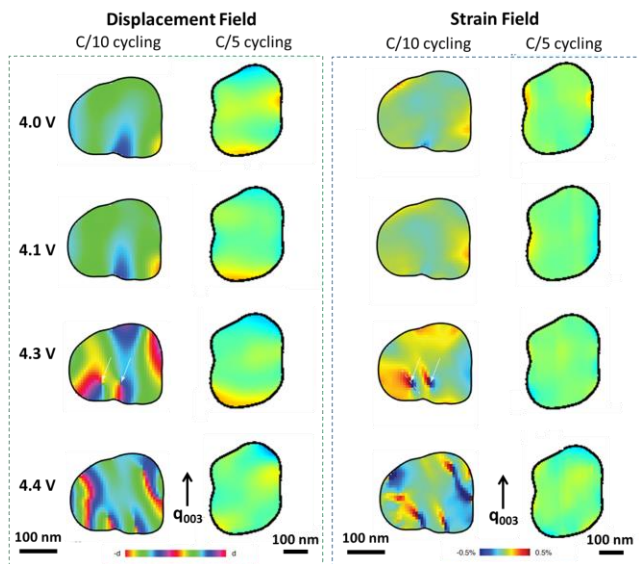


Figure II.5.C.3 Operando evolution of a LRLO nanoparticle during electrochemical charge at different rates including the changes in the displacement field along q_{003} and the strain along the [001] direction (perpendicular to the layers) inside of the nanoparticle calculated from the 3D displacement fields.

Note that up to 4.4 V, almost the same amount of lithium (one third of total lithium in $\text{Li}_{1.2}\text{Ni}_{0.133}\text{Mn}_{0.533}\text{Co}_{0.133}\text{O}_2$) is extracted out from the structure at both C/10 and C/5 rate. In other words, the influence of Li concentration difference on the structure changes until 4.4 V can be fairly excluded when comparing different charging rates. As shown in Figure II.5.C.3, from the beginning of the charge to 4.1 V, a continuous displacement field is observed in the nanoparticle and the displacement field changes slightly at both C-rates. When charged to 4.3 V, before the voltage plateau that signifies oxygen redox activity, the displacement field is qualitatively different and only lower rate charging shows singularities characteristic of dislocations as pointed out by white arrows. The discontinuity in the displacement field around a singularity is the projection of the Burgers vector along the scattering vector q_{003} . While, no obvious changes in the displacement field is found in the LRLO nanoparticle charged at a higher rate even until 4.4 V. The strain field distribution yields further insights into the

physical and electrochemical processes underpinning the formation of dislocations (see Figure II.5.C.3). For the nanoparticle charged at C/10 rate, the strain inhomogeneity in the slice shown increases between 4.0 V and 4.1 V and the strain is larger towards the bottom left edge of the particle. At 4.3 V, the strain is compressive

(reduced lattice spacing d) on the right and tensile on the left around dislocations revealing extra half-planes on the right in agreement with the displacement field analysis. Not surprisingly, no obvious strain characteristics are found in the bulk of the nanoparticle charged at the higher rate. At higher rate charging, less oxygen redox is activated due to sluggish kinetics so that less dislocation and strain network is formed in the bulk of LRLO particles.

HRTEM/ED characterization on structural recovery of single particle for LRLO

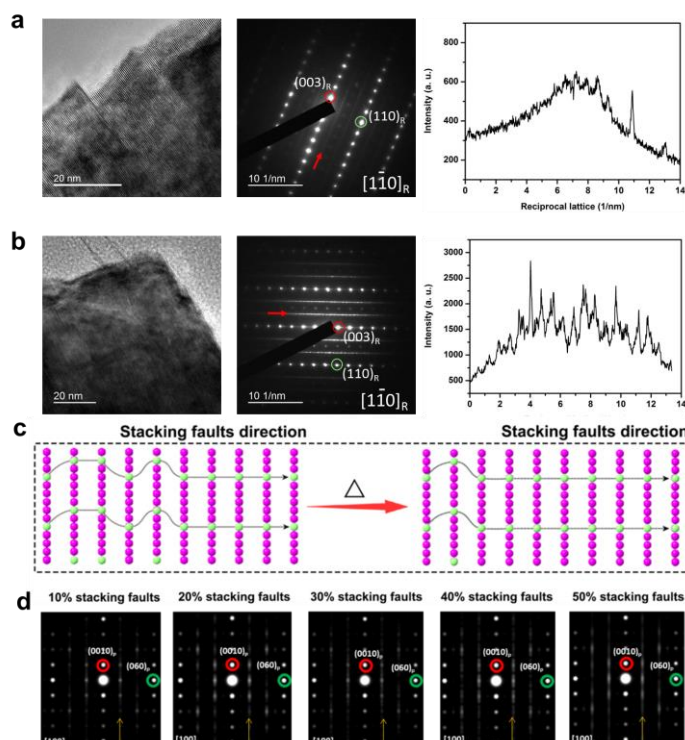


Figure II.5.C.4 HRTEM image, ED, and intensity of reciprocal lattice from line-scanning on single particle for the LRLO sample after 50 cycles (a) and after heat treatment at 300 °C (b). Models of cycled and heat treated LRLO for ED simulation (c). Simulated ED patterns for LRLO with different degree of stacking faults (d).

Previous report has demonstrated dislocations are generated and accumulated in the structure of LRLO material during electrochemical cycling. The nucleation of line defects dramatically modifies the local lithium environment by perturbing the ordering of oxygen stacking layers. In order to investigate stacking faults in detail, HRTEM combined with ED were applied for cycled LRLO material $\text{Li}[\text{Li}_{0.144}\text{Ni}_{0.136}\text{Co}_{0.136}\text{Mn}_{0.544}]\text{O}_2$. The diffraction streaks indicated by the red arrow in ED pattern represent superlattice ordering of single particle for LRLO. As shown in Figure II.5.C.4a, the diffraction streaks in ED pattern of cycled LRLO material are diffused, which indicates strong disorder in the layers stacking direction. After heat treatment at 300 °C for one hour, the bulk structure still maintains the layer phase (Figure II.5.C.4b). More importantly, the diffraction spots along the streaks in ED pattern becomes more obvious compared with the cycled bulk structure. To show the changes clearly for different samples, the diffraction streaks intensity were quantified from line-scanning with position presented by red arrows. The peaks are more noticeable after the heat treatment compared with the sample after cycling. This observation can be well

explained by the ED simulation result using SingleCrystal for LRLO material with different concentration of stacking faults (Figure II.5.C.4c and Figure II.5.C.4d). Stacking faults are allowed only in between the $-\text{O}-\text{TM}-\text{O}-\text{Li}-$ slabs and could never be generated inside the slabs. Three vectors defined as $[0, 0, 1]$, $[1/2, -1/6, 1]$, and $[1/6, -1/6, 1]$ in the unit cell with conventional monoclinic cell definition represent all possible atomic configurations generated by the stacking faults. Different concentration of stacking faults was associated with the stacking probabilities of these stacking vectors. The ED analysis implies the stacking faults generated in the bulk structure during the electrochemical cycling can be partially eliminated by the heat treatment. The structure ordering along the layers stacking direction is partially restored. These findings well support our proposed heat treatment strategy for structure and voltage recovery of cycled LRLO material.

The impact of defects generation on the structure metastability and voltage decay for LRLO

Previous report has demonstrated dislocations are generated and accumulated in the structure of LRLO material during electrochemical cycling. The nucleation of line defects dramatically modifies the local lithium environment by perturbing the sequence of oxygen layers. The influence of the oxygen stacking sequence on the system energy in LRLO material was investigated by first-principles calculations. For simplicity, a supercell model composed of three-formula units of $\text{Li}_{11}\text{Ni}_2\text{Mn}_5\text{O}_{18}$ was used for LRLO structure with

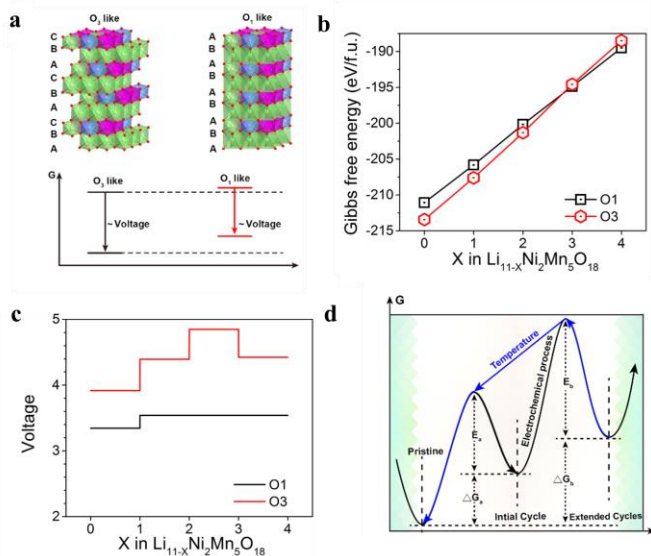


Figure II.5.C.5 Correlation between voltage decay and defects generation. a. Schematic illustration of free energy differences due to different oxygen stacking sequences (green, Li; red, O; purple, Mn; blue, Ni). b. The Gibbs free energy for each delithiation composition of the supercell with O3 and O1 stacking. c. Calculated voltage of supercell $\text{Li}_{11-x}\text{Ni}_2\text{Mn}_5\text{O}_{18}$ ($0 \leq x \leq 4$) for stacking sequence O3 and O1. d. Schematic illustration of the Gibbs free energy profiles for the conversion between pristine and cycled LRLO.

different oxygen stacking sequence (Figure II.5.C.5a). Oxygen stacking sequence changes from ABCABC (O3) to ABAB (O1) were considered since these transformations are easily accomplished via gliding of the MO_2 layers. In the energetically most favourable O3 structure, all lithium octahedral sites share edges with transition metal octahedral sites. The partial transition to O1 induces unfavourable face sharing between lithium and transition metal octahedral sites, thus raising the Gibbs free energy of the system (see Figure II.5.C.5b). The Gibbs free energy for O1 stacking is higher than that of O3 stacking for almost all tested delithiation compositions. This energy penalty is greater at high lithium concentration simply because more face-sharing sites are filled. Note, that the slope of the Gibbs free energy as a function of lithium concentration is a rough estimate for the average voltage. This results in a smaller average voltage for the structure with more defects (see Figure II.5.C.5c). In short, the highly cycled LRLO material is trapped in a metastable state with an energetically unfavourable local lithium environment, which is mainly responsible for the issue of voltage decay. Based on the mechanistic description above,

defects elimination is the key factor to achieve structure reversibility and voltage recovery. External driving force, such as heat treatment, is necessary to enable the system cross over the energy barrier to relax to the stable state as indicated by the blue arrows in Figure II.5.C.5d.

Influence of metal-ion electrolyte additive on electrochemically deposited Li metal (EDLi)

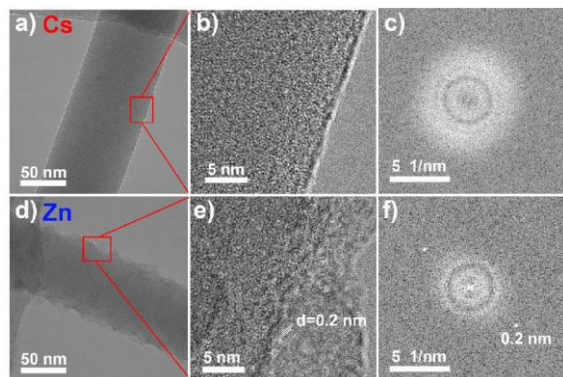


Figure II.5.C.6 Cryo-TEM images (a, b, d, e) with their corresponding area FFT analysis (c, f) of the deposited Li metal using electrolytes containing Cs^+ (a-c) and Zn^{2+} (d-f) additives at 400 kx magnification.

In order to disclose the effect of Cs^+ and Zn^{2+} electrolyte additives, cryo-TEM was applied to explore the nanostructure of the deposited Li metal. The cryo-TEM results (Figure II.5.C.6a, b and c) exhibit that the Li metal plated from Cs^+ -containing electrolyte has a dense, uniform and ultrathin SEI (< 1 nm) on the surface, which is similar to the SEI formed on graphite anode surface in the CsPF_6 -containing electrolyte, demonstrating the positive effect of Cs^+ additive on the SEI formation. On the other hand, a conformal thick surface film was found along the surface of the Li metal when the cell was cycled with Zn^{2+} containing electrolyte. The surface is rough and about 10 nm in average thickness. The EDLi is consistently amorphous in the bulk with a partially-crystallized SEI—composed of LiF given characteristic bright spots (Figure II.5.C.6f). Furthermore, the Li-Zn alloy is also amorphous without any characteristic bright rings and spots present in Figure II.5.C.6e and Figure II.5.C.6f. Note that the Zn^{2+} containing electrolyte has a higher CE and thicker surface layer than that of the pristine electrolyte. The Li-Zn alloy is believed to be

distributed on the surface and protect the Li metal from electrolyte corrosion. Overall, both of the EDLi from Cs^+ and Zn^{2+} -containing electrolytes are amorphous, suggesting there is little effect on the Li bulk structure, yet they differ significantly in their interfacial properties.

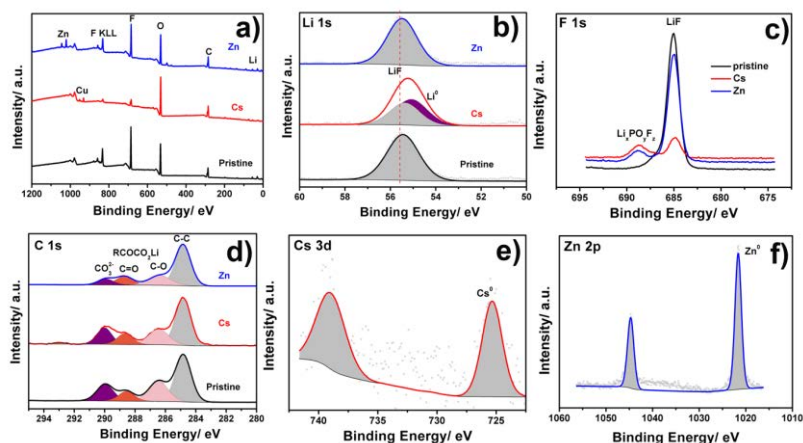


Figure II.5.C.7 Compared XPS spectra of the survey (a), C 1s (b), F 1s (c), Li 1s (d), Cs 3d (e) and Zn 2p (f) with the deposited Li metal from the pristine, Cs^+ and Zn^{2+} containing electrolytes.

and Li_2CO_3 in Figure II.5.C.7c) and organic species (e.g. esters, ethers and carboxylates in Figure II.5.C.7d). Some oxygenated fluorines ($\text{Li}_x\text{PO}_y\text{F}_z$) were observed when the Cs^+ and Zn^{2+} were added in the electrolyte (Figure II.5.C.7c). In addition, both ions are found to be partially reduced since there is a weak signal from metallic Cs (Figure II.5.C.7e) and a strong signal from metallic Zn (Figure II.5.C.7f). The latter confirms the presence of LiZn alloy on the surface of the EDLi.

The above observations were further confirmed by the surface sensitive XPS, obtaining the chemical compositions of the SEI. The presence of Cu signal in the survey spectra (Figure II.5.C.7a) and metallic Li in the Li 1s spectra (Figure II.5.C.7b) indicates an ultra-thin surface film from the Cs^+ -containing electrolyte, consistent with the SEI measured by cryo TEM. Figure II.5.C.7a and Figure II.5.C.7c demonstrate less fluorine species in Cs^+ than Zn^{2+} containing electrolyte, which could be due to the thinner SEI film thickness formed in Cs^+ -containing electrolyte. The SEI from all electrolytes is composed of inorganic compounds (e.g. LiF, Li_2O

Conclusions

Through rigorous characterization methods, a pathway to recover the LRLO structure and working voltage is designed through mild-temperature annealing. The treatment at mild temperature recovers the local Li-excess environments around oxygen, oxygen stacking sequence, and eliminates microstrain associated with different defects. BCDI measurements on LRLO single particle demonstrate significantly higher amount of defects generated when the material is charged at a lower rate. Cryogenic electron microscopy is a powerful tool to reveal the detailed structure of EDLi and the SEI composition on Li metal at the nanoscale while minimizing beam damage during imaging. Similar method will be applicable to highly charged cathode materials.

Key Publications

1. Y. S. Meng and M. Zhang, "Quantifying the Unusual Anion Redox Activity in Lithium Intercalation Compounds" American Physical Society Meeting, 2018, Los Angeles, U.S., Invited talk.
2. Singer, M. Zhang, Y. S. Meng, et al., "Nucleation of Dislocations and Their Dynamics in Layered Oxides Cathode Materials during Battery Charging", *Nature Energy*, 2018, 3, 641.
3. M. Zhang, H.D. Liu, Y. S. Meng, "Structure and Voltage Recovery Driven by Defects Elimination in Li-Rich Layered Oxide Cathode Materials" 233rd ECS Meeting, 2018, Seattle, U.S., Oral Presentation.
4. M. Zhang, H.D. Liu, Y. S. Meng, et al., "Modified Co-precipitation Synthesis of Meso-structure Controlled Li-rich Layered Oxides for Minimizing Voltage Degradation", *ACS Applied Energy Materials*, 2018, 1, 3369.

5. Y. S. Meng, M. Zhang, B. Qiu, A. Singer, “Role of Strain and Defects in Anion Redox Electrochemistry” The 19th International Meeting on Lithium Batteries, 2018, Kyoto, Japan, Keynote Lecture.
6. X. Wang, Y. Li, Y.S. Meng, “Cryogenic Electron-Microscopy for Characterizing and Diagnosing Batteries”, *Joule*, 2018, 2, 1.

References

1. B. Qiu, M. Zhang, Y. Xia, Z. Liu, Y. S. Meng, *Chemistry of Materials* 29 (2017): 908-915.
2. B. Qiu, M. Zhang, L. Wu, J. Wang, Y. Xia, D. Qian, H.D. Liu, S. Hy, Y. Chen, K. An, Y. Zhu, Z. Liu, Y. S. Meng, *Nature Communications* 7 (2016): 12108.

Acknowledgements

We thank Dr. Aaron D. Yocum (NETL manager) for supporting our work.

II.5.D Microscopy Investigation on the Fading Mechanism of Electrode Materials (PNNL)

Chongmin Wang, Principal Investigator

Pacific Northwest National Laboratory
902 Battelle Boulevard, Mail Stop K8-93
Richland, WA 99352
E-mail: Chongmin.wang@pnnl.gov

Tien Q. Duong, DOE Technology Development Manager

U.S. Department of Energy
E-mail: Tien.Duong@ee.doe.gov

Start Date: October 1, 2015 End Date: September 30, 2019
Project Funding (FY18): \$1,300,000 DOE share: \$1,300,000 Non-DOE share: \$0

Project Introduction

During the operation of a rechargeable battery, structural and chemical evolution of cathode, anode, electrolyte and the corresponding interfaces formed among them are critical factors that control the performance of the battery. A direct understanding of these structural and chemical evolution and their correlation with battery performance will be the key for designing electrode materials with better properties. This project will focus on establishing the structure and property relationship in rechargeable batteries using advanced in-situ and ex-situ microscopy and spectroscopy tools. This study will feed back to the battery materials fabrication group for designing of better materials with better properties. The project includes two tasks: Task 1 will focus on high capacity anode and interfaces and Task 2 will focus on Ni-rich Cathode and interfaces.

Objectives

The objective of this work will be using a combination of *ex-situ*, *in situ* and *operando and cryo* high-resolution transmission electron microscopy (TEM) and spectroscopy to probe the fading mechanism of both Li and Si as high capacity anode and Ni-rich NMC as high capacity cathode. For high capacity anode, the research task will focus on revealing how Li and Si interact with liquid electrolyte to critically affect their fading process. For the Ni-rich NMC cathode, the research task will focus on delineating the structural and chemical evolution of the Ni-rich NMC as their dependence on the operating voltage, charge rate and chemistry of electrolyte. To complement the high resolution TEM study, in-situ liquid cell SIMS and XPS will also be used to gain structural and chemical evolution of cathode and anode and correlate the structural and chemical evolution with battery performance. The diagnosis work will be in close combination with calculation and atomic level modeling.

Approach

In the proposed research, aberration-corrected STEM-HAADF and cryo-TEM imaging combined with EELS/EDX chemical analysis will be used to probe the microstructural and chemical evolution of the Ni-rich NMC layered cathode before and after cycling. EELS/EDX mapping, time-of-flight secondary ion mass spectrometry (TOF-SIMS), nano-SIMS, and XPS will be used to explore the elemental distribution and the thickness of SEI layer formed on the surface of the cathode material. Direct correlation of the structural and chemical information with battery properties will provide insight on the capacity degradation mechanism of the layered materials with different compositions and performance improvement mechanism with lattice doping/surface modification/electrolyte additives. These characterization results will be used to guide the materials optimization process and establish a solid knowledge base on the correlation between materials selections and structure evolution in the Ni-rich NMC layered cathode materials.

Results

Established the correlation of cycling rate with the structural evolution of the NMC cathode

The key new information of this work is to report the correlation between charge-discharge rate and structural phase transition of the layer structured cathode. We discover that high rate cycling leads to the layer to spinel transition, while low rate cycling leads to the layer to rock salt transition.

It is very well established that the battery performance critically depends on the charge and discharge rate. Fast cycling leads to performance deteriorations and the intrinsic roles that the cycling rate play in the battery performance are poorly understood and the correlation between cycling rate and cathode degradation, in terms of structure evolution, has not been established. Two well-recognized phase transitions usually take place in the layer structured cathode during the battery operation: layered-to-spinel and the layered-to-rock-salt phase transitions. Numerous studies have revealed the thermodynamic nature of such phase transitions to be a thermal decomposition process, where the reaction occurs as the temperature reaches the phase transition point. Most cathodes readily develop into the spinel-like or disordered rock salt phase on both surfaces and bulk upon cycling. However, the parameters associated the battery operation that control the phase transition products are far from clear. The two phase transition products developed upon cycling are of distinct crystal structure, and may affect the battery rate behavior in a different way. Nevertheless, the battery community usually categorizes the two configurations into one group-Li⁺ insulating layers, but, the differentiation of deterioration effects of the two reconstruction layers on the battery performance remain vague.

Using scanning transmission electron microscopy (STEM), we have systematically studied the structural features of LiNi_{0.76}Mn_{0.14}Co_{0.10}O₂ cycled at rate of ranging from 0.33C to 2C. We reveal that the phase transition products vary with the cycling rate and contribute distinctly different to the battery decay in Ni-rich cathode materials. We demonstrate the diverse phase transition paths in a range of battery operation rates, in which the layered-to-disordered rock salt transition occurs at below 1C, whereas layered-to-spinel takes place at the rate above 2C. By combing the electrochemical tests with atomistic simulations, we reveal that the abundant vacancies in the highly delithiated state, under the low charge/discharge rate, favor the thorough cation mixing between the Li and transition metal (TM) layers and result in the formation of disordered rock salt structure. In contrast, the limited vacancies resulted from the Li ions retention, at the high cycling rate, impede the fully cation mixing and give rise to the growth of spinel-like phase. Our subtle characterizations at the atomic scale bridge the gap between the structure evolution and cycling rate and may provide mechanistic insight into tailoring the battery rate capability.

We demonstrate the cycling rate-crystal structure-battery performance correlation in the Ni-rich cathode as illustrated in Figure II.5.D.1. We find the electrochemical reaction products of the layered materials are effectively controlled by the cycling rate, in which rock salt forms at the low cycling rate, whereas the spinel phase develops at the high cycling rate. The two kind of reconstruction layers deteriorate the cycling performance distinctly and a critical cycling rate at between 1C and 2C distinguishes the layered-to-spinel-like and layered-to-rock-salt phase transition. Our simulations reveal that cycling rate controls battery performance via forming different phase transition products, which are kinetically governed by the amount of vacancies generated during the battery operation.

Revealed the solid-liquid interfacial reaction controls the layer to spinel phase transition

The key new information of this work is to reveal the functioning mechanism of enhanced cycling stability of cathode secondary particle in terms of capacity retention and voltage stability when the grain boundary boundaries of the secondary particles is infused with a solid electrolyte.

The biggest challenge for the commercialization of layered structured nickel rich lithium transition metal oxide cathode is the capacity and voltage fading. Resolving this problem over the years follows an incremental progress. Tailoring of grain boundary structure and chemistry for optimization of materials behaviors and properties appears to be a classic protocol in material science. However, this strategy has ever hardly been used

for the case of rechargeable battery. Herein, a new approach, based on tailoring grain boundary structure and chemistry in the secondary particles, has been developed to tackle these critical barriers in the system of Ni-rich layered cathode material, $\text{LiNi}_{0.76}\text{Mn}_{0.14}\text{Co}_{0.10}\text{O}_2$ as a specific example.

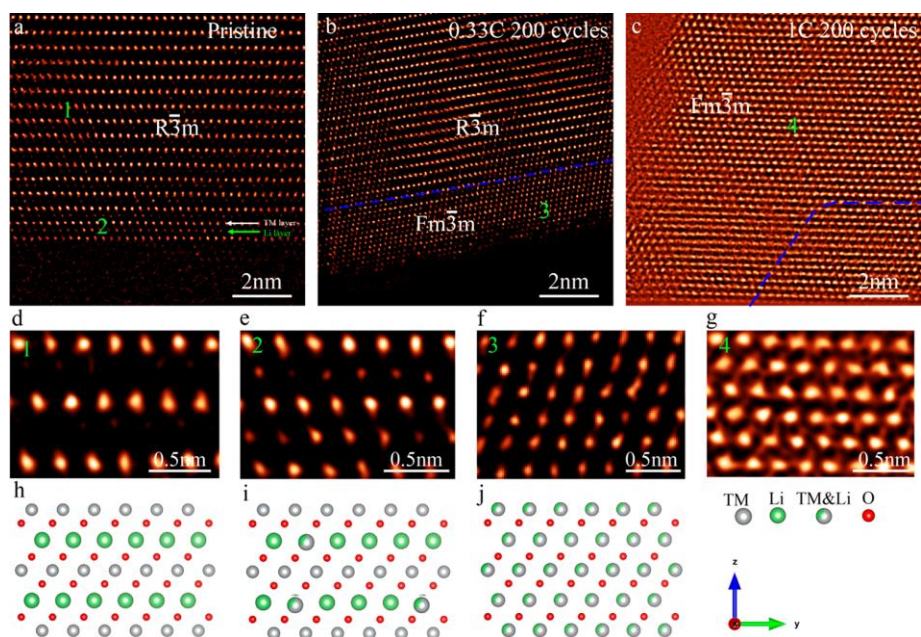


Figure II.5.D.1 HAADF-STEM images of layered-to-disordered rock salt phase transition at the low cycling rate. (a) HAADF-STEM image of the pristine sample showing the majority of the bulk maintains $R\bar{3}m$ structure. The white and green arrows point to the TM layer and Li layer, respectively. (b and c) HAADF-STEM image of the 200-cycle sample at 0.33C and 1C, respectively. The blue dashed lines outline the boundary of the converted phase, below and above which are the disordered rock salt and layered structure, respectively. (d–g) The enlarged view of the pristine bulk, pristine surface, 0.33C 200-cycle surface, and 1C 200-cycle surface from area 1, 2, 3, and 4 in panels a–c, respectively. (h–j) Atomic structure corresponding to the panels d, e, and f, respectively

It has been noticed that coating of NMC secondary particles with Li_3PO_4 and subsequent high temperature annealing can lead to dramatic enhanced cycling stabilities of battery in terms of capacity retention, voltage decay, and thermal stability. Based on details STEM structural and chemical analysis, it is demonstrated that following the high temperature annealing, the coated Li_3PO_4 is infused along the grain boundaries of the secondary particles. The infusion of grain boundary with solid electrolyte will eliminate penetration of liquid electrolyte into the grain boundaries of secondary particle, which subsequently eliminates the following detrimental factors: (1) intergranular cracking; (2) reaction of cathode with liquid; (3) layer to disorder phase transition as illustrated in Figure II.5.D.2.

Further, most importantly, the present work indicates that cathode-liquid electrolyte interfacial reaction controls some of the critical steps that have been observed previously to contribute to the cycling stability of cathode. Therefore, the core step for addressing the barrier of cathode stability is to minimize the cathode-liquid electrolyte interaction.

The present work, for the first time, reveals unprecedented insight as how the cathode behaves in the case of not contacting with the liquid electrolyte, ultimately points toward a general new route, via grain boundary engineering, for designing of better batteries of both solid-liquid and solid state systems.

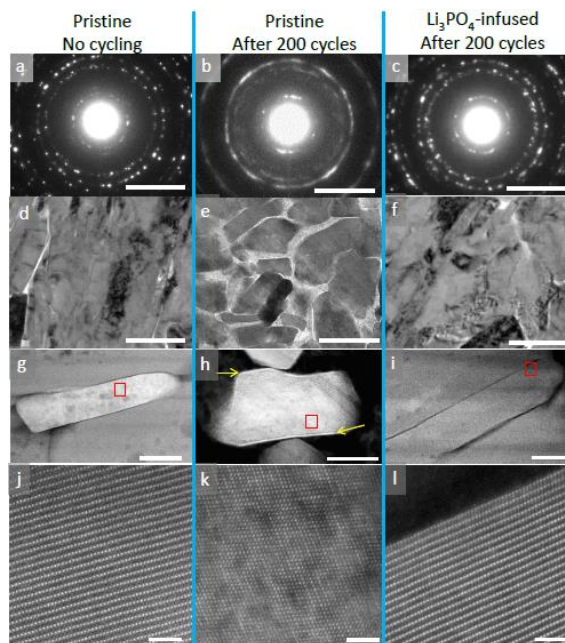


Figure II.5.D.2 Infusion of Li_3PO_4 into secondary particles eliminates structural degradation. The structural degradations are evaluated by a combination of SAED a-c, bright-field TEM imaging d-f, STEM-HAADF imaging g-i, and atomic-level STEM-HAADF imaging j-l (corresponding to the high magnification image of the redline marked regions). The left column corresponds to the pristine electrode without cycling, the middle column is the pristine electrode after 200 cycles, and the right column shows the Li_3PO_4 -infused electrode after 200 cycles. These observations demonstrate that after 200 cycles, the pristine electrode shows significant structural degradation, featuring intergranular cracking and formation of amorphous phase within the grain boundaries (e), formation of surface reaction layer on each grain surface (indicated in h by the yellow arrows), and layered-to-spinel transformation (k), while these degradation features do not occur in the Li_3PO_4 -infused electrode. The scale bars are 5 nm^{-1} in a-c, 500 nm in d-f, 100 nm in g-i, and 2 nm in j-l.

In-situ environmental TEM revealing that coupling of electrochemically triggered thermal and mechanical effects can aggravate failure of layered cathode

The key new information of this work is to use in-situ HRTEM to directly demonstrate the coupling effect among electrochemical induced thermal and mechanical effect, which will lead to the fading of the cathode in a way severe than that of a simple addition of each factor.

Electrochemical driven functioning of battery inevitably induces thermal and mechanical effects. Vast amount of work has been done in terms of elucidating the role of each of these three factors on the performance of rechargeable battery, typically such as thermal management and analysis of mechanical induced failure. However, during the operation of a battery, these three factors exist simultaneously and they are coupled and collectively govern the performance of the battery. However, such a coupling effect, favorable or detrimental, has never been explicitly elucidated in the past.

By using in-situ high resolution scanning transmission electron microscopy to deliberately demonstrate such a coupling effect among the electrochemical induced thermal and mechanical effects.

By integrating in situ transmission electron microscopy (TEM), in situ X-ray diffraction (XRD) and modeling, such a coupling effect on the intragranular cracking of a Ni-rich $\text{LiNi}_{0.6}\text{Mn}_{0.2}\text{Co}_{0.2}\text{O}_2$ (NMC622) layered cathode is demonstrated. It has been noticed that supplying a thermal perturbation to the delithiated $\text{LiNi}_{0.6}\text{Mn}_{0.2}\text{Co}_{0.2}\text{O}_2$ will lead to the nucleation and propagation of intragranular cracks in the lattice, often in an explosive way as shown in Figure II.5.D.3. It shows that in situ heating of delithiated NMC622 particles, even at the first delithiation from the pristine state, leads to explosive nucleation and propagation of intragranular cracking. Such a phenomenon is absent in fully discharged particles (with Li being reinserted).

Combining ex situ and in situ TEM observations with chemomechanical modeling, it reveals that in response to the temperature raise, electrochemically induced phase inhomogeneity and oxygen evolution cause, respectively, thermal stress and internal pressure, which constitute the two primary driving forces for the intragranular cracking. The present observation demonstrates that the intimate coupling of the electrochemical, thermal, and mechanical processes leads to a much severer effect on the degradation of the cathode.

Characteristically, the heating induced intragranular cracking is accompanied with surface phase transformation and oxygen gas release. Taken together, the observed intragranular cracking resembles the popcorn fracture mechanism under heating. The studies offer insights into how the electrochemical process triggers thermal and mechanical processes in battery operation, and how these effects are intimately coupled and mutually strengthened in the degradation of layered cathode materials. The fundamental understanding also shed light on the mitigation of the degradation of battery materials under complicated electrochemical and thermo-mechanical conditions.

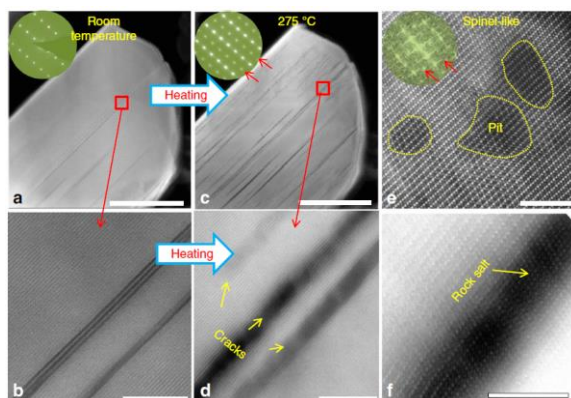


Figure II.5.D.3 In situ heating-induced crack nucleation and propagation. The $\text{LiNi}_0.6\text{Mn}_0.2\text{Co}_0.2\text{O}_2$ (NMC622) was delithiated by charging to 4.7 V vs. Li metal. a and b High angle annular dark field (HAADF) images from delithiated NMC622 before heating (room temperature). c-f HAADF images after heating to 275 °C. Selected area electron diffraction (SAED) patterns and fast Fourier transformation images in (a), (c), and (e) show the overall lattice change during heating. d, e, and f show local lattice structure change at crack regions and crack-free regions. The scale bars are 200 nm in (a) and (c); 10 nm in (b) and (d); and 4 nm in (e) and (f).

Conclusions

Based on in-situ and ex-situ electron microscopy study, we have revealed new information on the structural and chemical evolution of NMC cathode, providing key insight for optimization and designing of cathode materials with cycling stability. We discovered that the cycling rate will lead to different phase transition, which provides basis for tailoring the chemistry of the lattice to main the stability of the lattice while still allow a fast charge of the battery system. Another important observation is the interfacial reaction not only induce solid-liquid interphase layer, but also, most importantly, the interfacial reaction will control the bulk lattice behavior. A very insightful observation is the infusion of solid electrolyte into the grain boundary of secondary particle can eliminate the layer to bulk lattice transition, therefore enhanced cycling stability of the battery in terms of capacity and voltage. This observation points to the right direction for optimization of NMC cathode. By using in-situ TEM, we also revealed the coupling effect of electrochemical triggered thermal and mechanical effect. Leading to exaggerated failure of the battery. In the continuation of the work, we will focus on explore the origin of the intragranular cracks in the NMC. At the same time, we will also try to decipher the mechanism of the lithium dendrite growth on during lithium deposition. The microscopy work will be closely correlate with the battery materials design.

Key Publications

1. Pengfei Yan, Jianming Zheng, Jian Liu, Biqiong Wang, Xiaopeng Cheng, Yuefei Zhang, Xueliang Sun, Chongmin Wang, and Ji-Guang Zhang, "Tailoring Grain Boundary Structures and Chemistry of Ni-rich Layered Cathode for Enhanced Cycle Stability of Lithium-Ion Batteries", **Nature Energy**, **3**, 600-605(2018).
2. Pengfei Yan, Jianming Zheng, Tianwu Chen, Langli Luo, Yuyuan Jiang, Kuan Wang, Manling Sui, Ji-Guang Zhang, Sulin Zhang and Chongmin Wang, "Coupling of electrochemically triggered thermal and mechanical effects to aggravate failure in a layered cathode", **Nature Communications** **9**, 2437(2018).
3. Lianfeng Zou, Zhenyu Liu, Wengao Zhao, Haiping Jia, Jianming Zheng, Yong Yang, Guofeng Wang, Ji-Guang Zhang, and Chongmin Wang, "Solid-Liquid Interfacial Reaction Triggered Propagation of Phase Transition from Surface into Bulk Lattice of Ni-Rich Layered Cathode", **Chem. Mater.** **30**, 7016-7026(2018).
4. Lianfeng Zou, Wengao Zhao, Zhenyu Liu, Haiping Jia, Jianming Zheng, Guofeng Wang, Yong Yang, Ji-Guang Zhang, and Chongmin Wang, "Revealing Cycling Rate-Dependent Structure Evolution in Ni-Rich Layered Cathode Materials", **ACS Energy Lett.** **3**, 2433-2440(2018).
5. Hanlei Zhang, Brian M. May, Jon Serrano-Sevillano, Montse Casas-Cabanas, Jordi Cabana, Chongmin Wang and Guangwen Zhou, "Facet-Dependent Rock-Salt Reconstruction on the Surface of Layered Oxide Cathodes", **Chem. Mater.** **30**, 692-699(2018).
6. Qiaobao Zhang, Huixin Chen, Langli Luo, Bote Zhao, Hao Luo, Xiang Han, Jiangwei Wang, Chongmin Wang, Yong Yang, Ting Zhu and Meilin Liu, "Harnessing the concurrent reaction dynamics in active Si and Ge to achieve high performance lithium-ion batteries", **Energy Environ. Sci.**, **11**, 669-681(2018).
7. Jagjit Nanda, Chongmin Wang, and Ping Liu, "Frontiers of solid-state batteries", **MRS Bulletin**, **10** 741(2018).
8. Jaegwon Ryu, Tianwu Chen, Taesoo Bok, Gyu-jin Song, Jiyoung Ma, Chihyun Hwang, Langli Luo, Hyun-Kon Song, Jaephil Cho, Chongmin Wang, Sulin Zhang and Soojin Park, "Mechanical mismatch-driven rippling in carboncoated silicon sheets for stress-resilient battery anodes", **Nature Communications**, **9**, 2924(2018).
9. Pengfei Yan, Jianming Zheng, Ji-Guang Zhang, and Chongmin Wang, "Atomic Resolution Structural and Chemical Imaging Revealing the Sequential Migration of Ni, Co, and Mn upon the Battery Cycling of Layered Cathode", **Nano Lett.** **17**, 3946-3951(2017).
10. Hanlei Zhang, Fredrick Omenya, Pengfei Yan, Langli Luo, M. Stanley Whittingham, Chongmin Wang, and Guangwen Zhou, "Rock-Salt Growth-Induced (003) Cracking in a Layered Positive Electrode for Li-Ion Batteries", **ACS Energy Lett.** **2**, 2607-2615(2017).
11. Hanlei Zhang, Fredrick Omenya, M. Stanley Whittingham, Chongmin Wang, and Guangwen Zhou, "Formation of an Anti-Core-Shell Structure in Layered Oxide Cathodes for Li-Ion Batteries", **ACS Energy Lett.** **2**, 2598-2606(2017).
12. Won-Jin Kwak, Langli Luo, Hun-Gi Jung, Chongmin Wang, and Yang-Kook Sun, "Revealing the Reaction Mechanism of Na-O₂ Batteries using Environmental Transmission Electron Microscopy", **ACS Energy Lett.** **2**, 2607-2615(2017).

13. Xiaolin Li, Pengfei Yan, Xingcheng Xiao, Jae Ha Woo, Chongmin Wang, Jun Liu and Ji-Guang Zhang, “Design of porous Si/C–graphite electrode with long cycle stability and controlled swelling”, **Energy Environ. Sci.**, **10**, 1427-1434(2017).

II.5.E In-Operando Thermal Diagnostics of Electrochemical Cells (LBNL)

Ravi Prasher, Principal Investigator

Lawrence Berkeley National Lab
1 Cyclotron Rd
Berkeley, CA, 94720
E-mail: RSPrasher@lbl.gov

Tien Duong, DOE Technology Development Manager

U.S. Department of Energy
E-mail: Tien.Duong@ee.doe.gov

Start Date: October 1, 2017

End Date: September 30, 2018

Project Funding (FY18): \$145,000

DOE share: \$145,000

Non-DOE share: \$0

Project Introduction

Effective heat dissipation in batteries is important for many reasons, such as performance, reliability, and safety. Currently, the thermal management of battery cells is provided at the system level by either forced air or liquid cooling. This engineering solution has many shortcomings, such as a reduction in the energy density at the system level and complex system designs to allow for fluid flow. In spite of such high importance, so far no thermal transport measurements or diagnostics have been performed inside electrochemical batteries under operating conditions. An understanding of thermal transport through various interfaces within the electrochemical cell is of particular importance as interfacial thermal transport typically plays the dominant role (up to 90% of the overall thermal resistance according to our preliminary measurements) in determining the internal temperature rise and temperature gradients within various devices. Currently, no thermal model exists that can predict the spatially resolved internal temperature rise within an operating battery, accurate to the true heterogeneous multilayered internal structure of the battery.

Objectives

We will measure the dominant thermal resistances within the multilayered stack comprising the full battery cell. These measurements will be performed *in-operando* on a fully assembled and functioning battery. This will identify the layer(s) and layer interface(s) that dominate the total thermal resistance to heat flow within an operating battery, even if they are buried deep within the bulk of the battery cell, and quantify their contributions. From these measurements we will build a spatially resolved theoretical thermal model of the internal heat transfer within a battery. This model can then be used to accurately predict the internal temperature rise and temperature profile of a battery under various operating conditions, such as fast charging. This model can also be used to guide the thermal optimization of battery design and battery control software to improve performance, reliability, and safety. Such a model does not currently exist.

Approach

The thermal measurements will be achieved using a customized derivative of the 3-omega technique. This technique uses microfabricated sensors placed on the outer surfaces of the electrochemical cell stack (see Figure II.5.E.1) to launch thermal waves at multiple frequencies into the battery and interrogate the thermal transport properties at various depths within the bulk of the cell. Our technique simultaneously measures thermal transport properties as a function of depth into the cell as well as temperature. Because the measurement is performed in the frequency domain and not the time domain, it is very robust against ambient noise. Our design enables *in-operando* measurement during battery operation because our sensors and

measurements are immune to both electrical interference from the battery and thermal interference from any heat generated by the battery's own operation.

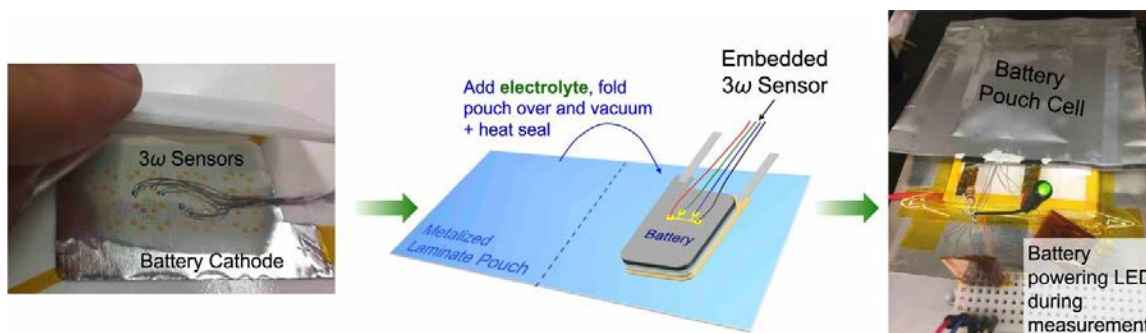


Figure II.5.E.1 Design of 3-omega thermal sensors and how they are incorporated into an electrochemical battery pouch cell for in-operando measurements.

We are working with the Battaglia group at LBNL in order to make lithium-ion electrochemical pouch cells inside of which we embed our sensors, and to perform electrical measurements on the batteries in addition to our thermal measurements. Because our sensors probe the interior of the battery from the surface of the multilayer stack, the sensors are non-invasive and do not disturb the local environment of the electrochemical multilayer stack. Sending in thermal waves at many different frequencies allows us to separate out the thermal transport properties at different locations throughout the depth profile of the cell.

Prior to performing any measurements, we fully simulate each experiment and numerically optimize the thermal design of the housing of our battery samples so as to maximize sensitivity to the properties of interest and minimize sensitivity to the outside environment and noise. All sensors are designed and fabricated in-house.

Results

This year we continued to improve our measurement system, built new equipment, and advanced the samples that we are able to measure. We succeeded in embedding 3-omega sensors into a full lithium-ion battery pouch cell and recording *in-operando* data while the battery was in use. The raw data from this measurement is shown in Figure II.5.E.2.

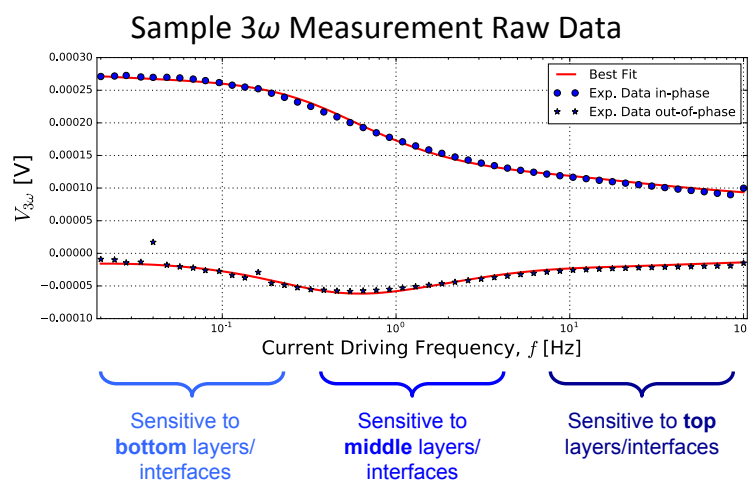


Figure II.5.E.2 Raw 3-omega data for an in-operando measurement of a full Li-ion battery showing the extended frequency range of our upgraded system.

We also finished upgrading our 3-omega measurement system to be able to go down to frequencies over an order of magnitude lower than before. This significantly increases our sensitivity to the more deeply buried layers and interfaces within the battery, allowing us to better measure thermal transport properties throughout the entirety of a full battery pouch cell. This is because lower frequency thermal waves can penetrate more deeply into the battery.

After a more careful examination of the available literature, we also found that currently available data for the thermal conductivity of battery materials is sparse and highly variable and therefore unreliable. Our 3-omega measurements require some of these values as inputs into the data analysis thermal model so as to measure other more important *in-operando* thermal properties. Therefore, we designed and built a new piece of equipment to perform *ex-situ* measurements of thermal conductivity of battery components. These measurements are then used in the data analysis of the *in-operando* 3-omega measurements. This new measurement system is a linear heat flow Cut Bar system as shown in Figure II.5.E.3.

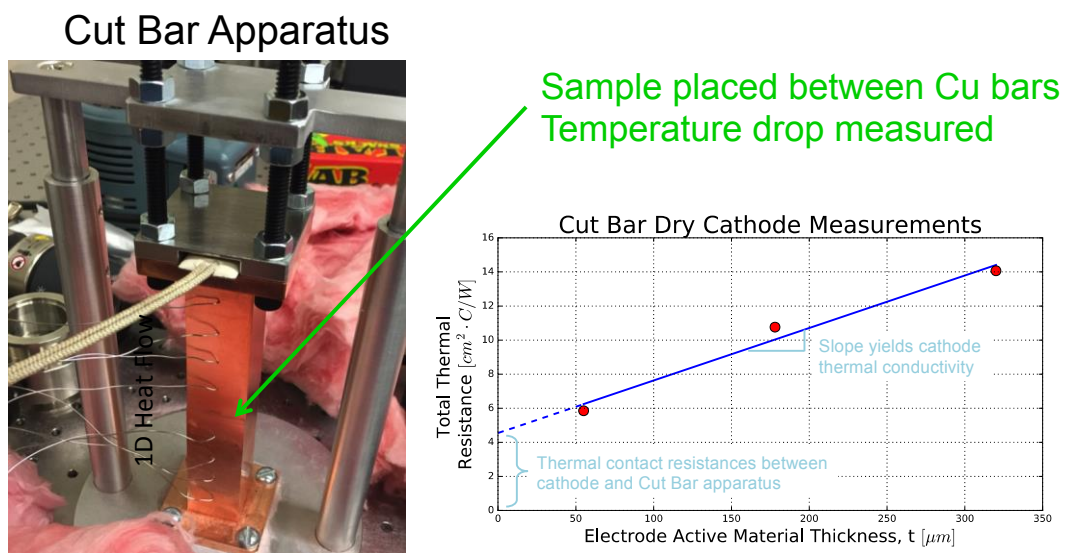


Figure II.5.E.3 Newly built Cut Bar system that uses linear heat flow to accurately measure the thermal conductivity of isolated battery components *ex-situ*. Bottom-right: data from Cut Bar measurements on dry cathode samples. By measuring samples of varying thickness, we can separate out the effects of thermal contact resistance and intrinsic thermal conductivity.

The Cut Bar works by sandwiching a sample between two highly thermally conductive Cu bars and measuring the temperature drop across the sample. The 1D heat flux passing through the sample is measured from the temperature gradient in the bars. From the heat flux and the temperature drop, the total thermal resistance of the sample is calculated. This includes the thermal contact resistance between the sample and the bars themselves. To separate out the thermal contact resistance from the sample's intrinsic thermal conductivity, we measure samples of varying thickness. An example of this is given for dry cathode materials, shown in Figure II.5.E.3.

Conclusions

We have successfully performed 3-omega measurements *in-operando* on functioning full lithium-ion battery pouch cells. We have finished upgrading our 3-omega measurement system to have increased sensitivity and probe deeper into the batteries. Finally, we have designed and built a new piece of equipment, the Cut Bar, to perform high accuracy *ex-situ* measurements of the thermal conductivity of individual battery components. We are continuing to perform Cut Bar measurements, which will provide the necessary input parameters to finalize the analysis of the *in-operando* 3-omega measurements.

Key Publications

This work has been presented in part at the 2018 International Technical Conference and Exhibition on Packaging and Integration of Electronic and Photonic Microsystems (InterPACK), the 16th International Heat Transfer Conference (IHTC) along with accompanying conference paper, and the 2018 Bay Area Battery Summit.

Acknowledgements

We thank Dr. Sean Lubner, Dr. Suman Kaur, Dr. Yanbau Fu, and Dr. Vince Battaglia for their help in carrying out the research in this project.

II.5.F Correlative Microscopy Characterization of Oxide Electrodes (SLAC National Accelerator Laboratory)

Yi Cui, William C. Chueh, Michael F. Toney

SLAC National Accelerator Laboratory
2575 Sand Hill Road
Menlo Park, CA 94025
E-mail: wchueh@stanford.edu

Tien Duong, DOE Technology Development Manager

U.S. Department of Energy
E-mail: Tien.Duong@ee.doe.gov

Start Date: January 1, 2016 End Date: September 30, 2018
Total Project Cost (FY18): \$ 975,000 DOE share: \$ 975,000 Non-DOE share: \$0

Project Introduction

A new cross-technique characterization platform will be developed to track lithiation dynamics at the single-particle level in Lithium- Manganese-rich Nickel Cobalt Oxide (LMR-NMC). Fundamental insights from this new diagnostic capability are expected to increase the power density and cycle life of oxide electrodes by improving electrode utilization, reducing electrochemical hotspots, decreasing capacity and voltage fade, and enhancing safety, which all improve the viability of lithium-ion batteries for vehicle transportation. By understanding lithiation at the single-particle level, this project's success will contribute to improving on-vehicle battery management, such as charging/discharging protocol, state-of-charge and state-of-health monitoring.

Due to the cost of Co, substituting Ni, Mn, Al, Mg, or Cr in the layered oxide cathode LiCoO_2 has become the focus of much research. LMR-NMC is of significant interest for use in electric vehicle applications due to its balance of cost and performance, with demonstrated specific capacities of 230- 280 mAh g^{-1} . Recharging time, power density, voltage/capacity fade, and thermal stability are important performance matrices for these battery chemistries to gain widespread use in vehicle transportation. Rational engineering of electrode chemistry and microstructure is expected to greatly increase these aspects of battery performance. However, due to the wide range of length scales involved – spanning nanometers to millimeters – a comprehensive understanding of kinetics and degradation in battery electrodes is lacking, especially at the single-primary-particle level. Part of the challenge lies in the characterization of lithiation dynamics across a wide range of length scales of realistic batteries during cycling.

This project is carried out in collaboration with scientists at Advanced Light Source and the Molecular Foundry, users facilities at Lawrence Berkeley National Laboratory.

Objectives

This study aims to develop and utilize a correlative microscopy platform to investigate the lithiation dynamics of LMR-NMC, with the specific goal of understanding factors that determine the rate capability and degradation mechanisms at the single primary particle length scale. By developing a nanoscale and single-particle understanding of lithiation, the project addresses specific engineering problems including electrochemical hotspot, electrode utilization, safety, and capacity/voltage fade. Chemistry-sensitive soft transmission X-ray microscopy, operating in standard and in ptychography mode, will be carried out on cycling electrodes in a liquid electrolyte using a microfluidic cell. A platform to transfer the identical electrode to the transmission electron microscope and Raman microscope will be developed to integrate the X- ray, electron and optical characterization with the goal of achieving a comprehensive understanding of the lithiation dynamics at the single-particle level. Ex-situ spectro- ptychography on electrodes cycled at low (-20°C) and

high (+80°C) temperatures will be conducted to understand the temperature dependence of lithiation dynamics, hotspots, and degradation in single particles.

Approach

Chemistry-sensitive soft transmission X-ray microscopy, operating in standard and in ptychography mode, will be carried out on cycling electrodes in a liquid electrolyte using a microfluidic cell while the electrode is cycled between the charged and the discharged state. The expected spatial resolution is 5 nm (ptychography mode) and 50 nm (standard mode). To attain even higher spatial resolution, a platform to transfer the same electrode to the transmission electron microscope will be developed. Finally, Raman microscopy, which is sensitive to the vibrational nature of chemical bonds, will also be used to characterize the same electrode. With the seamless integration the X-ray, electron and optical characterization, the goal is to achieve a complete understanding of the lithiation dynamics at the single-particle length scale.

Results

While many oxygen-redox-active materials have been developed, they almost universally exhibit a host of irreversible electrochemical behaviors such as voltage hysteresis and voltage fade. This is most notable in the anion-redox-active Li-rich layered oxides, $\text{Li}_{1+x}\text{M}_{1-x}\text{O}_2$, which exhibit capacities approaching 300 mAh g^{-1} but have yet to achieve commercial success due to such electrochemical behavior. It was recently proposed that these properties arise from a coupling between the oxidation of oxygen and the migration of M into Li sites – a widely observed phenomenon – creating structural disorder in the form of $\text{M}_{\text{Li}}/\text{V}_{\text{M}}$ antisite/cation vacancy defect pairs and an associated loss of in-plane honeycomb-like transition-metal (TM) ordering. However, the two main mechanistic models for oxygen redox, describing the nature of the oxidized oxygen species as either a $\sim 2.4 \text{ \AA}$ peroxo-like O_2^{n-} dimer or an isolated O^- anion, do not directly explain this coupling. As such, a robust understanding of the materials design criteria for achieving reversible anion redox remains elusive. In approaching this issue, we turn to layered Li_2IrO_3 (equivalently, $\text{Li}[\text{Li}_{0.33}\text{Ir}_{0.67}]\text{O}_2$ or LIO) as a model system which is reported to exhibit anion redox, yet, unlike other Li-rich layered oxides, exhibits highly reversible structural and electrochemical behavior during cycling.

LIO exhibits two well-defined voltage plateaus with average potentials of 3.45 V and 4.15 V versus Li/Li^+ and a capacity of $1.5e^-$ per Ir for several cycles without noticeable capacity or voltage fade (Figure II.5.F.1a). High-resolution synchrotron X-ray diffraction (XRD) shows two consecutive, completely reversible two-phase reactions. Rietveld refinement shows that pristine LIO exhibits a typical layered structure with monoclinic $C2/m$ symmetry, with the Li and TMs in the TM layers ordered into a honeycomb-like arrangement, and accommodates delithiation through changes in the stacking of the TM layers. We find that LIO changes from O3 to T3 to O1 stacking at the Li_2IrO_3 , Li_1IrO_3 , and $\text{Li}_{0.5}\text{IrO}_3$ compositions, respectively.

To quantify the cation vacancy/antisite formation during electrochemical cycling, we employed an iterative approach to simultaneously refine the in-plane and out-of-plane site disorder. This approach eliminates the difficulty in site occupancy determination resulting from the presence of stacking faults. We confirm the absence of $\text{V}_{\text{Ir}}/\text{Ir}_{\text{Li}}$ defects ($\leq 0.1 \pm 0.2\%$ of all Li sites occupied by Ir) in the discharged state both before and after the first electrochemical cycle. Out-of-plane refinement shows negligible Ir occupancy in the Li layer in the fully charged state. These results show why LIO exhibits reversible electrochemistry: minimal cation disordering occurs during cycling. This is unlike all other Li-rich materials in which anion redox is reported to occur.

To gain further insight into the bulk redox mechanism of LIO, we perform *operando* transmission X-ray absorption near edge structure (XANES) measurements at the Ir L_3 edge (Figure II.5.F.1b). Throughout the first galvanostatic charge and discharge, the white line (WL) energy increases and decreases linearly (Figure II.5.F.1c), nearly returning to its original value at the end of discharge. This is in striking contrast to the behavior of most anion redox active Li-rich oxides whose TM ions either stop being oxidized or are even reduced during the high voltage plateau. Principle component analysis and non-negative matrix factorization of the XANES spectra reveal the presence of three spectral end members corresponding to the Li_2IrO_3 , Li_1IrO_3 ,

and $\text{Li}_{0.5}\text{IrO}_3$ compositions, consistent with the two isosbestic points marked in Figure II.5.F.1b. A linear combination analysis using these end members confirms that the entire spectral evolution is well described by two consecutive two-phase reactions. The total shift in the Ir L_3 WL energy (1.2 eV) is consistent with Ir being oxidized by $\sim 1.5 e^-$, accounting for the entire capacity and strongly suggesting that LIO exhibits only cationic Ir redox.

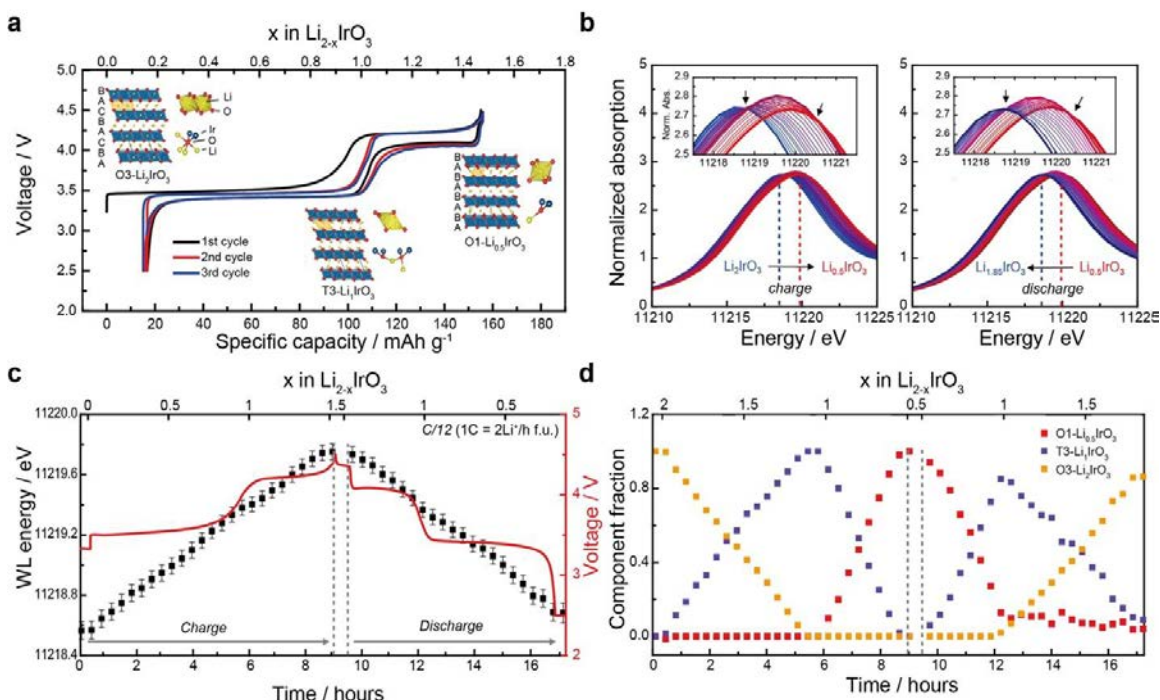


Figure II.5.F.1 **Reversible redox and phase behavior of $\text{Li}_{2-x}\text{IrO}_3$.** (a) Capacity-voltage curves of $\text{Li}_{2-x}\text{IrO}_3$ galvanostatically measured at a $C/12$ rate (17.58 mA g^{-1}) in 4.50–2.50 V for the initial three cycles and the stable phases during the two consecutive two-phase reactions of $\text{Li}_{2-x}\text{IrO}_3$ occurring at each voltage plateau obtained by combined XRD Rietveld refinements and DFT calculations. (b) Operando transmission XANES spectra of Ir L_3 edge for charging (left) and discharging (right) with two isosbestic points (arrows in insets). (c) Shift of the white line energy showing the continuous oxidation/reduction of iridium throughout the whole charge/discharge processes. Error (see methods) was determined to be reasonably small. (d) Linear combination analysis of the three end-members obtained through NMF, consistent with the phase behavior.

To directly assess the contribution of bulk O to the LIO redox mechanism, we perform soft X-ray absorption spectroscopy (sXAS) at the O K edge of LIO. Transmission and fluorescence yield (FY) detection modes with probing depths of hundreds of nm were employed (see methods). Figure II.5.F.2a shows the O K edge sXAS-FY and transmission sXAS spectra of LIO during the first electrochemical cycle. The peaks at $\sim 529 \text{ eV}$ and 532 eV are ascribed to the unoccupied Ir $5d\text{-O } 2p t_{2g}$ and e_g^* hybridized states, respectively. The difference plots taken between different states of charge (Figure II.5.F.2b) clearly show that the intensity of the t_{2g} peak increases and decreases throughout charge and discharge, mirroring the evolution of the Ir L_3 WL (Figure II.5.F.1c). Figure II.5.F.2c shows that the integrated area ratio of the two O K XAS pre-edge peaks follows the same trend in transmission sXAS, which probes the entirety of the particles, confirming that this is a bulk phenomenon. The correlated changes at the O K and Ir L_3 edges indicate redox of a hybridized Ir–O state, and are widely accepted as a fingerprint of conventional “TM–O” cation redox.

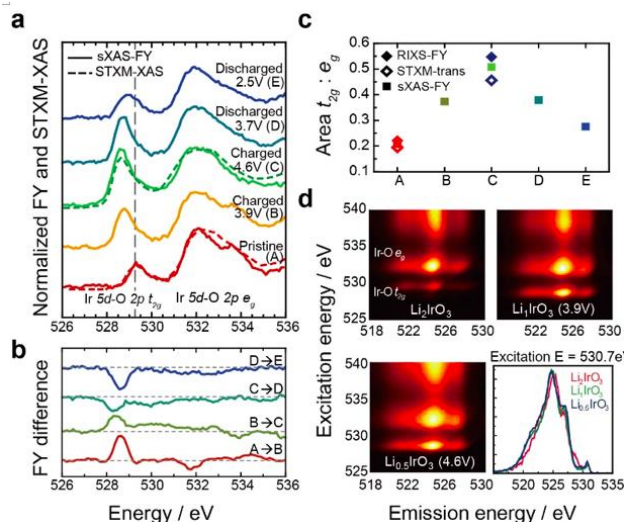


Figure II.5.F.2 **Hybridized Ir-O redox in $\text{Li}_{2-x}\text{IrO}_3$.** (a) sXAS fluorescence yield spectra (solid lines) and STXM (scanning transmission X-ray microscopy)-XAS spectra (dashed lines) of O K edge of $\text{Li}_{2-x}\text{IrO}_3$ at various states of charge in the first cycle. From bottom to top, pristine (red, A), charged to 3.9 V (yellow, B), charged to 4.6 V (green, C), discharged to 3.7 V after being charged to 4.6 V (olive, D), discharged to 2.5 V after being charged to 4.6 V (blue, E). (b) Difference plot of sXAS obtained from A showing the hole population evolution of Ir 5d-O 2p t_{2g} and e_g^* hybridized state. (c) Ratio of the area of Ir 5d-O 2p t_{2g} peak and Ir 5d-O 2p e_g^* peak measured by RIXS, STXM and sXAS. (d) O K edge RIXS maps of Li_2IrO_3 , Li_1IrO_3 and $\text{Li}_{0.5}\text{IrO}_3$ showing conventional Ir-O cationic redox. The right bottom panel shows the RIXS spectra of each composition at 530.7 eV excitation energy where the anion redox feature is expected to appear.

When Sn is substituted into Li_2IrO_3 to make solid-solution phase $\text{Li}_2\text{Ir}_{1-y}\text{Sn}_y\text{O}_3$, the electrochemistry changes dramatically and becomes typical of that of anion redox active materials (Figure II.5.F.1a). Regardless of Sn content, when charged beyond Ir5.5+, LISO exhibits a new plateau at ~ 4.35 V, followed by a large voltage drop on the subsequent discharge, a permanently sloped voltage profile, and voltage hysteresis that persists even at open circuit. Despite the drastic changes to the voltage profile, LISO25 exhibits reasonable capacity retention with cycling (74.5% after 192 cycles). The new high voltage plateau, in conjunction with the additional reversible capacity well beyond 1.5 e- per Ir (Figure II.5.F.1a), indicates the presence of a reversible redox partner beyond Ir4+/Ir5.5+.

In addition to this high-voltage redox partner, the average and local structural behavior of LISO differs from that of Sn-free LIO as reported in 2018Q2. Substantial degree of cation site disorder develops in LISO after first delithiation. Figure II.5.F.3b quantifies the extent of site disorder in LISO25 before and after electrochemical cycling with either a 4.25 or 4.60 V cutoff. As shown schematically in Figure II.5.F.1b, we assume that each in-plane and out-of-plane antisite defect results in a corresponding vacant M site. We therefore quantify the total amount of disorder by the fraction of VM, which reaches between $7.5 \pm 0.4\%$ (assuming all Ir_{Li}) and $10.2 \pm 0.6\%$ (assuming all Sn_{Li}) after a single cycle between 4.60-2.50 V, approximately evenly split between in-plane and out-of-plane antisite defects (since low concentrations of Sn_{Li} and Ir_{Li} have an identical effect on the Bragg peak intensity, XRD cannot be used to differentiate between the migrating species). This translates to at least 40.8% of Sn having migrated in fully charged LISO assuming all Sn_{Li} . Since the total accessed capacity is approximately the same between LIO and the various LISO compositions, by substituting with Sn we can conclude that the structural disordering is not due to inherent structural instability at low lithium contents. Furthermore, the disordering appears to be associated with the new redox partner giving rise to the high voltage plateau: the disorder in LISO25 after a full cycle is dramatically greater than in both LIO after the first cycle and LISO25 after a single cycle between 4.25-2.50 V, which are both zero within experimental error. Out-of-plane refinement of the fully charged O1 structure shows that the disorder is

increased substantially at 4.60 V providing a direct connection between the new redox partner, electrochemical irreversibility, and the onset of cation disordering.

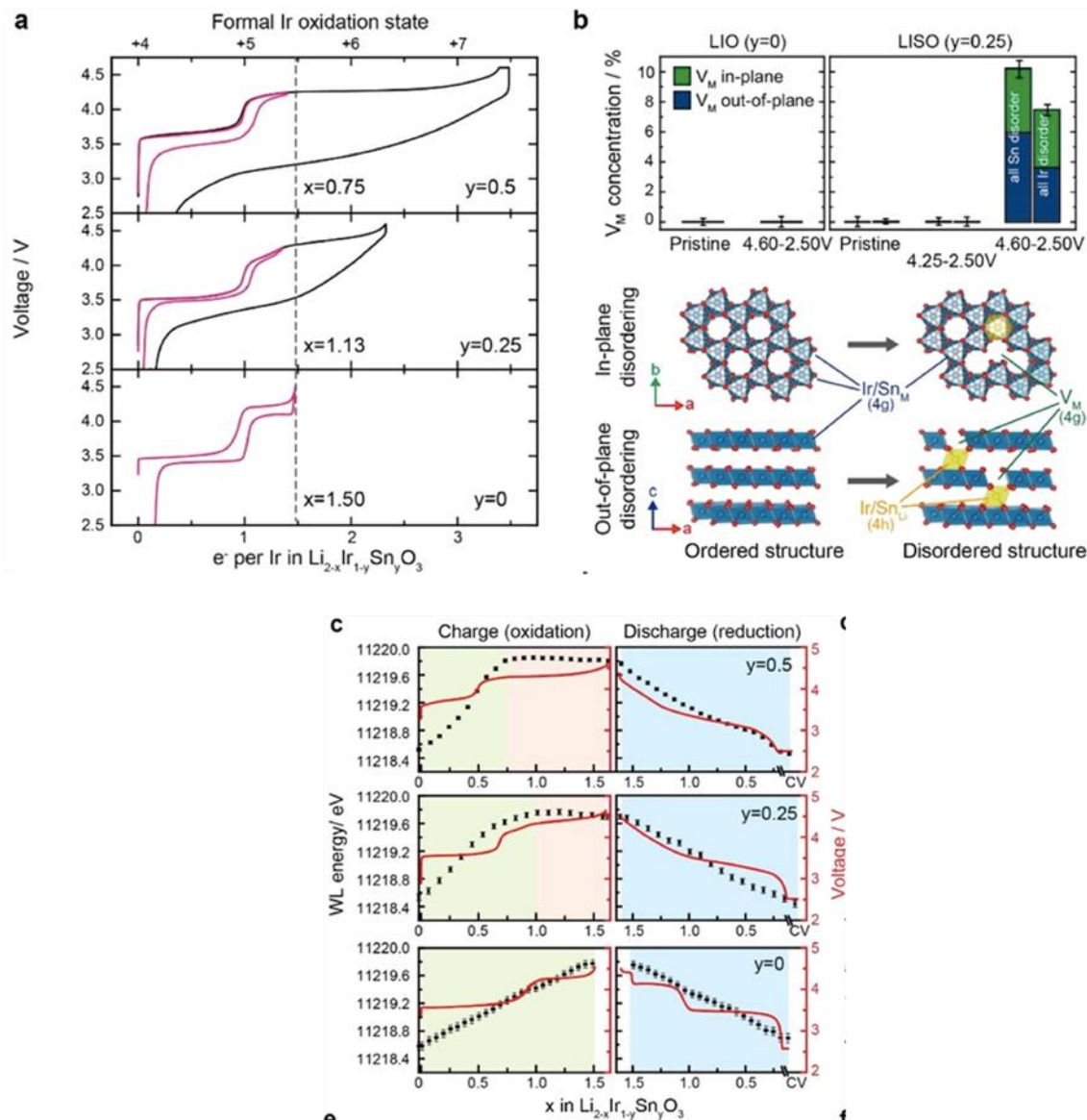


Figure II.5.F.3 (a) Charge/discharge profiles of $\text{Li}_{2-x}\text{Ir}_{1-y}\text{Sn}_y\text{O}_3$ ($y=0, 0.25, 0.5$) under a constant current density ($C/10$ rate) for a full cycle (black) and for an approximately 1.5 electron per Ir per f.u. cycle (pink). (b) In-plane and out-of-plane disordering mechanisms and quantification of V_M concentration. The scheme illustrates the in-plane (top) and out-of-plane (bottom) structural disordering mechanisms resulting in V_M , with the migrated cation octahedron shaded yellow and the Wyckoff positions indicated in parentheses. (c) Operando transmission XANES spectra of Ir L3 edge for the first cycle showing the continuous Ir oxidation up to 4.25 V, no shift beyond 4.25 V, and the continuous Ir reduction during discharge.

Conclusions

Oxygen anion redox has garnered intense interest for such applications, particularly lithium ion batteries, as it offers substantial redox capacity at > 4 V vs. Li/Li^+ in a variety of oxide materials. However, oxidation of oxygen is almost universally correlated with irreversible local structural transformations, voltage hysteresis, and voltage fade, which currently preclude its widespread use. By comprehensively studying the $\text{Li}_{2-x}\text{Ir}_1\text{O}_3$.

$y\text{Sn}_y\text{O}_3$ model system, which exhibits tunable oxidation state and structural evolution with y upon cycling, we reveal that this structure-redox coupling arises during oxygen redox, which occurs in $\text{Li}_{2-x}\text{Ir}_{1-y}\text{Sn}_y\text{O}_3$ through ligand-to-metal charge transfer. Crucially, formation of these oxidized oxygen species necessitates the decoordination of oxygen to a single covalent bonding partner through formation of vacancies at neighboring cation sites, driving cation disorder. These insights establish a point defect explanation for why anion redox often occurs alongside local structural disordering and voltage hysteresis during cycling. Our findings offer an explanation for the unique electrochemical properties of lithium-rich layered oxides, with implications generally for the design of materials employing oxygen redox chemistry.

Key Publications

J. Hong, W. E. Gent, P. Xiao, K. Lim, D.-H. Seo, J. Wu, P. M. Csernica, C. J. Takacs, D. Nordlund, C.-J. Sun, K. H. Stone, W. Yang, D. Prendergast, G. Ceder, M. F. Toney, W. C. Chueh. Metal-Oxygen Decoordination Stabilizes Anion Redox in Li-rich Oxides. *Nature Mater.* (2018).

II.5.G *In situ* Diagnostics of Coupled Electrochemical-Mechanical Properties of Solid Electrolyte Interphases on Lithium Metal for Rechargeable Batteries (General Motors)

Xingcheng Xiao, Principal Investigator

General Motors Research and Development Center
30470 Harley Earl Blvd.
Warren, MI 48092-2031
E-mail: xingcheng.xiao@gm.com

Tien Duong, DOE Technology Development Manager

U.S. Department of Energy
E-mail: Tien.Duong@ee.doe.gov

Start Date: October 1, 2016

End Date: September 30, 2019

Project Funding: \$580,174

DOE share: \$464,139

Non-DOE share: \$116,035

Project Introduction

Lithium (Li) metal-based batteries, including Li-air, Li sulfur batteries, and solid-state batteries, are among the most promising candidates of high energy density batteries, due to their ultrahigh capacity (3860 mAh g⁻¹), lowest reduction potential (~3.04 V vs. S.H.E), and low density (0.534 g cm⁻³). However, Li typically goes through large volume expansion and contraction during stripping/plating processes, leading to coupled mechanical/chemical degradation at multiple length scales, including the formation of mossy structures and dendrite growth. The mossy structure leads to low cycle efficiency due to the continuous decomposition of electrolyte. Dendrite formation leads to current shortage and sometime catastrophic failure. Both failures are initiated from the damage of the solid electrolyte interphase (SEI).

The fundamental understanding of the coupled mechanical/chemical degradation of the SEI layer during lithium cycling will enable the project to identify the desirable mechanical properties on SEI/lithium as a system and the specific transport properties that enable the homogenous lithium stripping/plating while avoiding the mossy structure. Furthermore, it will allow the project to develop a highly impactful strategy to protect lithium metal and achieve dendrite-free high cycle efficiency, which can dramatically increase the energy density of lithium batteries for EV applications.

Objectives

The project objective is to develop a comprehensive set of *in situ* diagnostic techniques combined with atomic/continuum modeling schemes to investigate and understand the coupled mechanical/chemical degradation of the SEI layer/lithium system during lithium cycling. The goal of this understanding is to develop a new coating design strategy to achieve high cycle efficiency/dendrite free and extend the cycle life of high-energy-density batteries with lithium as the anode for EV application.

Approach

Different *in situ* techniques, including AFM, nano-indentor, dilatometer, and stress-sensor, will be developed to investigate the mechanical compatibility between SEI and soft lithium and the relationship between surface morphology and current density distribution that results in an inhomogeneous lithium plating/stripping process. Multiple strategies will be developed to tailor the mechanical and transport properties of SEI and to properly engineer the protective coating/lithium interface.

Results

During the past year, we have further developed a comprehensive set of in-situ diagnostic tools and investigated the coupled mechanical/electrochemical behaviors of SEI/Li during striping/plating processes.

Based on that, we have gained fundamental understanding of coupled mechanical/chemical degradation of the SEI layer and Li metal electrode and developed a variety of Li protection strategies to achieve high cycle efficiency/dendrite free electrode.

Stress evaluation during Li plating and stripping

Stresses have been known to play a crucial role in affecting the evolution of the structure of Li metal electrodes upon electrochemical cycling. It has been shown that externally applied pressure can strongly affect the Li plating morphology, propensity for Li dendrite formation, and Li cycle-ability. At an applied pressure lower than a critical value, highly porous, needle like, and irregularly shape Li deposits would form after electrochemical cycling. Our studies indicated that compressive stress is heavily accompanied by Li plating on Au current collector (shown in Figure II.5.G.1 a.), as measured by in-situ multibeam optical stress sensor (MOSS). We believe this behavior was due to the messy SEI layer, composed of electrolyte decomposition products, dead Li, and porosity, which dominates the stress response during the cycling process.

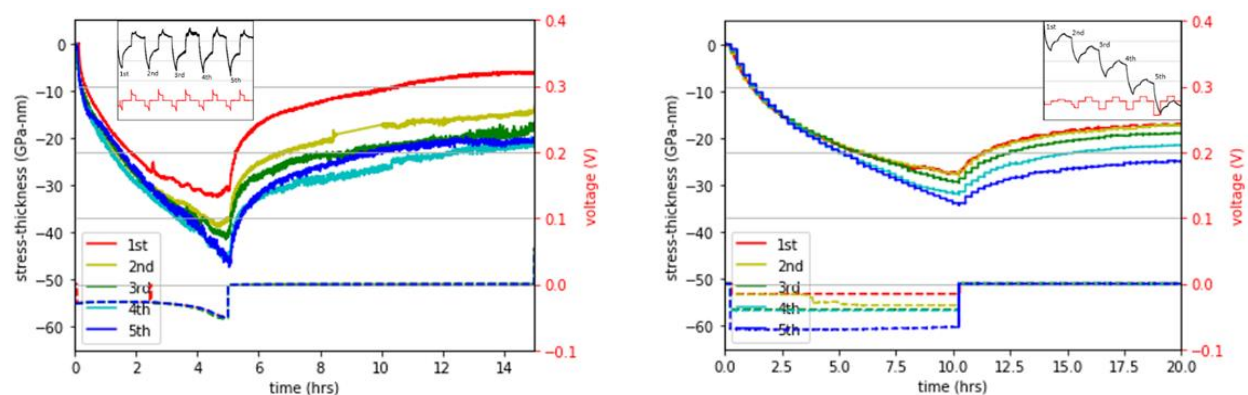


Figure II.5.G.1 Stress-thickness response during plating sequence and OCV hold of 5 consecutive symmetric cycles. a: -265uA/cm² for 5hrs; b: -265uA/cm² for 10hrs.

To validate this claim, we further designed experiments performed in asymmetric cycles; By doubling the current density during plating sequence compared to the stripping sequence for the same number of hours, Au current collector continuously increased thickness of plated Li as the cycles continued. This study would confirm which factor dominates the stress-thickness response. If the mechanical behavior of the system was largely dominated by plated Li metal, the stress-thickness change would be proportional to the increasing Li thickness. Conversely, stress-thickness change would not show much variance if the multi-phase SEI was the main contribution to the mechanics of the system.

Stress measurement on uniformly deposited Li under asymmetric cycling reveals that the in-plane compressive stress built up during Li plating is not mainly contributed from the deposited Li metal. To interpret the origin of the plating-induced stress, a porous structure of SEI with multiple types of conductive paths that Li atoms can flow into was proposed, as shown in Figure II.5.G.2.

To simplify the analysis, only the conductive paths that connect to the top surface of the Li metal have been considered due to their accessibility to the electrons from the Li metal side, as shown in Figure II.5.G.2. The SEI is assumed to be fully passivated and thus have a constant thickness H . The average distance between the conductive paths is set to L . During plating, Li atoms on the Li metal surface flow into the conductive paths due to the difference in chemical potential, creating compressive stress in the SEI layer.

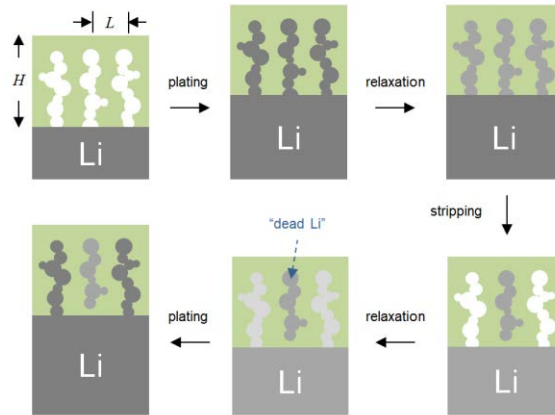


Figure II.5.G.2 Schematic of Li flow between the conductive paths and Li metal surface during plating/stripping cycles.

A kinetic model based on the aforementioned mechanisms have been developed, inspired by a model for stress generation during thin film growth [1]. The stress evolution during each plating, OCV hold, or stripping process takes the following form,

$$\sigma(t) = \left(\sigma_i + \frac{\Delta\mu}{\Omega} \right) \exp \left[-C_s \Gamma \frac{E\alpha\Omega^2}{(1-\nu)HL^2kT} \cdot t \right] - \frac{\Delta\mu}{\Omega} \quad (1)$$

where σ_i represents the initial stress, $\Delta\mu$ the chemical potential difference between the Li surface and conductive path, C_s the concentration of mobile Li on the surface, Γ the transition rate between the surface and the conductive path, α a geometric shape factor, Ω , E and ν the atomic volume, Young's modulus and Poisson's ratio of Li, respectively, κ the Boltzmann constant, T the temperature.

With parameters calibrated from the experimental data, the kinetic model predicts the stress-thickness evolution as plotted in Figure II.5.G.3, which is in good agreement with the results from the stress measurements. This model can account for the build-up of the compressive/tensile stress during plating/stripping, the observed stress relaxation during OCV hold, as well as the decrease in the magnitude of the stress variation during cycling, which supports the conclusion that the main contribution of the induced stress during Li plating is from SEI, rather than Li metal.

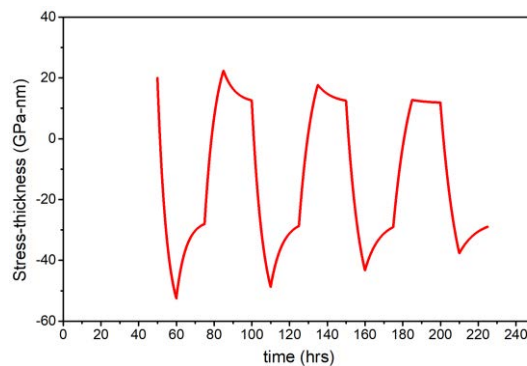


Figure II.5.G.3 Stress-thickness evolution predicted from the kinetic model.

Impact Stress on SEI Mechanical Stability

The stress measurements on Li plating/stripping also revealed that the magnitude of stress×thickness of the deposited Li film increases at the beginning of Li plating, followed by an abnormal small drop, and then increased again until the end of Li plating. As an attempt to understand this stress×thickness drop, an SEI

wrinkling mechanism was considered, in which a finite element model of an SEI layer on a Li thin film was built to simulate the cycling of Li plating/stripping (Figure II.5.G.4). In this model, the SEI was assumed to have a compressive stress of 2 GPa before Li plating, based on the observed compressive stress of ~ 1 GPa in the SEI layer on carbon electrodes during SEI formation and Li was assumed to be elastic and perfectly plastic experiencing isotropic volume expansion/shrinkage during Li plating/stripping. The Young's modulus and yield stress of Li metal were taken to be 3.5 GPa and 100 MPa, respectively. The SEI modulus was assumed to be 10 GPa. The bottom of the Li film was fixed and periodic boundary conditions were imposed on both sides of the simulation box. SEI remained flat at the beginning of the first Li plating half-cycle (Figure II.5.G.4a), but wrinkled as extensive plastic deformation occurred in the growing Li (Figure II.5.G.4b). Subsequently, during the first Li stripping half-cycle, SEI became wrinkled as the Li thickness shrank (Figure II.5.G.4c). The stress \times thickness response of the SEI/Li film calculated in the simulation was plotted in Figure II.5.G.4d. The drop in the magnitude of the stress \times thickness during the first Li plating half-cycle due to SEI wrinkling was similar to what was observed in MOSS measurements. However, the stress \times thickness drop did not appear in subsequent cycles. Direct evidence of SEI wrinkling on Li metal is required to support this proposed mechanism.

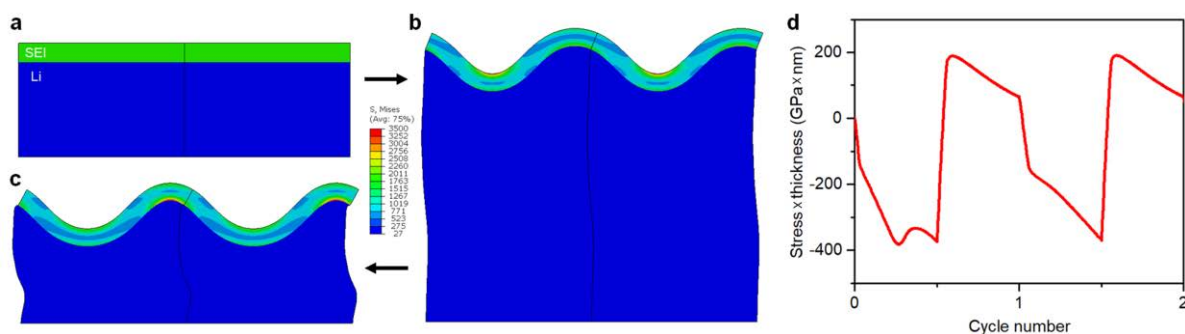


Figure II.5.G.4 (a-c) Finite element modeling of morphological evolution of SEI on Li metal anode (a) before 1st Li plating half-cycle; (b) after the 1st Li plating half-cycle; (c) after the 1st Li stripping half-cycle. (d) Stress \times thickness response of the SEI

A “wrinkling-to-ratcheting-to-delamination” failure mechanism of thin film coatings as artificial SEI layer on Li metal

In continuation of our previous studies on the wrinkling of a thin film protective coating on a Li metal electrode, a “wrinkling-to-ratcheting-to-delamination” failure mode was proposed and an analytical model was developed to predict the design space for a mechanically stable coating that prevents interfacial delamination. In this model, the coating wrinkles during the first Li deposition as the coating process induces a compressive stress in the coating. Thereafter, extensive plastic flow occurs in Li during cyclic Li deposition and stripping, leading to plastic ratcheting in the coating/Li system, which results in an accumulative increase of the amplitude of the wrinkled coating and thus increasing strain energy stored in the coating. After enough cycles, the delamination of the coating from its underlying Li metal becomes energetically favorable and occurs as the delamination energy release rate exceeds the interfacial toughness, which is detrimental to the battery performance due to the increased impedance through the loss of contact between the coating (as an artificial SEI layer) and Li electrode.

The analytical model predicted a phase diagram of the failure mode with respect to the modulus and compressive stress of the coating normalized by the yield stress of Li (Figure II.5.G.5). The compositional strain in Li, normalized interfacial toughness and elastic limit of the coating were assumed to be 100%, 0.1 and 0.3%, respectively. The orange line and red line in Figure 1 correspond to the predicted critical conditions for wrinkling and delamination, respectively. These two critical lines divide the phase diagram into three regions, representing three behaviors of the coating: no wrinkling, wrinkling, and wrinkling-induced interfacial delamination. The diagram affords a design space for a mechanically stable protective coating on Li metal. To

avoid delamination, the coating should have a moderate modulus, low compressive stress, high interfacial toughness and low thickness.

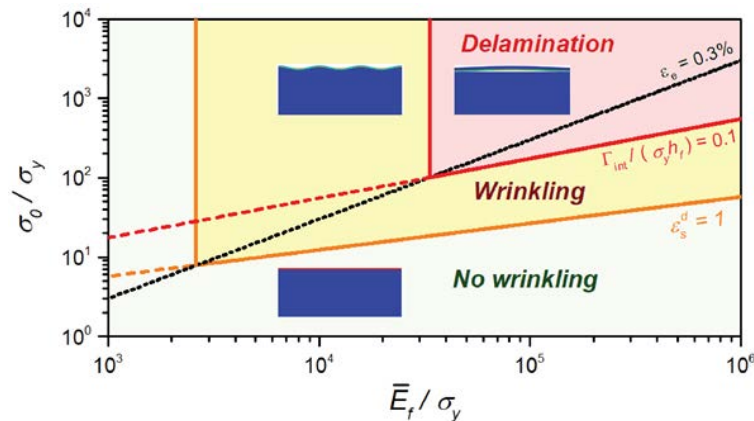


Figure II.5.G.5 A phase diagram of wrinkling and delamination of a thin film protective coating on a Li metal electrode.

Effects of Pressure on Li plating and stripping

Effects of stress on the formation of Li dendrites during long-term storage at room temperature have been investigated using nanoindentation. Indents were made on the surface of Li foils to induce stress as well as damage to the naturally formed SEI. Finite element modeling was used to obtain maximum stress and stress distribution beneath the indent, as shown in Figure II.5.G.6 (a). Li atoms may concentrate and form dendrites in areas with high compressive stress since the stress gradient will drive the diffusion of Li atoms to release the stress. Unlike Sn alloys, no Li dendrite was formed around or inside indents after storing the Li foil at room temperature (25°C) for 30 days, as shown in Figure II.5.G.6 (b). A possible explanation is that the stress gradient is not high enough to drive the diffusion of enough Li atoms to form dendrites since Li has very low yield strength and high creep tendency. Therefore, internal stress and interfacial stress (at Li/SEI) is unlikely a reason for the growth of Li dendrites.

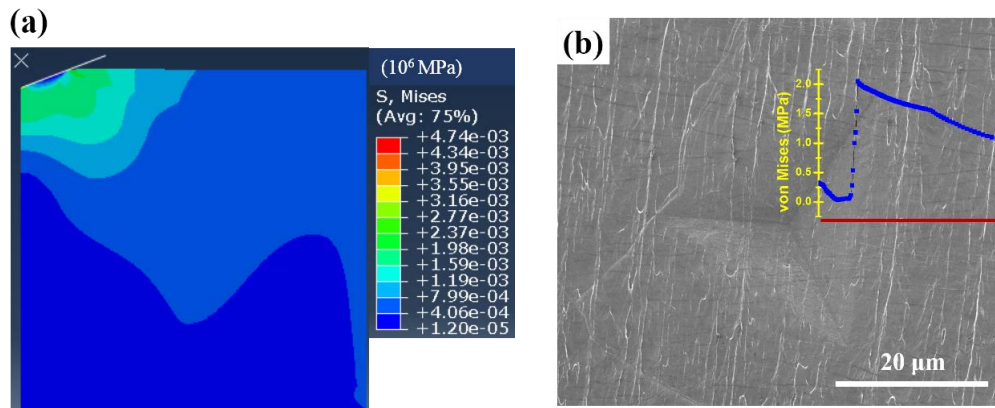


Figure II.5.G.6 (a) The distribution of von Mises stress in bulk Li after nanoindentation. (b) Microstructure of an indent in a Li foil after it is stored inside an Ar-filled glovebox for 30 days at room temperature. The insert shows the stress distribution on Li surface along the red line direction.

The influence of pressure on the morphology of Li dendrites has been studied by using Swagelock cells.

As shown in Figure II.5.G.7 (a), the pressure applied on Li metal electrodes is controlled by the compression deformation of the spring. Table II.5.G.1 shows that mossy Li plated under high pressure (~19.39 MPa) has lower porosity than that under low pressure (~4.85 MPa). Li dendrites plated under low pressure have needle-like shape. In contrast, round Li chunks form under high pressure, as shown in Figure II.5.G.7 (b) and (c). Two possible reasons may explain this phenomenon. (1) Thermodynamic, that is, the external pressure may

influence the thermodynamics in Li ion diffusion, nucleation rate, growth rate and their competition of Li dendrites. (2) Current density distribution. Li metal electrodes can be easily deformed. Under high pressure, they become more smooth and flat and the current density distribution would be more homogeneous than those under high pressure. Nanoindentation measurements with a flat punch indicate that the penetration depth of mossy Li at the maximum depth is about the same with bulk Li, but the creep displacement of mossy Li during the holding period is much smaller than that of bulk Li. In addition, the creep displacement of mossy Li plated under high pressure is about half of that plated under low pressure, which partially results from their difference in porosity. Further studies will be focused on understanding the role of pressure in the morphology of mossy Li and investigating the influence of pressure on the cycling life of Li metal electrodes in half cell and full cell configurations.

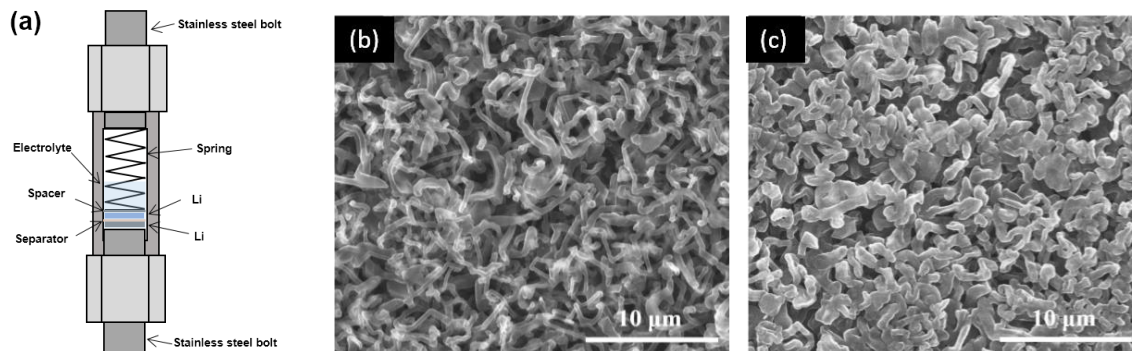


Figure II.5.G.7 (a) The schematic diagram of a Swagelok cell. Microstructure of mossy Li plated under (b) 4.85 MPa and (c) 19.39 MPa.

Surface compositions of Li electrodes cycled in four different electrolytes were analyzed with XPS.

To avoid air exposure, sample electrodes were stored in glove box and transferred to XPS and TOF-SIMS analysis chambers with respective special vessels. Same analyzing and sputtering parameters were applied to these samples. XPS analyzing region has a diameter of 250 μm and sputtering region has a diameter of 1250 μm . In raw data, C-C peak at 285 eV may shift to a higher binding energy in some samples. Spectra curves shown later are calibrated based on the C-C peak at 285 eV. Figure II.5.G.8 shows the XPS depth profiling spectra (Li_{1s} , C_{1s} , O_{1s} , F_{1s} , N_{1s} , S_{2p}) of Li electrodes after the first plating (0.5 mAcm^{-2} , 4 mAhcm^{-2}) in four different electrolytes. For the SEI formed in the 4 M LiFSI DME electrolyte, Li_2CO_3 , LiOH, LiF, Li_3N , Li_2S are present on the surface. S 2p spectra indicates that the amount of Li_2S increases with the sputtering depth, reaching peak value after about 6 mins. Li 1s and O 1s spectra show a small amount of Li_2O is on the surface and its concentration increases and becomes stable after about 6 mins of sputtering. On the contrary, F 1s spectra shows LiF is distributing through the SEI and its concentration decreases gradually. Similar phenomenon applies to Li_2CO_3 , LiOH, Li_3N and organic species such as RCOOLi, ROCO_2Li . For the SEI formed in the 0.4 M LiTFSI + 0.6 M LiNO_3 DOL-DME electrolyte, Li_2S only exists in the outer part of it and only a small amount of $\text{Li}_x\text{S}_y\text{O}_z$ species exist in the inner part. Other components have similar depth profiles compared with those formed in the 4 M LiFSI DME electrolyte. For the SEI formed in the 1 M LiTFSI DOL-DME electrolyte, learned from C 1s, F_{1s} , N_{1s} and S_{2p} spectra, its surface layer contains some amount of LiTFSI salt because Li_3N , Li_2S , $\text{Li}_x\text{S}_y\text{O}_z$ are decomposition products of LiTFSI. Residual LiTFSI disappeared after 30s of sputtering. The sputtering interval is 30s in this work. That means residual LiTFSI exists on the surface only. Other inorganic compounds on the surface include Li_2CO_3 , LiOH and LiF with decreasing concentrations and Li_2O with increasing concentration. For the SEI formed in the 1 M LiPF_6 EC-DEC electrolyte, Li_2CO_3 , LiOH, LiF and Li_2O are present on the surface. The concentration of Li_2O increases with sputtering depth. While other components have decreasing concentrations.

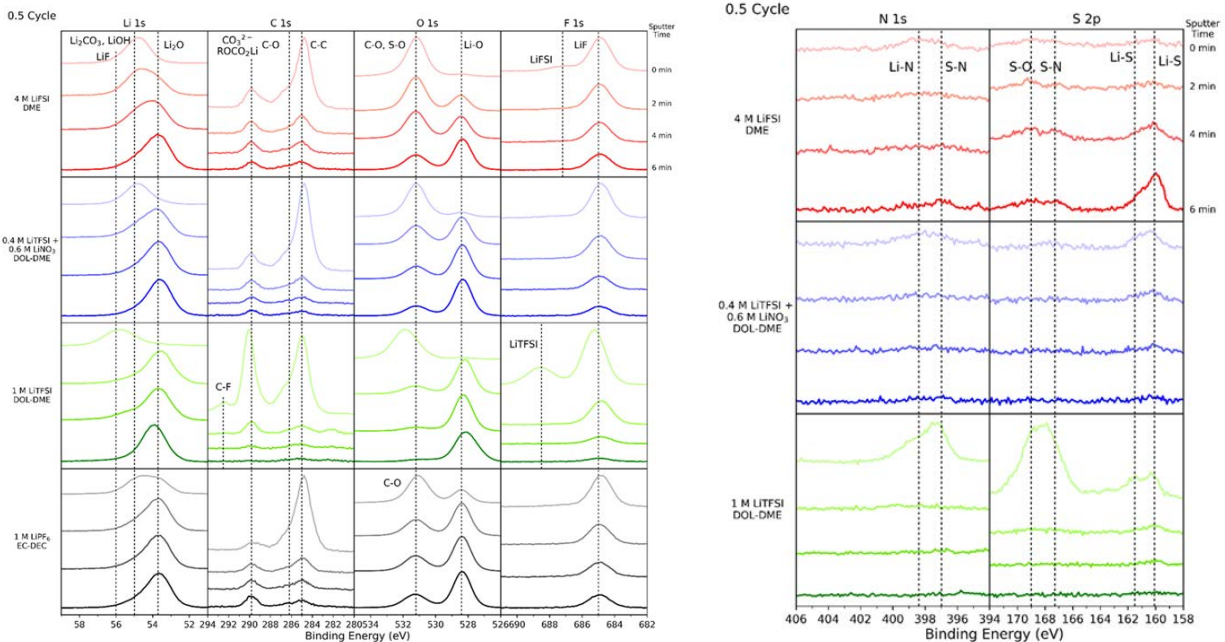


Figure II.5.G.8 XPS depth profiling spectra of plated Li surfaces after a half cycle (0.5 mA cm⁻², 4 mAh cm⁻²) in 4 different electrolytes (4 M LiFSI DME, 0.4 M LiTFSI + 0.6 M LiNO₃ DOL-DME, 1 M LiTFSI DOL-DME, and 1 M LiPF₆ EC-DEC)

Interface adhesion energy calculations at Li/Li₂CO₃, Li/LiF interfaces and predict where interface delamination will occur.

Based on the surface energy results and construction rules elaborated in the method section, two LiF/Li and two Li₂CO₃/Li interfaces were constructed. Since Li is rather isotropic, the two lowest energy surfaces, (001) and (110), are both considered in the interface model. On the other hand, LiF and Li₂CO₃ are rather anisotropic, only the orientations with the lowest surface energy were considered. The interfacial mismatches are less than ~3% for all interface supercells, and the strain energy contribution to the total interface formation energy is small (less than 3%, except one interface). Both Li/Li₂CO₃ and Li/LiF interfaces have relatively small work of adhesion. The work of adhesion at the interface is also lower than the decohesion energy of each phase, indicating interface delamination will occur under tensile stress.

Table II.5.G.1 DFT calculated energetics for different fully-relaxed interfacial supercells in comparison with the fracture energy of the bulk materials.

	Li(001)/ Li ₂ CO ₃ (001)	Li(110)/ Li ₂ CO ₃ (001)	Li(001)/ LiF(001)	Li(110)/ LiF(001)
Interfacial Energy (J/m²)	0.498	0.573	0.747	0.803
Work of Adhesion (J/m²)	0.167	0.124	0.093	0.065
Strain Energy (mJ/m³)	52.711	6.248	16.342	1.121
Strain Energy Contribution (%)	11.73%	1.32%	2.99%	0.23%
Decoherence energy of each phase (J/m²)	Li(001) 0.96	Li(001) 1.02	Li(001) 0.96	Li(001) 1.02
	Li ₂ CO ₃ (001) 0.36		LiF(001) 0.72	

Li plating kinetics at a Li/single-component SEI/electrolyte interface.

The first step to determine the Li-plating kinetics is to determine the electrochemical equilibrium, which changes in the different electrolyte. The half reaction at the Li/SEI/electrolyte interface can be written as



where the Li^+ ions dissolved in the electrolyte are reduced by the electrons, e^- , on the electrode to produce the Li^0 atoms depositing to the Li-metal electrode (forwarding reaction). The thermodynamic driving force is given by

$$\Delta G = \Delta G^0 + F\phi - RT \ln a_{Li^+} \quad (3)$$

where ΔG^0 is the standard free energy change for the electrode reaction (1) on a zero charged Li-metal, F is the Faraday constant. ϕ is the Galvani potential on the Li-metal electrode (assuming the potential in the electrolyte to be the zero). a_{Li^+} is the activity of Li^+ in the electrolyte, which depends on temperature, solvent, and the concentrations of ions. At the electrochemical equilibrium, the forward and backward currents are equal, or in other word, the chemical potential of Li^+ in the electrolyte equals to the chemical potential of a reduced Li^0 in the electrode, thus

$$\Delta G = \Delta G^0 + F\phi^0 - RT \ln a_{Li^+} = 0 \quad (4)$$

where ϕ^0 is the equilibrium potential. During the charge or discharge process, the thermodynamic driving force for the reaction can also be expressed as,

$$\Delta G = F(\phi - \phi^0) = F\eta \quad (5)$$

where η is the overpotential. If $\eta < 0$, the Li^+ is reduced (plating); whereas if $\eta > 0$, the Li^0 is being oxidized to Li^+ (stripping). The charge transfer reaction in Eq-1 can be rewritten to include the insulating effect of the SEI layer, assuming Li^+ dissolved in the solvents. One can compute or measure each energy term in the thermodynamic cycle like the following:

$$\Delta G^0 = -E_f(V_{Li}) - E_{vap} - E_{ion} + W_f + E_{sol}(Li^+) \quad (6)$$

Because the solvation energy of Li^+ in EC is 5.5eV, larger than that in DOL (5.06eV), ΔG^0 is 1.26 eV for Li in EC and 0.82eV in DOL. Negative charges must be applied to Li-metal in order reach the electrochemical equilibrium. Assuming $a_{Li^+} \sim 1M$, the equilibrium potential ϕ^0 is -1.26eV for Li in EC and -0.82 in DOL, suggesting the Li metal surface has less excess electron density at $\eta = 0$. This might be the fundamental reason for less SEI growth in ether-based electrolytes.

Fluorine-based polymer coating to protect Li metal electrode.

It has been found that adding FEC into the electrolyte can significantly improve the cycle stability by forming LiF and polymeric matrix in Solid Electrolyte Interphase (SEI). However, FEC is gradually consumed during the long-term cycling process. In addition, the gas generation from the reaction between FEC and Li metal could be a potential issue related with the abuse tolerance. We have developed a simplified process to coat Li metal electrode with fluorine-based polymer coatings. The defluorination will occur once C-F species from the plasma contact with Li, forming LiF nano-sized and carbonaceous polymer matrix immediately. The self-forming nanocomposite coating is conformal and dense, and effectively isolates Li metal from electrolyte (Figure II.5.G.9). The flexibility of the coating can accommodate the volume changes of the electrode. The highly conductivity can make the current distribution uniform to ensure the homogenous Li plating and stripping. The protected Li metal electrodes, combining with high concentration salt electrolyte developed at PNNL show significantly improved cycle stability in symmetrical cells under harsh testing conditions (Figure

II.5.G.10). The further validation will be carried out in large pouch cell paired with high energy NMC or S positive electrodes.

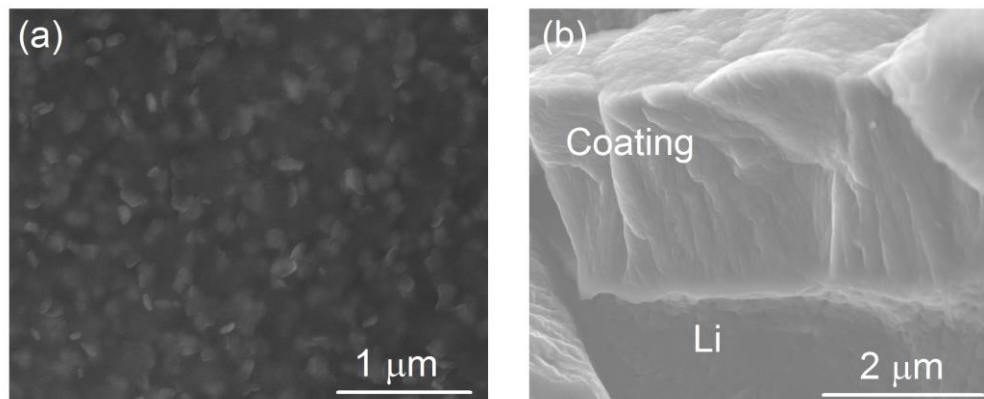


Figure II.5.G.9 Self-forming nanocomposite has a unique nanostructure where LiF nanocrystals embedded in polymeric matrix (a); The cross-section image showing the coating is dense and has good adhesion to Li metal (b).

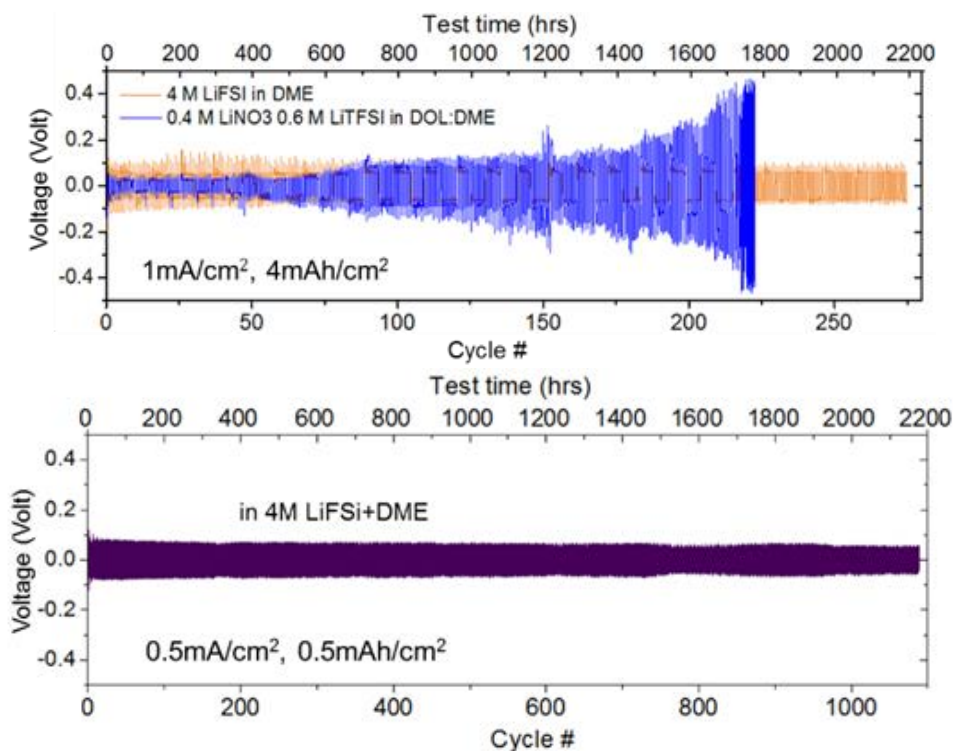


Figure II.5.G.10 The combination of the protective coating with high concentration LiFSi in DME enables the long cycle stability.

Conclusions

Various *in situ* techniques have been developed to understand Li plating/stripping behavior and SEI/Li interface. Possible failure mechanisms of the SEI/Li interface have been studied by electrochemical-mechanical modeling and provides insights into designing mechanically stable SEI layers for Li metal electrodes. Mechanical compatibility, interface strength, dynamic balance between Li diffusion in SEI and Li, and current distribution along the interface must be taken into account for controlling SEI formation or

developing artificial SEI layer. We have demonstrated fluorine-based polymer coatings as the artificial SEI layers can effectively improve the cycle stability of Li metal electrode.

Key Publications

Publications

1. Y. Liu, K. Guo, C. Wang, H. Gao, Wrinkling and ratcheting of a thin film on cyclically deforming plastic substrate: Mechanical instability of the solid-electrolyte interphase in Li-ion batteries, *Journal of the Mechanics and Physics of Solids*, 2018, doi.org/10.1016/j.jmps.2018.08.006..
2. Z Liu, P Lu, Q Zhang, X Xiao, Y Qi, LQ Chen, A Bottom-up Formation Mechanism of Solid Electrolyte Interphase (SEI) Revealed by Isotope-Assisted Time-of-Flight Secondary Ion Mass Spectrometry (TOF SIMS), *J. Phys. Chem. Lett.*, 2018, 9 (18), pp 5508–5514
3. Guo, K., and P. A. Tamirisa, B. W. Sheldon, X. Xiao, and H. Gao. Pop-Up Delamination of Electrodes in Solid-State Batteries. *Journal of The Electrochemical Society*, 2018, 165, A618-A625.
4. Wang, A.P., Kadam, S., Li, H., Shi, S.Q., Qi, Y., Review on Modeling of the Solid Electrolyte Interphase (SEI) for Lithium-Ion Batteries, *npj Computational Materials* 2018, 4, 15 (Invited Review)
5. C. Vinado, S. Wang, Y. Hec, X. Xiao, Y. Li, C. Wang, and J. Yang, Electrochemical and Interfacial Behavior of All Solid State Batteries Using Li₁₀SnP₂S₁₂ Solid Electrolyte, *Journal of Power Sources*, Vol. 396, Page 824-830, 2018.
6. Guo, K., and P. A. Tamirisa, B. W. Sheldon, X. Xiao, and H. Gao. Pop-Up Delamination of Electrodes in Solid-State Batteries. *Journal of The Electrochemical Society*, 165 (2018): A618-A625.
7. Su, X., Guo, K., Ma, T., Tamirisa, P. A., Ye, H., Gao, H., and Sheldon, B. W. Deformation and Chemomechanical Degradation at Solid Electrolyte–Electrode Interfaces. *ACS Energy Letters* 2 (2017): 1729–1733

Patents

1. X. Xiao, Method of Applying Self-forming Artificial Solid Electrolyte Interface(SEI) layer to Stabilize Cycle Stability of Electrode in Lithium Batteries. United States patent application P042557 (8540R-505), August 31, 2017
2. X. Xiao, Protective Coating for Lithium-containing Electrode and Methods of Making the Same. United States patent application P044686 (8540R-539), April 5, 2018
3. X. Xiao, B. Li, H. Gao, K. Guo, Coating system design for Lithium Electrode Protection, P045909, 2018
4. B. Li, X. Xiao, J. Xu, Q. Zhang, Surface treatment of Li metal for rechargeable batteries, P044686, TMS, 2018
5. B. Li, X. Xiao, A Reinforced Siloxane Coating for Lithium Metal Electrodes, P047263, 2018

Presentations

1. Yang-Tse Cheng³, Working towards Making Better and Cheaper Lithium-Ion Batteries,” 35th Annual International Battery Seminar & Exhibition, Fort Lauderdale, Florida, March 26-29, 2018.
2. X. Xiao, Advanced Electrode Materials for Next Generation Lithium Ion Batteries, 35th Annual International Battery Seminar & Exhibition, Fort Lauderdale, Florida, March 26-29, 2018 (Invited Talk)

3. B. W. Sheldon, “Mechanical Degradation and Optimization of Solid Electrolyte Interphases in Li Ion Batteries”, 10th European Solid Mechanics Conference, Bologna, Italy, July 3, 2018.
4. B. W. Sheldon, “Chemo-Mechanical Degradation and Optimization of Solid Electrolyte Interphases in Li Ion Batteries”, ACS National Meeting, Boston, Massachusetts, August 21, 2018.
5. B. W. Sheldon, “Chemo-Mechanical Degradation of Solid Electrolyte Interphases in Li Ion Batteries”, Society of Engineering Science Annual Meeting, Madrid, Spain, October 10, 2018.
6. Yang-Tse Cheng, “In situ mechanical characterization for understanding the coupled electrochemical-mechanical behavior of battery materials,” Detroit Section of the Electrochemical Society, Seminar, Thursday, September 13th, 2018
7. Yikai Wang, Dingying Dang, Ming Wang, Xingcheng Xiao, Yang-Tse Cheng. “Mechanical Behavior of Li Metal Electrodes Studied by Environmental Nanoindentation.” 2018 Beyond Lithium Ion XI, Cleveland, OH, 07/2018 (Poster)
8. X Xiao, J Xu, B Li, Q Zhang, In-Situ Diagnostics of Coupled Electrochemical-Mechanical Failures of Solid Electrolyte Interphases on Lithium Metal for Rechargeable Batteries, 233rd ECS MEETING, May 13-17, 2018, Seattle, WA
9. C Vinado, S Wang, Y Li, X Xiao, J Yang, Electrochemical Properties and Interfacial Behavior of All Solid State Batteries Using Li₁₀SnP₂S₁₂ Solid Electrolyte, 233rd ECS MEETING, May 13-17, 2018, Seattle, WA
10. Y Wang, Q Zhang, D Li, J Hu, J Xu, D Dang, X Xiao, YT Cheng, Mechanical Properties and Microstructure Evolution of Silicon Composite Electrodes, 233rd ECS MEETING, May 13-17, 2018, Seattle, WA
11. X. Xiao, In-situ Diagnostics of Coupled Electrochemical-Mechanical Properties of Solid Electrolyte Interphases on Lithium Metal for Rechargeable Batteries, DoE 2018 Annual Merit Review (AMR), June 18-21, 2018, Arlington, Virginia
12. K. Guo, Ratcheting-induced Deformation and Failure in Li-ion Batteries The 18th U.S. National Congress for Theoretical and Applied Mechanics (USNCTAM), June 8, 2018, Chicago, IL.

References

1. E. Chason, B.W. Sheldon, L.B. Freund, J.A. Floro, S.J. Hearne, Origin of compressive residual stress in polycrystalline thin films, *Phys. Rev. Lett.* 88 (2002).

Acknowledgements

The PI would like to acknowledge co-PIs: Prof. Brian W. Sheldon, Prof. Huajian Gao at Brown University, Prof. Yue Qi at Michigan State University, Prof. Yang-Tse Cheng at University of Kentucky, Dr. Qinglin Zhang, and Dr. Peng Lu at General Motors R&D Center, graduate students and postdocs: Dr. Binsong Li, Kai Guo, Yuxiao Lin, Yikai Wang.

The team would like to also acknowledge the support from Program Managers Tien Duong at DoE, Patricia Smith at NAVSEA-Carderock, and Aaron Yocum at NETL.

II.5.H Development of High Energy Battery System with 300Wh/kg (ANL)

Khalil Amine, Principal Investigator

Argonne National Laboratory
9700 S Cass Ave
Lemont, IL
E-mail: amine@anl.gov

David Howell, DOE Technology Development Manager

U.S. Department of Energy
E-mail: David.Howell@ee.doe.gov

Start Date: October 1, 2017

End Date: September 30, 2018

Project Funding (FY18): \$600,000

DOE share: \$600,000

Non-DOE share: \$0

Project Introduction

Transformational changes in battery technologies are critically needed to enable the effective use of renewable energy sources, such as solar and wind, and to allow for the expansion of the electrification of vehicles. For these applications, batteries must store more energy per unit volume and weight, and they must be capable of undergoing many thousands of charge-discharge cycles. Therefore, developing high-performance batteries is critical to meet these requirements, which certainly relies on material breakthroughs. In the meantime, to enhance the performance and lifetime of batteries (specifically lithium-ion batteries), it is very critical to understand, for example, the formation of the solid-electrolyte interphase (SEI) layer, and the degradation mechanisms in battery electrodes, oftentimes, at the nanometer scale. Under this circumstance, various state-of-the-art in-situ and operando characterization tools are very critical to understanding battery behavior and could help address all the major issues of lithium batteries and beyond. The collaborative work with our colleagues from china under CERC-CVC-2 consists of the following:

- Development of advanced in situ characterization tools to understand failure mechanism in different battery systems with focus on high voltage high energy cathode (230mAh/g)
- Characterization of Silicon-Based Anode Materials and their Solid-Electrolyte Interphase (SEI)
- Characterization of Lithium Sulfur Batteries
- Investigation of the safety of batteries at the component and pack level
- Characterization and development of new catalysts to improve the efficiency of Li-O₂ batteries and/or Zinc ion Battery

Objectives

The objective of this project is to conduct research on rechargeable Li-ion battery and beyond lithium ion to help develop the next generation of advanced batteries that can expand electrification of vehicles and enable smart grids. The main objective is to understand and develop advanced battery chemistries based on lithium ion and beyond lithium ion that meet 300wh/kg energy density.

Approach

Tasks 1 Development of advanced in situ characterization tool to understand failure mechanism in different battery systems with focus on high voltage high-energy cathode (230mAh/g).

For most of battery systems, there is a significant reactivity both at the bulk and the interface of electrodes that are not well understood and are the major cause of both poor cycle life, poor safety and poor efficiency. One task of this project is going to focus on developing advanced in-situ techniques at ANL, BNL and PNNL in collaboration with our Chinese partners at Tsinghua University, Xiamen University, Peking University and

BIT by making use of the advanced user facilities at the above organizations. The techniques developed includes synchrotron based in situ X-ray techniques (x-ray diffraction, hard and soft x-ray absorption) with other imaging and spectroscopic tools such as high resolution transmission electron microscopy (HRTEM), Scanning transmission electron microscopy (STEM), mass spectroscopy (MS), X-Ray fluorescence microscopy (XRF) and transmission x-ray microscopy (TXM). We uses the time-resolved x-ray diffraction TR-XRD and absorption (TR-XAS) developed at ANL and BNL to study the kinetic properties of electrode materials with structural sensitivity (TR-XRD) and elemental selectivity (TR-XAS). In-situ XANES is used to monitor oxidation state of active metal ions in cathode. This techniques can be used to understand failure mechanism of high voltage, and high energy cathode which will help us develop high capacity high voltage and stable cathode. Another important issue is the thermal stability of new cathode materials which is closely related to the safety of the batteries. This problem is studied using the combined TR-XRD, TR-XAS with mass spectroscopy (MS). This project also proposes to develop a novel in situ X-ray fluorescence (XRF) microscopy combined with X-ray absorption spectroscopy (XAS) technique, which will enable us to track the morphology and chemical state changes of the electrodes and the SEI layer formation and decomposition during cycling.

Task 2 Characterization of Silicon-Based Anode Materials and their Solid-Electrolyte Interphase (SEI)

This work is to investigate Si-based material as the anode including development of in-depth understanding of the SEI protective layer that can be formed on these materials and characterization of the lithium alloying properties of the bulk that will influence the formation of the SEI layers. Finding electrolytes additives that can provide a good protective SEI for silicon-based anodes, as well as operate at higher voltages, would provide for stable cycling performance needed for high energy and high power lithium ion batteries for PHEV and EV applications. The team combine characterization of silicon anode material, electrolytes and electrolyte additives to meet the desired criteria for high energy density Li ion batteries. For the characterization of SEI properties and formation mechanisms on the Si anode materials, we have access to and expertise in the following techniques: SEM, TEM, AFM and STEM Scanning electron microscopy (SEM), transmission electron microscopy (TEM), and scanning tunneling electron microscopy (STEM) are available through the electron microscopy center (EMC) and CNM. Atomic force microscopy (AFM) with electrochemical capability is available in our group. AFM study inside of a dry box is possible. The AFM can be used to study the formation of SEI layer, its thickness, morphology, and mechanical strength, etc.

XPS and SIMS Analysis X-ray photoelectron spectroscopy (XPS) is an ideal tool for surface characterization. Survey scans and high-resolution scans of the Si 2p, C 1s, O 1s, F 1s, Li 1s, and P 2p energy spectra are very informative for the identification of the compounds present on the surface, especially the solid electrolyte interface (SEI). Secondary ion mass spectrometry (SIMS) is a technique to analyze the composition of solid surfaces and thin films by sputtering the surface of the specimen with a focused primary ion beam and collecting and analyzing ejected secondary ions. These secondary ions are measured with a mass spectrometer to determine the elemental, isotopic, or molecular composition of the surface and films. SIMS is the most sensitive surface and thin film analysis technique, being able to detect elements present in the parts per billion range.

XANES X-ray absorption at near edge spectroscopy (XANES) of Si K-edge on a serial of discharge and charge Si-based samples can be carried out at Canadian Light Source (CLS). Our preliminary results using the XANES technique showed that the Si-containing species are involved in the SEI formation over Si anode, but it seems that the Si-containing SEI is dependent of the discharge and charge process, i.e. the potential applied.

Results

Evolution of Redox Couples in Li- and Mn-Rich Cathode Materials and Mitigation of Voltage Fade by Reducing Oxygen Release

Lithium- and Manganese-rich (LMR) layer-structured cathode materials have been considered as one of the most promising candidates for high energy density Lithium-ion batteries. They can deliver reversible capacities over 280 mAh/g, which almost doubles those of conventional cathode materials such as LiCoO₂ or LiFePO₄. However, these materials are still facing significant challenges for commercialization in large scale.

One of the major problems is known as voltage fade, which means that upon cycling, the discharge voltage of LMR materials keeps decreasing. To overcome this problem, we need to acquire fundamental understanding of the mechanism for voltage fade.

In collaboration with our Chinese partners at CAS, the Argonne team together with BNL carried out a systematic study on a typical LMR material $\text{Li}_{1.2}\text{Ni}_{0.15}\text{Co}_{0.1}\text{Mn}_{0.55}\text{O}_2$ by combining synchrotron X-ray absorption spectroscopy (XAS) with high penetration power and the capability to average through the whole cathode, STEM with the atomic level spatial resolution and the newly developed 3-D electron tomography, a very large number of in situ and ex situ synchrotron X-ray spectra, including both hard X-ray absorption spectroscopy (h-XAS) at transition metal K-edges and soft X-ray absorption spectroscopy (s-XAS) at oxygen and carbon K-edges were collected at various charge-discharge cycles and the capacity contribution from each transition metal redox couple were calculated for certain cycle number from these spectra. Through probing from surface to bulk, from individual to the whole ensembles of particles, we show that the average valence states of each type of transition metal cations are continuously reduced, which is attributed to the oxygen release from LMR. Such reductions activate the new lower voltage $\text{Mn}^{3+}/\text{Mn}^{4+}$ and $\text{Co}^{2+}/\text{Co}^{3+}$ redox couples in addition to the original ones like $\text{Ni}^{2+}/\text{Ni}^{3+}$, $\text{Ni}^{3+}/\text{Ni}^{4+}$, and O^{2-}/O^- , directly leading to the voltage fade (Figure II.5.H.1 Figure II.5.H.1). We also show that the oxygen release causes microstructural defects such as the formation of large pores within particles which also contributes to the voltage fading (Figure II.5.H.2). Comparing with the charge-discharge profiles, we demonstrated that the origin of voltage fade is the redox couple evolution during cycling. We also investigated the evolution of microstructure during cycling and studied how that relates to the chemical degradation of the material. In addition, we demonstrated that the surface coating or other surface modifications are quite effective in suppressing the voltage fade through reducing the oxygen release during charge-discharge cycling, which is well correlated with the improvement in thermal stability. Such a correlation between electrochemical cycling and thermal stability is not a coincidence but intrinsically caused by the fact that both cycling and heating can involve oxygen loss, and transition metal reduction and migration. This correlation provides a simple and quick procedure to test the effectiveness of a new surface modification or a new material developed on suppressing voltage fade without having to conduct time-consuming multiple cycling: If the material for surface modification has a better thermal stability (meaning that oxygen only releases at high temperature), it would have a better structural stability in resisting voltage fade during cycling.

This work has been published in *Nature energy*, 3(8), 690, 2018.

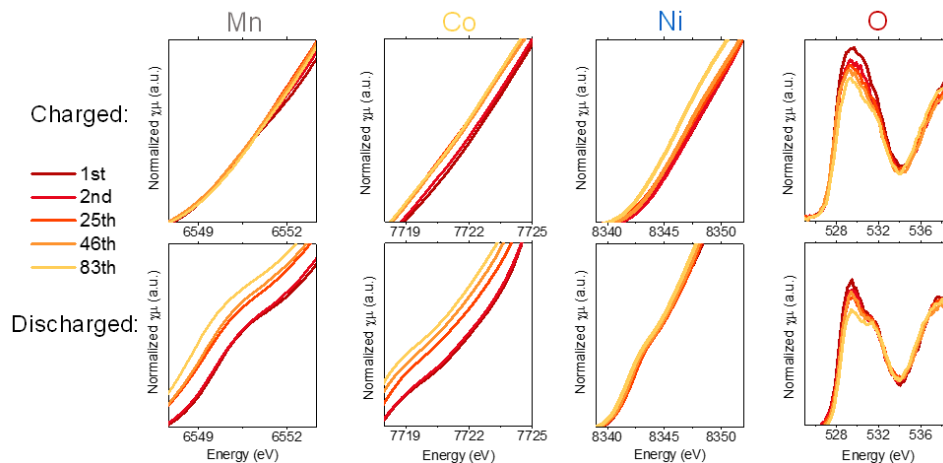


Figure II.5.H.1 XAS results of various elements in $\text{Li}_{1.2}\text{Ni}_{0.15}\text{Co}_{0.1}\text{Mn}_{0.55}\text{O}_2$ at different cycles. Transmission mode transition metal K-edge XAS spectra for Mn, Co and Ni, and fluorescence mode O K-edge XAS of samples at the 1st, 2nd, 25th, 46th, and 83th cycle. For each element, charged and discharged graphs are plotted using the same scale.

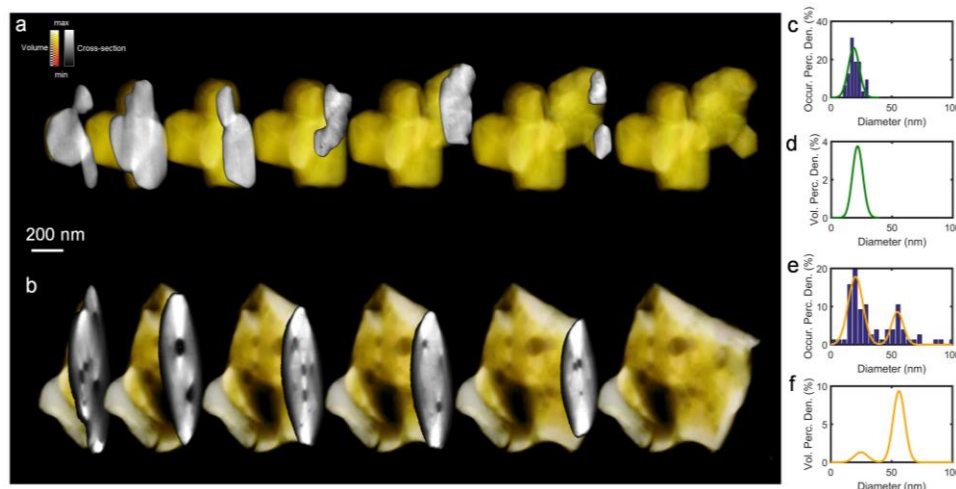


Figure II.5.H.2 Three-dimensional electron tomography reconstruction of $\text{Li}_{1.2}\text{Ni}_{0.15}\text{Co}_{0.1}\text{Mn}_{0.55}\text{O}_2$ materials. (a and b) volume rendition and progressive cross-sectional view of cathode particles at the (a) pristine state, and (b) after 15 cycles.

(c and d) Internal pore size distribution of the pristine sample weighted by occurrence (c) and by volume (d). (e and f) Internal pore size distribution of the cycled sample (15 cycles) weighted by occurrence (e) and by volume (f). The green and orange lines in (c) and (e) are single-Gaussian and bi-Gaussian fitting of the pore size histogram. The reweighting by volume in (d and f) are applied to the fitted curves.

In situ quantification of interphasial chemistry in Li-ion battery

Li-ion batteries (LIBs) have reshaped our life in the 21st century, and will continue to affect our energy future with larger applications in automotive and grid-storage technologies. However, much of the electrochemical processes governing this young chemistry remains to be understood. Amongst all, the solid-electrolyte-interphase (SEI) situating between the electrode and electrolyte remains to be the most elusive system in LIBs. In order to maximize energy densities, the electrodes in LIBs are designed to operate at extreme potentials; hence, electrolytes are forced to work under electrochemical strains far exceeding their thermodynamic stability limits at both anode and cathode surfaces. Under such “hostile” environments the kinetic stability of electrolytes is usually achieved through a passivation process, where trace amounts of electrolyte components decompose and form a dense and protective layer on the electrode surfaces. Since this passivation layer must insulate electron-tunneling so that the sustained electrolyte decomposition could stop, while remaining

conductive to ions essential to the cell chemistry, it is named “Solid-Electrolyte-Interphase (SEI)” after such “electrolyte” nature. It is the SEI that ensures the reversibility and rate-capability of LIB chemistries far from the equilibria.

In collaboration with Peking University, we developed a concerted approach to quantitatively monitor the interphasial components as they deposit on electrode surface at various potentials steps. Integrating the quantitative and in-situ/operando natures of electrochemical quartz crystal microbalance (EQCM) and atomistic-precision of AFM (Figure II.5.H.3), we applied these experiments on interphasial processes occurring on graphitic electrode surfaces that are cathodically polarized in a typical electrolyte composition (1.0 M LiPF_6 dissolved in equal molar mixture of ethylene carbonate (EC) and dimethyl carbonate (DMC)) extensively used in commercial LIBs. As a highly sensitive mass monitor, EQCM allows us to precisely measure what species is accumulated on or lost from the graphite electrode as function of applied potential, and AFM visually demonstrates how the graphene layers in a highly oriented pyrolytic graphite (HOPG) interact with the solvated Li^+ during the initial lithiation and de-lithiation processes. For the first time, the precise weighing of SEI during its initial lithiation process was realized with electrochemical quartz crystal microbalance, which unequivocally identifies lithium fluoride (LiF) and lithium alkylcarbonates as the main chemical components of the interphase at different potentials. In-situ gas analysis confirmed the preferential reduction of cyclic over acyclic carbonate molecules, making lithium ethylene dicarbonate (LEDC) the major product contributed from the solvent. This lithium alkylcarbonate, at least in its nascent form, was revealed to be re-oxidizable, despite general belief that the interphase is electrochemically inert and its formation irreversible. Meanwhile, atomic force microscope found that the presence of LEDC on graphitic surface started at edge sites, which does not seem to occur in an obvious staging manner as the intercalation of Li^+ does. These atomistic and quantitative observations provided unprecedented insights into the formation chemistry and mechanism of SEI that is hitherto unavailable. Such in-depth knowledge will serve as precious guideline in designing ideal interphases for future battery chemistries.

These unprecedented discoveries are summarized in a paper that was recently published by *Nature Nanotechnology*.

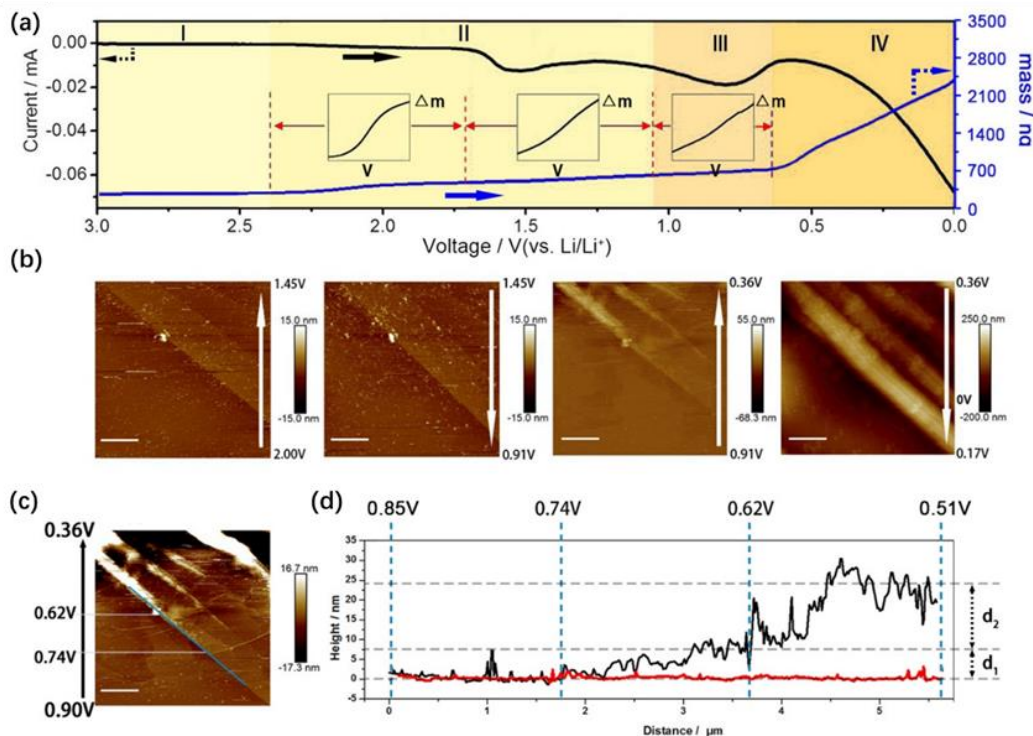


Figure II.5.H.3 (a) CV scan (black) of the fresh graphite electrode in 1 mol/L LiPF₆ EC/DMC at 1 mV/s from OCP (3.0 V) to 0.0 V, and the simultaneous EQCM responses (blue) recorded; (b) AFM topological imaging of HOPG during the CV scan, where the long white arrows indicate the scan directions, and the length of scale bar is 1.0 μm; (c) Further analysis of first SEI formation scanning from 0.90 V to 0.36 V, and the length of scale bar is 1.0 μm; (d) The height distribution (the black curve) of SEI on the stage labeled by a blue line, and the datum line of height (the red curve) is extracted from the first image of Figure 1b.

Thermal runaway of lithium-ion batteries without internal short Circuit

In collaboration with Tsinghua University, we demonstrate that not only internal short circuiting, but also chemical crossover, is the mechanism behind thermal runaway that can occur in lithium-ion batteries due to abuse conditions. In situ experiments showed that during thermal runaway, the cathode releases oxygen by a phase transition, and this oxygen is consumed by the lithiated anode. The released highly oxidative gas reacts with reductive LiC_x with tremendous heat generation centered at 274.2°C with heat flow of 87.8 W/g. To confirm the proposed mechanism, a battery undergoing the thermal runaway process was frozen by liquid nitrogen and was then subjected to detailed post-test analysis. Our results revealed the hidden thermal runaway mechanism of chemical crossover between the battery components without a severe internal short circuit. These findings provide an important insight into the rational design of automotive lithium-ion batteries as well as solid-state batteries.

At first the thermal runaway phenomenon of a 25-Ah vehicle used LIBs was reported without internal short circuits for the first time. The initial discharge capacity was 25.04 Ah, and the capacity remained high at 24.08 Ah after the 292th cycle, with capacity retention around 96%. The deliverable discharge capacity at 1/5C, 1/2C, 1C, 2C, 3C, 4C, and back to 1/2C was 24.9, 24.0, 23.1, 22.4, 22.0, 21.5, and 24.1 Ah respectively. These data indicate a stable long-term cycling as well as good rate performance of this battery. Moreover, a thermal resistant Al₂O₃ ceramic-Coated PET separator was adapted in this battery to eliminate the effect of internal short circuit. The DSC-TGA analysis and hot box result of the PET-based separator was shown in Figure II.5.H.4. Results show that the separator can resist the temperature as high as 257°C when PET starts to melt.

The ARC experiments showed that with a thermal stable PET/ceramic separator shown in Figure II.5.H.5, the NMC532/graphite cell did not undergo internal short circuit (voltage is not close to 0 below 600°C) during thermal runaway. However, the battery thermal runaway happened at 251°C and the temperature increased to more than 800°C immediately. The hidden reason to trigger the battery thermal runaway other than internal short circuit was founded to be the chemical crosstalk between the cathode and anode.

Our result shows that, the chemical crosstalk is the hidden reason of the battery TR. To design a safe high-energy-density automotive battery, the released oxygen from the cathode is the most critical factor to consider. If the cathode is vulnerable to high temperature, an advanced separator cannot guarantee the safety (or a battery with solid-state electrolyte). The rational design of the reliable high energy density battery needs careful verification at both the material level and automotive cell level.

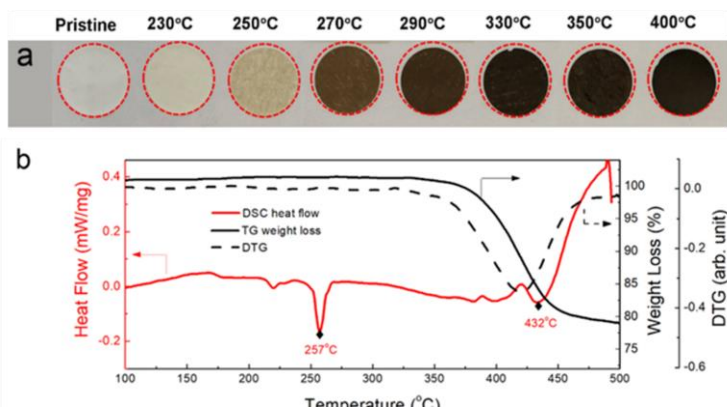


Figure II.5.H.4 the thermal stability of the PET-based separator

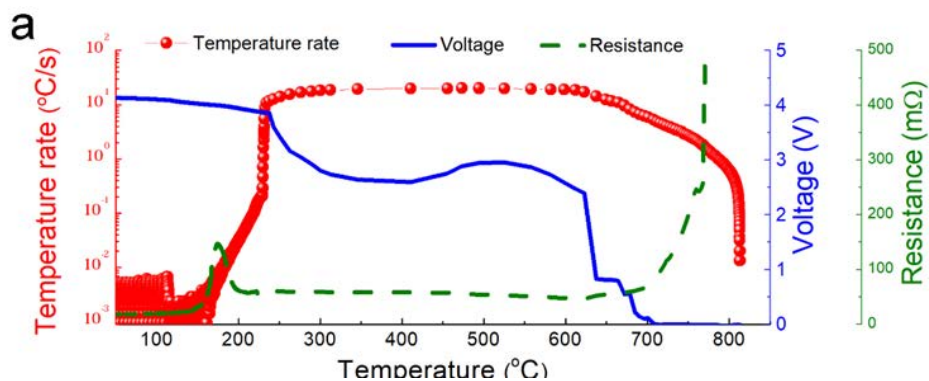


Figure II.5.H.5 Thermal runaway characterization of 25-Ah SC-NMC532/graphite cell

Conclusions

1) Through probing from surface to bulk, from individual to the whole ensembles of particles, we show that the average valence states of each type of transition metal cations are continuously reduced, which is attributed to the oxygen release from LMR. Such reductions activate the new lower voltage $\text{Mn}^{3+}/\text{Mn}^{4+}$ and $\text{Co}^{2+}/\text{Co}^{3+}$ redox couples in addition to the original ones like $\text{Ni}^{2+}/\text{Ni}^{3+}$, $\text{Ni}^{3+}/\text{Ni}^{4+}$, and O^{2-}/O^- , directly leading to the voltage fade. We also show that the oxygen release causes microstructural defects such as the formation of large pores within particles which also contributes to the voltage fading.

2) We developed a concerted approach to quantitatively monitor the interphasial components as they deposit on electrode surface at various potentials steps.

3) We demonstrated that the chemical crosstalk is the hidden reason of the battery TR. To design a safe high-energy-density automotive battery, the released oxygen from the cathode is the most critical factor to consider. If the cathode is vulnerable to high temperature, an advanced separator cannot guarantee the safety (or a battery with solid-state electrolyte). The rational design of the reliable high energy density battery needs careful verification at both the material level and automotive cell level.

Key Publications

1. Enyuan Hu, Xiqian Yu, Ruoqian Lin, Xuanxuan Bi, Jun Lu, Seongmin Bak, Kyung-Wan Nam, Huolin L. Xin, Cherno Jaye, Daniel A Fischer, Khalil Amine, Xiao-Qing Yang, “Evolution of redox couples in Li- and Mn-rich cathode materials and mitigation of voltage fade by reducing oxygen release”, *Nature Energy*, 3(8), 690, 2018
2. Tongchao Liu, Lingpiao Lin, Xuanxuan Bi, Leilei Tian, Kai Yang, Jijie Liu, Maofan Li, Zonghai Chen, Jun Lu, Khalil Amine, Kang Xu and Feng Pan, “In situ quantification of interphasial chemistry in Li-ion battery”, *Nature Nanotechnology*, 2018, ASAP
3. Yuruo Qi, Zizheng Tong, Junmei Zhao, Lu Ma, Tianpin Wu, Huizhou Liu, Chao Yang, Jun Lu, Yong-Sheng Hu, “Scalable Room-Temperature Synthesis of Multi-shelled Na₃(VOPO₄) 2F Microsphere Cathodes”, 2018, *Joule*, ASAP.
4. Wenru Hou, Xianwei Guo, Xuyang Shen, Khalil Amine, Haijun Yu, Jun Lu, “Solid electrolytes and interfaces in all-solid-state sodium batteries: progress and perspective”, *Nano Energy*, 52, 279-291, 2018
5. Feng Wu, Lu Liu, Yifei Yuan, Yu Li, Ying Bai, Tao Li, Jun Lu, Chuan Wu, “Expanding Interlayer Spacing of Hard Carbon by Natural K⁺ Doping to Boost Na-Ion Storage”, *ACS Applied Materials & Interfaces*, 10 (32), 27030-27038, 2018
6. Li Li, Jun Lu, Longyu Zhai, Xiaoxiao Zhang, Larry Curtiss, Yi Jin, Feng Wu, Renjie Chen, Khalil Amine, “A facile recovery process for cathodes from spent lithium iron phosphate batteries by using oxalic acid”, *CSEE Journal of Power and Energy Systems*, 4(2), 219-215, 2018
7. Yu Li, Yifei Yuan, Ying Bai, Yuanchang Liu, Zhaohua Wang, Limin Li, Feng Wu, Khalil Amine, Chuan Wu, Jun Lu, Insights into the Na⁺ Storage Mechanism of Phosphorus-Functionalized Hard Carbon as Ultrahigh Capacity Anodes, *Advanced Energy Materials*, 8, 1702781, 2018
8. Jiaxin Zheng, Wenjun Deng, Zongxiang Hu, Zengqing Zhuo, Fusheng Liu, Haibiao Chen, Yuan Lin, Wanli Yang, Khalil Amine, Rui Li, Jun Lu, Feng Pan, “An Asymmetric K/Li-ion Battery Based on Intercalation Selectivity”, *ACS Energy Letters*, 3 (1), 65-71, 2017
9. Xie, Y.; Xu, G. L.; Che, H.; Wang, H.; Yang, K.; Yang, X.; Guo, F.; Ren, Y.; Chen, Z.; Amine, K., Probing Thermal and Chemical Stability of Na_xNi_{1/3}Fe_{1/3}Mn_{1/3}O₂ Cathode Material toward Safe Sodium-Ion Batteries. *Chem. Mater.* 30, 4909-4918, 2018.
10. Liu, X.; Ren, D.; Hsu, H.; Feng, X.; Xu, G. L.; Zhuang, M.; Gao, H.; Lu, L.; Han, X.; Chu, Z., Thermal Runaway of Lithium-Ion Batteries without Internal Short Circuit. *Joule* 2018, doi.org/10.1016/j.joule.2018.06.015.
11. Xu, G. L.; Xiao, L.; Sheng, T.; Liu, J.; Hu, Y.-X.; Ma, T.; Amine, R.; Xie, Y.; Zhang, X.; Liu, Y., Electrostatic Self-Assembly Enabling Integrated Bulk and Interfacial Sodium Storage in 3D Titania-Graphene Hybrid. *Nano Lett.*, 18, 336-346, 2017.

12. Liu, R.; Xu, G. L.; Li, Q.; Zheng, S.; Zheng, G.; Gong, Z.; Li, Y.; Kruskop, E.; Fu, R.; Chen, Z., Exploring Highly Reversible 1.5-Electron Reactions ($V^{3+}/V^{4+}/V^{5+}$) in $Na_3VCr(PO_4)_3$ Cathode for Sodium-Ion Batteries. *ACS Appl. Mater. Interf.*, 9, 43632-43639, **2017**.
13. Li, Q.; Liu, Z.; Zheng, F.; Liu, R.; Lee, J.; Xu, G. L.; Zhong, G.; Hou, X.; Fu, R.; Chen, Z., Identifying the Structural Evolution of the Sodium Ion Battery Na_2FePO_4F Cathode. *Angew. Chem. Int. Ed.*, 57, 11918-11923, **2018**.
14. Xu, G. L.; Amine, R.; Abouimrane, A.; Che, H.; Dahbi, M.; Ma, Z.-F.; Saadoune, I.; Alami, J.; Mattis, W. L.; Pan, F.; Chen, Z.; Amine, K., Challenges in Developing Electrodes, Electrolytes, and Diagnostics Tools to Understand and Advance Sodium-Ion Batteries. *Adv. Energy Mater.*, 1702403, **2018**.

II.6 Next-Gen Lithium-Ion: Modeling Advanced Electrode Materials

II.6.A Electrode Materials Design and Failure Prediction (ANL)

Venkat Srinivasan, Principal Investigator

Argonne National Laboratory
9700 S. Cass Avenue,
Lemont, IL 60439
E-mail: vsrinivasan@anl.gov

Tien Q. Duong, DOE Technology Development Manager

U.S. Department of Energy
E-mail: Tien.Duong@ee.doe.gov

Start Date: October 1, 2017 End Date: September 30, 2018
Project Funding (FY18): \$1,000,000 DOE share: \$1,000,000 Non-DOE share: \$0

Project Introduction

Next generation lithium ion batteries require high energy density to meet the ever-increasing demands of the electronics and automobile industries. Lithium sulfur batteries are considered to be a potential candidate capable of fulfilling the future demands. This particular battery uses the phase change properties of sulfur cathodes to achieve very high energy densities. Due to relatively lower cathode potentials (as compared to transition metal oxides), these lithium sulfur chemistries require lithium metal-based anodes that help them to attain higher energy densities. However, dendrite growth during deposition of lithium at the anode side (at the time of charge), and carbon surface passivation due to precipitation of lithium-sulfide at the cathode side (during discharge process), is considered to be the largest bottlenecks preventing widespread implementation of lithium sulfur chemistries.

Based on the work conducted as part of this project, better understanding of the different mechanisms responsible for degradation in lithium metal anodes and lithium sulfur batteries can be developed. Based on these understandings, different strategies can also be devised to minimize the impact of degradation mechanisms and enhance the performance and lifetime of next generation lithium ion batteries. At the end of this project, mathematical models will be developed that can capture the impact of diffusivity, conductivity, transference number, solubility and mechanical stiffness of various species on the morphology of lithium and lithium-sulfide deposits on top of lithium metal and carbon substrates, respectively.

Objectives

The goal of this project is to develop a continuum-based mathematical model to (i) investigate the impact of solid electrolyte interphase (SEI) layer on the growth of dendritic protrusions, and (ii) elucidate the deposition mechanism and deposit morphology observed on top of the carbon substrate in lithium sulfur battery cathodes. Mechanical stiffness and transport mechanism of lithium through the SEI layer can significantly affect the nucleation of dendritic protrusions on top of lithium metal anodes. Effectiveness of protective layers in preventing the growth of lithium dendrites can also be studied by using this methodology. Next generation high energy density lithium-sulfur batteries experience limited capacity due to cathode surface passivation because of the precipitation of lithium-sulfides during the discharge process. Understanding the morphology of precipitates can significantly help to develop strategies that can minimize the surface passivation and improve the practical specific capacity of lithium sulfur batteries. The main focus of this project will be to develop microscale models capable of successfully capturing the multiscale multiphysics phenomena that occurs during lithium metal and lithium sulfide deposition processes.

Approach

In the present effort, both dendrite growth during lithium deposition, and surface passivation due to lithium-sulfide precipitation have been modeled. Two different approaches were adopted for modeling these two different physical phenomena. Both the techniques are briefly described below.

Modeling lithium dendrite growth: It has been argued by several researchers that inhomogeneous transport of lithium through the SEI layer leads to the formation and growth of dendritic protrusions. In this context, an SEI layer has been added at the lithium electrolyte interface, and its impact on the Butler-Volmer reaction current has been incorporated as an extra overpotential term. The Butler-Volmer equation is:

$$i_{BV} = (k_a^{\alpha_c})((k_c c_e)^{\alpha_a}) \exp(\alpha_a \Delta\mu_e / RT) [\exp(\alpha_a F\eta / RT) - \exp(-\alpha_c F\eta / RT)] \quad (\text{II.F.1.1})$$

Here, k_a and k_c are the anodic and cathodic reaction rate constants, and α_a and α_c are the anodic and cathodic transfer coefficients, respectively. Also, $\Delta\mu_e$ indicates the electrochemical potential change induced by mechanical stresses and surface curvature effects. Moreover, F denotes Faraday's constant, R denotes the universal gas constant and T signifies the local temperature on the Kelvin scale. For the reduction of lithium ions at the lithium metal anode, the anodic and cathodic rate constants are assumed to be equal ($k_a = k_c$). Also, following other researchers, the anodic and cathodic transfer-coefficients have been assumed to be equal for reduction of lithium metal, so that $\alpha_a = \alpha_c = (1/2)$. The overpotential at the lithium-electrolyte interface, which takes a negative value during the reduction process, is given by $\eta = \phi_s - \phi_e - U_{Li}$, where ϕ_s and ϕ_e indicate the solid phase and electrolyte phase potentials. The open circuit potential for lithium metal has been denoted by U_{Li} , which is defined to be zero.

The change in electrochemical potential due to the mechanical stress and surface curvature effects, which appears in Eq. (1) and varies along the x-direction, has been adopted from Monroe and Newman (*JES*, 2005, A396 – A404):

$$\Delta\mu_e(x) = -\frac{1}{2}(\bar{V}_{Li} + t_{A^-} \bar{V}_{Elec}) \left\{ -\gamma k + \bar{n} \cdot \left[\bar{n} \cdot (\Delta\tau^{Li} - \Delta\tau^{Elec}) \right] \right\} + \frac{1}{2}(\bar{V}_{Li} - t_{A^-} \bar{V}_{Elec}) \cdot (\Delta p^{Li} + \Delta p^{Elec}) \quad (\text{II.F.1.2})$$

Here, \bar{V}_{Li} and \bar{V}_{Elec} represent the partial molar volumes of lithium and electrolyte salt, respectively, t_{A^-} is the transference number of anions within the electrolyte, γ is the surface energy, and \bar{n} represents the normal vector at the lithium-electrolyte interface pointing into the electrolyte region. Contributions from hydrostatic stress ($\sigma_{kk} = \sigma_{11} + \sigma_{22} + \sigma_{33}$), deviatoric stress (s_{ij}), which is obtained by subtracting the hydrostatic component (σ_{kk}) from the total stress tensor (σ_{ij}), $s_{ij} = \sigma_{ij} - (1/3)\sigma_{kk}\delta_{ij}$, and local surface curvature (k) are present. The pressure term is calculated as $\Delta p^{Li} = -\sigma_{kk}^{Li}/3$ and $\Delta p^{Elec} = -\sigma_{kk}^{Elec}/3$, and the deviatoric stress terms are evaluated as $\Delta\tau^{Li} = -s_{ij}^{Li}$ and $\Delta\tau^{Elec} = -s_{ij}^{Elec}$. Repeated indices indicate implicit summation throughout this entire article wherever indicial notations have been used. In this 2D computational domain, the local curvature k has been calculated in a piece-wise fashion.

Transport of lithium through both the electrolyte and solid-electrolyte-interphase (SEI) layer has been modeled as a combination of diffusion and migration process. Mechanical stress distribution within the lithium metal electrode, electrolyte and SEI layer has been estimated by solving the equilibrium equation. Proper boundary conditions have also been assumed while solving the governing equations. Due to the presence of inhomogeneity in the SEI layer, propensity of lithium dendrite growth during deposition has been investigated. Effects of electrolyte thickness, stiffness and transport properties on the overall lithium deposition process will be elucidated as part of this research.

Modeling lithium-sulfide precipitation: Numerous published researches have indicated that active surface passivation caused by lithium-sulfide (Li_2S) precipitation can significantly reduce sulfur utilization, and greatly

limit battery charge-storage capacity and cycle life. Here, research work targets to evaluate this precipitation process of Li_2S on the active sulfur electrode surface by mathematical modeling. Based on the electrochemical kinetics and thermodynamics, a phase field modeling approach is developed to describe the ‘deposition’ of Li_2S during battery discharge process and the ‘removal’ of Li_2S during charge process on the active cathode surface. As illustrated in Figure II.6.A.1, a one-dimensional geometry is applied, in which two reactions are assumed to describe the Li_2S film generation (discharge) and removal (charge) respectively. A phase-field based model has been developed to capture the increase in thickness of the lithium-sulfide precipitate. During discharge, as soon as a critical thickness is reached, the simulation is stopped, because at that critical thickness, the lithium-sulfide precipitate is expected to cover the entire carbon surface and form a passivation film. Meanwhile, for simplicity, a few assumptions are applied: reactions are only considered on the active carbon surface, and the nucleation of Li_2S in the electrolyte is neglected. Besides, because Li_2S has very low electron conductivity ($\sim 10^{-13}$ S/m), the surface passivation process is simulated through the surface coverage increase of Li_2S on the active carbon surface along with the discharge process.

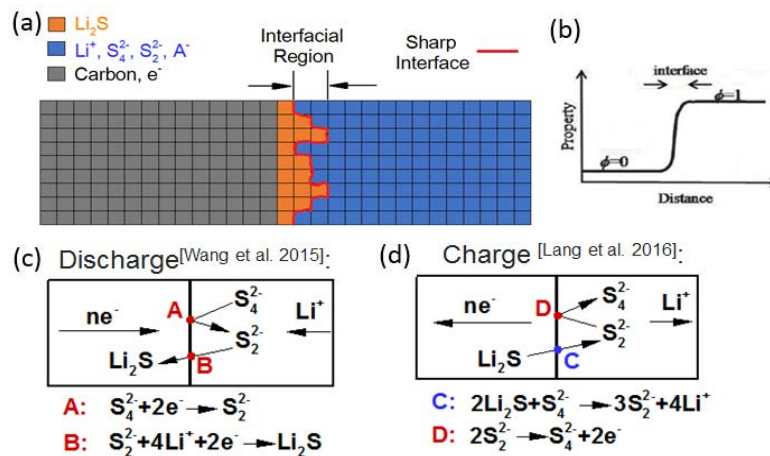


Figure II.6.A.1 (a) One dimensional model geometry for the electrode-electrolyte interfacial region; (b) phase field model converts the sharp interface into a continuous interfacial region by a phase parameter; (c) electrochemical reactions assumed for the Li_2S precipitation process in the battery discharge process; (d) electrochemical/ chemical reactions assumed for Li_2S removal during battery charge process.

Results

Lithium dendrite growth: While investigating the effect of SEI layer on the dendrite growth process, the problem was approached in two different ways. In the first attempt, the SEI layer was assumed to be extremely thin, and transport of lithium through the thin SEI layer was modeled. Effect of the resistance associated with the SEI layer (R_f) was captured as an extra polarization within the overpotential term: $\eta = \phi_s - \phi_e - (i_{BV} \cdot R_f)$. Figure II.6.A.2(a) demonstrates possible non-homogeneities of SEI resistance in the form of ‘‘sharp’’ and ‘‘wide’’ variations. Starting from flat lithium (see Figure II.6.A.2(b)), the corresponding dendrite morphologies have been depicted in Figure II.6.A.2(c) and Figure II.6.A.2(d), respectively. Please note that, mechanical equilibrium has not been solved in this particular case, which is similar to the case with liquid electrolytes. It is evident that a sharp variation in SEI resistance leads to a narrow dendrite growth, which has the potential to easily penetrate through the separator and eventually short the cell. Wider variation in SEI properties produce a relatively wide dendritic protrusion, which can be easily impeded by the separator/protective layer.

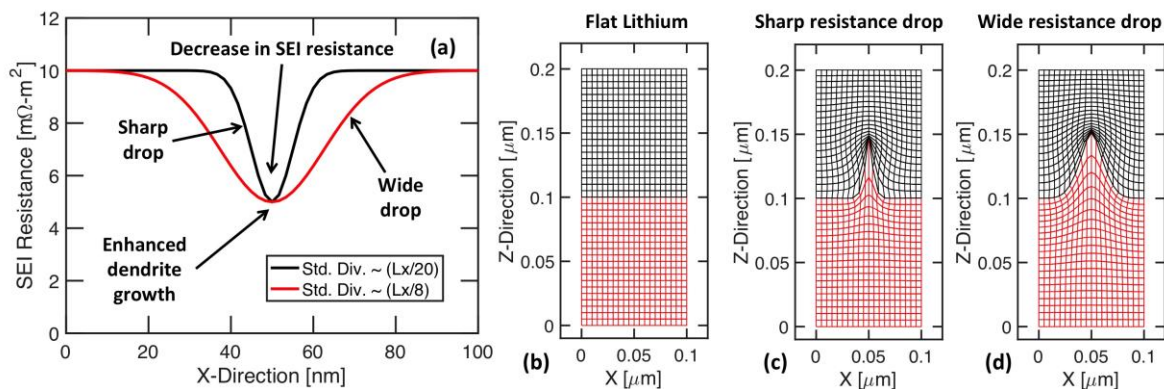


Figure II.6.A.2 (a) Demonstration of inhomogeneous SEI resistance, which may have a sharp variation (black line) or a wide drop (red line). (b) Initial lithium-electrolyte interface, which is flat. (c) Sharp drop in SEI resistance leads to growth of a thin dendritic protrusion. (d) Wider variation in SEI resistance forms a thick dendritic protrusion.

Heights of dendritic protrusions with increasing time have been demonstrated in Figure II.6.A.3(a). It is evident that the growth rate is not constant and decreases with time, which can be attributed to the increasing surface area of reaction and curvature induced suppression. Figure II.6.A.3(b) clearly demonstrates that by increasing the surface energy density between lithium and electrolyte, size of the propagating dendritic protrusion can be altered significantly. Lithium dendrites with higher aspect ratio are observed in liquid electrolytes, whereas, polymer electrolytes experience dendritic protrusion with lower aspect ratio, which appears as globule shaped. Significantly increasing the surface energy density may lead to prevention of dendrite growth altogether.

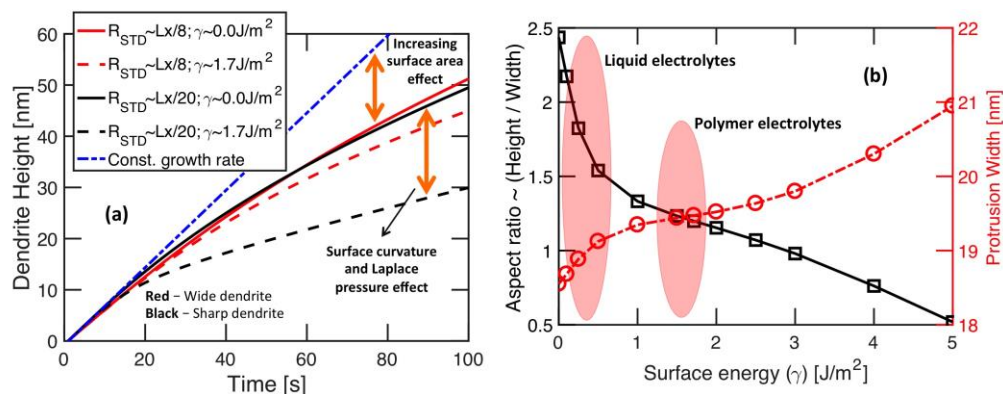


Figure II.6.A.3 (a) Increase in height of dendritic protrusions with time for sharp and wide drop in SEI resistance. Growth of dendrites decrease with time because of increase in surface area and surface curvature induced suppression mechanisms. (b) As the surface energy between lithium and electrolyte increases, the width of the dendritic protrusion increase (red circles), and the aspect ratio of the protrusions drop (black squares).

Next, the impact of thick SEI layers on dendrite growth was investigated. Mechanical stiffness and transport properties through the SEI layer were varied, and the changes in height of dendritic protrusion were studied. It has been assumed that, internal heterogeneity of transport properties within the SEI leads to development of non-uniform current distribution and formation of lithium nuclei. The computational mesh has been shown in Figure II.6.A.4(a), where the heterogeneity within the SEI layer has been assumed to exist at the left edge (highlighted in Figure II.6.A.4(a)). Enhanced transport of ions through this imperfection leads to formation of lithium nucleus. However, presence of a stiff SEI layer is expected to prevent the growth of any inhomogeneity. To capture the suppression of lithium dendrites by the SEI layer, a two-step computational mechanism has been adopted: (i) Based on the amount of lithium deposited, the lithium electrolyte interface is deformed. This produces excessive compression in electrolyte. (ii) Next, the stress in lithium is relaxed, and

the compressed electrolyte is allowed to push the lithium (with dendritic protrusion) back to equilibrium. This two-step mechanism ensures the evolution of compressive stresses within both lithium and electrolyte. Figures Figure II.6.A.4(b) and Figure II.6.A.4(c) demonstrates the distribution of potential and concentration, respectively, within the electrolyte, under specific operating conditions.

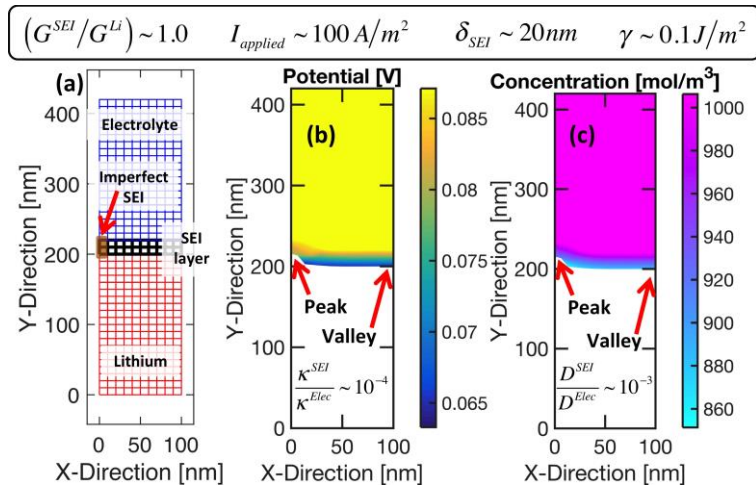


Figure II.6.A.4 (a) Computational mesh used to understand the growth of dendritic protrusions under the presence of SEI layer. Internal heterogeneity of the SEI at the left boundary leads to faster transport of reacting species, which eventually leads to the growth of dendritic protrusions. (b) Potential distribution within the electrolyte during operation under specified conditions. (c) Concentration distribution within electrolyte under the same operating condition specified above the figures. Larger gradients of both potential and concentration are observed within the SEI.

Figure II.6.A.5(a) demonstrates that increasing the SEI thickness helps to prevent growth of dendritic protrusions. Decrease in dendritic protrusion height with increasing SEI stiffness has been demonstrated in Figure II.6.A.5(b). Figure II.6.A.5(c) shows that higher surface energy density helps to stabilize the growth of dendrites, but the impact is more pronounced at lower current densities.

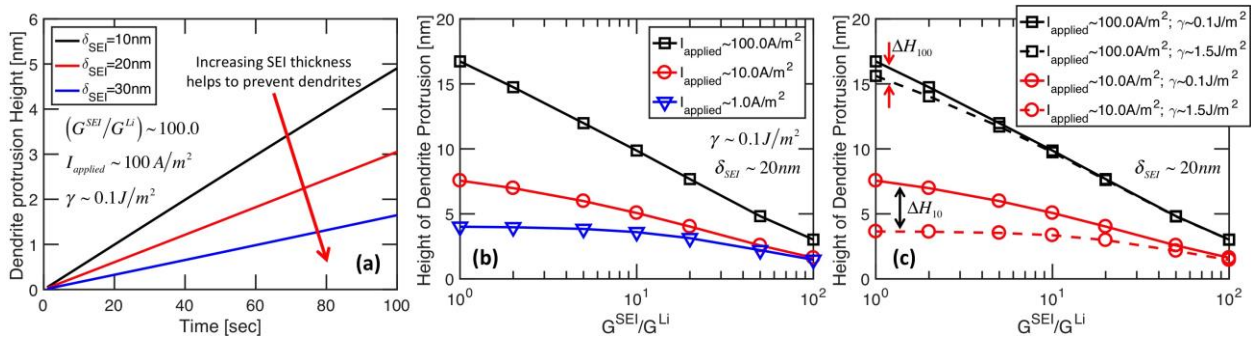


Figure II.6.A.5 (a) Growth of dendritic protrusions with time under applied current density of 100A/m². Increasing thickness of a stiff SEI layer helps to prevent dendrite growth. (b) Height of the dendritic protrusion with increasing SEI stiffness. Increase in applied current density helps to grow the dendritic protrusion. (c) Increasing surface energy density between lithium and electrolyte helps to suppress the dendritic protrusion. However, the impact of surface energy density minimizes at extremely high currents of operation (~100A/m²).

Lithium-sulfide precipitation: In the subsequent research, the impact of lithium-sulfide precipitation on the cell performance has been studied in details. As discussed in the “Approach” section, a phase field based methodology has been developed for capturing the evolution of Li₂S thickness. Modeling results are illustrated in Figure II.6.A.6. On the carbon surface, as shown in Figure II.6.A.6(a), Li₂S film growth (precipitation process) and removal in discharge-charge process follow different trends. This is originated from the different

electrochemical-chemical reactions taking place during discharge and charge. Under different discharge/charge current conditions, model indicates that current increase can greatly reduce the time needed for Li_2S growth till its surface coverage reaches 100% (Figure II.6.A.6(b)), while its influence on the time needed for Li_2S removal in the charge process is not comparable (Figure II.6.A.6(c)). This implies high C-rates can potentially lead to Li_2S accumulation on the active electrode surface in the discharge-charge cycles, since the time needed for Li_2S film growth could be longer than that needed for Li_2S film removal.

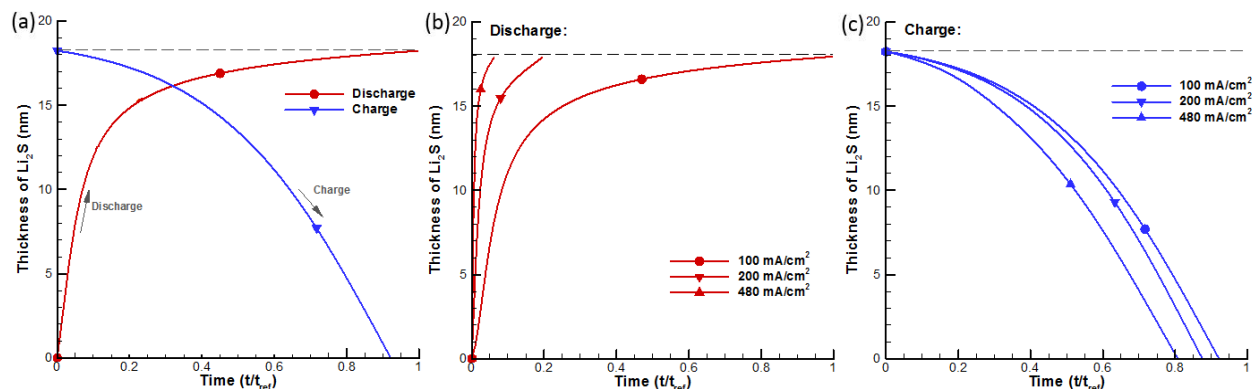


Figure II.6.A.6 (a) Modeled Li_2S film growth on the active carbon surface in the discharge, and Li_2S film removal in the charge; (b) Li_2S film thickness growth under different discharge current conditions: 100 mA/cm^2 , 200 mA/cm^2 and 480 mA/cm^2 ; (c) Simulated Li_2S film thickness variation under different charge current conditions.

According to the developed phase field model, Li_2S precipitates form due to the reaction between Li^+ cations and S_2^{2-} anions. Since S_2^{2-} gets generated through the reduction of S_4^{2-} , the concentration of S_2^{2-} should depend strongly on the concentration of S_4^{2-} , or its solubility. Figure II.6.A.7 demonstrates the impact of S_4^{2-} solubility on the evolution of Li_2S film thickness during discharge and charge processes (Figure II.6.A.7(a) and Figure II.6.A.7(b), respectively). During discharge, decreasing the solubility of S_4^{2-} helps to delay the surface passivation by precipitation of Li_2S film. Similarly, lower solubility of S_4^{2-} slows down the dissolution process during charge.

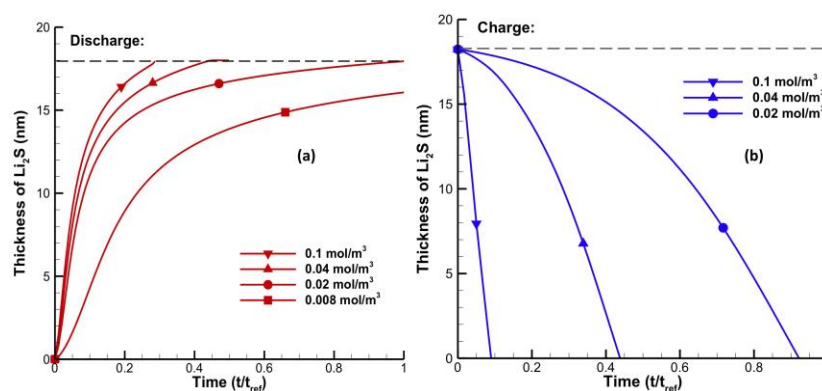


Figure II.6.A.7 Effect of the S_4^{2-} solubility on the evolution of Li_2S film thickness on top of carbon substrate. (a) During discharge, decreasing the solubility of S_4^{2-} helps to delay the surface passivation. (b) Similarly, at the time of charge, decreasing S_4^{2-} solubility slows down the dissolution of Li_2S film.

Conclusions

Detailed computational methodologies have been developed for understanding two different physical phenomena, which occur in the anode and cathode of lithium sulfur batteries.

1. Impact of SEI heterogeneity on lithium deposition and dendrite growth process during charge.

2. The effect of current density and polysulfide solubility on the precipitation of lithium-sulfide at the cathode surface during the discharge process.

Both these phenomena have significant impact on the cell performance, and affect not only the capacity, but also the lifetime of the energy storage device. From the obtained results, it is evident that increasing the surface energy density at the electrode/electrolyte interface, and increasing the stiffness of the SEI layer, can help in preventing the overall lithium dendrite growth. Regarding the precipitation of lithium-sulfide species, modeling results indicate that Li_2S film growth and removal follows different trends, and high C-rate can potentially lead to Li_2S accumulation on the active carbon surface. Also, decreasing the solubility of polysulfides can significantly slow down the surface passivation process, which is considered to be a major bottleneck in achieving high discharge capacity in lithium sulfide cells.

Key Publications

1. Pallab Barai, Kenneth Higa and Venkat Srinivasan. "Impact of External Pressure and Electrolyte Transport Properties on Lithium Dendrite Growth". *Journal of the Electrochemical Society* (2018) 165 (11) A2654 – A2666.
2. Yuanyuan Xie and Venkat Srinivasan, "Mathematical modeling of the Li_2S precipitation process in Li-S battery". Presented at: *The Electrochemical Society 233rd Meeting*, May 13-17, 2018 Seattle, WA, USA. (Conference Presentation)

Acknowledgements

The authors would like to acknowledge the collaboration with Prof. Partha Mukherjee and his group (Purdue University), for investigating the impact of pore size distribution, i.e. a range of curvatures, on the lithium-sulfide precipitation process. Their research findings indicate that positive curvature slows down the rate of precipitation. This work has been included within the quarterly report prepared for the fourth quarter.

II.6.B Predicting and Understanding Novel Electrode Materials from First Principles (LBNL)

Kristin A. Persson , Principal Investigator

Lawrence Berkeley National Laboratory
1 Cyclotron Rd.
Berkeley, CA, 94720
E-mail: KAPersson@lbl.gov

Tien Duong, DOE Technology Development Manager

U.S. Department of Energy
E-mail: Tien.Duong@ee.doe.gov

Start Date: October 1, 2017	End Date: September 30, 2018	
Project Funding (FY18): \$350,000	DOE share: \$350,000	Non-DOE share: \$0

Project Introduction

This project supports VTO's programmatic goal by developing next-generation, high-energy cathode materials and enabling stable cathode operation at high voltages through target particle morphology design, functional coatings and rational design of electrolytes.

Over the last year, we have focused on understanding the origin of conductivity of Li salts in low permittivity electrolytes. In such electrolytes, despite the very small dielectric constant compared to aqueous solutions ($\epsilon = 3$ vs $\epsilon = 80$), there is considerable conductivity at conventional Lithium Ion Battery salt concentrations (~ 1 M). The ability of low permittivity electrolytes to dissociate salt is surprising due to a majority of associated salt species, such as neutral (but polar) contact-ion pairs. However, at higher concentrations these polar clusters lead to a permittivity increase of the liquid and in turn, a larger fraction of dissociated free ions. Our research focused on studying the dielectric properties of low permittivity Li electrolytes and the interplay between the dielectric constant and salt association. This allows us to understand the general atomistic and molecular details relating to bulk speciation and conductivity in liquid electrolyte systems.

We also investigated surface oxides, in terms of conductivity and passivation, of alloy anode materials. The native surface oxide was assessed for Li ion conductivity as well as reactivity with Li and subsequent phase formation, and compared to the bulk alloy properties.

Objectives

- Understanding the solvation environment underlying salt speciation and conductivity in low permittivity Li electrolytes
- Understanding the role of the native SiO₂ layer in the cycling of Si based Li-ion batteries

Approach

- Determine the extent to which the various electrolyte components contribute to the dielectric constant of bulk electrolyte and subsequent change in salt speciation via first principles modelling and classical molecular dynamics
- Examine the stability of various Li_xSi and Li_xSiO₂ and predict their lithiation voltages through first principles calculations
- Assess the kinetics of Li diffusion in SiO₂ compared to Si using ab-initio molecular dynamics

This research used resources of the National Energy Research Scientific Computing Center, a DOE Office of Science User Facility supported by the Office of Science of the U.S. Department of Energy under Contract No.

DE-AC02-05CH11231. This research also used the Lawrence computational cluster resource provided by the IT Division at the Lawrence Berkeley National Laboratory (Supported by the Director, Office of Science, Office of Basic Energy Sciences, of the U.S. Department of Energy under Contract No. DE-AC02-05CH11231)

Results

This year's goals aimed towards modeling linear carbonate-based electrolytes (e.g. dimethyl carbonate with the addition of LiAsF_6 or LiPF_6), where the associated salt is believed to increase the dielectric constant ϵ of the overall electrolyte, allowing an exponential increase in conductivity as the concentration is increased (see Figure II.6.B.1).

In order to assess speciation of the electrolyte salt, we employed first principles calculations to determine the free energy of dissociation. We used a mean field polarizable continuum model (PCM), where the dielectric constant of the overall electrolyte is used to account for solvation effects. Figure II.6.B.2 shows the free energy of dissociation for LiAsF_6 and LiPF_6 as a function of the overall permittivity of the electrolyte. Here, first principles calculations results indicate that a higher dielectric constant promotes dissociation of contact ion pairs (CIPs) into free ions. An experimental value (black X) shows qualitative agreement

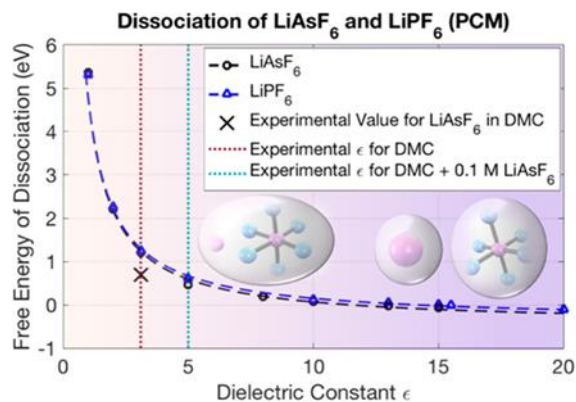


Figure II.6.B.2 Free energy of dissociation for LiAsF_6 (black) and LiPF_6 (blue) into their respective free ions as computed from first principles using the polarizable continuum model (PCM). [1]

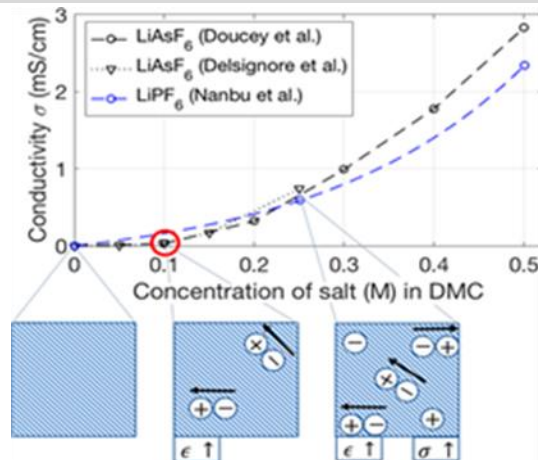


Figure II.6.B.1 Experimentally measured conductivity as a function of salt concentration for LiAsF_6 and LiPF_6 in dimethyl carbonate (DMC). The bottom rectangles (left to right) illustrate the neat solvent, an electrolyte with only associated salt (with dipole moments drawn as directed arrows), and finally an electrolyte with both associated (arrows) and dissociated salt (no arrows). [1]

for DMC ($\epsilon = 3.1$) with our calculated results

such that CIPs are the majority species for sufficiently low concentrations of salt. This is in agreement with the hypothesis that CIPs could increase the overall permittivity of the electrolyte to allow a higher fraction of charge carriers as concentration is increased. We notice a crossover for both LiAsF_6 and LiPF_6 , respectively at $\epsilon=13$ and $\epsilon=15$, indicating that, upon addition of salt, there should be a change in the solvation structure in that the majority of added species should be free ions as opposed to CIPs. An inverse relationship fit to the free energy as a function of the dielectric constant ϵ shows that computed results agree with the theoretical expectation of such systems. [1]

A further goal of the current BMR project is to examine the effect of surface phases on electrodes. Here, we focus on the effects of an amorphous thin SiO_2 present on a Si electrode surface.

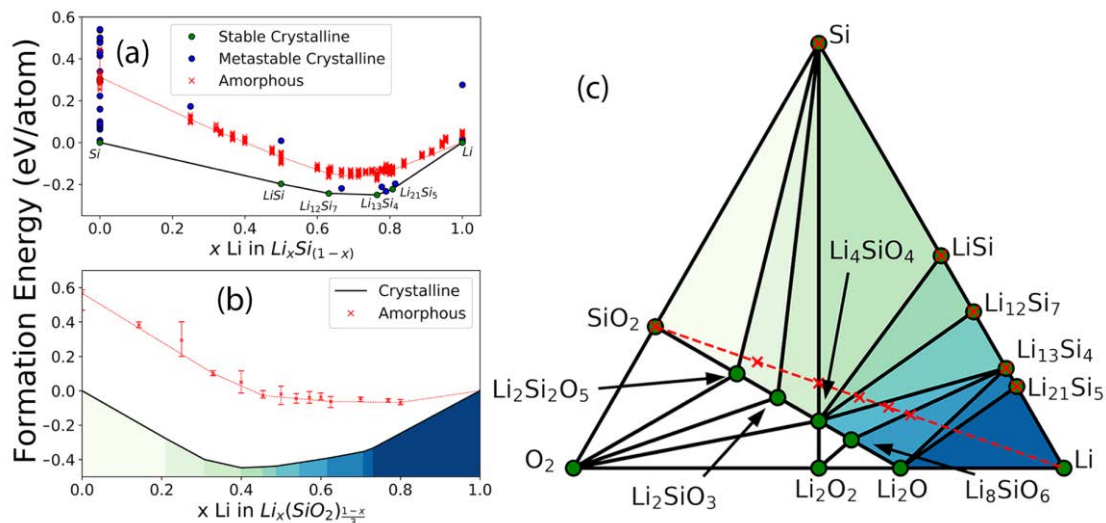


Figure II.6.B.3 Formation energy of crystalline and amorphous a) lithium silicides and b) lithium silicates, following lithiation path from Si and SiO_2 , respectively, as seen on the c) phase diagram

Figure II.6.B.3c shows the calculated Li-Si-O phase diagram at low temperature, which is constructed from the calculated formation energies, defined as $E_F = E_{\text{Li}_x\text{SiO}_2} - xE_{\text{Li}} - E_{\text{Si}} - E_{\text{O}_2}$, for the crystalline and amorphous phases respectively, as a function of Li content. The convex hull, which constructs the energy envelope of the thermodynamically stable phases, is depicted with lines and the stable phases as nodes along those lines. We emphasize that metastable compounds, e.g. those with energies above the convex hull, may be observed experimentally if the energy difference is small compared to the room temperature driving force for structural reorganization.

Figure II.F.2.3a shows the binary convex hull for the Li-Si composition line in the phase diagram, where the calculated metastable phases are also indicated. We note that the amorphous states exhibit a high degree of metastability, ranging from 10-500 meV/atom, however the amorphous convex hull follows a similar trend as for their crystalline counterparts, as a function of Li content. This suggests that the relative difference in formation energy between different compositions originates primarily from changes in short-range order Li-Si motifs. As indicated by the dashed line in Figure II.6.B.3c, SiO_2 is thermodynamically driven to lithiate. The predicted lithiation process passes through ten 3-phase regions consisting of lithium silicides, silicon, and stoichiometric lithium silicates, until the end products Li_2O and Li_xSi are formed. Following this compositional trajectory, we examine the calculated formation energies of a range of Li_xSiO_y amorphous compositions and compare to the combined energy of the crystalline phases as obtained through the convex hull of the phase diagram (illustrated by the same color scheme in Figure II.6.B.3c). Similar to the lithiation of Si, the amorphous structures are metastable as compared to the combination and the overall shape of the lithiation convex hull is similar for both crystalline and amorphous phases. Again, the common trend suggests that the energy differences between the compositions are dominated by the local Li-Si-O environments, rather than longer range interactions, which are not similar in crystalline and amorphous states. The initial charging (lithiation of the anode) will extrude Si, promoting more oxygen rich silicates. Further charging will produce various Li silicides until Li_2O and Li_xSi are formed.

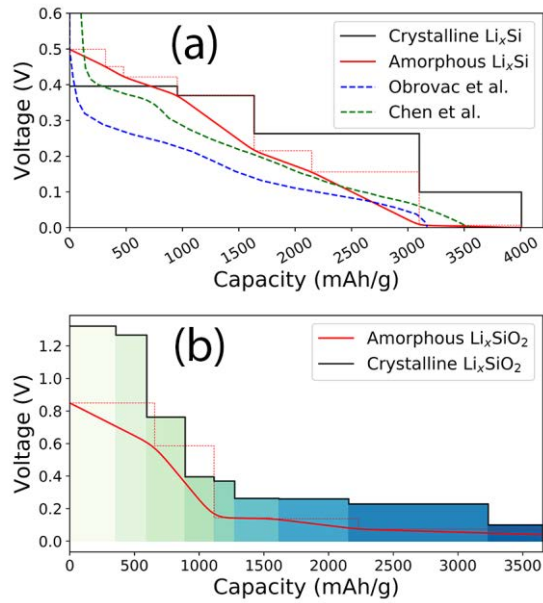


Figure II.6.B.4 Predicted potential profiles for a) Si and b) SiO₂ as referenced to the phase diagram in Figure II.6.B.3

Using the formation energies, the lithiation potential profiles (at equilibrium) of the systems were found as the chemical potential of Li in each multi-phase region. In the calculated voltage profile for Li_xSi, Figure II.6.B.4a, the crystalline states follow a discrete pathway from 0.39 V to 0 V. In the amorphous lithium silicides, the lithiation voltage is initially found to be higher than the crystalline voltage, 0.54 V until $x_{Li}=0.5$, where it drops below and follows the crystalline states.

Similar to the case of Si lithiation, the potential profile for Li_xSiO₂ was derived from the chemical potential of Li within the composition range between adjacent stable compositions. In the crystalline phases, the initial voltage of SiO₂ exceeds that of Si by almost 1 V. As lithiation progresses and a Li-Si environment forms, the voltage drops to values closer to that of Li_xSi. The amorphous phases follow a similar trajectory, initially exhibiting a high potential of 1.29 V, and ending at 0.06 V. These findings agree qualitatively with previous studies on bulk SiO₂ which exhibit voltage profiles higher than that of Si, between 1.00-1.50 V. The preferred equilibrium phase sequence upon lithiation shows the strength of, and

preference towards, the formation of Li-Si and Li-O bonds at the expense of Si-O bonds. The formation of Li_xSi and Li₂O local environments will occur, even in the first charge, if the anode voltage drops below ~100 mV vs Li metal. During discharge, the lithiated composite (surface phase and bulk) will delithiate in order of increasing potential such that the lithium silicides within the oxide layer and silicides in the bulk Si will delithiate first, forming Li_xSi and Li₄SiO₄. Only after the Li_xSi phases have been completely delithiated will the Li₄SiO₄ be delithiated to form SiO₂. Within the voltage/capacity limits batteries are typically cycled, it is likely that the delithiation of Li₄SiO₄ does not occur and the reaction can be viewed as a source of initial coulombic efficiency loss.

Lithium self-diffusivities were calculated from AIMD simulations, with a fixed number of atoms, volume, and temperature (NVT), through the Stokes-Einstein relation (Figure II.6.B.5) over 200 ps trajectories at 500 K, 1000 K, and 1500 K. Room temperature Li self-diffusivity is obtained from the Arrhenius relation. We find diffusivities on the order of 10⁻⁷ to 10⁻¹¹ cm²/s as shown in Figure II.6.B.5, which is comparable to the large range reported in literature, of 10⁻⁹ to 10⁻¹⁶ cm²/s. We observe an upward trend in diffusivity with decreasing voltage. Intuitively, as percolating Li-rich environments and pathways are formed within the amorphous matrix, we expect the Li diffusivity in Li-rich Si to approach that of Li-metal.

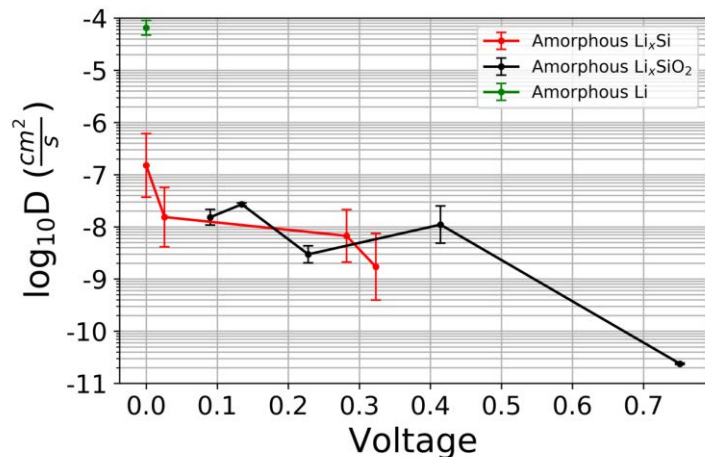


Figure II.6.B.5 Li self-diffusivity diffusion coefficients in lithium silicides and lithium silicates as a function of voltage vs Li/Li⁺.

Conclusions

In summary, our first-principles calculations have identified a concentration limit causing a change in Li^+ solvation structure between CIPs and SSIPs for not only LiAsF_6 in DMC but LiPF_6 in DMC as well. This provides notable insight into the effect of the electrolyte dielectric constant on the speciation of salt, between neutral CIPs and charge-carrying free ions. From our first principles calculations, we conclude that a surface phase SiO_2 is thermodynamically poised to lithiate. We find that the lithiation of SiO_2 occurs at higher potential than Si. Furthermore, the surface oxide presents a barrier to lithium diffusion towards the Si anode, with significantly lower Li conductivity, especially at low Li content.

Key Publications

1. Self, J.; Brandon, M. W.; Rajput, N. N.; Persson, K. A. The Interplay between Salt Association and the Dielectric Properties of Low Permittivity Electrolytes: The Case of LiPF_6 and LiAsF_6 in Dimethyl Carbonate. *J. Phys. Chem. C* **2017**.
2. Dielectric Properties of LiPF_6 in Dimethyl Carbonate, Self, J.; Brandon, M. W.; Rajput, N. N.; Persson, K. A. Gordon Battery Conference, Ventura, CA, 2018
3. Sivonxay, E.; Aykol M.; and Persson, K. A. The lithiation process and Li diffusion in amorphous Si and SiO_2 from first-principles, Submitted

II.6.C First Principles Calculations of Existing and Novel Electrode Materials (LBNL)

Gerbrand Ceder, Principal Investigator

Lawrence Berkeley National Laboratory
1 Cyclotron Rd, MS: 33-146
City, State Zip: Berkeley, CA 94720
E-mail: gceder@berkeley.edu

Duong Tien, DOE Technology Development Manager

U.S. Department of Energy
E-mail: Tien.Duong@ee.doe.gov

Start Date: October 1, 2015 End Date: September 30, 2019
Project Funding (FY18): \$1,204,226 DOE share: \$1,204,226 Non-DOE share: \$0

Project Introduction

There is a pressing need for the development of inexpensive, eco-friendly, high energy density cathode materials for lithium ion batteries. It was recently demonstrated that cathode materials based on Li-excess disordered transition metal oxides can deliver high capacities and sustain efficient Li transport provided Li is in an excess of at least 10% with respect to the transition metal concentration, creating a network of 0-TM channels through which Li can diffuse [1], [2], [3]. Modeling of diffusion through such disordered structures was developed in this part of the BMR program and has been used to develop novel compositions. In particular, compositions based on manganese are attractive candidates because of their low cost, high abundance, and intrinsic stability of Mn^{4+} . These cathodes have the potential to replace the nickel and cobalt in current battery cathodes. In our recent work, we used fluorination and high-valent cation substitution to develop Mn-based Li-excess cathodes that achieve ultrahigh capacity (> 300 mAh/g) and energy density (~ 1000 Wh/kg) within the voltage window of 1.5-5.0V at 10 mA/g, through Mn^{2+}/Mn^{4+} redox combined with a limited use of O redox [1].

In addition, modeling showed that these novel materials can be fluorinated due to the Li-rich environments in them. Fluorination of disordered rocksalt Li-ion cathodes have shown several advantages including reduced oxygen loss and improved capacity retention. Our modeling results also indicate that fluorination makes some of the Li inaccessible due to the presence of high-voltage Li sites created by the fluorine doping and the formation of tetrahedrally-coordinated Li. By considering these two effects, we investigated a series of disordered rocksalt oxyfluoride cathodes based on the combination of $Mn^{2+/4+}$ and $V^{4+/5+}$ couples [4].

Objectives

Develop very high capacity cathodes with high structural stability (> 250 mAh/g) and high surface stability. Clarify the role that Li-excess and cation disorder play in capacity and structural stability. Develop predictive modeling of oxygen charge transfer and oxygen loss and find ways to make oxygen redox beneficial in terms of increase capacity. Develop materials with engineered surface passivation which does not lead to impedance increase.

Approach

Thermodynamic evaluation of our systems is done using configurational Monte Carlo simulations, based on a cluster expansion Hamiltonian parametrized on the basis of first-principles density functional theory (DFT) calculations. Voltages and intercalation curves are calculated with GGA+U, and with the recently developed SCAN functional. Phase diagrams are calculated with the Materials Project infrastructure based on high-throughput computations. Configurational disorder for elevated temperature and off-stoichiometry is modeled with either point defect models (when off-stoichiometry is small) or with the cluster expansion for the larger disorder. Compounds have been synthesized by mechanochemical ball-milling, and experimental

characterization with XRD, TEM, NMR and XAS is used to evaluate existing and novel materials. Some of the computational work is performed in collaboration with Persson and with the Materials Project. Work on Li-excess materials is done in coordination with Persson (computational) and with the experimental efforts in the BMR Program (e.g. Chen and McCloskey).

Results

The viability of fluorination of disordered-rocksalt cathode materials

The high capacity generally observed for Li-excess disordered (rocksalt) transition metal oxides (DRX) cathodes relies on oxygen redox processes which can cause oxygen loss near the surface of the particles. This results in the creation of high impedance surface layers and large polarization of the voltage profile, leading to poor cycling performance. We recently showed that fluorine doping of DRX materials is feasible and results in a reduction of oxygen release as measured by differential electrochemical mass spectrometry (DEMS) [5]. We have used density functional theory (DFT) and cluster expansion Monte Carlo simulation methods to study the thermodynamics of fluorine incorporation into transition metal oxides to produce lithium-excess compositions.

Using ab-initio simulations, we constructed phase diagrams for the mixing of LiF into the lithium-metal oxide phase for the Ti, V, Cr, Mn, Fe, Co, and Ni systems. Figure II.6.C.1 shows an example phase diagram obtained for the LiCoO₂-LiF system. Our results indicate that, while fluorine solubility is very small in the cation ordered oxide phase (purple region on the left of Figure II.6.C.1), it is significantly increased upon disordering of the lithium and Co cations (dashed red region in Figure II.6.C.1). Similar results were obtained for all the transition metal systems of interest to this study.

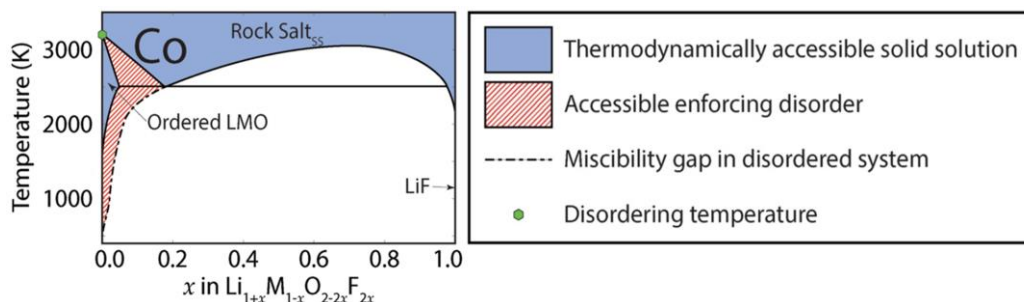


Figure II.6.C.1 LiCoO₂-LiF phase diagram [6].

We also carried out Monte Carlo simulations to determine the distribution of fluorine environments in representative cation-disordered $\text{Li}_{1.125}\text{M}_{0.875}\text{O}_{1.75}\text{F}_{0.25}$ compositions as a function of temperature (Figure II.6.C.2a). While there are three M-F bonds per F dopant in cation-ordered LMO structures, fluorine environments have fewer M-F bonds on average in the cation-disordered compounds. At the solubility limit (the lowest temperature at which the disordered $\text{Li}_{1.125}\text{M}_{0.875}\text{O}_{1.75}\text{F}_{0.25}$ forms), most fluorine ions are surrounded by one transition metal and five lithium atoms to minimize the number of high energy M-F interactions while still allowing for reasonable entropy in the system. Since disordering of the cation sublattice creates more of these metal-poor, lithium-rich local environments, it plays a central role in increasing LiF solubility in transition metal oxide systems.

Finally, due to the similar defect energetics of the disordered states, the miscibility gaps in the metastable disordered phase diagrams are very similar (Figure II.6.C.2b). The difference between the seven transition metal systems lies in the stability and disordering temperature of the stoichiometric LMO compound.

Our results indicate that for systems that can cation-disorder at typical sintering temperatures of 1000°C about 7.5% of O can be substituted by F.

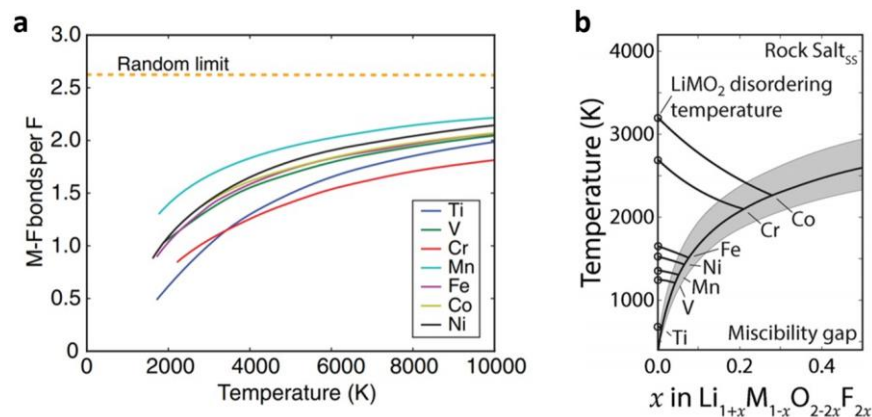


Figure II.6.C.2 (a) Local fluorine environments present in $\text{Li}_{1.125}\text{M}_{0.875}\text{O}_{1.75}\text{F}_{0.25}$ disordered rocksalt phases. (b) Superposition of the low fluorine region of the phase diagrams obtained for the Ti, V, Cr, Mn, Fe, Co, and Ni LMO systems [6].

Reversible $\text{Mn}^{2+}/\text{Mn}^{4+}$ double redox in lithium-excess cathode materials

It has been previously shown that high non-equilibrium fluorination levels can be achieved through mechanochemical synthesis methods such as high energy ball-milling. High F incorporation can lower the average transition metal valence in the as-synthesized discharged state. In a series of novel compounds with high level of fluorination, we were able to incorporate Mn^{2+} offering prospects for a very high theoretical $\text{Mn}^{2+}/\text{Mn}^{4+}$ redox capacity. Through the combined strategy of high valent cation (Nb^{5+} , Ti^{4+}) substitution and O^{2-} replacement by F^- , we achieved a very high transition metal redox and bypassed the negative effect of oxygen oxidation. Li-Mn-Nb-O-F (LMNOF) and Li-Mn-Ti-O-F (LMTOF) were synthesized by mechanochemical ball-milling. XRD, SEM, STEM-EDS were used to confirm that the material is a disordered rocksalt structure with homogenous fluorination (Figure II.6.C.3). Further evidence that fluorine is incorporated in the bulk of these materials has been provided by F-NMR.

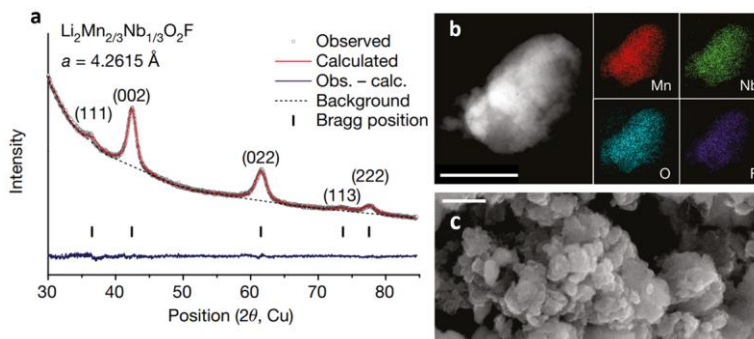


Figure II.6.C.3 (a) XRD, (b) STEM-EDS mapping from $\text{Li}_2\text{Mn}_{2/3}\text{Nb}_{1/3}\text{O}_2\text{F}$, (c) SEM [1].

Galvanostatic charge-discharge tests were carried out in LMNOF and LMTOF materials within different voltage windows and rates, demonstrating ultrahigh capacity (> 300 mAh/g) and energy density (~ 1000 Wh/kg) within the voltage window of 1.5-5.0V at 10 mA/g (Fig.4a). We also studied the redox mechanism by a combination of *ex-situ* XRD and X-ray absorption spectroscopy of manganese and oxygen K edge. The results showed that the $\text{Mn}^{2+}/\text{Mn}^{4+}$ redox partially overlaps with oxygen redox at high voltage. DFT calculations demonstrated that this overlap between oxygen redox and Mn redox arises from fluorination and from the large lattice constant of the materials (Figure II.6.C.4b).

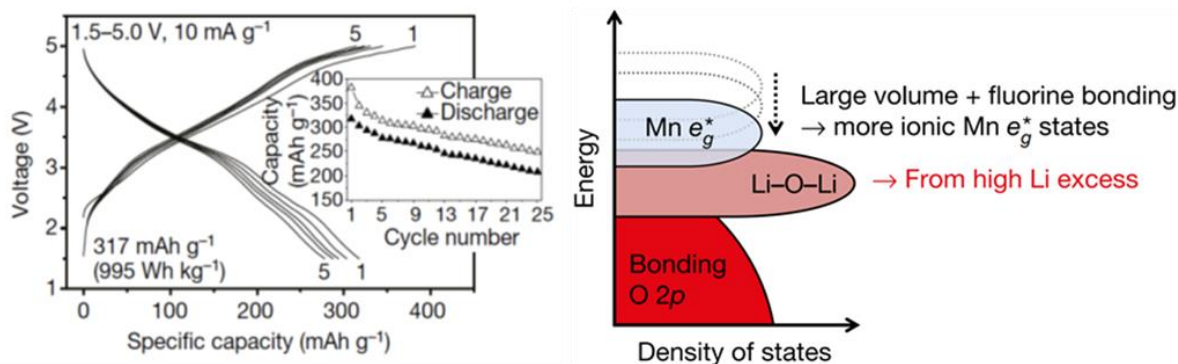


Figure II.6.C.4 (a) Electrochemical performance of LMNOF. (b) A schematic band structure of Li₂Mn_{2/3}Nb_{1/3}O₂F [1].

Design principle for high capacity disordered rocksalt Li-ion cathodes

We also explored the increasing capacity of DRX materials by replacing the inactive high-valent charge compensating element such as Nb⁵⁺, Mo⁶⁺, Ti⁴⁺ by V⁴⁺ as it can be oxidized further to V⁵⁺ and thereby provide additional transition metal redox capacity. For different redox couples we computed the full ternary phase diagram with V⁵⁺ and LiF so that the most optimal compositions could be picked out for experimental evaluation. For each system we computed the voltage curve and analyzed the delithiation mechanism.

Figure II.6.C.5 shows the computed phase diagram of the MnO/Li₂VO₃/LiF compositional space. According to the phase diagram, accessible compositions by both high-temperature solid-state synthesis (solid lines) and high energy ball-milling (dotted line) can be identified. The theoretical capacity of possible compositions in this chemical space is given as a color-coded overlay in Figure II.6.C.5. According to the theoretical capacity, the Mn^{2+/4+} and V^{4+/5+} redox couples are fully accessible, unless limited by the Li content in the structure. Because of the high content of light, redox-active transition metals the theoretical transition metal capacities are very high, reaching above 300 mAh/g for synthetically-accessible oxides and oxyfluorides. We picked a representative, Li_{1.166}Mn_{0.333}V_{0.500}O_{1.833}F_{0.166} (ST-LMVF) from the phase diagram, to study the delithiation behavior of these class of materials.

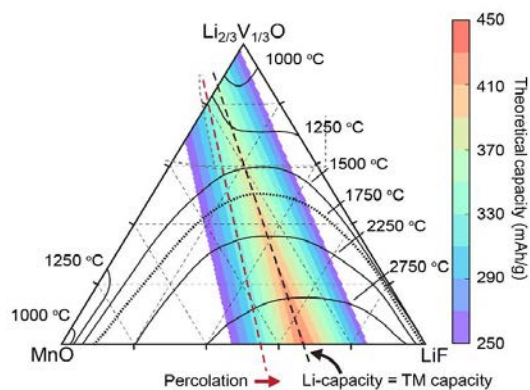


Figure II.6.C.5 Computed phase diagram of MnO - Li₂VO₃ - LiF. [4].

Figure II.6.C.6 shows the calculated voltage profile and valence states of each metal upon charge for ST-LMVF. Calculations suggest an initial mixed population of Mn^{2+} , Mn^{3+} , V^{3+} , and V^{4+} due to partial charge transfer from Mn^{2+} to V^{4+} . As Li is extracted from the structure, for $0 < x < 0.166$, the population of V^{3+} decreases rapidly while that of V^{4+} increases. For $0.166 < x < 0.666$ the population of V^{5+} increases at the expense of V^{4+} . Between $x = 0.666$ and $x = 0.916$, the population of Mn^{3+} increases at the expense of Mn^{2+} , while for $0.916 < x < 1.08$, Mn^{3+} starts to oxidize to Mn^{4+} . For $1.08 < x < 1.166$ oxygen commences. Based on our calculation, ST-LMVF shows a redox mechanism consisting of low voltage $\text{V}^{4+} / \text{V}^{5+}$ redox combined with high voltage $\text{Mn}^{2+} / \text{Mn}^{4+}$ redox, partially overlapping with oxygen oxidation at high voltage.

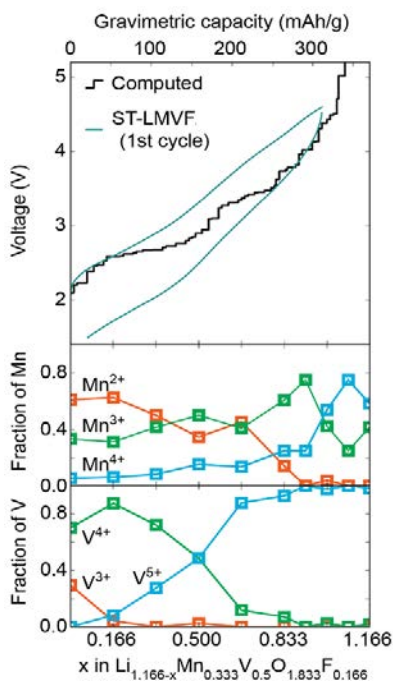


Figure II.6.C.6 Computed voltage profile and evolution of Mn and V oxidation states (from DFT) [4].

Electrochemical accessibility of Li in disordered rocksalt Li-Mn-V-O-F cathodes

We synthesized $\text{Li}_{1.143}\text{Mn}_{0.286}\text{V}_{0.572}\text{O}_2$ (STLMVO), $\text{Li}_{1.171}\text{Mn}_{0.343}\text{V}_{0.486}\text{O}_{1.8}\text{F}_{0.2}$ (ST-LMVF20), $\text{Li}_{1.133}\text{Mn}_{0.400}\text{V}_{0.467}\text{O}_{1.8}\text{F}_{0.2}$ (MR-LMVF20) and $\text{Li}_{1.23}\text{Mn}_{0.255}\text{V}_{0.515}\text{O}_{1.8}\text{F}_{0.2}$ (LR-LMVF20) using high-energy ball-milling in an argon atmosphere. As shown in Figure II.6.C.7, obtained capacities are lower than theoretical ones. Note that the Li theoretical capacity is based on the Li content of each composition, while the transition metal (TM) theoretical capacity is based on the total capacity of the $\text{Mn}^{2+/4+}$ and $\text{V}^{4+/5+}$ couples. Figure II.6.C.7 indicates that fluorination increases both Li and TM theoretical capacity from ST-LMVO to ST-LMVF20. By increasing the TM content from ST-LMVF20 to MR-LMVF20 the theoretical capacity is reduced but leaves the fraction of theoretical capacity that is obtained in experiments unchanged. For LR-LMVF20 the observed capacity becomes much closer to the theoretical value. In general, these trends illustrate that the limit on the performance of these compounds is not related to the accessibility of TM redox. Instead, the distribution of Li site energies in the disordered compounds can explain the observed sub-theoretical capacity.

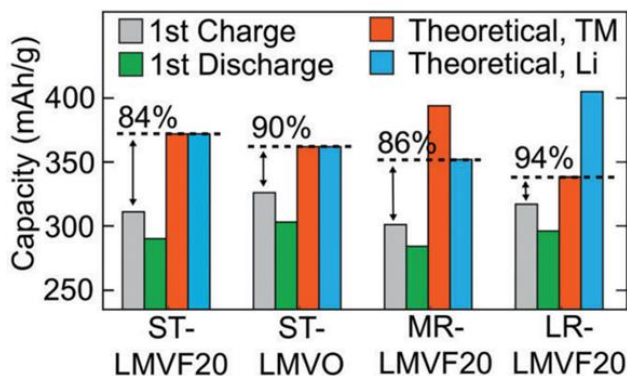


Figure II.6.C.7 Comparison between observed and theoretical capacities for ST-LMVF20, ST-LMVO, MR-LMVF20, and LR-LMVF20 compounds [4].

Figure II.6.C.8a shows the computed voltage range over which various F environments, characterized by their F-cation coordination number, appear within partially delithiated structures obtained from ST-LMVF20. Environments containing F with 1 nearest neighbor nearly always occur above 4.6 V indicating that for 75% of F sites, the delithiation of an F environment down to 1 remaining nearest neighbor cation charging above 4.6 V. Figure II.6.C.8b shows the Li-anion coordination number as a function of voltage for computed structures obtained from the delithiation of ST-LMVF20. The distribution of Li-anion coordination numbers shows that tetrahedral Li environments can form above 4 V. Above 4.5 V, nearly all Li remaining in the structure exist in a tetrahedral environment.

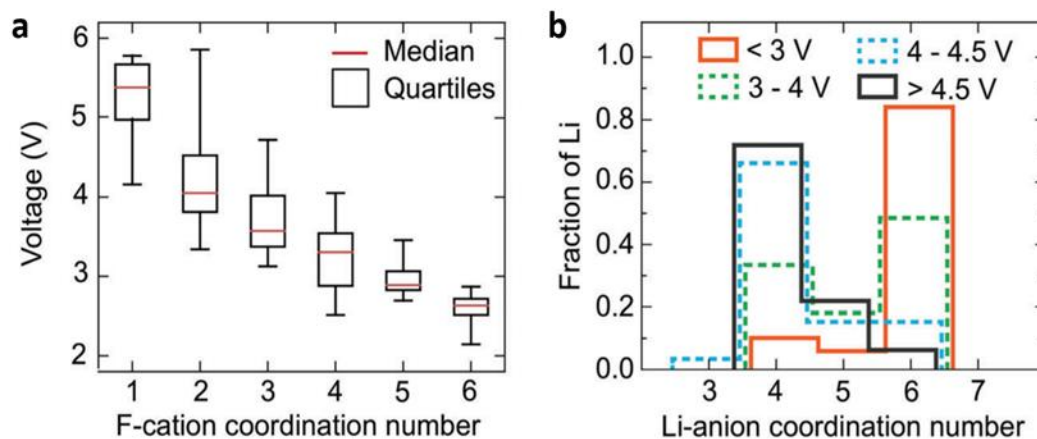


Figure II.6.C.8 Distribution of (a) F-cation and (b) Li-anion environments by coordination number, among simulated partially charged structures derived from ST-LMVF20, according to the voltage at which they appear [4].

Conclusions

Using computational modeling and experiments, we have shown several benefits related to fluorine substitution in disordered rocksalt materials: (i) lowering the average anion valence, (ii) allowing Li-excess compositions to be combined with lower valence metals, (iii) reducing oxygen loss during cycling, and (iv) improve capacity retention. However our results also indicate that in oxyfluorides 0.4-0.8 Li per F is inaccessible due to strong Li-F binding. In addition, the formation of high-voltage tetrahedral Li is another factor that causes 10-12% of Li present to be inaccessible at moderate voltages.

Our DFT-derived cluster expansion results show that the ability for fluorine incorporation into an oxide compound associates with the ease of cation disordering.

Using fluorination and high-valent cation substitution, we developed Mn-based Li-excess cathodes that achieve ultrahigh capacity (> 300 mAh/g) and energy density (~ 1000 Wh/kg) within the voltage window of 1.5-5.0V at 10 mA/g, through $\text{Mn}^{2+}/\text{Mn}^{4+}$ redox combined with a limited use of O redox

Key Publications

1. Kitchaev, D. A., Lun, Z., Richards, W. D., Ji, H., Clément, R. J., Balasubramanian, M., Kwon, D. H., Dai, K., Papp, J. K., Lei, T., McCloskey, B.D., Yang, W., Lee, J., & Ceder, G (2018). Design principles for high transition metal capacity in disordered rocksalt Li-ion cathodes. *Energy & Environmental Science*.
2. Lee, J., Kitchaev, D. A., Kwon, D. H., Lee, C. W., Papp, J. K., Liu, Y. S., Lun, Z., Clément, R.J., Shi, Tan., McCloskey, B.D., Guo, J., Balasubramanian, M., & Ceder, G (2018). Reversible $\text{Mn}^{2+}/\text{Mn}^{4+}$ double redox in lithium-excess cathode materials. *Nature*, 556(7700), 185.

References

1. Lee, J., Kitchaev, D. A., Kwon, D. H., Lee, C. W., Papp, J. K., Liu, Y. S., Lun, Z., Clément, R.J., Shi, Tan., McCloskey, B.D., Guo, J., Balasubramanian, M., & Ceder, G (2018). Reversible $\text{Mn}^{2+}/\text{Mn}^{4+}$ double redox in lithium-excess cathode materials. *Nature*, 556(7700), 185.
2. Lee, J., Urban, A., Li, X., Su, D., Hautier, G., & Ceder, G. (2014). Unlocking the potential of cation-disordered oxides for rechargeable lithium batteries. *Science*, 343(6170), 519-522.
3. Urban, A., Lee, J., & Ceder, G. (2014). The Configurational Space of Rocksalt-Type Oxides for High-Capacity Lithium Battery Electrodes. *Advanced Energy Materials*, 4(13), 1400478.
4. Kitchaev, D. A., Lun, Z., Richards, W. D., Ji, H., Clément, R. J., Balasubramanian, M., Kwon, D. H., Dai, K., Papp, J. K., Lei, T., McCloskey, B.D., Yang, W., Lee, J., & Ceder, G (2018). Design principles for high transition metal capacity in disordered rocksalt Li-ion cathodes. *Energy & Environmental Science*.
5. Lee, J., Papp, J.K., Clément, R.J., Sallis, S., Kwon, D.H., Shi, T., Yang, W., McCloskey, B.D. and Ceder, G. (2017). Mitigating oxygen loss to improve the cycling performance of high capacity cation-disordered cathode materials. *Nature communications*, 8(1), 981.
6. Richards, W. D., Dacek, S. T., Kitchaev, D. A., & Ceder, G. (2018). Fluorination of Lithium-Excess Transition Metal Oxide Cathode Materials. *Advanced Energy Materials*, 8(5), 1701533.

II.6.D Addressing Heterogeneity in Electrode Fabrication Processes (Brigham Young University)

Dean Wheeler, Principal Investigator

Brigham Young University
 Department of Chemical Engineering
 330 Engineering Building
 Provo, UT 84602
 E-mail: dean_wheeler@byu.edu

Brian Mazzeo, Principal Investigator

Brigham Young University
 Department of Electrical and Computer Engineering
 450 Engineering Building
 Provo, UT 84602
 E-mail: bmazzeo@byu.edu

Tien Duong, DOE Technology Development Manager

U.S. Department of Energy
 E-mail: Tien.Duong@ee.doe.gov

Start Date: October 1, 2017	End Date: September 30, 2019	
Project Funding (FY18): \$350,000	DOE share: \$350,000	Non-DOE share: \$0

Project Introduction

A lack of fundamental understanding about the relationships between fabrication parameters, microstructure, and performance prevents appropriate feedback and hurts the development of next-generation battery materials and process improvement in battery manufacturing. For instance, one problem with large-format batteries is ensuring uniformity in the manufacturing process, so that all components perform equally well and no component contributes unduly to performance limitations and failure. This improvement in manufacturing will not be possible without additional information on the nature of heterogeneities and how they relate to electrode fabrication steps. Even more beneficial is if the information is made available in a timely manner through the use of convenient and reliable experimental and modeling tools.

Objectives

The goal of this work is to better understand connections between fabrication conditions and undesired heterogeneity of thin-film electrodes by means of new non-destructive inspection techniques and computer models. This work will result in new diagnostic and modeling tools for rapidly and conveniently interrogating how well homogeneity has been maintained in electrodes during fabrication and in subsequent cycling. Real-time measurement of heterogeneity will enable manufacturer quality control improvements. The measurement and modeling tools will further enable researchers to compare different electrodes, improve formulations and processes, and anticipate cell performance of new designs.

Approach

Two non-destructive inspection techniques are being developed and improved which will characterize electrochemical and mechanical uniformity of the electrodes. The first tool is a flexible contact probe on a polymer substrate for rapidly measuring local electrical conductivity across electrodes of any geometry. The second tool is a new acoustic probe that measures local elasticity and density of the composite film. These two prototyping efforts are tied together by a particle-based microstructure model that allows prediction and correlation of electrode conductive and mechanical properties with fabrication conditions. Each of these tools involved one or more quarterly milestones. In addition to model and tool development, the tools were used to

begin examining electrodes sourced from other researchers, including from industry, in order to assess the effects of mixing and composition changes, and the effects of cycling.

Results

This year the project focused on improvements and validation of the new flexible conductivity probe. Work on the acoustic probe and fabrication model were ongoing, but are not part of reported milestones until FY2019.

Milestone 1. The flexible N-line probe has been shown to be robust and achieves accurate results as compared with the previous rigid probe iterations. Despite the advantages of the old rigid probe, measurements of large-format electrodes have not been possible and manufacturing of the probe was relatively time-consuming and costly. In order to make the N-line probe more attractive commercially, the first milestone of FY2018 was to integrate an off-the-shelf solution to replace the high-resolution 3-axis stage. The result had to be less expensive and cover a larger interrogation area without compromising significantly on the usefulness of the measurement apparatus.

Due to the prevalence of do-it-yourself 3-D printers and CNC devices, 3-axis stages have become both available and affordable. The stage seen in Figure II.6.D.1 is an off-the-shelf CNC stage sold by Carbide 3D. Samples up to 15 inches by 20 inches can be measured easily.

Measurements of Argonne National Labs AC006 electrode materials were performed on both the old high-resolution stage and on the new low-cost stage. As shown in Figure II.6.D.2 measurement results for the two stages are in statistical agreement. The results were further validated against the average film conductivity measured using the Van Der Pauw method and against our initial results with the rigid 4-line probe.

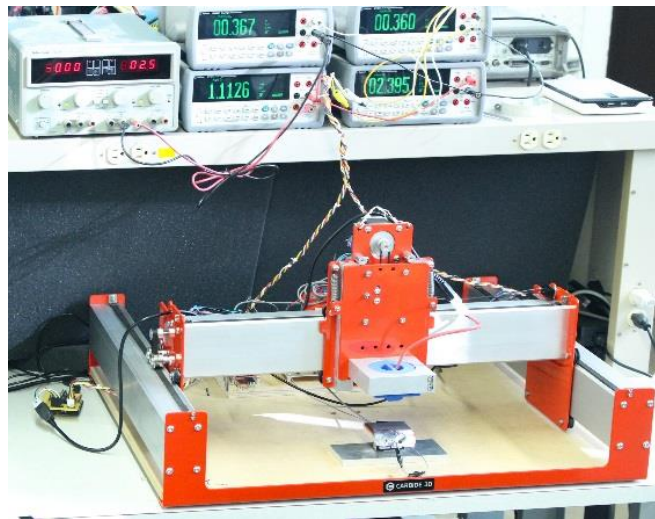


Figure II.6.D.1 Large-format Shapeoko CNC stage produced by Carbide 3D, with a custom made N-line probe attachment.

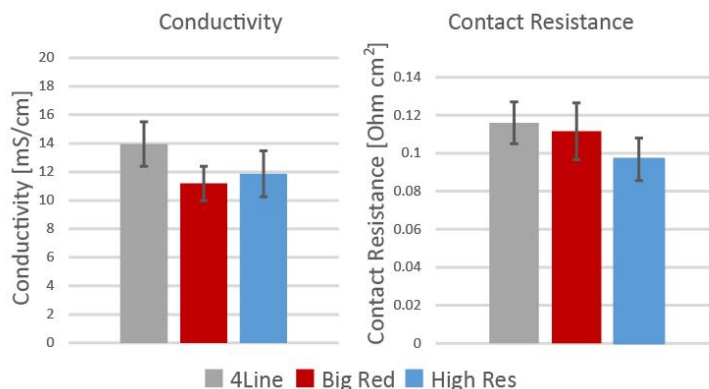


Figure II.6.D.2 Measured bulk conductivity and contact resistance values (with 95% confidence intervals) on ANL AC006 cathode film using both large-format (“Big Red”) and high-resolution stages, compared to results from the (old) rigid 4-line probe.

Milestone 2. The flexible N-line probe has provided the opportunity for a more robust way of taking electronic measurements of battery electrode films. With the flex probe integrated into an off-the-shelf CNC machine as a positioning system, the probe becomes more commercially attractive. The second milestone of FY2018 was to develop a proof-of-concept rolling probe, allowing for interrogation of continuous-roll electrode films without compromising the integrity of the films.

Using 3D printing, a series of designs were realized for the rolling apparatus. The flex probe is embedded along the circumference of the rolling apparatus, which in turn attaches to the head unit of the CNC positioning system, as shown in Figure II.6.D.3. Use of the CNC positioning system is a preliminary step to simulate a fully continuous rolling apparatus as might be used during roll-to-roll electrode manufacturing. Here the apparatus can complete two full rotations in one test, and therefore take two measurements at intervals on the electrode film.

Figure II.6.D.4 shows the results of a rolling measurement over 40 mm of travel distance. A nonzero current corresponds to the region where the N-line probe is in contact with a Li-ion electrode sample, and therefore allows a conductance to be computed. Figure II.6.D.4 shows the intermittent contact for 8 repetitions in which the roller is moved back and forth over the same location. The results for conductance show relatively high repeatability. Further work on this apparatus will continue in order to move toward a fully automated measurement tool.

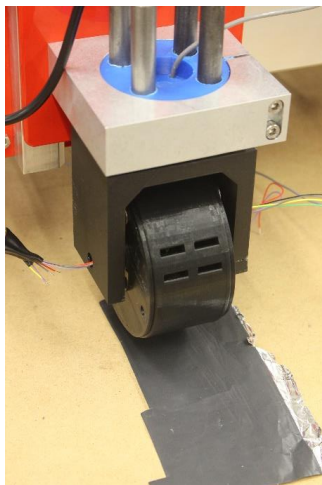


Figure II.6.D.3 Converted Carbide 3D CNC stage with custom rolling N-line probe attachment.

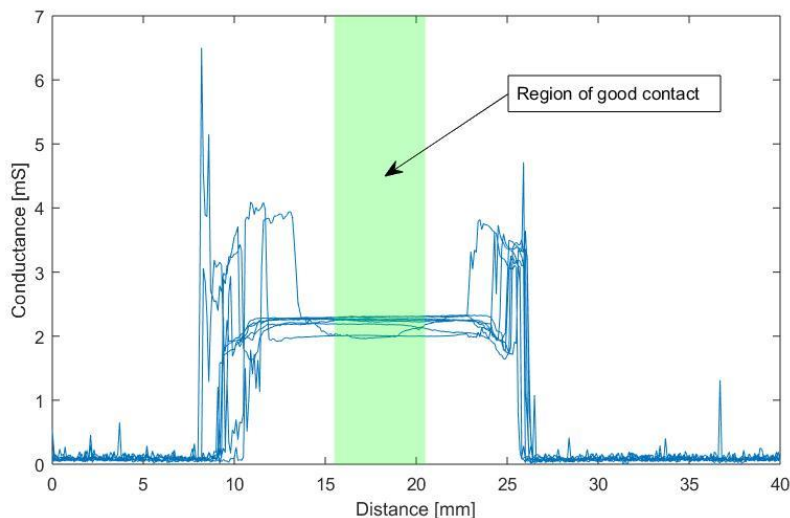


Figure II.6.D.4 Conductance measurements over a 40-mm segment of battery electrode film, showing areas of no, minimal, and good contact. The measurement is repeated eight times with the probe rolled back forth over the same segment.

Milestone 3. The blocking-electrolyte method and polarization-interrupt method have both been used at BYU to measure effective ionic conductivity or electrolyte diffusivity inside battery films. These methods as implemented measure average transport properties for films typically of size 2 cm x 2 cm. Taking measurements with a microprobe allows the possibility of determining local ionic conductivity and the degree of heterogeneity for this critical property. There is a great need to determine local ion transport as this correlates with active material utilization and, in the case of anodes, the cause of localized lithium plating during fast charging. This quarterly milestone was to show proof of concept of measuring ionic conductivity with the conductivity microprobe previously designed at BYU.

Measurements were taken separately with electrolyte only, separator, anode, and cathode. Results indicate that the method clearly distinguishes between different conductivity values of these materials. However, a more detailed computer model must be completed in order to properly invert the experiments and make the method quantitative. For this reason the milestone is considered partially complete.

Figure II.6.D.5 shows the experimental set-up with an electrolyte-soaked electrode on the microprobe. In a given test the probe is sampling conductivity for an electrode area of approximately $100\ \mu\text{m} \times 450\ \mu\text{m}$. When the conductivity is varied and other conditions are held constant, the EIS spectra show a clear trend with conductivity. Figure II.6.D.6 shows typical Nyquist curves for different electrolytes, demonstrating that the method can distinguish even modest variations in conductivity.

In further work, a microprobe was used to measure the ionic resistance of 7 electrodes of different average MacMullin numbers, a measure of how easy ions can move through the electrode. The MacMullin number was determined using the blocking-electrolyte method over the whole film. On each electrode, 30 locations were chosen randomly, and each location yielded a different ionic resistance using the microprobe, due to the heterogeneity of the electrode. Figure II.6.D.7 shows the average ionic resistance (by microprobe; vertical axis) of each electrode versus its MacMullin number (by blocking electrolyte method; horizontal axis), with a parity line showing the proportional level of agreement between the two methods. The trend shows that the microprobe measurement has the potential to distinguish electrodes of different tortuosity, though continuing work in FY2019 will be needed to make the method more quantitative. The method is also able to quantify the degree of heterogeneity in ionic transport for a given electrode

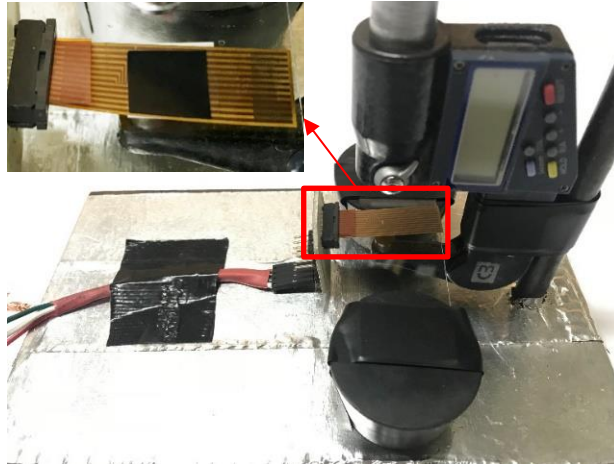


Figure II.6.D.5 The experimental setup of a microprobe in contact with a sample of delaminated cathode.

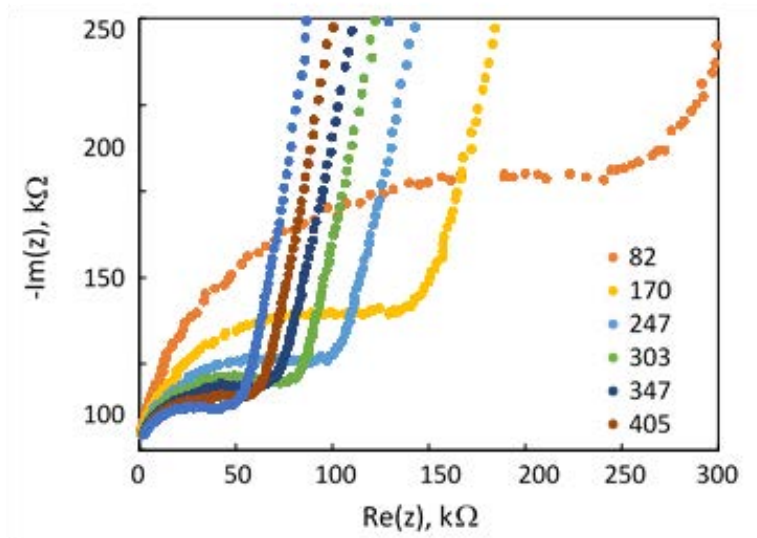


Figure II.6.D.6 Nyquist spectra of different electrolyte samples with conductivities varying from 82 to 443 $\mu\text{S}/\text{cm}$.

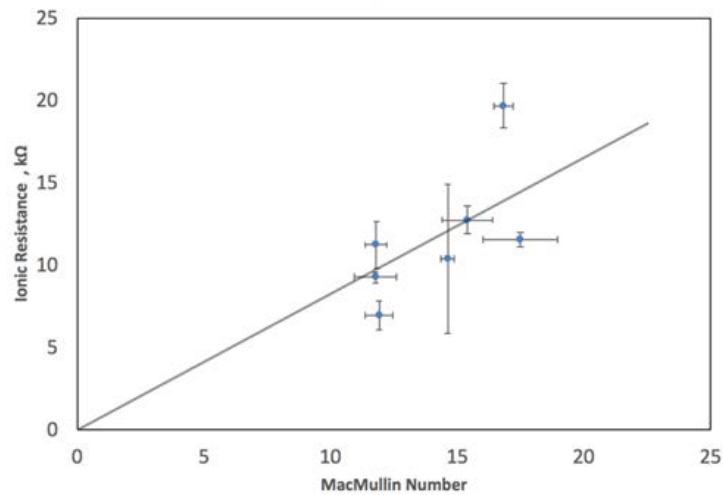


Figure II.6.D.7 Average MacMullin number versus localized ionic resistance for 7 different electrode films.

Milestone 4. In order for the new flex probes to be a viable method for laboratory or commercial analysis of electrodes, the probes must have satisfactory durability. The probes are made of polymer substrate with applied copper lines, but contact with active material on electrodes can lead to wear. Therefore, to complete the final milestone of FY2018, tests were performed to determine the durability of the flexible conductivity microprobes. The probe was used to perform 1,000-sampling-point tests on a commercial Li-ion cathode. Images of the probes were taken between such tests and the electrical data were also analyzed to determine the degradation of the flexible probe. Figure II.6.D.8 shows the image progression of the probe lines over the duration of these tests. As shown in the figure, slight degradation was shown over the course of a total of 10,000 points which demonstrates high durability, given that typical tests encompass several hundred points. The electrical data also showed that the probe lines consistently obtained good contact with the Li-ion electrode. Occasionally probes need to be cleaned, but nevertheless show satisfactory durability for their intended purpose.

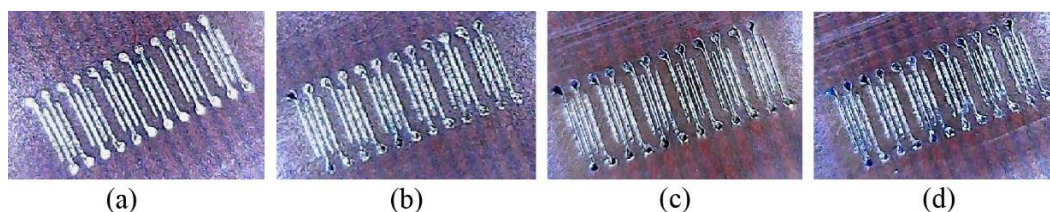


Figure II.6.D.8 Optical microscope images of probe surface (a) before durability tests, (b) after a total of 3,000 sampling points, (c) after a total of 7,000 points, and (d) after a total of 10,000 points.

Conclusions

This year the main theme of the project was to integrate the new flex probe with test fixtures suitable for assessment of large or continuous samples and to demonstrate measurement of localized ionic conductivity.

The primary deliverables were to

1. Integrate the flex probe with an off-the-shelf CNC positioning system to enable interrogation of large-format electrode films.
2. Integrate the flex probe with a prototype rolling apparatus to enable interrogation of continuous-roll electrode films.
3. Demonstrate that the localized conductivity probe has adequate reliability for continued development. Specifically, the results from the probe were compared to macroscopic results for multiple electrode samples.
4. Quantify the durability of multiple flex probes to validate the technology's suitability for industrial use.

This work has resulted in better understanding of the connections between fabrication conditions and undesired heterogeneity of thin-film electrodes. Non-destructive inspection techniques and computer models have been created to provide researchers with new tools to measure and model electrode properties. These techniques have been used to evaluate commercial electrodes in collaboration with researchers in academia and industry.

In the upcoming fiscal year the project will focus on assessing the effect of heterogeneity on cell charge and discharge performance and further improving the accuracy and reliability of probe and modeling technologies.

Key Publications

The following publications were made during FY2018 under VTO support. Additional manuscripts based on this work are under preparation.

1. F. Usseglio-Viretta, A. Colclasure, D. Finnegan, K. P. Yao Claver, D. Abraham, A. Mistry, P. Mukherjee, T. Heegan, P. Shearing, F. Pouraghajan, D.R. Wheeler, S. Cooper, K. Smith, “Resolving the discrepancy in tortuosity factor estimation for Li-ion battery electrodes through micro-macro modeling and experiment,” *J. Electrochem. Soc.* 165, A3403-A3426 (2018).
2. F. Pouraghajan, H. Knight, M. Wray, B. Mazzeo, R. Subbaraman, J. Christensen, D.R. Wheeler, “Quantifying tortuosity of porous Li-ion battery electrodes: comparing polarization-interrupt and blocking-electrolyte methods,” *J. Electrochem. Soc.* 165, A2644-A2653 (2018).
3. M. Forouzan, B.A. Mazzeo, and D.R. Wheeler, “Modeling the effects of electrode microstructural heterogeneities on Li-ion battery performance and lifetime,” *J. Electrochem. Soc.* 165, A2127-A2144 (2018).
4. K.L. Dallon, J. Yao, D.R. Wheeler, and B.A. Mazzeo, “Characterization of mechanical properties of battery electrode films from acoustic resonance measurements,” *J. Appl. Phys.* 123, 135102 (2018)

The following presentations at scientific conferences were based partially or completely on this work.

1. D.R. Wheeler, “Investigating heterogeneity in Li-ion battery electrodes,” Utah Energy Symposium, University of Utah, 2018.
2. D.R. Wheeler and B.A. Mazzeo, “Addressing heterogeneity in electrode fabrication processes,” U.S. Department of Energy 2018 Annual Merit Review Meeting, Washington, DC.
3. D.R. Wheeler, “(Invited) How to deal with electrode heterogeneity in cell-level battery modeling,” 233rd Meeting of The Electrochemical Society, Seattle, WA, 2018.
4. M.M. Forouzan, D.R. Wheeler, and B.A. Mazzeo, “Effects of local tortuosity and porosity heterogeneities on charge and discharge performance of Li-ion batteries,” 233rd Meeting of The Electrochemical Society, Seattle, WA, 2018.
5. J.E. Vogel, E.E. Hardy, S. Crawford, B.A. Mazzeo, and D.R. Wheeler, “Local variation in microstructure causes heterogeneity in the conductivity of commercial lithium-ion cathode films,” 233rd Meeting of The Electrochemical Society, Seattle, WA, 2018.
6. M. Nikpour, J. Cordon, D.R. Wheeler, and B.A. Mazzeo, “Slurry model for understanding fabrication of Li-ion battery electrodes,” 233rd Meeting of The Electrochemical Society, Seattle, WA, 2018.
7. F. Pouraghajan, A.I. Thompson, J.E. Vogel, B.A. Mazzeo, and D.R. Wheeler, “The effect of different mixing processes on the ionic and electronic conductivities of Li-ion battery electrodes,” 233rd Meeting of The Electrochemical Society, Seattle, WA, 2018.
8. B.A. Mazzeo, “(Invited) Measurement and Origins of Conductivity Variations in Commercial Li-Ion Electrode Films,” International Battery Seminar & Exhibit, Ft. Lauderdale, FL, 2018.
9. D.R. Wheeler, “(Invited) Variations in microstructure and conductive properties of Porous Li-ion electrodes,” Gordon Research Conference on Batteries, Ventura, CA, 2018.

Acknowledgements

Partners in this effort included Ram Subbaraman (Bosch), Daniel Abraham (ANL), Kandler Smith (NREL), Bryant Polzin (ANL), Chisu Kim (Hydro-Québec), and Henning Dreger (TU Braunschweig). Other commercial parties provided materials, discussions, or both, but do not wish to be publically identified at this time.

II.6.E Large Scale *ab initio* Molecular Dynamics Simulation of Liquid and Solid Electrolytes (LBNL)

Lin-Wang Wang, Principal Investigator

Lawrence Berkeley National Laboratory
One cyclotron road, MS-66
Berkeley, CA, 94760
E-mail: lwwang@lbl.gov

Tien Duong, DOE Technology Development Manager

U.S. Department of Energy
E-mail: Tien.Duong@ee.doe.gov

Start Date: October 1, 2016

End Date: September 30, 2017

Project Funding (FY18): \$225,000

DOE share: \$225,000

Non-DOE share: \$0

Project Introduction

One major obstacle for lithium sulfur battery is the dissolution of the lithium polysulfide in the electrolytes. The goal of this project is to use large scale *ab initio* calculation and molecular dynamics simulations to study the discharge mechanism in Li sulfur battery, especially for polysulfide interaction with liquid electrolyte solvent molecules, and cathode materials, as well as Li diffusion mechanism in superionic crystal solid electrolytes. We like to search for cathode materials and designs to prevent the dissolution based on thermodynamic principles. The long term goal is to use such theoretical understanding to provide guidance to develop better electrolyte and cathode systems to overcome the bottlenecks which currently prevent the commercialization of the Li/S battery.

Objectives

We have followed the work of last year, continue the study of lithium polysulfide interaction with substrate cathode materials, and to find such substrates to bind the lithium polysulfide with sufficient binding energies to overcome their dissolution. One objective is to screen a few cathode materials for their feasibilities for Li-S battery applications through *ab initio* calculation. We have also studied solid electrolytes for the lithium diffusion in such systems. One long term objective is to study the actual lithium polysulfide thermodynamic properties and morphology in the electrolyte. For this goal, we also need to develop the proper *ab initio* calculation methods to study such thermodynamic properties in liquid.

Approach

Several *ab initio* calculation methods will be used, and new methods will be tested and developed. Most of our calculations will be based on density functional theory (DFT). One approach is to use genetic algorithm to search for the minimum energy structure. This is important for Li-S battery since the cathode material and the binding morphology is usually complicated, not in simple crystal structure. Another issue is the dealing of the solvent effects. First, we will use implicit solvent model to deal with this solute-solvent interaction energy. The uncertainty of the interaction parameters will be fixed through the comparison with the experimental voltages in the dissolved Li_2S_n cases. In the future, we will test a molecular dynamics (MD) based method to study the solute-solvent interaction energy. One particular approach is the bi-canonical thermodynamics. In this approach, a small specie in the solution is allowed to disappear gradually by using weights of two systems, one with this specie another without this specie. This enables the thermodynamic integration to yield the Gibbs free energy of the solute specie inside a solvent. It has been shown this approach can yield accurate Gibbs free energies for simple ions in water. We will also explore other approaches, which combine classical force field molecular dynamics (FF-MD) with *ab initio* calculations, to use FF-MD to guide the *ab initio* calculations for energy average. For Li diffusion in solid electrolyte we are using the nudged elastic band (NEB) method to calculate the barrier height. However, the NEB is only applicable for systems with well defined structures and

local minima (e.g., in crystal structures), it cannot be applied to complicated amorphous like systems as in some of the lithium sulfur cathode materials we studied. For such cases, we have tested new approaches. One is to apply a force in one lithium atom, forcing it to move along one direction. The resulting potential landscape is analyzed to get the information for the barrier height. Finally, in the future, we will explore the use of neural network potential developed with machine learning techniques to simulate large systems with ab initio accuracy.

Results

Using our newly developed implicit solvent model, we have studied the use of 2D hexaaminobenzene, as a Li-S battery cathode. The 2D hexaaminobenzene is consisted with a carbon-nitride sheet with carbons in a benzene ring and nitrogen atom binding with a transition metal. This is a system similar to the C_2N nanosheet we studied last year, but with transition metal in the system. We have studied the system with Mn. Its atomic structure and electronic band structures are shown in Figure II.6.E.1. It is electric conductive. Such a system can absorb S_8 molecule, which in turn can serve as Li-S battery cathode. We show that the system can absorb Li, and be able to prevent the dissolution of lithium sulphur cluster, as indicated by their binding energies with the substrate (Figure II.6.E.2). The negative binding energies means the polysulfides will rather be bound with the substrate, instead of being dissolved in the solvent. When a Li-S cluster is absorbed, the S can bind with the Mn, while Li can bind with the N atoms. When fully charged, the energy capacity of the system can be around 1300 Wh/Kg. energy.

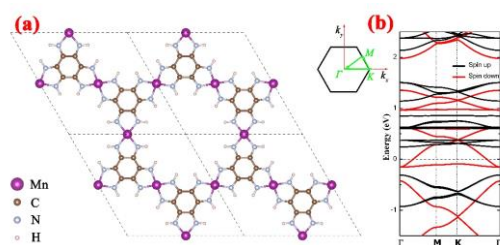


Figure II.6.E.1 A sandwich system with Li-S and Mn hexaaminobenzene system with the maximum lithiation of 20 Li per 8 S atoms. The top view and side view. The green ball is Li and yellow ball is S.

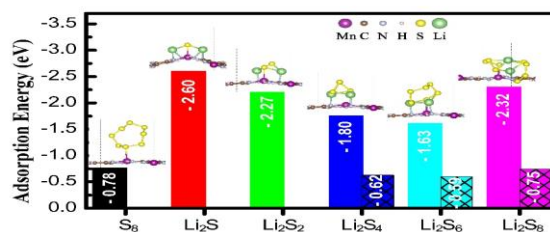


Figure II.6.E.2 The energy landscape by pulling one Li through the system. One can use such landscape to estimate the barrier height.

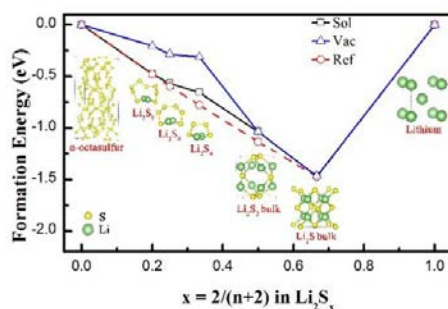


Figure II.6.E.3 The Li polysulphides free energies calculated with solvent model (Sol), compared with the results in vacuum (Vac), and the reference curve derived from experiment (Ref).

We have also recalibrated the theoretical Li_2S_n cluster energy in the solvent electrolyte. This is shown in Figure II.6.E.3. In the literature, we found that sometimes the solvent effects were not included in the calculations of Li_2S_n cluster energy, and Li metal clusters instead of Li crystal were used as the Li reference energy. Such calculations can lead to big errors.

One issue of the 2D material as cathode is how to increase their volumetric energy capacities. We have designed a sandwich structures with alternating 2D hexaaminobenzene and Li-S layers, as shown in Figure II.6.E.4. Surprisingly, such structure only has a few percent volume expansion upon full lithiation. The weight energy capacity of the system remains to be high, above 1000 Wh/kg. One issue is the lithium diffusion inside such a system. As can be seen from the top view in Figure II.6.E.4, there is a big hole of the structure, which allows the Lithium atoms to diffuse down, and the lithium atoms only need to diffuse a short distance side way between the layers. To calculate the Li diffusion constant in such an amorphous like system, we have developed a new computational method. In this new method, an artificial force is applied to one Li atom while doing an ab initio molecular dynamics. When the force is sufficiently large, the Li atom will move. The resulting energy landscape is analyzed as shown in Figure II.6.E.5. This landscape contains the information of potential barrier. We are testing different procedures to optimize the reliability of such method. If successful, this procedure can be used in the calculation of Li diffusion in many battery systems.

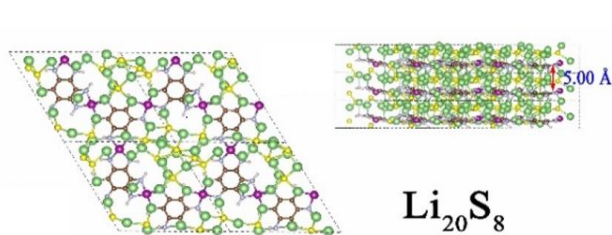


Figure II.6.E.4 A sandwich system with Li-S and Mn hexaaminobenzene system with the maximum lithiation of 20 Li per 8 S atoms. The top view and side view. The green ball is Li and yellow ball is S.

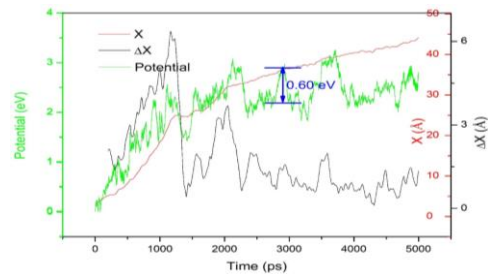


Figure II.6.E.5 The energy landscape by pulling one Li through the system. One can use such landscape to estimate the barrier height.

We have studied the design and improvement of solid electrolyte : $\text{Li}_{10}\text{GeP}_2\text{S}_{12}$ (LGPS). This germanium thiophosphate has one of the highest Li conductivities (20 mS/cm) among all the known solid electrolytes. Unfortunately, it is moisture unstable. Through ab initio calculation, we found that the instability comes from the PS_4 tetrahedron. It is possible to replace the PS_4 with PO_4 , hence we arrived at a new compound: $\text{Li}_{10}(\text{GeS}_4)(\text{PO}_4)_2$, as shown in Figure II.6.E.6.

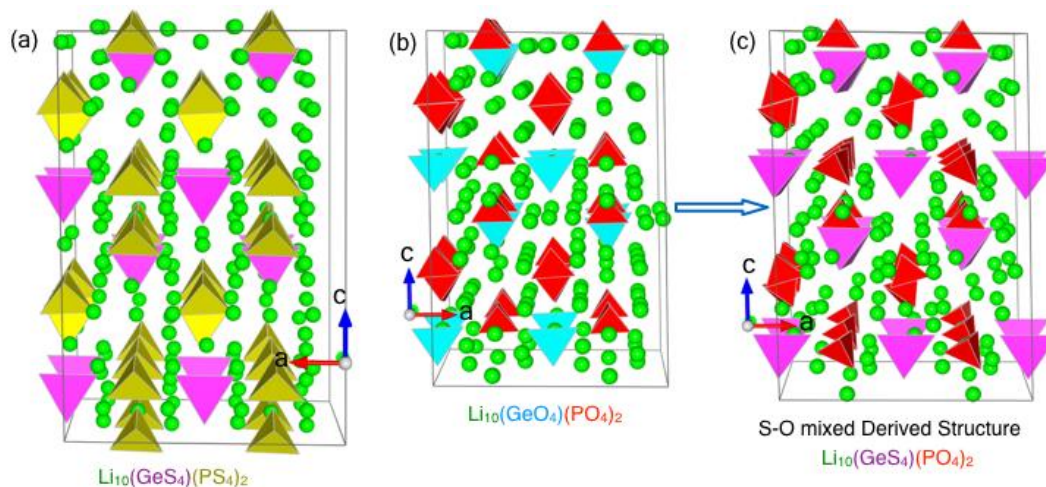


Figure II.6.E.6 The mixing of the $\text{Li}_{10}(\text{GeS}_4)(\text{PS}_4)_2$ structure and the $\text{Li}_{10}(\text{GeO}_4)(\text{PO}_4)_2$ structure to form the $\text{Li}_{10}(\text{GeS}_4)(\text{PO}_4)_2$ structure.

We found that this compound is moisture stable. This is because the original moisture instability comes from the reaction of $(\text{PS}_4)+4\text{H}_2\text{O} \rightarrow (\text{PO}_4)+4\text{H}_2\text{S}$. Now, with PS_4 being replaced by PO_4 , such reaction can no longer happen, and the $(\text{GeS}_4)+4\text{H}_2\text{O} \rightarrow (\text{GeO}_4)+4\text{H}_2\text{S}$ reaction is energetically unfavorable. Furthermore, using linear programming, we found that the $\text{Li}_{10}(\text{GeS}_4)(\text{PO}_4)_2$ is stable against decomposition into binary compounds, although it is thermal dynamically stable against the decomposing into ternary compounds of Li_4GeS_4 and Li_3PO_4 . But this is the same situation as for $\text{Li}_{10}\text{GeP}_2\text{O}_{12}$ which is also thermal dynamically unstable against the decomposition into Li_4GeO_4 and Li_3PO_4 . The situation is depicted in Figure II.6.E.7. We argue that a kinetic barrier exists against the decomposition into ternary compounds.

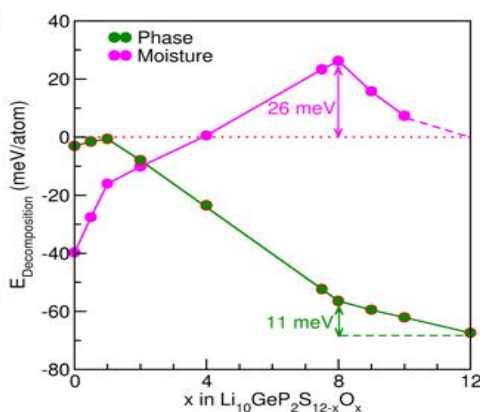


Figure II.6.E.7 The chemical decomposition energy of $\text{Li}_{10}\text{GeP}_2\text{S}_{12-x}\text{O}_x$ system (green), and the moisture caused reaction energy (purple). Negative energy indicates the instability, while positive energy indicates the stability against the reaction.

We have also calculated the Li mobility in the $\text{Li}_{10}(\text{GeS}_4)(\text{PO}_4)_2$ using direct ab initio molecular dynamics simulations. We found that its Li mobility is even higher than the original $\text{Li}_{10}(\text{GeS}_4)(\text{PS}_4)_2$. Furthermore, the original 1D diffusion channel has become a 3D diffusion network. Several reasons contribute to the increase Li mobility. First, the increased disorder in the $\text{Li}_{10}(\text{GeS}_4)(\text{PO}_4)_2$ as shown in Figure II.6.E.6 opens up more diffusion channels, making it changes from 1D transport to a 3D transport. Second, the Li diffusion is via a path from one $\text{Li}(\text{S/O})_n$ polyhedron to a neighboring $\text{Li}(\text{S/O})_n$ polyhedron. The transition point happens in a S-O-O or S-S-O triangle plan. The size of such triangle is larger than that of O-O-O triangle in the case of $\text{Li}_{10}(\text{GeO}_4)(\text{PO}_4)_2$, as a result, it avoids the stereohedron bottleneck. On the other hand, its chemical binding at this triangle is stronger than the S-S-S plane in $\text{Li}_{10}(\text{GeS}_4)(\text{PS}_4)_2$, this makes the transition state energy lower, thus it reduces the barrier height. Overall, we found that the existence of GeS_4 retains the Li diffusion channels. Lastly, we found that the $\text{Li}_{10}(\text{SnS}_4)(\text{PO}_4)_2$ has even better Li mobility than $\text{Li}_{10}(\text{GeS}_4)(\text{PO}_4)_2$. This can overcome the scarcity of Ge element. The ab initio calculated self-diffusion curves are shown in Figure II.6.E.8.

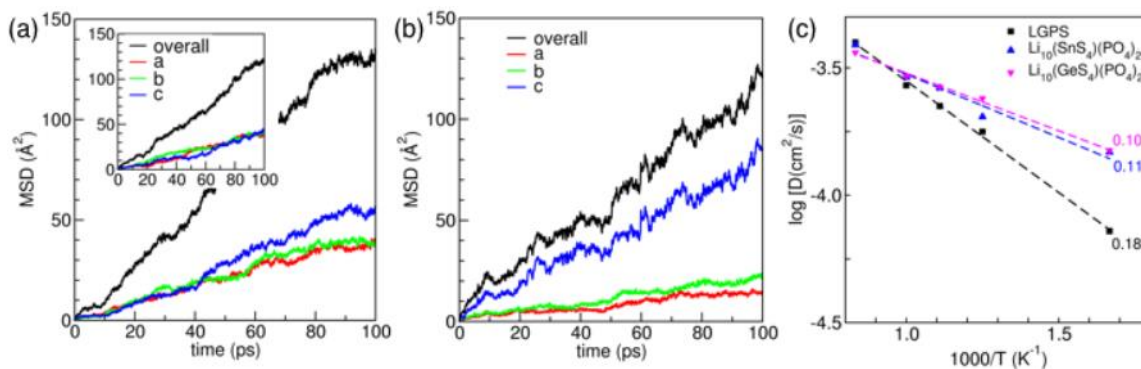


Figure II.6.E.8 Mean square displacements (MSD) of Li-ions along three different crystallographic directions as well as the overall value, obtained from the ab initio molecular dynamics trajectory at 800 K; within LGPSO: $\text{Li}_{10}(\text{GeS}_4)(\text{PO}_4)_2$ (a) and LGPS: $\text{Li}_{10}(\text{GeS}_4)(\text{PS}_4)_2$ (b). The a, b, c in (a) and (b) denotes for diffusion in the a, b, c directions. Inset shows the same for LSnPSO: $\text{Li}_{10}(\text{SnS}_4)(\text{PO}_4)_2$. (c) Li-diffusivity (D) at various temperature (T) are fitted linearly for: LGPS, LGPSO, LSnPSO and corresponding Li-migration barriers (in eV) are given.

Conclusions

In conclusion, we found that 2D hexaaminobenzene can be a very good Li-S cathode material, with a potential energy capacity of about 1300 Wh/Kg. We found that the Li polysulfide binding to the 2D hexaaminobenzene is strong enough to prevent its dissolution into the solvent. We developed a fine tuned solvent model based on the experimentally measured voltages for different Li_2S_n molecules in the solvent. We found that the Li-solvent interaction needs to be very strong in order to reproduce the experimental voltages. We have designed a Li-S/2D hexaaminobenzene sandwich structure to increase the volumetric capacity of the Li cathode system. We have tested a new procedure to estimate the diffusion constant of Li in such a disordered system. We have studied the $\text{Li}_{10}(\text{GeS}_4)(\text{PS}_4)_2$ and proposed a $\text{Li}_{10}(\text{GeS}_4)(\text{PO}_4)_2$ compound. We found that the proposed compound is moisture stable, and it also has a higher mobility than the original pure sulfur counterpart. We further proposed the $\text{Li}_{10}(\text{SnS}_4)(\text{PS}_4)_2$ system, which has a better performance than the Ge counterpart, and it can also resolve the element scarcity problem for Ge based system.

Key Publications

1. L. Yang, J. Zheng, M. Xu, Z. Zhuo, W. Yang, L.W. Wang, L. Dai, J. Lu, K. Amine, F. Pan, "Short hydrogen bonds on reconstructed nanocrystal surface enhance oxygen evolution activity", ACS Catal. 8, 466 (2018)
2. J. Wu, L.W. Wang, "2D frameworks C_2N as a potential cathode for lithium sulfur batteries: an ab initio density functional study", J. Mat. Chem. A 6, 2984 (2018).
3. Y. Li, F. Ma, L.W. Wang, "Phosphorene oxides as a promising cathode material for sealed non-aqueous Li-oxygen battery", J. Mat. Chem. A 6, 7815 (2018)
4. G. Gao, F. Pan, L.W. Wang, "Theoretical investigation of 2D hexaaminobenzene coordination polymers as Li-S battery", Adv. Energy Mat. 8, 1801823 (2018).
5. S. Banerjee, X. Zhang, L.W. Wang, "Motif based design of an oxysulfide class of lithium superionic conductor: towards improved stability and record high Li-ion conductivity", (submitted).

II.6.F Dendrite Growth Morphology Modeling in Liquid and Solid Electrolytes (MSU)

Yue Qi, Principal Investigator

Michigan State University
3509 Engineering Building
East Lansing, MI, 48824
E-mail: yueqi@egr.msu.edu

Tien Duong, DOE Technology Development Manager

U.S. Department of Energy
E-mail: Tien.Duong@ee.doe.gov

Start Date: January 1, 2017

End Date: December 31, 2019

Project Funding: \$1,135,125

DOE share: \$999,943

Non-DOE share: \$135,182

Project Introduction

In this project, we will first develop a phase-field model to incorporate the electrochemical driving forces predicted from first principles simulations in liquid electrolytes and then incorporate mechanical driving forces to simulate dendrite growth in solid electrolytes with resolved microstructures. The μm -thick solid electrolytes will allow easier, direct comparison of modeling and experimental results, thus facilitating the validation of the electrochemical-mechanically driven Li-dendrite growth model. Last but not the least, the computational model for solid electrolytes can also be applied to study and design nm-thin artificial SEI on Li metal surface. Therefore, this atomically-informed phase-field model will allow us to design the desired properties of artificial SEI coating to suppress dendrite growth in liquid-electrolyte and the microstructure of a solid-electrolyte to be dendrite-resistant during cycling. This model will enable the design of durable and safe Li-anodes for Li-S, Li-air, all-solid Li-ion batteries, as well as high energy density Li-ion batteries, lead to batteries that meet DOE's target for the high energy batteries cell density (>350 Wh/kg) for EV applications and cost below \$100/kWhuse.

Objectives

The ultimate goal of this project is to develop a validated model to predict Li dendrite morphology evolution in both liquid and solid electrolytes during electrodeposition and stripping, in order to accelerate the adoption of Li metal electrodes in current and emerging battery technologies. To achieve this goal, the project has four objects:

1. formulate a general framework that captures the electrochemical-mechanical driving forces for Li morphology evolution;
2. consider the role of the nm-thin SEI in liquid-electrolytes as well as the microstructures of mm-thick solid-electrolytes for Li morphology evolution;
3. connect micron-scale phase-field models and atomic-scale DFT-based simulations via parameter- and relationship-passing in order to predict Li dendrite nucleation and growth kinetics and morphology; and
4. validate the key input parameters and main conclusions of the multi-scale model as new capabilities being developed step-by-step.

Approach

This project will develop a multi-scale model that connects micron-scale phase-field models and atomic-scale DFT-based simulations via parameter- and relationship-passing in order to predict Li-metal dendrite morphology evolution, in both liquid and solid electrolytes. The key innovation of this project is to capture the electrochemical-mechanical driving forces and incorporate the roles of an nm-thin solid electrolyte interphase (SEI) in liquid electrolytes as well as of the microstructures of μm -thick solid electrolytes for all-solid-state

batteries. Our strategy to study Li dendrite morphology in both liquid and solid electrolytes allows us to share many similar governing equations and common mechanisms, to gradually increase the complexity of the model, and to validate the model step-by-step for its crucial input parameters and main conclusions through tailored experiments

Results

Task 1: Illuminate the role of SEI kinetics in Li dendrite growth in liquid electrolytes

Using the multiscale modeling developed in the first year of the project, we modeled two electrodes and compared with experiments. It has been observed that Li plating is more dendritic than Mg plating, which is more faceted (Figure II.6.F.1). The difference in the morphology evolution of the plated Li and Mg is related to the charge transfer kinetics at the electrode/electrolyte interface. One of the significant differences is that SEI always covers the lithium (Li) surface, but not the magnesium (Mg). At the atomistic scale, Li/Li₂CO₃/liquid-EC-electrolyte and Mg/liquid-THF-(with Cl⁻)-electrolyte interfaces were used to represent the two systems. The DFT results showed that the desolvation energy barrier for the reduction reaction is higher for Mg²⁺ than Li⁺ (1.38 eV for Mg²⁺ vs. 0.4 eV for Li⁺) at the similar voltage, due to its larger solvation energy for Mg²⁺ than Li⁺. Coupling with atomistic calculations, phase-field simulations were performed to investigate the Li/Mg plating morphological evolution at mesoscale. With thermodynamic and kinetic parametric inputs from first-principles calculation (i.e. interfacial energy and anisotropy of Li/Li₂CO₃, surface energy and anisotropy of Mg, diffusion coefficient of Li⁺ in Li₂CO₃, and relative difference in charge-transfer kinetics of Li/Mg plating), the implicit non-linear phase-field model captures the notable morphological evolution difference between dendritic Li plating and faceted Mg plating (as shown in Figure II.6.F.1). Therefore, we have determined (Go) that the effect of SEI on dendrite growth in the liquid electrolyte can be modeled implicitly.

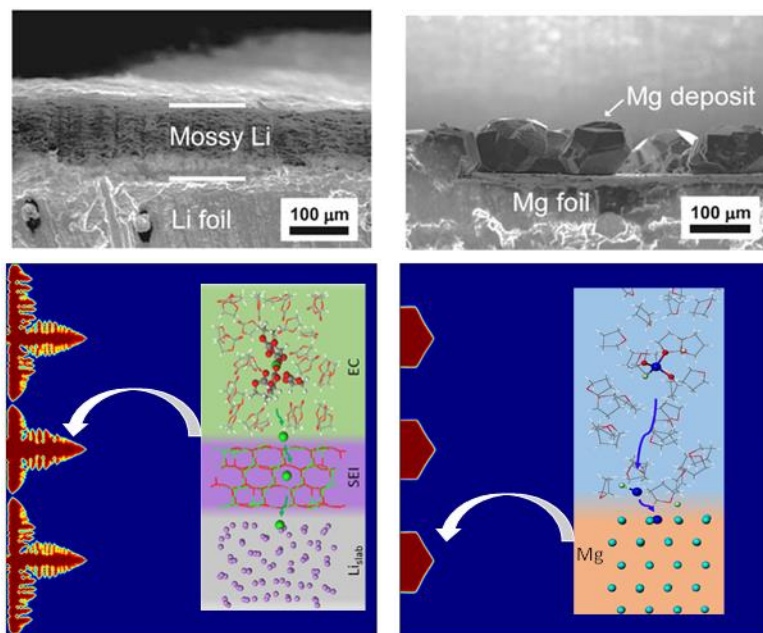


Figure II.6.F.1 upper panel, the observed Li (left) and Mg (right) plating morphology from Yoo et al.[1]. Lower panel, the simulated morphology difference of Li and Mg plating.

Furthermore, the simulation results indicate that, among all possible parameters for Li/Mg electrodeposition processes, the plating charge-transfer energy barrier difference is the dominating factor that accounts for the morphological discrepancy. Specifically, in our systematical tests on the impact of charge-transfer energy barrier on plating morphology (a range of 0.5-10 times of the reaction energy barrier height of the Li plating were tested), dendrites were prominently suppressed from around two times, and faceted morphology (hexagonal for Mg) were produced at about four times. Using this newly developed implicit Li morphology

model, the impact of surface energy, exchange current, and anisotropy on Li morphology was investigated. It was found that the most effective way to form smooth surface morphology during Li electrodeposition process is by reducing the relative exchange current, I_0 . This study result fundamentally explains the origin of the Li/Mg plating morphological difference and reveals that the proper elevation of the charge-transfer barrier height (e.g., by anodic surface treatment, protective coating, upgraded electrolyte, etc.) is a promising approach to dendrite suppression in Li metal batteries.

In order to vary I_0 experimentally, electronically conductive carbon coatings and ionically conductive $\text{Li}_{1.5}\text{Al}_{0.5}\text{Ge}_{1.5}\text{P}_3\text{O}_{12}$ solid electrolyte coatings were deposited on Li electrode via DC and RF magnetron sputtering systems, respectively. The thickness of the carbon layer was measured to be about 65 nm from a profiler. Figure II.6.F.2 shows the voltage profiles of Li-Li symmetrical cells cycled in ether-based electrolyte (0.4 M LiNO_3 + 0.6 M LiTFSI in DOL:DME=1:1, vol%) with a current density of 1 mAcm^{-2} and a capacity density of 4 mAhcm^{-2} . This aggressive capacity density was applied to examine the effect of carbon coating quickly. Prolonged cycle life was achieved in lithium electrodes coated with carbon. The mechanisms are proposed as (1) the solid SEI layer formed in carbon layer acts a protective layer to lithium by reducing the lithium-electrolyte reactions; (2) the carbon layer could improve the uniformity of current distribution. On the other hand, no improvements of cycling performance were found with the 245 nm thick solid electrolyte LiAlGePO coating. SEM observation shows that Li was deposited above and below the LiAlGePO coating. More efforts on developing Li-ion conductive coatings, such as conventional solid electrolyte materials, will be discussed in Task 2.

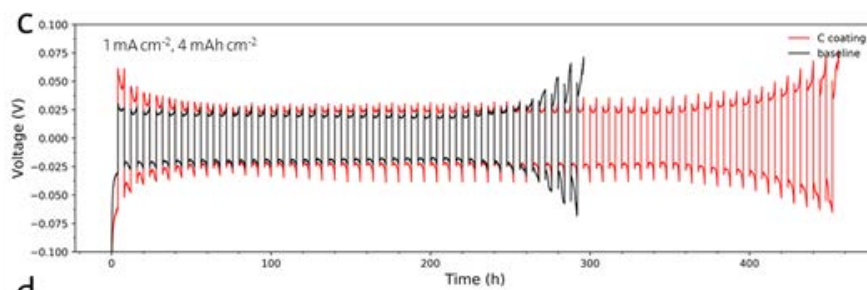


Figure II.6.F.2 Improved cycle life with carbon coated Li-electrode.

Task 2: Model the metallic Li precipitation in solid electrolytes of all-solid batteries

A new mechanism to explain the driving force for the metallic Li formation in some solid electrolytes is proposed. Although the bulk cubic $\text{Li}_7\text{La}_3\text{Zr}_2\text{O}_{12}$ (c-LLZO) has a large band gap, Density functional theory (DFT) based electronic structure calculation and analysis revealed that additional surface states exist in the bandgap of the (110) surface of c-LLZO (Figure II.6.F.3a) and t-LLZO. Here the surface can be the surface of pores, cracks or even grain boundaries in solid electrolytes. This means that the surface electronic states in LLZO can be the pathway for electron transport and the traps for excess electrons to nucleate metallic Li. Excess electrons would be trapped on LLZO surfaces, either around the La atoms on the surface of c-LLZO or dispersed on the nonstoichiometric surface of t-LLZO. It is also thermodynamically favorable for the excess electrons on La to reduce Li^+ forming metallic Li^0 . In contrast, there is no additional state on the (100) surface of $\text{Li}_2\text{PO}_2\text{N}$ (Figure II.6.F.3b), and the excess electrons will be localized on O or N underneath the surface in $\text{Li}_2\text{PO}_2\text{N}$, making Li^+ hard to be reduced. For comparison, γ and β Li_3PS_4 phases were investigated. Although they did not show additional surface state, the excess electrons are mainly localized on top of surface S atoms and around P atoms for both γ - Li_3PS_4 and β - Li_3PS_4 . Thus, the predicted order of Li nucleation tendency will be LLZO (cubic and tetragonal) > β - Li_3PS_4 > γ - Li_3PS_4 > $\text{Li}_2\text{PO}_2\text{N}$. However, Li_3PS_4 also has much lower fracture energy than the oxide solid electrolytes (LLZO and $\text{Li}_2\text{PO}_2\text{N}$), this will also contribute to the different Li dendrite morphology observed in sulfide and oxide-based electrolytes. A literature survey of experimental data on c-LLZO and β - Li_3PS_4 revealed that, despite similar Li ion conductivity, β - Li_3PS_4 sustained higher current density and areal capacity than c-LLZO, indicating a higher Li-dendrite resistance of β - Li_3PS_4 . Correlating this observation with all the computed basic material properties, including the shear modulus, fracture energy, bulk

band gap, surface band gap, and the reduction potential (Figure II.6.F.3c) shows that the Li dendrite resistance is mainly determined by the surface band gap (the higher, the better). Therefore, we propose that an interlayer of $\text{Li}_2\text{PO}_2\text{N}$ at the Li/c-LLZO or Li/ $\beta\text{-Li}_3\text{PS}_4$ interfaces would be more efficient and defect tolerant to suppress Li dendrite formation/growth.

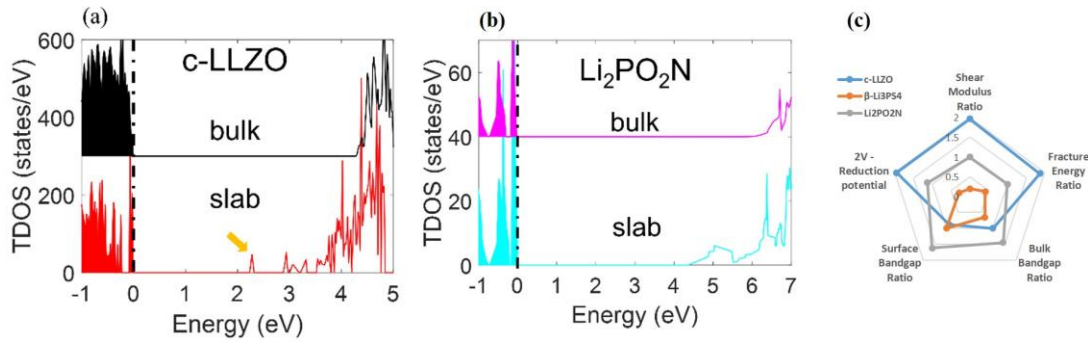


Figure II.6.F.3 Compare the total density of states between bulk and slabs of (a) c-LLZO and (b) LIPON and (c) the solid electrolyte properties that relate to Li-dendrite resistance.

The contribution of the surface electronic states to Li-dendrite growth needs to be captured in the mesoscale as a new implementation, by incorporating a consistent thermodynamics description of electrons to the phase-field model. More specifically, we have formulated the local static electron concentration based on the DOS data calculated from DFT and then incorporated it into a phase field model. Meanwhile, the chemical potential of electrons becomes a function of the distance to the surface/grain boundaries. We found it is computationally efficient to formulate the electron concentration as a function of the local structure (phase order parameter), voltage and the solid electrolyte materials surface states. An explicit nucleation process based on the classical nucleation theory was also integrated with the electrochemical reaction driven Li dendrite growth model. Elasticity and strain energies are also included in the phase field model.

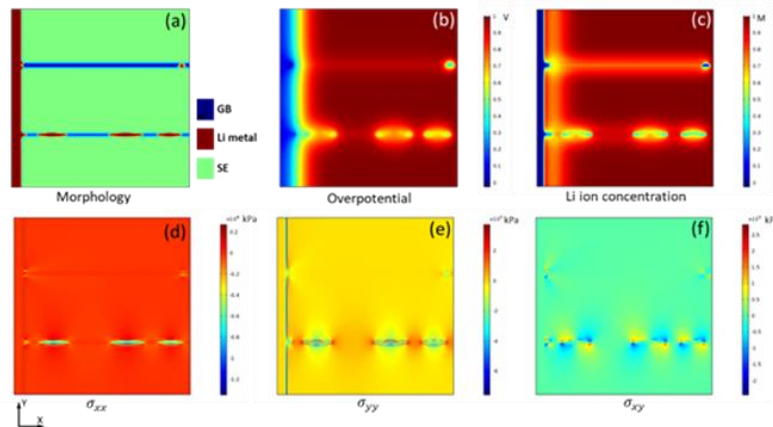


Figure II.6.F.4 Phase-field simulation results of Li dendrite growth and nucleation at straight grain boundaries with different widths under constant voltage condition at 100s: (a) Li dendrite morphology, (b) overpotential distribution, (c) Li-ion concentration distribution and (d-f) stress distribution.

The highly coupled electro-chemical-mechanical model was then used to simulate the Li plating process, and the effect of straight grain boundaries (can also be considered as cracks or pores) was investigated in a solid electrolyte half-cell system charged under constant voltage (1V) condition, as shown in Figure II.6.F.4. The dendrite morphology (Figure II.6.F.4a) demonstrated isolated Li dendrites nucleated and grew along the GBs, where the local overpotential (Figure II.6.F.4b) and Li-ion concentration (Figure II.6.F.4c) dropped due to the formation of Li metal. The stress was concentrated at the Li metal nucleation tip regions, where large elastic

deformation occurs. The model demonstrated that higher dendrite nucleation probability and growth rate at narrower GB due to the higher surface free electron and Li-ion concentration. On the other hand, since Li metal nucleation and growth at narrow GB needs to overcome larger elastic strain energy barrier compared to the wider GB, it can be concluded the electrochemical driving force plays a more dominant role in Li plating.

Task 3: Guide the design of artificial solid electrolytes on Li metal

Various coating design strategies have been drawn based on the modeling conclusions in Task 1 and 2, such as coating lower I_0 and LIPON coatings to be more Li-dendrite resistant. Another design idea is from the electrolyte additive, which decomposes on Li-surface to form the SEI layer. 1,2-propyleneglycol sulfite (PS) was explored to improve the stability of SEI formed in the conventional carbonate-based electrolyte. Figure II.6.F.5a shows the voltage profiles of Li-Li symmetrical cells cycled in baseline electrolyte (1 M LiPF₆ in a mixture of ethylene carbonate and diethyl carbonate with a mass ratio of 1:2) w/o 5 wt% PS at a current density of 1 mA cm⁻² and a capacity density of 4 mAh cm⁻². Two times more cycle life was achieved when PS was added to the baseline electrolyte. Cycled Li surface was analyzed with X-ray photoelectron spectroscopy (XPS). Figure II.6.F.5b demonstrates the existence of Li_xS_yO_z and Li₂S, which are reduction reaction products of Li and PS. We propose that Li₂S in the inner part of SEI could provide more resistance to mechanical breakdown of the SEI layer, thus relatively stable Li plating/stripping can be achieved, as shown in Figure II.6.F.5a. Furthermore, a practical thin 20 μm Li|LiFePO₄ system with a negative/positive capacity ratio of ~5.3 was used to evaluate the effects of PS additive. Figure II.6.F.5c confirms that PS results in double cycle life with an average Coulombic efficiency of 98%.

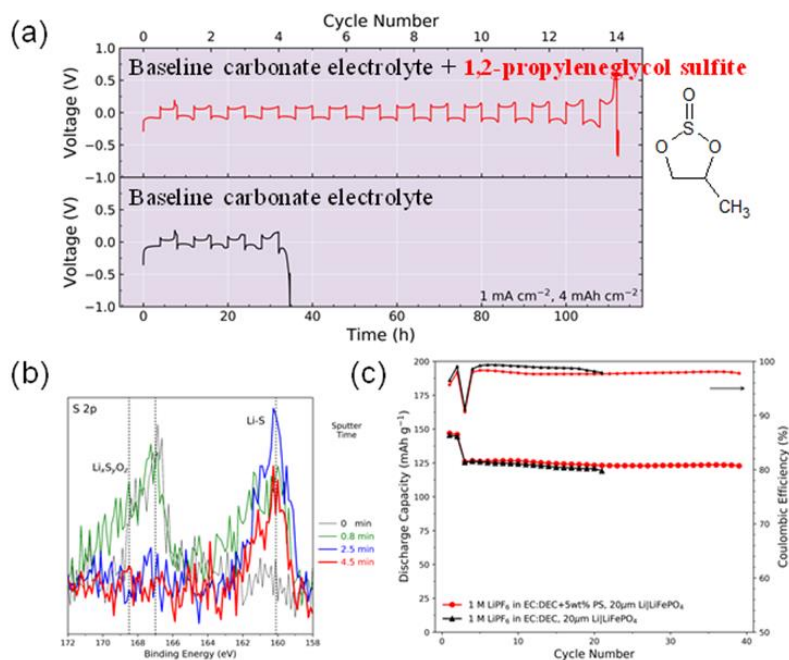


Figure II.6.F.5 (a) Voltage profiles of Li-Li symmetrical cells cycled in baseline electrolyte (1 M LiPF₆ in a mixture of ethylene carbonate and diethyl carbonate with a mass ratio of 1:2) with 5wt% additives. The current density is 1 mA cm⁻² and the capacity density is 4 mAh cm⁻². (b) C 1s, F 1s, and S 2p XPS spectra and (c) schematic of SEI compositions associated with Li metal electrode after one charge in baseline electrolyte with 5wt% 1,2-propyleneglycol sulfite.

We found two main mechanisms (volume compatibility and electronic property) for the stability of Li₂S in the SEI in comparison with Li₂O. PBR-ratio (PBR) was used to evaluate the volume compatibility of the common inorganic SEI components with Li. PBR is defined as the molar volume ratio of the oxide (or sulfide) and the metal. PBR assumes stress generation in the surface layer can cause crack formation (PBR<1), spallation of the surface oxide (PBR>2) due to the volume mismatch. It is interesting to note that the PBR is 0.60 for Li₂O and 1.16 for Li₂S. Cracks can easily form in the Li₂O layer as the layer forms. On the other hand, Li₂S has good

volume match with Li-metal, thus mechanically more stable in terms of protecting the Li-surface. If the Li_2O or Li_2S layer do crack, will Li metal nucleate on the cracked surface? To address this question, DFT calculations were performed. The band gap for the bulk Li_2O is around 5.0 eV, which is larger than that of bulk Li_2S (3.4 eV). However, there is a dramatic decrease in the band gap on the surface of Li_2O (111) surface, which is around 2.1 eV. In comparison, the surface band gap for Li_2S (111) surface is only 0.1eV lower than its bulk value (3.3eV). As it will be shown in Task 2, the Li dendrite resistance of a solid electrolyte is mainly determined by the surface band gap. Therefore, the electrons have a lower barrier to conduct on Li_2O surface than Li_2S , suggesting Li_2S is more Li-dendrite growth resistant comparing to Li_2O .

Conclusions

A fully first principle calculations informed phase-field model was developed to capture the electrochemically driven dendrite morphology evolution in a liquid electrolyte. The role of SEI was modeled implicitly. The implicit model successfully captured the plating morphology difference between Li and Mg anodes. It also predicts that the most effective way to form smooth surface morphology during Li electrodeposition process is by reducing the relative exchange current, I_0 . To capture the defects, microstructures in both solid electrolyte and SEI, an explicit model was developed. First, the metallic Li nucleation driving force inside LLZO has been proposed based on DFT calculations. It was found, any defects (such as the surface of pores, cracks or even grain boundaries) in solid electrolytes can have new electronic states and low band gap compared to the bulk form. These states form electron transport pathways and the traps for excess electrons to nucleate metallic Li. This effect has been incorporated into the phase-field model which also couples the elastic deformation of the solid electrolyte.

Key Publications

1. Wang, A.P., Kadam, S., Li, H., Shi, S.Q., Qi, Y., Review on Modeling of the Solid Electrolyte Interphase (SEI) for Lithium-Ion Batteries, *npj Computational Materials* 2018, 4, 15
2. Yulaev, A.; Oleshko, V.; Haney, P.; Liu, J.; Qi, Y.; Talin, A.A.; Leite, M; Kolmakov, A., From Microparticles to Nanowires and Back: Radical Transformations in Plated Li Metal Morphology Revealed via in situ Scanning Electron Microscopy, *Nano Letter* 2018, 18, 3, 1644-1650
3. Li, Y.S., and Qi, Y., Transferable SCC-DFTB Parameters for Li-Metal and Li-Ions in Inorganic Compounds and Organic Solvents“, *J. Phys. Chem. C* 122, 10755 (2018)
4. Tian, H.K., Xu, B., Qi, Y., Computational Study of Li Nucleation Tendency in LLZO and Rational Design of Interlayer Materials to Prevent Li Dendrites, *Journal of Power Source* 382, 79-86 (2018)
5. Q. Cheng, L. Wei, Z. Liu, N. Ni, Z. Sang, B. Zhu, W. Xu, L-Q. Chen, W. Min and Y Yang, “In-operando, Three Dimensional, and Simultaneous Visualization of Ion Depletion and Lithium Growth by Stimulated Raman Scattering Microscopy”, *Nature Comm.* 9, 2942 (2018)
6. G. Li, Z. Liu, Q. Huang, Y. Gao, M. Regula, D. Wang, L-Q. Chen, D. Wang, “Stable metal anodes enabled by electrokinetic phenomena”. *Nature Energy*, (2018)
7. Z. Liu, P. Lu, Q. Zhang, X. Xiao, Y. Qi and L.-Q. Chen, “A Bottom-up Formation Mechanism of Solid Electrolyte Interphase (SEI) Revealed by Isotope-Assisted Time-of-Flight Secondary Ion Mass Spectrometry (TOF SIMS)”. *J. Phys. Chem. Lett.*, 9 5508-5514 (2018).

References

1. H.D. Yoo, Y. Liang, Y. Li, Y. Yao, *ACS Appl. Mater. Interfaces* 7 (2015) 7001.

Acknowledgments

We acknowledge the collaboration with Dr. Lin and Dr. Rubloff at University of Maryland.

II.7 Beyond Li-ion R&D: Metallic Lithium and Solid Electrolytes

II.7.A Mechanical Properties at the Protected Lithium Interface (ORNL)

Nancy Dudney, Principal Investigator

Oak Ridge National Laboratory
PO Box 2008, MS6124
Oak Ridge, TN 37831
E-mail: dudneynj@ornl.gov

Erik Herbert, Principal Investigator

Michigan Technological University
604 M&M Building, 1400 Townsend Dr.
Houghton, MI 49931
E-mail: eherb@mtu.edu

Jeff Sakamoto, Principal Investigator

University of Michigan
2350 Hayward Ave.
Ann Arbor, MI 48109
E-mail: jeffsaka@umich.edu

Tien Duong, DOE Technology Development Manager

U.S. Department of Energy
E-mail: Tien.Duong@ee.doe.gov

Start Date: January 1, 2015	End Date: December 30, 2018	
Project Funding (FY18): \$1,150,000	DOE share: \$610,000	Non-DOE share: \$540,000

Project Introduction

A stable lithium anode is critical to achieve high energy density with excellent safety, lifetime and cycling efficiency. Instability and/or high resistance at the interface of lithium metal with various solid electrolytes limit the use of the metallic anode for batteries with high energy density batteries, such as Li-air and Li-S. The critical impact of this endeavor will be a much deeper analysis of the degradation for both the lithium metal and the solid electrolyte, so that materials can be engineered to fulfill the target level of performance for EV batteries, namely 1000 cycles and 15 year lifetime, with adequate pulse and charge power.

While other programs look at changes in the lithium morphology and the electrochemical performance, this project focuses on the mechanical properties of the lithium metal, typical solid electrolytes, and their interface. The mechanical properties are expected to influence the interface contact and adhesion, the formation and growth of cracks and dendrites, and changes in the microstructure and defects. Being buried by 2-20 μm of lithium, this interface is challenging to characterize, but is protected from reactions with other compounds present in the battery or environment. Developing methods to probe the buried interface is an important component of the study.

The structure and mechanical properties of the Li / solid electrolyte interface are expected to evolve in complex ways depending on details of the battery cycling and age. Understanding what factors control the evolution of the lithium metal and solid electrolytes will provide important information to understand degradation and develop mitigation strategies.

Objectives

This project will develop the understanding of the Li metal-solid electrolyte interface through state of the art nanoindentation and other mechanical methods coupled with solid electrolyte fabrication and electrochemical cycling. We will develop experimental tools to probe the structure, mechanical properties, and interfaces relevant to ultra-thin lithium films required for high energy density. Methods will include mechanical, imaging and electrochemical probes during mass transport and relaxation. Our goal is to provide the critical information that will enable transformative insights into the complex coupling between the microstructure, its defects and the mechanical behavior of Li metal anodes.

The practical objective for this project will be to understand the evolution of the lithium metal upon cycling in contact with a generic solid electrolyte under various intrinsic and extrinsic conditions to the point that we can develop stability maps. Different constructions for the stability maps will be explored which will illustrate the predominate mass transport process and defect structure evolution in the lithium metal. Simple maps may address the current density, areal capacity, and layer thickness. Then maps extending to many other cell designs, interfacial factors and duty cycle parameters are envisioned. A key activity will be to develop experimental tools with which to probe the lithium morphology in real time. While initial work will focus on experimental characterization, modeling will be introduced to interpret the kinetic processes and extrapolate for alternative properties and designs and extended cycling.

Approach

Generally, the cycling of lithium is investigated electrochemically. Here we are testing the mechanical properties the solid electrolyte and the lithium independently, and then the interfaces formed of lithium with the solid electrolyte. This provides not only important materials characterization, but a real-time measure of how lithium moves in response to cycling through a solid electrolyte. The solid electrolytes investigated included a glassy lithium phosphorus oxynitride (Lipon) electrolyte and the polycrystalline garnet electrolyte of lithium lanthanum zirconium oxide (LLZO). The lithium metal is applied to cleaned solid electrolyte surfaces by either vacuum vapor deposition (at ORNL) or by melt processing (at UM) using protocols developed under program III.B.1.ii, led by Jeff Sakamoto. In addition, Li metal is deposited on smooth nonreactive supports. In all cases the samples were well protected from air and humidity during processing and tests.

Mechanical properties studies through state of the art nanoindentation techniques are used to probe the surface properties of the solid electrolyte and the changes to the lithium that result from prolonged electrodeposition and/or dissolution at the interface. High speed mapping of large indentation arrays provides statistically relevant distributions of the properties relative to microstructural features. The nanoindentation approach benefitted from a close collaboration with associates at Nanomechanics, Inc. of Oak Ridge TN for continuing refinements in both hardware, software and firmware for the NanoFlip and iNano systems used in this investigation. Other tests of the Li/LLZO interface were performed using a precision Instron in an Ar-filled glove box, pulse-echo acoustic spectroscopy, contact angle, and imaging with electron microscopy and tomography. These probes are used to elucidate the relations between mechanical (stack) pressure applied to the lithium, the solid electrolyte surface preparation, the interface energy and resistance to ionic transport.

Results

Lithium metal studies using nanoindentation. Following careful analysis and models of the indentation results for thin Li metal films (5-18 μm) on glass substrates, the results interpreting both the elastic and plastic properties Li metal have been published. [\[Herbert, 2018\]](#) The unique mechanical behavior of Li at small length scales and high homologous temperature is of particular interest because of its potential impact on the performance of energy storage devices. During charging (Li deposition), gradients in the chemical potential will force Li to preferentially diffuse into defects at the Li/SE interface. In a manner that depends on the length scale of the defect and the imposed strain rate, for an initially low dislocation density ($\rho \leq 1.1 \times 10^{12} \text{ m}^{-2}$), Li can support pressures ranging from ~46 to 350 times higher than the nominal yield strength of bulk

polycrystalline Li. The highest pressures develop in the smallest interfacial defects exposed to the highest strain rates (related to the charging current density).

Grain boundary grooves, porosity and scratches in the SE (solid electrolyte) are among the potential small length-scale (≤ 500 nm) flaws that may occur at Li/SE interface. If during charging, these defects become filled with metallic Li, some defects at the SE interface may be physically too small to activate glide-controlled dislocation mechanisms such as Frank-Reed sources for the Li to flow. Under these conditions, dislocation plasticity will not be an efficient stress relief mechanism, allowing the hoop stress within the interfacial defect to initiate mode I crack fracture in the SE. Diffusional creep would also be expected to relieve stress when the diffusion distance is small relative to the current. Figure II.7.A.1 shows (left) examples of the stochastic pop-in behavior when diffusion distances and dislocation density result in a change in the creep mechanism; and (right) the statistical average of the hardness derived from many load displacement curves showing the volume and strain rate dependence.

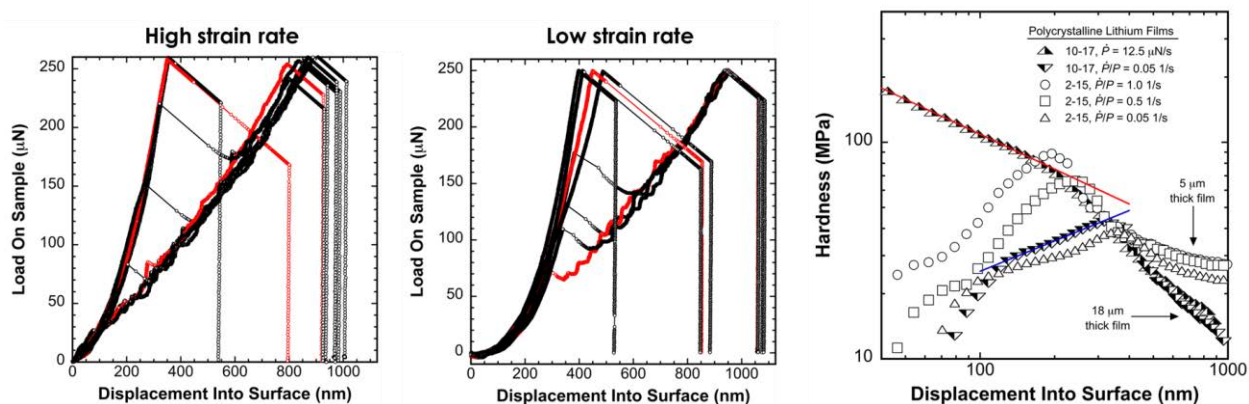


Figure II.7.A.1 Indentation of Li thin films. Plots at left are typical the load displacement curves to a maximum of $250\mu\text{N}$, followed by 60 sec hold and unload. At right are average values for the hardness collected for many indents and different samples. The indentations were conducted at different strain rates and different thicknesses of Li films.

Li-LLZO interface studies by imaging and adhesion tests. In other mechanics testing, a precision Instron housed in an inert glove box provided Li/LLZO interface adhesion results. [Wang, 2018] The sample set up and results are shown in Figure II.7.A.2. The adhesion strength was determined as Li/LLZO/Li cells were pulled in tension. Analysis of the fracture surfaces showed that at high area specific interface resistance (ASR), there is a clean separation of the Li from the LLZO surface, leaving behind negligible Li residue. In contrast, at the lowest ASRs, the adhesive strength of the Li/LLZO interface exceeds the tensile strength of the Li metal.

To support these results, the tensile strength of Li foil was measured to be $\sim 8\text{MPa}$, which is the maximum interface strength observed in Li/LLZO/Li stacks (red-dashed line in Figure II.7.A.2). The fact that the strength of the interface is stronger than the Li metal itself at low ASRs suggests that there is good surface chemistry and wettability of Li on LLZO. From these studies, it can be concluded that both the adhesive strength and ASR of the interface are governed by the surface chemistry and wettability of the LLZO surface.

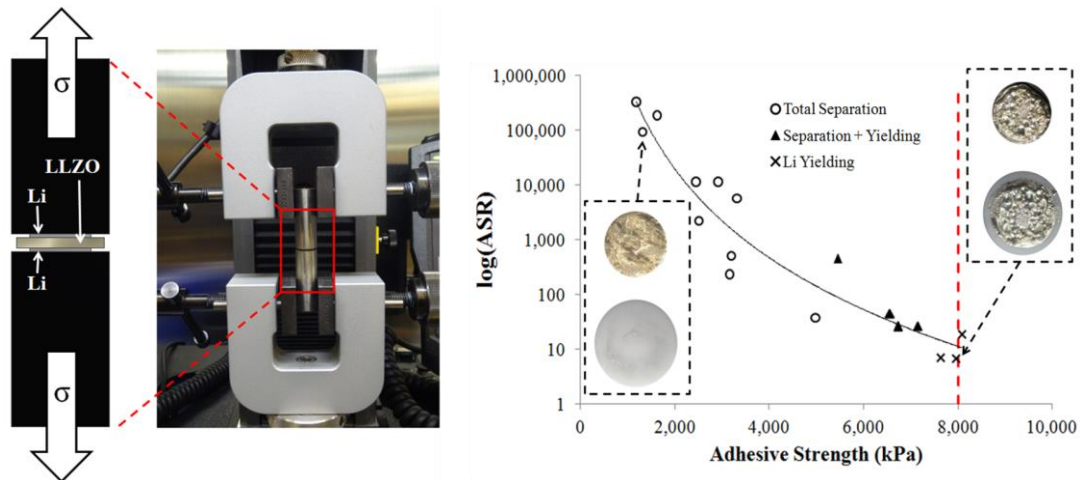


Figure II.7.A.2 Instron and sample setup for Li adhesion test (left). The area specific resistance of the Li/LLZO/Li determined by electrical impedance correlates with the Li-LLZO adhesion (right).

Li-LLZO electrochemical tests and models. Evidence for excellent cycling of Li with garnet LLZO solid electrolyte disks continues to be collected at MU. [Taylor 2018] Here the LLZO interface was carefully prepared and cleaned, but was free of any interface coatings. Symmetric Li/LLZO/Li samples were cycled at increasing currents to determine the critical current density (CCD) that leads to Li shorts at different temperatures. By testing many samples, statistical averages have been assessed, as summarized in Figure II.7.A.3. The CCD appears to follow Arrhenius behavior exhibiting an activation energy of 0.25 eV.

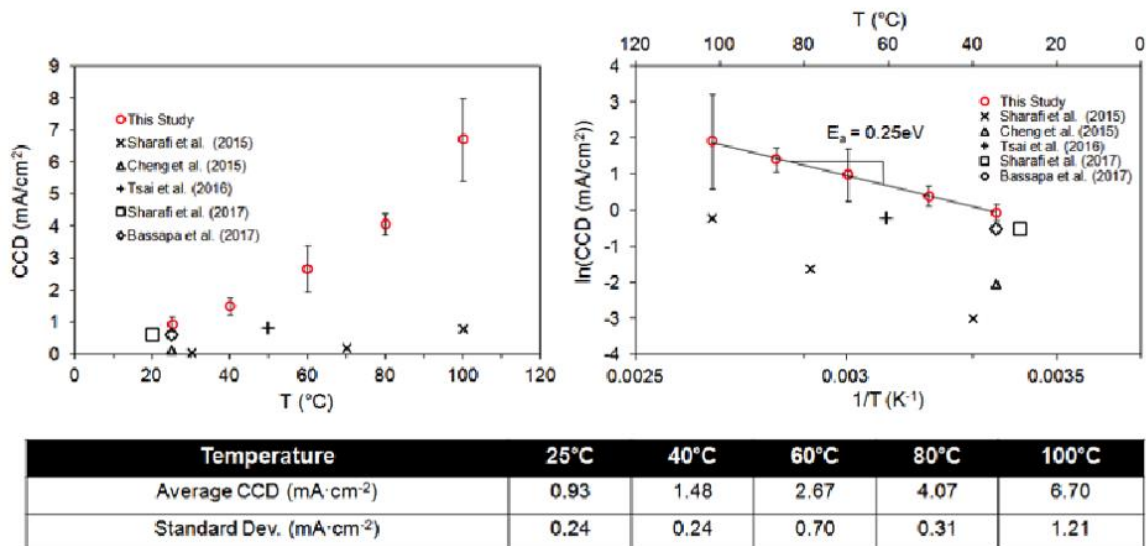


Figure II.7.A.3 Average CCD for our recent studies compared to earlier published results. Most of the studies showed little change with increasing temperatures (left). The Arrhenius plot (right) determines an activation energy.

Currently we are analyzing the data to fit the activation energy to a physical model, with an emphasis on balancing the Li flux at the Li-LLZO interface. The higher Li diffusivity in LLZO relative to the extrapolated self diffusivity for Li metal may lead to hot spots where vacancy defects are insufficient to accommodate the Li atoms forced to plate at the interface.

Nanoindentation studies to determine creep of Lipon. While indentation of LLZO are consistent with a uniform and rigid ceramic, it is interesting that the glassy electrolyte, Lipon, shows evidence of both creep and recovery processes which may influence the interfaces with lithium and also the cathode. Creep measurements, such as shown in Figure II.7.A.4, have been conducted at several different temperature and analyzed as viscoplastic flow behavior described by the constitutive equation $\dot{\epsilon} = B \sigma^n$ where $\dot{\epsilon}$ is the normalized strain rate, σ the stress and n the stress exponent. To date, the stress exponent for Lipon films is a high number, ~ 20 , and independent of temperature and displacement. A similarly high value has been reported for lithiated amorphous Si. [1] Such a high value may be understood as the rearrangement of small atomic clusters in the material, rather than single atoms. The exponent indicates an activated volume of 112 \AA^3 , whereas a possible cluster unit of Lipon, being 3 Li^+ plus a PO_4^{3-} unit, would occupy 81 \AA^3 in the dense glass.

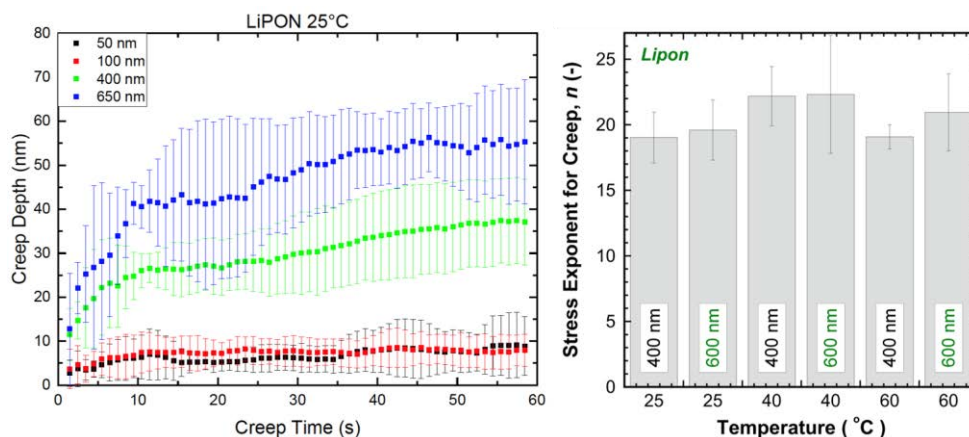


Figure II.7.A.4 Indentation of Lipon thin films showing creep behavior for constant load at different displacements from the surface (left). The stress exponent (right) was determined for the power law dependence strain rate dependence.

Conclusions

This investigation is rich with new information concerning the lithium, the solid electrolytes and their interface. For a stable, solid-state Li battery, this interface must maintain a full contact and low resistance to ion transport while moving a large amount of lithium across the battery. The plastic and elastic properties of each material are important to assess how the materials near the interface adjust to compressive and tensile stresses that develop during cycling at various currents and temperatures. Further, the tendency for Li metal dendrites or deposits to form and short the solid electrolyte must be inhibited by control of the surface and bulk flaws, purity and the current density. A variety of mechanical tests have been evaluated and correlated with the ion currents near and above room temperature and will be used to being to model the evolution of microstructure and defect structures at the interface.

Key Publications

1. M. Wang and J. Sakamoto, "Correlating the Interface Resistance and Surface Adhesion of the Li Metal-Solid Electrolyte Interface," *J Power Sources*, 377 (2018) 7-11.
2. Nathan J. Taylor, Sandra Stangeland-Molo, Catherine G. Haslam, Asma Sharafi, Travis Thompson, Michael Wang, Regina Garcia-Mendez, and Jeff Sakamoto. "Demonstration of high current densities and extended cycling in the garnet $\text{Li}_7\text{La}_3\text{Zr}_2\text{O}_{12}$ solid electrolyte." *Journal of Power Sources* 396 (2018) 314-318.
3. Sharafi, A., Kazyak, E., Davis, A.L., Yu, S., Thompson, T., Siegel, D.J., Dasgupta, N.P. and Sakamoto, J., Surface Chemistry Mechanism of Ultra-Low Interfacial Resistance in the Solid-State Electrolyte $\text{Li}_7\text{La}_3\text{Zr}_2\text{O}_{12}$," *Chemistry of Materials*, 29 (2017) 7961-7968.

4. E. G. Herbert, P. S. Phani, N. J. Dudney, and S. A. Hackney, “Nanoindentation of High Purity Vapor Deposited Lithium Films: The Elastic Modulus,” *J. Mat. Res.* 33 (2018) 1335.
5. E. G. Herbert, S. A. Hackney, N. J. Dudney, V. Thole and P. S. Phani, “Nanoindentation of High Purity Vapor Deposited Lithium Films: A Mechanistic Rationalization of Diffusion-Mediated Flow,” *J. Mat. Res.* 33 (2018) 1347.
6. E. G. Herbert, S. A. Hackney, N. J. Dudney, V. Thole and P. S. Phani, “Nanoindentation of High Purity Vapor Deposited Lithium Films: A Mechanistic Rationalization of the Transition to Dislocation-Mediated Flow,” *J. Mat. Res.* 33 (2018) 1361.

References

1. Lucas A. Berla, Seok Woo Lee, Yi Cui, William D. Nix, “Mechanical behavior of electrochemically lithiated silicon”, *J Power Sources*, 273 (2015) 41-51.

Acknowledgements

Prof. Steve Hackney (Michigan Technological University) played a key role in interpreting and developing models of the indentation studies for the lithium metal.

II.7.B Solid electrolytes for solid-state and lithium-sulfur batteries (Univ. of Michigan, ORNL, ARL, Oxford U.)

Jeff Sakamoto, Principal Investigator

University of Michigan
 Mechanical Engineering
 2350 Hayward Ave.,
 Ann Arbor, MI, 48109
 E-mail: jeffsaka@umich.edu

Tien Duong, DOE Technology Development Manager

U.S. Department of Energy
 E-mail: Tien.Duong@ee.doe.gov

Start Date: January 1, 2015	End Date: December 31, 2017	
Project Funding (FY18): \$1,200,000	DOE share: 1,200,000	Non-DOE share: \$0

Project Introduction

Batteries that surpass Li-ion systems require advanced anode, cathode, and electrolyte technology. In theory, the lithium-sulfur (Li-S) system offers over a six-fold increase in specific energy (2567 Wh/kg) compared to state-of-the-art (SOA) Li-ion (387 Wh/kg). However, the potential of the Li-S system has not been realized due to instabilities at the interface between the Li metal anode and the electrolyte. First, other than LIPON, no electrolyte has demonstrated stability against metallic Li. Second, dissolution of Li-polysulfides in SOA liquid electrolytes results in passivation of the Li anode. Thus, there is a compelling need to develop novel electrolyte technology to enable beyond Li-ion battery technologies employing Li metal anodes.

Objectives

Enable advanced Li-ion solid-state and lithium-sulfur EV batteries using LLZO solid-electrolyte membrane technology. Owing to its combination of fast ion conductivity, stability, and high elastic modulus, LLZO exhibits promise as an advanced solid-state electrolyte. To demonstrate relevance in EV battery technology, several objectives must be met. First, LLZO membranes must withstand current densities approaching ~ 1 mA/cm² (commensurate with EV battery charging and discharging rates). Second, low area specific resistance (ASR) between Li and LLZO must be demonstrated to achieve cell impedance comparable to conventional Li-ion technology (~ 10 Ohms/cm²). Third, low ASR and stability between LLZO and sulfur cathodes must be demonstrated.

Approach

Our effort will focus on the promising new electrolyte known as LLZO (Li₇La₃Zr₂O₁₂). LLZO is the first bulk-scale ceramic electrolyte to simultaneously exhibit the favorable combination of high conductivity (~ 1 mS/cm at 298K), high shear modulus (61 GPa) to suppress Li dendrite penetration, and apparent electrochemical stability (0-6V vs Li/Li⁺). While these attributes are encouraging, additional R&D is needed to demonstrate that LLZO can tolerate current densities in excess of 1mA/cm², thereby establishing its relevance for PHEV/EV applications. We hypothesize that defects and the polycrystalline nature of realistic LLZO membranes limit the critical current density. However, the relative importance of the many possible defect types (porosity, grain boundaries, interfaces, surface & bulk impurities), and the mechanisms by which they impact current density, have not been identified. Using our experience with the synthesis and processing of LLZO (Sakamoto and Wolfenstine), combined with sophisticated materials characterization (Nanda), we will precisely control atomic and microstructural defects and correlate their concentration with the critical current density. These data will inform multi-scale computation models (Siegel and Monroe) which will isolate and quantify the role(s) that each defect plays in controlling the current density. By bridging the knowledge gap between composition, structure, and performance we will determine if LLZO can achieve the current densities required for vehicle applications.

Results

As has previously been shown [1], the surface chemistry of LLZO is sensitive to air exposure. A contamination layer readily forms and is predominantly composed of lithium carbonate (Li_2CO_3), lithium hydroxide (LiOH), and other adventitious carbon species; which collectively result in high interfacial resistance between LLZO and metallic Li. It has been reported that dry polishing in an inert atmosphere can lower the interfacial resistance by partially cleaning the surface; however, the efficacy of this approach is limited to reducing the interface resistance from $\sim 1000 \text{ } \Omega \cdot \text{cm}^2$ to $\sim 100 \text{ } \Omega \cdot \text{cm}^2$. Here, several surface conditioning protocols, including dry polishing (DP), wet polishing (WP), and heat treatments (HT) were employed in an attempt to reduce the interfacial resistance, and their impact on LLZO surface chemistry was evaluated. Heat treatment between 200 and 500°C in an inert atmosphere was conducted after dry and wet polishing.

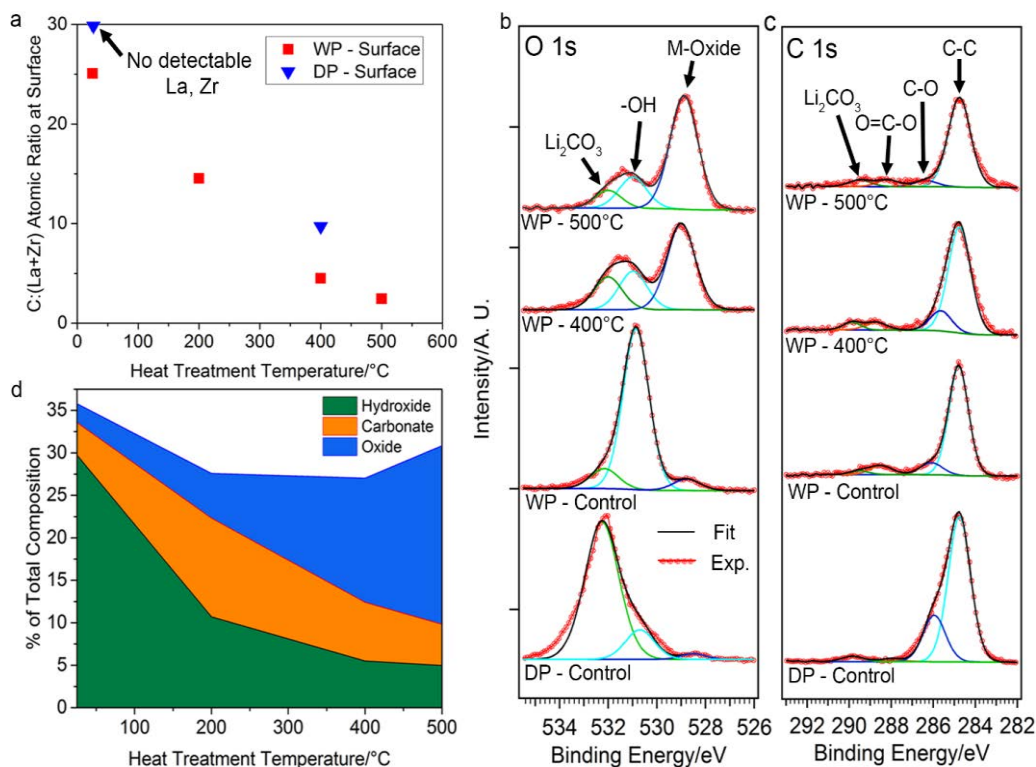


Figure II.7.B.1 XPS analysis of LLZO before and after heat treatment at 400 and 500°C . a) C:(La+Zr) atomic ratio as a function of heat treatment temperature, b) O 1s and c) C 1s core levels, d) percentage of total composition of different oxygen species on the LLZO surface as a function of heat treatment temperature after wet polishing (WP).

The surface chemistry of LLZO was analyzed using X-ray photoelectron spectroscopy (XPS) after each conditioning protocol (Figure II.7.B.1). Measurements were performed on samples transferred without air exposure between an argon-filled glovebox and the ultra-high vacuum XPS chamber. Figure II.7.B.1a shows that in samples conditioned with DP or WP (no HT) a surface layer blocks nearly all the signal attributed to La and Zr. Thus, in these cases the surface layer is composed almost entirely of H, Li, C, and O (H content cannot be directly detected by XPS, but can be observed as hydroxyl bonds). The nature of the bonds in which these species participate can be examined through high-resolution core-scans. The O 1s peak reveals a significant difference between the surface layer after wet vs. dry polishing (Figure II.7.B.1b). The WP surface consists of predominantly hydroxide species, while a greater concentration of carbonate species exists on the DP sample. This suggests that the use of polishing fluid protects the LLZO surface from reformation of carbonate species.

Samples that underwent HT were first polished (DP or WP in ambient air) and then immediately transferred into an argon-filled glovebox where the samples were heated to different temperatures. Subsequent XPS

analysis demonstrated significant variations in the surface chemistry of these samples. In Figure II.7.B.1a the plot of the ratio of the C content to the summed La and Zr contents is used as a metric to quantify the amount of surface contamination. The lower the ratio, the more closely the surface resembles bulk LLZO. Some adventitious carbon is always observed on the LLZO surface, even for samples kept continuously in an argon atmosphere after HT, Figure II.7.B.1c. The amount of contamination is observed to dramatically decrease after heating to 400 and 500°C. This is consistent with the O 1s core scans shown for these samples, which demonstrate that the predominantly hydroxide and carbonate surfaces before heating are converted to primarily oxide species (as expected in bulk LLZO) after heating (Figure II.7.B.1b). In contrast, heating a DP sample to 400°C did not change the surface as dramatically, with carbonate species still dominating (Figure II.7.B.1). A plot of the fractional surface composition of the oxygen-containing species is shown in Figure II.7.B.1d for WP samples heated to different temperatures. As the HT temperature increases to 500°C, the oxide fraction steadily increases, the hydroxide fraction decreases, and the amount of carbonate remains roughly constant. In total, these observations suggest that: (1) compared to dry polishing, wet polishing is more effective at achieving a surface with low carbonate content, (2) heat treatment up to 500°C can remove LiOH, but is less effective at removing Li₂CO₃, and (3) of the strategies examined, the successive combination of WP and HT is the most effective at removing surface contamination layers.

The wettability of a SSE by metallic Li has been proposed to influence interfacial resistance in SSBs. However, quantitative analysis of the Li contact angle and direct correlation with surface chemistry has not been reported. To characterize wettability, sessile drop tests were performed to measure the contact angle of molten Li on Li₂CO₃ and on LLZO samples after various surface conditioning processes (Figure II.7.B.2). Molten Li was deposited onto heated Li₂CO₃ or LLZO from a heated stainless-steel syringe. Importantly, the native layers (composed of oxide, nitride, and carbonate species) present on the surface of the Li foil did not melt, and thus were easily removed from the molten Li source. This allowed for deposition of purified molten Li onto the LLZO surface. The present approach differs from a scenario involving the melting of solid Li foil directly on LLZO, as wettability in the latter approach will be influenced by the presence of native layers on the Li surface and at the Li-LLZO interface. All experiments were performed inside an argon-filled glovebox, and high-resolution cross-sectional images were captured and digitally analyzed to determine contact angles.

As shown in Figure II.7.B.2, the DP-LLZO sample exhibited the highest contact angle amongst all LLZO samples, $\theta = 146^\circ$, which was nearly identical to the value measured for a pure Li₂CO₃ surface ($\theta = 142^\circ$). Such a large contact angle is consistent with a non-wetting interaction typical of an interface exhibiting weak adhesion. The similar wetting behavior between the DP-LLZO sample and Li₂CO₃ is expected, given that the DP-LLZO surface is composed predominantly of Li₂CO₃. Similarly, the WP-LLZO contact angle was 141° , which is consistent with the presence of the hydroxide and carbonate contamination layer which was observed with XPS. In contrast, the WP-LLZO heat treated at 500°C exhibited a significantly lower contact angle ($\theta = 95^\circ$). We hypothesize that this reduction in contact angle is caused by the removal of hydroxide and carbonate species, resulting in a surface more closely resembling bulk LLZO, which interacts more strongly with Li metal.

To validate the correlation between surface chemistry and wettability, the wetting angle of Li on LLZO, Li₂CO₃, and LiOH was evaluated using DFT calculations. Li-LLZO, Li-Li₂CO₃ and Li-LiOH interfaces were

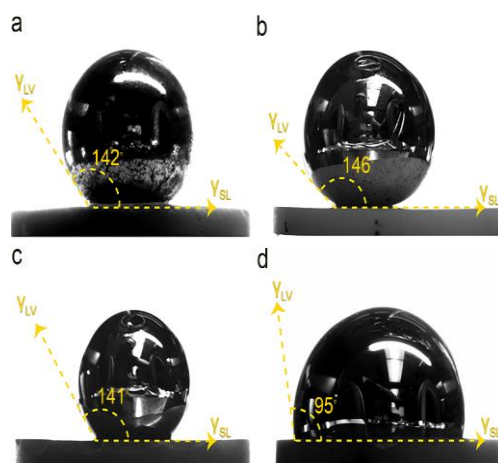


Figure II.7.B.2 Contact angle measurements of molten metallic Li on a) Li₂CO₃, b) DP-LLZO, c) WP-LLZO, d) WP-LLZO after heat treatment at 500°C.

constructed from the low-energy surfaces of each respective material. Large simulation cells were used, to accommodate geometries that minimize interfacial strain. The interfacial distance and translation state within the interfacial plane were optimized to identify the most energetically-favorable interface structures.

Figure II.7.B.3 shows the atomic structure of the low-energy interfaces for Li-LLZO and Li-Li₂CO₃. The contact angle, θ , for these interfaces was calculated by combining the Young-Dupré equation, $W_{ad} = \sigma_{Li}(1 + \cos\theta)$, with DFT calculations of the interfacial work of adhesion, W_{ad} , and the surface energy of Li, $\sigma_{Li} = 0.45 \text{ J.m}^{-2}$. Using the Li-LLZO interface as an example, W_{ad} was evaluated as: $W_{ad} = E_{int} - E_{Li-slab} - E_{LLZO-slab}$. Here E_{int} is the energy of the interface cell and E_{X-slab} refers to the energy of an isolated Li ($X = \text{Li}$) or LLZO slab ($X = \text{LLZO}$). The calculated values for W_{ad} and θ are shown in Figure 3 below their respective interfaces. The trend predicted by our calculations – that Li strongly wets LLZO, but not Li₂CO₃ – is consistent with the measurements shown in Figure 2. More specifically, the wetting angle predicted for the Li-Li₂CO₃ interface, $\theta = 142^\circ$, is in excellent agreement with the measured value (142° , Figure II.7.B.2a) indicating a weak interfacial interaction between Li and Li₂CO₃ ($W_{ad} = 0.10 \text{ J.m}^{-2}$). In contrast, the calculated W_{ad} for the Li-LLZO interface is nearly seven times larger, $W_{ad} = 0.67 \text{ J.m}^{-2}$, resulting in a relatively small wetting angle, $\theta = 62^\circ$. This value is qualitatively consistent with the measured value of 95° reported in Figure II.7.B.2d. The smaller value predicted by our calculations is expected, given that approximately 15% of carbonate and/or hydroxide remains on the LLZO surface after heating to 500°C (Figure II.7.B.2d). Calculations on the Li-LiOH interface predict a relatively large contact angle of 125° , similar to the non-wetting behavior observed for the Li-Li₂CO₃ system.

Electrochemical impedance spectroscopy (EIS) was performed on Li-LLZO-Li symmetric cells (Figure II.7.B.4a) to measure the LLZO bulk (R_{bulk}), grain boundary (R_{gb}), and Li-LLZO interfacial ($R_{Li-LLZO}$) resistances for WP and HT samples between 200 and 500°C . EIS data were modelled using an equivalent circuit shown in Figure II.7.B.4b. This approach allows for the direct measurement of the individual contributions to cell resistance and involves the correlation between characteristic frequencies and transport phenomena. Representative

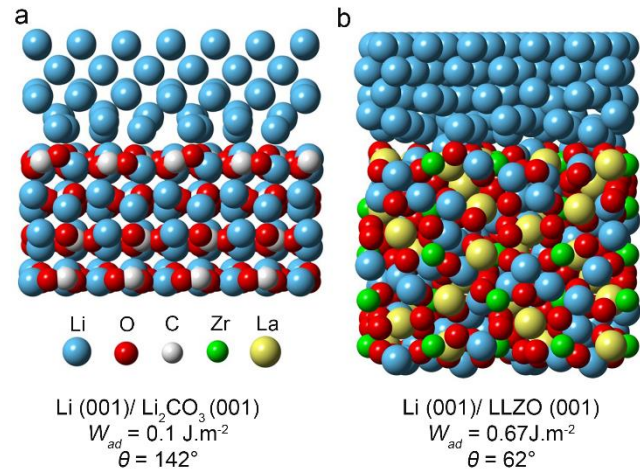


Figure II.7.B.3 Calculated work of adhesion (W_{ad}), contact angle (θ), and atomic structure for the a) Li-Li₂CO₃ and b) Li-LLZO interfaces.

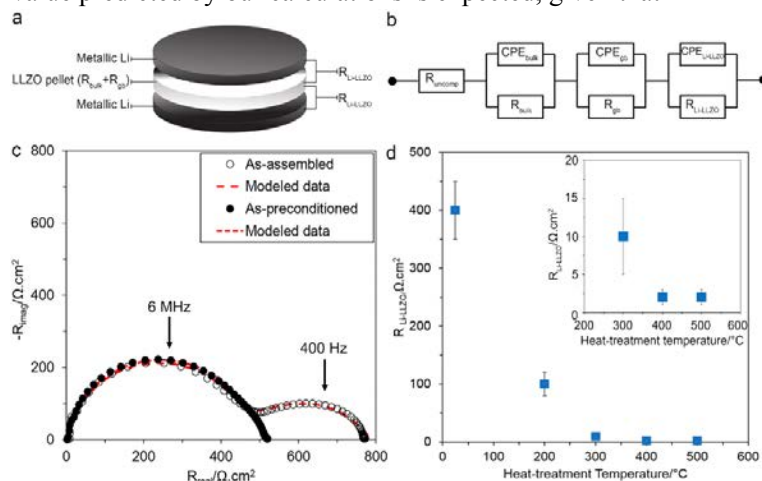


Figure II.7.B.4 a) Schematic of the all solid-state Li-LLZO-Li cell, b) the equivalent circuit used for modeling the EIS data c) representative Nyquist plot of the Li-LLZO-Li cell (for LLZO heat-treated at 500°C), as-assembled (\circ) and after preconditioning at 175°C (\bullet). Markers indicate experimental data and dotted lines are simulated lines extrapolated from the equivalent circuit modeling using the circuit shown in b, d) the Li-LLZO interfacial resistance after preconditioning at 175°C versus the heat-treatment temperature. $N=3$ for each HT condition. Error bars represent standard deviations.

EIS spectra for a cell consisting of a WP and HT at 500°C LLZO sample before and after preconditioning at 175°C are shown in Figure II.7.B.4c (Preconditioning was used to ensure good contact between metallic Li and LLZO by heating the Li-LLZO-Li cell to 175°C for 12 h).⁶ From Figure II.7.B.4c, it is apparent the LLZO total resistance ($R_{\text{bulk}} + R_{\text{gb}}$) has remained constant ($500 \Omega \cdot \text{cm}^2$) while $R_{\text{Li-LLZO}}$ dramatically decreased upon preconditioning at 175°C and cooling. Initially, $R_{\text{Li-LLZO}}$ was approximately $400 \Omega \cdot \text{cm}^2$ which is significantly lower than previous values reported for LLZO after dry polishing in literature.⁶ After preconditioning at 175°C, a further dramatic reduction in $R_{\text{Li-LLZO}}$ was observed. The combination of wet polishing, HT, and preconditioning results in an extremely small interfacial resistance of $2 \Omega \cdot \text{cm}^2$.

Figure II.7.B.4d shows $R_{\text{Li-LLZO}}$ after preconditioning for WP LLZO samples with no HT and HT at several temperatures between 200 and 500°C. With increasing HT temperature, $R_{\text{Li-LLZO}}$ decreases from 400 to $2 \Omega \cdot \text{cm}^2$. Importantly, the low interfacial resistance coincides with the removal of the surface contamination layer. Furthermore, the decrease in interfacial resistance closely follows the trend in surface chemistry with HT temperature observed in XPS measurements, and with the improved wettability of the LLZO surface after HT. Taken together, these observations provide quantitative evidence of the strong coupling between surface chemistry, wettability, and interfacial resistance.

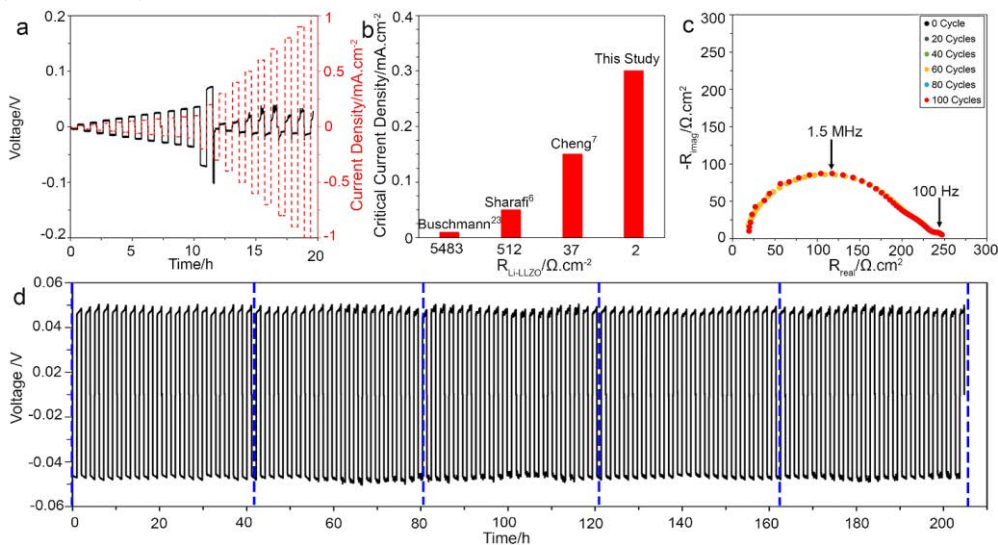


Figure II.7.B.5 a) DC cycling of Li-LLZO-Li cells (LLZO HT to 500°C after WP) at room temperature, stepping the current density from 0.01 to $1 \text{ mA} \cdot \text{cm}^{-2}$, b) the critical current density versus Li-LLZO interfacial resistance comparing the result of this study with other studies available in the literature, c) Nyquist plots of Li-LLZO-Li cell after each 20 cycles for cell cycled 100 time, d) Galvanostatic cycling of Li-LLZO-Li at $0.2 \text{ mA} \cdot \text{cm}^{-2}$ for 100 cycles at $0.4 \text{ mAh} \cdot \text{cm}^{-2}$. The blue dotted line shows the times at which EIS was collected and is shown in c.

The cycling behavior and critical current density (CCD) of a WP LLZO sample HT to 500°C (WP+HT) were characterized using a combination of DC cycling and EIS analysis (Figure II.7.B.5). The CCD is defined as the lowest current density at which cell shorting occurs due to Li metal penetration. After removal of the surface contamination, the CCD was determined to be $0.3 \text{ mA} \cdot \text{cm}^{-2}$ (Figure II.7.B.5a). The CCD from the WP+HT sample prepared here is compared in Figure II.7.B.5b to other Li-LLZO-Li symmetric cells reported in the literature. The CCD measured in this study is one of the highest values reported in literature for an LLZO SSE. Our data indicates that the CCD and $R_{\text{Li-LLZO}}$ are inversely correlated, suggesting that higher power density can be achieved by controlling interfacial chemistry, and thus $R_{\text{Li-LLZO}}$.

To evaluate the stability of the interface after WP+HT upon cycling, a Li-LLZO-Li cell was cycled for one hundred cycles at $\pm 0.2 \text{ mA} \cdot \text{cm}^{-2}$ at room temperature (Figure II.7.B.5d). After every 20 cycles, EIS analysis was conducted to assess changes in R_{bulk} , R_{gb} , and $R_{\text{Li-LLZO}}$. Figure II.7.B.5c shows that negligible changes in

the EIS spectra were observed, implying excellent stability of the interface and the absence of short-circuiting. Furthermore, the total cell resistance ($R_{\text{bulk}} + R_{\text{gb}} + R_{\text{Li-LLZO}}$) estimated using the DC cell polarization voltage ($230 \Omega \cdot \text{cm}^2$) (Figure II.7.B.5a) agrees well with the total cell resistance measured using EIS ($240 \Omega \cdot \text{cm}^2$). This confirms that the DC and EIS analyses are in good agreement, and further validates the interpretation of the EIS data to quantitatively decouple resistance values and correlate them to their respective transport phenomena.

The DC and EIS characterization illustrate the importance of achieving low and stable interfacial resistance. First, a low $R_{\text{Li-LLZO}}$ enables a path toward low resistance solid-state cell designs employing metallic Li anodes. Second, reducing $R_{\text{Li-LLZO}}$ increases the CCD. Although $0.3 \text{ mA} \cdot \text{cm}^{-2}$ is one of the highest reported CCD values, it must be further increased to demonstrate relevance to vehicle electrification; the data in Figure II.7.B.5b suggest further tuning surface chemistry and reducing $R_{\text{Li-LLZO}}$ may be an approach to achieve higher CCD. Lastly, a clean and discrete Li-LLZO interface is preferred to minimize side reactions and mechanical degradation. In preliminary cycling tests, the interface kinetics appear to be stable when cycling at $\pm 0.2 \text{ mA} \cdot \text{cm}^{-2}$ at room temperature.

Conclusions

This study has revealed the mechanism by which surface chemistry controls the resistance of the Li-LLZO interface. By exploiting this mechanism, very low interfacial resistances – $2 \Omega \cdot \text{cm}^{-2}$, comparable to solid-liquid interfaces in Li-ion cells – can be achieved *without the need for coatings*. The removal of LLZO surface contamination was demonstrated to enhance Li wetting of LLZO, which was quantitatively evaluated using molten Li contact angle measurements through sessile drop tests. The interfacial chemistry and wettability measurements agree with atomic-scale DFT calculations of interfacial adhesion and wetting angle. The lower interfacial resistance made possible by controlling surface chemistry resulted in a doubling of the critical current density. This study clarifies the relationships between interfacial chemistry, lithium wettability, interfacial resistance, and stable cycling. The knowledge gained enables the rational design of electrode/electrolyte interfaces, and has general implications for solid-state transport phenomena.

Key Publications

1. A. Sharafi, C. G. Haslam, R.D. Kerns, J. Wolfenstine, J. and J. Sakamoto, Controlling and correlating the effect of grain size with the mechanical and electrochemical properties of $\text{Li}_7\text{La}_3\text{Zr}_2\text{O}_{12}$ solid-state electrolyte. *Journal of Materials Chemistry A*, 5(40), pp.21491-21504, 2017.
2. Sharafi, S. Yu, M. Naguib, M. Lee, C. Ma, H. Meyer, J. Nanda, M. Chi, D. J. Siegel, and J. Sakamoto, "Impact of Air Exposure and Surface Chemistry on the Li- $\text{Li}_7\text{La}_3\text{Zr}_2\text{O}_{12}$ Interfacial Resistance" *J. Mater. Chem. A*, *J. Mater. Chem. A* 2017.
3. Yu, S. and Siegel, D. Grain Boundary Contributions to Li-ion Transport in the Solid Electrolyte $\text{Li}_7\text{La}_3\text{Zr}_2\text{O}_{12}$ (LLZO), *ChemMater*, 2017.
4. Sharafi, E. Kazyak, A. L. Davis, S. Yu, T. Thompson, D. J. Siegel, N. P. Dasgupta, and J. Sakamoto, "Achieving low resistance all-solid-state Li-LLZO interfaces through surface chemistry control" *ChemMater*, Accepted 2017.
5. E. J. Cheng, A. Sharafi, and J. Sakamoto, "Intergranular Li metal propagation through polycrystalline $\text{Li}_{6.25}\text{Al}_{0.25}\text{La}_3\text{Zr}_2\text{O}_{12}$ ceramic electrolyte" *Electrochim. Acta* 223, 85-91 (2017).
6. T. Thompson, S. Yu, L. Williams, R. D. Schmidt, R. Garcia-Mendez, J. Wolfenstine, J. A. Allen, E. Kioupakis, D. J. Siegel, and J. Sakamoto, "Electrochemical Window of the Li-Ion Solid Electrolyte $\text{Li}_7\text{La}_3\text{Zr}_2\text{O}_{12}$ " *ACS Energy Letters*, 2(2), 462-468 (2017).

7. Jeff Wolfenstine, Jan L. Allen, Jeff Sakamoto, Donald J. Siegel, and Heeman Choe³ “Mechanical Behavior of Li-Ion Conducting Crystalline Oxide-based Solid Electrolytes: A Brief Review,” IONICS, Accepted, (2017).
8. Priyamvada Goyal and Charles W. Monroe, “New Foundations of Newman’s Theory for Solid Electrolytes: Thermodynamics and Transient Balances,” *Journal of The Electrochemical Society*, 164 (11) E3647-E3660 (2017).
9. Smith, S., Thompson, T., Sakamoto, J., Allen, J. L., Baker, D. R., & Wolfenstine, J. (2017). Electrical, mechanical and chemical behavior of $\text{Li}_{1.2}\text{Zr}_{1.9}\text{Sr}_{0.1}(\text{PO}_4)_3$. *Solid State Ionics*, 300, 38-45.
10. Kim, Y., Yoo, A., Schmidt, R., Sharafi, A., Lee, H., Wolfenstine, J., & Sakamoto, J. (2016). Electrochemical Stability of $\text{Li}_{6.5}\text{La}_3\text{Zr}_{1.5}\text{M}_{0.5}\text{O}_{12}$ (M= Nb or Ta) against Metallic Lithium. *Frontiers in Energy Research*, 4, 20.
11. C. Ma, Y. Cheng, K. Yin, J. Luo, A. Sharafi, J. Sakamoto, J. Li, K. L. More, L., N. J. Dudney, and M. Chi, “Interfacial Stability of Li Metal–Solid Electrolyte Elucidated via in Situ Electron Microscopy: *Nano Letters*, 16(11), 7030-7036 (2016).
12. S. Yu, R. D. Schmidt, R. Garcia-Mendez, E. Herbert, N. J. Dudney, J. B. Wolfenstine, J. Sakamoto, and D. J. Siegel, “Elastic Properties of the Solid Electrolyte $\text{Li}_7\text{La}_3\text{Zr}_2\text{O}_{12}$ (LLZO)” *Chem. Mater.*, 2016, 28 (1), 197–206.
13. Y. Kim, H. Jo, J. L. Allen, H. Choe, J. Wolfenstine, and J. Sakamoto, “The Effect of Relative Density on the Mechanical Properties of Hot-Pressed Cubic $\text{Li}_7\text{La}_3\text{Zr}_2\text{O}_{12}$ ” *J. Am. Ceram. Soc.*, 99 [4] 1367–1374 (2016).
14. Sharafi, A., Meyer, H. M., Nanda, J., Wolfenstine, J., & Sakamoto, J. (2016). Characterizing the Li– $\text{Li}_7\text{La}_3\text{Zr}_2\text{O}_{12}$ interface stability and kinetics as a function of temperature and current density. *Journal of Power Sources*, 302, 135-139.

Patents

1. A. Sharafi and J. Sakamoto, Suppressing “Metal Propagation in Polycrystalline Solid Electrolytes U.S. application (File No.: 920357.00095) and PCT application (File No.: 920357.00096).

Acknowledgement

The information, data, or work presented herein was funded in part by the Office of Energy Efficiency and Renewable Energy (EERE), U.S. Department of Energy, under Award Number DE-EE0006821. Co-investigators included Prof. D. Siegel from the University of Michigan, J. Wolfenstine from the Army Research Laboratory, Prof. C. Monroe from Oxford University, and J. Nanda from the ORNL. The NETL manager was Kimberly Nuhfer.

II.7.C Composite Electrolytes to Stabilize Metallic Lithium Anodes (ORNL)

Nancy Dudney, Principal Investigator

Oak Ridge National Laboratory
 PO Box 2008, MS6124
 Oak Ridge, TN 37831
 E-mail: dudneynj@ornl.gov

Xi (Chelsea) Chen, Principal Investigator

Oak Ridge National Laboratory
 PO Box 2008, MS6124
 Oak Ridge, TN 37831
 E-mail: chenx@ornl.gov

Tien Duong, DOE Technology Development Manager

U.S. Department of Energy
 E-mail: Tien.Duong@ee.doe.gov

Start Date: October 1, 2017	End Date: September 30, 2018	
Total Project Cost (FY18): \$400,000	DOE share: \$400,000	Non-DOE share: \$0

Project Introduction

A stable lithium anode is critical to achieve high energy density with excellent safety, lifetime and cycling efficiency. This study will identify the key design strategies that should be used to prepare composite electrolytes to meet the challenging combination of physical and chemical and manufacturing requirements to protect and stabilize the lithium metal anode for advanced batteries. By utilizing well characterized and controlled component phases, the design rules developed for the composite structures will be generally applicable toward the substitution of alternative and improved solid electrolyte component phases as they become available. Success in this program will enable these specific DOE technical targets: 500-700Wh/kg, 3000-5000 deep discharge cycles, robust operation.

Objectives

- Prepare composites of representative polymer and ceramic electrolyte materials to achieve thin membranes which have the unique combination of electrochemical and mechanical properties required to stabilize the metallic lithium anode while providing for good power performance and long cycle life.
- Understand the lithium ion transport at the interface between polymer and ceramic solid electrolytes which is critical to the effective conductivity of the composite membrane. Utilize bi-layer and tri-layer samples in place of dispersed composites to focus on the interface.
- Identify key features of the composite composition, architecture and fabrication that optimize the performance.
- Using practical and scaleable processing, fabricate thin electrolyte membranes to use with a thin metallic lithium anode that provide good power performance and long cycle life.
- Incorporate new polymer and ceramic materials phases into the composite electrolyte and composite cathode to better optimize transport and electrochemical stability

Approach

This program seeks to develop practical solid electrolytes that will provide stable and long-lived protection for the lithium metal anode. Current electrolytes all have serious challenges when used alone: oxide ceramics are brittle, sulfide ceramics are air sensitive, polymers are too resistive and soft, and many electrolytes react with

lithium. Composites provide a clear route to address these issues and finite element simulations served as a guide to composites with promising compositions and architectures.^{[1], [2], [3]} In past years, this program did not seek discovery of new electrolytes, rather the goal was to study combinations of current well-known electrolytes that can provide critical understanding towards the effects of the interfaces and architecture on the ion transport and stability with the Li anode. In general, the ceramic phase is several orders of magnitude more conductive than the polymer electrolyte and therefore should carry the bulk of the ionic current. However, because the interfaces contribute an additional source of resistance, in reality most of the Li ion current flows through continuous polymer phase rather than across the ceramic/polymer interfaces. To focus the investigation toward the polymer-ceramic interfaces, samples are formed as bilayers and trilayers where the effects of the interface properties can be readily isolated.

While work continues to emphasize study of ceramic electrolyte / polymer electrolyte interfaces, effort has expanded to address (i) practical processing routes to fabricate full batteries using the better composite electrolytes with a composite cathode and thin lithium metal anode, and (ii) introduction of alternative polymer and ceramic phases to replace the well-known model materials and develop improved composite electrolytes. In addition to solid state devices, hybrid batteries are investigated utilizing a fluid or gel catholyte within the porous cathode. Coatings have also been employed to stabilize the electrode interfaces. These directions increase the complexity of the studies, but are needed to improve cycling stability, rate performance and advance practical implementation of the solid electrolyte and Li anode technology.

Results

Results are summarized for three topics: interface investigations using symmetric tri-layer samples (polymer/ceramic/polymer), efforts to fabricate robust full cells, and lastly introduction of new polymer electrolytes to replace the poly(ethylene oxide) (PEO) plus Li salt phase.

Trilayer studies to reveal the ceramic – polymer interface properties

To accurately isolate the Li ion transport across the interface between a polymer and a crystalline ceramic interface, samples were prepared using a commercial ceramic membrane (from Ohara Corp.) coated on both faces with a very thin coating of PEO+dissolved Li salt. Using a polymer electrolyte of PEO+LiTf salt, at 30°C the area specific resistance from the interface ($R_{\text{interface}}$) was 1600 Ω . Addition of tetraethylene glycol dimethyl ether (TEGDME), a tight-binding solvent of Li^+ , into the trilayer did not effectively decrease the interfacial resistance. However, when dimethyl carbonate (DMC), a loose-binding solvent of Li^+ , was introduced into the trilayer, $R_{\text{interface}}$ decreased to essentially zero. These results were obtained by optimizing the polymer thicknesses and detailed analysis of the impedance spectroscopy of the trilayer and single phase samples. Characterization was extended to 70°C as shown in Figure II.7.C.1.

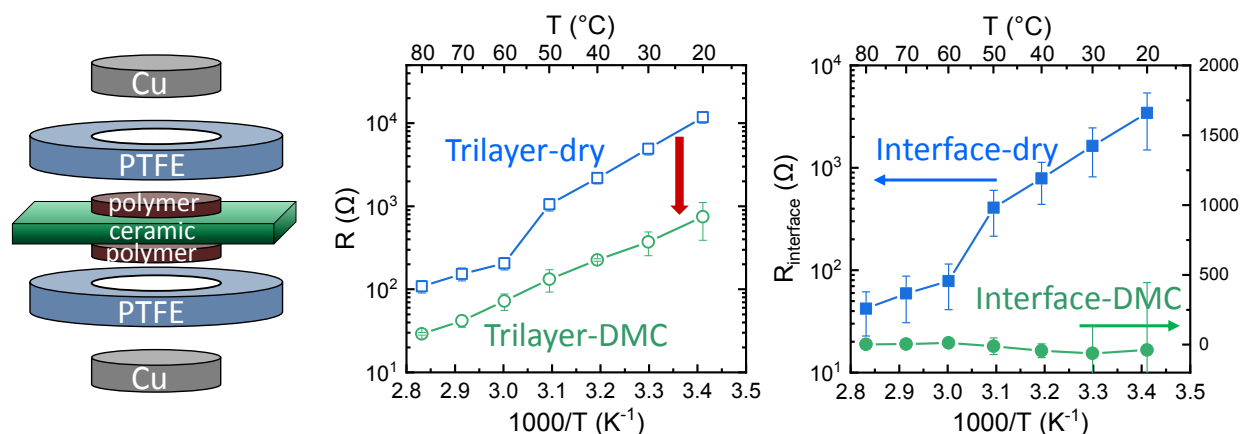


Figure II.7.C.1 Tri-layer sample configuration (left). Comparison of area specific resistance dry and with DMC additive (center). Extracted resistance attributed to polymer-ceramic interface (right).

Performance of full cells with the composite electrolyte

A series of cells were fabricated and cycled using the dispersed composite polymer electrolytes (CPE) of Ohara powder (< 50 vol%) in a PEO+Li salt matrix. On the cathode side, initial studies with aqueous spray-coated cathodes of 5:3:2 NMC with carbon and binder additives proved to have an electrochemical stability window mismatch with the composite electrolyte. In most cases the pores of the NMC cathode were wet with a controlled amount of $\text{LiPF}_6(\text{EC}+\text{DMC})$ liquid electrolyte, forming a hybrid battery. Improved adhesion between the cathode and CPE was obtained with a thin intermediate layer of the polymer electrolyte without the ceramic, but in all cases the resistance increased within 2 to 20 cycles as the liquid electrolyte dried and/or the cathode separated from the electrolyte membrane.

The cycling stability was greatly improved using LiFePO_4 cathodes with the polymer electrolyte acting as the catholyte within the porous cathode. Cycling at elevated temperatures (50-70°C) was required to achieve reasonable specific capacity, yet this was still less than expected perhaps owing to incomplete infiltration of the pores. Further improvement was obtained when using a composite cathode of LiFePO_4 + polymer + carbon obtained from a commercial partner in place of our homemade porous LiFePO_4 cathodes. Examples of the cycling results with the optimized LFP cathode are shown in Figure II.7.C.2. In these tests the CPE is free of plasticizers; no DMC was incorporated.

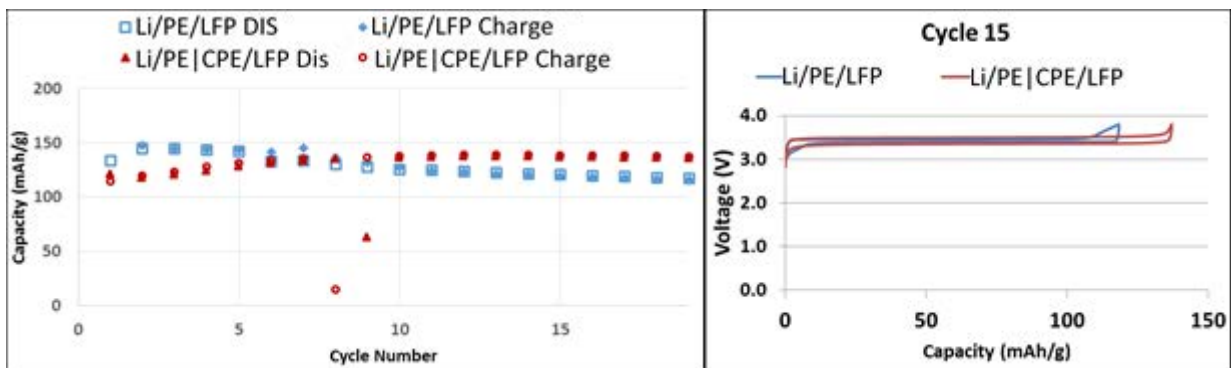


Figure II.7.C.2 Cycling of batteries comparing performance with PE-only with a bilayer electrolyte of PE coated CPE. Cycling capacities at 75°C (left). Voltage profiles for cycle 15 (right). Capacity is normalized to mass of the composite cathode.

The thin coating of the ceramic-free polymer electrolyte (PE) was used to form an improved interface with the Li metal anode. Presumably this limits the reaction of the Li metal with the Ohara particles which contain titanium. Similarly, a 1 μm -thick Lipon coating separating the Li from the CPE appears to inhibit reduction of the titanium.

Composite electrolyte with an alternative polymer gel

The Li ionic conductivity was greatly increased by forming a plasticized ceramic polymer composite gel.^[4] In this study, two different ceramic powders, two different plasticizers, and different loadings of the plasticizer were compared to the dry-polymer gel. Here the plasticizer greatly enhanced the conductivity while the ceramic powder reduced the overvoltage for Li symmetric cell cycling. See Figure II.7.C.3. Ongoing work will further characterize and evaluate the performance of these new solid electrolytes.

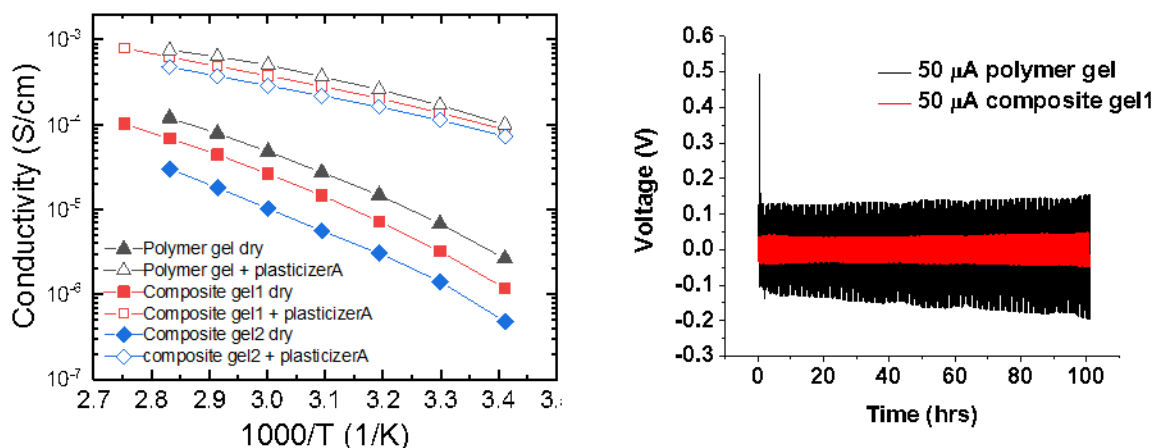


Figure II.7.C.3 Ionic conductivity comparing dry and plasticized electrolytes of different compositions (left). DC symmetric cycling at +/- 50μA/cm² for plasticized ceramic-free polymer gel versus composite gel (right).

Conclusions

A new composite electrolyte has been formulated with a promising room temperature conductivity of 10⁻⁴ S/cm. Preliminary results indicate good stability when cycling with Li contacts.

Tri-layer studies are in good agreement with earlier dispersed particle composite electrolytes for Ohara and PEO+Li salt electrolytes. In both cases, the polymer-ceramic interface is quite resistive unless a significant quantity of DMC is added to the composite. With the DMC plasticizer addition, the interface resistance is zero within experimental error. This contrasts sharply with addition of TEGDME as the plasticizer.

When fabricating full batteries using the dry composite electrolyte of Ohara ceramic dispersed in the polymer formed of PEO+Li salt, the best results were obtained with cathode composed of LiFePO₄ particles mixed with carbon and a polymer electrolyte. When the composite electrolyte was coated with a thin polymer electrolyte to form the contact to the Li metal, the theoretical capacity was realized with good cycling stability over more than 20 cycles. Cycling was conducted at elevated temperatures due to the resistance of the electrolyte and composite cathode.

Batteries fabricated with porous cathodes of NMC particles saturated with finite quantity of liquid catholyte did not cycle.

Key Publications

1. Pandian, A. S.; Chen, X. C.; Chen, J.; Lokitz, B. S.; Ruther, R. E.; Yang, G.; Lou, K.; Nanda, J.; Delnick, F. M.; Dudney, N. J., "Facile and scalable fabrication of polymer-ceramic composite electrolyte with high ceramic loadings," *Journal of Power Sources* 390 (2018) 153-164.
2. X. C. Chen, A. S. Pandian, X. Liu, K. Liu, F. M. Delnick, N. J. Dudney, "Facilitating Ion Transport at the Polymer-Ceramic Electrolyte Interface," in review.

3. Amaresh Samuthira Pandian, Frank M. Delnick, Nancy Dudney, "(PEO)₁₆LiCF₃SO₃+Ohara LICGC® Composite Polymer Ceramic Electrolyte for Lithium Secondary Batteries", presented at *MRS Fall Meeting*, November 2017.
4. X. Chelsea Chen, Amaresh Samuthira Pandian, Naresh Osti, Frank Delnick, Nancy Dudney, "Study of Ion Conductivity and Chain Dynamics in Polymer-Ceramic Composite Electrolytes", presented at *APS March Meeting 2018*, March 5–9, 2018, Los Angeles, California.

References

1. Keller, Marlou, Giovanni Battista Appetecchi, Guk-Tae Kim, Varvara Sharova, Meike Schneider, Jörg Schuhmacher, Andreas Roters, and Stefano Passerini. "Electrochemical Performance of a Solvent-Free Hybrid Ceramic-Polymer Electrolyte Based on Li₇La₃Zr₂O₁₂ in P(Eo)15litfsi." *Journal of Power Sources* 353, no. Supplement C (2017/06/15/ 2017): 287-97.
2. Li, Yutao, Biyi Xu, Henghui Xu, Huanan Duan, Xujie Lü, Sen Xin, Weidong Zhou, *et al.* "Hybrid Polymer/Garnet Electrolyte with a Small Interfacial Resistance for Lithium-Ion Batteries." *Angewandte Chemie International Edition* 56, no. 3 (2017): 753-56.
3. Zhang, Xue, Ting Liu, Shuofeng Zhang, Xin Huang, Bingqing Xu, Yuanhua Lin, Ben Xu, *et al.* "Synergistic Coupling between Li_{6.75}La₃Zr_{1.75}Ta_{0.25}O₁₂ and Poly(Vinylidene Fluoride) Induces High Ionic Conductivity, Mechanical Strength, and Thermal Stability of Solid Composite Electrolytes." *Journal of the American Chemical Society* 139, no. 39 (2017/10/04 2017): 13779-85.
4. Yoon-Sung, Lee, Lee Jae Ha, Choi Ji-Ae, Yoon Woo Young, and Kim Dong-Won. "Cycling Characteristics of Lithium Powder Polymer Batteries Assembled with Composite Gel Polymer Electrolytes and Lithium Powder Anode." *Advanced Functional Materials* 23, no. 8 (2013): 1019-27.

II.7.D High Conductivity and Flexible Hybrid Solid State Electrolyte (University of Maryland)

Eric Wachsman, Principal Investigator

University of Maryland
1206 Engineering Laboratory Building
College Park, MD 20742
E-mail: ewach@umd.edu

Tien Duong, DOE Technology Development Manager

U.S. Department of Energy
E-mail: Tien.Duong@ee.doe.gov

Start Date: October 1, 2016

End Date: September 30, 2019

Project Funding: \$1,250,000

DOE share: \$1,250,000

Non-DOE share: \$0

Project Introduction

Metallic lithium is considered the “Holy Grail” for high-energy density batteries. However, using lithium metal in organic liquid electrolyte systems faces many challenges in terms of battery performance and safety. A fundamental strategy is to develop a solid-state electrolyte (SSE) to mechanically suppress lithium dendrites and intrinsically eliminate SEI formation. Among the different types of SSEs, solid-polymer electrolytes have been the most extensively studied. In polymer-based composite SSEs, nanoparticles are incorporated to influence the recrystallization kinetics of the PEO polymer chains to promote local amorphous regions, thereby increasing the ionic conductivity of the Li salt/polymer system. The fillers can be either non-Li⁺ conductive nanoparticles, such as Al₂O₃, SiO₂, TiO₂, ZrO₂, and organic polymer spheres, or Li⁺ conductive nanoparticles, such as Li_{0.33}La_{0.557}TiO₃, and Li_{1.3}Al_{0.3}Ti_{1.7}(PO₄)₃. Developing nanostructured fillers is an essential approach to increase the ionic conductivity of composite electrolytes due to the increased surface area of the amorphous region and improved interface between fillers and polymers. Meanwhile, numerous solid-state inorganic Li⁺ electrolytes are being investigated to replace liquid organic electrolytes. Due to their high ion conductivity and excellent stability, Li-stuffed garnets exhibit the most promising physical and chemical properties for SSEs. However, major challenges still exist in garnet based electrolytes, including: (1) Being either too thick with corresponding high ASR or too mechanically fragile when thin (~20 μm); (2) High temperature processing that is incompatible with most anode/cathode materials; and (3) High interfacial impedance. Moreover, flexible SSEs with high ionic conductivity and excellent processability are completely lacking.

Recently, the PIs at the University of Maryland have pioneered thin garnet based solid state batteries that effectively address the interfacial impedance using gel/polymer layers and here propose to integrate these two materials (garnet and organic) to address the other issues. We have demonstrated the ability to overcome the solid-electrolyte/solid-electrode interfacial impedance using gel and polymer interfacial layers with solid-state garnet (e.g. Li₇La₃Zr₂O₁₂ LLZO) electrolytes under BMR contract DEEE0006860. We now are extending this to an integrated high-conductivity, conformal/flexible and low-interfacial impedance, hybrid (garnet-organic) solid electrolyte. Our approach is based on a continuous network of high-conductivity one-dimensional (1D) garnet electrolyte nanofibers that not only provide greater conductivity, but through microstructural optimization can block Li-dendrite propagation. We have already demonstrated the ability to synthesize 1D garnet nanofibers by electrospinning and that the corresponding hybrid electrolyte (after infiltrating the pore structure with a polymer electrolyte) is flexible with enhanced mechanical properties compared to the polymer matrix. Moreover, it has greater thermal stability than the polymer alone, high ion conductivity, excellent stability with Li metal and can be used to make solid-state metal anode batteries with S cathode, as well as low electrode interfacial impedance due to the intrinsic gel/polymer-interface developed in the current BMR project. Therefore, this can potentially revolutionize solid-state, metal-anode, battery technology.

Instability and/or high resistance at the interface of lithium metal with various solid electrolytes limit the use of the metallic anode for batteries with high energy density, such as Li-air and Li-S batteries. The critical impact of this endeavor will be focused on developing a new type of solid-state electrolyte (SSE) that is highly conductive, highly flexible and electrochemically stable. In particular, the new SSE will enable Li metal anodes with excellent interfacial impedance and blocking formation of Li dendrites.

Objectives

The objective of this project is to develop a flexible hybrid electrolyte with garnet nanofibers to achieve the following: (1) Flexibility with greater mechanical strength (~ 10 MPa) and thermal stability than polymer electrolytes; (2) High room temperature ionic conductivity, ~ 0.5 mS/cm; (3) Stable interface with Li metal and effectively block Li dendrites at current densities up to 3 mA/cm²; and (4) Battery performance with Li-S chemistry with an energy density of ≥ 450 Wh/kg and (≥ 1000 Wh/L), and maintain $\geq 80\%$ of capacity up to 500 cycles.

Approach

We will synthesize garnet nanofibers, fill the porous region with polymer electrolyte, and characterize and tune the flexible hybrid membrane properties. The flexible hybrid SSE microstructure will be analyzed by leveraging the UMD AIMLab Focused Ion Beam Scanning Electron Microscopy (FIB-SEM) tools and integrated with electrochemical methods at the UMERB Battery Fabrication Lab to investigate the properties and stability with Li metal anode. We will develop a fundamental understanding of the mechanism of Li ionic diffusion in garnet nanofibers and their mechanical properties, as well as these properties for hybrid garnet-fiber/polymer hybrids. Work will progress toward the study of the electrode assembly during electrochemical cycling of the anode.

Results

1. Characterization of electrochemical, mechanical and thermal properties of hybrid SSE

Hybrid SSEs were developed and characterized using garnet nanofiber membranes. Al-doped LLZO with the chemical composition of $\text{Li}_{6.28}\text{Al}_{0.24}\text{La}_3\text{Zr}_2\text{O}_{11.98}$ was prepared. The cellulose nanofiber template was soaked in the garnet precursor solution and then treated at high temperature of 800°C to obtain the ceramic membrane. The 3D structure of the garnet membrane was scanned using a LK-H082 semiconductor laser model. The reconstructed digital structure shows a typical over one-under one, plain weave textile pattern in Figure I.1.1. Height of the membrane was indicated to be generally $200\ \mu\text{m}$ by the cross-yarn junction areas in the pattern. The fiber structure was further analyzed by 3D FIB tomography in the Tescan XEIA FIB-SEM. The 3D sampling produced secondary electron images with good contrast between the ceramic fiber mat particles (which appeared bright) and the infiltrated epoxy (which appeared dark) in Figure II.7.D.1. The continuous ceramic fiber will provide structure reinforcement and abundant fast Li-ion conductive pathways within the composite electrolyte.

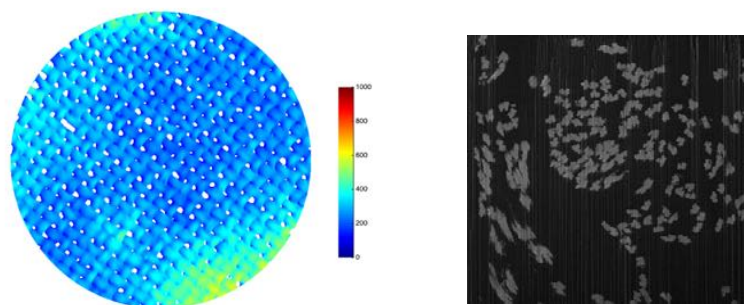


Figure II.7.D.1 Characterization of garnet fibrous membrane: left, Reconstructed model of garnet membrane flatness generated by 3D laser scanning; right, Focus ion beam analysis of the typical fiber bundle structure

Hybrid electrolyte was fabricated by infiltrating conductive polymer into the multi-level open space in the garnet fiber membrane. Surface morphology of the hybrid electrolyte was analyzed by AFM within an area of $10\ \mu\text{m} \times 10\ \mu\text{m}$ in Figure II.7.D.2. The polymer material has fully filled the open pores and covered the surface of the individual fibers. The surface roughness of the hybrid electrolyte was effectively limited to a value of less than $2\ \mu\text{m}$. Thermal performance of the hybrid electrolyte was analyzed by thermogravimetry measurement. The weight loss is caused by evaporation of the trapped solvent from room temperature to 300°C . The hybrid electrolyte shows thermal stability up to 450°C .

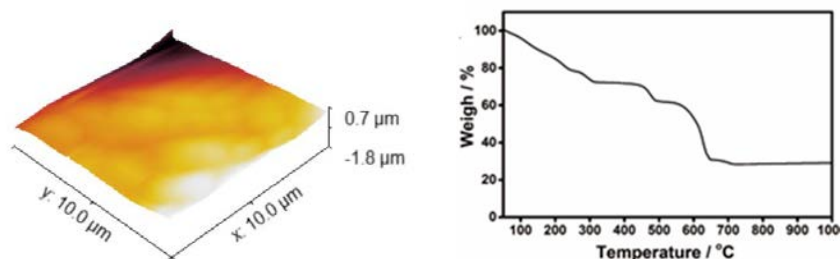


Figure II.7.D.2 Characterization of hybrid electrolyte membrane: left, AFM scanning of the hybrid electrolyte membrane; right, Thermal properties of the hybrid electrolyte membrane

2. Fabrication of thin hybrid electrolyte and study Li-SSE interface

We developed a nanofiber template membrane to further reduce the thickness of the hybrid electrolyte. PAN (Polyacrylonitrile) fiber membrane was electrospun and hot pressed as the sacrificial template. The pressed template was stabilized at 260°C for 10 h for garnet precursor soaking. The soaked membrane was sintered at 800°C in oxygen. Figure II.7.D.3 shows the SEM images of the sintered garnet nanofiber membrane. Thickness of the garnet nanofiber membrane is less than $30\ \mu\text{m}$ with a typical layered structure.

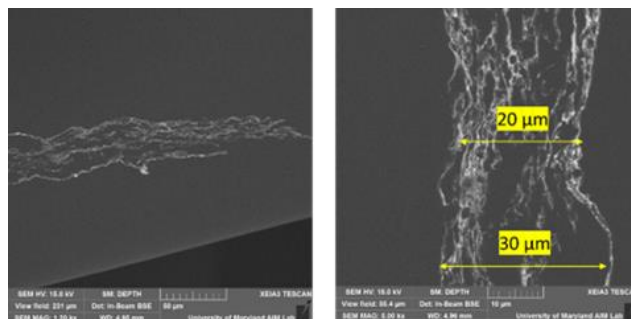


Figure II.7.D.3 Sintered garnet nanofiber membrane from PAN fiber template. Sample was impregnated with epoxy Li-ion conducting polymer was infiltrated into the porous garnet nanofiber membrane to make hybrid electrolytes. The as-infiltrated electrolyte was hot pressed to further reduce the thickness to as thin as $11\ \mu\text{m}$ (Figure II.7.D.4). The hybrid electrolyte appears to be homogenous, dense and flexible.

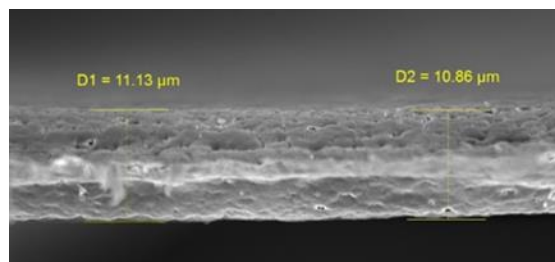


Figure II.7.D.4 Hybrid electrolyte membrane with $\sim 11\ \mu\text{m}$ thickness

3. Understanding lithium stripping and plating in thin SSE at a current density of $\sim 3\text{ mA/cm}^2$ without shorting

Using the thin hybrid electrolyte and lithium metal, we assembled symmetrical cells for electrochemical characterization. The symmetrical cells were fabricated by pressing two pieces of lithium metal on both sides of the electrolyte by hydraulic crimping. The cell was tested using Solatron 1260 and 1287 stations. The initial impedance of the cell was measured from 10^7 to 10 Hz with an AC amplitude of 100 mV at room temperature. Two arcs are observed for the cell as shown in Figure II.7.D.5. The first suppressed arc at high frequency range is from the resistance of electrolyte. The second arc at low frequency range originated from the interface between lithium metal and electrolyte. As we can see, the interface resistance is higher than that from the electrolyte due to the impurity phase on the surface of lithium metal. The electrochemical performance of the symmetrical cell was further evaluated by stripping and plating using Arbin electrochemical testing station at room temperature. Figure II.7.D.5 shows the preliminary cycling results. The voltage profiles of the cell show stable performance at different current densities of 0.1 mA/cm^2 and 0.5 mA/cm^2 . The resistance calculated from the cycling matched well the AC impedance. We further tested the Li plating/stripping performance at 3 mA/cm^2 . The symmetric Li/electrolyte/Li cell shows overpotential around 1 V without shorting.

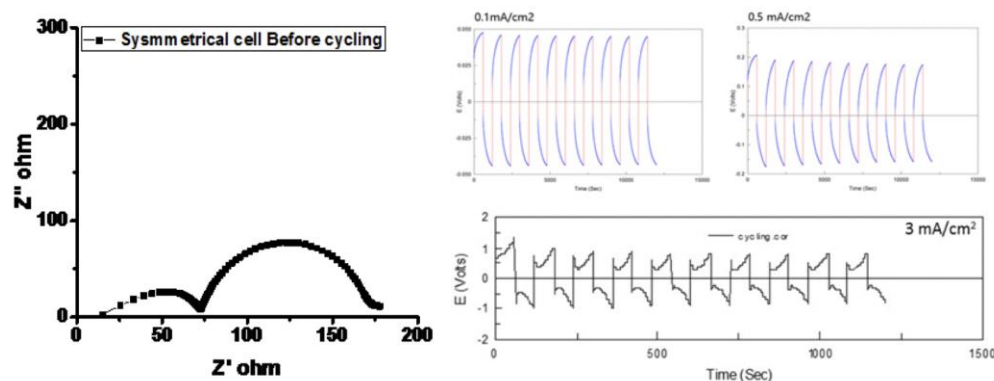


Figure II.7.D.5 Electrochemical impedance of the Li/electrolyte/Li symmetrical cell at room temperature (left); Cycling of the cell at different current densities of 0.1 mA/cm^2 , 0.5 mA/cm^2 and 3 mA/cm^2

Computational modeling

Computational modeling is performed to evaluate various fundamental processes that are related to the Li dendrite growth in SSEs, including defect chemistry and energetics, Li-ion diffusion in nanofibers and grain boundary, and local potential distribution. We performed DFT calculations on the formation of various point defects in garnet (Figure II.7.D.6), which may significantly impact Li dendrite growth mechanism within garnet solid electrolyte. Our calculation found Li^+ insertion into garnet may be energetically favorable in contact with Li metal, in agreement with previous experimental observations. The calculations also found oxygen vacancy formation may be favorable at Li-rich conditions, which may aid Li metal reduction and dendrite formation. The formation and transport of electron polaron is also evaluated in DFT calculations, which was speculated to contribute to Li reduction inside garnet SSE. In order to understand Li dendrite growth mechanism within garnet solid electrolyte, MD simulations were performed on garnet grain boundaries (Figure II.7.D.6). We observed the decrease of Li^+ diffusion observed near grain boundary core, caused by distortion of garnet crystal structural framework near grain boundary core. Grain boundaries may cause significant potential drop or field concentration, and may aid Li nucleation and Li dendrite growth, as shown by continuum modeling (Figure II.7.D.6).

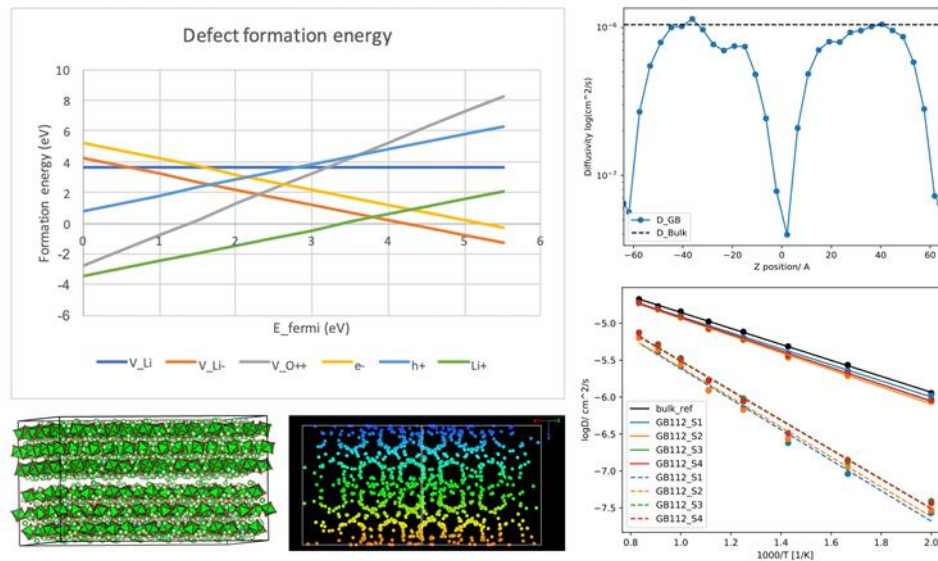


Figure II.7.D.6 Formation energy of point defects in LLZO (left) and Li ion diffusion in LLZO grain boundary (right) from atomistic modeling

Computer modeling was performed for Li nucleation and dendrite growth within the SSE. We modeled the electronic potential and ionic transport within the SSE with different microstructure features during Li cycling. For the SSE with Li dendrite formed inside, the modeling results (Figure II.7.D.7) show high ion current density near the tip of Li dendrite, indicating an increase of Li chemical potential and the driving force for Li dendrite growth. We also found that similar behavior exists in the intersection of grain boundaries in SSE, which are caused by the slow ionic diffusion and high resistances in the grain boundaries. This behavior also suggests favorability for Li dendrite growth in grain boundaries of SSEs, consistent with numerous reports in the literature. We found that the hybrid SSEs do not exist these hot spots for Li dendrite growth, because of the well-connected fast-ion conducting garnet fibers formed inside the hybrid SSE. This modeling result is consistent with the high current density as high as 3 mA/cm² observed in the Li cycling experiments of hybrid garnet SSEs.



Figure II.7.D.7 Hot map of Li dendrite formation in SSE with various microstructure features

4. Lithium plating and stripping in thin SSE at current density of 3 mA/cm² for 500 cycles

We assembled symmetrical cells in Li metal/ hybrid electrolyte/Li metal structure for electrochemical cycling. The symmetrical cell was fabricated by pressing two pieces of lithium metal on both sides of the electrolyte with proper interface modification. Figure II.7.D.8 shows voltage profiles of the cycling cell at different current densities of 0.1 mA/cm² and 3 mA/cm². The cell was initially cycled under low current density to stabilize the lithium metal/hybrid electrolyte interfaces. The cell shows stable and uniform lithium stripping/plating behavior with flat cycling plateaus. After stabilization, the cell was cycled at high current density of 3 mA/cm² for 500 cycles. As current density was increased by 30 times, overpotential of the cell increased. The cell was successfully cycled at 3 mA/cm² for 500 cycles without dendrite penetrating through the hybrid electrolyte, thus achieving the Budget Period 2 Go/No-Go metrics.

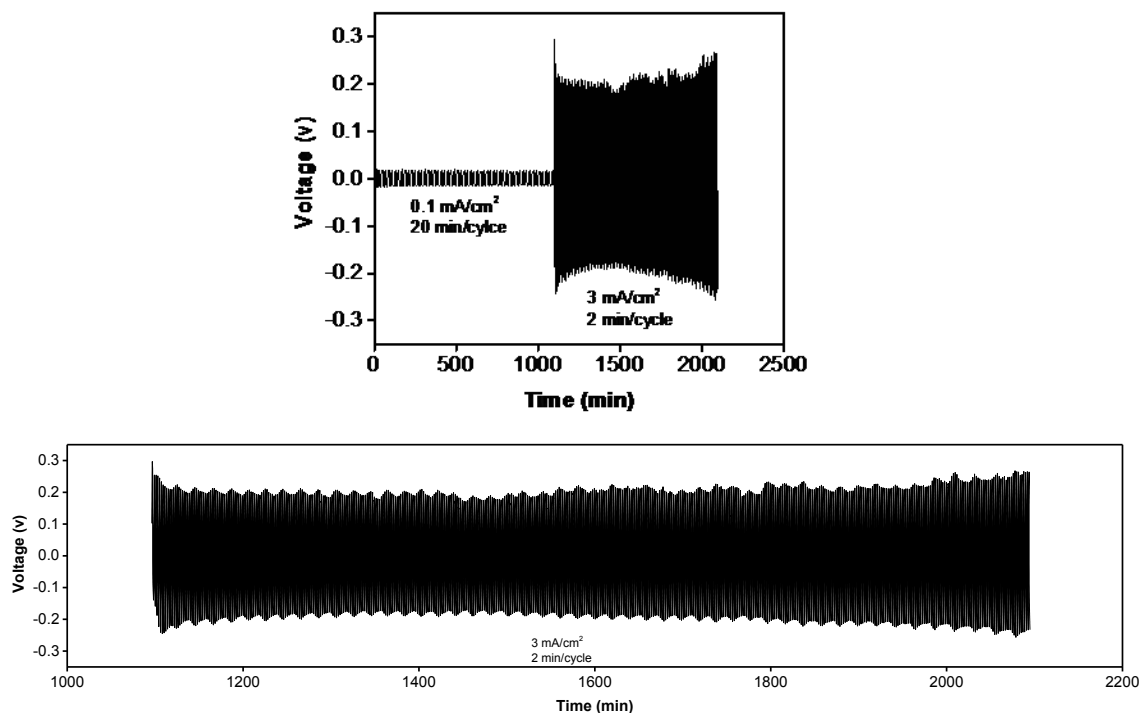


Figure II.7.D.8 Electrochemical cycling of the Li/electrolyte/Li symmetrical cell, including low current density stabilization at 0.1 mA/cm² and high current density cycling at 3 mA/cm² (top); enlarged plot at 3 mA/cm² for 500 cycles without lithium dendrite penetration (bottom)

Conclusions

We fully characterized garnet nanofiber membrane and its hybrid electrolyte for solid state lithium metal battery application. The hybrid electrolyte shows reasonably high ionic conductivity, mechanical strength and thermal stability. We synthesized thin garnet nanofiber membrane and hybrid electrolyte with thickness less than 20 micron. Fundamental understand of the Li cycling in hybrid and other SSE are provided by both experiments and computation modeling. Our garnet nanofiber membrane reinforced hybrid was cycled at high current density of 3 mA/cm² for 500 cycles without lithium dendrite penetration, thus achieving the Budget Period 2 Go/No-Go performance metrics.

Key Publications & Presentations

1. Eric Wachsman, “Beyond Dendrites, Cycling Li-Metal Across Garnet at High Current Densities”, Argonne National Lab, September 6, 2018, Lemont, IL

2. Y. Mo, “Computation Accelerated Design of Materials and Interfaces for Solid-State Batteries”, 21st International Conference on Ternary and Multinary Compounds, September 2018, Boulder, CO (Invited)
3. Y. Mo, “Computation Accelerated Design of Materials and Interfaces for Solid-State Batteries”, Applied Mechanics Seminar, Harvard University, April 2018, (Invited)
4. Y. Mo, “First-Principles Computation Study and Design for Solid Electrolyte–Electrode Interfaces in All-Solid-State Li-Ion Batteries”, Materials Research Society (MRS) Spring Meeting, April 2018, Phoenix AZ (Invited)
5. Y. Mo, “Computation Accelerated Design of Materials and Interfaces for All-Solid-State Li-ion Batteries”, Nature Conference on Materials Electrochemistry: Fundamentals & Applications, January 2018, Shenzhen, China (Invited)
6. X. He, Y. Mo, “Universal Strategy to Design Super-Ionic Conductors through First Principles Computation”, Materials Research Society (MRS) Spring Meeting, April 2018, Phoenix AZ
7. Y. Zhu, Y. Mo., “Atomistic Modeling of Interface Transport in All-Solid-State Li-ion Batteries”, Materials Research Society (MRS) Spring Meeting, April 2018, Phoenix AZ
8. Y. Zhu, Y. Mo., “Novel Strategies for Lithium Metal Anode Protection from Computation-Guided Materials Discovery”, Materials Research Society (MRS) Spring Meeting, April 2018, Phoenix AZ
9. Y. Gong, K. Fu, S. Xu, J. Dai, T. R. Hamann, L. Zhang, G. T. Hitz, X. Han, L. Hu, E. D. Wachsman, Lithium-Ion Conductive Ceramic Textile: A New Architecture for Flexible Solid-State Lithium Metal Batteries, *Materials Today*, Volume 21, 6, 594-601, 2018
10. Adelaide Nolan, Yizhou Zhu, Xingfeng He, Qiang Bai, Yifei Mo*, “Computation-Accelerated Design of Materials and Interfaces for All-Solid-State Lithium-Ion Batteries”, *Joule*, 2, 2016-2046, 2018 (Invited Review)
11. Kern Ho Park+, Qiang Bai, Dong Hyeon Kim, Dae Yang Oh, Yizhou Zhu, Yifei Mo, Yoon Seok Jung, “Design Strategies, Practical Considerations, and New Solution Processes of Sulfide Solid Electrolytes for All-Solid-State Batteries”, *Advanced Energy Materials*, 1800035, 2018 (Invited Review)
12. Qiang Bai, Lufeng Yang, Hailong Chen, Yifei Mo, “Computational Studies of Electrode Materials in Sodium-Ion Batteries”, *Advanced Energy Materials*, 1702998, 2018 (Invited Review)

II.7.E Lithium Dendrite Prevention for Lithium Batteries (Pacific Northwest National Laboratory)

Wu Xu, Principal Investigator

Pacific Northwest National Laboratory
902 Battelle Boulevard
Richland, WA 99354
E-mail: wu.xu@pnnl.gov

Ji-Guang Zhang, Principal Investigator

Pacific Northwest National Laboratory
902 Battelle Boulevard
Richland, WA 99354
E-mail: jiguang.zhang@pnnl.gov

Tien Duong, DOE Technology Development Manager

U.S. Department of Energy
E-mail: Tien.Duong@ee.doe.gov

Start Date: October 1, 2015

End Date: September 30, 2018

Project Funding (FY18): \$400,000

DOE share: \$400,000

Non-DOE share: \$0

Project Introduction

Lithium (Li) metal is the ideal anode material for rechargeable Li batteries due to its advantages including extremely low redox potential (-3.040 V vs. standard hydrogen electrode), ultrahigh theoretical specific capacity (3860 mAh g^{-1}), and very low density (0.534 g cm^{-3}). However, there are still several barriers for the practical application of Li metal anodes, including the uncontrollable growth of Li dendrites and low Coulombic efficiency (CE) of Li cycling. The repeated stripping/plating of a Li anode will form dendritic and mossy Li metal deposits, which will eventually cause safety hazards. In addition, Li is thermodynamically unstable in organic electrolytes and results in low CE, which will cause depletion of electrolyte, consumption of Li metal and consequently short cycle life. In our previous works, we have reported the mechanism behind the largely improved cycling stability of Li metal batteries when lithium hexafluorophosphate ($LiPF_6$) is used as an additive in lithium bis(trifluoromethanesulfonyl)imide ($LiTFSI$)-lithium bis(oxalato)borate ($LiBOB$) dual-salt electrolyte. We also got deep understanding on the effects of Li capacity utilization and charging current density on the stability of Li metal anode. However, the Li CE is still not high enough and the stability of Li metal battery with high loading and high current density is still a challenge. In FY18, our research works have been focused on the systematical study of effects of lithium salts, solvent compositions, additives and polymer electrolytes on ionic conductivity, Li CE, Li anode morphology, and battery performances. This will guide the development of Li metal anode to achieve higher efficiency and further suppress dendrite prevention in Li metal batteries.

Objectives

- Enable Li metal to be used as an effective anode in rechargeable Li metal batteries for long cycle life at a reasonably high current density.
- Investigate the effects of various lithium salt mixtures, inorganic fillers and polymer types on ionic conductivity, Li CE, Li anode morphology, and battery performances in terms of long-term cycling stability at room temperature and elevated temperatures and at various current densities, rate capability, and at low temperatures.

- Investigate the compatibility of such electrolytes with 4-V $\text{LiNi}_{1/3}\text{Mn}_{1/3}\text{Co}_{1/3}\text{O}_2$ (NMC333 or NMC) cathode.

Approach

The following approaches have been used to reach the objectives outlined above. First, four electrolytes of lithium imide (chosen from LiTFSI and lithium bis(fluorosulfonyl(imide (LiFSI)) and lithium orthoborate (chosen from LiBOB or lithium difluoro oxalato borate (LiDFOB)) dual-salt mixtures in organic carbonate solvents were investigated to identify the effects of different salt chemistries on the cycling stability of Li metal batteries. Second, high Li CE of LiTFSI-LiBOB/carbonate electrolyte system was obtained through optimization of solvent composition and addition of combinational additives. Third, the effects of lithium difluorophosphate (LiDFP) additive in conventional LiPF_6 /carbonate electrolyte on Li metal anode and Li metal batteries were investigated. Fourth, the effects of different separators (without and with surface coating layers) on Li CE and stability were investigated. Finally, hybrid polymer-in-salt electrolytes (HPISEs) were developed. Various characterization technologies, including high-resolution scanning electron microscopy (SEM), atomic force microscopy (AFM) and X-ray photoelectron spectroscopy (XPS) were used to analyze the morphology and composition of the interfacial films on Li-metal surfaces. The density functional theory (DFT) calculations were utilized to study the mechanism.

Results

1. Effects of imide-orthoborate dual-salts/carbonate electrolytes

Lithium salt chemistry is critical for enhancing the interfacial stability of Li metal anode. The effects of lithium imide and lithium orthoborate dual-salt mixtures in organic carbonate electrolytes on the stability of Li metal anode and the cycle life of Li metal batteries were systematically investigated. DFT calculations indicate that the chemical and electrochemical stabilities of the four imide-orthoborate dual-salt mixtures rank in the following order: $\text{LiTFSI-LiBOB} > \text{LiTFSI-LiDFOB} > \text{LiFSI-LiDFOB} > \text{LiFSI-LiBOB}$, the same order as demonstrated by the experimental results. The LiTFSI-LiBOB electrolyte shows the superior capability of enhancing the stability of Li metal anode (Figure II.7.E.1a) and improving the cycle life of Li metal batteries (Figure II.7.E.1b). XPS analysis reveals that there are more electrolytes decomposed on Li anodes to generate the surface film when using the LiFSI-LiBOB, LiFSI-LiDFOB, and LiPF_6 electrolytes than those using the LiTFSI-LiBOB and LiTFSI-LiDFOB electrolytes. The LiTFSI-LiBOB can effectively protect the Al substrate and form a more robust surface film on Li metal anode (Figure II.7.E.1a).

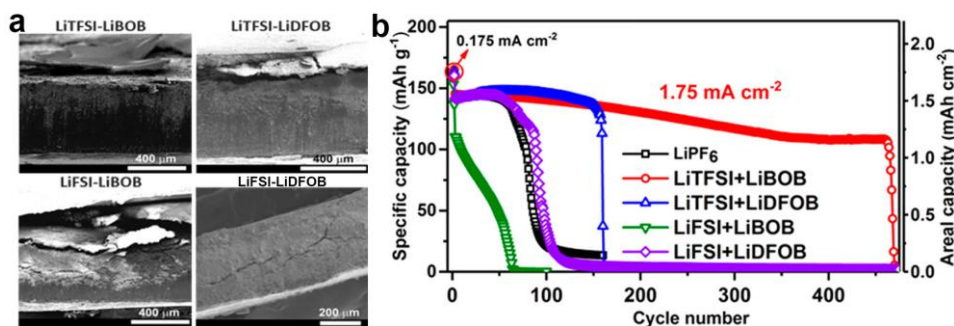


Figure II.7.E.1 (a) Cross-sectional views of Li metal anodes retrieved from Li||NMC cells after 100 cycles at 1.75 mA cm^{-2} using different dual-salt electrolytes. (b) cycling performances of the baseline LiPF_6 electrolyte and the four different dual-salt electrolytes at a current density of 1.75 mA cm^{-2} after three formation cycles at 0.175 mA cm^{-2} .

2. Optimization of LiTFSI-LiBOB in carbonate electrolytes

Based on the studies of dual-salt in carbonate electrolytes, the optimization of solvent compositions and the addition of combinational additives were further investigated. As shown in Figure II.7.E.2a, a high Li CE of 98.1% has been achieved for the electrolyte of 1 M LiTFSI-LiBOB dual-salt in ethylene carbonate-ethyl methyl carbonate (EC-EMC) (7:3 by wt.) plus the combinational additives of 0.05 M LiPF_6 , 2% vinylene

carbonate (VC) and 2% fluoroethylene carbonate (FEC). This electrolyte also shows long-term cycling stability in Li||NMC cells with an areal capacity loading of 2 mAh cm^{-2} . The capacity retention is 85.4% after 230 cycles at 30°C and 92.6% after 260 cycles at 60°C (Figure II.7.E.2b), respectively. The Li||NMC cells can be charged and discharged at 3C rate (where $1\text{C} = 2 \text{ mA cm}^{-2}$) with a capacity retention of 125 mAh g^{-1} . SEM analysis reveals that the optimized electrolyte enhances the formation of large size Li deposition, while the controls yield wire-like Li morphology. The additives VC and FEC are decomposed first due to their lower lowest-unoccupied-molecular-orbital (LUMO) energies to form solid electrolyte interphase (SEI) film prior to the decomposition of EC and EMC. The higher ratio of EC in the solvent mixture can lead to slightly more ring-opening polymerization of EC by the induction of LiPF_6 and to form polycarbonates in SEI on Li. The SEI films could enable the fast Li^+ ion transport through the SEI layer, thereby facilitating the growth of Li nuclei in large particle size. At the same time, the SEI layer enriched with polycarbonates constituents could well attach to the Li metal anode, thus effectively suppressing the further decomposition of electrolyte and the corrosion to Li metal anode. Furthermore, the surface film formed on the Li metal anode using the optimized electrolyte could be more ionic conductive, enabling the Li metal anode cycled in this electrolyte to have the low and stable polarization, fast chargeability and low interfacial impedance.

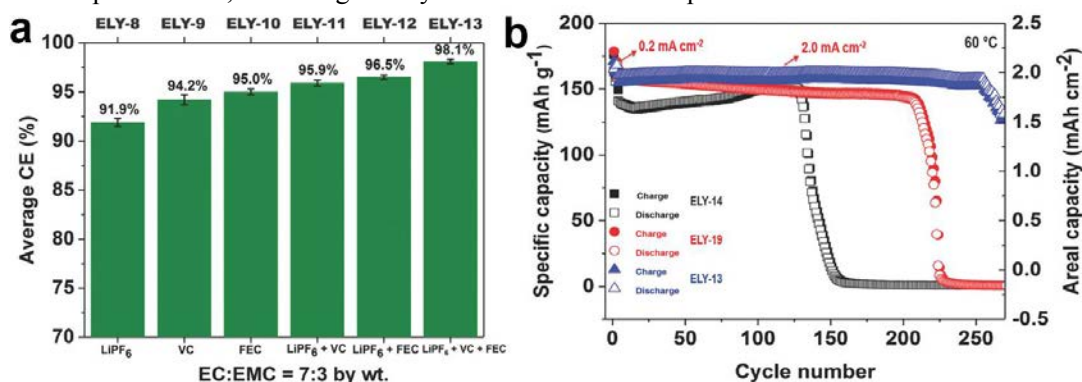


Figure II.7.E.2 (a) The average Li CE values of the LiTFSI-LiBOB/EC-EMC (7:3 by wt) electrolytes with single additive of LiPF_6 , VC, and FEC, and the combinational additives of LiPF_6 + VC, LiPF_6 + FEC, and LiPF_6 + VC + FEC. The weight percentages of LiPF_6 , VC, and FEC are 0.6, 2.0, and 2.0%, respectively. (b) Cycling performances of Li||NMC cells using the three electrolytes of ELY-14, ELY-19, and ELY-13 at the same charge and discharge current density of 2.0 mA cm^{-2} after 3 formation cycles at 0.2 mA cm^{-2} at 60°C .

3. Effect of LiDFP additive

An appropriate electrolyte additive is very useful to modify the SEI layer to suppress Li dendrites and increase Li CE. Lithium difluorophosphate (LiDFP) was used as an electrolyte additive to inhibit Li dendrite growth by forming a vigorous and stable SEI film on metallic Li anode. By the addition of an optimal concentration of 0.15 M LiDFP, the Li CE can be improved from 84.6% of the conventional LiPF_6 -based electrolyte to 95.2% (Figure II.7.E.3a). The optimal LiDFP-containing electrolyte can allow the Li||Li symmetric cells to cycle stably for more than 500 and 200 h at 0.5 and 1.0 mA cm^{-2} (Figure II.7.E.3b), respectively, much longer than the control electrolyte without LiDFP additive. The main reason of the high CE and enhanced stability is that LiDFP could introduce an SEI layer rich in LiF and phosphate compounds, which prevents the continuous decomposition of electrolyte and facilitates Li^+ deposition with dendrite-free. Consequently, the Li||NMC cells using this LiDFP-containing electrolyte exhibit largely enhanced cycle life.

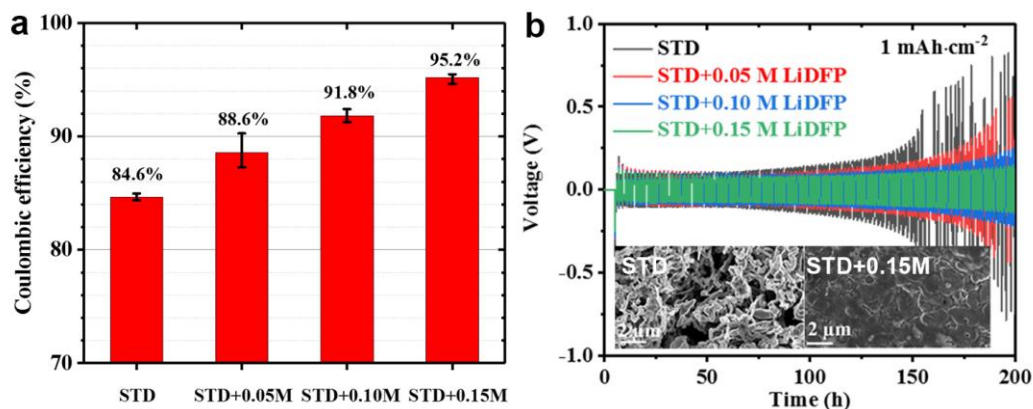


Figure II.7.E.3 (a) Average CE values of Li metal in electrolytes with LiDFP additive from 0 to 0.15 M. (b) Cycling stability of Li||Li symmetric cells in the electrolytes without and with various contents of LiDFP additive at the current density of 1.0 mA cm⁻² with 1 h plating/stripping time at 25 °C. Inserted are SEM images of Li anodes in Li||Li cells at 1.0 mA cm⁻² with 1 h plating/stripping time for 100 cycles without and with LiDFP.

4. Effects of polymer separators

The separator is an important part in rechargeable Li metal batteries. Besides electrolytes, the effects of polymer separators on Li CE and stability of Li metal anode were also systematically studied. The separators investigated in this work include polyethylene (PE) and polypropylene (PP) without and with surface coatings of ceramic (Al_xO_y), siloxy polymer, and PVDF; and the electrolytes are 1 M LiPF₆ in EC-EMC (4:6 by wt.) (always with trace amount of HF) and 0.6 M LiTFSI + 0.4 M LiBOB in EC-EMC (4:6 by wt.) (without HF). For the PE separator, the average Li CE value in Li||Cu cells and the cycling stability in Li||Li cells would not be affected no matter whether there is a trace amount of HF in the electrolytes. For the ceramic coated PE separator (e.g. Al_xO_y-PE), the average Li CE value and the cycling stability will be seriously affected by the electrolyte type, which should be mainly attributed to the side reactions among HF, Al_xO_y and Li metal. For the PP based separators, a correct average Li CE value and a good cycling stability can be achieved if the used electrolyte has no trace amount of HF, which is probably because the PP based separators have less thermodynamic stability in the HF containing electrolyte. Among these separators, the PE separator is the most stable one with Li metal while the ceramic and polysiloxo coating layers are not stable with Li metal in the presence of the LiPF₆ electrolyte.

5. Hybrid polymer-in-salt electrolytes

The HPISEs were developed in this fiscal year as well. The HPISE was composed of a lithium salt, a suitable polymer and a small amount of organic solvent, and was fabricated by using a facile mixing method. The HPISE is stable at a voltage as high as 4.8 V vs. Li/Li⁺ (Figure II.7.E.4a), which is well compatible with the 4-V class Li metal batteries. The HPISE without separator has an ionic conductivity of 2.3 mS cm⁻¹ and 5.1 mS cm⁻¹ at 30°C and 60°C, respectively, while the HPISE/GF (glass fiber) exhibits an ionic conductivity of 0.4 mS cm⁻¹ and 1.8 mS cm⁻¹ at 30°C and 60°C, respectively (Figure II.7.E.4b). The high conductivity and wide electrochemical window of the HPISE enable the Li||NMC333 cells (with an areal capacity loading of 2 mAh cm⁻²) to show a stable cycling in the voltage range of 3.0 – 4.2 V, having a high capacity retention of 88.7% after 125 cycles under charge rate of C/5 and discharge rate of C/3 at 60°C (Figure II.7.E.4c and Figure II.7.E.4d).

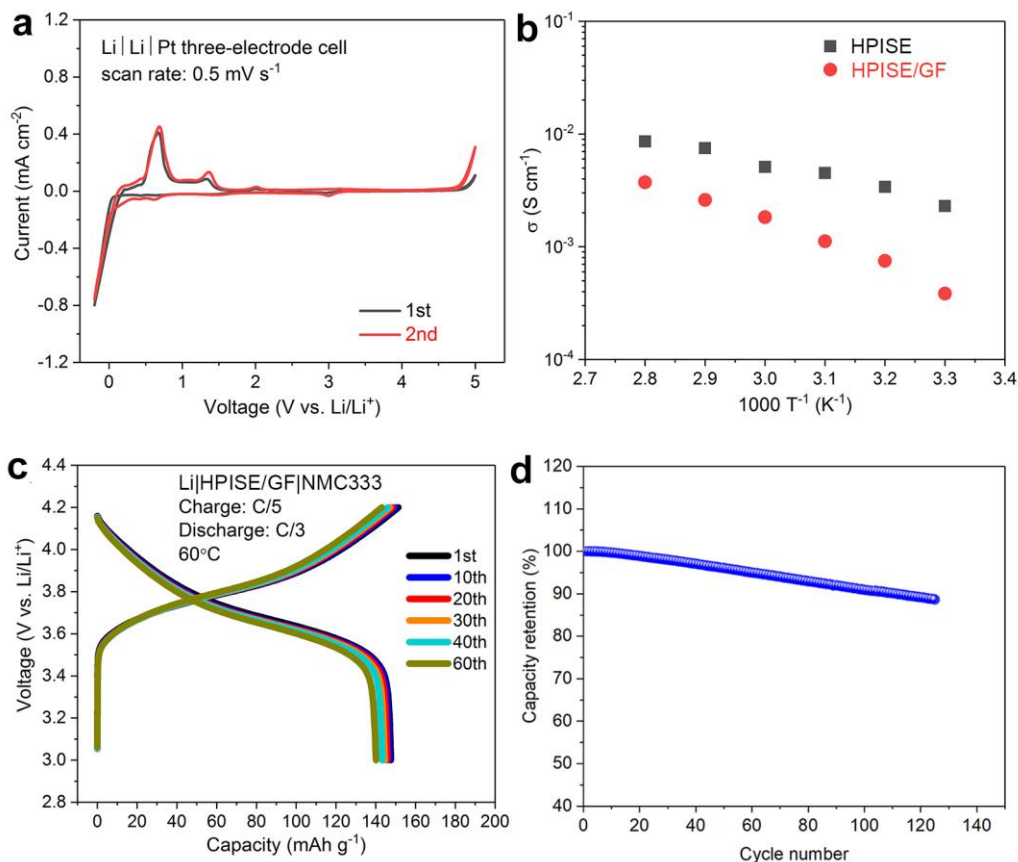


Figure II.7.E.4 (a) Cyclic voltammogram curves of Li|Li|Pt three-electrode cell containing HPISE at a scan rate of 0.5 mV s⁻¹ in the voltage window of -0.2 V to 5.0 V at room temperature. (b) Temperature dependence of ionic conductivity of HPISE without and with GF separator. (c) Voltage profiles of a coin cell of Li|NMC333 (2 mAh cm⁻²) with GF separator soaked with HPISE cycled using a charge rate of C/5 and a discharge rate of C/3 between 3.0 V and 4.2 V at 60 °C, where 1C = 2.0 mA cm⁻². (d) The corresponding cycling performance of the cell.

6. Advancing Li metal batteries

Based on our research on Li metal batteries and other groups' work, we summarized the strategies to stabilize Li metal anode and proposed some new research directions to further develop Li metal batteries. First, optimization of electrolytes such as additives and high concentration electrolytes can obtain dendrite-free Li morphology and high Li CE. Second, membrane and interfacial engineering such as solid-state electrolytes, artificial SEI layers and Janus separators are widely used to suppress Li dendrite growth. Third, rational design of Li anode structures, like three-dimensional porous copper current collectors and layered Li/reduced graphene oxide composites are proved to get uniform ion flux distribution and reduce volume change. For the further development of Li metal batteries, there are many critical issues needing to be carefully considered, which include: (1) deep understanding of SEI, (2) improving electrolyte durability, (3) evaluating Li metal stability from the practical requirements, (4) pursuing non-dendritic Li metal anodes, (5) suppressing change of Li metal upon cycling, (6) controlling Li deposition on anode current collector, (7) simplifying Li metal stabilization process, and (8) enabling relaxed environmental controls.

Conclusions

1. Among the four imide-orthoborate dual-salt mixtures, LiTFSI-LiBOB shows the best cycling stability because of its effective protection on Al substrate and formation of a more robust surface

film on Li metal anode. Optimization of solvent composition and addition of LiPF₆+VC+FEC additive mixture can further stabilize Li metal anode and increase Li CE to 98.1%, thus extending the cycling stability of Li metal batteries. The optimized electrolyte enables the Li||NMC333 cells with a medium capacity loading to have good cycling stability and superior rate capability.

- LiDFP as additive in conventional LiPF₆-carbonate electrolyte can increase the Li CE to 95.2% and show low polarization and enhanced cycling stability. The preferential reduction of LiDFP renders compact and stable SEI enriched with LiF and phosphates.
- Separators have large effects on the CE and cycling stability of Li metal cells, especially when using the LiPF₆ electrolyte. Among these separators, PE separator is the most stable one with Li metal while ceramic and polysiloxo coating layers are not stable with Li metal especially in the presence of the LiPF₆ electrolyte.
- An HPiSE composed of a lithium salt, a suitable polymer and a small amount of organic solvent has ionic conductivity over 1 mS cm⁻¹ at 30°C and high electrochemical stability above 4.5 V. The HPiSE can enable the Li||NMC333 cells to be cycled stably for more than 125 cycles at 60°C (where the cells are still under testing).

Key Publications, Presentations and Patent

- X. Li, J. Zheng, M. H. Engelhard, D. Mei, Q. Li, S. Jiao, N. Liu, W. Zhao, J.-G. Zhang*, and W. Xu*, “Effects of Imide-Orthoborate Dual-Salt Mixtures in Organic Carbonate Electrolytes on the Stability of Lithium Metal Batteries”, *ACS Appl. Mater. Interfaces*, 2018, **10**, 2469.
- X. Li, J. Zheng, X. Ren, M. H. Engelhard, W. Zhao, Q. Li, J.-G. Zhang*, and W. Xu*, “Dendrite-Free and Performance-Enhanced Lithium Metal Batteries through Optimizing Solvent Compositions and Adding Combinational Additives”, *Adv. Energy Mater.*, 2018, **8**, 1703022.
- P. Shi, L. Zhang, H. Xiang*, X. Liang, Y. Sun, and W. Xu*, “Lithium Difluorophosphate as a Dendrite-Suppressing Additive for Lithium Metal Batteries”, *ACS Appl. Mater. Interfaces*, 2018, **10**, 22201.
- X. Li, J. Tao, D. Hu, M. H. Engelhard, W. Zhao, J.-G. Zhang *, and W. Xu, “Stability of polymeric separators in lithium metal batteries in a low voltage environment”, *J. Mater. Chem. A*, 2018, **6**, 5006.
- B. Liu, J.-G. Zhang, and W. Xu*, “Advancing Lithium Metal Batteries”, *Joule*, 2018, **2**, 833.
- X. Li, J. Zheng, M. H. Engelhard, D. Mei, Q. Li, S. Jiao, N. Liu, W. Zhao, J.-G. Zhang, and W. Xu, “Effects of Imide-Orthoborate Dual-Salt Mixtures in Organic Carbonate Electrolytes on the Stability of Lithium Metal Batteries”, Oral presentation at *the 232nd ECS Meeting*, October 4, 2017, Boston, MA.
- W. Xu, S. Chen, X. Cao, J.-G. Zhang, “Nonflammable electrolytes for lithium-ion batteries”, Invited talk at the Energy Storage System Safety and Reliability Forum 2018, Seattle, WA, March 28-29, 2018.
- W. Xu, F. Ding, Y. Zhang, J. Qian, X. Ren, X. Li, J.-G. Zhang, “Guided growth and smooth deposition of lithium metal film through electrolyte strategy”, Invited talk at the 233rd Electrochemical Society Meeting, Seattle, WA, May 13-17, 2018.
- W. Xu, X. Li, J. Zheng, S. Jiao, H. Xiang, X. Chen, J.-G. Zhang, “Imide-orthoborate salts/carbonate electrolytes for fast charging and stable cycling of rechargeable lithium metal batteries”, Invited talk

at the 2018 China International Conference on the Frontier Technology of Advanced Batteries, Shenzhen, Guangdong, May 22-24, 2018.

10. W. Xu, J.-G. Zhang, “Lithium dendrite prevention for lithium batteries”, Poster presentation at the 2018 DOE Vehicle Technologies Office Annual Merit Review Meeting, Arlington, VA, June 18-21, 2018.
11. P. Shi, L. Zhang, H. Xiang, X. Liang, Y. Sun, W. Xu, “Lithium difluorophosphate as a dendrite-suppressing additive for lithium metal batteries”, Poster presentation at Beyond Lithium Ion XI, Cleveland, OH, July 24-26, 2018.
12. W. Xu, J.-G. Zhang, “Lithium dendrite prevention for lithium batteries”, Oral presentation at Lithium Metal Anode Project Deep Dive Meeting, Pittsburgh, PA, August 28-29, 2018.
13. W. Xu, H. Xiang, J.-G. Zhang, R. Cao. “Solid Electrolyte Interphase Film-Suppression Additives”. U.S. Patent Number **9,865,900**, granted date: 1/9/2018.

Acknowledgements

Key contributors including Drs. Xing Li, Linchao Zhang, Bin Liu, Mark H. Engelhard, Jianming Zheng, Qiuyan Li, Donghai Mei, Hongfa Xiang, Pengcheng Shi and Haiping Wu are greatly appreciated.

II.7.F Understanding and Strategies for Controlled Interfacial Phenomena in Li-Ion Batteries and Beyond (TAMU, Purdue Univ.)

Perla B. Balbuena, Principal Investigator

Texas A&M University
3122 TAMU
College Station, TX 77843
E-mail: balbuena@tamu.edu

Jorge M. Seminario, Principal Investigator

Texas A&M University
3122 TAMU
College Station, TX 77843
E-mail: seminario@tamu.edu

Partha P. Mukherjee, Principal Investigator

Purdue University
585 Purdue Mall
West Lafayette, IN 47907-2088
E-mail: pmukherjee@purdue.edu

Tien Duong, DOE Technology Development Manager

U.S. Department of Energy
E-mail: Tien.Duong@ee.doe.gov

Start Date: October 1, 2016
Project Funding: \$1,333,335

End Date: September 30, 2019
DOE share: \$1,200,000

Non-DOE share: \$133,335

Project Introduction

This project focuses on elucidating the roles of the electrolyte and electrode on the formation and evolution of the SEI layer and cell electrochemical performance on silicon and on Li metal anodes. For Si nano/microstructures we evaluate lithiation, volume changes, reactivity, and chemo-mechanical transformations as functions of nanoparticle size, shape, presence of coatings, electrolyte composition, electron leakage to the electrolyte, and cycling. For Li metal anodes we provide a detailed analysis of the electrode and electrolyte effects on reactivity and as a function of microstructural evolution and underlying stochasticity as dendrites nucleate and grow. We thoroughly investigate and test how the chemistry of the various components of the electrolyte and the electrode architecture may affect the electrochemical reactions as well as cell degradation. The analysis of Si electrodes was reported in the previous year. This report focuses on Li metal anodes issues.

Objectives

The knowledge gained by developing fundamental understanding of the issues associated with metal electrodeposition and stripping are aimed to elaborate strategies for solving practical issues associated with SEI instability, electrode expansion, and dendrite formation. These strategies are expected to emerge from electrolyte formulation and electrode morphology design.

Approach

A comprehensive multiscale modeling approach including first-principles ab initio static and dynamics, classical molecular dynamics, and coarse-grained mesoscopic models is used to characterize the roles of the electrolyte chemical, structural, and dynamical properties and of the electrode micro- and nanostructure on the formation and evolution of the SEI layer and associated electrochemical performance on silicon and on Li metal anodes. For Si nano/microstructures we evaluate lithiation, volume changes, reactivity, and chemo-

mechanical transformations as functions of nanoparticle size, shape, presence of coatings, electrolyte composition, electron leakage to the electrolyte, and cycling. For Li metal anodes we focus on a detailed analysis of the electrolyte effects on reactivity leading to solid electrolyte interphase formation, and as a function of electrode microstructural evolution and underlying stochasticity as dendrites are formed.

Results

Chemical Origin of Dendrite Nucleation: We investigated the reactions and electronic distribution existing when a Li ion (bare, complexed with one or more solvent molecules, or coupled with the salt anion) is in contact with a Li metal surface. We carried out DFT calculations to determine whether the competition of the reduction of the Li cation with the other electrolyte components. We observed that in most cases, the anion and some solvents are reduced first. However, when the cation is reduced, a large accumulation of electrons (much more than needed to reduce a single cation) appears in the vicinity of the site where that cation is reduced. This accumulation of electrons should induce further reduction of other species including electrolyte components but also other cations. We studied the effect of surface defects, and the presence of a nucleating SEI, on the deposition of reduced Li. Figure II.7.F.1 illustrates the DFT-calculated charge density difference (before and after electrodeposition) in the z-direction perpendicular to the surface for a pair Li^+PF_6^- located in the proximity of the Li surface. The negative ion is fixed to avoid the ion-pair formation. The surface has a defect of four Li atoms defining a hollow site where the new Li atom deposits. The charge density difference profile reveals how the charge accumulates in the vicinity of the deposited ion (yellow region), whereas it becomes depleted in the subsurface (light blue). This study evaluates for the first time the electronic distribution during electrodeposition and the effects of the surrounding environment (SEI layer components). When the Li ion arrives to the top of the SEI (represented by a monolayer of Li_2CO_3), it is not reduced. Instead, there is a driving force for Li diffusion toward the metal surface underneath the SEI layer, where it is reduced, and similar accumulation of electrons takes place. We suggest that this extreme reactivity of the Li surface and the subsequent uneven distribution of electrons in the Li metal is the chemical origin of the dendrite nucleation. These phenomena occur when the deposition is on a Li metal foil or on the current collector (after a thin film of Li is deposited). Thus, a comprehensive solution to the problem of the dendrite formation has to arise from controlling such reactions.

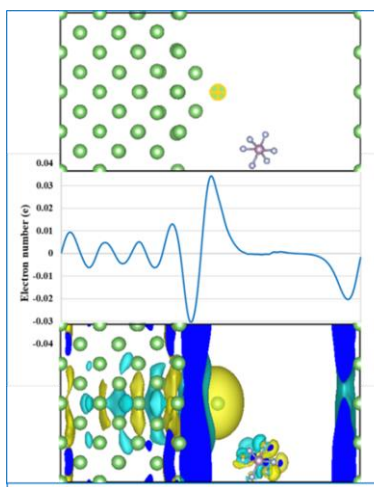


Figure II.7.F.1 Charge density difference profile when a Li ion is deposited on top of a defective Li surface. Yellow: charge density accumulation. Light blue: Charge density depletion.

We are currently analyzing various possible scenarios for accomplishing this goal. A manuscript has been published in *Electrochimica Acta* (listed under Key Publications) that discusses extensively our findings.

Surface Films due to Li Metal Dissolution and SEI Nucleation: The buildup of the SEI layer was studied using classical MD simulations to analyze possible reactions and rearrangements taking place at the electrolyte/Li-metal anode interface when a Li metal surface is in direct contact with an electrolyte phase. Note that in

contrast with the DFT analysis, here we are able to include much larger systems and examine longer time scales, although the chemistry is more accurate in the DFT description. Simulations with different electrolytes indicate that a porous phase develops immediately above the Li surface, which contains not only decomposed species due to electron transfer from the Li surface but also intact electrolyte molecules. Over the porous phase, two additional surface films are formed: the nest and the disperse phases. The nest phase is an amorphous matrix structure of connected partially oxidized Li atoms separated by nanochannels, through which the intact electrolyte and other products of its decomposition such as ethylene (molecules and radical anions) diffuse. In the disperse phase (the top layer in contact with the electrolyte), Li atoms in a higher oxidation state are connected in networks nucleating SEI blocks such as Li_2O and LiF , or more complex structures. These findings have been published in the J. of Phys. Chem. C (see Key Publications).

Li Deposition over Coated Current Collector: We demonstrated by combination of experimental and simulation techniques that 2-D films of graphene oxide (GO) can mitigate the dendrite growth by favoring a smooth deposition of Li over the current collector. The experimental characterizations included microscopy, *in operando* optical observations, and electrochemical measurements, carried out by our collaborators at the University of Illinois at Chicago. Our *ab initio* molecular dynamics (AIMD) and DFT simulations evaluated the modes of Li diffusion and deposition over the Cu substrate. AIMD simulations suggested that Li-ions initially get adsorbed onto the lithiophilic GO and then diffuse through defect sites. This delayed Li transfer eliminates the "tip effect" leading to a more homogeneous Li nucleation. Meanwhile, C-C bonds rupture observed in the GO during AIMD simulations creates more pathways for faster Li-ions transport. DFT calculations confirmed the lithiophilicity of GO coating. An important conclusion is that GO stores Li-ions for a limited amount of time before releasing them to the metal surface. This confined transfer slows down large fluxes of Li-ions, resulting in a uniform delivery of Li-ions to the electrode surface and a more homogeneous Li plating morphology. Diffusion pathways are illustrated in Figure II.7.F.2. This study was published in *Advanced Functional Materials* (see Key Publications).

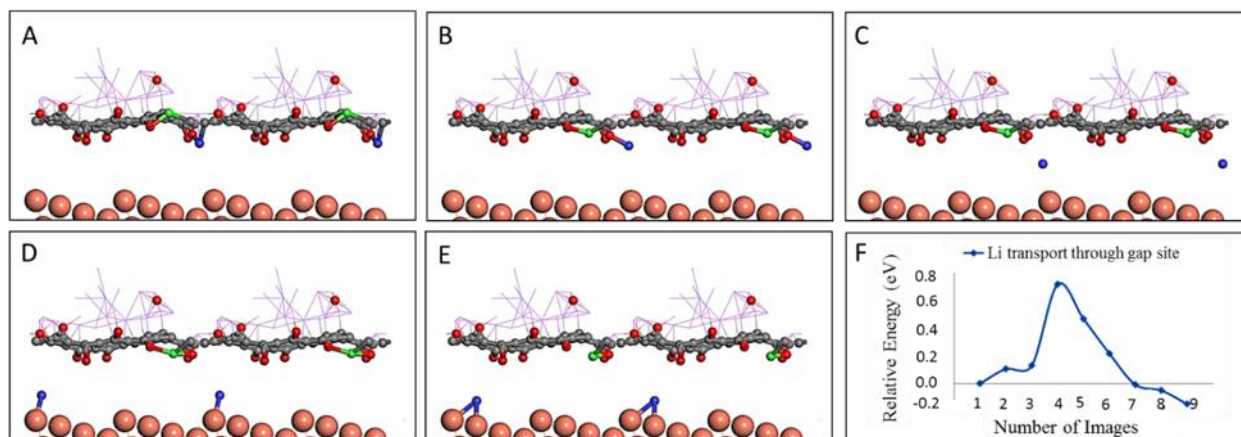


Figure II.7.F.2 Atomic configuration and energy profile of a knocked-off Li atom entering the gap site. Panels (A) through (E) show atomic configurations of the diffusion pathway of the Li atom knocked-off by a Li entering the gap site. Orange, grey and red spheres represent Cu, C and O atoms, respectively. Li atoms adsorbed at the GO layer are shown in a line display style for clarity. The green and blue spheres represent the Li atoms entering the gap site and the displaced Li atoms, respectively. (F) Energy profile for the Li transport through gap site.

Dendrites Nucleation and Growth: Classical MD simulations demonstrated the dendrite nucleation and growth by testing various charge distributions localized in a nanosized square representing a crack of the solid electrolyte interphase, where the electrolyte solution gets in direct contact with the fresh anode. Depending on the selected charge distributions, the dendrites grow when an external field is applied (Figure II.7.F.3). We found that dendrites grow when strong variations of charge exist on the surface of the crack. The results for dendrite growth on lithiated Si surfaces were published in *RSC Advances* (Key Publications). New studies have been performed for the dendrite growth on Li metal surfaces, as illustrated in Figure II.7.F.3.

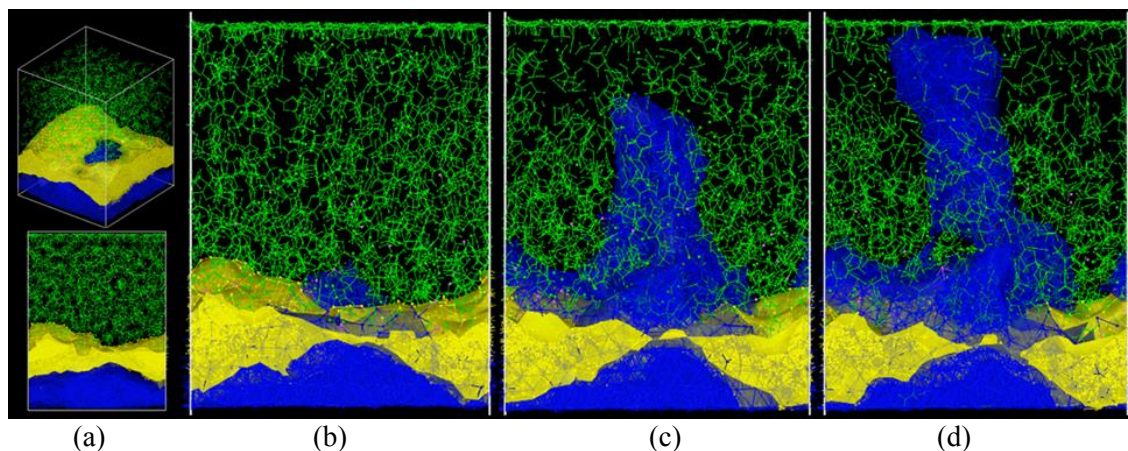


Figure II.7.F.3 (a) MD simulation setting (side views): anode surface (blue) covered by SEI (LiF, yellow). The SEI has a crack (shown as a blue spot in (a)). In green the electrolyte phase and Li ions are small purple spheres. Electrolyte (green) access the SEI crack in direct contact with the anode surface leading to Li⁺ deposition and dendrite formation. (b), (c) and (d) show time evolution of the dendrite growth as the Li ions are deposited and plated in the crack region.

On Li metal surfaces, it is observed that as the flow of Li ions arrives, it diffuses through the SEI layer film, and upon reduction, the metal nucleates in the space defined by the SEI crack (Figure II.7.F.3 b to d). As new metal atoms are deposited at the bottom of the nucleating structure, they exert pressure at the bottom that pushes the growth in the vertical direction. Thus, although there is also growth due to electrodeposition on the emerging needle surface, there is a bottom-up growth from the basis of the structure. As discussed below, atomic surface diffusion on the electrodeposited structure and ionic diffusion through the SEI are also determinant factors. Moreover, current studies focus on understanding how the SEI growth in the vicinity of the nucleating dendrite affects such dendrite nucleation and growth.

Mesoscopic Modeling Investigation of Li Deposition Morphology on Lithium and Copper Substrates: The non-dimensional Damköhler number, Da , defined as the ratio of the electrochemical reaction rate to surface diffusion rate, is used to characterize the deposition morphology. $Da \gg 1$ leads to dendritic structures, $Da \sim 1$ results in island-type deposits, whereas uniform film-type deposits arise for $Da \ll 1$ (Figure II.7.F.4 a). Using the aforementioned parameters for Li/Li and Li/Cu system, we determined the electrode operating regime, as delineated by the white boundaries in Figure II.7.F.4 a. Subsequently, 2D kinetic Monte Carlo simulations were carried out to ascertain the morphology of the obtained deposition and establish congruency with our predictions from the phase map. Figure II.7.F.4 b illustrates the morphology map of Li deposition on copper, which considers the effects of local overpotential and Li surface diffusion kinetics. It is evident that the deposition morphology strongly depends on the local overpotential and Li diffusion barrier. The map is divided into four regions: metal film, needle-like Li, porous metal film, and dendrite. When the reaction rate is low and the Li surface diffusion barrier is small, the deposited Li forms a metal film. If the reaction rate is high and Li surface diffusion barrier is small, needle-like/island-type Li is detected. If the local overpotential is low and Li surface diffusion barrier is large, the deposited Li gives a porous metal film. However, when the two parameters are both large, Li dendrite will grow on the substrate. For the porous metal film, we find that the porosity increases with increasing self-diffusion barrier. Figure II.7.F.4 b also demonstrates that Li-ion has a nonuniform distribution in the electrolyte when the local overpotential is high, and Li-ion concentration is low at the deposition layer-electrolyte interface. Interestingly, there are few Li-ions between the Li needles or below the dendrite.

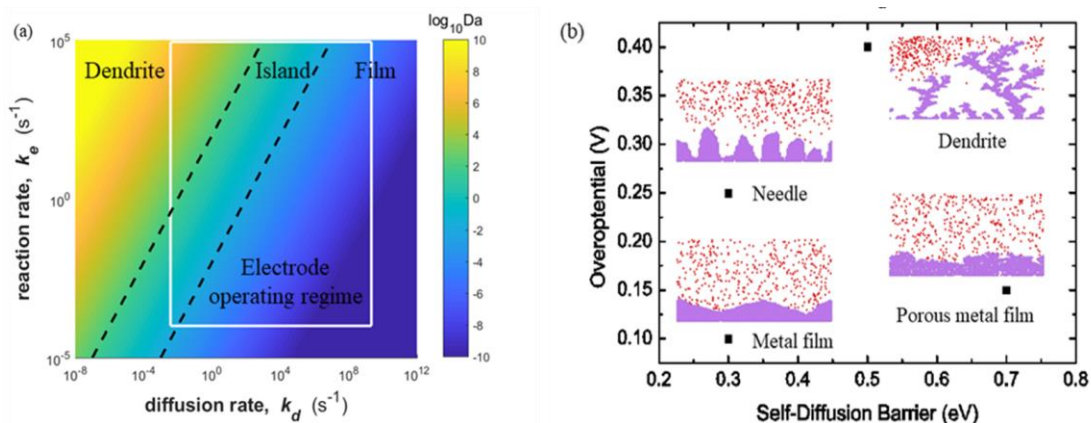


Figure II.7.F.4 (a) Electrodeposition morphology phase map for Li deposition as a function of Damkohler number. Yellow zone corresponds to $Da \gg 1$ (dendrite morphology), green zone corresponds to $Da \sim 1$ (island type deposits) and blue zone corresponds to $Da \ll 1$ (uniform film type deposits). Electrode operating regime for Li deposition on Li/Cu falls inside the white box. (b) KMC derived morphology map for Li deposition on the copper current collector in terms of local overpotential and surface self-diffusion, and four regions are presented: deposited Li can form metal film, needle-like Li, porous metal film, and dendrite. Purple is deposited Li, and red dots are Li-ions.

Lithium Electrodeposition in Intercalated Electrodes: A mesoscale Kinetic Monte Carlo model was developed linking rates of reduction of Li ions and diffusion of Li atoms into the anode and electrolyte and surface diffusion to operating conditions and material properties. The critical events determining electrodeposition occur at the anode-electrolyte interface. If the rate of Li diffusion into the anode is about the same order as the rate of reduction of Li ions on the anode surface, Li atoms accumulate on the anode surface as a film. There are two electrochemical reactions occurring on the anode surface, reduction on the graphite anode and reduction on the deposited Li film. The rate of Li reduction on the graphite anode is large compared to that on the surface. In the absence of surface diffusion of Li atoms on the electrodeposited film, if the reduction reaction on the graphite anode dominates compared to the reaction on the Li film, the morphology of the film deposited is that of a uniform layer. On the other hand, if the reduction reaction on the Li film dominates, a dendritic morphology is obtained. If the diffusion of the Li atoms on film is included, the morphology of the electrodeposited film changes from dendritic to columnar or mossy (Figure II.7.F.5) as the surface diffusion decreases.

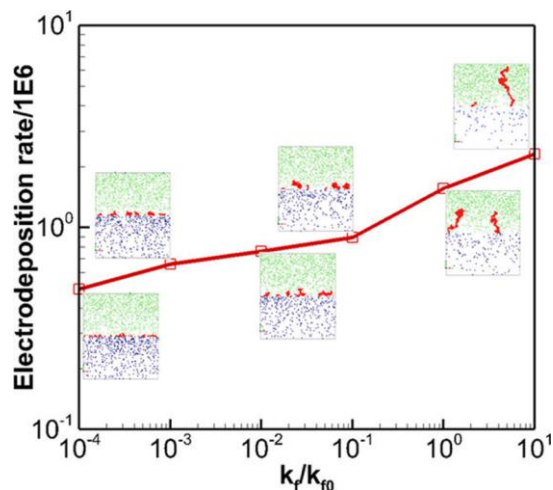


Figure II.7.F.5 Effect of the Li surface diffusion rate k_r on the electrodeposition rate and morphology of the deposited film; k_{r0} is the rate of diffusion calculated using activation energy of Li diffusion on the (100) plane.

If the rate of diffusion is small, the film is irregular due to diffusion of Li atoms into the anode but the morphology is mostly flat. At larger rates of surface diffusion, the film growth is mostly vertical.

These results were discussed in a paper published in the J. of Physical Chemistry C (Key Publications).

Conclusions

A multiscale modeling approach provided new insights into the Li electrodeposition on metal surfaces and into the possible factors that affect dendritic growth. An unusual accumulation of electrons detected as the electrochemical reduction takes place at the surface of the Li metal induces deposition of further cations in the vicinity and the subsequent heterogeneous nucleation. We concluded that it is essential to determine the role of the electrolyte chemical nature and concentration on altering such electronic distribution and promoting more homogeneous metal deposition. Dendrite nucleation and growth were further explored at the classical atomistic and mesoscopic levels. The mode of nucleation as a function of ionic current rate and surface structure were characterized by classical MD studies, and the influence of other factors such as surface diffusion, and local overpotentials defined phase mappings for the various types of growth morphologies.

Key Publications

1. X. Qin, M. Shao, and P. B. Balbuena, "Elucidating Mechanisms of Li Plating on Li Anodes of Lithium-Based Batteries," *Electrochim. Acta*, 264, 485-494, (2018).
2. D. Tewari, Z. Liu, P. B. Balbuena, and P. P. Mukherjee, "Mesoscale Understanding of Lithium Electrodeposition for Intercalation Electrodes," *J. Phys. Chem. C*, 122, 37, 21097-21107, (2018).
3. J. Han and P. B. Balbuena, "First-Principles Calculations of Oxidation Potentials of Electrolytes in Lithium-Sulfur Batteries and Their Variations with Changes in Environment," *Phys. Chem. Chem. Phys.*, 20, 18811-18827, (2018).
4. F. Hao, A. Verma and P. P. Mukherjee, "Mesoscale Complexations in Lithium Electrodeposition," *ACS Appl. Mater. Interfaces*, 10, 26320 (2018).
5. F. Hao, A. Verma, and P. P. Mukherjee, "Mechanistic Insight into Dendrite-SEI Interactions for Lithium Metal Electrodes," *J. Mater. Chem. A*, DOI: 10.1039/C8TA07997H (2018).
6. S. Bertolini and P. B. Balbuena, "Buildup of Solid Electrolyte Interphase on Lithium-Metal Anode: Reactive Molecular Dynamics Study," *J. Phys. Chem. C*, 122, 10783-10791, (2018).
7. Y. Horowitz, H-L. Han, F. A. Soto, W. T. Ralston, P. B. Balbuena, and G. A. Somorjai, "Fluoroethylene Carbonate as a Directing Agent in Amorphous Silicon Anodes - Electrolyte Interface Structure Probed by Sum Frequency Vibrational Spectroscopy and Ab-initio Molecular Dynamics," *NanoLetters*, 18, 1145-1151, (2018).
8. T. Foroozan, F. A. Soto, V. Yurkiv, S. Sharifi-Asl, R. Deivanayagam, Z. Huang, R. Rojaee, F. Mashayek, P. B. Balbuena, R. Shahbazian-Yassar, "Synergistic Effect of Graphene Oxide for Impeding the Dendritic Plating of Li," *Adv. Funct. Mater.*, 1705917, (2018).
9. L. Selis and J. M. Seminario, "Dendrite Formation in Anodes of Lithium-Ion Batteries," *RSC Advances*, 8, 5255-5267, (2018).
10. D. Galvez-Aranda and J. M. Seminario, "Simulations of a LiF Solid Electrolyte Interphase Cracking on Silicon Anodes Using Molecular Dynamics," *J. Electrochem. Soc.*, 165, A717-A730, (2018).
11. F. Hao, Z. Liu, P. B. Balbuena, and P. Mukherjee, "Mesoscale Elucidation of Solid Electrolyte Interphase Layer Formation in Li-ion Battery Anode," *J. Phys. Chem. C*, 121, 26233-26240 (2017).

II.7.G Engineering Approaches to Dendrite Free Lithium Anodes (University of Pittsburgh)

Dr. Prashant N. Kumta, Principal Investigator

University of Pittsburgh
815C Benedum Hall ,3700 O'Hara Street
Pittsburgh, PA 15261
E-mail: pkumta@pitt.edu

Dr. Moni K. Datta, Co-PI

University of Pittsburgh
815C Benedum Hall ,3700 O'Hara Street
Pittsburgh, PA 15261
E-mail: mkd16@pitt.edu

Dr. Oleg I. Vellkokhatnyl, Co-PI

University of Pittsburgh
815C Benedum Hall ,3700 O'Hara Street
Pittsburgh, PA 15261
E-mail: olv3@pitt.edu

Tien Duong, DOE Technology Development Manager

U.S. Department of Energy
E-mail: Tien.Duong@ee.doe.gov

Start Date: October 1, 2016
Project Funding: \$1,562,500

End Date: September 30, 2019
DOE share: \$1,250,000

Non-DOE share: \$312,500

Project Introduction

Dendrite formation in electrochemical systems occurs due to inhomogeneous current densities coupled with local diffusion gradients, surface roughness, and kinetic roughening of the surface of the anode systems. However, as complex and ubiquitous as it seems, the phenomenon of Li dendrite formation and growth are not very well-understood. Adding to the complexity and increasing the enigmatic nature is the formation of the solid-electrolyte interphase (SEI). Control and elimination of Li metal dendrite formation is a veritable challenge and, if overcome, would render the universal adoption of lithium anode batteries (LAB) for stationary and mobile applications. The current project is thus a scientific study of novel approaches undertaken and implemented to address the highly complex but ubiquitous problem of dendrite formation in LABs, combined with electrolyte decomposition, and associated cell-failure. Development of dendrite free high-performance Li anodes will enable the use of Li-free cathodes opening up a myriad possibilities pushing the envelope in terms of achieving the desired cathode capacity and battery energy density.

Objectives

This project will yield lithium metal anodes with specific capacity ≥ 2000 mAh/g (≥ 10 mAh/cm²), cycling stability of ~ 1000 cycles, coulombic efficiency loss $\leq 0.01\%$, coulombic efficiency: $\geq 99.99\%$ combined with superior rate capability. The goal is to systematically characterize the different approaches for generation of dendrite-free Li-metal anodes while also providing an understanding of the scientific underpinnings, and evaluating the microstructure and electrochemical performance of the dendrite free Li metal anodes. Generation of high performance dendrite free Li metal anodes will successfully demonstrate generation of novel sulfur cathodes affording the fabrication of Li-S batteries meeting the targeted gravimetric energy densities ≥ 350 Wh/kg and ≥ 750 Wh/l with a cost target \$125/kWh and cycle life of at least 1000 cycles for meeting the next generation *EV everywhere* blueprint.

Approach

This is a multi-year project comprised of three major phases to be successfully completed in three years.

- Phase – 1 (Year 1): Synthesis, characterization and scale up of suitable porous metal foams (PMFs) for use as current collectors for lithium anodes and Li-ion conductor (LIC) materials to prepare multilayer porous foams (MPFs).
- Phase – 2 (Year 2): Development of Li-rich structurally isomorphous alloy (SIA) anodes and Generation of composite multilayer anodes (CMAs).
- Phase-3 (Year 3): Advanced high energy density, high rate, and extremely cycleable cell development.

The project will involve collaboration with Dr. Moni Kanchan Datta (UPitt) and Dr. Oleg I. Velikokhatnyi (UPitt) as Co-PIs. In addition, collaborations will be undertaken and continued with Dr. D. Krishnan Achary (UPitt) for solid-state nuclear magnetic resonance (MAS-NMR) characterization.

Results

Metal Porous Foams:

In the previous year porous Cu foams have shown improved stability over plain Cu foils in terms of achieving stable plating efficiencies. However, the foams suffer from unstable Li plating and buildup of solid electrolyte interphase (SEI) layers that eventually result in instabilities causing cycling fade and loss in capacity. Efforts for phase-2 of the project have focused on modifications to the surface of the metal porous foams (MPFs) in order to control SEI formation and growth, specifically the use of a thin organic and lithium-ion conducting coatings.

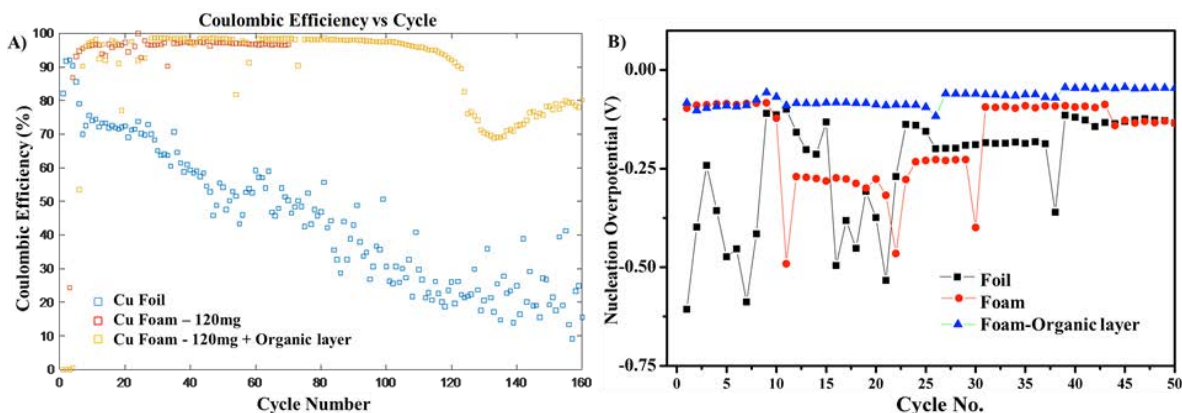


Figure II.7.G.1 a) Coulombic Efficiency of Li plating on MPF with organic coating, without coating, and on an unmodified copper foil. b) Nucleation overpotential for Cu foil, Cu foam, and organic layer-Cu foam during the first 50 cycle.

As shown in Figure II.7.G.1a, the use of organic layers embedded MPF improves the coulombic efficiency of the electrode, and increases the number of stable cycles achieved before fade (~70 cycles for unmodified MPF to ~120 cycles for the organic layer containing MPF). Furthermore, a drop in the nucleation overpotential of lithium was observed with the addition of this organic layer (Figure II.7.G.1b).

The erratic behavior of the nucleation overpotential for the unmodified foam and foil can be attributed to the instabilities of the SEI formed on the metallic copper surface. The addition of the organic layer results in the formation of a more stable SEI layer along with providing solid state Li^+ diffusion pathway, thus, resulting in improved reversible lithium plating and lower resistance to ionic conduction. Eventually, however, the SEI layer grows too thick and an efficiency fade is observed leading to capacity loss. Additional work is being done to improve the uniformity of the organic coating, as well as examine other surface additives to assist in the formation of a stable SEI or act as an artificial SEI. The wetting of the Li metal on Cu also influences the

stability and plating morphology of Li plating and hence, work has been focused to develop zero nucleation potential next generation anode substrate materials to replace Cu as substrate described in another section (Zero Nucleation Potential Electrodes).

Surface Modification of Li Metal:

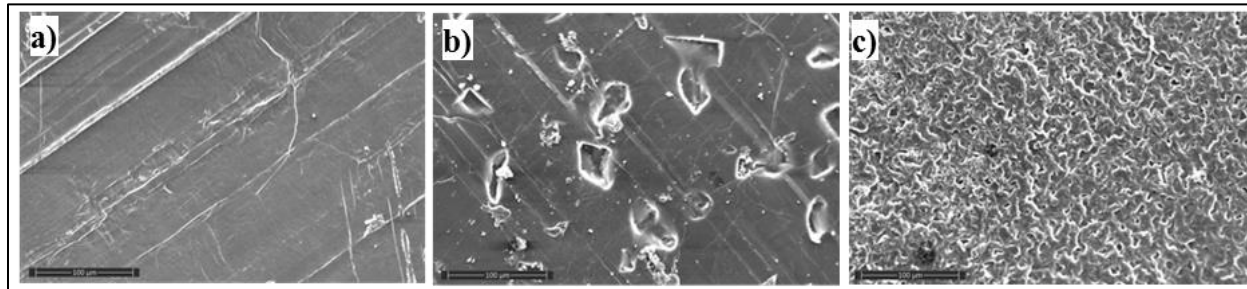


Figure II.7.G.2 SEM images of (a) pristine lithium foil, (b) lithium foil imprinted with 300 grit sandpaper, and (c) 2500 grit.

The surface of pristine lithium foil is modified by using various media corresponding to different grits (300 grit to 2500 grit) on the surface and the effect of surface modification on the nucleation and growth of lithium on the lithium foil was studied. Figure II.7.G.2 shows the SEM of the surface pattern with different roughness developed by using the surface patterning technique. By modifying the surface roughness, high energy sites for preferential plating can be obtained, thus controlling the plating location and morphology preventing both dendrite and high surface area lithium.

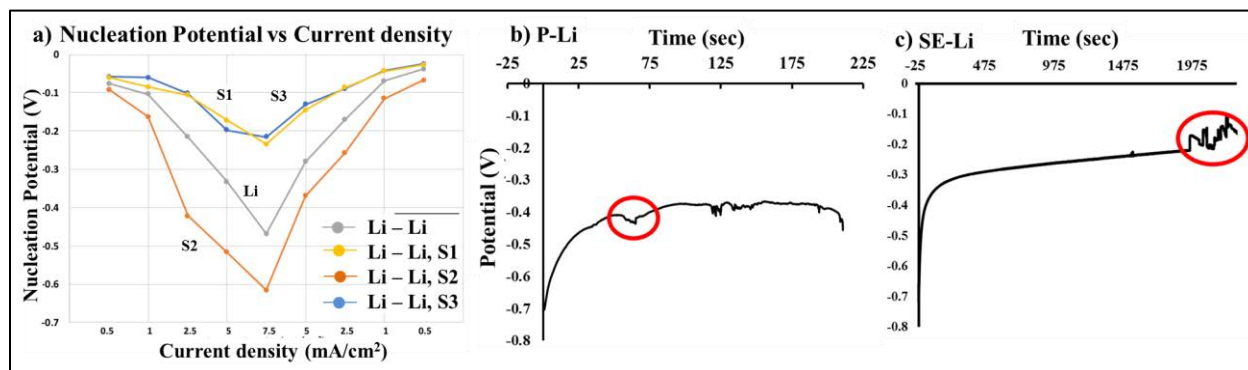


Figure II.7.G.3 a) Nucleation potential for various surface modified lithium-metal foils at different current densities. Sand's time experiment showing potential vs time for symmetric Li/Li cells for a) P-Li and b) SE-Li.

A reduction in nucleation overpotential is observed for the 300-grit imprinted lithium, however, the overpotential is unaffected when using the 2500-grit sand paper. The deep sites obtained by the 300-grit sandpaper provide a pre-active high energy sites for nucleation thus reducing the overpotential during Li plating. (Figure II.7.G.3a) shows the nucleation potential as a function of current density for many of the modified lithium surfaces (S1, S2, and S3). It is observed that large modifications in the engineered surface area (S1 and S3) of the structures created on the surface of the lithium metal helps to lower the nucleation potential. On the other hand, creation of small modification of the surface architecture and morphological structures create an undesired roughness and surface characteristics that actually increase the nucleation potential compared to the unmodified lithium-metal surface.

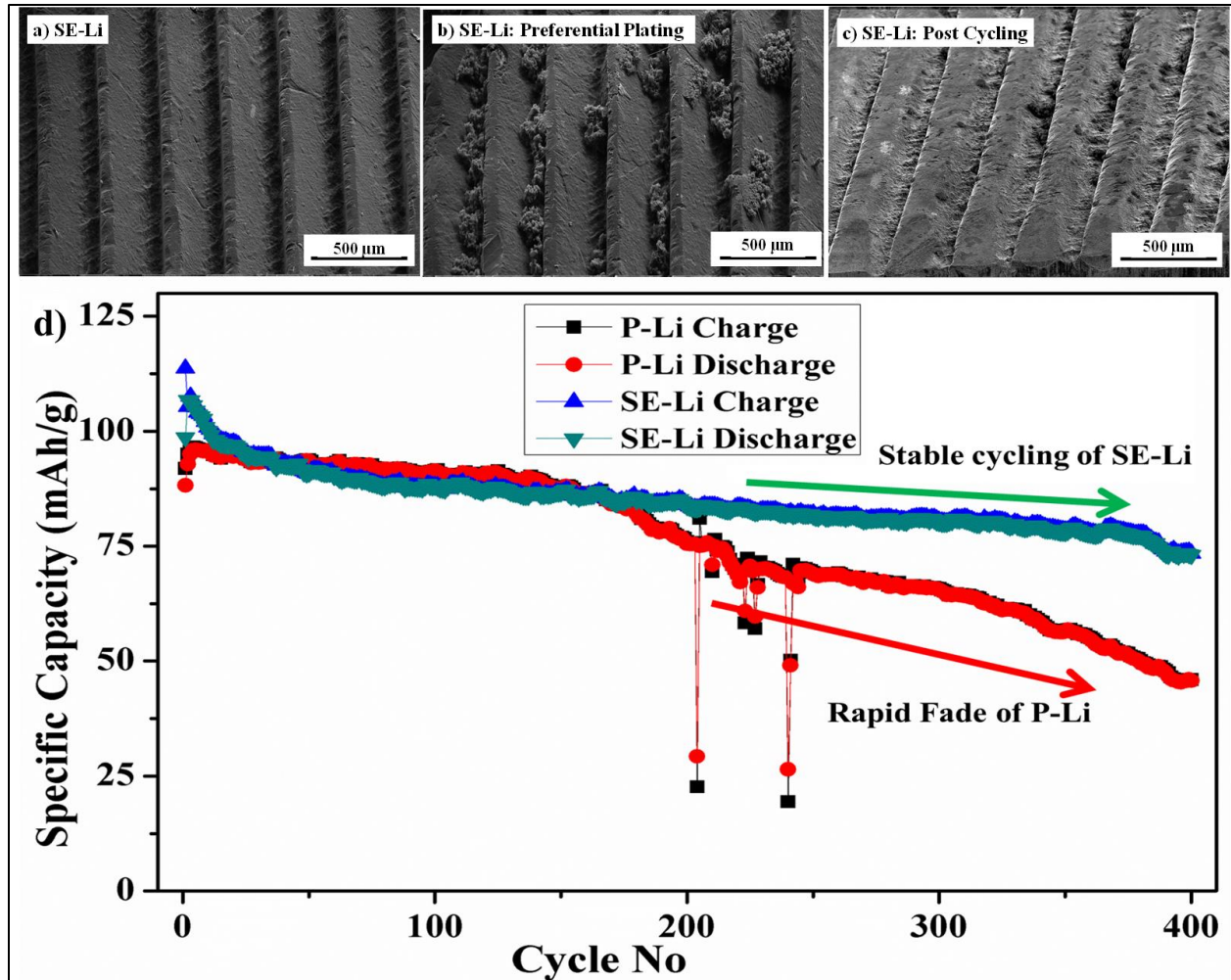


Figure II.7.G.4 SEM images of a) surface engineered Lithium, b) Li plating on SE-Li and c) cycled SE-Li. d) Cycling behavior of LiMn_2O_4 cathode tested against P-Li and SE-Li..

Based on this observation, considerable attention has been directed towards understanding the “planar/non-planar” growth behavior of the surface engineered Li metal (SE-Li) during long term cycling. Towards this end, Sand’s time analysis, post cycling SEM analysis, and full cell testing with high voltage LiMn_2O_4 cathode were conducted to study the planar/non-planar growth behavior of SE-Li in 1M LiPF_6 in EC:DEC:FEC=45:45:10 (%vol.) electrolyte. Sand’s time experiment (Figure II.7.G.3b, Figure II.7.G.3c) was conducted in a symmetric Li/Li in a three electrode Swagelok cell with SE-Li as the working electrode. The cell has been charged (Li plating) at an areal current density (I_{AD}) of $10\text{mA}/\text{cm}^2$. The onsets of voltage fluctuations indicate the onset of unstable Li plating (non-planar Li growth). As shown in Figure II.7.G.3b, Figure II.7.G.3c, pristine lithium (P-Li) and surface engineered Li (SE-Li) show fluctuations at $\sim 60\text{s}$ and $\sim 1940\text{s}$ corresponding to areal charge density (Q_{AD}) of $\sim 0.17\text{mAh}/\text{cm}^2$ and $\sim 5.39\text{mAh}/\text{cm}^2$ respectively. The increase in the Sand’s time indicates delay in the development of the high surface area mossy Li plating on SE-Li. The post plated SEM study (Figure II.7.G.4b) of SE-Li showed preferential plating ($I_{AD}=0.5\text{mA}/\text{cm}^2$, $t=1\text{h}$) in the high energy regions due to surface engineering. P-Li under the same conditions however, shows random plating of Li. Post cycling SEM image (Figure II.7.G.4c) of SE-Li after 10 cycles, ($I_{AD}=0.5\text{mA}/\text{cm}^2$, $t=1\text{h}$) shows a gradual buildup of SEI layer in the high energy regions, still retaining the engineered surface features.

Full cell cycling (Figure II.7.G.3) of SE-Li and P-Li with LiMn_2O_4 cathode (\sim loading: $11\text{--}15\text{ mg/cm}^2$) was further conducted in a coin cell cycled between $3\text{V--}4.3\text{V}$ at a current of 100mA/g ($I_{\text{AD}}\sim 1.5\text{mA/cm}^2$) with analysis of the cycling performance. P-Li/ LiMn_2O_4 shows rapid fade in specific capacity after 160 cycles while SE-Li/ LiMn_2O_4 shows stable cycling till 400 cycles (Figure II.7.G.3). Premature capacity fade seen in P-Li electrode can be attributed to the unstable mossy plating on P-Li leading to rapid SEI layer buildup contrasted to SE-Li.

Composite Polymer Electrolyte:

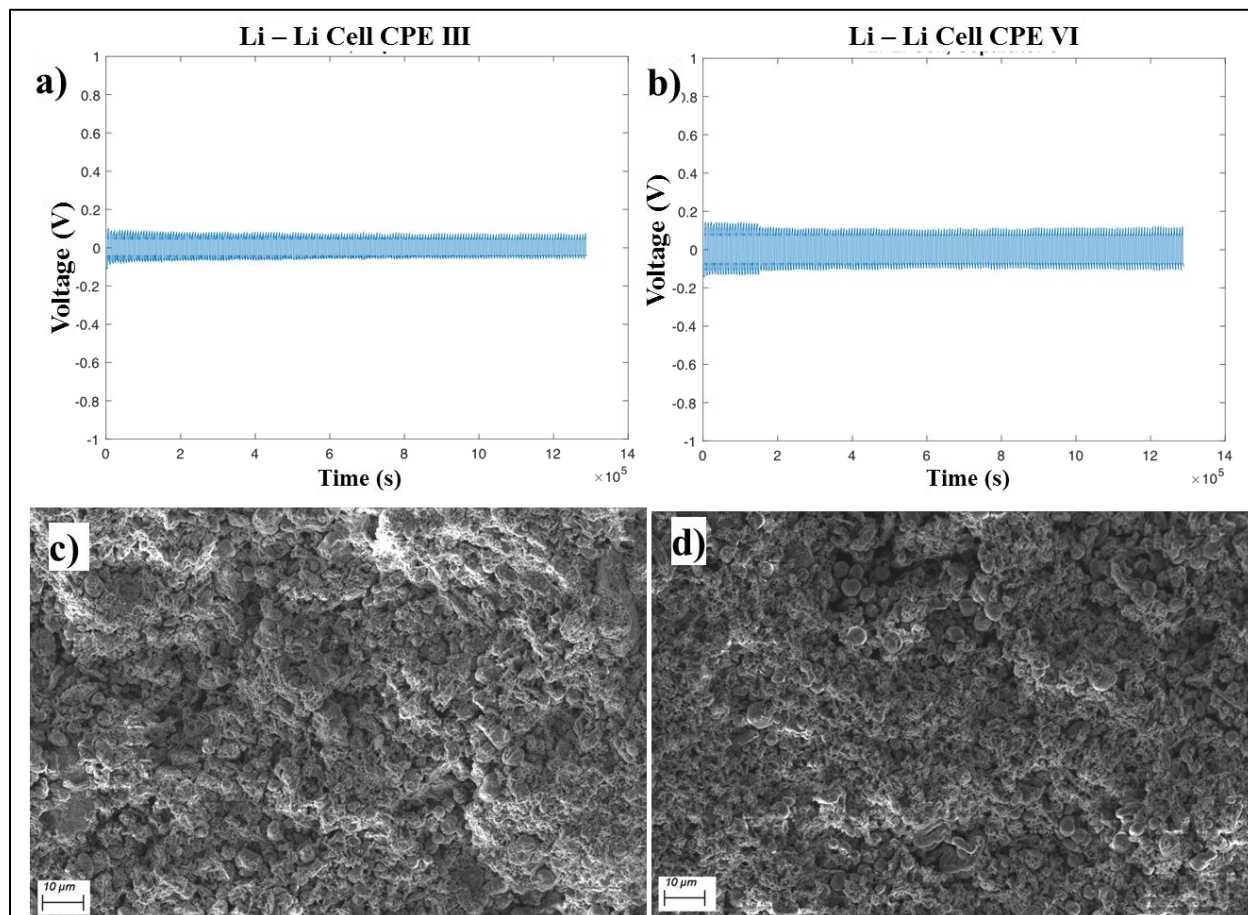


Figure II.7.G.5 Voltage-time curve for symmetric Li/Li cells using composite polymer electrolytes a) CPE-III and b) CPE-VI (~ 200 cycles). SEM images of lithium-metal after cycling in symmetric Li/Li cells with c) CPE-III and d) CPE-VI after ~ 200 cycles).

In order to stabilize the lithium-metal battery system further, studies have been focused on developing a flexible moving boundary solid state electrolyte system to modify the nucleation and growth of lithium-metal on the current collector. The first approach involved development of a composite polymer electrolyte (CPE) which would control the lithium-ion flux and thus modify the deposition conditions thereby inhibiting the dendritic growth. CPE separators were accordingly fabricated by electrospinning of polymer-blends, after which the electrospun mats were punched to yield the individual separators. The separators were then soaked in traditional liquid electrolyte ($50:50\text{ DOL:DME}$ by volume, 1.0M LiTFSI , 0.1M LiNO_3) before assembling the symmetric Li/Li coin cells. No additional liquid electrolyte was added beyond that used to activate the CPEs. Figure II.7.G.5a, Figure II.7.G.5b shows the potential-time curves generated for the two different CPEs (CPE III and CPE VI) after cycling for ~ 200 cycles in symmetric Li/Li cells. The SEM images collected on the lithium-metal foil after ~ 200 cycles indeed confirm the absence of dendrites (Figure II.7.G.5c, Figure

II.7.G.5d) and moreover indicate the formation of uniform Li metal plating due to homogenous Li^+ diffusion that is afforded by the improved Li-ion conduction processes occurring in these composite polymer electrolytes.

Zero Nucleation Potential Electrodes:

The concept of surface engineering of Li metal to control the nucleation and growth of dendritic structures was presented above. Additionally the findings from the above study confirmed the observation that Li metal plating on Cu substrates used traditionally was unstable leading to the failure of multilayer porous Cu foams due to high nucleation potential which arises from the poor wettability of Cu with respect to Li. Hence, a significant and more in-depth study was performed to identify suitable current collectors to serve as heterogeneous nucleation sites exhibiting zero or minimal nucleation barriers (i.e. zero nucleation underpotential) for Li metal plating. The heterogeneous nucleation feature, described in Figure II.7.G.6a, shows that if the contact angle between the Li metal and the current collector decreases below $\sim 20^\circ$ to 30° , affording improved wetting, the heterogeneous nucleation barrier, $[\Delta G_{\text{cr}}(\text{het})/\Delta G_{\text{cr}}(\text{hom})]$, approaches almost 0, and therefore, the rate of nucleation, J_{het} , is expected to increase significantly promoting uniform nucleation creating conditions for also favorably modifying the growth pattern. In this condition, it is expected that the nucleation underpotential for Li metal plating will be minimum leading to smooth homogeneous surface formation across the current collector if the associated contact angle is well below 30° . Furthermore, in the presence of an efficient nucleant/current collector, the columnar/needlelike growth of Li metal as well as dendrite formation can be minimized and also completely prevented by inhibiting the rapid and isotropic growth of the nucleated Li crystal.

Metal alloys as an efficient nucleant/current collector exhibiting negative heat of mixing (i.e. good wetting with Li metal) and exceptional lattice registry with Li metal have thus been identified and synthesized. Figure II.7.G.6b shows the plating/de-plating behavior of one of the synthesized novel current collector/substrate showing “zero nucleation underpotential” tested at a current density of $0.5\text{mA}/\text{cm}^2$ in the 1M LiPF_6 (EC:DEC) electrolyte system whereas the traditional Cu current collector exhibits large nucleation under-potential. In addition, the growth potential of Li metal (Figure II.7.G.6b), cycled at a current density of $0.5\text{mA}/\text{cm}^2$ for 1h, shows no significant change ($\sim 47\text{ mV}$) with time or cycle numbers suggesting minimal Gibbs-Thomson effect on the growth potential which mainly arises due to the formation of high surface area needlelike cellular or dendritic growth of the Li metal. However, most of the efficient current collector shows low coulombic efficiency ($\text{CE} \leq 90\%$) (Figure II.7.G.6c) due to the irreversible side reaction of the reactive electrolyte (EC:DEC) with the current collector resulting in the formation of the solid electrolyte interphase (SEI). This adventitious side reaction in the novel materials is minimized by further alloying with non-reactive metals to inhibit SEI formation as well as forming novel “zero nucleation under-potential” binary, ternary, and multicomponent alloys. Figure II.7.G.6d shows the preliminary results of the plating/stripping behavior of such a synthesized “zero nucleation underpotential” novel ternary alloy exhibiting high CE ($>99\%$) tested at a charge density of $1\text{mAh}/\text{cm}^2$ with a current density of $1\text{mA}/\text{cm}^2$ in the EC: DEC based electrolyte. The growth front morphology of the Li metal plated at low and high current density ($0.5\text{mA}/\text{cm}^2$ - $2\text{mA}/\text{cm}^2$) and charge density (0.05 - $4\text{mAh}/\text{cm}^2$) is currently under investigation and will be reported and published in the near future.

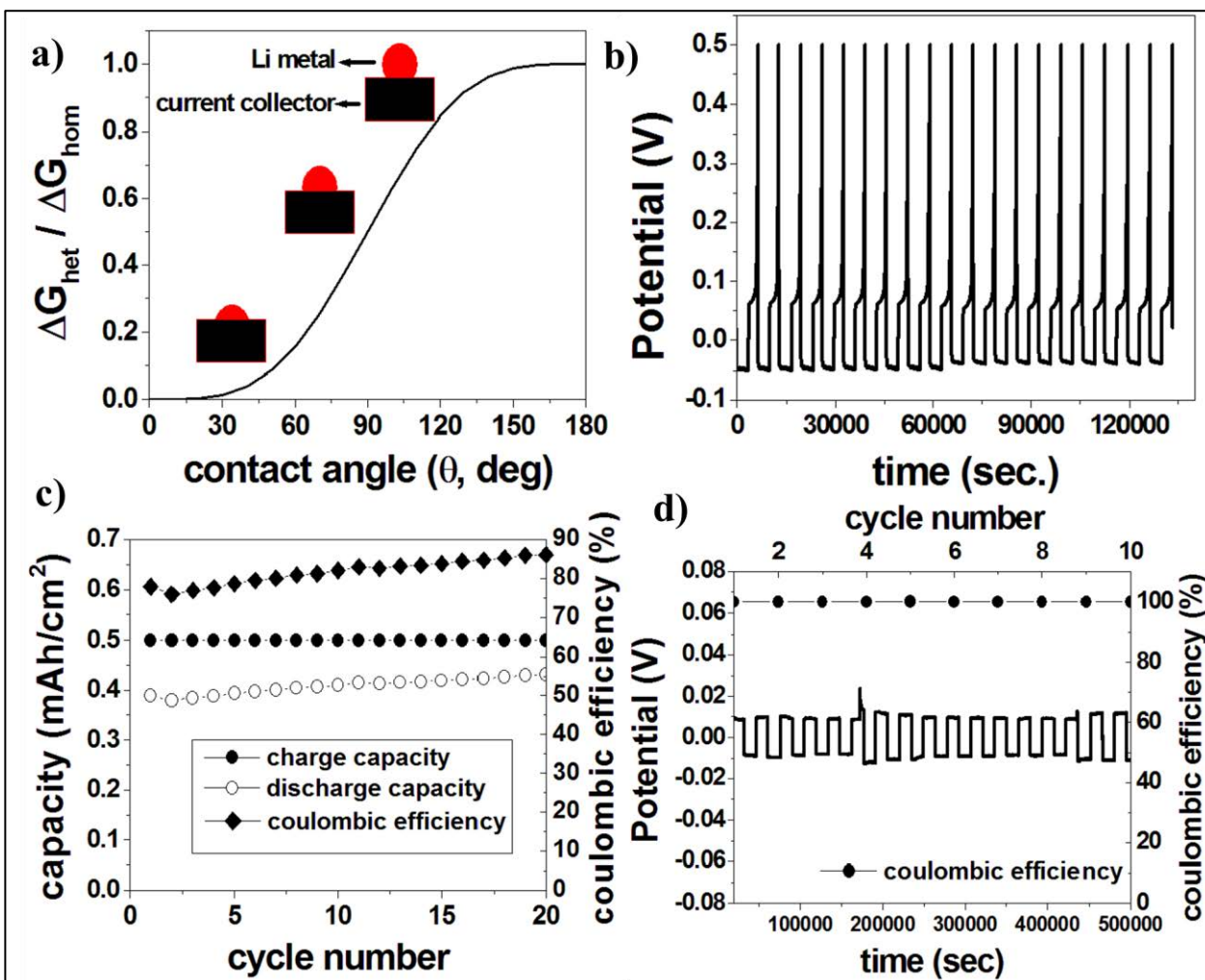


Figure II.7.G.6 a) Variation of heterogeneous nucleation barrier with contact angle, b) Plating/ stripping behavior of an efficient electrode showing zero nucleation underpotential and invariant growth potential with time and cycle numbers, c) the charge/discharge capacity along with coulombic efficiency of an efficient electrode, d) Plating/stripping behavior of multicomponent alloy showing high coulombic efficiency.

Conclusions

Phase – 2 of the current project was successful in developing organic layer embedded composite porous Cu foam architectures capable of eliminating dendrite formation during cycling of lithium metal with stable coulombic efficiency of ~96% till 130-160 cycles. The poor wettability of Cu with Li makes it undesirable framework for plating with Li and hence, new alloy systems with enhanced wettability and lattice registry were identified and developed to control the nucleation and growth of Li. The alloys developed under this approach show zero nucleation potential at a charge density of 1mAh/cm^2 with a current density of 1mA/cm^2 in EC:DEC based electrolyte with a high coulombic efficiency of ~99%. Long term plating - stripping studies indicate stable growth potential of ~47mV with respect to Li/Li^+ .

Surface engineering of Li (SE-Li) metal decreases the nucleation potential and creates high energy sites for preferential plating of lithium thus improving the performance in LIBs. The improvement in the performance of SE-Li was observed in terms of Sand's time, post cycling SEM analysis after repeated Li plating/deplating followed by full cell studies using LiMn_2O_4 as the cathode with plating/deplating charge densities of ~1.4-1.5 mAh/cm^2 .

Composite polymer electrolytes were developed as a part of electrolyte modification using electrospinning of various blend polymers with novel ceramic fillers to induce controlled Li flux during plating and deplating. The symmetric Li cells cycled using these CPEs showed no change in plating / deplating overpotentials till 200 cycles in a Li/Li symmetric cell with complete absence of dendritic Li plating as indicated in the post cycling SEM analysis.

Key Publications

1. Jampani, P.H.; Shanthi, P.M.; Day, B.A.; Gattu, B.; Velikokhatnyi, O.I.; Datta, M.K.; Kumta, P.N. Lithium Metal Anode based Rechargeable Batteries: Recent Advances and Challenges for the Future, *Progress in Materials Science* (2018) (under review)
2. B. Gattu, P. Murugavel Shanthi, P. Thanapisitikul, B. A. Day, M. K. Datta, O. I. Velikokhatnyi, and P. N. Kumta, "Suppression of Dendrites in Lithium Sulfur Batteries Using a Composite Polymer Electrolyte (CPE)", Presentation, 223rd ECS Meeting, Seattle, WA, May 13-17, 2018.
3. P. Thanapisitikul, B. Gattu, P. M. Shanthi, B. A. Day, M. K. Datta, and P. N. Kumta, "Surface Patterning of Lithium Metal: Novel Approach to Stable Li Metal Anodes", Presentation, 223rd ECS Meeting, Seattle, WA, May 13-17, 2018.
4. B. A. Day, B. Gattu, P. M. Shanthi, M. K. Datta, and P. N. Kumta, "Surface Modification of Porous Foam Electrodes: Stabilization of Solid Electrolyte Interphase Formation in Li-Metal Batteries", Presentation, 223rd ECS Meeting, Seattle, WA, May 13-17, 2018.

Acknowledgements

Research supported by the U.S. Department of Energy OVT-DE-EE0007797 and the Edward R. Weidlein Chair Professorship Funds, Nanomaterials for Energy Conversion and Storage Technology (NECST) Laboratories, and the Center for Complex Engineered Multifunctional Materials (CCEMM) for partial assistance and help with procuring the electrochemical equipment and facilities used in this research work.

II.7.H Solid-State Inorganic Nanofiber Network-Polymer Composite Electrolytes for Lithium Batteries (WVU)

Nianqiang Wu, Principal Investigator

West Virginia University
P.O. Box 6106
Morgantown, WV, 26506
E-mail: nick.wu@mail.wvu.edu

Tien Duong, DOE Technology Development Manager

U.S. Department of Energy
E-mail: Tien.Duong@ee.doe.gov

Start Date: October 1, 2016

End Date: September 30, 2019

Project Funding: \$1,400,193

DOE share: \$1,244,012

Non-DOE share: \$156,181

Project Introduction

Safety is of concern regarding the currently commercial lithium batteries due to the use of highly volatile and flammable organic solvent-based electrolytes. Use of solid-state electrolytes is an alternative solution to the safety issue, and improves the chemical and thermal stability of Li-ion batteries due to their good mechanical strength and potentially high electrochemical stability. [1], [2]

Objectives

The project objective is to develop the solid-state electrolytes based on the highly-conductive inorganic nanofibrous network in the polymer matrix for lithium-ion batteries.

Approach

Integration of the highly Li⁺-conductive inorganic nanofiber network into the polymer matrix not only provides the continuous Li⁺ transport channels, but also inhibits crystallization from the amorphous state of polymer electrolyte. The inorganic nanofibers are fabricated with an electrospinning technique. The ionic conductivity of inorganic nanofibers is improved by chemical substitution or doping. Highly ionic-conductive polymers are developed by cross-linking and/or creation of a block-copolymer structure. The composition and microstructure of the composite electrolyte are designed to suppress the lithium dendrite formation.

Results

Li_{0.33}La_{0.557}TiO₃ ceramic nanofiber-enhanced polyethylene oxide-based composite polymer electrolytes for all-solid-state lithium batteries.

A polyethylene oxide (PEO)-based composite solid polymer electrolyte filled with one-dimensional (1D) ceramic Li_{0.33}La_{0.557}TiO₃ (LLTO) nanofibers was designed and prepared. It exhibits a high ionic conductivity of 2.4×10^{-4} S cm⁻¹ at room temperature and a large electrochemical stability window up to 5.0 V vs. Li/Li⁺.

Thermogravimetric analysis (TGA) was used to study the formation process of the LLTO nanofibers during calcination, in the TGA curve that no obvious weight loss occurred above 730°C, which indicated the formation of stable ceramic LLTO nanofibers. XRD patterns of the LLTO nanofibers calcined at 700, 800 and 900°C for 2 h. The main peaks in the diffraction patterns of the LLTO nanofibers calcined at 700, 800 and 900°C were ascribed to the LLTO structure, and they are consistent with the JCPDS card 01-087-0935 with a tetragonal cell.

The PEO/LiTFSI/LLTO composite electrolytes were prepared by dispersing the LLTO nanofibers in PEO/LiTFSI salt/acetonitrile solution, followed by solvent removal. The ionic conductivities of PEO/LiTFSI/LLTO composite electrolytes were measured by EIS. The thickness of the solid composite electrolytes was around 100 ± 10 μm. The ionic conductivities of PEO/LiTFSI solid composite electrolytes at

room temperature reached the maximum value of $2.4 \times 10^{-4} \text{ S cm}^{-1}$ when 15 wt% LLTO was incorporated. The ionic conductivities were 1.75×10^{-5} , 6.2×10^{-5} and $5.5 \times 10^{-5} \text{ S cm}^{-1}$ for PEO/LiTFSI, PEO/LiTFSI/LLTO (10 wt%) and PEO/LiTFSI/LLTO (20 wt%) solid electrolytes, respectively. The PEO/LiTFSI/LLTO (15 wt%) composite electrolyte showed the lowest activation energy of 0.40 eV (0.52, 0.48 and 0.48 eV for the PEO/LiTFSI, PEO/LiTFSI/LLTO (10 wt%) and PEO/LiTFSI/LLTO (20 wt%) electrolytes, respectively).

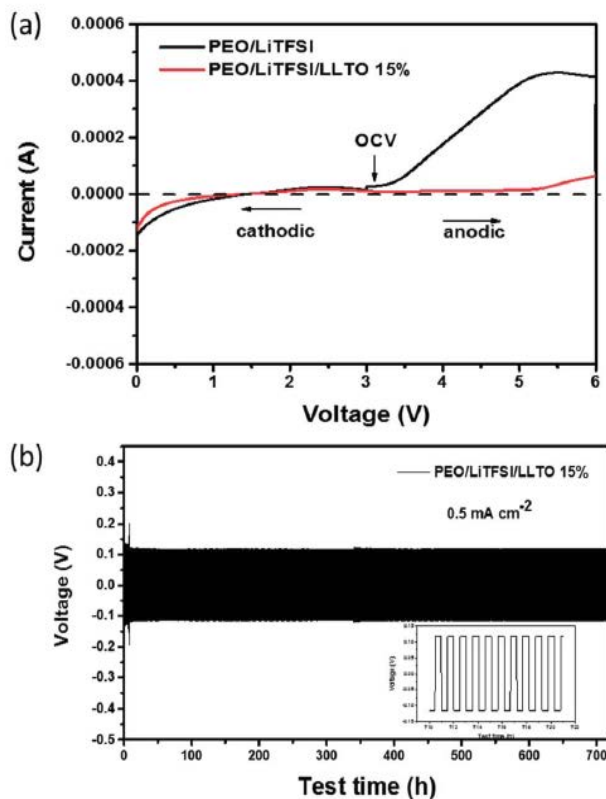


Figure II.7.H.1 (a) Linear sweep voltammetry curve of the PEO/LiTFSI and PEO/LiTFSI/LLTO 15 wt% solid composite electrolytes. (b) Voltage profile of the continued lithium plating/stripping cycling of PEO/LiTFSI/LLTO 15% electrolyte tested at a current density of 0.5 mA cm^{-2} at 25°C (inset: voltage profiles of the PEO/LiTFSI/LLTO 15% electrolyte tested at 710–720 h).

The PEO/LiTFSI/LLTO 15 wt% composite electrolyte exhibited a stable voltage window up to 5 V vs. Li/Li^+ , which indicated that this solid composite electrolyte could satisfy the requirements of most high-voltage lithium battery applications. To further identify the interface stability of the PEO/LiTFSI/LLTO 15 wt% composite electrolyte, a symmetric hybrid cell ($\text{Li/composite electrolyte/Li}$) was fabricated and tested for 0.5 h (each cycle) at a constant current density of 0.5 mA cm^{-2} at 25°C . The cell exhibited a relatively stable voltage of around $\pm 115 \text{ mV}$ after 720 h of cycling; and this voltage value was much lower than that reported previously for the symmetric cell with the LLZO/PEO polymer electrolyte ($\pm 300 \text{ mV}$) tested at the same current density (Figure II.7.H.1). [3]

Lithium Phosphate-Modified Lithium Lanthanum Titanium Oxide Nanofiber-Polymer Composite Electrolyte for Lithium Battery

A composite solid state electrolyte based on three dimensional (3D) aluminium-doped perovskite-type lithium lanthanum titanium oxide (LLATO) nanofibers was fabricated. Modified with lithium phosphate of the surface of nanofibers, the flexible solid-state electrolyte composite membrane exhibited high ionic conductivity of $5.1 \times 10^{-4} \text{ S/cm}$ at room temperature.

A narrow concentration range of Ti^{4+} was substituted by Al^{3+} , which enhanced the ionic conductivity of the LLTO nanofibers, changed the bond strength between the B-site cation and oxygen. [4] A thin layer of lithium phosphate was coated onto the surface of the LLTO nanofibers. After calcinations at $900^{\circ}C$ in air, all the diffraction peaks of LLTO matched well with those of perovskite-type $Li_{0.33}La_{0.56}TiO_3$ (JCPDS 54-1238). All the samples were perovskite-structured LLTO without any impurity phase, confirming the tetragonal crystalline structure (P4/mmm space group). After the modification with lithium phosphate, the XRD pattern didn't change after modification with Li_3PO_4 .

The composite electrolyte based on the 10 wt%-30 wt% LLATO nanofibers was by immersing the nanofiber membrane directly in the PVDF-HFP/LiTFSI acetone solution. The ionic conductivity of PVDF-HFP/LiTFSI composite electrolyte with 10%-30% LLATO nanofibers was $1.7\sim 4.0 \times 10^{-4} S cm^{-1}$. Coating of Li_3PO_4 on the nanofibers further increased the ionic conductivity to $5.1 \times 10^{-4} S/cm$.

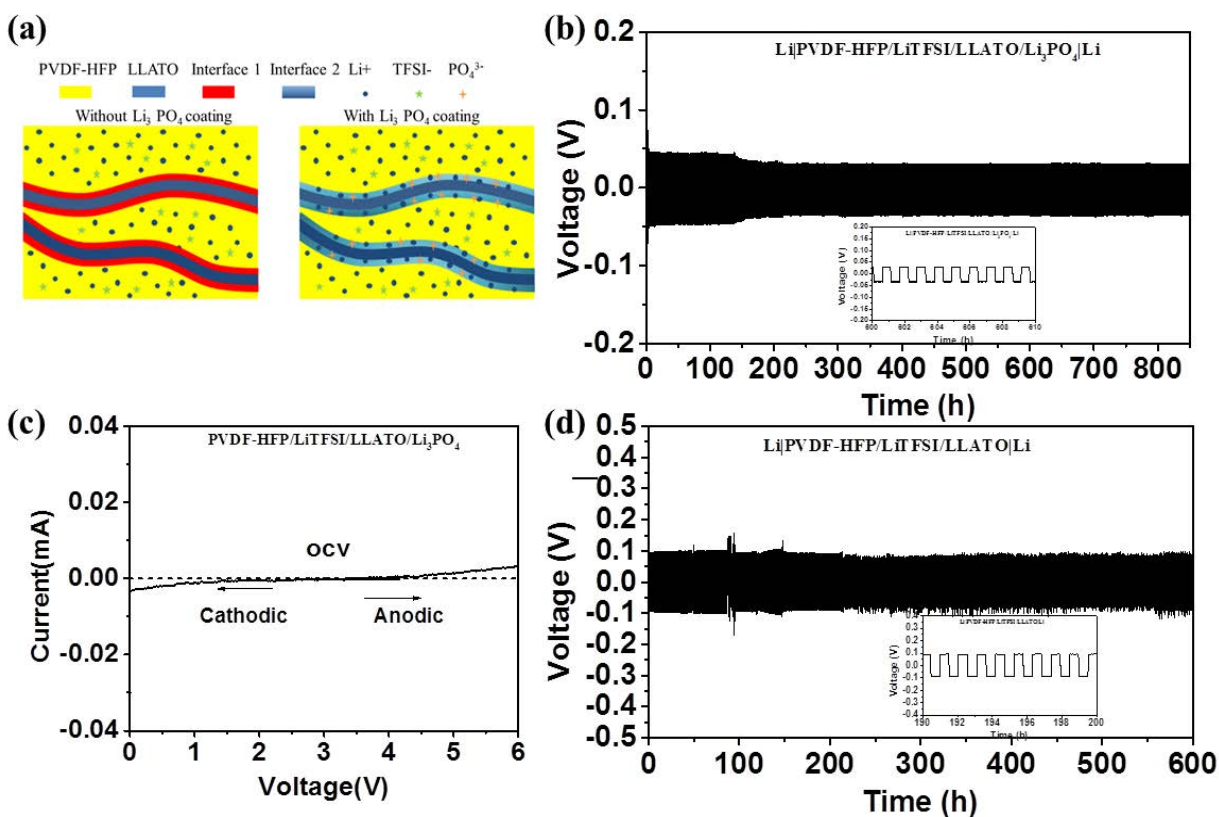


Figure II.7.H.2 (a) Schematic illustration showing the structure with and without Li_3PO_4 coating on the LLATO nanofibers. (b) Voltage profile of $Li|PVDF-HFP/LiTFSI/LLATO/Li_3PO_4|Li$ at a current density of $0.5 mA/cm^2$. (c) LSV curve of the FRPC electrolyte membrane to show the electrochemical stability window in the range of 0–6 V. (d) Voltage profile of $Li|PVDF-HFP/LiTFSI/LLATO|Li$ at a current density of $0.5 mA/cm^2$.

The PVDF-HFP/LiTFSI/LLATO/ Li_3PO_4 composite electrolyte exhibited a stable voltage window up to 5 V vs. Li/Li^+ . Structural stability of the solid electrolyte PVDF-HFP/LiTFSI, PVDF-HFP/LiTFSI/LLATO and PVDF-HFP/LiTFSI/LLATO/ Li_3PO_4 was evaluated through a symmetric $Li|Electrolyte|Li$ cell discharged at a constant current density of $0.5 mA/cm^2$ at room temperature. The $Li|PVDF-HFP/LiTFSI/LLATO/Li_3PO_4|Li$ cell stabilized at $\sim 50 mV$ without short-circuiting in 850 h (Figure II.7.H.2).

Composite Electrolyte with $\text{Li}_{0.33}\text{La}_{0.55}\text{TiO}_3$ Ceramic Nanofiller Induced Poly(ethylene oxide) based Cross-linked Polymer for Ambient All-Solid-State Lithium-ion Batteries

Incorporating active nanofiller within the polymer matrix demonstrates an effective method to fabricate composite solid electrolytes (CSE) [3], [5], [6]. In this work, we synthesized a highly ionic-conductive cross-linked poly(ethylene oxide) (PEO) polymer (Figure II.7.H.3). After plasticized with poly(ethylene glycol) (PEG), the solid polymer electrolyte showed an ionic conductivity of $1.65 \times 10^{-4} \text{ S} \cdot \text{cm}^{-1}$ at room temperature. Based on the synthesized cross-linked polymer, a composite solid electrolyte was developed by dispersing $\text{Li}_{0.33}\text{La}_{0.557}\text{TiO}_3$ (LLTO) nanofiller within the polymer matrix. Since LLTO nanofibers provided a 3D network and continuous Li^+ transfer channels within the polymer matrix, the composite electrolyte showed high ionic conductivity ($3.13 \times 10^{-4} \text{ S cm}^{-1}$), high lithium transference number (0.51), and excellent mechanical properties. The all-solid-state $\text{Li}|\text{LiFePO}_4$ cells with this composite solid electrolyte exhibited remarkable specific capacity and stable cycle performance at room temperature. Notably, it can deliver the specific capacity of 147 mAh g^{-1} at room temperature.

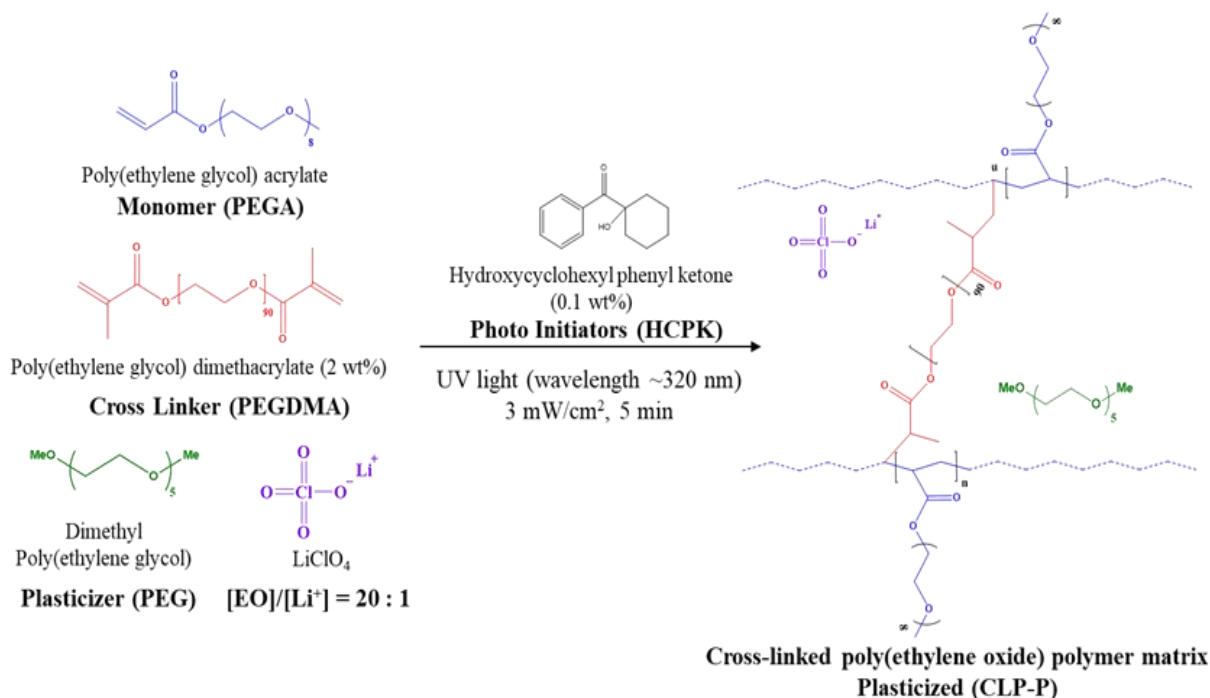


Figure II.7.H.3 The procedure for synthesis of cross-linked poly(ethylene oxide) solid-state electrolyte (CLPSE).

Flexible Electrolyte-Cathode Bilayer Framework with Stabilized Interface for Room-Temperature All-Solid-State Lithium-Sulfur Batteries

Lithium-sulfur batteries (LSBs) are promising next-generation energy storage system beyond state-of-the-art lithium-ion batteries because of their low cost and high energy density [7], [8]. However, liquid electrolyte-based LSBs suffer from “polysulfide shuttle”, raise a concern on safety due to the use of flammable organic electrolytes and the formation of lithium dendrites [9], [10]. In this work, we report a composite bilayer framework that was composed of a one-dimensional (1D) $\text{Li}_{0.33}\text{La}_{0.557}\text{TiO}_3$ (LLTO) ceramic nanofiber/poly(ethylene oxide) (PEO) composite electrolyte coupled to a three-dimensional (3D)-flexible carbon nanofiber/sulfur (CNF/S) cathode. This bi-layer served as both the electrolyte and the cathode for room-temperature all-solid-state LSBs, which can be placed on the top of anode surface to form a Li-S full cell without the use of an additional electrolyte or a separator (Figure II.7.H.4). The highly Li-ion conductive/mechanically robust solid composite polymer electrolyte with dual-conductive matrix was integrated in the bilayer structure, which reconciled the conductivity-rigidity inconsistency and met the multiple requirements for room-temperature all-solid-state LSBs. The bilayer structure have several

advantages: i) The 1D LLTO nanofibers are embedded in the polymer matrix, which provides the continuous ionic transport pathways and enhances amorphous region in the PEO matrix; ii) the LLTO nanofibers on/within the thin PEO electrolyte enable the ion transport and reduce the interfacial resistance at the electrolyte/electrode interface; iii) the PEO/LLTO solid electrolyte is infiltrated onto the surface and pores of CNF/S nanofiber membranes (similar to liquid electrolyte), which obtains a balanced conducting matrix with high electrical and ionic conductivities; iv) the uniform distribution of nano-sized S along the CNF axis shortens the diffusion distances for both Li ions and electrons; and v) the mechanically robust cathode with micro-/meso- pores could accommodate the large volume change in sulfur during continuous charge-discharge processes. As a result, the bilayer framework demonstrated favorable electrochemical performance at room temperature with high Coulombic efficiency of over 99%.

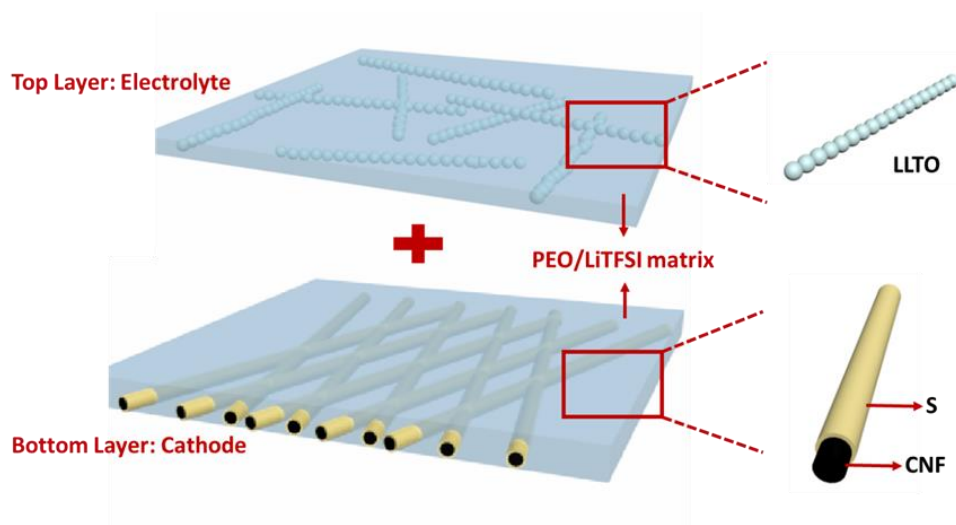


Figure II.7.H.4 Schematic illustration of the CNF/S-PEO/LLTO bilayer structure: the top thin PEO/LLTO solid composite electrolyte layer acts as the Li-ion conductor, enabling fast ion transport between cathode and anode; and the bottom PEO filled CNF/S nanofiber layer with intimate triple-phase contact of electrical conductive current collector (CNF), active material (S) and solid polymer electrolyte (PEO), providing a balanced dual-conductive architecture for continuous electron/ion transfer. The entire bilayer structure can be placed on the top of the anode surface to form a Li-S full cell without the use of an additional electrolyte or a separator.

Conclusions

1. The ceramic LLTO nanofibers with a high aspect ratio were dispersed into a PEO polymer, and formed a PEO/LLTO composite solid polymer electrolytes, achieving a considerably enlarged electrochemical stability window up to 5 V vs. Li/Li^+ . This could satisfy the need of most lithium based batteries.
2. The LLTO nanofibers were doped with aluminum and then coated with lithium phosphate to help form a continuous lithium-ion-conducting network, improving the lithium ion mobility at the LLTO nanofiber. The ionic conductivity of the PVDF-HFP/LiTFSI/LLATO/ Li_3PO_4 reached to 5.1×10^{-4} S/cm.
3. A highly ionic-conductive cross-linked poly(ethylene oxide) (PEO) polymer was synthesized by dispersing the LLTO nanofiller into the polymer matrix. This composite solid electrolyte showed high ionic conductivity (3.13×10^{-4} S cm^{-1}), high lithium transference number (0.51), and excellent mechanical properties.
4. A composite bilayer framework was fabricated, in which the LLTO ceramic nanofiber/poly(ethylene oxide) (PEO) composite electrolyte was coupled to a 3D flexible carbon nanofiber/sulfur (CNF/S) cathode. The bilayer framework demonstrated favorable electrochemical performance at room temperature with the Coulombic efficiency of over 99%.

Key Publications

1. Zhu, P., Yan, C., Dirican, M., Zhu, J., Zang, J., Selvan, R.K., Chung, C.C., Jia, H., Li, Y., Kiyak, Y. and Wu, N., 2018. $\text{Li}_{0.33}\text{La}_{0.557}\text{TiO}_3$ ceramic nanofiber-enhanced polyethylene oxide-based composite polymer electrolytes for all-solid-state lithium batteries. *Journal of Materials Chemistry A*, 6(10), pp.4279-4285.
2. X. Dong, P. Zhu, Z. Du, J. Zang, Y. Li, C. Yan, M. Dirican, H. Jia, C. Zhang, N. Q. Wu, J. Zhu, X. W. Zhang, 2018. Flexible Electrolyte-cathode bilayer framework with stabilized interface for room-temperature all-solid-state lithium-sulfur batteries, *Energy Storage Materials*, in press.

References

1. Yang, C., Fu, K., Zhang, Y., Hitz, E. and Hu, L. Protected Lithium-Metal Anodes in Batteries: From Liquid to Solid. *Advanced Materials*, 2017, 29(36), 1701169.
2. Sun, C. Liu, J., Gong, Y., Wilkinson, D. P. and Zhang, J., Recent advances in all-solid-state rechargeable lithium batteries, *Nano Energy*, 2017, 363–386.
3. Fu, K. K., Gong, Y., Dai, J., Gong, A., Han, X., Yao, Y., Wang, C., Wang, Y., Chen, Y. and Yan, C., Flexible, solid-state, ion-conducting membrane with 3D garnet nanofiber networks for lithium batteries. *Proceedings of the National Academy of Sciences* 2016, 113 (26), 7094-7099.
4. Thangadurai, V. and Weppner, W. Effect of B-site substitution of (Li, La) TiO_3 perovskites by di-, tri-, tetra- and hexavalent metal ions on the lithium ion conductivity. *Ionics*, 2000, 6, 70-77.
5. Liu, W., Liu, N., Sun, J., Hsu, P.-C., Li, Y., Lee, H.-W., Cui, Y., Ionic conductivity enhancement of polymer electrolytes with ceramic nanowire fillers. *Nano Letters* 2015, 15 (4), 2740-2745.
6. Zhu, P., Yan, C., Dirican, M., Zhu, J., Zang, J., Ramakrishnan, K. S., Chung, C.-C., Hao, J., Li, Y. and Kiyak, Y., $\text{Li}_{0.33}\text{La}_{0.557}\text{TiO}_3$ ceramic nanofiber-enhanced polyethylene oxide-based composite polymer electrolyte for all-solid-state lithium batteries. *Journal of Materials Chemistry A* 2018, 6, 4279-4285.
7. Manthiram, A., Fu, Y., Chung, S.-H., Zu, C. and Su, Y.-S., Rechargeable lithium-sulfur batteries. *Chemical Reviews* 2014, 114 (23), 11751-11787.
8. Yin, Y. X., Xin, S., Guo, Y. G. and Wan, L. J., Lithium-sulfur batteries: electrochemistry, materials, and prospects. *Angewandte Chemie International Edition* 2013, 52 (50), 13186-13200.
9. Zhang, S. S., Liquid electrolyte lithium/sulfur battery: fundamental chemistry, problems, and solutions. *Journal of Power Sources* 2013, 231, 153-162.
10. Zhu, J., Chen, C., Lu, Y., Zang, J., Jiang, M., Kim, D. and Zhang, X., Highly porous polyacrylonitrile/graphene oxide membrane separator exhibiting excellent anti-self-discharge feature for high-performance lithium-sulfur batteries. *Carbon* 2016, 101, 272-280.

II.7.1 Electrochemically Responsive Self-Formed Li-ion Conductors for High Performance Li Metal Anodes (Penn State Univ)

Donghai Wang, Principal Investigator

The Pennsylvania State University
134 Energy and the Environment Lab Building
University Park, PA 16802
E-mail: dwang@psu.edu

Tien Duong, DOE Technology Development Manager

U.S. Department of Energy
E-mail: Tien.Duong@ee.doe.gov

Start Date: October 1, 2016

End Date: September 30, 2019

Project Funding: \$1,266,052

DOE share: \$1,139,319

Non-DOE share: \$126,733

Project Introduction

The project will develop and optimize organo- Li_xS_y , organo- $\text{Li}_x\text{P}_y\text{S}_z$, and organo- Li_xS_y /organo- $\text{Li}_x\text{P}_y\text{S}_z$ composite materials as protective layers for Li metal anodes in Li-S batteries. The core focus will be on synthesis methods and precursors for new organic/inorganic hybrid Li-ion conductors, protective layer composition, and protective layer fabrication methods. This will be accompanied by property measurement and characterization (conductivity, mechanical properties, etc.) for the protective layer on Li metal, as well as detailed diagnostics and cell testing. At the conclusion of the project, twelve ~300 mAh pouch cells will be delivered which use the optimal protection layer.

Objectives

The objective of this project is to develop and deliver an electrochemically responsive self-formed hybrid Li-ion conductor as a protective layer for Li metal anodes, enabling Li metal anodes to cycle with a high efficiency of ~99.7% at high electrode capacity ($>6 \text{ mAh/cm}^2$) and high current density ($>2 \text{ mA/cm}^2$) for over 500 cycles. The project will also demonstrate prototype ~300 mAh Li-S battery cells with energy densities of ~200 Wh/kg and ~80% capacity retention for ~300 cycles at ~80% depth of discharge (DOD) using Li metal anodes with this protective layer.

Approach

The novel multiphase organo- Li_xS_y or organo- $\text{Li}_x\text{P}_y\text{S}_z$ hybrid ion conductors with tunable multifunctional organic components and controlled Li_xS_y and $\text{Li}_x\text{P}_y\text{S}_z$ inorganic components will be designed and prepared, and thus enable safe use of lithium metal with high Coulombic efficiency. In the second year, the team will develop the second generation of organo- Li_xS_y lithium protection layers with tuned functionality to further improve Li plating/stripping Coulombic efficiency: 1) finding appropriate composition, 2) developing appropriate synthesis and fabrication methods and 3) optimizing organic components in protection layer to further improve Coulombic efficiency and Li-S battery performance.

Results

To further strengthen the organo- Li_xS_y lithium protective layer, we screen the organic species based on their molecular conformation. Because the planar backbone conformation facilitates fabrication of the flat and uniform structure of SEI layer during the co-deposition of organic and inorganic components, so aromatic-based organic components with planar backbone conformation should be beneficial to preparing more stable lithium protection layer. We use aromatic compound (1, 3-diisopropenylbenzene (DIB)) which can react with sulfur to prepare the sulfur-containing polymer (poly(sulfur-random-1, 3-diisopropenylbenzene (PSD))). This polymer retains the electrochemical properties of elemental sulfur and can generate the inorganic lithium salt ($\text{Li}_2\text{S}/\text{Li}_2\text{S}_2$) and aromatic-based organic components during the charge/discharge process, the aromatic-based organic components could be co-deposit with $\text{Li}_2\text{S}/\text{Li}_2\text{S}_2$ to form more stable inorganic/organic hybrid film.

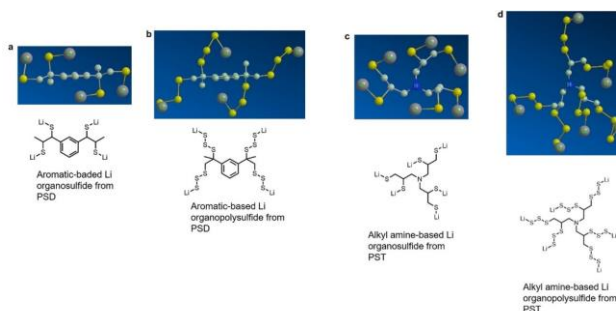


Figure II.7.1.1 Possible molecular conformation of aromatic-based Li organosulfide (a) and Li organopolysulfide (b) originating from PSD polymer; alkyl amine-based Li organosulfide (c) and Li organopolysulfide (d) originating from PST polymer.

Figure II.7.1.1 shows possible molecular conformation of different Li organosulfides, aromatic-based organic components show planar backbone conformation (Figure II.7.1.1a-b) rather than a branched structure of PST polymer (used for preparing our 1st generation organo-Li_xS_y lithium protective layer, Figure I.1c-d), this kind of organic components facilitates the initial “growth” of a flat and uniform morphology of hybrid protective layer and formation of a planar and smooth structure.

We prepare PSD polymers with various sulfur contents, as shown in Table II.7.1.1. PSDs with different various sulfur contents (50 wt%, 70 wt% and 90 wt%, designated as PSD-50, PSD-70 and PSD-90, respectively) were used as additives in the electrolyte. The solubility of PSDs in electrolyte decreases with the increment in sulfur content of the polymer. When PSD-90 is added in the electrolyte, a mixture is formed. However, it becomes homogeneous after the first cycle of Li plating/stripping due to the chemically/electrochemically reaction with Li metal (Figure II.7.1.2). The corresponding cycling performance of Li plating/stripping was first investigated. The electrolyte used here was 1 M LiTFSI (lithium bis(trifluoromethanesulfonyl)imide) and 1 wt% LiNO₃ in the dioxolane/dimethoxyethane (DOL/DME, V/V = 1). It is found that the cells using PSD-90 as an additive exhibit the best performance, and the cycling stability drops with the decrease of sulfur content in the PSDs (e.g., PSD-70, PSD-50), as shown in Figure II.7.1.3.

Table II.7.1.1 Prepared SCPs with different contents of sulfur.

Samples	Content (wt%)	
	Sulfur	DIB
PSD-50	50	PSD-50
PSD-70	70	PSD-70
PSD-90	90	PSD-90

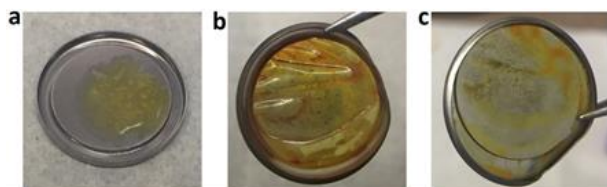


Figure II.7.1.2 The photos of PSD-90-Ely before cycling (a) and after 1st cycle of Li plating/stripping: (b) with separator covering on stainless steel, (c) separator was peeled off.

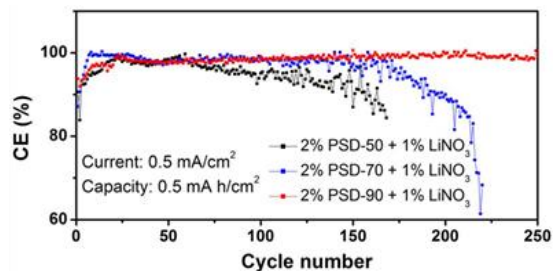


Figure II.7.1.3 Cycling performance of 2 wt% PSDs containing different sulfur contents as additives.

For the protection of the Li metal anode, poly(sulfur-random-1, 3-diisopropenylbenzene (PSD), which contain the sulfur chains and aromatic-based organic components, is used for fabrication of organo-Li_xS_y lithium protection layers. The PSD with 90 wt% sulfur (PSD-90) exhibited the best cycling performance. The content of PSD-90 as additives in the electrolyte affects the Li plating/stripping cycling performance. As show in Figure II.7.I.4, comparing the Li plating/stripping performance of using electrolyte containing 2 wt%, 5 wt%, 8 wt% and 10 wt% of PSD-90, we found that the cycling life is improved with increasing content of PSD-90 additive till reaching 8 wt%. When the content of PSD-90 in the electrolyte increased to 10 wt%, the cycling life deteriorates.

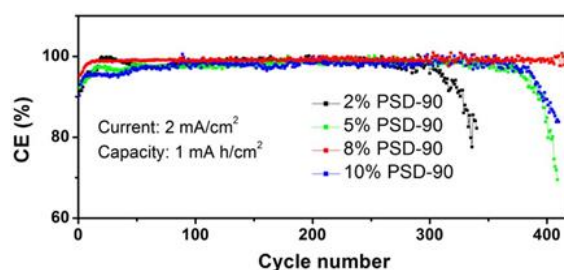


Figure II.7.I.4 Cycling performance of cells using electrolytes containing different contents of SCPs.

Therefore, the PSD-90 was investigated as the electrolyte additives to suppress the growth of the Li dendrite and enhance the CE. The control electrolyte used here was 1 M LiTFSI (lithium bis(trifluoromethanesulfonyl)imide) and 4 wt% LiNO₃ in the dioxolane/dimethoxyethane (DOL/DME = 1:1, V/V). The electrolyte containing 8 wt% PSD-90 was used in the following study. Figure II.7.I.5 shows scanning electron microscopy (SEM) images of the deposited Li after 10 cycles at a current density of 2 mA cm⁻² and a deposition capacity of 2 mA h cm⁻². For the control electrolyte, both the top (Figure I.5a-b) and the cross-section view (Figure II.7.I.5c) show typical dendritic and fluffy structure, indicating dendritic and mossy Li grows on the whole electrode. When 8 wt% PSD-90 was added in the electrolyte, the deposited Li shows a continuous, uniform and highly packed morphology not accompanied by any dendritic and mossy Li (Figure II.7.I.5d-e). The cross-section view displays the compact structure without any dendrite observed at the interior of Li layer (Figure II.7.I.5f).

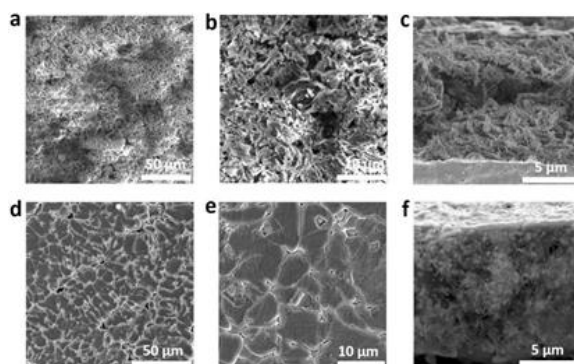


Figure II.7.I.5 Morphologies of Li metal deposited onto stainless steel substrates. SEM images of Li metal deposited onto bare stainless steel substrates in the control electrolyte (a-c), and the electrolyte containing 8 wt% PSD-90 (d-f) at a current density of 2 mA cm⁻² and a deposition capacity of 2 mA h cm⁻² after 10 cycles of Li plating/stripping.

Even after 100 cycles of Li plating/stripping, the deposited Li still exhibits very smooth, uniform surface and compact interior without any growth of Li dendrites (Figure II.7.I.6a-b). The growth of the compact and dendrite-free Li should be ascribed to the property change of the SEI layer in the presence of the PSD-90 additive. In comparison to Li morphologies using PSD-90 as additive, a large amount of typical dendritic and fluffy structure is observed using the control electrolyte at both surface and interior of the deposited Li layer after 100 cycles (Figure II.7.I.6c-d).

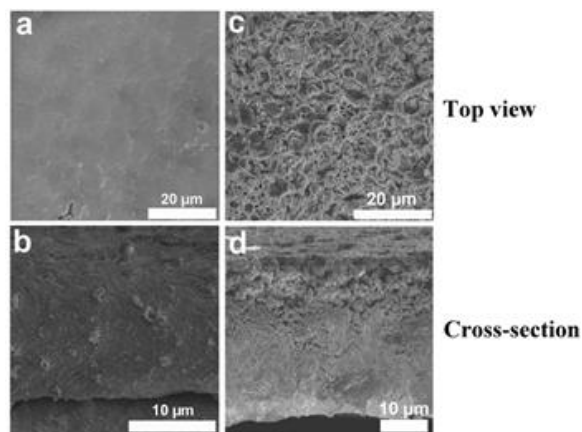


Figure II.7.1.6 SEM images of the deposited Li after 100 cycles at a current density of 2 mA cm⁻² and a deposition capacity of 2 mA h cm⁻². (a, b) Top view and cross-section view of deposited Li using the electrolyte containing 8wt% PSD-90. (c, d) Top view and cross-section view of deposited Li using the control electrolyte.

SEI layers formed from electrolyte containing PSD-90 were characterized. First, the composition of the SEI layers was investigated using X-ray photoelectron spectroscopy (XPS). The SEI layers were obtained from C-Ely (1M LiTFSI+4%LiNO₃/DOL+DME) and PSD-90-Ely (1M LiTFSI+8%PSD-90+4%LiNO₃/DOL+DME) after 100 cycles of Li deposition/dissolution and named C-SEI and PSD-90-SEI, respectively. In S 2p XPS spectra (Figure II.7.1.7a), two strong peaks at 160.5 and 161.7 eV for the PSD-90-SEI indicate the presence of Li₂S and Li₂S₂; and the peak located at 162.2 eV which corresponds to the S 2p_{3/2} for Li organosulfides (RS₄Li₄) confirms the Li organosulfides exist in the PSD-90-SEI layer. The peak at 163.3 eV is assigned to Li polysulfides (Li₂S_x) and organopolysulfides (RS_xLi₄) which overlap and make the peak stronger. The 2p XPS spectra of PSD-90-SEI reflect the existence of Li organosulfides/organopolysulfides along with the Li₂S/Li₂S₂ in the SEI layer. The C 1s XPS spectra of C-SEI (Figure II.7.1.7b) contains a peak at ~292.1 eV assigning to the functional group -CF₃ from the decomposition of LiTFSI. This peak almost disappears when PSD-90 is added in the electrolytes (PSD-90-Ely), indicating the decomposition of LiTFSI is dramatically suppressed in the presence of PSD-90. Moreover, the F 1s XPS spectra (Figure II.7.1.7c) display a relatively lower intensity of peak assigned to -CF₃ in the PSD-90-SEI, reconfirming the suppression of LiTFSI decomposition in the presence of PSD-90. Figure II.7.1.8 shows that Fourier-transform infrared (FT-IR) spectra of C-SEI and PSD-90-SEI are quite different. The FT-IR spectra of PSD-90-SEI show prominent peaks at 1600, 1575 and 1558 cm⁻¹, which correspond to the vibration of carbon-carbon double bond of the phenyl group. The peak at ~790 cm⁻¹ is the vibration characteristic of C-H bond of the 1, 3-substituted phenyl groups, which can prove the presence of 1, 3-substituted phenyl groups. All of the peaks can also be found in the pure PSD-90, demonstrating that the organosulfides originate from the PSD-90.

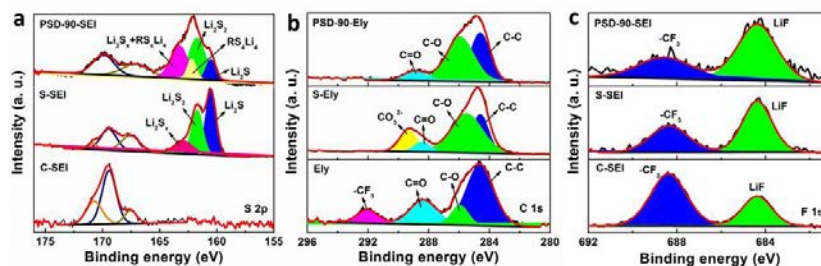


Figure II.7.1.7 The XPS spectra of SEI layers formed from the electrolytes containing different additives. S 2p XPS spectra (a), C 1s XPS spectra (b), and F 1s XPS spectra (c) of the SEI layers formed from different electrolytes.

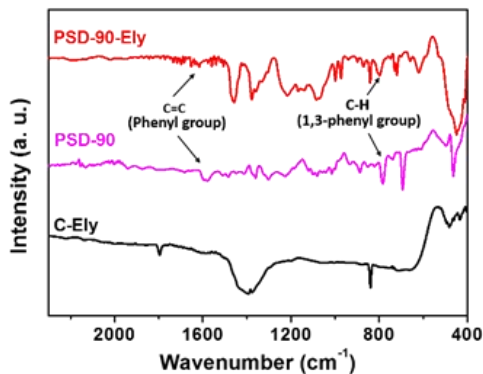


Figure II.7.1.8 FT-IR of SEI layers obtained from the C-Ely (C-SEI) and the PSD-90-Ely (PSD-90-SEI).

Surface morphologies of the C-SEI and PSD-90-SEI layers studied by AFM (Figure II.7.1.9a and b) and SEM (Figure II.7.1.9e and f) consistently show a porous, fractured, and loose structure observed in C-SEI (Figure II.7.1.9a and e), in comparison, a mostly planar, smooth and uniform structure in PSD-90-SEI layer (Figure II.7.1.9b and f). Indentation curve of C-SEI (Figure II.7.1.9c) shows the loading and unloading curves almost overlap and the slopes are very high, implying that the C-SEI layer is rigid and its viscoelasticity is negligible. The reduced modulus of the C-SEI is calculated to be 903 MPa from the Johnson-Kendall-Roberts (JKR) model fit (Table II.7.1.2). By contrast, a more substantial deformation and hysteresis between the loading and unloading curves of PSD-90-SEI layer (Figure II.7.1.9d) reflects flexible characteristic under the mechanical deformation. The PSD-90-SEI layer exhibits a lower modulus of 340 MPa (Table II.7.1.2), indicating this SEI layer becomes soft and viscoelastic.

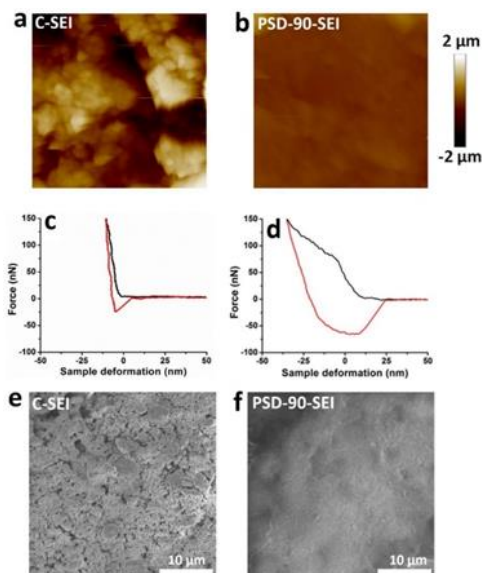


Figure II.7.1.9 AFM images and indentation study of SEI layers obtained from C-Ely (a, c) and PSD-90-Ely (b, d). SEM images of SEI layers obtained from C-Ely (e) and PSD-90-Ely (f). The scan size for AFM images is $10 \times 10 \mu\text{m}^2$.

Table II.7.I.2 The reduced modulus of SEI layers formed from the C-Ely and PSD-90-Ely.

Electrolyte	SEI layer	Reduce modulus (JKR model)/MPa
C-Ely	Inorganic layer (C-SEI)	903
PSD-90-Ely	Inorganic/organic layer (PSD-90-SEI)	340

The stable SEI layer fabricated from PSD-90-Ely dramatically improves the Li deposition/dissolution CE. The cycling performance of Li deposition/dissolution using PSD-90-Ely was shown in Figure II.7.I.10. At a capacity of 1 mA h cm⁻² and a deposition capacity of 2 mA cm⁻², a high average CE of 99.1% can be maintained for 420 cycles. The CE and cycling stability of Li deposition/dissolution at high current densities and deposition capacities are investigated. The stable hybrid SEI layer fabricated from PSD-90-Ely significantly improves the CE. The cycling performance of Li deposition/dissolution using PSD-90-Ely was shown in Figure II.7.I.11. At the current density of 2 mA cm⁻² and deposition capacity of 2 mA h cm⁻², the average CE achieved can be as high as 99% over 250 cycles (Figure II.7.I.11a). When the capacity of 3 mA h cm⁻² was applied, the cells delivered a high average CE of 98.9% over 250 cycles (Figure II.7.I.11b). Especially from 160th cycle to 220th cycle, the average CE is as high as ~99.5%. The voltage profiles of Li deposition/dissolution (Figure II.7.I.11c) indicate the cells using PSD-90-Ely show lower polarization than those with C-Ely. Moreover, in contrast to the cells using C-Ely, the batteries using PSD-90-Ely show more stable and smaller voltage hysteresis at ~47 mV over 200 cycles (Figure II.7.I.11d). Both the low polarization and the modest and stable hysteresis are mainly due to the durable and flexible SEI layer that enables the compact and uniform Li deposition leading to thin and uniform SEI accumulated over the electrode surface. At an extremely high capacity and current density (4 mA h cm⁻² and 4 mA cm⁻²), the stable hybrid SEI layer still enables improved CE. As show in Figure II.7.I.12, a high average CE of ~97% can be maintained over 150 cycles. From 95th cycle to 115th cycle, the average CE can reach as high as 99.5%.

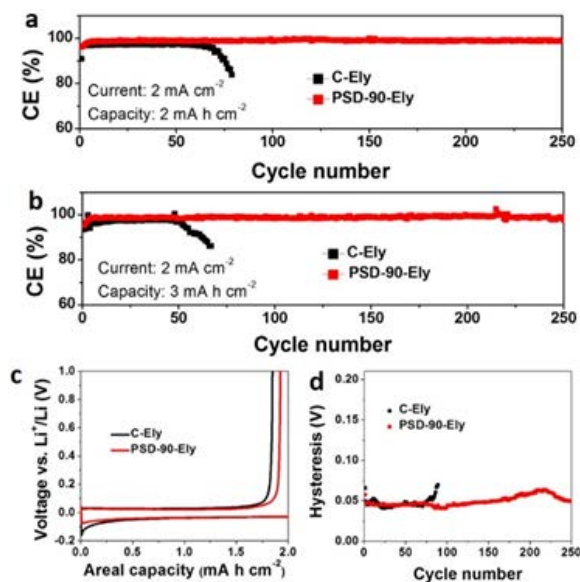


Figure II.7.I.10 Cycling performances of Li deposition/dissolution using the PSD-90-Ely and C-Ely at a current density of 2 mA cm⁻² and a deposition capacity of 2 (a) and 3 mA h cm⁻² (b). (c) Voltage profiles (the first cycle) and (d) average voltage hysteresis of (b).

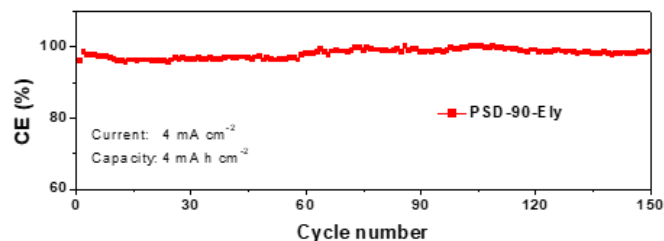


Figure II.7.I.11 Li deposition/dissolution cycling performances of the cells using PSD-90-Ely at a current density of 4 mA cm^{-2} with a deposition capacity of 4 mA h cm^{-2} .

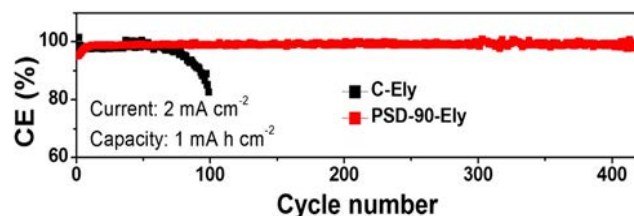


Figure II.7.I.12 Cycling performance of cells using PSD-90-Ely electrolyte.

After finishing the goals of Budget Period 2, we also conduct the preliminary study on Budget Period 3. We synthesized the polymers containing P_xS_y components (polymer- P_xS_y) through the reaction of sulfur anion (S_n^-) containing trifunctional crosslinker lithium polythiophosphate with a chlorine-rich polymer. Then the polymers were directly coated on the substrates (Figure II.7.I.13), during Li plating/stripping, the polymers react with Li metal and in situ release Li sulfides and $\text{Li}_x\text{P}_y\text{S}_z$ at the interface of polymer and Li metal to form organo- Li_xS_y /organo- $\text{Li}_x\text{P}_y\text{S}_z$ composite protection layer. Figure II.7.I.14 shows the scanning electron microscopy (SEM) images of the as-prepared polymer- P_xS_y film, which appears to be a very uniform coating layer with a thickness around $7.0 \mu\text{m}$.

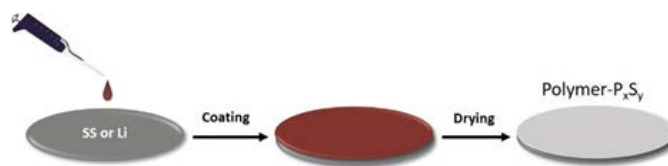


Figure II.7.I.13 Schematic illustration for the fabrication of polymer- P_xS_y protective layer on substrates.

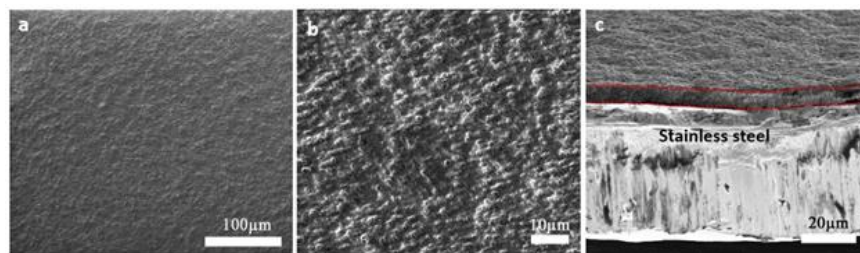


Figure II.7.I.14 SEM images of the as prepared polymer- P_xS_y film on SS foil.

Conclusions

We successfully developed a second generation organo- Li_xS_y lithium protection layers with the planar aromatic-based components, Aromatic-based sulfur-containing polymers (poly(sulfur-random-1,3-diisopropenylbenzene) (PSD)) was used to fabricate thi protection layer. The released aromatic-based organic components have a planar backbone conformation, facilitating the initial “growth” of a flat and uniform

morphology of the hybrid SEI layer and the formation of a planar and smooth structure. In addition, the noncovalent π - π interaction between benzene rings can promote self-assembly of the aromatic components to further improve the toughness and flexibility of the SEI layer. Meanwhile, the suitable inorganic species ($\text{Li}_2\text{S}/\text{Li}_2\text{S}_2$) can provide Li conductive pathway and necessary mechanical hardness in the protection layer. Using this protection layer, lithium anodes were effectively protected without any dendritic and mossy lithium, high Coulombic efficiency (CE) of lithium plating/stripping was achieved.

Key Publications

1. Li, G. X., Liu, Z., Huang, Q. Q., Gao, Y., Regula, M., Wang, D. W., Chen, L. Q., Wang, D. H., Stable Metal Battery Anodes Enabled by Polyethylenimine Sponge Hosts by Way of Electrokinetic Effects, *Nature Energy*, **2018**, <https://doi.org/10.1038/s41560-018-0276-z>.
2. Li, G. X., Huang, Q. Q., He, X., Gao, Y., Wang, D. W., Kim, S. H., Wang, D. H., Self-Formed Hybrid Interphase Layer on Lithium Metal for High Performance Lithium-Sulfur Batteries, *ACS Nano*, **2018**, 12(2), 1500-1507.
3. Gao, Y., Zhao, Y. M., Li, Y. C., Huang, Q. Q., Mallouk, T. E., Wang, D. H., Interfacial Chemistry Regulation via a Skin-Grafting Strategy Enables High-Performance Lithium-Metal Batteries, *Journal of the American Chemical Society*, **2017**, 139(43), 15288-15291.

Acknowledgements

The PI appreciates the support from NETL manager Kimberly Nuhfer in this project.

II.7.J Improving the Stability of Lithium-Metal Anodes and Inorganic-Organic Solid Electrolytes (LBNL)

Nitash Balsara, Principal Investigator

201 C Gilman Hall
University of California
Berkeley, CA 94720
E-mail: nbalsara@berkeley.edu

Tien Q. Duong, DOE Technology Development Manager

U.S. Department of Energy
E-mail: Tien.Duong@ee.doe.gov

Start Date: October 1, 2017	End Date: September, 30, 2020	
Project Funding (FY18): \$900,000	DOE share: \$900,000	Non-DOE share: \$0

Project Introduction

Polymer electrolytes offer increased stability in lithium batteries in comparison to more widely used liquid electrolytes. Nanostructured electrolytes containing both soft, ion-conducting domains and rigid non-conducting domains offer the opportunity to tune both mechanical and electrical properties separately. Such electrolytes are conveniently made by block copolymer self-assembly. Most of the block copolymer electrolytes studied thus far comprise organic polymer chains for both the conducting and rigid domains. The team hopes to synthesize new electrolytes that simultaneously have improved ion transport properties and exhibit greater stability against lithium metal in comparison to all-organic diblock copolymers. The project objective is to establish a new hybrid electrolyte that will be stable in cells with a Li-metal anode. In this project, we investigate an organic, lithium-ion-conducting poly(ethylene oxide) (PEO) block covalently bonded to an inorganic poly(acryloisobutyl polyhedral oligomeric silsesquioxane) (POSS) block.

Objectives

- Synthesize an initial series of hybrid inorganic-organic diblock and triblock copolymers
- Characterize the electrochemical properties of hybrid inorganic-organic block copolymers
- Fabricate lithium symmetric cells incorporating hybrid inorganic-organic block copolymer electrolytes and evaluate their promise as battery electrolytes using electrochemical techniques and X-ray tomography
- Systematically investigate current density as a key parameter in the lifetime of solid block copolymer electrolytes

Approach

Innovative Approach: First, the team synthesizes hybrid diblock and triblock copolymers by incorporating monomers that contain an inorganic component. Then, electrolytes are prepared by mixing these block copolymers with a lithium salt. Electrochemical and mechanical characterization of these materials are performed before carrying out cycling X-ray tomography experiments. The combination of these approaches enables rational design of materials that exhibit improved stability against lithium metal.

1. Synthesis of POSS-PEO block copolymer hybrid electrolyte. (Q1, FY 2018; Completed)
2. Measurement of conductivity of the hybrid copolymer. (Q2, FY 2018; Completed)

- Measurement of diffusion coefficient and transference number of electrolytes. (Q3, FY 2018; Completed)
- Completion of the first Li-electrolyte-Li tomography experiments. (Q4, FY 2018; Completed)

Results

Poly(ethylene oxide) *-b-* poly(acryloisobutyl polyhedral oligomeric silsesquioxane) (PEO-POSS) diblock copolymers were synthesized by nitroxide-mediated radical polymerization (NMP) as described in Figure II.7.J.1. An acryloisobutyl POSS monomer was polymerized using PEO-based macroalkoxyamine as initiator. Molecular weight of the POSS block ranged between 1 kg mol^{-1} to 18 kg mol^{-1} , determined using H-NMR. Gel-permeation chromatography (GPC) traces of PEO-POSS using tetrahydrofuran (THF) solvent in relation to PEO-Acrylate confirm the polymerization of the POSS block. A list of synthesized PEO-POSS systems are given in Table II.7.J.1, where we list the molecular weight of each block and the PEO volume fraction, f_{EO} . We studied PEO-POSS/LiTFSI mixtures with the molar ratio of lithium to ethylene oxide moieties, $[\text{Li}]/[\text{EO}]$, between 0.005 and 0.30. Poly(acryloisobutyl polyhedral oligomeric silsesquioxane) *-b-* Poly(ethylene oxide) *-b-* poly(acryloisobutyl polyhedral oligomeric silsesquioxane) with molecular weight of the PEO block 35 kg mol^{-1} and each POSS block 5 kg mol^{-1} (POSS-PEO-POSS(5-35-5) triblock copolymers were also synthesized by nitroxide-mediated radical polymerization with structure shown in Figure II.7.J.2.

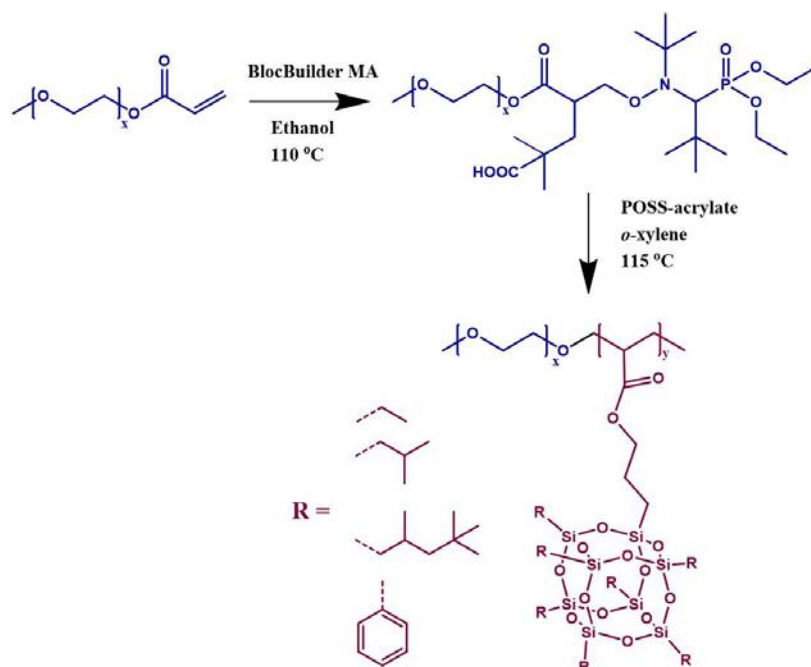


Figure II.7.J.1 Synthesis scheme for PEO-POSS block copolymers.

Table II.7.J.1 POSS-PEO diblock copolymers currently available with isobutyl-functionalized-POSS. The volume fraction of PEO is given and chain length N based on a reference volume of 0.1 nm^3 .

PEO-POSS	POSS units	$M_{\text{PEO}} (\text{kg mol}^{-1})$	$M_{\text{POSS}} (\text{kg mol}^{-1})$	$f_{\text{EO}} 90^\circ \text{C}$	N
(5-1)	1	5	0.9	.84	88
(5-2)	2	5	1.9	.76	97
(5-3)	3	5	2.8	.67	109
(5-4)	4	5	3.7	.61	121
(10-10)	11	10	10.2	.53	278
(15-15)	16	15	14.9	.54	411

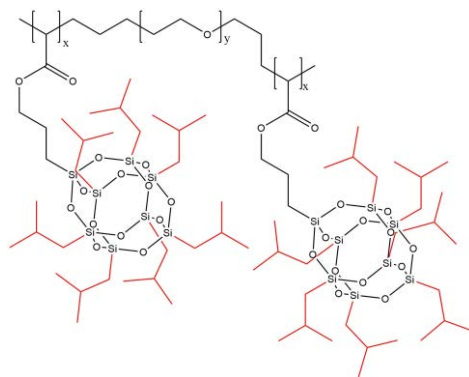


Figure II.7.J.2 Chemical structure of the POSS-PEO-POSS triblock copolymer. The triblock synthesized during this study has a molecular weight of 5-35-5 [kg/mol].

Measurement of conductivity of the hybrid copolymer

We have measured the ionic conductivity of the hybrid diblock copolymer for a range of molecular weights of the POSS chain between 1 kg mol^{-1} to 18 kg mol^{-1} . Electrolytes were prepared by mixing each polymer with lithium bis(trifluoromethane)sulfonimide (LiTFSI) salt at a concentration of $[\text{Li}]/[\text{EO}] = 0.10$ in Figure II.7.J.3a. Data at 90°C for salt concentrations ranging between $[\text{Li}]/[\text{EO}] = 0.02$ to 0.30 is shown in Figure II.7.J.3b. POSS-PEO-POSS(5-35-5) triblock copolymer membrane was cast and electrochemically characterized. The ionic conductivity with salt concentration $[\text{Li}]/[\text{EO}] = 0.04$ is demonstrated in Figure II.7.J.4.

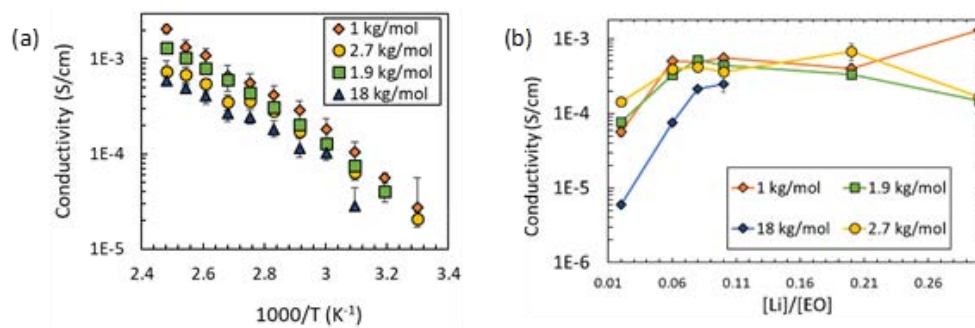


Figure II.7.J.3 Ionic conductivity of PEO-POSS. Conductivity is plotted for organic-inorganic diblock copolymer electrolytes with PEO molecular weight 5 kg mol^{-1} and POSS 1, 1.9, 2.7, and 18 kg mol^{-1} (a) between 30°C and 130°C with $[\text{Li}]/[\text{EO}] = 0.10$ and (b) at 90°C with salt concentration ranging between $[\text{Li}]/[\text{EO}] = 0.02$ to 0.30 . Conductivity decreases with POSS molecular weight and increases with temperature.

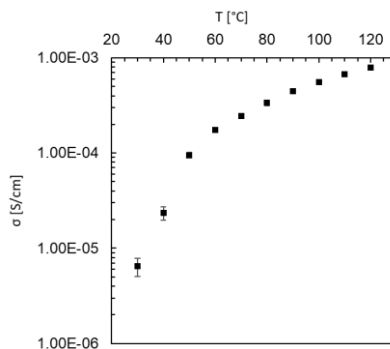


Figure II.7.J.4 Ionic conductivity of a POSS-PEO-POSS (5-35-5) electrolyte with LiTFSI salt concentration $r = [\text{Li}]/[\text{EO}] = 0.04$. The ionic conductivity is similar to previously studied polystyrene-*b*-poly(ethylene oxide) (PS-PEO) diblock copolymer electrolytes.

Measurement of diffusion coefficient and transference number of electrolytes:

Diffusion coefficient (D) and steady-state transference number ($t_{+,ss}$) of the POSS-PEO-POSS(5-35-5) electrolyte with salt concentration $r = 0.04$ is shown in Figure II.7.J.5. ($t_{+,ss}$) of PEO-POSS(5-6) (the molecular weight of the PEO block is 5 kg mol^{-1} and POSS block 6 kg mol^{-1}) was calculated for salt concentrations ranging between $0.02 \leq [\text{Li}]/[\text{EO}] \leq 0.20$. The results are shown in Figure II.7.J.6.

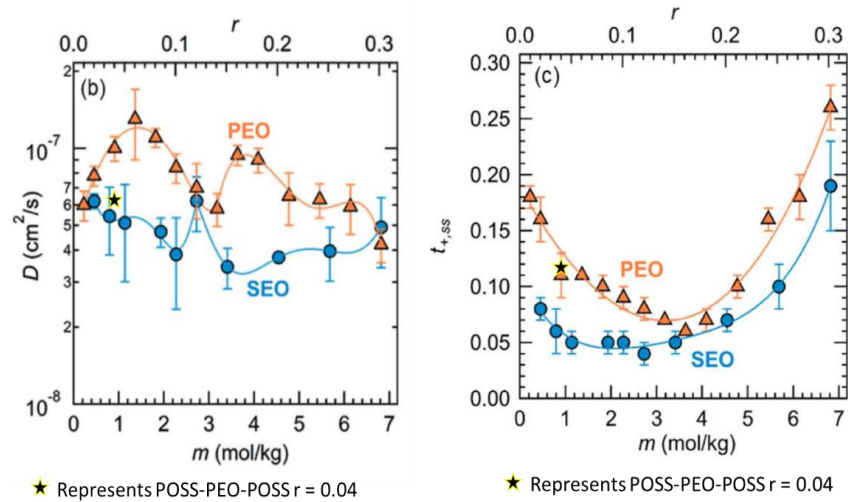


Figure II.7.J.5 Diffusion coefficient and transference number of the POSS-PEO-POSS (5-35-5) electrolyte. The values, marked by a star, are superimposed for comparison on a plot of previously reported values [1] for PEO homopolymer and PS-PEO diblock copolymer electrolytes.

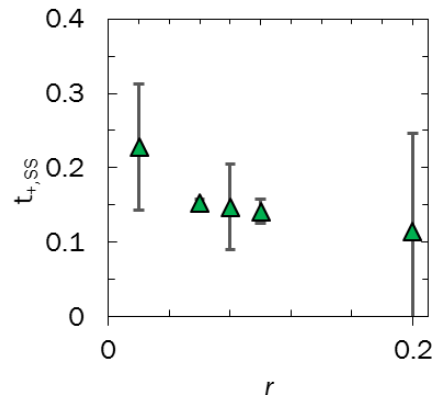


Figure II.7.J.6 Transference number measurements of PEO-POSS(5-6) as a function of salt concentration.

Completion of the first Li-hybrid electrolyte-Li cell cycling and tomography experiments:

Lithium symmetric cells were fabricated with the POSS-PEO-POSS (5-35-5 [kg/mol]) membrane, since this was the only hybrid electrolyte capable of forming a robust membrane. A set of three cells was fabricated and cycled until failure at 0.175 mA cm^{-2} . The cells were then imaged using hard X-ray microtomography at the Advanced Light Source beamline 8.3.2 to observe the mode of failure.

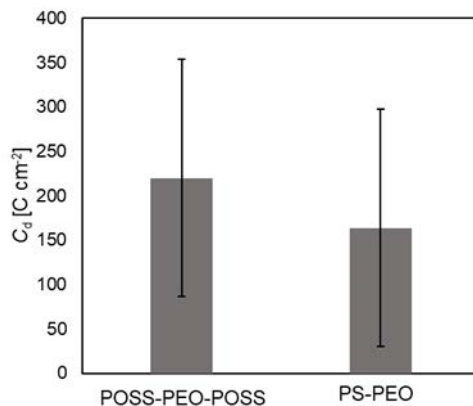


Figure II.7.J.7 Comparison of charge passed before failure, C_d , between Li symmetric cells fabricated from a POSS-PEO-POSS (5-35-5 [kg/mol]) electrolyte and a polystyrene-*b*-poly(ethylene oxide) (PS-PEO) (115-172 [kg/mol]) electrolyte. Each cycle consisted of a 4 hour discharge at 0.175 mA cm^{-2} , 1 hour rest, 4 hour charge at 0.175 mA cm^{-2} , and 1 hour rest at 90°C .

Figure II.7.J.7 shows a comparison of charge passed before failure, C_d , between Li symmetric cells fabricated from a triblock POSS-PEO-POSS (5-35-5 [kg/mol]) electrolyte and a diblock polystyrene-*b*-poly(ethylene oxide) PS-PEO (115-172 [kg/mol]) electrolyte. Despite the much higher molecular weight of the PS-PEO electrolyte, the cycle life of POSS-PEO-POSS is indistinguishable from that of the diblock. This indicates that the inorganic POSS block imparts mechanical resistance to lithium protrusions on the order of that imparted by an organic PS block more than an order of magnitude larger.

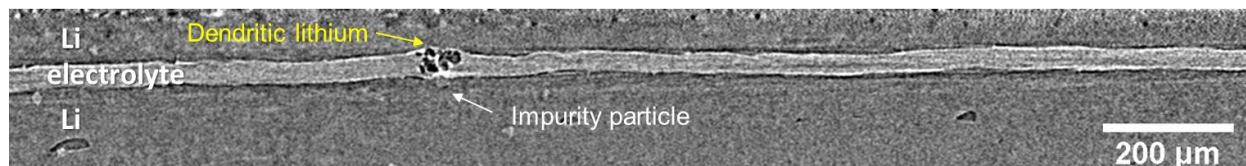


Figure II.7.J.8 Slice through a reconstructed volume imaged using X-ray tomography. This Li/POSS-PEO-POSS/Li cell was cycled at 0.175 mA cm^{-2} and failed after 17 cycles.

X-ray tomography, shown in Figure II.7.J.8, revealed a failure mechanism in the POSS-PEO-POSS which is identical to that seen in PS-PEO: multiglobular lithium protrusions nucleated on an impurity particle embedded in the lithium metal electrode.

Limiting current measurements of a POSS-PEO-POSS hybrid electrolyte

In Figure II.7.J.9, a routine used to test limiting current measurements is shown. The POSS-PEO-POSS hybrid triblock electrolyte showed an exceptionally high limiting current between 4.5 and 6 mA cm^{-2} for a membrane of 30 μm thickness.

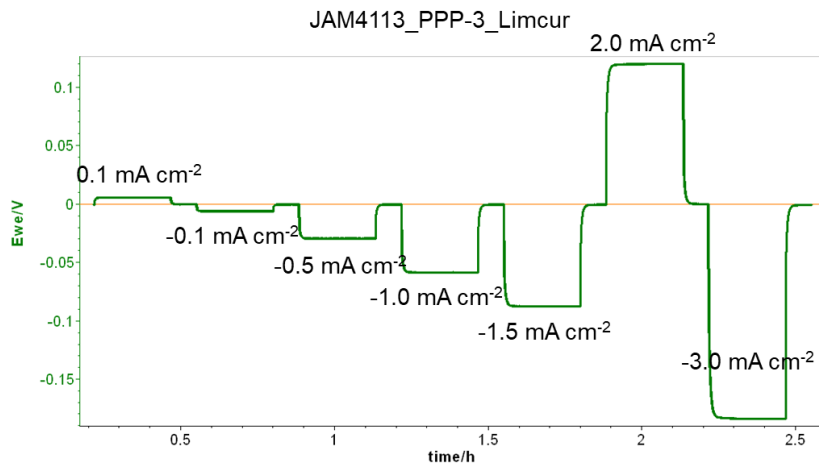


Figure II.7.J.9 Example of a routine used to test the limiting current of POSS-PEO-POSS (5-35-5). This 30 micron thick solid organic-inorganic polymer electrolyte was sandwiched between two lithium electrodes and polarized to electrodeposit Li from one electrode to the other. The current density was increased systematically until the potential diverged or the cell short-circuited.

For the first time, we have synthesized a system which achieved the estimated limiting current (4.5 mA cm^{-2}) based on Monroe and Newman's equation (Eq. 1) without the cell shorting immediately. [1] In all of our previous experiment on block copolymer electrolytes, cells shorted well before the limiting current was reached. We also note that the estimate of limiting current is based on complete characterization of solid polymer electrolytes using the Newman approach.

$$i_L = \frac{2c_B DF}{L(1 - t_{Li})} \quad (\text{Eq. 1})$$

The limiting current is implicated as a normalization factor in Barai et al.'s model of the propagation of lithium protrusions through solid polymer electrolytes. [2], [3] Thus, it is of relevance to study the effect of current density on the nucleation and growth of lithium protrusions. Due to limitations in triblock polymer material, the systematic study of current density effects was conducted with PS-PEO (115-172), which has been shown to have indistinguishable cycle life compared to equivalent cells fabricated with POSS-PEO-POSS (5-35-5).

Systematic study of effects of normalized current density on solid polymer electrolytes [4]

In this study, the effects of current density on lithium deposition through a solid block copolymer electrolyte were systematically evaluated. Li/PS-PEO/Li symmetric cells were polarized until failure, imaged using X-ray microtomography, and the resulting data was analyzed and compared with no adjustable parameters to the model proposed by Barai et al [3].

Figure II.7.J.10 is a schematic describing the three types of characteristic defective deposition observed when lithium is electrodeposited through a solid polymer electrolyte.

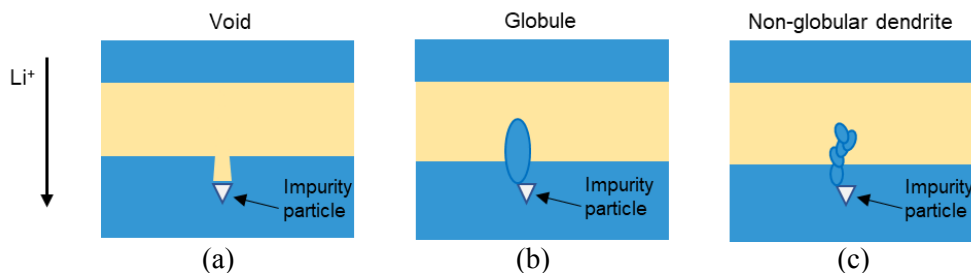


Figure II.7.J.10 A schematic showing the three types of defects observed in this study: (a) a void defect, (b) a protruding lithium globule, and (c) a protruding non-globular dendrite. In each case, the triangle signifies a crystalline impurity particle, which is observed to be the nucleating site for defective deposition.

Figure II.7.J.11 shows examples of defective lithium deposition inside failed cells observed by X-ray tomography. In Figure II.7.J.11a, X-ray tomography results obtained at $i = 0.08 \text{ mA cm}^{-2}$ are shown. This cell failed at $C_d = 50.1 \text{ C cm}^{-2}$, corresponding to 68 microns of lithium deposition. Most of the defects at this current density are voids, and lithium deposition is planar. Figure II.7.J.11b shows X-ray tomography results obtained at $i = 0.32 \text{ mA cm}^{-2}$. This cell failed at $C_d = 18.7 \text{ C cm}^{-2}$, corresponding to 25 microns of lithium deposition. Here, we see the formation of a globular defect. At intermediate current densities, such as $i = 0.32 \text{ mA cm}^{-2}$, we observe both voids and globular defects. In Figure II.7.J.11c, X-ray tomography results obtained at $i = 0.64 \text{ mA cm}^{-2}$ are shown. This cell failed at $C_d = 0.92 \text{ C cm}^{-2}$, corresponding to 1.2 microns of lithium deposition. Here, we see the formation of a non-globular dendrite. The protrusion shown exhibits branching and a small tip radius. At this current density, we observe voids, globular defects, and non-globular dendrites. Despite the relatively large current density, all protrusions were observed to nucleate at an impurity particle. Figure II.7.J.10 and Figure II.7.J.11 are parallel to each other: Figure II.7.J.11 shows data corresponding to the idealized schematics in Figure II.7.J.10.

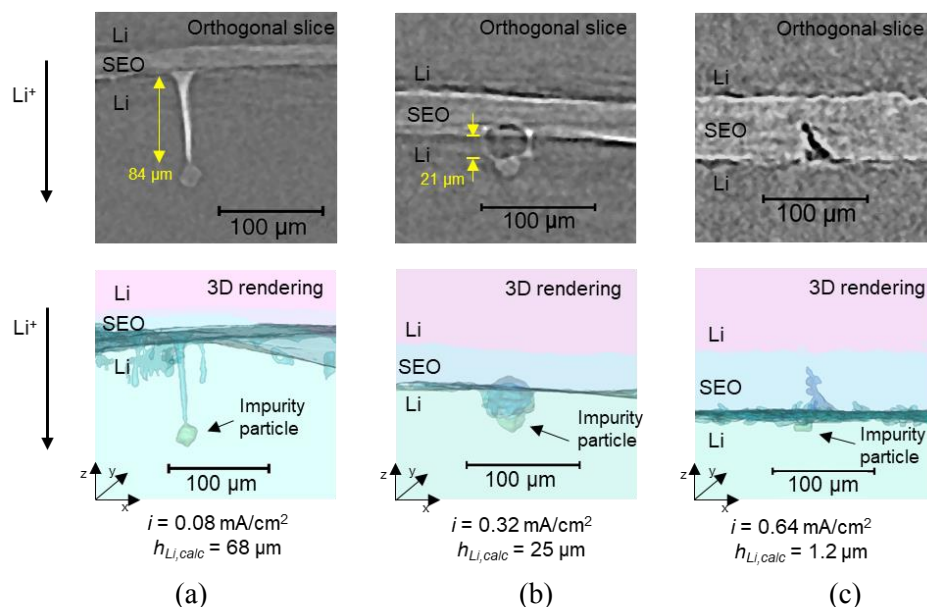


Figure II.7.J.11 Examples of defective lithium deposition observed by X-ray tomography. The top row shows an orthogonal cross-section through the defect. The bottom row shows a 3D rendered volume that includes the defect. In the 3D rendering, the lower interface between electrolyte and lithium is highlighted. The impurity particle, present in each tomogram, is colored green. Lithium is deposited from top to bottom. The current densities used to polarize the cells are indicated, along with the calculated average thickness of lithium, $h_{\text{Li,calc}}$, deposited on the bottom electrode. The yellow arrows are used to estimate the actual thickness of lithium deposited, using the impurity particle as a reference point. In the third cell, not enough lithium was deposited to label the figure. (a) a void defect, (b) a protruding lithium globule, and (c) a protruding non-globular dendrite.

In Figure II.7.J.12, we show planar lithium deposition at sufficiently low current densities: 0.04 mA cm^{-2} in this case. This cell was polarized for 900 h and did not short circuit.

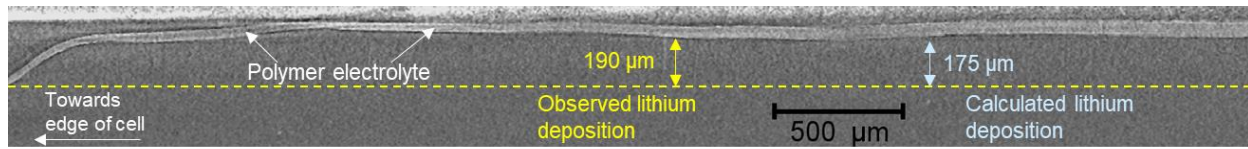


Figure II.7.J.12 Representative cross section of cell polarized at $i = 0.04 \text{ mA cm}^{-2}$ for $t = 900 \text{ h}$ acquired using X-ray tomography. Lithium was deposited downward through the polymer electrolyte, which appears as a light band extending across the cell near the top of the cross-section. No lithium protrusions were observed. This cell did not short circuit. The yellow arrow shows the thickness of the electrochemically deposited lithium, $190 \mu\text{m}$, at a representative location based on the analysis of the tomograms, using the electrolyte's original position at the edge of the cell as a reference point. The light blue arrow shows, for comparison, the estimated thickness of electrochemically deposited lithium, $175 \mu\text{m}$, based on the current passed through the cell.

Figure II.7.J.13 presents the areal density of lithium protrusions as a function of current density. It is apparent that the areal density of lithium protrusions increases monotonically with current density. This sheds new light on the nucleation mechanism of lithium protrusions at impurity particles: high current densities are more likely to nucleate a protrusion than a void on an impurity particle.

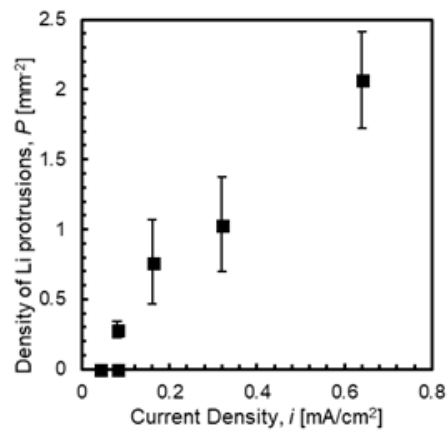


Figure II.7.J.13 Correlation between current density and defect density in failed cells. The areal density of protruding defects, P , increases with current density.

Figure II.7.J.14 frecasts the data in order to make a comparison to the theoretical work of Barai et al. [3] The qualitative trend demonstrated in Figure II.7.J.8 by experiment is consistent with the trend calculated theoretically by Barai et al., who predicted stable lithium deposition at low current densities and unstable lithium deposition at high current densities.

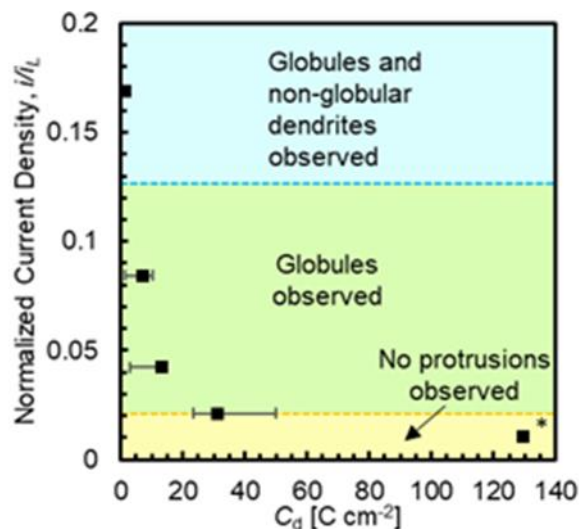


Figure II.7.J.14 Nature of observed lithium protrusions as a function of current density, i , and charge passed before failure, C_d . Observation of no protrusion nucleation at low current densities (yellow area), globules at medium current densities (green area) and non-globular dendrites at high current densities (blue area). The asterisk at $i = 0.04 \text{ mA cm}^{-2}$ indicates these cells had not failed at the time point used to calculate C_d , ($t = 900 \text{ h}$). Normalized current density, i/i_L , as a function of C_d , where i_L is theoretical limiting current (Eq. 1). [1]

The predicted value of i/i_L at the crossover between stable and unstable deposition for $G^{\text{SEO}}/G^{\text{Li}} \approx 0.006$ (we use $G^{\text{Li}} \approx 3.4 \text{ GPa}$ and $G^{\text{SEO}} = 0.02 \text{ GPa}$) is about 0.39. In contrast, the experimentally determined value of i/i_L at this crossover is about 0.02. The experimentally determined crossover from globular to dendritic protrusions, which occurs at i/i_L of about 0.13, is also significantly lower than theoretical prediction. The experimentally determined onset of non-planar lithium deposition occurred at a current density about a factor of twenty lower than that predicted by Barai et al. An important limitation of current lithium electrodes is the presence of numerous impurity particles. It is conceivable that the current density range over which planar lithium deposition occurs would increase dramatically if defect free electrodes were available.

Conclusions

A library of PEO-POSS diblock and triblock copolymers with varying molecular weights and volume fractions were successfully synthesized using nitroxide-mediated radical polymerization. Initial electrochemical characterization indicates PEO-POSS behaves much like an all-organic diblock copolymer with the same salt.

Despite the much higher molecular weight of the PS-PEO electrolyte, the cycle life of POSS-PEO-POSS is indistinguishable from that of the diblock. This indicates that the inorganic POSS block imparts mechanical resistance to lithium protrusions on the order of that imparted by an organic PS block more than an order of magnitude more massive.

The POSS-PEO-POSS hybrid triblock electrolyte showed an exceptionally high limiting current between 4.5 and 6 mA cm^{-2} for a membrane of 30 μm thickness. The operating current density is an important factor in the lifetime of lithium symmetric cells with solid polymer electrolytes. Organic and inorganic-organic block copolymer electrolytes must account for current density effects on lithium dendrite growth when optimizing cell lifetime.

Key Publications

1. Maslyn, J. A.; Loo, W. S.; McEntush, K. D.; Oh, H. J.; Harry, K. J.; Parkinson, D. Y.; Balsara, N. P. *J. Phys. Chem. C* **2018**.

References

1. Monroe, C.; Newman, J. J. *Electrochem. Soc.* 2003, 150 (10), A1377–A1384.
2. Barai, P.; Higa, K.; Srinivasan, V. J. *Electrochem. Soc.* 2017, 164 (2), 180–189.
3. Barai, P.; Higa, K.; Srinivasan, V. *Phys. Chem. Chem. Phys.* 2017, 19, 20493–20505.
4. Maslyn, J. A.; Loo, W. S.; McEntush, K. D.; Oh, H. J.; Harry, K. J.; Parkinson, D. Y.; Balsara, N. P. *J. Phys. Chem. C* 2018.

II.8 Beyond Li-ion R&D: Lithium Sulfur Batteries

II.8.A Novel Chemistry: Lithium-Selenium and Selenium-Sulfur Couple (ANL)

Khalil Amine, Principal Investigator

Argonne National Laboratory
9700 South Cass Avenue
Lemont, IL 60439-4837
E-mail: amine@anl.gov

Tien Duong, DOE Technology Development Manager

U.S. Department of Energy
E-mail: Tien.Duong@ee.doe.gov

Start Date: October 1, 2015

End Date: December 31, 2020

Project Funding (FY18): \$500,000

DOE share: \$500,000

Non-DOE share: \$0

Project Introduction

The rechargeable lithium/sulfur battery has attracted extensive attention for energy storage applications due to its much higher energy density and lower cost than that of the state-of-the-art lithium-ion battery. [1] However, the insulating nature of sulfur and the dissolution of intermediary polysulfides into the electrolyte significantly hinder its practical application. [1] Recently, selenium and selenium-sulfur systems have received considerable attention as cathode materials for rechargeable batteries because of the high electronic conductivity (20 orders of magnitude higher than sulfur) and high volumetric capacity (3254 mAh cm^{-3}) of selenium. [2] Selenium-sulfur mixtures are miscible in a wide concentration range, and many Se-S composites can be prepared, including Se_5S , Se_5S_2 , Se_5S_4 , SeS , Se_3S_5 , SeS_2 , SeS_7 , and even materials with a small amount of Se such as SeS_{20} . [2] These Se-S composites offer higher theoretical specific capacities than Se alone and improved conductivity compared to pure S. However, as a new chemistry, the electrochemistry of Se-S cathodes in different electrolytes is not well understood. [3] The lack of such knowledge significantly hinders the rational design of Li/electrolyte/Se-S chemistries with outstanding electrochemical performance.

Via advanced diagnostic tools including synchrotron X-ray probes and computational modeling, the team led by Dr. Khalil Amine at Argonne National Laboratory (ANL) is focusing on the development of rational cathode structure designs and exploration of novel electrolytes as well as understanding of the electrochemistry needed to effectively suppress the shuttle effect and lithium dendrite formation during long-term cycling.

Objectives

The objective of this project is to develop novel SeS_x cathode materials for rechargeable lithium batteries with high energy density (500 Wh/kg) and long life (>500 cycles) along with low cost and high safety.

Approach

To prevent the dissolution of polysulfides and increase the active material utilization, S or Li_2S is generally impregnated in a conducting carbon matrix. However, this approach makes it difficult to increase the loading density of practical electrodes. It is proposed here to solve the above barriers by the following approaches: (1) partial replacement of S with Se, (2) confinement of the SeS_x in a porous conductive matrix with high pore volume, and (3) exploration of low polysulfide/polyselenide dissolution electrolytes.

COLLABORATIONS:

- Cathode development (Prof. Chunsheng Wang at University of Maryland College Park)
- Synchrotron X-ray characterization (Dr. Yang Ren and Dr. Chengjun Sun at APS of ANL)
- Computational modeling (Dr. Larry Curtiss at MSD of ANL)

Results

Discovery of a novel class of concentrated siloxane-based electrolytes to suppress shuttle effect

High concentration electrolytes have recently attracted increased attention in the application of rechargeable batteries due to their attractive properties such as increased reductive stability, enhanced oxidative stability, and low solvent volatility. [4] High concentration electrolytes can also decrease the amount of free solvent in the electrolyte to interact with polysulfides by a common ion effect and can thus decrease the dissolution. However, the low ionic conductivity, high viscosity, and poor wettability of current high concentration electrolytes have increased the operation temperature of the Li/S battery. [5] Moreover, the nature of the solid-electrolyte interphase (SEI) and its formation mechanism with the high concentration electrolyte could be significantly different and could thus possess unusual features compared with the conventional electrolyte. Therefore, a search is underway for novel high concentration electrolytes with optimal concentration, anions, and so-solvents.

In FY2018, we obtained test results for a novel class of concentrated siloxane-based electrolytes that suppress the shuttle effect. Siloxanes, which have very low glass transition temperatures [$T_g = -123^\circ\text{C}$ for poly(dimethylsiloxane)] and extremely high free volumes, are expected to be good hosts for Li^+ transport when polar units are introduced onto the polymer backbone. Figure II.8.A.1a shows the cycling performance of a Li/S cell in a typical concentrated siloxane-based electrolyte during charge/discharge at C/10 within the 1.0-3.0 V voltage window at room temperature. The concentration of lithium bis(trifluoromethanesulfonyl)imide (LiTFSI) in the concentrated siloxane-based electrolyte is between 3M and 7M. As shown, the Li/S cell could deliver an initial discharge/charge capacity of 1400 and 1318 mAh/g, respectively, leading to an initial coulombic efficiency of 94.1% and a sulfur utilization of ca. 80%. After 100 cycles at room temperature, the cell still maintained a reversible capacity of ca. 800 mAh/g. Moreover, the coulombic efficiency within the 100 cycles was very close to 100%, indicating the parasitic reactions between polysulfides and Li metal that have plagued past Li/S systems have been effectively mitigated. Note that we have tested different concentrations of siloxane-based electrolytes, which all showed a significantly suppressed shuttle effect (composition optimization is undergoing).

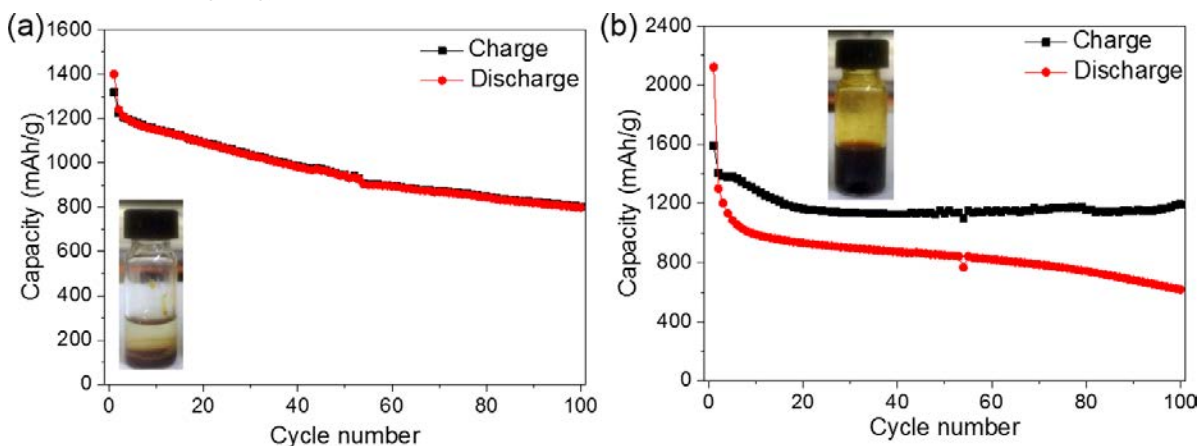


Figure II.8.A.1 Cycle performance of a Li/S cell in two different electrolytes at C/10 within 1.0-3.0 V voltage window at room temperature: (a) novel concentrated siloxane-based electrolyte and (b) 1M LiTFSI/DOL+DME+0.2M LiNO_3 . Insets in (a) and (b) show results from polysulfide solubility test in the two electrolytes.

By contrast, as can be clearly seen in Figure II.8.A.1b, the Li/S cell underwent a continuous capacity fading and severe shuttle effect in the common ether-based electrolyte of LiTFSI in dioxolane (DOL)/dimethoxyethane (DME) with LiNO_3 additive. The insets in Figure II.8.A.1 demonstrate that the solubility of polysulfides in the two different electrolytes is significantly different. Polysulfides are hardly dissolved in the concentrated siloxane-based electrolyte while high polysulfide solubility is evident in the common ether-based electrolyte. Polysulfide solubility is an important cause for the distinct electrochemical performance in the two electrolytes.

Understanding of the beneficial effects of novel concentrated electrolytes on morphology conservation of Li metal and S cathode

To elucidate the beneficial effects of the concentrated siloxane-based electrolyte, the cycled Li/S cells in the two electrolytes were disassembled, and the Li metal anode and S cathode were characterized by scanning electron microscopy (SEM). On the Li metal side, the morphology of the pristine Li anode is quite flat (Figure II.8.A.2a). However, after 20 cycles in the common ether-based electrolyte, the surface became very rough and porous (Figure II.8.A.2b), indicating severe Li metal corrosion by the polysulfides. The polysulfides are highly soluble in the common ether-based electrolytes, which can easily migrate from the cathode to anode side. With concentrated siloxane-based electrolyte, by contrast, the surface of the Li anode remained relatively flat (Figure II.8.A.2c), implying that the parasitic reactions between the polysulfides and Li anode are effectively mitigated. We concluded that the formation of soluble polysulfides in the concentrated siloxane-based electrolyte is suppressed. On the cathode side, after cycling in the common ether-based electrolytes, the deposition of Li_2S particles outside the pores of the carbon host can be clearly seen (Figure II.8.A.2d and Figure II.8.A.2e). No obvious morphology change was observed on the surface of the S cathode cycled with concentrated siloxane-based electrolyte (Figure II.8.A.2f).

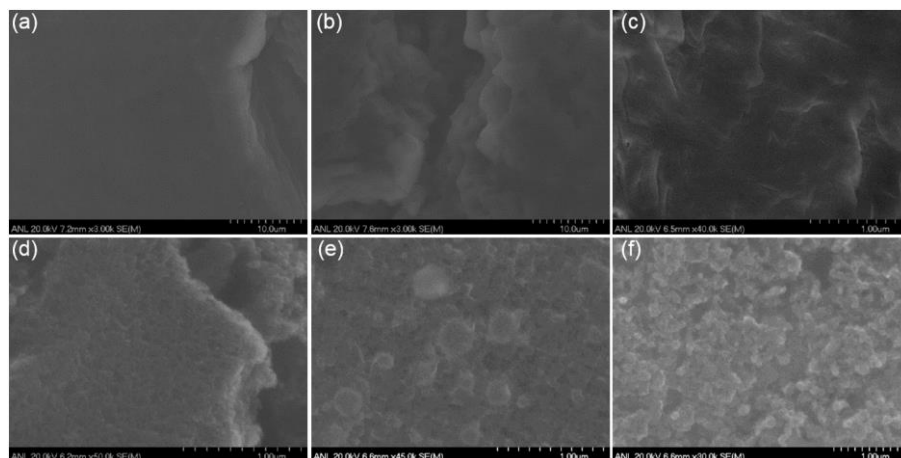


Figure II.8.A.2 SEM images of Li metal before (a) and after 20 cycles in (b) common ether-based electrolyte and (c) concentrated siloxane-based electrolyte. SEM images of S cathode before (d) and after 20 cycles in (e) common ether-based electrolyte and (f) concentrated siloxane-based electrolyte.

We have also used SEM elemental mapping to probe the composition of cycled Li metal and the separator for the two electrolytes to compare their shuttle effect. In the ether-based electrolyte (Figure II.8.A.3a), a large accumulation of sulfur was observed on the cycled Li metal. The sulfur is due to the migration of polysulfides from the cathode side to the Li metal. In the elemental mapping of the separator (Figure II.8.A.3c), we can see large Li_2S particles trapped by the separator, confirming the high dissolution of polysulfides in the ether-based electrolyte. On the contrary, with the concentrated siloxane-based electrolyte, the signals for S, O, and F in the cycled Li metal (Figure II.8.A.3b) and separator (Figure II.8.A.3d) are very weak. These elements originated from the decomposition of LiTFSI to form the SEI layer.

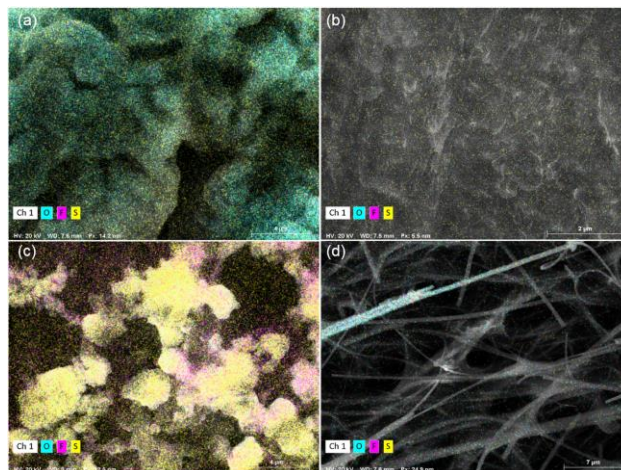


Figure II.8.A.3 SEM elemental mapping of Li metal after 20 cycles in (a) common ether-based electrolyte and (b) concentrated siloxane-based electrolyte. SEM elemental mapping of separator after 20 cycles in (c) common ether-based electrolyte and (d) concentrated siloxane-based electrolyte.

The SEM results clearly show that due to the much lower polysulfide solubility of concentrated siloxane-based electrolyte, the parasitic reactions between Li metal and polysulfides are effectively eliminated. This effect results in much better electrochemical performance compared to that with the common ether-based electrolyte.

In-operando characterization of the Se lithiation pathway in the concentrated siloxane-based electrolyte

To gain further insight into the electrochemical behavior of Li/Se cells in concentrated siloxane-based electrolyte, in-operando X-ray absorption near edge spectroscopy (XANES) was carried out to determine the average chemical environment of the elements in the liquid and solid phases, as well as crystalline and/or amorphous phases. Due to the interference of the sulfur signal from the LiTFSI salt, in-operando Se K-edge XANES measurement of a Li/Se instead of a Li/S cell was conducted because of the similarity between S and Se. Figure II.8.A.4a shows no obvious edge shift, while the absorption intensity decreases during discharge and then increases during charge. This behavior is significantly different from that of the ether-based electrolyte. [6] By selecting standard Se and Li_2Se as a reference, we found that the phase composition as a function of time over charge/discharge could be determined by using the Se- Li_2Se two-phase transition mode (Figure I.1.4b). As shown, the content of Se gradually decreased during discharge while that of Li_2Se increased. During charge, this process reversed.

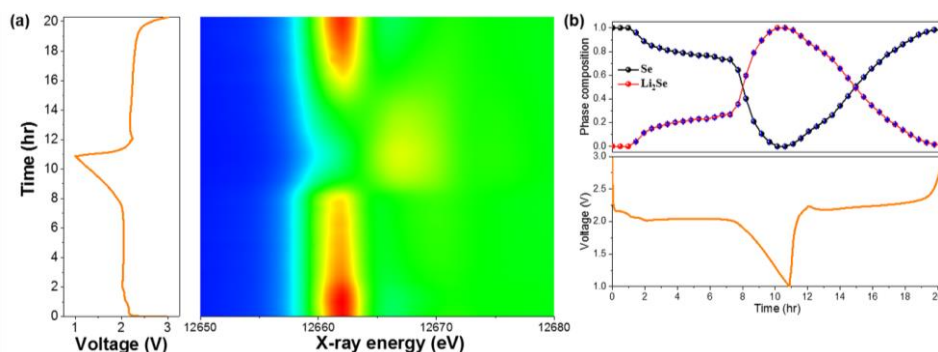


Figure II.8.A.4 (a) 2D contour plot of in-operando Se K-edge XANES of Li/Se cell in concentrated siloxane-based electrolyte at C/10 within 1.0-3.0 V voltage window at room temperature and (b) corresponding phase composition analysis using linear combination fitting at different charge/discharge states.

In addition, we performed in-operando extended X-ray absorption fine structure (EXAFS) Se K-edge measurement to probe the local structure changes of Se atoms during the discharge/charge. Figure II.8.A.5

clearly indicates a two-phase transition process. At the early discharge stage, the main composition is amorphous Se, which gradually decreases until the end of the discharge plateau at around 2.0 V. When further discharging the cell to 1.0 V, amorphous Li_2Se gradually forms, as evidenced by the change of bond distance peaks. The amorphous Li_2Se remains until the cell is charged over 2.3 V, which converts Li_2Se back to Se. By comparing the whole set of EXAFS data during discharge/charge, we found that the lithiation/de-lithiation process is highly reversible, leading to the high initial coulombic efficiency and good cycle stability. These results confirm that there is very little formation of highly soluble polyselenides during charge/discharge in the concentrated siloxane-based electrolyte, and this leads to the significantly improved shuttle effect and increased capacity retention.

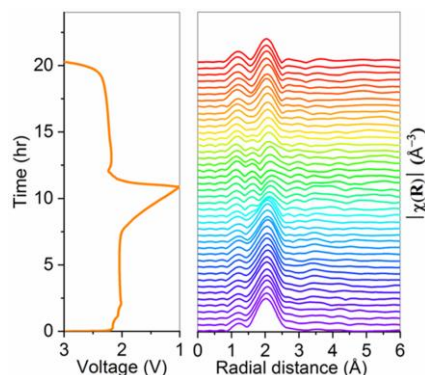


Figure II.8.A.5 In-operando Se K-edge EXAFS measurement of Li/Se cell in concentrated siloxane-based electrolyte at C/10 within 1.0-3.0 V voltage window at room temperature.

Computational simulation on the interaction of polysulfides with concentrated siloxane-based electrolyte

Using ab initio molecular dynamics simulation, we also evaluated the solvation of polysulfides (e.g., Li_2S_6) in the concentrated siloxane-based electrolyte to understand their interactions. Figure II.8.A.6 presents a snapshot of the simulated structure of Li_2S_6 in the concentrated siloxane-based electrolyte. The calculated results indicated no chemical bond breaking of Li_2S_6 , suggesting no interaction between Li_2S_6 and the surrounding environment, i.e., the concentrated siloxane-based electrolyte. This may be because in the concentrated siloxane-based electrolyte, the solvents are well coordinated with the Li^+ and TFSI⁻ in the form of contact ion pairs and cation-anion aggregates. Therefore, no free solvent molecules are available to solvate with Li_2S_6 , which significantly decreases the formation of soluble polysulfides and the parasitic activity with Li metal. This hypothesis explains the low solubility of polysulfides in the concentrated siloxane-based electrolyte and the absence of polysulfides during the discharge/charge.

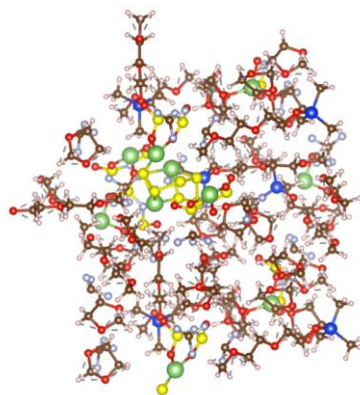


Figure II.8.A.6 Snapshot of simulated structure of Li_2S_6 in the concentrated siloxane-based electrolyte determined by ab initio molecular dynamics simulation.

Conclusions

In summary, we have discovered a novel class of concentrated siloxane-based electrolytes for Li/Se-S batteries, which can significantly suppress the detrimental shuttle effect and improve cycle stability. In-operando X-ray absorption spectroscopy revealed that the concentrated siloxane-based electrolyte can effectively suppress the formation of soluble polysulfides/polyselenides during cycling as all the solvents are well coordinated with $\text{Li}^+/\text{TFSI}^-$ as evidenced by ab initio molecular dynamics simulation. Therefore, the parasitic reactions between polysulfides and Li metal have been well mitigated, leading to the remarkably improved electrochemical performance of the Li/S cell. Future research will be focused on the development of high-energy and long-life Li/Se-S batteries with high concentrated siloxane-based electrolyte by tailoring the cathode structure and electrolyte composition.

Key Publications

Publications/Patents

1. Xu, G. L.; Sun, H.; Luo, C.; Estevez, L.; Zhuang, M. H.; Gao, H.; Amine, R.; Wang, H.; Zhang, X.; Sun, C. J.; Liu, Y. Z.; Ren, Y.; Heald, S.; Wang, C. S.; Chen, Z.; Amine, K., Solid-State Lithium/Selenium-Sulfur Chemistry Enabled *via* a Robust Solid-Electrolyte Interphase. *Adv. Energy Mater.* 2018, 1802235.
2. Xu, G.L.; Chen, Z.; Amine, K., Selenium-Doped Sulfur Cathodes for Rechargeable Batteries, U.S. Patent Application, US20180090751A1.
3. Xu, G.L.; Chen, Z.; Liu, J.; Amine, K., US. Patent Application no. 15/760,295.

Invited Talks

1. Gui-Liang Xu, Zonghai Chen and Khalil Amine. Novel Chemistry for Automotive Application: Lithium-Selenium and Selenium-Sulfur Couple. 2018 ACS Spring Meeting. March 31st- 4th, Orlando, FL, USA.
2. Gui-Liang Xu, Zonghai Chen and Khalil Amine. Novel Chemistry for Automotive Application: Lithium-Selenium and Selenium-Sulfur Couple. 2018 U.S. DOE Li-S Deep-dive Meeting. September 5-6, Austin, TX, USA.
3. Gui-Liang Xu, Zonghai Chen and Khalil Amine. Novel Chemistry for Automotive Application: Lithium-Selenium and Selenium-Sulfur Couple. 2018 Advanced Automotive Battery Conference. June 4-7, 2018, San Diego, CA, USA.

References

1. Pang, Q., Liang X., Kwok, C. Y., and Nazar, L. F. "Advances in Lithium-Sulfur Batteries Based on Multifunctional Cathodes and Electrolytes." *Nature Energy* 1 (2016): 16132. DOI: 10.1038/NENERGY.2016.132.
2. Abouimrane, A., Dambournet, D., Chapman, K. W., Chupas, P. J., Weng, W., and Amine, K. "A New Class of Lithium and Sodium Rechargeable Batteries Based on Selenium and Selenium-Sulfur as a Positive Electrode." *Journal of the American Chemical Society* 134, no. 10 (2012): 4505-4508. DOI: 10.1021/ja211766q.
3. Xu, G. L., Liu, J. Z., Amine, R., Chen, Z. H., and Amine, K. "Selenium and Selenium-Sulfur Chemistry for Rechargeable Lithium Batteries: Interplay of Cathode Structures, Electrolytes, and Interfaces." *ACS Energy Letters* 2, no. 3 (2017): 605-614. DOI: 10.1021/acsenerylett.6b00642.
4. Zheng, J. M., Lochala, J. A., Kwok, A., Deng, Z. D., and Xiao, J. "Research Progress towards Understanding the Unique Interfaces between Concentrated Electrolytes and Electrodes for Energy Storage Applications." *Advanced Science* 4, no. 8 (2017): 1700032. DOI:10.1002/advs.201700032.

5. Pang, Q., Shyamsunder, A., Narayanan, B., Kwok, C. Y., Curtiss, L., and Nazar, L. F. "Tuning the electrolyte network structure to invoke quasi-solid state sulfur conversion and suppress lithium dendrite formation in Li-S batteries." *Nature Energy* 3, no. 9 (2018): 783-791. DOI: 10.1038/s41560-018-0214-0.
6. Xu, G. L., Ma, T., Sun, C. J., Luo, C., Cheng, L., Ren, Y., Heald, S. M., Wang, C., Curtiss, L., Wen, J. G., Miller, D. J., Li, T., Zuo, X. B., Petkov, V., Chen, Z., and Amine, K. "Insight into the Capacity Fading Mechanism of Amorphous Se₂S₅ Confined in Micro/Mesoporous Carbon Matrix in Ether-Based Electrolytes." *Nano Letters* 16, no 4 (2016): 2663-2673. DOI: 10.1021/acs.nanolett.6b00318.

Acknowledgements

Support from Tien Duong of the U.S. DOE's Office of Vehicle Technologies Program is gratefully acknowledged. We also want to thank all our collaborators for their significant contribution to this project: Prof. Chunsheng Wang (UMD), Dr. Chao Luo (UMD), Dr. Yang Ren (ANL), Dr. Cheng-Jun Sun (ANL), Dr. Larry Curtiss (ANL), and Dr. Anh Tuan Ngo (ANL).

II.8.B Development of High Energy Lithium-Sulfur Batteries (PNNL)

Jun Liu, Principal Investigator

Pacific Northwest National Laboratory
902 Battelle Blvd, Richland, WA 99354
E-mail: jun.liu@pnnl.gov

Dongping Lu, Principal Investigator

Pacific Northwest National Laboratory
902 Battelle Blvd. Richland, WA 99354
E-mail: dongping.lu@pnnl.gov

Tien Duong, DOE Technology Development Manager

Vehicle Technologies Office
E-mail: Tien.Duong@ee.doe.gov

Start Date: October 1, 2015 End Date: September 30, 2019
Project Funding (FY18): \$400,000 DOE share: \$400,000 Non-DOE share: \$0

Project Introduction

The lithium-sulfur (Li-S) battery is a potential high-energy storage technology to meet DOE battery cost target of < \$80/kWh for vehicle electrification, owing to its high theoretical specific energy (~2300 Wh kg⁻¹) and the low cost and abundance of sulfur. However, the practical deployment of Li-S batteries is still hindered by the limited cycle-life when working at practical high-energy densities. Recent attempts to improve performance of Li-S batteries have been focused on the development of nanostructured sulfur host materials or functional material decoration, which demonstrate encouraging progresses in terms of either high sulfur utilization rate or stable battery cycling. However, most of those studies are based on thin-film electrodes with low sulfur loadings (<2 mg/cm²), and the use of excessive amounts of electrolyte (E/S>10, Electrolyte volume/Sulfur loading) and Li metal anode (N/P>20, anode areal capacity/cathode areal capacity). Our cell energy prediction and experimental results indicate that in order to reach energy density over 350 Wh/kg at cell level, the sulfur loading and E/S ratio should be >6 mg/cm² and <3 ul/mg, respectively, given the cell capacity < 3Ah. In addition, parasitic contents like carbon, current collectors, tabs, and package materials, are required to be minimized as much as possible. Unfortunately, under those practical conditions, low cell performance is usually observed for sulfur cathodes, compared to that demonstrated in thin-film electrodes. Possible reasons for the performance gap are 1) electrode wetting problems in high-loading electrodes, 2) non-uniform sulfur reactions and low sulfur utilization rate under lean electrolyte conditions, and 3) exacerbated side reactions of Li anode and electrolyte when high-loading sulfur cathodes and lean electrolyte are used simultaneously. Clear understanding of such problems at a practical level is critical for further development of materials, electrodes, and cells. However, it should be noted that reactions inside a Li-S cell are complicated by the entangled reactions of sulfur degradation, polysulfide shuttle, and Li anode corrosion. Particularly, the dissolution and crossover of soluble polysulfides between the cathode and anode are closely related to the irreversible sulfur loss and Li anode instability, which leads to cell capacity decay and even early failure. Hence, an effective method to achieve the decoupled understandings of sulfur cathode, electrolyte, and Li anode is highly demanded. In FY 2018, electrode wetting problems and sulfur utilization were investigated based on high-loading sulfur cathodes developed at PNNL (U.S. Patent No. 9,577,250). A generic liquid/solid hybrid cell was designed to realize the focused mechanism study on sulfur cathode and electrolyte by completely eliminating the interferences of Li metal anode and polysulfide crossover. Insights into the fundamental mechanism of those issues was gained and effective approaches were demonstrated to address the issues.

Objectives

- Understand fundamental reasons of low sulfur utilization rate and quick capacity decay in high-loading sulfur cathodes.
- Design a cell setup to completely eliminate polysulfide crossover and Li anode interferences for a focused mechanism study.
- Develop effective approaches to enhance sulfur utilization and improve Li anode cyclability in high energy Li-S batteries.

Approach

To understand and address the key problems that affect performance of high-loading sulfur electrodes, the following approaches were adopted:

- Investigate the factors that affect sulfur utilization in high-loading electrodes, including the effects of binder coating and electrolyte decomposition.
- Design a hybrid electrochemical cell by using a ceramic Li^+ conductor to prevent polysulfide crossover, and remove the interferences from Li anode.
- Study the electrode wetting process in high-loading sulfur electrodes at different E/S ratios using the designed hybrid electrochemical cell.
- Develop functionalized separators to enhance sulfur cathode wetting and improve interfacial stability of Li anode.

Results

1. Effects of electrode binder on sulfur utilization in high-loading sulfur cathodes

The full electrode wetting by electrolyte comprises electrolyte diffusion through the voids in between the secondary particles and followed infiltration into individual particles. The latter process is more sluggish compared to the former one, due to higher tortuosity inside of the particles. Electrode binder, which coats on material particles and stabilizes electrode architectures, may negatively affect electrolyte infiltration. Two types of solution and emulsion based binders were studied to understand their effects on sulfur reactions in high-loading electrodes. Electrodes were prepared by mixing 10 wt% of different binders with integrated Ketjen Black and carbon nanofiber (IKB/CNF), which are used as a sulfur host and electronic conductor, respectively, in sulfur electrode preparation. For comparison, here we take PAA (poly amide acid) and PTFE (Polytetrafluoroethylene) as examples of solution and emulsion based binder, respectively. It is found that both solution and emulsion binders have significant coating effects on the IKB/CNF carbon materials. As shown in Figure II.8.B.1a, BET surface area of IKB/CNF decreases significantly from the original $650 \text{ m}^2/\text{g}$ to $195 \text{ m}^2/\text{g}$ after mixed with the PTFE binder and further decreases to only $107 \text{ m}^2/\text{g}$ with a solution based PAA binder. Pore volume of IKB/CNF follows the same trend and decreases from 2.01 cc/g (no binder) to 1.05 and 0.8 cc/g after mixing with PTFE and PAA binder, respectively. In both cases, micropores are completely filled or blocked. Comparison of these two categories of binders indicates that solution based PAA has more profound coating effects than emulsion based PTFE due to its flow-ability and uniform distribution on the particles. Even more complete blocking effect is identified for CMC (carboxymethyl cellulose) binder because of its smaller molecular weight (Figure II.8.B.1). The BET surface loss induced by binder coating leads to apparent reduction of electrode active area. Figure II.8.B.1c compares CV responses of IKB/CNF electrodes prepared with different binders. An electrode made with PAA binder shows a reduction current peak of 0.2 mA at ca. 1.6 V , which is ascribed to the electrochemical reduction of LiNO_3 additive in electrolyte. From the second scan, the reduction peak almost disappears, indicating full passivation of the electrode. For the electrode with similar loading but comprised of PTFE binder, the reduction peak is much higher (0.85 mA) in the first scan, and reduces gradually in the subsequent scans, indicating larger active area and slower electrode passivation.

This is consistent with the BET surface and pore volume analysis. The surface coating from the binder has direct effects on electrode wetting and sulfur utilization. Figure II.8.B.1d compares the sulfur utilization rate of high loading electrodes ($>6.3 \text{ mg/cm}^2$) using different binders. At similar mass loadings, a PAA based electrode delivers a discharge capacity of 1073 mAh/g; while the PTFE based electrode shows a much higher capacity of 1196 mAh/g. This study suggests that a solution based binder has more profound coating effects on the cathode, and thus should be considered in high-loading electrode design and preparation.

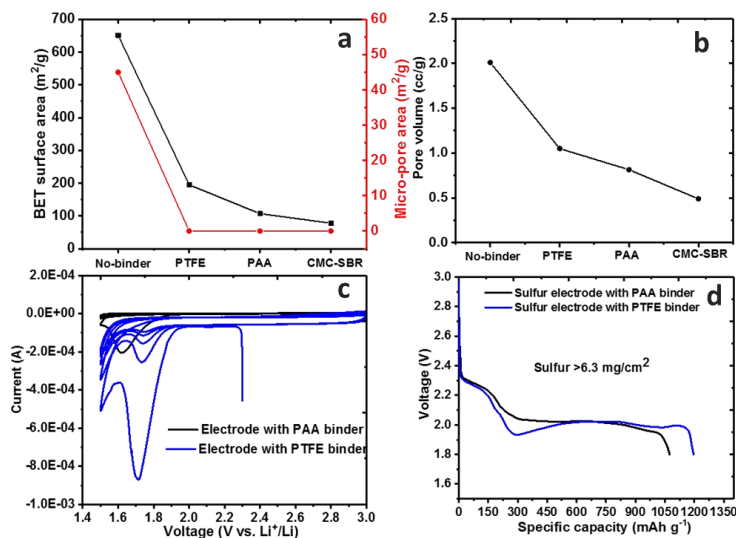


Figure II.8.B.1 (a) Comparison of BET surface areas of pristine IKB/CNF carbon materials and those mixed with 10 wt% of different types of binders and (b) corresponding pore volume. (c) Cyclic voltammetry (CV) of IKB/CNF electrodes with PAA and PTFE binders (1.5–3.0 V, 0.05 mV/s), and (d) first discharge curves of sulfur electrodes with PAA and PTFE binders (sulfur loading $>6.3 \text{ mg/cm}^2$, $E/S=4 \mu\text{L}/\text{mg}$, 0.05C).

2. Design of solid/liquid hybrid electrochemical cell to eliminate polysulfide shuttle and Li interferences

Clear understanding of sulfur reaction mechanism is critical for an improved design of Li-S batteries; however, such a study is complicated by the interferences from both the Li metal anode and the polysulfide crossover. Due to the lack of a stable surface protection layer, Li metal continuously reacts with electrolyte and polysulfides, which is the leading cause of capacity fading or cell failure. This also makes the mechanism understanding on sulfur cathode or electrolyte very complicated. To tackle those problems for focused mechanism study, we designed a generic hybrid cell that can be used to eliminate the interferences of Li anode and polysulfide crossover. Our methodology is to realize cathode operation with liquid electrolyte (LE) to mimic the reactions in conventional Li-S batteries, while the anode is all- solid-state to eliminate any interferences from Li metal. Figure II.8.B.2a depicts section view of the overall design. To completely block the “cross-talk” of Li with either electrolyte or polysulfides, a rigid and dense Garnet solid electrolyte (SE) was employed to separate the cathode and anode chambers. Sealing mechanism of the cell is guaranteed by three O-rings and meticulously designed sealing parts. This enables the durable testing of the setup outside of the glove box. To stabilize the SE-Li interface to enable high current operation of the SE without any short circuit, we used Li-In instead of pure Li as the anode, and the interface was enhanced by nanometer Au coating. The design was carefully optimized and verified by an In-SE-In symmetric cell test. Without a liquid electrolyte, the In-SE-In symmetric cell shows the typical impedance response of an only SE (Figure II.8.B.2b), which corresponds to an ionic conductivity of 0.6 mS/cm. The absence of interfacial processes indicates excellent contact between SE and In with the help of Au layer. When Li and liquid electrolyte are used to form an In-SE-LE-Li cell, a nearly identical bulk resistance is identified. This indicates a well maintained SE pellet and proper sealing of the system; otherwise, an obvious decrease of resistance will be observed if the SE cracks or if there is liquid leakage. The In electrode was lithiated electrochemically by capacity control, forming LiIn,

and the LiIn-SE-LE-S cell was assembled to verify functions of the design. The cell shows a high sulfur utilization of 1350 mAh/g without any shuttle in the following charging process by using excess amounts of electrolyte ($E/S > 10$) (Figure II.8.B.2c). This excludes any crossover of liquid electrolyte, and thus proves the functionality of the hybrid cell design.

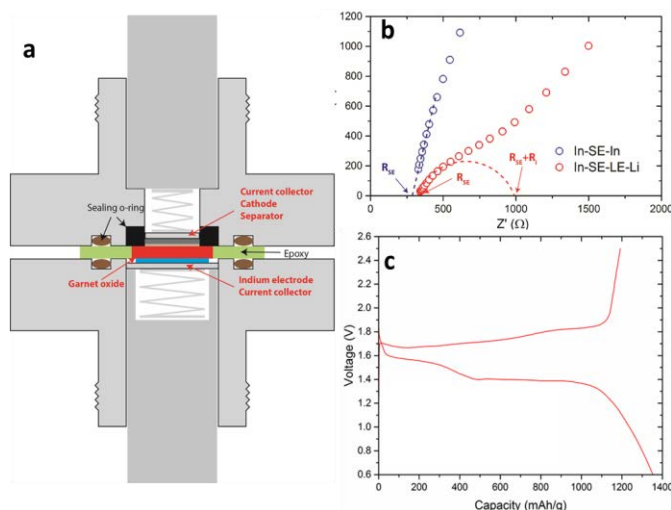


Figure II.8.B.2 (a) Cross-section view of the hybrid cell design, (b) electrochemical impedance of In-SE-In and In-SE-LE-Li (5 mv, 10^5 - 10^{-1} Hz). (c) charge/discharge curves of LiIn-SE-LE-S. (0.1C, V_{InLi} vs. $V_{\text{Li}} = 0.6\text{V}$).

3. Study of electrode wetting and sulfur reactions in high-loading electrode using the liquid/solid hybrid cell

With the hybrid cell structure and meticulously designed sealing parts, accurate electrolyte volume control in the cathode can be realized. This made it possible to quantify the minimum electrolyte amount required for a certain electrode architecture or composition. Before the study, the compatibility of the liquid and solid electrolyte was evaluated first. The Indium (In) and stainless steel (SS) blocking electrodes were used in such In-SE-LE-SS cell configuration, where solid electrolyte (SE) contacts with liquid electrolyte (LE) directly. In contrast to the published results, the DME solvent is found not compatible with the Garnet solid electrolyte (Figure II.8.B.3a). Formation of a new interfacial layer on Garnet pellet is possible. On the other hand, when DOL based electrolyte is used, the EIS is very stable throughout the whole test (Figure II.8.B.3b). Thus, 1M LiTFSI/DOL was used as the electrolyte in the subsequent studies of electrode wetting and cell performance. As one of the focuses of the study, the electrode wetting process in high loading sulfur electrodes was investigated under lean electrolyte conditions, which mimics electrode wetting in high energy Li-S pouch cells. The In electrode was lithiated electrochemically and used as an anode for InLi/SE/LE/SS cell configuration. Almost identical EIS spectra during the 22 hours' test further confirmed the stability of SE with DOL (Figure II.8.B.3c). Then, a sulfur electrode (sulfur mass loading $\sim 4 \text{ mg/cm}^2$) was added into the cathode chamber. A lean amount of electrolyte with $E/S < 4$ was applied. At the very beginning, the overall charge transfer resistance (R_{ct}) is low and comparable to that of a blank test without a sulfur electrode (Figure II.8.B.3c). However, the R_{ct} starts to increase, after only 1 hour of rest. The trend of resistance increase accelerates in the first 12 hours, then slows down and achieves stability after 18 hours (Figure II.8.B.3d and insert). The significant change of the EIS can be attributed to the slow electrolyte infiltration in the high loading sulfur electrode. During the resting period, the limited electrolyte between the sulfur electrode and SE will diffuse into the electrode and penetrate into the individual S/C secondary particles. After about 18 hours' rest, the cell resistance stabilizes, indicating the completion of electrolyte infiltration/distribution. This stabilization time has been applied in the test of high energy Li-S pouch cells with similar electrode loadings.

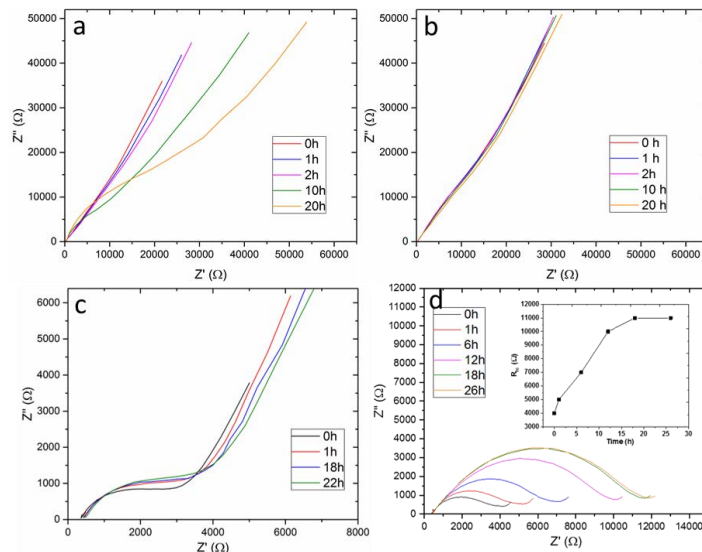


Figure II.8.B.3 Electrochemical impedance spectra (EIS) evolution in the first 20 hrs of In-SE-LE-SS cell with electrolytes (a) 1M LiTFSI/DME and (b) 1 M LiTFSI/DOL. (c) EIS evolution of InLi/SE/LE/SS and (d) InLi/SE/LE/S with 1 M LiTFSI/DOL. EIS test (5 mv, 10^5 - 10^{-1} Hz).

4. Development of functionalized separators to enhance sulfur cathode wetting and improve interfacial stability of Li anode

When high-loading sulfur cathodes (>4 mg/cm²) and lean electrolyte amounts (E/S=4 μ L/mg) were used simultaneously, Li-S cells suffer from limited cycle life. One cause of cell failure was identified as short-circuit. The nonuniform sulfur reactions under lean electrolyte conditions lead to localized lithium deposition and stripping, which results in the occurrence of a short-circuit. To circumvent those issues, a functionalized separator with double-side coatings was designed and applied. The coating layers are designed to realize the functions of 1) enhancing electrolyte distribution, 2) blocking polysulfide crossover, and 3) improving reaction uniformity of the Li anode. Figure II.8.B.4a shows a cross-sectional SEM image of the double-side coated Celgard separator. One side of the separator was coated with a mixture of polymer P1 and CNT with a mass loading of 0.2-0.6 mg/cm², which faced towards the sulfur cathode in the cell; the other side was coated by an ultra-thin layer of polymer P2, which has a loading of 0.1 mg/cm² and contacts the Li anode in the cell. The improved wettability of the coated Celgard separators with electrolyte (1M LiTFSI/DOL/DME+0.3M LiNO₃) was verified by comparing the static contact angles (Figure II.8.B.4b). Coin cells with high-loading cathodes (4 mg/cm²) and excess amount of electrolyte (E/S=16) were tested and compared. The coated separator (0.3 mg/cm²) boosts stable sulfur utilization from 600 mAh/g to greater than 900 mAh/g at P1/CNT=1:4, indicating a suppression of polysulfide crossover and irreversible loss. Interestingly, by the use of the double-side coated separator (loading: 0.3 mg/cm²), the cell life was extended from 20 cycles to 45 cycles when operated at practical conditions (S $>$ 4 mg/cm² and E/S=4 μ L/mg) (Figure II.8.B.4d). It is believed that the coating of functional polymers enhances uniform electrolyte distribution across the electrode surface, which regulates the reactions of both the sulfur cathode and Li anode in a more uniform way. This double-side coated separator has been applied in the fabrication of high energy Li-S pouch cells.

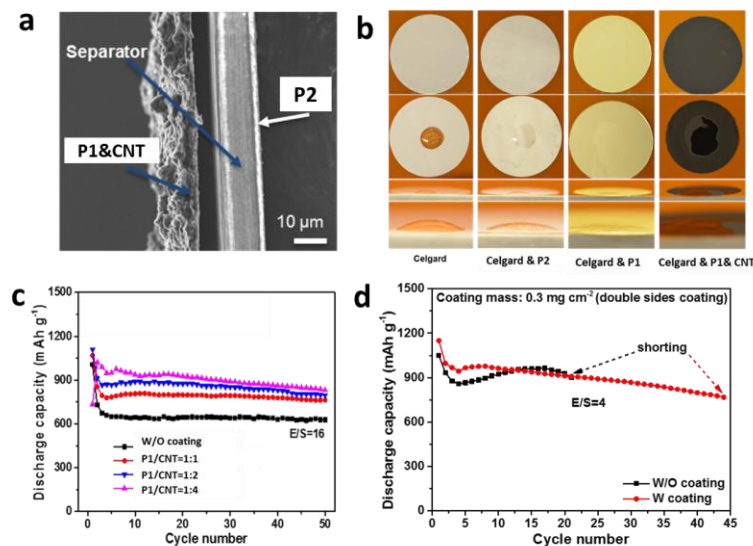


Figure II.8.B.4 (a) Cross-sectional SEM image of double-side coated Celgard 2500, (b) digital photographs of the static contact angles of the coated separators with electrolyte 1M LiTFSI/DOL/DME+0.3M LiNO₃, (c) effects of separator coating on sulfur utilization rate, and (d) cycling stability of cells at lean electrolyte conditions (E/S= 4 $\mu\text{L}/\text{mg}$) (S: 4 mg/cm^2).

Conclusions

1) Blocking effects of electrode binders were identified in high-loading sulfur electrodes. Compared to an emulsion based binder like PTFE, the solution based binders (PAA or CMC) slow down electrolyte infiltration and reduce electrode active surface area, therefore have more profound blocking effects on the electrodes. 2) To remove the interferences of the Li anode and polysulfide crossover for a dedicated mechanism study, a generic solid/liquid hybrid cell was designed. The design enables cathode operation with liquid electrolyte to mimic the reactions in conventional Li-S batteries, while the anode is all- solid-state, to eliminate any interferences from Li metal and polysulfide crossover. 3) With the hybrid cell design and meticulously designed sealing parts, accurate control of E/S ratio, which is one of the most critical parameters in high-energy Li-S batteries, can be realized. The study of the electrode wetting process under lean electrolyte conditions indicates that electrolyte infiltration into the high-loading electrode is a very slow process. A rest duration of >18 hrs is suggested to reach full electrode wetting for the electrodes with loadings > 6 mg/cm^2 and $E/S < 4 \mu\text{L}/\text{mg}$. 4) an internal short-circuit was identified as a main reason of cell failure when the cell is operated at practical conditions (sulfur loading >4 mg/cm^2 and $E/S < 4 \mu\text{L}/\text{mg}$). To circumvent those issues, a functionalized separator with double-side coatings was designed to improve the electrode wetting and reaction uniformity. Using a separator with double-side polymer coating of 0.3 mg/cm^2 , cell cycle life was extended significantly at practical conditions.

Key Publications

1. Wang Y, Lu D, Bowden M, El Khoury PZ, Han KS, Deng ZD, et al. Formation mechanism of Li₇P₃S₁₁ solid electrolytes through liquid phase synthesis. *Chem. Mater.*, 2018, 30 (3), 990–997
2. Liu J, Lu D, Zheng J, Yan P, Wang B, Sun X, Shao Y, Wang C, Zhang J, and Liu J. Minimizing Polysulfide Shuttle Effect in Lithium Sulfur Batteries by Anode Surface Passivation, *ACS Appl. Mater. Interfaces*, 2018, 10 (26), 21965–21972.
3. Lu D, Li Q, Liu J, Zheng J, Wang Y, Ferrara S, Xiao J, Zhang J and Liu J. Enabling High Energy Density Cathode for Lithium-Sulfur Batteries, *ACS Appl. Mater. Interfaces*, 2018, 10 (27), 23094–23102.

4. Lu D and Liu J, Development of High Energy Lithium-sulfur Batteries, Lithium-sulfur Deep-dive Meeting, September 2018, Austin, TX
5. Lu D, Xiao J, and Liu J, Development of high energy Lithium-sulfur Batteries: from Materials to Pouch cell, Battery Electric Vehicle Architectures (BEVA) USA 2018 Congress, September 2018, San Francisco, CA
6. Lu D, Shi L, Xiao J, Zhang J and Liu J, Rational Design of High Energy Sulfur Cathodes for Lithium-Sulfur Batteries, Americas International Meeting on Electrochemistry and Solid State Science, September 2018, Cancun, Mexico.
7. Lu D, Wang Y, Xiao J, Zhang J and Liu J, Sulfide Based Solid Conductor for Lithium-Sulfur Batteries, Americas International Meeting on Electrochemistry and Solid State Science, September 2018, Cancun, Mexico.

II.8.C Nanostructured Design of Sulfur Cathodes for High Energy Lithium-Sulfur Batteries (Stanford University)

Yi Cui, Principal Investigator

Stanford University
 Department of Materials Science and Engineering, Stanford University
 Stanford, CA 94305
 E-mail: yicui@stanford.edu

Tien Duong, DOE Technology Development Manager

U.S. Department of Energy
 E-mail: Tien.Duong@ee.doe.gov

Start Date: October 1, 2017	End Date: September 30, 2018	
Project Funding (FY18): \$300,000	DOE share: \$300,000	Non-DOE share: \$0

Project Introduction

Lithium-sulfur batteries can bring about significant improvements to the current state-of-the-art battery technologies due to its high specific energy density and cost saving. The capacity decay of lithium-sulfur battery during cycling is a multifaceted problem. There exist multiple materials challenges that prevent it from reaching the cycling performance suitable for portable electronics and electrical vehicles. The rapid capacity decay of sulfur cathode can be attributed to several reasons: 1) significant volumetric expansion (~80% change) when sulfur is reduced to lithium sulfide (Li_2S); 2) dissolution of intermediate lithium polysulfides (Li_2S_x , $4 \leq x \leq 8$) in the electrolyte; 3) low ionic and electronic conductivity of both sulfur and Li_2S .

Introducing anchoring materials, which can induce strong binding interaction with Li_2S_x species, has been demonstrated as an effective way to overcome this problem and achieve long-term cycling stability and high-rate performance. The interaction between Li_2S_x species and anchoring materials should be studied at the atomic level in order to understand the mechanism behind the anchoring effect and to identify ideal anchoring materials to further improve the performance of Li-S batteries. We elucidate different adsorption mechanisms and probe possible adsorption sulfide species. We expect our work will provide a useful strategy to screen for suitable candidate materials and valuable information for rational design of long cycle life Li-S batteries. We also develop an aqueous inorganic polymer, ammonium polyphosphate (APP), as a novel multifunctional binder to address the issues existing in Li-S batteries. The strong binding affinity of the main chain of APP with lithium polysulfides blocks diffusion of polysulfide anions and inhibits their shuttling effect. The coupling of APP with Li-ion facilitates ion transfer and promotes the kinetics of the cathode reaction. APP also bestows the sulfur cathode with significantly improved flame-retardant property, thus improving the safety of Li-S batteries. In order to provide direct evidence about a long-debated reaction pathway for sulfur electrode, we build *in situ* characterization platform to monitor nucleation/dissolution of sulfur, and provide avenues to the development of advanced Li-S batteries.

Objectives

The charge capacity limitations of conventional transition metal oxide cathodes are overcome by designing optimized nano-architected sulfur cathodes. This study aims to enable sulfur cathodes with high capacity and long cycle life by developing sulfur cathodes from the perspective of nanostructured materials design, which will be used to combine with lithium metal anodes to generate high-energy lithium-sulfur batteries. The selection criterion of anchoring materials is proposed to guide the rational design of cathode materials for advanced Li-S batteries. A standard procedure to quantitatively compare the polysulfide adsorption capability of candidate materials was established. Different adsorption mechanisms and probe possible adsorption species will be elucidated. Multi-functional sulfur cathode binder capable of controlling the polysulfide shuttling and facilitating Li-ion transport will be developed. The flame-retardant property of binder to improve safety and propose flame-retardant mechanism will be demonstrated. *In situ* characterization platform to monitor

nucleation/dissolution of sulfur/Li₂S_n will be built. A non-invasive imaging method with sub-micron, sub-second resolution for Li-S battery in label-free, native organic liquid electrolyte is under developing.

Approach

The approaches refer to three main parts: (I) advanced nanostructured sulfur cathodes design and synthesis, including (1) engineer empty space into sulfur cathode to solve the problem of electrode volume expansion; (2) develop novel sulfur nanostructures with multi-functional coatings for the confinement of sulfur/lithium polysulfides to address the issues of active materials loss and low conductivity; (3) develop/discover optimal nanostructured materials that can capture the polysulfide dissolved in the electrolyte; (4) develop space efficiently packed nanostructured sulfur cathode to increase the volumetric energy density and rate capability; (5) identify the interaction mechanism between sulfur species and different types of oxides/sulfides, and find the optimal material to improve the capacity and cycling of sulfur cathode. (II) Structure and property characterization, including (1) ex-situ scanning electron microscopy; (2) XPS analysis; (3) in operando X-ray diffraction and optical microscopy. (III) Electrochemical testing including (1) coin cells and pouch cells; (2) A set of electrochemical techniques.

Results

It is commonly assumed that the Li₂S₆ species stay intact and is the adsorbed species. This may not be true as the adsorbed species could be a mixture of different species, for example Li₂S₄ and Li₂S₂. Different candidate materials can have different preferences and mechanisms for the species adsorbed. Figure II.8.C.1a illustrates the sulfur to lithium content ratio of the supernatant solutions after Li₂S₆ adsorption tests. Based on the sulfur to lithium content, speculations can be made about the species present. A sulfur to lithium ratio of 3 corresponds with the original introduced species Li₂S₆, a ratio of 4 implies possible formation of the species Li₂S₈, while even higher ratios may suggest a mixture of S₈ and lithium polysulfide species such as Li₂S₆ and Li₂S₈. Figure II.8.C.1b illustrates the calculated sulfur to lithium content ratio of the adsorbed species based on ICP-AES data. For carbon black, a S:Li ratio of 3 for both the remaining supernatant solution and the adsorbed species suggests that Li₂S₆ may be the adsorbed species. For Al₂O₃, SiO₂, TiN, TiO₂ and Ti₄O₇, a S:Li ratio of higher than 3 remaining in the supernatant solution suggests relatively more sulfur is left behind than lithium, and thus the adsorbed species should have a lower S:Li ratio than 3, this may correspond to a S:Li ratio of 2 for Li₂S₄, a ratio of 1 for Li₂S₂, and a ratio of 0.5 for Li₂S. For MnO₂, V₂O₅ and V₂O₃, S:Li ratios of much higher than 3 remain in the supernatant solution, suggesting the adsorbed species would proportionally have higher lithium than the original Li₂S₆ species, and thus S:Li ratios much lower than 3. Therefore, it can be seen that the candidate materials can have different preferences for the proportional amount of sulfur and lithium adsorbed.

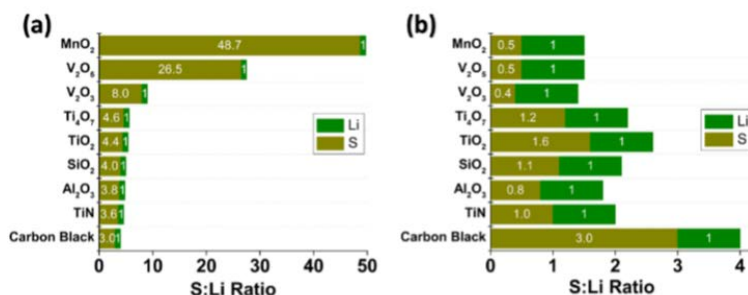


Figure II.8.C.1 ICP-AES data of S to Li atoms concentration ratio (a) remaining in supernatant solutions and (b) adsorbed onto candidate materials, after 3mM Li₂S₆ adsorption test.

We also develop an aqueous inorganic polymer, ammonium polyphosphate (APP), as a novel multifunctional binder to address the issues existing in Li-S batteries. APP is commercially used as a food additive, emulsifier, and fertilizer available at large scale and low cost (Figure II.8.C.2a). Here we employ it as a multifunctional binder. The absorptivity of APP and commonly used PVDF binder toward LiPSs was quantitatively evaluated

by adding different masses of binder with the same total surface area into a dioxolane/dimethoxyethane (DOL/DME, 1:1, v:v) solution containing 0.005 M Li_2S_6 . After adsorption and rest for 4h, there is no obvious color change of the polysulfide solution after adsorption by PVDF, suggesting weak adsorption of polysulfide (Figure II.8.C.2b). In sharp contrast, APP demonstrates significant polysulfide adsorption capability and the color of the polysulfide solution changes from yellow to nearly colorless, indicating strong interaction between Li_2S_6 and APP binder. In order to further probe the polysulfide trapping ability of different binders, the supernatant liquid of the three bottles after adsorption was analyzed by ultraviolet-visible (UV-vis) absorption spectroscopy, and the concentration variation of Li_2S_6 solution before and after adding various binders is shown in Figure II.8.C.2c. All samples exhibited a broad absorption region between 250 and 350 nm and the characteristic peaks located around 260, 280, 300 and 340 nm can be attributed to S_6^{2-} species. Compared with pristine Li_2S_6 solution, the peak intensities of the solution soaked with PVDF decreased slightly, while the absorption peak intensities of the APP solution decreased much more sharply. The APP binder adsorbs roughly twice as much polysulfide as the PVDF binder, as indicated by the much lower concentration of Li_2S_6 remaining in the solution and demonstrating the strong affinity of the S_6^{2-} species to the APP binder.

In order to clarify the enhancement of binding strength by inorganic APP polymer, first-principles simulations were carried out on the adsorption of Li-S species on APP and PVDF. The binding energies between the LiPS species and two polymers are computed to evaluate the interaction strength between them, which can be expressed as $E_b = E_P + E_{\text{LiS}} - E_{P-\text{LiS}}$ ($E_{P-\text{LiS}}$, E_P and E_{LiS} are the total energies for the adsorption system, isolated polymer and isolated Li-S species respectively). The Li-S species we chose for simulation are Li_2S , Li_2S_2 , Li_2S_4 , Li_2S_6 and Li_2S_8 , which can cover the whole lithiation process and represent all of the typical species in the fully-lithiated, middle-lithiated and under-lithiated stages. The chemical structures as well as adsorption conformations are illustrated in Figure II.8.C.2d-g. The binding strengths of various LiPS species on two kinds of polymer binders are demonstrated in Figure II.8.C.2h. It can be clearly seen that APP polymer can induce binding energies in the region of 2.16 - 2.30 eV, much higher than those of PVDF (0.58 - 0.74 eV).

Important requirements for binders include good swelling in the electrolyte to maintain electrolyte immersion and high viscosity to enable good mechanical properties of the electrode. To determine the electrolyte uptake ability of the two binders, the swelling ratios of APP and PVDF are tested at different times and shown in Figure II.8.C.2i. APP binder exhibits an electrolyte uptake of around 40% after 10 min, much higher than the uptake of PVDF binder with limited values of 20% measured after 30 min. APP binder's higher uptake suggests that it can effectively adsorb and maintain electrolyte in the electrode structure to improve ion accessibility and reaction kinetics.

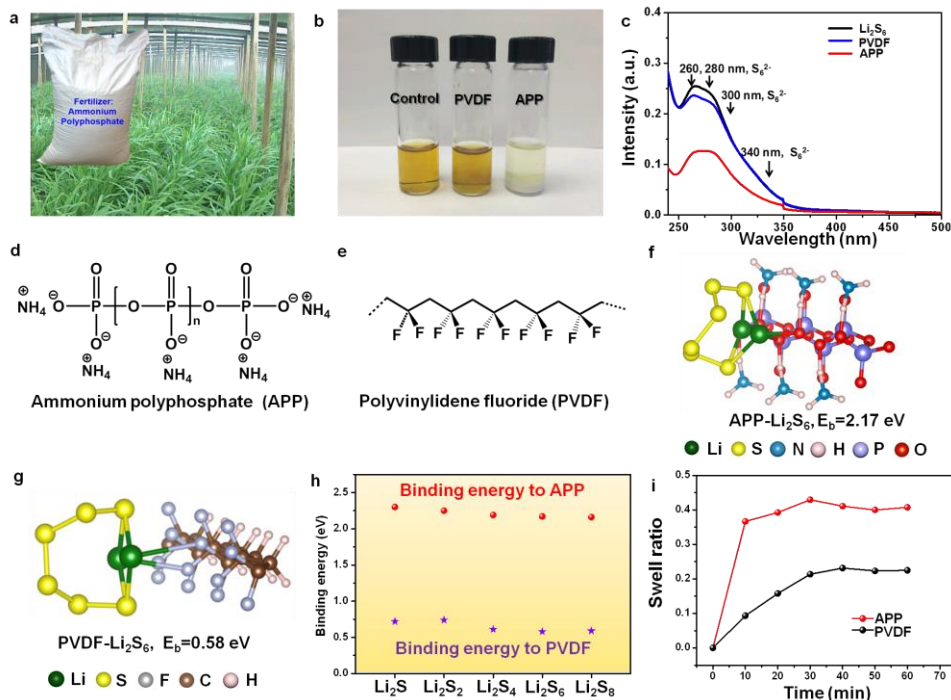


Figure II.8.C.2 (a) Commercially available APP used as fertilizer. (b) Digital image of the Li_2S_6 (0.005 M) captured by PVDF and APP in DOL/DME solution. (c) UV/Vis absorption spectra of Li_2S_6 solution before and after the addition of PVDF and APP. Chemical structures of (d) APP and (e) PVDF binders. Adsorption conformations and binding strengths for Li_2S_6 on (f) APP and (g) PVDF polymers. (h) Binding strengths for APP and PVDF with various Li-S species. (i) Swelling ratios of the APP and PVDF binders.

The safety issues of Li-S batteries originating from the flammability of lithium, sulfur electrodes and liquid electrolytes can be alleviated by engineering battery structure, employing solid-state electrolyte, and optimizing electrode design. APP binder employed here not only improves the polysulfide adsorption capability but also endows sulfur electrode flame-retardant properties to effectively improve the safety of Li-S batteries. To demonstrate the flame-retardant property of APP, sulfur cathodes with APP and PVDF binders were exposed to a direct flame until they are ignited, after which the direct flame was removed. Sulfur cathode with traditional PVDF binder was tested using this method as shown in Figure II.8.C.3a. Upon exposure to direct flame for ~ 1 s, the sulfur cathode was ignited and the flame burns vigorously and spreads quickly. The specific burning time, i.e. the burning time divided by the mass of sulfur, was calculated to be ~ 519 s g^{-1} , reflecting the high flammability of sulfur cathode (Figure II.8.C.3c). The sulfur cathode with APP binder was tested using the same method. In contrast, APP binder is efficient in reducing the burning time of the sulfur cathode. After being ignited, the flame is suppressed and finally self-extinguished (Figure II.8.C.3b, c). The specific burning time was significantly decreased to ~ 289 s g^{-1} , indicating the flame-retardant properties of the APP binder based sulfur cathode. The flame-retardant mechanism of the APP binder can be supposed as follows: During the combustion process, APP decomposes and releases ammonia/water gas, and crosslinks to form an insulating polymer layer (Figure II.8.C.3d). This insulating polymer layer acts as a physical barrier to heat, fuel, and oxygen transfer, thus building up an isolation layer between the condensed and gas phases and effectively protecting the underlying sulfur from catching fire (Figure II.8.C.3d).

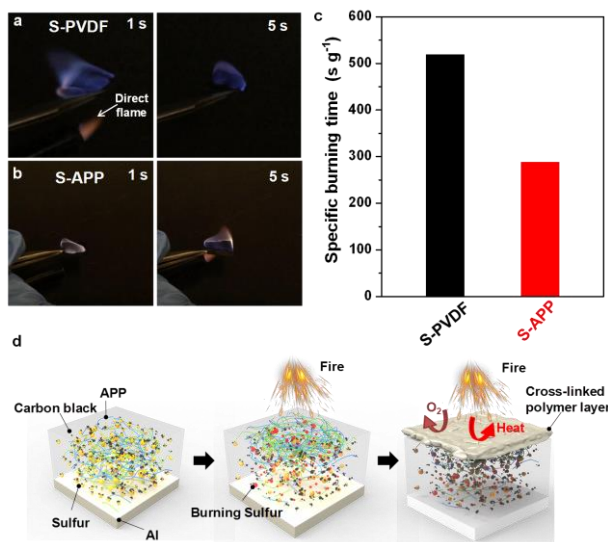


Figure II.8.C.3 The specific burning time test of sulfur electrodes with (a) S-PVDF electrode and (b) S-APP electrode. The time indicated in the pictures are counted as soon as the electrodes are exposed to the direct flame from a lighter (indicated by the white arrow in (a)). (c) The specific burning time of the sulfur cathodes with APP and PVDF binders. (d) Schematic showing the flame-retardant mechanism of the APP binder based sulfur electrode.

To confirm the proposed flame-retardant mechanism, we did a burning test on S-APP and S-PVDF electrodes and after the fire was self-extinguished, X-ray photoelectron spectroscopy (XPS) and scanning electron microscopy (SEM) were used to understand the mechanism. XPS analysis clearly shows the presence of nitrogen, sulfur, and phosphorous elements in the S-APP electrode from the survey spectrum (Figure II.8.C.4b). After burning, the intensity of the N 1s signal significantly decreases, while the intensity of the phosphorous signal is almost the same, indicating decomposition and release of NH_3 , as well as generating a crosslinked polymer, as proposed in Figure II.8.C.4a. It should be noted that the sulfur signal only slightly decreases, suggesting that the APP binder protects the underlying sulfur from burning and halts the further spread of the fire. This is quite different for the S-PVDF electrode based on the S 2p XPS spectrum analysis, in which the intensity of the sulfur signal obviously decreases, suggesting most of the sulfur materials are burned away. Further evidence can be obtained from the SEM postmortem analysis of the electrodes after burning. The overall morphology and structure were well preserved for S-APP electrode (Figure II.8.C.4d), demonstrating that the protective layer produced by APP decomposition helps prevent further combustion of sulfur. However, due to the weak protection offered by PVDF binder, a large quantity of sulfur is evaporated from the sulfur cathode, leaving many holes in the electrode after burning (Figure II.8.C.4h) which is in agreement with the previous analysis. The corresponding sulfur and phosphorus elemental maps of the S-APP electrode after burning indicate sulfur is protected and phosphorous is retained in the electrode (Figure II.8.C.4e, f), which is consistent with the EDS results that the intensity of the sulfur signal is much higher compared with the carbon signal from the electrode (Figure II.8.C.4g). In contrast, holes are found on the sulfur cathode with PVDF binder (Figure II.8.C.4h), and the sulfur signal is missing in these areas (Figure II.8.C.4i), indicating poor protection of sulfur combustion by PVDF. In addition, the sulfur signal is much lower than the carbon signal after burning (Figure II.8.C.4k), confirming the evaporation of sulfur from sulfur cathode during the burning process.

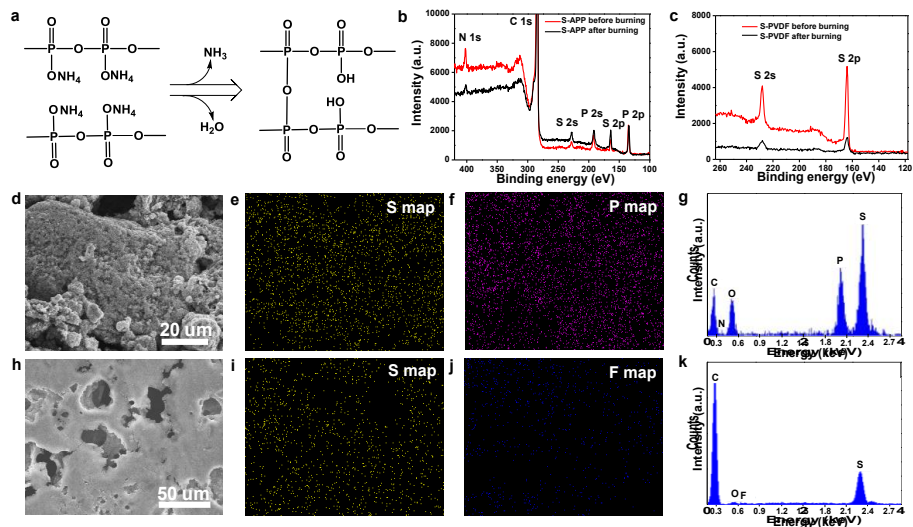


Figure II.8.C.4 (a) Chemical reaction for flame-retardant mechanism. (b) XPS spectra of the surface chemical composition of the S-APP electrode before and after burning. (c) S 2p XPS spectra of the S-PVDF electrode before and after burning. (d) SEM image and the corresponding (e) sulfur and (f) phosphorus elemental maps of the S-APP electrode after burning. (g) EDS of the S-APP electrode after burning. (h) SEM image and the corresponding (i) sulfur and (j) fluorine elemental maps of the S-PVDF electrode after burning. (k) EDS of the S-PVDF electrode after burning.

Probing sulfur electrochemistry has multiple challenges that include: a) sulfur and its reduced species are extremely sensitive to vacuum, electron beam irradiation and X-ray irradiation, which limits the diagnostic tools one can use; b) sulfur has a large family of intermediate species connected by interwoven reaction pathways, which could be easily disturbed by added indicators or labels; c) the materials easily change upon removing from native electrolyte, hence often requiring *in operando* study. Here we combine dark-field light microscopy (DFLM) and a planar electrochemical cell fabricated on a glass slide to visualize sulfur electrochemistry *in operando* (Figure II.8.C.5a). Visible light is a benign probe which allows non-invasive study in native ether-based liquid electrolyte, while dark-field illumination was used to enhance the sensitivity to small features on a flat background. Lithium polysulfide (Li_2S_8) was dissolved in dioxolane (DOL) and dimethyl ether (DME) and served as the electrolyte and sulfur source. A metal grid electrode (1 μm in line width, 50 nm in height) was deposited on a glass substrate via e-beam lithography and evaporation (Figure II.8.C.5b and c), while Li metal placed on the same plane was the counter/reference electrode. During galvanostatic charging/discharging at room temperature (Figure II.8.C.5d), sulfur deposits on/strips from the working electrode, while DFLM images of a $180 \mu\text{m} \times 135 \mu\text{m}$ region on the surface of the substrate were captured at 1 frame/second simultaneously. A white light source and a three-color-channel CMOS camera were used to record color information. Using this technique, we are able to directly observe multiple new phenomena in lithium-sulfur batteries for the first time, including the electrochemical generation of metastable liquid sulfur at room temperature, *etc.*

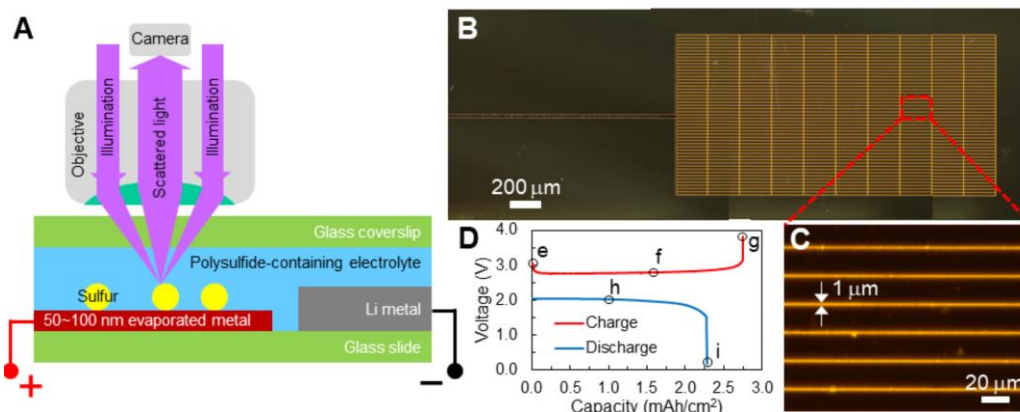


Figure II.8.C.5 (a) Schematic of the electrochemical cell design that allows in-operando dark field light microscopy (DFLM) observation. (b and c) DFLM images of the metal grid (50 nm thick, 1 μm wide) fabricated on glass slide as a substrate for the electrochemical cell. (d) Voltage profile of the cell.

Conclusions

In all, in the past one year, we have made great progress in understanding the mechanism of adsorption, diffusion, and flame-retardant property on anchoring materials and binders. Different adsorption mechanisms and probe possible adsorption species were elucidated. In general, stronger candidate materials seem to adsorb relatively more lithium than sulfur, compared to weaker candidate materials. This is particularly evident in MnO_2 , V_2O_5 and V_2O_3 . The trend is also consistent in metal sulfides, with TiS_2 , FeS and MoS_2 also exhibiting much higher preferences for lithium, however the S:Li ratios are not reported here because the metal sulfides themselves are a source of sulfur atoms and thus any powder particles that is suspended in supernatant solutions would severely undermine the validity of the S:Li ratio data for speculations of species adsorbed. Multi-functional sulfur cathode binder capable of controlling the polysulfide shuttling and facilitating Li-ion transport was developed. The flame-retardant property of binder to improve safety and propose flame-retardant mechanism was also demonstrated. This work offers a feasible and effective strategy for employing APP as an efficient multifunctional binder towards building next generation high-energy density Li-S batteries. Moreover, APP bestows the sulfur cathode with significantly improved flame-retardant property, thus improving the safety of Li-S batteries. *In situ* characterization platform to monitor nucleation/dissolution of sulfur/ Li_2S_n was built, which is a non-invasive imaging method with sub-micron, sub-second resolution for Li-S battery in label-free, native organic liquid electrolyte.

Key Publications

1. David Wu, Feifei Shi, Guangmin Zhou, Chenxi Zu, Chong Liu, Kai Liu, Yayuan Liu, Jiangyan Wang, Yucan Peng, Yi Cui*, Quantitative Investigation of Polysulfide Adsorption Capability of Candidate Materials for Li-S Batteries, *Energy Storage Materials*, **2018**, 13, 241-246.
2. Guangmin Zhou, Kai Liu, Yanchen Fan, Mengqi Yuan, Bofei Liu, Wei Liu, Feifei Shi, Yayuan Liu, Wei Chen, Jeffrey Lopez, Denys Zhuo, Jie Zhao, Yuchi Tsao, Xuanyi Huang, Qianfan Zhang, and Yi Cui*, An Aqueous Inorganic Polymer Binder for High Performance Lithium-Sulfur Batteries with Flame-Retardant Properties, *ACS Cent. Sci.*, **2018**, 4 (2), 260-267.

II.8.D Addressing Internal “Shuttle” Effect: Electrolyte Design and Cathode Morphology Evolution in Li-S Batteries (TAMU, Purdue Univ)

Perla B. Balbuena, Principal Investigator

Texas A&M University
3122 TAMU
College Station, TX 77843
Email: balbuena@tamu.edu

Partha P. Mukherjee, Principal Investigator

Purdue University
585 Purdue Mall
West Lafayette, IN 47907-2088
Email: pmukherjee@purdue.edu

Tien Duong, DOE Technology Development Manager

U.S. Department of Energy
E-mail: Tien.Duong@ee.doe.gov

Start Date: October 1, 2014	End Date: September 30, 2018	
Project Funding (FY18): \$990,000	DOE share: \$990,000	Non-DOE share: \$0

Project Introduction

This project focuses on developing new understanding of the main challenges of the Li/S cell obtained from first-principles atomistic and mesoscopic modeling and state of the art synthesis and characterization. The current report does not include the experimental section that ended 9-30-2017. Specifically, the work aims to elucidating: 1) Effects of the electrolyte chemistry on the formation of a solid-electrolyte interphasial film at the surface of the Li anode due to the shuttle of soluble polysulfide species; 2) Effects of electrolyte and shuttle on reactions occurring at the C/S cathode surface, 3) Relative contributions of the solid discharge products to the cathode performance, and associated morphology and volume changes of the C/S cathode microstructure; 3) Effects of the electrolyte chemistry and cathode microstructure on the coulombic and cyclic efficiency of composite C/S electrodes.

Objectives

The objective of this project is to elucidate the lithium-metal anode deterioration issues especially under the polysulfide shuttle environment, and the effects of the carbon/sulfur cathode morphology and synthesis on the cathode performance, and to develop and test strategies based on Li-metal protection advanced cathode structure design to mitigate these issues.

Approach

A mesoscale model including different realizations of electrode mesoporous structures based on a stochastic reconstruction method allows virtual screening of the cathode microstructural features and the corresponding effects on electronic/ionic conductivity and morphological evolution. Interfacial reactions at the anode due to the presence of polysulfide species are characterized with ab initio methods. For the cathode interfacial reactions, classical and ab initio molecular dynamics are used to follow the cathode synthesis structure and composition, as well as the voltage discharge reactions. Mesoscopic and continuum model evaluations of battery performance complement the microscopic analyses.

Results

Concentrated Solution Effects in Li-S Battery Electrolyte Transport: The electrolyte in a Li-S system is a continuously evolving system given the successive S reduction during discharge (or oxidation during charge). This leads to a coexistence of multiple species and the presence of each species influences the transport of the

rest. Such coupled interactions are modeled using a concentrated solution theory (Figure II.8.D.1). A distinguishing feature of such involved interactions is the decline in ionic conductivity at high enough ion concentrations. For the Li-S, the ionic concentration is the highest when high order polysulfides (PS) near completely convert to medium chain PS (shorter chain PS precipitate almost instantaneously, thus limiting their concentration), which takes place around the transition from an upper voltage to a lower voltage plateau. This sudden decrease in ionic conductivity reflects on increased overpotential and correspondingly a dip joining the two plateaus (Figure II.8.D.1a). Evolution of different cell resistances as a function of discharge capacity (Figure II.8.D.1b) reveal that the electrolyte phase resistance (transport N_t and concentration N_k) are the most dominant during this intermediate capacity range, while microstructural resistances (passivation and blockage) are the most influential during voltage plateaus.

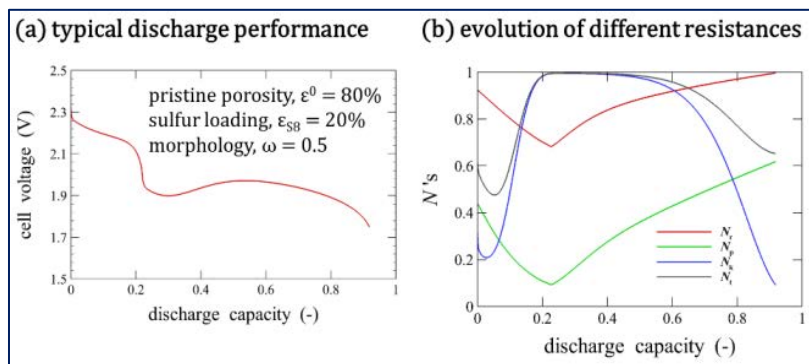


Figure II.8.D.1 (a) Effects of porosity, sulfur loading, and morphology on cell performance. (b) Evolution of resistance modes during discharge: Surface passivation resistance (red), pore block resistance (green), concentration resistance (blue) and transport resistance (black). As any N resistance value goes to 1, the mode becomes dominant.

Chemical Interactions of Li-anode and Electrochemical Complexations in Li-sulfur Cells: During electrochemical operation of a Li-sulfur cell, S is present in different forms in the electrolyte phase. Each of these species can reach the Li metal anode due to the shuttle effect. Since the Li metal is quite reactive, it can reduce the S species arriving at anode. This reduction, being chemical in nature, does not contribute to electrochemical capacity and gives rise to a capacity defect. Figure II.8.D.2a compares the electrochemical response of two cells with and without these deleterious reactions at the anode. The speciation also changes and in turn the cell potential profile changes its form. Each dissolved S, long-chain and medium-chain polysulfides (PSs) can partake in these reactions. Based on the availability of the species, various elemental reactions are active at different stages in electrochemical operation (Figure II.8.D.2b). [1] The reduction of a short-chain PS forms a solid species on the Li metal surface. [2], [3] This constitutes an irreversible capacity loss. In contrast, the reactions involving long-chain PS and S reduce them to lower oxidation states but the products are still present in the electrolyte phase and this S may not be irreversibly lost (referred to as the reversible capacity defect in Figure II.8.D.2c).

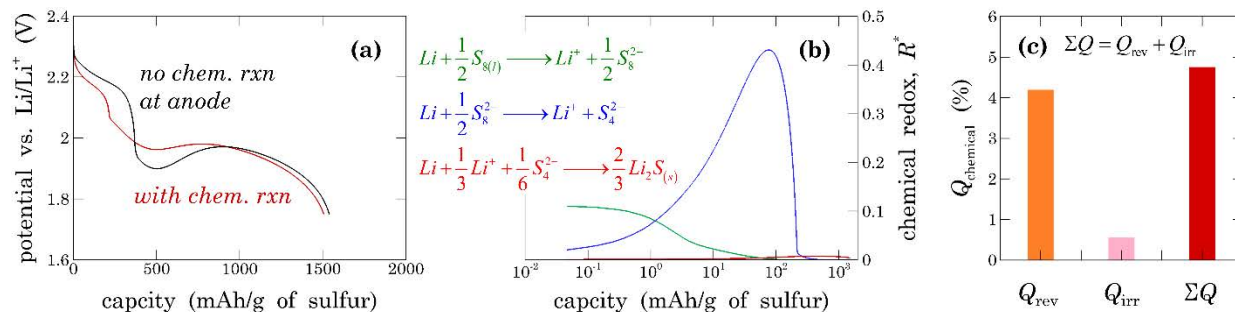


Figure II.8.D.2 Anode chemical reactions and electrochemical interactions at 1C. (a) With chemical redox reactions at Li anode, capacity decreases as well as qualitative nature of the potential profile changes with changes in speciation. (b) The dominant mode of chemical reduction at Li metal anode correlates the form of sulfur present at that instance. (c) This effect has both reversible and irreversible components.

Physicochemical Origins of Electrochemical Hysteresis in Li – S Cell: During discharge, S successively reduces to lower order PS and deposit in the form of solid Li_2S . During charging, since the electrode potential is greater than oxidation potentials for each of the intermediate S species, all the oxidation reactions take place concurrently and start forming solid S from a very early stage. This leads to partial coverage of the Li_2S surface by solid S. Based on the morphologies of Li_2S and solid S, the extent of this coverage varies. For example, a film-type S deposition covers more Li_2S . In the extreme event, freshly deposited S can completely overlap on the remaining Li_2S and prevent its further dissolution in the electrolyte. Such isolated Li_2S cannot be oxidized back to S and thus amounts to capacity decay. Another factor that further complicates such isolation is the affinity of S to deposit on the backbone substrate (e.g., carbon). If the substrate is sulfur-philic, Li_2S isolation is reduced; however, it makes for a more deteriorative surface passivation and in turn increases the overpotentials.

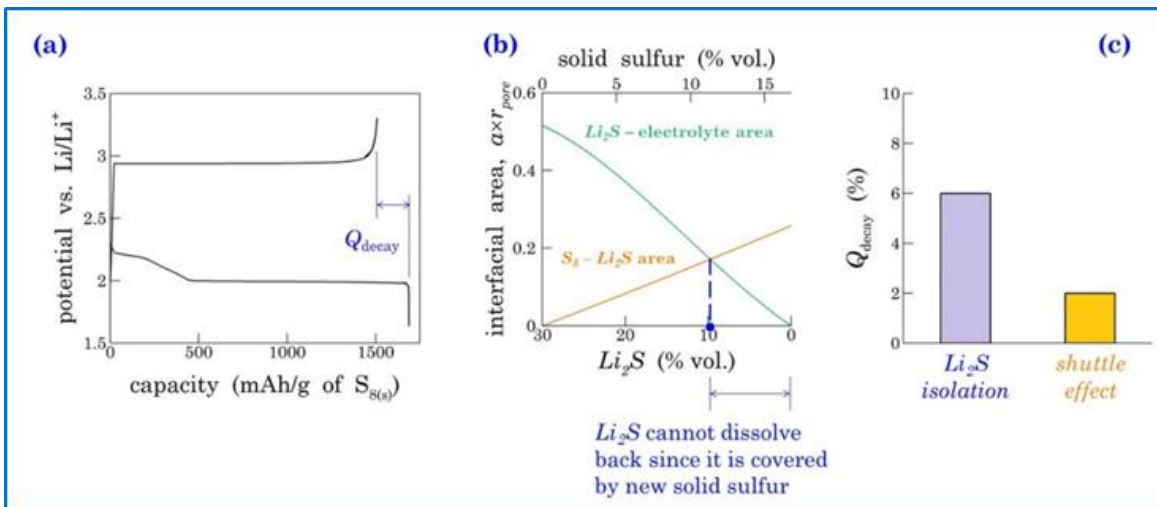


Figure II.8.D.3 (a) Charge-discharge hysteresis is composed of dissimilar potential profiles and unequal capacities (b) Dissolution of Li_2S does not often proceed to completion as freshly precipitated S covers Li_2S surface (c) Both Li_2S isolation and shuttle effect fundamentally lead to such hysteresis.

Effects of Carbon-Sulfur Morphology on Cathode Electrochemical Performance: Classical reactive molecular dynamics (MD) simulations were used to evaluate novel sulfur/graphene architectures that emulate the electrochemical behavior of the Li-S battery cathode, promoting the S-C interaction through the edges of graphene sheets. A random mixture of 8-membered S rings mixed with small graphene sheets was simulated at 64%-wt. S loading. Structural stabilization and S reduction calculations are performed with classical reactive

MD. This methodology allowed accounting for the collective behavior of the S and graphene structures. The S encapsulation induces ring opening and the S phase evolves into a distribution of small chain-like structures interacting with C through the graphene edges (Figure II.8.D.4). This new arrangement of the S phase not only leads to a less pronounced volume expansion during S reduction but also to a different discharge voltage profile, in qualitative agreement with earlier reports on S encapsulation in microporous carbon structures.

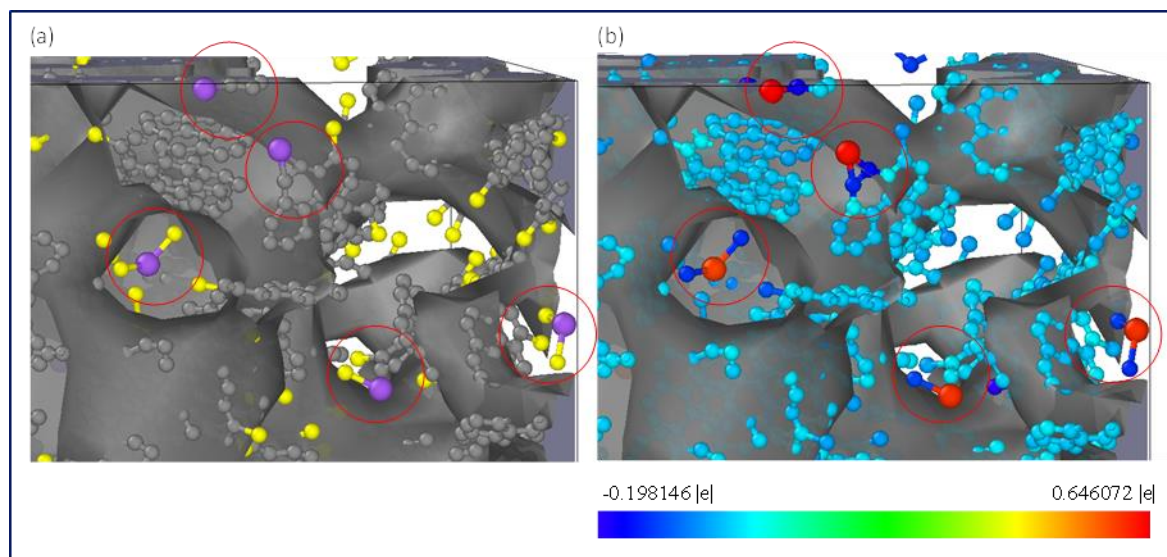


Figure II.8.D.4 (a) Lithium-sulfur bonding and lithium-carbon interaction at low lithium contents, (b) electronic charge distribution at low lithium contents. Color code: C grey, S yellow, Li purple. In (b) atoms are colored according to their electrostatic charge shown in the color bar.

The Li_2S phase was found to grow around ensembles of parallel graphene sheets during S reduction. No diffusion of S or Li between graphene sheets was observed, and extended Li_2S domains bridging the space between carbon ensembles were suppressed. The results emphasize the importance of morphology on the electrochemical performance of the composite material. The sulfur/graphene model outlined here provides new understanding of the graphene effects on the S reduction behavior and the role that van der Waals interactions may play in favoring S reduction reactions and enhanced polysulfide trapping. Thus, we demonstrated that the formation of S-C chemical bonds at the synthesis stage favors the discharge reaction during lithiation of S-C cathodes. Advantages include the suppression of the formation of long-chain polysulfide species, and the contribution of C to enhance the overall cathode capacity. This behavior is similar to that found experimentally using sulfurized poly-acrylonitrile (SPAN) as cathode material.

Our first model (Figure II.8.D.4) was only composed of carbon and sulfur. Our findings were published in *Chem.Sus.Chem* (2018) and *J. Mater. Chem.* (2018). But the sulfurized polyacrylonitrile composite (SPAN) rises itself as a very promising cathode material for LiS batteries due to its excellent polysulfide retention and cycling performance. Therefore, new ab initio molecular dynamics (AIMD) simulations were carried out to elucidate the role of N (Figure II.8.D.5). We computed the lithiation process and obtained the voltage profile which qualitatively agrees with the experimental reports. We studied the structural features and lithiation mechanisms of these materials. We found evidence of C-S chemical

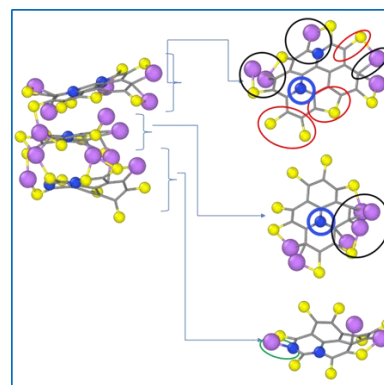


Figure II.8.D.5 Multilayer graphene structure showing the incorporation of N into the C rings in pyridinic (not shown), graphitic (blue circle), and pyrrolic (green circle) positions and their interactions with Li. Note that: a) Graphitic N does not interact with Li. b) Pyrrolic N bonds to Li. c) C backbone also participates in the electrochemical reduction of S.

bonding and no formation of long-chain PS during lithiation. Moreover, at high Li contents, we found significant C-Li and N-Li interactions that might contribute to an extended lithiation process beyond a Li:S 2:1 molar ratio in SPAN composites. Our calculations corroborate the experimental findings and pave the way to a rational design of SPAN-based cathodes for LiS batteries. Currently, we are aiming at a better understanding of long-term effects of these C- and N-Li interactions during battery cycling. A new manuscript is being written.

Charge Reactions of Nucleating Li₂S Structures: The ab-initio simulation method was used to study the delithiation process of ultra-small Li₂S nanoparticles represented by a Li₂₀S₁₀ cluster. It was found that although the overall delithiation is an oxidation reaction, local reductions and disproportionation reactions were observed. Long-chain PSs can be found as intermediate products. However, these PSs can be firmly bonded to insoluble S₂⁻ via Li atoms as mediators. The charge and discharge voltages were also estimated based on the energy profiles of changing Li content in the cluster. The charge process only requires 0.37 V overpotential. Although the discharge voltage of the Li₂₀S₁₀ particle is only 1.26 V, it can still deliver a theoretical specific energy density about 1480 Wh/kg of Li₂S. During the charging process, polarons can form in the ultra-small particles, providing charges to support oxidation reactions. This is the first study that probes reactions during the delithiation of an ultra-small Li₂S nanoparticle. It is still unclear if small nanoparticles would agglomerate during charge/discharge processes. Agglomeration of nanoparticles can increase the charge transport distance and slow down the kinetics. In addition, the electrolyte also plays a significant role in the Li-S electrochemical system. An interesting and important remaining question that will be pursued is whether side reactions may happen between the electrolyte and the nanoparticle, and then result in chemical degradation. The study was published in *Phys. Chem. Chem. Phys.* (2018).

Conclusions

The effect of the various resistances on the discharge curves was characterized as a function of the discharge capacity. It was found that at the transition between the first and second plateau the electrolyte resistances due to transport and concentration are the dominant effects, whereas the resistances due to surface passivation and pore blockage are more influential during each of the first and second plateaus. Due to the soluble PS migration, these species react at the surface of the Li anode. A model of the electrochemical response of the Li-S cell to these reactions illustrates how specific reactions may affect the discharge curve. Reduction of shorter chain PS species leads to insoluble products resulting in irreversible capacity; however, some reactions lead to soluble shorter PS could still return to the cathode thus being a reversible capacity defect. Another important issue is the irreversible capacity due to Li₂S insulation. Such isolated Li₂S cannot be oxidized back to S and thus increases the capacity decay. The Li₂S insulation effects were quantified and compared with the irreversibilities due to the shuttle effect.

The second focus of this study was on the understanding of the C-S composite synthesis and structure and their correlation with battery performance. Classical and quantum molecular simulations were employed to emulate the synthesis methods. In the most popular synthesis methods, C and S are physically coupled and this material yields the typical two-plateau discharge curves and the polysulfide shuttle effect. However, synthesis at higher temperatures may result in chemical C-S interactions. These alternative structures (an example are the S-PAN materials), do not produce long-chain PS species. The S8 ring is opened during synthesis and the open chains become chemically attached to the carbon edge structures. These hanging open chains are reduced to shorter chains during lithiation. Thus, a very different discharge curve is defined by a single plateau and a much higher capacity. Other elements such as nitrogen may also contribute favorably to increasing the capacity and stabilizing the products.

Key Publications

1. S. Perez Beltran and P. B. Balbuena, "Formation of Multi-layer Graphene Domains with Strong Sulfur-Carbon Interaction and Enhanced Sulfur Reduction Zones for Lithium-Sulfur Battery Cathodes," *ChemSusChem*, 11, 1970-1980, (2018).

2. Z. Liu, H. Deng, W. Hu, F. Gao, S. Zhang, P. B. Balbuena, P. P. Mukherjee, "Revealing Reaction Mechanisms of Nanoconfined Li_2S : Implications for Lithium-Sulfur Batteries," *Phys. Chem. Chem. Phys.*, 20, 11713-11721, (2018).
3. S. Perez Beltran and P. B. Balbuena, "First-Principles Explorations of the Electrochemical Lithiation Dynamics of a Multilayer Graphene Nanosheet-based Sulfur-Carbon Composite," *J. Mater. Chem. A*, 6, 18084-18094, (2018).
4. Mistry and P. P. Mukherjee, Electrolyte Transport Evolution Dynamics in Li-sulfur Batteries, *Journal of Physical Chemistry C*, 122, 18329 (2018) (doi: 10.1021/acs.jpcc.8b05442).
5. Mistry and P. P. Mukherjee, 'Shuttle' in Polysulfide Shuttle: Friend or Foe?, *Journal of Physical Chemistry C*, in press (2018) (doi: 10.1021/acs.jpcc.8b06077).

References

1. Juan C. Burgos, Perla B. Balbuena, Javier A. Montoya, *J. Phys. Chem. C*, 121 (2017): 18369-18377.
2. Luis E. Camacho-Forero, Taylor W. Smith, Samuel Bertolini, Perla B. Balbuena, *J. Phys. Chem. C*, 119 (2015): 26828-26839.
3. Zhixiao Liu, Samuel Bertolini, Partha P. Mukherjee, Perla B. Balbuena, *ACS Appl. Mater. & Interfaces*, 8 (2016): 4700-4708.

II.8.E Mechanistic Investigation for the Rechargeable Li-Sulfur Batteries (U of Wisconsin)

Deyang Qu, Principal Investigator

University of Wisconsin Milwaukee
3200 N Cramer Street
Milwaukee, WI, 53211
E-mail: qud@uwm.edu

Xiao-Qing Yang, Principal Investigator

Chemistry Department
Bldg. 555, Brookhaven National Lab.
Upton, NY 11973
E-mail: xyang@bnl.gov

Tien Duong, DOE Technology Development Manager

U.S. Department of Energy
E-mail: Tien.Duong@ee.doe.gov

Start Date: September 1, 2017
Project Funding: \$300,000

End Date: August 30, 2019
DOE share: \$300,000

Non-DOE share: \$0

Project Introduction

Rechargeable lithium sulfur (Li-S) batteries are considered as one of the potential candidates to replace state-of-art Li-ion batteries in EV, due to their high theoretical energy density (1672mAh*g⁻¹), safety, and low cost. A substantial amount of work has been done on Li-S batteries in the past decade. However, the low cycleability and the high capacity decay (self-discharge) are the two main issues that have been associated with Li-S batteries from the beginning. This is especially true for the Li-S batteries with elemental sulfur as redox materials and lithium salts in organic solvents as liquid electrolytes. The majority of the work is dedicated to improving the battery's performance through chemically and physically modifying the sulfur electrode, electrolytes, separator, and lithium anode. However, the single most important aspect, understanding the sulfur redox mechanism is sparse and overwhelmed by the huge volume of work done on improving the battery's performance. Besides the intrinsic complexity of the sulfur redox chemistry, the most challenging task is to find an effective analytical technique for the quantitative and qualitative determination of the dissolved and solid polysulfides, including elemental sulfur.

During 2017, we successfully established and further optimized the in-situ Electrochemical-HPLC-MS technique. So for the first time, all of the dissolved polysulfide ions can be qualitatively and quantitatively determined during the charge and discharge of a Li-S cell. Also, an in-situ electrochemical– microscopic technique for the in-situ investigation of Li anode during cycling was established, so the interaction between dissolved polysulfide ions and Li-anode can be investigated in real time.

Based on the achievements in 2017, the mechanism of the inhibition for the “shuttle effect” was investigated; new innovative electrode designs and inhibitors to mitigate the effect in the rechargeable Li-S cells were explored. The extensive scientific investigation was carried out taking the advantages of new in-situ electrochemical spectroscopic techniques developed in 2016 and 2017.

Objectives

The primary objectives were to conduct focused fundamental research on the mechanism of “shuttle effect” inhibition for the rechargeable Li-S batteries; to develop the electrode and electrolyte systems which can mitigate the “shuttle effect” so the low self-discharge and long cycle life can be achieved. In this objective, special attentions were paid to the investigation of the chemical interactions between the additives and

dissolved polysulfides, the management for the solubility of polysulfide ions, the formation of the SEI layer and dead Li on the surface of Li anode, and the exploration of electrode and cell designs. Through systematic investigation of Li-S chemistry and the scientific understanding of the inhibition mechanism for “shuttle effect”, the system engineering design can be guided. The ultimate goal for the project is to develop a practical rechargeable Li-S battery to meet the challenges of power for the next generation of electric vehicles beyond Li-ion technologies.

Approach

1. With the combination of *High Performance Liquid Chromatography (HPLC)/Mass Spectroscopy (MS)* together with *in-situ* electrochemical measurement in a specially designed cell, the dissolved polysulfide ions can be detected quantitatively and qualitatively, therefore the reactions between dissolved polysulfides with the Li anode and other components were accurately determined.
2. *In-situ* Keyence 3D microscope and electrochemical measurement in a specially designed cell to investigate the surface modification of Li with e.g. various additives and at different stage of charge/discharge.
3. Synthesis of the sulfur containing polymer in order to localize the polysulfide with the polymer composite material, and searching for the anode materials which don't react with dissolved polysulfide ions.
4. Extended collaboration with other U.S. and international academic institutions and U.S. industrial partners.

Results

1, Effectiveness of “shuttle effect” inhibitors:

High performance liquid chromatography (HPLC) can be used to systematically and rapidly screen the potential additives for the inhibition of the polysulfide shuttle effect in a Li-S battery. The method is proven effective by investigating the compounds which were reported in the literature as redox shuttle inhibitors for Li-S batteries. Figure II.8.E.1 shows the relative ratios of polysulfide ions for the electrolytes with 15 different additives and a baseline electrolyte without any additive before and after being in contact with Li metal at different periods of time. Ideally, when the shuttle reactions between Li metal and polysulfides (and elemental sulfur) were totally inhibited, the relative ratios for the different additives before and after being in contact with Li metal should not change with the time of exposure to Li metal. Unfortunately, none of the above additives can totally inhibit the shuttle reactions as shown in Figure II.8.E.1. There was always a large decrease of the relative ratio after being in contact with Li metal within 10 hours, which evidently indicates the reaction between the additives and polysulfide ions. The reaction occurred until either the reactants were consumed or a passive layer was formed. Clearly, the decline of the ratio varied, the ratio for the nitride additives which demonstrated decent inhibition declined much less (Figure II.8.E.1A) than those additives showing less inhibition (Figure II.8.E.1B). The hypothesis was that the reactions between the additives and polysulfide ions with the Li metal were competitive, a better inhibitor reacted with Li faster than that of the polysulfide ions forming an effective passivation layer to prevent the further reaction between Li and polysulfide ions. This observation demonstrated that the additives under investigation may not completely inhibit the shuttle reaction between Li metal and polysulfides (and elemental sulfur), although the nitride additives showed better inhibition. Therefore, the search for a better polysulfide shuttle inhibitor is ongoing and critical for improving the electrochemical performance of Li-S batteries.

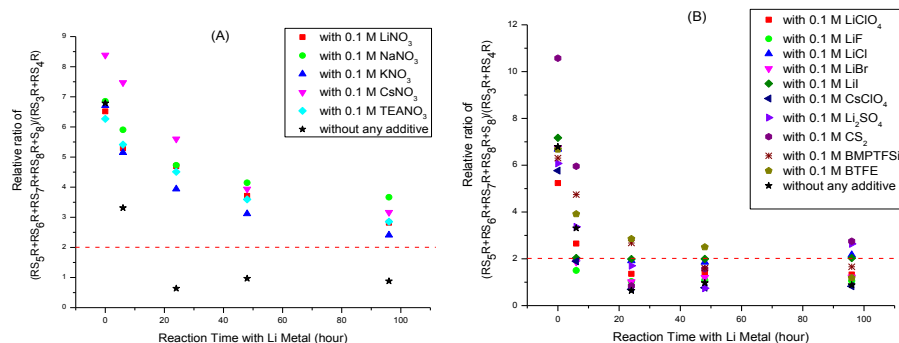


Figure II.8.E.1 The relative ratios of $(RS5R+RS6R+RS7R+RS8R+S8)/(RS3R+RS4R)$ for electrolytes (containing 16 mM Li_2S_6) without and with additives before and after contacted with Li metal for different period of time.

To eventually demonstrate the practical simplicity, clearness, and significance of our HPLC method for studying the inhibition effect of different additives. 7 Li-S cells with and without 6 different additives (including $LiNO_3$, $LiBr$, $LiClO_4$, $BMPTFSi$, $BTFE$, and CS_2) were discharged and charged in flooded three-electrode cells. The elemental sulfur was added into the electrolyte to form the catholyte as the sulfur source. By doing this, the quantity of the elemental sulfur can be easily analyzed by our HPLC method before discharge and after recharge. In theory, the sulfur recovery rate (ratio of the sulfur concentration in catholyte before discharge and after recharge) should be ONE when there is no shuttle effect. Since the shuttle effect will inevitably consume some of the sulfur source on the Li electrode, in reality, this recovery rate should be less than 1. By using the sulfur recovery rate of catholyte without any additives as a standard, one can easily compare the inhibition effects for different additives. Good additives have a recovery rate close to one and larger than the recovery rate of the catholyte without any additives. Borderline additives have a recovery rate similar to that of the catholyte without any additives and bad additives have a recovery rate much less than that of the catholyte without any additives. The recovery rates of sulfur and the coulombic efficiencies of the charge/discharge for the 7 investigated Li-S cells are summarized in Table II.8.E.1. Clearly, the Li-S cell with 0.1 M $LiNO_3$ in the catholyte has over a 95% recovery rate of elemental sulfur which is close to our FY17 report. This observation indicates the superior shuttle-inhibition effect for $LiNO_3$ (and other nitrate salts) and supports the HPLC results mentioned above. For others, some additives (such as $LiClO_4$, $BMPTFSi$) have the sulfur recovery rate similar to that of no additive, which may indicate the little or no shuttle-inhibition effect of these two additives. Some additives (such as $LiBr$, $BTFE$, and CS_2) surprisingly have the sulfur recovery rate much lower than that of no additive, the impact of these three additives on the shuttle effect is definitely controversial and counter to some previous reports, hence further studies may be needed. Overall, the electrochemical tests in tandem with chromatographic analysis clearly show that our HPLC method for studying the inhibition effect of additives in Li-S batteries is simple, sound and effective. However, one should be cautious of using coulombic efficiency (1st charge and 1st discharge ratio) to determine the effectiveness of an inhibitor as shown in Table II.8.E.1

2. Preventing the interaction of dissolved polysulfide ions with Li containing anodes:

The “shuttle effect” inhibitors are sacrificial additives, just like $LiNO_3$ which can delay the shuttle reaction by reacting with the Li anode forming a passive layer on the surface of Li metal. However, after the inhibitor is consumed, the shuttle reaction will start. Thus, unless a “renewable” inhibitor can be found, sacrificial inhibitors can only alleviate the “shuttle effect”, but cannot eliminate the problem. In addition, from our investigation in FY17, ALL common electrolytes failed to form a stable SEI layer to prevent the reaction between dissolved polysulfide ions with metallic Li anode.

Table II.8.E.1 Summary of the recovery rate of elemental sulfur and the coulombic efficiency for several Li-S cells with and without different catholyte additives

Catholyte With	Recovery Rate of S8 (%) [S8]after charge/[S8]before discharge	Coulombic Efficiency (%) 1 st Charge Capacity/1 st Discharge
No additive	81	99
0.1 M LiNO ₃	98	98
0.1 M LiBr	37	120
0.1 M LiClO ₄	82	93
0.1 M BMPTFSi	77	89
0.1 M BTFE	57	91
0.1 M CS ₂	69	105

In FY18, by means of the *in-situ* HPLC-MS electrochemical technique, we have tried investigating different Li containing anode materials. With the proprietary technology developed in Dr. Qu's lab, many anode materials ranging from carbon to Li-metal alloys can be formed through the prelithiation process. Figure II.8.E.2 shows the reaction between three different Li containing anode materials – metallic Li, Li loaded phosphorous and a proprietary Li pre-loaded anode material. Obviously, the distribution of polysulfide ions changed after contacting metallic Li and Li-P anode materials. However, there is no apparent changes of the polysulfide distribution after one contact to Li-XX, which is evidence that the Li containing anode material was stable in the electrolyte solution containing elemental sulfur and polysulfide ions.

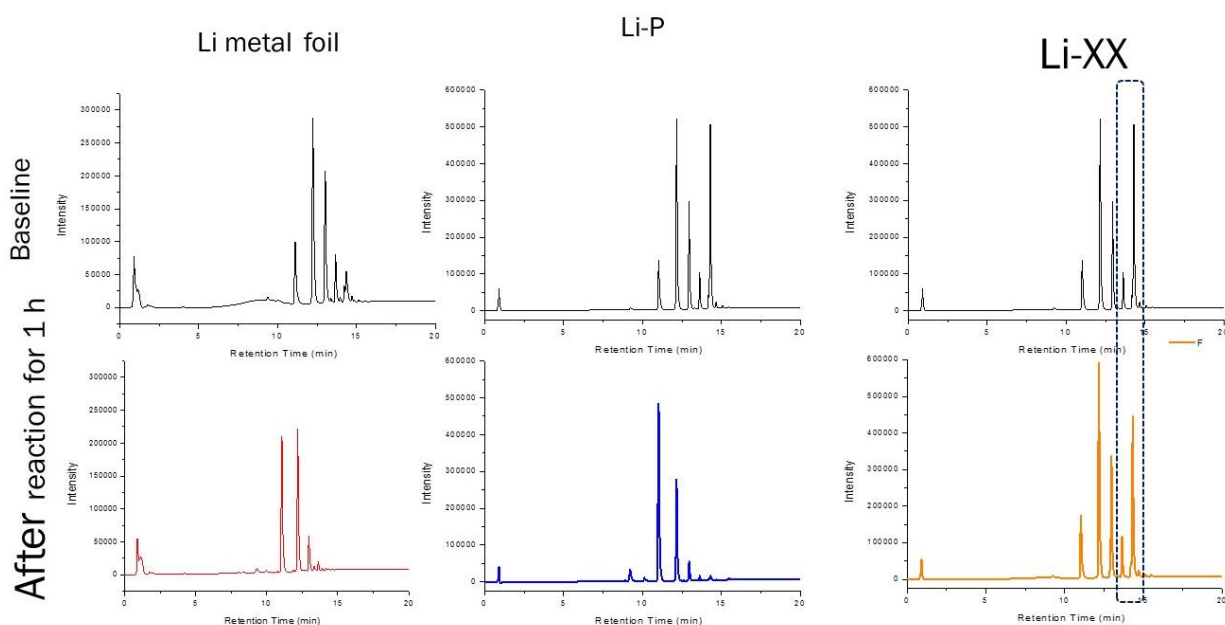


Figure II.8.E.2 Comparison of the reaction between dissolved polysulfide ions with metallic Li, Li-phosphorus and a proprietary Li containing anode (Li-XX). The HPLC peak on the far right (in the dash-line box) is elemental sulfur peak.

3, Synthesis and electrochemical testing of sulfur containing polymer cathode materials

To eventually eliminate the so-called “shuttle effect”, we should first try to prevent the chemical reactions between the anode and dissolved polysulfide ions as we described in section 1 and 2; secondly, to localize the dissolved polysulfide ions in the cathode matrix. In FY18, we explored synthesizing numerous sulfur containing polymer compounds and tested them as sulfur cathodes.

In order to better localize the polysulfide in the cathode matrix and prevent them from diffusing to the bulk electrolyte and making contact with Li anode, we tried to bond the polysulfide species on the backbone materials, either modified carbon or polymers through chemical bonds. One example was to copolymerize sulfur with *p*-Phenylene vinylene derivative (denoted as Xant-) to form a new conductive crosslinked Polysulfur-*random*-PPV (denoted as S/Xant-) copolymer cathode material in one pot. Taking advantage of the diradical character of *p*-Phenylene vinylene intermediate, the diradical polymeric sulfur can be intercepted and stabilized by the formation of strong covalent bonds between sulfur and carbon. The cross-linked polymer framework would help to self-protect and confine polysulfide and sulfur dissolution, and thus avoided the detrimental shuttle effects. Poly(*p*-Phenylene vinylene) (PPV) and its derivatives were conjugated conductive materials and with their inclusion in the cross-linked copolymer framework, fast electron conducting channels would be provided, which could improve the conductivity of the sulfur containing polymer. Figure II.8.E.3 shows the photographs of S/Xant-copolymer with different sulfur contents and the rate performance of as-synthesized S/Xant- (70 wt% S). The preliminary result indicated that the S/Xant- has a high initial capacity of 720 mAh g⁻¹ (based on S/Xant- or 1029 mAh g⁻¹ based on sulfur) at 100 mA g⁻¹ discharge rate. The capacity decreased as the discharge rate increases e.g. at high rate (> 1 A g⁻¹) it was relatively low, which probably results from the aggregation of S/Xant- copolymer in the electrode, which could limit the ionic diffusion. On one hand, the aggregation of S/Xant- copolymer could confine the polysulfide ions within the cathode; while on the other hand, it might also hinder the mass transfer of Li⁺ in and out of the cathode matrix. The limitation of the Li ion diffusion would induce the low capacity at high rates. As shown in Figure II.8.E.3, When the current density was back to 100 mA g⁻¹ after 30 cycles, the reversible capacity went back to ~ 610 mAh g⁻¹ (S/Xant-), suggesting a good stability of the electrode. The performance of S/Xant- electrode could be further improved by optimizing the electrode structure.

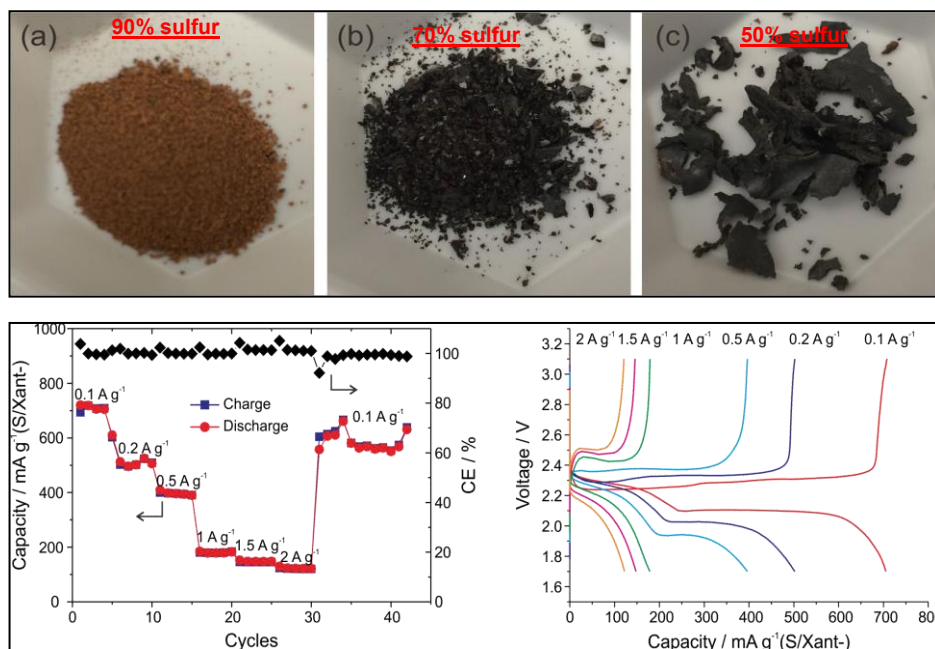


Figure II.8.E.3 The photograph of the synthesized S/Xant co-polymer with different sulfur contents (top); the cycle and rate performance of the co-polymer with 70% sulfur. The tests were done in a coin cell.

Together with the S/Xant co-polymer, we have synthesized a few copolymerize sulfur materials according to the various strategies to localize the polysulfide ions. We had limited success. The results are tabulated in Table II.8.E.2. It seems copolymer #1, #6 and #10 had relatively better cycleability than a sulfur anode, but the initial capacity of all anodes was lower than that of sulfur anode. More copolymerized sulfur compounds are being synthesized and tested.

**Table II.8.E.2 Test results of ten synthesized co-polymers.
The control is sulfur cathode with 75% sulfur.**

Sulfur polymer	1st discharge Capacity (mAh/g)	50th Discharge Capacity (mAh/g)	Retention (%)
1	626	455	73
2	623	238	45
3	554	253	46
4	448	201	45
5	905	412	45
6	333	249	75
7	591	228	39
8	345	134	39
9	176	69	39
10	473	288	61
11	1663	1247	75
Control (75% S)	672	267	40

Conclusions

1. *In-situ* HPLC-MS electrochemical essays were developed to quantitatively and qualitatively determine the polysulfide ions during the operation of Li-S batteries.
2. The techniques have been further proven as an effective method to investigate the mechanism of Li-sulfur redox mechanism, screening “shuttle effect” inhibitors and study the chemical/electrochemical reactions of the dissolved polysulfide ions since all the soluble elemental sulfur and polysulfide ions can be separated and qualitatively determined by HPLC-UV/MS with proper treatment.
3. LiNO₃ and other sacrificial inhibitors may SLOW-DOWN the Li-sulfide (sulfur) reactions, but cannot eliminate “shuttle effect”.
4. To mitigate “shuttle effect”, the polysulfide ions should be either restrained in the cathode matrix e.g. by strong chemical bonding in co-polymers, or made not to react with alternative Li containing anodes.

Key Publications

1. Dong Zheng, Gongwei Wang, Dan Liu, Jingyu Si, Tianyao Ding, Deyu Qu, Xiaoqing Yang, and Deyang Qu, “The Progress of Li-S batteries – understanding of the sulfur redox mechanism”, *Adv. Mater. Technology* <https://doi.org/10.1002/admt.201700233>
2. Dong Zheng, Gongwei Wang, Dan Liu, Joshua B. Harris, Tianyao Ding, Jingyu Si, Deyu Qu, Xiaoqing Yang, Deyang Qu, “Systematic and Rapid Screening for the Redox Shuttle Inhibitors in Lithium-Sulfur Batteries”, *Electrochim. Acta* 282(2018)687-693.

II.8.F Statically and Dynamically Stable Lithium-sulfur Batteries (UTA)

Arumugam Manthiram, Principal Investigator

The University of Texas at Austin

Austin, TX 78712

E-mail: manth@austin.utexas.edu

Tien Q. Duong, DOE Technology Development Manager

U.S. Department of Energy

E-mail: Tien.Duong@ee.doe.gov

Start Date: October 1, 2015

End Date: September 30, 2018

Project Funding (FY18): \$330,000

DOE share: \$297,000

Non-DOE share: \$33,000

Project Introduction

The commercialization of lithium-sulfur (Li-S) batteries is hampered by several intrinsic materials challenges: low electronic and ionic conductivity of the active material, severe polysulfide migration from the cathode to the anode, and instability of the Li-metal anode. The poor conductivity limits the electrochemical utilization of the active material and often necessitates a high content of electrochemically inactive, conductive carbon or functional polymers in the cathode region, which lowers the practical energy density. The polysulfide migration causes static and dynamic instabilities with high self-discharge, poisoning of Li-metal surface, and poor cycling efficiency, hindering the practical viability of Li-S batteries. Recently, it is becoming obvious that these intrinsic materials issues are very sensitive toward and even strongly impacted by the extrinsic cell-design parameters, such as the amount of sulfur in the cathode, the electrolyte/sulfur (E/S) ratio in the tested cells, and the type of testing cells. In response, the research community is invoking the necessity of studying the Li-S battery electrochemistry and the cell performance using cells fabricated with more practical parameters. The necessary parameters to develop high-energy-density Li-S batteries include a sulfur loading of at least 5 mg cm^{-2} , a sulfur content of over 65 wt.%, and a low E/S ratio of less than $11 \mu\text{L mg}^{-1}$. In terms of the testing cells used in research, coin-type cells offer a cost/time-effective way for fundamental research and initial designs. For practical application, the future focus should be devoted largely to pouch-type cells to make the Li-S technology a practically viable energy storage system.

To overcome the above challenges, our group has demonstrated that innovations in polysulfide-filter-coated separators and advanced electrode substrates can greatly enhance the electrochemical utilization and efficiency with reasonably high sulfur loadings and low E/S ratios in the cells. This is because Li-S batteries involve conversion reactions unlike the insertion-reaction electrodes in commercial Li-ion batteries, so cell components/designs directly borrowed from Li-ion batteries may need new architectures or chemical/physical characteristics to be adapted to sulfur cathodes. Our cell-component design provides the fabricated Li-S cells with enhanced electrochemical performance: high utilization of the active material, extended cycle life, and good storage properties. More importantly, these custom cell configurations allow the cells to employ the easily prepared sulfur cathodes with high sulfur loading ($> 6.0 \text{ mg cm}^{-2}$) and high sulfur content ($> 65 \text{ wt. \%}$) in both coin-type and pouch-type cells with low electrolyte/sulfur ratios of less than $11 \mu\text{L mg}^{-1}$. Our progress illustrates that the approaches presented and developed in this project are inexpensive and offer a practically viable solution for the Li-S technology development.

Objectives

The objective of this project is to develop statically and dynamically stable Li-S batteries by integrating polysulfide-filter-coated separators with an advanced cathode design and/or a protected Li-metal anode. The project includes demonstration of electrochemically stable cells with sulfur capacities of $> 1,000 \text{ mA h g}^{-1}$ and cycle life in excess of 500 cycles (dynamic stability) along with improved storage properties (static stability) at $> 70 \text{ wt. \%}$ sulfur content and $\sim 5 \text{ mg cm}^{-2}$ loading.

Approach

The electrochemical stability of the Li-S cells is improved by three approaches that are complementary to each other:

- The first approach focuses on the establishment of an electrochemically stable cathode environment by employing polysulfide-filter-coated separators. The polysulfide-filter coatings aim to suppress the severe polysulfide diffusion and improve the redox capability of the Li-S cells with high-sulfur loadings. The study includes an understanding of the materials characteristics, fabrication parameters, electrochemical properties, and battery performance of the polysulfide -filter-coated separators.
- The second approach focuses on electrode engineering from two aspects. First, the investigation of a Li-metal anode with coating- and additive-supporting approaches aim at improving the safety of Li-S cells. Second, the research on activated-Li₂S cathode with little or no charge-barrier aims at promoting the performance and safety of the C-Li₂S cells.
- The integration of the above two approaches aims at creating statically and dynamically stable Li-S batteries for electric vehicles.

Results

In Year 3 of the project, we have demonstrated our scientific success in developing (i) Li-metal anodes with high electrochemical stability and (ii) high-performance Li₂S cathodes with practically necessary parameters (Technical Milestones I and II in Quarters 1 and 2). Moreover, in order to demonstrate Li-S cells with good practical feasibility, we have investigated coin-type Li-S cells with a high-loading sulfur cathode at a lean electrolyte condition. We further applied the understanding to develop pouch-type Li-S cells (Technical Milestone III and Go/No-Go Milestone in Quarters 3 and 4). As a result, we have demonstrated that Li-S cells with a high-loading sulfur cathode (sulfur loading: 13 mg cm⁻² and sulfur content: 75 wt.%) can achieve excellent cycle stability at a low E/S ratio of 4.0 μL mg⁻¹. The cells attained a long cycle life of over 200 cycles and high capacity retention of 85%. The scientific and technical challenges that our team overcame this year have guided us to develop a time/cost-effective way to transition coin-type Li-S cells to pouch-type Li-S cells.

Key accomplishment 1: Li-metal anodes with high electrochemical stability

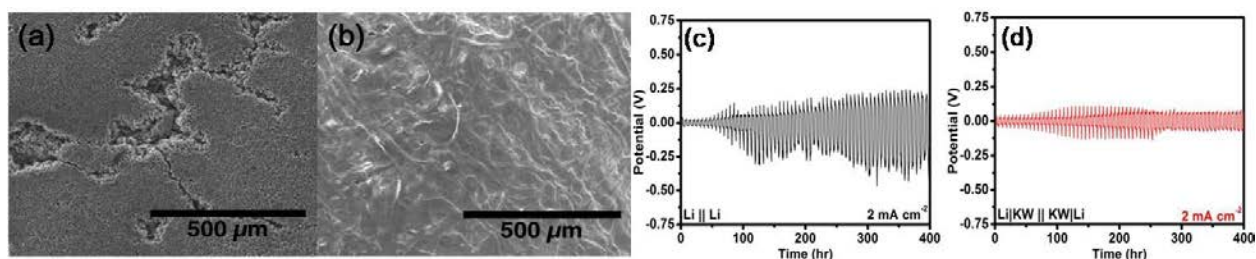


Figure II.8.F.1 Scanning electron microscope (SEM) images of Li deposits using Li-Cu cells (a) with and (b) without the KW-stabilization layer at 3 mA cm⁻² for 3 hours. Overpotential of Li-Li symmetric cells (c) with and (d) without the KW-stabilization layer at 2 mA cm⁻² for 400 hours.

In order to enhance the stability of the reacted Li-metal electrode during long-term cycling, we have applied a Kimwipe (KW) paper on the surface of Li-metal anode as a stabilization layer (KW-stabilization layer). The KW-stabilization layer aimed to create a uniform, smooth Li redeposition with no Li dendrites. Moreover, the fresh cellulose fibers of the KW paper have abundant polar functional groups like -OH and C-O-C, which can adhere to Li ions, improve the wettability with the electrolyte, and impede the inhomogeneous aggregation of Li ions around the protrusions of the deposited Li. To demonstrate these physical and chemical functions, cells with and without the KW-stabilization layer were prepared for the comparative research

Figure II.8.F.1a and Figure II.8.F.1b show the Li deposition tests of the Li-Copper (Cu) cells, respectively, with and without the KW-stabilization layer. We controlled the Li to be plated on the Cu-foil substrate at a current density of 3 mA cm^{-2} for 3 hours in both cases. The control cell without the KW-stabilization layer exhibited non-uniform and rough Li deposits with huge cracks, in which we could clearly observe the growth of Li dendrites (Figure II.8.F.1a). In contrast, at the same plating condition, Figure II.8.F.1b demonstrates that a KW-stabilization layer allowed the cycled Li-metal anode to possess a dendrite-free, smooth Li deposition layer. The KW-protected Li-metal anode exhibited a well-preserved integrity after cycling. The dendrite-free morphology and smooth surface observed in the KW-protected cell provide evidence of homogeneous Li-ion distribution and stabilized Li-metal electrodes. Figure II.8.F.1c and Figure II.8.F.1d show the electrochemical testing of the Li-Li symmetric cells, respectively, with and without the KW-stabilization layer. Without the KW-stabilization layer, the control cell showed a typical high and increasing voltage polarization ($\sim 700 \text{ mV}$) with unstable voltage fluctuations in the voltage versus cycling time profile during 400-hour cycling (Figure II.8.F.1c). In contrast, the symmetric cell with the KW-stabilization layer showed excellent cycling stability for 400 hours with a low polarization ($\sim 200 \text{ mV}$) at the same current density of 2 mA cm^{-2} (Figure II.8.F.1d). The high reversibility of the KW-protected cell suggests that the KW paper provides a polar lithiophilic interface for the Li-metal anode, which effectively eliminates inhomogeneous Li-ion distribution on the surface, resulting in a dendrite-free morphology of the deposited Li.

Key accomplishment 2: Develop high-performance Li_2S cathodes with practically necessary parameters

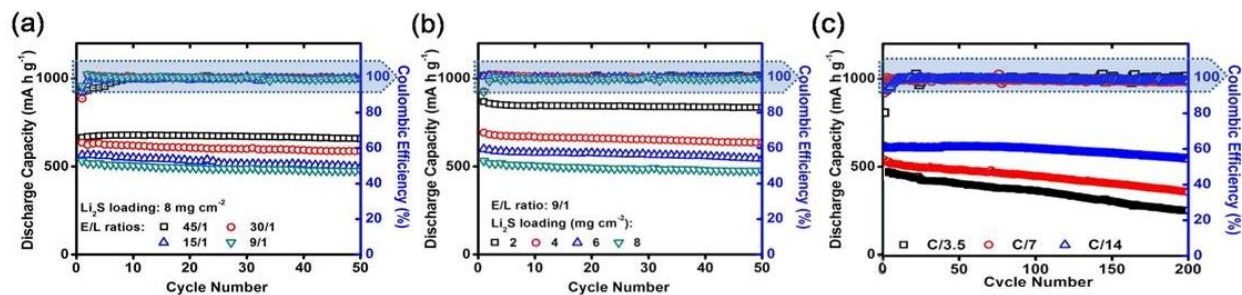


Figure II.8.F.2 Cyclability (a) with various E/L ratios from 45 to $9 \mu\text{L mg}^{-1}$ at a fixed Li_2S loading of 8 mg cm^{-2} and (b) with various Li_2S loadings from 2 to 8 mg cm^{-2} at a fixed E/L ratio of $9 \mu\text{L mg}^{-1}$. E/L ratio and Li_2S loading of, respectively, $45 \mu\text{L mg}^{-1}$ and 2 mg cm^{-2} are the average values reported in published Li_2S papers. (c) Performances of the cells with a Li_2S loading of 8 mg cm^{-2} and an E/L ratio of $9 \mu\text{L mg}^{-1}$ at various cycling rates.

We have demonstrated in this year a shell-shaped carbon architecture for developing pure lithium sulfide (Li_2S) cathodes with superior cell-design parameters and electrochemical characteristics. The key concept of the Li_2S core – carbon shell electrode aimed to encapsulate the insulating Li_2S and its redox products within the conductive shell to facilitate good electron/ion accessibility and limit the irreversible loss of the active material. In order to realize the best cell-design specification, the core-shell Li_2S cathode was initially carefully evaluated in relation to the critical cell-design parameters, such as the loading and content of Li_2S in the cathode and the electrolyte amount in the cells. Accordingly, our cells presented the highest Li_2S loading of 8 mg cm^{-2} (a value that is 5 times higher than the average value in the literature) with 100% Li_2S content (63 wt.%, including all cathode components), as shown in Figure II.8.F.2a, and the lowest electrolyte/ Li_2S (E/L) ratio of 9 (a value that is 5 times lower than the average value in the literature, Figure II.8.F.2b). Even with such strict cell-design parameters, Figure II.8.F.2c demonstrates that our core-shell Li_2S cathodes achieved a high peak charge-storage capacity of 601 mA h g^{-1} and kept a high reversible capacity of 540 mA h g^{-1} after 200 cycles at a C/14 rate. Such enhanced battery performance demonstrates (i) superior electrochemical Li_2S utilization, (ii) high capacity retention of 90%, and (iii) enhanced rate performance from C/14 – C/3.5 rates.

Key accomplishment 3: Develop coin-type Li-S cells with a high sulfur loading and lean electrolyte

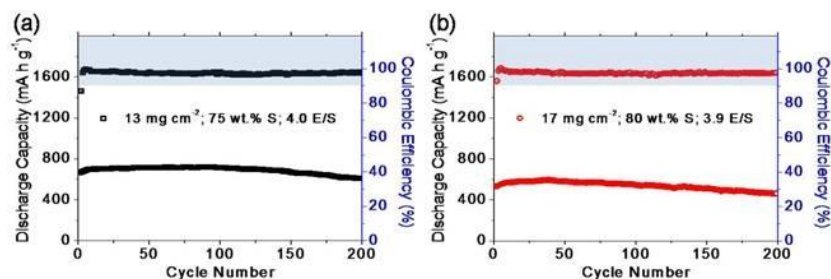


Figure II.8.F.3 (a) Cyclability of the cells fabricated with the carbon-paper cathodes with a sulfur loading, sulfur content, and E/S ratio of, respectively, (a) 13 mg cm⁻², 75 wt.%, and 4.0 μL mg⁻¹ and (b) 17 mg cm⁻², 80 wt.%, and 3.9 μL mg⁻¹.

It is recognized by the research community that the necessary parameters to develop high-energy-density Li-S batteries include a sulfur loading of at least 5 mg cm⁻², a sulfur content of over 65 wt.%, and a low E/S ratio of less than 11 μL mg⁻¹. This year, we demonstrated a high-loading, lean-electrolyte sulfur cathode by assembling two carbon-paper sheets as a cathode substrate, into which Li₂S₆ polysulfide catholyte was added. Two cathodes were fabricated with this design: one with 13 mg cm⁻² and 75 wt.% sulfur with an E/S ratio of 4.0 μL mg⁻¹ and the other with 17 mg cm⁻² and 80 wt.% sulfur with an E/S ratio of 3.9 μL mg⁻¹, based on the total mass of the cathode including the carbon paper. Operating under such strict cell-design conditions, the cells with 13 and 17 mg cm⁻² showed high charge-storage capacities of, respectively, 717 and 593 mA h g⁻¹ at a C/10 rate with high capacity-retention rates of 71% and 85% after 200 cycles (Figure II.8.F.3). With the extensive work we carried out this year with a high sulfur loading and lean electrolyte in the coin cells, we also applied the knowledge to fabricate pouch-type Li-S cells.

Key accomplishment 4: Transitioning from coin-type Li-S cells to pouch-type Li-S cells

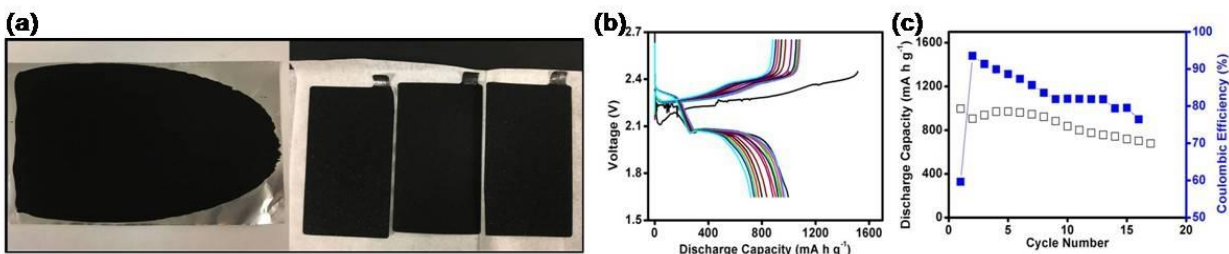


Figure II.8.F.4 (a) Sulfur cathodes fabricated for pouch-type Li-S cells. Electrochemical performance of the pouch-type Li-S cells: (b) voltage profiles and (c) cycling performance.

For practical application, it is necessary to develop the Li-S technology by transitioning from coin-type cells with small size electrodes to pouch-type cells with electrode sizes similar or close to that of practical battery electrodes. In order to develop and assess the design of pouch-type Li-S cells with a high sulfur loading, we focused on cathode engineering (Figure II.8.F.4a). In addition, we also considered the cost and environmental issues involved with high-loading cathode configurations in pouch cells. Thus, a simple sulfur-based active-material composite was used. The active-material composite with pristine sulfur (S), KetJen Black (KJB), and carbon nanotube (CNT) was prepared through a melt-diffusion process at 155 °C. The synthesized active-material composite (S/KJB/CNT) was mixed with additional conductive carbon and polymer binders. The resultant active-material slurry was then coated onto an aluminum foil and dried in a vacuum oven at 50 °C. All materials, including active sulfur and other inactive materials, and the heat-treatment methods are similar to those commonly used with Li-S cathodes. Thus, we make the cathode preparation as simple as possible. A simplified cathode-preparation method allows us to prepare a high volume of cathodes with high repeatability and stability, limiting the cost issues encountered in cathode optimization. The prepared cathode was cut in a size of 47.8 mm x 81.5 mm and had a sulfur content of 65 wt.% and a sulfur loading of 6 mg cm⁻². In the cell-

assembly process, a lithium foil was cut into the same size as large as the size of the cathode. A sheet of separator was then placed between the two electrodes and the assembled cell was sealed in a plastic film pouch with the E/S ratio fixed at $5 \mu\text{L mg}^{-1}$.

Figure II.8.F.4b shows the electrochemical performance of the pouch-type Li-S cells. The assembled cells were rested for 2 h and then cycled in the voltage window of 1.65 – 2.60 V at a C/20 rate. After the first cycle, the discharge-charge curves exhibit the typical two-step redox reaction of the Li-S chemistry. The discharge capacity at the first cycle reaches 995 mA h g^{-1} , corresponding to 60% electrochemical utilization. Considering the larger areal size of the cell (38.9 cm^2), the cell still shows outstanding performance. As a reference, the areal size of the regular coin cell is only 1.13 cm^2 . After 18 cycles, the discharge capacity remains at 661 mA h g^{-1} with a high capacity retention of 66% (Figure II.8.F.4c). Thus, we demonstrated the promising pouch cell performance by using simple sulfur-based active-material composites, which might offer a facile path forward to fabricate pouch-type Li-S cells with good consistency. This progress further allows us to avoid the concern of applying a high amount of toxic starting active materials, such as liquid-state polysulfide catholyte that has strong activity or lithium sulfide that has strong sensitivity toward air and moisture.

Conclusions

In Year 3, we have completed the investigation on the Li-anode stabilization and the development of Li_2S cathodes with high electrochemical performance and practically necessary parameters. (1) The KW-stabilization layer offers a sustainable and low-cost protection layer on the reacted Li-metal anode. (2) The Li_2S core – carbon shell electrode achieves the highest Li_2S loading and the lowest E/L ratio while still attaining a high electrochemical stability for 200 cycles. For the sake of practical application, we have demonstrated the high-loading, lean-electrolyte carbon-paper cathodes that attain excellent cyclability with 85% capacity retention after 200 cycles at a low E/S ratio of only $4.0 \mu\text{L mg}^{-1}$. With the extensive work we carried out with a high sulfur loading and lean electrolyte in coin cells, we applied the knowledge to fabricate pouch-type Li-S cells. Our pouch-type Li-S cells utilize the simple S/C composite cathode design with low-cost and commercially available materials as well as easy preparation processes to result in a high electrochemical performance.

Key Publications

Reports

1. DOE EE7218 Quarterly Report-01-18 (Jan. 29, 2018)
2. DOE EE7218 Quarterly Report-04-18 (Apr. 24, 2018)
3. DOE EE7218 Quarterly Report-07-18 (Jul. 27, 2018)
4. DOE EE7218 Quarterly Report-10-18 (Oct. 25, 2018)

Journal articles

1. C.-H. Chang and A. Manthiram, “Covalently-grafted Polysulfur-graphene Nanocomposites for Ultrahigh Sulfur-loading Lithium-polysulfur Batteries,” *ACS Energy Letters* **3**, 72 (2018).
2. S.-H. Chung and A. Manthiram, “Rational Design of Statically and Dynamically Stable Lithium-sulfur Batteries with High Sulfur Loading and Low Electrolyte/sulfur Ratio,” *Advanced Materials*, **30**, 1705951 (2018).
3. S.-H. Chung, L. Luo and A. Manthiram, “ TiS_2 -Polysulfide Hybrid Cathode with High Sulfur Loading and Low Electrolyte Consumption for Lithium-sulfur Batteries,” *ACS Energy Letters* **3**, 568 (2018).
4. S.-H. Chung and A. Manthiram, “Designing Lithium-Sulfur Batteries with Practically Necessary Parameters,” *Joule* **2**, 1 (2018).

5. L. Luo, S.-H. Chung, and A. Manthiram, "Rational Design of a Dual-function Hybrid Cathode Substrate for Lithium-sulfur Batteries," *Advanced Energy Materials* **8**, 1801014 (2018).
6. S.-H. Chung, C.-H. Chang, and A. Manthiram, "Progress on the Critical Parameters for Lithium-sulfur Batteries to be Practically Viable," *Advanced Functional Materials* **28**, 1801188 (2018).
7. S. Nanda, A. Gupta, and A. Manthiram, "A Lithium-sulfur Cell Based on Reversible Lithium Deposition from a Li₂S Cathode Host onto a Hostless-anode Substrate," *Advanced Energy Materials* **8**, 1801556 (2018).
8. L. Luo, S.-H. Chung, and A. Manthiram, "Long-Life Lithium-Sulfur Batteries with a Bifunctional Cathode Substrate Configured with Boron Carbide Nanowires," *Advanced Materials* **30**, 1804149 (2018).
9. S.-H. Chung, K.-Y. Lai, and A. Manthiram, "A Facile, Low-cost Hot-pressing Process for Fabricating Lithium-sulfur Cells with Stable Dynamic and Static Electrochemistry," *Advanced Materials* (2018) DOI: 10.1002/adma.201805571.
10. S.-H. Chung and A. Manthiram, "Constructing high-loading, lean-electrolyte lithium-sulfur battery cathodes with a conductive, low-surface-area cathode substrate," *ACS Applied Materials & Interfaces* (submitted).

Presentations

1. A. Manthiram, "Electrical Energy Storage: Next Generation Battery Technologies," *King Abdullah University of Science and Technology (KAUST)*, Thuwal, Saudi Arabia, October 26, 2017 (invited).
2. C.-H. Chang, S.-H. Chung, and A. Manthiram, "Oligoanilines as a suppressor of polysulfide shuttling in lithium-sulfur batteries," *2017 MRS Fall Meeting*, Boston, MA, November 26 – December 1, 2017.
3. C.-H. Chang and A. Manthiram, "Polymeric sulfur-graphene nanocomposites for high areal capacity lithium-sulfur batteries," *2017 MRS Fall Meeting*, Boston, MA, November 26 – December 1, 2017.
4. S.-H. Chung and A. Manthiram, "Lithium-sulfur batteries with the high sulfur loading/content and low electrolyte/sulfur ratio," *2017 MRS Fall Meeting*, Boston, MA, November 26 – December 1, 2017.
5. S.-H. Chung and A. Manthiram, "Lithium-sulfur batteries with the lowest self-discharge and the longest shelf-life," *2017 MRS Fall Meeting*, Boston, MA, November 26 – December 1, 2017.
6. Manthiram, "Electrical Energy Storage: Next Generation Battery Chemistries," *School on Clean and Renewable Energy Technologies via Chemical Route*, "International Institute for Complex Adaptive Matter, Jawaharlal Nehru Centre for Advanced Scientific Research, Bangalore, India, November 27 – December 2, 2017 (invited).
7. Manthiram, "Next Generation Battery Technologies," *Ford Motor Company*, Dearborn, MI, December 13, 2017 (invited).
8. Manthiram, "Electrical Energy Storage: Next Generation Battery Technologies," *University of Central Florida*, Orlando, FL, January 19, 2018 (invited).
9. Manthiram, "Next Generation Battery Chemistries," *NAATBatt Annual Meeting and Conference*, San Antonio, TX, March 21, 2018 (invited).

10. Manthiram, “Materials Challenges and Prospects of Electrical Energy Storage,” International Symposium on Functional Materials (ISFM-2018), Chandigarh, India, April 13 – 15, 2018 (invited plenary talk).
11. Manthiram, “Next Generation Battery Chemistries: Materials Challenges and Prospects,” Central Electrochemical Research Institute, Chennai, India, April 20, 2018 (invited talk).
12. Manthiram, “Next-generation Battery Technologies: Materials Challenges and Prospects,” 2nd International Materials Science and Engineering for Green Energy Conference, Rabat, Morocco, April 25, 2017 (invited plenary talk).
13. Manthiram, “Next-generation Rechargeable Battery Chemistries,” Hefei University, Hefei, China, July 14 – 15, 2018 (invited talk).
14. Manthiram, “Materials Challenges and Prospects of Electrical Energy Storage,” 3rd International Symposium on Renewable Energy Technologies, Gold Coast, Australia, July 19 – 22, 2018 (invited plenary talk).
15. Manthiram, “Where is Electrical Energy Storage Headed?” 16th Asian Conference on Solid State Ionics, Shanghai, China, August 5 – 9, 2018 (invited plenary talk).
16. Manthiram, “Lithium-Sulfur Batteries: Progress, Benchmarks, and Challenges,” Lithium-Sulfur Batteries Deep-dive Meeting, University of Texas at Austin, Austin, TX, September 5 – 6, 2018 (invited).

II.8.G Dual Function Solid State Battery with Self-forming Self-healing Electrolyte and Separator (Stony Brook University)

Distinguished Professor Esther Takeuchi, Principal Investigator

Stony Brook University
1000 Innovation Road
Stony Brook, NY 11794-6044
E-mail : esther.takeuchi@stonybrook.edu

Kenneth J. Takeuchi, Principal Investigator

Stony Brook University
1000 Innovation Road
Stony Brook, NY 11794-6044
E-mail: kenneth.takeuchi.1@stonybrook.edu

Amy C. Marschilok, Principal Investigator

Stony Brook University
1000 Innovation Road
Stony Brook, NY 11794-6044
E-mail: amy.marschilok@stonybrook.edu

Tien Duong, DOE Technology Development Manager

U.S. Department of Energy
E-mail : Tien.Duong@ee.doe.gov

Start Date: October 1, 2016	End Date: September 1, 2019	
Project Funding: \$1,200,000	DOE share: \$1,065,975	Non-DOE share: \$134,025

Project Introduction

The goal of this project is to demonstrate a solid-state rechargeable battery based on a lithium metal anode and iodine cathode with a self-forming, self-healing electrolyte and separator. The presence or formation of dendrites or pin holes can result in compromised cell performance or even failure for solid state cells which would be avoided by the proposed new technology. The theoretical energy density of the Li/I₂ couple is 560 W·h/kg, which provides the opportunity to meet or exceed the DOE target of 250 W·h/kg at the battery level.

The proposed concept is a solid-state battery utilizing lithium iodide (LiI) combined with silver iodide (AgI) as the electrolyte with lithium (silver) metal as the anode and iodine as the cathode with a self-forming self-healing separator/electrolyte. The battery will be assembled in the discharged state where the anode and cathode will be created during the first formation (charge) step. Silver ion, Ag⁺, will diffuse toward the negative electrode and be reduced to silver metal, Ag⁰ and lithium ion, Li⁺, will form a lithium metal-layer at the anode. Iodine ion, I⁻, will be oxidized to elemental iodine, I₂, at the cathode side. As formation of the battery continues, Lithium iodide will remain and serve as both the separator and electrolyte, as shown schematically in Figure II.8.G.1.

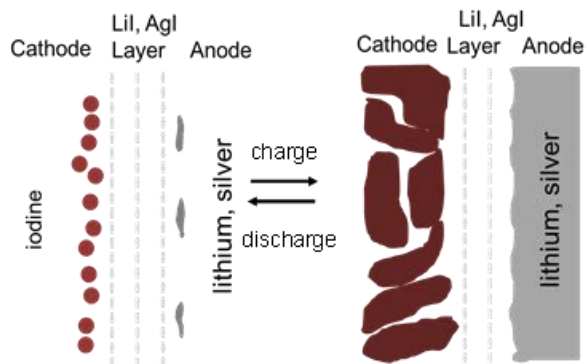


Figure II.8.G.1 Silver-lithium/iodine solid state dual function battery.

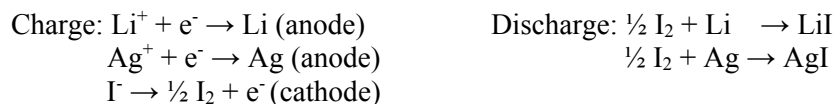
Objectives

The project goal will be addressed by focusing on the three major objectives outlined below:

- **Objective 1:** Develop a LiI/AgI based electrolyte with conductivity of $>10^{-3}$ S/cm at 30°C.
- **Objective 2:** Form Li/I₂ batteries through the charging of the composite solid-state electrolytes, determine relationship of coulombic efficiency to electrolyte type.
- **Objective 3:** Determine the role of Ag ion in the anode: electrolyte interface as a function of electrolyte composition and cell test parameters through in-situ and ex-situ analyses.

Approach

The proposed solid-state battery utilizes lithium iodide (LiI) combined with silver iodide (AgI) as the electrolyte with lithium (silver) metal as the anode and iodine as the cathode with a self-forming self-healing separator/electrolyte. The mechanism of the Ag-Li/I₂ solid state battery can be described as follows:



This is a multiyear program where the effort is divided into three major tasks.

Year 1 involves preparation and characterization of solid-state electrolytes and conductivity measurements.

Year 2 will focus on cell construction and testing including both *in-situ* and *ex-situ* analysis.

Year 3 will focus on cell characterization. Under the program, cycle life, efficiency, energy density, and the functional capacity of cells will be determined.

The proposed work will be executed in the Advanced Power Sources (APS) Laboratories in the Chemistry Building at Stony Brook University (SBU), the Advanced Energy Research and Technology Center (AERTC) at SBU, and at Brookhaven National Laboratory (BNL). BNL offers core capabilities for the proposed program, including the user facilities the National Synchrotron Light Source-II (NSLS-II) and Center for Functional Nanomaterials (CFN). Table II.8.G.1 lists the quarterly milestones and verification for year 2.

Table II.8.G.1 Quarterly Milestones and Verification for Year 2.

	Q1	Q2	Q3	Q4
Milestone	Identify 3 most conductive LiI based solid electrolytes	Develop cell construction A	Prepare construction A electrolyte candidates	Formation of LiO, AgO at anode and iodine at cathode
Verification	Conductivity measured	Charging dependence on formation of battery is obtained	Performance evaluation begins with electrolyte candidates	Cell voltage and analysis confirm products

Results

Solid electrolyte conductivity

LiI based solid electrolytes with or without additive were created and the conductivity was determined. This additive was initially combined with solid LiI and incorporated into electrolytes in varying ratios. The improvements in ionic conductivity were measured and quantified by Electrochemical Impedance Spectroscopy (EIS) and equivalent circuit modeling. Multiple ratios were tested, each with different amounts of additive, Figure II.8.G.2. These samples were compared to solid electrolytes of the same composition without additive. A select number of samples with additive across the temperature range from 28 to 42°C are shown in Figure II.8.G.2 where an increase in conductivity of up to 2 orders of magnitude is observed. The solid electrolyte compositions were selected for development of cell construction A.

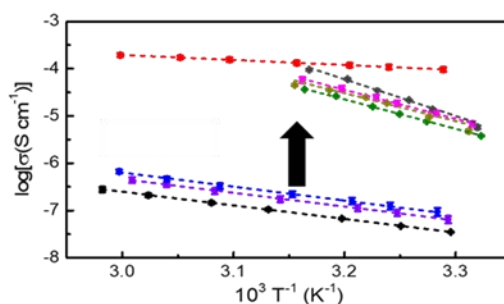


Figure II.8.G.2 Conductivity effects of additive

Preliminary cycling data was collected using a solid electrolyte containing LiI with additive. Cells were constructed with and without an additional Li source and were cycled to test feasibility (Figure II.8.G.3a) and to evaluate the Coulombic efficiency compared to cycle number. (Figure II.8.G.3b) Both sets of cells could be charged and functioned effectively, but the efficiency was higher for the Li metal containing cells.

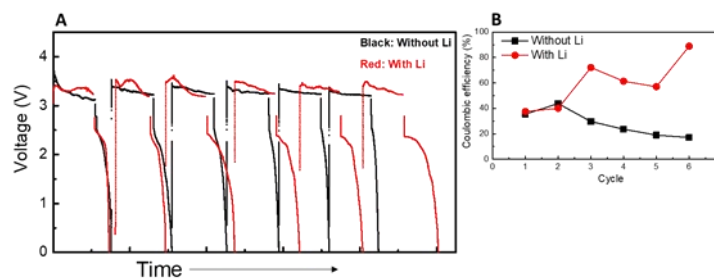


Figure II.8.G.3 (a) Cycling of cells containing additive with and without Li metal added, b) Coulombic efficiency.

Cell construction A for Li/I₂ batteries with or without additive

The milestone for the sixth quarter was the development of cell construction A for Li/I₂ batteries with the use of additive. The electrolyte used for the cell testing included the use of LiI composite with additive. The cell was charged under 10 $\mu\text{A}/\text{cm}^2$, and electrochemical impedance spectroscopy (EIS) data were collected at several states of charge ranging from <1% to ~10% of total capacity (Figure II.8.G.4). Notably, after each charge interval a stable open circuit voltage (OCV) of ~2.7 V was seen and is an indicator of a successfully formed Li/I₂ battery. Analysis of the EIS data reveal the decrease of the cell resistance with charging. A large impedance of ~316 k Ω was initially observed for the as prepared cell. Significant impedance decrease (factor of ~5 times) was observed after only 0.5% charge. The impedance then stabilized and remained at ~30-40 k Ω through the continuing charge steps. The data indicate that the impedance is not directly correlated to the quantity of electrolyte consumed.

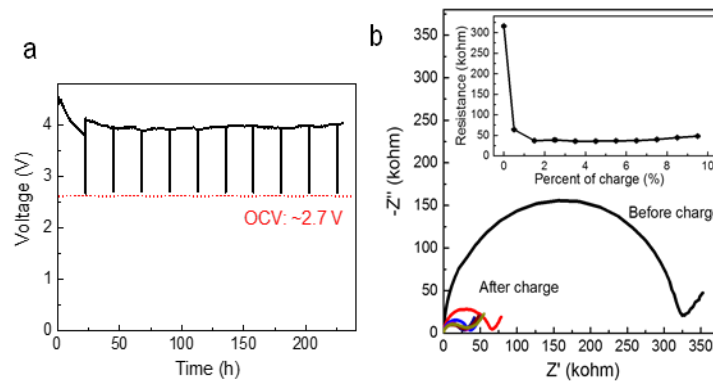


Figure II.8.G.4 (a) Intermittent charging and (b) AC impedance results for LiI electrolyte based cell.

Modification of the cathode interface of the LiI composite containing cells was studied by inclusion of polymeric additive. The additive is known to create conductive charge transfer complexes with iodine. For one cell design, a thin layer of polymer was used at cathode interface. Interestingly, EIS results indicated that the LiI composite containing cells with polymeric additive showed slightly higher impedance results before and after charging than the cells with no polymeric additive (Figure II.8.G.5).

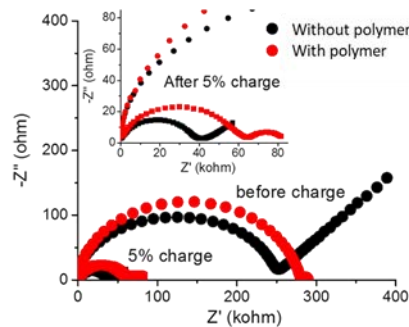


Figure II.8.G.5 AC impedance of LiI cells with and without polymer.

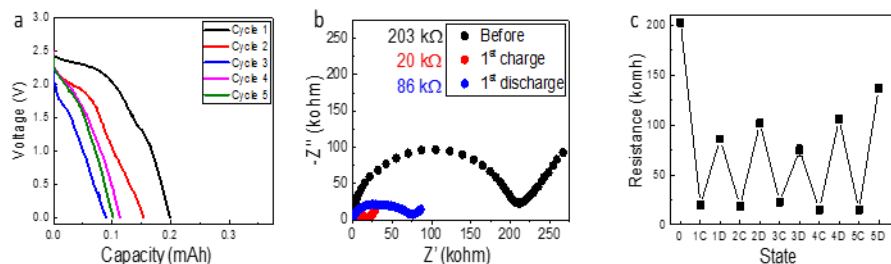


Figure II.8.G.6 (a) Discharge curves, (b) AC impedance, and (c) impedance results for LiI composite containing cell.

Electrochemical cycling using cell construction A

Galvanostatic cycling was performed for cell construction A. A solid electrolyte based on 80%LiI:20%LiI composite was used for the electrochemical cycling. Five full charge and discharge cycles were performed on the cell where full discharge was used for the test. The cell performance was evaluated by the discharge capacities and EIS after charge/discharge (Figure II.8.G.6). Notably, after initial charge, the impedance decreased significantly. Even when fully discharged, the cell impedance remained lower than the as prepared cell. A difference in the cell impedance was observed between each charge and discharge cycle.

Formation of Li^0 , Ag^0 at anode and iodine at cathode upon charging

The milestone for the Q4 was the identification of the formation of lithium metal and silver metal at the anode and iodine at the cathode upon charge. Figure II.8.G.7 depicts a schematic of the Li/I₂ battery detailing the in-situ generation of the lithium anode and iodine cathode after an initial charge. After the completion of the charging process, the cell was disassembled, parts recovered and investigated via x-ray diffraction (XRD).

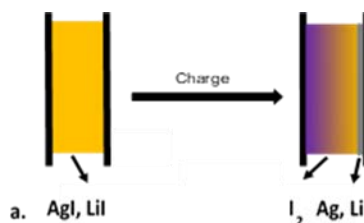


Figure II.8.G.7 Schematic of cell as assembled and after charge.

As a demonstration of the feasibility in forming an in-situ metal anode and iodine cathode, exemplary cells containing a solid electrolyte of reagent-grade XI, where $X = \text{Ag}$ or Li , were charged, and investigated by XRD. XRD of the anode side of the charged silver(I) iodide-containing solid electrolyte (Figure II.8.G.8a) confirmed the presence of elemental silver at the anode, as evidenced by several peaks which may be attributed to the 111, 200, and 220 crystallographic planes of the face-centered cubic silver crystals, respectively. Analysis of the cathode side (Figure II.8.G.8b) confirmed the presence of iodine, evinced by the appearance of peaks which may be ascribed to the 020 and 112 crystallographic planes of the orthorhombic iodine crystals. The diffraction pattern of the cathode of the LiI containing pouch cell (Figure II.8.G.9a) revealed peaks consistent with the 020, 111, 112, 113, and 201 crystallographic planes of the iodine crystals. Peaks consistent with Li can be observed on the anode side (Figure II.8.G.9b).

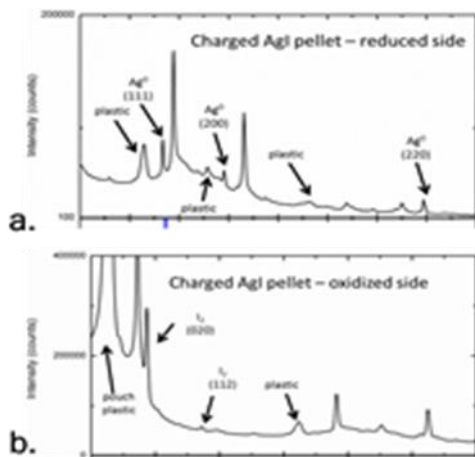


Figure II.8.G.8 X-ray diffraction of negative and positive electrodes after charge of AgI cell.

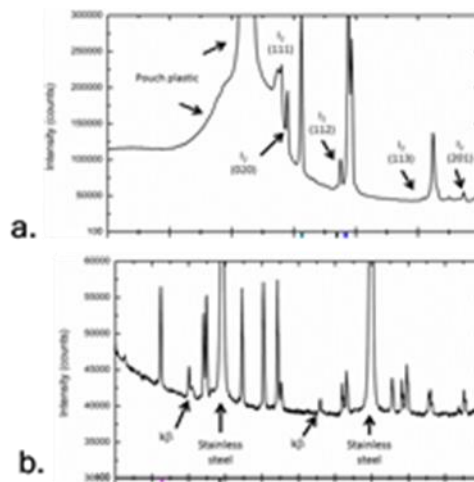


Figure II.8.G.9 X-ray diffraction of negative and positive electrodes after charge of LiI cell.

A cell containing a solid electrolyte charged to 5% capacity using a step-wise charging process. Examination of the recovered electrodes by XRD (Figure II.8.G.10) depicted several peaks appearing at 2-theta values of 8.6°, 16.9°, 25.3°, 33.8°, 42.4°, and 51.4° and can be assigned to the crystallographic planes of I₂-LiI composite, e.g. 001, 002, 003, 004, 005, and 006. [1], [2] These peaks indicate a layered atomic arrangement of iodine atoms along the lattice *c* direction of LiI composite. These results confirm the formation of the desired metal anode and iodine cathode. The results affirm project success for meeting the September 2018 go/no go metric.

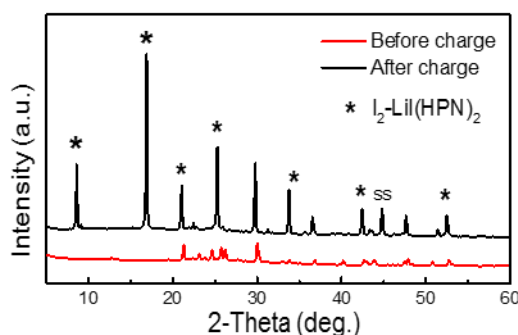


Figure II.8.G.10 X-ray diffraction of positive electrode after charge of LiI cell.

Feasibility demonstration

Initial charging data using coin cell type construction containing solid electrolytes, demonstrated proof of concept for the feasibility of *in situ* generation of anode, cathode with a solid electrolyte/separator. A notable decrease in charge transfer resistance as determined by EIS after charging was observed (Figure II.8.G.4- Figure II.1.A.6). Notably, the open circuit voltages of the cells were stable after the charging step demonstrating electrochemistry consistent with successful formation of an active cell. Disassembly of the cells followed by characterization using x-ray diffraction demonstrated *in situ* generation of Li or Ag and I₂ at the negative and positive interfaces, respectively (Figure II.8.G.8 and Figure II.8.G.9).

Conclusions

- A method for measuring conductivity was developed and methods were used to formulate solid electrolytes with conductivities higher than the base LiI or AgI materials.

- LiI based solid electrolytes with conductivities $\geq 10^{-3}$ S/cm were prepared.
- A cell design enabling demonstration of the solid state cell was developed.
- Decreased impedance as a result of cell charging was demonstrated.
- We have demonstrated a step-wise charging procedure with increasing current levels that decreases total charge time.
- OCV stability followed by ex-situ analysis of electrode interfaces after charge show successful *in situ* formation of a Li/I₂ cell.

References

1. Liu, Fang-Chao, Zulipiya Shadike, Fei Ding, Lin Sang, Zheng-Wen Fu. "Preferential orientation of I₂-LiI(HPN)₂ film for a flexible all-solid-state rechargeable lithium-iodine paper battery," *J. Power Sources* 274 (2015): 280-285. <https://doi.org/10.1016/j.jpowsour.2014.10.057>
2. Wang, Hongxia, Hong Li, Bofei Xue, Zhaoxiang Wang, Qingbo Meng, Liquan Chen. "Solid-State Composite Electrolyte LiI/3-Hydroxypropionitrile/SiO₂ for Dye-Sensitized Solar Cells" *J. Am. Chem. Soc.* 127 (2005): 6394-6401. <https://doi.org/10.1021/ja043268p>

Key Publications/Patents/Presentations

Publications

1. Alyson Abraham[†], Jianping Huang[†], Paul F. Smith, Amy. C. Marschilok, Kenneth J. Takeuchi, Esther S. Takeuchi, "Demonstration of a self-forming solid-state rechargeable Li/I₂ battery," *Journal of The Electrochemical Society*, **165** (10) A2115-A2118 (2018).

Presentations

1. Presentation: E. Takeuchi, A. Marschilok, K. Takeuchi, "Dual Function Solid State Battery with Self-forming Self-healing Electrolyte and Separator", Program Officer Site Visit, June 14, 2018, Stony Brook University, Stony Brook, NY 11794.
2. (Poster) Presentation: E. Takeuchi, A. Marschilok, K. Takeuchi, "Dual Function Solid State Battery with Self-forming Self-healing Electrolyte and Separator", DOE 2018 Annual Merit Review and Peer Evaluation Meeting (AMR) for the Vehicle Technologies Office, June 18-21, 2018, Washington, DC.
3. Presentation: E. Takeuchi, A. Marschilok, K. Takeuchi, "Dual Function Solid State Battery with Self-forming Self-healing Electrolyte and Separator", LBNL, October 12, 2018, Berkley, CA
4. Presentation: A. Abraham, J. Huang, P. F. Smith, A. Marschilok, K. Takeuchi, E. Takeuchi "Demonstration of a self-forming solid-state rechargeable Li/I₂ battery", MRS, December 2018 Boston, MA

II.8.H Advancing Solid-Solid Interfaces in Li-ion Batteries (Argonne National Laboratory)

Nenad Markovic, Principal Investigator

Argonne National Laboratory
9700 S Cass Ave
Lemont, IL 60439
E-mail: nmarkovic@anl.gov

Larry Curtiss, Principal Investigator

Argonne National Laboratory
9700 S Cass Ave
Lemont, IL 60439
E-mail: curtiss@anl.gov

Tien Duong, DOE Technology Development Manager

U.S. Department of Energy
E-mail: Tien.Duong@ee.doe.gov

Start Date: November 1, 2017	End Date: November 1, 2019	
Project Funding (FY18): \$1,200,000	DOE share: \$1,200,000	Non-DOE share: \$0

Project Introduction

Many challenges must be resolved in order to fully implement next generation Li-ion technologies, including: (i) development of high energy density cathode and anode materials with high activity and cyclability; (ii) enhancement of the stability of electrode materials and their corresponding electrolytes; (iii) improvement in the selectivity of electrochemical interfaces to minimize undesired side reactions at electrode surfaces; and (iv) mitigation of many safety issues related to the high flammability of organic solvents and Li dendrite formation at the anode. As a result, the focus of much research in the field of Li energy storage is centered on the development of methods that can enable dendrite-free Li metal anodes with minimal parasitic electrode-electrolyte interactions (required for high energy density Li-ion batteries), as well as the replacement of flammable organic solvents with solid electrolytes. One means of meeting these goals is the development of all-solid-state battery systems, composed of Li⁺ conductive solid electrolytes that connect the metal Li anode with high energy cathode materials. Various types of “hard” ceramic electrolytes have been developed with suitable bulk ionic conductivity and the general ability to suppress dendrite formation; however, most of these materials exhibit issues with interfacial stability to both anode and cathode materials and will require new manufacturing processes to assemble batteries at scale. Only by overcoming these issues will it be possible to enable Li-ion battery technology to move forward.

Objectives

The project objectives are multifaceted, including the development of a new mechanically and chemically stable and Li ion conductive ($\geq 2 \times 10^{-4}$ S/cm at 298K) solid electrolyte for a solid-state battery encompassing a metal Li anode, Li-oxide-based cathode and nonflammable crystalline and amorphous solid electrolytes that can operate at cathode potentials > 5V (denoted as a S_{Li-SEL-Sc} system)

Project Impact: Protective organic and inorganic compounds can enhance the stability of interface, improve Li ion interfacial transport, minimize dendrite formation and increase safety in Li ion batteries.

Approach

We propose to develop and use interdisciplinary, atomic-/molecular-level insight obtained from integrating both experimental- and computational-based methodologies to define the landscape of parameters that control

interfacial properties for new generations of Li-ion solid-solid battery systems. Our strategy will involve transferring the knowledge gained from well-characterized thin film materials to real-world materials. This strategy forms a closed loop wherein the knowledge gained from the model systems is used to design the more complex, real-world materials and vice-versa. The work will focus on utilizing existing in-house synthesis and characterization methods to enable rapid transition from fundamental science to realistic cells.

Results

LLTO Orientation-Dependent Interfacial Stability: $\text{Li}_{0.33}\text{La}_{0.55}\text{TiO}_3$ (LLTO) is a perovskite solid electrolyte with a tetragonal structure and ionic conductivity of $\sim 6.8 \times 10^{-4}$ S/cm at room temperature [1]. Its commercial application is mainly limited by instability against the Li anode, as Ti in the structure is reduced in contact with Li metal. To better understand the effect of crystal orientation on the stability of the LLTO/Li interface, (100), (110), (112) and (001)-oriented epitaxial LLTO films (~ 200 nm thick) were deposited on SrTiO_3 and NdGaO_3 substrates by pulsed laser deposition (PLD). Metallic lithium was sputtered onto these surfaces, which were then transferred under argon to the Advanced Photon Source at ANL to characterize the extent of Ti reduction in the bulk (~ 100 nm) via hard X-ray photoelectron spectroscopy (HAXPES). Only Ti^{4+} is observed prior to reaction with Li; however, partial reduction of Ti^{4+} to Ti^{3+} was observed after sputtering lithium, with the degree of reduction varying significantly between orientations (Figure II.8.H.1). Among all four orientations, LLTO(001) is the most unstable, with $\sim 33\%$ Ti reduction, whereas the LLTO(100) film is the most stable, with only $\sim 13\%$ Ti reduction. This result suggests that Li can migrate along the c-axis in the LLTO structure, enabling a more extensive reduction – a result that is consistent with theoretical calculations.

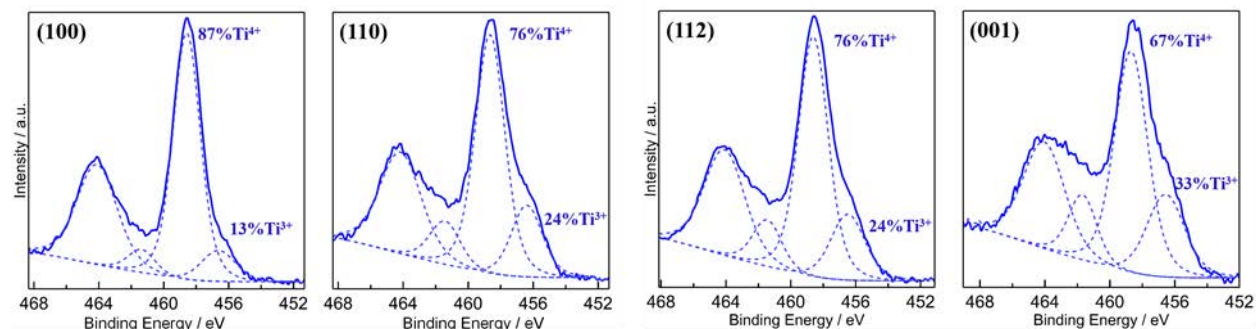


Figure II.8.H.1 Ti 2p core level HAXPES spectra after Li deposition demonstrating orientation-dependent reactivity of epitaxial LLTO thin films.

LLZO surface chemistry: $\text{Li}_7\text{La}_3\text{Zr}_2\text{O}_{12}$ (LLZO) garnet-based solid electrolytes are well known to form a variety of oxygen/carbon-containing reaction species due to reactivity with CO_2 and H_2O , leading to wide variations in interfacial impedance depending on the surface chemistry. [2] The presence of such reaction layers can further influence the interaction of LLZO with reactive Li metal, and as a result it is very important to understand the interfacial properties of LLZO with and without these surface layers. Annealing in ultrahigh vacuum (UHV) is an effective method to remove surface reaction layers (Figure II.8.H.2a-b). Before heating, the relative intensity of the carbonate peak in the C 1s core level is high, indicating that the surface is covered in Li_2CO_3 . In addition to the Li_2CO_3 oxidation layer, the O 1s peak also indicates that there are hydroxyl adsorption species on surface, with a characteristic peak at 532.9 eV, that disappears above 80°C . When heated to 500°C , both the C 1s and O 1s spectra show a clean LLZO surface with no carbonate or hydroxide peaks. The although no additional reactivity is detected during heating via XPS (i.e. no valence change of Zr or La species), heat treatment can induce the formation of secondary phases. In order to determine the window of structural stability on annealing, we heated LLZO up to 1173 K in UHV using a specially designed chamber at the APS that made it possible to monitor the structural evolution via X-ray diffraction *in situ* (Figure II.8.H.2c). From room temperature up to 800°C , the LLZO exhibits the pure cubic garnet phase as shown in green line. Above 600°C , a lithium deficient $\text{La}_2\text{Zr}_2\text{O}_7$ phase appears due to the loss of lithium and oxygen at

high temperature, as evidenced by a growing peak at 22.5°. As all annealing treatments are performed below 600°C, we conclude that no secondary phase formation takes place.

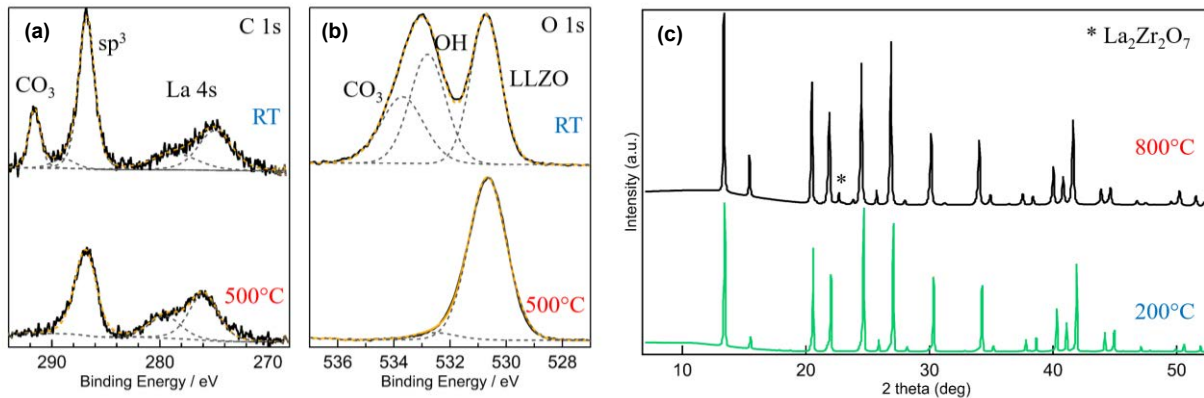


Figure II.8.H.2 (a) C1s and (b) O 1s XPS core level before (labeled RT) and after heating to 500 °C to remove surface contamination species. (c) XRD patterns of LLZO heated to 200 °C (green) and 800 °C (black).

(Electro)chemical stability of the LLZO-Li interface: Nb, Ta and Al are commonly used dopants to stabilize the cubic garnet phase and introduce Li⁺ vacancies that improve the conductivity of LLZO electrolytes. To understand the influence of dopant species on the intrinsic stability of doped LLZO surfaces in contact with Li metal, UHV annealed Nb-, Ta- and Al-doped LLZO were analyzed before and after lithium metal deposition via sputtering to characterize the chemistry of the buried LLZO-Li interface. Surprisingly, reduction of Zr⁴⁺ was observed for all three dopant types (Figure II.8.H.3), with the most significant reduction taking place on Al-doped LLZO (~9% Zr²⁺ and ~3% Zr⁰). Additional reactivity was observed on Nb-doped LLZO, with Nb reduction from 5+ to 4+ (~16%) 3+ (~9%) 2+ (~13%) and 1+ (~11%). Ta-doped LLZO was found to be the most stable surface (Figure II.8.H.3c), with no reduction of Ta and only a small amount (~2.4%) of Zr reduction. These results clearly demonstrate that the stability of the Li-LLZO interface is strongly dependent the dopant. In order to correlate the observed interfacial reactivity with electrochemical response, we performed electrochemical impedance spectroscopy (EIS) on Li-Li symmetric coin cells assembled with both vacuum-deposited Li and Li foil present on both sides of annealed LLZO samples. Among all three doped LLZMO samples (M = Al, Ta and Nb), Nb-doped LLZO exhibits the most reduction at the interface, whereas Ta-doped LLZO is relatively stable. This observed chemical instability directly correlates with the time-dependent increases in interfacial impedance of Nb-LLZO (Figure II.8.H.4a). Ta-doped LLZO, on the other hand, exhibits negligible changes in impedance with time (Figure II.8.H.4b), consistent with the low degree of reactivity between Ta-doped LLZO and Li metal.

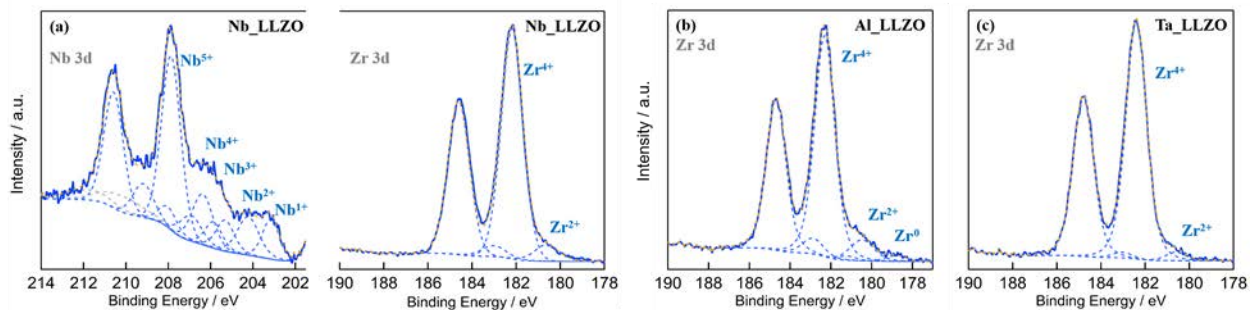


Figure II.8.H.3 XPS core level spectra after Li deposition on clean LLZO surface. Reduction of (a) Nb and Zr in Nb:LLZO; (b) Zr in Al:LLZO; and (c) Zr in Ta:LLZO.

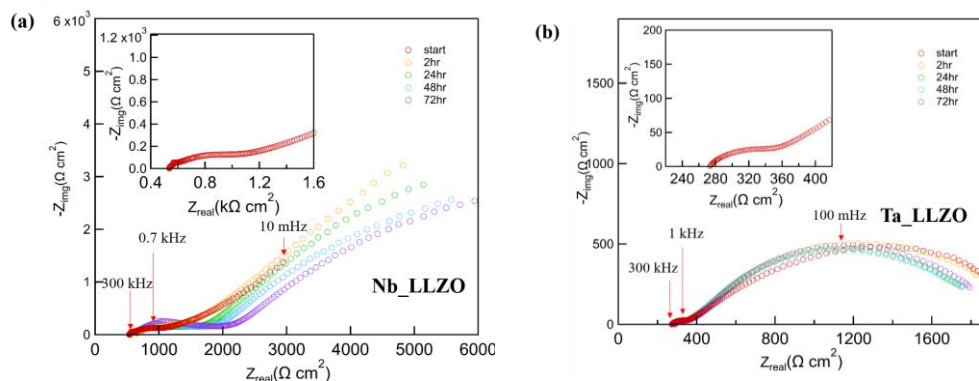


Figure II.8.H.4 EIS spectra of Li-Li symmetric cells with (a) Nb- and (b) Ta-doped LLZO at room temperature demonstrating the change in impedance over 72 hours due to reaction with Li metal.

Computational Characterization of LLZMO and its interaction with lithium metal: Density functional theory calculations were performed for LLZMO to understand the thermodynamic factors that drive the reactivity of LLZMO with lithium metal. In particular, using XPS and EIS we have observed considerable differences in Li-induced reactivity of Ta and Nb-doped LLZO, which is surprising. The LLZMO structure developed for first principles calculations is similar to that used by others, and we have used the Li-terminated LLZO (100) surface orientation for the interface with Li metal, as it is one of the most stable LLZO surfaces. We calculated several instances for each dopant and report averaged energy values, since energy deviations from these averages are, in most cases, below 0.1 eV per dopant atom. The interface energy does not depend significantly on the doping element, due to the fact that the top layer of the surface that interacts with deposited Li metal consists of Li and O atoms, with dopant atoms well underneath the top layer. This energy is -0.51 J/m^2 , -0.52 J/m^2 and -0.55 J/m^2 for average Nb-doped, Ta-doped and undoped material, respectively.

We also considered two different dopant distributions for each dopant type, with the dopants evenly distributed in the bulk or segregated towards the surface (Figure II.8.H.5a-b), and at least three different configurations calculated for each distribution. We find that, in the case of Ta-doped LLZO, the average energy of configurations with dopant atoms distributed near the surface vs. distributed in the bulk is nearly the same, favoring bulk by less than 0.01 eV/dopant atom both in the presence of Li on the surface and without Li metal (Figure II.8.H.5c). Strikingly, in case of Nb-doped LLZO there is a strong preference for Nb to be distributed near the surface as compared to distributed in the bulk, both with and without Li on the surface, with average energy differences for the two distributions of 0.23 eV/dopant and 0.19 eV/dopant, respectively. This clearly indicates that Nb has a thermodynamic preference to substitute Zr sites near the surface of LLZO, whereas Ta has about the same preference for surface and bulk sites. The preference of Nb to occupy Zr sites near the surface is slightly stronger in the presence of deposited Li metal, which suggests that segregation of Nb to the Li-LLZO interface may drive the high degree of Li-induced reactivity of this material. This high degree of reactivity may further lead to the observed propagation of the Li-induced reaction into the solid electrolyte.

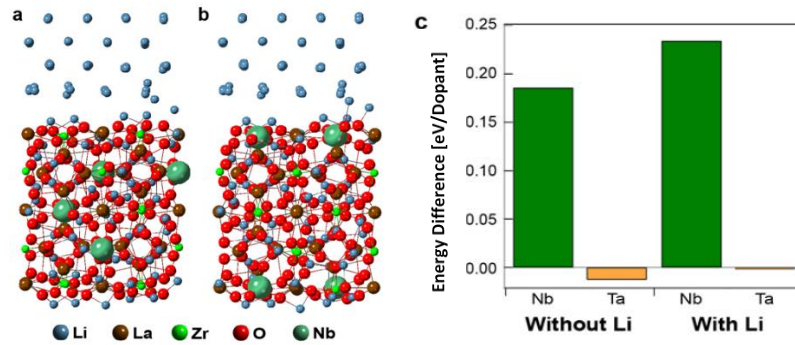


Figure II.8.H.5 Examples of DFT optimized structures with Nb dopants (a) distributed in the bulk and (b) segregated towards the surface for Nb-doped LLZO in contact with Li. (c) Bar chart showing differences in dopant energy near the surface and in the bulk for Nb- and Ta-doped LLZO without and with Li present.

Transition from well-ordered systems to disordered systems: Sulfide solid electrolytes: $75\text{Li}_2\text{S}-25\text{P}_2\text{S}_5$ (LPS) glass are amorphous materials with high ionic conductivities at room temperature ($10^{-4} - 10^{-3} \text{ S cm}^{-1}$) and have been reported to have a low charge-transfer resistance against metallic lithium despite the high reactivity expected when in contact with Li. Samples were synthesized through bulk processing from $\text{Li}_2\text{S} + \text{P}_2\text{S}_5$ (3:1), and as-synthesized material contains a reaction layer due to exposure to residual H_2O and O_2 during shipment. XPS spectra measured before (red) and after (black) Li sputtering onto as-received LPS samples (Figure II.8.H.6) clearly shows significant reactivity of this material in contact with Li, with the evolution of new features in the S 2p and P 2p core level spectra. Note that the Li target contains 2-3% Cu as an impurity from the target fabrication, leading to the observed Cu peaks in the survey and core level spectra; however, as Li is significantly more reactive than Cu, we do not anticipate any significant modification to the chemistry of the reaction. Surprisingly, the samples appear to be oxidized in contact with Li, with the appearance of peaks to higher binding energy relative to those present on the as-received samples; however, at this time we cannot rule out the presence of differential charging that would also lead to the presence of such peaks at higher binding energy. Recent work suggests that LPS decomposes to form Li_2S and Li_3P in contact with Li [3]; however, these results suggest the reactions that take place on air/moisture-exposed surfaces may be more complicated than simple decomposition.

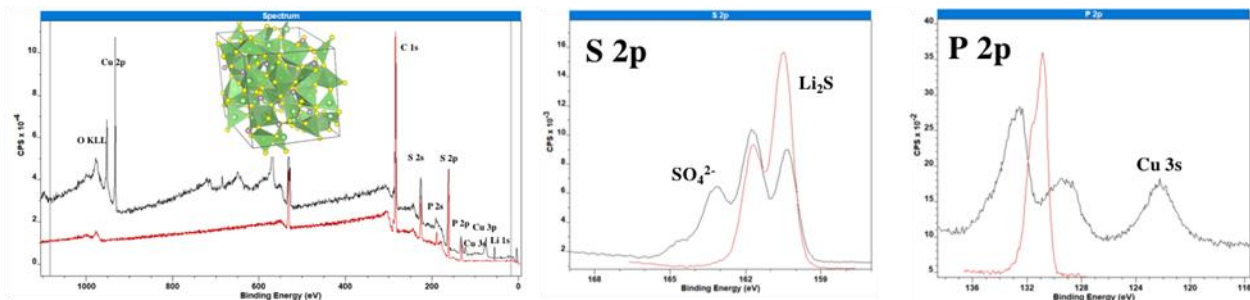


Figure II.8.H.6 Survey (left), S 2p (middle) and P 2p (right) core level XPS spectra before (red) and after (black) Li sputtering show clear reaction of LPS with Li metal

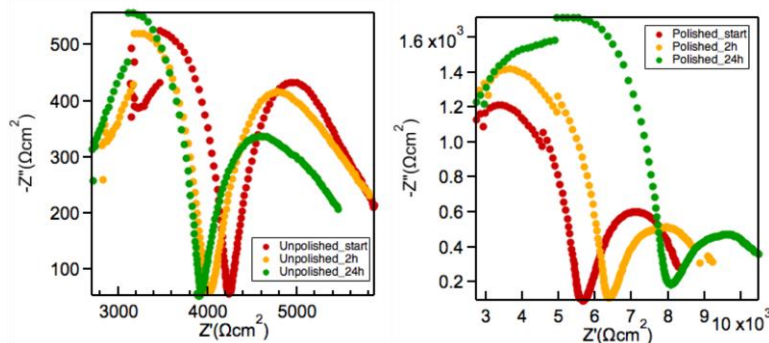


Figure II.8.H.7 The impedance spectrum of unpolished (left) and polished (right) Li-LPS-Li symmetric cells at room temperature.

LPS Interface Stability Correlation with Impedance: One of the biggest challenges in assembling LPS into functional electrochemical cells is its extreme moisture sensitivity that quickly degrades the sample surface. Li-LPS-Li symmetric coin cells were fabricated as before, with vacuum-deposited Li and cleaned Li foil pressed on both sides of unpolished and (sand-paper) polished LPS samples. We followed the evolution of impedance with time (Figure II.8.H.7) in order to understand how the reactivity observed from XPS evolves with time. We observed a slight decrease in impedance over first 24 hours for unpolished samples (Figure II.8.H.7, right), which can be attributed to slow removal of the oxidation layer on as-received material by reactive Li, improving Li contact with the glass surface. In contrast, both bulk and interfacial impedance is higher for polished samples, and the impedance further increases over first 24 hours (Figure II.8.H.7, right), likely due to the decomposition of LPS by Li metal. For both samples, however, it was not possible to measure impedance measurements after just two days, which is likely due to extensive reactivity with Li that ultimately resulted in loss of contact with the LPS.

Future Directions: During the coming year we will complete the current studies and expand this experimental/computational approach to studies of solid-solid interfaces on the cathode side with layered cathodes as model systems.

a) *Chemistry of LLZO dopants.* We will investigate the role of different dopants such as Nb, Ta and Al on solid electrolyte stability and reactivity vs. lithium metal. We will employ first-principles computational methods, spectroscopic surface and diffraction bulk techniques and electrochemical impedance testing.

b) *Crystalline vs Amorphous Solid Electrolyte.* We will synthesize amorphous and epitaxial film counterparts of common solid electrolytes or cathode materials. We will study model interfaces between crystalline solid electrolytes with either single or average orientation vs. amorphous solid electrolyte. We will also evaluate surface and bulk stability and reactivity of different crystallinity and orientation. These studies will help to predict which interface structures are favorable for real solid-state batteries.

c) *Chemical vs Electrochemical Reactivity.* We will carry out electrochemical testing of different solid-solid interfaces and compare interface and bulk changes during electrochemical cycling vs contact reactivity. This will be done in coin cells with a symmetric cell setup or full cell with layered perovskite cathodes.

d) *Computational Modeling.* Predictions of lithium behavior at different interfaces with solid state electrolytes.

Conclusions

First, we applied our unique, surface science-based approach to investigate the intrinsic stability of LLTO epitaxial films in contact with lithium with different orientations. Results indicate that the bulk stability is orientation dependent, with films that enable more out-of-plane Li interactions leading to more Ti reduction in the bulk. The same experiment strategy was applied to the more practical LLZO system with different dopants and surface oxidation states to study its intrinsic reactivity in contact with lithium. Experimental and

theoretical results reveal that the stability of the LLZO-Li interface is strongly related to both the initial surface chemistry and the type of dopant element present. As surface oxidation products are systematically removed, a general trend of increasing interfacial reactivity is observed. Reduction of Zr^{4+} is observed for all doped LLZO samples, and Nb-doped LLZO exhibits additional reduction of Nb^{5+} . EIS results indicate that the Nb-doped LLZO, which exhibits more intensive interface reaction compared to Ta-doped material, also yields much higher interfacial impedance with Li. Furthermore, the interfacial impedance of Nb-LLZO increases with time – consistent with propagation of the reaction into the bulk. DFT calculations suggest that Nb dopants have a thermodynamic preference to segregate to the LLZO surface and an even stronger preference for the Li/LLZO interface, whereas Ta dopants are nearly isoenergetic in the bulk and at the interface. This preference for surface segregation likely explains the poor stability of Nb-doped LLZO in the presence of Li. Finally, the amorphous solid electrolyte LPS was also characterized using the same methodology, revealing extensive decomposition of LPS in contact with Li metal, and corresponding time-dependent increases in impedance that ultimately resulted in cell failure.

Key Publications

1. Yisi Zhu, Justin G. Connell, Sanja Tepavcevic, Peter Zapol, Regina Garcia-Mendez, Nathan Taylor, Jeff Sakamoto, Brian J. Ingram, Larry A. Curtiss, John W. Freeland, Dillon D. Fong, Nenad M. Markovic, Dopant-Dependent Stability of Garnet Solid Electrolyte Interfaces with Lithium Metal, *Submitted to Advanced Energy Materials*

References

1. Y. Inaguma, C. Liqun, M. Itoh, T. Nakamura, T. Uchida, H. Ikuta, M. Wakihara, *Solid State Communications* **1993**, *86*, 689.
2. A. Sharafi, E. Kazyak, A. L. Davis, S. Yu, T. Thompson, D. J. Siegel, N. P. Dasgupta, J. Sakamoto, *Chemistry of Materials* **2017**, *29*, 7961.
3. K. N. Wood, K. X. Steirer, S. E. Hafner, C. Ban, S. Santhanagopalan, S.-H. Lee, G. Teeter, *Nature communications* **2018**, *9*, 2490.

II.8.1 Multifunctional, Self-Healing Polyelectrolyte Gels for Long-Cycle-Life, High-Capacity Sulfur Cathodes in Li-S Batteries (University of Washington)

Alex K.-Y. Jen, Principal Investigator

University of Washington
Seattle, WA 98195
Email: ajen@u.washington.edu

Jihui Yang, Principal Investigator

University of Washington
Roberts Hall 315, Box 352120
Seattle, WA 98195
Email: jihuiy@u.washington.edu

Tien Duong, DOE Technology Development Manager

U.S. Department of Energy
E-mail: Tien.Duong@ee.doe.gov

Start Date: January 1, 2017
Project Funding: \$1,388,888

End Date: December 31, 2019
DOE share: \$1,250,000

Non-DOE share: \$138,888

Project Introduction

The current electric vehicle (EV) battery market is dominated by lithium-ion batteries (LIBs). However, conventional LIBs based on this basic materials system have already begun to reach their performance limits due to progressive materials and device optimization over the past two decades. In order to meet EV Everywhere goals of 75% cost reduction and 50% weight reduction in electric vehicle batteries by 2022, radically new strategies must be employed.

One tantalizing solution is to look beyond traditional lithium-ion intercalation chemistry towards “beyond-lithium” systems such as the lithium-sulfur (Li-S) battery. A sulfur cathode has a theoretical gravimetric specific capacity of 1673 mAh/g at ~2V vs Li/Li⁺, rendering a theoretical energy density improvement of 500% as compared to the lithium metal oxide cathodes found in LIBs. This increase can be matched on the anode side by a movement to lithium metal, which possesses an intrinsic theoretical gravimetric specific capacity of 3860 mAh/g – an order of magnitude higher than graphite. Additionally, sulfur is cheap and earth-abundant, making this redox couple highly attractive for EV battery use.

However, a commercially-viable Li-S battery has remained elusive due to technical challenges. Many of them stem from the formation of polysulfides (Li₂S_x, 3 ≤ x ≤ 8) which are highly soluble in organic electrolytes, leading to self-discharge, passivation of the lithium anode, low coulombic efficiency due to the escape of polysulfides into the electrolyte, and voltage hysteresis from differences in forward and backward reaction mechanism. In addition, both the starting material (sulfur) and end products (Li₂S, Li₂S₂) are highly insulating, necessitating the use of a large amount of conductive carbon in the electrode. Furthermore, because the overall reaction is accompanied by a large volume change, this composite matrix is prone to cracking, promoting battery failure. Finally, on the anode side, lithium metal tends to form dendrites upon repeated stripping and plating, which puncture the cell separator and cause internal shorting.

Researchers have addressed these issues, to a certain degree of success, using a variety of creative strategies, including ionic liquid electrolytes, SEI-improving additives, mesoporous carbon hosts, advanced binders, and many others. Still, despite these myriad strategies, a safe Li-S battery with long cycle life based on scalable fabrication techniques remains elusive, as no single strategy or even combination of several has proven to be totally effective at both preventing dendrite growth and stopping efficiency/capacity loss due to dissolution of polysulfides.

Objectives

The objective of this project is to develop self-healing and polysulfide-trapping polyelectrolyte gels containing ionic liquid (IL) for the Li-S battery system. The Li-S battery design will be capable of achieving gravimetric and volumetric energy densities of ≥ 800 Wh/kg and ≥ 1000 Wh/L, respectively.

The project will achieve the following performance targets (all cycles at C/10 rate unless otherwise specified):

- A cathode gravimetric specific capacity of ≥ 675 mAh/g after 10 charge/discharge cycles between 2.8 and 1.7 V vs Li/Li⁺
- An average coulombic efficiency $\geq 99\%$ for the 10th cycle through the 100th
- $\geq 90\%$ capacity retention after 100 cycles as compared to the capacity of the 10th cycle.
- $\geq 30\%$ capacity retention when cycled at a C/2 rate, as compared to the capacity at C/10
- Ability to operate at temperatures between -20°C and 50°C.

Approach

During Budget Period 1 (quarters 1-6), we have synthesized a variety of starting materials for gel electrolytes and self-healing polymers, fabricated them into films both individually and together, and then tested their electrochemical/mechanical properties relevant to use in a Li-S battery. Additionally, we have synthesized a variety of sulfur/carbon (S/C) composites, utilizing mesoporous carbons with varying properties and various functionalities placed onto their surfaces.

Organic synthesis include NDI- (naphthalene diimide) and Py- (pyrene) containing materials, as well as monomers for the polyelectrolyte phase. Materials have been produced through established synthetic routes and characterized by nuclear magnetic resonance (NMR), gel permeation chromatography, and/or solution-phase cyclic voltammetry. Synthesis of S/C composites was achieved by mixing of sulfur and carbon at above the melting point of sulfur, and characterized by Brunauer–Emmett–Teller (BET) surface area and pore size analysis to confirm successful integration of sulfur into the pore structure. Surface functionality has been studied by thermal gravimetric analysis (TGA) and x-ray photoelectron spectroscopy (XPS).

Fabrication and testing of ionomer gels with varying ratios of IL and molecular starting materials have been performed. Basic electrochemical and mechanical properties of each gel composition have been tested and used to determine structure-property relationships, then gel compositions with favorable properties underwent more detailed testing on long-term interfacial stability with Li foil, Li dendrite suppression, and polysulfide diffusion. Conductivity and thermal properties have been assessed by A/C impedance, TGA, and differential scanning calorimetry. Tensile testing were carried out to determine mechanical properties. For advanced tests, Li/gel/Li symmetric cells have been constructed, and analyzed for development of interfacial resistance and dendrite suppression using cyclic stripping/plating. Polysulfide trapping ability were quantified by measuring absorption from a fixed-concentration solution.

Fabrication and testing of self-healing films, made from various structures and ratios of NDI- and Py-containing moieties, were performed. Mechanical and self-healing properties have been tested, as well as ionic conductivity. Static and dynamic mechanical testing have been carried out to determine tensile modulus, toughness modulus, and storage and loss modulus. Self-healing properties were measured by slicing films in two, contacting the pieces, and annealing at fixed temperature, followed by re-testing tensile properties.

This were followed by fabrication and testing of gel electrolytes containing both physically-crosslinked (self-healing) and chemically-crosslinked (ionomer) materials. All of the tests detailed in the two paragraphs above will be performed in order to determine how the performance of individual components of the gel translates to an interpenetrated structure containing all components.

Parallel to materials development efforts, we undertook fabrication and testing of small-capacity coin cells utilizing a variety of cell design concepts, including organic electrolytes, IL electrolytes, non-self-healing polyelectrolyte gels, and interpenetrating gels in order to benchmark performance and demonstrate an interpenetrating materials system that is capable of significantly improving performance. Cells were cycled for short periods (≤ 100 cycles) at rates ranging from $C/100$ or $C/50$ to $C/2$. A/C impedance spectra have been collected at various points in order to observe the evolution of internal impedances during cell cycling. Voltages traces during charge and discharge were observed and correlated to internal processes such as polysulfide speciation and insulating buildup of $\text{Li}_2\text{S}/\text{Li}_2\text{S}_2$ deposits. The origins of undesirable cell performance were investigated using a combination of experimental techniques, including targeted cycling tests, cyclic voltammetry, A/C impedance tests, scanning electron microscopy, and x-ray diffraction (XRD).

During Budget Period 2 (quarters 7-12), we will continue synthesis of molecular components of gels and S/C composites from raw starting materials. Synthesis will proceed according to literature, as well as any modifications we may make in order to produce materials more efficiently. We will continue testing of gel electrolytes containing both physically-crosslinked self-healing and chemically-crosslinked ionomer materials, as well as continue development of self-healing polymer films. Basic electrochemical and mechanical (including self-healing) behavior will be characterized, and gel compositions with favorable properties will undergo more detailed testing on long-term interfacial stability with Li foil, Li dendrite suppression, and polysulfide diffusion. Minor structural and compositional adjustments will be made to the gel electrolyte formulation based on cell performance details.

We will continue to fabricate coin cells with sulfur-based cathodes and lithium metal anodes which utilize electrolyte materials in the cell structure, and study their performance as a function of gel design. Initially, low-mass-loading demonstration cells will be constructed, followed by practical-loading cells. This task will culminate directly in the production of deliverable 10 mAh Li-S cells for DOE testing. All of the experiments previously mentioned for cell testing will be performed as cell design is optimized. We plan to utilize instrumentation at the new Washington Clean Energy Testbeds on the University of Washington campus, the University of Washington Molecular Analysis Facility, and NMR/microscopy instrumentation available at the Environmental Molecular Sciences Laboratory at Pacific Northwest National Lab.

Results

Ionomer Gels: Using our previously-developed gel fabrication method, we synthesized solvate ionogels (SIGs) containing varying ratios and structures of polymerizable components (Figure II.8.I.1a). All formulas produced transparent, freestanding films. We then measured the bulk ionic conductivity (κ) and lithium transference number (t_{Li^+}) of each sample at 23°C , plus $\text{Li}(\text{G4})\text{TFSI}$ as a control, using Electrochemical Impedance Spectroscopy (EIS) and/or potentiostatic polarization, as well as elastic modulus (E) using uniaxial compression with a 50N load cell. Following this, we fabricated $\text{Li}|\text{Li}$ symmetric cells using SIG films as separators, or $\text{Li}(\text{G4})\text{TFSI}/\text{glass fiber}$ as a control, and measured time-to-short-circuit (T_{sc}) under static polarization at $0.1 \text{ mA}/\text{cm}^2$. The results are summarized in Table II.8.I.1. Finally, $\text{Li}|\text{Li}$ symmetric cells containing SIG separators (SIG 2 or SIG 5) were subjected to cyclic polarization (period: 6 hr) at $\pm 0.1 \text{ mA}/\text{cm}^2$, and the results compared to $\text{Li}(\text{G4})\text{TFSI}/\text{glass fiber}$ (Figure II.8.I.1b).

We observed several distinct trends in electrochemical properties based on SIG composition. Most notably, we found that formulas based on longer-chain P_{3500} produced uniformly higher conductivity values, in some cases even exceeding $\text{Li}(\text{G4})\text{TFSI}$ in its liquid state. Lithium transference number also increases with PEG molecular weight, with two outliers: SIG 4, in which t_{Li^+} is decreased due to excess mobile anion content, and SIG 5, in which t_{Li^+} is vastly increased due to the inclusion of 1,4-dioxane as a diluent. Finally, we find that suppression of/resistance to lithium dendrites (as measured by T_{sc}) also increases for samples with P_{3500} , although the variability between such samples is large. As seen in Figure II.8.I.1b, best-performing formulas SIG 2 and SIG 5 are able to strip and plate lithium reversibly, at low overpotential, for ≥ 600 hrs without any signs of short-circuit. Detailed interpretation of these results may be found in our pending publication (*vide infra*).

Table II.8.I.1 Composition/Properties of Five Novel SIGs in Comparison to Li(G4)TFSI

Formula	Components (vol% added)						Properties			
	P ₇₅₀	P ₃₅₀₀	TEGMA	PyrTFSIMA	1,4-dioxane	Li(G4)TFSI	κ (mS/cm)	t_{Li^+}	E (kPa)	T _{sc} (hr)
SIG 1	20%	0%	0%	0%	0%	80%	0.73	0.21	369	10.8
SIG 2	0%	20%	0%	0%	0%	80%	1.05	0.28	254	113.9
SIG 3	0%	10%	10%	0%	0%	80%	0.92	0.24	249	25.0
SIG 4	0%	10%	0%	10%	0%	80%	1.07	0.16	401	99.3
SIG 5	0%	20%	0%	0%	13.3%	66.6%	2.15	0.57	228	118.3
Li(G4)TFSI	0%	0%	0%	0%	0%	100%	1.08	0.13	n/a	10.6

Following our investigation of basic SIG properties, we developed a fabrication process for S/C composite cathodes with SIGs cured *in-situ* within the pores (Figure II.8.I.1c), as well as a process for creating composite separators consisting of SIGs cured into a porous polypropylene film (Celgard 2500). We then assembled Li-S coin cells from these components and performed galvanostatic charge/discharge tests on them at a theoretical C/10 rate. Representative cycling results are shown in Figure II.8.I.1d. We observed that capacity loss occurs gradually over the first 20 cycles, followed by recovery and stabilization at about 900 mAh/g. Coulombic efficiency averaged roughly 97% per cycle (note: no LiNO₃ or any other anode-passivating additives were present in this cell). Further analysis of these results and optimization of our process is ongoing.

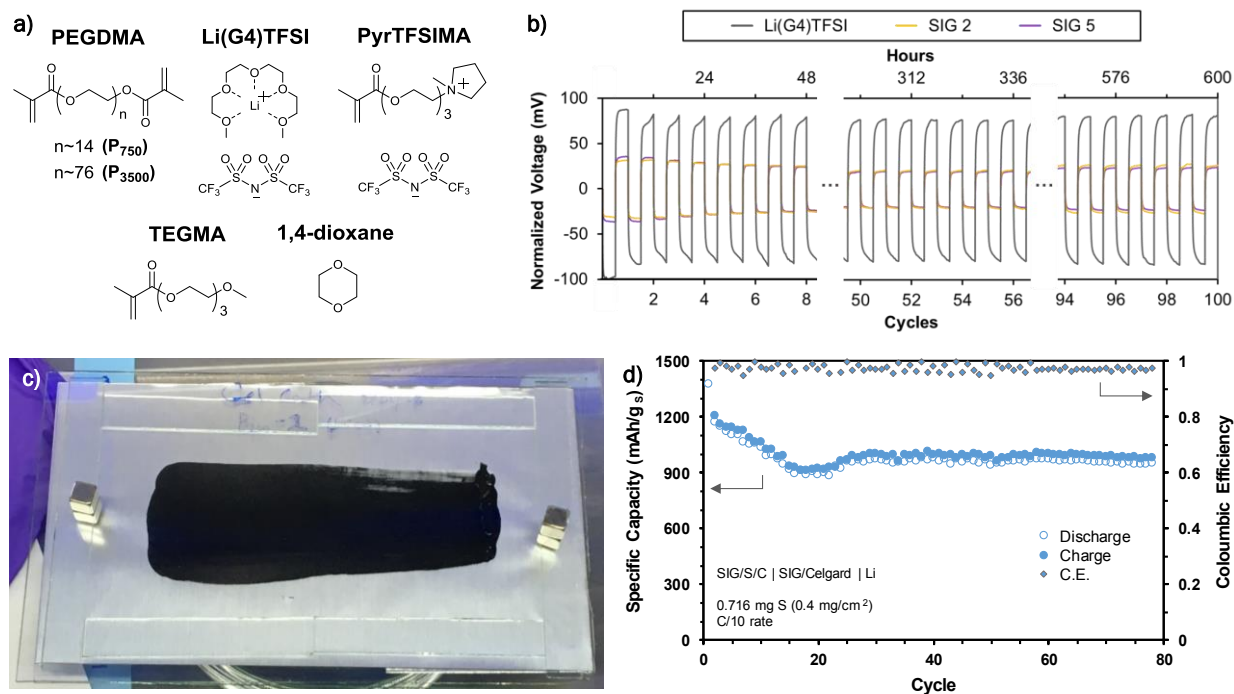


Figure II.8.I.1 a) Molecular structure of SIG components with their abbreviated names. b) Cycling data (0.1 mA/cm²) for Li|Li symmetric cells with SIG separators, along with Li(G4)TFSI/glass fiber for comparison. All cells completed 100 cycles (600 hrs) without developing short circuits. SIG separators required less overpotential (normalized to separator thickness) for Li stripping/plating than the solvate ionic liquid alone. c) Photograph of a SIG/S/C cathode, where SIG is cured *in-situ* within the pores of the electrode. d) Galvanostatic cycling data (theoretical C/10 rate) for an all-solid-state Li-S cell containing SIG in both the cathode and separator. Capacity retention (81%, 2nd → 75th cycle) and coulombic efficiency (~97%) are encouragingly high even without anode passivating additives (i.e. LiNO₃).

Self-Healing Materials: Previously, we have demonstrated a series of self-healing polymer composites with varying self-healing temperature termed PP-1, PP-Py, and PP-dbNDI. Extensive mechanical testing was carried out on these composites to demonstrate their tensile properties before and after healing. Representative films were sliced in two, contacted under minimal pressure, and healed for 12 hours at 40–60°C, followed by stress-strain testing. As shown in Figure II.8.I.2, even after heat treatment at only 40°C, all healed materials still possess high Young's moduli (> 60 MPa). We also demonstrated good compatibility of solvate ionic liquid Li(G4)TFSI with PP-1, which swells well with up to 33wt% liquid to form a freestanding gel with bulk ionic conductivity $\sim 10^{-5}$ S/cm at 25°C. Furthermore, the PP-1/Li(G4)TFSI gel showed complete self-healing ability at only 40°C, lower than the polymer alone.

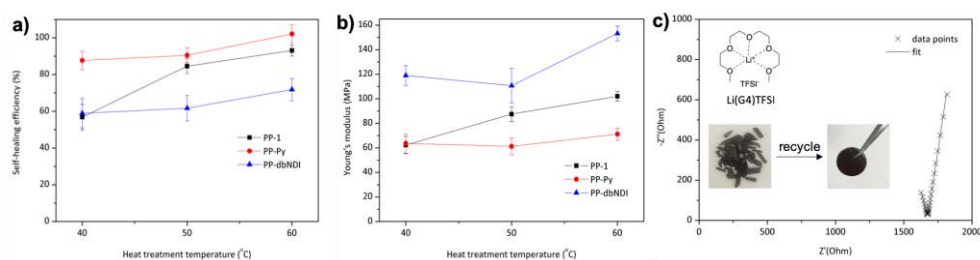


Figure II.8.I.2 a) Self-healing efficiency based on maximum tensile strength and, b) recovery of Young's modulus upon self-healing of composite films after heat treatment at different temperatures, c) Nyquist plots and curve fit of PP-1/Li(G4)TFSI at room temperature and recovery of PP-1/Li(G4)TFSI under 40°C for 12 h.

Following basic characterization, we tested the effects of PP materials on a Li-S battery system. We expected performance improvement from the two primary functions of PP: the polysulfide-trapping effect of naphthalene diimide (NDI) and PEG moieties, and resistance to/self-healing of cracks formed during cycling. In order to isolate the former effect for study, we have fabricated low-loading (~ 1 mg/cm²) cathodes using either PVDF or various combinations of PENDI-350/triPy (latest generation of PP) as binders. The low loading ensures that mechanical stresses play a minor role in cell performance compared to cathode chemistry.

Cells were configured with Li metal anodes, Celgard 2500 separators, DOL:DME-based organic electrolyte, and C/S composite cathodes. The polymer binders made up 20 wt% of the cathode materials. We achieved best results using a PP binder with a 3:1 NDI:Py molar ratio (Figure II.8.I.3), which displayed >74% capacity retention after 100 cycles, as compared to <44% for the PVDF control. The charge/discharge rate capability of cathodes with the 3:1 PP binder formulation was also slightly better than the PVDF control, with almost no capacity loss observed up to 1C rate. We are currently working to fabricate and test high-loading (>5 mg/cm²) cathodes with this PP binder formulation, in order to determine whether the self-healing properties of the supramolecular polymer result in additional performance improvement for cells with practical thickness.

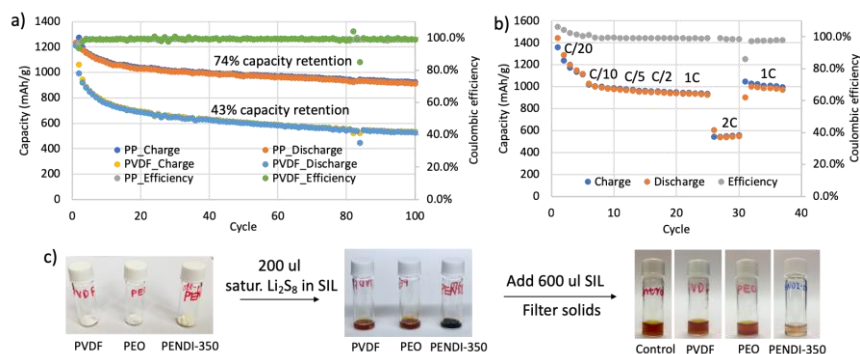


Figure II.8.I.3 a) Self-healing efficiency based on maximum tensile strength and, b) recovery of Young's modulus upon self-healing of composite films after heat treatment at different temperatures, c) Nyquist plots and curve fit of PP-1/Li(G4)TFSI at room temperature and recovery of PP-1/Li(G4)TFSI under 40°C for 12 h.

To additionally confirm the polysulfide-trapping properties of our material, we added a saturated solution of Li_2S_8 (~10mM) in $\text{Li}(\text{G4})\text{TFSI}$ to powdered PVDF, PEO ($M_w \sim 1,000\text{kDa}$), and PENDI-350 – all of which are virtually insoluble in the ionic liquid – followed by dilution, stirring, and filtering to remove the polymers along with any absorbed polysulfides. We observed a much lighter colored solution from which had been in contact with PENDI-350 than either PEO or PVDF, indicating a strong interaction between PENDI-350 and Li_2S_x species, which tend to remove them from solution, *i.e.*, polysulfide trapping.

Chemical Modification of Mesoporous Carbons for S/C Composite Cathodes: We have explored chemical surface modification of the carbon starting materials as an additional route to cathode performance improvement. Our procedure is based on well-studied diazonium chemistry, which attaches phenyl rings bearing customizable functional groups to unsaturated carbon surfaces. Functionalization was confirmed by pore shrinkage (determined by BET, as well as the appearance of nitrogen- or sulfur-associated peaks in XPS analysis and weight loss during TGA). The extent of functionalization, measured by %weight loss during TGA as compared to control samples, was easily varied by adjusting reaction conditions. We used this procedure to attach a variety of chemical functional groups to carbon surfaces, including primary amines, tertiary amines, and sulfides. In particular, we were interested in sulfide-based surface modifiers, as reversible covalent bonding between sulfide groups is well-known and has potential for containment of lithium polysulfides within the cathode pore structure. We have performed detailed study on S/C cathodes modified with phenylthiol functional groups by analyzing cell cycling data. Figure II.8.I.4 summarize data from this investigation.

We note several important trends. Firstly, the introduction of phenylthiol modifiers progressively inhibits the overcharging behavior at 2.37 V in the MJ430-S cathode (Figure II.8.I.4a and Figure II.8.I.4c), indicating an efficient protection of LiPS diffusion from the cathode to the Li anode, which is ascribed to the interaction of SH modifiers with LiPSs. In addition, Figure II.8.I.4b and Figure II.8.I.4d compares the long-term cycling performance of MJ430-S and 20% SH-MJ420-S cathodes with various S loading. As expected, the modified cathode displays an obvious improvement in capacity retention. The capacity of the unmodified MJ430-S decreased from 812 to 486 mAh g^{-1} at 0.25 C (a capacity retention of 60%) after 300 cycles. Over the same number of cycles, the 20% SH-MJ430-S device shows a capacity retention of 89%, with the discharge capacity dropping from 838 to 745 mAh g^{-1} . Due to the additional challenges of a cathode with a high S loading (e.g. poor wettability and severe LiPS dissolution), the thick MJ430-S cells show a poor cycling retention of 56% at 0.25C, whereas the capacity retention in the 20% SH-MJ430-S cells remains at 89% (Figure II.8.I.4d). Upon close examination of the discharge curves of modified cells at various discharge rates, we can find an increased polarization (Figure II.8.I.4e). The polarization could be gradually reduced as the concentration of SH modifier decreases (Figure II.8.I.4f).

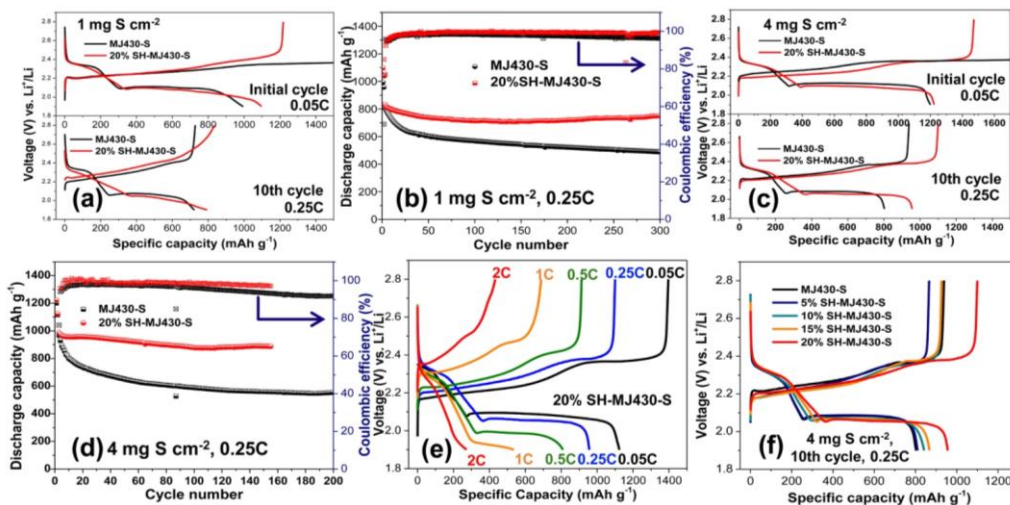


Figure II.8.1.4 (a) The discharge/charge voltage profiles of the MJ430-S and the 20% SH-MJ430-S electrodes based on S loading of 1 mg cm^{-2} at initial activation cycle (0.05 C) and 10th cycle (0.25C) and (b) the corresponding cycling performance within the first 300 cycles. (c) The discharge/charge voltage profiles and (d) the corresponding cycling performance of the MJ430-S and the 20% SH-MJ430-S electrodes based on S loading of 4 mg cm^{-2} . (e) The discharge/charge voltage profiles of the 20% SH-MJ430-S electrodes at various rates. (f) The discharge/charge voltage profiles of a series [SH]-MJ430 with increasing weight percentage of thiol modifier, from 5% to 20%, controlled via reaction conditions. Thiol modification largely increases capacity retention.

The improved capacity retention of MJ430-S cathodes with SH modifiers is presumed to strongly correspond to the multifunctional surface interacting with solvated active materials in many ways, such as reversible covalent disulfide interactions and electrostatic lithium bonding. These postulated interactions were verified by solid-state magic angle spinning (MAS) NMR and XPS test (Figure II.8.1.5a-d). Although the surface interaction increased the charge transfer resistance and cell overpotential (Figure II.8.1.5e-h), these side-effects can be balanced by fine-tuning the modifier concentration. Additionally, the polar, nucleophilic surface induced by thiol modifiers allows for a better wetting of the electrode surface by the electrolytes due to the dipole-dipole interaction of SH groups with Li^+ from the electrolyte (Figure II.8.1.5a-b). This improved wettability can lead to enhanced utilization of active materials during cycling, since better access to the electrolyte within pores would aid in solvation and confinement of solvated LiPSs, while maintaining the tethering of solvated LiPSs to the cathode surface. In summary, we have correlated the alteration of surface chemistry with electrochemical behavior of cycled cells. The fundamental insight on the thiol functionality suggests a further rational design of multi-functional interfaces to achieve better Li-S performance.

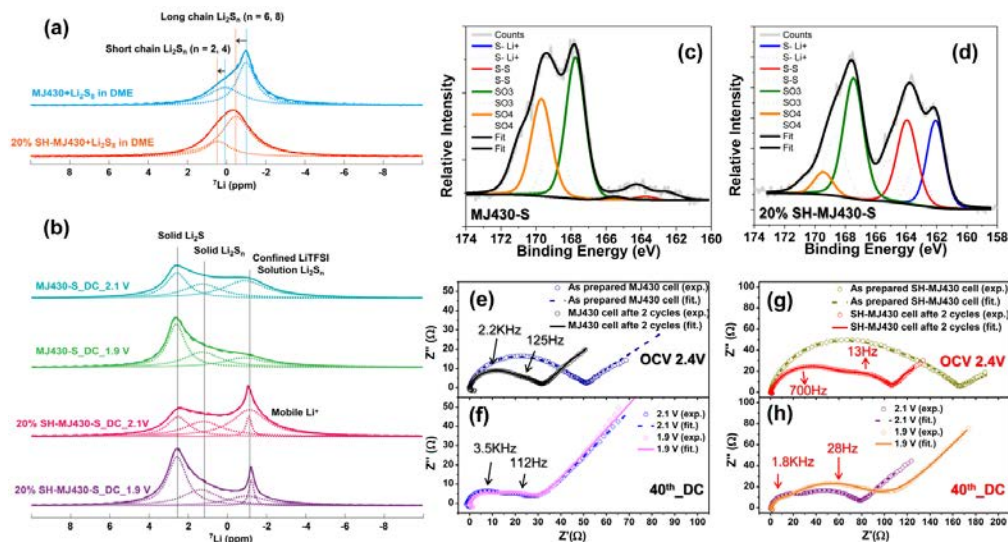


Figure II.8.1.5 (a) ^7Li MAS NMR spectra of the Li_2S_8 solution interacting with MJ430 and the 20% SH-MJ430. (b) ^7Li MAS NMR spectra of the cathode materials with MJ430-S and 20% SH-MJ430-S from Li-S cells that are discharged to different voltages, with experimental data in solid lines, deconvolution peaks in dot lines, and the sum of deconvolution peaks in dash lines. High resolution S2p XPS spectra of (c) the MJ430-S and (d) the 20% SH-MJ430-S cathodes, obtained from Li-S cells discharged to 1.9 V after 100 cycles. EIS analysis of (e-f) the MJ430-S and (g-h) the 20% SH-MJ430-S cells at different stages of discharge within 40 cycles.

Conclusions

Ionomer Gels

- We have fabricated freestanding solvate ionogels with conductivity $>10^{-3}$ S/cm and lithium transference number >0.5 , and demonstrated their utility as metallic-lithium-compatible electrolytes.
- We have developed fabrication procedures for all-solid-state Li-S cells containing solvate ionogel in both the cathode and separator, and demonstrated the potential of this system to produce good capacity retention and coulombic efficiency during galvanostatic cycling.

Self-Healing Materials

- We have demonstrated recovery of mechanical strength upon self-healing in our PP polymer materials, as well as high swellability in solvate ionic liquid $\text{Li}(\text{G4})\text{TFSI}$.
- We have fabricated low-loading Li-S cells using PP polymer formulations as binders, and demonstrated enhanced capacity retention after 100 cycles ($>74\%$) compared to PVDF ($<44\%$).

Chemical Modification of Mesoporous Carbons for S/C Composite Cathodes

- We have developed a procedure based on diazonium chemistry to covalently attach customizable functional groups to the surface of mesoporous carbons, and created S/C composites from both modified and unmodified samples.
- S/C cathodes based on phenylthiol-modified carbons display improved capacity and retention compared to unmodified samples. Voltage profiles exhibit significant changes upon modification, which may indicate covalent tethering of polysulfides to the carbon surface.

Key Publications

1. Hubble D., Qin J., Lin F., Murphy I. A., Jang S.-H., Yang J., Jen A. K.-Y., “Designing Lithium Solvate Ionogels with Very High Conductivity and Lithium Transference Number.” (*accepted to Journal of Materials Chemistry A*)
2. Hubble D., Qin J., “Multifunctional, Self-Healing Polyelectrolyte Gels for Long-Cycle-Life, High-Capacity Sulfur Cathodes in Li-S Batteries.” Presented at BMR Electrolytes Meeting, Berkeley, CA, Oct. 2018.
3. Hubble D., Qin J., Lin F., Murphy I. A., Li Y., Jang S.-H., Yang J., Jen A. K.-Y., “Rationally-Designed Solvate Ionogel Electrolytes for Improved Lithium-Sulfur Battery Performance.” Poster presented at 233rd ECS Meeting, Seattle, WA, May 2018.
4. Murphy I. A., Li Y., Chen Y., Lin F., Wang X., Wang S., Hubble D., Jang S.-H., Mueller K. T., Wang C., Yang J., Jen A. K.-Y., “Tunable Surface Modification of Mesoporous Carbon Particles for Polysulfide Trapping in Lithium Sulfur Batteries.” Poster presented at 233rd ECS Meeting, Seattle, WA, May 2018.
5. Qin J., Lin F., Hubble D., Wang Y., Li Y., Murphy I. A., Jang S.-H., Yang J., Jen A. K.-Y., “Tuning Self-Healing Properties of Stiff, Ion-Conductive Polymers” (*in preparation*)
6. Li Y.,* Murphy I. A.,* Chen Y., Lin F., Wang X., Wang S., Hubble D., Jang S.-H., Mueller K. T., Wang C., Jen A. K.-Y., Yang J., “Surface Functionalization of Mesoporous Carbon for Polysulfide Trapping in Lithium Sulfur Batteries” (*co-first author) (*in preparation*)

Acknowledgements

Project team includes Dr. Sei-Hum Jang, Dion Hubble, Jiaxu Qin, Ian Murphy, and Francis (Ray) Lin from the Jen group, as well as Dr. Shanyu Wang and Yun (April) Li from the Yang group. Special thanks to *PNNL people.* Special thanks to Ryan Toivola for assistance with ionogel mechanical testing. Dion Hubble acknowledges government support under and awarded by the Department of Defense, Air Force Office of Scientific Research, National Defense Science and Engineering Graduate (NDSEG) Fellowship, 32 CFR 168a.

II.8.J Self-Forming Thin Interphases and Electrodes Enabling 3-D Structures High Energy Density Batteries (Rutgers, the State University of New Jersey)

Glenn G. Amatucci, Principal Investigator

Rutgers, the State University of New Jersey
671 US Highway 1
North Brunswick, NJ 08902
E-mail: gamatucc@soe.rutgers.edu

Tien Duong, DOE Technology Development Manager

U.S. Department of Energy
E-mail: Tien.Duong@ee.doe.gov

Start Date: October 1, 2016

End Date: September 30, 2019

Project Funding: \$ 382,441

DOE share: \$ 317,544

Non-DOE share: \$ 64,894

Project Introduction

This project remains extremely relevant with the potential to bring a step change in energy density, cost, safety and high voltage scalability of battery technology compared to the current state of the art secondary battery technologies. The technology is based on an *in-situ* formed solid-electrolyte battery leading to high energy metal fluoride vs. lithium metal chemistry in a planar battery electrode format and provides the following advantages: 1) enabling the use of lithium metal electrodes via solid-state electrolytes, 2) eliminating Li metal in fabrication and handling of cells, 3) providing the highest practical energy density electrochemical system, and 4) enabling a unique pathway to high voltage systems.

Objectives

The project objective is to develop and implement a novel *in-situ* formed lithium-metal-based metal fluoride battery that will enable packaged 10 mAh batteries of energy density > 1000 Wh/L and specific energy > 400 Wh/kg at 12 V. Gradual yearly targets were established for each of the main components of the self-formed batteries in order to achieve the final deliverables. For FY18 the milestones included the goals to (1) establish negative current collector compositions that enable high efficiency lithium plating and stripping in excess of 90% during the in situ step and greater than 95% during subsequent cycles, (2) develop optimal bi-ion conductors that achieve ionic conductivities in excess of 1×10^{-4} S/cm after in situ formation, and (3) design cell stacks that achieve 75% utilization of the positive reactive current collector and 12 V. Finally, the go-no/go goals of FY18 were to achieve self-formed cell stacks with energy densities of greater than 750Wh/L and 200Wh/kg and greater than 80% capacity retention after 20 cycles at a rate of C/10, and to achieve 12 V output voltage in one planar design.

Approach

The *in-situ* self-formed battery enables the formation and implementation of high energy density Li/metal fluorides by simple polarization of a LiF-based bi-ion conducting glass between a positive and a negative reactive current collector. These solid state *in-situ* batteries are fabricated with a maskless scalable patterning technique. The rationale is that such maskless scalable patterning technique offers a pathway to high throughput, low material loss and fabrication of complex architectures. The resulting solid state *in-situ* cells have shown transport barriers in positive electrode that need to be addressed in order to optimize utilization and discharge rate and achieve our milestones. We have shown in FY17 that hybridization of transport pathways successfully improved discharge rates up to the desired C/10. This year we isolated the positive electrode in order to evaluate and optimize its properties in a more traditional stacking arrangement that we developed. In parallel, we also optimized the formation/priming protocols of the single planar architecture for long cycle life. Finally, the single solid state *in-situ* self-formed baseline technology was translated into a 12 V baseline technology.

Results

Bulk transport: Multicomponent nanolayered structured architectures. The early half of FY18 was directed at identifying and understanding the limitations of transport within the positive electrode. We isolated the positive electrode formation reaction and evaluated the cell components in a more traditional stacked arrangement. Such study determined transport properties were mainly limited by diffusion. In order to promote F^- ion transport, shorter pathways needed to be created. In response, we developed a unique vapor deposition technique that enabled the rapid fabrication of new multicomponent structured architectures with features in the nanoscale. These nanostructured composites of enhanced F^- ion transport resulted in the improvement of the positive reactive electrode utilization/capacity by a factor 2 leading to 78% and > 1000 mAh/cc, with areal capacity approaching 0.4 mAh/cm². Nanostructured architectures have also enabled improved cycling stability as shown in Figure II.8.J.1. In short, multicomponent nanolayered structured architectures demonstrated drastic improvement of cell electrochemical performance: positive electrode utilization / capacity / cycling stability.

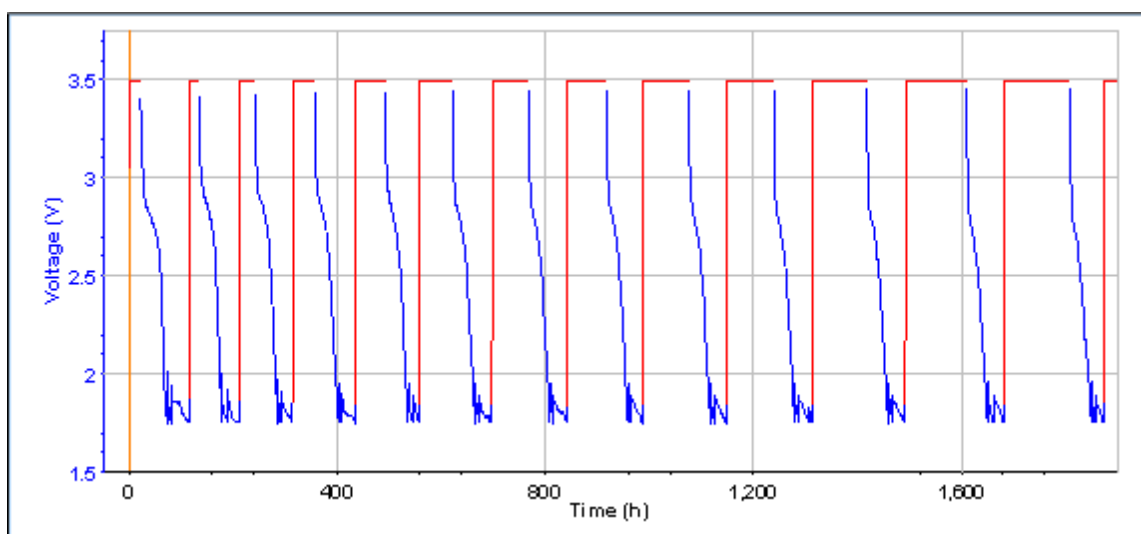


Figure II.8.J.1 Constant voltage charge (red) /constant current discharge (blue) profile representative of multicomponent structured architecture cells cycled between 1.75 and 3.5 V.

Bulk transport: Mixed conductor electrodes. Utilizing our unique nanolayering process enabled control of the chemistry of the multicomponent structure via additives to modify the type of conductivity, ionic (Li^+ and F^-) and/or electronic, and the amount of transport pathways within the bulk of the solid state electrode structure. Figure II.8.J.2 shows the three types of nanolayered additives investigated for the positive electrode. Layer additive “A” enhanced the ionic transport which resulted in a slight increase in capacity retention. Layer additive “B” enhanced electronic conductivity but resulted in a detrimental effect on capacity. Layer additive “C” was a hybrid composition that enhanced both electronic and ionic transport. This mixed conductor provided the best performance as it resulted in an increase in capacity by 40% and improved capacity retention. As such, transport limitations were identified as both ionic and electronic. In conclusion, mixed conductor

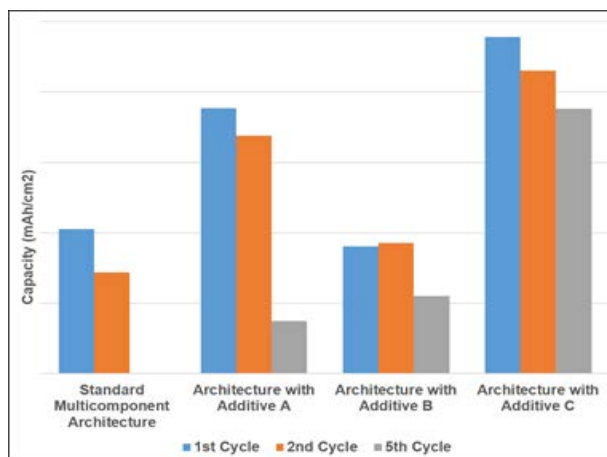


Figure II.8.J.2 Impact of transport additive composition on discharge capacities of solid state multicomponent nanolayered structured architecture cells in the 1st, 2nd and 5th cycles.

Additives A, B and C enhance ionic, electronic and mixed conductivity, respectively. Cells cycled between 1.75 and 3.5V.

multicomponent nanolayered structured architectures demonstrated enhanced electrochemical performance: positive electrode utilization / capacity / cycling stability.

Mechanical stability. In the third quarter we focused on the mitigation of stress/strain energy to produce more uniform transformations during reactions for longer cycle life. One particular area of focus was on optimization of cycling protocols. As previously reported, we included studies on pulsed charging steps and the addition of intermediate slow discharge formation steps prior to our standard discharge protocols. Our investigations concluded the most beneficial impact came from the additional slow intermediate discharge step. It was determined that this “priming” step allowed for a more uniform distribution in nucleation so that transformations during reactions are less likely to create highly concentrated areas of active components leading to mechanical failure. Finally, cells were encapsulated to apply light pressure and protect the chemistry from environment exposure. Encapsulation of chemistry seemed to improve reaction uniformity in the formation step as demonstrated by good capacity retention followed by increased capacity output at a higher rate. In short, “priming” with a slow intermediate step and encapsulation were beneficial to electrochemical cycling.

12 V cell architecture development. In the late third and fourth quarter, the focus of our research shifted from addressing transport limitations and mechanics to enabling another one of our goals: the development of a 12 V architecture. Our first high voltage design showed limited voltage output with 8 V revealing transport issues related to the structure. Optimization of the cell reorientation to simplify transport pathways enabled the successful achievement of an electrolytically formed cell with a 12 V output voltage. These new 12 V architectures have been fabricated reproducibly, charged to an excess of 12 V and subsequently successfully discharged. However, positive electrode utilization was poor since these initial cells were fabricated as baseline designs without any of the chemical and nanostructural improvements we developed at low voltage. As we previously reported, diffusion limitations prevent full access to the cell’s electrochemically active materials inducing inactive pockets thereby leading to low utilization. The first phase of improvement we conducted on the 12 V cell architecture focused on the design optimization at the electrode level and layout. This was executed with variations in the electrode design, aspect ratio, thickness and electrode width. Figure II.8.J.3 depicts some of the results for modifications of electrode thickness and width studies. From this investigation, it was determined that decreasing the aspect ratio of the electrodes and thereby increasing the surface area enhanced diffusion properties thereby enabling access to previously electrochemically inactive pockets within the cell. This increased utilization by 18%. Within the electrode design optimization, other limiting factors to the positive electrode utilization included discontinuity in electrolyte coverage. The presence of a physical break in the continuity of the reactive electrolyte was discovered only later during finer analysis. Increasing the reactive electrolyte thickness to ensure proper coverage significantly improved the positive electrode utilization to approximately 40%. Figure II.8.J.4 shows the voltage profile for the first cycle of a 12 V cell with both increased electrolyte thickness and electrode cell modifications charged to 14 V and subsequently discharged to 7.5 V in a stepped discharge protocol. Moving forward, we plan to aggregate the chemical and nanostructural advances we made on the 2.5 V format to the 12 V format and achieve > 75 % utilization within the 12 V architecture.

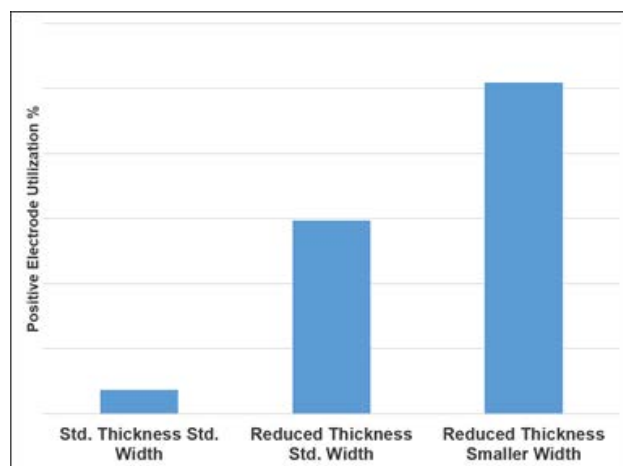


Figure II.8.J.3 Impact of electrode design, including electrode thickness and width, on the positive electrode utilization of 12 V *in-situ* cells. Cells were cycled between 7.5 and 13.5 V. By decreasing the aspect ratio of the electrodes and thereby increasing surface area, enhanced diffusion properties enabled access to previously electrochemically inactive areas leading to higher utilization.

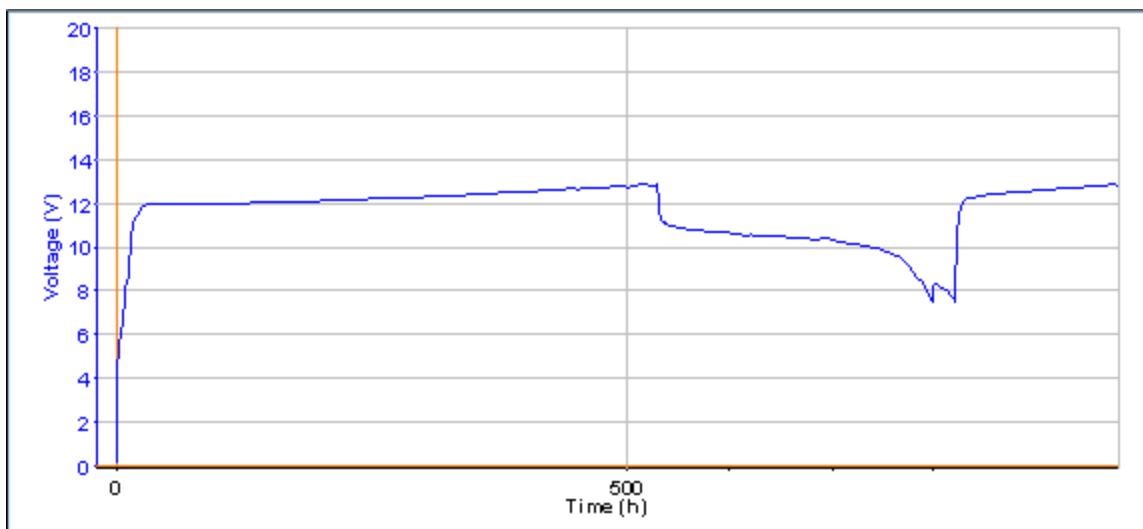


Figure II.8.J.4 First cycle voltage profile for self-formed 12 V cell with improved transport pathways due to cell design modifications and increased reactive electrolyte thickness. The cell was charged up to 14 V before undergoing a stepped discharge protocol down to 7.5 V.

Conclusions

Continued progress has been made toward the development of a high energy solid state battery technology and 12 V output platform. Characterizing the transport properties of the positive electrode enabled the identification of pathways to advance electrochemical performance including capacity, cycle life, and utilization. To date, we have achieved a positive electrode utilization of $> 75\%$ by moving towards multicomponent nanostructured architectures. Mixed conductive additives in these positive nanolayered electrodes have showed an increase in capacity by 40%. In addition, formation/priming protocols and chemistry encapsulation have demonstrated improvements in cycling stability. Finally, our 2.5 V single cell technology (baseline) was successfully translated into a 12 V planar cell (baseline) demonstrating parity in performance. In FY19, we plan to apply our positive electrode modifications to the 12 V cells in order to achieve next years' milestone of $> 90\%$ utilization and deliver 10 mAh cells that achieve energy densities of 1400 Wh/L and 600 Wh/kg per cell stack.

Acknowledgements

Kimberly Scott, Anna Halajko and Nathalie Pereira (Rutgers University) are acknowledged for their contribution as the research team of this program. Colleen Butcher is acknowledged as the National Energy Technology Laboratory Program Manager of this program. Yi Ding is acknowledged as TARDEC Program Manager of this effort. TARDEC and US Army is also thanked for their contribution to the research funding of this effort.

II.8.K Electrochemically Stable High Energy Density Lithium Sulfur Batteries (University of Pittsburgh)

Dr. Prashant N. Kumta, Principal Investigator

University of Pittsburgh
815C Benedum Hall ,3700 O'Hara Street
Pittsburgh, PA 15261
E-mail: pkumta@pitt.edu

Dr. Moni K. Datta, Principal Investigator

University of Pittsburgh
815C Benedum Hall ,3700 O'Hara Street
Pittsburgh, PA 15261
E-mail: mkd16@pitt.edu

Dr. Oleg I. Velikokhatnyi, Principal Investigator

University of Pittsburgh
815C Benedum Hall ,3700 O'Hara Street
Pittsburgh, PA 15261
E-mail: olv3@pitt.edu

Tien Duong, DOE Technology Development Manager

Vehicle Technologies Office, U.S. Department of Energy
E-mail: Tien.Duong@ee.doe.gov

Start Date: October 1, 2017
Project Funding: \$800,000

End Date: March 31, 2019
DOE share: \$800,000

Non-DOE share: \$0

Project Introduction

Lithium–sulfur battery (LSB) technology is widely investigated as an attractive alternative to currently used Li-ion battery (LIB) chemistries for the EV/PEV industry due to the superior theoretical capacity (1674 mAh/g) and specific energy density (2600 Wh/kg) of elemental sulfur. Moreover, the natural abundance of sulfur in the earth's crust makes it a more economical and highly attractive proposition compared to currently existing intercalation-based LIB's cathode materials systems. However, the dissolution of sulfur via formation of soluble polysulfides (PSs) (i.e. poor capacity retention) and the inferior electronic conductivity of S (barrier to complete active materials utilization) are one of the primary limitations of LSB's along with the concomitant development of the Li metal anode which together continue to hinder the much-awaited commercialization of the system. Current generation sulfur cathodes show low reversible specific storage capacity, very poor charging rates and low loading densities. There is hence, a vital need for conducting research to overcome the major issues impeding the development of high energy density LSB technology to enable next generation systems meeting the Battery 500 objectives.

Objectives

This project is a scientific study to obviate the primary problems of (a) low overall electrode capacity (mAh/g-active material) occurring due to low electronic conductivity of sulfur (b) poor cycling stability owing to polysulfide (PS) dissolution (c) voltage drop due to PS transport across and deposition at the lithium anode (d) poor coulombic efficiency (CE). The target of the Battery500 seedling projects is in-line with the overall objectives of the program with the target being to deliver either lithium metal/sulfur cells or lithium/NMC cells exhibiting in excess of 500 Wh/kg energy density and stable cycling over 1000 cycles shown in Table II.8.K.1 below. The proposed innovative and engineered strategies involving polysulfide confinement, sulfur

electrocatalyst (SEC), directly derived sulfur assembled (DDSA) electrodes of electronically conducting nanostructured doped sulfur yielding high sulfur loadings $> 10 \text{ mg/cm}^2$ will yield sulfur cathodes displaying specific capacity $\geq 1200 \text{ mAh/g}$ (electrode-level capacity), at $\geq 2.2 \text{ V}$ generating $\sim 600 \text{ Wh/kg}$ energy density systems higher than the target objectives. Full cells meeting the required deliverables will be made and performance tested in pouch cells. Successful completion of the proposed program will yield: (a) Targeted lithium-sulfur battery (LSB) specific energy ($\geq 500 \text{ Wh/kg}$) and energy density ($\geq 750 \text{ Wh/l}$), (b) Compact light-weight LSB, (c) Economical and scalable precursors; (d) Excellent life-cycle (~ 1000 cycle), calendar life (~ 15 years) and fast recharge-ability. Finally, full cells with optimized sulfur cathodes and dendrite free lithium metal anodes (LMA) will be generated with the following performance metrics: Specific energy $> 500 \text{ Wh/kg}$, cyclability (> 1000 cycles), loss per cycle $< 0.01\%$, Coulombic Efficiency (CE): $> 90\%$ capable of meeting MIL-STD-810G and IEC62133 industry safety standards.

Table II.8.K.1 Battery Specifications for the Battery 500 Program

Energy Storage Performance Requirements		Battery500
Characteristics	Unit	
Specific Energy	Wh/kg	> 500
Energy Density	Wh/l	> 750
Electrode Sulfur Loading	Mg/cm ²	> 10
Specific Capacity	mAh/g	≥ 1200
Voltage	V	≥ 2.2
Calendar Life	Year	~ 15
Cycle Life	Cycles	> 1000
Loss Per Cycle	%	< 0.01
Coulombic Efficiency	%	$> 90\%$

Approach

This project utilizes the use of chemical interactions of PSs with transition metal oxides and complex metal framework-based metal organic framework structures as well as trapping of sulfur in porous carbon or other porous matrix structures. Along with increasing sulfur utilization, the project aims to completely prevent PS dissolution into the electrolyte by confining them within the electrode architectures. It will also involve the translation of this design into electrodes with high sulfur loadings to deliver high overall electrode capacity. Another approach to reduce PS dissolution is electrolyte modification with suitable replacement of the polymer electrolyte (PE) component.

The proposed research which will be conducted in two phases, comprise four novel thrust areas and following major elements outlined below:

- **Thrust 1:** Use of ab-initio techniques, such as density functional theory (DFT) to simplify materials selection for sulfur cathodes comprising the following three sub-thrusts.
 - **Thrust 1a:** Study reaction pathways of polysulfide and disulfide formation, and identification of suitable catalysts ensuring faster reaction kinetics/pathways of conversion of polysulfide to Li_2S , thus enhancing the electrode stability.
 - **Thrust 1b:** Identify room-temperature lithium ion conductors (LIC) for coating sulfur nanoparticles (SNPs) and electrodes.
 - **Thrust 1c:** Use DFT for identifying dopants to enhance the electronic conductivity of sulfur.

- **Thrust 2:** Innovative materials engineering involving (a) Development of thin LIC coated sulfur particles; (b) Generating of complex framework materials (CFM); (c) Synthesis of directly derived doped sulfur assembled (DDSA) electrodes of high-sulfur loading ($> 10 \text{ mg/cm}^2$); (d) Engineering and design of composite polymer electrolyte (CPE) mats; and (e) Development of electrocatalyst and their incorporation promoting polysulfide conversion kinetics.
- **Thrust 3:** Morphological engineering to generate high-energy density electrode architectures exploiting advanced, rapid manufacturing methods utilizing insights from **Thrust 1** and **Thrust 2**.
- **Thrust 4:** Design and development of **Phase 1** technology via full cell implementation including benchmarking and prototype cell testing using standard field conditions.

Thrusters 1-3 will be executed in **Phase 1** with **Thrust 3** in tandem and **Thrust 4** to be pursued in **Phase 2**.

Phase 1 will deliver Li-S cells with specific energy of $\geq 500 \text{ Wh/kg}$ and $> 1,000$ cycles ($< 10\%$ capacity loss). Further, the goal will be to fabricate high loading ($\geq 10 \text{ mg/cm}^2$) sulfur-rich cathodes ($\geq 80\%$ sulfur) exhibiting $\geq 1200 \text{ mAh/g}$ (active material basis) capacity with excellent life-cycle (> 1000 cycles) and high $> 90\%$ CE when tested with dendrite-free lithium metal anodes (LMAs). **Phase 2** will involve implementation and testing of the lab-level pouch cell technology in field conditions.

Results

In 2018, the current project involved formulation and execution of project management plan, and designation of various tasks and technical aspects of the projects. The main technical objectives of FY2018 comprised theoretical modeling and identifying Lithium Ion Conductors (LICs) needed to achieve the targeted energy density ($\geq 500 \text{ Wh/kg}$, $\geq 750 \text{ Wh/l}$) of lithium sulfur batteries (LSBs). To meet the BATT-500 targeted goal, the following systems were generated: sulfur nanoparticles coated with high ionic conductivity LIC named as LIC coated Sulfur Nanoparticles (SNPs), Directly Doped Sulfur Nanoparticles (DSNs), Complex Framework Materials (CFMs) using wet-chemical methods, Directly Doped Sulfur Architectures (DDSA) using electrochemical deposition techniques.

Using density functional theory (DFT) approach and the nudged elastic band (NEB) method two prospective LIC materials Li_3PO_4 and Li_3PS_4 have been explored in terms of the Li-ion diffusivity. Different pathways have been considered and the most optimal ones were identified. Figure II.8.K.1a shows the interstitial channels in the crystal structure along the c-axis direction. The channel sizes are large enough to allow Li-ions to diffuse through these pathways with relatively low activation barriers E_a as shown in Figure II.8.K.1b. One can see, that E_a for Li_3PS_4 is slightly lower than that of Li_3PO_4 due to the weaker Li-S bonds compared to Li-O ones. As a continuation of the computational study initiated in 2018, two prospective LIC materials Li_3PO_4 and Li_3PS_4 have been explored from first principles in terms of the Li-ion mobility/diffusivity. Since introduction of different dopant elements may induce formation of Li-vacancies and/or interstitial Li-ions, there is an opportunity to increase the ionic conductivity of the materials even further. For these purposes different Li-ion migration pathways have been considered for calculations of the activation barriers E_a (see Figure II.8.K.1a). Figure II.8.K.1b&c demonstrate the calculated E_a in various pathways for pure as well as doped structures. Presence of dopants marginally decreases the activation barriers, thus resulting in slight improvement in the Li-ion conductivity. Further study to explore the effects of other dopants on enhancing the ionic conductivity/diffusivity will be conducted theoretically as well as experimentally to validate the computational data during the second phase of the project.

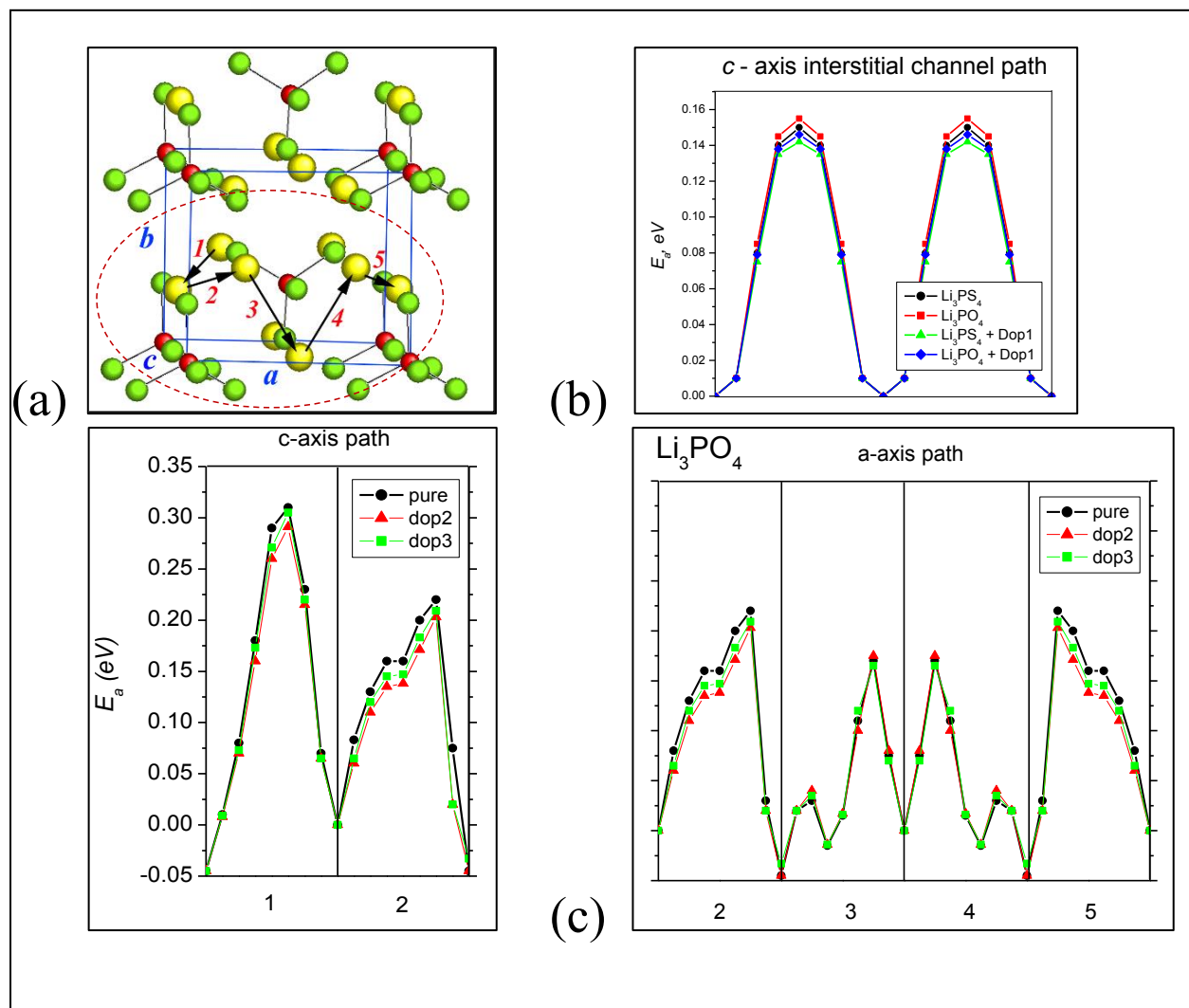


Figure II.8.K.1 **a)** Crystal structure of Li_3PO_4 and Li_3PS_4 with hopping pathways of Li-ions; **1b)** potential energy for migration paths of Li-ions along c-axis interstitial channels in pure and doped Li_3PS_4 and Li_3PO_4 with Dop1; **1c)** the same for vacancy hopping mechanism along a- and c-axis in pure Li_3PO_4 and doped Li_3PO_4 with Dop2 and Dop3.

Synthesis and characterization of lithium ion conducting (LIC) membranes identified by theoretical calculation has been performed as separator/electrolyte complexes for LSB. Two different LIC membranes (LIC-1 and LIC-2) were prepared by electrospinning 50:50 wt% of two polymers namely, Polymer-1 and Polymer-2 and by incorporating two types of inorganic filler molecules IFM-1 and IFM-2. The synthesized polymeric based LIC membranes exhibited good room temperature lithium ion conductivity (Table II.8.K.2) comparable to that of organic liquid electrolyte (1M $\text{LiCF}_3\text{SO}_3 + 0.1\text{M LiNO}_3$ in 50:50 vol% Dioxalane: Dimethoxyethane) as evident from the Nyquist plot (Figure II.8.K.2a). In addition, the IFM incorporated LICs (LIC-1 and LIC-2) exhibited excellent mechanical properties as compared to the parent polymers, Polymer-1, Polymer-2 and the polymer mixture (50:50 wt% Polymer-1:Polymer-2) without filler (Figure II.8.K.2b). Both, LIC-1 and LIC-2 also exhibited tensile strengths of 687 kPa and 723 kPa, respectively which are almost two-fold higher than the polymer mixture (320 kPa).

Table II.8.K.2 Ionic conductivity of different LIC membranes.

LIC Composition	Ionic Conductivity (mS cm ⁻¹)
Polymer-1 + IFM-1	1.351
Polymer-1 + IFM-2	2.253
Polymer-2 + IFM-1	2.654
Polymer-2 + IFM-2	2.997
Polymer-1/Polymer-2 (50:50 wt%) + IFM-1 (LIC-1)	2.091
Polymer-1/Polymer-2 (50:50 wt%) + IFM-2 (LIC-2)	2.839
Liquid Electrolyte	4.283

The LIC membranes (LIC-1 and LIC-2) were further tested as separator/electrolyte complexes in LSBs after activation by dipping into organic liquid electrolyte (1M LiCF₃SO₃ + 0.1M LiNO₃ in 50:50 vol% Dioxalane: Dimethoxyethane). Figure II.8.K.2c shows the electrochemical cycling performance of the Li/LIC/commercial sulfur cells along with that of the commercial sulfur cell cycled with liquid electrolyte (1M LiCF₃SO₃ + 0.1M LiNO₃ in 50:50 vol% Dioxalane: Dimethoxyethane). The LSBs cycled with LIC-1 as separator shows an initial capacity of 1001 mAh/g and a stable capacity of 752 mAh/g after 60 cycles and the LIC-2 shows an initial capacity of 894 mAh/g and a stable capacity of 744 mAh/g. On the other hand, the Li/commercial S cell cycled with the organic liquid electrolyte shows a low initial capacity of 697 mAh/g and poor cyclability displaying 124 mAh/g specific capacity after 60 cycles. The superior cycling performance of the LICs is attributed to their better polysulfide trapping properties and their ability to inhibit the sulfide shuttling.

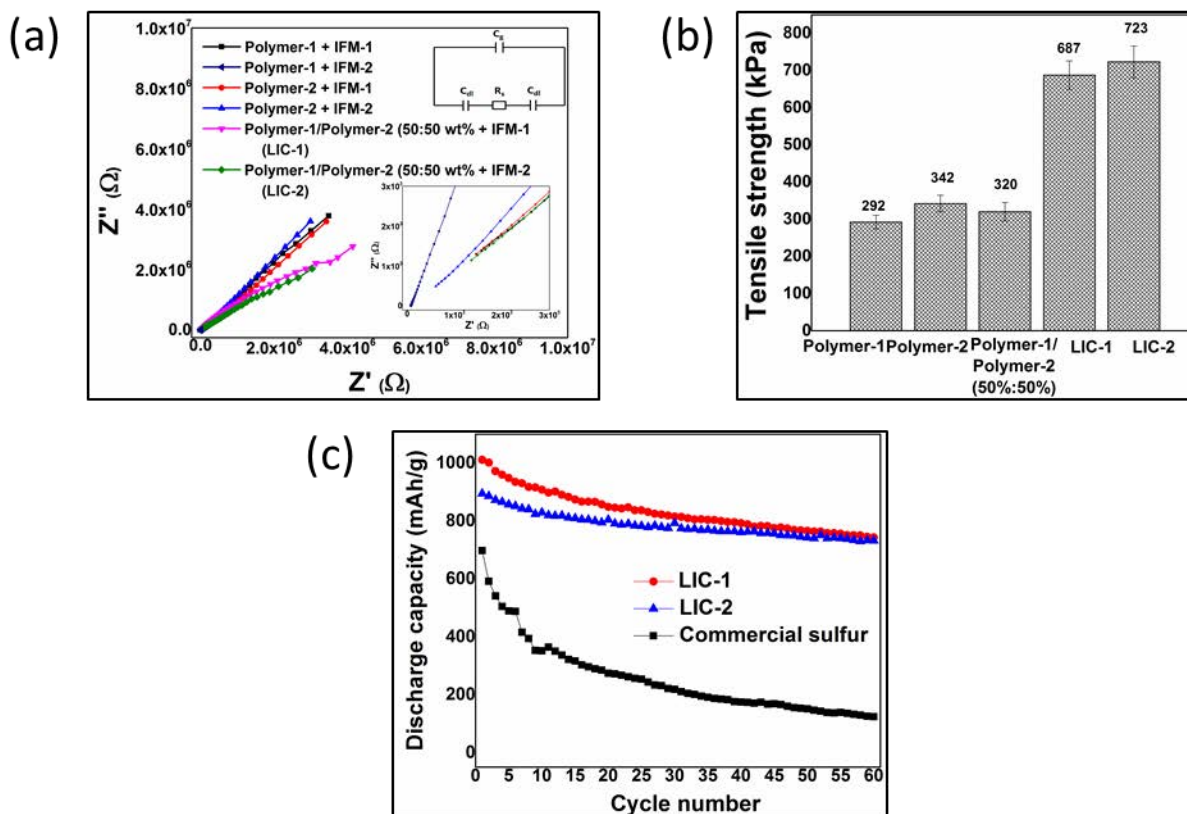


Figure II.8.K.2 a) Nyquist plot from lithium ion conductivity measurements performed on the LIC membranes. b) Mechanical property analysis of the LIC membranes c) Electrochemical cycling performance of the LIC membranes.

As a continuation of the computational study, a prospective garnet-type LIC oxide $\text{Li}_7\text{La}_3\text{Zr}_2\text{O}_{12}$ (LLZO-LIC) was also explored by first principles calculations for studying the Li-ion mobility/diffusivity (see Figure II.8.K.3a for the crystal structure). Introduction of various dopants can induce Li-vacancy formation, increasing the partially occupied Li-site occupation numbers, and/or enlarge the open channels allowing facile diffusion pathways. There is hence, an opportunity to increase the Li-ion conductivity of the garnet oxide even further. Following this approach, different Li-ion migration pathways were considered for calculations of the activation barriers, E_a using the nudged elastic band (NEB) computational method. Figure II.8.K.3b illustrates the calculated E_a values for various pathways in pure and doped garnets. Introduction of dopants as shown decreases the activation barriers pointedly (for example, from 0.23eV to 0.148eV for pure and garnet with dopant 3, respectively).

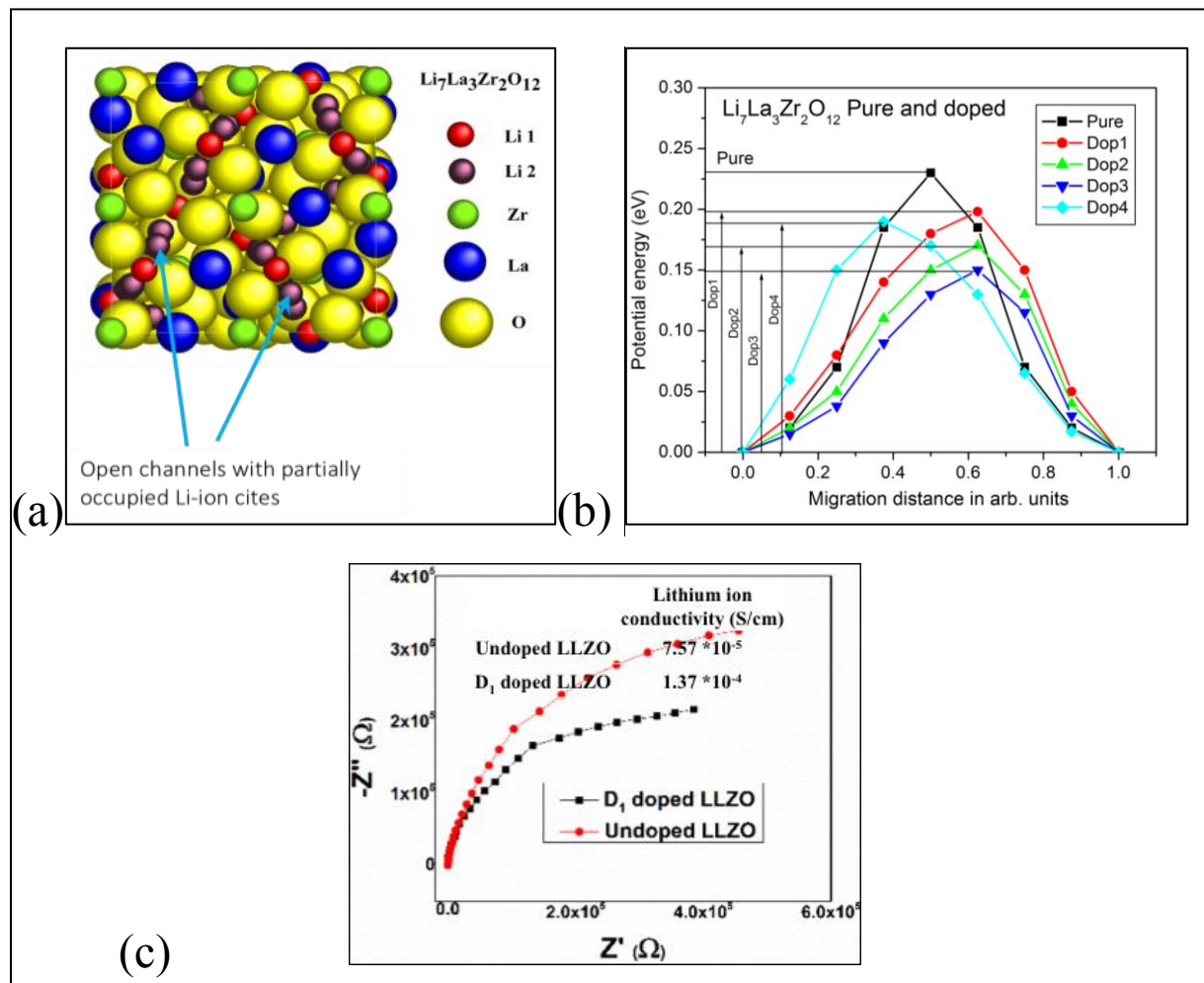


Figure II.8.K.3 **a**) Crystal structure of the cubic garnet-type $\text{Li}_7\text{La}_3\text{Zr}_2\text{O}_{12}$ with partially occupied Li-ion sites denoted by arrows, **b**) potential energy for the migration paths of Li-ions in pure garnet and the oxide doped with dopants 1-4, **c**) Nyquist plot of the undoped and D_1 -doped LLZO-LIC.

This in turn, yields ~ 20 fold increase in the corresponding ionic diffusion coefficients enhancing the Li-ion diffusivity values to increase from $1.5 \times 10^{-6} \text{cm}^2/\text{s}$ to $3.2 \times 10^{-5} \text{cm}^2/\text{s}$, thus facilitating Li-ion conductivity improvements. Correspondingly, when LLZO-LIC is doped with a D_1 dopant, the room temperature ionic conductivity increased from $7.57 \times 10^{-5} \text{S/cm}$ to $1.37 \times 10^{-4} \text{S/cm}$ (Figure II.8.K.3c). This improvement is promising validating the theoretical studies and inspiring continued theoretical studies to be executed to explore the effect of other dopants on ionic conductivity/diffusivity of various garnet-type oxides.

Experimental studies will also be accordingly conducted in the second phase to validate the theoretical predictions and findings.

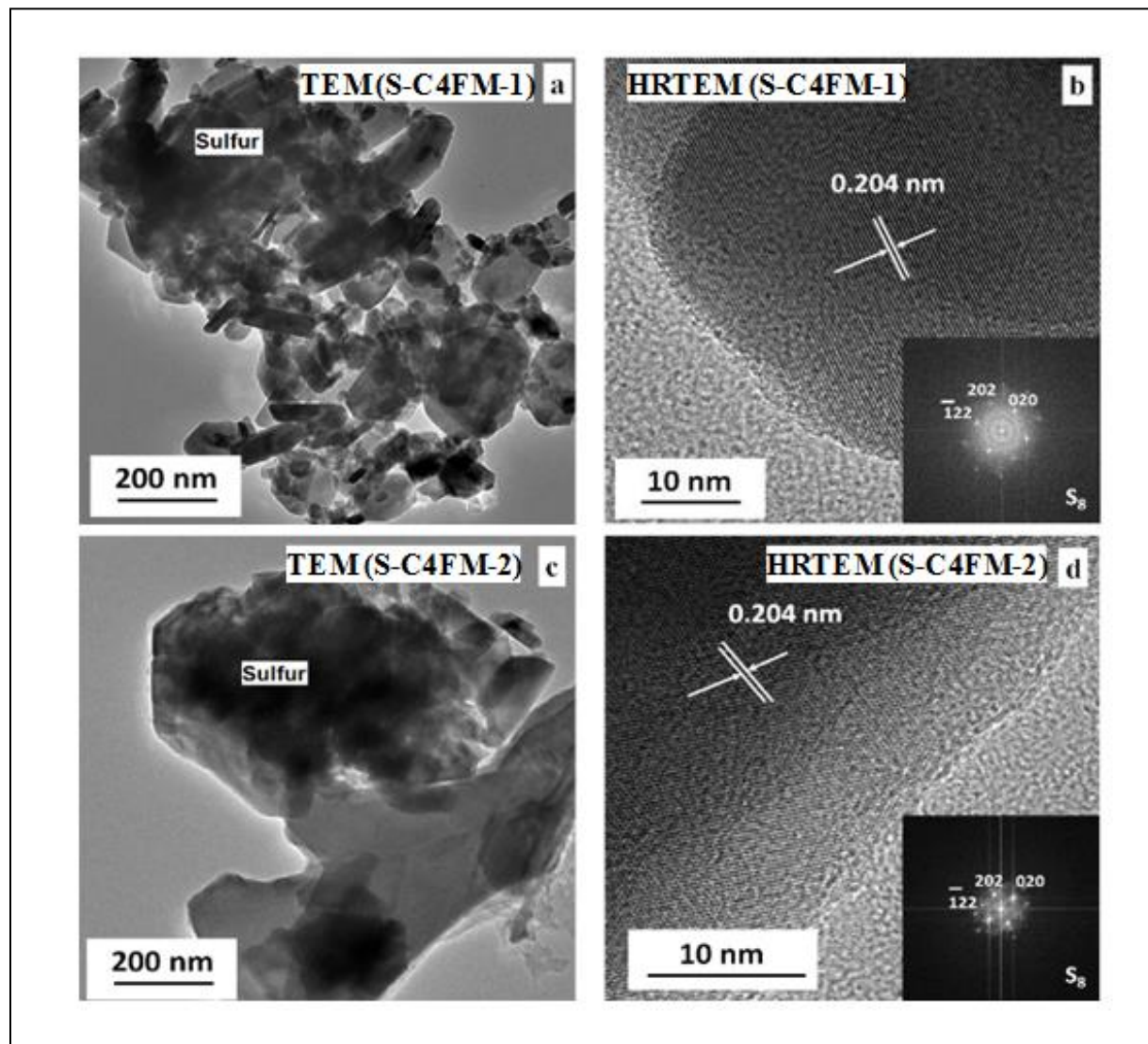


Figure II.8.K.4 **a&b**) TEM images of S-C4FM-1 at two different magnifications along with the corresponding SAED pattern (inset) and **c&d**) TEM images of S-C4FM-2 at two different magnifications along with the corresponding SAED pattern (inset).

Phase 1 also involved the characterization of gen-2 Chemically Coupled Conducting Complex Framework Materials (C4FM), S-C4FM-1 and S-C4FM-2. Sulfur was infiltrated into the chemically synthesized C4FMs using a vapor phase infiltration process. To confirm the nanoporous characteristic of the C4FMs and the presence of crystalline sulfur inside the C4FMs, TEM analysis was conducted on the S-C4FM-1 and S-C4FM-2 following infiltration of sulfur. High and low resolution TEM micrographs of the C4FMs are shown in Figure II.8.K.4.a-d. The low resolution TEM images of the C4FMs (Figure II.8.K.4a&c) clearly show islands of sulfur generated inside the S-C4FM-1 and S-C4FM-2 crystals. The high-resolution images (Figure II.8.K.4b&d), on the other hand, additionally shows very clearly the fringe patterns with a d-spacing of 0.204nm corresponding to crystalline sulfur confirming the infiltration of sulfur into the two C4FMs structures. In addition, the SAED pattern of the sulfur infiltrated C4FMs (inset Figure II.8.K.4b&d) clearly shows the

diffraction pattern corresponding to the presence of crystallographic sulfur planes involving the following planes: $(\bar{1}22)$, (202) and (020) .

The effect of chemical binding between the C4FMs and sulfur on the electrochemical performance of the S-

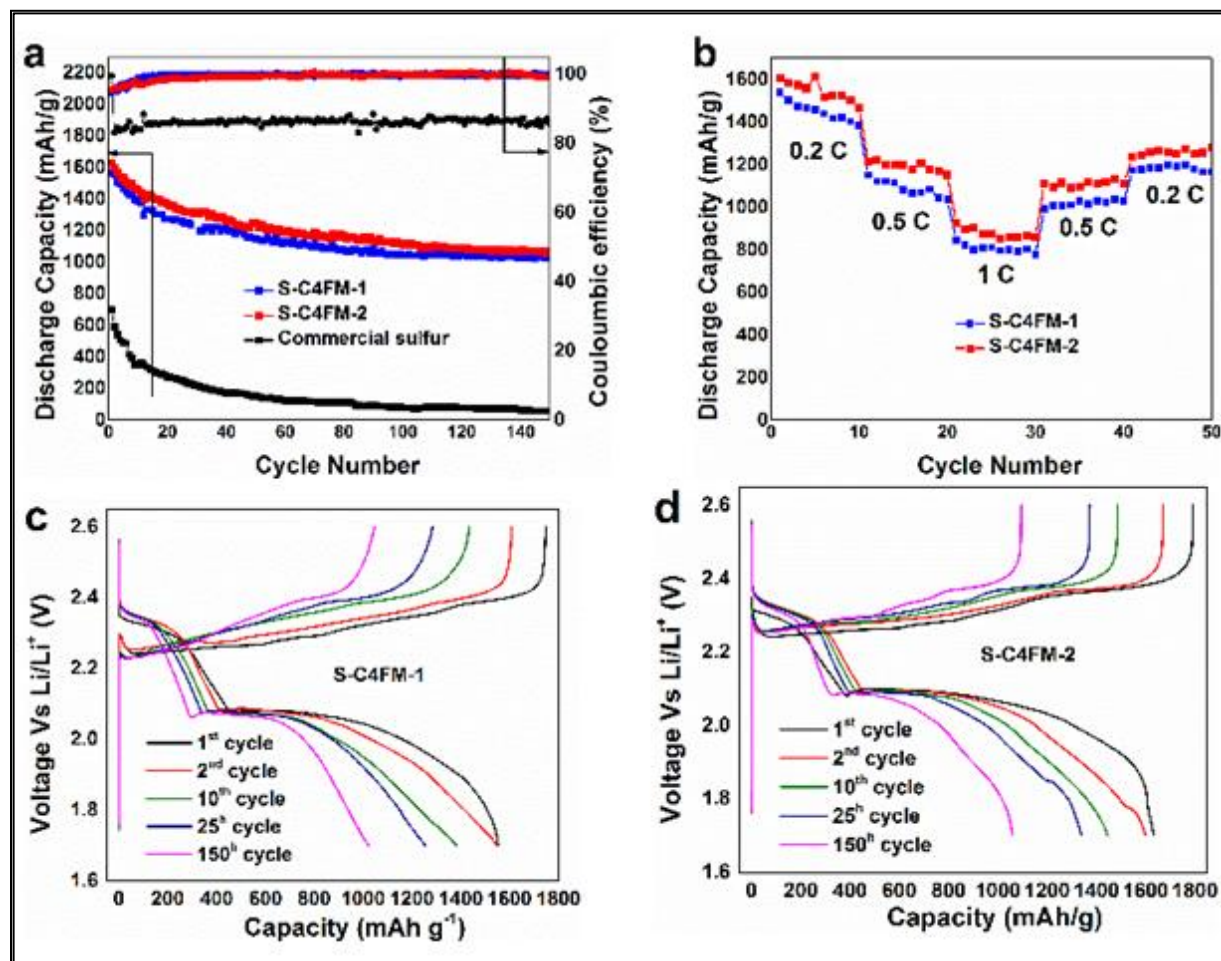


Figure II.8.K.5. **a**) Cycling performance of S-C4FM-1 and S-C4FM-2 cycled at 0.2C rate, **b**) rate capability plot of S-C4FM-1 and S-C4FM-2, **c**) charge-discharge plot of S-C4FM-1 and **d**) charge-discharge plot of S-C4FM-2.

C4FMs was further studied by electrochemically cycling the S-C4FM-1 and S-C4FM-2 electrodes. Figure II.8.K.5a represents the results of the electrochemical cycling experiments and Figure II.8.K.5b represents the rate capability experiments of S-C4FM-1 and S-C4FM-2. The S-C4FM-1 shows an initial discharge capacity of 1565 mAh/g that stabilizes at a discharge capacity of 1025 mAh/g after 150 cycles with a fade rate of (0.0022%/ cycle). The S-C4FM-2 also shows a high initial discharge capacity of 1626 mAh/g and a stable 1063 mAh/g discharge capacity after 150 cycles (fade-rate of 0.0023%/cycle). Both the S-C4FM-1 and S-C4FM-2 electrodes systems show good rate capability as seen from Figure II.8.K.5b. This is a significant improvement in performance as compared to the commercial sulfur cathodes that shows an initial capacity of only 697 mAh/g that fades down to 57 mAh/g by the end of 150 charge-discharge cycles. However, it is important to note that both the C4FMs (S-C4FM-1 and S-C4FM-2) exhibit a fade of ~35% of the initial discharge capacity during the initial ~25 cycles followed by a stable cycling performance. Efforts were concentrated on identifying the cause of this fade and the results showed that this fade is mainly arising from the chemical components of the C4FM system binding the Li ions and is not due to the dissolved polysulfide species which was affirmed by X-ray photoelectron spectroscopy (XPS) studies.

Phase 1 also involved the optimization and chemical and electrochemical characterization of the C4FM-3 system. TEM analysis was performed on the experimentally synthesized C4FM-3 to confirm the nanoporous nature of the sulfur infiltrated C4FM-3 structures, S-C4FM-3 to confirm that the sulfur had indeed infiltrated within the experimentally generated C4FM-3 structure (Figure II.8.K.6a-d). The HR-TEM image of the C4FM-3 at low magnification shows the macroscopic structure of the C4FM-3 and the high-resolution image (Figure II.8.K.6b) similar to the systems studied earlier further shows the highly ordered nature while the corresponding SAED diffraction pattern of the S-C4FM-3 (inset Figure II.8.K.6b) indicates the expected long-range order of the C4FM-3 channels. Figure II.8.K.6c represents the HR-TEM image of the sulfur-infiltrated C4FM-3 (S-C4FM-3). HR-TEM of the S-C4FM-3 at a higher magnification (dFigure II.8.K.6) shows the presence of fringe patterns with an interplanar spacing value of 0.2046 nm corresponding to that of crystalline sulfur (S_8). The inset in Figure II.8.K.6d also shows the SAED pattern corresponding to S-C4FM-3. Upon further analysis, the SAED pattern shows spots corresponding to the (202), (020) and ($\bar{1}22$) crystalline planes of S_8 , thus confirming the presence of crystalline sulfur inside the S-C4FM-3 framework structures.

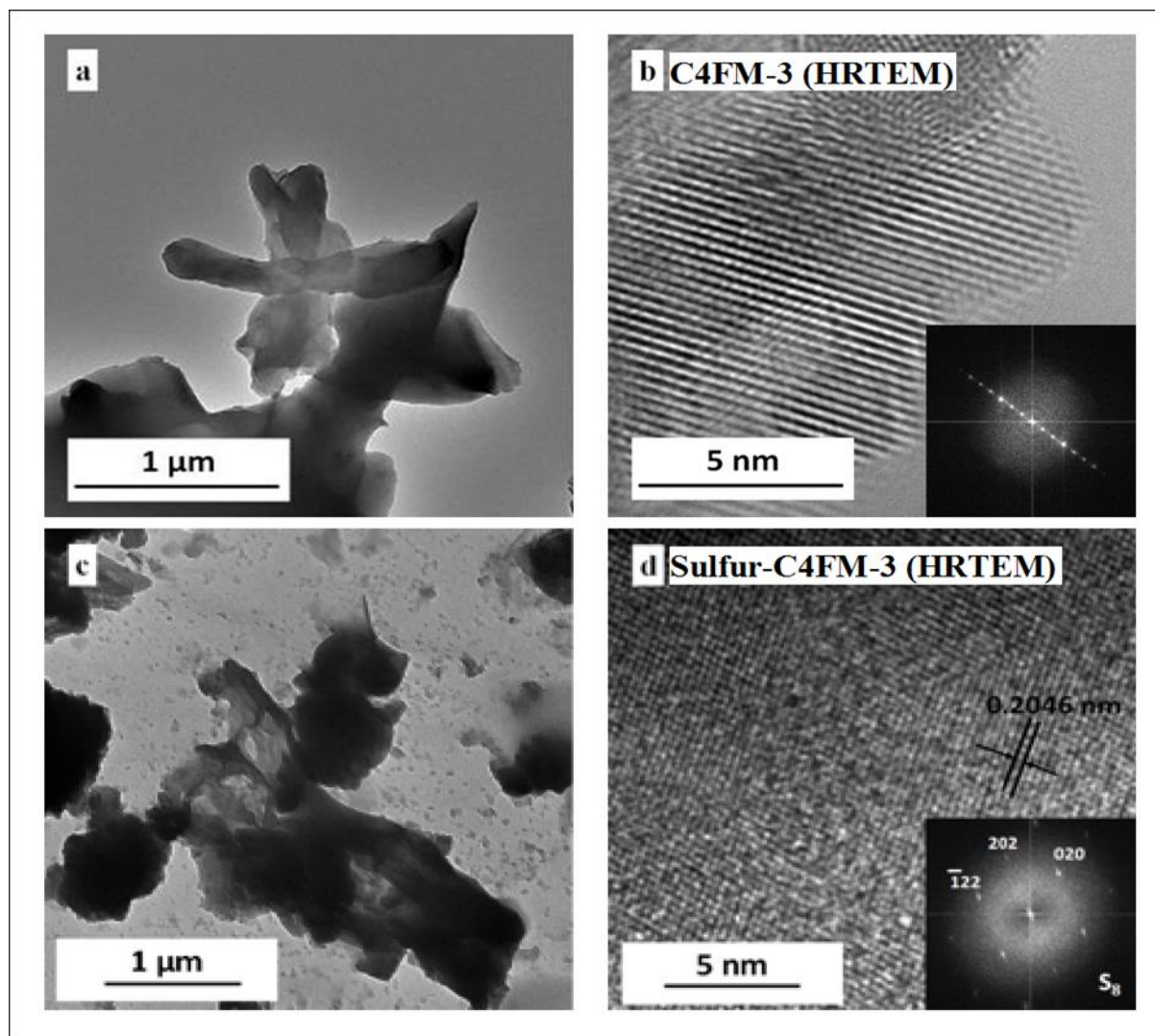


Figure II.8.K.6. **a&b)** TEM images of C4FM-3 at two different magnifications and **c&d)** TEM images of S-C4FM-3 at two different magnifications along with the corresponding SAED pattern (Figure II.M.8.6d inset).

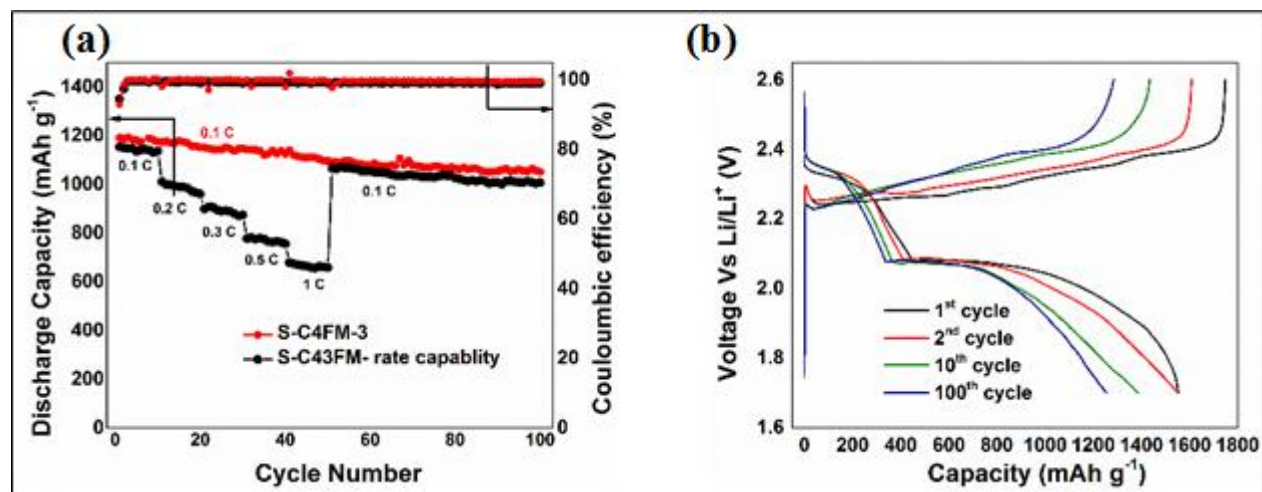


Figure II.8.K.7.a) Cycling and rate capability plot of the S-C4FM-3 and b) Specific capacity plot of the S-C4FM-3.

The results of the electrochemical charge-discharge response on the S-C4FM-3 at 0.1C rate ($\sim 1.5\text{-}2\text{ mg/cm}^2$ sulfur loading) and corresponding rate capability study is shown in Figure II.8.K.7a. The S-C4FM-3 shows an initial discharge capacity of 1190 mAh/g which stabilizes at 1044 mAh/g after the 100th cycle demonstrating promising electrochemical response with a fade rate of $\sim 0.0012\%/ \text{cycle}$. Detailed studies are on-going and will be reported in the near future.

Conclusions

The aim of Phase-1 in 2018 was to improve the cycling characteristics and reduce the polysulfide dissolution in Li-S batteries by identifying solid state lithium ion conductors (LICs) using DFT calculations. At the same time, efforts were directed to synthesize composite polymer electrolytes (CPEs) with various inorganic framework material (IFM) nanofillers with enhanced Li-ion conductivities. In addition, work was directed at developing sulfur architectures by infiltrating sulfur into chemically coupled conducting complex framework materials (C4FMs). By implementing such a unique approach various complex framework materials system (S-C4FM-1, S-C4FM-2 and S-C4FM-3) were derived and evaluated as cathodes in lithium sulfur batteries. The S-C4FM-1 showed an initial discharge capacity of 1565 mAh/g and stabilizes at a discharge capacity of 1025 mAh/g after 150 cycles with a fade rate of (0.0022%/ cycle) (Figure II.8.K.5a), S-C4FM-2 exhibited a high initial discharge capacity of 1626 mAh/g and a stable 1063 mAh/g discharge capacity after 150 cycles (fade rate of 0.0023%/cycle) (Figure II.8.K.5a) and S-C4FM-3 demonstrated a high initial capacity of 1190 mAh/g, with stable capacity of 1044 mAh/g for over 100 cycles (fade rate of $\sim 0.0012\%/ \text{cycle}$) (Figure II.8.K.5a).

Key Publications

1. Jampani, P.H.; Gattu, B.; Shanthi, P.M.; Damle, S.S.; Basson, Z.; Bandi, R.; Datta, M.K.; Park, S.K.; Kumta, P.N. Flexible sulfur wires (Flex-SWs) – A Versatile platform for lithium-sulfur batteries, *Electrochimica Acta* Vol. 212, pp. 286 - 293 (2016)
2. Shanthi, P.M.; Jampani, P.H.; Gattu, B.; Sweeney, M.; Datta, M.K.; Kumta, P.N. Nanoporous Non-Carbonized Metal Organic Frameworks (MOFs): Understanding the Origin of Irreversible Capacity loss in Non-Carbonized Carbonate – based Metal Organic Framework (MOF) Sulfur hosts for Lithium – Sulfur battery, *Electrochimica Acta*, Vol, 229, pp 208–218 (2017)
3. Shanthi, P.M., Jampani, P.H., Gattu, B., Albuquerque T., Datta, M.K., Kumta, P.N., “Novel electrospun PVdF – HFP Composite Polymer Electrolytes (CPEs) with enhanced Ionic Conductivities for Lithium – Sulfur batteries”, *ACS Applied Energy Materials*, 2018, 1 (2), 483–494.

4. Jampani, P.H.; Gattu, B.; Shanthi, P.M.; Kumta, P.N. Novel electro-spun sulfur wires for fabricating mattes of lithium-sulfur batteries, International Patent Number: WO 2016/145429 A1, U.S. Provisional Patent, Application Number: PCT/US2016/022283 (Filing date: 03/14/2016)
5. Shanthi, P. M, Jampani, P.H., Gattu, B.; Datta, M K, Velikokhatnyi, O. I., Kumta, P.N., “Electrospinning of PVdF-HFP: Novel Composite Polymer Electrolytes (CPEs) with enhanced ionic conductivities for Lithium-Sulfur batteries.” U.S. Provisional Appln. Serial No. 62/529,638 (2017).
6. Jampani, P.H., Shanthi, P. M., Gattu, B., Datta, M K, Velikokhatnyi, O.I., Kumta, P.N., “High capacity, air-stable, Structurally Isomorphous lithium Alloy (SIA), Multilayer Porous Foams (MPFs) and Composite Multilayer Anodes (CMAs) for dendrite-free lithium metal anodes for Li-ion batteries”, U.S. Provisional Patent Appln. No. 62/529,588 (2017).

Acknowledgements

Research supported by the U.S. Department of Energy OVT-DE-EE0006825 and the Edward R. Weidlein Chair Professorship Funds, Nanomaterials for Energy Conversion and Storage Technology (NECST) Laboratories, and the Center for Complex Engineered Multifunctional Materials (CCEMM) for partial assistance and help with procuring the electrochemical equipment and facilities used in this research work.

II.9 Beyond Li-ion R&D: Lithium-Air Batteries

II.9.A Rechargeable Lithium-Air Batteries (Pacific Northwest National Laboratory)

Ji-Guang Zhang, Principal Investigator

Pacific Northwest National Laboratory
902 Battelle Boulevard
Richland, WA 99354
E-mail: jiguang.zhang@pnnl.gov

Wu Xu, Principal Investigator

Pacific Northwest National Laboratory
902 Battelle Boulevard
Richland, WA 99354
E-mail: wu.xu@pnnl.gov

Tien Duong, DOE Technical Development Manager

U.S. Department of Energy
E-mail: Tien.Duong@ee.doe.gov

Start Date: October 1, 2015

End Date: September 30, 2019

Project Funding (FY18): \$200,000

DOE share: \$200,000

Non-DOE share: \$0

Project Introduction

It is well known that the state of the art lithium (Li)-ion batteries is a mutual technology and may reach their practical limit on specific energy ($\sim 300\text{-}350 \text{ Wh kg}^{-1}$) in the near future. Therefore, a worldwide effort has been made to explore new battery chemistries that may far exceed the specific energy of Li-ion batteries. Among the alternative energy storage systems, Li-air batteries have triggered worldwide research interest since the first nonaqueous Li-air battery was unveiled in 1996 due to their extremely high theoretical specific energy density ($\sim 5,200 \text{ Wh kg}^{-1}$ when the weights of Li and O_2 are included). However, before the commercialization of Li-air batteries, considerable challenges still face Li-air batteries and need to be overcome. These challenges include instability of electrolyte, high overpotential, and severe corrosion of Li anodes. These problems cause poor round-trip efficiency and short cycle life in the state of the art Li-air batteries. Thus, efficient strategies for further development of ultrahigh-energy-density Li-air batteries suitable for application in electric vehicles include development of electrolytes that are more stable against superoxide and Li metal anodes, design of alternative catalysts and carbon-based or carbon-free air electrodes, stabilization of Li metal anodes, and exploration of new insights into the mechanisms of oxygen reduction/evolution reactions (ORR/OER).

Objectives

The objective of this project is to develop rechargeable lithium-oxygen (Li-O_2) batteries with long-term cycling stability through in-depth research on more stable electrolytes and highly efficient catalysts for air electrodes, protection of Li metal anodes, and deeper insight into the ORR/OER mechanisms behind the electrochemical performance of Li-O_2 cells.

Approach

Stability of Li metal anode when exposed to an oxygen saturated non-aqueous electrolyte is critical for the long term calendar life and cycle life of Li-O_2 batteries. A stable solid electrolyte interphase (SEI) layer will be formed in situ through selected electrolytes and treatment protocols before Li-O_2 cell operation. In addition, ex situ formation of stable inorganic/polymeric hybrid electrolyte layers will be developed through dip-coating or tape casting method to coat the inorganic/polymeric hybrid electrolyte layer on Li-metal surface. Thick carbon/catalyst composite air electrodes based on carbon nanotubes (CNTs) and transient metal oxides such as ruthenium oxide (RuO_2) and with $\geq 4 \text{ mg/cm}^2$ areal loading will be developed.

Results

Significant progresses have been made in protection of electrodes (both carbon based air-electrode and Li anode), efficient catalysts, and high-loading air-electrodes in Li-O₂ batteries in FY18. The details are described below.

1. In-situ induced protection films produced on both air electrode and Li metal anode of Li-O₂ cells

A low cost, one-step electrochemical pre-charging strategy has been developed to simultaneously generate protective thin films on both the CNTs air electrode and Li metal anode in argon (Ar) gas. Thus, during the subsequent Li-O₂ battery cycling, these thin films can protect both electrodes and significantly suppress the attack of highly reactive reduced oxygen species (superoxide radical anions) against carbon-based air-electrode and Li anode, as well as minimize Li anode corrosion, as shown in Figure II.9.A.1a. The pre-treatment of the assembled Li||CNTs cells was conducted by charging the cells in an Ar filled container from open-circuit voltage (OCV) to 4.3 V at 0.1 mA cm⁻² and then holding the cells at 4.3 V for 0, 5, 10, 15, and 20 min, respectively. After pre-treatment process (e.g., 4.3 V/10 min), the protective thin films can be formed on CNTs air-electrode surface (Figure II.9.A.1b) and Li anode surface (Figure II.9.A.1c), respectively. The numbers of stable cycles of the Li-O₂ cells with the pre-treatment (4.3 V/0 min, 4.3 V/5 min, 4.3 V/10 min, 4.3 V/15 min, and 4.3 V/20 min) and without pretreatment are 62, 63, 110, 95, 72, and 43, respectively (Figure II.K.1.1d). This demonstrated that the simple pre-treatment did enhance the cycling stability of the Li-O₂ cells even without mediators in the electrolytes or catalysts on the air electrodes. After cycling, the surface layer of Li metal anode after 110 cycles with pre-treatment (4.3 V/10 min) retains relatively flat and compact with only a few cracks (Figure II.9.A.1e). However, a large amount of corrosion products are loosely packed on the Li metal surface (Figure II.9.A.1f) for the un-treated Li metal anode after 70 cycles. This shows that the optimal pre-charging treatment could significantly improve the stability of both CNT electrode and Li metal anode during long-term cycling, thus leading to greatly enhanced cycling stability of Li-O₂ cells.

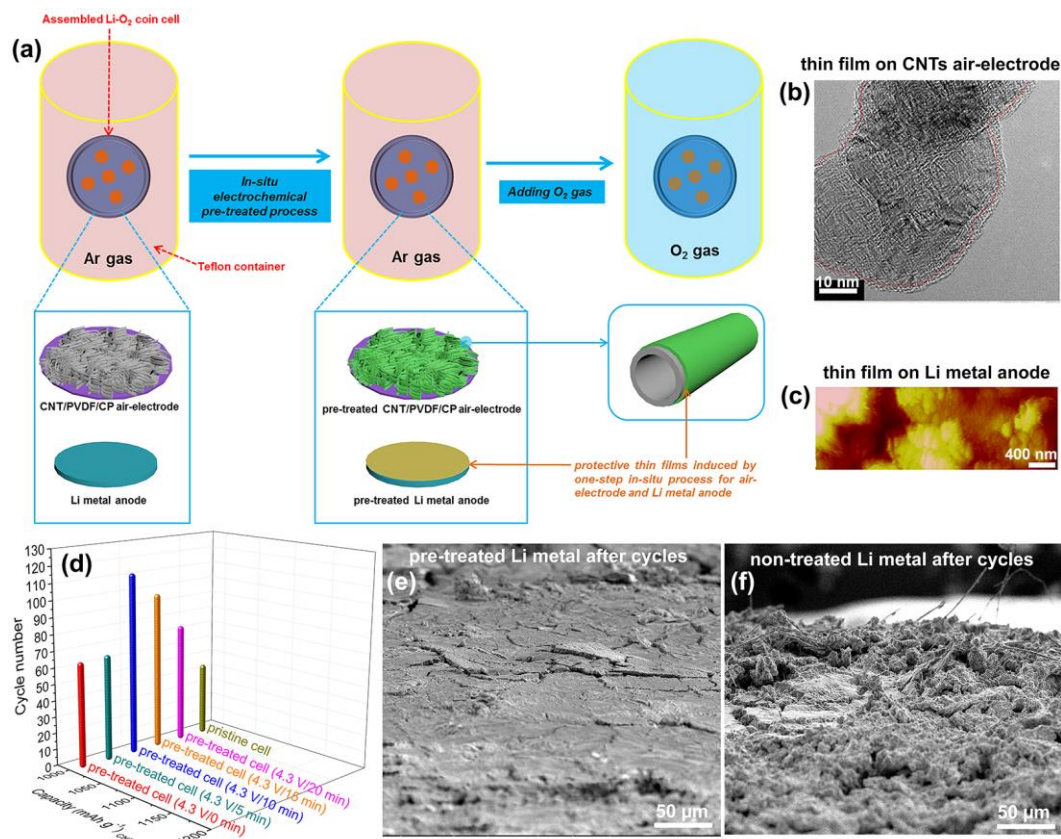


Figure II.9.A.1 (a) Schematic of the operation principle of the simple one-step electrochemical pre-charging treatment process for CNTs air electrode and Li metal anode. (b) TEM image of protective thin film produced on CNTs air-electrode after pre-treatment (4.3 V/10 min). (c) Atomic force microscopy (AFM) image of protective thin film produced on Li metal anode after pre-treatment (4.3 V/10 min). (d) Stable cycling life of Li-O₂ cells without and with pretreatment cycled at 0.1 mA cm⁻² in common 1 M lithium trifluoromethanesulfonate (LiTf) in tetraethylene glycol dimethyl ether (Tetra glyme) electrolyte at room temperature. Scanning electron microscopy (SEM) top-view images of Li metal anode with pre-treatment (4.3 V/10 min) after 110 cycles (e), and Li metal anode without pre-treatment after 70 cycles (f).

2. Long-lasting lithium-oxygen battery using optimized RuO₂/CNTs catalysts

In our previous work, we found that Li metal experienced severe corrosion after than 100 cycles at 0.1 mA cm⁻² in Li-O₂ cells containing RuO₂/CNTs air-electrodes and Li anodes. On the other hand, the cycled, RuO₂/CNTs air-electrode still remains very stable after even long-term cycles (over 300 cycles). Reassembled cells with cycled RuO₂/CNTs air-electrodes and fresh Li anode were still able to show at least 125 cycles at a higher rate (0.2 mA cm⁻²). These results indicate that corrosion of Li metal anode is the main reason for the shortened cycle life in these Li-O₂ cells. Considering the fact that instability of Li anode may prevent the accurate evaluation of optimized air-electrodes, we further replaced Li metal with more stable LiFePO₄ (LFP) counter electrode so we can focus on the evaluation of air-electrode and electrolyte during ORR/OER reactions. The Li-O₂ cells based on optimal RuO₂/CNTs air-electrode and LFP counter electrode can be cycled for 800 times and 430 times under constant-capacity protocols of 800 mAh g⁻¹ and 1000 mAh g⁻¹, respectively (Figure II.9.A.2a). These results reveals the highly efficient optimal RuO₂/CNTs for ORR/OER process of Li-O₂ cells during long-term cycling. Here, capacities and current densities were calculated on the basis of total mass of RuO₂ and CNTs. After 430th discharge, discharge products were uniformly distributed on the air-electrode surface (Figure II.9.A.2b), whereas they have been identified as Li₂O₂ (Figure II.9.A.2d). After the subsequent charge process, almost all of discharge products can be decomposed (Figure II.9.A.2c and Figure II.9.A.2d), while RuO₂ catalysts are still intact on the air-electrode after long term cycles due to its high stability (Figure II.9.A.2e). The above results clearly reveal that the optimal RuO₂/CNTs catalysts could

significantly improve the cycle life of Li-O₂ cells. It's highly expected to further enhance the cycling stability of Li-O₂ batteries containing this kind of optimal RuO₂/CNTs air-electrodes and well-protected Li metal anodes.

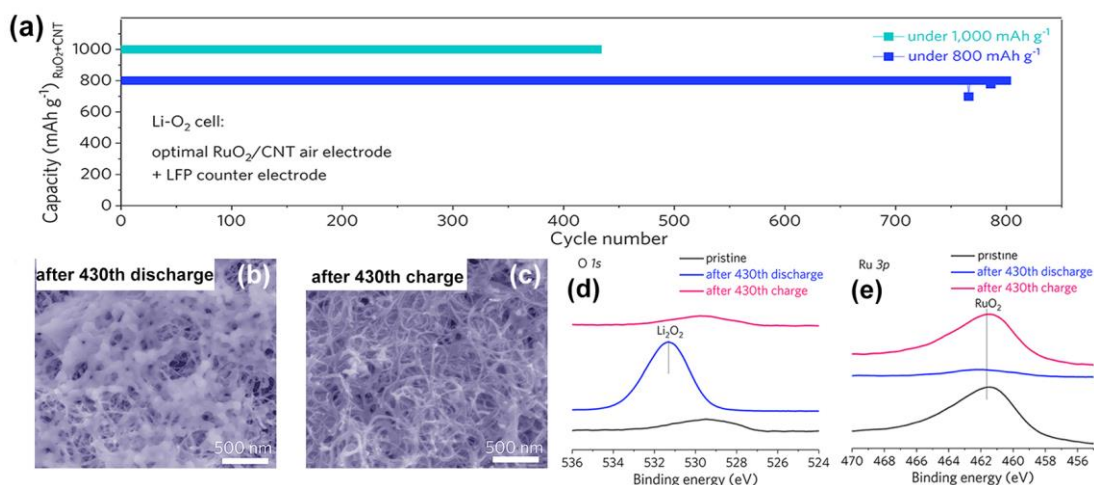


Figure II.9.A.2 (a) Cycling performance of Li-O₂ cells with optimized RuO₂/CNT air electrode and LiFePO₄ (LFP) counter electrode cycled at 0.1 mA cm⁻² in 1 M LiTf-Tetraglyme electrolyte under capacity-fixed protocols of 1,000 mAh g⁻¹ and 800 mAh g⁻¹, respectively. (b) SEM images of cycled air-electrode after 430th discharge (b) and 430th charge (c). XPS spectra of O 1s (d) and Ru 3p (e) of cycled air-electrodes.

3. Development of inorganic/polymeric composite hybrid electrolyte membranes to protect Li metal anode in Li-O₂ batteries

During the last year, we have synthesized an inorganic/polymeric composite membrane composed of Li_{6.75}La₃Zr_{1.75}Ta_{0.25}O₁₂ (LLZTO), lithium bis(trifluoromethanesulfonyl)imide (LiTFSI), and poly(vinylidene fluoride) (PVDF) by a facile method to protect Li metal anode in Li-O₂ batteries. PVDF and LiTFSI (7:3 weight ratio) were first dissolved in N,N-dimethylformamide (DMF) with a polymer concentration of 10 wt.% followed by mechanical stirring to obtain a homogeneous solution. LLZTO was then added into the homogeneous solution with a LLZTO to PVDF weight ratio of 1:10. The mixture was then cast with a doctor blade on a clean polytetrafluoroethylene (PTFE) plate. Finally, the free-standing solid LiTFSI-LLZTO-PVDF (LLP) composite thin membranes (~20 μm in thickness) were obtained after drying under vacuum at 80 °C for 24 h to remove the DMF solvent, as shown in Figure II.9.A.3a and Figure II.9.A.3b. The effect of the LLP hybrid protective membrane on Li-O₂ cell performance was investigated. Compared to the limited cycle life of the Li-O₂ cells without Li metal protection membranes (Figure II.9.A.3c and Figure II.9.A.3d), the addition of LLP protective membrane on Li metal anode surface in Li-O₂ cells largely enhanced Li metal stability upon cycling, leading to more stable operation of Li-O₂ cells (Figure II.9.A.3e and Figure II.9.A.3f) due to significantly decreased side reaction between Li metal and electrolyte. Thus, it has been proved that this kind of inorganic/polymeric composite membrane composed of LLZTO, LiTFSI and PVDF facilitates Li metal protection in Li-O₂ cell, which is beneficial for cycling improvement of high-energy Li-O₂ battery.

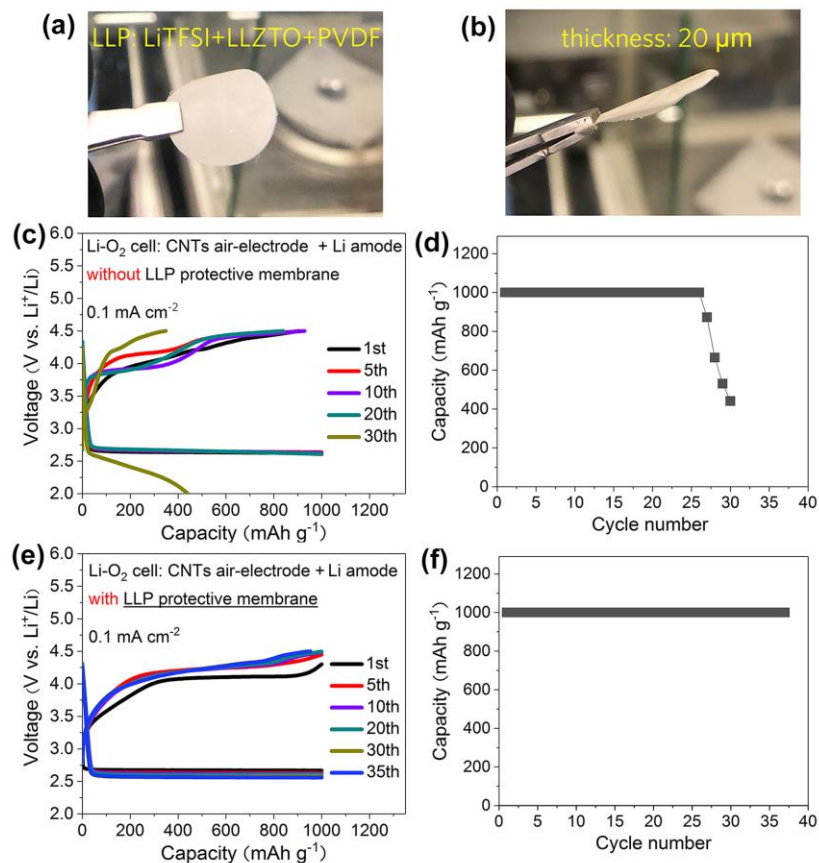


Figure II.9.A.3 (a, b) Optical images of as-prepared free-standing thin composite LiTFSI-LLZTO-PVDF (LLP) membrane with good flexibility. Cycling performance of Li-O₂ cells composed of CNTs air-electrode and Li anode without LLP membrane (c, d), and with LLP membrane (e, f) cycled at 0.1 mA cm⁻² under a limited capacity of 1,000 mAh g⁻¹.

4. Evaluation on cycling performance of Li-O₂ batteries composed of high-loading air-electrode and protected Li metal anode

Although many progresses have been made in improving cycling stability of Li-O₂ batteries in recent years, very small mass loading of the air electrodes (generally less than 1 mg cm⁻²) in these batteries makes it questionable for the practical application of high energy density of Li-O₂ batteries. Realization of high energy-density Li-O₂ batteries relies on effective utilization of high loading air-electrodes with long-lasting cycling stability. During the last year, Li-O₂ cells containing optimized RuO₂/CNTs air cathodes with high loading and Li metal anodes with or without composite protective membrane (LiTFSI/LLZTO/PVDF) have been tested in 1 M LiTf-Tetraglyme electrolyte, and the corresponding cell design can be found in Figure II.9.A.4a. Here, the glass fiber filter paper (GF-B) was used as the separator, and the thickness of the composite polymer membrane was about 20 μm. After using pre-treatment process to optimize RuO₂/CNTs air electrode, these Li-O₂ cells were cycled in a voltage window between 2.2 V and 4.2 V at a current density of 0.1 mA cm⁻² in O₂ atmosphere at room temperature. It is observed from Figure II.9.A.4b that Li-O₂ cell with the optimal air electrode and the protected Li metal anode with composite protective membrane demonstrates better stability over 14 cycles, compared to the poor cycling performance of cells with optimal air electrode but un-protected Li metal anode. After 14 cycles, the areal capacity of Li-O₂ cells with composite protective membrane is still more than 4 mAh cm⁻². Moreover, the capacities of Li-O₂ cells with composite protective membrane on Li metal anode are higher than those of cells without composite protective membrane on Li anode, which means that the addition of composite protective membrane on Li metal surface leads to significantly increased capacity retention of Li-O₂ cells due to the effective protection for Li metal anode during discharge/charge processes. The well-protected Li metal anode paired with high loading air-electrode in a non-aqueous Li-O₂

battery has delivered high areal capacity (i.e., over 4 mAh cm⁻²) required for high utilization of Li metal in each cycle and reliable stabilization of Li metal anode.

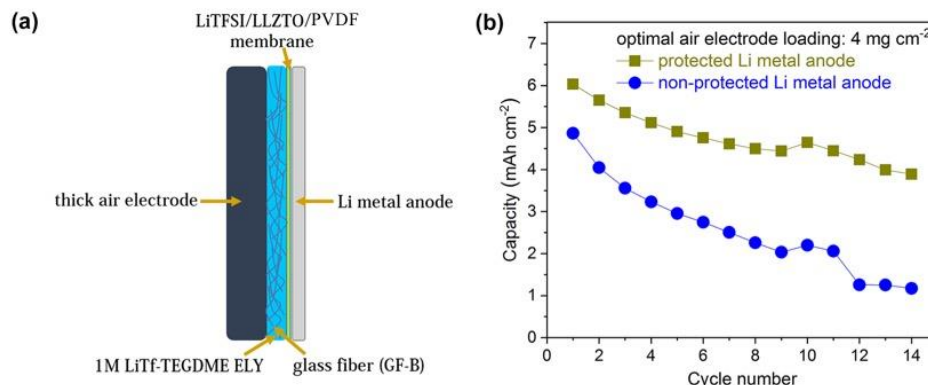


Figure II.9.A.4 (a) Schematic of high energy-density Li-O₂ cell design. (b) Cycling performance of Li-O₂ cells containing optimal RuO₂/CNTs air electrodes (high loading: 4 mg cm⁻²) and Li metal anodes with and without composite protective membrane (LiTFSI/LLZTO/PVDF) cycled in voltage window between 2.2 V and 4.2 V at a current density of 0.1 mA cm⁻² in 1 M LiTf-Tetraglyme electrolyte at room temperature.

Conclusions

- A low-cost in-situ electrochemical pre-charging method has been developed to simultaneously produce ultrathin protective films on both CNTs air electrodes and Li metal anodes. These protective films can significantly suppress and mitigate the well-known oxidation of CNTs air electrodes by reduced oxygen species and severe corrosion of Li metal anode upon cycling; thus, the cycling life of pretreated Li-O₂ cells can be extended to more than 110 cycles in common 1 M electrolyte without using efficient catalysts or redox mediators.
- Li-O₂ cells based on the optimized RuO₂/CNTs air electrode demonstrated superior cycling stability (as long as 800 times under a capacity protocol of 800 mAh g⁻¹) due to the extremely high stability and catalytic capability of the optimal RuO₂ catalyst-decorated air electrodes.
- LiTFSI-LLZTO-PVDF composite protective membrane has been successfully developed for Li metal protection in Li-air batteries, which is beneficial for cycling improvement of the high-energy Li-O₂ battery.
- Cycling performance of Li-O₂ cells with high-loading optimized RuO₂/CNTs air-electrode and protected Li anode has been successfully evaluated. Our results indicated that the combination of the optimized efficient air-electrode and the protected Li anode could result in the desired enhancement in cycling of high energy-density Li-O₂ batteries.

Key Publications and Paten Application

1. B. Liu, W. Xu, J.-G. Zhang, "Stability of Li metal anode in Li-air batteries", *Wiley*, Invited book chapter, **2018**, DOI:10.1002/9783527807666.
2. B. Liu, W. Xu,* J. Tao, P. Yan, J. Zheng, M. H. Engelhard, D. Lv, C. Wang, J.-G. Zhang,* "Enhanced cyclability of lithium-oxygen batteries with electrodes protected by surface films induced via in-situ electrochemical process", *Advanced Energy Materials* **2018**, 8, 1702340. DOI:10.1002/aenm.201702340.
3. B. Liu, W. Xu,* J. Zheng, P. Yan, E. D. Walter, N. Isern, M. E. Bowden, M. Engelhard, S. T. Kim, J. Read, B. D. Adams, X. Li, J. Cho, C.-M. Wang, J.-G. Zhang,* "Temperature dependence of oxygen

reduction mechanism in non-aqueous Li-O₂ batteries”, *ACS Energy Letters* **2017**, 2, 2525. DOI: 10.1021/acsenergylett.7b00845.

4. W. Xu, B. Liu, J.-G. Zhang, “Preformation of solid electrolyte interphase on electrodes for rechargeable lithium metal batteries”, WO2018071503A1.

Acknowledgements

Key contributors including Drs. Bin Liu, Mark H. Engelhard, Jianming Zheng, Jinhui Tao, Pengfei Yan, and Chongmin Wang are greatly appreciated.

II.9.B Lithium-Air Batteries (Argonne National Laboratory)

Khalil Amine, Principal Investigator

Argonne National Laboratory
9700 S. Cass Ave
Argonne, IL 60516
Email: amine@anl.gov

Larry Curtiss, Principal Investigator

Argonne National Laboratory
9700 S. Cass Ave
Argonne, IL 60516
Email: curtiss@anl.gov

Jun Lu, Principal Investigator

Argonne National Laboratory
9700 S. Cass Ave
Argonne, IL 60516
Email: junlu@anl.gov

Tien Duong, DOE Technical Development Manager

U.S. Department of Energy
E-mail: Tien.Duong@ee.doe.gov

Start Date: October 1, 2014 End Date: December 31, 2018
Project Funding (FY18): \$1,600,000 DOE share: \$1,600,000 Non-DOE share: \$0

Project Introduction

Lithium-oxygen batteries can be considered the ‘holy grail’ of lithium-ion batteries because they offer, in principle, ten times the energy density of conventional lithium-ion systems. The inherent energy potential of lithium metal approaches that of gasoline, but today’s battery manufacturers have not yet been able to unlock this potential. While today’s lithium-ion batteries may provide acceptable power for hybrid electric vehicles and all-electric vehicles, they do not as yet provide sufficient energy for driving distance desired by consumers. A breakthrough in Li-oxygen battery technology would significantly increase the possibility of extending the electric range of these vehicles with the added advantages of reducing battery cost and weight. [\[1\]](#)

Li-oxygen battery technology has many challenges and requires significant research efforts to meet these challenges and to unlock its full potential. The successful implementation of non-aqueous Li-air cells has been hampered because of severe materials problems that have limited electrochemical performance. These include (1) the non-aqueous electrolytes can be unstable under both the charge and discharge conditions, thereby seriously limiting cycle life; (2) during discharge, the solid and insoluble Li_2O_2 and/or other Li_2O products are deposited on the surface or within the pores of the carbon cathode, thereby passivating the surface as well as clogging the pores and restricting oxygen flow; (3) degradation of the lithium anode due to oxygen crossover destroys the integrity and functioning of the cell; and (4) commonly used transition metal cathode catalysts, do not access the full capacity of the oxygen electrode or enable sufficiently high rates.

The team led by Dr. Khalil Amine, Dr. Larry Curtiss, and Dr. Jun Lu at Argonne National Laboratory is working on problems that limit the electrochemical performance of the Li-oxygen battery, including the stability of the organic electrolytes, development of new cathode catalysts, and the stability of the lithium anode under oxygen-crossover conditions. This effort will lead to the development of a reversible lithium oxygen battery that provides much higher energy density than state-of-the-art lithium ion batteries for electric

vehicles. The technology, if successful, can also benefit many military applications that require very high energy density such as satellite, military vehicles for silent watch and operation.

Objectives

The objective is to develop stable electrolytes and new cathode architectures for lithium air batteries to lower the charge overpotential, improve the cell efficiency, and increase cycle life. Commonly used carbons and cathode catalysts do not access the full capacity of the oxygen electrode and can cause significant charge overpotentials, which lowers efficiency and limits cycle life. Therefore, there is a need for improved catalysts and how they can control the discharge product morphology, which affects the overpotentials. New more stable electrolytes are needed to prevent gradual electrolyte decomposition that occurs in the presence of the reduced oxygen species, especially superoxide anion (O_2^-) from the discharge process. Understanding the oxygen crossover effect at the anode on the electrochemical performance of Li-air battery is important to understanding the lithium electrode degradation due to oxygen crossover and thus reduces the cycle life.

Approach

Issues that limit the performance of the Li-air battery include (1) electrolytes decomposition; (2) inefficient cathode materials; and (3) lithium electrode degradation. This project addresses the cycle life problem of Li- O_2 batteries through experimental and theoretical investigation of (a) the discharge formation mechanism and relationship to electrolytes, (b) investigation of the morphology and composition of the discharge product, and (c) investigation of electrolyte decomposition mechanisms. This understanding is being used to (1) develop new cathode materials to promote formation of discharge morphologies such as those involving superoxides with better conductivity to decrease charge overpotentials, (2) cathode and electrolyte materials that do not degrade with cycling and (c) electrolyte modification to protect the lithium anode. The experimental work to create advanced electrolytes, carbons, catalysts, cathodes, and anodes is guided by theory and modeling. The experimental results will be thoroughly analyzed with very sophisticated analytical techniques and used to fine-tune the computational studies. Fundamental understanding of the underlying principles will be provided to greatly facilitate the next steps in the development cycle

Collaborators include Professor Kah Chun Lau (University of California-Norridge), Professor Yiying Wu (Ohio State University), Professor Amin Salehi (University of Illinois-Chicago), Dr. Dengyun Zhai (China). We utilize several facilities at Argonne National Laboratory including the Advanced Photon Source, the Center for Nanoscale Materials, and the Argonne Leadership Computing Facility.

Results

Metal-organic framework-derived catalysts

Metal-organic framework-derived catalysts have received increasing attention as promising cathode materials for Li- O_2 batteries because of their superior catalytic activity and high theoretical capacity. However, further optimization of their structural and electrochemical properties is necessary to promote practical applications. We have used a bulk-doping approach to encapsulate platinum nanocomponents into the bulk of the catalyst. The fabricated cathode architecture features highly uniform Pt and Pt₃Co nanoparticles within biphasic nitrogen-doping (BND) cobalt@graphene heterostructures. Because of the improvement in the materials for optimizing catalytic and electrical properties and maximizing active regions, such a cathode design has enabled promising electrochemical performance in our testing. This has included higher specific capacity and a dramatic reduction in charge overpotential to 0.4 V. Density functional theory calculations have provided mechanistic insights into the promotional effect of the Pt and Pt₃Co nanoparticles in reducing the charge overpotential. In addition, there is a dramatically different structural evolution of lithium peroxide\ dependent on the platinum modification approach. This dependence contributes to the influence of platinum component on the formation and decomposition mechanism of lithium peroxide.

The synthetic routes are illustrated in Figure II.9.B.1. Firstly, we synthesized a cobalt-based zeolitic imidazolate framework-derived, biphasic nitrogen-doped cobalt@graphene catalyst via a co-precipitation and calcination process. Then we fabricated the electrodes by pasting the catalysts with poly(vinylidene fluoride) onto carbon fibers, followed by sputtering Pt nanoparticles onto the electrode surface by employing a thin-film deposition system, forming a Pt surface-coated cathode. The other approach was to infuse the Pt^{2+} solution within the same base catalyst followed by H_2 reduction to form a well-defined Pt bulk-doped structure. This latter cathode architecture with highly uniform catalytic nanocomponents and abundant active regions in the material bulk gave improved catalytic efficiency and provides a new strategy for development of cathode architectures for future research.

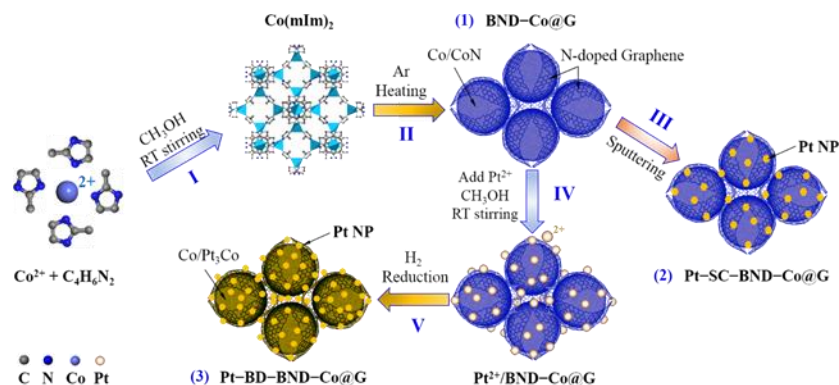


Figure II.9.B.1 Schematic of Pt modified MOF-derived catalysts. BND-Co@G = biphasic N-doped cobalt@graphene, Pt-SC-BND-Co@G = Pt surface-coating BND-Co@G, and Pt-BD-BND-Co@G = Pt bulk-doping BND-Co@G.)

Lithium superoxide as a discharge product on cathodes with well-defined Ir nanoparticles

One of the major challenges for Li-oxygen batteries is the high charge overpotential, which results in a low energy efficiency. It has recently been shown that lithium superoxide, which is a good electronic conductor and has a low charge overpotential, can be formed in a Li- O_2 battery using iridium as a catalyst, [2] but little is known about the role of iridium in the lithium superoxide formation. In Ref. 2 was speculated that an Ir_3Li alloy forms that acts as effective template for growth of the LiO_2 . In this work size-selected subnanometer Ir clusters were used to generate uniformly sized Ir nanoparticles on reduced graphene oxide based cathodes to gain new insight into the mechanism by which the iridium particles evolve and function during discharge when the LiO_2 forms. It is found that during discharge the Ir nanoparticles surprisingly evolve to larger ones while incorporating Li from LiO_2 to form core-shell structures with Ir_3Li shells.

The cathode material for the Li- O_2 cell used in this study was prepared by depositing ligand-free subnanometer Ir_n clusters of a specific size on reduced graphene oxide (rGO). The rGO surface is covered by a fraction of a monolayer with size-selected Ir_n clusters of sizes 2, 4, and 8 atoms. The size and crystallinity of the deposited nanoclusters were further tuned by annealing of the samples under vacuum. For the Ir clusters we have chosen one size ($n=8$), which have been annealed to larger particles (~ 1.5 nm). From high resolution transmission electron microscopy (HRTEM) studies the Ir nanoparticles have crystalline facets as shown in Figure II.9.B.2. During discharge it is found that LiO_2 forms in the Li- O_2 cell with a TEGDME electrolyte. The evidence for LiO_2 formation was from Raman spectra and titration of the discharge product, as well as DEMS measurement during discharge that showed one electron used per O_2 .

HRTEM was used to characterize the evolution of the Ir nanoparticles. The HRTEM images showed that the Ir nanoparticles, which started out as ~ 1.5 nm particles, had unexpectedly evolved during the discharge process and formed larger particles, most being ~ 5 to 10 nm in size. From HRTEM imaging the shell has a lattice spacing of ~ 0.41 nm,

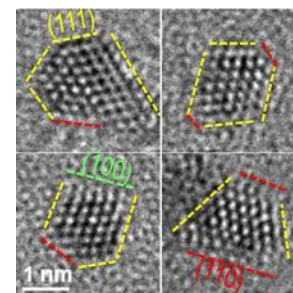


Figure II.9.B.2 HRTEM image of annealed Ir_8 clusters on an rGO cathode showing crystalline facets of the Ir nanoparticles.

which matches with that of an Ir_3Li lattice. Electron diffraction patterns also confirm that the shell is Ir_3Li as it shows an additional diffraction ring with dots corresponding to the double lattice spacing of Ir_3Li . Thus, these results show that the 1.5 nm Ir particles grow during discharge to form larger core-shell Ir/ Ir_3Li nanoparticles. The Ir_3Li shell can act as a template for the growth and stabilization of crystalline LiO_2 . The Ir_3Li core-shell nanoparticles discovered here provide a new direction in nanomaterials research for reducing charge overpotentials and finding a closed system in Li- O_2 batteries.

Dependence of lithium superoxide formation on electrolytes

In this work the size-selected subnanometer Ir clusters were used to gain new insight into whether the electrolyte affects the composition of the discharge product and also how it can stabilize the lithium superoxide. We have examined several aspects including whether disproportionation depends on the ether chain length and whether different electrolytes at the interface can suppress disproportionation. The results are based on both experimental and theoretical investigations.

The first question was investigated by using dimethoxyethane (DME) and comparing it with tetraglyme (TEGDME). The Li- O_2 cell was tested under identical conditions with annealed Ir_8 clusters on the cathode surface. The cell was discharged to 1000 mAh/g using 1 M LiCF_3SO_3 in dimethyl ether (DME) as the electrolyte and then was charged. The cell discharged at ~ 2.7 V similar to the results for TEGDME, but charged at ~ 4.1 V significantly higher than what was found for TEGDME. These differing charge potentials suggest that the discharge product with DME is different from the LiO_2 formed with TEGDME. This was confirmed when a Ti(IV)OSO₄ based titration technique was used on the DME discharge product. A strong UV peak was obtained in the UV-Vis spectra, which showed a Li_2O_2 content of 42%.

We performed computational studies to investigate whether the shorter chain DME solvent favors disproportionation of LiO_2 in solution to form Li_2O_2 as a reason for these differing results. We first carried out density functional calculations to determine whether for DME the interaction of two LiO_2 leading to disproportionation would be more favorable than for TEGDME because of the shorter length of the DME. The results of these calculations indicated that disproportionation should be no more favorable for DME than for TEGDME and would not explain the results. A more likely explanation is the differences in viscosity. TEGDME, due to its long chain length, is more viscous than DME which may result in much slower Li cation conductivity in TEGDME compared to DME. Based on various reports of ionic conductivity in related species, we estimate that the ionic conductivity in DME is about two orders of magnitude larger than in TEGDME. The faster diffusion of Li^+ or LiO_2 in DME may enhance formation of LiO_2 dimers for disproportionation in solution, accounting for the preference for Li_2O_2 formation in DME as opposed to TEGDME.

The second question we investigated was the role of the electrolyte in the stability of LiO_2 . For this study we carried out calculations for the barrier to the elimination of O_2 from a crystalline surface of lithium superoxide at an interface with DME and TEGDME solvents needed for disproportionation. The barriers were 1.51 and 1.66 eV for TEGDME and DME, respectively. The barrier for TEGDME is shown in Figure II.9.B.3. This is larger than compared to vacuum (0.9 eV) suggesting that the lifetime of LiO_2 will increase significantly in the presence of an electrolyte at the surface. This is consistent with our previous experimental studies, which indicated that the presence of a TEGDME based electrolyte decreases the disproportionation of LiO_2 compared to when it is aged for 24 hours in vacuum. [3] In addition, the barriers indicate that disproportionation from the surface in the presence of DME should be similar to that of TEGDME.

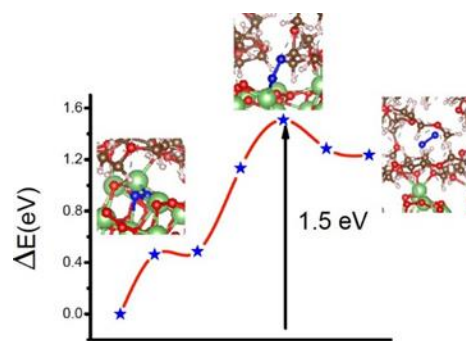


Figure II.9.B.3 Density functional calculation of the barrier for dissolution of O_2 into the TEGDME.

Conclusions

Various new catalysts have been investigated. We have used a bulk-doping approach to encapsulate platinum nanocomponents into the bulk of a cathode material. The fabricated cathode architecture features highly uniform Pt and Pt₃Co nanoparticles within a cobalt-based zeolitic imidazolate framework. This cathode design has enabled lithium peroxide formation with promising electrochemical performance including a low charge overpotential. A second catalyst design was based on size-selected subnanometer Ir clusters used to generate uniformly sized Ir nanoparticles on reduced graphene oxide based cathodes. It was found that during discharge the Ir nanoparticles surprisingly evolve to larger ones while incorporating Li from LiO₂ to form core-shell structures with Ir₃Li shells. The discharge product was LiO₂ that had a small charge overpotential. We ALSO found that LiO₂ disproportionation can depend on the ether chain length used as an electrolyte. The Li-O₂ cell was tested under identical conditions with THE annealed Ir₈ clusters on the cathode surface with both dimethyl ether (DME) and tetraglyme (TEGDME) as the electrolyte solvent. The DME resulted in the discharge product with a large lithium peroxide component compared to TEGDME, which was LiO₂.

Key Publications

1. "Identification and Implications of Lithium Superoxide in Li-O₂ Batteries," Avik Halder, Hsien-Hau Wang, Kah Chun Lau, Rajeev S. Assary, Jun Lu, Stefan Vajda, Khalil Amine, and Larry A. Curtiss, *ACS Energy Lett.* 2018, 3, 1105–1109. DOI: 10.1021/acseenergylett.8b00385
2. "Fundamental Understanding and Material Challenges in Rechargeable Nonaqueous Li–O₂ Batteries: Recent Progress and Perspective," Lu Ma, Tongwen Yu, Evangelos Tzoganakis, Khalil Amine, Tianpin Wu, Zhongwei Chen, and Jun Lu, *Adv. Energy Mater.* 2018, 8, 1800348
3. Dendrite-Free Potassium–Oxygen Battery Based on a Liquid Alloy Anode, W. Yu, K. C. Lau, Y. Lei, R. Liu, L. Qin, W. Yang, B. Li, L. A. Curtiss, D. Zhai, and F. Kang, *ACS Appl. Mater. Interfaces*, 2017, 9, 31871–31878 DOI: 10.1021/acsaami.7b08962
4. "Mass and charge transport relevant to the formation of toroidal lithium peroxide nanoparticles in an aprotic lithium-oxygen battery: An experimental and theoretical modeling study," X. Y. Luo, R. Amine, K. C. Lau, J. Lu, C. Zhan, L. A. Curtiss, S. Al Hallaj, B. P. Chaplin, K. Amine, *NANO RESEARCH* 10 4327-4336 (2017).

References

1. "Aprotic and aqueous Li-O₂ batteries," J. Lu, L. Li, J. B. Park, Y. K. Sun, F. Wu, K. Amine, *Chem Rev* 2014, 114, 5611.
2. "A lithium-oxygen battery based on lithium superoxide," J. Lu, Y. J. Lee, X. Luo, K. C. Lau, M. Asadi, H.-H. Wang, S. Brombosz, J. G. Wen, D. Zhai, Z. Chen, D. J. Miller, Y. S. Jeong, J.-B. Park, Z. Z. Fang, B. Kumar, A. Salehi-Khojin, Y.-K. Sun, L. A. Curtiss, K. Amine, *Nature* 2016, 529, 377.
3. "Interfacial Effects on Lithium Superoxide Disproportionation in Li-O₂ Batteries," D. Zhai, K. C. Lau, H.-H. Wang, J. Wen, D. J. Miller, J. Lu, F. Kang, B. Li, W. Yang, J. Gao, E. Indacochea, L. A. Curtiss, and K. Amine *Nano Lett.*, 2015, 15, 1041.

II.10 Beyond Li-ion R&D: Sodium-Ion Batteries

II.10.A Exploratory Studies of Novel Sodium-Ion Battery Systems (BNL)

Xiao-Qing Yang, Principal Investigator

Chemistry division, Brookhaven National laboratory
Bldg. 555, Brookhaven National Lab.
Upton, NY 11973
E-mail: xyang@bnl.gov

Seongmin Bak, Principal Investigator

Chemistry division, Brookhaven National laboratory
Bldg. 555, Brookhaven National Lab.
Upton, NY 11973
E-mail: smbak@bnl.gov

Tien Duong, DOE Technical Development Manager

U.S. Department of Energy
E-mail: Tien.Duong@ee.doe.gov

Start Date: October 1, 2017

End Date: September 30, 2018

Project Funding (FY18): \$400,000

DOE share: \$400,000

Non-DOE share: \$0

Project Introduction

In order to meet the challenges of powering PHEVs, the next generation of rechargeable battery systems with higher energy and power density, lower cost, better safety characteristics, and longer calendar and cycle life beyond lithium-ion batteries, which is today's state-of-the-art technology, need to be developed. Recently, Na-ion battery systems have attracted more and more attention due to the more abundant and less expensive nature of Na resources. However, building a sodium battery requires redesigning battery technology to accommodate the chemical reactivity and larger size of sodium atoms. Since Na-ion battery research is an emerging technology, new materials to enable Na electrochemistry and the discovery of new redox couples and the related diagnostic studies of these new materials and redox couples are quite important. In sodium electrochemical systems, the greatest technical hurdles to overcome are the lack of high-performance electrode and electrolyte materials which are easy to synthesize, safe, non-toxic, with long calendar and cycling life and low cost. Furthermore, fundamental scientific questions need to be further elucidated, including (1) the difference in transport and kinetic behaviors between Na and Li ions in analogous electrodes; (2) Na insertion/extraction mechanism; (3) solid electrolyte interphase (SEI) layer on the electrodes from different electrolyte systems; and (4) charge transfer in the electrolyte–electrode interface and Na⁺ ion transport through the SEI layer. This project has been using the synchrotron based in situ x-ray diagnostic tools developed at BNL to evaluate the new materials and redox couples, to explore in fundamental understanding of the mechanisms governing the performance of these materials and provide guidance for new material developments. This project also has been focusing on developing advanced diagnostic characterization techniques to investigate these issues, providing solutions and guidance to solve the problems. The synchrotron based in situ X-ray techniques (x-ray diffraction and hard and soft x-ray absorption) are combined with other imaging and spectroscopic tools such as high resolution transmission electron microscopy (HRTEM), mass spectroscopy (MS), as well transmission x-ray microscopy (TXM). In FY2018, this BNL team has built a good working relationship with several beamlines at Synchrotron Light Source II (NSLSII) with assigned beamtime at hard x-ray nanoprobe (HXN) beamline and x-ray Powder diffraction (XPD) beamline. By collaborating with Dr. Dong Su and Dr Huoling Xin, this team also has sufficient time using the HRTEM. The BNL team has been working closely with top scientists on new material synthesis at ANL, LBNL, SLAC, and PNNL, with U.S. industrial collaborators at General Motors and Johnson Controls, and international collaborators in Japan

and South Korea. In FY2018, results through these collaborations were published on high impact journals such as JACS and Advanced Energy Materials.

Objectives

The primary objective of this proposed project is to develop new advanced in situ material characterization techniques and apply these techniques to explore the potentials, challenges, and feasibility of new rechargeable battery systems beyond the lithium-ion batteries (LIBs), namely the sodium-ion battery systems for plug-in hybrid electric vehicles (PHEV). In order to meet the challenges of powering PHEVs, new rechargeable battery systems with high energy and power density, low cost, good abuse tolerance, and long calendar and cycle life need to be developed. This project will use the synchrotron based in situ x-ray diagnostic tools, combined with HRTEM, STEM, and TXM imaging techniques developed at BNL to evaluate the new materials and redox couples to enable a fundamental understanding of the mechanisms governing the performance of these materials and provide guidance for new material and new technology development regarding Na-ion battery systems.

Approach

A combination of time resolved X-ray diffraction (TR-XRD) and mass spectroscopy (MS), together with in situ soft and hard X-ray absorption (XAS) during heating and transmission electron microscopy (TEM) to study the thermal stability of the Na battery electrode materials.

Synchrotron based X-ray diffraction (XRD), X-ray absorption spectroscopy (XAS), to elucidate and differentiate the contribution from each component and element to the capacity and structural changes of various cathode and anode materials for Na-ion batteries.

Extended collaboration with other US and international academic institutions and US industrial partners.

Results

In FY2018, BNL has completed the *in situ* XRD and *ex situ* XAS studies and the evaluation of lattice parameter changes of new NaCrS₂ layer structured cathode materials for sodium-ion batteries during the charge-discharge cycling. Through our XRD and XAS studies, it is found that Na ions can successfully move out and into the NaCrS₂ without changing its lattice parameter *c*, as shown in Figure II.10.A.1. In addition, it is very interesting to discover that in NaCrS₂, the electrochemical reactions are through S₂²⁻/S²⁻ redox instead of Cr⁴⁺/Cr³⁺ that accompanies the deintercalation/intercalation reactions of Na ions from/into layered structure, as shown in Figure II.10.A.2.

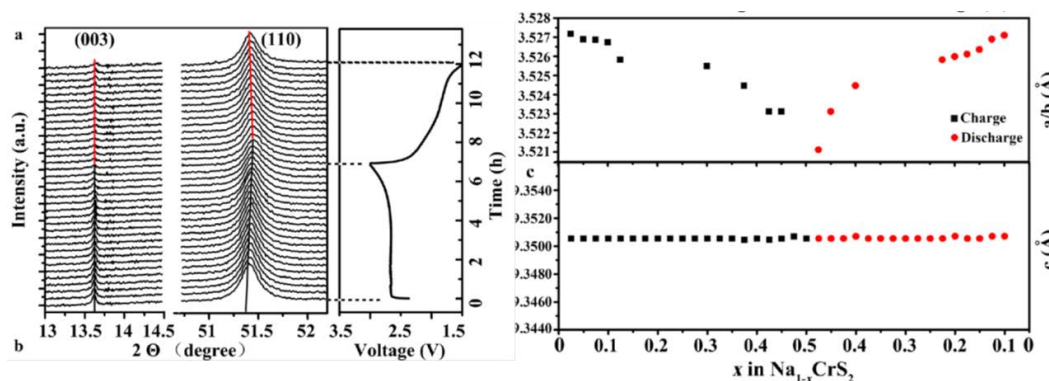


Figure II.10.A.1 **Na-driven structural behavior on cycling.** (a) In situ XRD patterns collected during the first charge-discharge cycle for NaCrS₂, corresponding time vs. voltage profile is shown on the right. (The 2θ is converted to the corresponding angle for $\lambda=1.54$ Å (Cu-K α) from the real wavelength $\lambda=0.7747$ Å used for synchrotron XRD experiments). (b) Evolution of lattice parameters calculated from the in situ X-ray diffraction during the first charge/discharge process

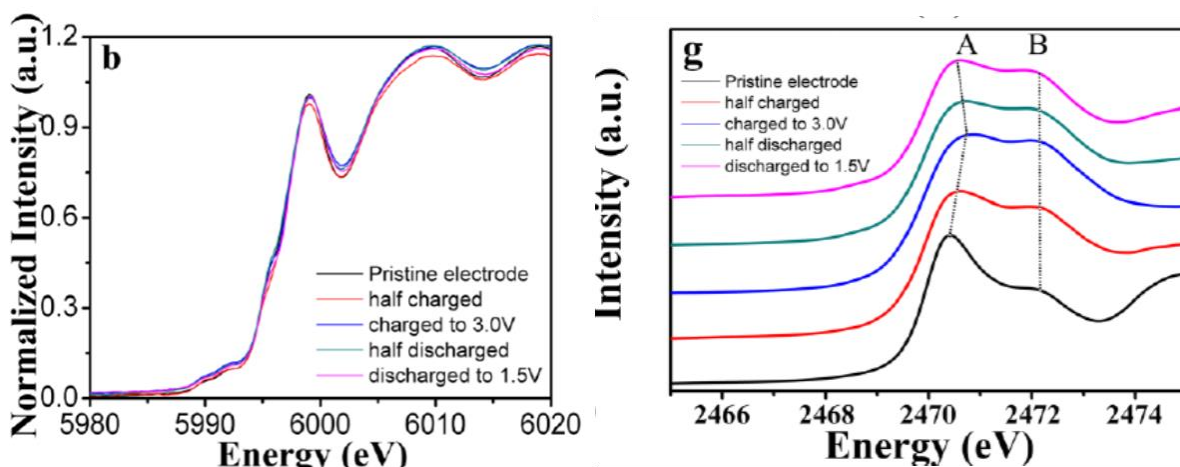


Figure II.10.A.2 Ex situ XAS Studies of Cr (b) and S (g) valence state during various charge-discharge stages

In FY2018, BNL has carried out the XRD studies of $\text{Na}_3\text{VP}_3\text{O}_9\text{N}$ cathode materials which can be used in both Na-ion and Li-ion (after ion exchange of Na by Li) systems. *Ex situ* X-ray diffraction patterns collected after each ion exchange procedure of $\text{Na}_3\text{VP}_3\text{O}_9\text{N}$ are shown in Figure II.10.A.3. It can be seen that three distinct phases formed after initial ion exchange at 330°C for 20 hours, indicating there is not a complete solid solution between pristine $\text{Na}_3\text{VP}_3\text{O}_9\text{N}$ and the fully ion exchanged $\text{Li}_3\text{VP}_3\text{O}_9\text{N}$. After another ion exchange at 310°C for 18 hours (2nd ion exchange), the initial phase with largest lattice parameter (labeled as A in Figure II.10.A.1) disappeared while the second phase (labeled as B) and the third phase (labeled as C) remained. It took another ion exchange to obtain the fully exchanged product.

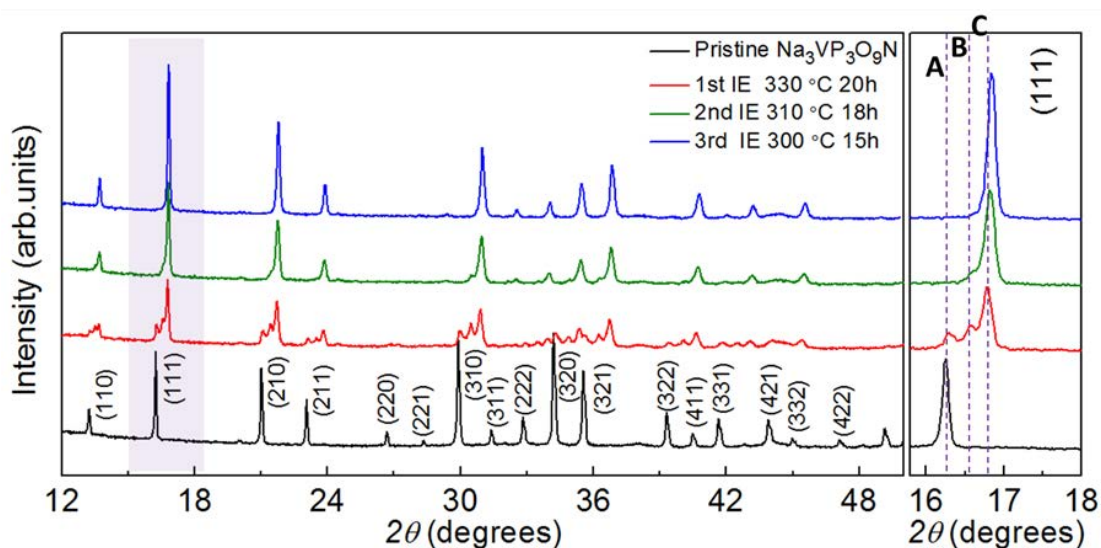


Figure II.10.A.3 X-ray diffraction patterns of $\text{Li}_x\text{Na}_{3-x}\text{VP}_3\text{O}_9\text{N}$ collected before starting and after each ion exchange (IE) process. The zooming (111) reflections are shown on the right side, the initial phase, second phase and third phase are labeled as A, B and C separately.

In FY2018, BNL team has been carried out the in situ XRD studies of $\text{Na}_{0.66}\text{Mn}_{0.6}\text{Ni}_{0.2}\text{Mg}_{0.2}\text{O}_2$ as new cathode materials for Na-ion batteries. To monitor the structural changes of $\text{Na}_{0.66}\text{Mn}_{0.6}\text{Ni}_{0.2}\text{Mg}_{0.2}\text{O}_2$ during Na extraction and insertion, in situ XRD was conducted at various charge/discharge states in a voltage range of 1.5-3.8 V vs. Na^+/Na . The results are presented in Figure II.10.A.4. During the charge process, most of diffraction peaks shift continuously to higher angles, indicating the shrinking of the unit cells of

$\text{Na}_{0.66}\text{Mn}_{0.6}\text{Ni}_{0.2}\text{Mg}_{0.2}\text{O}_2$ upon sodium deintercalation in a solid-solution behavior. At the end of the charge, a new peak can be observed indicating a new phase is formed.

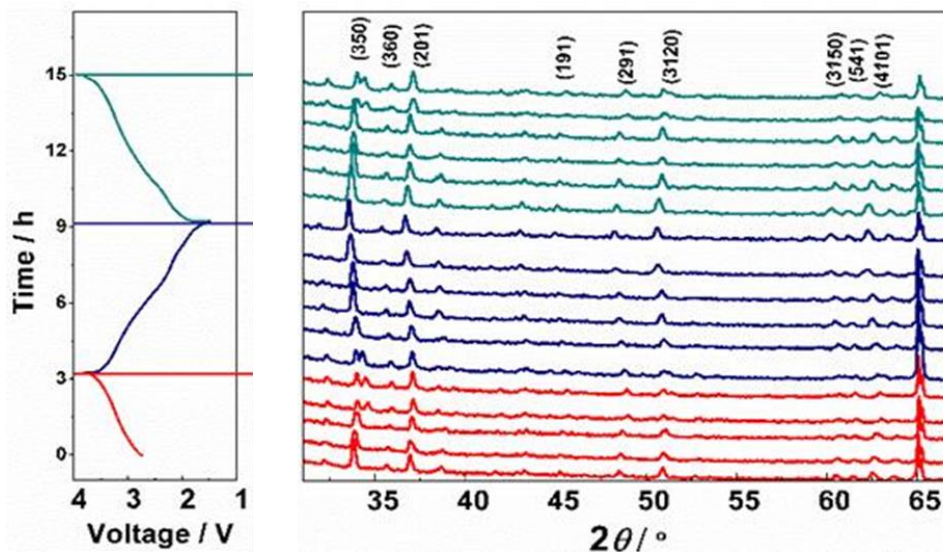


Figure II.10.A.4 In-situ X-ray diffraction patterns collected during the first charge/discharge and the second charge of $\text{Na}_{0.66}\text{Mn}_{0.6}\text{Ni}_{0.2}\text{Mg}_{0.2}\text{O}_2$ cells at a current rate of 0.2 C in the potential range between 1.5 and 4.3 V.

In FY2018, BNL has carried out the in situ XAS studies of $\text{Na}_{0.66}\text{Mn}_{0.6}\text{Ni}_{0.2}\text{Mg}_{0.2}\text{O}_2$ (MNM) as new cathode materials for Na-ion batteries. Synchrotron-based XAS was employed to investigate the valence state and local structure changes of the MNM-2 electrode during charge and discharge process. XANES spectra of Mn and Ni during the first charge, first discharge and second charge processes are illustrated in Figure II.10.A.5. To quantitative analysis the K-edge position of Mn and Ni, Figure II.10.A.5g shows the change of the half edge energy ($E_{0.5}$) of Mn and Ni deduced by the half-height method. In the first charge process, no edge shift for Mn K-edge XANES can be observed, indicating Mn^{4+} ions are maintained with no valence change during the initial charge. However, the white line for Ni K-edge XANES shifts to higher energy obviously, suggesting that the Ni cations are oxidized to higher valence state during charge. The energy shift of Ni K-edge is about 1.6 eV, which can be roughly estimated that the valence state of Ni is changing from 2^+ to 3.3^+ , compared with the XANES of NiO and LiNiO_2 references.

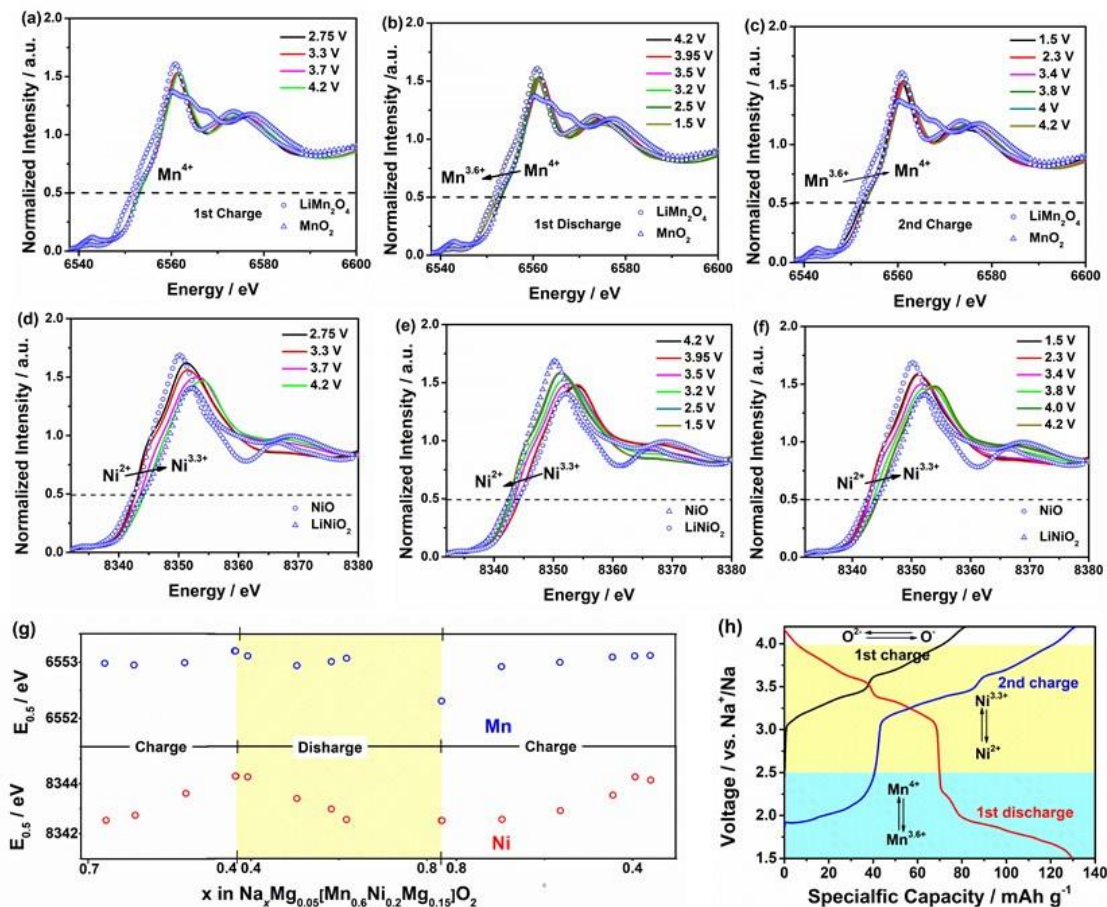


Figure II.10.A.5 Charge compensation mechanism of MNM-2 during charge and discharge processes. a), b) and c) Mn and d), e) and f) Ni K-edge XANES of MNM-2 at various stages during the first charge/discharge and the second charge process, respectively. g) The half edge energy ($E_{0.5}$) at different content of Na in $\text{Na}_x\text{Mg}_{0.05}[\text{Mn}_{0.6}\text{Ni}_{0.2}\text{Mg}_{0.15}]\text{O}_2$. h) The charge compensation of different elements contribution during the charge and discharge process.

Conclusions

1. NaCrS_2 as an anionic redox cathode material for sodium ion batteries has been studied using XRD and XAS.
2. Air-stable O3-Type cathode materials $\text{NaNi}_{0.45}\text{Cu}_{0.05}\text{Mn}_{0.4}\text{Ti}_{0.1}\text{O}_2$ as cathode materials for Na-ion batteries have been studied using synchrotron based XANES and EXAFS.
3. Honeycomb ordered $\text{Na}_3\text{Ni}_{1.5}\text{M}_{0.5}\text{BiO}_6$ ($M = \text{Ni}, \text{Cu}, \text{Mg}, \text{Zn}$) as high voltage layered cathode materials for sodium-ion batteries have been studied

Key Publications

1. Zulipiya Shadike, Enyue Zhao, Yong-Ning Zhou*, Xiqian Yu*, Yong Yang, Enyuan Hu, Seongmin Bak, Lin Gu, Xiao-Qing Yang*, "Advanced Characterization Techniques for Sodium-Ion Battery Studies", *Adv. Energy Mater.* Publication Date: February 19, 2018, DOI: 10.1002/aenm.201702588.
2. Qin-Chao Wang, Qi-Qi Qiu, Na Xiao, Zheng-Wen Fu, Xiao-Jing Wu, Xiao-Qing Yang, Yong-Ning Zhou. "Tunnel-structured $\text{Na}_{0.66}[\text{Mn}_{0.66}\text{Ti}_{0.34}]\text{O}_2\text{-xFx}$ ($x < 0.1$) cathode for high performance

sodium-ion batteries“, *Energy Storage Materials*, Publication Date: March 13, 2018, DOI: 10.1016/j.ensm.2018.03.007

3. Jue Liu, Lei Yu, Enyuan Hu, Beth S. Guiton, Xiao-Qing Yang, and Katharine Page, “Large-Scale Synthesis and Comprehensive Structure Study of δ -MnO₂”, *Inorg. Chem.*, 2018, 57 (12), pp 6873–6882, DOI: 10.1021/acs.inorgchem.8b00461, Publication Date (Web): May 30, 2018.
4. Shuyin Xu, Jinpeng Wu, Enyuan Hu, Qinghao Li, Jienan Zhang, Yi Wang, Eli Stavitski, Liwei Jiang, Xiaohui Rong, Xiqian Yu, Wanli Yang, Xiao-Qing Yang*, Liquan Chen and Yong-Sheng Hu*, “Suppressing the voltage decay of low-cost P2-type iron-based cathode materials for sodium-ion batteries”, *J. Mater. Chem. A*, Advance Article, published on 24th September 2018. DOI: 10.1039/C8TA07933A

II.11 Beyond Li-ion R&D: Battery500

II.11.A Battery500 Innovation Center (PNNL)

Jun Liu, Principal Investigator

Pacific Northwest National Laboratory
902 Battelle Boulevard
Richland, WA 99354
E-mail: jun.liu@pnnl.gov

Yi Cui, Principal Investigator

Stanford University/SLAC
450 Serra Mall
Stanford, CA 94305
E-mail: yicui@stanford.edu

Tien Duong, DOE Technical Development Manager

U.S. Department of Energy
E-mail: Tien.Duong@ee.doe.gov

Start Date: October 1, 2017
Project Funding: \$8,000,000

End Date: September 30, 2018
DOE share: \$8,000,000

Non-DOE share: \$0

Project Introduction

Lithium (Li)-ion batteries play a critical role in modern day technologies, but their specific energy (Wh kg^{-1}) and energy density (Wh L^{-1}) are approaching the maximum practically achievable values based on existing manufacturing processes with the conventional cathode and anode materials. The large scale deployment of electric vehicles and ever-increasing demand of modern technologies require further increase in cell energy and cost reduction. Li-metal batteries are regarded as “Holy Grail” of high-energy-density systems because Li metal has an ultrahigh theoretical specific capacity (3860 mAh g^{-1}), an extremely low redox potential (-3.040 V vs. standard hydrogen electrode), and a very low gravimetric density (0.534 g cm^{-3}). However, the practical application of Li metal anode still faces several big challenges, including safety concerns due to Li dendrite growth, limited cycle life because of low Li Coulombic efficiency, and infinite volume change during Li stripping and redeposition if a two-dimensional (2D) flat Li foil is used. In addition, developing the next generation rechargeable Li metal batteries with a specific energy higher than 300 Wh kg^{-1} , up to 500 Wh kg^{-1} , is still a significant challenge. Many groups are focusing on the fundamental breakthroughs in electrode materials and control the unnecessary side reactions in such new battery concepts. Solid-state Li batteries using solid electrolytes have recently received wide attention due to the inherent high safety and decent energy. There have been intense efforts to improve the bulk conductivity, interfacial charge transport and stability for the manufacturing of the solid-state cells. A very desirable strategy is to take advantage of the electrode materials that are commercially or nearly commercially available and introduce the least perturbation to the cell configuration and manufacturing process of the current technologies. Based on these considerations, two battery chemistries, high nickel content lithium nickel-manganese-cobalt oxide (high-Ni $\text{LiNi}_x\text{Mn}_y\text{Co}_z\text{O}_2$ (NMC), $\text{Ni}>60\%$), coupled with Li metal anode, and Li-sulfur (S) chemistry, with the potential to achieve a specific energy higher than 500 Wh kg^{-1} are selected for this Battery500 innovation center project.

Objectives

The Battery500 Consortium aims to develop commercially viable Li battery technologies with a cell level specific energy of 500 Wh/kg through innovative electrode and cell designs that enable the extraction of the maximum capacity from advanced electrode materials. In addition, the project aims to be able to achieve 1000 cycles for the developed technologies.

Approach

The Battery500 Consortium will utilize first class expertise and capabilities in battery research in the United States and develop an integrated and multidisciplinary approach to accelerate the development and deployment of advanced electrode materials in commercially viable high energy batteries. The Li metal anode combined with compatible electrolyte systems and two types of cathodes—one high-Ni NMC and another S—will be studied and developed to reach high specific energy. The project focus is to design novel electrode and cell architectures to meet the 500 Wh/kg goal. The Consortium will work closely with R&D companies, battery/materials manufacturers and end-users/OEMs to ensure that the developed technologies are aligned with industry needs and can be transferred to production. The out-year goals for FY2018 include: (1) completion of first phase full cell fabrication and testing based on the Consortium recommended protocols, demonstrating the 300 Wh/kg full cell capability, (2) provision of analytical results for materials selection, cell design and fabrication, and further refinement, and (3) completion of the selection and launching of seedling projects for Battery500. All of these goals were successfully achieved in FY2018 through the approaches described below.

Results

1. Project management and coordination

The whole Consortium team has organized various teams, including the research teams, the Leadership Team, the Executive Committee, the Advisory Board, carrying out different roles and responsibilities. A total of 14 projects were defined. A Working Committee, made of one representative from each institution was formed with the function of keeping the whole Consortium updated of the research progresses through biweekly telephone conferences. Several large core groups, including the NMC cathode group, the anode group, the diagnostic group, and the S group, were formed. The coordinator for each large core group is responsible for organizing biweekly tele-conferences to exchange research results and discuss important issues within each project throughout the whole year. These teleconferences were also announced through the whole Consortium to welcome PIs, research scientists, postdocs, and students from other projects to attend and provide their inputs. Most of the presentation slides were distributed to all PIs meeting attendees. In addition, several subgroups were also formed, including the electrolyte group, the characterization group, the diagnostic and electrochemical characterization group, and the cell design and fabrication group. These subgroups are responsible for ensuring regular communications and meeting program goals on the project level. A drop box folder dedicated to Battery500 has also been set for communications and file exchanges within the Consortium, which contains all presentation slides (both orals and posters) for quarterly review meetings.

The integrated efforts of the Consortium team have been very efficient and successful. The biweekly teleconferences for the leader team, the Working Committee, as well as for each Keystone project and special task teams (such as cathode, anode, and diagnostic teams) were held regularly. The summaries of the teleconferences for the Working Committee were emailed to all PIs afterward, while the presentations of the technical conferences were distributed even more widely including staff scientists, postdocs and students who are working on the Battery500 projects. At many tele-conferences, the young scientists (postdocs and students) are the main presenters and their active involvements during and after tele-conferences are the key factors to achieve the milestones of FY2018.

The FY2018 first quarterly review/annual meeting was held at Berkeley, California on February 8th (the first quarterly review meeting for Battery500 seedling was held at Berkeley on February 9th, 2018). The other three quarterly review meetings were held at University of Washington (UW) in Seattle from May 10th to 11th 2017 (Q2), at Berkeley on August 2nd and 3rd, 2018 (Q3), and at PNNL in Richland Washington State on November 1st and 2nd, 2018, respectively. Averagely about 50 people attended these review meetings, including DOE Program managers, the Executive Committee members, the PIs, staff scientists, and a big group of postdocs and students. At each review meeting, the DOE Program managers gave updates of the DOE programs, the Consortium Director (Jun Liu) gave overviews of the Consortium, and invited PIs and postdocs gave the updates of the keystone projects and technical progresses related to quarterly review topics. A poster session

was included to exchange the progresses of different projects among the Consortium. For every quarterly review meeting, two posters were voted to get the best poster awards to acknowledge the great contributions of postdocs/students and their teams. All oral and poster presentations for the Q4 review meeting were given by postdocs and students and all sessions were chaired by them too. In addition, three breakout sessions were organized and chaired by these young scientists as well. All the meeting attendees felt this was an excellent new form of the review meeting and decided to do it again for one of the FY2019 quarterly review meetings. The second Advisory Board meeting was held at Berkeley on August 3rd, 2018 with participation from the DOE program managers, representatives from USABC, IBM, FMC, and Naatbatt.

2. Keystone project 1: Materials and interfaces

2.1. High Nickel NMC

We have addressed three critical questions on the high-Ni NMC: (i) environmental sensitivity, (ii) impact of thick electrodes on capacity and capacity retention, and (iii) a recommendation on the NMC beyond 622.

A moist environment was shown to be detrimental to the capacity of high-Ni NMCs, as shown in Figure II.11.A.1a for a 94% Ni sample. The capacity decreases with time and has lost more than 50% of its capacity after 30 days. The addition of a little aluminum (Al) helps ameliorate these major losses, but does not completely eliminate the losses. This is consistent with our reports on NCA and indicates that all these high Ni materials must be handled carefully in a dry atmosphere.

Two NMC622 thick electrodes were provided by Maxwell Technologies: Maxwell24 (19% porosity, 95% active material ratio, 24 mg/cm² areal active mass loading and 75 μm thickness) and Maxwell30 (31% porosity, 94% active material ratio 30 mg/cm² areal mass loading and 100 μm thickness). The Maxwell24 shows the better capacity retention (Figure II.11.A.1b) and has a higher rate capability, possibly due to its greater density that might lead to a higher electrode overall electronic conductivity.

A comparison of NMC811, NMC622 and NCA showed that 811 was overall superior to 622 in capacity, capacity retention and rate capability (Figure II.11.A.1c). Although NCA showed the highest capacity at rates of 2C and greater, its capacity retention at the desired rates from C/5 to 1C was the lowest. So, Keystone 1 is recommending that NMC811 with some Al doping be the cathode of choice for the next year.

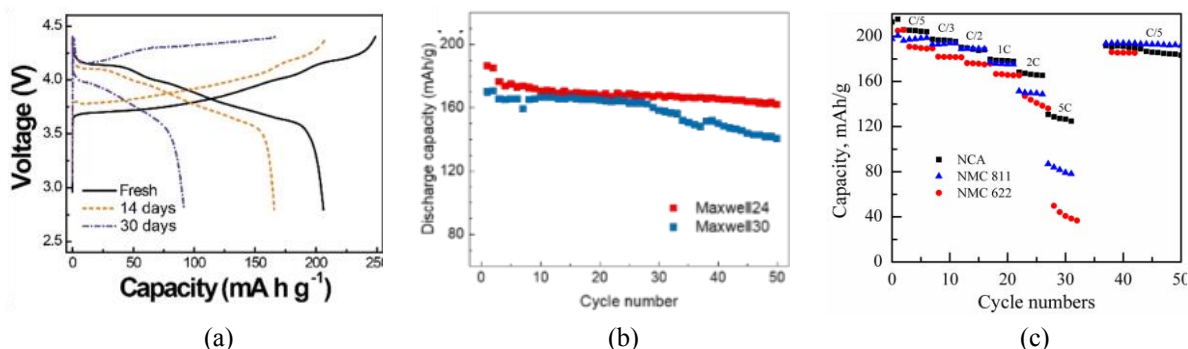


Figure II.11.A.1 (a) 1st cycle charge/discharge voltage profiles of LiNi_{0.94}Mn_{0.06}O₂ at fresh and after exposure to a moist atmosphere for 14 and 30 days. (b) Cycling performance of Maxwell24 and Maxwell30, 2 cycles at C/10, then 3rd - 50th cycle at C/3, 2.8-4.4 V. (c) Comparison of rate capability and capacity of NMC811, NMC622 and NCA, 12 mg/cm².

Determine attributes of NMC811 vs NCA: The thermal stability of NCA vs NMC 811 charged to either 4.4 V or 4.7 V was determined. It was reported that the presence of Al in the layered oxide structure can improve the thermal stability of layer structured cathode materials. Our results in Figure II.11.A.2 (a) and (b) show that in the presence of electrolyte, both delithiated NMC 811 and NCA have similar thermal stabilities. Both decompose at temperatures below 250 °C; the similarity indicates that in operating battery, NCA does not have significant thermal stability advantage over NMC 811. The different cut-off voltage results further showed that

samples charged to 4.4 V and 4.7 V have similar thermal stabilities in NMC 811 and NCA. However, we physically observed much more gassing from 811 than from NCA; i.e. the DSC holders popped open for 811 but not for NCA. These observations are consistent with our earlier discussions that in Li metal batteries the Li anode is the major concern rather than the cathode. Therefore, we have initiated a study of the thermal stability of the anode/electrolyte combinations. The cell capacity retention for Li||NMC811 cells using lean electrolyte are much worse than for flooded electrolyte cells and have been associated with reaction of the Li metal with the electrolyte. We have confirmed that graphite anodes do not have the same capacity fade issue for lean electrolyte as shown in Figure II.11.A.2(c).

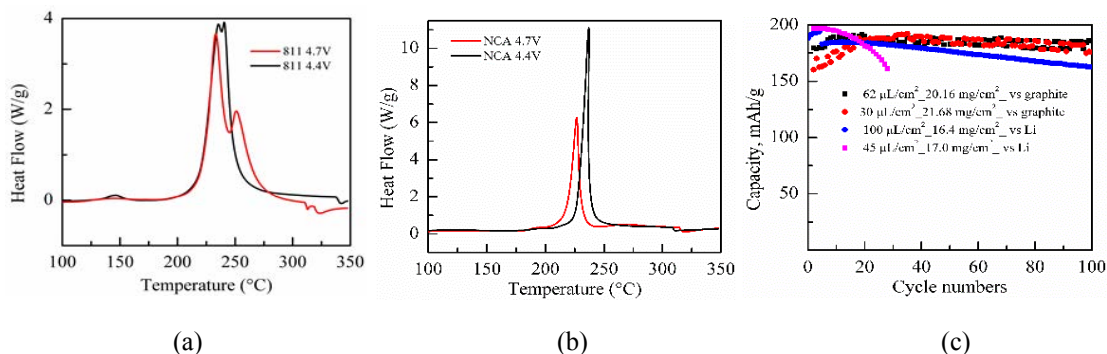


Figure II.11.A.2 DSC profiles of (a) NMC 811 and (b) NCA charged to different cut-off voltages. (c) Capacity retention of a graphite/NMC 811 cell, compared with a Li || NMC 811 cell.

2.2. New Electrolytes

Electrochemical performance: A range of new class electrolytes called localized high-concentration electrolytes (LHCEs) was continuously studied in this fiscal year for the Li||NMC cells. Modifications of the first LHCE, consisting of 1.2 M lithium bis(fluorosulfonyl)imide (LiFSI) in a mixture of dimethyl carbonate (DMC) and bis(2,2,2-trifluoroethyl) ether (BTFE) (1:3 by mol) studied in FY2017, were conducted in the first two quarters. Replacing DMC with ethylene carbonate (EC)-ethyl methyl carbonate (EMC) mixture and adding lithium difluoro oxalato borate (LiDFOB) additive further improves the long-term cycling stability. The LHCE containing LiFSI in a mixture of sulfolane and 1,1,2,2-tetrafluoroethyl-2,2,3,3-tetrafluoropropyl ether (TTE) shows better stability than the DMC-based LHCE as well. However, these two LHCEs still perform inferior to the flame-retarding LHCE based on flame-retardant triethyl phosphate (TEPa) (developed in latter FY2017) in Li||NMC811 pouch cells. Our newly developed LHCE ED1123 exhibits much improved thermal stability than other LHCEs reported before. The electrochemical performance of ED1123 was verified in Li||NMC811 coin cells and currently in pouch cells. Baseline electrolyte 1 M LiPF₆ in EC/EMC (3/7) + 2% VC and high concentrated electrolyte (HCE) were presented for comparison. Figure II.11.A.3 (a) shows that ED1123 has great stability in Li||NMC811 cell with an average Coulombic efficiency of 99.7% and capacity retention of ca. 80% after 300 cycles even with limited Li (50 μm) used in cells. Baseline and HCE electrolytes show fast capacity decay and cell failure after 30 or 50 cycles, respectively. Beyond the significantly improved long-term cycling stability, Figure II.11.A.3 (b) and (c) shows that ED1123 electrolyte also leads to great rate performances. Specific capacity of 135 mAh/g can be achieved at 4C (6 mA/cm²) charge rate with a discharge rate of C/3, and 170 mAh/g specific capacity is obtained at 4C discharge rate with a charge rate of C/3. These results indicate that ED1123 electrolyte is suitable for fast charge and fast discharge for Li||NMC811 cells.

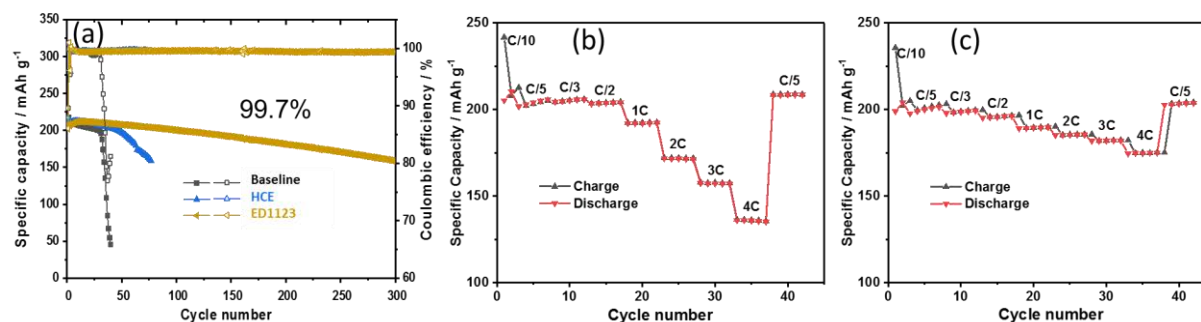


Figure II.11.A.3 Electrochemical performance of Li||NMC811 with investigated electrolytes (a) cycling performance at C/3 charge/discharge processes (b) Different charge rate performance in ED1123 electrolyte with constant charge rate of C/3. (c) Different discharge rate performance in ED1123 electrolyte with constant charge rate of C/3, all Li||NMC cells are cycled between 2.8 and 4.4 V vs. Li/Li⁺

Minimized thickness expansion during cycling: Li consumption and volume expansion caused by Li/electrolyte side reactions are two of the biggest barriers for the practical use of Li metal batteries, which lead to limited cycle life and severe safety concerns. ED1123 electrolyte has led to significant reduced Li consumption and volume expansion over cycling. Figure II.11.A.4 shows the cross-sectional SEM image of the cycled Li anode in Li||NMC811 cells with baseline and ED1123 electrolytes after 100 cycles. In this study, 50 μm thick Li metal was used as the anode. After 100 cycles in baseline electrolyte, 50 μm thick Li metal is fully utilized and the final thickness of reacted Li anode is of ca. 290 μm . In contrast, for Li anode cycled in the ED1123 electrolyte, two distinguished Li layer are observed. One layer is non-reacted Li, which is ca. 48 μm and has the same state as the fresh Li, the other one is reacted Li (residue Li) on the surface of the non-reacted Li foil. This result indicates that majority of Li metal foil was not used during cycling. The porous layer shown in Figure II.11.A.4 is mainly formed by the reaction of electrolyte and Li comes from NMC cathode instead of Li metal anode. This phenomenon will lead to long-term cycling stability of Li metal batteries. The reacted Li layer (ca. 48 μm thick) collected from Li||NMC811 cell using ED1123 electrolyte contains large particle size as shown in Figure 4b instead of much fine particles shown in Figure II.11.A.4a for the reacted Li layer collected from Li||NMC811 cell using baseline electrolyte.

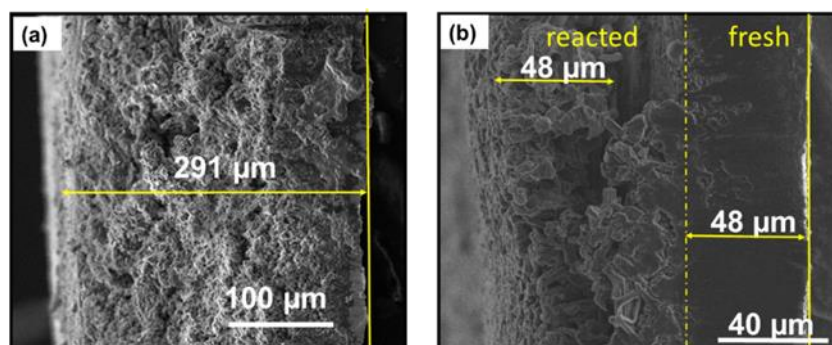


Figure II.11.A.4 Cross-section of cycled Li (100 cycles) collected from Li||NMC811 cells with (a) baseline and (b) ED1123 electrolytes.

2.3. Sulfur cathode

A novel inorganic binder, ammonium polyphosphate (APP), has been designed which combines several attractive properties for high performance Li-S batteries including (1) moderate binding strength to maintain integrity of the electrode material; (2) strong affinity with lithium polysulfides (LiPSs) *via* chemical interactions to suppress the dissolution of LiPSs since the main chain of the inorganic polymer binder has highly polarized chemical bonds, which can bind LiPS more efficiently; (3) flame-retarding property to improve safety, a property that conventional organic polymer binders do not have; (4) facilitation of Li ion

transport to accelerate redox chemistry and promote the reaction kinetics; and (5) water solubility for environmentally friendly processing. The S cathodes with this inorganic polymer binder demonstrated good electrochemical performance with a high-rate capacity of 520 mAh g^{-1} at 4C and excellent cycling stability of $\sim 0.038\%$ capacity decay per cycle at 0.5C for 400 cycles. Even with a high S loading of 5.6 mg cm^{-2} , the electrode still exhibits good cycling performance with reversible discharge capacities reaching 530 mAh g^{-1} at 0.5C rate after 200 cycles.

3. Keystone project 2: Electrode architectures

The goal of Keystone 2 is to design, model, fabricate and characterize the effect of electrode architecture on electrode and cell performance in support of reaching the project of 500 Wh/kg cell specific energy. Included in this Keystone are architecturally designed thick cathodes, Li metal electrode architectures, inorganic electrolytes and polymer electrolytes (Stanford), and electrode performance modeling. The team has continued its effort in optimizing the fabrication of thick cathodes as well as the evaluation of electrodes with exceptionally low porosities. Figure II.11.A.5 shows that binder choice is critical for achieving high quality electrodes with uniform carbon coating on the particle surface. The copolymer, PVDF-HFP, which absorbs organic solvents more readily, results in a much less uniform coating of carbon than PVDF-HSV, a homopolymer. Under similar processing conditions and polymer loading (2%), the later results in highly uniform distribution of carbon on the oxide surface while the former has carbon agglomeration.

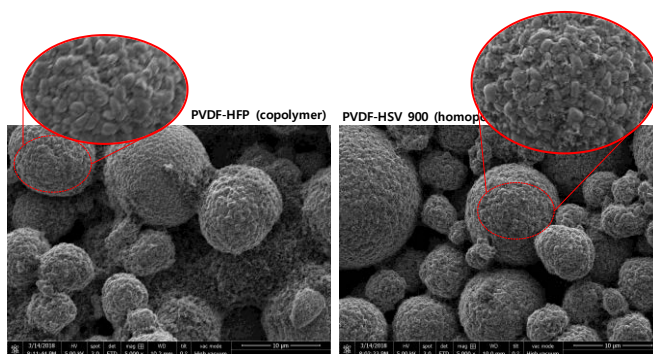


Figure II.11.A.5 SEM images of NMC811 electrodes fabricated with two different binders, PVDF-HFP copolymer and PVDF-HSV 900 homopolymer.

In Li metal architecture, the team has previously demonstrated that 2D atomic crystal layers of hexagonal boron nitride (h-BN) can be used as interfacial protection layers for Li metal anodes. However, it is difficult to grow pristine, electrode-scale, high quality BN due to defects that form and the small grain sizes. Here, we demonstrate the selective atomic layer deposition (ALD) of LiF on defect sites of h-BN prepared by chemical vapor deposition. The LiF deposits primarily on the line and point defects of h-BN, thereby creating seams that hold the h-BN crystallites together. The selective deposition allows us to visualize the location of defects in h-BN using scanning electron microscopy (SEM), atomic force microscopy (AFM), and transmission electron microscopy (TEM). The chemically and mechanically stable hybrid LiF/h-BN film successfully suppresses Li dendrite formation during both the initial electrochemical deposition onto a Cu foil and the subsequent cycling. Li metal that is deposited on the LiF/h-BN-protected current collector is highly dense and nearly free of void spaces, with its density matching that of bulk Li. The protected Li electrodes exhibit good cycling behavior with more than 300 cycles at relatively high Coulombic efficiency ($>95\%$) in an additive-free carbonate electrolyte, as compared to the unprotected Li anodes, which had rapidly decaying Coulombic efficiency and overall mossy Li morphology.

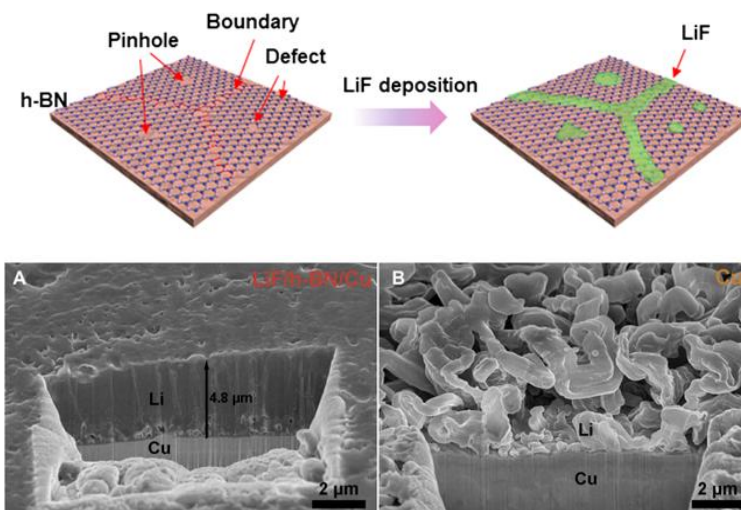


Figure II.11.A.6 Schematics (top) of LiF deposition on h-BN to heal the defects. This approach enables dense, void-free Li metal cycling (bottom, A). In contrast, Li deposits on bare Cu surface in a carbonate based electrolyte is dendritic and porous (bottom, B)

4. Keystone project 3: Cell fabrication, testing and diagnosis

To advance beyond successful efforts in FY2017, which saw the development of a 1 Ah, 300 Wh/kg pouch cell which could effectively cycle for over 50 complete cycles, key focal points for Keystone 3 for the first quarter of FY2018 were the development of parameters to achieve a cell design of 350 Wh/kg, identification of means to extend the cycling stability of Li metal pouch cells and to better understand fading mechanism associated with Li metal. With respect to cell design, detailed plans using realistic components and loadings were developed for both a Li||S cell design and a Li||NMC design which uses a high Ni content NMC. To better facilitate these cell designs, distinct material evaluation protocols for FY2018 were developed and sent to the entire Battery500 team to enable uniformity across all three Battery500 Keystones. On the cell design front, a pseudo-two-dimensional (P2D) model was also developed to better provide real-time impedance analysis that uses various cell design input parameters. Using the resulting computed Nyquist plots it is more readily feasible to understand how distinct changes to the cell design will impact the cell impedance and ultimately performance.

When developing the protocols for uniform evaluation across Battery500 several analyses were employed including understanding the role of using thin, realistic Li and lean electrolyte. For the lean electrolyte conditions it was found that the reduction in electrolyte quantity resulted in a significant impact on cycle life (Figure II.11.A.7). Similar, dramatic reductions in cycle life were seen when thin Li was employed. For both lean electrolyte and thin Li which mirror what is needed to achieve a high specific energy cell it was also found that alteration in the failure mechanism of the cells occurred.

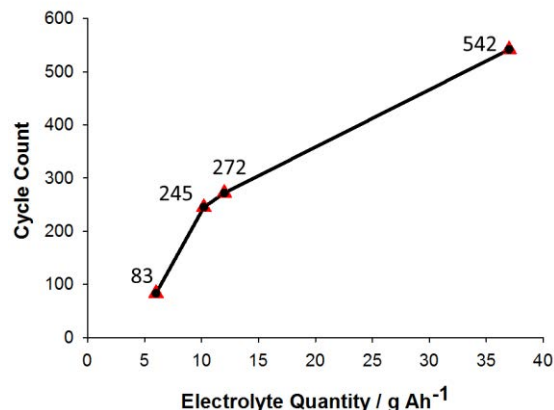


Figure II.11.A.7 Cycle life of cells (as specified by the cycle number at completely no capacity) as a function of electrolyte content (in g Ah⁻¹) to illustrate the impact of electrolyte quantity on cycle aging.

Understanding the cell failure and particularly the role that the Li metal anode plays is a distinct challenge. To address this challenge multiple institutions within the Battery500 team have employed a range of different methods including direct electrochemical evaluation, X-ray absorption spectroscopy (XAS), scanning transmission X-ray microscopy (STXM), X-ray photoelectron spectroscopy (XPA) and cryogenic focused-ion beam (cryo-FIB) SEM. The overarching goal of these activities is to understand how Li protection schemes affect the Coulombic efficiency and growth of Li. Using XAS and STXM the chemical compositions of the solid electrolyte interphase (SEI) from initial formation through several cycles have been investigated to better understand if there is an evolution of the chemical and physical properties of the SEI. Cryo-FIB-SEM was performed to reduce the beam damage to Li metal. With the reduced beam damage, more distinct variation between the Li morphology for different electrolytes was observed. When comparing electrolytes using LiPF_6 and high concentration LiFSI electrolytes it was found that the more traditional LiPF_6 electrolyte yielded a more porous structure while the LiFSI resulted in a lower porosity Li deposit. Additional work using different electrolytes has also distinctly found that as salt concentration is altered there are changes not just to the cycle life of the cell, but also to the overall SEI composition. While the chemistry and materials properties strongly dictate the overall performance of Li-metal cells additional attention also needs to be paid to the mechanical alteration which occurs over cycling. One route to directly impact the mechanics of a cell is through the application of pressure. During experiments on a full, 300 Wh/kg pouch cell it was found that moderate amounts of pressure distinctly improve the performance of cells by over 2-fold. A key to this result is that the pressure alters the interfacial boundary of the Li metal as the cell cycles. To better understand this relationship, a continuum model that captures the dynamics of Li deposition and stripping during repeated cycling of a Li-metal cell was developed and compared with experimental data from a Li||Li symmetric cell.

Distinct focal points for FY2018 were on refining modeling architectures to advance understanding of Li metal electrodes and thick electrode architectures, development and early evaluation of higher specific energy Li||NMC pouch cell designs, identifying means to increase cycle life and in performing advanced scientific diagnostics of Li metal electrodes. With respect to the modeling activities the Battery500 team performed two-dimensional modeling of novel electrode architectures to understand the effect of architecture design and material parameters on Li ion transport, and thus overall rate performance. In conjunction with developing this modeling framework the team also focused on developing codes which enable simulations to be performed in a computationally efficient manner. The result of the new codes is that simulations are faster and more robust than simulations run on commercial software. A continuum model that captures the dynamics of Li deposition and stripping during repeated cycling was also developed that includes a moving boundary representation to the standard Butler-Volmer method.

In FY2018, pouch cells with a specific energy of 340 Wh/kg have been developed using a Li metal anode and a high Ni-NMC cathode. Thus far cells have demonstrated at least 50 cycles. The ability to extend life was also a key area of research. Combined methods looking to more distinctly control pressure and the initial conditioning of Li have extended the cycle life from just over 50 cycles with no control to over 225 cycles (still cycling) for a cell with a design of 310 Wh/kg. Analysis on the calendar life of Li||NMC cells has also begun. For both pouch and coin cells the electrochemical characterization standard methods for evaluation are also in place.

With respect to diagnostics analysis of Li metal deposited from different electrolytes were analyzed using a newly developed Cryo-FIB-SEM. This method significantly minimizes beam damage to the Li sample. For investigations roughly $\sim 5 \mu\text{m}$ of Li was deposited from two different electrolytes. From the top view, the conventional carbonate electrolyte (1 M LiPF_6 in EC-DMC) generates needlelike dendrites with highly porous surface (Figure II.11.A.8a). In contrast, close packed large Li particles with dense surface are formed in the liquefied gas-based electrolyte of LiTFSI-fluoromethane (FM): CO_2 -Additive01 (Figure II.11.A.8b). From the cross-section view, the Li metal film from the conventional electrolyte has porous structure with large voids resulting in a thickness of $\sim 10 \mu\text{m}$. On the contrary, the use of LiTFSI-FM: CO_2 -Additive01 electrolyte forms a dense Li deposit with a thickness of $5.2 \mu\text{m}$. The dense deposition formed in liquefied gas-based electrolyte prevents dendrite formation and severe electrolyte consumption from SEI formation.

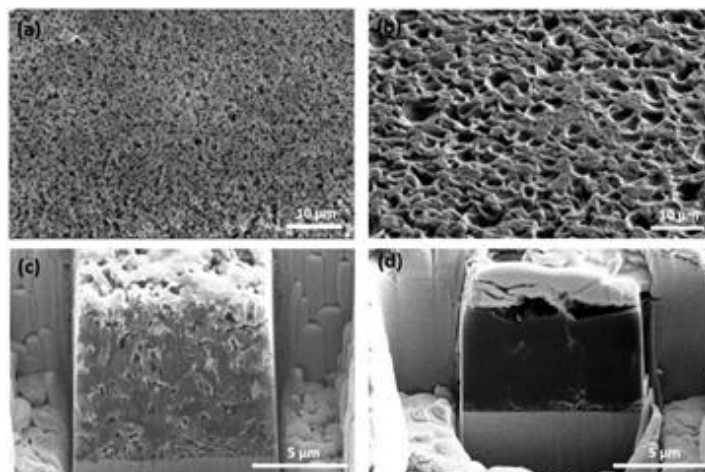


Figure II.11.A.8 Cryo FIB-SEM images of the plated lithium at the first cycle and the corresponding cross-section images when the cells are cycled in (a, c) 1M LiPF₆ EC: DMC, and (b, d) 0.1M LiTFSI in fluoromethane: CO₂ 19:1 with 0.1M Additive01

Efforts to better understand electrode structure and cell failure highlighted our activities in FY2018. On the electrode structure side two distinct computational efforts were undertaken. In the first, novel structures with arrays of electrode material and fixed width, low tortuosity gaps were investigated. Finite-element simulations (FEM) of these architectures using macro-homogeneous models of Newman and co-workers were undertaken to help determine the optimal distribution of electrode mass for a fixed thickness and overall capacity, and to understand material utilization at high rates of galvanostatic discharge. Figure II.11.A.9 depicts discharge curve simulations for an NMC cathode. The discharge simulation is terminated either when the cell voltage falls below the cutoff value, or when the electrolyte concentration in the cathode towards the current collector drops below a certain minimum value. When used to identify enhanced utilization of cathode material it was identified that increased utilization is obtained over the homogeneous $W_d/L_p = 1$ for and lower. At a configuration of $W_d/L_p = 0.5$ nearly 95% utilization is achieved where W_d is the domain width and L_p is the domain thickness. The pseudo-3D model permits parametric variations that allow simulation of low electronic-conductivity regimes, and as such is a generalized framework that can be used to simulation any combinations of anode/cathode chemistries, and different property combinations of electrodes, separator, and electrolytes.

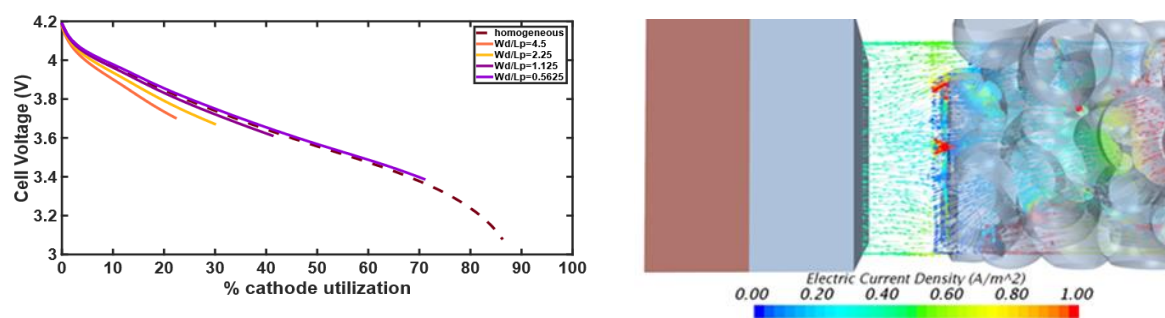


Figure II.11.A.9 Discharge curves at ~ 6 mA/cm² to understand cathode utilization (right). Current density variation computations (left) cathode chemistries.

During FY2018 distinct progress was made in combined experimental and modeling efforts to understand design and performance limitations for high specific energy Li metal batteries. At the end of the fiscal year the Battery500 team had developed a 2.5 Ah Li||NMC pouch cell that had achieved 100 cycles with only 2.5% capacity fade (Figure II.11.A.10). The cell, which fulfilled the annual milestone for the program, had a specific energy of 350 Wh/kg at the beginning of life and was still cycling at the end of the fiscal year. The cell

displayed a 40 Wh/kg improvement over the end of FY2017. To achieve the high performance the team capitalized on improvements in electrolyte, mechanical cell management and the use of thick NMC cathodes. A key to the cell design is the use of low volumes of electrolyte and thin Li foil.

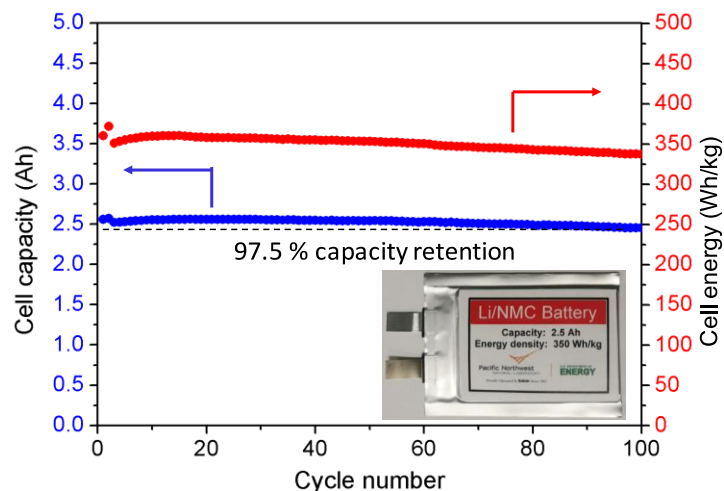


Figure II.11.A.10 Final deliverable cell for FY2018. The Li||NMC pouch cell was still cycling at the end of FY2018

Conclusions

1. The 1st cycle loss of Li||NMC cells is independent of cathode loading but is decreased by increased calendaring.
2. The thermal instability of NMC cathodes is a function of both the Ni content and the degree of Li removal.
3. Localized high concentration electrolytes (LHCE) have been developed. One good example is the ED1123, for which, much improved thermal stability, high CE, and higher rate capability have been demonstrated in Li||NMC811 coin cells.
4. A one-dimensional model is developed to describe the Li metal deposition process that correlates with experimental setup.
5. Ion transport resistance through thick electrodes is quantified with a d.c. through membrane measurement technique.
6. Pouch cells with greater than 350 Wh/kg specific energy and over 100 cycles have been demonstrated and the cells are still cycling.
7. The amount of inactive Li in high energy cells was quantified at the end of life.

Key Publications

1. M. Lee, J. Hong, J. Lopez, Y. Sun, D. Feng, K. Lim, W. C. Chueh, M. F. Toney, Y. Cui, Z. Bao, "High-performance sodium-organic battery by realizing four-sodium storage in disodium rhodizonate", *Nature Energy*, 2017, 2, 861–868.
2. Y. Tsao, Z. Chen, S. Rondeau-Gagné, Q. Zhang, H. Yao, S. Chen, G. Zhou, C. Zu, Y. Cui, Z. Bao, "Enhanced cycling stability of sulfur electrodes through effective binding of pyridine-functionalized polymer", *ACS Energy Lett.*, 2017, 2, 2454–2462.

3. E. C. Miller, R. M. Kasse, K. N. Heath, B. R. Perdue, M. F. Toney, "Operando Spectromicroscopy of Sulfur Species in Lithium-Sulfur Batteries", *J. Electrochem Soc.*, accepted.
4. Y. Qi, T. Jang, V. Ramadesigan, D. T. Schwartz, and V. R. Subramanian, "Is there a benefit in employing graded electrodes for lithium-ion batteries?", *J. Electrochem. Soc.*, 2017, 164(13), A3196-A3207.
5. K. Park and J. B. Goodenough, "Dendrite-Suppressed Lithium Plating from a Liquid Electrolyte via Wetting of Li_3N ", *Adv. Energy Mater.* 2017, 1700732, 1–7.
6. L. Chen, Y. Li, S.-P. Li, Li-Z. Fan, C.-W. Nan, and J. B. Goodenough, "PEO/Garnet Composites for Electrolyte Solid-state Lithium Batteries: from "Ceramic-in-Polymer" to "Polymer-in-Ceramic," *Nano Energy*, 2017, DOI: [10.1016/j.nanoen.2017.12.037](https://doi.org/10.1016/j.nanoen.2017.12.037).
7. Y. Lyu, E. Hu, D. Xiao, Y. Wang, X. Yu*, G. Xu, S. N. Ehrlich, K. Amine, L. Gu*, X.-Q. Yang, and H. Li*, "Correlations between Transition Metal Chemistry, Local Structure and Global Structure in $\text{Li}_2\text{Ru}_{0.5}\text{Mn}_{0.5}\text{O}_3$ Investigated in a Wide Voltage Window", *Chem. Mater.*, 2018, DOI: 10.1021/acs.chemmater.7b02299.
8. K. Zhang, F. Ren, X. Wang, E. Hu, Y. Xu, X.-Q. Yang, H. Li, L. Chen, P. Pianetta, A. Mehta, X. Yu*, Y. Liu*, "Finding a Needle in the Haystack: Identification of Functionally Important Minority Phases in an Operating Battery", *Nano Lett.*, 2017, 17 (12), 7782–7788.
9. G. Zhou, K. Liu, Y. Fan, M. Yuan, B. Liu, W. Liu, F. Shi, Y. Liu, W. Chen, J. Lopez, D. Zhuo, J. Zhao, Y. Tsao, X. Huang, Q. Zhang, Y. Cui, "An aqueous inorganic polymer binder for high performance lithium-sulfur batteries with flame-retardant properties", *ACS Central Sci.*, 2018, 4, 260-267.
10. J. Alvarad, M. Schroeder, O. Borodin, E. Gobrogge, M. Olguin, M. Ding, M. Gobet, S. Greenbaum, Y. S. Meng, K. Xu "Solvent-Salt Synergy Offers Fresh Pathway to Unlock Next Generation Li-Ion Chemistries", *Mater. Today*, accepted.
11. M. S. Whittingham, F. Omenya, and C. Siu, "Solid State Ionics - the key to the discovery, introduction and domination of lithium batteries for portable energy storage", *Solid State Ionics*, 2018, 318, 60-68.
12. E. Hu, X. Wang, X. Yu, and X.-Q. Yang, "Probing the Complexities of Structural Changes in Layered Oxide Cathode Materials for Li-Ion Batteries during Fast Charge–Discharge Cycling and Heating", *Account Chem. Research*, 2018, 51, 290–298.
13. N. Dawson-Elli, S. B. Lee, M. Pathak, K. Mitra, and V. R. Subramanian, "Data Science Approaches for Electrochemical Engineers: An Introduction through Surrogate Model Development for Lithium-Ion Batteries", *J. Electrochem. Soc.*, 2018, 165(2), A1-A15.
14. T. Munaoka, X. Yan, J. Lopez, J. W. F. To, J. Park, J. B.-H. Tok, Y. Cui, Z. Bao, "Ionically conductive self-healing binder for low cost Si microparticles anodes in Li-ion batteries", *Adv. Energy Mater.*, 2018, 1703138
15. S. Wang, H. Xu, W. Li, A. Dolocan, and A. Manthiram, "Interfacial Chemistry in Solid-state Batteries: Formation of Interphase and Its Consequences," *J. Am. Chem. Soc.*, 2017, 140, 250-257.
16. W. Li, X. Liu, H. Celio, P. Smith, A. Dolocan, M. Chi, and A. Manthiram, "Mn vs. Al in Layered Oxide Cathodes in Lithium-Ion Batteries: A Comprehensive Evaluation on Long-term Cyclability," *Adv. Energy Mater.*, 2018, 8, 20173154.

17. L. Chen, Y. Li, S.-P. Li, Li-Z. Fan, C.-W. Nan, and J. B. Goodenough, "PEO/Garnet Composite Electrolyte Solid-state Lithium Batteries: from "Ceramic-in-Polymer" to "Polymer-in-Ceramic," *Nano Energy*, 2018, 46, 176-184.
18. L. Xue, H. Gao, Y. Li, and J. B. Goodenough, "Cathode Dependence of Liquid-Alloy Na–K Anodes," *J. Am. Chem. Soc.*, 2018, 140, 3292–3298.
19. Y. You, H. Celio, J. Li, A. Dolocan, and A. Manthiram, "Stable Surface Chemistry against Ambient Air of Modified High-nickel Cathodes for Lithium-ion Batteries," *Angew. Chem. Int. Ed.*, 2018, DOI: <https://doi.org/10.1002/anie.201801533>.
20. S. Chen, J. Zheng, D. Mei, K. S. Han, M. H. Engelhard, W. Zhao, W. Xu, J. Liu and J.-G. Zhang, "High-voltage lithium metal batteries enabled by localized high concentration electrolytes," *Adv. Mater.*, 2018, 30, 1706102.
21. L. Yu, N. L. Canfield, S. Chen, H. Lee, M. H. Engelhard, Q. Li, J. Liu, W. Xu and J.-G. Zhang, "Enhanced Stability of Li Metal Anode Enabled by 3D Porous Nickel Substrate," *ChemElectroChem*, 2018, 5, 1–10.
22. G. Hu, C. Shen, L.-Z. Cheong, S. Wang, S. Huang, J.-G. Zhang, D. Wang, "Direct Observation of Lithium Dendrite Growth by Operando EC-AFM," *Small Methods*, 2018, 2, 1700298.
23. K. N. Heath, B. R. Perdue, M. F. Toney, E. C. Miller, R. M. Kasse, "Operando Spectromicroscopy of Sulfur Species in Lithium-Sulfur Batteries", *J. Electrochem Soc.*, 2018, 165, A6043-A6050.
24. J. Li, W. Li, S. Wang, K. Jarvis, J. Yang, and A. Manthiram, "Facilitating the Operation of Lithium-Ion Cells with High-Nickel Layered Oxide Cathodes with a Small Dose of Aluminum," *Chem. Mater.*, vol. 30, no. 9, pp. 3101–3109, April 2018.
25. Y. Li, X. Chen, A. Dolocan, Z. Cui, S. Xin, L. Xue, H. Xu, K. Park, and J. B. Goodenough, "Garnet Electrolyte with an Ultralow Interfacial Resistance for Li-Metal Batteries," *J. Am. Chem. Soc.*, vol. 140, no. 20, pp. 6448–6455, April 2018.
26. J. Liu*, L. Yin, X.-Q. Yang*, and P. G. Khalifah, "Li₃VP₃O₉N as a Multielectron Redox Cathode for Li-Ion Battery", *Chem. Mater.*, 2018, DOI: 10.1021/acs.chemmater.8b01114.
27. J. Liu*, L. Yu, E. Hu, B. S. Guiton, X.-Q. Yang, and K. Page*, "Large-Scale Synthesis and Comprehensive Structure Study of δ-MnO₂", *Inorg. Chem.*, 2018, 57 (12), pp 6873–6882.
28. X. Fan, E. Hu, X. Ji, Y. Zhu, F. Han, S. Hwang, J. Liu, S. Bak, Z. Ma, T. Gao, S.-C. Liou, J. Bai, X.-Q. Yang, Y. Mo, K. Xu, D. Su, and C. Wang, "High energy-density and reversibility of iron fluoride cathode enabled via an intercalation-extrusion reaction", *Nature Commun.*, DOI: 10.1038/s41467-018-04476-2.
29. S. Chen, J. Zheng, L. Yu, X. Ren, C. Niu, H. Lee, X. Wu, J. Xiao, J. Liu and J. Zhang, "High Efficiency Lithium Metal Batteries with Fire-Retardant Electrolytes", *Joule*, 2018, 2 (8), 1548-1558.
30. S. Jiao, X. Ren, R. Cao, M. H. Engelhard, Y. Liu, D. Hu, D. Mei, J. Zheng, W. Zhao, Q. Li, N. Liu, B. D. Adams, C. Ma, J. Liu, J.-G. Zhang, and W. Xu, "Stable Cycling of High-Voltage Lithium Metal Batteries in Ether Electrolytes", *Nature Energy*, 2018, 3(9), 739-746.
31. Y. Li, H. Xu, P. Chien, N. Wu, S. Xin, L. Xue, K. Park, Y. Hu, and J.B. Goodenough, "A Perovskite Electrolyte That Is Stable in Moist Air for Li-ion Batteries", *Angew. Chem. Int. Ed.*, 2018, 57 (28), 8587-8591.

32. L. Xue, W. Zhou, S. Xin, H. Gao, Y. Li, A. Zhou, and J. B. Goodenough "Room-Temperature Liquid Na-K Anode Membranes", *Angew. Chem. Int. Ed.*, 2018, 130 (43), 14380-14383.
33. L. Yu, S. Chen, H. Lee, L. Zhang, M. H. Engelhard, Q. Li, S. Jiao, J. Liu, W. Xu, J.-G. Zhang. "A Localized High-Concentration Electrolyte with Optimized Solvents and Lithium Difluoro(oxalate)borate Additive for Stable Lithium Metal Batteries." *ACS Energy Lett.*, 2018, 3(9), 2059-2067.
34. X. Ren, S. Chen, H. Lee, D. Mei, M. H. Engelhard, S. D. Burton, W. Zhao, J. Zheng, Q. Li, M. S. Ding, M Schroeder, J Alvarado, K. Xu, Y. S. Meng, J. Liu, J.-G. Zhang, W. Xu. "Localized High-Concentration Sulfone Electrolytes for High-Efficiency Lithium-Metal Batteries." *Chem*, 2018, 4(8), 1877-1892.
35. S.-M. Bak, Z. Shadik, R. Lin, X. Yu, X.-Q. Yang, "In situ/operando synchrotron-based X-ray techniques for lithium-ion battery research", *NPG Asia Mater.*, 2018, DOI 10.1038/s41427-018-0056-z.
36. E. Hu, X. Yu, R. Lin, X. Bi, J. Lu, S. Bak, K.-W. Nam, H. L. Xin, C. Jaye, D. A. Fischer, K. Amine, and X.-Q. Yang, "Evolution of redox couples in Li- and Mn-rich cathode materials and mitigation of voltage fade by reducing oxygen release", *Nature Energy*, 2018, 3, 690–698.
37. J.-Y. Piao, Y.-G. Sun, S.-Y. Duan, A.-M. Cao, X.-L. Wang, R.-J. Xiao, X.-Q. Yu, Y.-G., L. Gu, Y. Li, Z.-J. Liu, Z.-Q. Peng, R.-M. Qiao, W.-L. Yang, X.-Q. Yang, J. B. Goodenough, L.-J. Wan, "Stabilizing Cathode Materials of Lithium-Ion Batteries by Controlling Interstitial Sites on the Surface", *Chem*, 2018, 4 (7), 1685-1695.
38. X.-Y. Yue, W.-W. Wang, Q.-C. Wang, J.-K. Meng, Z.-Q. Zhang, X.-J. Wu, X.-Q. Yang, Y.-N. Zhou, "CoO nanofiber decorated nickel foams as lithium dendrite suppressing host skeletons for high energy lithium metal batteries", *Energy Storage Mater.*, 2018, 14, 335–344.
39. L. Yin, G. Mattei, Z. Li, J. Zheng, W. Zhao, F. Omenya, C. Fang, W. Li, J. Li, Q. Xie, J.-G. Zhang, M.S. Whittingham, Y.S. Meng, A. Manthiram and P. Khalifah. "Extending the limits of powder diffraction analysis: diffraction parameter space, occupancy defects, and atomic form factors" *Rev. Sci. Instrum.*, 2018, 89, 093002.
40. Lopez, A. Pei, J. Y. Oh, G.-J. N. Wang, Y. Cui, Z. Bao, "Effects of Polymer Coatings on Electrodeposited Lithium Metal", *J. Am. Chem. Soc.*, 2018, 140 (37), 11735-11744.
41. D. G. Mackanic, W. Michaels, M. Lee, D. Feng, J. Lopez, J. Qin, Y. Cui, Z. Bao, "Crosslinked Poly(tetrahydrofuran) as a Loosely Coordinating Polymer Electrolyte", *Adv. Energy Mater.*, 2018, 8 (25), 1800703.
42. F. Shi, A. Pei, D. T. Boyle, J. Xie, X. Yu, X. Zhang, and Y. Cui, "Lithium metal stripping beneath the solid electrolyte interphase", *Proc. Natl. Acad. Sci. U. S. A.*, 2018, 115 (34), 8529–8534.
43. Y. Liu, D. Lin, Y. Li, G. Chen, A. Pei, O. Nix, Y. Li, and Y. Cui, "Solubility-mediated sustained release enabling nitrate additive in carbonate electrolytes for stable lithium metal anode", *Nat. Commun.*, 2018, 9, 3656.
44. J. Xie, J. Wang, H. R. Lee, K. Yan, Y. Li, F. Shi, W. Huang, A. Pei, G. Chen, R. Subbaraman, J. Christensen, and Y. Cui, "Engineering stable interfaces for three-dimensional lithium metal anodes", *Sci. Adv.*, 2018, 4, eaat5168.

45. S. Wang, M. Yan, Y. Li, C. Vinado, and J. Yang, "Separating Electronic and Ionic Conductivity in Mix-Conducting Layered Lithium Transition Metal Oxides", *J. Power Sources*, 2018, 393, 75-82.
46. S. M. Wood, C. Fang, E. J. Dufek, S. C. Nagpure, S. V. Sazhin, B. Liaw, Y. S. Meng, "Predicting Calendar Aging in Lithium Metal Secondary Batteries: The Impacts of Solid Electrolyte Interphase Composition and Stability", *Adv. Energy Mater.*, 2018, DOI: 10.1002/aenm.201801427.

Patents (Invention Disclosure and Patent Applications)

1. (Invention Disclosure) X. Cao, J.-G. Zhang, W. Xu. "Electrolytes for Stable Cycling of Rechargeable Li Metal and Li Ion Batteries", IPID 31452-E. Sept. 4, 2018.
2. (Invention Disclosure) C. Fang, X. Wang, Y. S. Meng, TGC Method and System for Metal Quantification, UD00000763, May 2018.
3. (U.S. Non-Provisional Patent Application) J.-G. Zhang, S. Chen, W. Xu. "Low Flammability Electrolytes for Stable Operation of Electrochemical Devices", IPID 31111-E CIP. Application No. 15/788,188, filed date: 10/2017 (U.S. Patent Application 20180251681, publication date: 9/6/2018)
4. (U.S. Non-Provisional Patent Application) S. Wang, J. Yang, H. Pan, J. Xiao, and J. Liu, "Battery Separator with Lithium Ion Conductor Coating", 62/687,125, June 19, 2018.
5. (Foreign Patent Application) J.-G. Zhang, S. Chen, W. Xu, X. Cao, X. Ren. "Low Flammability Electrolytes for Stable Operation of Electrochemical Devices", IPID 31111-E CIP PCT. PCT Application No. PCT/US2018/049141, filed date: 8/2018.

II.11.B Battery500 Seedling Projects (NAVSEA)

Patricia H. Smith, Ph.D., Project Coordinator

NAVSEA-Carderock
 Non-Metallic Materials Research & Engineering Branch, 617
 9500 MacArthur Blvd.
 West Bethesda, MD 20817-5700
 E-mail: patricia.h.smith1@navy.mil

Tien Duong, DOE Technology Development Manager

U.S. Department of Energy
 E-mail: Tien.Duong@ee.doe.gov

Start Date: October 1, 2017	End Date: September 30, 2020	
Project Funding: \$8,000,000	DOE share: \$8,000,000	Non-DOE share: \$0

Introduction/Objectives

Proof-of-concept or seedling projects were awarded to support the Battery500 Program. The projects are high-risk, high-payoff efforts that if successful will provide an infusion of novel technology into the Consortium's effort. The objective of the Battery500 Consortium is to research, develop, and demonstrate lithium battery technologies capable of achieving a cell specific energy of ≥ 500 Wh/kg and 1,000 cycles. The two electrochemistries being developed are lithium metal/sulfur and lithium metal/high nickel lithium nickel manganese cobalt (NMC) cells, using solid or concentrated liquid electrolytes.

Promising phase I awardees will be competitively down-selected at the end of 18 months for a second phase of research.

Approach

The goal of the Battery500 seedlings is to jump-start emerging technologies that could lead to a cell delivering an energy density of 500 Wh/kg over 1,000 cycles. The fifteen Seedling projects and their corresponding approaches are listed below:

500Wh/Kg Batteries with Fluoride Conversion Cathodes and LiPON-Protected Lithium Anodes (Chunsheng Wang, University of Maryland, College Park)

Electrolytes need to satisfy often conflicting requirements that cannot be achieved with only one solvent and salt. The philosophy behind all-fluorinated electrolytes is to form a LiF-rich SEI on Li and F-rich CEI on high energy cathodes, while simultaneously achieving high ionic conductivity, low viscosity and good wettability of the separator. By tuning the salts, solvents, and concentrations, this effort will maximize the cycling efficiency and stability of the lithium anodes. In addition, the oxidation stability of the electrolytes on the cathode will be enhanced. The understanding of the degradation processes of lithium anode and high-voltage cathode will guide the design of next-generation electrolytes.

Multifunctional Lithium-Ion Conducting Interfacial Materials for Lithium-Metal Batteries (Donghai Wang, Pennsylvania State University Park Research)

The overall approach will focus on development and optimization of synthesis methods and precursors for multifunctional lithium-ion conducting interfacial materials, protective layer composition, and protective layer fabrication methods. This will be accompanied by property measurement and characterization (conductivity, mechanical properties, etc.) for the protective layer on lithium metal, along with cell testing.

Scalable Polymer Precursor Based LiPON Type Lithium-Metal Interface Enabled High-Performance Lithium-Sulfur Battery (Tobias Glossmann, Mercedes-Benz Research & Development North America, Inc.)

The project includes the synthesis of LiPON and LiOAl precursors with controlled compositions and lithium contents; optimization of coating and ceramization processes, characterization, and modeling of LiPON and LiOAl films with different lithium, nickel, and P/Al contents; and the fabrication of solid-state membranes of c-LLZO and $\text{Li}_{1.7}\text{Al}_{0.3}\text{Ti}_{1.7}\text{Si}_{0.4}\text{P}_{2.6}\text{O}_{12}$ (LATSP) to which optimized barrier precursors are then applied and transformed to LiPON and/or LiOAl. Coated membranes will be cycled in symmetrical cells against lithium metal. Stability of LiPON and LiOAl films will be tested and modeled/predicted using *ab initio* quantum chemical computer models. The project will develop a process for coating the solid-state electrolyte with LiPON and/or LiOAl precursors and ceramizing them. Scalable methods to heat the very thin precursor coatings with the potential to “glue” components during ceramization so as to simplify assembly will be developed. A baseline sulfur cathode will be fabricated, and an initial electrolyte will be selected. The project also includes coin cell assembly, characterization, and analysis.

3D Printed, Low Tortuosity Garnet Framework for Beyond 500 Wh/kg Batteries (Eric Wachsman, University of Maryland, College Park)

LLZ garnet inks will be developed to 3D print solid electrolyte high-porosity, low-tortuosity patterns, including lines, grids, and columns. Using 3D printing enables rapid comparison of different electrolyte structure types as well as variations in structure characteristics (column height, width, etc.). These structures will be used in porous-dense-porous trilayer structures and assembled into batteries for testing. At the same time, 3D solid-state ionic and electronic transport models will be developed to understand how the 3D structure affects the ionic and electronic transport rates and how to increase electrode loading while maintaining high C-rates. The models will be validated by experiment, and used to optimize the 3D electrolyte structure.

Design, Processing, and Integration of Pouch-Format Cell for High-Energy Lithium-Sulfur Batteries (Mei Cai, General Motors LLC)

The concept of design, processing, and integration of pouch-format high-energy Li-S batteries will be validated. Deposition technologies will be applied for thin lithium anode fabrication. Various treatments of the lithium surface will be applied to achieve the stability target of the lithium anode. For the sulfur cathode, polymer binders and binding additive adjustments will be explored. A Corona discharge technology will be applied on the current collector to improve the interface condition. The calendaring process with tuned parameters will be integrated with the binder and interface efforts to achieve porosity control on the sulfur cathode. The relationship between the electrolyte-to sulfur ratio and electrochemical performance will be determined. With development of each major component, integration and full-cell design will proceed through the combined efforts of the pilot cell validation and the algorithm modeling tool developed inside GM. The pouch-format cell will be fabricated accordingly. The deliverable will be a pouch format cell with energy density of 500 Wh/kg with cycle life of 500 cycles.

Electrochemically Stable High Energy Density Lithium-Sulfur Batteries (Prashant Kumta, University of Pittsburgh)

This research will generate high sulfur loading electrode configurations exhibiting high energy densities without any polysulfide dissolution meeting the EV everywhere blueprint target. Approaches include: (1) Generation of novel high loading directly doped sulfur architecture (DDSA) cathodes and unique polysulfide trapping agent (PTA) configurations, (2) Generation of novel composite framework materials (CFM) enabling high sulfur loading and polysulfide confinement, (3) Generation of high Li-ion conducting (LIC) and polysulfide dissolution resistant coatings on sulfur nanoparticles, and (4) Generation of new polysulfide conversion electrocatalysts enabling rapid kinetics of lithium disulfide formation.

Highly Loaded Sulfur Cathode and Coated Separator for High-Rate Lithium-Sulfur Batteries (Yong Joo, Cornell University)

The project reduces the mesoporous carbon substrate amount by creating a compact mesoporous carbon and graphene assembly as the cathode, and eliminates the use of the interlayer by coating mesoporous carbon and/or functionalized graphene directly on the separator. This compact hybrid assembly of substrate and separator with reduced interfacial resistance and more functional group will allow the team to increase sulfur loading further and achieve enhanced rate capability without sacrificing capacity retention. In addition, gel electrolytes based on functionalized silsesquioxanes is employed to Li-S batteries to eliminate the issues of leaking and shuttle effect, especially for pouch cells. Coin cells are initially used for evaluating and optimizing the cell performance with highly loaded cathode and carbon-coated separator. The team will scale up the cathode and separator coating via air-controlled electrospray and fabricate large format pouch cells in collaboration with EIC Labs, who will also carry out in situ Raman monitoring of polysulfide redox reactions during cycling of Li-S batteries.

Identification of Efficient and Stable Electrochemical Interfaces for Lithium-Sulfur Batteries (Perla Balbuena, Texas A&M Engineering Experiment Station)

First-principles simulations and in situ experimentation and analysis constitute the basis of this project. The innovation aspects are: (a) detailed DFT and ab initio molecular dynamics (AIMD) analysis and characterization at the interfaces coupled with well-designed XPS, X-ray absorption spectroscopy (XAS), NMR, and electrochemical tests of half cells and complete cells; (b) use of classical molecular dynamics simulations that extend the length and time scales of the interfacial models integrated with the microscopic chemical information regarding reactivity and composition of interphases obtained from DFT, AIMD, XPS, NMR, and chemical imaging techniques, will allow characterization of slower kinetics phenomena not usually properly addressed.

Solvent-Free and Non-Sintered 500 Wh/kg All-Solid-State Battery (Pu Zhang, Navitas Advanced Solutions Group, LLC)

This effort focuses on both the material limitations and process challenges facing large format solid-state battery production. At present, sulfide solid state electrolytes have two major limitations to be solved before being adopted for large-scale battery production: (1) low (electro)chemical stability against air and common cathode materials, and (2) lack of scalable fabrication processes. This project will address the first by modifying the sulfide structure to improve its stability and will address the second challenge by adopting and scaling a Dry Process Electrode Fabrication technology developed successfully at Navitas.

High-Energy Lithium-Metal Batteries Based on 3D Architectures of MnO₂ as Cathodes (Da Deng, Wayne State University)

Lithium-free MnO₂ based cathode will be synthesized under various experimental conditions and fully characterized. For the anodes, the focus will be on lithiated anodes that are based on metallic lithium or lithiated silicon. The couples will be assembled to make full cells. The electrochemical properties of those full cells, in terms of capacity, rate performances, and cycling stability, will be evaluated; cell performances will be optimized.

Tuned Li₂S@Graphene Cathode for Lean Electrolyte Lithium-Sulfur Batteries and Induced SEI on Lithium-Metal Anode (Ji Xiulei, Oregon State University)

The project will tune the surface properties of a nanocomposite of Li₂S@Graphene as the cathode of Li-S batteries so that this cathode material can be highly electrolyte-philic. This is to dramatically increase the energy density of Li-S batteries by reducing the necessary volume of the electrolyte—the usage of lean electrolytes. The goal is to decrease the electrolyte-volume/sulfur active mass ratio to be below 2 mL/g. As another goal, we investigate the formula of electrolytes that contain solid-electrolyte-interphase (SEI) formation additives, which facilitates both dendrite-free lithium plating as well as high Coulombic efficiency values.

Sulfur Loaded MS2 Barrier for Control of Polysulfide Shuttling in Lithium-Sulfur Batteries (Amy Marschilok, SUNY University at Stony Brook Research)

The proposed Li-S battery concept utilizes 2D-nanosheet transition metal (TM) dichalcogenides (MS₂, M = Mo, Ti), to capitalize on the positive TM center, facilitating trapping of negatively charged polysulfide chains before entering bulk solution to reduce polysulfide shuttling. Sulfur will be embedded between the MS₂ nanosheets to create a 2D MS₂/S₈ composite cathode, which will enable material homogeneity with high-sulfur loading in the cathode. In addition to improving capacity retention by trapping polysulfide species, the MS₂ nanosheets will aid in improving the electrical conductivity of the composite cathode, with orders of magnitude improvement in electrical conductivities relative to S₈.

High-Energy Solid-State Lithium Batteries with Organic Cathode Materials (Yan Yao, University of Houston)

Among the few cathode materials that could potentially achieve the specific energies of ≥ 500 Wh/kg at the cell level, both sulfur and high nickel manganese cobalt chemistries face challenges. This project introduces organic insertion materials (OIMs) as a new class of cathode materials for high-energy solid-state lithium batteries. They offer a unique combination of moderately high operating potential, high specific capacity without large volume change, decent electronic/ionic conductivity, resource abundance, low cost, and favorable mechanical formability. The success of solid-state OIM-Li batteries will be enabled by interdependent tasks including: (1) selection/molecular design of high-energy stable OIMs, (2) development of sufficiently conductive and chemically robust solid-state electrolytes, and (3) dedicated device configuration designs that connect the two.

Composite Cathode Architectures Made by Freeze-Casting for All-Solid-State Lithium Batteries (Marca Doeff, Lawrence Berkeley National Laboratory Research)

An innovative freeze tape-casting technique is used to produce scaffolds of a Li-ion conducting ceramic material, which is then infiltrated with active material and conductive additives to produce thick (~100 μ m) composite electrodes for all solid-state lithium batteries. The low tortuosity pores produced by the freeze tape-casting process facilitate infiltration and minimizes lithium diffusion distances in the composite, which is good for rate performance.

500 Wh/Kg Batteries with Fluoride Conversion Cathodes and LiPON-Protected Lithium Anodes (Chunsheng Wang, University of Maryland, College Park)

1D ordered mesoporous carbon thin films are synthesized by using a triblock copolymer, and highly cross-linked resorcinol-formaldehyde resin (RFR) as the soft-templates and carbon precursor. The radio frequency magnetron sputtering technique is used for LiPON coating to seal the porous carbon, or a highly concentrated electrolyte is used to form LiF-rich SEI to seal the porous carbon. Scanning electron microscopy (SEM), transmission electron microscopy (TEM), and atomic force microscopy (AFM) are used to check the LiPON coating on carbon surface. The performance of the Li-C@LiPON/Fe_{1.0-y}MyOF cell is evaluated by Arbin test station.

Results

500Wh/Kg Batteries with Fluoride Conversion Cathodes and LiPON-Protected Lithium Anodes (Chunsheng Wang, University of Maryland, College Park)

A nonflammable all-fluorinated electrolyte (1M LiPF₆ in FEC/FEMC/HFE, 2/6/2) was developed to enhance the cycling stability of both Li metal anode and high energy cathodes. The all-fluorinated electrolyte enables a high coulombic efficiency (CE) of 99.2% for Li plating/stripping during 500 cycles, and 99.9% for NMC811 during 450 cycles at a high areal capacity of 1.0 mAh/cm². In addition to NMC811, this electrolyte also enables 5.0 V LiCoPO₄, 5.3 V LiCoMnO₄ and >1000 Wh/Kg Fe_{0.9}Co_{0.1}OF cathodes to be stably charged/discharged for 1000 cycles at a high CE of >99.9%. Using lithiated Si at 2.0 mAh/cm² as a Li host, this electrolyte enables the Li plating/stripping to achieve a record high CE of 99.8% even at a high Li

plating/stripping capacity of 2.0 mAh/cm² and also enable NMC811(2 mAh)/Li_xSi (2mAh) full cell to achieve 300 cycles without capacity decay.

Multifunctional Lithium-Ion Conducting Interfacial Materials for Lithium-Metal Batteries (Donghai Wang, Pennsylvania State University Park Research)

The effort focused on optimizing the structure of the multifunctional Li-ion conducting interfacial materials, which serve as protective layers for Li anodes, and enabling safe, high-performance lithium metal batteries. Major innovations included the development of Li-ion conducting materials having 1) multiple tunable functionalities, morphologies and corresponding tunable physical properties, and 2) a spontaneous formation process after exposure to lithium, enabling uniform Li deposition and superior cycling efficiency. In the phase I, the team demonstrated that the use of this material enables high-efficiency Li deposition (99.1% CE at a deposition amount of 4.0 mAh/cm²) and stable cycling (over 200 cycles) of 4V Li|NCM cells under lean-electrolyte (7 μL/mAh), lean-anode (1.9-fold excess of Li), and high-capacity (3.4 mAh/cm²) conditions.

Scalable Polymer Precursor Based LiPON Type Lithium-Metal Interface Enabled High-Performance Lithium-Sulfur Battery (Tobias Glossmann, Mercedes-Benz Research & Development North America, Inc.)

A sulfur-poly(acrylonitrile) composite (SPAN) / solid-state electrolyte + LiPON / lithium-metal cell system was developed as an approach to achieving a 500 Wh/kg, high cycle life battery. In contrast to ceramic solid-state electrolytes, LiPON is known for forming a stable interface with Li-metal. Unfortunately, thin, costly, gas-deposited layers had to be used in the past due to its low conductivity. New LiPON type glasses were developed by the Laine group as polymer-precursor based, scalable coatings. SPAN, through covalent bonding of sulfur and Li-S intermediates, essentially eliminates elemental sulfur and poly-sulfides. Thus, the cycle life reducing shuttle effect is essentially eliminated and carbonate electrolytes, not compatible with poly-sulfides can be utilized for higher rate cycling capability. Several pre-cursors based on O=P(NH₂)₃ or O=P(NHSiMe₃)₃ followed by lithiation with LiNH₂ were prepared and treated at different temperatures resulting in PON, LiPON and LiSIPON coatings with surprisingly high Li⁺ conductivities orders of magnitude higher (10⁻⁴ vs 10⁻⁶ S/cm) than expected from gas-phase deposited LiPON. SPAN/LATSP+LiPON/Li cells cycled at 0.25C showed initial discharge capacities of ~ 1250 mAh/g_{sulfur}, 75 % of the theoretical capacity for a Li-S battery. The half-cell charges/discharges to the targeted potentials with minimal polarization. (See Figure II.11.B.1)

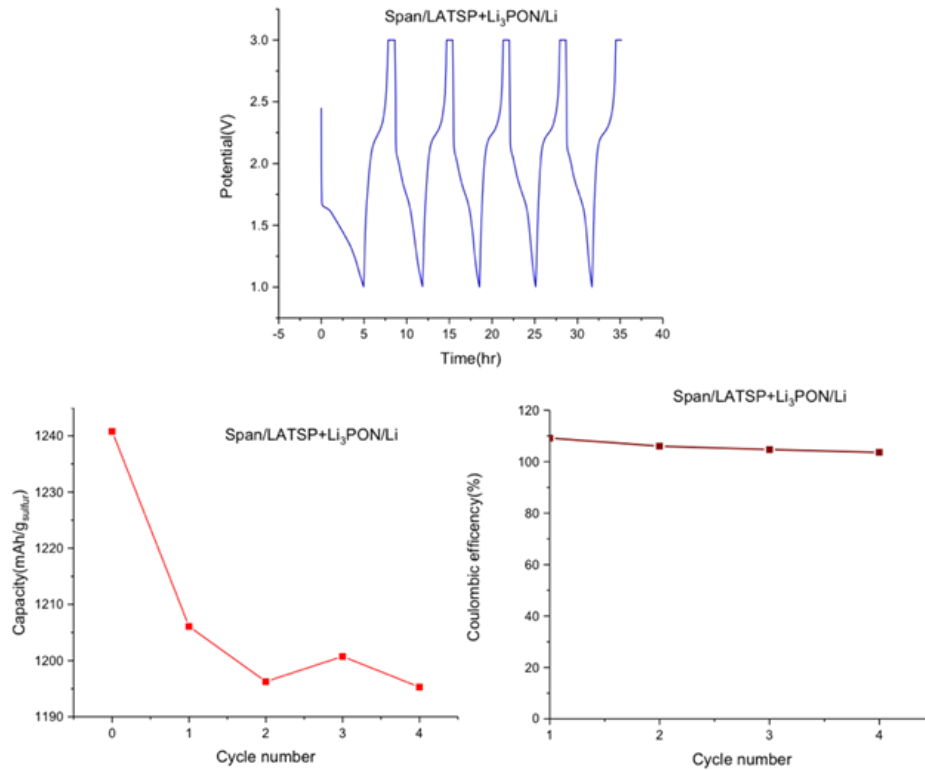


Figure II.11.B.1 Potential vs. time (bottom right), capacity vs. cycle number (bottom left), and coulombic efficiency (top) plots of SPAN/LATSP+LiPON/Li half cells at 0.25 C rate.

3D Printed, Low Tortuosity Garnet Framework for Beyond 500 Wh/kg Batteries (Eric Wachsman, University of Maryland, College Park)

The team successfully 3D printed solid state electrolyte column and grid structures and related structural parameters (e.g., diameter) to relative C-rate (see Figure II.11.B.2). In addition, we fabricated and evaluated initial cells using this 3D printed cathode architecture with Li-metal anodes.

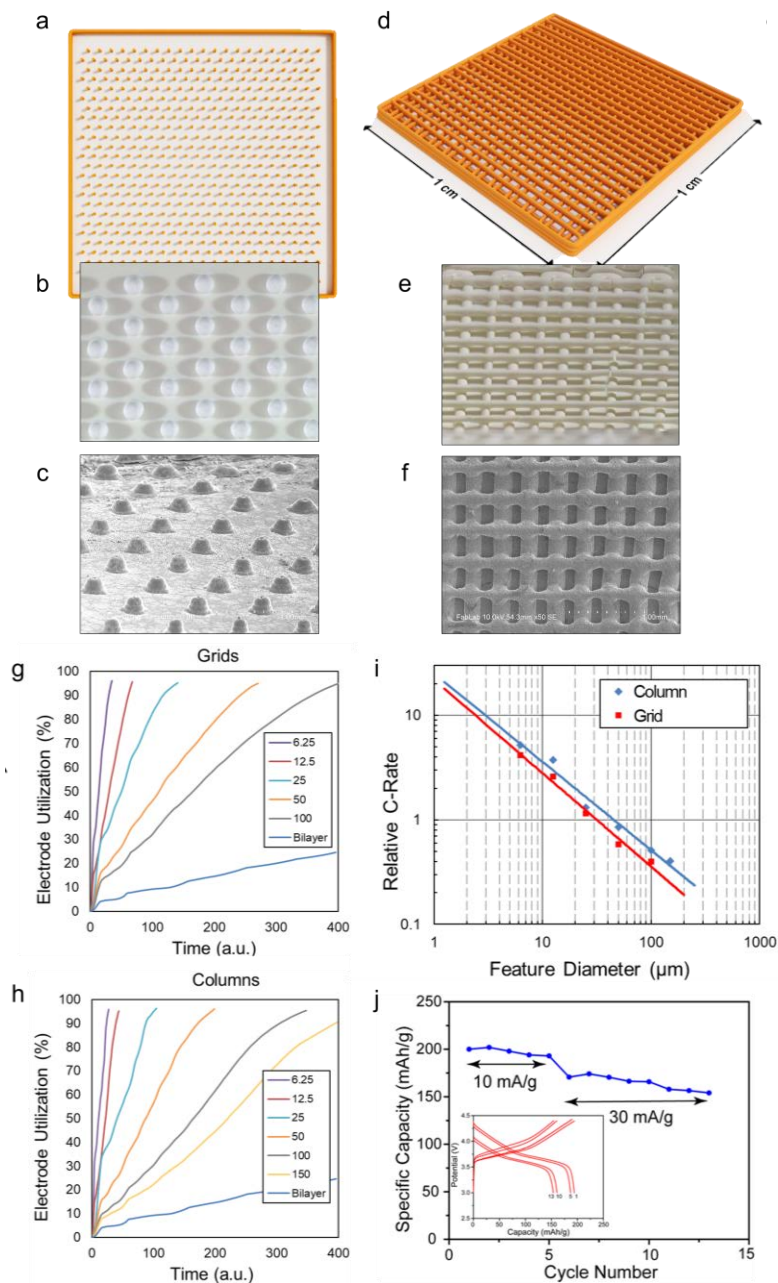


Figure II.11.B.2 (a,d) Computer generated schematics, (b,e) stereomicroscope images of as-printed structures, and (c,f) SEM images of sintered structures for the (a-c) columns and (d-f) multilayer grid designs. (g-h) Modeling results predicting the electrode utilization during discharge as a function of time and feature diameter, from 6.25 to 150 μm . (i) Model results showing the enhancement of relative C-rate with smaller feature size at constant cathode layer porosity (85 v%) and loading. (j) Cycling at C/20 (10 mA/g) and C/7 (30 mA/g) rates with 3D printed garnet grid structure filled with 811 NMC on the cathode side with Li metal filling random pores on anode side

Design, Processing, and Integration of Pouch-Format Cell for High-Energy Lithium-Sulfur Batteries (Mei Cai, General Motors LLC)

For thin lithium anode optimization, we utilized a thermal deposition method developed at GM R&D with a high deposition rate (up to 100nm/min) and precisely controlled the thickness to make lithium film electrodes on copper current collectors. A thickness of lithium above 10 μm can be obtained which has the equal electrochemical performance compared to that of commercial lithium foil. In addition, a laser welding process of nickel or copper tabs on lithium metal was introduced, which enables current collector free design for lithium anode to achieve desired cell-level specific energy. For cathode porosity control, we screened additives and optimized the binder formulation. A surface treatment by Corona discharge process was further validated on aluminum current collector with improved slurry adhesion. Porosity control (45% - 70%) of sulfur cathodes was also investigated by optimized calendaring process. With optimized electrode formulation, a moderated porosity (50% - 60%) was found to provide a balanced electrochemical performance and energy density. Electrolyte-to-sulfur (E/S) ratio studies in both coin and pouch format cells also showed that higher E/S ratio may provide better cycling stability, while lower E/S ratio may provide better cell-level energy density. To achieve the optimized cell level energy density, a modeling tool previously developed at GM R&D was utilized to guide the cell design by tuning the parameters at component level. This modeling tool was experimentally validated with the measured pouch cell data to improve the accuracy. In addition, we developed another mathematic model based on the saturation of polysulfide controlled mechanism, which reveals the relationship between the porosity, sulfur loading and corresponding cell energy density. Finally, a stacking cell design was adopted for fabricating several 1 Ah multi-layer pouch cells. With a E/S ratio of 2.8:1, a 1Ah pouch cell with medium sulfur loading and moderate porosity ($\sim 4.5 \text{ mAh/cm}^2$, 65% porosity) showed energy density of $> 400 \text{ Wh/kg}$.

Electrochemically Stable High Energy Density Lithium-Sulfur Batteries (Prashant Kumta, University of Pittsburgh)

The progress made during this effort included the follow: (1) PTA-DDSA with $\sim 12.5 \text{ mg/cm}^2$ sulfur loadings showed a stable areal capacity of $\sim 12.5 \text{ mAh/cm}^2$ for over 100 cycles when tested using Battery500 test protocol with $\sim 96\%$ capacity retention (Patent disclosure filed), (2) Novel high Li-ion conductivity ($1.3 \times 10^{-3} \text{ S cm}^{-1}$) polysulfide dissolution resistant composite polymer membranes (CPEs) were developed to achieve high capacity $\sim 895 \text{ mAh/g}$ and excellent capacity retention of 0.055% capacity loss/cycle over 100 cycles when tested under Battery 500 protocol (<https://pubs.acs.org/doi/abs/10.1021/acsaem.7b00094>), (3) Commercially scalable high sulfur loading ($8\text{-}12 \text{ mg/cm}^2$) inorganic framework material (IFM) electrodes when tested under Batt 500 protocol exhibited high energy density of $\sim 1150\text{-}1200 \text{ Wh/kg-S}$ and an aerial capacity of $4.5\text{-}5 \text{ mAh/cm}^2$ @ $0.7\text{C} - 1\text{C}$ rate with a capacity/energy retention of $\sim 99\%$ at the end of 60 cycles, and (4) Demonstrated initial feasibility testing of single layer pouch cell of IFM-S system under Battery500 protocol showing high energy density of $\sim 1100 \text{ Wh/kg}$ for 4 mg/cm^2 sulfur loading with a total area of $\sim 20 \text{ cm}^2$. Further optimization of the system and pouch cell fabrication process is in progress (Patent disclosure filed). (See Figure II.11.B.3.)

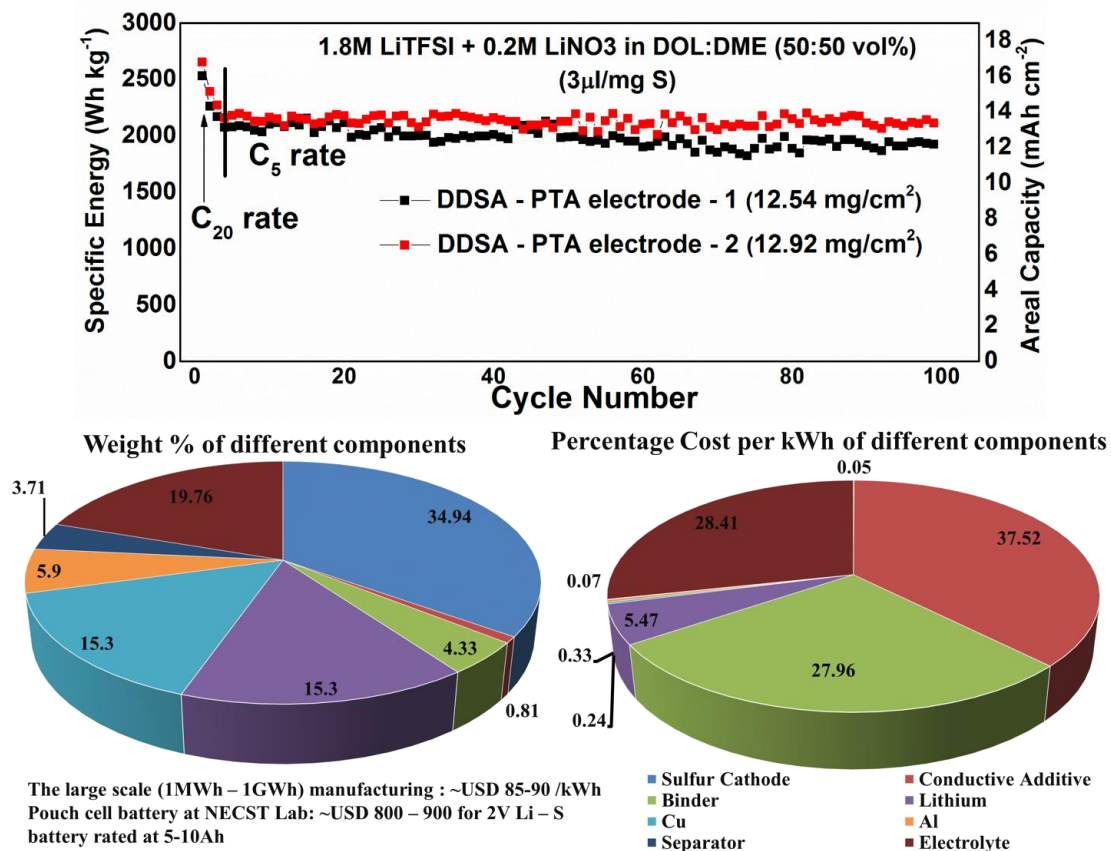


Figure II.11.B.3 (Top) - High performance of Directly Derived Doped Sulfur Architectures (DDSA) with polysulfide trapping agents (PTA); (Bottom) - weight analysis and cost analysis for large scale manufacturing and laboratory scale battery testing of the DDSA-PTA system at the Nanomaterials for Energy Conversion and Storage Technology (NECST) laboratories at the Energy Innovation Center (EIC), University of Pittsburgh.

Highly Loaded Sulfur Cathode and Coated Separator for High-Rate Lithium-Sulfur Batteries (Yong Joo, Cornell University)

The resulting layered cathodes and coated separators exhibited higher capacity and capacity retention (about 1,000 mAh/g capacity with less than 0.02% fade/cycles) than a single layer cathode or cathode prepared by conventional slurry cast and pristine separator without coating. We also evaluated Li-S pouch cells to confirm the improved performance which was observed in coin cells. The capacity of the pouch cells was shown to be comparable to those of the coin cells. (See Figure II.11.B.5.)

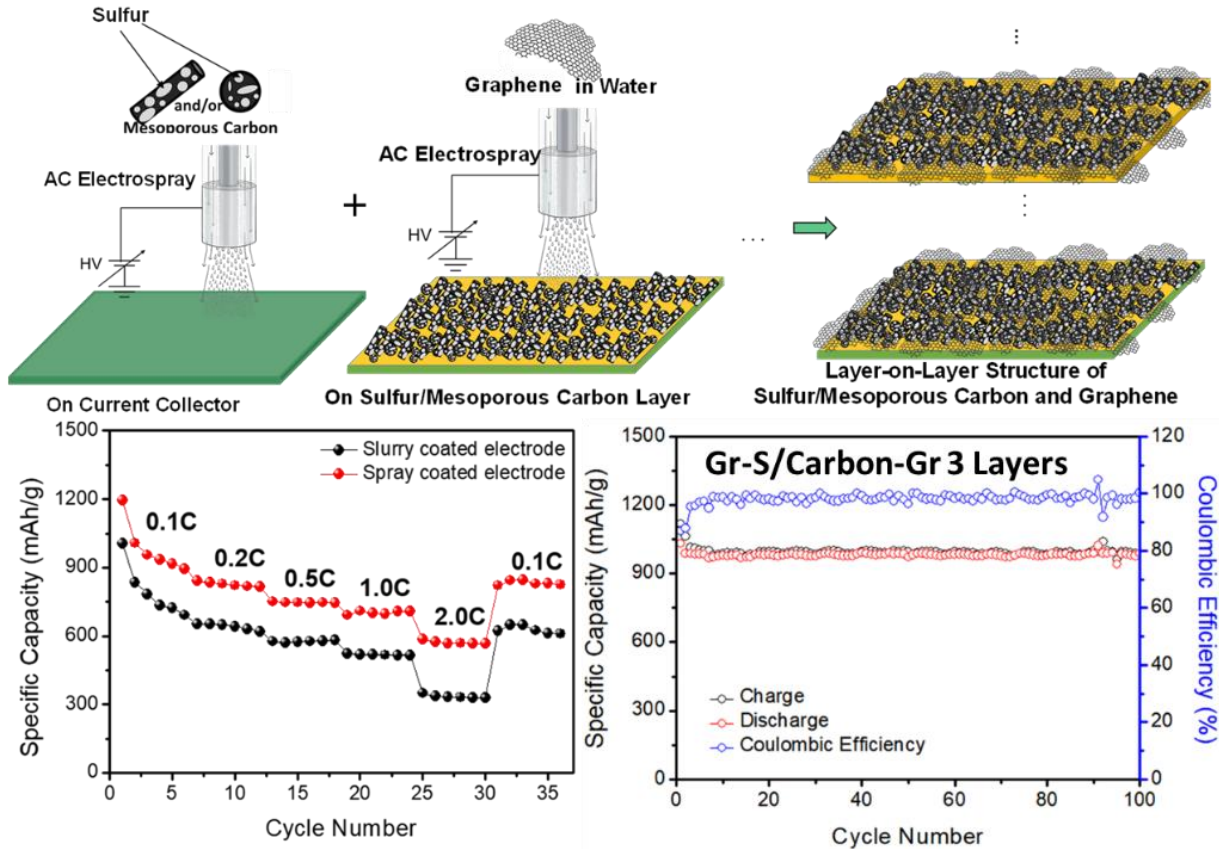


Figure II.11.B.4 Schematic of direct alternating deposition of S/carbon and graphene by layer-on-layer via air-controlled electro spray (ACES) and enhanced cell performance (rate capability and capacity retention) of layered cathodes.

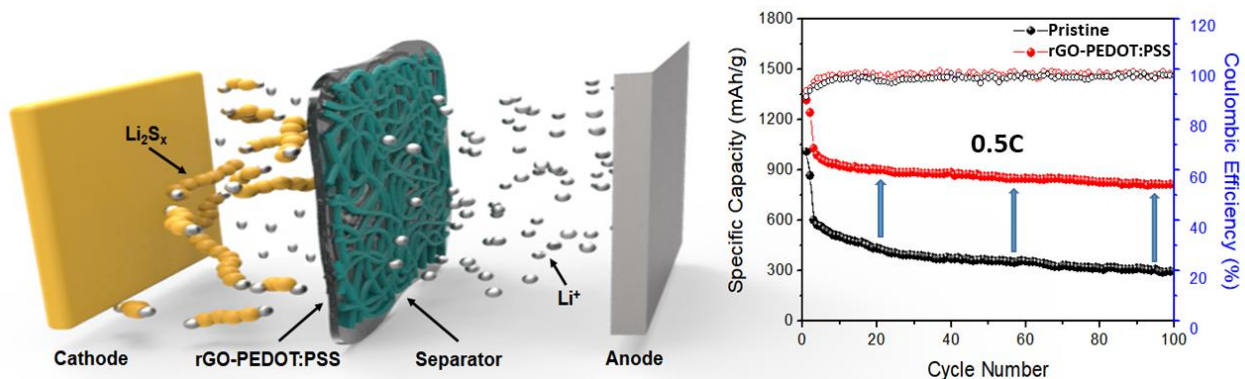


Figure II.11.B.5 Schematic of direct coating of PEDOT:PSS-rGO coating on a separator and enhanced cell performance due to the separator coating.

Identification of Efficient and Stable Electrochemical Interfaces for Lithium-Sulfur Batteries (Perla Balbuena, Texas A&M Engineering Experiment Station)

We have found that the nature and concentration of the electrolyte as well as the associated solvation structures play a fundamental role on Li electrodeposition and into the formation of solid-electrolyte interphases. Because of surface polarization, such solvation and complexation structures are very sensitive to the applied potential. Our new first-principles methods allow characterizing the interphase products as a function of potential, identifying stable electrolytes, and following Li electrodeposition and nucleation. Figure II.11.B.6 shows Li electrodeposition on a Cu surface. A strong stable solvation is observed. However, notable differences are found depending on the effects of the various chemical species. At low salt concentration, the DME solvent is

able to keep the cation in the solvated structure for longer times, delaying decomposition of anion and deposition of cation. As the salt concentration increases, the anion is attracted by the polarized surface and reduces first, thus generating specific SEI components on the surface. When DOL is used instead of DME, the anion decomposition takes place earlier (see CF_3 separation from LiTFSI). When LiNO_3 is present in solution, its dipole moment causes fast deposition on the polarized surface and simultaneous deposition of DME on the surface. Higher potentials show a larger number of simultaneous reactions. This example clearly illustrates how the electrolyte composition could be modulated to generate specific SEIs. A manuscript is ready to be submitted reporting these findings.

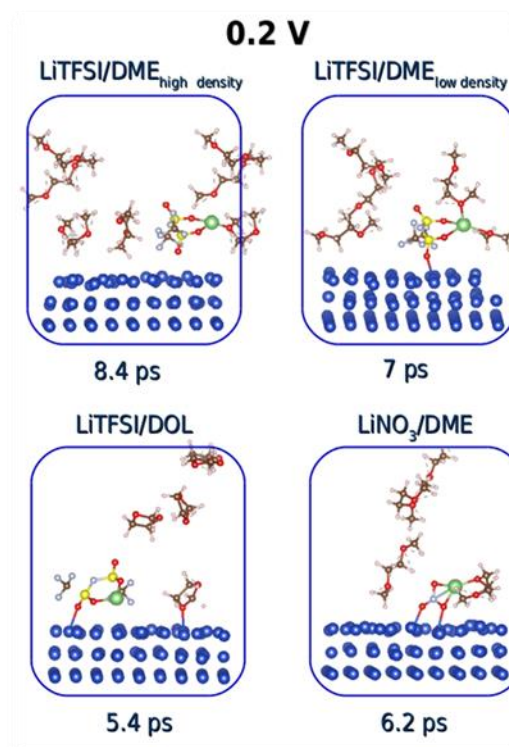


Figure II.11.B.6 Electrodeposition of solvated Li (green) at constant potential. Top left: High density DME solvent (low LiTFSI salt concentration). Top right: Low density DME solvent (high LiTFSI salt concentration). Bottom left: LiTFSI in DOL solvent. Bottom right: LiNO_3 in DME solvent. Color code: O: red, C: brown, F: light blue, H: white, Li: green, N: grey.

Solvent-Free and Non-Sintered 500 Wh/kg All-Solid-State Battery (Pu Zhang, Navitas Advanced Solutions Group, LLC)

A doped sulfide SSE material was developed with >2hr air stability and conductivity of 0.2 mS/cm. Li metal was protected by either vapor deposition of LiPON (dry) or in-situ SEI formation (wet) on its surface. Surface protection significantly improved the cycling capability. A mixture of cathode powder, SSE, carbon, and polymer binder was dry blended, followed by a calendaring process. A stand-alone cathode film was formed. A SSE film was formed similarly by combining only SSE powder and binder. A cathode/SSE bilayer film was then fabricated by laminating the two stand-alone films. The cathode/SSE bilayer and Li metal anode were assembled into solid state cells. Swagelok cells were initially assembled for performance evaluation. Single-layer-pouch (SLP) cells are being assembled for the final demonstration. Li metal anode (with or without artificial SEI), the doped LPS electrolyte, and a surface modified LCO cathode were used in the film fabrication and cell assembly. The SSB prototype cell showed promising rate capability and cycle, retaining 83% of initial capacity at 0.2C, 65% at 0.5C, and 50% at 1C, respectively. When cycled at 0.1C and 2.5 - 4.2V, the cell with protected Li anode retained 83% of the initial capacity after 100 cycles. The cell with pristine Li anode showed a rapid degradation due to Li cycling limitation.

High-Energy Lithium-Metal Batteries Based on 3D Architectures of MnO₂ as Cathodes (Da Deng, Wayne State University)

The new lithium-ion batteries using lithium-free cathodes and lithiated anodes were found to be tolerant to overcharge, therefore improving safety, as compared to the existing batteries using fully lithiated cathodes. Lithium-free MnO₂-based cathodes demonstrated impressively high initial capacity of 460 mAh/g (Figure II.11.B.7a). 3-D MnO₂ synthesized demonstrated a six-fold increase in specific capacity as compared to that of monolayer MnO₂ (Figure II.11.B.7b). In addition, a prototypic coin cell demonstrated specific energy over 400 Wh/kg for 80 cycles without optimization.

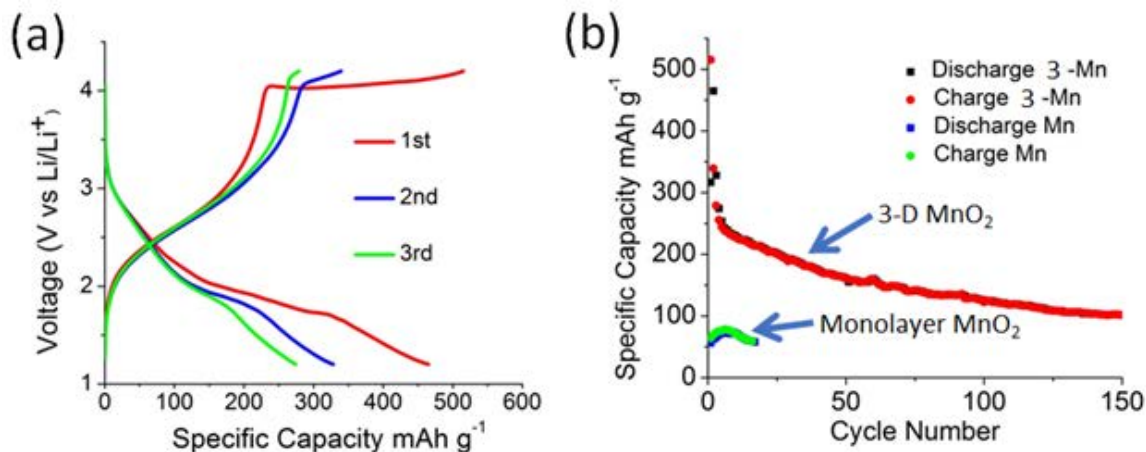


Figure II.11.B.7 Preliminary electrochemical results of the as-prepared 3-D MnO₂ based cathode materials: (a) First three cycle charge-discharge profiles; (b) Capacity vs. cycle number plots. The cycling performance of monolayer MnO₂ nanosheets without 3-D structure tested under the same conditions was plotted in (b) for comparison.

Tuned Li₂S@Graphene Cathode for Lean Electrolyte Lithium-Sulfur Batteries and Induced SEI on Lithium-Metal Anode (Ji Xiulei, Oregon State University)

An energy density represented by the combination of cathode and electrolyte equivalent to 433 Wh/kg at the full-cell level was achieved. We identified the coating composition for the composite electrode of Li₂S@Graphene that facilitates a very low electrolyte/sulfur active mass (E/S) of 2 (Figure II.11.B.8). We have gained in-depth understanding on what enables the affinity between the electrolyte and the surface of the cathode. We have made significant progress on protecting the lithium metal anode by preferentially reacting an oxidizing additive with lithium to form a more inorganic solid electrolyte interphase. The treated lithium metal anode is completely dendrite free; the average Coulombic efficiency of the lithium metal anode has reached nearly 99.0%.

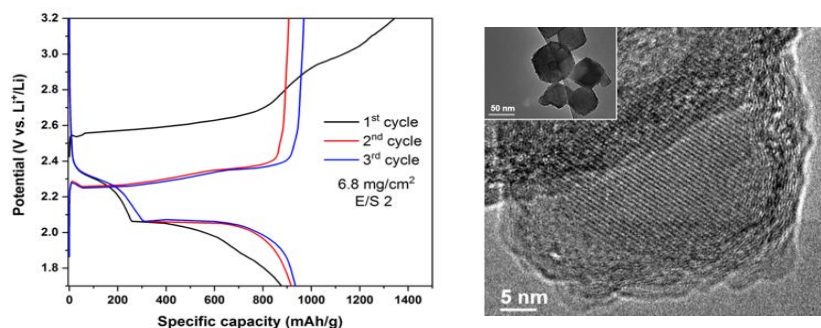


Figure II.11.B.8 First three cycles of galvanostatic charge and discharge (GCD) profiles of surface tuned Li₂S@graphene at A. E/S ratio of 2 with mass loading of 6.8 mg/cm² B. A TEM image of Li₂S@Graphene.

Sulfur Loaded MS_2 Barrier for Control of Polysulfide Shuttling in Lithium-Sulfur Batteries (Amy Marschilok, SUNY University at Stony Brook Research)

Lithium sulfur batteries incorporating these cathodes using a novel environmentally friendly electrolyte exhibited improved rate capability and cycle stability (20% higher retention rate) and 10-fold capacity increase per electrode weight relative to coated foil electrodes even with 2X higher areal sulfur loading. The improvement is attributed to the synergistic effect of efficient polysulfide trapping by the MoS_2 nanosheets and a conductive framework from the interconnected macroporous structure of the CNT interlayers. (See Figure II.11.B.9.)

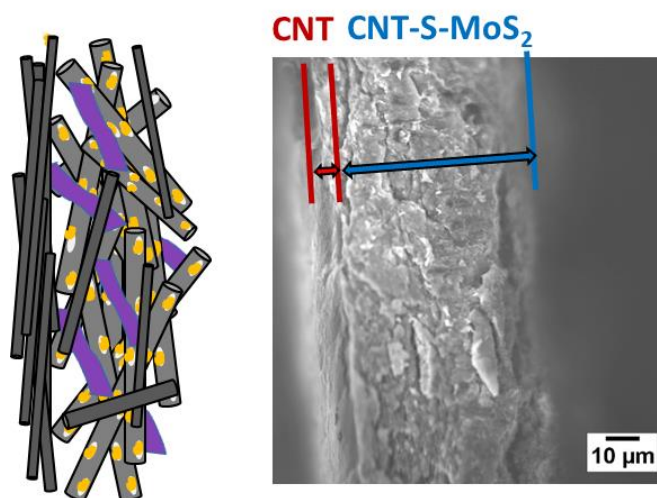


Figure II.11.B.9 MoS_2 nanosheet-carbon nanotube-sulfur composites. Left: conceptual figure, Right: scanning electron micrograph.

High-Energy Solid-State Lithium Batteries with Organic Cathode Materials (Yan Yao, University of Houston)

A class of organic cathode materials was established for building high-energy solid-state lithium batteries. Designed polymer and sulfide solid electrolytes and organic cathode materials stabilized each other to give long cycle life. Up to 767 Wh/kg based on active mass and a capacity retention of 61% over 1000 cycles were demonstrated.

Composite Cathode Architectures Made by Freeze-Casting for All-Solid-State Lithium Batteries (Marca Doeff, Lawrence Berkeley National Laboratory Research)

During Phase 1 of this project, ceramic scaffolds were successfully fabricated, infiltrated, and incorporated in hybrid and all solid-state cells. For the latter, dense layers were combined with either one porous layer (bilayer configuration) or sandwiched between two porous layers (trilayer configuration). Planar lithium anodes were attached to the bilayers to form the solid-state cells, where the porous layer was infiltrated with cathode active material. For the trilayer cells, anode active material was infiltrated into one of the porous layers and cathode material into the other. (See Figure II.11.B.10.)

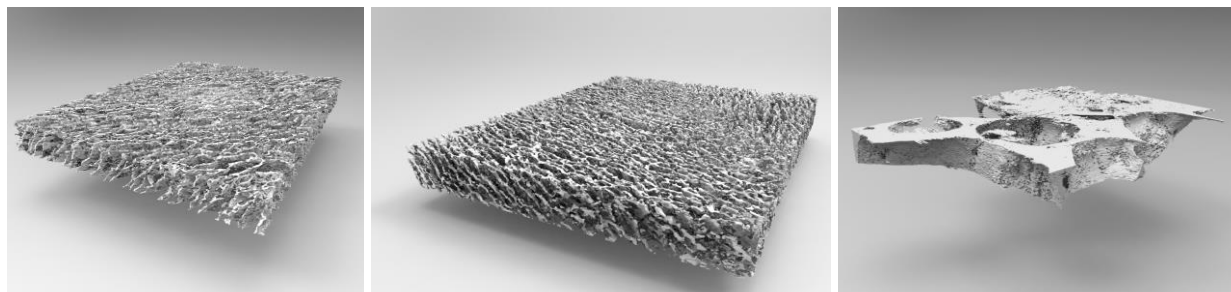


Figure II.11.B.10 Synchrotron tomographic images of aqueous freeze-cast LLZO scaffolds (subvolume view 1046x1403x128 μm). Left to right: 7.5% LLZO, 12.5% LLZO, and 17.5% LLZO loading in the aqueous slurries.

**500 Wh/Kg Batteries with Fluoride Conversion Cathodes and LiPON-Protected Lithium Anodes
(Chunsheng Wang, University of Maryland, College Park)**

Bi-intercalated graphite enabled the Li plating/ stripping Coulombic efficiency (CE) in all fluorinated electrolyte to reach 82.4% at 1.0 mAh/cm² capacity in the first cycle, and jumped to 99.8% after 10 cycles. When the areal capacity increased to 2.0 and 3.0 mAh/cm², the CE still maintained 99.6% for 200 cycles, which is the highest Li plating/ stripping CE reported to date. Over 90% capacity was contributed from Li plating/stripping at 1.0 mAh/cm², corresponding to 2000 mAh/g (of Graphite). For the conversion LiFe_{0.9}Co_{0.1}OF cathode, a high capacity of 420 mAh g⁻¹, high energy density of ~1000 Wh kg⁻¹, and a high reversibility over 1000 cycles with a decay rate of 0.03% per cycle was simultaneously achieved after the concerted doping of cobalt and oxygen into iron fluoride. In addition, Co and O substitution of FeF₃ also significantly reduced the potential hysteresis to 0.27V.

List of Principal Investigators

Principal Investigator	Project Title	APR Section
Abraham, Daniel P.	Advanced Computer Aided Battery Engineering Consortium (NREL/ANL/SNL/Purdue Univ.)	I.3.A
	Advanced Tool for Computer Aided Battery Engineering (ANL)	I.3.E
	Electrochemical Analysis and Evaluation (ANL, LBNL, ORNL)	II.3.A
Ahmed, Shabbir	BatPaC Model Development (ANL)	I.7.A
Amatucci, Glenn G.	Self-Forming Thin Interphases and Electrodes Enabling 3-D Structures High Energy Density Batteries (Rutgers, The State University of New Jersey)	II.8.J
Amine, Khalil	Development of high energy battery system with 300wh/kg (ANL)	II.5.H
	Lithium-Air Batteries (ANL)	II.9.B
	Novel Chemistry: Lithium-Selenium and Selenium-Sulfur Couple (ANL)	II.8.A
Arnold, John	Development of UV Curable Binder Technology to Reduce Manufacturing Cost and Improve Performance of Lithium Ion Battery Electrodes (Miltec UV International)	I.2.D
Bae, Chulheung	Development and Validation of a Simulation Tool to Predict the Combined Structural, Electrical, Electrochemical and Thermal Responses of Automotive Batteries (Ford Motor Company)	I.3.G
Bai, Jianming	In situ Solvothermal Synthesis of Novel High-Capacity Cathodes (BNL)	II.3.G
Bak, Seongmin	Advanced in situ Diagnostic Techniques for Battery Materials (BNL)	II.5.B
	Exploratory Studies of Novel Sodium-Ion Battery Systems (BNL)	II.10.A
Balbuena, Perla B.	Addressing Internal "Shuttle" Effect: Electrolyte Design and Cathode Morphology Evolution in Li-S Batteries (TAMU, Purdue)	II.8.D
	Understanding and Strategies for Controlled Interfacial Phenomena in Li-Ion Batteries and Beyond (TAMU, Purdue)	II.7.F
Balsara, Nitash	Improving the Stability of Lithium-Metal Anodes and Inorganic-Organic Solid Electrolytes (LBNL)	II.7.J
Bao, Zhenan	Advanced Polymer Materials for Li-ion and Correlative Microscopy Characterization of Electrochemical Hotspots in Oxide Electrodes (SLAC)	II.1.B
Battaglia, Vincent	Higher Energy Density via Inactive Components and Processing Conditions (LBNL)	II.1.A
Bloom, Ira	Battery Performance and Life Testing (ANL)	I.7.B
	Post-test Analysis of Lithium-Ion Battery Materials (ANL, ORNL, SNL)	I.7.H
Burrell, Anthony	Beyond Batteries: Behind the Meter Storage (NREL, INL, ORNL, SNL)	I.5.G

Principal Investigator	Project Title	APR Section
	Silicon Electrolyte Interface Stabilization (SEISta) (NREL, ANL, ORNL, LBNL, SNL)	II.2.B
Ceder, Gerbrand	First Principles Calculations of Existing and Novel Electrode Materials	II.6.C
Chen, Guoying	Materials and Characterization (ANL, LBNL, ORNL)	II.3.B
	Model-System Diagnostics for High-Energy Cathode Development (LBNL)	II.3.L
Chen, Xi (Chelsea)	Composite Electrolytes to Stabilize Metallic Lithium Anodes (ORNL)	II.7.C
Chueh, William C.	Correlative Microscopy Characterization of Oxide Electrodes (SLAC National Accelerator Laboratory)	II.5.F
Costantino, Henry R.	Low Cost Manufacturing of Advanced Silicon-Based Anode Materials (Group14 Technologies, Inc.)	I.2.A
Croy, Jason R.	Novel Cathode Materials and Processing Methods (ANL)	II.3.H
Cui, Yi	Advanced Polymer Materials for Li-ion and Correlative Microscopy Characterization of Electrochemical Hotspots in Oxide Electrodes (SLAC)	II.1.B
	Battery500 Innovation Center (PNNL)	II.11.A
	Correlative Microscopy Characterization of Oxide Electrodes (SLAC National Accelerator Laboratory)	II.5.F
	Nanostructured Design of Sulfur Cathodes for High Energy Lithium-Sulfur Batteries (Stanford University)	II.8.C
	Pre-Lithiation of Silicon Anode for High Energy Li Ion Batteries (Stanford University)	II.2.D
Curtiss, Larry	Advancing Solid-Solid Interfaces in Li-ion Batteries (Argonne National Laboratory)	II.8.H
	Lithium-Air Batteries (Argonne National Laboratory)	II.9.B
Dahlberg, Kevin	12V Start-Stop Development Program (XALT Energy)	I.1.K
Dai, Sheng	Research on high power, doped titanium-niobium oxide anodes (ORNL)	I.5.E
Datta, Moni K.	Electrochemically Stable High Energy Density Lithium Sulfur Batteries (University of Pittsburgh)	II.8.K
	Engineering Approaches to Dendrite Free Lithium Anodes (University of Pittsburgh)	II.7.G
Dees, Dennis	Next Generation Anodes for Lithium-Ion Batteries: Silicon (ANL, LBNL, ORNL, SNL, NREL)	II.2.A
Doeff, Marca M.	Advanced Cathode Materials for High Energy Lithium Ion Batteries (LBNL)	II.3.I
Du, Zhijia	Novel Liquid/Oligomer Hybrid Electrolyte with High Li Ion Transference Number (Hi-LiT) for Extreme Fast Charging (ORNL)	I.5.D

Principal Investigator	Project Title	APR Section
	Towards Solventless Processing of Thick Electron-Beam (EB) Cured LIB Cathodes (ORNL)	I.2.E
Dudney, Nancy	Composite Electrolytes to Stabilize Metallic Lithium Anodes (ORNL)	II.7.C
	Mechanical Properties at the Protected Lithium Interface (ORNL)	II.7.A
Dufek, Eric	XFC R&D: Battery Testing Activities (INL)	I.5.B
Falzone, Alec	Advanced Lithium Ion Battery Technology - High Voltage Electrolyte (Daikin America, Inc.)	II.4.C
Fenton, Kyle R.	Post-test Analysis of Lithium-Ion Battery Materials (ANL, ORNL, SNL)	I.7.H
Gaines, Linda	Battery Production and Recycling Materials Issues (ANL)	I.4.B
Goodenough, John B.	Lithium Batteries with Higher Capacity and Voltage (UTA)	II.3.J
Gutierrez, Arturo	Novel Cathode Materials and Processing Methods (ANL)	II.3.H
Hellring, Stuart	Electrodeposition for Low-Cost, water-Based Electrode Manufacturing (PPG Industries, ANL, Navitas, ORNL)	I.2.C
	Enabling Thicker Cathode Coatings for Lithium Ion EV Batteries (PPG)	I.1.D
Hendershot, Ron	Advanced Lithium Ion Battery Technology - High Voltage Electrolyte (Daikin America, Inc.)	II.4.C
Herbert, Erik	Mechanical Properties at the Protected Lithium Interface (ORNL)	II.7.A
Iddir, Hakim	Theory and Modeling (ANL, LBNL, ORNL)	II.3.C
Jansen, Andrew N.	Cell Analysis, Modeling, and Prototyping (CAMP) Facility Research Activities (Argonne National Laboratory)	I.7.F
Jen, Alex K.-Y.	Multifunctional, Self-Healing Polyelectrolyte Gels for Long-Cycle-Life, High-Capacity Sulfur Cathodes in Li-S Batteries (University of Washington)	II.8.I
Karulkar, Mohan	Research three-dimensional hierarchical graphite architectures for anodes for fast charging (SNL)	I.5.F
Kelly, Jarod C.	Life Cycle Assessment of Li-ion Batteries (ANL)	I.4.A
Keyser, Matthew	Battery Thermal Analysis and Characterization Activities (NREL)	I.7.E
	XFC R&D: MSMD Modeling & Thermal Testing (NREL)	I.5.C
Kostecki, Robert	Interfacial Processes (LBNL)	II.5.A
Krumdick, Gregory K.	Advanced Active Battery Materials: Active Cathode Materials with Component Concentration Gradient Structures (ANL)	I.2.G
	Process R&D and Scale up of Critical Battery Materials (ANL)	I.2.K
Kumta, Prashant N.	Electrochemically Stable High Energy Density Lithium Sulfur Batteries (University of Pittsburgh)	II.8.K
	Engineering Approaches to Dendrite Free Lithium Anodes (University of Pittsburgh)	II.7.G

Principal Investigator	Project Title	APR Section
Lamb, Joshua	Advanced Computer Aided Battery Engineering Consortium (NREL/ANL/SNL/Purdue Univ.)	I.3.A
	Advanced Tool for Computer Aided Battery Engineering (SNL)	I.3.F
	Battery Safety Testing (SNL)	I.7.D
Li, Jianlin	Performance Effects of Electrode Processing for High-Energy Lithium-Ion Batteries (ORNL)	I.2.F
	Research on high power, doped titanium-niobium oxide anodes (ORNL)	I.5.E
Li, Xiaolin	Development of Si-based High-Capacity Anodes (Pacific Northwest National Laboratory)	II.2.C
Libera, Joseph	Process R&D for Droplet-Produced Powdered Materials	I.2.H
Liu, Jun	Battery500 Innovation Center (PNNL)	II.11.A
	Development of High Energy Lithium-Sulfur Batteries (PNNL)	II.8.B
Lopez, Herman	High Energy Lithium Batteries for Electric Vehicles (Zenlabs Energy)	I.1.A
Lu, Dongping	Development of High Energy Lithium-Sulfur Batteries (PNNL)	II.8.B
Lu, Jun	Lithium-Air Batteries (Argonne National Laboratory)	II.9.B
Lu, Wenquan	Materials Benchmarking Activities for CAMP Facility (Argonne National Laboratory)	I.7.G
Manev, Veselin	12V Start-Stop Development Program (XALT Energy)	I.1.K
Manthiram, Arumugam	Statically and Dynamically Stable Lithium-sulfur Batteries	II.8.F
Markovic, Nenad	Advancing Solid-Solid Interfaces in Li-ion Batteries (Argonne National Laboratory)	II.8.H
	Stability of cathode/electrolyte interfaces in high voltage Li-ion batteries (ANL)	II.4.A
Marschilok, Amy C.	Dual Function Solid State Battery with Self-forming Self-healing Electrolyte and Separator (Stony Brook University)	II.8.G
Mazzeo, Brian	Addressing Heterogeneity in Electrode Fabrication Processes (Brigham Young University)	II.6.D
Meng, Ying Shirley	Advanced Microscopy and Spectroscopy for Probing and Optimizing Electrode-Electrolyte Interphases in High Energy Lithium Batteries (UCSD)	II.5.C
Monroe, C.	Solid electrolytes for solid-state and lithium-sulfur batteries, Univ. of Michigan, ORNL, ARL, Oxford	II.7.B
Mukherjee, Partha P.	Addressing Internal "Shuttle" Effect: Electrolyte Design and Cathode Morphology Evolution in Li-S Batteries (TAMU, Purdue)	II.8.D
	Advanced Computer Aided Battery Engineering Consortium (NREL/ANL/SNL/Purdue Univ.)	I.3.A

Principal Investigator	Project Title	APR Section
	Understanding and Strategies for Controlled Interfacial Phenomena in Li-Ion Batteries and Beyond (TAMU, Purdue)	II.7.F
Nanda, Jagjit	Solid electrolytes for solid-state and lithium-sulfur batteries, Univ. of Michigan, ORNL, ARL, Oxford	II.7.B
	Studies on High Capacity Cathodes for Advanced Lithium-Ion (ORNL)	II.3.D
Persson, Kristin A.	Predicting and Understanding Novel Electrode Materials from First Principles	II.6.B
Pesaran, Ahmad	Lithium-ion Battery Recycling Prize Support (NREL)	I.4.E
Pintauro, Peter N.	High Performance Li-Ion Battery Anodes from Electrospun Nanoparticle/Conducting Polymer Nanofibers (Vanderbilt University)	I.2.J
Prasher, Ravi	In-Operando Thermal Diagnostics of Electrochemical Cells (LBNL)	II.5.E
Qi, Yue	Dendrite Growth Morphology Modeling in Liquid and Solid Electrolytes (MSU)	II.6.F
Qu, Deyang	Mechanistic Investigation for the Rechargeable Li-Sulfur Batteries (U of Wisconsin)	II.8.E
Rao, Ranjeet	Co-Extrusion (CoEx) for Cost Reduction of Advanced High-Energy-and-Power Battery Electrode Manufacturing (PARC)	I.2.B
Roberts, Scott A.	Consortium for Advanced Battery Simulation (SNL)	I.3.C
Sakamoto, Jeff	Mechanical Properties at the Protected Lithium Interface (ORNL)	II.7.A
	Solid electrolytes for solid-state and lithium-sulfur batteries, Univ. of Michigan, ORNL, ARL, Oxford	II.7.B
Santhanagopalan, Shriram	Advanced Computer Aided Battery Engineering Consortium (NREL/ANL/SNL/Purdue Univ.)	I.3.A
Siegel, D.	Solid electrolytes for solid-state and lithium-sulfur batteries, Univ. of Michigan, ORNL, ARL, Oxford	II.7.B
Slater, Michael	Li-Ion Cell Manufacturing Using Directly Recycled Active Materials (Farasis Energy)	I.1.H
Smith, Ian	Perform USABC/USCAR Benchmarking Activities (Southwest Research Institute)	I.1.J
Smith, Kandler	Advanced Computer Aided Battery Engineering Consortium (NREL/ANL/SNL/Purdue Univ.)	I.3.A
	High Energy, Long Life Lithium-Ion Battery (NREL)	I.2.L
Spangenberg, Jeffrey	Closed-loop Battery Recycling Model (ANL)	I.4.C
	Li-ion Battery Recycling R&D Center (ANL)	I.4.D
Srinivasan, Venkat	Consortium for Advanced Battery Simulation (ANL, LBNL)	I.3.D
	Electrode Materials Design and Failure Prediction (ANL)	II.6.A
	XFC R&D: CAMP, Testing & Post-Test Characterization and Modeling (ANL)	I.5.A

Principal Investigator	Project Title	APR Section
Stamenkovic, Vojislav	Stability of cathode/electrolyte interfaces in high voltage Li-ion batteries (ANL)	II.4.A
Stefan, Ionel	Advanced High-Performance Batteries for Electric Vehicle Applications (Amprius)	I.1.E
	Rapid Commercialization of High Energy Anode Materials (SiNode Systems)	I.1.F
Strmcnik, Dusan	Stability of cathode/electrolyte interfaces in high voltage Li-ion batteries (ANL)	II.4.A
Sun, Xiao-Guang	Research on high power, doped titanium-niobium oxide anodes (ORNL)	I.5.E
Sunstrom, Joseph	Advanced Lithium Ion Battery Technology - High Voltage Electrolyte (Daikin America, Inc.)	II.4.C
Surampudi, Bapiraju	Perform USABC/USCAR Benchmarking Activities (Southwest Research Institute)	I.1.J
Taggougui, Mohamed	High-Performance Semi-Solid Cell for EV Applications (24M Technologies, Inc.)	I.1.B
Takeuchi, Esther	Dual Function Solid State Battery with Self-forming Self-healing Electrolyte and Separator (Stony Brook University)	II.8.G
Takeuchi, Kenneth J.	Dual Function Solid State Battery with Self-forming Self-healing Electrolyte and Separator (Stony Brook University)	II.8.G
Thakur, Madhuri	Development of High Performance Li-ion Cell Technology for EV Applications (Farasis Energy)	I.1.C
Toney, Michael F.	Correlative Microscopy Characterization of Oxide Electrodes (SLAC National Accelerator Laboratory)	II.5.F
Tong, Wei	Discovery of High-Energy Li-Ion Battery Materials (LBNL)	II.3.K
Turner, John A.	Consortium for Advanced Battery Simulation (ORNL)	I.3.B
Vaughey, Jack	Materials and Characterization (ANL, LBNL, ORNL)	II.3.B
	Next Generation Anodes for Lithium-Ion Batteries: Silicon (ANL, LBNL, ORNL, SNL, NREL)	II.2.A
Velikokhatnyi, Oleg I.	Electrochemically Stable High Energy Density Lithium Sulfur Batteries (University of Pittsburgh)	II.8.K
	Engineering Approaches to Dendrite Free Lithium Anodes (University of Pittsburgh)	II.7.G
Wachsman, Eric	High Conductivity and Flexible Hybrid Solid State Electrolyte (University of Maryland)	II.7.D
Walker, Lee	Electrochemical Performance Testing (INL)	I.7.C
Wang, Chongmin	Microscopy Investigation on the Fading Mechanism of Electrode Materials (PNNL)	II.5.D

Principal Investigator	Project Title	APR Section
Wang, Donghai	Electrochemically Responsive Self-Formed Li-ion Conductors for High Performance Li Metal Anodes	II.7.I
Wang, Feng	In situ Solvothermal Synthesis of Novel High-Capacity Cathodes (BNL)	II.3.G
Wang, Lin-Wang	Large scale ab initio molecular dynamics simulation of liquid and solid electrolytes (Lawrence Berkeley National Laboratory)	II.6.E
Wang, Yan	A Closed Loop Recycling Process for End-of-Life Electric Vehicle Li-ion Batteries (Worcester Polytechnic Institute)	I.1.I
Wheeler, Dean	Addressing Heterogeneity in Electrode Fabrication Processes (Brigham Young University)	II.6.D
White, Eric	Advanced Separators for Vehicle Lithium Battery Applications (Celgard, LLC)	I.1.G
Whittingham, M. Stanley	High Energy Density Lithium Battery (Binghamton University)	II.3.E
Wolfenstine, J.	Solid electrolytes for solid-state and lithium-sulfur batteries, Univ. of Michigan, ORNL, ARL, Oxford	II.7.B
Wood III, David L.	Performance Effects of Electrode Processing for High-Energy Lithium-Ion Batteries (ORNL)	I.2.F
	Post-test Analysis of Lithium-Ion Battery Materials (ANL, ORNL, SNL)	I.7.H
	Towards Solventless Processing of Thick Electron-Beam (EB) Cured LIB Cathodes (ORNL)	I.2.E
Wu, Nianqiang	Solid-State Inorganic Nanofiber Network-Polymer Composite Electrolytes for Lithium Batteries	II.7.H
Xiao, Xingcheng	In situ Diagnostics of Coupled Electrochemical-Mechanical Properties of Solid Electrolyte Interphases on Lithium Metal for Rechargeable Batteries (General Motors)	II.5.G
Xing, Yangchuan	Integrated Flame Spray Process for Low Cost Production of Battery Materials for Lithium Ion Batteries and Beyond (University of Missouri)	I.2.I
Xu, Wu	Lithium Dendrite Prevention for Lithium Batteries (Pacific Northwest National Laboratory)	II.7.E
	Rechargeable Lithium-Air Batteries (Pacific Northwest National Laboratory)	II.9.A
Yang, Jihui	Multifunctional, Self-Healing Polyelectrolyte Gels for Long-Cycle-Life, High-Capacity Sulfur Cathodes in Li-S Batteries (University of Washington)	II.8.I
	Advanced in situ Diagnostic Techniques for Battery Materials (BNL)	II.5.B

Principal Investigator	Project Title	APR Section
Yang, Xiao-Qing	Exploratory Studies of Novel Sodium-Ion Battery Systems (BNL)	II.10.A
	Mechanistic Investigation for the Rechargeable Li-Sulfur Batteries (U of Wisconsin)	II.8.E
Zhang, Ji-Guang	Development of High-Energy Cathode Materials (PNNL)	II.3.F
	Development of Si-based High-Capacity Anodes (Pacific Northwest National Laboratory)	II.2.C
	Lithium Dendrite Prevention for Lithium Batteries (Pacific Northwest National Laboratory)	II.7.E
	Rechargeable Lithium-Air Batteries (Pacific Northwest National Laboratory)	II.9.A
Zhang, Zhengcheng	Fluorinated Deep Eutectic Solvent (FDES)-Based Electrolytes (ANL)	II.4.B
Zheng, Jianming	Development of High-Energy Cathode Materials (PNNL)	II.3.F

U.S. DEPARTMENT OF
ENERGY

Office of
**ENERGY EFFICIENCY &
RENEWABLE ENERGY**

For more information, visit:
energy.gov/eere/vehicles

DOE/EE-1831 April 2019